

A. V. Narlikar (Ed.)

Frontiers in Superconducting Materials

 Springer

A.V. Narlikar

Frontiers in Superconducting Materials

A.V. Narlikar (Ed.)

Frontiers in Superconducting Materials

With 635 Figures and 61 Tables

 Springer

Prof. Dr. Anant V. Narlikar
UGC-DAE Consortium for Scientific Research
University Campus
Khandwa Road
Indore-452017, MP
India

ISBN 3-540-24513-8 **Springer Berlin Heidelberg New York**
ISBN 3-540-24513-1 **Springer Berlin Heidelberg New York**

Library of Congress Control Number: 2005923312

This work is subject to copyright. All rights are reserved, whether the whole or part of the material is concerned, specifically the rights of translation, reprinting, reuse of illustrations, recitation, broadcasting, reproduction on microfilm or in other ways, and storage in data banks. Duplication of this publication or parts thereof is permitted only under the provisions of the German Copyright Law of September 9, 1965, in its current version, and permission for use must always be obtained from Springer-Verlag. Violations are liable to prosecution under German Copyright Law.

Springer is a part of Springer Science+Business Media

springeronline.com

© Springer-Verlag Berlin Heidelberg 2005
Printed in Germany

The use of general descriptive names, registered names, trademarks, etc. in this publication does not imply, even in the absence of a specific statement, that such names are exempt from the relevant protective laws and regulations and therefore free for general use.

Typesetting: Data conversion by the author.
Final processing by PTP-Berlin Protago- \TeX -Production GmbH, Germany
Cover-Design: medionet AG, Berlin
Printed on acid-free paper 62/3141/Yu - 5 4 3 2 1 0

CONTRIBUTORS

AKIMITSU, *J.*

Department of Physics and Mathematics
Aoyama-Gakuin University
5-10-1 Fuchinobe
Sagamihara
Kanagawa 229-8558
JAPAN

AWANA, *V.P.S.*

National Physical Laboratory
Dr K.S. Krishnan Road
New Delhi-110012
INDIA

BLANK, *Dave H.A.*

Faculty Science & Technology,
MESA+ Institute for Nanotechnology,
University of Twente,
P.O.Box 217,
7500 AE Enschede,
THE NETHERLANDS

BOOTHROYD, *A.T.*

Clarendon Laboratory,
Department of Physics,
University of Oxford,
Parks Road,
Oxford OX1 3PU,
UK.

BRAUN, *Hans H.*

Physikalisches Institut,
Universität Bayreuth,
Bayreuth,
GERMANY

CHENG, C.H.

Superconductivity R&D Center,
Southwest Jiaotong University
Chengdu
Sichuan, 610031
CHINA
and
Superconductivity Research Group
School of Materials Science and Engineering
University of New South Wales
Sydney, 2052, NSW,
AUSTRALIA

CHU, C.W.

Department of Physics and Texas Center for Superconductivity
University of Houston
Houston
Texas 77204-5002
USA,
Lawrence Berkeley National Laboratory,
1 Cyclotron Road,
Berkeley, CA 94720
USA
and
Hong Kong University of Science and Technology
Hong Kong
CHINA

CLAYTON, N

Department of Condensed Matter Physics (DPMC)
University of Geneva
24, quai E.-Ansermet
CH-1211 Genève 4
SWITZERLAND

CRESPI, Vincent H.

Department of Physics
The Pennsylvania State University
University Park
Pennsylvania 16802-6300
USA

DAHM, *Thomas*

Institut für Theoretische Physik
Universität Tübingen
Auf der Morgenstelle 14
D-72076 Tübingen,
GERMANY

DOU, *S.X.*

Institute for Superconducting and Electronic Materials
University of Wollongong
Northfields Ave.
Wollongong
NSW 2522
AUSTRALIA

ERDIN, *Serkan*

School of Physics and Astronomy
University of Minnesota
Minneapolis, MN 55455
USA

FENG, *Y.*

Northwest Institute for Nonferrous Metal Research
P.O. Box 51
Xi'an
Shaanxi, 710016
CHINA

FLÜKIGER, *R.*

Department of Condensed Matter Physics (DPMC)
University of Geneva
24, quai E.-Ansermet
CH-1211 Genève 4
SWITZERLAND

GIANNINI, *E.*

Department of Condensed Matter Physics (DPMC)
University of Geneva
24, quai E.-Ansermet
CH-1211 Genève 4
SWITZERLAND

GLADYSHEVSKII, R

Dept. Inorganic Chemistry,
Ivan Franko National University of L'viv
Kyryla i Metodiya str. 6
UA-79005 L'viv
UKRAINE

GLOWACKI, Bartek A.

Department of Materials Science and Metallurgy
University of Cambridge
Pembroke Street
Cambridge CB2 3QZ
ENGLAND
and
IRC in Superconductivity
Cavendish Laboratory
University of Cambridge
Madingley Road
Cambridge CB3 0HE
ENGLAND

GOLDACKER, W.

Forschungszentrum Karlsruhe
Institut für Technische Physik
P.O. Box 3640,
76021 Karlsruhe,
GERMANY

GUNNARSSON, O.

Max-Planck-Institut für Festkörperforschung
D-70506, Stuttgart
GERMANY

GUPTA, Anurag

National Physical Laboratory
Dr K.S. Krishnan Road
New Delhi-110012
INDIA

GUPTA, L.C.

Department of Physics,
University of Mumbai,
Mumbai 400 098,
INDIA

HAN, J.E.

Department of Physics
State University of New York at Buffalo
Buffalo
New York 14260
USA

HERRMANNSDÖRFER, T.

Forschungszentrum Rossendorf
D-01314 Dresden
GERMANY

HOSSAIN, Z.

Department of Physics,
Indian Institute of Technology,
Kanpur 208016,
INDIA

HOTT, Roland

Forschungszentrum Karlsruhe
Institut für Festkörperphysik
P. O. Box 3640
76021 Karlsruhe
GERMANY

JORDA, J-L.

Université de Savoie,
LAIMAN-ESIA,
Domaine Universitaire,
B.P.806
F-74016 ANNECY cedex
FRANCE

JÉROME, D.

Laboratoire de Physique des Solides
UMR 8502
Université Paris-Sud
91405 Orsay,
FRANCE

KARPPINEN, M.

Materials and Structures Laboratory
Tokyo Institute of Technology
Yokohama 226-8503
JAPAN

KIMOTO, K.

High Voltage Electron Microscopy Station (HVEMS)
National Institute for Materials Science (NIMS)
Tsukuba 305-0044
JAPAN
and
Advanced Materials Laboratory (AML)
National Institute for Materials Science (NIMS)
Tsukuba 305-0044
JAPAN

KISHAN, Hari,

National Physical Laboratory
Dr K.S. Krishnan Road
New Delhi-110012
INDIA

KLEINER, Reinhold

Physikalisches Institut - Experimentalphysik II
Universität Tübingen
72076 Tübingen
GERMANY

KOSHIZUKA, N.

Superconductivity Research Laboratory
International Superconductivity Technology Center
1-10-13 Shinonome
Koto-ku
Tokyo, 135-0062
JAPAN

LORENZ, B.

Department of Physics and Texas Center for Superconductivity
University of Houston
Houston
Texas 77204-5002
USA

MATSUI, Y.

High Voltage Electron Microscopy Station (HVEMS)
National Institute for Materials Science (NIMS)
Tsukuba 305-0044
JAPAN
and
Advanced Materials Laboratory (AML)
National Institute for Materials Science (NIMS)
Tsukuba 305-0044
JAPAN

MAZUMDAR, Chandan

Saha Institute of Nuclear Physics,
Kolkata 700064,
INDIA

MENG, R.L.

Department of Physics and Texas Center for Superconductivity
University of Houston
Houston
Texas 77204-5002
USA

MILLIKEN, *Damion*

Institute for Superconducting and Electronic Materials
University of Wollongong
Northfields Ave.
Wollongong
NSW 2522
AUSTRALIA

MURAKAMI, *Masoto*

Department of Materials Science and Engineering
Shibaura Institute of Technology
Shibaura 3-9-14
Minato-ku,
Tokyo 108-8548
JAPAN

MURANAKA, *T.*

Department of Physics and Mathematics
Aoyama-Gakuin University
5-10-1 Fuchinobe
Sagamihara
Kanagawa 229-8558
JAPAN

MUSOLINO, *N.*

Department of Condensed Matter Physics (DPMC)
University of Geneva
24, quai E.-Ansermet
CH-1211 Genève 4
SWITZERLAND

NAGAI, *T.*

High Voltage Electron Microscopy Station (HVEMS)
National Institute for Materials Science (NIMS)
Science, 1-1 Namiki,
Tsukuba 305-0044,
JAPAN

NAGARAJAN, R.

Tata Institute of Fundamental Research
Mumbai 400005
INDIA

NARLIKAR, A.V.

Inter-University Consortium for DAE Facilities
University Campus, Khandwa Road,
Indore-452017, MP,
INDIA

NISHIYAMA, M.

Superconductivity Research Laboratory
International Superconductivity Technology Center
1-10-13 Shinonome
Koto-ku
Tokyo, 135-0062
JAPAN

PAN, A.V.

Institute for Superconducting and Electronic Materials
University of Wollongong
Northfields Ave.
Wollongong
NSW 2522
AUSTRALIA

PASQUIER, C.R.

Laboratoire de Physique des Solides
UMR 8502
Université Paris-Sud
91405 Orsay
FRANCE

POBELL, F.

Forschungszentrum Rossendorf
D-01314 Dresden
GERMANY

PRABHAKARAN, D.

Clarendon Laboratory,
Department of Physics,
University of Oxford,
Parks Road,
Oxford OX1 3PU,
UK.

QIN, M.J.

Institute for Superconducting and Electronic Materials
University of Wollongong
Northfields Ave.
Wollongong
NSW 2522
AUSTRALIA

RIJNDERS, *Guus*

Faculty Science & Technology,
MESA+ Institute for Nanotechnology,
University of Twente,
P.O.Box 217,
7500 AE Enschede,
THE NETHERLANDS

SAKURAI, H.

Superconducting Materials Center,
National Institute for Materials Science,
1-1 Namiki,
Tsukuba, 305-0044
JAPAN

SAMANTA, S.B.

National Physical Laboratory
Dr K.S. Krishnan Road
New Delhi-110012
INDIA

SCHLACHTER, S.I.

Forschungszentrum Karlsruhe
Institut für Technische Physik
P.O. Box 3640,
76021 Karlsruhe,
GERMANY

SHIMOYAMA, J.

Faculty of Engineering,
University of Tokyo
Hongo 7-3-1,
Bunkyo-ku,
Tokyo 113-8656,
JAPAN

SILVER, Tania

Institute for Superconducting and Electronic Materials
University of Wollongong
Northfields Ave.
Wollongong
NSW 2522
AUSTRALIA

SPARN, G.

Max-Planck-Institut für Chemische Physik fester Stoffe,
01187 Dresden
GERMANY

STEGLICH, F.

Max-Planck-Institut für Chemische Physik fester Stoffe,
01187 Dresden
GERMANY

STOCKERT, O.

Max-Planck-Institut für Chemische Physik fester Stoffe,
01187 Dresden
GERMANY

TAKADA, K

Advanced Materials Laboratory,
National Institute for Materials Science,
1-1 Namiki,
Tsukuba, 305-0044
JAPAN

TAKAYAMA-MUROMACHI, E.

Superconducting Materials Center,
National Institute for Materials Science,
1-1 Namiki,
Tsukuba, 305-0044
JAPAN

TALLON, J.L.

MacDiarmid Institute for Advanced Materials and Nanotechnology
Industrial Research Ltd.
and Victoria University of Wellington
P.O. Box 31310
Lower Hutt
NEW ZEALAND

THALMEIER, P.

Max-Planck-Institut für Chemische Physik fester Stoffe,
01187 Dresden
GERMANY

WANG, J.S.

Applied Superconductivity Laboratory
Southwest Jiaotong University
Chengdu
Sichuan 610031
CHINA

WANG, S.Y.

Applied Superconductivity Laboratory
Southwest Jiaotong University
Chengdu
Sichuan 610031
CHINA

WOLF, Thomas

Forschungszentrum Karlsruhe
Institut für Festkörperphysik
P. O. Box 3640
76021 Karlsruhe
GERMANY

XI, X.X.

Department of Physics,
Department of Materials Science and Engineering
and
Materials Research Institute
The Pennsylvania State University
University Park
Pennsylvania 16802
USA

XUE, Y.Y.

Texas Center for Superconductivity
University of Houston,
Houston, Texas 77204-5002,
USA

YAMAUCHI, H.

Materials and Structures Laboratory
Tokyo Institute of Technology
Yokohama 226-8503
JAPAN

YOKOSAWA, T.

Advanced Materials Laboratory,
National Institute for Materials Science,
Namiki,
1-1 Tsukuba 305-0044,
JAPAN
and
Arrhenius Laboratory,
Stockholm University,
S-106 91, Stockholm,
SWEDEN

ZENITANI, Y.

Department of Physics and Mathematics
Aoyama-Gakuin University
5-10-1 Fuchinobe
Sagamihara
Kanagawa 229-8558
JAPAN

ZHANG, H.

State Key Lab for Mesophysics
Department of Physics
Peking University
Beijing 100871,
CHINA

ZHAO, Y.

Superconductivity R&D Center,
Southwest Jiaotong University
Chengdu
Sichuan, 610031
CHINA
and
Superconductivity Research Group
School of Materials Science and Engineering
University of New South Wales
Sydney, 2052, NSW,
AUSTRALIA

ZWICKNAGL, *Gertrud*

Institut für Mathematische Physik
Technische Universität Braunschweig
38106 Braunschweig
GERMANY

PREFACE

Since the discovery of mercury as the very first superconductor in 1911 by Kamerlingh Onnes, thousands of materials have been found to exhibit this exciting phenomenon in the temperature range of mK to 165K. Its occurrence among pure elements reveal that more than half the members of the periodic table become superconducting at temperatures, however low, under one condition or another, e.g., as thin films, fine powders, under pressure, in the disordered state or when made amorphous. Besides pure elements, almost all categories of materials seem to exhibit the phenomenon, including metallic alloys and compounds, intermetallics, metallic glasses, ceramics, both inorganic and organic polymers, organic charge transfer salts, various forms of carbon like fullerenes and nanotubes. Over the last 9 decades, the field has proved itself to be extraordinarily rich and dynamic with exciting new discoveries, in the form a novel material or phenomenon that occurred in intervals of every 2-3 years. The most recent of these superconducting materials is sodium-cobalt-oxide-hydrate, announced in 2003, while the previous one was superconducting magnesium diboride, discovered in 2001.

In this edited book, *Frontiers in Superconducting Materials*, the focus is on those materials and related phenomenas which are presently serving as arenas for intense topical research or applications. While choosing such areas for a book, one clearly has to follow a selective rather than exhaustive approach. Here, instead of all the topics only those making a greater impact, or so to say –the frontal or front runners, are included. Inherent in the above process is the risk of some topics inadvertently getting overemphasized while some, in the worst case, inadvertently or unavoidably getting altogether left out. In the case of superconductivity, where the significant developments seem too many, the above risk is especially nontrivial.

Frontiers in Superconducting Materials includes the following broad areas; superconductivity at ultra-low temperatures, heavy fermion superconductors, organic superconductors, superconducting fullerides, high T_c cuprate superconductors, their structural chemistry, important role of oxygen, their wires and tapes, their coated conductors, bulk materials for applications, their thin film processing, TEM studies, rutheno-cuprates and magnetic superconductors, their phase diagrams, superconducting borocarbides, heterogeneous magnetic superconductors, superconducting magnesium diborides, making of its wires and tapes, thin films and theory, single crystals and polycrystalline sodium-cobalt-oxide, pressure effects on superconductors, disordered superconductors, irradiation effects on superconductors, superconductors with nano-size pinning centres, niobium-based conductors for AC and DC applications.

Frontiers in Superconducting Materials comprises 30 chapters on the mentioned topical areas, written by noted international experts in the field. It should be of central interest to researchers and specialists in physics and materials science faculties of academic institutes as well as relevant industries. Given the multidisciplinary character of the field, the book should prove useful to electrical and device engineers while some of the reviews and overviews might answer the queries and curiosities of a nonspecialist interested in superconductors. The book is also likely to be of relevance for final year undergraduates reading physics and materials science.

XX

I would like to thank all the contributors for their splendid and timely cooperation. Thanks are further extended to the IUC, Indore and UGC-DAE Consortium for Scientific Research, Indore for providing the necessary infrastructure facilities.

November, 2004

Anant V. Narlikar

CONTENTS

| | |
|--------------|-----|
| CONTRIBUTORS | V |
| PREFACE | XXI |

SUPERCONDUCTING MATERIALS – A TOPICAL OVERVIEW

Roland Hott, Reinhold Kleiner, Thomas Wolf, and Gertrud Zwicknagl

| | |
|--|----|
| Introduction | 1 |
| Applications | 4 |
| Cuprate High Temperature Superconductors | 6 |
| Other Oxide Superconductors | 33 |
| Heavy Fermion Superconductors | 35 |
| Organic and Other Carbon Based Superconductors | 44 |
| Borides and Borocarbides | 46 |
| References | 50 |

SUPERCONDUCTIVITY AT ULTRA-LOW TEMPERATURES AND ITS INTERPLAY WITH NUCLEAR MAGNETISM

T. Herrmannsdörfer and F. Pobell

| | |
|---|-----|
| Introduction | 71 |
| Experimental Methods at Microkelvin Temperatures | 73 |
| The Noble Metals Cu, Ag, and Au | 75 |
| The Platinum Metals Rh, Pd, and Pt | 77 |
| Nuclear Ferromagnetism and Its Interplay with Superconductivity in AuIn ₂ | 83 |
| The Dependence of the Critical Field on Nuclear Magnetization in Nuclear Paramagnets | 91 |
| Hyperfine Enhanced Nuclear Magnetism and Its Interplay with Superconductivity in Pr _{1-x} La _x Cu ₆ | 98 |
| Summary | 104 |
| References | 106 |

SUPERCONDUCTIVITY IN HEAVY FERMION COMPOUNDS

P. Thalmeier, G. Zwicknagl, O. Stockert, G. Sparn, and F. Steglich

| | |
|--|-----|
| Introduction | 109 |
| Theories for the Normal HF State | 111 |
| Cerium-Based HF Superconductors | 120 |
| Microscopic SC Pairing Mechanism in HF Compounds | 149 |
| U-Based HF Superconductors | 155 |
| Summary and Outlook | 167 |
| References | 171 |

ONE DIMENSIONAL ORGANIC SUPERCONDUCTORS

D. Jérôme and C.R. Pasquier

| | |
|-----------------------------------|-----|
| Towards Organic Superconductivity | 183 |
| The (TM) ₂ X Period | 186 |
| Concluding Remarks | 222 |
| References | 223 |

SUPERCONDUCTIVITY IN FULLERIDES

J.E. Han, O. Gunnarsson, and Vincent H. Crespi

| | |
|--|-----|
| Introduction | 231 |
| C ₆₀ Molecule and Lattice Models | 235 |
| Mott Insulator Transition | 238 |
| Local Pairing via Local Quantum Fluctuations | 240 |
| Conclusions | 249 |
| References | 251 |

**CHEMICAL DESIGN OF COPPER-OXIDE SUPERCONDUCTORS:
– HOMOLOGOUS SERIES AND OXYGEN ENGINEERING –**

M. Karppinen and H. Yamauchi

| | |
|--------------------------------------|-----|
| Introduction | 255 |
| Structural Categorization | 256 |
| Redox Tailoring | 272 |
| Charge/Carrier Distribution | 278 |
| Fine-Structure and Superconductivity | 286 |
| References | 287 |

OXYGEN IN HIGH-T_c CUPRATE SUPERCONDUCTORS

J.L. Tallon

| | |
|-------------------------------|-----|
| Introduction | 295 |
| Structure | 296 |
| Electronic Structure | 300 |
| Doping | 301 |
| Oxygen Ordering | 306 |
| Oxygen Diffusion | 309 |
| Oxygen and Superfluid Density | 311 |
| ¹⁷ O NMR | 314 |
| Oxygen Isotope Effect | 322 |
| Conclusions | 326 |
| References | 327 |

RUTHENO-CUPRATES: THE SUPERCONDUCTING FERROMAGNETS

C.W. Chu, B. Lorenz, R.L. Meng, and Y.Y. Xue

| | |
|---|-----|
| Introduction | 331 |
| Synthesis | 333 |
| Superconductivity and Granularity | 342 |
| Magnetism | 350 |
| Meissner State and Spontaneous Vortex Phase | 359 |
| Conclusions | 361 |
| References | 362 |

A PHASE DIAGRAM APPROACH TO MAGNETIC SUPERCONDUCTORS

Hans H. Braun

| | |
|---|-----|
| Introduction | 365 |
| Phase Diagrams and Phase Properties | 366 |
| Crystal Structure and Occurrence of the Ruthenocuprates | 369 |
| Phase Equilibria in the Sr-Gd-Ru-Cu-O System | 370 |
| Preparation and Properties of Ruthenocuprates | 377 |
| Concluding Remarks | 384 |
| References | 386 |

SUPERCONDUCTIVITY IN QUATERNARY BOROCARBIDES

R. Nagarajan, Chandan Mazumdar, Z. Hossain, and L.C. Gupta

| | |
|--|-----|
| Introduction | 393 |
| Discovery of Superconductivity in Y-Ni-B-C System | 394 |
| Structure and Materials of Quaternary Borocarbide Family | 396 |
| Nonmagnetic Superconductors YNi_2B_2C and $LuNi_2B_2C$ | 399 |
| Magnetic Superconductors – RNi_2B_2C (R=Tm,Er,Ho,Dy) and $NdPt_2B_2C$ | 401 |
| The Heavy Fermion Borocarbide – $YbNi_2B_2C$ | 403 |
| Anisotropy in Superconducting Properties | 404 |
| Summary | 415 |
| References | 416 |

HETEROGENEOUS MAGNETIC SUPERCONDUCTING SYSTEMS

Serkan Erdin

| | |
|---|-----|
| Introduction | 425 |
| Theory | 427 |
| FM Dot on SC Film | 433 |
| Ferromagnetic – Superconducting Bilayers | 438 |
| Conclusions | 447 |
| Appendix A: The Pearl Vortex | 448 |
| Appendix B: Integrals of Bessel Functions | 449 |
| Appendix C: Calculation of Series | 452 |
| References | 455 |

HIGH PRESSURE EFFECTS ON SUPERCONDUCTIVITY

B. Lorenz and C.W. Chu

| | |
|---|-----|
| Introduction | 459 |
| Pressure Effects in Low Temperature Superconductors | 461 |
| Pressure Effects in High temperature Superconductors | 469 |
| Pressure Effects in Some Unconventional Superconductors | 483 |
| Summary | 489 |
| References | 492 |

DISORDERED SUPERCONDUCTORS

Anurag Gupta, V.P.S. Awana, S.B. Samanta, Hari Kishan, and A.V. Narlikar

| | |
|--|-----|
| Introduction | 499 |
| Amorphous Disorder and Superconductivity in Simple Metals | 500 |
| Amorphous Disorder and Superconductivity in Transition Metals, Alloys, and Metallic Glasses | 503 |
| Crystalline and Amorphous Disorders in A-15 Superconductors | 506 |
| Crystalline Disorder in High T _c Cuprates | 508 |
| Conclusions | 550 |
| References | 551 |

IRRADIATION OF HTS FOR ENHANCEMENT OF CRITICAL CURRENT

Damion Milliken, Tania Silver, and Shi Xue Dou

| | |
|-----------------------------|-----|
| Introduction | 555 |
| Gamma Ray Irradiation | 555 |
| Electron Irradiation | 556 |
| Neutron Irradiation | 556 |
| Ion Irradiation | 558 |
| Low Energy Ion Irradiation | 560 |
| High Energy Ion Irradiation | 561 |
| Fission Irradiation Methods | 565 |
| U/N Method | 570 |
| Uranium BSCCO Interaction | 579 |
| References | 580 |

STACKING MANNER OF CHARGE RESERVOIR BLOCKS IN SUPERCONDUCTING COPPER OXIDES

T. Nagai, T. Yokosawa, K. Kimoto, and Y. Matsui

| | |
|----------------------------|-----|
| Introduction | 589 |
| Experimental | 593 |
| Ru-System | 594 |
| Co-System | 604 |
| Discussion and Conclusions | 616 |
| References | 618 |

SUPERCONDUCTORS WITH NANOSCALE FLUX PINNING CENTRES

C.H. Cheng, Y. Zhao, Y. Feng, H. Zhang, M. Nishiyama,
N. Koshizuka, and M. Murakami

| | |
|---|-----|
| Introduction | 619 |
| NiO Induced Nano-Pinning Centres in Melt Textured YBCO Superconductor | 622 |
| Nanoscale Defects by Y211 Additions in Melt Textured YBCO Superconductor | 626 |
| Nano-Diamond Induced Flux Pinning in MgB ₂ | 630 |
| Nano-SiO ₂ Induced Flux Pinning in MgB ₂ | 635 |
| Flux Pinning Induced by Composition Fluctuations in Overdoped Cu-Rich Bi ₂ Sr ₂ CaCu ₂ O _{8+x} Single Crystals | 639 |
| Summary | 647 |
| References | 647 |

**PHYSICS AND CHEMISTRY
OF THE COBALT OXIDE HYDRATE SUPERCONDUCTOR**

K. Takada, H. Sakurai, and E. Takayama-Muromachi

| | |
|--|-----|
| Introduction | 651 |
| Layered Cobalt Oxide Systems | 652 |
| Superconductivity in Two Dimensional CoO ₂ Layers | 655 |
| Summary | 676 |
| References | 677 |

PROGRESS IN Na_xCoO₂ SINGLE CRYSTAL GROWTH

D. Prabhakaran and A.T. Boothroyd

| | |
|------------------------|-----|
| Introduction | 683 |
| Experimental Method | 684 |
| Results and Discussion | 685 |
| Conclusions | 693 |
| References | 694 |

DEVELOPMENT OF NB-BASED CONDUCTORS

Bartek A. Glowacki

| | |
|--|-----|
| Introduction | 697 |
| Outline of Critical Parameters and Global Pinning Force for Nb-Based Conductors | 698 |
| Nb-Ti Conductors | 700 |
| Nb ₃ Sn Conductors | 703 |
| Nb ₃ Al Conductors | 728 |
| Nb ₃ Ga Conductors | 733 |
| Mechanical Strain vs. J _c in Nb Based Conductors | 733 |
| Conclusions | 735 |
| References | 736 |

BI-BASED SUPERCONDUCTING CUPRATES: MATERIALS ASPECTS, CRYSTAL GROWTH AND PROPERTIES

E. Giannini, N. Clayton, N. Musolino, R. Gladyshevskii, and R. Flükiger

| | |
|---|-----|
| Introduction | 739 |
| Bi-Based Cuprates: General Features and Crystal Structure | 741 |
| Crystal Growth of Bi-Based Superconductors | 744 |
| Superconducting Properties and Vortex Phase Diagram of Bi ₂ Sr ₂ Ca ₂ Cu ₃ O ₁₀ | 750 |
| Structure and Superconducting Properties of Modulation-Free (Bi,Pb) ₂ Sr ₂ CaCu ₂ O _{8+□} | 755 |
| Concluding Remarks | 759 |
| References | 761 |

(RE)Ba₂Cu₃O₇ COATED CONDUCTORS FOR AC AND DC APPLICATIONS

Bartek A. Glowacki

| | |
|---|-----|
| Introduction | 765 |
| Material Design and Processing Considerations | 766 |
| Metal Substrates | 770 |
| Buffer Layer | 774 |
| Superconducting Layer | 776 |
| Ion-Beam-Assisted-Deposition, IBAD | 800 |

| | |
|---|-----|
| Metal Organic Deposition | 801 |
| Sol-Gel Technology | 802 |
| Liquid Phase Epitaxy | 808 |
| Magnetic Alignment and Thermo-Magnetic Growth of (RE)Ba ₂ Cu ₃ O ₇ | 814 |
| Cryomagnetic Stabilization of Ag/YBa ₂ Cu ₃ O ₇ /Buffer/Ni-Based Coated Conductor | 820 |
| Final Remarks | 823 |
| References | 824 |

THALLIUM-BASED SUPERCONDUCTING CUPRATES

J-L. Jorda

| | |
|---|-----|
| Introduction | 833 |
| Structural and Crystal Chemistry Aspects of Tl _m Ba ₂ Ca _{n-1} Cu _n O _x | 835 |
| The Phase Stability of the Substituted Thallium Cuprates Substituted or Unsubstituted TlBa ₂ Ca ₂ Cu ₃ O _{9-δ} : | 843 |
| Comparative Superconducting Properties | 855 |
| Thallium Coated Superconductors | 858 |
| Conclusion | 860 |
| References | 861 |

MATERIALS DEVELOPMENTS AND APPLICATIONS OF BULK RE-BA-CU-O SUPERCONDUCTORS

Masato Murakami

| | |
|------------------------------|-----|
| Introduction | 869 |
| Materials Developments | 870 |
| Applications of Bulk HTSs | 876 |
| Summary and Future Prospects | 882 |
| References | 883 |

SYNTHESIS OF BULK SUPERCONDUCTORS AND THEIR PROPERTIES FOR PERMANENT MAGNET GUIDEWAY

J.S. Wang and S.Y. Wang

| | |
|---|-----|
| Introduction | 885 |
| HTS Bulk Synthesis | 886 |
| Magnetic Levitation of HTS Bulk | 888 |
| Normal Permanent Magnetic (NPM) Guideway | 890 |
| HTS Maglev Measurement System | 891 |
| Magnetic Levitation Force | 894 |
| Magnetic Guidance Force | 900 |
| Influence of YBCO Bulk Size and Shape on the Levitation Properties | 902 |
| HTS Maglev Test Vehicle | 905 |
| References | 910 |

HIGH TC CUPRATES – THIN FILM PROCESSING, ATOMIC LAYER CONTROLLED DEPOSITION

Guus Rijnders and Dave H.A. Blank

| | |
|---|-----|
| Introduction | 913 |
| Nucleation Stage and Initial Growth | 914 |
| Influence of Substrate Properties on RE123 Growth | 917 |
| Experiments: REBa ₂ Cu ₃ O _{7-δ} on SrTiO ₃ | 919 |
| Conclusions | 932 |
| References | 934 |

SUPERCONDUCTIVITY IN MgB₂

T. Muranaka, Y. Zenitani, J. Shimoyama, and J. Akimitsu

| | |
|--|-----|
| Introduction | 937 |
| Crystal and Electronic Structure of MgB ₂ | 939 |
| Physical Properties of MgB ₂ | 946 |
| Potential of MgB ₂ for Practical Applications | 963 |
| Conclusion | 972 |
| References | 973 |

**SUPERCONDUCTIVITY OF MAGNESIUM DIBORIDE:
THEORETICAL ASPECTS**

Thomas Dahm

| | |
|--|------|
| Introduction | 983 |
| The Picture Suggested by Band Structure Calculations | 984 |
| Two Gap Superconductivity in Magnesium Diboride | 985 |
| Upper Critical Field Anisotropy | 988 |
| Microwave Conductivity | 994 |
| Summary | 1001 |
| Appendix | 1003 |
| References | 1008 |

CRITICAL CURRENT DENSITY IN SUPERCONDUCTING MgB₂

S.X. Dou, A.V. Pan, M.J. Qin, and T. Silver

| | |
|---|------|
| Introduction | 1011 |
| Two Gap Superconductivity of MgB ₂ | 1012 |
| MgB ₂ Material and Wire Development | 1013 |
| Effect of Substitution and Addition | 1014 |
| Activation Energy | 1027 |
| Sample Size Dependence of the Magnetic Critical Current Density | 1029 |
| Overcritical Currents in MgB ₂ Wires with Ferromagnetic Sheathing | 1032 |
| J _c Enhancement by Irradiation | 1038 |
| References | 1044 |

PREPARATION AND PROPERTIES OF ADVANCED MgB₂ WIRES AND TAPES

W. Goldacker and S.I. Schlachter

| | |
|--|------|
| Introduction | 1049 |
| Preparation of MgB ₂ Wires and Tapes | 1051 |
| Sheath Materials and Composite Structure of Mono-Filamentary Conductors | 1053 |
| The PIT Process | 1055 |
| Alternative Preparation Routes | 1056 |
| Superconducting Properties of MgB ₂ Wires and Tapes | 1056 |
| Technical Application of MgB ₂ Conductors | 1064 |
| Conclusions | 1065 |
| References | 1067 |

MgB₂ THIN FILMS

X.X. Xi

| | |
|---|-------------|
| Introduction | 1073 |
| Difficulties in Depositing MgB ₂ Films | 1074 |
| Deposition Techniques for MgB ₂ | 1076 |
| Properties of Clean Epitaxial HPCVD Films | 1078 |
| Properties of Carbon-Doped HPCVD Films | 1080 |
| Substrates and Heterostructures | 1082 |
| MgB ₂ Thin Film Devices | 1084 |
| Conclusions | 1085 |
| References | 1086 |
| | |
| SUBJECT INDEX | 1093 |

SUPERCONDUCTING MATERIALS – A TOPICAL OVERVIEW

Roland Hott¹, Reinhold Kleiner², Thomas Wolf¹, and Gertrud Zwicknagl³

¹ Forschungszentrum Karlsruhe, Institut für Festkörperphysik,
P. O. Box 3640, 76021 Karlsruhe, GERMANY

² Physikalisches Institut - Experimentalphysik II, Universität Tübingen,
72076 Tübingen, GERMANY

³ Institut für Mathematische Physik, Technische Universität Braunschweig,
38106 Braunschweig, GERMANY

1. INTRODUCTION

The phenomenon of superconductivity has not lost its fascination ever since its discovery in 1911. The flow of electric current without friction amounts to the realization of the old human dream of a perpetuum mobile. The ratio of resistance between the normal-conducting and the superconducting (“SC”) state has been tested to exceed 10^{14} , i. e., it is at least as large as between a usual insulator and copper as the best normal-conducting material [1].

But superconductivity is more than just the disappearance of resistance: The *Meißner effect*, the expulsion of magnetic fields from a superconductor, discovered in 1933, shows that superconductivity is a true thermodynamical state of matter since, in contrast to the situation for a merely perfect conductor, the expulsion is independent of the experimental history [1]. As the progress of cooling technique gave access to lower and lower temperatures, superconductivity established as common low-temperature instability of most, possibly all metallic systems (see Fig. 1). As the apparent $T \rightarrow 0$ K state of metals, the zero-entropy postulate of thermodynamics for this limit points to its nature as a macroscopic quantum state.

| H ? | s | | s-d | | | | | | | | | | s-p | | | | | | He |
|--------------------|---------------------|--|------------|-----------|-------------|-----------|---------------------|--------------|----|----|------------|--------------------|---------------------|----------------------|---------------------|----------------------|----|--|----|
| Li 20 55 GPa | Be 0.026 | <div style="border: 1px solid black; padding: 5px; display: inline-block;"> Elements T_c[K] applied pressure </div> | | | | | | | | | | B 11 293 GPa | C 4 9 GPa | N 6 | O 8.6 152 GPa | F 17 | Ne | | |
| Na | Mg | | | | | | | | | | | Al 1.19 | Si 8.5 12 GPa | P 6 17 GPa | S 17 169 GPa | Cl | Ar | | |
| K | Ca 15 138 GPa | Sc 0.3 21 GPa | Ti 0.4 | V 5.3 | Cr | Mn | Fe 2 21 GPa | Co | Ni | Cu | Zn 0.9 | Ga 1.1 | Ge 5.4 11 GPa | As 2.7 24 GPa | Se 7 132 GPa | Br 1.4 152 GPa | Kr | | |
| Rb | Sr 4 36 GPa | Y 2.8 10 GPa | Zr 0.6 | Nb 9.2 | Mo 0.92 | Tc 7.8 | Ru 0.5 21 GPa | Rh 0.0003 | Pd | Ag | Cd 0.55 | In 3.4 | Sn 3.72 | Sb 3.6 8.5 GPa | Te 7.4 30 GPa | I 1.2 29 GPa | Xe | | |
| Cs 1.5 3 GPa | Ba 5 36 GPa | La 5.9 | Hf 0.13 | Ta 4.4 | W 0.01 | Re 1.7 | Os 0.65 | Ir 0.14 | Pt | Au | Hg 4.15 | Tl 2.39 | Pb 7.2 | Bi 8.5 8 GPa | Po | At | Rn | | |
| Fr | Ra | Ac | Rf | Db | Sg | Bh | Hs | Mt | | | | | | | | | | | |
| s-f | | Ce 1.7 5 GPa | Pr | Nd | Pm | Sm | Eu | Gd | Tb | Dy | Ho | Er | Tm | Yb | Lu 1.3 18 GPa | | | | |
| | | Th 1.4 | Pa 1.4 | U 0.2 | Np 0.075 | Pu | Am 0.8 | Cm | Bk | Cf | Es | Fm | Md | No | Lr | | | | |

Fig. 1. Periodic table with the distribution and T_c [K] of chemical elements for which superconductivity has been observed with or without application of pressure [1,2,3,4].

The respective explanation of superconductivity by the *BCS theory* in 1957 [5] was a desperately awaited breakthrough of theoretical solid state physics. The starting point was the consideration that phonons introduce an attractive interaction between electrons close to the Fermi surface (“overscreening”). The key idea is that an (isotropic) attractive interaction leads here to bound electron pair states (“Cooper pairs”). These pair states are no longer obliged to obey the Fermi-Dirac statistics, which enforced the electrons to occupy high kinetic energy single particle states due to the Pauli principle. The energy gain of the SC state with respect to the normal state does not result from the small binding energy of the pairs but it is the condensation energy of the pairs merging into the macroscopic quantum state. It can be measured as an energy gap for electron excitations into single particle states.

In spite of the great impact of BCS theory¹, the discovery of *oxide “high-temperature superconductors” (“HTS”)* in 1986 [6] made it very clear that new theoretical concepts will be required here. The problem is not the high T_c of up to 138 K under normal pressure² [7], far above the pre-HTS record of 23 K [10]. However, in contrast to the “deep” Fermi sea of quasi-free electrons in the case of classical metals where the Cooper-pair condensed electrons amount only to a small part of the valence electron system ($k_B T_c \ll E_{\text{Fermi}}$), in these layered cuprate compounds there is only a “shallow” reservoir of charge carriers ($k_B T_c \sim E_{\text{Fermi}}$) which

¹ It had an impact not only on solid state physics but also on elementary particle physics where it was further developed to the idea of the Higgs mechanism of elementary particle mass generation.

² There is no theoretical argument why a textbook phonon BCS superconductor should not achieve such a high T_c . In the McMillan-Rowell formula [8], for example, as a commonly used theoretical- T_c approximation, T_c depends in a very sensitive way on the involved materials parameters. The HTS T_c range is readily accessible with a still reasonable parameter choice [9].

have to be introduced in the insulating antiferromagnetic (“AF”) stoichiometric parent compound by appropriate doping. The thus generated normal state corresponds to a “bad metal” in which Coulomb correlations strongly link the charge and spin degrees of freedom. This intrinsic proximity of metal-insulator, magnetic and SC transitions continues to present a great challenge to theory, which is sensibly more complicated than the classical superconductivity problem. The SC instability in cuprate HTS, as well as in the structurally and chemically related layered cobaltate and ruthenate compounds, is hence believed to stem predominantly from a magnetic and not from a phononic interaction as in the case of the classical metallic superconductors where magnetism plays only the role of an alternative, intrinsically antagonistic long range order instability.

A magnetic mechanism had been suspected already before the HTS discovery for “*Heavy-Fermion*” superconductors, discovered in 1979 [11]. In these intermetallic compounds the electronic degrees of freedom which are responsible for superconductivity are directly linked with magnetic moments of partially filled f-shells of Ce or U atoms³. The superconductivity below a typical $T_c \sim 1$ K seems to arise here from the delicate balance between the localized magnetic moments which try to imprint their magnetic signature on the shielding conduction electrons, and the conduction electrons which try to neutralize these magnetic moments by spin flipping, e. g., via the Kondo effect.

The search for *organic superconductors* had been boosted in the 1960s by the idea that conductive polymer chains with polarizable molecular groups may provide a highly effective Cooper pair coupling for electrons running along the polymer chains by means of an energy exchange via localized excitons [13]. Since the first discovery of an organic superconductor in 1980 [14] remarkable critical temperatures $T_c > 10$ K have been achieved [15]. However, the origin of superconductivity has turned out to be certainly far from the suggested excitonic mechanism. The electric conduction stems here from π -electrons in stacked aromatic rings, which form one- or two-dimensional delocalized electron systems. Similar to HTS, the restriction of the effective dimensionality⁴ and strong Coulomb repulsion effects push the systems towards metal-insulator, magnetic and SC transitions.

Fullerenes (C_{60} , C_{70} , ...) attracted much attention since their discovery in 1985 as a third modification of elementary carbon. The superconductivity in C_{60} introduced by doping and intercalation of alkali-metal atoms⁵, with T_c values up to 33 K at normal pressure [17], well above the pre-HTS record of 23 K [10] followed soon as another surprise. In spite of this high

³ PuCoGa₅ is a recently found “Medium Heavy Fermion” superconductor with $T_c = 18.5$ K [12].

⁴ The verdict of the Mermin-Wagner theorem [16] that long-range order can not exist in two dimensions at finite temperature due to the influence of fluctuations has long been believed to restrict superconductivity to the physical dimension $d = 3$. However, HTS have shown that the limiting case $d = 2 + \epsilon$ ($\epsilon \rightarrow 0$), i. e., a basically two-dimensional layer-oriented superconductivity scenario with a slight coupling of neighbouring layers, can be enormously beneficial for SC long-range order.

⁵ The chemically appropriate denotation of metal-doped fullerenes is “fullerides”. The semiconductor-impurity based view of “doping” amounts here to denoting common salt as “sodium-doped chlorine”.

T_c , the explanation of superconductivity seems to be well within reach of conventional BCS theory based on intramolecular phonons [18].

Borides had been investigated systematically with respect to high- T_c superconductivity already in the 1950s. The rationale was the BCS T_c -formula [8] where a high characteristic phonon frequency, as provided by the light boron atoms, was predicted to be particularly helpful with respect to a high T_c . In the 1990s, the borocarbide superconductors RE Ni₂B₂C with T_c up to 16.5 K [19] seemed to fulfill this promise at least halfway. However, phonons are here only one of the candidates of contributing superconductivity mechanisms⁶.

The huge surprise came in 2001 with the discovery of superconductivity up to $T_c = 40$ K in MgB₂, a compound which was well-known since the 1950s and which was in 2001 already commercially available in quantities up to metrical tons [20]. As for the fullerides, in spite of the high T_c a phononic mechanism is highly plausible: Strong Coulomb correlation effects are not expected since the conduction electron system does neither involve inner atomic shells nor a reduction of the effective dimensionality. Nevertheless, new theoretical ingredients are required for a satisfactory explanation of the experiments [21].

This recent example demonstrates which scientific surprises can be encountered even in seemingly well-investigated research areas, and that superconductivity will certainly remain for a long time to come at the forefront of physics and materials research.

2. APPLICATIONS

Besides the scientific interest, the search for applications has always been a driving force for superconductor materials science [22]. Right from the discovery, it had been envisioned that SC coils with high persistent current might be used to generate strong magnetic fields. However, in the first generation of SC materials (“*type-I*”) superconductivity was easily suppressed by magnetic fields: The magnetic self-field generated by the injected current prevented high-field as well as high-current applications. A first step towards this goal was the discovery of *type-II* superconductors where the magnetic penetration depth λ exceeds the SC coherence length ξ . This enables a coexistence of superconductivity and magnetic fields, which are allowed to penetrate into the SC bulk in the quantized form of vortices. The concomitant substantial reduction of the loss of SC condensation energy that has to be paid for magnetic field penetration facilitates the survival of superconductivity even in strong magnetic fields, at least up to a certain critical field H_{c2} where the SC state no longer survives the “vortex swiss cheesing”. The last ingredient required for technically applicable “*hard*” superconductors was the discovery and engineering of pinning centers which fix penetrated magnetic flux and prevent its Lorentz force driven flow through the superconductor that otherwise generates power dissipation.

⁶ For Rare Earth borocarbides there is additional magnetism due to localized RE ³⁺ 4f-electrons which is weakly interacting with superconductivity associated with the 3d-electrons of the Ni₂B₂ layers.

Today, NbTi and Nb₃Sn conductors are the basis of a billion Euro SC wire industry which delivers magnets that cannot be realized by means of conventional metal wire conductors, e. g., for Magnetic Resonance Imaging (MRI) systems and High-Energy Physics (HEP) particle accelerators⁷ [1,22,23]. The enormously high critical fields $H_{c2} \sim 100$ T of HTS [24] indicate their potential for extremely high-field applications. However, HTS vortex physics has turned out to be much more complex than what had been known from classical superconductors [25]. This implies strong restrictions for high-field, high-temperature HTS magnet hopes⁸. Nevertheless, in spite of earlier concerns about the ceramic nature of HTS, flexible⁹ HTS-based conductors are steadily progressing towards applications where a substantial size decrease justifies the cryogenic efforts. HTS current leads are just being introduced worldwide in HEP accelerators to transport kA-sized feed currents at a substantially reduced heat leakage from a liquid-nitrogen (“LN₂”) temperature region to LHe cooled SC NbTi coil systems [28]¹⁰.

Nb-based SC rf-cavities represent another recent technological progress of HEP accelerators: An extremely high quality factor provides here a much better transfer of acceleration energy to the particle bunches than in conventional cavities¹¹. Miniaturized microwave filters, e. g., for mobile phone base stations, are at present the most advanced HTS electronics application [31]: The low loss of thin film HTS resonator stripes with a typical size $50 \mu\text{m} \times 1 \text{cm}$ (see Fig. 17 of this article) allows a complex coupling of a large number of such resonators on a chip which enables filters with sharp frequency cut-offs.

Josephson junctions [1], well-defined weak links of SC regions, can be coupled to “Superconducting QUantum Interferometric Devices” (“SQUIDS”) [32,33], magnetic flux detectors with quantum accuracy that are the most sensitive magnetic field detectors presently

⁷ Only persistent-current mode operation fulfills the MRI temporal field stability requirements of ~ 1 ppm / hour. This can not be achieved by active stabilisation. Moreover, conventional multi-Tesla magnet systems would require a much more complicated and much more expensive cooling systems than the liquid He (“LHe”) cooling of SC coils. The Large Hadron Collider (LHC), presently under construction at CERN, will employ SC 9 T dipole coils to keep the high-energy protons on their orbit in a 9 km diameter circular tunnel. The high cost of the in total more than 8000 SC beam guiding magnets on the order of ~ 500 million Euro is still a bargain compared to the alternative of building a ~ 100 km diameter circular tunnel that would be required by conventional magnet technology.

⁸ The generation of an extra 5 T field by an HTS coil at 4.2 K on top of a 20 T background field, adding up to a total field of the SC coil system of > 25 T has just been demonstrated [26]. At low temperature, the actual field limit of HTS will always be determined by the mechanical reinforcement that has to be provided to prevent the HTS wire or bulk from being disrupted by the Lorentz forces. At liquid nitrogen temperature, YBCO tapes are promising candidates for field levels up to ~ 10 T.

⁹ Bending such HTS tapes around a finger does not deteriorate their critical current capacity [27].

¹⁰ Superconductors are not restricted by the Wiedemann-Franz coupling of electric and thermal transport since supercurrents do not transport entropy.

¹¹ At CERN, this energy increase has allowed the recently discussed “glimpse at the Higgs Boson” [29]. For the next generation of Nb cavities, the rf-magnetic fields will be increased up to 50% of H_{c2} of Nb [30].

available. SQUIDs based on Nb/AIO_x/Nb Josephson junctions achieve today at LHe temperature a magnetic noise floor $\sim 1 \text{ fT}/\sqrt{\text{Hz}}$ which enables diagnostically relevant magnetic detection of human brain signals (“magnetoencephalography”, “MEG” [34]). HTS SQUIDs at liquid nitrogen operation have approached this magnetic sensitivity within one order of magnitude [35] and are already in commercial use for the nondestructive evaluation (NDE) of defects in complex computer chips [36] and aircrafts [37].

In the 1970s and 1980s, IBM as well as a Japanese consortium including Fujitsu, Hitachi, and NEC tested in large projects the fast switching of Josephson junctions from the SC to the normal state with respect to a post-semiconductor computer generation [38]. Unfortunately, the switching from the normal to the SC state turned out to limit the practical performance to several GHz instead of the theoretical $\sim 1 \text{ THz}$ ¹². Meanwhile, new device concepts based on the transport of single magnetic flux quanta reestablished the feasibility of THz operation [1]. The hottest topic of present Josephson circuit investigations¹³ is the realization of quantum computing [39] with “Qubits” encoded by the SC wave function around μm -sized loops containing single [40] or even half [41] flux quanta¹⁴. At present, among all demonstrated Qubit realizations a SC electronics implementation appears to have the largest potential of upscalability to the size of several kQubit, which is required for first real applications: The lithographic requirements of $\sim 1 \mu\text{m}$ minimum feature size are already common practice in present semiconductor circuits.

For all these applications of superconductivity, the necessity of cryogenics is at least a psychological burden. Nevertheless, with the present progress of small cryocoolers [42] SC devices may evolve within foreseeable future to push-button black-box machines that may be one day as common practice as nowadays vacuum tube devices in ordinary living rooms¹⁵.

3. CUPRATE HIGH-TEMPERATURE SUPERCONDUCTORS

Cuprate High-Temperature Superconductors (“HTS”) play an outstanding role in the scientific development and for the present understanding of superconductivity. Except for semiconductors, no other class of materials has been investigated so thoroughly by thousands and thousands of researchers worldwide:

- A huge number of samples has been produced, in quantities of the order of metrical tons.
- Details of materials science have been diligently elaborated.
- High reproducibility has thus been achieved taking the materials complexity into account.
- The whole tool-set of experimental solid-state physics has been applied. For some techniques such as photoelectron spectroscopy [43,44], inelastic neutron scattering [45] or

¹² The practical problem is to avoid a “punch through“, i. e., the jump from a $V = +V_0$ to the $V = -V_0$ instead of the targeted $V = 0$ voltage state.

¹³ which may even be combined with the former

¹⁴ There are even several possibilities for such an encoding of a Qubit, e. g., it can be represented in terms of the polarity of the flux quanta.

¹⁵ such as old-fashioned TV sets

scanning tunneling microscopy [46,47] HTS have become a “drosophila”-like favorite object of investigation which still challenges further methodological development.

- HTS still represent a great challenge to theoretical solid-state physics since not only the superconducting but even more the “normal” conducting state of HTS is awaiting a satisfactory explanation.

It is due to this extraordinary importance that a large part of this book on superconductors and of this topical overview on SC materials is dedicated to cuprate HTS.

3.1 INTRODUCTORY REMARKS

The discovery of superconductivity above liquid-nitrogen temperature in cuprate materials (“High-Temperature Superconductors”, “HTS”) [6] raised an unprecedented scientific euphoria¹⁶ and challenged research in a class of complicated compounds which otherwise would have been encountered on the classical research route of systematic investigation with gradual increase of materials complexity only in a far future. The plethora of preparational degrees of freedom, the inherent tendency towards inhomogeneities and defects, in combination with the very short SC coherence length of the order of the dimensions of the crystallographic unit cell did not allow easy progress in the preparation of these materials. Nevertheless, after enormous preparation efforts HTS arrived meanwhile at a comparatively mature materials quality [49] that allows now a clearer experimental insight in the intrinsic physics which is still awaiting a satisfactory theoretical explanation [50,51,52].

The present situation of HTS materials science resembles in many aspects the history of semiconductors half a century ago [53]. The new dimension in the development of HTS materials, in particular in comparison with the case of silicon, is that HTS are *multi-element* compounds based on complicated sequences of *oxide layers* [54,55,56]. In addition to the impurity problem due to undesired additional elements, which gave early semiconductor research a hard time in establishing reproducible materials properties, intrinsic local stoichiometry defects arise in HTS from the insertion of cations in the wrong layer and defects of the oxygen sublattice. As additional requirement for the optimization of the SC properties, the oxygen content has to be adjusted in a compound-specific off-stoichiometric ratio [57], but nevertheless with a spatially homogeneous microscopic distribution of the resulting oxygen vacancies or interstitials [58]. Today, reproducible preparation techniques for a number of HTS material species are available which provide a first materials basis for applications. As a stroke of good fortune, the optimization of these materials with respect to their SC properties seems to be in accord with the efforts to improve their stability in technical environments in spite of the only metastable chemical nature of these substances under such conditions [59,60,61].

¹⁶ It has been estimated that in the hottest days of this “Woodstock of physics“ in 1987 [48] about one third of *all* physicists all over the world tried to contribute to the HTS topic.

3.2 STRUCTURAL ASPECTS

The structural element of HTS compounds related to the location of mobile charge carriers are stacks of a certain number $n = 1, 2, 3, \dots$ of CuO_2 layers which are "glued" on top of each other by means of intermediate Ca layers (see Fig. 2&3) [54,55,62,63]. Counterpart of these "active blocks" of $(\text{CuO}_2/\text{Ca})_{n-1}\text{CuO}_2$ stacks are "charge reservoir blocks" $\text{EO}/(\text{AO}_x)_m/\text{EO}$ with $m = 1, 2$ monolayers of a quite arbitrary oxide AO_x ($A = \text{Bi}$ [55], Pb [62], Tl [55], Hg [55], Au [64], Cu [55], Ca [65], B [62], Al [62], Ga [62]; see Table 1)¹⁷ "wrapped" on each side by a monolayer of alkaline earth oxide EO with $E = \text{Ba}, \text{Sr}$ (see Fig. 2&3). The HTS structure results from alternating stacking of these two block units. The choice of BaO or SrO as "wrapping" layer is not arbitrary but depends on the involved AO_x since it has to provide a good spatial adjustment of the CuO_2 to the AO_x layers.

The general chemical formula¹⁸ $\text{A}_m\text{E}_2\text{Ca}_{n-1}\text{Cu}_n\text{O}_{2n+m+2+y}$ (see Fig. 3) is conveniently abbreviated as $\text{A-m}2(\text{n-1})\text{n}$ [63] (e. g. $\text{Bi}_2\text{Sr}_2\text{Ca}_2\text{Cu}_3\text{O}_{10}$: Bi-2223) neglecting the indication of the alkaline earth element¹⁹ (see Tab.1). The family of all $n = 1, 2, 3, \dots$ representatives with common AO_x are often referred to as "A-HTS", e. g. Bi-HTS. The most prominent compound $\text{YBa}_2\text{Cu}_3\text{O}_7$ (see Fig. 2), the first HTS discovered with a critical temperature T_c for the onset of superconductivity above the boiling point of liquid nitrogen [67], is traditionally abbreviated as "YBCO" or "Y-123" ($\text{Y}_1\text{Ba}_2\text{Cu}_3\text{O}_{7-\delta}$). It also fits into the general HTS

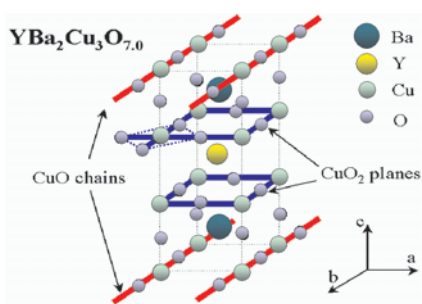


Fig. 2. Crystal structure of $\text{YBa}_2\text{Cu}_3\text{O}_7$ ("YBCO"). The presence of the CuO chains introduces an ortho-rhombic distortion of the unit cell ($a = 0.382$ nm, $b = 0.389$ nm, $c = 1.167$ nm [66]).

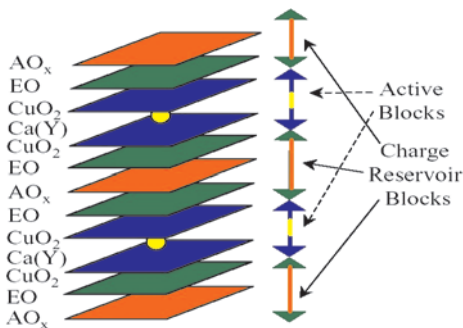


Fig. 3. General structure of a cuprate HTS $\text{A-m}2(\text{n-1})\text{n}$ ($\text{A}_m\text{E}_2\text{Ca}_{n-1}\text{Cu}_n\text{O}_{2n+m+2+y}$) for $m = 1$. For $m = 0$ or $m = 2$ the missing (additional) AO_x layer per unit cell leads to a $(a/2, b/2, 0)$ "side step" of the unit cells adjoining in c -axis direction.

¹⁷ HTS compounds based on "oxide mixtures" $\text{A}^{(1)}_s\text{A}^{(2)}_{1-s}\text{O}_x$ are omitted in this consideration.

¹⁸ $y = m(x - 1)$ in the oxygen stoichiometry factor.

¹⁹ A more precise terminology $\text{A-m}^{(E)}2(\text{n-1})\text{n}$ has been suggested [63].

classification scheme as a modification of Cu-1212 where Ca is completely substituted by Y. This substitution introduces extra negative charge in the CuO_2 layers²⁰ due to the higher valence of Y (+3) compared to Ca (+2). The HTS compounds $\text{REBa}_2\text{Cu}_3\text{O}_{7-\delta}$ ("RBCO", "RE-123") where RE can be La [55] or any rare earth element [68] except for Ce or Tb [69] can be regarded as a generalization of this substitution scheme. The lanthanide contraction of the RE ions provides an experimental handle on the distance between the two CuO_2 layers of the active block of the doped Cu-1212 compound [70,71,72]. $\text{Y}_1\text{Ba}_2\text{Cu}_4\text{O}_8$ ("Y-124") is the $m = 2$ counterpart Cu-2212 of YBCO.

The "214" HTS compounds $\text{E}_2\text{Cu}_1\text{O}_4$ (s. Tab1), e. g. $\text{La}_{2-x}\text{Sr}_x\text{CuO}_4$ ("LSCO") or $\text{Nd}_{2-x}\text{Ce}_x\text{CuO}_4$ ("NCCO") are a bit exotic in this ordering scheme but may also be represented here as "0210" with $m = 0$, $n = 1$ and $\text{E}_2 = \text{La}_{2-x}\text{Sr}_x$ and $\text{E}_2 = \text{Nd}_{2-x}\text{Ce}_x$, respectively.

Further interesting chemical modifications of the basic HTS compositions are the introduction of fluorine [73,74] or chlorine [75] as more electronegative substituents of oxygen. For Hg-1223, $T_c = 135$ K can thus be raised to 138 K [7], the highest T_c reported by now under normal pressure conditions (164 K at 30 GPa [76]).

3.3 METALLURGICAL ASPECTS

Within 18 years since their discovery, cuprate HTS samples have greatly improved towards high materials quality and can in fact nowadays be prepared in a remarkably reproducible way. The enormous worldwide efforts for this achievement may be estimated from the plain number of more than 100 000 articles which meanwhile have been published on cuprate high- T_c superconductivity, strongly outnumbering the only about 15 000 publications [77, 78,79] that appeared within a whole century on the remaining superconducting materials.

Nevertheless, the HTS materials quality level is still far from the standards of classical superconductors. The reason is the larger number of at least four chemical elements from which the various cuprate HTS phases have to be formed: The majority of the classical SC compounds, e. g. B1 or A15 compounds, is made of only two elements. Each element contributes an additional degree of freedom to the preparation route towards new compounds. For the metallurgist, this translates roughly into one order of magnitude more elaborate exploratory efforts. A new cuprate HTS compound requires therefore typically as much metallurgical optimization work as 100 binary compounds.

As a further complication, the large number of adjacent phases in the phase diagram constituted by the contributing elements hamper the preparation of phase pure quaternary or quinary cuprates. The HTS layer structure based on $(\text{CuO}_2/\text{Ca})_{n-1}\text{CuO}_2$ stacks with a certain CuO_2 layer number n (see Fig. 3) introduces another dimension of preparation challenges: As the formation enthalpy of a compound, e. g. with a single CuO_2 layer ($n = 1$), differs only little from that of the ($n = 2$)-compound with two adjacent CuO_2 layers, these materials tend to form polytypes [80]. A sophisticated process control during sample preparation is essential in order to reduce the amount of such stacking faults.

²⁰ Since the CuO_2 layers in YBCO are hole-doped this amounts to a reduction of the hole doping compared to the (hypothetical) canonical Cu-1212 compound.

The big metallurgical challenge introduced by the cuprate HTS materials in a previously unknown extent is the large number of chemical degrees of freedom of such materials. Binary compounds may have a 1-dimensional homogeneity range, e. g., NbN_{1-x} . In quaternary compounds, e. g., for RE-123 this range is in general 3-dimensional! In all cuprate HTS materials the oxygen degree of freedom O_x can be adjusted quite arbitrarily far from the stoichiometric ratio. The issue how to do this has been the subject of intensive investigations. As will become clear in chapter 3G, the oxygenation is an extraordinarily important experimental handle to introduce even radical changes of the physical properties of the material, e. g., to turn it from an insulator into a high-temperature superconductor! [81] The critical current capability steering the ampacity of technical conductors is another vital issue with respect to applications that depends critically not only on the content but also on the atomic-scale distribution of the oxygen atoms which are in the form of oxygen vacancy clusters probably the most important pinning centers [82] (see chapter 3F).

With respect to the cation stoichiometry, for the RE-123 phase as a particularly well-investigated HTS example the RE/Ba ratio represents the second chemical degree of freedom which may also deviate from the stoichiometric value 1/2. Y-123 (YBCO) represents here a remarkable exception. However, RE-123 compounds where the Y ions are replaced by larger RE ions like Gd or Nd exhibit a pronounced homogeneity range. For Nd-123, the Nd/Ba ratio encountered in such solid solutions may vary from 0.49 to 2, with the oxygen content being still a fully independent chemical variable. The Cu/(EA=Ba or Sr) ratio as chemical degree of freedom of all “hole-doped” HTS compounds (see Table 1) has up to now not been studied in great detail. For the 123 phase as a particularly complicated HTS example with respect to the Cu stoichiometry featuring two CuO_2 layers and an additional CuO chain structure in the unit cell, the present assumption is that the Cu/Ba ratio sticks to the stoichiometric value 3/2. For samples prepared close to their peritectic temperatures or at very low temperatures close to the boundary of the stability field of the 123 phase this may no longer be the case.

Chemical purity of the starting material is still a topical issue for a reproducible preparation of cuprate HTS. The use of chemicals with a purity of 99.99% and better is mandatory but still not sufficient. The frequently used Ba source material BaCO_3 is usually not completely reacted and may thus lead to the incorporation of carbonate ions into the HTS cuprate phase. During the preparation procedure, the formation of even a small amount of liquid has to be carefully avoided since this may corrode the substrate or crucible and may thus introduce impurities into the sample. This corrosion process is particular harmful for crystal growth experiments where the complete melt encounters the crucible wall. BaO/CuO melts are highly corrosive and attack all conventional types of crucible materials forming new solid phases. Some of these reaction products have turned out to be well suited as materials for corrosion resistant crucibles for the preparation of cuprate HTS. BaZrO_3 is here the best-known example [49], BaHfO_3 and BaSnO_3 are promising candidates.

Bearing in mind all these drawbacks and problems, the surprisingly high quality achieved nowadays for HTS cuprate materials, in particular for single crystals with respect to low impurity content, composition close to the desired stoichiometry, low concentration of defects such as inclusions, stacking faults or dislocations is rather amazing. However, a lot still remains to be done before the HTS sample quality becomes really comparable to that of binary classical superconductors.

3.4 STRUCTURE AND T_c

Experimentally, for all HTS families A-m2(n-1)n the optimized T_c is found to increase from $n = 1$ to $n = 3, 4$ and to decrease again for higher n (s. Tab.1). It is still unclear whether this T_c maximum is an intrinsic HTS property since the synthesis of higher- n members of the HTS families turns out to be more and more complicated [107,108,109,110]. In particular, there is at present no preparation technique that allows to adjust here a sufficiently high oxygen content²¹ or to provide otherwise sufficient electronic doping that would allow to clarify the possible range of T_c optimization for higher n HTS A-m2(n-1)n²² [107,110]. Hence the question is still open if such an optimized T_c may eventually continue to increase towards higher n , possibly up to $T_c \sim 200$ K as can be estimated for optimized infinite-layer HTS based on model-independent theoretical considerations extrapolating from $T_c(n = 1) \sim 100$ K of Hg-1201 [121].

Another well-investigated experimental T_c trend is the slight increase of the optimized T_c of the RE-123 HTS with increasing distance between the two CuO₂ layers in the active block²³. It has been explained in terms of a higher effective charge transfer to the CuO₂ layers [68,70]. For RE-123 HTS with larger RE ions (La, Pr, Nd), sufficient oxygenation with respect to T_c optimization becomes increasingly difficult. In this respect, La-123 is apparently beyond the present practical limit [49]: The intrinsic $T_c \sim 100$ K, estimated from optimized T_c values of the other RE-123 as a function of oxygenation [49], has not been achieved yet.

As a further complication, these larger RE ions are comparable in size with the Ba ions. This favors cation disorder with respect to the RE and Ba lattice sites [123] which leads to substantial T_c degradation [124]. This disorder effect, oxygen deficiency and / or impurities had been suggested as reasons for the non-appearance of superconductivity in Pr-123 [125] and Tb-123 as the only non-SC members of the 123-HTS family. However, in 1998 first superconducting Pr-123 samples with $T_c \sim 80$ K [126] (105 K at 9.3 GPa [127]) could be synthesized which lost their SC properties within few days after their preparation. The nature of this SC Pr-123 phase is still unclear. It has been suggested that it consisted of Ba-rich Pr-123 which is unstable at room temperature with respect to spinodal decomposition. The c-axis lattice parameter of these SC Pr-123 samples fits well in the series of the other SC RE-123 compounds, in remarkable contrast to the c-axis lattice parameter of the usual non-SC Pr-123 samples [126,127] where the absence of superconductivity is attributed to a hybridisation of the Pr 4f electrons with O 2p_π electrons depriving mobile charge carriers [128,129].

²¹ The microscopic distribution of oxygen [111] is neither easily observed [112,113,114] nor easily controlled [115]: Experimentally, oxygen content and distribution are adjusted by means of (oxygen partial) pressure, temperature and sufficient holding time to achieve thermal equilibrium [116].

²² The T_c depression is believed to arise from a redistribution of doping charge in the CuO₂ layer stacks from the interior to the outer CuO₂ layers [117] which has been confirmed by NMR measurements [118,119]. Based on these experimental results, a reasonable theoretical description of $T_c(n)$ has recently been modeled in a phenomenological Ginzburg-Landau free energy approach [120].

²³ On hydrostatic pressure application, dT_c/dP shows the same trend which further increases the T_c differences of the RE-123 [68]. On uniaxial pressure application, T_c increases if the pressure effect is to reverse the tetragonal-to orthorhombic lattice distortion [122].

Table 1. Classification and reported T_c values of HTS compounds.

| HTS Family | Stoichiometry | Notation | Compounds | Highest T_c |
|---------------------------|---|---|--|----------------|
| Bi-HTS | $\text{Bi}_m\text{Sr}_2\text{Ca}_{n-1}\text{Cu}_n\text{O}_{2n+m+2}$ $m = 1, 2$ $n = 1, 2, 3 \dots$ | Bi-m2(n-1)n, BSCCO | Bi-1212 | 102 K [83] |
| | | | Bi-2201 | 34 K [84] |
| | | | Bi-2212 | 96 K [85] |
| | | | Bi-2223 | 110 K [55] |
| Pb-HTS | $\text{Pb}_m\text{Sr}_2\text{Ca}_{n-1}\text{Cu}_n\text{O}_{2n+m+2}$ | Pb-m2(n-1)n | Pb-1212 | 70 K [87] |
| | | | Pb-1223 | 122 K [88] |
| Tl-HTS | $\text{Tl}_m\text{Ba}_2\text{Ca}_{n-1}\text{Cu}_n\text{O}_{2n+m+2}$ $m = 1, 2$ $n = 1, 2, 3 \dots$ | Tl-m2(n-1)n, TBCCO | Tl-1201 | 50 K [55] |
| | | | Tl-1212 | 82 K [55] |
| | | | Tl-1223 | 133 K [89] |
| | | | Tl-1234 | 127 K [90] |
| | | | Tl-2201 | 90 K [55] |
| | | | Tl-2212 | 110 K [55] |
| | | | Tl-2223 | 128 K [91] |
| Hg-HTS | $\text{Hg}_m\text{Ba}_2\text{Ca}_{n-1}\text{Cu}_n\text{O}_{2n+m+2}$ $m = 1, 2$ $n = 1, 2, 3 \dots$ | Hg-m2(n-1)n, HBCCO | Hg-1201 | 97 K [55] |
| | | Hg-1212 | 128 K [55] | |
| | | Hg-1223 | 135 K [93] | |
| | | Hg-1234 | 127 K [93] | |
| | | Hg-1245 | 110 K [93] | |
| | | Hg-1256 | 107 K [93] | |
| | | | Hg-2212 | 44 K [94] |
| | | | Hg-2223 | 45 K [95] |
| | | | Hg-2234 | 114 K [95] |
| Au-HTS | $\text{Au}_m\text{Ba}_2\text{Ca}_{n-1}\text{Cu}_n\text{O}_{2n+m+2}$ | Au-m2(n-1)n | Au-1212 | 82 K [64] |
| 123-HTS | $\text{REBa}_2\text{Cu}_3\text{O}_{7-\delta}$ RE = Y, La, Pr, Nd, Sm, Eu, Gd, Tb, Dy, Ho, Er, Tm, Yb, Lu | RE-123, RBCO | Y-123, YBCO | 92 K [70] |
| | | | Nd-123, NBSCO | 96 K [70] |
| | | | Gd-123 | 94 K [96] |
| | | | Er-123 | 92 K [49] |
| | | | Yb-123 | 89 K [68] |
| | | | | |
| Cu-HTS | $\text{Cu}_m\text{Ba}_2\text{Ca}_{n-1}\text{Cu}_n\text{O}_{2n+m+2}$ $m = 1, 2$ $n = 1, 2, 3 \dots$ | Cu-m2(n-1)n | Cu-1223 | 60 K [55] |
| | | | Cu-1234 | 117 K [97] |
| | | | Cu-2223 | 67 K [55] |
| | | | Cu-2234 | 113 K [55] |
| | | | Cu-2245 | < 110 K [55] |
| Ru-HTS | $\text{RuSr}_2\text{GdCu}_2\text{O}_8$ | Ru-1212 | Ru-1212 | 72 K [98] |
| B-HTS | $\text{B}_m\text{Sr}_2\text{Ca}_{n-1}\text{Cu}_n\text{O}_{2n+m+2}$ | B-m2(n-1)n | B-1223 | 75 K [99] |
| | | | B-1234 | 110 K [99] |
| | | | B-1245 | 85 K [99] |
| 214-HTS | E_2CuO_4 | LSCO "0201" | $\text{La}_{2-x}\text{Sr}_x\text{CuO}_4$ | 51 K [100] |
| | | | Sr_2CuO_4 | 25 (75)K [101] |
| | | <i>Electron-Doped HTS</i> PCCO NCCO | $\text{La}_{2-x}\text{Ce}_x\text{CuO}_4$ | 28 K [102] |
| | | | $\text{Pr}_{2-x}\text{Ce}_x\text{CuO}_4$ | 24 K [103] |
| | | | $\text{Nd}_{2-x}\text{Ce}_x\text{CuO}_4$ | 24 K [103] |
| | | | $\text{Sm}_{2-x}\text{Ce}_x\text{CuO}_4$ | 22 K [104] |
| | | | $\text{Eu}_{2-x}\text{Ce}_x\text{CuO}_4$ | 23 K [104] |
| | $\text{Ba}_2\text{Ca}_{n-1}\text{Cu}_n\text{O}_{2n+2}$ | "02(n-1)n" | "0212" | 90K [105] |
| | | | "0223" | 120K [105] |
| | | | "0234" | 105K [105] |
| | | | "0245" | 90K [105] |
| <i>Infinite-Layer HTS</i> | ECuO_2 | <i>Electron-Doped I. L.</i> | $\text{Sr}_{1-x}\text{La}_x\text{CuO}_2$ | 43 K [106] |

In Bi-HTS, cation disorder at the Sr crystallographic site is inherent and strongly affects the value of T_c . In Bi-2201, partial substitution of Sr by RE = La, Pr, Nd, Sm, Eu, Gd, and Bi was shown to result in a monotonic decrease of T_c with increasing ionic radius mismatch [85]. For Bi-2212, partial substitution of Ca by Y results in a T_c optimum of 96 K at 8% Y doping, apparently due to a trade-off between the respective disorder effect and charge doping [85].

In 214-HTS without BaO or SrO “wrapping” layers around the CuO₂ layers (see Table 1), T_c seems to be particularly sensitive with respect to oxygen disorder [130]. The electron doped 214-HTS such as Nd_{2-x}Ce_xCuO₄ (“NCCO”) have here the additional complication of a different oxygen sublattice where oxygen ions on interstitial lattice positions in the Nd_{2-x}Ce_xO₂ layer (which are yet for hole doped 214-HTS the regular oxygen positions in the non-CuO₂ layer!) tend to suppress T_c [131].

With respect to the T_c dependence of the A-m2(n-1)n HTS families on the cation A of the charge reservoir blocks, there is an increase moving in the periodic table from Bi to Hg (see Tab. 1). However, continuing to Au, the reported T_c is already substantially lower²⁴. This T_c trend seems to be related to the chemical nature of the A-O bonds in the AO_x layers [94].

The correlation of T_c with the buckling angles of the CuO₂ layer is less pronounced [132]. Such and other deviations from a simple tetragonal crystal structure are found in most of the HTS compounds as a chemical consequence of the enforced AO_x layer arrangement in the cuprate HTS structure. These structural modifications certainly influence the SC properties.

However, these peculiarities can not be essential for high-temperature superconductivity, since there *are* cuprate HTS with a simple tetragonal crystal structure *and* high T_c : Tl-2201 [133,134] and Hg-1201 [135] are such HTS model compounds based on a single CuO₂ layer in the unit cell²⁵ with T_c values of 90 K and 97 K, respectively. Tl-2201 has already been used several times for experimental falsification of HTS theory predictions [136,137]. These simple model compounds represent also a much more natural starting point for the theoretical ab-initio understanding of HTS than YBCO and LSCO which are for historic reasons still favorites of present computational HTS materials science.

The rationale that the phenomenon of superconductivity in HTS can be conceptually reduced to the physics of the CuO₂ layers [51] has evolved to a more and more 2-dimensional view in terms of CuO₂ *planes*. The superconductive coupling between these planes within a given (CuO₂/Ca)_{n-1}CuO₂ stack (“interplane coupling”) is much weaker than the intraplane coupling, but still much stronger than the superconductive coupling between the (CuO₂/Ca)_{n-1}CuO₂ stacks which can be described as Josephson coupling (see Fig. 4).

The charge reservoir blocks EO/(AO_x)_m/EO play in this idealized theoretical picture only a passive role in providing the doping charge as well as the “storage space” for extra oxygen ions and cations introduced for additional doping. However, the huge pressure dependence of

²⁴ Earlier reports of Ag-HTS with AgO_x integrated in the HTS lattice have not been confirmed [62].

²⁵ Strictly speaking, the primitive unit cell of Tl-2201 has only rhombohedral crystal symmetry due to the “diagonal side step“ of the EO/(AO_x)_m/EO blocks common to all A-m2(n-1)n compounds with even m, i. e., m = 0, 2 (see Fig. 2). The tetragonal symmetry can be conceptually recovered enlarging the unit cell to include two primitive cells on top of each other.

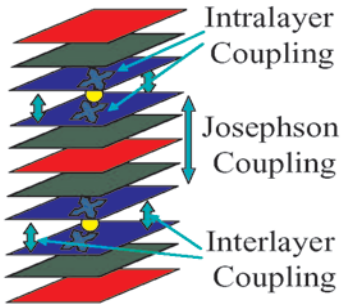


Fig. 4. Hierarchy of the SC coupling between the different structural elements of cuprate HTS.

T_c [76] in combination with the large quantitative variation of this effect for the various $A-m2(n-1)n$ HTS families points to a more active role where the cations change not only their valency but also their transmission behavior for the interstack tunneling of Cooper pairs [138].

This becomes most evident for the Cu-HTS family, in particular for YBCO or the RE-123 HTS where the AO_x layer is formed by 1-d CuO chain structures (see Fig. 2). There is experimental evidence that these CuO chains become SC, probably via proximity effect. The intercalation of superconductive CuO chain layers in-between the $CuO_2/Ca/CuO_2$ bilayer stacks is most likely the origin of the strong Josephson coupling between these bilayer stacks. This explains the remarkable reduction of the superconductive anisotropy in c-axis direction as compared to the other HTS families. Moreover, in contrast to the usually isotropic SC behavior within the a-b-plane, the CuO chains seem to introduce a substantially higher SC gap in b- compared to the a-direction [139]. This particular SC anisotropy renders YBCO and the RE-123 HTS exceptional among the cuprate HTS.

3.5 SYMMETRY OF THE SUPERCONDUCTING ORDER PARAMETER

The long search for superconductors with a nonisotropic energy gap Δ arrived finally in the 1980s with a small list of plausible candidates. The observation of power law temperature dependencies of physical properties such as specific heat and thermal transport coefficients instead of the $\exp(-2\Delta_0/k_B T)$ dependence of “s-wave” superconductors gave here the only clue to the structure of the energy gap nodes and their topology, and hence to the symmetry of the “unconventional” order parameter. Meanwhile, cuprate HTS have been established as a textbook example of a d-wave symmetric SC order parameter which can be observed directly by means of tricky “Superconducting QUantum Interference (Device)” (“SQUID”) circuits²⁶. Essential prerequisite for the applicability of these experimental techniques is a high quality single crystal and epitaxial thin film preparation.

First convincing experimental evidence of d-wave superconductivity of cuprate HTS was provided by a SQUID configuration based on YBCO-Au-Pb Josephson junctions which were

²⁶ Recent success with respect to YBCO-Nb Josephson junctions [41] enables now even the use of d-wave symmetry as a new functional principle for the construction of novel electronic devices.

fabricated on the a and b edges and straddling the a-b corners of a YBCO single crystal ("corner-SQUID") [140,141]. The most striking proof came from experiments performed on epitaxial c-axis oriented HTS thin films on "tricrystal substrates", substrates composed of three single-crystalline parts with different in-plane orientations which enforce the HTS films to a corresponding alignment of the a-b-crystal axes [142,143]. By suitable choice of the relative angles between these in-plane orientations, the boundary conditions for the SC order parameter connecting the three $d_{x^2-y^2}$ -wave subsystems impose a π -shift on any path circulating around the meeting point of these three film areas²⁷ (see Fig. 5) [144,145]. Since the SC wave function has to return to the same (complex) value, a compensating odd number of half-integer multiples of the magnetic flux quantum Φ_0 , i. e. $\pm \Phi_0/2$ in the ground state, must be encountered at this meeting point in the case of a $d_{x^2-y^2}$ -wave SC order parameter, whereas an s-wave order parameter symmetry requires here integer multiples of the full magnetic flux quantum, i. e. $\pm n \Phi_0$ [146,147]. Magnetic microscopy experiments²⁸ with a flux resolution of a minute fraction of Φ_0 clearly resolved at this tricrystal meeting point for all investigated cuprate HTS systems $\Phi_0/2$ vortices²⁹ (see Fig. 6) [142,143]. A particular SQUID circuit based on a tricrystal configuration (" π -SQUID") allows determining admixtures of other symmetries to the $d_{x^2-y^2}$ SC order parameter [148,149,150,151]. Up to now, no s-admixture has been observed within experimental error.

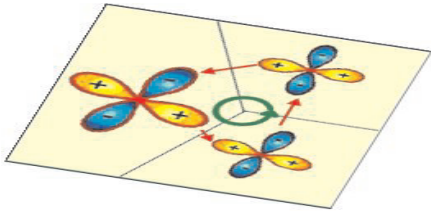


Fig. 5. Basic idea of tricrystal experiments for the verification of the $d_{x^2-y^2}$ symmetry of the SC order parameter of cuprate HTS.

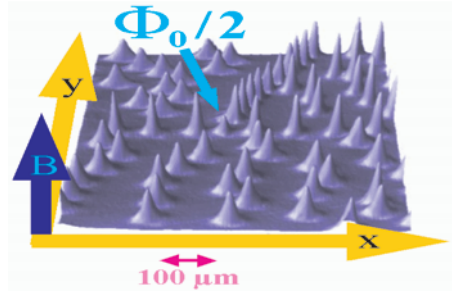


Fig. 6. Spatial distribution of magnetic flux in a Bi-2212 thin film deposited on such a tricrystal substrate in an applied field of 3.7 mG (adapted from [143]).

²⁷ Actually, due to the technical problem of providing a high quality substrate environment around the tricrystal point, tetracrystal substrates with identical crystal orientations of two neighboring single-crystal pieces of the four substrate parts have been used in most of these experiments.

²⁸ LTS SQUIDs are used in these experiments as external, at present most powerful research tools for the magnetic field sensing of microscopic samples with a spatial resolution $\sim 1 \mu\text{m}$.

²⁹ in external fields surrounded by regular Abrikosov Φ_0 vortices in the remaining film (see Fig. 6)

In contrast to the clear-cut experimental situation for hole-doped HTS representing the majority of the cuprate HTS compounds (see Table 1), the results for electron-doped HTS are still contradictory. Magnetic microscopy of NCCO and PCCO thin films on tricrystal substrates revealed $\Phi_0/2$ vortices at the tricrystalline “meeting point” demonstrating $d_{x^2-y^2}$ -symmetry [142,152]. π -SQUID experiments on $\text{La}_{2-x}\text{Ce}_x\text{CuO}_4$ [153] and photoelectron spectroscopy on NCCO [154] arrived at the same result. However, the temperature dependence of the London penetration depth $\lambda_{ab}(T)$ [103,155,156] as well as tunneling spectra derived from microbridges connecting epitaxial c-axis film areas with different in-plane orientations [157,158] seem to speak more in favor of an s-wave-symmetric SC order parameter: Tunneling spectra on hole-doped HTS show a distinct zero-(voltage-)bias anomaly (ZBA) with an amplitude that is directly proportional to the in-plane misorientation angle [159]. This can be readily explained as a (“Andreev”) bound state located in the transition region between the two film areas [157,159,160,161,162]. The d-wave related π -phase shift (see Fig. 5) is an essential quantization condition for the existence of such a bound state. For the electron-doped HTS NCCO and PCCO clear tunneling spectra have been obtained without any indication of such a ZBA [157,158]. At present, no reconciling explanation of these contradictory experimental facts has been found yet³⁰. Experimentally, the preparation of electron-doped HTS is much more demanding than of hole-doped HTS: Superconductivity occurs in a narrower doping range ($\text{Nd}_{2-x}\text{Ce}_x\text{CuO}_4$: $0.14 < x < 0.17$, $\text{Pr}_{2-x}\text{Ce}_x\text{CuO}_4$: $0.13 < x < 0.2$ [142]; $\text{La}_{2-x}\text{Sr}_x\text{CuO}_4$: $0.05 < x < 0.27$; $\text{YBa}_2\text{Cu}_3\text{O}_{6+x}$: $0.35 < x < 1.0$ [167]). Photoelectron spectroscopy revealed a switching from electron to hole-like states on doping [168] which may match the switching from s- to d-wave superconductivity concluded from London penetration depth measurements³¹ [169].

3.6 SUPERCONDUCTIVE COUPLING

HTS are extreme type-II superconductors [172] with $\lambda > 100$ nm and $\xi \sim 1$ nm. Superconductivity in HTS is believed to have its origin in the physics of the CuO_2 layers where the mobile charges are located [50,51]. The superconductive coupling between these CuO_2 layers within a given $(\text{CuO}_2/\text{Ca})_{n-1}\text{CuO}_2$ stack (“interlayer coupling”) is much weaker than the *intralayer coupling* within the CuO_2 layers, but still much stronger than the coupling between the $(\text{CuO}_2/\text{Ca})_{n-1}\text{CuO}_2$ stacks which can be described as Josephson coupling (see Fig. 4). This quasi-2-dimensional nature of superconductivity in HTS leads to a pronounced anisotropy of the SC properties with much higher supercurrents along the CuO_2 planes than in

³⁰ In NCCO low-energy excitations are observed for $T < 1$ K which presumably have their origin in the interaction of the magnetic Nd ions [163,164]. However, this additional physics is not an intrinsic peculiarity of electron-doped HTS: $\text{GdBa}_2\text{Cu}_3\text{O}_{7-\delta}$ shows similar effects attributed to the magnetic Gd ions [165,166] but the same “high energy” superconducting behavior as other RE-123 HTS.

³¹ A possibly related quantum phase transition of $\text{Pr}_{2-x}\text{Ce}_x\text{CuO}_4$ at $x_c = 0.165$ has been reported [170]. The presence of both charge carriers suggested by magnetothermopower measurements [171] could be due to local doping inhomogeneities and the strong doping sensitivity of the SC properties.

the perpendicular direction, a property which is not appreciated for technical applications but which can be dealt with by additional engineering efforts [173,174].

However, being type-II superconductor is not enough for a flow of strong currents without dissipation: The magnetic vortices that are introduced into the SC material by a magnetic field, in particular by the self-field generated by injected current, need to be fixed by *pinning centers*, or else dissipation by *flux flow* of the vortices is induced. In technical “hard” superconductors, material imperfections of the dimension of the coherence length do this job by blocking superconductivity from these regions. This provides a natural “parking area” for vortex cores where no SC condensation energy needs to be “paid”.

Material imperfections of the dimension of the coherence length are easily encountered in HTS due to their small coherence lengths, e. g., for optimally doped YBCO $\xi_{ab} = 1.6$ nm, $\xi_c = 0.3$ nm for $T \rightarrow 0$ K [175] which are already comparable to the lattice parameters (YBCO: $a = 0.382$ nm, $b = 0.389$ nm, $c = 1.167$ nm [66]). However, the low ξ_c , i. e. the weak superconductive coupling between the $(\text{CuO}_2/\text{Ca})_{n-1}\text{CuO}_2$ stacks causes new problems. The thickness of the charge reservoir blocks $\text{EO}/(\text{AO}_x)_m/\text{EO}$ in-between these stacks is larger than ξ_c with the result that due to the low Cooper pair density vortices are here no longer well-defined (see Fig. 7). This leads to a quasi-disintegration of the vortices into stacks of “*pancake vortices*” which are much more flexible entities than the continuous quasi-rigid vortex lines in conventional superconductors and therefore require individual pinning centers.

The extent of this quasi-disintegration is different for the various HTS compounds since ξ_c is on the order of the thickness of a single oxide layers: Hence the number of layers in the charge reservoir blocks $\text{EO}/(\text{AO}_x)_m/\text{EO}$ makes a significant difference with respect to the pinning properties and thus to their supercurrents in magnetic fields. This is one of the reasons why YBCO (“Cu-1 212”) has a higher supercurrent capability in magnetic fields than the Bi-HTS Bi-2 212 and Bi-2 223 which for manufacturing reasons are still the most prominent HTS conductor materials³².

Beside these intrinsic obstacles for the transport of supercurrent in single-crystalline HTS materials there are additional hurdles since HTS materials are not a homogeneous continuum but rather a network of linked grains (see Fig. 8). The mechanism of crystal growth is such that all material that cannot be fitted into the lattice structure of the growing grains is pushed forward into the growth front with the consequence that in the end all remnants of secondary phases and impurities are concentrated at the boundaries in-between the grains. Such barriers impede the current transport and have to be avoided by careful control of the growth process, in particular of the composition of the offered material.

³² In addition, in the Cu-HTS family the AO_x layer is formed by CuO chain structures (see Fig. 2). There are indications that the CuO chains become superconducting via proximity effect. This leads to stronger Josephson coupling in c-axis direction and thus to the smallest superconductive anisotropy among all HTS families [177].

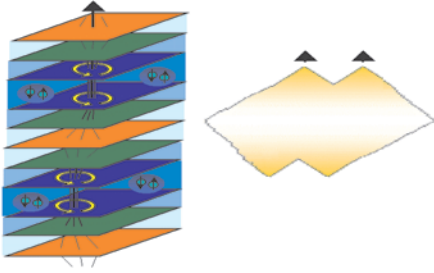


Fig. 7. Quasi-disintegration of magnetic vortex lines into “pancake” vortices due to weak SC interlayer coupling and schematic overlap of neighboring vortices [176].

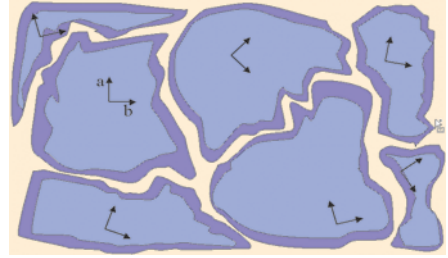


Fig. 8. Schematics of the HTS microstructure: Differently oriented single crystal grains are separated by regions filled with secondary phases. In addition, oxygen depletion may occur at grain boundaries.

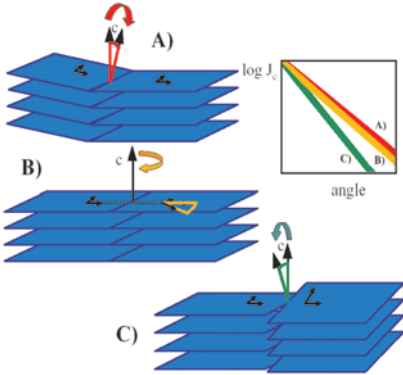


Fig. 9. Basic grain boundary geometries and experimentally observed J_c reduction $J_c \sim e^{-\alpha/\alpha_0}$ as function of the misalignment angle α : $\alpha_0 \approx 5^\circ$ for A) and B), $\alpha_0 \approx 3^\circ$ for C) independent of temperature [178,179].

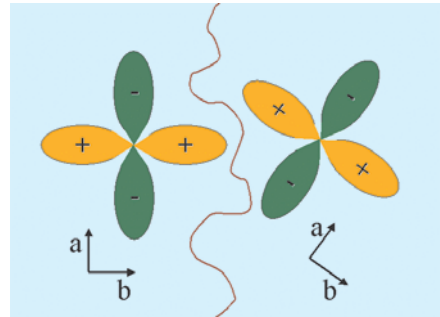


Fig. 10. Schematics of a boundary between HTS grains. Misorientation of the SC d-wave order parameter leads to partial cancellation of the supercurrents modified by the faceting of the grain boundaries.

Another obstacle for supercurrents in HTS is misalignment of the grains: Exponential degradation of the supercurrent transport is observed as a function of the misalignment angle (see Fig. 9). One of the reasons for this behavior is the d-symmetry of the SC order parameter (see Fig. 10) [142]. However, the J_c reduction as a function of the misalignment angle α turns out to be much larger than what is expected from d-wave symmetry alone [178,179,180,181]. This extra J_c degradation as well as the change of the current-voltage characteristics of the transport behavior³³ [182] are believed to arise from structural defects such as dislocations [183] and deviations from stoichiometry. In particular, the loss of oxygen at the grain surfaces [184] leads to a decrease of doping with respect to the grain bulk value and thus to a local degradation of the SC properties according to the temperature-doping phase diagram of HTS (see Fig. 13) [185]. For YBCO this can be partially eliminated by means of Ca-doping [186], which widens the range of acceptable grain misalignment in technical HTS material.

3.7 BASIC PHYSICS

The CuO_2 layers are believed to be the location of the mobile charge carriers in the cuprate HTS compounds [50]. This is in agreement with band structure calculations (see Fig. 11 a) [187,188]. However, in contrast to these results based on the independent electron approximation the stoichiometric compounds are actually antiferromagnetic (“AF”) insulators due to strong correlation effects: In HTS cuprates, the copper 3d-shells are filled with nine electrons, resulting in Cu^{2+} ions in d^9 configuration which are subject to a strong Jahn-Teller effect³⁴. The deformation of the oxygen octahedra which surround each Cu ion make the $d_{x^2-y^2}$ orbital the only unoccupied Cu 3d orbital, i. e., it accomodates the single hole [190]. This copper $d_{x^2-y^2}$ state hybridizes with the $p\sigma$ -orbitals of the surrounding four oxygen atoms (see Fig. 12). Due to the strong Coulomb repulsion for adding another hole at a Cu site these holes cannot move to neighboring Cu sites. This Coulomb correlation effect prevents a metallic behavior and turns the stoichiometric HTS compounds into insulators³⁵ (see Fig. 11 b). Virtual charge fluctuations generate a "superexchange" interaction, which favors antiparallel alignment of neighboring spins [192]. The result is long-range AF order up to rather high Néel temperatures $T_N = 250 - 400$ K [50].

³³ In addition to the quantitative effect on increasing misalignment angles of a reduction of the supercurrents, the current-voltage characteristics shows in addition a qualitative change from a flux-flow behavior for smaller misalignment angles [25,178,179] to overdamped Josephson junction behavior for larger misalignment angles [32].

³⁴ The starting point of K. A. Müller’s investigations on copper oxides were considerations that this might be used to achieve a large electron-phonon coupling with beneficial effects for an onset of superconductivity.

³⁵ Actually, the metal-insulator transition of copper oxides is more complicated than this classical Mott scenario. The gap for electronic excitations is here not determined by the mutual Coulomb repulsion of copper 3 $d_{x^2-y^2}$ holes but by the energy required to transfer a charge from an oxygen ion to the copper ion since the highest occupied electronic states are derived from oxygen 2p orbitals (see Fig. 11 b) with only a small admixture of Cu character (see Fig. 11 c) [189]. Hence, undoped copper oxides are not “Mott-(Hubbard) insulators” but “Charge-Transfer insulators”.

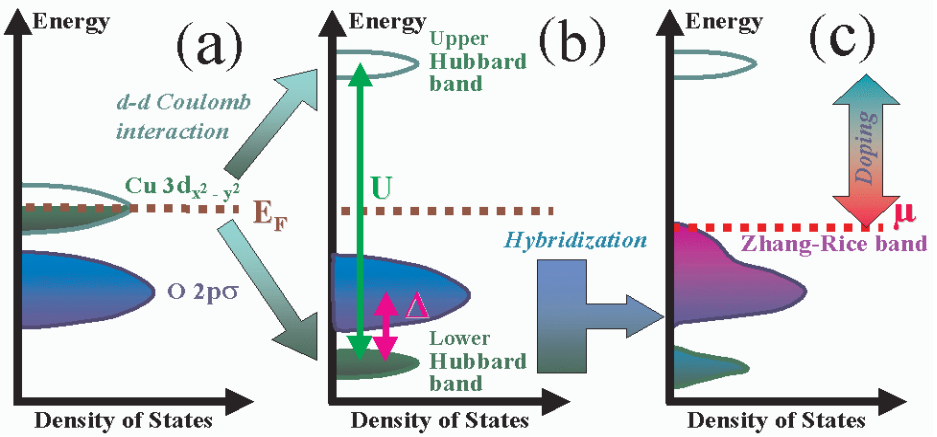


Fig. 11. Schematics of the electronic energy states involved in the charge transport in HTS (a) in an independent electron model, (b) including on-site Coulomb repulsion of the Cu 3d $_{x^2-y^2}$ states, (c) and hybridization of oxygen 2p σ states and the lower Hubbard Cu 3d band [191].

What is special about copper oxides in the big zoo of conducting oxides is that they are composed of CuO $_2$ layers which form 2-dimensional spin-1/2 Heisenberg AF subsystems that are subject to particularly strong quantum spin fluctuations³⁶.

³⁶ This is the starting point for many theoretical descriptions of the High-Temperature Superconductivity in cuprate compounds such as the Resonating Valence Bond (“RVB”) [51,52] or the Quantum Critical Point (“QCP”) scenario [193].

In the RVB picture, the antiferromagnetic lattice is perceived as a network of spin singlets made up of pairs of antiparallel Cu spins of the AF lattice. The ground state of the antiferromagnetic lattice is in this view a “resonating” superposition of such configurations of “valence bonds” in close analogy to the chemical picture of resonating double bonds in benzene. Putting an additional oxygen hole on a certain lattice site compensates the corresponding Cu spin by means of a singlet formation and leaves somewhere an unpaired spin of the related broken valence bond. The same holds true for the removal of a Cu hole (along with its spin). The many-body ground state of such a system with broken valence bonds is suggested to be a liquid-like state made up of the remaining resonating valence bonds and the decoupled charges (“holons”) and unpaired spins (“spinons”) as independent degrees of freedom.

Mathematically, the RVB wave function can be generated by projecting out double (lattice site) occupations from a d-wave BCS wavefunction used as a variational testfunction. However, due to the mathematical complexity of this approach, practical computations could be performed only on the basis of rather crude approximations. A recent refinement [194, 195] was claimed to show that RVB is able to explain many experimental features, but the criticism that the RVB concept is rather vague did not fall silent [196]. A recent RVB derivative is the “gossamer” superconductor wavefunction where the double occupations are only partially removed [197]. The new idea is that in the limit of small doping HTS do not become real insulators but remain superconductors, however, with an extremely large gap and an extremely rarefied superfluid density [198].

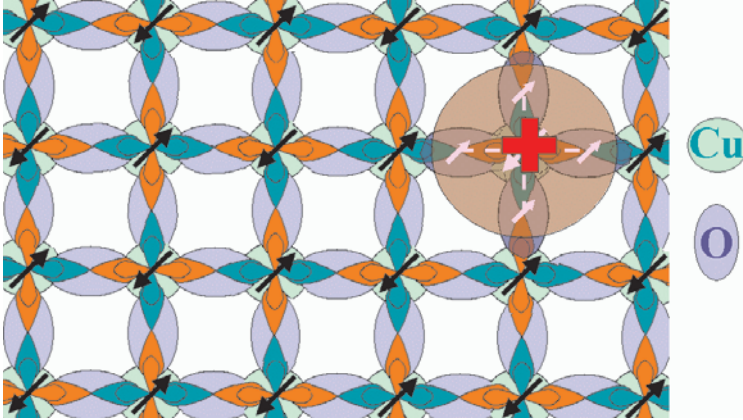


Fig. 12. Schematics of the spin-charge distribution atomic orbitals in the CuO_2 planes³⁷ with an additional hole charge. Doped holes are believed to enter a bonding combination of four oxygen $p\sigma$ -orbitals surrounding a copper ion. Antiparallel orientation of the involved spins leads to the formation of a “Zhang-Rice” singlet state with charge $Q = +e$ and spin $S = 0$ [199,200]. Doped electrons, in contrast, are believed to go to the copper sites and to eliminate there directly the hole in the $3d_{x^2-y^2}$ state along with its spin.

The following scenario applies for *hole-* [50] (see Fig. 12) as well as for *electron-doping* [201]: Adding charge carriers by variation of the oxygen content or by suitable substitution of cations relaxes the restrictions of spin alignment due to the interaction of these additional spin-1/2-particles with the spin lattice. T_N decreases and the insulator turns into a “bad metal”: The room-temperature mobility of the charge carriers increases gradually, in direct inverse proportionality to the AF correlation length [202]. At low temperature, however, the electric transport shows a dramatic change within a small doping range from an insulating behavior with an divergent upturn of the resistivity on decreasing temperature, to a superconducting behavior with a respective sudden downturn of resistivity next to T_c [202]. For $\text{La}_{2-x}\text{Sr}_x\text{CuO}_4$ this happens at a critical hole concentration $x = 0.05$ in the CuO_2 planes³⁸ (see Fig. 13). On stronger doping, superconductivity can be observed up to an increasingly higher critical temperature until for “optimal doping” ($x \approx 0.16$ for $\text{La}_{2-x}\text{Sr}_x\text{CuO}_4$) the maximum T_c is

³⁷ The indicated in-plane spin orientations are encountered in LSCO [204]. Most interestingly, in lightly doped antiferromagnetic LSCO this in-plane spin orientation is manifestly linked with the orthorhombic lattice distortion: LSCO can be magnetically detwinned applying a 10 T in-plane magnetic field [203]. This gives evidence of a close connection of spin and lattice degrees of freedom in cuprate HTS.

In YBCO the spins are in-plane aligned parallel to the CuO bonds [205].

³⁸ For $\text{La}_{2-x}\text{Sr}_x\text{CuO}_4$, a spin-glass like state has been reported at this critical doping $x \sim 0.05$. However, due to the tendency of HTS towards spatial doping inhomogeneities it is unclear whether this kind of decay of the long-range AF order is intrinsic.

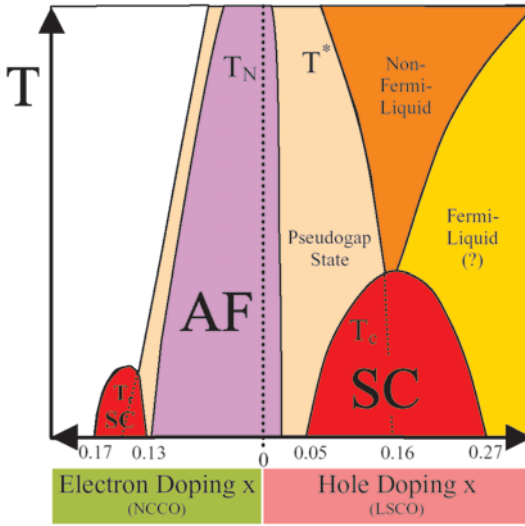


Fig. 13. Schematic HTS temperature-doping phase diagram dominated by the interplay of antiferromagnetism (“AF”) and superconductivity (“SC”) [50, 206, 207, 208].

achieved. On further doping, the critical temperature decreases again until finally ($x \geq 0.27$ for $\text{La}_{2-x}\text{Sr}_x\text{CuO}_4$) only normal conducting behavior is observed³⁹.

The rise and fall of T_c as a function of doping leads to the classification of the corresponding regions of the chemical phase diagram (see Fig. 13) as “underdoped” and “overdoped” regimes, respectively. At a first glance, the physical properties of these two regimes seem to be not so different for the SC state⁴⁰, but they are dramatically different for the normal state: In the underdoped regime for temperatures far above T_c , even up to room temperature, a peculiar redistribution of electronic states in the energy spectrum is observed in the vicinity of the Fermi energy resembling the features of a SC energy gap [214,215]. The critical temperature T^* associated with this “*pseudogap*” energy decreases monotonically on doping, in stark contrast to the monotonic increase of T_c in this doping regime (see Fig. 13). In the overdoped regime, in electron spectroscopy only a regular SC gap is identified. This is widely interpreted as coincidence of the SC gap and the pseudogap, which is hence regarded as a precursor of the SC gap [216]. However, from other experiments it has been concluded that $T^*(x)$ may actually continue its rapid decrease as a function of doping x “inside of the SC

³⁹ This doping scenario has been suggested to be even quantitatively universal with respect to the concentration x of holes or electrons in the CuO_2 planes [206] albeit with a large asymmetry between hole- and electron-doping (actually, there is no principal reason for electron-hole doping symmetry since different electronic states are affected; see Fig. 11), and with individual T_c and T_N parameters for each HTS compound (see Fig. 13). However, at least for the R-123 HTS family there is a substantial deviation of $T_c(x)$ from this “Tallon” parabola, with a T_c maximum around $x \sim 0.25$ and a “dent” or “plateau” at $x \sim 0.15$ [209,210,211].

⁴⁰ The SC condensation energy is lower [212] and the SC anisotropy is stronger in the underdoped regime [213], featuring an even more 2-dimensional character with stronger SC fluctuations.

dome”, i. e., below T_c , and that the pseudogap actually vanishes at a critical value x_c close or even identical to the optimal doping [206].

The so-called normal state of HTS is not at all "normal" according to the laws of conventional metal physics. In fact, it is now considered to be even more astonishing than the SC state. Early on, the dependencies of its physical properties were found to be highly unusual [217,218]. For *optimally doped* HTS, a linear temperature dependence of the electrical resistance $\rho(T) = \rho_0 + \rho_1 T$ is observed over the entire accessible temperature range up to 1000 K with essentially the same slope ρ_1 for all HTS compounds⁴¹ [217]. In spite of a well-developed Fermi surface [219,220,221,222], a Landau Fermi-liquid (“FL”) description of these dependencies necessitates the assumption of a strangely modified excitation spectrum (“Marginal Fermi Liquid”) [223]. As another indication of the breakdown of the Landau FL theory, in optimally (electron-)doped $\text{Pr}_{2-x}\text{Ce}_x\text{CuO}_4$ with the SC state quenched by a magnetic field the Wiedemann-Franz relation of charge and heat transport seems to be not obeyed even in the limit $T \rightarrow 0$ K⁴² [224].

In photoelectron spectroscopy, in the energy spectrum of the normal state no sharp quasiparticle peaks are observed, but only very broad features [50,230,231]. This can no longer be attributed to insufficient sample quality⁴³ or intrinsic problems of photoelectron spectroscopy [233,234]: In the SC state, already even slightly above T_c , on top of these broad features distinct quasiparticle peaks appear at energies right above the pseudogap. These peaks

⁴¹ $\rho(T) \approx \rho_0 + \rho_1 T^\alpha$ with $\alpha < 1$ for underdoped HTS. $\alpha \rightarrow 2$ for overdoping indicates the “normalisation” towards a regular Fermi liquid description of the normal state resistivity.

⁴² PCCO was selected for this experiment since a comparatively low, technically readily accessible $H_{c2} \leq 14$ T is believed to allow a magnetic suppression of superconductivity [224]. However, even if such a magnetic field is sufficient to destroy the phase coherence of the Cooper pairs in HTS, the SC pairing appears to be rather insensitive to these fields [225]. This argument, derived for hole-doped HTS, may also apply to electron-doped HTS such as PCCO where magnetic fields of the order of 10 T have a much more dramatic effect on the physical properties than for hole-doped HTS [208]. Nevertheless, measurement of the voltage induced by vortex flow in a driving temperature gradient (Nernst effect [226]) in magnetic fields up to 45 tesla seems to allow a more precise determination of H_{c2} [24]. Such measurements indicate in fact, e. g., $H_{c2}(T \rightarrow 0) = 10$ T for optimally electron-doped $\text{Nd}_{2-x}\text{Ce}_x\text{CuO}_4$ (“NCCO”; $x_{\text{opt}} = 0.15$) in contrast to $H_{c2}(T \rightarrow 0) \sim 60$ T for optimally hole-doped Bi-2212. Recent experiments on overdoped Tl-2201 [227], LSCO [228] and optimally doped Bi-2201 [229] indicate the validity of the Wiedemann-Franz relation for these hole-doped HTS compounds.

⁴³ Bi-2212 is the HTS best-suited for photoelectron spectroscopy experiments [232] since the lattice can easily be cleaved in-between two adjacent BiO layers which are only weakly (“van-der-Waals”) bonded. This leads to a micaceous material consistency (pure single-crystalline films can easily be wiped away by cotton wool) which offers good prospects for undegraded sample surfaces after cleaving in vacuum. Detwinned YBCO single crystals have meanwhile reached sufficient surface perfection as well [139]. However, the analysis of the quasiparticle peaks is complicated here by a low-energy surface state which is probably due to the cleaving of the lattice in-between a CuO chain layer and a BaO layer. Similar concerns have to be borne in mind for other HTS materials without a suitable cleavage plane.

become continuously sharper towards lower temperatures⁴⁴ [237]. This looks quite like the opposite of the familiar BCS scenario of a condensation of elementary normal state quasiparticles into a complex SC many-particle state [5,238] and gave rise to the speculation that charge may not be a good quantum number for the quasiparticles associated with the pseudogap state⁴⁵.

Another amazing experimental finding was the discovery of vortex-like excitations in the pseudogap phase of underdoped HTS well above T_c [240,241,242,243], which indicate the presence of strong SC fluctuations [216,225,244] even in this normal state. This points to the idea of "preformed (Cooper) pairs" [245] which exist already above T_c as noncoherent fluctuations and achieve coherent behavior only at lower temperature after condensation into the SC state. For spatially localized pairs as suggested for HTS by their small coherence length (e. g. for (optimally doped) YBCO: $\xi_{ab} = 1.6$ nm, $\xi_c = 0.3$ nm for $T \rightarrow 0$ K [175]; lattice parameters: $a = 0.382$ nm, $b = 0.389$ nm, $c = 1.167$ nm [66]), such a preforming of pairs is much easier to imagine than for the cloud of spatially strongly overlapping pair states associated with the BCS description of conventional superconductors.

In this spirit, the difference between the underdoped and the overdoped regime has been attributed to a doping-induced crossover from the Bose-Einstein ("BE") condensation of preformed pairs in underdoped HTS, to a BCS pair-state formation in overdoped HTS [246,247]. The assumption that the pseudogap is a redistribution of the electronic states due to incoherent pair formation is tantamount to identifying the pseudogap as precursor of the BCS gap Δ which directly measures the binding of electrons into Cooper pairs. Even in the description of conventional superconductors the superfluid density ρ_s introduces a second temperature scale besides Δ [246]: ρ_s plays the role of a phase stiffness which measures the ability of the SC state to carry a supercurrent. In conventional superconductors, Δ is much smaller than the energy associated with ρ_s , and the destruction of superconductivity begins with the breakup of electron pairs. However, in cuprates the two energy scales seem to be more closely balanced. Actually, in underdoped materials the ordering is apparently reversed, with the phase stiffness now being the weaker link. When the temperature exceeds the critical temperature associated with ρ_s , thermal agitation destroys the ability of the superconductor to carry a supercurrent while the pairs continue to exist [248,249]. According to this phenomenological interpretation of the pseudogap, T_c would be defined here by ρ_s and not by Δ as in the case of conventional superconductors.

Another suggestion is that the pseudogap is due to a "hidden order" [250]. The favorite candidate for HTS cuprates is a $d_{x^2-y^2}$ density wave state (see Fig. 14) which was already

⁴⁴ The peak amplitude is apparently proportional to the superfluid density: In experiments on Bi-2212 samples with a broad variety of doping levels [235], the amplitude of these quasiparticle peaks measured at low temperature has been determined to show more or less a T_c -parabola-like behavior as a function of doping, very similar to the behavior of the low temperature superfluid density measured in μ SR, or of the jump of the specific heat coefficient at T_c [236].

⁴⁵ The charge-detection principle of photoelectron spectroscopy would then imply the observation of superpositions of quasiparticle states with the consequence of a respective energy broadening. This argument has been discussed in the context of spin-charge separation as predicted by RVB theory [51,52,167,239].

discussed in the late 1980s as ground state in HTS-oriented model calculations⁴⁶ [251,252], and which is also in agreement with the d-wave characteristics of the pseudogap as observed in photoelectron spectroscopy [253,254]. This $d_{x^2-y^2}$ density wave state is a particular example for a recently suggested extension of charge density waves (CDWs) to more general density waves based on the condensation of particle-hole pairs of a certain angular momentum into a BCS-like many-particle state [255]. This results in an energy gap for single-particle excitations, in close analogy with the usual BCS formalism. Conventional CDWs are conceived in this framework as s-density wave states where the charges are subject to a coherent, but in this case merely translatory motion. For non-zero angular momentum density wave states, additional synchronization of orbital motion comes into play. On a lattice, non-zero angular momentum density wave states correspond to patterns of circular bond currents (see Fig. 14), which describe perfectly synchronized hopping processes. This mechanism enables a charge transport without strong hindrance by mutual Coulomb repulsion.

Another attractive feature of the $d_{x^2-y^2}$ density wave state approach to the pseudogap is that the universal HTS- T_c parabola as a function of doping can be explained quantitatively in a Ginzburg-Landau approach in terms of a competition between $d_{x^2-y^2}$ superconductivity based on particle-particle (hole-hole) pairing, and the $d_{x^2-y^2}$ density wave state based on particle-hole pairing [250]. A major difference between the respective energy gaps is that the SC gap remains fixed at the Fermi energy while the $d_{x^2-y^2}$ density wave depends on the doping. In mean-field approximation it is found to be fully developed only at half filling of the energy band. It becomes reduced for both doping directions and vanishes towards either complete filling or full depleting. Physically this can be understood from the discussed property of the $d_{x^2-y^2}$ density wave state that it allows a charge transport avoiding strong Coulomb repulsion. This energy reduction is most effective for half filling whereas no gain of correlation energy can be expected for the motion of single electrons or holes across the empty lattice.

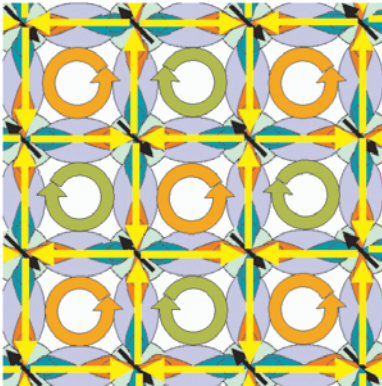


Fig. 14. $d_{x^2-y^2}$ density wave on a CuO_2 lattice based on bond currents (yellow) summing up to circulating currents of alternating orientation (orange/green).

⁴⁶ Here it was called “Staggered Flux“ state due to the magnetic flux generated by the circulating currents (see Fig. 14).

The neighborhood of the pseudogap and superconductor phases to the AF phase in the temperature-doping phase diagram points to a spin-related superconductivity mechanism. Starting out from static AF order for the undoped case, it is plausible that on increasing the doping strong AF correlations will persist in the underdoped pseudogap regime. Actually, neutron scattering experiments show that the Bragg peaks which result from the doubling of the real space unit cell due to antiferromagnetism survive in broadened versions, at least in the form of spin fluctuation patterns which can be probed by inelastic neutron scattering (INS) [256,257]. Surprisingly, in the underdoped regime for $T < T^*$ the single peaks in reciprocal space found in the insulator split into four, each displaced in orthogonal directions by a small amount (see Fig. 15 a) [256,257,258,259,260,261,262,263,264].

This scattering had at first been interpreted in terms of spin fluctuations described by linear response theory, which corresponds to sinusoidal spin density waves (SDW) fluctuating slowly in space and time⁴⁷ [265]. Spin waves are the Goldstone modes with respect to the AF order parameter and are therefore expected as low energy excitations. However, the measured energy dispersion is not compatible with conventional SDWs. Nevertheless, the INS k-space pattern points to modified spin waves [257]. A prominent suggestion was that the charges introduced by doping into the AF spin lattice may align in equidistant rows to form parallel "stripes" in transversal orientation to the spin wave, thus forming a charge density wave running in the same direction but with half the spatial period of the corresponding spin wave⁴⁸ [266,267,268;261,262]. This construction results in perfect commensurate AF spin domains extending over half a spin wave period, enclosed by charge stripes. Here a phase jump occurs so that the spin pattern of the neighboring AF domains appears to be spatially shifted by one lattice position. Stripes have been suggested to constitute a fundamental structural element of the ground state of all doped AF insulators arising from a competition between phase separation (the tendency of an AF insulator to expel doped holes) and the long-range part of the Coulomb interaction⁴⁹ [272,273]. The incommensurability ϵ ⁵⁰ increases monotonically with doping up to optimal doping where it saturates at $\epsilon \sim \pi/4$. A quantitative description of this experimental incommensurability-doping relation [50] was given by the concept of "metallic stripes" [275,276,277,278] where only every other "spin", i. e., hole along with its spin, is removed from the stripe positions: The remaining spins delocalize along the stripe forming metallic zone separating the AF domains.

The original stripe proposal [261,262] assumed one-dimensional stripes following a much earlier theoretical suggestion [266,267]. The four peaks ($\pi \pm \epsilon$, $\pi \pm \epsilon$) were believed to stem from a superposition of the signals ($\pi \pm \epsilon$, π) and (π , $\pi \pm \epsilon$), e. g., from the two twin domains

⁴⁷ An effective correlation length of ~ 20 nm has been derived from the width of the scattering peaks [262]. This corresponds to an extension of the spin fluctuations over ~ 50 unit cells.

⁴⁸ INS observations of a broadening of the linewidth of phonons stemming from the motion of planar oxygen atoms had been interpreted as evidence for the existence of charge stripe fluctuations [269,270]. However, this interpretation has been disproved by later INS measurements [271].

⁴⁹ This interpretation was inspired by measurements on $\text{La}_{2-x}\text{R}_x\text{Sr}_x\text{CuO}_4$ where partial substitution of La by R = Nd [261] or R = Eu [274] condenses the spin fluctuation into a static spin wave.

⁵⁰ measured as the splitting of the AF Bragg peak $(\pi,\pi) \rightarrow (\pi \pm \epsilon, \pi \pm \epsilon)$

of the usually twinned single crystal samples. INS measurements on partially detwinned samples seemed to back up this argument [279]. However, recent INS experiments on fully detwinned YBCO single crystals [280] as well as LSCO [281] showed that this decomposition is not appropriate. The correct Fourier transformation of the full INS k -space pattern leads to the 2-dimensional real space pattern as shown in Fig. 15 where the stripes run in “diagonal” spatial directions, in stark contrast to the reported naive interpretation of the INS Fourier peaks. Assuming again half-filling of the metallic stripes, the 2-dimensional stripe pattern reproduces equally well the experimental incommensurability-doping relation. Surprisingly, this stripe pattern was already presented in the original “stripe” paper as an alternate suggestion [267].

What has not yet been noticed is that it fits perfectly the “checkerboard” pattern which is observed in atomic resolution Scanning Tunneling Microscopy (STM) on Bi-2212 samples⁵¹ [284] (Fig. 15 (e)) ! The caveat is that the STM pictures reproduce a static phenomenon whereas INS measures dynamic excitations⁵² [285]. Nevertheless, pinning forces acting on these non-conventional spin-and-charge density waves may explain the actually observed tiny static spatially periodic charge accumulations⁵³. The “checkerboard” pattern was first seen in STM only in the low-temperature SC regime. It has been interpreted in terms of elastic scattering between characteristic regions (gap nodes) of the Fermi surface as observed in photoelectron spectroscopy [286,287]. The observed spatial periodicity was attributed to the difference of the k -space wave vectors around the gap nodes on the Fermi surface to where the scattering is energetically restricted by the SC gap (see Fig. 16). Recent STM measurements on slightly underdoped Bi-2212 found such modulations above T_c as well and attributed it to the energetic restrictions introduced by the pseudogap [288].

The topical question is whether this scattering is only an artifact of the STM observation or if it is already present in the HTS material as a particular spin-charge density wave [289]. The indicated compatibility of the collective spin excitation “stripe” pattern derived from INS with the STM “checkerboard” charge pattern speaks in favor of the latter one as the basic physical entity and against the idea that this real space pattern is only a mirage generated by the STM observation due to interference of single-particle excitations.

⁵¹ Erroneous indications of the real space direction of the experimental stripes are widely encountered in literature. This confusion is mainly due to the counterintuitive result of the Fourier transformation (see caption of Fig. 15). The different crystallographic notations used for orthorhombic and tetragonal LSCO where the first stripe formation was observed by INS may be additionally confusing: The so-called orthorhombic a - and b - directions of LSCO are rotated by 45° with respect to their tetragonal counterparts which are commonly denoted in literature as “HTS a and b axes” [282,283].

⁵² Only in the case of $\text{La}_{2-x-y}\text{R}_y\text{Sr}_x\text{CuO}_4$ with partial substitution of La by R = Nd [261] or R = Eu [274] for the doping $x = 1/8$ the spin fluctuation is condensed to a static spin wave, however, with the consequence of the disappearance of superconductivity [260].

⁵³ The dislocations in the STM picture Fig. 15 e indicate the presence of such pinning centers.

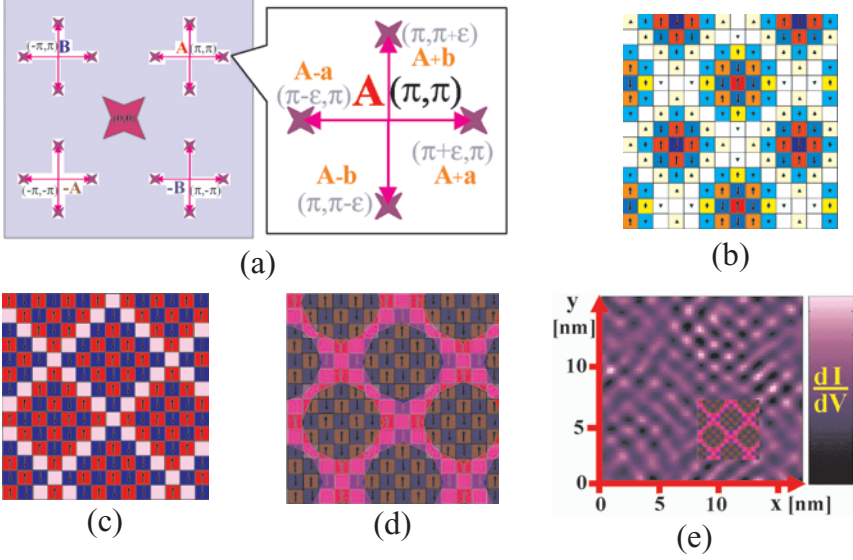


Fig. 15. (a) Schematics of the incommensurate low-energy INS k-space spectrum [263]. (b) Schematics of the corresponding harmonic spin wave real space pattern for $\varepsilon = \pi/4$, the incommensurability observed for optimally and overdoped HTS [259]:

$$\begin{aligned}
 f(x,y) &= \cos(\pi x) \times \cos(\pi y) \times \cos\{\pi/8\}\{x+y\} \times \cos\{\pi/8\}\{x-y\} \\
 &= [\cos(\mathbf{A}\mathbf{R}) + \cos(\mathbf{B}\mathbf{R})] \times [\cos(\mathbf{a}\mathbf{R}) + \cos(\mathbf{b}\mathbf{R})] / 4 \\
 &= [\cos(\{\mathbf{A}+\mathbf{a}\}\mathbf{R}) + \cos(\{\mathbf{A}-\mathbf{a}\}\mathbf{R}) + \cos(\{\mathbf{A}+\mathbf{b}\}\mathbf{R}) + \cos(\{\mathbf{A}-\mathbf{b}\}\mathbf{R}) \\
 &\quad + \cos(\{\mathbf{B}+\mathbf{a}\}\mathbf{R}) + \cos(\{\mathbf{B}-\mathbf{a}\}\mathbf{R}) + \cos(\{\mathbf{B}+\mathbf{b}\}\mathbf{R}) + \cos(\{\mathbf{B}-\mathbf{b}\}\mathbf{R})] / 8 \\
 &= [\exp(i\{\mathbf{A}+\mathbf{a}\}\mathbf{R}) + \exp(i\{\mathbf{A}-\mathbf{a}\}\mathbf{R}) + \exp(i\{\mathbf{A}+\mathbf{b}\}\mathbf{R}) + \exp(i\{\mathbf{A}-\mathbf{b}\}\mathbf{R}) \\
 &\quad + \exp(i\{\mathbf{B}+\mathbf{a}\}\mathbf{R}) + \exp(i\{\mathbf{B}-\mathbf{a}\}\mathbf{R}) + \exp(i\{\mathbf{B}+\mathbf{b}\}\mathbf{R}) + \exp(i\{\mathbf{B}-\mathbf{b}\}\mathbf{R}) \\
 &\quad + \exp(-i\{\mathbf{A}+\mathbf{a}\}\mathbf{R}) + \exp(-i\{\mathbf{A}-\mathbf{a}\}\mathbf{R}) + \exp(-i\{\mathbf{A}+\mathbf{b}\}\mathbf{R}) + \exp(-i\{\mathbf{A}-\mathbf{b}\}\mathbf{R}) \\
 &\quad + \exp(-i\{\mathbf{B}+\mathbf{a}\}\mathbf{R}) + \exp(-i\{\mathbf{B}-\mathbf{a}\}\mathbf{R}) + \exp(-i\{\mathbf{B}+\mathbf{b}\}\mathbf{R}) + \exp(-i\{\mathbf{B}-\mathbf{b}\}\mathbf{R})] / 8
 \end{aligned}$$

with $\mathbf{R} = (x, y)$, $\mathbf{A} = (\pi, \pi)$, $\mathbf{B} = (\pi, -\pi)$, $\mathbf{a} = (\pi/4, 0)$, $\mathbf{b} = (0, \pi/4)$.⁵⁴

(c) 2d-stripe distortion of the harmonic spin wave pattern (b). (d) Schematical representation of pattern (y) with “diagonal” metallic stripes separating insulating AF spin domains. (e) Fourier-filtered dI/dV real space pattern observed in STM over a 16 nm x 16 nm scan area of a slightly overdoped Bi-2212 single crystal (adapted from [284]). Figure (y) is integrated as appropriately scaled inset.

⁵⁴ $\cos(\alpha + \beta) + \cos(\alpha - \beta) = 2 \cos(\alpha) \cos(\beta)$. The high-energy part of the incommensurate INS k-space spectrum has recently been determined to be described alike [264], but by $\mathbf{a} = (\varepsilon, \varepsilon)$ and $\mathbf{b} = (\varepsilon, -\varepsilon)$. This leads thus to $f(x,y) = \cos(\pi x) \times \cos(\pi y) \times \cos(\varepsilon x) \times \cos(\varepsilon y)$, i. e., a “parallel” 2d-stripe pattern.

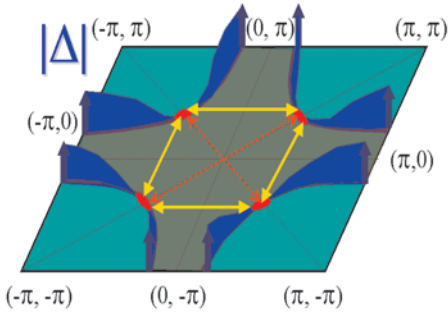


Fig. 16. Schematics of the HTS Fermi surface with a d-wave-like gap and indicated scattering between the nodal points of the energy gap.

This discussion has interesting aspects for general physics. For a $d_{x^2-y^2}$ -gapped Fermi surface, quasiparticles in the nodal regions make up the low-energy excitations (see Fig. 16). Time reversal symmetry connects the four nodal regions into two nonequivalent, but symmetry related pairs. Quasiparticles of either of these two pairs can be regarded as identical particles except for different “flavor” in the language of elementary particle physics. If the discussed “stripe-checkerboard” spin-charge agglomerations represent the basic physical entities these two pairs of quasiparticle excitations would also be intrinsically connected as a consequence of the energetic preference of the 2-d compared to the 1-d stripe configuration. As a nice toy model for quarks, this amounts to a “confinement” of two such single-flavor 2-d particles. It is charming to speculate that in our 3-d real world this argument would require a respective “confinement” of three 3-d particles as it is in fact observed for quarks. Moreover, this reasoning puts a question mark on the very idea of “elementary particles” which may turn out as artificial constructions for a single-particle description of many-body phenomena.

As a speculative summary of the presented HTS physics concepts, the stripe idea of an electronic phase separation in doped AF insulators may be extended into the following picture: The AF insulator bulk likes to get rid of the holes in order to maximize the exchange energy. The d- density wave state with its energetic preference for a “half-filling” environment provides a suitable mechanism for the formation and coherent connection of pure AF islands. The holes like to aggregate in a spatially extended metal state in order to reduce their kinetic exchange energy. An electronic phase separation into AF insulator islands surrounded by metallic 2-d network of stripes as shown in Fig. 15 c + d may be the energetically most favorable compromise⁵⁵. As long as this spin-charge agglomeration is subject only to minor pinning forces it remains a mobile phenomenon, with the d-density wave as collective transport mechanism based on coherent particle-hole currents. The occurrence of superconductivity in the metallic stripe channels would hence be only a parasitic effect.

These recent findings and speculations show that the investigations on cuprate HTS gave and still give rise to novel theoretical concepts in solid state physics which may provide again new input for elementary particle physics.

⁵⁵ 1-d stripes were shown to face the “spaghetti” stability problem of getting in too close touch with each other [290]. Model simulations seem to result usually in electronic 2d-foam with metallic membranes around AF islands [268].

3.8 TECHNICAL APPLICATIONS

The development of technically applicable HTS materials has progressed on several routes. Epitaxial YBCO [291,292] and Tl-HTS (Tl-2212) [293] *thin films* achieve excellent SC properties ($T_c > 90$ K; critical current density $J_c(77\text{ K}, 0\text{ T}) > 10^6\text{ A/cm}^2$; microwave surface resistance $R_s(77\text{ K}, 10\text{ GHz}) < 500\ \mu\Omega$, $R_s(T,f) \propto f^2$) that are well suited for superconductive electronics. They are already in use in commercial and military microwave filter systems (see Fig. 17). Since the HTS deposition takes place at $650 - 900\text{ }^\circ\text{C}$ the thermal expansion coefficients of the substrates and the HTS films have to match or else the different contraction of HTS film and substrate on cooling to room or even cryogenic temperature will lead to mechanical stress which can be tolerated by the film only up to a certain maximum thickness without crack formation [295]. This limits the thickness of YBCO films on the technically most interesting substrates silicon and sapphire to $\sim 50\text{ nm}$ [296] and $\sim 250 - 300\text{ nm}$ [297], respectively.

YBCO *Josephson junctions* based either on Josephson tunneling through ultra-thin artificial barriers [298,299,300,301] or on the Josephson junction behavior of HTS grain boundaries [302,303,304,305,306,307] have become available with a reproducibility of the critical currents of about $\pm 10\%$. They can be used for the construction of highly sensitive SQUID magnetic field sensors. For 77 K operation a field resolution of $\sim 10\text{ fT}$ has already been demonstrated [35] which compares favorably with the record resolution of $\sim 1\text{ fT}$ of Nb SQUIDS operated at 4 K . Recent success in the fabrication of YBCO-Au-Nb ramp-type junctions [308] enables now the use of the d-wave symmetry related π phase shift as a new functional principle for the construction of novel electronic devices.

Among other types of HTS contacts, intrinsic Josephson junctions (IJJs) in Bi-HTS [309,310,311,312] are of technical interest. These junctions are formed by the layered crystal structure itself, with adjacent CuO_2 double layers acting as the superconducting electrodes and

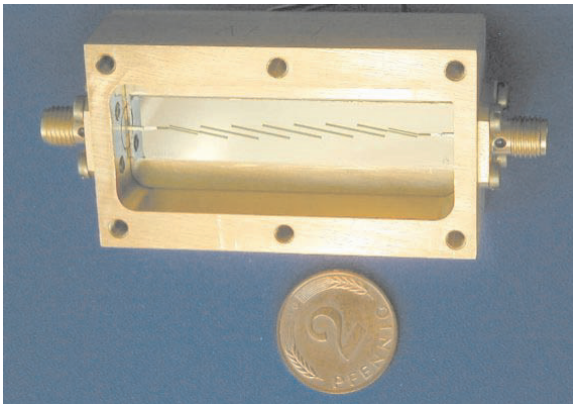


Fig. 17. Microwave filter based on seven YBCO resonator stripes [294].

the BiO and SrO layers acting as the nonsuperconducting barrier layers. Stacks of IJJs can be realized by patterning single crystals or thin films into mesa structures consisting of between one and up to some hundreds of IJJs. Even two-dimensional arrays containing many thousands of IJJs can be formed using a two-dimensional fabrication technique. Besides from Bi-HTS stacks of IJJs have been realized from Tl-HTS [313] and also from oxygen deficient YBCO [314].

HTS single crystals are not suitable for applications due to their small size and their low J_c values as a consequence of a low density of pinning centers. However, the “quick and dirty” version *melt-textured* 123-HTS *bulk material* can be grown reproducibly in sizes up to a diameter $d = 6$ cm even in complex shapes⁵⁶ [315], it shows superb magnetic pinning properties and is already tested as high-field permanent magnets, e. g., in magnetic bearings and motors [316]. Strong pinning allows the “freezing” of high magnetic fields, e. g., in single domain cylinders with a diameter of 30 mm an induction of 1.3 T can thus be fixed at 77 K [315], 17 T at 29 K has been demonstrated in-between two such samples [317]. This exceeds the potential of conventional permanent magnets based on ferromagnetic spin polarization by an order of magnitude and can be used for high-field “cryomagnets”. The present field limit does not stem from the pinning, but from the involved mechanical forces, which exceed at high fields the fracture toughness of the YBCO ceramic [318]. The combination of melt-textured YBCO with permanent magnets leads to levitation properties that are attractive for bearing applications. In contrast to classic magnetic bearings, SC magnetic bearings are self-stabilizing due to flux pinning. The levitation forces with densities > 10 N/cm² and the stiffness are already limited by the magnetic field strength of the permanent magnet [319,320,321].

In spite of the ceramic nature of the cuprate oxides, flexible HTS *wire* or *tape conductor* material can be obtained either by embedding thin HTS filaments in a silver matrix or by HTS coating of metal carrier tapes.

Bi-HTS /Ag tapes with cross sectional areas of ~ 1 mm² (Bi-HTS fill factor < 40 % [322]) are commercially available and can transport critical currents $I_c(77$ K, 0 T) up to 130 A [323] over km lengths. In the “Powder-in-Tube” fabrication, Ag tubes are filled with Bi-HTS precursor powder and are subject to various thermomechanical processing steps where the tubes are flattened out to tapes that include the Bi-HTS material as thin filaments. The fragility of the Bi-22(n-1)n grains along neighboring Bi-oxide planes⁵⁷ is the physical origin for the successful mechanical alignability of the Bi-HTS grains by means of rolling or pressing which orients the grains preferably with the ab-planes parallel to the tape surface. Silver is the only matrix material that does not chemically react with HTS compounds and allows in addition sufficient oxygen diffusion. The common melting of Ag and Bi-HTS around $\sim 850^\circ\text{C}$ leads to a close mechanical and electrical contact that helps to bridge non-SC regions by means of low-resistivity shorts. Critical issues for technical applications of Bi-HTS/Ag conductors are the cost and the softness of Ag.

⁵⁶ comparable to what has been achieved in NdFeB permanent magnets.

⁵⁷ The two BiO_x layers in the charge reservoir layers SrO/(BiO_x)₂/SrO of the Bi-HTS are attached to each other only by weak van-der-Waals-like bonding.

Bi-2223/Ag tapes with $T_c > 100$ K allow operation at LN₂ temperature [324,325,326]. However, the upper field limit of ~ 1 T at 77 K due to the pancake vortex disintegration of magnetic flux lines (see Fig. 7) [327] restricts the LN₂ operation of Bi-2223 tapes to low-field applications such as cables [328,329] or transformers. For extremely high magnetic field applications at low temperature operation, Bi-2212 conductors are economically more attractive than Bi-2223 tapes due to simpler processing and thus lower fabrication cost [330]. The fabrication of a complex standard conductor for accelerator magnets has already been demonstrated [331]. Another development aims at insertion magnets for 30 T class magnets where the Bi-HTS coils have to generate an additional field of several Tesla in a background field of ~ 20 T⁵⁸ [332]. The targeted high-field NMR application requires the persistent mode operation of the SC magnet system in order to fulfill the extreme temporal stability requirements based on an extremely slow decay of the supercurrents [333].

Cost arguments have always been in favor of HTS coating of simple robust metal carrier tapes. However, the major advantage would be the high-current operation in magnetic fields up to ~ 10 T at liquid nitrogen temperature. Meanwhile, $J_c(77\text{ K}, 0\text{ T}) \sim 1\text{ MA/cm}^2$ is achieved in YBCO-coated tapes over a length of ~ 10 meters⁵⁹. If this performance can be extended within the next few years to a commercial status comparable to the present situation for Bi-2223/Ag conductors, the US military would be highly interested in respective small-size/high-power transformers, motors, generators, cables etc. for the next generation of “purely electric” tactical aircrafts without hydraulics [334] and “stealth” battleships [335].

Comparing the 18 years since HTS discovery with the time frame of about 50 years that classical superconductors and semiconductors required to establish as reliable high-tech materials these achievements of HTS applications are truly amazing. Nevertheless, there is still no “killer application” where HTS could prove its ability to provide a unique technical solution required in order to realize a broad-impact technology as it had been the case with MRI magnets for classical superconductors. The lesson from this example is that this breakthrough will probably happen in an application field which no one has even thought of today [336]. Until then, again in analogy with classical superconductors, HTS materials will probably find their main use in some niche applications, in particular in scientific research, where they have the chance to finally reach the status of a readily available mature technology.

⁵⁸ Present state of the art is the generation of an extra 5 T field by a Bi-HTS coil (at 4.2 K) on top of a 20 T background field, adding up to a total field of the SC coil system of > 25 T [26].

⁵⁹ For HTS conductor materials, the current density criterion $J_c(77\text{ K}, 0\text{ T}) \geq 1\text{ MA/cm}^2$ has turned out to be good practical indicator for a sufficiently weak-link free microstructure. In principal, a lower J_c level would be satisfactory as long as a total current capability of the conductor of ≥ 100 A can be achieved. However, with the only exception of Bi-HTS/Ag tapes $J_c(77\text{ K}, 0\text{ T}) < 1\text{ MA/cm}^2$ have been found to show a large reduction of the current capability in external magnetic fields due to weak links. In addition, it indicates that the reproducibility is not yet sufficient with respect to the fabrication of longer length conductor material.

4. OTHER OXIDE SUPERCONDUCTORS

The discovery of superconductivity in the *bismuthate* $\text{BaPb}_{1-x}\text{Bi}_x\text{O}_3$ in 1975 with a (in those days) rather high $T_c \sim 13$ K for $x \sim 0.25$ [337,338] raised great interest in the mechanism of superconductivity in this (at that time) quite exotic oxide compound with a low density of states at the Fermi level. The HTS cuprates soon chased away that exotic touch in spite of the rise of T_c to > 30 K in $\text{Ba}_{1-x}\text{K}_x\text{BiO}_3$ (“BKBO”; $x \sim 0.35$) in the middle of the HTS bonanza days [339]: Tunneling showed clean gap structures consistent with weak-to-moderate coupling BCS theory [340]. The simple pseudocubic ABO_3 solid solution structure of a nonlayered nature derived for BKBO [341,342], with barium and potassium randomly occupying the A position, seemed to exclude for the SC phase the ordered, 3D charge-density wave (“CDW”) arrangement of $\text{Bi}^{(4-\delta)+}\text{O}_6$ and $\text{Bi}^{(4+\delta)+}\text{O}_6$ octahedra ($0 < \delta \ll 1$) that renders the parent compound BaBiO_3 insulating.

In contrast to the HTS cuprates, it is not Coulomb correlation but this structural instability – in combination with charge disproportionation and in a 3D analog of the 1D Peierls gap formation – that causes the gap at the Fermi level for the undoped parent compounds. Just like in HTS cuprates, superconductivity is effected by introducing hole carriers into the stoichiometric parent compound, in this case by K or Pb doping. However, the doping dependence of T_c is very different from the HTS doping scenario: For BKBO, the maximum occurs right at the metal-insulator transition at $x = x_c \sim 0.35$ when metallicity sets in; for $x > x_c$, T_c rapidly decreases and finally disappears at the K solubility limit $x \sim 0.65$.

Actually, recent investigations indicate that CDWs do survive, in part, for all K or Pb doping levels and coexist with the doped hole states, which, in the case of BKBO, turn out to be bipolaronic in nature and originate from Bi^{5+}O_6 octahedra. In fact, a complex interplay of the remaining CDWs with the different electronic states introduced by the two doping routes is responsible for metallicity and superconductivity [338]. Recently, evidence has been reported for a non-cubic, non-centrosymmetric crystal structure of SC BKBO. This would point to a more layered electronic character and a closer analogy to the cuprate HTS compounds [343], but without their restrictions of the spin degrees of freedom by d-shell Coulomb correlation effects.

The extensive search for other SC transition metal oxides following the discovery of the cuprate HTS came in 1994 across strontium *ruthenate* (Sr_2RuO_4), a layered perovskite with an almost identical crystal structure as the cuprate HTS $\text{La}_{2-x}\text{Sr}_x\text{CuO}_4$ (“LSCO”), albeit only with a $T_c \sim 1.5$ K [344]. In both materials the conduction electrons stem from partially filled d-bands (of the Ru or Cu ions, respectively) that are strongly hybridized with oxygen p-orbitals. In contrast to the nearly filled Cu 3d-shell in HTS with only one hole state, in Sr_2RuO_4 , in the formal oxidation state of the ruthenium ion Ru^{4+} four electrons are left in the 4d-shell. The closely related ferromagnetic material SrRuO_3 shows the inherent tendency of Ru^{4+} towards ferromagnetism. Hence, in analogy with the HTS cuprates, where on doping the AF ground state of the parent compounds seems to “dissolve” in spin-singlet Cooper pairs in a d-wave orbital channel, it was suggested that the superconductivity in Sr_2RuO_4 is brought about by spin-triplet pairing where the Ru ions “release” parallel-spin, i. e., triplet Cooper pairs in p-wave or even higher odd order angular orbital channels.

$\text{RuSr}_2\text{GdCu}_2\text{O}_8$ (Ru-1212) is a *ruthenate-cuprate hybrid* containing both CuO_2 and RuO_2 layers. It fits into the elucidated cuprate HTS layer structure scheme (see Fig. 3) substituting the Ca of the canonical 1212-HTS structure (or the Y in YBCO, or the RE in RE-123, respectively) by Gd to render $\text{CuO}_2/\text{Gd}/\text{CuO}_2$ stacks, separated by a SrO “wrapping layer” from the RuO_2 layers as “charge reservoir layers”. Like rare-earth borocarbides (see chapt. 7), Ru-1212 and some other closely related rutheno-cuprate compounds display ferromagnetism and superconductivity coexisting on a microscopic scale [345], with $T_{\text{Curie}} \sim 135$ K and T_c up to 72 K for Ru-1212. The $\text{CuO}_2/\text{Gd}/\text{CuO}_2$ stacks are believed to be responsible for the superconductivity, whereas the (ferro)magnetic ordering arises from the RuO_2 layers. A clear intrinsic Josephson effect shows that the material acts as a natural superconductor-insulator-ferromagnet-insulator-superconductor superlattice [346]. Electronic phase separation as discussed for underdoped cuprates resulting in domains that are both SC and AF separated by ferromagnetic boundaries has been suggested as a possible explanation [347].

Cobaltates are a very recent entry in the SC oxide zoo. $T_c = 4.5$ K has been achieved in hydrated sodium cobaltate $\text{Na}_{0.3}\text{CoO}_2 \cdot 1.4 \text{H}_2\text{O}$ [348]. Na provides here the doping charge. The intercalation of water which increases the separation between the CoO_2 layers seems to be essential for the onset of superconductivity: $\text{Na}_{0.3}\text{CoO}_2 \cdot 0.6 \text{H}_2\text{O}$, with the same Co formal oxidation state but substantially less separation between the CoO_2 layers is not SC [349]. This triggered theoretical interest in this compound, since it could hence provide an experimental test field for investigating the transition from a 3-dimensional to a 2-dimensional nature of the charge carriers which is believed to play a major role for the high T_c of cuprate HTS. A major difference is the triangular lattice geometry of the CoO_2 layers (see Fig. 18) which introduces magnetic frustration into the Co spin lattice, in contrast to the square lattice geometry of Cu ions in cuprate HTS which favors unfrustrated AF spin orientation.

A recent report on superconductivity in *pyrochlore oxides* ($T_c = 9.6$ K in KO_2O_6 , $T_c = 6.3$ K in RbOs_2O_6 , $T_c = 3.3$ K in CsOs_2O_6) [351] with a triangle-based crystal structure which is even more subject to magnetic frustration is a further indication that magnetic frustration is apparently not a no-go criterion for superconductivity [352].

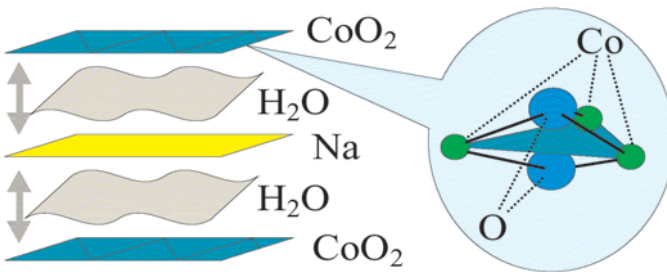


Fig. 18. Schematics of the layer structure of hydrated sodium cobaltate $\text{Na}_{0.3}\text{CoO}_2 \cdot 1.4 \text{H}_2\text{O}$ and atomic microstructure of the basic cobalt oxide triangular plaquettes [350].

5. HEAVY FERMION SUPERCONDUCTORS

Heavy-Fermion (HF) systems are stoichiometric lanthanide or actinide compounds whose qualitative low-temperature behavior in the normal state closely parallels the one well-known from simple metals. The key features are the specific heat which varies approximately linearly $C \sim \gamma T$, the magnetic susceptibility which approaches a temperature independent constant $\chi(0)$ and the electrical resistivity which increases quadratically with temperature $\rho(T) = \rho_0 + AT^2$. The coefficient $\gamma \sim 1 \text{ J / mole K}^2$ as well as $\chi(0)$ are enhanced by a factor of 100–1000 as compared to the values encountered in ordinary metals while the Sommerfeld-Wilson ratio $[\pi (k_B)^2 \chi(0)] / [3(\mu_B)^2 \gamma]$ is of order unity. The large enhancement of the specific heat is also reflected in the quadratic temperature coefficient A of the resistivity $A \sim \gamma^2$. These features indicate that the normal state can be described in terms of a Fermi liquid. The excitations determining the low-temperature behavior correspond to heavy quasiparticles whose effective mass m^* is strongly enhanced over the free electron mass m . The characteristic temperature T^* which can be considered as a fictitious Fermi temperature or, alternatively, as an effective band width for the quasiparticles is of the order 10 – 100 K. Residual interactions among the heavy quasiparticles lead to instabilities of the normal Fermi liquid state. A hallmark of these systems is the competition or coexistence of various different cooperative phenomena which results in highly complex phase diagrams. Of particular interest are the SC phases which typically form at a critical temperature $T_c \leq 2 \text{ K}$ ⁶⁰.

The discovery of superconductivity in CeCu_2Si_2 [11] forced condensed-matter physicists to revise the generally accepted picture of the electrons occupying the inner shells of the atoms. Traditionally, the corresponding states were viewed as localized atomic-like orbitals which are populated according to Hund's rules in order to minimize the mutual Coulomb repulsion. This leads to the formation of local magnetic moments which tend to align and which are weakly coupled to the delocalized conduction electrons. The latter were viewed as "free" fermions which occupy coherent Bloch states formed by the valence orbitals of the atoms. An attractive residual interaction among the conduction electrons causes the normal metallic state to become unstable with respect to superconductivity. The Cooper pairs which characterize a superconducting phase are broken by magnetic centers. The damaging effect of 4f- and 5f-ions was well established by systematic studies of dilute alloys.

The key to the understanding of the origin and the nature of the unanticipated superconductivity in CeCu_2Si_2 [11] lies in a better appreciation of the physics of the highly unusual normal state out of which it forms. The characteristic features summarized above show that the magnetic degrees of freedom of the partially filled f-shells form a strongly correlated paramagnetic Fermi liquid with an effective Fermi energy of the order of 1-10 meV. The existence of a Fermi liquid state with heavy quasiparticles involving the f-degrees of freedom has been confirmed experimentally.

The superconducting phases of HF materials are characterized by BCS-type pair-correlations among the heavy quasiparticles of the normal state [353]. This picture is inferred

⁶⁰ The exceptionally high transition temperature of $\sim 18.5 \text{ K}$ was recently reported for the actinide compound PuCoGa_5 [12].

from the fact that the discontinuities observed in various thermodynamic properties at the superconducting transition scale with the large effective masses of the normal state. The unusual energy and length scales in HF superconductors, however, lead to novel phenomena. First, the effective Fermi temperature typically exceeds the superconducting transition temperature only by one order of magnitude. This fact implies that standard weak-coupling theory which keeps only the leading contributions in an expansion with respect to the ratio T_c/T^* can provide only qualitative results. Pronounced strong-coupling corrections are reflected in deviations from the universal behavior predicted for weak-coupling systems. Second, the small characteristic energy $k_B T^*$, or, equivalently, the narrow width of the quasiparticle bands implies a small value of the Fermi velocity v_F . As a result, the size of the Cooper pairs in the HF systems, i. e., the coherence length $\xi_0 = \frac{\hbar v_F}{k_B T_c}$ is much less than in a typical "ordinary" superconductor. Many of the systems can be considered as "clean" with the mean-free paths exceeding the coherence length. As a result, anisotropic pair states can form which are strongly suppressed by impurity scattering in "ordinary" superconductors with large coherence lengths.

Although we know the correlations which characterize the superconducting state we are still far from a complete theory of superconductivity in these materials. Major questions are still open. Among the prominent is the question of which order parameters characterize the superconducting states and what is the origin of the attraction between the quasiparticles. The correct microscopic description of the interaction would yield, of course, the superconducting transition temperatures as well as the detailed form of the order parameter.

To describe ordered phases, the determination of the type and the symmetry of the order parameter is of central importance. The latter restricts the possible excitations in the ordered phases and hence determines the low-temperature properties. Order parameters given in terms of expectation values of physical observables like spin- and charge densities can be directly measured by x-ray or neutron diffraction. The magnetic phases of the lanthanide and actinide compounds are therefore rather well characterized. Superconductivity, however, corresponds to an off-diagonal long-range order parameter which is not directly observable. The usual procedure to determine the symmetry of the superconducting order parameter is to select plausible candidate states corresponding to irreducible representations of the symmetry group, calculate expected behavior of physical quantities and compare the predictions with experiment.

The occurrence of long-range order described by an order parameter is most frequently associated with spontaneous symmetry breaking. The simplest superconductors where only gauge invariance is broken are called conventional. In this case the superconducting state has the same symmetry as the underlying crystal. It should be noted that conventional is not a synonym for isotropic. A superconductor who has additional broken symmetries besides gauge symmetry, i. e., whose symmetry is lower than that of the underlying crystal is called unconventional. Considerable progress has been made recently in detecting unconventional order parameter symmetries. Angle-resolved studies of thermodynamic and transport properties in the vortex phase determine the position of order parameter nodes relative to the crystal axes.

In several systems, the order parameter has been shown to be unconventional. This was inferred mainly from anisotropies displayed by thermal transport in the presence of an external magnetic field. The most spectacular examples of unconventional superconductors are UPt_3 [354] and $\text{PrOs}_4\text{Sb}_{12}$ [355] where the split transition points to a multicomponent order parameter. In all the other HF superconductors, the order parameter seems to be a complex scalar function.

The fact that HF superconductors can be considered as "clean" systems with the mean-free path exceeding the coherence length has rekindled speculations so as to find inhomogeneous superconductivity phases (Fulde-Ferrel-Larkin-Ovchinnikov states; "FFLO" / "LOFF") at sufficiently low temperatures in sufficiently high magnetic fields [356]. In fact, the order of the phase transition in an applied magnetic field has been found to change from second to first order with decreasing temperature – in agreement with long-standing theoretical predictions [357].

An indispensable prerequisite to a microscopic theory of superconductivity is a microscopic theory of the normal state, of the quasiparticles and their interactions. The Landau theory does not make assumptions or predictions concerning the microscopic nature of the ground state and the low-lying excitations. It does not address the question how the latter emerge in an interacting electron system. During the past decade it became clear that there are different routes to heavy fermion behaviour.

In Ce-based compounds, the heavy quasiparticles with predominantly 4f-character arise through the Kondo effect in the periodic lattice. The Kondo picture for the Ce-based heavy-fermion compounds is supported by the fact that the thermodynamic properties at low temperatures (e. g., the specific heat, the magnetic susceptibility) as well as the temperature-dependence of the spectroscopic data can be reproduced by an Anderson model. This picture has been confirmed in detail by deHaas-vanAlphen and photoemission studies [358]. The strongly renormalized quasiparticles can be described by a semiphenomenological ansatz, the Renormalized Band Method which yields realistic quasiparticle bands [359]. The nesting features of the calculated Fermi surfaces can serve as a useful guideline in the search for instabilities with respect to modulated structures [360]. In particular, the calculations provide realistic models for the study of the competition/coexistence phase diagrams. Despite the efforts to implement modern many-body methods for strong correlations into realistic electronic structure calculations there is still no general concept for quantitative microscopic correlations. In particular, the subtle interplay between local and intersite effects continues to challenge theorists. The latter may lead to long-range order while the former favor the formation of a Fermi liquid state at low temperatures.

A microscopic picture for the heavy quasiparticles has finally emerged for the actinide compounds [361]. Increasing experimental evidence points towards a dual character of the 5f-electrons with some of them being delocalized forming coherent bands while others stay localized reducing the Coulomb repulsion by forming multiplets. The hypothesis of the dual character is translated into a calculational scheme which reproduces both the Fermi surfaces and the effective masses determined by deHaas-vanAlphen experiments without adjustable parameter. The method yields a model for the residual interaction leading to various

instabilities of the normal phase. The dual model should also provide insight into the mysterious hidden order phases of U compounds.

In both cases, i. e., in Ce and in U HF compounds, the coherent heavy quasiparticles are derived from the partially filled f-shells whose degrees of freedom have to be (partially) included into the Fermi surface. The situation is different for the Pr skutterudites where the quasiparticles are derived from the conduction states whose effective masses are strongly renormalized by low-energy excitations of the Pr 4f-shells. From a microscopic point of view we are dealing with three different classes of HF superconducting materials.

It is generally agreed that the pairing interaction in HF superconductors is of electronic origin. Theoretical models usually involve the exchange of a boson. It is therefore convenient to classify the various mechanisms according to the boson which is exchanged [362]. The majority of models construct effective interactions based on the exchange of spin-fluctuations. Neither these models nor their refined variants which account for the internal orbital f-electron structure are able to properly predict the symmetry of the order parameter, e. g., in UPt₃. In particular, the calculations do not reproduce a multicomponent order parameter as stable solution. Recently, a model based on the exchange of weakly damped propagating magnetic excitons was suggested for U-based HF compounds [363,364]. First estimates of the transition temperature yield a value of the correct order of magnitude. Pairing due to intra-atomic excitations may also occur in the Pr-skutterudite HF superconductor. In this case, however, quadrupolar instead of magnetic excitons should be involved [365].

Superconductivity in HF compounds is usually found to coexist or to compete with various cooperative phenomena. Of particular importance in this context is itinerant antiferromagnetism as realized in a spin density wave (SDW). Since both order parameters appear in the itinerant quasiparticle system the observed behavior results from a subtle interplay between Fermi surface geometry and gap structures.

Many HF systems are on the verge of magnetic instability. By application of pressure these materials may be tuned in their normal states through a quantum critical point (QCP) from an antiferromagnet to a paramagnetic metal. The theoretical picture, however, is at present still rather controversial and contentious.

5.1 Ce-BASED HF COMPOUNDS

The discovery of superconductivity in CeCu₂Si₂ ($T_c = 1.5$ K; see Fig. 19) [11] initiated the rapid development of HF physics. For nearly two decades, this material was the only Ce-based heavy fermion superconductor at ambient pressure. Only recently, superconductivity at ambient pressure was found in the new class of heavy fermion materials CeM_mIn_{3+2m} (M = Ir or Co; m = 0, 1) [366,367]. The most prominent member of this family is CeCoIn₅ which has a relatively high $T_c = 2.3$ K (see Fig. 12) [368]. Of fundamental interest is the discovery of HF superconductivity in CePt₃Si which crystallizes in a lattice without inversion symmetry.

The superconducting phases in the Ce-based HF compounds are characterized by anisotropic order parameters which reflect the on-site repulsion introduced by the strong correlations of the partially filled Ce 4f shells.

The current experimental and theoretical research focuses on the question which factors determine the character of the low-temperature phases. The subtle interplay between local singlet-formation via Kondo effect and long-range magnetic order can be monitored experimentally in pressure studies where isostructural relatives of the HF superconductors are tuned from magnetic phases at ambient pressure to SC states, e. g., CeCu_2Ge_2 [369], CePd_2Si_2 [370,371] CeNi_2Ge_2 [372] and CeRh_2Si_2 [373], CeSn_3 [374] and CeIn_3 (see Fig. 12 [370]). Similar behavior is found in doping experiments where constituents of the metallic host are successively replaced.

In CeCu_2Si_2 a highly interesting type of competition between (anisotropic) superconductivity and magnetic order is encountered. In this material, the heavy Fermi liquid is unstable with respect to both superconductivity and a spin-density wave. The actual ground state realized in a sample depends sensitively on the composition of the sample [360].

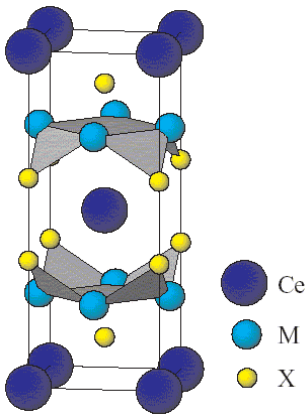


Fig. 19. Conventional unit cell of CeM_2X_2 ($M = \text{Cu, Ni, Ru, Rh, Pd, Au, \dots}$; $X = \text{Si, Ge}$) and URu_2Si_2 .

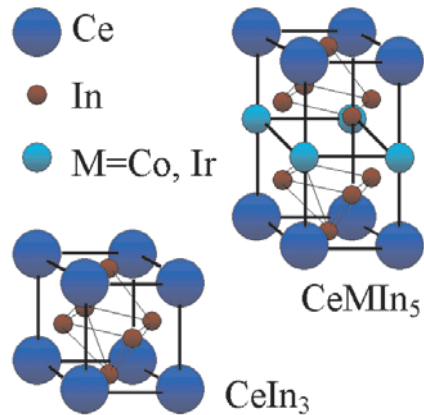


Fig. 20. Unit cell of CeIn_3 and CeMIn_5 ($M = \text{Co, Ir}$).

5.2 U-BASED HF COMPOUNDS

Heavy Fermion superconductivity is found more frequently in intermetallic U-compounds than in Ce-compounds. This may be related to the different nature of heavy quasiparticles in U-compounds where the 5f-electrons have a considerable, though orbitally dependent, degree of delocalization. The genuine Kondo mechanism is not appropriate for heavy quasiparticle formation as in Ce-compounds. This may lead to more pronounced delocalized spin fluctuations in U-compounds which mediate unconventional Cooper pair formation. Antiferromagnetic (“AF”) order, mostly with small moments of the order $10^{-2} \mu_B$ is frequently found to envelop and coexist with the SC phase.

The hexagonal compound UPt_3 (see Fig. 21) [375] exhibits triplet pairing. It sticks out as the most interesting case of unconventional superconductivity with a multicomponent order parameter whose degeneracy is lifted by a symmetry-breaking field due to a small moment AF order. In contrast, in UPd_2Al_3 (see Fig. 22) [376] superconductivity coexists with large moment antiferromagnetism. Probably spin singlet pairing is realized. There is experimental evidence for a new kind of magnetic pairing mechanism mediated by propagating magnetic exciton modes. The sister compound UNi_2Al_3 [377] is an example of coexistence of large moment antiferromagnetism with a SC triplet order parameter. In URu_2Si_2 [378] the SC order parameter symmetry is still undetermined. The interest in this compound is focused more on the enveloping phase with a "hidden" order parameter presumably of quadrupolar type or an "unconventional" spin density wave (SDW). The oldest cubic U-HF superconductor UBe_{13} [379] and its thorium alloy $\text{U}_{1-x}\text{Th}_x\text{Be}_{13}$ is also the most mysterious one. While for the pure system there is a single SC phase of yet unknown symmetry, in the small Th concentration range two distinct phases exist which may either correspond to two different SC order parameters or may be related to a coexistence of superconductivity with a SDW phase. In addition, in UBe_{13} SC order appears in a state with clear non-Fermi liquid type anomalies. More recently the coexistence of ferromagnetism and superconductivity in UGe_2 [380] has been found. Due to the ferromagnetic polarization the triplet gap function contains only equal spin pairing.

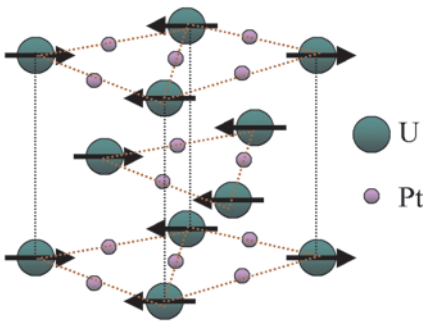


Fig. 21. Crystal structure of UPt_3 ($a = 0.5764$ nm, $c = 0.4884$ nm) and AF magnetic structure ($T < T_N = 5.8$ K).

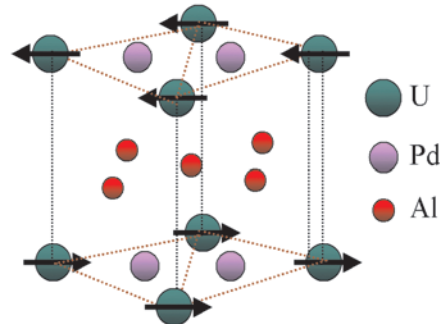


Fig. 22. Conventional unit cell of UPd_2Al_3 ($a = 0.5350$ nm, $c = 0.4185$ nm) and simple AF magnetic structure.

The hexagonal heavy fermion compound UPt_3 (see Fig. 21) is the "flagship" of unconventional superconductivity, despite its rather low critical temperature of slightly less than 1 K. It is set aside from all other unconventional superconductors insofar as it exhibits two SC phase transitions. The exciting discovery of the split superconductive transitions in UPt_3 at $T_{c1} = 530$ mK and $T_{c2} = 480$ mK in specific heat measurements [354] has led to an enormous amount of experimental and theoretical work on UPt_3 [381]. The additional small moment antiferromagnetism observed in UPt_3 ($T_N = 5.8$ K, $\mu = 0.035 \mu_B$) plays a key role in the identification of the SC order parameter since the in-plane staggered magnetization acts as

a symmetry breaking field (SBF) to the SC multicomponent order parameter. The SBF is believed to be responsible for the appearance of two SC transitions which otherwise would merge into one. Therefore one can identify three distinct SC phases. Despite the wealth of experimental results on UPt_3 there is no unequivocal consensus on the symmetry and node structure of the SC gap.

UPd_2Al_3 (see Fig. 22) [376] is a rather special case among the U-based HF superconductors. There is also AF order below $T_N = 14.3$ K with almost atomic size local moments ($\mu = 0.85 \mu_B$) in contrast to the small moments in other U-compounds. The AF order coexists with superconductivity below $T_c = 1.8$ K. This suggests that in addition to the heavy itinerant quasiparticles nearly localized 5f-electrons should be present. They result from the dominating $5f^2$ configuration of the U^{4+} ion [382]. This dual nature of 5f-electrons is even more obvious than in UPt_3 as is seen in various experiments. A direct confirmation of this dual nature of 5f-electrons in UPd_2Al_3 was obtained from inelastic neutron scattering (INS) [383] which found excitations that originate from local CEF transitions and disperse into bands of “magnetic excitons” due to intersite exchange. Complementary tunneling experiments with epitaxial $\text{UPd}_2\text{Al}_3\text{-AlO}_x\text{-Pb}$ heterostructures probed the response of the itinerant quasiparticles and their SC gap. Strong coupling features in the tunneling density of states were reported [384] suggesting that the magnetic excitons identified in INS are the bosonic “glue” which binds the electrons to Cooper pairs [363]. This new mechanism for superconductivity is distinctly different from both the electron-phonon and spin fluctuation mechanism known so far. The pairing potential is mediated by a propagating boson (the magnetic exciton) as in the former case but depends on the spin state of conduction electrons as in the latter case.

The possibility of coexisting ferromagnetism and superconductivity was first considered by Ginzburg [385] who noted that this is only possible when the internal ferromagnetic field is smaller than the thermodynamic critical field of the superconductor. Such a condition is hardly ever fulfilled except immediately below the Curie temperature T_C where coexistence has been found in a few superconductors with local moment ferromagnetism and $T_C < T_c$ such as ErRh_4B_4 and HoMo_6S_8 . If the temperature drops further below T_C the internal ferromagnetism molecular field rapidly becomes larger than H_{c2} and superconductivity is destroyed. The reentrance of the normal state below T_C has indeed been observed in the above compounds. The only compound known so far where local moment ferromagnetism coexists homogeneously with superconductivity for all temperatures below T_c is the borocarbide compound $\text{ErNi}_2\text{B}_2\text{C}$ [386] (see chapter 6). The competition between ferromagnetism and superconductivity becomes more interesting if ferromagnetic order is due to itinerant electrons which also form the SC state. If the interaction slightly exceeds a critical value one has weak ferromagnetic order such as in ZrZn_2 with large longitudinal ferromagnetic spin fluctuations. In this case p-wave superconductivity may actually be mediated by the exchange of ferromagnetic spin fluctuations and coexist with the small ferromagnetic moments [387]. p-wave superconductivity was predicted to exist in this case both on the ferromagnetic as well as on the paramagnetic side of this critical parameter region. The discovery of unconventional superconductivity under pressure in the itinerant ferromagnets UGe_2 [380] and later for URhGe [388] and the 3d ferromagnet ZrZn_2 [389] under ambient pressure has opened this theoretical scenario to experimental investigation.

URu₂Si₂ (see Fig. 19), a “moderately heavy” fermion compound has mystified experiment-
 alists and theorists alike with the discovery of AF order and another still unidentified “hidden
 order” phase. In addition, the compound becomes a nodal superconductor below $T_c = 1.2$ K
 [378, 390, 391]. The simple tetragonal AF order with wave vector in c-direction has tiny
 moments $\mu \sim 0.02 \mu_B$ along c-axis [392, 393] which are of the same order as in UPt₃.
 However, unlike in UPt₃, very large thermodynamic effects, e. g., in specific heat, thermal
 expansion etc., occur which are hard to reconcile with the small ordered moments. These
 pronounced anomalies were interpreted as evidence for the presence of a second “hidden
 order” parameter, which cannot be seen in neutron or x-ray diffraction. In the itinerant models
 the order parameter is due to an unconventional pairing in the particle-hole channel leading to
 an unconventional SDW which has vanishing moment in the clean limit and also does not
 break time reversal invariance. The small staggered moments may then be induced in the
 condensate due to impurity scattering. Finally, in the dual models one assumes a localized
 singlet-singlet system in interaction with the itinerant electrons to cause induced moment
 magnetism with small moments but large anomalies. In all models it was previously taken for
 granted that both the primary “hidden” order parameter and AF order coexist homogeneously
 within the sample. However, hydrostatic and uniaxial pressure experiments [394, 395] have
 radically changed this view, showing that the order parameters exist in different parts of the
 sample volume; the tiny AF moment is not intrinsic but due to the small AF volume fraction
 under ambient pressure. Applying hydrostatic pressure or lowering the temperature increases
 the AF volume fraction and hence the ordered moment until it saturates at an atomic size
 moment of $0.4 \mu_B$ per U atom. This means that the evolution of antiferromagnetism arises
 from the increase of AF volume with pressure rather than the increase of the ordered moment
 μ per U-atom.

The cubic compound UBe₁₃ and U_{1-x}Th_xBe₁₃ was discovered rather early [379, 396] as a
 SC HF system. The U atom in this structure is embedded in an icosahedral cage of 12 Be-
 atoms. A global understanding of the normal state and symmetry breaking in both SC and
 magnetic state is still elusive. Firstly, UBe₁₃ single crystals do not yet achieve the quality as,
 e. g., UPt₃ single crystals so that the symmetry of the anisotropic SC gap functions could not
 be identified yet. Furthermore, the Th-doped crystals U_{1-x}Th_xBe₁₃ show a perplexing variety of
 SC and possibly also magnetic phases whose microscopic origin and order parameter
 symmetries are not understood. Already in the normal state UBe₁₃ is a rather anomalous
 metal, e. g. non-Fermi-liquid behavior has been observed and attributed to a multichannel
 Kondo effect. The T_c values for superconductivity, which occurs in the non-Fermi-liquid state,
 depend considerably on the type of sample. There are two classes with ‘high’ $T_c \sim 0.9$ K and
 ‘low’ $T_c \sim 0.75$ K which, however, are not much different in their impurity content.

5.3 RARE-EARTH SKUTTERUDITES

The recently discovered heavy fermion superconductor PrOs₄Sb₁₂ [355] is potentially of
 similar interest as UPt₃ because it represents the second example of multiphase
 superconductivity [397] with a critical temperature $T_c = 1.85$ K. The skutterudites RT₄X₁₂
 (R = alkaline earth, rare earth or actinide; T = Fe, Ru or Os and X=P, As or Sb) show a cage
 structure where large voids formed by tilted T₄X₁₂ octahedrons can be filled with R atoms (see

Fig. 23). They are however rather loosely bound and are therefore subject to large anharmonic oscillations (“rattling”) in the cage. In addition, the presence of several equivalent equilibrium positions may give rise to tunneling split states. Both effects may lead to interesting low temperature elastic and transport phenomena, such as thermoelectric effects [398,399]. Depending on the cage-filling atom this large class of compounds displays also a great variety of interesting effects of strong electron correlation. Mixed valent and HF behavior, magnetic and quadrupolar order, non-Fermi liquid and Kondo insulating behavior has been found [355,399]. Recently the superconductivity in non-stoichiometric skutterudites $\text{Pr}(\text{Os}_{1-x}\text{Ru}_x)\text{Sb}_{12}$ has been investigated throughout the whole concentration range of $0 \leq x \leq 1$ [400]. While for $x = 0$ one has an unconventional HF superconductor, the $x = 1$ compound $\text{PrRu}_4\text{Os}_{12}$ on the other hand is a conventional superconductor with $T_c \sim 1$ K. The type of superconductivity changes at $x \sim 0.6$ where the transition temperature $T_c(x)$ has a minimum value of 0.75 K.

In the HF multiphase superconductor $\text{PrOs}_4\text{Sb}_{12}$ ($x = 0$) the specific heat jump due to superconductivity is superposed on a Schottky anomaly due to the lowest CEF excitation. Nevertheless, its detailed analysis provides clear evidence for a split superconductivity transition [355,401] at $T_{c1} = 1.85$ K and $T_{c2} = 1.75$ K. The total jump of both transitions amounts to $\Delta_{SC} C/\gamma T_c \sim 3$ which considerably exceeds the BCS value 1.43 for a single transition. It also proves that the SC state is formed from the heavy quasiparticles that cause the enhanced γ -value of the electronic low-temperature specific heat contribution. A T_c -splitting of similar size also was clearly seen in thermal expansion measurements [402]. The two SC transitions are reminiscent of the split transition in UPt_3 . There, a twofold orbitally degenerate SC state is split by weak AF order that reduces the hexagonal symmetry to an orthorhombic one. This also leads to two critical field curves in the B-T phase diagram. In $\text{PrOs}_4\text{Sb}_{12}$ no such symmetry breaking field exists.

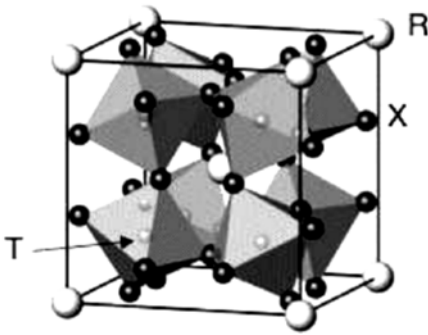


Fig. 23. Cubic crystal structure of the filled skutterudite RT_4X_{12} . The T atoms are located in the center of the X octahedra. For $\text{PrOs}_4\text{Sb}_{12}$ the lattice constant is $a = 0.93017$ nm.

In this still rather early stage of investigation, various experiments gave inconclusive results on the question of the nature of gap anisotropy. As a preliminary conclusion, it seems clear that $\text{PrOs}_4\text{Sb}_{12}$ is a very unconventional multiphase HF superconductor of potentially the same interest as UPt_3 . Since that heavy quasiparticles are presumably caused by coupling with

virtual quadrupolar excitations from the nonmagnetic 5f ground state one is lead to speculate that superconductivity in $\text{PrOs}_4\text{Sb}_{12}$ might also result from an unprecedented pairing mechanism based on the exchange of quadrupolar fluctuations. At the moment, this quadrupolar superconductivity mechanism in $\text{PrOs}_4\text{Sb}_{12}$ as a third possibility for Cooper pair formation in heavy fermion compounds in addition to the spin-fluctuation and magnetic-exciton exchange mechanisms is still a conjecture.

6. ORGANIC AND OTHER CARBON BASED SUPERCONDUCTORS

Carbon, being perhaps the most important element for life, has not played a big role in superconductivity for a long time. Things changed in 1980 when superconductivity was discovered below 0.9 K in the compound $(\text{TMTSF})\text{PF}_6$, with the organic molecule TMTSF (tetra-methyl-tetra-selenium-fulvalene; see Fig. 24) [14]. To suppress a metal-insulator transition the material had to be kept under a hydrostatic pressure of 12 kbar. In 1991 it was found that compounds based on the “soccer ball” C_{60} (see Fig. 25) become superconductors when doped with alkali atoms [403]. In 1994 superconductivity in Boron carbides was reported [404,405] (see the chapter 7), in 2001 there was evidence that carbon nanotubes when imbedded in a zeolite matrix can become superconductors with a T_c of about 15 K [406]. Most recent are reports on superconductivity in diamond with T_c up to 4 K when doped with boron [3], and in yttrium carbide compounds with T_c as high as 18 K [407,408].

Regarding superconductors based on the TMTSF molecule a variety of compounds are known by now, exhibiting transition temperatures around 1 K. An example is $(\text{TMTSF})_2\text{ClO}_4$, which also under normal pressure remains metallic down to the lowest temperatures and becomes superconducting at 1 K [409]. The general formula is $(\text{TMTSF})_2\text{X}$ where X denotes an electron acceptor such as PF_6 , ClO_4 , AsF_6 or TaF_6 . In the TMTSF compounds, the organic molecules are stacked upon each other (see Fig. 24).

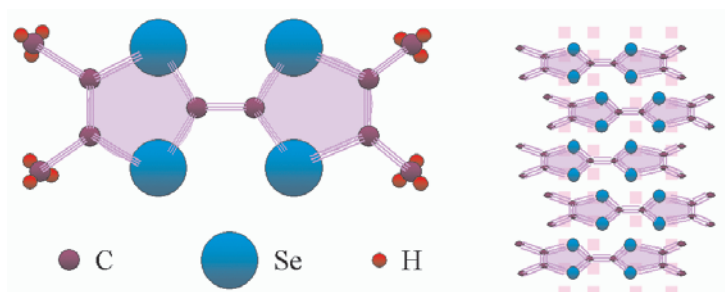


Fig. 24. Structure of the organic molecule tetra-methyl-tetra-selenium-fulvalene (TMTSF) and staple arrangement of the molecules forming one-dimensional conduction channels.

In the normal state, the TMTSF compounds have a relatively large electric conductivity along the stacks, but only a small conductivity perpendicular to the stacks, thus forming *nearly-one-dimensional conductors*. The TMTSF compounds are type-II superconductors with highly anisotropic properties. For example, in $(\text{TMTSF})_2\text{ClO}_4$ along the stacks the Ginzburg-Landau coherence length is about 80 nm, whereas along the two perpendicular directions of the crystal axes it is about 35 nm and 2 nm, respectively. The latter value is of the same order of magnitude as the lattice constant along the c axis. Hence, the compound nearly represents a *two-dimensional superconductor* [410].

Another important class of organic superconductors, often exhibiting T_c well above 1 K is based on the bis-ethylene-dithia-tetra-thiafulvalene molecule, abbreviated as “BEDT-TTF” or “ET”. For example, the compound $(\text{BEDT-TTF})_2\text{Cu}[\text{N}(\text{CN})_2]\text{Br}$ becomes superconducting at 11.2 K [411]. The transition temperature of $(\text{BEDT-TTF})_2\text{Cu}(\text{NCS})_2$ is 10.4 K. The ET-compounds are also highly anisotropic. However, in contrast to the TMTSF-compounds, in the normal state they form two-dimensional layered structures with a large electric conductivity in two dimensions. Like the TMTSF based materials the ET-compounds are type-II superconductors as well, with very short out-of-plane coherence lengths. These compounds thus also represent superconducting layered structures making them in many respects similar to HTS. Like for HTS, the pairing mechanism of the organic superconductors is at present still unclear. At least some compounds appear to be d-wave superconductors. However, in the compound $(\text{TMTSF})_2\text{PF}_6$ one may even deal with a spin-triplet superconductor [412].

Fullerides are compounds of the form A_3C_{60} . They can become superconducting at surprisingly high temperatures [18,413,414]. By now, a number of SC fullerides based on the admixture of alkali atoms or of alkaline earth atoms are known. Rb_3C_{60} has a value of T_c of 29.5 K, and the present record under pressure is held by Cs_3C_{60} with $T_c = 40$ K. The crystal structure of the fullerides is face centered cubic, with the alkali atoms occupying interstitial sites between the large C_{60} molecules. Fullerides are BCS-like s-wave superconductors. Intramolecular C_{60} phonons (see Fig. 25) seem to contribute the most important part of the pairing interactions [18].

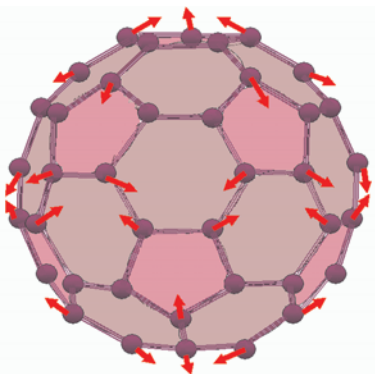


Fig. 25. Structure of the C_{60} molecule. The red arrows indicate one of the intramolecular H_g phonon modes which are believed to be mainly responsible for the SC pairing [18].

7. BORIDES AND BOROCARBIDES

Rare-earth borocarbide superconductors have provided the first example of a homogeneous coexistence of superconductivity and ferromagnetism for all temperatures below T_c : The two antagonistic long-range orders are carried by different species of electrons that interact only weakly through contact exchange interaction leading to a small effect of the local moment molecular field on the SC conduction electrons. This allows a much better understanding of coexistence behavior as compared to the HF systems. Moreover, the nonmagnetic rare earth borocarbides have extremely large gap anisotropy ratios $\Delta_{\max}/\Delta_{\min} \geq 100$. Surely the standard electron-phonon mechanism has to be supplemented by something else, perhaps anisotropic Coulomb interactions to achieve this “quasi-unconventional” behavior in borocarbides.

The SC class of layered transition metal borocarbides RNi_2B_2C (nonmagnetic $R = Y, Lu, Sc$; magnetic $R =$ lanthanide elements in a R^{3+} state; see Fig. 26) was discovered in 1994 [404,415,416,417]. The crystal structure consists of RC rock salt type planes separated by Ni_2B_2 layers built from NiB_4 tetrahedra and stacked along the c -axis. More general structures with more than one RC layer are possible [416]. The nonmagnetic borocarbides have relatively high T_c values around 15 K. There is evidence that the SC mechanism is primarily of the electron-phonon type although this cannot explain the large anisotropy of the SC gap. At first sight the layered structure is similar to the HTS cuprates. However, unlike the copper oxide planes the NiB_2 planes show buckling. As a consequence, the electronic states at the Fermi level in the borocarbides do not have quasi-2-dimensional $d_{x^2-y^2}$ character and, therefore, have much weaker correlations excluding the possibility of AF spin-fluctuation mediated superconductivity.

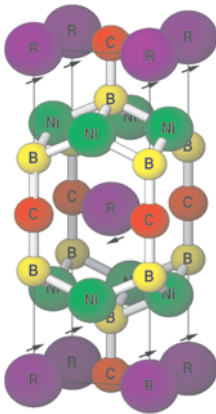


Fig. 26. Tetragonal crystal structure of RNi_2B_2C ($a = 0.352$ nm, $c = 1.053$ nm for $R = Ho$) and low temperature AF magnetic structure with $[110]$ easy axis as indicated by the arrows.

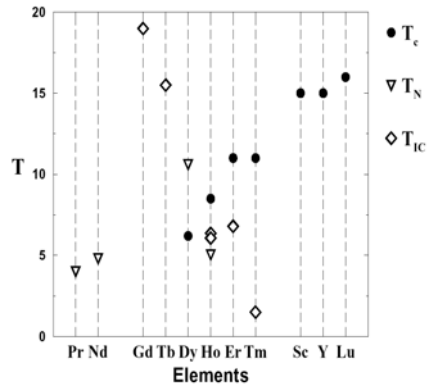


Fig. 27. Magnetic (T_{IC} : incommensurate magnetic structure, T_N : simple AF structure) and SC (T_c) transition temperatures in Kelvin for the RNi_2B_2C series.

The nonmagnetic borocarbides serve as a kind of reference point to separate the fascinating effects of AF and SC order parameter coupling in the magnetic $\text{RNi}_2\text{B}_2\text{C}$. However, the former have their own peculiarities, which are not yet completely understood. Foremost, despite their alleged electron-phonon nature, $\text{LuNi}_2\text{B}_2\text{C}$ and $\text{YNi}_2\text{B}_2\text{C}$ have strongly anisotropic gap functions and low energy quasiparticle states as is evident from specific heat and thermal conductivity. Furthermore, an anomalous upturn in H_{c2} has been observed.

The magnetic $\text{RNi}_2\text{B}_2\text{C}$ are an excellent class of materials to study the effects of competition of magnetic order and superconductivity for the following reasons: The T_c values are relatively high, and the T_c / T_N ratio varies systematically across the R-series (see Fig. 27). Especially interesting are the cases of $\text{RNi}_2\text{B}_2\text{C}$ with $R = \text{Dy}, \text{Ho}$ and Er where T_c and T_N (or T_C) are not too different, leading to strong competition of the magnetic and superconductivity order parameters. Furthermore, the SC condensate and magnetic moments are carried by different types of electrons, namely itinerant 3d-electrons for the Ni_2B_2 layers and localized R^{3+} 4f-electrons for the R C layers, respectively. Finally, they are well separated and their coupling which is of the local exchange type can be treated in a controlled perturbative way, somewhat akin to the situation in the well known classes of Chevrel phase [418] and ternary compound [419] magnetic superconductors.

The AF molecular field establishes a periodic perturbation characterized by a length scale of the order of the Fermi wavelength. This implies that the spatial extent of the Cooper pairs extends over many periods of the alternating molecular field. The latter is therefore effectively averaged to zero and does not suppress superconductivity via an orbital effect. The system is invariant under the combined operation of time inversion followed by a translation with a lattice vector which allows to form Cooper pairs in a spin singlet state with vanishing (crystal) momentum in the AF lattice. This pair-state can be considered as a natural generalization of the pairing in time-reversed states encountered in usual non-magnetic superconductors.

The nonmagnetic $\text{YNi}_2\text{B}_2\text{C}$ and $\text{LuNi}_2\text{B}_2\text{C}$ compounds with comparatively high T_c values of 16.5 K and 15.5 K serve as reference systems for the more difficult systems $\text{RNi}_2\text{B}_2\text{C}$ with both magnetic and SC phases. The electron-phonon nature of superconductivity in $\text{YNi}_2\text{B}_2\text{C}$ and $\text{LuNi}_2\text{B}_2\text{C}$ is inferred from a substantial s-wave character of the order parameter as witnessed by the appearance of a moderate Habel-Slichter peak in the ^{13}C NMR relaxation rate [420].

On the other hand, the gap function is strongly anisotropic as can be seen both from temperature and field dependence of thermodynamic and transport quantities [416,421] indicating the presence of gap nodes [422]. More precisely, within experimental accuracy, there must be at least a gap anisotropy $\Delta_{\text{max}}/\Delta_{\text{min}} \geq 100$ [422]. For an electron-phonon superconductor this would be the largest anisotropy ever observed. This conjecture is also supported by the field dependence of the low temperature specific heat [423] and of the thermal conductivity along (001) [421]. Since in the latter case the heat current is perpendicular to the vortices this proves that quasiparticles must be present in the inter-vortex region. This is also required to explain the observation of dHvA oscillations far in the vortex phase. Experimental evidence therefore demands a nodal gap function for borocarbides. A s+g wave model [424] fulfills the requirements. In addition, it explains recent results on ultrasonic attenuation, which also confirmed the existence of gap nodes in the cubic plane [425].

The classical argument in favor of the electron-phonon mechanism is the observation of an isotope effect characterized by the isotope exponent for a specific atom with mass M as given by $\alpha_X = d [\ln T_c] / d [\ln M_X]$. However, this cannot be applied easily to complex layered superconductors, as is evident from the existence of an isotope effect in the probably nonphononic cuprate superconductors with nonoptimal doping. The boron isotope effect found in $\text{YNi}_2\text{B}_2\text{C}$ ($\alpha_B = 0.2$) and $\text{LuNi}_2\text{B}_2\text{C}$ ($\alpha_B = 0.11$) is much smaller than the BCS value $\alpha_X = 0.5$. A nonphononic origin stemming from the influence of boron on the charge density in the B_2Ni_2 layers has therefore been suggested [426]. The most direct support for phonon-mediated Cooper pairing comes from scanning tunneling spectroscopy (“STS”)[427] which has shown the existence of a strong coupling signature in the tunneling DOS due to a soft optical phonon close to the Fermi surface nesting wave vector Q . The STS-derived electron-phonon coupling constant $\lambda = 0.5 - 0.8$ is compatible with the value $\lambda = 0.53$ obtained from resistivity data.

The discovery of superconductivity in MgB_2 (see Fig. 28) in early 2001 with $T_c \sim 40 \text{ K}$ ⁶¹, almost twice the record value before HTS [20] brought back a bit of the HTS bonanza spirit of the late 1980s [429,430,431,432,433]. The fact that such a simple material which was known since the early 1950s had been missed in the systematic research for superconductivity on this class of compounds was as amazing as the "materials preparation" that was usually practiced immediately after the discovery by most of the research groups for reestablishing this high T_c value: They simply ordered MgB_2 powder from chemicals wholesale where it was commercially available in quantities of metric tons already for years!

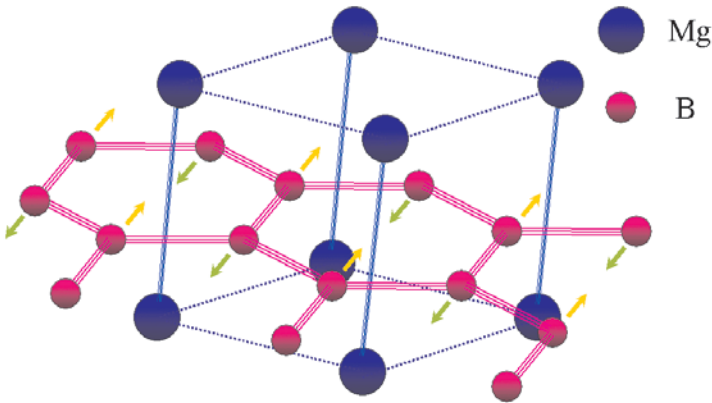


Fig. 28. Hexagonal crystal structure of MgB_2 . The arrows indicate the B-phonon mode, which presumably introduces the strongest SC coupling.

⁶¹ Isotopically pure Mg^{11}B_2 and Mg^{10}B_2 show sharp superconducting transitions in resistivity with $T_c(\text{Mg}^{11}\text{B}_2) = 39.2 \text{ K}$ and $T_c(\text{Mg}^{10}\text{B}_2) = 40.2 \text{ K}$ [428].

No strong Coulomb correlation effects can be expected in MgB₂: No atomic d- or f-shells are involved in the conduction electron system of this binary compound of light elements. In addition, the simple crystal structure consisting of graphite-like B-layers with intercalated Mg clearly favors conduction along these layers and a respective superconductive and normal state anisotropy, but it does not introduce a reduction of the effective dimensionality, as in the case of organic superconductors due to the stacking of isolated aromatic rings. The coupling of the conduction electrons to a particular boron phonon mode (see Fig. 28) was hence identified right from the start as basic origin of superconductivity in MgB₂ [434, 435]. The observation of two energy gaps (at 1.8 and 6.8 meV [436, 437]) and the considerable superconductive anisotropy as large as 6–9 [428] challenged a more thorough theoretical investigation which tries at present to explain these findings in terms of two-band superconductivity [439] on the basis of the large anharmonicity of the involved phonon mode and a refined treatment of its coupling with the different sheets of the electronic conduction band [436,438,440,441].

MgB₂ shows great promise as material for both large-scale and electronic *applications* [4]:

- low cost and abundant availability of the raw materials
- high T_c
- extreme type-II SC nature as a consequence of a large coherence lengths $\xi_0 \sim 4.4$ nm and an even larger penetration depth $\lambda \sim 132$ nm in combination with the occurrence of suitable pinning centers
- both SC gaps larger than that of Nb (1.5 meV)
- high critical current densities J_c (10 K, 0 T) ~ 10 MA/cm²
- high critical fields ($H_{c2}(0$ K) ~ 16 T in bulk, > 40 T achieved for thin films)
- transparency of grain boundaries to current
- remarkably low normal state resistivity $\rho(42$ K) = 0.38 $\mu\Omega$ cm⁶² [428]

MgB₂ has already been fabricated in the form of bulk, single crystals, thin films [442], tapes and wires [443]. Serious difficulties in depositing MgB₂ films, such as the volatility of Mg, the phase stability of MgB₂, the low sticking coefficients of Mg at elevated temperatures, and the reactivity of Mg with oxygen have meanwhile been overcome. Epitaxial MgB₂ films with superior superconducting properties have been produced [444]. MgB₂ wires are already used in first real applications [443].

MgB₂ is hence a further excellent example for the progress and excitement of the present research on superconductors. Superconductivity with its wide range from the most fundamental aspects of physics to hands-on applications is, one century after its discovery, still one of the most fascinating topics of modern science.

⁶² This value is comparable to that of copper wire and over a factor of 20 times lower than that of polycrystalline Nb₃Sn [436]. It means that MgB₂ can carry in the normal state substantially higher current densities than other superconductors with less Joule heating. This combination of a high T_c and a low normal state resistivity makes MgB₂ particularly appealing for wire applications [428].

ACKNOWLEDGEMENT

Besides many others who helped us in the preparation of this overview we would like to thank Robert Eder, Christoph Meingast, Lothar Pintschovius, Christof Schneider and Stefan Schuppler for their critical reading of the manuscript and for many helpful comments.

REFERENCES

- [1] W. Buckel, R. Kleiner, *Supraleitung – Grundlagen und Anwendungen*, WILEY-VCH Verlag, Weinheim (2004);
W. Buckel, R. Kleiner, *Superconductivity - Fundamentals and Applications*, WILEY-VCH Verlag, Weinheim (2004)
- [2] T. H. Geballe, *Science* **293** (2001) 223
- [3] E. A. Ekimov, V. A. Sidorov, E. D. Bauer, N. N. Mel'nik, N. J. Curro, J. D. Thompson, S. M. Stishov, *Nature* **428** (2004) 542
- [4] C. Buzea, T. Yamashita, *Supercond. Sci. Techn.* **14** (2001) R115
- [5] J. Bardeen, L. N. Cooper, J. R. Schrieffer, *Phys. Rev* **108** (1957) 1175
- [6] J. G. Bednorz, K. A. Müller, *Z. Phys. B* **64** (1986) 189
- [7] S. N. Putilin, E. V. Antipov, A. M. Abakumov, M. G. Rozova, K. A. Lokshin, D. A. Pavlov, A. M. Balagurov, D. V. Sheptyakov, M. Marezio, *Physica C* **338** (2001) 52
- [8] W. L. McMillan, J. M. Rowell, *Phys. Rev. Lett.* **14** (1965) 108
- [9] R. Zeyer, G. Zwirgagl, *Z. Phys. B* **78** (1990) 175
- [10] J. R. Gavaler, *Appl. Phys. Lett.* **23** (1973) 480
- [11] F. Steglich, J. Aarts, C. D. Bredl, W. Lieke, D. Meschede, W. Franz, H. Schäfer, *Phys. Rev. Lett.* **43** (1979) 1892
- [12] J. L. Sarrao, L. A. Morales, J. D. Thompson, B. L. Scott, G. R. Stewart, F. Wastin, J. Rebizant, P. Boulet, E. Colineau, G. H. Lander, *Nature* **420** (2002) 297
- [13] W. A. Little, *Phys. Rev. A* **134** (1964) 1416
- [14] D. Jérôme, A. Mazaud, M. Ribault, K. Bechgaard, *J. Phys. (Paris), Lett.* **41** (1980) L95;
D. Jerome, A. Mazaud, M. Ribault, K. Bechgaard; *C. R. Hebd. Seances Acad. Sci. Ser. B* **290** (1980)
- [15] G. Saito, H. Yamochi, T. Nakamura, T. Komatsu, M. Nakashima, H. Mori, K. Oshima, *Physica B* **169** (1991) 372
- [16] N. D. Mermin, H. Wagner, *Phys. Rev. Lett.* **17** (1966) 1133 & 1307
- [17] K. Tanigaki, T. W. Ebbesen, S. Saito, J. Mizuki, J. S. Tsai, Y. Kubo, S. Kuroshima, *Nature* **352** (1991) 222
- [18] O. Gunnarsson, *Rev. Mod. Phys.* **69** (1997) 575
- [19] P. C. Canfield, P. L. Gammel, D. J. Bishop, *Physics Today*, October 1998, p. 40
- [20] J. Nagamatsu, N. Nakagawa, T. Muranaka, Y. Zenitani, J. Akimitsu, *Nature* **410** (2001) 63
- [21] T. Dahm, this volume

- [22] R. Hott, *High Temperature Superconductivity 2 - Engineering Applications* (Ed. A. V. Narlikar), Springer Verlag, Berlin (2004) pp.35; cond-mat/0306444;
<http://www.wifp.fzk.de/ISAS/>
Handbook of Applied Superconductivity (Ed. B. Seeber), Institute of Physics Publishing, Bristol and Philadelphia (1998)
- [23] P. Komarek, *Supercond. Sci. Technol.* **13** (2000) 456
- [24] Y. Wang, S. Ono, Y. Onose, G. Gu, Y. Ando, Y. Tokura, S. Uchida, N. P. Ong, *Science* **299** (2003) 86
- [25] G. Blatter, M. V. Feigel'man, V. B. Geshkenbein, A. I. Larkin, V. M. Vinokur, *Rev. Mod. Phys.* **66** (1994) 1125
- [26] H. W. Weijers, U. P. Trociewitz, K. Marken, M. Meinesz, H. Miao, J. Schwartz, *Supercond. Sci. Technol.* **17** (2004) 636
- [27] http://www.lanl.gov/superconductivity/wire_conductors.shtml
- [28] CERN Weekly Bulletin No. 21/2004
- [29] P. Renton, *Nature* **428** (2004) 141
- [30] *Physics Today* **54**, May 2001, pp.27
- [31] H. J. Chaloupka, T. Kässer, *High Temperature Superconductivity 2 - Engineering Applications* (Ed. A. V. Narlikar), Springer Verlag, Berlin (2004) pp.411
- [32] K. K. Likharev, *Dynamics of Josephson Junctions and Circuits*, Gordon & Breach Science Publishers (1986) p.30
- [33] *SQUID Handbook* (Ed. J. Clarke, A. Braginski), WILEY-VCH Verlag, Berlin (2003)
- [34] J. Malmivuo, V. Suihko, H. Eskola, *IEEE Trans. Biomed. Eng.* **44** (1997) 196
- [35] D. Koelle, R. Kleiner, F. Ludwig, E. Dantsker, J. Clarke, *Rev. Mod. Phys.* **71** (1999) 631;
 H. J. Barthelmeß, F. Ludwig, M. Schilling, D. Drung, T. Schurig, *High Temperature Superconductivity 2 -Engineering Applications* (Ed. A. V. Narlikar), Springer Verlag, Berlin (2004) pp.299
- [36] L. A. Knauss, A. B. Cawthorne, N. Lettsome, S. Kelly, S. Chatraphorn, E. F. Fleet, F. C. Wellstood, W. E. Vanderlinde, *Microelectronics Reliability* **41** (2001)1211
- [37] M.v.Kreutzbruck, *High Temperature Superconductivity 2 - Engineering Applications* (Ed. A. V. Narlikar), Springer Verlag, Berlin (2004) pp.223
- [38] *WTEC Panel Report on Electronic Applications of Superconductivity in Japan*, International Technology Institute, Maryland (1998);
<http://www.wtec.org/loyola/scel96/toc.htm>
- [39] A. Ekert, R. Jozsa, *Rev. Mod. Phys.* **68** (1996) 733;
<http://www.cs.caltech.edu/~westside/quantum-intro.html>;
<http://www.qubit.org/library/intros/comp/comp.html>
- [40] I. Chiorescu, Y. Nakamura, C. J. P. M. Harmans, J. E. Mooij, *Science* **299** (2003) 1869
- [41] H. Hilgenkamp, Ariando, H.-J. H. Smilde, D. H. A. Blank, G. Rijnders, H. Rogalla, J. R. Kirtley, C. C. Tsuei, *Nature* **422** (2003) 50

- [42] R. Hott, *High Temperature Superconductivity*, Vol. II *Engineering Applications*, (Ed. A. V. Narlikar), Springer Verlag, Berlin (2004) pp.41;
H. J. M. ter Brake, G. F. M. Wiegerinck, *Cryogenics* **42** (2002) 705
- [43] A. Damascelli, Z. Hussain, Z.-X. Shen, *Rev. Mod. Phys.* **75** (2003) 473
- [44] J. C. Campuzano, M. R. Norman, M. Randeria, in *Physics of Superconductors*, Vol. II, (Ed. K. H. Bennemann & J. B. Ketterson), Springer Verlag, Berlin (2004), p. 167-273;
cond-mat/0209476;
M. R. Norman, C. Pepin, *Rep. Prog. Phys.* **66** (2003) 1547
- [45] *Neutron Scattering in Layered Copper-Oxide Superconductors* (Ed. A. Furrer), Kluwer Academic Publishers (1998), ISBN 0-7923-5226-2
- [46] B. W. Hoogenboom, M. Kugler, B. Revaz, I. Maggio-Aprile, Ø. Fischer, Ch. Renner, *Phys. Rev. B* **62** (2000) 9179
- [47] K. McElroy, D.-H. Lee, J. E. Hoffman, K. M. Lang, E. W. Hudson, H. Eisaki, S. Uchida, J. Lee, J. C. Davis, cond-mat/0404005
- [48] R. F. Service, *Science* **271** (1996) 1806
- [49] A. Erb, E. Walker, R. Flükiger, *Physica C* **245** (1995) 245;
A. Erb, E. Walker, J.-Y. Genoud, R. Flükiger, *Physica C* **282-287** (1997) 89
- [50] J. Orenstein, A. J. Millis, *Science* **288** (2000) 468
- [51] P. W. Anderson, *Science* **235** (1987) 1196
- [52] P. W. Anderson, *The Theory of Superconductivity in High- T_c Cuprates Superconductors*, Princeton University Press, Princeton (1997)
- [53] A. B. Fowler, *Physics Today*, October 1993, 59
- [54] C. W. Chu, *J. Supercond.* **12** (1999) 85
- [55] C. W. Chu, *IEEE Trans. Appl. Supercond.* **7** (1997) 80
- [56] B. Raveau, in *High- T_c Superconductivity 1996: Ten Years after the Discovery*, NATO ASI Series E Vol. **343**, Kluwer Academic Publishers (1997) p.109
- [57] J. L. Tallon, G. V. M. Williams, J. W. Loram, *Physica C* **338** (2000) 9
- [58] H. Lütgemeier, S. Schmenn, P. Meuffels, O. Storz, R. Schöllhorn, Ch. Niedermayer, I. Heima, Yu. Baikov, *Physica C* **267** (1996) 191
- [59] R. Bormann, J. Nölting, *Appl. Phys. Lett.* **54** (1989) 2148
- [60] A. Mawdsley, J. L. Tallon, M. R. Presland, *Physica C* **190** (1992) 437
- [61] E. L. Brosha, P. K. Davis, F. H. Garzon, I. D. Raistrick, *Science* **260** (1993) 196
- [62] H. Yamauchi, M. Karppinen, S. Tanaka, *Physica C* **263** (1996) 146
- [63] H. Yamauchi, M. Karppinen, *Supercond. Sci. Technol.* **13** (2000) R33
- [64] P. Bordet, S. LeFloch, C. Chailout, F. Duc, M. F. Gorius, M. Perroux, J. J. Capponi, P. Toulemonde, J. L. Tholence, *Physica C* **276** (1997) 237
- [65] N. L. Wu, Z. L. Du, Y. Y. Xue, I. Rusakova, D. K. Ross, L. Gao, Y. Cao, Y. Y. Sun, C. W. Chu, M. Hervieu, B. Raveau, *Physica C* **315** (1999) 227
- [66] D. R. Harshman, A. P. Mills, Jr., *Phys. Rev. B* **45** (1992) 10684

- [67] M. K. Wu, J. R. Ashburn, C. J. Torng, P. H. Hor, R. L. Meng, L. Gao, Z. J. Huang, Y. Q. Wang, C. W. Chu, *Phys. Rev. Lett.* **58** (1987) 908
- [68] J. G. Lin, C. Y. Huang, Y. Y. Xue, C. W. Chu, X. W. Cao, J. C. Ho, *Phys. Rev. B* **51** (1995) 12900
- [69] J. W. Chu, H. H. Feng, Y. Y. Sun, K. Matsuishi, Q. Xiong, C. W. Chu, *HTS Materials, Bulk Processing and Bulk Applications* - Proceedings of the 1992 TCSUH Workshop (Ed. C. W. Chu, W. K. Chu, P. H. Hor and K. Salama), World Scientific, Singapore (1992), p. 53; TCSUH preprint 92:043
- [70] G. V. M. Williams, J. L. Tallon, *Physica C* **258** (1996) 41
- [71] M. Guillaume, P. Allenspach, W. Henggeler, J. Mesot, B. Roessli, U. Staub, P. Fischer, A. Furrer, V. Trounov, *J. Phys.: Condens. Matter* **6** (1994) 7963
- [72] M. Guillaume, P. Allenspach, J. Mesot, B. Roessli, U. Staub, P. Fischer, A. Furrer, *Z. Phys. B* **90** (1993) 13
- [73] M. Al-Mamouri, P. P. Edwards, C. Greaves, M. Slaski, *Nature* **369** (1994) 382
- [74] T. Kawashima, Y. Matsui, E. Takayama-Muromachi, *Physica C* **257** (1996) 313
- [75] Z. Hiroi, N. Kobayashi, M. Takano, *Nature* **371** (1994) 139
- [76] L. Gao, Y. Y. Xue, F. Chen, Q. Xiong, R. L. Meng, D. Ramirez, C. W. Chu, J. H. Eggert, H. K. Mao, *Phys. Rev. B* **50** (1994) 4260
- [77] B. W. Roberts, *J. Phys. Chem. Ref. Data* **5** (1976) 581
- [78] B. W. Roberts, NBS Technical Note **983** (1978), *Properties of Selected Superconductive Materials* 1978 Supplement
- [79] Landolt-Börnstein, New Series, Group III, Vol. **21**, *Superconductors* (1990-2002)
- [80] R. K. Williams; D. M. Kroeger, P. M. Martin, J. R. Mayotte, E. D. Specht, J. Brynstad, *J. Appl. Phys.* **76** (1994) 3673;
W. Zhang, K. Osamura, *Physica C* **190** (1992) 396;
G. F. Voronin, S. A. Degterov, *Physica C* **176** (1991) 387;
J. Karpinski, S. Rusiecki, B. Bucher, E. Kaldis, E. Jilek, *Physica C* **161** (1989) 618;
J. Karpinski, S. Rusiecki, B. Bucher, E. Kaldis, E. Jilek, *Physica C* **160** (1989) 449;
J. Karpinski, E. Kaldis, E. Jilek, S. Rusiecki, B. Bucher, *Nature* **336** (1988) 660
- [81] R. Liang, D. A. Bonn, W. N. Hardy, J. C. Wynn, K. A. Moler, L. Lu, S. Larochelle, L. Zhou, M. Greven, L. Lurio, S. G. J. Mochrie, *Physica C* **383** (2002) 1
- [82] Th. Wolf, A.-C. Bornarel, H. K pfer, R. Meier-Hirmer, B. Obst, *Phys. Rev. B* **56** (1997) 6308
- [83] P. Zoller, J. Glaser, A. Ehmann, C. Schultz, W. Wischert, S. Kemmler-Sack, T. Nissel, R. P. Huebener, *Z. Phys. B* **96** (1995) 505
- [84] D. L. Feng, A. Damascelli, K. M. Shen, N. Motoyama, D. H. Lu, H. Eisaki, K. Shimizu, J.-i. Shimoyama, K. Kishio, N. Kaneko, M. Greven, G. D. Gu, X. J. Zhou, C. Kim, F. Ronning, N. P. Armitage, Z.-X. Shen, *Phys. Rev. Lett.* **88** (2002) 107001
- [85] H. Eisaki, N. Kaneko, D. L. Feng, A. Damascelli, P. K. Mang, K. M. Shen, Z.-X. Shen, M. Greven, *Phys. Rev. B* **69** (2004) 064512

- [86] S. Lösch, H. Budin, O. Eibl, M. Hartmann, T. Rentschler, M. Rygula, S. Kemmler-Sack, R. P. Huebener, *Physica C* **177** (1991) 271
- [87] H. Yamauchi, T. Tamura, X.-J. Wu, S. Adachi, S. Tanaka, *Jpn. J. Appl. Phys.* **34** (1995) L349
- [88] T. Tamura, S. Adachi, X.-J. Wu, T. Tatsuki, K. Tanabe, *Physica C* **277** (1997) 1
- [89] A. Iyo, Y. Tanaka, Y. Ishiura, M. Tokumoto, K. Tokiwa, T. Watanabe, H. Ihara, *Supercond. Sci. Technol.* **14** (2001) 504
- [90] A. Iyo, Y. Aizawa, Y. Tanaka, M. Tokumoto, K. Tokiwa, T. Watanabe, H. Ihara, *Physica C* **357-360** (2001) 324
- [91] D. Tristan Jover, R. J. Wijngaarden, R. Griessen, E. M. Haines, J. L. Tallon, R. S. Liu, *Phys. Rev. B* **54** (1996) 10175
- [92] Z. Y. Chen, Z. Z. Sheng, Y. Q. Tang, Y. F. Li, L. M. Wang, D. O. Pederson, *Supercond. Sci. Technol.* **6** (1993) 261
- [93] E. V. Antipov, A. M. Abakumov, S. N. Putilin, *Supercond. Sci. Technol.* **15** (2002) R31
- [94] C. Acha, S. M. Loureiro, C. Chaillout, J. L. Tholence, J. J. Capponi, M. Marezio, M. Nunez-Regueiro, *Solid State Comm.* **102** (1997) 1
- [95] T. Tatsuki, A. Tokiwa-Yamamoto, A. Fukuoka, T. Tamura, X.-J. Wu, Y. Moriwaki, R. Usami, S. Adachi, K. Tanabe, S. Tanaka, *Jpn. J. Appl. Phys.* **35** (1996) L205
- [96] E. Stangl, S. Proyer, M. Borz, B. Hellebrand, D. Bäuerle, *Physica C* **256** (1996) 245
- [97] H. Ihara, *Physica C* **364-365** (2001) 289
- [98] P. W. Klamut, B. Dabrowski, S. M. Mini, M. Maxwell, S. Kolesnik, J. Mais, A. Shengelaya, R. Khasanov I. Savic, H. Keller, T. Graber, J. Gebhardt, P. J. Viccaro, Y. Xiao, *Physica C* **364-365** (2001) 313;
B. Lorenz, R. L. Meng, J. Cmaidalka, Y. S. Wang, J. Lenzi, Y. Y. Xue, C. W. Chu, *Physica C* **363** (2001) 251
- [99] T. Kawashima, Y. Matsui, E. Takayama-Muromachi, *Physica C* **254** (1995) 131
- [100] I. Bozovic, G. Logvenov, I. Belca, B. Narimbetov, I. Sveklo, *Phys. Rev. Lett.* **89** (2002) 107001
- [101] S. Karimoto, H. Yamamoto, T. Greibe, M. Naito, *Jpn. J. Appl. Phys.* **40** (2001) L127
- [102] M. Naito, M. Hepp, *Jpn. J. Appl. Phys.* **39** (2000) L485
- [103] L. Alff, S. Meyer, S. Kleefisch, U. Schoop, A. Marx, H. Sato, M. Naito, R. Gross, *Phys. Rev. Lett.* **83** (1999) 2644
- [104] C. Q. Jin, Y. S. Yao, S. C. Liu, W. L. Zhou, W. K. Wang, *Appl. Phys. Lett.* **62** (1993) 3037
- [105] A. Iyo, Y. Tanaka, M. Tokumoto, H. Ihara, *Physica C* **366** (2001) 43
- [106] C. U. Jung, J. Y. Kim, S. M. Lee, M.-S. Kim, Y. Yao, S. Y. Lee, S.-I. Lee, D. H. Ha, *Physica C* **364-365** (2001) 225
- [107] P. Majewski, *J. Mater. Res.* **15** (2000) 854
- [108] M. P. Siegal, E. L. Venturini, B. Morosin, T. L. Aselage, *J. Mater. Res.* **12** (1997) 2825

- [109] J. J. Capponi, J. L. Tholence, C. Chaillout, M. Marezio, P. Bordet, J. Chenavas, S. M. Loureiro, E. V. Antipov, E. Kopnine, M. F. Gorius, M. Nunez-Regueiro, B. Souletie, P. Radaelli, F. Gerhards, *Physica C* **235-240** (1994) 146
- [110] T. Ito, H. Suematsu, M. Karppinen, H. Yamauchi, *Physica C* **308** (1998) 198
- [111] D. Monster, P.-A. Lindgard, N. H. Andersen, *Phys. Rev. B* **60** (1999) 110
- [112] C. L. Jia, K. Urban, *Science* **303** (2004) 2001
- [113] Y. Yan, M. G. Blanchin, *Phys. Rev. B* **43** (1991) 13717
- [114] S. H. Pan, J. P. O'Neal, R. L. Badzey, C. Chamon, H. Ding, J. R. Engelbrecht, Z. Wang, H. Eisaki, S. Uchida, A. K. Gupta, K.-W. Ng, E. W. Hudson, K. M. Lang, J. C. Davis, *Nature* **413** (2001) 282
- [115] M. Karppinen, A. Fukuoka, L. Niinistö, H. Yamauchi, *Supercond. Sci. Technol.* **9** (1996) 121
- [116] S. Sadewasser, J. S. Schilling, A. M. Hermann, *Phys. Rev. B* **62** (2000) 9155
- [117] Y. Ohta, T. Tohyama, S. Maekawa, *Phys. Rev. B* **43** (1991) 2968
- [118] H. Kotegawa, Y. Tokunaga, K. Ishida, G.-q. Zheng, Y. Kitaoka, K. Asayama, H. Kito, A. Iyo, H. Ihara, K. Tanaka, K. Tokiwa, T. Watanabe, *J. Phys. Chem. Solids* **62** (2001) 171
- [119] H. Kotegawa, Y. Tokunaga, K. Ishida, G.-q. Zheng, Y. Kitaoka, H. Kito, A. Iyo, K. Tokiwa, T. Watanabe, H. Ihara *Phys. Rev. B* **64** (2001) 064515
- [120] S. Chakravarty, H.-Y. Kee, K. Völker, *Nature* **428** (2004) 53;
P. Coleman, *Nature* **428** (2004) 26
- [121] J. Leggett, *Phys. Rev. Lett.* **83** (1999) 392
- [122] C. Meingast, O. Kraut, T. Wolf, H. Wühl, A. Erb, G. Müller-Vogt, *Phys. Rev. Lett.* **67** (1991) 1634
- [123] K. Kuroda, K. Abe, S. Segawa, J.-G. Wen, H. Unoki, N. Koshizuka, *Physica C* **275** (1997) 311
- [124] J. P. Attfield, A. L. Kharlanov, J. A. McAllister, *Nature* **394** (1998) 157
- [125] M. W. Pieper, F. Wiekhorst, T. Wolf, *Phys. Rev. B* **62** (2000) 1392;
A. J. Markwardsen, A. T. Boothroyd, B. Buck, G. J. McIntyre, Th. Wolf, *J. Magn. Mater.* **177-181** (1998) 502
- [126] K. Oka, Z. Zou, J. Ye, *Physica C* **300** (1998) 200;
Z. Zou, J. Ye, K. Oka, Y. Nishihara, *Phys. Rev. Lett.* **80** (1998) 1074
- [127] J. Ye, Z. Zou, A. Matsushita, K. Oka, Y. Nishihara, T. Matsumoto, *Phys. Rev. B* **58** (1998) 619
- [128] Z. Hu, R. Meier, C. Schüßler-Langeheine, E. Weschke, G. Kaindl, I. Felner, M. Merz, N. Nücker, S. Schuppler, A. Erb, *Phys. Rev. B* **60** (1999) 1460
- [129] M. Merz, S. Gerhold, N. Nücker, C. A. Kuntscher, B. Burbulla, P. Schweiss, S. Schuppler, V. Chakarian, J. Freeland, Y. U. Idzerda, M. Kläser, G. Müller-Vogt, Th. Wolf, *Phys. Rev. B* **60** (1999) 9317
- [130] Y. S. Lee, F. C. Chou, A. Tewary, M. A. Kastner, S. H. Lee, R. J. Birgeneau, *Phys. Rev. B* **69** (2004) 020502

- [131] P. K. Mang, S. Larochelle, A. Mehta, O. P. Vajk, A. S. Erickson, L. Lu, W. J. L. Buyers, A. F. Marshall, K. Prokes, M. Greven, cond-mat/0403258, submitted to Phys. Rev. **B**
- [132] O. Chmaissem, J. D. Jorgensen, S. Short, A. Knizhnik, Y. Eckstein, H. Shaked, Nature **397** (1999) 45
- [133] F. Izumi, J. D. Jorgensen, Y. Shimakawa, Y. Kubo, T. Manako, S. Pei, T. Matsumoto, R. L. Hitterman, Y. Kanke, Physica C **193** (1992) 426
- [134] Z. F. Ren, J. H. Wang, D. J. Miller, Appl. Phys. Lett. **69** (1996) 1798
- [135] A. Yamato, W. Z. Hu, F. Izumi, S. Tajima, Physica C **351** (2001) 329
- [136] K. A. Moler, J. R. Kirtley, D. G. Hinks, T. W. Li, M. Xu, Science **279** (1998) 1193
- [137] A. A. Tsvetkov, D. Van der Marel, K. A. Moler, J. R. Kirtley, J. L. De Boer, A. Meetsma, Z. F. Ren, N. Koleshnikov, D. Dulic, A. Damascelli, M. Grüninger, J. Schützmann, J. W. van der Eb, H. S. Somal, J. H. Wang, Nature **395** (1998) 360
- [138] T. H. Geballe, B. Y. Mozyzhes, Physica C **341-348** (2000) 1821
- [139] D. H. Lu, D. L. Feng, N. P. Armitage, K. M. Shen, A. Damascelli, C. Kim, F. Ronning, Z.-X. Shen, D. A. Bonn, R. Liang, W. N. Hardy, A. I. Rykov, S. Tajima, Phys. Rev. Lett. **86** (2001) 4370
- [140] D. A. Wollman, D. J. Van Harlingen, J. Giapintzakis, D. M. Ginsberg, Phys. Rev. Lett. **74** (1995) 797
- [141] D. J. Van Harlingen, J. E. Hilliard, B. L. T. Blourde, B. D. Yanoff, Physica C **317-318** (1999) 410
- [142] C. C. Tsuei, J. R. Kirtley, Rev. Mod. Phys. **72** (2000) 969;
C. C. Tsuei, J. R. Kirtley, Physica C **367** (2002) 1
- [143] J. R. Kirtley, C. C. Tsuei, H. Raffy, Z. Z. Li, A. Gupta, J. Z. Sun, S. Megert, Europhys. Lett. **36** (1996) 707
- [144] L. N. Bulaevskii, V. V. Kuzii, A. A. Sobyenin, JETP Lett. **25** (1977) 290
- [145] V. B. Geshkenbein, A. I. Larkin, A. Barone, Phys. Rev. B **36** (1987) 235
- [146] V. G. Kogan, J. R. Clem, J. R. Kirtley, Phys. Rev. B **61** (2000) 9122
- [147] J. R. Kirtley, C. C. Tsuei, K. A. Moler, Science **285** (1999) 1373
- [148] B. Chesca, Ann. Phys. (Leipzig) **8** (1999) 511
- [149] B. Chesca, Physica B **284-288** (2000) 2124
- [150] R. R. Schulz, B. Chesca, B. Goetz, C. W. Schneider, A. Schmehl, H. Bielefeldt, H. Hilgenkamp, J. Mannhart, C. C. Tsuei, Appl. Phys. Lett. **76** (2000) 912
- [151] B. Chesca, R. R. Schulz, B. Goetz, C. W. Schneider, H. Hilgenkamp, J. Mannhart, Phys. Rev. Lett. **88** (2002) 177003
- [152] C. C. Tsuei, J. R. Kirtley, Phys. Rev. Lett. **85** (2000) 182
- [153] B. Chesca, K. Ehrhardt, M. Mößle, R. Straub, D. Koelle, R. Kleiner, A. Tsukada, Phys. Rev. Lett. **90** (2003) 057004
- [154] T. Sato, T. Kamiyama, T. Takahashi, K. Kurahashi, K. Yamada, Science **291** (2001) 1517

- [155] M.-S. Kim, J. A. Skinta, T. R. Lemberger, A. Tsukada, M. Naito, Phys. Rev. Lett. **91** (2003) 087001
- [156] J. A. Skinta, T. R. Lemberger, T. Greibe, M. Naito, Phys. Rev. Lett. **88** (2002) 207003
- [157] S. Kashiwaya, Y. Tanaka, M. Koyanagi, K. Kajimura, Phys. Rev. B **53** (1996) 2667
- [158] S. Kleefisch, B. Welter, A. Marx, L. Alff, R. Gross, M. Naito, Phys. Rev. B **63** (2001) 100507
- [159] I. Iguchi, W. Wang, M. Yamazaki, Y. Tanaka, S. Kashiwaya, Phys. Rev. B **62** (2000) R6131
- [160] C.-R. Hu, Phys. Rev. Lett. **72** (1994) 1526
- [161] L. Alff, A. Beck, R. Gross, A. Marx, S. Kleefisch, Th. Bauch, H. Sato, M. G. Koren, Phys. Rev. B **58** (1998) 11197
- [162] R. Krupke, G. Deutscher, Phys. Rev. Lett. **83** (1999) 4634
- [163] E. Maiser, W. Mexner, R. Schäfer, T. Schreiner, P. Adelman, G. Czjzek, J. L. Peng, R. L. Greene, Phys. Rev. B **56** (1997) 12961
- [164] P. Fulde, Ann. Phys. (Leipzig) **9** (2000) 871
- [165] D. Dunlap, M. Slaski, Z. Sungaila, D. G. Hinks, K. Zhang, C. Segre, S. K. Malik, E. E. Alp, Phys. Rev. B **37** (1988) 592
- [166] R. J. Ormeno, C. E. Gough, G. Yang, Phys. Rev. B **63** (2001) 104517
- [167] J. C. Wynn, D. A. Bonn, B. W. Gardner, Yu-Ju Lin, R. Liang, W. N. Hardy, J. R. Kirtley, K. A. Moler, Phys. Rev. Lett. **87** (2001) 197002
- [168] N. P. Armitage, D. H. Lu, D. L. Feng, C. Kim, A. Damascelli, K. M. Shen, F. Ronning, Z.-X. Shen, Y. Onose, Y. Taguchi, Y. Tokura, Phys. Rev. Lett. **86** (2001) 1126
- [169] J. A. Skinta, M.-S. Kim, T. R. Lemberger, T. Greibe, M. Naito, Phys. Rev. Lett. **88** (2002) 207005
- [170] Y. Dagan, M. M. Qazilbash, C. P. Hill, V. N. Kulkarni, R. L. Greene, Phys. Rev. Lett. **92** (2004) 167001
- [171] R. C. Budhani, M. C. Sullivan, C. J. Lobb, R. L. Greene, Phys. Rev. B **66** (2002) 052506
- [172] E. H. Brandt, cond-mat/0104518
- [173] G. Grasso, R. Flükiger, Supercond. Sci. Technol. **10** (1997) 223
- [174] J. Sato, K. Ohata, M. Okada, K. Tanaka, H. Kitaguchi, H. Kumakura, T. Kiyoshi, H. Wada, K. Togano, Physica C **357-360** (2001) 1111;
M. Okada, Supercond. Sci. Technol. **13** (2000) 29
- [175] N. P. Plakida, *High-Temperature Superconductivity*, Springer-Verlag Berlin Heidelberg (1995)
- [176] E H Brandt, Rep. Prog. Phys. **58** (1995) 1465; condmat/9506003
- [177] K. Tanaka, A. Iyo, Y. Tanaka, K. Tokiwa, M. Tokumoto, M. Ariyama, T. Tsukamoto, T. Watanabe, H. Ihara, Physica B **284-288** (2000) 1081;
T. Watanabe, S. Miyashita, N. Ichioka, K. Tokiwa, K. Tanaka, A. Iyo, Y. Tanaka, H. Ihara, Physica B **284-288** (2000) 1075

- [178] B. Götz, “*Untersuchung der Transporteigenschaften von Korngrenzen in Hochtemperatur-Supraleitern*”, PhD-thesis, University of Augsburg, 2000
- [179] H. Hilgenkamp, J. Mannhart, Rev. Mod. Phys. **74** (2002) 485
- [180] H. Hilgenkamp, J. Mannhart, B. Mayer, Phys. Rev. B **53** (1996) 14586
- [181] P. A. Nilsson, Z. G. Ivanov, H. K. Olsson, D. Winkler, T. Claeson, E. A. Stepantsov, A. Ya. Tzalenchuk, J. Appl. Phys. **75** (1994) 7972
- [182] J. Betouras, R. Joynt, Physica C **250** (1995) 256
- [183] J. Alarco, E. Olsson, Phys. Rev. B **52** (1995) 13625
- [184] D. Agassi, D. K. Christen, S. J. Pennycook, Appl. Phys. Lett. **81** (2002) 2803
- [185] H. Hilgenkamp, J. Mannhart, Appl. Phys. Lett. **73** (1998) 265
- [186] G. Hammerl, A. Schmehl, R. R. Schulz, B. Goetz, H. Bielefeldt, C. W. Schneider, H. Hilgenkamp, J. Mannhart, Nature **162** (2000) 162;
C. W. Schneider, R. R. Schulz, B. Goetz, A. Schmehl, H. Bielefeldt, H. Hilgenkamp, J. Mannhart, Appl. Phys. Lett. **75** (1999) 850;
H. Hilgenkamp, C. W. Schneider, R. R. Schulz, B. Goetz, A. Schmehl, H. Bielefeldt, J. Mannhart, Physica C **326-327** (1999) 7
- [187] W. M. Temmermann, H. Winter, Z. Szotek, A. Svane, Phys. Rev. Lett. **86** (2001) 2435
- [188] O. K. Andersen, A. I. Liechtenstein, O. Jepsen, F. Paulsen, J. Phys. Chem. Solids **56** (1995) 1567
- [189] J. Zaanen, G. Sawatzky, J. W. Allen, Phys. Rev. Lett. **55** (1985) 418;
A. Fujimori, F. Minami, Phys. Rev. B **30** (1984) 957
- [190] R. J. Cava, J. Am. Ceram. Soc. **83** (2000) 5
- [191] E. Dagotto, Rev. Mod. Phys. **66** (1994) 763
- [192] R. M. White and T. H. Geballe: *Long Range Order in Solids*, Academic Press, New York – San Francisco – London (1979)
- [193] S. Sachdev, Rev. Mod. Phys. **75**, 913-932 (2003)
- [194] A. Paramekanti, M. Randeria, N. Trivedi, Phys. Rev. Lett. **87** (2001) 217002
- [195] P. W. Anderson, P. A. Lee, M. Randeria, T. M. Rice, N. Trivedi, F. C. Zhang, J. Phys. Condens. Matter **16** (2004) R755
- [196] C. M. Varma, cond-mat/0312385
- [197] B. A. Bernevig, G. Chapline, R. B. Laughlin, Z. Nazario, D. I. Santiago, cond-mat/0312573
- [198] P. Coleman, Nature **424** (2003) 625
- [199] F. C. Zhang, T. M. Rice, Phys. Rev. B **37** (1988) 3759
- [200] T. M. Rice, Physica B **241-243** (1997) 5
- [201] Y. Onose, Y. Taguchi, K. Ishizaka, Y. Tokura, Phys. Rev. Lett. **87** (2001) 217001
- [202] Y. Ando, A. N. Lavrov, S. Komiya, K. Segawa, X. F. Sun, Phys. Rev. Lett. **87** (2001) 017001
- [203] A. N. Lavrov, S. Komiya, Y. Ando, Nature **418** (2002) 385
- [204] M. A. Kastner, R. J. Birgenau, G. Shirane, Y. Endoh, Rev. Mod. Phys. **70** (1998) 897

- [205] J. M. Tranquada, D. E. Cox, W. Kunnmann, H. Moudden, G. Shirane, M. Suenaga, P. Zolliker, D. Vaknin, S. K. Sinha, M. S. Alvarez, A. J. Jacobson, D. C. Johnston, *Phys. Rev. Lett.* **60** (1988) 156
- [206] J. L. Tallon, J. W. Loram, *Physica C* **349** (2001) 53
- [207] C. M. Varma, *Phys. Rev. B* **55** (1997) 14554
- [208] L. Alff, Y. Krockenberger, B. Welter, M. Schonecke, R. Gross, D. Manske, M. Naito, *Nature* **422** (2003) 698
- [209] B. W. Veal, A. P. Paulikas, *Physica C* **184** (1991) 321
- [210] K. Segawa, Y. Ando, *J. Low Temp. Phys.* **131** (2003) 821
- [211] U. Tutsch, P. Schweiss, H. Wühl, B. Obst, Th. Wolf, to be published
- [212] J. W. Loram, K. A. Mirza, J. M. Wade, J. R. Cooper, W. Y. Liang, *Physica C* **235-240** (1994) 134
- [213] T. Schneider, H. Keller, *cond-mat/0404702*
- [214] T. Timusk, B. Statt, *Rep. Prog. Phys.* **62** (1999) 61
- [215] M. Buchanan, *Nature* **409** (2001) 11
- [216] C. Meingast, V. Pasler, P. Nagel, A. Rykov, S. Tajima, P. Olsson, *Phys. Rev. Lett.* **86** (2001) 1606
- [217] B. Batlogg, *Solid State Comm.* **107** (1998) 639
- [218] J. Ruvalds, *Supercond. Sci. Technol.* **9** (1996) 905
- [219] H. Ding, M. R. Norman, J. C. Campuzano, M. Randeria, A. F. Bellman, T. Yokoya, T. Takahashi, T. Mochiku, K. Kadowaki, *Phys. Rev. B* **54** (1996) 9678
- [220] P. V. Bogdanov, A. Lanzara, X. J. Zhou, S. A. Kellar, D. L. Feng, E. D. Lu, H. Eisaki, J.-I. Shimoyama, K. Kishio, Z. Hussain, Z. X. Shen, *Phys. Rev. B* **64** (2001) 180505
- [221] T. Valla, A. V. Fedorov, P. D. Johnson, Q. Li, G. D. Gu, N. Koshizuka, *Phys. Rev. Lett.* **85** (2000) 828
- [222] A. A. Kordyuk, S. V. Borisenko, M. S. Golden, S. Legner, K. A. Nenkov, M. Knupfer, J. Fink, H. Berger, L. Forro, *Phys. Rev. B* **66** (2002) 014502
- [223] C. M. Varma, P. B. Littlewood, S. Schmitt-Rink, E. Abrahams, A. E. Ruckenstein, *Phys. Rev. Lett.* **63** (1989) 1996
- [224] R. W. Hill, C. Proust, L. Taillefer, P. Fournier, R. L. Greene, *Nature* **414** (2001) 711
- [225] R. Lortz, C. Meingast, A. I. Rykov, S. Tajima, *Phys. Rev. Lett.* **91** (2003) 207001
- [226] N. P. Ong, Y. Wang, S. Ono, Y. Ando, S. Uchida, *Annalen der Physik* **13** (2004) 9
- [227] C. Proust, E. Boaknin, R. W. Hill, L. Taillefer, A. P. Mackenzie, *Phys. Rev. Lett.* **89** (2002) 147003
- [228] S. Nakamae, K. Behnia, N. Mangkorntong, M. Nohara, H. Takagi, S. J. C. Yates, N. E. Hussey, *Phys. Rev. B* **68** (2003) 100502
- [229] R. Bel, K. Behnia, C. Proust, P. van der Linden, D. Maude, S. I. Vedenev, *Phys. Rev. Lett.* **92** (2004) 177003
- [230] T. Tohyama, S. Maekawa, *Supercond. Sci. Technol.* **13** (2000) R17
- [231] B. Keimer, *Science* **292** (2001) 1498

- [232] G. Yang, J. S. Abell, C. E. Gough, *Appl. Phys. Lett.* **75** (1999) 1955
- [233] R. Joynt, *Science* **284** (1999) 777
- [234] S. V. Borisenko, M. S. Golden, S. Legner, T. Pichler, C. Dürr, M. Knupfer, J. Fink, G. Yang, S. Abell, H. Berger, *Phys. Rev. Lett.* **84** (2000) 4453
- [235] D. L. Feng, D. H. Lu, K. M. Shen, C. Kim, H. Eisaki, A. Damascelli, R. Yoshizaki, J.-I. Shimoyama, K. Kishio, G. D. Gu, S. Oh, A. Andrus, J. O'Donnell, J. N. Eckstein, Z.-X. Shen, *Science* **289** (2000) 277
- [236] A. Junod, A. Erb, C. Renner, *Physica C* **317-318** (1999) 333
- [237] A. V. Fedorov, T. Valla, P. D. Johnson, Q. Li, G. D. Gu, N. Koshizuka, *Phys. Rev. Lett.* **82** (1999) 2179
- [238] J. R. Schrieffer, M. Tinkham, *Rev. Mod. Phys.* **71** (1999) S313
- [239] P. A. Lee, *Physica C* **317-318** (1999) 194
- [240] Z. A. Xu, N. P. Ong, Y. Wang, T. Kakeshita, S. Uchida, *Nature* **406** (2000) 486
- [241] P. A. Lee, *Nature* **406** (2000) 467
- [242] I. Iguchi, T. Yamaguchi, A. Sugimoto, *Nature* **412** (2001) 420
- [243] Y. Wang, Z. A. Xu, T. Kakeshita, S. Uchida, S. Ono, Y. Ando, N. P. Ong, *Phys. Rev. B* **64** (2001) 224519
- [244] V. Pasler, P. Schweiss, C. Meingast, B. Obst, H. Wühl, A. I. Rykov, S. Tajima, *Phys. Rev. Lett.* **81** (1998) 1094
- [245] A. S. Alexandrov, N. F. Mott, *Rep. Prog. Phys.* **57** (1994) 1197
- [246] V. J. Emery, S. A. Kivelson, *Nature* **374** (1995) 434
- [247] M. Randeria, in *Bose-Einstein condensation* (Ed. A. Griffin, D. W. Snoke, S. Stringari), Cambridge University Press 1995, pp.355
- [248] J. Corson, R. Mallozzi, J. Orenstein, J. N. Eckstein, I. Bozovic, *Nature* **398** (1999) 221
- [249] A. J. Millis, *Nature* **398** (1999) 193
- [250] S. Chakravarty, R. B. Laughlin, D. K. Morr, C. Nayak, *Phys. Rev. B* **63** (2001) 094503
- [251] I. Affleck, J. B. Marston, *Phys. Rev. B* **37** (1988) 3774
- [252] J. B. Marston, I. Affleck, *Phys. Rev. B* **39** (1989) 11538
- [253] A. G. Loesser, Z.-X. Shen, D. S. Dessau, D. S. Marshall, C. H. Park, P. Fournier, A. Kapitulnik, *Science* **273** (1996) 325
- [254] H. Ding, T. Yokoya, J. C. Campuzano, T. Takahashi, M. Randeria, M. R. Norman, T. Mochiku, K. Kadowaki, J. Giapintzakis, *Nature* **382** (1996) 51
- [255] C. Nayak, *Phys. Rev. B* **62** (2000) 4880
- [256] G. Aeppli, D. J. Bishop, C. Broholm, E. Bucher, S.-W. Cheong, P. Dai, Z. Fisk, S. M. Hayden, R. Kleiman, T. E. Mason, H. A. Mook, T. G. Perring, A. Schroeder, *Physica C* **317-318** (1999) 9
- [257] P. Bourges, *The Gap Symmetry and Fluctuations in High Temperature Superconductors* (Eds. J. Bok, G. Deutscher, D. Pavuna, S. A. Wolf), Plenum Press (1998); Proc. NATO ASI summer school, September 1-13, 1997 in Cargèse, France; cond-mat/9901333

- [258] M. Arai, T. Nishijima, Y. Endoh, T. Egami, S. Tajima, K. Tomimoto, Y. Shiohara, M. Takahashi, A. Garrett, S. M. Bennington, *Phys. Rev. Lett.* **83** (1999) 608
- [259] K. Yamada, C. H. Lee, K. Kurahashi, J. Wada, S. Wakimoto, S. Ueki, H. Kimura, Y. Endoh, S. Hosoya, G. Shirane, R. J. Birgeneau, M. Greven, M. A. Kastner, Y. J. Kim, *Phys. Rev. B* **57** (1998) 6165
- [260] J. M. Tranquada, J. D. Axe, N. Ichikawa, A. R. Moodenbaugh, Y. Nakamura, S. Uchida, *Phys. Rev. Lett.* **78** (1997) 338
- [261] J. M. Tranquada, *Physica B* **241-243** (1998) 745
- [262] J. M. Tranquada, J. D. Axe, N. Ichikawa, Y. Nakamura, S. Uchida, B. Nachumi, *Phys. Rev. B* **54** (1996) 7489
- [263] J. M. Tranquada, H. Woo, T. G. Perring, H. Goka, G. D. Gu, G. Xu, M. Fujita, K. Yamada, *Nature* **429** (2004) 534
- [264] S. M. Hayden, H. A. Mook, Pengcheng Dai, T. G. Perring, F. Dogan, *Nature* **429** (2004) 531
- [265] G. Grüner, *Rev. Mod. Phys.* **66** (1994) 1
- [266] K. Machida, *Physica C* **158** (1989) 192
- [267] J. Zaanen, O. Gunnarsson, *Phys. Rev. B* **40** (1989) 7391
- [268] J. Zaanen, *Nature* **404** (2000) 714
- [269] H. A. Mook, F. Dogan, *Physica C* **364-365** (2001) 553
- [270] H. A. Mook, F. Dogan, *Nature* **401** (1999) 145
- [271] L. Pintschovius, W. Reichardt, M. Kläser, T. Wolf, H. v. Löhneysen, *Phys. Rev. Lett.* **89** (2000) 037001
- [272] M. I. Salkola, V. J. Emery, S. A. Kivelson, *Phys. Rev. Lett.* **77** (1996) 156
- [273] S. A. Kivelson, E. Fradkin, V. J. Emery, *Nature* **393** (1998) 550
- [274] H.-H. Klauss, W. Wagener, M. Hillberg, W. Kopmann, H. Walf, F. J. Litterst, M. Hücker, B. Büchner, *Phys. Rev. Lett.* **85** (2000) 4590
- [275] T. Tohyama, C. Gazza, C. T. Shih, Y. C. Chen, T. K. Lee, S. Maekawa, E. Dagotto, *Phys. Rev. B* **59** (1999) R11649
- [276] M. G. Zacher, R. Eder, E. Arrigoni, W. Hanke, *Phys. Rev. Lett.* **85** (2000) 2585
- [277] G. B. Martins, C. Gazza, J. C. Xavier, A. Feiguin, E. Dagotto, *Phys. Rev. Lett.* **84** (2000) 5844
- [278] A. L. Chernyshev, A. H. Castro Neto, A. R. Bishop, *Phys. Rev. Lett.* **84** (2000) 4922
- [279] H. A. Mook, P. Dai, F. Dogan, R. D. Hunt, *Nature* **404** (2000) 729
- [280] B. Keimer, DPG-AKF meeting, Regensburg, March 8 – 12, 2004
- [281] N. B. Christensen, D. F. McMorrow, H. M. Ronnow, B. Lake, S. M. Hayden, G. Aeppli, T. G. Perring, M. Mangkorntong, M. Nohara, H. Tagaki, cond-mat/0403439
- [282] Y. S. Lee, R. J. Birgeneau, M. A. Kastner, Y. Endoh, S. Wakimoto, K. Yamada, R. W. Erwin, S.-H. Lee, G. Shirane, *Phys. Rev. B* **60** (1999) 3643
- [283] M. Fujita, K. Yamada, H. Hiraka, P. M. Gehring, S. H. Lee, S. Wakimoto, G. Shirane, *Phys. Rev. B* **65** (2002) 064505

- [284] C. Howald, H. Eisaki, N. Kaneko, M. Greven, A. Kapitulnik, *Phys. Rev. B* **67** (2003) 014533;
A. Fang, C. Howald, N. Kaneko, M. Greven, A. Kapitulnik, *cond-mat/0404452*
- [285] S. A. Kivelson, I. P. Bindloss, E. Fradkin, V. Oganesyan, J. M. Tranquada, A. Kapitulnik, C. Howald, *Rev. Mod. Phys.* **75** (2003) 1201
- [286] J. E. Hoffman, K. McElroy, D.-H. Lee, K. M Lang, H. Eisaki, S. Uchida, J. C. Davis, *Science* **297** (2002) 1148
- [287] K. McElroy, R. W. Simmonds, J. E. Hoffman, D.-H. Lee, J. Orenstein, H. Eisaki, S. Uchida, J. C. Davis, *Nature* **422** (2003) 592
- [288] M. Vershinin, S. Misra, S. Ono, Y. Abe, Y. Ando, A. Yazdani, *Science* **303** (2004) 1995;
K. McElroy, D.-H. Lee, J. E. Hoffman, K. M Lang, J. Lee, E. W. Hudson, H. Eisaki, S. Uchida, J. C. Davis, *cond-mat/0406491*
- [289] M. Norman, *Science* **303** (2004) 1985
- [290] L. P. Pryadko, S. A. Kivelson, V. J. Emery, Y. B. Bazaliy, E. A. Demler, *Phys. Rev. B* **60** (1999) 7541
- [291] W. Prusseit, S. Furtner, R. Nemetschek, *Supercond. Sci. Technol.* **13** (2000) 519
- [292] V. Matijasevic, Z. Lu, T. Kaplan, C. Huang, *Inst. Phys. Conf. Ser. No.* **158** (1997) 189
- [293] D. W. Face, R. J. Small, M. S. Warrington, F. M. Pellicone, P. J. Martin, *Physica C* **357-360** (2001) 1488;
D. W. Face, C. Wilker, J. J. Kingston, Z.-Y. Shen, F. M. Pellicone, R. J. Small, S. P. McKenna, S. Sun, P. J. Martin, *IEEE Trans. Appl. Supercond.* **7** (1997) 1283
- [294] R. Aidam, J. Geerk, G. Linker, F. Ratzel, J. Reiner, R. Schneider, R. Smithey, A. G. Zaitsev, E. Gaganidze, R. Schwab, *IEEE Trans. Appl. Supercond.* **11** (2001) 357
- [295] Y. Yamada, J. Kawashima, J. G. Wen, Y. Niiori, I. Hirabayashi, *Jpn. J. Appl. Phys.* **39** (2000) 1111
- [296] P. Seidel, S. Linzen, G. Kaiser, F. Schmidl, Y. Tian, A. Matthes, S. Wunderlich, H. Schneidewind, *Proc. SPIE* **3481** (1998) 366
- [297] A. G. Zaitsev, G. Ockenfuss, R. Wördenweber, *Inst. Phys. Conf. Ser. No.* **158** (1997) 25
- [298] D. H. A. Blank, H. Rogalla, *J. Mater. Res.* **12** (1997) 2952;
K. Verbist, O. I. Lebedev, M. A. J. Verhoeven, R. Wichern, A. J. H. M. Rijnders, D. H. A. Blank, F. Tafuri, H. Bender, G. Van Tendeloo, *Supercond. Sci. Technol.* **11** (1998) 13;
K. Verbist, O. I. Lebedev, G. Van Tendeloo, M. A. J. Verhoeven, A. J. H. M. Rijnders, D. H. A. Blank, H. Rogalla, *Appl. Phys. Lett.* **70** (1997) 1167
- [299] J. Talvacchio, M. G. Forrester, B. D. Hunt, J. D. McCambridge, R. M. Young, X. F. Zhang, D. J. Miller, *IEEE Trans. Appl. Supercond.* **7** (1997) 2051
- [300] Y. Soutome, T. Fukazawa, A. Tsukamoto, K. Saitoh, K. Takagi, *Physica C* **372-376** (2002) 143

- [301] T. Satoh, M. Hidaka, S. Tahara, J. G. Wen, N. Koshizuka, S. Tanaka, *IEEE Trans. Appl. Supercond.* **11** (2001) 770
- [302] J. Mannhart, P. Chaudhari, *Physics Today*, November 2001, p.48
- [303] F. Herbstritt, T. Kemen, A. Marx, R. Gross, *J. Appl. Phys.* **91** (2002) 5411
- [304] Z. G. Ivanov, E. A. Stepantsov, T. Claeson, F. Wenger, S. Y. Lin, N. Khare, P. Chaudhari, *Phys. Rev. B* **57** (1998) 602
- [305] T. Minotani, S. Kawakami, T. Kiss, Y. Kuroki, K. Enpuku, *Jpn. J. Appl. Phys.* **36** (1997) L 1092
- [306] H. Q. Li, R. H. Ono, L. R. Vale, D. A. Rudman, S. H. Liou, *Appl. Phys. Lett.* **71** (1997) 1121
- [307] F. Schmidl, S. Linzen, S. Wunderlich, P. Seidel, *Appl. Phys. Lett.* **72** (1998) 602
- [308] H. J. H. Smilde, H. Hilgenkamp, G. Rijnders, H. Rogalla, D. H. A. Blank, *Appl. Phys. Lett.* **80** (2002) 4579;
H. J. H. Smilde, H. Hilgenkamp, G. J. Gerritsma, D. H. A. Blank, H. Rogalla, *Physica C* **350** (2001) 269;
H. J. H. Smilde, Ariando, D. H. A. Blank, G. J. Gerritsma, H. Hilgenkamp, H. Rogalla, *Phys. Rev. Lett.* **88** (2002) 057004
- [309] R. Kleiner, F. Steinmeyer, G. Kunkel, P. Müller, *Phys. Rev. Lett.* **68** (1992) 2394;
R. Kleiner, P. Müller, *Phys. Rev. B* **49** (1994) 1327
- [310] D. Winkler, N. Mros, E. J. Tarte, A. Yurgens, V. M. Krasnov, D. T. Foord, W. E. Booij, M. G. Blamire, *Supercond. Sci. Technol.* **12** (1999) 1013;
for a review, see A. Yurgens, *Supercond. Sci. Technol.* **13** (2000) R85
- [311] H. B. Wang, L. X. You, J. Chen, P. H. Wu, T. Yamashita, *Supercond. Sci. Technol.* **15** (2002) 90;
H. B. Wang, J. Chen J, P. H. Wu, T. Yamashita, D. Vasyukov, P. Müller, *Supercond. Sci. Technol.* **16** (2003) 1375
- [312] T. Clauss, V. Oehmichen, M. Mößle, A. Müller, A. Weber, D. Koelle, R. Kleiner, *Supercond. Sci. Technol.* **15** (2002) 1651
- [313] K. Schlenga, R. Kleiner, G. Hechtfisher, M. Mößle, S. Schmitt, P. Müller, Ch. Helm, Ch. Preis, F. Forsthofer, J. Keller, H. L. Johnson, M. Veith, E. Steinbeiß, *Phys. Rev. B* **57** (1998) 14518
- [314] M. Rapp, A. Murk, R. Semerad, W. Prusseit, *Phys. Rev. Lett.* **77** 1996) 928
- [315] D. Litzkendorf, T. Habisreuther, R. Müller, S. Kracunovska, O. Surzhenko, M. Zeisberger, J. Riches, W. Gawalek, *Physica C* **372-376** (2002) 1163
- [316] G. Desgardin, I. Monot. B. Raveau, *Supercond. Sci. Technol.* **12** (1999) R115
- [317] M. Tomita, M. Murakami, *Nature* **421** (2003) 517
- [318] M. Tsuchimoto, H. Takashima, M. Tomita, M. Murakami, *Physica C* **378-381** (2002) 718
- [319] H. Teshima, M. Sawamura, M. Morito, M. Tsuchimoto, *Cryogenics* **37** (1997) 505
- [320] P. Stoye, W. Gawalek, P. Görmert, A. Gladun, G. Fuchs, *Inst. Phys. Conf. Ser. No.* **158** (1997) 1535

- [321] W. Hennig, D. Parks, R. Weinstein, R.-P. Sawh, Appl. Phys. Lett. **72** (1998) 3059
- [322] K. Tanaka, M. Okada, K. Ohata, J. Sato, H. Kitaguchi, H. Kumakura, K. Togano, Physica C **357-360** (2001) 1102;
K. Ohata, J. Sato, M. Okada, K. Tanaka, H. Kitaguchi, H. Kumakura, K. Togano, T. Kiyoshi, H. Wada, Physica C **357-360** (2001) 1107
- [323] L. Masur, D. Parker, M. Tanner, E. Podtburg, D. Buczek, J. Scudiere, P. Caracino, S. Spreafico, P. Corsaro, M. Nassi, IEEE Trans. Appl. Supercond. **11** (2001) 3256
- [324] J. Kellers, L. J. Masur, Physica C **372-376** (2002) 1040
- [325] T. J. Arndt, B. Fischer, J. Gierl, H. Krauth, M. Munz, A. Szulczyk, M. Leghissa, H.-W. Neumueller, IEEE Trans. Appl. Supercond. **11** (2001) 3261
- [326] J. Fujikami, T. Kaneko, N. Ayai, S. Kobayashi, K. Hayashi, H. Takei, K. Sato, Physica C **378-381** (2002) 1061
- [327] Q. Li, M. Suenaga, T. Kaneko, K. Sato, Ch. Simmon, Appl. Phys. Lett. **71** (1997) 1561
- [328] P. Corsaro, M. Bechis, P. Caracino, W. Castiglioni, G. Cavalleri, G. Coletta, G. Colombo, P. Ladiè, A. Mansoldo, R. Mele, S. Montagnero, C. Moro, M. Nassi, S. Spreafico, N Kelley, C. Wakefield, Physica C **378-381** (2002) 1168
- [329] T. Masuda, T. Kato, H. Yumura, M. Watanabe, Y. Ashibe, K. Ohkura, C. Suzawa, M. Hirose, S. Isojima, K. Matsuo, S. Honjo, T. Mimura, T. Kuramochi, Y. Takahashi, H. Suzuki, T. Okamoto, Physica C **378-381** (2002) 1174
- [330] H. Kitaguchi, K. Itoh, T. Takeuchi, H. Kumakura, H. Miao, H. Wada, K. Togano, T. Hasegawa, T. Kizumi, Physica C **320** (1999) 253;
T. Hasegawa, T. Koizumi, N. Ohtani, H. Kitaguchi, H. Kumakura, K. Togano, H. Miao, Supercond. Sci. Technol. **13** (2000) 23
- [331] Y. Aoki, T. Koizumi, N. Ohtani, T. Hasegawa, L. Motowidlo, R. S. Sokolowski, R. M. Scanlan, S. Nagaya, Physica C **335** (2000) 1
- [332] T. Wakuda, M. Okada, S. Awaji, K. Watanabe, Physica C **357-360** (2001) 1293
- [333] T. Hase, Y. Murakami, S. Hayashi, Y. Kawate, T. Kiyoshi, H. Wada, S. Sairate, R. Ogawa, Physica C **335** (2000) 6;
K. Fukushima, K. Tanaka, T. Wakuda, M. Okada, K. Ohata, J. Sato, T. Kiyoshi, H. Wada, Physica C **357-360** (2001) 1297
- [334] J. Cloyd, "2002 DOE Wire Workshop", January 22, 2002, St. Petersburg, FL, http://www.eren.doe.gov/superconductivity/docs/10mil_perspective_cloyd.ppt
- [335] M. Gouge, "2002 DOE Wire Workshop", January 22, 2002, St. Petersburg, FL, http://www.eren.doe.gov/superconductivity/docs/09dod_perspective_gouge.ppt
- [336] M. Wood, *Trials and Triumphs in Superconductivity: The Making of Oxford Instruments*, IEEE Trans. Appl. Supercond. **5** (1995) 152
- [337] A. W. Sleight, J. L. Gillson, P. E. Bierstedt, Solid State Commun. **17** (1975) 27
- [338] M. Merz, N. Nücker, S. Schuppler, D. Arena, J. Dvorak, Y. U. Idzerda, S. N. Ustinovich, A. G. Soldatov, S. V. Shiryayev, S. N. Barilo, to be published
- [339] L. F. Mattheiss, E. M. Gyorgy, D. W. Johnson Jr., Phys. Rev. B **37** (1988) 3745
- [340] E. S. Hellman, E. H. Hartford, Jr., Phys. Rev. B **52** (1995) 6822

- [341] R. J. Cava, B. Batlogg, J. J. Krajewski, R. Farrow, L. W. Rupp, Jr., A. E. White, K. Short, W. F. Peck, T. Kometani, *Nature* **332** (1988) 814
- [342] S. Pei, J. D. Jorgensen, B. Dabrowski, D. G. Hinks, D. R. Richards, A. W. Mitchell, J. M. Newsam, S. K. Sinha, D. Vaknin, A. J. Jacobson, *Phys. Rev. B* **41** (1990) 4126
- [343] L. A. Klinkova, M. Uchida, Y. Matsui, V. I. Nikolaichik, N. V. Barkovskii, *Phys. Rev. B* **67** (2003) 140501
- [344] Y. Maeno, T. M. Rice, M. Sigrist, *Physics Today*, January 2001, p. 42
- [345] C. Bernhard, J. L. Tallon, Ch. Niedermayer, Th. Blasius, A. Golnik, E. Brücher, R. K. Kremer, D. R. Noakes, C. E. Stronack, E. J. Asnaldo, *Phys. Rev. B* **59** (1999) 14099
- [346] T. Nachtrab, D. Koelle, R. Kleiner, C. Bernhard, C. T. Lin, *Phys. Rev. Lett.* **92** (2004) 117001
- [347] B. Lorenz, Y. Y. Xue, C. W. Chu, this volume
- [348] K. Takada, H. Sakurai, E. Takayama-Muromachi, F. Izumi, R. A. Dilanian, T. Sasaki, *Nature* **422** (2003) 53
- [349] M. L. Foo, R. E. Schaak, V. L. Miller, T. Klimczuk, N. S. Rogado, Y. Wang, G. C. Lau, C. Craley, H. W. Zandbergen, N. P. Ong, R. J. Cava, *Solid State Commun.* **127** (2003) 33
- [350] J. W. Lynn, Q. Huang, C. M. Brown, V. L. Miller, M. L. Foo, R. E. Schaak, C. Y. Jones, E. A. Mackey, R. J. Cava, *Phys. Rev. B* **68** (2003) 214516
- [351] S. Yonezawa, Z. Muraoka, Y. Matsushita, Z. Hiroi, *J. Phys.: Condensed Matter* **16** (2004) L9;
S. Yonezawa, Z. Muraoka, Z. Hiroi, *cond-mat/0404220*;
S. Yonezawa, Y. Muraoka, Y. Matsushita, Z. Hiroi, *J. Phys. Soc. Jpn.* **73** (2004) 819;
Z. Hiroi, S. Yonezawa, Y. Muraoka, *cond-mat/0402006*
- [352] N. P. Ong, R. J. Cava, *Science* **305** (2004) 52
- [353] L. Taillefer, G. G. Lonzarich, *Phys. Rev. Lett.* **60** (1988) 1570;
H. Aoki, S. Uji, A. K. Albessard, Y. Onuki, *Phys. Rev. Lett.* **71** (1993) 2110;
F. S. Tautz, S. R. Julian, G. J. McMullen, G. G. Lonzarich, *Physica B* **206-207** (1995) 29
- [354] R. A. Fisher, S. Kim, B. F. Woodfield, N. E. Phillips, L. Taillefer, K. Hasselbach, J. Flouquet, A. L. Giorgi, J. L. Smith, *Phys. Rev. Lett.* **62** (1989) 1411
- [355] E. D. Bauer, N. A. Frederick, P.-C. Ho, V. S. Zapf, M. B. Maple, *Phys. Rev. B* **65** (2002) 100506
- [356] T. Watanabe, Y. Kasahara, K. Izawa, T. Sakakibara, C. vanderBeek, T. Hanaguri, H. Shishido, R. Settai, Y. Onuki, Y. Matsuda, *Phys. Rev. B* **70** (2004) 020506
- [357] A. Bianchi, R. Movshovich, C. Capan, A. Lacerda, P. G. Pagliuso, J. L. Sarrao, *Phys. Rev. Lett.* **91** (2003) 187004

- [358] J. D. Denlinger, G.-H. Gweon, J. W. Allen, C. G. Olson, M. B. Maple, J. L. Sarrao, P. E. Armstrong, Z. Fisk, H. Yamagami, J. Electron. Spectrosc. Relat. Phenom. **117&118** (2001) 347;
F. Reinert, D. Ehm, S. Schmidt, G. Nicolay, S. Hübner, J. Kroha, O. Trovarelli, C. Geibel, Phys. Rev. Lett. **87** (2001) 106401
- [359] G. Zwicknagl, Adv. Phys. **41** (1992) 203
- [360] O. Stockert, E. Faulhaber, G. Zwicknagl, N. Stüßer, H. S. Jeevan, M. Deppe, R. Borth, R. KÜchler, M. Loewenhaupt, C. Geibel, F. Steglich, Phys. Rev. Lett. **92** (2004) 136401
- [361] G. Zwicknagl, A. N. Yaresko, P. Fulde, Phys. Rev. B **63** (2002) 081103
G. Zwicknagl, A. N. Yaresko, P. Fulde, Phys. Rev. B **68** (2003) 052508
- [362] For a recent review see P. Thalmeier, G. Zwicknagl, *Handbook on the Physics and Chemistry of Rare Earths*, Vol. 36, chapter "Unconventional Superconductivity and Magnetism in Lanthanide and Actinide Intermetallic Compounds"; cond-mat/0312540
- [363] N. K. Sato, N. Aso, K. Miyake, R. Shiina, P. Thalmeier, G. Varelogiannis, C. Geibel, F. Steglich, P. Fulde, T. Komatsubara, Nature **410** (2001) 340
- [364] P. McHale, P. Thalmeier, P. Fulde, cond-mat/0401520
- [365] P. Thalmeier, G. Zwicknagl, G. Sparn, F. Steglich, "Superconductivity in Heavy Fermion Compounds", this volume
- [366] J. D. Thompson, R. Movshovich, Z. Fisk, F. Bouquet, N. J. Curro, R. A. Fisher, P. C. Hammel, H. Hegger, M. F. Hundley, M. Jaime, P. G. Pagliuso, C. Petrovic, N. E. Phillips, J. L. Sarrao, J. Magn. Mat. **226-230** (2001) 5
- [367] C. Petrovic, R. Movshovich, M. Jaime, P. G. Pagliuso, M. F. Hundley, J. L. Sarrao, Z. Fisk, J. D. Thompson, Europhys. Lett. **53** (2001) 354
- [368] C. Petrovic, P. G. Pagliuso, M. F. Hundley, R. Movshovich, J. D. Sarrao, J. D. Thompson, Z. Fisk, P. Monthoux, J. Phys.: Condens. Matter **13** (2001) L337
- [369] D. Jaccard, K. Behnia, J. Sierro, Phys. Lett. A **163** (1992) 475
- [370] F. M. Grosche, S. R. Julian, N. D. Mathur, G. G. Lonzarich, Physica B **223&224** (1996) 50
- [371] N. D. Mathur, F. M. Grosche, S. R. Julian, I. R. Walker, D. M. Freye, R. K. W. Haselwimmer, G. G. Lonzarich, Nature **394** (1998) 39
- [372] F. M. Grosche, P. Agarwal S. R. Julian, N. J. Wilson, R. K. W. Haselwimmer, S. J. S. Lister, N. D. Mathur, F. V. Carter, S. S. Saxena, G. G. Lonzarich, J. Phys. Condens. Matter. **12** (2000) L533
- [373] R. Movshovich, T. Graf, D. Mandrus, J. D. Thompson, J. L. Smith, Z. Fisk, Phys. Rev. B **53** (1996) 8241
- [374] I. R. Walker, F. M. Grosche, D. M. Freye, G. G. Lonzarich, Physica C **282** (1997) 303
- [375] G. R. Stewart, Z. Fisk, J. O. Willis, J. L. Smith, Phys. Rev. Lett. **52** (1984) 679
- [376] C. Geibel, C. Schank, S. Thies, H. Kitazawa, C. D. Bredl, A. Böhm, M. Rau, A. Grauel, R. Caspary, R. Helfrich, U. Ahlheim, G. Weber, F. Steglich, Z. Phys. B **84** (1991) 1

- [377] C. Geibel, S. Thies, D. Kczorowski, A. Mehner, A. Grauel, B. Seidel, U. Ahlheim, R. Helfrich, K. Petersen, C. D. Bredl, F. Steglich, *Z. Phys.* **83** (1991) 305
- [378] T. T. M. Palstra, A. A. Menovsky, J. van den Berg, A. J. Dirkmaat, P. H. Res, G. J. Nieuwenhuys, J. A. Mydosh, *Phys. Rev. Lett.* **55** (1985) 2727
- [379] H. R. Ott, H. Rudigier, Z. Fisk, J. L. Smith, *Phys. Rev. Lett.* **80** (1983) 1595
- [380] S. S. Saxena, P. Agarwal, K. Ahllan, F. M. Grosche, R. W. K. Haselwimmer, M. J. Steiner, E. Pugh, I. R. Walker, S. R. Julian, P. Monthoux, G. G. Lonzarich, A. Huxley, I. Shelkin, D. Braithwaite, J. Flouquet, *Nature* **406** (2000) 587
- [381] R. Joynt, L. Taillefer, *Rev. Mod. Phys.* **74** (2002) 237
- [382] A. Grauel, A. Böhm, H. Fischer, C. Geibel, R. Köhler, R. Modler, C. Schank, F. Steglich, G. Weber, *Phys. Rev. B* **46** (1992) 5818
- [383] T. E. Mason, G. Aeppli, *Matematisk-fysiske Meddelelser* **45** (1997) 231
- [384] M. Jourdan, M. Huth, H. Adrian, *Nature* **398** (1999) 47
- [385] V. Ginzburg, *JETP* **4** (1957) 153
- [386] P. C. Canfield, S. L. Bud'ko, *Physica C* **262** (1996) 249
- [387] D. Fay, J. Appel, *Phys. Rev. B* **22** (1980) 3173
- [388] D. Aoki, A. Huxley, E. Ressouche, D. Braithwaite, J. Flouquet, J.-P. Brison, E. Lhotel, *Nature* **413** (2001) 613
- [389] C. Pfleiderer, *J. Magn. Magn. Mat.* **226-230** (2001) 23
- [390] W. Schlabit, J. Bauman, B. Politt, U. Rauchschwalbe, H. M. Mayer, U. Ahlheim, C. D. Bredl, *Z. Phys. B* **52** (1986) 171
- [391] A. de Visser, F. E. Kayzel, A. A. Menovsky, J. J. M. Franse, J. van der Berg, G. J. Nieuwenhuys, *Phys. Rev. B* **34** (1986) 8168
- [392] C. Broholm, J. K. Kjems, W. J. L. Buyers, P. Matthews, T. T. M. Palstra, A. A. Menovsky, J. A. Mydosh, *Phys. Rev. Lett.* **58** (1987) 1467
- [393] M. B. Walker, W. J. L. Buyers, Z. Tun, W. Que, A. A. Menovsky, J. D. Garrett, *Phys. Rev. Lett.* **71** (1993) 2630
- [394] H. Amitsuka, M. Sato, N. Metoki, M. Yokohama, K. Kuwahara, T. Sakakibara, H. Morimoto, S. Kawarazaki, Y. Miyako, J. A. Mydosh, *Phys. Rev. Lett.* **83** (1999) 5114
- [395] H. Amitsuka, M. Yokoyama, S. Miyazaki, K. Tenya, T. Sakakibara, W. Higemoto, K. Nagamine, K. Matsuda, Y. Kohori, T. Kohara, *Physica B* **312-313** (2002) 390
- [396] H. R. Ott, H. Rudigier, T. M. Rice, K. Ueda, Z. Fisk, J. L. Smith, *Phys. Rev. Lett.* **82** (1984) 1915
- [397] K. Izawa, Y. Nakajima, J. Goryo, Y. Matsuda, S. Osaki, H. Sugawara, H. Sato, P. Thalmeier, K. Maki, *Phys. Rev. Lett.* **90** (2003) 117001
- [398] B. C. Sales, D. Mandrus, R. K. Williams, *Science* **272** (1996) 1325
- [399] B. C. Sales, *Handbook on the Physics and Chemistry of the Rare Earths*, Vol. 33, Elsevier (2003) chapter 211, p. 1
- [400] N. A. Frederick, T. D. Do, P.-C. Ho, N. P. Butch, V. S. Zapf, M. B. Maple, *Phys. Rev. B* **69** (2004) 024523

- [401] R. Vollmer, A. Faißt, C. Pfeleiderer, H. v. Löhneysen, E. D. Bauer, P.-C. Ho, V. Zapf, M. B. Maple, *Phys. Rev. Lett.* **90** (2003) 5700
- [402] N. Oeschler, P. Gegenwart, F. Steglich, N. A. Frederick, E. D. Bauer, M. B. Maple, *Acta Phys. Pol. B* **34** (2003) 959
- [403] A. Hebard, M. J. Rosseinsky, R. C. Haddon, D. W. Murphy, S. H. Glarum, T. T. M. Palstra, A. P. Ramirez, A. R. Kortam, *Nature* **350** (1991) 600;
R. M. Fleming, A. P. Ramirez, M. J. Rosseinsky, D. W. Murphy, R. C. Haddon, S. M. Zahurak, A. V. Markhija, *Nature* **352** (1991) 787
- [404] R. J. Cava, H. Takagi, H. W. Zandbergen, J. J. Krajewski, W. F. Peck, Jr., T. Siegrist, B. Batlogg, R. B. van Dover, R. J. Felder, K. Mizuhashi, J. O. Lee, H. Eisaki, S. Uchida, *Nature* **367** (1994) 252;
- [405] J. Cava, H. Takagi, B. Batlogg, H. W. Zandbergen, J. J. Krajewski, W. F. Peck Jr., R. B. van Dover, R. J. Felder, K. Mizuhashi, J. O. Lee, H. Eisaki, S. A. Carter, S. Uchida, *Nature* **367** (1994) 146
- [406] Z. K. Tang, L. Zhang, N. Wang, X. X. Zhang, G. W. Wen, G. D. Li, J. N. Wang, C. T. Chan, P. Sheng, *Science* **292** (2001) 2462
- [407] G. Amano, S. Akutagawa, T. Muranaka, Y. Zenitani, J. Akimitsu, *J. Phys. Soc. Jpn.* **73** (2004) 530
- [408] T. Nakane, T. Mochiku, H. Kito, J. Itoh, M. Nagao, H. Kumakura, Y. Takano, *Appl. Phys. Lett.* **84** (2004) 2859
- [409] K. Bechgaard, K. Carneiro, M. Olsen, R. B. Rasmussen, C. B. Jacobsen, *Phys. Rev. Lett.* **46** (1981) 852
- [410] P. A. Mansky, G. Danner, P. M. Chaikin, *Phys. Rev. B* **52** (1995) 7554
- [411] G. Saito, H. Yamochi, T. Nakamura, T. Komatsu, M. Nakashima, H. Mori, K. Oshima, *Physica B* **169** (1991) 372
- [412] I. J. Lee, S. E. Brown, W. G. Clark, M. J. Strouse, M. J. Naughton, W. Kang, P. M. Chaikin, *Phys. Rev. Lett.* **88** (2002) 017004
- [413] C. H. Pennington, V. A. Stenger, *Rev. Mod. Phys.* **68** (1996) 855
- [414] V. Buntar, H. W. Weber, *Supercond. Sci. Technol.* **9** (1996), 599
- [415] R. Nagarajan, C. Mazumdar, Z. Hossain, S. K. Dhar, K. V. Gopalakrishnan, L. C. Gupta, C. Godart, B. D. Padalia, R. Vijayaraghavan, *Phys. Rev. Lett.* **72** (1994) 274
- [416] G. Hilscher, H. Michor, *Studies in High Temperature Superconductors*, Vol. 28, Nova Science Publishers (1999) pp. 241–286
- [417] K.-H. Müller, V. N. Narozhnyi, *Rep. Prog. Phys.* **64** (2001) 943
- [418] O. Fischer, *Magnetic Superconductors*, Vol. 5, North Holland, Amsterdam (1990)
- [419] *Topics in Current Physics* (Eds. O. Fischer & M. B. Maple), Vol. 32 and 34, Springer Verlag, Berlin (1982)
- [420] K. Mizuno, T. Saito, H. Fudo, K. Koyama, K. Endo, H. Deguchi, *Physica B* **259-261** (1999) 594
- [421] E. Boaknin, R. W. Hill, C. Proust, C. Lupien, L. Taillefer, P. C. Canfield, *Phys. Rev. Lett.* **87** (2001) 237001

- [422] K. Izawa, K. Kamata, Y. Nakajima, Y. Matsuda, T. Watanabe, M. Nohara, H. Takagi, P. Thalmeier, K. Maki, *Phys. Rev. Lett.* **89** (2002) 137006
- [423] M. Nohara, M., Isshiki, H., Takagi, R. Cava, *J. Phys. Soc. Jpn.* **66** (1997) 1888
- [424] K. Maki, P. Thalmeier, H. Won, *Phys. Rev. B* **65** (2002) 140502
- [425] T. Watanabe, M. Nohara, T. Hanaguri, H. Takagi, 2003, preprint
- [426] S. -L. Drechsler, H. Rosner, S. V. Shulga, I. Opahle, H. Eschrig, J. Freudenberger, G. Fuchs, K. Nenkov, K. -H. Müller, H. Bitterlich, W. Löser, G. Behr, D. Lipp, A. Gladun, *Physica C* **364-365** (2001) 31
- [427] H. Suderow, P. Martinez-Samper, N. Luchier, J. P. Brison, S. Vieira, P. C. Canfield, *Phys. Rev. B.* **64** (2003) 020503
- [428] S. L. Bud'ko, P. C. Canfield, V. G. Kogan, *Physica C* **382** (2002) 85
- [429] P. Grant, *Nature* **411** (2001) 532
- [430] A. M. Campbell, *Science* **292** (2001) 65
- [431] R. F. Service, *Science* **291** (2001) 1476
- [432] R. F. Service, *Science* **291** (2001) 2295
- [433] S. Tomlin, *Nature* **410** (2001) 407
- [434] J. Kortus, I. I. Mazin, K. D. Belashchenko, V. P. Antropov, L. L. Boyer, *Phys. Rev. Lett.* **86** (2001) 4656
- [435] K.-P. Bohnen, R. Heid, B. Renker, *Phys. Rev. Lett.* **86** (2001) 5771
- [436] H. J. Choi, D. Roundy, H. Sun, M. L. Cohen, S. G. Louie, *Nature* **418** (2002) 758
- [437] P. C. Canfield, G. Crabtree, *Phys. Today* **56** (March 2003) 34
- [438] Y. Kong, O. V. Dolgov, O. Jepsen, O. K. Andersen, *Phys. Rev. B* **64** (2001) 020501
- [439] G. Binnig, A. Baratoff, H. E. Hoenig, J. G. Bednorz, *Phys. Rev. Lett.* **45** (1980) 1352
- [440] I. I. Mazin, O. K. Andersen, O. Jepsen, A. A. Golubov, O. V. Dolgov, J. Kortus, *Phys. Rev. B* **69** (2004) 056501
- [441] H. J. Choi, D. Roundy, H. Sun, M. L. Cohen, S. G. Louie, *Phys. Rev. B* **69** (2004) 056502
- [442] M. Naito, K. Ueda, *Supercond. Sci. Technol.* **17** (2004) R1
- [443] W. Goldacker, this volume
- [444] X. X. Xi, A. V. Pogrebnnyakov, X. H. Zeng, J. M. Redwing, S. Y. Xu, Qi Li, Zi-Kui Liu, J. Lettieri, V. Vaithyanathan, D. G. Schlom, H. M. Christen, H. Y. Zhai, A. Goyal, *Supercond. Sci. Technol.* **17** (2004) S196

SUPERCONDUCTIVITY AT ULTRALOW TEMPERATURES AND ITS INTERPLAY WITH NUCLEAR MAGNETISM

T. Herrmannsdörfer and F. Pobell

Forschungszentrum Rossendorf, D-01314 Dresden, Germany*

1. INTRODUCTION

In this article we will describe experiments at microkelvin temperatures which were performed to give – at least partly – answers to the following questions:

- a. will all nonmagnetic metals become superconducting if refrigerated to low enough temperatures,
- b. what is the impact of the weakest version of magnetism, nuclear magnetism, on superconductivity.

a. The first question has intrigued low temperature physicists since the discovery of superconductivity by H. Kamerlingh-Onnes in 1911. He wrote already in 1913 “There is left little doubt that if Au and Pt could be obtained absolutely pure, they could also pass into the superconducting state at helium temperatures”. And in 1929 W. Meissner wrote “At present it does not seem unlikely that, opposite to former expectations, all metals will become superconducting at low enough temperature”. One can pose the question in more general terms: “Is the electron-phonon interaction or another possible pairing mechanism in all metals strong enough so that they will eventually become superconducting, if this transition is not hindered by other phenomena, like magnetic properties?” After all, somehow the conduction electrons have to get rid of their entropy when approaching absolute zero, and one way is a transition to a superconducting state.

Looking at the periodic system of the elements (Fig.1), one realizes that superconductivity is rather the rule than the exception. Most metallic elements become superconducting if they show no magnetic order like some 3d- and 4f-elements. Even most insulators, like S or O, if

* The experiments described in this article have been performed at the Forschungszentrum (formerly: Kernforschungsanlage) Jülich and at the University of Bayreuth.

| | | | | | | | | | | | | | | | | | |
|----|----|----|----|----|----|----|----|----|----|----|----|----|----|----|----|----|----|
| H | | | | | | | | | | | | | | | | | He |
| Li | Be | | | | | | | | | | | B | C | N | O | F | Ne |
| Na | Mg | | | | | | | | | | | Al | Si | P | S | Cl | Ar |
| K | Ca | Sc | Ti | V | Cr | Mn | Fe | Co | Ni | Cu | Zn | Ga | Ge | As | Se | Br | Kr |
| Rb | Sr | Y | Zr | Nb | Mo | Tc | Ru | Rh | Pd | Ag | Cd | In | Sn | Sb | Te | I | Xe |
| Cs | Ba | La | Hf | Ta | W | Re | Os | Ir | Pt | Au | Hg | Tl | Pb | Bi | Po | At | Rn |
| Fr | Ra | Ac | | | | | | | | | | | | | | | |

| | | | | | | | | | | | | | |
|----|----|----|----|----|----|----|----|----|----|----|----|----|----|
| Ce | Pr | Nd | Pm | Sm | Eu | Gd | Tb | Dy | Ho | Er | Tm | Yb | Lu |
| Th | Pa | U | Np | Pu | Am | Cm | Bk | Cf | Es | Fm | Md | No | Lw |

Fig. 1. Periodic system of the elements. \square : magnetically ordering; \blacksquare : superconducting; \square with diagonal lines : superconducting under pressure; \bigcirc : investigated at ultralow temperatures and discussed in this article.

forced into a metallic state by high pressure, eventually enter the superconducting state. When we started our research, there were only two small “islands” in the periodic system of the elements where metals had shown neither a superconducting nor a magnetic transition: some alkali and alkaline-earth metals and the noble and platinum metals (Cu, Ag, Au, Rh, Pd, Pt).

Until the beginning of the eighties of the last century, the lowest superconducting transition temperatures observed were 15.4 mK for the element W [1] and 6 mK for alloys (Ir-Rh, [2]). However, at the end of the 1970s, the microkelvin temperature range had become accessible by adiabatic nuclear refrigeration [3]. Hence, one of us (F.P.) started a program to investigate the low temperature state of the noble and platinum metals; the results of this research will be described in Sects. 3 and 4 of this article.

b. Superconductivity in its simplest version – s-wave, singlet pairing of conduction electrons mediated by electron-phonon interaction – is counteracted by magnetic interactions. This has been well demonstrated by the depression of the superconducting transition temperature when magnetic impurities are introduced [4]. The large variety of “magnetic interactions” has varying impacts on superconductivity. The clearest demonstration of its detrimental impact is the vanishing of the superconducting state when a superconducting metal enters a ferromagnetic state. This was demonstrated in 1977 by Matthias et al. for ErRh_4B_4 and by Ishikawa and Fischer for HoMo_8S_8 [5].

The weakest known version of magnetism is caused by the interaction of nuclear magnetic moments. Hence, it was a natural question to investigate the impact of *nuclear* ferromagnetism on superconductivity. This investigation became possible when we had observed a nuclear ferromagnetic transition of the superconductor AuIn_2 at 35 μK in 1994 [6]. The results of the investigation of the interplay between *nuclear ferromagnetism* and

superconductivity in AuIn₂ [7] – some of it are not yet understood – will be described in Sect. 5. Further investigations of the impact of *nuclear paramagnetism* in AuAl₂, Al, Sn, AuIn₂, In, Rh, as well as TiH_{2+x} on superconductivity are discussed in Sect. 6. In Sect. 7, a first study of the interplay of *hyperfine enhanced nuclear magnetism* and superconductivity is presented. Eventually, in Sect. 8, we will summarize our results.

However, before starting with the discussion of the experimental results we will give a short review of the experimental methods of our microkelvin research.

2. EXPERIMENTAL METHODS AT MICROKELVIN TEMPERATURES

The experiments to be described in this article have been performed in the double-stage nuclear refrigerators at the Forschungszentrum (formerly: Kernforschungsanlage) Jülich [8] and at the University of Bayreuth [9]. They were the most powerful refrigerators for the microkelvin temperature range, with minimum temperatures of 38 μ K achieved in Jülich in 1979 [8], as well as 12 μ K in 1987 [9] and 1.5 μ K in 1995 [10] in Bayreuth. All these temperatures as well as all the temperatures mentioned in this article are equilibrium temperatures ($T_{\text{electron}}=T_{\text{phonon}}=T_{\text{nuclei}}$) measured at metallic samples refrigerated in these apparatus.

For thermometry in our experiments, we used NMR thermometers ($f = 62.5, 125, \text{ or } 250$ kHz) made of 25 μ m Pt wire and mounted on a cold finger on the nuclear refrigeration stage. The Pt nuclear susceptibility is calibrated by the electronic susceptibility of a $\text{Pd} + 15$ ppm Fe spin glass at $T > 10$ mK [3, 9]. This spin glass thermometer eventually is calibrated by five superconducting transitions at 15 mK $< T < 200$ mK of the calibrated commercial superconductive fixed point device SRM 768 of NIST [3, 8, 9].

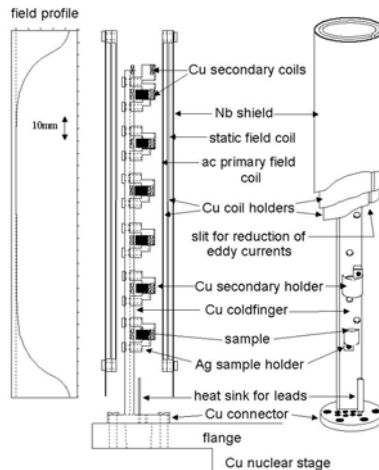


Fig. 2. Schematics of the ac susceptometer, designed for six samples, which is screwed to the top flange of the Cu nuclear stage of the nuclear demagnetization refrigerator. The empty secondary coil on top of the cold finger is used as a reference. In addition, the calculated static field profile is shown. See Ref. [18].

In the susceptibility (Fig. 2), magnetization and transport (Fig. 3) experiments, one end of the samples was screwed, clamped, or glued under pressure with silver containing epoxy (in the case of brittle samples) to a Ag or Cu cold finger connected to the refrigerating Cu nuclear stage of the refrigerator. In the heat capacity measurements (Fig. 4), in addition a superconducting Al foil heat switch to thermally couple or decouple the sample to or from the nuclear stage and a separate Pt-NMR thermometer to measure the temperature of the sample have been used.

A pick-up coil around but not in thermal contact to the free end of the samples was used to measure their low-frequency ac susceptibility. In most cases we used the highly sensitive commercial mutual induction bridges LR 400 or LR 700. In the case of tiny signals, a flux transformer connected to a SQUID sensor served as the input circuit. As the critical magnetic fields of the very-low- T_c samples are very small, careful magnetic shielding by a combination of superconducting field compensation coils, superconducting Nb, and soft magnetic “degaussed” Cryoperm shields to measured values of below $0.1 \mu\text{T}$ was arranged in the “hostile” high-field environment of our nuclear refrigerators.

Several hours or – at the lowest temperatures – even days have been waited to assure thermal equilibrium between nuclear stage, samples, and thermometers. Details of the refrigeration, thermometry, and measuring techniques can be found in our relevant publications, in particular Refs. [3, 6, 8, 9].

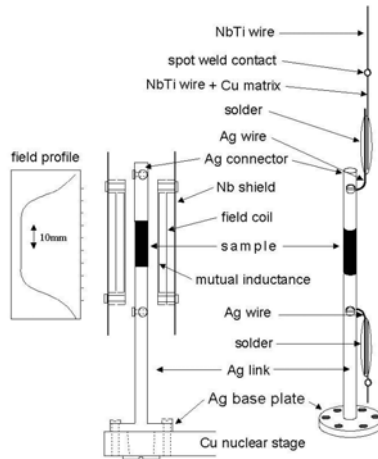


Fig. 3. Schematics of the resistivity setup and field profile. In order to minimize the electrical contact resistances in the current joints as well as to isolate the sample from parts of the cryostat at higher temperatures, thin superconducting NbTi wires are used for the leads of current and voltage. Smallest contact resistances for the current input have been achieved by spot welding NbTi wire to a NbTi wire with copper matrix which is then soldered to 1 mm diameter Ag wire screwed to Ag connectors glued with Ag containing epoxy to the sample. In addition to resistance, ac susceptibility can be measured simultaneously using the mutual inductance coils installed inside the shielded superconducting static field coil.

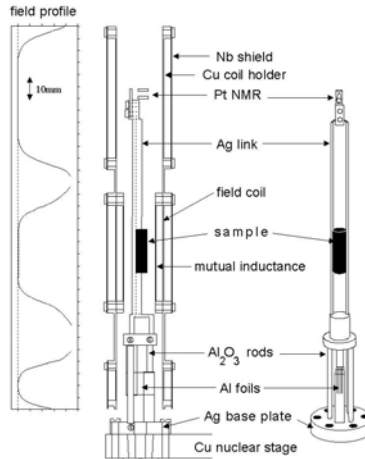


Fig. 4. Schematics of the calorimeter and field profile. There are three separately shielded superconducting static field coils for the superconducting Al foil heat switch, the sample, and the Pt NMR thermometer. In addition to heat capacity measurements (heat pulses are applied by a tiny PtW wire heater glued to the sample), ac susceptibility can be measured simultaneously using the mutual inductance coils installed inside of the shielded superconducting static field coil. See Ref. [6].

3. THE NOBLE METALS Cu, Ag, Au

A superconducting transition of noble metals – if it occurs – can only be expected at very low temperatures because of their weak electron-phonon interaction and their small s-electron density of states at the Fermi energy.

3.1 Gold

Gold was one of the first metals whose metallic resistance was investigated by Kamerlingh-Onnes at the beginning of the last century. He as well as Meissner and Voigt in the thirties of the last century did not find a superconducting transition down to about 1 K. In 1974, Buhman and Halperin could show that T_c of Au is below 2 mK [11]. Eventually in 1976, Hoyt and Mota extrapolated from their investigations of $Au_{1-x}In_x$, $Au_{1-x}Ga_x$, and $Au_{1-x}Al_x$ alloys with $x \geq 6\%$ and at $T_c > 8$ mK that T_c of Au should be at around 0.2 mK [12]. We have investigated samples to higher Au concentrations and lower temperatures with the following results (Fig. 5), [13]:

| | | |
|------------------------|---|------------------------------|
| $Au_{0.9}In_{0.1}$ | : | $T_c = 77$ mK |
| $Au_{0.915}In_{0.085}$ | : | $T_c = (31 \pm 1)$ mK |
| $Au_{0.978}In_{0.022}$ | : | $T_c = (500 \pm 70)$ μ K |
| $Au_{0.99}In_{0.01}$ | : | $T_c < 55$ μ K |
| Au | : | $T_c < 38$ μ K. |

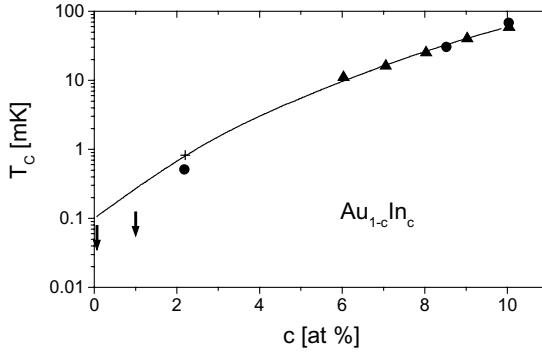


Fig. 5. Superconducting transition temperatures of Au-In alloys. (\blacktriangle) are data by Hoyt and Mota (12), (\bullet) denote measured T_c -values for our samples, (+) indicates $T_{c,0}$ for our sample calculated from measured T_c and dB_c/dT (see text). The sample ($c = 1\%$) was not superconducting at $T \geq 55 \mu\text{K}$, the Au samples were not superconducting at $T \geq 38 \mu\text{K}$. The line is the BCS-extrapolation of [12]. See Ref. [13].

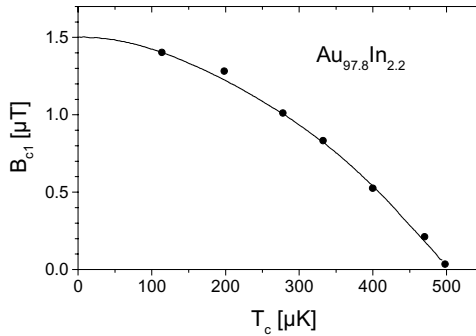


Fig. 6. Measured critical field as a function of temperature for $\text{Au}_{97.8}\text{In}_{2.2}$. The line is $B_{c1} = B_{c1}(0)(1 - T^2/T_c^2)$. See Ref. [13].

The 3d-impurity concentrations were Fe(2 ± 1 ppm), Cr(1.4 ppm), Mn(0.2 ppm), Co(<1 ppm), Ni (< 1ppm) for the alloys, and Fe(1.4 ppm), Ni(< 0.4 ppm), Co(< 0.1 ppm), Mn(< 0.1 ppm) for the Au sample [13]. After annealing this Au sample in air, a RRR = 10.000 was obtained. A second, even purer investigated sample had a RRR = 70.000.

To investigate the dependence of T_c of our samples on the 3d-impurity concentrations, we have measured T_c of $\text{Au}_{0.9}\text{In}_{0.1}$ with various Fe concentrations as well as the $B_c(T)$ curve of $\text{Au}_{0.978}\text{In}_{0.022}$ (Fig. 6). Correcting the measured T_c -values of the alloys with $x \geq 2.2\%$ for the depression of T_c by 3d-impurities and extrapolating these values to $x = 0$, we expect $T_c = 100$

μK for pure Au. However, even sub-ppm concentrations of 3d-impurities may be enough to depress T_c of Au with its very weak electron-phonon-interaction to below $38 \mu\text{K}$ and of $\text{Au}_{0.99}\text{In}_{0.01}$ to below $55 \mu\text{K}$.

3.2 Copper and Silver

Hoyt and Mota [12] had shown that T_c – values of $\text{Cu}_{1-x}\text{Ga}_x$ and $\text{Ag}_{1-x}\text{Ga}_x$ alloys are below the corresponding values of $\text{Au}_{1-x}\text{Ga}_x$ at the same x . Hence, very likely, T_c 's of pure Cu and Ag are below $T_c(\text{Au})$. Because we did not observe the latter value in the accessible temperature range, it was not meaningful to search for $T_c(\text{Cu or Ag})$. Furthermore, in almost every of our experiments performed to low μK temperatures, pure Cu or Ag sample holders, heat sinks or other parts of the setups were involved. From none of these parts we have received hints (through stray signals, changes in thermal conductivity etc.) for superconductivity in these metals. Anyway, the discussed experiments seem to indicate that the weak electron-phonon interaction in very pure Au is strong enough to make this element superconducting with $T_c = 100 \mu\text{K}$, and that $T_c(\text{Ag, Cu}) < 10 \mu\text{K}$.

4. THE PLATINUM METALS Rh, Pd, Pt

The possible superconducting transition in noble metals occurs at very low temperatures due to their weak electron-phonon interaction and small s-electron density of states at the Fermi energy. The situation is completely different in the platinum metals. They have a substantial electron-phonon interaction and a rather high d-electron density of states at the Fermi energy. Hence, one might expect a superconducting transition at Kelvin temperatures. The absence of superconductivity of them at these temperatures therefore must have other reasons.

All these elements show strongly exchange-enhanced Pauli paramagnetism, with Stoner enhancement factors of 2.2, 4.1, 10 for Rh, Pt, Pd, respectively, and the last one is very close to a ferromagnetic transition. The associated spin - fluctuations in the platinum metals are supposed to be detrimental for their superconductivity. As a result, Webb et al. in 1978 did not observe superconducting transitions of them to 1.7 mK [14]. We have investigated the properties of these metals in more detail at microkelvin temperatures.

4.1 Rhodium

Mota et al. had investigated the superconducting transitions of Rh-Ir and Rh-Os alloys to 6 mK [2]. From their data, they extrapolated to a $T_c(\text{Rh}) \sim 0.2 \text{ mK}$. We have searched for a superconducting transition of pure Rh in the microkelvin temperature range [15].

Various Rh samples with different impurity concentrations and different annealing treatments were investigated. The one with the highest RRR (450) showed a sharp superconducting transition and a fully developed Meissner effect. As the data at $160 \mu\text{K}$ in Fig. 7 demonstrate, this sample shows strong supercooling effects. It supercools to a field of only $0.2 \mu\text{T}$ which is more than an order of magnitude lower than its critical field. This observation is expected for a first order transition at such a low temperature and with the small Ginzburg-Landau parameter $\kappa \sim 10^{-2}$ of Rh.

The $B_c(T)$ values measured at $65 \mu\text{K} \leq T \leq 265 \mu\text{K}$ for this as well as for a sample with $\text{RRR}=130$ are shown in Fig. 8. They extrapolate to $T_c(0) = (325 \pm 10) \mu\text{K}$ and $B_c(0) = (4.9 \pm 0.2) \mu\text{T}$, by far the lowest values ever measured for a superconducting element and three orders of magnitude lower than for its neighbouring elements Ir and Ru.

The BCS coherence length $\xi_0 = v_{\text{Fermi}} \cdot \tau \sim 1\text{mm}$ is much larger than the electronic mean free path of about $3 \mu\text{m}$ in these samples [15]. Hence, they are type I superconductors in the dirty limit. A further analysis of the properties of Rh showed that spin fluctuations may contribute $\lambda_{\text{sf}} \sim 0.1$ to the total mass enhancement $\lambda = 0.44$ of Rh. Taking this into account, one may expect $T_c(\text{Rh}) \sim 0.5 \text{ K}$ if spin fluctuations could be suppressed.

Superconductivity in these samples was observed in spite of the rather high concentration of 3d-impurities (Fe: ~ 15 ppm; others: several ppm). This is probably due to the fact that 3d-elements form no or very small local moments in Rh [16]. Our analysis showed that – opposite to the noble metals – the impurities depress T_c of Rh only slightly, possibly from about 500 to 600 μK to the observed 325 μK [15]. However, at higher impurity concentrations, both T_c as well as the supercooling effects were strongly affected; a sample containing about 100 ppm Fe showed no transition at $T > 65 \mu\text{K}$.

In their investigations of nuclear magnetic interactions in nuclear spin polarized Rh (see also Chap. 6f), Knuuttila et al. could confirm superconductivity of Rh (99.99%; 10 to 15 ppm Fe; $\text{RRR} = 740$) at $60 \mu\text{K} < T_c < 140 \mu\text{K}$, extrapolating to $T_c(0) = 210 \mu\text{K}$ and $B_c(0) = 3.4 \mu\text{T}$ [17]. These lower values than the ones observed by Buchal et al. [15] and the absence of superconductivity of Rh in the earlier Helsinki experiments confirm the strong supercooling and the dependence of $T_c(\text{Rh})$ on the quality of the sample.

4.2 Palladium

Palladium is the metallic element with the strongest Stoner enhancement factor $S = 10$; it is almost ferromagnetic. Opposite to Rh, Fe impurities create giant moments in their polarized Pd surrounding with moments of up to $(15 \pm 1) \mu_B$; these giant moments show spin glass freezing at millikelvin temperatures (Fig. 9) [18]. However, even below the spin glass freezing temperature of the giant moments, no superconducting transition was observed – even in our “cleanest” samples with only 2.2 and 2.5 ppm Fe, respectively, to a temperature of 35 μK [15, 18].

Gyorffy et al. had predicted that the addition of Ag to Pd – which diminishes the d-electron density of states at the Fermi energy - should evoke superconductivity at $T > 10 \text{ mK}$ [19]. However, we could not observe a superconducting transition even to $T \sim 0.1 \text{ mK}$ in high-purity $\text{Pd}_{1-x}\text{Ag}_x$ for $0.065 \leq x \leq 0.55$ [20]. On the other hand, alloying Pd with H or irradiating it at helium temperatures – both procedures supposedly also reduce the electronic density of states at the Fermi energy – lead to superconductivity at 9 K and 3 K, respectively [21].

4.3 Platinum

Platinum is the element which we have refrigerated to the lowest equilibrium temperature ever achieved in condensed matter. In these experiments a sample of $\text{Pt Fe}_{11\text{ppm}}$ was refrigerated to an equilibrium temperature of 1.5 μK (and a nuclear spin temperature of 0.2 μK), (Fig. 10) [10]. Neither for this nor for other bulk Pt samples refrigerated to low

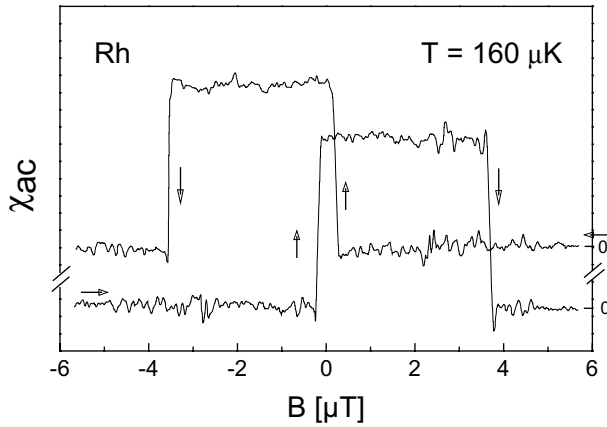


Fig. 7. Susceptibility of Rh as a function of applied field at $160 \mu\text{K}$. The vertical axis shows two shifted traces of the pickup signal amplitude in arbitrary units. The upper trace is a slow sweep ($1 \mu\text{T}/\text{min}$) from $+6 \mu\text{T}$ to $-6 \mu\text{T}$, and the lower one runs in the reverse direction. The ac drive field had an amplitude of 1.2 nT rms at 11 Hz . Note the strong supercooling and the sharp transitions. See Ref. [15].

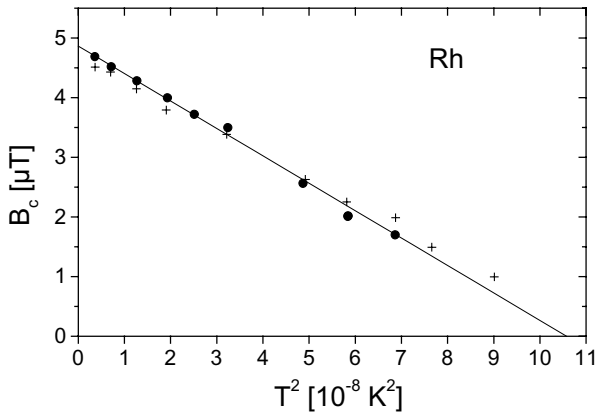


Fig. 8. Critical magnetic field data for two Rh samples. The straight line is given by $B_c(T)/B_c(0) = 1 - T^2/T_c^2$ with $B_c(0) = 4.9 \mu\text{T}$ and $T_c = 325 \mu\text{K}$. See Ref. [15].

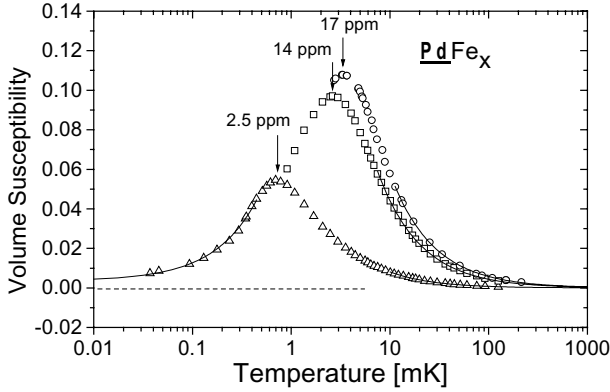


Fig. 9. Real part χ' of the volume ac(16 Hz) susceptibility of PdFe_x ($x = 2.5, 14, 17$ ppm) versus temperature at $40 \mu\text{K} \leq T \leq 200$ mK. The spin glass freezing temperature T_f (temperature of maximum) scales with impurity concentration x . The high temperature behaviour at $T > 9$ mK follows a Curie-Weiss law with small Weiss temperatures $\theta \simeq 0.1 T_f$. The low temperature behaviour at $T < T_f/2$ follows $\chi'(x, T) = \chi'_0(x) + \alpha T$. The horizontal dashed line indicates $\chi'_0 = 0$ for comparison. See Ref. [18].

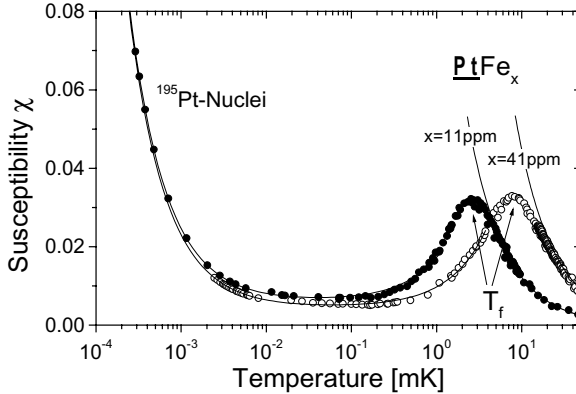


Fig. 10. Ac(16 Hz) susceptibility of PtFe_x ($x = 11$ and 41 ppm). The solid lines at $T > T_f$, where T_f is the freezing temperature of the giant electronic magnetic moments of the impurities, show the Curie behaviour. The Curie constants, determined in a SQUID magnetometer at $1.6 \leq T \leq 40$ K, are used to calibrate the data at lower temperatures. The solid lines at $T < 50 \mu\text{K}$ show the Curie behaviour of the ^{195}Pt nuclei. At $T < 1.5 \mu\text{K}$, the nuclear susceptibility data refer to temperatures of the nuclear spin system only, whereas at $T \geq 1.5 \mu\text{K}$ the Pt samples have been studied in their thermal equilibrium, $T_{\text{nuclear}} = T_{\text{electron}} = T_{\text{phonon}}$. See Ref. [10].

microkelvin temperatures we did observe a superconducting (or nuclear spin) transition. However, superconductivity surprisingly was observed at millikelvin temperatures in platinum powder as discussed in the next section.

4.4 Platinum Powder

Platinum powder is a favorite material for the construction of ultralow-temperature heat exchangers with very large surface areas [3]. For this application, various properties of compacted Pt powders were investigated. In investigations of how the magnetic properties of Ag and Pt powder containing a few ppm Fe might assist in cooling liquid ^3He via magnetic coupling [3, 22], as a great surprise superconductivity was observed in compacted Pt powder with an average grain size of $2\mu\text{m}$ at $T_c = 1\text{ mK}$ (Fig. 11), [23].

An investigation of the magnetic properties of purest available Pt powders in the Kelvin temperature range gave a first indication that the magnetic behaviour of 3d impurities in Pt grains is different to that in bulk platinum although the Stoner enhancement, $S(\text{Pt}) = 4$, has been found unchanged. Compared to bulk platinum in which Fe giant magnetic moments of $8\mu_B$ with an infinite spin quantum number have been found [18], in Pt powders 3d impurity induced moments with only about $6\mu_B$ and a finite average spin quantum number $J \simeq 4$ have been observed. Extending the magnetic study to the mK temperature range showed that the impurity magnetism of compacted Pt powder is clearly weakened (Fig. 11) compared to bulk Pt; the ac susceptibility of compacted granular Pt is about one order of magnitude smaller at mK temperatures. Moreover, the spin glass behaviour of PtFe (which in the bulk case is very similar to PdFe at millikelvin temperatures, see Fig. 10, [18]) is clearly affected in compacted granular Pt. A first significant drop of the ac susceptibility occurs at about 2 mK, whereas a clear transition from the tiny paramagnetic susceptibility to perfect diamagnetism, i.e. $\chi = -1$, occurs at $T_c = 1\text{ mK}$. This result has then been confirmed by measurements of electrical conductivity (Fig.12) and magnetization, the latter showing the full Meissner effect of the sample [23].

The weakened impurity magnetism in powdered Pt may play the crucial role in adjusting the balance between electron-phonon interaction and competing magnetic interactions. As a proof we have also investigated Pt powders with a higher impurity content observing lower T_c values. However, due to the large surface area of the order of $1\text{ m}^2/\text{g}$ also acoustic properties could be of importance for the creation of superconductivity in compacted granular Pt; additional so called “soft phonon modes” (lower frequency phonons at the surface) could influence the electron-phonon interaction. The enhancement of the electron-phonon interaction and the related increase of the superconducting transition temperature by granularity has already been reported for other systems [24]. In agreement with this interpretation, we found that the superconducting transition temperature strongly depends on the packing fraction $f = V_{\text{Pt}}/V_{\text{sample}}$ and related surface area of the compacted powder. Performing experiments on samples with $0.50 \leq f \leq 0.80$, we observed superconducting transition temperatures $1.38\text{ mK} \geq T_c \geq 0.62\text{ mK}$. In addition, the critical magnetic field of superconductivity strongly varies as function of the packing fraction in these experiments in the range $67\mu\text{T} \geq B_c \geq 7\mu\text{T}$ [23].

In further susceptibility measurements, where the ac amplitude has been varied, we have been able to distinguish between intragranular (within single grains) and intergranular (whole sample becomes superconducting) transitions of our granular Pt compacts [25]. Similar

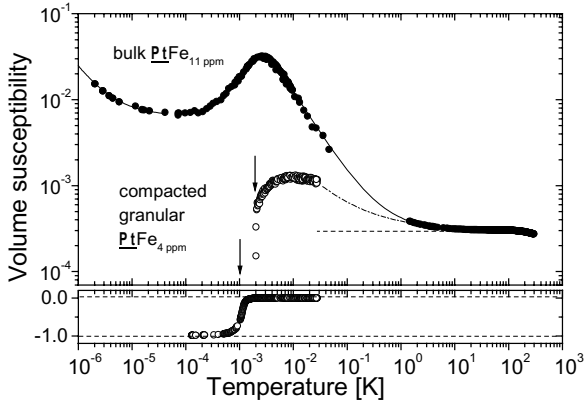


Fig. 11. Ac(16 Hz) susceptibility (at $T < 0.1\text{K}$) and static susceptibility measured in a SQUID magnetometer (at $T > 1\text{K}$) of bulk $\text{PtFe}_{11\text{ppm}}$ compared to the results for compacted granular $\text{PtFe}_{4\text{ppm}}$ of $2\ \mu\text{m}$ grains on a logarithmic scale. In the lower frame, the superconducting transition of the compacted $\text{PtFe}_{4\text{ppm}}$ powder is shown separately on a linear scale for the susceptibility. The arrows mark the onset of the strong decrease of susceptibility (at 2 mK) and the jump to $\chi = -1$ (at 1 mK). The horizontal dashed line indicates the Stoner enhanced susceptibility of Pt at Kelvin temperatures.

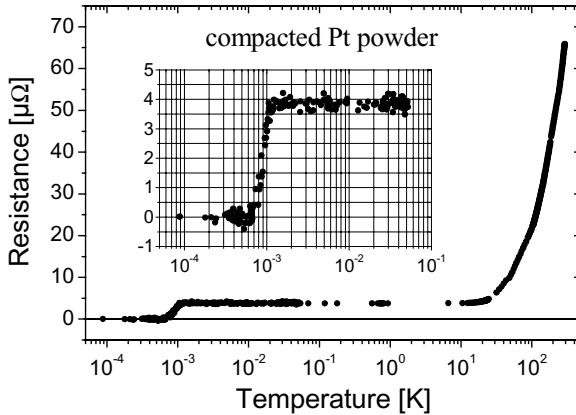


Fig. 12. Ac(16 Hz) resistance of compressed $\text{PtFe}_{4\text{ppm}}$ powder cooled from room temperature to ultralow temperatures. The nominal purity of the used Pt powder is 99.999%. The $2\ \mu\text{m}$ grains have been compacted for 1 hour to a packing fraction $V_{\text{Pt}}/V_{\text{sample}} = 63.3\%$. From the data we receive $\text{RRR} = 17$, $\text{RR} = 3.8\ \mu\Omega$. In the inset, the superconducting transition is shown in more detail. See Ref. [23].

features have already been observed and discussed for granular cuprate high- T_c superconductors [26].

In recent experiments performed on samples with a distinctively smaller - submicrometer - grain size we have observed an enhancement of T_c of up to 20 mK [27]. For a deeper understanding of superconductivity in compacted granular Pt, further investigations are necessary in which the impact of the magnetic (controlled variation of concentration and type of magnetic impurities), microscopic structural (grain size and crystal quality), topological (surface roughness), and macroscopic structural parameters (packing fraction) have to be investigated independently from each other.

We have extended these studies to other metal powders, e.g. Ag, Au, Pd without observing superconductivity at temperatures down to 0.1 mK. In the case of Ag [22] and Pd, the magnetic purity was even better than in the investigated Pt compacts.

5. NUCLEAR FERROMAGNETISM AND ITS INTERPLAY WITH SUPER-CONDUCTIVITY IN AuIn_2

5.1 Nuclear Ferromagnetic Ordering of In nuclei in AuIn_2

Because of the typically 10^6 times lower characteristic temperatures for nuclear magnetic phenomena compared to their electronic counterparts, spontaneous *nuclear* magnetic ordering occurs at extremely low temperatures. In metals it had been reported only for two representatives from two quite different groups. Nuclear antiferromagnetic transitions have been observed for Ag and Cu at nanokelvin *nuclear spin* temperatures [28]. In these experiments, the rather weak conduction electron – nuclear coupling allowed refrigeration of the nuclear spins only to the required nanokelvin temperatures while leaving the conduction electrons at typically 100 μK . The other group are the hyperfine-enhanced van Vleck paramagnets, PrCu_6 and PrNi_5 for example, where the Pr nuclear moments induce an electronic magnetic moment in the singlet ground state of Pr. The resulting coupled electron-nuclear system has been observed to order ferromagnetically at $0.1 \leq T \leq 2.5$ mK in thermal equilibrium of the subsystems ($T_{\text{nuclear}} = T_{\text{electron}} = T_{\text{phonon}}$)[29].

The large nuclear magnetic moment ($\mu = 5.5 \mu_n$) and nuclear spin ($I = 9/2$) as well as its small Korringa constant ($\kappa = 0.09$ Ks) make In, in principle, a favorable candidate for studying nuclear magnetic ordering phenomena at thermal equilibrium in the sample. Unfortunately, the large nuclear electric quadrupole interaction in tetragonal In and its rather high superconducting critical field of 28 mT are severe obstacles (see Sect. 6e) for the investigation of a spontaneous nuclear magnetic phase transition. To avoid these disadvantages, one can study In in the *cubic* intermetallic compound AuIn_2 , which has a superconducting critical field of only 1.45 mT (for its properties see Tab. 1). Because of its small nuclear magnetic moment ($\mu = 0.14\mu_n$), the contribution of Au to the nuclear magnetic interactions in AuIn_2 is negligible. Fortunately, the Korringa constant of In in AuIn_2 is similarly small as in pure In, indicating a similar strength for the conduction electron-nuclear coupling.

In 1995, we could report on the first observation of a spontaneous nuclear magnetic ordering transition in a “simple”, not-hyperfine-enhanced metal with $T_{\text{nuclear}} = T_{\text{electron}} = T_{\text{phonon}}$. By measuring nuclear heat capacity, nuclear ac susceptibility, and nuclear magnetic

resonance for In nuclei in AuIn_2 at $30 \mu\text{K} \leq T \leq 10 \text{ mK}$ and $2 \leq B \leq 115 \text{ mT}$ we observed its nuclear magnetic ordering at $35 \mu\text{K}$ [6]. The nuclear magnetization deduced from the NMR amplitude, the nuclear ac susceptibility, and the nuclear heat capacity are shown in Figs. 13 and 14. Particularly convincing are the specific heat data taken in the smallest external field 2 mT, where they reach a maximum value of 58 J/mol K , which is almost 3 orders of magnitude larger than the value for noninteracting In moments [6]. These data give a nuclear Weiss temperature $\Theta = (+43 \pm 11) \mu\text{K}$, a nuclear magnetic Curie temperature $T_{\text{cn}} = (35 \pm 3) \mu\text{K}$, and an internal field in the nuclear paramagnetic state of 7 mT. The positive nuclear Weiss temperature indicates that the magnetic interactions between the nuclear moments of In in AuIn_2 are dominantly ferromagnetic. The ferromagnetic tendency is also supported by a calculation of the exchange sum in a simple free electron model [6]. The ratio $T_{\text{cn}} / \Theta \cong 0.82$ is in good agreement with the value 0.72 calculated for a Heisenberg ferromagnet with simple cubic symmetry and with large spin.

Nuclear dipolar interactions between In nuclei in AuIn_2 are only of order $1 \mu\text{K}$. Hence the interactions causing the spontaneous nuclear ferromagnetic transition at $35 \mu\text{K}$ must be strong indirect Ruderman-Kittel exchange interactions between the In nuclei mediated by the conduction electrons. This is confirmed by the small Korringa constant $\kappa = 0.112 \text{ K s}$.

Our AuIn_2 samples for these as well as the samples of the experiments described in the following section were prepared by melting Au (99.999%, only detected impurities 1 ppm Ag and 2.5 ppm Si) and In (99.9999%) in a graphite crucible. The samples were annealed for 40 h at 420°C , resulting in residual resistivity ratios of up to 550. From measurements of the

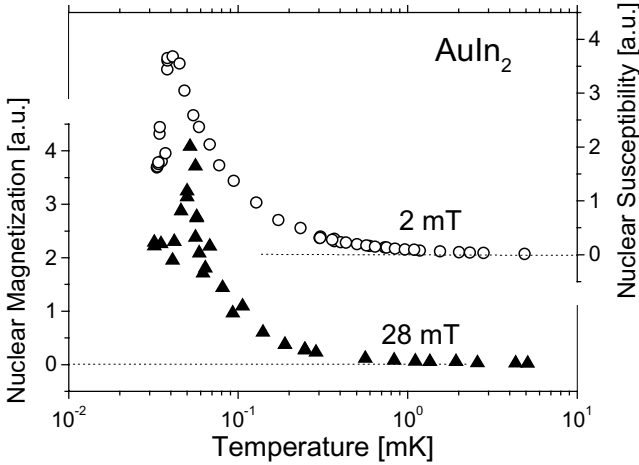


Fig. 13. Nuclear magnetization of ^{115}In (a) and ac susceptibility of $^{113}, ^{115}\text{In}$ (b) in AuIn_2 . (a) Deduced from NMR spectra taken at 266 kHz in 28.4 mT; (b) obtained from mutual inductance measurements at 16 Hz in 2 mT. These data are $\chi_n = \chi'_n + (\chi''_n)^2 / \chi'_n$ calculated from the measured real, χ'_n , and imaginary part, χ''_n , of the complex nuclear susceptibility. See Ref. [6].

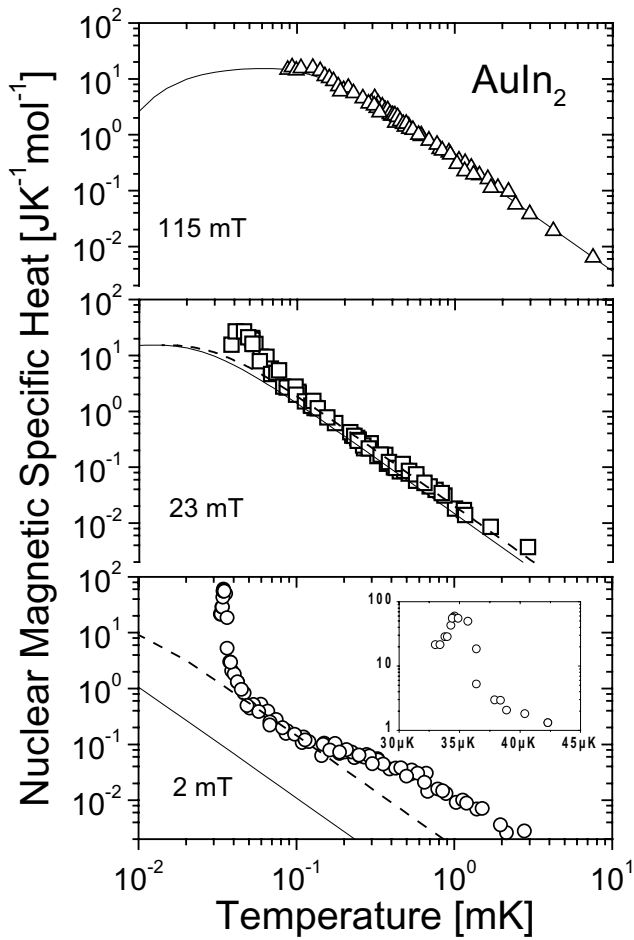


Fig. 14. Nuclear magnetic specific heat C_n of In nuclei in AuIn_2 per mole compound (per 2 moles In) in the three indicated magnetic fields. The full lines are the Schottky curves for a non-interacting nuclear paramagnet with the properties of $^{113,115}\text{In}$ in the given external fields. The dashed lines in the lower two figures are these curves with $B_{\text{eff}} = 27 \text{ mT}$, $b_{\text{int}} = 14 \text{ mT}$, and $B_{\text{eff}} = 7.3 \text{ mT}$, $b_{\text{int}} = 7 \text{ mT}$, respectively. The inset shows the behaviour in 2 mT near $T_{c,n} = 35 \mu\text{K}$. See Ref. [6].

static susceptibility at $2 \leq T \leq 30 \text{ K}$, we obtain an upper limit of 0.5 ppm for the concentration of electronic magnetic impurities and of 1 ppm for possibly segregated superconducting In. X-ray and neutron diffraction data showed that the investigated samples are single crystals.

5.2 The Impact of Nuclear Ferromagnetism on Superconductivity in AuIn₂

Studies on the interplay between *electronic* magnetism and superconductivity have led to an understanding of many effects associated with the interaction of these two phenomena. Most of these studies were concerned with the coexistence of antiferromagnetism and superconductivity. The destruction of superconductivity at a critical temperature T_{c2} due to the onset of electronic ferromagnetism below the temperature T_{c1} , where superconductivity appears, was discovered in 1977 for ErRh₄B₄ and HoMo₆S₈ [5]. For these materials it was found that oscillatory magnetic order can only coexist with superconductivity in a very narrow temperature range just above T_{c2} . However, the interplay of *nuclear* magnetic ordering and superconductivity had never been observed because spontaneous nuclear magnetic ordering in metals had been reported only for the non-superconducting metals Ag and Cu [28] as well as for intermetallic van Vleck compounds like PrCu₆ and PrNi₅ [29]. As described above, we have observed a nuclear ferromagnetic ordering of In nuclei in AuIn₂ at $T_{cn} = 35$ μ K [6]. This compound is also a type-I superconductor with $T_c(B = 0) = 207$ mK and $B_c(T = 0) = 1.45$ mT.

All the measurements described in the preceding section were performed in $B \geq 2$ mT to suppress the superconducting state of AuIn₂ [6]. It was a natural extension of these experiments to investigate the field range $B < 2$ mT to study the interplay between nuclear ferromagnetism and superconductivity in AuIn₂ [7].

The nuclear refrigerator precooled the sample in 115 mT to 80 μ K. We then thermally isolated the sample from the nuclear refrigerator by a superconducting heat switch (Fig. 4) and demagnetized it to a minimum temperature of 25 μ K from where we started the warm-up stepwise. The normal to superconducting transition of AuIn₂ was determined by driving the magnetic field from $B = 2$ mT to zero and watching the ac susceptibility. Before further increasing the temperature, the field was driven back to 2 mT. B_c was defined as the field value where 50% of the normal to superconducting transition is passed.

The critical field measured at $4 < T \leq 207$ mK agrees well with the BCS equation $B_c(T) = 1.45$ mT $(1 - (T/207 \text{ mK})^2)$ with known parameters of AuIn₂ (Fig. 15). At $42 \mu\text{K} \leq T \leq 4$ mK the critical field decreases slightly with decreasing temperature to a value $B_c(42 \mu\text{K}) = 1.41$ mT. However, decreasing the temperature further from 42 to 35 μ K, the critical field is strongly reduced to $B_c(35 \mu\text{K}) = 0.95$ mT in the nuclear ferromagnetic phase (Figs. 15 to 17). A further decrease of the temperature to 25 μ K reduces B_c only weakly to an approximately constant value $B_c(25 \mu\text{K}) = 0.87$ mT. This means that the main part of the drop of the critical field takes place between $T_c(\chi_{\max}) = 42 \mu\text{K}$ and $T_c(C_{\max}) = 35 \mu\text{K}$, where the maxima of the nuclear ac susceptibility and nuclear magnetic specific heat occur, respectively [6]. The finite and approximately temperature independent B_c at $T < 35 \mu\text{K}$ is interpreted as appearance of a new stable coexistence region of nuclear ferromagnetism and superconductivity.

The superconducting transition in the magnetically ordered state is strongly broadened at $T \leq (37 \pm 1) \mu\text{K}$ to a value of (0.20 ± 0.03) mT, using the 90% - 10% criterion, compared to its width in the paramagnetic state where it was too small to be detectable with the used field steps of 5 μ T. The broadening may result from the appearance of nuclear ferromagnetic domains below the nuclear Curie temperature (see below). The change from a sharp to a broadened transition takes place in a narrow temperature interval of about 1 μ K around

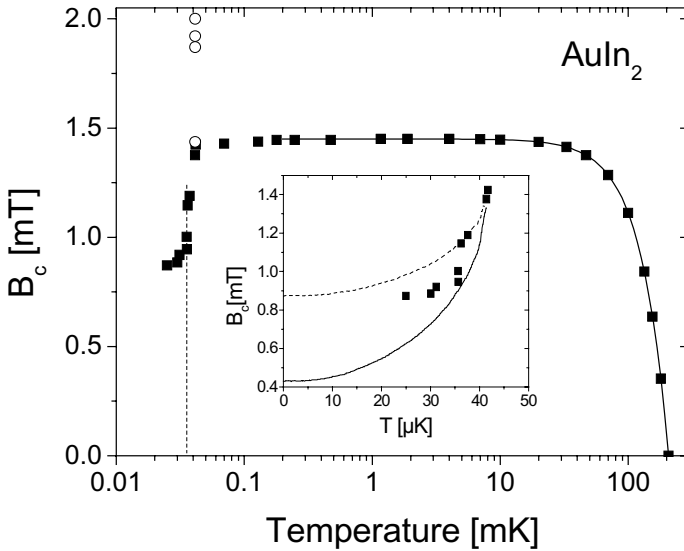


Fig. 15. Phase diagram of AuIn_2 . Critical field B_c of the superconducting transition of AuIn_2 (closed squares) as a function of temperature. The solid line represents the $B_c(T)$ behaviour according to BCS theory. The dotted line indicates the change from sharp superconducting transitions ($\Delta B_c < 5 \mu\text{T}$) to broadened transitions ($\Delta B_c = 0.2 \text{ mT}$) (see Fig. 16). The open circles indicate the temperatures $T_{\text{cn}}(\chi_{\text{max}})$ of the maximum of the nuclear magnetic susceptibility χ . The inset shows the calculations $\Delta B_c \propto M$ for $T < 42 \mu\text{K}$ [dotted line for $B_c(T = 0) \equiv 0.87 \text{ mT}$ and solid line for $B_c(T = 0) \equiv 0.44 \text{ mT}$, see text], where M_0 is the spontaneous magnetization of ferromagnetically ordered In nuclear magnetic moments in AuIn_2 . See Ref. [7].

$T_c = 37 \mu\text{K}$. In comparison with $T_c(C_{\text{max}})$ and $T_c(\chi_{\text{max}})$ this characteristic temperature with its small error bar may define the nuclear magnetic ordering temperature more exactly. Furthermore, from the calibration of our susceptometer we know that at $T < 37 \mu\text{K}$ the sample is still fully diamagnetic, $\chi = -1$ at $B = 0$, in the nuclear ferromagnetic state.

The measurements of the critical fields were performed during warm-up starting after demagnetizing the sample from different precooling conditions of $70 \leq B \leq 115 \text{ mT}$ and $T \geq 80 \mu\text{K}$, corresponding to entropy reductions $\Delta S_{\text{pre}}/S_{\infty}$ up to 29% ($S_{\infty} = 2R \ln(2I + 1)$ with $I = 9/2$, the high temperature entropy of the nuclear spin system). Some representative $B_c(T)$ curves with different $\Delta S_{\text{pre}}/S_{\infty}$ values are shown in Fig.17. For $T > 42 \mu\text{K}$ the critical field is independent from the precooling conditions. But below this temperature, the reduction of B_c seems to be the stronger the larger the entropy reduction was, with values of $0.87 \text{ mT} \leq B_{\text{cmin}} \leq 1.25 \text{ mT}$ depending on the precooling conditions. The maximum reduction $\Delta B_{\text{cmax}} =$

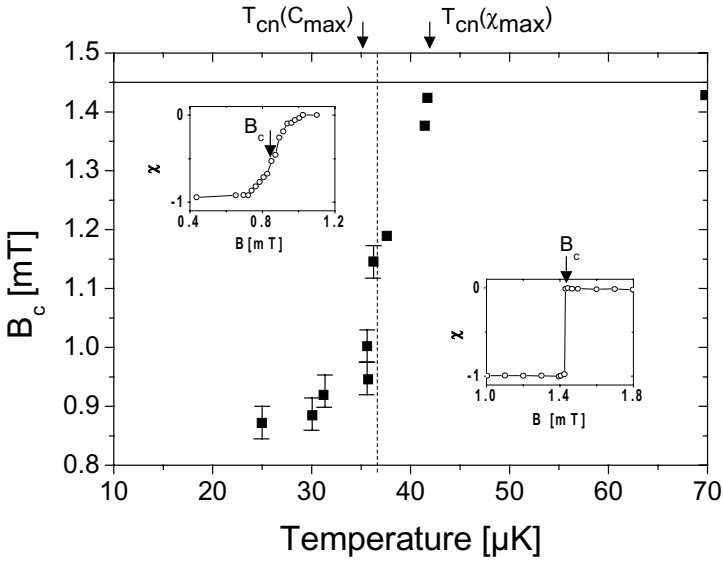


Fig. 16. Critical field B_c of the superconducting transition of AuIn_2 as a function of temperature. The solid line represents the critical field $B_c = 1.45$ mT. The dotted line indicates the nuclear ferromagnetic phase transition obtained from the broadening of the superconducting transition, $T_{\text{cn}} = (37 \pm 1)$ μK . The error bar of B is ± 0.03 mT at $T < 37$ μK . For $T > 37$ μK the error bar is < 5 μT . Insets (a) and (b) show typical susceptibility versus magnetic field curves of the superconducting transition in the nuclear ferromagnetic and paramagnetic regimes, respectively. For comparison, the “critical” temperatures where the nuclear heat capacity and the nuclear magnetic susceptibility, respectively, show their maxima are indicated on top. See Ref. [7].

1.45 mT - B_{cmin} seems to be proportional to the reduction of nuclear entropy and to the square of the nuclear polarization (see inset of Fig. 17). Assuming this dependence of ΔB_{cmax} on $\Delta S_{\text{pre}}/S_{\infty}$ to be valid also at higher entropy reductions, one would expect the full depression of B_c after an entropy reduction of 70%. This would yield re-entrant superconductivity (however, see below).

The observed dependence ΔB_{cmax} on the precooling conditions could be qualitatively explained if domains would occur in the nuclear ferromagnetic phase (see above). The polarization of the nuclear spin system in the paramagnetic region due to an external magnetic field possibly gives rise to the growth of those domains magnetized parallel to the applied field when the ferromagnetic state is entered. This would lead to a spontaneous magnetization of the nuclear ferromagnetic system increasing with polarization in the paramagnetic state.

The calculated saturation magnetization of the nuclear spin system in AuIn_2 is $\mu_0 M_0 = \mu_0 N_0 \mu_{\text{n}} g_{\text{n}} I / V_{\text{mol}} = 1.01$ mT at $T = 0$ K, which is smaller than $B_c(T \ll T_c) = 1.45$ mT.

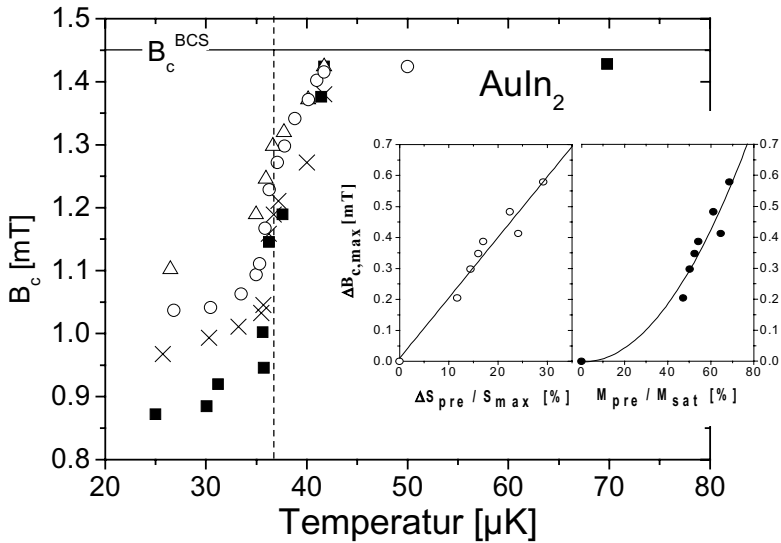


Fig. 17. Critical field B_c of the superconducting transition of AuIn_2 as a function of temperature of four representative measurements with the precooling conditions $\Delta S_{\text{pre}}/S_{\text{max}} = 16\%$, 24% , 22% , and 29% , resulting in $B_{c,\text{min}} = 1.10$ mT (open triangles), 1.04 mT (open circles), 0.97 mT (crosses), and 0.87 mT (closed squares), respectively. The solid line represents the critical field $B_c = 1.45$ mT. The insets show the reduction $\Delta B_{c,\text{max}} = B_c - B_{c,\text{min}}$ as a function of entropy reduction $\Delta S_{\text{pre}}/S_{\text{max}}$ and polarization M_{pre}/M_0 after precooling. The full lines in the insets indicate the behaviour $\Delta B_{c,\text{max}} \propto \Delta S_{\text{pre}}/S_{\text{max}}$ and $\Delta B_{c,\text{max}} \propto (M_{\text{pre}}/M_0)^2$, respectively. See Ref. [7].

Assuming that the reduction of B_c is only due to the saturation magnetization (see below), it follows that the maximum available reduction should be 1.01 mT and therefore $B_{c,\text{min}} = B_c(T \ll T_s) - \mu_0 M_0 = 0.44$ mT. Hence a full suppression of superconductivity seems to be impossible even at the lowest temperatures. This might explain the absence of complete destruction of superconductivity by nuclear magnetic order. On the other hand, the above mentioned possibility of complete destruction of superconductivity at $\Delta S_{\text{pre}}/S_{\infty} = 70\%$ (corresponding to a nuclear polarization $P_{\text{pre}} = M_{\text{pre}}/M_0 = 93\%$) contradicts this conclusion. Unfortunately, we can not clarify this question with our data.

There are two phenomena, electromagnetic and exchange interactions, which are responsible for the interplay of superconductivity and magnetism in electronic magnetic systems. Both are interactions between the magnetic moments (or an applied field) on one hand and the momentum and spin of the conduction electrons on the other hand. From the multiple pairbreaking theory of Fulde and Maki [30] the upper critical field B_{c2} of a type-II superconductor influenced by electronic magnetism can be described as $B_{c2}(T) = B_{c02}(T) -$

$\Delta B_{c2}(T) = B_{c02}(T) - \mu_0 M(B_{c2}, T)$ in the case of negligible exchange interaction and therefore dominating electromagnetic induction, where $B_{c02}(T)$ is the upper critical field in the absence of magnetic influence and $M(B_{c2}, T)$ is the magnetization. Ginzburg [4] considered this situation already in 1957 for type-I superconductivity influenced by the magnetization of magnetic ions. In order to determine the possible origin of the reduction of the (type-I) superconducting critical field B_c of AuIn_2 we take $B_c \equiv B_{c2}$ and the spontaneous magnetization of the nuclear ferromagnet $M(T) = M_0 B(\alpha) \equiv M(B_{c2}, T)$ in the equation of Fulde and Maki with the Brillouin function $B(\alpha)$, ($\alpha = \mu B_i(M(T))/k_B T$), and the interaction field $B_i(M(T))$ given in [31] and calculated $B_c(T)$ for $T < 42 \mu\text{K}$. However, taking as parameter either $B_c(T = 0) \equiv B_{c\text{min}} = 0.87 \text{ mT}$ from the experimental results (Fig. 15) or $B_c(T = 0) = 1.45 \text{ mT} - \mu_0 M_0 = 0.44 \text{ mT}$ from the saturation magnetization, both simulations with $\Delta B_c \propto M$ deviate clearly from the measured reduction of the critical field (Fig. 15). Obviously, additional effects might be responsible for the reduction of B_c . For example, in the case of negligible electromagnetic interaction and dominating effective exchange field $H_J \propto \mu_0 M(B_c, T)$, the critical field $B_{c2}(T) = B_{c02}(T) - \text{const} \cdot H_J^2(M, T)$, and therefore $B_{c2}(T) = B_{c02}(T) - \text{const} \cdot M^2(B_{c2}, T)$ [30]. However, the equation $\Delta B_c = \mu_0 M_0 B(\alpha)$ is a qualitative approximation for the slight decrease of B_c at $42 \mu\text{K} \leq T < 4 \text{ mK}$ for the case that instead of the temperature T , the difference of T and the Weiss temperature θ of AuIn_2 is used (see Sect. 6d, Fig. 18).

Up till now we have discussed the influence of magnetic ordering on the superconducting properties. Vice versa, the influence of superconductivity on magnetism is considered to be weak, because the superconducting coherence length in AuIn_2 , $\xi_0 = 4.9 \mu\text{m}$ (using $\xi_0 = 2\hbar^2 k_F / \pi m_{\text{eff}} \Delta$ with $k_F^{-1} = 1.448 \text{ \AA}^{-1}$, effective mass $m_{\text{eff}} = 1.0 m_{e0}$ [6], gap energy $2\Delta = 3.5 k_B T_c$) is large compared to the characteristic length of the RKKY interaction (of the order of a few nm) responsible for nuclear magnetic ordering. After a cycle of field sweeps, driving the sample superconducting at a temperature $T < T_c$ and again normal conducting, no increase of the temperature within the error bar of $1 \mu\text{K}$ occurred, and the nuclear susceptibility was nearly unchanged still showing the characteristic temperature dependence in the ordered state [6]. The observation that the increase of entropy is negligible after driving the sample superconducting starting from the normal conducting and nuclear ordered state and going back to this state means that the nuclear spin arrangement kept its entropy and enthalpy and seems to be still ferromagnetically ordered in the superconducting state, even at $B = 0$. Otherwise a significant increase of entropy and a change of the nuclear susceptibility should have occurred (remember that the lattice and electronic contributions to the entropy are negligible in the μK temperature range). This is a very remarkable result taking into account that the nuclear order in AuIn_2 is caused by indirect exchange interactions between the nuclear moments mediated by normal conduction electrons (see Sect. 5.a).

In summary, these results show the first observation of the weakening of superconductivity due to long-range nuclear ferromagnetic order and the coexistence of both phenomena. It seems that the nuclear magnetic interactions are not significantly influenced by superconductivity. In addition, AuIn_2 is the first system where type-I superconductivity competes with magnetic order. Obviously, more investigations are necessary to understand some of the observations for this new type of magnetic superconductor.

The interplay between superconductivity and nuclear magnetism in AuIn_2 has recently been treated theoretically in three papers [32,33,34]. In particular Kuli et al. [33] did arrive at

the result that the hyperfine interaction dominates, giving rise to a spiral or domain like magnetic structure caused by the exchange interaction in the superconducting state. They then calculate a reduction of B_c in this state of about a factor of two in good agreement with our experimental result. Sonin [34] has considered the electromagnetic interaction only. He arrives at $\Delta B_c \propto M$ for a spatially uniform ferromagnetic state which according to his discussion can only appear as a metastable state compared to a more stable spiral state for which Sonin expects a much smaller reduction of B_c , in disagreement with Ref. [33]. Both papers give a decrease of B_c in the paramagnetic state of AuIn_2 in reasonable agreement with our experimental result discussed in Sect. 6d (see below). Obviously, more theoretical studies are necessary to understand the interplay of superconductivity and nuclear magnetism in metals.

6. THE DEPENDENCE OF THE CRITICAL FIELD ON NUCLEAR MAGNETIZATION IN NUCLEAR PARAMAGNETS

In the preceding chapter we have reported on the first study of the interplay of nuclear ferromagnetism and superconductivity in the intermetallic compound AuIn_2 . It would be desirable to perform such experiments also on other nuclear magnetic superconductors. However, because of the lack of any other material which undergoes both a spontaneous nuclear magnetic ordering transition and is also a type-I superconductor, we had to restrict ourself to the study of nuclear *paramagnets*. Due to the observed weak decrease of the superconducting critical field already in the nuclear paramagnetic range of AuIn_2 (see Sect. 5b and Figs. 15 – 17), we looked for similar effects in other type I superconductors. A search on the periodic table and among simple intermetallic compounds [35] led us to Al, AuAl_2 , Sn, and In as further possible candidates. We have chosen these systems because of their nuclear magnetizations and strongly varying hyperfine couplings (expressed by their Korringa constants), as well as their type-I superconducting properties which are given in Tab.1.

Table 1. Nuclear magnetic and superconducting properties of the investigated type-I superconductors: isotope(s), natural abundance, nuclear spin I, nuclear magnetic moment μ , nuclear saturation magnetization $\mu_0 M_0$, Korringa constant κ , superconducting transition temperature T_c , and superconducting critical field B_c .

| | Isotope(s) | Nat. Abun. [%] | I | μ [μ_n] | $\mu_0 M_0$ [mT] | κ [K·sec] | T_c [K] | B_c [mT] |
|-------------------------|---------------------------|-------------------|---------------|---------------------|----------------------|---------------------|---------------------|-------------------|
| AuAl₂ | ²⁷ Al | 100 | 5/2 | 3.64 | 0.92 | 18 | 0.163 | 1.21 |
| Al | ²⁷ Al | 100 | 5/2 | 3.64 | 1.3 | 1.8 | 1.175 | 10.5 |
| Sn | ^{115,117,119} Sn | 0.35, 7.6, 8.7 | 1/2, 1/2, 1/2 | -0.9, -1.0, -1.1 | 0.031 | 0.05 | 3.70 | 30.9 |
| AuIn₂ | ^{113,115} In | 4.3, 95.7 | 9/2, 9/2 | 5.50, 5.51 | 1.01 | 0.11 | 0.207 | 1.45 |
| In | ^{113,115} In | 4.3, 95.7 | 9/2, 9/2 | 5.50, 5.51 | 0.22 (1) 1.33 (2) | 0.09 | 3.404 | 29.3 |
| Rh | ¹⁰³ Rh | 100 | 1/2 | -0.088 | 0.03 | 8.1 | $3.3 \cdot 10^{-4}$ | $5 \cdot 10^{-4}$ |

(1) at $B \leq 0.1$ T, i.e. In is quadrupolar dominated.

(2) at $B > 1$ T, i.e. In is dominated by nuclear Zeeman interaction.

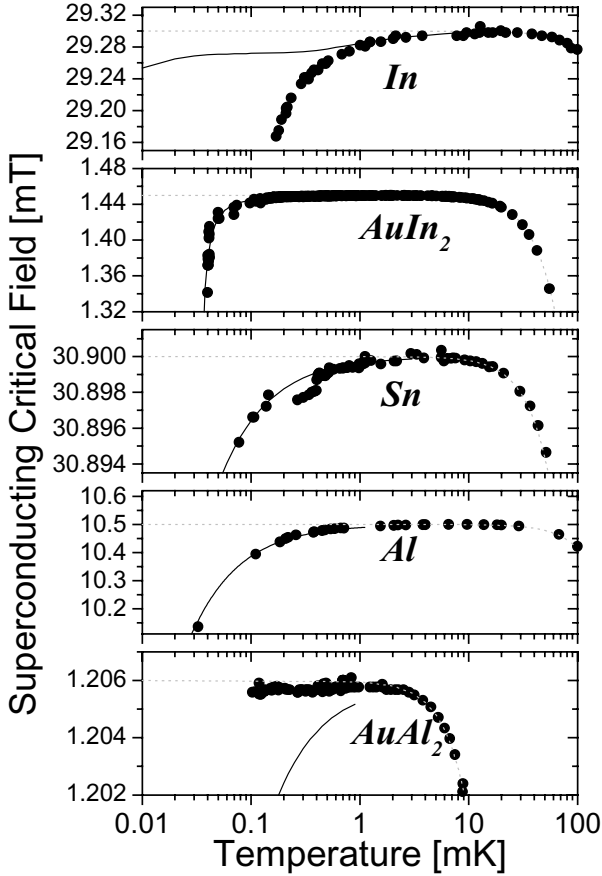


Fig. 18. Critical field B_c of the superconducting transitions of the type-I superconductors $AuAl_2$, Al, Sn, $AuIn_2$, and In as a function of temperature in their nuclear paramagnetic range. The dashed lines show the BCS type temperature dependence $B_c = B_{c0}(1-(T/T_c)^2)$. The solid lines are the reductions $\Delta B_c = \alpha N \mu_0 M_n(B_c, T)$ of the superconducting critical field due to the paramagnetic nuclear magnetization M_n , where $N = 1 - D + L$ is the correction for the demagnetization factor D as well as for the Lorentz factor L . The values of the fit parameter α are given in the text. For $AuIn_2$ and In nuclear spin-spin interactions, described by the Weiss temperature θ , contribute to the breaking of Cooper pairs. Hence, T has to be replaced by $T - \theta$. For $AuIn_2$, the fit (steeper line through the data points) gives $\theta = 35 \mu K$. For In a rather high $\theta = 150 \mu K$ is the result of the fit (steeper line through the data points). For details, see text.

The succeeding investigations have been performed on very pure samples, being analysed by SQUID magnetometry and showing the content of electronic magnetic impurities to be below 0.1 ppm in all of our samples. Compared to the results discussed in Chap. 5b, we have improved the resolution of the field steps from 5 μT to below 0.1 μT in these experiments which were performed at $17 \mu\text{K} \leq T \leq 1\text{K}$. Again, the B_c values were taken by slowly reducing the applied magnetic field from slightly above the superconducting critical field to below with B_c taken at $\chi = -0.5$.

A summary of the results is presented in succession of the strength of hyperfine coupling of the samples in paragraphs a) to e), starting with the weakest representative AuAl_2 with the large Korringa constant of $\kappa = 18 \text{ Ks}$. The results of the measurements of $B_c(T)$ in the vicinity of B_{c0} are compared to the equation $B_c = B_{c0}(1 - T^2/T_c^2) - \Delta B_c$, where $\Delta B_c = \alpha N \mu_0 M(B_c, T)$ is a term linear in the nuclear magnetisation $M(B_c, T)$ according to the multiple pairbreaking theory by Fulde and Maki [30] for the case of dominance of electromagnetic induction. In this equation we include $N = 1 - D + L$ as a correction for the demagnetization factor D and Lorentz factor L . The constant α serves as a free fit parameter. In Fig. 18, our data of B_c of the various materials are compared to this equation (solid lines). Whereas the nuclear spin-spin interactions in AuAl_2 , Al , and Sn are weak and estimations lead to nuclear magnetic ordering temperatures $T_{\text{cn}} \leq 1 \mu\text{K}$, for AuIn_2 and In we had to consider their stronger nuclear spin-spin interactions. For this reason, for AuIn_2 and In we have also fitted the equation to the data by replacing in $M(B_c, T)$ the temperature T with $T - \theta$, where θ is the Weiss temperature. In addition, it seems that in the equation for ΔB_c one has to include a term quadratic in M to explain the AuIn_2 data; the term results from exchange interaction [30]. Further, in paragraph f) the results of Rh and in g) of the possible candidate TiH_{2+x} are reported.

6.1 AuAl_2

Opposite to the other investigated systems, there is almost no reduction of the critical field in the intermetallic cubic (CaF_2 -structure) compound AuAl_2 (with its large Korringa constant $\kappa = 18 \text{ Ks}$), compared to the BCS behaviour of a nonmagnetic weakly coupled superconductor, i.e. $B_c(T) = B_{c0} (1 - (T/T_c)^2)$. For the parameter α a small value of 0.08 ± 0.03 has been found. This finding is of particular importance cause AuAl_2 serves concerning its superconducting parameters as well as concerning its nuclear saturation magnetisation as a reference material for AuIn_2 (see Table). Furthermore, due to its identical ^{27}Al nuclei, it also serves as a reference for pure Al . The almost absence of a suppression of B_c compared to AuIn_2 and Al with their much smaller Korringa constants may indicate that the strength of the hyperfine coupling plays an important role in the interplay of nuclear magnetism and superconductivity (however, see the results for AuIn_2 below).

6.2 Al

Compared to AuAl_2 , in Al ($\kappa = 1.8 \text{ Ks}$) the suppression of the superconducting critical field is clearly enhanced (Fig. 18 and Ref. [36]). Starting with 10.5 mT at 2 mK, the critical field decreases to 10.1 mT at 30 μK . This suppression fits to a much larger parameter $\alpha = 1.00 \pm 0.05$. The stronger hyperfine interaction in Al seems to create a stronger competition between

nuclear paramagnetism and superconductivity than in AuAl₂. In Ref. [36] we have presented a detailed analysis of the data taken on our Al sample.

6.3 Sn

Sn has an even smaller Korringa constant ($\kappa = 0.05$ Ks) than Al and AuAl₂. However, its small number of nuclear magnetic isotopes with their small nuclear magnetic moments lead to a saturation magnetization of only 31 μ T. Because of the small size of nuclear magnetization we had to improve our field measurements in presence of a comparably large background superconducting critical field, $B_{c0} = 30.9$ mT. We solved this through an optimized coil system and using several high precision power supplies in parallel for applying the current to the field coils [37]. Again on a coarse scale, the superconducting critical field of Sn appears to be proportional to the nuclear magnetization (Fig. 18). As already observed for Al, for Sn we receive a parameter $\alpha = 1.0 \pm 0.05$ as well. However, on a fine scale (Fig. 19), unexpected anomalies occur in the $B_c(T)$ curve, in particular at about 0.3 mK. These data have been confirmed in several runs. We have no quantitative explanation for this non-monotonous step-like behaviour of $\Delta B_c(T)$, however, we like to mention that under these field and temperature conditions, the electron density of states already starts to occupy separate Landau levels.

6.4 AuIn₂

Additionally, we have performed a detailed investigation of the superconducting critical field of AuIn₂, focusing on the nuclear paramagnetic range. A fit to the data taken at $0.2 \text{ mK} \leq T \leq 4 \text{ mK}$ reveals a fitting parameter $\alpha = 0.3 \pm 0.05$. This value is surprisingly small compared to the results for Al and Sn, inspite of the strong hyperfine interaction in AuIn₂. As mentioned above, to take the strong influence of the nuclear spin-spin interactions in AuIn₂ into account, we had to replace in the equation of $M(B_c, T)$ the temperature T by $T - \theta$. The fit yields a Weiss temperature $\theta = 35 \mu\text{K}$. This value for θ is in reasonable agreement with $\theta = 42 \mu\text{K}$ obtained from the 16 Hz nuclear susceptibility data (see Sec. 5a, [6]). In addition, a contribution where the nuclear magnetization appears quadratically in the suppression of the critical field in AuIn₂ may also be present, because the linear term alone does not describe the data points too well (Fig. 18). Such a quadratic term is expected from exchange interactions [30].

6.5 In

As already mentioned in Sec. 5a, Indium shows a more complicated nuclear magnetic behaviour compared to the above discussed compounds. In Indium, due to its (noncubic) tetrahedral crystal structure, the nuclear electrical quadrupole interaction has to be considered in addition to the nuclear Zeeman interaction and exchange contributions ($\kappa = 0.09$ Ks). In order to determine the properties of the nuclear electrical quadrupole interaction, we have also performed measurements of its nuclear heat capacity at $0.2 \text{ mK} \leq T \leq 8 \text{ mK}$ (Fig. 20). Our data help to distinguish between a positive and a negative product of nuclear quadrupolar moment Q and electrical field gradient EFG [38]. They clearly favour a positive value, $Q \cdot \text{EFG} > 0$, and support former results for the nuclear heat capacity as well as from nuclear quadrupole resonance experiments [39]. In consequence, in Indium the lowest nuclear energy

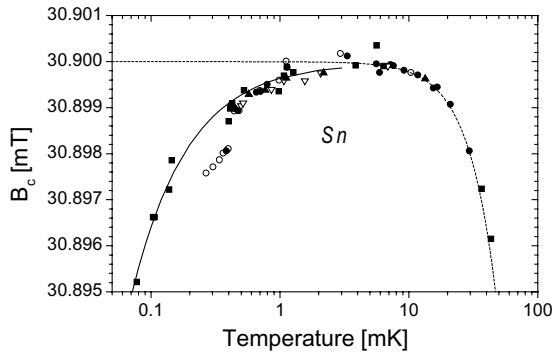


Fig. 19. Critical field B_c of the superconducting transitions of Sn as a function of temperature. The displayed field range is only $6 \mu\text{T}$ in the vicinity of $B_{c0} = 30.9 \text{ mT}$. The various symbols indicate different experimental runs. During the course of the investigations, the nuclear demagnetization cryostat has been warmed up to room temperature one time [37]. The dashed line shows the BCS type temperature dependence $B_c = B_{c0}(1-T^2/T_c^2)$. The solid line indicates the deviation $\Delta B_c = \alpha N\mu_0 M(B_c, T)$ from the BCS dependence (for details see text). See Ref. [37].

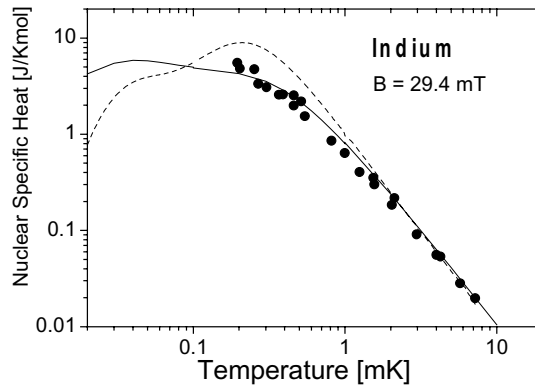


Fig. 20. Nuclear magnetic heat capacity of In (which is dominated by the nuclear electric quadrupole interaction) measured in a magnetic field slightly above the superconducting critical field. The solid line shows the calculated specific heat for the case that the product of electrical field gradient (EFG) and nuclear electrical quadrupolar moment Q is positive (full line) and vice versa the dashed line shows the case that $EFG \cdot Q$ is negative. The data clearly favour the positive case. See Ref. [38].

state is a $I = 1/2$ low spin state. Therefore, in In at small applied magnetic fields ($B < 0.1$ T, i.e. under dominance of the nuclear electrical quadrupole interaction) the nuclear saturation magnetization is only $\mu_0 M_0^{Q,Z} = 0.22$ mT. In particular, this saturation magnetization is valid in the vicinity of the superconducting critical field B_{c0} of about 29.3 mT.

Surprisingly, we found that the depression of the superconducting critical field is clearly stronger than expected for the electromagnetic contribution $\Delta B_c = N \mu_0 M_{In}^{Q,Z}(B_c, T)$, where $\mu_0 M_{In}^{Q,Z}(B_c, T)$ is the magnetization considering both the electrical quadrupolar as well as nuclear magnetic Zeeman interaction. Possibly, strong exchange contributions cause an enhanced suppression of the superconducting critical field [38]. Here we fit $\Delta B_c = \alpha N \mu_0 M_{In}^{Q,Z}(B_c, T - \theta)$ to the data points and receive $\alpha = 1.0$ as well as a surprisingly high Weiss temperature $\theta = (150 \pm 20) \mu\text{K}$. This result is a clear motivation for further studies of Indium at ultralow temperatures. The latter value may indicate that In will undergo a spontaneous nuclear magnetic ordering transition at a T_{cn} even higher than observed for AuIn_2 ($35 \mu\text{K}$; see Sect. 5a).

In summary, for the investigated nuclear paramagnets we have observed a variety of interesting interplay phenomena with superconductivity. In particular, we find for the fit parameter α , describing the strength of the impact of nuclear magnetization on the critical magnetic field of superconductivity, that this parameter $\alpha = 1.0$ for the investigated elements Al, Sn, and In. However, we find smaller values (0.08 for AuAl_2 , 0.3 for AuIn_2) for the investigated intermetallic compounds. Hence, the competition between nuclear magnetism and superconductivity is not simply proportional to the strength of the hyperfine interaction. Obviously, several of the observations remain to be understood, e.g. the relative small value of $\alpha = 0.3$ for AuIn_2 .

6.6. Rh

A further study of the interplay of nuclear magnetism and superconductivity has been performed under nonequilibrium thermal conditions at nK nuclear spin temperatures and $T_{\text{electron}} \sim 100 \mu\text{K}$ in the weakly hyperfine coupled nuclear magnet Rh by Knuutila et al. [17]. These data have been obtained from measurements of the nuclear spin lattice relaxation rates of Rh. It remains an open question whether the reduction of the critical field is directly proportional to the nuclear magnetization in Rh because at fields of the order of μT in the vicinity of the critical superconducting field (see Chap. 4a), the authors of Ref. [17] did not have a possibility to measure the nuclear polarization. A calculation of the nuclear polarization is perhaps not conclusive, because of the presence of nuclear magnetic exchange and dipolar contributions of unknown size. The authors report a weak suppression of the superconducting critical field at nonequilibrium thermal conditions for nuclear magnetic moments and conduction electrons, however, for Rh the factor α remains undefined so far.

Among the elements, there are without any doubt, further candidates for studies of the interplay between nuclear magnetism and superconductivity. Ref. [35] gives an overview of relevant superconducting critical parameters and nuclear magnetic properties of the elements. In addition, we have identified compacted Pt powder as a new superconductor (see Sect. 4d). The small Korringa constant ($\kappa = 0.030$ Ksec) of ^{195}Pt nuclei rises the hope of a strong nuclear magnetic influence on the superconducting critical field B_c . However, due to the very small values of B_c observed in the compacts so far (see Sect. 4d), an interplay study requires

to perform experiments at $T \leq 10 \mu\text{K}$ in order to get large enough nuclear magnetic polarizations.

Of course, among the many intermetallic compounds, one will find candidates with features that are suitable for studies of the interplay of nuclear magnetism and superconductivity. One possible group comprises metal hydrides as well as superconducting hyperfine enhanced nuclear spin systems, which we will discuss in the following chapters.

6.7 TiH_{2+x} as a further candidate

Superconductivity in metal hydrides has already been reported. As an example, PdH has been observed to undergo a superconducting phase transition (see Sect. 4b, [21]). We have concentrated our investigation on titanium hydride which has the highest hydrogen density in metal hydrides with up to a 28% higher proton density than solid hydrogen [40]. However, superconductivity has never been reported in this system before.

In the course of our investigations, we have identified highly saturated TiH_x metal hydride as a new superconducting nuclear spin system [35]. In particular, during the preparation of our samples with various hydrogen concentrations we have surprisingly been able to create $\text{TiH}_{2.07}$ in which the whole hydrogen content is still single atomically embedded (a heat release analysis gave us no hint for ortho-para conversion of molecular hydrogen). It had been expected that the maximum possible hydrogen content is 2.00 at the full occupation of tetrahedral sites. However, the occupation of octahedral sites could give an explanation for our results which had already been observed for the metal hydride YH_x for $x > 2.00$ [41]. In $\text{TiH}_{2.07}$ the superconducting transition is most pronounced (Fig. 21). We found a broadened superconducting phase transition at about 15 mK, which strongly depends on the amplitude of the applied ac field. In future, this system may be an interesting candidate for studies of the

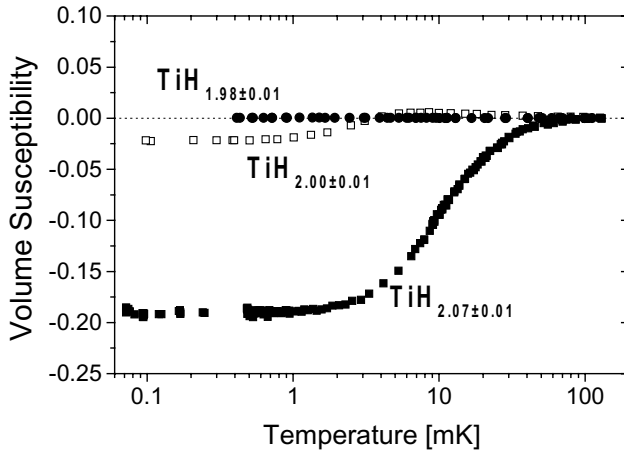


Fig. 21. Ac(16Hz) susceptibility of TiH_x for three different hydrogen concentrations. Superconductivity appears for $x \geq 2.00$.

interplay of superconductivity and nuclear magnetism due to its large nuclear saturation magnetization $\mu_0 M_0 = 1.7$ mT resulting from the high proton density. However, a deeper understanding of the strength of the hyperfine coupling in these hydrides is required. It has been observed that the hyperfine coupling in titanium hydride crucially depends on tiny concentrations of electronic magnetic impurities [42]. Probably, the Korringa constant can be tuned by the addition of impurities in this system.

7. HYPERFINE ENHANCED NUCLEAR MAGNETISM AND ITS INTERPLAY WITH SUPERCONDUCTIVITY IN $\text{Pr}_{1-x}\text{La}_x\text{Te}$ and $\text{Pr}_{1-x}\text{La}_x\text{Cu}_6$

In Sects. 5 and 6 we have presented the first studies of the interplay of *nuclear* magnetism and superconductivity. All nuclear magnetic moments involved in this interplay have hyperfine couplings dominantly with s- and p-conduction electrons and almost negligible electronic enhancements (Knight shifts $\leq 1\%$). In the following, we will discuss studies where the nuclei are in hyperfine contact with 4f-electrons, too, and are dramatically enhanced by this interaction (hyperfine enhancement factors of about 1000 %).

7.1 The Interplay of van Vleck Paramagnetism and Superconductivity in $\text{Pr}_{1-x}\text{La}_x\text{Te}$

Compared to superconductors doped with magnetic 3d-impurities and described by the theory of Abrikosov and Gorkov [43], electronic singlet ground state systems doped with magnetic 4f-ions can have a much larger critical concentration of magnetic impurities, as observed for $\text{La}_{1-x}\text{Pr}_x\text{Pb}_3$ by Bucher et al. [44]. In these systems, the magnetic moments of the $4f^{3+}$ ions are quenched in their lowest crystal electrical field state. As a result, their competition with superconductivity is clearly weakened compared to ions which keep their full or even enhanced electronic magnetic moment. Keller and Fulde [45] in their theory have introduced the ratio Δ/T_c of crystal field splitting Δ and superconducting transition temperature T_c as the decisive scaling parameter for a description of these systems. The maximum magnetic impurity concentration is large when the crystal field splitting Δ (i.e. the energy difference between the singlet ground state and the first excited state) is large relative to T_c .

We have focused our interest on the van Vleck paramagnets $\text{Pr}_{1-x}\text{La}_x\text{Te}$. For LaTe, made of 4N5 for Pr and 6N for Te, we have observed a superconducting transition temperature of 5.7 K (Fig. 22). Together with the crystal field splitting of 76 K [46], we have a ratio $\Delta/T_c = 13$ in LaTe, which is a good precondition for a high critical concentration of singlet ground state ions. Our recent measurements on the diluted superconducting van Vleck paramagnet $\text{Pr}_{1-x}\text{La}_x\text{Te}$ revealed a high critical Pr^{3+} concentration slightly above 0.50 (Fig. 22). This result has enabled us to investigate the influence of hyperfine enhanced nuclear magnetism on superconductivity for the first time, as described in the following section.

7.2 The Impact of Hyperfine Enhanced Nuclear Magnetism on Superconductivity in $\text{Pr}_{0.50}\text{La}_{0.50}\text{Te}$

The *electronic* singlet ground state, which forces the susceptibility to follow the so called van Vleck type behaviour and in consequence to show a temperature and field independent constant van Vleck susceptibility χ_{v} at temperatures much smaller than the crystal field

splitting Δ (Fig. 23), is not the only magnetic contribution. In addition, *nuclear* magnetic moments of La and Pr are contributing. By far, the contribution of ^{141}Pr nuclei is dominating because the nuclear magnetic moments are hyperfine enhanced by a factor of $(1+h_f\chi_{sv}) = 10.2$ in PrTe due to the hyperfine interaction expressed by the hyperfine factor h_f of the Pr 4f electrons, leading to a second increase of the susceptibility below 1 K (Fig. 23). The Ruderman-Kittel exchange interaction of the hyperfine enhanced nuclear magnetic moments in PrTe is large enough to cause a nuclear magnetic phase transition at $T_{\text{cn}} = 0.6$ mK with a clear antiferromagnetic tendency (Fig. 23, [47]).

In order to study the interplay of hyperfine enhanced nuclear magnetization and superconductivity at a high concentration of nuclear magnetic moments, we have focused our study on $\text{Pr}_{0.50}\text{La}_{0.50}\text{Te}$ which showed the lowest superconducting transition temperature, $T_c = 0.20$ K, of all samples investigated (Fig. 22) and is likely to suppress superconductivity at this critical Pr concentration.

We have investigated the electrical resistance and ac(16 Hz) susceptibility of $\text{Pr}_{0.50}\text{La}_{0.50}\text{Te}$ to μK temperatures. The resistance data have been taken using a bulk sample whereas the susceptibility has been measured both for a bulk and a powder composite sample (compacted mixture of powdered $\text{Pr}_{0.50}\text{La}_{0.50}\text{Te}$ with grain sizes smaller than $20\ \mu\text{m}$ and Ag powder with an average grain size of $70\ \text{nm}$; mass ratio of compound to Ag = 1:10), the latter in order to reduce thermal relaxation times.

Whereas the superconducting transition measured resistively appears to be quite conventional (Fig. 24), the susceptibility provides a more detailed and interesting picture (Fig. 25). It does not reach $\chi = -1$, as a possible consequence of type-II superconductivity with an extremely small value of B_{c1} , but passes through a minimum at about 30 mK from which it starts to increase at further cooling. At temperatures $T < 20\text{mK}$, we find a clear reentrance of the susceptibility towards its normal conductive value (Fig. 25).

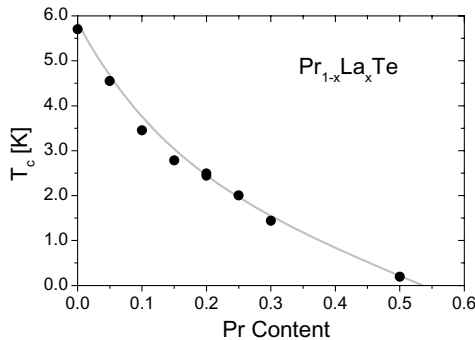


Fig. 22. Superconducting transition temperatures $T_c(x)$ of the superconducting van Vleck paramagnets $\text{La}_{1-x}\text{Pr}_x\text{Te}$ versus Pr content x . The solid line is the result of the theory by Keller and Fulde [44] for magnetic impurities with a singlet nonmagnetic groundstate. In contrast to the strong influence of magnetic impurities in the absence of crystal field effects on T_c as described in the Abrikosov-Gorkov theory [42], the singlet groundstate Pr^{3+} ions in $\text{La}_{1-x}\text{Pr}_x\text{Te}$ cause a much weaker depression of T_c . As a result we have observed a high maximum concentration x_{max} defined by $T_c(x_{\text{max}}) \rightarrow 0$ close above $x = 0.50$ in $\text{La}_{1-x}\text{Pr}_x\text{Te}$.

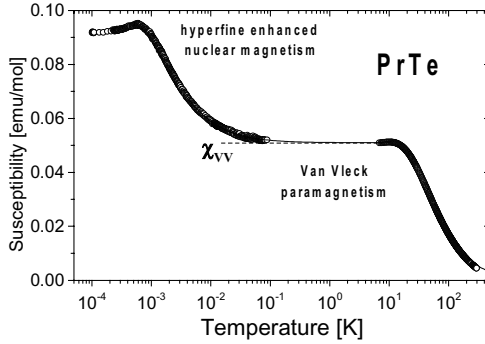


Fig. 23. Static susceptibility measured with a SQUID magnetometer at $T > 4$ K and ac (16Hz) susceptibility at $100 \mu\text{K} \leq T \leq 100$ mK of PrTe. The nonmagnetic singlet crystal electrical field ground state of Pr in PrTe leads to a constant van Vleck susceptibility χ_{VV} at $T \leq 10$ K (indicated by the dashed horizontal line). However, the nuclear magnetic ^{141}Pr moments in PrTe are strongly hyperfine enhanced. The resulting large effective nuclear magnetic Curie constant causes a significant increase of the total susceptibility. At $T_{\text{cn}} = 0.60$ mK a maximum of the hyperfine enhanced nuclear magnetic susceptibility occurs indicating the transition to a nuclear magnetic ordered state [47]. The Curie-Weiss law (solid line) fitted to the data at $T_{\text{cn}} \leq T \leq 100$ mK suggests an antiferromagnetic type of hyperfine enhanced nuclear magnetic ordering.

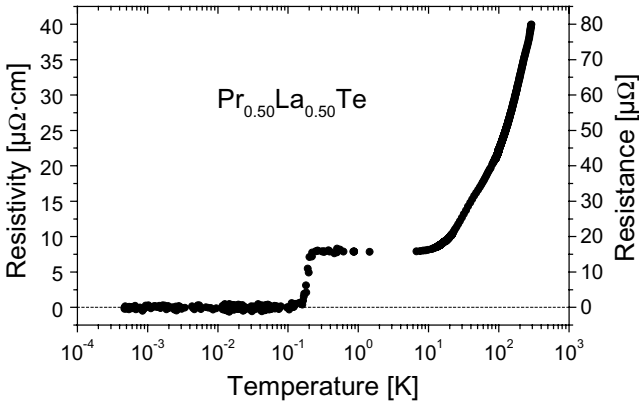


Fig. 24. Ac(16 Hz) resistivity of $\text{La}_{0.50}\text{Pr}_{0.50}\text{Te}$ measured in a field of $30 \mu\text{T}$. From the data, we get $RR = 15 \mu\Omega\text{cm}$ and a value of $RRR = 5.3$ typical for samples of diluted intermetallic van Vleck paramagnets. The super-conducting transition occurs at $T_c = 0.20$ K in this compound.

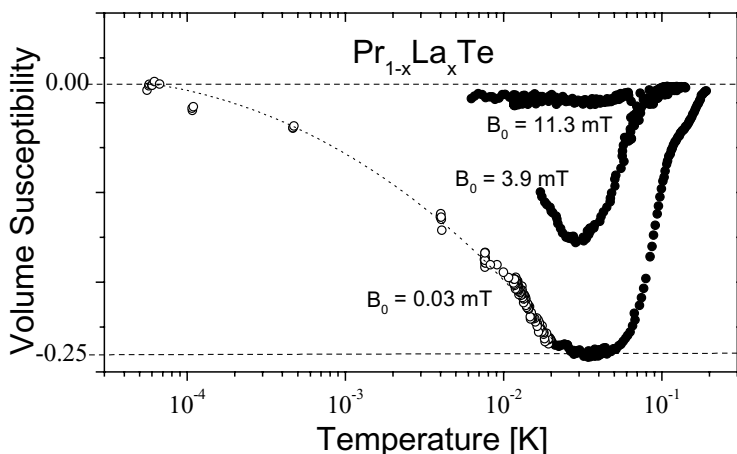


Fig. 25. Ac(16 Hz) susceptibility of $\text{La}_{0.50}\text{Pr}_{0.50}\text{Te}$ at very low temperatures. The closed circles show results taken for bulk samples. The open circles indicate data taken for powder composite samples, which have been investigated in order to reduce the huge thermal relaxation times observed for the bulk sample in the same temperature range. Even for the powder composite sample, relaxation times of the order of days have been observed at $T < 10$ mK. For details, see text.

In summary, in $\text{Pr}_{0.50}\text{La}_{0.50}\text{Te}$ the superconducting state with $T_c = 0.20$ K is not stable down to zero temperature but undergoes a reentrant transition below about 20 mK. This reentrant transition is likely caused by the *hyperfine enhanced nuclear magnetic* moments of ^{141}Pr . Although the hyperfine enhanced nuclear magnetic moments are not in a magnetically ordered ground state at $T = 20$ mK, their impact on superconductivity seems to be even stronger than the influence of a nuclear ferromagnetic transition of the *bare nuclear magnetic* In moments in AuIn_2 (see Sect. 5b). In order to study the possible influence of a nuclear magnetic ordering transition in $\text{Pr}_{0.50}\text{La}_{0.50}\text{Te}$, more extended investigations are required.

In addition to the observation reported in Sect. 5 and 6, the results presented here underline the strong impact of hyperfine interaction on Cooper pair breaking at ultralow temperatures.

7.3 $\text{Pr}_{1-x}\text{La}_x\text{Cu}_6$ as a further candidate

The isostructural intermetallic rare earth copper compounds of stoichiometry RECu_6 (RE = La, Ce, Pr, Nd) reveal an interesting variety of physical phenomena. CeCu_6 is a classical heavy fermion system which exhibits dynamic and static spin correlations. NdCu_6 is well known as an electronic antiferromagnet. PrCu_6 is a classical Van Vleck paramagnet and in regard of its nuclear magnetic properties, a hyperfine enhanced nuclear spin system which undergoes a spontaneous nuclear magnetic ordering transition at mK temperatures [29]. In detail, nuclear magnetic ordering transition temperatures between 2.15 and 2.7 mK have been

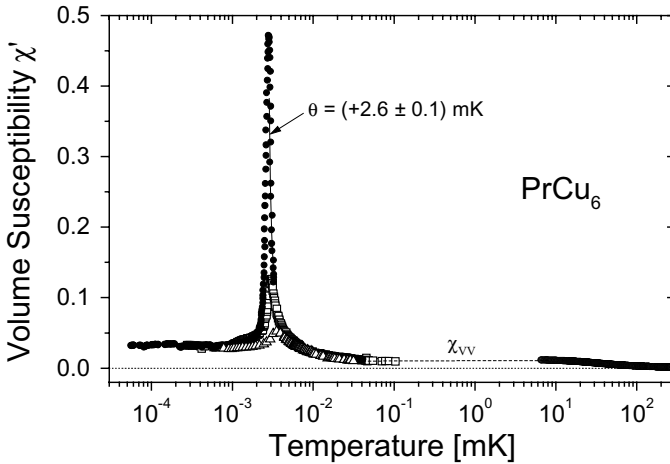


Fig. 26. Static susceptibility measured with a SQUID magnetometer at $T > 4$ K and ac (16Hz) susceptibility at $55 \mu\text{K} \leq T \leq 110$ mK of PrCu_6 . The nonmagnetic singlet crystal electrical field ground state of Pr in PrCu_6 leads to a constant van Vleck susceptibility χ_{vV} at $T \leq 5$ K (indicated by the dashed horizontal line). The hyperfine enhanced nuclear magnetic ^{141}Pr moments in PrCu_6 show an exceptionally large increase to a maximum of the total susceptibility χ close to 0.5 (for comparison: note the comparably small value of χ_{vV}). The temperature dependence (full line) follows an archetypal ferromagnetic Curie-Weiss law with a clearly positive Weiss temperature of the size of the nuclear magnetic ordering temperature $T_{\text{cn}}(B < 0.1 \text{ mT}) = 2.75$ mK as indicated in the figure. Furthermore, the increase of the nuclear magnetic ordering temperature [$T_{\text{cn}}(5 \text{ mT}) = 3.0$ mK (open squares), $T_{\text{cn}}(25 \text{ mT}) = 3.5$ mK (open triangles)] at increasing the field applied to the sample clearly supports the occurrence of a hyperfine enhanced *nuclear ferromagnetic* ordering transition in PrCu_6 .

reported [29]. Our own investigation on this compound yields clear hints for a nuclear hyperfine enhanced ferromagnetic ground state at $T \leq T_{\text{cn}} = 2.75$ mK and with $\theta = +2.6$ mK (Fig. 26). The hyperfine enhanced nuclear ac susceptibility shows all features of an archetypal ferromagnet (Fig. 26). In particular, the positive Weiss temperature of the size of the nuclear magnetic ordering temperature $T_{\text{cn}} = 2.75$ mK and its increase at increasing the field applied to the sample clearly demonstrates the occurrence of *hyperfine enhanced nuclear ferromagnetism* in PrCu_6 .

If superconductivity could be observed in the Pauli paramagnet LaCu_6 than this nuclear ferromagnetic transition would make the intermetallic compounds $\text{Pr}_{1-x}\text{La}_x\text{Cu}_6$ interesting candidates for the study of the interplay of hyperfine enhanced nuclear ferromagnetism and superconductivity. However, our search in the literature during the time of our experiments resulted in no hint of a previous successful effort to find a superconducting transition in LaCu_6 (but see also our later finding of Ref. [48]).

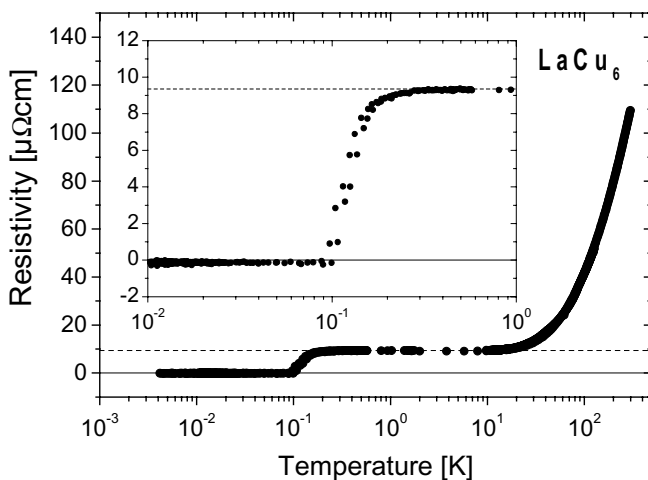


Fig. 27. Resistivity of polycrystalline LaCu_6 at $4 \text{ mK} \leq T \leq 300 \text{ K}$. The inset shows the superconducting transition at 120 mK in more detail. During its cooldown from room temperature, the bulk LaCu_6 sample has been exposed to a static field $B_0 \leq 10 \mu\text{T}$.

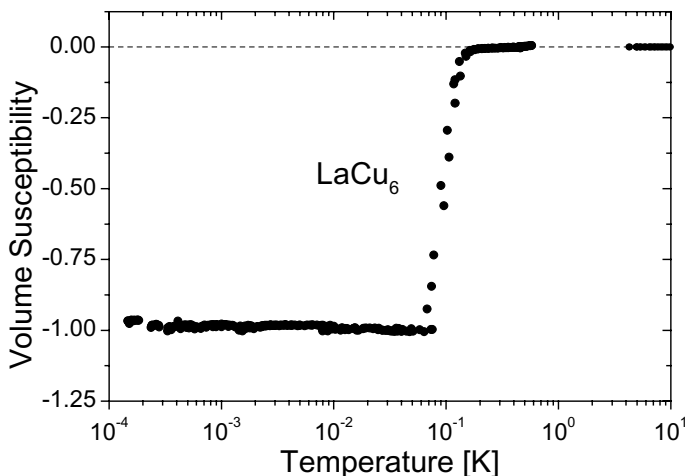


Fig. 28. Ac susceptibility of LaCu_6 at $140 \mu\text{K} \leq T \leq 10 \text{ K}$. As already seen in the resistivity data, the superconducting transition occurs at around 0.12 K . The static field has been compensated to $B_0 \leq 10 \mu\text{T}$. 16Hz ac primary field amplitudes $B_{16\text{Hz}} \leq 1.0 \mu\text{T}$ have been used.

For the search of superconductivity in LaCu_6 [49], we have prepared polycrystalline samples by arc melting of the elements (99.99 % La, 99.9999 % Cu). We have added 5 atom % of Cu to the stoichiometric ratio in order to compensate for the higher volatility of Cu from the melt [49]. The x-ray diffraction data for the sample agree with calculated diffraction patterns. The content of magnetic impurities in our LaCu_6 sample have been obtained by polarising the impurity moments in a field of 3.0 T at Kelvin temperatures, $4.3 \text{ K} \leq T \leq 40 \text{ K}$. By fitting the Brillouin function to the magnetization data, we have obtained average values $x = (26 \pm 2)$ ppm of the concentration of impurities with magnetic moments $\mu = (11.7 \pm 0.9) \mu_B$ and average spin quantum number $J = 2.5 \pm 0.6$, probably caused by remanent magnetic rare earth impurities from the used La of 4N quality.

We have measured the ac resistivity and the ac susceptibility (ac amplitudes less than $1 \mu\text{T}$, remanent magnetic field less than $10 \mu\text{T}$) of LaCu_6 at a frequency of 16 Hz. In order to get a reasonable thermal coupling of the used bulk sample to the thermal reservoir, it has been glued to a silver link which is connected to the nuclear refrigeration stage. Resistivity data have been taken from room temperature to a few mK. As it is typical for such intermetallic compounds, we have observed a rather small residual resistivity ratio $\text{RRR} = 11$ for our sample (Fig.27). The reduction of R to 90 % RR, 50 % RR, and 10 % RR occurs at 160, 120, and 100 mK, respectively. Below 100 mK the resistivity remains zero within our resolution. The superconducting transition of our sample appears to be clearly broadened. The susceptibility data (Fig. 28) exhibit similar features. We suspect that the broadening is at least partly caused by an inhomogeneous distribution of magnetic rare earth impurities. During writing of our manuscript [48], we have realized, that superconductivity had already been observed in LaCu_6 by Sumiyama et al. [47] at $T_c = 42 \text{ mK}$. This lower value could be the result of a higher magnetic impurity content or larger magnetic field applied to the sample used in this experiment.

As a result, there is indeed the possibility to study interplay phenomena between superconductivity and hyperfine enhanced nuclear magnetism with ferromagnetic tendency in $\text{Pr}_{1-x}\text{La}_x\text{Cu}_6$ (and possibly in other van Vleck compounds as well). Due to the quenched electronic magnetic properties of PrCu_6 through the singlet crystal field ground state we expect a much smaller influence of Pr doping on the superconducting transition of LaCu_6 compared to other 4f impurities.

8. SUMMARY

In the preceding sections, we have described experimental results obtained at milli- and micro- Kelvin temperatures which have given the following informations on superconductivity at ultralow temperatures and its interplay with nuclear magnetism.

- Very pure Au (3d impurity concentration less than 10^{-2} ppm) seems to be a superconductor with $T_c = 100 \mu\text{K}$. However, Ag and Cu are – if at all – only superconducting at $T < 10 \mu\text{K}$.
- For the platinum metals, we find Rh to be superconducting with $T_c = 325 \mu\text{K}$, whereas Pd and Pt do not superconduct to a few microKelvin, probably because of their strongly Stoner enhanced paramagnetism. However surprisingly, compacted Pt powder is a superconductor with T_c depending on grain size and packing fraction (for example, $T_c = 1 \text{ mK}$ for $d = 2 \mu\text{m}$

and $V/V_0 = 63\%$). It remains to be shown whether this superconducting transition is caused by the weakened magnetism or/ and by additional soft surface phonons of the compacted powders compared to the bulk material.

- We discuss the first observation of a spontaneous nuclear ferromagnetic transition in a simple not hyperfine enhanced metal in thermal equilibrium in AuIn_2 at $T_{\text{cn}} = 35 \mu\text{K}$, as well as its interplay with type I superconductivity in this intermetallic compound. At $T < T_{\text{cn}}$, the critical field of superconductivity is depressed from 1.45 mT in the nuclear paramagnetic state to values between 1.1 and 0.87 mT in the nuclear ferromagnetic state, depending on the field induced nuclear polarization in the nuclear paramagnetic state. Hence, in the nuclear ferromagnetic state superconductivity is weakened but does not vanish. Vice versa, the nuclear ferromagnetic state does not seem to be influenced by field induced transitions from and to the superconducting state. However, various details of the observations are not yet understood and wait for a further theoretical interpretation.

- For Al, Sn, In, AuAl_2 , and AuIn_2 we observe a small reduction ΔB_c of the critical field of superconductivity already in the nuclear paramagnetic state at very low temperatures. This reduction is proportional to the nuclear magnetization M , as expected for dominant electromagnetic interaction. The proportionality parameter α between ΔB_c and M expressing the strength of this reduction is 1 for the three investigated elements but only 0.08 for AuAl_2 and 0.3 for AuIn_2 . This result shows that the interplay is not simply proportional to the hyperfine coupling expressed by the Korringa constant, and it remains to be understood. For the two samples with strong indirect nuclear exchange interactions, In and AuIn_2 , the temperature T in the equations has to be replaced by $T - \Theta$ (Θ : nuclear Weiss temperature). This section is concluded by some comments on possibly relevant behaviour of metal hydrides, in particular on the here investigated $\text{TiH}_{2.07}$ ($T_c = 15 \text{ mK}$).

- Eventually, we have discussed investigations of the superconducting and nuclear magnetic properties of the mixed hyperfine enhanced compounds $\text{Pr}_{1-x}\text{La}_{1-x}\text{Te}$ and $\text{Pr}_{1-x}\text{La}_x\text{Cu}_6$. In particular, we find reentrant behaviour of superconducting $\text{Pr}_{0.5}\text{La}_{0.5}\text{Te}$ ($T_c = 0.2\text{K}$) below $T = 20 \text{ mK}$, probably caused by the hyperfine enhanced nuclear magnetic moments of ^{141}Pr . Obviously, these enhanced moments in the nuclear paramagnetic state have an even stronger impact on superconductivity than the nuclear ferromagnetic transition of the bare nuclear moments of In in superconducting AuIn_2 . It would be of interest to extend these studies to other van Vleck compounds, in particular $\text{Pr}_{1-x}\text{La}_x\text{Cu}_6$, starting from the here investigated nuclear ferromagnet PrCu_6 ($T_{\text{cn}} = 2.75 \text{ mK}$) to LaCu_6 for which we have observed a superconducting transition at $T_c = 120 \text{ mK}$.

The above discussed investigations have given a wealth of first and new informations on the investigated problems. However, various aspects of our results remain to be understood and many more investigations of superconductivity at ultralow temperatures and its interplay with nuclear magnetism, be it a nuclear ordered state, nuclear paramagnetism or hyperfine enhanced nuclear magnetism wait for further experimental as well as theoretical studies.

ACKNOWLEDGEMENT

We gratefully acknowledge the contributions of our co-workers in Jülich, Ch. Buchal, H. R. Folle, M. Kubota, R. M. Mueller, and J. R. Owers-Bradley, as well as in Bayreuth, R. König, S. Rehmann, A. Schindler, B. Schröder-Smeibidl, M. Seibold, P. Smeibidl, and W. Wendler to the experiments described in this article.

REFERENCES

- [1] W. C. Black, R. T. Johnson, J. C. Wheatly, *J. Low Temp. Phys.* 1 (1969) 641; T. L. Thorp, B. B. Triplett, W. D. Brewer, M. L. Cohen, N. E. Phillips, D. A. Shirley, J. E. Tempton, R. W. Stark, P. H. Schmidt, *J. Low Temp. Phys.* 3 (1970) 589.
- [2] A. C. Mota, W. C. Black, P. M. Brewster, A. C. Lawson, R. W. Fitzgerald, J. H. Bishop, *Phys. Lett.* 34A (1971) 160
- [3] Frank Pobell, *Matter and Methods at Low Temperatures*, Springer Verlag, Berlin-Heidelberg; 1. ed. 1992, 2. ed. 1996
- [4] V. L. Ginzburg, *Sov. Phys. JETP* 4 (1957) 153; A. A. Abrikosov, L. P. Gorkov, *Sov. Phys. JETP* 12 (1961) 1243; B. T. Matthias, H. Suhl, E. Corenzwit, *Phys. Rev. Lett.* 1 (1958) 92 and 449.
- [5] W. A. Fertig, D. C. Johnston, L. E. DeLong, R. W. McCallum, M. B. Maple, B. T. Matthias, *Phys. Rev. Lett.* 38 (1977) 987; M. Ishikawa, O. Fischer, *Sol. State Comm.* 24 (1977) 747.
- [6] T. Herrmannsdörfer, P. Smeibidl, B. Schröder-Smeibidl, F. Pobell, *Phys. Rev. Lett.* 74 (1995) 1996; T. Herrmannsdörfer, F. Pobell, *J. Low Temp. Phys.* 100 (1995) 253.
- [7] S. Rehmann, T. Herrmannsdörfer, F. Pobell, *Phys. Rev. Lett.* 78 (1997) 1122.
- [8] R. M. Mueller, Ch. Buchal, H. R. Folle, M. Kubota, F. Pobell, *Cryogenics* 26 (1980) 395; F. Pobell, *Physica B* 109-110 (1982) 1485.
- [9] K. Gloos, P. Smeibidl, C. Kennedy, A. Singsaas, P. Sekowski, R. M. Mueller, F. Pobell, *J. Low Temp. Phys.* 73 (1988) 101.
- [10] W. Wendler, T. Herrmannsdörfer, S. Rehmann, F. Pobell, *Europhys. Lett.* 38 (1997) 619.
- [11] R. A. Buhrman, W. P. Halperin, *J. Low Temp. Phys.* 16 (1974) 409.
- [12] R. F. Hoyt, A. C. Mota, *Sol. State Comm.* 18 (1976) 139.
- [13] Ch. Buchal, R. M. Mueller, F. Pobell, M. Kubota, H. R. Folle, *Sol. State Comm.* 42 (1982) 43.
- [14] R. A. Webb, J. B. Ketterson, W. P. Halperin, J. J. Vuillemin, N. B. Sandesara, *J. Low Temp. Phys.* 32 (1978) 659.
- [15] Ch. Buchal, F. Pobell, R. M. Mueller, M. Kubota, J. R. Owers-Bradley, *Phys. Rev. Lett.* 50 (1983) 64.
- [16] B. R. Coles, *Phys. Lett.* 8 (1964) 243; G. S. Knapp, *J. Appl. Phys.* 38 (1967) 1267; A. B. Kaiser, S. Doniach, *Int. J. Magn.* 1 (1970) 11.
- [17] T. A. Knuutila, J. T. Tuoriniemi, K. Lefman, K. J. Juntunen, F. B. Rasmussen, K.K. Nummila, *J. Low Temp. Phys.* 123 (2201) 65.
- [18] T. Herrmannsdörfer, S. Rehmann, W. Wendler, F. Pobell, *J. Low Temp. Phys.* 104 (1996) 49; T. Herrmannsdörfer, S. Rehmann, F. Pobell, *J. Low Temp. Phys.* 104 (1996) 67.

- [19] B. L. Gyorffy, A. Pindor, W. M. Temmerman, Phys. Rev. Lett. 43 (1979) 1343.
- [20] Ch. Buchal, B. Stritzker, M. Kubota, R. M. Mueller, F. Pobell, Sol. State Comm. 39 (1981) 771.
- [21] B. Stritzker, W. Buckel, Z. Physik 257 (1972) 1; B. Stritzker, Phys. Rev. Lett. 42 (1979) 1796; J. D. Meyer, B. Stritzker, Phys. Rev. Lett. 48 (1982) 502.
- [22] R. König, T. Herrmannsdörfer, D. Riese, W. Jansen, J. Low. Temp. Phys. 106 (1997) 581; R. König, T. Herrmannsdörfer, I. Batko, Phys. Rev. Lett. 80 (1998) 4787; T. Herrmannsdörfer, R. König, J. Low. Temp. Phys. 118 (2000) 450.
- [23] R. König, A. Schindler, T. Herrmannsdörfer, Phys. Rev. Lett. 82 (1999) 4528.
- [24] M. Strongin, Physica 55 (1971) 154 ; H. Zeller, I. Giaever, Physica 55 (1971) 173; B. Abeles, *Granular Metal Films* in Applied Solid State Sci. 6 (1976) 1.
- [25] A. Schindler, R. König, T. Herrmannsdörfer, H. F. Braun, Phys. Rev. B 62 (2000) 14350.
- [26] J. Clem, Physica 153 (1988) 50.
- [27] A. Schindler, R. König, T. Herrmannsdörfer, H. F. Braun, G. Eska, D. Günther, M. Meissner, M. Mertig, R. Wahl, W. Pompe, Europhys. Lett. 58 (2002) 885.
- [28] A. S. Oja, O. V. Lounasmaa, Rev. Modern Phys. 69 (1997) 1.
- [29] J. Babcock, J. Kiely, T. Manley, W. Weyhmann, Phys. Rev. Lett. 43 (1979) 380 and K. Akashi, K. Kawabata, A. Matsubara, O. Ishikawa, T. Hata, H. Ishii, T. Kodama; Y. Onuki, Phys. Rev. Lett. 82 (1999) 1297 ; M. Kubota, H. R. Folle, Ch. Buchal, R. M. Mueller, F. Pobell, *ibid.* 45 (1980) 1812.
- [30] P. Fulde, K. Maki, Phys. Rev. 141 (1966) 275.
- [31] R. S. Tebble, D. J. Craik, *Magnetic Materials*, John Wiley & Sons Ltd., London, (1969)
- [32] A. Dyugaev, I. Vagner, P. Wyder, JETP Lett. 65 (1997) 810
- [33] M. Kulic, A. Duzdin, L. Bulaevskii, Phys. Rev. B 56 (1997) R11 415
- [34] E. Sonin, J. Low Temp. Phys. 110 (1998) 411
- [35] T. Herrmannsdörfer, S. Rehmann, M. Seibold, F. Pobell, J. Low Temp. Phys. 110 (1998) 405.
- [36] M. Seibold, T. Herrmannsdörfer, F. Pobell, J. Low Temp. Phys. 110 (1998) 363.
- [37] T. Herrmannsdörfer, Physica B 280 (2000) 368.
- [38] T. Herrmannsdörfer, D. Tayurskii, J. Low Temp. Phys. 124 (2001) 257.
- [39] Y. Karaki, M. Kubota, H. Ishimoto, Physica B 194-196 (1994) 461; L. Pollack, E. N. Smith, R. C. Richardson, J. Low Temp. Phys. 106 (1997) 93.
- [40] W. Heeringa, R. Aures, R. Maschuw, F. K. Schmidt, Cryogenics 25 (1985) 365.
- [41] U. Stuhr, D. Steinbinder, H. Wipf, B. Frick, Europhys. Lett. 20 (1992) 117.
- [42] J. Li, I. Roggatz, Y. Kondo, E. Rössler, F. Pobell, Proc. 21. Int. Conf. Low Temp. Phys., Prague, Vol. S 4 (1996) 2193.
- [43] A. Abrikosov, L. Gorkov, Sov. Phys. JETP 12 (1961) 1243.
- [44] E. Bucher, K. Andres, J. Maita, G. Hull, Jr., Helv. Phys. Acta 41 (1968) 723.
- [45] J. Keller, P. Fulde, J. Low Temp. Phys. 4 (1971) 289.
- [46] K. C. Turberfield, L. Passel, R. J. Birgeneau, E. Bucher, Phys. Rev. Lett. 25 (1970) 752.
- [47] T. Herrmannsdörfer, J. Sebek, to be published.
- [48] A. Sumiyama, Y. Oda, H. Nagano, Y. Onuki, T. Komatsubara, J. Phys. Soc. Jap. 54 (1985) 877.
- [49] T. Herrmannsdörfer, F. Pobell, J. Sebek, P. Svoboda, Physica C 388-389 (2003) 565.

SUPERCONDUCTIVITY IN HEAVY FERMION COMPOUNDS

P Thameier¹, G Zwirner², O Stocert¹, G Sparn¹, and F Steglich¹

¹Max-Planck-Institut für Chemische Physik fester Stoffe,
01187 Dresden, GERMANY

²Institut für Mathematische Physik,
Technische Universität Braunschweig,
38106 Braunschweig, GERMANY

1 INTRODUCTION

The heavy electron state in intermetallic lanthanide and actinide compounds has its origin in the interplay of strong Coulomb repulsion in the 4f- and 5f- shells and their hybridisation with conduction band states. Heavy quasiparticles have mostly been observed in Ce- and U-based intermetallics which are therefore at the focus of this review. Ideally the ground state in these strongly correlated electron compounds may be described as a Landau Fermi liquid (LFL) state with large enhancement of the effective mass and associated large values of the linear specific heat coefficient γ , Pauli susceptibility χ_0 and A-coefficient of the resistivity. It has recently become clear that the microscopic origin of mass enhancement is quite different in Ce- and U-compounds, as described by the Kondo lattice model and dual model respectively.

The renormalised LFL state is however prone to instabilities at low temperatures due to residual heavy quasiparticle interactions and the sharpness of the Fermi distribution. The most common instabilities are the spontaneous appearance of (spin-)density wave (SDW) and superconducting (SC) order parameters which break at least some of the underlying spatial or internal symmetries like time reversal or gauge symmetry. Via their associated gap functions both type of order parameters are reflected in the modified energies and densities of low lying excitations.

This also changes low temperature properties in the ordered state and may in turn be used as a means to obtain information on the symmetry class of the order parameter. Both SC and SDW gap functions $\Delta(\mathbf{k})$ may be conventional or unconventional depending on whether their \mathbf{k} -dependence has the same or a lower spatial symmetry as the Fermi surface. In the latter case particles (SC) or particles and holes (SDW) pair preferentially at neighboring sites and avoid the strong on-site repulsion of quasiparticles. For this reason the SC states in Ce- and U-based HF compounds are usually of the unconventional type. Their intriguing properties have led to a rich and flourishing field of research, not only in the genuine HF compounds but also in oxides, ruthenates and organic solids.

The stability of the ordered phase may be influenced by changing microscopic control parameters via application of pressure or by chemical substitution. In this way the SDW state may be tuned to a magnetic quantum critical point (QCP) where the staggered moment vanishes. On theoretical grounds it has long been suspected that unconventional SC pairing is favored by magnetic instabilities, triplet pairing in the ferromagnetic and singlet pairing in the antiferromagnetic case. This correlation, however, cannot always be upheld for real HF materials.

The accumulated evidence in the Ce122 (e.g. CeCu_2Si_2), Ce115 (e.g. CeCoIn_5) and Ce218 (e.g. Ce_2CoIn_8) classes of superconductors seems to vindicate this picture, since the SC appears mostly in small 'domes' around the QCP. The connection between critical spin fluctuation properties and the stability of SC pair states has been analysed within strong coupling Eliashberg type theories. The QCP has additional implications beyond SC. In the normal state above the SC dome thermodynamic and transport behaviour show distinctly anomalous non-Fermi liquid (NFL) behaviour as function of temperature and field. This is thought to be the result of a dressing of quasiparticles with soft spin fluctuations leading to entirely different scaling exponents for specific heat, resistivity etc. as compared to the LFL state. This scenario is accepted for most NFL anomalies in Ce-HF compounds. Alternatively they may be caused by the existence of a 'pseudo-gap' associated with a 'hidden order' parameter, e.g. an unconventional SDW. This may indeed play a role in CeCoIn_5 and CeIrIn_5 in a similar way as invoked for the pseudo-gap phase of underdoped cuprates.

In U-based HF superconductors quantum critical behaviour does not play an important role with the possible exception of UBe_{13} . Instead of appearing close to the destruction of SDW order, SC in U-HF compounds is mostly embedded within a stable AF phase of reduced (sometimes very small) ordered moments. Like the different origin of mass enhancement this may be connected with the multi-orbital structure and multiple occupation of 5f shells. Instead of the Kondo lattice picture, a dual model with partly localised and partly itinerant electrons caused by a strongly orbital dependent effective hybridisation is more appropriate for U-HF compounds. In turn this suggests a new SC mechanism: Pair formation is caused by the exchange of magnetic excitons which are CEF excitations of the localised 5f-electrons that have acquired dispersion due to intersite-exchange. Contrary to the critical spin fluctuations in Ce-compounds these propagating bosonic modes are not overdamped. This mechanism has been vindicated in UPd_2Al_3 by the complementary results of quasiparticle tunneling and inelastic neutron scattering (INS) experiments. An equivalent experimental support for the spin fluctuation mechanism is still lacking.

This article reviews the present understanding of Ce-based and some of the U-based HF superconductors, with emphasis on the former. We will not discuss the physics of HF su-

perconductors containing other 4f or 5f elements like Pr skutterudites or trans-uranium based superconductors. For Ce-compounds we focus on the connection to magnetic quantum critical behaviour and the implications of the dual 5f-electron nature are discussed extensively for U-compounds. In sect. 2 we give the theoretical foundation of the different heavy quasiparticle origin in Ce- and U- compounds and present a brief summary of NFL properties in the normal state close to a QCP. In sect. 3 we discuss the known classes of Ce-HF superconductors with emphasis on the Ce122 compounds. We also discuss the new non-centrosymmetric SC CePt₃Si. In sect. 4 we give a description of the different microscopic pairing mechanisms present in the Ce- and U- intermetallics. In sect. 5 we discuss only those two U-based HF superconductors where new results have been obtained recently, namely UBe₁₃ and UPd₂Al₃. Finally sect. 6 gives the summary.

Of the many already existing review articles and monographies on HF systems and their superconducting state we mention here a small selection: The normal state properties of HF metals are at the focus in [1–4]. General reviews on HF superconductors are given in [5, 6] and the monography [7]. The exceptional case of the multicomponent SC UPT₃ is discussed in detail in [8, 9].

2 THEORIES FOR THE NORMAL HF STATE

The theoretical understanding of superconductivity and magnetism in the heavy fermion systems is still in the state of rather schematic or illustrative models. A major difficulty is that the normal state quasiparticles can sofar be described only within effective single-particle renormalised band pictures with empirical input parameters. For some compounds like UBe₁₃ and Ce- compounds close to the quantum critical point the SC transition may even take place in a state where the low energy excitations are not simple LFL quasiparticles but are dressed by soft spin fluctuations. This is witnessed by the observation of non-Fermi liquid (NFL) behaviour in thermodynamic and transport quantities. A fully microscopic description in the case where inter-site effects become important is not available. Typical lattice effects are the formation of coherent heavy quasiparticle bands whose Fermi surfaces were observed experimentally. We first discuss the renormalised band theory which provides a way to describe the coherent heavy quasiparticle bands within a Fermi liquid approach. The latter can be calculated from single-particle Hamiltonians where the effective potential is constructed to account for many-body effects. The residual interaction among the quasiparticles eventually leads to the instability of the normal Fermi liquid phase.

2.1 RENORMALISED BAND THEORY FOR HF Ce-COMPOUNDS

The Landau theory assumes that there exists a one-to-one correspondence between the states of the complex interacting system and those of a gas of independent fermions, which may move in an external potential [10–12], [13]. The single-particle orbitals and energies are determined from an effective Hamiltonian. The characteristic properties of a system are reflected in an effective and not necessarily local potential which describes the field of the nuclei and the modifications arising from the presence of the other electrons. The essential many-body aspects

of the problem are then contained in the prescription for constructing the effective potentials which have to be determined for specific problems.

The Landau theory of Fermi liquids is a phenomenological theory. The characteristic properties of the quasiparticles which can hardly be calculated from microscopic theories are expressed in terms of parameters which are determined from experiment. The quasiparticle energies in a crystal

$$\varepsilon(\mathbf{k}) = \mathbf{v}_F(\hat{\mathbf{k}}) \cdot (\mathbf{k} - \mathbf{k}_F(\hat{\mathbf{k}})) \quad (1)$$

are given in terms of the (anisotropic) Fermi wave vector \mathbf{k}_F and the Fermi velocity \mathbf{v}_F which depend upon the direction $\hat{\mathbf{k}}$. The key idea of the renormalized band method is to determine these quantities by computing the band structure for a given effective potential which accounts for the many-body effects. The periodic potential leads to multiple-scattering processes involving scattering off the individual centers as well as the propagation between the centers. The characteristic properties of a given material enter through the information about single center scattering. They can be expressed in terms of properly chosen set of phase shifts $\{\eta_v^i(\varepsilon)\}$ specifying the change in phase of a wave incident on site i with energy E and symmetry v with respect to the scattering center. Within the scattering formulation of the band structure problem the values of the phase shifts at the Fermi energy $\{\eta_v^i(\varepsilon_F)\}$ together with their derivatives $\left\{ \left(\frac{d\eta_v^i}{d\varepsilon} \right)_{\varepsilon_F} \right\}$ determine the Fermi wave vectors \mathbf{k}_F and the Fermi velocity \mathbf{v}_F . The scattering formulation of the effective band structure problem provides a highly efficient parametrisation scheme for the quasiparticles. To further reduce the number of phenomenological parameters we refer to the microscopic model for Ce-based HF compounds.

The similarities in the behavior of Ce-based heavy-fermion systems to that of dilute magnetic alloys have led to the assumption that these systems are "Kondo lattices" where the observed anomalous behavior can be explained in terms of periodically repeated resonant Kondo scattering. This ansatz provides a microscopic model for the formation of a singlet ground-state and the existence of heavy quasiparticles. An extensive discussion is given in [4]. Direct evidence for the Kondo scenario comes from photoelectron spectroscopy. The characteristic features of a Kondo system can be summarized as follows [14, 15]: At high temperatures, the combined PES/BIS spectra from photoemission and inverse photoemission exhibit two distinct peaks below and above the Fermi energy. These two features correspond to the valence transitions $f^n \rightarrow f^{n\pm 1}$, respectively. The changes in the occupation of the Ce 4f- shells are associated with energies of order eV. The high-temperature state can be modelled by weakly correlated conduction electrons which are weakly coupled to local f-moments. The f-derived low-energy excitations are those of a system of local moments. The direct manifestation of the low-energy scale is the appearance of a sharp peak near the Fermi energy at low temperatures. In Ce systems, this many-body feature known as "Abrikosov-Suhl" or "Kondo" resonance, is centered at $\varepsilon_F + kT^*$ slightly above the Fermi edge ε_F . The "Kondo temperature" T^* determines the energy scale of the dynamical screening of the impurity spin by conduction electrons [4]. The evolution of the Kondo resonance with temperature was recently observed by high-resolution photoemission experiments [16].

The resonance is a genuine many-body feature reflecting the small admixture of f^0 configurations to the ground state and the low-lying excitations which are mainly built from f^1 -configurations. At sufficiently low temperatures $T \ll T^*$, the contribution of the narrow reso-

nance peak to the thermodynamic and transport properties can be described in terms of a Landau theory with heavy fermionic quasiparticles [17]. Based on the corresponding effective Hamiltonian Nozières [18] introduced a resonant phase shift to account for the impurity contribution to the low-energy properties.

The novel feature observed in stoichiometric Ce-compounds is the formation of narrow coherent bands of low-energy excitations. The heavy fermions arise from a decoherence-coherence crossover occurring at low temperatures.

The calculation of realistic quasiparticle bands in Ce-based Heavy Fermion compounds proceeds in several steps. For a detailed description see [19]. The first step is a standard LDA band structure calculation by means of which the effective single-particle potentials are self-consistently generated. The calculation starts, like any other ab-initio calculation, from atomic potentials and structure information. In this step, no adjustable parameters are introduced. The effective potentials and hence the phase shifts of the conduction states are determined from first principles to the same level as in the case of “ordinary” metals. The f -phase shifts at the lanthanide and actinide sites, on the other hand, are described by an empirical resonance type expression

$$\eta_{\hat{f}} \simeq \tan^{-1} \frac{\Gamma_{\hat{f}}}{\varepsilon - \varepsilon_{\hat{f}}} \quad (2)$$

charactered by the position $\varepsilon_{\hat{f}}$ and the width $\Gamma_{\hat{f}}$ of the many-body resonance. One of these free parameters is eliminated by imposing the condition that the charge distribution is not significantly altered as compared to the LDA calculation by introducing the renormalisation. The renormalised band method devised to calculate the quasiparticles in heavy-fermion compounds thus is essentially a one-parameter theory. We mention that spin-orbit and CEF splittings can be accounted for in a straight-forward manner [20].

The strong local correlations in Kondo lattices lead to an observable many-body effect, i. e., the change with temperature of the volume of the Fermi surface. At high temperatures, the f -degrees of freedom appear as localised magnetic moments, and the Fermi surface contains only the itinerant conduction electrons. At low temperatures, however, the f degrees of freedom are now tied into itinerant fermionic quasiparticle excitations and accordingly, have to be included in the Fermi volume following Luttinger’s theorem. Consequently the Fermi surface is strongly modified. This scenario [21] was confirmed experimentally by measurements of the de Haas-van Alphen (dHvA) effect [22–24].

2.2 DUAL MODEL FOR U-BASED SYSTEMS

The Kondo picture, however, does not apply in the case of the actinide compounds. The difficulties with this model have been discussed in [25]. The difference between the Ce-based heavy-fermion compounds and their U-counterparts can be seen directly from the photoemission spectra [14]. In U-based heavy-fermion compounds, the fingerprint character of the transitions $f^n \rightarrow f^{n\pm 1}$ is lost. Instead of the well defined f -derived peaks familiar from the Ce systems we encounter a rather broad f -derived feature. This fact shows that the f -valence in the actinide heavy-fermion systems is not close to integer value as it is the case in Ce-based HF compounds. In fact, the f -valence of the U ions has been discussed rather controversially.

Increasing experimental and theoretical evidence points towards a dual nature of the $5f$ -electrons in actinide-based intermetallic compounds, with some of the $5f$ electrons being localised and others delocalised. The dual model which assumes the coexistence of both delocalised and localised $5f$ -electrons provides a scheme for microscopic calculations of the heavy quasiparticle bands in actinide compounds. The concept is summarised as follows: The “delocalised” $5f$ -states hybridise with the conduction states and form energy bands while their “localised” atomic-like counterparts form multiplets to reduce the local Coulomb repulsion. The two subsystems interact which leads to the mass enhancement of the delocalised quasiparticles. The situation resembles that in Pr metal where a mass enhancement of the conduction electrons by a factor of 5 results from virtual crystal field (CEF) excitations of localised $4f^2$ electrons [26]. The underlying hypothesis is supported by a number of experiments. For an extensive discussion we refer to [27]. Calculations based on the dual model as described above reproduce the dHvA data in UPt₃ [28] and UPd₂Al₃ [29]. The results of the latter calculation will be discussed in sect. 5.2.

The dual nature of the $5f$ states which is found in many actinide intermetallic compounds is a consequence of the interplay between local Coulomb correlations and hybridisation with the conduction electrons. The underlying microscopic mechanism is an area of active current research (see [30] and references therein). LDA calculations show that the effective hopping matrix elements for different $5f$ orbitals are unequal. But it is of interest to understand why only the largest among them is important and why the others are suppressed.

The reason lies in the competition between anisotropic hybridisation and angular correlations in the $5f$ shell which can be seen by exact diagonalisation of small clusters modelling the U sites in heavy fermion compounds [30]. Keeping only the degrees of freedom of the $5f$ shells while accounting for the conduction states by (effective) anisotropic $5f$ -intersite hopping leads to the model Hamiltonian

$$H = - \sum_{\langle nm \rangle, j_z} t_{j_z} \left(c_{j_z}^\dagger(n) c_{j_z}(m) + h.c. \right) + H_C \quad (3)$$

The first sum is over neighboring sites $\langle nm \rangle$. Furthermore $c_{j_z}^\dagger(n)$ ($c_{j_z}(n)$), creates (annihilates) an electron at site n in the $5f$ $j = 5/2$ state with $j_z = -5/2, \dots, 5/2$. The effective hopping between sites results from the hybridisation of the $5f$ states with the orbitals of the ligands and depends generally on the crystal structure. Rather than trying to exhaust all possible different lattice symmetries, we shall concentrate here on the special case that hopping conserves j_z . While this is certainly an idealisation, it allows us to concentrate on our main topic, i. e., a study of the influence of atomic correlations on the renormalisation of hybridisation matrix elements. The parameters $t_{j_z} (= t_{-j_z})$ are chosen in accordance with density-functional calculations for bulk material which use jj_j basis states. The local Coulomb interactions can be written in the form

$$H_C = \frac{1}{2} \sum_n \sum_{j_{z1}, \dots, j_{z4}} U_{j_{z1}j_{z2}j_{z3}j_{z4}} c_{j_{z1}}^\dagger(n) c_{j_{z2}}^\dagger(n) c_{j_{z3}}(n) c_{j_{z4}}(n) \quad (4)$$

where the Coulomb matrix elements $U_{j_{z1}j_{z2}j_{z3}j_{z4}}$ are expressed in terms of the expectation values U_J of the repulsion between electron pairs in states with total angular momentum J . The

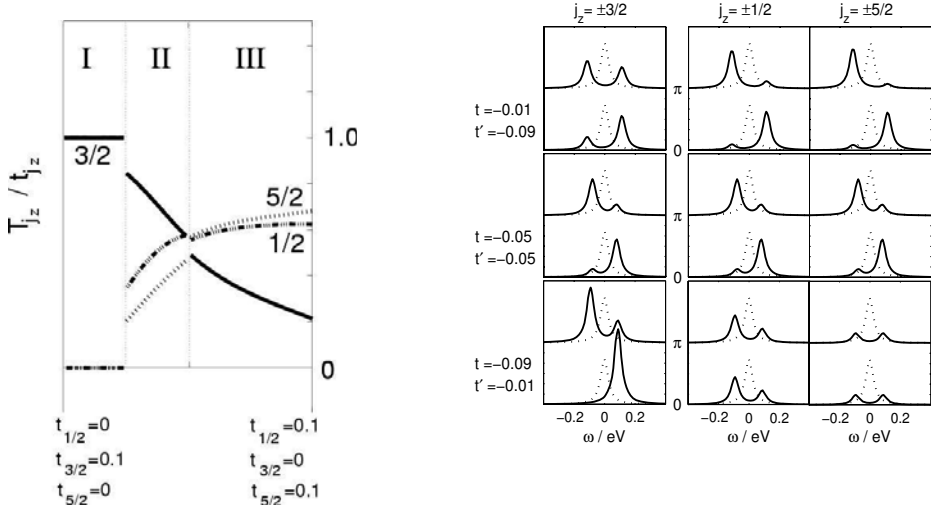


Figure 1: Left panel: Enhancement of hopping anisotropies due to intra-atomic correlations in a two-site cluster. The orbital-projected expectation value of the kinetic energy T_{j_z}/t_{j_z} along the lines connecting linearly the points is written below the figure. Regions with $\mathcal{J}_z=15/2, 5/2$ and $3/2$, are labeled I, II and III respectively. Right panel: Dispersion of the low-energy peak in the spectral functions ($A_{j_z}(\mathbf{k}, \omega) + A_{-j_z}(\mathbf{k}, \omega)$) for strongly anisotropic systems ($|t_{3/2}| = |t| \ll |t'| = |t_{1/2}| = |t_{5/2}|$) as well as in the isotropic limit ($|t_{3/2}| = |t| = |t'| = |t_{1/2}| = |t_{5/2}|$). For each parameter set of hopping parameters, the spectral functions for $\mathbf{k}=0$ and $\mathbf{k}=\pi$ are compared. The dotted curve denotes the isotropic peak in the atomic limit.

actual calculations U_J values used in the calculation were determined from LDA wavefunctions for UPT_3 [28], i. e., $U_{J=4} = 17.21$ eV, $U_{J=2} = 18.28$ eV, and $U_{J=0} = 21.00$ eV. We expect $U_{J=4} < U_{J=2} < U_{J=0}$ always to hold for Coulomb interactions, independently of the chemical environment. In contrast, the relative order of the hopping matrix elements will vary strongly from one compound to the next. The average Coulomb repulsion is irrelevant for the low-energy physics of the model. It simply restricts the relevant configurations to states such that each site is occupied either by 2 or 3 f electrons. The low-energy sector is exclusively determined by the differences of the U_J values, which are of the order of 1eV and thus slightly larger than typical bare f -band widths. The latter are obtained, e.g., from LDA calculations for metallic uranium compounds like UPT_3 . To mimic the situation in the U-based heavy-fermion compounds we consider the intermediate valence regime. The Hamiltonian eq. (3) conserves $\mathcal{J}_z = \sum_n J_z(n)$ where \mathcal{J}_z is the z -component of the total angular momentum of the system and the $J_z(n)$ refer to angular momentum projections on individual sites. We shall therefore characterise the eigenstates by their \mathcal{J}_z value. Strong on-site correlations result in a considerable enhancement of anisotropies in the bare hopping matrix elements. This can lead to a localisation of electrons in orbitals with relatively weak hybridisation. The latter is effectively reduced to zero in those cases.

The degree of localisation or, alternatively, of the reduction of hopping of a given j_z orbital by local correlations, is quantified by the ratio of the j_z -projected kinetic energy T_{j_z} and the bare matrix element t_{j_z}

$$\frac{T_{j_z}}{t_{j_z}} = \sum_{\langle nm \rangle, \pm} \langle \Psi_{\text{gs}} | (c_{\pm j_z}^\dagger(n) c_{\pm j_z}(m) + h.c.) | \Psi_{\text{gs}} \rangle. \quad (5)$$

The ground-state wavefunction $|\Psi_{\text{gs}}\rangle$ contains the strong on-site correlations. A small ratio of T_{j_z}/t_{j_z} indicates partial suppression of hopping for electrons in the $\pm j_z$ orbitals. Two kinds of correlations may contribute to that process. The first one is based on the reduction of charge fluctuations to atomic f^2 and f^3 configurations. This is a result for large values of U_J and can be studied by setting all U_J equal to a value much larger than the different t_{j_z} . The second one is due to differences in the U_J values, i. e., $U_{J=4} < U_{J=2} < U_{J=0}$. The differences in the U_J values are the basis of Hund's rules. Hopping counteracts Hund's rule correlations and vice versa. What we want to stress is the fact that those correlations can lead to a complete suppression of hopping channels except for the dominant one which shows only little influence.

Results for the ratios T_{j_z}/t_{j_z} are shown in fig. 1 for a two-site model [30]. As the relevant correlations are local the general results qualitatively agree with those found for a three-site cluster and four-site clusters [31]. We can distinguish three different regimes with $\mathcal{J}_z = 15/2$, $5/2$ and $3/2$, labeled I, II and III respectively. One observes that in region I only the dominant hybridisation of the $j_z = 3/2$ orbital survives while that of the $j_z = 1/2$ and $j_z = 5/2$ orbitals is completely suppressed. On the other hand in regions II and III the correlation effects on different orbitals are not very different. These findings demonstrate that in particular Hund's rule correlations strongly enhance anisotropies in the hopping. For a certain range of parameters this may result in a complete suppression of the effective hopping except for the largest one, which remains almost unaffected. This provides a microscopic justification of partial localisation of $5f$ electrons which is observed in a number of experiments on U compounds and which is the basis for further model calculations described later on.

Many aspects of partial localisation in the ground state are described appropriately by both a Gutzwiller type variational wave function and by a treatment which keeps only those interactions which are present in LDA+U calculations [32]. This finding should encourage further applications of LDA+U and related approaches as SIC-LDA for ground-state properties of actinide heavy-fermion materials. The subtle angular correlations which determine the magnetic character are accounted for only in limiting cases. In addition, we cannot expect these schemes to reproduce the small energy scales responsible for the heavy fermion character of the low-energy excitations. The dual nature of the $5f$ states is manifest in the spectral functions $A_{j_z}(\mathbf{k}, \omega)$ and the density of states (DOS) $N(\omega)$ given by

$$N(\omega) = \sum_{\mathbf{k}} \sum_{j_z} A_{j_z}(\mathbf{k}, \omega) \quad . \quad (6)$$

The spectral functions which are defined by

$$\begin{aligned} A_{j_z}(\mathbf{k}, \omega) = & \sum_n \left| \left\langle \psi_n^{N+1} \left| c_{j_z}^\dagger(\mathbf{k}) \right| \psi_0^N \right\rangle \right|^2 \delta(\omega - (E_n^{N+1} - E_0^N)) + \\ & + \sum_n \left| \left\langle \psi_n^{N-1} \left| c_{j_z}(\mathbf{k}) \right| \psi_0^N \right\rangle \right|^2 \delta(\omega + (E_n^{N-1} - E_0^N)) \end{aligned} \quad (7)$$

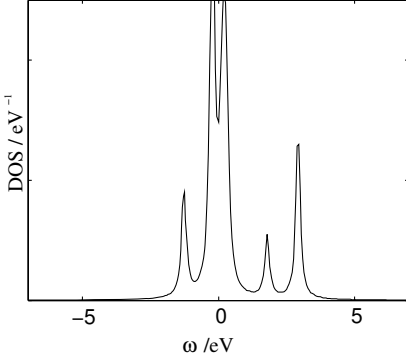


Figure 2: Density of states for a linear chain calculated within CPT. The short-range correlations are treated within a two-site cluster. The hopping parameters are $|t_{3/2}| = 0.2$ eV and $|t_{1/2}| = |t_{5/2}| = 0$. The high-energy side-bands have predominantly $j_z = \pm 5/2$ character.

measure the weights for removing an electrons in state $(\mathbf{k}j_z)$ from the ground state (negative energies) or adding on to it (positive energies). Here $|\psi_0^N\rangle$ denotes the exact ground state of an N -particle system with ground state energy $E_0^{(N)}$ while $|\psi_n^{N+1}\rangle$ and $|\psi_n^{N-1}\rangle$ are complete sets of eigenstates of the $N+1$ - and $N-1$ -particle systems with energies $E_n^{(N+1)}$ and $E_n^{(N-1)}$, respectively. Technically, the spectral functions are obtained from the one-particle Green's functions according to

$$A_{j_z}(\mathbf{k}, \omega) = -\frac{1}{\pi} \text{Im} G_{j_z}(\mathbf{k}, \omega) \quad (8)$$

which are approximately calculated for a cluster following [33]. As a first step towards a microscopic treatment of partial localisation in extended systems the one-particle Green's functions are calculated within cluster perturbation theory. The method combines exact diagonalisation of small clusters with strong-coupling perturbation theory [34]. The many-particle states of the clusters are determined by means of the Jacobi-Davidson method [35]. The formation of the heavy quasiparticles, i. e., the enhancement of the effective mass over the bare band mass is related to the transfer of spectral weight from low energies to high-energy satellites. Different kinds of processes may contribute to this phenomenon. First, there is the suppression of charge fluctuations which effectively restricts the ground state in the mixed-valent regime to f^2 and f^3 configurations. Neglecting angular correlations, the spectral function will have a low-energy peak from the transitions $f^2 \rightarrow f^3$ and $f^3 \rightarrow f^2$ whose weight will be reduced due to the atomic valence transitions $f^2 \rightarrow f^1$ and $f^3 \rightarrow f^4$. These transition appear in the spectrum at energies well separated from the Fermi level. Second, there are the angular correlations as described by Hund's rules. They transfer spectral weight to atomic side bands which appear at energies $\sim 1 - 2$ eV below (or above) the Fermi edge. These structures can be seen from the DOS displayed in fig. 2. Experimentally, the "Hund's rule structures" are observed as "humped features" in photoemission experiments [36]. Due to the atomic transitions the overall width is much larger than the value predicted by standard band structure calculations.

Suppression of charge fluctuations and angular correlations reduce the weight of the low-energy peak to 0.41. This reduction corresponds to an isotropic enhancement of the quasiparticle mass by ~ 2.5 . The quasiparticle weight is further reduced by hopping between the sites. The latter introduces dispersion effects and orbital-dependence as can be seen from fig. 1 (right

panel). The spectral weight of the isotropic “atomic” peak is distributed over a rather broad energy range. The strong local correlations result in a considerable enhancement of anisotropies in the bare hopping matrix elements. The j_z channels with the dominant hopping exhibit well-defined dispersive quasiparticle peaks in the low-energy regime whereas the remaining channels contribute a non-dispersive incoherent background. The results are consistent with previous results the orbital-projected expectation values of the kinetic energy.

2.3 THE NFL STATE AND ITS SCALING LAWS

In the vicinity of a second order phase transition the behavior of various physical properties exhibit singularities which can be characterised by critical exponents [37]. The latter are universal in the sense that they do not depend upon the detailed microscopic nature of the system. They are determined by the dimensionality of the system and the degrees of freedom associated with the long-range correlations in the ordered phase. As a consequence, the critical exponents have been successfully used to classify the critical behavior in classical systems. The universality reflects the fact that the characteristic length and time scales, i.e., the correlation length ξ and the relaxation time τ diverge like

$$\xi \sim |g|^{-\nu} \text{ and } \tau \sim |g|^{-\nu z} \quad (9)$$

for $|g| \rightarrow 0$ (see e. g. [38, 39]) where $g = t, r$ measures the distance to the critical point according to

$$t = \frac{T - T_c}{T_c}, \quad r = \frac{p - p_c}{p_c} \quad \text{or} \quad r = \frac{H - H_c}{H_c} \quad (10)$$

Here T , p and H are temperature, pressure and field while T_c , p_c and H_c are their critical values. It is important to note that the critical exponents are not independent. They are related by scaling relations and, in addition, they are connected with the dimension d of the system by hyperscaling relations. On approaching T_c from above ($t \rightarrow 0^+$) the growing amplitude of thermally excited collective modes drives the system to a new state with spontaneously broken symmetry characterised by an order parameter.

On the other hand quantum phase transitions (QPT) which take place at zero temperature ($T_c=0$) are driven by the contribution of quantum fluctuations to the ground state energy which depends on a control parameter $r \rightarrow 0^+$ associated with pressure or field. In this case the effective dimensionality d_{eff} is given by

$$d_{eff} = d + z \quad (11)$$

where z is the dynamical exponent introduced above. Due to the effective increase in dimensionality the latter may reach the upper critical dimension. As a consequence, the critical exponents associated with the QPT may assume mean-field values [40]. In general, the characterisation of a continuous quantum phase transition is more subtle than that of a classical one.

Besides specific heat, susceptibility and resistivity the Grüneisen ratio Γ has turned out to be a sensitive quantity to characterise the vicinity of the QCP. Zhu et al. [41] have shown that the

Γ ratio defined in terms of the molar specific heat $c_p = \frac{T}{V}(\partial S/\partial T)_p$ and the thermal expansion $\alpha = \frac{1}{V}(\partial V/\partial T)_{p,N} = \frac{1}{V}(\partial S/\partial p)_{T,N}$, namely

$$\Gamma = \frac{\alpha}{c_p} = -\frac{1}{V_m T} \frac{(\partial S/\partial p)_T}{(\partial S/\partial T)_p} \quad (12)$$

diverges at any QCP. Here S is the entropy and $V_m = \frac{V}{N}$ is the molar volume. Away from the QCP when the low-temperature behavior is characterised by a single energy scale E^* the Grüneisen ratio in eq. (12) reduces to

$$\Gamma \simeq \frac{1}{V_m E^*} \frac{\partial E^*}{\partial p} \quad (13)$$

This form was already introduced and discussed in [42–45]. Instead of pressure, an external magnetic field H may be used as control parameter. In this case, the ratio

$$\Gamma_H = -\frac{1}{c_H} \left(\frac{\partial M}{\partial T} \right)_H = -\frac{1}{T} \frac{(\partial S/\partial H)_T}{(\partial S/\partial T)_H} = -\frac{1}{T} \left(\frac{\partial T}{\partial H} \right)_S \quad (14)$$

can be determined directly from the magneto-caloric effect. The Grüneisen ratio Γ and its magnetic counterpart Γ_H owe their importance to the fact that at the critical value $r = 0$ the temperature dependence is given by

$$\Gamma(T, r = 0) \sim T^{-\frac{1}{\nu z}} \quad (15)$$

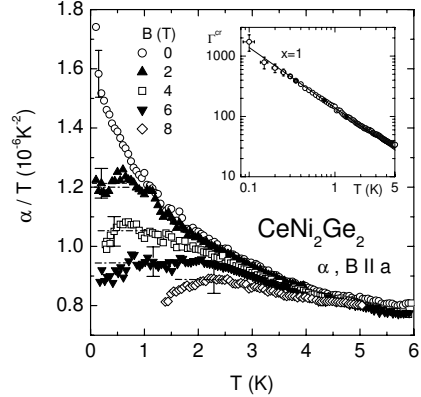
and consequently permits to measure νz . Comparison with experiment usually requires to account for corrections to the simple scaling ansatz from which eq. (15) is derived. The corrections, however, have to be evaluated from a microscopic model. For a discussion of the validity of eq.(15) we refer to [46, 47].

Neutron diffraction results for the A-phase in CeCu_2Si_2 suggest that the magnetic quantum phase transition in stoichiometric heavy fermion compounds arises from the instability of the strongly renormalised Fermi liquid with respect to the formation of a SDW. Model studies for the SDW transition therefore deserve special attention. Using the Ginzburg-Landau-Wilson functional for the effective action [40]

$$\begin{aligned} S[\phi] &= \sum_{\mathbf{q}, i\omega_n} \left(r + q^2 + \frac{|\omega_n|}{\Gamma q} \right) |\Phi_{\mathbf{q}, i\omega_n}|^2 + S^{(4)} \quad \text{with} \quad \Gamma_{\mathbf{q}} = \Gamma_0 q^{z-2} \\ S^{(4)} &= u \int_0^\beta \int d^d \mathbf{r} |\Phi(\mathbf{r}, \tau)|^4 \end{aligned} \quad (16)$$

the thermal expansion and Grüneisen ratio were calculated on the nonmagnetic side of the phase diagram [41]. Here Φ is the order parameter that fluctuates in space and imaginary time, $\beta = 1/kT$ is the inverse temperature and $\omega_n = 2n\pi T$ are bosonic Matsubara frequencies. The parameter r controls the distance from the critical point. The Landau damping which is linear in $|\omega|$ is due to the scattering of quasiparticles by spin fluctuations. It is characterised by the dynamical exponent z . The theory starts on the Fermi liquid side ($r > r_c$) which is characterised by a large Fermi surface including the f-degrees of freedom. The low-energy excitations are

Figure 3: Thermal expansion showing the suppression of NFL behaviour as function of field. The inset shows that for $B = 0$ the critical contribution to the Grüneisen ratio of CeNi_2Ge_2 (sect. 3.2) scales like $\Gamma \sim 1/T^x$ with $x = 1$. After eq.(15) this means (assuming $z = 2$ for AF SDW) a mean field correlation length exponent $\nu = 1/2$ which is in agreement with $d_{eff} = d+z = 5$ for the effective dimension [48].



fermionic quasiparticles and their collective excitations. Close to the QCP the static susceptibility is assumed to diverge at a specific wave vector \mathbf{Q} which signifies the transition into the SDW state. The quasiparticles are strongly scattered along “hot lines” which are connected by \mathbf{Q} [49]. This strong scattering modifies the low-temperature thermodynamic and transport properties which exhibit anomalous scaling relations close to QCP. They differ from those familiar from Fermi liquids. The scaling relations are derived adopting the renormalisation scheme of Millis [50, 51] which proceeds in close analogy to the spin-fluctuation theory of ferromagnetism [52]. The scaling behavior obtained for various models and many non-Fermi liquid compounds are summarised in [53].

The model calculations in [41] classify transitions according to various types of magnetic order. Two-dimensional ($d=2$) as well as three-dimensional ($d=3$) systems are considered assuming the values $z = 2, 3$ for the dynamical exponents. Comparison of calculated Grüneisen ratios with experiments in CeNi_2Ge_2 [48] shows that the QCP in this stoichiometric HF compound are consistent with the SDW scenario for three-dimensional critical AF spin fluctuations (fig. 3).

3 CERIUM-BASED HF SUPERCONDUCTORS

Since the discovery of heavy electrons and their superconducting state [54] in CeCu_2Si_2 the Ce-based tetragonal 112-compounds (space group $I4/mmm$, see fig. 4) have been at the focus of investigation. This class of materials offers a unique stage to watch the interplay of quantum-criticality, heavy Landau Fermi liquid (LFL) and non-Fermi liquid (NFL) behaviour as well as unconventional superconductivity. Although it has a long history, major aspects of the parent compound CeCu_2Si_2 of this class where only understood very recently: Firstly the long mysterious ‘A-phase’ associated with the low pressure quantum critical point, has finally been identified as an incommensurate (IC) SDW phase caused by the nesting of heavy quasiparticle FS sheets [55]. In fact it is now possible to follow the continuous evolution of the SDW wave vector and moment size of magnetic phases in $\text{CeCu}_2(\text{Si}_{1-x}\text{Ge}_x)_2$ from the small moment IC-SDW in CeCu_2Si_2 to the atomic moment commensurate antiferromagnetism in CeCu_2Ge_2 [56].

Secondly the anomalous stability of SC in CeCu_2Si_2 for pressures far above the A-phase QCP [57] which did not exhibit the typical dome-shape around the QCP pressure has now been understood. Likewise CeCu_2Ge_2 does not have a dome-shaped SC $T_c(p)$ curve once AF order is suppressed. Employing a negative pressure shift caused by the larger Ge- radius it looks rather similar to that of CeCu_2Si_2 . Artificial reduction of the SC condensation energy in CeCu_2Si_2 by Ge- alloying and applying positive shifts with hydrostatic pressure leads to a breakup of the SC region into two isolated domes which are associated with the previous A-phase magnetic QCP and a new high pressure valence transition QCP respectively [58]. This also suggests that SC phases and pairing mechanisms in the isolated SC regimes are different. Quantum criticality in the $\text{CeCu}_2(\text{Si}_{1-x}\text{Ge}_x)_2$ system is connected with distinct NFL anomalies that can only partly be explained within the standard nearly AF Fermi liquid picture, notably the discrepancy of the temperature scaling of resistivity and γ - coefficients at higher fields close to the A- phase QCP may require different concepts.

The HF compounds CeRh_2Si_2 and CePd_2Si_2 also become superconducting only under application of pressure like CeCu_2Ge_2 . As in CeCu_2Ge_2 AF order in CeRh_2Si_2 vanishes in a first order phase transition at the critical pressure p_c . SC in the latter appears only in an extremely narrow region around p_c , unlike in the former compound. Due to the first order transition both CeCu_2Ge_2 and CeRh_2Si_2 are in a LFL state close to p_c . For CePd_2Si_2 on the other hand a QCP where AF order vanishes continuously leads to a SC p-T phase diagram which is of the canonical single dome shape centered at p_c where clear cut NFL behaviour in the resistivity is observed. Finally CeNi_2Ge_2 is quite unique because it is not magnetic but rather displays almost ideal NFL behaviour at ambient pressure although incipient superconductivity is found at very low temperatures in highest-purity samples.

A comparison of the various Ce122 compounds leads one to conclude that the existence of an AF QCP with associated NFL behaviour is sufficient to induce superconductivity around p_c . Indeed the AF spin fluctuation theory (sect. 4) predicts a stabilisation of the SC state when the QCP is approached. However, as the examples of CeCu_2Ge_2 and CeRh_2Si_2 show, SC in Ce122 compounds may just as well appear in the normal LFL state.

It took more than 20 years to discover an additional class of Ce-based HF superconductors with the general formula $\text{Ce}_n\text{M}_m\text{In}_{3n+2m}$ ($M = \text{Co}, \text{Ir}$ and Rh). This belongs to the tetragonal layer type materials derived from the 'infinite layer' parent compound CeIn_3 by stacking n 'CeIn₃' and m 'MIn₂' subunits along the tetragonal axis. While CeCoIn_5 and CeIrIn_5 are single layer ($n=1$) HF compounds which are superconducting at ambient pressure [59], CeRhIn_5 is a local moment AF which becomes SC only under pressure. Likewise in the bilayer ($n=2$) compounds SC appears both at ambient pressure for Ce_2CoIn_8 and Ce_2IrIn_8 and at finite pressure for Ce_2RhIn_8 . Especially CeCoIn_5 has turned out to be of great interest. Its comparatively large T_c has allowed to determine the d-wave symmetry of the SC gap function by field-angle resolved magnetothermal conductivity [60] and specific heat [61] measurements. High-field specific heat [62] and ultrasonic attenuation measurements [63] have indicated that firstly the SC transition evolves to first order at larger fields, and secondly evidence for the long-sought FFLO phase with SC pairing at finite momentum exists. As in the Ce122 class SC appears preferably in the vicinity of magnetic QCPs and the corresponding AF/SC phase diagrams have been determined in pressure experiments. Likewise NFL phenomena above the AF QCP have been observed.

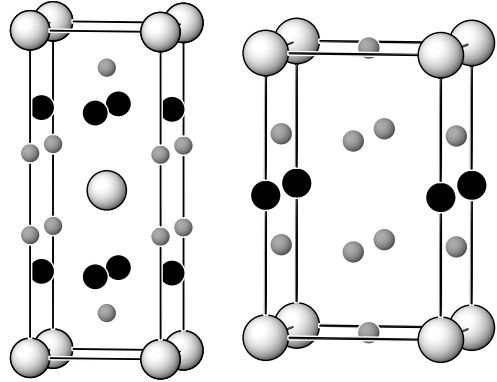


Figure 4: Left: Tetragonal unit cells of the ThCr₂Si₂ and CeM₂X₂ (Ce122) structure where M = Cu, Ni, Ru, Rh, Pd, Au, .. (black circles); X = Si, Ge (small grey circles) and Ce (large grey circles). Right: Conventional unit cell of the CeMIn₅ (Ce115) structure whith M = Co, Ir, Rh (black circles); In (small grey circles) and Ce (large grey circles).

Another exotic HF Ce- superconductor, CePt₃Si has now been discovered which is the first with a non-centrosymmetric structure [64]. Superconductivity in crystals without inversion center was discussed theoretically first in [65]. The lack of inversion symmetry raises fundamental questions of classification of the SC states according to odd and even parity [66]. It remains to be seen whether this compound is the first member of a new class of HF SC.

3.1 QUANTUM CRITICAL BEHAVIOUR AND SUPERCONDUCTIVITY IN CeCu₂Si₂ AND THE ALLOY SERIES CeCu₂(Si_{1-x}Ge_x)₂

The first Ce- based HF metal and superconductor [54] has for a considerable time served as a most fruitful model for investigating strongly correlated electron systems. Until rather recently it was also the only HF Ce compound exhibiting superconductivity. Most importantly in CeCu₂Si₂ Si can be continuously substituted by Ge while the compound changes from a HF superconductor to a normal antiferromagnet [56]. The Ge substitution acts like a negative chemical pressure, likewise fully substituted CeCu₂Ge₂ under positive hydrostatic pressure behaves similar as CeCu₂Si₂ under ambient pressure. Ge- substitution and application of hydrostatic pressure therefore allows to vary the coexistence and competition behaviour of superconducting and other order parameters in the alloy series CeCu₂(Si_{1-x}Ge_x)₂.

Indeed already stoichiometric CeCu₂Si₂ at ambient pressure shows an additional 'A-phase' which envelops SC in the B-T phase diagram [67] (fig. 5). When T_c and T_A are close they do not coexist and the A-phase is expelled from the SC region of the B-T plane. Ge-substitution or suitable deficit of Cu however stabilises the A-phase (T_A > T_c) and coexistence of both phases results. Hydrostatic pressure and Cu excess on the other hand reduces T_A to zero at the quantum critical point (QCP). Even after single crystals became available [68] the nature of the A-phase has remained mysterious. Later, neutron diffraction on weakly Ge- substituted CeCu₂(Si_{1-x}Ge_x)₂ samples have shown that the magnetic order observed in the stoichiometric CeCu₂Ge₂ compound is still present, although with continuously decreasing moment [69]. The slightly incommensurate (IC) modulation vector did not change very much as function of x (Ge concentration). Finally IC magnetic order with $\mathbf{Q} = (0.215, 0.215, 0.530)$ (r.l.u) has been found in the stoichiometric compound CeCu₂Si₂ by neutron diffraction [55], which identified the A-phase as a conventional IC-SDW phase with rather low moment $\sim 0.1 \mu_B$ per Ce

Table 1: Material parameters of Ce- based HF superconductors. ⁽¹⁾ Value extrapolated to $T = 0$ by fitting the $S=1/2$ Bethe ansatz result to data for $T > T_N$ using $T^* = 6\text{K}$.

| | γ [mJ/molK ²] | T_N [K] | μ [μ_B] | $T_c(p=0)$ [K] | $T_c^m(p_m)$ [K] |
|-----------------------------------|----------------------------------|-----------|-------------------|----------------|------------------|
| CeCu ₂ Si ₂ | 700 | 0.8 | 0.10 | 0.7 | 2.3 (3 GPa) |
| CeCu ₂ Ge ₂ | 1200 ⁽¹⁾ | 4.3 | 1.05 | - | 1.7 (16 GPa) |
| CeNi ₂ Ge ₂ | 350 | - | - | - | 0.4 (2.2 GPa) |

site (fig. 6). The ordering wave vector nicely agrees with the nesting wave vector of heavy FS sheets in CeCu₂Si₂ found by Zwicknagl et al. [20, 55]. It is clear now that the A-phase of CeCu₂Si₂ evolves continuously from the magnetic phase of CeCu₂Ge₂, when x is reduced from $x = 1$ progressively. Taken together the pressure and Ge- substitution dependences at first sight do not support the idea that SC appears around the QCP of the A-phase because the $T_c(x,p)$ curve (full dots in fig. 7) lacks the typical 'dome shape'. Specifically $T_c(p)$ strongly increases for increasing hydrostatic pressure p [57] and reaches its maximum far away from the QCP (fig. 7). This feature is very different from the conventional SC/AF QCP phase diagram which applies for other Ce- based HF superconductors like CePd₂Si₂ and CeRh₂Si₂ (fig. 16). However it is now clear [58] that this anomalous high pressure maximum in T_c is due to the presence of an additional high pressure QCP associated with an only weakly first order valence phase transition of Ce which does not break any symmetry [70]. The charge fluctuations associated with the valence transition have been proposed to mediate the SC pairing around the high pressure maximum [71] which is distinct from both spin fluctuation and magnetic exciton mechanism invoked for other Ce- and U-HF compounds respectively. The appropriate dome shape of two separated QCPs has been revealed by using simultaneous tuning with Ge-substitution and hydrostatic pressure. The latter compensates the effect of the former, but the mean free path is decreased which destabilises the unconventional SC order parameter and reduces its T_c . In this way the large stability region of stoichiometric CeCu₂Si₂ may be broken into the two domes associated with the magnetic and valence transition QCPs (fig.7). It seems now that CeCu₂Si₂ and substitutes also fit into the generic QCP scenario of Ce-HF superconductors albeit with the surprise of an additional qualitatively new QCP.

3.1.1 QUANTUM CRITICAL POINTS AND THE B-T PHASE DIAGRAM

Like the other Ce122 compounds the CeCu₂(Si_{1-x}Ge_x)₂ series crystallises in the tetragonal body centered ThCr₂Si₂ structure (fig. 4). The stability of A and SC phases is extremely sensitive to the stoichiometry of the constituent elements. The homogeneity range of CeCu₂Si₂ in the ternary chemical Ce-Cu-Si phase diagram is quite limited and comprises three regions where either A or SC alone are present or A/SC coexist [72]. This agrees with the observation that in the combined Ge- doping and pressure phase diagram shown in (fig. 5) the crossing of T_c and T_A curves is located around the stoichiometric case at ambient pressure. Around the first low pressure magnetic QCP where $T_A \rightarrow 0$ NFL behaviour with $\Delta\rho(T) \sim T^{3/2}$ and $\gamma(T) = \gamma_0 - \alpha T^{1/2}$ was observed for moderately low temperatures and moderately high fields [75]. This low temperature phase diagram which has been composed of different transport and susceptibility mea-

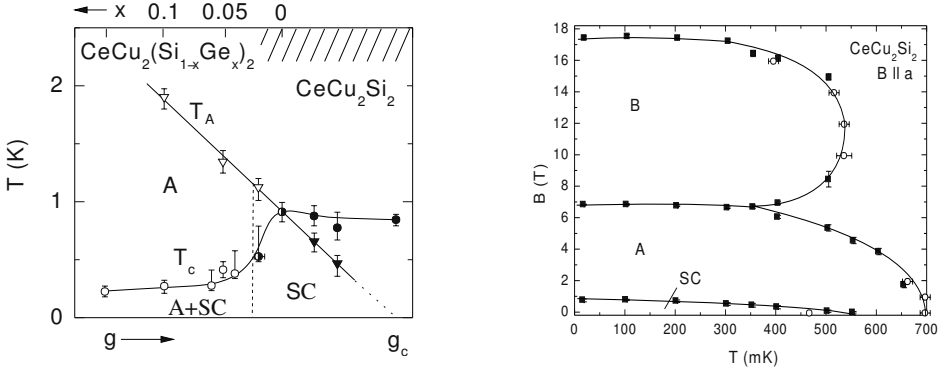
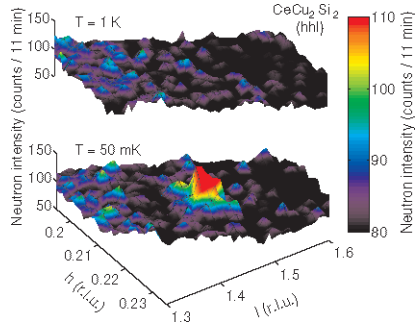


Figure 5: Left panel: Coexistence/competition phase diagram of SC and magnetic A phases close to the magnetic QCP1. Phase boundaries are obtained from susceptibility and resistivity measurements and composed of alloying (negative pressure) and hydrostatic pressure results, separated by a dashed line. Here $g \sim 1-x$ on the left and $g \sim p$ on the right [72] (c.f. theoretical results in fig. 10). Right panel: B-T phase diagram of CeCu_2Si_2 for $B \parallel a$. Original version in [73], completed version from [74]. For this sample the A-phase is expelled from the SC region (no coexistence).

measurements already shows that T_C saturates in a plateau after the T_A -crossing instead of forming the canonical QCP dome shape. Indeed on increasing pressure even further T_C increases steeply reaching a maximum around 3 GPa [76] to 4 GPa [57] (fig. 7). The delicate competition and coexistence behaviour for stoichiometric single crystals of CeCu_2Si_2 has already been obvious from earlier investigations on the B-T phase diagram obtained with ultrasonic methods and dilatometry [73, 74] which is shown in fig. 5 (right panel). For this sample $T_C \leq T_A$ and A/SC phases do not coexist. The expulsion of the A-phase from the SC region in fig. 5 can be clearly seen from sound velocity anomalies across the A and SC phase boundaries. The still poorly understood B phase might be another SDW phase with different propagation vector \mathbf{Q} and/or SDW moment polarisation.

Figure 6: Neutron diffraction intensity in reciprocal (hhl) plane in CeCu_2Si_2 at temperatures above and below the A-phase transition temperature T_A . The magnetic peak appears at $(0.215, 0.215, 1.470)$ corresponding to an incommensurate SDW modulation vector $\mathbf{Q} = (0.215, 0.215, 0.530)$ [55].



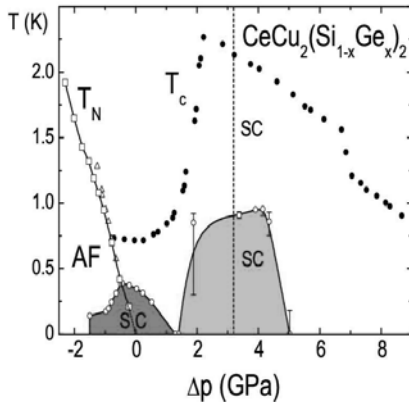


Figure 7: p - T phase diagram of $\text{CeCu}_2(\text{Si}_{1-x}\text{Ge}_x)_2$ composed from pressure (p) dependence and Ge-doping (x) dependence of $\rho(T)$, $C(T)$ and $\chi(T)$. For different substitution level x , the pressure is shifted by the value of its corresponding critical pressure $p_{c1}(x)$ for the magnetic QCP ($\Delta p = p - p_{c1}(x)$). Two SC domes are associated with QCP1(p_{c1}) (left dome) of the A-phase and QCP2(p_{c2}) of the integer valence (Kondo) phase (right dome) [58]. The dashed line indicates the valence transition in CeCu_2Ge_2 and T_c (dots [76]) corresponds to stoichiometric CeCu_2Si_2 .

To unravel the puzzling anomalous stability of T_c at high pressure systematic studies with slightly Ge doped single crystal CeCu_2Si_2 were performed [58]. It has been long suspected that the anomalous $T_c(p)$ behaviour is associated with the presence of a second QCP connected with a Ce-valence transition [70]. To support this scenario one has to prove that the region around $T_c \simeq T_A$ and around the maximum T_c correspond to distinct SC phases. This is achieved by the following strategy [58]: i) Due to larger Ge ionic radius slight Ge doping corresponds to application of internal negative pressure which may be compensated again by application of external positive pressure, returning to zero effective pressure. ii) Because the electronic mean free path has decreased due to scattering from Ge impurities, the condensation energy and hence T_c of the anisotropic SC phase will be decreased, destabilising SC. In this way the continuous SC region of stoichiometric CeCu_2Si_2 indeed breaks up into two separate SC domes as shown in fig. 7. The first one centered at $p_{c1}(x)$ is the magnetic QCP associated with the A-phase and its critical line $T_N(\Delta p)$, the second QCP at $p_{c2}(x)$ is supposed to describe the $\text{Ce}^{3+}/\text{Ce}^{4+}$ valence transition where the 4f electron of Ce^{3+} becomes delocalised. This transition does not break any symmetry and therefore its critical line $T_V(\Delta p)$ (not shown in fig. 7) is assumed to end in a critical endpoint. The critical line and its endpoint, however, have so far not been confirmed for these doped $\text{CeCu}_2(\text{Si}_{1-x}\text{Ge}_x)_2$ systems by independent methods. However for pure CeCu_2Ge_2 a weak, symmetry-conserving valence transition was observed via x-ray diffractometry [77] near $p \simeq 15$ GPa, where also $T_c(p)$ assumes its maximum value [57]. Certainly a large volume collapse signifying the 4f delocalisation as in the $\alpha - \gamma$ Ce transition would not be compatible with the presence of the SC phase around $p_{c2}(x)$.

3.1.2 THE A-PHASE AND ELECTRONIC STRUCTURE OF CeCu_2Si_2

The incommensurate magnetic order of the A-phase suggests a SDW origin associated with the itinerant heavy electron FS in CeCu_2Si_2 . To support this conjecture the static magnetic

susceptibility $\chi(\mathbf{q})$ has to be calculated within the context of renormalised band theory [20]. In this approach (sect. 2) resonant phase shifts $\eta_{\hat{f}_m}$ for the 4f-states are introduced empirically into the LDA scheme to generate the heavy bands at the Fermi level while charge neutrality and proper f-count are preserved. For the three CEF split Kramers doublets of Ce^{3+} ($J=\frac{5}{2}$) the ansatz for the phase shift is

$$\eta_{\hat{f}_m}(\varepsilon) = \tan^{-1} \frac{\Gamma_{\hat{f}}}{\varepsilon - \varepsilon_{\hat{f}_m}} \quad \varepsilon_{\hat{f}_m} = \varepsilon_{\hat{f}} + \Delta_m \quad (17)$$

Here $\varepsilon_{\hat{f}_m}$ defines the centers of heavy bands with $\varepsilon_{\hat{f}}$ denoting the renormalised 4f- level and Δ_m the energies of the three Kramers doublets taken from neutron scattering. The resonance width $\Gamma_{\hat{f}}$ is an empirical parameter which determines the width kT^* or mass m^* of the heavy electron band. It is adjusted to reproduce the proper experimental value of $\gamma = C/T$. The main heavy electron sheet obtained in [19] is shown in fig. 8. It consists of stacked columns along c . Obviously there are large flat parts on the columns with a nesting vector \mathbf{Q} as indicated. Indeed this leads to a pronounced maximum of $\chi(\mathbf{q})$ at $\mathbf{q} = \mathbf{Q}$ as shown in the contour plot of fig. 8. The experimental IC ordering vector of the A-phase (fig. 6) agrees well with the maximum position of $\chi(\mathbf{q})$ giving credence to the SDW picture for the A phase.

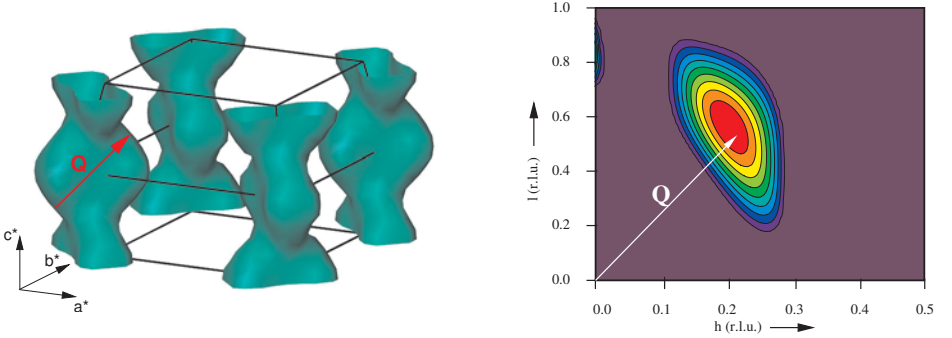


Figure 8: Left panel: Main heavy FS sheet in CeCu_2Si_2 where columnar nesting with wave vector \mathbf{Q} is indicated. Parameters for renormalised band calculations are: $T^* \sim 10$ K and $\Delta_{\text{CEF}} = 330$ K overall CEF splitting. Right panel: Comparison of experimental propagation vector (fig. 6) and contour map of theoretical $\chi(\mathbf{q})$ in (hh) plane [55].

3.1.3 THE HIGH PRESSURE MIXED VALENT PHASE TRANSITION

The present experimental evidence for the second QCP at high pressure connected with Ce-valence change was described in [70]. A valence transition does not break any spatial symmetry but charge fluctuations and volume strain are strongly coupled which commonly leads to a first order valence transition as in the famed γ - α transition of Ce. No such volume change has been found at p_{c2} of CeCu_2Si_2 making it a rather exceptional case. On the other hand this feature may provide a link to superconductivity as discussed in the next section. The only direct evidence for

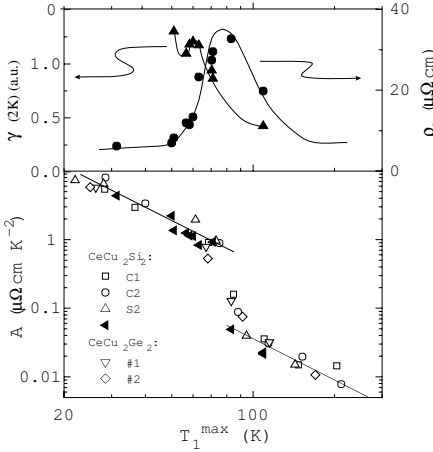


Figure 9: Behaviour of γ -coefficient, residual resistivity ρ_0 and A-coefficient in $\rho(T) = \rho_0 + AT^2$ against $T_1^{\max} \sim T^*$ which scales monotonously with pressure [70].

a small valence change was obtained earlier in L_{III} - x-ray absorption experiments [78]. There is however considerable indirect support for the valence change. The gradual delocalisation of the $4f^1$ - electron under pressure leads to a less strongly correlated electron state, i.e. the effective mass will be reduced according to

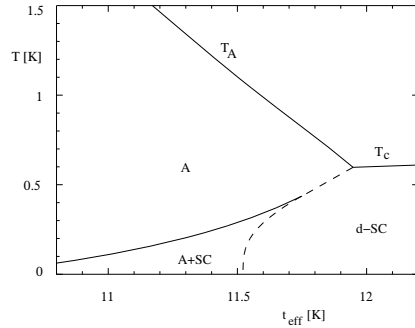
$$\frac{m^*}{m} = \frac{1 - n_f/2}{1 - n_f} \quad (18)$$

when the f-level occupation n_f is reduced significantly below its value in the Kondo limit $n_f \leq 1$. The linear specific heat coefficient $\gamma = C(T)/T$ should reflect this decrease. Likewise the Kadowaki-Woods ratio A/γ^2 should decrease across the valence transition [70]. If it is not of first order, critical valence fluctuations should also lead to a strong increase in the residual resistivity around the transition. These expected fundamental features of a valence transition are indeed present in $CeCu_2Si_2$ as shown in fig. 9. Theoretical models for the present case of a rapid but continuous valence transition under pressure are based on the extended periodic Anderson model (PAM) including a Coulomb repulsion U_{fc} between conduction and f- electrons, in addition to the on-site U_{ff} Coulomb term in the common PAM. Within the more simple impurity model this term has the tendency to decrease the f-occupation and when the energy of the $4f^1$ state, $\epsilon_f + U_{fc}$ approaches ϵ_F , i.e. the energy of the $4f^0$ hole state, n_f is rapidly reduced to values much less than one (fig. 11). External pressure is thought to tune primarily U_{fc} which is an inter-site Coulomb integral and thus cause the valence transitions. For the lattice model the valence change as function of U_{fc} has been calculated within slave boson fluctuation approximation [71].

3.1.4 UNCONVENTIONAL SUPERCONDUCTIVITY AND THE TWO QCP'S

The breakup of the SC region into two independent domes in fig. 7 allows one to speculate that the SC pairing mechanism at each QCP involves exchange of fluctuations of the associated order parameters, magnetic (A-phase transition) or charge fluctuations (valence transition)

Figure 10: Theoretical phase diagram for A and d_{xy} -SC order from a two band model. Full and dashed line correspond to second and first order transitions. A+SC is the coexistence region. The effective tight binding hopping integral t_{eff} scales with p or $1-x$ (c.f. experimental results in fig. 5) [72]



respectively. This may possibly imply a different type of superconducting gap symmetry, although not much is known about the SC state in both regimes, especially for the high pressure SC region. In the magnetic QCP regime Cu NQR experiments under pressure for polycrystalline $\text{CeCu}_2(\text{Si}_{1-x}\text{Ge}_x)_2$ [79] and under ambient pressure for Cu and Ce off-stoichiometric polycrystalline samples [80] show i) $1/T_1 \sim T^3$ behaviour indicating a SC state with gap nodes and ii) the presence of soft magnetic fluctuations close to a pressure or doping regime where the SC is stabilised. This suggests that the magnetic QCP scenario for unconventional HF-SC in CeCu_2Si_2 may be correct. Further knowledge about the nature of the SC gap function can only come from field-angle resolved pure single crystal investigations, e.g. $C(\mathbf{H}, T)$ measurements at very low temperatures.

Model for SC at the magnetic A- phase QCP:

A 2D two-band model for SDW-SC states in $\text{CeCu}_2(\text{Si}_{1-x}\text{Ge}_x)_2$ has been studied in some detail [72]. The microscopic origin of the pair potential is not specified in the BCS type model. A tight binding (TB) band centered at the $\Gamma(0,0)$ point and with $\mathbf{Q} = (\frac{1}{2}, \frac{1}{2})$ nesting feature represents a simplified version of the FS columns in fig. 8 whose nesting properties are known to be responsible for the SDW A-phase. In addition spherical electron pockets which represent the remaining FS sheets of CeCu_2Si_2 are included. The former carries both SDW and SC order parameters, the latter only SC. Therefore a d_{xy} SC state is favored. The A/SC competition-coexistence phase diagram resulting from the coupled gap equations is shown in fig. 10. There t_{eff} is the hopping element of the TB band which is thought to scale linearly with the control parameter g which is $1-x$ ($x = \text{Ge doping}$) or the pressure p . The comparison of the theoretical (fig. 10) and experimental phase diagram (fig. 5) shows a striking resemblance. In this model the tail of the coexistence A+SC regime is stabilised by the SC pairing on the spherical FS sheets. A more elaborate discussion of this issue using the real FS of CeCu_2Si_2 is given in sect. 3.1.6.

Model for SC at the valence transition QCP:

A more microscopic model for the SC mechanism around the high pressure valence transition has been proposed in [71]. The extended PAM mentioned above leads to an electron pairing mainly via the exchange of $c \leftrightarrow f$ charge fluctuations with small wavelength. In weak coupling approximation a d-wave state is found to be stabilised in the regime where appreciable charge

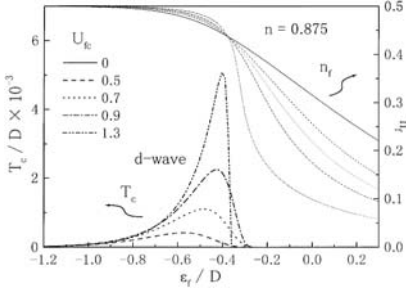


Figure 11: Valence (n_f) transition in the extended (impurity) Anderson model as function of the f-level position ϵ_f ($D =$ conduction band width, $\epsilon_F \equiv 0$). Associated T_c dependence of d-wave SC is also shown. [71]

fluctuations, controlled by the pressure dependent U_{fc} - parameter, set in but the quasiparticle DOS (the mass enhancement) is still sizable. The maximum in T_c scales with the steepness of the continuous valence transition as seen in fig. 11. This does not incorporate realistic FS features but assumes a single spherical conduction band. Also the real change in n_f across the valence transition will certainly be much less than in the theoretical model (fig. 11). Therefore it should be taken as an illustration of the mechanism and not literally as explanation for high pressure SC in $\text{CeCu}_2(\text{Si}_{1-x}\text{Ge}_x)_2$.

3.1.5 NON-FERMI LIQUID STATE AND QUANTUM CRITICAL BEHAVIOUR

Above the SC domes the two QCP's in $\text{CeCu}_2(\text{Si}_{1-x}\text{Ge}_x)_2$ lead to pronounced NFL anomalies in thermodynamic and transport properties. Naturally one would invoke here the quasiparticle scattering from low energy fluctuations of the associated order parameters [49] as one possible mechanism behind NFL behaviour. For the A-phase QCP a detailed comparison of experimentally observed T,B-scaling laws for $\rho(T) = \rho_0 + \Delta\rho(T)$, $\chi(T)$ and $\gamma(T)$ for single crystal CeCu_2Si_2 and polycrystalline samples of various Ge-dopings has been performed [75, 81]. It was found that for samples slightly above $T_A(x) = 0$ the expected NFL scaling laws at a 3D AF QCP

$$\Delta\rho(T) = \beta T^{\frac{3}{2}} \quad \gamma(T) = \gamma_0 - \alpha T^{\frac{1}{2}} \quad (19)$$

are indeed well fulfilled. However there are also distinct deviations, notably the high-field behaviour of $\Delta\rho(T)$ where a crossover of the resistivity exponent from 3/2 to the FL exponent 2 is observed. In contrast $\gamma(T)$ remains qualitatively unchanged [75] at moderately low T and exhibits an upturn at the lowest temperatures which is not yet understood. Such disparities in the scaling of $\Delta\rho(T)$ and $\gamma(T)$ are now also known from other NFL systems and proposals how to account for them have been made [75]. The study of NFL behaviour at the high pressure valence transition QCP on the other hand is still in its beginning. The NFL behaviour in $\Delta\rho(T)$ above the two distinct SC domes of fig. 7 is illustrated in fig. 12.

3.1.6 COEXISTENCE OF SUPERCONDUCTIVITY AND A-PHASE IN CeCu_2Si_2

The central goal in this section is to study the competition-coexistence phase diagram within a more realistic model than above. We start from the real FS sheets of CeCu_2Si_2 as obtained

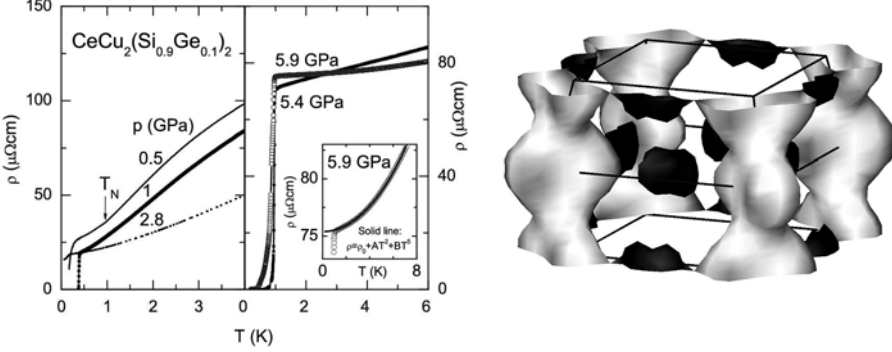


Figure 12: Left panel: NFL behaviour of $\Delta\rho(T)$ in $\text{CeCu}_2(\text{Si}_{1-x}\text{Ge}_x)_2$ close to QCP1 (left) and QCP2 (right) [58]. Right panel: Variation of the SC gap function amplitude $|\Delta(\mathbf{k})|/|\Delta_0(T)| = |\phi_{\Gamma_3}(\mathbf{k})|$ for the (pseudo-) singlet wave function with Γ_3 -symmetry $\phi_{\Gamma_3}(\mathbf{k}) \sim \cos k_x a - \cos k_y a$ on the main sheet of the paramagnetic FS [82, 83]. The amplitude of this SC order parameter is maximal on the kidney-shaped surfaces centered along the Σ -direction which are (almost) unaffected by the formation of the A-phase (dark grey). The dominant contributions to the latter come from the nesting parts on the heavy columns where the superconducting amplitude is small (light grey).

by renormalised band structure calculations. The FS nesting properties determine the observed magnetic structure. Of particular interest are the superconducting states which can either coexist with the A-phase or expel it. The model Hamiltonian is given by

$$H = \sum_{\mathbf{k}s} \epsilon_{\mathbf{k}} c_{\mathbf{k}s}^\dagger c_{\mathbf{k}s} + H_{int} \quad (20)$$

where the first term describes heavy quasiparticles and H_{int} their residual interactions. The creation (annihilation) operators are for quasiparticles with wavevector \mathbf{k} , (pseudo) spins $s = \uparrow, \downarrow$ and energy $\epsilon_{\mathbf{k}}$ are denoted by $c_{\mathbf{k}s}^\dagger$ ($c_{\mathbf{k}s}$). The energies which are measured relative to the Fermi level are calculated within the renormalised band scheme. The residual interactions in the strongly renormalised Fermi liquid is assumed to be repulsive for short separations while being attractive for two quasiparticles of opposite momenta on neighboring sites. The former favors the formation of a SDW while the latter gives rise to the superconducting instability. Within mean-field approximation one has $H_{int} = H_{SDW} + H_{SC}$ where

$$H_{SDW} = - \sum_{\mathbf{k}s} s \frac{1}{2} \sum_{\mathbf{Q}_j} [h(\mathbf{Q}_j) c_{\mathbf{k}s}^\dagger c_{\mathbf{k}+\mathbf{Q}_j s} + h.c.] \quad (21)$$

$$H_{SC} = \frac{1}{2} \sum_{\mathbf{k}s s'} [\Delta_{ss'}(\mathbf{k}) c_{\mathbf{k}s}^\dagger c_{-\mathbf{k}s'}^\dagger + h.c.] \quad (22)$$

The periodically modulated magnetisation $h(\mathbf{Q}_j)$ associated with the eight equivalent SDW propagation vectors \mathbf{Q}_j defined below as well as the superconducting pair potential Δ have to

be determined selfconsistently

$$h(\mathbf{Q}_j) = \frac{U}{L} \sum_{\mathbf{k}_s} \frac{s}{2} \left\langle c_{\mathbf{k}+\mathbf{Q}_j, s}^\dagger c_{\mathbf{k}_s} \right\rangle \quad (23)$$

$$\Delta_{ss'}(\mathbf{k}) = \frac{1}{L} \sum g_{ss',s''s'''}(\mathbf{k}, \mathbf{k}') \left\langle c_{-\mathbf{k}', s''} c_{\mathbf{k}', s'''} \right\rangle \quad (24)$$

where the strength U of the local Hubbard-type repulsion is of the order of the quasiparticle band width $k_B T^*$ and $g_{ss',s''s'''}(\mathbf{k}, \mathbf{k}')$ is the effective pair attraction. The \mathbf{k} -summation runs over the entire paramagnetic Brillouin zone and L denotes the number of lattice sites. The expectation values denoted by $\langle \dots \rangle$ have to be evaluated with the eigenstates of the total mean-field Hamiltonian $H_{MF} = H_0 + H_{SDW} + H_{SC}$, and, consequently, depend upon the order parameters. The selfconsistency equations are therefore coupled. The mean-field Hamiltonian implicitly assumes that the amplitudes of both order parameters are small. In particular, we neglect here the pairing amplitudes of the form $\langle c_{-\mathbf{k}', s''} c_{\mathbf{k}', s'''} \rangle$. The latter are important when the gaps introduced by the antiferromagnetic order into the quasiparticle spectrum are large on the scale set by superconductivity. For a discussion of this point we refer to [84, 85]. The periodically modulated magnetisation associated with the SDW acts on the conduction electrons like a periodic spin-dependent potential which we approximate by

$$h(\mathbf{x}) = \sum_{\mathbf{Q}_j} h(\mathbf{Q}_j) e^{i\mathbf{Q}_j \cdot \mathbf{x}} \quad (25)$$

with identical amplitudes $h(\mathbf{Q}_j) = h_0$ for the eight commensurate wave vectors $\mathbf{Q}_j \in \{(\pm \frac{\pi}{2a}, \pm \frac{\pi}{2a}, \pm \frac{\pi}{c})\}$ which are used for a commensurate approximation to the experimentally found IC SDW. The magnetic superstructure breaks the translational invariance of the underlying lattice but it conserves the point group symmetry. However the mean-field Hamiltonian is invariant under translations with the lattice vectors

$$\mathbf{a}'_1 = (2a, 2a, 0); \quad \mathbf{a}'_2 = (2a, -2a, 0); \quad \mathbf{a}'_3 = (2a, 0, c) \quad (26)$$

The volume of the magnetic supercell is 32 times the volume of the paramagnetic unit cell. As a result, the Brillouin zone is reduced and the quasiparticle states are modified by extra Bragg planes. The opening of new gaps is important at sufficiently low temperatures $T \ll T_A$ where T_A is the SDW transition temperature.

Before proceeding with the SC/SDW coexistence analysis of CeCu_2Si_2 we have to give a brief description of the symmetry classification of unconventional SC gap functions. The fundamental property of $\Delta_{ss'}(\mathbf{k})$ is its behaviour as a two-fermion wave function in many respects. This expresses the fact that an ODLRO order parameter is not the thermal expectation value of a physical observable but rather a complex pseudo-wave function describing quantum phase correlations on the macroscopic scale of the SC coherence length. Its phase is a direct signature of the broken gauge invariance in the SC condensate. The Pauli principle requires $\Delta_{ss'}(\mathbf{k})$ to be antisymmetric under the interchange of particles

$$\Delta_{ss'}(\mathbf{k}) = -\Delta_{s's}(-\mathbf{k}) \quad (27)$$

In addition, it transforms like a two-fermion wave function under rotations in position and spin space and under gauge transformations. The transformation properties yield a general classification scheme for the superconducting order parameter which is represented by a 2×2 -matrix in (pseudo-) spin space. It can be decomposed into an antisymmetric (s) and a symmetric (t) contribution according to $\Delta(\mathbf{k}) = \Delta_s(\mathbf{k}) + \Delta_t(\mathbf{k})$ with

$$\Delta_s(\mathbf{k}) = \phi(\mathbf{k})i\sigma_2 \quad \Delta_t(\mathbf{k}) = \sum_{\mu=1}^3 d_\mu(\mathbf{k})\sigma_\mu i\sigma_2 \quad (28)$$

where σ_μ denote the Pauli matrices. Antisymmetry $\Delta(\mathbf{k}) = -\Delta^T(-\mathbf{k})$ requires

$$\phi(\mathbf{k}) = \phi(-\mathbf{k}) \quad \text{and} \quad d_\mu(\mathbf{k}) = -d_\mu(-\mathbf{k}) \quad (29)$$

for the complex orbital functions $\phi(\mathbf{k})$ and $d_\mu(\mathbf{k})$ ($\mu = 1-3$). For brevity we will frequently write $\Delta(\mathbf{k})$ for $\phi(\mathbf{k})$ or $|\mathbf{d}(\mathbf{k})|$.

The order parameter can be chosen either as purely antisymmetric (Δ_s) or purely symmetric (Δ_t) when spin-orbit interaction can be neglected. In the 4f- and 5f- based heavy fermion superconductors spin-orbit interaction is strong. As a consequence classification according to physical pair spins cannot be used. If their high-temperature crystal structures, however, have an inversion center classification according to parity is still possible as is the case in CeCu_2Si_2 .

The general classification scheme for superconducting order parameters proceeds from the behavior under the transformations of the symmetry group \mathcal{G} of the Hamiltonian. It consists of the crystal point group G , the spin rotation group $\text{SU}(2)$, the time-reversal symmetry group \mathcal{K} , and the gauge group $\text{U}(1)$. The appropriate choice of rotations corresponding to weak or strong spin-orbit coupling case is determined by microscopic considerations. Using the above transformation properties the singlet and triplet gap functions $\phi(\mathbf{k})$ and $\mathbf{d}(\mathbf{k})$ respectively may further be decomposed into basis functions $\phi_\Gamma^n(\mathbf{k})$ or $\mathbf{d}_\Gamma^n(\mathbf{k})$ of the irreducible representations Γ (degeneracy index n) of $G \times \text{SU}(2)$ (weak s.o. coupling) or G (strong s.o. coupling). In the latter case the pseudo spin associated with Kramers degeneracy replaces the physical conduction electron spin.

The occurrence of long-range order at a phase transition described by an order parameter is most frequently associated with spontaneous symmetry breaking. The simplest superconductors where only gauge symmetry is broken are called *conventional*. In this case the SC order parameter has the same spatial symmetry as the underlying crystal, i.e. it transforms as a fully symmetric even parity singlet Γ_1 representation of G . It should be noted, however, that conventional is not a synonym for isotropic, for any G one can form Γ_1 representations from angular momentum orbitals of higher order l , for example $l \geq 2$ for tetragonal and hexagonal symmetry and $l \geq 4$ for cubic symmetry. On the other hand, a superconductor with additional broken symmetries besides gauge symmetry is called *unconventional*. It can have either parity. A recent summary is found in the monography [7].

NMR experiments [79, 80] in slightly Ge-doped or Cu-off-stoichiometric samples suggest that the SC gap is unconventional and has line nodes. In our discussion we restrict ourselves to a singlet pair state as revealed by strong Pauli limiting seen in early H_{c2} studies [86]. The singlet state is characterised by a scalar order parameter

$$\Delta(\mathbf{k})_{ss'} = \phi(\mathbf{k})(i\sigma_2)_{ss'} \quad (30)$$

The anisotropic effective pair interaction in the (pseudo-) spin singlet channel can be expanded according to

$$g(\mathbf{k}s, -\mathbf{k}s'; -\mathbf{k}'s'', \mathbf{k}'s''') \rightarrow (i\sigma_2)_{ss'} (i\sigma_2)_{s''s'''} \times \sum_j \frac{1}{2} g(\Gamma^{(j)}) \sum_{\kappa=1}^{d^{(j)}} \phi_{\kappa}^{(j)}(\mathbf{k}) \phi_{\kappa}^{(j)*}(\mathbf{k}') \quad (31)$$

where $\phi_{\kappa}^{(j)}(\mathbf{k})$ is a basis function which belongs to the κ th row, $\kappa = 1, \dots, d^{(j)}$, of the $d^{(j)}$ -dimensional representation $\Gamma^{(j)}$ of the symmetry group. In principle we have to classify the order parameters with respect to the antiferromagnetic lattice. Since the two ordering temperatures are so close we focus on pair states which are compatible with the translational symmetry of the paramagnetic lattice. The corresponding basis functions are listed in [5, 19, 87, 88]. In the explicit calculations, we restrict ourselves to one-dimensional representations for simplicity. The generalisation to multi-dimensional representations is rather straightforward [82].

We further simplify the problem by focussing on the symmetry Γ which yields the strongest quasiparticle attraction g_{Γ} . Assuming that this most stable order parameter is non-degenerate yields the separable interaction kernel

$$g(\mathbf{k}s, -\mathbf{k}s'; -\mathbf{k}'s'', \mathbf{k}'s''') \rightarrow (i\sigma_2)_{ss'} (i\sigma_2)_{s''s'''} \frac{g_{\Gamma}}{2} \phi_{\Gamma}(\mathbf{k}) \phi_{\Gamma}^*(\mathbf{k}') \quad (32)$$

and the selfconsistency condition

$$\Delta(\mathbf{k}) = -g_{\Gamma} \phi_{\Gamma}(\mathbf{k}) \frac{1}{L} \sum_{\mathbf{k}'} \phi_{\Gamma}^*(\mathbf{k}') \langle c_{-\mathbf{k}'\downarrow} c_{\mathbf{k}'\uparrow} \rangle \quad (33)$$

We adopt the Nambu formalism to diagonalise the mean-field Hamiltonian in eq. (22) which allows us to reduce it to single-particle form:

$$H = \sum_{\mathbf{k}}^{AFBZ} \Psi_{\mathbf{k}}^{\dagger} \{ \epsilon(\mathbf{k}) \hat{\tau}_3 + \mathbf{h} \hat{1} + \Delta(\mathbf{k}) \hat{\tau}_1 \} \Psi_{\mathbf{k}} \quad (34)$$

where we explicitly exploited the fact that the (pseudo) spin is conserved. The Nambu spinors $\Psi_{\mathbf{k}}$ have 32 components and are defined as

$$\Psi_{\mathbf{k}} = \left(c_{\mathbf{k}\uparrow}, c_{\mathbf{k}+\mathbf{Q}_1\uparrow}, \dots, c_{-\mathbf{k}\downarrow}, c_{-\mathbf{k}-\mathbf{Q}_1\downarrow}, \dots \right) \quad (35)$$

They account for the coherent superposition of particles and holes which is the characteristic feature of the superconducting state. Here $\hat{1}$, $\hat{\tau}_1$ and $\hat{\tau}_3$ denote the unit matrix and the Pauli matrices in particle-hole space. The 16 wave vectors $\mathbf{Q}_0 = 0, \mathbf{Q}_1, \dots, \mathbf{Q}_{15}$ are the reciprocal lattice vectors appearing in the antiferromagnetic phase. The set includes the eight propagation vectors of the SDW and their harmonics. The \mathbf{k} -summation is restricted to the reduced Brillouin zone (AFBZ) of the antiferromagnetic state defined by the SDW. The structure of the Hamiltonian matrix in particle-hole space is

$$\hat{H} = \begin{pmatrix} \epsilon(\mathbf{k}) + \mathbf{h} & \Delta \\ \Delta & -\epsilon(\mathbf{k}) + \mathbf{h} \end{pmatrix} \quad (36)$$

where the 16×16 -diagonal matrix contains the quasiparticle energies of the paramagnetic normal phase

$$\epsilon(\mathbf{k})_{\mathbf{Q}_i, \mathbf{Q}_j} = \delta_{\mathbf{Q}_i, \mathbf{Q}_j} \epsilon(\mathbf{k} + \mathbf{Q}_i) \quad (37)$$

The magnetic Umklapp scattering associated with the modulated spin density is accounted for by the matrix

$$\mathbf{h} = -h_0(T) \mathbf{m} \quad (38)$$

whose temperature-dependent amplitude $h_0(T)$ has to be determined selfconsistently while \mathbf{m} is a given matrix. The diagonal matrix

$$\Delta(\mathbf{k})_{\mathbf{Q}_i, \mathbf{Q}_j} = \Delta_0(T) \Phi(\mathbf{k})_{\mathbf{Q}_i, \mathbf{Q}_j} = \delta_{\mathbf{Q}_i, \mathbf{Q}_j} \Delta_0(T) \phi_\Gamma(\mathbf{k} + \mathbf{Q}_i) \quad (39)$$

contains the superconducting order parameters with the given \mathbf{k} -dependent function $\phi_\Gamma(\mathbf{k})$ and a temperature-dependent amplitude $\Delta_0(T)$. The selfconsistency equations in eq. (24) can be formulated in terms of the off-diagonal elements of the 32×32 -matrix Green's function

$$\hat{G}(i\epsilon_n, \mathbf{k}) = (i\epsilon_n \hat{1} - \hat{H}(\mathbf{k}))^{-1} \quad (40)$$

according to

$$\begin{aligned} h_0(T) &= \frac{U}{L} T \sum_{i\epsilon_n} \sum_{\mathbf{k}}^{AFBZ} \frac{1}{16} \text{Tr}[\mathbf{m} \hat{\mathbf{G}}(i\epsilon_n, \mathbf{k})] \\ \Delta_0(T) &= -\frac{g_\Gamma}{L} T \sum_{i\epsilon_n} \sum_{\mathbf{k}'}^{AFBZ} \frac{1}{2} \text{Tr}[\Phi(\mathbf{k}') \hat{\tau}_1 \hat{\tau}_3 \mathbf{G}(i\epsilon_n, \mathbf{k}') \hat{\tau}_3] \end{aligned} \quad (41)$$

Here $i\epsilon_n = \pi T(2n+1)$ denote the T-dependent Matsubara frequencies and ϵ_c is the energy cut-off required in weak-coupling theory. The coupling constants U and g_Γ as well as the cut-off ϵ_c are eliminated in the usual way in favor of the decoupled transition temperatures $T_A^{(0)}$ and $T_c^{(0)}$. The temperature dependence of SDW (A-phase) and SC order parameters is shown in the right panel of fig. 13. On entering the SC regime the A-phase is expelled in a finite temperature interval. This is nicely confirmed by recent neutron diffraction results [89] shown in the left panel of the figure.

3.2 THE (ALMOST) IDEAL NFL COMPOUND CeNi_2Ge_2

This is one of the few Ce-HF compounds which neither order magnetically nor become superconducting, except for incipient SC at very low temperatures in very clean samples. Instead it exhibits clear cut NFL anomalies over more than two temperature decades. Together with the recently discovered YbRh_2Si_2 , CeNi_2Ge_2 is one of the rare cases where one is accidentally very close to a QCP at ambient pressure. This is supported further by the x (Pd-concentration) dependence of the Néel temperature in the alloy series $\text{Ce}(\text{Ni}_{1-x}\text{Pd}_x)_2\text{Ge}_2$ [90]. It is found that $T_N(x)$ extrapolates to zero at a very small positive concentration x_c . Thus CeNi_2Ge_2 is (in contrast to YbRh_2Si_2) slightly on the nonmagnetic side of the QCP. After

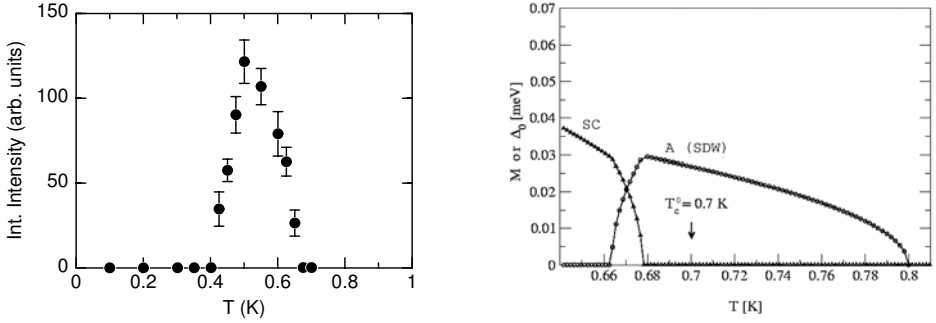


Figure 13: Left panel: Integrated neutron diffraction intensity of the A-phase SDW satellite corresponding to $\mathbf{Q} \simeq (0.215, 0.215, 0.530)$ as a function of temperature. It is proportional to the square of the A-phase order parameter in CeCu_2Si_2 [89]. Right panel: Variation with temperature of the A-phase (SDW) and superconducting order parameters with Γ_3 -symmetry, $\phi_{\Gamma_3}(\mathbf{k}) \sim \cos k_x a - \cos k_y a$ calculated for $T_A^{(0)} = 0.8\text{K} > T_c^{(0)} = 0.7\text{K}$ [82, 83]. For this choice of parameters, the magnetic A-phase initially suppresses the superconducting state which forms at $T_c < T_c^{(0)}$. The two ordering phenomena coexist in a narrow temperature range below T_c . The superconducting correlations, however, suppress the long-range magnetic order which disappears continuously at $T_A' < T_c < T_A^{(0)}$.

some initial doubts [75] it is now accepted [91] that the 3D-SDW QCP scenario analysed in detail in [49] is realised in CeNi_2Ge_2 . This predicts a scaling $\gamma(T) = \gamma_0 - cT^{\frac{1}{2}}$ which is well fulfilled in CeNi_2Ge_2 (fig. 14) down to temperatures around 0.3 K. For even lower temperatures sample dependent upturns in $\gamma(T)$ of unknown origin are present. Likewise the expected NFL resistivity behaviour $\rho(T) = \rho_0 + \beta T^\epsilon$ with $\epsilon \geq 1.5$ depending on the sample quality (ρ_0) is found. The very closeness of the AF QCP implies an extreme sensitivity of the scaling to an external field. With increasing field strength one crosses rapidly into a Fermi liquid regime as witnessed by the appearance of a widening plateau in $\gamma(T)$ (fig. 14) and a LFL type resistivity $\rho(T) = \rho_0 + A(B)T^2$. The boundary between the T^ϵ and T^2 scaling marks the transition from the NFL to the LFL regime (fig. 14). As this boundary is approached from $B > B_c$ the A(B)-coefficient diverges indicating a singular energy dependence of the scattering rate. Thus as the QCP is approached by varying B and T the quasiparticle mass and scattering rates in CeNi_2Ge_2 grow in agreement with the predictions of the 3D SDW scenario for quantum criticality. More recently the NFL behaviour in CeNi_2Ge_2 has also been found in a low temperature divergence of the Grüneisen ratio obtained from thermal expansion as discussed in sect. 2.3.

3.3 SUPERCONDUCTIVITY AND QUANTUM CRITICALITY UNDER PRESSURE IN CePd_2Si_2 AND CeRh_2Si_2

At ambient pressure CeCu_2Si_2 and $\text{CeCu}_2(\text{Si}_{1-x}\text{Ge}_x)_2$ together with CeCoIn_5 and CeIrIn_5 are still the only Ce-based HF superconductors, aside from incipient superconductivity around 100

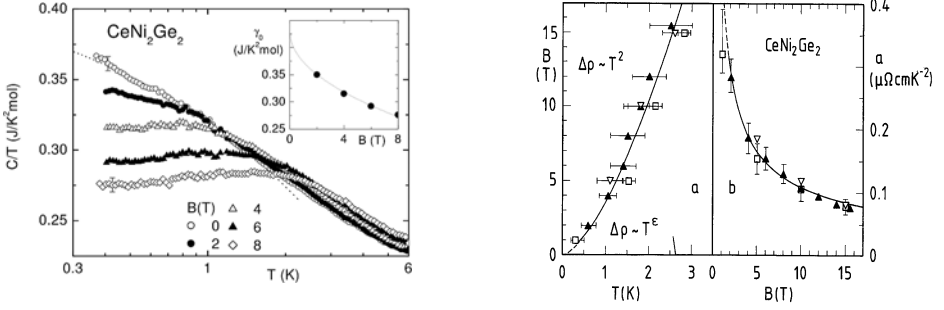


Figure 14: Left panel: Field dependence of $\gamma = C/T$. Dotted line ($B = 0$) indicates $\gamma(T) = \gamma_0 - \beta\sqrt{T}$. Inset shows $\gamma(B)$ in FL (plateau) regime [91]. Right panel: (a) B-T phase boundary separating the FL/NFL regimes; (b) Field dependence of the A-coefficient, solid line indicates $A \sim B^{-0.6}$ [91].

mK in CeNi_2Ge_2 in exceptionally clean samples and the recently discovered non-centrosymmetric SC in CePt_3Si [64]. In the former case this may be due to the accidental closeness of the A-SDW phase QCP at ambient pressure, witnessed by the phase diagram in fig. 5 and the associated NFL anomalies. To find more examples of Ce-based HF superconductors it is therefore an obvious strategy to look for magnetically ordered Ce-HF compounds and drive them to a QCP with applied pressure, hoping that a SC 'dome', however small, might appear. This has been successful for CeCu_2Ge_2 [92] and more recently for CeRh_2Si_2 [93] and also CeIn_3 and CePd_2Si_2 [94]. Note however that strictly speaking CeRh_2Si_2 is not a HF system due to its small mass enhancement visible from the low γ -value at ambient pressure.

The magnetism of these compounds (table 2) and of the Pd-alloy series $\text{Ce}(\text{Rh}_{1-x}\text{Pd}_x)_2\text{Si}_2$ at ambient pressure has been subject to many investigations [94–96]. While there is unanimous agreement on the localised moment nature of CePd_2Si_2 , the interpretation of magnetism in CeRh_2Si_2 is controversial, partly favoring the itinerant picture from resistivity and specific heat measurements [97] and partly a localised picture from dHvA experiments and their interpretation and comparison with band structure calculations for the reference compound LaRh_2Si_2 [98].

The commensurate AF structure of CePd_2Si_2 consists of FM (110) sheets stacked alternately with a wave vector $\mathbf{Q} = (\frac{1}{2}, \frac{1}{2}, 0)$ and moments oriented along [110]. The local moment nature of CePd_2Si_2 can directly be inferred from susceptibility measurements and INS experiments [99]. The former give a tetragonal CEF level scheme of the localised $\text{Ce}^{3+} 4f^1$ electrons as a sequence of three Kramers doublets $\Gamma_7^{(1)}(0)$, $\Gamma_6(19 \text{ meV})$ and $\Gamma_7^{(2)}(24 \text{ meV})$. Well developed AF spin waves with an uniaxial anisotropy gap $\Delta = 0.83 \text{ meV}$ and a dispersion of 2 meV were observed which can be explained within the AF Heisenberg model for local moments. This is further supported by the magnetic phase diagram of the $\text{Ce}(\text{Rh}_{1-x}\text{Pd}_x)_2\text{Si}_2$ alloy series shown in fig. 15 on the Pd-rich side: The monotonous decrease of T_N and simultaneous strong increase of the characteristic HF temperature T^* with Rh-doping (1-x) corresponds to the QCP of a Doniach phase diagram for a Kondo-lattice type local moment system. There the destruction of AF

Table 2: Material parameters and magnetic properties of the sister compounds CeRh_2Si_2 and CePd_2Si_2 .

| | $\gamma(p=0)$ [mJ/molK ²] | T_N [K] | μ [μ_B] | $T_c^m(p_m)$ [K] | p_m [GPa] |
|----------------------------|---------------------------------------|-----------|-------------------|------------------|-------------|
| CePd_2Si_2 | 250 | 10 | 0.62 | 0.4 | 2.71 |
| CeRh_2Si_2 | 23 | 36 | 1.42 | 0.4 | 1.05 |

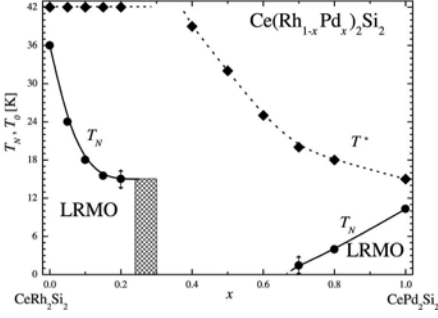


Figure 15: Magnetic x - T phase diagram of $\text{Ce}(\text{Rh}_{1-x}\text{Pd}_x)_2\text{Si}_2$ with Néel temperature $T_N(x)$ (circles) and Kondo temperature $T^*(x)$ (diamonds). Rh-rich side: Itinerant SDW regime. Pd-rich side: Local moment regime with Doniach type phase diagram [97].

order is due to the compensation of magnetic moments in the Fermi sea of conduction electrons.

The magnetism in $\text{Ce}(\text{Rh}_{1-x}\text{Pd}_x)_2\text{Si}_2$ is less well understood. The origin of the exceptionally high $T_{N1} = 36$ K is a longstanding mystery which defies understanding in the local moment system if deGennes scaling of T_{N1} with respect to GdRh_2Si_2 is applied. Like CePd_2Si_2 it orders with $\mathbf{Q} = (\frac{1}{2}, \frac{1}{2}, 0)$, first with a single \mathbf{q} -structure at T_{N1} which changes to a $4\mathbf{q}$ -structure below $T_{N2} = 24$ K (fig. 16). Also the (partly) plateau-like behaviour of $T_N(x)$ and $T^*(x)$ on the Rh-rich side of fig. 15 speaks against the local moment Kondo lattice picture and therefore an itinerant SDW origin of AF in $\text{Ce}(\text{Rh}_{1-x}\text{Pd}_x)_2\text{Si}_2$ has been proposed in [97]. On the other hand the moment size ($1.5\mu_B$, $\mathbf{m} \parallel \mathbf{c}$) can be explained within a CEF-split localised $4f^1$ model for Ce which is supported by the entropy gain $\Delta S(T_N) \simeq R \ln 2$ indicating a CEF Kramers doublet. From dHvA experiments [98] it was found that some Fermi surface branches are well explained by LDA results for LaRh_2Si_2 which advocates that $4f$ - electrons in CeRh_2Si_2 do not contribute to the Fermi surface. Alloying leads to an increase of the mean free path and may easily destroy unconventional superconducting states. Therefore, unlike in the $\text{CeCu}_2(\text{Si}_{1-x}\text{Ge}_x)_2$ system, no superconductivity has been found around the magnetic QCPs of the above T - x magnetic phase diagrams. However the magnetic QCP may also be approached by applying hydrostatic pressure to the pure compounds. Detailed studies of CePd_2Si_2 [95] have revealed the QCP to lie at $p_c = 2.86$ GPa. The almost linear scaling $T_N(p) \sim (p_c - p)$ observed above 1.5 GPa is not in agreement with 3D spin fluctuation theory which predicts a pressure exponent $2/3$. The resistivity at p_c exhibits a NFL-type dependence of $\rho(T) = \rho_0 + BT^\alpha$ with an exponent $\alpha \simeq 1.2$. For samples with sufficiently small ρ_0 an approximately symmetric superconducting dome was indeed identified around p_c as shown in fig. 16. From upper critical field studies the coherence length was estimated as $\xi_0 \simeq 150\text{\AA}$.

Likewise hydrostatic pressure application destroys AF in CeRh_2Si_2 [100] at $p_c = 1.05$ GPa. The transition seems to be of first order. Nevertheless in good polycrystalline samples it was

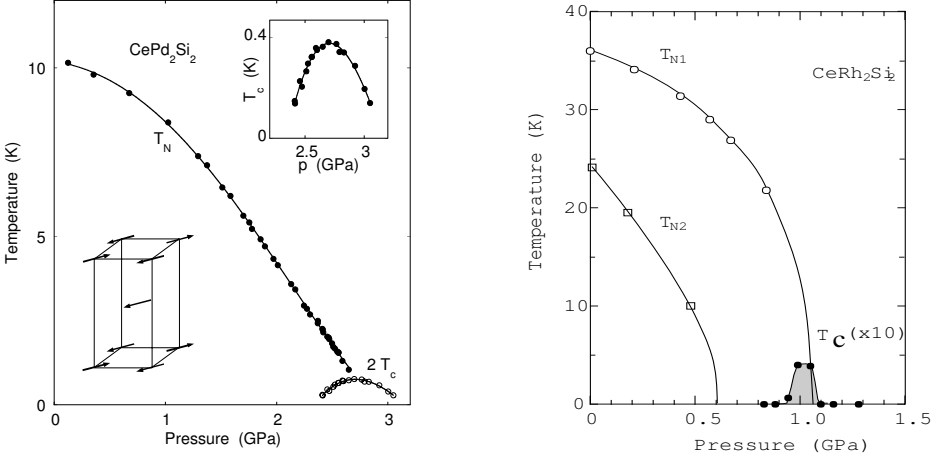


Figure 16: Magnetic and SC phase boundaries under hydrostatic pressure in CePd₂Si₂ (left panel) [95] and CeRh₂Si₂ (right panel) [100]; note the enlarged scales of T_c. In CeRh₂Si₂ the AF structure changes at T_{N2}.

found that SC appears around p_c , albeit in a very small pressure interval from 0.97 to 1.20 GPa, much smaller than previously thought (fig. 16). Again the optimal $T_c \simeq 0.4$ K. From the H_{c2} curves [98] at p_c the coherence lengths $\xi_c \simeq 240\text{\AA}$ and $\xi_a \simeq 310\text{\AA}$ are obtained. The anisotropy of $H_{c2}^{a,c}(0)$ may be caused by the anisotropic paramagnetic limiting effect ($\chi_c/\chi_a = 4$), its observation also suggests a SC singlet pairing state. The dHVA results [100] show a discontinuous change of FS topology at p_c , also the effective masses increase by almost an order of magnitude to $m^*/m \simeq 30$ above p_c . Therefore the transition across the QCP was interpreted as change from the low pressure AF local moment phase with light electrons to the paramagnetic heavy electron state above p_c [100].

Although the superficial appearance of quantum critical phase diagrams in fig. 16 is quite similar for both compounds, there is an important difference: quite opposite to CePd₂Si₂, CeRh₂Si₂ does not show any signature of NFL behaviour around p_c , $\gamma(T)$ has no significant T-dependence below 10 K and its value even increases up to 80 mJ/molK² at p_c due the suppression of AF order [101]. This means there is no direct connection between NFL behaviour in the QCP regime and the appearance of a SC dome. This conclusion can also be drawn from the investigation of Ce155 compounds (sect. 3.4).

Indeed from the theoretical point of view there is no reason to expect such a connection as can be concluded from the discussion in sect. 4. At the QCP the magnetic correlation length ξ_m diverges as described by eq. (9). Accordingly the spectral maximum at an energy $\sim \xi_m^{-2}$ of critical spin fluctuations responsible for NFL behaviour shifts to zero on approaching the QCP (eq.(45)). As explained in sect. 4, this increases the pair breaking effect due to low lying spin excitations and hence should lead even to a suppression of T_c close to the QCP. The soft spin fluctuations responsible for NFL behaviour in the Ce122 compounds close to the QCP are

therefore not essential for the SC pair formation. Therefore compounds like CeCu_2Ge_2 and CeRh_2Si_2 which are in the LFL state around p_c may form the same kind of SC state as NFL compounds like CePd_2Si_2 .

3.4 THE NEW Ce_{115} AND Ce_{218} CLASS OF HF SUPERCONDUCTORS

Only recently a new class of promising Ce-based HF superconductors with the general formula $\text{Ce}_n\text{M}_m\text{In}_{3n+2m}$ ($\text{M} = \text{Co}, \text{Ir}, \text{Rh}$) has been discovered. Again the guiding principle of looking for SC close to magnetic QCP's has been successful, which naturally means that for the members of the family the SC transition takes place out of a pronounced NFL-like normal state. These tetragonal compounds (space group $\text{P4}/\text{mmm}$) are composed of alternating n -fold CeIn_3 layers and m -fold MIn_2 layers derived from the parent compound CeIn_3 ($n=\infty$). The $n=1, m=1$ compounds (fig. 4) CeCoIn_5 and CeIrIn_5 are ambient pressure superconductors and the AF CeRhIn_5 becomes superconducting under pressure similar to the AF $n=2, m=1$ family members Ce_2CoIn_8 and Ce_2RhIn_8 . Although they partly have FS sheets with 2D character like slightly warped cylinders oriented along c , the physical properties, e.g. resistivity and upper critical field are not excessively anisotropic. In fact, an analysis of uniaxial pressure effects of both normal-state and SC properties based on high-resolution thermal expansion measurements reveals that the SC T_c is strongly affected by at least two factors: The lattice anisotropy and the 4f-conduction electron hybridisation which is most sensitive to c -axis lattice distortions [102].

Their electronic structure is well understood and the ambient pressure superconductors CeCoIn_5 and CeIrIn_5 have conduction band states with strong 4f admixture, contrary to the ambient pressure AF compounds which have well localised 4f states witnessed by the similarity of their FS to the La parent compound. Large mass enhancements and specific heat γ coefficients are found but achieving the FL state may require application of a sufficiently large field. Maximum $T_{c,s} \simeq 2.5$ K are achievable under pressure and already realised at ambient pressure for CeCoIn_5 . This is higher than in other families of Ce- or U-HF superconductors, except for CeCu_2Si_2 under pressure, and a factor of ten larger than in the parent compound CeIn_3 . A compilation of physical data is given in table 3, see also [103]. Certainly CeCoIn_5 has turned out to be the most interesting system and is also most thoroughly investigated, partly due to its large ambient pressure T_c and large H_{c2} as well as availability of excellent single crystals. Its unconventional superconducting state with d-wave symmetry is possibly the first which exhibits a change from a second to first order SC transition at $H_{c2}(T)$ below a temperature $T_0 < T_c$. Furthermore specific heat, NMR and ultrasonic attenuation suggest that CeCoIn_5 is the first SC which exhibits the elusive Fulde-Ferrell-Larkin-Ovchinnikov (FFLO) phase at high field and low temperature.

3.4.1 BASICS OF THE ELECTRONIC STRUCTURE

There are extensive LDA calculations and dHvA investigations of the CeMIn_5 and Ce_2MIn_8 electronic structure and FS topology [100, 104–106]. For the reference compound LaRhIn_5 excellent agreement is found and the dHvA frequencies of a few sheets exhibit clear 2D cylindrical structure. The AF compound CeRhIn_5 has localised 4f electrons which are CEF split into three Kramers doublets $\Gamma_7^2(0)$, $\Gamma_7^1(6.9 \text{ meV})$ and $\Gamma_6(23.6 \text{ meV})$ [107]. Therefore CeRhIn_5 should have

Table 3: Material parameters of Ce115 and Ce218 HF superconductors.

| | γ [mJ/molK ²] | T_N [K] | μ [μ_B] | $T_c(p=0)$ [K] | $T_c^m(p_m)$ [K] |
|-----------------------------------|----------------------------------|-----------|-------------------|----------------|------------------|
| CeIn ₃ | 130 | 10.2 | 0.65 | - | 0.25 (2.6 GPa) |
| CeCoIn ₅ | 350 | - | - | 2.3 | 2.5 (1.56 GPa) |
| CeIrIn ₅ | 750 | - | - | 0.4 | - |
| CeRhIn ₅ | 400 | 3.8 | 0.37 | - | 2.2 (2.5 GPa) |
| Ce ₂ CoIn ₈ | 500 | - | - | 0.4 | - |
| Ce ₂ IrIn ₈ | 700 | - | - | - | - |
| Ce ₂ RhIn ₈ | 400 | 2.8 | 0.55 | - | 2.0 (2.3 GPa) |

a similar FS as the La parent. Its AF order introduces many new sheets by folding into the AF BZ but the main FS sheets are indeed in good agreement. On the other hand the almost identical FS of CeCoIn₅ and CeIrIn₅ are well explained by including the 4f states as itinerant electrons in the FS volume which makes them highly different from the above LaRhIn₅ and CeRhIn₅ FS. The selfconsistently calculated f-level occupations for CeCoIn₅ and CeIrIn₅ are indeed close to one [105]. The enhanced γ values are given in table 3 and are generally larger for the itinerant 4f-electron compounds. The different size of mass enhancement for CeCoIn₅ and CeIrIn₅ was attributed to the influence of CEF effects [105]. The mass anisotropies as obtained from upper critical field measurements [104] are considerable, $m_c^*/m_a^* = 4.8$ in CeIrIn₅ and $m_c^*/m_a^* = 5.6$ in CeCoIn₅, reflecting the partly 2D FS topology. As in CeRhIn₅ the AF bilayer compound Ce₂RhIn₈ has largely localised 4f states and therefore again the FS sheets are very similar to the La₂RhIn₈ parent compounds [106], three similar sheets with 2D cylindrical appearance have been found in dHvA experiments and LDA calculations.

3.4.2 AF QUANTUM CRITICAL POINTS AND SUPERCONDUCTIVITY

When magnetic order changes to a different symmetry or vanishes as a function of an external or internal parameter this may be interpreted as a quantum phase transition provided the respective ground state energies are largely determined by the contribution from quantum fluctuations. If the transition is of second order the critical parameter value then defines a proper magnetic quantum critical point (QCP). In its vicinity NFL behaviour and a superconducting phase transition may be induced by spin fluctuations of the type discussed in sect. 4. The Ce115 and Ce218 compounds give considerable support for this scenario.

In the T-p phase diagrams of Ce115 and Ce218 and also Ce122 compounds which are AF at ambient pressure and SC under pressure two typical idealised situations may occur [108]: (1) When $T_N(p=0) \gg T_c(p_c)$ a symmetric SC dome around p_c appears and FL behaviour is observed above T_c and for $p > p_c$, AF order is suppressed inside the SC region. This situation is realised for CeRh₂Si₂ and CePd₂Si₂ as seen in fig. 16. (2) When $T_N(p=0) \geq T_c(p_c)$ the SC region is commonly asymmetric around the QCP and AF order partly coexists with SC. Around p_c and above T_c an extended region of NFL behaviour is observed. This holds for CeCu₂(Si_{1-x}Ge_x)₂, CeRhIn₅ and CeRh_{1-x}Co_xIn₅ (fig.18). This picture is, however, oversimplified as is obvious from the case of CeIn₃ where the conditions (1) are fulfilled but nevertheless

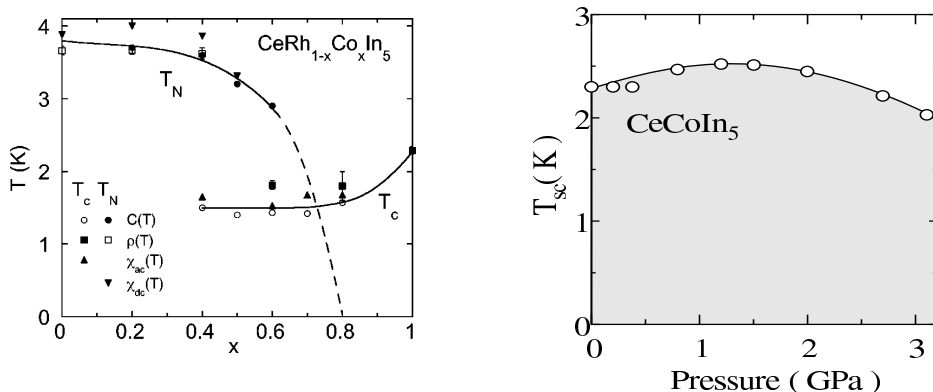


Figure 17: Left panel: Coexistence of AF order and SC in $\text{CeRh}_{1-x}\text{Co}_x\text{In}_5$ ('negative pressure' side) [109]. Right panel: Hydrostatic pressure dependence of T_c in CeCoIn_5 . The critical pressure where $T_c = 0$ is not known [100].

coexistence SC/SDW has been identified in NMR experiments [79]. In fact these results suggest that instead of having a QCP within the SC dome a first order transition with AF/PM phase separation occurs. It remains to be seen whether this also holds true for CePd_1Si_1 . Especially the quantum criticality of CeCoIn_5 and its connection to superconductivity has been clarified by external field and pressure application and by internal pressure through Rh substitution of Co. At ambient pressure CeCoIn_5 is nonmagnetic and the 'large' T_c is almost independent in hydrostatic pressure up to 3 GPa and no magnetic order appears. Apparently doping with Rh, which has a larger ionic radius compared to Co, exerts a 'negative pressure' which for $1-x > 0.2$ Rh doping achieves AF order (fig. 17) while SC persists, albeit with slightly reduced T_c . Thus a considerable regime of AF/SC coexistence appears. Taken together Rh-doping and hydrostatic pressure do not present an ideal dome-shaped SC region, it is rather reminiscent of slightly doped $\text{CeCu}_1(\text{Si}_{1-x}\text{Ge}_x)_1$ under pressure. The combined x, p - T phase diagram of the Rh-doped compound $\text{CeRh}_{1-x}\text{Ir}_x\text{In}_5$ [110] and CeIrIn_5 under hydrostatic pressure [111] is quite similar to fig. 17. $\text{CeRh}_{1-x}\text{Ir}_x\text{In}_5$ also develops AF order that coexists with SC between $0.35 < x < 0.5$ [112]. The $T_c(p)$ curve of CeIrIn_5 starts at $T_c(p=0) = 0.4$ K and reaches $T_c(p_m) = 1.05$ K at $p_m = 2.2$ GPa and finally drops to zero at $p_c = 6$ GPa. This critical pressure for the CeCoIn_5 sister compound is not yet known.

Other family members which are AF at ambient pressure but not SC naturally exhibit better realisations of the canonical AF/SC quantum critical phase diagrams under hydrostatic pressure. This is already true for the AF parent compound CeIn_3 ($T_N = 10$ K) of the Ce115 family [100] with an optimum $T_c = 0.2$ K at 2.5 GPa and especially for the localised 4f compound CeRhIn_5 ($x = 0$ in fig. 17) as is shown in fig. 18. The related AF bilayer compound Ce_1RhIn_8 is another exciting example of AF/SC quantum critical phase diagram (fig. 18). The remarkably high optimum T_c rivals that of ambient pressure CeCoIn_5 and is comparable to its own $T_N(p=0) = 2.8$ K.

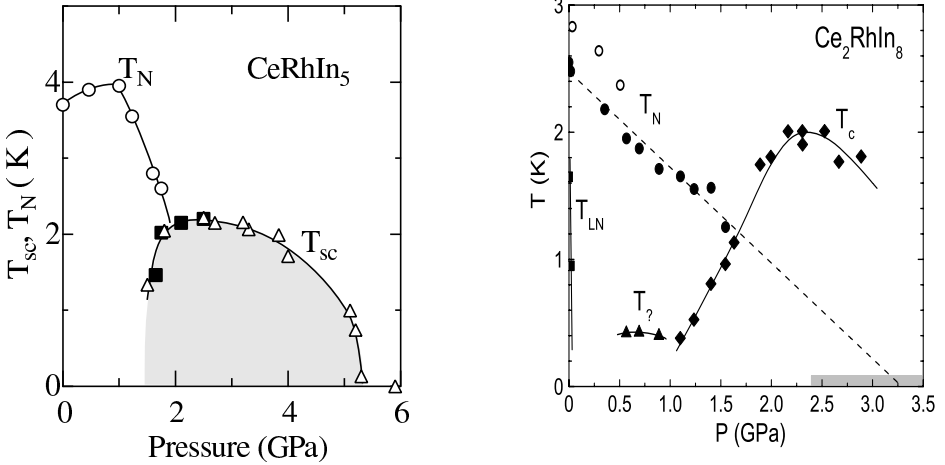


Figure 18: Quantum critical p-T phase diagrams for CeRhIn₅ [100] and Ce₂RhIn₈ [113]. When $T_N \sim T_c^m$ as in Ce₂RhIn₈, AF and SC coexist over considerable pressure range, contrary to the situation in CeRhIn₅ where $T_N \gg T_c^m$.

3.4.3 NFL ANOMALIES IN FIELD AND PRESSURE INDUCED QCP'S

The common signature of a NFL state are anomalous temperature and field scaling exponents for thermodynamic quantities like specific heat, susceptibility, Grüneisen parameters (thermal expansion) and transport quantities like resistivity or Hall coefficient. Their origin and appearance has been briefly discussed in sect. 2.3.

Pronounced NFL anomalies have been identified in the ambient pressure SC CeCoIn₅ and CeIrIn₅, pointing to the closeness of the QCP [114]. This is well illustrated by $\rho(T)$ data for CeCoIn₅ at ambient pressure and zero field. They exhibit linear temperature behaviour above T_c and the logarithmic $\gamma(T)$ variation between 0.4 K and 8 K for fields larger than $H = H_{c2}^{[001]} = 5$ T but smaller than $H = 8$ T (fig. 19) [62]. From systematic $\rho(T, H)$ investigations of CeCoIn₅ a B-T phase diagram may be mapped out showing the development of a field-tuned QCP and associated with it two different NFL regimes. They are characterised by $\rho(T) = \rho_0 + BT^n$ where $n=1$ or $n=\frac{2}{3}$ and a low temperature crossover at T^* to the LFL regime [115] is observed. The $n=1$ regime is similar to the underdoped regime in high T_c superconductors and speculations about the existence of a spin pseudo-gap in CeCoIn₅ and CeRhIn₅ have been made [116]. This is supported by normal state Hall angle and magnetoresistance (MR) measurements [117] which show that in the $n=1$ NFL regime the Hall angle $\Theta_H \sim T^2$ whereas Kohlers rule $\Delta_{xx}(H) \sim H^2$ which holds for LFL systems is strongly violated and a different scaling law is obeyed. The similarities of transport coefficients in CeCoIn₅ to high T_c materials suggests a common origin of NFL behaviour in the critical 2D AF spin fluctuations in both type of compounds. This idea is also supported by an observed giant Nernst effect [118] as in the cuprates. Clear signature of NFL behaviour has also been seen in thermal expansion measurements [119] and the associated

Grüneisen ratio. A compilation of various scaling laws in the NFL regime of the Ce115 and Ce218 compounds may be found in [103, 114]. A kind of inverted behaviour compared to CeCoIn₅ shown in fig. 19 is seen in Ce₂IrIn₈, because in this nonmagnetic HF compound LFL behaviour at zero field changes to NFL behaviour at a field of 13 T, which is interpreted as the appearance of a field induced magnetic QCP [120].

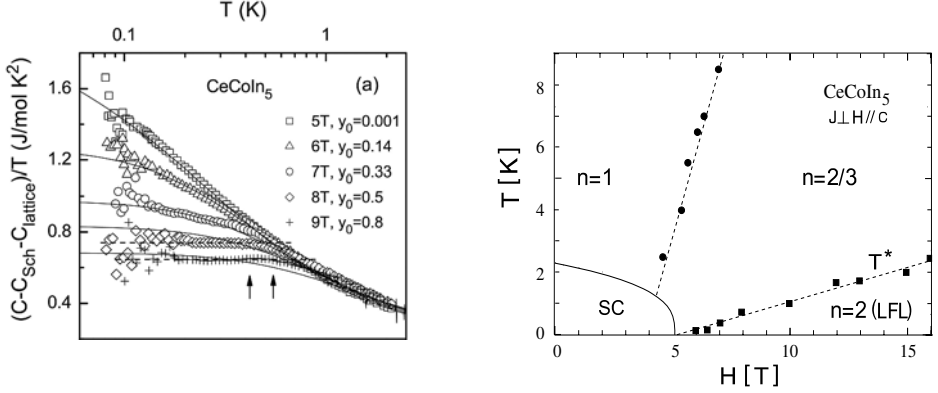
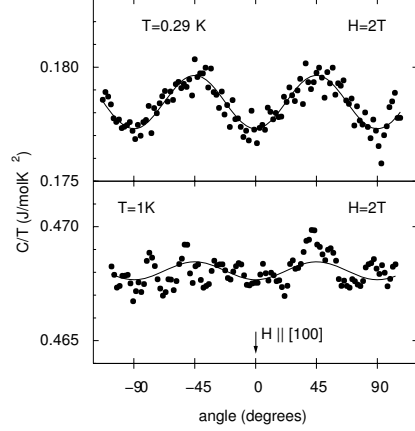


Figure 19: Left panel: Field dependence of $\gamma = C/T$ for $\mathbf{H} \parallel [001]$. Solid lines are fits by Moriya's SCR spin fluctuation theory [62]. Right panel: B-T phase diagram of CeCoIn₅ showing the evolution of two distinct NFL regimes (characterised by different exponents n of $\Delta\rho(T) \sim T^n$) and the high field LFL phase [115].

3.4.4 THE SUPERCONDUCTING GAP FUNCTION IN CeCoIn₅

Heavy Fermion systems are unconventional superconductors regarding their pairing mechanism which is of magnetic origin in most cases and also with respect to non-s-wave symmetry of the order parameter, generally belonging to a non-trivial representation of the total symmetry group. Often, but not necessarily, this is connected with the appearance of nodes or zeroes in the gap function $\Delta(\mathbf{k})$. CeCoIn₅ is the prime and best studied example of unconventional SC in the new family. It is a strong coupling SC with very large BCS ratio $2\Delta/kT_c = 8.86$ at ambient pressure [121] and the gap function is believed to exhibit d-wave symmetry. This has already been suspected from the T^3 -power law behaviour of NMR and NQR relaxation rate $1/T_1$ and the absence of a Hebel-Slichter peak [122]. The same result was found for CeIrIn₅. In addition CeCoIn₅ shows a ¹¹⁵In- Knight shift reduction $K \sim T$ for field along a and c, indicating an isotropic reduction of spin susceptibility in the SC state. The T- dependence of $1/T_1$ and K consistently suggest a singlet pair state with line nodes, e.g. a d-wave state for CeCoIn₅. In subsequent field-angle resolved magnetothermal conductivity [60] and specific heat experiments [61] the position of line nodes, in \mathbf{k} -space have been investigated to identify which irreducible D_{4h} representation among the five d-wave states is realised. In this method a peculiar feature of nodal superconductors in the vortex phase is used as has been first discussed by Volovik [123]. Because of $\Delta(\mathbf{k}) = 0$ along certain directions in \mathbf{k} -space, quasiparticles can

Figure 20: Specific heat γ -coefficient for CeCoIn₅ as function of field angle ϕ with respect to [100] ($\mathbf{H} \perp c$ -axis) in the ab plane. Maxima at [110] correspond to antinodal direction for $\Delta(\mathbf{k})$, suggesting a d_{xy} -gap function. The oscillation amplitude decreases with increasing temperature [61].



tunnel into the inter-vortex region where they acquire a Doppler shift energy $\mathbf{v}_s \cdot \mathbf{k}$ due to the superfluid velocity field $\mathbf{v}_s(\mathbf{r})$. This leads to a finite, field induced residual quasiparticle DOS. For a gap with line nodes one has ($E \ll \Delta$):

$$\frac{N_s(E, \mathbf{H})}{N_n} \simeq \frac{1}{\Delta} \langle \langle |E - \mathbf{v}_s(\mathbf{r}) \cdot \mathbf{k}| \rangle \rangle \quad (42)$$

where a double average over the Fermi surface and the vortex coordinate has to be taken. This contributes to the specific heat and most importantly supports a heat current \perp to the vortices which is not possible in s -wave superconductors for $T \ll T_c$. For $H \ll H_{c2}$ the residual DOS and hence $\gamma(H)$ has a \sqrt{H} dependence characteristic of nodal superconductors [124]. In addition $N_s(E, \mathbf{H})$ depends on the field *direction* with respect to crystal axes and the position of node lines. As a function of polar field angles θ and ϕ the residual DOS and hence the specific heat and thermal conductivity will exhibit angular oscillations whose type and phase allows one to draw direct conclusions on the \mathbf{k} -space positions of nodes in $\Delta(\mathbf{k})$. The Doppler shift phenomenon has now been exploited successfully to clarify the nodal gap structure in many unconventional superconductors [60, 125–128] including CeCoIn₅; see also [129]. There both $\kappa_{xx}(\theta, \phi)$ [60] and $C(\theta, \phi)$ [61] exhibit fourfold oscillations in the azimuthal angle ϕ which means that the gap function $\Delta(\mathbf{k})$ has four line nodes parallel to the c -axis on the main cylindrical FS of CeCoIn₅. The maximum in the oscillation will be achieved when each of them gives a Doppler shift contribution in eq. (42), i.e. when \mathbf{H} points along the anti-nodal direction, the minimum occurs in the nodal direction. Surprisingly the two measurements presently disagree on the position of the line nodes: Thermal conductivity results suggest line nodes along c at [110] and equivalent directions. This means a $d_{x^2-y^2}$ (B_{1g}) symmetry of the SC gap in CeCoIn₅ as for high T_c compounds. On the other hand in the specific heat results of fig. 20 the maxima in the ϕ -oscillations are shifted by 45° , therefore node lines along c should be situated at the tetragonal [100] and equivalent positions meaning a d_{xy} (B_{2g})-type symmetry of the SC gap. This discrepancy is not fully resolved so far.

3.4.5 VORTEX STATE AND FFLO PHASE IN CeCoIn₅

Besides providing important clues on gap function symmetry the vortex state of CeCoIn₅ has proved highly interesting, even unique, in its own right. It was known already for a long time that for low temperatures the SC transition at H_{c2} should change from second to first order. This is due to a competition of orbital- and Pauli-pair breaking effects characterised by the Maki parameter $\alpha = \sqrt{2}H_{c2}/H_P$ where $H_P = \Delta_0/\sqrt{2}\mu_B$ (for $g = 2$) is the Pauli limiting field. Conditions are favorable if the former is weak (large H_{c2} or $\alpha > 1$) compared to the latter and if spin-orbit scattering by impurities is negligible. Neglect of the orbital effect ($\alpha \rightarrow \infty$) leads to $T_0 = 0.55T_c$ for the appearance of the first order transition in an s-wave SC. Apparently these conditions have never been met in superconductors investigated so far. In CeCoIn₅, due to the large effective mass $m^* \simeq 100 m$ and resulting extremely high $H_{c2}^{[110]}(0) = 11.9$ T, and due to excellent sample quality they are much better fulfilled. Indeed in this compound a change from second to first order superconducting transition for field $\mathbf{H} \parallel [001]$ has been found at $T_0 \simeq 0.3T_c$ (corresponding to $\alpha = 3.5$) by specific heat [130, 131] and thermal expansion [102] measurements. The first order transition was also found for $\mathbf{H} \parallel [110]$ from magnetisation [132] and specific heat [62] measurements below $T_0 = 0.5T_c$. (fig 21). The same favorable

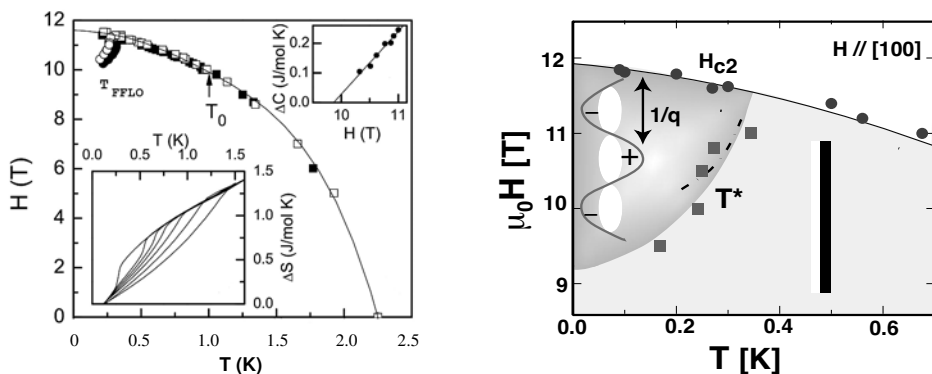


Figure 21: Left panel: H_{c2} curve from specific heat results. At $T_0 \simeq 1.1$ K the SC transition changes from 1st to 2nd order. Lower inset shows entropy gain. Upper inset shows specific heat jump at T_{FFLO} line [62]. Right panel: enlarged FFLO corner determined from sound velocity measurements. Segmentation of vortices in FFLO phase with wave length $1/q$ is indicated [63].

circumstances may explain an even more exotic observation in CeCoIn₅ for $\mathbf{H} \parallel [110]$. At very small temperatures an additional phase appears in the vortex state (fig. 21). It is now considered as the first realisation of the Fulde-Ferrell-Larkin-Ovchinnikov (FFLO) phase where the electrons form Cooper pairs with a finite momentum q . It appears when the Pauli effect largely dominates the orbital effect ($\alpha > 1.8$ [133]) and spin orbit scattering is very small. Apparently CeCoIn₅ is the first SC compound where these conditions are fulfilled leading to the spatially modulated FFLO SC pair state with a wave number $q \simeq 2\mu_B H/\hbar v_F$. In this state the order parameter should have planar nodes perpendicular to the field leading to a segmentation

of vortex lines along the vortex direction. A definite proof for this conjecture by small angle neutron scattering is still lacking, but indirect evidence for the segmentation has been found by sound velocity measurements [63]. The segmentation of vortices on crossing the T_{FFLO} line changes their pinning properties which in turn leads to a Lorentz force anomaly for sound modes with displacement vector $\mathbf{u} \perp \mathbf{H}$. The estimated segmentation length is remarkably close to the calculated modulation length $1/q = 60 \text{ \AA}$. Also this method allows an independent determination of specific heat results and assures that the new phase is not due to field induced magnetic order since the latter should not have any effect on the vortex pinning. The FFLO corner is clearly visible for \mathbf{H} in the ab - plane but hard to identify for \mathbf{H} along [001] with the smaller H_{c2} in agreement with theoretical predictions. Evidence for the FFLO state for $\mathbf{H} \parallel [110]$ has recently also been found from ^{115}In -NMR measurements [134] which give a $T_{\text{FFLO}}(\mathbf{H})$ -line similar to that from specific heat and sound velocity results and provide direct evidence for the spatial texture of the order parameter in the FFLO phase.

3.5 HF SUPERCONDUCTIVITY WITHOUT INVERSION SYMMETRY IN CePt_3Si

All previously discussed Ce- intermetallic compounds and in fact all HF superconductors known possess centrosymmetric space groups which contain an inversion center. This leads one to a natural classification of SC pairs into even and odd parity or singlet and triplet states. For the singlet channel only time reversal invariance is required in order to assure the necessary degeneracy of paired electron states with opposite momenta and spins. For the formation of triplet pairs however, electron states with opposite momenta but equal spins must also be degenerate which requires inversion symmetry as an additional necessary condition [135]. The lack of an inversion center may also strongly affect the magnetic properties of a superconductor as shown in [65].

The discovery of the first HF superconductor CePt_3Si [64] without inversion symmetry is therefore of considerable fundamental interest. CePt_3Si belongs to the tetragonal space group $P4/m$ (fig. 22) where the removal of the inversion center leads to the Ce-point group C_{4v} meaning the loss of the basal plane as mirror plane ($z \rightarrow -z$). The structure can be derived from the hypothetical cubic CePt_3 structure (the same as for CeIn_3) by tetragonal distortion with $c/a=1.336$ and by filling the voids with Si. The $\text{Ce}^{3+}4f$ states of CePt_3Si are well localised as evident from sharp CEF excitations found in INS experiments [137] where the C_{4v} level scheme was determined as $\Gamma_7^{(1)}(0)$, $\Gamma_6(1 \text{ meV})$ and $\Gamma_7^{(2)}(24 \text{ meV})$. At $T_N = 2.2 \text{ K}$ AF magnetic order appears where FM planes are staggered along c with $\mathbf{Q} = (0,0,\frac{1}{2})$. Below $T_c = 0.75 \text{ K}$ superconductivity sets in (fig. 23) and coexists microscopically with AF order. Only the second time after A-type CeCu_2Si_2 (fig. 5) this has now been observed for a stoichiometric Ce-compound at ambient pressure. The ordered moments $\mu = 0.16\mu_B$ however are much less than the value of the localised $\Gamma_7^{(1)}$ ground state doublet which suggests a large Kondo screening, and indeed there is an associated mass enhancement of itinerant quasiparticles as is evident from $\gamma_n(\text{CePt}_3\text{Si}) = 390 \text{ mJ/mol K}^2$ as compared to $\gamma_n = 9 \text{ mJ/mol K}^2$ for LaPt_3Si . A considerable residual $\gamma_s = 180 \text{ mJ/mol K}^2$ and a $\Delta C/\gamma_n T_c = 0.25$ much smaller than the BCS value 1.43 has been observed. This raises questions on the quality of the polycrystalline samples although the ξ estimate from H_{c2} indicates that one is not in the dirty limit. Later resistivity measurements on single crystals [138] in a field indeed have identified a coherence length $\xi \simeq 100 \text{ \AA} \ll 1$ (mean

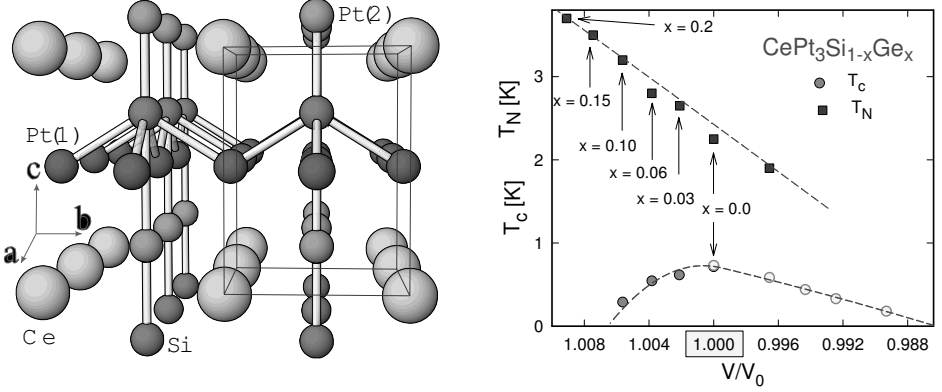


Figure 22: Left panel: Crystal structure of CePt_3Si belongs to the tetragonal space group $P4mm$, the conventional unit cell ($a = 4.072 \text{ \AA}$, $c = 5.442 \text{ \AA}$) is indicated [64]. It lacks the reflection symmetry $z \rightarrow -z$. Right panel: Phase diagram of $\text{CePt}_3\text{Si}_{1-x}\text{Ge}_x$ from ambient pressure (mainly T_N) and hydrostatic pressure results (mainly T_c). Here 1% volume reduction corresponds to 1.5 GPa [136].

free path). There the almost isotropic upper critical fields has been determined as $H_{c2}^a(0) = 3.2 \text{ T}$ and $H_{c2}^c(0) = 2.9 \text{ T}$ (fig. 23) which is considerably larger than the Pauli-Clogston limiting field estimated by $H_P \sim \Delta/\sqrt{2}\mu_B \sim 1.2 \text{ T}$ for $g = 2$. The pressure dependence of T_c which vanishes around $p_c = 1.5 \text{ GPa}$ has still some uncertainty due to the broad appearance of the resistive transition [138]. Nevertheless a combined $p(V)$ - T phase diagram from Ge-doping and hydrostatic pressure results is shown in fig. 22. Whether the AF T_N and the ordered moment vanish continuously and the SC dome extends on both sides of the magnetic phase is presently not known.

The observation of $H_{c2}(0) \gg H_P$ would rather advocate for triplet pairing, this confronts one with two major problems: i) the lack of inversion symmetry should disfavor triplet pairing according to the above arguments. ii) coexistence with fully developed AF order should be destructive for triplet pairs. Proposals to avoid this contradiction have been made in theoretical investigations [66, 139] which include an explicit inversion symmetry breaking but time reversal conserving term in the single particle part of the BCS Hamiltonian. It has the form of a Rashba-type antisymmetric spin-orbit coupling for conduction electrons $c_{\mathbf{k}s}$ which is of the form ($\sigma =$ Pauli matrices)

$$H_P = \alpha \sum_{\mathbf{k}, ss'} \mathbf{g}_{\mathbf{k}} \cdot \sigma_{ss'} c_{\mathbf{k}s}^\dagger c_{\mathbf{k}s'} \quad (43)$$

where $\mathbf{g}_{\mathbf{k}} = -\mathbf{g}_{-\mathbf{k}}$ is an antisymmetric function which may be obtained from the periodic potential of Bloch states and is conveniently normalised to one on the Fermi surface. For finite α this term lifts the twofold spin degeneracy of conduction bands (but preserves the \mathbf{k} , $s \rightarrow -\mathbf{k}$, $-s$ symmetry). It leads to i) modifications for both singlet and triplet gap equations, ii) a mixing term for singlet and triplet gaps which, however, is of the order $\alpha/\varepsilon_F \ll 1$ and therefore can be

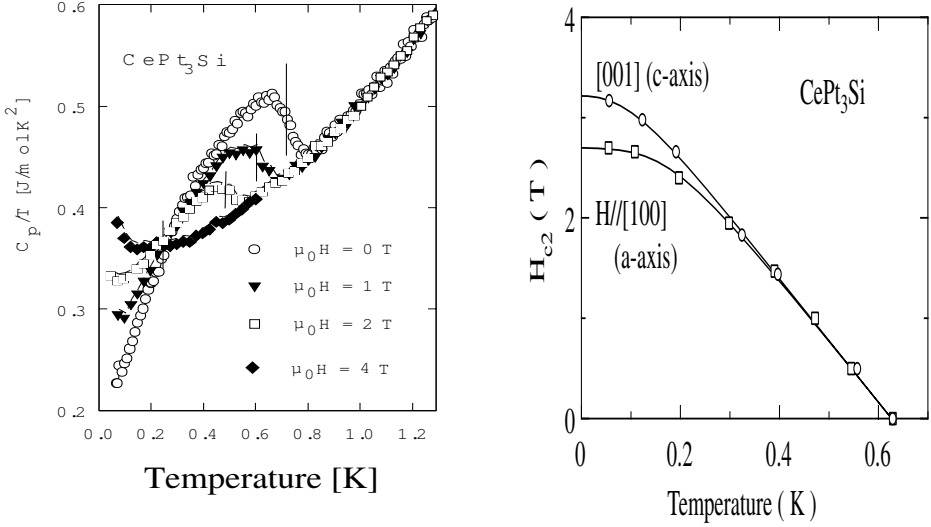


Figure 23: Left panel: Field dependence of C/T in polycrystalline CePt_3Si with SC transition indicated by vertical lines [64]. Right panel: Upper critical field in single crystals from ρ [138].

neglected. Likewise T_c reduction in the singlet case is of order $(\alpha/\varepsilon_F)^2 \ll 1$. The triplet case is more involved and provides important clues on the effect of H_p . For $\alpha = 0$ all triplet states of a given odd l and described by a $\mathbf{d}(\mathbf{k})$ vector gap function have the same T_c . Turning on the I-symmetry breaking ($\alpha > 0$) lifts this degeneracy, the expected T_c -reduction however does not affect all triplet states indiscriminantly, those triplet states with $\mathbf{d}(\mathbf{k}) \parallel \mathbf{g}_\mathbf{k}$ are well protected and have no T_c reduction as in the singlet case. From the C_{4v} point group one may expect $\mathbf{g}_\mathbf{k} \cdot \boldsymbol{\sigma} = k_x \sigma_y - k_y \sigma_x$ and then the protected triplet state with unaffected T_c corresponds to the A_{2u} gap function $\mathbf{d}(\mathbf{k}) = \hat{x}k_y - \hat{y}k_x$ which has point nodes. Other triplet states are strongly suppressed for $\alpha \gg T_c$. Thus in principle favorable triplet states are not destroyed by inversion symmetry breaking.

On the other hand the loss of inversion symmetry described by eq. (43) weakens the Pauli-Clogston limiting argument against singlet pairing considerably. It is known that spin-orbit impurity scattering reduces the effect of paramagnetic limiting, the same is true for the anti-symmetric spin-orbit coupling of paired conduction electrons in eq. (43). With increasing α the renormalised H_p increases above its starting value $\Delta/\sqrt{2}\mu_B$ for $\alpha = 0$. For $\alpha/T_c \gg 1$ it becomes arbitrarily large. As a result the observation of a large $H_{c2}(0) \gg \Delta/\sqrt{2}\mu_B$ does not contradict singlet pairing, which in addition would be more compatible with the coexisting AF order.

As a preliminary conclusion one may say that there is no compelling theoretical reason why triplet pairing for SC without inversion symmetry should be prohibited. Likewise the upper critical field observations do not contradict singlet pairing so that the question of gap symmetry in CePt_3Si remains open. Recent NMR relaxation experiments [140] on Pt-sites also did not clarify this question but rather added new puzzles: The low temperature $1/T_1$ behaviour is

neither described by the usual T^3 power law generally observed in HF SC, nor by an exponential decay indicative of an isotropic gap. However the latter is more compatible with the observation of a small coherence peak below T_c and a Balian-Werthamer type relaxation rate immediately below it.

4 MICROSCOPIC SC PAIRING MECHANISM IN HF COMPOUNDS

In this section we illustrate to some detail microscopic concepts and theories that were proposed to describe the superconducting pairing in HF systems or, more generally, in strongly correlated electron compounds including the cuprates and ruthenates. The long history of the subject of non-phononic superconductivity will not be recounted and we refer to the literature for this purpose [6, 141, 142].

Far below the Kondo temperature T^* the ideal HF compound is in a LFL state with quasiparticles that have an effective mass m^* much enhanced compared to the band mass m_b . However due to the presence of virtual high energy excitations a residual on-site quasiparticle repulsion appears. The low energy excitations may then be described by a spectrum of spin fluctuations characterised by a dynamic susceptibility matrix $\chi(\mathbf{q}, \omega)$. In the vicinity of a magnetic instability, for example AF order close to a QCP, overdamped critical spin fluctuations called antiferromagnetic paramagnons appear whose spectral density is concentrated around the AF \mathbf{Q} -vector and which has a typical energy $T_{sf} < T^*$ at the maximum of $\chi(\mathbf{Q}, \omega)$. The virtual exchange of these excitations mediates an effective interaction between quasiparticles which may lead to a superconducting instability. In contrast to conventional phonon-mediated superconductors the pair states have to be of unconventional (non s-wave) type whose order parameter exhibits a sign change in \mathbf{k} -space to avoid the strong on-site repulsion of quasiparticles. A brief symmetry classification of unconventional SC order parameters was given in sect. 3.1.

Originally the spin fluctuation mechanism in the case of nearly FM systems with paramagnon exchange was proposed to explain superfluidity in ^3He [143, 144]. It was later extended to HF [145] and cuprate superconductors [146]. In the latter one has simple tight binding (TB) hole bands which allows one to carry out fully microscopic calculations based on the fluctuation exchange (FLEX) approximation [147, 148] for the Hubbard model. However the theory in its original single band form is not able to describe the complications of SC pairing in real HF materials, for the following reasons: i) Orbital (spin-orbit) and crystal field effects lead to complicated renormalised band structures with multisheeted FS, therefore the dynamic susceptibility $\chi(\mathbf{q}, \omega)$ cannot be reliably calculated, instead empirical forms have to be assumed which also incorporate the vicinity to a possible QCP frequently present in Ce-HF compounds. ii) In the U-compounds 5f- electron have a dual nature, partly localised and partly itinerant. The internal CEF excitations (magnetic excitons) of the former may dominate the effective interactions between itinerant quasiparticles, which is an alternative to the spin fluctuation mechanism that involves only the itinerant 5f electrons.

We shall discuss both electronic pairing mechanisms in the following. While the spin fluctuation mechanism may be appropriate for the Kondo-like Ce HF superconductors, the magnetic exciton mechanism is a serious candidate for a number of U-compounds.

4.1 SPIN FLUCTUATION MECHANISM FOR Ce-BASED HF COMPOUNDS

If one is not too close to the QCP of magnetic order one may assume that the frequency dependence of spin fluctuations is negligible on the scale of the cutoff energy for SC pairing. Then in the effective interaction $V(\mathbf{q}, \omega)$ between quasiparticles $\chi(\mathbf{q}, \omega)$ may be replaced by the non-retarded RPA expression $\chi(\mathbf{q})$. For the spin dependent part one obtains the spin rotationally invariant interaction

$$V_{\alpha\beta;\gamma\rho}(\mathbf{q}) = V(\mathbf{q})\sigma_{\alpha\gamma} \cdot \sigma_{\beta\rho} \quad \text{with}$$

$$V(\mathbf{q}) = -\frac{1}{2} \frac{I}{1 - I\chi_0(\mathbf{q})} \simeq -\frac{1}{2} I^2 \chi(\mathbf{q}) \quad \text{and} \quad \chi(\mathbf{q}) = \frac{\chi_0(\mathbf{q})}{1 - I\chi_0(\mathbf{q})} \quad (44)$$

Here I is the residual on-site quasiparticle interaction and $\chi_0(\mathbf{q}) \leq I^{-1}$ their static noninteracting susceptibility. The interaction may be split into singlet ($S=0$) and triplet ($S=1$) channels according to $V_0 = -3V$ and $V_1 = V$, the factor 3 is due to the fact that only longitudinal spin fluctuations contribute in the triplet channel whereas both longitudinal and transverse parts contribute in the singlet channel. In this approximation the SC pairing is completely determined by the static susceptibility $\chi(\mathbf{q})$ which may in principle be obtained from diffuse neutron scattering. Its \mathbf{q} -dependence together with the characteristics of the Fermi surface determines the dominant angular momentum component V_S^l of $V_S(\mathbf{q})$ that leads to the stable SC pair state ($l = \text{even}$ for $S=0$ and odd for $S=1$). Obviously the s -wave state is not stable because $V_0^{l=0}$ is always positive (repulsive), pair states with $l > 0$, however, may have attractive $V_l < 0$ and become stable depending on the characteristics of $\chi(\mathbf{q})$. The model has been analysed in some detail in [145] by assuming a spherical FS and a plausible behaviour for $V(\mathbf{q})$ in a cubic lattice with a peak near the AF wave vector \mathbf{Q} to simulate the AF spin fluctuations observed in HF compounds. This analysis predicts that the unconventional even singlet SC state ($l > 0$), e.g. $l = 2$ d-wave state, should be stable because $V_l < 0$ is attractive in this orbital channel.

This result led to the general expectation that AF spin fluctuations favor singlet pairing. While it is true in the simple case of cuprates, and it may be true for some Ce-based HF compounds like CeCoIn_5 (sect. 3.4), it turned out to be misleading for a number of U-compounds like UPt_3 or UNi_2Al_3 and possibly UBe_{13} which exhibit triplet pairing as concluded e.g. from Knight shift results [149]. Therefore the above prediction of singlet pairing may be partly an artefact of the model simplifications and point to the inadequacy of the spin fluctuation model for U-HF superconductors. Indeed the model has obvious deficiencies: i) It completely ignores the orbital structure strongly influenced by spin orbit coupling and CEF effects. ii) It does not take into account the uniaxial crystal anisotropy present in most HF superconductors which possess either tetragonal or hexagonal space groups. iii) It ignores the spin space anisotropy of the pair potential which is assumed as rotationally invariant in eq.(44). In case this symmetry is reduced the triplet state will be less disfavored.

From the low temperature 'power laws' in various thermodynamic and spectroscopic quantities it is also concluded that most HF SC have gap functions with nodes $\Delta(\mathbf{k}) = 0$ along lines on the FS. However if one assumes the strong spin orbit coupling case for quasiparticles, i.e. the crystal double group as symmetry group, 'Blount's theorem' states that triplet pair states can have only point nodes in the SC gap [150]. Therefore the observed power laws which support

line nodes have also been used as an argument for singlet pairing. This argument is misleading however, since the spin orbit coupling is so large that it has to be included already in the orbital basis for band structure calculations within the jj -coupling scheme. The scale of SC pairing energies is much smaller than band energies and therefore it is the 'pseudo-spin' degrees of freedom connected with Kramers degeneracy of quasiparticle band states which are involved in the singlet and triplet pair wave functions. Therefore the pseudo-spins may be assumed to have an effectively weak (pseudo-)spin orbit coupling, and then no contradiction between the existence of line nodes and SC pairing in triplet states for U-compounds appears. We note however that ironically, in UPd₂Al₃, which is the one U compound where the spin fluctuation model is known to be inappropriate probably a singlet SC pair state is realised.

In a series of papers the spin fluctuation mechanism has also been studied within the non-retarded strong-coupling Eliashberg approach [151–154] including the frequency dependence of the pairing interaction and assuming a simple tight binding band with n.n. and n.n.n hopping t and t' respectively for conduction electrons. The frequency dependence is especially important close to a magnetic QCP when the typical energy of spin fluctuations becomes comparable to $2\pi T_c$. Instead of starting from a microscopic model Hamiltonian, a phenomenological effective interaction kernel $V(\mathbf{q}, \omega)$ was used as input for the Eliashberg equation which determines the quasiparticle self energy $\Sigma(\mathbf{k}, i\omega_n)$ and anomalous self energy ('gap function') $\Delta(\mathbf{k}, i\omega_n)$. For singlet ($S=0$) and triplet ($S=1$) pairing it is given in the AF case by

$$\begin{aligned} V_S(\mathbf{q}, \omega) &= a_S I^2 \chi(\mathbf{q}, \omega) \quad \text{with } a_0 = -1 \text{ and } a_1 = \frac{1}{3} \\ \chi(\mathbf{q}, \omega) &= \frac{\chi_0 \kappa_0^2}{\kappa^2 + \hat{q}^2 - i \frac{\omega}{\eta(\hat{q})}} \quad \text{where } \eta(\hat{q}) = T_{sf} \hat{q}_-, \quad \hat{q} = \hat{q}_+ \\ \hat{q}_\pm^2 &= (4 + 2\alpha_m) \pm 2[\cos q_x + \cos q_y + \alpha_m \cos q_z] \end{aligned} \quad (45)$$

Here κ and κ_0 denote the nearly critical and background inverse magnetic correlation lengths respectively (in units of the inverse lattice spacing a^{-1}). In Stoner-RPA theory $\kappa_0^2/\kappa^2 = (1 - I\chi_0)^{-1}$ and $\kappa_0 \sim 2k_F a$. This interaction is mediated by *overdamped* spin fluctuations since the pole of $\chi(\mathbf{q}, \omega)$ is at a purely imaginary frequency, i.e. the spin excitation does not have a real group velocity and therefore is not propagating. This is a natural assumption close to the QCP where the restoring force for spin excitations due to the molecular field breaks down. It is completely different from the phonon case and also the magnetic exciton mechanism discussed later which are both characterised by the exchange of propagating bosons which have a real frequency bigger than the line width. In eq.(45) α_m determines the crystal anisotropy of the spectrum, it is of 2D character when $\alpha_m = 0$ and 3D character for $\alpha_m = 1$. It is still fully isotropic in (pseudo-) spin space as evident from the singlet and triplet classification. According to eq.(45) the interaction in the AF case peaks at the zone boundary vector \mathbf{Q} with a spread given by κ ($\kappa =$ inverse magnetic correlation length ξ_m^{-1}) and a frequency maximum at $\omega_{max} = \eta(\hat{q})\kappa^2$. The same type of expression holds for FM spin fluctuations where one has to replace $\hat{q} = \hat{q}_-$. Using the effective pairing in eq. (45) the Eliashberg equation for the gap function $\Delta(\mathbf{k}, i\omega_n)$ ($\omega_n =$ Matsubara frequencies) is

$$\Lambda(T)\Delta(\mathbf{k}, i\omega_n) = a_S \frac{T}{N} \sum_{\omega_m} \sum_{\mathbf{k}} \chi(\mathbf{k} - \mathbf{q}, i\omega_n - i\omega_m) |G(\mathbf{q}, i\omega_m)|^2 \Delta(\mathbf{q}, i\omega_m) \quad (46)$$

where $G(\mathbf{q}, i\omega_m)$ is the quasiparticle Green's function renormalised by the normal self energy $\Sigma(\mathbf{q}, i\omega_m)$ that satisfies a similar equation. The solution of this set of self consistent equations determines T_c via the condition that the eigenvalue $\Lambda(T_c) = 1$. The fixed parameters of the model are t, t' (hopping elements), κ_0 (inverse background correlation length), and T_{sf} (spin fluctuation energy scale). The critical temperature $T_c(\lambda, \kappa)$ is studied as function of the dimensionless coupling constant $\lambda = I^2 \chi_0/t$ and the inverse magnetic correlation length κ which determines the width of the AF spin fluctuation peak in \mathbf{k} -space. In reality this parameter may be varied experimentally by applying pressure, i.e. tuning the distance to the magnetic QCP where $\kappa = 0$. In the spirit of Ginzburg-Landau theory, at T_c the gap function should belong to a single representation Γ of the spatial symmetry group whose \mathbf{k} -dependence is characterised by the basis function $\Phi_\Gamma(\mathbf{k})$. The stable SC state is the one which has the highest T_c among the representations Γ and pair spins $S = 0, 1$. The $T_c(\lambda, \kappa)$ variation of the stable state may then be calculated. This has been done e.g. for the $d_{x^2-y^2}$ - state in the 2D case appropriate for cuprates, or, with suitable redefinition of bandwidth and T_{sf} also for CeCoIn_5 . Without going to great detail the essential results with the above procedure can be summarised as follows [151–153]:

- When $\mathbf{Q} = 0$ (FM) the p-wave state ($S=1$) is favored (has the largest T_c) and for the AF $\mathbf{Q} = (\frac{1}{2}, \frac{1}{2})$ (2D) or $\mathbf{Q} = (\frac{1}{2}, \frac{1}{2}, \frac{1}{2})$ (3D) the d-wave state ($S=0$) is preferred.
- In both cases T_c increases monotonously with coupling constant λ for any κ . For constant λ it first increases with κ and reaches a maximum at $\kappa^2 \simeq 0.5$ and then shows slow monotonic decrease with κ . When λ decreases the optimum T_c position moves towards $\kappa = 0$, i.e. to the AF QCP.
- Generally the achievable T_c 's under equal conditions are larger in 2D than in 3D, and they are much larger for AF spin fluctuations leading to even pair states as compared to FM spin fluctuations associated with the odd SC states. The latter also depend more strongly on parameters, e.g. on κ .

This result is somewhat counter-intuitive: In the FM case the effective interaction in real space is purely attractive while it is oscillating in the AF case. However as mentioned above, for triplet pairing only longitudinal spin fluctuations contribute, leading to the reduction factor $a_1=1/3$ in eq. (45) whereas in the AF singlet pairing case the additional transverse contributions lead to $|a_0|=1$. This advantage of singlet pairing depends on the isotropy of the effective interaction in spin space. In the opposite limit with maximal Ising type anisotropy in spin space, the disadvantage of triplet pairing is removed as will be discussed in sect. 5.2.

4.2 T_c -DEPENDENCE ON SPECTRAL PROPERTIES OF SPIN FLUCTUATIONS

In the above considerations the change of T_c under variation of global interaction parameters and characteristics is considered. This does not answer the question how the variation of the spectrum of spin fluctuations for a specific \mathbf{q}^* and ω_0 influences T_c , specifically one would like to know which parts of the spectrum are most favorable for achieving a large T_c for a given pair state. For the electron-phonon superconductor this has been first investigated in [155]. It was found that every part of the e-ph interaction function $\alpha^2 F(\omega)$ contributes positively with $2\pi T_c$

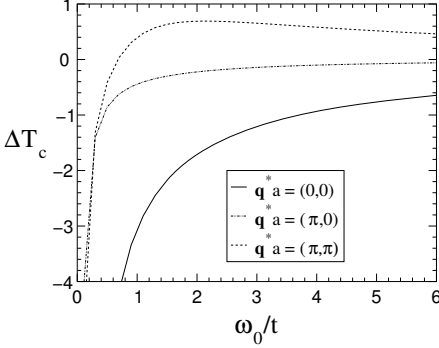


Figure 24: Dependence of ΔT_c on spin fluctuation frequency ω_0 ($t =$ hopping energy) for various momenta \mathbf{q}^* in the 2D AF case with $\mathbf{Q} = (0.5, 0.5)$ (in r.l.u.). Coupling constant $I^2\chi_0/t = 10$; $\kappa^2 = \xi_m^{-2} = 0.5$, $\kappa_0^2 = 12$ and $T_{sf} = 0.67t$. Only spin fluctuations at $\mathbf{q}^* = (\pi/a, \pi/a) \equiv \mathbf{Q}$ or close to \mathbf{Q} contribute positively to T_c above the crossover frequency $\omega_{cr}(\mathbf{q}^*) \simeq 0.5t$. Below $\omega_{cr}(\mathbf{q}^*)$ they are pair breaking. [154].

being the optimum phonon frequency while phonons with frequencies much larger or much smaller frequencies contribute little to T_c .

This analysis has been extended later [156] to the spin fluctuation model for HF systems, albeit using an unrealistic effective interaction that factorises with respect to frequency and momentum. As a main result it was found that, for any momentum \mathbf{q} , adding spectral weight below a crossover frequency ω_{cr} reduces T_c , i.e. low energy spin fluctuations act pair breaking. However a subsequent analysis by McHale and Monthoux [154] using the more realistic effective interaction in eq. (45) has modified this picture considerably. By adding an infinitesimal amount of spectral weight to $\chi(\mathbf{q}, \omega)$ at fixed wave vector \mathbf{q}^* and frequency ω_0 and $-\omega_0$, i.e. adding two delta-functions, the change in the critical temperature $\Delta T_c(\mathbf{q}^*, \omega_0)$ was computed numerically. A representative result in 2D for three different \mathbf{q}^* is shown in fig. 24 for the nearly AF spin fluctuation spectrum with 2D incipient ordering vector $\mathbf{Q} = (\frac{1}{2}, \frac{1}{2})$. It clearly shows that the effect of the added intensity to the spectrum also depends strongly on \mathbf{q}^* , i.e. where it is added in the BZ, in addition to the ω_0 dependence. For $\mathbf{q}^* = (0,0)$ or $(\frac{1}{2}, 0)$ which are far away from the AF $\mathbf{Q} = (\frac{1}{2}, \frac{1}{2})$ the added intensity reduces T_c for all frequencies ω_0 . Only when it is added at the incipient ordering wave vector \mathbf{Q} or close to it one has $\Delta T_c > 0$ for frequencies $\omega > \omega_{cr}(\mathbf{q}^*)$. The crossover frequency ω_{cr} from pair breaking to pair formation therefore strongly depends on the wave vector \mathbf{q}^* of the added intensity relative to \mathbf{Q} . Sufficiently far away from their spectral maximum at \mathbf{Q} spin fluctuations with *all* frequencies ω_0 are pair breaking ($\Delta T_c(\mathbf{q}^*, \omega_0) < 0$). The pair forming fluctuations are constrained to the region around \mathbf{Q} which means that the pairing occurs mostly through the short range magnetic fluctuations, except very close to the QCP ($\kappa \rightarrow 0$). The analysis again shows that $\Delta T_c(\mathbf{q}^*, \omega_0)$ is much more robust in the AF case as compared to FM case ($\mathbf{Q} = 0$). From the $\Delta T_c(\mathbf{q}^*, \omega_0)$ curves in the AF case it is also found that the optimum ω_0 where ΔT_c is largest lies above the spectral maximum of $\chi(\mathbf{q}, \omega)$ for $\kappa^2 \ll 1$ (nearly critical case) and vice versa for $\kappa^2 \gg 1$. Despite the complications the optimum ω_0 is of the same order of magnitude given by $2\pi T_c$ as for the electron-phonon mechanism.

These results show that the formation of the SC state is not determined by the very low energy critical spin fluctuations which are responsible for the NFL anomalies in compounds like CePd_2Si_2 . It explains qualitatively why compounds like CeCu_2Ge_2 or CeRh_2Si_2 which exhibit LFL behaviour around the critical pressure for destruction of AF order may nevertheless be spin fluctuation mediated superconductors (see also sect. 3.3).

The previous analysis also suggests another reason why triplet pairing should be relatively scarce. In strongly correlated electron systems not too close to a QCP dominant spin fluctuations involve mostly nearest neighbors, i.e. they have wave vectors \mathbf{Q} at the zone boundary, these are however triplet-pair breaking for all frequencies in the spin fluctuation mechanism. Considering this fact and the observation that most U-based HF superconductors seem to have triplet pairs it seems doubtful whether the spin fluctuation model is appropriate for them and one has to think about other possibilities.

4.3 MAGNETIC EXCITON MECHANISM FOR SUPERCONDUCTIVITY IN U- BASED HF COMPOUNDS

The origin of mass enhancement in Ce- and U-based compounds is not the same as explained in sect. 2. This is due to the multiple 5f-shell occupation and strongly orbital dependent hybridisation in U compounds which, in some cases like UPd₂Al₃, UPt₃ and possibly UBe₁₃ leads to a partly itinerant and partly localised nature of 5f electrons. In a strong-coupling theory for the quasiparticles, mass enhancement and effective pair interactions are two sides of the same coin. Therefore we discuss now the origin of SC pairing within the dual model of 5f electrons. This idea has been proposed and explored to some extent in [157–159] for UPd₂Al₃ as discussed further in sect. 5.2.

In the dual model the localised 5f² electrons occupy specific total angular momentum orbitals which are split by the CEF. For simplicity we consider only the two lowest CEF states which are assumed to be nonmagnetic singlets. They are then described by a pseudo-spin ($S=\frac{1}{2}$) variable where $S_z = \pm\frac{1}{2}$ correspond to singlet CEF states with energies $\pm\frac{\delta}{2}$. They have an effective inter-site coupling (superexchange) as well as a coupling to the itinerant 5f electrons of the conduction band $\epsilon_{\mathbf{k}}$. The latter couples only with the σ_z - conduction electron spin component due to the (Ising-type) anisotropy introduced by the singlet CEF states which have only transition matrix elements for the local S_x pseudo-spin operator. This dual 5f-model is described by [159]

$$H = \sum_{\mathbf{k}\sigma} \epsilon_{\mathbf{k}} c_{\mathbf{k}\sigma}^\dagger c_{\mathbf{k}\sigma} + \delta \sum_i S_{iz} - J_{ff} \sum_{\langle ij \rangle} S_x^i S_x^j - I \sum_i \sigma_{iz} S_{ix}. \quad (47)$$

The localised part may be diagonalised separately. Due to the effective inter-site interaction $J(\mathbf{q})$ which contains the superexchange J_{ff} and a RKKY contribution from the last term the local CEF excitations at an energy δ evolve into propagating magnetic exciton modes with a dispersion given by

$$\omega_E(\mathbf{q}) = \delta \left[1 - \frac{J(\mathbf{q})}{2\delta} \tanh \frac{\beta}{2} \delta \right] \quad (48)$$

If $J(\mathbf{q})$ has its maximum $J_e = J(\mathbf{Q})$ at an AF zone boundary vector \mathbf{Q} the mode frequency becomes soft at \mathbf{Q} at the Néel temperature where induced AF appears;

$$T_N = \frac{\Delta}{2 \tanh^{-1}(\frac{1}{\xi})} \quad \xi = \frac{J_e}{2\Delta} \quad (49)$$

provided one has $\xi > 1$ for the control parameter. In reality the softening will be arrested at a finite magnetic exciton gap due to the effect of higher lying CEF states which may shift T_{NI}

slightly to higher temperatures. The magnetic excitons associated with the localised 5f system may be seen in INS as discussed for UPd₂Al₃ in sect. 5.2. For $T \ll \delta$ they are bosonic modes like phonons and then a canonical transformation on eq. (47) leads to a more convenient dual model Hamiltonian [159]

$$H = \sum_{\mathbf{k}\sigma} \varepsilon_{\mathbf{k}} c_{\mathbf{k}\sigma}^\dagger c_{\mathbf{k}\sigma} + \sum_{\mathbf{q}} \omega_E(\mathbf{q}) (\alpha_{\mathbf{q}}^\dagger \alpha_{\mathbf{q}} + \frac{1}{2}) - I \int d\mathbf{r} \psi_{\alpha}^\dagger(\mathbf{r}) \sigma_{\alpha\beta}^z \psi_{\beta}(\mathbf{r}) \phi(\mathbf{r}) \quad (50)$$

where $c_{\mathbf{k}\sigma}^\dagger$ and $\alpha_{\mathbf{q}}^\dagger$ create conduction electrons and magnetic excitons respectively and $\psi_{\alpha}^\dagger(\mathbf{r})$, $\phi(\mathbf{r})$ are the associated field operators. It is indeed very similar to the electron-phonon Hamiltonian, except that magnetic excitons do not couple to the electronic density but (in this simplified model) only to the z-component of the itinerant spin density. The resulting normal self energy of conduction electrons due to dressing by virtual magnetic excitons has been discussed before. Complementary virtual exchange processes involving magnetic excitons lead to an effective quasiparticle interaction given by ($v_n = 2\pi nT$) [159]

$$\hat{V}(\mathbf{q}, iv_n) = -I^2 D^0(\mathbf{q}, iv_n) \hat{\sigma}^z \hat{\sigma}^z = \left(\frac{I^2 \Delta}{2} \right) \frac{\hat{\sigma}^z \hat{\sigma}^z}{v_n^2 + \omega_E(\mathbf{q})^2} \quad (51)$$

This effective pairing breaks spin rotational symmetry in a maximal (Ising type) manner. This is enforced by the anisotropy of the CEF states and has important consequences for the classification of SC pair states, one now has to use the equal spin pairing (ESP) states $|\chi\rangle = |\uparrow\uparrow\rangle$ and $|\downarrow\downarrow\rangle$, and opposite spin pairing (OSP) states, given by

$$|\chi\rangle = \begin{cases} \frac{1}{\sqrt{2}} (|\uparrow\downarrow\rangle - |\downarrow\uparrow\rangle) \\ \frac{1}{\sqrt{2}} (|\uparrow\downarrow\rangle + |\downarrow\uparrow\rangle) \end{cases} \quad (52)$$

This aspect is completely different from the previous spin fluctuation theory which leads to a spin rotationally invariant pairing potential and the pair states are classified as (pseudo-) spin singlet ($S = 0$) and triplet ($S = 1$) states. As a consequence, because $p = \langle \chi | \hat{\sigma}^z \hat{\sigma}^z | \chi \rangle$ is +1 for ESP and -1 for OSP respectively, the coupling strength of the effective potential in eq. (51) is equal for OSP and ESP states, in contrast to the enhancement factor 3 of singlet vs. triplet pair interaction in the spin fluctuation model. Thus the present mechanism with its Ising type spin anisotropy in eq. (51) does not disfavor the odd parity states over even parity states, in fact they may be degenerate as will be discussed for a concrete case in UPd₂Al₃.

The magnetic exciton mediated pairing mechanism is due to the interaction between itinerant 5f electrons caused by the exchange of excitations within the localised 5f-CEF states. On one hand it is similar to the electron-phonon mechanism because propagating modes are involved and not overdamped spin fluctuations, on the other hand it is repulsive in the s-wave channel and contains the conduction electron spin variables leading to the possibility of unconventional or nodal pair states.

5 U-BASED HF SUPERCONDUCTORS

Most ambient pressure HF superconductors are intermetallic U compounds like UBe₁₃ [160], UPt₃ [161], URu₂Si₂ [162], UPd₂Al₃ [163] and UNi₂Al₃ [164]. This may partly be caused by

the enhanced delocalisation of 5f as compared to 4f electrons. Due to the multiply occupied 5f shell in U which hosts between two and three electrons, the origin of heavy electron mass enhancement in U compounds is in fact quite different as compared to Ce compounds with nearly singly occupied 4f orbitals. In the latter, heavy quasiparticles originate from coherent resonant scattering in the Kondo lattice [4]. For some U-HF systems however the dual, i.e. localised and itinerant nature of 5f electrons in different orbitals generates the mass enhancement [28, 29] (sect. 2) and may also dominate the SC pairing mechanism. The AF QCP scenario so prevalent in Ce-compounds is not of general importance in U-based HF superconductors with the possible exception of UBe_{13} . One rather observes that SC phases in U-compounds are embedded in a region of reduced moment AF order. In the more recently discovered FM U-based superconductors like UGe_2 or URhGe however QCP of FM or even hidden order may indeed be associated with the observed unconventional SC phases. On the other hand these superconductors are not really HF materials as witnessed by their low γ -values and they will not be discussed here.

In this review we shall not give a complete overview on U-based HF superconductors but shall focus on two examples, $\text{U}_{1-x}\text{Th}_x\text{Be}_{13}$ and UPd_2Al_3 where new results have been obtained recently. Some of the other classical U-compounds, notably the unique multicomponent superconductor UPt_3 are reviewed in [6, 8, 9] while URu_2Si_2 is reviewed in [6].

5.1 MULTIPHASE SUPERCONDUCTIVITY IN THE NON-FERMI LIQUID COMPOUND $\text{U}_{1-x}\text{Th}_x\text{Be}_{13}$

The cubic Be-cage compound UBe_{13} was the second HF superconductor discovered [160, 165] but remains only partly understood. The SC transition takes place in a normal state with pronounced NFL behaviour, as can be seen from the C/T behaviour for fields above H_{c2} . The thorated UBe_{13} has a complicated x -T phase diagram with two distinct SC phases and possibly a coexisting magnetic phase. In fact it is surprising that SC survives up to about $x = 0.06$ since the potential scattering of normal Th impurities should lead to a strong pair breaking for an unconventional SC state and an ensuing rapid reduction of T_c . Instead a pronounced non-monotonic behaviour of $T_c(x)$ is found. The x -T phase boundaries are still partly a conjecture and may have to be revised according to recent flux creep experiments [166]. The most interesting issue is doubtlessly the origin of small magnetic moments in the low temperature SC phase (C) in the regime $0.02 < x < 0.045$. They may either be caused by a non-unitary SC C-phase which breaks time reversal symmetry as suggested by μSR experiments [167] or they may be associated with the formation of a long range SDW order suggested by thermal expansion experiments [168–170]. Theoretically the former scenario has been explored within the context of a Ginzburg-Landau approach assuming that the $T_c(x)$ of two distinct SC phases cross [5]. The SC/SDW scenario on the other hand has been theoretically proposed in [171]. It should be noted however that assumptions on the gap function symmetry remain purely speculative. Even in the pure UBe_{13} it is not known although the presence of nodes in the gap function and hence its unconventional nature is assured, e.g. from the existence of a zero-bias conductance peak in tunneling experiments [172] which provides evidence for a sign change of the gap function $\Delta(\mathbf{k})$.

5.1.1 ELECTRONIC STRUCTURE AND NFL-LIKE NORMAL STATE

The 5f states in UBe_{13} show both signatures of localisation and itineracy. On one hand the 5f-orbital energy is close to the Fermi level according to photoemission results. This disfavors the Kondo picture with a localised $5f^3$ configuration as origin of the extremely large mass enhancement characterised by $\gamma = 1100 \text{ mJ/mol K}^2$ corresponding to a quasiparticle band width of $T^* \simeq 8 \text{ K}$. LDA calculations [173] with fully itinerant 5f electrons however lead to only $\gamma_b = 13 \text{ mJ/mol K}^2$ implying a large many body enhancement factor of $m^*/m_b = 85$. The Fermi surface consists of two closed hole sheets with nesting properties and one closed electron sheet.

On the other hand Schottky-type specific heat anomalies [174] suggest the presence of CEF excitations $\simeq 180 \text{ K}$ out of a $\Gamma_6(5f^3)$ Kramers doublet ground state. An alternative model [175] assuming a nonmagnetic $\Gamma_3(5f^2)$ ground state can be ruled out because it predicts the wrong sign of the nonlinear susceptibility $\chi^{(3)}(T)$ at low temperatures [176]. A mixed valent model involving both nonmagnetic Γ_3 and magnetic Γ_6 doublets has also led to the conclusion that the ground state must be the magnetic Γ_6 to obtain qualitative agreement with the observed $\chi^{(3)}(T)$ behaviour [177]. In the pure Γ_6 picture the Kondo effect would lead to a LFL state with enhanced m^* . However a further temperature scale below T^* given by $T_m \simeq 2 \text{ K}$ has been found from a clear maximum structure in resistivity, specific heat and thermal expansion [169, 170]. This indicates that UBe_{13} has not yet reached a true LFL state when SC sets in at $T_c \simeq 0.9 \text{ K}$. Indeed for fields above H_{c2} a pronounced NFL behaviour with logarithmic increase in $\gamma(T)$ and no saturation to the lowest temperatures has been observed [178, 179] in UBe_{13} . In addition a universal field-independent $\rho(T)/\rho_{1K}$ behaviour is observed for $T \geq 1.2K$ and $4T \leq H \leq 10T$ in the normal state. One finds $\rho(T) \sim T$ at elevated and $(\rho(T) - \rho_0) \sim T^{3/2}$ at lower T [179, 180]. The origin of NFL behaviour may reside in the vicinity of a QCP for SDW or possibly hidden order, this would be in accordance with the nesting properties of electronic bands in UBe_{13} and with the evolution of $T_m(x)$ which hits the maximum of $T_c(x)$ in $\text{U}_{1-x}\text{Th}_x\text{Be}_{13}$ as concluded from resistivity measurements [169, 170]. Another possibility is provided by the $T_m(B^*)$ dependence, implying $T_m \rightarrow 0$ for $B^* \rightarrow 5T$ (fig. 25), i.e. a field-induced QCP of short-range AF correlations [179].

5.1.2 THE SUPERCONDUCTING PHASE DIAGRAM OF $\text{U}_{1-x}\text{Th}_x\text{Be}_{13}$

The symmetry of the SC state in pure UBe_{13} is not known with any confidence, but its anisotropic nature is suggested by power law behaviour of specific heat, penetration depth and NMR relaxation and by tunneling results mentioned before. As usual from the power law exponents no consensus has emerged whether the gap function is characterised by point or line nodes and therefore we do not discuss these results. A strong indication of nonconventional SC is obtained from a giant ultrasonic absorption anomaly immediately below T_c [181, 182] which was attributed to damping by domain walls formed by a multicomponent SC order parameter [5]. Also the B-T phase diagram (fig. 25) is quite anomalous, it exhibits a line of anomaly $B^*(T)$ deep in the SC regime which starts at $T_L(x=0) = 0.7 \text{ K}$ signifying the onset of short range AF correlations. As function of x they eventually develop into a long range SDW order discussed below. The SC phase diagram of thoriated $\text{U}_{1-x}\text{Th}_x\text{Be}_{13}$ ($x \leq 0.1$) has required a great effort to unravel and the task is still not finished. It displays a bewildering richness of different phases and lines of anomalies which have been obtained mostly from specific heat, resistivity and ther-

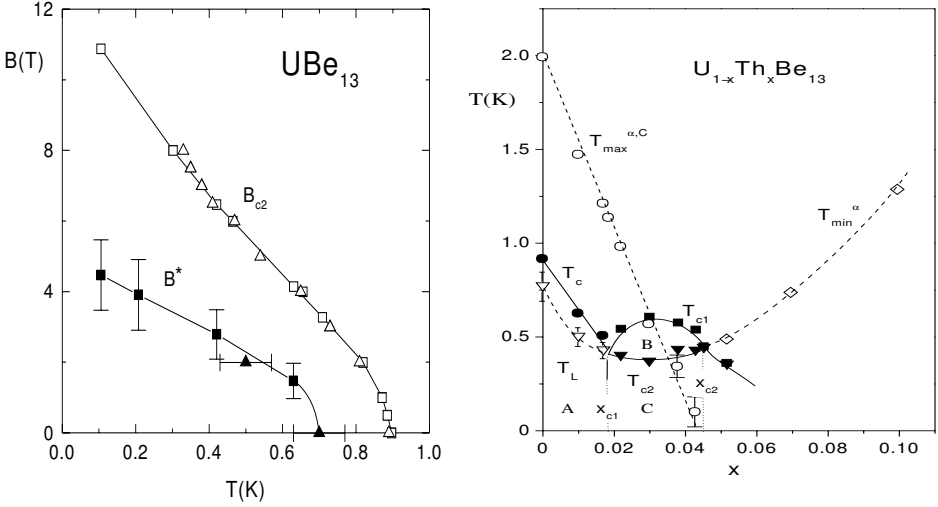


Figure 25: Left panel: B-T phase diagram of UBe_{13} with additional anomaly line $B^*(T)$ obtained from specific heat (squares) and thermal expansion (triangles) experiments. Right panel: SC phase diagram of $\text{U}_{1-x}\text{Th}_x\text{Be}_{13}$. Full lines and symbols denote boundaries of different thermodynamic phases, broken lines and open symbols denote lines of anomalies. T_L and T_{min}^{α} are anomaly lines obtained from the minimum in thermal expansion $\alpha(T)$. $T_{max}^{\alpha, C} \equiv T_m$ is the line of anomalies from the maximum in $C(T)$ and $\alpha(T)$. A, B and C are the distinct SC phases in the T_c -crossing model. [169, 170, 183]

mal expansion (magnetostriction) measurements [169, 170]. The salient feature of the phase diagram is a nonmonotonic variation of the $T_c(x)$ curve with a cusp at $x_{c1} \approx 0.02$ and associated with it a splitting in two SC transitions $T_{c1}(x)$ and $T_{c2}(x)$ in the range $x_{c1} < x < x_{c2}$ with $x_{c2} \approx 0.045$ [184]. This leads to three distinct SC regions A, B and C in the x - T plane. When crossing from B to C, H_{c1} exhibits a sudden change in slope [185] and small magnetic moments $\mu \approx 10^{-3}\mu_B$ seen in μSR experiments [167] appear which are absent below x_{c1} (A) and above x_{c2} . There are presently two distinct scenarios, denoted by I and II, to explain these observations.

(I) The T_c -crossing model

The most widely accepted interpretation has been given quite early in [5, 186] in terms of a Ginzburg-Landau model involving only SC order parameters. The fundamental assumption is that two SC phases with gap functions belonging to different representations, e.g. Γ_1 and Γ_5 of the cubic symmetry group O_h , have close transition temperatures $T_c(\Gamma_1, x)$ and $T_c(\Gamma_5, x)$ which cross at a critical concentration x_{c1} . Below x_{c1} $T_c(\Gamma_5, x) > T_c(\Gamma_1, x)$ and the unconventional Γ_5 (A) phase which has gap nodes is stable. Above x_{c1} the inequality is reversed and the conventional (fully symmetric) Γ_1 (B) phase is stable immediately below $T_{c1} = T_c(\Gamma_1, x)$. For lower temperatures ($T < T_{c2}(x)$) higher order mixing terms in the GL free energy functional stabilise a mixed $\Gamma_1 \otimes \Gamma_5$ (C) SC phase with a different H_{c1} , hence the observed kink. The C- phase gap

function may be non-unitary and time reversal symmetry breaking, thus leading to condensate magnetic moments induced around impurities and defects which allegedly have been observed in the μ SR experiments. For even larger concentrations enhanced pairbreaking or the reduction of the spin excitation energy scale $T_m(x)$ involved in pair formation leads to a decrease in $T_c(\Gamma_1, x) = T_{c1}$ and a second crossing point appears. However a GL expansion around x_{c1} cannot naturally explain the second crossing.

(II) *The SC/SDW coexistence model*

An alternative scenario to explain the phase diagram in fig. 25 (right panel) has appeared as a result of investigations of the differential thermal expansion $\alpha = l^{-1}\partial l/\partial T$ [169, 170]. In this explanation the SC phases A and B are assumed as identical unconventional SC phases as inferred from the almost equal pressure dependence away from the critical x_{c1} . In phase C the SC order parameter is unchanged by a SDW modulation which appears within the unconventional SC phase. This was previously already proposed theoretically in [171] within the context of a model calculation for coexistence of a necessarily unconventional SC and a SDW phase. The moments seen in the C phase are then associated with the SDW. The main reason for this alternative interpretation of the x -T phase diagram is the discovery of a new line of anomaly $T_L(x)$ in $\alpha(T)$ for subcritical $x < x_{c1}$ which starts at a $T_L(0)$ identical to the temperature for which $B^*(T) = 0$ as seen in the B-T phase diagram. With growing x the $\alpha(T)$ anomaly becomes increasingly sharp and $T_L(x)$ exactly joins the T_{c2} line at x_{c2} . This suggests to interpret $T_L(x)$ as the onset temperature of short range magnetic correlations which turn into the long range SDW state at x_{c1} . The $\alpha(T)$ anomaly line is seen to continue even far above x_{c2} . The shape of the $\alpha(T)$ anomaly above x_{c1} is indeed familiar from other magnetic transitions. It is also in accord with the interpretation of a huge (Cr-type) anomaly in the ultrasonic attenuation [187]. The SC/SDW coexistence scenario lacks however a natural explanation for the observed kink in H_{c1} at T_{c2} .

Recent flux-creep experiments [166, 188] have further complicated the picture. A steep drop in the flux creep rate was observed below T_{c2} which may naturally be explained within the T_c -crossing model because the nonunitary C-phase may have domain walls which pin vortices very effectively [189]. Using this effect for mapping out the C/A-phase boundary it was found that contrary to the original view shown in fig. 25 the C-phase boundary is not perpendicular at x_{c1} but rather has a low temperature tail extending down to $x = 0$, i.e. the drop in flux creep indicating a transition into the C-phase is even seen in pure UBe_{13} .

5.2 NODAL SUPERCONDUCTIVITY IN UPd_2Al_3 MEDIATED BY MAGNETIC EXCITONS

Since its discovery in 1991 by Geibel et al. [163] the extensive experimental studies on this antiferromagnetically ordered moderate HF superconductor (see table 4) have lead to two important conclusions: Firstly the 5f electrons have a dual nature, partly localised and partly itinerant where the former carry the magnetic moments and the latter become superconducting [190, 191]. Secondly there is now compelling evidence that the internal low energy excitations of the localised 5f subsystem mediate an effective pairing potential between the itinerant electrons. This leads to a superconducting state which has an anisotropic gap function with line

nodes [157]. Moreover the virtual low energy excitations of localised 5f electrons lead to a quasiparticle mass enhancement factor m^*/m_b , which is thought to be the origin of the normal HF state of UPd₂Al₃ [29]. Indeed this new mechanism gives consistent T_c and mass enhancement factor within a strong coupling approach based on a dual 5f electron model Hamiltonian [159]. As discussed in sect. 4, HF superconductivity is assumed to exhibit a non-phononic SC pairing mechanism leading to nodal gap functions because the strong on-site repulsion of quasi-particles prevents the (nearly) isotropic SC state most favored by the electron-phonon mechanism. However, UPd₂Al₃ is the only case known so far where this theoretical conjecture has actually been proven by experiment. This was achieved by complementary INS [192–195] and quasiparticle tunneling experiments [196] which, respectively, probe the two aspects of the dual nature of 5f electrons: (1) The internal singlet-singlet CEF excitations ($\delta \simeq 6$ meV) of localised 5f electrons which form propagating magnetic exciton bands in the range of 1-8 meV due to inter-site interactions. (2) The tunneling current which probes the superconducting gap of itinerant 5f electrons in epitaxially grown UPd₂Al₃-AlO_x-Pb tunneling devices. There is a considerable interaction between localised and itinerant 5f electrons signified on one hand by the appearance of a resonance in the INS scattering function associated with the SC gap. On the other hand, even more compelling is the presence of typical 'strong coupling' signatures in the tunneling DOS at about the magnetic exciton energy in the center of the AF BZ as determined in INS. This is a direct proof that the exchange of these magnetic bosons mediates the SC pairing in UPd₂Al₃. This important new mechanism is distinctly different from both the electron-phonon and the spin fluctuation mechanism (sect.4).

5.2.1 PHYSICAL PROPERTIES

Further experimental evidence for the dual nature of 5f electrons comes from susceptibility measurements [197] above T_c where $\chi(T)$ for field perpendicular to c shows a pronounced maximum below $T = 50$ K, typical for the effect of CEF states which originate from the 5f² configuration of the U⁴⁺ ions. The presence of localised states is also seen in Knight shift measurements [191] and optical experiments [198]. There in addition the formation of heavy itinerant quasiparticles below T^* was concluded from an analysis of the Drude peak in the optical conductivity. The low lying CEF states of localised 5f electrons are of singlet-singlet (doublet) type with a splitting $\delta \simeq 6$ meV as obtained from a fit to the overall magnetic exciton dispersion [158]. This means that the AF ordering (table 4) found below T_N is of the induced moment type. The FM ordered ab planes are stacked along c with an AF wave vector $\mathbf{Q} = (0,0,0.5)$ (r.l.u.) [199, 200] and an easy axis [100]. Moment reorientation can only be observed for fields in the ab plane and the phase diagram was determined in [200].

The superconducting state below T_c was investigated in numerous experiments, but a definite conclusion on the symmetry of the pair state has not been achieved yet. Upper critical field measurements show a flattening of $H_{c2}(T)$ for low temperatures [201] which is interpreted as the effect of Pauli limiting in a spin singlet pair state. This hypothesis was further investigated by ²⁷Al Knight shift experiments [202] which shows a considerable reduction below T_c again in favor of singlet pairing, however, the interpretation is not unambiguous due to a large local moment contributions to K_s . The ²⁷Al NMR relaxation rate T_1^{-1} was found to exhibit clear T³ power law [202], naively interpreted as evidence for line nodes in the gap function $\Delta(\mathbf{k})$ leading

Table 4: Material parameters of UPd₂Al₃ and its isostructural sister compound UNi₂Al₃.

| | $\gamma \left[\frac{mJ}{molK^2} \right]$ | T_N [K] | μ [μ_B] | T_c [K] | $\frac{\Delta C(T_c)}{\gamma T_c}$ [K] | $\frac{\Delta S(T_N)}{R \ln 2}$ |
|----------------------------------|---|-----------|-------------------|-----------|--|---------------------------------|
| UPd ₂ Al ₃ | 140 | 14.3 | 0.85 | 1.8 | 1.2 | 0.67 |
| UNi ₂ Al ₃ | 120 | 4.6 | 0.20 | 1.2 | 0.2-0.4 | 0.12 |

to a quasiparticle DOS $\sim |E|$. This was also suggested by ¹⁰⁵Pd NMR/NQR [203]. Conclusions from the low temperature specific heat $C(T)$ which should be $\sim T^2$ for line nodes are hampered by the difficult subtraction of the nuclear contribution. A $C(T) = \gamma_0 T + aT^3$ behaviour was found where the residual value γ_0 scales with the width of the SC transition [204] that characterises sample quality. The isostructural sister compound UNi₂Al₃ is also a superconductor with co-existing incommensurate magnetic order (table 4). However, contrary to UPd₂Al₃ its 5f states have all a delocalised character as is obvious from the much smaller moment, the incommensurate ordering wave vector and the small entropy release ΔS at T_N which is only one sixth of the value in UPd₂Al₃. Therefore, superconductivity in this compound is thought to be mediated by spin fluctuations of conduction electrons rather than localised 5f excitations as in UPd₂Al₃. However, as in UPt₃, a spin triplet gap function has been proposed for UNi₂Al₃ [205] which according to NMR results should have a line node. Note that this is in conflict with the simple theory of isotropic AF spin fluctuations proposed for U-HF compounds since they would rather prefer spin singlet pairing (sect. 4) [145]. Also it suggests that Blount's theorem which predicts the absence of line nodes for strong spin-orbit coupling cannot naively be applied to real U-HF superconductors (sect. 4). Finally we note that from recent H_{c2} -measurements on epitaxially grown thin films [206] a considerable paramagnetic Pauli-limiting effect was deduced for both a and c directions which led the authors to the opposite conclusion that UNi₂Al₃ should also have a SC singlet pair state.

5.2.2 ELECTRONIC STRUCTURE, THE DUAL MODEL

Within conventional LDA type band structure calculations for UPd₂Al₃ [207–209] there is no way to treat the partly localised and partly itinerant character of 5f electrons properly, all 5f orbitals are incorporated in the basis set for the band states. While the FS topology corresponds reasonably to dHvA results [210] the effective masses of the various sheets are far too small. Even within a modified LSDA (local spin density approximation) treatment including self interaction corrections [211] the effective masses are still too small by an overall factor of ten. The dual model opens an attractive way to remove this discrepancy [29]. The coupling of itinerant 5f- electrons to the low lying discrete CEF excitations of the localised subsystem offers an effective mechanism of mass enhancement (sect. 2). In this approach the calculation of heavy bands proceeds in three steps: 1) 5f orbitals in the jj-coupling limit ($j = \frac{5}{2}$) are used and those with $j_z = \pm \frac{5}{2}, \pm \frac{1}{2}$ are excluded from the basis set of LDA bands which comprises only $j_z = \pm \frac{3}{2}$ states. The band center is fixed to obtain the correct 5f count. 2) The multiplet structure of localised states 5f is calculated using the proper intra-shell Coulomb interactions. The ground

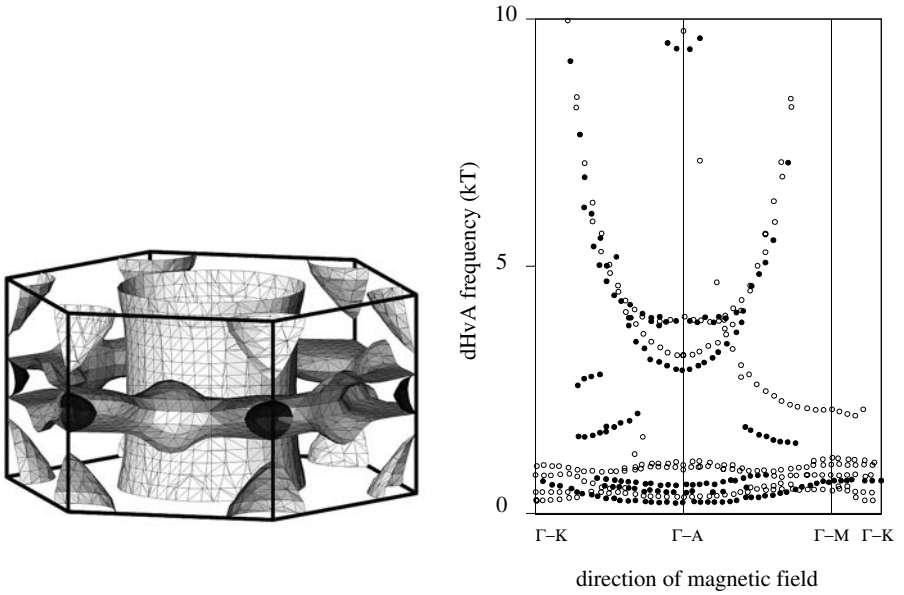


Figure 26: Left panel: Fermi surface of UPd_2Al_3 calculated within the dual model [29]. The main cylinder part has a heavy mass with $m^* = 19 - 33 m$ and the torus ('crown') has $m^* = 65 m$. Right panel: Comparison of experimental dHvA frequencies (black symbols) from [209] and calculated frequencies (open symbols) from the dual model [29]. Large parabolas correspond to the corrugated main FS cylinder. Small arc on top of Γ -A corresponds to the crown sheet.

state is a doublet $|J = 4, J_z = \pm 3\rangle$ which is further split by the CEF potential into two singlets

$$|\Gamma_{3,4}\rangle = \frac{1}{\sqrt{2}}(|J = 4; J_z = 3\rangle \pm |J = 4; J_z = -3\rangle) \quad (53)$$

The splitting energy $\delta \simeq 6 \text{ meV}$ is taken as an empirical parameter obtained from INS. 3) The scattering of localised band states from CEF excitations leads to the mass renormalisation of the former. In the simplest case, without including the dispersion which turns the localised CEF transitions with energy δ into a band of magnetic excitons and neglecting strong coupling effects the mass enhancement would be given by

$$\frac{m^*}{m_b} = 1 + 2 \frac{I^2 N(\epsilon_F)}{\delta} \quad (54)$$

with I defined in eqs. (47) and (50). A more refined treatment for $\frac{m^*}{m_b}$ appropriate for UPd_2Al_3 is described below. In this approach the different treatment of $5f$ orbitals with $j = \frac{5}{2}$ and different j_z cannot be explained on the single particle level because their hybridisation matrix elements are rather similar. The amplification of the orbital dependence of hybridisation due to many body effects has been proposed in [30] and is described in detail in sect. 2.2.

Although the starting point is indeed very different from standard LDA, with only a single delocalised 5f electron, the main FS sheets are reproduced quite well as is obvious from fig. 26. The most prominent FS sheet has the form of a slightly corrugated cylinder oriented along c . It has also a large mass enhancement of $m^*/m \simeq 33$ (m = free electron mass). In the following model discussion one may therefore restrict to this main FS sheet.

5.2.3 MASS ENHANCEMENT AND SC PAIRING DUE TO MAGNETIC EXCITONS

The great advantage of the dual model as compared to the pure LDA approach is its natural explanation of the mass enhancement factor of $m^*/m_b \simeq 10$ (m_b = LDA band mass) which is due to the contribution of virtual singlet-singlet CEF excitations to the conduction electron self energy. Assuming the value of $\delta = 6$ meV from INS the proper mass enhancement is predicted without further adjustable parameters. In addition to the mass enhancement the interaction between the subsystems leads to induced AF magnetic order [157, 158] of localised 5f moments and superconductivity in the itinerant part [157–159]. In its most rudimentary form a model Hamiltonian is given by eq. (50). In UPd₂Al₃ the conduction electrons corresponding to the main FS cylinder in fig. 26 have only dispersion $\perp c$ with $\varepsilon_{\perp\mathbf{k}} = \varepsilon_{\perp}(\mathbf{k}_{\perp}/k_0)^2$. The magnetic exciton dispersion $\omega_E(\mathbf{q})$ which originates from the $\Gamma_3 \leftrightarrow \Gamma_4$ CEF transitions given by eq. (48) is of central importance. For large T eq. (48) describes isolated CEF transitions at an energy δ which develop a dispersion at lower temperature due to an effective exchange $J(\mathbf{q})$. In this RPA expression a complete softening at the Néel temperature T_N in eq. (49) for induced AF order is expected at the AF ordering wave vector $\mathbf{Q} = (0, 0, \frac{1}{2})$. Note that, unlike spin waves the magnetic excitons which originate in singlet-singlet CEF transitions may exist already above T_N and their softening signifies the approaching induced AF order. The experimental investigation of magnetic excitons was undertaken in many INS studies [157, 194, 212, 213]. In the former the overall dispersion up to the maximum $\simeq 8$ meV was determined and theoretically analysed in [158]. The latter focused on high resolution analysis of the low energy excitations around the AF wave vector \mathbf{Q} . The result is shown in the left panel of fig. 27. Indeed, contrary to the above simple RPA singlet-singlet result a magnetic exciton gap of about 1 meV appears. This may be caused by the effect of higher magnetic CEF states whose contribution to the staggered susceptibility leads to AF order slightly before complete softening is achieved and also by self energy effects beyond RPA. The dispersion along c is much larger than in the hexagonal ab -plane which may lead to a considerable DOS for the low energy magnetic excitons around 1 meV. The spectral shape of magnetic excitons is Lorentzian above T_c and evolves into a double peak structure where the lower has the appearance of a sharp resonance within the SC gap region [157, 213]. This is a signature of the strong residual interaction between itinerant (SC) electrons and the excitations within the localised 5f subsystem. A model analysis of the INS spectra at \mathbf{Q} leads to conclude that $\Delta/\omega_E(\mathbf{Q}) \simeq 1$, i.e. SC gap amplitude and magnetic exciton gap are nearly degenerate.

Complementary evidence for this interaction was found in the quasiparticle tunneling spectra of c -axis oriented epitaxially grown UPd₂Al₃ films [196] which probe the SC electrons. The differential conductivity dI/dV of the UPd₂Al₃-AlO_x-Pb tunneling barrier is proportional to the quasiparticle DOS $N_S(\omega)$. In the weak coupling BCS limit it shows the monotonic square root singular behaviour above $\Delta(\mathbf{k} \parallel c)$. However, retardation effects in the strong coupling limit for

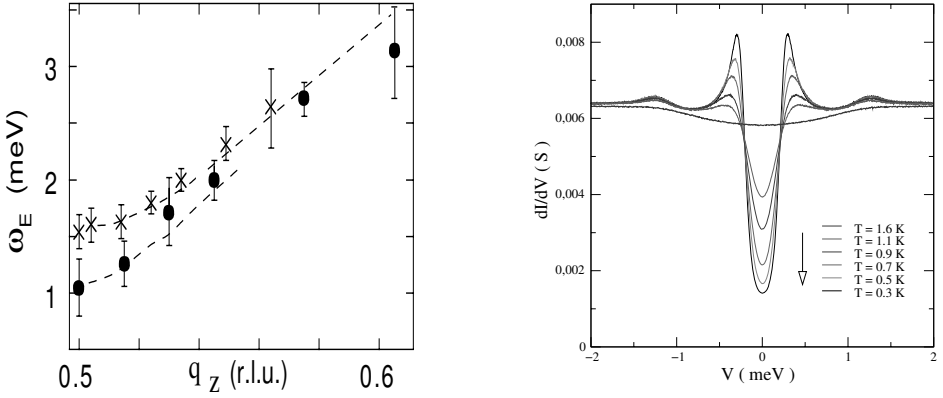


Figure 27: Left panel: Magnetic exciton dispersion $\omega_E(\mathbf{q})$ ($\mathbf{q}=(0,0,q_z)$) derived from low energy INS [157] for temperatures above (crosses) and below (circles) T_c . Right panel: Differential conductivity from tunneling for various temperatures (the arrow indicates the sequence of curves). The hump at 1 meV is a strong coupling signature of the magnetic exciton at $\mathbf{Q}=(0,0,0.5)$ (cf. left panel) which mediates Cooper pairing [196].

the effective pairing interaction lead to characteristic signatures in $dI/dV \sim N_S(\omega)$ at an energy which corresponds to typical energies of the bosons which mediate the interaction. This is well known in the case of strong-coupling electron-phonon superconductors. In their breakthrough tunneling experiment in UPd_2Al_3 Jourdan et al. [196] have for the first time seen evidence of the boson that mediates superconductivity in a HF metal. Its signature can clearly be seen in the tunneling spectra in the right panel of fig. 27 at an energy slightly above 1 meV. This is far too small for characteristic phonon frequencies, since the Debye energy is of the order 13 meV. Instead it corresponds directly to the magnetic exciton energy at the AF vector \mathbf{Q} for $T < T_c$ in the left panel. This strongly suggests that magnetic excitons mediate SC pair formation in UPd_2Al_3 . The coupling between the itinerant heavy quasiparticles and the magnetic exciton in the center of the AF BZ ($q_z = 0.5$) shows substantial retardation because the group velocity ($\partial\omega_E/\partial q_z$) of the latter is much smaller than the Fermi velocity v_F^* of heavy quasiparticles due to the flatness of $\omega_E(q_z)$ over a considerable part of the BZ along c^* [213]. Within Eliashberg theory the quasiparticle DOS can be explained by using a phenomenological retarded potential centered at $\omega_E(\mathbf{Q})$, the analysis [157] leads to the conclusion $2\Delta/T_c = 5.6$ in agreement with the gap estimate above and also with NMR results [214]. Together the two complementary results shown in fig. 27 present the first direct evidence for a non-phononic SC pairing mechanism in a HF superconductor. The magnetic exciton-mediated pairing identified here is distinctly different from both the conventional electron-phonon mechanism and the common spin-fluctuation mechanism (sect. 4) which does not involve any localised electron component.

5.2.4 SYMMETRY OF THE SC GAP FUNCTION AND ELIASHBERG THEORY

The question of the symmetry of the gap function $\Delta(\mathbf{k})$ is most difficult to resolve in unconventional superconductors, and perhaps with the exception of UPt_3 (see [6, 9] for a review) has not been unambiguously achieved for any of the HF superconductors. And yet this is very important because the nodal structure of the gap function and the associated low temperature thermodynamic and transport properties are directly determined by the symmetry class of the gap function. It was suggested [195, 215] that the INS double peak structure for $T \ll T_c$ mentioned previously requires the translational symmetry property $\Delta(\mathbf{k} + \mathbf{Q}) = -\Delta(\mathbf{k})$. Furthermore Knight shift and H_{c2} results mentioned above have lead to the proposal of a spin singlet gap with $\Delta(-\mathbf{k}) = \Delta(\mathbf{k})$. Together this suggest a gap function with node lines $\Delta(\mathbf{k}) = 0$ perpendicular to c at the AF Bragg planes $\mathbf{k} = \pm \frac{1}{2}\mathbf{Q}$ (A_{1g} in table 5). To investigate the consistency of the magnetic exciton model strong coupling calculations based on the Hamiltonian in eq. (50) have been performed [159]. Such model calculations cannot predict reliably the symmetry of the gap function, but they may decide which one is the most favorable within a restricted class of possible gap functions. In addition one may at the same time obtain the mass enhancement (m^*/m_b) of normal quasiparticles from the self energy and T_c from the Eliashberg equations. Both quantities are determined by the effective retarded potential due to magnetic exchange given in eq. (51). For simplicity we use an empirical form for $\omega_E(\mathbf{q})$ with a finite gap and no dispersion $\perp c$, given by

$$\omega_E(q_z) = \omega_E^0 [1 + \beta \cos(q_z)] \quad (55)$$

The parameters ω_E^0 , α and β (fig. 28) are chosen to describe the experimental dispersion along c obtained from INS [212]. The effective interaction of eq. (51) breaks spin rotational symmetry in a maximal (Ising type) manner. As explained in sect. 4 this leads to a classification into ESP and OSP pair states with spin projection factors $p = \pm 1$. The Eliashberg equation for the gap function is then given by

$$\Lambda(T)\Delta(\mathbf{k}, i\omega_n) = p \frac{T}{N} \sum_{\mathbf{k}'\omega'_n} V(\mathbf{k} - \mathbf{k}', i\omega_n - i\omega'_n) |G(\mathbf{k}', i\omega'_n)|^2 \Delta(\mathbf{k}', i\omega'_n). \quad (56)$$

where $G(\mathbf{k}, i\omega_n)$ is the renormalised conduction electron Green's function and T_c is obtained from $\Lambda(T_c) = 1$. The result for the T_c of various gap function candidates as function of the dimensionless coupling parameter \hat{g} are shown in fig. 28. Likewise the dependence of m^*/m_b on \hat{g} which is roughly linear may be calculated. From dHvA results the enhancement factor for the main FS cylinder in fig. 26 is $m^*/m_b \simeq 10$. This would imply $\hat{g} = 2$. The corresponding theoretical value $T_c = 2.9$ K for the degenerate A_{1g} and A_{1u} states from fig. 28 is a factor 1.6 larger than the experimental value of 1.8 K. Given that the latter is reduced due to the action of static AF order, this result shows that the magnetic exciton mechanism gives both mass enhancement and a T_c which are consistent. This supports the previous empirical conjecture for this new mechanism of HF superconductivity.

The dispersion of $\omega_E(\mathbf{k})$ and hence the \mathbf{k} -dependence of the interaction is strongest along c . Therefore one may restrict to SC candidate states of the type $\Delta(\mathbf{k}) = \Delta \Phi(k_z)$ with a few possible form factors $\Phi(k_z)$ given in table 5. It is seen in fig. 28 that the A_{1g} and A_{1u} OSP spin pairing states have the highest and equal T_c 's. This degeneracy between even and odd parity

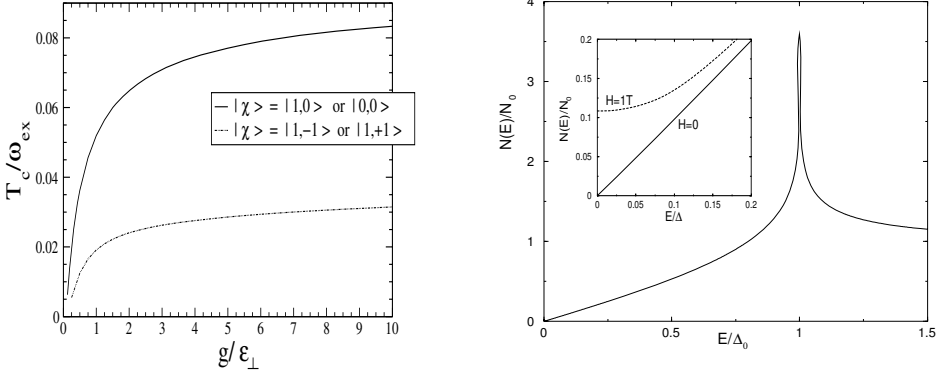


Figure 28: Left panel: Critical temperature as function of the dimensionless coupling constant $\hat{g} = g/\epsilon_{\perp} = \frac{t^2 \Delta N(\epsilon_F)}{2 \omega_E^0}$. Model parameters for $\omega_E(\mathbf{q})$ are $\omega_E^0 = 0.01 \epsilon_{\perp}$ (ϵ_{\perp} = conduction band width) and $\beta = 0.8$. Full (dashed) curve: OSP (ESP) SC states (see table 5) [159]. Right panel: DOS in the A_{1g} state of table 5 with $N(E) \sim E$ for $E \ll \Delta_0$. Inset shows the DOS for field of 1T and orientation $\parallel c$ ($\theta = 0$). Finite $N(0)$ is induced by the Doppler shift of quasiparticles and contributes to specific heat and transport [216].

states is due to the Ising type anisotropy of the effective interaction in spin space signified by their equal spin projection factors $p = -1$ (table 5). It will be lifted by the interaction of the SC order parameters with the background AF order. The respective node lines for $\Phi(k_z)$ would be at $k_z = \pm \pi/c$ (zone boundary) for A_{1g} and $k_z = 0$ for A_{1u} (zone center). Note that both states have $S_z = 0$ and therefore both should show Pauli limiting of H_{c2} and a Knight shift reduction below T_c . For the odd parity state this is due to the fact that the other 'triplet' components with $S_z = \pm 1$ are not stable, i.e. the \mathbf{d} - vector is pinned along c . Note that although A_{1g} with $\Delta(\mathbf{k}) = \Delta_0 \cos k_z$ has a node line, it is not an unconventional order parameter in the strict sense since it has the full D_{6h} symmetry. The quasiparticle DOS of the A_{1g} state is shown in fig. 28 is linear for $E \ll \Delta_0$ due to the node line at $k_z = \pm \frac{\pi}{2}$. The inset shows that an external field induces a finite residual DOS at $E = 0$ according to the Doppler shift expression of eq. (42). The residual DOS depends on the field direction relative to the nodal position. This leads to a polar field-angle dependent residual $\gamma(\theta)$ -coefficient and thermal conductivity $\kappa_{ii}(\theta)$. There is no azimuthal ϕ -dependence due to cylindrical FS symmetry. The residual κ_{ii} normalised to the normal state κ_n is given by

$$\begin{aligned} \kappa_{ii}(T, \theta) / \kappa_n &= \frac{3}{4\pi^2} \frac{1}{T^3} \int_0^{\infty} \frac{d\omega \omega^2}{\cosh^2(\omega/2T)} \hat{t}(\omega) \langle v_{ik}^2 \rangle_{FS}^{-1} \langle \langle v_{ik}^2 K(\omega, \hat{\mathbf{k}}, \hat{\mathbf{r}}) \rangle \rangle_{FS,V} \\ K(\omega, \hat{\mathbf{k}}, \hat{\mathbf{r}}) &= \frac{2}{|\hat{\omega}|} [\hat{\omega}^2 - \Delta(\hat{\mathbf{k}})^2]^{\frac{1}{2}} \Theta_H(\hat{\omega}^2 - \Delta(\hat{\mathbf{k}})^2) \end{aligned} \quad (57)$$

Table 5: Spin and orbital structure of the possible gap functions which are solutions of the Eliashberg equations for the dual model of UPd₂Al₃. The A_{1g} OSP state is fully symmetric and its node line ($k_z = \pm\pi/c$) is not enforced by symmetry.

| p | $ \chi\rangle = S, S_z\rangle$ | D _{6h} repres. | spin pairing | $\Phi(k_z)$ |
|-----|--|---------------------------------|--------------|---------------|
| -1 | $ 0, 0\rangle = \frac{1}{\sqrt{2}}(\uparrow\downarrow\rangle - \downarrow\uparrow\rangle)$ | Γ_1^+ (A _{1g}) | OSP | $\cos(ck_z)$ |
| -1 | $ 1, 0\rangle = \frac{1}{\sqrt{2}}(\uparrow\downarrow\rangle + \downarrow\uparrow\rangle)$ | Γ_1^- (A _{1u}) | OSP | $\sin(ck_z)$ |
| +1 | $ 1, \pm 1\rangle = \uparrow\uparrow\rangle, \downarrow\downarrow\rangle$ | Γ_1^- (A _{1u}) | ESP | $\sin(2ck_z)$ |

Here $\hat{\omega} = \omega - \mathbf{v}_s(\mathbf{r}, \hat{\theta}) \cdot \mathbf{k}$ is the Doppler shifted energy of the quasiparticle, \mathbf{k} and \mathbf{r} are its momentum and its position with respect to the vortex core oriented along $\hat{\theta}$. The double average is performed over the FS and the inter-vortex region and Θ_H is the Heaviside function. Furthermore $\hat{\tau}(\omega)$ is the effective quasiparticle lifetime. As already mentioned in sect. 3.4 for CeCoIn₅ angle-resolved measurements of thermal conductivity give important information the position of the node lines of $\Delta(\mathbf{k})$ with respect to the crystal axes. This is of great help in the determination of gap symmetry. One should have $H \ll H_{c2}$ to minimise the background effect of the H_{c2} anisotropy. These experiments, which were proposed in [158], have recently been performed on UPd₂Al₃ single crystals [217] in a rotating field geometry with heat current perpendicular to the field (vortex) direction to probe the itinerant quasiparticle contribution (fig. 29). For fields rotated in the hexagonal ab-plane no oscillations have been found excluding the presence of node lines perpendicular to the ab plane as has been proposed in the model of [218]. On the other hand field rotation in the ac-plane clearly leads to twofold oscillations for $H \ll H_{c2}$ proving the existence of a node line which is parallel to the ab-plane as is predicted by the magnetic exciton model of SC in UPd₂Al₃ [159] (fig. 29). Because of the cylindrical FS geometry the oscillations are qualitatively similar for the three gap functions of table 5. Thus thermal transport measurements alone are in this case not able to fix the position of the horizontal node line. However if one accepts that the Knight shift results point to singlet (OSP) pairing, then the A_{1g}-gap function in table 5 is the proper one for UPd₂Al₃.

6 SUMMARY AND OUTLOOK

The understanding of the heavy fermion state in Ce- and U- intermetallics and its SC phases has made great progress in recent years. In the normal state it has become clear that the origin of quasiparticle mass enhancement may be profoundly different. It is described by the Kondo lattice mechanism in 4f-Ce compounds and by a dual (multiorbital) model of localised and itinerant 5f electrons in U compounds. For Ce systems the heavy electron bands may be described by the renormalised band theory where the single 4f electron is treated as itinerant with a resonant phase shift. Within the dual model for U-compounds, two electrons are treated as being localised in CEF states. The remaining 5f electron forms itinerant conduction bands and its coupling to magnetic excitons, i.e. propagating CEF excitations, leads to the mass enhancement. These different approaches lead to realistic Fermi surfaces in cases like CeCu₂Si₂, UPt₃, UPd₂Al₃ and the mass enhancement may be incorporated naturally.

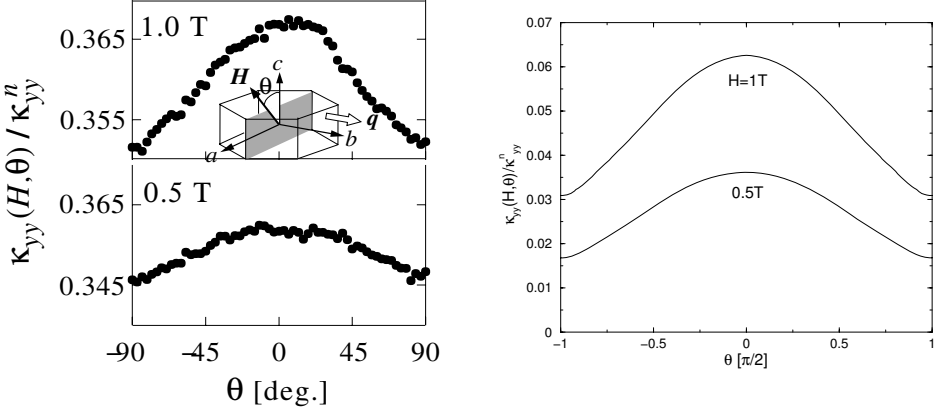


Figure 29: Left panel: Angular variation of the normalised b-axis thermal conductivity $\kappa_{yy}(\mathbf{H}, \theta)$. Field is rotated in the ac -plane \perp to the heat current \mathbf{q} [217]. Right panel: Theoretical calculation of $\kappa_{yy}(\mathbf{H}, \theta)$ according to eq. (57) for the corrugated FS cylinder of UPd_2Al_3 and the A_{1g} gap function. Twofold oscillations in θ proves the existence of a node line in the ab plane [216].

The Kondo lattice mechanism in Ce-compounds implies the competition between HF state and AF ordering as illustrated in the Doniach phase diagram. When AF order is destroyed by variation of a control parameter, pressure or chemical substitution, the normal state behaviour around the QCP shows distinct NFL behaviour. It is characterised by anomalous scaling exponents in the temperature and field dependences of specific heat, resistivity, thermal expansion and other properties. In Ce-compounds these NFL exponents may largely be understood by considering the dressing of quasiparticle with a spectrum of soft magnetic spin fluctuations, this picture seems especially appropriate for CeNi_2Ge_2 but also for CeCu_2Si_2 and CePd_2Si_2 . Simultaneously effective quasiparticle interactions mediated by soft spin fluctuations favor SC pair formation as predicted by Eliashberg theory. In fact in many Ce-compounds SC domes exist around the QCP and frequently but not necessarily is associated with NFL behaviour.

Mass enhancement and SC pairing are closely related. The importance of virtual magnetic exciton exchange for SC pair formation in HF-U compounds with dual 5f electron behaviour may therefore be supposed. Indeed this novel mechanism has been identified in the model compound UPd_2Al_3 by complementary tunneling and INS measurements. The former exhibit a characteristic strong coupling feature at the energy of the zone center magnetic exciton mode which identifies the latter as the exchanged boson that mediates pairing. This observation is quite unique for HF-compounds, it has not been achieved for the spin fluctuation Ce-compounds which is explicable since the latter are overdamped modes whereas magnetic excitons are propagating modes with a real group velocity. Whether SC in other U-HF compounds may be explained with a similar mechanism is a matter of debate. UBe_{13} is the only SC U compound which possibly exhibits a magnetic QCP and may therefore be more similar to Ce-based SC, while UPt_3 and URu_2Si_2 where SC is embedded in a magnetic (or hidden

order) phase are more plausible candidates for the magnetic exciton mechanism. Also the AF spin fluctuation model in its simple versions strongly favors singlet pairing whereas a number of U-HF compounds, notably UPt₃, exhibit triplet pairing. The latter is not disfavored in the magnetic exciton model due to an inherent spin space anisotropy of the effective interaction.

The most important property of unconventional HF SC is the symmetry class of the gap function. Progress in understanding these symmetries for specific compounds has been slow in the past since the traditional method, i.e. interpreting 'power law' behaviour of thermodynamic and transport quantities etc. is ambiguous and often contradictory. Recently the situation has improved considerably with the advent of angle-resolved specific heat and magnetotransport measurements that can identify or restrict nodal positions of the gap functions in **k**-space. Together with Knight shift measurements they are the most powerful tool to investigate the gap symmetry in ultra-pure stoichiometric samples. Up to now the SC gap is known with some certainty only for three cases: f-wave triplet (E_{2u}) in UPt₃, nodal singlet (A_{1g}) in UPd₂Al₃ and d-wave singlet (B_{1g} or B_{2g}) in CeCoIn₅.

An issue of permanent interest in HF SC is the coexistence/competition with long range AF or SDW order away from the QCP. This is now fairly well understood for the 'A-phase' SDW state in CeCu₂Si₂ and CeCu₂(Si_{1-x}Ge_x)₂, both experimentally and within theoretical models involving a realistic FS geometry. A similar approach may be possible for Ce115 materials like CeRh_{1-x}Co_xIn₅.

The vortex phase can give further insight into the SC state. For UPt₃ the appearance of three distinct SC regions in the B-T plane was a sure sign of a multicomponent SC order parameter. More recently the observation of a distinct SC vortex phase in the low temperature and high field corner close to H_{c2} for CeCoIn₅ has been interpreted as the long-sought FFLO phase where SC pairs have finite momentum which leads to a segmentation of vortices.

Many fundamental issues in HF materials, like the importance of unconventional density wave states for NFL behaviour, QCP scenarios with a local breakup of quasiparticles, the effect of time reversal and inversion symmetry breaking in unconventional SC states, the vortex and FFLO phase for nodal SC gap functions and many others, are still incompletely understood. This guarantees that heavy fermion physics will be a thriving field in the future.

Acknowledgements

The authors are grateful for collaboration and discussion with numerous colleagues, especially T. Dahm, E. Faulhaber, P. Fulde, P. Gegenwart, C. Geibel, K. Izawa, K. Maki, Y. Matsuda, P. McHale, M. Neef, F. Pollmann, N. Sato, B. Schmidt, G. Varelogiannis, T. Watanabe, A. Yaresko, H.Q. Yuan and Q. Yuan.

List of acronyms

| | |
|---------|--|
| AF | antiferromagnet, antiferromagnetism, antiferromagnetic |
| AFBZ | antiferromagnetic Brillouin zone |
| ARPES | angle resolved photoemission spectroscopy |
| BIS | bremstrahlung isochromat spectroscopy |
| BZ | Brillouin zone |
| CDW | charge density wave |
| CEF | crystalline electric field |
| CPT | cluster perturbation theory |
| dHvA | de Haas-van Alphen |
| DLRO | diagonal long range order |
| DOS | density of states |
| ESP | equal spin pairing |
| FFLO | Fulde-Ferrell-Larkin-Ovchinnikov |
| GL | Ginzburg-Landau |
| LFL | Landau-Fermi liquid |
| FLEX | fluctuation exchange |
| FM | ferromagnet, ferromagnetism, ferromagnetic |
| FS | Fermi surface |
| HF | heavy fermion |
| IC | incommensurate |
| INS | inelastic neutron scattering |
| LDA | local density approximation |
| LSDA | local spin density approximation |
| mf | mean field |
| NFL | non-Fermi liquid |
| n.n. | next neighbor |
| n.n.n. | next nearest neighbor |
| NMR | nuclear magnetic resonance |
| NQR | nuclear quadrupole resonance |
| ODLRO | off-diagonal long range order |
| OSP | opposite spin pairing |
| PES | photoemission spectroscopy |
| QCP | quantum critical point |
| RPA | random phase approximation |
| RKKY | Ruderman-Kittel-Kasuya-Yoshida |
| SC | superconductor, superconductivity, superconducting |
| SIC-LDA | self interaction corrected local density approximation |
| SDW | spin density wave |
| s.o. | spin orbit |
| TB | tight binding |

REFERENCES

- [1] P. Fulde, *J. Phys. F* 18 (1988) 601.
- [2] N. Grewe and F. Steglich, *Handbook on the Physics and Chemistry of Rare Earths* (Elsevier Science Publishers B. V., Amsterdam, 1991), vol. 14, chap. Heavy Fermions, p. 343.
- [3] Y. Kuramoto and Y. Kitaoka, *Dynamics of Heavy Electrons*, vol. 105 of *International Series of Monographs in Physics* (Clarendon Press, Oxford, 2000).
- [4] A. C. Hewson, *The Kondo Problem to Heavy Fermions* (Cambridge University Press, 1993).
- [5] M. Sigrist and K. Ueda, *Rev. Mod. Phys.* 63 (1991) 239.
- [6] P. Thalmeier and G. Zwicknagl, *Handbook on the Physics and Chemistry of Rare Earths (cond-mat/0312540)* (Elsevier, 2004), vol. 34.
- [7] V. P. Mineev and K. V. Samokhin, *Introduction to Unconventional Superconductivity* (Gordon and Breach Science Publishers, 1999).
- [8] J. A. Sauls, *Adv. Phys.* 43 (1994) 113.
- [9] R. Joynt and L. Taillefer, *Rev. Mod. Phys.* 74 (2002) 237.
- [10] L. D. Landau, *Sov. Phys. JETP* 3 (1956) 920.
- [11] L. D. Landau, *Soviet Physics - JETP* 32 (1957) 59.
- [12] L. D. Landau, *Soviet Physics - JETP* 35 (1958) 97.
- [13] A. A. Abrikosov, L. P. Gorkov, and I. E. Dzyaloshinski, *Methods of Quantum Field Theory in Statistical Physics* (Dover, New York, 1975).
- [14] J. W. Allen, *Resonant Photoemission of Solids with Strongly Correlated Electrons* (Plenum Press, New York, 1992), vol. 1 of *Synchrotron Radiation Research: Advances in Surface and Interface Science*, chap. 6, p. 253.
- [15] D. Malterre, M. Grioni, and Y. Baer, *Adv. Phys.* 45 (1996) 299.
- [16] F. Reinert, D. Ehm, S. Schmidt, G. Nicolay, S. Hübner, J. Kroha, O. Trovarelli, and C. Geibel, *Phys. Rev. Lett.* 87 (2001) 106401.
- [17] K. G. Wilson, *Rev. Mod. Phys.* 47 (1975) 773.
- [18] P. Nozières, *J. Low Temp. Phys.* 17 (1974) 31.
- [19] G. Zwicknagl, *Adv. Phys.* 41 (1992) 203.

- [20] G. Zwicknagl and U. Pulst, *Physica B* 186 (1993) 895.
- [21] G. Zwicknagl, *Physica Scripta T* 49 (1993) 34.
- [22] G. G. Lonzarich, *J. Magn. Magn. Mat.* 76 / 77 (1988) 1.
- [23] H. Aoki, S. Uji, A. K. Albessard, and Y. Onuki, *Phys. Rev. Lett.* 71 (1993) 2110.
- [24] F. S. Tautz, S. R. Julian, G. J. McMullen, and G. G. Lonzarich, *Physica B* 206-207 (1995) 29.
- [25] D. L. Cox and A. Zawadowski, *Exotic Kondo effects in retals: Magnetic ions in a crystalline electric field and tunnelling centres* (Taylor and Francis, 1999).
- [26] R. White and P. Fulde, *Phys. Rev. Lett.* 47 (1981) 1540.
- [27] G. Zwicknagl and P. Fulde, *J. Phys. Condens. Matter* 15 (2003) S1911.
- [28] G. Zwicknagl, A. N. Yaresko, and P. Fulde, *Phys. Rev. B* 65 (2002) 081103(R).
- [29] G. Zwicknagl, A. Yaresko, and P. Fulde, *Phys. Rev. B* 68 (2003) 052508.
- [30] D. V. Efremov, N. Hasselmann, E. Runge, P. Fulde, and G. Zwicknagl, *Phys. Rev. B* 69 (2004) 115114.
- [31] F. Pollmann, Diplomarbeit, Techn. Universität Braunschweig (2004).
- [32] E. Runge, P. Fulde, D. V. Efremov, N. Hasselmann, and G. Zwicknagl, *Phys. Rev. B* 69 (2004) 155110.
- [33] E. Dagotto, *Rev. Mod. Phys.* 66 (1994) 763.
- [34] D. Senechal, D. Perez, and D. Plouffe, *Phys. Rev. B* 66 (2002) 075129.
- [35] G. L. G. Sleijpen and H. A. V. der Vorst, *SIAM J. Matrix Anal. Appl. (SIMAX)* 17 (1996) 401.
- [36] S. Fujimori, Y. Saito, M. Seki, K. Tamura, M. Mizuta, K. Yamaki, K. Sato, T. Okane, A. Tanaka, N. Sato, T. Komatsubara, Y. Tezuka, S. Shin, S. Suzuki, and S. Sato, *Journal of Electron Spectroscopy and Related Phenomena* 101-103 (1999) 439.
- [37] S.-K. Ma, *Modern Theory of Critical Phenomena*, *Frontiers in Physics* (W. A. Benjamin Inc., Reading, Massachusetts, 1976).
- [38] S. Sachdev, *Quantum Phase Transitions* (Cambridge University Press, 1999).
- [39] M. A. Continentino, *Quantum Scaling in Many-Body Systems* (World Scientific Publishing, Singapore, 2001).
- [40] J. A. Hertz, *Phys. Rev. B* 14 (1976) 1165.

- [41] L. Zhu, M. Garst, A. Rosch, and Q. Si, *Phys. Rev. Lett.* 91 (2003) 066404.
- [42] R. Takke, M. Nicksch, W. Assmus, B. Lüthi, R. Pott, R. Schefzyk, and D. K. Wohlleben, *Z. Phys. b* 44 (1981) 33.
- [43] P. Thalmeier and P. Fulde, *Europhys. Lett.* 1 (1986) 367.
- [44] P. Fulde, J. Keller, and G. Zwicky, in *Solid State Physics*, edited by F. Seitz, D. Turnbull, and H. Ehrenreich (Academic Press, New York, 1988), vol. 41, p. 1.
- [45] P. Thalmeier and B. Lüthi, *Handbook on the Physics and Chemistry of Rare Earths* (North-Holland, 1991), vol. 14, chap. 96, p. 225.
- [46] M. A. Continentino, *cond-mat/0408217* (2004).
- [47] L. Zhu, M. Garst, A. Rosch, and Q. Si, *cond-mat/0408230* (2004).
- [48] R. Kuchler, N. Oeschler, P. Gegenwart, T. Cichorek, K. Neumaier, O. Tegus, C. Geibel, J. A. Mydosh, F. Steglich, L. Zhu, and Q. Si, *Phys. Rev. Lett.* 91 (2003) 066405.
- [49] A. Rosch, *Phys. Rev. Lett.* 82 (1999) 4280.
- [50] A. J. Millis, *Phys. Rev. B* 48 (1993) 7183.
- [51] U. Zülicke and A. J. Millis, *Phys. Rev. B* 51 (1995) 8996.
- [52] T. Moriya, *Spin Fluctuations in Itinerant Electron Magnets* (Springer Verlag, Berlin, 1985).
- [53] G. R. Stewart, *Rev. Mod. Phys.* 73 (2001) 797.
- [54] F. Steglich, J. Aarts, C. Bredl, W. Lieke, D. Meschede, W. Franz, and H. Schäfer, *Phys. Rev. Lett.* 43 (1979) 1892.
- [55] O. Stockert, E. Faulhaber, G. Zwicky, N. Stuesser, H. Jeevan, T. Cichorek, R. Loewenhaupt, C. Geibel, and F. Steglich, *Phys. Rev. Lett.* 92 (2004) 136401.
- [56] O. Trovarelli, M. Weiden, R. Müller-Reisener, M. Gómez-Berisso, P. Gegenwart, M. Deppe, C. Geibel, J. G. Sereni, and F. Steglich, *Phys. Rev. B* 56 (1997) 678.
- [57] D. Jaccard, H. Wilhelm, K. Alami-Yadri, and E. Vargoz, *Physica B* 259-261 (1999) 1.
- [58] H. Q. Yuan, F. M. Grosche, M. Deppe, C. Geibel, G. Sparn, and F. Steglich, *Science* 302 (2003) 2104.
- [59] C. Petrovic, R. Movshovich, M. Jaime, P. G. Pagliuso, M. F. Hundley, J. L. Sarrao, Z. Fisk, and J. D. Thompson, *Europhys. Lett.* 53 (2001) 354.
- [60] K. Izawa, H. Yamaguchi, Y. Matsuda, H. Shishido, R. Settai, and Y. Onuki, *Phys. Rev. Lett.* 87 (2001) 05700.

- [61] H. Aoki, T. Sakakibara, H. Shishido, R. Settai, Y. Onuki, P. Miranovic, and K. Machida, *J. Phys. Condens. Matter* 16 (2004) L13.
- [62] A. Bianchi, R. Movshovich, C. Capan, A. Lacerda, P. G. Pagliuso, and J. L. Sarrao, *Phys. Rev. Lett.* 91 (2003) 187004.
- [63] T. Watanabe, Y. Kasahara, K. Izawa, T. Sakakibara, C. van der Beek, T. Hanaguri, H. Shishido, R. Settai, Y. Onuki, and Y. Matsuda, *cond-mat/0312062* (2003).
- [64] E. Bauer, G. Hilscher, H. Michor, C. Paul, E. W. Scheidt, A. Griбанov, Y. Seropegin, H. Noel, M. Sigrist, and P. Rogl, *Phys. Rev. Lett.* 92 (2004) 027003.
- [65] L. N. Bulaevskii, A. A. Guseinov, and A. I. Rusinov, *Sov. Phys. JETP* 44 (1976) 1243.
- [66] P. Frigeri, D. Agterberg, A. Koga, and M. Sigrist, *Phys. Rev. Lett* 92 (2003) 097011.
- [67] G. Bruls, D. Weber, B. Wolf, P. Thalmeier, B. Lüthi, A. de Visser, and A. Menovsky, *Phys. Rev. Lett* 65 (1990) 2294.
- [68] W. Sun, M. Brand, G. Bruls, and W. Assmus, *Z. Phys. B* 80 (1990) 249.
- [69] O. Stockert, M. Deppe, E. Faulhaber, H. Jeevan, R. Schneider, N. Stüsser, C. Geibel, M. Loewenhaupt, and F. Steglich, preprint (2004).
- [70] A. T. Holmes, D. Jaccard, and K. Miyake, *Phys. Rev. B* 69 (2004) 024508.
- [71] Y. Onishi and K. Miyake, *J. Phys. Soc. Jpn.* 69 (2004) 3955.
- [72] F. Steglich, P. Gegenwart, C. Geibel, P. Hinze, M. Lang, C. Langhammer, G. Sparn, T. Tayama, O. Trovarelli, N. Sato, T. Dahm, and G. Varelogiannis, *More is different- fifty years of condensed matter physics* (Princeton University Press, 2001), chap. 13, p. 191.
- [73] G. Bruls, B. Wolf, D. Finsterbusch, P. Thalmeier, I. Kouroudis, W. Sun, W. Assmus, B. Lüthi, M. Lang, K. Gloos, F. Steglich, and R. Modler, *Phys. Rev. Lett.* 72 (1994) 1754.
- [74] F. Weickert, unpublished.
- [75] P. Gegenwart, C. Langhammer, C. Geibel, R. Helfrich, M. Lang, G. Sparn, F. Steglich, R. Horn, L. Donnevert, A. Link, and W. Assmus, *Phys. Rev. Lett.* 81 (1998) 1501.
- [76] F. Thomas, J. Thomasson, C. Ayache, C. Geibel, and F. Steglich, *Physica B* 186-188 (1993) 303.
- [77] A. Onodera, S. Tsuduki, Y. Onishi, T. Watanuki, K. Ishida, Y. Kitaoka, and Y. Onuki, *Solid State Commun.* 123 (2002) 113.
- [78] J. Roehler, J. Klug, and K. Keulertz, *J. Magn. Magn. Mater* 76-77 (1988) 340.

- [79] Y. Kawasaki, K. Ishida, S. Kawasaki, T. Mito, G. q. Zheng, Y. Kitaoka, C. Geibel, and F. Steglich, *J. Phys. Soc. Jpn.* 73 (2004) 194.
- [80] K. Ishida, Y. Kawasaki, K. Tabuchi, K. Kashima, Y. Kitaoka, and K. Asayama, *Phys. Rev. Lett.* 82 (1999) 5353.
- [81] F. Steglich and S. Suellow, *Encyclopedia of Materials: Science and Technology* (2001).
- [82] M. Neef, *Diplomarbeit, Techn. Universität Braunschweig* (2004).
- [83] M. Neef and G. Zwircknagl, preprint (2004).
- [84] G. Zwircknagl and P. Fulde, *Z. Phys. B* 43 (1981) 23.
- [85] P. Fulde and G. Zwircknagl, *J. Appl. Phys.* 53 (1982) 8064.
- [86] U. Rauchschwalbe, W. Lieke, C. D. Bredl, F. Steglich, J. Aarts, K. M. Martini, and A. C. Mota, *Phys. Rev. Lett.* 49 (1982) 1448.
- [87] R. Konno and K. Ueda, *Phys. Rev. B* 40 (1989) 4329.
- [88] M. Ozaki and K. Machida, *Phys. Rev. B* 39 (1989) 4145.
- [89] O. Stockert, unpublished (2004).
- [90] G. Knebel, M. Brando, J. Hemberger, M. Nicklas, W. Trinkl, and A. Loidl, *Phys. Rev. B* 59 (1999) 12390.
- [91] P. Gegenwart, J. Custers, T. Tayama, K. Tenya, C. Geibel, G. Sparn, N. Harrison, P. Kersch, D. Eckert, K.-H. Müller, and F. Steglich, *J. Low Temp. Phys.* 133 (2003) 3.
- [92] D. Jaccard, K. Behnia, and J. Sierro, *Phys. Lett. A* 163 (1992) 475.
- [93] R. Movshovich, T. Graf, D. Mandrus, J. D. Thompson, and a. Z. F. J. L. Smith, *Phys. Rev. B* 53 (1996) 8241.
- [94] N. D. Mathur, F. M. Grosche, S. R. Julian, I. R. Walker, D. M. Freye, R. K. W. Haselwimmer, and G. G. Lonzarich, *Nature* 394 (1998) 39.
- [95] F. M. Grosche, I. R. Walker, S. R. Julian, N. D. Mathur, D. M. Freye, M. J. Steiner, and G. G. Lonzarich, *J. Phys.: Condens. Matter* 13 (2001) 2845.
- [96] A. Demuer, A. T. Holmes, and D. Jaccard, *J. Phys. Condens. Matter* 14 (2002) L529.
- [97] M. G. Berisso, P. Pedrazzini, J. G. Sereni, O. Trovarelli, C. Geibel, and F. Steglich, *Eur. Phys. J. B* 30 (2002) 343.
- [98] S. Araki, R. Settai, T. C. Kobayashi, H. Harima, and Y. Onuki, *Phys. Rev. B* 64 (2001) 224417.

- [99] N. H. van Dijk, B. Fak, T. Charvolin, P. Lejay, and J. M. Mignot, *Phys. Rev. B* 61 (2000) 8922.
- [100] Y. Onuki, R. Settai, K. Sugiyama, T. Takeuchi, T. C. Kobayashi, Y. Haga, and E. Yamamoto, *J. Phys. Soc. Jpn.* 73 (2004) 769.
- [101] T. Graf, J. D. Thompson, M. Hundley, R. Movshovich, Z. Fisk, D. Mandrus, R. A. Fisher, and N. E. Philips, *Phys. Rev. Lett.* 78 (1997) 3769.
- [102] N. Oeschler, P. Gegenwart, M. Lang, R. Movshovich, J. L. Sarrao, J. D. Thompson, and F. Steglich, *Phys. Rev. Lett.* 91 (2003) 076402.
- [103] J. D. Thompson, M. Nicklas, A. Bianchi, R. Movshovich, A. Llobet, W. Bao, A. Malinowski, M. F. Hundley, N. O. Moreno, P. G. Pagliuso, J. L. Sarrao, S. Nakatsuji, Z. Fisk, R. Borth, E. Lengyel, N. Oeschler, G. Sparn, F. S. E. Lengyel, N. Oeschler, G. Sparn, and F. Steglich, *Physica B* 329-333 (2003) 446.
- [104] H. Shishido, R. Settai, D. Aoki, S. Ikeda, H. Nakawaki, N. Nakamura, T. Iizuka, Y. Inada, K. Sugiyama, T. Takeuchi, K. Kindo, T. C. Kobayashi, Y. Haga, H. Harima, Y. Aoki, T. Namiki, H. Sato, and Y. Onuki, *J. Phys. Soc. Japan* 71 (2002) 162.
- [105] T. Maehira, T. Hotta, K. Ueda, and A. Hasegawa, *J. Phys. Soc. Jpn.* 72 (2003) 854.
- [106] T. Ueda, H. Shishido, S. Hashimoto, T. Okubo, M. Yamada, Y. Inada, R. Settai, H. Harima, A. Galatanu, E. Yamamoto, N. Nakamura, K. Sugiyama, T. Takeuchi, K. Kindo, T. Namiki, Y. Aoki, H. Sato, and Y. Onuki, *J. Phys. Soc. Jpn.* 73 (2004) 649.
- [107] A. D. Christianson, J. M. Lawrence, P. G. Pagliuso, N. O. Moreno, J. L. Sarrao, J. D. Thompson, P. S. Riseborough, S. Kern, E. A. Goremychkin, and A. H. Lacerda, *Phys. Rev. B.* 66 (2002) 193102.
- [108] Y. Kitaoka, S. Kawasaki, Y. Kawasaki, T. Mito, and G. q. Zheng, *cond-mat/0405348* (2004).
- [109] V. S. Zapf, E. J. Freeman, E. D. Bauer, J. Petricka, C. Sirvent, N. A. Frederick, R. P. Dickey, and M. B. Maple, *Phys. Rev. B* 65 (2001) 014506.
- [110] P. G. Pagliuso, C. Petrovic, R. Movshovich, D. Hall, F. Hundley, J. L. Sarrao, J. D. Thompson, and Z. Fisk, *Phys. Rev. B* 64 (2001) 100503(R).
- [111] T. Muramatsu, T. C. Kobayashi, K. Shimizu, K. Amaya, D. Aoki, Y. Haga, and Y. Onuki, *Physica C* 388-389 (2003) 539.
- [112] G. Zheng, Y. Yamaguchi, H. Kan, Y. Kitaoka, J. L. Sarrao, P. G. Pagliuso, N. O. Moreno, and J. D. Thompson, *Phys. Rev. B* 70 (2004) 014511.
- [113] M. Nicklas, V. A. Sidorov, H. A. Borges, P. G. Pagliuso, C. Petrovic, Z. Fisk, J. L. Sarrao, and J. D. Thompson, *Phys. Rev. B.* 67 (2003) 020506(R).

- [114] J. S. Kim, J. Alwood, G. R. Stewart, J. L. Sarrao, and J. D. Thompson, *Phys. Rev. B* 64 (2001) 134524.
- [115] J. Paglione, M. A. Tanatar, D. G. Hawthorn, E. Boaknin, F. Ronning, R. W. Hill, M. Sutherland, L. Taillefer, C. Petrovic, and P. C. Canfield, *cond-mat/0405157* (2004).
- [116] V. A. Sidorov, M. Nicklas, P. G. Pagliuso, J. L. Sarrao, Y. Bang, A. V. Balatsky, and J. D. Thompson, *Phys. Rev. Lett.* 89 (2002) 157004.
- [117] Y. Nakajima, K. Izawa, Y. Matsuda, S. Uji, T. Terashima, H. Shishido, R. Settai, Y. Onuki, and H. Kotani, *J. Phys. Soc. Jpn.* 73 (2004) 5.
- [118] R. Bel, K. Behnia, Y. Nakajima, K. Izawa, Y. Matsuda, H. Shishido, R. Settai, and Y. Onuki, *Phys. Rev. Lett.* 92 (2004) 217002.
- [119] N. Oeschler, P. Gegenwart, F. Steglich, N. A. Frederick, E. D. Bauer, and M. B. Maple, *Acta Phys. Pol. B* 34 (2003) 959.
- [120] J. S. Kim, N. O. Moreno, J. L. Sarrao, J. D. Thompson, and G. R. Stewart, *Phys. Rev. B* 69 (2004) 024402.
- [121] M. Yashima, S. Kawasaki, Y. Kawasaki, G. Zheng, Y. Kitaoka, H. Shishido, R. Settai, Y. Haga, and Y. Onuki, *J. Phys. Soc. Jpn.* 73 (2004) 2073.
- [122] Y. Kohori, Y. Yamato, Y. Iwamoto, T. Kohara, E. D. Bauer, M. B. Maple, and J. L. Sarrao, *Phys. Rev. B* 64 (2001) 134526.
- [123] G. E. Volovik, *JETP Lett.* 58 (1993) 469.
- [124] N. Nagai, P. Miranović, M. Ichioka, and K. Machida, preprint (2004).
- [125] K. Izawa, H. Takahashi, H. Yamaguchi, Y. Matsuda, M. Suzuki, T. Sasaki, T. Fukase, Y. Yoshida, R. Settai, and Y. Onuki, *Phys. Rev. Lett.* 86 (2001a) 2653.
- [126] K. Izawa, H. Yamaguchi, T. Sasaki, and Y. Matsuda, *Phys. Rev. Lett.* 88 (2002) 027002.
- [127] K. Izawa, K. Kamata, Y. Nakajima, Y. Matsuda, T. Watanabe, M. Nohara, H. Takagi, P. Thalmeier, and K. Maki, *Phys. Rev. Lett.* 89 (2002a) 137006.
- [128] K. Izawa, Y. Nakajima, J. Goryo, Y. Matsuda, S. Osaki, H. Sugawara, H. Sato, P. Thalmeier, and K. Maki, *Phys. Rev. Lett.* 90 (2003) 1170013.
- [129] P. Thalmeier and K. Maki, *Acta Physica Polonica B* 34 (2003) 557.
- [130] A. Bianchi, R. Movshovich, N. Oeschler, P. Gegenwart, F. Steglich, J. D. Thompson, P. G. Pagliuso, and J. L. Sarrao, *Phys. Rev. Lett.* 89 (2002) 137002.
- [131] H. A. Radovan, N. A. Fortune, T. P. Murphy, S. T. Hannahs, E. C. Palm, S. W. Tozer, and D. Hall, *Nature* 425 (2003) 51.

- [132] T. Tayama, A. Harita, T. Sakakibara, Y. Haga, H. Shishido, R. Settai, and Y. Onuki, *Phys. Rev. B.* 65 (2002).
- [133] L. W. Gruenberg and L. Gunther, *Phys. Rev. Lett.* 16 (1966) 996.
- [134] K. Kakuyanagi, M. Saito, K. Kumagai, S. Takashima, M. Nohara, H. Takagi, and Y. Matsuda, *cond-mat/0405661* (2004).
- [135] P. W. Anderson, *Phys. Rev. B* 30 (1984) 1549.
- [136] E. Bauer, G. Hilscher, H. Michor, M. Sieberer, E. W. Scheidt, A. Griбанov, Y. Seregin, P. Rogl, A. Amato, W. Y. Song, J. G. Park, D. T. Adroja, M. Nicklas, G. Sparn, M. Yogi, and Y. Kitaoka, *cond-mat/0408244* (2004).
- [137] N. Metoki, K. Kaneko, T. D. Matsuda, A. Galatanu, T. Takeuchi, S. Hashimoto, T. Ueda, R. Settai, Y. Onuki, and N. Bernhoeft, *J. Phys. Condens. Matter* 16 (2004) L207.
- [138] T. Yasuda, H. Shishido, T. Ueda, S. Hashimoto, R. Settai, T. Takeuchi, T. D. Matsuda, Y. Haga, and Y. Onuki, *J. Phys. Soc. Jpn.* 73 (2004) 1657.
- [139] P. A. Frigeri, D. F. Agterberg, and M. Sigrist, *cond-mat/0405179* (2004).
- [140] M. Yogi, Y. Kitaoka, S. Hashimoto, T. Yasuda, R. Settai, T. D. Matsuda, Y. Haga, Y. Onuki, P. Rogl, and E. Bauer, *cond-mat/0405493* (2004).
- [141] T. Moriya and K. Ueda, *Adv. Phys.* 49 (2000) 555.
- [142] D. Vollhardt and P. Wölfle, *The superfluid phases of ^3He* (Taylor and Francis, New York, 1990).
- [143] S. Nakajima, *Prog. Theor. Phys.* 50 (1973) 1101.
- [144] P. W. Anderson and W. F. Brinkman, *Phys. Rev. Lett.* 30 (1973) 1108.
- [145] K. Miyake, S. Schmitt-Rink, and C. M. Varma, *Phys. Rev. B* 34 (1986) 6554.
- [146] D. J. Scalapino, E. Loh, and J. E. Hirsch, *Phys. Rev. B* 34 (1986) 8190.
- [147] C. H. Pao and N. E. Bickers, *Phys. Rev. Lett.* 72 (1994) 1870.
- [148] T. Dahm and L. Tewordt, *Phys. Rev. Lett.* 74 (1995) 793.
- [149] H. Tou, K. Ishida, and Y. Kitaoka, *cond-mat/0308562* (2003).
- [150] G. E. Volovik and L. P. Gor'kov, *Sov. Phys. JETP* 61 (1985) 843.
- [151] P. Monthoux and G. G. Lonzarich, *Phys. Rev. B* 59 (1999) 14598.
- [152] P. Monthoux and G. G. Lonzarich, *Phys. Rev. B* 63 (2001) 054529.
- [153] P. Monthoux and G. G. Lonzarich, *Phys. Rev. B* 66 (2002) 224504.

- [154] P. McHale and P. Monthoux, *Phys. Rev. B* 67 (2003) 214512.
- [155] G. Bergmann and D. Rainer, *Z. Phys.* 263 (1973) 59.
- [156] A. J. Millis, S. Sachdev, and C. M. Varma, *Phys. Rev. B* 37 (1988) 4975.
- [157] N. K. Sato, N. Aso, K. Miyake, R. Shiina, P. Thalmeier, G. Varelogiannis, C. Geibel, F. Steglich, P. Fulde, and T. Komatsubara, *Nature* 410 (2001) 340.
- [158] P. Thalmeier, *Eur. Phys. J. B* 27 (2002) 29.
- [159] P. McHale, P. Fulde, and P. Thalmeier, *Phys. Rev. B* 70 (2004) 014513.
- [160] H. R. Ott, H. Rudigier, Z. Fisk, and J. L. Smith, *Phys. Rev. Lett.* 50 (1983) 1595.
- [161] G. R. Stewart, Z. Fisk, J. O. Willis, and J. L. Smith, *Phys. Rev. Lett.* 52 (1984) 679.
- [162] W. Schlabitz, J. Baumann, B. Pollit, U. Rauchschwalbe, W. M. Meyer, U. Ahlheim, and C. C. Bredl, *Z. Phys. B* 62 (1986) 171, (and abstracts of the ICVF, Cologne, 1984).
- [163] C. Geibel, C. Schank, S. Thies, H. Kitazawa, C. D. Bredl, A. Böhm, M. Rau, A. Grauel, R. Caspary, R. Helfrich, U. Ahlheim, G. Weber, and F. Steglich, *Z. Phys. B* 84 (1991) 1.
- [164] C. Geibel, S. Thies, D. Kaczorowski, A. Mehner, A. Grauel, B. Seidel, U. Ahlheim, R. Helfrich, K. Petersen, C. D. Bredl, and F. Steglich, *Z. Phys.* 83 (1991) 305.
- [165] H. R. Ott, H. Rudigier, T. M. Rice, K. Ueda, Z. Fisk, and J. L. Smith, *Phys. Rev. Lett.* 82 (1984).
- [166] A. C. Mota and T. Cichorek, unpublished (2003).
- [167] R. H. Heffner, J. L. Smith, J. O. Willis, P. Birrer, C. Baines, F. N. Gygax, B. Hitti, E. Lippelt, H. R. Ott, A. Schenk, E. A. Knetsch, J. A. Mydosh, and D. E. MacLaughlin, *Phys. Rev. Lett.* 65 (1990) 2816.
- [168] F. Kromer, R. Helfrich, M. Lang, F. Steglich, C. Langhammer, A. Bach, T. Michels, J. Kim, and G. Stewart, *Phys. Rev. Lett.* 81 (1998) 4476.
- [169] F. Kromer, M. Lang, N. Oeschler, P. Hinze, C. Langhammer, and F. Steglich, *Phys. Rev. B* 62 (2000) 12477.
- [170] F. Kromer, N. Oeschler, T. Tayama, K. Tenya, T. Cichorek, M. Lang, F. Steglich, J. S. Kim, and G. R. Stewart, *J. Low Temp. Phys.* 126 (2002) 815.
- [171] M. Kato and K. Machida, *J. Phys. Soc. Jpn.* 56 (1987) 2136.
- [172] C. Wälti, H. R. Ott, Z. Fisk, and J. L. Smith, *Phys. Rev. Lett.* 84 (2000) 5616.
- [173] T. Maehira, A. Higashiya, M. Higuchi, H. Yasuhara, and A. Hasegawa, *Physica B* 312-313 (2002) 103.

- [174] R. Felten, F. Steglich, G. Weber, H. Rietschel, F. Gompf, B. Renker, and J. Beuers, *Europhys. Lett.* 2 (1986).
- [175] D. L. Cox, *Phys. Rev. Lett.* 59 (1987) 1240.
- [176] A. P. Ramirez, P. Chandra, P. Coleman, Z. Fisk, J. L. Smith, and H. R. Ott, *Phys. Rev. Lett.* 73 (1994) 3018.
- [177] A. Schiller, F. B. Anders, and D. L. Cox, *Phys. Rev. Lett.* 81 (1998) 3235.
- [178] R. Helfrich, Dissertation, TU Darmstadt (1996).
- [179] P. Gegenwart, C. Langhammer, R. Helfrich, N. Oeschler, M. Lang, J. S. Kim, G. R. Stewart, and F. Steglich, *cond-mat/0307420* (2004).
- [180] P. Gegenwart, Dissertation, TU Darmstadt (1997).
- [181] B. Golding, D. J. Bishop, B. Batlogg, W. H. Haemmerle, Z. Fisk, J. L. Smith, and H. R. Ott, *Phys. Rev. Lett.* 55 (1985) 2479.
- [182] V. Müller, D. Maurer, E. W. Scheidt, C. Roth, K. L. amd E. Bucher, and H. E. Bömmel, *Solid State Commun.* 57 (1986) 319.
- [183] F. Kromer, Dissertation, TU Dresden (2000).
- [184] H. R. Ott, H. Rudiger, Z. Fisk, and J. L. Smith, *Phys. Rev. B* 31 (1985) 1651.
- [185] U. Rauchschwalbe, F. Steglich, G. R. Stewart, A. L. Giorgi, P. Fulde, and K. Maki, *Europhys. Lett.* 3 (1987) 751.
- [186] M. Sigrist and T. M. Rice, *Phys. Rev. B* 39 (1989) 2200.
- [187] B. Batlogg, D. Bishop, B. Golding, C. M. Varma, Z. Fisk, J. L. Smith, and H. R. Ott, *Phys. Rev. Lett.* 55 (1985) 1319.
- [188] E. Dumont and A. C. Mota, *Phys. Rev. B* 65 (2002) 144519.
- [189] M. Sigrist and D. Agterberg, *Prog. Theor. Phys.* 102 (1999) 965.
- [190] R. Caspary, P. Hellmann, M. Keller, C. Wassilew, R. Köhler, G. Sparn, C. Schank, C. Geibel, F. Steglich, and N. E. Phillips, *Phys. Rev. Lett.* 71 (1993) 2146.
- [191] R. Feyerherm, A. Amato, F. N. Gygax, A. Schenck, C. Geibel, F. Steglich, N. Sato, and T. Komatsubara, *Phys. Rev. Lett.* 73 (1994) 1849.
- [192] N. Sato, N. Aso, G. H. Lander, B. Rössli, T. Komatsubara, and Y. Endoh, *J. Phys. Soc. Jpn.* 66 (1997) 1884.
- [193] N. Sato, N. Aso, G. H. Lander, B. Rössli, T. Komatsubara, and Y. Endoh, *J. Phys. Soc. Jpn.* 66 (1997) 2981.

- [194] N. Bernhoeft, N. Sato, B. Roessli, N. Aso, A. Hiess, G. H. Lander, Y. Endoh, and T. Komatsubara, *Phys. Rev. Lett.* 81 (1998) 4244.
- [195] N. Bernhoeft, *Eur. Phys. J. B* 13 (2000) 685.
- [196] M. Jourdan, M. Huth, and H. Adrian, *Nature* 398 (1999) 47.
- [197] A. Grauel, A. Böhm, H. Fischer, C. Geibel, R. Köhler, R. Modler, C. Schank, F. Steglich, and G. Weber, *Phys. Rev. B* 46 (1992) 5818.
- [198] M. Dressel, N. Kasper, K. Petukhov, B. Gorshunov, G. Grüner, M. Huth, and H. Adrian, *Phys. Rev. Lett.* 88 (2002) 186404.
- [199] A. Krimmel, P. Fischer, B. Roessli, H. Maletta, C. Geibel, C. Schank, A. Grauel, A. Loidl, and F. Steglich, *Z. Phys. B* 86 (1992) 161.
- [200] H. Kita, A. Dönni, Y. Endoh, K. Kakurai, N. Sato, and T. Komatsubara, *J. Phys. Soc. Jpn.* 63 (1994) 726.
- [201] J. Hessert, M. Huth, M. Jourdan, H. Adrian, C. T. Rieck, and K. Scharnberg, *Physica B* 230-232 (1997) 373.
- [202] H. Tou, Y. Kitaoka, K. Asayama, C. Geibel, C. Schank, and F. Steglich, *J. Phys. Soc. Jpn.* 64 (1995) 725.
- [203] K. Matsuda, Y. Kohori, and T. Kohara, *Phys. Rev. B.* 55 (1997) 15223.
- [204] F. Steglich, B. Buschinger, P. Gegenwart, C. Geibel, R. Helfrich, P. Hellmann, M. Lang, A. Link, R. Modler, D. Jaccard, and P. Link, *Physical Phenomena in High Magnetic Fields -II* (World Scientific, Singapore, 1996), p. 125.
- [205] K. Ishida, K. Okamoto, Y. Kawasaki, Y. Kitaoka, O. Trovarelli, C. Geibel, and F. Steglich, *Phys. Rev. Lett.* 89 (2002) 107202.
- [206] M. Jourdan, A. Zakharov, M. Foerster, and H. Adrian, *Phys. Rev. Lett* 93 (2004) 097001.
- [207] L. M. Sandratskii and J. Kübler, *Phys. Rev. B* 50 (1994).
- [208] K. Knöpfle, A. Mavromaras, L. M. Sandratskii, and J. Kübler, *J. Phys. Condens. Matter* 8 (1996) 901.
- [209] Y. Inada, H. Yamagami, Y. Haga, K. Sakurai, Y. Tokiwa, T. Honma, E. Yamamoto, Y. Onuki, and T. Yanagisawa, *J. Phys. Soc. Jpn.* 68 (1999) 3643.
- [210] Y. Inada, A. Ishiguro, J. Kimura, N. Sato, A. Sawada, T. Komatsubara, and H. Yamagami, *Physica B* 206-207 (1995) 33.
- [211] L. Petit, A. Svane, W. M. Temmerman, Z. Szotek, and R. Tyer, *Europhys. Lett.* 62 (2003) 391.

- [212] T. E. Mason and G. Aeppli, *Matematisk-fysiske Meddelelser* 45 (1997) 231.
- [213] A. Hiess, N. Bernhoeft, N. Metoki, G. H. Lander, B. Roessli, N. K. Sato, N. Aso, Y. Haga, Y. Koike, T. Komatsubara, and Y. Onuki, preprint (2004).
- [214] M. Kyogaku, Y. Kitaoka, K. Asayama, C. Geibel, C. Schank, and F. Steglich, *J. Phys. Soc. Jpn.* 62 (1993) 4016.
- [215] N. Bernhoeft, A. Hiess, N. Metoki, G. H. Lander, and B. Roessli, preprint (2004).
- [216] P. Thalmeier and P. McHale, preprint (2004).
- [217] T. Watanabe, K. Izawa, Y. Kasahara, Y. Haga, Y. Onuki, P. Thalmeier, K. Maki, and Y. Matsuda, *cond-mat/0405211* (2004).
- [218] Y. Nishikawa and K. Yamada, *J. Phys. Soc. Jpn.* 71 (2002) 237.

ONE DIMENSIONAL ORGANIC SUPERCONDUCTORS

D. Jérôme and C.R. Pasquier

Laboratoire de Physique des Solides, UMR 8502, Université Paris-Sud, 91405 Orsay, France

1. TOWARDS ORGANIC SUPERCONDUCTIVITY

The new state of matter (superconductivity) has been discovered somehow unexpectedly in mercury with a critical temperature of $T_c = 4.15K$ by Kamerlingh Onnes in 1911 just after he had mastered the liquefaction of helium [1]. However, the phenomenon of superconductivity in particular its T_c , is strongly dependent on the material in which it is to be observed. Therefore, over the years a lot of new metals and intermetallic compounds have been discovered with increased values of T_c reaching a maximum which was apparently leveling off at about 24 K in the fifties, see figure 1. The absence of any satisfactory theory until 1957 did not prevent the applications of superconductivity which developed after World War Two but all these applications were bound to the use of liquid helium as the cooling agent which is necessary to stabilize the superconducting state. It is only in 1986 that totally new types of copper oxides discovered by Bednorz and Müller led to drastically higher T_c [2]. This remarkable discovery was actually an outcome of the quest for new materials able to show superconductivity under conditions as close as possible to ambient temperature. As to the possibility of superconductivity in materials other than metals, F.London in 1937 had been the first to suggest that aromatic compounds under magnetic fields might exhibit a permanent current running along aromatic ring systems (anthracene, naphthalene,...) under magnetic field[3].

The first practical attempt to promote metal-like conduction between open shell molecular species came out in 1954 with the molecular salt of perylene oxidized with bromine [4] although this salt was not very stable. In the sixties when superconductivity had already turned into practical applications people were worrying about the existence of new

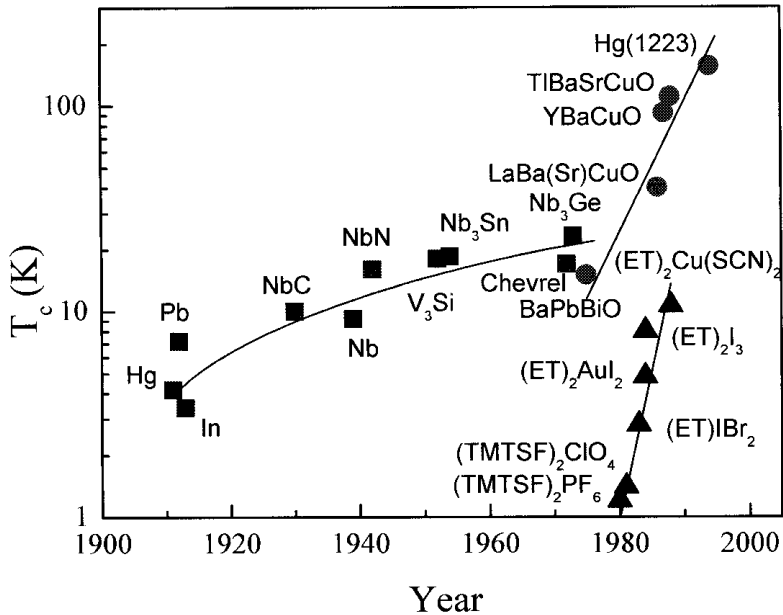


Fig 1. Evolution of the superconducting critical temperature in metals and intermetallic compounds, cuprates, organic conductors (one and two dimensional).

superconductors which would no longer require the need of liquid helium, W.A.Little made an interesting suggestion [5,6]. This was a new mechanism expected to lead to superconductivity at room temperature and to be observed in especially designed macromolecules. The idea of Little's mechanism was indeed strongly rooted in the isotope effect which has been one of the great successes of the theory proposed in 1957 by Bardeen Cooper and Schrieffer [7] for the interpretation of most superconducting compounds known up to that date. The attractive interaction between electrons (or holes) which is a prerequisite for the Bose condensation of electron pairs into the superconducting state since the heart of the BCS theory relies on the mass M of the ions which undergo a small displacement when the electrons are passing closeby namely, ($T_c \propto M^{-1/2}$). In the excitonic mechanism of Little it is an electronically polarizable entity which is used instead of the usual polarizable ionic lattice. Consequently, the small electronic mass m_e would lead to an increased T_c of the order of $(M/m_e)^{1/2}$ times what is observed in a conventional superconductor. This has been the beginning of the concept of room temperature superconductivity, still a dream for scientists in the twenty first century [8]. As far as materials are concerned, the model of Little was based on the use of a long conjugated polymer such as polyacetylene together with the grafting of polarizable side groups [9]. This formidable task in synthetic chemistry did not succeed but the idea to link organic metallicity and one dimensionality happened to be stimulating for the

development of organic superconductors although a lot of basic physical problems had been overlooked in the seminal paper of Little [5]. One of the positive aspects of Little's suggestion is that all organic conductors making up the first generation of organic conductors are given by linear arrays of organic molecules.

The prerequisite for the formation of a molecular conductor is first the requirement for having charged molecules in a solid and second to allow their charge to delocalize between molecular entities. Charging the molecules can be achieved either by a charge transfer reaction between molecules of different species or by the formation of an organic salt. The first case has been realized in TTF-TCNQ by a transfer of charge between the donor molecule TTF and the acceptor molecule TCNQ leading to open shell donor and acceptor molecules [10,11]. TTF-TCNQ has really marked the beginning of the research's effort in organic conductors keeping in mind organic superconductivity as the ultimate goal. This system is remaining famous for the experimental evidence of a Peierls transition in a one dimensional conductor responsible for a metal to insulator transition at low temperature. The physical properties have been extensively summarized in a review article [12].

The second route gave rise to the synthesis of the first organic superconductor $(\text{TMTSF})_2\text{PF}_6$ in 1979 [13]. Actually, it is the study of the two-chain charge transfer compounds $(\text{TMTSF}-\text{DMTCNQ})$, $(\text{TM}-\text{DM})$ where the donor is the tetramethyl selenide derivative of TTF which drew chemists and physicists's attention on the role of the TMTSF molecule. The outcome of this study has been decisive for the quest of organic superconductivity [14]. This 1-D conductor undergoes a Peierls transition at 42 K [15] where unlike TTF-TCNQ a distortion occurs simultaneously on both chains [16]. Several other results have triggered the attention. X-ray experiments had shown that the charge transfer is only $\rho = 0.5$ leading to a quarter-filled band situation [16]. Transport and thermopower data emphasized the dominant role played by the TMTSF chain in the mechanism driving the Peierls transition and also in its contribution to the conduction at high temperature [17]. The really new and unexpected finding has been the suppression of the Peierls transition under pressure and the conductivity remaining metal-like reaching the unprecedented value of $10^5(\Omega\text{cm})^{-1}$ under 10 kbar at the temperature of liquid helium [18]. The conducting state of TM-DM was also remarkable in displaying a huge transverse magnetoresistance below 50 K [19].

Since all these phenomena, were new and unexpected the effort was put on a structure made of only one organic stack comprising the lucky TMTSF molecule. Such a structure was already known from the early work of the Montpellier chemistry group who synthesized and studied the series of isostructural $(\text{TMTTF})_2\text{X}$ organic salts [20] where TMTTF is the sulfur analog of TMTSF and X is a monoanion such as ClO_4 , BF_4 or SCN . All these compounds turn into strong insulators at low temperature. This is the reason why they did not attract much interest until recently when they have been practically rediscovered after twenty years of studies which were mainly devoted to the selenide series, $(\text{TMTSF})_2\text{X}$.

While the research on 1D conductors was developing the same fulvalene had been used to synthesise a new molecule containing only sulfur atoms as the heteroatom in the fulvalene ring. This is the bisethyldithio-tetrathiafulvalene also abbreviated BEDT-TTF or (ET) in short. The ET molecules can give rise to several 2:1 phases with various polymeric

anions exhibiting usually a very pronounced two-dimensional metallic character. For instance, the beta phase $\beta-(\text{ET})_2\text{I}_3$ with the triiodide anion I_3^- reveals a columnar stacking of ET molecules arranged in layers like in the $(\text{TM})_2\text{X}$ structure. But the stronger interlayer interactions via S...S bonds makes the side by side interaction as strong as the face to face coupling. Consequently, the band structure becomes 2D with a half filled conduction band [21]. $\beta-(\text{ET})_2\text{I}_3$ has been the first 2D organic conductor to reveal superconductivity below 1.5K at ambient pressure [22]. Additional pressure work has shown an usual pressure dependence for T_c which is *at variance* with the regular pressure dependence of the $(\text{TM})_2\text{X}$ series. Instead of a steady decrease T_c has been found to increase discontinuously up to 8K around 1 kbar [23,24,25]. This behavior has been studied in details using the gas pressure technique, performing a pressure-temperature-pressure cycling known as the Orsay process pointing out the existence of two crystallographic phases for this salt, the low T_c phase β_L characterized by the onset of a displacive modulation below 200K [26] and the high T_c phase β_H free from any distortion [27]. Textbooks examples for two dimensional magnetoresistance oscillations have been observed in the β_H -phase stabilized at low temperature after the appropriate pressure cycling [28]. Although a large number of other crystalline structures have been synthesized using the ET molecule, let us mention only some materials with the κ structure [29], namely $\kappa-(\text{ET})_2\text{Cu}(\text{NCS})_2$ which held the record for organic superconductivity for some time [30] and $\kappa-(\text{ET})_2\text{Cu}[\text{N}(\text{CN})_2]\text{Cl}$ where the highest organic T_c of 13K can be stabilized under a pressure of 300 bar [31]. In the κ structure two ET molecules are paired with their planes almost parallel forming dimers arranged in sheets separated by insulating anion sheets. 2D organic conductors have been the subject of extensive reviews [32,33,34,35]. Their properties will only be discussed in this review when we shall be touching specific topics such as the superconducting state and the interplay between superconductivity and antiferromagnetism.

2. THE $(\text{TM})_2\text{X}$ PERIOD

2.1 Organic superconductivity in $(\text{TMTSF})_2\text{X}$

In 1979, the Copenhagen group succeeded in the synthesis of a new series of conducting salts all based on the TMTSF molecule namely, $(\text{TMTSF})_2\text{X}$ where X is an inorganic anion with various possible symmetry, spherical (PF_6^- , AsF_6^- , SbF_6^- , TaF_6^-), tetrahedral (BF_4^- , ClO_4^- , ReO_4^-) or triangular (NO_3^-) [36]. All these compounds but the one with $\text{X} = \text{ClO}_4^-$ did reveal an insulating ground state with a metal-insulator transition ranging from 180K in $\text{X} = \text{ReO}_4^-$ down to 12K in $\text{X} = \text{PF}_6^-$, figure 2. In this latter compound the conductivity reached the value of $10^5 \Omega^{-1}\text{cm}^{-1}$ at 12K with still a very strong temperature dependence. This behavior for the transport properties together with the absence of any lattice modulation [16,37] as precursors to the metal-insulator transition were new features in this field still dominated by the CDW philosophy stimulated further investigations under pressure and allowed the stabilization of a metallic state down to liquid helium temperature at a pressure of about 9kbar. The finding of

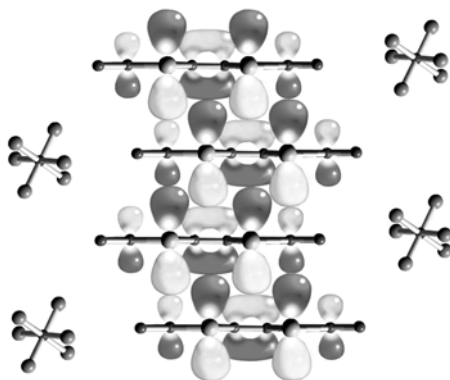


Fig.2. Side view of $(TM)_2X$ conductors.

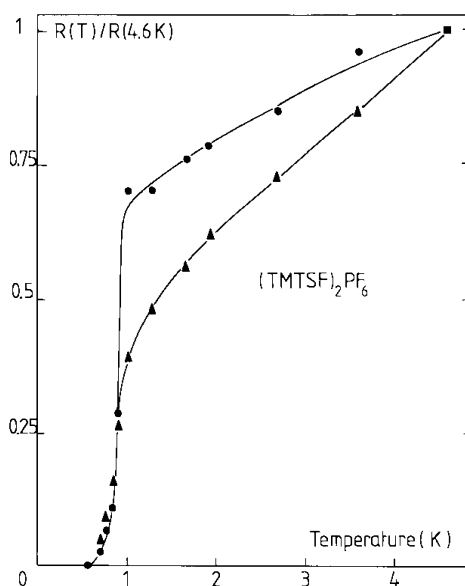


Fig. 3. $(TMTSF)_2PF_6$, first observation of organic superconductivity under pressure [13] obtained by hand recording the resistivity data.

a very small and still non-saturating resistivity at $1.3 K$ extrapolating linearly to a nearly zero value at $T = 0 K$ was a strong enough motivation to trigger further studies under pressure in a dilution refrigerator which rapidly led to the discovery of a zero resistance state below $1 K$. As this zero resistance state was easily suppressed by a magnetic field transverse to the most conducting direction, superconductivity was claimed [13].

The discovery of superconductivity in the $(\text{TMTSF})_2\text{X}$ family was a very exciting phenomenon since it was the first time such an instability could be stabilized in an organic compound. This happened about 15 years after the publication of Little and 10 years after the meeting of an international symposium organized by W.A. Little at Hawai'i on the Physical and Chemical Problems of Possible Organic Superconductors [9].

2.2 A variety of ground states in the $(\text{TM})_2\text{X}$ series

The discovery of superconductivity in an organic conductor has triggered subsequent investigations of the $(\text{TMTSF})_2\text{X}$ series which have shown that the superconducting ground state is only one among a variety of other ground states which can be stabilized in the isostructural series depending either on the nature of the anion or on the applied pressure. Shortly after the discovery of superconductivity in $(\text{TMTSF})_2\text{PF}_6$ it has been realized that the mechanism driving the metal-insulator transition at 12K in $(\text{TMTSF})_2\text{PF}_6$ at ambient pressure is the onset of itinerant antiferromagnetism which sets a magnetic modulation called a spin density wave (SDW). SDW formation had been proposed earlier for the interpretation of the magnetic transition in chromium due to the nested regions of the peculiar Fermi surface of this 3-D metal [38,39]. However, what makes the onset of a SDW particularly damaging for a 1-D conductor like $(\text{TMTSF})_2\text{PF}_6$ is the planarity of the Fermi surface. With a band filled up to $\pm k_F$ the exchange term of the Hartree-Fock potential characterized by wave vector $2k_F$ in the SDW phase opens a gap at the Fermi level over the entire surface giving rise in turn to an insulating ground state.

Shortly after the discovery of superconductivity in $(\text{TMTSF})_2\text{PF}_6$, many other members of the same series with a variety of anions have also been found superconducting in the vicinity of 1 K in the 10 kbar pressure domain [41]. The compound $(\text{TMTSF})_2\text{NO}_3$ is however the only system in the selenide series in which superconductivity has not been

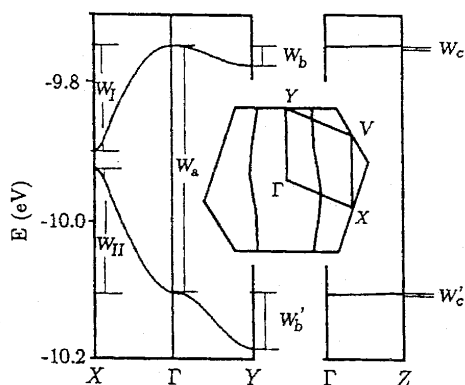


Fig.4. Band structure and Fermi surface of $(\text{TMTSF})_2\text{PF}_6$ [40].

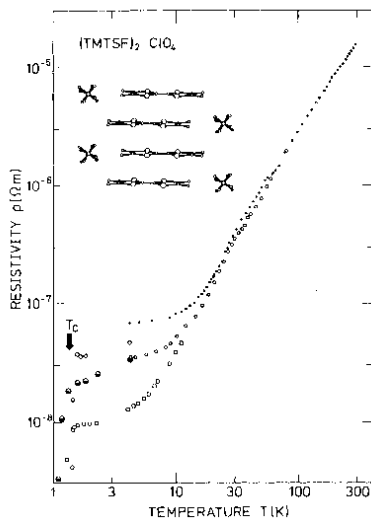


Fig. 5. $(\text{TMTSF})_2\text{ClO}_4$, first observation of organic superconductivity at ambient pressure [42].

stabilized for reasons related to the peculiar ordering of the anions at low temperature. $(\text{TMTSF})_2\text{ClO}_4$ is the only member of the $(\text{TMTSF})_2\text{X}$ series to show superconductivity under atmospheric pressure [42].

In the mid-eighties the isostructural family comprising the sulfur molecule TMTTF with the same series of mono-anions has been investigated under pressure and quite interesting new results obtained [43]. Thanks to studies performed at higher pressures it has been realized that $(\text{TMTTF})_2\text{X}$ and $(\text{TMTSF})_2\text{X}$ salts both belong to the same family forming the generic $(\text{TM})_2\text{X}$ phase diagram [44], figure 6. At this stage, it is instructive to look at the band structure which can be foreseen for these materials on the basis of a single particle model using a tight binding scheme and few simplifications. One assumption is the use of the highest occupied molecular orbital (HOMO) as the starting wave function for the tight binding calculation which is justified by the only weak interaction existing between molecules in the solid state. The other is the extended Hückel method which leads to an appropriate band description. The band structure parameters thus obtained can be used to define the following model of the energy spectrum [12,45] :

$$\varepsilon(\vec{k}) = -2t_a \cos(k_a a) - 2t_{\perp b} \cos(k_{\perp b} b) - 2t_{\perp c} \cos(k_{\perp c} c) \quad (1)$$

where it is assumed that the underlying lattice is orthorhombic. The symmetry of the lattice in the $(\text{TM})_2\text{X}$ being triclinic with the $P\bar{1}$ space group the above expression then represents a simplified model of the actual spectrum of figure 4 but it retains the essential and is easier to manipulate. The conduction band along the chain direction has an overall width $4t_a$ ranging between 0.4 and 1.2 eV, depending on the chemical nature of the donor molecule. As the overlap between electron clouds of neighbouring molecules along the stacking direction is

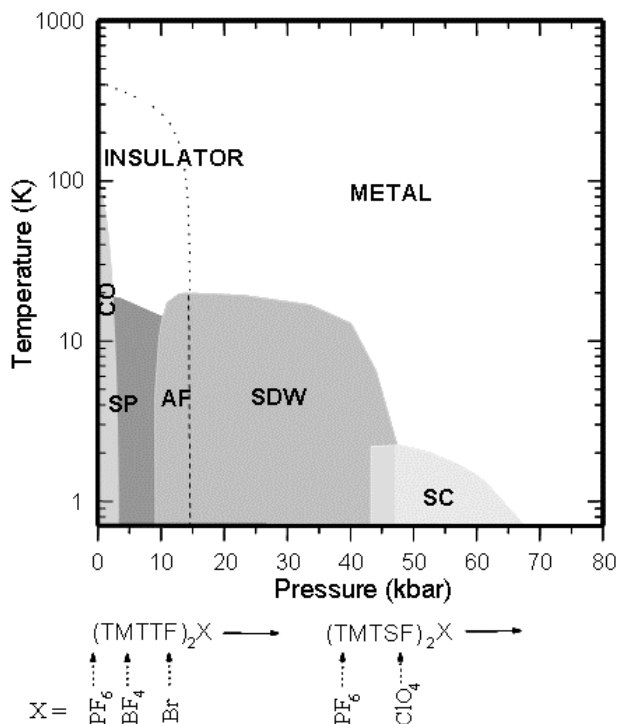


Fig.6. Generic phase diagram for the $(\text{TM})_2\text{X}$ compounds [44] with the zero pressure point fixed at the compound $(\text{TMTTF})_2\text{PF}_6$. The small shaded area at low pressure schematizes the region of the phase diagram in which charge disproportionation arises in $(\text{TMTTF})_2\text{AsF}_6$.

about 10 times larger than the overlap between the stacks in the transverse b direction and 500 times larger than that along the c direction, the electronic structure can be viewed at first sight as one-dimensional with an open and slightly warped Fermi surface centered at the Fermi wave vector $\pm k_F$ defined for isolated chains, figure 4.

The anions located in centrosymmetrical cavities lie slightly above or below the molecular planes. This structure results in a dimerization of the intermolecular distance (overlap) with a concomitant splitting of the HOMO conduction band into a filled lower band separated from a half-filled upper (hole-like) band by a gap Δ_D at $\pm 2k_F$, called the dimerization gap which is shown in figure 4 at the point X of the new Brillouin zone. However, on account of the finite transverse dispersion, this dimerization gap does not lead to a genuine gap in the middle of the density of states as shown from the extended-Hückel band calculation (figure 7). The only claim which can be made is that these conductors have a commensurate band filling (0.75) coming from the 2:1 stoichiometry with a tendency toward half filling which is more pronounced for sulfur (with enhanced structural dimerization) than for selenium compounds, while it differs from compound to compound within a given series.

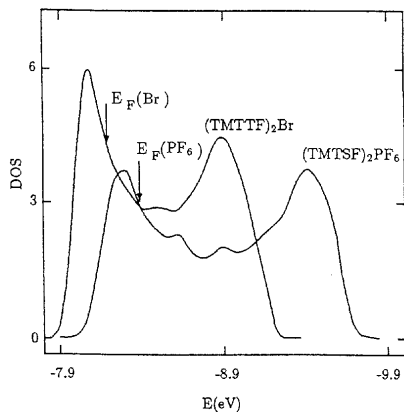


Fig. 7. Extended Hückel density of states for $(\text{TMTSF})_2\text{PF}_6$ and $(\text{TMTTF})_2\text{Br}$ [40].

Table 1. Calculated band parameters for three representative members of the $(\text{TM})_2\text{X}$ series according to the crystallographic data of reference 46. The average intra and interstacks interactions are given in lines 4 and 6 respectively. The bound dimerization is shown in line 5. All energies are counted in meV.

| | $(\text{TMTTF})_2\text{PF}_6$ | $(\text{TMTSF})_2\text{PF}_6$ | $(\text{TMTSF})_2\text{ClO}_4$ |
|----------------------|-------------------------------|-------------------------------|--------------------------------|
| t_1 | 137 | 252 | 258 |
| t_2 | 93 | 209 | 221 |
| \bar{t} | 115 | 230 | 239 |
| $\frac{\Delta t}{t}$ | 0.38 | 0.187 | 0.155 |
| \bar{t}_\perp | 13 | 58 | 44 |

Consequently, according to the single particle band calculation all compounds in the $(\text{TM})_2\text{X}$ series should be found conducting. On Table 1 we have reported the band parameters of different members of the $(\text{TM})_2\text{X}$ family as they can be computed from the crystallographic data [46]. The sulfur compounds exhibit bands which are significantly narrower and more dimerized than the selenide ones.

The gross features of the $(\text{TM})_2\text{X}$ phase diagram are the followings. First, compounds at the left in the diagram such as $(\text{TMTTF})_2\text{PF}_6$ are insulators below room temperature while those right of $(\text{TMTTF})_2\text{Br}$ exhibit an extended temperature regime with a metallic behavior, see figure 8. Therefore, the cause for the insulating nature of some members in the $(\text{TM})_2\text{X}$ series will have to be searched in the joint role of e-e repulsion and low dimensionality as we shall show later on in this article.

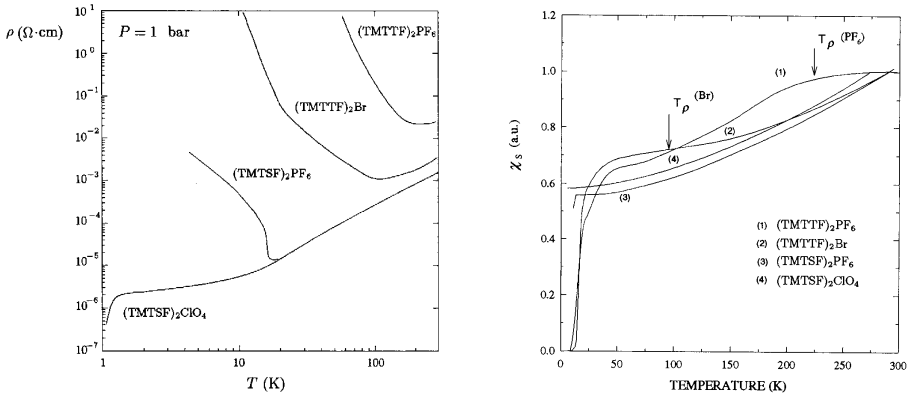


Fig.8. $(\text{TM})_2\text{X}$, resistivity and susceptibility. An illustration for the charge-spin separation [48].

The salient feature of the $(\text{TM})_2\text{X}$ diagram is the existence of a wide variety of ground states occurring below 20K or so. Moving toward the right across the $(\text{TM})_2\text{X}$ phase diagram, a succession of ground states is revealed either changing compounds or changing pressure on a given compound. All these ground states have been discovered from the study of the temperature dependence of the spin degrees of freedom (susceptibility, EPR and NMR) and from structural data [47]. The compound at the extreme left in the $(\text{TM})_2\text{X}$ diagram, $(\text{TMTTF})_2\text{PF}_6$ is the only one which can be moved by pressure through the entire series of ground states, Spin-Peierls, Néel antiferromagnetism, SDW phase with an incommensurate magnetic modulation and ultimately superconductivity. It is this latter compound which has established the universality of the generic phase diagram [44].

2.3 $(\text{TM})_2\text{X}$ at high temperature: from the 1-D Mott insulator to the 2D conductor

Given the unified $(\text{TM})_2\text{X}$ phase diagram established experimentally which suggests that apparently so different systems such as the superconducting $(\text{TMTSF})_2\text{ClO}_4$ and the strongly insulating $(\text{TMTTF})_2\text{PF}_6$ belong to the same class of materials *i.e.* physical properties of the latter can be made equivalent to those of the former provided a large enough pressure is applied we shall try to explain how recent theoretical ideas in 1-D physics have contributed to a better understanding. Therefore, we intend to summarize very briefly the physics of the high temperature phase in the rest of this article. Extended reviews have been published in ref [48] also in a recent textbook [49].

What 1-D physics means is that instead of the usual description of low lying excitations in terms of quasi particle states in the Landau-Fermi liquid model, a collective mode description with decoupled spin and charge modes is a more appropriate starting point [50,51]. Such a model for 1D conductors has been proposed starting from a linearized energy spectrum for excitations close to the Fermi level and adding the relevant Coulomb repulsions

which are responsible for electron scattering with momentum transfer $2k_F$ and 0. This is the popular Tomonaga-Luttinger model for a 1-D conductor in which the spatial variation of all correlation functions (spin susceptibility at $2k_F$ or $4k_F$, CDW, Superconductivity) exhibit a power law decay at large distance, characterized by a non-universal exponent K_ρ (which is a function of the microscopic coupling constants) [52]. This experimental review is not the place to discuss extensively the significance of the 1-D exponent but let us just say to be extremely brief that K_ρ is a positive exponent. When K_ρ is larger than unity, interactions between carriers become attractive and favor superconducting correlations at low temperature while if K_ρ is less than unity, repulsive interactions together with magnetic correlations are enhanced at low temperature [53].

Furthermore, there exists an added peculiarity in $(TM)_2X$ conductors since the stoichiometry imposes half a carrier (hole) per TM molecule (and this filling cannot be modified by the applied pressure). Consequently, uniformly spaced molecules along the stacking axis should lead to the situation where the unit cell contains $\frac{1}{2}$ carrier, *i.e.* the conduction band is quarter-filled. However, non-uniformity of the molecular packing had been noticed from the early structural studies of $(TMTTF)_2X$ crystals [46]. There exists a dimerization of the overlap between molecules along the stacks, a situation which is more developed in the sulfur series although it is still encountered in some members of the $(TMTSF)_2X$, see Table 1. The impact of the dimerization on the electronic structure is usually quantified by the modulation of the intra-stack overlap integral as both longitudinal and transverse molecular displacements are able to contribute to the modulation of the intermolecular overlap could contribute to make them half-filled band compounds. The commensurate band filling opens a new scattering channel for the carriers between both sides of the Fermi surface as then the total momentum transfer for two (four) electrons from one side of the 1-D Fermi surface to the other is equal to a reciprocal lattice vector (Umklapp scattering for half (quarter)-filled bands).

Commensurability leads to important modifications in the model of the gapless Luttinger liquid which instead becomes a Mott-Hubbard type insulator with a gap in the charge sector although on account of the spin-charge separation of the 1-D physics the spin sector remains gap-less [53]. The amplitude of the charge gap relies very strongly on the band filling and the strength of the e-e repulsions of the 1-D electronic spectrum. For half-filled band 1-D conductors the Mott Hubbard gap opens up as soon as interactions between carriers are infinitesimally repulsive namely, $K_\rho < 1$, see figure 9. Quarter-filled band conductors however can afford more repulsive interactions before turning into 1-D insulators. They become insulating when the condition $K_\rho < 0.25$ is fulfilled.

The gap in the density of states at the Fermi energy reads :

$$2\Delta_\rho \approx W \left(\frac{g_U}{W} \right)^{1/(2-2n^2K_\rho)} \quad (2)$$

where g_U is the coupling constant $g_U = W \left(\frac{U}{W} \right)^3$ and $n = 2$ (1) for the $\frac{1}{4}$ ($\frac{1}{2}$)-filled situation respectively in the Hubbard limit.

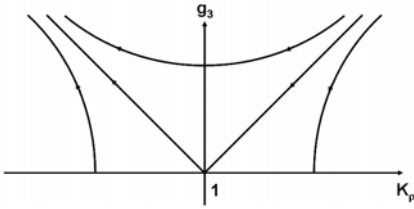


Fig.9. Temperature flow of interactions g_3 (strength of the Umklapp interaction) and K_ρ for the half filled band situation.

2.4 The 1-D physics high temperature regime

The first important question to be settled is whether there exists a part of the generic $(\text{TM})_2\text{X}$ diagram where 1-D physics is relevant and second where is this region located. According to band calculations, the transverse overlap t_\perp along the b -direction is of order 120 K and 200 K for sulfur and selenium compounds respectively [48]. Therefore, it is quite natural to expect first 1-D theory to govern the physics of these quasi 1-D conductors, at least in the high temperature regime when $T > t_\perp$ [54] and second, to observe a cross-over toward higher dimensionality physics below room temperature.

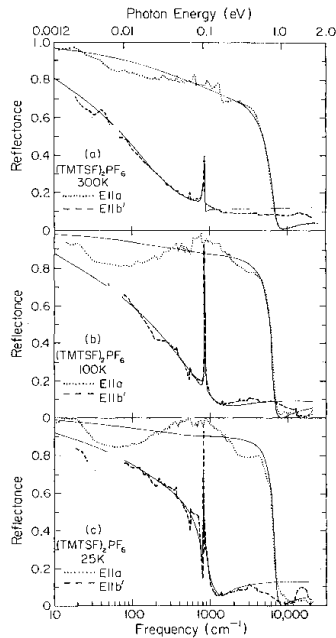


Fig.10. Reflectance data for $(\text{TMTSF})_2\text{PF}_6$ at decreasing temperatures from top to bottom with the light polarized along a or the b' transverse axis. A transverse plasma edge is observed at low temperature [56].

As observed very early in the polarized reflectance studies of $(\text{TMTSF})_2\text{PF}_6$, a plasma edge for a light polarized along the transverse b -axis becomes observable only below 100K [55,56] and therefore suppresses the relevance of 1-D physics restricted to the high temperature limit, see fig.10. The situation is more delicate for $(\text{TMTTF})_2\text{PF}_6$ which is already a semiconductor from 300K according to the frequency dependence of the conductivity showing a peak of oscillator strength around 2000cm^{-1} at room temperature [57]. More recent optical investigations performed on the same compound at low temperature [58] concluded to the existence of a gap in the single particle spectrum of order 800cm^{-1} . In the following we shall see that this insulating character is indeed a direct consequence of strong electron-electron repulsions and one-dimensionality.

2.4.1 The charge ordering in the insulating state of $(\text{TMTTF})_2\text{X}$

The charge reorganization which is observed in the insulating regime at high temperature of some of the insulating salts is discussed in this section although it concerns a real ordering phenomenon because it is not the actual ground state of the materials observed at low temperature.

The dominant role of Coulomb interactions between one dimensional carriers of these salts has been illustrated by the observation of a new electronic state detected long time ago in the $(\text{TMTTF})_2\text{X}$ members of the $(\text{TM})_2\text{X}$ series but understood only recently: the charge-ordered (CO) state. The early evidences came from the study of the transport properties showing sharp anomalies of resistivity, thermopower [59] and microwave dielectric constant [60] in the salts with $\text{X} = \text{SbF}_6$, AsF_6 , and ReO_4 of the $(\text{TMTTF})_2\text{X}$ family at $T_{CO} = 154$, 100 and 225K respectively. In addition it had been noticed that none of these anomalies were accompanied by structural modifications and thus the name of structure-less transitions was given to them [61]. Similarly, the absence of any change for the spin degrees of freedom was taken as an evidence for the spin-charge separation of the 1-D electron gas physics. Recent NMR [62,63] and low frequency dielectric [64,65] measurements ascribed the anomalies at T_{CO} to the existence of an electronic phase transition and the onset of a charge disproportionation occurring between near neighbor molecules along the molecular stacks. As shown by the splitting of the NMR lines [62], the charge redistribution removes the inversion symmetry $P\bar{1}$ existing at high temperature and gives rise to a modulation at wave vector $4k_F$ of the molecular site energy leading in turn to an additional increase of the preexisting charge gap due to on-site correlations and Umklapp scattering [66] (*vide-infra*). The case of $(\text{TMTTF})_2\text{SbF}_6$ is indeed quite peculiar as it is a metal-insulator transition which is observed at T_{CO} instead of the usual insulator-insulator transition with a concomitant increase of the activation energy observed in all other compounds such as $(\text{TMTTF})_2\text{AsF}_6$ [65] and even recently in $(\text{TMTTF})_2\text{BF}_4$ [67]. The strengthening of the dimerization gap (and in turn of the localization) has been anticipated in two different theoretical approaches. It was first shown from numerical calculations of the 1-D extended Hubbard model that the nearest neighbour interaction V added to the on-site repulsion U resulted in a CDW singularity at $4k_F$ [68]. Subsequently, the calculation of the ground state of a quarter-filled 1-D band within a mean field approximation of the extended Hubbard chain [69] showed how the long range part of the Coulomb interaction is essential to stabilize a charge disproportionated state

(leaving spin excitations unaffected). As 1-D correlations only are unable to explain long range order and the existence of finite temperature phase transitions, a uniform displacement of the anion lattice has been suggested as the 3-D stabilizing agent [65] leading to a ferroelectric ground state [70] through the second order transition where the permittivity is found to be diverging with a Curie law [65]. High pressure studies have shown that the CO state survives the formation of the spin-singlet (spin-Peierls) ground state and may coexist with it in a narrow pressure domain [63] in agreement with the 1-D extended Hubbard calculation adding the electron-lattice coupling [71]. In conclusion, the phenomenon of charge ordering observed in practically all members of the $(\text{TMTTF})_2\text{X}$ sub-family has emphasized the importance of the long-range Coulomb interactions besides on-site repulsions. The fast suppression under pressure, *see* figure 11 is also suggestive of a rather modest influence on the properties of the more metallic compounds which become superconducting at low temperature. The phenomenon of charge ordering is not restricted to salts with centrosymmetrical anions but in the case of the tetrahedral anion ReO_4 charge ordering is observed first at a transition with $T_{\text{CO}} = 225\text{K}$ (the structure-less transition) and it is followed at lower temperature by an anion ordering transition at $T_{\text{AO}} = 154\text{K}$ (see next section) leading to a superstructure $(1/2, 1/2, 1/2)$ and an increase of the activation energy [59,60].

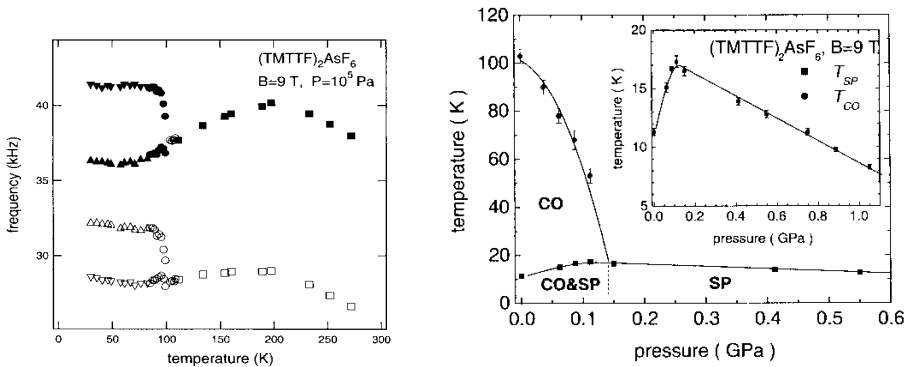


Fig. 11. $(\text{TMTTF})_2\text{AsF}_6$, Knight shift data (left) revealing the charge-ordering at low temperature and P-T phase diagram (right) [63].

2.4.2 Longitudinal versus transverse transport

Studies of the DC transport have provided important clues regarding the domain of 1D physics. The striking behavior of the transport properties emerges from a comparison between the temperature dependence of longitudinal and transverse components of the resistivity [72]. In particular, a lot can be learned about the physics of the a - b layers from the temperature dependence of the transverse transport even (especially) when this latter is incoherent between the layers.

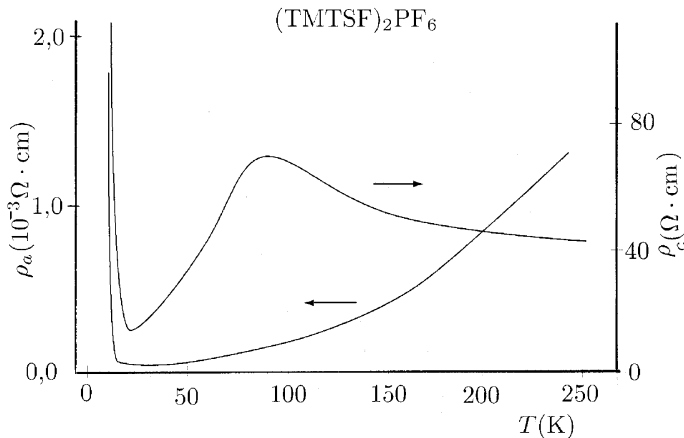


Fig.12. $(\text{TMTSF})_2\text{PF}_6$, temperature dependence of the parallel and transverse (c -axis) resistivity [72].

From the early measurements in $(\text{TMTSF})_2\text{PF}_6$ opposite temperature dependences for ρ_a and ρ_c had been reported in the high temperature regime [55]. This phenomenon has been revisited later including a high pressure study in $(\text{TMTSF})_2\text{PF}_6$ and $(\text{TMTTF})_2\text{PF}_6$ [72] and recently in the extensive high pressure investigation of $(\text{TMTTF})_2\text{PF}_6$ [67].

The behavior of the resistance along the direction of weakest coupling *i.e.* along the c -axis displays an insulating character with a maximum around 120 K and becomes metallic at lower temperatures although remaining several orders of magnitude above the Mott-Ioffe critical value which marks the limit between metal-like and insulating-like transport, figure 12 [73].

The existence of opposite temperature dependences between transverse and in-chain transport is not restricted to organic conductors and even to 1-D conductors as this property has been observed in a large number of anisotropic conductors. Some examples are given by underdoped high T_c cuprates [74] and layered conductors, $(\text{Bi}_{0.5}\text{Pb}_{0.5})_2\text{Ba}_3\text{Co}_2\text{O}_y$ and NaCo_2O_4 [75] or the quasi 1-D cuprate $\text{PrBa}_2\text{Cu}_4\text{O}_8$ [76]. The insulating character of the transverse transport has been interpreted as the signature of a non Fermi-Landau behavior for the carriers within the planes (chains). When the transverse transport is incoherent, the carriers are scattered many times in layers or chains before they hop to the neighboring plane (chain), the conductivity in the tunneling approximation in terms of the transverse coupling t_\perp thus reads,

$$\sigma_\perp(\omega, T) \propto t_\perp^2 \int dx \int d\omega' A_{1D}(x, \omega') A_{1D}(x, \omega + \omega') \frac{f(\omega') - f(\omega' + \omega)}{\omega} \quad (3)$$

where $A_{1D}(x, \omega)$ is the one-electron spectral function of a single chain (or a plane in case of layered materials). The transverse conduction derived from equation 3 is also related to the weight of quasi-particles (QP) at the Fermi energy. Angle resolved photoemission studies

(ARPES) in inorganic low dimensional systems have actually confirmed the existence of a correlation between the insulating character of ρ_{\perp} and the absence of quasi particle peaks in the above-mentioned layered materials [75]. Furthermore, the emergence of a quasi particle peak in ARPES at low temperature correlates with the transverse transport becoming metal-like. In case of a Landau-Fermi electron gas in which electron states are characterized by an in-chain (or in-plane) lifetime τ the previous equation recovers the proportionality between σ_{\perp} and σ_{\parallel} which had been established at the time of TTF - TCNQ using the Fermi Golden rule for incoherent transverse transport [77]. The temperature at which the transverse transport changes from insulating to metallic temperature dependence corresponds to a cross-over between two regimes; a high temperature regime with no QP weight at Fermi energy (possibly a TL liquid in the 1-D case) and another regime in which QP weight grows going toward low temperature. This interpretation does not necessarily imply that the transport along the c -direction must also become coherent below the cross-over. The c axis transport may well remain incoherent with a Fermi liquid establishing in the a - b plane with the temperature decreasing below T^* . In case of $(\text{TMTSF})_2\text{PF}_6$, it has been noticed that the Hall voltage which involves the conduction in the a - b plane displays a marked minimum at the same T^* where the c -axis resistivity displays a maximum [72]. Since the theory of the Hall effect for coupled TL chains is not yet very much advanced we cannot tell more about the interpretation of the Hall voltage [78].

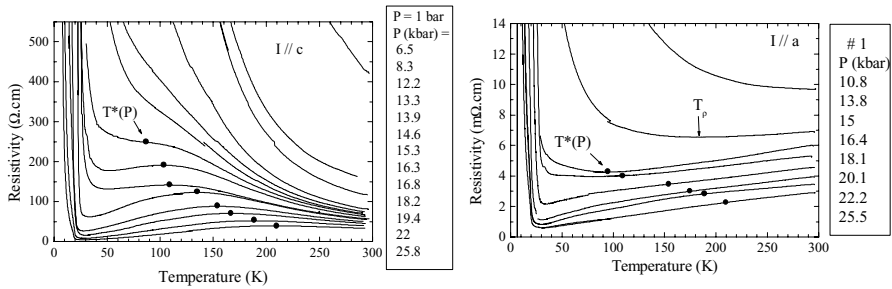


Fig. 13. $(\text{TMTTF})_2\text{PF}_6$ longitudinal (left) and transverse (right) resistance versus temperature at different pressures [67].

2.4.3 The $(\text{TMTTF})_2\text{PF}_6$ phase diagram under pressure

The study of the strongly insulating system $(\text{TMTTF})_2\text{PF}_6$ under high pressure has been very rewarding not only because it enabled the stabilization of superconductivity in a sulfur compound but also its location at the left end of the $(\text{TM})_2\text{X}$ diagram allows several key properties of quasi 1-D conductors to be studied under pressure; longitudinal *versus* transverse transport and one dimensional deconfinement [67]. The phase diagram in figure 14 has been obtained with $(\text{TMTTF})_2\text{PF}_6$ taken as the reference compound from the pressure dependence of $\rho_c(T)$ and $\rho_a(T)$. In the low pressure region ($P < 10$ kbar), both $\rho_c(T)$ and

$\rho_a(T)$ are activated although an important difference is noticed between activation energies, $\Delta_a < \Delta_c$. Moving towards higher pressures, the activation of ρ_c persists with a gentle decrease of Δ_c under pressure while Δ_a collapses at a pressure of ≈ 14 kbar which also marks the onset of the cross-over temperature T^* as shown by the T dependence of ρ_c . The different values and pressure dependences of the activation energies have been taken as an evidence for an in-chain conduction provided by thermally excited 1-D objects similar to the solitons in conducting polymers [79] whereas transverse transport requires the excitation of quasi-particles through a Mott-Hubbard gap larger than the soliton gap. More recent studies performed in other compounds of the $(\text{TMTTF})_2\text{X}$ series with $\text{X} = \text{ReO}_4$, BF_4 and Br have shown that the main features observed in $(\text{TMTTF})_2\text{PF}_6$ under pressure are also observed in the other systems, in particular the signature of the cross-over is recovered and does not depend on the symmetry of the anion [80].

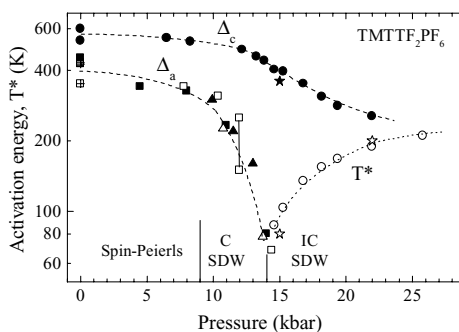


Fig. 14. $(\text{TMTTF})_2\text{PF}_6$ temperature-pressure phase diagram derived from parallel and transverse transport. The activation for the c axis transport (Δ_c) although decreasing survives up to high pressure while the longitudinal transport (Δ_a) is no longer activated above 15 kbar. when a dimensional cross-over occurs at finite temperature [67]. Given the measured values of Δ_c and T^* , for $(\text{TMTSF})_2\text{PF}_6$ under ambient pressure (stars), the latter compound would correspond to $(\text{TMTTF})_2\text{PF}_6$ under 15kbar. The open star on the right corresponds to $(\text{TMTSF})_2\text{PF}_6$ under 9kbar.

2.4.4 Dimensionality cross-over under pressure

The temperature T^* corresponding to the c -resistance maximum moves up under pressure and reaches room temperature under 10 kbar. This temperature can be attributed to the beginning of a cross-over between 1-D and 2-D regimes. The strong pressure dependence of the cross-over temperature T^* is a remarkable phenomenon of the $(\text{TM})_2\text{X}$ physics. According to the pressure data of ρ_c for different compounds belonging to the $(\text{TM})_2\text{X}$ series, the pressure

dependence of T^* is about ten times larger than that of t_{\perp} (which is typically $2\%kbar^{-1}$). This feature suggests that T^* is actually a renormalized version of the bare temperature t_{\perp} due to the 1-D confinement via intrastacks electron-hole interactions [81]. As far as insulating $(TMTTF)_2X$ compounds are concerned the cross-over is meaningless as the strong one dimensionality renormalization makes T^* irrelevant [81] and transport remains 1-D down to the lowest temperature.

2.4.5 $(TM)_2X$ compounds: $\frac{1}{2}$ or $\frac{1}{4}$ filled band conductors ?

When the density of states is gapped $2\Delta_{\rho}$ by correlation effects then the longitudinal transport is expected to vary according to a power law,

$$\rho_{||} \approx T^{4n^2K_{\rho}-3} \quad (4)$$

in the high temperature regime *i.e.* $T > \Delta_{\rho}$ [53]. The material looks like a metal although this may be true only for the parallel direction with a transport along the c direction remaining incoherent showing an insulating dependence in the same temperature domain probing the density of quasiparticle states in the a - b planes following equation 3.

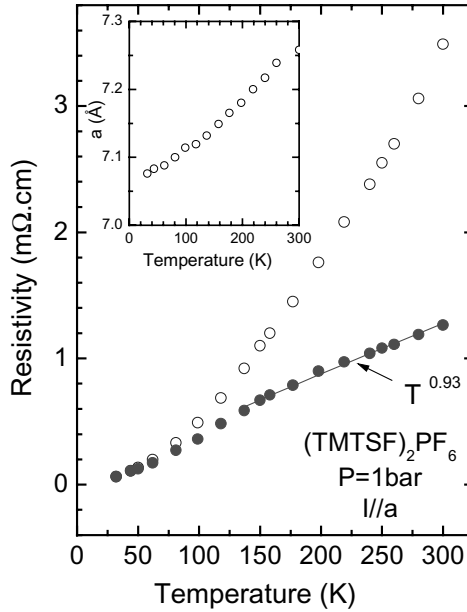


Fig. 15. Temperature dependence of the $(TMTSF)_2PF_6$ longitudinal resistance at constant volume showing a quasi linear T-dependence with the thermal dependence of the a parameter displayed in the inset [82].

In the high T regime, the picture of non-coupled chains is approached. Therefore, the density of quasiparticle states should resemble the situation which prevails in a Luttinger liquid namely, $N(E) \approx |\omega|^\alpha$ where α is related to K_ρ by $\alpha = \frac{1}{4}(K_\rho + 1/K_\rho - 2)$ neglecting the influence of the Mott gap small compared to the temperature. Experimentally, the longitudinal resistivity of $(\text{TMTSF})_2\text{PF}_6$ is metal-like down to the SDW transition at 12 K, varying sublinearly ($\approx T^{0.93}$) from 300 to 150 K once the constant volume correction is taken into account and more like T^2 below 150 K [82], see figure 15.

The experimental power law of the longitudinal resistivity leads inturn to $n^2 K_\rho = 0.98$ according to equation 4.

An other approach to the correlation coefficient is provided by optical studies. The study of the far infrared (FIR) conduction of $(\text{TMTSF})_2\text{PF}_6$ has been very helpful for the determination of K_ρ since the FIR gap of about $\Delta_\rho = 200 \text{ cm}^{-1}$ in $(\text{TMTSF})_2\text{PF}_6$ has been attributed to the signature of the Mott-Hubbard gap [83]. The theory predicts a power law dependence for the optical conductivity at frequencies larger than the Mott gap [53] namely,

$$\sigma(\omega) \approx \omega^{4n^2 K_\rho - 5} \quad (5)$$

at $\omega > 2\Delta_\rho$. According to the optical experimental data [83], $\sigma(\omega) \approx \omega^{-1.3}$ at high frequency and thus a value of $n^2 K_\rho = 0.93$ is obtained. This value for the correlation coefficient is fairly close to the one derived from parallel transport data but none of these experiments allow to discriminate between half or quarter filled Umklapp scattering.

In the early days of the $(\text{TM})_2\text{X}$ compounds the lattice dimerization was believed to govern the amplitude of the Mott-Hubbard gap [84,85]. However, later, an alternative interpretation based on new experimental results has been proposed, assuming that the $1/4$ -filled scattering could justify the existence of the Mott gap in the whole $(\text{TM})_2\text{X}$ series [53].

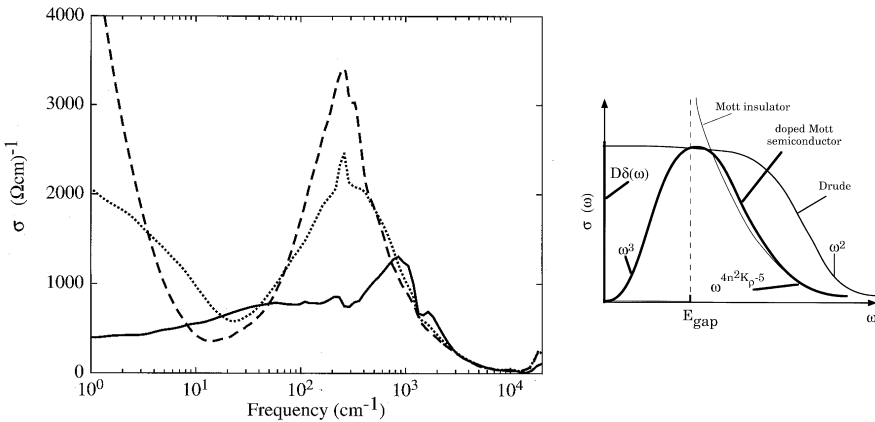


Fig.16. Far infra red data of $(\text{TMTSF})_2\text{PF}_6$, experiment [83] (left) and theory [53] (right).

If we choose the half filled hypothesis ($n=1$) thus K_ρ is closed to unity implying that the system is weakly coupled. This situation of very weak coupling is hard to reconcile with the enhancement of the spin susceptibility [48] but an additional argument against weak coupling is given by the unusual behavior of the transverse transport.

As far as the transverse transport is concerned, a temperature dependence such as $\rho_c(T) \approx T^{1-2\alpha}$ can be anticipated in the 1-D regime ($T > T^*$) [86] if the density of states of a Luttinger liquid is governing the density of excited quasiparticles at high temperature. The weak coupling value for K_ρ derived from the temperature dependence of the longitudinal transport and the optical data would imply $\alpha \approx 0$ and consequently a metal-like temperature dependence for $\rho_c(T)$ which is *at variance* with the data.

If we take now the quarter filled hypothesis $n=2$, then the fit of the experimental data would lead to $K_\rho = 0.23$ and $\alpha=0.64$ [83]. This value for K_ρ agrees fairly well with the $1/4$ filled scenario and $W = 12000K$ (from band structure calculations and plasma edge measurements), $\Delta_\rho = 200 \text{ cm}^{-1}$ (from FIR data) and $U/W = 0.7$ (which is in fair agreement with the enhancement of the spin susceptibility at low temperature) [48]. Such a strong coupling value for K_ρ implies that a system such as $(\text{TMTSF})_2\text{PF}_6$ lies at the border between a 1D Mott insulator and a Luttinger liquid though slightly on the insulating side.

Since studies of parallel and transverse transport have been carried on in $(\text{TMTTF})_2\text{PF}_6$ under pressure this latter compound provides the possibility to study the gentle evolution from Mott insulation to Luttinger liquid induced by pressure. Turning to the evaluation of the correlation coefficient from the temperature dependence of ρ_c and the law $\rho_c(T) \approx T^{1-2\alpha}$ which is expected to hold in the regime of uncoupled Luttinger chains we end up fitting the data for $(\text{TMTTF})_2\text{PF}_6$ in the pressure domain around 12 kbar , figure 14, with very small values of K_ρ (large values of α) which are not compatible with the value $K_\rho = 0.23$ derived from FIR and NMR data [48]. Consequently, we are forced to accept that the preexistence of a Mott gap cannot be forgotten and that the excitation of single particle through the remnence of the Mott gap of the order of $220K$ in $(\text{TMTSF})_2\text{PF}_6$ is still the dominant factor for the temperature dependence of the transverse transport along c [86] with a transverse resistivity behaving as $\rho_c(T) \propto T^{1-2\alpha} \exp(\Delta_\rho / T)$. The neglect of the Mott gap may become a valid approximation at higher pressures.

Since the Mott -Hubbard gap varies exponentially with K_ρ , even a small variation of the ratio between the Coulomb interaction and the bandwidth under pressure can explain a large decrease of $2\Delta_\rho$ moving from the left to the right in the generic phase diagram. Both optical and transport data give $2\Delta_\rho = 800 - 1000K$ in $(\text{TMTTF})_2\text{PF}_6$ at ambient pressure [67]. The difference between K_ρ for selenium and sulfur compounds ($K_\rho = 0.18$ for the latter material) can be afforded by the difference of their bare bandwidths as the on-site repulsion being a molecular property is likely to be less sensitive to pressure than the intermolecular overlap along the stacking axis. The lesson from this section is that all members in the phase diagram $(\text{TM})_2\text{X}$ are indeed 1-D confined Mott insulators with a

correlation gap evolving rapidly under pressure due to the pressure-induced band broadening. $(\text{TMTSF})_2\text{PF}_6$ under ambient pressure looks like a 1-D metal at high temperature because the temperature is large compared to the Mott gap. This compound remains a metal below the cross-over temperature T^* only because one dimensional carriers become deconfined by a transverse coupling which becomes then larger than the Mott gap [53].

2.4.6 Pseudogap and zero frequency mode

It is also most illuminating to have a look at the conductivity in the far infrared regime. A large gap of order $1000K$ is observed in the frequency dependence of the FIR conductivity of sulfur compounds [57]. This is in line with the activation energy of the DC conductivity in those compounds. However, the surprise arose for selenium compounds which behave apparently like normal metals as far as DC transport is concerned in spite of the marked gap observed in the FIR regime at low temperature. The apparent normal behaviour of the resistivity varying quadratically in temperature for $(\text{TMTSF})_2\text{ClO}_4$ or $(\text{TMTSF})_2\text{PF}_6$ above the SDW transition could lead to the misleading conclusion of a 2 or 3-D Fermi gas in which the temperature dependence of the transport is governed by e-e scattering. However, the analysis of the conductivity in terms of the frequency reveals quite a striking breakdown of the Drude theory for single-particles. The inability of the Drude theory to describe the optical conductivity has been noticed by a number of experimentalists working on $(\text{TMTSF})_2\text{X}$ with $\text{X}=\text{ClO}_4$, PF_6 or SbF_6 [87]. When the reflectance of $(\text{TMTSF})_2\text{ClO}_4$ in the near-infrared is analyzed with the Drude model in the whole range of temperatures from 300 down to $30K$ the electron scattering rate is found to decrease gradually from $2.5 \times 10^{14} \text{ s}^{-1}$ at room temperature to $1.3 \times 10^{14} \text{ s}^{-1}$ at 30 K [88]. Even if the RT value is not far from the value from DC conductivity, a drastic difference emerges at low temperature as σ_{DC} increases by a factor about 100 between RT and $30K$ [42] as compared to the factor 2 for the optical lifetime.

An other striking feature of the optical conductivity has been noticed when the Kramers-Krönig transformation of the reflectance is performed in a broad frequency domain for $(\text{TMTSF})_2\text{ClO}_4$ as well for all conducting materials at low temperature. Given the usual Drude relation $\sigma_{DC} = \omega_p^2 \tau / 4\pi$ between transport lifetime and plasma frequency data (the plasma frequency has been found nearly temperature independent [88,56]) and the measured resistance ratio for ρ_a of about 800 between RT and $2K$ obtained in good quality measurements, the Drude conductivity in the frequency range $\approx 40 \text{ cm}^{-1}$ should amount to at least $4000 \Omega \text{ cm}^{-1}$ [89,90]. The measured optical conductivity is at most of the order of $500 \Omega \text{ cm}^{-1}$ [89]. Consequently, the rise in the conductivity as $\omega \rightarrow 0$ has been taken in $(\text{TMTSF})_2\text{ClO}_4$ as well as in the other salts with PF_6 or SbF_6 as an evidence for a hidden zero frequency mode. This mode is actually so narrow that it escapes a direct determination from K-K analysis of the reflectance which is limited to the frequency domain above 10 cm^{-1} . Estimates of the mode width have been obtained using the DC conductivity and the oscillator strength Ω_p^2 of the mode using the Drude relation $\sigma_{DC} = \Omega_p^2 \tau_c / 4\pi$ where Ω_p is measured

from the first zero crossing of the dielectric constant. This procedure gives $\Gamma_c = 0.005 \text{ cm}^{-1}$ ($1/\tau \approx 10^9 \text{ s}^{-1}$) and 0.09 cm^{-1} at 2 and 25 K respectively in $(\text{TMTSF})_2\text{ClO}_4$ [90]. The confirmation of a very long scattering time for the DC conduction has also been brought by the rapid suppression of T_c by non-magnetic defects in the non conventional superconductor $(\text{TMTSF})_2\text{ClO}_4$ leading to $\Gamma_c = 0.13 \text{ cm}^{-1}$ at low temperature [91] meaning that the electron lifetime at low temperature is actually much longer than the value inferred from a Drude description.

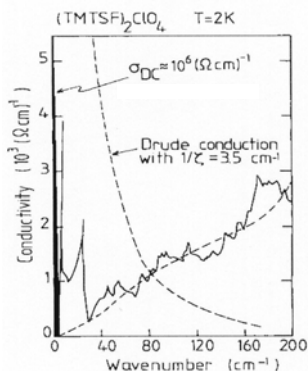


Fig. 17. Far infrared data of $(\text{TMTSF})_2\text{ClO}_4$ from reference 90. The dashed line is the Drude behaviour with $1/\tau = 3.5 \text{ cm}^{-1}$ and $\omega_p = 10^4 \text{ cm}^{-1}$.

There is now a wealth of experimental evidences showing the development of a narrow frequency mode in the Mott gap of $(\text{TMTSF})_2\text{ClO}_4$ and related conducting compounds. From FIR data in $(\text{TMTSF})_2\text{PF}_6$, it has also been shown that the narrow mode carries only a small fraction (a few percent) of the total spectral weight [83,56] but it is this mode which explains the very large value of the DC conduction observed at low temperature [47].

2.4.7 The symmetry of the anions

Although most of the physics of organic conductors is governed by the organic molecules, the anions, the presence of which is essential for electric neutrality may in some case suppress the stability of the conducting phase. As a matter of fact the possibility for $(\text{TM})_2\text{X}$ compounds having non centro-symmetrical anions to undergo a structural phase transitions can modify the band structure and the topology of the Fermi surface. Anions such as ClO_4 , ReO_4 , NO_3 , SCN have two equivalent orientations corresponding to short and long contacts between Se (resp. S) atoms of TMTSF (resp. TMTTF) molecule and a peripheral electronegative atom of the anion. Consider the case of $(\text{TMTSF})_2\text{ClO}_4$, the anion lattice orders at 24K leading to a superstructure of the Se-O contacts with a wave vector $\mathbf{q}_A = (0, 1/2, 0)$ here expressed in units of the reciprocal lattice vector [92,66]. The periodic potential thus created connects two Fermi points along the b direction and opens a gap which

doubles the unit cell along that direction. The folding of the Fermi surface that results introduces two warped Fermi surfaces near $\pm k_F$. Anion lattice superstructure has thus important consequences on the one-particle spectrum and in particular the nesting properties of the Fermi surface. This plays an important role in the efficiency of electron-electron interactions at low temperature and on the nature of the ground states. It also controls the stability of the superconducting phase in $(\text{TMTSF})_2\text{ClO}_4$ below 1.2 K at ambient pressure when long range orientation is defective. The variety of features induced by a magnetic field such as the so-called quantization of the Fermi surface nesting in the spin-density-wave phase ordering namely, field induced spin density wave phases (FISDW) [93,94,95,96,97,98], and the Lebed resonances [99] is also sensitive to the symmetry of the anions. This is particularly manifest when it is compared to compounds with spherical anions such as PF_6 or AsF_6 for which the absence of alteration of the Fermi surface via anion ordering enables for example the stabilization of spin-density-wave long-range order in zero magnetic field even under ambient ambient pressure. As previously mentioned, the anion potential produced by spherical anions like PF_6 and AsF_6 leads to a modulation of the charge along the organic stack with the same periodicity as the dimerization [100]. It may independently contribute to the half-filled character of the band and then enhances the strength of electron-electron interaction at low temperature [54].

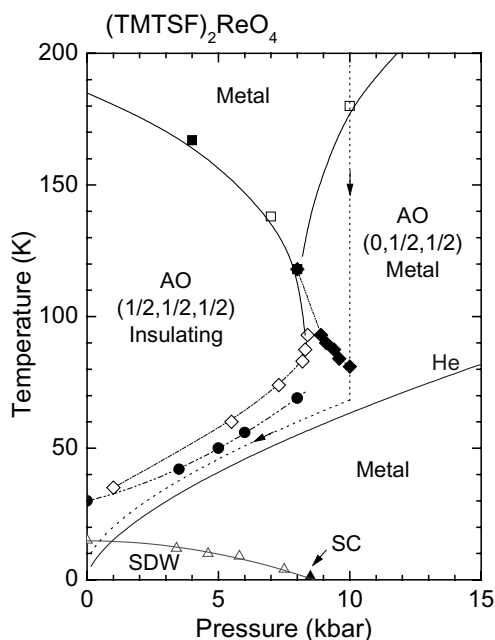


Fig. 18. $(\text{TMTSF})_2\text{ReO}_4$, phase diagram displaying the SDW ground state obtained after "Orsay process" [101].

For other compounds with a non-centrosymmetrical anion like ReO_4 , the structural ordering is different and takes place at $\mathbf{q}_A = (1/2, 1/2, 1/2)$; its impact on the electronic structure, however, turns out to be stronger since the anion potential at this wave vector creates a gap over the whole Fermi surface which is so large in amplitude ($\sim t_a$) that it leads to an insulating state although not due to the existence of strong electron-electron interactions. The application of hydrostatic pressure is then required to restore the metallic state with anions ordered according to $\mathbf{q}_A = (0, 1/2, 1/2)$ and the possibility of stabilization of superconductivity as in $(\text{TMTSF})_2\text{ClO}_4$ [102,103]. The use of an helium gas pressure experiment allowing depressurization at low temperature, see fig. 18, has shown that the actual interplay occurs between SC and SDW as observed in $(\text{TMTSF})_2\text{PF}_6$ as well.

The case of $(\text{TMTSF})_2\text{NO}_3$ is quite special since it is the only member among $(\text{TM})_2\text{X}$ salts where superconductivity cannot be stabilized although the SDW ground state is suppressed by a pressure of 7 kbar [104,105]. What makes $(\text{TMTSF})_2\text{NO}_3$ peculiar is the existence of an ordering of the triangular anions with the wave vector $\mathbf{q}_A = (1/2, 0, 0)$ at 45K which is responsible for a change of the electronic structure from a nearly flat Fermi surface at high temperature to a 2D semimetallic one below T_{AO} [106]. While the SDW ground state can be easily suppressed under pressure, the ordered anion state survives up to high pressures as illustrated by a strong anomaly of the resistivity [104,103] lowering the large density of states at the Fermi level needed for the stabilization of superconductivity.

2.5 Some features of the superconducting state

We shall not talk about the detailed features of the insulating (spin-Peierls or magnetic) ground states of the $(\text{TM})_2\text{X}$ diagram which can be found in various reference articles and textbooks [32] but shall devote some space to the discussion of the superconducting state itself and to the interplay between superconductivity and antiferromagnetism which remains the dominant peculiarity of the $(\text{TM})_2\text{X}$ phase diagram.

2.5.1 The superconducting transition

We intend to review briefly some physical features related to the onset of the superconducting state in $(\text{TMTSF})_2\text{X}$ limiting ourselves only to some of the experiments which have been used to characterize this state. The observation of superconductivity in the $(\text{TMTSF})_2\text{X}$ series requires the extended use of high pressure [41,107] with the notable exception of $(\text{TMTSF})_2\text{ClO}_4$ which is superconducting under ambient pressure [42] and $(\text{TMTSF})_2\text{NO}_3$ which never becomes a superconductor even under pressure [106]. For all cases the first evidence for superconductivity has been provided by a drop of the resistivity below the critical temperature and the suppression of this drop under magnetic field. We shall focus the presentation on the two members of the $(\text{TMTSF})_2\text{X}$ series which have attracted most attention ;

i) $(\text{TMTSF})_2\text{PF}_6$, because this has been the first superconductor to be found by transport measurements [14] and confirmed by magnetic shielding [108,109] and also because

the electronic properties of the 1-D electron gas on the organic stacks are only weakly (if at all) affected by the centrosymmetrical anions,

ii) $(\text{TMTSF})_2\text{ClO}_4$, because it is the only member on which some experiments such as specific heat [110] or Meissner expulsion [111] have been performed [111,112]. However, the study of the superconducting state in $(\text{TMTSF})_2\text{ClO}_4$ is facing the problem of the ClO_4 anions ordering at 24K doubling the periodicity along the b -axis [113]. Consequently, great care must be taken to cool the sample slowly enough in order to reach a well ordered state (R-state) at low temperature otherwise superconductivity is faced to its great sensitivity to disorder which will be discussed below.

The limitation for $(\text{TMTSF})_2\text{PF}_6$ is quite different. It is the proximity under pressure between SDW and superconducting phases which prevents the study of an homogeneous superconducting state unless the pressure is well above the critical pressure suppressing the SDW phase (*vide-infra*).

Other evidences of superconductivity have been provided by magnetic and calorimetric studies. First, a confirmation of the superconducting state in $(\text{TMTSF})_2\text{PF}_6$ under pressure has been carried out using an AC susceptibility experiment showing a signal below 1K indicative of a transition into a diamagnetic state [108]. The Meissner effect (*i.e.*, flux expulsion on cooling in a field) has subsequently confirmed the bulk nature of superconductivity (under 17.7 kbar) as well as the strongly anisotropic character of the critical fields [109]. The Meissner effect has been measured in more details in $(\text{TMTSF})_2\text{ClO}_4$ since superconductivity in that compound does not necessitate high pressure [111,114]. These studies have led to a measurement of the lower critical fields, namely $H_{c1} = 0.2, 1, 10(\text{Oe})$ along the respective a, b and c directions [111]. Combining lower critical field determinations with the thermodynamical field, the derivation of anisotropic and very large Landau-Ginzburg parameters shows that these materials are strong type II superconductors.

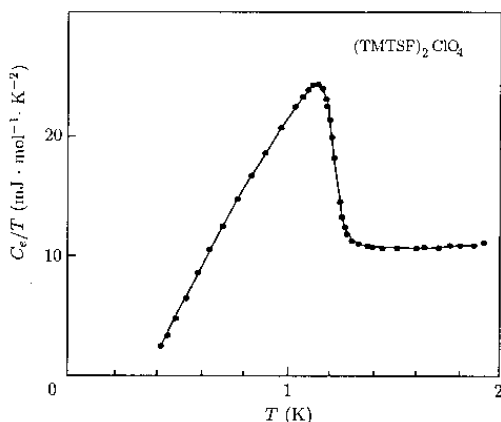


Fig. 19. $(\text{TMTSF})_2\text{ClO}_4$, the electronic C/T versus T [110].

The anisotropic character of the electronic structure already known from the anisotropy of the optical data in the normal phase is reflected in a pronounced anisotropy of the critical fields H_{c2} measured along the three principal directions in $(\text{TMTSF})_2\text{ClO}_4$ [112, 115, 116, 117]. The linearity of the critical fields with temperature in the vicinity of the T_c suggests an orbital limitation in the Ginzburg-Landau formalism for the critical field and rules out a Pauli limitation which would favour a $(1 - T/T_c)^{1/2}$ dependence [115,118]. However, the a/b anisotropy measured from upper critical fields is at least a factor two below the anisotropy derived from plasma edge studies. The interpretation of the upper critical fields in $(\text{TM})_2\text{X}$ is still waiting for an answer since several experimental results seem to imply that critical fields values could overcome the Pauli limit at low temperature by factors two or more [119,120]. At this stage great care must be taken to measure the critical field in an homogeneous superconducting phase as we shall discuss below.

The specific heat of $(\text{TMTSF})_2\text{ClO}_4$ in a $(\text{TMTSF})_2\text{ClO}_4$ versus T plot, figure 19, displays a very large anomaly around 1.2K [110]. Above 1.22K , the specific heat obeys the classical relation in metals $C/T = \gamma + \beta T^2$ where $\gamma = 10.5 \text{ mJ mol}^{-1} \text{K}^{-2}$, ($\beta = 11.4 \text{ mJ mol}^{-1} \text{K}^{-4}$) corresponding to $N(E_F) = 2.1 \text{ states eV}^{-1} \text{mol}^{-1}$ for the two spin directions. The specific heat jump at the transition amounts then to $\Delta C / \gamma T_c = 1.67$ i.e. only slightly larger than the BCS ratio. The behaviour of $C(T)$ in the superconducting state leads to the determination of the thermodynamical critical field $H_c = 44 \pm 2 \text{ Oe}$ and the single particle gap $2\Delta = 4\text{K} \cdot T_c$ is depressed at a rate of 1.1 mK Oe^{-1} when a magnetic field is applied along the c^* axis [121]. Comparing the value of the density of states derived from the specific heat and the value of the Pauli susceptibility [122] lends support to a weak coupling Fermi liquid picture (at least in the low temperature range) [48]. The thermal conductivity along the chains of $(\text{TMTSF})_2\text{ClO}_4$ as a function of temperature [123], presents the characteristics of a nodeless gap superconductor. The data in the superconducting state were successfully analyzed in the framework of a conventional Bardeen-Rickaysen-Tewordt (BRT) theory [124] where the only fitting parameter is the ratio $\Delta(0)/k_B T_c$. The best fit is obtained for

$$\Delta(0)/k_B T_c = 2.3. \text{ On the other hand, using the classical phonon gas equation } \kappa_{ph} = \frac{1}{3} c_{ph} v_s l_{ph}$$

where the ph index stands for the phonon contribution, v_s is the sound velocity and c_{ph} is the lattice specific heat, the authors estimated that the phonon mean-free path reaches $l_{ph} = 100 \mu\text{m}$ at 200mK .

2.5.2 Superconductivity under pressure

The pressure dependence of T_c is admittedly a remarkable feature for the $(\text{TMTSF})_2\text{X}$ compounds since it is pressure which enabled organic superconductivity to be discovered. As far as $(\text{TMTSF})_2\text{PF}_6$ is concerned, the strong pressure dependence observed above 10 kbar (T_c is only 0.2K under 24 kbar [125]) leads to a Gruneisen constant $\delta \ln T_c / \delta \ln T = 11$ at 9 kbar [125] using the compressibility data at 16 kbar [126], $\delta \ln V / \delta P = 0.7\% \text{ kbar}^{-1}$. This value of 11 is indeed larger than what has been derived for tin (7), the classical

superconductor which reveals the strongest sensitivity to pressure. The stability of superconductivity in $(\text{TMTSF})_2\text{ClO}_4$ is even more dramatic since then $\delta \ln T_c / \delta \ln T = 36$ [127] using the compressibility of $1\% \text{kbar}^{-1}$ measured for $(\text{TMTSF})_2\text{PF}_6$ at ambient pressure [126]. However, this remarkable sensitivity of T_c in $(\text{TMTSF})_2\text{ClO}_4$ might actually be related to the very specific problem of anion ordering in this compound as it has been suggested from the recent study of the sensitivity of T_c against the presence of non-magnetic disorder [91]. Anion ordering reveals an uprise of the ordering temperature under pressure [128,24,127] which can be derived from the pressure dependence of a small kink in the resistivity, the signature of the ordering, moving from 24 K up to 26.5 K under 1.5 kbar [128] and even up to 41 K at 11 kbar [129]. Connected to this uprise under pressure, there exists a slowing down in the dynamics needed for the ordering of the anions. Hence, high pressure studies require a special attention to the cooling rate which must be kept low enough to allow anion ordering at low temperature. Consequently, the decrease of T_c under pressure may be the consequence of two effects: an intrinsic modification of the electronic structure and the influence of imperfect anion ordering as discussed in Sec.2.6.1. The slowing down of the anion dynamics may also provide an explanation for the discrepancy between high pressure data showing the signature of anion ordering up to 8 kbar [24] and the absence of ordering claimed from the interpretation of magneto-angular oscillations [130].

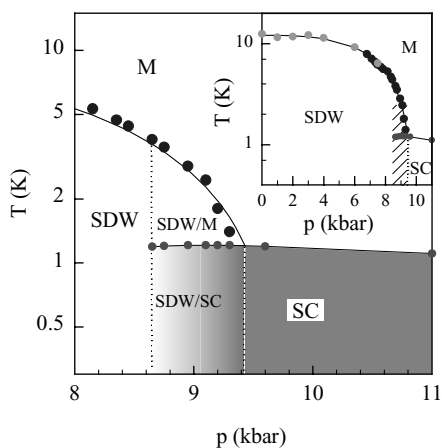


Fig. 20. Coexistence between SDW and Superconductivity in $(\text{TMTSF})_2\text{PF}_6$ in the vicinity of the critical pressure for the suppression of the SDW ground state [133].

2.5.3 Interplay between superconductivity and antiferromagnetism

The likeliness of superconducting domains appeared to be important already in the early days of organic superconductivity as Greene *et al.* [131] in the first repetition of organic superconductivity in $(\text{TMTSF})_2\text{PF}_6$ suggested the possibility of a coexistence of SDW and SC states. Furthermore, they attributed the strong depression of the critical temperature with

pressure to a filamentary superconductivity. On the other hand, EPR studies performed by Azevedo *et al.* [132] concluded that in the whole pressure range of existence, the superconducting phase is an homogeneous phase. The interplay between superconductivity and the spin density wave has been recently carefully revisited in $(\text{TMTSF})_2\text{PF}_6$ [133]. At ambient pressure, $(\text{TMTSF})_2\text{PF}_6$ exhibits a phase transition towards a spin-density wave state with a critical temperature $T_{SDW} \approx 12\text{K}$. As pressure is increased, T_{SDW} decreases and falls down rapidly above $P=6\text{ kbar}$ [134]. For $P \geq 9\text{ kbar}$, superconducting features appear below 1.2K . The critical temperature remains more or less constant up to $P \geq P_c = 9.4\text{ kbar}$ where the SDW state disappears and at higher pressures, the superconducting critical temperature, T_c , decreases monotonically with increased pressure as shown in figure 20. For $P \geq 9.5\text{ kbar}$, superconductivity can be reasonably considered as homogeneous with a low temperature critical current density along the a -axis, $J_c = 200\text{ A.cm}^{-2}$. However, for $P \leq 9.4\text{ kbar}$, the critical current decreases by four orders of magnitude in less than 1 kbar while the critical temperature remains constant. This experimental observation is in favor of a phase coexistence of the SDW and SC states with a superconducting fraction of the sample increasing with pressure. In addition, Lee *et al.* [135] observed a strong enhancement of the upper critical field for $H//c$ as pressure is decreased below P_c , a phenomenon which was already noticed by Brusetti *et al.* [121] in $(\text{TMTSF})_2\text{AsF}_6$.

Similar features have also been observed in $(\text{TMTTF})_2\text{PF}_6$ [136] and $(\text{TMTTF})_2\text{BF}_4$ [137,138]. When the SDW state is present at high temperatures, the superconducting critical temperature remains more or less constant in these Fabre salts and the upper critical field is shown to be enhanced by a factor of nearly ten. Table 2 summarizes the upper critical field for $H//c$ in different quasi-1D organic superconductors and for different pressures. Similarly to $(\text{TMTSF})_2\text{PF}_6$, the critical current strongly increases with pressure, in $(\text{TMTTF})_2\text{BF}_4$, as shown in figure 21. For the lowest pressures, strong spikes in the dV/dI versus current characteristics are clearly visible. This is an apparent signature of filamentary

Table 2. Critical temperature and upper critical field of various quasi-1D organic superconductors for different pressures. h stands for homogeneous superconductivity (obtained at high pressures), i for inhomogeneous superconductivity in the phase coexistence regime. (*= US pressure scale).

| Compound | Pressure | Coexistence | T_c | $\mu_0 H_{c2} // c$ | Reference |
|--------------------------------|-----------|-------------|-------|---------------------|-----------|
| $(\text{TMTSF})_2\text{AsF}_6$ | 11 kbar | h | 1.2K | 0.15T | [121] |
| | 8.5 kbar | i | 1.1K | 0.35T | [121] |
| $(\text{TMTSF})_2\text{PF}_6$ | 10.5 kbar | h | 1.1K | 0.15T | [13] |
| | 5.5 kbar* | i | 1.1K | 1T | [135] |
| $(\text{TMTTF})_2\text{PF}_6$ | 61.4 kbar | h | 1.3K | 0.08 T | [141] |
| | 52.6 kbar | i | 2.0K | 0.57 T | [141] |
| | 47.3 kbar | i | 2.2K | 0.75 T | [141] |
| $(\text{TMTTF})_2\text{BF}_4$ | 38.5 kbar | i | 1.2K | 0.08 T | [142,143] |
| | 33.5 kbar | i | 1.1K | 2 T | [142,143] |

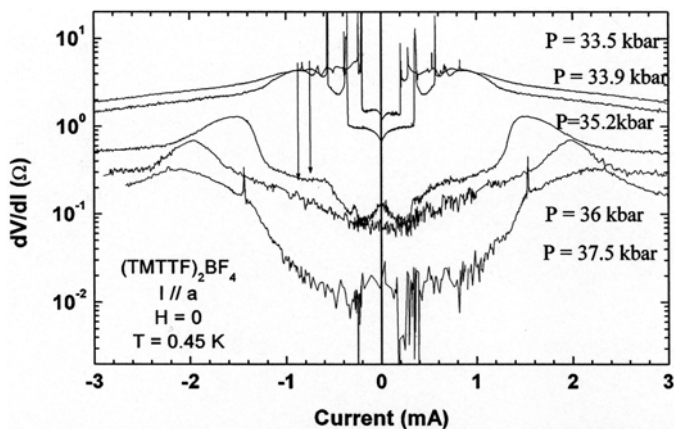


Fig. 21. dV/dI versus current characteristics as a function of pressure in $(\text{TMTTF})_2\text{BF}_4$. From [137].

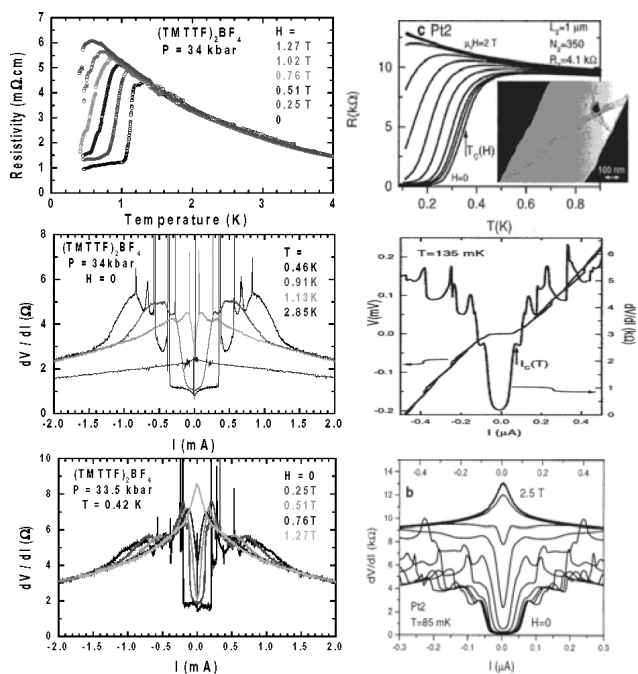


Fig. 22. Comparison of transport characteristics in $(\text{TMTTF})_2\text{BF}_4$ (left) from refs.137,138,142 and in SWNT ropes (right) from ref.140 as a function of temperature, magnetic field and applied current.

superconductivity as these observations are similar to previously reported data on Sn whiskers [139] and more recently in ropes of single wall carbon nanotubes (SWNT) [140]. Figure 22 presents a direct comparison of the different electrical characteristics of superconductivity in $(\text{TMTTF})_2\text{BF}_4$ and in SWNT ropes. The similarities are striking and the only difference is the zero field critical temperature which is three times larger in $(\text{TMTTF})_2\text{BF}_4$ than in SWNT ropes.

The interplay between superconductivity and an insulating state is a common feature in many strongly correlated electron systems. Among organic superconductors, a special attention has been focused on quasi-two dimensional organic superconductors of the κ -(BEDT-TTF) $_2$ X family. In these compounds, superconductivity competes with an antiferromagnetic phase and a Mott insulator state [144,145]. At low temperature, a quantitative determination of the superconducting fraction as a function of pressure has been obtained in κ -(BEDT-TTF) $_2$ Cu[N(CN) $_2$]Cl using NMR and AC susceptibility [144]. However, even at ambient pressure, this salt exhibits some traces of superconductivity as shown by all electrical transport measurements performed along the conducting planes [146]. This discrepancy may be explained by the fact that NMR probes only domains with sizes larger than the magnetic penetration depth. In α -(BEDT-TTF) $_2$ KHg(SCN) $_4$, superconductivity appears below a charge density wave state with a tendency for an increase of the onset critical temperature as pressure is lowered [147]. The tendency of evolution of the upper critical field as a function of pressure [148] is similar to the observations in $(\text{TMTSF})_2\text{PF}_6$. More recently, in the Mott insulator, β' -(BEDT-TTF) $_2$ ICl $_2$, superconducting features were shown to appear above *70kbar* with a critical temperature about *14.2K*, nearly constant up to *90kbar* while the high temperature insulating state disappears only above *82kbar* [149]. In inorganic materials, such phase competition involving superconductivity has also been observed in a wide range of compounds such as NbSe $_3$ [150], heavy fermions [151,152,153,154] and cuprates [155]. A more complete review can be found in ref. 156. However, in these systems and in the κ -(BEDT-TTF) $_2$ X superconductors, whenever sufficient data are available, a strong enhancement of the upper critical field is not observed to the best of our knowledge. Forgetting superconductivity, Metal-Insulator phase coexistence is a common feature in electronic systems. For example in cuprates [157] or valence mixed oxides such as V $_2$ O $_3$ [158], antiferromagnetism may coexist with metallic stripes. As far as organic materials are concerned, various states can coexist and the phenomenon has been often observed when charge ordering (CO) is present. For example, Spin-Peierls (SP)-charge ordering phase coexistence has been clearly identified in the Fabre salts [63] as shown in figure 11. Another important example is $(\text{TMTSF})_2\text{ReO}_4$ where different anion orderings are present, fig.18. The $(1/2,1/2,1/2)$ insulating anion ordering coexists under pressure with the $(0,1/2,1/2)$ metallic anion ordering as shown by X-ray diffraction [102]. Furthermore, at low temperatures, when the insulating order is suppressed, SDW-SC phase coexistence is also observed [103].

Various theoretical models have been developed in strongly correlated electron systems for the interplay between superconductivity or metal and antiferromagnetism. Such models range from microscopic models to Landau expansions. Microscopic models based on

the Coulomb-Coulomb interaction through the Mott-Hubbard Hamiltonian predict the formation of stripes where the different orders alternate. These stripes have been clearly observed in cuprates [157] and extensively studied in these materials and we therefore refer the reader to the chapters of the present book devoted to cuprates for detailed references and informations.

As far as superconductivity is concerned in the quasi-1D organic conductors, the existence of superconducting stripes between SDW domains at the microscopic scale is likely to be excluded as the observed non linear transport measurements suggest superconducting domain sizes of the order or larger than the coherence length which is much larger than a typical interchain distance (figure 21). More experiments would be useful to rule out completely this possibility. An other model to explain this phase coexistence is to consider that the phenomenon occurs in the real space. The model discussed in detail in ref. 133 explains most experimental features of SC-SDW (or metal-SDW) phase coexistence. This model is applicable to any second order phase transition and takes into account a phase A whose stability *versus* a phase B strongly depends on an extensive parameter u (in the thermodynamic sense) as shown in figure 23. Eventually, at low temperatures, the phase B can condense into an ordered phase C, but, for simplicity, we will skip this phase. If phase coexistence exists in a small range of parameter u larger than u_c , the fraction of phase B is denoted c and this part is characterized by a parameter $u=u_B$, the fraction of phase A is therefore $1-c$ and we have $u_A > u_c > u_B$ in these regions. In most cases, u is the volume and we will suppose that u is for example one of the lattice parameters. At the lowest order, when

phase coexistence occurs, the energy gain is given by $\left. \frac{\partial F_A}{\partial u} \right|_{\delta u_A}$ while the cost of elastic

energy is proportional to $(1-c)(\delta u_A)^2 + c(\delta u_B)^2$ where $\delta u_A = u_A - u$, $\delta u_B = u - u_B$ and F_A is the free energy of phase A as a function of u . As a result, if the phase transition is abrupt which means that F_A varies strongly enough with u , phase coexistence may occur even for a second order phase transition. The introduction of the third phase C does not change the conclusion [133]. These simple predictions explain the observed phase coexistence in organic superconductors : when superconductivity is involved, the phase A is the SDW phase, phase B is the metallic phase and phase C the superconducting phase and the driving parameter is the b lattice parameter which decreases with increasing pressure and controls the unnesting of the Fermi surface. This model may be extended to the CO-SP transition where phase A is the charge ordered phase, phase B is again the metallic phase and phase C the spin-Peierls phase [159]. The driving parameter is now the a lattice parameter which also decreases with increasing pressure and controls the interaction along the conducting chains so the charge disproportionation. In both cases, the experimentally determined critical temperature for phase C (SC or SP) is experimentally shown to be nearly constant when phase coexistence occurs for the ordered phases. Anion ordering coexistence might be understood also in the framework of this model. This simple model also predicts the shape of the domains to be slabs or stripes of width which depends on the applied pressure : the sample is formed of slabs with alternating parameters u_A and u_B . A more complete model would require taking into account the interface energy between the domains of different order parameters. However, various domain topologies can be expected [160] and filamentary superconductivity is therefore plausible at low concentrations of metal or superconductivity.

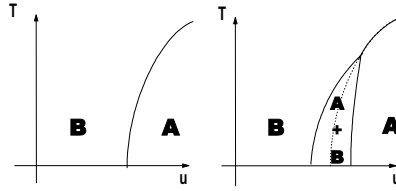


Fig. 23. Left : generic phase diagram for the competition of two phases A and B. The phase transition is supposed to be of second order. Right: the real phase diagram showing the phase coexistence. (Adapted from ref. 133).

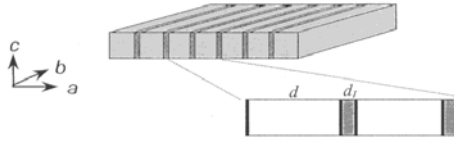


Fig. 24. Slab arrangement of superconducting and insulating (SDW) sandwiches for $H//c$. From [162].

Around u_c , the slab geometry is the most plausible and has been detailed by Lee *et al.* [135,161,162] (figure 24). The authors consider that slabs of alternating SDW and SC orders appear parallel to the applied magnetic field. Upon increasing magnetic field, the reduction of the critical temperature, T_c is due to the energy cost of the introduction of interfaces between the SC and SDW phases and screening currents. The formation of slabs is characterized by slab thicknesses d and d_i of the SC and SDW slabs respectively, the surface tension, γ and the magnetic penetration depth, λ . The deduced form of the upper critical field as a function of the critical temperature T_c is :

$$H_{c2} \propto \frac{\lambda}{\gamma} (T_c - T_{c0})^{3/2} \quad (6)$$

where T_{c0} is the zero field critical temperature. The authors effectively observe the $T^{3/2}$ dependence for $H//a$ or $H//b$ but a T^2 dependence for $H//c$. This model explains in a very simple way the observed divergence of the upper critical field.

On the other hand, the strong enhancement of the upper critical field can be understood as we deal with anisotropic type II superconductors. In a strongly anisotropic quasi-2D superconductor, when the field is applied parallel to the superconducting planes, the upper critical field is strongly enhanced. Usually, in the inorganic high T_c superconductors, the out of plane coherence length is about 0.05 nm while the interlayer distance is about 1.2 to 1.5 nm depending on the different compounds so that a high- T_c superconductors can be understood as a Superconductor-Insulator-Superconductor (SIS) stack. Similar values are observed in the quasi-2D organic superconductors of the κ -(BEDT-TTF) $_2$ X family and these compounds can be understood as SIS stacks also [163]. The advantage of both quasi-1D and quasi-2D organic superconductors is that the upper critical field is reachable

experimentally in all crystallographic directions [164,119,161]. For instance, in κ -(BEDT-TTF)₂I₃, the upper critical field when the field is applied perpendicular to the plane is about $0.2 T$ and the upper critical field when the field is applied parallel to the superconducting layers is about $8 T$ [165]. These values are quite similar to the measured values in (TMTSF)₂PF₆ [164,119,161] except the critical temperature which is about $4K$ in the BEDT salt. However, the measurements of the upper critical field for $H//a$ or $H//b'$ in (TMTSF)₂PF₆ are always performed in a region of pressure so close to the critical pressure that the enhancement of the upper critical field may be connected to this phase coexistence [161]. This is a real possibility as their measured upper critical field for $H//c$ is much larger than the expected $0.1-0.15T$ for homogeneous superconductivity [166,164]. On the other hand, in the sister compound (TMTSF)₂ClO₄, the large value of the upper critical field for $H//b'$ is not associated with an upward curvature of the upper critical field line except at ultra low temperatures [166]. The enhancement of the upper critical field observed in all quasi-1D organic superconductors for $H//c$ when the pressure is decreased may then be attributed to a partial or a full penetration of the magnetic field in the insulating (SDW) regions of the sample. Indeed, the magnetic field will penetrate partly in the superconducting regions creating usual Abrikosov vortices and also in the SDW regions in which vortices like Josephson vortices [167] may appear. As penetration of the field is favored in the insulating regions, the effective magnetic field which penetrates the superconducting regions is reduced so the observed upper critical field is enhanced. As pressure is further decreased, the size of the SC domains can reach the coherence length as shown in (TMTTF)₂BF₄ (fig. 21) and the magnetic field will fully penetrate the insulating regions and the upper critical field might be about its value for an homogeneous superconductor with $H//a$ or $H//b$. In a certain way, decreasing the pressure in a sample at the SDW-SC border (so decreasing the SC fraction of the sample) is equivalent to rotate the strongly anisotropic homogeneous superconductor in a magnetic field from the situation $H//c$ to the aligned situation where $H//a$ or $H//b$.

2.6 Peculiarities of the superconducting coupling

2.6.1 Pairing symmetry

Very little is still known experimentally regarding the symmetry of the superconducting pairing in 1D organic superconductors. An early theoretical work of Abrikosov [168] performed within the self consistent approximation has concluded that both scenarios could be envisaged for quasi one dimensional (Q-1D) conductors namely, singlet or triplet spin pairing depending on the properties of the electron-electron interaction. It was also anticipated that the stability of the triplet state would be very sensitive to the presence of non magnetic impurities. An other approach based on the exchange of antiferromagnetic fluctuations between neighbouring chains has led to an exotic d -like pairing [169]. This model is singlet in the spin sector and leads to a superconducting gap which exhibits a sign reversal along the open Fermi surface of these Q-1D conductors. Experiments available up today are unable to settle without ambiguity the question of the pairing symmetry in organic superconductors. Key experiments are uncomplete. Among those experiments we can cite the determination of the Knight shift below the critical temperature and a possible existence of a Hebel-Slichter(HS) coherence peak, the crossing or not of the Pauli limit for special alignment of the

Table 3. Characteristics of superconductivity of two members of the κ -(BEDT-TTF)₂X family. $\mu_0 H_{c2\perp}$ denotes the extrapolated upper critical field at $T=0$ when the magnetic field is applied perpendicular to the conducting planes. $\mu_0 H_{c2\parallel}$ denotes the extrapolated upper critical field when the magnetic field is applied parallel to these conducting planes.(*: the transition to zero resistivity is called the melting line and lies in the superconducting state but confusion between the two definitions is made sometimes)

| | Br | NCS |
|---|--|--|
| T_c | 11.6 K | 9.4 K |
| $\mu_0 H_{c2\perp}$ | 10 T [170] | 5.2 T [171] |
| $\mu_0 H_{c2\parallel}$ (resistivity kink) | 40 T ? [172,173] | 35 T [173,174,175] |
| $\mu_0 H_{c2\parallel}$ (zero resistivity)* | > 28 T [172] | 26 T [175] |
| $\mu_0 H_p^{BCS}$ | 21.3 T | 17.3 T |
| NMR Knight shift | Singlet SC [170, 176] | |
| NMR $1/T_1$ | T^3 law [170,176,177] | |
| Specific heat (C_v/T) | T^2 law [178] Exponential [179] | Exponential [179,180] |
| Thermal conductivity | | Power law [181,182] |
| Tunnelling | | [183] (nodes) |
| Penetration depth | Power law [184,185,186] Exponential [189] | Power law [184,185,187,188] Exponential [190,191] |

magnetic field with respect to the crystallographic axes or the low temperature variation of various quantities such as thermal conductivity, specific heat and penetration depth. Among organic superconductors, two families have attracted most interest : on the one hand, the genuine Bechgaard salt (TMTSF)₂PF₆ and the R-state of (TMTSF)₂ClO₄ and on the other hand the strongly two dimensional κ -(BEDT-TTF)₂X family (for a recent review, see ref. 34,35). Before discussing in large details, the pairing symmetry of the quasi-1D organic systems, it is important to list some characteristics of the 2D organic superconductors which have been intensively studied since it may in turn imply important remarks on the experimental data in the quasi-1D organic superconductors. Table 3 summarizes what is known in this family for the most studied members of the family : κ -(BEDT-TTF)₂Cu[N(CN)₂]Br (Br in short) and κ -(BEDT-TTF)₂Cu(NCS)₂ (NCS in short).

At first sight, all these results seem incompatible as the upper critical field for a magnetic field applied parallel to the planes is twice the Pauli (or Clogston-Shandrasekhar [192,193]) paramagnetic limit and implies necessarily a spin-triplet pairing. Such observations have been confirmed in κ -(BEDT-TTF)₂Cu[N(CN)₂]Cl under pressure [194]. This is in contradiction with all the NMR measurements performed by many groups which supports a spin-singlet superconductivity. On the other hand, the question of the presence or the absence of nodes in the superconducting gap remains open but recent penetration depth measurements may reconcile all groups [195] as the disorder induced by the terminal ethylene

groups of the BEDT - TTF molecules might induce additional density of states at low energy. However, the data can be compatible if the Pauli limit is reestimated. Indeed, the critical field, H_P which gives the Pauli limit is given by [192] :

$$U_c = \frac{\mu_0}{2} \chi_e H_P^2 \quad (7)$$

where U_c is the superconducting condensation energy density and χ_e is the finite metallic Pauli spin susceptibility. Using the standard BCS theory in the weak coupling limit, this leads to the well-known formula :

$$\mu_0 H_P = \mu_0 H_P^{BCS} = 1.84 k_B T_c \quad (8)$$

Including strong coupling effects [196] or changing the symmetry of the order parameter from s to d-wave pairing [197] does not change strongly the factor 1.84 and cannot explain the observed 3.7 prefactor. On the other hand, many-body effects can renormalize the mass of the carriers and enhance the value of H_P [196]. Zeeman splitting may also be taken into account and the value of g affects also the Pauli limit. In the BEDT - TTF salts, Zuo *et al.* [175] take another point of view and consider a theory-independent model and determine H_P from experimental data using equ.7. They obtained $\mu_0 H_P = 30 \pm 5 T$ which is in fair agreement with the experimental data. An alternative explanation is to consider an inhomogeneous superconductivity and the existence of a Fulde-Ferrell-Larkin-Ovchinnikov (FFLO) [198,199] state at high fields [174,34].

We now go back to the quasi 1D organic superconductors $(TMTSF)_2PF_6$ and $(TMTSF)_2ClO_4$. Table 4 summarizes the available data.

In these two Bechgaard salts, the amount of experimental results is rather limited and furthermore experiments have often been carried out by a single group only. Here again, the Pauli limit is much less than the upper critical field along the a or b' directions. Forgetting about models for a while we can perform the same estimate as in the BEDT - TTF salts :

Table 4. Characteristics of superconductivity of $(TMTSF)_2PF_6$ at 9.5kbar and $(TMTSF)_2ClO_4$ at ambient pressure. $\mu_0 H_{c2d}$ denotes the upper critical field when the magnetic field is applied along the direction d . The values of the upper critical fields correspond to the 'kink' of the transition.

| | $(TMTSF)_2PF_6$ @ 9.5kbar | $(TMTSF)_2ClO_4$ @ 1 bar |
|-------------------------|---------------------------|--------------------------|
| T_c | 0.9 K | 1.2 K |
| $\mu_0 H_{c2c}$ | 0.2 T [13] | 0.16 T [111] |
| $\mu_0 H_{c2b'}$ | 7 T ? [164] | 4-5 T [116,117,166,120] |
| $\mu_0 H_{c2a}$ | 5 T ? [164] | 0.25 T [116,117] |
| $\mu_0 H_P^{BCS}$ | 1.8 T | 2.2 T |
| NMR Knight shift | Triplet SC [200] | |
| NMR $1/T_1$ | | T^3 law [201] |
| Specific heat (C_v) | | nodeless [110] |
| Thermal conductivity | | nodeless [123] |
| Tunnelling | [202] | [203] |
| Penetration depth | | |

using the thermodynamical critical field determined through specific heat measurements [110]: $H_{th} = 44Oe$ and assuming that H_{th} is the same in the PF_6 and in the ClO_4 salt (a plausible assumption), using the spin susceptibility $\chi_e = 1.43emu\ mol^{-1}$ [200], we get $\mu_0 H_p \cong 2.4T$ with a large error bar but it still remains somewhat larger than the BCS value given in table 4. We can first notice that the obtained value is much closer to the BCS value than in the κ -(BEDT-TTF)₂X salts and that all experimental determinations of the superconducting gap through specific heat, thermal conductivity or tunnelling [110,123,202,203] lead to the ratio $2\Delta(0)/k_B T_c \approx 2.1 \pm 0.3$.

We first discuss the case of $(TMTSF)_2PF_6$. The fact that the NMR Knight shift (or spin susceptibility) shows no variation below the critical temperature¹ and that the upper critical fields for $H//a$ or $H//b'$ are far above the Pauli limit have been taken as a strong support in favor of a triplet pairing in the quasi-1D organic superconductors. However, this is not so simple as it might be. In particular, in Sr_2RuO_4 (for a review, see ref. 204) where triplet superconductivity seems plausible also from NMR Knight shift data, the upper critical field, when the field is applied parallel to the superconducting planes, is still far below the Pauli limit. On the other hand, as shown before in the κ -(BEDT-TTF)₂X salts, an upper critical field above the BCS Pauli limit is not the signature of triplet superconductivity. So both conditions are not necessary to support triplet superconductivity. Moreover, in 1D organic superconductors, the upper critical field for $H//a$ or $H//b'$ has always been determined through resistivity criteria until recently [120]. However, for these field orientations, the 'normal' state above typically $1T$ is no longer metallic but insulating [166,164]. So, for these particular field orientations (but may be for other field directions as well), there is a metal-insulator-superconductor 'imbroglio' in the magnetic field-temperature phase diagram which looks like the pressure-temperature phase diagram near the SDW-metal transition at zero field. In this sense, the possibility of insulator-superconductor (metal) phase coexistence should not be excluded : the magnetic field would be now the experimental driving parameter

¹ NMR Knight shift data coupled with resistance measurements obtained in ref. 200 had been taken as strong arguments in favour of triplet SC in $(TMTSF)_2PF_6$. To be sure that the injected energy by the rf pulses is not enough to drive the sample into the normal state, the authors measured the time relaxation of the resistance at a time $t > 1msecond$ and extrapolated the value of the resistance back to $t=0$ allowing an evaluation of the sample temperature. One strong criticism that might be highlighted is that the 'dead time' of about $1msecond$ is much larger than the NMR time scale measurement ($\approx 50\mu seconds$) and can be large enough for the sample to relax from the normal state back to the superconducting state after the heat pulse. To check this point, non-linear resistivity measurements have been performed and even with short pulse length, the resistive superconducting transition can be observed during the pulse together with a rapid relaxation [143]. Therefore, the results of ref. 200 would have been more convincing if the sample resistance had been measured simultaneous to the rf pulses which means a time resolution for the resistance measurement better than $1\mu second$ as the sample may relax very rapidly. However, the question still remains open as thermalisation may strongly vary from one experiment to another. As also mentioned by thermal conductivity data [123], the phonon mean free path is quite large at low temperatures and even with a weak electron-phonon interaction, a fast thermal equilibrium of the electrons can be achieved.

and would also explain the divergence (at least the upward curvature) of the upper critical field using the slab geometry model developed by Lee *et al.* [135]. Similar to the phase coexistence already discussed, the effective magnetic field seen by the superconducting regions could be much lower than the applied field. This possibility has also been extensively discussed in the framework of the FFLO model to explain the possibility of reentrant superconductivity for fields larger than the paramagnetic (Pauli) limit [205,206]. An alternative or complementary explanation of the divergence of the upper critical field is that the temperature of the 'resistance peak' observed in resistance versus temperature measurements is no longer the superconducting critical temperature but an insulator-metal critical temperature as the mean free path for the electrons may increase at low temperatures in these ultra-pure materials that are the quasi-1D organic superconductors. Such metal-insulator-metal transitions have been already observed in clean 2D electron gas at the metal-insulator border in such a low temperature range [207,208,209]. In our 1D materials, the origin of this insulating phase is still a mystery and understanding of this phase still a challenge in this field.

As far as $(\text{TMTSF})_2\text{ClO}_4$ is concerned, the situation appears no more clear. The specific heat data [110] can be fully analyzed in the framework of a fully developed gap. The thermal conductivity data [123] are also not compatible with a gap function vanishing on any point of the Fermi surface. However, NMR relaxation measurements performed down to $T_c/2$ by Takigawa *et al.* [201] suggested the existence of nodes. It can be argued that the observed power law in this temperature range may be not enough to conclude for the existence of nodes in the superconducting gap.

However, a nodeless gap is not necessarily associated to *s*-wave superconductivity and Hasegawa and Fukuyama [210,211] showed that a pseudo-triplet gap with no nodes is possible. On the other hand, the divergence of the upper critical field for $H//b'$ is not fully understood and ideas developed for $(\text{TMTSF})_2\text{PF}_6$ may also be pertinent. The main difference between the two salts namely the possibility for the existence of nodes in the PF_6 salt and their absence in ClO_4 could be related to the anion ordering of the latter salt at 24K [212,213]. This anion ordering doubles the unit cell along the *b* direction so modifies the Fermi surface and in turn replaces the two-sheets Fermi surface by a four-sheets surface.

The quantum states of the partners entering into the formation of a Cooper pair of a BCS *s*-wave superconductor are related to each other by a time reversal symmetry. Hence no pair breaking is expected from the scattering of electrons against spinless impurities [216]. Experimentally, this property has been verified in non-magnetic dilute alloys of *s*-wave superconductors and brought a strong support for the BCS model of conventional *s*-wave superconductors. However, the condition for time reversal symmetry is no longer met for the case of *p*-wave pairing and consequently T_c for these superconductors should be strongly affected by even a small amount of such non-magnetic scattering. It is the extreme dependence of the critical temperature of Sr_2RuO_4 [204] on non-magnetic disorder which has provided besides Knight shift data a strong support in favour of triplet superconductivity in this compound.

2.6.2 Superconductivity and non-magnetic defects

The remarkable sensitivity of organic superconductivity to irradiation [215,216] has led Abrikosov to suggest the possibility of triplet pairing in these materials [168]. Although irradiation was recognized to be an excellent method for the introduction of defects in a controlled way [217], defects thus created can be magnetic [218] and the suppression of superconductivity by irradiation induced defects as a signature of non-conventional pairing must be taken with "a grain of salt" since local magnetic moments can also act as strong pair-breakers on *s*-wave superconductors. Several routes have been followed to introduce an intrinsically non-magnetic perturbation modulating the potential seen by the carriers on the organic stacks. Substituting TMTSF for TMTTF on the cationic stacks of (TM)₂X salts non disorder has been achieved with PF₆ [43] and ClO₄ salts [219]. However in both situations cationic alloying induces drastic modification of the normal state electronic properties since the SDW transition of (TMTSF)₂PF₆ is quickly broadened and pushed towards higher temperature upon alloying [220].

Leaving the cation stack uniform, scattering centers can also be created on the anion stacks with the solid solution (TMTSF)₂(ClO₄)_(1-x)(ReO₄)_x where Tomi *et al.* first mentioned the suppression of superconductivity upon alloying with a very small concentration of ReO₄ anions [221]. In the case of a solid solution with tetrahedral anions such as ClO₄ or ReO₄ one is confronted to two potential sources of non-magnetic disorder which act additively on the elastic electronic lifetime according to the Mathiessen's law. First the modulation due to the different chemical natures of the anions and second a disorder due to a progressive loss of long range ordering at T_{AO} in the (TMTSF)₂(ClO₄)_(1-x)(ReO₄)_x solid solution although X-ray investigations have revealed that long range order is preserved up to 3% ReO₄ with a correlation length $\xi_a > 200 \text{ \AA}$ [222]. Studies of superconductivity in (TMTSF)₂(ClO₄)_(1-x)(ReO₄)_x conducted under extremely slow cooling conditions have shown that T_c is a fast decreasing function of the non-magnetic disorder [91] where the residual resistivity along the c^* axis has been used for the measure of the disorder in the alloys with different concentrations, figure 25. The suppression of T_c must be related to the enhancement of the scattering rate in the solid solution. Since the additional scattering cannot be ascribed to magnetic scattering according to the EPR checks showing no additional traces of localized spins in the solid solution the data in figure 25 cannot be reconciled with the picture of a superconducting gap keeping a constant sign over the whole $\pm k_F$ Fermi surface. They require a picture of pair breaking in a superconductor with an unconventional gap symmetry. The conventional pair breaking theory for magnetic impurities in usual superconductors has been generalized to the case of non-magnetic impurities in unconventional materials and T_c reads [223,199],

$$\ln\left(\frac{T_{c0}}{T_c}\right) = \Psi\left(\frac{1}{2} + \frac{\alpha T_{c0}}{2\pi T_c}\right) - \Psi\left(\frac{1}{2}\right) \quad (9)$$

with Ψ being the digamma function, $\alpha = \hbar/2\tau k_B T_{c0}$ the depairing parameter, τ the elastic scattering time and T_{c0} the limit of T_c in the absence of any scattering. From the data in figure 25, the best fit leads to $T_{c0} = 1.22 K$ and a critical scattering for the suppression of

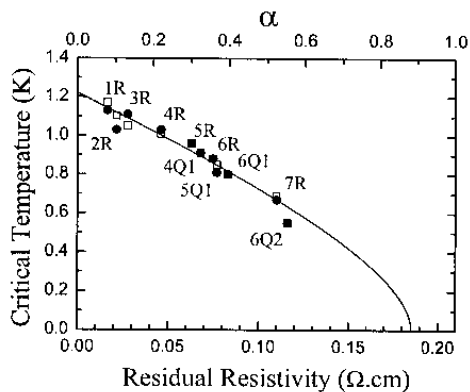


Fig. 25. Superconducting critical temperature as a function of the residual resistivity for samples with different amounts of disorder either chemical (nR) or orientational (nQ) [91]. The solid line is a least square fit of the digamma pair-breaking function to the data which reaches zero at $\alpha = 0.88$.

superconductivity of $1/\tau_{cr} = 1.44 \text{ cm}^{-1}$, $\tau_{cr} = 3.5 \text{ ps}$ (following the definition of α). Accordingly, $1/\tau$ amounts to 0.13 cm^{-1} ($\tau = 40 \text{ ps}$) in the pristine $(\text{TMTSF})_2\text{ClO}_4$ sample. The sensitivity of T_c to non-magnetic disorder cannot be reconciled with a model of conventional superconductors. The gap must show regions of positive and negative signs on the Fermi surface which can be averaged out by a finite electron lifetime due to elastic scattering. As these defects are local the scattering momentum of order $2k_F$ can mix + and - k_F states and therefore the sensitivity to non-magnetic scattering is still unable to tell the difference between p or d orbital symmetry for the superconducting wave function. A noticeable progress could be achieved paying attention to the spin part of the wave function. In the close vicinity of T_c orbital limitation for the critical field is expected to prevail and therefore the analysis of the critical fields close to T_c [118] not necessarily implies a triplet pairing. When the magnetic field is oriented along the intermediate b -axis, violations of the Pauli limitation have been claimed in the $(\text{TMTSF})_2\text{PF}_6$ [119] and recently $(\text{TMTSF})_2\text{ClO}_4$ [120] superconductors. However, it must be kept in mind that in all these experiments performed under transverse magnetic field the electronic structure is profoundly affected by the application of the field (as an electron localization is observed at low temperature) and it is still unclear whether the superconducting phase remains homogeneous under strong transverse field. Older data in $(\text{TMTSF})_2\text{ClO}_4$ [117] are not in contradiction with the picture of singlet pairing but no data were given below 0.5 K , the temperature domain where it would be most rewarding to see how H_{c2} compares with the Pauli limit when H is perfectly aligned along the a axis.

3. CONCLUDING REMARKS

Organic superconductivity in quasi-one dimensional Bechgaard salts belonging to the large class of $(\text{TM})_2\text{X}$ compounds is a direct outcome of the constant quest for superconducting materials at high temperatures. Although the critical temperature of one dimensional organic superconductors is still fairly modest in the one Kelvin range, these materials have provided a wealth of new physical phenomena. One dimensionality of the electronic spectrum is a common feature to all conductors of the $(\text{TM})_2\text{X}$ series as shown by anisotropic optical and transport properties. Furthermore, the one dimensionality together with electron-electron Coulombic interactions are responsible for the Mott localization observed at high temperature. This is due to the Umklapp scattering of the electrons in a quarter filled-band conductor. Such an electron localization can be suppressed in the $(\text{TM})_2\text{X}$ series via the enhancement of the interchain overlap either chemically in different compounds or by the application of an hydrostatic pressure giving a way to a metallic state and in turn to superconductivity at low temperature. In addition, the metallic phase is characterized by the unsuitability of the classical Drude model to explain the very peculiar behaviour of the frequency dependent conduction with a narrow zero frequency mode which is observed in a far infrared pseudogap. Organic superconductivity is certainly non conventional with sign changes of the gap over the Fermi surface as required by the unusually large sensitivity of the superconducting state to non magnetic defects. However, a final answer discriminating between p -triplet and d -singlet pairings should await more experimental studies. In addition, the $(\text{TM})_2\text{X}$ family shows a clear case of phase coexistence at the border between insulating-itinerant antiferromagnetic and superconducting ground states. Organic conductors gather most of the relevant problems in modern condensed matter physics. This 25 years old subject still holds a very promising future.

4. ACKNOWLEDGMENTS

This article is the opportunity to acknowledge the cooperation of our co-workers at Orsay, P.Auban-Senzier, P.Wzietek, and all visitors including post docs and students who have stayed in the Orsay laboratory. We also wish to acknowledge the cooperation with the groups at Copenhagen (K.Bechgaard), Montpellier (J.M.Fabre and students) and Angers (P.Batail and colleagues) who have contributed to the development of the physics and chemistry of 1D organic superconductors. This work has greatly benefited from a close cooperation with the theory group at Orsay : T.Giamarchi, M.Héritier and also C.Bourbonnais at Sherbrooke, Canada.

REFERENCES

- [1] H.K. Onnes, Proc. Akad. Wetenschappen 11 (1911) 113
- [2] J.Bednorz and K.A.Müller, Z. Phys. B 64 (1986) 189
- [3] F.London, Jour. of Chem. Phys. 5 (1937) 837
- [4] H.Akamatsu, H.Inokuchi and Y.Matsunaga, Nature 173 (1954) 168
- [5] W.A.Little, Phys. Rev. A 134 (1964) 1416
- [6] W.A.Little, Scientific American 212 (1965) 21
- [7] J.Bardeen, L.N.Cooper and J.R.Schrieffer, Phys. Rev. 108 (1957) 1175
- [8] V.L.Ginzburg, J. Polymer Sci. C 29 (1970) 3
- [9] W.A.Little, J.Polymer Sci. C 29 (1970) 17
- [10] L.B.Coleman, Solid State Comm. 12 (1973) 1125
- [11] J.Ferraris, D.O.Cowan, W.Walatka, and J.H.Pearlstein, J. Am. Chem. Soc. 95 (1973) 948
- [12] D.Jérome and H.J.Schulz, Adv. In Physics 31 (1982) 299
- [13] D.Jérome, A.Mazaud, M.Ribault, and K.Bechgaard, J. Phys. Lett. (Paris) 41 (1980) L45
- [14] J.R.Andersen, K.Bechgaard, C.S.Jacobsen, G.Rindorf, H.Soling, and N.Thorup, Acta Cryst.B 34 (1978) 1901
- [15] C.S.Jacobsen, K.Mortensen, J.R.Andersen, and K.Bechgaard, Phys. Rev. B 18 (1978) 905
- [16] J.P.Pouget, Chemica Scripta 55 (1981) 85
- [17] Y.Tomkiewicz, J.R.Andersen and A.R.Taranko, Phys. Rev. B 17 (1978) 1579
- [18] A.Andrieux, C.Duroire, D.Jérome, and K.Bechgaard, J. Phys. Lett. (Paris) 40 (1979) L381
- [19] A.Andrieux, P.M.Chaikin, C.Duroire, and D.Jérome, J.Phys. (Paris) 40 (1979) 1199
- [20] G.Brun, S.Peytavin, B.Liautard, E.Toreilles, M.Maurin, J.M.Fabre, and L.Giral, C. R. Acad. Sc. (Paris) 284C (1977) 211
- [21] T.Mori, A.Kobayashi, Y.Sasaki, H.Kobayashi, G.Saito, and H.Inokuchi, Chem. Lett. 1984 (1984) 957
- [22] E.B.Yagubskii, I.F.Shegolev, V.N.Laukhin, P.N.Kononovich, M.V.Kartsovnik, A.V.Zvarykina, and L.I.Buravov, JETP Lett. 39 (1984) 12
- [23] V.N.Laukhin, E.Kostyvchenko, Y.V.Sushko, I.F.Shegolev, and E.B.Yagubskii, JETP Lett. 41 (1985) 81
- [24] K.Murata, L.Brossard, R.C.Lacoe, M.Ribault, D.Jérome, K.Bechgaard, and A.Moradpour, Mol. Cryst. Liq. Cryst. 119 (1985) 245
- [25] G.Creuzet, J.R.Cooper, F.Creuzet, D.Jérome, and A.Moradpour, J. Phys. Lett. (Paris) 46 (1985) L1133
- [26] T.J.Emge, P.C.W.Leung, M.A.Beno, A.J.Schultz, H.H.Wang, L.M.Sowa, and J.M.Williams, Phys. Rev. B 30 (1984) 6780
- [27] W.Kang, D.Jérome, C.Lenoir, and P.Batail, Synth. Metals 27 (1988) A353
- [28] W.Kang, G.Montambaux, J.R.Cooper, D.Jérome, P.Batail, and C.Lenoir, Phys. Rev. Lett. 62 (1989) 2559
- [29] A.Kobayashi, R.Kato, H.Kobayashi, S.Moriyama, Y.Nishino, H.Kajita, and W.Sasaki, Chem. Lett. 1987 (1987) 459

- [30] H.Urayama, H.Yamochi, G.Saito, S.Sato, A.Kawamoto, J.Tanaka, T.Mori, Y.Mruyama, and H.Inokuchi, *Chem. Lett.* 1988 (1988) 463
- [31] J.M.Williams, A.M.Kini, H.H.Wang, K.D.Carlson, U.Geiser, L.K.Montgomery, G.J.Pyrka, D.M.Watkins, J.M.Kommers, S.J.Boryschuk, A.V.Strieby-Crouch, W.K.Kwok, J.E.Schirber, D.L.Overmeyer, D.Jung, and M.-H.Whangbo, *Inorg. Chem.* 29 (1990) 3272
- [32] T.Ishiguro, K.Yamaji, and G.Saito, *Organic Superconductors*, Springer Verlag, Berlin (1998)
- [33] J.Wosnitzer, *Fermi Surfaces of Low Dimensional Organic Metals and Superconductors*, Springer Verlag Berlin (1996)
- [34] J.Singleton and C.Mielke, cond-mat/0202442
- [35] M.Lang and J.Müller, cond-mat/0302157
- [36] K.Bechgaard, C.S.Jacobsen, K.Mortensen, H.J.Pedersen, and N.Thorup, *Solid State Comm.* 33 (1979) 1119
- [37] J.P.Pouget and S.Ravy, *Synth. Metals* 85 (1997) 1523
- [38] A.W.Overhauser, *Phys. Rev. Lett.* 9 (1960) 462
- [39] W.M. Lomer, *Proc. Phys. Soc.* 80 (1962) 489
- [40] L.Balicas, K.Behnia, W.Kang, E.Canadell, M.Ribault, P.Auban-Senzier, D.Jérome, and J.M.Fabre, *J.Phys. I (France)* 4 (1994) 1539
- [41] S.S.Parkin, M.Ribault, D.Jérome and K.Bechgaard, *J.Phys. C* 14 (1981) L445
- [42] K.Bechgaard, M.Carneiro, M.Olsen, and F.B.Rasmussen, *Phys. Rev. Lett.* 46 (1981) 852
- [43] C.Coulon, P.Delhaes, S.Flandrois, R.Lagnier, E.Bonjour, and J.M.Fabre, *J.Phys. (France)* 43 (1982) 1059
- [44] D.Jérome, *Science* 252 (1991) 1509
- [45] J.Friedel and D.Jérome, *Contemp. Phys.* 23 (1982) 583
- [46] L.Ducasse, A.Abderraba, J.Hoarau, M.Pesquer, B.Gallois, and J.Gaultier, *J. Phys. C* 39 (1986) 3805
- [47] For more references on the ground states of the insulating compounds, see articles in [222]
- [48] C.Bourbonnais and D.Jérome, *Advances in Synthetic Metals*, (Eds P.Bernier, S.Lefrant and G.Bidan), Elsevier, (1999), pp. 206
- [49] T.Giamarchi, *Quantum Physics in One-Dimension*, Clarendon Press, Oxford (2004)
- [50] H.J.Schulz, *Phys. Rev. Lett.* 64 (1990) 2831
- [51] J.Voit, *Rep. Prog. Phys.* 58 (1995) 977
- [52] J.Solyom, *Adv. Phys.* 28 (1979) 201
- [53] T.Giamarchi, *Physica B* 230-232 (1997) 975
- [54] V.J.Emery, *J. Phys. (Paris) Coll.* 44 (1983) C3-977
- [55] C.S.Jacobsen, D.B.Tanner, and K.Bechgaard, *Phys. Rev. Lett.* 46 (1981) 1142
- [56] C.S.Jacobsen, D.B.Tanner, and K.Bechgaard, *Phys. Rev. B* 28 (1983) 7019
- [57] C.S.Jacobsen, *Low Dimensional Conductors and Superconductors*, (Eds D.Jérome and L.G.Caron), Plenum Press, New York (1987)
- [58] V.Vescoli, L.Degiorgi, W.Henderson, G.Grüner, K.P.Starkey, and L.K.Montgomery, *Science* 281 (1998) 1181
- [59] C.Coulon, S.S.Parkin, and R.Laversanne, *Phys. Rev. B* 31 (1985) 3583
- [60] H.H.S.Javadi, R.Laversanne, and A.J.Epstein, *Phys. Rev. B* 37 (1988) 4280

- [61] R.Laversanne, C.Coulon, B.Gallois, J.P.Pouget, and R.Moret, *J.Phys. Lett. (Paris)* 45 (1984) L393
- [62] D.S.Chow, F.Zamborsky, B.Alavi, D.J.Tantillo, A.Baur, C.A.Merli, and S.E.Brown, *Phys. Rev. Lett.* 85 (2000) 1698
- [63] F.Zamborsky, W.Yu, W.Raas, S.E.Brown, B.Alavic, C.A.Merli, A.Baur, S.Lefebvre, and P.Wzietek, *J.Phys. IV (France)* 12 (2002) Pr9-139
- [64] F.Nad, P.Monceau, and J.M.Fabre, *J.Phys. IV (France)* 9 (1999) Pr10-361
- [65] F.Nad and P.Monceau, *J.Phys. IV (France)* 12 (2002) Pr9-133
- [66] J.P.Pouget and S.Ravy, *J.Phys. I (France)* 6 (1996) 1501
- [67] P.Auban-Senzier, D.J erome, C.Carcel, and J.M.Fabre, *J.Phys. IV (France)* 114 (2004) 41
- [68] J.E.Hirsch and D.J.Scalapino, *Phys. Rev. B* 27 (1983) 7169
- [69] H.Seo and H.Fukuyama, *J. Phys. Soc. Jpn.* 66 (1997) 1249
- [70] S.Brazovskii, *J.Phys. IV (France)* 12 (2002) Pr9-149
- [71] H.Seo, M.Kuwabara, and M.Ogata, *J.Phys. IV (France)* 12 (2002) Pr9-205
- [72] J.Moser, M.Gabay, P.Auban-Senzier, D.J erome, K.Bechgaard, and J.M.Fabre, *Eur. Phys. J. B* 1 (1998) 39
- [73] N.F.Mott, *Metal-Insulator Transitions*, Taylor and Francis, London (1974)
- [74] P.W.Anderson, *The Theory of Superconductivity in the High T_c Cuprates*, Princeton Univ. Press (1997)
- [75] T.Valla, P.D.Johnson, Z.Yusof, B.Wells, W.Li, S.M.Loureiro, R.J.Cava, M.Mikami, Y.Mori, M.Yoshimura, and T.Sasaki, *Nature* 417 (2002) 627
- [76] N.E. Hussey, M.N. Mc Brien, L. Balicas, J.S. Brooks, S. Horii, and H. Ikuta, *Phys.Rev. Lett.* 89 (2002) 086601
- [77] M.Weger, *J. Phys. (Paris)* 39 (1978) C6-1456
- [78] V.Yakovenko, cond-mat/9802172.
- [79] S.Brazovskii and S.A. Gordyunin, *JETP Letters* 31 (1980) 371.
- [80] P.Auban-Senzier, D.J erome, C.Carcel, and J.M.Fabre, *J.Phys.IV (France)*, 114 (2004) 41 and to be published.
- [81] C.Bourbonnais, *High Magnetic Fields*, Springer Verlag, (Eds. C. Berthier, L.P. Levy and G. Martinez), Berlin, (2002), pp 236
- [82] P.Auban-Senzier, D.J erome, and J.Moser, *Physical Phenomena at High Magnetic Fields*, (Eds Z.Fisk, L.Gorkov, R.Schrieffer), World Scientific, Singapore, (1999), pp 211
- [83] A.Schwartz, M.Dressel, G.Gr uner, V.Vescoli, L.Degiorgi, and T. Giamarchi, *Phys. Rev. B* 58 (1998) 1261
- [84] S.Barisi and S.Brazovskii, *Recent Developments in Condensed Matter Physics*, v 1 (Eds J. T. Devreese), Plenum Press, New York, (1981), pp 327
- [85] V.J.Emery, R.Bruinsma, and S.Barisi, *Phys. Rev. Lett.* 48 (1982) 1039
- [86] A.Georges, T.Giamarchi, and N.Sandler, *Phys. Rev. B* 61 (2000) 16393
- [87] T.Timusk, *Low Dimensional Conductors and Superconductors*, (Eds. D.J erome and L.G. Caron), Plenum Press, New York, (1987) pp 275
- [88] K.Kikuchi, I.Ikemoto, K.Yakushi, H.Kuroda, and K. Kobayashi, *Solid State Commun.* 42 (1982) 433
- [89] H.K.Ng, T.Timusk, D.J erome, and K.Bechgaard, *Phys. Rev. B* 32 (1985) 8041
- [90] H.K.Ng, T.Timusk, and K. Bechgaard, *J. Physique (France)* 44 (1983) C3-867

- [91] N.Joo, C.R.Pasquier, P.Auban-Senzier, P .Monod, and D. Jérôme, Eur.Phys.Jour.B 40 (2004) 43.
- [92] R.Moret, J.P.Pouget, R. Comès, and K.Bechgaard, J. Phys. (France) 46 (1985) 1521
- [93] M.Ribault, D.Jérôme, J.Tuchendler, C.Weyl, and K. Bechgaard, J. Phys. Lett. (Paris) 44 (1983) L-953
- [94] J.R.Cooper, W.Kang, P.Auban, G.Montambaux, D.Jérôme, P.Batail, and K.Bechgaard, Phys. Rev. Lett. 12 (1985) 1984.
- [95] W.Kang, J.R.Cooper, and D.Jérôme, Phys. Rev. B.43 (1991) R11467
- [96] M.J.Naughton, R.V.Chamberlin, P.M.Chaikin, X.Yan, S.Y.Hsu, L.Y.Chiang, and M.Y.Azbel, Phys. Rev. Lett. 61 (1995) 621
- [97] S.K.McKernan, S.T.Hannahs, U.M.Scheven, G.M.Danner, and P.M.Chaikin, Phys. Rev. Lett., 75 (1995) 1630
- [98] W.Kang, S.T.Hannahs, and P.M.Chaikin, Phys. Rev. Lett. 70 (1993) 3091
- [99] A.G.Lebed, J. Phys. I (France) 6 (1996) 1819 and references therein.
- [100] F.Wudl, D.Nalewajek, J.M.Thorup, and N. W. Extine, Science 22 (1983) 415
- [101] S.Tomi , J.R.Cooper, D.Jérôme, and K. Bechgaard, Phys. Rev. Lett. 62 (1989) 462
- [102] R.Moret, S.Ravy, J.P.Pouget, R.Comès, and K. Bechgaard, Phys. Rev. Lett. 57 (1986) 1915
- [103] S.Tomi and D. Jérôme, J. Phys. : Cond.Matter.,1 (1989) L4451
- [104] A.Mazaud, PhD thesis, Univ. Paris Sud (1981)
- [105] W.Kang, S.T.Hannahs, L.Y.Chiang, R.Upasani, and P.M.Chaikin, Phys. Rev. Lett. 65 (1990) 2812
- [106] W.Kang, K.Behnia, D.Jérôme, L.Balicas, E.Canadell, M.Ribault, and J.M.Fabre, Europhys. Lett. 29 (1995) 635
- [107] H.Wilhelm, D.Jaccard, R.Duprat, C.Bourbonnais, D.Jérôme, J. Moser, C.Carcel, and J.M. Fabre, Eur. Phys. Jour. B 21(2001) 175
- [108] M.Ribault, G.Benedek, D.Jérôme, and K. Bechgaard, J. Phys. Lett. (Paris) 41 (1980) L397
- [109] K.Andres, F.Wudl, D.B.McWhan, G.A.Thomas, D.Nalewajek, and A.L.Stevens, Phys. Rev. Lett. 45 (1980) 1449
- [110] P.Garoche, R.Bruseti, and K.Bechgaard, Phys. Rev. Lett. 49 (1982) 1346
- [111] D.Mailly, M.Ribault, and K.Bechgaard, J. Phys. (France) 44 (1983) C3-1037
- [112] D.U.Gubser, W.W.Fuller, T.O.Poehler, J.Stokes, D.O.Cowan, M.Lee, and A.N.Bloch, Mol. Cryst. Liq. Cryst. 79 (1982) 225
- [113] J.P.Pouget, *Low Dimensional Conductors and Superconductors*, (Eds. D.Jérôme and L.G. Caron), Plenum Press, New York, (1987), pp 17
- [114] H.Schwenk, K.Andres, and F.Wudl, Solid State Commun. 49(1984) 723
- [115] R.L.Greene, P.Haen, S.Z.Huang, E.M.Engler, M.Y.Choi, and P.M.Chaikin, Mol. Cryst. Liq. Cryst. 79(1982) 183
- [116] K.Murata, H.Anzai, K.Kajimura, T.Ishiguro, and G.Saito, Mol. Cryst. Liq. Cryst. 79 (1982) 283
- [117] K.Murata, M.Tokumoto, H.Anzai, K.Kajimura, and T. Ishiguro, Japanese Jour. of Appl. Physics Suppl. 26-3 (1987) 1367
- [118] L.P.Gorkov, and D.Jérôme, J.Phys.Lett. 46 (1985) L643
- [119] I.J.Lee, P.M.Chaikin, and M.J.Naughton, Phys. Rev. B 62 (2000) R14669
- [120] J.L.Oh, and M.J.Naughton, Phys. Rev. Lett. 92(2004) 067001

- [121] R.Brusetti, M. Ribault, D.Jérôme, and K.Bechgaard, *J. Phys. IV (France)*,43 (1982) 801
- [122] N.Miljak, J.R.Cooper, and K.Bechgaard, *J. Physique (France)* 44 (1983) C3–893
- [123] S.Belin, and K.Behnia, *Phys. Rev. Lett.* 79(1997) 2125
- [124] J.Bardeen, G.Rickaysen, and L.Tewordt, *Phys. Rev.* 113 (1959) 982
- [125] H.J.Schulz, D.Jérôme, M.Ribault, A.Mazaud, and K.Bechgaard, *J. Phys. Lett. (Paris)* 42 (1981) L51
- [126] B.Gallois, PhD thesis, Univ. Bordeaux I, 1987
- [127] D.Mailly, PhD thesis, Univ. Paris-Sud, 1983
- [128] F.Creuzet, D.Jérôme, and A. Moradpour, *Mol. Cryst. Liq. Cryst.* 119 (1985) 297
- [129] F.Guo, K.Murata, H.Yoshino, S.Maki, S.Tanaka, J.Yamada, S.Nakatsuji, and H.Anzai, *J. Phys. Soc. Jpn.* 67 (1998) 3000
- [130] W.Kang, S.T.Hannahs, and P.M.Chaikin, *Phys. Rev. Lett.* 70 (1993) 3091
- [131] R.L.Greene and E.M.Engler, *Phys. Rev. Lett.* 45 (1980) 1587
- [132] L.J.Azevedo, J.E.Schirber, J.M.Williams, M.Beno, and D.Stephens, *Phys. Rev. B* 30 (1984) R1570
- [133] T.Vuleti , P.Auban-Senzier, C.Pasquier, S.Tomi , D.Jérôme, M.Héritier, and K.Bechgaard, *Eur. Phys. Jour. B* 25 (2002) 319
- [134] N.Biskup, S.Tomi , and D.Jérôme, *Phys. Rev. B* 51(1995) 17972.
- [135] I.J.Lee, P.M.Chaikin, and M.J.Naughton, *Phys. Rev. Lett.* 88 (2002) 207002.
- [136] D.Jaccard, H.Wilhelm, D.Jérôme, C.Carcel, and J.M.Fabre, *J. Phys. : Condens. Matter* 13 (2001) L89.
- [137] C.Pasquier, P.Auban-Senzier, T.Vuleti , S.Tomi , M.Héritier, and D.Jérôme, *J. Phys. IV (France)* Pr9 (2002) 197
- [138] P.Auban-Senzier, C.Pasquier, D.Jérôme, C.Carcel, and J.M.Fabre, *Synth. Metals* 133-134 (2003) 11.
- [139] J.D.Meyer and G.V.Minnigerode, *Phys. Lett.* 38A (1972) 529.
- [140] M.Kociak, A.Yu.Kasumov, S.Guéron, B.Reulet, I.I.Khodos, Yu.B.Gorbatov, V.T.Volkov, L.Vaccarini, and H.Bouchiat, *Phys. Rev. Lett.* 86 (2001) 2416.
- [141] H. Wilhelm et al, (2004) unpublished data.
- [142] P.Auban-Senzier, C.R.P asquier, and D.Jérôme, unpublished data.
- [143] C.R.Pasquier, habilitation thesis, Université Paris-Sud, Orsay, France (2003).
- [144] S.Lefebvre, P.Wzietek, S.Brown, C.Bourbonnais, D.Jérôme, C.Mézière, M.Fourmigué, and P.Batail, *Phys. Rev. Lett.* 85 (2000) 5428.
- [145] P.Limelette, P.Wzietek, S.Florens, A.Georges, T.A.Costi, C.Pasquier, D.Jérôme, C.Mézière, and P.Batail, *Phys. Rev. Lett.* 91 (2003) 16401.
- [146] H.Ito, T.Ishiguro, M.Kubota, and G.Saito, *J. Phys. Soc. Jpn* 69 (1996) 2987.
- [147] D.Andres, M.V.Kartsovnik, W.Biberacher, K.Neumaier, and H.Müller, *J. Phys. IV (France)* Pr9 (2002) 87
- [148] M.V.Kartsovnik, D.Andres, W.Biberacher, P.D.Grigoriev, E.A.Schuberth, and H.Müller, *J. Phys. IV (France)* 114 (2004) 191.
- [149] H.Taniguchi, M.Miyashita, K.Uchiyama, K.Satoh, N.Mori, H.Okamoto, K.Miyagawa, K.Kanoda, M.Hedo, and Y.Uwatoko, *J. Phys. IV (France)* 114 (2004) 273
- [150] A.Briggs, P.Monceau, M.Nunez-Regueiro, M.Ribault, and J.Richard, *J. Physique (France)* 42 (1981) 1453.

- [151] N.D.Mathur, F.M.Groche, S.R.Julian, J.R.Walker, D.M.Freye, R.K.W.Haselwimmer, and G.G.Lonzarich, *Nature* 394 (1998) 39.
- [152] I.Shaikin, D.Braithwaite, J.-P.Brison, A.Buzdin, and W.Assmus, *PhysicaB* 259-261 (1999) 683.
- [153] G.R.Stewart, *Rev. Mod. Phys.* 73 (2001) 797.
- [154] R.A.Fisher, F.Bouquet, N.E.Philips, M.F.Hundley, P.G.Pagliuso, J.L.Sarrao, Z.Fisk, and J.D.Thompson, *Phys. Rev. B* 65 (2002) 224509.
- [155] H.Takagi, B.Batlogg, H.L.Kao, J.Kow, R.J.Cava, J.J.Krajewski, and W.F.Peck Jr, *Phys. Rev. Lett.* 69 (1992) 2975.
- [156] A.M.Gabovich, A.I.Voitenko, and A.Ausloos, *Phys. Rep.* 367 (2002) 583
- [157] J.M.Tranquada, B.J.Sternlieb, J.D.Axe, Y.Nakamura, and S.Uchida, *Nature* 375 (1995) 561.
- [158] E.Semel, P.Auban-Senzier, C.R.Pasquier, and D.J erome, internal report, Universit  d'Orsay (France) (2002).
- [159] H.Seo and H.Fukuyama, *J. Phys. Soc. Jpn.* 69 (2000) 805.
- [160] M.Seul and D.Andelman, *Science* 267 (1995) 476.
- [161] I.J.Lee, P.M.Chaikin, and M.J.Naughton, *Phys. Rev. B* 65 (2002) R180502.
- [162] I.J.Lee, W.Wu, M.J.Naughton, and P.M.Chaikin, *J. Phys. IV (France) Pr9* (2002) 189.
- [163] P.M uller, *Festk rperprobleme/Advances in Solid State Physics*, v34.(R.Helbig editor), Springer Verlag, Vieweg, Braunschweig/Wiesbaden,(1994).
- [164] I.J.Lee, M.J.Naughton, G.M.Danner, and P.M.Chaikin, *Phys. Rev. Lett.* 78 (1997) 3555.
- [165] S.Wanka, D.Beckmann, J.Wosnitza, E.Balthes, D.Schweitzer, W.Strunz, and H.J.Keller, *Phys. Rev. B* 53 (1996) 9301.
- [166] I.J.Lee, A.P.Hope, M.J.Leone, and M.J.Naughton, *Synth. Met.* 70 (1995) 747.
- [167] D.Feinberg and C.Villard, *Phys. Rev. Lett.* 65 (1990) 919.
- [168] A.A.Abrikosov, *Jour.Low.Temp.Physics* 53 (1983) 359.
- [169] C. Bourbonnais and L.G. Caron, *Europhys. Lett.* 5 (1988) 209.
- [170] H.Mayaffre, P.Wzietek, C.Lenoir, D.J erome, and P.Batail, *Phys. Rev. Lett.* 75 (1995) 4951
- [171] S.Belin, T.Shibauchi, K.Behnia, and T.Tamegai, *J. of Superconductivity* 12 (1999) 497.
- [172] Y.Shimojo, A.E.Kovalev, S.Kamiya, E.Ohmichi, T.Ishiguro, H.Yamochi, G.Saito, A.Ayari, and P.Monceau, *Physica B* 294-295 (2001) 427.
- [173] S.Kamiya, Y.Shimojo, M.A.Tanatar, T.Ishiguro, H.Yamochi, and G.Saito, *Phys. Rev. B* 65 (2002) 134510.
- [174] J.M. Singleton, J.A.Symington, M.-S.Nam, A.Ardavan, M. Kurmoo, and P. Day, *J. Phys.: Condens. Matter* 12 (2000) L641.
- [175] F.Zuo, J.S.Brooks, R.H.McKenzie, J.A.Schlueter, and J.M.Williams, *Phys. Rev. B* 61 (2000) 750.
- [176] S.M.DeSoto, C.P.Slichter, A.M.Kini, H.H.Wang, U.Geiser, and J.M.Williams, *Phys. Rev. B* 52 (1995) 10364.
- [177] K.Kanoda, K.Miyagawa, A.Kawamoto, and Y.Nakazawa, *Phys. Rev. B* 54 (1996) 76.
- [178] Y.Nakazawa, and K.Kanoda, *Phys. Rev. B* 55 (1997) R8670.

- [179] H.Elsinger, J.Wosnitzer, S.Wanka, J.Hagel, D.Schweitzer, and W.Strunz, *Phys. Rev. Lett.* 84 (2000) 6098.
- [180] J.Müller, M.Lang, R.Helfrich, F.Steglich, and T.Sasaki, *Phys. Rev. B* 65 (2002) 140509.
- [181] S.Belin, K.Behnia, and A.Deluzet, *Phys. Rev. Lett.* 81 (1998) 4728.
- [182] K.Izawa, H.Yamaguchi, T.Sasaki, and Y.Matsuda, *Phys. Rev. Lett.* 88 (2002) 27002.
- [183] T.Arai, K.Ichimura, K.Nomura, S.Takasaki, J.Yamada, S.Nakatsuji, and H.Anzai, *Phys. Rev. B* 63 (2001) 104518.
- [184] L.P.Le, G.M.Luke, B.J.Sternlieb, W.D.Wu, Y.J.Uemura, J.H.Brewer, T.M.Riseman, C.E.Stronach, G.Saito, H.Yamochi, H.H.Wang, A.M.Kini, K.D.Carlson, and J.M.Williams, *Phys. Rev. Lett.* 68 (1992) 1923.
- [185] A.Carrington, I.J.Bonalde, R.Prozorov, R.W.Giannetta, A.M.Kini, J.Schlueter, H.H.Wang, U.Geiser, and J.M.Williams, *Phys. Rev. Lett.* 83 (1999) 4172.
- [186] M.Pinteri, S.Tomi, M.Prester, D.Drobac, O.Milat, K.Maki, D.Schweitzer, I.Heinen, and W.Strunz, *Phys. Rev. B* 61 (2000) 7033.
- [187] K.Kanoda, K.Akiba, K.Suzuki, T.Takahashi, and G.Saito, *Phys. Rev. Lett.* 65 (1990) 1271.
- [188] D.Achkar, M.Poirier, C.Bourbonnais, G.Quirion, C.Lenoir, P.Batail, and D.Jérôme, *Phys. Rev. B* 47 (1993) 11595.
- [189] M.Lang, N.Toyota, T.Sasaki, and H.Sato, *Phys. Rev. B* 46 (1992) R5822.
- [190] D.R.Harshman, R.N.Kleiman, R.C.Haddon, S.V.Chichester-Hicks, M.L.Kaplan, L.W.Rupp Jr., T.Pfiz, D.L.Williams, and D.B.Mitzi, *Phys. Rev. Lett.* 64 (1990) 293.
- [191] M.Lang, N.Toyota, T.Sasaki, and H.Sato, *Phys. Rev. Lett.* 69 (1992) 1443.
- [192] A.M.Clogston, *Phys. Rev. Lett.* 9 (1962) 266.
- [193] B.S.Shandrasekhar, *Appl. Phys. Lett.* 1 (1962) 7.
- [194] Y.Shomijo, T.Ishiguro, H.Yamochi, and G.Saito, *J. Phys. Soc. Jpn* 71 (2002) 1716.
- [195] M.Pinteri, S.Tomi, M.Prester, D.Drobac, and K.Maki, *Phys. Rev. B* 66 (2002) 174521.
- [196] A.Perez-Gonzalez, *Phys. Rev. B* 54 (1996) 16053.
- [197] K.Yang and S.L.Sondhi, *Phys. Rev. B* 57 (1998) 8566.
- [198] P.Fulde and R.A.Ferrell, *Phys. Rev.* 135 (1964) A550.
- [199] A. I. Larkin, *JETP Lett.* 2 (1965) 130.
- [200] I.J. Lee, M.J. Naughton, and P.M. Chaikin, *Phys. Rev. Lett.* 88 (2002) 207002.
- [201] M.Takigawa, H.Yasuoka, and G.Saito, *J. Phys. Soc. Jpn* 56 (1987) 873.
- [202] C.More, G.Roger, J.P.Sorbier, D.Jérôme, and K.Bechgaard, *J. Physique Lett.* 42 (1981) L445.
- [203] A.Fournel, B.Oujia, and J.P.Sorbier, *J. Physique Lett.* 46 (1985) L417.
- [204] A.P.Mackenzie and Y.Maeno, *Rev. Mod. Phys.* 75 (2003) 657.
- [205] A.G.Lebed, *JETP Lett.* 44 (1986) 114.
- [206] N. Dupuis, G. Montambaux, and C. A. R. Sá de Melo, *Phys. Rev. Lett.* 70 (1993) 2613.
- [207] S.V.Kravchenko, G.V.Kravchenko, J.E.Furneaux, V.M.Pudalov, and M.D'Iorio, *Phys. Rev. B* 50 (1994) 8039.
- [208] P.T.Coleridge, R.L.Williams, Y.Feng, and P.Zawadzki, *Phys. Rev. B* 56 (1997) R12764.

- [209] Y.Hanein, U.Meirav, D.Shahar, C.C.Li, D.C.Tsui, and H.Shtrikman, Phys. Rev. Lett. 80 (1998) 1288.
- [210] Y.Hasegawa and H.Fukuyama, J. Phys. Soc. Jpn. 55 (1986) 3978.
- [211] Y.Hasegawa and H.Fukuyama, J. Phys. Soc. Jpn. 56 (1987) 877.
- [212] H.Shimahara, Phys.Rev. B 61 (2000) 14936
- [213] K.Sengupta, and N.Dupuis, Phys. Rev. B 65 (2002) 035108
- [214] P.W.Anderson, J. Phys. Chem. Solids 11 (1959) 26.
- [215] S. Bouffard, M.Ribault, R. Brusetti, D. Jérôme, and K.Bechgaard, J. Phys. C 15 (1982) 295.
- [216] M.Y.Choi, P.M.Chaikin, S.Z.Huang, P.Haen, E.M.Engler, and R.L.Greene, Phys. Rev. B. 25 (1982) 6208.
- [217] L.Zuppiroli, *Low Dimensional Conductors and Superconductors*, (Eds. D.Jérôme and L.G. Caron), Plenum Press, New York, (1987), pp 307
- [218] M.Sanquer and S.Bouffard, Mol. Cryst. Liq. Cryst. 119 (1985) 147.
- [219] I.Johannsen, K.Bechgaard, C.S.Jacobsen, G.Rindorf, N.Thorup, K.Mortensen, and D.Mailly, Mol. Cryst. Liq. Cryst. 119 (1985) 277.
- [220] K.Mortensen and E.M.Engler, Phys. Rev. B 29 (1984) 842.
- [221] S.Tomi , D.Jérôme, D.Mailly, M.Ribault, and K.Bechgaard, J. Physique (France) 44 (1983) C3:1075.
- [222] S.Ravy, R.Moret, J.P.Pouget, and R.Comès, PhysicaB 143 (1986) 542.
- [223] K.Maki, H.Won, and S.Haas, Phys. Rev. B 69 (2004) 012502.
- [224] *Organic Conductors*, (Ed J.P.Farges), Marcel Dekker, New York, (1994).

UPERCONDUCTIVITY IN FULLERIDE

J. E. Han¹, O. Gunnarsson², and Vincent H. Crespi³

¹) Department of Physics, State University of New York at Buffalo
Buffalo, New York 14260, USA

²) Max-Planck-Institut für Festkörperforschung, D-70506, Stuttgart, Germany

³) Department of Physics, The Pennsylvania State University
University Park, Pennsylvania 16802-6300, USA

1. INTRODUCTION

Since the discovery[1] of C_{60} as the third form of pure carbon structures, fullerene systems have attracted a great deal of interest from a wide range of scientists in different disciplines for their unique molecular chemistry [2], solid state properties [3, 4], and recently for a vehicle of nanotechnology. The availability of the mass production of C_{60} molecules and their solid formation [5] has initiated an intense research in condensed matter physics. By intercalation of alkali atoms, the C_{60} lattice were found to be metallic [6] at A_3C_{60} ($A = \text{Rb}, \text{K}$). Fig. 1 illustrates the lattice structure of A_3C_{60} compounds with the alkali atoms occupying the interstitial space of the face-centered cubic crystal of C_{60} .

One of the great excitements in the fullerene research has been the unusually strong superconductivity in solid C_{60} when doped with alkali atoms [7, 8]. The main role of the alkali atoms is to fill up the empty C_{60} orbitals with their valence electrons without much changing the band structure near the Fermi energy. The transition temperature of the system reaches a maximum of $T_c = 33$ K for $\text{Rb}_2\text{CsC}_{60}$ [9] which has only been surpassed recently by MgB_2 [10] among the phonon-mediated superconductors. Fig. 2 (from Yildirim *et al.* [11]) shows T_c for a collection of alkali-doped compounds with two different kinds of lattice structure. It is remarkable that the alkali-doped fullerene is superconducting at all, since it has been pointed out that the system goes through Mott metal-insulator

transitions with varying alkali concentrations [12]. The Mott insulator transition (MIT) is a phenomenon of localization of charge carriers driven by the dominant Coulomb repulsion at the cost of smaller kinetic energy. The main puzzle is then how the attractive pairing interaction not only overcomes the strong Coulomb repulsion but also survives to produce a very strong superconductor. There has generally been a consensus that the fullerene superconductors are phonon-driven, and the strong electron correlations present near the MIT has been considered harmful to superconductivity.

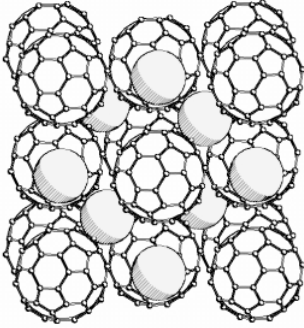


Fig. 1: Schematic picture of alkali-doped C_{60} solid. Three alkali atoms (solid spheres) are intercalated into interstitial voids of C_{60} lattice of face-centered cubic crystal symmetry.

The conventional theory of superconductivity [13] is based on the large discrepancy in time scales between electron and lattice dynamics. With slow phonons, a lattice distortion created by an electron remains unchanged until a next-approaching electron feels an effective attractive force from the electric field generated by the distortion. Migdal approximation takes into account this energy hierarchy and significantly simplifies the diagrammatic theory by ignoring complicated vertex corrections [13]. Furthermore, when the Coulomb interaction is seen in the relevant energy scale of pairing interaction, the effective electron-electron (el-el) interaction is dramatically reduced, since by the time the second electron feels an attractive interaction via the lattice distortion, the first electron is long gone [14, 15]. This retardation effect is very important in reducing strong Coulomb interaction in conventional systems.

However, the energy scale of C_{60} systems does not guarantee the validity of the above conventional approximations. Weak inter-molecular bonding makes the conduction bandwidth of the lowest unoccupied molecular orbital (LUMO) of C_{60} only $0.5 - 0.6$ eV. On the other hand, due to the light mass of carbon atoms and the stiff bonding from the curved geometry of the C_{60} molecule, the molecular vibration frequency is rather high. The high curvature of C_{60} surface also makes the electron-phonon (el-ph) coupling strong compared to the alkali-intercalated graphite [16] and contributes to the high superconducting transition temperatures. H_g vibration modes, corresponding to molecular distortions known to be responsible for the pairing, have an average frequency $\omega_{ph} \sim 0.1$ eV. For A_3C_{60} (A =alkali element), this gives $\omega_{ph}/E_F \sim 0.3$ while the conventional el-ph superconductors have the ratio of few thousandths. Furthermore, the el-ph coupling strengths are in the strong coupling regime with the el-ph mass-renormalization factor $\lambda = 0.5 - 1.0$. These conditions put the validity of the Migdal approximation on shaky grounds.

The Coulomb interaction strength between two extra electrons on a single molecular site of C_{60} lattice has been estimated in Auger spectroscopy experiments [17, 18] to be $1.2 - 1.5$ eV, substantially larger than the conduction bandwidth. This immediately

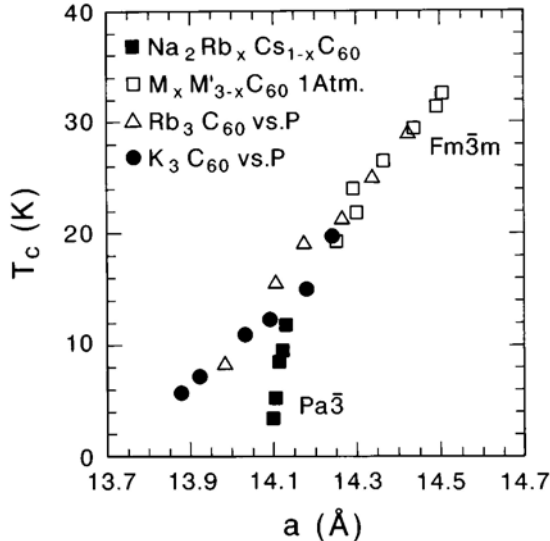


Fig. 2: Transition temperature T_c as a function of the lattice parameter a for the $Fm\bar{3}m$ (triangles, circles, and open squares) and $Pa\bar{3}$ (filled squares) superconductors. Regardless of chemical composition, T_c increases with a due to the increasing density of states at the chemical potential from band narrowing. After Yildirim, Fisher, *et al.* [11].

addresses the possibility of a Mott metal-insulator transition. Indeed, some alkali-doped systems A_4C_{60} are insulators although the LUMO band is supposed to be partially filled. Interestingly, when doped with 3 alkali atoms per C_{60} , A_3C_{60} systems turn metallic [12]. These facts suggest that the superconducting A_3C_{60} is in the vicinity of the MIT. The conventional wisdom is that such strong el-el interaction reduces the coherent part of the electronic wavefunction to a fraction of that in the non-interacting limit, further undermining the assumptions used in the Migdal approximation and the retardation argument. The competition between these energy scales radically alters the electronic structure to the vicinity of an MIT and invalidates the conventional perturbative approaches. The energy parameters in the C_{60} solid are summarized in Table 1.

Table 1: Energy parameters for solid C_{60} system.

| | |
|---|--------------|
| conduction bandwidth, W | 0.5 – 0.6 eV |
| average phonon frequency, ω_{ph} | 0.1 eV |
| electron-phonon mass renormalization, λ | 0.5 – 1.0 |
| on-site Coulomb interaction, U | 1.3 – 1.6 eV |

It is important to understand that the superconducting and Mott-insulating phases are close to each other in the C_{60} compounds. In order to address the issue correctly, the el-ph and el-el interactions need to be dealt with in a nonperturbative scheme. The interplay of el-ph and el-el interactions has received a great deal of interest [19, 20]. Recently, this issue has been revitalized with the suggestion that the phonons may play significant roles in the cuprate high-temperature superconductors [21]. However, there has been no clear understanding of this problem.

Another important aspect that the conventional theories overlooked is the symmetry of locally degenerate states. The crucial input to the Eliashberg-Migdal theory is the energy hierarchy of electrons and phonons without local symmetries playing any substantial role. With increasing Coulomb interaction, electron movement is hindered and the local limit of the electrons becomes relevant. For C_{60} , the LUMO level has orbital degeneracy of three which can accommodate on-ball electron density distortions. This electron density distortion then couples to the molecular distortion. This coupling lifts the degeneracy of local electronic configurations and form local multiplets in the dynamic limit. Fluctuations among the local multiplets generate electron correlations which lead to electron pairing. We call this mechanism local pairing. Since the local pairing is driven by fluctuations between different local multiplets within the same-charge manifold, the attractive pairing interaction does not suffer directly from charging interactions such as the Coulomb repulsion. What is unique in the fullerene superconductivity when compared to other atomic solids is the intramolecular degeneracy and fluctuations therein, which becomes possible due to weak molecular bonding in the solid.

Experimental Results

The LUMO orbitals of t_{1u} symmetry only couples to two types of vibrations given by the point group symmetry [22]: A_g symmetric and H_g distortion modes. The 8 different H_g modes have vibration frequencies in the range of 0.03 – 0.2 eV. The mass renormalization factor due to the electron-phonon coupling with the H_g modes has been estimated to be 0.5 – 1.0 from various measurements: isotope effect ($\lambda = 0.9$ for Rb_3C_{60} [23]), photoemission (1.0 for Rb_3C_{60} , K_3C_{60} [24]), transport (0.65 – 0.80 for Rb_3C_{60} [25]), optical data (0.8 – 1.2 for K_3C_{60} [26]), Raman scattering (0.5 for K_3C_{60} [27]).

Since the discovery of superconductivity in fullerenes, general superconducting properties have been well studied [3, 4]. The ratio $2\Delta/T_c$ (with the superconducting gap Δ) is important to determine how close the system is to the BCS superconductors. Numerous groups have measured the gap Δ using different techniques (point contact [28], break junction [29] tunneling, NMR [30, 31, 32, 33], muon spin relaxation [34], optical measurements [35], and photoemission [36, 37]). $2\Delta/T_c$ ranges from the BCS value 3.53 to rather high 4.0 – 4.2. Although the larger numbers indicate the strong coupling limit [13], their origin is not well understood. Isotope effect is of particular interest in studying phonons in superconductors. The isotope exponent α is defined as

$$T_c \sim M^{-\alpha} \quad (1)$$

with the carbon mass M . With complete substitution of ^{12}C by ^{13}C , $\alpha = 0.30 \pm 0.06$ [38] for K_3C_{60} and $\alpha = 0.30 \pm 0.06$ [39], 0.21 [23] for Rb_3C_{60} . These finite α values are a

strong indication that the fullerene superconductors are induced by phonons. Unusual α 's larger than 0.5 observed in systems with incomplete substitution of ^{13}C [39, 40] are not understood. Isotope effects on the substitution of alkali atoms have not been observed [41, 42]. This shows that alkali-phonons do not participate in the pairing interaction, and alkali atoms may influence the superconductivity only indirectly by changing electronic or lattice structures.

Behavior of superconducting transition temperatures have been extensively studied. The lattice constant dependency of T_c received much attention [43, 11]. The results are summarized in Fig. 2 from Yildirim, Fischer *et al.* [11]. The lattice constant a of K_3C_{60} and Rb_3C_{60} has been changed by applying pressure, while in $\text{Na}_2\text{Rb}_x\text{Cs}_{1-x}\text{C}_{60}$ and $M_xM'_{3-x}\text{C}_{60}$ ($M, M' = \text{K, Rb, Cs}$) a was changed by different chemical composition. It is remarkable that the T_c is an increasing function of the lattice constant a . Despite some deviation in $\text{Na}_2\text{Rb}_x\text{Cs}_{1-x}\text{C}_{60}$, most of the data points fall on the same curve, which suggests that the superconductivity is determined by the C_{60} lattice, not by the chemistry of alkali atoms. An increase of a reduces the overlap of t_{1u} orbitals on neighboring C_{60} molecules and the conduction bandwidth. The narrow band results in larger density of states at the Fermi energy and the electron-phonon coupling λ [9, 44]. Therefore T_c increases monotonically until system goes through a Mott insulator transition.

Interesting but much less understood results have been the dependence of T_c on concentration of alkali atoms [45, 46]. T_c is maximum when 3 alkali atoms are doped per C_{60} molecule at A_3C_{60} , i.e., by half-filling the triply degenerate t_{1u} orbital with electrons. T_c sharply decreases when the doping moved away from 3. Since there are no reasons for a sharp structure in the el-ph coupling λ or the Coulomb interaction due to rather smooth density of states, conventional theories have been unable to explain the result. This unexpected behavior has led to speculations [47] for electronic pairing mechanisms. Recently, Han *et al.* [48] showed that the symmetry of local orbital degeneracy in A_3C_{60} is crucial for strong phonon-driven superconductivity and the doping dependency results from the el-ph coupling symmetry of local Jahn-Teller phonons on C_{60} molecules without the need for an electronic mechanism.

2. C_{60} MOLECULE AND LATTICE MODEL

C_{60} Molecules

A fullerene molecule is made up of 60 carbon atoms with each atom sitting on the vertices of a soccer-ball-shaped cage. With the geometry so symmetric (truncated icosahedral symmetry), the molecule inherits the high structural symmetry to its electronic orbitals and molecular vibration modes. As shown in Fig. 3(a), the symmetry results in degenerate molecular levels on a free C_{60} molecule. The t_{1u} level has the orbital degeneracy of three with the wavefunction of odd parity about the center of the molecule. When the molecules are put together in a lattice, the shortest distance between carbon atoms on neighboring molecules ($\sim 3.1 \text{ \AA}$) is more than twice as long as the C-C bond ($\sim 1.4 \text{ \AA}$) on the same C_{60} ball. This tends to make the bands formed from different molecular orbitals well-separated

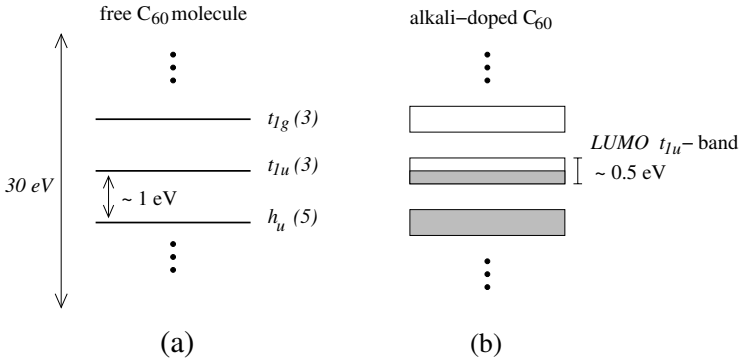


Fig. 3: (a) Schematic molecular energy levels of an isolated C₆₀ molecule. Molecular states spanning over 30 eV split into degenerate energy levels with spacing of roughly 1 eV. C₆₀ molecule has the completely filled h_u HOMO states and empty t_{1u} LUMO states. The numbers in the parenthesis are the orbital degeneracy. (b) Upon electron doping by infiltrating alkali atoms, the t_{1u} conduction band is filled up. Due to the small bandwidths (0.5 – 0.6 eV), bands near the Fermi energy with different symmetry do not overlap.

from each other as sketched in Fig. 3(b). For many low temperature phenomena, it is often reasonable to ignore bands which are well separated from the conduction band. This approximation simplifies the C₆₀ solid system to a lattice model with each site resided by t_{1u} -orbitals whose degenerate degrees of freedom act as internal variables.

Isotope effect experiments suggest that the superconductivity in alkali-doped C₆₀ compounds is driven by phonons coming from carbon atoms. The molecular vibration modes, well-identified in Raman scattering [49, 50] experiments, can be classified into two groups: symmetric modes with respect to the icosahedral symmetry and unsymmetrical modes associated with molecular distortions. The direct intermolecular coupling of the vibrations is very weak in the undoped C₆₀ and the molecular modes can be well described by optic phonons. Like the electronic states, the high symmetry of the truncated icosahedral group results in degenerate molecular vibration modes. Most important are the 5-fold degenerate H_g distortion modes, which are believed to be mainly responsible for the superconductivity. These distortion modes, called molecular Jahn-Teller (JT) phonons, only couple to the distorted electronic density, i.e., to configurations of unevenly occupied t_{1u} orbitals. On the other hand, the symmetric modes (A_g phonons) couple to the symmetric part of the electronic wavefunction, i.e., the total electron density on the t_{1u} orbitals. As will be discussed later, this symmetry consideration has critical significance to the strong superconductivity in the fullerene system.

Model for C₆₀ solid

To fully consider the el-ph and el-el interactions on the same footing in a nonperturbative manner, we use a model system given by a Hamiltonian, $H = H_{\text{el}} + H_{\text{ph}} + H_{\text{el-ph}} + H_{\text{el-el}}$,

with each term representing electron hopping, phonon vibration modes, el-ph coupling, and el-el interaction, respectively.

$$H_{\text{el}} = - \sum_{ijmm'\sigma} t_{im,jm'} d_{im\sigma}^\dagger d_{jm'\sigma} - \mu \sum_{im\sigma} n_{im\sigma}, \quad (2)$$

where $d_{im\sigma}^\dagger$ is creation operator of a spin- σ electron on the m -th t_{1u} orbital ($m = 1, 2, 3$) at the i -th C_{60} site. μ is the chemical potential and $n_{im\sigma} = d_{im\sigma}^\dagger d_{im\sigma}$ is the occupation number operator. Although detailed lattice structure can be important in MIT [51], we use here a generic featureless density of states (DOS) of semicircular shape to focus on the influence of el-ph interaction. We represent the 8 different H_g modes on each C_{60} by a single H_g mode at the average phonon frequency ω_{ph} ,

$$H_{\text{ph}} = \omega_{\text{ph}} \sum_i \sum_{\nu=1,\dots,5} \left(b_{i\nu}^\dagger b_{i\nu} + \frac{1}{2} \right), \quad (3)$$

with the phonon creation operator $b_{i\nu}^\dagger$ of the ν -th vibration state at the i -th site. The el-ph coupling interaction with H_g phonons is specified by the coupling constant g as

$$H_{\text{el-ph}} = g \sum_i \sum_{\nu} \sum_{mm'\sigma} V_{mm'}^{(\nu)} (b_{i\nu}^\dagger + b_{i\nu}) d_{im\sigma}^\dagger d_{im'\sigma}. \quad (4)$$

The traceless matrix $V^{(\nu)}$ is determined by rotational symmetry of t_{1u} and H_g modes alone [22]. For a frozen configuration of the H_g mode, the electronic states tend to conform to the molecular distortion which in turn splits the degenerate t_{1u} orbitals. It is then energetically favorable to fill up the nondegenerate states with alternating spins, resulting in low-spin ground state configuration. Quantum fluctuations between the frozen phonon configurations recover the symmetry between orbitals [52] in the dynamic Jahn-Teller limit, and the ground state multiplet retains the low-spin symmetry. Throughout this chapter, the electron-phonon coupling strength is parametrized by the mass renormalization factor λ defined in a perturbative form [53, 4]

$$\lambda = \frac{5}{3} \frac{g^2 N(0)}{\omega_{\text{ph}}}, \quad (5)$$

with the non-interacting density of states per spin $N(0)$.

Finally, the Coulomb repulsion is parametrized by an on-site interaction,

$$H_{\text{el-el}} = U \sum_i \frac{N_i(N_i - 1)}{2}, \quad (6)$$

with $U > 0$ and $N_i = \sum_{m\sigma} n_{im\sigma}$. This Hamiltonian accounts for the charging energy of C_{60} molecules. Intersite Coulomb repulsion, smaller than the on-site interaction, are ignored. Like in atomic systems, the Pauli exclusion principle results in the Hund's rule coupling at the molecular level. Hund's rule coupling in C_{60} molecule reduces the manifold of same-charge d^n configurations into several multiplets by favoring high-spin configuration. The Hund's rule coupling is in competition with the JT coupling, as discussed in the previous paragraph, with the ground state of opposite spin symmetry. C_{60} is believed to have stronger JT coupling [54], consistent with the nonmagnetic insulators in $A_4\text{C}_{60}$ systems and spin-singlet superconductors in $A_3\text{C}_{60}$.

3. MOTT INSULATOR TRANSITION

Metal-insulator transition driven by the electron-electron interaction has become one of the most fascinating subjects of condensed matter physics, in systems including cuprate high-temperature superconductors, transition metal oxides, and alkali-doped fullerenes. Strong Coulomb interaction favors locally charge-neutral configurations and suppresses the electron hopping, leading to a Mott insulator. The metallic A_3C_{60} at the large U/W ($= 1.5 - 2.5$) ratio has puzzled many researchers because such a large U/W typically implies a Mott insulator. It has been pointed out [55] that the orbital degeneracy of three with the t_{1u} LUMO states stabilize the metallic state of A_3C_{60} . Traditionally, most of the research on the MIT phenomena has focused on the role of Coulomb interaction. However, the Coulomb interaction alone cannot explain the transition between the insulating A_4C_{60} and the metallic A_3C_{60} as the alkali-doping level is changed [56, 57] in C_{60} solid. Both the lattice structure effects due to frustration and the coupling to JT phonons are important to explain the doping dependency of MIT [51]. Here we focus on the effects of the JT phonons, which becomes crucial in explaining the doping dependency of the superconducting transition temperature [45].

To attack the multiple interactions in the above Hamiltonian nonperturbatively, we use the dynamical mean field theory [58] (DMFT). The DMFT maps a lattice model to a model of a quantum impurity imbedded in a self-consistently determined electron bath. Unlike the Weiss mean-field theory in statistical mechanics, this mapping preserves the local quantum fluctuations in time and has proved extraordinarily successful in describing the Mott insulator transition. The quantum impurity model is numerically solved by the quantum Monte Carlo (QMC) technique [59] using the Hirsch-Fye algorithm [60]. The DMFT is expected to be a reasonable approximation for the fullerene system since it is close to the MIT and its large coordination number in the fcc lattice structure makes the spatial average more accurate.

We approach from the insulating state and examine the insulating gap defined as

$$E_g = E(N + 1) + E(N - 1) - 2E(N), \quad (7)$$

where $E(N)$ is the ground state of the insulating solid and $E(N \pm 1)$ is the lowest excited energy of a singly charged electron/hole excitation. When the electrons are localized in the insulating state, the energy gain due to the JT coupling approaches the local limit which is depicted as dots in Fig. 4. With the JT coupling favoring the low-spin states, the el-ph coupling energy gains maximum at fillings of $n = 2$ and 4. Due to the electron-hole symmetry in the coupling matrix $V^{(\nu)}$ in Eq. (4), the coupling energy has the symmetric form. The unit of the JT coupling energy Δ_{JT} is g^2/ω_{ph} . Creating a charge excitation, with an extra electron on one site and an extra hole on a different site, costs a Coulomb energy U . However, once created, the electron and the hole can delocalize without further cost in Coulomb energy. Due to the delocalization energy determined primarily by the electron hopping integral which is comparable or larger than Δ_{JT} , the local JT coupling energy is only a fraction of the local limit. The JT coupling contribution to the excitation energy falls somewhere in the shaded area in Fig. 4. Comparing the ionization energies in Fig. 4(a) and (b), the insulating gap E_g in Eq. (7) tend to be larger for A_4C_{60} cases and

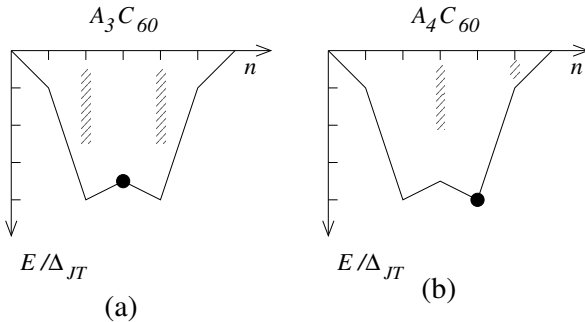


Fig. 4: (a) The electron-phonon coupling energy for Ground state and charge excited states in the insulating regime of A_3C_{60} . The solid curve shows the energy gain due to coupling to the H_g Jahn-Teller phonons in the atomic limit. The insulating ground state (dot) has the same coupling energy as the atomic limit. The charge excitation becomes delocalized and the coupling energy to the local phonons is only a fraction (somewhere in the shaded region) of the atomic limit. (b) Same for the A_4C_{60} system. A_4C_{60} has higher ionization energy and therefore favors insulating state.

the insulating state is more favored in A_4C_{60} systems. This is summarized in a schematic phase diagram in Fig. 5(a) with $U - \lambda$ parameters. The A_3C_{60} system has the larger metallic region than the A_4C_{60} system. Quantitatively, this result should be taken with some caution due to the negligence of the lattice structure and inaccurate λ from partial cancellation of the JT effect by the Hund's rule coupling.

We come to an opposite conclusion with a coupling to the symmetric non-Jahn-Teller (nJT) A_g phonons. The symmetric nJT modes couple to the total number of on-site electrons with the el-ph term given as $g(b^\dagger + b)(\hat{N} - \langle N \rangle)$ with the electron number operator \hat{N} , its average value $\langle N \rangle$ and the creation operator b^\dagger of the nondegenerate nJT phonons. As often adopted in the negative- U Hubbard model, the el-ph contribution to the energy becomes proportional to $-(g^2/\omega_{ph})(\hat{N} - \langle N \rangle)^2$ after the phonon variables are approximately integrated out. This el-ph contribution acts to reduce the total repulsive interaction between electrons, which results in higher critical Coulomb parameter U_c for the MIT.

Fig. 5(b) shows the DMFT results for one-particle Green function $G(\tau)$ as a function of the Coulomb repulsion parameter U at the imaginary time $\tau = \beta/2$ (inverse temperature $\beta = 1/T$). The temperature is finite at $T = W/32$. With the chemical potential inside an insulating gap E_g , $G(\tau)$ decays exponentially and the small $G(\beta/2)$ indicates a Mott insulator. The open circles are without the el-ph interaction ($\lambda = 0$) and solid circles/diamonds are with coupling to JT/nJT phonons (note the scale difference between the plots). With $\lambda = 0$, $U_c/W \approx 2.3$. With the H_g -JT phonons, an insulating solution is reached at the smaller $U_c/W \approx 1$ while the coupling to the A_g -nJT phonons expanded the metallic region with higher U_c . It is also interesting to note that for small U ,

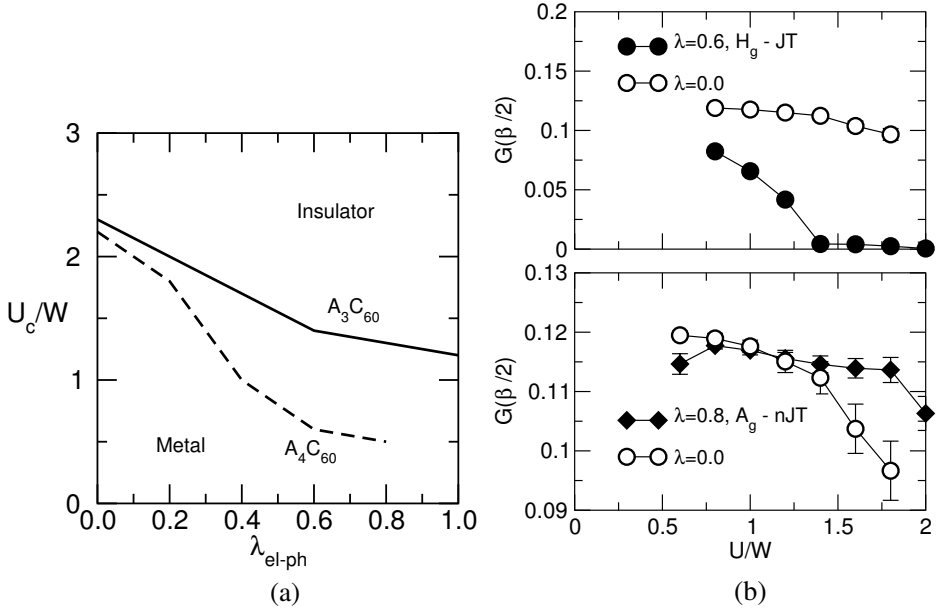


Fig. 5: (a) Diagram for metallic and insulating phases in the $U - \lambda$ parameter space for A_nC_{60} ($n = 3, 4$). The symmetry of el-ph coupling predicts larger parameter space for the metallic solution for the half-filled A_3C_{60} , in agreement with the experiments. (b) Green function $G(\tau)$ at the imaginary time $\tau = \beta/2$ with the inverse temperature $\beta = 1/T$. Decaying $G(\beta/2)$ shows that the metallic regime shrinks with the coupling to H_g Jahn-Teller (JT) phonons in contrast to the A_g non-Jahn-Teller (nJT) phonons.

the coupling to JT and nJT phonons acts additively in the same manner as to increase the electron renormalization effect, which agrees with the perturbation theory.

4. LOCAL PAIRING VIA LOCAL QUANTUM FLUCTUATION

Due to the fast local molecular phonons in C_{60} , the underlying assumptions for the Migdal approximation and the Coulomb pseudopotential argument are no longer justified in the superconducting A_nC_{60} . The incipient Mott insulator further complicates the problem. Koch *et al.* [61] examined this question by studying the effectiveness of metallic screening by the t_{1u} band. Their projection QMC calculations performed on finite C_{60} lattice with the Hubbard on-site interaction have shown that the screening is remarkably effective nearly up to the Mott transition, which matched the random-phase-approximation well.

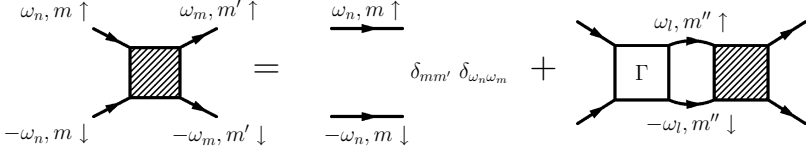


Fig. 6: Local pair susceptibility χ expanded in terms of propagators of two independent electrons χ_0 and the irreducible vertex function Γ . χ is defined to probe the spin singlet pairing. For the static limit of the pair susceptibility, the incoming and outgoing pairs have zero net frequency.

The critical Hubbard parameter $U_c/W \sim 2.5$ [55] were consistent with the experimental estimate. However, with phonons being the primary pairing medium, the calculations were unable to directly address the effectiveness of the phonon-mediated pairing.

It is widely agreed that the pairing in fullerene systems are driven by the electron-phonon coupling as suggested by the isotope experiments [23]. The nodeless superconducting order parameter, as opposed to the cuprate high-temperature superconductors or other exotic superconductors, is commonly believed to be destroyed by the Coulomb repulsion between pairing electrons. Conventional perturbation theory with el-ph and el-el interactions, such as the Migdal-Eliashberg theory, would not properly address the aforementioned shortcomings. As summarized in the McMillan formula [62]

$$T_c = \frac{\omega_{\text{ln}}}{1.2} \exp \left[\frac{1.04(1 + \lambda)}{\lambda \mu^*(1 + 0.62\lambda)} \right] \quad (8)$$

with the characteristic phonon frequency ω_{ln} and the Coulomb pseudopotential parameter μ^* , the perturbation theory predicts that the el-ph and el-el interactions act additively in the factor $\lambda - \mu^*$.

As discussed in the previous section, the nonperturbative effects in the strongly interacting regime change drastically depending on the el-ph coupling symmetry. The JT and nJT el-ph coupling symmetry influenced the MIT in opposite ways. In a similar way, the coupling symmetry turns out to be crucial [48] in the unusually strong superconductivity in the fullerene systems.

Attractive Pairing Interaction

From DMFT calculations, existence of the surprisingly strong pairing from the JT coupling is shown below. At the same time, the pairing due to nJT phonons is shown to be suppressed by Coulomb interaction which confirms the conventional view of the *s*-wave pairing. We assume along the line of DMFT that the interaction is dominantly local, given the strong local coupling of electronic orbitals to molecular phonons. The local interaction can be extracted from the local pair correlation function χ defined by

$$\chi_{mm'}(\tau_1, \tau_2, \tau_3, \tau_4) = \langle T_\tau c_{im\uparrow}(\tau_1) c_{im\downarrow}(\tau_2) d_{im'\downarrow}^\dagger(\tau_3) d_{im'\uparrow}^\dagger(\tau_4) \rangle \quad (9)$$

with the time-ordering operator T_τ in the Matsubara space. χ is a two-particle Green function for creating two electrons of spin singlet on the same site. From the Bethe-Salpeter equation, χ can be formally expanded in a series [63]

$$\chi = \chi_0 + \chi_0 \Gamma \chi_0 + \chi_0 \Gamma \chi_0 \Gamma \chi_0 + \cdots = [\chi_0^{-1} - \Gamma]^{-1}. \quad (10)$$

This is a shorthand of matrix equation where the indices run for the orbital variables and the imaginary-time (or Fourier transformed Matsubara frequency). As illustrated in Fig. 6, χ can be expressed in terms of the correlation function χ_0 of two independently propagating local electrons (represented as two disjoint electron propagators) and the irreducible vertex Γ . Γ is interpreted as the effective interaction $V_{\text{eff}} (\equiv -\beta\Gamma)$ between pairing electrons, which should reduce to $g^2 D_{\text{ph}}$ (with phonon Green function D_{ph}) in the limit of the Migdal-Eliashberg theory. Since χ is directly obtained from the QMC calculations and χ_0 is a product of one-particle Green function, Γ is derived from Eq. (10).

Superconductivity as a collective phenomenon is probed by computing the uniform pairing susceptibility instead of the local susceptibility Eq. (10). With the assumption of local interaction, the pair susceptibility $\chi(Q)$ with the net momentum Q of the electron pair can be expressed by the Bethe-Salpeter equation similar to Eq. (10),

$$\chi(Q) = \chi_0(Q) + \chi_0(Q) \Gamma \chi_0(Q) + \chi_0(Q) \Gamma \chi_0(Q) \Gamma \chi_0(Q) + \cdots = [\chi_0^{-1}(Q) - \Gamma]^{-1}, \quad (11)$$

where $\chi_0(Q)$ is the correlation function of two independently propagating electrons with the net momentum Q defined as $\chi_0(Q; \tau_1, \tau_2, \tau_3, \tau_4) = \Omega^{-1} \sum_{\mathbf{k}} G(\mathbf{k} + \mathbf{Q}, \tau_1 - \tau_4) G(\mathbf{k}, \tau_2 - \tau_3)$ (with $\Omega = \text{unit volume}$). The uniform susceptibility corresponds to $Q = 0$.

When the system goes through a superconducting transition, small perturbation of creating electron pairs leads to an instability which shows up as a singularity in the static limit of $\chi(Q = 0)$. $\chi(Q = 0)$ diverges as the maximum eigenvalue of $\chi_0(Q = 0)\Gamma$ in Eq. (11) approaches 1. With a finite metallic weight at the Fermi energy, $\chi_0(Q = 0) \approx zN(0)/\pi|\omega_n|$ with the total electron renormalization factor z , non-interacting density of states $N(0)$ and Matsubara frequency $\omega_n = (2n + 1)\pi T$. As the temperature lowers, the lowest Matsubara frequency approaches zero and $\chi_0(Q)$ diverges. With a finite attractive interaction ($V_{\text{eff}} < 0$ or $\Gamma > 0$), the maximum eigenvalue of $\chi_0(Q)\Gamma$ is then expected to cross 1 at a finite temperature. Although the Bethe-Salpeter equation is in the similar formal structure of the Eliashberg theory, the crucial difference is that we compute the pairing interaction V_{eff} from the nonperturbative χ and χ_0 , numerically exact within controllable errors, instead of *assigning* diagrams for V_{eff} in a perturbative scheme.

The numerical results for V_{eff} is plotted in Fig. 7 as a function of incoming and outgoing Matsubara frequencies ω_n, ω_m . In (a) without the Coulomb interaction, the effective interaction is consistent with the Eliashberg theory. The attractive part lies within the width of the phonon frequency along the line of low energy transfer $\omega_n = \omega_m$. As the Coulomb interaction is turned on to $U/W = 1.0$, the attractive part becomes much narrower and stronger, which indicates that the interaction induced by the el-ph interaction grows stronger as electrons are localized by the Coulomb repulsion. Qualitatively, this is in agreement with the increasing JT el-ph coupling energy discussed in the previous section. The charge interaction does not suppress the JT el-ph coupling induced by internal

fluctuations of the degenerate local orbitals. The renormalization effects in V_{eff} is quite significant and detailed quantitative understanding of the results needs further investigation. By the shape of V_{eff} , one can still view the pairing interaction as mediated by some highly renormalized low energy excitations, which we will discuss in more detail below. As noted earlier, the transition temperature is determined by the balance between the metallic weight in $\chi_0(Q)$ and the effective interaction V_{eff} . Even though V_{eff} is enhanced by the interaction, the renormalization of the metallic weight leads to a reduced $\chi_0(Q)$. Therefore the behavior of T_c can only be known given fully self-consistent solutions.

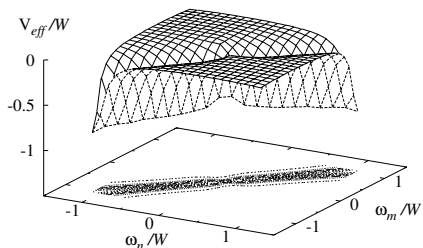
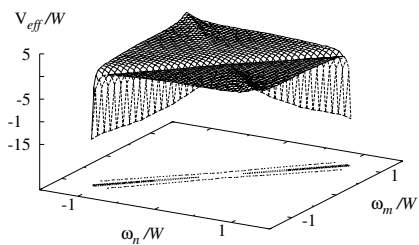
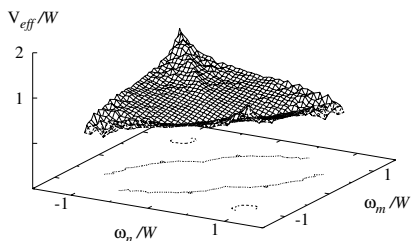
(a) $U/W=0.0$ (Jahn-Teller)(b) $U/W=1$. (Jahn-Teller)(c) $U/W= .5$ (non-Jahn-Teller)

Fig. 7: Effective interaction V_{eff} ($\equiv \Gamma/T$) between pairing electrons as defined in Fig. 6 with incoming and outgoing frequencies ω_n, ω_m . (a) The attractive interaction without Coulomb repulsion ($U = 0$) runs along the small energy transfer $\omega_n = \omega_m$, consistent with pairing mediated with a low energy fluctuation. (b) With large U , the attractive interaction due to Jahn-Teller phonons persists. The pairing medium is highly renormalized from the non-interacting phonons. (c) The attractive interaction induced by non-Jahn-Teller phonons is canceled by finite U . The shallow dip in V_{eff} shows the reduced el-ph coupling due to frozen charge fluctuation by finite U .

Fig. 7(c) for coupling to the A_g nJT modes displays a qualitatively different behavior from the JT coupling. First, the finite Coulomb interaction lifted up the effective inter-

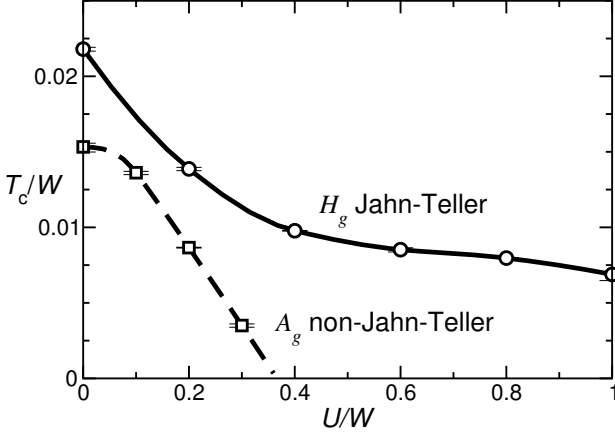


Fig. 8: Transition temperature T_c as a function of U with coupling to H_g Jahn-Teller and A_g non-Jahn-Teller phonons. T_c remains strong with coupling to H_g phonons as U approached the Mott transition ($U_c/W \sim 1.4$). However, the superconductivity vanishes with A_g phonons well before the Mott insulator phase ($U_c/W > 2.4$).

action upward and removed the negative part of V_{eff} . Therefore, no pairing is expected with the A_g phonons. Without the Coulomb interaction ($U = 0$, not plotted here), the nJT coupling produced a very similar V_{eff} to the one in (a) with JT phonons. With $U/W = 0.5$, the depth of the negative part along the $\omega_n = \omega_m$ has been significantly reduced in contrast to the JT case. When U is turned on, the charge fluctuation is increasingly frozen and the A_g phonons then have no dynamic electronic degrees of freedom to couple to. Therefore, the effective local el-ph coupling constant is renormalized away by the Coulomb interaction. These observations are in agreement with conventional beliefs on how el-ph and el-el interplay. For instance, the el-ph and el-el interactions counteract each other, as similarly in the McMillan formula Eq. (8), although with highly renormalized parameters λ and μ^* . The comparison of the JT and nJT couplings in the pairing suggests that the local fluctuation effects in the strongly correlated regime are important in pairing beyond the screening and retardation of the Coulomb interaction.

While the attractive interaction due to local JT phonons is enhanced by the Coulomb interaction, the manybody effects reduce the weight of the coherent states at the Fermi energy. Fully converged DMFT calculation is needed to obtain self-consistent transition temperatures. Fig. 8 shows the transition temperature with U for the alkali doping of A_3C_{60} at $\lambda = 0.6$. With the H_g JT coupling, T_c decreased monotonically but remained finite and surprisingly high for large U . The overestimation of T_c due to the systematic discretization errors [64] in QMC is not large enough to change the conclusion. Although calculations for higher U could not be performed due to the computing time, T_c is expected to remain finite up to the Mott transition at $U_c/W \approx 1.4$. Capone *et al.* [65] have

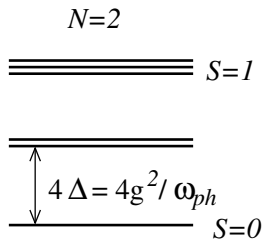


Fig. 9: Schematic energy level scheme in the atomic limit of local $e \times E$ JT coupling with 2 electrons on site.

JT el-ph coupling

also found strong superconducting instability in the JT coupled systems close to MIT in different parameter regimes from those discussed here. On the other hand, with coupling to the A_g nJT phonons superconductivity ceased to exist well before the Mott transition ($U_c/W > 2.4$), as has been anticipated from the absence of an attractive part in Fig. 7(c). The effective interaction with A_g JT phonons can be approximately written

$$\frac{U_{\text{tot}}}{W} \approx \frac{\pi}{4} + \frac{U}{W}, \quad (12)$$

where the first term is the negative- U contribution induced by A_g phonons. With $\lambda = 0.6$, the total interaction becomes repulsive when $U/W \approx 0.47$ in good agreement with the metal-superconductor transition in the full DMFT calculation. The same argument cannot be applied to the H_g JT phonon coupling. It would be very interesting to see whether the transition temperature in the JT coupling goes to zero continuously across the MIT. In a system with a different JT phonon model [66] from C_{60} systems, T_c did not decrease monotonically and dropped discontinuously to zero at MIT.

Local Pairing Mechanism

In order to understand the underlying ideas of the local pairing mechanism, let's consider a simpler model of JT coupling with lower local degeneracy. The system, often called $e \times E$ model, has doubly degenerate e local orbitals and doubly degenerate E_g phonon modes. Due to symmetry, the el-ph coupling can be written as (site index i suppressed)

$$H_{\text{el-ph}} = g \sum_{\sigma} \left[\varphi_1 (n_{1\sigma} \quad n_{2\sigma}) + \varphi_2 (d_{2\sigma}^{\dagger} d_{1\sigma} + h.c.) \right], \quad (13)$$

with the phonon amplitude $\varphi_{\nu} = \sqrt{2}^{-1} (b_{\nu}^{\dagger} + b_{\nu})$. We first examine the local eigenstates. When a site is half-filled with two electrons, there are 6 Fock states. As shown in Fig. 9, these states split into 3 multiplets when coupled to the E_g JT phonons. To the leading order of the el-ph coupling constant g , the lowest states are split by $4\Delta_{\text{JT}} = 4g^2/\omega_{\text{ph}}$. The ground multiplet is a nondegenerate spin singlet $S = 0$. Within this local picture, the important fluctuation is between the multiplets with the excitation energy of order Δ_{JT} . For the moment we view the local system as electronic multiplets in the lowest order of

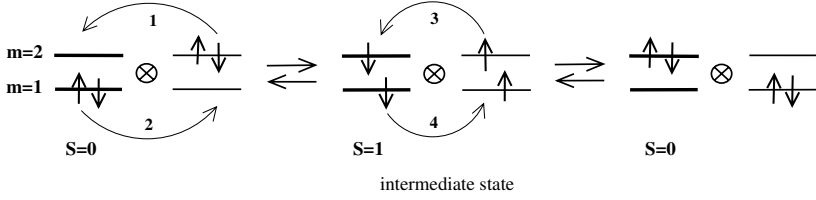


Fig. 10: Equivalent spin-singlet configurations on the left and right panels are coupled by 4 electron hoppings. The impurity site is represented as two (degenerate) levels marked with $m = 1$ and $m = 2$ on the left hand side of the \otimes symbol and the quasi-particle levels are on the right. The energetically favorable intermediate configurations are charge-neutral states as shown in the middle panel for an example. The intermediate state has the local excitation to JT multiplets illustrated in Fig. 9.

the el-ph coupling and ignore fluctuations to phonon satellite states of excitation energy ω_{ph} , which may be significant in real fullerene regime.

With increasing U , electronic states in solid tend to evolve into two classes. The low energy manybody states are coherent throughout the lattice and are mainly responsible for low temperature phenomena. They are commonly called quasi-particle (QP) states which often emerge as a resonance pinned at Fermi energy. Other high energy states are incoherent and usually have short lifetime. Within the DMFT, the energy spectrum of the two states becomes separated as the system approaches the strongly correlated limit [58]. Here, we make a simplification by throwing away the high energy incoherent states and keep the quasi-particle resonant states. Near the Mott transition, the QP peak becomes narrow and we represent the resonant state as a single energy level. Now the system is stripped down to a two site model with one interacting site and the other non-interacting site at Fermi energy level. Although this procedure is probably an oversimplified view on the fullerene system, it is nevertheless useful to conceptualize the local pairing.

As U grows, the spectral weight of the QP peak diminishes and so does the hopping rate onto QP states. Therefore, we treat the effective hopping parameter \tilde{t} as a perturbation to the local basis states. One of the basis state configurations is shown in the left panel of Fig. 10. The degenerate orbitals (marked with $m = 1$ and $m = 2$) on the impurity site is on the left hand side and the QP medium states at zero excitation energy are on the right. The spin singlet basis on the impurity site are part of the local JT ground state

$$|\text{gs}\rangle_{\text{loc}} = \frac{1}{\sqrt{2}} (d_{1\uparrow}^\dagger d_{1\downarrow}^\dagger + d_{2\uparrow}^\dagger d_{2\downarrow}^\dagger) |\text{vac}\rangle_{\text{loc}}. \quad (14)$$

An exchange of electrons with the suggested hoppings 1 and 2 in the diagram results in the intermediate state in the middle panel of Fig. 10. This is via one of many transition paths which involve charge-neutral intermediate states. The d^0 or d^4 configurations on the impurity site are doubly charged states and energetically unfavorable. The intermediate states are excitations from the ground JT multiplet. (See Fig. 9.) The example shown in

Fig. 10 is a high-spin state. The initial state is brought to another degenerate spin-singlet basis by successive electron exchange, for example, via transitions 3 and 4 in Fig. 10. These exchanges of electrons via the intermediate excited state induce coupling between the two equivalent configurations. The process described here can be carried out in a perturbation theory up to the fourth order in \tilde{t} . The pairing correlation energy can be estimated in the simplified model by

$$E_{\text{pair}} = E(N+2) - E(N) - 2[E(N+1) - E(N)], \quad (15)$$

where E_{pair} quantifies the energy gain of adding two interacting electrons together over adding single electron twice independently. For the simplified two site model with the $e \times E$ JT coupling, $E_{\text{pair}} = -7\tilde{t}^4/\Delta_{\text{JT}}U^2$ up to the fourth order of the hopping integral \tilde{t} , consistent with the attractive V_{eff} . The JT coupling parameter Δ_{JT} in the denominator of E_{pair} indicates that the pairing is mediated by local multiplet fluctuations. For nJT coupling, the possible excitations (orthogonal to the degenerate same-charge basis states) are to doubly charged configurations of d^0 and d^4 and results in positive E_{pair} , which agrees with the lack of superconductivity with the nJT coupling at large U in Fig. 8.

Although the above explicit expression for E_{pair} is a result of a somewhat oversimplified model, it points out that the important pairing correlation is through coupling to the local fluctuations which become well-defined as U increases. The above attractive interaction can be also interpreted as correlation of electron pairs. In the example of Fig. 10, the spin singlet electron pair hops to the non-interacting site through processes labeled as 2 and 4. The other pair on the non-interacting site hops back via processes 1 and 3, thereby overlapping in time with the former pair of electrons. To avoid the doubly charged intermediate states, an electron pair must be extended in time and interact in exchange with other electron pairs due to the coupling provided by the overlap in time.

At the heart of the the local pairing mechanism is the attractive interaction due to local fluctuations induced by the Coulomb interaction and multiplet interaction. The JT coupling can be generalized to other types of intrasite interactions. It has been suggested [66] that the Hund's rule coupling, with its symmetry opposite to that of the JT coupling, induces a spin-triplet pairing mediated by the local spin fluctuations when the Coulomb interaction is turned up.

Doping Dependence of T_c

It was pointed out earlier that the transition temperature is determined by the balance between the effective interaction V_{eff} and the coherent metallic weight provided in the uniform (non-interacting) pair susceptibility $\chi_0(Q=0)$. This is most interestingly demonstrated in the doping dependence of T_c . (See Fig. 11.) The doping dependency in the $A_x\text{C}_{60}$ observed by Yildirim *et al.* [45] and others [46] has been one of the major puzzles in the field. Within the conventional el-ph theories, the sharp peak of T_c can only be explained when the electron-phonon coupling strength λ or the Coulomb pseudopotential μ^* (see Eq. (8)) changes abruptly around the half-filling of the t_{1u} -band at $A_3\text{C}_{60}$. However, there are no such fine-tuned features in the DOS of the t_{1u} conduction band. With

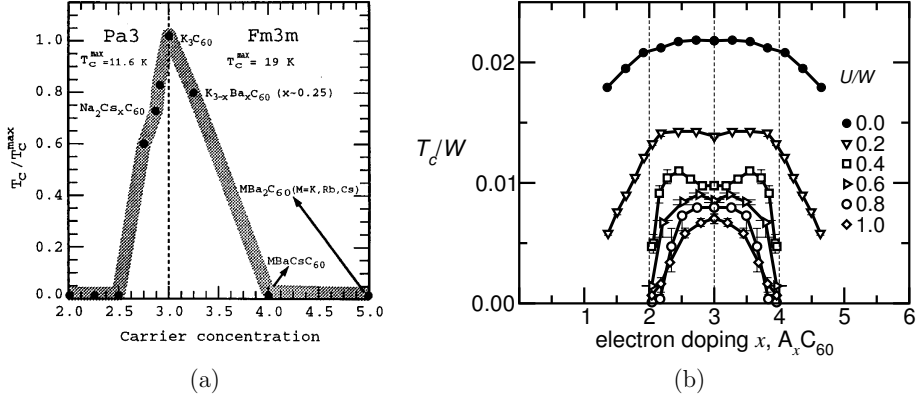


Fig. 11: (a) Superconducting transition temperature T_c as the electron doping level is changed with invariant lattice structure. T_c drops rapidly as the electron doping moves away from the half-filling (carrier concentration = 3) of the t_{1u} conduction band. (After Yildirim, Barbedette *et al.*[45]). (b) DMFT calculation for T_c with electron doping at various Coulomb interaction strength U . The el-ph mass renormalization λ is fixed at 0.6. With increasing U the superconducting transition becomes confined to the doping range of 2–4.

the rotational disorder of C_{60} molecules in the lattice reduces the DOS nearly featureless [67]. These observations have prompted some researchers [47] to propose electronic mechanisms for the pairing in C_{60} .

The DMFT calculation with the JT coupling explains the qualitative features of the experimental results without introducing the electronic mechanism. Although the local pairing is strongly influenced by the Coulomb interaction, the principal pairing medium is the H_g JT phonons. As shown in Fig. 11(b), the region of finite T_c gradually shrinks to $x = 2-4$ as the Coulomb interaction is turned on. When $U = 0$, T_c extends from $x = 0$ to $x = 6$ with the line shape primarily determined by the DOS. A DOS of semi-elliptical shape was used here. As U increases, the superconductivity at $x < 2$ and $x > 4$ becomes quickly suppressed. In the local pairing, the splitting of multiplets of reduced symmetry was crucial. However, at the single electron doping at $x = 1$ (or equivalently $x = 5$ for hole doping), the coupling to JT phonons does not generate multiplet splitting of the d^1 , d^5 space in the dynamic JT limit. Without the local pairing, the system behaves similarly to the non-Jahn-Teller phonon system and the superconductivity is destroyed easily by the Coulomb interaction as pointed out in Figs. 7 and 8.

As the doping changes from 3 towards 2 or 4, T_c drops to zero. This is mainly due to the approaching Mott insulator transition at $x = 2, 4$. As suggested in Fig. 7(b), the effective interaction V_{eff} becomes stronger near $x = 2, 4$ as the system comes closer to the MIT. However, the enhanced V_{eff} is overshadowed by the diminishing coherent part of the electronic states. The overall shape of the T_c curve is self-consistently determined by

these competing effects. It seems that the bumps in the T_c curves for $U/W = 0.4$ and 0.6 are due to a temporary domination by V_{eff} .

Before concluding this section, we discuss parameters used in the calculations shown here. Estimates from photoemission and density of states data has the el-ph coupling $\lambda \sim 1$. However, the Hund's rule coupling is believed to modify this value significantly. The singlet-triplet splitting [54] measured in magnetic response in A_4C_{60} samples suggests that nearly $2/3$ of the JT coupling is compensated by the Hund's rule coupling. The overestimated $\lambda = 0.6$ used in Fig. 11 gave $T_c \sim 50$ K with $W = 0.6$ eV. Although much more time-consuming, calculations with $\lambda = 0.3$ gave improved results. First, read off from Fig. 5(a) for A_3C_{60} , $U_c/W \approx 1.8$ at the MIT is within the experimental bounds $U/W = 1.5 - 2.5$. Second, using the lower end value of $U/W = 1.5$, DMFT calculation with $\lambda = 0.3$ gave $T_c = 15 - 20$ K in reasonable agreement with $T_c = 19$ K for K_3C_{60} [7] and $T_c = 29$ K for Rb_3C_{60} [8].

5. CONCLUSION

Alkali-doped fullerene systems stand as an excellent example where the electron-phonon coupling interacts with the electron-electron interaction and local degeneracy in a highly non-trivial way. Large degeneracy of molecular orbitals and molecular vibrations serves as internal degrees of freedom on each C_{60} sites of the lattice and their fluctuation develops for pairing medium of superconductivity. With the degeneracy, the symmetry of the interaction proves crucial in electron pairing. Although the fullerene system has often been regarded as conventional el-ph superconductors, a close examination reveals much richer superconductivity arising from the high symmetry of the molecular structure and strong manybody interactions. The system also provides a wonderful testing ground of basic assumptions of superconductivity theory which have been taken for granted for many years.

There still remain several key questions to be resolved in the local pairing theory. The local pairing is crucial for the strong superconductivity in fullerene systems, but not much of its property is known. Detailed study of the multiplet fluctuations and the pairing mechanism should follow. Isotope effect is one of the most interesting superconducting properties to check. The isotope exponent α is significantly smaller than 0.5 but still within the prediction of the Eliashberg theory. In the simplified limit of the local pairing as in the argument following Fig. 9, the multiplet level spacing is determined by $\lambda \propto \Delta_{\text{JT}}$. Changing ω_{ph} , while keeping Δ_{JT} constant, will have little effects on the pairing in the local limit. However, in the real C_{60} systems, the anti-adiabatic phonon limit is not accurate and excitations to phonon satellites could be important. Therefore it would be interesting to see how much α is reduced by the local pairing effect in the realistic parameter range. Some of other superconducting properties such as the ratio $2\Delta/T_c$ ($\Delta =$ superconducting order parameter) also lie within the bounds of the conventional theories. It will be important to check the consistency of the local pairing with those experimental results.

Recent developments [4] in the fullerene research have brought the manybody effects in the fulleride system into attention. Full-fledged manybody calculations have been

instrumental for the establishment. The DMFT has been very effective in including various manybody interactions on the same footing and studying the Mott transition and superconductivity in a coherent manner. However, there are some open problems in the field yet to be understood in the manybody framework. Without the momentum dependence as assumed in the DMFT the specific heat enhancement has to be large near the Mott transition, where experiments produced only a small change from the non-interacting limit. It is of interest to investigate how much of the frequency-dependent contribution is canceled by the momentum dependency. Along the similar line, the lattice constant dependence of the Hall coefficient [68] should be addressed by including lattice structure effect.

REFERENCES

- [1] H. W. Kroto, J. R. Heath, S. C. O'Brien, R. F. Curl, and R. E. Smalley, *Nature* **318** (1985) 162.
- [2] Harold Kroto, *Rev. Mod. Phys.* **69** (1997) 703.
- [3] A. P. Ramirez, *Superconductivity Review* **1**, (1994), pp.1-101.
- [4] O. Gunnarsson, *Rev. Mod. Phys.* **69** (1997) 575.
- [5] W. Krätschmer, L. D. Lamb, K. Fostiropoulos, and D. R. Huffman, *Nature* **347** (1990) 354.
- [6] R. C. Haddon, A. F. Hebard, M. J. Rosseinsky, D. W. Murphy, S. J. Duclos, K. B. Lyons, B. Miller, J. M. Rosamilia, R. M. Fleming, A. R. Kortan, S. H. Glarum, A. V. Makhija, A. J. Muller, R. H. Eick, S. M. Zahurak, R. Tycko, G. Dabbagh, and F. A. Thiel, *Nature* **350** (1991) 320.
- [7] A. F. Hebard, M. J. Rosseinsky, R. C. Haddon, D. W. Murphy, S. H. Glarum, T. T. M. Palstra, A. P. Ramirez and A. R. Kortan, *Nature* **350** (1991) 600.
- [8] M. J. Rosseinsky, A. P. Ramirez, S. H. Glarum, D. W. Murphy, R. C. Haddon, A. F. Hebard, T. T. M. Palstra, A. R. Kortan, S. M. Zahurak, and A. V. Makhija, *Phys. Rev. Lett.* **66** (1991) 2830.
- [9] K. Tanigaki, T. W. Ebbesen, S. Saito, J. Mizuki, J. S. Tsai, Y. Kubo, and S. Kuroshima, *Nature* **352** (1991) 222.
- [10] J. Nagamatsu, N. Nakagawa, T. Muranaka, Y. Zenitani, and J. Akimitsu, *Nature* **410** (2001) 63.
- [11] T. Yildirim, J. E. Fischer, R. Dinnebier, P. W. Stephens, and C. L. Lin, *Solid State Commun.* **93** (1995) 269.
- [12] D.W. Murphy, M.J. Rosseinsky, R.M. Fleming, R. Tycko, A.P. Ramirez, R.C. Haddon, T. Siegrist, G. Dabbagh, J.C. Tully, R.E. Walstedt, *J. Phys. Chem. Solids* **53** (1992) 1321; R.F. Kiefl, T. L. Duty, J. W. Schneider, A. MacFarlane, K. Chow, J. Elzey, P. Mendels, G. D. Morris, J. H. Brewer, E. J. Ansaldo, C. Niedermayer, D. R. Noakes, C. E. Stronach, B. Hitti, and J. E. Fischer, *Phys. Rev. Lett.* **69** (1992) 2005.
- [13] J. R. Schrieffer, *Theory of superconductivity*, Addison-Wesley Publishing Company, New York (1994).
- [14] P. Morel and P. W. Anderson, *Phys. Rev.* **125** (1962) 1263.
- [15] O. Gunnarsson, and G. Zwicknagl, *Phys. Rev. Lett.* **69** (1992) 957.
- [16] M. Schluter, M. Lannoo, M. Needels, G. A. Baraff, and D. Tomanek, *Phys. Rev. Lett.* **68** (1992) 526.
- [17] R. W. Lof, M. A. van Veenendaal, B. Koopmans, H. T. Jonkman, and G. A. Sawatzky, *Phys. Rev. Lett.* **68** (1992) 3924.
- [18] P. A. Brühwiler, A. J. Maxwell, A. Nilsson, N. Mårtensson, and O. Gunnarsson, *Phys. Rev. B* **48** (1993) 18296.
- [19] D. M. Newns, H. R. Krishnamurthy, P. C. Pattnaik, C. C. Tsuei, and C. L. Kane, *Phys. Rev. Lett.* **69** (1992) 1264.
- [20] J. K. Freericks and M. Jarrell, *Phys. Rev. Lett.* **75** (1995) 2570.

- [21] A. Lanzara, P. V. Bogdanov, X. J. Zhou, S. A. Kellar, D. L. Feng, E. D. Lu, T. Yoshida, H. Eisaki, A. Fujimori, K. Kishio, J.-I. Shimoyama, T. Noda, S. Uchida, Z. Hussain, and Z.-X. Shen, *Nature* **412** (2001) 510.
- [22] M. Lannoo, G. A. Baraff, M. Schluter, and D. Tomanek, *Phys. Rev. B* **44** (1991) 12106.
- [23] M. S. Fuhrer, K. Cherrey, A. Zettl, M. L. Cohen, and V. H. Crespi, *Phys. Rev. Lett.* **83** (1999) 404.
- [24] O. Gunnarsson, H. Handschuh, P. S. Bechthold, B. Kessler, G. Ganteför, and W. Eberhardt, *Phys. Rev. Lett* **74** (1993) 13944.
- [25] W. A. Vareka and A. Zettl, *Phys. Rev. Lett.* **72** (1994) 4121.
- [26] F. Marsiglio, T. Startseva, and J. P. Carbotte, *Phys. Lett. A* **245** (1998) 172.
- [27] J. Winter and H. Kuzmany, *Phys. Rev. B* **53** (1996) 655.
- [28] Z. Zhang, C.-C. Chen, S. P. Kelty, H. Dai, and C. M. Lieber, *Nature* **353** (1991) 333.
- [29] D. Kollar, M. C. Martin, and L. Mihaly, *Phys. Rev. Lett.* **77** (1996) 4082.
- [30] R. Tycho, G. Dabbagh, M. J. Rosseinsky, D. W. Murphy, A. P. Ramirez, and R. M. Fleming, *Phys. Rev. Lett.* **68** (1992) 1912.
- [31] S. Sasaki, A. Matsuda, and C. W. Chu, *J. Phys. Soc. Japan* **63** (1994) 670.
- [32] P. Auban-Senzier, G. Quirion, D. Jerome, P. Bernier, S. Della-Negra, C. Fabre, and A. Rassat, *Synthetic Metals* **56** (1993) 3027.
- [33] V. A. Stenger, C. H. Pennington, D. R. Buffinger, and R. P. Ziebarth, *Phys. Rev. Lett.* **74** (1995) 1649.
- [34] R. F. Kiefl, W. A. MacFarlane, K. H. Chow, S. Dunsiger, T. L. Duty, T. M. S. Johnston, J. W. Schneider, J. Sonier, L. Brard, R. M. Strongin, J. E. Fischer, and A. B. Smith III, *Phys. Rev. Lett.* **70** (1993) 3987.
- [35] L. Degiorgi, P. Wachter, G. Grüner, S.-M. Huang, J. Wiley, and R. B. Kaner, *Phys. Rev. Lett.* **69** (1992) 2987; L. Degiorgi, B. Briceno, M. S. Fuhrer, A. Zettl, and P. Wachter, *Nature* **369** (1994) 541; L. Degiorgi, *Mod. Phys. Lett. B* **9** (1995) 445.
- [36] C. Gu, B. W. Veal, R. Liu, A. P. Paulikas, P. Kostic, H. Ding, K. Gofron, J. C. Campuzano, J. A. Schluter, H. H. Wang, U Geiser, and J. M. Williams, *Phys. Rev. B* **50** (1994) 16566.
- [37] R. Hesper, L. H. Tjeng, A. Heeres, G. A. Sawatzky, *Phys. Rev. Lett.* **85** (2000) 1970.
- [38] C.-C. Chen and C. M. Lieber, *J. Am. Chem. Soc.* **114** (1992) 3141.
- [39] C.-C. Chen and C. M. Lieber, *Science* **259** (1993) 655.
- [40] T. W. Ebbesen, J. S. Tsai, K. Tanigaki, J. Tabuchi, Y. Shimakawa, Y. Kubo, I. Hirose, and J. Mizuki, *Nature* **355** (1992) 620; A. A. Zakhidov, K. Imaeda, D. M. Petty, K. Yakushi, H. Inokuchi, K. Kikuchi, I. Ikemoto, S. Suzuki, and Y. Achiba, *Phys. Lett. A* **164** (1992) 355; A. P. Ramirez, A. R. Kortan, M. J. Rosseinsky, S. J. Duclos, A. M. Muzsca, R. C. Haddon, D. W. Murphy, A. V. Makhija, S. M. Zahurak, and K. B. Lyons, *Phys. Rev. Lett.* **68** (1992) 1058.
- [41] T. W. Ebbesen, J. S. Tsai, K. Tanigaki, H. Hiura, Y. Shimakawa, Y. Kubo, I. Hirose, and J. Mizuki, *Physica C* **203** (1992) 163.

- [42] B. Burk, V. H. Crespi, A. Zettl, and M. L. Cohen, Phys. Rev. Lett. **72** (1994) 3706.
- [43] J. Diederichs, J. S. Schilling, K. W. Herwig, and W. B. Yelon, J. Phys. Chem. Soc. **122** (2000) 12352.
- [44] R. M. Fleming, A. P. Ramirez, M. J. Rosseinsky, D. W. Murphy, R. C. Haddon, S. M. Zahurak, and A. V. Makhija, Nature **352** (1991) 787.
- [45] T. Yildirim, L. Barbedette, J. E. Fischer, C. L. Lin, J. Robert, P. Petit, and T. T. M. Palstra, Phys. Rev. Lett. **77** (1996) 167.
- [46] M. Kosaka, K. Tanigaki, K. Prassides, S. Margadonna, C. M. Brown, A. Lappas, and A. N. Fitch, Phys. Rev. B **59** (1999) R6628; S. Margadonna, K. Prassides, A. N. Fitch, M. Kosaka, and K. Tanigaki, J. Am. Chem. Soc. **121** (1999) 6318.
- [47] S. Chakravarty, M. P. Gelfand, and S. Kivelson, Science **254**, 970 (1991); S. Chakravarty and S. Kivelson, Europhys. Lett. **16** (1999) 751.
- [48] J. E. Han, O. Gunnarsson, and V. H. Crespi, Phys. Rev. Lett. **90** (2003) 167006.
- [49] D. S. Bethune, G. Meijer, W. C. Tang, H. J. Rosen, W. G. Golden, H. Seki, C. A. Brown, and M. S. de Vries, Chem. Phys. Lett. **179** (1991) 181.
- [50] M. G. Mitch, S. J. Chase, and J. S. Lannin, Phys. Rev. Lett. **68**, 883 (1992); M. G. Mitch, S. J. Chase, and J. S. Lannin, Phys. Rev. B **46** (1992) 3696.
- [51] J. E. Han, E. Koch, and O. Gunnarsson, Phys. Rev. Lett. **84** (2000) 1276.
- [52] A. Auerbach, N. Manini, and E. Tosatti, Phys. Rev. B **49** (1994) 12998.
- [53] P. B. Allen, Phys. Rev. B **6** (1972) 2577.
- [54] G. Zimmer, M. Helme, M. Mehring, and Rachdi, Europhys. Lett. **27** (1994) 543; I. Lukyanchuk, N. Kirova, F. Rachdi, C. Goze, P. Molinie, and M. Mehring, Phys. Rev. B **51** (1995) 3978; G. Zimmer, M. Mehring, C. Goze, and F. Rachdi, Phys. Rev. B **52** (1995) 13300.
- [55] O. Gunnarsson, E. Koch, and R. M. Martin, Phys. Rev. B **54** (1996) R11026.
- [56] E. Koch, O. Gunnarsson, and R. M. Martin, Phys. Rev. B **60** (1999) 15714.
- [57] J. E. Han, M. Jarrell and D. L. Cox, Phys. Rev. B **58** (1998) R4199.
- [58] A. Georges, Gabriel Kotliar, Werner Krauth and Marcelo J. Rozenberg, Rev. Mod. Phys. **68** (1996) 13.
- [59] R. Blankenbecler, D. J. Scalapino, and R. L. Sugar, Phys. Rev. D **24** (1981) 2278.
- [60] R. M. Fye and J. E. Hirsch, Phys. Rev. B **38** (1988) 433.
- [61] E. Koch, O. Gunnarsson, and R. M. Martin, Phys. Rev. Lett. **83** (1999) 620.
- [62] W. L. McMillan, Phys. Rev. **167** (1968) 331.
- [63] C. Owen and D. J. Scalapino, Physica (Amsterdam) **55** (1971) 691.
- [64] For the worst case of $U/W = 1.0$, T_c was overestimated by about 20 %.
- [65] M. Capone, M. Fabrizio, C. Castellani, and E. Tosatti, Science **296** (2002) 2364.
- [66] J. E. Han, cond-mat/0401104 (to appear in Phys. Rev. B)
- [67] S. Satpathy, V. P. Antropov, O. K. Andersen, O. Jepsen, O. Gunnarsson, and A. I. Liechtenstein, Phys. Rev. B **46**, (1992) 1773.
- [68] L. Lu, V. H. Crespi, M. S. Fuhrer, A. Zettl, and M. L. Cohen, Phys. Rev. Lett. **74** (1995) 1637.

CHEMICAL DESIGN OF COPPER-OXIDE SUPERCONDUCTORS: – HOMOLOGOUS SERIES AND OXYGEN ENGINEERING –

M. Karppinen and H. Yamauchi

Materials and Structures Laboratory, Tokyo Institute of Technology,
Yokohama 226-8503, Japan

1. INTRODUCTION

Two-dimensional CuO_2 planes in which copper atoms nominally possess an intermediate valence value between II and III have appeared to be essential for superconductivity of copper oxides with holes as charge carriers. Contrary to this, in *n*-type superconductive copper oxides, copper atoms have an intermediate valence state of I/II. In both cases, control over the charge carrier concentration has been achieved by tuning the precise mixed-valence value of copper atoms in the superconductive CuO_2 plane(s). In terms of valence tuning, structures allowing for oxygen nonstoichiometry are advantageous. At the same time, within the conductive copper-oxide framework the charge has to be uniformly distributed between each copper-oxygen polyhedron to ensure itinerancy of the charge carriers. Therefore high electrical conductivity is expected only in CuO_2 planes that consist of equivalent Cu-O polyhedra. In line with this, high- T_c superconductivity occurs in layered structures built up with (i) conductive copper-oxide layers in which the oxygen content is stoichiometric and (ii) spacing layer(s) with oxygen and/or cation nonstoichiometry, *i.e.* tunable charge.

In the structure of the first high- T_c superconductor, $(\text{La,Ba})_2\text{CuO}_{4\pm\delta}$ [1], a single CuO_2 plane is combined with a $[(\text{La,Ba})\text{O}_{1\pm\delta/2}]_2$ double-layer block only. Since this discovery, a variety of superconductive copper-oxide phases with a number of different layers being involved have been synthesized. Depending on the piling sequence of the layers various structure blocks with different characteristics in terms of charge balance and doping are formed. Based on the

types of layers involved, the structures of superconductive and related layered copper oxides have successfully been classified into “two main categories” [2,3], and further understood as members of different “homologous series” [4-6], *viz.* Chapter 2. With such a large number of superconductive copper-oxide phases synthesized and thoroughly characterized, it has become easier to recognize the “yet-missing” phases and design the strategies for searching for such. It has also become possible to find various trends and draw general conclusions related to the functions of the different structure blocks in terms of redox characteristics and charge balance, as being reviewed in Chapters 3 and 4, respectively. Here one of the key concepts is “oxygen engineering” [7]. It is also important to recognize that, even though ideal rather than real structures are considered for the purpose of classification, it is the small and delicate deviations from the ideal structures that control the material properties such as charge/carrier distribution and superconductivity [6,8,9]. Such factors and their fine-tuning are shortly discussed in Chapter 5.

2. STRUCTURAL CATEGORIZATION

Copper-oxide superconductors are all derived from an oxygen-vacancy-ordered perovskite (P) block, $Q_{n-1}Cu_nO_{2n}$, in which oxygen-free Q metal layers alternate with vacancy-free CuO_2 planes. Piling such superconductive $Q_{n-1}Cu_nO_{2n}$ blocks with other structural units, *i.e.* other types of perovskite block, rock-salt (RS) layers and/or fluorite (F) layers, results in a c -axis-elongated multi-layered unit cell known for high- T_c superconductors. Depending on the involvement of the differently structured layers the existing superconductive copper-oxide phases are categorized into two main categories: Category-A contains the phases which are built up with P- and RS-structured layers only, whereas the phases of Category-B contain F-structured layers as well (Fig. 1) [2,3]. Within the two categories, the phases are further divided into homologous series on the basis of the number and cation composition of the layers in the nonsuperconductive portion of the structure, *i.e.* “blocking block”.

2.1. Homologous Series of Category-A

As shown in Fig. 1, the structures of Category-A phases contain alternating $M_mO_{m\pm\delta}$ “charge-reservoir” blocks with m units of $MO_{1\pm\delta/m}$ layers ($M = Cu, Bi, Pb, Tl, Hg, Al, Ga, C, B, etc.$) and superconductive $Q_{n-1}Cu_nO_{2n}$ blocks with n CuO_2 planes and $n-1$ Q metal layers [$Q = Ca, rare-earth\ element\ (R)$] [4]. The $M_mO_{m\pm\delta}$ and $Q_{n-1}Cu_nO_{2n}$ blocks are separated from each other by a single AO layer ($A = Ba, Sr, La, etc.$) such that the structure repeats the layer sequence of $AO-(MO_{1\pm\delta/m})_m-AO-CuO_2-(Q-CuO_2)_{n-1}$ and the stoichiometry of the phase is given by $M_mA_rQ_{n-1}Cu_nO_{m+r+2n\pm\delta}$. Each such phase is denoted in an unambiguous way by $M-m^{(A)}r^{(Q)}(n-1)n$ or in short $M-mr(n-1)n$. Sometimes it is also useful to indicate the crystallographic structure of the charge-reservoir block, *e.g.* RS or P, and/or the possible halogen substituent, X , using the somewhat longer formula of $M-m^{(A)}r^{(Q)}(n-1)n[X]:RS/P$ [6].

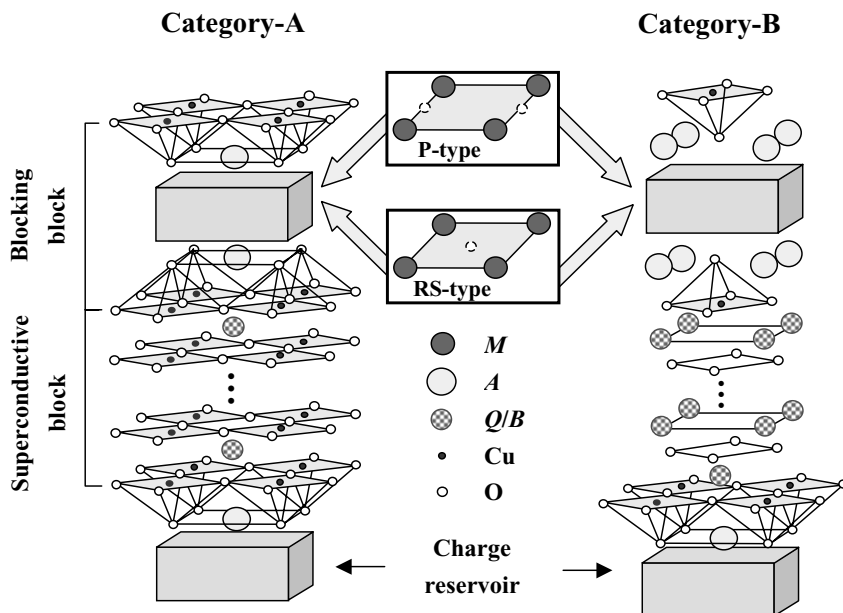


Fig. 1. Schematic illustration of crystal structures of Category-A (left) and Category-B (right) multi-layered copper oxides.

In Table 1, the multi-layered $M-mr(n-1)n$ copper-oxide structures together with some representative compounds are arranged in the order of increasing m (0~3), r (1, 2) and n (1~4). Note that, as far as the structures known to exist at the moment are concerned the table could be continued up to $n=9$ [10]. In each $M-mr(n-1)n$ phase with $m > 0$ the number of AO layers between two superconductive $Q_{n-1}Cu_nO_{2n}$ blocks sandwiching the charge-reservoir block is fixed at $r=2$. Also in the case of $m=0$, superconductive phases have been so far obtained only for $r=2$, i.e. the “zero” $02(n-1)n$ phases (see Section 2.1.3). To be able to include the “not-yet-superconductorized” $01(n-1)n$ phases in the general classification scheme, we, however, consider r as a variable having two possible values of 1 and 2, with the condition that: $r=1$ or 2 for $m=0$ and $r=2$ for $m \geq 1$ [6]. For $r=2$ and odd m values, i.e. $m=1$ and 3, the unit cell possesses primitive (P) symmetry and contains only one $M-m2(n-1)n$ formula unit, while for even m values, i.e. $m=0$ and 2, the unit cell is doubled along c axis to contain two $M-m2(n-1)n$ formula units. At the same time P symmetry changes to body-centered (I) symmetry.

By definition, $M_m A_r Q_{n-1} Cu_n O_{m+r+2n \pm \delta}$ or $M-m^{(A),r^{(Q)}}(n-1)n$ phases for which the $AO-(MO_{1 \pm \delta/m})_m AO$ portion is common, form a homologous series [4,6]. In order to establish a homologous series, realizing at least (the first) three members experimentally may be considered as a proper requirement. This is partly based on the belief that the phase-formation

Table 1. Multi-layered copper-oxide structures of Category-A: $M_m A_r Q_{n-1} Cu_n O_{m+r+2n\pm\delta}$ or $M_{mr}(n-1)n$, together with representative compounds as arranged in the order of increasing m , r and n . Here, in terms of n the table extends only up to $n = 4$ even though phases up to $n = 9$ have been experimentally detected. Also note that when $n \rightarrow \infty$, the formula ends up with 0011 which is the name for the so-called “infinite-layer” structure (see Section 2.3).

| 01($n-1$)n | 02($n-1$)n | $M-12(n-1)n$ | $M-22(n-1)n$ | $M-32(n-1)n$ |
|---|--|---|--|--|
| 0101 LaCuO ₃ | 0201 (La,Sr,Ba) ₂ CuO ₄ Sr ₂ CuO ₄ Sr ₂ CuO ₂ F ₂ | $M-1201$ HgBa ₂ CuO ₄ Tl(Ba,Y) ₂ CuO ₅ | $M-2201$ Bi ₂ Sr ₂ CuO ₆ Tl ₂ Ba ₂ CuO ₆ | $M-3201$ (Pb _{2/3} Cu _{1/3}) ₃ (Sr,La) ₂ CuO ₆ |
| 0112 BaY(Cu,Fe) ₂ O ₃ | 0212 La ₂ SrCu ₂ O ₆ Sr ₂ CaCu ₂ O ₆ Ba ₂ CaCu ₂ O ₆ Sr ₂ CaCu ₂ O ₄ F ₂ | $M-1212$ HgBa ₂ CaCu ₂ O ₆ TlBa ₂ CaCu ₂ O ₇ CuBa ₂ YCu ₂ O ₇ | $M-2212$ Bi ₂ Sr ₂ CaCu ₂ O ₈ Tl ₂ Ba ₂ CaCu ₂ O ₈ | $M-3212$ (Pb _{2/3} Cu _{1/3}) ₃ Sr ₂ (Y,Ca)Cu ₂ O ₈ |
| | 0223 Sr ₂ Ca ₂ Cu ₃ O ₈ Ba ₂ Ca ₂ Cu ₃ O ₈ Sr ₂ Ca ₂ Cu ₃ O ₆ F ₂ | $M-1223$ HgBa ₂ Ca ₂ Cu ₃ O ₈ TlBa ₂ Ca ₂ Cu ₃ O ₉ CuBa ₂ Ca ₂ Cu ₃ O ₉ | $M-2223$ Bi ₂ Sr ₂ Ca ₂ Cu ₃ O ₁₀ Tl ₂ Ba ₂ Ca ₂ Cu ₃ O ₁₀ | $M-3223$ (Cu,C,Ba) ₃ Ba ₂ Ca ₂ Cu ₃ O ₉ |
| | 0234 Sr ₂ Ca ₃ Cu ₄ O ₁₀ Ba ₂ Ca ₃ Cu ₄ O ₁₀ | $M-1234$ HgBa ₂ Ca ₃ Cu ₄ O ₁₀ TlBa ₂ Ca ₃ Cu ₄ O ₁₁ CuBa ₂ Ca ₃ Cu ₄ O ₁₁ | $M-2234$ Tl ₂ Ba ₂ Ca ₃ Cu ₄ O ₁₂ | $M-3234$ (Cu,C,Ba) ₃ Ba ₂ Ca ₃ Cu ₄ O ₁₁ |

mechanism for phases with $n \geq 3$ in the same homologous series is the same, but most likely different from those of phases with $n = 1$ and 2.

By the end of year 1992 only four homologous series fulfilling the above definitions, *i.e.* Bi-2^(Sr)2($n-1$) n [11-13], Tl-2^(Ba)2($n-1$) n [14,15], Tl-1^(Ba)2($n-1$) n [16] and Tl-1^(Sr)2($n-1$) n [17], had been verified, but since January 1993 many other homologous series have been discovered. All these later series, with the exception of Hg-1^(Ba)2($n-1$) n [18,19], are obtained only through high-pressure (HP) synthesis [20,21]. The best established examples of these HP-synthesized series are: 0^(Sr)2($n-1$) n [22], Cu-1^(Ba)2($n-1$) n [23,24], Pb-1^(Sr)2($n-1$) n [25,26], (Cu,C)-1^(Ba)2($n-1$) n [27], (C,B)-1^(Sr)2($n-1$) n [28], Al-1^(Sr)2($n-1$) n [29], Ga-1^(Sr)2($n-1$) n [30], B-1^(Sr)2($n-1$) n [31], [(Cu,C)_{2/3}Ba_{1/3}]-3^(Ba)2($n-1$) n [32], (Cu,S)-1^(Sr)2($n-1$) n [33], (Cu,P)-1^(Sr)2($n-1$) n [34], (Hg,Tl)-2^(Ba)2($n-1$) n [35,36], 0^(Sr)2($n-1$) n [F] [37,38], (Cu,Ge)-1^(Sr)2($n-1$) n [39], (Cr,Cu)-1^(Sr)2($n-1$) n [10], (Cu,V)-1^(Sr)2($n-1$) n [40], (Cu,N,C)-1^(Sr)2($n-1$) n [41] and 0^(Ba)2($n-1$) n [42-44]. In the following Sections 2.1.1-2.1.4, some of these series are discussed in more detail.

From the knowledge accumulated for the various homologous series of Category-A, we make the following four empirical observations:

- (1) For phases with $n \geq 3$, the Q -cation site is solely occupied by Ca [4]: both isovalent and aliovalent substitution attempts for Ca have all been unsuccessful so far.
- (2) No trace of oxygen is detected in the Q -cation layer. (Here the nature seems to favour the occurrence of high- T_c superconductivity, as it is believed that even small amounts of excess oxygen atoms in the Q layer would be detrimental for the superconductivity!)
- (3) Within each homologous series, the highest T_c belongs to the $n = 3$ member [6].
- (4) M - $m^{(\text{Ba})}2(n-1)n$ phases show higher T_c 's than the corresponding M - $m^{(\text{Sr})}2(n-1)n$ phases [45].

It is amazing to note that even though these simple empirical facts are rather widely recognized, they have not been completely understood from the fundamental chemistry and/or physics points of view. This applies especially to the first three points. The last one is understood by the smaller size of Sr as compared to Ba (*viz.* Section 3.2): the smaller Sr-O layer puts the CuO_2 plane(s) under compressive stress that then results in stronger in-plane O-Cu-O buckling and thereby in the lower T_c values.

2.1.1. M - $m2(n-1)n$:RS phases

The Bi-based phases comprised the first homologous series, *i.e.* $\text{Bi-}2^{(\text{Sr})}2(n-1)n$:RS. For this series only the first three members, *i.e.* $\text{Bi}_2\text{Sr}_2\text{CuO}_{6+\delta}$ (Bi-2201), $\text{Bi}_2\text{Sr}_2\text{CaCu}_2\text{O}_{8+\delta}$ (Bi-2212) and $\text{Bi}_2\text{Sr}_2\text{Ca}_2\text{Cu}_3\text{O}_{10+\delta}$ (Bi-2223), have been experimentally verified [11-13]. The real structures of the Bi-22($n-1$) n phases are more complex than those suggested by the basic model of Fig. 1. The origin of this is in the mismatch between the preferred ab -plane dimensions of the CuO_2 and $\text{BiO}_{1\pm\delta/2}$ layers, which leads to an incommensurate structural modulation due to atomic rearrangements and incorporation of excess oxygen in the $\text{Bi}_2\text{O}_{2\pm\delta}$ charge-reservoir block [46]. Moreover, the "lonely" s^2 electron pair of trivalent bismuth requires extra space around the Bi^{III} ion, and thus contributes to the deformation of the Bi-O coordination sphere.

Simultaneous replacements of Bi and Sr by Tl and Ba yielded the first thallium-based homologous series, $\text{Tl-}2^{(\text{Ba})}2(n-1)n$:RS [14,15]. For the $n = 3$ member of this series a T_c value was recorded that for the first time exceeded 130 K [47]. The $\text{Tl-}1^{(\text{Ba})}2(n-1)n$:RS series in which the charge-reservoir block is a single layer of $\text{TlO}_{1\pm\delta}$ was the first homologous series of the $m = 1$ type [16]. Later another thallium-based series, $\text{Tl-}1^{(\text{Sr})}2(n-1)n$:RS [17], and many other series including the record-high- T_c series $\text{Hg-}1^{(\text{Ba})}2(n-1)n$:RS [18,19] have been discovered at $m = 1$.

In principle the $\text{Hg-}1^{(\text{Ba})}2(n-1)n$:RS phases are isostructural with the corresponding $\text{Tl-}1^{(\text{Ba})}2(n-1)n$:RS phases. However, the oxygen coordination polyhedra around the trivalent Tl and the divalent Hg atoms are quite different, since the oxygen site of the $MO_{1-\delta}$ layer is almost fully occupied in the case of thallium but more than 50 % vacant in the case of mercury, *i.e.* $\delta > 0.5$ for the $\text{HgO}_{1-\delta}$ charge-reservoir block [48]. Thus, Hg atoms in the $\text{Hg-}1^{(\text{Ba})}2(n-1)n$:RS phases possess a two-fold linear oxygen coordination commonly observed for Hg atoms in Hg^{II} compounds. In the BaO layer, the oxygen atom (apical oxygen) is shifted from the ideal rock-salt position to the vicinity of the $\text{HgO}_{1-\delta}$ block, while the barium atom is rather close to the

CuO_2 - $(Q\text{-CuO}_2)_{n-1}$ block. As a result of this crystallographic feature, the CuO_2 plane just beneath the Ba plane is nearly flat [48]. This may be considered as one of plausible explanations to rationalize the fact that for each n , it is the Hg-based phase that possesses the highest T_c value. Most profoundly, for the $n=3$ member of the $\text{Hg-1}^{(\text{Ba})}2(n-1)n$ series the record values of T_c are as follows: 135 K [19] and 138 K [49] for nonsubstituted and fluorine-substituted samples, respectively, as measured under ambient pressure, and > 150 K [50] and 166 K [51] for the same compositions, respectively, when measured under high pressures.

After the $\text{Hg-1}^{(\text{Ba})}223$ phase was recognized to possess the highest-ever-recorded value of T_c , efforts were made to synthesize Hg-based phases with $m=2$ [35,36], since among the thallium copper oxides the $m=2$ phases possess higher T_c values than the corresponding $m=1$ phases. However, the T_c values recorded for Hg-2223 never exceeded those for Hg-1223.

2.1.2. $M\text{-}m2(n-1)n\text{:P}$ phases

The most thoroughly characterized superconductive compound, $\text{YBa}_2\text{Cu}_3\text{O}_{7-\delta}$ or the so-called “Y-123” phase [52], has a multi-layered structure with the layer sequence, $\text{BaO-CuO}_{1-\delta}\text{-BaO-CuO}_2\text{-Y-CuO}_2$, and thus a single $\text{CuO}_{1-\delta}$ chain with an oxygen-deficient perovskite-type arrangement of the Cu and O atoms as the charge-reservoir constituent. The initial dream to insert additional CuO_2 planes (and additional Q layers to fulfill the charge-neutrality condition) into the $\text{YBa}_2\text{Cu}_3\text{O}_{7-\delta}$ structure in order to increase T_c in this system became true when the $n=3\sim 6$ phases of the $\text{Cu-1}^{(\text{Ba})(\text{Ca})}2(n-1)n\text{:P}$ series were discovered utilizing HP synthesis techniques [23,24]. As had been expected, the highest T_c value achieved for the Cu-1223 phase, *i.e.* ~ 120 K [53-55], clearly exceeded that of $\text{YBa}_2\text{Cu}_3\text{O}_{7-\delta}$. Even more importantly, this discovery demonstrated that the $\text{YBa}_2\text{Cu}_3\text{O}_{7-\delta}$ compound is not just an “exceptional” phase but an $n=2$ member of the $\text{Cu-1}^{(\text{Ba})}2(n-1)n\text{:P}$ homologous series, and should thus be called as Cu-1212:P or $\text{CuBa}_2\text{YCu}_2\text{O}_{7-\delta}$ [4,6].

The lead-based compound $(\text{Pb}_{2/3}\text{Cu}_{1/3})_3\text{Sr}_2(\text{Y,Ca})\text{Cu}_2\text{O}_{9\pm\delta}$ [55] was the first superconductive copper oxide with a three-layer charge-reservoir block, *i.e.* $m=3$. In the middle $\text{CuO}_{1\pm\delta}$ layer of the $\text{PbO-CuO}_{1\pm\delta}\text{-PbO}$ charge reservoir, the extra oxygen atoms arrange at perovskite positions to form a CuO_2 plane when $1\pm\delta\approx 2$, and the phase may thus be expressed as $(\text{Pb}_{2/3}\text{Cu}_{1/3})\text{-}3212\text{:P}$. The $(\text{Pb}_{2/3}\text{Cu}_{1/3})\text{-}3201\text{:P}$ phase has also been synthesized and found to superconduct [57,58], whereas the higher ($n\geq 3$) members of the $(\text{Pb}_{2/3}\text{Cu}_{1/3})\text{-}32(n-1)n\text{:P}$ series remain to be discovered yet. On the other hand, $m=3$ superconductors with $n=3\sim 5$ were stabilized through HP synthesis in the Ba-Ca-Cu-C-O system, *i.e.* $[(\text{Cu,C})_{2/3}\text{Ba}_{1/3}]\text{-}32(n-1)n$ for which the three-layer charge-reservoir block obeys the layer sequence of $(\text{Cu,C})\text{O}_{1-\delta/2}\text{-BaO-(Cu,C)}\text{O}_{1-\delta/2}$ [32].

2.1.3. “Zero” $02(n-1)n$ phases and their water derivatives

Among the different Category-A superconductors, those with an $A_2Q_{n-1}\text{Cu}_n\text{O}_{2+2n}$ or $02(n-1)n$ structure are unique in the sense that they lack the $M_m\text{O}_{m\pm\delta}$ charge-reservoir block. Due to the lack of the charge reservoir these phases are called “zero” phases [59]. The first high- T_c superconductor of Bednorz and Müller [1], *i.e.* $(\text{La,Ba/Sr})_2\text{CuO}_4$ with the layer sequence of

AO - AO - CuO_2 ($A = \text{La, Ba, Sr}$), is nothing but the first superconductive zero copper-oxide phase, *i.e.* 0201. Note that several nonsystematic names for this structure have been used as well, including “214”, “ K_2NiF_4 ” and “ T ”. In a $02(n-1)n$ structure in general, adjacent CuO_2 - $(Q\text{-CuO}_2)_{n-1}$ superconductive blocks are separated from each other by a rock-salt-type (AO)₂ double layer only (Fig. 2). The rock-salt-type atomic arrangement of the (AO)₂ double layer causes the successive AO - AO - CuO_2 - $[(Q\text{-CuO}_2)_{n-1}]$ units to be translated by $\frac{1}{2}$ in the $[110]$ direction of the primitive tetragonal unit cell such that the unit cell contains two $02(n-1)n$ formula units and accordingly possesses body-centered symmetry.

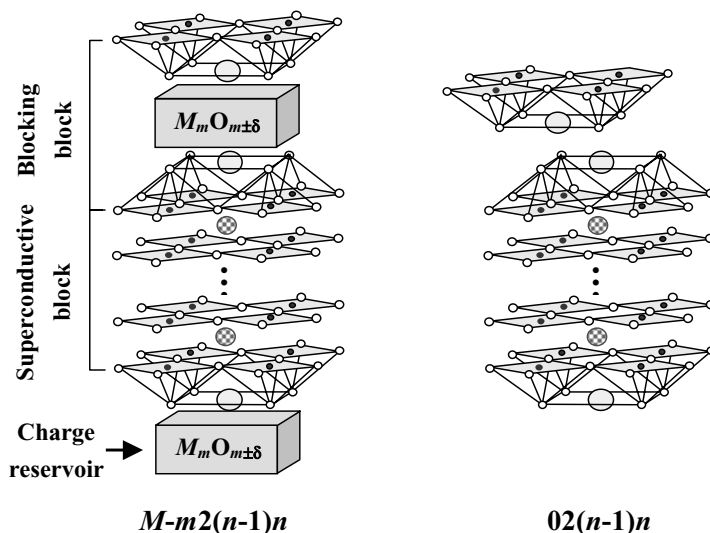


Fig. 2. Derivation of the zero $02(n-1)n$ crystal structure from the general $M-m2(n-1)n$ structure of Category-A.

The first complete zero homologous series was discovered in 1993 in the Sr-Ca-Cu-O system, *i.e.* $\text{Sr}_2\text{Ca}_{n-1}\text{Cu}_n\text{O}_{2+2n}$ or $0^{(\text{Sr})}2^{(\text{Ca})}(n-1)n$ phases with $n = 2 \sim 4$ [22]. These phases are obtained by means of HP (~ 5 GPa) synthesis only. Later, Ca-free analogs were reported to exist as well, *i.e.* $\text{Sr}_2\text{Sr}_{n-1}\text{Cu}_n\text{O}_{2+2n}$ or $0^{(\text{Sr})}2^{(\text{Sr})}(n-1)n$ [60]. Note that the $n = 1$ member is common for both series, $0^{(\text{Sr})}2^{(\text{Ca})}(n-1)n$ and $0^{(\text{Sr})}2^{(\text{Sr})}(n-1)n$. Also note that the formula of the $\text{Sr}_2\text{Sr}_{n-1}\text{Cu}_n\text{O}_{2+2n}$ phases may alternatively be written as $\text{Sr}_{n+1}\text{Cu}_n\text{O}_{2+2n}$ to emphasize that they are oxygen-deficient Ruddlesden-Popper [61] phases, $A_{n+1}T_n\text{O}_{3n+1\pm\delta}$ ($T = \text{transition metal}$).

The Ba-based zero series, $\text{Ba}_2\text{Ca}_{n-1}\text{Cu}_n\text{O}_{2+2n}$ [$0^{(\text{Ba})}2(n-1)n$], was discovered more recently. The $n = 2 \sim 4$ members have been experimentally verified to exist in bulk form in HP-synthesized samples [42-44], whereas the $n = 1$ member has so far been obtained in a thin-film form only [62] (see Fig. 3 for the crystal structures). For the $n = 3$ member remarkably high T_c values up to ~ 126 K are detected [42]. In Fig. 3, plotted is the lattice parameter c against the number of CuO_2 planes for both the $0^{(\text{Ba})}2(n-1)n$ [$c = (8.9 + 6.5n)$ Å] [43,44] and the $0^{(\text{Sr})}2(n-$

1) n [$c = (7.6 + 6.55n)$ Å] [63] series. The two c -versus- n lines lie in parallel but separated by ~ 1.3 Å from each other. This c parameter difference of ~ 1.3 Å of corresponding $\text{Ba}_2\text{Ca}_{n-1}\text{Cu}_n\text{O}_{2+2n}$ and $\text{Sr}_2\text{Ca}_{n-1}\text{Cu}_n\text{O}_{2+2n}$ phases is precisely accounted for by the difference in the ionic radii (r) [64] of the nine-coordinated Ba^{2+} and Sr^{2+} ions: $8[r(\text{Ba}^{2+}) - r(\text{Sr}^{2+})] = 8(1.47 - 1.31 \text{ Å}) = 1.28 \text{ Å}$. (There are four BaO layers in the unit cell.)

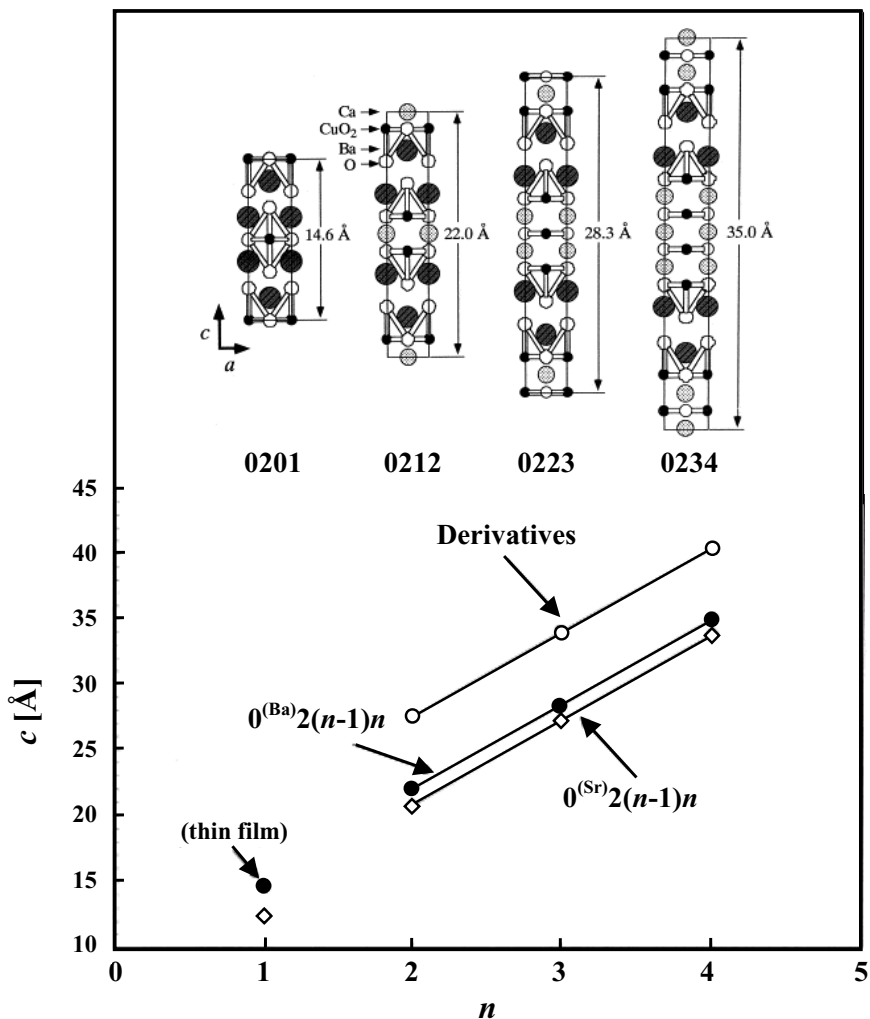


Fig. 3. Crystal structures of the first four members of the $\text{Ba}_2\text{Ca}_{n-1}\text{Cu}_n\text{O}_{2+2n}$ or $0^{(\text{Ba})}2(n-1)n$ series, and the c -versus- n relation for these $0^{(\text{Ba})}2(n-1)n$ phases and their water-derivatives [43,44], and also for the Sr analogs, $0^{(\text{Sr})}2(n-1)n$ [63], for reference.

Besides the pure oxides, also oxyhalogenides of the $02(n-1)n$ structure, *i.e.* phases in which the AO -layer oxygen site is substituted by fluorine or chlorine, have been synthesized [37,38,65,66]. These phases are rather more stable than the corresponding oxide zero phases. Here one should recognize that among the $02(n-1)n$ phases, those which do not contain halogen ions or trivalent A -site cations are extremely highly oxidized, at least nominally [6]. For example for $(\text{Sr}/\text{Ba})_2\text{Ca}_2\text{Cu}_3\text{O}_8$ [$0^{(\text{Sr}/\text{Ba})2^{(\text{Ca})}223$], the nominal value of Cu valence is as high as 2.67 if the phase is assumed to be stoichiometric in terms of oxygen content. For the Ba-based phase, the presence of oxygen vacancies was ruled out by means of wet-chemical redox analysis that corroborated the high nominal valence state of copper [67]. The highly oxidized nature of the $0^{(\text{Sr}/\text{Ba})2^{(\text{Ca})}(n-1)n$ phases is along with the fact that they are obtained only under highly oxidizing conditions. Another manifestation is that they (especially the Ba-based ones [42-44]) have been found to be highly unstable in open air. In the most plausible way, the high overall oxidation state of these phases would be understood by the presence of highly oxidized “peroxide-type” O species in the $(AO)_2$ double layer.

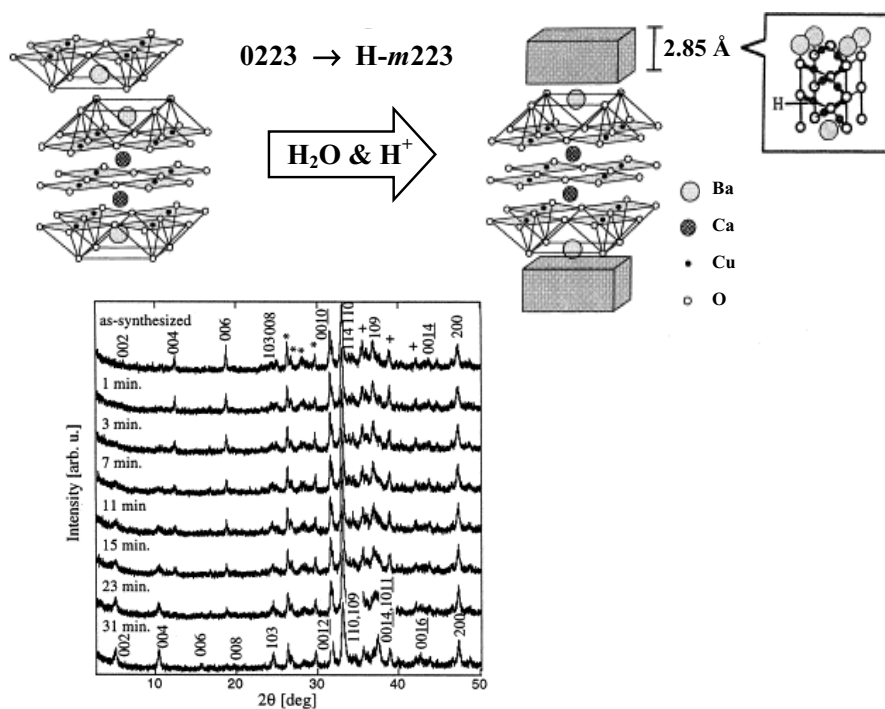


Fig. 4. Schematic illustration of the phase transformation of $\text{Ba}_2\text{Ca}_2\text{Cu}_3\text{O}_8$ (0223) into its water derivative, H- $m223$. Also shown are x-ray diffraction patterns to demonstrate the speed of the phase transformation when an as-HP-synthesized 0223 sample is exposed to $\text{H}_2\text{O}/\text{N}_2$ gas: the 31-min pattern is indexed for the H- $m223$ phase [68].

Interestingly, even though the $0^{(\text{Ba})}_2{}^{(\text{Ca})}(n-1)n$ phases are not stable in open (humid) air, they do not actually decompose but rather incorporate water into their zero charge-reservoir blocks (see Fig. 4 for the case of $n = 3$). The incorporation results in the formation of well-defined derivative phases with an expanded c -axis lattice parameter, *i.e.* $5.4 \sim 5.7 \text{ \AA}$ longer than that of the parent phase, and a charge-reservoir block that presumably consists of hydrogen and oxygen atoms only [42-44] (see Fig. 4 for a possible charge-reservoir structure). For the derivative of the $0^{(\text{Ba})}_2{}^{(\text{Ca})}23$ phase, superconductivity was verified ($T_c = 78 \sim 90 \text{ K}$ [42,67,68]), while in the cases of the other derivatives some ambiguity has remained in terms of their superconductivity properties. In Fig. 4, the speed of the phase transformation is illustrated by the sequence of x-ray powder diffraction patterns collected for an as-HP-synthesized $0^{(\text{Ba})}_2{}^{(\text{Ca})}23$ phase upon exposing it to humid air [68]. Among the Sr-analogs, *i.e.* $0^{(\text{Sr})}_2{}^{(\text{Ca})}(n-1)n$, a similar phase transformation (though much slower) has been so far confirmed for $n = 3$ [69].

Among the water-derivatives, wet-chemical redox analysis has so far been carried out for the derivative of the $0^{(\text{Ba})}_2{}^{(\text{Ca})}23$ phase [67]. The result clearly indicated a considerably lower (overall) oxidation state for the $\text{H-}m^{(\text{Ba})}_2{}^{(\text{Ca})}23$ derivative in comparison to that of its $0^{(\text{Ba})}_2{}^{(\text{Ca})}23$ parent. Therefore, it is believed that the driving force for the fast phase transformation of the $0^{(\text{Ba})}_2{}^{(\text{Ca})}(n-1)n$ phases is their strong tendency to be reduced. Moreover, since accommodation of neutral H_2O molecules alone should not change the oxidation state of the phase, it is believed that additional protons are incorporated as well. Here it is interesting to refer to the newly discovered “watery” CoO_2 -layer-based superconductor, $\text{Na}_x\text{CoO}_{2-\delta}\cdot y\text{H}_2\text{O}$ [70]: for this layered superconductor too, the presence of excess protons has been suggested [71,72].

2.1.4. “Zero” $01(n-1)n$ phases

The partly virtual $r = 1$ or $01(n-1)n$ series may be considered as the parent series for all the layered copper oxides of Category-A. So far the two first members of this series have been realized, but both of them have remained to be “superconductorized” yet. The first member at $n = 1$ is the $\text{LaCuO}_{3-\delta}$ perovskite [73] with single CuO_2 planes and LaO layers only, *i.e.* 0101 , whereas the second ($n = 2$) member is the Ba-R cation-ordered $\text{BaR}(\text{Cu,Fe})_2\text{O}_{5+\delta}$ double perovskite [74], *i.e.* 0112 .

Various efforts have been made to induce superconductivity in the three-dimensional $\text{LaCuO}_{3-\delta}$ perovskite phase [75-77]. All of these efforts have been unsuccessful so far. By oxygen stoichiometry tuning the average valence of copper can be continuously varied in the range of II and III, *i.e.* $0 \leq \delta \leq 0.5$, but introduction of oxygen vacancies results in a mixture of five-coordinated Cu^{II} and six-coordinated Cu^{III} rather than uniformly mixed-valent $\text{Cu}^{\text{II/III}}$ [77]. Tetravalent-for-trivalent cation substitution at the La site with oxygen-stoichiometric composition would in principle promote a three-dimensional network of mixed-valent $\text{Cu}^{\text{II/III}}$. However, solubility limits for the possible tetravalent cations, *e.g.* Ce^{IV} and Zr^{IV} , are far too low for the $(\text{La,Ce/Zr})\text{CuO}_3$ phase to reach a valence value close to $+2.2$ for copper [75,76]. On the other hand, with the oxygen-deficient stoichiometry at $\delta = 0.5$, Sr^{II} -for- La^{III} substitution has been successfully accomplished and shown to result in hole-doped copper-oxygen ladders, but not in superconductivity [78].

An $n=2$ member of the $01(n-1)n$ series, *i.e.* the $\text{BaR}(\text{Cu,Fe})_2\text{O}_{5+\delta}$ double perovskite, has so far been stabilized only with some portion of the copper site being occupied by iron. In order to increase the solubility limit of copper in the $(\text{Cu,Fe})\text{O}_2$ planes, application of ultra-high pressures was found advantageous [79].

2.2. Homologous Series of Category-B

Layered copper-oxide structures containing a fluorite-structured layer-block of $B\text{-}[\text{O}_2\text{-}B]_{s-1}$ [$B = (\text{Ce,R})$] are defined to form Category-B [2,5,6]. The first high- T_c superconductor to contain fluorite-structured layers was discovered in the Ce-Nd-Sr-Cu-O system as early as 1988 [80,81]. The so-called T^* structure of this $(\text{Ce,Nd,Sr})_2\text{CuO}_4$ compound is a 1:1 piling of La_2CuO_4 (T structure [82,83]) and Nd_2CuO_4 (T' structure [84]) type slabs with a layer sequence of $[(\text{Nd,Sr})\text{O}-(\text{Nd,Sr})\text{O}]_{\text{RS}}\text{-}[\text{CuO}_2]_{\text{P}}\text{-}[(\text{Ce,R})\text{-O}_2\text{-}(\text{Ce,R})]_{\text{F}}\text{-}[\text{CuO}_2]_{\text{P}}$, where the subscript, RS, P or F, refers to the structure type of the corresponding layer/block. The second copper-oxide superconductor with the F-structured layers was found soon after [85], *i.e.* $(\text{Ce,Nd})_2\text{CuO}_4$ of the bare T' structure. These first Category-B phases are zero phases, *i.e.* they lack the charge-reservoir block [59]. In an analogy to the Category-A phases, in Category-B as well the two RS-structured AO [$A = e.g.$ (Nd,Sr)] layers may sandwich an additional $M_m\text{O}_{m\pm\delta}$ charge-reservoir block ($M = \text{Cu, Bi, Pb, Tl, Hg, etc.}; 0 \leq m \leq 3$). This results in multi-layered structures with a layer sequence of $[AO]_{\text{RS}}\text{-}[(MO_{1\pm\delta})_m]_{\text{P/RS}}\text{-}[\text{CuO}_2]_{\text{P}}\text{-}[(\text{Ce,R})\text{-O}_2\text{-}(\text{Ce,R})]_{\text{F}}\text{-}[\text{CuO}_2]_{\text{P}}$, as was illustrated in Fig. 1. The third Category-B superconductor, *i.e.* $\text{Cu}(\text{Ba,R})_2(\text{Ce,R})_2\text{Cu}_2\text{O}_{9\pm\delta}$ [86] with a layer sequence of $[(\text{Ba,R})\text{O}]_{\text{RS}}\text{-}[\text{CuO}_{1\pm\delta}]_{\text{P}}\text{-}[(\text{Ba,R})\text{O}]_{\text{RS}}\text{-}[\text{CuO}_2]_{\text{P}}\text{-}[(\text{Ce,R})\text{-O}_2\text{-}(\text{Ce,R})]_{\text{F}}\text{-}[\text{CuO}_2]_{\text{P}}$, is such a charge-reservoir-containing phase.

With later discoveries, it has turned out that all the aforementioned three phases are just examples of a larger group of multi-layered copper oxides that contain F-structured layers between two adjacent CuO_2 planes and have a stoichiometry of $M_m A_{2k} B_s \text{Cu}_{1+k} \text{O}_{m+4k+2s\pm\delta}$ or $M\text{-}m^{(A)}(2k)^{(B)}s(1+k)$ [or $M\text{-}m(2k)s(1+k)$ in short] [2,5,6]. Here $m = 0, 1, 2, 3, \dots, s \geq 1$ and $k = 0$ or 1 , with the conditions that for $k = 0, m = 0$, and for $k = 1, m \geq 0$. Within Category-B, phases with the $[AO]\text{-}[(MO_{1\pm\delta/m})_m]\text{-}[\text{CuO}_2]$ blocking block fixed but the number, s , of the fluorite-structured cation layers varying form a homologous series [5,6]. In Table 2, Category-B structures together with some representative compounds are given.

An interesting point to note is that whereas each Category-A phase has only one type of (nonsuperconductive) blocking block besides the superconductive block that contains the CuO_2 planes, Category-B phases have two distinct blocking blocks (refer to Fig. 1). One of these blocks is the common $[AO]_{\text{RS}}\text{-}[(MO_{1\pm\delta/m})_m]_{\text{P/RS}}\text{-}[\text{CuO}_2]$ ($A = \text{Ba, Sr, etc.}; M = \text{Cu, Pb, Tl, Hg, etc.}$) block with/or RS- and P-structured layers. This block is glued (through AO layers) to the adjacent CuO_2 planes by sharing the ‘‘apical’’ oxygen atoms of the CuO_5 pyramids that constitute the CuO_2 planes. The other blocking block of $(\text{Ce,R})\text{-}[\text{O}_2\text{-}(\text{Ce,R})]_{s-1}$ (valence states, Ce^{IV} and R^{III} , are assumed) is then inserted between the basal planes of the CuO_2 -plane pyramids, and is of the F structure. In both categories, blocking blocks are believed not only to provide (proper) spacing between the superconductive CuO_2 planes but also to control the hole-doping level of these planes.

Table 2. Multi-layered copper-oxide structures of Category-B: $M_m A_{2k} B_s \text{Cu}_{1+k} \text{O}_{m+4k+2s}$ or $M_m(2k)s(1+k)$ together with representative compounds as arranged in the order of increasing m , k and s . Note that in terms of s , the table could be continued up to 7. Also note that the 0212, M -1212, M -2212 and M -3212 phases belong to Category-A as well.

| 00s1 | 02s2 | M -12s2 | M -22s2 | M -32s2 |
|--|--|--|--|--|
| 0011 (Sr,Nd)CuO ₂ | 0212 La ₂ SrCu ₂ O ₆ Sr ₂ CaCu ₂ O ₆ Ba ₂ CaCu ₂ O ₆ Sr ₂ CaCu ₂ O ₄ F ₂ | M-1212 HgBa ₂ CaCu ₂ O ₆ TlBa ₂ CaCu ₂ O ₇ CuBa ₂ RCu ₂ O ₇ RuSr ₂ RCu ₂ O ₈ | M-2212 Bi ₂ Sr ₂ CaCu ₂ O ₈ Tl ₂ Ba ₂ CaCu ₂ O ₈ | M-3212 (Pb _{2/3} Cu _{1/3}) ₃ Sr ₂ (Y,Ca)Cu ₂ O ₈ |
| 0021 (Nd,Ce) ₂ CuO ₄ | 0222 (Nd,Sr,Ce) ₂ CuO ₄ | M-1222 Cu(Ba,Eu) ₂ (Ce,Eu) ₂ Cu ₂ O ₉ CoSr ₂ (Ce,Y) ₂ Cu ₂ O ₉ RuSr ₂ (Ce,R) ₂ Cu ₂ O ₁₀ (Hg,W)Sr ₂ (Ce,R) ₂ Cu ₂ O ₉ (Cu,Mo)Sr ₂ (Ce,Y) ₂ Cu ₂ O ₉ | M-2222 Bi ₂ Sr ₂ (Ce,Gd) ₂ Cu ₂ O ₁₀ | M-3222 (Pb _{2/3} Cu _{1/3}) ₃ Sr ₂ (Ce,Eu) ₂ Cu ₂ O ₁₁ |
| | | M-1232 (Pb,Cu)Sr ₂ (Ce,Ho) ₃ Cu ₂ O ₁₁ (Fe,Cu)Sr ₂ (Ce,Y) ₃ Cu ₂ O ₁₁ CoSr ₂ (Ce,Y) ₃ Cu ₂ O ₁₁ (Hg,W)Sr ₂ (Ce,Eu) ₃ Cu ₂ O ₁₁ (Cu,Mo)Sr ₂ (Ce,R) ₃ Cu ₂ O ₁₁ | | |
| | | M-1242 (Fe,Cu)Sr ₂ (Ce,Y) ₄ Cu ₂ O ₁₃ | | |

Versatile understanding of high- T_c superconductivity and the behavior of materials showing this phenomenon is not possible without extending the understanding over both the categories of layered copper-oxide phases. For Category-A phases, the amount of accumulated experimental data is huge and accordingly various relations among the layer piling, crystallographic fine-structures, doping and superconductivity characteristics have been fairly well uncovered. As compared to the Category-A phases, those of Category-B have been much less investigated and therefore remained rather poorly understood. For example, in the known phases of Category-B, m varies from 0 up to 3, whereas s can be increased even up to 7 or 8 (though single-phase bulk samples have been realized only up to $s = 3$) [87-89]. Phases with $s \geq 3$ are rather rare and up to very recently none of them had been superconductorized [90]. At the same time, no definite explanation had been given why these phases do not show superconductivity [91]. In the following Sections 2.2.1-2.2.4, some of the Category-B phases are discussed in more detail.

2.2.1. Zero phases

Within Category-B, four zero structures have been experimentally verified. The structure adopted by $(\text{Ce,Nd,Sr})_2\text{CuO}_4$ should be denoted 0222 [2,5,6]. This 0222 phase together with the different 0212 phases that are common with Category-A (*viz.* Tables 1 and 2) comprise the first two members of the series 02s2. On the other hand, the $(\text{Ce,Nd})_2\text{CuO}_4$ phase is the $s = 2$ member of the 00s1 series, whereas the so-called infinite-layer structure of $(\text{Sr,R})\text{CuO}_2$ (discussed in detail in Section 2.3.) is the $s = 1$ member, *i.e.* 0011, of this series.

The most interesting feature of the 00s1 phases of $(\text{Sr,R})\text{CuO}_2$ ($s = 1$) and $(\text{Ce,Nd})_2\text{CuO}_4$ ($s = 2$) is that they are the only two phases among the high- T_c superconductive copper oxides that have not holes but electrons as charge carriers. These are also the only two phases that lack the rock-salt-type AO layers and thus the apical oxygen atoms. Here it is worthwhile to note that successful synthesis of the “so-far-virtual” 0031 phase would help us to clarify whether the n -type superconductivity is a universal/unique feature of the 00s1 series. Actually, one of the important challenges yet remaining is to elucidate the role of the “apical oxygen” or “apical anion” in the occurrence of high- T_c superconductivity.

2.2.2. Superconductive M-12s2 phases

The Cu-12s2 homologous series is one of the most interesting target systems for deeper understanding of Category-B phases. The first member, Cu-1212, is nothing but the prototype superconductor, $\text{CuBa}_2\text{RCu}_2\text{O}_{7\pm\delta}$ (“R-123”; note that the $s = 1$ phase of Category-B is equal to the corresponding $n = 2$ phase of Category-A), the second member, Cu-1222, is the first charge-reservoir-containing Category-B superconductor [86], whereas the third member, Cu-1232, very recently turned out to be the first “triple-fluorite-layer” superconductor [92].

The first samples of the Cu-1222 ($s = 2$) phase were obtained with the stoichiometry of $\text{Cu}(\text{Ba,R})_2(\text{Ce,R})_2\text{Cu}_2\text{O}_{9\pm\delta}$ or $\text{Cu-1}^{(\text{Ba,R})}222$: the highest T_c of 43 K was achieved for an $R = \text{Eu}$ sample synthesized under ambient pressure but oxygenated under elevated O_2 pressures [86]. The role of the trivalent R substituent at the A (= Ba) site was to stabilize the structure. The Cu-1222 structure is also stabilized for $A = \text{Sr}$ by substituting the charge-reservoir Cu partially by a higher-valent element, *e.g.* $(\text{Cu,Mo})\text{Sr}_2(\text{Ce,Y})_2\text{Cu}_2\text{O}_{9\pm\delta}$ [92,93]. With Sr at the A site, the Cu-1222 structure is formed even without structure-stabilizing substituents, *i.e.* $\text{CuSr}_2(\text{Ce,Y})_2\text{Cu}_2\text{O}_{9\pm\delta}$, though only under high O_2 pressures [94]. At least with the original composition, $\text{Cu}(\text{Ba}_{0.67}\text{Eu}_{0.33})_2(\text{Ce}_{0.33}\text{Eu}_{0.67})_2\text{Cu}_2\text{O}_{9\pm\delta}$, the Cu-1222 phase is rather flexible for oxygen-content control. By means of a set of deoxygenation (in N_2) and oxygenation (under high O_2 pressures) annealing treatments the hole-doping level of the phase could be continuously adjusted from a nondoped (nonsuperconductive) state to a slightly overdoped state. For the optimally-doped sample T_c was found at 62 K [95]. For the same sample, the average valence of copper was determined to be ~ 2.2 from Cu L -edge XANES spectroscopy data [95]. In comparison to the average value of Cu valence in optimally-doped Cu-1212, *i.e.* ~ 2.3 in $\text{CuBa}_2\text{RCu}_2\text{O}_{6.95}$, the value obtained for Cu-1222 looks unexpectedly low. However, O K -edge XANES data revealed that in Cu-1222 [at least with the cation stoichiometry of $\text{Cu}(\text{Ba}_{0.67}\text{Eu}_{0.33})_2(\text{Ce}_{0.33}\text{Eu}_{0.67})_2\text{Cu}_2\text{O}_{9\pm\delta}$] holes are distributed in a way that the CuO_2 plane gets more holes than the $\text{CuO}_{1\pm\delta}$ charge reservoir [95], whereas the situation is opposite in

Cu-1212 [6,96] (see Section 4.1). Therefore, the CuO_2 -plane hole concentration in optimally-doped Cu-1222 may not be much different from that in optimally-doped Cu-1212.

The Cu-1232 structure was also realized long time ago, *i.e.* multi-phase samples of $\text{CuSr}_2(\text{Ce},\text{Ho})_3\text{Cu}_2\text{O}_{11+\delta}$ and nearly single-phase samples of $(\text{Cu},M)\text{Sr}_2(\text{Ce},\text{Ho})_3\text{Cu}_2\text{O}_{11+\delta}$ ($M = \text{Pb}, \text{Fe}, \text{Al}$) [97-99]. None of these samples containing the $s = 3$ phase, however, showed superconductivity, which was for long time rather believed to be the general characteristics of phases with $s \geq 3$. Recently single-phase $(\text{Cu},\text{Mo})\text{-1}^{(\text{Sr})232}$ samples were synthesized with the composition of $(\text{Cu}_{0.75}\text{Mo}_{0.25})\text{Sr}_2(\text{Ce}_{0.67}\text{Y}_{0.33})_3\text{Cu}_2\text{O}_{11+\delta}$. As-synthesized samples of $(\text{Cu},\text{Mo})\text{-1}^{(\text{Sr})232}$ were not superconductive either, but superconductivity was successfully induced in these air-synthesized samples by means of high-pressure oxygenation carried out in a cubic-anvil-type high-pressure apparatus at 5 GPa and 500 °C in the presence of Ag_2O_2 as an excess oxygen source. Moreover found was that with increasing ratio of Ag_2O_2 to the $(\text{Cu},\text{Mo})\text{-1232}$ phase the c -axis lattice parameter gradually decreased and T_c increased up to 53 K [92]. Together with the phases, $(\text{Cu},\text{Mo})\text{-1}^{(\text{Sr})212}$ and $(\text{Cu},\text{Mo})\text{-1}^{(\text{Sr})222}$, this new $s = 3$ phase forms a homologous series of $(\text{Cu},\text{Mo})\text{-1}^{(\text{Sr})2s2}$. With the parameter s increasing from 1 to 3 the members of the $(\text{Cu},\text{Mo})\text{-1}^{(\text{Sr})2s2}$ series have two adjacent CuO_2 planes separated from each other by a single R -cation layer for $s = 1$, a “double-fluorite-layer” block of $(\text{Ce},R)\text{-O}_2\text{-}(\text{Ce},R)$ for $s = 2$, and a “triple-fluorite-layer” block of $(\text{Ce},R)\text{-O}_2\text{-}(\text{Ce},R)\text{-O}_2\text{-}(\text{Ce},R)$ for $s = 3$. In Fig. 5, the highest so-far obtained T_c value for these three phases is plotted against s . Tentatively it seems that once the two pyramidal CuO_2 planes are separated from each other with a somewhat thicker blocking block, further increase in the thickness of this block does not necessarily decrease the T_c value. To corroborate this, the first “quadruple-fluorite-layer” superconductor should be hunted.

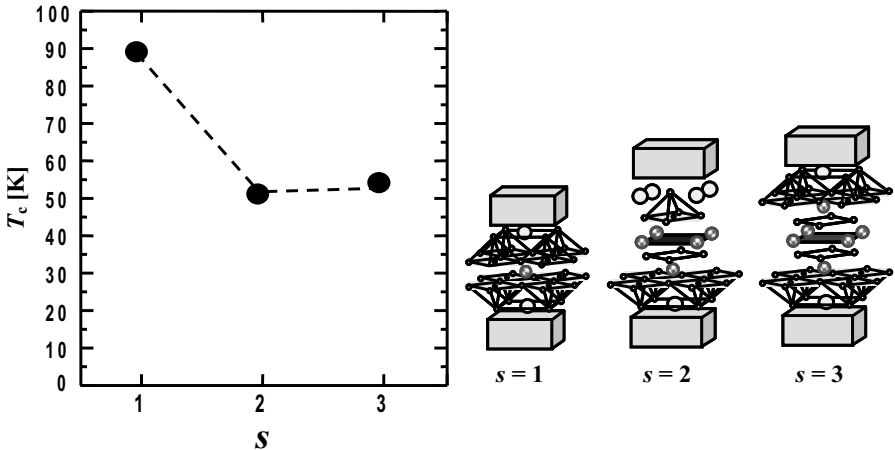


Fig. 5. T_c versus s for the homologous series $(\text{Cu},\text{Mo})\text{-12s2}$. The given T_c values are the highest values so far obtained for these phases [92], but not necessarily optimized yet.

2.2.3. Ru-12s2 magnetosuperconductors

The ruthenium-based Category-B phase, Ru-1222, was the first to show “coexistence of high- T_c superconductivity and high- T_C ferromagnetism”, first in $\text{RuSr}_2[(\text{Eu,Gd})_{0.7}\text{Ce}_{0.3}]_2\text{Cu}_2\text{O}_{10-\delta}$ samples [100]. Later the Ru-1212 phase ($\text{RuSr}_2\text{GdCu}_2\text{O}_{8-\delta}$) was shown to be another “magnetosuperconductor” [101]. Very recently the third ($s = 3$) member of the homologous series, Ru-12s2, was successfully synthesized [102]. As a potential new magnetosuperconductor, its further characterization is now highly awaited. Even though the Ru-12s2 phases have received continuous attention since the first indication of their possible magnetosuperconductivity [103], further discussion is omitted within the scope of the present contribution.

2.2.4. Nonsuperconductive M-12s2 phases

Various M-12s2-type phases have been experimentally observed even up to $s = 7$ (for $M = (\text{Fe,Cu})$ [88]). However, most of these phases have yet remained to be superconductorized. For example, for (Fe,Cu)-12s2 only the $s = 1$ member (that actually does not contain fluorite-structured layers) is superconductive.

Among the nonsuperconductive Category-B phases, the $\text{Co-1}^{(\text{Sr})}_2^{(\text{Ce,Y})}_s2$ homologous series forms one of the most well-established systems: all the three first members are readily obtained in single-phase forms through solid-state-synthesis in air [104]. (The first two members have been known for a long time [105-108].) Like in any other (ideal) homologous series of Category-B, the three first members of the Co-12s2 ($s = 1, 2, 3$) series differ from each other only in terms of the $(\text{Ce,Y})\text{-}[\text{O}_2\text{-}(\text{Ce,Y})]_{s-1}$ layer block between two identical CuO_2 planes. The precise cation and oxygen contents [104] as well as crystallographic features [109] are well established for the as-air-synthesized samples: all the three phases are essentially stoichiometric in terms of oxygen content, *i.e.* $\delta \approx 0$ for the $\text{CoO}_{1+\delta}$ charge-reservoir. They are also all nonsuperconductive. At $\delta = 0$, the charge reservoir of all of them consists of zigzag chains of corner-linked CoO_4 tetrahedra that run diagonally relative to the perovskite base [109]. By means of high-pressure oxygenation it is possible to gradually dope the phases with holes [110]. Utilizing Cu *L*-edge XANES spectroscopy it is possible to follow changes in the valence state of copper accordingly. It has been found that the positive charge induced by oxygen loading is not completely directed into the CuO_2 planes but is rather effectively trapped by the charge-reservoir Co atoms. For Co-1212 ($\text{CoSr}_2\text{YCu}_2\text{O}_{7+\delta}$) superconductivity appears in the samples when the valence of copper exceeds 2.1, whereas for Co-1222 [$\text{CoSr}_2(\text{Ce}_{0.25}\text{Y}_{0.75})_2\text{Cu}_2\text{O}_{9+\delta}$] and Co-1232 [$(\text{CoSr}_2(\text{Ce}_{0.67}\text{Y}_{0.33})_3\text{Cu}_2\text{O}_{11+\delta})$] the CuO_2 -plane hole concentration does not increase strongly enough for superconductivity to be induced [110]. Thus, depending on the system, the charge balance between the charge reservoir and the CuO_2 plane may be affected differently upon increasing the F-block thickness, s : for Co-12s2 the balance shifts to the charge-reservoir direction, whereas an opposite trend was suggested for Cu-12s2 (*cf.* Section 2.2.2).

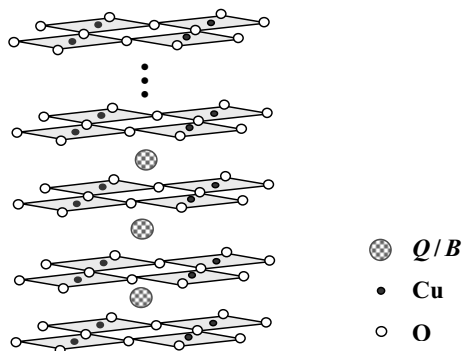


Fig. 6. Crystal structure of the infinite-layer or 0011 phase.

2.3. “Infinite-Layer” Phases

The naming schemes for the two categories, A and B, are consistent at common limits. As already discussed, the $s = 1$ phases of Category-B are identical to the corresponding $n = 2$ phases of Category-A. Here, it is interesting to note that the so-called “infinite-layer” superconductor, $(\text{Sr}/\text{Ca}, R)\text{CuO}_2$ [111], that consists of an infinite stacking of oxygen-free Q or B cation layers and CuO_2 planes only (see Fig. 6), can be alternatively imagined as the “infinite” limit ($n \rightarrow \infty$) of the $M\text{-}mr(n-1)n$ structure of Category-A (Table 1) or as the “parent” ($s = 1$) of the $M\text{-}m(2k)s(1+k)$ structure (at $m = 0$ and $k = 1$) of Category-B (Table 2). In both cases, the structure is consistently denoted 0011 [5,6,59].

With the SrCuO_2 stoichiometry the 0011 structure with an infinite, two-dimensional stacking of CuO_2 planes and oxygen-vacant Sr layers along the c axis, is obtained through high-pressure synthesis only. (When synthesized at ambient pressure the same stoichiometry adopts a structure in which copper atoms are arranged with oxygen atoms in quasi-one-dimensional, edge-sharing double chains.) The infinite-layer structure is obtained also at ambient pressure but only in a narrow compositional range of $\text{Ca}_{0.86}\text{Sr}_{0.14}\text{CuO}_2$ [112]. With the $\text{Ca}_{0.86}\text{Sr}_{0.14}\text{CuO}_2$ composition the infinite-layer phase is semiconductive. Under high pressures the composition range of Q in the infinite-layer phase, $Q\text{CuO}_2$, is much wider [113], *i.e.* Q may contain Sr, Ca, Ba, La, Pr, Nd, Sm and Gd [111,114-121]. The $Q\text{CuO}_2$ samples containing trivalent R ions are electron-doped superconductors with a large Meissner volume fraction and $T_c = 40 \sim 43$ K, being quite independent of the R content [111,114-121]. These samples are typically synthesized under reducing conditions. On the other hand, much higher T_c values of $90 \sim 110$ K were reported for HP-synthesized Ba-Sr-Cu-O and Sr-Ca-Cu-O samples obtained under oxidizing conditions [122,123]. However, the phase(s) responsible for superconductivity are believed not to be of the 0011 structure [124].

As was discussed in Section 2.1., it has been an “empirical fact” that the cation Q must be divalent Ca in a superconductive $Q_{n-1}\text{Cu}_n\text{O}_{2n}$ block for the $M\text{-}mr(n-1)n$ phases containing more than two CuO_2 planes, *i.e.* $n \geq 3$ [4,6]. In this sense the 0011 phase in which the oxygen-free cation layer may contain not only trivalent (as discussed above) but also monovalent

cations as in $(\text{Ca,Li})\text{CuO}_2$ [125], is an obvious exception. Here note that the $(\text{Ca,Li})\text{CuO}_2$ samples that were p -type doped did not show superconductivity.

2.4. Other Types of Layered Copper Oxides

Besides the tens of different crystal structures/phases that belong to the aforementioned two categories, A and B, there are yet a handful of phases that can not be counted as members of Category-A or Category-B homologous series. One of these is the $R\text{Ba}_2\text{Cu}_4\text{O}_{8-\delta}$ or “ R -124” phase that was first detected as an intergrowth in “ R -123” or Cu-1212 thin films [126]. Later it was revealed that R -124 is rather more stable than R -123 at lower temperatures [127]. The R site may be occupied not only by Y but also by various other rare-earth elements [128]. Using the general Category-A naming scheme, the “124” structure may be written as Cu-2212, though the charge-reservoir block structure, in which CuO_4 squares share their O-O edges to form two parallel CuO chains, belongs to neither P nor RS type. In this kind of shear-type charge-reservoir structure in which the Cu atoms on the different chains are shifted from each other by the Cu-O distance such that each oxygen atom is bonded to three different copper atoms in the Cu_2O_2 double chain, is very rigid in terms of oxygen-content variations; wet-chemical redox analysis confirmed $\delta \approx 0$ for variously synthesized samples [129], in contrast to the single $\text{CuO}_{1-\delta}$ chain of the Cu-1212 phase. Note that no other members of the “virtual homologous series, Cu-22($n-1$) n ,” have been synthesized. The related “247” phase has an ordered structure consisting of alternative piling of the “123” and “124” structures along the c axis of the both structures.

Various layered copper oxycarbonate phases containing CO_3^{2-} groups have also been synthesized, such as CSr_2CuO_5 [130]. The basic structures of CSr_2CuO_5 and related oxycarbonate phases may be expressed as members of the homologous series, C-12($n-1$) n . However, since the neighbouring charge-reservoir units characteristically tend to combine each other, the sizes of crystallographically defined unit cells of these copper oxycarbonates are much larger than a single cell containing only one C-12($n-1$) n formula unit. For CSr_2CuO_5 , for example, the unit cell consists of eight C-1^(Sr)201 formula units [131]. Among the oxycarbonates, $(\text{C,Cu})(\text{Sr,Ba})_2\text{CuO}_5$ or C-1^(Sr,Ba)201 was the first to show super-conductivity [132]. Also the $n = 2$ oxycarbonate phase was superconductorized with the stoichiometry of (C,Cu) -1^(Sr)2^(Y,Ca)12 [133]. Later various Bi-, Tl- and Hg-based oxy-carbonate superconductors have been successfully synthesized [134-136]. Utilizing high-pressures for the synthesis it has also been possible to synthesize higher- n phases, e.g. (C,Cu) -1^(Ba)2^(Ca)($n-1$) n ($n = 3, 4$) [27], (C,Cu,Ba) -3^(Ba)2^(Ca)($n-1$) n ($n = 3 \sim 5$) [32] and (C,B) -1^(Sr)2^(Ca,Sr)($n-1$) n [28].

In terms of the structural elements, not only the P, RS and F structured layers but also layers of other simple structures may be involved in multi-layered copper-oxide phases. This is true at least for the cesium-chloride (CC) structure: in $\text{Pb}_3\text{Sr}_3\text{Cu}_3\text{O}_{8+\delta}\text{Cl}$ [137] a CC-structured block of $(\text{Pb}_{0.5}\text{Sr}_{0.5})\text{-Cl-(Pb}_{0.5}\text{Sr}_{0.5})$ is sandwiched by the two CuO_2 planes, whereas the $\text{PbO-CuO}_8\text{-PbO}$ layer piling serves as the charge reservoir. Accordingly the formula should be written as $(\text{Pb}_{2/3}\text{Cu}_{1/3})_3\text{Sr}_2(\text{Pb}_{0.5}\text{Sr}_{0.5})_2\text{Cu}_2\text{O}_{8+\delta}\text{Cl}$ to show the relation to the categorized structures. Moreover, immediately seen is a further possibility to design a novel homologous series as expressed with the layer sequence of $[\text{PbO-CuO}_8\text{-PbO}]_P\text{-}[\text{SrO}]_{\text{RS}}\text{-}[\text{CuO}_2]_P\text{-}\{(\text{Pb}_{0.5}\text{Sr}_{0.5})\text{-}[\text{Cl-(Pb}_{0.5}\text{Sr}_{0.5})]_{i-1}\}_{\text{CC}}\text{-}[\text{CuO}_2]_P\text{-}[\text{SrO}]_{\text{RS}}$. So far no superconductivity has been reported for $\text{Pb}_3\text{Sr}_3\text{Cu}_3\text{O}_{8+\delta}\text{Cl}$.

3. REDOX TAILORING

In the multi-layered copper oxides the redox (= reduction-oxidation) state of the CuO_2 planes(s) is most straightforwardly controlled by tuning the oxygen (non)stoichiometry of the phase. "Oxygen engineering" [7] is therefore one of the most important tools for "on-demand tailoring" of these materials, and should cover methods of not only precisely controlling but also precisely analyzing the degree of oxygen stoichiometry/nonstoichiometry. Moreover, in the case of a multi-layered phase it is important to elucidate the functions of individual layers in terms of oxygen-content tunability and charge accommodation. The various chemical techniques for oxygen-content analysis and their applicability have been extensively reviewed in Refs. [6,7,138] and thus left outside of the scope of the present contribution. In this Chapter, we discuss the redox tendency and oxygen-content tunability of layered copper oxides, whereas charge distribution and layer-specific carrier concentrations are discussed in Chapter 4.

3.1. Oxygen Nonstoichiometry

Common to all metal oxides is that the Gibbs free energy of formation becomes less negative with increasing temperature [139]. In other words, metal oxides tend to be reduced (*i.e.* lose oxygen) when the temperature is increased. Obviously, if the partial pressure of oxygen is decreased the temperature at which the reduction occurs becomes lower. For some metal oxides, *e.g.* Ag_2O_2 [7], reduction to the metallic state occurs even in air at reasonably low temperatures, while for others temperatures much higher than what can be achieved by ordinary techniques are required for complete reduction. For a majority of metal oxides, reduction occurs in one or two discrete steps, each step corresponding to an integer oxidation number of the metal concerned. Only for some transition metal oxides oxygen nonstoichiometry, *i.e.* continuous variation in oxygen stoichiometry, is possible [6,7]. The variation range furthermore depends on the specific crystal structure. In each case oxygen tends to incorporate back upon cooling. Only if the cooling is carried out in an (essentially) oxygen-free atmosphere an oxygen-deficient sample is obtained [6,7,140,141]. On the other hand, according to thermodynamics it is impossible to synthesize metal oxides with an intermediate oxygen-content value in an oxygen-containing atmosphere just by "controlling the annealing time" or using "rapid cooling from a high temperature". Such treatments - though sometimes employed - would end up with a mixture of oxygenated and reduced phases but not with homogeneous intermediate oxygen content throughout the whole sample.

Oxygen nonstoichiometry and thereby mixed copper valency are common characteristics to the simple perovskite, $\text{LaCuO}_{3-\delta}$ (0101 phase), and the whole family of the multi-layered copper oxides derived from the perovskite structure. The fully-oxygenated $\text{LaCuO}_{3-\delta}$ ($\delta \approx 0$) perovskite itself (obtained through HP synthesis only) loses oxygen gradually within $0 \leq \delta \leq 0.5$ upon annealing in an inert atmosphere [77]. Consequently it is possible to synthesize a series of $\text{LaCuO}_{3-\delta}$ samples with oxygen contents precisely controlled by the choice of annealing temperature, *i.e.* temperature-controlled oxygen-depletion (TCOD) [6,7,140-143]. By performing such a TCOD annealing in a thermobalance allows one to *in-situ* thermogravimetrically (TG) monitor the amount of depleted oxygen [77], see Fig. 7(a).

Moreover, initially the choice of the proper annealing temperature is conveniently established on the basis of the TG data.

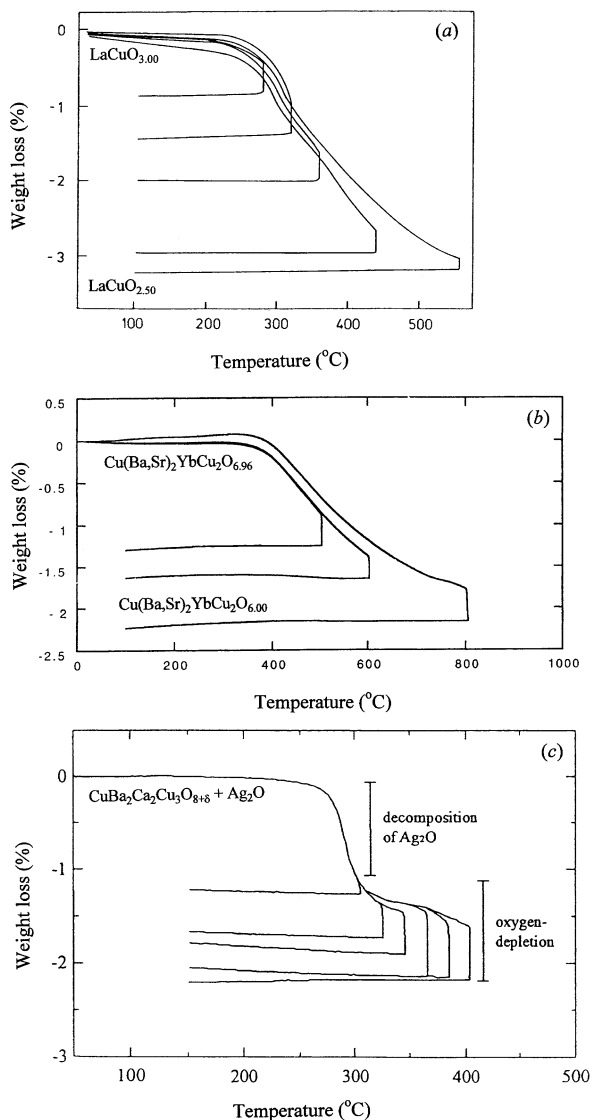


Fig. 7. TGA annealings carried out in inert gas for (a) LaCuO_{3-δ} (0011), (b) Cu(Ba,Sr)₂RCu₂O_{7-δ} (Cu-1212), and (c) CuBa₂Ca₂Cu₃O_{9-δ} (Cu-1223), to obtain oxygen-depleted samples.

In a similar manner samples of the $\text{Cu}(\text{Ba},\text{Sr})_2\text{RCu}_2\text{O}_{7-\delta}$ or Cu-1212 phase (“oxygen-deficient triple perovskite”) with any intermediate oxygen-content value within $0 < \delta < 1$ (*i.e.* $\Delta\delta \approx 1$) are conveniently prepared through TCOD annealings carried out in a thermobalance in an inert atmosphere at prefixed temperatures [140-143], see Fig. 7(b). The TCOD method works equally well for other superconductive copper oxides too. In Fig. 7(c), examples of TCOD annealing curves are shown for the HP-synthesized $\text{CuBa}_2\text{Ca}_2\text{Cu}_3\text{O}_{9-\delta}$ or Cu-1223 phase (“oxygen-deficient quadruple perovskite”) [54,55]. Here it should be noted that only the second weight-loss step seen in the TG curves is due to the oxygen loss from the Cu-1223 phase; the first step is due to decomposition of the leftover $\text{Ag}_2\text{O}/\text{Ag}_2\text{O}_2$ that exists in the samples since Ag_2O_2 is used as an excess-oxygen source in the HP synthesis to promote the phase formation. The two weight-loss steps are distinguishable and from the total weight loss observed in the temperature range from 300 °C to 420 °C (second weight-loss step) the amount of removable oxygen in the Cu-1223 phase is calculated at $\Delta\delta \approx 0.4$ [54,55]. For the $n = 4$ member of the Cu-12($n-1$) n series, *i.e.* the Cu-1234 phase or the “oxygen-deficient quintuple perovskite”, no detectable changes in oxygen content are seen upon different normal-pressure annealing treatments, *i.e.* $\Delta\delta \approx 0$ [144]. It may thus be concluded that within the homologous series, Cu-12($n-1$) n , with increasing number of consecutively stacked CuO_2 planes in the superconductive block the amount of removable oxygen decreases. Empirically, this seems to apply to other (Category-A) homologous series too.

The wide-range oxygen-content tunability seen for many of the copper-oxide superconductors is commonly explained by their perovskite-derived structures. In line with this, among the superconductive copper oxides most prominent changes in oxygen content are detected for the Cu-1212:P ($\Delta\delta \approx 1.0$) and $(\text{Pb}_{2/3}\text{Cu}_{1/3})$ -3212:P ($\Delta\delta \approx 1.8$ [145]) phases in which the charge reservoir consists of perovskite-type $\text{CuO}_{1-\delta}$ and $\text{Pb}_2\text{CuO}_{2+\delta}$ blocks, respectively, whereas the phases with a RS-type charge reservoir are much less flexible for oxygen-content tuning, *e.g.* for the $\text{Hg}-1^{(\text{Ba})}2(n-1)n$:RS phases with $n = 1 \sim 3$, $\Delta\delta$ as achieved by normal-pressure annealings is around 0.15 [146]. At the same time it is interesting and rather important to note that even though the superconductive CuO_2 -(Q - CuO_2) $_{n-1}$ block has an ordered-oxygen-vacancy perovskite structure the oxygen content of it does not show even a slightest deviation from $2n$, *i.e.* the oxygen content changes occur in the $M_m\text{O}_{m\pm\delta}$ charge-reservoir block only.

3.2. Layer-Matching and Redox Characteristics

Manipulation of the composition and the sequence of the different layers in the unit cell provides us with a chemical means of controlling the extent of compression or tension of the CuO_2 planes and further the redox characteristics of the phase. As the first criterion, to facilitate coherent connections between adjacent layers and therewith the phase formation the naturally preferred *ab*-plane dimensions of the different layers should match well enough. [Such “preferred *ab*-plane dimensions” are estimated based on the empirical room-temperature ionic radii (r) of the constituent elements at an assumed valence state (V) and coordination number (CN)]. The so-called “tolerance factor” (t) [147] gives us a quantitative measure of the bond-length mismatch across an interface of the two different layers. In the structures of superconductive copper oxides (both categories), the outermost CuO_2 plane of

the superconductive block is connected to the $M_m O_{m \pm \delta}$ charge-reservoir block *via* an AO layer, *i.e.* $-MO_{1 \pm \delta/m} AO-CuO_2-$. Since the nonstoichiometric $MO_{1 \pm \delta/m}$ layer is (in most cases) quite flexible in terms of the ab -plane dimension, the degree of mismatch between the AO and CuO_2 layers is assumed to be most essential to the phase stability. For each layer-pair, t by definition equals to 1 at ideal matching. Thus, for the interface between the RS-type AO layer and the P-type CuO_2 plane, t is given by:

$$t = \frac{r(A^{II} / A^{III}) + r(O^{-II})}{\sqrt{2} [r(Cu^{II/III}) + r(O^{-II})]} \quad (1)$$

In terms of the phase stability, small deviations from the ideal matching are allowed. However, such deviations tend to lead to structural distortions and/or nonstoichiometry. An $M_m A_2 Q_{n-1} Cu_n O_{m+2+2n \pm \delta}$ or $M_m A_{2k} B_s Cu_{1+k} O_{m+4k+2s \pm \delta}$ phase typically responds to internal stress caused by layer-mismatch by adjusting the oxygen nonstoichiometry and thereby the redox state of copper in the CuO_2 plane(s): under compression ($t < 1$)/tension ($t > 1$) the CuO_2 plane tends to be oxidized/reduced to shorten/lengthen the expected ionic radius of $Cu^{II/III}$ [148,149]. From the t value calculated at a stoichiometric composition, redox tendency of the phase may thus be predicted/rationalized [6,45]. Besides the changeable oxygen content, the Jahn-Teller effect provides an additional degree of freedom for copper-oxide (Cu^{II} : $t_{2g}^6 e_g^3$) phases to adjust the ab -plane dimension, as it enables the four in-plane Cu-O bonds to become shorter at the expense of the two out-of-plane Cu-O bonds [148,149].

Table 3. Tolerance parameter, t , calculated using the tabulated values of ionic radii, r [64], for some layered copper-oxide structures. Also given is the redox tendency, *i.e.* either $\delta > 0$ (tends to be oxidized) or $\delta < 0$ (tends to be reduced), as predicted from the t value.

| Structure | r [Å] | t | δ |
|------------------------------|--|------|----------|
| $LaCuO_{3+\delta}$ | $r_{La(III;12)} = 1.36$; $r_{Cu(III;6)} = 0.54$; $r_{O(-II)} = 1.40$ | 1.01 | < 0 |
| $La_2CuO_{4+\delta}$ | $r_{La(III;9)} = 1.22$; $r_{Cu(II;6)} = 0.73$; $r_{O(-II)} = 1.40$ | 0.87 | > 0 |
| $HgBa_2CuO_{4+\delta}$ | $r_{Ba(II;8)} = 1.42$; $r_{Cu(II;6)} = 0.73$; $r_{O(-II)} = 1.40$ | 0.94 | > 0 |
| $TlBa_2CuO_{5+\delta}$ | $r_{Ba(II;9)} = 1.47$; $r_{Cu(III;6)} = 0.54$; $r_{O(-II)} = 1.40$ | 1.05 | < 0 |
| $CuBa_2YCu_2O_{7+\delta}$ | $r_{Ba(II;10)} = 1.52$; $r_{Cu(II;5)} = 0.65$; $r_{O(-II)} = 1.40$ | 1.01 | < 0 |
| $Bi_2Sr_2CaCu_2O_{8+\delta}$ | $r_{Sr(II;9)} = 1.31$; $r_{Cu(II;5)} = 0.65$; $r_{O(-II)} = 1.40$ | 0.93 | > 0 |

In Table 3, t values calculated for some representative superconductive and related copper-oxide phases are given together with the redox tendency as predicted for the phases on the basis of the obtained t value: for $t > 1$, δ is expected to be < 0 , and *vice versa*. In the $LaCuO_3$ perovskite the CuO_2 plane is attached to a LaO layer in which the A -site cation, La^{III} , has a large CN value of 12 and accordingly a large ionic radius. The obtained t value of 1.01,

i.e. slightly higher than unity, is in accordance with the strong tendency of LaCuO_3 to be reduced [77]. When the AO layer is connected from the other side to another AO layer [as in the $02(n-1)n$ phases] or an $MO_{1\pm\delta/m}$ layer [as in the $M-m-2(n-1)n$ phases] rather than directly to the next CuO_2 plane (as in LaCuO_3 of the 0011 structure), the number of nearest-neighbour oxygen atoms about the A cation is less than 12 owing to the smaller number of oxygen atoms in the $MO_{1\pm\delta/m}/AO$ layer as compared to their number in the CuO_2 plane. For example, in La_2CuO_4 with a layer sequence of LaO-LaO-CuO_2 , La^{III} is 9-coordinated and Cu^{II} has an octahedral coordination with $\text{CN} = 6$. Here t becomes 0.87. The fact that $t < 1$ means that the CuO_2 plane in La_2CuO_4 is under compression and the compound thus accepts excess oxygen.

Alkaline earths, Ba^{II} and Sr^{II} , are the most common A -site cations in the superconductive copper oxides. With $A = \text{Sr}$, the AO layer is usually too small to match perfectly with the CuO_2 plane, *i.e.* t is significantly smaller than unity (see Table 3). Moreover, since a spherical coordination sphere is favoured by the alkaline earths due to their s -orbital bonding, SrO layers (and to some extent BaO layers too) in layered structures of the $AO-(MO_{1\pm\delta/m})_m-AO-\text{CuO}_2-(Q-\text{CuO}_2)_{n-1}$ type tend to be buckled such that the oxygen atom is shifted towards the $MO_{1\pm\delta/m}$ layer. This effect is especially pronounced in phases with strongly oxygen-deficient $MO_{1\pm\delta/m}$ layers. As the degree of SrO -layer buckling increases the ab -plane dimension preferred by it decreases, and the mismatch becomes more severe. Increasing the amount of excess oxygen in the $M_mO_{m\pm\delta}$ charge-reservoir block increases the CN of the A -site Sr and thus enhances the stability of an $M_m\text{Sr}_2Q_{n-1}\text{Cu}_n\text{O}_{m+2+2n\pm\delta}$ phase. There are three reasons for this. Firstly - as already discussed above - when the buckling diminishes the ab dimension preferred by the SrO layer increases. Secondly, effective size of Sr increases when the CN about it increases. Thirdly, the excess oxygen increases the oxidation state of copper in the CuO_2 plane and thereby makes the plane compressed.

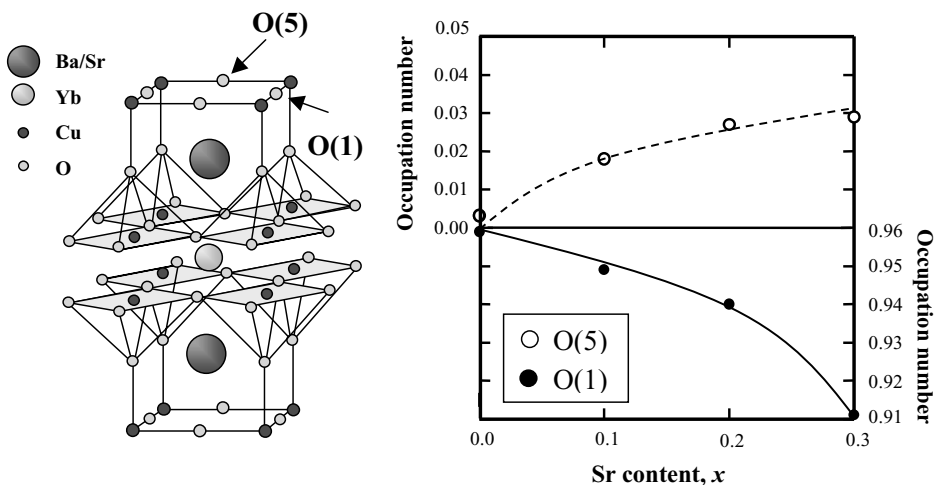


Fig. 8. Gradual shift of oxygen occupation from the characteristics $O(1)$ position to the $O(5)$ position with increasing Sr -substitution level in the $\text{Cu}(\text{Ba}_{1-x}\text{Sr}_x)_2\text{YbCu}_2\text{O}_{6.95}$ samples of the $\text{Cu-1}^{(\text{Ba},\text{Sr})}_2^{(R)}12$ phase [151]. Note that the overall oxygen content remains essentially constant.

Along the above scenario, it was found that when Ba is partially substituted by the smaller Sr in the $\text{Cu-1}^{(\text{Ba,Sr})2^{(R)}}12$ system the charge-reservoir oxygen shifts partly from the characteristic b -axis O(1) site to the a -axis O(5) site [150,151], as shown in Fig. 8. This is to satisfy the need for Sr to possess - against the Pauling's first rule - a higher CN than that required by Ba. In other words, in each unit cell where the A site is occupied by Sr, the tendency is towards the both oxygen sites to be occupied, whereas for the Ba-containing unit cells even the b -axis site is less occupied than in the Sr-free samples. An outcome is that the Sr-for-Ba substitution partly breaks the charge-reservoir copper-oxygen chains. This is believed to cause a decrease in the number of mobile holes in the charge-reservoir block and be the origin for the suppression of magnetic irreversibility (H_{irr}) characteristics that is seen for the $\text{Cu-1}^{(\text{Ba,Sr})2^{(R)}}12$ phases as a consequence of increasing Sr content [150,151].

3.3. Hole Doping Level

Obviously, hole concentration of a CuO_2 -plane, $p(\text{CuO}_2)$, is related to the "chemical" valence state of copper, *i.e.* $p(\text{CuO}_2) = V_{\text{Cu}} - 2$. Therefore, for an $M_m A_2 Q_{n-1} \text{Cu}_n \text{O}_{m+2+2n\pm\delta}$ phase one may calculate the value of $p(\text{CuO}_2)$ from the cation and oxygen stoichiometry values, m , n and δ , and the cation valence values, V_M , V_A and V_Q , as follows [6,7]:

$$p(\text{CuO}_2) = \frac{4 + 2m + 2n - mV_M - 2V_A - (n-1)V_Q \pm 2\delta}{n} \quad (2)$$

However, there are some uncertainties. Firstly, Eq. (2) assumes the same hole-concentration value for each CuO_2 plane across the superconductive CuO_2 - $(Q\text{-CuO}_2)_{n-1}$ block [6,8]. Secondly, even though the valences of cations A and Q can be guessed with good confidence (*e.g.* II for Ca, Sr, Ba and III for R) that is not necessarily the case with all the charge-reservoir constituents, as many of them (*e.g.* $M = \text{Cu, Bi, Pb}$ and Tl) are likely to possess mixed-valence values [138] (see Chapter 4). Thirdly, Eq. (2) gives an estimation for the "excess positive charge" in the CuO_2 planes, but this may not be exactly equivalent with the concentration of "mobile hole carriers".

Nevertheless, from Eq. (2) it is clear that the $M_m \text{O}_{m\pm\delta}$ block acts as a positive charge reservoir that "absorbs" part of the holes from the $AO\text{-CuO}_2\text{-}(Q\text{-CuO}_2)_{n-1}\text{-AO}$ block. Actually, for the known $M\text{-}m^{(A)}2^{(Q)}(n-1)n$ phases, charge of the $M_m \text{O}_{m\pm\delta}$ block is always positive, the magnitude varying from 0 to 2 [6,7]. A decrease in the positive charge of the charge reservoir increases the average hole concentration of the CuO_2 planes. The unusually high oxidation state of the zero $(\text{Sr}^{\text{II}}, \text{Ba}^{\text{II}})_2 \text{Ca}^{\text{II}}_{n-1} \text{Cu}_n \text{O}_{2+2n}$ phases is also evident from Eq. (2) that reduces for the given composition to: $p(\text{CuO}_2) = 2/n$. Thus at $n=3$, the average nominal Cu valence is as high as 2.67 [67]. Here it is interesting to recall that the overall oxidation state of an $M\text{-}m^{(A)}2^{(Q)}(n-1)n$ superconductor may also be unusually low, *i.e.* the average valence of copper may be lower than II, even though the CuO_2 plane(s) are doped with holes. An example is $(\text{Pb}_{2/3}\text{Cu}_{1/3})_3\text{Sr}_2(\text{Y,Ca})\text{Cu}_2\text{O}_{8.0}$ [152-154]: the CuO_2 -plane copper atom with CN = 5 is at a mixed-valence II/III state, whereas the charge-reservoir copper atom with CN = 2 is monovalent. (The valence of lead is II.) Another example of a similar situation is the oxygen-deficient, Ca^{II} -for- R^{III} substituted $\text{CuBa}_2(\text{Y,Ca})\text{Cu}_2\text{O}_{6.0}$ phase [143,155,156].

4. CHARGE/CARRIER DISTRIBUTION

From bond-valence-sum (BVS) calculations for differently oxygenated samples of Hg-12($n-1$) n and Tl-22($n-1$) n ($n = 1, 2$) an interesting observation was made: it seems that only in the underdoped region the changes that occur in the actual CuO₂-plane hole concentration upon oxygen loading follow the value calculated for $p(\text{CuO}_2)$ from Eq. (2) (on an assumption that the valence of Hg/Tl remains constant), whereas in the overdoped region the actual $p(\text{CuO}_2)$ is much smaller than that estimated with Eq. (2) [8,157]. Experimentally a similar observation was made for various $n = 1$ and 2 phases from optical conductivity data [158]. Also theoretical calculations for Hg-1201 pointed out to the same direction [159]. Such behaviour is explained by accommodation of (either mobile or localized) holes in the charge-reservoir block. The capability of the charge-reservoir block to accommodate holes is easily understood for phases in which the M cation is likely to exhibit variable oxidation states, *e.g.* Cu^{I/II/III}, Bi^{III/IV}, Pb^{II/IV}, Tl^{I/III} and even Hg^{0/II} [6,138,141].

Therefore, we conclude that before it is possible to establish a valence value for copper from a result of oxygen content analysis [through Eq. (2)], precise valence values of the other possibly multi-valent cations have to be determined. Moreover, in the M - m 2($n-1$) n phases with $n \geq 3$ (of Category-A) there are at least two types of inequivalent CuO₂ planes in the superconductive CuO₂-[Q -(CuO₂) _{$n-1$}] block, *i.e.* outer (pyramidal) and inner (square-planar) CuO₂ planes, among which holes are likely to be inhomogeneously distributed [6,8]. Full understanding of high- T_c superconductors would not be possible unless we are able to measure the distribution of charge/carriers among all the different layers. However, powerful experimental tools to detect layer-specific hole concentrations are yet to be devised [6]. In this Chapter, some illustrative examples of successful approaches and systems for which it is possible to analyze and/or control the charge/carrier balance are high-lighted.

4.1. XANES Spectroscopy

At present, x-ray absorption near-edge structure (XANES) spectroscopy is one of the few (and probably most straightforward) techniques for the studies on individual cation valences and layer-specific hole concentrations: it definitely probes local concentration of holes as the x-ray absorption spectrum is determined by electronic transitions from a selected atomic core level to the unoccupied electronic states near the Fermi level. For the superconductive copper oxides, absorption measurements at both the Cu L and the O K edges have been found effective. Due to the dipole selection rule, the Cu $L_{2,3}$ -edge absorption spectrum is governed by transitions from the Cu $2p_{1/2,3/2}$ core levels into the hole states of Cu $3d$ character. On the other hand, in the O K -edge spectrum, the O $2p$ hole states are accessible.

As an illustrative example, in Fig. 9 shown are Cu $L_{2,3}$ -edge XANES spectra for a series of CuBa₂YCu₂O_{7- δ} samples with different oxygen contents [160]. The narrow peak centered at ~931 eV (in the L_3 area) is due to divalent copper, whereas its high-energy shoulder about ~932 eV arises from trivalent copper [96,156,161]. Similar features have been observed for many other p -type doped copper-oxide superconductors, *e.g.* 0201 [162] Bi-22($n-1$) n [163-166], Tl-22($n-1$) n [167,168], Hg-12($n-1$) n [169-171], Cu-1223 [55] and (Pb_{2/3}Cu_{1/3})-3212 [154]. With decreasing oxygen content in CuBa₂YCu₂O_{7- δ} the relative intensity of the

shoulder decreases as the portion of Cu^{III} decreases. Parallel with this an additional peak emerges about ~ 934 eV. This is due to monovalent copper (with $\text{CN} = 2$) in the $\text{CuO}_{1-\delta}$ charge reservoir [96,154,156,172,173]. From the relative spectral intensities of the three peaks, accurate estimates are obtained for the (relative) amounts of Cu^{I} , Cu^{II} and Cu^{III} and thereby for the average valence state of copper. In the case of the Cu-1212 phase (and other phases with more than one type of Cu atoms) the information from the L -edge XANES data, however, is not enough to explicitly reveal the actual CuO_2 -plane hole concentration. Here absorption measurements at the O K edge may be utilized to gain layer-specific information, see Fig. 9 for a fully-oxygenated $\text{CuBa}_2\text{YCu}_2\text{O}_{6.92}$ sample for example. The pre-edge peak about ~ 528.5 eV is the well-known signature of hole states in the p -type doped CuO_2 planes in high- T_c superconductors [55,96,151,154,156,165,166,169]. For Cu-1212, partly over-lapping with this peak we can distinguish another lower-energy pre-edge peak at ~ 527.5 eV. This is due to the hole states in the $\text{CuO}_{1-\delta}$ charge reservoir [96,151,156]. By fitting these peaks, layer-specific hole concentrations are obtained. In $\text{CuBa}_2\text{YCu}_2\text{O}_{6.92}$, the $\text{CuO}_{0.92}$ charge reservoir is more heavily doped with holes than the CuO_2 plane.

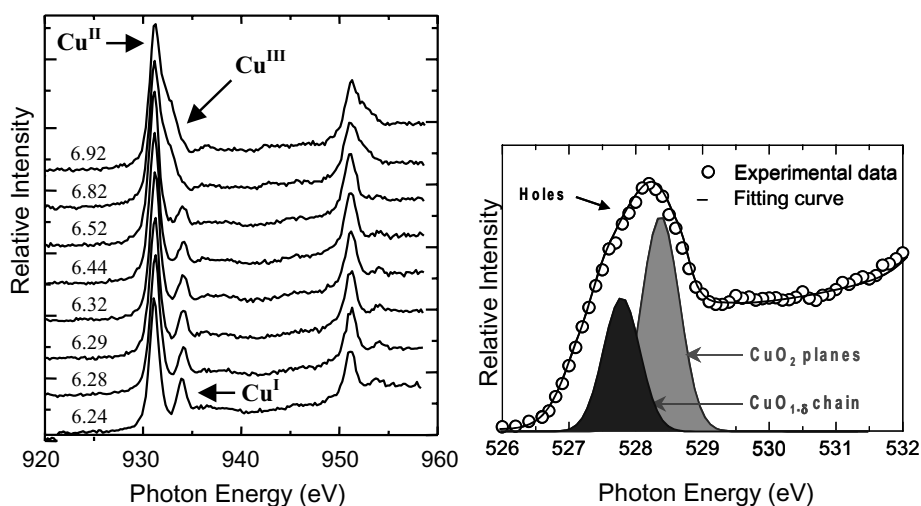


Fig. 9. Left: Cu $L_{2,3}$ -edge XANES spectra for a series of $\text{CuBa}_2\text{YCu}_2\text{O}_{7-\delta}$ samples with different oxygen contents, $7-\delta$ [160]. Right: Pre-edge portion of the O K -edge XANES spectrum and its fitting for the $\text{CuBa}_2\text{YCu}_2\text{O}_{6.92}$ sample. Note that the spectral weight due to the CuO_2 -plane hole states corresponds to two copper-oxygen planes, whereas that of the $\text{CuO}_{1-\delta}$ charge reservoir corresponds to one copper-oxygen layer only.

4.2. Cu-1212: $\text{CuBa}_2\text{RCu}_2\text{O}_{6.93}$

For the known superconductive copper-oxide phases having a trivalent rare earth element as a constituent a common feature has been that any one of the R^{III} ions is changeable by most of the others. Such “isovalent” or “size-only-dependent” cation substitutions may be used for fine-tuning the hole distribution. Here note that by replacing an R^{III} ion by another the overall hole concentration remains constant if the oxygen content is kept constant, but the distribution of holes among the different layers over the unit cell is likely to be influenced. For a series of $\text{Cu-1}^{(\text{Ba})2(R)}12$ -phase samples of $\text{CuBa}_2\text{RCu}_2\text{O}_{7-\delta}$ with the oxygen content, $7-\delta$, precisely fixed at $6.93(1)$, the isovalent smaller-for-larger R^{III} substitution was found to result in an inter-block hole shift from the $\text{BaO-CuO}_{1-\delta}\text{-BaO}$ blocking block to the superconductive $\text{CuO}_2\text{-R-CuO}_2$ block [150,174]. Since fully-oxygenated samples of the $\text{Cu-1}^{(\text{Ba})2(R)}12$ phase are in a slightly overdoped state, such an increase in the CuO_2 -plane hole concentration decreases the T_c value slightly as it makes the phase more heavily overdoped. At the same time, the distribution of holes over the unit cell becomes more homogeneous, which should be an advantage in terms of the H_{irr} characteristics [6]. Indeed, it was found that by means of decreasing the size of the R constituent it was possible to gradually enhance the H_{irr} property [174]. For the sample with the smallest R constituent, *i.e.* $\text{CuBa}_2(\text{Yb}_{0.6}\text{Lu}_{0.4})\text{Cu}_2\text{O}_{6.92}$, record-high $H_{\text{irr}}(T)$ values were achieved [174]. In Fig. 10, plotted is the 77-K H_{irr} value against the ionic radius, $r(R^{\text{III}})$, for the entire $\text{CuBa}_2\text{RCu}_2\text{O}_{6.93(1)}$ sample series. Also given is the $p(\text{CuO}_2)$ value as estimated for the $\text{Cu-1}^{(\text{Ba})2(R)}12$ system through BVS calculation.

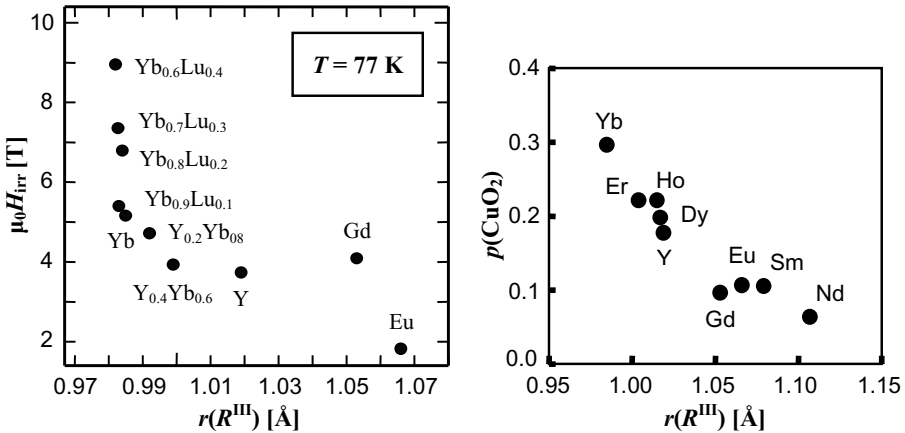


Fig. 10. Left: 77-K H_{irr} characteristics for a series of $\text{CuBa}_2\text{RCu}_2\text{O}_{6.93\pm 0.01}$ samples [174]. Right: $p(\text{CuO}_2)$ versus $r(R^{\text{III}})$ for “fully-oxygenated” $\text{CuBa}_2\text{RCu}_2\text{O}_{7-\delta}$ samples, where the $p(\text{CuO}_2)$ ’s are from BVS calculation (neutron powder diffraction data used are from Ref. [175]).

4.3. (Cu,Mo)-1232: $(\text{Cu}_{0.75}\text{Mo}_{0.25})\text{Sr}_2(\text{Ce}_{0.67}\text{R}_{0.33})_3\text{Cu}_2\text{O}_{11+\delta}$

Having the results obtained for the $\text{CuBa}_2\text{RCu}_2\text{O}_{7-\delta}$ (Cu-1212) system (Section 4.2.) in mind, one may wonder what happens if Y is replaced by other R s in the newly-discovered (Cu,Mo)-1232-phase superconductor, $(\text{Cu}_{0.75}\text{Mo}_{0.25})\text{Sr}_2(\text{Ce}_{0.67}\text{Y}_{0.33})_3\text{Cu}_2\text{O}_{11+\delta}$ [92]. In Fig. 11, the T_c value for a series of similarly HP-oxygenated $(\text{Cu}_{0.75}\text{Mo}_{0.25})\text{Sr}_2(\text{Ce}_{0.67}\text{R}_{0.33})_3\text{Cu}_2\text{O}_{11+\delta}$ samples is plotted against $r(R^{\text{III}})$ [176]. For the same samples Cu L -edge XANES data confirmed that the average valence of copper remains constant within the entire $r(R^{\text{III}})$ range. For these (Cu,Mo)-1232 samples T_c increases with decreasing $r(R^{\text{III}})$. For Cu-1212, a hole shift was found to occur from the $\text{CuO}_{1-\delta}$ charge reservoir to the CuO_2 plane when the size of the R constituent was decreased. Now, assuming that for the (Cu,Mo)-1232 phase too, holes would be gradually shifted from the $(\text{Cu,Mo})\text{O}_{1\pm\delta}$ charge-reservoir block to the CuO_2 plane with decreasing $r(R^{\text{III}})$, one comes to a conclusion that the $(\text{Cu}_{0.75}\text{Mo}_{0.25})\text{Sr}_2(\text{Ce}_{0.67}\text{R}_{0.33})_3\text{Cu}_2\text{O}_{11+\delta}$ samples studied must be underdoped. This is actually what can be concluded also from the fact that T_c monotonically increased upon loading these samples with increasing amounts of oxygen [92,176]. Here, for comparison, one should recall that for the $\text{RBa}_2\text{Cu}_4\text{O}_{8.0}$ series (“ R -124” or Cu-2212) T_c also largely increases with decreasing $r(R^{\text{III}})$ [177]; at the same time it is known that the R -124 phases are underdoped (unless part of the R^{III} ions are substituted by divalent calcium).

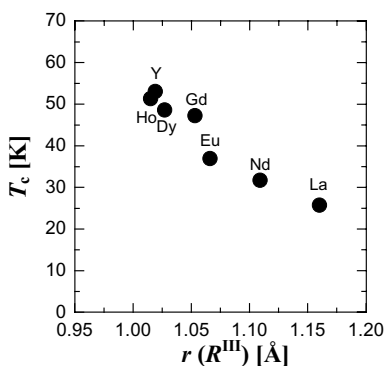


Fig. 11. T_c versus $r(R^{\text{III}})$ for a series of (similarly) HP-oxygenated (Cu,Mo)-1232-phase samples of $(\text{Cu}_{0.75}\text{Mo}_{0.25})\text{Sr}_2(\text{Ce}_{0.67}\text{R}_{0.33})_3\text{Cu}_2\text{O}_{11+\delta}$ [176].

4.4. Bi-2212: $\text{Bi}_2\text{Sr}_2(\text{Y,Ca})\text{Cu}_2\text{O}_{8+\delta}$

In the case of the Bi-2212 phase, difficulties in determining the CuO_2 -plane hole concentration arise from the fact that, besides copper, bismuth also exhibits mixed valence states. Therefore, one needs to distinguish the individual valences of Cu and Bi. This is achieved by combining information from various characterization methods [165]. By means of coulometric $\text{Cu}^+/\text{Cu}^{2+}$ redox titration it is possible to accurately analyze the total amount of

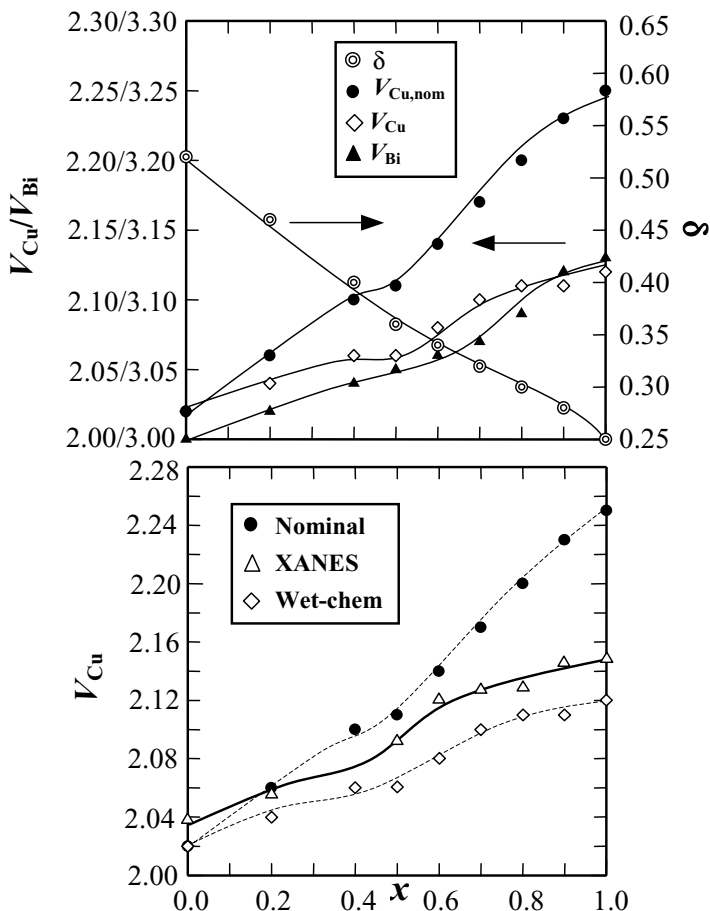


Fig. 12. Upper: wet-chemical redox analysis results for sample series, $\text{Bi}_2\text{Sr}_2(\text{Y}_{1-x}\text{Ca}_x)\text{Cu}_2\text{O}_{8+\delta}$, *i.e.* oxygen excess, δ , nominal Cu valence, $V_{\text{Cu,nom}}$ [calculated from δ through Eq. (2) assuming Bi^{III}], and the actual valences of Cu and Bi, V_{Cu} and V_{Bi} . Lower: Cu *L*-edge XANES analysis results for the valence of Cu in the same samples (for comparison, $V_{\text{Cu,nom}}$ and V_{Cu} are replotted from the upper figure).[165]

high-valent copper and bismuth species, *i.e.* Cu^{III} and Bi^{V} , and thus the oxygen content of the sample, *i.e.* δ [138,153,178]. The valence of bismuth, V_{Bi} , may then be determined with another redox experiment, *i.e.*, $\text{Fe}^{2+}/\text{Fe}^{3+}$ coulometric titration. This experiment yields selectively the amount of Bi^{V} in the presence of Cu^{III} [138,153,178]. The valence of copper, V_{Cu} , is then obtained from the values of δ and V_{Bi} , taking into account the cation

stoichiometry of the phase. The analysis can yield valence values with a high precision of ± 0.01 , but at the same time it requires sample dissolution *prior* the analysis. Therefore it is important to corroborate the wet-chemical valence-analysis results by analyzing the same samples by means of a direct (though often less accurate) solid-state analysis technique such as XANES spectroscopy. For Bi-2212 both Cu *L*-edge and O *K*-edge data are highly useful [165]; here we refer only to the former results.

Figure 12 summarizes the results from both wet-chemical redox analysis and Cu *L*-edge XANES analysis for a Bi-2212-phase sample series, $\text{Bi}_2\text{Sr}_2(\text{Y}_{1-x}\text{Ca}_x)\text{Cu}_2\text{O}_{8+\delta}$, in which holes are gradually doped through the aliovalent cation substitution, Ca^{II} -for- Y^{III} [165]. From wet-chemical redox analysis, it is revealed that the amount of excess oxygen, δ , decreases continuously from 0.52 to 0.25 when the Ca content, x , increases from 0 to 1. As the Ca^{II} -for- Y^{III} substitution proceeds, both copper and bismuth are oxidized concomitantly even though δ decreases: V_{Cu} increases from 2.03 to 2.14 and V_{Bi} from 3.00 to 3.13. In other words, holes are induced not only in the superconductive CuO_2 plane but also in the $\text{Bi}_2\text{O}_{2+\delta}$ charge reservoir. The variation range of V_{Cu} as determined from the Cu *L*-edge XANES data is 2.04-2.15, in good agreement with the wet-chemical analysis results. In Fig. 12, also given is so-called nominal Cu valence, $V_{\text{Cu,nom}}$; it is calculated from the determined value of δ through Eq. (2) assuming that Bi is trivalent. It is clearly seen that the actual valence of Cu significantly deviates from the $V_{\text{Cu,nom}}$ value thorough the sample series. This underlines the importance of precise determination of the *M* cation (here Bi) valence state in order to properly understand the doping state of superconductive copper oxides in general.

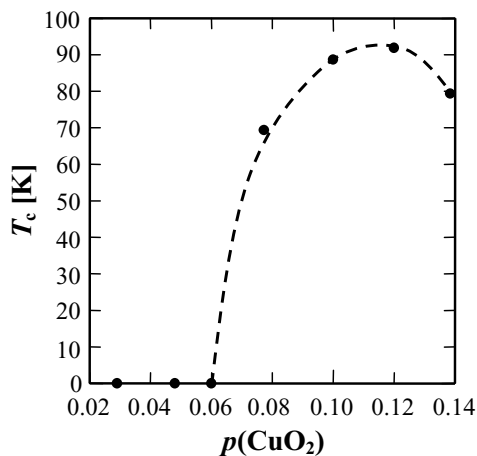


Fig. 13. T_c versus (real) $p(\text{CuO}_2)$ for sample series, $\text{Bi}_2\text{Sr}_2(\text{Y}_{1-x}\text{Ca}_x)\text{Cu}_2\text{O}_{8+\delta}$; V_{Cu} is an average of the experimental values determined from wet-chemical and Cu *L*-edge XANES analyses [165].

After determining the actual valence state of copper in the $\text{Bi}_2\text{Sr}_2(\text{Y}_{1-x}\text{Ca}_x)\text{Cu}_2\text{O}_{8+\delta}$ system, we may furthermore establish the real T_c versus $p(\text{CuO}_2)$ ($\equiv V_{\text{Cu}} - 2$; see Section 3.3). relation for the Bi-2212 phase (doped with holes through the Ca^{II} -for- Y^{III} substitution), as shown in Fig. 13, where V_{Cu} has been taken as an average of the values determined from wet-chemical and XANES analyses. Most interestingly, the threshold CuO_2 -plane hole concentration for the appearance of superconductivity is determined at 0.06(1) [165], to coincide with the value previously established for the $(\text{La,Sr})_2\text{CuO}_{4\pm\delta}$ system [179,180]. Here it should be emphasized that among the variety of $M\text{-}m2(n\text{-}1)n$ phases only a handful, e.g. $(\text{La,Sr})_2\text{CuO}_{4\pm\delta}$ (0201), $\text{CuBa}_2\text{RCu}_2\text{O}_{7-\delta}$ (Cu-1212), $\text{Bi}_2\text{Sr}_2(\text{R,Ca})\text{Cu}_2\text{O}_{8+\delta}$ (Bi-2212) and $(\text{Tl}_{0.5}\text{Pb}_{0.5})\text{Sr}_2(\text{R,Ca})\text{Cu}_2\text{O}_{7\pm\delta}$ ((Tl,Pb)-1212) [179-183], allow us to experimentally observe the actual appearance of superconductivity adjacent to the insulator-metal boundary. At the same time, the actual V_{Cu} or $p(\text{CuO}_2)$ values are straightforwardly obtained (from the cation and oxygen stoichiometry parameters) only for $(\text{La,Sr})_2\text{CuO}_{4\pm\delta}$.

4.5. Bi-2223: $(\text{Bi,Pb})_2\text{Sr}_2\text{Ca}_2\text{Cu}_3\text{O}_{10+\delta}$

For the three- CuO_2 -plane Bi-based superconductor, $\text{Bi}_2\text{Sr}_2\text{Ca}_2\text{Cu}_3\text{O}_{10+\delta}$ (Bi-2223), partial Pb-for-Bi substitution is commonly employed to enhance the otherwise sluggish and incomplete phase formation. Despite the apparent importance of Pb in (Bi,Pb)-2223, the actual role of it and its effect on the charge balance were not investigated until very recently. Rather intuitively valence states of II for Pb and III for Bi had been assumed, and accordingly believed that such a substitution should increase the concentration of holes in the CuO_2 planes. Recent careful oxygen-content and cation-valence analyses, utilizing a similar combination of wet-chemical redox titration and XANES spectroscopy techniques as described in Section 4.4 for the Bi-2212 phase, however, showed that this very intuitive scenario is not correct [166]. Table 4 summarizes results for two air-synthesized samples, $\text{Bi}_2\text{Sr}_2\text{Ca}_2\text{Cu}_3\text{O}_{10+\delta}$ and $(\text{Bi}_{0.85}\text{Pb}_{0.15})_2\text{Sr}_2\text{Ca}_2\text{Cu}_3\text{O}_{10+\delta}$.

Table 4. Redox characteristics for air-synthesized $(\text{Bi}_{1-x}\text{Pb}_x)_2\text{Sr}_2\text{Ca}_2\text{Cu}_3\text{O}_{10+\delta}$ samples [166]: δ , V_{Bi} , V_{Pb} , V_{Cu} , $p(\text{SB+CR})$ (= holes *per* formula unit) and $p(\text{CR})$ (holes *per* charge reservoir) from wet-chemical redox analysis, and V_{Cu}^* (= average Cu valence) and p^* (= average CuO_2 -plane hole concentration) from Cu *L*-edge/O *K*-edge XANES data, respectively.

| x | δ | $p(\text{SB+CR})$ | $p(\text{CR})$ | V_{Bi} | V_{Pb} | V_{Cu} | V_{Cu}^* | p^* |
|------|----------|-------------------|----------------|-----------------|-----------------|-----------------|-------------------|-------|
| 0.00 | 0.28 | 0.56 | 0.14 | 3.07 | - | 2.14 | 2.07 | 0.14 |
| 0.15 | 0.19 | 0.68 | 0.41 | 3.07 | 2.97 | 2.09 | 2.05 | 0.09 |

From coulometric $\text{Cu}^+/\text{Cu}^{2+}$ titrations, the amount of excess oxygen is found to decrease upon Pb substitution from $\delta = 0.28$ for the pristine (Pb-free) sample to $\delta = 0.19$ for the Pb-substituted one. However, counting the excess holes as those beyond the valence states of

Bi^{III} , Pb^{II} and Cu^{II} , the total number of holes *per* formula unit, $p(\text{SB}+\text{CR})$, is obtained at 0.56 for $\text{Bi}_2\text{Sr}_2\text{Ca}_2\text{Cu}_3\text{O}_{10.28}$ and at 0.68 for $(\text{Bi}_{0.85}\text{Pb}_{0.15})_2\text{Sr}_2\text{Ca}_2\text{Cu}_3\text{O}_{10.19}$. Thus, despite the lower oxygen content the Pb-substituted sample is in overall more strongly doped with holes (= excess positive charge) than the pristine Bi-2223 phase. These holes, however, are mostly located in the $(\text{Bi,Pb})_2\text{O}_{2+\delta}$ charge reservoir. This is concluded from coulometric $\text{Fe}^{2+}/\text{Fe}^{3+}$ titrations. For the Pb-free sample, V_{Bi} is seen to be not precisely III but 3.07. For the Pb-substituted sample, the method yields the total number of holes in the $(\text{Bi}_{0.85}\text{Pb}_{0.15})_2\text{O}_{2.19}$ charge reservoir. Assuming that the valence of Bi remains constant (at 3.07) upon Pb substitution, an estimation is obtained at 2.97 for V_{Pb} in (Bi,Pb) -2223. In Table 4, also given is the total amount of positive charge (in excess with respect to Bi^{III} and Pb^{II}) in the charge reservoir: upon Pb substitution $p(\text{CR})$ increases from 0.14 to 0.41. (The degree of localization of these holes is not known from this analysis.) At the same time, the average value of V_{Cu} , calculated as: $V_{\text{Cu}} = [p(\text{SB}+\text{CR}) - p(\text{CR})] / 3$, decreases from 2.14 to 2.09. Thus, as judged from the results of wet-chemical redox analyses, Pb substitution does not increase but rather decreases the average Cu valence/ CuO_2 -plane hole concentration in (Bi,Pb) -2223. From Table 4, seen is that the Cu *L*-edge and O *K*-edge XANES data for the same two samples confirmed this trend (despite some deviation in absolute values) [166].

4.6. Inequivalent CuO_2 Planes

For understanding the roles of individual CuO_2 planes of the $n \geq 3$ phases of Category-A, we should be able to accurately and reliably determine the distribution of charge/carriers among the inequivalent CuO_2 planes of the CuO_2 - $[\text{Q}-(\text{CuO}_2)_{n-1}]$ block. However, no single experimental tool has been established to accomplish direct probing of local hole amounts of individual CuO_2 planes. For example, O *K*-edge XANES spectroscopy, that has been successfully employed in hole distribution analysis of the various the $n = 2$ phases (*cf.* Sections 4.1 - 4.4), has not been made selective enough to distinguish the different oxygen sites among the inequivalent CuO_2 planes of $n \geq 3$ phases [169,184]. Since the $n = 3$ phases are the highest T_c superconductors, we should not give up our efforts to search for solutions to this challenging task

Indirectly, experimental fine-structure data, preferably extracted from neutron diffraction experiments, may be used to calculate charge balances from interatomic distances. Although various approaches have been reported [185-187], the BVS concept [188-192] provides us with most versatile possibilities [6,8]. It is worthwhile to recognize that for the $n \geq 3$ phases precise position of the Q cation (= Ca) between the different CuO_2 planes the superconductive CuO_2 - $(\text{Q}-\text{CuO}_2)_{n-1}$ block crucially controls the (inhomogeneous) distribution of holes among these planes: shifting the position of Ca atom towards the outer, pyramidal CuO_2 plane increases the hole concentration in the inner, square-planar CuO_2 plane, and *vice versa* [6,8]. Here the most interesting fact to note is that for all the known Category-A copper oxides with $n = 3$, the position of Ca is always closer to the oxygen atom of the outer CuO_2 plane than to that of the inner CuO_2 plane. This could be a manifestation of the relatively higher hole concentration of the inner portion of the CuO_2 - $(\text{Q}-\text{CuO}_2)_{n-1}$ block [6,8].

5. FINE-STRUCTURE AND SUPERCONDUCTIVITY

As stated in previous Chapters, there are yet many simple but not-yet-solved questions, such as:

- Why the value of T_c that corresponds to the optimized hole concentration varies so widely among the more-than-hundred different copper-oxide superconductors known to date?
- Why it is always the $n = 3$ phase within each homologous series of Category-A that exhibits the highest T_c value?
- What are the real roles of apex oxygen, CuO_2 -plane buckling, in-plane Cu-O bond length, *etc.*?

An early dream seems to be already forgotten to find a single structural parameter that could explicitly determine the T_c value of all the copper-oxide superconductors. On the other hand, accumulated empirical knowledge tells us that the high- T_c superconductivity characteristics have strong correlation with various crystal-chemistry parameters. The difficulty in understanding these correlations arises from the fact that the various chemical and fine-structural parameters that probably together govern the superconductivity characteristics are highly interrelated. Therefore it is impossible to have a single parameter to vary without affecting the others, and further to interpret the effects of the varied parameter without taking the variations of the other correlated parameters into account. Therefore, to assess the relationships between the atomic arrangements and superconductivity characteristics, techniques of “chemometrics” or “statistical multivariate data analysis” should be useful. The first such approach was reported in 2001 [9]: the relations between structural variables, such as the cation-oxygen bond lengths and bond angles, and the value of T_c were successfully modeled and qualitatively evaluated for a large number of $\text{Cu-1}^{(A)2^{(Q)}}12$ samples with widely varied compositions.

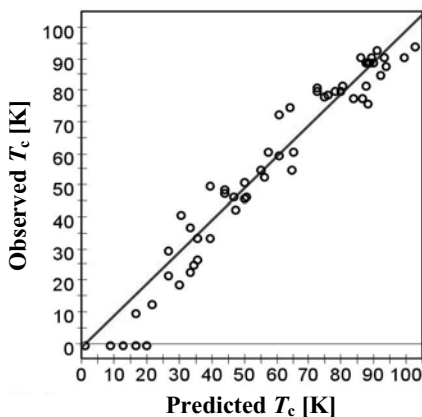


Fig. 14. Statistical multivariate data analysis result: observed *versus* predicted T_c for a series of “home-made” $\text{Cu}(\text{Ba},\text{Sr})_2(\text{R},\text{Ca})\text{Cu}_2\text{O}_{7-\delta}$ (Cu-1212) samples. The data set consists of 62 samples, each described by multiple (up to 38) structural/chemical parameters [9,193].

The first multivariate data analysis results demonstrated that the value of T_c is well explained by real-spatial crystal-chemistry parameters only (Fig. 14). This may be taken as one of the manifestations of the essential importance of chemistry rules and tools for understanding, on-demand tailoring and new-material design of high- T_c superconductive and related multi-layered strongly-correlated-electron oxides not only in the past but in the future too.

REFERENCES

- [1] J.G. Bednorz and K.A. Müller, *Z. Phys. B* 64 (1986) 189.
- [2] H. Yamauchi, *New Ceramics* 3(10) (1990) 47. (in Japanese)
- [3] T. Wada, A. Ichinose, H. Yamauchi and S. Tanaka, *J. Ceram. Soc. Jpn. Int. Ed.* 99 (1991) 420.
- [4] H. Yamauchi, M. Karppinen and S. Tanaka, *Physica C* 263 (1996) 146.
- [5] H. Yamauchi and M. Karppinen, *Superlatt. Microstruct.* 21A (1997) 127.
- [6] M. Karppinen and H. Yamauchi, *Mater. Sci. Eng. R* 26 (1999) 51.
- [7] M. Karppinen and H. Yamauchi, *Oxygen Engineering for Functional Oxide Materials, International Book Series: Studies of High Temperature Superconductors*, Vol. 37, (Ed. A.V. Narlikar), Nova Science Publishers, New York (2001), pp. 109-143.
- [8] M. Karppinen and H. Yamauchi, *Philos. Mag. B* 79 (1999) 343.
- [9] K. Lehmus and M. Karppinen, *J. Solid State Chem.* 162 (2001) 1.
- [10] S.M. Loureiro, Y. Matsui and E. Takayama-Muromachi, *Physica C* 302 (1998) 244.
- [11] C. Michel, M. Hervieu, M.M. Borel, A. Grandin, F. Dreslandes, J. Provost and B. Raveau, *Z. Phys. B* 68 (1987) 421.
- [12] H. Maeda, Y. Tanaka, M. Fukutomi and T. Asano, *Jpn. J. Appl. Phys.* 27 (1988) L209.
- [13] J.L. Tallon, R.G. Buckley, P.W. Gilberd, M.R. Presland and I.W.M. Brown, *Nature* 333 (1988) 153.
- [14] Z.Z. Sheng and A.M. Hermann, *Nature* 332 (1988) 55; *Nature* 332 (1988) 138.
- [15] C.C. Torardi, M.A., M.A. Subramanian, J.C. Calabrese, J. Gopalakrishnan, K.J. Morrissey, T.R. Askew, R.B. Flippin, U. Chowdry and A.W. Sleight, *Science* 240 (1988) 631.
- [16] S.S.P. Parkin, V.Y. Lee, A.I. Nazzal, R. Savoy, R. Beyers and S.J. La Place, *Phys. Rev. Lett.* 61 (1988) 750.
- [17] S. Matsuda, S. Takeuchi, A. Soeta, T. Suzuki, K. Aihara and T. Kamo, *Jpn. J. Appl. Phys.* 27 (1988) 2062.
- [18] S.N. Putilin, E.V. Antipov, O. Chmaissem and M. Marezio, *Nature* 362 (1993) 226.
- [19] A. Schilling, M. Cantoni, J.D. Guo and H.R. Ott, *Nature* 363 (1993) 56.
- [20] E. Takayama-Muromachi, *Chem. Mater.* 10 (1988) 2686.
- [21] H. Yamauchi and M. Karppinen, *Supercond. Sci. Technol.* 13 (2000) R33.
- [22] S. Adachi, H. Yamauchi, S. Tanaka and N. Mōri, *Physica C* 208 (1993) 226; *Physica C* 212 (1993) 164.

- [23] M.A. Alario-Franco, C. Chaillout, J.J. Capponi, J.L. Tholence and B. Souleite, *Physica C* 222 (1994) 52.
- [24] C.-Q. Jin, S. Adachi, X.-J. Wu, H. Yamauchi and S. Tanaka, *Physica C* 223 (1994) 238; X.-J. Wu, S. Adachi, C.-Q. Jin, H. Yamauchi and S. Tanaka, *Physica C* 223 (1994) 243.
- [25] T. Maeda, K. Sakuyama, S. Koriyama, H. Yamauchi and S. Tanaka, *Phys. Rev. B* 43 (1991) 7866.
- [26] H. Yamauchi, T. Tamura, X.-J. Wu, S. Adachi and S. Tanaka, *Jpn. J. Appl. Phys.* 34 (1995) L349.
- [27] T. Kawashima, Y. Matsui and E. Takayama-Muromachi, *Physica C* 224 (1994) 69.
- [28] M. Uehara, M. Uoshima, S. Ishiyama, H. Nakata, J. Akimitsu, Y. Matsui, T. Arima, Y. Tokura and N. Mori, *Physica C* 229 (1994) 310.
- [29] M. Isobe, T. Kawashima, K. Kosuda, Y. Matsui and E. Takayama-Muromachi, *Physica C* 234 (1994) 120.
- [30] E. Takayama-Muromachi and M. Isobe, *Jpn. J. Appl. Phys.* 33 (1994) L1399.
- [31] E. Takayama-Muromachi, Y. Matsui and K. Kosuda, *Physica C* 241 (1995) 137.
- [32] T. Kawashima, Y. Matsui and E. Takayama-Muromachi, *Physica C* 227 (1994) 95.
- [33] E. Takayama-Muromachi, Y. Matsui and J. Ramirez-Castellanos, *Physica C* 252 (1995) 221.
- [34] M. Isobe, Y. Matsui and E. Takayama-Muromachi, *Physica C* 273 (1996) 72.
- [35] P.G. Radaelli, M. Marezio, M. Perroux, S. De Brion, J.L. Tholence, Q. Huang and A. Santoro, *Science* 265 (1994) 380.
- [36] A. Tokiwa-Yamamoto, T. Tatsuki, X.-J. Wu, S. Adachi and K. Tanabe, *Physica C* 259 (1996) 36; *Physica C* 268 (1996) 191.
- [37] M. Al-Mamouri, P.P. Edwards, C. Greaves and M. Slaski, *Nature* 369 (1994) 382.
- [38] T. Kawashima, Y. Matsui and E. Takayama-Muromachi, *Physica C* 257 (1996) 313.
- [39] A.T. Matveev, J. Ramirez-Castellanos, Y. Matsui and E. Takayama-Muromachi, *Physica C* 262 (1996) 279.
- [40] N. Zhigadlo and E. Takayama-Muromachi, *Advances in Superconductivity XI*, (Eds. N. Koshizuka and S. Tajima), Springer, Tokyo (1999), pp. 375-378.
- [41] N.D. Zhigadlo, A.T. Matveev, Y. Ishida, Y. Anan, Y. Matsui and E. Takayama-Muromachi, *Physica C* 307 (1998) 177.
- [42] T. Hosomi, H. Suematsu, H. Fjellvåg, M. Karppinen and H. Yamauchi, *J. Mater. Chem.* 9 (1999) 1141.
- [43] M. Karppinen, H. Yamauchi, T. Hosomi, H. Suematsu and H. Fjellvåg, *J. Low Temp. Phys.* 117 (1999) 843.
- [44] H. Yamauchi, M. Karppinen, T. Hosomi and H. Fjellvåg, *Physica C* 338 (2000) 38.
- [45] P.P. Edwards, G.B. Peacock, J.P. Hodges, A. Asab and I. Gameson, *Proc. NATO ASI, Materials Aspects of High Temperature Superconductivity: 10 Years After the Discovery* (Eds. E. Kaldis and E. Liarokapis), Kluwer Academic Publ. (1997).
- [46] Y. Syono, *J. ISTEC* 4/2 (1991) 35.
- [47] T. Kaneko, H. Yamauchi and S. Tanaka, *Physica C* 178 (1991) 377.
- [48] M. Marezio, J.-J. Capponi, P.-G. Radaelli, P.P. Edwards, A.R. Armstrong and W.I.F. David, *Eur. J. Solid State Inorg. Chem.* 31 (1994) 843.
- [49] K.A. Lokshin, D.A. Pavlov, S.N. Putilin, E.V. Antipov, D.V. Sheptyakov and A.M. Balagurov, *Phys. Rev. B* 63 (2001) 64511.

- [50] L. Gao, Y.Y. Xue, F. Chen, Q. Xiong, R.L. Meng, D. Ramirez, C.W. Chu, J.H. Eggert and H.K. Mao, *Phys. Rev. B* 50 (1994) 4260.
- [51] M. Monteverde, M. Núñez-Regueiro, C. Acha, K.A. Lokshin, D.A. Pavlov, S.N. Putilin and E.V. Antipov, *Physica C* (2004) in press.
- [52] M.K. Wu, J.R. Ashburn, C.J. Torng, P.H. Hor, R.L. Meng, L. Gao, Z.J. Huang, Y.Q. Wang and C.W. Chu, *Phys. Rev. Lett.* 58 (1987) 908.
- [53] C. Chailout, S. Le Floch, E. Gautier, P. Bordet, C. Acha, Y. Feng, A. Sulpice, J.L. Tholence, M. Marezio, *Physica C* 266 (1996) 215.
- [54] T. Ito, H. Suematsu, K. Isawa, M. Karppinen and H. Yamauchi, *Physica C* 308 (1998) 9.
- [55] M. Karppinen, H. Yamauchi, Y. Morita, M. Kitabatake, T. Motohashi, R.S. Liu, J.M. Lee and J.M. Chen, *J. Solid State Chem.* 177 (2004) 1037.
- [56] R.J. Cava, B. Batlogg, J.J. Krajewski, L.W. Rupp, L.F. Schneemeyer, T. Siegrist, R.B. van Dover, P. Marsh, W.F. Peck Jr, P.K. Gallagher, S.H. Glarum, J.H. Marshall, R.C. Farrow, J.V. Waszczak, R. Hull and P. Trevor, *Nature* 336 (1988) 211.
- [57] H.W. Zandbergen, W.T. Fu, J.M. van Ruitenbeek, L.J. de Jongh, G. van Tendeloo and S. Amelinckx, *Physica C* 159 (1989) 81.
- [58] F.J.M. Benshop, W.T. Fu and W.J.A. Maaskant, *Physica C* 184 (1991) 311.
- [59] H. Yamauchi and M. Karppinen, *Physica C* 335 (2000) 273.
- [60] Z. Hiroi, M. Takano, M. Azuma and Y. Takeda, *Nature* 364 (1993) 315.
- [61] S.N. Ruddlesden and P. Popper, *Acta Cryst. Sect. A* 10 (1957) 538; *Acta Cryst. Sect. A* 11 (1958) 54.
- [62] H. Yamamoto, M. Naito and H. Sato, *Jpn. J. Appl. Phys.* 36 (1997) L341.
- [63] T. Kawashima and E. Takayama-Muromachi, *Physica C* 267 (1996) 106.
- [64] R.D. Shannon, *Acta Cryst. A* 32 (1976) 751.
- [65] Z. Hiroi, N. Kobayashi and M. Takano, *Nature* 371 (1994) 139.
- [66] C.-Q. Jin, X.-J. Wu, P. Laffez, T. Tatsuki, T. Tamura, S. Adachi, H. Yamauchi, N. Koshizuka and S. Tanaka, *Nature* 375 (1995) 301.
- [67] M. Karppinen, T. Hosomi and H. Yamauchi, *Physica C* 382 (2002) 276.
- [68] T. Hosomi, H. Suematsu, M. Karppinen and H. Yamauchi, *Physica C* 324 (1999) 65.
- [69] H. Yamauchi, M. Karppinen, T. Hosomi and H. Suematsu, *Physica C* 338 (2000) 46.
- [70] K. Takada, H. Sakurai, E. Takayama-Muromachi, F. Izumi, R.A. Dilanian and T. Sasaki, *Nature* 422 (2003) 53.
- [71] M. Karppinen, I. Asako, T. Motohashi and H. Yamauchi, *Chem. Mater.* 16 (2004) 1693.
- [72] K. Takada, K. Fukuda, M. Osada, I. Nakai, F. Izumi, R.A. Dilanian, K. Kato, M. Takata, H. Sakurai, E. Takayama-Muromachi and T. Sasaki, *J. Mater. Chem.* 14 (2004) 1448.
- [73] G. Demazeau, C. Parent, M. Pouchard, and P. Hagenmuller, *Mater. Res. Bull.* 7 (1972) 913.
- [74] L. Er-Rakho, C. Michel, Ph. Lacorre and B. Raveau, *J. Solid State Chem.* 73 (1988) 531.
- [75] A.W. Webb, E.F. Skelton, S.B. Qadri, V. Browning and E.R. Carpenter Jr., *Phys. Rev. B* 45 (1992) 2480.
- [76] A.W. Webb, E.F. Skelton, S.B. Qadri and E.R. Carpenter Jr., *J. Solid State Chem.* 102 (1993) 519.

- [77] M. Karppinen, H. Yamauchi, H. Suematsu, K. Isawa, M. Nagano, R. Itti and O. Fukunaga, *J. Solid State Chem.* 130 (1997) 213.
- [78] Z. Hiroi and M. Takano, *Nature* 377 (1995) 41.
- [79] M. Nagase, J. Lindén, H. Suematsu, M. Karppinen and H. Yamauchi, *Phys. Rev. B* 59 (1999) 1377.
- [80] Akimitsu, S. Suzuki, M. Watanabe and H. Sawa, *Jpn. J. Appl. Phys.* 27 (1988) L1859.
- [81] H. Sawa, S. Suzuki, M. Watanabe, J. Akimitsu, H. Matsubara, H. Watabe, S. Uchida, K. Kokusho, H. Asano, F. Izumi and E. Takayama-Muromachi, *Nature* 337 (1989) 347.
- [82] J.M. Longo and P.M. Raccah, *J. Solid State Chem.* 6 (1973) 526.
- [83] B. Grande, Hk. Müller-Buschbaum and M. Schweizer, *Z. Anorg. Allg. Chem.* 428 (1977) 120.
- [84] Hk. Müller-Buschbaum and W. Wollschlaeger, *Z. Anorg. Allg. Chem.* 414 (1975) 76.
- [85] Y. Tokura, H. Takagi and S. Uchida, *Nature* 337 (1989) 345.
- [86] H. Sawa, K. Obara, J. Akimitsu, Y. Matsui and S. Horiuchi, *J. Phys. Soc. Jpn.* 58 (1989) 2252.
- [87] A. Tokiwa, T. Oku, M. Nagoshi and Y. Syono, *Physica C* 181 (1991) 311.
- [88] T. Wada, A. Nara, A. Ichinose, H. Yamauchi and S. Tanaka, *Physica C* 192 (1992) 181.
- [89] S. Ikegawa and Y. Motoi, *Appl. Phys. Lett.* 68 (1996) 2430.
- [90] In two published works [Chen Xianhui *et al.*, *Phys. Rev. B* 48 (1993) 9799, and Y. Akagi *et al.*, *Physica C* 388-389 (2003) 387] possible superconductivity in an *M*-1232 type phase has been claimed/mentioned. However, both the works lack the most crucial experimental evidence required to verify bulk superconductivity of the given phase.
- [91] S. Ikegawa, K. Nakayama and M. Arai, *Physica C* 384 (2003) 61.
- [92] Y. Morita, T. Nagai, Y. Matsui, H. Yamauchi and M. Karppinen, *Phys. Rev. B* (2004) in press.
- [93] A. Ono, *Jpn. J. Appl. Phys.* 32 (1993) 4517.
- [94] A. Ono, *Jpn. J. Appl. Phys.* 32 (1993) L1599.
- [95] M. Arai, J.M. Lee, J.M. Chen, R.S. Liu, Y. Morita, T. Motohashi, H. Yamauchi and M. Karppinen, (2004) manuscript.
- [96] N. Nücker, E. Pellegrin, P. Schweiss, J. Fink, S. L. Molodtsov, C.T. Simmons, G. Kaindl, W. Frentrop, A. Erb and G. Müller-Vogt, *Phys. Rev. B* 51 (1995) 8529.
- [97] T. Wada, A. Ichinose, H. Yamauchi and S. Tanaka, *Physica C* 171 (1990) 344.
- [98] T. Wada, A. Ichinose, F. Izumi, A. Nara, H. Yamauchi, H. Asano and S. Tanaka, *Physica C* 179 (1991) 455.
- [99] H.W. Zandbergen, T. Wada, A. Nara, H. Yamauchi and S. Tanaka, *Physica C* 183 (1991) 149.
- [100] I. Felner, U. Asaf, Y. Lavi and O. Milio, *Phys. Rev. B* 55 (1997) 3374.
- [101] C. Bernhard, J.L. Tallon, Ch. Niedermayer, Th. Blasius, A. Golnik, E. Brücher, R.K. Kremer, D.R. Noakes, C.E. Stronack and E.J. Asnaldo, *Phys. Rev. B* 59 (1999) 14099.
- [102] H. Sasakura, Y. Akagi, S. Noguchi, S. Tsukui, T. Oka and M. Adachi, *J. Supercond.* 16 (2003) 961.

- [103] V.P.S. Awana, M. Karppinen and H. Yamauchi, Magneto-superconductivity in Rutheno-cuprates $\text{RuSr}_2\text{GdCu}_2\text{O}_{8-\delta}$ (Ru-1212) and $\text{RuSr}_2(\text{Gd}_{0.75}\text{Ce}_{0.25})_2\text{Cu}_2\text{O}_{10-\delta}$ (Ru-1222): A Critical Review, *International Book Series: Studies of High Temperature Superconductors*, Vol. 46, (Ed. A.V. Narlikar), Nova Science Publishers, New York (2003), pp. 77-98.
- [104] M. Karppinen, V.P.S. Awana, Y. Morita and H. Yamauchi, *Physica C* 392-396 (2003) 82.
- [105] Q. Huang, R.J. Cava, A. Santoro, J.J. Krajewski and W.F. Peck, *Physica C* 193 (1992) 196.
- [106] T. Krekels, O. Milat, G. van Tendeloo, S. Amelinckx, T.G.N. Babu, A.J. Wright and C. Greaves, *J. Solid State Chem.* 105 (1993) 313.
- [107] V.P.S. Awana, S.K. Malik, W.B. Yelon, M. Karppinen and H. Yamauchi, *Physica C* 378-381 (2002) 155.
- [108] R.J. Cava, H.W. Zandberger, J.J. Krajewski, W.F. Peck Jr., B. Hessen, R.B. Van Dover and S.-W. Cheong, *Physica C* 198 (1992) 27.
- [109] T. Nagai, V.P.S. Awana, E. Takayama-Muromachi, A. Yamazaki, M. Karppinen, H. Yamauchi, S.K. Malik, W.B. Yelon and Y. Matsui, *J. Solid State Chem.* 176 (2003) 213.
- [110] Y. Morita, H. Fjellvåg, T. Nagai, J.M. Lee, J.M. Chen, R.S. Liu, B.C. Hauback, V.P.S. Awana, Y. Matsui, H. Yamauchi and M. Karppinen, (2004) manuscript.
- [111] M.G. Smith, A. Manthiram, J. Zhou, J.B. Goodenough and J.T. Markert, *Nature* 351 (1991) 549.
- [112] T. Siegrist, S.M. Zahurak, D.W. Murphy and R.S. Roth, *Nature* 334 (1988) 231.
- [113] M. Takano, Y. Takeda, H. Okada, M. Miyamoto and T. Kusaka, *Physica C* 159 (1989) 140.
- [114] G. Er, Y. Miyamoto, F. Kanamaru and S. Kikkawa, *Physica C* 181 (1991) 206.
- [115] G. Er, S. Kikkawa, F. Kanamaru, Y. Miyamoto, S. Tanaka, M. Sera, M. Sato, Z. Hiroi, M. Takano and Y. Bando, *Physica C* 196 (1992) 271.
- [116] Z. Hiroi, M. Azuma, M. Takano and Y. Takeda, *Physica C* 208 (1993) 286.
- [117] N. Ikeda, Z. Hiroi, M. Azuma, M. Takano, Y. Bando and Y. Takeda, *Physica C* 210 (1993) 367.
- [118] J.D. Jorgensen, P.G. Radaelli, D.G. Hinks, J.L. Wagner, S. Kikkawa, G. Er and F. Kanamaru, *Phys. Rev. B* 47 (1993) 14654.
- [119] H. Shaked, Y. Shimakawa, B.A. Hunter, R.L. Hitterman, J.D. Jorgensen, P.D. Han and D.A. Payne, *Phys. Rev. B* 51 (1995) 11784.
- [120] G. Er, S. Kikkawa, M. Takahashi, F. Kanamaru, M. Hangyo, K. Kisoda and S. Nakashima, *Physica C* 290 (1997) 1.
- [121] B. Wiedenhorst, H. Berg, R. Gross, B.H. Freitag and W. Mader, *Physica C* 304 (1998) 147.
- [122] M. Takano, M. Azuma, Z. Hiroi, Y. Bando and Y. Takeda, *Physica C* 176 (1991) 441.
- [123] M. Azuma, Z. Hiroi, M. Takano, Y. Bando and Y. Takeda, *Nature* 356 (1992) 775.
- [124] S. Adachi, N. Sugii, H. Yamauchi, S. Tanaka and N. Mōri, *J. Ceram. Soc. Jpn.* 101 (1993) 815. (in Japanese)
- [125] K. Kubo, M. Ichikawa, N. Sugii, K. Yamamoto and H. Yamauchi, *Phys. Rev. B* 49 (1994) 6919.
- [126] H.W. Zandbergen, R. Gronski, K. Wang and G. Thomas, *Nature* 331 (1988) 596.

- [127] E. Kaldis, P. Fischer, A.W. Hewat, E.A. Hewat, J. Karpinski and S. Rusiecki, *Physica C* 159 (1989) 668.
- [128] Y. Yaegashi, S. Adachi, T. Wada, S. Takano and H. Yamauchi, *Physica C* 190 (1992) 433.
- [129] A. Fukuoka, M. Karppinen, N. Seiji, J. Valo, A. Kareiva, L. Niinistö, M. Leskelä, N. Koshizuka and H. Yamauchi, *Supercond. Sci. Technol.* 8 (1995) 673.
- [130] D.V. Fomichev, A.L. Kharlanov, E.V. Antipov and L.M. Kovba, *Fizika Khimiya Tekhnika* 3 (1990) 1280. (in Russian)
- [131] Y. Miyazaki, H. Yamane, T. Kajitani, T. Oku, K. Hiraga, Y. Morii, K. Fuchizaki, S. Funahashi and T. Hirai, *Physica C* 191 (1992) 434.
- [132] K. Kinoshita and T. Yamada, *Nature* 357 (1992) 313.
- [133] J. Akimitsu, M. Uehara, M. Ogawa, H. Nakata, K. Tomimoto, Y. Miyazaki, H. Yamane, T. Hirai, K. Kinoshita and Y. Matsui, *Physica C* 201 (1992) 320.
- [134] D. Pelloquin, M. Caldes, A. Maignan, C. Michel, M. Hervieu and B. Raveau, *Physica C* 208 (1993) 121.
- [135] F. Goutenoire, M. Hervieu, A. Maignan, C. Michel, C. Martin and B. Raveau, *Physica C* 210 (1993) 359.
- [136] M. Uehara, S. Sahoda, H. Nakata, J. Akimitsu and Y. Matsui, *Physica C* 222 (1994) 27.
- [137] R.J. Cava, P. Bordet, J.J. Capponi, C. Chaillout, J. Chevasnas, T. Fournier, E.A. Hewat, J.L. Hodeau, J.P. Levy, M. Marezio, B. Batlogg and L.W. Rupp Jr., *Physica C* 167 (1990) 67.
- [138] M. Karppinen, A. Fukuoka, L. Niinistö and H. Yamauchi, *Supercond. Sci. Technol.* 9 (1996) 121.
- [139] F.D. Richardson and J.H.E. Jeffes, *J. Iron Steel Inst.* 160 (1948) 261.
- [140] E. Ikonen, J. Hietaniemi, K. Härkönen, M. Karppinen, T. Katila, J. Lindén, L. Niinistö, H. Sipola, I. Tittonen and K. Ullakko, *High- T_c Superconductors*, (Ed. H. W. Weber), Plenum Publishing Corporation, New York (1988), pp. 209-215.
- [141] M. Karppinen, *Annales Academiae Scientiarum Fennicae, Series A II. Chemica* 249 (1993) 51 p.
- [142] M. Karppinen, L. Niinistö and H. Yamauchi, *J. Therm. Anal.* 48 (1997) 1123.
- [143] K. Fujinami, M. Karppinen and H. Yamauchi, *Physica C* 300 (1998) 17.
- [144] T. Ito, H. Suematsu, M. Karppinen and H. Yamauchi, *Physica C* 308 (1998) 198.
- [145] T. Karlemo, M. Karppinen, L. Niinistö, J. Lindén and M. Lippmaa, *Physica C* 292 (1997) 225.
- [146] A. Tokiwa-Yamamoto, A. Fukuoka, M. Itoh, S. Adachi, H. Yamauchi and K. Tanabe, *Physica C* 269 (1996) 354.
- [147] V.M. Goldschmidt, *Geochemische Verteilungsgesetze der Elemente, Skrifter Norske Videnskaps-Akad.*, Oslo, I. Mat-Naturr. K1 (1926).
- [148] J.B. Goodenough, *Supercond. Sci. Technol.* 3 (1990) 26.
- [149] J.B. Goodenough and A. Manthiram, *J. Solid State Chem.* 88 (1990) 115.
- [150] M. Karppinen, N. Kiryakov, Y. Yasukawa, T. Nakane and H. Yamauchi, *Physica C* 382 (2002) 66.
- [151] T. Nakane, K. Isawa, R.S. Liu, J.M. Chen, H. Yamauchi and M. Karppinen, *J. Solid State Chem.* 177 (2004) 1925.
- [152] M. Marezio, *Acta Crystallogr. A* 47 (1991) 640.

- [153] M. Karppinen, A. Fukuoka, J. Wang, S. Takano, M. Wakata, T. Ikemachi and H. Yamauchi, *Physica C* 208 (1993) 130.
- [154] M. Karppinen, M. Kotiranta, H. Yamauchi, P. Nachimuthu, R.S. Liu and J.M. Chen, *Phys. Rev. B* 63 (2001) 184507.
- [155] M. Karppinen, H. Yamauchi, K. Fujinami, K. Peitola, T. Nakane, H. Rundlöf and R. Tellgren, *Phys. Rev. B* 60 (1999) 4378.
- [156] M. Karppinen, H. Yamauchi, T. Nakane, K. Fujinami, K. Lehmus, P. Nachimuthu, R.S. Liu and J.M. Chen, *J. Solid State Chem.* 166 (2002) 229.
- [157] M. Karppinen and H. Yamauchi, *J. Supercond.* 11 (1998) 39.
- [158] A.V. Puchkov, P. Fournier, T. Timusk and N.N. Kolesnikov, *Phys. Rev. Lett.* 77 (1996) 1853.
- [159] C. Ambrosch-Draxl, P. Süle, H. Auer and E. Ya. Sherman, *Phys. Rev. B* 67 (2003) R100505.
- [160] Y. Morita, M. Karppinen, H. Yamauchi, R.S. Liu and J.M. Chen, *J. Low Temp. Phys.* 131 (2003) 381.
- [161] A. Bianconi, M. DeSantis, A. Di Ciccio, A.M. Flank, A. Fronk, A. Fontaine, P. Legarde, H. K. Yoshida, A. Kotani and A. Marcelli, *Phys. Rev. B* 38 (1988) 7196.
- [162] C.T. Chen, L.H. Tjeng, J. Kwo, H.L. Kao, P. Rudolf, F. Sette and R.M. Fleming, *Phys. Rev. Lett.* 68 (1992) 2543.
- [163] A.Q. Pham, F. Studer, N. Merrien, A. Maignan, C. Michel and B. Raveau, *Phys. Rev. B* 48, 1249 (1993).
- [164] N.L. Saini, D.S.-L. Law, P. Pudney, K.B. Garg, A.A. Menovsky and J.J.M. Franse, *Phys. Rev. B* 52 (1995) 6219.
- [165] M. Karppinen, K. Kotiranta, T. Nakane, S.C. Chang, J.M. Chen, R.S. Liu and H. Yamauchi, *Phys. Rev. B* 67 (2003) 134522.
- [166] M. Karppinen, S. Lee, J.M. Lee, J. Poulsen, T. Nomura, S. Tajima, J.M. Chen, R.S. Liu and H. Yamauchi, *Phys. Rev. B* 68 (2003) 54502.
- [167] A. Krol, C.S. Lin, Y.L. Soo, Z.H. Ming, Y.H. Kao, J.H. Wang, M. Qi and G.C. Smith, *Phys. Rev. B* 45 (1992) 10051.
- [168] P. Srivastava, F. Studer, K.B. Garg, Ch. Gasser, H. Murray and M. Pompa, *Phys. Rev. B* 54 (1996) 693.
- [169] E. Pellegrin, J. Fink, C.T. Chen, Q. Xiong, Q.M. Lin and C.W. Chu, *Phys. Rev. B* 53 (1996) 2767.
- [170] B.R. Sekhar, F. Studer, K.B. Garg, Y. Moriwaki, C. Gasser and K. Tanabe, *Phys. Rev. B* 56 (1997) 14809.
- [171] T. Watanabe, N. Kiryakov, J. Poulsen, J.M. Lee, J.M. Chen, R.S. Liu, H. Yamauchi and M. Karppinen, *Physica C* 392-396 (2003) 93.
- [172] M. Grioni, J. B. Goedkoop, R. Schoorl, F. M. F. de Groot, J. C. Fuggle, F. Schäfers, E. E. Koch, G. Rossi, J.-M. Esteve, R. C. Karnatak, *Phys. Rev. B* 39 (1989) 1541.
- [173] M. Grioni, J.F. van Acker, M.T. Czyżyk, J.C. Fuggle, *Phys. Rev. B* 45 (1992) 3309.
- [174] Y. Yasukawa, T. Nakane, H. Yamauchi and M. Karppinen, *Appl. Phys. Lett.* 78 (2001) 2917.
- [175] M. Guillaume, P. Allenspach, W. Henggeler, J. Mesot, B. Roessli, U. Staub, P. Fischer, A. Furrer and V. Trounov, *J. Phys. Condens. Matter* 6 (1994) 7963.
- [176] Y. Morita, J.M. Chen, R.S.Liu, H. Yamauchi and M. Karppinen, (2004) manuscript.

- [177] Y. Yaegashi, S. Adachi, T. Wada, S. Takano and H. Yamauchi, *Physica C* 190 (1992) 433.
- [178] M. Karppinen, H. Yamauchi and S. Tanaka, *J. Solid State Chem.* 104 (1993) 276.
- [179] M.W. Shafer, T. Penney and B.L. Olson, *Phys. Rev. B* 36 (1987) 4047.
- [180] J.B. Torrance, Y. Tokura, A.I. Nazzal, A. Bezing, T.C. Huang and S.S.P. Parkin, *Phys. Rev. Lett.* 61 (1988) 1127.
- [181] Y. Tokura, J. B. Torrance, T.C. Huang and A.I. Nazzal, *Phys. Rev. B* 38 (1988) 7156.
- [182] J.-M. Tarascon, P. Barboux, G.W. Hull, R. Ramesh, L.H. Greene, M. Giroud, M.S. Hedge and W.R. McKinnon, *Phys. Rev. B* 39 (1989) 4316.
- [183] R.S. Liu, P.P. Edwards, Y.T. Huang, S.F. Wu and P.T. Wu, *J. Solid State Chem.* 86 (1990) 334.
- [184] J.M. Chen, S.C. Chung and R.S. Liu, *Solid State Commun.* 99 (1996) 493.
- [185] M. Di Stasio, K.A. Müller and L. Pietronero, *Phys. Rev. Lett.* 64 (1990) 2827.
- [186] E.M. Haines and J.L. Tallon, *Phys. Rev. B* 45 (1992) 3172.
- [187] D.T. Jover, R.J. Wijngaarden, R. Griessen, E.M. Haines, J.L. Tallon and R.S. Liu, R.S., *Phys. Rev. B* 54 (1996) 10175.
- [188] I.D. Brown and D. Altermatt, *Acta Crystallogr. B* 41 (1985) 244.
- [189] I.D. Brown, *J. Solid State Chem.* 82 (1989) 122.
- [190] I.D. Brown, *Physica C* 169 (1990) 105.
- [191] J.L. Tallon, *Physica C* 168 (1990) 85.
- [192] M. Karppinen and H. Yamauchi, *Int. J. Inorg. Mater.* 2 (2000) 589.
- [193] M. Karppinen, J. Poulsen and H. Yamauchi, (2004) manuscript.

OXYGEN IN HIGH- T_c CUPRATE SUPERCONDUCTORS

J. L. Tallon

MacDiarmid Institute for Advanced Materials and Nanotechnology, Industrial Research Ltd.,
and Victoria University of Wellington, P.O. Box 31310, Lower Hutt, New Zealand.

1. INTRODUCTION

It goes without saying that oxygen plays a vital role in the structure and properties of cuprate high- T_c superconductors (HTS). That is clear from the very fact that superconductivity originates in the corner-shared square-planar CuO_2 planes which are common to all HTS [1]. Central as this fact is to the modern understanding of HTS physics, it continues to be questioned in some quarters [2]. However, there can be no doubt that superconductivity (SC) does develop exclusively in the orbitals which comprise the CuO_2 plane. Heavy substitutional disorder can be injected into any of the non- CuO_2 layers with little or no effect on T_c or superfluid density, ρ_s [3]. But the incorporation of disorder at the Cu or O site of the CuO_2 plane is pathological and both T_c and ρ_s are suppressed exactly as expected for a d -wave order parameter in the unitarity limit [4,5]. Perhaps more significantly, superconductivity has been demonstrated in a single CuO_2 plane in layer-by-layer MBE-deposited thin films[6].

So it is clear that oxygen is a key component of the structural matrix in which SC originates. But is that all? Or does it play a more intimate role in the essential physics of superconductivity? Just how important is the role of oxygen may be assessed from the following:

(a) the exchange interaction from which the antiferromagnetism (AF) of the undoped parent compound derives is mediated via O 2p orbitals [7]. Short-range AF in some form, perhaps dressed by phonons, probably mediates the Cooper pairing;

- (b) the doped hole carriers that pair up to form the superconducting condensate have a dominant O 2p character [8,9];
- (c) the onset, beyond optimal doping, of mixed O 2p_z character associated with apical oxygens [10] appears to signal the closure of the pseudogap, the onset of coherent *c*-axis transport [11] and the demise of superconductivity (SC). T_c begins an abrupt fall;
- (d) internal stress between the Cu-O bonds in the CuO₂ planes and the structural matrix in which they reside governs both the thermodynamic stability [12] of the compounds and the maximal T_c achievable [13];
- (e) oxygen non-stoichiometry plays a central role in determining doping state and carrier concentration; at the same time slow oxygen diffusion provides a severe limitation to our ability to fully control doping (and especially to achieve full oxygenation);
- (f) and, the use of oxygen isotopes allows powerful probes of the electronic state. These include ¹⁷O NMR measurements of spin susceptibility and spin relaxation, and
- (g) ¹⁸O isotope effects in both the pairing strength given by the SC gap, Δ_0 , and in the condensate strength given by ρ_s , the superfluid density.

Here we review these various important features that underscore the central role of oxygen in both the fundamental physics of HTS cuprates and their applied technology.

2. STRUCTURE

HTS cuprates are members of a class of defect layered perovskite oxides which are known to be subject to substantial oxygen nonstoichiometry. These cuprates are no exception. They comprise corner-shared square planar CuO₂ layers stacked, in perovskite fashion, one, two, three or four layers thick which are then separated by “blocking layers” which may be ionic, molecular, organic or, in the case of the bismuth, thallium and mercury families a rocksalt structure such as Bi₂O₂ or Tl₂O₂. There are many variations of these structures and they are thoroughly summarized by Hazen [1]. Because they are layered they tend to be electronically very anisotropic with quasi-two-dimensional electron dynamics in-plane and tunneling or Josephson characteristics normal to the plane.

2.1 YBCO family

Fig. 1 shows an important subgroup represented by YBa₂Cu₃O_{7- δ} , YBa₂Cu₄O₈, and Y₂Ba₄Cu₇O_{15- δ} , where Y may be yttrium or any of the lanthanide rare earth elements. They will be referred to as Y-123, Y-124 and Y-247, and the pure compounds have maximal T_c values of 93.5K, 81K and 95K [14,15], respectively. In the first of these the layer sequence is CuO_{1- δ} -BaO-CuO₂-Y-CuO₂-BaO-CuO_{1- δ} where δ may range from 0 to 1 depending upon annealing conditions. The value of δ determines, amongst other things, the carrier concentration. When $\delta=0$ and the material is fully ordered the CuO layer forms one-dimensional chains extending in the *b*-direction. So the material is formed of -CuO₂-Y-CuO₂- bilayers of fixed stoichiometry separated by blocking layers of -BaO-CuO_{1- δ} -BaO- with variable oxygen stoichiometry. The CuO chains are conductive and as a consequence YBa₂Cu₃O₇ has additional in-plane anisotropy that plays an important role in the high critical current density (J_c) achievable in this material, especially in a magnetic field. The structure is

an orthorhombic tripled defect perovskite with structure Pmmm and lattice parameter $c \approx 3b \approx 1.17\text{nm}$. Annealing this compound at elevated temperatures in, for example, reduced oxygen partial pressure ($p\text{O}_2$) results in egress of oxygen from the chain layers. Quantification of the equilibrium state is discussed in §5.1. When $\delta=1$ the material is fully oxygen deficient in the chain layer and therefore now tetragonal with $a = b$. The Cu1 atoms in the “chain layer” are monovalent Cu^+ and the addition of a single O atom to this layer converts the adjacent Cu atoms to divalent Cu^{++} and as a consequence there are no holes initially doped into the CuO_2 layers by introducing a small random distribution of O atoms in the “chain layer”. Only when there is sufficient density to form chain segments exceeding two coppers in length does hole doping occur. This will be examined in more detail in §4.3 and §5.1. The development of chain segments and the impact of ionic radius of the rare-earth has been investigated in detail by Lutgemeier *et al.* using NQR [16]. At intermediate values of δ , orthorhombic Y-123 tends to twin because chains can randomly nucleate in either direction and twinning also provides a means of releasing stress in a sintered body of randomly oriented grains. These twins cause a defect potential within the CuO_2 planes that can significantly affect normal state and superconducting properties.

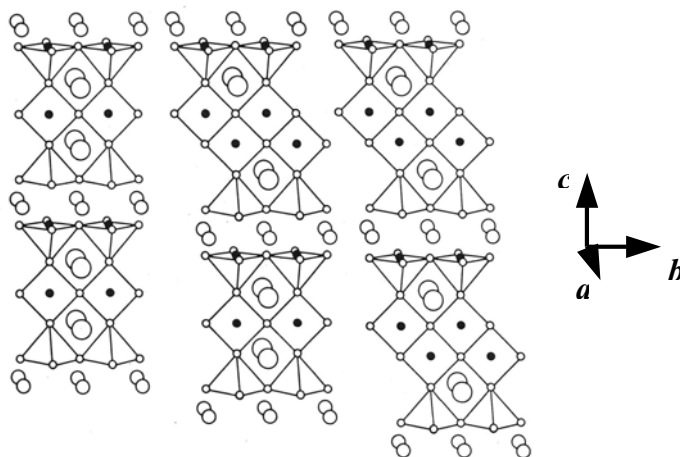


Fig. 1. The structure of Y-123, Y-247 and Y-124 showing square pyramid oxygen coordination about the planar Cu atoms and linear CuO chains in the b -direction. Y-123 has single chains, Y-124 double chains and in Y-247 single and double chains alternate.

The Y-124 material has a double chain (or ladder) extending in the b -direction with each chain offset by $b/2$. This causes a doubling of the unit cell length to $2 \times 1.37 = 2.74 \text{ nm}$. The double chain is very stable and as a consequence stoichiometric. Annealing of this compound at elevated temperatures in reduced oxygen partial pressure does not result in egress of oxygen from these double chains. This condition applies right up to the stability boundary shown in Fig. 2 where Y-124 decomposes to $\text{CuO} + \text{YBa}_2\text{Cu}_3\text{O}_{7-\delta}$, with some equilibrium value of δ . The decomposition is very rapid and can be used to effectively introduce pinning defects to enhance J_c [17]. Because of its fixed stoichiometry, Y-124 has a fixed doping state

irrespective of thermal history and as a consequence is a useful material for undertaking oxygen isotope effect studies because two parallel exchanged samples (one with ^{16}O and one with ^{18}O) will assume exactly the same doping state during the exchange anneal. The fixed stoichiometry, combined with absence of twinning, means that Y-124 generally is the most defect-free HTS. This is most important for NMR studies where electric field gradients and chemical shifts due to disorder can seriously broaden out the resonance as in the Bi family or $\text{La}_{2-x}\text{Sr}_x\text{CuO}_4$ (referred to as La-214).

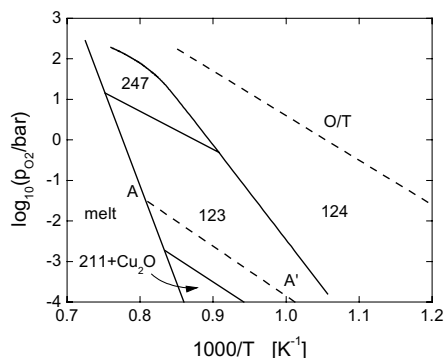


Fig. 2. The oxygen phase diagram for the Y/Ba/Cu/O system with Y-247 composition. The line O/T marks the orthorhombic/tetragonal transition in Y-123 and the line A-A' marks the phase boundary between Cu_2O and CuO . The line below this shows where Y-123 decomposes to $\text{Cu}_2\text{O} + \text{Y}_2\text{BaCuO}_5$ (referred to as 211).

Y-247, as shown in Fig. 1, is an ordered intergrowth system comprising alternating layers of Y-123 and Y-124. As expected the oxygen nonstoichiometry is confined to each of the single chains in the Y-123 blocks [14] and the double chains in the Y-124 blocks provide a preferred direction which ensures absence of twinning as the single chains load up oxygen. We will see in §7 that the double chains in combination with ordered single chains provide for a very high superfluid density, and this compound as a consequence has the highest irreversibility field, for its doping state, of all HTS. Fig. 2 shows the stability domains for the three compounds, together with the location of the orthorhombic/tetragonal transition in Y-123 (marked O/T), the decomposition line for Y-123 to suboxides, and the boundary (A-A') between Cu_2O and CuO . It is fortunate that Y-247 has a small stability window at 1 bar oxygen pressure between 860 and 870°C. This allowed synthesis of this compound at atmospheric pressure [14] and the low-temperature synthesis material exhibits a remarkably high T_c (= 95K). In contrast, high pressure synthesized Y-247 showed rather low T_c values (40 – 60K) [18].

The fully oxygenated Y-123, Y-247 and Y-124 compounds form a series with doping states of 0.19, 0.16, and 0.13 holes per planar Cu, respectively. Interestingly (though not significantly) these compounds reside almost precisely on critical doping, optimal doping and $1/8^{\text{th}}$ doping respectively. They have T_c values of 91K, 95K and 81K respectively and stoichiometric $\text{YBa}_2\text{Cu}_3\text{O}_7$ is lightly overdoped with $T_{c,max} = 93.5\text{K}$. When fully deoxygenated, Y-123 and Y-247 have doping states of 0 and 0.065 holes per planar Cu with

T_c values of 0 and 25K [14], respectively. The five compounds Y-123, Y-247 and Y-124 with $\delta=0$ and 1 represent a set of model compounds, each quite free of disorder.

2.2 BSCCO family

These, like the thallium- and mercury-based HTS, form a Ruddleston-Popper series of homologous compounds with single, bilayer, trilayer and tetralayer CuO_2 stacks separated usually by Ca ions. The general formula is approximately $\text{Bi}_{2-1}\text{Sr}_2\text{Ca}_{n-1}\text{Cu}_n\text{O}_{4+2n+\delta}$, $n=1, 2, 3, 4, \dots$ [19] and these possess $T_{c,\text{max}}$ values of 32, 95, 109 and 112K, respectively. The utility of the BSCCO family is that the $\text{Bi}_2\text{O}_{2+\delta}$ blocking layer is relatively wide with weak van der Waals bonding between the BiO sheets. This gives these materials a micaceous or graphitic character with a slip system that allows deformation induced texturing. By rolling composite tapes from BSCCO in silver tube a high degree of grain alignment can be achieved with atomically smooth “railway junction” grain boundaries [20] which can support high J_c values. The Bi-2223 ($n=3$) material is currently the only HTS material which is manufactured commercially in long lengths for magnet, cable, transformer and motor applications.

Since the charge transfer that induces hole doping in the CuO_2 multi-layers comes only from the $\text{Bi}_2\text{O}_{2+\delta}$ layer with its excess oxygen, the doped hole concentration is distributed over the n layers and thus is progressively diluted as n increases. The homologous series thus moves from the overdoped side back to the underdoped side of the generic T_c phase curve as n increases [21]. As noted in the formula there seems to be excess Bi, which may account for a structural modulation along the b-axis with superlattice length $\approx 4.5a$ [19], and in addition some Bi can substitute on the Sr site. For $n=1$ and 2 some Sr and Ca can intersubstitute [1]. This makes for a complex defect distribution and the broad NMR linewidths clearly evidence this disorder. Of interest to us here is the location of oxygen in the $\text{Bi}_2\text{O}_{2+\delta}$ blocking layer. The natural Bi-O bondlength of ~ 0.22 nm is significantly less than the ideal value enforced by the Cu-O bond ($0.192 \times \sqrt{2} = 0.27\text{nm}$). As a consequence each oxygen atom sits closer to one in-plane Bi neighbour than the other three [22] and the excess oxygen, denoted by δ , results in a curious structural modulation [23]. The dominant structure of the Bi_2O_2 layer is a rocksalt packing (two interpenetrating FCC lattices) with the distorted oxygen locations as noted above. But every 2.57nm the structure reverts to a strip of pseudo-perovskite packing as shown in Fig. 3 [24]. It is in this layer that the labile oxygen may be adjusted in order to

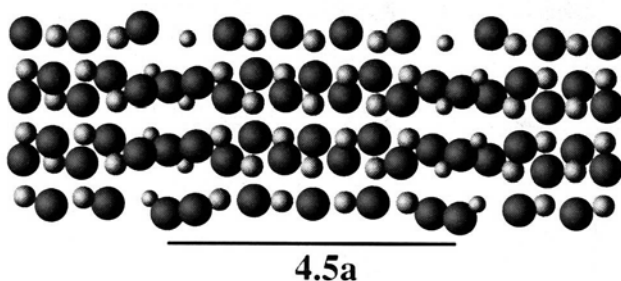


Fig. 3. The modulated structure of the BiO plane. Narrow periodic strips of oxygen-deficient pseudo-perovskite pack in a ‘rocksalt’ sheet. Large atoms denote oxygen and smaller atoms are Bi^{3+} . In the perovskite strips the smallest atoms denote Bi^{5+} .

control the doping state of the CuO_2 layers [25]. The combination of variable doping via oxygen content and cleavability under UHV to render pristine surfaces has allowed extensive characterization of the electronic properties of $\text{Bi}_2\text{Sr}_2\text{CaCu}_2\text{O}_{8+\delta}$ using e.g. ARPES [26], scanning tunneling microscopy [27] and transport properties [28].

3. ELECTRONIC STRUCTURE

The magnetism, normal state transport properties and SC in HTS cuprates derive from electron dynamics within hybridised Cu 3d and O 2p orbitals. The electronic configuration for Cu is $3d^9$ and the degeneracy of these orbitals is first broken by the octahedral crystal field to produce an upper e_g level comprising $d_{x^2-d_{y^2}}$ and d_{z^2} orbitals and a lower t_{2g} level arising from degenerate d_{xy} , d_{yz} and d_{zx} orbitals. Further, the Jahn-Teller distortion pushes back the apical oxygen lifting the degeneracy of the $d_{x^2-d_{y^2}}$ and d_{z^2} orbitals, raising the energy of the former above the latter. (It also lifts the d_{zx} level above that of the d_{xy} and d_{yz} orbitals).

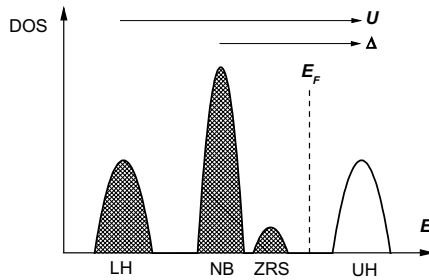


Fig. 4. The density of states scheme for HTS cuprates at low doping. LH and UH are the lower (occupied) and upper (unoccupied) Hubbard Cu 3d bands, NB is the non-bonding O $2p_\sigma$ band and ZRS is the Zhang-Rice singlet band for doped holes.

The nine 3d electrons fill all lower levels and could, in principle, leave the $d_{x^2-d_{y^2}}$ band half filled and hence metallic. However, strong on-site Coulomb repulsion results in a splitting of the $d_{x^2-d_{y^2}}$ band into an empty upper Hubbard (UH) band and a full lower Hubbard (LH) band separated by the Mott-Hubbard gap, U . Hence the undoped state is an insulator with a single spin, $s=1/2$, localized on each Cu site and its ground state is antiferromagnetic (AF). This is illustrated schematically in Fig. 4.

Early studies [8,9] showed that when holes are doped into the CuO_2 layer they reside within the oxygen O $2p_\sigma$ orbitals. This occurs because the HTS cuprates are charge-transfer insulators in which, as shown in Fig. 4, the energy separation Δ between the non-bonding O $2p_\sigma$ orbitals and the UH band is less than the separation of the LH and UH bands. The charge transfer gap, Δ , is governed by the difference in Madelung energy between a hole on an O and a hole on a Cu and hence is a function of the crystal structure and the CuO bond length. This variability is confirmed by infrared spectroscopy [29,30]. At the same time, the single spin

residing on each Cu site may be viewed as a localized hole on the Cu 3d orbitals. Zhang and Rice showed that strong hybridization results in doped holes on O 2p orbitals forming a singlet state with the localized Cu hole such that the doped hole is distributed over the four adjacent in-plane oxygen orbitals. This yields the Zhang-Rice singlet band shown in Fig. 4 as the highest occupied states. Optical transitions between the ZRS band and the UH band may be observed at about 2eV [31].

At low doping it is known that AF correlations lead to an attractive interaction between holes. As a consequence the lightly doped Mott insulator is unstable with respect to phase separation of spins and doped holes and this can lead to the formation of nanoscale stripes in which spins assemble into antiphase AF strips separated by charged domain walls on which the holes are located. Evidence for such stripes has been deduced from inelastic neutron scattering [32] and NMR [33]. A second possibility is that the attractive interaction between holes afforded by the AF background leads to pairing and a *d*-wave SC state [34]. And yet a third possibility is that the spin gap associated with the formation of stripes overcomes coulomb repulsion and leads to SC pairing [35]. These possibilities will be discussed in more detail below.

4. DOPING

4.1 Control of doping state

The doped carrier concentration in HTS may be controlled by alteration of their cation or anion stoichiometry or by atomic substitution of altrivalent species. Thus, for example, substitution of Sr^{2+} for La^{3+} in $\text{La}_{2-x}\text{Sr}_x\text{CuO}_4$ introduces holes which have a dominantly O 2p character, that is, they reside substantially but not fully on the in-plane oxygen orbitals. This provides for a doping state given by $p = x$ holes per Cu which is fixed from synthesis. At higher levels of $x > 0.2$ the as-prepared compound tends to be a little oxygen deficient and full oxygen stoichiometry is only achieved by slow-cooling and annealing in oxygen following the last synthesis step. Post synthesis variation of the doped hole concentration may also be achieved by electrochemical insertion of excess oxygen in compounds of the form $\text{La}_2\text{CuO}_{4+\delta}$. Here the doping is not continuous but appears to proceed in discrete steps called staging. There is a miscibility gap for $0 \leq \delta \leq 0.055$ [36].

For the remaining HTS the doping state is usually adjusted by annealing the sample in a controlled oxygen partial pressure at a particular temperature to achieve oxygen equilibrium, and then quenching the sample, preferably into liquid nitrogen. Since 1987 we have annealed in a vertical furnace with a magnetic release that drops the sample into liquid nitrogen in order to rapidly freeze in the oxygen state. The oxygen exchange rate can be so high, especially in low density samples, that quenching is absolutely necessary to ensure uniform oxygen (and hence doping) concentration across the sample. Changes in oxygen content can be determined rather accurately simply by mass change or by titration [37]. An alternative method is to anneal in a sealed quartz tube with a suitable oxygen getter or source [38] and single crystals may be annealed in such fashion with a polycrystalline pellet that has been annealed and quenched. In this way the oxygen content of the crystal may be adjusted to that already established for the pellet.

4.2 Doping phase diagram

In spite of their variable band structure HTS cuprates appear to follow a universal phase behaviour with doping which is summarized in Fig. 5 [39,40]. This seems to arise from the dominant strong correlations that over-ride band-structure considerations. The undoped state, $p=0$, corresponds to an AF insulator with $300\text{K} < T_{Neel} < 400\text{K}$, and as holes are doped in magnetic correlations are frustrated and T_{Neel} falls rapidly to zero at $p \approx 0.05$. Superconductivity spans the range $0.05 < p < 0.27$ with T_c rising up and down a roughly parabolic phase curve given by [21]

$$T_c = T_{c,max} [1 - 82.6 (p-0.16)^2] \quad (1)$$

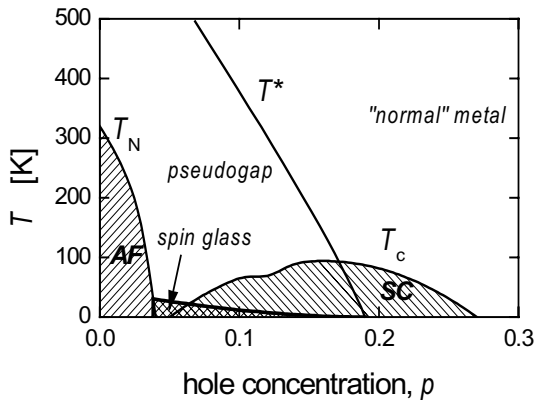


Fig. 5. The universal phase diagram for hole-doped HTS superconductors showing a region of antiferromagnetic (AF) ordering at low p and superconductivity (SC) at higher doping. The normal state pseudogap energy scale $T^* = E_g/k_B$ falls to zero at critical doping $p = p_{crit} = 0.19$ holes/Cu. There is a spin-glass state at intermediate doping and the system progresses towards a “normal” Fermi liquid at high doping.

This relation seems to be satisfied by the broad class of hole doped HTS cuprates. Short-range AF correlations continue to persist across at least half of this phase curve but apparently die out rather abruptly around a critical doping state, $p_{crit} \approx 0.19$ holes/Cu. In this region quasiparticles are heavily damped, presumably due to scattering from AF spin fluctuations near the $(\pi,0)$ ‘hot spots’ on the Fermi surface. With increasing doping the material proceeds from a strongly correlated systems towards a more Fermi-liquid-like electronic system and $(\pi,0)$ quasiparticle lifetimes lengthen out rather abruptly at p_{crit} [41]. The ‘optimal doping’ state where $T_c = T_{c,max}$ occurs at $p = p_{opt} \approx 0.16$ holes/Cu and the so-called ‘underdoped region’ refers to hole concentrations less than this value while the ‘overdoped region’ refers to values exceeding p_{opt} . In the neighbourhood of $p \approx 0.125$ the T_c phase curve exhibits an

anomaly associated with the freezing out of spin/charge stripe fluctuations. The possible role of these stripes in the pseudogap and pairing interaction will be discussed further in §9.

Across the underdoped region the normal state ($T > T_c$) exhibits a gap in the density of states that results in a T -dependent spin susceptibility and a loss of spectral weight that is evident in most normal-state and SC physical properties. This is referred to as the pseudogap though its origins remain uncertain. The pseudogap causes a reduction in T_c and in superfluid density, even at $T=0$, and so must arise from an independent correlation that competes with SC. This is most evident from intrinsic tunneling studies which expose the SC gap on the flanks of the pseudogap with each having very different doping dependence. The SC gap is states-conserving and, in BCS fashion, closes at T_c , while the pseudogap is non-states-conserving and remains unaltered on passing through T_c . The energy scale of the pseudogap, E_g , decreases with increasing doping and closes abruptly at $p = p_{\text{crit}}$, as shown in Fig. 5 by the line $T^* = E_g/k_B$. It is evident then that the pseudogap is closely linked to short-range AF correlations and the incoherent quasiparticles at $(\pi,0)$. It should be noted that this summary reflects the views of the author and a consensus on these points is yet to be established [40].

4.3 Measuring the doping level

In the case of $\text{La}_{2-x}\text{Sr}_x\text{CuO}_4$ the doped hole concentration is just given by $p = x$. But for most other HTS compounds the doping state cannot be directly determined in this way. For example, the Y-123 compound has both CuO_2 planes and CuO chains in which doped holes may reside. Indeed, the latter takes the major fraction. It is not straightforward to deduce the planar hole concentration even though the total doped hole concentration per unit cell can be deduced from e.g. titration measurements.

There are, nonetheless, several available approaches to this problem. Consider the fully deoxygenated Ca-doped Y-123 compound $\text{Y}_{1-x}\text{Ca}_x\text{Ba}_2\text{Cu}_3\text{O}_6$. Because the Cu1 atoms in the chain layer are Cu^{1+} and remain so irrespective of Ca content then the doping level in the CuO_2 planes is just $p=x/2$. The thermoelectric power (TEP) of this compound and other HTS follows a universal dependence upon p which allows a simple two-minute measurement of the room temperature TEP to determine the doping state [42]. The countable doping state in $\text{Y}_{1-x}\text{Ca}_x\text{Ba}_2\text{Cu}_3\text{O}_6$ allows an absolute scale to be established for the TEP which can then be applied to the other cuprates. In addition the universal SC phase curve given by eq. (1) may be inverted to determine p and the result always agrees rather closely with that obtained from the TEP [39]. This is not exact because all the cuprates exhibit some degree of phase curve anomaly near $p=1/8$ probably due to the formation of spin/charge stripes.

A further method that works in the case of some HTS is the use of bond valence sums (BVS) [43]. Most use has focused on the Cu BVS:

$$V_{\text{Cu}} = \sum_j \exp [-(r_j - r_0)/0.37] \quad (2)$$

Here r_j are the bond lengths for the oxygen atoms neighbouring the Cu atom of interest and r_0 is a characteristic length for Cu-O bonds tabulated by Brown and Altermatt [44]. The sum is over the set of neighbours which is usually 6, 5 or 4. In the spirit of this approach, for planar coppers, $p = V_{\text{Cu}} - 2$. However, in view of the dominantly O2p character of the doped holes it has been argued that the oxygen BVS must also be included in any estimate of the total doped hole concentration [13]. Thus we introduce the parameter V_- such that

$$p \approx V_- = 2 + V_{\text{Cu}} - V_{\text{O2}} - V_{\text{O3}} \quad (3)$$

where O2 and O3 are the two oxygen sites in the CuO_2 plane. This allows for the possibility that $V_{\text{O2}} \neq V_{\text{O3}}$ when there is in-plane anisotropy, as in the case of Y-123, Y-124 and Y-247. This scheme seems remarkably successful in the case of $\text{Y}_{1-x}\text{Ca}_x\text{Ba}_2\text{Cu}_3\text{O}_{7-\delta}$ as is shown in Fig. 6 for $x = 0, 0.1$ and 0.2 [39]. This shows the relation between p (i.e. V_-) and δ for each case and we note in particular the fact we have already noted, namely that the doping is independent of δ when δ is close to 1 i.e. close to full deoxygenation. In our view each of these curves must be bodily displaced up by about $\Delta p \approx 0.01$ holes/Cu. This is evidenced at $\delta = 1$ where p should be $x/2$. This scheme works well when, as in the present case, there is only weak internal stress arising from mismatch between natural bondlengths. But it fails when this internal stress is large. Thus, V_- is a measure of the total hole density and we can introduce an additional parameter, V_+ , that is a measure of its relative distribution between Cu and O orbitals.

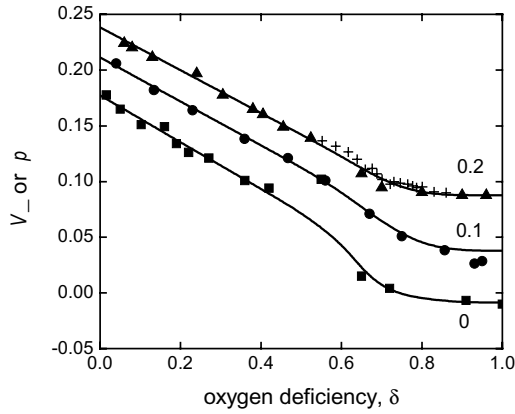


Fig. 6. The variation of p , estimated from the BVS parameter V_- , with oxygen deficiency in $\text{Y}_{1-x}\text{Ca}_x\text{Ba}_2\text{Cu}_3\text{O}_{7-\delta}$. Values of x are shown for each curve. Near full oxygenation the curves are linear with slope 0.21 holes/oxygen while as $\delta \rightarrow 1$ the hole density is independent of δ . Actual values of p are probably 0.01 larger in all cases.

The V_+ parameter is given by:

$$V_+ = 6 - V_{\text{Cu}} - V_{\text{O2}} - V_{\text{O3}} \quad (4)$$

V_+ is also a measure of stress in the CuO_2 plane in the sense that negative values indicate a compressive stress (as well as stronger copper character in the doped holes) while positive values indicate an in-plane tensile stress (as well as stronger oxygen character in the doped holes). It emerges that the optimal T_c value correlates rather well with V_+ such that $T_{c,max}$ is greatest under tensile stress and strong O2p character. This is summarised in Fig. 7 and one

may thus construct a 3-dimensional topographic map of $T_c(V_-, V_+)$ which incorporates both the doping dependence and stress-dependence of T_c . This is strongly peaked at $T_c(0.16, 0.3)$ in a manner rather suggestive of the near proximity of a quantum critical point. These basic ideas were subsequently independently inferred by the group of Bianconi [45]. This suggests a strategy of stretching the Cu-O bond length by substitution of a larger cation in the blocking layers of an HTS cuprate. It is for this reason that $T_{c,max}$ for the L-123 system increases with increasing lanthanide radius [46]. On this basis we expect that the highest $T_{c,max}$ achievable in a cuprate system would be for $\text{HgR}_{a_2}\text{Ca}_2\text{Cu}_3\text{O}_8$. The attendant complications of radioactive radium have thus far prevented the synthesis of this compound!

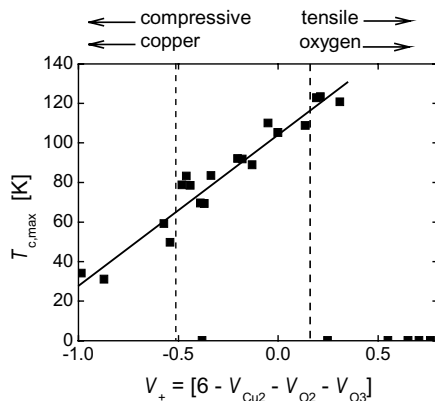


Fig. 7. The correlation of $T_{c,max}$ with the bond valence sum parameter V_+ . Negative values of V_+ correspond to a compressive in-plane stress and holes tending to reside more on Cu 3d orbitals while positive values correspond to a tensile in-plane stress and holes tending to reside more on oxygen 2p orbitals.

An interesting outcome of this correlation concerns the thermodynamic stability of cuprates. All of the compounds plotted in Fig. 7 were synthesized and their phase stability was investigated at the line A-A' in the phase diagram shown in Fig. 2. This is the stability boundary between Cu_2O and CuO and annealing across this boundary has been used to synthesize high quality thin films of $\text{YBa}_2\text{Cu}_3\text{O}_{7-\delta}$ [47]. It was found [12] that all HTS compounds between the two vertical dashed lines in Fig. 7 decomposed at the phase boundary A-A' where CuO would decompose to Cu_2O . Those compounds outside of these dashed lines were stable to much lower $p\text{O}_2$ or higher temperature. Because those compounds within the lines have little stress exerted on the CuO_2 planes by the blocking layers the stability appears to be determined primarily by the CuO_2 layer which decomposes at A-A'. Those compounds lying outside of the lines experience a strong tensile or compressive stress on the CuO_2 layers and here the stability seems to be determined primarily by the blocking layers. These materials thus survive to well below the A-A' boundary. Y-123 is an exception, presumably because of the $\text{CuO}_{1-\delta}$ chains.

5. OXYGEN ORDERING

5.1 CuO chain ordering in Y-123

As noted, the Y-123 structure progresses from tetragonal structure, when δ is near unity, to an orthorhombic structure when δ is small due to the ordering of oxygen into CuO chains extending in the b-direction. This transformation is via a second-order phase transition. Twinning may diminish or even nullify the macroscopic orthorhombicity but the material will remain microscopically orthorhombic. Twinning in orthorhombic single crystals may be removed by applying a uniaxial stress at elevated temperature (350–400°C) in oxygen. Viewed under polarized light microscopy one may observe an abrupt transition to the detwinned state. The crystal must then be cooled while maintaining the applied stress. Such detwinned crystals have been used for optical, magnetotransport, magnetization and inelastic neutron scattering studies to probe the effects of in-plane anisotropy on electron dynamics.

Oxygen ordering and equilibrium stoichiometry may be simply described as follows [48]. At the microscopic level we may define the ideal chain oxygen sites as O1 with fractional occupancy x_1 and the ideally vacant sites as O5 with fractional occupancy x_5 . When $\delta \approx 1$ an inserted oxygen atom may equally reside in an O1 or O5 site with binding energy, ϵ . As δ is reduced with oxygen loading, sites will initially be randomly occupied but eventually adjacent O1 and O5 sites will be faced with the prospect of joint occupancy. A repulsive interaction ϵ_r tends to minimize such contiguity and it is this that promotes the development of extended chain segments and the onset of orthorhombicity. The oxygen equilibrium state can be calculated using a Bragg-Williams mean-field order/disorder calculation which results in the following two general relations [48]:

$$[x_1/(1-x_1)][x/(1-x)] = (p/p_0)^{1/2} \exp[(\epsilon-zx_5\epsilon_r)/k_B T] \quad (5)$$

$$[x_5/(1-x_5)][x/(1-x)] = (p/p_0)^{1/2} \exp[(\epsilon-zx_1\epsilon_r)/k_B T] \quad (6)$$

where x is the total occupancy and z ($=4$) is the nearest-neighbour coordination number. Above the orthorhombic/tetragonal transition, T_{OT} , we have $x_1 = x_5 = x/2$ so that

$$x^2/[(2-x)(1-x)] = (p/p_0)^{1/2} \exp[(\epsilon-0.5zx\epsilon_r)/k_B T] \quad (7)$$

and the OT transition occurs at

$$k_B T_{OT} = \frac{1}{4} z\epsilon_r x(2-x). \quad (8)$$

This provides a rather good description of the observed behaviour for Y-123. Fig. 8 shows calculated constant-composition plots in the oxygen-partial-pressure/temperature Arrhenius diagram (lines) with experimental data points from Gallagher [49]. The dashed curve and square data points delineate the calculated and experimental OT transition line. The overall agreement is excellent.

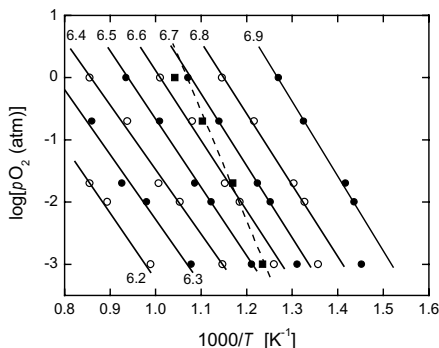


Fig. 8. Constant oxygen composition plots for $\text{YBa}_2\text{Cu}_3\text{O}_{7-\delta}$ calculated using eqs. (5) and (6) and OT transition line calculated using eq. (8). Data is from Gallagher [49].

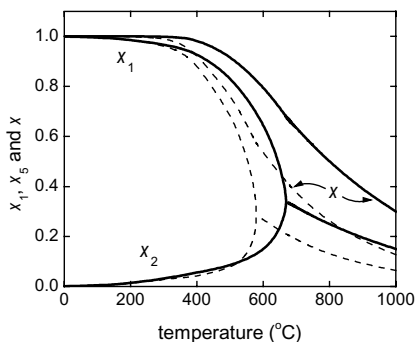


Fig. 9. Site occupancies x_1 and x_5 , and total chain-oxygen content, x , calculated using eqs. (5) and (6) for $p\text{O}_2 = 1$ atm (solid curves) and 0.01 atm (dashed).

It is also instructive to consider the temperature dependence of the compositions x_1 , x_5 and x . These are shown in Fig. 9 for oxygen partial pressures of 1 atm and 0.01 atm. We note that full oxygenation does not occur until below 380°C so that no amount of annealing at higher temperatures will achieve this result. More importantly full oxygen ordering does not occur until below 100°C . This has major implications for ensuring high J_c because the doping state is not so much dependent upon the total oxygen content as the degree of ordering. Full chain order ensures maximal charge transfer to the CuO_2 planes. The repulsive energy E_r is greatest when the in-plane lattice parameters a and b are smallest, as for example when Y is replaced by a smaller lanthanide rare-earth element such as Er, Tm, Yb or Lu. These compounds exhibit the best oxygen ordering while in the larger lanthanides increasing occupation of the O5 site occurs and the charge transfer is accordingly diminished.

5.2 Other ordered phases

This kind of calculation has been refined to allow for repulsive interaction between nearest interchain O1 sites. This leads to an additional form of oxygen ordering known as “ortho-II” in which, for $\delta=0.5$, every second chain is empty and the intervening chains are full and ordered [50]. This presents a superlattice doubling of the a -parameter. Other ordered structures are observed when e.g. $\delta = 0.333$ corresponding to one empty and two full chains [51]. Again, ordered phase single crystals like this can be detwinned [52] and these provide very high quality crystals which are relatively free of oxygen disorder and its associated perturbations to physical properties.

5.3 The Y-247 and (Y,Ca)-123 compounds

It was a surprise in the first synthesis of Y-247 at atmospheric pressure that these materials were superconducting with $T_c \approx 94\text{K}$ on removal from the furnace without cooling [14]. These were porous due to low temperature synthesis (865°C) using KNO_3 as a reaction rate enhancer. As a consequence they loaded oxygen very rapidly, merely in the process of removal from the tubular furnace, at temperature. By annealing in a vertical furnace, quenching into liquid nitrogen and measuring mass change, the value of δ in $\text{Y}_2\text{Ba}_4\text{Cu}_7\text{O}_{15-\delta}$, was found to be the same as the value of δ in $\text{YBa}_2\text{Cu}_3\text{O}_{7-\delta}$ [14], thus indicating that the equilibrium thermodynamics for oxygen loading is the same in the single chains of Y-247 as it is in Y-123. However, for several years since the first discovery of Y-247 it was found [53] to have a much lower T_c than the values ($92\text{-}95\text{K}$) noted above. This proved to be due to the formation of [100] 90° rotation twins in the intermediate Y-123 compound where the c -axis unit cell built onto three a -axis unit cells [54,55], thus hindering oxygen diffusion and preventing full oxygenation. These samples all tended to be underdoped. A further problem was found with the incorporation of CO_2 molecules into the chain layer [56]. This is a significant materials issue for all Y-123, Y-247 and (Y,Ca)-123 materials for CO_2 molecules block the chain layer and thus hinder oxygen diffusion. Any sample that is removed from the controlled atmosphere of its synthesis oven and exposed to the atmosphere tends to take up some CO_2 . It may initially be merely adsorbed, but if reannealed in a closed environment the CO_2 becomes incorporated into the chains and it is then difficult to fully oxygenate the chains. This is not readily noticeable in Y-123 because T_c is on the 90K plateau so there is little change in T_c with a small amount of oxygen deficiency. But there is a serious reduction in e.g. critical current density. In the case of Y-247 it results in underdoping [57] with a clear reduction in T_c and, on the other hand, (Y,Ca)-123 samples cannot be so fully overdoped with a consequent increase in T_c . This is a central issue with the synthesis of high-quality YBCO materials and it particularly frustrates ability to achieve heavily overdoped samples of $\text{Y}_{0.8}\text{Ca}_{0.2}\text{Ba}_2\text{Cu}_3\text{O}_{7-\delta}$. Samples must be oxygen loaded during synthesis and if they are deoxygenated and reoxygenated they must be reheated under oxygen to $T > 970^\circ\text{C}$, rapidly cooled to $\approx 700^\circ\text{C}$, then very slowly cooled under oxygen without removal at any stage from the furnace. The effect of Ca substitution is to displace the curves in Fig. 9 to lower T (by about 40°C). They must therefore be annealed at lower temperature than pure Y-123 and typically $\sim 350^\circ\text{C}$. The lower temperature nominally results in a significantly lower diffusion rate (due to thermal activation) except for the fact that Ca-substitution typically enhances the

oxygen diffusion coefficient by a factor of ~ 100 [58]. Nonetheless, because the samples are synthesized at such high temperature, they are very dense and their final anneal in oxygen at ~ 350 °C should last for at least a week.

6. OXYGEN DIFFUSION

Because oxygen loading and equilibration is essential to the optimization of HTS cuprates, and particularly so in Y-123 like materials, the issue of oxygen diffusion becomes exceedingly important. The fact is that the oxygen diffusion coefficient is sufficiently low that single crystals or dense polycrystalline ceramics may take many weeks, even months, to oxygenate. Oxygen diffusion has been directly measured in single crystals [59,60] by exposure to ^{18}O gas at a given temperature and $p\text{O}_2$. The concentration of ^{18}O has then been measured by SIMS as a function of depth by progressive ion milling. From the concentration profile the diffusion coefficient may be deduced for those annealing conditions. The process is then continued for a variety of temperatures or pressures.

Another technique is that of ultrasonic relaxation. Because the displacement of an oxygen atom from an interchain O5 site to an intrachain O1 site results in a local elongation of the b -axis the application of an oscillatory longitudinal stress causes local hopping of oxygen atoms between the two sites. This leads to a Debye relaxation which exhibits a peak in the mechanical damping when the characteristic relaxation rate corresponds to the frequency of the applied stress. In this way the hopping rate may be measured and the self-diffusion coefficient deduced [61,62].

Such measurements have been carried out using an ultrasonic composite oscillator [63]. This comprises a long assembly of 70mm quartz drive and gauge crystals, a 300mm-long spacer fused quartz rod and a 50mm long rod-shaped HTS sample, usually a polycrystalline sintered ceramic. The components are precisely cut to the same resonant frequency, glued end to end and the fused quartz spacer allows the placement of the sample in a furnace while the quartz drive and gauge crystals are maintained at room temperature. In this arrangement the drive crystal is activated at ~ 40 kHz and the strain in the gauge crystal is detected by an induced voltage across electrodes formed orthogonal to those on the drive crystal (to minimize electrical pickup). The gauge voltage is amplified, re-phased and fed back into the drive crystal in closed-loop mode. The system thus automatically adjusts to its resonant frequency which of course changes as the elastic modulus of the HTS sample alters with change in temperature or $p\text{O}_2$. Measurements with and without the sample allow determination of the variation in sample modulus and the ratio of the gauge to the drive crystal voltage yields the mechanical damping of the system and thus of the sample.

Fig. 11 shows the Young's modulus determined in this way for $\text{YBa}_2\text{Cu}_3\text{O}_{7-\delta}$ [63]. It reveals a cusp in the stiffness arising from orthorhombic fluctuations near the O-T transition. Repeating the experiment with a torsional composite oscillator (with both sample and spacer rod of cylindrical shape) allows measurement of the shear or rigidity modulus. This also reveals a marked softening near the O-T transition associated with strain fluctuations of the type $\epsilon_{22} - \epsilon_{11}$. The shift in the O-T transition with variation in $p\text{O}_2$ is evident in the figure by the shift in the cusp, depending upon ambient atmosphere.

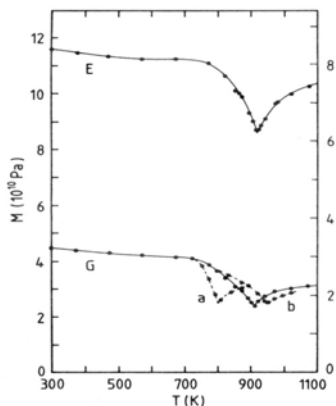


Fig. 11. Young's modulus, E , and shear modulus, G , for $\text{YBa}_2\text{Cu}_3\text{O}_{7-\delta}$ using longitudinal or torsional oscillators at ~ 40 kHz. Solid curves: measurements in air. Curves (a) and (b) are for $p\text{O}_2 = 0.01$ atm and 1.0 atm, respectively. The cusp results from orthorhombic fluctuations near the O-T transition which is seen to shift with $p\text{O}_2$.

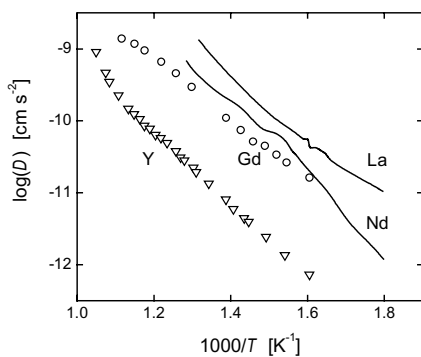


Fig. 12. Oxygen self diffusion coefficient determined for $\text{LnBa}_2\text{Cu}_3\text{O}_{7-\delta}$ in an ultrasonic composite oscillator at 40 kHz from the Debye relaxation. Ln = Y, Gd, Nd and La.

The mechanical damping peak associated with the Debye relaxation allows a determination of the relaxation time, τ . The oxygen self-diffusion coefficient is calculated from $D = f\ell^2/2d\tau$, where f is the correlation factor, of order unity, ℓ ($= 0.276$ nm) is the hop distance between adjacent O1 and O5 sites and d ($= 2$) is the dimensionality of the diffusion.

Diffusion coefficients measured in this way are shown in Fig. 12 as a function of temperature for four different lanthanide rare earths. This shows a marked increase in diffusivity with increasing size of the rare-earth element as one might expect due to the

expansion of the lattice and a consequent reduction of the energy barrier to hopping between sites. Other estimates of the diffusion coefficient for Y [59] agree well with the above results and confirm a very slow diffusivity. A fully dense sample just 1mm thick should take a year to fully oxygenate and equilibrate. The fact that this can be achieved in a matter of weeks illustrates the presence of structural defects which assist in-diffusion. A further point of practical import is the fact that the oxygen diffusion coefficient through silver at all times exceeds that in these Y-123 like systems. For wire applications HTS are frequently coated or canned in silver and their final equilibration requires in-diffusion of oxygen. The oxygen permeability of silver is an important factor in its selection.

Oxygen diffusion along the c -axis of Y-123 has also been measured using SIMS [59], and D_{ab} is found to exceed D_c by a factor exceeding 10^7 . This is not surprising given the fact that oxygen must traverse the CuO_2 bilayer in which the central Y layer is completely devoid of oxygen and the O2 and O3 sites are very strongly bound. These facts allows selective exchange of planar, apical or chain sites with the ^{18}O isotope and the ability to probe partial isotope effects associated with each of these sites [64]. This will be discussed further in §9.3.

7. OXYGEN AND SUPERFLUID DENSITY

7.1 Uemura relation

The superfluid density, $\rho_s(T) = \lambda_{ab}^{-2} = \mu_0 e^2 (n_s/m^*)$, is a fundamental SC parameter describing the density of Cooper pairs and the robustness of the SC condensate. Here μ_0 is the vacuum permeability, e the electronic charge, n_s is the pair density, m^* is their effective mass and λ_{ab} is the in-plane London penetration depth. ρ_s is a measure of the phase stiffness of the condensate [65] and plays a major role in governing the irreversibility field [66]. Careful measurement of the T -dependence of ρ_s has helped establish the d -wave symmetry of the HTS order parameter [67]. As to its magnitude, Uemura has inferred a linear relation between T_c and ρ_s that has been interpreted by some as indicating the Bose-Einstein condensation of preformed bosons [67]. Emery and Kivelsen took the view that the superfluid density is so low in the cuprates that phase fluctuations prevent the establishment of a phase-coherent state at the mean field T_c^{MF} and it is not until a lower temperature, the observed T_c , that long-phase phase coherence sets in [65]. In this picture T_c is naturally linear in the phase stiffness, ρ_s , and the phase-incoherent state is identified with the pseudogap that extends across the underdoped regime. This Uemura relation was shown to be sustained across a broad range of HTS cuprates as well as extending across the underdoped regime for many of these. There are several problems with these inferences and we note just those associated with the data itself. Firstly, it was observed that, after passing through a maximum, the superfluid density surprisingly falls rapidly on the overdoped side when p exceeds p_{crit} [68]. Consequently, within this picture one would expect the pseudogap to open up again in that region, contrary to observation. (This backtracking behaviour is unexpected as the carrier density continues to increase in the overdoped region. It has been interpreted in terms of developing pairbreaking [68], but we will see in §8 that low-temperature NMR Knight shifts and specific heat reveal a full nodal gap with no activated quasiparticle states). Secondly, it is beginning to emerge that the linear Uemura relation is not in fact satisfied by the cuprates [69]. In fact the specific heat

shows that the phenomenology is more consistent with k -space pairing of carriers within Δ_0 of E_F (i.e. the BCS picture) rather than Bose-Einstein condensation of real-space pairs [70].

7.2 Chain-layer superfluid density

When we consider the detailed doping dependence of ρ_s in Y-123 and related materials we find a broad plateau near optimal doping that is not observed in other cuprates [71]. This is associated with incorporation and ordering of the last 10% of chain oxygens and occurs in a region where T_c changes little while ρ_s about doubles. This certainly cannot be understood within the Uemura picture. In order to understand this we note that the CuO chains contribute significantly to the conductivity of Y-123 (and of Y-124) giving rise to a marked in-plane anisotropy [72]. The NMR spin-lattice relaxation rate $1/^{63}T_1$ associated with the chain Cu atoms is fast when the chains are fully ordered [73] indicating a metallic environment and suggesting that the chains are metallic. A two-band (plane+chain) picture gives a good representation of the in-plane anisotropy of the conductivity [73], and infrared reflectivity shows a strongly enhanced conductivity when the electric field is aligned along the b -axis, consistent with the DC conductivity [74]. If indeed the electronic carriers on the chains are mobile then they may contribute to the condensate density by proximity effect, and this is indeed what is found. For b -axis electron dynamics the effective superfluid density is enhanced over that for a -axis dynamics. For a randomly oriented sample one observes the geometric mean ρ_s which is enhanced over that for other chain-free cuprates *at the same doping state*.

The oxygen concentration dependence of these effects was determined by investigating a series of samples of $Y_{1-x}Ca_xBa_2Cu_3O_{7-\delta}$ with different x values in which the doping state was controlled to be the same [71]. Because the bare planar superfluid density is a strong function of hole concentration it is essential to maintain all comparative samples at the same doping state. A convenient common value is optimal doping, $p = 0.16$ hole/Cu. Thus for each value of x the value of δ is adjusted to achieve optimal doping. As x increases so does the optimal value of δ and the chains are progressively destroyed. In this way the additional contribution to ρ_s arising from the chains may be determined.

The superfluid density may be measured using transverse-field muon spin relaxation (μ SR) where the muon spin depolarisation rate $\sigma(T)$ is directly proportional to ρ_s according to

$$\sigma(T) = 7.09 \times 10^{-4} [\lambda_{ab}(T)]^{-2} \quad (9)$$

where σ is in μs^{-1} and λ is in nm. Fig. 13 shows the zero-temperature depolarization rate σ_0 as a function of δ determined in this way for $Y_{1-x}Ca_xBa_2Cu_3O_{7-\delta}$. The first three data points are for $x=0$, the next five are for optimally doped samples with $x = 0, 0.03, 0.06, 0.13$ and 0.2 , and the last data point is for brominated $YBa_2Cu_3O_{6.2}$ with $T_c = 92\text{K}$. As the chain contribution to the superfluid density is progressively destroyed σ_0 falls to a plateau at $2.95 \mu\text{s}^{-1}$ which represents the plane contribution only. This corresponds to a value $\lambda_a = 155 \text{ nm}$ which is consistent with other optimally-doped bilayer cuprates without chains. Under the assumption that the total effective in-plane superfluid density is the geometric mean of the two in-plane components, then for $\lambda_c \gg \lambda_a$ we have $\lambda_{\text{eff}}^{-2} = \lambda_a^{-1} \lambda_b^{-1}$. This allows λ_b to be calculated as a function of oxygen deficiency, δ , and this is plotted in the insert in Fig. 13. It falls to as low as

$\lambda_b = 80\text{nm}$ as $\delta \rightarrow 0$. These results agree nicely with measurements by Basov *et al.* of the penetration depth using infrared reflectivity on detwinned single crystals of Y-123 [74]. These authors found $\lambda_a = 160\text{nm}$ and $\lambda_b = 100\text{nm}$. Their value of λ_b is larger than the μSR value (80nm) obtained for polycrystalline samples and this may be attributed to incomplete oxygen loading, typical of single crystals.

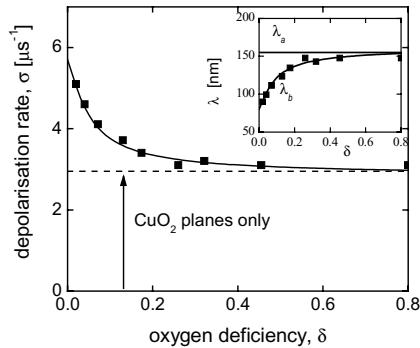


Fig. 13. The depolarization rate (\propto superfluid density) as a function of δ in optimally-doped $\text{Y}_{1-x}\text{Ca}_x\text{Ba}_2\text{Cu}_3\text{O}_{7-\delta}$. The plane contribution, only, is shown by the dashed line. Inset: λ_a and λ_b values determined from this data assuming $\lambda_{\text{eff}}^2 = \lambda_a \times \lambda_b$.

7.3 Irreversibility field

In summary, the chains in Y-123 afford a large enhancement in superfluid density arising from the additional proximity-induced condensate on the conducting chains. It is this that produces the large irreversibility field in this compound. The compounds Y-124 and Y-247 also exhibit a strong enhancement in superfluid density arising here from the double chains in the former and the combination of double and single chains in the latter [71]. It is of note that the irreversibility field in Y-247 is as high as in Y-123 (11 Tesla at $0.75T_c$) even though the former has a significantly lower doping state. Were Y-247 to be doped up to $p = p_{\text{crit}}$ using e.g. Ca substitution for Y then it is likely to exhibit the highest irreversibility field of any of the cuprates.

These ideas can be tested in a surprisingly effective manner. A simple tunneling model of c -axis transport shows that the c -axis resistivity is proportional to $\exp(+d_b/\xi)$ where d_b is the block layer spacing which separates the CuO_2 bilayers and ξ is a c -axis correlation length. Within a simple decoupling model of the irreversibility field in which the thermal energy exceeds the Josephson coupling between layers one finds that the irreversibility field is [75]:

$$H_{\text{irr}}(T) \propto \exp(-d_b/\xi) \times f(T/T_c) \quad (10)$$

where $f(T/T_c)$ is a universal function of T/T_c . Fig. 14 shows $H_{\text{irr}}(0.75T_c)$ plotted against the block layer spacing, d_b , for a variety of HTS cuprates all carefully controlled to optimal

doping, and this relation appears to be well satisfied. This statement is qualified by the following. Because of the proximity-induced superconductivity on the chains in Y-123 the effective block layer spacing is not the 0.84nm separating successive bilayers but the 0.42nm separating a bilayer from the adjacent chain layer. It is the latter number which is plotted in Fig. 14 while the former evidently does not satisfy eq. (10). If this idea is correct then it may be tested by destroying the chains while keeping the doping state fixed and investigating the consequent reduction in irreversibility field. This may be achieved in $Y_{0.8}Ca_{0.2}Ba_2Cu_3O_{7-\delta}$. When adjusted to optimal doping one finds $\delta \approx 0.39$ and the heavy oxygen deficiency, according to Fig. 13, should substantially eliminate any chain superfluid density. The block layer spacing for this compound should then effectively be the true spacing, $d_b = 0.84$ nm. For this sample $H_{ir}(0.75T_c)$ dropped significantly. This is the data point annotated Ca-123 in Fig. 14 and it lies lower on the correlation curve, consistent with eq. (10). Similarly, the data point annotated Br-123 refers to $YBa_2Cu_3O_{6.2}Br_{0.8}$. This is a sample which was deoxygenated to $\delta = 0.8$ (and therefore non-SC) then annealed in Br gas to intercalate 0.8 Br atoms per formula unit. Bromination is a doping process which reestablishes optimal doping with SC occurring at $T_c = 92$ K but, again, the chain SC is extinguished. This data point, like that for Ca-123, is consistent with an inert chain layer and a resultant block-layer spacing of 0.84nm.

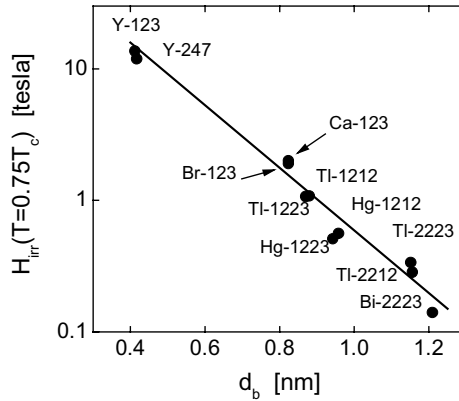


Fig. 14. The irreversibility field at $0.75 T_c$ for optimal doped cuprates as a function of block-layer spacing, d_b . Ca-123 denotes $Y_{0.8}Ca_{0.2}Ba_2Cu_3O_{6.61}$ and Br-123 denotes $YBa_2Cu_3O_{6.2}Br_{0.8}$. For Y-123 d_b is taken to be 0.42nm, the chain-to-plane distance.

8. ^{17}O NMR

Spin dynamics clearly play a central role in the physics of HTS cuprates. Superconductivity in these materials straddles the region, between the AF insulator and the metallic region, where short-range AF fluctuations persist. Scattering of quasiparticles from these fluctuations results in heavy quasiparticle damping near the $(\pi, 0)$ zone boundary [76]. The formation of these

“hot spot” sections of the Fermi surface is intimately associated with the pseudogap and strongly affects c-axis electron dynamics. AF fluctuations are thought to play a role in the pairing interaction: a magnetic resonance appears with the onset of SC [77] and the \mathbf{q} -width of magnetic excitations has been correlated with T_c [78]. The magnetic spectrum has been extensively studied by NMR and by inelastic neutron scattering, which can access the full \mathbf{q} and ω dependence of the dynamical susceptibility. NMR is more limited in the spectral information it can access but it gives important information at the AF wavevector $\mathbf{q}_{AF} = (\pi, \pi)$ and at $\mathbf{q} = (0, 0)$. Moreover, though the Knight shift and spin-lattice relaxation rate, T_1^{-1} , are effectively zero frequency measurements the spin-spin relaxation rate, T_{2G}^{-1} , may be expressed (via a Kramers-Kronig transformation) as an integral over all energy. Thus comparison of T_1^{-1} with T_{2G}^{-1} may be used to deduce spectral weight shift from low to high energy [79]. In addition, NMR is a local probe which has the capacity to explore the local susceptibility e.g. in the neighbourhood of substituent atoms.

8.1 Knight shift

The nuclear spin Hamiltonian contains a dominant term arising from the Zeeman coupling of nuclear spins to the external applied field. This gives a nuclear resonance at the Larmor frequency, ω_L , which is very low in comparison with the quasiparticle fluctuations rates. (For this reason one considers ω_L to be effectively zero). The local field is modified by the induced local hyperfine field which is proportional to the applied field. As a consequence the nuclear resonance is shifted away from ω_L and the normalised shift is referred to as the Knight shift. In general, the magnetic hyperfine shift tensor, $K_{\alpha\alpha}$, has spin, orbital and diamagnetic components but for the cuprates the latter is negligible and the orbital part is T -independent, so we focus just on the spin component which is related to the spin susceptibility as follows:

$$K_{\alpha\alpha} = A_{\alpha\alpha} \chi_{\alpha\alpha} / g_{\alpha} \mu_B. \quad (11)$$

Here $A_{\alpha\alpha}$ is the hyperfine field, $\chi_{\alpha\alpha}$ is the static spin susceptibility, g_{α} is the electronic Landé factor and μ_B is the Bohr magneton. In the cuprates $K_{\alpha\alpha}$ and $\chi_{\alpha\alpha}$ are quite strongly T -dependent, and in the underdoped region they decrease effectively to zero as $T \rightarrow 0$. This is contrary to normal metals for which Pauli spin susceptibility is constant, reflecting a constant density of states (DOS). For a Fermi liquid the static spin susceptibility, χ_s , is given by:

$$\chi_s = 2\mu_B^2 \int_{-\infty}^{\infty} N(E) \left[-\frac{\partial f(E)}{\partial E} \right] dE \quad (12)$$

where $N(E)$ is the DOS and $f(E)$ is the Fermi function. Thus the strong reduction in the normal-state (NS) Knight shift observed in HTS with decreasing T may be interpreted as due to the opening of a gap in the DOS and this is generally referred to as the pseudogap (less frequently as the “spin gap”). Use of a Fermi liquid approach is very much open to question in strongly correlated systems but χ_s is dominated by the nodal regions of the Fermi surface well away from the so-called “hot spots” near $(\pi, 0)$. Here quasiparticles are long-lived with well-defined momentum and energy. This assumption is confirmed by the observation that χ_s and

the electronic entropy, S_{el} are linearly related according to $S_{\text{el}} = a_W \chi_s T$, as expected for a Fermi liquid [70]. Here a_W is the Wilson ratio for nearly free electrons.

8.2 Spin-lattice relaxation

When nuclear spins are magnetically perturbed they relax back to thermal equilibrium due to fluctuations in the magnetic hyperfine field. This couples the spins to the lattice and the relaxation rate may be written as [80]:

$$1/{}^n T_1 T = \frac{k_B \gamma_n^2}{\mu_B^2 g^2} \sum_{\mathbf{q}} |A(\mathbf{q})|^2 \frac{\chi''(\mathbf{q}, \omega_L)}{\omega_L}. \quad (13)$$

Here we have dropped the tensorial notation. $A(\mathbf{q})$ are the hyperfine coupling form factors, the subscript or superscript n refers to the particular nucleus ($n = 63$ for ${}^{63}\text{Cu}$ or 17 for ${}^{17}\text{O}$) and $\chi''(\mathbf{q}, \omega)$ is the imaginary part of the dynamical spin susceptibility. For the HTS cuprates the form factors in $1/{}^{63}\text{T}_1$ maximise at $\mathbf{q}_{\text{AF}} \equiv (\pi, \pi)$ [81] while $\chi''(\mathbf{q}, \omega)$ also maximises at \mathbf{q}_{AF} . Therefore $1/{}^{63}\text{T}_1 T$ is dominated by the response at the AF wavevector. Values of the relaxation rate are rather large due, as is generally believed, to scattering from antiferromagnetic (AF) spin fluctuations. As a consequence $1/{}^{63}\text{T}_1 T$ adopts a Curie-like $1/T$ dependence at high temperature. At a lower temperature this quantity passes through a maximum then falls rapidly as shown by the two curves for Y-124 in the inset to Fig. 17. This temperature is often taken as the spin-gap or pseudogap opening temperature and is distinguished from the pseudogap opening temperature determined from the T -dependent Knight shift, but this will be seen to be misleading.

In contrast, the form factor for ${}^{17}\text{O}$ (like that for ${}^{89}\text{Y}$) is peaked at $\mathbf{q} = (0, 0)$ and falls to zero at \mathbf{q}_{AF} [81]. It is thus insensitive to AF correlations and so provides a test for the Korringa relationship, $K^2 T_1 T = \text{const}$, that is satisfied by normal metals. In fact it seems that $1/{}^{17}\text{T}_1 T$ satisfies a linear scaling with ${}^{17}K(T)$ so that both quantities reflect the T -dependence of the spin susceptibility.

8.3 Single-spin fluid

In the early days of HTS studies there was considerable debate as to whether the cuprates could be described by a simple one-band Hamiltonian [82] or whether both Cu and O bands should be incorporated. As noted in §3 Zhang and Rice introduced the idea of a *single-spin fluid* comprising Z-R singlets. Here the doped hole localizes on the four nearest-neighbour oxygens and hops from one hub Cu to the next in the same fashion as hopping in the single-band t - J model. The discovery that the T -dependence of the ${}^{89}\text{Y}$ Knight shift scaled with the static susceptibility [83] confirmed this picture, since Y couples to the spin susceptibility via the O2 and O3 orbitals. Then, Takigawa *et al.* [84] showed that the T -dependence of the various tensor components of the ${}^{63}\text{Cu}$ and ${}^{17}\text{O}$ Knight shifts all scaled with $\chi_s(T)$, thus further validating the single-spin fluid model. We thus can presume that ${}^{17}K(T)$, ${}^{63}K(T)$ and ${}^{89}K(T)$ each scale with the spin susceptibility and we will see examples of this in the following figures in this section.

8.4 Pseudogap

It was Alloul *et al.* [83] who first showed that the ^{89}Y Knight shift was systematically reduced with decreasing temperature and doping suggesting the occurrence of a gap in the NS DOS. Specific heat measurements by Loram *et al.* [70] revealed exactly the same behaviour for S_{el}/T and, as noted, these authors demonstrated the nearly-free electron scaling of S_{el}/T with χ_s . From this they argued that the observed gap is a gap in the quasiparticle spectrum not merely in the spin spectrum and that it is pinned to the Fermi level for all doping levels. The gap energy E_g decreases with increasing doping, falling abruptly to zero at $p = p_{\text{crit}} = 0.19$ holes/Cu in the lightly overdoped region [85,40]. This, amongst other data, has led to the proposal that the physics of HTS is dominated by quantum fluctuations above a quantum critical point at p_{crit} [86]. At this doping level the resistivity is linear down to the lowest temperatures above T_c and various properties including the Knight shift exhibit scaling behaviour with the scaling separatrix lying at p_{crit} . In Fig. 15 we summarise the doping and temperature dependence of the spin susceptibility determined using $^{89}\text{K}_s(T)$ [87]. According to the above discussion such data could equally have been deduced from the oxygen $^{17}\text{K}_s(T)$. The NS data was modeled then extrapolated to $T=0$ to infer the expected behaviour if pairing interactions were suppressed. In the pseudogap regime, based on tunneling data, a triangular gap that fills with increasing T was assumed, giving

$$^{89}\text{K}_s = ^{89}\text{K}_s^0 \times \{1 - \epsilon^{-1} \tanh(\epsilon) \times \ln[\cosh(\epsilon)]\}, \quad (14)$$

where $\epsilon = E_g/2k_B T$. For $p > p_{\text{crit}}$ the Knight shift was assumed to adopt a Kondo-like T -dependence $\propto 1/(T+\theta)$.

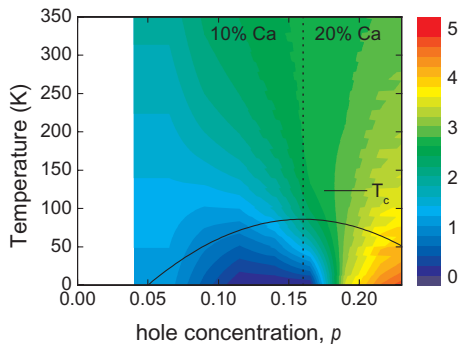


Fig. 15. Color contour plot of the Knight shift, $^{89}\text{K}_s(T)$, for $\text{Y}_{1-x}\text{Ca}_x\text{Ba}_2\text{Cu}_3\text{O}_{7-\delta}$ in the normal state extrapolated to $T=0$. The plot is a composite from data for $x = 0.1$ and 0.2 as indicated. The closure of the pseudogap is seen at $p \approx 0.18$. Note also the filling of the pseudogap below $p=0.12$, possibly due to stripe formation.

The closure of the pseudogap around $p \approx 0.18$ can be seen (it has been artificially displaced down by 0.01 hole/Cu in the smoothing process for forming the colour contours) and

interestingly one can also see the filling of the pseudogap for $p < 0.12$, possibly associated with stripe formation. For $p > p_{\text{crit}}$ there is a peak in χ_s associated with the low-energy pile up in DOS possibly associated with the Fermi energy crossing a van Hove singularity (vHS) at higher doping [26].

8.5 Antiferromagnetic fluctuations

The persistence of short-range AF fluctuations at higher doping beyond the Néel state results in a strong peak in the NS dynamical susceptibility that is observed in inelastic neutron scattering. This peak is centred on $\mathbf{q} = (\pi, \pi)$ (except in La-214 where the peak has an incommensurate split suggestive of stripe correlations) and its amplitude decreases with increasing doping, disappearing at p_{crit} [88], as will be seen in Fig. 18. This in itself suggests that AF fluctuations die out at critical doping and while the large background could conceal persistent magnetic correlations beyond p_{crit} it is clear that something pathological occurs in the susceptibility at this point. In contrast, in the SC state an AF resonance mode is observed centred on 41meV which does persist beyond p_{crit} [89, 90]. One way to view this is that, in the NS, spin-flip scattering of mobile carriers effectively reduce the spin lifetime to zero while, in the SC state, the absence of scattering extends the spin lifetime.

The strong peak in the dynamical susceptibility led Millis, Monien and Pines (MMP) to propose a phenomenological enhanced susceptibility given by [91]:

$$\chi(\mathbf{q}, \omega) = \frac{\chi_s(T)}{1 - i\omega/\Gamma_0} + \frac{\beta\xi^2}{[1 + (\mathbf{q} - \mathbf{q}_{AF})\xi^2 - i\omega/\omega_{SF}]} \quad (15)$$

where Γ_0 is the (T -independent) effective bandwidth, β is a parameter which in the original MMP formalism was just $\chi_s(T)$, ξ is the AF correlation length in units of the lattice parameter a , and ω_{SF} is the paramagnon frequency. The first term in the eq. (15) is the Fermi liquid term while the second is the enhanced susceptibility, peaked at \mathbf{q}_{AF} due to the AF correlations.

The MMP susceptibility provides us with the means now to understand the relationship between the Knight shift (for any nucleus – ^{63}Cu , ^{17}O or ^{89}Y) and the relaxation rates $^{17}\text{T}_1^{-1}$ and $^{63}\text{T}_1^{-1}$. By substituting eq. (15) in eq. (13), taking the limit $\xi \gg 1$ and allowing for the \mathbf{q} -dependence of the form factors one may show that $^{63}\text{T}_1 T = a_1 \omega_{SF}/\beta$ and $^{17}\text{T}_1 T = a_2 \Gamma_0/\chi_s(T)$. If we take $\beta = \chi_s(T)$ as originally suggested by MMP and note that $\omega_{SF} \propto T$ then:

$$1/^{63}\text{T}_1 \propto \chi_s(T) \propto 1/^{17}\text{T}_1 T \propto ^{17}\text{K}_s(T) \propto ^{63}\text{K}_s(T) \propto ^{89}\text{K}_s(T). \quad (16)$$

We will show that these are all satisfied. Evidently, the way to interpret $1/^{63}\text{T}_1 T$ is as $(1/T) \times \chi_s(T)$, where the first factor reflects the presence of AF correlations. Thus, in the underdoped region a Curie T -dependence is observed at high T , with a peak and strong reduction at low T reflecting the pseudogap in the second term, $\chi_s(T)$. We point out that many workers have deduced a T^* point where $\chi_s(T)$ first reduces and a second (lower) T^*_2 where $1/^{63}\text{T}_1 T$ reaches a maximum. In this way they construct an upper and a lower pseudogap temperature. But eq. (16) shows that, to be consistent, one must determine T^*_2 as the point where $1/^{63}\text{T}_1 T$ first departs from a Curie T -dependence. When this is done T^*_2 is identically equal to T^* .

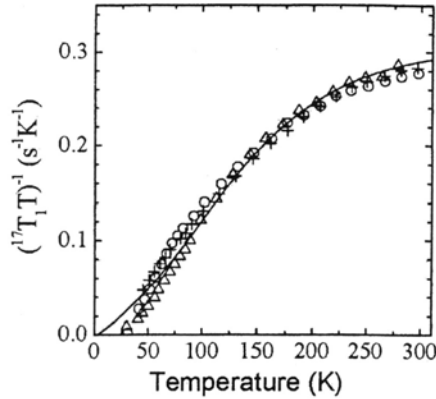


Fig. 16. Comparison of the T -dependence of $(^{17}T_1T)^{-1}$ (crosses) with $(^{63}T_1)^{-1}$ (circles) and $^{17}K_s(T)$ (triangles) for $\text{YBa}_2\text{Cu}_3\text{O}_{6.63}$.

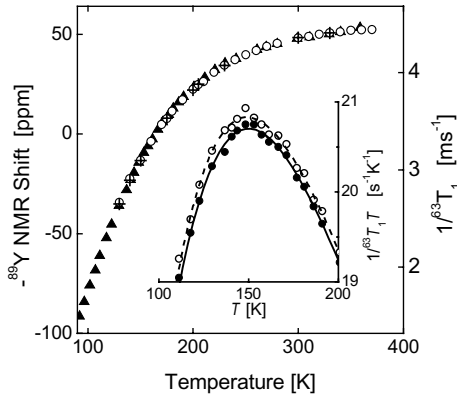


Fig. 17. Comparison of $(^{63}T_1)^{-1}$ (triangles) with $^{89}K_s(T)$ (circles for ^{16}O , crosses for ^{18}O) for Y-124 illustrating that both of these quantities have the same T -dependence and are proportional to $\chi_s(T)$. No oxygen isotope effect is evident in $^{89}K_s(T)$. Inset: $(^{63}T_1)^{-1}$ for Y-124 with oxygen isotopes ^{16}O (\circ) and ^{18}O (\bullet).

Fig. 16 shows the T -dependence of $^{63}T_1^{-1}$, $(^{17}T_1T)^{-1}$ and $^{17}K_s$ for $\text{YBa}_2\text{Cu}_3\text{O}_{6.63}$ together with the curve eq. (14) for a triangular gap. The data is from references [84] and [92]. It is evident that these quantities are all proportional, thus confirming eq. (16). Here the linewidths are quite broad and so the correspondence in Fig. 16 is not especially precise. However, Raffa *et al.* [93] have carried out very precise NQR measurements of $(^{63}T_1)^{-1}$ on Y-124 which, of all the cuprates, is probably the most free of defects and disorder. Their data is plotted as

triangles in Fig. 17. By way of comparison, the circles show magic-angle-spinning ^{89}Y NMR shift data for Y-124 which have extremely narrow linewidths (100 Hz). The precise correspondence between $(^{63}\text{T}_1)^{-1}$ and $^{89}\text{K}_s(T)$ in what are probably the most accurate measurements available of these two quantities, strongly supports the analysis leading to eq. (16).

The inset in Fig. 17 also shows the same $(^{63}\text{T}_1)^{-1}$ data for samples exchanged with ^{16}O and ^{18}O . There is an apparent isotope effect here from which the authors inferred an isotope effect in the pseudogap. However, our magic-angle spinning ^{89}Y Knight shift data for ^{18}O exchanged Y-124 (crosses) showed no discernible isotope shift thus clearly negating the possibility of an isotope effect in the pseudogap. In view of the fact that $^{63}\text{T}_1 T = a_1 \omega_{\text{SF}} / \chi_s(T)$ this implies that the observed isotope effect in the inset to Fig. 17 must rather be one in ω_{SF} . Further, because the isotope effect equals that observed in the value of T_c [94] this implies, rather suggestively, that the isotope effect in T_c equals the isotope effect in ω_{SF} , giving strong credence to a spin fluctuation pairing mechanism. We return to oxygen isotope effects in §9.

Finally in this section we consider the ratio $^{17}\text{T}_1 / ^{63}\text{T}_1$. As noted, the Curie-like T -dependence of $1/^{63}\text{T}_1 T$ at high-temperature is viewed as a signature of AF correlations. Now, La-214 exhibits Curie-like behaviour across the entire overdoped region [95] thus suggesting the persistence of spin fluctuations throughout this region. However, reference to eq. (16) shows that this can be misleading because $1/^{63}\text{T}_1 T \propto (1/T) \times \chi_s(T)$. For overdoped La-214, χ_s exhibits a strong and growing upturn at lower temperatures [96]. Though weaker, this is also present in other HTS cuprates as shown in Fig. 15. This clearly makes ambiguous the inference of AF correlations from the T -dependence of $1/^{63}\text{T}_1 T$. A better route is to consider the ratio $^{17}\text{T}_1 / ^{63}\text{T}_1$. Because $^{63}\text{T}_1 T = a_1 \omega_{\text{SF}} / \chi_s(T)$ and $^{17}\text{T}_1 T = a_2 \Gamma_0 / \chi_s(T)$, then $^{17}\text{T}_1 / ^{63}\text{T}_1 = a_2 \Gamma_0 / a_1 \omega_{\text{SF}}$ which is independent of χ_s . The effects of both the pseudogap and the proximate vHS are thus effectively removed in this ratio and we are left with a measure of the AF fluctuation spectrum alone. More generally,

$$^{17}\text{T}_1 / ^{63}\text{T}_1 = a_4 \langle 1 + f_q^2 \rangle_q = a_4 [1 + C_{\text{AF}} / T] \quad (17)$$

where f_q is the ratio of the right-hand term in eq. (15) to the left-hand term and the average is over q . C_{AF} thus measures the strength of AF correlations in the normal state. The value of C_{AF} has been extracted by fitting [97] the data for the T -dependence of $^{17}\text{T}_1 / ^{63}\text{T}_1$ for Y-123, Y-124 and oxygen-deficient Y-123 and its p -dependence is plotted in Fig. 18 (diamonds). This falls progressively towards zero at p_{crit} suggesting that the pseudogap itself is intimately associated with short-range AF correlations which disappear abruptly at critical doping (at least on the NMR time scale of 10^{-7} s). This appears to be consistent with inelastic neutron scattering. Bourges [88] has integrated $\chi''(\mathbf{q}_{\text{AF}}, \omega)$ up to 50 meV to obtain the total AF weight for a variety of Y-123 single crystals with different oxygen contents. Converting the δ values to p -values using Fig. 6 we plot his data (circles) in Fig. 18. The linear fall to zero at p_{crit} again indicates that AF correlations die out at p_{crit} . If they do not then something pathological must occur in the doping dependence of $\chi''(\mathbf{q}, \omega_0)$ at this point. This is also borne out by susceptibility measurements on induced moments in Zn-substituted Y-123. Though Zn is non-magnetic Alloul et al. [98] consider that a moment is induced on the four nearest Cu neighbours due to the local frozen AF background. We plot in Fig. 18 the square of their measured effective moment ($\times 6000$) and this also progresses towards zero at p_{crit} , again suggesting the demise of the background AF correlations at this point.

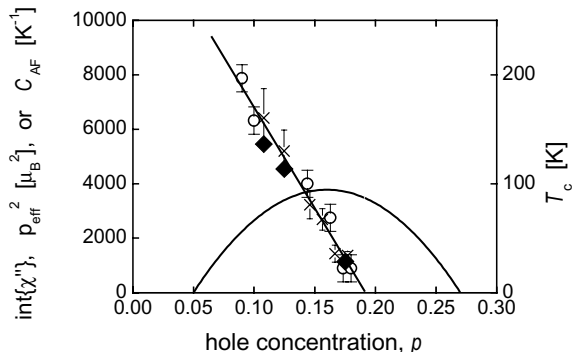


Fig. 18. Plot of the doping dependence of C_{AF} determined from eq. (17) for Y-123 and Y-124 (diamonds). In addition the total AF weight given by $\int_0^{50meV} \chi''(\mathbf{q}_{AF}, \omega) dE$ from Bourges [88] is plotted (\circ) and the square of the effective Zn moment (\times).

8.6 Phase separation

As noted, the HTS cuprates exhibit a tendency to phase separation. At low doping isolated holes are unstable in the AF background and tend to segregate onto domain walls [99]. The parent compound $\text{La}_2\text{CuO}_{4+\delta}$ exhibits staging and a miscibility gap in the range $0.01 < \delta < 0.055$ [36]. Overdoped $\text{La}_{2-x}\text{Sr}_x\text{CuO}_4$, when slow-cooled, can exhibit phase separation into optimal and strongly overdoped phases [100]. This can be avoided by quenching from high temperature then subsequently oxygenating at lower temperature.

We have already noted in Fig. 15 the abrupt filling of the pseudogap for $p < 0.12$ holes/Cu presumably associated with stripe formation, but the corollary is that, across the remaining region up to $p = 0.19$, the pseudogap is a full gap at $T = 0$ (as determined from the normal-state data) and in the SC state a full gap is observed across the entire domain for $p > 0.12$ [87,101]. Phase separation into SC and NS regions would result in normal quasiparticle excitations that would show up as gap-filling at low T . On the other hand phase separation into SC and insulating regions would result in a reduction of the normal state $\gamma \equiv C_p/T$. This quantity remains constant independent of T and p , across a broad doping range [101]. There is therefore no evidence of phase separation in specific heat measurements for samples with $p > 0.125$. Further, we will see in §9 that scattering in the presence of phase separation should introduce an isotope effect in the superfluid density. This is absent in the overdoped region suggesting that any phase separation in the materials studied ($\text{La}_{2-x}\text{Sr}_x\text{CuO}_4$) is insignificant.

^{17}O Knight shift studies on overdoped $\text{Y}_{0.8}\text{Ca}_{0.2}\text{Ba}_2\text{Cu}_3\text{O}_{7-\delta}$ present the same picture. Fig. 19 shows $^{17}K_s(T)$ for a sample with $p = 0.23$ holes/Cu and $T_c = 55\text{K}$ [102]. The precipitate fall in the oxygen NMR shift is evident at T_c and significantly, it drops to a value equal to the T -independent orbital shift at $T = 0$ indicating the presence of a full gap. The only way in which phase separation could occur, while the spin part of $^{17}K_s(T \rightarrow 0)$ remains zero, is if the phase separation is nanoscale, with spatial scales $\sim \xi_0$ ($=1.7\text{nm}$). Then proximity effects in the NS regions may induce a gap. But in this case one would expect excessive fluctuations at T_c , which are found to be absent [101].

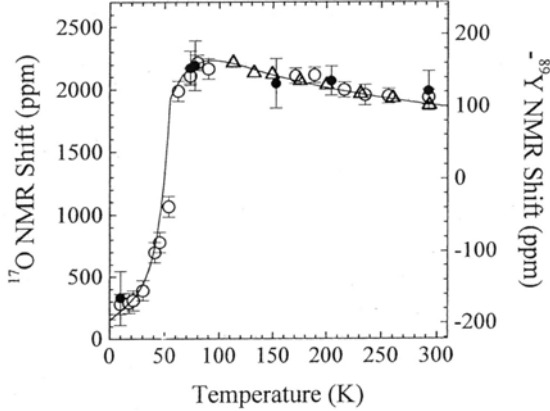


Fig. 19. The T -dependence of the ^{17}O NMR Knight shift for the central (\circ) and first satellite (\bullet) line for overdoped $\text{Y}_{0.8}\text{Ca}_{0.2}\text{Ba}_2\text{Cu}_3\text{O}_{7.8}$ with $p \approx 0.23$. Also shown is the ^{89}Y shift (Δ). There is no gap filling due to phase separation into SC and NS

We certainly recognize the propensity for phase separation in the HTS cuprates but the strong evidence for electronic homogeneity in a number of samples and at various doping levels, especially for $p > 0.12$ holes/Cu, show that inhomogeneity is not a universal property of these materials and therefore may only play an incidental role in their central physics.

9. OXYGEN ISOTOPE EFFECTS

9.1 Introduction

The discovery of an isotope effect in T_c for Sn by Allen *et al* [103] was the key observation leading to the development of the BCS theory of superconductivity and in particular phonon-induced Cooper pairing. The isotope exponent $\alpha(E)$ in any given property E is defined as $\alpha(E) = -(\Delta E/E)/(\Delta M/M)$ where M is the isotopic mass. The property E in conventional SC is either T_c or the SC gap parameter, Δ_0 . But in HTS one may also contemplate an isotope effect in the pseudogap energy scale, E_g , (which, as noted above, we reject) and surprisingly an isotope effect was discovered in the superfluid density, ρ_s [104]. In conventional BCS superconductors $\alpha(T_c) \approx 0.5$ reflecting the fact that the energy scale for the pairing derives from phonon exchange. With the discovery of HTS there was early interest in establishing a possible role for phonons in these materials and the oxygen isotope effect was investigated by several groups [105,106]. Typically, identical samples are annealed in separate quartz tubes containing ^{16}O and ^{18}O oxygen gas mounted side by side in a furnace to ensure identical thermal history. The samples may be annealed at $\sim 750^\circ\text{C}$ and several repeat anneals may be used to ensure nearly complete oxygen exchange, depending upon the size of the sample relative to the volume of gas in the tube. Samples then must be slow cooled to ensure complete oxygenation. The degree of exchange can be measured directly from the mass

change or indirectly from the shift in oxygen phonon modes using Raman spectroscopy. Usually, following measurement of the magnitude of the isotope effect one carries out a back exchange to the other isotope to be sure of the absence of systematic differences between the two tubes. Measurements of $\alpha(T_c)$ for several HTS are summarized in Fig. 20 for different p [107]. The isotope exponent is seen to be small around optimal doping but, with underdoping, $\alpha(T_c)$ was found to increase and ultimately diverge as $T_c \rightarrow 0$. The overdoped region remains uncertain as to whether $\alpha(T_c)$ remains constant or grows with further reduction in T_c .

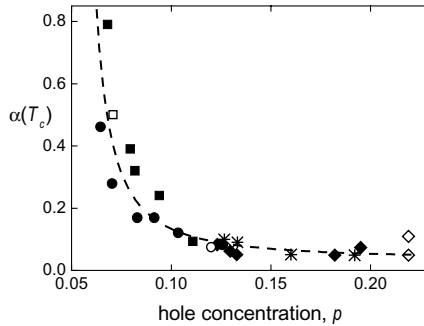


Fig. 20. The isotope effect $\alpha(T_c)$ as a function of hole concentration for several HTS, from ref. [107]. The curve shows the calculated value assuming a competing pseudogap with a bare value of $\alpha(\Delta_0)=0.05$.

9.2 Effect of pseudogap

The rise in $\alpha(T_c)$ with underdoping occurs because of the opening of the pseudogap which reduces (eventually to zero) the magnitude of the SC order parameter and the value of T_c . The observation of an isotope effect in ρ_s is unexpected because, according to Leggett's theorem [108], ρ_s is rigorously just the total integrated spectral weight of the free carriers i.e. the total carrier density divided by the effective electronic mass. Thus ρ_s should be isotope independent. But in the presence of a pseudogap (and in the presence of impurity scattering) both T_c and ρ_s develop a strong isotope dependence and both diverge as $T_c \rightarrow 0$. According to this model $\alpha(\rho_s)$ reduces to zero as $p \rightarrow p_{crit}$ and the pseudogap closes. We develop the theory as follows. The pseudogap is an approximately triangular gap in the NS DOS and we have elsewhere calculated its effect on weakening the SC state [69]. One finds $T_c \rightarrow 0$ when $E_g \rightarrow 2.397k_B T_c^0$, where k_B is Boltzmann's constant and $T_c^0 = T_c(E_g=0)$. Consider therefore the scaled gap parameter $\zeta = E_g / (2.397k_B T_c^0)$. As ζ increases with underdoping $T_c(\zeta)$ reduces at first slowly then more rapidly as $\zeta \rightarrow 1$ and $T_c \rightarrow 0$. In contrast $\rho_s(\zeta)$ falls rapidly at first then slows as $\zeta \rightarrow 1$. Let us define the functions h and g given by $\rho_s(\zeta)/\rho_{s0} = h(\zeta)$ and $T_c(\zeta)/T_{c0} = g(\zeta)$. Then the isotope effects in ρ_s and T_c are given by

$$\alpha(\rho_s) = -\zeta (h'/h) \alpha(T_{c0}) \quad (18)$$

and

$$\alpha(T_c) = [1 - \zeta (g'/g)] \alpha(T_{c0}) . \quad (19)$$

where $\alpha(T_{c0})$ (≈ 0.05) is the bare isotope effect in T_c in the absence of the pseudogap. Eliminating $\alpha(T_{c0})$ we find

$$\alpha(\rho_s) = \zeta (h'/h) [1 - \zeta (g'/g)]^{-1} \alpha(T_c) . \quad (20)$$

We plot $\alpha(\rho_s)$ against $\alpha(T_c)$ calculated in this way by the solid line in Fig. 21. The effects of impurity scattering are calculated in exactly the same way and the result is almost identical to this line. Notably, at the left hand limit, $\alpha(\rho_s)$ falls to zero when the pseudogap closes but $\alpha(T_c)$ remains finite and falls to 0.05. The value of $\alpha(\rho_s)$ may be determined from the isotope-induced fractional change in slope of the magnetization curve ($= \alpha(\rho_s) - \alpha(T_c)$) while $\alpha(T_c)$ is obtained from the isotopic fractional change in T_c . Experimental values determined in this way are shown in the figure for $\text{La}_{2-x}\text{Sr}_x\text{CuO}_4$ and for Y-123 and Y-124 (see ref. [109] for more details). The agreement with the canonical pseudogap behaviour is excellent and, in particular, is consistent with the vanishing of $\alpha(\rho_s)$ at p_{crit} .

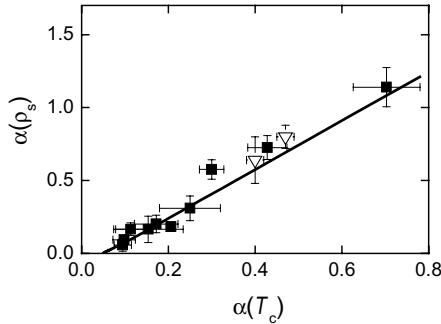


Fig. 21. $\alpha(\rho_s)$ plotted versus $\alpha(T_c)$. The line is calculated for a pseudogap competing with SC. The left-hand end corresponds to $p > p_{crit}$ where the pseudogap is absent. Both $\alpha(\rho_s)$ and $\alpha(T_c)$ diverge as the pseudogap suppresses T_c to zero.

The data in Fig. 21 intentionally omits values for $\text{La}_{2-x}\text{Sr}_x\text{CuO}_4$ where $p = x = 0.125$. This is the so-called $1/8^{\text{th}}$ point where, in this compound, various anomalies are observed that are generally interpreted in terms of the formation of nanoscale spin/charge “stripes”. In this picture doped holes are unstable in the AF background and spatially separate to form AF strips separated by linear domain walls on which the holes reside with 50% occupancy. This yields the following sequence $\dots \bullet \uparrow \downarrow \uparrow \circ \downarrow \uparrow \downarrow \bullet \uparrow \downarrow \uparrow \circ \dots$ which has a wavelength of $8a$ and corresponds to a doping level of $1/8$ holes/Cu. It is believed that objects like this fluctuate in space and time in the neighbourhood of this doping state and freeze out at low temperature. Further, it has been proposed that these stripe fluctuations may be the microscopic origin of the pseudogap [35]. When we measure the isotope effects for $\text{La}_{2-x}\text{Sr}_x\text{CuO}_4$ in this doping

range we observe the huge anomaly shown in Fig. 22. This breaks away sharply from the canonical pseudogap behaviour, presumably because of the strong electronic coupling to the lattice in the presence of the stripe-induced charge and spin density waves. Most importantly, it shows that stripes and pseudogap are unrelated because of the anomalously non-canonical behaviour observed near $p = 1/8$ holes/Cu. That these stripe objects are largely confined to the La-214 system is illustrated by the fact that the upward triangle in Fig. 22 is Pr-substituted Y-123 with doping state very close to $p = 1/8$ holes/Cu. This data point sits on the canonical pseudogap line with no suggestion of the stripe-induced anomaly.

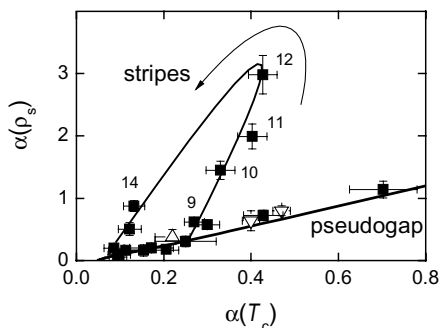


Fig. 22. The isotope effect in the superfluid density plotted versus $\alpha(T_c)$ as in Fig. 20 but now including data for $\text{La}_{2-x}\text{Sr}_x\text{CuO}_4$ near $p = 1/8$. The numbers annotating the data points are the Sr composition expressed as $100x$.

9.3 Site selective isotope effects

The huge difference in oxygen diffusion coefficient in Y-123 between in-plane and out-of-plane migration [59] opens up the potential for selective isotope exchange of oxygen sites. Because the activation energy for c -axis diffusion is larger than that for ab -plane diffusion the ratio D_{ab}/D_c grows rapidly with decreasing temperature and below 400°C exceeds 10^7 (and is probably more like 10^{10}). At the same time ab -plane diffusion occurs along the $\text{CuO}_{1.8}$ chains so that if the radius, r , of the grains is small enough (and a low enough temperature is employed) oxygen can diffuse along the entire length of chains before they have diffused 0.42nm from the chain layer to the plane layer. The necessary condition is that $(r/0.42)^2 \ll (D_{ab}/D_c)$ i.e. $r \ll 40 \mu\text{m}$. Thus a polycrystalline sample sintered at relatively low temperature to ensure small grain size may be annealed at 350°C in ^{18}O for an extended period (≥ 150 hours) to achieve dominantly ^{16}O on the CuO_2 planes and ^{18}O on the chains and apical sites. We can refer to this as $^{16}\text{O}_p^{18}\text{O}_{ca}$. Alternatively, a sample may be annealed at elevated temperature to ensure full ^{18}O exchange, then annealed at 350°C in ^{16}O to invert the isotope distribution, giving $^{18}\text{O}_p^{16}\text{O}_{ca}$. These shifts in distribution can be tracked using Raman spectroscopy. Fig. 23 shows the Raman scattering spectrum for a single crystal of $\text{YBa}_2\text{Cu}_3\text{O}_{6.8}$ fully exchanged with either ^{16}O or ^{18}O . Mode 'a' refers to antiphase motion of the planar O2 and O3 atoms while mode 'b' is associated with motion of the apical oxygen.

This mode is sensitive to oxygen stoichiometry and its shift may be used as a measure of oxygen content [110]. Mode 'c' (absent in the fully oxygenated state) is a chain oxygen mode arising from oxygen defects and the associated loss of inversion symmetry. In the figure these modes are all shifted by the ratio $(16/18)^{1/2}$. Site-selective substitution results in a shift only of the apical and chain modes or only of the planar mode. Examples of such site selective Raman spectra are given in the paper by Khasanov *et al.* [64].

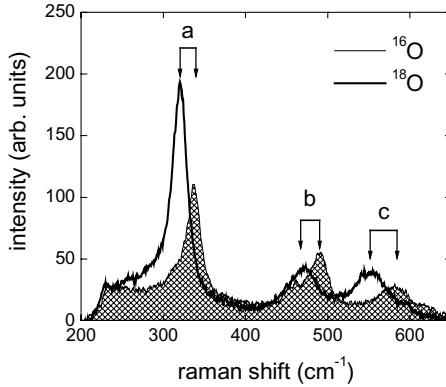


Fig. 23. The Raman spectra for $\text{YBa}_2\text{Cu}_3\text{O}_{6.8}$ with ^{16}O (bordering shaded region) and ^{18}O exchange, showing the $(16/18)^{1/2}$ shift in phonon modes. Mode 'a' is the out-of-phase motion of the in-plane O2 and O3. Mode 'b' is the bond-stretching mode for the O4 apical oxygen and mode 'c' is a chain oxygen defect mode.

These authors recently carried out site-selective isotope exchange in $\text{Y}_{0.6}\text{Pr}_{0.4}\text{Ba}_2\text{Cu}_3\text{O}_7$ and by determining the change in superfluid density using μSR concluded that both $\alpha(T_c)$ and $\alpha(\rho_s)$ are, within errors, governed completely by the mass effect on the CuO_2 planes only. They obtain $\alpha(T_c) = 0.331(36)$ for $^{18}\text{O}_{\text{pac}}$, $0.297(33)$ for $^{18}\text{O}_p^{16}\text{O}_{\text{ca}}$ and $-0.007(29)$ for $^{16}\text{O}_p^{18}\text{O}_{\text{ca}}$, while $\alpha(\rho_s) = 0.56(9)$ for $^{18}\text{O}_{\text{pac}}$, $0.61(8)$ for $^{18}\text{O}_p^{16}\text{O}_{\text{ca}}$, and $0.07(8)$ for $^{16}\text{O}_p^{18}\text{O}_{\text{ca}}$. Data such as this clearly refutes claims [2] that SC arises outside of the CuO_2 planes. These results are also quantitatively consistent with the canonical pseudogap behaviour summarized in Fig. 21 and reflect the absence of any stripe-like anomaly in this Y,Pr-123 system.

10. CONCLUSIONS

And so we conclude this brief sketch of some of the oxygen effects in HTS cuprates. Evidently oxygen plays an important role in the basic physics of the normal and SC states and has proved a useful tool via NMR and isotope effects to probe the electronic correlations which are present in these materials. Because it is labile it has proved an enormously useful means to reversibly alter doping state and thus has led to the discovery of the universal doping phase behaviour of these materials. In many metallic systems this objective can only be achieved through the application of high pressure, as for example in the case of the heavy

fermion systems. But it is probably the case that this ease of doping in HTS materials has led to the surprising lack of high pressure studies on the cuprates. Certainly there have been many studies of the pressure dependence of T_c and this reveals a dominant pressure-induced charge transfer from the block layers to the CuO_2 layers [111]. But beyond that, very few studies have addressed the pressure dependence of the excitation spectrum. In particular pressure offers a means to control the exchange coupling between Cu spins via oxygen orbitals and it is a point of great interest as to what is the effect on the universal phase behaviour when the magnetism is altered in this way. This kind of study could reveal important aspects of the role of short-range magnetism in the pairing mechanism as well as the nature of the pseudogap state and the relative importance of stripes as a competing correlation. Evidently there is still much scope for further investigation in this heavily-studied class of fascinating materials.

ACKNOWLEDGEMENTS

The author wishes to thank and acknowledge the many close collaborators who have shared the HTS journey with him over the past 17 years. Of particular note are Dr John Loram (specific heat), Dr John Cooper (transport and magnetism), Dr Grant Williams (NMR and materials), Dr Christian Bernhard (μSR), Dr Christos Panagopoulos (penetration depth and μSR) and the HTS team at Industrial Research Ltd. Cambridge University has been a regular host and my research described here has been supported by the N.Z. Foundation for Research Science and Technology, the Marsden Fund, The James Cook Fellowship, Trinity College, Victoria University and the MacDiarmid Institute for Advanced Materials and Nanotechnology.

REFERENCES

- [1] R. M. Hazen, in *Physical Properties of High Temperature Superconductors II*, (Ed. D. M. Ginsberg) World Scientific, Singapore (1990), p. 121.
- [2] J. D. Dow, H. A. Blackstead, and D. R. Harshman, *Int. J. Mod. Phys. B* 14 (2000) 3444.
- [3] C. Bernhard *et al.*, *Phys. Rev. B* 52 (1995) 10488.
- [4] C. Bernhard *et al.*, *Phys. Rev. Lett.* 77 (1996) 2300.
- [5] J. Tallon *et al.*, *Phys. Rev. Lett.* 79 (1997) 5294.
- [6] M. E. Klausmeier-Brown *et al.*, *Appl. Phys. Lett.* 60 (1992) 2806.
- [7] P. W. Anderson, *Science* 235 (1987) 1196.
- [8] A. Fujimori *et al.*, *Phys. Rev. B* 35 (1987) 8814.
- [9] N. Nucker *et al.*, *Z. Phys. B* 67 (1987) 9.
- [10] C. T. Chen, *et al.*, *Phys. Rev. Lett.* 68 (1992) 2543.
- [11] R. Henn *et al.*, *Phys. Rev. B* 56 (1997) 6295.
- [12] A. Mawdsley, J. L. Tallon and M. R. Presland, *Physica C* 190 (1992) 437.
- [13] J. L. Tallon, *Physica C* 168 (1990) 85.
- [14] J. L. Tallon *et al.*, *Phys. Rev. B* 41 (1990) 7220.
- [15] J. -Y. Genoud, G. Triscone, A. Junod and J. Muller, *Physica C* 235 (1994) 443.
- [16] H. Lutgemeier *et al.*, *Physica C* 267 (1996) 191.

- [17] J. L. Tallon *et al.*, Appl. Phys. Lett. 59 (1991) 1239.
- [18] P. Bordet *et al.*, Nature (London) 334 (1988) 596.
- [19] J. L. Tallon *et al.*, Nature 333 (1988) 153.
- [20] B. Hensel, G. Grasso, and R. Flukiger, Phys. Rev. B 51 (1995) 15456.
- [21] M. R. Presland *et al.*, Physica C 176 (1991) 95.
- [22] J. M. Tarascon *et al.*, Phys. Rev. B 37 (1988) 9382.
- [23] Y. Le Page *et al.*, Phys. Rev. B 40 (1989) 6810.
- [24] T. Stoto, D. Pooke, L. Forro, and K. Kishio, Phys. Rev. B 54 (1996) 16147.
- [25] R. G. Buckley *et al.*, Physica C 156 (1988) 629.
- [26] J. C. Campuzano, M. R. Norman, and M. Randeria, in *Physics of Conventional and Unconventional Superconductors* (Ed. K. H. Bennemann and J. B. Ketterson) Springer-Verlag, Berlin, 2002.
- [27] Ch. Renner *et al.*, Phys. Rev. Lett., 80 (1998) 149.
- [28] T. Watanabe, T. Fujii, and A. Matsuda, Phys. Rev. Lett., 79 (1997) 2113.
- [29] Y. Ohta, T. Tohyama and S. Maekawa, Phys. Rev. Lett. 66 (1991) 1228.
- [30] M. Imada, A. Fujimori and Y. Tokura, Rev. Mod. Phys. 70 (1998) 1039.
- [31] S. Uchida *et al.*, Phys. Rev. B 43 (1991) 7942.
- [32] J. M. Tranquada *et al.*, Phys. Rev. Lett. 78 (1998) 338.
- [33] P. M. Singer, and T. Imai, Phys. Rev. Lett. 88 (2002) 187601.
- [34] S. R. White *et al.*, Phys. Rev. B 39 (1989) 839.
- [35] V. J. Emery, S. A. Kivelson, and O. Zachar, Phys. Rev. B 56 (1997) 6120.
- [36] P. G. Radaelli *et al.*, Phys. Rev. B 49 (1994) 6239.
- [37] R. Liang, and T. Nakamura, Jpn. J. Appl. Phys. 27 (1988) L1277.
- [38] D. C. Johnston *et al.*, in *Chemistry of High Temperature Superconductors* (Ed. D. L. Nelson, M. S. Whittingham, T. F. George) ACS Symposium Series 351, p. 136.
- [39] J. L. Tallon *et al.*, Phys. Rev. B. 51 (1995) 12911.
- [40] J. L. Tallon, and J. W. Loram, Physica C 349 (2001) 53.
- [41] J. L. Tallon, J. W. Loram, and C. Panagopoulos, J. Low Temp. Phys., 131 (2003) 387.
- [42] S. D. Obertelli, J. R. Cooper, and J. L. Tallon, Phys. Rev. B 46 (1992) 14928.
- [43] I. D. Brown, J. Sol. State Chem. 82 (1989) 122.
- [44] I. D. Brown, and D. Altermatt, Acta Cryst. B 41 (1985) 244.
- [45] A. Bianconi *et al.*, J. Phys. Condens. Matter 12 (2000) 10655.
- [46] G. V. M. Williams, and J. L. Tallon, Physica C 258 (1996) 41.
- [47] R. H. Hammond, and R. Bormann, Physica C 162-164 (1989) 703.
- [48] J. L. Tallon, Phys. Rev. B 39 (1989) 2784.
- [49] P. K. Gallagher, Adv. Ceram. Mater. 2 (1987) 306.
- [50] R. McCormack, D. de Fontaine, and G. Ceder, Phys. Rev. B 45 (1992) 12976.
- [51] M. V. Zimmermann *et al.*, Phys. Rev. 68 (2003) 104515.
- [52] Z. Yamani *et al.*, Physica C 405 (2004) 227.
- [53] P. Bordet *et al.*, Nature (London) 334 (1988) 596.
- [54] H. W. Zandbergen *et al.*, phys. stat. solidi a 103 (1987) 45; Physica C 166 (1990) 255.
- [55] T. Stoto *et al.*, (unpublished).
- [56] J. Karpinski *et al.*, Physica C 227 (1994) 68.
- [57] G. V. M. Williams *et al.*, Physica C 258 (1996) 273.
- [58] J. L. Tallon *et al.*, Physica C 171 (1990) 61.
- [59] S. J. Rothman, J. L. Routbort, U. Welp, and J. E. Baker, Phys. Rev. B 44 (1991) 2326.

- [60] M. Runde *et al.*, Phys. Rev. B 45 (1992) 7375.
- [61] J. L. Tallon, and M. P. Staines, J. Appl. Phys. 68 (1990) 3998.
- [62] J. L. Tallon, and B. -E. Mellander, Science 258 (1992) 781.
- [63] J. L. Tallon, A. H. Schuitema, and N. J. Tapp, Appl. Phys. Lett. 52 (1988) 507.
- [64] R. Khasanov *et al.*, Phys. Rev. B 68 (2003) 220506, and references therein.
- [65] V. J. Emery, and S. A. Kivelsen, Nature (London) 374 (1995) 434-437.
- [66] G. V. M. Williams *et al.*, Phys. Rev. B 62 (2000) 9132.
- [67] W. N. Hardy *et al.*, Phys. Rev. Lett. 70 (1993) 3999
- [68] Ch. Niedermayer *et al.*, Phys. Rev. Lett. 71 (1993) 1764.
- [69] J. L. Tallon *et al.*, Phys. Rev. B 68 (2003) R180501.
- [70] J.W. Loram *et al.*, Physica C 235-240 (1994) 134.
- [71] J.L. Tallon *et al.*, Phys. Rev. Lett. 74 (1995) 1008.
- [72] B. Bucher *et al.*, Phys. Rev. Lett. 70 (1993) 2012.
- [73] A. Vega *et al.*, Phys. Rev. B 39 (1989) 2322.
- [74] D. N. Basov *et al.*, Phys. Rev. Lett. 74 (1995) 598.
- [75] J. L. Tallon *et al.*, Phys. Rev. B 53 (1996) R11618.
- [76] P. Monthoux, Phys. Rev. B 68 (2003) 064408.
- [77] H. A. Mook *et al.*, Phys. Rev. Lett. 70 (1993) 3490.
- [78] A. V. Balatsky and P. Bourges, Phys. Rev. Lett. 82 (1999) 5337.
- [79] Y. Itoh *et al.*, J. Phys. Soc. Jpn. 61 (1992) 1287.
- [80] T. Moriya, J. Phys. Soc. Jpn. 18 (1963) 516-523.
- [81] C. P. Slichter *et al.*, Appl. Mag. Reson. 3 (1992) 423.
- [82] e.g. the *t-J* model: P.W. Anderson, Science 235 (1987) 1196.
- [83] H. Alloul, T. Ohno and P. Mendels, Phys. Rev. Lett. 63 (1989) 1700.
- [84] M. Takigawa *et al.*, Phys. Rev. B 43 (1991) 247-257.
- [85] J. W. Loram *et al.*, J. Phys. Chem. Solids 62 (2001) 59.
- [86] J. L. Tallon *et al.*, phys. stat. solidi (b) 215 (1999) 531.
- [87] J. L. Tallon, T. Benseman, G. V. M. Williams and J. W. Loram, *The phase-diagram of high- T_c superconductors*, Physica C (in press).
- [88] P. Bourges, in *Neutron Scattering in Novel Materials*, (Ed. A. Furrer) World Scientific, 2000.
- [89] P. Bourges, in *Gap Symmetry and Fluctuations in High Temperature Superconductors* (Ed. J. Bok, G. Deutscher, D. Pavuna and S.A. Wolf) Plenum Press, 1998, 349. (Vol. 371 in NATO ASI series, Physics).
- [90] H. He *et al.*, Phys. Rev. Lett. 86 (2001) 1610.
- [91] A. J. Millis, H. Monien and D. Pines, Phys. Rev. B 42 (1990) 167.
- [92] G. V. M. Williams, J. L. Tallon, and J. W. Loram, Phys. Rev. B 58 (1998) 15053.
- [93] F. Raffa *et al.*, Phys. Rev. Lett. 81 (1998) 5912.
- [94] T. Ohno and K. Asayama, Phys. Lett. A 258 (1999) 367.
- [95] S. Ohsugi *et al.*, J. Phys. Soc. Japan 60, 2351 (1991).
- [96] J.W. Loram *et al.*, *10th Anniversary HTS Workshop* (World Scientific, 1996), p. 341.
- [97] J.L. Tallon, *Advances in Superconductivity XII* (Springer, Tokyo, 2000) p. 185; cond-mat/9911422.
- [98] H. Alloul *et al.*, in *High Temperature Superconductivity* (Ed. S. E. Barnes *et al.*) AIP Conference Proceedings, 483 (1999) 161.
- [99] J. Zaanen, and O. Gunnarsson, Phys. Rev. B 40 (1989) 7391.

- [100] P. G. Radaelli *et al.*, Phys. Rev. B 49 (1994) 4163.
- [101] J. W. Loram, J. L. Tallon and W. Y. Liang, Phys. Rev. B 69 (2004) R060502.
- [102] G. V. M. Williams, J. L. Tallon, R. Michalak, and R. Dupree, Phys. Rev. B 57 (1998) 146.
- [103] W. D. Allen, *et al.*, Nature (London) 166 (1950) 1071.
- [104] G-M. Zhao, *et al.*, Phys. Rev. B 52 (1995) 6840.
- [105] B. Batlogg, *et al.*, Phys. Rev. Lett. 58 (1987) 2333.
- [106] J. P. Franck in *Physical Properties of High Temperature Superconductors* vol. 4 (Ed. D. M. Ginsburg) World Scientific, Singapore, 1994, p. 189.
- [107] D. J. Pringle, G. V. M. Williams, and J. L. Tallon, Phys. Rev. B 62 (2000) 12527.
- [108] A. J. Leggett, J. Stat. Phys. 93 (1998) 927.
- [109] J. L. Tallon *et al.*, Phys. Rev. Lett. (submitted); cond-mat/0407782.
- [110] R. M. MacFarlane *et al.*, Phys. Rev. B 38 (1988) 284.
- [111] S. I. Schlachter *et al.*, Physica C 328 (1999) 1.

RUTHENO-CUPRATES: THE SUPERCONDUCTING FERROMAGNETS

C.W. Chu^{1,2,3}, B. Lorenz¹, R.L. Meng¹, and Y.Y. Xue¹

¹) Texas Center for Superconductivity, University of Houston, Houston, Texas 77204-5002, USA

²) Lawrence Berkeley National Laboratory, 1 Cyclotron Road, Berkeley, CA 94720, USA

³) Hong Kong University of Science and Technology, Hong Kong, China

1. INTRODUCTION

The investigation of the occurrence of and interaction between various cooperative phenomena in a solid has long been an important part of condensed matter physics research. It helps elucidate the very nature of the various phenomena and provides additional degrees of freedom for device designs. Among the phenomena, superconductivity and magnetism are of particular interest because of their known antagonistic natures, especially when coexistence is detected. For decades, they have attracted great attention from condensed matter physicists, both theoretical and experimental. Superconductivity and magnetism interact via exchange and electromagnetic interactions between conduction electrons and the local moments in the same compound. As early as 1956, Ginzburg [1] examined the electromagnetic effect on superconductivity and concluded that ferromagnetism suppresses superconductivity leading to a reduction of the superconducting transition temperature T_s , and that a uniform superconductivity and a ferromagnetic order cannot coexist. Later, Matthias et al. [2] found in 1958 that the exchange field in a magnetically ordered state aligns the spins of the Cooper pairs and thus breaks the pairs. Pair-breaking and thus superconductivity suppression due to exchange scattering between the superconducting electrons and the local moments were pointed out by Abrikosov and Gor'kov in 1960 [3]. On the other hand, Anderson and Suhl [4] found in 1959 that superconductivity suppresses magnetism and a nonuniform magnetic

structure with a proper wave vector can exist in a superconducting state. Doping a superconductor with a magnetic rare-earth element was first employed by Matthias in 1958 [2] to explore the interaction between them. In the ensuing 18 years, great progress was made and a region of coexistence at very low temperatures was predicted by extrapolation and later observed at a low enough temperature. However, the possible formation of magnetic clusters in an otherwise superconducting background often complicated the explanation of the observation. This doubt was removed only after the discoveries of the superconducting tertiary rare earth compounds (RRh_4B_4 , RMO_6S_8 , and RMO_6Se_8 , where R = rare-earth) in 1976 by Matthias et al. [5] and Fischer et al. [6]. In addition to the superconducting transition at T_s , these compounds undergo a ferromagnetic transition at T_C or an antiferromagnetic transition at T_N on further cooling, depending on the strength of the exchange interactions of the rare-earth elements. They display a wide variety of complex interplays between these long-range orders that include the coexistence of superconductivity and antiferromagnetism, and the exclusion of superconductivity from ferromagnetism leading to the appearance of a re-entrance transition and the intriguing existence of an inhomogeneous ferromagnetic order in the superconducting state within a narrow temperature range below T_C [4, 7–9]. The inhomogeneous ferromagnetic order has been predicted to have the spiral structure [10], the domain structure [11], or the spontaneous vortex structure [12]. It should be noted that while the superconducting and the different magnetic orders do coexist in the same compound, not all occur at the same temperature range. Only the antiferromagnetic and the inhomogeneous ferromagnetic orders coexist with the superconducting order in the same temperature range in some of these compounds. For instance, the spiral and domain magnetic structures have been reported to appear in some superconducting tertiary rare-earth compounds but over only a narrow temperature region below T_C [13, 14], except for HoMo_6Se_8 , where superconductivity and ferromagnetism coexist below T_C to the lowest experimental temperature [15]. No clear experimental evidence for the spontaneous vortex state has ever been reported in this class of compounds, known as magnetic superconductors where $T_s > T_C$ or T_N .

A spontaneous vortex state is supposed to appear in a Type II superconductor when the demagnetizing field $H_d = 4\pi M$ originated from the spontaneous magnetization M is greater than the lower critical field H_{c1} but smaller than the upper critical field H_{c2} of the coexisting superconductivity. As a result, H_d cannot be expelled from and thus trapped inside the sample when the sample enters the superconducting state. The trapped field is expected to be quantized and to form the spontaneous vortex state in the superconducting state. This is the coexistence of the superconducting and ferromagnetic orders in its true sense, albeit the latter is nonuniform. Meissner effect, the salient signature of a superconductor below T_s , will then be absent and cannot be detected. In the **ferromagnetic superconductors** discussed above, T_s is always higher than T_C . The exact evolution of the macroscopic H_d in the superconducting ambient, however, remains non-trivial [e.g. Leo Radzihovsky et al., Phys. Rev. Lett. 87 (2001) 27001]. The situation becomes more comprehensible for materials that enter the ferromagnetic state at a higher T_C before they become superconducting on further cooling to below T_s . Compounds that exhibit a magnetic transition at a temperature T_m (either T_C or T_N) higher than their T_s therefore will serve as an ideal platform for the search for the spontaneous vortex state.

In an attempt to broaden the high temperature superconducting (HTS) material base and to further improve the flux pinning force, two general groups of ruthenocuprate compounds, $\text{RuSr}_2(\text{R,Ce})_2\text{Cu}_2\text{O}_x$ (Ru1222) and $\text{RuSr}_2\text{RCu}_2\text{O}_8$ (Ru1212), where R = rare-earth, were

synthesized and found to be superconducting with a T_s up to ~ 30 's K in 1995 by modifying the layered $\text{YBa}_2\text{Cu}_3\text{O}_7$ (or YBCO = $\text{CuBa}_2\text{YC}_2\text{O}_7 = \text{Cu1212}$) [16]. Both Ru1222 and Ru1212 compounds have a tetragonal symmetry with a space group $I4/mmm$ and $P4/mmm$, respectively. Ru1222 can be regarded as the result of substituting the CuO linear-chain layer, the BaO layer, and the Y layer in YBCO with the RuO_2 square-planar layer, the SrO layer and the $(\text{R,Ce})_2\text{O}_2$ fluorite-type layer block, respectively, while Ru1212 can be regarded as the result of replacing the CuO linear-chain layer, the BaO layer and the Y layer with the RuO_2 square-planar layer, the SrO layer, and the R layer, respectively, as shown in Fig. 1. They were later found to be weak ferromagnets with a magnetic onset temperature T_m above T_s , i.e. up to ~ 180 K for Ru1222 and ~ 133 K for Ru1212. These compounds with their $T_C > T_s$ were first called **superconducting ferromagnets** (SCFMs) by Felner [17] to differentiate them from the ferromagnetic superconductors with their $T_C < T_s$, discussed earlier. The discovery of these SCFMs has attracted intense interest over the past few years. The appearance of magnetism and superconductivity in Ru1212 and Ru1222 does not seem to be surprising in view of the layer blocks of $[(\text{RuO}_2)(\text{SrO}) = \text{RuSrO}_3]$ and $[(\text{CuO}_2)(\text{R})(\text{CuO}_2)]$ in the compounds, since the former represents the itinerant ferromagnet RuSrO_3 with a $T_C \sim 160$ K and the latter is the active component of the superconductor YBCO with a $T_s \sim 93$ K. While the simultaneous occurrence of superconductivity and magnetism in these compounds has been established, many issues remain open [18]. They include the absence of a bulk Meissner effect, the large variation in T_s , the nature of the magnetic state, the nature of the superconducting state, and the possible occurrence of the spontaneous vortex state in this fascinating class of compounds. In this article, we shall address these issues in the following sections: Synthesis, Superconductivity and Granularity, Magnetism, and Meissner State and Spontaneous Vortex Phase.

2. SYNTHESIS

Although Ru1222 [$\text{RuSr}_2(\text{R,Ce})_2\text{Cu}_2\text{O}_x$] was the first SCFM discovered [17], Ru1212 ($\text{RuSr}_2\text{RCu}_2\text{O}_8$) appeared to attract more attention at least at the beginning of the extensive study on these compounds. This may have something to do with the simpler structure and the almost fixed doping level in Ru1212 (Fig. 1). Almost all studies on Ru1212 reported the detection of a dc magnetization (M) rise below a temperature T_m , a diamagnetic shift in both the ac magnetic susceptibility (χ_{ac}) and zero-field-cooled dc magnetic susceptibility ($\chi_{dc,ZFC}$), a change of slope in the field-cooled dc magnetic susceptibility ($\chi_{dc,FC}$), and a resistivity (ρ) drop near T_s , suggesting a magnetic transition at T_m and a superconducting transition at T_s , as schematically shown in Fig. 2 [18–21]. However, the salient signature of a superconducting transition, i.e. a bulk Meissner effect characterized by a large diamagnetic shift, $\approx -1/4\pi$, in the $\chi_{dc,FC}$, is missing. When a diamagnetic shift of $\chi_{dc,FC}$ was observed later in some samples, it was extremely small and only noticeable under very low fields, but as a slight change in the slope $d\chi_{dc,FC}/dT$ [22]. In contrast with T_m , the T_s varies greatly from report to report. The differences have been attributed to impurity, grain size, oxygen disorder, and doping level. For example, both the small grain sizes comparable to or smaller than the magnetic penetration depth and strong pinning forces should suppress the $\chi_{dc,FC}$ observed. The small or absent Meissner signal and the low T_s are often attributed to deficiencies in sample preparation. It is therefore essential to verify the sample quality.

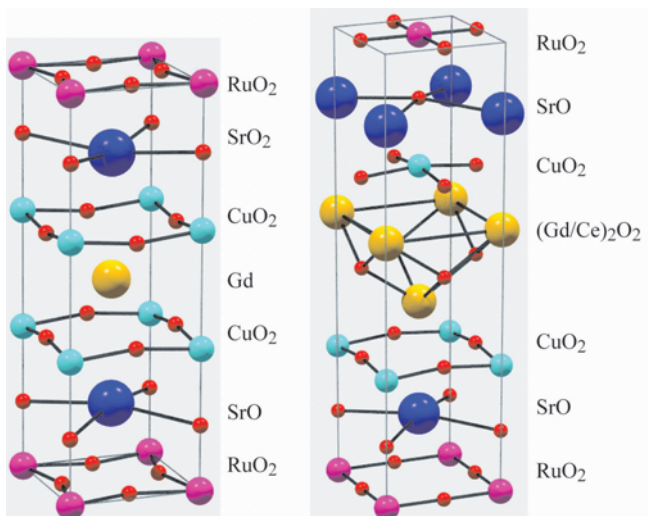


Fig. 1. Crystal structures of Ru1212 (left) and Ru1222 (right). For Ru1222 only one-half of the unit cell is shown.

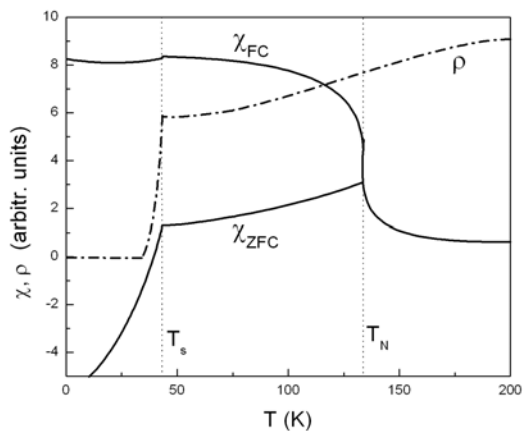


Fig. 2. Schematic temperature dependence of the field-cooled (FC) and zero-field-cooled (ZFC) magnetic susceptibilities χ and the resistivity ρ of RuSr₂GdCu₂O₈.

In spite of the different T_s and the presence or absence of the small superconducting diamagnetic signals, however, all samples investigated were reported to be carefully prepared and to be pure to within the resolution of x-ray diffraction. Unfortunately, no consensus emerged concerning the underlying reasons for the diverse observations. A systematic investigation has been carried out on factors related to compound synthesis that affect the T_s ,

$\chi_{dc,FC}$, and ρ . The factors include the particle size of the precursors before calcination, the particle size of the material prior to sintering, the temperature and time duration of sintering, the cooling speed after the sintering, and the annealing atmosphere. Since Ru1212 and Ru1222 are very similar, except that Ru1222 is less robust against the loss of oxygen than Ru1212, only results for Ru1212 are summarized and reviewed here.

As for most previous experiments, the synthesis method employed by us for the preparation of polycrystalline samples is the standard solid-state reaction. For Ru1212, high purity starting materials RuO₂, SrCO₃, Gd₂O₃, and CuO are individually preheated to 600–800 °C for 12 h to remove any possible absorbed H₂O and CO₂. The thoroughly mixed oxides with a cation ratio Ru:Sr:Gd:Cu = 1:2:1:2 then undergoes the following treatment: 1) calcination at a temperature T_{calc} for a time period of t_{calc} ; 2) pulverization followed by compaction; 3) sintering at a temperature T_{sint} for a time period of t_{sint} ; 4) repeating steps 2 and 3 several times; 5) final sintering at a temperature $T_{sint,1}$ for a longer time period $t_{sint,1}$ in an oxygen atmosphere before cooling at a specific temperature-time profile to room temperature; and an optional step 6) annealing at a temperature T_{ann} in a specific atmosphere.

The samples so prepared are subjected to a series of characterizations: x-ray diffraction, and electrical, magnetic, and thermoelectric measurements. The T_{calc} has an effect on the formation of Ru1212 as exemplified by the XRD patterns in Fig. 3 for two sets of samples after step 1 at different T_{calc} 's. An increase in T_{calc} from 960 to 1000 °C reduces the SrRuO₃ impurity phase from 40% (a) to 20% (c). Repetitive pulverization and sintering followed by a long time sintering at the same final temperature do remove the impurity completely in both samples (spectra b and d in Fig. 3). According to our observations, we have chosen a $T_{calc} = 960\text{--}1000$ °C to calcinate our samples for the present study. Samples prepared under such a T_{calc} followed by repetitive pulverization and sintering exhibit the pure Ru1212 phase with the basic structural, magnetic, electric, and thermoelectric properties shown in Fig. 4, similar to those of the previously published results. The Ru1212 sample has a tetragonal symmetry with space group P4/mmm and lattice parameters $a = 3.8375(8)$ Å and $c = 11.560(2)$ Å. The scanning electron microscopy data show grain dimensions of a few μm and energy dispersive spectroscopy displays uniform composition across the sample. The magnetic properties at low temperatures depend on the magnetic field used for the measurements. For most of the ceramic samples cooled in a field ~ 10 Oe, the $\chi_{dc,FC}$ rises sharply at $T_m \sim 132$ K, indicating a magnetic transition, and continues to increase with further cooling at a much slower rate and flattens out below ~ 30 K. On warming after zero-field-cooling under a field below 10 Oe, the $\chi_{dc,ZFC}$ displays a diamagnetic signal at 4 K, corresponding to a shielded volume fraction up to 100%, bends over at $T_s \sim 30$ K, increases only slightly above T_s , and merges with $\chi_{dc,FC}$ at a temperature slightly below T_m (Fig. 4a). The difference between $\chi_{dc,FC}$ and $\chi_{dc,ZFC}$ between T_s and T_m shows that there exists a magnetic hysteresis and thus a ferromagnetic M in this temperature region. From room temperature to ~ 70 K, ρ decreases with cooling, but increases slightly below 70 K before reaching a small maximum at ~ 52 K followed by a precipitous drop starting at ~ 45 K and reaching zero at ~ 30 K (Fig. 4b). The Seebeck coefficient S increases with cooling from room temperature, exhibits a broad maximum at ~ 200 K, and decreases almost linearly with temperature below 150 K. S decreases more rapidly below 50 K and reaches zero slightly above ~ 30 K where $\rho = 0$ (Fig. 4b). It should be noted that the superconducting transition defined by $\chi_{dc,ZFC}$ and ρ of the pure Ru1212 samples in general is broad with a width $\sim 15\text{--}20$ K, similar to the Ru1212 data previously published

[20, 21, 23–25]. Fine structures are apparently discovered within this broad transition as one plots dp/dT vs. T in the inset of Fig. 4b, which shows two peaks, indicative of two transitions at T_1 and $T_2 < T_1$, which are tentatively attributed to intragrain and intergrain transitions, respectively, for reasons to be given later.

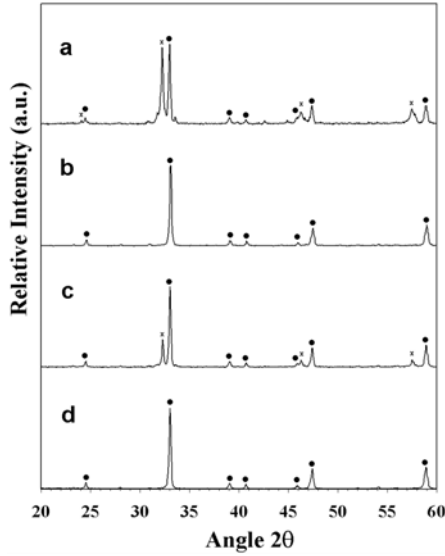


Fig. 3. X-ray spectra of two samples of $\text{RuSr}_2\text{GdCu}_2\text{O}_8$ synthesized at 960°C (a, b) and 1000°C (c, d). The dot indicates reflections assigned to the Ru1212 structure. Crosses show the presence of SrRuO_3 . The spectra a and c are measured immediately after step 1; b and d, after step 5, long time sintering at 1065°C .

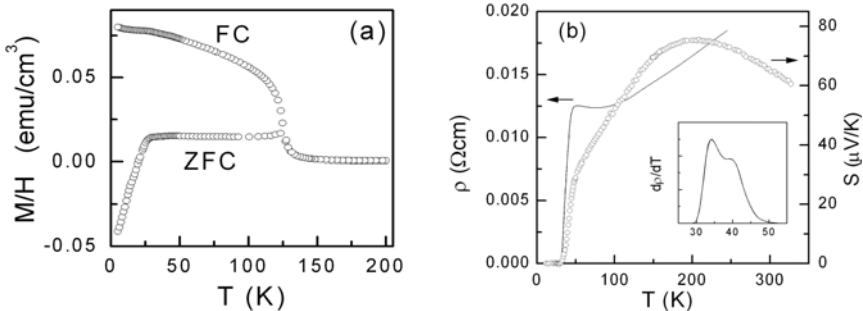


Fig. 4. (a) Magnetic susceptibility, M/H , of $\text{RuSr}_2\text{GdCu}_2\text{O}_8$ at 7 Oe for field cooling (FC) and zero field cooling (ZFC). (b) Resistivity (line) and thermoelectric power (circles) of $\text{RuSr}_2\text{GdCu}_2\text{O}_8$. The inset shows the derivative, dp/dT .

Low T_{calc} leads to a higher level of the SrRuO_3 impurity phase and repetitive pulverization and sintering are required to remove the impurity, as was pointed out earlier (Fig. 3). However, the lower T_{calc} of 960 °C appears to give a lower ρ and higher T_s than the T_{calc} of 1000 °C after proper processing. This is exemplified by two samples that are synthesized according to the following steps (the first step is calcination and the rest are sintering): (T_{calc} , 16 h) \Rightarrow (1015 °C, 10 h) \Rightarrow (1060 °C, 10 h) \Rightarrow (1060 °C, 10 d), where h = hours and d = days with $T_{\text{calc}} = 960$ and 1000 °C, as shown in Fig. 5 as a solid line and a dashed line, respectively. It is evident that ρ is enhanced and the superconducting transition is shifted downward in parallel by 5 K by increasing the T_{calc} from 960 to 1000 °C (Fig. 5). The same downward shifts were detected in T_1 and T_2 . Since the intergrain phase lock does not depend only on the superconducting transition of the grain but also on the physical and chemical conditions in the grain boundaries, the fact that T_1 and T_2 are shifted in parallel by different T_{calc} is puzzling.

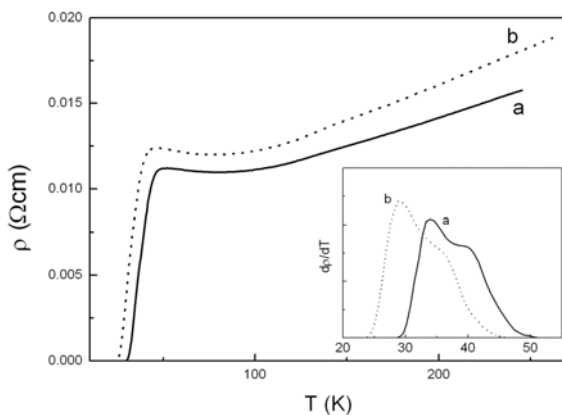


Fig. 5. Resistivities of two samples calcinated at (a) 960 °C and (b) 1000 °C. Inset: Temperature derivative of resistivity.

While repeated grinding after calcination and before sintering is usually expected to promote homogeneity and produce better samples as for the HTS cuprates, they do not show noticeable improvement in the superconducting properties of Ru1212 . It is surprising to find that repeated grinding actually results in lowering T_1 and T_2 , although it also reduces the ρ . The effect is displayed in Fig. 6 where results for samples that are repeatedly ground (dashed line) and ground once (solid line) are shown. The parallel shifts of T_1 and T_2 are again evident.

Prolonged annealing is considered to be good for enhancing formation, promoting order, reducing strain, and thus helping to achieve better samples. Indeed, this is the case for Ru1212 . Fig. 7 shows the results of two samples prepared according to the following two processing schedules (the first step is calcination and the rest are sintering): a) (960 °C, 16 h) \Rightarrow (1015 °C, 24 h) \Rightarrow (1060 °C, 24 h) \Rightarrow (1065 °C, 14 d); and b) (960 °C, 16 h) \Rightarrow (960 °C, 12 h) \Rightarrow (1015 °C, 16 h) \Rightarrow (1060 °C, 24 h) \Rightarrow (1065 °C, 14 d) \Rightarrow (1070 °C, 4 d). Additional

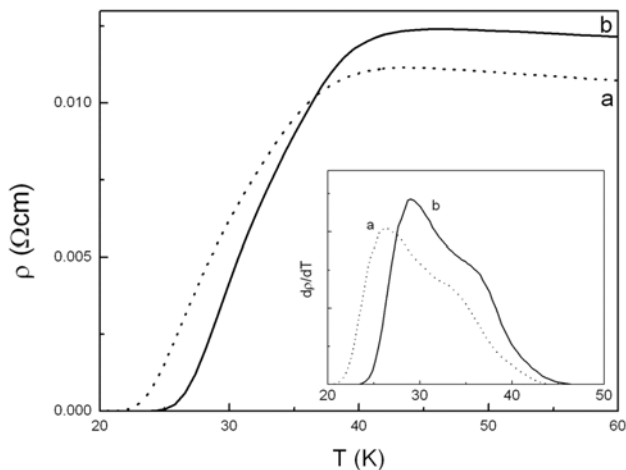


Fig. 6. Effect of grinding on the resistivity of $\text{RuSr}_2\text{GdCu}_2\text{O}_8$. (a) Frequently reground sample; (b) ground only after the calcination step. Inset: Temperature derivative of resistivity.

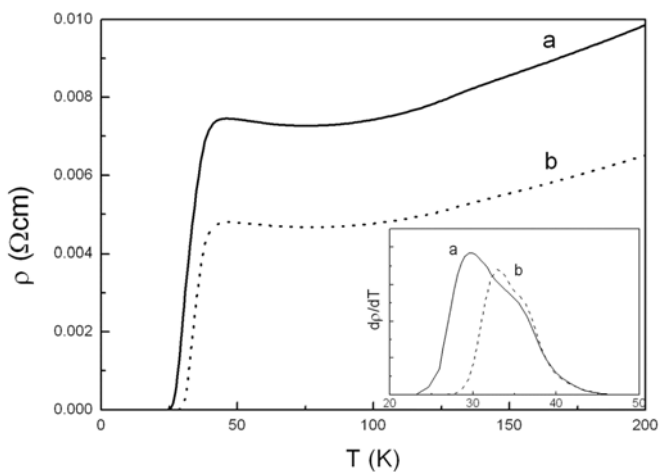


Fig. 7. Effect of sintering and annealing on the resistivity of $\text{RuSr}_2\text{GdCu}_2\text{O}_8$. (a) Sample prepared according to our standard procedure; (b) including additional steps of sintering and annealing. Inset: Temperature derivative of resistivity.

grinding and sintering steps and prolonged annealing reduce ρ and raise T_2 but barely affect T_1 , consistent with the idea that these steps improve the connectivity of the samples but cannot account for the observations mentioned above.

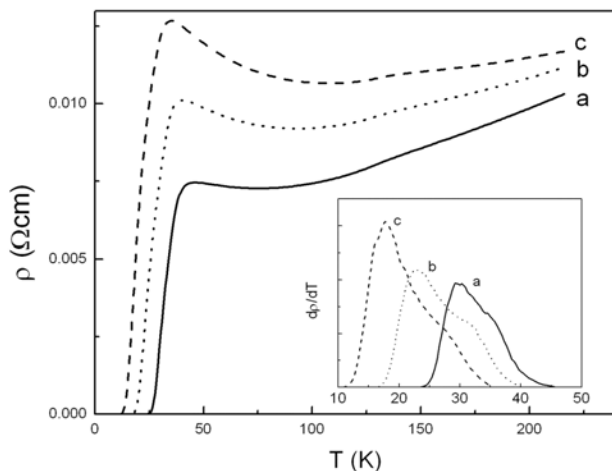


Fig. 8. Influence of particle size of the precursor powders. (a) Coarse-grain powder; (b) mixed fine- and coarse-grain powder; (c) fine grained powder. Inset: Temperature derivative of resistivity.

The particle size of the starting material for sintering is known to influence the chemical homogeneity, density, and microstructure of the final product. We have decided to determine its effect on the superconducting properties of Ru1212. Calcinated ruthenocuprate is grounded to powder of different sizes, and compressed and sintered by the same temperature-time schedule. Results of three samples are shown in Fig. 8: (a) prepared from coarse grains; (b) from intermediate coarse grains; and (c) from fine grains. While samples from fine grains have the highest density, they possess the lowest T_1 and T_2 . However, the coarse grain sample shows the highest T_1 and T_2 . The observation suggests that pulverization can introduce unfavorable grain boundaries and microstructures to the superconducting properties of Ru1212.

Since the microscopic grain structure appears to affect the superconducting properties it is expected that the cooling process to room temperature (RT) after finishing the sample synthesis at 1060 °C will be important. As shown in Fig. 9, one sample (a) was slowly cooled at 15 °C per hour to 900 °C and from 900 °C to RT at 150 °C per hour; and the other sample (b) was slowly cooled (15 °C/h) all the way down to 400 °C and then faster to RT. It is clear from Fig. 9 that sample (b) exhibits a much higher transition temperature, indicating that the slow cooling between 900 and 400 °C enhanced the superconducting properties. Both the intragrain T_1 and the intergrain T_2 are shifted by about 6 K. Since the x-ray spectra of both samples are nearly identical, the higher T_s 's of sample (b) should be due to improvements of the intergrain connectivity and the microscopic grain structure.

The influence of post-sintering annealing in different atmospheres was investigated and the results are summarized in Fig. 10. The parent sample (a) was synthesized in the following sequence (the first step is calcination and the rest are sintering): (960 °C, 16 h) \Rightarrow (1015 °C, 25 h) \Rightarrow (1060 °C, 10 h) \Rightarrow (1065 °C, 7 d). After the synthesis was finished three pieces of

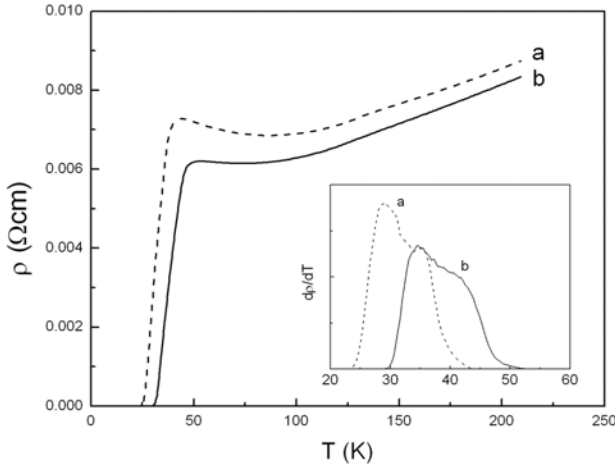


Fig. 9. Resistivity data for two samples subjected to different cooling procedures. (a) Slow cooling from 1060 to 900 °C; (b) slow cooling from 1060 to 400 °C. Inset: Temperature derivative of resistivity.

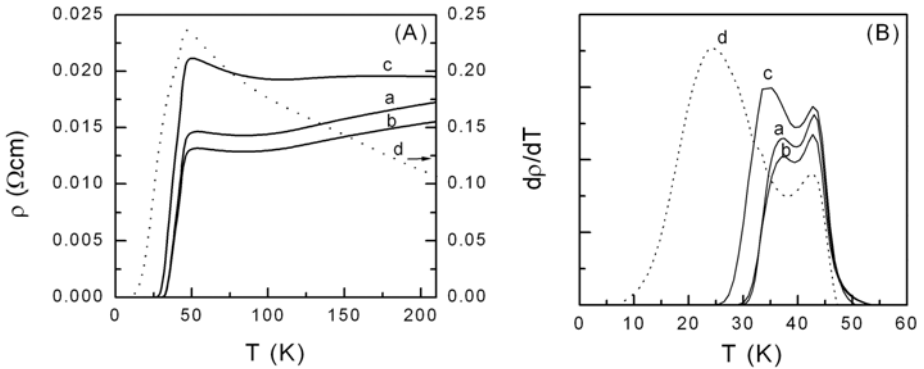


Fig. 10. Comparison of the resistivity (A) and its derivative (B) for samples annealed in different atmospheres. (a) No additional annealing; (b) annealed in oxygen; (c) annealed in air; (d) annealed in argon (note the reduced scale for this curve, right axis).

this sample were annealed once again at 600 °C for 24 h in different atmospheres: oxygen (b); air (c); and argon (d). The ρ data (Fig. 10) for samples (a) and (b) are almost identical, i.e. annealing in oxygen does not change the superconducting properties (neither T_1 nor T_2), although it reduces the normal state ρ . However, annealing in air (sample c) clearly reduces T_2 and the zero- ρ temperature, indicating degrading grain boundaries and intergrain coupling. These detrimental effects are enhanced by annealing in argon (sample d). The high temperature resistivity tends to become semiconducting (Fig. 10, sample d) as a result of

dominating grain boundary resistance. However, the intragrain transition at T_1 is barely affected as indicated by the vertical dashed line in Fig. 10. The decrease of the intergrain superconducting transition temperature, T_2 , can be understood assuming a depletion of the oxygen content in the grain boundaries if samples are annealed in other than pure oxygen atmosphere. Therefore, T_2 is not associated with the bulk superconducting effect since the intragrain transition remains unchanged after the annealing.

It is evident that, depending on the synthesis conditions, the T_s of Ru1212 can change by 10 to 15 K. Although changes in intergrain coupling may account for the large T_2 difference, the variation of T_1 has to be attributed to the alteration in the carrier density of the compound if T_1 represents the transition temperature of the grains as assumed. For the cuprate high temperature superconductors, a universal T_c - carrier density relation has long been established. Similarly, a universal T_c - room temperature thermopower (S) was also obtained. This is not surprising since the carrier density is closely related with S . Therefore, we have measured the S of Ru1212 with different T_c 's processed under different conditions. The values of S are spread in a narrow band between 65 and 77 $\mu\text{V}/\text{K}$. According to the universal T_c - S relation, the relatively small differences in S cannot account for the large differences in T_1 and T_2 (Fig. 11). This leads us to the conclusion that the carrier density for all of our samples is about constant and the change of the transition temperature for different synthesis conditions cannot be explained in terms of the doping effect. The observation is in accordance with thermogravimetric analysis [19] showing that the oxygen deficiency in Ru1212 systems is very small and not sensitive to annealing conditions. The foregoing discussion is based on the assumption that the superconductivity in Ru1212 compounds is a bulk state and not due to minor impurity phases, which is supported by x-ray diffraction and EDX measurements that do not show any impurity phase within the resolution of a few percent.

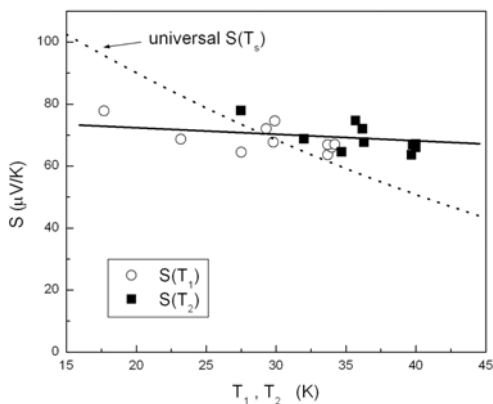


Fig. 11. Thermoelectric power at ambient temperature versus intergrain (T_1) and intragrain (T_2) transition temperatures. The universal $S(T_s)$ relation is shown by the dotted line, assuming a maximum $T_s \approx 90$ K.

From the above, it is clear that, indeed, the samples used in reported studies are pure as claimed and the spread of T_s 's cannot be caused by variation of carrier density. This is in strong contrast to assertions that factors associated with the oxygen content and detailed synthesis are responsible for the large T_s variation reported. Our observation suggests that the T_s 's reported do not reflect the change of the superconducting properties of the bulk Ru1212. Although the transition observed at T_2 and assigned to an intergrain phase-lock transition can be understood, the large change in T_1 without the corresponding change in S or carrier density casts a serious question on the nature of the so-called intragrain superconducting transition at T_1 . In other words, the superconducting grains may have further microstructures within them.

3. SUPERCONDUCTIVITY AND GRANULARITY

The absence of a bulk Meissner signal in $\chi_{dc,FC}$ initially led us to question the bulk nature of superconductivity in Ru1212 [18]. To address the question, we have examined Ru1212 (as well as Ru1222) samples optimally prepared and characterized by XRD to be phase-pure to the XRD resolution (Fig. 12) using EDS, showing them to be chemically homogeneous to within $\sim 1 \mu\text{m}$, and SEM, showing them to possess grains of dimensions 1–5 μm . However, given the resolution of XRD of a few percent, it remains to be seen if the possible presence of superconducting filaments associated with a minor superconducting impurity phase, such as the Ru-stabilized $\text{YSr}_2\text{Cu}_3\text{O}_7$, in the Ru1212 samples can exist beyond detection by our XRD. We decided to determine the electrical homogeneity of the samples by measuring magnetically the superconducting current density J_c of samples of different particle sizes d ranging from 0.01 to 1 mm at 5 K. The results are displayed in Fig. 13. J_c is found to be constant, suggesting that the sample is electrically homogeneous to within $\sim 10 \mu\text{m}$ and its superconductivity cannot be caused by superconducting impurity filaments at least down to this dimension. Specific heat anomaly was also detected [23, 26] in Ru1212 and Ru1222, confirming unambiguously that the superconductivity in these compounds is bulk.

In a Type II superconductor such as Ru1212, flux pinning can reduce the size of the Meissner signal. For strong flux pinning, the Meissner effect can be completely suppressed. To remove the pinning effect as well as the magnetic background of Ru1212, we have determined the reversible magnetization (M_r) of Ru1212, which is obtained as $M_r \equiv (M_+ + M_-)/2$, where M_+ and M_- are the magnetizations measured from the increasing and decreasing field branches of the $M - H$ loop, respectively. The M_r of a SCFM has two components, one (M_s) due to superconductivity and the other (M_m) due to ferromagnetism.

To discriminate between M_m and M_s , we have measured the M_r of both the superconducting Ru1212 and the nonsuperconducting Ru1212Zn ($\text{RuSr}_2\text{GdCu}_{1.94}\text{Zn}_{0.06}\text{O}_8$), which has a T_m similar to the superconducting Ru1212, at 5 K below T_s and 50 K above T_s . The superconducting component of the reversible magnetization (M_s) of Ru1212 at 5 K is thus obtained as $M_s = [M_r(\text{Ru1212 at 5 K}) - M_r(\text{Ru1212Zn at 5 K})] - [M_r(\text{Ru1212 at 50 K}) - M_r(\text{Ru1212Zn at 50 K})]$. The results of M_s as a function of field are shown in Fig. 14. No Meissner effect greater than a few percent of that of a bulk superconductor is detected at a field as low as 0.25 Oe. The M_s at 5 K of the underdoped superconducting YBCO with a $T_s \sim 40$ K is also shown in the same figure for comparison. If the superconductivity in Ru1212 is similar to that in the underdoped YBCO, the $M_s - H$ of Ru1212 can be obtained from the YBCO data by shifting the H axis by $H_d = 4\pi M \sim 400$ Oe, as indicated by the vertical dashed

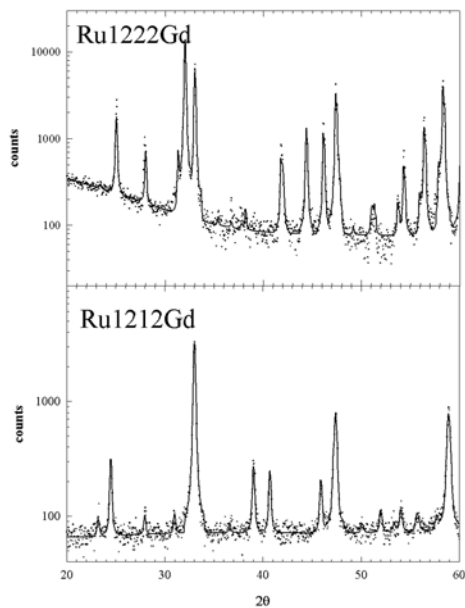


Fig. 12. The XRD pattern of Ru1222 and that of Ru1212Gd. The dots are data and the solid lines are the Rietveld refinements.

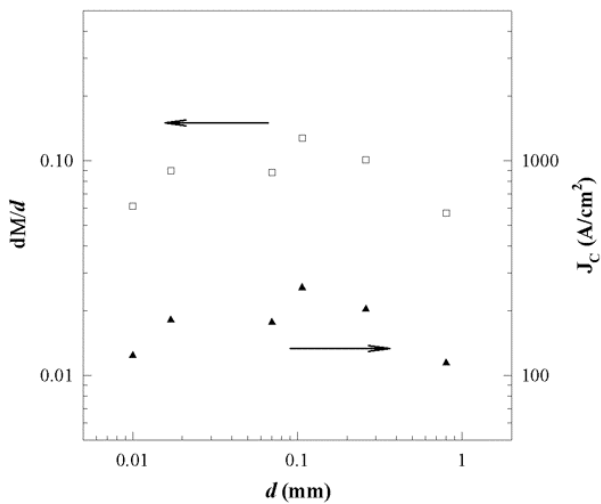


Fig. 13. ΔM and J_c as functions of particle size.

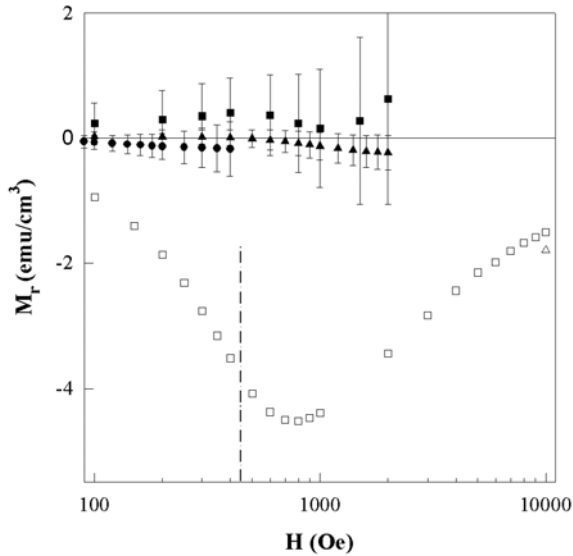


Fig. 14. The reversible magnetization associated with the superconductivity of Ru1212Gd (filled symbols) and YBCO (open squares)

line. However, this is clearly not the case. Instead, Ru1212 exhibits negligible diamagnetic shift, not more than 1–2% of that for YBCO with a comparable T_s , demonstrating the absence in Ru1212 of the bulk Meissner effect that is a common characteristic feature of bulk superconductors. Granularity of Ru1212 with the presence of microdomains inside the crystal grains of dimensions comparable to or smaller than the penetration depth is therefore proposed to account for the absence of a bulk Meissner effect.

The existence of crystal grains of 1–5 μm in Ru1212 polycrystalline samples is revealed by the SEM data and by the appearance of two superconducting transitions at T_1 and T_2 , designated as the intragrain and intergrain transition temperatures, respectively (Fig. 4). The two transitions so designated are expected to show different responses to the external pressure and magnetic field applied, with dT_2/dP being more positive than dT_1/dP and dT_2/dH more negative than dT_1/dH . This is because of the large pressure-induced improvement in grain-grain contact and the accompanying enhancement in intergrain Josephson coupling, as well as the greater field effect on the weaker intergrain Josephson coupling than on the intragrain one. We have measured the pressure effects on T_1 and T_2 of Ru1212 both resistively and magnetically. While both are found to increase with pressure, T_2 rises at a rate of 1.8 K/GPa, about two times that of T_1 as displayed in Fig. 15, as expected and consistent with the designation of T_2 as the intergrain phase-lock transition temperature. The magnetic field is found to suppress both T_1 and T_2 , but at a higher rate for T_2 , as expected. However, even the suppression rate of T_1 of ~ 100 K/T at low H (Fig. 16) is unexpectedly large for a bulk superconductor. The overall field dependence of T_1 , therefore, should be very different from what has been predicted by the Ginzburg-Landau theory for a homogeneous bulk

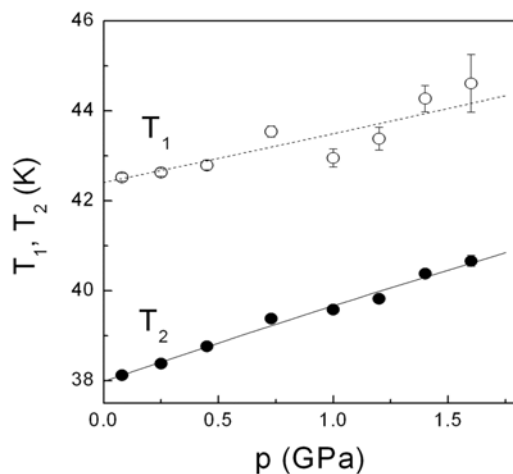


Fig. 15. Pressure dependence of the intragrain (T_1 , open symbols) and intergrain (T_2 , solid symbols) transition temperatures of $\text{RuSr}_2\text{GdCu}_2\text{O}_8$.

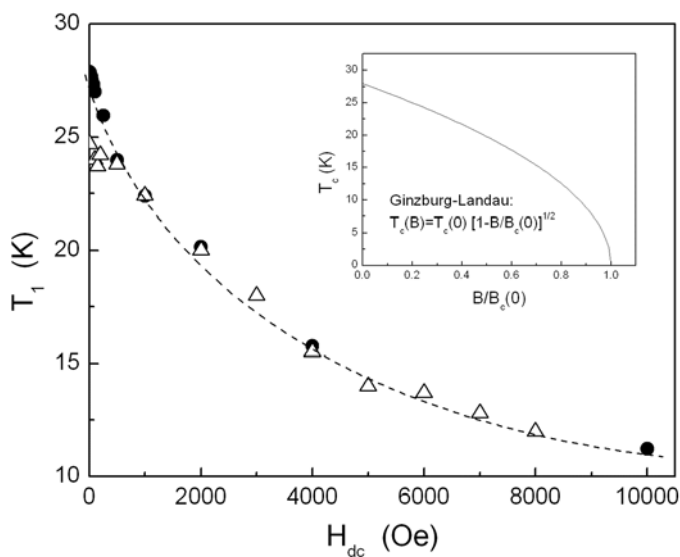


Fig 16. Field dependence of the intragrain superconducting transition temperature T_1 from resistivity (open triangles) and ac susceptibility (solid circles) measurements. Inset: Ginzburg-Landau theory for a homogeneous bulk superconductor.

superconductor as shown in the insert of Fig. 16. This strongly suggests that T_1 may also be a phase-lock transition temperature between microdomains within the crystal grains. We conjecture that these microdomains are coupled as a Josephson junction array and the interdomain coupling is sensitive to the magnetic field applied. The large dT_1/dH observed can thus be understood.

In fact, similar granularity has been widely observed. The suggested existence of domains within the crystalline grains should be reflected in the existence of at least two different length scales. It is known that the diamagnetic shift of the real part of the ac magnetic susceptibility χ' is a measure of the volume shielded by the connected superconducting path. For a granular superconductor, χ' will decrease drastically with pulverization when the particles size reaches the characteristic length scale, but much slower after that.

The χ' of several Ru1212 powder samples from the same ingot with particle sizes ranging from 0.3 to $3 \times 10^4 \mu\text{m}$ are shown in Fig. 17. On cooling, $\chi'(T)$ of the solid sample of dimension of 3 mm first displays two anomalies: a small peak at ~ 42 K and then a rapid drop at ~ 32 K. By comparing the resistivity data, the two anomaly temperatures are identified as $T_1 \sim 42$ K and $T_2 \sim 32$ K for the interdomain and the intergrain phase-lock transitions. The diamagnetic shift below T_2 is found to decrease as the particle size is reduced to $\sim 10 \mu\text{m}$, while χ' between T_2 and T_1 remains unchanged. However, when the particle dimension is decreased to below $\sim 10 \mu\text{m}$, the overall drop of χ' below T_1 decreases. When the particle size is $\sim 0.3 \mu\text{m}$, χ' continues to increase with the decrease in temperature and shows no magnetic sign of superconductivity. The results show that there exist two length scales in our Ru1212 sample: one greater than $\sim 10 \mu\text{m}$ and the other much smaller than $\sim 10 \mu\text{m}$. The change of the diamagnetic shift with particle dimension is in agreement with the crystalline grain size under SEM, i.e. about $10 \mu\text{m}$. The further decrease (or even absence) of the superconducting

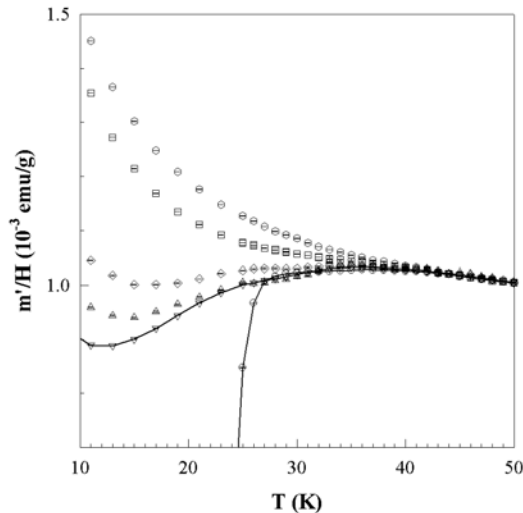


Fig. 17. $\chi'(T)$ of Ru1212Gd powders with different particle sizes. From top to bottom: 0.8, 3, 8, 20, and 40 μm , and a 3 mm bulk ceramic.

signal with the size below $10\ \mu\text{m}$ may thus have to be attributed to a penetration depth λ much larger than $0.3\ \mu\text{m}$. The actual superconducting transition temperature T_0 , therefore, should be higher than T_1 .

We have therefore decided to determine and analyze the λ of the crystal grains by measuring the χ' of the Ru1212 samples with particles of different sizes d from the same ingot between $T_2 \sim 32\ \text{K}$ and $T_1 \sim 42\ \text{K}$, as shown in Fig. 17. χ' for these samples at $5\ \text{K}$ decreases from $+0.007$ for $d \sim 40\ \mu\text{m}$ powder sample to $-1/4\pi$ for $d \sim 3\ \text{mm}$. However, χ' between 32 and $42\ \text{K}$ remains unchanged with d decreasing to $\sim 10\ \mu\text{m}$. We deduced λ from χ' using the relation for a magnetically aligned powder sample $\chi' = -3/(8\pi)[1-6(\lambda/d)\coth(d/2\lambda) + 12(\lambda/d)^2] \sim (1/500)(d/\lambda)^2$ for $d < 2\lambda$. For randomly oriented powder samples of ours, a geometric factor of $1/3$ has to be included to account for the high anisotropy of superconductivity in cuprate HTS. The χ' of Ru1212 samples with particles of $d = 0.3, 0.8, 1.5, 3,$ and $8\ \mu\text{m}$ are shown in Fig. 18. χ' between 32 and $42\ \text{K}$ starts to move up as $d < 8\ \mu\text{m}$. It is interesting to note that values of the χ' of the 0.3 and $0.8\ \mu\text{m}$ powder samples are almost the same and appear to be a continuation from the magnetic background from above $42\ \text{K}$, suggesting a $\lambda \gg 1\ \mu\text{m}$. The magnetic background (solid line in Fig. 18) was estimated from the χ' of the $0.8\ \mu\text{m}$ powder sample. A $\lambda(0) \sim 3\ \mu\text{m}$ is consequently deduced based on the χ'/d^2 of the $0.8, 1.5$ and $3\ \mu\text{m}$ powder samples. The estimated uncertainty is less than 10% , mainly arising from the uncertainty in d . An even longer penetration depth up to $30\ \mu\text{m}$ was also obtained from χ' below T_2 , using samples with particle sizes $> 10\ \mu\text{m}$, reflecting the microstructure of the samples due to the crystal grains in the sintered ceramics. The observation of two different

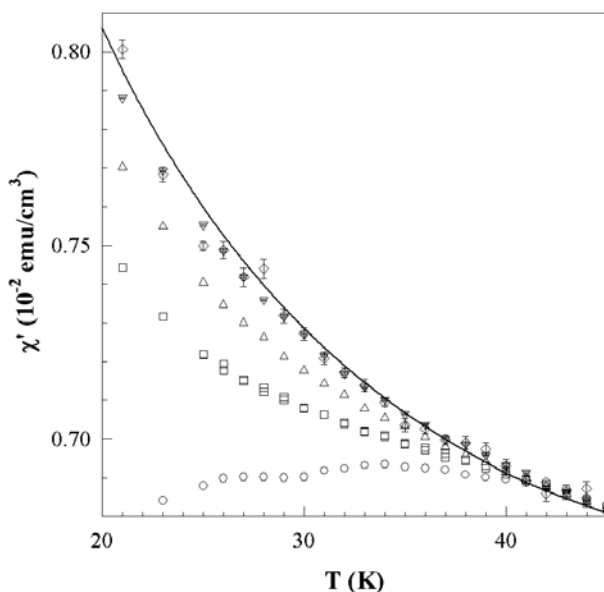


Fig. 18. χ' of Ru1212 powders with sizes of \diamond : $0.3\ \mu\text{m}$; ∇ : $0.8\ \mu\text{m}$; \triangle : $1.5\ \mu\text{m}$; \square : $3\ \mu\text{m}$ and \circ : $8\ \mu\text{m}$.

length scales in Ru1212 ceramic samples is therefore a result of the two different microstructures in the samples, i.e. typical crystal grains of micron size in ceramic material and unusual domains of submicron size within the crystal grains. The submicron domains may originate from phase separation that occurs quite commonly in cuprate HTS.

As mentioned earlier, Ru1212 is rather robust against the loss of oxygen and thus carrier density. However, affinity of oxygen in Ru1222 is less than that in Ru1212. As a result, the superconducting properties of Ru1222 can be adjusted to a greater extent by high pressure oxygen annealing. We have therefore investigated the Ru1222 samples to determine if submicron domains are common in ruthenocuprates. Methods similar to those described above for Ru1212 are used to determine the granular microstructures within the crystal grains of Ru1222.

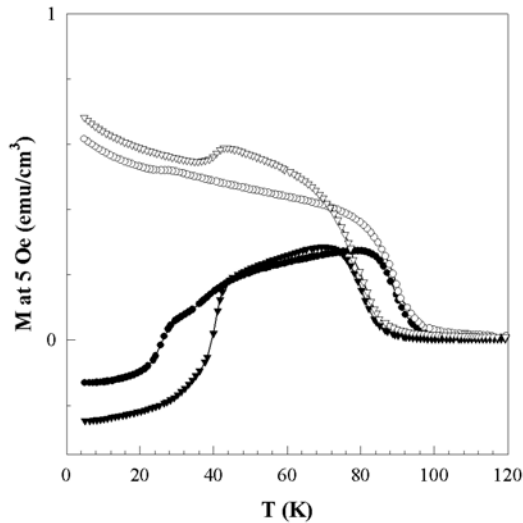


Fig. 19. $\chi_{dc,FC}$ (open symbols) and $\chi_{dc,ZFC}$ (filled symbols) for the as-synthesized Ru1222 sample (circles) and that after 300 atm. O_2 annealing for 8 h (triangles).

In contrast to most Ru1212 samples, the $\chi_{dc,FC}$ of Ru1222 ceramic samples at fields below ~ 50 Oe shows a small but relatively sharp diamagnetic drop at a transition temperature, as defined by the inflection point in $\chi_{dc,FC}(T)$. This transition temperature exhibits a systematic rise from 26 to 40 K with increasing oxygen intake, as exemplified by the $\chi_{dc,FC}$ and $\chi_{dc,ZFC}$ of two Ru1222 ceramic samples in Fig. 19: one as-synthesized (a) and the other after annealing in 300 atm oxygen at 600 K for 8 h. It is designated as T_1 for the intragrain transition, since a second transition, arising from intergrain coupling at T_2 below 20 K is also easily detected, especially in the ac χ' of these samples at very low field. This relatively weaker intergrain coupling of the Ru1222 ceramic seems to be typical in previously published reports, where a less than 100% shielding in $\chi_{dc,ZFC}$ was observed. To estimate the carrier density, the thermoelectric power S was measured. Using the universal T_s - carrier density and T_s - $S(300\text{ K})$ relations, the increase in carrier density due to the high pressure oxygen annealing

could only result in a T_s increase of < 6 K, which is much smaller than the 14 K T_s difference observed between samples (a) and (b). Adopting the procedure developed for Ru1212, the penetration depth λ is deduced from the d dependence of χ' for samples annealed. Similar to Ru1212, $\lambda(0\text{ K}) > 0.5\ \mu\text{m}$ is relatively large and $\lambda(0\text{ K})$ for sample (a) is about twice as large as that for sample (b). T_s has been shown to vary linearly with $1/\lambda^2$ and to cross the origin in the T_s versus $1/\lambda^2$ plot for bulk cuprate HTS, known as the Uemura line. The $1/\lambda^2$ dependence of T_1 of Ru1222 ceramic samples with different oxygen contents is shown in Fig. 20. While a linear dependence is observed, the line is shifted to the left-hand side of the Uemura line, suggesting that microstructures must exist inside the Ru1222 grains and that Josephson couplings exist between these microstructures, which may be designated as domains, as for Ru1212. A large $dT_1/dH \sim 100\text{ K/T}$ is also observed in Ru1222, further supporting the existence of domain structure in Ru1222.

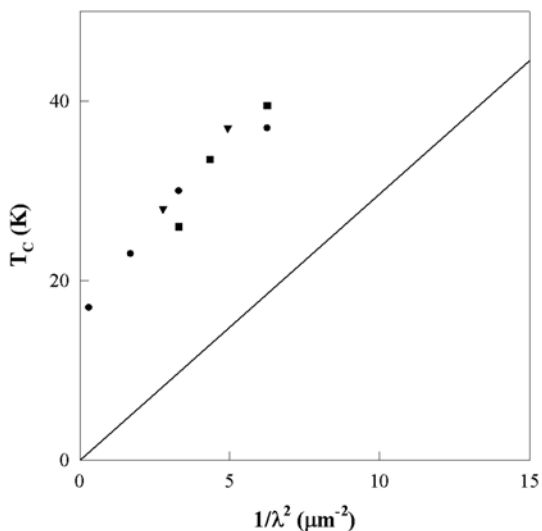


Fig. 20. T_1 vs. $1/\lambda^2$ for annealed Ru1222 samples.

From the above studies, it is concluded that the ruthenocuprate SCFM's unusual granular nature with two length scales is found to be responsible for the absence of the bulk Meissner effect and for the appearance of multiple superconducting transitions in the compounds. Although single-crystal ruthenocuprates will remove the intergrain phase-lock transition, single crystallinity may not be able to overcome the interdomain weak links and the associated unusually long penetration depth. With the additional presence of the ferromagnetic component in ruthenocuprates, the appearance of a novel superconducting state is not impossible.

4. MAGNETISM

The magnetic structure of Ru1212/Ru1222 is the key to understanding the coexistence of magnetism and superconductivity. Such coexistence, on the one hand, can be well accommodated with existing theoretical models if the Ru spins are antiferromagnetically (AFM) aligned. The antiferromagnetic ordering of the R = Gd, Nd, or Er in the superconducting $\text{RBa}_2\text{Cu}_3\text{O}_{7-\delta}$, for example, is experimentally established and theoretically well understood [27]. According to the band-structure calculations, on the other hand, the superconducting order parameter may have to either be spatially modulated, i.e. in so-called FFLO state, or totally suppressed if the Ru spins are ferromagnetically ordered [28, 29]. Actually, the calculated exchange splitting of the carriers would be 26 meV or higher, a significant value compared to the superconducting gap [28]. The spin dependency of the carrier momentums at the Fermi surface, therefore, makes the Cooper pairs possess large net wave vectors, i.e. the order parameter will either rapidly oscillate in the ab planes at the length scale of a few tens nm or alternate the sign from layer to layer [28]. It should be pointed out that such non-negligible coupling between the RuO- and the CuO_2 -layers is in line with both the proximity superconductivity observed in the chains of $\text{YBa}_2\text{Cu}_3\text{O}_7$ and the mixing Ru valences reported [30, 31]. It has been further pointed out that even the d-wave superconductivity in the CuO_2 planes is very unstable against such exchange splitting [29]. In the case of canted antiferromagnetism, the situation is less clear, although a spatial modulation of the superconductivity, i.e. an FFLO state, seems to be unavoidable. However, the most likely FFLO state [28], the so-called π phase, seems to be in disagreement with experiment [32].

Unfortunately, the experimental situation is similarly controversial. Two major microscopic probes, i.e. powder neutron diffraction (NPD) and zero field nuclear magnetic resonance (ZFNMR), suggest different magnetisms while both claim that the magnetic structure is homogeneous [31, 33]. Similar contradictions exist in the macroscopic magnetization [17, 34-36], the ESR [37], the μSR [38], and the Mössbauer spectrum [17] observed. On the other hand, the magnetic structures suggested by a given probe are surprisingly consistent among various groups even when the samples measured vary significantly. This suggests, in our opinion, that the key is the data interpretation rather than the sample-to-sample variations or the data uncertainties.

Three sets of NPD data, for example, have been reported thus far about the spin structures of Ru1212Gd, Ru1212Y, and Ru1212Eu, respectively [33, 39, 40]. In all three cases, the G-type antiferromagnetic spin order is suggested with the ordered spin $\approx 1 \mu_B/\text{Ru}$ along the c direction (Table 1). The possible minor ferromagnetic component is suggested to be < 0.1 , $0.28(8)$, and $< 0.3 \mu_B/\text{Ru}$, respectively.

Two detailed $^{99,101}\text{Ru}$ ZFNMR experiments have also been carried out for Ru1212Y and Ru1212Gd, respectively (Table 2) [31, 42]. Despite some details, the two data sets are in good agreement: both show a signal enhancement (compared with paramagnetic salts) of 100–200; a mixture of Ru^{4+} and Ru^{3+} with the moments of 0.9 and $2 \mu_B/\text{Ru}$, respectively; and, especially, an in-plane spin alignment. The in-plane alignment suggested is in line with the ferromagnetic resonance (FMR) data [37]. The valence mixture suggested is also in agreement with both the macroscopic magnetization and the x-ray absorption near-edge structure (XANES) [35, 43].

Table 1. Summary of the NPD data

| compound | AFM aligned spins (μ_B/Ru) | spin direction | FM component μ_B/Ru | FM moment based on the spontaneous magnetization |
|----------|---|----------------|--------------------------------|--|
| Ru1212Gd | 1.18(6) | c | < 0.1 | ≈ 0.28 [41] |
| Ru1212Y | 1.15(9) | c | 0.28(8) | ≈ 0.2 [38] |
| Ru1212Eu | ≈ 1 | c | < 0.3 | 0.08 |

Table 2. Summary of the ZFNMR data

| compound | ordered spins μ_B/Ru | Orientation* | signal enhancement |
|----------|---|--------------|--------------------|
| Ru1212Y | Ru^{4+} and Ru^{5+} | in-plane | 200 |
| Ru1212Gd | 0.9 (Ru^{4+} , 40%) and 2 (Ru^{5+} , 60%) | in-plane | 100 |

*Based on the interference between the hyperfine field and the electric field gradient at the Ru site.

It is interesting to note that the magnetic structure sensed by the ZFNMR is qualitatively different from those by the NPD data. Even the spin orientations differ by 90° . This is the very reason that Tokunaga et al. call for a re-examination of the NPD data [31]. However, the conclusion of the c-oriented spin alignment is repeatedly confirmed in two later independent NPD experiments, including one on the same Ru1212Y ceramic as that examined by ZFNMR [39, 40]. This contradiction, it should be pointed out, cannot be accommodated even in canted antiferromagnetic models, and it directly challenges the widely held belief that the magnetic structure of Ru1212/Ru1222 is microscopically homogeneous.

Similar controversies also exist for the observed remnant magnetization, which consistently shows a spontaneous moment of Ru1212Gd larger than that sensed in NPD (Table 1); for the magnetic susceptibility, which leads to a positive Curie-Weiss temperature [35]; and with the FMR data, which suggest an internal field ≈ 600 G (a dipole field far larger than that expected if the sample is a homogeneous canted antiferromagnet) at the Gd site [37].

It is interesting to note that such discrepancies have previously been reported in manganites. An early neutron diffraction investigation found that the magnetic structure of $\text{La}_{0.35}\text{Ca}_{0.65}\text{MnO}_3$ can be described as homogeneously antiferromagnetic [44], although a later ZFNMR/NMR investigation discovered that up to 8% of the compound is actually ferromagnetically aligned [45]. The conflict is interpreted as the result of the “biased” sensitivities of the probes. The lines in the diffraction data, in principle, will be suppressed or even disappear if the size of the coherent scattering domains is comparable to the wavelength used, \approx a few Å in most neutron diffraction measurements. Mesoscopic phase separation with the possible ferromagnetic species a few nm thick, therefore, may well escape the detection as demonstrated in the case of $\text{La}_{0.35}\text{Ca}_{0.65}\text{MnO}_3$. The amplitude of the ZFNMR signals, on the other hand, is essentially the transition probability of the nuclear spins under the rf excitation field, which will be either enhanced (proportional to the magnetic anisotropy in the case of ferromagnets) or suppressed (by a factor proportional to the exchange field in

antiferromagnets) by the ordered local electron spins. A moderate enhancement factor ≈ 10 in $\text{La}_{0.35}\text{Ca}_{0.65}\text{MnO}_3$ already makes the resonance corresponding to the minor ferromagnetic phase the dominant one. In the case of Ru1212, the larger enhancement factor may explain the absence of the expected lines corresponding to the c-oriented antiferromagnetically aligned spins observed in the neutron diffraction.

Many investigations, however, placed an emphasis on evidence for homogeneous magnetic structures and argued against possible mesoscopic phase separation. One of the strongest pieces of evidence is the reported $1/(T T_1)$ suppression of the ^{101}Ru ZFNMR signal below T_c , which is similar to that of ^{63}Cu [31]. Such suppression of the relaxation indeed demonstrates that the carriers in the RuO layers, whose coupling with ^{101}Ru dominates the relaxation, experience the superconducting transition. As demonstrated both experimentally and theoretically, however, a mesoscopic phase separation may also be able to satisfy such a constraint if the size of the nonsuperconducting species is comparable to the coherence length [46, 47]. It is interesting to note that another ^{101}Ru $1/TT_1$ peak was observed around 20 K, where the resistance R reaches zero. This has been interpreted by the authors as a presumed transition between the spontaneous vortex phase and the Meissner state [31]. In our opinion, however, this $R = 0$ temperature is nothing but a phase-locking transition of the ceramic samples as demonstrated by many groups [24, 36, 48]. The assumed SVP - Meissner transition should actually not happen in ceramic Ru1212/Ru1222 samples, where the condition of $\lambda \gg d$ makes the lower critical field H_{c1} determined by the T-independent grain diameter d instead of the T-dependent penetration depth λ [49, 50]. Instead, plasma oscillations may occur along weak links during the phase-locking transition [33], which stimulates the rf ZFNMR relaxation. The large amplitude of this 20 K $1/TT_1$ peak in such a case suggests that a significant part of the ^{101}Ru sensed by ZFNMR is actually in proximity of the weak links, an indication that the ZFNMR signal may come disproportionately from a small part of the sample.

The data on various Ru1222 compounds, fortunately, offer a clue to the puzzle: as pointed out by Felner et al., the magnetic transition in various single-phase Ru1222R samples is multi-stage in nature [17, 48]. The main jump in the field-cooled magnetization, for example, appears around $T_{M1} \approx 90$ K in a Ru1222Gd sample. Noticeable FM-like steps, however, appear up to $T_M \approx 160$ K under $H < 100$ Oe and merge into the main jump at higher fields (Fig. 21) [34]. The hyperfine field at the Ru site, probed by ^{57}Fe Mössbauer spectroscopy, further suggests that the spin order actually begins above 160 K, almost twice the T_{M1} [17]. This multistage transition has been interpreted either as the flips of the canting angle in the homogeneous magnetic models or as a multistage precipitation of the ferromagnetic clusters in the phase-separation models [34, 51].

Experimental verifications, therefore, are needed. Felner et al. observed that the $M(H)$ of Ru1222 becomes reversible but highly nonlinear, i.e. with a non-zero extrapolated interception between T_{M1} and a higher temperature $\approx T_M$. Below T_{M1} , the magnetization further becomes irreversible, and therefore FM-like [48]. By interpreting the nonlinear $M(H)$ as a field-induced spin cant in antiferromagnets, they suggested that the magnetic state between T_{M1} and T_M is antiferromagnetic but evolves into a canted state below T_{M1} .

To explore the issue, we measured the isothermal $M(H)$ at various temperatures and found that the H dependence of the magnetization can be fitted to the well known Langevin function $\coth(\mu H/k_B T) - k_B T/\mu H$ of superparamagnetic particles with an additional linear term

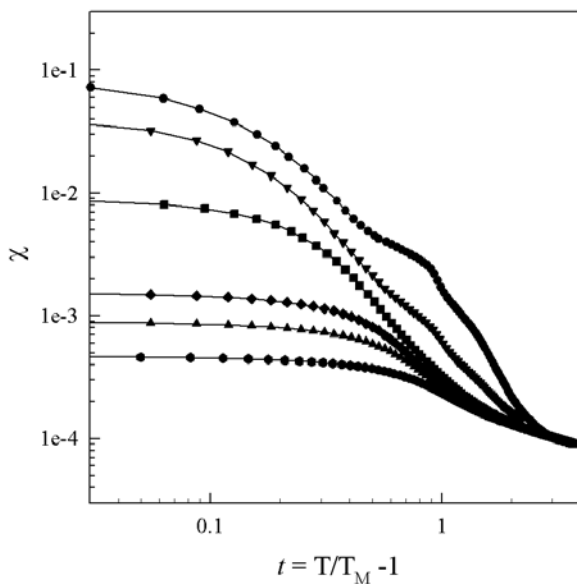


Fig. 21. The field-cooled M/H of a Ru1222Eu sample under fields (from top to bottom: 0.005, 0.01, 0.1, 1, 2, and 5 T). The multistage transition is clear below 0.01 T, but merges into a broad one at higher fields.

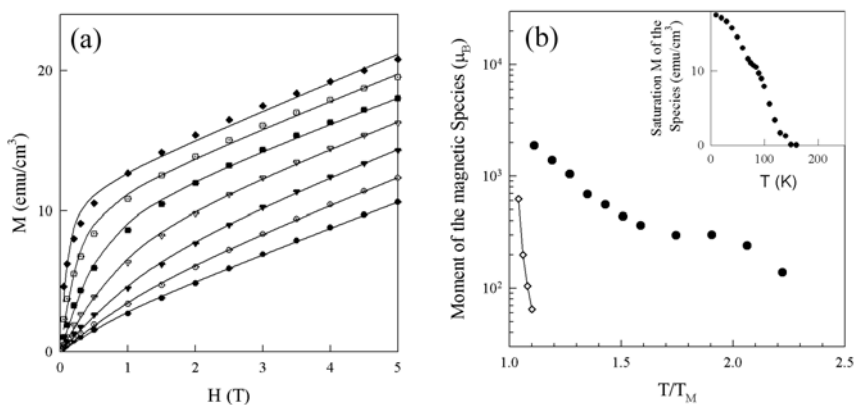


Fig. 22. (a) M vs. H for Ru1222Eu at 70, 80, 90, 100, 110, 120, and 130 K from top to bottom. Symbols: data. Solid line: fit to the Langevin function with a linear term (see text).

(b) The estimated cluster size in the Ru1222Eu sample (\bullet) and in Ni (\diamond). Inset: The saturation moment m of the proposed magnetic species in Ru1222Eu.

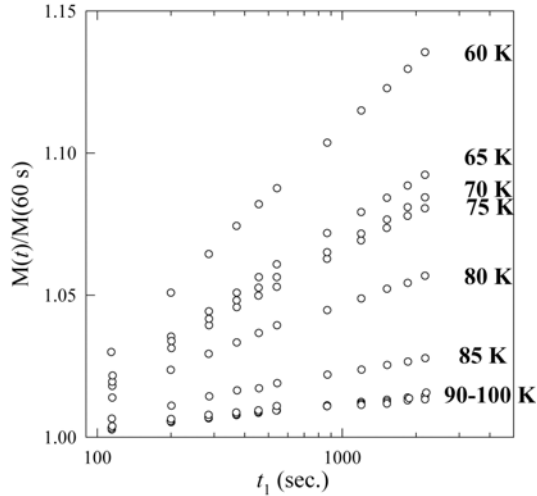


Fig. 23. The relaxation of the Ru1212Eu sample after a sudden field increase from $H = 0$ to 5 Oe

associated with the contributions from ions other than Ru (Fig. 22a), where μ is the full moment of the clusters [34]. The μ so deduced suggests that the cluster size is already noticeably large near T_M , continuously increases with further cooling, and becomes nondetectably large around T_{M1} (Fig. 22b), precisely what the phase-separation model expected.

It should be noted that such a highly nonlinear $M(H)$ is a common property of Ru1212/Ru1222. Several previous investigations, however, interpret it as either a short-range correlation or due to a peculiar magnetic anisotropy that is small in-plane but very large in the c -direction [35]. To verify the superparamagnetic cluster nature, the relaxation of the magnetizations was also measured [34]. The balance between the thermal energy and the barrier associated with the magnetic anisotropy would determine the relaxation rate, and noticeable relaxation should be observed only in a narrow time window of $(10-15) \cdot k_B T / H \mu$, i.e. only for clusters with $10-10^4 \mu_B$ with the typical time window of 10–1000 sec. Indeed, the relaxation can be clearly seen even below T_{M1} , demonstrating that the ferromagnetically aligned Ru spins are in clusters smaller than $10^4 \mu_B$, i.e. 1000 nm^3 using the aligned spin amplitude of $1-2 \mu_B/\text{Ru}$ (Fig. 23). This may explain why neutron diffraction persistently underestimates the ferromagnetic component in Ru1212/Ru1222. The observation is also in rough agreement with the spin-glass behavior, which is essentially interacting ferromagnetic clusters, of Ru1222Gd as reported by Cardoso *et al.* [52], where similar relaxation and a systematic frequency dependency of the ac susceptibility is observed.

There are also some indications about the antiferromagnetic ordering in Ru1212/Ru1222. As pointed out by Butera *et al.*, the high field susceptibility of Ru1212Eu shows an antiferromagnet-like maximum at a temperature slightly above the temperature where a ferromagnet-like transition appears in the field-cooled magnetization [35].

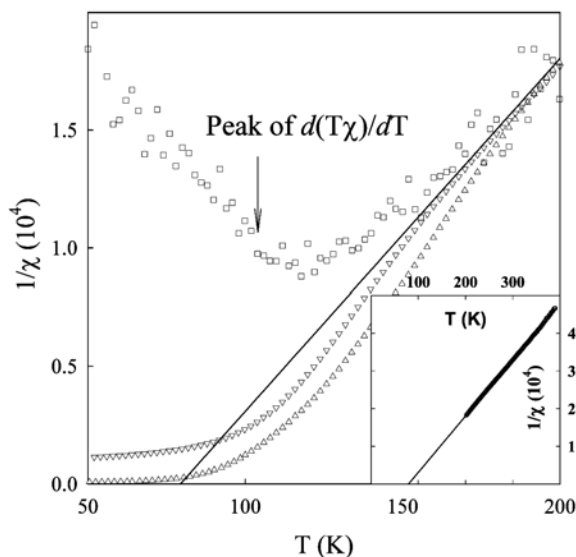


Fig. 24. The T dependence of the Ru contribution to the $1/\chi = H/M_{FC}$. Δ : at 1 T; ∇ : at 5 T; \square : the differential susceptibility at 5 T. Solid line: the Curie-Weiss fit. Inset: $1/\chi$ between 200 and 400 K. \bullet : data. Solid line: the C-W fit.

To further verify the situation, we studied Ru1222Eu. A similar trend appears: an antiferromagnet-like minimum of the inverse susceptibility appears around 100–150 K even in raw data. However, the ferromagnet-like jump in the field-cooled magnetization is at a much lower temperature of 65 K [34]. The two transitions seem to be separated by more than 50 K. The contributions from Eu are further calculated and subtracted from the magnetization measured (Fig. 24). The high temperature susceptibility $1/\chi$ deviated from the C-W fit significantly below 180 K and the deviation increases with the field. Such deviation typically suggests the appearance of either spin clusters or short-range magnetic correlations, as demonstrated above based on the nonlinear $M(H)$ and the relaxation. The trend, however, evolved with further cooling. A minimum of the inverse differential susceptibility clearly appears around 120 K, indicating AFM transitions (Fig. 24). To identify the AFM transition, we follow Fisher's argument that the magnetic specific heat is proportional to $\partial(T\chi)/\partial T$ on rather general grounds [53]. A broad peak does appear in the $\partial(T\chi)/\partial T$ at 5 T, but with the corresponding Néel temperature at 104 K in the sample, i.e. the antiferromagnetic transition appears 40 K above the ferromagnetic transition in the same sample (Fig. 24).

Very recently, a zero-field μ SR measurement of Ru1222Gd showed that there are several different muon stop sites corresponding to different possible magnetic transitions. Although the raw data show anomalies at 200, 95, and 77 K, the authors suggest that the 95 K and 77 K anomalies may actually be the same transition due to the limited resolution [38]. Between 77 and 200 K, the magnetically ordered species occur only in 20% of the volume. This is strong

evidence that phase separation does occur in Ru1222, and in good agreement with the above analysis of Ru1222Eu [34]. In particular, the deduced volume fraction, $\approx 15\%$, of the magnetic clusters is in a good agreement with our estimated fraction, $\approx 20\%$, of the ferromagnetic clusters. The Néel temperature, ≈ 104 K, estimated above may correspond to the 95 K anomaly observed.

However, the situation in Ru1212 remains in debate. In addition to the above ZFNMR and NPD data, an early zero-field μ SR investigation [41], in which the data can be well fit as in a homogeneous ferromagnet, was frequently used as evidence for a homogeneous magnetic structure. We, however, would argue that the corresponding resolution, i.e. with the sensitivity of ≈ 10 – 20% of the sample volume and an H-resolution $\approx 20\%$ of 720 G given by the authors, may miss the possible ferromagnetic clusters with a volume fraction of 10–20%. Actually, the authors of Ref. 41 concluded that the dipole field of ferromagnetically aligned Ru spins with the assumed in-plane orientation might produce an internal field at the expected muon stop sites that may also be consistent with the internal field of 720 G observed, i.e. the internal field of the AFM species.

To address the issue, we compared Ru1212Eu and Ru1222Eu, as well as doping the Ru with Cu [54]. An obvious similarity between Ru1212Eu and Ru1222Eu is the highly nonlinear $M(H)$ far above T_{M1} . The Langevin function of superparamagnetic particles is again used to estimate the cluster size. It should be noted that later evidence suggested that the interactions between these clusters, which cause irreversible glass behaviors [52], need to be considered. These interactions, however, may affect the equilibrium magnetization less severely, and can only make the apparent cluster size larger, i.e. the deduced size can still serve as an upper size limit [55]. The size so deduced suggests that the clusters in Ru1212Eu are almost one order of magnitude smaller than that in Ru1222Eu at the same reduced temperature (Fig. 22b and the $x = 0$ sample in Fig. 25a), which may explain their differences in the macroscopic magnetizations. The essential features, however, are rather similar. The relaxation far above T_{M1} , for example, can also be observed in Ru1212Eu if a proper condition is created, i.e. to prepare an initial state deviating from the equilibrium as far as possible. In our case, clear relaxation is observed after setting $H = 0$ after a field-cooling procedure (Fig. 25b).

The absence of a multi-stage transition in undoped Ru1212 is also a puzzle. The Cu-doping, therefore, is used to adjust the competition between the antiferromagnetism and the ferromagnetism. We estimated the two magnetic transitions through the macroscopic magnetization, i.e. using the peaks in the low-field dM/dT and the high-field $d(T\chi)/dT$ for the ferromagnetic and antiferromagnetic transitions, respectively (Fig. 26a). The specific heat is also used to verify the deduced transition temperature (Fig. 26b). The data suggest that the coincidence of the two transitions in the undoped Ru1212Eu is an accident, and that the multistage feature appears with the Cu doping. It is interesting to note that the separation between the two transitions in both Ru1212 and Ru1222 actually follows the same trend with the change of the ferromagnet-like transition temperature (Fig. 26c).

The magnetization data, therefore, suggest a rather similar magnetic structure in both Ru1212 and Ru1222: spatially separated ferromagnetic nanoclusters and an antiferromagnetically coupled matrix. A bulk antiferromagnetic transition occurs in the matrix while the ferromagnetic clusters experience a global transition through the intercluster interactions. These two transitions may be independently adjusted through doping.

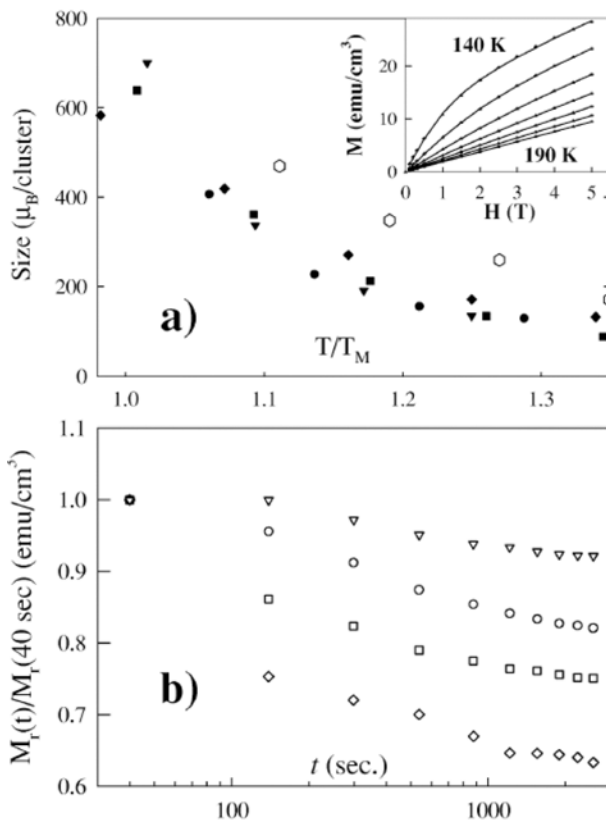


Fig. 25. (a) Cluster sizes for samples with \bullet : $x=0$; \blacktriangledown : $x=0.05$; \blacksquare : $x=0.10$; and \blacklozenge : $x=0.15$ and for \circ : as-synthesized $\text{Ru}_{1222}\text{Eu}$ ($\times 4$). Inset: The isothermal $M(H)$ of the $x=0$ sample. (b) Relaxation of the remnant magnetizations at 160, 150, 140, and 130 K (from top to bottom) after field cooling at 50 Oe.

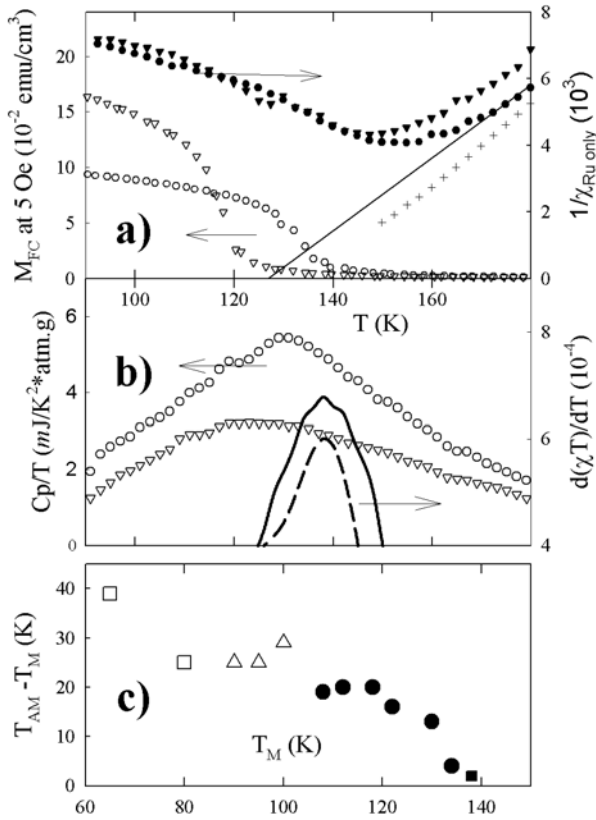


Fig. 26. (a) Magnetizations of the $(Ru_{1-x}Cu_x)Sr_2EuCu_2O_8$ samples. For $x = 0$, \circ : $M_{FC}(5 \text{ Oe})$; $+$: $H/M_{FC}(1 \text{ T})$; \bullet : $1/\chi_{Ru}$ only; solid line: C-W fit. For $x = 0.1$, ∇ : $M_{FC}(5 \text{ Oe})$; \blacktriangledown : $1/\chi_{Ru}$ only. (b) Spin entropy. \circ : the magnetic C_p/T of the $x = 0$ sample; ∇ : that of the $x = 0.1$ sample; solid line: $\partial(T\chi)/\partial T$ of the $x = 0$ sample; dashed line: that of the $x = 0.1$ sample. (c) The evolution of the separation between the two transitions, $T_{AM} - T_M$, with the FM-like transition T_M . \bullet : Cu-doped Ru1212Eu; \blacksquare : Ru1212Eu of Butera et al. (Ref. 35); \triangle : annealed Ru1222Gd; \square : as-synthesized Ru1222Eu.

5. MEISSNER STATE AND SPONTANEOUS VORTEX PHASE

The competition between superconductivity, which expulses the field to reduce the free energy of the supercurrents associated, and ferromagnetism, which leads to a spontaneous demagnetizing field of $4\pi M_0$, extends to macroscopic electrodynamics. Spontaneous vortex phase (SVP) should be formed when the spontaneous magnetization is larger than the lower critical field H_{c1} associated with the superconductivity. This is based on a rather general thermodynamic argument, and should not be affected by details such as the possible phase separation discussed above. Especially in the case of Ru1212/Ru1222, where the ferromagnetic spin order is established at the magnetic transition temperature T_M far higher than T_c , SVS seems to be inevitable slightly below T_c . Many previous investigations, therefore, attributed most unusual observations to the possible SVP in Ru1212/Ru1222. In particular, a transition between SVP and Meissner state was proposed for the sudden increase of the M_{FC} [22], the peak in the ZFNMR $1/TT_1$ of ^{101}Ru [31]. However, later data indicated that the proposed transition may simply be an intergrain phase-locking transition [24, 36, 48]. Whether SVP exists in Ru1212/Ru1222, therefore, need to be directly verified.

A procedure was developed to extract the equilibrium magnetization associated with the superconductivity. A small piece of Pb was added in the SQUID probe 5 cm below the Ru1212Eu sample to measure the local field in situ. The residual field of the SQUID magnetometer was deduced to a few mG before every zero-field measurement. The interference between the Pb piece and the sample are negligible within the 4-cm scanning length used. The estimated H uncertainty is $\approx 0.001H + 1$ mG. A Ru1212Eu was then crushed into single-grain powder with the average particle size ≈ 5 μm to avoid the complications associated with intergrain coupling. The intragrain T_c appears at 23.5 K. The sample was first cooled from 150 K $> T_{FM}$ to 32 K $> T_c$ under a chosen field H_1 , which determines the FM-domain alignment. The external field was then switched to $H_0 \approx 0$ at 32 K $\gg T_c$, followed by a dc-magnetization (M_1) measurement from 40 K to 8 K. The field was then increased to H_2 at 6 K. The zero-field-cooled magnetization (M_{ZFC}) and the field-cooled one (M_{FC}) were consequentially measured in a thermal cycle of 8 to 40 K (ZFC branch) and 40 to 8 K (FC branch). A typical data set in a powder sample of Ru1212Eu with $H_1/H_0/H_2$ being 0.5/-0.025/0.614 Oe, respectively, is show in the inset of Fig. 27. It is interesting to note that the M_1 differs from both the M_{ZFC} and the M_{FC} only by a constant offset C above T_c . This suggests that $M_1 + C$ may serve as a good estimation of the FM background below T_c . The SC contributions ($\Delta\chi$), therefore, are taken as $(M_{ZFC} - M_1 - C)/(H_2 - H_0)$ and $(M_{FC} - M_1 - C)/(H_2 - H_0)$ for the ZFC and FC branches, respectively. These two $\Delta\chi$'s, however, are almost the same (inset, Fig. 26). This leads us to believe that the data obtained, in the FC branch for example, are actually the *equilibrium* superconductivity properties under the external field H_2 and the corresponding demagnetizing field $4\pi M_1$.

Features resembling the lower critical fields can be seen clearly in Fig. 27 around 8 Oe. Below 8 Oe, the $\Delta\chi$ is H-independent within an experimental resolution of a few percent, suggesting that the major part of the sample is in a Meissner state. The apparent vortex-entry field, however, seems to be temperature-independent up to 22 K $\approx 0.9T_c$. The intragrain penetration depth λ of the same sample, on the other hand, has been measured and shows a more-than-three-fold increase, i.e. from 2 μm at 5 K to 6 μm at 20 K, over a narrower temperature range [50]. To explore the issue, the Ru1212Eu powder was classified according

to the particle size, and the $\Delta\chi$'s of three sets with the average particle sizes of 3.5, 2.1, and 1.5 μm , respectively, were measured (Fig. 28). Our data demonstrate that the apparent H_{c1} changes significantly with the particle size, i.e. from 8 to 50 Oe.

Such d -dependent-only H_{c1} has been previously observed in mesoscopic superconducting samples [49]. The vortex entering in Type-II superconductors is essentially the result of a free-energy competition between the magnetostatic part and the vortex-associated supercurrent part. When the energy cost of creating a vortex is only weakly dependent on the sample size d if $d \gg \xi$, the magnetostatic-energy gain varies as $(d/\lambda)^2$ when $d \leq \lambda$, where ξ is the coherence length [49]. In the case of Ru1212/Ru1222, the unusually large λ and the ceramic samples used, therefore, make the case for resembling the scenario of mesoscopic superconductors. A direct result of the observation is that the proposed SVP-to-Meissner state transition cannot occur, and the unusual properties previously associated with it have to be reconsidered.

The status of the Ru1212/Ru1222 ceramic samples below T_c , therefore, appears to be rather exotic even without an external field, and different from both traditional Meissner state and the SVP. With the average demagnetizing field ranging from 0–30 Oe, the sample may actually be a mixture, with some large grains in the SVP state but the smaller ones in the Meissner state. Such a mixture, although independent of the temperature directly, may make the apparent magnetic properties somewhat between those predicated for the SVP and those of the traditional Meissner state.

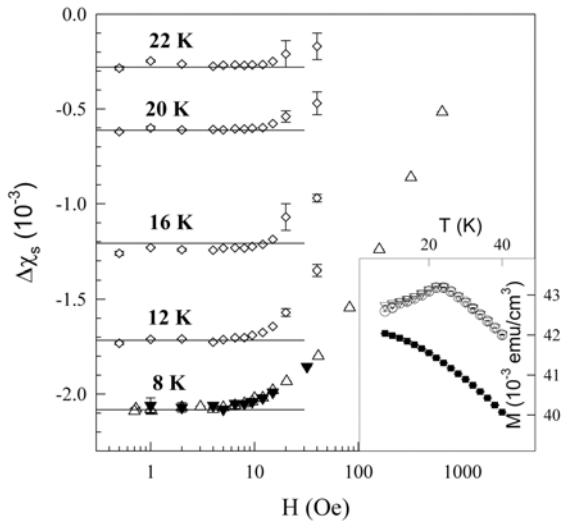


Fig. 27. The dc $\Delta\chi$ at the FC branch. The horizontal lines represent the ac susceptibility with the excitation field of 0.1 Oe. Open symbols: with $H_{dm} = 0$; Filled triangles: with $H_{dm} = 10$ G at 8 K. The statistic uncertainties are smaller than the symbol size when there is no error bar attached. Inset: The M_I (■), M_{ZFC} (○) and M_{FC} (▽) with $H_1/H_0/H_2$ being 0.5/-0.025/0.614 Oe, respectively.

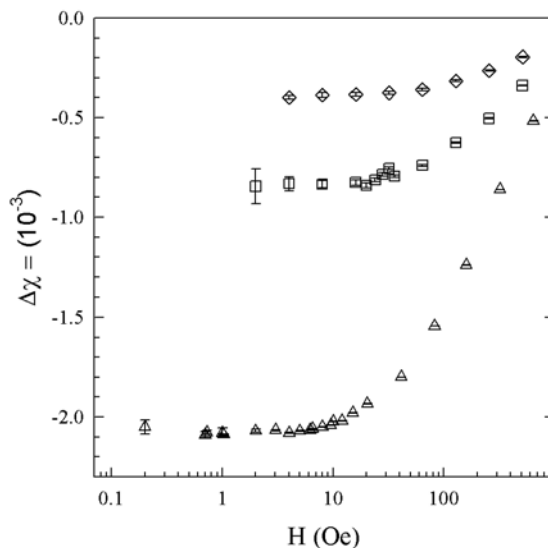


Fig. 28. The dc $\Delta\chi$ in the FC branch at 8 K for powders with average particle size $d = 3.5$ (Δ), 2.1 (∇) and 1.5 (\diamond) μm .

6. CONCLUSIONS

The synthesis conditions as well as the magnetic and superconducting properties of superconducting ferromagnets, Ru1212 and Ru1222, have been extensively investigated. The superconducting properties depend very sensitively on the synthesis conditions, especially the 1050 °C long-time heat treatment. We show that the superconducting transition temperatures of $\text{RuSr}_2\text{GdCu}_2\text{O}_8$ can be changed by varying the synthesis conditions, although the carrier density is barely affected. The intragrain superconducting transition and the intergrain phase-lock temperatures are clearly distinguished in resistivity experiments and in ac-susceptibility measurements of sorted powders of different average particle size.

Several magnetic phase transitions starting as high as 180 K have been observed in Ru1222. We show that the major magnetic order in both compounds, Ru1212 and Ru1222, is antiferromagnetic in nature with a small ferromagnetic (FM) component detectable at lower temperature in Ru1222 but at the AFM temperature in Ru1212. We argue that the latter coincidence of the AFM transition and the FM moment in Ru1212 is accidental and that the experimentally observed small FM moment is due to the formation of nanometer-sized FM clusters. The superconducting state develops in microscopic AFM domains existing within the single grain. The observed onset of superconductivity at a critical temperature T_1 with an extremely small Meissner signal can then be understood as a phase-lock transition between superconducting domains of nanometer size. This can also explain the unusually large magnetic penetration depth observed in recent experiments.

The superconducting state was investigated for sorted powders of $\text{RuSr}_2\text{EuCu}_2\text{O}_8$ and it is concluded that mesoscopic superconductivity, spontaneous vortex phase, and Meissner state have to be considered in a ceramic sample with varying grain size to understand the exotic properties of superconducting ferromagnets.

ACKNOWLEDGMENTS

The work in Houston is supported in part by NSF Grant No. DMR-9804325, the T. L. L. Temple Foundation, the John J. and Rebecca Moores Endowment, and the State of Texas through the Texas Center for Superconductivity and Advanced Materials at the University of Houston; and at Lawrence Berkeley Laboratory by the Director, Office of Science, Office of Basic Energy Sciences, Division of Materials Sciences and Engineering of the U.S. Department of Energy under Contract No. DE-AC03-76SF00098.

REFERENCES

- [1] V. L. Ginzburg, *Zh. exsp. teor. Fiz.* 31 (1956) 202.
- [2] B. T. Matthias, H. Suhl, and E. Corenzwit, *Phys. Rev. Lett.* 1 (1958) 92.
- [3] A. A. Abrikosov and L. P. Gor'kov, *Zh. exsp. teor. Fiz.* 39 (1960) 1781.
- [4] P. W. Anderson and H. Suhl, *Phys. Rev.* 116 (1959) 898.
- [5] B. T. Matthias, E. Corenzwit, J. M. Vandenberg, and H. E. Barz, *Proc. Nat. Acad. Sci. USA* 74 (1977) 1334.
- [6] O. Fischer, A. Treyvaud, R. Chevrel, and M. Sergent, *Solid State Commun.* 17 (1975) 721.
- [7] E. I. Blount and C. M. Varma, *Phys. Rev. Lett.* 42 (1979) 1079.
- [8] R. A. Ferrell, J. K. Bhattacharjee, and A. Bagchi, *Phys. Rev. Lett.* 43 (1979) 154.
- [9] H. Matsumoto, H. Umezava, and M. Tachiki, *Solid State Commun.* 31 (1979) 157.
- [10] L. N. Bulaevskii, A. I. Rusinov, and M. L. Kulin, *Solid State Commun.* 30 (1979) 59.
- [11] P. Fulde and R. A. Ferrel, *Phys. Rev. A* 135 (1964) 550.
- [12] C. G. Kuper, M. Revzen, and A. Ron, *Phys. Rev. Lett.* 44 (1980) 1545.
- [13] D. E. Moncton, D. B. McWhan, P. H. Schmidt, G. Shirane, W. Thomlinson, M. B. Maple, H. B. MacKay, L. D. Woolf, Z. Fisk, and D. C. Johnston, *Phys. Rev. Lett.* 45 (1980) 2060.
- [14] S. K. Sinha, G. W. Crabtree, and D. G. Hinks, *Phys. Rev. Lett.* 48 (1982) 950.
- [15] J. W. Lynn, J. A. Gotaas, R. W. Erwin, R. A. Ferrell, J. K. Bhattacharjee, R. N. Shelton, and P. Klavins, *Phys. Rev. Lett.* 52 (1984) 133.
- [16] L. Bauernfeind, W. Widder, and H. F. Braun, *Physica C* 254 (1995) 151.
- [17] I. Felner, U. Asaf, Y. Levi, and O. Millo, *Phys. Rev. B* 55 (1997) R3374.
- [18] C. W. Chu, Y. Y. Xue, Y. S. Wang, A. K. Heilman, B. Lorenz, R. L. Meng, J. Cmaidalka, and L. M. Dezaneti, *J. Supercond.* 13 (2000) 679.
- [19] K. Otschi, T. Mizukami, T. Hinouchi, J. Shimoyama, and K. Kishio, *J. Low Temp. Phys.* 117 (1999) 855.
- [20] R. L. Meng, B. Lorenz, Y. S. Wang, J. Cmaidalka, Y. Y. Xue, and C. W. Chu, *Physica C* 353 (2001) 195.
- [21] B. Lorenz, R. L. Meng, J. Cmaidalka, Y. S. Wang, J. Lenzi, Y. Y. Xue, and C. W. Chu, *Physica C* 363 (2001) 251.
- [22] C. Bernhard, J. L. Tallon, E. Brücher, and R. K. Kremer, *Phys. Rev. B* 61 (2000) R14960.
- [23] J. L. Tallon, J. W. Loram, G. V. M. Williams, and C. Bernhard, *Phys. Rev. B* 61 (2000) R6471.
- [24] B. Lorenz, Y. Y. Xue, R. L. Meng, and C. W. Chu, *Phys. Rev. B* 65 (2002) 174503.
- [25] A. Fainstein, P. Etchegoin, H. J. Trodahl, and J. L. Tallon, *Phys. Rev. B* 61 (2000) 15468.
- [26] X. H. Chen, Z. Sun, K. Q. Wang, S. Y. Li, Y. M. Xiong, M. Yu, and L. Z. Cao, *Phys. Rev. B* 63 (2001) 064506.
- [27] A. B. Maclsaac, J. P. Whitehead, K. De'Bell, and K. Sowmya Narayanan, *Phys. Rev. B* 46 (1992) 6387.
- [28] W. E. Pickett, R. Weht, and A. B. Shick, *Phys. Rev. Lett.* 83 (1999) 3713.
- [29] J. X. Zhu, C. S. Ting, and C. W. Chu, *Phys. Rev. B* 62 (2000) 11369.

- [30] C. Bernhard, Ch. Niedermayer, U. Binniger, A. Hofer, Ch. Wenger, J. L. Tallon, G. V. M. Williams, E. J. Ansaldo, J. I. Budnick, C. E. Stronach, D. R. Noakes, and M. A. Blankson-Mills, *Phys. Rev. B* 52 (1995) 10488.
- [31] Y. Tokunaga, H. Kotegawa, K. Ishida, Y. Kitaoka, H. Takagiwa, and J. Akimitsu, *Phys. Rev. Lett.* 86 (2001) 5767.
- [32] J. W. Lynn, B. Keimer, C. Ulrich, C. Bernhard, and J. L. Tallon, *Phys. Rev. B* 61 (2000) 14964.
- [33] H. Shibata, *Phys. Rev. B* 65 (2002) 180507.
- [34] Y. Y. Xue, B. Lorenz, D. H. Cao, and C. W. Chu *Phys. Rev. B* 67 (2003) 184507.
- [35] A. Butera, A. Fainstein, and E. Winkler, *Phys. Rev. B* 63 (2001) 54442.
- [36] Zivkovic, D. Drobac, D. Ariosa, H. Berger, D. Pavuna, and M. Prester, *Europhys. Lett.* 60 (2002) 917.
- [37] A. Fainstein, E. Winkler, and A. Butera, *Phys. Rev. B* 60 (1999) 12597.
- [38] A. Shengelaya, R. Khasanov, D. G. Eshchenko, I. Felner, U. Asaf, I. M. Savi, H. Keller, and K. A. Müller, *Phys. Rev. B* 69 (2004) 24517.
- [39] H. Takagiwa, J. Akimitsu, H. Kawano-Furukawa, and H. Yoshizawa, *J. Phys. Soc. Jpn.* 70 (2001) 333.
- [40] J. D. Jorgensen, O. Chmaissem, H. Shaked, S. Short, P. W. Klamut, B. Dabrowski, and J. L. Tallon, *Phys. Rev. B* 63 (2001) 54440.
- [41] C. Bernhard, J. L. Tallon, Ch. Niedermayer, Th. Blasius, A. Golnik, E. Brücher, R. K. Kremer, D. R. Noakes, C. E. Stronach, and E. J. Ansaldo, *Phys. Rev. B* 59 (1999) 14099.
- [42] K. I. Kumagai, S. Takada, and Y. Furukawa, *Phys. Rev. B* 63 (2001) 180509.
- [43] R. S. Liu, L. Y. Jang, H. H. Hung, and J. L. Tallon, *Phys. Rev. B* 63 (2001) 212507.
- [44] M. R. Ibarra, J. M. De Teresa, J. Blasco, P. A. Algarabel, C. Marquina, J. García, J. Stankiewicz, and C. Ritter, *Phys. Rev. B* 56 (1997) 8252.
- [45] Cz. Kapusta, P. C. Riedi, M. Sikora, and M. R. Ibarra, *Phys. Rev. Lett.* 84 (2000) 4216.
- [46] For example, V. T. Petrashov, I. A. Sosnin, I. Cox, A. Parsons, and C. Troadec, *Phys. Rev. Lett.* 83 (1999) 3281.
- [47] Z. Sefrioui, D. Arias, V. Peña, J. E. Villegas, M. Varela, P. Prieto, C. León, J. L. Martinez, and J. Santamaria, *Phys. Rev. B* 67 (2003) 214511.
- [48] I. Felner, E. Galstyan, B. Lorenz, D. Cao, Y. S. Wang, Y. Y. Xue, and C. W. Chu, *Phys. Rev. B* 67 (2003) 134506.
- [49] A. K. Geim, I. V. Grigorieva, S. V. Dubonos, J. G. S. Lok, J. C. Maan, A. E. Filippov, and F. M. Peeters, *Nature* 390 (1997) 259.
- [50] Y. Y. Xue, B. Lorenz, A. Baikalov, J. Cmaidalka, F. Chen, R. L. Meng, and C. W. Chu, *Physica C* 408-410 (2004) 638.
- [51] I. Felner, U. Asaf, and E. Galstyan, *Phys. Rev. B* 66 (2002) 24503.
- [52] C. A. Cardoso, F. M. Araujo-Moreira, V. P. S. Awana, E. Takayama-Muromachi, O. F. de Lima, H. Yamauchi, and M. Karppinen, *Phys. Rev. B* 67 (2003) 20407.
- [53] M. E. Fisher, *Philos. Mag.* 7 (1962) 1731.
- [54] Y. Y. Xue, F. Chen, J. Cmaidalka, R. L. Meng, and C. W. Chu, *Phys. Rev. B* 67 (2003) 224511.
- [55] For example, P. Allia, M. Coisson, M. Knobel, P. Tiberto, and F. Vinai, *Phys. Rev. B* 60 (1999) 12207.

A PHASE DIAGRAM APPROACH TO MAGNETIC SUPERCONDUCTOR

Hans F. Braun

Physikalisches Institut, Universität Bayreuth, Bayreuth, Germany

1. INTRODUCTION

The interplay of magnetism and superconductivity has been a fascinating field of study for more than forty years. Starting with dilute alloys of magnetic impurities in a superconducting matrix [1], the focus of research moved to ternary compounds in the seventies. In these compounds, a lanthanide (Ln) occupies a crystallographically ordered sublattice like in the rhodium boride $LnRh_4B_4$ and the molybdenum chalcogenides $LnMo_6S_8$ (Chevrel phases). At low temperatures, the localized moments of the lanthanides Ln with partially filled f -shell show long-range magnetic ordering of antiferromagnetic (AF) or ferromagnetic (FM) type. For a review, see *e.g.* [2–4].

In most compounds, the AF ordering of the Ln moments occurs in the superconducting state and leads to coexistence on a microscopic scale of both ordering phenomena. The notable effect on superconductivity is a depression of the upper critical field near the AF ordering temperature [3]. In $ErRh_4B_4$ [5] and $HoMo_6S_8$ [6] superconductivity, which appears at an upper transition temperature T_{c1} , is destroyed by FM ordering of the Ln moments at a lower transition temperature T_{c2} which roughly coincides with the Curie temperature; this phenomenon was named “re-entrant superconductivity”. In these compounds, the interplay of superconductivity and ferromagnetism leads to the appearance of a modulated magnetic structure with a wavelength of the order of 10 nm that coexists with superconductivity in a narrow temperature range around the re-entrant T_{c2} [4]. In the third known ordered re-entrant superconductor, $Tm_2Fe_3Si_5$, pressure-induced super-

conductivity is suppressed at lower temperatures at the onset of AF ordering of the Tm moments [7, 8].

The discovery of the quaternary borocarbides $LnNi_2B_2C$ [9, 10] renewed the interest in the interplay of magnetism and superconductivity. These compounds, showing a rich variety of magnetic behavior, provide a new approach, since depending on Ln , the AF ordering temperature may be above or below the superconducting T_c . Due to the early discovery of a suitable flux (Ni_2B), single crystals became available (see, *e.g.* [11]). Early conflicting reports on the appearance of a re-entrant transition in $HoNi_2B_2C$ could be resolved through phase diagram studies. The physical properties of these phases depend on pressure [12], chemical composition within the homogeneity range of single phase material [13, 14], and on annealing temperature [15] due to B/C ordering [16, 17].

The layered ruthenocuprates $RuSr_2GdCu_2O_8$ (Ru-1212) [18, 19] and $RuSr_2(Gd_{1-x}Ce_x)_2Cu_2O_{10}$ (Ru-1222) [18, 20], discovered in 1995, appear to provide the first example of superconductivity developing at temperatures far below the transition into a weakly ferromagnetic state, with coexistence of both ordering phenomena [21–24]. The weak ferromagnetism (WFM) is associated with the ordered antiferromagnetic state of the Ru moments which appears at about 138 K in Ru-1212, while the Gd moments order antiferromagnetically below 3 K [25–27]. The potential of T -1212-type compounds for high- T_c superconductivity was pointed out by Mattheis [28]. A thorough analysis of the factors which would permit the coexistence of superconductivity and ferromagnetism in $RuSr_2GdCu_2O_8$ has been given by Pickett *et al.* [29].

Coexistence of *nuclear* ferromagnetism (below 35 μ K) with superconductivity (below 207 mK) has been reported for $AuIn_2$ [30]. More recently, superconductivity has been discovered on the border of itinerant electron ferromagnetism in UGe_2 [31] and coexistence of superconductivity and ferromagnetism was found in the d -band metal $ZrZn_2$ [32].

While superconductivity was readily observed in Ru-1222, Ru-1212 has been a more problematic case, with strong effects of the details of sample preparation on its superconducting properties and reports on the absence of superconductivity. We are convinced that answers to the apparent contradictions must be sought in the nature of the phase diagram of these systems consisting of five (Ru-1212) or six (Ru-1222) elemental constituents. In this review, we present a brief overview of the properties of the ruthenocuprates and then concentrate on Ru-1212, examining the common sample preparation methods in the light of our knowledge of the quinary system Sr–Gd–Ru–Cu–O.

The naming scheme of the chemical formulae and their shorthand notation used throughout this paper follows that introduced with the discovery of bismuth-, thallium-, or mercury-containing cuprates. It has the advantage to reflect the different crystal-chemical nature of the cationic sites in the CuO_2 conducting layers and the interspersed “charge reservoirs”, see *e.g.* [33–35]. However, we keep the popular notation Y-123 for $YBa_2Cu_3O_7$ which should be replaced by $CuBa_2YCu_2O_7$ (Cu-1212) in the above scheme.

2. PHASE DIAGRAMS AND PHASE PROPERTIES

In the materials approach to superconductivity in multinary compounds, the study of phase diagrams is relevant for two main reasons. The first is fundamental in nature: If we

are to understand why a phase forms and has certain properties, we might learn from the way homologs with different elemental substitutions or neighboring phases with different crystallographic structure and chemical composition differ or show similarities.

The second reason is more circumstantial: As long as a multinary compound can be obtained reproducibly by following a defined procedure, we may choose to ignore the metallurgy of this phase and the existence of other phases in this system. However, if “sample dependence” of some properties is found we ought to examine these questions. In particular, if a phase is metastable, or if “impurity” phases are suspected to obscure the determination of physical properties, an inspection of the phase diagram is called for.

2.1. MULTINARY SYSTEMS

Consider a sample prepared from a number of elemental constituents and assume that it has reached thermal equilibrium. The state of such a sample is described by appropriate variables such as pressure, temperature, and chemical composition. Of these variables depend the phases present in the sample and their physical properties, such as unit cell volume, electronic and phononic properties, the occurrence of superconducting or magnetic ordering transitions and the corresponding ordering temperatures. Sample characterization is essential: Unexpected or unexplained properties may reflect that not all state variables are known with sufficient precision.

Usually, we will be interested in the properties of a given phase. If the phase under consideration has a homogeneity range, its properties may vary as a function of chemical composition. The interpretation of such composition dependent properties, straightforward in binary systems, requires some care in multinary systems.

In a ternary system (with constituents A, B, and C), for example, the values of properties associated with a phase are invariant everywhere in three-phase regions and along tie-lines in two-phase regions, but they may vary as a function of composition inside the homogeneity range (except along iso-parametric contours which are thus defined) and, impossible in binary systems in equilibrium, in two-phase regions if tie-lines are crossed.

This is illustrated in Fig. 1 for two properties, say unit cell volume V and superconducting critical temperature T_c . If nominal composition is changed along the section 1–2, both properties will vary in the two-phase region $\alpha + \kappa$, within the single-phase homogeneity range α and in the two-phase region $\alpha + \gamma$, but no variation will be observed in

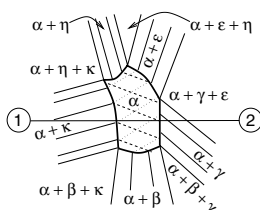


Fig. 1. Portion of an isothermal section of a ternary system showing a single-phase domain and five adjacent two- and three-phase regions. Tie-lines are indicated in two-phase regions, iso-parametric contours for two properties in the single-phase domain.

the three-phase region $\alpha + \gamma + \epsilon$. Assume that along the section 1–2 only the concentration of component A is changed, then in this example the properties will vary in region $\alpha + \gamma$ despite the fact that the concentration of A in phase α does not change. The variation of a property of the majority phase with the nominal concentration of one constituent in such a multiphase sample does not necessarily mean that the concentration of this constituent in the phase under consideration is changing.

2.2. SUPERCONDUCTING AND MAGNETIC PROPERTIES

The claim of superconductivity for a given compound should ideally be based on measurements that are sensitive to the volume of material showing superconductivity, such as the Meissner effect or specific heat. Both have their drawbacks. The Meissner effect, flux expulsion from the superconducting volume as the sample is cooled below T_c in a weak magnetic field (below the lower critical field H_{c1} of the material examined) may be suppressed in a material with strong pinning or if the size of the superconducting particles is comparable to or smaller than the magnetic penetration depth. In the presence of magnetization, the Meissner effect may be absent in a “superconducting magnet” in favor of a spontaneous vortex phase (SVP) [36]. Thus, failure to observe the Meissner effect is no unambiguous proof of non-superconductivity of the sample under consideration. The specific-heat jump at T_c may be difficult to observe in a sample with a spread of transition temperatures or if magnetic contributions to the heat capacity are present. Interpretation of the specific-heat jump at T_c depends on assumptions about the nature of the superconducting state.

The possibility of filamentary shorting due to minor amounts of superconducting “impurity” phases distributed along grain boundaries renders resistance measurements as “proof” of superconductivity problematic. Similarly, the ac susceptibility or the “zero field cooled” (ZFC) dc magnetization probe the magnetic shielding and may be dominated by strategically distributed minority “impurity” phases. A shielding signal corresponding to a large volume fraction of the sample is no proof for a large superconducting volume fraction. This complex has been critically reviewed by Hein [37].

On the other hand, failure to establish superconductivity in one sample of a given phase does not constitute proof that this phase cannot be superconducting at all. The phase may have a homogeneity range and the superconducting properties may strongly depend on the actual composition. Further, the homogeneity range may vary with temperature. It can therefore be considered good practice to study at least part of a multinary phase diagram if reliable results are desired.

However, inhomogeneities may be present in single phase samples, even in single crystals, for a variety of reasons, as *e.g.* temperature dependent vacancy formation, elemental ordering, strains introduced by anisotropic thermal expansion of the crystallites in a polycrystalline specimen. Finally, even within a chemically homogeneous material, domains with differing electronic or magnetic properties may form.

Sometimes, it is difficult to reach an equilibrium state. One particular problem for the study of ruthenocuprates is the formation of oxide phases as minor impurities which, once formed, are difficult to remove and could simulate a weak ferromagnetic behavior

of the majority phase (for SrRuO_3 impurities) or mask the heat capacity contribution of the superconducting transition (for $\text{Sr}_2\text{GdRuO}_6$ impurities). Thus, one of the tasks is to search ways to avoid the formation of such impurities or, if present, to quantitatively account for their contributions to observed sample properties.

3. CRYSTAL STRUCTURE AND OCCURRENCE OF THE RUTHENOCUPRATES

The structure of the ruthenocuprates shown in Fig. 2 is closely related with that of the cuprates of the $\text{YBa}_2\text{Cu}_3\text{O}_7$ type. In the Y-123-structure, the layers of CuO_5 pyramids (forming the superconducting Cu-O-planes) are connected by CuO_4 squares forming chains, in Ru-1212 they are connected by corner-sharing RuO_6 octahedra forming planar sheets (Fig. 2). This “T-1212” structure has been observed with the transition metals $T = \text{Nb, Ta}$ [38, 39] and in solid solutions (Nb,Ru) [40], with a variety of lanthanide and alkaline earth elements replacing the Y and Ba of Y-123. It has been described in primitive tetragonal spacegroup $P4/mmm$ [26, 38, 40] (with $a \simeq 0.384$ nm, $c \simeq 1.155$ nm for $\text{RuSr}_2\text{GdCu}_2\text{O}_8$ [20, 41]) leading to straight T-O-T bonds in the octahedron layer. This description might, however, correspond to an average structure.

A $\sqrt{2}a \times \sqrt{2}a \times c$ supercell has been found in electron diffraction [42]. The appearance of this superstructure depends on details of sample preparation [43]. It arises from ordered rotations of the RuO_6 octahedra around the c direction which are required to accommodate the mismatch between Cu-O and Ru-O distances [25, 42]. The structure with RuO_6 rotations has been described in primitive tetragonal $P4/mbm$ [25] or, doubling c , in body centered tetragonal $I4/mcm$ [44, 45]. Such rotations may be of crucial importance for the magnetic and electronic properties of Ru-1212. First-principle calculations taking into account the rotations predict an AF ordering of the Ru moments [46] instead of FM ordering. Ru-1212 is found to be cation and oxygen stoichiometric [42].

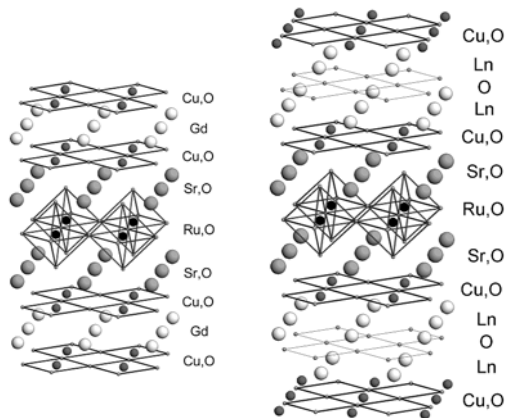


Fig. 2. The structures of Ru-1212 (left) and Ru-1222 (right, part of unit cell shown).

A number of substitutions on the Ru site have been reported. While complete solubility is observed for (Ru,Nb)-1212 [47], the solubilities of Sn [48], Ti, and V [47] on the Ru site are limited. A wide solid solution range is reported with Cu substituting for Ru if prepared in a high-pressure oxygen atmosphere [49] while under standard conditions samples $(\text{Ru}_{1-x}\text{Cu}_x)\text{Sr}_2\text{GdCu}_2\text{O}_8$ are multiphase for $x = 0.1$ [41].

The Ru-1212 structure was observed with Sr and the lanthanides Sm, Eu, and Gd [41] when prepared under ambient pressure. While partial substitution of Gd by Dy in Ru-1212 was reported [50], no Ru-1212 type phase is formed at the nominal Ru-1212 composition with $A = \text{Sr}$ and lanthanides of smaller radius $Ln = \text{Tb-Lu}$ and Y or $A = \text{Ba}$ and $Ln = \text{La-Gd}$ and Y, but a mixture of CuO and ordered perovskites of the type $A_2Ln\text{RuO}_6$ is obtained [41]. For perovskites of this type with $A = \text{Sr}$, $Ln = \text{Y}$, Wu *et al.* [51–53] report superconductivity when part of the Ru is substituted by Cu. With $A = \text{Sr}$ and lanthanides with ionic radii larger than that of samarium, $Ln = \text{La-Nd}$, disordered perovskites of the type $(A_{1-x}R_x)(\text{Ru}_{1-y}\text{Cu}_y)\text{O}_3$ are formed instead of Ru-1212 [41]. High-pressure synthesis is required to obtain the Ru-1212 compounds with $A = \text{Sr}$ and $Ln = \text{Y}$ [54–57], Tb [56], Dy, Ho [55–57], and Er [55, 57].

In the Ru-1222-type structure, a fluorite-like $(Ln_{1-x}\text{Ce}_x)_2\text{O}_2$ -layer is added between the Cu-O-planes (Fig. 2) which introduces a body-centering operation (spacegroup $I4/mmm$ [58–60]; $a \simeq 0.384$ nm, $c \simeq 2.855$ nm for $\text{RuSr}_2(\text{Gd}_{1-x}\text{Ce}_x)_2\text{Cu}_2\text{O}_{10}$ [18, 20]). The phase forms for a range of cerium concentrations $0.5 \leq x \leq 1.0$ [18].

For $\text{RuSr}_2(\text{Gd}_{1.3}\text{Ce}_{0.7})_2\text{Cu}_2\text{O}_{10-\delta}$, Knee *et al.* find rotations about c and tilts of the RuO_6 octahedra and determine $\delta \simeq 0.22$ by neutron powder diffraction [61]. As for Ru-1212, the occupation of the Ln site in Ru-1222 is restricted to Sm, Eu, and Gd [19] under standard preparation conditions. Gd may be replaced by Ho, Dy, and Y under high pressure conditions [62].

This “ T -1222” structure was found with the transition metals Nb, Ta [58, 59, 63], Ti [64, 65], Ru [18–20, 22, 66, 67], and solid solutions (Ru,Fe) [21, 68], (Ru,Sb) [69], and (Ru,Mo) [70]. Sr/ Ln disorder [71] and solubility of Cu and Ce [71], Pd, Os, and Rh [72] on the Ru site have also been reported, however, the Sb and Mo-substituted samples were not single phase, and no phase purity was reported for the platinum group substitutions.

In general, these compounds can be made superconducting by adjusting the Ln/Ce -concentration [18] or by oxygen-doping [18], however, superconductivity was not observed by Ono [66] in the pure Ru compound, and is suppressed with Fe substitution [21]. The Ru valence was established by X-ray absorption spectroscopy and is close to five [73, 74], independent of the Ce concentration [74] and in contrast to Ru-1212 (see Sect. 4).

Layers of corner-sharing RuO_6 octahedra are also characteristic for the ruthenates $\text{Sr}_{n+1}\text{Ru}_n\text{O}_{3n+1}$, isotypical with Ruddlesden-Popper-phases. The compound with $n = 1$, Sr_2RuO_4 , is superconducting at about 1 K [75]. The other known ruthenates of this series, $\text{Sr}_3\text{Ru}_2\text{O}_7$ [76], $\text{Sr}_4\text{Ru}_3\text{O}_{10}$ [77], and SrRuO_3 [78] ($n = \infty$) are itinerant ferromagnets.

4. PHASE EQUILIBRIA IN THE Sr–Gd–Ru–Cu–O SYSTEM

$\text{RuSr}_2\text{GdCu}_2\text{O}_8$ (Ru-1212) was the first known quinary phase in the system Sr–Gd–Ru–Cu–O. With respect to synthesis and, eventually, single crystal growth of the Ru-1212

phase, knowledge of the corresponding phase diagram is of particular interest at temperatures in the range of 1000°C and above and at oxygen partial pressures of the order of $10^5 \text{ Pa} = 1 \text{ bar}$, for example in air under ambient conditions $p_{\text{O}_2} \approx 0.21 \text{ bar}$.

Under these conditions, the metal oxides often have a fixed cation/oxygen ratio and in such a case it is possible to treat the system consisting of N metallic elements and oxygen as a system consisting of N constituents, the binary metallic oxides. Likewise, it is tempting to treat this system of five elemental components as a quaternary system made up of the four binary metal oxides: $\text{SrO-GdO}_{1.5}\text{-RuO}_2\text{-CuO}$. This is perfectly possible for strontium and gadolinium which are strictly divalent (Sr) and trivalent (Gd), respectively. However, both copper and ruthenium show variable valences and thus the oxygen concentration is not fixed by cationic composition (we use valence and oxidation state as synonyms). The preferred formal valence of copper in the solid phases of the system is two or somewhat higher as in $(\text{Sr}_{14-x}\text{Gd}_x)\text{Cu}_{24}\text{O}_{41-z}$, where it reaches 2.25+. In liquid phases, copper tends to assume a valence below two, but for the subsolidus phase diagrams we may suppose copper to be divalent, since in air, the decomposition of $4 \text{ CuO(s)} \rightarrow 2 \text{ Cu}_2\text{O(s)} + \text{O}_2\text{(g)}$ proceeds above the solidus temperature of the systems under consideration.

In contrast, solid phases with tetravalent and pentavalent ruthenium are known. Among the former are RuO_2 , $\text{Gd}_2\text{Ru}_2\text{O}_7$, and the strontium based ruthenates $\text{Sr}_{n+1}\text{Ru}_n\text{O}_{3n+1}$ ($n = 1, 2, \infty$). Phases with pentavalent ruthenium are, *e.g.*, $\text{Sr}_2\text{GdRuO}_6$ and Gd_3RuO_7 . In Ru-1212, the (average) Ru valence is between four and five, with 40-50% Ru^{4+} and 60-50% Ru^{5+} [79-81], in doped $(\text{Ru}_{1-x}\text{M}_x)\text{Sr}_2\text{GdCu}_2\text{O}_8$ ($\text{M}=\text{Sn, Nb}$) the average Ru valence is 4.8 [82] independent of x . This opens the possibility of charge segregation in the RuO_6 layer [79, 81]. We show below that there exist solid solutions $\text{Sr}(\text{Ru}_{1-x}\text{Cu}_x)\text{O}_3$ in which the average valence of ruthenium varies from four to five in a continuous fashion. Higher valences however, as do occur in RuO_3 and RuO_4 [83, 84], were not observed for solid phases at high temperatures.

Because of the variable cation/oxygen ratio and the possible loss of volatile RuO_x at elevated temperature, we are working in an open quinary system, and our *pseudoquaternary* representation $\text{SrO-GdO}_{1.5}\text{-RuO}_{2+\delta}\text{-CuO}$ ($0 \leq \delta \leq 0.5$) is to be considered an approximation which we have chosen for the convenience of visualization.

In the constitutional tetrahedron depicted in Fig. 3, only phases of immediate interest are indicated by a black sphere (that is, neglecting any homogeneity ranges), while phases without relevance for our considerations have been omitted. Among the latter is, for example, $\text{SrCu}_3\text{Ru}_4\text{O}_{12}$ [85], which decomposes above 950°C. For convenience, we consider only subsolidus equilibria. Since the solidus temperature is determined by “low melting point” copper-rich phases, we should keep in mind that some considerations presented below also apply at higher temperatures in the Ru-rich part of the system.

In the next Sects. which are based on work by Bauernfeind *et al.* [18, 19, 41], the pseudoternary boundary systems will be discussed as well as a section of the pseudoquaternary system where $(X_{\text{Sr}} + X_{\text{Gd}})/(X_{\text{Cu}} + X_{\text{Ru}}) = 1$. Here, the X_{M} are cationic mole fractions defined according to $X_{\text{M}} = n_{\text{M}}/(n_{\text{Sr}} + n_{\text{Gd}} + n_{\text{Ru}} + n_{\text{Cu}})$, and n_{M} is the number of moles present of element M. This section is represented by the square outlined in Fig. 3 and contains both the Ru-1212 phase and the solid solution $(\text{Sr}_{1-x}\text{Gd}_x)(\text{Ru}_{1-y}\text{Cu}_y)\text{O}_3$.

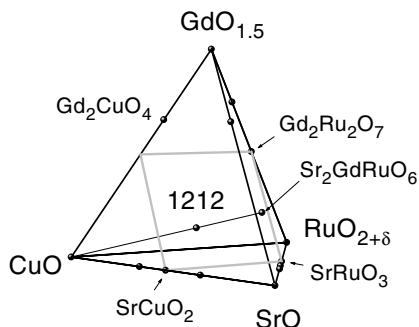


Fig. 3. Schematic view of the system $\text{SrO-GdO}_{1.5}\text{-CuO-RuO}_{2+\delta}$ at 1000°C in air. For clarity, all homogeneity ranges and all pseudoternaries except $\text{Sr}_2\text{GdRuO}_6$ have been omitted. *Grey square*: section parallel to the $\text{SrO-GdO}_{1.5}$ and $\text{RuO}_{2+\delta}\text{-CuO}$ edges, see Sect. 4.2. *Solid line* connecting CuO and $\text{Sr}_2\text{GdRuO}_6$: see Sect. 5.2

4.1. PSEUDOTERNARY SUBSOLIDUS PHASE DIAGRAMS

The samples used for the study of phase equilibria were prepared from the binary oxides or carbonate in the case of strontium by calcination and sintering at appropriate temperatures, with intermediate grindings [18, 19, 41]. Sample properties were monitored by resistivity, ac susceptibility, and dc magnetization measurements. The interior of the pseudoquaternary system has not been examined in detail, however, there is reasonable evidence that besides solid solutions extending from the border systems, Ru-1212 is the only stable phase inside the constitutional tetrahedron under the conditions chosen.

$\text{SrO-GdO}_{1.5}\text{-CuO}$

Gadolinium is intermediate in ionic size between La and Y and therefore one might expect the $\text{SrO-GdO}_{1.5}\text{-CuO}$ phase diagram to reflect properties of the well-studied $\text{SrO-LaO}_{1.5}\text{-CuO}$ and $\text{SrO-YO}_{1.5}\text{-CuO}$ systems [86, 87]. Although the sole binary oxide is Ln_2CuO_4 for both $\text{Ln} = \text{Gd}$ and La (with different crystal structures, though) while it is $\text{Ln}_2\text{Cu}_2\text{O}_5$ for $\text{Ln} = \text{Y}$, gadolinium in many oxides behaves more like the slightly smaller yttrium than like the larger lanthanum.

The pseudoternary subsolidus phase diagram of the system $\text{SrO-GdO}_{1.5}\text{-CuO}$ is depicted in Fig. 4, where, for the sake of simplicity, the phase $\text{Sr}_{2-x}\text{Gd}_{1+x}\text{Cu}_2\text{O}_{5.5\pm\delta} = (\text{Sr,Gd})_3\text{Cu}_2\text{O}_z$ is assumed to have the unique composition $\text{Sr}_{1.8}\text{Gd}_{1.2}\text{Cu}_2\text{O}_{5.6}$. In fact, a homogeneity range of this phase $0.1 \leq x \leq 0.3$ has been reported [88]. However, neglecting this homogeneity range and the resulting omission of various narrow two-phase regions in this representation of the phase diagram has no severe consequences for its gross features.

The phase with the lowest melting point is $\text{Sr}_{14}\text{Cu}_{24}\text{O}_{41}$. Its peritectic decomposition temperature varies with oxygen partial pressure and has been reported between 955°C [89] and 982°C [90] in air and at 1030°C at $p_{\text{O}_2} = 1$ bar [90]. These temperatures

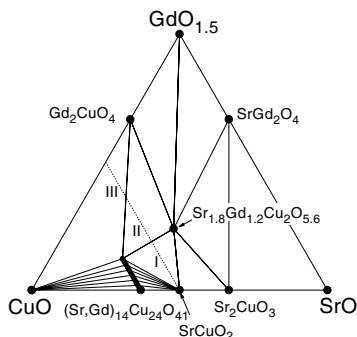


Fig. 4. Subsolidus phase equilibria in the system $\text{SrO-GdO}_{1.5}\text{-CuO}$ in air. I, II, and III denote three-phase regions touched along the *dotted line*: see text

are only slightly higher than the eutectic temperatures of the system Sr-Cu-O , reported at 955°C [89] to 973°C [90] in air and 1011°C at $p_{\text{O}_2} = 1$ bar [90].

The dotted line connecting SrCuO_2 and the point of equimolar ratio between CuO and Gd_2CuO_4 is of particular interest. Along this line we move across the three-phase regions (I) $\text{SrCuO}_2\text{-(Sr,Gd)}_{14}\text{Cu}_{24}\text{O}_{41}\text{-(Sr,Gd)}_3\text{Cu}_2\text{O}_z$, (II) $\text{Gd}_2\text{CuO}_4\text{-(Sr,Gd)}_{14}\text{Cu}_{24}\text{O}_{41}\text{-(Sr,Gd)}_3\text{Cu}_2\text{O}_z$ and (III) $\text{CuO-Gd}_2\text{CuO}_4\text{-(Sr,Gd)}_{14}\text{Cu}_{24}\text{O}_{41}$, and the corresponding two-phase regions. These regions mark the left boundary of the section of the pseudoquaternary system with $(X_{\text{Sr}} + X_{\text{Gd}})/(X_{\text{Cu}} + X_{\text{Ru}}) = 1$, depicted in Figs. 3 and 8 and discussed in Sect. 4.2.

$\text{SrO-GdO}_{1.5}\text{-RuO}_{2+\delta}$

None of the phases appear to have non-negligible homogeneity ranges. Therefore, all phases are considered *point compounds*, yielding the rather simple subsolidus phase diagram depicted in Fig. 5. The solidus temperatures were not determined, but are believed

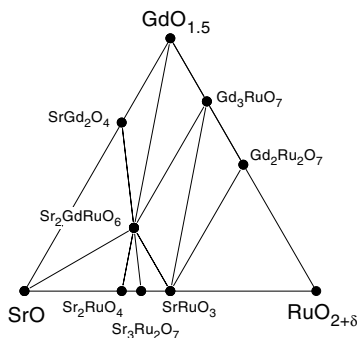


Fig. 5. Phase equilibria in the system $\text{SrO-GdO}_{1.5}\text{-RuO}_{2+\delta}$ at 1000°C in air

to be much higher than the melting temperature of Ru-1212, which is found to be about 1120-1130°C [41] (see Sect. 4.2) at $p_{O_2} = 1$ bar.

In the open system, however, where the investigations have been carried out, $Gd_2Ru_2O_7$ tends to be unstable with respect to decomposition into Gd_3RuO_7 (s) and RuO_x (g) already above 1050°C. No loss of ruthenium was observed from Sr-Ru-O phases, from Gd_3RuO_7 and Sr_2GdRuO_6 below 1200°C. The latter phase is stable after 12 h at 1500°C in flowing oxygen, while $SrRuO_3$ decomposes into $Sr_3Ru_2O_7$, Sr_2RuO_4 , and RuO_x (g) under these conditions [41].

The only pseudoternary phase in this system is Sr_2GdRuO_6 which shows magnetic ordering below about 35 K and a magnetization peak around 20 K [91, 92].

$GdO_{1.5}$ - $RuO_{2+\delta}$ -CuO

This system (Fig. 6) is even simpler than the previous one since it contains neither ternary phases nor extended homogeneity ranges nor a pseudobinary phase in the system $RuO_{2+\delta}$ -CuO. The dotted line represents the horizontal upper boundary of the square section shown in Figs. 3 and 8 and discussed in Sect. 4.2. Along this line, one moves from the three-phase region (A) $Gd_2Ru_2O_7$ - Gd_3RuO_7 -CuO into the three-phase region (B) Gd_2CuO_4 - Gd_3RuO_7 -CuO.

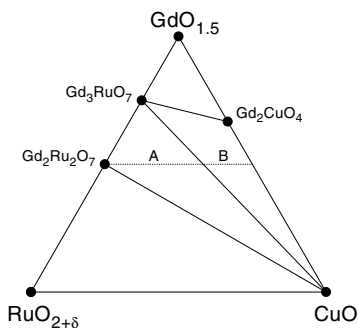


Fig. 6. Phase equilibria in the system $GdO_{1.5}$ - $RuO_{2+\delta}$ -CuO at 1000°C in air. A and B denote three-phase regions touched along the *dotted line*: see text

SrO- $RuO_{2+\delta}$ -CuO

Much more interesting is this system, presented in Fig. 7. Here, copper substitutes for ruthenium in all strontium based ruthenates with general formula $Sr_{n+1}Ru_nO_{3n+1}$ ($n = 1, 2, \infty$; compounds with other values of n could not be synthesized [41]). The solubility limit is the same in all three phases: copper replaces up to one third of ruthenium, which is enormous for elements of different valence. However, this striking behavior can be explained quite naturally if one assumes that for each divalent copper ion substituted, two ruthenium ions transform from tetra- to pentavalent, whereby the structure is left intact

and the oxygen content does not change: $\text{Sr}(\text{Ru}_{1-x}\text{Cu}_x)\text{O}_3 = \text{Sr}(\text{Ru}_{1-3x}^{4+}\text{Ru}_{2x}^{5+}\text{Cu}_x^{2+})\text{O}_3$, and similar for the other phases. At $x = 1/3$, only Ru^{5+} is present and both further oxidation of ruthenium and depletion of oxygen do not occur, instead, impurity phases form for $x > 1/3$.

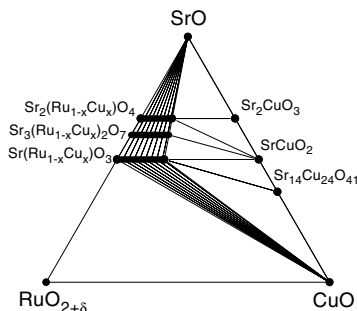


Fig. 7. Phase equilibria in the system $\text{SrO-RuO}_{2+\delta}\text{-CuO}$ at 1000°C in air

Although SrRuO_3 is orthorhombic, the deviation from cubic metric is only slight and the X-ray powder diagram corresponds qualitatively to a perovskite cell with $a_p \simeq 0.3925(4)$ nm. Substitution of copper for ruthenium leaves this value almost unchanged for $x < 1/6$. This unexpected behavior can be explained by the fact that the mean ionic radius [93] of the elements at the octahedral site is left unchanged $r(\text{Ru}^{4+}) = (r(\text{Cu}^{2+}) + 2r(\text{Ru}^{5+}))/3$ upon this substitution.

At higher concentrations of copper ($x \geq x_{\text{JT}} \simeq 1/6$), the Jahn-Teller character of the divalent copper ion apparently begins to break through and the lattice undergoes an abrupt orthorhombic to tetragonal structural transition with tetragonal lattice parameters $a = 0.3895(5)$ nm and $c = 0.400(1)$ nm. The magnetic transition temperature T_{M} was found to decrease linearly with increasing copper content: $T_{\text{M}} \approx (1 - 4x) \times 160$ K. For $x > 0.19$, no magnetic transition was observed. This value is in close vicinity of x_{JT} , but the correlation is not clear, since three samples with $0.17 \leq x \leq 0.19$ that were tetragonal at room temperature did show magnetic transitions at low temperatures; possibly, x_{JT} increases with decreasing temperature [41]. The synthesis of SrRuO_3 under high-pressure oxygen produces a nonstoichiometric form with randomly distributed vacancies on the Ru sites, along with a significantly reduced ferromagnetic ordering temperature [94].

4.2. THE SECTION $(X_{\text{Sr}} + X_{\text{Gd}})/(X_{\text{Cu}} + X_{\text{Ru}}) = 1$

Three corners of the square of Fig. 8 are formed by the pseudobinary phases SrCuO_2 , SrRuO_3 , and $\text{Gd}_2\text{Ru}_2\text{O}_7$. In the fourth corner, CuO and Gd_2CuO_4 coexist in equimolar ratio. Along the lower and right hand edges of the square, $\text{SrCuO}_2\text{-SrRuO}_3$ and $\text{SrRuO}_3\text{-Gd}_2\text{Ru}_2\text{O}_7$, respectively, form pseudobinary equilibria. Along the left and upper edges we cut across two- and three-phase regions of the border systems; the latter are denoted I, II, III, and A, B as defined above (compare Figs. 4 and 6). In this section we

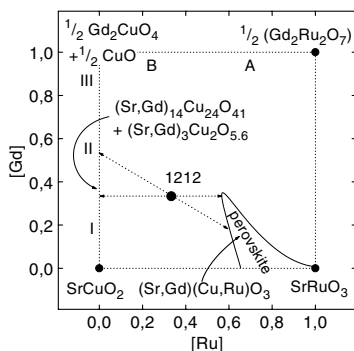


Fig. 8. Section of the pseudoquaternary system at $(X_{\text{Sr}} + X_{\text{Gd}})/(X_{\text{Cu}} + X_{\text{Ru}}) = 1$, containing Ru-1212 and the solid phase which forms at its peritectic decomposition, after [41]

find the Ru-1212 phase and the SrRuO₃-derived solid solution (Sr,Gd)(Ru,Cu)O_{3±δ}. It is likely that there occur deviations from the nominal oxygen content in this Gd-substituted phase. Bauernfeind [18, 41] synthesized a series of samples with nominal compositions Ru_{1-y}Sr_{2-x}Gd_{1+x}Cu_{2+y}O_z at 1030°C/72 h/pO₂ = 0.21 bar. The existence of a homogeneity range of the Ru-1212 phase is indicated by a variation of its unit cell *c/a* ratio in these samples and of other properties, like *T_c* [18, 41]. Although a slight reduction of the impurity content was achieved for the samples with moderate nominal excess of Cu and Gd ($x, y \approx 0.1$), this should not be taken as indication that the stoichiometric compound does not exist, since the sintering temperature may have been too low to reach equilibrium.

Thermogravimetric measurements at pO₂ = 1 bar show (Fig. 9) that the Ru-1212 phase starts to decompose at about 1120°C with the peak at 1130°C [41], in agreement with other investigations (1113°C [95], 1118°C [96]) discussed in Sect. 5.2. The weight loss, which corresponds to 1/2 oxygen per formula unit, is reversible upon cooling, and the liquid solidifies at about 1030°C (in Al₂O₃ crucibles). X-ray and microprobe investigations of the solidified ingots reveal the presence of the disordered perovskite (Sr,Gd)(Ru,Cu)O_{3±δ}, of (Sr_{14-x}Gd_x)Cu₂₄O₄₁ with $x \approx 5$, and, to a much smaller extent (sometimes only trace amounts), of CuO, Gd₂CuO₄, and (Sr,Gd)₃Cu₂O_z [41]. This implies that Ru-1212 undergoes a peritectic decomposition into a liquid which is rich in copper and poor in – possibly almost free from – ruthenium and a disordered solid perovskite (Sr,Gd)(Ru,Cu)O_{3±δ}. Two such possible decompositions of Ru-1212 are indicated by arrows in Fig. 8. The Ru-1212 phase (here represented as a point compound) is in equilibrium with the disordered perovskite phase (Sr_{1-x}Gd_x)(Ru_{1-y}Cu_y)O_{3±δ} with $x \approx 0.25(10)$, $y \approx 0.35(10)$, and $\delta \approx 0$. In contrast to pure SrRuO₃, no magnetic ordering was observed in the solid solution at this composition and in fact everywhere near the Cu-rich boundary of its homogeneity range depicted in Fig. 8. Ruthenium most likely is nearly pentavalent along this boundary.

With these values of x and y , the composition of the liquid is estimated to be between $X_{\text{Sr}} : X_{\text{Gd}} : X_{\text{Cu}} = 0.25 : 0.25 : 0.5$ and $0.35 : 0.15 : 0.5$. The region of primary crystallization

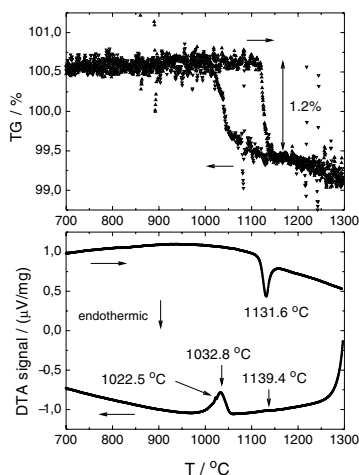


Fig. 9. Differential thermal analysis (DTA) and thermo-gravimetric (TG) study of the peritectic decomposition of Ru-1212 at $p_{\text{O}_2} = 1$ bar. After [41]

of Ru-1212 may be expected in the tetrahedron spanned by these two compositions, Ru-1212, and CuO [41]. Lin *et al.* obtained their best single crystals with a starting composition somewhat more rich in ruthenium [97]. This higher Ru concentration might be the reason that complete melting did not occur at 1300°C in their experiments. Other thermal investigations of Ru-1212 are discussed in Sect. 5.2.

5. PREPARATION AND PROPERTIES OF RUTHENOCUPRATES

The sometimes contradicting reports on the superconducting and magnetic properties of ruthenocuprates may have their origin in the complex nature of the multinary phase diagrams in question. Thus, an overview of the common preparation procedures and the ensuing properties will be given.

5.1. $\text{RuSr}_2(\text{Gd}_{1-x}\text{Ce}_x)_2\text{Cu}_2\text{O}_{10}$

Ono studied solid solutions of the Nb and Ru “1222” compounds, but did not establish superconductivity in the pure Ru samples [66]. In contrast to Ru-1212, doping of the CuO_2 -planes can be achieved by the mutual replacement of tetravalent Ce and the trivalent $Ln = \text{Sm}, \text{Eu}, \text{Gd}$ [18], and by a variable oxygen content in the fluorite block [18, 98–100]. The simultaneous occurrence of superconductivity and unusual magnetism in $\text{RuSr}_2(\text{Gd}_{1-x}\text{Ce}_x)_2\text{Cu}_2\text{O}_{10}$ was first pointed out by Bauernfeind *et al.* [20] based on ac susceptibility measurements similar to those shown in Fig. 10. They found that oxygenation or lowering the Ce concentration increases the superconducting T_c and decreases the magnetic ordering temperature [18, 20]. Fig. 10 shows the variation of both the magnetic and

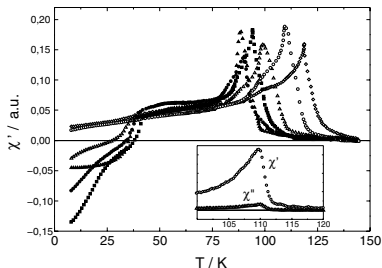


Fig. 10. Ac susceptibility for $\text{RuSr}_2(\text{Gd}_{1-x}\text{Ce}_x)_2\text{Cu}_2\text{O}_{10}$ as a function of cationic composition: $x = 0$ (open diamond), 0.1 (open circle), 0.2 (open triangle), 0.3 (solid circle), 0.4 (solid square), 0.5 (solid triangle). Inset: Dissipation at the magnetic transition ($x = 0.1$) is indicated by the peak in χ'' . After [20, 41]

the superconducting transition temperatures as a function of Gd concentration. Note the dissipative contribution at the FM transition, which has not been observed for Ru-1212.

The coexistence of ferromagnetism and superconductivity in Ru-1222 on a microscopic scale was first claimed by Felner *et al.* who used Mössbauer studies to establish uniformity of the magnetically ordered state and tunneling spectroscopy to establish uniformity of the superconducting gap [22] in Eu and Gd materials. From magnetization measurements they concluded on a WFM state which they proposed to arise by the Dzyaloshinsky-Moriya mechanism [101, 102] due to a symmetry lowering at the Ru site [21]. In contrast to Ru-1212, magnetization curves are clearly hysteretic. Hydrogen doping reversibly increases the magnetic ordering temperature of the Ru moments and suppresses superconductivity [103, 104], oxygen doping enhances T_c [104]. The formation of a spontaneous vortex phase in Ru-1222 was suggested by Sonin and Felner [36]. Ru-1222 exhibits unexpected magnetic dynamics in low magnetic fields with time relaxation, switching behavior, and “inverted” hysteresis loops, while neither Ru-1212 nor SrRuO_3 exhibit such magnetic dynamics [105] which may be explained by a magnetic multilayer model [105].

5.2. $\text{RuSr}_2\text{GdCu}_2\text{O}_8$

In the first study of Ru-1212 [18], the samples were prepared by solid state reaction from the oxides and strontium carbonate. The stoichiometric mixtures were calcined at 970°C for 24 h in air, pressed to pellets and sintered between 1000°C and 1040°C in air. As-sintered samples were semiconducting, but with resistivities about three orders of magnitude lower than the Nb analogues. Resistive transitions to superconductivity were reported in samples that were slowly cooled or annealed under oxygen pressure (see Fig. 2 of [18]), but since no shielding signal was detected, the superconductivity of this phase remained unclear. The samples contained a small amount of impurity of the SrRuO_3 type, with Sr partially replaced by the lanthanide (and Ru by Cu [106]). The SrRuO_3 -type impurity appears at temperatures as low as 600°C and is present in the calcined powders [18, 50, 95, 107].

In flowing oxygen, the impurity content was even higher than in air [19], while in flowing nitrogen, the Ru-1212 phase did not form, but a mixture of $\text{Sr}_2\text{GdRuO}_6+(\text{Cu}_2\text{O})$ was obtained instead. Preparation paths involving precursors in which the Sr is bound to ternary or quaternary oxides containing Cu or Ru were examined in [19]. While reactions starting from $2(\text{SrCuO}_2)+\text{RuO}_2 + \frac{1}{2}(\text{Gd}_2\text{O}_3)$, $\text{Sr}_2\text{CuO}_3+\text{CuO}+\text{RuO}_2 + \frac{1}{2}(\text{Gd}_2\text{O}_3)$, and $\text{Sr}_2\text{RuO}_4+2(\text{CuO})+\frac{1}{2}(\text{Gd}_2\text{O}_3)$ could not suppress the formation of SrRuO_3 type impurities, no impurities were detected in powder X-ray patterns of samples prepared in oxygen atmosphere from $\text{Sr}_2\text{GdRuO}_6+2(\text{CuO})$ or from the intermediate product of the treatment in flowing nitrogen [19].

Samples sintered in flowing oxygen without pre-reaction in flowing nitrogen had semi-conducting resistivities and did not show traces of superconductivity, while those pre-reacted in nitrogen were metallic down to 80 K, showing a slight semiconducting-like upturn at lower temperatures and a transition to zero resistivity between 30-20 K [19]. Synthesis in 1% oxygen at 930°C leads to non-superconducting Ru-1212 in which superconductivity subsequently can be induced with oxygen annealings without observable stoichiometric changes [108], while in other reports, non-superconducting Ru-1212 cannot be made superconducting by oxygen annealing [109].

Prolonged sintering at the optimum temperature of 1060°C improves the metallic behavior and enhances the onset of the resistive transition to superconductivity to about 48 K, with zero resistance achieved at 35 K [41, 106] (Fig. 11).

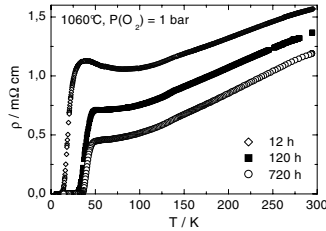


Fig. 11. Resistivity of $\text{RuSr}_2\text{GdCu}_2\text{O}_8$ prepared via the precursor route after prolonged sintering at 1060°C under flowing oxygen ($p_{\text{O}_2} = 1$ bar)

Samples prepared under optimum conditions show sharp transitions to full diamagnetic shielding ($97 \pm 3\%$ after correction for geometric demagnetization of the spherical sample) at ≈ 33 K [41, 106] as shown in Fig. 12. The apparent depression of T_c and decrease of the shielding fraction with ac field amplitude in the susceptibility measurements is indicative of granular superconductivity with a low inter-granular critical (Josephson) current density [41]. Superconductivity is not destroyed at 32 G, since in a dc magnetic field of 5 T superimposed on a small ac field (1/4 G), the onset is at 8 K and the shielded volume fraction higher than one third at 5 K. Granularity effects are also seen in the shape of the resistive transition in an applied dc magnetic field, while the midpoint of the resistive transition shifts down from $T_c \approx 38$ K to $T_c \approx 10$ K at 9 T [41].

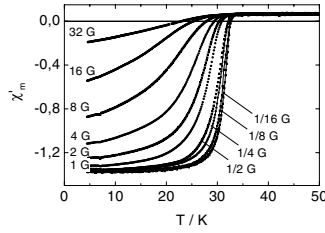


Fig. 12. Diamagnetic screening as a function of ac field amplitude of a spherical sample of $\text{RuSr}_2\text{GdCu}_2\text{O}_8$ prepared via the precursor route (720 h, 1060°C , $p_{\text{O}_2} = 1$ bar)

Scanning electron microscope investigations indicate that the improved transport properties are (at least partly) due to an increase of grain size and improved contacts between grains [41]. The apparent changes of resistivity with different oxygen treatment observed in the first investigation of Ru-1212 [18] must thus be attributed to a variation (due to the oxygen treatment) of the type and amount of foreign phases present in those samples. Grain boundary depletion of oxygen as a possible consequence of the annealing has been suggested in [107]. The decrease of resistivity after hot isostatic pressing in oxygen of 400 bar is attributed to physical changes in the grain boundary [57].

Other effects of the long-term heat treatment could be the loss of ruthenium, cation disorder [49,71], and structural defects [42] as *e.g.* long range ordering of RuO_6 -octahedra rotations. This in turn could affect the average Ru valence, magnetic, electronic, and transport properties of the Ru-1212 phase. With pentavalent ruthenium, we expect insulating or semiconducting behavior in our simple valence-counting scheme. The loss of ruthenium at fixed oxygen content would contribute to doping according to $\text{Ru}^{5+} + \text{Cu}_2^{2+} \rightarrow \text{Ru}_{1-\delta}^{5+} + \text{Cu}_2^{(2+5\delta/2)+}$. As already suggested by Bauernfeind [41], a change of the average Ru valence gives rise to a doping of the CuO_2 layers according to $\text{Ru}^{5+} + \text{Cu}_2^{2+} \rightarrow \text{Ru}^{(5-\epsilon)+} + \text{Cu}_2^{(2+\epsilon/2)+}$. Such deviations with a mixture of Ru^{4+} and Ru^{5+} have indeed been observed [79, 80].

The substitution of Ce^{4+} for Gd^{3+} (electron doping) lowers, substitution of Ca^{2+} (hole doping) enhances the superconducting T_c [110]. Both Sn^{4+} and Nb^{5+} suppress the ferromagnetism in the RuO_2 layers when substituted for Ru, but they respectively enhance and diminish superconducting T_c through hole transfer to and from the CuO_2 layers [111]. All doping experiments are consistent with the interpretation that Ru-1212 is underdoped with an estimated maximum T_c of 65 K [111, 112]. Superconducting T_c up to 72 K has indeed been observed in $(\text{Ru}_{1-x}\text{Cu}_x)\text{Sr}_2\text{GdCu}_2\text{O}_8$ solid solutions synthesized in a high-pressure oxygen atmosphere [49]. The maximum temperature of the superconducting transition is obtained for $x = 0.3, 0.4$ [49].

The preparation route with an intermediate treatment in flowing nitrogen or argon was essential to avoid the appearance of trace amounts of SrRuO_3 [19, 41, 106], and has subsequently been adopted by [23, 24, 42] and many others. The formation of Ru-1212 from the precursor $\text{Sr}_2\text{GdRuO}_6 + 2(\text{CuO})$ was extensively studied by Bauernfeind *et al.* [41] and Chen *et al.* [95] through thermal analysis and X-ray diffraction.

The best phase purity for thoroughly ground and pelletized powders of $\text{Sr}_2\text{GdRuO}_6$ and CuO sintered in flowing oxygen ($p_{\text{O}_2} \approx 1$ bar) for 12 h was obtained for sintering temperatures around 1050–1060°C. At temperatures below 1050°C, the reaction was not complete after 12 h, while above 1060°C the formation of impurity phases was observed (Fig. 13).

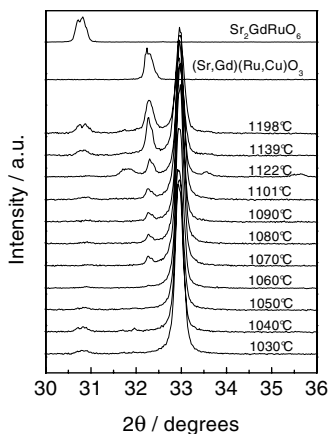


Fig. 13. Powder X-ray diffraction ($\text{CuK}\alpha$) of samples prepared via the precursor route. The main peaks of Ru-1212 , $\text{Sr}_2\text{GdRuO}_6$, and $(\text{Sr,Gd})(\text{Ru,Cu})\text{O}_3$ are visible, see the upper two traces included for comparison

The resistivity of these samples reveals a correlation between phase purity and metallic behavior. Samples sintered below 1050°C show semimetallic behavior at room temperature with $\varrho(T)$ only slightly varying and a semiconducting increase in resistivity below 100 K (Fig. 14). Samples sintered between 1050–1110°C at $p_{\text{O}_2} = 1$ bar are metallic with positive $d\varrho/dT$ down to about 100 K, where a less pronounced increase in resistivity occurs. Samples sintered above 1110°C are semiconducting over the whole temperature range, all

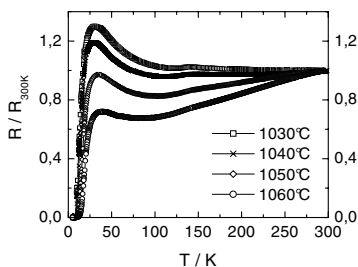


Fig. 14. Resistivity of Ru-1212 prepared via the precursor route in flowing oxygen at different sintering temperatures

others show a broad transition into the superconducting state, with an onset below 30 K which is almost independent of sintering temperature.

Should this improvement be due to an increase of the oxygen content of Ru-1212, then the absolute change is very small and below the limit of resolution of thermogravimetry [41]. No weight change was detected during the reaction $\text{Sr}_2\text{GdRuO}_6 + 2\text{CuO} \rightarrow \text{RuSr}_2\text{GdRuCu}_2\text{O}_{8\pm\delta}$ and thus the oxygen content was assumed to be quite close to eight: $0 \simeq \delta < 0.05$ [41]. This is compatible with the observation by Henn *et al.* who for non-superconducting Ru-1212 find only a negligible change in oxygen content, independent of heat and Ar/O gas flow treatment [109].

The kinetics of the reaction were studied in [95]. The precursor was prepared from dried oxides and strontium carbonate, calcined at $950^\circ\text{C}/\text{air}$ and reacted at $1250^\circ\text{C}/16\text{ h}/\text{O}_2$. From isochronal annealing at $800\text{--}1000^\circ\text{C}$ and isothermal annealing at 1000°C they find that Ru-1212 forms in a diffusion-controlled reaction with an activation energy of 530 kJ/mol in a single step without other phases intervening [95]. Apparently, the reaction path follows the straight line of Fig. 3 involving pseudobinary equilibria and thus giving no room for the appearance of other phases. Under flowing oxygen, they report Ru-1212 to decompose at 1113°C [95].

Li *et al.* [113] synthesized the precursor $\text{Sr}_2\text{GdRuO}_6$ by solid-state reaction in flowing oxygen and water vapor. The dried oxides and strontium carbonate were calcined ($950^\circ\text{C}/30\text{ h}/\text{O}_2+\text{H}_2\text{O}$) and reacted to form $\text{Sr}_2\text{GdRuO}_6$ at this temperature. Ru-1212 prepared from this precursor at $930^\circ\text{C}/24\text{ h}/\text{air}$ is reported to be phase-pure and not superconducting, while samples prepared in oxygen at higher temperature ($950^\circ\text{C}/24\text{ h}/\text{O}_2$ followed by $1050^\circ\text{C}/24\text{ h}/\text{O}_2$) contain $\text{Sr}_2\text{GdRuO}_6$ and SrRuO_3 impurities but are superconducting. These findings are in contrast with [95] who find only a 60% fraction of Ru-1212 after 120 h at 930°C , and with the X-ray results cited above.

Based on thermogravimetric analysis, Matveev *et al.* [114] propose that in an atmosphere with more than 35% oxygen concentration, Ru-1212 decomposes in a three-step process: a loss of Ru by sublimation of RuO_2 , decomposition into $\text{Sr}_2\text{GdRuO}_6$, Cu_2O , CuO-rich liquid and oxygen, and occupation of the Ru vacancies in Ru-1212 by Cu. They give an upper limit for the stability of the Ru-1212 phase in oxygen at 1060°C [114].

A more homogeneous starting composition and a higher reactivity of the reactants than by standard sintering of oxide powders can in general be achieved by the sol-gel method. A modified sol-gel method was reported in [96]. They decompose the gel at $700^\circ\text{C}/24\text{ h}/\text{N}_2$ to remove the organics (but SrCO_3 is still present) and form Ru-1212 at $950^\circ\text{C}/18\text{ h}/\text{air}$. SrRuO_3 impurities disappear after a treatment at $1020^\circ\text{C}/48\text{ h}/\text{O}_2$ flow. In-situ high-temperature X-ray diffraction reveal no transformation up to 1050°C in flowing oxygen, but a decomposition into $\text{Sr}_2\text{GdRuO}_6+\text{SrRuO}_3$ plus liquid above that temperature. Upon cooling, the Ru-1212 apparently is recovered with fast kinetic [96], which appears difficult to reconcile with the observed activation energy for this reaction [95] unless there is a strong effect of particle size [95]. A DTA feature at 1118°C is interpreted as liquidus event [96]. Since neither pure $\text{Sr}_2\text{GdRuO}_6$ nor pure SrRuO_3 show transformations in this temperature range, the reaction at 1118°C may rather be the peritectic decomposition of the not yet transformed Ru-1212, consistent with [41,95]. Samples quenched from 1185°C contain $\text{Sr}_2\text{GdRuO}_6$, SrRuO_3 , $\text{Sr}_3\text{Ru}_2\text{O}_7$ and $\text{Cu}_2\text{O}/\text{CuO}$ [96].

A preparation via nitrates is reported by [72]. The pelletized powders are treated at 800, 950, 1050 and 1060°C in air or oxygen. The samples contain sizable amounts of SrRuO₃ and are not superconducting after annealing for 20 h in oxygen but are said to become superconducting after annealing for 48 h [72]. Absence of superconductivity in RuSr₂GdCu₂O₈ was also reported by [109, 115, 116].

The ferromagnetic transition of Ru-1212 is clearly established in dc magnetization measurements [23, 41] (Fig. 15). Muon-spin relaxation [23] and Gd³⁺ EPR measurements [117] reveal a spatially homogeneous FM ordered state which remains unchanged below the superconducting transition. Magnetic excitations have been studied by Raman scattering [118]. A characterization through magnetization measurements reveals an effective magnetic moment $\mu_{\text{eff}} = 3.15(4) \mu_B$ per Ru in agreement with the Ru valence between 4–5, with predominant ferromagnetic interaction among the Ru ions [119].

The magnetic structure of RuSr₂GdCu₂O₈ has been determined by neutron powder diffraction. Chmaissem *et al.* [25] find no evidence for a ferromagnetic component perpendicular to the *c*-axis with an upper limit of about $0.3 \mu_B$. However, ferromagnetism along the *c* axis, itinerant ferromagnetism or a canted antiferromagnetism could not be excluded [25]. Lynn *et al.* [26] find antiferromagnetic order of the Ru moments with a Néel temperature coincident with the previously reported onset of ferromagnetism, a Ru moment of $1.18 \mu_B$ along the *c* axis and an upper limit of $0.1 \mu_B$ to any zero-field ordered moment. The Gd moments order antiferromagnetically below ~ 2.8 K. It appears possible that the weak ferromagnetism develops from the basically AF Ru ordering due to the crystallographic disorder introduced by the rotation of the RuO₆ octahedra, *e.g.* by a canting of the Ru moments through the Dzyaloshinsky-Moriya mechanism [101, 102] as suggested for Ru-1222 by Felner *et al.* [21]. WFM arising from a polarization of the Gd moments due to a lowering of the tetragonal symmetry at the Cu site without involving a canting of the AF Cu moments has been suggested for Gd₂CuO₄ [120]. Antiferromagnetic ordering of the Ru moment at $T_N = 145$ K is observed by neutron diffraction in RuSr₂YCu₂O₈ [54], with a ferromagnetic component at low temperatures of $\simeq 0.28 \mu_B$ [54].

The discrepancy between magnetic measurements which give evidence for ferromagnetic interactions [119] and the AF ordering found in the structure determinations [25–27, 54] and calculations [46] remains puzzling.

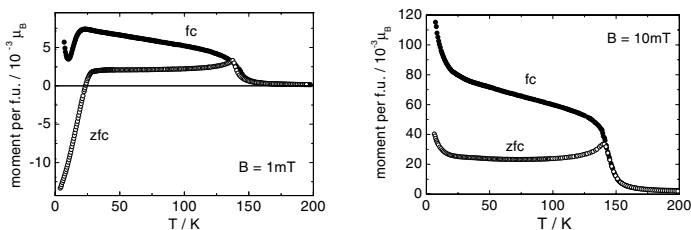


Fig. 15. Magnetic moment of RuSr₂GdCu₂O₈ in different external fields. The Meissner fraction observed at 1 mT has disappeared at 10 mT. After [41, 106]

At least a partial Meissner effect, flux expulsion in *field-cooled* (FC) measurements, has been observed by Bauernfeind [41, 106] in an applied field of 1 mT as shown in Fig. 15. In a field of 10 mT, the Meissner signal and even the *zero-field-cooled* (ZFC) shielding has disappeared [41], indicating that the lower critical field has been exceeded. Even higher Meissner fractions have been reported, *e.g.* corresponding to bulk superconductivity in [121] or to 50% Meissner volume in [79]. The Meissner effect is observed at temperatures far below the superconducting T_c [121] as determined in ZFC susceptibility measurements, which together with the observation of characteristic hysteresis effects is suggestive of the formation of a spontaneous vortex phase [121]. Thermopower measurements as well as the heat capacity difference between pure superconducting and Zn-substituted, non-superconducting $\text{RuSr}_2\text{GdCu}_2\text{O}_8$ suggest bulk superconductivity [122, 123]. A clear peak in the specific heat at the superconducting transition is also observed by Chen *et al.* [124]. The onset of the specific heat jump is independent of the applied field (up to 6 T) while the amplitude of the anomaly decreases and the peak shifts to lower temperature [124]. This is in contrast to [123] where the maximum slope of the differential Sommerfeld constant shifts to higher temperature with magnetic field. Chu *et al.* argued that traces of $\text{Sr}_2\text{GdRuO}_6$ with an antiferromagnetic transition between 31 and 35 K [92, 116] could give rise to such an anomaly. Chen *et al.* exclude this possibility since non-superconducting Ru-1212 prepared from their superconducting Ru-1212 by a treatment 500°C/48 h/nitrogen flow should contain at least the same amount of the impurity but did not show specific heat anomalies.

Chu *et al.* report on the absence of a Meissner effect in their samples and suggest non-uniform, non-bulk superconductivity [125–128] with evidence for phase separation [107, 129, 130]. Given the strong effect of details of the sample preparation [131] and the granular nature of sintered $\text{RuSr}_2\text{GdCu}_2\text{O}_8$ [41, 42, 107, 132], these findings might not contradict the above evidence for a bulk homogeneous superconducting phase.

6. CONCLUDING REMARKS

Both Ru-1222 and Ru-1212 appear to have a non-negligible homogeneity range which very likely encloses the stoichiometric composition. It is evident for Ru-1212 that Cu can substitute Ru. While sizable Cu-substitution is possible only in a high-pressure oxygen atmosphere [49], a small homogeneity range in this direction cannot be excluded under standard preparation conditions. The increase of T_c with Cu-substitution [49] makes it tempting to assume that *all* superconducting Ru-1212 has either such a non-stoichiometric Cu-rich composition or is maybe stoichiometric but with Ru/Cu disorder, however, this is not strictly proven. Both extrinsic (*e.g.* impurity phases at grain boundaries) and intrinsic (*e.g.* cationic order, RuO_6 rotations) properties appear to be affected by annealing.

The magnetic nature of Ru-1212 is more firmly established. One serious problem of Ru-1212 synthesis is the formation of magnetic impurity phases which proved to be very stable under the synthesis conditions generally used – oxidizing atmosphere and temperatures in the range of 1000°C – and thus the magnetic signals observed in the early work near 160 K were attributed to possibly undetected traces of residual SrRuO_3 [19]. However, phase diagram work has shown that in equilibrium, such impurities would be disordered

perovskites $(\text{Sr,Gd})(\text{Ru,Cu})\text{O}_3$ which are not magnetically ordered near that temperature. The magnetic behavior of Ru-1222 is clearly more complex than that of Ru-1212 [105].

The precursor route, reacting $\text{Sr}_2\text{GdRuO}_6$ and CuO in an oxygen atmosphere, permits to avoid the formation of such disordered perovskite impurities. $\text{Sr}_2\text{GdRuO}_6$ shows magnetic ordering below about 35 K with a magnetization peak around 20 K [91, 92]. In dc magnetization measurements of Ru-1212, a peak in this temperature range has been observed occasionally [92, 131], which could have been due to traces of precursor material present in the samples. A quantitative study reveals, however, that the observed magnetization anomalies of Ru-1212 are associated with its superconductivity [92] and not due to $\text{Sr}_2\text{GdRuO}_6$ impurities.

While the formation of Ru-1212 via the precursor route appears to be understood, the reaction path for the preparation from the oxides is yet unknown. Phase formation of Ru-1212 appears to be kinetically hindered due to the stability of impurity phases forming at comparatively low temperatures [18, 50, 95, 107] prior to Ru-1212. The possible volatility of RuO_x plays a role in the final Ru/Cu composition reached. The sublimation of pure RuO_2 in Ar/O_2 atmosphere becomes discernible above about 850°C at a heating rate of 5 K/min [114]. However, appreciable amounts of SrRuO_3 are found at temperatures as low as 600°C when the Ru-1212 phase is synthesized from the binary oxides in air or oxygen, while non-negligible formation of Ru-1212 was observed only at temperatures approaching 1000°C. Since SrRuO_3 and $\text{Sr}_2\text{GdRuO}_6$ are not susceptible to loss of volatile RuO_x under these preparation conditions, the danger of Ru-loss in the precursor route appears much smaller than what the experiments with pure RuO_2 [114] would suggest.

The thermal investigations on the Ru-1212 indicate its peritectic decomposition near 1120°C in oxygen. The stability limits of Ru-1212 as a function of oxygen partial pressure and phase composition are currently not well understood.

From the investigations of Ru-1222 and Ru-1212 it appears reasonably established that these phases are both magnetically ordered and superconducting. There is no evidence that other phases in these multinary systems, which might be present as impurities in samples of nominally Ru-1222 or Ru-1212 compositions, are responsible for the observed behavior. While some experiments clearly indicate homogeneous coexistence of magnetic order and superconductivity in these compounds, the existence of a homogeneity range very naturally opens the possibility of domain formation and complex magnetic behavior in inhomogeneous sintered materials.

ACKNOWLEDGMENTS

The discovery of superconductivity in $\text{RuSr}_2\text{GdCu}_2\text{O}_8$ and $\text{RuSr}_2(\text{Gd}_{1-x}\text{Ce}_x)_2\text{Cu}_2\text{O}_{10}$ would not have been possible without the dedication and perseverance of L. Bauernfeind. I sincerely thank him and E. Casini, S. Chen, T. Ernst, W. Ettig, T. Herrmannsdörfer, O. Korf, C. Lottes, T. Mai, T. P. Papageorgiou, E. Srinivasan, and W. Widder for their fruitful collaboration.

REFERENCES

1. B. T. Matthias, H. Suhl, and E. Corenzwit, *Phys. Rev. Lett.* 1 (1958) 449
2. Ø. Fischer and M. B. Maple, eds., *Superconductivity in Ternary Compounds I*, vol. 32 of *Topics in Current Physics*. Springer, Berlin (1982)
3. M. B. Maple and Ø. Fischer, eds., *Superconductivity in Ternary Compounds II*, vol. 34 of *Topics in Current Physics*. Springer, Berlin (1982)
4. M. B. Maple, *Physica B* 215 (1995) 110
5. W. A. Fertig, D. C. Johnston, L. E. DeLong, R. W. McCallum, M. B. Maple, and B. T. Matthias, *Phys. Rev. Lett.* 38 (1977) 387
6. M. Ishikawa and Ø. Fischer, *Solid State Commun.* 23 (1977) 37
7. J. A. Gootas, J. W. Lynn, R. N. Shelton, P. Klavins, and H. F. Braun, *Phys. Rev. B* 36 (1987) 7277
8. H. Schmidt, M. Weber, and H. F. Braun, *Physica C* 256 (1996) 393
9. R. Nagarajan, C. Mazumdar, Z. Hossain, S. K. Dhar, K. V. Gopalakrishnan, L. C. Gupta, C. Godart, B. D. Padalia, and R. Vijayaraghavan, *Phys. Rev. Lett.* 72 (1994) 274
10. R. J. Cava, H. Takagi, H. W. Zandbergen, J. J. Krajewski, W. F. Peck, Jr., T. Siegrist, B. Batlogg, R. B. van Dover, R. J. Felder, K. Mizuhashi, J. O. Lee, H. Eisaki, and S. Uchida, *Nature* 367 (1994) 252
11. P. C. Canfield, P. L. Gammel, and D. J. Bishop, *Physics Today* 51 (1998) 40
12. H. Schmidt and H. F. Braun, *Physica C* 229 (1994) 315
13. H. Schmidt, M. Weber, and H. F. Braun, *Physica C* 246 (1995) 177
14. H. Schmidt and H. F. Braun, *Studies of high temperature superconductors*, (Ed. A. Narlikar), vol. 26. Nova Science Publishers (1998), p. 47
15. H. Schmidt, A. Dertinger, B. Ernstberger, and H. F. Braun, *J. Alloys Compounds* 262-263 (1997) 459
16. A. Dertinger, R. E. Dinnebier, A. Kreyssig, P. W. Stephens, S. Pagola, M. Loewenhaupt, S. van Smaalen, and H. F. Braun, *Phys. Rev. B* 63 (2001) 184518
17. A. Dertinger, *Supraleitung und Magnetismus in Holmium-Nickel-Borkarbid vom Strukturtyp LuNi₂B₂C*. Berichte aus der Physik, Dissertation Universität Bayreuth, Shaker Verlag, Aachen (2001)
18. L. Bauernfeind, W. Widder, and H. F. Braun, *Physica C* 254 (1995) 151
19. L. Bauernfeind, W. Widder, and H. F. Braun, *J. Low Temp. Phys.* 105 (1996) 1605
20. L. Bauernfeind, W. Widder, and H. F. Braun, *High T_c superconductors*, (Eds. A. Barone, D. Fiorani, and A. Tampieri), vol. 6 of *Fourth Euro Ceramics*. Gruppo Editoriale Faenza S.p. A., Faenza, Italy (1995)
21. I. Felner and U. Asaf, *Physica C* 292 (1997) 97
22. I. Felner, U. Asaf, Y. Levi, and O. Millo, *Phys. Rev. B* 55 (1997) R3374
23. C. Bernhard, J. L. Tallon, C. Niedermayer, T. Blasius, A. Golnik, E. Brücher, R. K. Kremer, D. R. Noakes, C. E. Stronach, and E. J. Ansaldo, *Phys. Rev. B* 59 (1999) 14099
24. J. L. Tallon, C. Bernhard, M. E. Bowden, P. W. Gilberd, T. M. Stoto, and D. J. Pringle, *IEEE Transactions on Applied Superconductivity* 9 (1999) 1696

25. O. Chmaissem, J. D. Jorgensen, H. Shaked, P. Dollar, and J. L. Tallon, Phys. Rev. B 61 (2000) 6401
26. J. W. Lynn, B. Keimer, C. Ulrich, C. Bernhard, and J. L. Tallon, Phys. Rev. B 61 (2000) 14964
27. J. D. Jorgensen, O. Chmaissem, H. Shaked, S. Short, P. W. Klamut, B. Dabrowski, and J. L. Tallon, Phys. Rev. B 63 (2001) 054440
28. L. F. Mattheiss, Phys. Rev. B 45 (1992) 2442
29. W. E. Pickett, R. Weht, and A. B. Shick, Phys. Rev. Lett. 83 (1999) 3713
30. S. Rehmman, T. Herrmannsdörfer, and F. Pobell, Phys. Rev. Lett. 78 (1997) 1122
31. S. S. Saxena, P. Agarwal, K. Ahilan, F. M. Grosche, R. K. W. Haselwimmer, M. J. Steiner, E. Pugh, I. R. Walker, S. R. Julian, P. Monthoux, G. G. Lonzarich, A. Huxley, I. Sheikin, D. Braithwaite, and J. Flouquet, Nature 406 (2000) 587
32. C. Pfleiderer, M. Uhlarz, S. M. Hayden, R. Vollmer, H. v. Löhneysen, N. R. Bernhoeft, and G. G. Lonzarich, Nature 412 (2001) 58. See erratum, Nature 412, (2001) 660
33. A. W. Sleight, Science 242 (1988) 1519
34. C. Park and R. L. Snyder, J. Am. Ceram. Soc. 78 (1995) 3171
35. M. Karppinen and H. Yamauchi, Materials Science and Engineering 26 (1999) 51
36. E. B. Sonin and I. Felner, Phys. Rev. B 57 (1998) R14000
37. R. A. Hein, Phys. Rev. B 33 (1986) 7539
38. N. Murayama, E. Sudo, K. Kani, A. Tsuzuki, S. Kawakami, M. Awano, and Y. Torii, Jpn. J. Appl. Phys. 27 (1988) L1623
39. C. Greaves and P. R. Slater, Physica C 161 (1989) 245
40. B. Hellebrand, X. Z. Wang, and P. L. Steger, J. Solid State Chem. 110 (1994) 32
41. L. Bauernfeind, *Supraleitung und Magnetismus in rutheniumhaltigen Kupraten*. Ph.D. thesis, Universität Bayreuth (1998)
42. A. C. McLaughlin, W. Zhou, J. P. Attfield, A. N. Fitch, and J. L. Tallon, Phys. Rev. B 60 (1999) 7512
43. D. J. Pringle, J. L. Tallon, B. G. Walker, and H. J. Trodahl, Phys. Rev. B 59 (1999) R11679
44. M.-J. Rey, P. Dehault, J. Joubert, and A. W. Hewat, Physica C 167 (1990) 162
45. M. Vybornov, W. Perthold, H. Michor, T. Holubar, G. Hilscher, P. Rogl, P. Fischer, and M. Divis, Phys. Rev. B 52 (1995) 1389
46. K. Nakamura, K. T. Park, A. J. Freeman, and J. D. Jorgensen, Phys. Rev. B 63 (2001) 024507
47. S. Malo, D. Ko, J. T. Rijssenbeek, A. Maignan, D. Pelloquin, V. P. Dravid, and K. R. Poeppelmeier, Int. J. Inorg. Mater. 2 (2000) 601
48. A. C. McLaughlin and J. P. Attfield, Phys. Rev. B 60 (1999) 14605
49. P. W. Klamut, B. Dabrowski, S. Kolesnik, M. Maxwell, and J. Mais, Phys. Rev. B 63 (2001) 224512
50. K. Otzsch, T. Mizukami, T. Hinouchi, J. Shimoyama, and K. Kishio, J. Low Temp. Phys. 117 (1999) 855
51. M. K. Wu, S. R. Sheen, D. C. Ling, C. Y. Tai, G. Y. Tseng, D. H. Chen, D. Y. Chen, F. Z. Chien, and F. C. Zhang, Czechoslovak Journal of Physics 46 (1996) 3381

52. D. Y. Chen, F. Z. Chien, D. C. Ling, J. L. Tseng, S. R. Sheen, M. J. Wang, and M. K. Wu, *Physica C* 282-287 (1997) 73
53. M. K. Wu, D. Y. Chen, F. Z. Chien, S. R. Sheen, D. C. Ling, C. Y. Tai, G. Y. Tseng, D. H. Chen, and F. C. Zhang, *Z. Phys. B* 102 (1997) 37
54. H. Takagiwa, J. Akimitsu, H. Kawano-Furukawa, and H. Yoshizawa, *J. Phys. Soc. Jpn.* 70 (2001) 333
55. E. Takayama-Muromachi, T. Kawashima, N. D. Zhigadlo, T. Drezen, M. Isobe, A. T. Matveev, K. Kimoto, and Y. Matsui, *Physica C* 357-360 (2001) 318
56. R. Ruiz-Bustos, J. M. Gallardo-Amores, R. Sáez-Puche, E. Morán, and M. A. Alario-Franco, *Physica C* 382 (2002) 395
57. T. Kawashima and E. Takayama-Muromachi, *Physica C* 398 (2003) 85
58. R. Li, Y. Zhu, Y. Qian, and Z. Chen, *Physica C* 176 (1991) 19
59. R. J. Cava, J. J. Krajewski, H. Takagi, H. W. Zandbergen, R. B. van Dover, W. F. Peck, jr., and B. Hessen, *Physica C* 191 (1992) 237
60. Y. Zhu, Y. Qian, R. Li, S. Wang, Z. Chen, Z. Chen, N. Wang, and G. Zhou, *Chinese Phys. Lett.* 9 (1992) 398
61. C. S. Knee, B. D. Rainford, and M. T. Weller, *J. Mater. Chem.* 10 (2000) 2445
62. V. P. S. Awana and E. Takayama-Muromachi, *Physica C* 390 (2003) 101
63. T. J. Goodwin, H. B. Radousky, and R. N. Shelton, *Physica C* 204 (1992) 212
64. R. Li, Y. Zhu, C. Xu, Z. Chen, Y. Qian, and C. Fan, *J. Solid State Chem.* 94 (1991) 206
65. H. A. Blackstead, J. D. Dow, I. Felner, and D. B. Pulling, *Phys. Rev. B* 61 (2000) 6303
66. A. Ono, *Jpn. J. Appl. Phys.* 34 (1995) L1121
67. K. Tang, Y. Qian, Y. Zhao, L. Yang, Z. Chen, and Y. Zhang, *Physica C* 259 (1996) 168
68. I. Felner, *Hyperfine Interactions* 113 (1998) 477
69. L. Shi, G. Li, X. D. Zhang, S. J. Feng, and X. G. Li, *Physica C* 383 (2003) 450
70. G. M. Kuz'micheva, A. S. Andreenko, I. E. Kostyleva, A. Zalevski, and J. Warchulka, *Physica C* 400 (2003) 7
71. G. M. Kuz'micheva, V. V. Luparev, E. P. Khlybov, I. E. Kostyleva, A. S. Andreenko, and K. N. Gavrilov, *Physica C* 350 (2001) 105
72. G. K. Strukova, I. I. Zver'kova, L. A. Dorosinskii, D. V. Shovkun, V. N. Zverev, and U. Topal, *Physica C* 387 (2003) 359
73. I. Felner, U. Asaf, C. Godart, and E. Alleno, *Physica B* 259-261 (1999) 703
74. G. V. M. Williams, L.-Y. Jang, and R. S. Liu, *Phys. Rev. B* 65 (2002) 064508
75. Y. Maeno, H. Hashimoto, K. Yoshida, S. Nishizaki, T. Fujita, J. G. Bednorz, and F. Lichtenberg, *Nature* 372 (1994) 532
76. G. Cao, S. McCall, and J. E. Crow, *Phys. Rev. B* 55 (1997) R672
77. G. Cao, S. K. McCall, J. E. Crow, and R. P. Guertin, *Phys. Rev. B* 56 (1997) R5740
78. A. Callaghan, C. W. Moeller, and R. Ward, *Inorg. Chem.* 5 (1966) 1572
79. K. Kumagai, S. Takada, and Y. Furukawa, *Phys. Rev. B* 63 (2001) 180509
80. R. S. Liu, L.-Y. Jang, H.-H. Hung, and J. L. Tallon, *Phys. Rev. B* 63 (2001) 212507

81. K. Yoshida, M. Nakamura, H. Kojima, and H. Shimizu, *Physica C* 388-389 (2003) 385
82. A. C. McLaughlin, J. P. Attfield, R. S. Liu, L. Y. Jang, and W. Z. Zhou, *J. Solid State Chem.* 177 (2004) 834
83. H. Schäfer, G. Schneidereit, and W. Gerhardt, *Z. anorg. allgem. Chemie* 319 (1963) 327
84. H. Schäfer, A. Tebben, and W. Gerhardt, *Z. anorg. allgem. Chemie* 321 (1963) 41
85. M. Labeau, B. Bochu, J. C. Joubert, and J. Chenavas, *J. Solid State Chem.* 33 (1980) 257
86. J. D. Whittler and R. S. Roth, eds., *Phase Diagrams for High T_c Superconductors*. American Ceramic Soc., Westerville, Ohio (1991)
87. T. A. Vanderah, R. S. Roth, and H. F. McMurdie, eds., *Phase Diagrams for High T_c Superconductors II*. American Ceramic Soc., Westerville, Ohio (1997)
88. N. Nguyen, J. Choisnet, and B. Raveau, *Mater. Res. Bull.* 17 (1982) 567
89. N. M. Hwang, R. S. Roth, and C. J. Rawn, *J. Am. Ceram. Soc.* 73 (1990) 2531
90. M. Nevřiva and H. Kraus, *Physica C* 235-240 (1994) 325
91. I. Nowik and I. Felner, *J. Magn. Magn. Mater.* 237 (2001) 1
92. T. P. Papageorgiou, T. Herrmannsdörfer, R. Dinnebier, T. Mai, T. Ernst, M. Wunschel, and H. F. Braun, *Physica C* 377 (2002) 383
93. R. D. Shannon, *Acta Cryst. A* 32 (1976) 751
94. Z. H. Han, J. I. Budnick, M. Daniel, W. A. Hines, D. M. Pease, P. W. Klamut, B. Dabrowski, S. M. Mini, M. Maxwell, and C. W. Kimball, *Physica C* 387 (2003) 256
95. S. Chen, H. F. Braun, and T. P. Papageorgiou, *J. Alloys Compounds* 351 (2003) 7
96. N. D. Zhigadlo, P. Odier, J. C. Marty, P. Bordet, and A. Sulpice, *Physica C* 387 (2003) 347
97. C. T. Lin, B. Liang, C. Ulrich, and C. Bernhard, *Physica C* 364-365 (2001) 373
98. I. Felner, U. Asaf, Y. Levi, and O. Millo, *Int. J. Mod. Phys. B* 13 (1999) 3650
99. I. Felner, U. Asaf, Y. Levi, and O. Millo, *Physica C* 334 (2000) 141
100. I. Felner, U. Asaf, F. Ritter, P. W. Klamut, and B. Dabrowski, *Physica C* 364-365 (2001) 368
101. I. Dzyaloshinsky, *J. Phys. Chem. Solids* 4 (1958) 241
102. T. Moriya, *Phys. Rev.* 120 (1960) 91
103. I. Felner, U. Asaf, S. D. Goren, and C. Korn, *Phys. Rev. B* 57 (1998) 550
104. I. Felner, U. Asaf, Y. Levi, and O. Millo, *Physica B* 280 (2000) 370
105. I. Zivkovic, Y. Hirai, B. H. Frazer, M. Prester, D. Drobac, D. Ariosa, H. Berger, D. Pavuna, G. Margaritondo, I. Felner, and M. Onellion, *Phys. Rev. B* 65 (2002) 14420
106. H. F. Braun, *Rare Earth Transition Metal Borocarbides (Nitrides), Superconducting, Magnetic and Normal State Properties*, (Eds. K.-H. Müller and V. N. Narozhnyi). Kluwer Academic Publishers, Dordrecht (2001)
107. B. Lorenz, R. L. Meng, J. Cmaidalka, Y. S. Wang, J. Lenzi, Y. Y. Xue, and C. W. Chu, *Physica C* 363 (2001) 251

108. P. W. Klamut, B. Dabrowski, S. M. Mini, M. Maxwell, S. Kolesnik, J. Mais, A. Shengelaya, R. Khasanov, I. Savic, H. Keller, T. Graber, J. Gebhardt, P. J. Viccaro, and Y. Xiao, *Physica C* 364-365 (2001) 313
109. R. W. Henn, H. Friedrich, V. P. S. Awana, and F. Gmelin, *Physica C* 341-348 (2000) 457
110. P. W. Klamut, B. Dabrowski, J. Mais, and M. Maxwell, *Physica C* 350 (2001) 24
111. A. C. McLaughlin, V. Janowitz, J. A. McAllister, and J. P. Attfield, *Chem. Commun.* (2000) 1331
112. A. C. McLaughlin, V. Janowitz, J. A. McAllister, and J. P. Attfield, *J. Mater. Chem.* 11 (2001) 173
113. M. Li, M. Yu, Z. Wang, H. Yang, Y. Hu, Z. Chen, Z. Li, and L. Cao, *Physica C* 382 (2002) 233
114. A. T. Matveev, A. Kulakov, A. Maljuk, C. T. Lin, and H. U. Habermeier, *Physica C* 400 (2003) 53
115. K. B. Tang, Y. T. Qian, L. Yang, Y. D. Zhao, and Y. H. Zhang, *Physica C* 282 (1997) 947
116. I. Felner, U. Asaf, S. Reich, and Y. Tsabba, *Physica C* 311 (1999) 163
117. A. Fainstein, E. Winkler, A. Butera, and J. Tallon, *Phys. Rev. B* 60 (1999) R12597
118. V. G. Hadjiev, A. Fainstein, P. Etchegoin, H. J. Trodahl, C. Bernhard, M. Cardona, and J. L. Tallon, *Phys. Stat. Sol. B* 211 (1999) R5
119. A. Butera, A. Fainstein, E. Winkler, and J. Tallon, *Phys. Rev. B* 63 (2001) 054442
120. J. D. Thompson, S.-W. Cheong, S. E. Brown, Z. Fisk, S. B. Oseroff, M. Tovar, D. C. Vier, and S. Schultz, *Phys. Rev. B* 39 (1989) 6660
121. C. Bernhard, J. L. Tallon, E. Brücher, and R. K. Kremer, *Phys. Rev. B* 61 (2000) 14960
122. J. L. Tallon, C. Bernhard, and J. W. Loram, *J. Low Temp. Phys.* 117 (1999) 823
123. J. L. Tallon, J. W. Loram, G. V. M. Williams, and C. Bernhard, *Phys. Rev. B* 61 (2000) R6471
124. X. H. Chen, Z. Sun, K. Q. Wang, S. Y. Li, Y. M. Xiong, M. Yu, and I. Z. Cao, *Phys. Rev. B* 63 (2001) 064506
125. C. W. Chu, Y. Y. Xue, R. L. Meng, J. Cmaidalka, L. M. Dezaneti, Y. S. Wang, B. Lorenz, and A. K. Heilman, Absence of a bulk Meissner state in $\text{RuSr}_2\text{GdCu}_2\text{O}_8$. *cond-mat/9910056* (1999)
126. C. W. Chu, Y. Y. Xue, S. Tsui, J. Cmaidalka, A. K. Heilman, B. Lorenz, and R. L. Meng, *Physica C* 335 (2000) 231
127. Y. Y. Xue, S. Tsui, J. Cmaidalka, R. L. Meng, B. Lorenz, and C. W. Chu, *Physica C* 341-348 (2000) 483
128. Y. Y. Xue, R. L. Meng, J. Cmaidalka, B. Lorenz, L. M. Desaneti, A. K. Heilmann, and C. W. Chu, *Physica C* 341-348 (2000) 459
129. Y. Y. Xue, B. Lorenz, R. L. Meng, A. Baikalov, and C. W. Chu, *Physica C* 364-365 (2001) 251
130. R. L. Meng, B. Lorenz, Y. S. Wang, J. Cmaidalka, Y. Y. Xue, and C. W. Chu, *Physica C* 353 (2001) 195

131. P. W. Klamut, B. Dabrowski, M. Maxwell, J. Mais, O. Chmaissem, R. Kruk, R. Kmiec, and C. W. Kimball, *Physica C* 341-348 (2000) 455
132. L. Bauernfeind, T. P. Papageorgiou, and H. F. Braun, *Physica B* 329-333 (2003) 1336

SUPERCONDUCTIVITY IN QUATERNARY BOROCARBIDES

R. Nagarajan¹, Chandan Mazumdar², Z. Hossain³ and L.C. Gupta^{4,*}

¹ Tata Institute of Fundamental Research, Mumbai 400005, INDIA

² Saha Institute of Nuclear Physics, Kolkata 700064, INDIA

³ Department of Physics, Indian Institute of Technology, Kanpur 208016, INDIA

⁴ Department of Physics, University of Mumbai, Mumbai 400 098, INDIA

1. INTRODUCTION

After the revolutionary discovery of superconductivity in high T_c oxide materials by Bednorz and Muller [1] in 1986, discovery of superconductivity in intermetallic quaternary borocarbide [2, 3, 4, 5, 6] is a landmark in the field of superconductivity. The discovery revived research in superconductivity in intermetallics for a variety of reasons and led to the new subject of *superconductivity and magnetism in quaternary borocarbides*. The field quaternary borocarbides originated with the discovery of superconductivity at an elevated temperature $T_c \sim 12-15$ K in Y-Ni-B-C system at TIFR, Bombay (Mumbai), India [2, 3, 4, 5, 6] followed by the findings of superconductivity in Y-Pd-B-C system ($T_c \sim 23$ K) [7] and in RNi_2B_2C ($R = Y, Lu, Tm, Er, Ho$) ($T_c \sim 15.5$ K, 16 K, 11 K, 10.5 K, and 8 K, respectively) [8, 9]. In this review we present briefly our experiments that led to the discovery of superconductivity in Y-Ni-B-C and an outline of subsequent developments indicating certain unique aspects of superconductivity and its interplay with magnetism in quaternary borocarbides. Several experiments studies which emphasize unusual superconducting properties of these materials are presented. We particularly stress upon the two most important features of these materials, namely, the energy gap and the flux line lattice. Several review articles and publications [10, 11, 12, 13, 14, 15, 16, 17, 18, 19, 20, 21, 22, 23, 24, 25,

* DAE-BRNS Senior Scientist

26, 27, 28, 29] are suggested for detailed information on a variety of phenomena in borocarbides.

2. DISCOVERY OF SUPERCONDUCTIVITY IN Y-Ni-B-C SYSTEM

The discovery of superconductivity in quaternary borocarbides arose out of our investigations of the intermetallic series RNi_4B (R = rare earth, Y) [2, 3, 4, 5, 6], [30, 31, 32, 33, 34,35]*.

The historic results on our argon arc melted sample of essentially single phase YNi_4B , which initiated this new field of quaternary borocarbides, is shown in Fig. 1. The non zero resistance drop around 12K and the drop in dc susceptibility around the same temperature is due to occurrence of trace superconductivity ($\sim 2\%$) in this sample, as confirmed by the observation of diamagnetism at low magnetic fields below 12K. Heat capacity of the material did not rule out bulk superconductivity, as the Sommerfeld coefficient was nearly zero. The results were found to be reproducible with $T_c \sim 12 - 15$ K [3, 5, 6] though the resistance drop was not the same in several independently prepared batches of YNi_4B (using starting materials from different sources) (elements with nominal purity $> 99.9\%$, except for B which was 99.8%). Powder x-ray diffraction pattern and electron microprobe analysis (EPMA and EDAX) indicated the sample to be highly homogeneous and did not reveal any significant impurity phases [3]. Therefore, initially it was speculated that superconductivity in this material might be related to the crystallographic superstructure of YNi_4B [3]. Finding of superconductivity in YNi_4B was a remarkable and surprising result as: (i) till then, only a few Ni containing superconductors were known and in all these cases T_c was less than 4.2 K (ii) Ni is known to suppress superconductivity even in small concentrations, e.g., 2% Ni suppresses T_c of $Lu_2Fe_3Si_5$ from ~ 6 K to ~ 2 K [36], and (iii) Only a few intermetallics are known with $T_c > 10$ K [37], which may be considered high T_c for intermetallics.

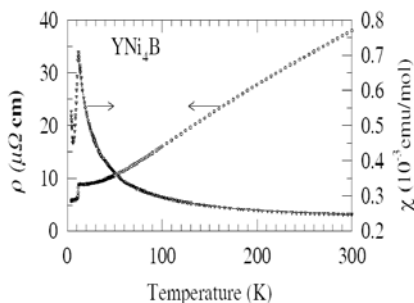


Fig. 1. Temperature dependence of resistivity (ρ) and magnetic susceptibility (χ) (measured at 6 kOe) of our sample of YNi_4B as a function of temperature. The anomaly at ~ 12 K is due to trace superconductivity (from Ref. 3).

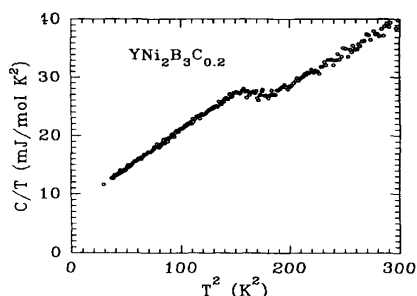


Fig. 2. Specific heat (C/T vs T^2) of the material with nominal composition $YNi_2B_3C_{0.2}$. The anomaly around 13 K confirms the occurrence of bulk superconductivity in the sample (from Ref. 4).

* Refs. 30 – 35, give several details that are not given in Refs. 2 – 6.

As the drop in resistivity was different in different batches of YNi_4B , we pursued the possibility of superconductivity arising from a phase of Y-Ni-B system, other than YNi_4B . Accordingly, we synthesized (by arc melting) materials with various compositions $\text{Y}_x\text{Ni}_y\text{B}_z$ (those reported in the phase diagram of Y-Ni-B system as well those not reported) and investigated them for superconductivity. In this process three more materials (nominal composition, YNi_2B_3 , YNi_3B_2 and YNi_4B_3) were found exhibiting superconductivity around the same temperature [35]. Superconducting phase in all of them, however, was still only a minor fraction of the materials. These results strongly suggested that superconductivity in our samples may be due to a phase stabilized by the presence of yet another element in our samples of YNi_4B . Considering various impurities carbon was considered a possibility. In order to test this conjecture, a sample of YNi_4B was re-melted with deliberate addition of 0.2 atom fraction of carbon. The new material, $\text{YNi}_4\text{BC}_{0.2}$ showed dramatic result of the superconducting fraction being similar to a bulk superconductor [4], and unlike YNi_4B , it exhibited zero resistance around 12 K, diamagnetic response of the bulk material increased by about 20 times compared to that of YNi_4B and powdered $\text{YNi}_4\text{BC}_{0.2}$ also exhibited diamagnetism [4].

A comparison of x-ray diffraction patterns of YNi_4B and $\text{YNi}_4\text{BC}_{0.2}$ showed that addition of carbon did not alter the XRD pattern except for the suppression of the line due to superstructure and the presence of a minor line around $2\theta = 40$ (intensity $< 10\%$ of 100% line). Careful EDAX analysis of the material showed that there were no regions that were free of Ni [4]. These investigations, therefore, ruled out the possibility that the observed superconductivity was due to Y_2C_3 (a high pressure, high temperature phase with the Pu_2C_3 structure) with $T_c \sim 11$ K [38]. Meissner signal (diamagnetic susceptibility under field cooled (FC) condition) at 5 K and small but distinct anomaly in heat capacity across T_c and small Sommerfeld coefficient were consistent with the possibility of bulk superconductivity in this material [4].

We also reinvestigated the other compositions YNi_2B_3 , YNi_3B_2 and YNi_4B_3 which had shown weak superconductivity, by re-melting each of them with 0.2 atomic fraction of carbon. In all of them we found enhanced superconducting properties, but all of them were multiphase. Of these, multiphase sample $\text{YNi}_2\text{B}_3\text{C}_{0.2}$ with $T_c \sim 13$ K showed a large Meissner fraction and had the maximum specific heat anomaly across T_c (Fig. 2) [4]. This confirmed that $\text{YNi}_2\text{B}_3\text{C}_{0.2}$ definitely had a bulk superconducting phase [4, 5, 6]. From our EDAX analysis (our instrument was not sensitive to B and C) we argued that the major phase responsible for the bulk superconductivity in our multiphase $\text{YNi}_2\text{B}_3\text{C}_{0.2}$ sample [4] contains Y and Ni in the ratio $\text{Y}:\text{Ni} = 1:2$. By preparing and studying samples with various combinations of the elements we showed that all the four elements are required for the formation of this new superconducting phase. All these results together established that the system Y-Ni-B-C has a bulk superconducting phase containing all the four elements [4, 5, 6]. Thus, the first quaternary intermetallic superconducting material was discovered, giving a new direction to research in intermetallic superconductors.

While our further efforts to synthesize the single phase material were in progress, Cava *et al.*, reported superconductivity in multiphase $\text{YPd}_5\text{B}_3\text{C}_{0.35}$ with $T_c \sim 23$ K [7] and in single phase materials of the composition $\text{RNi}_2\text{B}_2\text{C}$, $\text{R} = \text{Y, Lu, Tm, Er, Ho}$ ($T_c \sim 15.5$ K, 16.5 K, 11 K, 10.5 K, 8 K, respectively) [8]. Siegrist *et al.*, [9] showed that the structure of $\text{LuNi}_2\text{B}_2\text{C}$ is a filled variant of the well known ThCr_2Si_2 tetragonal structure with C atoms located in the Lu (R)-planes (Fig. 3).

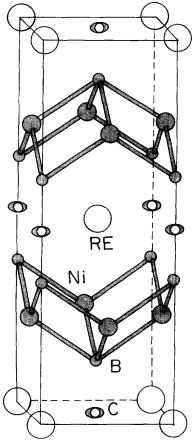


Fig. 3. Unit cell of the tetragonal (space group $I4/mmm$) structure of $RENi_2B_2C$ (RE = Y, rare earth)-materials (based on Fig. from Ref. 9). The oblong representation of C atoms indicates the highly anisotropic thermal vibrations of C [43].

landmark in superconductivity. It triggered intense activity in the general area of superconductivity and magnetism in intermetallics and brought out many new facets associated with it.

3. STRUCTURE AND MATERIALS OF QUATERNARY BOROCARBIDE FAMILY

Majority of the members are of the type RM_2B_2C (R = rare earth, Y, Sc, Th, U; M = *d* metal) (not all combinations of R and M form) with $LuNi_2B_2C$ -type tetragonal structure (space group $I4/mmm$) (Fig. 3). The structure is highly anisotropic with the ratio of the two lattice parameters of the tetragonal unit cell, c/a , being ~ 3 . The structure is derived from the well known $ThCr_2Si_2$ structure with C atoms in the rare earth planes. The structure is most stable for Ni and the entire rare earth series form and these materials are the most investigated. These materials have been prepared in polycrystalline form (arc melting), single crystal form (by flux method [49], and floating zone method [50, 51]) and in thin film form [52, 53, 54]. It is the availability of large single crystals, having large electron mean free path (compared to the coherence length of superconductivity) which could be regarded as clean limit superconductor, of RNi_2B_2C (R = Y, rare earth) which has enabled detailed investigation of the physical properties of these interesting materials.

These developments generated excitement [39] for the following reasons. The observed T_c in quaternary borocarbides is high ($> 10K$) for intermetallics. $T_c \sim 23$ K in the Pd- system was the highest then known for *bulk* intermetallics. Such a high T_c has been observed two decades after the observation of $T_c \sim 23$ K in *thin* films of Nb_3Ge [40]. It is to be noted that bulk samples of Nb_3Ge are multiphase and non superconducting. The highest then known T_c in a bulk material was 21 K in Nb_3Ga [37]. Since then, MgB_2 has been shown to superconduct at 39 K [41]. Apart from high T_c 's, quaternary borocarbides have acquired importance also because of the exotic phenomenon of coexistence of superconductivity and magnetism, observed in $TmNi_2B_2C$ [42], $ErNi_2B_2C$ [42,43], $HoNi_2B_2C$ [42] and $DyNi_2B_2C$ [44,45,46,47] ($T_c \sim 11$ K, 10.5 K, 8 K & 6 K, and $T_N \sim 1.5$ K, 6 K, 8 K & 11 K, respectively). These quaternary magnetic superconductors appeared about two decades after the ternary magnetic superconductors RRh_4B_4 and $RMo_6S(Se)_8$ [48]. The quaternary borocarbide magnetic superconductors have high coexistence temperatures, known thus far, providing scope for detailed experiments. They exhibit certain unique features not observed before. Thus, discovery of superconductivity in the system Y-Ni-B-C is a

The structure type is intermediate between the two well known superconducting families, the HTSC materials and the ternary borides RRh_4B_4 series. The HTSC materials are tetragonal and layered [55] with the rare earth layer almost isolated with respect to the superconducting CuO plane. The RRh_4B_4 structure has clusters of Rh_4B_4 and the clusters were thought to be important for superconductivity in intermetallics [48]. Quaternary borocarbide structure is layered - can be viewed as layers of RC, and Ni_2B_2 [9], but normal state electronic properties are nearly three dimensional as indicated by band structure calculations [56] and almost isotropic normal state resistivity [57].

The variation of a lattice parameter in RNi_2B_2C (R = rare earth) series exhibits the classic lanthanide contraction with decreasing free R ion radius, but the c parameter increases [58]. This shows that the R-R bond dominates the structure, squeezing and distorting the NiB_4 tetrahedron in the structure as the size of R decreases. Ni-Ni distance (2.45 Å) is shorter than that in Ni-metal (2.5 Å) and implies a strong metallic system.

Since many members of RNi_2B_2C rare earth series (R = Dy, Ho, Er, Tm, Lu) are superconductors, and La being a non magnetic rare earth, one might expect $LaNi_2B_2C$ to be a superconductor, but no superconductivity is observed down to 0.3 K [59]. This absence of superconductivity in this material as well as in lighter rare earths is attributed to larger ionic size resulting in a distortion of NiB_4 tetrahedron (because of rigidity of Ni-B bonds) from the optimum configuration that is conducive for superconductivity. This structural distortion changes electronic density of states (DOS) at E_F which is an important parameter for superconductivity. Band structure calculations show that both T_c and DOS scale the same way as B-Ni-B angle (a measure of distortion of the NiB_4 tetrahedron) [60]. In this sense, the suppression of superconductivity appears to be structurally driven. The material with perfect NiB_4 tetrahedron should have highest T_c . The NiB_4 tetrahedron is closest to the perfect in $LuNi_2B_2C$ having highest T_c in the series and far away from being perfect in non superconducting $LaNi_2B_2C$. The requirement of near ideal NiB_4 tetrahedron for superconductivity has also been seen in investigations of effect of doping on superconductivity in YNi_2B_2C . As the doping concentration (or element) is changed, a linear relation has been obtained between T_c and unit cell volume [61]. Such a structure- T_c relationship of this type is unusual for intermetallic superconductors [60]. However, it may be noted that the high T_c ($\sim T_{c,onset} \sim 16$ K) of metastable superconductor $ScNi_2B_2C$ does not follow the above structural correlation [60].

No change in structure was observed in RNi_2B_2C down to 5 K [58]. a parameter of the unit cell changes with temperature considerably, mimicking the R-C and Ni-Ni bond. However, the c parameter does not change much as a function of temperature implying the non stretchable nature of B-B bond [62, 61]. In YNi_2B_2C , there is no change in structure under pressure up to 6 GPa at room temperature [63]

The quaternary borocarbide system Y-Pd-B-C deserves special mention as it has a phase with $T_c \sim 23$ K [7], which equaled the highest T_c known for intermetallics prior to the discovery of superconductivity in MgB_2 ($T_c \sim 39$ K) in 2001 [41]. But, it has not been possible to prepare single phase material of the superconducting phase. Strong signal of superconductivity is obtained in a multiphase material of nominal composition $YPd_5B_3C_{0.35}$. The superconducting phase is found to form only as a metastable high temperature phase which is obtained by quenching the melt. On annealing, superconductivity vanishes.

In the absence of single phase sample, it has been difficult to identify the composition of superconducting phase of Y-Pd-B-C system. Indirectly, it has been inferred that the phase is

YPd₂B₂C with LuNi₂B₂C tetragonal structure, may be with variations in site occupancy of B and C [64, 65, 66, 67, 68]. One systematic study of heat treatment of YPd₅B₃C_{0.35} and correlation of intensities of x-ray diffraction peaks of 1221 phase with strength of diamagnetic signal seems to suggest that superconducting phase is cubic [69]. However, a recent work on micro-grain single phase specimen [70] seems to confirm the phase to be 1221-type tetragonal structure. Interestingly, investigations on the phase diagram of the pseudo quaternary Y(Ni_{1-x}Pd_x)₂B₂C [71] have shown that stable and superconducting tetragonal phase can be obtained on substitution of Ni by Pd up to $x = 0.38$. In contrast to metastable YPd₂B₂C phase, in the partial substituted system, the phase is stable even after annealing up to 1300°C. But with increasing Pd content, T_c decreases from 15.5 K for $x = 0$ to 10.4 K for $x = 0.4$ [71].

The quaternary borocarbides form in homologous series (RC)_m(Ni₂B₂)_n [9] with the structure having more sheets of R-C layers between Ni₂B₂ layers. For $m = 2$, $n = 1$ only the heavier members (smaller ionic radius) of the rare earth series RNiBC form [9, 72, 73]. In this series, LuNiBC and YNiBC are superconductors with T_c ~2.9 K [74] and ~0.8 K [75], respectively. On partial replacement of Ni by Cu, the T_c in YNi_{1-x}Cu_xBC increases to as high as ~9 K (for $x = 0.4$) [75, 76, 77] and T_c in LuNi_{1-x}Cu_xBC increases to 6.6 K [78]. These are the only known cases in quaternary borocarbides where T_c is increased on partial substitution of an element. In the case of YNi₂B₂C, doping with Cu decreases the T_c. In YNi_{1-x}Cu_xBC, the T_c of 9 K has been found to be very sensitive to B concentration. For B stoichiometry ≤ 0.95 , T_c does not exceed 6 K [75].

One compound is known for $m = 3$ and $n = 1$, but it is a nitride La₃Ni₂B₂N₃ [79] and is only the third material outside 1221-type, which is a superconductor (T_c ~12 K). When prepared in pure form, this compound is stable [80]. Neutron diffraction measurements of this compound indicate that N-sites are not fully occupied [81].

For $m = 4$, $n = 1$, two compounds have been reported, viz., Lu₄Ni₂B₂C₄ (*i.e.*, Lu₂NiBC₂) [82] and Y₄Ni₂B₂C₄ (*i.e.*, Y₂NiBC₂) [83]. However, later detailed investigations have shown that, in Y₄Ni₂B₂C₄, between two pairs of RC layers there is a B layer, giving Lu₄Ni₂B₃C₄ [84], as the correct chemical composition and suggesting that a four layer RC as a unit, is perhaps unstable as such and needs a B layer for stability. However, recently it has been found [85] that the structure has a slight monoclinic distortion - Lu₄Ni₂B₃C₄ has the lattice parameters: $a \sim 5 \text{ \AA}$, $b \sim 5 \text{ \AA}$, $c \sim 27.4 \text{ \AA}$, $\beta \sim 93$. It has also been reported [85] that this structure is very likely a stable one, and a large number of borocarbide compounds can be formed with many rare earth and d metal combinations. This seems to be the only structure in quaternary borocarbides which has a Fe member.

One member of the series $m = 3$ and $n = 2$, Y₃Ni₄B₄C₃ has been reported to form and is claimed to be a superconductor with T_c ~12 K [86]. Our studies confirm the formation of the phase but not in phase pure form. We believe that the reported superconductivity originates from the presence of 1221 phase in their sample. Recently, structures with $m = 5$, $n = 6$ (Y₅Ni₆B₆C₅) or with $m = 5$, $n = 8$ (Y₅Ni₈B₈C₅) have been reported to exist locally as metastable phases in as cast / annealed samples of YNi_{2-x}B_{2-x}C [87]. From the observation of stacking faults, possible occurrence of structures with $m = 2$, $n = 3$ (Y₂Ni₃B₃C₂) and $m = 4$, $n = 7$ (Y₄Ni₇B₇C₄) have also been claimed [87].

About 60 materials of the quaternary borocarbide family are known of which about 20 are superconductors, many of them having T_c > 5 K. A list of the materials can be found in Ref. 22.

Before we end this section, we point out that quaternary borocarbides may have boron/carbon vacancies depending on the preparation conditions and superconductivity seem to be somewhat sensitive to these vacancies. Positron annihilation studies [88] in $\text{YNi}_2\text{B}_2\text{C}$ have indicated the presence of carbon vacancies and ^{11}B NMR experiments [89] have shown two sets of signal below T_c , one shifting with temperature and the other remaining same as that above T_c . The unshifted signal is perhaps due to those regions which are non superconducting. Sensitivity of superconductivity to boron / carbon stoichiometry / vacancy is severe in the case of the magnetic superconductor members $\text{HoNi}_2\text{B}_2\text{C}$ and $\text{DyNi}_2\text{B}_2\text{C}$ (see below).

4. NON MAGNETIC SUPERCONDUCTORS $\text{YNi}_2\text{B}_2\text{C}$ AND $\text{LuNi}_2\text{B}_2\text{C}$

$\text{YNi}_2\text{B}_2\text{C}$ ($T_c \sim 15.5$ K) [43, 90] and $\text{LuNi}_2\text{B}_2\text{C}$ ($T_c \sim 16.5$ K) [91] are type-II superconductors with upper critical field $H_{c2}(0) \sim 10$ T. The basic superconducting parameters of these materials are intermediate to those of superconducting elements of type-I and HTSC oxides, e.g., at $T \rightarrow 0$ the penetration depth $\lambda(0) \sim 1000$ Å, coherence length $\xi(0) \sim 100$ Å, and energy gap $\Delta(0) \sim 2.2$ meV [27]. Initial studies suggested that these are conventional BCS type superconductors. The ratio $\Delta C / \gamma T_c$ (ΔC is the jump in heat capacity at T_c , and γ is the coefficient of electronic specific heat) obtained from heat capacity measurements, is 1.8, as against 1.43 expected from BCS theory. Inelastic neutron scattering and tunneling experiments in $\text{LuNi}_2\text{B}_2\text{C}$ show that superconducting energy gap is of the order of 2.5-4.5 meV which gives $\Delta/k_B T_c$ in the range 2-3.5 as against the value of 1.76 from BCS theory. These indicate intermediate to strong coupling in these superconductors. Isotope effect on T_c with ^{10}B or ^{11}B isotopes has been observed in $\text{YNi}_2\text{B}_2\text{C}$ and $\text{LuNi}_2\text{B}_2\text{C}$ [92, 93] supporting electron-phonon interaction as the mechanism of pairing. The total isotope exponent α of the BCS relation for isotope effect on $T_c = M^{-\alpha}$ ideally should be 0.5. The value of α estimated theoretically (using estimates of coulomb coupling constant and Debye temperature) for $\text{YNi}_2\text{B}_2\text{C}$ and $\text{LuNi}_2\text{B}_2\text{C}$ are 0.38 and 0.41, respectively. Experimentally the partial isotope exponent for boron isotopes 10 and 11 were found to be 0.21 and 0.11 respectively [93] which is smaller than the theoretical estimate. It is therefore, expected that a reasonably large partial isotope effect would come from other elements in these compounds [93]. It is pertinent to note that a large anisotropic thermal amplitude of carbon atom has been observed in R-C plane of $\text{YNi}_2\text{B}_2\text{C}$ [43, 94]. A rare and remarkable direct evidence of electron phonon interaction comes from the inelastic neutron scattering experiments on single crystals of $\text{YNi}_2\text{B}_2\text{C}$ [95] and $\text{LuNi}_2\text{B}_2\text{C}$ [96] where a dramatic change has been observed in the phonon spectra on the onset of superconductivity. A narrow phonon peak ($Q = 0.525, 0.8$; $E = 4.75$ meV) is observed below T_c . It is also found that the intensity of this peak depends on the strength of an external field in manner similar to the temperature dependence of H_{c2} confirming that this peak is associated with superconductivity [95]. While Kawano *et al.*, [95] have interpreted the peak as due a new excitation, others [96, 97] have interpreted it as due to narrowing of the phonon width as a result of increased phonon life time due to opening up of the superconducting gap. An important and interesting aspect is that the Q vector direction matches with that of the incommensurate vectors of magnetic ordering in $\text{RNi}_2\text{B}_2\text{C}$ family [58]. This suggests intimate relationship of superconductivity and magnetism, magnetic order also being controlled by conduction electrons (see below).

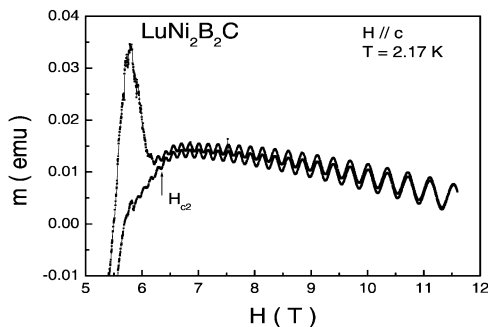


Fig. 4. dHvA oscillations in the m - H plot in $\text{LuNi}_2\text{B}_2\text{C}$ for applied field (H) \parallel c -axis of the crystal at 2.17 K with. The data also shows the peak effect (based on figure from Ref. 99).

NbSe_2 , perhaps borocarbide is the only other ideal material with availability of crystals in the clean limit and having optimum superconducting parameters for detailed investigations of vortex lattice dynamics through peak effect [101]. Along with the dHvA oscillations, Fig. 4 also shows the peak effect in $\text{LuNi}_2\text{B}_2\text{C}$ at 2 K [99].

Band structure calculations show that at the fermi energy, major part of the contribution comes from Ni $3d$ electron states and the remaining contribution come from s and p electron states of C and B and d electronic states of Y or Lu [102,103,104,105,106,107]. The Ni- $3d$ band is very narrow, but B-C s - p electronic states give a broad manifold band and Lu- $5d$ /Y- $4d$ band is a minority contribution. The narrow Ni- $3d$ band produces relatively high DOS at E_F and is mainly responsible for superconductivity. Broad s - p manifold band also seems to have a role in superconductivity in these compounds and this is related to NiB_4 tetrahedral geometry [103]. This also explains the absence of superconductivity in $\text{LaNi}_2\text{B}_2\text{C}$ where the DOS at E_F is only half of that in superconducting $\text{LuNi}_2\text{B}_2\text{C}$. Relationship of superconductivity and distortion of NiB_4 tetrahedron has been discussed in the earlier section. The width of d -band observed in photoemission experiment of $\text{YNi}_2\text{B}_2\text{C}$ [108] is narrower than that indicated by band structure calculations. The coefficient of electronic specific heat γ in $\text{LuNi}_2\text{B}_2\text{C}$ is ~ 18 mJ/mol K^2 which is about 1.6 times larger than that obtained from band structure calculation and suggests a stronger electron-phonon coupling [18]. Most band structure calculations show that rare earth ions are not fully ionized. However, isomer shift of ^{161}Dy Mössbauer resonance of superconducting $\text{DyNi}_2\text{B}_2\text{C}$ is similar to that of a non metallic system [109] which would imply fully ionized Dy and R-C layer is insulating, thereby suggesting that superconductivity arises from Ni_2B_2 layers.

In quaternary borocarbides, the dHvA oscillations have been seen down to unusually low magnetic fields (~ 2 T) [98]. The oscillations in normal state have been seen at relatively high temperatures (~ 10 K) [99]. Fig. 4 shows the dHvA oscillations observed in a single crystal of $\text{LuNi}_2\text{B}_2\text{C}$ [99]. The observed frequencies are consistent with band calculations. However, the large oscillations of F_β branch observed both in $\text{YNi}_2\text{B}_2\text{C}$ and $\text{LuNi}_2\text{B}_2\text{C}$ are not found in the band structure calculations and is surmised that the branch may be due to electronic correlation effects [100]. Apart from 2H-

5. MAGNETIC SUPERCONDUCTORS - RNi_2B_2C ($R = Tm, Er, Ho, Dy$) AND $NdPt_2B_2C$

Occurrence of superconductivity and its coexistence with local magnetism in $TmNi_2B_2C$, $ErNi_2B_2C$, $HoNi_2B_2C$, and $DyNi_2B_2C$, has been one of the most exciting aspects of quaternary borocarbides. Magnetism and superconductivity are normally, mutually exclusive phenomena. It is well known that dilute paramagnetic impurities would break the paired electrons (magnetic pair breaking) and suppresses superconductivity [110, 111]. 0.01 atomic fraction of Gd in La suppresses T_c of La from ~ 6 K to ~ 1 K [110]. The surprising fact about the magnetic superconductors of quaternary borocarbides is that superconductivity survives in the presence of large amount of rare earth magnetic ions. One could argue that in the magnetically ordered state, there is no net magnetic moment within coherence length. However, it is to be noted that both in $ErNi_2B_2C$ and $TmNi_2B_2C$ there is large temperature region (~ 6 K to ~ 11 K and ~ 1.5 K to ~ 11 K, respectively) where superconductivity is sustained in presence strong paramagnetism. Heat capacity and neutron scattering studies have established bulk superconductivity and long range magnetic order in these magnetic superconductors [43, 46, 58, 112]. Superconductivity has been shown to coexist with long range antiferromagnetic order, in materials like RRh_4B_4 , ($R = Pr, Nd, Sm, Tm$) [48]. In these cases, the magnetic ordering temperature (T_N) is rather low (< 2 K) implying that the magnetic order arises essentially due to dipolar interactions between the rare earth magnetic moments and the conduction electrons do not take part in the magnetic order. The same is true in the case of HTSC materials. In fact, the magnetic ordering temperature is ~ 2 K, both in $GdBa_2Cu_3O_7$ which is conductor and in $GdBa_2Cu_3O_6$ which is an insulator, clearly showing that conduction electrons have no role in the magnetic order in HTSC [113]. The major remarkable property of the magnetic superconductors of quaternary borocarbide materials is that the materials show coexistence of superconductivity and magnetism with high magnetic ordering temperatures ($T_N > 5$ K). The high T_N implies that the magnetic order is mediated by the conduction electrons (through the well known Ruderman-Kittel-Kasuya-Yoshida (RKKY) interaction [114] in magnetism of metallic systems) which in turn implies intimate interaction of superconductivity and magnetism. This is a surprising and exciting situation for the otherwise mutually exclusive phenomena. Further, the coexistence occurs in this system in all the three possible kinds of competition between superconductivity and magnetism, *viz.*, T_c (11 K) $>$ T_N (1.5 K) in $TmNi_2B_2C$ [42]; T_c (11 K) $>$ T_N (6 K) in $ErNi_2B_2C$ [42,43] *i.e.*, in these two materials as one cools the material, superconductivity occurs first then the magnetic order; T_c (8 K) \sim T_N (8 K) in $HoNi_2B_2C$ [42]; T_c (6 K) $<$ T_N (11 K) in $DyNi_2B_2C$ [44, 45, 46, 47] *i.e.*, superconductivity occurs in an already magnetically ordered lattice. With the above properties and with both T_c and T_N occurring at accessible temperatures (> 5 K), and as well as the availability of large and clean single crystals make these systems ideal and model systems for detailed investigations of interaction of superconductivity and local magnetism [115]. A large body of work now exists on these magnetic superconductors. A few highlights are mentioned here. More detailed accounts may be found in the reviews cited in the Introduction section, in particular in Refs. [17, 20, 24].

The double reentrant behavior of $HoNi_2B_2C$ in zero external magnetic field (normal $T > \sim 8.5$ K, superconducting ~ 8.5 K $>$ $T > \sim 5.5$ K, tendency to go normal ~ 5.5 K $>$ $T > \sim 4.5$ K and finally regains superconductivity below ~ 4.5 K) which has not been seen earlier in any other system [17, 42 116]. Neutron diffraction studies of $HoNi_2B_2C$ show that in the region 5-

8 K, immediately below the magnetic ordering temperature T_m , magnetic structure is quite complex and below 5 K, it settles down to a commensurate antiferromagnetic structure [58, 117, 118]. In the theoretical calculations based on normal state electronic structure, electronic susceptibility has been shown to have a maximum at $\chi(q) = (0.6, 0, 0)$ [119]. In several of these magnetic borocarbides, the magnetic structure corresponds to this $\chi(q)$ wave vector which confirms that magnetic order is mediated by conduction electrons. In the reentrance region, the magnetic structure has an a -axis modulated component which is believed to be responsible for the re-entrance [118]. A theoretical model that into account certain band structure details has been proposed to understand the the reentrance feature and anisotropy of H_{c2} in $\text{HoNi}_2\text{B}_2\text{C}$ [120]. According to this model, it is the helical component of the magnetic structure (the structure has an incommensurate c -axis spiral component in the reentrance temperature region [118]) which is responsible for the reentrance behaviour in the temperature region ~ 6 -4 K. Apart from these aspects, we also point out that in quaternary borocarbides, stoichiometry of B and C affects superconducting properties. In $\text{HoNi}_2\text{B}_2\text{C}$, the competition of superconductivity and magnetism is so delicate that the stoichiometry severely affects the superconductivity and the reentrance [121].

In $\text{DyNi}_2\text{B}_2\text{C}$ superconductivity sets in below T_N ($T_N \sim 11$ K, $T_c \sim 6$ K) [44, 45, 46, 47]. The other two materials where such a phenomenon has been observed are $\text{Er}_2\text{Fe}_3\text{Si}_5$ ($T_c \sim 0.9$ K, $T_N \sim 2.5$ K) [122] and $\text{Tb}_2\text{Mo}_3\text{Si}_4$ ($T_c \sim 2$ K, $T_N \sim 19$ K) [123]. However, T_N and T_c in $\text{DyNi}_2\text{B}_2\text{C}$ are high enough to allow detailed studies of this unique situation. An important implication of $T_c < T_N$ is that T_c might get suppressed even by non magnetic impurities which had been theoretically anticipated [17, 124]. Substitution of 0.1 atomic fraction of Dy by Lu [125] or Y [126] depresses of T_c of $\text{DyNi}_2\text{B}_2\text{C}$ by ~ 3 K which is as strong as T_c suppression of 4 K due to magnetic pair breaking by 0.1 atomic fraction of Gd in $\text{YNi}_2\text{B}_2\text{C}$ [127, 116]. This effect may be viewed as pair breaking due to creation of magnetic holes. Such an effect has been observed for the first time. Thus, superconductivity in materials with $T_c < T_N$ will be very sensitive to impurities and identifying such materials require extreme care. Superconductivity in $\text{DyNi}_2\text{B}_2\text{C}$ is very sensitive to conditions of preparation [47] and due to the reason mentioned above, superconductivity was not identified in $\text{DyNi}_2\text{B}_2\text{C}$ in the early investigations.

Recently coexistence of superconductivity and magnetism has been established in $\text{NdPt}_2\text{B}_2\text{C}$ system [128, 129]. Pt-based quaternary borocarbides $\text{RPt}_2\text{B}_2\text{C}$ form only for lighter rare earth members ($R = \text{La, Ce, Pr, Nd, Y}$) [130]. Even in these cases, the phase purity is not very good. It has been shown that the phase purity can be improved if Pt is partially replaced by Au, such as $\text{LaPt}_{1.5}\text{Au}_{0.6}\text{B}_2\text{C}$ [131] or with a nominal composition such as $\text{LaPt}_{2.1}\text{B}_{2.4}\text{C}_{1.2}$ [132]. In these Pt-borocarbides, superconductivity had been reported for La-, and Pr- compounds, but not for the Nd-compound. Earlier reports on magnetic order were conflicting for the Nd-compound [130, 131, 132]. Recent investigations showed superconductivity with $T_{c,\text{onset}} \sim 3$ K and magnetic order ~ 1.7 K in samples of both $\text{NdPt}_{1.5}\text{Au}_{0.6}\text{B}_2\text{C}$ and $\text{NdPt}_{2.1}\text{B}_{2.4}\text{C}_{1.2}$ [128, 129]. Superconductivity survives even below the magnetic ordering temperature [129]. Earlier studies [131, 132] suggested that Au helps in reducing the annealing temperature and that it does not enter the lattice. In the recent findings it has been found that superconductivity is more robust in Au containing samples than Au free non-stoichiometric single phase samples which suggests that very likely Au enters the lattice and plays a role in the superconductivity of the material [129].

6. THE HEAVY FERMION BOROCARBIDE - $\text{YbNi}_2\text{B}_2\text{C}$

The members $R = \text{Pr}, \text{Nd}, \text{Sm}, \text{Gd}, \text{Tb}$ of the $\text{RNi}_2\text{B}_2\text{C}$ series are magnetically ordered below ~ 4 K, 5 K, 10 K, 19 K, 15 K, respectively [46] and have a variety of magnetic structures [58]. This article being on superconductors, we do not discuss these magnetic members. Detailed discussion may be found in the review articles mentioned in the Introduction. However, we briefly discuss $\text{YbNi}_2\text{B}_2\text{C}$ which though non-superconducting, is a very important member of the quaternary borocarbide family. Considering that the two neighbouring members of $\text{YbNi}_2\text{B}_2\text{C}$ in the rare earth series are superconducting – $\text{LuNi}_2\text{B}_2\text{C}$ ($T_c \sim 16.5$ K) and $\text{TmNi}_2\text{B}_2\text{C}$ ($T_c \sim 11$ K), from the deGennes scaling systematics of T_c of magnetic superconductors of $\text{RNi}_2\text{B}_2\text{C}$ [42] with respect to rare earth, one would expect $\text{YbNi}_2\text{B}_2\text{C}$ to exhibit superconductivity around 12 K. However, surprisingly, $\text{YbNi}_2\text{B}_2\text{C}$ does not exhibit superconductivity down to 2 K [133, 134]. In contrast, it is to be noted that among the members of RMO_6S_8 series, YbMo_6S_8 has the highest T_c (~ 9 K) [48].

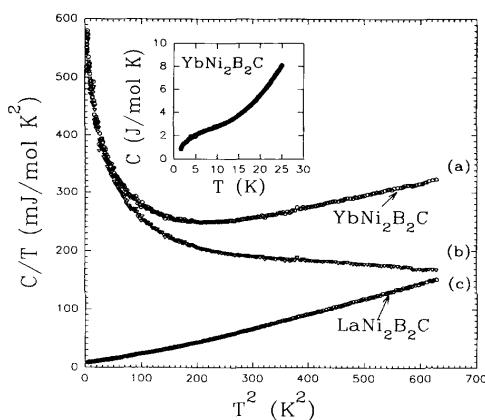


Fig. 5. Heat capacity (C) of (a) $\text{YbNi}_2\text{B}_2\text{C}$ and (c) $\text{LaNi}_2\text{B}_2\text{C}$ plotted in the form of C/T vs T^2 . (b) is the heat capacity of $\text{YbNi}_2\text{B}_2\text{C}$ after subtracting the non magnetic contribution using the data of $\text{LaNi}_2\text{B}_2\text{C}$ (from Ref. 133)

results [134]. These results show that $\text{YbNi}_2\text{B}_2\text{C}$ is a heavy fermion system and that $4f$ -electrons of Yb in $\text{YbNi}_2\text{B}_2\text{C}$ are hybridized with conduction electrons resulting in a dense Kondo system. Temperature independent x-ray L_{III} edge line shape and position signifying single $3+$ valence state of Yb [133], confirms that $\text{YbNi}_2\text{B}_2\text{C}$ is not a charge fluctuation system but a spin fluctuation system. ^{170}Yb Mössbauer measurements show no magnetic ordering of Yb ions down to 70 mK [135] indicating that spin fluctuations persist down to 70 mK.

Since there is no structural anomaly, the absence of superconductivity in $\text{YbNi}_2\text{B}_2\text{C}$ has to be attributed to the moderate heavy fermion nature of the material. From the value of γ , the

The resistivity of $\text{YbNi}_2\text{B}_2\text{C}$ is nearly temperature independent in the high temperature interval (50 K-300 K) [133, 134] and a relatively sharp fall around 50 K. The valence state of Yb is $3+$ as inferred from high temperature susceptibility. The coefficient γ of electronic specific heat extrapolated from heat capacity in the temperature interval 12-25 K of the polycrystalline material is ~ 200 mJ/mol.K^2 (Fig. 5) [133] (as against a few mJ/mol.K^2 encountered in normal metallic systems). The value of γ may be temperature dependent (as there is an upturn in C/T (Fig. 5)) and extrapolation of the data below 2 K gives even a larger value of γ (~ 580 mJ/mol.K^2). Measurements on single crystal of the material yielded similar

Kondo temperature (T_K) is estimated to be ~ 11 K [134] (T_K is estimated to be ~ 25 K from inelastic neutron scattering results – see below) which is comparable to the superconducting energy scale for the system. In the competition of Kondo interactions and superconductivity, the later is suppressed. In fact, the effect of hybridization is so strong that even substitution of 0.1 atomic fraction of Y by Yb in $\text{YNi}_2\text{B}_2\text{C}$ ($T_c \sim 15.5$ K), depresses T_c by ~ 12 K [127]. This is the largest suppression of T_c observed for Yb substitution in an intermetallics superconductor. This can be contrasted against the depression of 4 K by substitution of 0.1 atomic fraction of Y by Gd in $\text{YNi}_2\text{B}_2\text{C}$ [127, 116] (substitution by Gd ion is expected to give the maximum depression of T_c in a rare earth series of substitution). It is relevant to note that substitution of 0.1 atomic fraction of Y by Ce (the parent non superconducting $\text{CeNi}_2\text{B}_2\text{C}$ is also a 4f-electron hybridized system with Ce ions in valence fluctuation state with average valence close to non magnetic 4+ valence state) in $\text{YNi}_2\text{B}_2\text{C}$ does not have as drastic effect on depression of T_c as Yb – the depression is ~ 5 K [136] which is slightly larger than that caused by the substitution of 0.1 atomic fraction of Y by Nd and is in the range of depression by lighter rare earth substitution [116]. 4f-electron hybridization is present in the case of Ce substitution also, as the depression in the absence of hybridization should have been less than that by equivalent Nd substitution. Thus, it is clear that suppression of superconductivity in $\text{YbNi}_2\text{B}_2\text{C}$ is due to Kondo interaction and evolution of heavy fermion state.

X-ray absorption studies on Ni edge in $\text{RNi}_2\text{B}_2\text{C}$ show that Ni-*d* band in $\text{YbNi}_2\text{B}_2\text{C}$ is less filled than that in other members of the series [137]. It appears that Kondo interaction may be causing a reduction in electron density of states at E_F . Recent inelastic neutron scattering (INS) results [138] are also consistent with the Kondo lattice / heavy fermion nature of $\text{YbNi}_2\text{B}_2\text{C}$. A quasi-elastic peak with a width (FWHM) $\Gamma = 2.1$ meV was observed which correspond to a Kondo temperature of 25 K ($k_B T_K = \Gamma$). An interesting observation from INS is a significant increase (by a factor of two) of the crystal electric field (CEF) potential compared to other members of $\text{RNi}_2\text{B}_2\text{C}$ series of compounds [139, 140]. This increase has to be due to hybridization of 4f-electrons with neighbouring atomic orbitals as there is no lattice distortion. The low temperature properties of $\text{YbNi}_2\text{B}_2\text{C}$ have strong similarity with those of YbRh_2Si_2 which is located on the magnetic side ($T_N = 70$ mK) of the quantum critical point (QCP) [141]. Absence of magnetic order in $\text{YbNi}_2\text{B}_2\text{C}$ suggests that this material may be situated on the non magnetic side of QCP. It may be possible to tune this system to QCP by application of pressure.

7. ANISOTROPY IN SUPERCONDUCTING PROPERTIES

Even though the structure of quaternary borocarbides has high anisotropy ($c/a \sim 3$), the normal state electronic properties are almost isotropic [57] and initial studies indicated that $\text{YNi}_2\text{B}_2\text{C}$ and $\text{LuNi}_2\text{B}_2\text{C}$ are conventional and isotropic superconductors. However, later detailed investigations on single crystals (in the clean limit $l/\xi \sim 3$, where ξ is the superconducting coherence length and l is the electron transport mean free path) of these materials, revealed unusual behaviours, such as, anisotropy of H_{c2} in the basal *a-b* plane of the tetragonal structure [142, 143], square vortex lattice and its structural phase transformation [144, 145, 146, 147, 148, 149, 150], which could be due to anisotropy in Fermi surface and / or anisotropy in gap function of superconductivity. Another unusual feature observed was $H^{0.5}$ (instead of linear H) dependence of linear coefficient of electronic specific heat in the

superconducting state of $\text{LuNi}_2\text{B}_2\text{C}$ [18]. More recently, anisotropic behaviour has been observed in these materials in heat capacity [151] and thermal conductivity [152, 153] ultrasonic attenuation [154], directional point contact spectroscopy [155], *etc.* Anisotropy effects could arise from Fermi surface anisotropy or anisotropy of the superconducting gap function. Results from heat capacity and thermal conductivity have provided strong evidence for strongly anisotropic *s*-wave superconducting gap function in this system. The anisotropy reflects non local effects [156, 157, 158] which become observable when l is larger than ξ . Quaternary borocarbides, having $\xi \sim 100 \text{ \AA}$, $\{\kappa (= \lambda / \xi) \sim 15$, where κ is the Ginzburg-Landau parameter and λ is the penetration depth $\}$, with availability of large and good crystals in the clean limit with $l \sim 300 \text{ \AA}$, are ideal systems to study the effect of non locality and hence the effects of anisotropy. Symmetry of the gap function or the order parameter is an important and a key feature to understand the mechanism of superconductivity in a material. For example, if there are nodes in the gap function, it is believed that the pairing interaction would be unconventional and of electronic origin instead of conventional phonon mediated interaction. Some of the experimental results and discussions involving anisotropic effects are presented below.

7.1 FLUX LATTICE AND ITS STRUCTURAL PHASE TRANSFORMATIONS

The investigations of flux line lattice (FLL) or vortex lattice (VL) in superconducting quaternary borocarbides, both non magnetic and magnetic, have produced many surprising results, such as, the occurrence of *square* vortex lattice as against the usually expected hexagonal flux line lattice [144, 145, 146, 147], field and temperature dependent vortex lattice orientation and symmetry [149, 159, 160, 161, 162, 163], interaction between microscopic magnetic order and superconductivity [144, 147, 148]. Most of the investigations have been carried out through small angle neutron scattering (SANS) and a few using scanning tunneling microscopy (STM) [146, 150]. The favourable combination of κ and l and the moderate value of H_{c2} (compared to H_{c2} in HTSC materials) has enabled investigation of non local effects in VL over the complete H-T plane. The observed effects have been interpreted in terms of the anisotropy of the Fermi surface arising from the crystal structure [160], and the effects arising from the anisotropy of the unconventional superconducting gap function [164, 165].

In the VL observations in single crystals of superconducting borocarbides [144, 145, 146, 147, 148, 149, 150], with applied field $H \parallel c$ -axis of the crystal, the conventional hexagonal VL is observed only at low fields (typically $< \sim 50$ mT). At higher fields, a square VL is observed. Though square VL has been seen earlier in materials like Nb [166, 167] and PbBi [168], they were observed only with respect to certain crystallographic orientations, whereas in the case of quaternary borocarbides, the appearance of square lattice is field and temperature dependent. The orientation of the VL with respect to crystal lattice is not arbitrary, but locks to a certain direction of the crystal. – for the hexagonal VL, the diagonal of the rhombus unit cell is parallel to *a*- or *b*-axes of the crystal lattice and for the square VL lattice, the diagonal of the square unit cell is parallel to *a*-axis. This relation of the orientation of VL to the crystal structure is a reflection of the anisotropy of the Fermi surface and the anisotropy of the gap-function.

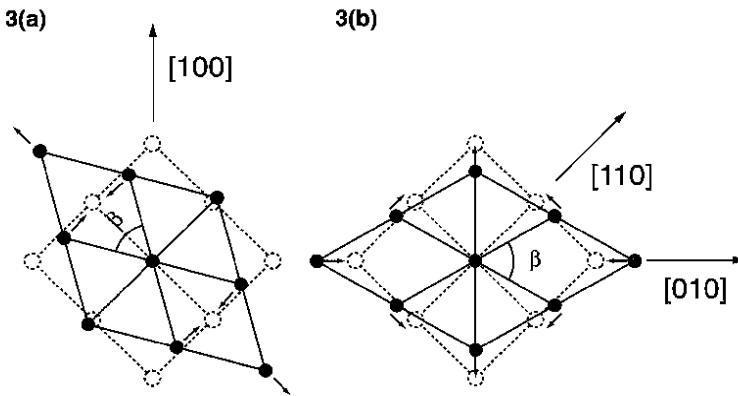


Fig. 6. A representation of how a hexagonal lattice, solid lines and symbols, would distort, at constant unit cell area, to match a square lattice, dotted lines and symbols, aligned along a $[110]$ direction, depending on the initial alignment of the hexagonal lattice. **(a)** Orientation of rhombic unit cell diagonal along $[110]$; **(b)** rhombic unit cell diagonal along $[010]$. Note that in **(a)** a decrease in β makes $[110]$ the nearest neighbour direction, while in **(b)** distortion towards a square lattice corresponds to an increase in β , as observed and predicted by Kogan *et al.* [159]. It is also clear from this diagram that it is possible to smoothly distort **(b)** to form a square lattice; hence a second order transition is possible at H_2 , while it is not possible to simply shift the orientation from **(a)** to **(b)** suggesting a first order transition at H_1 (From Ref. 161).

To explain the observed VL structure, Kogan *et al.*, [160, 169, 170] formulated an extension of the London model by incorporating higher order terms (arising from the anisotropy of the Fermi surface) in the free energy density of the VL. These terms explicitly take care of effects associated with nonlocality between the fields and currents. This corrected model accounts well for the unusual features of the VL-phase observed in borocarbide superconductors. The Fermi surface anisotropy was taken into account in terms of Fermi velocity averages in different directions obtained from band structure calculations. As the VL structure goes from hexagonal to square, the angle between two sides of VL rhombic unit cell, the apex angle, β , changes from 60° to 90° . By minimizing the free energy with respect to β , Kogan *et al.*, [160, 170] were able to predict the stable VL structure for a given field and temperature and the manner in which the structural transition would occur. The model could successfully explain many of the observations such as the transformation of the VL structure from hexagonal to square proceeding through a distortion, reorientation at a critical field H_1 as a first order transition and then a further continuous distortion of the rhombic unit cell, finally stabilizing into a square lattice at a second critical field H_2 [160].

As an example, the SANS results of VL of single crystal of $\text{YNi}_2\text{B}_2\text{C}$ (having enriched ^{11}B to reduce neutron absorption) reported by Mck. Paul *et al.*, [161] are described here. In this experiment, the crystal was aligned with its a -axis vertical and measurements were made

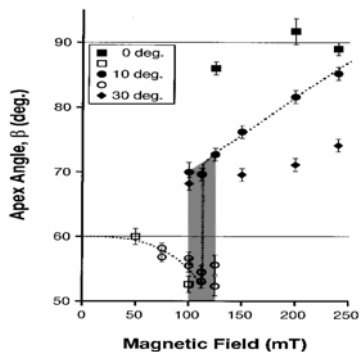


Fig 7. The derived apex angle (β) for the rhombic unit cell as a function of magnetic field at three orientations of the applied field to the c -axis. Open symbols, on the lower branch, correspond to an alignment of the diagonal of the unit cell near to $[110]$, while closed symbols, upper branch, refer to a $[100]$ orientation (from Ref. 161).

for the three cases, with H at angle (with respect to c -axis in the b - c plane) $\varphi = 0^\circ$ (i.e., $H \parallel c$ -axis), 10° , and 30° . Fig. 6 [161] gives a geometrical representation of the hexagonal to square VL transformation and Figs. 7 and 8 show the results. For the cases $\varphi = 0^\circ$, and $\varphi = 10^\circ$ at low field the diagonal of the rhombic unit cell is directed along a $[110]$ direction (Fig. 6 left) and the apex angle β decreases from 60° (the value for hexagon) as the field is increased ($H < 100$ mT region in Fig. 7). Around the critical field H_1 (~ 100 mT) the reorientation of the unit cell takes place with the rhombic diagonal orienting along $[010]$ direction (Fig. 6 right). This reorientation transition being first order around the critical field, both the orientations co-exist. This is clearly seen from the dual values of β in Fig. 7 around 100-125 mT. The splitting of the diffraction spot due to the presence of two orientations can be seen in Fig. 8 (top) for the case of $\varphi = 10^\circ$. At a higher field, the reorientation is complete and the diffraction spots are no longer split (Fig. 8 bottom).

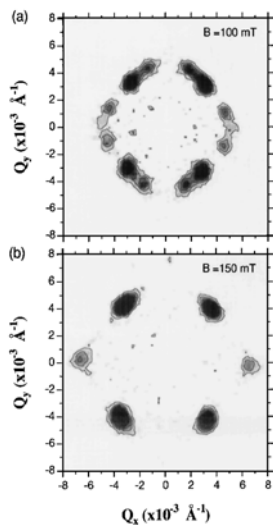


Fig. 8. Images of the diffraction pattern from the vortex lattice in YNi_2B_2C with a magnetic field of 100 and 150 mT applied at a 10° clock-wise rotation of the c axis, about the vertical $[100]$ axis, with respect to the applied field and the neutron beam. The splitting of the spots near the horizontal axis at low field has been removed at high field by the reorientation transition (from Ref. 161).

The model of Kogan *et al.*, [160] predicts that the behaviour of β (H) above H_1 depends on φ - with increasing φ , the field H_2 at which the VL locks to a square structure ($\beta = 90^\circ$) would be higher and that such a transition would be of second order. Experimental results [161] show that for H \parallel *c*-axis ($\varphi = 0^\circ$), the VL becomes almost square (at $H_2 = 125$ mT, $\beta \sim 86^\circ$) along with the first order reorientation, and after that the VL structure remains square for higher fields. For $\varphi = 10^\circ$, β slowly distorts and square VL is achieved above 250 mT ($H_2 \sim 250$ -300 mT) as a second order transition. For the case of $\varphi = 30^\circ$, the value of β is only $\sim 75^\circ$ at 250 mT and H_2 (not observed in the range of applied field) is higher than the other two cases. The qualitative behaviour are consistent with the predictions of Kogan *et al.* [160]. With increasing value of φ , the anisotropy in the *ac* plane (or *bc* plane) would start dominating and the VL behaviour for $\varphi \gg 20^\circ$ would be different from that for $\varphi \ll 20^\circ$.

For H \parallel *a*-axis of the crystal (*i.e.*, $\varphi = 90^\circ$), according to Kogan *et al.* [160], the orientation of the hexagonal (slightly distorted) VL is such that at low fields the diagonals of the rhombus unit cell would be already locked to the *b* (or *a*) and the *c*-axes of the crystal (instead of being oriented along [110] for H \parallel *a*-axis) and there would be no sudden reorientation as the field is increased (H_1 does not exist). The angle β of the distorted hexagon would continuously change with increasing field from about 53° at low fields to $\beta \sim 81.3^\circ$ at H_2 and remaining stable for higher fields (final stable VL not being square). The field H_2 for $\varphi = 90^\circ$ would be the highest compared to that of other values of φ . The VL structure investigations on single crystal of $\text{YNi}_2\text{B}_2\text{C}$ through STM [150] have confirmed these predictions. It is found that for H \parallel *a*-axis, H_2 is ~ 1 T (compared to ~ 0.1 T for H \parallel *c*-axis) with the stable value of β of the distorted hexagon being 85° at high field. However, while β does change in a continuous way, as predicted, but there is still a hint of a reorientation of VL. In this case the reorientation being an interchange of the long and short diagonals of the rhombus – the longer diagonal of the rhombus is parallel to the *a* axis below 0.75 T, and above 0.85 T it is parallel to the *c* axis [150]. This needs confirmation and understanding.

Further details of vortex physics have been obtained from the studies of the doped systems. Kogan *et al.*, [160, 169, 170] model predicts that when the mean free path of electrons l becomes shorter, the hexagonal to square VL transition should occur at higher field. This prediction has been tested in the SANS investigations of Co (non magnetic in this lattice) doped single crystals of $\text{Lu}(\text{Ni}_{1-x}\text{Co}_x)_2\text{B}_2\text{C}$ [162]. For the undoped ($x = 0$) and the maximum doped ($x = 0.09$) samples, the relevant parameters were $T_c = 16.0$ K & 9.5 K; $H_{c2} = 9$ T & 2.2 T; $\rho_0 = 1.5 \mu\Omega \text{ cm}$ & $14.5 \mu\Omega \text{ cm}$, respectively. From the value of ρ_0 , the value of l was estimated as ~ 27 nm and 3 nm. For the intermediate concentration of doping, the parameters roughly scale with x . The studies revealed that not only the onset-field of hexagonal to square transition was found to be higher in the doped material, as predicted by the theory, but this field was also found to vary nearly linearly with doping. There is an excellent agreement between the theoretical and experimental values. The manner of square to hexagonal phase transition can be quantified in terms of the splitting of the VL diffraction peak in the process of the transition. A $H^{0.5}$ dependence of the magnitude of the split in the course of transition predicted by the model was also found. Thus, quaternary borocarbides are not only ideal systems per se, but for the first time they have also given opportunity to suitably modify the system to bring the VL structure transitions to accessible temperature-field regimes enabling detailed understanding of vortex physics at microscopic scale.

The phase diagram of the VL structure has been determined for $\text{LuNi}_2\text{B}_2\text{C}$ and it has been found that as H approaches H_{c2} , square VL is not stable and the structure would tend to

become hexagonal [149]. It has been argued that as the flux line density is increased with increasing field, the repulsion of vortices would increase which may lead to the VL going over to hexagonal structure close to H_{c2} [149]. However, detailed VL studies in YNi_2B_2C seems to indicate that the VL remains square close to H_{c2} [163]. The structure of VL close to H_{c2} needs further study and elucidation.

It may be noted that the structure of VL undergoing series of transitions and resulting in non hexagonal lattice and going over to square lattice, has also been reasoned out on the basis of unconventional superconductivity having a $d_{x^2-y^2}$ -type gap function for a system (in the clean limit) with cylindrical Fermi surface [164]. In this case, the anisotropy arises from the selective population of quasiparticles in the nodal regions of the gap. However, this treatment has not been applied specifically to the case of quaternary borocarbides.

In the VL investigations of magnetic superconductors $ErNi_2B_2C$ [144, 159] and $TmNi_2B_2C$ [147, 148], all the features of VL observed in non magnetic YNi_2B_2C , $LuNi_2B_2C$ discussed above have been observed. In correlation with SANS results of $ErNi_2B_2C$, signatures of square to hexagonal VL transition has also been seen in rf kinetic inductance [159]. Most importantly, effect of local magnetic order on the VL structure, has been observed both in $ErNi_2B_2C$ [144] and $TmNi_2B_2C$ [147]. In $ErNi_2B_2C$, below 4 K, with the applied field (H) (0.25 T to 0.55 T) in the direction of c -axis of the crystal, the orientation of the VL begins to deviate away from the direction of H, towards the direction of the a -axis, but still remaining in the a - c plane. The angle between the orientation of the VL and the direction of H increases with decreasing temperature and increasing H, the maximum angle being about 1° at 1.5 K and 5.5 KOe. This deviation happens because of the magnetic ordering appearing in $ErNi_2B_2C$. In this magnetic superconductor ($T_c \sim 11$ K), antiferromagnetic order sets in at ~ 6 K and a ferromagnetic component appears below 2.4 K [171]. The internal field due to the onset of ferromagnetic component adds to the externally applied field and causes the deviation of the square VL from the applied field direction [144]. This is the first time a direct and clear evidence of intimate interaction and direct coupling of internal magnetic order with superconductivity at microscopic scale has been obtained in any magnetic superconductor

In the case of $TmNi_2B_2C$ ($T_c \sim 11$ K and $T_N \sim 1.5$ K), the VL as a function of temperature and magnetic field has been studied in right down into the magnetically ordered state ($T \sim 0.1$ K) [147, 148]. This system distinguishes itself from all the other magnetic superconductors of the borocarbide family in terms of orientation of the magnetic moment (moment parallel to c -axis) and rather small magnetic q -vector (0.093, 0.093, 0.000). Extremely rich effects, including the simultaneous changes in the magnetic structure and the symmetry of the VL, have been observed in this system which is a very important observation in the context of *interdependence* of magnetism and superconductivity [148].

Such interesting interplays of superconductivity and local magnetism at microscopic scale as described above in magnetic superconductors of borocarbides have not been observed before in any magnetic superconductor. Apart from demonstrating novel phenomena, the studies on quaternary borocarbides have established VL structure as an important microscopic tool to examine the details of superconductivity, its interaction with the crystal structure and magnetism.

7.2 ANISOTROPY AND SYMMETRY OF SUPERCONDUCTING GAP FUNCTION

In the above section effect of anisotropy in quaternary borocarbides as observed in the VL structure was discussed. We discuss below the anisotropy effects observed in other measurements and point out that some of the studies indicate that the energy gap may have extreme anisotropy having point nodes. Such an energy gap has not been observed before in any other superconducting material.

Metlushko *et al.*, [142] measured magnetization of $\text{LuNi}_2\text{B}_2\text{C}$ with applied field H parallel to the crystal axis directions $\langle 100 \rangle$, $\langle 001 \rangle$ or $\langle 110 \rangle$ and found different values in different directions. Such an anisotropy in superconducting properties cannot be understood within the framework of simple London / G-L theory for s -wave superconductors. As in the case of VL structure of quaternary borocarbides, non local effects and anisotropy arising from Fermi surface and / or gap function have to be taken into account to understand the observations.

The out of plane anisotropy, γ , in H_{c2} ($= 0.5(H_{c2}(T)^{\langle 100 \rangle} + H_{c2}(T)^{\langle 110 \rangle}) / H_{c2}(T)^{\langle 001 \rangle}$) was found to be ~ 1.16 and independent of temperature. This value corresponds to an effective mass anisotropy ($(m_{\max}/m_{\min}) = \gamma^2$) as 1.34 which agrees well with that predicted by band structure calculations [102, 172]. Jhonston-Halperin *et al.*, [173] reported a much smaller value of out-of-plane anisotropy for $\text{YNi}_2\text{B}_2\text{C}$ corresponding to effective mass anisotropy of 1.01 which perhaps is the smallest anisotropy ever reported for a non cubic lattice [173] and is consistent with that (1.02) obtained from band structure calculations of Dugdale *et al.* [174]. However, Civale *et al.*, [143] reported for $\text{YNi}_2\text{B}_2\text{C}$, an experimental (magnetization measured in SQUID magnetometer) out of plane mass anisotropy $\gamma \sim 1.15$ which is consistent with

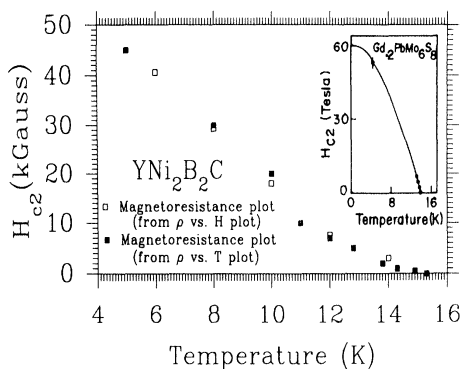


Fig. 9. Temperature dependence of H_{c2} (T) in $\text{YNi}_2\text{B}_2\text{C}$ obtained from magnetoresistance measurements. Solid squares are values of H_{c2} obtained from resistance vs T data at various fields and open squares are values of H_{c2} obtained from resistance vs H data at various temperatures (from Ref. 43). Note the positive curvature of H_{c2} near T_c . The inset shows the temperature dependence of $H_{c2}(T)$ in a conventional type-II superconductor $\text{Gd}_{0.2}\text{PbMo}_6\text{S}_8$.

that obtained (1.1) from the band structure calculations of D.J. Singh for $\text{YNi}_2\text{B}_2\text{C}$ [106]. The difference in the two experimental values may also be because, in one case the anisotropy was measured close to T_c (the smaller value in the case of Jhonston-Halperin *et al.*, by torque magnetometer where the reversible region of magnetization was available only close to T_c [173]), whereas in the other case, it was measured well below T_c (the larger value in the case of Civale *et al.*, where a much larger region of reversibility was found in their SQUID magnetometer measurements [143]).

Metlushko *et al.*, [142] reported a clear angular dependence of $H_{c2}(T)$ in $\text{LuNi}_2\text{B}_2\text{C}$ in the basal plane (applied magnetic field direction varied from 0° to 95° with respect to $\langle 100 \rangle$ direction in the basal plane). The results were symmetrical with respect to 45° , effectively implying a four fold symmetry of magnetization in the basal a - b plane.

The in-plane anisotropy in H_{c2} ($H_{c2}(T)^{\langle 100 \rangle} / H_{c2}(T)^{\langle 110 \rangle}$) was found to be 1.1 at 4.5 K and is temperature dependent (goes to 1.0 close to T_c). They also observed the positive curvature of $H_{c2}(T)$ near T_c which is an unusual behaviour. Such a positive curvature of $H_{c2}(T)$ was first observed by us in polycrystalline samples of $\text{YNi}_2\text{B}_2\text{C}$ (Fig. 9) [43, 175] and later confirmed by others in both in $\text{YNi}_2\text{B}_2\text{C}$ [176] and in $\text{LuNi}_2\text{B}_2\text{C}$ [142, 177, 178]. This behaviour is observed in single crystal of $\text{LuNi}_2\text{B}_2\text{C}$ in all the three directions, $H \parallel \langle 100 \rangle$, $H \parallel \langle 110 \rangle$, and $H \parallel \langle 001 \rangle$ [142]. Metlushko *et al.*, [142] could satisfactorily fit the observed temperature and angular dependence of $H_{c2}(T)$ in terms of a nonlocal extension of G-L equations with isotropic pairing interactions and anisotropic Fermi surface. The value of the Fermi velocity averages obtained from fitting agreed reasonably well with those obtained from band structure calculations. With the lowest order non-local correction the model fits well the observed positive curvature of $H_{c2}(T)$ only in the high temperature region $1 > T/T_c > \sim 0.6$ ($T_c \sim 16$ K). Including a term involving T^2 , which takes care of next order correction for non local extension to G-L equation, Metlushko *et al.*, were able to get satisfactory extended fit to lower temperatures also, without seriously affecting the values of the parameters obtained in the fit

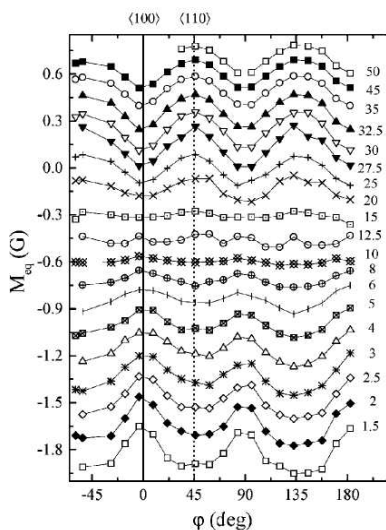


Fig. 10. Reversible magnetization M_{eq} at $T=7$ K, as a function of the angle ϕ between the applied field H (contained in the a - b plane) and the a axis. The fields (in kOe) are indicated next to each curve. The scale is the same for all of the curves, but data at different H have been vertically shifted. (from Ref. 143)

with only the first order corrections. We point out that other explanations have also been given for the positive curvature in H_{c2} , such as granularity [179], two bands involved in superconductivity with medium coupling between slow and fast electrons [180]. Effect of anisotropy of gap function (see below) is not ruled out.

More detailed measurements in single crystal of $\text{LuNi}_2\text{B}_2\text{C}$ [181] and $\text{YNi}_2\text{B}_2\text{C}$ (Fig. 10) [143] confirmed superconducting anisotropy in the basal plane from the observation of four fold symmetry in the angular dependence of magnetization in the basal a - b plane of these materials deep in the H - T plane. The observed angular and temperature dependence of magnetization in these materials could be interpreted well in terms of the earlier mentioned model of Kogan *et al.*, [169]. The logarithmic field (H) dependence of equilibrium reversible magnetization M_{eq} (which is the average of magnetization obtained in the increasing and decreasing

branches of an isothermal loop) in the superconducting state *i.e.* $M_{eq} \propto \ln(H)$, predicted by the model of Kogan *et al.*, [169], has also been seen in YNi_2B_2C [143].

More interestingly, the model of Kogan *et al.*, [169, 181] also predicts, close to T_c (when measured as function of temperature in a constant field) or H_{c2} (when measured as a function of field at a constant temperature), a change of sign in magnetization, and also predicts the maximum becoming a minimum (and vice-versa) in the four fold symmetric variation of magnetization. These have also been observed in both $LuNi_2B_2C$ [181] and YNi_2B_2C [143], more clearly in the later case. In YNi_2B_2C , the four fold symmetric variation in magnetization is seen in the normal state also [143]. This is interesting and important as it shows once again that at least part of the observed anisotropy arises out of Fermi surface anisotropy.

A confirmation of the significance of non local effects in the above studies has been obtained by investigating suitably doped materials. In the presence of scattering by impurities, mean free path is reduced and hence the effect of non locality is reduced. In such a case, the observed angular anisotropy should decrease or may even be absent. Indeed it is so, is confirmed in the investigation of magnetization of 6% Co doped $LuNi_2B_2C$ single crystal (with residual resistivity of about eight times the value for the undoped $LuNi_2B_2C$) wherein the four fold symmetry is absent in the superconducting state [181].

In the above, the results exhibiting anisotropy were interpreted in terms of Fermi surface anisotropy with the superconducting gap function being isotropic *s*-wave. Anomalous

behaviour in heat capacity and angular dependence in thermal conductivity strongly point to superconducting gap function being anisotropic *s* wave type. Some of these are discussed below.

Measurements of specific heat on polycrystalline and single crystal samples have led to important information with respect to strong anisotropy of the superconducting gap function. Electronic heat capacity $\gamma(T)$ depends on the quasiparticle density of states $N_0(H)$. measurements of both $LuNi_2B_2C$ (polycrystalline) [182] and YNi_2B_2C (single crystal) [183] have shown that $\gamma(T)$ follows a T^3 behaviour below T_c , instead of exponential behaviour expected for a conventional isotropic energy gap. Further, the magnetic field (H) dependence of $\gamma(H)$ ($= \gamma_N H/H_{c2}$) in the mixed state, instead of being proportional to H as expected for a *s*- wave superconductor with isotropic gap, is found to

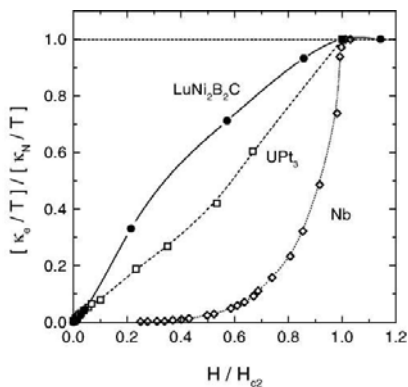


Fig. 11. Magnetic field dependence of the electronic thermal conductivity κ/T at $T \rightarrow 0$, normalized to its value at H_{c2} . Circles are for $LuNi_2B_2C$, squares for UPT_3 [H. Suderow *et al.*, J. Low Temp. Phys. 108 (1997) 11], and diamonds for Nb [J. Lowell and J.B. Souza, J. Low Temp. Phys. 3 (1970) 65]. Note the qualitative difference between the activated conductivity of *s*-wave superconductor Nb and the roughly linear growth seen in UPT_3 , a superconductor with a line of nodes. The lines are a guide to the eye (from Ref. 152).

be proportional to $H^{0.5}$ ($= \gamma_N(H/H_{c2})^{0.5}$) in $\text{LuNi}_2\text{B}_2\text{C}$ [18, 182] which is similar to that for d -wave superconductors with line nodes [184]. Theoretical investigations based on d -wave symmetry [164] also qualitatively explained the basal plane anisotropy results of Metlushko *et al.*, [142] discussed above. In an indirect support to d -wave superconductivity, it was found [185] that in a single crystal of $\text{YNi}_{1.6}\text{Pt}_{0.4}\text{B}_2\text{C}$, $\gamma(H) \propto H$, as one observes in a conventional s -wave superconductor. It is clear that because of the presence of Pt-impurities, the gap function has become more isotropic [185]. Further, Nohara *et al.*, [185] also observed the positive curvature of $H_{c2}(T)$ (mentioned earlier) near T_c . They suggest that the positive curvature of $H_{c2}(T)$ could be understood in terms of shrinking of vortex radius with H which may be happening because the vortex-vortex interaction may be involving delocalized quasiparticles outside the vortex cores. Delocalization of quasiparticles would happen if the superconductivity is of d -wave type. They also found that the positive curvature of $H_{c2}(T)$ vanishes on doping with Pt which could happen because impurities could smear out the delocalization effect.

Thermal conductivity measurements are important in inferring nature of gap function as electronic thermal conductivity in the superconducting state would have contribution from the low lying excitations if nodes are present in the gap function. Fig. 11 shows the results of thermal conductivity measurements of single crystal of $\text{LuNi}_2\text{B}_2\text{C}$ [152] as a function of field at very low temperature (around 70 mK) along with that of the conventional superconductor Nb (having exponential dependence characteristic of s -wave) and the heavy fermion superconductor UPt_3 having unconventional superconductivity with line nodes. The difference in thermal conductivity amongst the three is very clear and shows $\text{LuNi}_2\text{B}_2\text{C}$ to be a class apart from others. From an analysis of the results of Nohara *et al.* in $\text{LuNi}_2\text{B}_2\text{C}$ [186], and Izawa *et al.* in $\text{YNi}_2\text{B}_2\text{C}$ [187], and from their own results, Boaknin *et al.*, [152] estimate the gap anisotropy factor ($\Delta_{\text{max}} / \Delta_{\text{min}}$) to be ~ 10 . This is an unusually large value never encountered before (*e.g.*, in elemental superconductors a factor of ~ 2 is found) [152]. By comparison of the result with UPt_3 which is believed to have line nodes, it is expected that gap function in borocarbides would also have nodes and mechanism of superconductivity unconventional.

Later, measurements of electronic thermal conductivity along the c -axis K_{zz} (the heat current being in a direction parallel to c -axis of the crystal) in the superconducting state in single crystal of $\text{YNi}_2\text{B}_2\text{C}$ were reported by Izawa *et al.*, [153] as function of temperature, field and angle between the direction of the field and the heat current. In the angular dependence measurements, the field (H) was applied at an angle θ with respect to the heat current direction (c -axis) and K_{zz} was measured as a function of ϕ (the azimuthal angle of the field direction measured with respect to the a -axis) (see Fig. 12 [153] for the geometry). A clear four fold variation of K_{zz} in the a - b plane was found (Fig. 12) [153] which shows that the gap function is anisotropic and the minimum in K_{zz} at $\phi = 0^\circ$ and 90° indicates presence of nodes along $[100]$ and $[010]$ directions (*i.e.*, along a and b axes). The ϕ dependence of the K_{zz} is essentially in the nature of a cusp. The magnitude of the cusp strongly depends on θ , for $\theta = 90^\circ$, the magnitude of the cusp is maximum and decreases with decreasing θ and almost gets smeared out at $\theta = 45^\circ$. This cusp structure of K_{zz} with respect to θ is sensitive to the gap function. The dependence of $K_{zz}(\phi)$ on θ has been calculated for gap function with $s+g$ symmetry having a point node [188] and for a gap symmetry with d -wave with line node [189]. The gap structure and the functional variation of K_{zz} are shown in Fig. 13 [153]

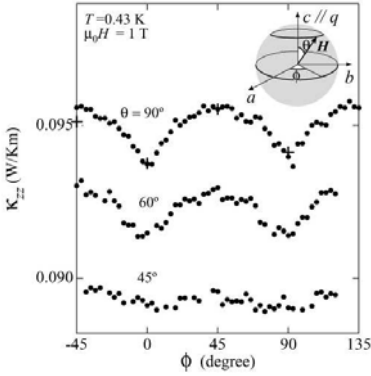


Fig. 12. Angular variation of K_{zz} at $H = 1$ T and $T = 0.43$ K ($q \parallel c$ -axis). K_{zz} are measured by rotating $H = H(\sin\theta \cos\phi, \sin\theta \sin\phi, \cos\theta)$ conically as a function of ϕ at fixed $\theta = 90^\circ, 60^\circ,$ and 45° (see the inset). The crosses represent the data obtained under the field cooling condition at each angle (from Ref. 153).

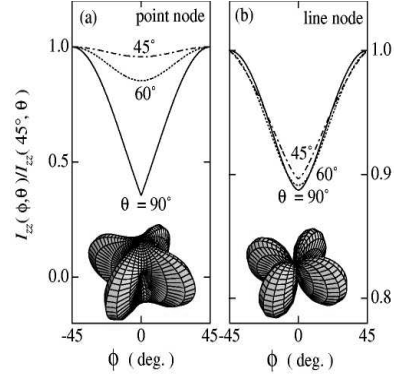


Fig. 13. Angular variation of $I_{zz}(\phi, \theta)$ normalized by $I_{zz}(45^\circ, \theta)$ as a function of ϕ at $\theta = 90^\circ$ (solid lines), 60° (dashed lines), and 45° (dash-dotted lines), which are calculated by the gap functions with (a) point node and (b) line node. For the definition of θ and ϕ , see the inset of Fig. 12. The corresponding gap functions are illustrated in the insets (from Ref. 153).

(where $I_{zz}(\phi, \theta)$ is the angular dependent functional factor in K_{zz}). It can be seen that for $s+g$ wave symmetry, K_{zz} is sensitive to θ whereas it is insensitive in the case of d -wave symmetry.

The very recent point contact spectroscopy results in single crystal of $\text{YNi}_2\text{B}_2\text{C}$ [155] also enable discrimination between d -wave and $s+g$ wave symmetries. Fig. 14 [155] shows the results with current I parallel to a -axis of the crystal and I parallel to c -axis of the crystal. The out of plane gap anisotropy is clearly evident, the value for I parallel to c -axis is 4.5 times larger than that for I parallel to a -axis. Comparing the two gap function symmetries that have been suggested, *viz.*, d -wave and $s+g$ wave (see Fig. 13 for the shape of the functions), the large value of $\Delta_{I\parallel c} / \Delta_{I\parallel a}$ observed at low temperature suggests that the gap function has sharp minima in the basal plane and the gap is maximum close to the poles, which supports the $s+g$ symmetry for the gap function.

These results clearly show that the gap function in $\text{YNi}_2\text{B}_2\text{C}$, and perhaps in other superconducting quaternary borocarbides too, has point nodes located along $[100]$ and $[010]$ directions.

Recently, Tuson Park *et al.*, [151] have observed four-fold variation in field-angle dependent heat capacity in single crystal of $\text{YNi}_2\text{B}_2\text{C}$. They point out that the symmetric variations observed in heat capacity measurements have stronger validity as thermal conductivity measurements would be sensitive to Fermi surface topology. These authors suggest that there may be nodes in the momentum space. In such a case, four fold pattern would be observed for both d -wave and anisotropic s -wave gaps with nodes [151] The

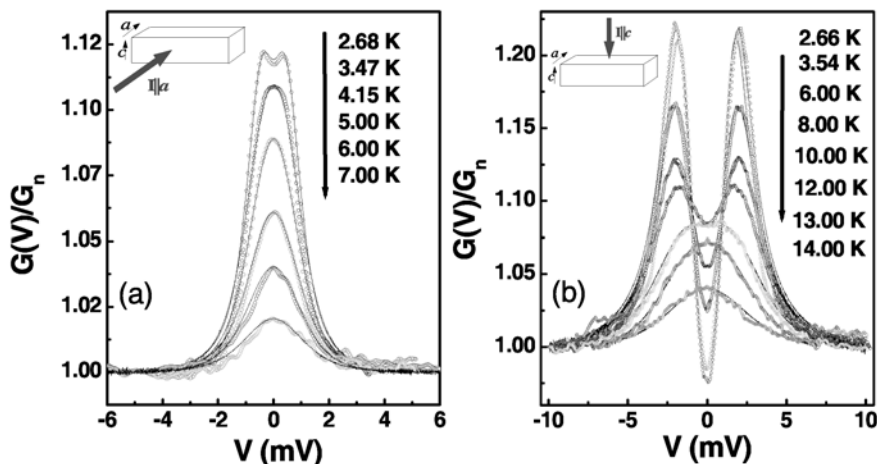


Fig. 14. Point contact spectra at different temperatures for (a) $I \parallel a$ -axis and (b) $I \parallel c$ -axis. Open circles are experimental data and solid lines are Blonder-Tinkham-Klapwijk model fits to the spectra. The conductance curves are normalized by their respective values at high bias (from Ref. 155).

unprecedented $s+g$ gap function raises questions on the pairing mechanism in borocarbides [153].

8. SUMMARY

Discovery of the superconducting quaternary borocarbide system Y-Ni-B-C has led to a new family of materials, quaternary borocarbides, *i.e.*, rare earth transition metal borocarbides [190] $(RC)_m(Ni_2B_2)_n$. The series RNi_2B_2C ($R = Y$, rare earth) has been extensively investigated. The members of the family have a range of properties, superconductivity with $T_c \sim 10$ K, coexistence of superconductivity and magnetism with high T_c and T_N , valence fluctuation behaviour, heavy fermion behaviour *etc.* Apart from high T_c , quaternary borocarbide superconductors show a variety of interesting phenomenon. Square vortex lattice is observed deep inside H-T plane and it undergoes remarkable symmetry transformations as a function of magnetic field and temperature. Anisotropy is seen in superconducting state in the square basal plane (a - b plane of the tetragonal lattice). Availability of large and good quality crystals with clean limit electronic transport has enabled detailed investigations and understanding of these phenomena. Anisotropic effects seen in detailed investigations of superconductivity in YNi_2B_2C and $LuNi_2B_2C$ point to occurrence of the effects of arising due to the anisotropy in Fermi surface and anisotropic superconducting gap function. Present evidence strongly suggests that the gap function to be of the $s+g$ symmetry having point nodes in the $[100]$ directions. This kind of gap structure is

unprecedented and cannot be understood in terms of electron-phonon interaction alone. Magnetic superconductors of the family have given scope to investigate details of the interaction of superconductivity and magnetism. For the first time, an intimate interaction of superconductivity and magnetism has been observed at microscopic scale in $\text{ErNi}_2\text{B}_2\text{C}$. Complex magnetic order and transformations in its structure in H-T plane in the superconducting state in $\text{TmNi}_2\text{B}_2\text{C}$, has given a chance for investigation of possible *interdependence* of superconductivity and magnetic order. The above mentioned considerations are keeping quaternary borocarbides in the forefront of research activity in superconductivity.

Acknowledgements

Prof. R. Vijayaraghavan, and Prof. S.K. Dhar are acknowledged for their collaboration in the work of quaternary borocarbides at TIFR. Prof. S. Ramakrishnan, Prof. C.V. Tomy, and Dr. P. Raychaudhuri are thanked for useful discussions. R. Shiva is acknowledged for his help in many ways in the preparation of this manuscript.

REFERENCES

- [1] J.G. Bednorz, K.A. Müller, Z. Phys. B 64 (1986) 189.
- [2] Tata Institute of Fundamental Research Annual Report, 1991-92, p77.
- [3] Chandan Mazumdar, R. Nagarajan, C. Godart, L.C. Gupta, M. Latroche, S.K. Dhar, C. Levy Clement, B.D. Padalia, and R. Vijayaraghavan, Solid State Commun. 87, (1993) 413.
- [4] R. Nagarajan, Chandan Mazumdar, Zakir Hossain, S.K. Dhar, K.V. Gopalakrishnan, L.C. Gupta, C. Godart, B.D. Padalia, and R. Vijayaraghavan, Phys Rev Lett, 72, (1994) 274.
- [5] Chandan Mazumdar, R. Nagarajan, C. Godart, L.C. Gupta, M. Latroche, S.K. Dhar, C. Levy-Clement, B.D. Padalia, and R. Vijayaraghavan, Oral presentation of results with and without carbon at 20th Int. Conf. on Low Temperature Physics (LT20), 4-11 August 1993, Eugene, Oregon, U.S.A. Results without addition of carbon appeared in the proceedings, Physica B 194-196 (1994) 1985.
- [6] Chandan Mazumdar, R. Nagarajan, C. Godart, L.C. Gupta, M. Latroche, S.K. Dhar, C. Levy-Clement, B.D. Padalia, and R. Vijayaraghavan, Poster presentation of results with and without carbon at Int. Conf. on Strongly Correlated Electron Systems (SCES93) 16-19 August 1993, San Diego, California, U.S.A., Poster KE56.
- [7] R.J. Cava, H. Takagi, B. Batlogg, H.W. Zandbergen, J.J. Krajewski, W.F. Peck, R.B. Van Dover, R.J. Felder, T. Siegrist, K. Mizuhashi, J.O. Lee, H. Eisaki, S.A. Carter, and S. Uchida, Nature 367 (1994) 146.
- [8] R.J. Cava, H. Takagi, H.W. Zandbergen, J.J. Krajewski, W.F. Peck, T. Siegrist, B. Batlogg, R.B. Van Dover, R.J. Felder, K. Mizuhashi, J.O. Lee, H. Eisaki, and S. Uchida, Nature 367 (1994) 252.
- [9] T. Siegrist, H.W. Zandbergen, R.J. Cava, J.J. Krajewski, and W.F. Peck, Nature, 367 (1994) 254.
- [10] See for example, contributions on quaternary borocarbides in the Proc. of Int. Confs: M2S-HTSC-IV, Grenoble, Physica C 235-240 (1994); SCES'94, Amsterdam, Physica B 206-207 (1995); SCES'95, Goa, Physica B 223-224 (1996); MOS'96, Karlsruhe, J. Low Temp. Phys., 105 (1996) & 107 [5/6] (1997); LT21, Prague, Czech. J. Phys. 46 Suppl. S1-S6 (1996); SCES'96, Physica B 230-232 (1996); M2S-HTSC-V, Beijing, Physica C 282-287 (1997); 12th International Symposium on boron, borides, and related compounds, Baden, Austria, 25-30 Aug. 1996, J. Solid State Chem. 133 (1997); 12th Int. Conf. on transition metal compounds, St. Malo, France, (1997), J. Alloys and Compounds 262-263 (1997).
- [11] R. Nagarajan, Indian J. Pure and Applied Physics, 33 (1995) 473.
- [12] L.C. Gupta, Physica B 223-224 (1996) 56
- [13] R. Nagarajan, J. Low Temp. Phys. 107 (1997) 517.
- [14] R. Nagarajan, Physica C 282-287 (1997) 69.
- [15] Articles on quaternary borocarbide superconductors in *Studies of High Temperature Superconductors*, Vol. 26 (1998) and Vol. 28 (2000) (Ed. A. Narlikar), Nova Sci. Publishers, NY.
- [16] R. Nagarajan and L.C. Gupta, Chapter 1, in Vol. 26 in Ref. 15.
- [17] L.C. Gupta, Phil. Mag. 77 (1998) 717, and references therein.
- [18] H. Takagi, M. Nohara, and R.J. Cava. Physica B 237-238 (1997) 292.

- [19] C. Godart, E. Alleno, E. Tominez, L.C. Gupta, R. Nagarajan, Z. Hossain, J. Lynn, P. Bonville, J.A. Hodges, J.P. Sanchez, I. Felner, J. Solid State Chem. 133 (1997) 169.
- [20] P.C. Canfield, P.L. Gammel, and D.J. Bishop, Physics Today, Vol. 51 (1998) No. 10 pp40
- [21] S.-L. Drechsler, S.V. Shulga, K.-H. Muller, G. Fuchs, J. Freudenberger, G. Behr, H. Eschrig, I. Schultz, M.S. Golden, H. von Lips, J. Fink, V.N. Narozhnyi, H. Rosner, P. Zahn, A. Gladun, D. Lipp, a. Kreyssig, M. Loewenhaupt, K. Koepernik, K. Winzer, K. Krug, Physica C 317-318 (1999) 117.
- [22] E. Tominez, E. Alleno, P. Berger, M. Bohn, Chandan Mazumdar, and C. Godart, J. Solid State Chem. 154 (2000) 114.
- [23] L.C. Gupta, J. Phys. Soc. Jpn 69 (Suppl. A) (2000) 138.
- [24] Proc. NATO Advanced Research Workshop on *Rare earth transition metal borocarbides (Nitrates): Superconducting, magnetic and normal state properties*, 13-18 June, 2000, Dresden, Germany, Eds. K.-H. Muller and V. Narozhnyi, NATO Science Series, Kluwer Acad. Pub., Dordrecht (2001).
- [25] R. Nagarajan, in Ref. 24, pp. 1.
- [26] L.C. Gupta, in Ref. 24, pp. 413.
- [27] K.-H. Muller and V.N. Narozhnyi, Rep. Prog. Phys. 64 (2001) 943.
- [28] K.-H. Muller, G. Fuchs, S.-L. Drechsler, and V.N. Narozhnyi, *Handbook of Magnetic Materials*, Vol. 14, Elsevier Science B.V., (2002), Chapter 3, pp199.
- [29] Chandan Mazumdar and R. Nagarajan, (to appear in Current Science, Jan. 2005)
- [30] Chandan Mazumdar, R. Nagarajan, L.C. Gupta, B.D. Padalia, R. Vijayaraghavan, Proc. Solid State Phys. Symp. of Dept. of Atomic Energy, Bombay, 1-4 Jan 1991, 33C (1991) 265.
- [31] R. Vijayaraghavan, Chandan Mazumdar, R. Nagarajan, L.C. Gupta, and B.D. Padalia, Abstracts Int. Conf. Magnetism, Edinburgh, 2-6, Sept 1991, Abstract PE 3.23.
- [32] Chandan Mazumdar, R. Nagarajan, S.K. Dhar, L.C. Gupta, B.D. Padalia, R. Vijayaraghavan, Proc. Solid State Phys. Symp. of Dept. of Atomic Energy, Varanasi, 21-24 Dec. 1991, 34C (1991) 241.
- [33] R. Nagarajan, L.C. Gupta, Chandan Mazumdar, Zakir Hossain, S.K. Dhar, C. Godart, B.D. Padalia, and R. Vijayaraghavan J. Alloys and Compounds 225 (1995) 571.
- [34] Chandan Mazumdar, R. Nagarajan, L.C. Gupta, B.D. Padalia, and R. Vijayaraghavan, Appl. Phys. Lett., 77 (2000) 895.
- [35] Chandan Mazumdar, Ph.D. Thesis, I.I.T. Bombay, 1995.
- [36] Youwen Xu and R.N. Shelton Solid State Commun., 68 (1988) 395.
- [37] J.C. Philips, (1989) Physics of High-Tc Superconductors, Academic Press, Inc., San Diego, California, U.S.A.
- [38] M.C. Krupka, A.L. Giorgi, N.H. Kirkorian, E.G. Szklarz, J. Less-Common Metals, 19 (1969) 113.
- [39] Z. Fisk, Nature, 367 (1994) 117.
- [40] J.R. Gavaler, M.A. Janocko, and C.K. Jones, J. App. Phys. 45 (1974) 3009; L.R. Testardi, J.H. Wernick, and W.A. Royer, Solid State Commun., 15 (1974) 1
- [41] J. Nagamatsu, N. Nakagawa, T. Muranaka, Y. Zenitani, and J. Akimitsu, Nature 410 (2001) 63.

- [42] H. Eisaki, H. Takagi, R.J. Cava, K. Mizuhashi, J.O. Lee, B. Batlogg, J.J. Krajewski, W.F. Peck Jr., and S. Uchida, *Phys. Rev. B* 50 (1994) 647.
- [43] C. Godart, L.C. Gupta, R. Nagarajan, S.K. Dhar, H. Noel, M. Potel, Chandan Mazumdar, Z. Hossain, C. Levy-Clement, G. Schiffmacher, B.D. Padalia, R. Vijayaraghavan, *Phys Rev B*, 51 (1995) 489.
- [44] B.K. Cho, P.C Canfield, and D.C. Jhonston, *Phys. Rev. B* 52 (1995) R3844.
- [45] C.V. Tomy, G. Balakrishnan, and D. McK Paul, *Physica C* 248 (1995) 349.
- [46] Z. Hossain, S.K. Dhar, R. Nagarajan, L.C. Gupta, C. Godart, and R. Vijayaraghavan, *IEEE Trans. Magn.* 31 (1995) 4133.
- [47] Z. Hossain, L.C. Gupta, R. Nagarajan, S.K. Dhar, C. Godart, and R. Vijayaraghavan, *Physica B* 223&224 (1996) 99.
- [48] See, *e.g.*, *Ternary Superconductors*, (1981) Eds. G.K. Shenoy, B.D. Dunlop, and F.Y. Fradin, North-Holland, Amsterdam.
- [49] B.K. Cho, P.C. Canfield, L.L. Miller, D.C. Johnston, W.P. Beyermann, and A. Yatskar, *Phys. Rev. B* 52 (1995) 3684.
- [50] H. Takeya, T. Hirano, K. Kadowaki, *Physica C* 256 (1996) 220; H. Takeya, K. Kadowaki, K. Hirata, and T. Hirano, *J. Alloys & Compounds*, 245 (1996) 94.
- [51] G. Behr *et al.*, *J. Crystal Growth* 198/199 (1999) 642.
- [52] R. Vaglio *et al.*, *Phys. Rev. B* 56 (1997) 934 and references therein.
- [53] S.C Wimbush *et al.*, *J. Phys.: Cond. Matter* 13 (2001) L355 and references therein.
- [54] M. Reibold *et al.*, *J. Alloys and Compounds*, 347 (2002) 24 and references therein.
- [55] See for example, B. Raveau, C. Michel, M. Hervieu, in *Studies of High Temperature Superconductors*, Vol. 2, (Ed. A. Narlikar), Nova Sci. Publishers, NY (1989) pp1.
- [56] W.E. Pickett and D.J. Singh, *Phys. Rev. Lett.*, 72 (1994) 3702.
- [57] I.R. Fisher, J.R. Cooper, and P.C. Canfield, *Phys. Rev. B*. 56 (1997) 10820.
- [58] J.W. Lynn, S. Skanthakumar, Q. Huang, S.K. Sinha, Z. Hossain, L.C. Gupta, R. Nagarajan, C. Godart, *Phys. Rev. B* 55 (1997) 6584.
- [59] M. El Massalami, R.E. Rupp, and G.J. Neuwenhuys, *Physica C* 304 (1998) 184.
- [60] S.M. Lourerio *et al.*, *Solid State Commun.* 119 (2001) 675.
- [61] Belger *et al*, *Physica C* 306 (1998) 277
- [62] W.B. Yelon, Z. Hu, M. Paranthaman, W.J. James, L. Menon, S.K. Malik, *Physica B* 223-224 (1996) 105.
- [63] S. Meenakshi, V. Vijaykumar, R.S. Rao, B.K. Godwal, S.K. Sikka, P. Ravindran, Z. Hossain, R. Nagarajan, L.C. Gupta, and R. Vijayaraghavan, *Phys. Rev. B* 58 (1998) 3377.
- [64] H.W. Zandbergen, W.G. Sloof, R.J. Cava, J.J. Krajewski, W.F. Peck, *Physica C*, 226 (1994) 365.
- [65] H. Fujii *et al.*, *Jpn. J. Appl. Phys.* 33 (1994) L590.
- [66] S. Ikeda *et al.*, *Jpn. J. Appl. Phys.* 33 (1994) 3896.
- [67] Y.Y. Sun *et al.*, *Physica C* 230 (1994) 435.
- [68] E. Tominez, P. Berger, E. Alleno, B. Décamps, G. Schiffmacher, M. Bohn, and C. Godart, *J. Alloys and Compounds*, 275-277 (1998) 123.
- [69] V. Strom, K.S. Kim, A.M. Grishin, and K.V. Rao, *J. Mater. Res.* 11 (1996) 572; V. Strom, K.S. Kim, A.M. Grishin, and K.V. Rao, *J. Appl. Phys.* 79 (1996) 5860.

- [70] L.M. Dezaneti, Y.Y. Xue, Y.Y. Sun, K. Ross, and C.W. Chu, *Physica C* 334 (2000) 123.
- [71] Bitterlich, W. Löser, and G. Behr, *Material Letters*, 57 (2002) 59.
- [72] M. El Massalami, E.M. Baggio-Saitovitch, A. Sulpice, *J. Alloys and Compounds*, 228 (1995) 49.
- [73] L.J. Chang, C.V. Tomy, D. Mck. Paul, N.H. Anderson, M. Yethiraj, *J. Phys. Condens. Mater.* 8 (1996) 2119.
- [74] L. Gao, X.D. Qui, Y. Cao, R.L. Meng, Y.Y. Sun, Y.Y. Xue, and C.W. Chu, *Phys. Rev. B* 50 (1994) 9445.
- [75] G. Graw, K. Günther, G. Behr, W. Löser, K. Nenkov, and U. Krämer, *J. Alloys and Compounds*, 319 (2001) 162.
- [76] A.K. Gangopadhyay *et al.*, *Physica C* 246 (1995) 317.
- [77] A.K. Gangopadhyay, and J.S. Schilling, *Phys. Rev. B* 54 (1996) 10107.
- [78] X.D. Qui, L. Gao, R.L. Meng, Y.Y. Sun, Y.Y. Xue, and C.W. Chu, *Phys. Rev. B* 53 (1996) 12318.
- [79] R.J. Cava, H.W. Zandbergen, B. Batlogg, H. Eisaki, H. Takagi, J.J. Krajewski, W.F. Peck Jr., E.M. Gyorgy, and S. Uchida, *Nature*, 372 (1994) 245.
- [80] H. Michor, R. Krendelsberger, G. Hilscher, E. Bauer, C. Dusek, R. Hauser, L. Naber, D. Werner, P. Rogl, and H.W. Zandbergen, *Phys. Rev. B* 54 (1996) 9408.
- [81] Huang *et al.*, *Physica C* 244 (1995) 101.
- [82] H.W. Zandbergen, R.J. Cava, J.J. Krajewski, and W.F. Peck Jr., *J. Solid State Chem.* 110 (1994) 196.
- [83] Li Rukang, Xiong Chaoshui, Zhu Hong, Lu Bin, and Yang Li, *J. Alloys and Compounds* 223 (1995) 53.
- [84] H.W. Zandbergen, D. Tang, J. Jensen, and R.J. Cava, *Ultramicroscopy* 64 (1996) 231.
- [85] J.R. Link, S.M. Loureiro, C. Kealhofer, H.W. Zandbergen, and R.J. Cava, *J. Solid State Chem.*, 164 (2002) 246.
- [86] H. Kito, S. Ikeda, S. Takegawa, H. Abe, and H. Kitazawa, *Physica C* 291 (1997) 332.
- [87] W. Yang-Bitterlich *et al.*, *J. Alloys and Compounds* 347 (2002) 131.
- [88] C. Sundar, A. Bharathi, Y. Hariharan, T.S. Radhakrishnan, Z. Hossain, R. Nagarajan, L.C. Gupta, R. and Vijayaraghavan, *Phys. Rev. B* 53 (1996) R2971.
- [89] T. Kohara, T. Oda, K. Ueda, Y. Yamada, A. Mahajan, K. Elankumaran, Zakir Hossain, L.C. Gupta, R. Nagarajan, R. Vijayaraghavan, and Chandan Mazumdar, *Phys. Rev. B* 51 (1995) 3985.
- [90] Ming Xu *et al.*, *Physica C* 227 (1994) 321.
- [91] J.S. Kim *et al.*, *Phys. Rev. B* 50 (1994) 3485.
- [92] D.D. Lawrie and J.P. Franck, *Physica C*, 245 (1995) 159.
- [93] K.O. Cheon, I.R. Fisher, P.C. Canfield, *Physica C* 312 (1999) 35.
- [94] Chandan Mazumdar, E. Alleno, O. Sologub, P. Salamakha, H. Noel, M. Potel, Arvind D. Chinchure, R. Nagarajan, L.C. Gupta, and C. Godart, *J. Alloys and Compounds*, 339 (2002) 18.
- [95] H. Kawano, H. Yoshizawa, H. Takeya, and K. Kadowaki, *Phys. Rev. Lett.* 77 (1996) 4628.
- [96] C. Stassis *et al.*, *Phys. Rev. B* 55 (1997) R8678.
- [97] M. Bullock *et al.*, *Phys. Rev. B* 57 (1998) 7916.

- [98] T. Terashima, C. Haworth, H. Takeya, S. Uji, H. Aoki, and K. Kadowaki, *Phys. Rev. B* 56 (1997) 5120.
- [99] D. Jaiswal-Nagar, A.D. Thakur, M.R. Eskildson, P.C. Canfield, Y.M. Yusuf, S. Ramakrishnan, and A.K. Grover, *Proc. SCES'04, Karlsruhe*, To appear in *Physica B* (2004).
- [100] K. Winzer and K. Krug, p 63 in Ref. 24.
- [101] S.S. Banerjee, S. Ramakrishnan, D. Pal, S. Sarkar, A.K. Grvoer, G. Ravikumar, R.K. Mishra, T.V. Chandrasekhar Rao, V.C. Sahni, C.V. Tamy, M.J. Higgins, and S. Bhattacharya, *J. Phys. Soc. Jpn.*, 69 (2000) 262.
- [102] L.F. Mattheis, *Phys. Rev. B* 49 (1994) 13279.
- [103] L.F. Mattheis, T. Siegrist, and R.J. Cava, *Solid State Commun.*, 91 (1994) 587.
- [104] Coehroon, *Physica C* 228 (1994) 331.
- [105] Lee et al., *PRB* 50 (1994) 4030.
- [106] D.J. Singh, *Solid State Commun.*, 98 (1996) 899.
- [107] C. Felser, *J. Solid State Chemistry*, 160 (2001) 93
- [108] A. Fujimori *et al.*, *Phys. Rev. B* 50 (1994) 9660.
- [109] J.P. Sanchez, P. Vulliet, C. Godart, L.C. Gupta, Z. Hossain, and R. Nagarajan, *Phys. Rev. B* 54 (1996) 9421.
- [110] B.T. Matthias, H. Suhl, and E. Corenzwit, *Phys. Rev. Lett.* 1 (1959) 92.
- [111] A.A. Abrikosov and L.P. Gorkov, *Sov. Phys. JETP* 12 (1961) 1243.
- [112] L.C. Gupta, R. Nagarajan, S.K. Dhar, Chandan Mazumdar, Z. Hossain, C. Godart, C. Levy-Clement, B.D. Padalia, and R. Vijayaraghavan., *Proc. Int. Conf. on Physical Metallurg, B A R C, Bombay, March 9-11, 1994*, Eds. S. Banerjee and R.V. Ramanujan, Pub. Gordon & Breach, New York, pp 494.
- [113] B.D. Dunlap *et al.*, *Phys. Rev. B* 37 (1998) 592.
- [114] K. Yosida, *Phys. Rev.*, 106 (1957) 893 and references therein.
- [115] L.C. Gupta, *Phil. Mag.* 77 (1998) 717, and references therein.
- [116] Zakir Hossain, Ph.D. Thesis, Bombay University, 1997.
- [117] K. Everman, A. Handstein, G. Guchs, L. Cao, and K.-H. Muller, *Physica C* 266 (1996) 27 and references therein.
- [118] K.-H. Muller, A. Kreyssig, A. Handstein, G. Guchs, C. Ritter, and M. Lowenhaupt, *J. Appl. Phys.* 81 (1997) 4240 and references therein.
- [119] J.Y. Rhee, X. Wang, and B.N. Harmon, *Phys. Rev. B* 51 (1995) 15585.
- [120] A. Amici, P. Thalmeier, and P. Fulde, *Phys. Rev. Lett.*, 84 (2000) 1800.
- [121] H. Schmidt, M. Weber, and H.F. Braun, *Physica C* 246 (1995) 177
- [122] S. Nagochi, and K. Okuda, *Physica B* 194-196 (1994) 1975.
- [123] F.G. Aliev, V.V. Prayadun, S. Vieira, R. Pillar, A.P. Levanyuk, and V.I. Yerovets, *Euro. Phys. Lett.*, 25 (1994) 143.
- [124] M.J. Nass, K. Levin, and G.S. Grest, *Phys. Rev. B* 25 (1982) 4541.
- [125] B.K. Cho, P.C. Canfield, and D.C. Jhonston, *Phys. Rev. Lett.*, 77 (1996) 163.
- [126] Z. Hossain, R. Nagarajan, S.K. Dhar, L.C. Gupta, *Physica B* 259-261 (1999) 606.
- [127] Z. Hossain, R. Nagarajan, S.M. Patalwar, S.K. Dhar, L.C. Gupta and C. Godart, *Physica B* 230-232 (1997) 865.
- [128] S.K. Dhar, A.D. Chinchure, E. Alleno, C. Godart, L.C. Gupta, and R. Nagarajan, *Pramana - J. Phys.* 58 (2002) 885.

- [129] P.L. Paulose, S.K. Dhar, A.D. Chinchure, E. Alleno, C. Godart, L.C. Gupta, and R. Nagarajan, *Physica C* 399 (2003) 165.
- [130] R.J. Cava, B. Batlogg, T. Siegrist, J.J. Krajewski, W.F. Peck Jr., S. Carter, R.J. Felder, H. Takagi, and R.B. van Dover, *Phys. Rev. B* 50 (1994) 12384.
- [131] R.J. Cava, B. Batlogg, J.J. Krajewski, W.F. Peck, T. Siegrist, R.M. Flemeing, S. Carter, H. Takagi, R.J. Felder, R.B. Van Dover, L.W. Rupp, *Physica C* 226 (1994) 170.
- [132] M. Buchgeister, G. Fuchs, J. Klosowski, U. Wiesner, J. Zawadzki, *Physica C* 255 (1995) 19.
- [133] S.K. Dhar, R. Nagarajan, Z. Hossain, E. Tominez, C. Godart, L.C. Gupta and R. Vijayaraghavan, *Solid State Commun.*, 98 (1996) 985.
- [134] A. Yatskar, N.K. Budraa, W.P. Bayerman, P.C. Canfield, and S.L. Bud'ko, *Phys. Rev. B* 54 (96) R3772.,
- [135] P. Bonville, J.A. Hodges, Z. Hossain, R. Nagarajan, S.K. Dhar, L.C. Gupta, E. Alleno, and C. Godart, *Euro Phys. J.*, B 11 (1999) 377.
- [136] E. Alleno, Z. Hossain, C. Godart, R. Nagarajan, L.C. Gupta, *Phys. Rev. B* 52 (1995) 7428.
- [137] Chandan Mazumdar, Z. Hu, H. von Lips, M.S. Golden, J. Fink, P.C. Canfield, and G. Kaindle, *Phys. Rev. B* 64 (2001) 020504.
- [138] A.T. Boothroyd, J.P. Barratt, P. Bonville, P.C. Canfield, A. Murani, A.R. Wildes, and R.I. Bewley, *Phys. Rev. B* 67 (2003) 104407.
- [139] U. Gasser, P. Allenpach, and A. Furrer, *Physica B* 241-243 (1997) 789.
- [140] U. Gasser, P. Allenpach, F. Fauth, W. Henggeler, J. Mesot, A. Furrer, S. Rosenkranz, P. Worderwisch, and M. Bucheister, *Z. Phys. B: Condens. Matter*, 101 (1996) 345.
- [141] O. Trovarelli, C. Geibel, S. Mederle, C. Langhammer, F.M. Grosche, P. Gegenwart, M. Lang, G. Sparn, and F. Steglich, *Phys. Rev. Lett.*, 85 (2000) 626.
- [142] V. Metlushko, U. Welp, A. Koshelev, I Aronson, G.W. Carbtree, and P.C. Canfield *Phys. Rev. Lett.*, 79 (1997) 1738.
- [143] L. Civale, A.V. Silhanek, J.R. Thompson, K.J. Song, C.V. Tomy, and D.Mck. Paul *Phys. Rev. Lett.*, 83 (1999) 3920.
- [144] U. Yaron, P.L. Gammel, A.P. Ramirez, D.A. Huse, D.J.K. Bishop, A.I. Goldman, C. Stassis, P.C. Canfield, K. Moretensen, and M.R. Eskildsen, *Nature* 382 (1996) 236.
- [145] M. Yethiraj, D. Mck. Paul, C.V. Tomy, and E.M. Forgen, *Phys. Rev. Lett.*, 78 (1997) 4849.
- [146] Y. De Wilde, M. Iavarone, U. Welp, V. Melushko, A.E. Koshelev, I. Aranson, G.W. Crabtree, and P.C. Canfield, *Phys. Rev. Lett.*, 78 (1997) 4273.
- [147] M.R. Eskildsen, K. Harada, P.L. Gammel, A.B. Abrahamsen, N.H. Andersen, G. Ernnst, A.P. Ramirez., D.J. Bishop, K. Mortensen, D.G. Naugle, K.D.D. Ratnanayaka, and P.C. Canfield, *Nature* 393 (1998) 242.
- [148] K. Nørgaard, M.R. Eskildsen, N.H. Andersen, J. Jensen, P. Hedegård, S.N. Klausen, and P.C. Canfield, *Phys. Rev. Lett.*, 84 (2000) 4982
- [149] M.R. Eskildsen, A.B. Abrahamsen, V.G. Kogan, P.L. Gammel, K. Mortensen, N.H. Andersen, and P.C. Canfield, *Phys. Rev. Lett.*, 86 (2001) 5148.
- [150] H. Sakata, M. Oosawa, K. Matsuba, N. Nishida, H. Takeya, K. Hirata, *Phys. Rev. Lett.*, 84 (2000) 1583.

- [151] Tuson Park, M.B. Salamon, Eun Mi Choi, Heon Jung Kim, and Sung-Ik Lee, *Phys. Rev. Lett.* 90 (2003) 177001.
- [152] Etienne Boaknin, R.W. Hill, Cyril Proust, C. Lupien, Louis Taillefer, and P.C. Canfield, *Phys. Rev. Lett.* 87 (2001) 237001.
- [153] K. Izawa, K. Kamata, Y. Nakajima, Y. Matsuda, T. Watanabe, M. Nohara, H. Takagi, P. Thalmeier, and K. Maki, *Phys. Rev. Lett.*, 89 (2002) 137006.
- [154] T. Watanabe, M. Nohara, T. Hanaguri, and H. Takagi, *Phys. Rev. Lett.*, 92 (2004) 147002.
- [155] P. Raychaudhuri, D. Jaiswal-Nagar, Goutam Sheet, S. Ramakrishnan, and H. Takeya, *Phys. Rev. Lett.* 93 (2004) 156802.
- [156] E. Helfand and N.R. Werthamer, *Phys. Rev.* 147 (1966) 288
- [157] P.C. Hoenberg and N.R. Werthamer *Phys. Rev.* 153 (1967) 493.
- [158] For a review, see *Anisotropy Effects in Superconductors*, Ed., H. Weber; (Plenum, New York, 1977).
- [159] M.R. Eskildsen, P.L. Gammel, B.P. Barber, U. Yaron, A.P. Ramirez, D.A. Huse, D.J. Bishop, C. Bolle, C.M. Lieber, S. Oxx, S. Sridhar, N.H. Andersen, K. Mortensen, and P.C. Canfield, *Phys. Rev. Lett.*, 78 (1997) 1968.
- [160] V.G. Kogan, M. Bullock, B. Harmon, P. Miranovi , Lj. Dobrosavljevi -Gruji , P.L. Gammel, and D.J. Bishop, *Phys. Rev. B* 55 (1997) R8693.
- [161] D. McK. Paul, C.V. Tomy, C.M. Aegerter, R. Cubitt, S.H. Lloyd, E.M. Forgan, S.L. Lee, and M. Yethiraj, *Phys. Rev. Lett.* 80 (1998) 1517.
- [162] P.L. Gammel, D.J. Bishop, M.R. Eskildsen, K. Mortensen, N.H. Andersens, I.R. Fisher, K.O. Cheon, P.C. Canfield, and V.G. Kogan, *Phys. Rev. Lett.*, 82 (1999) 4082.
- [163] Dewhurst, S.J. Levett, D. Mck. Paul, *Physica C* 388-89 (2003) 189.
- [164] G. Wang and K. Maki, *Phys. Rev. B* 58 (1998) 6493.
- [165] M. Franz, I. Affleck, and M.H.S. Amin, *Phys. Rev. Lett.*, 79 (1997) 1555.
- [166] J. Schelten, G. Lippmann, and H. Ullmaier, *J. Low Temp. Phys.* 14 (1974) 213.
- [167] D.K. Christen, H.R. Kerchner, S.T. Sekula, and P. Thorel, *Phys. Rev. B* 21 (1980) 102.
- [168] J. Schelten in *Anisotropy Effects in Superconductors*, Ed., H. Weber; (Plenum, New York, 1977), pp 113; B. Obst *ibid.*, pp 139.
- [169] V.G. Kogan, A. Gurevich, .H. Cho, D.C. Jhonston, Ming Xu, J.R. Thompson, and A. Martynovich, *Phys. Rev. B* 54 (1996) 12386,
- [170] V.G. Kogan, P. Miranovi , Lj. Dobrosavljevi -Gruji , W.E. Pickett, and D.K. Christen, *Phys. Rev. Lett.*, 79 (1997) 741.
- [171] P.C. Canfield, S.L. Bud'ko, and B.K. Cho, *Physica C* 262 (1996) 249.
- [172] J.Y. Rhee, X. Wang, and B.N. Harmon, *Phys. Rev. B* 51 (1995) 15585.
- [173] E. Jhonston-Halperin, J. Fiedler, D.E. Ferrell, Ming Xu, B.K. Cho, P.C. Canfield, D.K. Finnemore, and D.C. Jhonston, *Phys. Rev. B* 51 (1995) 12852.
- [174] S.B. Dugdale, M.A. Alam, I. Wilkinson, R.J. Hughes, I.R. Fisher, P.C. Canfield, T. Jarlborg, and G. Santi, *Phys. Rev. Lett.*, 83 (1999) 4824.
- [175] S. Kalavathi, T. Geetha Kumari, Y. Hariharan, M.C. Valsakumar, M.P. Janawadkar, T.S. Radhakrishnan, Z. Hossain, R. Nagarajan, L.C. Gupta, and R. Vijayaraghavan, *Physica B* 223-224 (1996) 96.
- [176] Mi-Ock Mun *et al.*, *Physica C* 303 (1998) 57.
- [177] J.S. Kim, W.W. Kim, and G.R. Stewart, *Phys. Rev. B* 50 (1994) 3485.

- [178] S.V. Shulga, S.-L. Drechsler, G. Fuchs, K.-H. Müller, K. Winzer, M. Heinecke, and K. Krug, *Phys. Rev. Lett.*, 80 (1998) 1730.
- [179] T.V. Chandrasekhar Rao, P.K. Mishra, G. Ravikumar, V.C. Sahni, K. Ghosh, S. Ramakrishnan, A.K. Grover, Girish Chandra, *Physica C* 249 (1995) 271.
- [180] S.-L. Drechsler *et al*, *Physica C*, 364-365 (2001) 31.
- [181] V.G. Kogan, S.L. Bud'ko, P.C. Canfield, and P. Miranovi , *Phys. Rev. B* 60 (1999) 12577.
- [182] M. Nohara, M. Isshiki, H. Takagi, R.J. Cava, *J. Phys. Soc. Jpn.*, 66 (1997) 1888.
- [183] K.J. Song, C. Park, S.S. Oh, Y.K. Kwon, J.R. Thompson, D.G. Mandrus, D. Mck. Paul, C.V. Tomy, *Physica C* 398 (2003) 107.
- [184] G.E. Volovik, *JETP Lett.*, 58 (1993) 469.
- [185] M. Nohara, M. Isshiki, F. Sakai, and H. Takagi, *J. Phys. Soc. Jpn.*, 68 (1999)1078.
- [186] M. Nohara, H. Suzuki, N. Mangkorntong, H. Takagi, *Physica C* 341-348 (2000) 2177.
- [187] K. Izawa, A. Shibata, Y. Matsuda, Y. Kato, H. Takeya, K. Hirata, C.J. van der Beek, and M. Konczykowski, *Phys. Rev. Lett.*, 86 (2001) 1327.
- [188] K. Maki, P. Thalmeier, and H. Won, *Phys. Rev. B* 65 (2002) 140502.
- [189] P. Thalmeier and K. Maki, *Acta Phys. Pol. B* 34 (2003) 557.
- [190] Physics and Astronomy Classification Scheme (PACS) of American Institute of Physics has introduced Quaternary Borocarbides in its subject index – “74.70.Dd. – “Quaternary and multinary borocarbides.”

HETEROGENEOUS MAGNETIC SUPERCONDUCTING SYSTEMS

Erkan Erdin

School of Physics and Astronomy
University of Minnesota, Minneapolis, MN 55455, U.S.A.

1. INTRODUCTION

Heterogeneous magnetic superconducting systems (HMCS) represent a new class of nanostructures. They are made of ferromagnetic (FM) and superconducting (SC) pieces separated by thin layers of insulating oxides. In contrast to the case of a homogeneous ferromagnetic superconductor studied during the last two decades, the two order parameters, the magnetization and the SC electron density do not suppress each other [1, 2]. In HMCS, the interaction between the two order parameters is due to the magnetic field created by the magnetic and SC textures. Strong interaction of the FM and SC systems not only gives rise to a new class of novel phenomena and physical effects, but also shows the important technological promise of devices whose transport properties can be easily tuned by comparatively weak magnetic fields.

The interplay between ferromagnetism and superconductivity has long been the focus of studies both experimental and theoretical [3–6]. In 1957, Ginzburg pointed out [7] that the two phenomena can occur in thin films and wires, due to the small FM induction and relatively large SC critical fields. Afterwards, Anderson and Hühner [8] described the conditions for both phenomena to appear simultaneously in the bulk. The domain-like magnetic structure in the coexistence phase was noted independently by two different groups [9, 10]. Later, Hühner developed the detailed version of the Landau-Ginzburg theory of ferromagnetic superconductors [11], e.g. HoMo_6S_8 and ErRh_4B_4 . The first experiment in this context was carried out by Mathias *et al.* [12]. The coexistence of ferromagnetism and superconductivity in the bulk has been observed

recently in the cuprates $\text{Ru}_{1-x}\text{Gd}_x\text{Cu}_2\text{O}_{8-\gamma}$ [13] and $\text{Ru}_{1-x}\text{Gd}_x\text{Ce}_x\text{Cu}_2\text{O}_{10}$ [14, 15] below their T_C transition temperatures $T_C = 15 - 40$ K and $T_C = 37$ K (for $x = 0.2$) respectively. It is possible to avoid the mutual suppression of the FM and T_C order parameters by separating them in space [1]. Such structures can be made with modern nanofabrication techniques. The proximity effect and spin diffusion which suppress both order parameters can be easily avoided by growing a thin insulating oxide layer between the FM and T_C components. Several theoretical studies have proposed different possibilities for realization of HM: arrays of magnetic dots on the top of a T_C film [1, 16], single magnetic dot of various geometries on top of a T_C film [17–19], ferromagnetic/superconducting bilayers (F/B) and multilayers (F/M) [20–23], magnetic nanorods embedded into a superconductor [24, 25] and semi-infinite HM [26].

In HM, the strong interaction between FM and T_C components stems from the magnetic fields generated by the inhomogeneous magnetization and the supercurrents as well as T_C vortices. T_C vortices were widely studied, both experimentally and theoretically, in the literature [28]. Vortices in T_C films were first studied by J. Pearl [29]. He realized that their current decays in space more slowly than those in the bulk.

Similar models of HM were studied theoretically by other groups in different configurations. Marmorosk *et al.* investigated the giant vortex state created by a magnetic dot, of size on the order of the coherence length ξ , embedded in a T_C film by solving the nonlinear Landau-Ginzburg equations [17]. Kayali [18, 19] and Peeters *et al.* [30] studied vortex creation by both in-plane and out-of-plane magnetized ferromagnets of different shapes on a T_C thin film. Asik and Santos *et al.* considered an array of FM dots on a T_C film [31, 32]. They treated the dots as magnetic dipoles, ignoring their real geometry and showed that they excite and pin T_C vortices. Carneiro studied interaction between vortices in T_C films and magnetic dipole arrays, and showed that the arrays with antiferromagnetic order is more effective in vortex creation than the arrays with ferromagnetic order [33]. Symmetry violation in T_C thin films with regular arrays of magnetic dots are reported by two different studies [16, 34]. Bulaevskii *et al.* discussed the pinning of vortices in ferromagnet-superconductor multilayers [35]. The same group also examined the effect of the screening magnetic field on a thick magnetic layer which is placed on top of a bulk superconductor [36]. They found that the magnetic domains shrink in the presence of the T_C film. In the most of theoretical studies, hard magnets are considered. Recently, Helseth found that identical vortices can attract each other in the presence of soft magnets [37].

To date, only sub-micron magnetic dots covered by thin T_C films have been prepared and studied [38–44]. The experimental samples of FM- T_C hybrid systems were prepared by means of electron beam lithography and lift-off techniques [45]. Both in-plane and out-of-plane magnetization was experimentally studied. The dots with magnetization parallel to the plane were fabricated from Co, Ni, Fe, Gd-Co and m-Co alloys. For the dots with magnetization perpendicular to the plane, Co/Pt multilayers were used. The FM dots were deposited on thin T_C films made of either Nb or Pb, whose transition temperatures are around 7–10 K. In these experiments, the effect of commensurability on the transport properties (e.g. magnetoresistance oscillations and matching anomalies) was observed. However, this effect is not limited to the magnets interacting with superconductors and was first found many years ago by Martinoli and his group [46]. They studied the transport properties of T_C films with periodically modulated thickness in an external magnetic field. They found oscillations of critical current versus magnetic field. Recently, several experimental groups observed commensurability effects caused by a periodic array of magnetic dots or holes [47–50]. These results confirm that the FM dots create and pin vortices. However, much more interesting and promising would be effects specific

for the HM , which are associated with the violation of the time reversal symmetry. Some of them include spontaneous currents in the ground state [24, 51–53]. So far only one such effect was experimentally observed: an asymmetry of the C hysteresis in the presence of magnetic dots [39].

In HM , the magnetic field induced by inhomogeneous magnetization penetrates into a superconductor through C vortices, while the magnetic field generated by the supercurrents and C vortices acts on the magnetic system. The mutual interaction between FM and C subsystems offer interesting physical effects such as spontaneous symmetry violation [16], shrinkage of FM domains and a magnetic domain wall [21, 36, 54], C transition temperature shift [23] and Bean-Livingstone-like energy barrier for vortices [26].

We recently developed a method based on London-Maxwell equations to study theoretical realizations of HM [27]. In this article, we first review this method and its extension to periodic systems and finite systems. Next, some of our recent results on a C film with a FM dot grown upon it and domain structures in F/B and further studies in these systems are briefly discussed. This review is prepared as a progress report and aims to give reader the basic aspects of HM . This article is organized as follows: In the next section, a method to calculate inhomogeneous magnetization and supercurrents including C vortices in the London approximation is presented with great details. In section II, a FM dot on top of a C film and vortex states in the ground state are discussed. Section III is devoted to the recent theoretical results on F/B . We conclude with discussions and summary in section IV. To help reader follow easily the theoretical analysis in this chapter, we give details of calculations with Bessel functions and series in the appendices.

2. THEORY

In both theoretically proposed and experimentally realized HM , the magnetic texture interacts with the superconducting (C) current. An inhomogeneous magnetization generates a magnetic field outside the magnets that in turn generates screening currents in the superconductor, which subsequently change the magnetic field. The problem must be solved self-consistently. In the literature, HM have been studied through Landau-Ginzburg equations [17] and linear London method . Though the C vortices are treated more accurately in the former in which C electron density n_s changes in the vicinity of the vortex core, solving non-linear Landau-Ginzburg equations is numerically difficult. In London approach, n_s is assumed to be constant, and vortices are treated as points. However, London's approximation is sufficient when the sizes of all the structures in the problem greatly exceed the coherence length , and offers more analytical insight. For this reason, we have been studying the several realizations of HM through a method based on London-Maxwell equations. Here we present the method to calculate inhomogeneous magnetization and supercurrents including the C vortices in the London approximation. In the next section a method for the most general 3-dimensional HM is given. In section B, this method is applied to the case of very thin ferromagnetic (FM) and C films. In section C, the method is extended to periodic heterogeneous magnetic superconducting systems (PHM). In the last section, we show how this method can be applied to semi-infinite and finite systems.

A. Three Dimensional Systems

The total energy of a stationary FM- C system reads [55]

$$U = \int \left[\frac{\mathbf{B}^2}{8\pi} + \frac{m_s n_s \mathbf{v}_s^2}{2} - \mathbf{B} \cdot \mathbf{M} \right] dV. \quad (1)$$

where \mathbf{B} is the magnetic induction, \mathbf{M} is the magnetization, n_s is the density of C electrons, m_s is their effective mass and \mathbf{v}_s is their velocity. We assume the C density n_s and the magnetization \mathbf{M} to be separated in space. We also assume that the magnetic field \mathbf{B} and its vector-potential \mathbf{A} asymptotically approaches zero at infinity. After the static Maxwell equation $\nabla \times \mathbf{B} = \frac{4\pi}{c} \mathbf{j}$, and $\mathbf{B} = \nabla \times \mathbf{A}$ are employed, the magnetic field energy can be transformed as follows:

$$\int \frac{\mathbf{B}^2}{8\pi} dV = \int \frac{\mathbf{j} \cdot \mathbf{A}}{2c} dV. \quad (2)$$

Although the vector potential enters explicitly in the last equation, it is gauge invariant due to current conservation $\text{div} \mathbf{j} = 0$. When integrating by parts, we neglect the surface term. This approximation is correct if the field, vector potential and current decrease sufficiently fast at infinity. The current \mathbf{j} can be represented as a sum: $\mathbf{j} = \mathbf{j}_s + \mathbf{j}_m$ of the C and magnetic currents, respectively [56]:

$$\mathbf{j}_s = \frac{n_s \hbar e}{2m_s} (\nabla \varphi - \frac{2\pi}{\phi_0} \mathbf{A}), \quad (3)$$

$$\mathbf{j}_m = c \nabla \times \mathbf{M}. \quad (4)$$

where $\phi_0 = hc/2e$ is the C flux quantum. We separately consider the contributions from magnetic and C currents to the integral (2), starting with the integral:

$$\frac{1}{2c} \int \mathbf{j}_m \cdot \mathbf{A} dV = \frac{1}{2} \int (\nabla \times \mathbf{M}) \cdot \mathbf{A} dV. \quad (5)$$

Integrating by parts and neglecting the surface term again, we arrive at

$$\frac{1}{2c} \int \mathbf{j}_m \cdot \mathbf{A} dV = \frac{1}{2} \int \mathbf{M} \cdot \mathbf{B} dV. \quad (6)$$

We have omitted the integral over a distant surface:

$$\oint (\mathbf{n} \times \mathbf{M}) \cdot \mathbf{A} dS. \quad (7)$$

Such an omission is justified if the magnetization is confined to a limited volume. But for infinite magnetic systems it may be wrong even in the simplest problems.

We next consider the contribution of the C current \mathbf{j}_s to the integral (2). In the gauge-invariant Eq.(3), φ is the phase of the C carriers wave-function. Note that the phase gradient $\nabla \varphi$ can be incorporated in \mathbf{A} as a gauge transformation. The exception is vortex lines, where φ is singular. We use the equation (3) to express the vector potential \mathbf{A} in terms of the supercurrent and the phase gradient:

$$\mathbf{A} = \frac{\phi_0}{2\pi} \nabla \varphi - \frac{m_s c}{n_s e^2} \mathbf{j}_s. \quad (8)$$

Plugging Eq.(8) into Eq.(2), we find

$$\frac{1}{2c} \int \mathbf{j}_s \cdot \mathbf{A} dV = \frac{\hbar}{4e} \int \nabla \varphi \cdot \mathbf{j}_s dV - \frac{m_s}{2n_s e^2} \int j_s^2 dV. \quad (9)$$

ince the superconducting current is

$$\mathbf{j}_s = en_s \mathbf{v}_s. \quad (10)$$

The last term in Eq.(9) equals the negative of the kinetic energy and thus exactly compensates the kinetic energy in the initial expression for the energy (1). Collecting all the remaining terms, we obtain the following expression for the total energy:

$$U = \int \left[\frac{n_s \hbar^2}{8m_s} (\nabla \varphi)^2 - \frac{n_s \hbar e}{4m_s c} \nabla \varphi \cdot \mathbf{A} - \frac{\mathbf{B} \cdot \mathbf{M}}{2} \right] dV. \quad (11)$$

This expression is complete except for a possible surface term for infinite magnetic systems. Note that integration volume includes both superconductors and magnets. Eq. (11) allows us to separate the energy of the vortices, the energy of magnetization and the energy of their interaction. Indeed, as we noted earlier, the phase gradient can be ascribed to the contribution of vortex lines alone. It can be represented as a sum of independent integrals over distinct vortex lines. The vector-potential and the magnetic field can also be presented as a sum of magnetization induced and vortex induced parts: $\mathbf{A} = \mathbf{A}_m + \mathbf{A}_\nu$, $\mathbf{B} = \mathbf{B}_m + \mathbf{B}_\nu$, where \mathbf{A}_k , \mathbf{B}_k (the index k is either m or ν) are determined as solutions of the London-Maxwell equations generated by the magnetization and the vortices. The effect of the C screening of the magnetic field due to the magnetization is already included in the vector fields \mathbf{A}_m and \mathbf{B}_m . If such separation of fields is applied, then the total energy, (11) becomes a sum of terms containing vortex contributions alone, magnetic contributions alone and the interaction terms. The purely magnetic component can be represented as a non-local quadratic form of the magnetization. The purely superconducting part becomes a non-local double integral over the vortex lines. Finally, the interaction term may be presented as a double integral over the vortex lines and the volume occupied by the magnetization, and is bi-linear in magnetization and vorticity.

B. Two Dimensional Textures and Vortices

Below we show a detailed analysis in the case of parallel FM and C films, both very thin and positioned close to each other. Neglecting their thickness, we assume both films to be located approximately at $z = 0$. In some cases we need a higher degree of accuracy. We then introduce a small distance d between the films, which in the end approaches zero. Although the thickness of each film is assumed to be small, the 2-dimensional densities of super-carriers $n_s^{(2)} = n_s d_s$ and magnetization $\mathbf{m} = \mathbf{M} d_m$ remain finite. Here d_s is the thickness of the C film and d_m is the thickness of the FM film. The 3d super-carrier density in the C film is $n_s(\mathbf{R}) = \delta(z) n_s^{(2)}(\mathbf{r})$ and the 3d magnetization in the FM film is $\mathbf{M}(\mathbf{R}) = \delta(z-d) \mathbf{m}(\mathbf{r})$, where \mathbf{r} is the two-dimensional radius-vector and the z -direction is chosen to be perpendicular to the films. In what follows the 2d C density $n_s^{(2)}$ is assumed to be a constant and the index (2) is omitted. The energy (11) for this special case takes the following form:

$$U = \int \left[\frac{n_s \hbar^2}{8m_s} (\nabla\varphi)^2 - \frac{n_s \hbar e}{4m_s c} \nabla\varphi \cdot \mathbf{a} - \frac{\mathbf{b} \cdot \mathbf{m}}{2} \right] d^2\mathbf{r}, \quad (12)$$

where $\mathbf{a} = \mathbf{A}(\mathbf{r}, z=0)$ and $\mathbf{b} = \mathbf{B}(\mathbf{r}, z=0)$. The vector potential satisfies the Maxwell-London equation, which is derived from the static Maxwell equation $\nabla \times \mathbf{B} = \frac{4\pi}{c} \mathbf{j}$, where \mathbf{j} is the total current density on the surface of the superconductor, and is given by $\mathbf{j} = (\mathbf{j}_s + \mathbf{j}_m) \delta(z)$. The supercurrent and the magnetic current densities are given in Eqs.(3, 4). Using $\mathbf{B} = \nabla \times \mathbf{A}$, the Maxwell-London equation reads

$$\nabla \times (\nabla \times \mathbf{A}) = -\frac{1}{\lambda} \mathbf{A} \delta(z) + \frac{2\pi \hbar n_s e}{m_s c} \nabla\varphi \delta(z) + 4\pi \nabla \times (\mathbf{m} \delta(z)). \quad (13)$$

Here $\lambda = \lambda_L^2/d_s$ is the effective screening length for the C film, and $\lambda_L = (\frac{m_s c^2}{4\pi n_s e^2})^{\frac{1}{2}}$ is the London penetration depth [57].

According to our general arguments, the term proportional to $\nabla\varphi$ in Eq. (13) describes vortices. A plane vortex characterized by its vorticity n and by the position \mathbf{r}_0 of its center on the plane, contributes a singular term to $\nabla\varphi$:

$$\nabla\varphi_0(\mathbf{r}, \mathbf{r}_0) = n \frac{\hat{z} \times (\mathbf{r} - \mathbf{r}_0)}{|\mathbf{r} - \mathbf{r}_0|^2}, \quad (14)$$

and generates a Pearl vortex vector potential (see Appendix A for details):

$$\mathbf{A}_{v0}(\mathbf{r} - \mathbf{r}_0, z) = \frac{n\phi_0}{2\pi} \frac{\hat{z} \times (\mathbf{r} - \mathbf{r}_0)}{|\mathbf{r} - \mathbf{r}_0|} \int_0^\infty \frac{J_1(q|\mathbf{r} - \mathbf{r}_0|) e^{-q|z|}}{1 + 2\lambda q} dq, \quad (15)$$

where $J_1(x)$ is Bessel function of the first order. Different vortices contribute independently in the vector potential and magnetic field. In the limit of zero film thickness, the usual Coulomb gauge, $\text{div}\mathbf{A} = 0$, leads to strong singularity in the vector potential, due to the surface currents in the C and FM films, which leads to the discontinuity at $z = 0$. Therefore, we choose to employ another gauge $A_z = 0$. The calculations become simple in the Fourier-representation. Following the previous section, we write the Fourier transform of the vector potential $\mathbf{A}_{\mathbf{k}}$ as a sum $\mathbf{A}_{\mathbf{k}} = \mathbf{A}_{m\mathbf{k}} + \mathbf{A}_{v\mathbf{k}}$ of independent contributions from magnetization and vortices. Using the following definitions of the Fourier transform:

$$\mathbf{A}_{\mathbf{k}} = \int \mathbf{A}(\mathbf{r}, z) e^{-i\mathbf{q}\cdot\mathbf{r} - ik_z z} d^3r, \quad (16)$$

$$\mathbf{a}_{\mathbf{q}} = \int \mathbf{a}(\mathbf{r}, z=0) e^{-i\mathbf{q}\cdot\mathbf{r}} d^2r. \quad (17)$$

The equation for the magnetic part of the vector-potential reads

$$\mathbf{k}(\mathbf{k} \cdot \mathbf{A}_{m\mathbf{k}}) - k^2 \mathbf{A}_{m\mathbf{k}} = \frac{\mathbf{a}_{m\mathbf{q}}}{\lambda} - 4\pi i \mathbf{k} \times \mathbf{m}_{\mathbf{q}} e^{ik_z d}, \quad (18)$$

where \mathbf{q} is the projection of the wave vector \mathbf{k} onto the plane of the films: $\mathbf{k} = k_z \hat{z} + \mathbf{q}$. An arbitrary vector field $\mathbf{V}_{\mathbf{k}}$ in wave-vector space can be fixed by its coordinates in a local frame of reference formed by the vectors $\hat{z}, \hat{q}, \hat{z} \times \hat{q}$:

$$\mathbf{V}_{\mathbf{k}} = V_{\mathbf{k}}^z \hat{z} + V_{\mathbf{k}}^{\parallel} \hat{q} + V_{\mathbf{k}}^{\perp} (\hat{z} \times \hat{q}). \quad (19)$$

The solution to equation (18) with $A_z = 0$ is found by taking the inner product of equation (19) with \hat{q} , \hat{z} and $\hat{z} \times \hat{q}$, respectively as below:

$$A_{mk}^{\parallel} = -\frac{4\pi i m_{\mathbf{q}}^{\perp}}{k_z} e^{ik_z d} - \frac{a_{m\mathbf{q}}^{\parallel}}{k_z^2 \lambda}, \quad (20)$$

$$A_{mk}^{\parallel} = -\frac{4\pi i m_{\mathbf{q}}^{\perp}}{k_z} e^{ik_z d}, \quad (21)$$

$$A_{mk}^{\perp} = -\frac{1}{\lambda k^2} a_{\mathbf{q}}^{\perp} + \frac{4\pi i (k_z m_{\mathbf{q}}^{\parallel} - q m_{\mathbf{q}z})}{k^2} e^{ik_z d}. \quad (22)$$

Integration of the latter equation over k_z gives the perpendicular component of $\mathbf{a}_{\mathbf{q}}^{(m)}$:

$$a_{m\mathbf{q}}^{\perp} = -\frac{4\pi \lambda q (m_{\mathbf{q}}^{\parallel} + i m_{\mathbf{q}z})}{1 + 2\lambda q} e^{-qd}. \quad (23)$$

It follows from Eqs.(20, 21) that $a_{m\mathbf{q}}^{\parallel} = 0$. Note that Eq. (21) for the parallel component of the vector potential A_{mk}^{\parallel} does not contain any information on the C film. This component corresponds to zero magnetic field outside the FM film. Therefore, it is not essential for our problem. The vortex part of the vector potential $\mathbf{A}_{\mathbf{v}\mathbf{k}}$ also has not a z -component since the supercurrents flow in the plane. The vortex-induced vector potential is [57]

$$\mathbf{A}_{\mathbf{v}\mathbf{k}} = \frac{2i\phi_0(\hat{q} \times \hat{z})F(\mathbf{q})}{\mathbf{k}^2(1 + 2\lambda q)}, \quad (24)$$

where $F(\mathbf{q}) = \sum_j n_j e^{i\mathbf{q} \cdot \mathbf{r}_j}$ is the vortex form-factor; the index j labels the vortices, n_j denotes the vorticity of the j th vortex and \mathbf{r}_j are coordinates of the vortex centers. The Fourier-transform of the vortex-induced vector potential at the surface of the C film $\mathbf{a}_{\mathbf{v}\mathbf{q}}$ reads

$$\mathbf{a}_{\mathbf{v}\mathbf{q}} = \frac{i\phi_0(\hat{q} \times \hat{z})F(\mathbf{q})}{q(1 + 2\lambda q)}. \quad (25)$$

We express the energy (12) in terms of the fields and vector-potential Fourier-transforms separating the purely magnetic, purely vortex and the interaction parts:

$$U = U_{vv} + U_{mm} + U_{mv}. \quad (26)$$

The vortex energy U_{vv} is the same as it would be in the absence of the FM film:

$$U_{vv} = \frac{n_s \hbar^2}{8m_s} \int \nabla \varphi_{-\mathbf{q}} \cdot \left(\nabla \varphi_{\mathbf{q}} - \frac{2\pi}{\phi_0} \mathbf{a}_{\mathbf{v}\mathbf{q}} \right) \frac{d^2 q}{(2\pi)^2} \quad (27)$$

However, the magnetic energy U_{mm} :

$$U_{mm} = -\frac{1}{2} \int \mathbf{m}_{-\mathbf{q}} \cdot \mathbf{b}_{m\mathbf{q}} \frac{d^2 q}{2\pi^2} \quad (28)$$

contains the screened magnetic field \mathbf{b} and therefore differs from its value in the absence of the C film, but it does not depend on the vortex positions. The interaction energy reads

$$U_{mv} = -\frac{n_s \hbar e}{4m_s c} \int (\nabla\varphi)_{-\mathbf{q}} \cdot \mathbf{a}_{m\mathbf{q}} \frac{d^2q}{(2\pi)^2} - \frac{1}{2} \int \mathbf{m}_{-\mathbf{q}} \cdot \mathbf{b}_{v\mathbf{q}} \frac{d^2q}{(2\pi)^2}. \quad (29)$$

Note that only the form-factor $F(\mathbf{q})$ conveys any information about the vortex arrangement.

C. Periodic Systems

A periodic heterogeneous magnetic superconducting system (PHM) such as a magnetic dot array or a periodic domains in ferromagnet-superconductor bilayers can be studied with the method described in the previous section. However, it is necessary to modify the equations given above for the periodic structures of interest. In this section, we extend the above method to study PHMs. In doing so, we still assume that PHMs are made of very thin magnetic textures with the magnetization perpendicular to the plane and C films. Their energy is calculated over the surface of the C film. We start with the energy of the 2d systems (12). In the plane of the PHM, the magnetic field \mathbf{b} , the magnetization \mathbf{m} , the phase gradient $\nabla\varphi$ and the vector potential \mathbf{a} are 2d periodic functions. Therefore, we need to express them in terms of Fourier series. For any function $f(\mathbf{r})$, the Fourier expansion is given by

$$\mathbf{f}(\mathbf{r}) = \sum_{\mathbf{G}} \mathbf{f}_{\mathbf{G}} e^{i\mathbf{G}\cdot\mathbf{r}} \quad \mathbf{f}_{\mathbf{G}} = \frac{1}{\mathcal{A}} \int \mathbf{f}(\mathbf{r}) e^{-i\mathbf{G}\cdot\mathbf{r}} d^2\mathbf{r}. \quad (30)$$

The \mathbf{G} s are the reciprocal vectors of the periodic structure of interest, and \mathcal{A} is the elementary cell area. We first express \mathbf{a} , \mathbf{b} , \mathbf{m} and $\nabla\varphi$ in terms of the Fourier series as in (30), then substitute them back in (12). Performing the integral over the infinite area of the 2d system and using $\int e^{i(\mathbf{G}+\mathbf{G}')\cdot\mathbf{r}} d^2\mathbf{r} = \mathcal{A} \delta_{\mathbf{G},-\mathbf{G}'}$, we obtain the energy per unit cell u for the 2d PHM expressed in terms of Fourier components as follows:

$$u = \sum_{\mathbf{G}} \left[\frac{n_s \hbar^2}{8m_s} |(\nabla\varphi)_{\mathbf{G}}|^2 - \frac{n_s \hbar e}{4m_s c} (\nabla\varphi)_{\mathbf{G}} \cdot \mathbf{a}_{-\mathbf{G}} - \frac{\mathbf{b}_{\mathbf{G}} \cdot \mathbf{m}_{-\mathbf{G}}}{2} \right]. \quad (31)$$

The Fourier coefficients of the vector potentials, \mathbf{a}_m and \mathbf{a}_v for both the magnetic part and the vortices in terms of continuous Fourier vectors are already given in (23) and (25). They can be rewritten in terms of reciprocal vectors as

$$\mathbf{a}_{m\mathbf{G}} = \frac{4\pi\lambda i \mathbf{G} \times \hat{z} m_z \mathbf{G}}{1 + 2\lambda G}, \quad (32)$$

$$\mathbf{a}_{v\mathbf{G}} = \frac{i\phi_0 (\hat{G} \times \hat{z}) F_{\mathbf{G}}}{\mathcal{A} G (1 + 2\lambda G)}. \quad (33)$$

Using the Fourier coefficients of the magnetic field and the phase gradient:

$$\mathbf{b}_{\mathbf{G}} = i\mathbf{G} \times \mathbf{a}_{\mathbf{G}}, \quad (34)$$

$$(\nabla\varphi)_{\mathbf{G}} = 2\pi i(\mathbf{G} \times \hat{z}F_{\mathbf{G}})/(\mathcal{A}G^2), \quad (35)$$

and replacing the vector potentials in (31) by (32) and (33), the energy of the PHM per unit cell is found term by term as

$$u_{vv} = \frac{\Phi_0^2}{4\pi\mathcal{A}^2} \sum_{\mathbf{G}} \frac{|F_{\mathbf{G}}|^2}{G(1+2\lambda G)}, \quad (36)$$

$$u_{mv} = -\frac{\Phi_0}{\mathcal{A}} \sum_{\mathbf{G}} \frac{m_z \mathbf{G} F_{-\mathbf{G}}}{1+2\lambda G}, \quad (37)$$

$$u_{mm} = -2\pi\lambda \sum_{\mathbf{G}} \frac{G^2 |\mathbf{m}_z \mathbf{G}|^2}{1+2\lambda G}. \quad (38)$$

D. Finite Systems

In the most of theoretical studies, C subsystem is considered to be infinite size for the sake of computational simplicity. Although it is relatively hard to handle C system's boundaries in both Landau-Ginzburg and London equations, several groups have studied finite or semi-finite realizations of HM. We recently considered semi-infinite HM elsewhere [26], by benefiting from the ideas of Kogan's study of Pearl vortex near the edge of C film[58]. Here, we propose an alternative method to treat semi-infinite and finite realizations of HM. To this end, we modify London-Maxwell equation (see Eq.(13)). The boundary condition can be incorporated into Maxwell-London equation by using step function, namely supercurrent is zero outside the C system's boundary. Together with step function, Maxwell-London equation reads

$$\nabla \times \nabla \times \mathbf{A} = \frac{4\pi}{c} (\mathbf{j}_s \theta(\mathbf{r}' - \mathbf{r}) + \mathbf{j}_m), \quad (39)$$

where $\mathbf{j}_s = \frac{c\Phi_0}{8\pi^2\lambda} \nabla\varphi - \frac{c}{4\pi\lambda} \mathbf{a}$ and $\theta(\mathbf{r}' - \mathbf{r})$ is step function that equals 0 or 1 when \mathbf{r} is greater than the boundary's position \mathbf{r}' or otherwise. For semi-infinite system in which 2-d C film lies on x-y plane and its edge is located at x=0, step function is $\theta(x)$. For a finite circular C disk of radius R, step function becomes $\theta(R - r)$. Eq.(39) can be solved by similar techniques used in the previous sections, however its solution gives rather complicated integral equations. We leave the details of the solution to further works.

3. FM DOT ON SC FILM

In this section, we review the studies related to the ground state of a superconducting (C) film in the presence of a circular FM dot grown upon it (see (see Fig. 1)). In this case, the magnetization is assumed to be fixed and homogeneous within the dot, and directed perpendicular to the C film. This problem is previously discussed elsewhere [27], in which we predicted the geometrical pattern formed by vortices in the ground state. Here, we give further details of analysis and some new results. The problems we discuss are: i) under what conditions do vortices appear in the ground state; ii) where they appear, and iii) the magnetic fields and currents in these states. As in the previous section, we assume the C film to be a very thin plane, and infinite in the lateral directions. Since the magnetization is confined within the finite dot, no

integrals over infinitely remote surfaces or contours arise. In the next section, we treat the first case using the method described in the previous chapter.

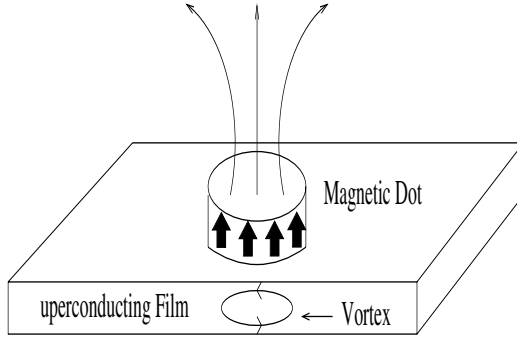


FIG. 1: Magnetic dot on a superconducting film.

Let both C and FM films be infinitely thin and placed at heights $z = 0$ and $z = d$, respectively. The C film is infinite in lateral directions, whereas the FM film is finite and has the shape of circle with radius R (magnetic dot). The 2d magnetization of the magnetic dot is $\mathbf{m}(\mathbf{r}) = m\hat{z}\sigma(R-r)\delta(z-d)$, where $\sigma(x)$ is the step function, equal to +1 for $x > 0$ and 0 for $x < 0$. We first find the vector potential and magnetic field induced by the dot in the presence of the C film, using Eqs. (22,23). The Fourier-component of \mathbf{d} at magnetization necessary for this calculation is

$$\mathbf{m}_{\mathbf{k}} = \hat{z} \frac{2\pi m R}{q} J_1(qR) e^{ik_z d}, \quad (40)$$

where $J_1(x)$ is the Bessel function. From (25) with (40), the calculations employ Fourier-transform of the vector potential at the superconductor surface:

$$a_{m\mathbf{q}}^\perp = -\frac{i8\pi^2 \lambda m R}{1 + 2\lambda q} J_1(qR). \quad (41)$$

In the last equation we have replaced e^{-qd} by 1. The Fourier-transform of the vector potential reads

$$A_{m\mathbf{k}}^\perp = -\frac{i8\pi^2 m R J_1(qR)}{k^2} \left[e^{-qd} \frac{2q\lambda}{1 + 2\lambda q} + (e^{ik_z d} - e^{-qd}) \right]. \quad (42)$$

Though the difference in the round brackets in equation (42) appears to be small (recall that d must be set to zero in the final answer), we cannot neglect it since it implies a finite, not small

discontinuity in the parallel component of magnetic field at the two film faces. From equation (42) we can immediately find the Fourier-transforms of the magnetic field components via

$$B_{mk}^z = iqA_{mk}^\perp; B_{mk}^\perp = -ik_z A_{mk}^\perp. \quad (43)$$

The inverse Fourier-transformation of Eqs. (43,42) gives the magnetic field in real space:

$$B_m^z(\mathbf{r}, z) = 4\pi\lambda mR \int_0^\infty \frac{J_1(qR)J_0(qr)e^{-q|z|}}{1+2\lambda q} q^2 dq, \quad (44)$$

$$B_m^r(\mathbf{r}, z) = -2\pi mR \int_0^\infty J_1(qR)J_1(qr)e^{-q|z|} \left[\frac{2q\lambda}{1+2\lambda q} \text{sign}(z) + \text{sign}(z-d) - \text{sign}(z) \right] q dq, \quad (45)$$

where $\text{sign}(z)$ is the function equal to the sign of its argument. Note that B_m^r has discontinuities at $z=0$ and $z=d$ due to surface currents in the C and FM films respectively; whereas, the normal component B_m^z is continuous.

ymmetry arguments imply that a vortex, if it appears, must be located at the center of the dot. Indeed, for $R \gg \lambda$, an analytical calculation shows that the central position of the vortex provides minimal energy. We have checked numerically that the central position is always energy favorable for one vortex. This fact is not trivial since the magnetic field of the dot is stronger near its boundary and a violation of symmetry could be naively expected. However, the gain of energy due to interaction of the magnetic field generated by the vortex with the magnetization of the dot decreases when the vortex approaches the boundary.

Another interesting problem is the sign of the perpendicular component of the magnetic field. The vector potential generated by a vortex is given by Eq. (24) with $F(\mathbf{q}) = 1$. The perpendicular component of the magnetic field generated by the vortex is

$$B_v^z = \frac{\Phi_0}{2\pi} \int_0^\infty \frac{J_0(qr)e^{-q|z|}}{1+2\lambda q} q dq. \quad (46)$$

Numerical calculation based on Eqs. (44, 46) shows that, in the presence of the vortex centered at $r=0$, B_z on the C film ($z=0$) changes sign for some $r > R$ (see Fig. 2), but it is negative for all $r > R$ without the vortex. The physical explanation of this fact is as follows. The dot itself is an ensemble of parallel magnetic dipoles. Each dipole generates a magnetic field whose z -component on the plane passing through the dot has sign opposite to the dipolar moment. However, the field exactly over and under the dipole has the same sign as the dipole and is strongly singular. The fields from different dipoles compete at $r < R$, but they have the same sign at $r > R$. The C current tends to screen the magnetic field of the magnetic dot and have the opposite sign. The field generated by a vortex at large distances decays more slowly than the screened dipolar field ($1/r^3$ vs. $1/r^5$). Thus, the sign of B_z is opposite to the magnetization at small values of r (but larger than R) and positive at large r . Measurement of the magnetic field near the film may serve as a diagnostic tool to detect a C vortex bound by the dot. To our knowledge, so far there are no experimental measurements of this effect.

The energy of the system in the presence of many vortices with arbitrary vorticities n_i can be calculated using Eqs.(26-29). The appearance of N vortices with arbitrary positions \mathbf{r}_i in the system changes the energy by an amount:

$$\Delta_N = \sum_{i=1}^N n_i^2 \epsilon_v + \frac{1}{2} \sum_{i \neq j}^N n_i n_j \epsilon_{vv}(r_{ij}) + \sum_{i=1}^N n_i \epsilon_{mv}(r_i). \quad (47)$$

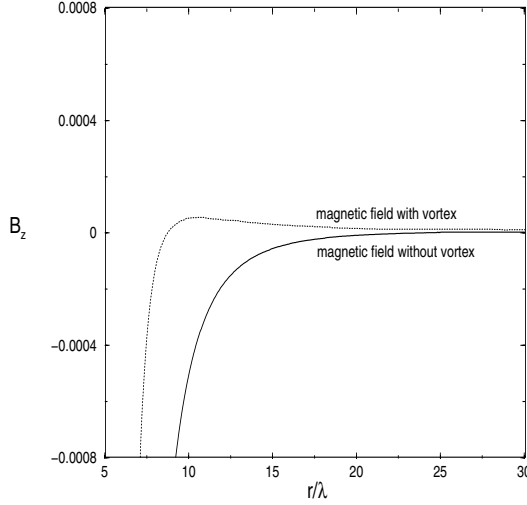


FIG. 2: Magnetic field of a dot with and without vortex for $R/\lambda = 5$ and $\phi_0/8\pi^2 mR = 0.05$.

Here $\epsilon_v = \epsilon_0 \ln(\lambda/)$ is the energy of a vortex without a magnetic dot, $\epsilon_0 = \phi_0^2/(16\pi^2\lambda)$ and ϵ_{vv} is the vortex-vortex interaction and ϵ_{mv} is the vortex-magnetic dot interaction. substituting (25) into the vortex energy ϵ_{vv} of (27), we get

$$\epsilon_{vv}(r_{ij}) = \frac{\epsilon_0}{\pi} \left[H_0\left(\frac{r_{ij}}{2\lambda}\right) - Y_0\left(\frac{r_{ij}}{2\lambda}\right) \right], \tag{48}$$

where $r_{ij} = |\mathbf{r}_j - \mathbf{r}_i|$, $H_0(x)$ and $Y_0(x)$ are the true function of the zeroth order and the modified Bessel function of the second kind of the zeroth order, respectively [59]. For ϵ_{mv} of (29), direct substitution of the vector potential, magnetic field and the phase gradient (see Eqs. (41,44)) into (29) gives

$$\epsilon_{mv}(r_i) = -m\phi_0 R \int_0^\infty \frac{J_1(qR)J_0(qr_i)dq}{1 + 2\lambda q}. \tag{49}$$

In order for N vortices to appear, the necessary condition is that $\Delta_N < 0$ and $\Delta_N < \Delta_{N-1}$. Using this criteria, we can determine in what configurations and order the vortices appear. To this end, we study only vortices with positive vorticity which are situated under the dot. Under the assumption that the dot's diameter is larger than λ , it is reasonable to think that vortices with multiple vorticities, the so-called giant vortices, do not appear, since the vortex energy grows as the square of its vorticity (see Eq.(47)). For large dots $R \gg \lambda$ and sufficiently small m , the giant vortex is definitely energy unfavorable. However for $R < \lambda$ and $mR \gg \phi_0$, it can be favorable. This question has not yet been analyzed completely.

The next step is to minimize (47) with respect to the positions of the vortices. We first start with one vortex. It turns out that it appears at the center of the dot. Δ_1 is a function of two dimensionless variables $m\phi_0/\epsilon_v$ and R/λ . $\Delta_1 = 0$ defines a critical curve separating regions

with and without vortices, and is depicted in Fig. 3. Stability occurs ($\Delta_N < 0$) for the regions in Fig. 3 below the critical curves. The asymptotic behavior of ε_{mv} for large and small values of R/λ can be found analytically (see Appendix C for details):

$$\varepsilon_{mv} \approx -m\phi_0 \quad \left(\frac{R}{\lambda} \gg 1\right), \quad (50)$$

$$\varepsilon_{mv} \approx -m\phi_0 \frac{R}{2\lambda} \quad \left(\frac{R}{\lambda} \ll 1\right). \quad (51)$$

Thus, asymptotically the curve $\Delta_1 = 0$ turns into a horizontal straight line $m\phi_0/\varepsilon_v = 1$ at large R/λ and into a logarithmically distorted hyperbola $(m\phi_0/\varepsilon_v)(R/\lambda) = 2$ at small R/λ .

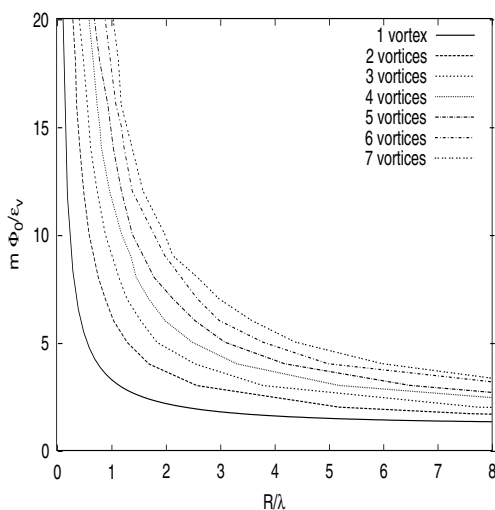


FIG. 3: Magnetic dot on a superconducting film.

For further increase of either $m\phi_0/\varepsilon_v$ or R/λ , the second vortex becomes energetically favorable. Due to symmetry, the centers of the two vortices are located on a straight line connecting the vortices with the center of the dot at equal distances from the center. The curve 2 on Fig. 3 corresponds to this second phase transition. The occurrence of 2 vortices can be experimentally detected as the violation of circular symmetry of the field. For three vortices, the equilibrium configuration is a regular triangle. The further increase of $m\phi_0/\varepsilon_v$ or R/λ makes other vortex states more energetically favorable. In principle there exists an infinite series of such transitions. Here, we limit ourselves to the first seven transitions by considering the next four vortex states. In equilibrium, for vortices sit on the corners of a square, whereas five vortices form a pentagon. We find that geometrical pattern for six vortices is hexagon. For the case of seven vortices, equilibrium configuration is different from the first six states. Namely, one vortex is situated at the dot's center, while other six vortices form a hexagonal shape (see Fig.4).

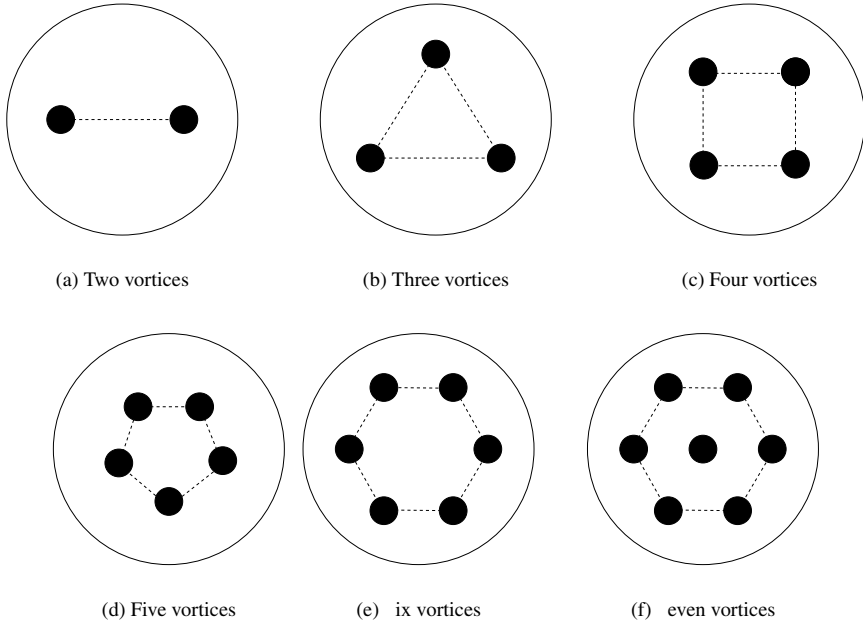


FIG. 4: Vortex states

It is not yet clear what is the role of configurations with several vortices confined within the dot region and antivortices outside. Note that these results are valid for infinite systems. When the FM dot is placed on top of a finite C film, we suspect that the geometrical patterns formed by vortices will be quite different. To investigate this hypothesis, we recently studied the FM dot on a semi-infinite C film, and found that the vortex is shifted either towards or away from the C film's boundary due to the competition between the attraction of a vortex with the C film's edge via its image vortex and the interaction between the dot and the vortex [26].

4. FERROMAGNETIC-SUPERCONDUCTING BILAYERS

Earlier Lyuksyutov and Pokrovsky noticed [20, 53] that in a bilayer consisting of homogeneous superconducting (C) and ferromagnetic (FM) films with the magnetization normal to the plane, C vortices occur spontaneously in the ground state, even though the magnet does not generate a magnetic field in the C film. In previous work [21], we presented a theory of such vortex-generation instability and the resulting vortex structures, and showed that due to this instability, domains with alternating magnetization and vortex directions occur in ferromagnetic-superconducting bilayers (F/B). In this chapter, we review the theory of F/B

and the domain structures. In the next section, we treat these domain structures in the continuum regime in which the domain size is much larger than the effective penetration depth. This approximation does not work when the equilibrium size of the domains is on the order of the effective penetration depth. However, it can be recovered by considering the discrete lattice of vortices instead. In the second section, we report our preliminary results on the possible equilibrium structure in the discrete case and calculate the vortex positions, which depend on the magnetization and domain wall energy [60].

A. The Continuum Regime

We start by refining previous arguments establishing a topological instability in the F/B [20, 53]. We assume that the magnetic anisotropy is strong enough to keep the magnetization exactly perpendicular to the film (in the z -direction). The homogeneous FM film creates no magnetic field outside itself and hence does not alter the state of the C film. The magnetic field generated by a single vortex in the superconducting film, with magnetic flux $\phi_0 = hc/2e$, interacts with the magnetization \mathbf{m} of the FM film and lowers the total energy by $-m\phi_0$ for a proper sign of vorticity. The energy to create a Pearl vortex in an isolated C film is $\varepsilon_v = \varepsilon_0 \ln(\lambda/\xi)$ [29], where $\varepsilon_0 = \phi_0^2/16\pi^2\lambda$, $\lambda = \lambda_L^2/d$ is the effective penetration depth [57], λ_L is the London penetration depth, and ξ is the coherence length. Thus, the total energy of a single vortex in the F/B is

$$\varepsilon_v^{eff} = \varepsilon_v - m\phi_0, \quad (52)$$

and the F/B becomes unstable with respect to spontaneous formation vortices as soon as ε_v^{eff} turns negative. Note that close enough to the C transition temperature T_s , ε_v^{eff} is definitely negative since the C electron density n_s and, therefore, ε_v is zero at T_s (Recall that $\varepsilon_v(T) = \varepsilon_v(T=0)(1 - T^2/T_s^2)$). For small m value, $\varepsilon_v^{eff} > 0$ at $T = 0$, the instability exists in the temperature interval $T_v < T < T_s$, where $\varepsilon_v^{eff}(T_v) = 0$, otherwise instability persists until $T = 0$.

A newly appearing vortex phase cannot consist only of vortices of one sign. Indeed, any system with average vortex density n_v would generate a constant magnetic field $B_z = n_v\phi_0$ along the z direction. The energy of this field for a finite film of the linear size L_f grows as L_f^3 , which quickly exceeds the gain in energy due to creation of vortices, proportional to L_f^2 . Hence, in order for the vortex array to survive, the film should split in domains with alternating magnetization and vortex directions. We show below that if the domain size L is much greater than the effective penetration length λ , the most favorable arrangement is the stripe domain structure. To this end we write the total energy of the bilayer in the form

$$U = U_{sv} + U_{vv} + U_{mv} + U_{mm} + U_{dw}, \quad (53)$$

where U_{sv} is the effective energy of single vortices; U_{vv} is the vortex-vortex interaction energy; U_{mv} is the energy of interaction between the vortices and magnetic field generated by domain walls; U_{mm} is the self-interaction energy of the magnetic layer; and U_{dw} is the linear tension energy of magnetic domain walls [60]. We assume that the 2d periodic domain structure consist of two equivalent sublattices, so that the magnetization $m_z(\mathbf{r})$ and density of vortices $n(\mathbf{r})$ alternate when crossing from one sublattice to another. The magnetization is assumed to have a constant absolute value: $m_z(\mathbf{r}) = ms(\mathbf{r})$, where $s(\mathbf{r})$ is the periodic step function equal to ± 1

at one sublattice and -1 at the other one. We consider a dilute vortex system where the vortex spacing is much larger than λ . Then the effective single-vortex energy becomes

$$U_{sv} = \varepsilon_v^{eff} \int n(\mathbf{r})s(\mathbf{r})d^2x. \quad (54)$$

Note that $n(\mathbf{r})s(\mathbf{r}) > 0$ in all cases. Due to ‘‘average neutrality’’ of the periodic stripe system, the energy of a single vortex in equation (54) is different from (52): $\varepsilon_v^{eff} = \varepsilon_v - m\phi_0/2$. Note that, $-\frac{1}{2} \int \mathbf{b}^v \cdot \mathbf{m}d^2x$ term in Eq.(29) contributes $-m\phi_0/2$ in the effective single-vortex energy. In the periodic systems, the contribution of the surface term is zero. The vortex-vortex interaction energy is

$$U_{vv} = \frac{1}{2} \int n(\mathbf{r})V(\mathbf{r}-\mathbf{r}')n(\mathbf{r}')d^2xd^2x', \quad (55)$$

where $V(\mathbf{r}-\mathbf{r}')$ is the pair interaction energy between vortices located at points \mathbf{r} and \mathbf{r}' . Its asymptotic value at large distances $|\mathbf{r}-\mathbf{r}'| \gg \lambda$ is [55]

$$V(\mathbf{r}-\mathbf{r}') = \frac{\phi_0^2}{4\pi^2|\mathbf{r}-\mathbf{r}'|}. \quad (56)$$

This long-range interaction is induced by the magnetic field generated by the Pearl vortices and their slowly decaying currents. By Eq.(29), the energy of the vortex interaction with the magnetic field generated by the magnetic film is [27]

$$U_{mv} = -\frac{\phi_0}{16\pi^2\lambda} \int \nabla\varphi(\mathbf{r}-\mathbf{r}')n(\mathbf{r}') \cdot \mathbf{a}^{(m)}(\mathbf{r})d^2xd^2x'. \quad (57)$$

Here $\varphi(\mathbf{r}-\mathbf{r}') = \arctan \frac{y-y'}{x-x'}$ is a phase shift created at a point \mathbf{r} by a vortex centered at a point \mathbf{r}' and $\mathbf{a}^{(m)}(\mathbf{r})$ is the value of the vector-potential induced by the FM film upon the C one. By Eq.(28), the magnetic self-interaction reads

$$U_{mm} = -\frac{m}{2} \int B_z^{(m)}(\mathbf{r})s(\mathbf{r})d^2x. \quad (58)$$

Finally, each magnetic domain wall’s linear energy is $U_{dw} = \varepsilon_{dw}L_{dw}$, where ε_{dw} is the linear tension of the magnetic domain wall and L_{dw} is the total length of the magnetic domain walls. Let us analyze the vortex-domain-wall interaction U_{mv} . The magnetic vector-potential $\mathbf{A}^{(m)}$ obeys the London-Pearl magneto-static equation (see Eq.(13)):

$$\nabla \times \left(\nabla \times \mathbf{A}^{(m)} \right) = \left[-\frac{1}{\lambda} \mathbf{a}^{(m)} + 4\pi \nabla \times (\hat{z}m(\mathbf{r})) \right] \delta(z). \quad (59)$$

We consider $L \gg \lambda$, where the term $\nabla \times (\nabla \times \mathbf{A}^{(m)})$ is negligible and then

$$\mathbf{a}^{(m)} \approx -4\pi m \lambda \hat{z} \times \nabla s(\mathbf{r}). \quad (60)$$

The phase gradient entering Eq. (57) can be rewritten as: $\nabla\varphi(\mathbf{r}) = \hat{z} \times \nabla \ln |\mathbf{r}-\mathbf{r}'|$. Plugging this expression into (57), integrating by part and employing relation $\nabla^2 \ln |\mathbf{r}-\mathbf{r}'| = -2\pi\delta(\mathbf{r}-\mathbf{r}')$, we arrive at

$$U_{mv} = -\frac{\phi_0}{2} \int m(\mathbf{r})n(\mathbf{r})d^2x. \quad (61)$$

This result implies that the vortex-domain-wall interaction renormalizes the single-vortex to

$$\tilde{\epsilon}_v = \epsilon_v - m\phi_0. \quad (62)$$

Thus, the term U_{mv} can be removed from the total energy (53) if the single-vortex contribution U_{sv} is replaced by \tilde{U}_v , which differs from (54) on replacing ϵ_v^{eff} by $\tilde{\epsilon}_v$. In physical terms, it means that the vortex attraction to the magnetic domain walls lowers the threshold for the spontaneous appearance of the vortex-domain structure. The next step is the minimization of energy with respect to $n(\mathbf{r})$ the vortex density, which appears only in the first three terms of the total energy (see Eq.(53)). Their sum can be conveniently denoted by $U_v \equiv \tilde{U}_{sv} + U_{vv}$. To simplify the minimization, we Fourier-expand the periodic functions: $s(\mathbf{r}) = \sum_{\mathbf{G}} s_{\mathbf{G}} e^{i\mathbf{G}\cdot\mathbf{r}}$ and $n(\mathbf{r}) = \sum_{\mathbf{G}} n_{\mathbf{G}} e^{i\mathbf{G}\cdot\mathbf{r}}$. The energy U_v in the Fourier-representation then reads

$$U_v = U_{sv} + U_{vv} + U_{mv} = \sum_{\mathbf{G}} \left(\tilde{\epsilon}_v s_{\mathbf{G}} n_{-\mathbf{G}} + \frac{1}{2} V_{\mathbf{G}} n_{\mathbf{G}} n_{-\mathbf{G}} \right), \quad (63)$$

where $V_{\mathbf{G}} = \int V(\mathbf{r}) e^{i\mathbf{G}\cdot\mathbf{r}} d^2x = \phi_0^2 / 2\pi |\mathbf{G}|$. Minimization of Eq.(63) over $n_{\mathbf{G}}$ leads to

$$n_{\mathbf{G}} = -\frac{\tilde{\epsilon}_v s_{\mathbf{G}}}{V_{\mathbf{G}}} = -\frac{2\pi\tilde{\epsilon}_v |\mathbf{G}| s_{\mathbf{G}}}{\phi_0^2}, \quad (64)$$

$$U_v = -\frac{\pi\tilde{\epsilon}_v^2}{\phi_0^2} \sum_{\mathbf{G}} |\mathbf{G}| |s_{\mathbf{G}}|^2. \quad (65)$$

Note that the solution becomes physically meaningless at positive $\tilde{\epsilon}_v$. We now apply these general results to analyze the stripe domain structure. In this case the density of vortices $n(x)$ depends only on one coordinate x perpendicular to the magnetic domain walls. The vectors \mathbf{G} are directed along the x -axis. The allowed wave numbers are $G = \pi(2r+1)/L$, where L is the domain width and r runs over all integers. The Fourier-transform of the step function is $s_G = \frac{2i}{\pi(2r+1)}$. The inverse Fourier-transform of Eq. (64) for the stripe domain case is (see Appendix C for details)

$$n(x) = -\frac{4\pi\tilde{\epsilon}_v}{\phi_0^2 L} \frac{1}{\sin \frac{\pi x}{L}}. \quad (66)$$

Note the strong singularity of the density near the domain walls. Our approximation is invalid at distances of the order of λ , and the singularities must be smeared out in a band of the width λ around the magnetic domain wall. Conversely, the approximation of the zero-width magnetic domain wall is invalid within the range of the magnetic domain wall width l . Fortunately, we do not need more detailed information on the distribution of vortices in the vicinity of the magnetic domain walls. Indeed, by substituting the Fourier-transform of the step function into equation (65), we find a logarithmically divergent series in the form of $\sum_r 1/(2r+1)$. It must be cut off at $\pm r_{max}$ with $r_{max} \sim L/\lambda$. The summation can be performed using the Euler asymptotic formula [65] with the following result (see Appendix C for details):

$$U_v^{str} = -\frac{4\tilde{m}^2 \mathcal{A}}{L} \left(\ln \frac{L}{\lambda} + C + 2 \ln 2 \right), \quad (67)$$

where $\tilde{m} = m - \epsilon_v / \phi_0$, \mathcal{A} is the domain area and $C \sim 0.577$. Now the problem is to analyze the proper cut-off for any lattice. As we have seen in the stripe domain structure, the energy U_v

diverges logarithmically due to the strong singularity of the vortex density near each magnetic domain wall (see Eq. (66)). Thus, the logarithmic term is proportional to the total magnetic domain wall length (see Eq.(67)). The singularity of the vortex density contributes the similar logarithmic term to the energy for any lattice. However, this logarithmic accuracy is not sufficient to distinguish the domain structures. In order to solve this problem, we need the next approximation to the energy U_v , i.e. a term α , proportional to the length of the magnetic domain wall, without the logarithmic factor. Together with this term, the energy for any lattice looks like $U_v \sim \ln(L\alpha/\lambda)$. Now, the problem is to find this term accurately. Such a term includes a non-local contribution from large distances between λ and L and a local contribution from the vicinity of the magnetic domain walls. The non-local contribution is accurately accounted for by the summation over the integers; whereas, the local contribution requires a cut-off at large r , which is not well defined. However, due to its local character it must be the same for all magnetic domain walls. Therefore, it is possible to choose the maximal wave-vector in the direction normal to the magnetic domain wall as $2\pi/\lambda$. Such a procedure renormalizes the magnetic domain wall's linear tension, in the same for any domain lattice. This remark allows calculation of the energy U_v for the square and triangular lattices. For the square checkerboard lattice, the allowed wave-vectors are $\mathbf{G} = \frac{\pi}{L} [(2r+1)\hat{x} + (2s+1)\hat{y}]$. The Fourier-transform of the step function is: $s_{\mathbf{G}} = \frac{4}{\pi^2(2r+1)(2s+1)}$. The maximal values of r and s are identical and equal to L/λ where L is the side of a square domain. The summation, similar to the case of stripe structure although somewhat more complicated, leads to the following expression (see Appendix C for details):

$$U_v^{sq} = -\frac{8\tilde{m}^2\mathcal{A}}{L} \left(\ln \frac{L}{\lambda} + C + 2\ln 2 - \gamma \right), \quad (68)$$

where the numerical constant γ is defined below:

$$\gamma = (2 - \sqrt{2}) \frac{7}{\pi^2} \zeta(3) + \frac{16}{\pi^2} \sum_{r=0}^{\infty} \sum_{s=r+1}^{\infty} S(r, s). \quad (69)$$

Here $\zeta(x)$ is the Riemann zeta-function; $\zeta(3) \approx 1.2020$ and,

$$S(r, s) = \frac{2(r+s+1) - \sqrt{(2r+1)^2 + (2s+1)^2}}{(2r+1)^2(2s+1)^2}. \quad (70)$$

Direct numerical calculation gives $\gamma \approx 0.9 > \ln 2$.

The reciprocal lattice vectors for the regular triangular domain lattice are

$\mathbf{G} = \frac{2\pi}{L} \left[r \left(\hat{x} - \frac{1}{\sqrt{3}}\hat{y} \right) + s \frac{2}{\sqrt{3}}\hat{y} \right]$. The analysis is remarkably simplified in the ‘‘triangular coordinate frame’’: $u = x - y/\sqrt{3}$; $v = 2y/\sqrt{3}$. The step function inside one elementary cell is $s(u, v) = +1$ for $u+v < L$ and $s(u, v) = -1$ for $u+v > L$, where L is the side of the elementary triangle. The Fourier-transform of the step function $s_{\mathbf{G}}$ is not zero at either $r \neq 0, s = 0$, or $r = 0, s \neq 0$, or $r = s \neq 0$. For all these cases $|s_{\mathbf{G}}|^2 = 1/(\pi^2 q^2)$, where q is either r or s , depending on which of these numbers differs from zero. For this case, the summation in equation (65) gives

$$U_v^{tri} = -\frac{32\mathcal{A}\tilde{m}^2}{L\sqrt{3}} (\ln r_{\max} + C). \quad (71)$$

However, the value r_{\max} is different from the stripe and square cases since the coordinates are skewed, here it equals $\frac{\sqrt{3}}{2} \frac{l}{\lambda}$.

Our next step is to show that the magnetization self-interaction can be included into the renormalized magnetic domain wall linear tension. For the isolated FM stripe domain structure, the magnetization self-interaction energy is equal to $U_{mm} = -m^2 L_{dw} \ln \frac{l}{\lambda}$, where l is the magnetic domain wall width [61–63]. The superconducting screening enhances the magnetic field very near the magnetic domain walls and reduces it away from the magnetic domain walls. In the stripe geometry, from Eq.(60), $b_z^{(m)} = da^{(m)}/dx = -4\pi m \lambda (d^2s/dx^2)$ implying that the screened magnetic field is confined to an interval $\sim \lambda$ near magnetic domain walls. Thus, its contribution to the energy does not contain a large logarithm. By (58), U_{mm} gives $-L_{dw} m^2$, which can be incorporated into the renormalized value of the magnetic domain wall linear tension. Note that this contribution is negative. We assume that it is less than the initial positive linear tension ε_{dw} . We do not consider here the interesting but less likely possibility of a negative renormalized linear tension, which probably results in domain wall branching.

Now we are in position to minimize the total energy U over the domain width L and compare the equilibrium energy. The equilibrium domain width and the equilibrium energy for the stripe structure are

$$L_{eq}^{(str)} = \frac{\lambda}{4} \exp\left(\frac{\varepsilon_{dw}}{4\tilde{m}^2} - C + 1\right), \quad (72)$$

$$U_{eq}^{(str)} = -\frac{16\tilde{m}^2 \mathcal{A}}{\lambda} \exp\left(-\frac{\varepsilon_{dw}}{4\tilde{m}^2} + C - 1\right). \quad (73)$$

Calculating the corresponding values for the square and triangular lattice, we obtain: $L_{eq}^{(sq)} = L_{eq}^{(str)} \exp(\gamma)$; $U_{eq}^{(sq)} = 2U_{eq}^{(str)} \exp(-\gamma)$; and $U_{eq}^{(tri)} = (3/4)U_{eq}^{(str)}$. Comparing these energies to the energy of the stripe structure, for which $U_{eq}^{(str)} < 0$, we conclude that the stripe structure wins. The domains become infinitely wide at $T = T_s$ and at $T = T_v$. The expression in the exponent (73) at $T = T_s$ is four times less than the corresponding expression for domains in an isolated magnetic film [56]. Therefore, stripe domains in the bilayer can be energetically favorable even if the isolated magnetic film remains in a monodomain state. If stripe domains in the magnetic film exist above the C transition, then they shrink dramatically below the transition. The physical reason behind this effect is as follows. There are two contributions to the energy that determines the domain width; magnetic energy and the domain wall energy. While the latter contribution prefers the larger domain width, the former contribution causes the smaller width. In the presence of superconductor, the magnetic field is screened due to the Meissner effect, which makes the magnetic energy contribution dominant. As a result, the domain width is smaller than that in the case of ferromagnet only. Bulaevsky and Chudnovsky [36] found that the domain width in a *thick* magnetic layer above a *bulk* superconductor is proportional to $d_m^{1/3}$ instead of $d_m^{1/2}$, a well-known result for an isolated magnetic layer. Here d_m is the thickness of the magnetic layer; "thick" means that $d_m \gg l$. Our problem is fundamentally different on two counts: first, we consider a *thin* FM film $d_m \ll l$ above a *thin* C film and, second, the main effect is due to the interaction of vortices with the magnetization rather than from the screening of the magnetic field as in [36]. The vortex-magnetization interaction effect is much stronger, leading to a totally different dependence.

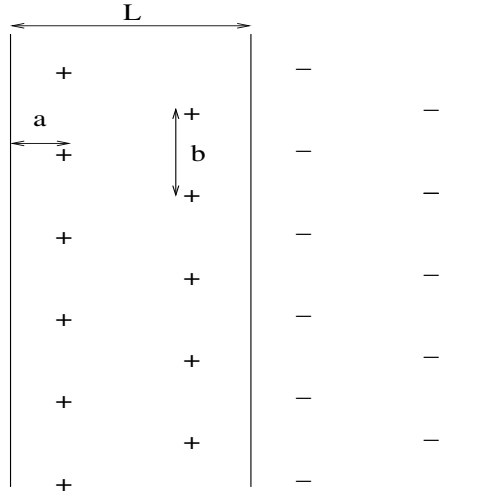


FIG. 5: The vortex lattice.

B. The Discrete Regime

If $\epsilon_{dw} \leq 4\tilde{m}^2$, the continuum approximation becomes invalid, since L_{eq} becomes on the order of or less than λ (see Eq.(72)). Instead a lattice of discrete vortices must be considered. In this section, we present a method which works in both continuum and the discrete regimes. We study the lattices of discrete vortices only in the stripe phase, since the system favors that phase in equilibrium. In the continuum approximation, it is found that the vortex density increases at the closer distances to the magnetic domain walls. Based on this fact and the symmetry of the stripe domain structure, it is reasonable to consider that the vortices and antivortices form periodic structures on straight chains along the y direction. Even though it is not clear how many chains are associated with each domain, we can still make progress toward understanding discrete vortex lattices. In this section, we report our preliminary results on the problems; i) how the vortices and the antivortices are positioned on the chains; ii) how the equilibrium domain size changes, depending on the magnetization and the magnetic domain wall energy in the presence of the vortices. In order to solve these problems, we propose a configuration of the vortex and the antivortex chains in which two chains per stripe is considered. According to our results in the continuum regime, the vortex density increases near the domain walls. Therefore, we can have at least two chains per stripe in a possible configuration. Chains are situated at distance a from the magnetic domain walls. Another problem is how to place vortices and antivortices on the chains. If vortices are next to each other on the either side of the magnetic domain wall, the magnetic fields they produce cancel out each other. As a result, the gain in energy is diminished. However, the system has the largest gain when the vortices and antivortices are shifted by a half period $b/2$ (see Fig. 5).

Our next step is to write the energies of the proposed structure. To this end, we use (36,37,38). In those equations, the vortex configurations differ by their form-factors. We can obtain them from $F_{\mathbf{G}} = \sum_{\mathbf{r}_i} n_i e^{i\mathbf{G}\cdot\mathbf{r}_i}$, where the \mathbf{G} 's are the reciprocal vectors of the periodic structures, the \mathbf{r}_i are the positions of the vortex centers, and n_i are the charge of the vortex. In our proposed model, $\mathbf{G} = ((2r+1)\frac{\pi}{L}, 2s\frac{\pi}{b})$, $n_i = \pm 1$ and $F_{\mathbf{G}} = e^{iG_x a} - (-1)^s e^{-iG_y a}$. In our calculations, the divergent part of the series must be extracted carefully. We show below the detailed analysis of series equations for each candidate. We start with the self interaction energy of the magnetic layer U_{mm} , since it is the same for each configuration. For the periodic structures, it is given by (38). Direct substitution of the Fourier coefficient of the stripe phase $m_z \mathbf{G} = \frac{2im}{\pi(2r+1)}$ into Eq.(38) gives the self-interaction of the magnetic layer per unit cell as

$$u_{mm} = -\frac{8m^2}{L} \sum_{r=0}^{\infty} \frac{1}{\frac{L}{2\pi\lambda} + 2r + 1}. \quad (74)$$

This series is logarithmically divergent. However, it can be pulled out easily by adding and subtracting $1/(2r+1)$ in the series above. Thus, we get two terms; one convergent, the other divergent. Summing over r on the divergent part up to the cutoff $r_{max} = L/l$, where l is the magnetic domain wall width, we obtain the following:

$$u_{mm} = -\frac{4m^2}{L} \left(\ln \frac{L}{l} - \psi^{(0)}\left(\frac{1}{2} + \frac{L}{4\pi\lambda}\right) \right), \quad (75)$$

where $\psi^{(0)}(x)$ is the polygamma function of zeroth order [59]. In our numerical calculations, we write the logarithmic term in (75) as $\ln(\lambda/l) + \ln(L/\lambda)$ and then incorporate the $-4m^2 \ln(\lambda/l)$ term in the renormalized ϵ_{dw}^{ren} . Another energy term with a divergent series is the vortex energy, in general given by (36). The logarithmic divergence in this term stems from the vortex self-energies. We first split (36) into two parts as follows:

$$u_{vw} = \frac{\pi\epsilon_0}{2L^2 b^2} \sum_{\mathbf{G}} \left[\frac{|F_{\mathbf{G}}|^2}{G^2} - \frac{|F_{\mathbf{G}}|^2}{G^2(1+2\lambda G)} \right]. \quad (76)$$

Note that the area of the elementary cell is $2Lb$. The first term of the series above contributes to the self-energies of the vortices; whereas, the second term is the vortex-vortex energy and will be left in the series form. The series in the first term can be transformed to the form of $\sum_{r=-\infty}^{\infty} \sum_{s=-\infty}^{\infty} 1/((2r+1)^2 x^2 + s^2)$ where x is constant, and depends on the form-factor. A detailed analysis of such series is given in Appendix B.

The next step is to find the vortex energy and the interaction energy of the magnetization and vortices for each configuration. In the calculation of u_{mv} , we take the Fourier coefficient of the magnetization to be $\frac{4im}{(2r+1)} \delta(G_y)$. The fact that the stripe is infinite along the y direction results in the additional term $2\pi\delta(G_y)$. However, it does not play any role in the calculation of u_{mm} . For numerical analysis, these energies must be expressed in terms of dimensionless parameters. To this end, we define dimensionless variables $\tilde{\lambda} = \lambda/L$, $\tilde{b} = b/L$ and $\tilde{\epsilon}_{dw} = \epsilon_{dw}^{ren} \lambda / \epsilon_0$. The total energy \tilde{U} is measured in units of ϵ_0/λ^2 . In addition, we introduce the dimensionless magnetic energy as $\tilde{U}_{mm} = u_{mm}/(\epsilon_0/\lambda^2)$. In the fourth configuration, the square of the form-factor is: $|F_{\mathbf{G}}|^2 = 2 - 2(-1)^s \cos((2r+1)\pi\tilde{a})$. Even and odd values of s give different contributions. Then, we can calculate the vortex energy for even s and odd s separately. In terms of these parameters, we find

$$\tilde{U} = \frac{\tilde{\lambda}^2}{2\tilde{b}} \left(\ln\left(\frac{\lambda}{\tilde{\lambda}}\right) - 2f_v(\tilde{\lambda}, \tilde{a}) - \frac{4}{\tilde{b}\pi} f_{vv}(\tilde{\lambda}, \tilde{a}, \tilde{b}) - \frac{16m\phi_0}{\epsilon_0} f_{mv}(\tilde{\lambda}) \right) + \tilde{U}_{mm} + \tilde{\epsilon}_{dw}\tilde{\lambda}, \quad (77)$$

where

$$\begin{aligned} f_v &= \sum_{r=0}^{\infty} \frac{\coth((2r+1)\frac{\pi\tilde{b}}{4}) - 1}{2r+1} \sin^2((2r+1)\pi\tilde{a}) \\ &+ \sum_{r=0}^{\infty} \frac{\tanh((2r+1)\frac{\pi\tilde{b}}{4}) - 1}{2r+1} \sin^2((2r+1)\pi\tilde{a}), \\ f_{vv} &= \sum_{r,s=-\infty}^{\infty} \frac{\sin^2((2r+1)\pi\tilde{a})}{((2r+1)^2 + \frac{16s^2}{\tilde{b}^2})(1 + 2\pi\tilde{\lambda}\sqrt{(2r+1)^2 + \frac{16s^2}{\tilde{b}^2}})}, \\ &+ \sum_{r,s=-\infty}^{\infty} \frac{\cos^2((2r+1)\pi\tilde{a})}{((2r+1)^2 + \frac{4(2s+1)^2}{\tilde{b}^2})(1 + 2\pi\tilde{\lambda}\sqrt{(2r+1)^2 + \frac{4(2s+1)^2}{\tilde{b}^2}})}, \\ f_{mv} &= \sum_{r=0}^{\infty} \frac{\sin((2r+1)\pi\tilde{a})}{(2r+1)(1 + 2\pi\tilde{\lambda}(2r+1))}. \end{aligned} \quad (78)$$

In the numerical minimization of Eq.(77), we take $\ln(\lambda/\tilde{\lambda}) = 5$. Changing $m\phi_0/\epsilon_0$ at fixed $\tilde{\epsilon}_{dw}$, which initially is fixed at 0.5, we calculate the minimal energy of the proposed configuration. We first investigate when this configurations becomes energetically favorable in the system. To this end, we check where the equilibrium energies of the configuration first become negative.

TABLE I: The numerical results for the fourth configuration at $\tilde{\epsilon}_{dw} = 0.5$. The column on the left is input.

| $m\phi_0/\epsilon_v$ | L/λ | a/λ | b/λ |
|----------------------|-------------|-------------|-------------|
| 2.00 | 2.50 | 0.56 | 0.18 |
| 3.00 | 1.67 | 0.38 | 0.12 |

In numerical calculations, we also found that the vortex lattice is stable for $\epsilon_{dw} > 4\tilde{m}^2$. At this point, the domain size is noticeably larger than the effective penetration depth λ , so the continuum approximation is valid. Therefore, we expect that the domain nucleation starts in the continuum regime. This problem is left for the future research. As seen in Table I, at constant $\tilde{\epsilon}_{dw}$, with increasing $m\phi_0/\epsilon_v$, the equilibrium size of the domain decreases. In addition, the vortices on the chain get closer to each other. These results agree with those obtained in the continuum approximation. As $\epsilon_{dw}/4\tilde{m}^2$ increases, we expect that new vortex chains develop within the domains. We leave this problem to future research.

5. CONCLUSIONS

We reviewed theory of the heterogeneous magnetic superconducting systems (HM) based on London-Maxwell equations and the application of the theory on two realizations: ferromagnetic (FM) dots and their square array on a superconducting (C) film, and ferromagnetic-superconducting bilayers (F B). In the first chapter, we presented a general formalism for the interaction between magnetic textures and superconductors in the Londons approximation. The problem is formulated as a variational principle. The variational functional (energy) is an integral over regions occupied either by magnet or by superconductor. It allows us to find directly the positions of vortices and magnetization. Afterwards, the formalism is extended to the case of periodic structures and finite systems.

As applications of the formalism, we have shown that vortices in superconducting films can be generated by magnetic dots magnetized normal to the film. We have found phase transition curves separating the state without vortices from the state with one vortex and the latter from the state with two vortices. Up to 7 vortices, the vortex-configurations on the ground state of a C film with the FM dot on it are determined. For one vortex under a dot we have shown that the perpendicular component of magnetic field changes sign at some distance from the dot. This fact can be used for diagnostics of the vortex generation.

However, we treat only vortices under the FM dot. In a more realistic picture, the antivortices outside the dot become important and most likely affect the configurations of the vortices confined within the dot's region. This problem still remains open.

In the fourth chapter, we studied ferromagnetic-superconducting bilayers (F B). We predicted that in a finite temperature interval below the C transition the F B is unstable with respect to C vortex formation. The slow decay ($\propto 1/r$) of the long-range interactions between Pearl vortices makes the structure that consists of alternating domains with opposite magnetization and vorticity energetically favorable. The distribution of vortices inside each domain is highly inhomogeneous, with density increasing near the magnetic domain walls. As long as the domain width is larger than the effective penetration depth, the energy of the stripe domain structure is minimized. These new topological structures can be observed directly. A strong anisotropy in current transport would provide indirect evidence of the stripe texture: the bilayer may be superconducting for current parallel to the domains and resistive for current perpendicular to the domains.

If $\epsilon_{dw} \leq 4\tilde{m}^2$, the continuum approximation becomes invalid. Instead, we considered the discrete lattice of vortices. We analyzed the vortex configurations in two vortex chains. Depending on the magnetization and the magnetic domain wall energy, the positions of the vortices and the equilibrium domain size are calculated.

It is possible that the long domain nucleation time can interfere with the observation of described textures. We expect, however, that the vortices that appear first will reduce the barriers for domain walls and, subsequently, expedite domain nucleation. Quantitative study of this dynamic process is still in progress.

Our purpose was to consider quantitatively a new class of phenomena provided by the interaction between superconductivity and ferromagnetism in heterogeneous systems. This review article focuses on unusual equilibrium structures of vortices and magnetization occurring in such systems. As the simplest specific examples we considered single magnetic dots and also C-FM bilayers. We have shown that, because of the numerous parameters for the system, such as

temperature, magnetization, thickness etc., these systems display a complex phase diagram. We did not exhaust all possible states. Moreover, dynamic effects and transport properties are beyond the scope of this article. However, we believe that our primary results are of experimental interest and have technological promise.

We believe that the most experimentally interesting and challenging predictions are: (1), the existence of domain structures with alternating magnetization and vortex polarity in FM- C bilayers and their shrinking below the C transition temperature; (2), the formation of several vortices under the magnetic dots placed on top of a C film; (3), the symmetry violation in the periodic array of the magnetic dots on C films. Although, antivortices outside the single magnetic dot are not analyzed in this article, they are expected to occur in real systems. All these effects can be observed directly by scanning tunnelling microscopy, scanning Hall probe microscopy and micro-QUID measurements.

In conclusion, our results not only confirm some old results found by means of different methods, but also present a class of new physical effects in HM. In this sense, they manifest a new direction and motivation for the possible experiments in the future.

APPENDIX A: THE PEARL VORTEX

The vortices in thin superconducting(C) films are first studied by J. Pearl [29]. Here, we give the detailed calculations of vector potential and magnetic field for Pearl vortex located at \mathbf{r}_0 on the C film. We start with the London-Pearl equation:

$$\nabla^2 \mathbf{A}(\mathbf{r}, z) = \frac{1}{\lambda} \mathbf{a}(\mathbf{r}) \delta(z) - \frac{\phi_0}{2\pi\lambda} \nabla \varphi(\mathbf{r} - \mathbf{r}_0) \delta(z), \quad (\text{A1})$$

where $\mathbf{a}(\mathbf{r}) = \mathbf{A}(\mathbf{r}, z=0)$. It is easy to find the vector potential due to the vortex by employing the Fourier transformation to Eq.(A1). In doing so, we use

$$\mathbf{A}(\mathbf{r}, z) = \int \mathbf{A}_{\mathbf{k}} e^{i\mathbf{q}\cdot\mathbf{r} + ik_z z} \frac{d\mathbf{k}}{(2\pi)^3}. \quad (\text{A2})$$

In the Fourier representation, the London-Pearl equation reads

$$\mathbf{A}_{\mathbf{k}} = -\frac{1}{\lambda k^2} \mathbf{a}_{\mathbf{q}} + \frac{\phi_0}{2\pi\lambda} \frac{(\nabla\varphi)_{\mathbf{q}}}{k^2}, \quad (\text{A3})$$

where $(\nabla\varphi)_{\mathbf{q}} = 2\pi \frac{i\hat{q} \times \hat{z}}{q} \tilde{e}^{-i\mathbf{q}\cdot\mathbf{r}_0}$ [57]. Employing integral over k_z to Eq.(A3) and using $\mathbf{a}_{\mathbf{q}} = \int_{-\infty}^{\infty} \frac{dk_z}{2\pi} \mathbf{A}_{\mathbf{k}}$, we obtain the Fourier-transform of the vortex-induced vector potential at the C film as

$$\mathbf{a}_{\mathbf{q}} = \frac{i\phi_0(\hat{q} \times \hat{z})e^{-i\mathbf{q}\cdot\mathbf{r}_0}}{q(1+2\lambda q)}. \quad (\text{A4})$$

substituting the above equation in Eq.(A3), the 3d vortex-induced vector potential is found as

$$\mathbf{A}_{\mathbf{k}} = \frac{2i\phi_0(\hat{q} \times \hat{z})e^{-i\mathbf{q}\cdot\mathbf{r}_0}}{\mathbf{k}^2(1+2\lambda q)}. \quad (\text{A5})$$

The direct substitution of Eq.(A5) back in Eq.(A2) leads to

$$\mathbf{A}(\mathbf{r}, z) = \int \frac{2i\phi_0(\hat{q} \times \hat{z})e^{-i\mathbf{q} \cdot (\mathbf{r} - \mathbf{r}_0) + ik_z z}}{\mathbf{k}^2(1 + 2\lambda q)} \frac{d^2 q dk_z}{(2\pi)^3}. \quad (\text{A6})$$

First, we perform integral over k_z , and find

$$\mathbf{A}(\mathbf{r}, z) = \int \frac{i\phi_0(\hat{q} \times \hat{z})e^{-i\mathbf{q} \cdot (\mathbf{r} - \mathbf{r}_0)} e^{-q|z|}}{q(1 + 2\lambda q)} \frac{d^2 q}{(2\pi)^2}. \quad (\text{A7})$$

Let

$$\mathbf{q} = q \cos(\theta + \phi) \hat{u} + q \sin(\theta + \phi) \hat{v} \quad (\text{A8})$$

$$\mathbf{r} - \mathbf{r}_0 = |\mathbf{r} - \mathbf{r}_0| \cos \phi \hat{u} + |\mathbf{r} - \mathbf{r}_0| \sin \phi \hat{v}, \quad (\text{A9})$$

where \hat{u} and \hat{v} are unit vectors in a plane perpendicular to the z -direction, θ is the angle between \mathbf{q} and $\mathbf{r} - \mathbf{r}_0$, and ϕ is the angle between $\mathbf{r} - \mathbf{r}_0$ and \hat{u} . By (A8), $\hat{q} \times \hat{z}$ in Eq.(A7) reads

$$\hat{q} \times \hat{z} = -\cos(\theta + \phi) \hat{v} + \sin(\theta + \phi) \hat{u}. \quad (\text{A10})$$

substituting (A10) in Eq.(A7), and using $\hat{u} \times \hat{z} = -\hat{v}$, $\hat{v} \times \hat{z} = \hat{u}$, $\int_0^{2\pi} e^{ix \cos \theta} \cos \theta d\theta = 2\pi i J_1(x)$ and $\int_0^{2\pi} e^{ix \cos \theta} \sin \theta d\theta = 0$, we find

$$\mathbf{A}(\mathbf{r}, z) = \frac{n\phi_0 \hat{z} \times (\mathbf{r} - \mathbf{r}_0)}{2\pi |\mathbf{r} - \mathbf{r}_0|} \int_0^\infty \frac{J_1(q|\mathbf{r} - \mathbf{r}_0|) e^{-q|z|}}{1 + 2\lambda q} dq. \quad (\text{A11})$$

Note that in the above equation, $\cos \phi \hat{v} - \sin \phi \hat{u} = \frac{\hat{z} \times (\mathbf{r} - \mathbf{r}_0)}{|\mathbf{r} - \mathbf{r}_0|}$. From $\mathbf{B} = \nabla \times \mathbf{A}$, the magnetic field components of the Pearl vortex are found as follows:

$$B_r(\mathbf{r}, z) = \frac{n\phi_0}{2\pi} \text{sign}(z) \int_0^\infty \frac{J_1(q|\mathbf{r} - \mathbf{r}_0|) q e^{-q|z|}}{1 + 2\lambda q} dq, \quad (\text{A12})$$

$$B_z(\mathbf{r}, z) = \frac{n\phi_0}{2\pi} \int_0^\infty \frac{J_0(q|\mathbf{r} - \mathbf{r}_0|) q e^{-q|z|}}{1 + 2\lambda q} dq. \quad (\text{A13})$$

APPENDIX B: INTEGRALS OF BESSEL FUNCTIONS

In this appendix, the asymptotic values and the exact results of the Bessel integrals used in this article are introduced. First, we present the integrals containing one Bessel function. These integrals are in the form of

$$\int_0^\infty \frac{J_m(kr) k^n}{1 + 2k\lambda} dk, \quad (\text{B1})$$

where $m = 0, 1$ and $n = 0, 1$. For $m = 0, 1$ and $n = 0$, the exact results can be obtained as follows [64]:

$$\int_0^\infty \frac{J_0(kr)}{1 + 2k\lambda} dk = \frac{\pi}{4\lambda} [H_0\left(\frac{r}{2\lambda}\right) - Y_0\left(\frac{r}{2\lambda}\right)], \quad (\text{B2})$$

$$\int_0^\infty \frac{J_1(kr)}{1+2k\lambda} dk = \frac{\pi}{4\lambda} [H_{-1}(\frac{r}{2\lambda}) + Y_1(\frac{r}{2\lambda})] + \frac{1}{r}, \tag{B3}$$

where $H_l(x)$ and $Y_l(x)$ are the Struve function and the second kind of the Bessel function of the l th order [59]. The respective asymptotic values of Eqs.(B2, B3) are found as follows: When $r \ll \lambda$, which corresponds to $k\lambda \gg 1$, the integral in (B2) becomes [65]

$$\int_0^\infty \frac{J_0(kr)}{2k\lambda} dk = \frac{1}{2\lambda} [\ln(\frac{\lambda}{r}) - C]. \tag{B4}$$

For $r \gg \lambda$, which is equivalent to $k\lambda \ll 1$, the integral in (B2) becomes [65]

$$\int_0^\infty J_0(kr) dk = \frac{1}{r}. \tag{B5}$$

Using the same techniques, the asymptotic values of the integral in (B3) are

$$\int_0^\infty \frac{J_1(kr)}{1+2k\lambda} dk \approx \int_0^\infty \frac{J_1(kr)}{2k\lambda} dk = \frac{1}{2\lambda} \quad r \ll \lambda \tag{B6}$$

$$\int_0^\infty \frac{J_1(kr)}{1+2k\lambda} dk \approx \int_0^\infty J_1(kr) dk = \frac{1}{r} \quad r \gg \lambda. \tag{B7}$$

In order to find the asymptotic values for $m = 0, 1$ and $n = 1$, we use

$$\int_0^\infty J_m(kr) k^n dk = \lim_{\alpha \rightarrow 0} \frac{\partial^n}{\partial \alpha^n} \int_0^\infty J_m(kr) e^{-\alpha k} dk. \tag{B8}$$

With similar techniques and (B8), the asymptotic values are given as follows:

$$\int_0^\infty \frac{J_0(kr)}{1+2k\lambda} k dk \approx \int_0^\infty \frac{J_0(kr)}{2\lambda} dk = \frac{1}{2\lambda r} \quad r \ll \lambda. \tag{B9}$$

For $r \gg \lambda$, the integral becomes $\int_0^\infty J_0(kr) k dk$, which equals zero [65]. In order to find nonzero result, we do the following approximation: $r \gg \lambda$ is equivalent to $k\lambda \ll 1$. Therefore, the fraction in (B1) can be rewritten as

$$\frac{1}{1+2k\lambda} = 1 - 2k\lambda + \dots \tag{B10}$$

By (B10), we obtain

$$\int_0^\infty \frac{J_0(kr)}{1+2k\lambda} k dk \approx -2\lambda \int_0^\infty J_0(kr) k^2 dk = \frac{2\lambda}{r^3} \quad r \gg \lambda, \tag{B11}$$

and,

$$\int_0^\infty \frac{J_1(kr)}{1+2k\lambda} k dk \approx \int_0^\infty \frac{J_1(kr)}{2\lambda} dk = \frac{1}{2\lambda r} \quad r \ll \lambda \tag{B12}$$

$$\int_0^\infty \frac{J_1(kr)}{1+2k\lambda} k dk \approx \int_0^\infty J_1(kr) k dk = \frac{1}{r^2} \quad r \gg \lambda. \tag{B13}$$

We give only the asymptotic values of the integrals with two Bessel functions. We start with the following integral:

$$\int_0^{\infty} \frac{J_1(kR)J_0(kr)}{1+2k\lambda} dk. \quad (\text{B14})$$

For the above integral, we first analyze the case, in which $R \ll \lambda$. In this case, we can replace $J_1(kR)$ by $kR/2$ in (B14). In doing so, we get

$$\int_0^{\infty} \frac{J_1(kR)J_0(kr)}{1+2k\lambda} dk \approx \frac{R}{2} \int_0^{\infty} \frac{J_0(kr)}{1+2k\lambda} k dk. \quad (\text{B15})$$

Using the asymptotic values for the integral on the left in (B9) and (B11), we find

$$\int_0^{\infty} \frac{J_1(kR)J_0(kr)}{1+2k\lambda} dk = \frac{R}{4\lambda r} \quad R \ll r \ll \lambda \quad (\text{B16})$$

$$= \frac{2\lambda R}{r^3} \quad R \ll \lambda \ll r. \quad (\text{B17})$$

For $R > \lambda$ and $r > \lambda$, we can neglect $2k\lambda$ in Eq.(B14). In doing so, we obtain

$$\int_0^{\infty} \frac{J_1(kR)J_0(kr)}{1+2k\lambda} dk \approx \int_0^{\infty} J_1(kR)J_0(kr) dk. \quad (\text{B18})$$

The above integral equals [65]

$$\int_0^{\infty} J_1(kR)J_0(kr) dk = 0 \quad R < r \quad (\text{B19})$$

$$= \frac{1}{2R} \quad R = r \quad (\text{B20})$$

$$= \frac{1}{R} \quad r < R. \quad (\text{B21})$$

The other integral of interest containing two Bessel functions is

$$\int_0^{\infty} \frac{J_1(kR)J_0(kr)k^2}{1+2k\lambda} dk. \quad (\text{B22})$$

For $R < \lambda$, using $J_1(kR) \approx kR/2$, the integral in Eq.(B22) becomes

$$\frac{R}{2} \int_0^{\infty} \frac{J_0(kr)k^3}{1+2k\lambda} dk. \quad (\text{B23})$$

By (B8) and (B10), the asymptotic values of the above integral can be calculated as follows: for $r \ll \lambda$, (B22) can be rewritten as

$$\frac{R}{4\lambda} \int_0^{\infty} J_0(kr)k^2 dk = \frac{R}{4\lambda r^3}. \quad (\text{B24})$$

For $R \ll r$, (B23) becomes

$$-R\lambda \int_0^\infty J_0(kr)k^4 dk = -\frac{9R\lambda}{r^5}. \quad (\text{B25})$$

Now, we can write the asymptotic values of (B22) as

$$\int_0^\infty \frac{J_1(kR)J_0(kr)k^2}{1+2k\lambda} dk \approx \frac{R}{4\lambda r^3} \quad R \ll r \ll \lambda \quad (\text{B26})$$

$$\int_0^\infty \frac{J_1(kR)J_0(kr)k^2}{1+2k\lambda} dk \approx -\frac{9R\lambda}{r^5}. \quad R \ll \lambda \ll r. \quad (\text{B27})$$

APPENDIX C: CALCULATION OF SERIES

In this appendix, the detailed analysis of series is given. First, the series in the energy calculations of the periodic systems are analyzed; second, the detailed calculation of the vortex density is shown. The series we encounter in the energy calculations fall into two categories. In the first category, we sum over one variable. The series in this category are in the form of $\sum_{r=1}^{r_{max}} 1/r$. Employing the Euler-Maclaurin summation formula [66], the summation is found with logarithmic accuracy as

$$\sum_{r=1}^{r_{max}} \frac{1}{r} \approx \ln r_{max} + C. \quad (\text{C1})$$

where $C \sim 0.577$ is the Euler-Mascheroni constant. If the summation is performed over only odd integers, we can still transform our series to (C1). Namely,

$$\sum_{r=0}^{r_{max}} \frac{1}{2r+1} \approx \sum_{r=1}^{2r_{max}+1} \frac{1}{r} - \frac{1}{2} \sum_{r=1}^{r_{max}/2} \frac{1}{r}, \quad (\text{C2})$$

$$\approx \ln(2r_{max}+1) + C - \ln\left(\frac{r_{max}}{2}\right) - \frac{C}{2}, \quad (\text{C3})$$

$$\approx \frac{1}{2}(\ln r_{max} + C + 2\ln 2). \quad (\text{C4})$$

The second category is the double series. In this aspect, we first show the calculation of square domain energy in the continuum approximation. The corresponding energy contains the series

$$S = \sum_{r,s=0}^{\infty} \frac{\sqrt{(2r+1)^2 + (2s+1)^2}}{(2r+1)^2(2s+1)^2}. \quad (\text{C5})$$

Our goal is to calculate the logarithmic contribution due to the self-vortex energies and the constant as a next approximation. The sum in (C5) diverges logarithmically in two regions: $r \gg s$ and $s \gg r$. Keeping this in mind, (C5) can be rewritten as

$$S = \sum_{r,s=-\infty}^{\infty} \frac{\max(2r+1, 2s+1)}{(2r+1)^2(2s+1)^2} + \sum_{r,s=-\infty}^{\infty} \frac{\sqrt{(2r+1)^2 + (2s+1)^2} - \max(2r+1, 2s+1)}{(2r+1)^2(2s+1)^2}. \quad (C6)$$

The first term in the above series contributes the logarithmic term S_{log} , and here it is

$$S_{log} = 2 \sum_{r_{max}} \frac{1}{2r+1} \sum_{s=0}^{\infty} \frac{1}{(2s+1)^2} \quad (C7)$$

$$\approx \frac{\pi^2}{8} (\ln r_{max} + C + 2 \ln 2). \quad (C8)$$

We used the result in Eq.(C4), and $\sum_{s=0}^{\infty} \frac{1}{(2s+1)^2} = \frac{\pi^2}{8}$ [67]. The other term in (C6) contributes the constant S_{cons} . For three regions $r = s$, $r > s$ and $s > r$, the second series in (C6) is rewritten as follows:

$$S_{cons} = (\sqrt{2} - 2) \sum_{r=0}^{\infty} \frac{1}{(2r+1)^3} + 2 \sum_{r=0}^{\infty} \sum_{s=r+1}^{\infty} \frac{\sqrt{(2r+1)^2 + (2s+1)^2} - (2r+2s+2)}{(2r+1)^2(2s+1)^2}. \quad (C9)$$

Numerical calculation gives $S_{cons} = -1.19$.

The other double series of interest here are in the form of

$$I(x) = \sum_{r=-\infty}^{r=\infty} \sum_{s=-\infty}^{s=\infty} \frac{1}{x^2 r^2 + s^2}, \quad (C10)$$

where x is an arbitrary constant. Although (C10) is logarithmically divergent, the sum over one of the variables can be done easily. To this end, we perform the sum over s first. In doing so, Eq. (C10) becomes $(2\pi/x) \sum_{r=1}^{\infty} \coth(\pi x r)/r$ [67]. This series is logarithmically divergent. In order to get the logarithmic term, we add and subtract $1/r$. Using the result in (C1), finally we get

$$I(x) \approx \frac{2\pi}{x} \left[\sum_{r=1}^{\infty} \frac{\coth(\pi x r) - 1}{r} + \ln r_{max} + C \right]. \quad (C11)$$

Employing the same techniques, we give the results of the different versions of Eq. (C10) below:

$$\sum_{r=-\infty}^{r=\infty} \sum_{s=-\infty}^{s=\infty} \frac{1}{x^2(2r+1)^2 + s^2} \approx \frac{2\pi}{x} \left[\sum_{r=0}^{\infty} \frac{\coth((2r+1)\pi x) - 1}{2r+1} + \frac{\ln r_{max}}{2} + \frac{C}{2} \right], \quad (C12)$$

$$\sum_{r=-\infty}^{r=\infty} \sum_{s=-\infty}^{s=\infty} \frac{1}{x^2(2r+1)^2 + (2s+1)^2} \approx \frac{\pi}{x} \left[\sum_{r=0}^{\infty} \frac{\tanh((2r+1)\frac{\pi x}{2}) - 1}{2r+1} + \frac{\ln r_{max}}{2} + \frac{C}{2} \right]. \quad (C13)$$

In (C12) and (C13), we use $\sum_{s=0}^{\infty} 1/(y^2 + (2s+1)^2) = \pi \tanh(\pi y/2)/(4y)$. In the presence of $\sin^2((2r+1)y)$ or $\cos^2((2r+1)y)$, the series can be calculated in a similar way, using $\sin^2((2r+1)y) = (1 - \cos(2(2r+1)y))/2$ or $\cos^2((2r+1)y) = (1 + \cos(2(2r+1)y))/2$. For example,

$$\sum_{r=-\infty}^{\infty} \sum_{s=-\infty}^{\infty} \frac{\sin^2((2r+1)y)}{(x^2(2r+1)^2 + s^2)} = \frac{2\pi}{x} \left[\sum_{r=0}^{\infty} \frac{\sin^2((2r+1)y)(\coth((2r+1)\pi x) - 1)}{2r+1} + \frac{\ln r_{max}}{4} - \frac{\ln |\cot(y/2)|}{4} + \frac{C}{4} \right], \quad (C14)$$

$$\sum_{r=-\infty}^{\infty} \sum_{s=-\infty}^{\infty} \frac{\cos^2((2r+1)y)}{(x^2(2r+1)^2 + s^2)} = \frac{2\pi}{x} \left[\sum_{r=0}^{\infty} \frac{\sin^2((2r+1)y)(\coth((2r+1)\pi x) - 1)}{2r+1} + \frac{\ln r_{max}}{4} + \frac{\ln |\cot(y/2)|}{4} + \frac{C}{4} \right]. \quad (C15)$$

We use

$$\sum_{r=0}^{\infty} \frac{\cos((2r+1)\theta)}{2r+1} = \frac{\ln |\cot(\theta/2)|}{2}. \quad (C16)$$

The Fourier transform of the vortex density $n_{\mathbf{G}}$ for the stripe domain structure is found by substituting the corresponding reciprocal lattice vectors $G = \pi(2r+1)/L$ and the Fourier transform of the step function $s_{\mathbf{G}} = \frac{2i}{\pi(2r+1)}$ in Eq.(64). In doing so, we obtain

$$n_{\mathbf{G}} = -\frac{4\pi i \tilde{\epsilon}_v}{L\phi_0^2} \sum_{r=-\infty}^{\infty} \text{sign}(2r+1). \quad (C17)$$

Employing the inverse Fourier transform to Eq.(C17) gives the following series:

$$F(x) = \sum_{r=-\infty}^{\infty} \text{sign}(2r+1) e^{i(2r+1)\frac{\pi x}{L}} = 2i \sum_{r=0}^{\infty} \sin((2r+1)\frac{\pi x}{L}). \quad (C18)$$

In order to calculate the above series, we integrate both sides over x . In doing so, by (C16) we find

$$\int F(x) dx = -2i \frac{L}{\pi} \sum_{r=0}^{\infty} \frac{\cos((2r+1)\frac{\pi x}{L})}{2r+1} = -i \frac{L}{\pi} \ln |\cot(\frac{\pi x}{2L})|. \quad (C19)$$

The derivative of the above equation with respect to x gives

$$F(x) = -\frac{i}{\sin(\frac{\pi x}{L})}. \quad (C20)$$

By (C17) and (C20), the vortex density $n(x)$ becomes

$$n(x) = -\frac{4\pi \tilde{\epsilon}_v}{L\phi_0^2} \frac{1}{\sin(\frac{\pi x}{L})}. \quad (C21)$$

REFERENCES

- [1] I.F. Lyuksyutov and V.L. Pokrovsky, Phys. Rev. Lett. **81**, (1998) 2344.
- [2] I.F. Lyuksyutov and V.L. Pokrovsky, *Superconducting Superlattices II: Native and Artificial*, Vol. 3480 (Eds. Ivan Bozovic and Davor Pavuna), PIE-International society for Optical Engineering, Bellingham, WA, (1998), pp. 230.
- [3] L.N. Bulaevskii, A.I. Buzdin, M.L. Kubic and V. Panyukov, Adv. Phys. **34**, (1985) 175.
- [4] O. Fisher, *Magnetic Superconductors*, Vol. 5 (Eds. K.H.J. Buschow and E.P. Wohlfarth), North-Holland, Amsterdam, (1990), pp. 465.
- [5] M. Belic and M.V. Jaric, Phys. Rev. Lett. **42**, (1979) 1015.
- [6] H. Greenside, E.I. Blount and C.M. Varma, Phys. Rev. Lett. **46**, (1981) 49.
- [7] V.L. Ginzburg, Zh. E'ksp. Teor. Fiz. **31**, (1957) 202 [Sov. Phys. JETP **4**, (1957) 153].
- [8] P.W. Anderson and H. Uhl, Phys. Rev. **116**, (1959) 898.
- [9] P. Fulde and R.A. Ferrell, Phys. Rev. **135**, (1964) 550.
- [10] A.I. Larkin and Yu.N. Ovchinnikov, Zh. E'ksp. Teor. Fiz. **47**, (1964) 1136 [Sov. Phys. JETP **20**, (1965) 762].
- [11] H. Uhl, J. Less-Common Metals **62**, (1978) 225.
- [12] B.T. Mathias, H. Uhl and E. Corenzwit, Phys. Rev. Lett. **1**, (1958) 92.
- [13] C. Bernhard, J.L. Tallon, Ch. Niedermayer, Th. Blasius, A. Golnik, E. Brucher, R.K. Kremer, D.R. Noakes, C.E. Stronach and E.J. Ansaldo, Phys. Rev. B **59**, (1999) 14099.
- [14] L. Bauernfeind, W. Widder and H. Braun, *Fourth Euro Ceramics*, Vol. 6 Faenza Editrice S.p.A., Italy, (1995).
- [15] I. Felner, U. Asaf, Y. Levi and O. Millo, Phys. Rev. B **55**, (1997) R3374.
- [16] Erdin, Physica C **391**, (2003) 140.
- [17] I.K. Marmoros, A. Matulis and F.M. Peeters, Phys. Rev. B **53**, (1996) 2677.
- [18] M. A. Kayali, Phys. Lett. A, **298**, (2002) 432.
- [19] M. A. Kayali, Phys. Rev. B, **69**, (2004) 012505.
- [20] I.F. Lyuksyutov and V.L. Pokrovsky, cond-mat/9903312 (unpublished).
- [21] Erdin, I.F. Lyuksyutov, V.L. Pokrovsky and V.M. Vinokur, Phys. Rev. Lett. **88**, (2002) 017001.
- [22] M.A. Kayali and V.L. Pokrovsky, Phys. Rev. B **69**, (2004) 132501.
- [23] V.L. Pokrovsky and H. Wei, Phys. Rev. B **69**, (2004) 104530.
- [24] I.F. Lyuksyutov and D.G. Naugle, Modern Phys. Lett. B **13**, (1999) 491.
- [25] I.F. Lyuksyutov and D.G. Naugle, Int. J. Mod. Phys. B **17**, (2003) 3713.
- [26] Erdin, in press Phys. Rev. B **69** (2004).
- [27] Erdin, A.M. Kayali, I.F. Lyuksyutov and V.L. Pokrovsky, Phys. Rev. B **66**, (2002) 014414.
- [28] E.H. Brandt, Rep. Prog. Phys. **58**, (1995) 1465.
- [29] J. Pearl, Appl. Phys. Lett. **5**, (1964) 65.
- [30] M.V. Milosovic and F.M. Peeters, Phys. Rev. B **69**, (2004) 104522.
- [31] J.E. Santos, E. Frey and F. Schwabl, Phys. Rev. B **63** (2001) 4439.
- [32] R. Sasik and T. Hwa, cond-mat/0003462 (unpublished).
- [33] G. Carneiro, Physica C **404**, (2004) 78.

- [34] D.J. Priour Jr. and H.A. Fertig, *Physica C* **404**, (2004) 293.
- [35] L.N. Bulaevskii, E.M. Chudnovsky and M.P. Maley, *Appl. Phys. Lett.* **76**, (2000) 2594.
- [36] L.N. Bulaevskii and E.M. Chudnovsky, *Phys. Rev. B* **63** (2001) 2502.
- [37] L.E. Helseth, *Phys. Lett. A*, Vol.315, (2003) 399.
- [38] J.I. Martin, M. Velez, J. Nogues and I.K. Schuller, *Phys.Rev. Lett.* **79**, (1997) 1929.
- [39] D.J. Morgan and J.B. Ketterson *Phys. Rev. Lett.* **80**, (1998) 3614.
- [40] Y. Otani, B. Pannetier, J.P. Nozieres and D. Givord, *J. Magn. Mag. Mat.* **126**, (1993) 622.
- [41] O. Geoffroy, D. Givord, Y. Otani, B. Pannetier and F. Ossart, *J. Magn. Mag. Met.* **121**, (1993) 223.
- [42] Y. Nozaki, Y. Otani, K. Runge, H. Miyajima, B. Pannetier, J.P. Nozieres and G. Fillion, *J. Appl. Phys.* **79**, (1996) 8571.
- [43] M.J. Van Bael, L. Van Look, K. Temst, M. Lange, J. Bekaert, U. May, G. Guntherodt, V.V. Moshchalkov and Y. Bruynseraede, *Physica C* **332**, (2000) 12.
- [44] A. Terentiev, D.B. Watkins, L.E. De Long, D.J. Morgan and J.B. Ketterson, *Physica C* **332**, (2000) 5.
- [45] M.J. Van Bael, K. Temst, V.V. Moshchalkov and Y. Bruynseraede, *Phys. Rev. B* **59**, (1999) 14674.
- [46] P.Martinoli, N. Nsabimana, G.A. Racine, H. Beck and R. Clem, *Helv. Phys. Acta.* **56**, (1983) 765.
- [47] V.V. Metlushko, M. Baert, R. Jonckheere, V.V. Moshchalkov and Y. Bruynseraede, *Solid State Comm.* **91**, (1994) 331.
- [48] M. Baert, V.V. Metlushko, R. Jonckheere, V.V. Moshchalkov and Y. Bruynseraede *Phys. Rev. Lett.* **74**, (1995) 3269.
- [49] V.V. Moshchalkov, M. Baert, V.V. Metlushko, E. Rosseel, M.J. VanBael, K. Temst, R. Jonckheere and Y. Bruynseraede *Phys. Rev. B* **54**, (1996) 7385.
- [50] V.V. Metlushko, L.E. DeLong, M. Baert, E. Rosseel, M.J. VanBael, K. Temst, R. Jonckheere and Y. Bruynseraede, *Europhys. Lett.* **41**, (1998) 333.
- [51] I.F. Lyuksyutov and D.G. Naugle, *Physica C* **341**, (2000) 1267.
- [52] I.F. Lyuksyutov, D.G. Naugle and V.L. Pokrovsky, *Superconducting and Related Oxides: Physics and Nanoengineering IV*, Vol. 4058 (Eds. Davor Pavuna and Ivan Bozovic), *PIE-International Society for Optical Engineering*, Bellingham, WA, (2000), pp. 376.
- [53] I.F. Lyuksyutov and V.L. Pokrovsky, *Modern. Phys. Lett.* **14**, (2000) 409.
- [54] L.E. Helseth, P.E. Goa, H. Hauglin, M. Baziljevich and T. Johansen, *Phys. Rev. B* **65**, (2002) 132514.
- [55] P.G. de Gennes, *Superconductivity of Metals and Alloys*, Addison-Wesley, (1989).
- [56] L.D. Landau and E.M. Lifshitz, *Electrodynamics of Continuous Media*, Butterworth-Heinemann, (1995), 2nd ed.
- [57] A.A. Abrikosov, *Introduction to the Theory of Metals* North Holland, (1986).
- [58] V.G. Kogan, *Phys. Rev. B* **49**, (1994) 15874.
- [59] M. Abramowitz and I. A. Stegun, *Handbook of Mathematical Functions*, Dover Publications, (1970).
- [60] A.P. Malozemoff and J.C. Bonczewski, *Magnetic Domain Walls in Bubble Materials*, Academic Press, (1979).
- [61] Y. Yafet and E.M. Gyorgy, *Phys. Rev. B* **38**, (1988) 9145.
- [62] A. Kashuba and V.L. Pokrovsky, *Phys. Rev. B* **48**, (1993) 10335.
- [63] A. Abanov, V. Kalatsky, V.L. Pokrovsky, W.M. Saslow, *Phys. Rev. B* **51**, (1995) 1023.
- [64] Y.L. Luke, *Integrals of Bessel Functions*, McGraw-Hill, (1962).

- [65] I. . Gradstein and I.M. Ryzhik, *Tables of Integrals, Sums, Series and Products*, Academic Press, (1994), 5th ed.
- [66] G.B. Arfken and H.J. Weber, *Mathematical Methods for Physicists*, Academic Press, (2000), 5th ed.
- [67] E.R. Hansen, *A Table of Series and Products*, Prentice-Hall, (1975).

HIGH PRESSURE EFFECTS ON SUPERCONDUCTIVITY

B. Lorenz¹ and C.W. Chu^{1,2,3}

¹) Department of Physics and Texas Center for Superconductivity, University of Houston, Houston, Texas 77204-5002, USA

²) Lawrence Berkeley National Laboratory, 1 Cyclotron Road, Berkeley, CA 94720, USA

³) Hong Kong University of Science and Technology, Hong Kong, China

1. INTRODUCTION

Since the discovery of superconductivity at 4 K in mercury by Kamerlingh Onnes in 1911 the search for higher transition temperatures has been the primary goal for many decades. In the early 1950's B. Matthias discovered a correlation between T_c and the number of valence electrons per atom (R) of a large number of superconducting elements and compounds [1, 2]. While there was no superconducting compound with $R \leq 2$ at the time Matthias showed the existence of a maximum of $T_c(R)$ close to $R = 4.75$ [1] and a second maximum at $R \approx 6.4$ [2]. Most of the intermetallic superconductors with a high T_c exhibit lattice instabilities. The application of external pressure to these high T_c superconductors can drive the compounds towards or away from lattice instabilities by varying the principal parameters determining the superconducting properties (the electronic density of states at the Fermi energy, $N(E_F)$, the characteristic phonon frequency, and the coupling constant of electrons and phonons), and it can be used to tune the T_c and the superconducting properties. Almost all of the superconducting metallic elements show a decrease of T_c with pressure. This negative pressure coefficient was attributed to the volume dependence of $N(E_F)$ and of the effective interaction between the electrons mediated by the electron-phonon coupling [3]. However, a few elemental superconductors such as Tl and Re show a more complex pressure dependence of T_c that was explained by pressure-induced changes of the Fermi surface topology [4,5].

Some aspects of the pressure dependence of T_c of low-temperature superconductors (LTS) will be discussed in more detail in Section 2.

New techniques for creating higher pressures have been developed over the last couple of decades pushing the limits of static pressure generation to a few hundred GPa. At high enough pressure almost every ambient pressure structure becomes unstable and transforms into a structure of higher density and, frequently, of higher symmetry. Some elements or compounds undergo a sequence of structural transitions into several different phases under applied pressure. Many of these new structures are metallic and superconductivity was observed in a large number of high-pressure phases even when the compound was not superconducting at ambient pressure. Among the elements of the periodic table, superconductivity induced by pressure has raised the total number of superconducting elements from 29 (at ambient pressure) to 52 including non-metallic elements like sulfur or oxygen and alkali metals with only one valence electron such as Li.

The latter alkali metal is of particular interest since it is one of the elements of the first column of the periodic system that should not be superconducting according to the Matthias rules. In 1969 Allen and Cohen [6], based on their pseudopotential calculations, proposed Li to be superconducting but no evidence of superconductivity has been found at temperatures as low as 4 mK [7]. However, it was predicted that superconductivity should occur in Li under high pressure with transition temperatures of up to 80 K [8]. Early high-pressure experiments [9] revealed a drop of resistivity in Li at 7 K between 22 and 32 GPa but the data were not conclusive enough to be interpreted in terms of superconductivity. Only recent measurements of electrical transport and magnetic properties have unambiguously shown that superconductivity exists in Li at pressures above 20 GPa and at temperatures up to 20 K [10, 11, 12]. The large interest in the superconductivity in dense lithium is also motivated by the fact that it is the “simplest” metal with only one valence electron, no d-electrons in sight, and it is the superconducting element closest to hydrogen. There appears to be new hope in the continuous search for superconductivity in metallic hydrogen that has been predicted to become superconducting at high pressure with an extraordinary high T_c [13].

A new chapter in the ongoing search for new superconducting compounds with higher T_c values was opened with the discovery of superconductivity at T_c 's as high as 35 K in the La-Ba-Cu-O (LBCO) cuprate compound in 1986 [14] bypassing the highest known T_c of Nb_3Ge ($T_c=23.2$ K, [15]) by more than 50 %. Soon after this remarkable event Chu et al. [16] reported an unprecedented large positive pressure coefficient of T_c of LBCO that led the authors to conclude that fine-tuning of material parameters by physical and chemical means could lead to even higher transition temperatures. In fact, simulating the effects of external pressure (variation of the lattice constants) by replacing La with the smaller isovalent Y ion (“chemical pressure”) led to the next giant leap in raising T_c above the temperature of liquid nitrogen as first demonstrated in the Y-Ba-Cu-O (YBCO) cuprate [17]. A detailed discussion of the pressure effects in this new class of high-temperature superconductors (HTS) is given in Section 3.

With all the success of high-pressure investigations in superconductivity there arises the question what we can learn from these experiments about the microscopic mechanisms, the pairing symmetry, and the validity of theoretical models. High-pressure investigations in conjunction with other experimental data and available theories have been found extremely useful leading to a deeper understanding of the superconducting state and to a possible discrimination between different proposed models. In Section 4 we discuss several recent

examples where the results of high-pressure experiments have significantly contributed to a better understanding of the superconductivity in specific compounds or have raised new questions about the mechanisms of superconductivity.

2. PRESSURE EFFECTS IN LOW-TEMPERATURE SUPERCONDUCTORS

Soon after the first high-pressure investigations of superconductors had been accomplished it became obvious that the majority of superconducting elements responded to the imposed pressure with a decrease of T_c . The fundamental question was raised whether pressure could suppress superconductivity completely if it was just increased to high enough values. The main difficulty at the time was the limited experimentally accessible pressure range of several GPa and the need to extrapolate the experimental data of $T_c(p)$ to much higher pressures to estimate the $T_c=0$ intercept. In many cases $T_c(p)$ turned out to be a non-linear function of p at higher pressures, however, it was proposed [3] that T_c was roughly linear when plotted as function of volume, V . The linear $T_c(V)$ relationship was later shown to hold for a large number of superconducting metals and the critical pressures above which superconductivity cannot persist have been derived from a linear extrapolation of $T_c(V)$ [18]. An impressive example of this linear T_c vs. V relation is shown in Fig. 1. Based on the extrapolation of the results shown in Fig. 1 and using the known compressibility data the critical pressures for Al, Cd, and Zn were estimated as 6.7 GPa, 3.8 GPa, and 4.1 GPa, respectively [18].

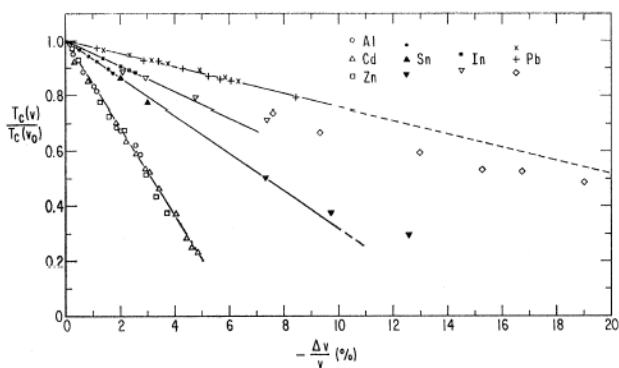


Fig. 1. The relative pressure shift of T_c as function of the relative volume change for a large number of superconducting metallic elements (Figure reproduced from Ref. [18]).

Contrary to the suppression of superconductivity by reducing the volume (or lattice constants), an increase of T_c could be expected by expanding the lattice. This possibility that was already discussed in the 1950's eventually led B. Matthias to enlarge the lattice parameters in a solid solution of NbC and NbN and to set a new record for T_c (17.8 K) at this time [1].

2.1 The Pressure Dependence of T_c in BCS and Strong-Coupling Theory of Superconductivity

The pressure dependence of T_c can be derived from microscopic theories of phonon-mediated superconductivity such as the weak-coupling BCS model [19] or the Eliashberg theory of strong-coupling superconductivity [20]. For a specific superconductor the knowledge about the pressure dependence of its microscopic parameters such as the average phonon frequency, ω_D , the electronic density of states, $N(E_F)$, etc. is than needed to estimate T_c as function of imposed pressure.

According to the weak-coupling BCS theory T_c is expressed by [19]

$$k_B T_c = 1.13 \hbar \omega_D \exp\{-1/\lambda\} \quad (1)$$

k_B and \hbar are Boltzman's and Planck's constant, respectively, $\lambda = N(E_F)V_{eff}$, and V_{eff} is the effective interaction between the electrons mediated by the electron-phonon coupling. Since ω_D commonly increases with pressure (phonon hardening) the frequently observed decrease of T_c with p must be due to a decrease of λ . The average value of the electronic density of states is expected to decrease under pressure because of the pressure-induced band broadening effect. However, the pressure dependence of $N(E)$ can be very different at the Fermi energy E_F , depending on the details and the topology of the Fermi surface in a particular compound. The pressure dependence of V_{eff} is even more difficult to estimate and it needs a microscopic treatment of the coupled system of electrons and phonons. It should be noted that the BCS-equation (1) applies only in the weak-coupling case when the electron-phonon coupling constant λ is small.

Most superconducting elemental metals (except Al) exhibit an intermediate to strong electron-phonon coupling with λ of the order of 1 or larger [21] and their superconductivity is not well described by the weak-coupling BCS equation (1). Extending the original BCS theory [19], Eliashberg developed the theory of strong-coupling superconductivity [20] that provides, together with the pseudopotential treatment of the screened Coulomb interaction [22], the fundamental equations describing the physics of superconductors with phonon mediated pairing of any coupling strength. By solving the finite-temperature Eliashberg equations McMillan [23] derived an equation for the transition temperature valid in the strong coupling case that was later slightly modified by Dynes [24]:

$$k_B T_c = \frac{\hbar \langle \omega \rangle}{1.2} \exp\left\{-\frac{1.04(1+\lambda)}{\lambda - \mu^*(1+0.62\lambda)}\right\} \quad (2)$$

μ^* is the Coulomb pseudopotential calculated in [23]:

$$\mu^* = \frac{N(E_F)V_c}{1 + N(E_F)V_c \ln \frac{E_B}{\hbar \omega_0}} \quad (3)$$

V_c is the matrix element of the screened Coulomb interaction averaged over the Fermi surface, E_B is the electronic bandwidth and ω_0 is the cut-off (or maximum) phonon frequency. The electron-phonon coupling constant λ is given by [23]

$$\lambda = 2 \int \frac{d\omega \alpha^2(\omega) F(\omega)}{\omega} = \frac{N(E_F) \langle I^2 \rangle}{M \langle \omega^2 \rangle} . \quad (4)$$

$\alpha(\omega)$ and $F(\omega)$ are the strength of an average electron-phonon interaction and the phonon density of states, respectively. $\langle I^2 \rangle$ is the average over the Fermi surface of the square of the electronic matrix element of the change of the crystal potential induced by a displacement of an atom. M stands for the atomic mass. $\langle \omega^n \rangle$ in equations (2), $n=1$, and (4), $n=2$, is the n -th moment of the normalized weight function:

$$\langle \omega^n \rangle = \frac{2}{\lambda} \int d\omega \alpha^2(\omega) F(\omega) \omega^{n-1}$$

From equations (2) to (4) it becomes obvious that the pressure dependence of T_c is very complex and depends on various parameters of the electron and phonon systems. The pressure effects on μ^* and on $\langle I^2 \rangle$ are frequently neglected which simplifies the evaluation and reduces the pressure dependence to two parameters, the density of states $N(E_F)$ and the average phonon energy $\langle \omega \rangle$ (or $\langle \omega^2 \rangle$). The McMillen formula (2) has been used successfully in a number of examples in deriving $T_c(p)$ from first principle calculations of the pressure effect on the band structure and the phonon spectrum. For example, Olsen et al. [25] have demonstrated that equation (2) can be used to estimate the pressure dependence of T_c for a number of non-transition-metal superconductors in qualitative agreement with experiments.

The pressure dependence of the superconducting T_c of lead was investigated very thoroughly, experimentally [18, 26] as well as theoretically [27]. For the high-pressure experimentalist the use of lead as an in-situ manometer at temperatures below 7 K appeared to be very attractive. Since lead is easily available in high purity (99.9999 %), its superconducting transition is extremely sharp, and the initial pressure coefficient, $dT_c/dp = -0.386 \text{ K/GPa}$, is of a reasonable magnitude it has advanced to a secondary pressure gauge that allows the accurate pressure measurement at low temperature in various pressure cells. A detailed theoretical treatment of the pressure effects on T_c of lead was presented by Hodder [27]. Neglecting the pressure dependence of μ^* in equation (2) and assuming a multiple-cutoff Lorentzian model [28] for the phonon density of states $F(\omega)$ the pressure dependence of the electron-phonon coupling constant could be related to the pressure dependence of the longitudinal (ω_l) and transverse (ω_t) phonon frequencies. The pressure effect on the electronic matrix element was calculated from a pseudopotential theory and found to be small compared with the pressure shift of the phonon energies. With the known values of $d \ln \omega_l / dp$ and $d \ln \omega_t / dp$ the pressure coefficient of the T_c of lead was estimated as $d \ln T_c / dp = -0.05 \text{ GPa}^{-1}$. This value is in very good agreement with the known experimental data [18].

2.2 The Non-Linear $T_c(p)$ of Thallium and Rhenium - Pressure Revealing Electronic Instabilities of the Fermi Surface

The majority of the superconducting elements show a rather monotonous decrease of T_c with pressure and a linear $T_c(V)$ as shown in Fig. 1. However, there are a few exceptions, thallium and rhenium, that exhibit a very unusual $T_c(p)$. The critical temperature of thallium was found to increase at low pressures. It passes through a maximum at about 0.2 GPa and decreases at higher p [3,4]. Since no structural transition was observed under pressure it was suspected that the unusual $T_c(p)$ dependence might be due to a modification of the electronic configuration under pressure [4]. Lazarev et al. [29] proposed a change in the Fermi surface topology as the possible explanation for the anomalous pressure dependence of T_c of Tl. A non-linear contribution to the pressure dependence of T_c was indeed shown [30] to result from a change of the Fermi surface topology (Lifshitz instability, [31]) from a closed surface to an open one by forming of a neck. This topological transition causes changes of the density of states, thermodynamic parameters, as well as the superconducting gap.

A similar anomalous change of T_c , but in opposite direction, with pressure was also observed in rhenium [5]. T_c of Re first decreases at low pressure, passes through a minimum close to 0.7 GPa, and increases slightly above this pressure. $T_c(p)$ measured for a Re single-crystal [32] is shown in Fig. 2.

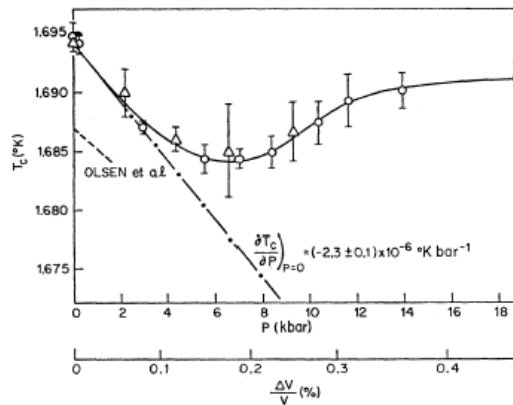


Fig. 2. The pressure shift of T_c of a single crystal of rhenium (Figure reproduced from Ref. [32]).

Based on the $T_c(p)$ data shown in Fig. 2 and the similarity to the thallium data Chu et al. proposed to adopt the approach of Ref. [29] and to express the pressure dependence of T_c of rhenium by the superposition of a linear variation of T_c with p and a nonlinear contribution due to a pressure-induced change of the Fermi surface topology. The model is supported by the observation that alloying rhenium with a minor amount of other metals (like osmium, tungsten, or molybdenum) has a dramatic effect on the anomalous $T_c(p)$ dependence [5,32].

For example, for Re-Os alloys the minimum in the $T_c(p)$ curves shifts to lower pressure with increasing Os concentration and, eventually, disappears at a critical concentration of about 0.2 %. The $T_c(p)$ data for the Re-Os alloys are displayed in Fig. 3. At Os concentrations in excess of 2.75 % the pressure dependence of T_c is close to linear and can be considered as “normal”. A similarly strong effect was observed in Re-W alloys but, in contrast to the Re-Os alloy, the critical pressure defined by the minimum of $T_c(p)$ increased quickly with the tungsten concentration [32]. This qualitatively different behavior can be understood by taking in mind that Os adds one electron thus raising the Fermi energy whereas W decreases the number of electrons and lowers E_F . Both contributions to the pressure dependence of T_c , the “normal” linear decrease of T_c with p and the nonlinear part (due to the change of Fermi surface topology) could be separated and it was found that in pure Re the nonlinear contribution starts at pressures above 0.2 GPa. A more detailed discussion of the topological changes of the Fermi surface that will appear if the Fermi energy passes through critical points in the reciprocal space and its relation to the nonlinear component of $T_c(p)$ is given in Ref. [32]. It should be noted that a band structure calculation for rhenium [33] revealed the existence of such critical points near the Fermi surface and provided evidence for the change of Fermi surface topology similar to that discussed above when the Fermi Energy is raised.

The anomalous pressure shifts of T_c observed in thallium and rhenium reveal the important influence of the electronic structure, the density of states, and the Fermi surface topology on the superconducting properties of LTS.

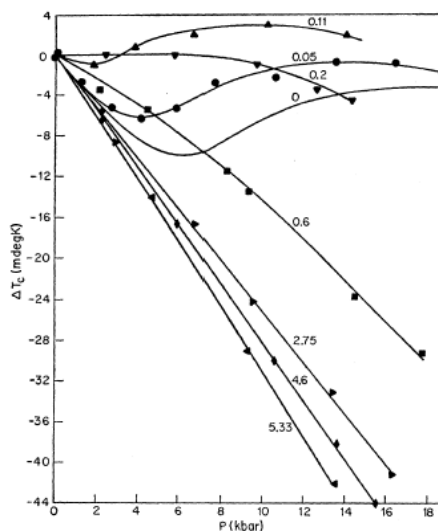


Fig. 3. The pressure shift of T_c for Re-Os alloys. The Os concentration in at. % is indicated by the numbers next to the curves. (Figure reproduced from Ref. [32]).

2.3 Pressure Dependence of T_c and Lattice Instabilities – The Common Electronic Origin of Superconductivity and Structural Transformations

The A15 intermetallic compounds A_3B have attracted attention because of the high transition temperatures shown (up to 23.2 K for Nb_3Ge). Some A15 compounds, such as V_3Si , are weakly coupled BCS-like superconductors but others (e.g. Nb_3Sn , Nb_3Ge) exhibit strong electron-phonon coupling and are better described by the strong-coupling theory. A number of A15 compounds undergo a structural phase transition at $T_L > T_c$ from the high-temperature cubic phase to a low-temperature tetragonal phase (although the tetragonal distortion is very small). A soft phonon mode has been observed in almost all A15 intermetallics with high T_c and it is the driving force for the cubic-to-tetragonal distortion at T_L observed in some compounds. Therefore, it was speculated that the soft phonon modes play a major role in stabilizing superconductivity at high critical temperatures.

To investigate the interplay between electronic excitations and soft phonon modes leading to structural instabilities and its significance for stabilizing superconductivity with high T_c 's it is desirable to tune the structural transition temperature closer to the superconducting T_c by either chemical or physical means. Since the A15 compounds $A_{3+x}B_{1-x}$ have very narrow ranges x of homogeneity it is more difficult to change T_L and T_c by tuning the chemical composition. The application of pressure, however, was shown to be a powerful tool to control the cubic-to-tetragonal transition in several A15 compounds [34,35].

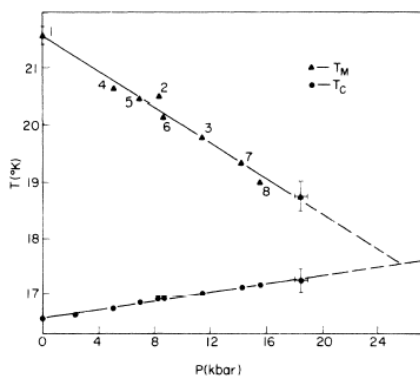


Fig. 4. The pressure shifts of T_L (triangles) and T_c (circles) in V_3Si . (Figure reproduced from Ref. [34]).

The pressure dependences of $T_L(p)$ and $T_c(p)$ were simultaneously measured in V_3Si single crystals [34] and a strong correlation was found between T_L and T_c (Fig. 4). Whereas T_L decreases linearly with pressure the superconducting T_c increased towards T_L . At the critical pressure of $p_c \approx 2.4$ GPa (estimated by extrapolation) both transitions happen at the same temperature, $T_L(p_c) = T_c(p_c)$, i.e. the lattice transformation is suppressed down to the superconducting state. The structural transition was theoretically described within the Weger-Labbé-Friedel (WLF) linear-chain model [36] and it was shown that good agreement with the

experimentally derived pressure coefficient dT_L/dp was only obtained for V_3Si when the interband charge transfer under pressure was properly taken into account [37]. The calculation shows that the pressure effect on the electronic structure and the pressure-induced charge transfer from s to d -bands are essential to explain the experimental data. However, the experimental results shown in Fig. 4 up to 1.8 GPa are also consistent with the suggestion that T_c in V_3Si could be enhanced by the softness of the lattice induced by pressure [38]. Within this model $T_c(p)$ is expected to pass through a maximum at p_c ($T_c=T_L$) where the lattice softness is also at its maximum [38]. To distinguish between the proposed mechanisms for the lattice instability and the T_c -enhancement under pressure it appeared necessary to measure $T_c(p)$ at and beyond the critical pressure p_c .

V_3Si is a special A15 compound in that the cubic-to-tetragonal transition can be suppressed depending on the sample preparation and conditions. The nontransforming (NT) samples show a weaker phonon softening effect and their T_c 's are found only slightly higher than those of transforming samples. The pressure coefficient of T_c of the NT V_3Si single crystal, however, was shown to be positive and lower (by about 30 %) than dT_c/dp of the V_3Si single crystal that exhibits the structural change from cubic to tetragonal symmetry [39]. This result suggests that the T_c of a transforming sample should still increase with pressure if p exceeds the critical value p_c above which the structural instability is completely suppressed. Extending the experimental pressure range to 2.9 GPa Chu and Diatschenko could later confirm this prediction [40]. By comparing the pressure coefficients of T_c of transforming as well as NT V_3Si single crystals it was unambiguously shown that $T_c(p)$ of the transforming sample does not exhibit the maximum predicted by the soft-phonon model but it changes slope above p_c and the pressure coefficient for $p>p_c$ was found to be very close to the value of the NT sample. Close to the highest pressure of this experiment a sudden drop of T_c of the NT sample indicated a pressure-induced phase transition, possibly into a non-superconducting phase, as was previously inferred from the negative pressure coefficient of the shear modulus [41].

In the WLF model T_L and T_c are non-monotonous functions of the number of d -electrons Q in the sub-band. The pressure-induced redistribution of charges between different bands will change Q and the position of the Fermi level. At ambient pressure E_F is close to a peak of the density of states and the application of pressure can enhance or suppress the lattice instability (T_L) if E_F is moved either towards or away from the peak, respectively. The analytic dependence of the two critical temperatures $T_L(Q)$ and $T_c(Q)$ have been calculated within the WLF model for V_3Si and Nb_3Sn [42]. It was shown that the functions $T_L(Q)$ and $T_s(Q)$ exhibit a maximum at Q_L and Q_c , respectively, and $Q_L < Q_c$ for V_3Si and $Q_c < Q_L$ for Nb_3Sn . For values of Q in between Q_L and Q_c the changes of $T_L(Q)$ and $T_c(Q)$ are opposite in sign [42]. Since pressure increases Q (charge transfer to the d -band) the p -induced increase of T_L and decrease of T_c observed in V_3Si is qualitatively understood ($Q_L < Q < Q_c$). A quantitative analysis is given in Ref. [39]. In Nb_3Sn , however, the charge transfer must result in the opposite changes of T_L (increasing with Q) and T_c (decreasing with Q) as long as $Q_c < Q < Q_L$. The enhancement of the lattice instability in Nb_3Sn and the decrease of T_c with pressure were in fact observed (see Fig. 5) and a qualitative interpretation of the pressure effects based on the WLF model was given [35]. The success of the WLF model with the inclusion of the pressure-induced interband charge transfer in describing the pressure dependence of $T_L(p)$ and $T_c(p)$ in a number of A15 compounds unambiguously demonstrates the superior role of the electronic excitation spectrum with peaks or singularities of the density of states close to the

Fermi energy for inducing the phonon softness and lattice instabilities as well as superconductivity with high T_c -values. The high-pressure experiments in A15 compounds discussed in the last paragraphs have shed new light onto the complex problem of structural instabilities, superconductivity, and the electronic structure. Similar phenomena are to be expected in other materials where superconductivity and structural instabilities exist in close neighborhood.

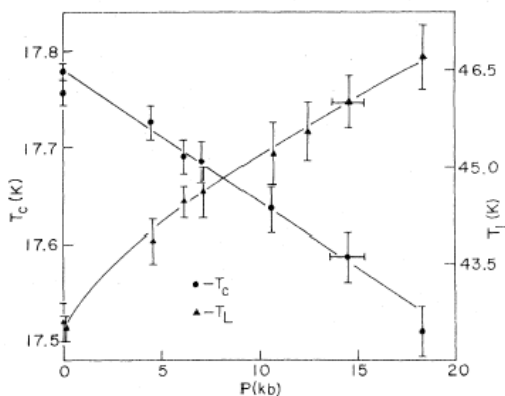


Fig. 5. The pressure shifts of T_L (triangles) T_c (circles) in Nb_3Sn . (Figure reproduced from Ref. [35]).

The vanadium-ruthenium alloys close to the equiatomic composition undergo a cubic to tetragonal transition upon cooling. T_L decreases with decreasing Ru concentration and the transition disappears below a critical value of $C_{crit} \approx 45.5$ at.% of Ru. Just above C_{crit} superconductivity was shown to arise with a sharp peak of T_c right at the critical concentration [43]. From ambient pressure measurements of transport and magnetic properties of a series of V-Ru alloys with compositions around C_{crit} it was suggested that the origin of the structural transition into the tetragonal phase lies in an electronic instability arising from a substantial reduction of the Fermi surface area and the associated decrease of the electronic contribution to the free energy in the tetragonal structure. Alternatively, the soft phonon model based upon the maximum of the lattice softness at C_{crit} and its effect on the superconducting temperature was proposed to explain the sharp maximum of T_c [44]. High-pressure experiments have been conducted to discriminate between the different proposals [45]. Fig. 6 (left graph) shows that the tetragonal phase of $V_{0.54}Ru_{0.46}$ is completely suppressed at a critical pressure of $p_c \approx 1.4$ GPa. The pressure dependence of T_c is displayed in Fig. 6, right graph. At low pressures T_c increases linearly with p , it changes slope at p_c and it increases further at a reduced rate for $p > p_c$. This observation cannot be explained by the lattice softening mechanism that predicted a distinct maximum of $T_c(p)$ right at p_c but it lends strong support to the model of electronic instability [44,45].

The systematic investigation of the pressure effects on the superconducting T_c and the structural instabilities in various compounds have led to the proposition that the electronic spectrum plays the major role in both, superconducting and lattice transformations. The

suggestion is also supported by the correlation between the structural instability and superconductivity as revealed by high-pressure experiments in layered charge-density-wave compounds, for example 2H-NbSe₂ [46].

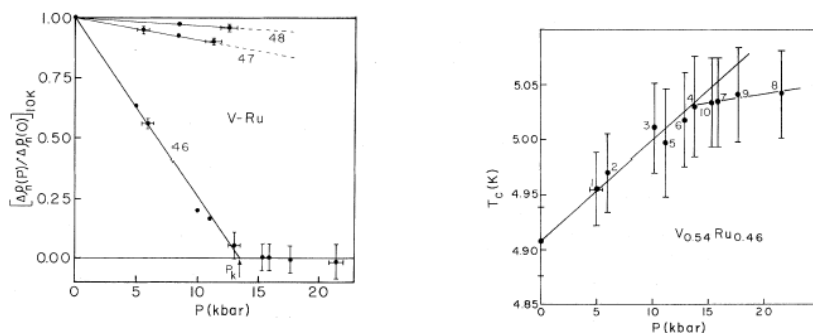


Fig. 6. Suppression of the tetragonal phase in V-Ru alloys with pressure (left) and the pressure dependence of T_c for $V_{0.54}Ru_{0.46}$ (right). (Figure reproduced from Ref. [45]).

3. PRESSURE EFFECTS IN HIGH-TEMPERATURE SUPERCONDUCTORS

The discovery of superconductivity in the La-Ba-Cu-O compound system [14] with unprecedented high transition temperatures of 35 K has revived a tremendous activity in the field of superconductivity. The positive pressure coefficient frequently observed in these new compounds have directed scientists to synthesize new materials with even higher T_c 's. In the following Sections we focus our discussion on a few topics of high-pressure investigations of HTS.

3.1 The Increase of T_c to New Records Under Imposed Pressure

The very first experiment on the pressure shift of T_c of the new La-Ba-Cu-O (LBCO) compound revealed a surprising result. The superconducting transition temperature was raised above 40 K with pressure at an unusually large rate [16]. The $T_c(p)$ data of Ref. [16] are shown in Fig. 7. The enormous increase of $T_c(p)$ at pressures up to 1.3 GPa (the data at higher pressure are invalid since the sample was destroyed under pressure) and the missing signs of saturation of T_c immediately led to the conclusion that even higher T_c values should be achievable at higher pressures and for optimized samples. Furthermore, it became obvious that the superconducting phase in the LBCO system is the one with the K_2NiF_4 structure, i.e. $La_{2-x}Ba_xCuO_{4-\delta}$ [16]. With this knowledge in mind C. W. Chu et al. [47] succeeded to optimize the sample preparation and to synthesize compounds with the nominal composition $La_{1.8}Ba_{0.2}CuO_{4-\delta}$. The onset of superconductivity in these compounds increased under hydrostatic pressure to 52.5 K [47], a new record T_c in early 1987.

There are two remarkable results from the early investigations of the new class of superconducting compounds: (i) The superconducting phase was identified as the perovskite (K_2NiF_4) structure. (ii) Pressure increases T_c at an exceptionally high rate (more than 6 K/GPa in the example shown in Fig. 7). This is in contrast to many low- T_c compounds showing a negative pressure coefficient of T_c . The LTS with an increasing $T_c(p)$ (such as V_3Si , Section 2.3) exhibit a much smaller coefficient dT_c/dp than that observed in the La-Ba-Cu-O system.

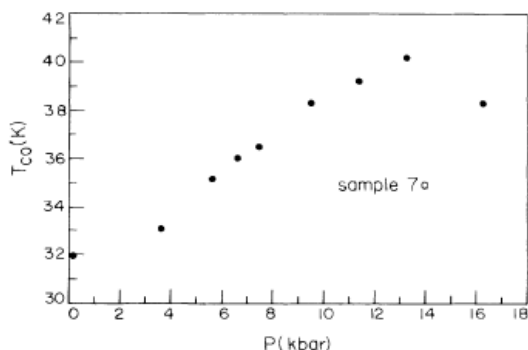


Fig. 7. Pressure dependence $T_c(p)$ of the HTS superconductor $La_{2-x}Ba_xCuO_{4-y}$. (Figure reproduced from Ref. [16]).

The large positive effect of external pressure on T_c of LBCO led to the next important step in the search for new superconducting compounds that eventually raised the transition temperature above the temperature of liquid nitrogen. In simulating the external pressure effect (lattice contraction) by replacing La^{3+} with the smaller ion Y^{3+} a new superconducting compound system, Y-Ba-Cu-O (YBCO), was synthesized with an onset temperature of $T_c=93$ K [17]. Interestingly, the application of external pressure did not change the T_c notably but rather caused a broadening of the resistive transition into the superconducting state [48]. The origin of this striking difference to the large pressure coefficient of LBCO was attributed to the presence of the large chemical pressure associated with the smaller Y^{3+} ions. The superconducting phase in the YBCO system was later identified as the tetragonal $YBa_2Cu_3O_{6+\delta}$ and it was shown that a homologous series of isostructural compounds can be derived by replacing Y with different rare earth ions, such as La, Nd, Sm, Eu, Gd, Ho, Er, and Lu, with superconducting T_c 's all above 90 K [49]. These results are particularly interesting because they prove that not the size of the A-ion in the structure of $A-Ba_2Cu_3O_{6+\delta}$ determines the high T_c but it is the layered structure with CuO_2 -Ba-CuO $_{2+\delta}$ -Ba-CuO $_2$ slabs separated by the A-ions and stacked along the c-axis that gives rise to the large T_c values.

In the following years other HTS compounds with even higher T_c 's have been synthesized with an increasing structural complexity (for a systematic review of HTS structures see Ref. [50]). The replacement of the (relatively expensive) rare earth ions by non-group-IIIb elements led to the discovery of the Tl-based superconducting compounds Tl-Ba-Cu-O ($T_c \approx 90$ K, [51]) and Tl-Ca-Ba-Cu-O (TCBCO, $T_c > 100$ K, [52]) as well as the Bi-Al-Ca-Sr-

Cu-O compound system (onset- $T_c=114$ K, [53]). The effect of hydrostatic pressure on T_c was investigated for the Bi-HTS compound. Initially, T_c increases with pressure at a rate of 3 K/GPa, it passes through a maximum and decreases above 1.2 GPa [53]. This was the first time that a maximum of $T_c(p)$ was observed in an HTS compound.

The TCBCO high-temperature superconductors can be synthesized in different layered structures described by the general formula $Tl_2Ca_{n-1}Ba_2Cu_nO_{2n+4-\delta}$ with e.g. $n=1$ (Tl-2021), $n=2$ (Tl-2122), and $n=3$ (Tl-2223). The ambient-pressure T_c of this series varies between 0 and 125 K. Tl-2021 is of particular interest since it is an overdoped HTS and T_c can be changed between 0 and 90 K by solely varying the oxygen content. The pressure dependence of T_c of TCBCO ($n=1,2,3$) was investigated by Lin et al. [54]. For Tl-2122 and Tl-2223 the T_c was found to increase at a moderate rate of 1.8 K/GPa and 2.4 K/GPa, respectively, in accordance with all previous high-pressure data of HTS. However, the pressure coefficients of T_c of Tl-2021 samples at different doping levels were all shown to be negative with dT_c/dp between -3.9 K/GPa and -1.4 K/GPa, depending on the doping state (or the oxygen content). The large negative values of dT_c/dp for Tl-2021 were also reported almost simultaneously by Mōri et al. [55] and Sieburger et al. [56]. The significance of $dT_c/dp < 0$ of a hole-doped HTS compound for the understanding of HTS was pointed out in Ref. [54]. In particular, the proposed asymmetry between the pressure dependence of T_c of hole-doped and electron doped HTS compounds [57] seemed not to be valid. Based on all available data for dT_c/dp of HTS materials a correlation between $d \ln T_c / dp$ and T_c , shown in Fig. 8, was shown to exist [50,54]. From this correlation it was proposed that there exists one pressure-sensitive parameter that determines T_c of all hole-doped HTS, such as the carrier concentration n or n/m^* (m^* effective carrier mass), as also suggested from Hall effect [58] and penetration depth measurements [59]. The carrier number dependence of T_c and its effect on the pressure coefficient of T_c based on a charge transfer model will be discussed in Section 3.2.

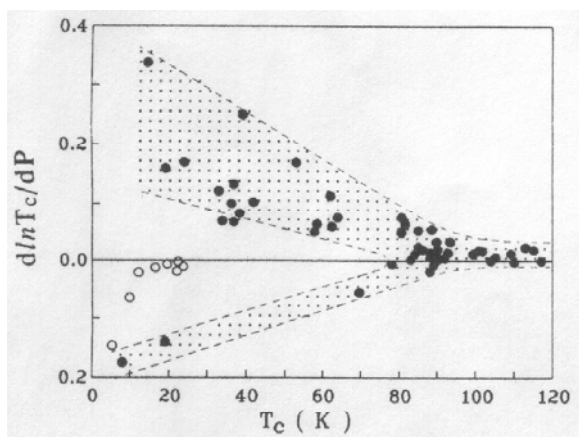


Fig. 8. $d \ln T_c / dp$ vs. T_c for a large number of HTS compounds. The data for hole-doped HTS (closed circles) can be grouped into two bands joining at the highest T_c 's close to $d \ln T_c / dp = 0$. Open circles: data for electron-doped HTS. (Figure reproduced from Ref. [50]).

The continuous enhancement of T_c with p of Tl-2223 observed at pressures below 2 GPa [54,60] suggested that even higher T_c values could be achieved in this compound if the pressure was further increased. For a slightly under-doped single crystal of $Tl_2Ca_2Ba_2Cu_3O_{10-\delta}$ Berkley et al. [61] reported an increase of T_c from 116 K ($p=0$) to 131.8 K at 7.5 GPa. This was a new record T_c at this time.

The search for new HTS materials with even higher T_c 's culminated in 1993 with the discovery of the mercury based HTS compounds. After the successful synthesis of the one-layer compound $HgBa_2CuO_{4+\delta}$ (Hg-1201) with $T_c=94$ K [62] Schilling et al. [63] reported superconductivity below 133.5 K in the three-layer system $HgBa_2Ca_2Cu_3O_{8+\delta}$ (Hg-1223). This remarkable result was immediately confirmed by other groups [64] with onset transition temperatures of the resistivity drop as high as 140 K. Until today no other compound has been found with higher superconducting temperature than Hg-1223. The positive pressure coefficient of T_c ($dT_c/dp=1.8$ K/GPa, [64]) indicated that superconductivity at even higher temperatures could be stabilized under high-pressure conditions. Upon further increase of the imposed pressure the T_c of Hg-1223 (as derived from the onset of the resistive transition) was shown to increase to 153 K at 15 GPa [65], 157 K at 23.5 GPa [66], and 150 K at 11 GPa [67], respectively. No maximum or saturation of $T_c(p)$ was detected at the highest pressures of 23.5 GPa although the pressure coefficient appeared to decrease with increasing p . Far higher pressures were needed to get to the largest possible T_c in the Hg-1223 compound. Extending the experimental pressure range to 45 GPa Gao et al. [68] achieved the highest ever reported superconducting transition temperature of 164 K in Hg-1223. The data for $T_c(p)$ for the three Hg-based HTS structures, Hg-1201, Hg-1212, and Hg-1223, are shown in Fig. 9.

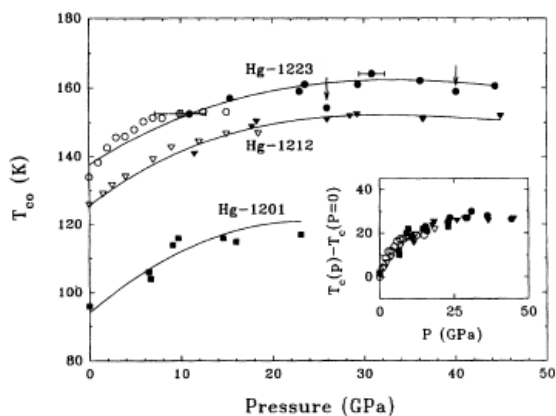


Fig. 9. Pressure dependence of T_c for Hg-1201, Hg-1212, and Hg-1223. Open symbols: data from previous reports, solid symbols: data from the diamond anvil cell experiment. (Figure reproduced from Ref. [68]).

There is clear evidence from the $T_c(p)$ data of Fig. 9 that a maximum of T_c exists close to 30 GPa. At higher pressures T_c finally decreases again. This tendency is characteristic for HTS compounds with an initial positive dT_c/dp [50,69]. However, the magnitude of the T_c

enhancement, $\Delta T_c(p) = T_c(p) - T_c(0)$, of up to 30 K is unusually large. Interestingly, $\Delta T_c(p)$ is nearly independent of the number of CuO_2 layers, as shown in the inset of Fig. 9 where $\Delta T_c(p)$ is plotted for Hg-1201, Hg-1212, and Hg-1223. The large $\Delta T_c(p)$ could be related to the enhanced compressibility (as compared to other HTS materials) of the Hg-HTS compounds [70]. Despite intense research to further increase the superconducting critical temperature of HTS by chemical or physical means the 164 K T_c of Hg-1223 under pressure is still, after more than one decade, the accepted record value for all known superconducting compounds. Whether higher T_c values can be achieved in the known HTS structures or in completely new compounds in the near future is uncertain and any projection has to be speculative.

3.2 The Unified Phase Diagram, the Charge Transfer Model, and the Understanding of Pressure Effects in HTS

Many attempts have been undertaken to understand the pressure effects in HTS materials. The key lies in the highly anisotropic layered structure of the HTS compounds, where superconductivity arises in nearly 2-dimensional CuO_2 layers. With a few exceptions (like the LBCO-214 structures of HTS) the active CuO_2 plane is next to a layer of e.g. SrO or BaO including an apical oxygen ion close to the CuO_2 plane. This block is considered a “charge reservoir” since charges are transferred to the CuO_2 planes via the apical oxygen resulting in an intermediate valence of the Cu in the active layer. Additional layers are inserted into the structure forming a wealth of HTS compounds [50]. The superconducting HTS compounds are derived from insulating parent structures by introducing hole carriers into the CuO_2 layers. The hole density n (or the ratio n/m^*) was shown to be one of the crucial parameters of HTS [50,58,59]. An empirical formula correlating the T_c of HTS with the hole density in the CuO_2 planes was proposed by Tallon and shown to hold for a large number of HTS compounds [71]:

$$T_c / T_{c,\max} = 1 - a(n - n_{\text{opt}})^2, \quad n_{\text{opt}} \approx 0.16, \quad a = 82.6 \quad (5)$$

According to the parabolic dependence (5) $T_c(n)$ exhibits a maximum at the optimal hole density in the CuO_2 planes, n_{opt} . Depending on the doping level the HTS compounds are classified as under-doped, optimally doped, and over-doped for $n < n_{\text{opt}}$, $n = n_{\text{opt}}$, and $n > n_{\text{opt}}$, respectively. The $T_c(n)$ dependence adds an additional degree of freedom to the pressure effect on T_c of HTS. Whereas most hole-doped HTS compounds show a positive pressure coefficient of T_c it was demonstrated that compounds with the highest T_c values (i.e. close to optimal doping) exhibit a very small pressure effect only and in some over-doped cuprates (e.g. $\text{Tl}_2\text{Ba}_2\text{CuO}_{6-\delta}$) T_c actually decreases with pressure. A universal trend correlating $\text{dln}T_c/\text{dp}$ with T_c was proposed and the different magnitudes and signs of $\text{dln}T_c/\text{dp}$ for under-doped, optimally doped, and over-doped HTS were attributed to a pressure-induced increase of the hole density due to a charge transfer from the reservoir to the CuO_2 layers [54]. Further experimental evidence from positron lifetime investigations [50] and Hall effect measurements [72] under pressure provides additional support of the charge transfer model. It is the strength of the model that, based on the known parabolic dependence $T_c(n)$, it explains

naturally the crossover of $d\ln T_c/dp$ with increasing degree of doping from positive values in the under-doped region to negative numbers in the over-doped range. The carrier density n increases roughly linearly with pressure and is of the order of 8 to 10%/GPa [50, 72]. Since the universal parabolic $T_c(n)$ relation is symmetric around n_{opt} (the optimal hole concentration) the pressure coefficient dT_c/dp should be an anti-symmetric function of $n - n_{opt}$, changing sign exactly at n_{opt} . However, experimental data indicate deviations from the perfectly anti-symmetric dependence and additional factors have to be taken into account to understand the pressure effects in HTS. In particular, the suggested negative pressure coefficient of T_c for over-doped materials could not be experimentally confirmed for several compounds [73]. Neumeier and Zimmermann [74] proposed to separate different contributions to the pressure coefficient of T_c and postulated the following relation

$$\frac{dT_c}{dp} = \frac{dT_c^i}{dp} + \frac{\partial T_c}{\partial n} \frac{dn}{dp} . \quad (6)$$

The first term in (6) represents the part of the pressure coefficient that is not due to a change of carrier density while the last term takes account of the pressure-induced charge transfer and its effect on T_c . This equation has successfully been used to interpret the pressure coefficients of several HTS compounds such as Y-123, Y-124, and other rare earth-123 superconductors [75]. It should be noted that the structure of the 214-LBCO class of HTS compounds is exceptional in that it has no charge reservoir layer near the CuO_2 planes. Consequently, pressure cannot transfer charges from a reservoir to the active layer and the second term in (6) does not contribute. Indeed, it was reported that dT_c/dp of LBCO and LSCO (S for Sr) is positive over the whole doping range [50, 76] and it can be considered as a measure of the first term, dT_c^i/dp .

Employing the parabolic relation (5) the pressure derivative of T_c can be written in the more general form [77]

$$\frac{dT_c}{dp} = \frac{\partial T_c}{\partial T_{c,max}} \frac{dT_{c,max}}{dp} + \frac{\partial T_c}{\partial a} \frac{da}{dp} + \frac{\partial T_c}{\partial n} \frac{dn}{dp} + \frac{\partial T_c}{\partial n_{opt}} \frac{dn_{opt}}{dp} . \quad (7)$$

The four terms of equation (7) contribute to the total pressure effect on T_c with different magnitude and sign, depending on the actual carrier density (under-doped or over-doped), and dT_c/dp can be a rather complex function. Besides the pressure-induced charge transfer it is not known how n_{opt} , $T_{c,max}$, or the parameter a will change with pressure and what the microscopic mechanisms for the assumed changes are.

Changes in the electronic structure as well as Fermi surface instabilities similar to those discussed in Section 2 for LTS compounds could also play an important role in the unusual pressure dependence of T_c of some HTS superconductors. The anomalous doping dependence of dT_c/dp in $\text{La}_{2-x}\text{Sr}_x\text{CuO}_4$ and $\text{La}_{2-x}\text{Ba}_x\text{CuO}_4$ in conjunction with the anomalous isotope effect reported in both compounds have been interpreted in terms of an abrupt change of the Fermi surface topology (Lifshitz transition) [78]. In the HTS series $\text{RSr}_2\text{Cu}_{2.7}\text{Mo}_{0.3}\text{O}_y$ (R rare earth element) an abrupt change of dT_c/dp with increasing rare earth ionic radius was reported and a

possible electronic transition was proposed [79]. Van Hove singularities (large peaks of the electronic density of states) are common in low-dimensional electronic structures and can cause abnormal behavior upon doping or application of pressure whenever the Fermi energy is close to the singularity. The existence of Van Hove singularities and a pressure-induced change of the Fermi surface topology were proposed to explain the unusual change of slope of dT_c/dp observed in oxygenated $\text{HgBa}_2\text{CaCu}_2\text{O}_{6+\delta}$ [80]. Deviations from the parabolic $T_c(n)$ dependence (5) as, for example, reported in $\text{HgBa}_2\text{CuO}_{4+\delta}$ [81] will also lead to a more complex pressure dependence of T_c than predicted by the charge transfer model. High-pressure investigations of $\text{HgBa}_2\text{CuO}_{4+\delta}$ over a wide range of δ show indeed a change from linear to non-linear $T_c(p)$ behavior with increasing δ that was ascribed to a possible pressure dependence of the optimal hole density n_{opt} [77].

Another factor that needs to be considered in understanding how pressure affects high-temperature superconductivity is the possible change of the oxygen arrangement in the HTS structure induced by external pressure. The oxygen content in most HTS compounds deviates from the ideal stoichiometric composition contributing to the doping of carriers. For example, in $\text{YBa}_2\text{Cu}_3\text{O}_{7-\delta}$ not all of the possible lattice positions in the CuO -chains are occupied by oxygen and the mobility of oxygen ions along the chains at room temperature is substantial. In the oxygen-doped $\text{La}_2\text{CuO}_{4+\delta}$ the excess oxygen occupies interstitial positions and can easily be moved as a function of temperature or pressure. This leads to unusual but interesting effects such as macroscopic chemical phase separation in very under-doped $\text{La}_2\text{CuO}_{4+\delta}$ ($\delta < 0.05$) [82]. The re-arrangement of mobile oxygen in HTS induced by pressure will be discussed in more detail in the following Section.

3.3 Pressure-Induced Redistribution of Mobile Oxygen in HTS

It is a peculiarity of HTS cuprates that the superconducting state emerges from the insulating state of the “parent” compound by proper doping of charge carriers. This can be achieved by substitution of cations with different valence and by changing the oxygen content of the compound. The latter doping process creates either excess oxygen occupying interstitial sites as in the lattice of $\text{La}_2\text{CuO}_{4+\delta}$ or oxygen vacancies as, for example, in the CuO chains of $\text{YBa}_2\text{Cu}_3\text{O}_{7-\delta}$. Due to its strong electrostatic potential the mobile oxygen (interstitial or along the chains) will interact with the hole distribution in the CuO_2 planes and, if present, with cationic dopants of different valence. In fact, relaxation effects in HTS have been observed as early as 1990. Veal et al. [83] reported a strong dependence of T_c of high-temperature quenched single crystals and ceramic samples of $\text{YBa}_2\text{Cu}_3\text{O}_{7-\delta}$ upon annealing at room temperature resulting in a gradual increase of the superconducting transition temperature by up to 15 K. The annealing effect on T_c was explained by oxygen-vacancy ordering at ambient temperature in the chain region of the structure. Based on a chemical valence model Veal and Paulikas showed a correlation between the oxygen-vacancy distribution and the carrier density in the active CuO_2 layer explaining some peculiarities in the T_c versus δ phase diagram of $\text{YBa}_2\text{Cu}_3\text{O}_{7-\delta}$ [84].

It appears natural that external pressure can have an effect on the oxygen distribution and, consequently, on the properties of the superconductivity and the value of T_c in HTS compounds. This adds additional complexity to the chapter of high-pressure effects in

cuprates that was not discussed in detail in the previous sections. The first indication for pressure-induced redistribution of oxygen ions was found in 1991 in the over-doped $Tl_2Ba_2CuO_{6+\delta}$ [56]. In recent years similar effects have been observed in quite different HTS cuprates (under-doped as well as over-doped) and it is suspected that this phenomenon is more or less universal for high-temperature superconductors with mobile oxygen ions.

$Tl_2Ba_2CuO_{6+\delta}$ is a typical over-doped high- T_c cuprate with a maximum T_c close to 90 K at $\delta \approx 0.1$ and zero T_c at $\delta \approx 0.22$ [85]. An unusually large negative pressure coefficient, $d \ln T_c / dp = -0.183 \text{ GPa}^{-1}$, was reported for this compound close to $\delta = 0.18$ in a piston-cylinder high-pressure clamp (pressure is applied at room temperature) [86]. However, Sieburger and Schilling found striking differences in the pressure dependence of T_c of $Tl_2Ba_2CuO_{6+\delta}$ depending on the temperature at which pressure was applied. Using a He-gas pressure system the large negative pressure effect on T_c of Ref. [86] was confirmed when pressure was increased at room temperature. In contrast, the value of $d \ln T_c / dp$ was positive and much smaller in its magnitude (of the order of 0.01 GPa^{-1}) when pressure was imposed below 100 K [56], as shown in Fig. 10. This led to the conclusion that pressure-induced diffusion of mobile interstitial oxygen plays a major role at high temperatures and that application of pressure at low enough temperatures does not change the oxygen configuration since any ionic diffusion process is inhibited at low T.

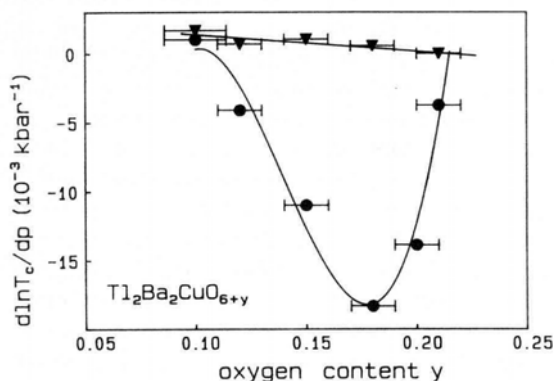


Fig. 10. The relative pressure coefficient of $Tl_2Ba_2CuO_{6+\delta}$. Circles: Pressure applied at room temperature. Triangles: Pressure applied at low temperature. (Figure reproduced from Ref. [56]).

Close to the maximum T_c (optimal doping) the two pressure coefficients (for pressure applied at high or low T) are almost identical so that the pressure-induced redistribution of oxygen does not seem to be essential close to the optimal doping level. This result was confirmed by Schirber et al. [87] for $Tl_2Ba_2CuO_{6+\delta}$ with $\delta = 0$ ($T_c = 92 \text{ K}$). In the $\delta \rightarrow 0$ limit of doping there is no interstitial oxygen in the structure that could be re-arranged by high pressure. Consequently, the value of $d \ln T_c / dp = 0.022 \text{ GPa}^{-1}$ does not depend on the temperature at which pressure was impressed.

The kinetic process of pressure-induced oxygen diffusion and the typical relaxation behavior of T_c were investigated in detail for $Tl_2Ba_2CuO_{6+\delta}$ [88]. A typical T_c -relaxation experiment is described in Fig. 11. Two separate relaxation processes have been identified, one low-temperature (LT) relaxation that appears to strongly depend on the concentration of interstitial oxygen δ and a high temperature (HT) relaxation process the magnitude of which (1 to 2 K change of T_c) was found to be independent of δ [88]. Two characteristic activation energies E_A of 0.25 eV and 0.72 eV have been estimated for LT and HT relaxations, respectively. The value for the HT process is comparable with the activation energy $E_A=0.96$ eV derived from the T_c relaxation in the quenching and annealing experiments of $YBa_2Cu_3O_{7-\delta}$ [83]. E_A for the LT relaxation was shown to be independent of pressure whereas E_A for the HT relaxation of T_c was found to increase with p [89]. The mobile oxygen ions in $Tl_2Ba_2CuO_{6+\delta}$ are interstitial ions residing in bi-layers of Tl_2O_2 . A hard-sphere model for the diffusion of interstitial oxygen along different diffusion paths was proposed in Ref. [89] and the authors come to the conclusion that the LT relaxation of T_c in $Tl_2Ba_2CuO_{6+\delta}$ is caused by an intra-unit cell migration of oxygen between two equivalent sites with a low activation energy and a vanishing diffusion volume. In contrast, the HT relaxation was ascribed to the diffusion of oxygen ions between different unit cells that requires a partial expansion of the lattice along the diffusion path and is, therefore, characterized by the higher activation energy and a finite diffusion volume.

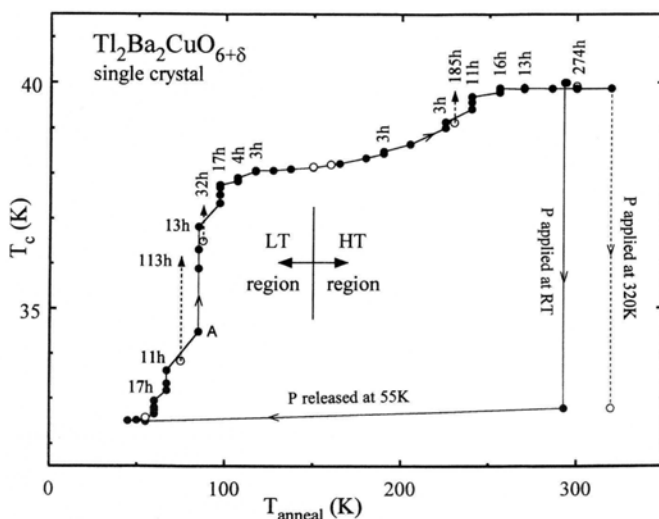


Fig. 11. Annealing effect on T_c of a $Tl_2Ba_2CuO_{6+\delta}$ single crystal ($T_c=40$ K). Hydrostatic pressure of 0.6 GPa was first applied at room temperature and then released at 55 K. Subsequent annealing at increasing temperatures for times indicated in the figure results in an increase of T_c towards its ambient value. Two distinct relaxation steps can be distinguished. (Figure reproduced from Ref. [88]).

T_c relaxations under external pressure and subsequent annealing have also been observed in the over-doped $TlSr_2CaCu_2O_{7-\delta}$ (Tl-1212, $T_{c,max} \approx 80$ K) [88]. T_c decreases with increasing oxygen content. The pressure coefficient of T_c when pressure is applied at room temperature significantly depends on the doping state and changes sign from strongly negative close to optimal doping (high T_c) to a relatively small, but positive value at higher doping level (lower T_c). However, when pressure is changed at low temperature $d \ln T_c / dp$ appeared to be positive over the whole doping range [90]. Relaxation effects of T_c have been observed only at annealing temperatures exceeding 210 K.

$YBa_2Cu_3O_{7-\delta}$ was the first HTS compound with T_c above the temperature of liquid nitrogen [17]. A large amount of scientific work was devoted to this particular compound. In its optimal doping state ($\delta=0.05$, $T_c=93$ K) the application of pressure had a negligible effect on T_c [48], a property that is common for many of the optimally doped HTS compounds. With increasing δ $YBa_2Cu_3O_{7-\delta}$ becomes under-doped and more oxygen vacancies are created in the CuO chains. A giant pressure coefficient dT_c/dp of up to 30 K/GPa was reported for very under-doped $YBa_2Cu_3O_{7-\delta}$ [91] (see Fig. 12) when pressure was imposed at room temperature. However, application of pressure below 100 K resulted in a moderate increase of T_c (2 to 4 K/GPa) even for the lowest doping levels. The pressure coefficients of T_c of $YBa_2Cu_3O_{7-\delta}$ are plotted for the whole doping range in Fig. 12 and the enhancement of dT_c/dp for room temperature pressure application is very obvious. This enhancement was attributed to the pressure-induced ordering of the chain oxygen in analogy to the results of the annealing experiments of Veal et al. [83].

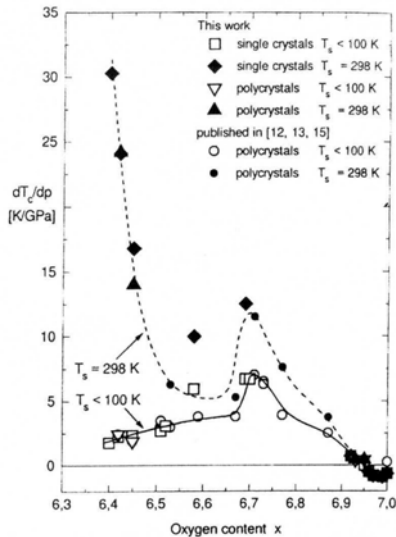


Fig. 12. The pressure coefficient of T_c of $YBa_2Cu_3O_{7-\delta}$. Solid curve (open symbols): Pressure applied at low temperature. Broken line (filled symbols): Pressure applied at high temperature. (Figure reproduced from Ref. [91]).

The pressure-induced redistribution of oxygen was investigated in more detail with respect to the characteristic time relaxation of T_c at different temperatures [91,92]. Changing pressure abruptly at room temperature and measuring T_c at different times after storing the pressurized sample at 298 K a typical relaxation behavior as shown in Fig. 13 was observed. The T_c relaxation was suppressed for storage temperatures below 240 K [92]. The time dependence of T_c after each change of pressure is well described by a stretched exponential function, as shown for data on $\text{YBa}_2\text{Cu}_3\text{O}_{6.41}$ [93]. The characteristic relaxation time, τ , increases dramatically with pressure and it was suggested that the T_c relaxation is due to the thermally activated diffusion of O^{2-} ions with $\tau(p,T) = \tau_0 \exp\{E_A(p)/k_B T\}$. The ambient-pressure value of $E_A \approx 0.97$ eV is in excellent agreement with the data of Fietz et al. [91], Veal et al. [83] and with the results of ^{18}O tracer diffusion experiments [94]. From the pressure dependence of E_A the activation volume for diffusion could be calculated and was found to be close to the molar volume of O^{2-} [93,95].

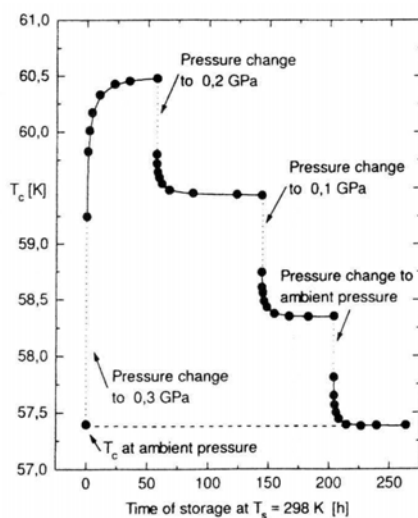


Fig. 13. T_c relaxation effects of an under-doped $\text{YBa}_2\text{Cu}_3\text{O}_{6.58}$ single crystal. The sample was annealed at 298 K after pressure changes as indicated. (Figure reproduced from Ref. [91]).

The observed changes of T_c in YBCO with the re-distribution of the chain oxygen was explained by a charge transfer to the active CuO_2 layers that depends sensitively on the specific oxygen configuration [83,84]. This charge transfer also affects the electrical transport properties in the normal state. The time-relaxation of the electrical resistivity of $\text{YBa}_2\text{Cu}_3\text{O}_{7-\delta}$ observed after hydrostatic pressure was applied (or released) at room temperature followed exactly the same stretched exponential relaxation function as the corresponding data for T_c with very similar relaxation times, activation energies, and migration volumes [95]. This obvious correlation between the relaxation of T_c and that of the normal-state resistivity provides evidence for the common origin of both effects.

The ordering of oxygen vacancies at ambient pressure was also observed near optimal doping in $\text{YBa}_2\text{Cu}_3\text{O}_{6.95}$, most notably in thermal expansion measurements [96]. Upon cooling from high temperature a glass-like transition with distinct anomalies in the thermal expansion coefficients around 280 K indicates the rearrangement of the oxygen ions. The largest anomaly is seen in the expansivity along the orthorhombic b-axis. The kinetics of this glass transition is determined by the energy barrier of $E_A=0.98$ eV [96], in agreement with other oxygen ordering studies discussed above. Under hydrostatic pressure the glass transition temperature increased at a rate of 25 K/GPa [97] supporting the assumption that pressure indeed facilitates the rearrangement of the mobile oxygen in the structure of YBCO. There arises the question why for the optimally doped $\text{YBa}_2\text{Cu}_3\text{O}_{6.95}$ the pressure coefficient of T_c was found to be independent of the temperature at which pressure was applied (see e.g. Fig. 12). According to the universal phase diagram of HTS the $T_c(n)$ inverted parabola exhibits a maximum at the optimal carrier density, n_{opt} . Any pressure-induced charge transfer mediated by the rearrangement of the mobile oxygen should therefore have a negligible effect on T_c since $dT_c/dn=0$ for $n=n_{\text{opt}}$. Furthermore, the number of oxygen vacancies in $\text{YBa}_2\text{Cu}_3\text{O}_{6.95}$ is small ($\delta=0.05$) and the change of carrier density in the active layer can be very small at optimal doping although the thermal expansivities show clear anomalies [96]. Therefore, no relaxation effects of T_c or resistivity could be observed in the optimally doped $\text{YBa}_2\text{Cu}_3\text{O}_{6.95}$.

The study of pressure-induced oxygen diffusion in $\text{HgBa}_2\text{CuO}_{4+\delta}$ is of particular interest since this compound is stable in the whole doping range. The T_c of this compound is a smooth parabolic function of δ covering the under-doped as well as the over-doped region of the phase diagram with a maximum $T_{c,\text{max}}=97$ K at $\delta=0.22$ [81]. dT_c/dp was found to be positive and of the order of 2 K/GPa as long as $\delta \leq 0.22$ (under-doped to optimally doped) [77]. In the over-doped range ($\delta > 0.22$) the shift of T_c was relatively small and a non-linear function of pressure. In the experiments of Ref. [77] pressure was imposed at room temperature. Pressure-induced relaxation processes of T_c have also been observed in over-doped $\text{HgBa}_2\text{CuO}_{4+\delta}$ with typical activation energies of about 0.9 eV (comparable with values of other HTS compounds) and activation volumes of $11 \text{ cm}^3/\text{mol}$ [98].

The La-214 HTS system allows for the simultaneous doping with cations (e.g. Sr^{2+}) and anions (O^{2-}) and its chemical formula is written in the general form $\text{La}_{2-x}(\text{Sr/Ba})_x\text{CuO}_{4+\delta}$. It is important to emphasize that there is a fundamental difference between these two doping options. The cationic dopants (Sr^{2+} or Ba^{2+}) replace the La^{3+} ions and reside in lattice site positions. Therefore, they are tightly bounded, immobile at ambient temperature, and randomly distributed among the La positions in the structure. We will use the notation “hard doping” because the dopants are literally frozen at ambient or even elevated temperatures. In contrast, the anionic doping by excess oxygen (notated as “soft doping” hereafter) creates interstitial O^{2-} ions that are highly mobile and will adjust to the change of thermodynamic parameters such as temperature or pressure. In a quantum statistical sense the two types of doping are well distinguished by the way thermodynamic and configuration averaging is conducted. Since doped systems are in general “disordered” systems and many different configurations contribute to the partition function the configuration average has to be performed in addition to the usual thermal average. As pointed out by Brout [99] for the case of hard doping the configuration average has to be taken after the thermal average and it is applied to the thermodynamic potential (free energy) that was calculated for all different dopant configurations. In the case of soft doping, however, the sequence of averaging is the

opposite, i.e. the configuration average is applied to the partition function before the thermodynamic averaging.

In $\text{La}_{2-x}\text{Sr}_x\text{CuO}_{4+\delta}$ the total hole density is determined by two parameters, x and δ , and the effects of hard and soft doping can be revealed by controlling both parameters independently. The crucial parameter is δ , the amount of soft excess oxygen doping, that gives rise to a number of interesting physical phenomena not observable in exclusively hard-doped compounds. Structural transitions and macroscopic phase separation have been observed in the super-oxygenated $\text{La}_2\text{CuO}_{4+\delta}$ [100-107]. For $\delta > 0.05$ the superconducting transition proceeds in two well-separated steps with two T_c 's at 15 K and 30 K, respectively, suggesting the possibility of electronic phase separation [100]. Interestingly, the two subsequent transitions appear in $\text{La}_2\text{CuO}_{4+\delta}$ and in $\text{La}_{1.985}\text{Sr}_{0.015}\text{CuO}_{4+\delta}$ above the same critical hole density of $n_h \approx 0.085$, as shown in Fig. 14. Care has to be taken in estimating the average carrier density in the CuO_2 layers. Similar to the reduced doping efficiency of oxygen observed in $\text{HgBa}_2\text{CuO}_{4+\delta}$ [81] it was shown that the doping efficiency of oxygen in $\text{La}_{2-x}\text{Sr}_x\text{CuO}_{4+\delta}$ is reduced to 1.3 holes per oxygen when the total hole density exceeds the value of 0.06 holes per Cu [108]. Oxygen-doped and oxygen-strontium co-doped La-214 compounds compared at the same total carrier density (but at different δ , depending on the amount of Sr) exhibit very similar superconducting properties, as demonstrated in Fig. 14 [109]. One superconducting transition is observed with $T_c \approx 30$ K in the low-doping range, $n_h < 0.085$. At higher doping ($n_h > 0.085$) two transitions at 15 and 30 K, respectively, are observed in the magnetic susceptibility. This was interpreted as a signature of electronic phase separation into two superconducting (hole-rich and hole-poor) states that has been predicted to be a general property of two-dimensional hole-like systems [110,111].

The effect of hydrostatic pressure on the superconducting phases in the one- as well as two-transition regions of the phase diagram (Fig. 14) and possible p-induced oxygen migration effects have been investigated in $\text{La}_2\text{CuO}_{4+\delta}$ and $\text{La}_{1.985}\text{Sr}_{0.015}\text{CuO}_{4+\delta}$ [109]. Hydrostatic pressure was imposed either at room temperature allowing the redistribution of the interstitial oxygen or below 100 K where oxygen diffusion is kinetically inhibited. An unusually large pressure coefficient, $dT_c/dp = 10$ K/GPa, was detected in the low doping range ($n_h < 0.085$) for pressures applied at 296 K. In contrast, the p-shift of T_c was much smaller (2 to 3 K/GPa) when pressure was changed at low T. This remarkable difference led to the conclusion that pressure induces a redistribution of the soft dopants (interstitial oxygen), similar to the effects observed in YBCO. The extraordinary large dT_c/dp in $\text{La}_{2-x}\text{Sr}_x\text{CuO}_{4+\delta}$, however, cannot be explained by a charge transfer from a charge reservoir to the active CuO_2 layers (as in YBCO) since there is no charge reservoir in the 214-structure. Hall effect measurements have confirmed that the average density of free carriers does not change with the application of pressure [112,113]. It was therefore suggested that the pressure facilitates a redistribution of charges resulting in a local enhancement of the carrier density and the separation into hole-rich and hole-poor phases [109]. This charge separation is made possible by the mobile oxygen ions that adjust their distribution to provide the needed screening and to compensate the Coulomb repulsion between the holes in the CuO_2 layers. When the oxygen ions are frozen in their positions and p is changed at low T the O^{2-} act like pinning centers for the holes and the p-induced charge separation is largely suppressed. This explains the smaller dT_c/dp for low-temperature application of pressure.

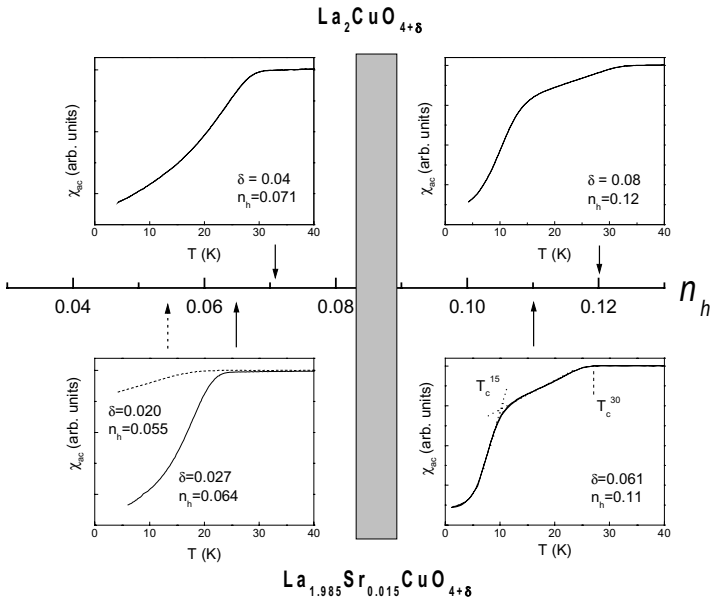


Fig. 14. Typical ac susceptibility curves in the phase diagram of $\text{La}_2\text{CuO}_{4+\delta}$ and $\text{La}_{1.985}\text{Sr}_{0.015}\text{CuO}_{4+\delta}$ as function of the average hole concentration, n_h . Two superconducting transitions are observed for $n_h > 0.085$. (Figure reproduced from Ref. [109]).

The pressure effects on the 15 K and 30 K superconducting transitions for higher doping levels ($n_h > 0.085$) are opposite in sign ($T_c^{(15)}$ decreases and $T_c^{(30)}$ increases with p) when p is applied at 296 K. Changing pressure at low T (< 100 K), however, barely affects the 15 K transition temperature but it increases $T_c^{(30)}$ at a moderate rate of about 3 K/GPa. These differences in the pressure effects on $T_c^{(15)}$ and $T_c^{(30)}$ and their dependence on the temperature at which pressure is changed show the important role the mobile oxygen dopants play in $\text{La}_{2-x}\text{Sr}_x\text{CuO}_{4+\delta}$ in stabilizing superconductivity. The results have been interpreted in terms of pressure-induced electronic phase separations. Further details can be found in Ref. [109].

The fundamental difference of cationic (hard) and anionic (soft) doping becomes drastically visible in the high-pressure investigation of very different HTS compounds as discussed above. Wherever doping is achieved by introducing mobile oxygen ions (or vacancies) the application of pressure at room temperature results in a redistribution of the O^{2-} ions and an increased response of the superconducting state (e.g. enhancement of dT_c/dp). The thermodynamically stable state under imposed pressure is characterized by a different oxygen configuration than the ambient-pressure state. This has to be taken into account as an additional dimension in the understanding of the pressure effects in HTS. When pressure is

applied at low temperature and oxygen diffusion is inhibited the resulting high-pressure state is actually away from thermodynamic equilibrium. The resulting pressure effects do not reflect the complex response of the superconductor to external compression that has to include the correlation between the hole carriers and the oxygen ions. The T_c -relaxation experiments discussed above therefore indicate the transition from a metastable state to the thermodynamically stable state at a given pressure.

4. PRESSURE EFFECTS IN SOME UNCONVENTIONAL SUPERCONDUCTORS

4.1 Pressure Effects in MgB_2 and Isostructural Intermetallic Compounds

Soon after the discovery of superconductivity in MgB_2 at temperatures as high as 39 K [114] one of the most disputed questions was whether or not the superconductivity in this simple intermetallic compound can be understood on the basis of a phonon-mediated BCS-like pairing mechanism. The unusually high T_c was attributed to the strong electron-phonon interaction and the high phonon frequency of lattice vibrations involving mainly the light boron element [115]. Alternatively, Hirsch proposed an explanation in terms of a “universal” theory of hole superconductivity conjecturing that the mechanism of superconductivity in MgB_2 is similar to that in cuprate superconductors and that the pairing of heavily dressed holes in almost completely filled bands is driven by a gain in kinetic energy. An increase of T_c with pressure was predicted if pressure does reduce the in-plane boron-boron distance [116]. Evidence for hole-type carriers was indeed derived from early measurements of the thermoelectric power [117]. The pressure coefficient of T_c of MgB_2 was first measured in a piston-cylinder clamp with liquid pressure transmitting medium. The results are shown in Fig. 15.

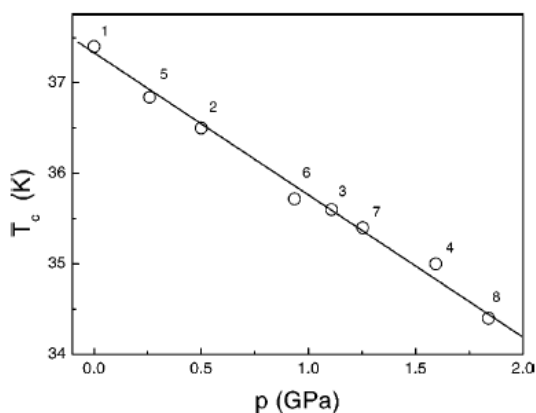


Fig. 15. Effect of hydrostatic pressure on the superconducting transition temperature of MgB_2 . The numbers next to the data points indicate the sequence of pressure changes. (Figure reproduced from Ref. [117]).

The pressure coefficient of T_c was found to be negative and of the order of -1.6 K/GPa [117] in very good agreement with calculations of the elastic and electronic properties of MgB_2 [118]. Therefore, the theory of hole superconductivity appeared to be less favorable to explain the mechanism of superconductivity in MgB_2 . Since the pressure coefficient of T_c is essential to discriminate between the different proposed models for MgB_2 , a large number of follow-up high-pressure experiments have been conducted. In all experiments employing hydrostatic pressure dT_c/dp was found to be negative but its value scattered between -1 and -2 K/GPa in most investigations. The different values of dT_c/dp reported by various groups have been a matter of a separate discussion (see for example Ref. [119, 120]). It was suggested that the larger values of dT_c/dp up to -2 K/GPa might be related to the sensitivity of the superconducting state of MgB_2 to stress introduced by the freezing of the liquid pressure medium upon cooling [121]. However, this suggestion could not be confirmed in alternative experiments [122]. Instead, a correlation between “sample quality” as expressed by small variations of T_c and the magnitude of dT_c/dp was proposed [123]. The role of defects in the structure of MgB_2 was discussed in detail and it was found that the increase of the defect density results in an increase of the lattice strain, an increase of the c -axis length, a decrease of the resistivity ratio $\rho(300K)/\rho(T_c)$, and a decrease of T_c [120,124]. The linear increase of $|dT_c/dp|$ with decreasing T_c could therefore be related to the increase of the defect density in “poor” samples [120,123].

The current microscopic understanding of the superconductivity in MgB_2 reveals an unusual superconducting gap structure where supercarriers are formed simultaneously in two bands at the Fermi energy and two superconducting gaps of different magnitude open at T_c [125]. This two-gap scenario was confirmed experimentally by a number of investigations including heat capacity measurements [126], Raman scattering [127], and tunneling spectroscopy [128]. To understand the pressure effects in superconducting MgB_2 the p -induced changes of the microscopic parameters of the two bands as well as the coupling between the bands need to be taken into account. Experimentally, the measurement of the heat capacity (C_p) under high-pressure conditions appears to be of interest since changes in the superconducting gap structure are reflected in the temperature dependence of C_p [126]. No such experiments have been conducted so far.

The excitement about the high superconducting transition temperature of MgB_2 initiated the search for similar intermetallic compounds with the same lattice structure. The most prominent materials found superconducting are $CaAlSi$ and $SrAlSi$ as well as the Ga-based series $(Ca,Sr,Ba)GaSi$ [129]. These compounds are isostructural to MgB_2 with Al (or Ga) and Si occupying randomly the boron sites in the C32 structure of MgB_2 . The critical temperatures of these new materials turned out to be moderate with the highest $T_c=8$ K found in $CaAlSi$. Although $CaAlSi$ and $SrAlSi$ are very similar electronically as well as structurally (the major difference is the 7.5 % larger c -axis lattice parameter of $SrAlSi$), the application of hydrostatic pressure revealed a fundamental difference of their superconducting states [130]. The superconducting T_c of $SrAlSi$ decreases linearly at a rate of -0.12 K/GPa, as shown in Fig. 16. However, T_c of $CaAlSi$ increases with pressure in a nonlinear way with an initial pressure coefficient of 0.21 K/GPa (Fig. 16). Heat capacity experiments (Fig. 17) indicate that superconductivity in $SrAlSi$ is well described by the BCS theory in the weak-coupling limit, however, the data for $CaAlSi$ show the typical signature of a very strong-coupling superconductor [21,130].

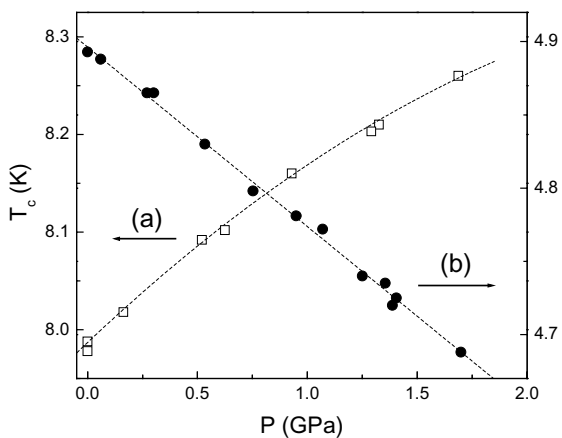


Fig. 16. Effect of hydrostatic pressure on the superconducting transition temperatures of (a) CaAlSi (open squares, left scale) and (b) SrAlSi (filled circles, right scale).

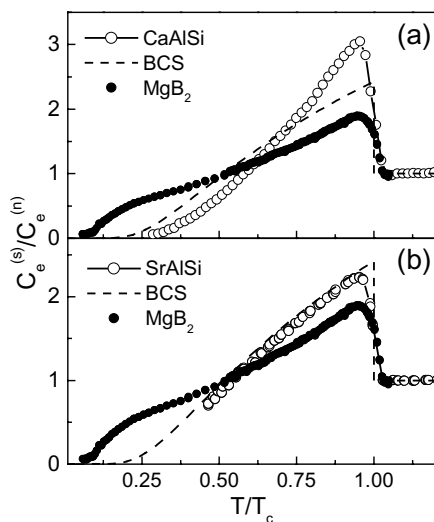


Fig. 17. Normalized heat capacity of (a) CaAlSi and (b) SrAlSi. The dashed line shows the BCS function. For comparison the heat capacity of MgB₂ is included (filled symbols).

Calculations of the electronic band structure and the electron-phonon coupling could not explain the qualitative disparity in the superconducting properties of the two compounds [131]. It was therefore speculated [131] that a soft mode in CaAlSi could lead to an enhancement of the electron-phonon coupling in CaAlSi and to an unusual structure of the Eliashberg function [21]. The possible existence of a soft mode in CaAlSi might be an indication that the compound is very close to an electronic or structural instability with the dramatic effect on its superconductivity resulting in the “unusual” behavior discussed above. The experimental search for this soft mode and its consideration in a theoretical description of superconductivity in the C32 intermetallic compounds will facilitate our principal understanding of superconductivity in “unconventional” compounds.

4.2 Pressure Control of Dimensionality in the New Superconductor $\text{Na}_x\text{CoO}_2 \cdot y\text{H}_2\text{O}$

The important role of dimensionality in superconductivity has been considered for many decades. With the rising age of HTS cuprates other low-dimensional superconductors have attracted renewed attention. The recent discovery of superconductivity in the sodium-doped cobalt oxyhydrate $\text{Na}_x\text{CoO}_2 \cdot y\text{H}_2\text{O}$ ($x \approx 1/3$, $y \approx 4/3$) has raised fundamental questions about the role of low dimensionality, the pairing symmetry, and the unusual properties of this unconventional superconductor [132]. The intercalation of water molecules in between the CoO_2 layers forces the c-axis lattice constant to expand by 77 % and increases the anisotropy of the structure in reducing the coupling between the CoO_2 layers. It was, therefore, suggested that the superconductivity observed below 5 K arises in the quasi-2d CoO_2 layers and analogies to the CuO_2 layers of the HTS cuprates have been drawn [132]. Indeed, experimental evidence for a nodal superconducting order parameter and the existence of line nodes in the gap function below T_c suggests a strong similarity of the superconducting state in $\text{Na}_x\text{CoO}_2 \cdot y\text{H}_2\text{O}$ to the d-wave superconductivity in HTS cuprates [133,134]. With the weak interactions between the CoO_2 layers the compressibility along the c-direction is expected to be particularly large. Application of hydrostatic pressure can be used to tune the coupling between the superconducting CoO_2 layers and it provides vital insight into the role of dimensionality in stabilizing the superconducting state.

We have found that pressure reduces the critical temperature with an unusual non-linear pressure dependence of T_c [135], as shown in Fig. 18. The negative dT_c/dp of $\text{Na}_x\text{CoO}_2 \cdot y\text{H}_2\text{O}$ was explained by the larger compression of the c-axis that drives the structure away from the two-dimensional character. Subsequent high-pressure x-ray investigations have confirmed our suggestion and have shown that the compressibility of the c-axis indeed exceeds the a-axis value by a factor of 4.5 [136]. The pressure effects on T_c and the lattice constants provide strong evidence for the two-dimensional character of superconductivity in $\text{Na}_x\text{CoO}_2 \cdot y\text{H}_2\text{O}$. A further increase of the c-axis should result in higher T_c values and, possibly, new superconducting phenomena could be detected. A very recent structural study [137] of $\text{Na}_x\text{CoO}_2 \cdot y\text{H}_2\text{O}$ single crystals has shown that the water content can be increased to $y=1.8$ with an increase of the c-axis lattice parameter from 19.71 Å ($y=1.3$) to 22.38 Å ($y=1.8$). However, low-temperature studies and the search for superconductivity in this compound have not yet been conducted.

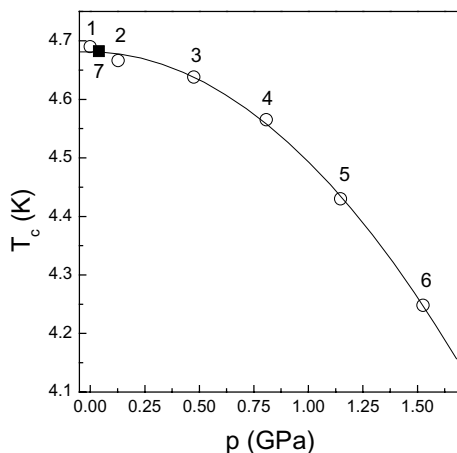


Fig. 18. Pressure dependence of T_c of the layered cobalt oxyhydrate $\text{Na}_x\text{CoO}_2 \cdot y\text{H}_2\text{O}$. The numbers indicate the sequence of pressure changes. The ambient-pressure T_c recovered after complete release of pressure (filled square).

The non-linearity of $T_c(p)$ is interesting by itself and it suggests the possible existence of large dispersion in the energy spectrum near the Fermi surface [135]. The average pressure change of T_c is $d \ln T_c / dp = -0.07 \text{ GPa}^{-1}$. Above 1 GPa T_c decreases at a rate of $d \ln T_c / dp = -0.1 \text{ GPa}^{-1}$. It is interesting to note that these values compare favorably with the pressure coefficients of electron-doped high-temperature superconductors with a similar T_c [138]. In $\text{Na}_x\text{CoO}_2 \cdot y\text{H}_2\text{O}$ the charge carriers are electrons. The current high-pressure results may suggest an interesting similarity of the layered $\text{Na}_x\text{CoO}_2 \cdot y\text{H}_2\text{O}$ and the HTS cuprates.

4.3 Competition of Superconducting and Magnetic Orders in Superconducting Ferromagnets as Revealed by High-Pressure Experiments

In the field of high-temperature superconductivity the coexistence of ferromagnetism and superconductivity in a class of Ru-based HTS compounds has raised considerable attention. In these materials (e.g. $\text{RuSr}_2\text{GdCu}_2\text{O}_8$) ferromagnetic order arises at relatively high temperature (≈ 130 K) and superconductivity sets in at about 45 K. The question if and how these two antagonistic states of matter can coexist has been a focal point of intense discussion (for a short review of the topic see e.g. Ref. [139]). The response of the two states, magnetism and superconductivity, to applied pressure will provide more insight into the way they coexist with one another.

The superconducting ferromagnets are commonly synthesized in polycrystalline form with relatively weak grain-grain connectivity. The weak links across the grain boundaries give rise to unusual effects, for example in the magnetoresistance measurements below T_c [140]. The superconducting transition as observed in resistivity or zero-field cooling magnetization measurements proceeds in two steps, the intra-grain transition is followed by an inter-grain transition (phase coherence across the grain boundaries) at lower temperature. Both transitions can be separated in ac-susceptibility or transport measurements [141,142]. It is essential to focus the high-pressure investigation onto the pressure effects on the bulk superconducting properties and the intra-grain superconducting T_c .

The pressure dependences of both, the ferromagnetic transition temperature, T_m , and the intra-grain superconducting T_c , of $\text{RuSr}_2\text{GdCu}_2\text{O}_8$ were estimated by measuring the ac susceptibility in a piston-cylinder clamp cell [143]. The results for $T_c(p)$ and $T_m(p)$ are shown in Fig. 19. Both transition temperatures increase with pressure, but at different rates. The magnitude of the relative pressure shift of T_m , $d \ln T_m / dp = 0.054 \text{ GPa}^{-1}$, was found to be about twice as large as $d \ln T_c / dp = 0.025 \text{ GPa}^{-1}$, indicating that the stabilizing effects of pressure on the magnetic state are much stronger than on the superconductivity.

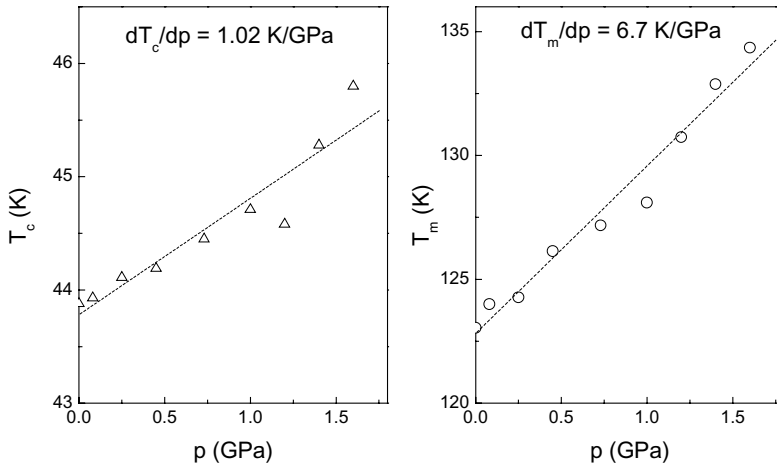


Fig. 19. Pressure dependences of the intra-grain T_c (left) and the ferromagnetic T_m (right) of $\text{RuSr}_2\text{GdCu}_2\text{O}_8$.

The absolute pressure coefficient of the intra-grain T_c , $dT_c / dp \approx 1 \text{ K/GPa}$, is surprisingly small if compared with similar, but non-magnetic high- T_c compounds in a comparable doping state. $\text{RuSr}_2\text{GdCu}_2\text{O}_8$ is known to be a typical under-doped cuprate with a hole density of about 0.06 to 0.07 [141]. The pressure coefficients of T_c of different HTS cuprates at a similar doping level, as for example $\text{La}_{2-x}(\text{Sr, Ba})_x\text{CuO}_4$, $\text{YBa}_2\text{Cu}_3\text{O}_{7-\delta}$, or $\text{YBa}_2\text{Cu}_{3-x}\text{M}_x\text{O}_{7-\delta}$, are all

larger by a factor of 3 to 4 than the dT_c/dp of the superconducting ferromagnet $\text{RuSr}_2\text{GdCu}_2\text{O}_8$. This leads us to propose that the magnetic and superconducting states are not completely independent but they compete with each other [143]. Due to this competition the stronger enhancement of the ferromagnetic phase results in a reduced (as compared to similar HTS compounds) pressure effect on T_c . Under external pressure the magnetism in $\text{RuSr}_2\text{GdCu}_2\text{O}_8$ is stabilized on the expense of the superconducting state.

5. SUMMARY

Since the discovery of superconductivity in 1911 the effects of high pressure on the superconducting state and T_c have been of prominent interest. Pressure was very successful in inducing superconductivity in elements and compounds that are not superconducting at ambient pressure. The total number of elements that turn superconducting at high pressure now almost equals the number of ambient pressure superconducting elements. Especially the high-pressure superconductivity detected in the alkali metal lithium sparks new hope in the ongoing search for superconductivity with an expected unprecedented high T_c in dense metallic hydrogen. The developments of new techniques have pushed the limits of static pressure generation into the range of several hundred GPa and the dream to squeeze hydrogen superconducting may be realized very soon. Large positive pressure coefficients of T_c found in the high-temperature superconducting cuprates have revealed the final clues that led to the synthesis of the first HTS compounds with T_c 's above the temperature of liquid nitrogen. The current record $T_c=164$ K was achieved in $\text{HgBa}_2\text{Ca}_2\text{Cu}_3\text{O}_{8+\delta}$ under high-pressure conditions.

The physical understanding of the pressure effects on superconductivity is very complex, even for conventional superconductors. Within the phonon-mediated pairing models (BCS in weak-coupling limit or Eliashberg theory for strong coupling) a number of electronic and phononic parameters that depend on pressure with an immediate effect on the transition temperature have to be considered. The equation for T_c derived by McMillen, for example, involves three parameters, the average phonon frequency, the electron-phonon coupling constant, and the screened Coulomb pseudopotential. All three parameters depend on pressure via the phonon energy, the density of states, the electronic matrix elements, the screened Coulomb interaction, etc. in a non-trivial analytical way. A first-principle theory of the pressure effects in superconductivity has to account for the pressure dependence of all parameters of the phonon and electron systems as well as their interactions. In a semi-empirical treatment the pressure dependence of the density of states and the phonon frequency is frequently considered and all other parameters are assumed to be independent of pressure. This simplified procedure was successful in describing the pressure effects on T_c in some simple compounds such as superconducting lead.

Abnormal pressure effects observed in several superconducting elements (Tl, Re) have been explained by electronic instabilities of the Fermi surface (change of topology from closed to open Fermi surface) induced by pressure. High-pressure investigations of superconductivity in some A15 compounds have revealed the superior role of the electronic excitation spectrum with peaks or singularities close to the Fermi energy in stabilizing superconductivity with relatively high T_c -values and inducing the phonon softness that leads to structural instabilities close to the superconducting transition.

In high-temperature superconducting cuprates the effect of pressure on T_c strongly depends on the doping state, i.e. the number of holes in the active CuO_2 layer. The universal parabolic law that applies to a majority of HTS compounds expresses T_c as an inversed parabolic function of the hole number, n , with an optimal hole density (maximum T_c) near 0.16. Because of this $T_c(n)$ dependence $T_c(p)$ is largely determined by a pressure-induced charge transfer from the charge-reservoir block to the CuO_2 layer. This charge-transfer model explains the observed sign change of the pressure coefficient of T_c in crossing from the under-doped region ($n < 0.16$) into the over-doped range ($n > 0.16$). However, there are several exceptions in the class of HTS compounds that either do not follow the parabolic $T_c(n)$ dependence in the full range of doping or that show a more complex pressure dependence of T_c contradicting the simple charge transfer model. The existence of Van Hove singularities and the pressure-induced change of the Fermi surface topology have therefore been proposed (e.g. in $\text{HgBa}_2\text{CaCu}_2\text{O}_{6+\delta}$) to account for the abnormal behavior of $T_c(p)$.

An increased complexity of pressure effects have been reported in HTS systems with weakly bound, mobile oxygen ions, such as vacancies in the CuO -chains of Y-123 (YBCO) providing the possibility of oxygen migration along the chains, or interstitial excess oxygen in Tl-2201 and La-214. It is shown that, for several different HTS compounds, the application of pressure results in a change of the distribution of these mobile oxygen ions with a large impact on the pressure dependence of T_c . Therefore, the pressure effects depend on the temperature at which pressure is imposed. If this temperature is low enough the oxygen migration is inhibited and the application of pressure drives the HTS system away from thermal equilibrium with a qualitatively different dependence $T_c(p)$. Consequently, T_c relaxation effects have been observed with relaxation times characteristic for diffusion of oxygen ions along specific diffusion paths.

In the superoxygenated La-214 HTS compound the interstitial oxygen facilitates the electronic phase separation into hole-poor and hole-rich states at different doping levels. Pressure applied at ambient temperature increases the tendency to phase separation. The pressure-induced re-arrangement of oxygen ions also results in an enhancement of the pressure coefficient of T_c up to 10 K/GPa. The high-pressure investigations reveal the fundamental difference of cation doping and oxygen doping in HTS compounds and emphasize on the important role of mobile oxygen in stabilizing superconductivity with high T_c . Since similar effects have been observed in quite different HTS cuprates it was suggested that the tendency to electronic phase separation and the oxygen ordering phenomena (also induced by pressure) are correlated and represent a universal feature of HTS.

Several examples are discussed where high-pressure investigations have led to a deeper understanding of the underlying physics of specific superconductors or have raised new questions about it. Among them are the pressure effects on superconductivity in MgB_2 and the isostructural intermetallic compounds CaAlSi and SrAlSi . In the former case the negative pressure coefficient of T_c provided strong support for the phonon-mediated BCS-like pairing mechanism in contrast to alternative theories. For the latter two compounds the opposite pressure coefficients of T_c in conjunction with large differences in the electron-phonon coupling strengths derived from heat capacity measurements led to speculations about the possible existence of a soft phonon in CaAlSi driving the system close to a structural instability. The suggestion is still awaiting experimental or theoretical verification.

In the sodium-doped cobalt oxyhydrate, $\text{Na}_x\text{CoO}_2 \cdot y\text{H}_2\text{O}$, the decrease of T_c with hydrostatic pressure was understood in terms of an increased coupling between the CoO_2

layers due to a larger compressibility of the c-axis as compared to the a-axis. The compression reduces the 2d character of the water-intercalated structure and the negative pressure coefficient of T_c lends indirect support to the assumption that the high anisotropy (or the low-dimensionality) of the structure is crucial for the understanding of the superconductivity in the compound.

Pressure effects on the ferromagnetic and superconducting transitions of the HTS superconducting ferromagnet $\text{RuSr}_2\text{GdCu}_2\text{O}_8$ are discussed and lead to the conclusion that both antagonistic states of matter compete with one another in the compound. The imposed pressure favors the magnetic state on the expense of the superconducting state that leads to a smaller than expected pressure coefficient of the superconducting T_c .

Acknowledgements

This work is supported in part by NSF Grant No. DMR-9804325, the T.L.L. Temple Foundation, the John J. and Rebecca Moores Endowment, and the State of Texas through the Texas Center for Superconductivity at the University of Houston and at Lawrence Berkeley Laboratory by the Director, Office of Energy Research, Office of Basic Energy Sciences, Division of Materials Sciences of the U.S. Department of Energy under Contract No. DE-AC03-76SF00098.

REFERENCES

- [1] B. T. Matthias, *Phys. Rev. B* 92, 874 (1953).
- [2] B. T. Matthias, *Phys. Rev. B* 97, 74 (1955).
- [3] L. D. Jennings and C. A. Swenson, *Phys. Rev.* 112, 31 (1958).
- [4] J. Hattton, *Phys. Rev.* 103, 1167 (1956).
- [5] C. W. Chu, T. F. Smith, and W. E. Gardner, *Phys. Rev. Letters* 20, 198 (1968).
- [6] P. B. Allen and M. L. Cohen, *Phys. Rev.* 187, 525 (1969).
- [7] K. M. Lang, A. Mizel, J. Mortara, E. Hudson, J. Hone, M. L. Cohen, A. Zettl, and J. C. Davis, *J. Low Temp. Phys.* 114, 445 (1999).
- [8] N. E. Christensen and D. L. Novikov, *Phys. Rev. Letters* 86, 1861 (2001).
- [9] T. H. Lin and K. J. Dunn, *Phys. Rev. B* 33, 807 (1986).
- [10] K. Shimizu, H. Ishikawa, D. Takao, T. Yagi, and K. Amaya, *Nature (London)* 419, 597 (2002).
- [11] V. Struzhkin, M. I. Erements, W. Gan, H.-K. Mao, and R. J. Hemley, *Science* 298, 1213 (2002).
- [12] S. Deemyad and J. S. Schilling, *Phys. Rev. Letters* 91, 167001 (2003).
- [13] N. W. Ashcroft, *Phys. Rev. Letters* 26, 1748 (1968).
- [14] J. G. Bednorz and K. A. Müller, *Z. Physik B* 64, 189 (1986).
- [15] J. R. Gavaler, *Appl. Phys. Letters* 23, 480 (1973).
- [16] C. W. Chu, P. H. Hor, R. L. Meng, L. Gao, Z. J. Huang, and J. Q. Wang, *Phys. Rev. Letters* 58, 405 (1987).
- [17] M. K. Wu, J. R. Ashburn, C. J. Torng, P. H. Hor, R. L. Meng, L. Gao, Z. J. Huang, Y. Q. Wang, and C. W. Chu, *Phys. Rev. Letters* 58, 908 (1987).
- [18] T. F. Smith and C. W. Chu, *Phys. Rev.* 159, 353 (1967).
- [19] J. Bardeen, L. N. Cooper, and J. R. Schrieffer, *Phys. Rev.* 108, 1175 (1957).
- [20] G. M. Eliashberg, *Soviet Phys.-JEPT* 11, 696 (1960); 12, 1000 (1961).
- [21] J. P. Carbotte, *Rev. Mod. Phys.* 62, 1027 (1990).
- [22] P. Morel and P. W. Anderson, *Phys. Rev.* 125, 1263 (1962).
- [23] W. L. McMillan, *Phys. Rev.* 167, 331 (1967).
- [24] R. C. Dynes, *Solid State Commun.* 10, 615 (1972).
- [25] J. L. Olsen, K. Andres, and T. H. Geballe, *Phys. Letters* 26A, 239 (1968).
- [26] M. Garfinkel and D. E. Mapother, *Phys. Rev.* 122, 459 (1961).
- [27] R. E. Hodder, *Phys. Rev.* 180, 530 (1969).
- [28] D. J. Scalapino, J. R. Schrieffer, and J. W. Wilkins, *Phys. Rev.* 148, 263 (1966).
- [29] B. G. Lazarev, L. S. Lazareve, and V. I. Makarov, *Zh. Eksperim. i Teor. Fiz.* 44, 481 (1963); B. G. Lazarev, L. S. Lazareva, V. I. Makarov, and T. I. Ignat'eva, *Zh. Eksperim. i Teor. Fiz.* 46, 829 (1964); *ibid.* 48, 1065 (1965); N. B. Brandt, N. I. Ginzburg, T. A. Ignat'eva, B. G. Lazarev, L. S. Lazareva, and V. I. Makarov, *Zh. Eksperim. i Teor. Fiz.* 49, 85 (1965).
- [30] V. I. Makarov and V. G. Bar'yakhtar, *Zh. Eksperim. i Teor. Fiz.* 48, 1717 (1965).
- [31] I. M. Lifshitz, *Zh. Eksperim. i Teor. Fiz.* 38, 1569 (1960).
- [32] C. W. Chu, T. F. Smith, and W. E. Gardner, *Phys. Rev. B* 1, 214 (1970).
- [33] L. F. Mattheiss, *Phys. Rev.* 151, 450 (1966).
- [34] C. W. Chu and L. R. Testardi, *Phys. Rev. Letters* 32, 766 (1974).
- [35] C. W. Chu, *Phys. Rev. Letters* 33, 1283 (1974).

- [36] J. Labbé and J. Friedel, *J. Phys. (Paris)* 27, 153 (1966); *ibid.* 27, 303 (1966).
- [37] C. S. Ting and A. K. Ganguly, *Phys. Rev. B* 9, 2781 (1974)
- [38] L. R. Testardi, *Phys. Rev. B* 5, 4342 (1972).
- [39] S. Huang and C. W. Chu, *Phys. Rev. B* 10, 4030 (1974).
- [40] C. W. Chu and V. Diatschenko, *Phys. Rev. Letters* 41, 572 (1978).
- [41] R. E. Larsen and A. L. Ruoff, *J. Appl. Phys.* 44, 1021 (1973).
- [42] J. Labbé, *Phys. Rev.* 172, 451 (1968).
- [43] C. W. Chu, E. Bucher, A. S. Cooper, and J. P. Maita, *Phys. Rev. B* 4, 320 (1971).
- [44] L. R. Testardi, *Phys. Lett. A* 35, 117 (1971).
- [45] C. W. Chu, S. Huang, T. F. Smith, and E. Corenzwit, *Phys. Rev. B* 11, 1866 (1975).
- [46] C. W. Chu, V. Diatschenko, C. Y. Huang, and F. J. DiSalvo, *Phys. Rev. B* 15, 1340 (1977).
- [47] C. W. Chu, P. H. Hor, R. L. Meng, L. Gao, and Z. J. Huang, *Science* 235, 567 (1987).
- [48] P. H. Hor, L. Gao, R. L. Meng, Z. J. Huang, Y. Q. Wang, K. Forster, J. Vassiliou, and C. W. Chu, *Phys. Rev. Letters* 58, 911 (1987).
- [49] P. H. Hor, R. L. Meng, Y. Q. Wang, L. Gao, Z. J. Huang, J. Bechthold, K. Forster, and C. W. Chu, *Phys. Rev. Letters* 58, 1891 (1987).
- [50] C. W. Chu, P. H. Hor, J. G. Lin, Q. Xiong, Z. J. Huang, R. L. Meng, Y. Y. Xue, and Y. C. Jean, in: *Frontiers of High-Pressure Research*, Edts. H. D. Hochheimer and R. D. Ethers, Plenum Press, New York 1991, p. 383.
- [51] Z. Z. Sheng, A. M. Hermann, A. El Ali, C. Almasan, J. Estrada, T. Datta, and R. J. Matson, *Phys. Rev. Lett.* 60, 937 (1988).
- [52] R. M. Hazen, L. W. Finger, R. J. Angel, C. T. Prewitt, N. L. Ross, C. G. Hadidiacos, P. J. Heaney, D. R. Veblen, Z. Z. Sheng, A. El Ali, and A. M. Hermann, *Phys. Rev. Lett.* 60, 1657 (1988).
- [53] C. W. Chu, J. Bechthold, L. Gao, P. H. Hor, Z. J. Huang, R. L. Meng, Y. Y. Sun, Y. Q. Wang, and Y. Y. Xue, *Phys. Rev. Letters* 60, 941 (1988).
- [54] J. G. Lin, K. Matsuishi, Y. Q. Wang, Y. Y. Xue, P. H. Hor, and C. W. Chu, *Physica C* 175, 627 (1991).
- [55] N. Môri, H. Takahashi, Y. Shimakawa, T. Manako, and Y. Kubo, *J. Phys. Soc. Jpn.* 11, 3839 (1990).
- [56] R. Sieburger and J. S. Schilling, *Physica C* 173, 403 (1991).
- [57] J. T. Markert, J. Beille, J. J. Neumeier, E. A. Early, C. L. Seaman, T. Moran, and M. B. Maple, *Phys. Rev. Lett.* 64, 80 (1990).
- [58] Z. Z. Wang, J. Clayhold, N. P. Ong, J. M. Tarascon, L. H. Greene, W. R. McKinnon, and G. W. Hull, *Phys. Rev. B* 36, 7222 (1987).
- [59] Y. J. Uemura et al., *Phys. Rev. Letters* 62, 2317 (1989).
- [60] R. Kubiak, K. Westerholt, G. Pelka, and H. Bach, *Physica C* 166, 523 (1990).
- [61] D. D. Berkley, E. F. Skelton, N. E. Moulton, M. S. Ososky, W. T. Lechter, and V. M. Browning, *Phys. Rev. B* 47, 5524 (1993).
- [62] S. N. Putilin, E. V. Antipov, O. Chmaissem, and M. Marezio, *Nature (London)* 362, 226 (1993).
- [63] A. Schilling, M. Cantoni, J. D. Guo, and H. R. Ott, *Nature (London)* 363, 56 (1993).
A. Schilling, M. Cantoni, J. D. Guo, and H. R. Ott, *Physica C* 178, 183 (1993).
- [64] L. Gao, Z. J. Huang, R. L. Meng, J. G. Lin, F. Chen, L. Beauvais, Y. Y. Sun, Y. Y. Xue, and C. W. Chu, *Physica C* 213, 261 (1993).

- [65] C. W. Chu, L. Gao, F. Chen, Z. J. Huang, R. L. Meng, and Y. Y. Xue, *Nature (London)* 365, 323 (1993).
- [66] M. Nuñez-Regueiro, J.-L. Tholence, E. V. Antipov, J.-J. Capponi, and M. Marezio, *Science* 262, 97 (1993).
- [67] H. Takahashi, A. Tokiwa-Yamamoto, N. Môri, S. Adachi, H. Yamauchi, and S. Tanaka, *Physica C* 218, 1 (1993).
- [68] L. Gao, Y. Y. Xue, F. Chen, Q. Xiong, R. L. Meng, D. Ramirez, C. W. Chu, J. H. Eggert, and H. K. Mao, *Phys. Rev. B* 50, 4260 (1994).
- [69] J. S. Schilling and S. Klotz, in: *Physical Properties of High Temperature Superconductors III*, edited by D. M. Ginsberg (World Scientific, Singapore, 1992), p. 59.
- [70] J. H. Eggert, J. Z. Hu, H. K. Mao, L. Beauvais, R. L. Meng, and C. W. Chu, *Phys. Rev. B* 49, 15299 (1994).
- [71] M. R. Presland, J. L. Tallon, R. G. Buckley, R. S. Liu, and N. E. Flower, *Physica C* 176, 95 (1991).
J. L. Tallon, C. Bernhard, H. Shaked, R. L. Hitterman, and J. D. Jorgensen, *Phys. Rev. B* 51, 12911 (1995).
- [72] C. Murayama, Y. Iye, T. Enomoto, N. Mori, Y. Yamada, T. Matsumoto, Y. Kubo, Y. Shimakawa, and T. Manako, *Physica C* 183, 277 (1991).
- [73] T. Miyatake, T. Wada, M. Kosuge, Y. Yaegashi, A. Ichinose, H. Yamauchi, N. Koshizuka, N. Môri, and S. Tanaka, *Phys. Rev. B* 44, 11971 (1991).
J. L. Tallon, J. Lusk, and M. R. Presland, *Physica C* 174, 345 (1991).
Y. Cao, T. L. Hudson, Y. S. Wang, S. H. Xu, Y. Y. Xue, and C. W. Chu, *Phys. Rev. B* 58, 11201 (1998).
- [74] J. J. Neumeier and H. A. Zimmermann, *Phys. Rev. B* 47, 8385 (1993).
- [75] J. G. Lin, C. Y. Huang, Y. Y. Xue, C. W. Chu, X. W. Cao, and J. C. Ho, *Phys. Rev. B* 51, 12900 (1995).
- [76] Q. Xiong, PhD.-Thesis, University of Houston, 1993.
- [77] Y. Cao, Q. Xiong, Y. Y. Xue, and C. W. Chu, *Phys. Rev. B* 52, 6854 (1995).
- [78] Q. Xiong, J. W. Chu, Y. Y. Sun, H. H. Feng, S. Bud'ko, P. H. Hor, and C. W. Chu, *Phys. Rev. B* 46, 581 (1992).
- [79] Q. Xiong, Y. Y. Xue, J. W. Chu, Y. Y. Sun, Y. Q. Wang, P. H. Hor, and C. W. Chu, *Phys. Rev. B* 47, 11337 (1993).
- [80] F. Chen, Z. J. Huang, R. L. Meng, Y. Y. Sun, and C. W. Chu, *Phys. Rev. B* 48, 16047 (1993).
- [81] Q. Xiong, Y. Y. Xue, Y. Cao, F. Chen, Y. Y. Sun, J. Gibson, C. W. Chu, L. M. Liu, and A. Jacobson, *Phys. Rev. B* 50, 10346 (1994).
- [82] P. H. Hor, H. H. Feng, Z. G. Li, J. F. DiCarlo, S. Bhavaraju, and A. J. Jacobson, *J. Phys. Chem. Solids* 57, 1061 (1996).
- [83] B. W. Veal, A. P. Paulikas, H. You, H. Shi, Y. Fang, and J. W. Downey, *Phys. Rev. B* 42, 6305 (1990).
- [84] B. W. Veal and A. P. Paulikas, *Physica C* 184, 321 (1991).
- [85] M. Kikuchi, S. Nakajima, Y. Syono, K. Nagase, R. Suzuki, T. Kajitani, N. Kobayashi, and Y. Muto, *Physica C* 166, 497 (1990).
C. Allgeier and J. S. Schilling, *Physica C* 168, 499 (1990).

- [86] N. Môri, H. Takahashi, Y. Shimakawa, T. Manako, and Y. Kubo, *J. Phys. Soc. Jpn.* 59, 3839 (1990).
- [87] J. E. Schirber, D. L. Overmeyer, E. L. Venturini, D. S. Ginley, and B. Morosin, *Physica C* 193, 126 (1992).
- [88] A.-K. Klehe, C. Looney, J. S. Schilling, H. Takahashi, N. Môri, Y. Shimakawa, Y. Kubo, T. Manako, S. Doyle, and A. M. Hermann, *Physica C* 257, 105 (1996).
C. Looney, J. S. Schilling, S. Doyle, and A. M. Hermann, *Physica C* 289, 203 (1997).
- [89] S. Sadewasser, S. J. Schilling, and A. M. Hermann, *Phys. Rev. B* 62, 9155 (2000).
- [90] C. Looney, J. S. Schilling, and Y. Shimakawa, *Physica C* 297, 239 (1998).
- [91] W. H. Fietz, R. Quenzel, H. A. Ludwig, K. Grube, S. I. Schlachter, F. W. Hornung, T. Wolf, A. Erb, M. Kläser, and G. Müller-Vogt, *Physica C* 270, 258 (1996).
- [92] J. Metzger, T. Weber, W. H. Fietz, K. Grube, H. A. Ludwig, T. Wolf, and H. Wühl, *Physica C* 214, 371 (1993).
- [93] S. Sadewasser, Y. Wang, J. S. Schilling, H. Zheng, A. P. Paulikas, and B. W. Veal, *Phys. Rev. B* 56, 14168 (1997).
- [94] S. J. Rothman, J. L. Routbort, and J. E. Baker, *Phys. Rev. B* 40, 8852 (1989).
- [95] S. Sadewasser, J. S. Schilling, A. P. Paulikas, and B. W. Veal, *Phys. Rev. B* 61, 741 (2000).
- [96] P. Nagel, V. Pasler, Ch. Meingast, A. I. Rykov, and S. Tajima, *Phys. Rev. Letters* 85, 2376 (2000).
- [97] H. Leibrock, K. Grube, W. H. Fietz, S. I. Schlachter, K.-P. Weiss, A. I. Rykov, S. Tajima, B. Obst, P. Schweiss, and H. Wühl, *Physica C* 341-348, 439 (2000).
- [98] S. Sadewasser, J. S. Schilling, J. L. Wagner, O. Chmaissem, J. D. Jorgensen, D. G. Hinks, and B. Dabrowski, *Phys. Rev.* 60, 9827 (1999).
- [99] R. Brout, *Phys. Rev.* 115, 824 (1959).
- [100] P. H. Hor, H. H. Feng, Z. G. Li, J. F. DiCarlo, S. Bhavaraju, and A. J. Jacobson, *J. Phys. Chem. Solids* 57, 1061 (1996).
- [101] D. Vaknin, J. L. Zaretsky, D. C. Johnston, J. E. Schirber, and Z. Fisk, *Phys. Rev. B* 49, 9057 (1994).
- [102] B. W. Statt, P. C. Hammel, Z. Fisk, S.-W. Cheong, F. C. Chou, D. C. Johnston, and J. E. Schirber, *Phys. Rev. B* 52, 15575 (1995).
- [103] J. D. Jorgensen, B. Dabrowski, S. Pei, D. G. Hinks, L. Soderholm, B. Morosin, J. E. Schirber, E. L. Venturini, and D. S. Ginley, *Phys. Rev. B* 38, 11337 (1988).
- [104] E. J. Ansaldo, J. H. Brewer, T. M. Riseman, J. E. Schirber, E. L. Venturini, B. Morosin, D. S. Ginley, and B. Sternlieb, *Phys. Rev. B* 40, 2555 (1989).
- [105] M. F. Hundley, J. D. Thompson, S.-W. Cheong, Z. Fisk, and J. E. Schirber, *Phys. Rev. B* 41, 4062 (1990).
- [106] P. C. Hammel, A. P. Teyes, Z. Fisk, M. Takigawa, J. D. Thompson, R. H. Heffner, S.-W. Cheong, and J. E. Schirber, *Phys. Rev. B* 42, 6781 (1990).
- [107] P. Zolliker, D. E. Cox, J. B. Parise, E. M. McCarron III, and W. E. Farneth, *Phys. Rev. B* 42, 6332 (1990).
- [108] Z. G. Li, H. H. Feng, Z. Y. Yang, A. Hamed, S. T. Ting, P.-H. Hor, S. Bhavaraju, J. F. DiCarlo, and A. J. Jacobson, *Phys. Rev. Letters* 77, 5413 (1996).
- [109] B. Lorenz, Z. G. Li, T. Honma, and P.-H. Hor, *Phys. Rev. B* 65, 144522 (2002).
- [110] V. J. Emery, S. A. Kivelson, and H. Q. Lin, *Phys. Rev. Letters* 64, 475 (1990).
- [111] S. A. Kivelson, V. J. Emery, and H. Q. Lin, *Phys. Rev. B* 42, 6523 (1990).

- [112] S. Yomo, M. Kawakami, H. H. Feng, Z. G. Li, P.-H. Hor, and N. Mori, *Advances in Superconductivity IX*, (Springer Verlag, Tokyo, 1997), p. 81.
- [113] S. Yomo, K. Soga, Z. G. Li, P.-H. Hor, and N. Mori, *Physica C* 341-348, 1851 (2000).
- [114] J. Nagamatsu, N. Nakagawa, T. Muranaka, Y. Zenitani, and J. Akimitsu, *Nature (London)* 410, 63 (2001).
- [115] J. Kortus, I. I. Mazin, K. D. Belashchenko, V. P. Antropov, and L. L. Boyer, *Phys. Rev. Letters* 86, 4656 (2001).
- [116] J. E. Hirsch, *Physics Letters A* 282, 392 (2001).
J. E. Hirsch and F. Marsiglio, *Phys. Rev. B* 64, 144523 (2001).
- [117] B. Lorenz, R. L. Meng, and C. W. Chu, *Phys. Rev. B* 64, 012507 (2001).
- [118] I. Loa and K. Syassen, *Solid State Commun.* 118, 575 (2001).
- [119] J. S. Schilling, in: *Frontiers of High Pressure Research II*, Edts. H. D. Hochheimer, B. Kuchta, P. K. Dorhout, and J. L. Yarger, Kluwer Academic Publ., Dordrecht/Boston/London 2001, p. 345.
- [120] B. Lorenz, Y. Y. Xue, R. L. Meng, and C. W. Chu, in: *New Trends in Superconductivity*, Edts. J. F. Annett and S. Kruchinin, Kluwer Academic Publ., Dordrecht/Boston/London 2001, p. 213.
- [121] T. Tomita, J. J. Hamlin, J. S. Schilling, D. G. Hinks, and J. D. Jorgensen, *Phys. Rev. B* 64, 092505 (2001).
- [122] B. Lorenz, R. L. Meng, and C. W. Chu, cond-mat/0104303 (2001), unpublished.
- [123] V. G. Tissen, M. V. Nefedova, N. N. Kolesnikov, and M. P. Kulakov, *Physica C* 363, 194 (2001).
- [124] Y. Y. Xue, R. L. Meng, B. Lorenz, J. K. Meen, Y. Y. Sun, and C. W. Chu, *Physica C* 377, 7 (2002).
- [125] A. Y. Liu, I. I. Mazin, J. Kortus, *Phys. Rev. Lett.* 87, 087005 (2001).
- [126] F. Bouquet, R. A. Fisher, N. E. Phillips, D. G. Hinks, and J. D. Jorgensen, *Phys. Rev. Lett.* 87, 047001.
- [127] X. K. Chen, M. J. Konstantinovi, J. C. Irwin, D. D. Lawrie, and J. P. Franck, *Phys. Rev. Lett.* 87, 157002 (2001).
- [128] F. Giubileo, D. Roditchev, W. Sacks, R. Lamy, D. X. Thanh, J. Klein, S. Miraglia, D. Fruchart, J. Marcus, and Ph. Monod, *Phys. Rev. Lett.* 87, 177008 (2001).
- [129] R. L. Meng, B. Lorenz, Y. S. Wang, J. Cmaidalka, Y. Y. Sun, Y. Y. Xue, J. K. Meen, and C. W. Chu, *Physica C* 382, 113 (2002).
B. Lorenz, J. Lenzi, J. Cmaidalka, R. L. Meng, Y. Y. Sun, Y. Y. Xue, and C. W. Chu, *Physica C* 383, 191 (2002).
R. L. Meng, B. Lorenz, J. Cmaidalka, Y. S. Wang, Y. Y. Sun, J. Lenzi, J. K. Meen, Y. Y. Xue, and C. W. Chu, *IEEE Trans. Appl. Supercond.* 13, 3042 (2003).
- [130] B. Lorenz, J. Cmaidalka, R. L. Meng, and C. W. Chu, *Phys. Rev. B* 68, 014512 (2003).
- [131] I. I. Mazin and D. A. Papaconstantopoulos, *Phys. Rev. B* 69, 180512(R) (2004).
- [132] K. Takada, H. Sakurai, E. Takayama-Muromachi, F. Izumi, R. A. Dilanian, and T. Sasaki, *Nature (London)* 422, 53 (2003).
- [133] T. Fujimoto, G. Zheng, Y. Kitaoka, R. L. Meng, J. Cmaidalka, and C. W. Chu, *Phys. Rev. Letters* 92, 047004 (2004).
- [134] B. Lorenz, J. Cmaidalka, R. L. Meng, and C. W. Chu, *Physica C* 402, 106 (2004).
- [135] B. Lorenz, J. Cmaidalka, R. L. Meng, and C. W. Chu, *Phys. Rev. B* 68, 132504 (2003).
- [136] S. Park, Y. Lee, A. Moodenbaugh, and Th. Vogt, *Phys. Rev. B* 68, 180505(R) (2003).

- [137] C. T. Lin, D. P. Chen, P. Lemmens, X. N. Zhang, A. Maljuk, and P. X. Zhang, preprint cond-mat/0407086 (2004), unpublished.
- [138] J. T. Markert, J. Beille, J. J. Neumeier, E. A. Early, C. L. Seaman, T. Moran, and M. B. Maple, *Phys. Rev. Lett.* **64**, 80 (1990).
- [139] B. Lorenz, Y. Y. Xue, and C. W. Chu, *Studies of High Temperature Superconductors*, Vol.46 (Ed. A. Narlikar), Nova Sci. Publishers, NY (2003), pp. 1
- [140] I. Felner, E. Galstyan, B. Lorenz, D. Cao, Y. S. Wang, Y. Y. Xue, and C. W. Chu, *Phys. Rev. B* **67**, 134506 (2003).
- [141] B. Lorenz, R. L. Meng, J. Cmaidalka, Y. S. Wang, J. Lenzi, Y. Y. Xue, and C. W. Chu, *Physica C* **363**, 251 (2001).
- [142] B. Lorenz, Y. Y. Xue, R. L. Meng, and C. W. Chu, *Phys. Rev. B* **65**, 174503 (2002).
- [143] B. Lorenz, R. L. Meng, Y. Y. Xue, and C. W. Chu, *Physica C* **383**, 337 (2003).

DISORDERED SUPERCONDUCTORS

Anurag Gupta¹, V.P.S. Awana¹, S.B. Samanta¹, Hari Kishan¹, and A.V. Narlikar²

¹National Physical Laboratory, Dr K.S. Krishnan Road, New Delhi-110012, INDIA

²Inter-University Consortium for DAE Facilities, University Campus, Khandwa Road, Indore-452017, MP, INDIA

1. INTRODUCTION

Disorder in solids is primarily of two types: *crystalline* and *amorphous*. The former may result from deviations in site occupancy of different species of its constituent ions with the crystal lattice otherwise essentially remaining intact. In the amorphous disorder there is a breakdown of the lattice framework that represents its long range order. Clearly, the crystalline disorder holds for alloys and compounds comprising more than one type of ion occupying well defined lattice sites, characteristic of the ordered state. Here the disorder would result with their mutual intermixing, essentially in a random fashion, giving rise to the so called anti-site defects. Here one type of ion, say A, occupies the lattice site that was originally (in the ordered state) the lattice site of the ion B. The situation may get further complicated by incorporation of impurity elements or vacancies at the lattice sites or by ions occupying the interstitial sites. The presence of impurities and vacancies produces compositional disorder with altered stoichiometry. Turning to the second form of disorder related to the lattice framework, the amorphous state represents the extreme situation where the long range order is drastically affected. Basically the structure of amorphous state varies from ultra small crystallites (about 2.0 nm diameter) with short range order preserved within nano-grains, the so called micro- or nanocrystalline amorphous, to a phase where the lattice structure is totally disordered, known as liquid-like amorphous. The amorphous disorder is commonly realized by rapid quenching of the material from its molten state (by using splat quenching or melt spinning techniques) or by quench condensation as thin films at low temperatures. Likewise, the techniques such as sputtering, electron beam evaporation, CVD,

various forms of vapour quenching methods as well as ion beam irradiation have been used to create amorphous disorder. Both pure elements and alloys can be turned from crystalline to amorphous. It is worth mentioning that in metallic systems, the crystalline disorder formed with anti-site defects is invariably more stable than the amorphous disorder. The latter occurs as a metastable state having a local minimum in the Gibbs free energy curve which is separated from the lowest minimum corresponding to the thermodynamic equilibrium (crystalline state) by energy barriers. The impurity atoms and defects commonly serve as barriers that stabilize the metastable state, as without them the system, with thermal excitation, gradually reverts to the crystalline order of the lowest energy.

How does superconductivity respond when a material gets disordered? As with many physical and chemical properties, such as mechanical, electrical, magnetic, thermal, chemical reactivity, corrosion etc., superconducting properties too reveal marked changes with disorder. Historically, the problem was first conceived by Shalnikov [1] who, in 1938, showed that the amorphous thin films of Sn and Pb produced by quench condensation (vapour condensation on liquid helium cooled substrate) had their critical temperature T_c raised from their respective bulk (crystalline) values of 3.7K and 7.3K to 4.7K and >7.5 K. The work was systematically pursued further by Buckel and Hilsch [2,3] who studied superconductivity in thin amorphous films of Pb, Bi and of various simple metals produced by quench condensation. Their most interesting result was for Bi-films which in the crystalline state were semi-metallic and nonsuperconducting, but when formed as amorphous by quench condensation showed metallic behaviour and superconductivity close to 6K. But, upon warming up to about 20K the films got reverted to their original crystalline form and showed no superconductivity upon re-cooling. Since this early work a considerable effort has gone into the study of superconductivity in relation to disorder in both low and high T_c superconductors (LTS and HTSC) and a wealth of data is now available in literature. It may be interesting to note that whereas in low T_c simple metals and alloys it is the amorphous disorder which holds its mainstay in significantly influencing T_c , for superconducting compounds such as A-15s, Laves and Chevrel phases, and high T_c cuprates, for instance, the cationic and anionic disorders resulting from deviations in their site occupancies play the most dramatic role in affecting superconductivity. In this respect, HTSC cuprates are perhaps the unique systems known to date that depict the highest level of structure sensitivity in respect of their superconductivity. Disorder resulting from small deviations in site occupancy and relatively minute changes in cationic and anionic dopings, including the oxygen content, have a devastating influence on superconductivity of these interesting materials. In this chapter, Disordered Superconductors, we first take a hurried look to assess the role of disorder in simple metals, transition metals, alloys and A-15s and then move to high T_c cuprates, where we essentially try to consolidate some of our recent cationic and anionic substitutional studies that are intimately linked with disorder effects.

2. AMORPHOUS DISORDER AND SUPERCONDUCTIVITY IN SIMPLE METALS

Host of available superconductivity data pertaining to disorder effects in elemental simple metals and their alloys focus on their amorphous thin films synthesized by quench condensation or by ion beam techniques. In majority of instances the amorphous disorder is found to enhance the superconducting critical temperature T_c of simple metals. This seems consistent with McMillan's extension of the BCS theory for the situation of strong electron-phonon coupling, which gives [4]

$$T_c = \frac{\theta_D}{1.45} \exp \left\{ \frac{-1.04 (1 + \lambda_e)}{\lambda_e - \mu^* (1 + 0.62 \lambda_e)} \right\} \quad (1)$$

where θ_D is Debye temperature and μ^* being the repulsive coulomb pseudopotential. The dimension-less parameter λ_e , which measures the electron-phonon interaction strength is given by

$$\lambda_e = 2 \int_0^{\infty} \frac{\alpha^2 F(\omega)}{\omega} d\omega, \quad (2)$$

where $F(\omega)$ is the phonon density of states at the Fermi surface and α relates to the electron-phonon pair potential. The parameter λ_e can be expressed in terms of the electron density of states $N(0)$, the ion mass M , electron matrix element $\langle I^2 \rangle$ and the mean square phonon frequency $\langle \omega^2 \rangle$ through the relation,

$$\lambda_e = \frac{N(0) \langle I^2 \rangle}{M \langle \omega^2 \rangle} \quad (3)$$

For strongly coupled superconductors $\lambda_e > 1$. Amorphous disorder, in general, leads to weakening of the bonds between atoms and should promote softening of the average phonon spectrum. This would correspond to a reduction in $\langle \omega^2 \rangle$ in equation (3) above, and thereby enhance the electron-phonon interaction strength and T_c .

As mentioned in the beginning, for stabilizing a high degree of disorder characteristic of the amorphous state, the presence of impurities is often found useful. In fact some metals can be realized amorphous only when impurities are present. Al, for example, which has T_c of 1.2 K in the crystalline state, shows higher T_c of 3.3 K when it is quench condensed [3] and still higher T_c of 4.5 K when condensed in the presence of O and H, and 6 K and 6.6 K when coevaporated with Ge and Si respectively [5]. Interestingly, T_c of Al gets enhanced further to 7.3 K and 8.35 K respectively when Ge and Si are incorporated by implantation instead of by evaporation. Higher T_c values observed are ascribed to a greater disorder produced in implantation. Implantation of H, D, He, C, O and Al in Al have been found to enhance T_c [6,7]. With H implanted films which show T_c of 6.75 K formation of AlH_2 has been suggested [6] where the optical phonon branch is thought to enhance T_c through electron-optical phonon interaction. A similar explanation had previously been suggested by Stritzker and Buckel [8] to explain the anomalously high T_c of about 11 K observed for Pd-H system.

A comparative study of disorder and superconductivity in quench condensed and ion implanted In films was carried out by Bauriedl et al. [9]. They implanted indium ions into annealed ($T_c=3.6$ K) and quench condensed ($T_c=4.25$ K) In films. Their results showed that ion implantation of quench condensed In films produced the highest T_c of 4.54K. However, the most prominent case of T_c enhancement due to amorphous disorder is that of Be, where T_c enhancement occurs from 0.03K to 9K. Incorporation of impurities is found to degrade T_c . Some data for simple metals and their alloys in the amorphous state are listed in Table 1 [10] below.

It may be interesting to note from the above table that the electron-phonon interaction parameter λ_e for amorphous simple metals and alloys generally exceeds 1.0 which makes them strongly coupled. Their gap coefficient $2\Delta/k_B T_c$ too, where 2Δ represents superconducting energy gap, is larger than the BCS weak coupling value of 3.50, which is

Table 1. Superconducting parameters of amorphous simple metals and alloys

| Metal/Alloy | Average Valence | T _c (K) | 2Δ/k _B T _c | λ _e |
|---------------------------------------|-----------------|--------------------|----------------------------------|----------------|
| Au _{0.84} Si _{0.16} | 1.48 | 1.4 | | |
| Mg _{0.7} Zn _{0.3} | 2.0 | 1.4 | | |
| Be | 2.0 | 9.0 | 3.5 | 0.5 |
| Be _{0.90} Al _{0.10} | 2.1 | 7.2 | | |
| Be _{0.70} Al _{0.3} | 2.3 | 6.1 | 3.57 | |
| Cd _{0.90} Ge _{0.10} | 2.3 | 1.6 | 3.00 | |
| Ga | 3.0 | 8.4 | 4.40 | 2.0 |
| Tl _{0.90} Te _{0.10} | 3.3 | 4.2 | 4.60 | 1.70 |
| In _{0.80} Sb _{0.20} | 3.4 | 5.6 | 4.40 | 1.69 |
| Sn _{0.90} Cu _{0.10} | 3.7 | 6.76 | 4.76 | 1.84 |
| Pb | 4.0 | 7.16 | 4.63 | |
| Pb _{0.90} Cu _{0.10} | 3.7 | 6.5 | 4.75 | 2.0 |
| Pb _{0.75} Bi _{0.25} | 4.25 | 6.91 | 4.99 | 2.76 |
| Pb _{0.50} Bi _{0.50} | 4.50 | 6.99 | 5.00 | |
| Bi | 5.0 | 6.1 | 4.6 | 2.35 |

again consistent with their strong coupling nature. As may be seen from the above table, the amorphous metals of low average valence of 1 or 2 have lower T_c than those having a larger valence. The only exception is perhaps Be whose unexpected high T_c is ascribed to a relatively large Debye temperature θ_D of around 1300 K which raises the critical temperature through the pre-exponent part of eq. (1). While studying the valency dependence of T_c, Johnson found [11] that the weighted T_c, that is T_c/T_p=k_B T_c/ħω_p, systematically increases with valency Z. Here, T_p=ħω_p / k_B is the characteristic phonon temperature and ω_p being the ionic plasma frequency. Johnson has argued that such a relationship follows directly from the McMillan theory [4]. For nearly free electrons,

$$\lambda_e = \frac{E_F}{K_F e^2} \frac{\langle V_q^2 \rangle}{[\langle \omega^2 \rangle / \omega_p^2]} \quad (4)$$

where E_F is the Fermi energy, K_F the wave number of Fermi electrons and <V_q²> the mean square of fourier transform of the bear pseudopotential. For free electron systems, <V_q²> varies as Z², while <ω²>/ω_p² varies as Z and consequently λ_e and hence also the T_c increase with valency. For Bi, Ga, Pb, Sn, In, Tl, in amorphous state, various measurements like temperature dependence of resistivity, Hall voltage and thermoelectric power have confirmed the validity of free electron model [12-15].

It is interesting to mention that in the case of semimetals like Si, Ge, P, As, Sb, Bi, S, Se and Te the application of external pressure [10] has qualitatively similar effect as of amorphous disorder. At the ambient pressure, while their resistive behaviour remains semi-metallic and none of them exhibits superconductivity, under the imposed external pressure they become more metal-like and also turn superconducting. Quench condensed films, as mentioned earlier, show a similar behaviour [2,3]. The semi-metals, unlike metals, have relatively open crystal structures and their Bloch energy of electrons is lower which reduces the Fermi surface and hence the bare density of states. Moreover, the Bloch electrons screen the lattice potential quite effectively as their concentration lies primarily in the potential valleys. This is believed to reduce the electron phonon interaction parameter λ_e and thus there

is no superconductivity. Under pressure, when the structure becomes more close packed the density of states at E_F is increased and so also λ_e which make them metallic and also superconducting. Essentially similar argument has been applied in the case of amorphous disorder.

Clearly, λ_e is the controlling parameter for superconductivity. The quasiparticle tunneling technique has been effectively used to study the parameter λ_e for simple metals in the amorphous state. In general, the effect of disorder is to smear out peaks in $\alpha^2 F(\omega)$, but at the same time the results [16] on amorphous Pb films showed that there is a simultaneous increase in the composite parameter $\alpha^2 F(\omega)$ on low frequency side of the spectra, which from equ.(2) corresponds to increase in λ_e that accounts for the observed T_c increase. It is natural to ask whether the increase in λ_e due to amorphous disorder owes to the change in the electronic part α^2 or in the phononic part represented by $F(\omega)$. Measurements of both Debye-Waller factor using Mossbauer technique [17] and the relative specific heat of amorphous samples and their crystalline counterparts [18] reveal that the observed changes in the phonon density of states $F(\omega)$ due to amorphous disorder alone are not sufficient to explain the T_c enhancement. On the other hand Bergmann [10] found the T_c enhancement due to amorphous disorder stemmed primarily from the resulting change in the electronic component α^2 . Presently it seems reasonable to believe that in simple metals and alloys where amorphous disorder enhances T_c , both α^2 and $F(\omega)$ are simultaneously affected by disorder.

3. AMORPHOUS DISORDER AND SUPERCONDUCTIVITY IN TRANSITION METALS, ALLOYS, AND METALLIC GLASSES

The pioneering work on superconductivity in relation to amorphous disorder in transition metals and alloys was due to Collver and Hammond [19,20]. They primarily followed the quench condensation method and deposited amorphous thin films by evaporation on cryogenically cooled substrates. In the case of disordered transition metals and alloys the annealing temperatures for recrystallization were higher than for simple metals, where annealing to 100K was sufficient to restore the crystallographic order.

Fig. 1 depicts the results [19,20] of Collver and Hammond for amorphous metals and alloys of 4d series showing T_c as a function of average valence electrons per atom. In the background are shown for comparison two characteristic peaks in T_c for e/a values of 4.75 and 6.5 of Matthias' rules for crystalline transition metals and alloys. As may be seen, the two peak structure has almost disappeared and instead one finds a single broad maximum for e/a of 6.5. In the case of group V metals, such as V, Nb and Ta the amorphous disorder is found to lower T_c while for metals of group VI and VII, i.e., Mo, W and Re, T_c is raised by disorder. For transition metals, in general, Schroeder et al. [21] had however found that for pure materials the amorphous disorder was difficult to realize in quench condensed thin films and such samples synthesized under ultra high vacuum of 10^{-10} torr, and low substrate temperature of 4.2K were still crystalline. Consequently, most of the reported data [19,20] on amorphous thin films of transition metals prepared under poorer vacuum of 10^{-7} torr really represent the impurity stabilized amorphous state. Nevertheless, Collver and Hammond's systematics of Fig. 1 is found to hold for a host of amorphous systems produced by ion implantation [22,23], and also for a large variety of metallic glasses [24] such as $Zr_{75}Rh_{25}$ [25,26], $Zr_{70}Pd_{30}$ [27,28], $Zr_{70}Be_{30}$ [29], as well as for a series of Phosphate glasses [30] of the type $(TM_{1-x}Ru_x)_{80}P_{20}$ produced by melt spinning technique.

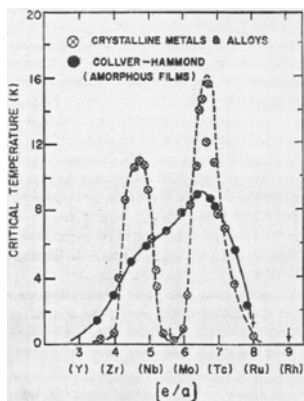


Fig. 1. T_c as a function of average valence electrons per atom for amorphous metals and alloys of 4d series taken from references [19,20].

Among pure transition elements Mo and Pd in the amorphous state are of particular interest. The former perhaps represents the most studied case where T_c is enhanced from its low value of 0.9K in the crystalline state to around 5 K to 9 K found for quench condensed amorphous films (Table 3). The techniques of ion implantation and heavy ion irradiation were extensively used by Meyer [23] to synthesize disordered Mo films. Thin films prepared at room temperature with different levels of impurities like O, N etc., were subjected to ion beam irradiation and implantation at 4.2K using different species of ions of varying electronegativity to produce amorphous films of varying T_c values. The results are presented in Table 2. As may be seen, incorporation of chemically active impurities with the electronegativity greater than that of Mo, which is close to 2.0, generally enhances the pristine T_c . A greater electro-negativity of the implanted ions would promote the electron transfer from Mo to the doped ion, making the outer d-band (including the probability of s- electron coming into d) of the former exactly half filled and thus give rise to a higher electronic density of states at the Fermi level E_F . This seems consistent with the results of ultra violet photoemission spectroscopic studies [21] which revealed that the effect of amorphous disorder was to shift the peak in $N(0)$ to E_F and thereby enhance T_c . Amorphous Nb and V films synthesized in the presence of N show a decrease in T_c from their crystalline value. Here the electron transfer from Nb or V to N would leave their d-band less than half filled and their T_c would thus get degraded.

As per above discussion, the high T_c of amorphous Mo is due to a peak in $N(0)$ at E_F , but interestingly the reverse seems to hold for achieving superconductivity in disordered Pd, which in the crystalline state, down to the lowest temperatures studied, does not turn superconducting. Interestingly, Stritzker [31] found Pd films deposited at 4.2 K show superconductivity at 3.2 K after they were irradiated with He-ions at low temperatures. The crystalline Pd is otherwise nonsuperconducting, which is believed to be due to the presence of strong Stoner enhanced spin fluctuations or paramagnons, resulting from high $N(0)$ at E_F . They serve as pair breakers to destroy superconductivity. It is therefore believed that with irradiation some Frenkel type defects are presumably formed in amorphous or highly disordered Pd which smear and broaden the density of states and thereby lower $N(0)$. This

Table 2. T_c of Mo alloy films prepared by irradiating/implanting ions of different electronegativity

| Ion | T_c optimum (K) | Atomic % | Electronegativity |
|-----|-------------------|----------|-------------------|
| B | 8.7 | 16 | 2.0 |
| C | 8.3 | 17 | 2.5 |
| N | 9.2 | 23 | 3.0 |
| Ne | 1.7 | 20 | – |
| Al | 1.7 | 35 | 1.5 |
| P | 9.2 | 27 | 2.1 |
| S | 9.2 | 25 | 2.5 |
| As | 7.6 | 30 | 2.0 |
| Sb | 1.7 | 35 | 1.9 |
| Bi | 1.7 | 35 | 1.9 |

way, when paramagnon effect is lowered the amorphous thin films of Pd show superconductivity. In this respect Pd holds some similarity to Pt whose powders when highly compressed exhibit superconductivity at 60 to 100 mK. Large surface area of Pt grains with its surface phonons leads to a decrease in the mean square phonon frequency $\langle\omega^2\rangle$ which, through equ.(3) favours superconductivity. Also, in the compressed Pt powders Stoner enhanced paramagnons of conduction electrons is markedly lowered due to broadening and decrease of $N(0)$ which, like in Pd, would support superconductivity

Some of the superconductivity and related data for various amorphous metals, alloys and melt spun glasses of transition metals are summarized [21,24] in Tables 3 and 4. Unlike in simple metals, the gap coefficient $2\Delta/k_B T_c$ for superconducting transition metals and alloys in the amorphous state is found close to the weak coupling value. As may be seen (Table 3), T_c of A15 superconductors, in most cases, is drastically lowered when produced as amorphous. Before the advent of high T_c cuprates these materials were known for their highest T_c values in the range of 20K and also possessed high critical fields and commendably high transport current densities. However the A-15 compounds, as described in the next section, are equally sensitive to both crystalline and amorphous disorders. Degradation of their properties with disorders poses a serious drawback in their use in various accelerator based applications.

Table 3. Superconductivity parameters for amorphous thin films of transition metals and compounds

| Thin films | T_c (K) | $2\Delta/k_B T_c$ |
|---------------------------------------|------------|-------------------|
| V | 2.3 to 4.6 | 3.5 to 3.9 |
| Nb | 8.0 | 3.0 |
| Mo | 5.0 to 9.0 | 3.5 to 3.7 |
| Nb ₃ Ge | 3.6 | 3.5 |
| Nb ₃ Si | 3.9 | 3.6 |
| Nb ₃ Sn | 3.0 to 4.0 | |
| Mo _{0.68} Si _{0.32} | 6.7 | 3.4 |
| Mo _{0.8} N _{0.2} | 8.3 | 3.6 |
| Re _{0.70} Mo _{0.30} | 8.6 | 3.7 |

Table 4. Superconductivity and related parameters for transition metal alloy glasses

| Metallic Glasses | T_c (K) | dH_{c2}/dT (T/K) | ρ_n ($\mu\Omega\text{cm}$) |
|--|-----------|--------------------|-----------------------------------|
| $\text{La}_{80}\text{Au}_{20}$ | 3.5 | 2.30 | 200 |
| $\text{La}_{80}\text{Ga}_{20}$ | 3.8 | 2.25 | 170 |
| $\text{Zr}_{75}\text{Rh}_{25}$ | 4.55 | 2.63 | 220 |
| $\text{Zr}_{70}\text{Pd}_{30}$ | 2.4 | 2.65 | |
| $\text{Zr}_{70}\text{Be}_{30}$ | 2.80 | 2.38 | 290 |
| $(\text{Mo}_{0.80}\text{Ru}_{0.20})_{80}\text{P}_{20}$ | 7.31 | 2.45 | 300 |
| $(\text{Mo}_{0.60}\text{Ru}_{0.40})_{80}\text{P}_{20}$ | 6.18 | 2.55 | 300 |
| $(\text{Mo}_{0.40}\text{Ru}_{0.60})_{80}\text{P}_{20}$ | 4.68 | 2.68 | 330 |
| $(\text{Mo}_{0.20}\text{Ru}_{0.80})_{80}\text{P}_{20}$ | 3.43 | 2.76 | 320 |
| $(\text{Mo}_{0.60}\text{Ru}_{0.40})_{90}\text{P}_{10}$ | 7.10 | 2.54 | 130 |
| $(\text{Mo}_{0.60}\text{Ru}_{0.40})_{78}\text{P}_{22}$ | 5.42 | 2.45 | 210 |
| $(\text{W}_{0.50}\text{Ru}_{0.50})_{60}\text{P}_{20}$ | 4.57 | 2.22 | |
| $(\text{Mo}_{0.8}\text{Re}_{0.20})_{80}\text{P}_{10}\text{B}_{10}$ | 8.71 | 2.42 | |

In the above respect the transition metal glasses, produced by melt spinning technique [24-30], seem to hold competitive advantages over A-15 superconductors. As may be seen from Table 4, although their T_c values are lower, their normal state resistivity ρ_n is commendably large which makes them high field superconductors, as indicated by their appreciable dH_{c2}/dT values in Table 4. For instance $H_{c2}(0)$ of $(\text{Mo}_{0.8}\text{Re}_{0.20})_{80}\text{P}_{10}\text{B}_{10}$ exceeds 16 T, a value intermediate between that of Nb-Ti and Nb₃Sn. Besides, these glasses often have superior mechanical properties than A-15, which are brittle materials and need special processing routes for their fabrication. The metallic glasses very often possess considerable ductility in shear and limited ductility in tension and moreover their tensile strength approaches the limit for a perfect crystal. Also, they being inherently amorphous, their superconducting properties remain unaffected with further disorder. Unfortunately, the measured values of the critical current for glasses are low. The problem being that their coherence length is around 5.0 nm, while the disorder present in the glasses is too fine for the flux vortices “to see” and consequently the pinning is poor. The problem might be effectively tackled by introducing inhomogeneities in the form of crystalline precipitates of about 5 nm dimensions in amorphous matrix which should pin the flux vortices more effectively.

4. CRYSTALLINE AND AMORPHOUS DISORDERS IN A-15 SUPERCONDUCTORS

4.1 Crystalline Disorder

There is a weight of evidence to show that T_c of ordered compounds like Laves phases, Chevrel compounds and A-15s etc., is affected by perturbation in the long range order. Of these, A-15 superconductors, due to their high T_c values, have been studied most extensively [32-34]. In this class of materials, whose binary chemical composition is represented by A_3B , there are three mutually orthogonal densely packed chains of transition metal ions A, located on the faces of BCC lattice formed by nontransition or transition metal ions B (see Fig. 2).

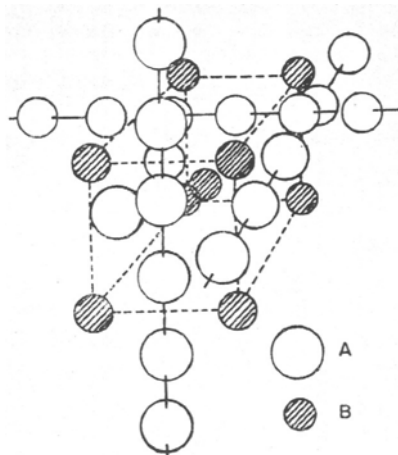


Fig. 2. Crystal structure of A-15 compounds (A_3B).

Typically, T_c values of some of the prominent compounds are Nb_3Sn ($T_c=18.5$ K), Nb_3Ge ($T_c=23.2$ K), Nb_3Ga ($T_c=20.7$ K), Nb_3Al ($T_c=19.2$ K), V_3Si ($T_c=17.2$ K), V_3Ga ($T_c=16.9$ K), $Nb_3(Al,Ge)$ ($T_c=21$ K). Relatively high T_c values noted for such a structure, known as β -tungsten, owe much to the three orthogonal chains of transition metal ions. These densely packed chains, as first pointed out by Weger [35], cause the d-band at the Fermi surface to become sharp, resulting in high $N(0)$ which is responsible for their observed high T_c . Consequently, any adulteration or disruption of A-chains, for example caused by B-ions, foreign impurity ions, or even vacancies occupying some of the A-sites would result in the broadening of the d-band and drastically reduce $N(0)$ and T_c . During heavy ion irradiation, some of the A-ions can get readily knocked off with their continuity getting interrupted by vacant lattice sites or this could as well lead to interchange of A and B sites, and T_c thereby gets degraded. Departure from the correct stoichiometry necessarily means the excess concentration of either A or B element. The excess B-ions would adulterate A-chains while the excess A would cause disorder in the BCC lattice of B-ions. Normally the B-site is considered less sensitive for T_c than the A-site. However, the transition metal A-ions at the B-site would have its d-band overlapping the narrow d-band due to A-chains, thereby making the latter broader with reduced $N(0)$. Extensive pseudobinary and ternary systems studied [32-34] show that in almost all instances corresponding to $(A,A')_3B$, where A and A' are both from the transition metal group, T_c is reduced. On the other hand, there seems little adverse effect on superconductivity with similar disorder on the B-site. In fact, there are instances where the pseudo-binary $A_3(BB')$ formed by A_3B and A_3B' has an optimum T_c that exceeds the T_c of the two constituent binaries. Here B and B' are both non-transition ions. Examples of these are Nb_3AlGe , Nb_3AlGa and Nb_3AuPt [33-34]. If B or B' are transition elements then their d-band overlaps the narrow d-band of A-chains and T_c is thereby significantly lowered due to decrease in $N(0)$. Some examples of the binary system where both A and B ions are transition metals are Cr_3Ir ($T_c=0.17$ K), V_3Rh ($T_c=0.38$ K), V_3Ni ($T_c=0.57$ K). In such a situation, the mutual intermixing of A and B does not seriously affect T_c . They are therefore called 'atypical' superconductors [32-34]. Their critical temperature is presumably already too low and any disorder has little further deteriorative effect on T_c .

4.2 Amorphous Disorder

A-15 superconductors have also been synthesized as thin films in the amorphous state, but in the situations such as for Nb₃Ge, Nb₃Sn and Nb₃Si, where in the crystalline state the T_c was high, in the amorphous state T_c was found to get significantly degraded (see Table 3). With amorphous disorder the chain structure is totally destroyed and it is really not surprising that the resulting T_c values are therefore significantly lowered. A-15 compounds of Mo, however, provide an interesting exception. Mo_{0.68}Si_{0.32}, Mo_{0.8}N_{0.2}, Re_{0.70}Mo_{0.30} (Table 3) which show low T_c (<2 K) in their crystalline state depict a substantially higher T_c when turned amorphous as quench condensed films. Similarly, crystalline films of Mo₃Ge and Mo₃Si with T_c of around 1.5 K, have their T_c raised by more than 6 K when they are turned amorphous with heavy ion irradiation [36]. The unusual behaviour of these Mo compounds is ascribed to superconductivity of the amorphous Mo sites, described in sec.2.

5. CRYSTALLINE DISORDER IN HIGH T_c CUPRATES

In general as T_c goes up superconducting state becomes increasingly more sensitive to disorder the relevant parameter closely linked with this issue is the range of coherence, ξ which decreases as T_c becomes larger. This is implicit in the relation which follows from the BCS theory,

$$\xi = hv_F / \pi \Delta_0 = 0.18 hv_F / k_B T_c \quad (5)$$

where v_F is the Fermi velocity, Δ₀ is half the energy gap and k_B is the Boltzmann constant. For classical simple elemental superconductors ξ = 50 to 100 nm, but for HTSC cuprate superconductors with T_c of around 90-100 K the coherence length drops down to around 0.2 to 1.5 nm. This value becomes comparable to the size of the crystallographic unitcell of high T_c cuprates. As a consequence, even very small disorder on the unitcell scale can interfere with the long range coherence of the superconducting state and thereby destroy superconductivity. The atomic disorder, such as resulting from the cationic dopings thus becomes a non-trivial issue in influencing the high T_c phenomenon.

High T_c superconducting cuprates (HTSC) seem to hold some similarity with A-15s in that here, instead of densely packed A-chains of transition metal ions of the A-15 structure, we have quasi-two dimensional CuO₂ planes (see Fig. 3) where any disorder makes the maximum impact on T_c. However, the underlying electronic structure in high T_c cuprates is thought to be very different from normal metals [37,38]. The main reasons for this are: HTSC are essentially doped Mott insulators with lower carrier concentration than typical metals; they are highly anisotropic/ quasi-two dimensional (CuO₂ planes), where the electrical transport along c-direction (across [CuO₂] planes) is neither metal- nor insulator- like. In the normal state, up to optimal doping, it is still unclear as to whether the Fermi-Liquid treatment of conventional metals holds in them. Along the [CuO₂] planes the electrical transport is unusual due to the features like linear resistivity over a wide temperature range (from T_c – 1000 K!) [39] and presence of pseudo-gap [40]. Along the c-direction, i.e. across the [CuO₂] planes, it is not even clear whether the electrical transport results from scattering of electronic waves or hopping of localized electrons/holes. However, these materials do show 3-D bulk superconductivity at a characteristic T_c. In such a situation, the way disorder is going to effect these materials can be radically different from classical examples given in earlier sections. In this section, focusing on one of the most extensively studied HTSC systems (RE)Ba₂Cu₃O_{7-δ}

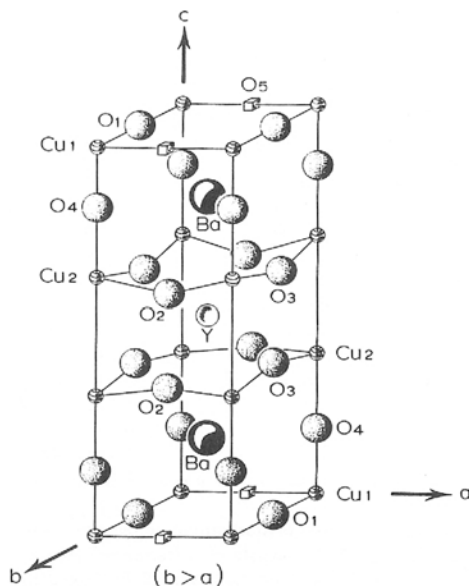


Fig. 3. Crystal structure of $\text{YBa}_2\text{Cu}_3\text{O}_7$ compound. The box at O(5) sites represents a vacancy.

(i.e. (RE)BCO-123, RE=Y or rare earth, see Fig. 3), we consolidate our studies of disorder induced by cationic substitution. In particular, the cases discussed are Pr and Ca substitutions at RE site, Sr at Ba site, Zn and Ni at Cu(2) site, and Fe, Co and Ga at Cu(1) site. The results reveal that in all the situations where T_c depression is more pronounced the origin of T_c degradation is directly linked with the incipient disorder resulting in the copper-oxide planes, where superconductivity is primarily believed to reside. We first provide evidence in several cases that $[\text{CuO}_2]$ planes are vulnerable to oxygen disorder in case of various cationic substitutions. Next we identify and discuss some interesting situations where T_c is dramatically influenced by various cation dopings at different crystallographic sites. Further, based on electrical transport and T_c studies on them, we discuss how the underlying electronic structure and the effect of disorder may be different from conventional superconductors considered in earlier sections.

5.1 Oxygen vacancy disorder in CuO_2 planes

5.1.1 Case of substituted $\text{Y}_{1-x}\text{Pr}_x\text{Ba}_2\text{Cu}_3\text{O}_{7-\delta}$

The HTSC samples investigated were bulk single crystals of Y(Pr)-123, with the nominal Pr content varying from 0 to 100%, which had been grown by using the flux method [41] at the Clarendon Laboratory, Oxford. The samples with 0% (i.e. Y-123) and 8% Pr (having a reduced T_c) exhibited the metallic character from room temperature down to T_c , while 20% Pr doped sample possessed a further reduced T_c with the normal state behaviour partly metallic-partly semiconducting, intermediate between 8% and 50% Pr doped crystals. XRD and STM / STS studies of the above single crystals were carried out under ambient conditions [42].

Table 5. Lattice constants of the samples determined by X-ray diffraction.

| Pr content | 8% | 20% | 30% | 50% | 90% | 100% |
|------------------|---------|---------|---------|---------|---------|---------|
| a-parameter (nm) | 0.38518 | 0.38813 | 0.38992 | 0.38993 | 0.39021 | 0.39153 |
| b-parameter (nm) | 0.39085 | 0.38987 | 0.39048 | 0.39046 | 0.39060 | 0.39201 |
| c-parameter (nm) | 1.16650 | 1.16851 | 1.17470 | 1.15688 | 1.17707 | 1.16474 |

i. Results and discussion

The observed variation of the lattice parameters as a function of Pr doping for the present series of Y(Pr)-123 single crystals was very similar to that reported earlier for Pr doped polycrystalline samples [43,44]. In all these cases, the a-parameter (about 0.383 nm) increases with Pr doping and approaches the value of the b-parameter (0.390 nm) when the level of Pr content becomes 100%. Thus, the orthorhombicity is gradually diminished and, for the full replacement of Y by Pr the crystal turns essentially tetragonal. There is no evidence of b-parameter decreasing, but instead all the earlier reported data on polycrystalline samples show a marginal increase in the b-parameter. The c-parameter, on the other hand, shows no specific trend in its increase or decrease with Pr doping. All these features, previously observed for polycrystalline samples, are corroborated by the lattice parameters measured on the Pr-doped single crystals of the present series as depicted in Table 5.

The fact that the a-parameter increases and approaches b shows only a slight increase with Pr-doping, suggests that the orthorhombicity is lowered by the filling-up of the empty O-5 sites without any change in the occupancy of the filled O-1 sites of the 1-2-3 unitcell. Intermixing of O-1 and O-5 sites would have led to a decrease of the b-parameter, which is not observed. Filling-up of O-5 site at the expense of O-1 is thus ruled out in the O-T transformation that results from Pr doping.

A direct manifestation of the Pr doped O-T transformation can also be seen by the studies of twin morphology of the doped samples. Figs. 4a and 4b respectively show STM images of the typical twin boundary structure observed in 1% and 20% Pr doped samples. Above 750° C YBCO is tetragonal with the dissolved oxygen distributed uniformly between O-1 and O-5 sites. At the processing stage when the sample is cooled to room temperature, the material is transformed to the orthorhombic structure with all O-1 sites filled and all O-5 sites empty. The shear strains associated with transformation are relieved by twinning. If, for some reason, like Pr-doping, the orthorhombicity at the ambient temperature is lowered the number density of the twin boundaries would be decreased. This is depicted in Fig. 5. The orthorhombicity, as given by the parameter $2(b-a)/a+b$, shown on the left ordinate, and twin boundary spacing - on the right ordinate, have been plotted as a function of Pr concentration, and are depicted by open and filled circles respectively. As orthorhombicity decreases and saturates the twin boundary spacing accordingly also increases and saturates with Pr-doping. This provides a direct correlation between the twin boundary formation and Pr-doping.

The observed increase in the a-parameter, by filling up of vacant O-5 site of the unitcell can in general take place only by aliovalent substitutions [45] when dopant cation has a higher valency than the on-site cation, which is being substituted. This suggests two relevant possibilities: (1) Pr^{3+} occupying Ba^{2+} sites and (2) Pr^{4+} occupying Y^{3+} sites. There have been many reports (see e.g., Ref. [46] and references therein) supporting Pr substituting at Ba anti-site easily, which may result in off-stoichiometric Y(Pr)-123 crystals and contribute in the

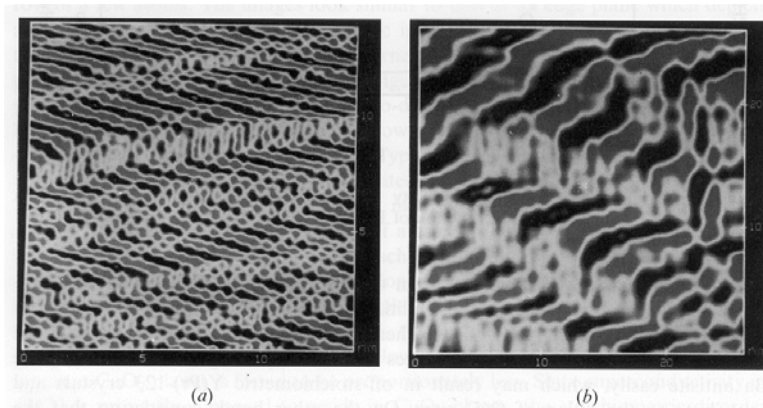


Fig. 4. STM image of twin boundaries in samples doped with (a) 1% Pr and (b) 20% Pr.

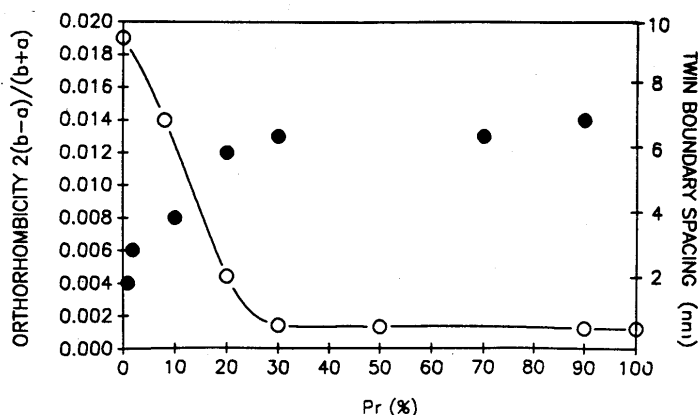


Fig. 5. Variation in the orthorhombicity (left ordinate, open circles) and twin boundary spacing (right ordinate, filled circles) as a function of Pr doping.

filling of the O-5 sites. On the other hand, considering that the ionic size of Pr^{4+} (0.099 nm) matches well with that of Y^{3+} (0.102 nm), the substitution of Pr^{4+} at Y^{3+} site in Y(Pr)-123 may also contribute in the filling of the O-5 sites, which, as will be seen, does not however fit in with other observations. The filling-up of vacant O-5 sites is expected to have a further effect on the radius of Cu(I), i.e. copper ions in the chains. Their coordination would increase from 4 to 6, with the effect that their ionic radius should show a small increase. This would account for the observed marginal increase in the b-parameter. This increment would obviously be present also in the a-parameter which is primarily increased by filling-up of O-5 sites.

ii. Atomic level lattice defects, rows of oxygen vacancies

The filling-up of O-1 and O-5 sites of the unitcell with Pr doping has interesting consequence, hitherto not explored in literature. In the situation when most of the O-1 and O-5 sites are occupied, the oxygen stoichiometry of the unitcell ought to increase from O_7 to O_8 . All the reported data [43, 44, 47] however confirm that even after full replacement of Y by Pr the oxygen stoichiometry remains unaltered and stays at 6.90-6.95. This implies that there is no fresh intake of oxygen but it is presumably transferred from some other parts of the unitcell. Since O-4 site in the Ba-O plane is crucial to the formation of the 1-2-3 structure without which the unitcell will collapse, it is most unlikely that oxygen from O-4 is transferred to the previously empty O-5 site. The only place from where the oxygen might get depleted are O-2 or O-3 sites of the two CuO_2 planes. In order to bring down the oxygen stoichiometry from 8 to 7, effectively 1/2 O-atom per CuO_2 plane should be transferred to the chains in Pr-123. Since each CuO_2 plane of the unitcell contains 2 oxygen atoms, we expect that 25% oxygen atoms must get depleted from each of the CuO_2 planes. In 50% Pr doped sample which shows a higher orthorhombicity, a simple argument would imply that 12.5% oxygen atoms are given out from planes to chains. Our experimental observations depicted below seem entirely consistent with the above reasoning.

Since the electronic states at E_f are essentially O-2p states, the low voltage imaging ($\leq |500|$ mV) of CuO_2 planes primarily reveals the oxygen atoms forming the characteristic square grid of 0.27 nm size. With increasing Pr content there was a noticeable increase observed in the missing of part of oxygen rows in the oxygen grid of CuO_2 planes. The partial removal of a row yields an appearance of an extra row of a few atoms being added. The images look similar to that of an edge plane which depicts an edge dislocation by the characteristic inverted T symbol. In the conventional three dimensional situation one is concerned with an extra half plane, either incorporated or removed, and the resulting edge dislocation is a line defect formed in a plane normal to the edge plane. In the two dimensional situation, such as considered now, the removal or incorporation of a row of atoms from a plane would imply creation of an atom-length dislocation. Typical images of CuO_2 planes for samples with 8%, 50% and 100% Pr doping are presented in Figs. 6a to 6c respectively. The places where the oxygen rows are missing are indicated by the inverted T symbol. Counting the missing number of atoms in a grid of oxygen atoms, observed in at least 5 to 10 different images of each sample, we find that from the 0.27 nm grid of 169 oxygen atoms of 100% Pr doped sample, roughly 35 to 45 atoms to be missing, while for 50% Pr doped sample, this number was approximately half i.e. about 15 to 25 atoms being lost from plane to the chains. In the case of samples with lower Pr content the number of missing oxygen atoms in CuO_2 planes is found to be proportionately less. Since superconductivity in YBCO is primarily supposed to reside in CuO_2 planes the stoichiometric disorder described above is expected to be of overriding importance in the problem of destruction of superconductivity due to Pr doping.

Interestingly, our STM observations on a fairly large number of pure and stoichiometric YBCO single crystals grown at various centres under different growth conditions reveal that CuO_2 networks are particularly susceptible to formation of missing oxygen rows, although as compared to the Pr-doped samples, the concentration of these defects is comparatively far less. Fig. 6a shows a typical oxygen grid of the CuO_2 plane with 2 or 3 vacancy sites which could bring down the net oxygen content from 7 to 6.9. It is worth pointing out that despite prolonged oxygen sintering, it is in general found unfeasible to realize to date the ideal oxygen stoichiometry of O_7 for any pure 123 system, and at best one attains a value anywhere

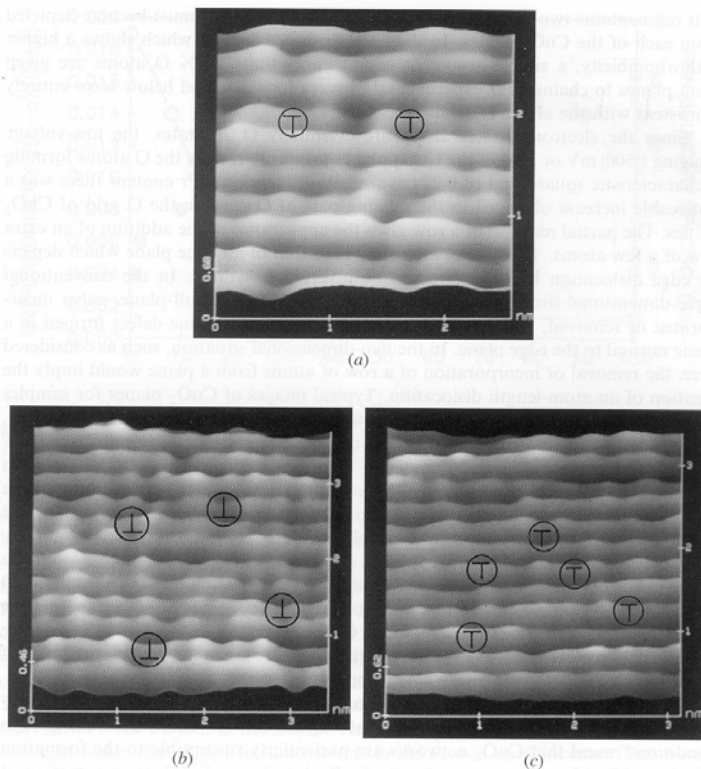


Fig. 6. STM images showing rows of oxygen vacancies in CuO₂ plane of samples doped with (a) 8% Pr, (b) 50% Pr and (c) 100% Pr.

between 6.90 to 6.95. The possible reason for this, we feel, might be that CuO₂ planes are buckled and are under considerable strain. The strains are released by breaking up of bonds leading to the creation of oxygen vacancies. In the case of Pr substitution, the neutron data show [48] that with Pr substituting the Y-site, there is an anomalous shrinkage in the Pr-O(2) distance which tends to enhance the buckling of the CuO₂ planes. This would enhance the strains and favour the oxygen depletion.

In contrast with CuO₂ planes the Ba-O plane (Fig. 7b) and Cu-O chains (Fig. 7c) are relatively free from the above defects. The only defect which the chains tend to acquire is the filling up of the O-5 sites which in the present case takes place by Pr substitution. Fig. 7d shows the chain structure of Fig. 7c getting adulterated by filling up of some of the O-5 sites caused by 20% Pr doping. The origin of oxygen loss from CuO₂ planes is ascribed to the antisites of Ba at Pr sites. The ionic size of Ba in 8-fold coordination is too large and in order to match with that of Pr³⁺ in y-plane it prefers 6-fold coordination. As a consequence oxygen from the neighbouring CuO₂ planes gets depleted. On the other hand Pr³⁺ at the Ba-site draws oxygen to fill empty O-5 sites of the Cu-O chains. In contrast to this, Pr⁴⁺ at Y³⁺ site should result only in filling-up of O-5 site without causing oxygen depletion from CuO₂ planes.

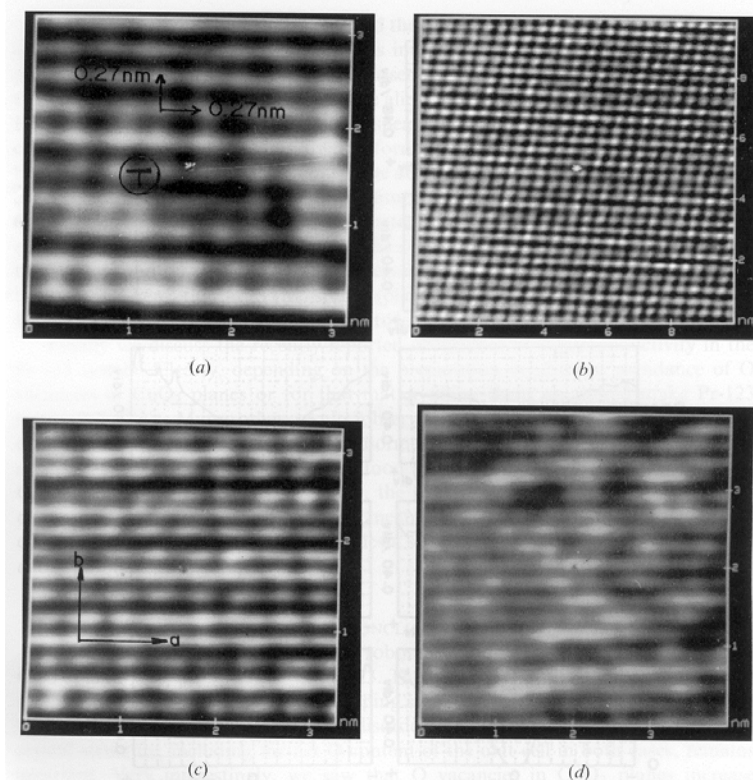


Fig. 7. STM images of (a) vacancies in CuO_2 plane of pure single crystal, (b) Ba-O plane (c) Cu-O chains in pure single crystal and (d) Cu-O chains with O-5 site partly filled in 20% Pr doped sample.

iii. Electronic structure

Turning to the changes in the electronic structure, the results of conductance spectra obtained for CuO_2 planes and Cu-O chains for the above Pr substituted samples are presented in Fig. 8. The normalized conductance $d\ln I/d\ln V$ is plotted as a function of bias voltage. These results were obtained by studying each sample in at least at 3 to 5 different regions, giving 20 spectra for each region. The spectra were remarkably repetitive near $V=0$ (i.e., near E_f), showing only a modest variation at the higher ramping voltage of the scan. As may be seen, up to 8% substitution, both CuO_2 planes and Cu-O chains have the conductance spectra characteristic of metallic nature, whereas for higher concentrations of Pr, the CuO_2 planes dramatically turn quasi-insulating without any noticeable change, however, in the metallic nature of the chains. Beyond 8% Pr, the conductance spectra of Fig. 8 reveal a gradual opening-up of a gap-like structure which widens to about 1.6 eV for the 100% Pr-substituted crystal. Incidentally, this value closely matches with the semiconducting energy gap of Y-123-O(6) compound. Further,

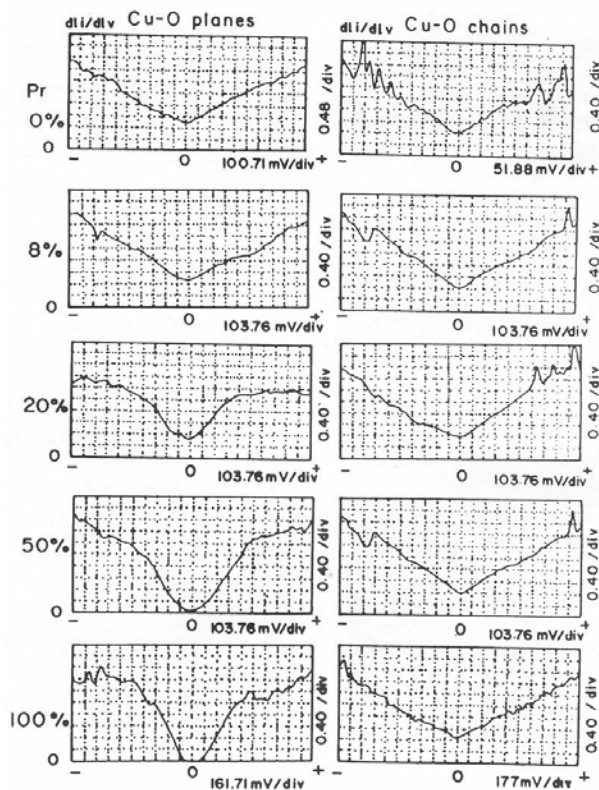


Fig. 8. Normalized conductance spectra, $d(I)/d(V)$ against bias voltage for CuO_2 planes and Cu-O chains in 0%, 8%, 20%, 50% and 100% Pr-doped samples. Note that Pr substitution makes CuO_2 planes quasi-insulating while Cu-O chains continue to exhibit metallic character.

the normalized conductance is directly proportional to the local density of states (LDOS) and, as one may note from the conductance spectra of 50% Pr sample, it touches the zero base line at $V=0$ (i.e. at E_f). Once the CuO_2 planes become fully insulating, superconductivity is no longer to be expected. It is worth recalling that, at this level of Pr concentration superconductivity indeed is destroyed. On the other hand, LDOS for chains is little affected by 100% Pr substitution.

iii. Summary

It follows that antisite formation between Pr^{3+} at Ba^{2+} sites [49] directly leads to oxygen vacancy disorder in CuO_2 networks and simultaneous filling up of O-5 sites. Very interestingly, we saw that oxygen vacancies in CuO_2 planes increase monotonically with increasing Pr in Y(Pr)-123; Pr-123 may have nearly twenty times more oxygen vacancies as compared to Y-123 with $\sim O_{6.95}$. We suggest that the disorder generated by the presence of such oxygen vacancies is responsible for the loss of (super)conductivity in Y(Pr)-123 systems.

5.1.2 Case of substituted $R_{1-x}Ca_xBa_2Cu_3O_{7-\delta}$ (R = Er, Y, Sm and Nd)

Samples of the series $R_{1-x}Ca_xBa_2Cu_3O_{7-\delta}$ (R = Er, Y, Sm and Nd), for different values of x ranging from 0.0 to 0.50, were synthesized through standard solid state reaction and furnace-cooled-in-oxygen method [50]. The lattice parameters were determined from a least-square fit of the observed d values. The resistivity was measured in the temperature range of 30 – 300 K using four-probe technique in a closed cycle refrigerator. The oxygen content of all the samples was determined by iodometric titration. AC magnetic susceptibility measurements were carried out in the temperature range of 4.2 – 300 K, using a quantum design SQUID magnetometer, in an applied field of 0.01 mT at 117 Hz.

i. Experimental Results

Figs. 9a-9d show the room temperature X-ray patterns of $R_{1-x}Ca_xBa_2Cu_3O_{7-\delta}$ (i.e., $R_{1-x}Ca_x:123$, where $R_x =$ Er, Y, Sm and Nd) samples. It is evident from these figures that for all the four series Ca substitutes isostructurally in most of the x range. However, a few unidentified low intensity lines for $x = 0.50$ samples mark the solubility limit of Ca in all the tried R:123 system. In general, the b -parameter is found to decrease along with a small increase in a -parameter, resulting in a decreased orthorhombic distortion (o.d. = $(b-a)/b$). The o.d. remains nearly invariant until $x = 0.30$ for Er and Y samples, and later decreases slightly for $x = 0.40$ and 0.50. The c -lattice parameter for both Er and Y samples increases slightly with Ca doping. Lattice parameters a , b and c , and the o.d. are listed in Table 6 for all the samples of Y and Er series. Interestingly, unlike as for Er and Y samples, the o.d. decreases continuously with x for Ca doping in Sm and Nd based samples. The c -lattice parameter of Sm and Nd samples increases with x . The increment in c -parameter with Ca doping is comparatively more for the Sm / Nd samples than that observed for Er / Y samples. The lattice parameters for all the samples along with orthorhombic distortion are given in Table 6.

A careful survey of the x -ray patterns, e.g., Fig. 9d for Nd series further shows formation of orthorhombic II phase. The double peaks at $2\theta \sim 46.5^\circ$ with increasing x show a clear evolution towards a triplet peak structure which has been identified [51] with the appearance of ortho II phase. As shown in the next section, increase of x leads to an increase in oxygen loss (δ) for all the four series of samples (see Table 6). For Nd based series, all the three peaks attain same intensity for $x \geq 0.3$ sample endorsing the formation of ortho II phase. In contrast, for Er based samples, even though the third peak does make a small appearance for $x \geq 0.3$, the relative intensity of the peaks in the original ($x=0$) doublet diminishes much less (see Fig. 9a). Another interesting feature occurs at $2\theta \sim 58^\circ$ (see Figs. 9a-9d), where the relative intensity of the double peak structure shows a change with increasing x . For the Nd series, the two peaks become equal in intensity for $x \geq 0.3$, see Fig. 9d. This observation strongly suggests [52] that with increasing x ordering / disordering of oxygen occurs at chain sites in Nd based samples, which supports the previous observation. In comparison, for Er based samples, the relative intensity of the double peaks at $2\theta \sim 58^\circ$ gets little effected with increasing x (see Fig. 9a), reflecting not much change in the order/disorder at chain sites with x . Sm and Y samples show similar behavior as that of Nd and Er based samples, respectively, which is consistent with the trends of o.d. and c -parameter change discussed above. Detailed structural comparisons of Ca substituted Er, Y, Sm and Nd series will be presented separately elsewhere.

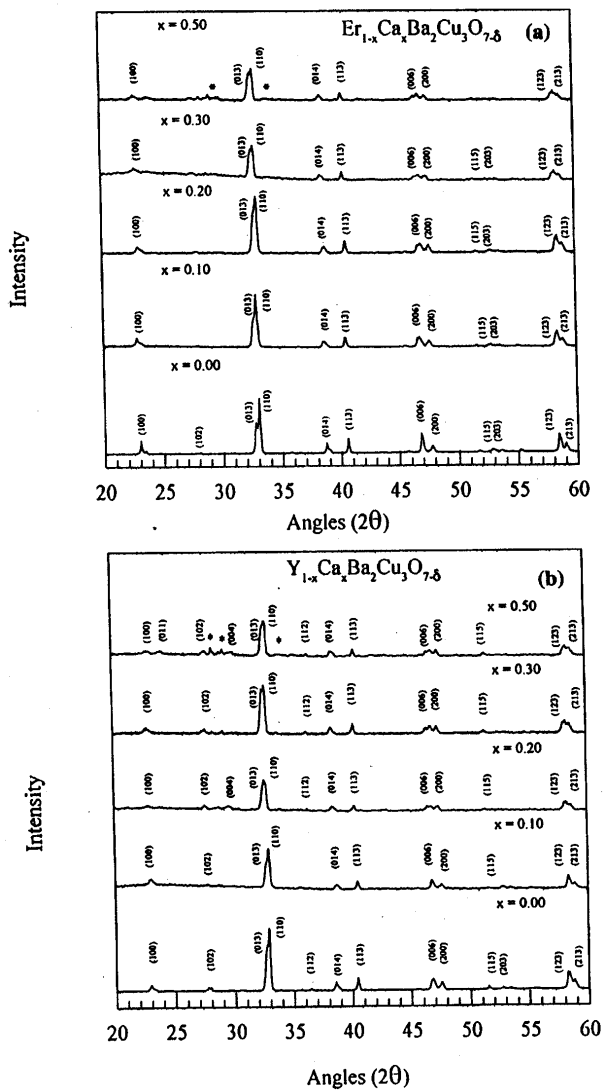


Fig. 9. X-ray diffraction patterns of (a) $\text{Er}_{1-x}\text{Ca}_x\text{Ba}_2\text{Cu}_3\text{O}_{7-\delta}$, (b) $\text{Y}_{1-x}\text{Ca}_x\text{Ba}_2\text{Cu}_3\text{O}_{7-\delta}$, (c) $\text{Sm}_{1-x}\text{Ca}_x\text{Ba}_2\text{Cu}_3\text{O}_{7-\delta}$ and (d) $\text{Nd}_{1-x}\text{Ca}_x\text{Ba}_2\text{Cu}_3\text{O}_{7-\delta}$. The symbol '*' represent impurities.

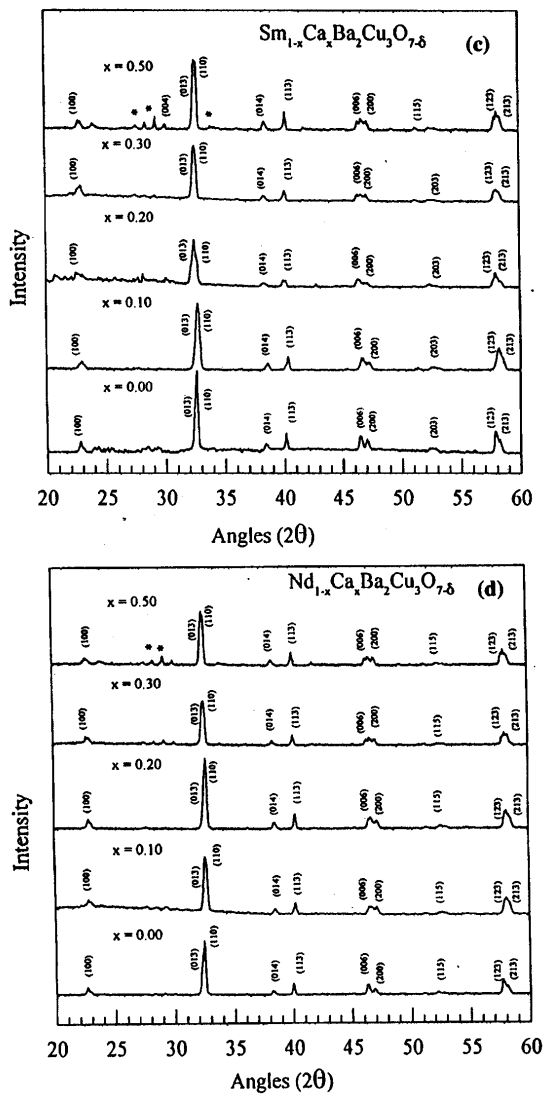


Fig. 9. (Continued)

Table 6. Lattice parameters a, b and c, orthorhombic distortion $\{(b-a)/b\}$, T_c ($\rho = 0$), average copper valance (Cu^{P+}) and the total oxygen content ($7-\delta$) for $\text{R}_{1-x}\text{Ca}_x\text{Ba}_2\text{Cu}_3\text{O}_{7-\delta}$.

| R | x | a(Å) | b(Å) | c(Å) | (b-a)/b | T_c (K) ($\rho = 0$) | p | $7-\delta$ |
|----|------|--------|--------|---------|---------|--------------------------|-------|------------|
| Er | 0.0 | 3.8163 | 3.8707 | 11.6789 | 0.014 | 90 | 2.295 | 6.943 |
| Er | 0.10 | 3.8109 | 3.8763 | 11.6743 | 0.017 | 78 | 2.271 | 6.856 |
| Er | 0.20 | 3.8193 | 3.8823 | 11.6803 | 0.016 | 64 | 2.267 | 6.800 |
| Er | 0.30 | 3.8207 | 3.8763 | 11.6863 | 0.014 | 54 | 2.271 | 6.756 |
| Er | 0.50 | 3.8293 | 3.8703 | 11.6894 | 0.011 | 44 | 2.270 | 6.655 |
| Y | 0.0 | 3.8195 | 3.870 | 11.6777 | 0.013 | 90 | 2.284 | 6.926 |
| Y | 0.10 | 3.8161 | 3.8811 | 11.6852 | 0.017 | 78 | 2.278 | 6.867 |
| Y | 0.20 | 3.8229 | 3.8884 | 11.6826 | 0.017 | 67 | 2.277 | 6.815 |
| Y | 0.30 | 3.8288 | 3.8813 | 11.6923 | 0.014 | 55 | 2.266 | 6.749 |
| Y | 0.50 | 3.8361 | 3.8746 | 11.6951 | 0.010 | 46 | 2.276 | 6.660 |
| Sm | 0.0 | 3.8247 | 3.8895 | 11.7103 | 0.017 | 89 | 2.271 | 6.906 |
| Sm | 0.10 | 3.8279 | 3.8802 | 11.7187 | 0.014 | 79 | 2.258 | 6.837 |
| Sm | 0.20 | 3.8367 | 3.8706 | 11.7234 | 0.012 | 73 | 2.241 | 6.761 |
| Sm | 0.30 | 3.8401 | 3.8645 | 11.7306 | 0.009 | 68 | 2.245 | 6.720 |
| Sm | 0.50 | 3.8468 | 3.8601 | 11.7396 | 0.008 | 64 | 2.248 | 6.622 |
| Nd | 0.0 | 3.8207 | 3.8863 | 11.7059 | 0.017 | 88 | 2.277 | 6.915 |
| Nd | 0.10 | 3.8263 | 3.8813 | 11.7113 | 0.014 | 82 | 2.265 | 6.848 |
| Nd | 0.20 | 3.8291 | 3.8763 | 11.7234 | 0.008 | 74 | 2.261 | 6.792 |
| Nd | 0.30 | 3.8307 | 3.8643 | 11.7297 | 0.006 | 71 | 2.254 | 6.731 |
| Nd | 0.50 | 3.8317 | 3.8623 | 11.7369 | 0.004 | 70 | 2.254 | 6.630 |

For all the four Er, Y, Sm and Nd sets of samples, the oxygen content, as determined by iodometric titration, is found to decrease with increasing x. This means, the Ca substitution at R-site in Er, Y, Sm and Nd :123 samples create oxygen vacancies. The oxygen content and the average Cu valance for all samples are given in Table 6.

In Figs. 10a - 10d, we plot the resistivity as a function of temperature for all the samples of series $\text{R}_{1-x}\text{Ca}_x\text{Ba}_2\text{Cu}_3\text{O}_{7-\delta}$ (R= Er, Y, Nd and Sm with $x = 0.0$ to 0.50). The increase of the room temperature resistivity with increasing x endorses the substitution of Ca in the lattice. Interestingly, the $\rho(T)$ curves show distinct upward curvature for the Er / Y series of sample, while the same is absent in case of the Sm / Nd samples. The only exception being the $x = 0.5$ Nd based sample. However, since $x = 0.5$ samples do show impurity phases, the curvature shown by $x=0.5$ Nd based sample is to be taken only cautiously. A glance at Fig. 10 shows the depression in T_c with increasing x. It is remarkable to note, that, the relative decrease in $T_c(\rho = 0)$ is more for Er and Y samples, when compared with those of Sm and Nd ones.

For all the four series, the superconducting transitions were also measured by ac magnetic susceptibility. The behavior of diamagnetically observed shift in transitions with x, corroborates in general well with the resistively measured transitions. Fig. 11 depicts typical ac susceptibility transitions for the Y based samples. Clearly, the diamagnetic onset and the transition shifts to lower temperatures with increasing x. However, we observe a decrease in the screening fraction for all the samples with increasing x, which is presently unclear. We

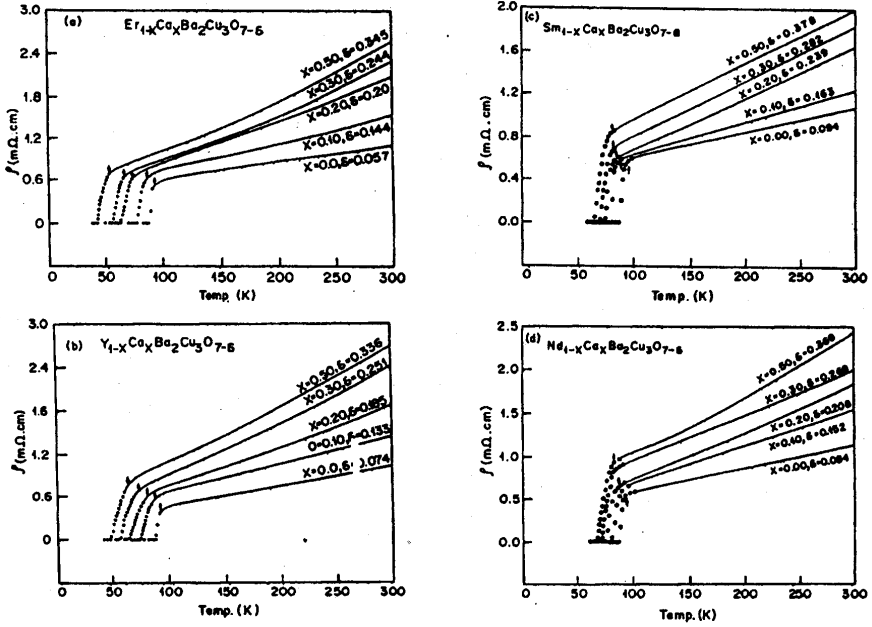


Fig. 10. Resistivity versus temperature plots for (a) $Er_{1-x}Ca_xBa_2Cu_3O_{7-\delta}$, (b) $Y_{1-x}Ca_xBa_2Cu_3O_{7-\delta}$, (c) $Sm_{1-x}Ca_xBa_2Cu_3O_{7-\delta}$ and (d) $Nd_{1-x}Ca_xBa_2Cu_3O_{7-\delta}$. The arrows in the figure mark the onset of the superconducting transition T_{on} .

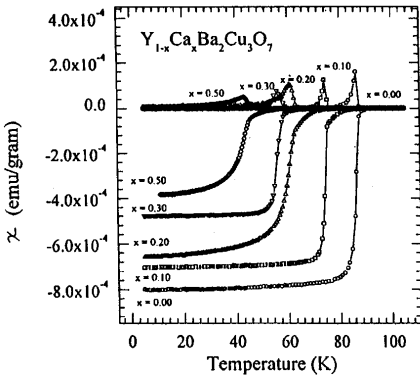


Fig. 11. AC susceptibility versus temperature plots for $Y_{1-x}Ca_x:123$.

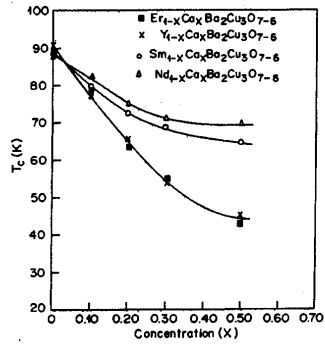


Fig. 12. $T_c(p=0)$ vs. x (Ca content) for $R_{1-x}Ca_x:123$.

would like to make a comment here, that, an incomplete Meissner / screening fractions and its dependence on doping in HTSC, has often been observed (e.g. see [53,54]). This might reflect an inherent disorder / inhomogeneity in the multicomponent HTSC materials.

To show more explicitly the T_c dependence on x , for all the four series of samples, the $T_c(\rho = 0)$ is plotted as a function of x in Fig. 12. As can be easily marked the T_c change with x is steeper for Er / Y than in Sm / Nd samples. Notice also that the $T_c(x)$ tends to saturate, in Sm / Nd samples, the origin of which is related with oxygen loss and will be discussed shortly. The saturation in T_c with x is nearly absent for Er / Y series (see Fig. 12). To cross check, that our samples represent the intrinsic behavior of the Ca substituted 1-2-3 compounds, we compare in Fig. 13 the $T_c(x)$ graphs of Er and Y with those of the cited earlier in the literature [55-57]. The agreement is found to be good.

Since Ca substitution leads to a change in oxygen content for all the samples (see section III.B), we also plot their $T_c(\rho = 0)$ as a function of oxygen content (δ) in Fig. 14. For comparison we have also included the well known $T_c(\delta)$ curve for pure Y:123 [53] in the same figure. As seen from the figure the T_c decreases sharply, and without any saturation, with increasing δ for Er and Y based samples. In contrast, the Nd and Sm based samples show a behavior which tends to mimic the pure Y:123 compound, i.e. the $T_c(\delta)$ after an initial decrease tends to show a plateau near $\delta = 0.30$.

ii. Discussion

The results of x-ray diffraction, iodometric titration, normal state resistivity and T_c measurements can be summarized as follows:

(1) Ca substitutes isostructurally in Er, Y, Sm and Nd based $R_{1-x}Ca_x:123$ samples, with only a little impurity phase(s) for $x = 0.50$ in all the four cases. The o.d. is only weakly affected for Er / Y, however the same decreases faster with x for Sm / Nd samples. The c-lattice parameter in general increases with x , and the increase is much stronger for Sm / Nd samples. For $x \geq 0.3$, Er/Y based samples clearly show a transformation to Ortho II phase, as against only traces of the same could be detected in the case of Sm/Nd samples.

(2) Ca substitution leads to a proportionately increasing loss of oxygen in all Er, Y, Sm and Nd based samples. The average Cu valence slightly decreases (as compared to pure R:123), but stays nearly independent of x for all the series.

(3) The normal state $\rho(T)$ curves show curvature for Er / Y based samples, while the same is absent in case (except $x = 0.5$ Nd:123) of Sm / Nd. The $T_c(\rho = 0)$ decreases with x and δ for all the four set of samples, and the decrease is stronger in case of Er / Y samples.

Now we demonstrate that all the above mentioned points consistently indicate an oxygen loss occurring from different sites in Er/Y set and Sm/Nd set of samples.

Firstly we show that how points 1 and 2, along with the ionic radii and coordination number considerations, suggest a different site preference for oxygen vacancies in different samples. In 8-fold coordination the trivalent Er, Y, Sm and Nd ions have a radii 1.00Å, 1.02Å, 1.09Å, and 1.12Å, respectively. For divalent Ca, in 8-fold coordination, the ionic radius is 1.12Å. Clearly, in 8-fold coordination, the ionic size of Ca^{2+} matches well with the size of Sm and Nd ions, and is much bigger when compared to that of Er and Y ions. However, interestingly, the ionic size of 6-fold coordinated Ca^{2+} (1.00Å) matches well with that of 8-fold coordinated Er and Y ions. This indicates that for Sm and Nd based R:123, Ca on substitution can acquire the same coordination number of eight as of the R-site. The loss of

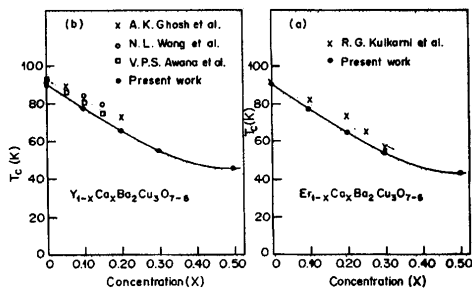


Fig. 13. Comparison of $T_c(x)$ variation for (a) $Er_{1-x}Ca_x:123$ and (b) $Y_{1-x}Ca_x:123$ taken from different works.

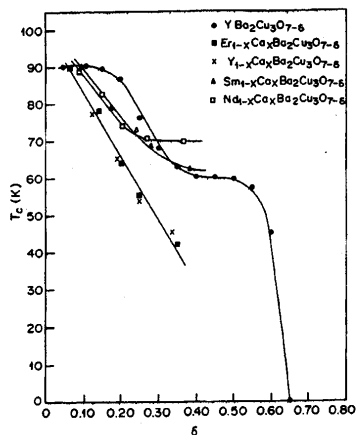


Fig. 14. $T_c(\rho=0)$ vs. δ (oxygen content) for $R_{1-x}Ca_x:123$ and pure $Y:123$. The lines are a guide to the eye.

oxygen (point 2) in Sm and Nd samples can thus be accounted for by the loss from chain site O(1) oxygen. This is also supported by the decrease in o.d. (point 1) in Sm and Nd based samples. On the other hand, it seems highly probable that Ca substitutes in 6-fold coordination at the site of 8-fold coordinated Er and Y ions in the R:123 lattice. The 6-fold coordinated Ca necessitates the creation of oxygen vacancies in the adjacent CuO_2 planes, which might be the case of Er and Y based samples to account for the oxygen loss. This is also in good agreement with the nearly invariant o.d. (point 1) in Er and Y samples, which reflect that the chain site oxygen O(1) is left relatively untouched. The creation of oxygen vacancies at CuO chain sites (CuO_2 plane sites) for Nd/Sm (Er/Y) is supported by the relative presence (absence) of ortho II phase (point 1), respectively.

Further evidence of oxygen being lost, from CuO_2 planes for Er / Y and from CuO chains in case of Sm / Nd, is suggested by the normal state $\rho(T)$ behavior (point 3). Note that the average Cu valence (point 2) in the studied samples, although invariant with x , decreases slightly with respect to the pure ($x=0$) samples. Thus the curvature in $\rho(T)$ for Ca substituted Er and Y samples can't be due to overdoping, and can be understood only by disorder induced localization. Considering that electrical transport essentially involves the CuO_2 planes, the $\rho(T)$ curvature is an indication of disorder in CuO_2 planes. In contrast, the Ca substituted Sm and Nd samples show no sign of curvature in $\rho(T)$, reflecting more orderly CuO_2 planes. The $x = 0.5$ Nd sample, which does show a curvature is not clear, however, due to the presence of impurity phases, it calls for a separate investigation.

Next piece of evidence, that it might be the different site preference of the oxygen vacancies in case of Sm / Nd as compared to Er / Y samples, is hinted from $T_c(x, \delta)$ behavior (point 3). The $T_c(\delta)$ graph for Ca substituted Sm / Nd samples was shown (see Fig. 14) to follow qualitatively the $T_c(\delta)$ graph of pure Y:123. The latter is understood [58] in terms of the oxygen vacancy creation and ordering in CuO chains of R:123 lattice, and by analogy may hold for Sm / Nd samples as well. The observed plateau in $T_c(\delta)$ of Sm/Nd, for $x \geq 0.3$, is in line with the transformation to ortho II phase seen by x-rays (point 1), and well known for

pure oxygen deficient Y:123 material. In clear contrast, the $T_c(\delta)$ of Ca substituted Er / Y samples shows a steeper slope and no plateau. This behavior does not fit with the known (pure Y:123) CuO chains scenario, and calls for oxygen vacancy creation elsewhere (“CuO₂ planes”) in the unit cell for Er / Y samples. Note also that, for $x \geq 0.3$ in these two series only traces of ortho II phase (point 1) could be detected, which supports the near absence of plateau in $T_c(\delta)$.

In addition, we would like to say something more about the $\rho(T)$ behavior of all the four sets of samples. We do observe that the onset of the superconducting transitions (T_{on} , marked by arrows in Figs. 10a-10d) as a function of x shifts maximum for the Er based samples and minimum for the Nd based samples. This observation appears to be more than a coincidence, as we illustrate it now. At the moment, admittedly, the mechanism by which the oxygen disordering of CuO chains can lead to a decrease of T_{on} is not very clear. However, decreasing the conductivity of the chains by increasing the disorder is expected to broaden the $\rho(T)$ transition width without effecting the onset T_{on} [59,60]. On the other hand, disorder in CuO₂ planes should lead to a direct suppression of the superconducting transition [59,60], i.e. the T_{on} should also shift to lower T . Note that Er (and Nd) represent the extremes of the R (= Er, Y, Sm, Nd) series in terms of their ionic radius 1.00 Å (and 1.12 Å), which match perfectly with 6-fold (and 8-fold) coordinated Ca²⁺. Therefore, ideally we expect, the loss of oxygen purely from the CuO₂ planes (CuO chains) for the end members Er (Nd), where as for samples based on middle members Y (Sm) the oxygen loss may partially also occur from the CuO chains (CuO₂ planes) for Y (Sm) based samples. For Nd based samples (see Fig. 10d), the near absence of the shift in T_{on} and at the same time the shift in $T_c(\rho = 0)$ to lower T with increasing x , is consistent with the disorder in chains. On the other hand, for Er based samples (see Fig. 10a), a clear strong shift in T_{on} with increasing x , is consistent with the disorder in planes. Note also that the curvature of $\rho(T)$ is more pronounced in Er based samples, which lies at the other end of tried R series, and where more disorder is expected in the CuO₂ planes.

iii. Summary

We investigated the structural and superconducting properties of $R_{1-x}Ca_xBa_2Cu_3O_{7-\delta}$ system, with R = Er, Y, Nd and Sm, and for $0.50 \geq x \geq 0.00$. We have shown that substitution of divalent Ca leads to a loss of oxygen in all the samples irrespective of the chosen R in R:123 system. The loss of oxygen compensates for the extra hole contribution due to Ca²⁺/R³⁺ aliovalence, resulting in an average Cu valence nearly independent of x for all R. The variation of orthorhombic distortion, c -lattice parameter and $\rho(T)$ with x , and the $T_c(x, \delta)$ behavior is significantly different in Er and Y with respect to Sm and Nd based R:123 system. We suggest and provide evidence that these differences are a consequence of different structural order / disorder of oxygen vacancies created by Ca substitution. Presumably, the oxygen loss occurs predominantly in CuO₂ planes for Er/Y based samples and in CuO chains for Sm/Nd based samples.

Finally, we would like to comment on certain reports [61,53] where the decrease in T_c of the optimally oxygenated $Y_{1-x}Ca_x:123$ samples has been solely attributed to the over doping due to Ca²⁺ / Y³⁺ aliovalence. However, there are clear pitfalls in the results of [61,53]: (1) the value of $T_{c,max}$ depends on the amount of substituted Ca (see the inset of Fig. 1 of [61]); (2) for a change of $T_c/T_{c,max}$ from 1 to 0.6, the corresponding change of hole concentration differs by a factor 3 in [61] and [53]. We believe, these discrepancies cannot be understood without taking into account the disorder due to oxygen vacancies in $Y_{1-x}Ca_x:123$ system.

5.1.3 Case of substituted Er Ba₂Cu_{3-x}M_xO_{7-y} (M = Fe, Co, Ni, and Ga)

Polycrystalline samples of ErBa₂Cu_{3-x}M_xO_{7-y} (M = Fe, Co, Ni and Ga) with $x = 0.0, 0.03, 0.045$ and 0.06 were synthesized via standard solid state reaction route [62]. Three series of samples were made for each M, namely: one with “full” oxygen content (oxygenated), one with “reduced” (400 °C argon annealing) oxygen content, and the other with “doubly reduced” (400 °C + 450 °C argon annealing) oxygen content. These samples will be referred to as O, A₁ and A₂ set of samples, respectively. X-ray diffraction (XRD) was performed to determine the unit cell parameters of all the samples of the sets O and A₂ at room temperature with the help of a D-500 Siemens diffractometer using CuK_α radiation. The oxygen content of all the samples of all three sets O, A₁ and A₂ was determined using a conventional iodometric technique, within a maximum error of ± 0.02 .

i. Experimental results and discussion

XRD patterns of all the samples of sets O and A₂ showed the presence of only a single phase. The lattice parameters for oxygenated samples of set O are given in Table 7. With progressive doping of Fe, Co and Ga, we observe a reduction in the o.d., see Table 7. In contrast, the Ni based samples show no change in the o.d., neither with respect to pure Er:123 and nor with increase in x . These results are in complete agreement with the earlier literature [45, 63-67]. The change in o.d. can also be directly appreciated by following the relative evolution of 020 and 200 reflections at $\sim 47^\circ$, and 123 and 213 reflections at $\sim 58^\circ$ in the XRD patterns. Left hand side of Fig. 15 shows such an evolution for the pure, Fe and Ni substituted Er:123 samples. Co and Ga doped samples follow a behavior similar to that of Fe. In Fig. 15, for the O set of samples, the relative intensity of the peaks in both the doublets change continuously with increasing Fe substitution, whereas they are invariant for Ni doped samples. This observation supports the decrease of o.d. in Fe doped samples and a constant o.d. in Ni doped samples of the set O, and are in accord with the results shown in Table 7.

The lattice parameters for the oxygen deficient samples of set A₂ are given in Table 8. For the pure ($x=0$) sample, as expected [54,68], the o.d. has decreased along with a corresponding increase in c -parameter. Substitution by all four elements (M= Fe, Co, Ni and Ga) leads to a further decrease in the o.d. with increasing x , see Table 8. This feature of set A₂, for Fe, Co and Ga doped samples, is similar to the one observed for set O. However, the decrease in o.d. for Ni doped samples of set A₂, unlike the set O, indicates a possible substitution of Ni³⁺ at the Cu(1)-site in Cu-O chains in oxygen deficient Er:123. Also note that (see the right hand side of Fig. 15), for both Fe and Ni doped samples of set A₂, the relative peak intensities in both the (020, 200) and (123, 213) doublets show a continuous change with increase in x . This feature observed in the XRD patterns endorses the change of o.d. in both Fe and Ni doped samples of set A₂.

We show in Tables 7 and 8 the iodometrically determined oxygen content in the samples for all three sets - O, A₁ and A₂. Consistent with the heat treatment, the pure ($x=0$) sample of these three sets have an overall oxygen content $7-y = 6.91, 6.76$ and 6.68 . For all substitutions, the samples of all the three sets show only a small change in the oxygen content as compared with the pure ($x=0$) ones. Considering the valence state of the substituting cations Fe³⁺, Co³⁺, Ga³⁺ and Ni³⁺ (Ni²⁺ in the samples of set O, where it occupies a Cu(2)-site in the CuO₂ planes) at Cu(1)-sites in Cu-O chains, the iodometrically determined oxygen content, and the charge balance, we can determine the average Cu valence (p^+) in all the samples. The values are given in Tables 7 and 8 for all the samples. None of the substitutions leads to any appreciable change in the average Cu valence.

Table 7. Lattice parameters (in Å) a, b and c, orthorhombic distortion [(b-a)/b]x100, oxygen content (7-y) and average Cu valence (p^+). The lattice parameters are rounded off at last decimal place and maximum error in y is ± 0.02 .

| Sample | a | b (Set O) | c | [(b-a)/b]*100 (Set O) | 7-y (Set O) | p^+ (Set O) | 7-y (Set A1) |
|-----------|-------|--------------|--------|--------------------------|----------------|------------------|-----------------|
| Pure(0.0) | 3.819 | 3.883 | 11.671 | 1.648 | 6.91 | 2.27 | 6.76 |
| Fe(0.03) | 3.825 | 3.875 | 11.670 | 1.290 | 6.92 | 2.27 | 6.77 |
| Fe(0.045) | 3.834 | 3.874 | 11.669 | 1.032 | 6.92 | 2.27 | 6.78 |
| Fe(0.06) | 3.833 | 3.872 | 11.650 | 1.007 | 6.93 | 2.27 | 6.80 |
| Co(0.03) | 3.821 | 3.879 | 11.670 | 1.495 | 6.92 | 2.27 | 6.77 |
| Co(0.045) | 3.829 | 3.877 | 11.691 | 1.238 | 6.93 | 2.28 | 6.77 |
| Co(0.06) | 3.824 | 3.874 | 11.687 | 1.291 | 6.93 | 2.27 | 6.78 |
| Ni(0.03) | 3.816 | 3.881 | 11.670 | 1.675 | 6.91 | 2.28 | 6.76 |
| Ni(0.045) | 3.808 | 3.872 | 11.672 | 1.653 | 6.90 | 2.27 | 6.76 |
| Ni(0.06) | 3.811 | 3.875 | 11.670 | 1.652 | 6.90 | 2.27 | 6.76 |
| Ga(0.03) | 3.820 | 3.870 | 11.670 | 1.292 | 6.92 | 2.27 | 6.76 |
| Ga(0.045) | 3.823 | 3.868 | 11.671 | 1.163 | 6.92 | 2.27 | 6.77 |
| Ga(0.06) | 3.826 | 3.868 | 11.670 | 1.085 | 6.93 | 2.27 | 6.78 |

Table 8. Lattice parameters (in Å) a, b and c, orthorhombic distortion [(b-a)/b]x100, oxygen content (7-y) and average Cu valence (p^+). The lattice parameters are rounded off at last decimal place and maximum error in y is ± 0.02 .

| Sample | a | b (Set A2) | c | [(b-a)/b]*100 (Set A2) | 7-y (Set A2) | p^+ (Set A2) | p^+ (Set A1) |
|-----------|-------|---------------|--------|---------------------------|-----------------|-------------------|-------------------|
| Pure(0.0) | 3.827 | 3.875 | 11.701 | 1.290 | 6.68 | 2.12 | 2.17 |
| Fe(0.03) | 3.829 | 3.874 | 11.696 | 1.162 | 6.69 | 2.12 | 2.17 |
| Fe(0.045) | 3.830 | 3.874 | 11.691 | 1.136 | 6.69 | 2.11 | 2.17 |
| Fe(0.06) | 3.832 | 3.873 | 11.690 | 1.061 | 6.70 | 2.12 | 2.18 |
| Co(0.03) | 3.830 | 3.872 | 11.690 | 1.085 | 6.69 | 2.12 | 2.17 |
| Co(0.045) | 3.836 | 3.870 | 11.687 | 0.888 | 6.69 | 2.11 | 2.17 |
| Co(0.06) | 3.839 | 3.870 | 11.676 | 0.801 | 6.70 | 2.12 | 2.17 |
| Ni(0.03) | 3.824 | 3.874 | 11.700 | 1.290 | 6.68 | 2.11 | 2.17 |
| Ni(0.045) | 3.825 | 3.871 | 11.698 | 1.188 | 6.69 | 2.11 | 2.16 |
| Ni(0.06) | 3.827 | 3.872 | 11.690 | 1.162 | 6.70 | 2.12 | 2.16 |
| Ga(0.03) | 3.831 | 3.874 | 11.694 | 1.110 | 6.69 | 2.12 | 2.17 |
| Ga(0.045) | 3.833 | 3.872 | 11.686 | 1.007 | 6.70 | 2.12 | 2.17 |
| Ga(0.06) | | | | 0.930 | | 2.13 | 2.17 |

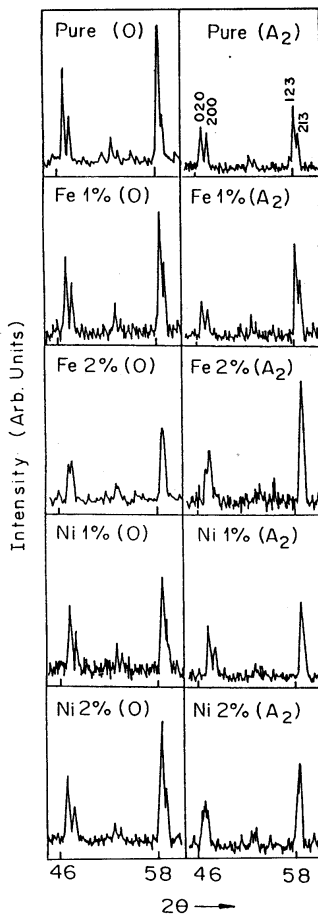


Fig. 15. Evolution of the double peaks at $\sim 47^\circ$ and $\sim 58^\circ$, determined by X-ray diffraction, in pure, Fe and Ni substituted $\text{ErBa}_2\text{Cu}_{3-x}\text{M}_x\text{O}_{7-y}$ samples of the sets O and A2.

For metal substitutions at Cu(1) chain sites in Er:123 the decrease in o.d. can occur owing to the O(5) chain sites (adjacent to the dopant) getting partially filled and its occupancy coming closer to O(1) chain sites. One obvious reason for this could be a preference of a six-fold oxygen coordinated environments by Fe, Co and Ga, where their respective ionic radii 0.55 \AA , 0.53 \AA and 0.62 \AA are ideal for substituting the Cu(1)-site in Cu-O chains with 0.65 \AA as ionic radius. The filling of the O(5)-sites should lead to an increase in the total oxygen content of the substituted samples. Considering that the Cu(1)-site has an occupancy of $1/8$ and the O(5)-site has an occupancy of $1/4$, and that we require to fill two O(5)-sites to provide six-fold coordination, each doped Fe atom will require an addition of 4 oxygen atoms. Note that this argument holds only for small amounts of M and for random substitution in the

grains. However, in our Fe, Co and Ga (and oxygen deficient set of Ni) doped samples the decrease of o.d. is not accompanied by any significant change in the total oxygen content (e.g., for $x = 0.03$, y should have increased by 0.12; compare it with the max. change observed in $y \approx 0.02$ shown in Table 7). The only way these facts can be reconciled, is, if the required oxygen gets transferred from either CuO_2 planes and / or from the filled O(1)-sites (next to the Cu(1)) to the empty O(5)-sites (next to the dopants). Such a transfer would indeed create oxygen vacancy disorder in the CuO_2 planes and/ or Cu-O chains of the Fe, Co and Ga doped Er:123 samples. Also note that for oxygen deficient sets A1 and A2, in comparison to set O, larger number of oxygen vacancies would be required to satisfy the six-fold coordination of doped trivalent M.

ii. Summary

Substitution of trivalent M cations preferring six-fold oxygen coordination at Cu(1)-site in Cu-O chains might result in removal of oxygen from CuO_2 planes and/or Cu-O chains (O(1)-sites next to Cu(1)) creating oxygen vacancy disorder. In oxygenated Er:123 samples with divalent Ni substitution, it is the Ni-site disorder in CuO_2 planes which replaces the oxygen vacancy disorder suggested in the cases of Fe, Co and Ga. However, in the oxygen deficient Er:123, the Ni substituted samples show results similar to those of Fe, Co and Ga, suggesting substitution of trivalent Ni at Cu(1)-site in Cu-O chains. Such a disorder could also account for the observed correlation between resistivity behaviour and suppression of T_c in the same samples with increasing substitution [62].

5.2 Normal State Resistivity, Striped Phase and Cationic Disorder

5.2.1 Co-doped $\text{ErBa}_2\text{Cu}_{3-x-y}\text{Zn}_x\text{Fe}_y\text{O}_{7-\delta}$ system

Polycrystalline samples of the series $\text{ErBa}_2\text{Cu}_{3-x-y}\text{Zn}_x\text{Fe}_y\text{O}_{7-\delta}$, at different values of x and y ($0 \leq x \leq 0.45$ and $0 \leq y \leq 0.18$), were synthesised through standard solid-state reaction method. For preparation details see Ref. [69]. Specifically, we have considered Zn and Fe as the two kinds of impurities co-doped in the $\text{ErBa}_2\text{Cu}_3\text{O}_{7-\delta}$ (1-2-3) system. The reason for choosing these impurities for doping the 1-2-3 system is that, it is known for this system [45,64,65,70,71], Zn substitutes at Cu(2)-site in the CuO_2 plane, while Fe, at least for low concentrations, substitutes at Cu(1)-site in the Cu-O chain. The samples were characterised for their phase purity by X-ray diffraction (XRD) and the lattice parameters were determined from a least-squares fit of the observed d values. The resistivity was measured, in the temperature range of 14 to 300 K, using four-probe technique in a closed cycle refrigerator.

i. X-ray diffraction and iodometric titration

In Figs. 16a-16d we show the x-ray patterns of all the four series of samples of $\text{ErBa}_2\text{Cu}_{3-x-y}\text{Zn}_x\text{Fe}_y\text{O}_{7-\delta}$, for $y = 0, 0.03, 0.09, 0.18$ respectively, and for varying Zn content. All the samples were found to be single phase. The calculated a , b and c lattice parameters, and iodometrically measured oxygen content for all the samples investigated in the present study are listed in Table 9. The observed variation of the lattice parameters and oxygen content as a function of Fe doping for the present series of the sample was very similar to that reported by other workers earlier [45,64,65,70,71]. As expected, the oxygen content was found to increase slightly with the increased doping of Fe in the samples. The samples of $y = 0.0$ and 0.03 series show an orthorhombic ($a \neq b$) structure, where as those of $y = 0.09$ and 0.18 series are all

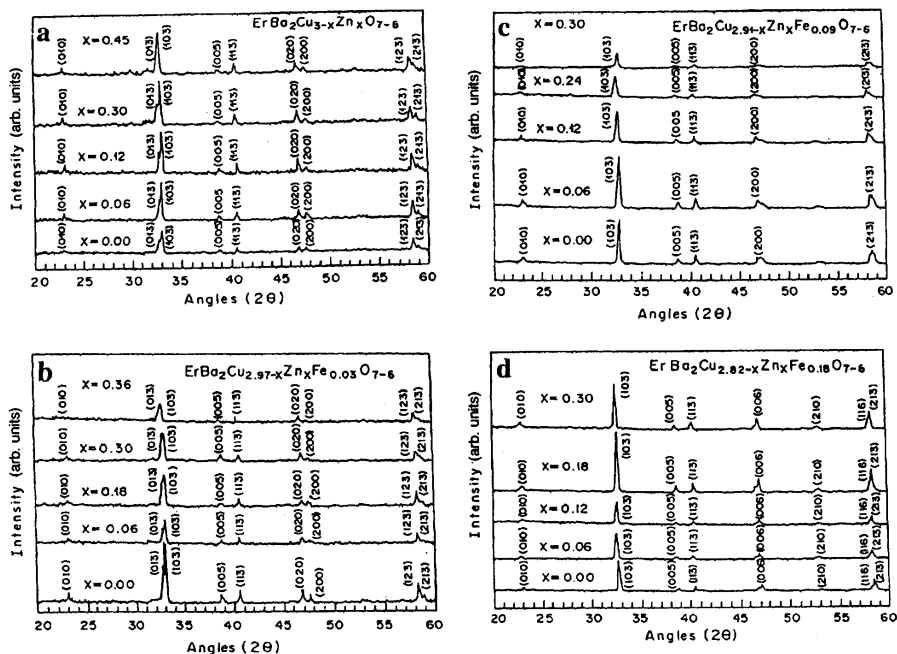


Fig. 16. X-ray diffraction patterns of $\text{ErBa}_2\text{Cu}_{3-x}\text{Zn}_x\text{Fe}_y\text{O}_{7-\delta}$ samples with varying Zn content and constant Fe content: (a) $y = 0.0$, (b) $y = 0.03$, (c) $y = 0.09$ and (d) $y = 0.18$.

tetragonal ($a=b$). Same can also be appreciated by the observed splitting (Figs. 16a and 16b) of the (020) - (200) and (123) - (213) reflections showing orthorhombic nature of $y=0.0$ and 0.03 based series. Whereas the suppression of the splitting of (020) and (123) reflections (Figs. 16c and 16d) illustrate the tetragonal nature of $y = 0.09$ and 0.18 based series. As a function of Zn content, both the former series of samples with respective constant Fe contents of $y = 0.0$ and 0.03, show no change in orthorhombic distortion (o.d) for $x < 0.24$, where after for $x \geq 0.24$ a decrease in the o.d is observed (see Table 9). All the four series of samples, with different constant Fe contents, also show a small oxygen loss with increasing Zn content. However, the Cu valence (p^+ , see Table 9), calculated from charge neutrality condition for all the samples over the entire studied x and y range, does not show any significant difference compared to the optimum value of 2.28^+ observed for $x=0, y=0$ sample.

ii. Normal state resistivity and T_c

Resistivity data as a function of temperature, $\rho(T)$, of the $\text{ErBa}_2\text{Cu}_{3-x}\text{Zn}_x\text{Fe}_y\text{O}_{7-\delta}$ system for $0 \leq x \leq 0.45$ and $0 \leq y \leq 0.18$ are presented in Figs. 17a-17d. In general the ρ - T curves involve a linear region, which for low x and y (including $x=y=0$) extends down to a temperature close to $T \approx T_c$, while for higher x and y , the linear region is reduced and persists only until $T > T_c$. The linear part of the ρ - T curves has a positive slope $d\rho/dT$ and its extrapolation to $T=0$ K provides the residual resistivity, say ρ_0 . While the ρ_0 is connected with impurity scattering, the

Table 9. a, b and c lattice parameters (in Å), orthorhombic distortion (o.d.=(b-a)/b), total oxygen content (7- δ), effective Cu valence (p^+), and $T_c(\rho=0)$ of a co-doped $\text{ErBa}_2\text{Cu}_{3-x-y}\text{Zn}_x\text{Fe}_y\text{O}_{7-\delta}$ system for different values of x and y.

| x | y | a | b | C | o.d. | 7- δ | p^+ | $T_c(\text{K})$ |
|------|------|-------|-------|--------|-------|-------------|-------|-----------------|
| 0.00 | 0.00 | 3.816 | 3.886 | 11.683 | 0.018 | 6.93 | 2.28 | 90.5 |
| 0.03 | 0.00 | 3.814 | 3.882 | 11.684 | 0.018 | 6.93 | 2.29 | 80.5 |
| 0.06 | 0.00 | 3.813 | 3.887 | 11.683 | 0.019 | 6.92 | 2.29 | 69 |
| 0.12 | 0.00 | 3.819 | 3.881 | 11.683 | 0.016 | 6.92 | 2.29 | 52 |
| 0.18 | 0.00 | 3.818 | 3.884 | 11.689 | 0.017 | 6.91 | 2.29 | 50 |
| 0.24 | 0.00 | 3.821 | 3.880 | 11.690 | 0.015 | 6.89 | 2.28 | 36 |
| 0.30 | 0.00 | 3.829 | 3.876 | 11.699 | 0.012 | 6.86 | 2.27 | 32 |
| 0.36 | 0.00 | 3.834 | 3.854 | 11.701 | 0.005 | 6.82 | 2.24 | |
| 0.45 | 0.00 | 3.838 | 3.848 | 11.705 | 0.003 | 6.80 | 2.23 | |
| 0.00 | 0.03 | 3.836 | 3.867 | 11.683 | 0.008 | 6.94 | 2.29 | 88 |
| 0.03 | 0.03 | 3.838 | 3.860 | 11.682 | 0.006 | 6.94 | 2.29 | 76 |
| 0.06 | 0.03 | 3.834 | 3.865 | 11.683 | 0.008 | 6.93 | 2.29 | 63 |
| 0.12 | 0.03 | 3.839 | 3.863 | 11.683 | 0.006 | 6.94 | 2.30 | 50 |
| 0.18 | 0.03 | 3.840 | 3.859 | 11.686 | 0.005 | 6.93 | 2.30 | 45.5 |
| 0.24 | 0.03 | 3.836 | 3.858 | 11.688 | 0.006 | 6.92 | 2.30 | 43 |
| 0.30 | 0.03 | 3.842 | 3.856 | 11.689 | 0.004 | 6.88 | 2.27 | |
| 0.36 | 0.03 | 3.850 | 3.855 | 11.690 | 0.001 | 6.85 | 2.25 | |
| 0.00 | 0.09 | 3.854 | 3.854 | 11.681 | 0.00 | 6.96 | 2.29 | 83 |
| 0.03 | 0.09 | 3.859 | 3.859 | 11.681 | 0.00 | 6.95 | 2.29 | 65 |
| 0.06 | 0.09 | 3.856 | 3.856 | 11.680 | 0.00 | 6.96 | 2.29 | 46 |
| 0.12 | 0.09 | 3.863 | 3.863 | 11.680 | 0.00 | 6.95 | 2.29 | 41.5 |
| 0.18 | 0.09 | 3.860 | 3.860 | 11.678 | 0.00 | 6.94 | 2.29 | 36.5 |
| 0.24 | 0.09 | 3.861 | 3.861 | 11.675 | 0.00 | 6.94 | 2.29 | 31.5 |
| 0.30 | 0.09 | 3.857 | 3.857 | 11.670 | 0.00 | 6.90 | 2.27 | |
| 0.00 | 0.18 | 3.853 | 3.853 | 11.680 | 0.00 | 6.97 | 2.27 | 71.5 |
| 0.03 | 0.18 | 3.853 | 3.853 | 11.683 | 0.00 | 6.97 | 2.27 | 44 |
| 0.06 | 0.18 | 3.856 | 3.856 | 11.684 | 0.00 | 6.97 | 2.27 | 24.5 |
| 0.12 | 0.18 | 3.856 | 3.856 | 11.683 | 0.00 | 6.95 | 2.27 | 22.5 |
| 0.18 | 0.18 | 3.851 | 3.851 | 11.684 | 0.00 | 6.95 | 2.27 | 20.5 |
| 0.24 | 0.18 | 3.854 | 3.854 | 11.686 | 0.00 | 6.94 | 2.27 | |
| 0.30 | 0.18 | 3.851 | 3.851 | 11.689 | 0.00 | 6.91 | 2.25 | |

slope $d\rho/dT$ determined from the linear region of the ρ -T curve is connected with carrier-carrier scattering. In the following we shall consider only such a resistivity slope and denote it by $(d\rho/dT)_{cc}$, where cc stands for 'carrier-carrier'. For increasing x and/or y, the ρ -T curves tend to show an upturn (-ve $d\rho/dT$) for decreasing temperatures. This upturn corresponding to a minimum in $\rho(T)$, at T_{\min} , may be accounted by a negative $\ln T$ term [72-74]. As shown in Figs. 17a-17d, in general the ρ -T curves can indeed be fitted well by

$$\rho = \rho_0 + \rho_1 T - \rho_2 \ln T \quad (6)$$

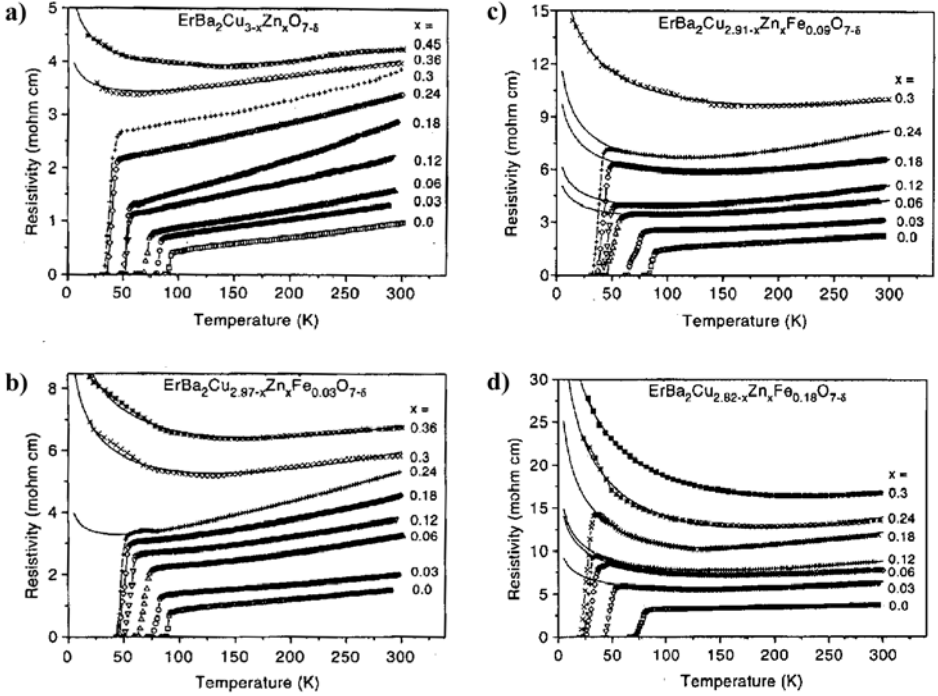


Fig. 17. Resistivity versus temperature for $\text{ErBa}_2\text{Cu}_{3-x}\text{Zn}_x\text{Fe}_y\text{O}_{7-\delta}$ samples for different values of Zn content, with (a) $y=0.0$, (b) $y=0.03$, (c) $y=0.09$, and (d) $y=0.18$. The solid lines represent a fit of the equ.6.

The origin of the logarithmic divergence of the resistivity at lower temperatures, in principle, may lie in the Kondo effect [75], localization [76], interaction effect [77] or pinning of the dynamically fluctuating striped phase [78-80], shall be taken up later in the discussion.

iii. $\rho(T)$ of samples containing either Zn or Fe

The $\rho(T)$ data of the Fe-free ($y=0$) Zn-doped samples are shown in Fig. 17a. Up to $x=0.12$ (4% Zn) the ρ varies almost linearly with T . In contrast, the $x=0.18$ and 0.30 samples show a non-linear $\rho(T)$ behaviour, which appears to be due to a cross over of one linear region into another linear region of different slope around 175 K and 150 K, respectively [81]. Such a behaviour of ρ vs. T plots in the Zn doped system has been reported previously by several authors [82] (see also [83]). The samples with $x \geq 0.36$ show an upturn in $\rho(T)$. The temperature T_{\min} where the upturn just begins is found to increase with Zn content. T_{\min} as a function of x is shown in Fig. 18. Another feature of the Fe-free Zn doped samples is that the ρ_0 increases monotonically with the Zn concentration, as depicted in Fig. 19a. The slope $(d\rho/dT)_{cc}$ increases gradually with increasing Zn concentration until $x=0.3$, where after it starts to decrease. This has been shown in Fig. 20. The critical temperatures T_c (estimated

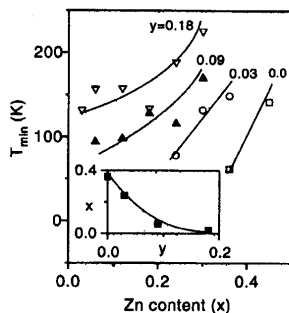


Fig. 18. T_{\min} versus Zn content x for different values of Fe content y . Inset: x versus y ; x and y correspond to the values where the upturn in $\rho(T)$ is first observed in 1-2-3 system in Figs. 17a-17d. The solid lines are a guide to the eye.

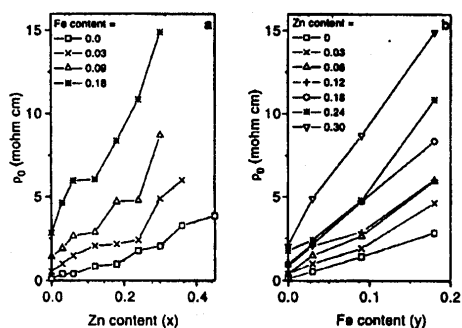


Fig. 19. Residual resistivity ρ_0 versus: (a) Zn content x for different values of Fe content y , (b) Fe content y for different values of Zn content x .

from $\rho=0$ condition) also decrease monotonically with the Zn concentration (cf. Fig. 21a). For up to $x=0.12$ the rate of T_c degradation $|dT_c/dx|$ is about 10 K/at% Zn. This is consistent with earlier observations of other workers on both polycrystalline [45,64,65,70,71] and single crystalline material (see Fig. 21a for a comparison with results on Zn-substituted single crystals taken from Refs.[82,84]). Thereafter T_c degrades slowly up to $x=0.3$, followed by a rapid suppression again (as seen in Fig. 17, the $\rho(T)$ curves of the samples with $x \geq 0.36$ do not show any sign of superconducting drop down to 15 K).

The behaviour of the $\rho(T)$ for the Zn-free ($x=0$) Fe doped samples may be seen in the lowest curves of each of the Figs. 17a-17d. It turns out that ρ varies linearly with T for all the Fe concentration considered here ($y \leq 0.18$). In particular, the T dependence of ρ for the 6% Fe sample ($y=0.18$, $x=0$) is qualitatively different from the 6% Zn sample ($x=0.18$, $y=0$). Moreover, the residual resistivity ρ_0 is significantly higher in the case of Fe-doped samples of the same concentration as for Zn. For instance (from Figs. 19a and 19b), $\rho_0(x=0.18, y=0) = 1 \text{ m}\Omega\text{cm} < \rho_0(x=0, y=0.18) = 2.9 \text{ m}\Omega\text{cm}$. Despite this, the rate of T_c degradation by Fe (cf. Fig. 21b), $|dT_c/dy|$, is much less than that for the corresponding concentration of Zn. In fact,

$|dT/dy|_{x=0}$ is about 3 K/at.% Fe, which is consistent with the earlier reports on both polycrystalline [45,64,65,70,71] and single crystalline material (see Fig. 21b for a comparison with results on Fe-substituted single crystals taken from Ref.[85]).

While the Fe-free Zn doped samples and the Zn-free Fe doped samples show a remarkable difference in their ρ_0 and T_c values, it is surprising to note that for low concentrations in both the cases the slope $(dp/dT)_{cc}$ seem to be affected by similar magnitudes (Fig. 20). In fact, up to a concentration of 3 at% of Zn or Fe, $(dp/dT)_{cc}$ increases monotonically by about the same magnitudes. For larger concentrations of Zn or Fe, the behaviour of $(dp/dT)_{cc}$ differs qualitatively as well as quantitatively.

iv. $\rho(T)$ of samples containing both Zn and Fe

First we consider the variation of $T_{min}(x,y)$ as shown in Fig. 18 and its inset. The Zn content (x), where an upturn in $\rho(T)$ is first observed in the co-doped 1-2-3 samples (see Figs. 17a-17d), goes down rapidly as a function of increasing Fe content (y) (see inset Fig. 18). From Fig. 18 we find that, for constant Fe content, the T_{min} increases rapidly with further addition of Zn, and vice-a-versa. For instance, the T_{min} of the Fe-free ($x=0.3,y=0$) sample increases from 60 K to 150 K just by an addition of $y=0.03$ Fe for the ($x=0.3,y=0.03$) sample. Whereas, increasing the Zn content by $x=0.03$ in the Fe-free ($x=0.3,y=0$) sample would have increased the T_{min} to around 90 K (cf. Fig. 18) only. Similarly, in the case of Zn-free ($x=0.0,y=0.18$) sample T_{min} increases from $T < 80$ K to 130 K just by an addition of $x=0.03$ Zn for the ($x=0.03,y=0.18$) sample. These are clear signatures of mutual interference of Zn and Fe in determining the normal state transport behaviour of the 1-2-3 system.

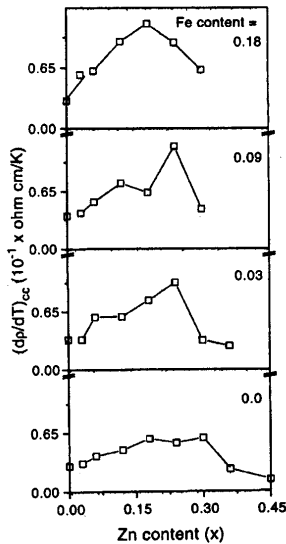


Fig. 20. Slope $(dp/dT)_{cc}$ versus Zn content x for different values of Fe content y .

The next quantity we consider for the situation of simultaneous presence of Zn and Fe is the residual resistivity $\rho_0(x,y)$. An interesting behaviour would be when the combined effect of Zn and Fe, as represented by $\rho_0(x,y)$, is not a direct summation of the individual effects of Zn and Fe, i.e., when

$$\rho_0(x,y) \neq \rho_0(x,0) + \rho_0(0,y) - \rho_0(0,0) \quad (7)$$

Here $\rho_0(0,0)$ is subtracted in the right-hand-side because the residual resistivity of the pure sample is contained in all $\rho_0(x,y)$, $\rho_0(x,0)$ and $\rho_0(0,y)$. For $\rho_0(x,y)$ to be a direct summation of $\rho_0(x,0)$ and $\rho_0(0,y)$ (to within the residual resistivity of the pure sample, $\rho_0(0,0)$), the $\rho_0(x,y)$ vs. x curves, or equivalently the $\rho_0(x,y)$ vs. y curves, should be parallel to each other. From Figs. 19a and b we see that this is not the case except for certain portion of the curves. Thus in general, $\rho_0(x,y)$ is not a direct sum of $\rho_0(x,0)$ and $\rho_0(0,y)$. For example, the $\rho_0(x,0)$ vs. x curve is generally superlinear for $x=0.03$ to $x=0.24$. On the other hand $\rho_0(x,0.03)$ is sublinear for the same range of x . This means that these two curves cannot be connected by a constant change of $\rho_0(0,0.03)$, so that $\rho_0(x,0.03)$ will show a significant interference effect (equ.7).

We now turn to the behaviour of $(dp/dT)_{cc}$ under the combined effect of Zn and Fe. From Fig. 20 it follows that, for different y , $(dp/dT)_{cc}$ as a function of x goes through a maxima, and the corresponding value of x decreases with increasing y . Clearly, for samples with $y=0.0$ ($y=0.18$) the maxima occurs at $x=0.36$ ($x=0.24$). From Fig. 20 we also see that $(dp/dT)_{cc}$ vs. x curves below the maxima differ qualitatively for different y . For example, for $x=0.03$, the value of $(dp/dT)_{cc}$ increases from 0.31 to 0.57 when y increases from 0.0 to 0.18 respectively.

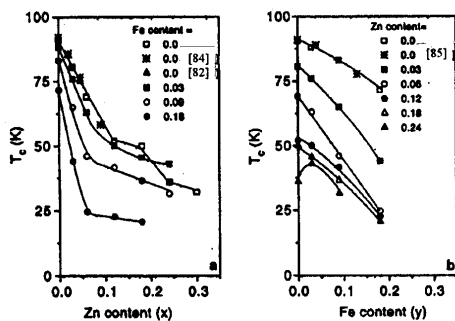


Fig. 21. Superconducting transition temperatures $T_c(\rho=0)$ as a function of x and y for $\text{ErBa}_2\text{Cu}_{3-x-y}\text{Zn}_x\text{Fe}_y\text{O}_{7-\delta}$ samples. (a) For varying Zn content and constant Fe content in the samples. Also shown are the data of Zn-doped (Fe-free) 1-2-3 single crystals from Refs. [82,84]. Note that the data from Ref.[82] has been shifted up by 3 K for comparison and limited up to $x \leq 0.052$, as crystals in Ref.[82] with higher x show a step in the superconducting transition. (b) For varying Fe content and constant Zn content in the samples. Also shown are the data of Fe-doped (Zn-free) 1-2-3 single crystals from Ref. [85].

In contrast, for the same change in y , the maximum value attained by $(dp/dT)_{cc}$ as a function of x increases from 0.60 to 1.12. This means that the combined effect of Zn and Fe for determining $(dp/dT)_{cc}$ is not a direct summation of their individually determined $(dp/dT)_{cc}$'s.

We next turn to the behaviour of the T_c under the simultaneous presence of the Zn and Fe atoms. From Fig. 21a we see that for low concentrations of Zn ($x \leq 0.06$), addition of Fe

impurities increases the rate of suppression of T_c . After $x = 0.06$ a cross over takes place in that now, because of the presence of Fe, the rate of suppression of T_c with Zn is less than that for the Fe-free samples. At higher concentrations of Zn ($x \geq 0.18$), with exact value of x depending upon the Fe content y , T_c gets suppressed rapidly again (refer to the ρ - T curves which do not show a T_c in Figs. 17a-17d). Another interesting feature of the T_c variation with Zn and Fe is that for the $x=0.24, y=0.03$ sample the T_c is higher than that for the $x=0.024, y=0$ sample (see Fig. 21a). This means that while Zn and Fe both suppress T_c individually, their combined effect may lead to a situation where $T_c(x_1+y_1) > T_c(x_1+y_2)$ with $y_1 > y_2$ (here x_i and y_i ($i=1,2$) are the values of x and y respectively).

v. Correlation of T_c with T_{min} , ρ_0 and $(dp/dT)_{cc}$

We now examine the possible correlation of T_c with ρ_0 , $(dp/dT)_{cc}$ and T_{min} on the basis of their variation extracted above from the data presented in Figs. 17a-17d.

(1) From Figs. 18 and Fig. 21a, it can be appreciated that in general higher the T_{min} , lower is the T_c . In other words, it seems that the temperature, at which the logarithmic divergence in $\rho(T)$ occurs, correlates with the T_c of the sample. However, it is interesting to note that such a correlation is strictly true only for the samples compared within any of the four ($y=0.0, 0.03, 0.09, 0.18$) series. It might not work for samples cross-compared among different series. For instance, the sample $x=0.03, y=0.18$ has a $T_{min}=131$ K and $T_c=44$ K, whereas the sample $x=0.36, y=0.0$ has a $T_{min}=62$ K and $T_c < 15$ K.

(2) A comparison of Figs. 19a and 21a makes it clear that the suppression of T_c with x (for a given y) becomes large or small depending upon whether the corresponding increase of ρ_0 is large or small. This means that T_c correlates with ρ_0 . In general, larger the ρ_0 smaller is the T_c of the samples. However, as noted above for T_{min} , a strict correlation of T_c and ρ_0 also occurs only for the samples compared within the same series of the samples, and not always for the ones cross-compared among different series. For instance, the sample $x=0.03, y=0.18$ has a $\rho_0=4.63$ m Ω cm and $T_c=44$ K, where as the sample $x=0.30, y=0.0$ has a $\rho_0=2.049$ m Ω cm and $T_c=32$ K. Similarly, comparing the $x=0.24, y=0.0$ sample to the $x=0.24, y=0.03$ sample, T_c increases despite an increase of ρ_0 .

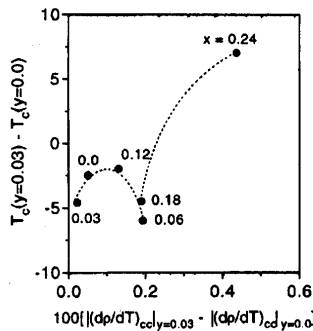


Fig. 22. Relation between $T_c(y=0.03) - T_c(y=0.0)$ versus $|(dp/dT)_{cc}|_{y=0.03} - |(dp/dT)_{cc}|_{y=0.0}$ for samples with varying Zn content.

(3) In order to examine how T_c relates with $(dp/dT)_{cc}$ we compare Figs. 20 and 21a. The correlation of T_c with $(dp/dT)_{cc}$ is found to be opposite to that shown by ρ_0 . For instance, for the values of x , corresponding to the region just below the maxima of $(dp/dT)_{cc}$ (see Fig. 20), the rate of decrease of $T_c(x)$ reduces (see Fig. 21a) substantially. And for the values of Zn content, corresponding to the region after the maxima of $(dp/dT)_{cc}$, the T_c tends to vanish rapidly (refer to the ρ - T curves which do not show superconducting transitions in Figs. 17a - 17d). These results imply that an increase in $(dp/dT)_{cc}$ may favour an enhancement in T_c and vice-a-versa. In order to further illustrate that how general this result is, we consider the Zn doped samples for $0 \leq x \leq 0.24$, and $y=0.0$ and 0.03 . The special feature of these samples is that for them ρ_0 changes relatively by a smaller amount for a large range of x . We plot $T_c(y=0.03) - T_c(y=0.0)$ vs. $(dp/dT)_{cc}|_{y=0.03} - (dp/dT)_{cc}|_{y=0.0}$ for different values of x ($0 \leq x \leq 0.24$) in Fig. 22. It is clear that with increased $(dp/dT)_{cc}$ the suppression of T_c is reduced, except for the $x=0.06$ and 0.18 samples. Indirectly, this means that in general the increase of $(dp/dT)_{cc}$ tends to increase T_c . The increase of T_c of the $x=0.24$, $y=0.03$ sample as compared to the $x=0.24$, $y=0.0$ sample is explained naturally on this basis. In fact, according to Fig. 18 there is a considerable enhancement of $(dp/dT)_{cc}$ while going from the $(x,y)=(0.24,0.00)$ sample to the $(x,y)=(0.24,0.03)$ sample. On the other hand ρ_0 increases relatively only by a smaller amount for the same change in the sample composition (cf. Fig. 19a). Thus it is quite likely that the effect of $(dp/dT)_{cc}$ on T_c overpowers the effect of ρ_0 , resulting in a net enhancement of T_c .

Further support in favour of this observation comes from the data of the $(x=0.12, y=0.09)$, $(x=0.12, y=0.18)$, $(x=0.18, y=0.09)$ and $(x=0.18, y=0.18)$ samples. For these samples (cf. Fig. 19b) $[\rho_0(y=0.18) - \rho_0(y=0.09)]_{x=0.12} \approx [\rho_0(y=0.18) - \rho_0(y=0.09)]_{x=0.18}$. On the other hand the corresponding difference of $(dp/dT)_{cc}$ for $y=0.09$ and $y=0.18$ are much different for $x=0.12$ and $x=0.18$. In fact, $[(dp/dT)_{cc}|_{y=0.18} - (dp/dT)_{cc}|_{y=0.09}]_{x=0.12} \approx 0.15/100$, while $[(dp/dT)_{cc}|_{y=0.18} - (dp/dT)_{cc}|_{y=0.09}]_{x=0.18} \approx 0.50/100$. The decrease of T_c for the case of the $x=0.18$ sample of $y=0.09$ and $y=0.18$ is about 14 K, while it is about 18 K for the $x=0.12$ samples. Since the difference of ρ_0 's are almost the same for the two set of samples, and since the difference of $(dp/dT)_{cc}$ is more for the $x=0.18$ samples, it supports that an increase in $(dp/dT)_{cc}$ helps increasing T_c . It may be noted that similar situation arises also for the $x=0.06$, 0.12 and $y=0.09$, 0.18 samples.

vi. Possible origin of superconductivity

We have seen that increasing T_{min} and ρ_0 in general tends to degrade T_c , while increasing $(dp/dT)_{cc}$ enhances T_c . In cuprate superconductors this kind of effect of ρ_0 on T_c may arise mainly in two ways. (1) The cuprate superconductors are mainly d-wave superconducting systems. So potential scattering will lead to pair breaking. Since the potential scattering is proportional to ρ_0 , increasing ρ_0 implies enhanced pair breaking. Thus T_c will reduce with increasing ρ_0 . (2) The other source of reduction of T_c with increasing ρ_0 lies in the pinning of the dynamically fluctuating striped phase. It has been [86-89] suggested that pinning of the dynamically fluctuating striped phase may lead to suppression of superconductivity.

In order to see which of these two possibilities, as supported by the present data, determine the connection of T_c with ρ_0 we proceed as follows. We first address the issue of the observed logarithmic divergence of $\rho(T)$ at lower temperatures in both superconducting as well as non-superconducting samples (cf. Figs. 17a-17d). Recently [78-80], in the underdoped regime, for both La(Sr)-214 and Zn-substituted Y-123 systems, the pinning of dynamically striped phase has been argued as a possible source of the -ve $\ln T$ behaviour of $\rho(T)$. It is interesting to note that although our samples are not in an underdoped regime (see Table 9), they still show a logarithmic divergence of $\rho(T)$. We suggest that the observed T_{min} in our doped 1-2-3 samples

may mark a change from depinned ($T > T_{\min}$) to relatively pinned ($T < T_{\min}$) striped phase resulting from substitutional disorder due to Zn and Fe.

Now we discuss that how such a possibility further determines the connection of T_c with ρ_0 . On the basis of the present data we have seen that the suppression of T_c with Zn or Fe is reduced with increasing $(dp/dT)_{cc}$. The way we have defined $(dp/dT)_{cc}$ makes it clear that its physical origin lies in the carrier-carrier scattering. In fact we do not expect a T-dependent resistivity from carrier-impurity scattering. There may, however, be a T-dependent contribution to the resistivity from electron-phonon scattering. But in cuprates such a contribution is significantly weaker than the contribution due to carrier-carrier scattering. We may, therefore, overlook the electron-phonon scattering rate as compared to the carrier-carrier scattering rate. Increase of $(dp/dT)_{cc}$ implies increase of carrier-carrier scattering rate unless there is a change in the carrier density and/or density of states at the Fermi level E_F . The Cu valence (p^+ , see Table 9), over the entire x and y range studied in present work, does not show any significant variation. We may thus assume that substitution of either Zn and / or Fe does not change the carrier density. This is also supported by earlier studies [90], in the case of Zn substitution in 1-2-3 system, where no change was observed in carrier density and density of states at the Fermi level E_F . So, the viewpoint that Zn doping increases the $(dp/dT)_{cc}$ implies increase of carrier-carrier scattering rate.

For zinc-free Fe-doped samples the resistivity ρ varies linearly with temperature for all the Fe doped samples considered here (cf. the lowest ρ -T plots in Figs. 17a-17d). Thus, there is no signature of (weak) localization in these ($x=0$) samples in the measured temperature range. Moreover, the variation of $(dp/dT)_{cc}$ with Fe is about the same as for the same concentration of Zn up to $x,y \leq 0.09$. Since Fe substitutes in the Cu-O chains, the density of states at E_F determined mainly by the Cu(3d) and O(2p) hybridized band of CuO_2 planes may not get affected straightforwardly. On these bases we hope that the increase of $(dp/dT)_{cc}$ due to Fe doping also primarily implies increase of carrier-carrier scattering rate in the samples considered here, although the rate of increment may be quantitatively different from the Zn case.

Thus, in general, increase of $(dp/dT)_{cc}$ appears to imply enhanced carrier-carrier scattering rate $1/\tau_{cc}(T)$ in the samples considered here. But the increase of carrier-carrier scattering rate is known to suppress T_c [74,91]. This contradicts what we have found above on the basis of the present data. A plausible solution of such a discrepancy is that suppression of T_c due to Zn and /or Fe arises due to pinning of the dynamically fluctuating striped phase. When this is so, ρ_0 will signify the extent of pinning of the striped phase for a given kind of impurity. An impurity tends to pin the dynamically fluctuating striped phase because the impurity is fixed in the sample. For the case of the carrier-carrier scattering the situation is different because now the source of scattering, a carrier itself, is mobile. Thus, we expect that it (the carrier) will tend to depin the striped phase. This, in turn, will tend to relatively enhance T_c . In this way, suppression of T_c due to pinning of the striped phase appears to be consistent with the observed correlation of T_c with $(dp/dT)_{cc}$ also.

vii. Interference effects of the Fe and Zn dopants

We have seen that in general the effect of simultaneous presence of (x/3) at.% Zn and (y/3) at.% Fe is not equal to the simple addition of the effects of (x/3) at.% Zn (in Fe-free samples) and (y/3) at.% Fe (in Zn-free samples) on the residual resistivity ρ_0 , resistivity slope $(dp/dT)_{cc}$, T_{\min} and on the transition temperature T_c . We illustrate now, that the interference effects of Fe and Zn dopant are expected and follow directly from their different site-dependent impacts on the properties of 1-2-3 system. Considering that Zn substitutes directly

in the CuO_2 plane and Fe occupies the Cu-site in the Cu-O chains, the latter can disorder the chains significantly [92] and reduce the coupling of the CuO_2 planes (i.e., more anisotropic) along the c-axis [60]. Thus in principle, each of the four series with different constant Fe content ($y=0.0, 0.03, 0.09, 0.18$) should represent series of samples with different anisotropy. In such a case, depending on the value of Fe content in Cu-O chains, Zn-doping in CuO_2 planes may result in different functional forms for $\rho_0(x)|_{y=\text{const}}$, $(d\rho/dT)_{\text{cc}}(x)|_{y=\text{const}}$, $T_{\text{min}}(x)|_{y=\text{const}}$, and $T_c(x)|_{y=\text{const}}$. In other words, change in the anisotropy of the 1-2-3 system leads to a change in the electrical transport in the CuO_2 planes which does not fit with a direct summation of the individual effects of Fe and Zn dopants. The observation of interference effects of Fe and Zn in 1-2-3 system can explain certain discrepancies and has interesting consequences which we point out below.

An apparent discrepancy that is related with ρ_0 , and was not discussed until now, has been that although the rise in ρ_0 is significantly higher in the case of Zn-free Fe-doped samples as compared to the Fe-free Zn-doped samples, the suppression of T_c is much higher in the latter case (see subsection iii). Since the striped phase resides in the CuO_2 planes, and Zn (Fe) substitutes directly in the CuO_2 planes (Cu-O chains), it should pin the striped phase strongly (weakly), leading to a faster (slower) suppression of T_c . Moreover, since Fe doping can cause severe disorder in Cu-O chains, the higher ρ_0 can result partly from the loss of chain conductivity and partly from the increased anisotropy of the 1-2-3 system. The latter cause for increased ρ_0 , which probably is linked up with the c-axis transport or the interplanar striped phase interactions, is not completely clear at present.

One interesting occasion where the interference effects of Fe and Zn showed up significantly, was, the observation of continuous decrease in the Zn content with increasing Fe content in the samples for the evolution of -ve $d\rho/dT$ (see inset Fig. 18) in the 1-2-3 system. Since the increase of Fe in Cu-O chains increases the anisotropy of the 1-2-3 system, we infer that higher anisotropy favours the pinning of the dynamically fluctuating striped phase, which is then achieved at smaller Zn content. This can also explain the fact that the increase in T_{min} (Fig. 18) and decrease in T_c (Fig. 21a) becomes faster as a function of Zn with the increased co-doping of Fe in our samples.

viii. Summary

We presented results of resistivity vs. temperature behaviour for the co-doped $\text{ErBa}_2\text{Cu}_{3-x-y}\text{Zn}_x\text{Fe}_y\text{O}_{7-\delta}$ system. From the ρ -T curves we have extracted the residual resistivity $\rho_0(x,y)$, resistivity slope corresponding to the carrier-carrier scattering $(d\rho/dT)_{\text{cc}}$, a characteristic temperature marking the upturn in ρ -T curves T_{min} , and the critical temperature T_c . On the basis of these parameters it is found that in general the impurities Zn and Fe interfere with each other significantly. The plausible reason for this has been identified with different site-dependent impacts of Zn (goes in CuO_2 planes) and Fe (goes in Cu-O chains), where the latter effects the anisotropy of the 1-2-3 system. As a consequence of this ρ_0 , $(d\rho/dT)_{\text{cc}}$, T_{min} or T_c cannot be expressed, in general, as a direct sum of the individual effects of Zn and Fe.

An attempt has been made to understand the correlation of T_c with T_{min} , ρ_0 and $(d\rho/dT)_{\text{cc}}$. It is found that increasing T_{min} and ρ_0 tends to suppress T_c , while increasing $(d\rho/dT)_{\text{cc}}$ tends to enhance T_c . On the basis of the generally acclaimed belief that the cuprate superconductors are d-wave superconductors, it has been argued that potential scattering is not adequate for explaining the correlation of T_c with T_{min} , ρ_0 and $(d\rho/dT)_{\text{cc}}$ simultaneously. We proposed that T_{min} , which marks the onset of logarithmic divergence of $\rho(T)$ observed at low temperatures, may characterize a crossover temperature from a depinned to a relatively pinned striped phase. In furtherance, pinning of the dynamically fluctuating striped phase in accordance with

T_{\min} and ρ_0 , and depinning of this phase due to $(dp/dT)_{cc}$ gives a plausible explanation for the observed correlation of T_c with T_{\min} , ρ_0 and $(dp/dT)_{cc}$.

5.2.2 $\text{Yb}_{1-x}\text{Pr}_x\text{Ba}_2\text{Cu}_3\text{O}_{7-\delta}$ system

Polycrystalline samples of the series $\text{Yb}_{1-x}\text{Pr}_x\text{Ba}_2\text{Cu}_3\text{O}_{7-\delta}$, with x ranging from 0 to 1, were synthesized through standard solid state reaction method. For preparation and structural characterization details see Ref. [93]. The samples were then characterized for their phase purity and lattice parameters by x-ray diffraction. The resistivity measurements were obtained using standard four-probe technique. The dc magnetization as a function of temperature (1.5 to 100 K) was measured using a commercial squid-magnetometer in field range of 0 - 50 kOe.

i. Experimental results

Owing to the small ionic size of Yb as compared to most other rare-earths, the x-ray pattern of pure Yb-123 generally shows a few low intensity impurity peaks. Interestingly however our present studies revealed that substitution of Yb by the larger Pr ion resulted in a phase pure material. As depicted in Fig. 23, the x-ray patterns of Yb(Pr)-123 with varying x show a single phase nature of the samples. Table 10 shows the variation of lattice parameters a , b and c , and orthorhombic distortion for all values of x . The increase of c -axis parameter with Pr indicates the substitution of larger Pr^{3+} ion (1.14 Å) in the place of smaller Yb^{3+} ion (0.98 Å). For all values of x the samples show an orthorhombic structure. However, with an increase in x (see Table 10) the orthorhombic distortion decreases monotonically. The evolution of the crystallographic splittings (see Fig. 23), for instance [020], [200] and [123], [213] supports the change in the orthorhombic distortion. It is also worth pointing out that, for a change in x from 0 to 1, the c -axis increases by 0.08 Å in case of Yb(Pr)-123 as compared to 0.04 Å for Y(Pr)-123 [94]. This may indicate that, due to a smaller size of Yb^{3+} ion (0.98 Å) in comparison to Y^{3+} ion (1.02 Å), the enveloping CuO_2 planes in the former case are relatively compressed for $x < 1$.

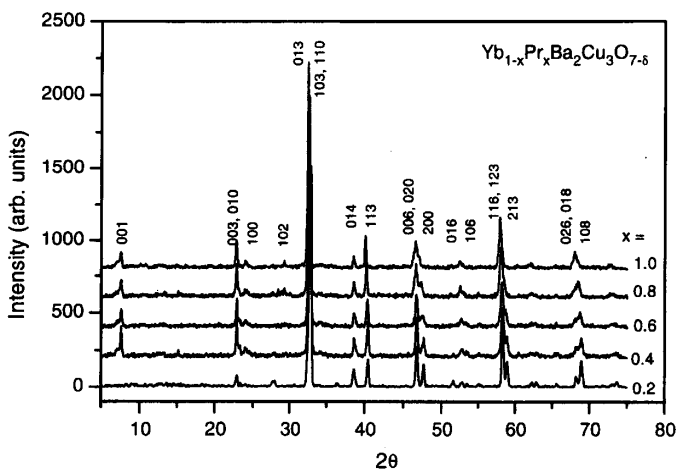


Fig. 23. X-ray diffraction patterns for various x values in $\text{Yb}_{1-x}\text{Pr}_x\text{Ba}_2\text{Cu}_3\text{O}_{7-\delta}$.

Table 10. Lattice parameters (in Å) a, b and c, and orthorhombic distortion (o.d.= $[(b-a)/b] \times 100$) for $\text{Yb}_{1-x}\text{Pr}_x\text{Ba}_2\text{Cu}_3\text{O}_{7-\delta}$ system.

| x | a | b | c | o.d. |
|-----|---------|---------|---------|--------|
| 0 | 3.80326 | 3.87311 | 11.6433 | 1.8035 |
| 0.1 | 3.80472 | 3.87534 | 11.6425 | 1.8223 |
| 0.2 | 3.80950 | 3.87649 | 11.6477 | 1.7281 |
| 0.3 | 3.81653 | 3.88025 | 11.6578 | 1.6422 |
| 0.4 | 3.82074 | 3.88449 | 11.6677 | 1.6411 |
| 0.5 | 3.83080 | 3.88215 | 11.6797 | 1.3227 |
| 0.6 | 3.83464 | 3.88714 | 11.6824 | 1.3506 |
| 0.7 | 3.84709 | 3.89292 | 11.6994 | 1.1773 |
| 0.8 | 3.85670 | 3.89522 | 11.7028 | 0.9889 |
| 0.9 | 3.86585 | 3.89501 | 11.7312 | 0.7487 |
| 1.0 | 3.87991 | 3.90213 | 11.7279 | 0.5694 |

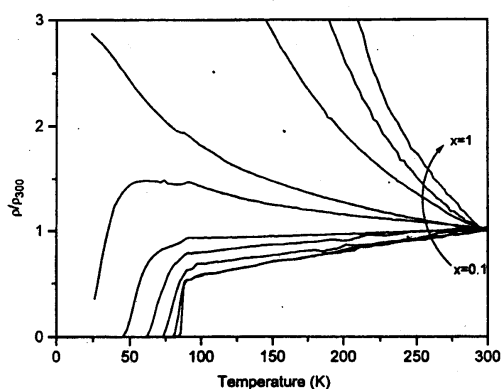


Fig. 24. Reduced resistivity (ρ/ρ_{300}) as a function of temperature for various x values (from 0.1 to 1 in steps of 0.1) in $\text{Yb}_{1-x}\text{Pr}_x\text{Ba}_2\text{Cu}_3\text{O}_{7-\delta}$.

Fig. 24 shows the normalized resistivity (ρ/ρ_{300}) as a function of temperature for all the samples of Yb(Pr)-123. As is evident from the figure, the $\rho(T)$ behaviour anomalously changes from metallic to semiconductor-like for values of $x \geq 0.6$. All samples with $x \leq 0.6$ show a transition to superconducting state. Fig. 25 shows the variation of reduced critical temperature ($T_c(x)/T_c(0)$) with Pr concentration. Similar data, taken from the literature, for the extrapolated value of critical concentration of Pr to quench superconductivity, x_c , is ~ 0.65 for Yb(Pr)-123 and ~ 0.55 for Y(Pr)-123 system. The observed increase of x_c with a decrease in R's ionic size is in line with the previous reports [43, 95, 97-102].

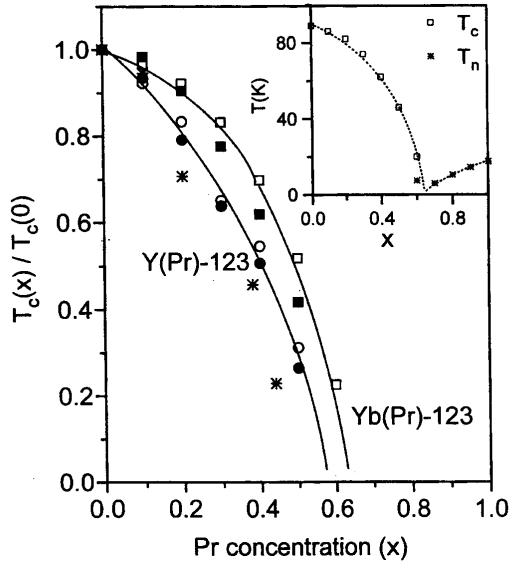


Fig. 25. Reduced critical temperature ($T_c(x) / T_c(0)$) as a function of Pr concentration x in $Yb_{1-x}Pr_xBa_2Cu_3O_{7-\delta}$ (present work), $Y_{1-x}Pr_xBa_2Cu_3O_{7-\delta}$ (filled circles [94] and open circles [95]) and single crystal $Y_{1-x}Pr_xBa_2Cu_3O_{7-\delta}$ (stars [96]). In the former the T_c determination by both $\rho=0$ (hollow squares) and diamagnetic onset (filled squares) are shown. Inset: T_c ($\rho=0$) and T_n as a function of x in $Yb_{1-x}Pr_xBa_2Cu_3O_{7-\delta}$.

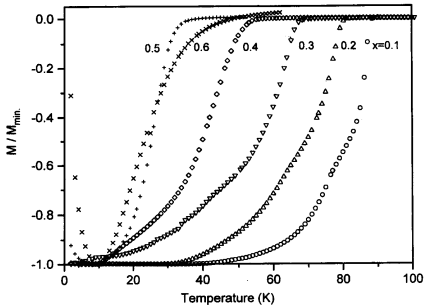


Fig. 26. M/M_{min} in an applied field $H=10$ Oe as a function of temperature for $x=0$ to 0.6 in $Y_{1-x}Pr_xBa_2Cu_3O_{7-\delta}$.

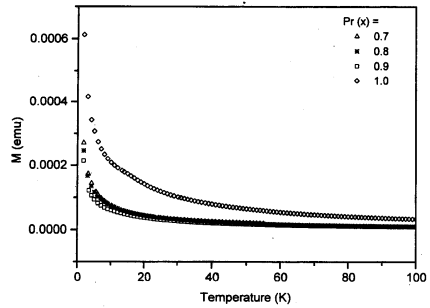


Fig. 27. M in an applied field $H=10$ Oe as a function of temperature for $x=0.7$ to $x=1$ in $Y_{1-x}Pr_xBa_2Cu_3O_{7-\delta}$.

Fig. 26 shows dc magnetization as a function of temperature, under an applied field $H=10$ Oe, for Yb(Pr)-123 samples with $x = 0$ to 0.6. The magnetization data shown in Fig. 26 is normalized by M_{\min} (the minimum value of M observed at low temperature side of the transition) to magnify the transitions for higher values of x . Values of M_{\min} , related with shielding fraction, decrease drastically with increase in x (results not shown). It decreases by over 25 times for sample with $x=0.6$ when compared to sample with $x=0.1$. Incomplete Meissner effect and similar dependence of shielding fraction on doping in HTSC has been always observed (e.g. see [53,54]) and are not yet completely understood. However, all the samples show a clear diamagnetic onset in $M(T)$, marking the superconducting transition. The $T_c(x)$ defined by the diamagnetic onset, also plotted in Fig. 25, show a decrease with an increase in x similar to that measured resistively. However, the diamagnetic onset for $x=0.6$ sample was expected at a temperature lower than that for the $x=0.5$ sample, whereas the observed behaviour is found contrary to that (see Fig. 26). This shows that for $x=0.6$ sample the diamagnetic onset has become anomalously broad. For samples with $x=0.7$ to 1.0 the $M(T)$ plots (see Fig. 27), under an applied field $H=10$ Oe, follow a Curie-Weiss- like and show no trace of superconductivity down to under 1.5 K. It is already known [43, 95, 97-102] that non-superconducting R(Pr)-123 system shows an antiferromagnetic ordering of Pr ions at a characteristic temperature $T_n(x)$. For our $x=1$ sample one could easily notice an anomaly corresponding to T_n at 17 K which became clear by plotting dM/dT vs. T . But for the other three samples of Fig. 27 the same was not so apparent. Following the work of Ref. [102], besides plotting dM/dT we tried also, by plotting M^{-1} vs. T and $\log(M)$ vs. $\log(T)$ to extract the $T_n(x)$ values from the $M(T)$ data. $T_n(x)$ values were most conspicuous only in $\log(M)$ versus $\log(T)$ plot, where a change in the slope for all the samples with $x \geq 0.7$ was observed, see Fig. 28a. The change in the slopes are also visible as peaks, typically observed at slightly lower (by ~ 3 K) temperatures, in the plots of $d\log(M)/d\log(T)$ vs. $\log(T)$, see Fig. 28b. The values of $T_n(x)$ (see inset of Fig. 25) corresponding to the change in slope, and their increase is in accord with the general trend reported for R(Pr)-123 system [43, 95, 97-102].

The superconducting samples of Yb(Pr)-123 with $x=0.5$ and 0.6 also showed upturns in $M(T)$ at low temperatures (see Fig. 26). These upturns presumably indicate the paramagnetic effect due to Pr ions competing with diamagnetism due to superconductivity. To check that the upturns are not due to magnetic ordering in these samples, the $M(T)$ measurements were carried out under high-applied fields up to 50 kOe. For instance, for $x=0.6$ sample, the $M(T)$ data under $H=10$ kOe is also included in Fig. 26. Interestingly, we observe a break in the slope at a characteristic temperature that may apparently indicate a T_n . However, firstly, as seen from the inset of Fig. 25, this value of $T_n(x=0.6)$ does not follow the same curve as that for non-superconducting samples with $x \geq 0.7$. Secondly, on a closer look at the data in Fig. 28, we see that the change in slope of $\log(M)$ vs. $\log(T)$ and the peak in $d\log(M)/d\log(T)$ plots at T_n gets weaker with decrease in x until $x=0.7$. However, for $x=0.6$, there is a fresh enhancement in the break of the slope and the peak (see Fig. 28). Considering that $x=0.6$ sample is superconducting, this may actually indicate a diamagnetic decrease occurring at a lower temperature when $H=10$ kOe as compared to that observed with smaller $H = 10$ Oe (see Fig. 26). Thirdly, the detailed heat capacity studies carried out in the temperature range of 2 -15 K for this sample failed to show even a broad hump that could be related to T_n as coexisting with T_c . Thus the break in $M(T)$ observed for superconducting samples need to be considered only cautiously as far as magnetic ordering is concerned.

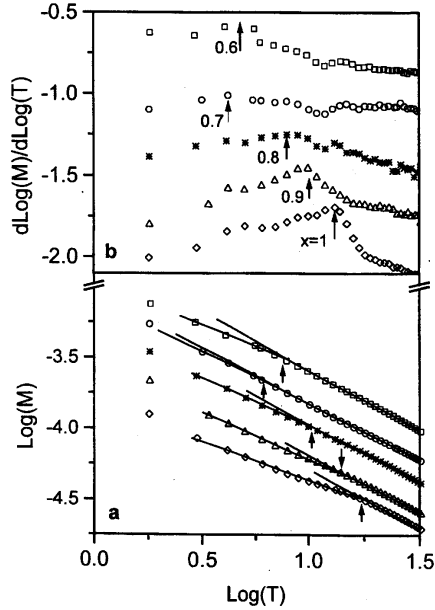


Fig. 28. (a) $\text{Log}(M)$ versus $\text{Log}(T)$ and (b) $d\text{Log}(M)/d\text{Log}(T)$ versus $\text{Log}(T)$ for various x values in $\text{Yb}_{1-x}\text{Pr}_x\text{Ba}_2\text{Cu}_3\text{O}_{7-\delta}$. M for $x=0.6$ is measured in an applied field $H=10$ kOe (see text also), whereas for all other samples $H=10$ Oe.

ii. Discussions

We look for a possible correlation of T_c with residual resistivity (ρ_0) as extracted from the extrapolation of linear $\rho(T)$ region to $T=0$ K and resistivity slope $((d\rho/dT)_{cc})$ corresponding to the linear $\rho(T)$ region in our Yb(Pr)-123 samples. However, considering the use of substituted polycrystalline samples in the present work, it is important to consider the possible extrinsic contributions that may interfere with the intrinsic values of these parameters in the material. We first discuss three such sources of error that may arise due to inhomogeneous substitution, anisotropic nature of R-123 system and defects in the grain boundaries. Next we delineate the intrinsic nature of ρ_0 and $(d\rho/dT)_{cc}$ in Yb(Pr)-123 samples by a comparison with both polycrystalline and single crystalline Y(Pr)-123 samples, and discuss that how their correlation with T_c may indicate the presence of dynamically fluctuating striped phase as a common source of superconductivity and antiferromagnetism in these systems.

Few results obtained in the present work, e.g., at higher values of x (> 0.2) the $T_c(x)$ determined by $\rho=0$ is higher in comparison to that estimated by diamagnetic onset (see Fig. 25); the shielding fraction decreases with an increase in Pr doping as mentioned in the experimental results; broad diamagnetic response below the onsets in $M(T)$ (see Fig. 26), seem to reveal something about the nature of superconductivity in our Yb(Pr)-123 samples. They probably indicate that, with increased Pr doping, higher T_c filamentary-superconducting paths start to evolve in the samples before a weak bulk superconductivity emerges at lower

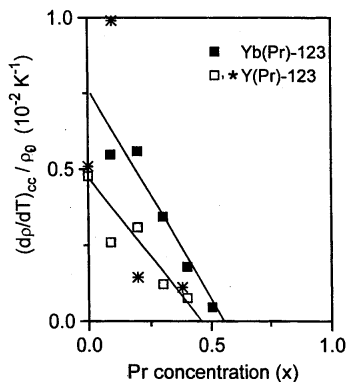


Fig. 29. Ratio of resistivity slope $(d\rho/dT)_{cc}$ and residual resistivity ρ_0 as a function of Pr concentration x in $\text{Yb}_{1-x}\text{Pr}_x\text{Ba}_2\text{Cu}_3\text{O}_{7-\delta}$ (filled squares represent present work), $\text{Y}_{1-x}\text{Pr}_x\text{Ba}_2\text{Cu}_3\text{O}_{7-\delta}$ (open squares [94]) and single crystals $\text{Y}_{1-x}\text{Pr}_x\text{Ba}_2\text{Cu}_3\text{O}_{7-\delta}$ (stars [96]). The solid lines represent linear fit of the data.

temperatures. This raises an important question - what is the origin of such superconductivity observed in our samples? Is it due to some macroscopic inhomogeneity, for instance, inhomogeneous cation (Pr, Yb) distribution along the Josephson-coupled grain boundaries? Or can it have some intrinsic origin? The former line of reasoning is apparently not supported by our XRD results, and the observed $T_c(x)$ and $T_n(x)$ behaviour. The presence of inhomogeneous cation (Pr, Yb) distribution should lead to broadening of the XRD peaks that should enhance further with an increase in Pr, and no systematic change in lattice parameters should occur, which are not observed (see Fig. 23 and Table 10). Second, the systematic and expected [43, 95, 97-102] decrease observed in $T_c(x)$ measured both by $M(T)$ and $\rho(T)$, and the emergence of $T_n(x)$, (see Fig. 25) is not accidental and is definitely connected with the intrinsic substitutional effects in Yb(Pr)-123 system. Thus, we propose to look for answers that may be generic to highly doped HTSC and where microstructural details of the sample are irrelevant as far as the origin of superconductivity is concerned. Good starting points in this direction are offered by various models, for instance, of quantum percolation in the presence of nanolevel inhomogeneities [103] and tunneling of cooper pairs across the static striped phases [104] (see below also).

Due to anisotropic nature of HTSC, the measured resistivity in the polycrystalline sample seems to represent sum of the contribution along and across the CuO_2 planes. However, we believe that the resistivity of R-123 samples will be mainly determined by the transport along well-connected CuO_2 planes across the grain boundaries. This assumption follows from the fact that the resistivity of the R-123 system, due to anisotropy, is roughly 20 times smaller along the CuO_2 planes than along the c -axis (i.e., across the CuO_2 planes) [105]. Moreover, as reported [106], in R(Pr)-123 system the anisotropy increases further with Pr doping. Thus the main error may arise only from the microstructure dependent effective cross section area and length for electrical transport in different samples. Considering the ratio of $(d\rho/dT)_{cc}/\rho_0$ should cancel out these geometrical factors. The third source of error, i.e., defects in the grain boundaries may contribute to the temperature independent part of the resistivity, namely ρ_0 . This aspect can be cross-checked by a comparison with single crystal data, that we could find

only for Y(Pr)-123 system [96]. The ratio of $(dp/dT)_{cc}/\rho_0$ as a function of x is shown in Fig. 29 for polycrystalline Yb(Pr)-123 (present work) and Y(Pr)-123 (taken from ref. [94]), and single crystals of Y(Pr)-123 (taken from ref. [96]). Values of ρ_0 are extracted from the extrapolation of linear $\rho(T)$ region to $T=0$ K, and thus represent only a lower limit to the true value. Due to an increasing curvature of the $\rho(T)$ for single crystals with $x \geq 0.4$ in Ref. [96], the ratio could not be determined reliably for higher values of x . The data on Y(Pr)-123 single crystal samples had to be normalized by a constant factor of 4 to match it with that of polycrystalline samples in Fig. 29. This factor reveals a definite contribution of grain boundaries to ρ_0 , as mentioned above, in case of the latter samples. However, as seen in Fig. 29, the behaviour of the polycrystalline samples does qualitatively resemble that of the single crystals, giving credence to the fact that the ratio of $(dp/dT)_{cc}/\rho_0$ in the former is indeed related to the intrinsic property of the material. From Fig. 29 and Fig. 25, we may thus infer two interesting observations: (a) the ratio $(dp/dT)_{cc}/\rho_0$ decreases with increasing x , in both Y(Pr)-123 and Yb(Pr)-123, as does the $T_c(x)$ in them; and (b) the ratio tends to go to zero at Pr concentration that is roughly 0.1 smaller for Y(Pr)-123 than Yb(Pr)-123, that also matches with the observed difference of x_c in them. These observations reveal a definite correlation of T_c with ρ_0 and $(dp/dT)_{cc}$ in these systems.

Now we show that superconductivity due to dynamically fluctuating striped phase in CuO_2 planes can consistently explain the observed correlation of T_c with $(dp/dT)_{cc}/\rho_0$. The increase of residual resistivity ρ_0 reflects an increase of impurities/defects, which can suppress the superconductivity by pinning the fluctuating stripes. The T_c should, as observed, correlate as inversely proportional to ρ_0 . On the other hand, the increase of resistivity slope $(dp/dT)_{cc}$ reflects either an increase in carrier concentration or an increase in carrier-carrier scattering. The increase of carrier density should amount to an increase in the density of charged stripes, which we expect would then require larger disorder to get pinned. For the latter case, because now the source of scattering is a carrier itself that is mobile, we expect that it (the carrier) will tend to depin the striped phase. In both the cases the increase of $(dp/dT)_{cc}$ will thus tend to relatively enhance T_c . The T_c should, as observed, correlate as directly proportional to $(dp/dT)_{cc}$. One may also say that, based on the decreasing ratio of $(dp/dT)_{cc}/\rho_0$ with x in Fig. 29, with an increase in Pr substitution the dynamically fluctuating striped phase in CuO_2 planes slows down more and more. Above x_c the fluctuating striped phase may get static, which then leads to the ordering of the Pr ions by a mechanism involving hybridization of Pr-4f with O-2p of CuO_2 planes. And with increasing x (above x_c), more number of Pr ions participate in magnetic ordering to give an increasing $T_n(x)$, as seen in the inset of Fig. 25. It is tempting to conclude that x_c in the phase-diagram for R(Pr)-123 marks the transition from static to fluctuating charge dynamics in CuO_2 planes. As also seen in Fig. 24, the non-superconducting Yb(Pr)-123 samples with $x \geq 0.7$, i.e. just above and greater than $x_c \sim 0.65$, show an increasing tendency of exponentially dependent $\rho(T)$ at low temperatures. This may be an indication of inter / intra - charge hopping in a static striped phase [104]. The superconducting sample with $x = 0.6$, i.e. just below $x_c \sim 0.65$, shows a negative dp/dT along with a very broad diamagnetic onset extending much above its $T_c(\rho=0) \sim 20$ K (see Figs. 24 and 26). This may reflect the precursor of a "spin-gap" at $T > T_c$ due to critical slowing down of fluctuating stripe dynamics in samples with x near and below x_c . This is corroborated by the fact that the diamagnetic onset becomes relatively sharp as one moves away and to smaller values of x (see Fig. 26). It may be interesting in future to study more samples with Pr concentration around and near to x_c . We would like to mention here that the observed unusual-broadening of $M(T)$ for $x=0.6$ sample cannot be straight forwardly related with inhomogeneity. As then it should have been present in all the superconducting samples, prepared in identical conditions, for values of $x \leq 0.6$, which is not the case.

Finally, we discuss a possible physical origin for the ionic-size dependence of x_c in R(Pr)-123. It may come from the dependence of anti-site substitution of Pr^{3+} at Ba^{2+} site [49] and/or Pr^{4+} at R^{3+} site [42] on the ionic size of R. It was shown in Y(Pr)-123 single crystals that these aliovalent substitutions directly lead to the creation of oxygen vacancies in CuO_2 planes [42]. Such vacancies can be an important source of impurities in CuO_2 planes that can pin the fluctuating stripes. However, the impact of such anti-site substitution on $(d\rho/dT)_{cc}$ is not a priori clear, which needs to be studied in more detail for various R(Pr)-123 systems. In the present case, however, because of smaller ionic size of Yb the possibility of anti-site defect formation should be less in comparison to Pr substitution in Y-123 [42]. Thus, comparatively the oxygen disorder is expected to be less as corroborated by the lattice parameter data, showing fewer O(5) sites getting filled-up. As a result the pinning of fluctuating stripes is less in Yb(Pr)-123 and the value of x_c is higher.

iii. Summary

The gradual destruction of superconductivity with increasing Pr, in both Yb(Pr)-123 and Y(Pr)-123 systems, seems to show up in the change of normal state parameters ρ_0 and $(d\rho/dT)_{cc}$, which can be extracted from the $\rho(T)$ curves. In both cases, it is found that the ratio of $(d\rho/dT)_{cc}/\rho_0$ tends to decrease with increasing x as does the $T_c(x)$. The difference in the values of Pr concentration where this ratio tends to go to zero matches with the observed difference of x_c in them. Moreover, for the Pr content near x_c , several properties like $\rho(T)$, the diamagnetic onset in $M(T)$ and the antiferromagnetic ordering of Pr ions show anomalous behaviour. These results can also be consistently explained by the presence of dynamically fluctuating striped phase in them. The critical Pr concentration, x_c , in R(Pr)-123 probably marks a transition from dynamic to static striped phase, where simultaneously superconductivity gets destroyed and magnetic ordering of Pr ions originates.

5.2.3 $\text{Y}_{1-x}\text{Pr}_x\text{BaSrCu}_3\text{O}_{7-\delta}$ system

Polycrystalline samples of the series $\text{Y}_{1-x}\text{Pr}_x\text{BaSrCu}_3\text{O}_{7-\delta}$ (i.e., Y(Pr)-1113), with x ranging from 0 to 1, were synthesized through a solid state reaction method. For preparation details see Ref. [94]. The samples were then characterized for their phase purity and lattice parameters by x-ray diffraction. The resistivity measurements were obtained using standard four-probe technique. The oxygen content in all the samples was determined by iodometric titrations.

i. Experimental results

Fig. 30 shows x-ray patterns of both Y(Pr)-1113 and Y(Pr)-123 samples with varying x. All the samples showed a single phase nature, except for two samples of Y(Pr)-1113 series with $x=0.75$ and 1.0, which show some low intensity peaks probably belonging to an impurity phase. Table 11 shows the variation of lattice parameters a, b and c, and orthorhombic distortion for both the systems. The c- parameter increases with Pr in both the systems, indicating the substitution of larger Pr^{3+} ion in the place of smaller Y^{3+} ion. Also, the c parameter of Y(Pr)-1113 samples is smaller than Sr-free Y(Pr)-123 samples, in agreement with the reported data [67, 107-109]. This substantiates that smaller Sr (1.32 Å) ion substitutes the bigger Ba (1.52 Å) ion with the same 10-fold coordination in Y(Pr)-1113.

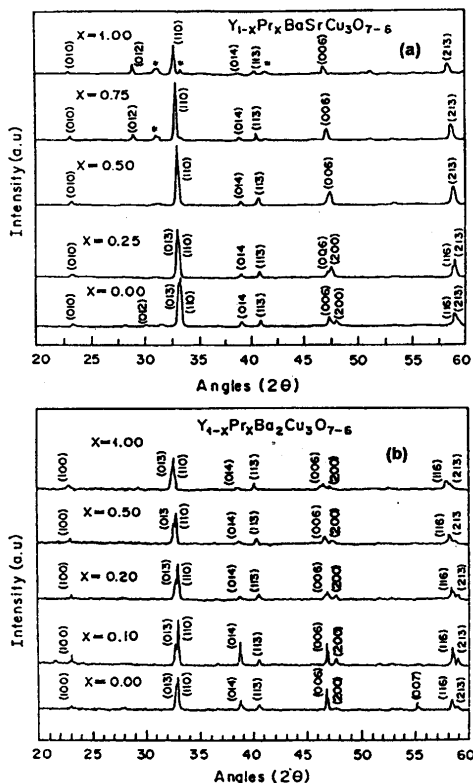


Fig. 30. X-ray diffraction patterns with various x values for (a) $Y_{1-x}Pr_xBaSrCu_3O_{7-\delta}$; (b) $Y_{4-x}Pr_xBa_2Cu_3O_{7-\delta}$.

However, as a function of increase in x , the orthorhombic distortion decreases and goes to zero at $x \approx 0.6$ in the case of Y(Pr)-1113, whereas, the same is found to be affected much less in the case of Y(Pr)-123. The evolution of the crystallographic splitting (see Figs. 30a and 30b) of [020], [200] and [123], [213] supports the change in the orthorhombic distortion for both the systems. As seen from the splitting, the samples of Y(Pr)-1113 with $x = 0.0$ and 0.25 are clearly orthorhombic. For higher values of x the splitting of both the doublets is reduced, before vanishing completely for the samples with $x \geq 0.6$ revealing a tetragonal structure. Whereas, in the case of Y(Pr)-123 the splitting of both [020], [200] and [123], [213] is maintained, revealing an orthorhombic structure for all the samples with $x = 0$ to 1. The measured oxygen content by iodometric titrations show no significant change with increasing Pr for both Y(Pr)-1113 and Y(Pr)-123 series (see Table 11). This observation is in agreement with previous reports [97, 110, 111].

Table 11. Lattice parameters (in Å) a, b and c, orthorhombic distortion (o.d.=[(b-a)/b]x100) and total oxygen content (7- δ). The lattice parameters are rounded off at last decimal place and maximum error in δ is ± 0.02 .

| x | Y _{1-x} Pr _x BaSrCu ₃ O _{7-δ} | | | | | Y _{1-x} Pr _x Ba ₂ Cu ₃ O _{7-δ} | | | | |
|------|---|-------|--------|------|-------------|---|-------|--------|------|-------------|
| | a | b | c | o.d. | 7- δ | a | B | c | o.d. | 7- δ |
| 0 | 3.784 | 3.842 | 11.523 | 1.59 | 6.94 | 3.825 | 3.886 | 11.667 | 1.57 | 6.94 |
| 0.1 | 3.790 | 3.841 | 11.524 | 1.33 | 6.94 | 3.832 | 3.893 | 11.672 | 1.57 | 6.94 |
| 0.2 | 3.805 | 3.840 | 11.530 | 0.91 | 6.93 | 3.836 | 3.898 | 11.682 | 1.60 | 6.94 |
| 0.25 | 3.812 | 3.839 | 11.535 | 0.70 | 6.93 | — | — | — | — | — |
| 0.3 | 3.818 | 3.838 | 11.540 | 0.52 | 6.93 | 3.838 | 3.900 | 11.687 | 1.59 | 6.94 |
| 0.4 | 3.821 | 3.837 | 11.549 | 0.42 | 6.93 | — | — | — | — | 6.93 |
| 0.5 | 3.826 | 3.835 | 11.552 | 0.24 | 6.93 | 3.842 | 3.902 | 11.698 | 1.54 | 6.93 |
| 0.6 | 3.831 | 3.834 | 11.563 | 0.08 | 6.92 | — | — | — | — | 6.93 |
| 0.75 | 3.834 | 3.834 | 11.573 | 0 | 6.92 | 3.844 | 3.900 | 11.705 | 1.44 | 6.93 |
| 1.0 | 3.841 | 3.841 | 11.584 | 0 | 6.92 | 3.843 | 3.904 | 11.711 | 1.56 | 6.92 |

Figs. 31a-31d show the measured resistivity as a function of temperature for all the samples of both Y(Pr)-1113 and Y(Pr)-123. As is evident from the figure, the normal state resistivity increases with Pr in both systems. The $\rho(T)$ behaviour turns from metallic to semiconductor-like for values of $x \geq 0.70$ for Y(Pr)-1113 and $x \geq 0.6$ for Y(Pr)-123. All samples of Y(Pr)-1113 (Y(Pr)-123) with $x < 0.6$ ($x < 0.7$) show a transition to superconducting state. Fig. 32 shows the variation of reduced critical temperature ($T_c(x) / T_c(0)$) with Pr concentration for both the systems. For comparison, similar data from literature of polycrystalline Y(Pr)-1113 [111], Y(Pr)-123 [95] and single crystal Y(Pr)-123 [96] are also plotted in Fig. 32. Slightly lower values of $T_c(\rho=0)$ for single crystals are mainly due to tail-like broadening of $\rho(T)$ when ρ goes to zero in them [96]. The values of x_c , to quench superconductivity is ~ 0.7 for Y(Pr)-1113 system and ~ 0.55 for Y(Pr)-123 system.

ii. Discussions

In general the $\rho(T)$ curves involve a high temperature ($T > T_c$, see Figs. 31a-31d) linear region for all the samples of both Y(Pr)-1113 and Y(Pr)-123 series, except for values of x in the vicinity of x_c . The linear part of the $\rho(T)$ curves has a positive slope $(dp/dT)_{cc}$ and its extrapolation to $T=0$ K provides the residual resistivity, say ρ_0 . While the ρ_0 is connected with impurity scattering, the slope $(dp/dT)_{cc}$ determined from the linear region of the ρ -T curve is connected with carrier-carrier scattering. In the following we shall consider only such a resistivity slope.

To appreciate the change in ρ_0 and $(dp/dT)_{cc}$ as a function of x , we plot these quantities for both Y(Pr)-1113 and Y(Pr)-123 in Figs. 33a and 33b. For comparison we plot similar data determined for single crystals of Y(Pr)-123 from the literature [96]. The data of ρ_0 and $(dp/dT)_{cc}$ for single crystals was normalized by factors 0.1 and 0.45. Normalization factors less than 1 are actually expected as a result of effectively smaller cross section area and longer length for electrical transport in polycrystalline samples as compared to the crystals. As seen from the Fig. 33a, $\rho_0(x)$ increases monotonically for both the systems. Since, simultaneously, the $T_c(x)$ shows a decrease for both the series (see Fig. 32), it may be concluded that T_c does inversely correlate with the ρ_0 in these systems. However, we note that although the values of $\rho_0(x)$ are higher and increase faster for the Y(Pr)-1113 system as compared to Y(Pr)-123

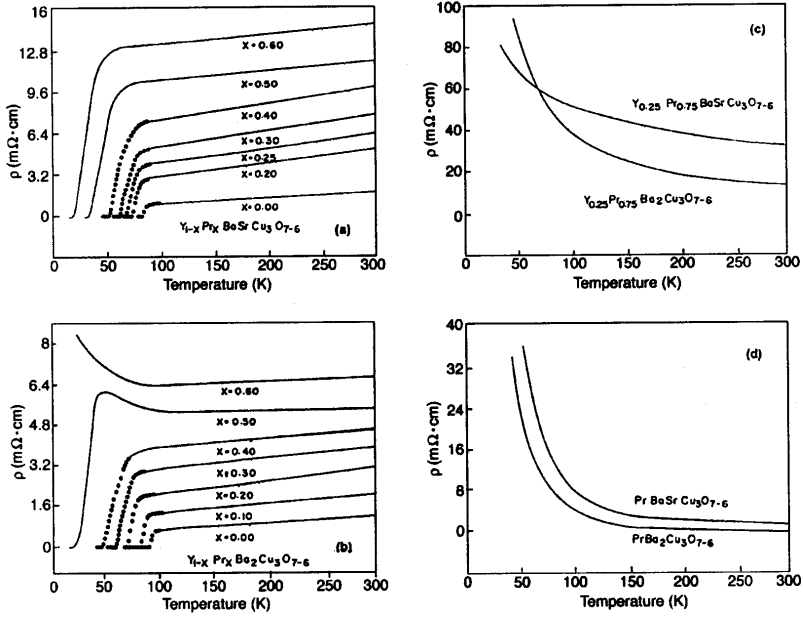


Fig. 31. (a–d) Resistivity as a function of temperature with various x values for $Y_{1-x}Pr_xBaSrCu_3O_{7-\delta}$ and $Y_{1-x}Pr_xBa_2Cu_3O_{7-\delta}$.

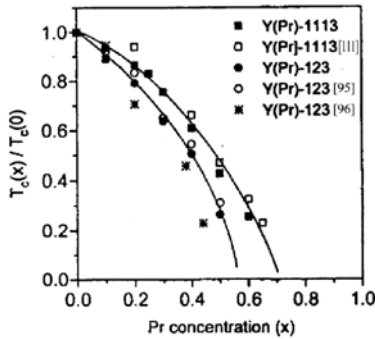


Fig. 32. Reduced critical temperature [$T_c(x) / T_c(0)$] as a function of Pr concentration x for $Y_{1-x}Pr_xBaSrCu_3O_{7-\delta}$ and $Y_{1-x}Pr_xBa_2Cu_3O_{7-\delta}$. Similar data on both the systems taken from the literature is also included in the figure.

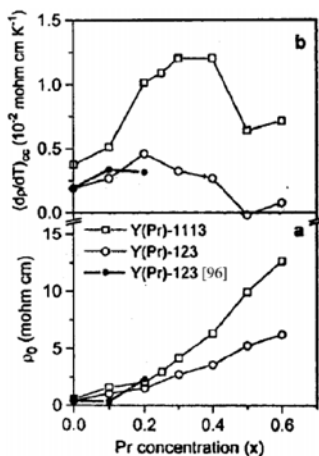


Fig. 33. (a) Residual resistivity ρ_0 and (b) slope $(dp/dT)_{cc}$ as a function of Pr concentration x for $Y_{1-x}Pr_xBaSrCu_3O_{7-\delta}$ and $Y_{1-x}Pr_xBa_2Cu_3O_{7-\delta}$. Similar data on single crystals of the latter system taken from the literature is also included in the figure.

system, the decrease of $T_c(x)$ is faster in the latter case. This indicates that there are other parameter(s) influencing $T_c(x)$ in these systems.

We now discuss the behaviour of resistivity slope $(dp/dT)_{cc}$ for both Y(Pr)-1113 and Y(Pr)-123. From Fig. 33b we see that an increase of Pr content in both the series results in a non-monotonic behaviour. In case of Y(Pr)-1113, the slope $(dp/dT)_{cc}$ increases until $x \sim 0.4$ and tends to zero at $x \sim 0.7$ (note that $(dp/dT)_{cc}$ becomes negative for $x = 0.75$, see Fig. 31c). Whereas, in case of Y(Pr)-123, it increases only until $x \sim 0.2$ and goes to zero at $x \sim 0.5$. Now we would like to point out a couple of observations: (a) for all the values of x shown in Fig. 33b, the values of slope $(dp/dT)_{cc}$ are remarkably higher in case of Y(Pr)-1113 as compared to Y(Pr)-123. For instance, at $x = 0.4$, $(dp/dT)_{cc}$ is around factor five higher in Y(Pr)-1113 than that in Y(Pr)-123. (b) The values of $x \sim 0.7$ and 0.5 , where $(dp/dT)_{cc}$ goes to zero, match quite well with the observed $x_c \sim 0.7$ and 0.55 where superconductivity is destroyed for Y(Pr)-1113 and Y(Pr)-123, respectively. These observations, along with the fact that the suppression of $T_c(x)$ is slower in Y(Pr)-1113 when compared with Y(Pr)-123, reveal that an increase of slope $(dp/dT)_{cc}$ correlates with an enhancement of $T_c(x)$ in these systems.

The above correlations indicate that underlying processes responsible for a change of ρ_0 and $(dp/dT)_{cc}$ are affecting the superconductivity in opposite ways in both Y(Pr)-1113 and Y(Pr)-123 systems. Now we discuss these processes and how they throw light on a possible mechanism of superconductivity. The increase of $\rho_0(x)$ clearly indicates an increase of temperature independent impurity scattering introduced by substitution of Pr in both Y(Pr)-1113 and Y(Pr)-123. We had earlier reported that Y(Pr)-123 is vulnerable to creation of oxygen vacancies, in CuO_2 planes [42], that increase with Pr concentration and constitute an additional scattering source. It has been recently [86-89] suggested that pinning of the dynamically fluctuating striped phase may lead to suppression of superconductivity. The impurities/vacancies in the lattice tend to pin the dynamically fluctuating striped phase and can explain the observed correlation between T_c and ρ_0 , where ρ_0 would signify the extent of pinning. Now turning towards $(dp/dT)_{cc}$, we have to remember that it has been defined only

for the observed linear ρ -T region. A linear ρ -T dependence especially in HTSC due to classical electron-phonon scattering can be ruled out, and the physical reason for it may lie only in carrier-carrier scattering. Thus the increase of $(d\rho/dT)_{cc}$ implies mainly an increase in hole carrier concentration and/or an increase in carrier-carrier scattering rate. There are no reports till date showing an increase of hole carriers with Pr substitution in these systems. The increase of $(d\rho/dT)_{cc}$ thus primarily implies an increase in carrier-carrier scattering rate. Now, unlike impurity/vacancy that is fixed in the sample, the carrier is mobile and will tend to depin the striped phase. An increase in carrier-carrier scattering would mean enhanced depinning of the striped phase. In this way, suppression of T_c due to pinning of the striped phase appears consistent with the observed correlation of T_c with $(d\rho/dT)_{cc}$ also. We would also mention here that, for samples with $x > x_c$ of both Y(Pr)-1113 and Y(Pr)-123, the observed semiconductor-like upturn of the ρ -T curves at low temperatures is also in accord with pinned striped phase [78-80].

ii. Summary

The gradual destruction of superconductivity with increasing Pr, in both Y(Pr)-1113 and Y(Pr)-123 systems, seems to show up in the change of normal state parameters ρ_0 and $(d\rho/dT)_{cc}$, which can be extracted from the $\rho(T)$ curves. In general, it is found that increase in ρ_0 correlates with a suppression in T_c , while an increase in $(d\rho/dT)_{cc}$ correlates with an enhancement of T_c . The difference in the values of critical Pr concentration for destruction of superconductivity in Y(Pr)-1113 and Y(Pr)-123 coincides with the values of x where $(d\rho/dT)_{cc}$ tends to zero. The origin of superconductivity in these systems also looks consistent with a presence of dynamically fluctuating striped phase.

6. CONCLUSIONS

In conventional low T_c superconductors, that include simple metals, alloys, A-15 materials, Laves and Chevrel phases, the effect of disorder can be understood within the classical Fermi Liquid framework in the normal state along with a phonon mediated BCS mechanism for superconductivity. The disorder in these materials can change the phonon spectra affecting the electron-phonon coupling or Debye temperature or density of states at E_F , as a result of which T_c can get influenced in them. However, the situation is quite complex in high T_c superconducting cuprates. They are doped Mott insulators with lower carrier concentration than typical metals, with highly anisotropic/ quasi-two dimensional CuO_2 planes and a probable breakdown of the Fermi liquid description. Thus to understand the effect of disorder in them the nature of the conducting electrons/holes in these systems need to be freshly hypothesized/discovered. One novel scenario is the presence of dynamically fluctuating striped phase of conducting charges in CuO_2 planes and the resulting superconductivity. Within such an arrangement, the role of disorder can be to pin the dynamic charge stripes and suppress the T_c . The electrical transport results on substitutionally disordered HTSC, shown in the present work, apparently supports the origin of superconductivity in these systems due to the dynamically fluctuating striped phase, the pinning and depinning of which can explain the observed correlation of T_c with ρ_0 and $(d\rho/dT)_{cc}$, respectively. It was shown that significant disorder in HTSC can result due to the vulnerability of CuO_2 planes to the formation of oxygen vacancies. However, it is still a long way to settle the mechanism-question of sensitivity of HTSC to disorder.

REFERENCES

- [1] P. Shalnikov, *Nature* 142 (1938) 74.
- [2] W. Buckel and R. Hilsch, *Z.Physik* 138 (1954) 109.
- [3] W. Buckel and R. Hilsch, *Z.Physik* 146 (1956) 27.
- [4] W.L. McMillan, *Phys.Rev* 167 (1968) 331.
- [5] G.V. Minnigerode and J. Rothenberg, *Z. Physik* 213 (1968) 397.
- [6] A.M. Lamoise, J. Chaumont, F. Meunier and H. Barnes, *J. Physique Letts.* 36 (1975) L271.
- [7] A.M. Lamoise, J. Chaumont,, F. Lalu, F. Meunier and H. Barnes, *J. Physique Letts.* 37 (1976) L287.
- [8] B. Stritzker and W. Buckel, *Z. Physik* 257 (1972) 1.
- [9] W. Bauriedl, G. Heim and W. Buckel, *Phys Letts A57* (1976) 282.
- [10] G. Bergmann, *Phys.Reports* 27C (1976) 159.
- [11] W.L. Johnson, *Proc. of the 3rd International Conf. on Rapidly Quenched Metals*, British Metals Society, London (1978) p.471.
- [12] O. Hunderi and R. Ryberg, *J.Phys.F* 4 (1974) 2096.
- [13] O. Hunderi, *J. Phys.F* 5 (1975) 2214.
- [14] D. Korn, W. Murier and G. Zibold, *Phys Letts* 47A (1974) 117.
- [15] H. Weibking, *Z.Physik* 232 (1970) 126.
- [16] K. Knorr and N. Bath, *J.Low Temp.Phys.*, 4 (1971) 464.
- [17] J. Bolz and F. Pobell, *Z.Physik* B20 95.
- [18] W. Buckel and Ch. Ohlerich, *Proc.Int.Conf. on Low Temp.Phys.*,LT-13, Plenum, NY (1972) p. 437.
- [19] M.M. Collver and R.H. Hammond, *Phys.Rev.Letts* 30 (1973) 92.
- [20] M.M. Collver and R.H. Hammond, *Sol.State Communs* 22 (1977) 55.
- [21] B. Schroeder, W. Grobman, W.L. Johnson, C.C. Tsuei and P. Chaudhari, *IV Int.Conf. on Phys. of Non-Cryst. Solids* (Ed. G.H. Frischat), Chausthal-Zellerfeld (1976) 190
- [22] O. Meyer, H. Mann and E. Philing, *Applications of Ion Beams to Metals* (Ed. S.T. Pieraax, E.P. Erilisse and F.L. Vook) Plenum, NY (1974) p.15.
- [23] O. Meyer, *New Uses of Ion Accelerators* (Ed. J.F. Ziegler) Plenum, NY (1975) p. 323
- [24] C.C. Tsuei, W.L. Johnson, R.B. Laibowitz and J.M. Viggiano, *Sol.State Communs.* 24 (1977) 615.
- [25] K. Togano and K. Tachikawa, *Phys Letts* 54A (1975) 205.
- [26] E. Domb and W.L. Johnson, *J.Low Temp.Phys.*, 33 (1978) 29.
- [27] W.L. Johnson, S.J. Poon and P. Duwez, *Phys.Rev* B11 (1975) 150.
- [28] J.E. Graebner, B. Golding, R.J. Schultz, F.S.L. Hsu and H.S. Chen, *Phys.Rev.Letts* 39 (1977) 1480.
- [29] R. Hasegawa and L.E. Tanner, *Phys.Rev.* B16 (1977) 3925.
- [30] W.L. Johnson, S.J. Poon, J. Dusand and P. Duwez, *Phys Rev.* B18 (1978) 206
- [31] B. Stritzker, *Phys.Rev.Letts* 42 (1979) 1769.
- [32] D. Dew-Hughes, *Cryogenics* 15 (1975) 435.
- [33] T. Luhman and D. Dew-Hughes (Ed) *Metallurgy of Superconducting Materials*, Academic Press, NY (1979).
- [34] J. Muller, *Rep.Prog.Phys.* 43 (1980) 41.
- [35] M. Weger, *Rev.Modern Phys.* 36 (1964) 175.
- [36] M. Lehmann, G. Saemann-Ischenko, H. Adrian and C. Nolscher, *Physica* 107B (1981) 473.
- [37] P. W. Anderson, *Science*, 256 (1992) 1526.

- [38] V. J. Emery and S. A. Kivelson, Phys. Rev. Lett., 74 (1995) 3253.
- [39] H.Takagi et al., Phys. Rev. Lett. 69 (1992) 2975.
- [40] H.Ding et al., Nature 382 (1996) 51.
- [41] Chen Changkang, A.T. Boothroyd, Hu Yongle, F.R.Wondre, B.M.Wanklyn and J.W.Hodby(1993), Physica C 214 (1993) 231.
- [42] A.V. Narlikar, Anurag Gupta, S.B.Samanta, C.Chen, Y.Hu, F.Wandre, B.M.Wanklyn and J.W.Hodby, Phil. Mag. B 79, (1999) 717.
- [43] I.Felner, U.Yaron, Y.I.Nowik, E.R.Bauminger, Y.Wolfus, E.R.Yacoby, G.Hilscher, and Pillmayr, Phys. Rev. B 40 (1989) 6739.
- [44] J.L. Peng, P.K. Klavins, R.N. Shelton, H.B. Radousky, P.A.Hahn and L. Bernardez Phys. Rev.B 40 (1989) 4517.
- [45] A.V.Narlikar, C.V.N. Rao and S.K. Agarwal, in *Studies of High Temperature Superconductors*, edited by A.V.Narlikar, Nova Science Publishers, Vol.1 (1989) 341.
- [46] H.A.Blackstead, and J.D.Dow, Phys.Rev. B 51 (1995) 11830.
- [47] S.K.Malik, W.B.Yelon, J.J.Rhyne, W.J.James, R. Prasad, K.Adhikary and N.C. Soni, Solid State Commun. 89 (1994) 383.
- [48] M.P.Guillaume, J.Allenspach, B.Masot, Z.Roessli, U.Stoub, P.Fishes, and A.Fusser, Z. Physik B 90 (1993) 13.
- [49] H.A.Blackstead, J.D.Dow, D.B.Chrisey, J.S.Horwitz, M.A.Black, P.J.McGinn, A.E.Klunzinger, and D.B.Pulling, Phys.Rev. B 54 (1996) 6122.
- [50] A. Sedky, Anurag Gupta, V.P.S. Awana and A.V. Narlikar, Phys. Rev. B 58 (1998) 12495.
- [51] W. E. Farneth, R. K. Bordia, E. M. McCarron III, M. K. Crawford and R. B. Flippen, Solid State Comm. 66 (1988) 953.
- [52] V.S. Melnikov, V.M. Pan and A.V. Zhalko-Titarenko, in *Studies of High Temperature Superconductors*, edited by A.V.Narlikar, Nova Science Publishers, Vol.7, (1991) 266.
- [53] G. Bottger, I. Magelschots, E. Kaldis, P. Fischer, Ch Kruger and F. Fauth, J. Phys. Condens. Matter 8, (1996) 8896.
- [54] R. J. Cava, B. Batlogg, K. M. Rabe, E. A. Rietman, P. K. Gallagher, L. W. Rupp Jr, Physica C 156, (1988) 523.
- [55] N. L. Wang, M. C. Tan, J. S. Wang, S. Y. Zhang, H. B. Jiang, J. Sha and Q. R. Zhang, Supercond. Sci. Technol. 4, (1991) S307.
- [56] R. G. Kulkarni, R. L. Raibagkar, G. K. Bichile, A. Shaikh, J. A. Bhalodia, G. J. Baidha and D.G. Kuberkar, Supercond. Sci. Technol. 6, (1993) 678.
- [57] A. K. Ghosh, S. K. Bandhopadhyay, P. Barat, P. Sen and A. N. Basu, Physica C 264 (1996) 255.
- [58] J. D. Jorgensen, Physics Today, June 1991, Page 34.
- [59] A. V. Narlikar, P. K. Dutta, S. B. Samanta and V. P. S Awana, in *Studies of High Temperature Superconductors*, edited by A. V. Narlikar, Nova Science Publishers, Vol.10, (1991) 1.
- [60] A. K. Bandyopadhyay, D. Varandani, E. Gmelin and A. V. Narlikar, Phys Rev. B 50 (1994) 462.
- [61] J. L. Tallon, C. Bernhard, H. Shaked, R. L. Hitterman and J. D. Jorgensen, Phys Rev. B 51 (1995) 12911.
- [62] Anurag Gupta, Rajvir Singh, D.P.Singh and A.V.Narlikar, J. Phys.:Condens. Matter 12 (2000) 7381.
- [63] Y. Maeno, T. Tomita, M. Kyogoku, S. Awaji, Y.A. Oki, K. Hoshino, A.A. Minami and T.Fujita, Nature 328 (1987) 512.

- [64] J. M. Tarascon, P. Barboux, P.F. Miceli, L.H. Greene, G.W. Hull, M. Eibschutz and S.A.Sunshine, *Phys. Rev. B* 37 (1988) 7458.
- [65] G. Xiao, M. Z. Cieplak, A. Gavrin, F.H. Streitz, A. Bakhshai and C.L. Chien, *Phys. Rev. Lett.* 60 (1988) 1446.
- [66] Y. Xu, R.L. Sabatini, A.R. Moodenbaugh, Y. Zhu, S.G. Shyu, M. Suenaga, K.W. Dennis and R.W. McCallum, *Physica C* 169 (1990) 205.
- [67] J. M. Tarascon and B. G. Bagley, in *Chemistry of Superconductor Materials*, edited by T.A.Vanderah (NOYES, New Jersey) (1993) p 310.
- [68] R.J. Cava, A.W. Hewat, E.A. Hewat, B. Batlogg, M. Marezio, K.M. Rabe, J.J. Krajewski, W.F.Peck and L.W. Rupp Jr, *Physica C* 165 (1990) 419.
- [69] Anurag Gupta, Ratan Lal, A.Sedky, A.V.Narlikar and V.P.S. Awana, *Phys. Rev.B* 61 (2000) 11752.
- [70] M.Mehbod, P.Wyder, R.Deltour, Ph.Duvigneaud and G.Maessens, *Phys. Rev. B* 36 (1987) 8819.
- [71] Y. Xu, R.L. Sabatini, A.R. Moodenbaugh, Y. Zhu, S.G. Shyu, M. Suenaga, K.W. Dennis and R.W. McCallum, *Physica C* 169 (1990) 205.
- [72] V.Kataev, Yu.Greznev, G.Teitel'baum, M.Breuer and N.Knauf, *Phys.Rev.B* 48 (1993) 13042.
- [73] Rajvir Singh, R.Lal, U.C.Upreti, D.K.Suri, A.V.Narlikar, V.P.S.Awana, J.Albino Aguiar and Md.Shahabuddin, *Phys.Rev.B* 55 (1997) 1216.
- [74] Very recently Musa et.al. [J.E.Musa, S.Garcia, M.Rothier de Amaral, Jr. and H.Salim de Amorim, B.Giordanengo, E.M.Baggio-Staitovitch, P.J.G.Pagliuro, C.Rettori, W.B.Yelon and S.K.Malik, *Phys.Rev.B* 59 (1999) 6557] have measured the resistivity of the $(La_{1-x}Pr_x)_{1.85}Sr_{0.15}CuO_4$ system for different values of Pr concentration x. They have fitted their data with equ.(1) of this article. They have found that T_c of the $(La_{1-x}Pr_x)_{1.85}Sr_{0.15}CuO_4$ system correlates well with ρ_2 . This observation of Musa et al. is incomplete in that the T_c of the samples considered by them also correlates well with the resistivity slope $(dp/dT)_{cc}$, such that increasing $(dp/dT)_{cc}$ enhances T_c suppression.
- [75] J. Kondo, in "Solid State Physics: Advances in Research and Applications", edited by Ehrenreich, F.Seitz and D.Turnbull (Academic, New York, 1969), Vol. 23, p.183.
- [76] M.V. Sadovskii, in *Studies of High Temperature Superconductors*, edited by A.V. Narlikar, Nova Science Publishers, Vol. 11 (1993) 131.
- [77] B.L.Altshuler and A.G.Aronov, *Solid State Commun.* 39 (1979) 115.
- [78] Y.Ando, G.S.Boebinger, A.Passner, T.Kimura and K.Kishio, *Phys.Rev.Lett.* 75 (1995) 4662.
- [79] J.M.Tranquada, J.D.Axe, N.Ichikawa, Y.Nakamura, S.Uchida and B.Nachumi, *Phys.Rev.B* 54 (1996) 7489.
- [80] Kouji Segawa and Yoichi Ando, *Phys.Rev.B* 59 (1999) R3948.
- [81] A possible reason for such a behaviour may be activation of certain phonon modes for certain dopant concentration above a suitable temperature. Such modes may couple with electrons to increase the electron-electron scattering rate in an effective way.
- [82] Chien et al [T.R.Chien, Z.Z.Wang and N.P.Ong, *Phys.Rev.B* 67 (1991) 2088] have found that the single crystal of $YBa_2Cu_3O_{7-\delta}$ doped with 0.53% Zn shows a superlinear ρ -T behaviour, similar to that observed for the $ErBa_2Cu_3O_{7-\delta}$ sample of 6.0% Zn in the present case. The temperature where the superlinear behaviour of ρ -T appears to be a crossover of two linear behaviours is $T^* \approx 160$ K for the 0.53% Zn samples of $YBa_2Cu_3O_{7-\delta}$, as compared to $T^* \approx 175$ K in the present case. There are other cases also where ρ -T curve show a superlinear behaviour. The 2%, 8/3% and 10/3% Zn doped samples of polycrystalline $DyBa_2Cu_3O_{7-\delta}$ also show superlinear behaviour near $T^* \approx 170$

- K [S.S.Ata-Allah, Y.Xu and Ch.Heiden, *Physica C* 221(1994) 39]. A superlinear behaviour of ρ vs. T curve is also seen in the 3% Zn sample of polycrystalline $YBa_2Cu_3O_{6.95}$ and with $T^* \approx 180$ K [D.J.C.Walker, A.P.Mackenzie and J.R.Cooper, *Phys.Rev.B* 51 (1995) 15653].
- [83] For the samples where ρ - T behaviour may be approximated as a crossover from one linear region with lower slope to another with higher slope, we have defined $(dp/dT)_{cc}$ by the linear region nearer to T_c . Similar specification for dp/dT has been considered earlier [D.J.C.Walker, A.P.Mackenzie and J.R.Cooper, *Phys.Rev.B* 51 (1995) 15653].
- [84] Kouichi Semba, Azusa Matsuda and Takao Ishu, *Phys. Rev. B* 49 (1994) 10043.
- [85] M.D.Lan, J.Z.Liu, Y.X.Jia, Y. Nagata, P.Klavins and R.N.Shelton, *Phys. Rev.B* 47 (1993) 457.
- [86] G.D.Liu, Z.X.Zhao and G.C.Che, *Solid State Commun.* 109 (1999) 495.
- [87] J.S.Zhou, J.B.Goodenough, H.Sato and M.Naito, *Phys.Rev.B* 59 (1999) 3827
- [88] R.F.Service, *Science* 283 (1999) 1106.
- [89] N.Hasselmann, A.H.Castro Neto, C.Morair Smith and Y.Dimashko, *Phys.Rev.Lett.* 82 (1999) 2135.
- [90] G.V.M. Williams, J. L. Tallon and R. Meinhold, *Phys. Rev. B* 52 (1995) 7034.
- [91] As we have already clarified $(dp/dT)_{cc}$ corresponds to carrier-carrier scattering. But carrier-carrier scattering amounts to reduce the mean free path of the carrier. Such a situation tends to reduce T_c by breaking Cooper pairs near T_c [A.J.Millis, S. Sachdev and C.M. Verma, *Phys. Rev. B* 37 (1988) 4975].
- [92] G.G.Li, F.Bridges, J.B.Boyce and W.C.H.Jainer, *Phys.Rev.B* 47 (1993) 12110.
- [93] Anurag Gupta, H. Narayan, P. N. Lisboa-Filho, C. A. Cardoso, F. M. Aranzujo Moreira, O. F.de Lima and A. V. Narlikar, *Mod. Phys. Lett. B* 16 (2002) 261.
- [94] Anurag Gupta, A. Sedky and A. V. Narlikar, *Phys. Stat. Sol. b* 241 (2004) 895.
- [95] S. K. Malik, C. V. Tomy and P. Bhargava, *Phys. Rev. B* 44 (1991) 7042.
- [96] Y.X.Jia, J.Z.Liu, A.Matsushita, M.D.Lan, P.Klavins and R.N.Shelton, *Phys. Rev. B* 46 (1992) 11745.
- [97] L. Soderholm, K. Zhang, D. G. Hinks, M. A. Beno, J. D. Jorgensen, C. V. Segree and I. K.Schuller, *Nature* 328 (1987) 604.
- [98] D. W. Cooke, R. S. Kwok, R. L. Lichti, T. R. Adams, C. Boekema, W. K. Dawson, A. Kebede, J. Schwegler, J. E. Crow and T. Mihalisin, *Phys. Rev. B* 41 (1990) 4801.
- [99] Y.Xu and W.Guan, *Solid State Commun.* 80 (1991) 105.
- [100] H.B. Radousky, *J. Mat. Res.* 7 (1992) 1917.
- [101] H. Jhans, S. K. Malik, S. K. Dhar, R. Vijayaraghavan, *Physica C* 207 (1993) 247.
- [102] W. Guan, Y. Xu, S. R. Sheen, Y. C. Chen, J. Y. T. Wei, H. F. Lai, M. K. Wu and J. C. Ho, *Phys. Rev. B* 49 (1993) 15993.
- [103] J.C.Phillips, *Proc. Natl. Acad. Sci. (USA)* 94 (1997) 12774.
- [104] V. J. Emery and S. A. Kivelson, *J. Low Temp. Phys.* 189 (1999) 189.
- [105] K. Takenaka, K. Mizuhashi, H. Takagi, and S. Uchida, *Phys. Rev. B* 50 (1994) 6534.
- [106] T.R.Chien, W.R.Datars, J.Z.Liu, M.D.Lan and R.N.Shelton, *Physica C* 221 (1994) 428.
- [107] H. Jhans, S.K. Malik and R. Vijayaraghavan, *Solid State Commun.* 85 (1993) 105.
- [108] T.Wada, S.Adachi, T.Mihira and R. Inaba, *Jap. J. Appl. Phys.* 20 (1987) L 706.
- [109] E. Oliber, C. Gonzalez Oliver, F. Parado, A. Serquis, A. Caneiro and D. Esparza, *Physica C* 235-240 (1994) 469.
- [110] G. Cao, Y.Qian, X.Li, Z.Chen and Y.Zhang, *Phys. Lett. A* 196 (1994) 263.
- [111] A. Das, I. Zelenay and R. Suryanarayanan, *Physica C* 295 (1998) 47.

IRRADIATION OF HTS FOR ENHANCEMENT OF CRITICAL CURRENT

Damion Milliken, Tania Silver, and Shi Xue Dou

Institute for Superconducting and Electronic Materials, University of Wollongong, NSW,
2522, Australia

1. INTRODUCTION

Of the various techniques employed to introduce defects into high T_c superconducting material with the goal of pinning flux, radiation techniques are among the most promising [1-4]. Radiation defect generating procedures allow close control of the defect size, shape, morphology, and density, allowing them to tailor damage to most effectively pin magnetic flux [3,5]. It is fortunate that the approximate size of damage introduced by radiation techniques is on the same order of magnitude as the coherence length in many high T_c superconductors. However, the introduction of pinning centres by means of irradiation induced defects is not a simple, nor necessarily a cost effective process, and it, too, is limited in the degree of improvement that is readily achievable in physical performance.

2. GAMMA RAY IRRADIATION

The superconducting properties of HTS can be affected by γ -ray irradiation, with the influence particularly great in the vicinity of grain boundaries, which tend to be strongly depleted in charge carriers. Irradiation of bulk $TlBa_2Ca_2Cu_3O_y$ showed a sudden drop in T_c of 4 K with a 100 MR gamma dose, and a much slower decrease up to 400 MR. The normal state resistance was also increased after irradiation, and J_c increased up to 50% at temperatures well below T_c . The results were attributed to the improvement of grain

boundaries and weak links such that SNS (superconductor-normal metal-superconductor) junctions in the Josephson coupling became dominant [6]. Similar effects on T_c were reported for YBCO and also attributed gamma irradiation improvement to inter-grain Josephson coupling [7].

3. ELECTRON IRRADIATION

Perhaps the easiest, cheapest, and most readily available irradiation technique is electron bombardment. This process employs a beam of high energy (1-30 MeV) electrons, which strike the target superconductor [8]. Elastic interactions between the energetic electrons and atoms in the superconductor result in movement of the superconductor atoms from their ideal positions in the crystal lattice. Due to the charged nature of electrons, much energy is lost in interactions between the incident electrons and the shell electrons of atoms in the target [8]. This generates small defects, typically considered point defects (with zero dimension), as they usually only effect a single atom [8]. If sufficient energy is transferred to the primary atom, then it may cause knock on movement of secondary, and subsequent, atoms [8]. Thus, some defects are clusters of point defects, or Frenkel pairs, rather than discreet individual point defects [8,9]. Important parameters of the incident electrons are their energy and their number (dose) [8].

In YBCO, electron irradiation with 1 MeV electrons increased pinning through introduction of point defects or very small cluster defects (< 2 nm) [10]. Electron bombardment improves J_c and $H^*(T)$ of Bi-2223 at low temperatures and low fields (between 5 and 60 K) [11,12]. It would seem that at higher temperatures and fields, electron bombardment has either little effect on superconducting performance, or actually decreases the observed physical properties of the material [11]. Results for Bi-2212 are similar [9,13], but higher energy electrons (28 MeV compared to 1-4 MeV) expanded the temperature range of enhancement (from 5 to 60 K) [14]. The activation energy for flux jumping after bombardment by electrons was calculated to be scarcely different to that prior to electron irradiation [13]. It would appear that the defects created by electron bombardment are too small to effectively pin magnetic flux, and so are only useful at low temperatures and low magnetic fields when thermal fluctuations and driving forces are small [8].

4. NEUTRON IRRADIATION

Neutron irradiation is similar to electron irradiation in that energetic neutrons, for example from a reactor, bombard a superconductor [8]. Similar to electron irradiation, critical parameters are the energy of the incident particles, and their density (fluence) [8]. Unlike electrons, neutrons do not lose energy in electronic interactions. However, thermal neutrons have relatively low initial energy, and are unlikely to cause significant damage, or if they do, the minor damage they cause will be easily annealed, even during the irradiation [15,16]. Even fast neutrons may not have large energy (perhaps 2 MeV; comparable to some electron beam energies) [8]. Again, similar to electron bombardment, neutron bombardment of HTS generates single point defects, or cascades of point defects as a result of knock on effects [8].

A cascade cluster defect is of the order of 1 to 6 nm in size, typically around 2.5 nm in Y-123 and 3.5 nm in Bi-2212 [17-21]. Surrounding the cluster is a vacancy strain field (directed inwards), which produces an effectively spherical defect of around 5-6 nm in size [19,20,22]. The precise structure of the defects is largely amorphous, with some indication of re-crystallisation having occurred [21]. High resolution TEM on YBCO has revealed further details, involving Cu-O chain defects [23]. Neutron irradiation has an advantage over electron irradiation and ion irradiation in that the penetrating power of neutrons is quite large, and the resulting homogeneity of defect distribution is superior [1]. It has the disadvantage of weak interactions (because neutrons have comparatively huge penetration depths), thus requiring large irradiation doses or long irradiation times [24]. Results almost identical to those of fast neutron irradiation have been produced in (Nd, Eu, Gd)Ba₂Cu₃O_y (NEG-123) by long term ball-milling with Gd-211 so as to introduce a secondary phase of modified NEG-211 with particle sizes of 20-50 nm [25].

Flux creep, and the effective activation energy were found to significantly improve (decrease and increase, respectively) in neutron irradiated high-T_c material [1,26-28]. Neutron irradiation can, however, reduce superconducting performance due to exacerbation of existing weak links in the material [1,29-31]. This damaging effect of fast neutron irradiation is most often observed at lower magnetic fields, while the same material will out-perform un-irradiated material at higher fields [22,32]. For both Tl-2223 and Tl-1223, fast neutron irradiation had the negative effect of reducing T_c with increasing neutron dose [33]. Excessive fast neutron irradiation of Tl-2223 single crystals decreased J_c at all temperatures and fields as a result of the introduction of large numbers of defects, to the point of disordering the superconducting nature of the sample, probably due to overlapping defect structures [33].

Fast neutron irradiation of Y-123 single crystals enhanced J_c by 10,000% at 77 K, but reduced T_c [34,35]. This commonly observed increase in J_c with commensurate decrease in T_c was attributed to the presence of small defects (eg oxygen vacancies) which provide strong collective pinning, but which decrease T_c due to changes in oxygen stoichiometry [2,35]. The same irradiation of melt-textured bulk samples gleaned a 1000% J_c increase at the same temperature, but no improvement was observed in thin film samples [36]. This difference was attributed to the pre-existing defect structures in these materials [37]. Those materials with less existing pinning defects experienced greater enhancement of J_c following neutron irradiation [37]. Neutron irradiation of RE-123 and thallium based superconducting materials generally improved flux pinning [33,36,38-41]. Tl₂Ca₂Ba₂Cu₃O₁₀ (Tl-2223) irradiated by fast neutrons showed an enhancement of J_c by a factor of 52 at 40 K and 1 T, and an upward shift of H*(T) [42]. Less significant improvements in H*(T) were observed for (TlPb)(SrBa)₂Ca₂Cu₃O₈ (Tl-1223) [42], and post-irradiation J_c results for Tl-1223 were disappointing, with minimal improvements, or reductions, in J_c at all fields measured [22,42]. These results were attributed to poor grain connectivity in the Tl-1223 material, which consequently rendered the material largely unconnected after neutron irradiation further disrupted the already poorly connected grains [22]. In Sm-123 bulk there was a five-fold increase in J_c after neutron irradiation to a fluence of 1.5 × 10¹⁷ n/cm² without any change in T_c [43]. The increase was stronger at lower fields and temperatures [43].

Single crystals of Bi-2212 irradiated with fast neutrons showed enormous improvement in properties and performance [44,45]. Fast neutron irradiated Bi-2212 was found to have superior J_c at low magnetic fields and low temperatures (5 K), with the enhancement moving

to higher fields with increasing neutron fluence [46]. At higher temperatures (40 to 60 K) J_c enhancement was found to be quite significant [47]. The irreversibility line also shifted to higher fields and temperatures [48].

Results for Bi-2223 are similar to those for Bi-2212, but at higher temperatures (35 K), the irradiation decreased J_c [49]. The enhanced J_c was attributed to an increase in the magnitude of high energy pinning sites, as determined by magnetic relaxation measurements [49]. $H^*(T)$ was found to increase with low neutron fluence irradiation at low fields, and at higher fields with increasing fluence [46]. The shift of $H^*(T)$ was especially marked when the applied field was parallel to the a-b axis [18]. Additionally, the temperature dependence of $H^*(T)$ was found to no longer follow the usual form [18]. Transport J_c measurements of fast neutron irradiated Bi-2223/Ag tapes showed that flux pinning is important even in the extremely 2D magnetic microstructure [50]. The defects created by fast neutron irradiation of Bi-2223/Ag tapes decreased J_c slightly due to radiation-induced damage of weak links at low fields (the weak link dominated region), but increased J_c at higher fields due to improved flux pinning [22,32,50,51]. Normalised J_c results showed superior performance for the irradiated samples at all fields, as did volume pinning results [32]. The non-dimensionality (point nature) of these defects caused insignificant change in the anisotropy of the Bi-2223/Ag composites, as the misalignment angle (θ_{eff}) was 6.8° before irradiation, and 7.0° after [22,50-52].

An innovative enhancement to neutron irradiation is to dope the irradiated material with an element with a high neutron capture cross section. This principle allows the use of lower doses of fast neutrons, or even the use of thermal neutrons, in order to achieve the same effects as would otherwise require large neutron irradiations [1]. Gadolinium doping of Y-123 (with gadolinium replacing 0.1 of the yttrium) allowed thermal neutrons to induce J_c improvements comparable to fast neutron irradiated un-doped Y-123 [53].

5. ION IRRADIATION

One of the problems with electron and neutron irradiation is that the energy transfer from bombarding particle to superconductor lattice atom is comparatively low, roughly 40 eV for electrons, and 63 eV for neutrons [8]. This allows for creation of, at best, point defect cascades or clusters. Irradiation with ions, however, allows a high mass incident particle, which if accelerated sufficiently, can have great energy. Additionally, the energy transfer between large highly charged ions and the superconductor crystal lattice is much more efficient, leading to the creation of semi-continuous or continuous defects.

These defects are typically columnar in shape and amorphous in structure, their radius may be several atomic spacings, and their length many microns (~ 10 -100) [54-59]. For lower energy ion bombardment, the semi-continuous defects produced are inhomogeneous along the length of the defect, and deviate from a cylindrical shape to form a defect that is more like a string of bubbles or beads, in which the round defect portions may be elongated [60]. Such extended defects (in particular fully columnar defects) make for ideal pinning sites, as their morphology matches the shape of flux vortices, and their dimensions (width) closely match the ξ value of high- T_c superconductors (being several nm). Pinning by columnar ion track defects is effective under field and temperature regimes where other types of defects are ineffective [54,56-58,61-71]. In addition to the amorphous columnar ion track, there is often a

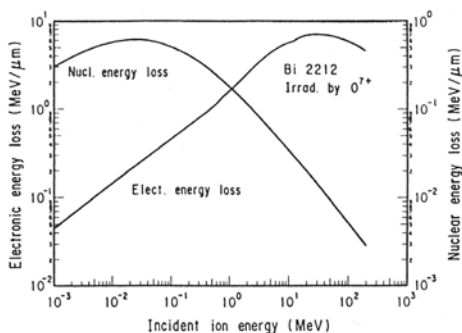


Fig. 5-1. Dissipation of incident O^{7+} ion energy by electronic and nuclear interactions with Bi-2212. (Reprinted with permission from [8] courtesy of Marcel Dekker, Inc.)

electronic interactions with the target material [8]. For a charged proton (hydrogen nucleus) of incident energy around the MeV range, the electronic to nuclear energy loss ratio is around 1000:1 [8]. The nuclear energy loss is the energy transferred from the incident ion directly to the nuclei of the target [8]. Due to interaction effects, the relative electronic and nuclear energy losses vary greatly with incident particle energy [8]. The variation for Bi-2212 bombarded by O^{7+} ions is shown in Fig. 5-1 [8]. Additionally, energy is lost by the incident ion in the formation of Cerenkov and “bremstrahlung” radiation [56]. For columnar defects to be generated, an electronic energy loss of over ~ 20 keV/nm is required [8,55,68,73,74], although for continuous defects, slightly more energy loss is required, in the region of ~ 28 -35 keV/nm [75]. Values of energy loss below around 11 keV/nm produce discreet spherical defects (similar to fast neutron induced collision cascades) in a line [60]. Higher energy losses produce larger columnar defects, for example 40 keV/nm 6 GeV lead ions create columnar defects 9 nm wide in Tl-1223, while 50 keV/nm 6 GeV uranium ions create columnar defects 11 nm wide in the same material [76].

However, the precise structure, size, and density of defects formed depends upon parameters such as the type and energy of ions, their incident direction relative to the crystallographic orientation of the target, the chemical state of the target (in particular, the oxygen content), and the target’s thermal conductivity [56,58,77]. Ions that impinge on the target material in a direction closer to the c -axis direction do less damage than those that strike more parallel to the a - b plane, with the difference in magnitude of damage being 2-5 nm of column radius [56,71,78]. Oxygen substoichiometry greatly increased the extent of damage to Y-123; defects more than halved in size when $YBa_2Cu_3O_{6.3}$ samples were ozone treated to full stoichiometry [56]. Both of these observations may be explained as being due to the lower thermal conductivity of the materials in question (i.e. c -axis Y-123 or BSCCO, and semi-conducting $YBa_2Cu_3O_6$, as compared to a - b axis Y-123 or BSCCO, and metallic $YBa_2Cu_3O_7$, respectively).[56] The presence of intrinsic planar defects such as stacking faults

radial strain or displacement of the crystal lattice surrounding the defects, which may be some two to three times the diameter of the track itself [56]. This region contains severe lattice distortion [56,72]. Extending further than this in samples irradiated with large heavy ions, to some three to five times the size of the columnar defect, are stacking faults created by the irradiation [56]. The nature of these faults are chemical, and could not have been produced by dislocation motion [56]. The weakly (or non) superconducting region introduced by a columnar defect extends to some twice the size of the defect itself, however, as a result of reductions in hole concentration nearby in the distorted lattice region [56].

Due to the charged nature of the incident particles, much of their energy is dissipated in

and grain boundaries, which often have reduced oxygen content, increases the size of generated defects, especially if their plane is normal to the incident ion beam [56,58,77,79]. BSCCO is more damaged by ion beam radiation than Y-123 [58,77]. There is evidence from Bi-2212 single crystals irradiated with different heavy ions that the diameter of columnar defects increases with electronic stopping power (how much energy is lost per unit distance due to inelastic collisions between the ion and the electrons of the target material), while for the same stopping power higher ion velocities produce smaller diameter defects [80].

When the incident ions excite electrons in the target material, the highly energetic electron gas melts a nearby region of the material [56]. Materials (or crystallographic directions in a material) with lower thermal conductivity will melt more slowly, and produce smaller defects [56,81]. It is hypothesised that the original molten volume due to the incident ion was the full size of the observed amorphous core plus the region containing the introduced chemical stacking faults (described above) [56]. During cooling from the molten state, outer regions cooled sufficiently slowly to recrystallise to a nominally correct structure, but with the formation of stacking faults (typically extra Cu-O planes) and corresponding sessile dislocation [56]. However, the theory of “thermal spikes” [82,83] is not the only explanation for ion induced amorphisation of the target material [1,56]. “Coulomb blockade”, “ion explosion”, or “Coulomb explosion” models have also been proposed to explain the phenomena [1,56,84-86]. In these theories, positively charged particles ionise the material as they travel through, and the residual mutually repulsive interactions between positively charged lattice ions result in damage to the crystallographic lattice [1].

6. LOW ENERGY ION IRRADIATION

Bombardment of Y-123 with ~1 MeV protons forms defects similar to electron or neutron bombardment [17]. Except at low temperatures and/or fields, there was little change in magnetisation, thus presumably little change in the effective pinning activation energy, insignificant changes in flux pinning, and no shift of $H^*(T)$ [87,88]. Y-123 irradiated with 182 MeV Si^{13+} ions showed no continuous defects [56]. Structures observed were similar to those produced by neutron and proton irradiation [18,89]. Irradiation of the same material with 236 MeV Cu^{18+} ions produced columnar defects in only small amounts, when the incident ion beam happened to be aligned with the *a-b* axis of the material [56]. Ag^{21+} ions produced columnar defects about 50% of the time (ie, the incident ion dose doubled the observed occurrence of columnar defects) [56]. 300 MeV Au^{24+} ions were required for each incident ion to reliably produce a columnar defect [56]. The diameter of the defects produced also increased with increasing ion energy, charge, and size: 2.36 nm for Cu^{18+} , 5.9 nm for Ag^{21+} , and 10.6 nm for Au^{24+} [56]. In a different approach, improved J_c (by about 30%) was produced in YBCO film by irradiating the SrTiO_3 substrate with 30 keV gallium ions before deposition of the optimally doped film so as to create hillocks 6 nm in height on the surface that formed a square lattice with a lattice parameter of 450 nm [90]. This lattice of hillocks caused defects to nucleate at the substrate-film interface and grow over the whole film thickness [90]. The current enhancement increased with temperature, probably because increasing ξ at higher temperatures caused a better match in terms of size between the defects and the flux vortices [90].

Irradiation of Bi-2212 single crystals with 120 MeV oxygen ions (sufficient to generate point defects and clusters) enhanced J_{cm} at all temperatures from 20 to 77 K, with an enhancement, for example, of 200 fold at 40 K and 0.1 T [8]. The dependence of J_{cm} on the externally applied magnetic field after irradiation was comparable to the same material after neutron irradiation [8]. Irradiation can, however, prove damaging to the material's physical performance. Bi-2212 single crystals irradiated with heavy doses of 30 MeV N^+ ions suffered impaired superconductivity, probably as a result of a change in oxygen content [91]. Bi-2212 films irradiated by 400 keV helium ions showed decreased J_{ct} that was later recovered by annealing at 400 °C [92,93].

Melt-processed Bi-2212 irradiated with 400 MeV oxygen ions (sufficient to only create point defect clusters) showed a decrease in T_c of 7 K, but a substantial increase in irreversible magnetisation (ΔM) at lower temperatures (< 60 K) [94]. The activation energy for flux creep was determined, and found to be no higher after irradiation than before [94]. This indicates that the defects introduced were not stronger pinning sites for magnetisation currents than existing intrinsic defects such as oxygen vacancies, and that the enhanced performance was due more to an increase in pinning sites than an increase in pinning strength [94]. However, for transport J_c measurements, the effect of irradiation at low temperatures (15 K) was negligible, while the improvement of transport J_c with increasing magnetic field was readily apparent at higher temperatures (up to 60 K) [94].

Bi-2212 tapes irradiated by 120 MeV oxygen ions showed a decreased T_c (82 to 76.9 K), but ΔM increased with increasing fluence, especially at higher temperatures and fields [95]. $H^*(T)$ increased with increasing fluence, and the effective activation energy also increased, the latter most markedly at higher temperatures [95]. Bi-2223/Ag tapes irradiated by 250 MeV gold ions exhibited continuous columnar defects (as produced by high energy irradiation, §7), but only for approximately 5% (5 μm) of the Bi-2223 core width [96]. Even with these relatively short columnar defects, significant improvements in $H^*(T)$ and J_c , as well as the anisotropy of $H^*(T)$ and J_c were observed [96].

7. HIGH ENERGY ION IRRADIATION

When an external magnetic field is applied in a direction parallel to that of columnar defects, flux pinning is observed at high fields and high temperatures, and $H^*(T)$ improves [67,70]. The presence of columnar defects, with their almost one-dimensional morphology, gives high pinning when applied fields are parallel to the defect direction. This anisotropy in pinning behaviour can be a disadvantage, or an advantage, depending on the application and design of devices that incorporate such defect material.

The columnar defects produced in YBCO film by Au ions at 250 MeV have been visualised in TEM and related to the results of quantitative magneto-optical analysis (QMO) before and after irradiation, which allows local measurement of $B_z(x,y)$ and the current density distribution [97]. The defects were insulating columns a few nanometers in diameter surrounded by an amorphous zone [97]. The QMO results showed that in transverse geometry the magnetic field lines increasingly curve (increase their tilt angle θ) towards the flux free region inside the sample as this region is approached [97]. These lines straighten towards the centre as more vortices are introduced [97]. After irradiation there was increased current

density, enhanced Meissner zone width and a more linear gradient of B_z curves inside the sample [97]. A huge current density gain with increasing θ was observed causing the authors to conclude that curvature effects were responsible for the changes in local critical current due to the strong pinning at the columnar defects in the z direction [97].

580 MeV tin ion irradiated YBCO crystals exhibited a J_c of 4.5×10^5 A.cm⁻² under an applied external field of 3T; except at low temperatures (5 K) the same material irradiated by protons showed a zero J_c [67,86,87]. The observed pinning enhancement was much greater when the applied field was parallel to the defect tracks [67,70]. Irradiation by 5.3 GeV lead ions produced similar results, with $H^*(T)$ shifting to higher fields and temperatures, and changing in curvature, and a substantial decrease in the flux creep rate [61]. However, improvements in flux creep rate are only possible up until defect saturation with vortices, and are dependent on temperature [86]. The pinning by columnar defects is so strong that ion tracks created at 45° to the c -axis direction still pin vortices when a field is applied parallel to the c -axis under high fields [98-100]. It is more energetically favourable to extend the length of the defect (with the associated suppression of the superconducting order parameter) so that it matches the morphology of the extended columnar defects than to minimise the vortex length [99]. This effect is more pronounced with defects that are continuous, and thus better able to trap entire lengths of vortices [101]. Conversely, the effect is less pronounced in more anisotropic materials, as in these cases the energy for kink formation is lower, and there is less of an energy advantage to be had by forcing a vortex to follow an inclined defect track [102]. Similar results are reported for lead-doped Bi-2212 single crystal irradiated with 7.2 GeV Ta ions, with smaller anisotropy making columnar defects more effective [103]. Heavy ion (for example 3.5 GeV xenon, or 5.3 or 5.8 GeV lead) irradiation dramatically improved J_c and magnetic irreversibility, and reduced magnetic relaxation in RE-123 [54,57,61,104-107]. Similarly, thallium based HTS (Tl-2212, Tl-1223, Tl-2223) irradiated by 6 GeV lead ions showed a higher $H^*(T)$ [76], and that irradiated by 3.6 GeV and 5.8 GeV xenon showed an improved J_c [63].

Irradiation by 0.5 GeV ¹²⁷I ions linearly reduced T_c of Bi-2212 single crystals with increasing dose, but significantly increased J_{cm} performance (5-10 fold) at all magnetic fields up to 5 T (the maximum tested) at 10 K [62]. The same material irradiated with 580 MeV tin ions showed 5-50 fold enhancement of J_{cm} in the temperature range 5-50 K under an applied field of 1 T [108]. Both sets of experiments tested with the applied field parallel to the c -axis, which was also parallel to the direction of the columnar defects [62,108]. However, the second set of experiments by Thompson *et al.* found that in Bi-2212 single crystals, the extent of angularly selective pinning was small compared to Y-123 samples [108]. The 0.5 GeV ¹²⁷I ion irradiated samples showed a largely unchanged activation energy (30-35 meV) for flux motion at 10 K and 0.1 T until the number of columnar defects was greater than the number of vortices [62]. A maximum in pinning energy (70 meV) was observed when the number of defects roughly doubled the number of vortices [62]. The observed pinning energies compare very well to Clem's pancake-vortex model, as do results for 0.65 GeV nickel ion irradiated crystals, which supports the hypothesis that the low angular dependence of the pinning energy was as a result of 2D vortex dissociation [108-111]. For comparison, irradiation by 5.3 GeV lead ions gave an effective activation energy of 50 meV at 60 K and 300 G [112].

Irradiation by 6 GeV lead ions created 7 nm diameter columnar defects in Bi-2212 single crystals and produced a sharp increase in pinning force at particular applied fields, the value

of which increased with dosage [113]. The field at which the maximum pinning force occurred was proportional to the dose, unlike neutron irradiation, which shifts the maximum point without correlation to the dose, or proton irradiation, which does not shift the maximum point at all [8,113]. The linear dependence of the maximum field is a characteristic of the presence of columnar type defects, rather than point defects or clusters [8]. 5.8 GeV lead ion irradiation of Bi-2212 produced similar results, and showed a large improvement in ΔM [8]. Precisely controlled irradiation of Bi-2212 single crystals by 240 MeV Au¹⁴⁺ ions using Lorentz microscopy and sample masks showed higher flux line density and a smaller relaxation rate in irradiated regions [114].

Bi-2212 single crystals irradiated by 6 GeV lead ions showed distinct changes in the positions of their irreversibility lines [113,115,116]. At low temperatures ($T/T_c < 0.3$) $H^*(T)$ for all fluences (including no irradiation) coincided, indicating that in this low temperature region the critical mechanism determining the position of $H^*(T)$ was unchanged by the presence of columnar defects [76,113,117]. At higher temperatures ($0.3 < T/T_c < 0.6$), increasing the density of columnar defects increased the position of $H^*(T)$ to higher fields [76,113]. It would appear that each columnar defect pins a vortex [76,113,115,118]. Although it has been proposed that even once all columns have pinned a vortex, a form of collective pinning in which vortex-vortex interactions become significant allows additional vortices to be pinned between columnar defects [119]. At even higher temperatures ($T/T_c > 0.6$), the $H^*(T)$ lines for all fluences once again began to merge, although less strongly than at low temperatures [113,116]. This sharp shift in the $H^*(T)$ line was attributed to the transition of the vortex lattice from 3D to 2D and showed a strong correlation to the decoupling line [113,120]. However, JPR experiments show that even in this higher temperature regime, decoupled vortices can be re-coupled by the presence of columnar defects, forming vortex lines [116,121]. Pinning force analysis determined that at low temperatures the post-irradiation $H^*(T)$ was composed of the temperature dependence of the field at maximum pinning force prior to irradiation, and at high temperatures it was based upon the temperature dependence of the field at maximum pinning force after irradiation [120]. This change in dependence typically occurred around 20-30 K [120]. In general, irradiation by high energy heavy ions (such as 5.8 GeV lead ions) significantly shifts $H^*(T)$ to higher fields at all temperatures [8,62,67,69,100,108,117,122].

The $H^*(T)$ of single crystals of Bi-2212 irradiated with 5.8 GeV lead ions was found to be determined by the flux-creep rate [123]. They exhibited giant, strongly non-logarithmic magnetic relaxation as a result of pinning by columnar defects [123]. Flux-creep was ascertained to occur as a result of a vortex-loop nucleation process [123]. In addition to the crossover from single-rod de-pinning to variable range hopping, a new crossover from combined pinning by both pre-existing defects and introduced defects to purely introduced defect pinning was observed [124]. In such films irradiated with 2.7 GeV ²³⁸U ions, the occurrence of the Bose-glass transition was rationalised as vortex localisation as a result of correlated disorder increasing the tilt modulus of the vortex ensemble [125].

Pinning by columnar defect tracks created by 17.7 GeV uranium ions in Bi-2212 single crystals was strong enough to prevent thermal fluctuation of vortex positions at all temperatures for magnetic fields up to 150 mT [126]. Single crystals of Bi-2212 irradiated by 2.25 GeV silver ions showed suppressed dynamic creep rates as compared to unirradiated

crystals, and this depression became more pronounced at higher temperatures [117]. At fields exceeding the matching field, however, the suppression was reduced [117].

Melt-textured layers of Bi-2212 on silver tape irradiated by 502 MeV ^{127}I ions showed enhanced J_{cm} from 4.2 to 60 K; with improvement being 1000 times at 30 K under a 2 T field [127]. J_{ct} , however, showed less significant enhancement, up to 5 fold at most [127]. The granularity of samples may be neglected for unirradiated samples, but limited the enhancement of J_{ct} possible by irradiation [8]. This result was similar to that observed in the above mentioned 400 MeV oxygen irradiated melt-processed Bi-2212, in which J_{ct} improvement would appear to have been limited by granularity effects [94]. Flux motion activation energies change in a manner similar to single crystal material irradiated with the same ions (above), but with twice the dose being required in the melt-textured material to achieve the same activation energies (i.e., approximately 4 times the density of columnar defects compared to the number of vortices is required for maximum pinning) [62,127]. Irradiation of Bi-2212 melt textured tapes with 580 MeV silver ions resulted in a 1-2 T increase in the magnetic hysteresis, evidencing significantly higher persistent current densities [128]. Energetic uranium ion irradiation of Bi-2212 single crystals and Bi-2212 melt textured tapes showed J_{c} (at 40 K) improvements of two orders of magnitude and one order of magnitude, respectively [129]. At higher magnetic fields, the improvement was up to five orders of magnitude and three orders of magnitude, respectively [129].

Polycrystalline Bi-2212 tapes irradiated by 180 MeV Cu^{11+} ions showed little reduction in T_{c} at low fluences (up to 10^{11} ions.cm $^{-2}$), but a more rapid decline at higher fluences (e.g., a 10 degree reduction at 10^{12} ions.cm $^{-2}$) [13]. The effect of irradiating with Br^{11+} ions was similar, with the reductions starting slightly sooner, and the extent of reduction being considerably larger (e.g., 60 degrees at the same 10^{12} ions.cm $^{-2}$ dose level) [13]. For comparison, electron irradiation barely changes T_{c} up to dose levels of 10^{18} electrons.cm $^{-2}$ [13]. ΔM was enhanced under all magnetic fields at temperatures up to 60 K by all three processes, and at 77 K by electron and Cu^{11+} irradiation [13]. Br^{11+} irradiation reduced T_{c} so significantly that this effect overrode any ΔM improvements [13]. J_{ct} improved only at low fluences, with high fluence drops in J_{ct} being attributed to irradiation induced exacerbation of weak links [13]. Changes in $H^*(T)$ with irradiation by Cu^{11+} and Br^{11+} were of an upward shifting form, with the magnitude of increase ranging from 2 to 10 fold depending on temperature, much higher than the 50% increase due to electron irradiation [13]. At high and low temperatures, the increase was less (2 to 4 fold) due to intrinsic pinning (at low temperatures) and degradation of T_{c} and anisotropy (at high temperatures) [13]. This observation is the same as that made by Hardy *et al.* for single crystal Bi-2212 irradiation [113]. The activation energy at 0.2 T changed from 15 meV before irradiation to 40 meV after [13]; both values were around 50% lower than those reported by other authors [62,94,127].

Single crystals of Bi-2223, with no contact between crystals, and weak intrinsic pinning, were irradiated with 0.8 GeV protons [130]. At all temperatures, the irradiated crystals' J_{c} was around an order of magnitude higher than that of the unirradiated crystals [130]. Civale *et al.* irradiated Bi-2223/Ag tapes with 1 GeV Au^{23+} ions and induced columnar defects with diameters of 10 nm; the irreversible region was greatly enlarged, and ΔM improved significantly for all measured fields and temperatures [131]. $H^*(T)$ showed a considerable upward movement with the irradiation, most markedly at higher temperatures [131]. Irradiation of Bi-2223/Ag tapes with 0.65 GeV and 2.65 GeV gold ions considerably

increased the critical current [110,132]. 0.8 GeV proton irradiation of Bi-2223/Ag tapes resulted in the creation of long defect tracks, and samples showed a large dose-dependent increase of J_c under applied magnetic fields parallel to the track direction, with little to no loss of J_c under self-field [133].

One of the potential problems with ion irradiation techniques (other than their prohibitive cost) is that defects with a single orientation are most effective in only a single applied field direction [67,134]. With kink formation being relatively easy, especially in 2D BSCCO materials, dissipation can easily occur when vortices form kinks [1]. In fact, identical parallel columnar defects are completely ineffective at preventing expansion of double kinks once relaxation has moved out of the initial stage of nucleation of half loops [135-137]. More randomly oriented columns have the advantages of an entangled flux line ground state and of inhibiting large scale low energy excitations (such as kink formation), thus reducing dissipative losses [1,135]. Crossed linear defect structures provide greater pinning in 2D systems than aligned linear defect structures, as they inhibit superfast vortex creep via variable-range vortex hopping [137-139]. Additionally, in a crossed linear defect structure, flux line de-pinning due to kink-pair creation is inhibited [32]. However, in more isotropic (3D) superconductors, such as Y-123, in which kink formation is not such a common occurrence, too great a splay of orientation of columnar defects can be detrimental [140].

Rutherford scattering as a result of collisions between incident ions and lattice ions can generate a small amount of angular variation in the defect orientation [58,86]. The difference in J_c performance between YBCO crystals irradiated with tin (low mass, and lower energy of 0.58 GeV) and gold (high mass, and higher energy of 1.08 GeV) ions was an order of magnitude at 80 K [141]. The difference was determined to be largely a consequence of the difference in the splay of the columnar tracks, with the lighter tin ions being more prone to deflection due to Rutherford scattering [141].

Tilting or rocking of a sample during ion beam bombardment would lead to such a splayed arrangement of defect columns [135,138,141,142]. Such configurations of tilted or splayed columnar defects have shown greater performance than linearly parallel arrangements [86]. However, even highly splayed arrangements will never achieve a truly random or anisotropic arrangement of columnar defects. This is not necessarily a disadvantage, depending on the superconductor involved and the direction of the external magnetic field. If the direction of the applied field is well known and stable, then optimum pinning effects, and thus J_c , will be obtained if the angular dispersion of columnar defects with respect to the applied field direction is a particular value, which depends on the electronic anisotropy of the superconductor [71,86,143]. For YBCO, it was determined that a discrete planar misorientation of $\pm 5^\circ$ to the external magnetic field was superior to parallel orientation or a gaussian splayed distribution [140]. The value for Bi-2212 was closer to 60-75° [71].

8. FISSION IRRADIATION METHODS

While in theory it might be effective to establish precisely controlled misorientations of columnar defects with the applied external magnetic field, in practice it is usually not possible to control the environment to such a degree so as to have a consistent direction of applied magnetic field [134]. For example, superconducting cable employed as windings in an

electromagnetic coil turns through 360° , requiring either a continuously varying misorientation of the defect structure, or a completely isotropic defect structure. The former option is nigh on impossible. The latter option is not possible with any columnar defect produced by the ion irradiation technique.

However, fission techniques are able to produce wholly directionally isotropic columnar defect structures because fission reactions, if they occur within the structure of the material on a microscopic scale, will produce daughter atoms with large momentum in completely random directions. It is impossible to predict the direction in space that the two daughter atoms of a fission reaction will be propelled, other than to say that each will go in the exact opposite direction to the other. With the energy released in a fission reaction being large, and the mass of many fissionable elements high, the effects of fission reactions can be comparable to fast heavy ion irradiation. Thus, by using fission techniques, columnar defects can be generated with isotropic arrangements. Such an isotropic arrangement, if sufficiently dispersed so as to create more or less continuous defects, can result in 100 times the fluxoid entanglement that relatively parallel columnar defects can engender [3].

The flip side of this otherwise advantageous sounding idea is that for these techniques to function at all, fissionable isotopes must be incorporated into the structure of the superconductor. This may be as simple as replacing an otherwise non-fissionable isotope of a component element with a fissionable one, or it may involve incorporating a fissionable element into the structure of the material. The former option is only viable if a suitably easily fissioned isotope of an existing component element is available. The latter presents problems related to elemental dispersion and distribution [144], not to mention concerns about chemical compatibility and phase stability. However, the very nature of utilising a fissionable isotope that is distributed throughout the structure of the superconductor helps fission based processes avoid one of the pitfalls of ion irradiation techniques, namely, low ion penetrating power. Many ion irradiation processes are only suitable for thin films or suitably thinly processed bulk samples, and are often unsuitable for sheathed tapes as the outer layers may completely block the ions [145-147].

Another potential negative is residual radioactivity, either from the incorporated elements themselves, from their daughter isotopes, or from the process employed to engender fission. Nonetheless, these techniques are powerful and versatile, and work can be carried out to minimise the problems and achieve maximum benefit from the processes.

While fission product damage is usually compared to fast heavy ion damage, there are some noteworthy differences. One of the more obvious is that heavy ion induced columnar defects necessarily extend to the edge of the material. As a result of the amorphous material being less dense than the surrounding matrix, a stress mismatch occurs. This stress is often relieved by slow forcing of amorphous material out of the sample though the surface ion penetration points [148]. With fission tracks often being entirely internal, these stress fields are not able to be so easily relieved, and the entire effect of a columnar defect may be significantly larger than the defect itself (perhaps twice as large) as a result of elastic strain [58,149,150].

Schwartz and Wu doped Bi-2212 with lithium and irradiated the polycrystalline powders with mixed energy neutrons (both thermal and high energy) [16,145]. This both resulted in neutron induced defects (§4) and caused some of the lithium to fission into tritium and an alpha particle (lithium is 7.6 % ^6Li which has a neutron capture cross section of 945 b), with

an energy release of 4.8 MeV [16,24,145]. The low energy of the fission event and the low mass of the daughter atoms makes this ion damage more comparable to low energy ion bombardment (§6). The fission induced damage from even these light low energy ions was significant enough to markedly increase (150% - 330%) magnetisation at most fields as compared to the modest 20% - 50% improvement from the neutron irradiation alone [145]. At higher fields (> 1 T) the increase was greater than 30 fold [16]. Additionally, the irreversibility line was extended to higher fields in the lithium doped samples, and these samples showed increased magnetisation at higher temperatures [145].

Manton *et al.* doped YBCO with lithium and induced fission by neutron irradiation [24]. Their results indicated a change in pinning regime, but were overall disappointing, as lithium doping degraded the general performance of un-irradiated YBCO to the point where even though the J_c gains after irradiation were twice that of undoped material, the gross magnitude was still lower [24]. These results may be improved with refinement of the initial processing of the lithium doped YBCO, but they highlight the inherent difficulties of adding elements to carefully synthesised HTS.

Krusin-Elbaum *et al.* irradiated Bi-2212 thick films (3-4 μm thick) with 0.8 GeV protons, causing fission of the ^{209}Bi nuclei (fission cross section 155 mb as a result of a resonant proton absorption event) [1,133,151]. A typical fission reaction between an incident proton and a bismuth nuclei produces an 80 MeV xenon nucleus and a 100 MeV krypton nucleus [151,152]. These daughter atoms have ranges of 7-12 μm though the Bi-2212 matrix [151]. TEM analysis showed a typical track diameter of ~ 7 nm, and a widely varying degree of track splay [151]. Magnetisation hysteresis increased 2-6 fold at lower temperatures (5 K) up to 5

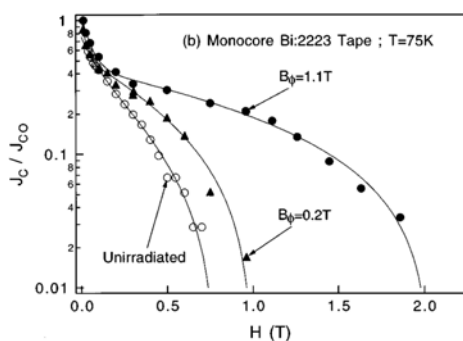


Fig. 8-1. Variation of J_c (normalised) in an externally applied magnetic field ($H \parallel c$ -axis/tape surface) for 0.8 GeV proton irradiated Bi-2223/Ag composite tape. B_0 is the matching field for the irradiation dose (the field at which each track is occupied by 1 vortex); higher matching fields indicate more columnar defects (due to larger irradiation doses). (Reprinted with permission from [133].)

T, and at higher temperatures (30 K) the effect was much more pronounced, with increases being effectively infinite at fields above approximately 0.5 T [151]. Similar results for magnetic hysteresis loop widths were also observed by Ossandon and Thompson [152]. Critical currents were dramatically enhanced at all measured fields and temperatures (1-4 orders of magnitude), with large J_c values present in irradiated samples at temperatures and fields well above the irreversibility line of unirradiated samples [151]. In the work of both Krusin-Elbaum *et al.* and Ossandon and Thompson, the irreversibility line was shifted to higher fields and temperatures, in one example with the shift being 22 K at 1 T [151,152]. Krusin-Elbaum *et al.* compared the physical enhancements with high energy heavy ion irradiation experiments, and it was found that for comparable improvements only a third of the dose was required, indicating the greater efficiency of splayed defects [151]. As an

additional benefit for engineering production, the penetrative power of high energy protons is typically around 0.5 m, which would allow treatment of fully clad materials or even entire manufactured pieces [146,151]. Similar enhancements of J_c and a strong reduction in equilibrium magnetisation were observed in bulk $Tl_2Ba_2CaCu_2O_x$ irradiated with 0.8 GeV protons by the same group [153].

Safar *et al.* employed the method of Krusin-Elbaum *et al.* and irradiated Bi-2223/Ag composite tapes with 0.8 GeV protons [133]. The tapes were then characterised by transport measurements, and an example of the variation in tape performance is shown in Fig. 8-1 [133]. The improvement in critical current drop with increasing field is immense and is most particularly obvious at fields above 0.5 T. Results for lower temperatures than 75 K, for example 64 K, were even more pronounced, with the rapid low field drop in J_c almost eliminated and the entire curve shifted half an order of magnitude higher [133]. The irreversibility line was determined to increase by approximately 15 K in the range 1-8 T [133].

Maley *et al.* used the technique of Krusin-Elbaum *et al.* and irradiated Bi-2212 single crystals and Bi-2223/Ag composite tapes with 0.8 GeV protons [147]. They found similar enhancements of J_c after irradiation, but also determined that the decoupling transition temperature of pancake vortices was increased as a result of the fission irradiation [147]. Ossandon and Thompson, who irradiated Bi-2212 thick films with the method of Krusin-Elbaum *et al.*, also observed large increases in J_c as a result of irradiation, but also established that proton irradiated Bi-2212 thick films trapped five times the flux of virgin films [152]. Additionally, they also found that the persistent current decay rate due to flux creep was improved by a factor of 10 after irradiation [152]. All of these results indicate stronger pinning as a result of irradiation. Cho further explored the persistent current decay rate due to flux creep, and found a lesser rate at fields less than the matching field, although the matching field was found to vary with temperature, likely as a result of a reduction in the effective pinning centres as temperature increases [154].

Thompson *et al.* measured quantum creep in 0.8 GeV irradiated Bi-2212/Ag tapes and found that irradiation halved the persistent current decay rate caused by quantum creep [155,156]. Thermal creep was still influencing the persistent current decay rate in un-irradiated tapes at around 5 K under a field of 10 kOe [155,156]. After irradiation, thermally induced creep was negligible at around 10 K under the same applied field, and the persistent current decay rate due to quantum creep was halved [155,156]. Even so, quantum creep at temperatures as low as 2 K still accounted for some two orders of magnitude loss in J_c from the theoretical maximum predicted by the de-pairing current density [156]. Qualitatively similar results were obtained for proton irradiated Tl-2212 polycrystals (in which the incident proton induces fission of thallium nuclei) [156].

Furthering the comparative work of Krusin-Elbaum *et al.*, Cho *et al.* compared Bi-2212 single crystals irradiated with similar doses of unidirectional columnar defects (produced by irradiation with 1 GeV uranium ions) and isotropic splayed columnar defects (produced by irradiation with 0.8 GeV protons) [157]. They found a much sharper zero resistance transition temperature for the proton irradiated samples at all applied magnetic fields (from 0.1 T to 7 T) [157]. However, contrary to the observations of Krusin-Elbaum *et al.*, the isotropically irradiated crystals had around a third of the effective matching field of the unidirectional irradiated crystals [157,158]. Samples with unidirectional columnar defects showed a sharp

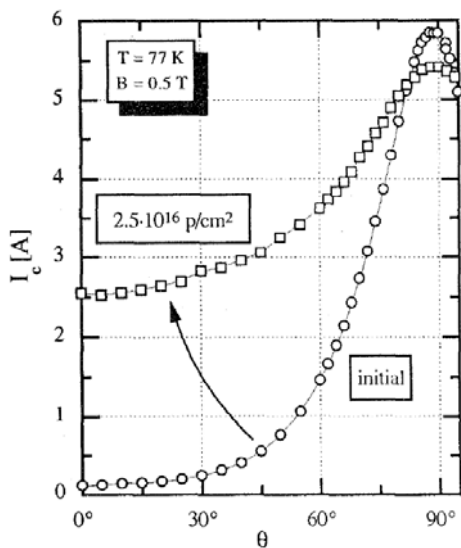


Fig. 8-2. Variation of critical current with applied field angle of both un-irradiated and proton irradiated Bi-2223/Ag tape at 77 K under an applied magnetic field of 0.5 T. (Reprinted with permission from [78] © 2004 IEEE.)

change in activation energy at around the matching field; the samples with isotropic columnar defects showed less variation of activation energy with magnetic field [157]. At fields lower than the matching field, the activation energy of crystals with an isotropic defect distribution was slightly lower, which is plausible when the energy requirement for slightly tilting vortices is taken into account [157]. At fields above the matching field, the isotropically irradiated samples had higher activation energies than the unidirectionally irradiated samples [157]. At these higher magnetic fields point defect-like pinning becomes important, and there are more point defect-like defects present in the sample with perfectly splayed columnar defects [157]. Additionally, vortex-vortex interactions were found to become significant at around a third of the matching field material with an isotropic defect distribution [158]. It would be expected that these results would be markedly different, in favour of the material with the isotropic distribution, for applied magnetic field orientations other than perpendicular to the a - b axis.

Hensel *et al.* also made use of the proton/bismuth nuclear reaction to produce splayed columnar tracks in Bi-2223/Ag tapes by irradiating with 600 MeV protons [78]. One of their most interesting results is shown in Fig. 8-2, and demonstrates the significant reductions in critical current anisotropy that are achievable with fission based techniques [78]. At the dosages employed (matching fields of around 0.5 T) the irreversibility field was found to dramatically increase in the useful temperature regime of 25 - 85 K [78]. However, a decrease in the irreversibility field was observed at higher temperatures (closer to 100 K) as a result of T_c depression of the material after irradiation [78]. Similar T_c depression (from 94 K 88 K) was observed in Bi-2212 thick films by Ossandon and Thompson after 0.8 GeV proton irradiation [152].

A potentially negative effect of splayed columnar defects was observed in Hensel *et al.*'s low temperature magnetisation results in which at 20 K the normalised magnetisation dropped off faster at fields above 1 T in the irradiated tapes than the un-irradiated ones [78]. They attributed this behaviour to the interplay of defect topology and vortex localisation [78,140,159]. Dhalle *et al.* further studied this phenomenon and found that at temperatures below 30 K irradiation increased the creep rate [160]. They modelled this behaviour by noting that it is generally agreed that a 3D to 2D crossover in vortex dynamics occurs at around 30 K in Bi-2223 HTS [160]. With this in mind, they were able to define a "localisation length" which related to the splay of defects and the correlation length of the vortices [160]. When

vortices were 3D, the localisation length was larger than the grain size, and vortices were equally well pinned at any position (i.e., they were able to move freely, resulting in creep) [160]. When vortices were 2D, their localisation length was much smaller (comparable to the spacing between CuO planes) and a discreet position on a defect was able to pin each pancake individually [160].

The work of Maley *et al.* on Bi-2223/Ag composite tapes also demonstrated that, at least up to irradiation doses producing equivalent track densities of 1 T, there was no intergranular connectivity degeneration [147]. Additional work by Budhani *et al.* demonstrated that higher irradiations (2 T matching field) produced a lesser field dependence of J_c on applied magnetic field, but a lower J_c overall [149]. This overall reduction of J_c was attributed to radiation induced damage of the crystal lattice and grain boundaries [149].

Additional interesting work carried out by Hensel *et al.* related to post-irradiation annealing of the tapes [78]. In this experiment, they found that a short (1 hour) anneal of the irradiated tape at 700 °C dramatically increased the critical current, by a factor 2-4, for applied fields up to 0.8 T [78]. It was hypothesised by the authors that this increase was due to relaxation of mechanical strain introduced as a result of the expanded amorphous defects [78]. Annealing at higher temperatures (825°C) resulted in a decrease of performance to near before-irradiation levels, with the hypothesis that extensive re-crystallisation of the amorphous defects had occurred [78]. Budhani *et al.* carried out similar annealing experiments and found that a 3 hour anneal at 400°C changed the low temperature (55 K) properties of 800 MeV proton irradiated Bi-2223/Ag tapes little, but such annealing significantly improved the critical current-magnetic field behaviour at higher temperatures (63 and 77 K) [149]. They explained this observation by speculating that the low temperature anneal removes point defects such as cation vacancies and oxygen disorder [149].

Krusin-Elbaum *et al.* repeated their Bi-2212 proton irradiation experiment with Hg-1201 and Hg-1212, in which 0.8 GeV protons induced a fission reaction in ^{200}Hg (fission cross section 110 mb) [161,162]. Fission products of the reaction could be zirconium and niobium, for example, with energies of around 100 MeV, which produce columnar tracks of 8-9 nm diameter and 8-9.5 μm length through the superconductor matrix [162]. The irradiation of Hg-1212 increased J_c by an order of magnitude or more at fields up to several tesla (5.5 T), and increased the temperature range at which a finite J_c was measurable to over 100 K (irreversibility temperature increases of around 25 K) [161,162]. It was proposed by the authors that the impressive results are only obtainable in highly anisotropic superconductors, in which splay angles are renormalised as a result of the anisotropy [161,163,164]. For less anisotropic superconductors such as Y-123, too great a splay angle ($> 10^\circ$) actually enhances vortex motion [140]. This observation was found to be true to a degree in Hg-1201, in which irradiation lowered J_c at low fields (0.1 T), but increased it by two orders of magnitude at high fields (1-2 T) [162]. At fields around the matching field of 1.2 T, the irreversibility line for Hg-1201 was increased by some 35 K [162].

9. U/N METHOD

The most effective fission methods employ high atomic number atom fissions. These methods ensure a high energy and relatively heavy mass of daughter atoms, which result in fully

amorphous, long columnar tracks. Fission techniques that rely on fission of low atomic mass nuclei only generate light and less energetic daughter atoms, and thus produce less effective pinning centres. As such, lithium fission techniques [16,24,145] are less effective than proton fission techniques, such as those suitable for bismuth [1,78, 133,140,146,147,149,151,152,154-157,159,160], mercury [161,162] and thallium [156] containing superconductors.

However, the fission techniques listed above also rely on highly energetic protons of around 1 GeV energy. Proton beams of this extremely high energy are rare, exceptionally expensive, their beam time is in high demand, and they can only irradiate a tiny area at a time (perhaps 1 cm by 1 cm) [133,144]. Similar problems are inherent with external ion irradiation techniques, with small sample size and tiny sample penetration hindering large scale use of these enhancement methods [165,166]. Even though work is under way to scale up the proton induced fission procedure with methods such as reeling superconducting tape through an irradiation chamber, the process is inherently limited by the requirement for expensive and rare ultra-high energy proton beams [147,165].

Alternative methods involve doping the superconducting material with an element that is more readily fissionable [144]. The best known example of this is uranium, which has a large thermal neutron capture cross section and fissions readily when exposed to thermal neutrons. ^{235}U fissions upon capture of a thermal neutron, and produces two daughter atoms with an average mass of around 116 amu and a combined energy of around 200 MeV [167-170]. Due to the proliferation of nuclear reactors, and the general availability of ^{235}U , doping with uranium is achievable, and exposure to thermal neutrons is comparatively readily available (at least compared with the availability of GeV proton beams). The process of doping with uranium and exposing the material to thermal neutrons to induce fission has become known as the "U/n method" [169-171].

Compared to proton beam irradiation methods, and other irradiation techniques, the U/n method has several practical advantages. In comparison to ion irradiation methods or proton irradiation methods, the enhancements possible with U/n processing are some two to four times larger [5,165,170,172]. Additionally, because the U/n method can be applied with low energy thermal neutrons, rather than high energy ions, or ultra-high energy protons, damage to the grain boundaries and reduction of inter-grain currents due to weak links can be reduced [4]. The cost of processing and irradiation using the U/n method is some 10 to 60 times lower than that of an ion beam irradiation technique [165,169]. Proton induced fission, with its requirement for unusually high proton energies, more than doubles this cost difference again [3,5,170].

For YBCO materials, the residual radioactivity is between three fold and around two orders of magnitude lower for the U/n method when compared to proton irradiation processes [3,165,169,173]. Fast neutron irradiation approaches also require much larger fluences than the U/n method, which means more irradiation time, necessitating an order of magnitude more cost, and results in three to five times the residual radioactivity [3,165,173]. Optimised U/n processed Y-123 has a residual γ radioactivity after six months of around 7 kBq.g⁻¹, which is approximately a fifth of that of a household smoke detector [3,174]. At 10 cm with no shielding, the biological dose as a result of emissions from the material is less than that adsorbed from cosmic rays [3].

For Bi-2223/Ag materials, the residual radioactivity is approximately 14 times lower for the U/n method when compared to proton irradiation fission processes [5,170,172]. Fast neutron irradiation approaches also require much larger fluences than the U/n method, which means more irradiation time, necessitating around 30 times the cost, and resulting in around 100 times the residual radioactivity [170,172,175].

Table 9-1. Adsorption distance at which incident thermal neutrons are diminished by a factor of $\frac{1}{e} \approx 0.368$.

(Reprinted with permission from [5].)

| HTS | d_e (cm) |
|---------|------------|
| Y-123 | 4.44 |
| Sm-123 | 0.0367 |
| Nd-123 | 2.16 |
| Gd-123 | 0.00406 |
| Bi-2223 | 4.6 |
| Tl-2223 | 4.55 |

performance improved by the U/n method. When compared to ion irradiation techniques, which typically have penetration depths of some tens of microns, 4 cm is considerable [134,172].

Work employing the U/n method in HTS was pioneered by Fleischer *et al.* [167], who in combination with other authors had employed a similar technique over two decades earlier with low temperature superconducting Nb_3Al and V_3Si [176]. Their earlier work with Nb_3Al and V_3Si showed improved flux pinning attributed to fission induced damage after thermal neutron irradiation [176]. In their more recent work with sintered bulk YBCO, Fleischer *et al.* doped the superconductor with 150 and 380 ppm of uranium [167]. The uranium was added as 0.08 and 0.2 wt% UO_2 , and natural, rather than enriched uranium, was used [167]. A range of irradiation fluences were employed, resulting in varying densities of fission tracks, which were approximately 16 μm in length [167].

Fleischer *et al.* found that the uranium doping decreased magnetic hysteresis by a small amount, but that after irradiation the magnetic hysteresis was markedly increased by some 4 to 20 times [167]. The increase was dependent on temperature, and indicated a much larger pinning energy for irradiated samples [167]. A portion of the increase was attributable to thermal neutron irradiation effects (§4), but the magnitude of this portion was less than 5% of the total improvement [167]. T_c transition onset was reduced as a result of irradiation by only 1 or 2 K, but the transition width increased two to three times [167].

Interestingly, there were no fission tracks observed by TEM in the uranium doped and irradiated YBCO of Fleischer *et al.* [167]. Weinstein *et al.*, however, observed broken tracks, or so called “string-of-beads” defects in uranium doped and irradiated Y-123, as shown in Fig. 9-1 [173]. This is not entirely surprising, as materials with resistivities below around 2000 $\Omega \cdot cm$ do not ionise sufficiently to result in fully amorphised fission tracks, as the energy

One potential problem with the U/n method, however, is the reliance on thermal neutrons. Thermal neutrons, of typical energy 25 meV, have relatively low penetrating power compared to fast neutrons, of typical energy 1.5 MeV, or ultra-high energy protons, of typical energy 800 MeV [5]. Typical penetration depths of thermal neutrons in different HTS materials are given in Table 9-1 [5]. Fortunately, Bi-2223 has one of the highest penetration depths, as its constituent elements have relatively low capture cross sections for thermal neutrons. With a penetration depth of around 4 cm, even bulk Bi-2223 electrical devices can have their

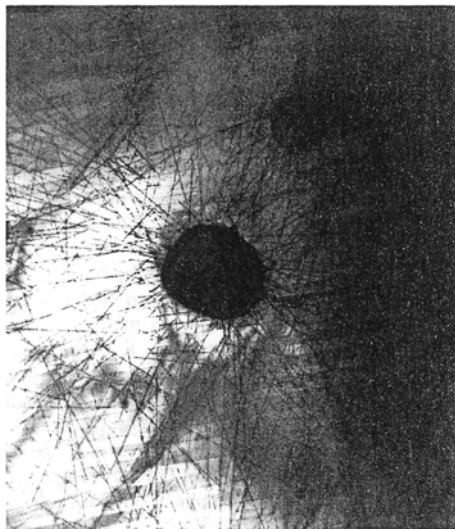


Fig. 9-1. Fission tracks as observed by TEM in uranium doped YBCO. The central dark area is a roughly spherical ($U_{0.6}Pt_{0.4}$) YBa_2O_6 particle of approximately 300 nm diameter. Most fission tracks emanate from this particle. (Reprinted with permission from [173].)

loss for fission products of energy around 100 MeV is slightly under the $2 \text{ keV}\text{\AA}^{-1}$ requirement for creation of continuous tracks [3,67,174,177]. However, due to the statistically varying ionisation energy loss per unit length, the actual energy loss fluctuates by $\pm 75\%$ [3,5,174,178]. As a result of the combination of these effects, the damage tracks formed are short columnar defects, broken columns, and “string-of-beads” type defects [169,170,173,174]. In YBCO, the effective track length is 2-12 μm , with the majority of columnar damage occurring in the initial 2-4 μm [3,165,170,173]. After the fission products have travelled this distance, they have lost sufficient energy to cause significant columnar damage [3,165,173]. At low energies, such as towards the end of the “track”, damage induced is as a result of the approximately 5% of fission energy that transfers by way of direct atomic collisions [179]. Nonetheless, the damage as a result of a fission event will be strongly localised to within 10 μm or so of the uranium atom, and will be significantly larger than the damage resultant from lower energy irradiation, such as electrons or fast neutrons [3,167].

Eisterer *et al.* calculated that with the energy and atomic mass of typical uranium fission products in YBCO, tracks would be predominantly fully columnar at distances of 2-5 μm [180]. These columnar tracks should be some 10 nm in diameter [180]. At distances up to around 10 μm , they determined that the ionic interactions would be sufficient to generate atomic collision cascades of roughly spherical morphology and an approximate size of 6 nm [180]. Calculations taking into account flux line interactions determined that the “effective” size of defects induced by the U/n method was some 10 - 20 nm, as only a small portion of the length of a flux line would fully align with any given defect track [180]. Weinstein *et al.* observed tracks in YBCO using TEM to be approximately 5 nm in diameter [170].

Luborsky *et al.* doped a variety of HTS with UO_2 and irradiated them with thermal neutrons [181]. Polycrystalline YBCO bulk samples were doped with 0.08 wt% natural UO_2 (150 ppm), while 0.4 μm thick YBCO epitaxial thin films were covered with a 60 μm thick foil of natural uranium metal during irradiation [181]. For the bulk Y-123 material, Luborsky *et al.* obtained similar results to Fleischer *et al.*, with substantial improvements of 2-6 fold in ΔM at primarily intermediate temperatures, and a large improvement of around an order of magnitude in the field dependence of ΔM at all measured fields [181]. They found no change in T_c , but a decrease in overall transport J_c [181]. This latter effect was attributed to irradiation induced damage to weak link grain boundaries [181]. Results for the Y-123 thin films showed

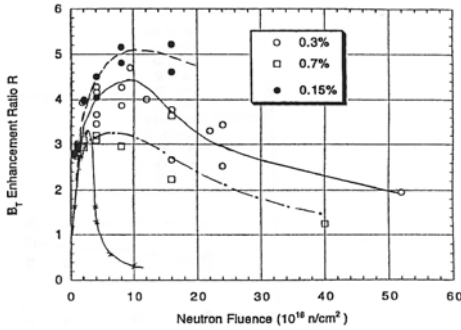


Fig. 9-2. Trapped field measurements of neutron irradiated Y-123 doped with uranium. Curves show the enhancement ratio of trapped field (directly proportional to J_c) for a range of neutron fluences and a number of uranium doping levels (● 0.15%, ○ 0.3%, □ 0.7%). For comparison, a curve showing the enhancement provided by ion irradiation with xenon ions in a parallel configuration is also shown (x). (Reprinted with permission from [173].)

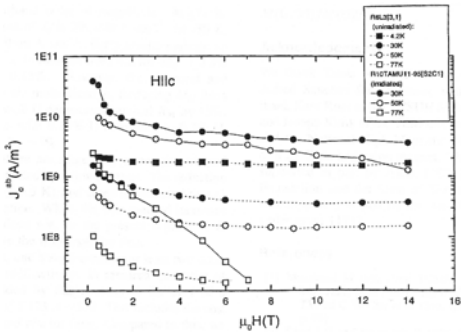


Fig. 9-3. Variation of J_c with magnetic field for uranium doped YBCO both before and after irradiation, at temperatures of 30 K, 50 K, and 77 K. (Reprinted with permission from [173].)

negligible change in physical performance after irradiation, which could be due to the lower fission fragment dose, or to the already high density of existing defects in the thin films [181]. Interestingly, the pinning energy for flux creep in both the polycrystalline material and the thin film was increased by a factor of two to three [181,182].

Weinstein *et al.*, Ren *et al.*, Sawh *et al.*, and Eisterer *et al.*, after optimising the chemical interaction between Y-123 and $UO_2 \cdot 2H_2O$ [165,183-185], doped melt textured Y-123 with ^{235}U and irradiated the material [5,165,169,171,173,174,180]. Under trapped field, J_c increases after irradiation were up to 5 fold, depending on the uranium doping level and fluence employed, as shown in Fig. 9-2 [165,169,171,173,174]. The J_c performance of the irradiated doped material was higher at all fields and temperatures, but the enhancement varied with these parameters as shown in Fig. 9-3 [173,174]. For example, at 77 K and 0.25 T, J_c increased 30 times [3,173]. With increasing temperature, J_c of U/n YBCO samples falls off linearly, as compared to the more rapid quadratic fall off of proton irradiated YBCO [165,186,187]. Additionally, J_c anisotropy ($\frac{J_c(H \parallel ab)}{J_c(H \parallel c)}$) is reduced from ~ 3 to ~ 2 as a result of doping and irradiation [5,174]. In work applying the U/n method to Nd-123, improvements in trapped field of around four fold were observed, similar to enhancements found in Y-123 [5,188].

For the U/n method developed for Y-123, at the optimum fluence level used, the creep rate increased by around 20% (from 5% to 6% decrease per decade of time), and T_c decreased from around 92 K to 91 K [169,171,173,180]. Based on trapped field measurements, the irreversibility point also appeared to have increased as a result of the irradiation [169], although subsequent measurements indicated that there was little change in the irreversibility line [3]. The effects on the irreversibility line will depend on the spacing between uranium deposits, and the number of fission incidents at each deposit [3]. These

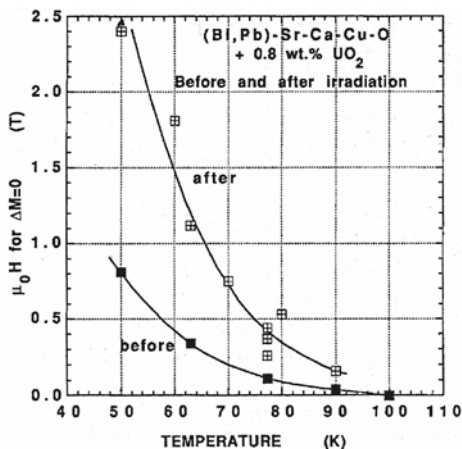


Fig. 9-4. Irreversibility line for 0.8 wt% natural UO_2 doped Bi-2223 powders before and after irradiation with thermal neutrons. The data are the fields and temperatures above which there is no observable magnetic hysteresis. (Reprinted with permission from [27] © 2004 IEEE.)

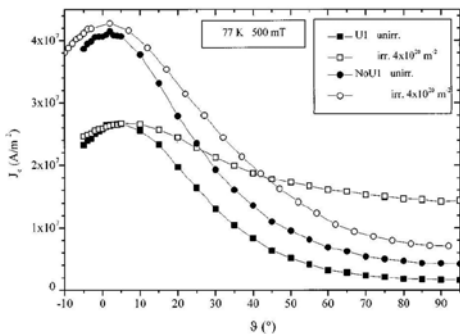


Fig. 9-5. Angular dependence of J_c at 77 K and 500 mT; $\phi=0^\circ$ refers to $H \parallel (a,b)$, and $\phi=90^\circ$ refers to $H \parallel c$. (Reprinted with permission from [190].)

factors vary the spacing between fission induced defects and the angle between fission induced defects, and with variation of these parameters increases in the irreversibility line could be achieved [3].

Luborsky *et al.* also doped Bi-2212 and Bi-2223 powders with natural uranium in the form of UO_2 up to 0.8 wt% [181]. After thermal neutron irradiation, ΔM increased with increasing UO_2 content, reaching a saturation point somewhere between 0.4-0.8 wt% UO_2 [181]. Interestingly, this saturation point is approximately the same as the UO_2 content independent point for decrease of apparent superconducting volume fraction, indicating that 0.3-0.4 wt% UO_2 is the point at which either the solid solubility of UO_2 in Bi-2223 is exceeded, or the point at which all of the Bi-2223 grains are coated in UO_2 [189]. Significant improvements of up to 13 fold for the Bi-2212 (at 0.2 T and 50 K), and 70 fold for the Bi-2223 (at 0.8 T and 50 K) were recorded for ΔM [181]. The impressive results with Bi-2223 were attributed to the largely poor inherent pinning in undoped and un-irradiated Bi-2223 material [181].

Hart *et al.* further investigated thermal neutron irradiated 0.8 wt% natural UO_2 doped powdered Bi-2223 [27]. They found that after irradiation T_c decreased from 107.5 K to 105.5 K, but thermally activated flux creep was greatly reduced as a result of significant increases (some two to three fold) in pinning energy [27]. Additionally, the irreversibility line was found to increase as a result of irradiation, as shown in Fig. 9-4 [27]. Luborsky *et al.* expanded the work of Hart *et al.* by varying the uranium additions, and found that the improvements scaled with the doping level, with no change due to uranium doping alone [189]. However, the dramatic improvements in physical performance (J_c , ΔM , flux pinning) found by Luborsky *et al.*

and Hart *et al.* were largely lost at temperatures higher than 60 K, with enhancements being less than two fold [27].

Schulz *et al.* doped Bi-2223/Ag composite tapes with 0.3 wt% $\text{UO}_2 \cdot 2\text{H}_2\text{O}$ and irradiated the tapes with thermal neutrons [190]. As a result of neutron adsorption by ^{109}Ag , which composes around 48% of natural silver and has a large neutron capture cross section of 91 barns, a radioactive $^{110\text{m}}\text{Ag}$ isotope is produced [191,192]. This leads to a residual radioactivity of one month after irradiation of $12 \text{ MBq} \cdot \text{g}^{-1}$ [190]. In spite of the large residual radioactivity of the material, significant physical gains were made as a result of application of the U/n method to Bi-2223/Ag. T_c was only reduced by 1 K, and normal state resistivity increased by 5% [190]. Transport J_c measurements indicated limited changes in performance at low fields ($< 0.7 \text{ T}$) as a result of irradiation, but considerable enhancement at higher fields, such as an order of magnitude increase in J_c at 3 T [190]. An upward shift of the irreversibility lines at 77 K was also observed, with a doubling of the magnetic field, contrary to YBCO results [3,190]. Additionally, as shown in Fig. 9-5, for fields less than the irreversibility field, a dramatic reduction in angular anisotropy of J_c (J_c with $H \parallel c$ as compared to J_c with $H \parallel (a,b)$) was observed, with anisotropy decreasing from 12 to 1.6 [190]. The results are impressive, with significantly greater gains than point defect inducing irradiation methods such as fast neutron irradiation and similar results to much more expensive ultra-high energy proton irradiation techniques [190]. The authors make special note that the large residual radioactivity could be reduced with better optimisation of the doping level and thermal neutron fluence [190].

Weinstein *et al.* continued the work of Schulz *et al.*, doped Bi-2223/Ag tapes with highly enriched uranium, and exposed the doped tapes to thermal neutrons [170]. The premise behind employing highly enriched uranium of 98% ^{235}U purity was to reduce the necessary irradiation fluence and time, and hence reduce the residual radioactivity of the final material [170]. Irradiated Bi-2223/Ag tapes doped with 0.3 wt% uranium had a residual radioactivity after eight months of $34 \text{ MBq} \cdot \text{g}^{-1}$ [170]. Doping with 0.15 wt% of highly enriched uranium allowed this post-irradiation residual radioactivity level after eight months to be reduced to 2

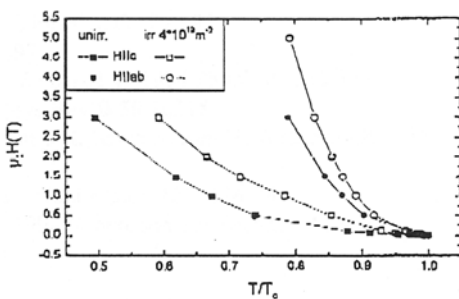


Fig. 9-6. Irreversibility lines for un-irradiated and irradiated 0.15 wt% uranium (as $\text{UO}_2 \cdot 2\text{H}_2\text{O}$) doped Bi-2223/Ag composite tapes in both $H \parallel c$ and $H \parallel (a,b)$ orientations. (Reprinted with permission from [193].)

$\text{MBq} \cdot \text{g}^{-1}$ [170,172]. Physical results obtained were superior, but comparable, to those of Schulz *et al.*, with reductions in zero field J_c only for high irradiation levels [170]. Large enhancements of J_c such as a 76 fold increase at 0.8 T with $H \parallel c$, an upward shift of the position of the irreversibility line by 1.9 times for $H \parallel c$ and 2.7 times for $H \parallel (a,b)$, and a reduction in J_c angular anisotropy of two orders of magnitude were observed [5,170].

Tönies *et al.* continued the work of Schulz *et al.* and Weinstein *et al.* and irradiated Bi-2223/Ag tapes doped with $\text{UO}_2 \cdot 2\text{H}_2\text{O}$ at levels of 0.15 wt%, 0.4 wt%, and 0.6 wt% uranium [193]. Low fluence irradiations in primarily thermal neutrons allowed the residual radioactivity for the 0.15 wt% doped material to be limited to 300

kBq.g⁻¹ after one week, compared to 2 MBq.g⁻¹ after eight months for previously irradiated 0.15 wt% doped material [170,193]. Large enhancements of J_c under applied magnetic field were observed, such as a 60 fold enhancement at 0.7 T for $H \parallel c$ [193]. Reductions in J_c anisotropy similar to those observed by Schulz *et al.* were found, with the magnitude of anisotropy reduction exceeding an order of magnitude at 77 K and 0.5 T [193]. Confirming the results of Schulz *et al.* and Weinstein *et al.*, Tönies *et al.* also found a large increase in the irreversibility line at all temperatures and in both $H \parallel c$ and $H \parallel (a,b)$ orientations [193]. This significant result, in which the irreversibility field is more than doubled, is reproduced in Fig. 9-6 [193]. A small reduction in T_c of around 0.5 K was found for all doping levels [193].

Prior to irradiation there was no distinguishable difference between the inter-grain J_c and the intra-grain J_c of the material, and irradiation did not change this relationship, indicating no worsening of weak links as a result of irradiation [193]. This result was promising, as the high field improvements due to irradiation are able to be achieved without the often experienced low field reductions in performance due to weak link induced radiation damage [193]. The authors make particular note that residual radiation could be reduced even further if additional uranium could be incorporated into the material [193].

Dou *et al.* also continued the work of Schulz *et al.* and Weinstein *et al.* and irradiated Bi-2223/Ag tapes doped with $UO_2 \cdot 2H_2O$ at levels of 0.15 wt%, 0.2 wt%, 0.4 wt%, and 0.6 wt% enriched uranium [194]. Very large enhancements of J_c were observed, for example 500 fold at 0.7 T for $H \parallel c$ and an order of magnitude at 3 T for $H \parallel (a,b)$, both at 77 K [194]. One of the most significant results of their work is reproduced in Fig. 9-7, and shows the reduction in anisotropy of a thermal neutron irradiated 0.6 wt% uranium oxide doped Bi-2223/Ag tape from around 50 to around 2.2 at 500 mT; more than a 20 fold decrease [194]. The enhancement of the irreversibility field was calculated to be more than 100% for $H \parallel (a,b)$ and more than 200% for $H \parallel c$ in the same 0.6 wt% doped tape [194]. The fission tracks resulting from thermal neutron irradiation, and which were contributing to the greatly enhanced flux pinning, were imaged using TEM and found to be amorphous, randomly distributed, with diameters of around 5 nm, and lengths of a few microns [194]. The fission tracks and their associated lattice strain did not influence either T_c or zero field J_c of the tapes [194].

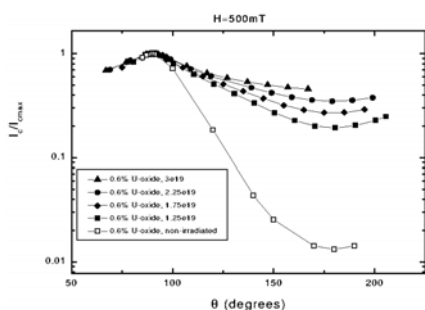


Fig. 9-7. Anisotropy of J_c before and after irradiation to various thermal neutron fluences for 0.6 wt% uranium doped Bi-2223/Ag tape. (Reprinted with permission from [194].)

Tönies *et al.* continued their work and synthesised Bi-2223/Ag tapes with up to 1 wt% 96% $^{235}UO_2 \cdot 2H_2O$ and irradiated them under low primarily thermal neutron fluences [4,195]. This allowed the residual radioactivity to be reduced to 30 $\mu Sv \cdot h^{-1}$ after one week [195]. Additionally, using low neutron fluences also avoided damage to weak links and associated loss of critical current at low fields, which was verified by SQUID measurements that found inter-grain and intra-grain critical currents to be the same for low doped samples [195,196]. In addition, employing low neutron fluences avoids concerns of reduction in T_c and H_{irr} [172]. Samples with higher uranium doping levels showed a reduction

in inter-grain critical currents after irradiation, which accounted for their lower performance in low fields, even after irradiation with lower neutron fluences to induce the same level of defect density [196]. Undoped samples showed no neutron induced variations of physical properties, while doped samples exhibited much higher J_c values, particularly at high fields where J_c increased two orders of magnitude [4,195]. Additionally, irradiated doped samples exhibited an order of magnitude reduced J_c anisotropy, and a doubling of the irreversibility field [4,195,196]. Intra-grain J_c values of $3.8 \times 10^{10} \text{ A.m}^{-2}$ became $9.7 \times 10^{10} \text{ A.m}^{-2}$ after doping and irradiation [195]. Irradiation slightly reduced T_c , with a reduction of 2 K for the highest fluence level employed [4].

Interestingly, the sample with the best low field performance after neutron dose optimisation was doped with only 0.15 wt% $^{235}\text{UO}_2.2\text{H}_2\text{O}$, and the best high field performance was exhibited by the intermediately doped 0.4 wt% sample [195,196]. This was contrary to the authors' expectations, and while the possible explanation of uranium segregation was offered, this unexpected result indicates a materials structure related issue such as inhomogenous uranium dispersion or phase equilibrium disruption as a result of higher doping levels [196].

Tönies *et al.* employed the U/n method on Tl-1223 thick films, doping with 0.15 wt% of 96% enriched ^{235}U [197]. J_c enhancements of 3-5 at high fields of around 4 T were found after irradiation and low field enhancements of 40% were observed, contrary to the Bi-2223 results [197]. Anisotropy of J_c was reduced at low field, but increased at high fields [197]. These results are attributed to the bi-layer structure of the Tl-1223 material, which contains a single crystalline portion and a granular portion, each of which carries the bulk of the current at different fields [197]. T_c reductions of around 0.5 K and minor increases in the irreversibility field of 7-33% were also observed [197].

Knowing the results of Schulz *et al.*, Weinstein *et al.*, Tönies *et al.*, and Dou *et al.*, Marinaro *et al.* doped Bi-2223/Ag composite tapes with 0.15 to 2 wt% $^{235}\text{UO}_2.2\text{H}_2\text{O}$ and irradiated the material with a wide range of highly moderated thermal neutrons [134,198]. The aim of the experiments was to minimise the neutron fluence by maximising $^{235}\text{UO}_2.2\text{H}_2\text{O}$ content and optimising neutron fluence levels for maximum gain, and to investigate changes in flux pinning strength as a result of the U/n method [134,198]. Dou and co-workers observed the fission induced defects by TEM and found them to be approximately 5 nm in diameter, and a few μm in length [175]. A slight reduction in T_c of 1 K was found, but a 46 fold reduction in J_c anisotropy occurred [134,198]. An increase in the effective pinning energy, U_{eff} , of 50% at high currents, and 100 - 200% at low currents, was found after irradiation, and the flux dynamics (hopping distance and attempt frequency) were determined to have changed [134,198,199]. J_c improvements were considerable, for example, a 500 fold increase at 5 T for $H \parallel c$ in the 0.6 wt% doped sample [134]. However, even with substantial J_c losses due to high doping levels of 2 wt% $^{235}\text{UO}_2.2\text{H}_2\text{O}$, similar final (post irradiation) performance to 0.15 wt% doped Bi-2223/Ag was achieved with a six fold reduction in irradiation levels required [134].

Shan *et al.* undertook study of the vortex phase in Bi-2223/Ag with isotropic defects introduced by the U/n method [200]. They observed no variable-range vortex hopping, implying a high level of entanglement of vortices by the splayed defects [200]. Additionally, they found that isotropic crossed defects enhance the coherence of vortex lines on a small scale, but destroy the coherence of vortex lines on a larger scale [200]. This phenomenon

occurs as a result of vortex “segments” being pinned on favourably oriented fission tracks, which happen to align for a short length (greater than a single pancake vortex in size), but which rarely align for the entire dimension of the vortex line [200]. Marinaro *et al.* corroborated these findings and determined the field dependent crossover from a 3D elastic creep regime to 2D plastic creep increased from $\mu_0 H_{cr} \approx 0.37$ T to $\mu_0 H_{cr} \approx 0.65$ T as a result of introduction of isotropic quasi-columnar defects in Bi-2223/Ag by the U/n method [199]. This increase was related to enhancement of c-axis vortex correlation [199].

Marinaro *et al.* discussed the relative merits of different doping and irradiation schedules [134]. They concluded that at the time of writing, a moderately doped (eg 0.3 or 0.6 wt%) material with a moderate irradiation fluence was optimum if performance over a wide range of fields was desirable, but that a high level of residual radioactivity would result [134]. However, if high flux pinning was desired, then a high doping level with minor irradiation was the best choice, and resulted in minimal residual radioactivity of the material, but at the expense of low field performance [134]. Particular mention is made of the possibility that if high levels of uranium could be incorporated into the material without significant degradation of the low field performance, then high doping levels and low irradiation levels would be optimum for all situations and requirements [134].

Babi *et al.* carried out a systematic study of the influence of uranium doping level and neutron irradiation fluence on various physical properties of Bi-2223/Ag [166]. They found that B_{irr} and B^* (the field of maximum pinning force, $F_{p\ max} = J_c B^*$) increased linearly with fission track density, indicating that pinning capacity was directly related to the number of defects present [166]. A competing effect, however, was the reduction of J_c with increasing uranium doping level [166]. Similarly, a weak dependence of B^* on neutron fluence was ascribed to non-uniform distribution of uranium within the Bi-2223 [166]. Additionally, some evidence of enhanced flux creep as a result of the presence of fission defects was found [166]. This observation, which is contrary to theoretical predictions, was attributed to randomness in the distances between nearest fission tracks and in their orientations [166]. However, B_{irr} results were extremely promising, with 4 fold increases for some combinations of uranium doping level and neutron fluence over an extended temperature range [166]. With their results, Babi *et al.* were able to formulate and solve an equation taking into consideration J_c variation with fission defect densities as a result of uranium doping and thermal neutron irradiation, and to determine an optimum combination of doping and fluence for a theoretical maximum performance increase [166]. It was proposed that if uranium doping levels could be increased without commensurate losses in J_c , then performance of Bi-2223/Ag materials could exceed even sophisticated U/n processed YBCO material [166].

10. URANIUM BSCCO INTERACTION

Milliken *et al.* investigated the chemical and phase interactions of uranium dopant compounds with the Bi-2223 matrix in Bi-2223/Ag composite tapes [201-203]. Until this work, all dopants employed with Bi-2223/Ag tapes were uranium oxides or uranium oxide hydrates [4,5,27,134,166,170,172,175,181,189,190,193,195,196,198-200]. It was found that uranium oxides caused serious disruption to the Bi-2223/Bi-2212 phase balance, as well as inducing significant porosity in the core microstructure [202,203]. This was as a result of chemical

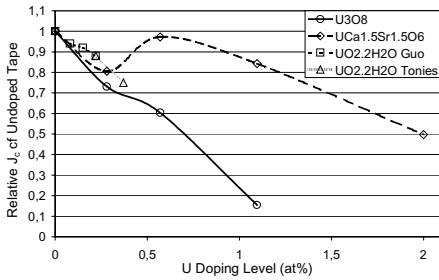


Fig. 10-1. Variation of J_c with doping level of uranium compound doped tapes after optimised thermomechanical processing. J_c values are normalised to that of an optimally processed undoped tape [4,195,196,204].

Fig. 10-1 [4,195,196,204]. The potential benefit of such a dramatic increase in uranium content with a comparatively small loss in J_c is that much smaller neutron fluences could be employed, resulting in significantly less residual radiation after processing.

interactions between the BSCCO core and the uranium dopants. Due to the poor chemical compatibility between the previously used uranium dopants and the Bi-2223 superconductor, additions of even moderate amounts (0.6 at%) of uranium resulted in loss of approximately half the J_c [201]. Work carried out focussing on alternative uranium containing dopant compounds discovered the more chemically compatible uranium compound $\text{UCa}_{1.5}\text{Sr}_{1.5}\text{O}_6$. With this compound, 1.1 at% (approximately 6 wt%) of uranium could be added to the Bi-2223 core with only around 15% loss in J_c . A comparison between the optimised unirradiated J_c values of tapes doped with U_3O_8 , $\text{UO}_2 \cdot 2\text{H}_2\text{O}$, and $\text{UCa}_{1.5}\text{Sr}_{1.5}\text{O}_6$ by Milliken *et al.*, Guo *et al.*, and Tönies *et al.* is shown in

REFERENCES

- [1] M.E. McHenry and R.A. Sutton, *Prog. Mater. Sci.*, 38 (1994) 159-310.
- [2] A. Umezawa, G.W. Crabtree, J.Z. Liu, H.W. Weber, W.K. Kwok, L.H. Nunez and C.H. Sowers, *Phys. Rev. B*, 36 (1989) 7151.
- [3] R. Weinstein, R. Sawh, Y.R. Ren and D. Parks, *Mater. Sci. Eng. B*, 53:1-2 (1998) 38-44.
- [4] S. Tonies, H.W. Weber, Y.C. Guo, S.X. Dou, R. Sawh and R. Weinstein, *Appl. Phys. Lett.*, 78:24 (2001) 3851-3.
- [5] R. Weinstein, *Proceedings of 12th International Symposium on Superconductivity* (1999)
- [6] B.A. Albiss, A. El-Ali, K. Khasawinah, M.K. Hasan, I. Al-Omari, K.A. Azez and J. Shobaki, 321:1-4 (2002) 324-7.
- [7] B.I. Belevtsev, I.V. Volchok, N.V. Dalakova, V.I. Dotsenko, L.G. Ivanchenko, A.V. Kuznichenko and I.I. Logvinov, *Phys. Status Solidi A*, 181:2 (2000) 437-50.
- [8] Y. Kazumata, S. Okayasu and H. Kumakura, *Bismuth-Based High-Temperature Superconductors*, (Eds. H. Maeda and K. Togano), Marcel Dekker, Inc. (1996), p. 177-213.
- [9] S.N. Barilo, V.I. Gatal'skaya, G.V. Gatal'skii, A.P. Ges, F.P. Korshunov, L.A. Kurochkin and D.I. Zhigunov, *Phys. Status Solidi A*, 126:2 (1991) K153-K7.
- [10] J. Giapintzakis, W.C. Lee, J.P. Rice, D.M. Ginsberg, I.M. Robertson, R. Wheeler, M.A. Kirk and M.O. Ruault, *Phys. Rev. B*, 45:18 (1992) 10677-83.

- [11] K. Shiraishi, Y. Kazumata and T. Kato, *Jpn. J. Appl. Phys.*, 30:4A (1991) L578-L81.
- [12] M. Akamatsu, R. Ikeda, R. Yoshizaki and T. Iwata, *Proceedings of Advances in Superconductivity V: The 5th International Symposium on Superconductivity*, Springer-Verlag, Tokyo (1993), p. 439.
- [13] H. Kumakura, H. Kitaguchi, K. Togano, H. Maeda, J. Shimoyama, S. Okayasu and Y. Kazumata, *J. Appl. Phys.*, 74:1 (1993) 451-7.
- [14] T. Terai, T. Masegi, K. Kusagaya, Y. Takahashi, K. Kishio, N. Motohira and K. Nakatani, *Physica C*, 185-89:pt 4 (1991) 2383-4.
- [15] K.E. Sickafus, J.O. Willis, P.J. Kung, W.B. Wilson, D.M. Parkin, M.P. Maley, F.W. Clinard, Jr., C.J. Salgado, R.P. Dye and K.M. Hubbard, *Phys. Rev. B*, 46:18 (1992) 11862-70.
- [16] J. Schwartz, S. Wu, G.W. Raban, Jr. and J.C. Rynes, *IEEE Trans. Appl. Supercond.*, 3:1 (1993) 1652-8.
- [17] M.A. Kirk, *Cryogenics*, 33:3 (1993) 235-42.
- [18] H.W. Weber, *Supercond. Sci. Technol.*, 5:1S (1992) S19-24.
- [19] M.C. Frischherz, M.A. Kirk, J.P. Zhang and H.W. Weber, *Philos. Mag. A*, 67:6 (1993) 1347-63.
- [20] M.C. Frischherz, M.A. Kirk, J. Farmer, L.R. Greenwood and H.W. Weber, *Physica C*, 232:3-4 (1994) 309-27.
- [21] M. Aleksa, P. Pongratz, O. Eibl, F.M. Sauerzopf, H.W. Weber, T.W. Li and P.H. Kes, *Physica C*, 297:3-4 (1998) 171-5.
- [22] G.W. Schulz, C. Klein, H.W. Weber, H.W. Neumuller, R.E. Gladyshevskii and R. Flukiger, *Appl. Supercond.*, 30:2 (1997) 1105-8.
- [23] M. Akiyoshi, K. Hashimoto and T. Yano, *Physica C*, 338:1 (2000) 103-9.
- [24] S.J. Manton, C. Beduz, Y. Yang, K. Deligiannis and P.A.J. Degroot, *Mater. Sci. Eng. B*, 53:1-2 (1998) 182-4.
- [25] M. Muralidhar, N. Sakai, M. Jirsa, N. Koshizuka and M. Murakami, *Appl. Phys. Lett.*, 83:24 (2003) 5005-7.
- [26] H.S. Lessure, S. Simizu, B.A. Baumert, S.G. Sankar, M.E. McHenry, M.P. Maley, J.R. Cost and J.O. Willis, *IEEE Trans. Magn.*, 27:2 (1991) 1043-6.
- [27] H.R. Hart, Jr., F.E. Luborsky, R.H. Arendt, R.L. Fleischer, J.E. Tkaczyk and D.A. Orsini, *IEEE Trans. Magn.*, 27:2 (1991) 1375-8.
- [28] W. Schindler, *J. Appl. Phys.*, 70:3 (1991) 1877-9.
- [29] H. Kupfer, I. Apfelstedt, W. Schauer, R. Flukiger, R. Meier-Hirmer, H. Wuhl and H. Scheurer, *Z. Phys. B*, 69:2-3 (1987) 167-71.
- [30] H. Kupfer, I. Apfelstedt, R. Flukiger, C. Keller, R. Meier-Hirmer, B. Runtsch, A. Turowski, U. Wiech and T. Wolf, *Cryogenics*, 28:10 (1988) 650-60.
- [31] D.W. Cooke, M.S. Jahan, R.D. Brown, K.C. Ott, E.R. Gray, J.L. Smith, J.O. Willis, B.L. Bennett, M.A. Maez, E.J. Peterson, W.L. Hults, J.Y. Coulter, A.M. Portis, H. Piel, N. Klein, G. Muller and M. Hein, *Appl. Phys. Lett.*, 56:24 (1990) 2462-4.
- [32] S.X. Dou, X.L. Wang, Y.C. Guo, Q.Y. Hu, P. Mikheenko, J. Horvat, M. Ionescu and H.K. Liu, *Supercond. Sci. Technol.*, 10:7A (1997) A52-A67.
- [33] G. Brandstatter, F.M. Sauerzopf, H.W. Weber, A. Aghaei and E. Schwarzmann, *Proceedings of 7th International Workshop on Critical Currents in Superconductivity (7th IWCC)*, World Scientific, Singapore (1994), p. 303-6.
- [34] F.M. Sauerzopf, H.P. Wiesinger, H.W. Weber and G.W. Crabtree, *Phys. Rev. B*, 51:9 (1995) 6002-12.

- [35] F.M. Sauerzopf, Phys. Rev. B, 57:17 (1998) 10959-71.
- [36] C. Czurda, M. Wacenovskiy, H.W. Weber and M. Murakami, Adv. Cryog. Eng., 40 (1994) 1015.
- [37] R.M. Schalk, K. Kundzins, H.W. Weber, E. Stangl, S. Proyer and D. Bauerle, Physica C, 257:3-4 (1996) 341-54.
- [38] J.W. Lee, H.S. Lessure, D.E. Laughlin, M.E. McHenry, S.G. Sankar, J.O. Willis, J.R. Cost and M.P. Maley, Appl. Phys. Lett., 57:20 (1990) 2150-2.
- [39] H.W. Zandbergen, J. Kulik and B. Nieuwendijk, Physica C, 179:1-3 (1991) 43-51.
- [40] H.W. Weber, Physica C, 185-89:pt 1 (1991) 309-14.
- [41] F.M. Sauerzopf, H.P. Wiesinger, W. Kritscha, H.W. Weber, G.W. Crabtree and J.Z. Liu, Phys. Rev. B, 43:4 (1991) 3091-100.
- [42] G. Brandstatter, F.M. Sauerzopf and H.W. Weber, Phys. Rev. B, 55:17 (1997) 11693-701.
- [43] U. Topal, L. Dorosinskii, H. Ozkan and H. Yavuz, Physica C, 388-389 (2003) 403-4.
- [44] G. Brandstatter, G. Samadi Hosseinali, G.W. Schulz, W. Straif, X. Yang, H.W. Weber, F. Ladenberger, E. Schwarzmann, S.L. Yan, M. Manzel, W.Y. Liang and R. Flukiger, *Proceedings of Fourth Euro Ceramics*, Gruppo Editoriale Faenza Editrice S.p.A. (1995), p. 57-64.
- [45] W. Kritscha, F.M. Sauerzopf, H.W. Weber, G.W. Crabtree, Y.C. Chang and P.Z. Jiang, Physica C, 179:1-3 (1991) 59-68.
- [46] F.M. Sauerzopf, H.P. Wiesinger, W. Kritscha, H.W. Weber, M.C. Frischherz and H. Gerstenberg, Cryogenics, 33:1 (1993) 8-13.
- [47] K. Kusagaya, T. Terai, Y. Takahashi, T. Kobayashi, S. Komiya and K. Kishio, *Proceedings of Advances in Superconductivity V: The 5th International Symposium on Superconductivity*, Springer-Verlag, Tokyo (1993), p. 435.
- [48] W. Kritscha, F.M. Sauerzopf, H.W. Weber, G.W. Crabtree, Y.C. Chang and P.Z. Jiang, Europhys. Lett., 12:2 (1990) 179-84.
- [49] M. Akamatsu, R. Yoshizaki and T. Iwata, Physica B, 194-96:pt 2 (1994) 2195-6.
- [50] Q.Y. Hu, H.W. Weber, F.M. Sauerzopf, G.W. Schulz, R.M. Schalk, H.W. Neumuller and S.X. Dou, Appl. Phys. Lett., 65:23 (1994) 3008-10.
- [51] M.C. Frischherz, M.A. Kirk, J. Farmer and H.W. Weber, *Proceedings of 7th International Workshop on Critical Currents in Superconductivity (7th IWCC): Critical Currents in Superconductors*, World Scientific Publishing Company, Singapore (1994), p. 34-9.
- [52] Q.Y. Hu, H.K. Liu, S.X. Dou, H.W. Neumuller and H.W. Weber, *Studies of High Temperature Superconductors*, (Ed. A. Nalika) (1997), p. 185-224.
- [53] J.O. Willis, K.E. Sickafus and D.E. Peterson, *Proceedings of Advances in Superconductivity IV (4th International Symposium on Superconductivity)* (1991), p. 323.
- [54] D. Bourgault, S. Bouffard, M. Toulemonde, D. Groult, J. Provost, F. Studer, N. Nguyen and B. Raveau, Phys. Rev. B, 39:10 (1989) 6549-54.
- [55] D. Bourgault, M. Hervieu, S. Bouffard, D. Groult and B. Raveau, Nucl. Instrum. Methods Phys. Res. Sect. B, B42:1 (1989) 61-8.
- [56] Z.-X. Cai and Y. Zhu, *Microstructures and Structural Defects in High-Temperature Superconductors*, World Scientific, Singapore (1998).
- [57] V. Hardy, D. Groult, M. Hervieu, J. Provost, B. Raveau and S. Bouffard, Nucl. Instrum. Methods Phys. Res. Sect. B, B54:4 (1991) 472-81.

- [58] Y.M. Zhu, Z.X. Cai, R.C. Budhani, M. Suenaga and D.O. Welch, *Phys. Rev. B*, 48:9 (1993) 6436-50.
- [59] F. Rullier-Albenque, A. Legris, S. Bouffard, E. Paumier and P. Lejay, *Physica C*, 175:1-2 (1991) 111-8.
- [60] R. Wheeler, M.A. Kirk, A.D. Marwick, L. Civale and F.H. Holtzberg, *Appl. Phys. Lett.*, 63:11 (1993) 1573-5.
- [61] M. Konczykowski, F. Rullier-Albenque, E.R. Yacoby, A. Shaulov, Y. Yeshurun and P. Lejay, *Phys. Rev. B*, 44:13 (1991) 7167-70.
- [62] W. Gerhauser, G. Ries, H.W. Neumuller, W. Schmidt, O. Eibl, G. Saemann-Ischenko and S. Klaumunzer, *Phys. Rev. Lett.*, 68:6 (1992) 879-82.
- [63] V. Hardy, D. Groult, J. Provost, M. Hervieu, B. Raveau and S. Bouffard, *Physica C*, 178:4-6 (1991) 255-65.
- [64] R.C. Budhani, Y. Zhu and M. Suenaga, *Appl. Phys. Lett.*, 61:8 (1992) 985-7.
- [65] R.C. Budhani, M. Suenaga and S.H. Liou, *Phys. Rev. Lett.*, 69:26 (1992) 3816-19.
- [66] R.C. Budhani and M. Suenaga, *Solid State Commun.*, 84:8 (1992) 831-4.
- [67] L. Civale, A.D. Marwick, T.K. Worthington, M.A. Kirk, J.R. Thompson, L. Krusin-Elbaum, Y. Sun, J.R. Clem and F. Holtzberg, *Phys. Rev. Lett.*, 67:5 (1991) 648-51.
- [68] B. Hensel, B. Roas, S. Henke, R. Hopfengartner, M. Lippert, J.P. Strobel, M. Vildic, G. Saemann-Ischenko and S. Klaumunzer, *Phys. Rev. B*, 42:7-A (1990) 4135-42.
- [69] V. Hardy, J. Provost, D. Groult, M. Hervieu, B. Raveau, S. Durcok, E. Pollert, J.C. Frison, J.P. Chaminade and M. Pouchard, *Physica C*, 191:1-2 (1992) 85-96.
- [70] V. Hardy, D. Groult, J. Provost and B. Raveau, *Physica C*, 190:3 (1992) 289-98.
- [71] V. Hardy, A. Ruyter, A. Wahl, A. Maignan, D. Groult, J. Provost, C. Simon and H. Noel, *Physica C*, 257:1-2 (1996) 16-24.
- [72] B. Roas, B. Hensel, S. Henke, S. Klaumunzer, B. Kabius, W. Watanabe, G. Saemann-Ischenko, L. Schultz and K. Urban, *Europhys. Lett.*, 11:7 (1990) 669-74.
- [73] B. Roas, B. Hensel, G. Endres, L. Schultz, S. Klaumunzer and G. Saemann-Ischenko, *Physica C*, 162-64:pt1 (1989) 135-6.
- [74] H. Watanabe, B. Kabius, K. Urban, B. Roas, S. Klaumunzer and G. Saemann-Ischenko, *Physica C*, 179:1-3 (1991) 75-84.
- [75] A.D. Marwick, L. Civale, L. Krusin-Elbaum, R. Wheeler, J.R. Thompson, T.K. Worthington, M.A. Kirk, S.Y. R., H.R. Kerchner and F. Holtzberg, *Proceedings of 8th International Conference on Ion Beam Modification of Materials* (1992)
- [76] C. Simon, J. Provost, D. Groult, V. Hardy, A. Wahl, C. Goupil and A. Ruyter, *Nucl. Instrum. Methods Phys. Res. Sect. B*, B 107 (1996) 384-92.
- [77] Y. Zhu, H. Zhang, M. Suenaga and D.O. Welch, *Philos. Mag. A*, 68:5 (1993) 1079-89.
- [78] B. Hensel, F. Marti, G. Grasso, M. Dhalle, R. Flukiger, F. Paschoud and M. Victoria, *IEEE Trans. Appl. Supercond.*, 7:2 (1997) 2030-3.
- [79] G.J. Clark, A.D. Marwick, R.H. Koch and R.B. Laibowitz, *Appl. Phys. Lett.*, 51:2 (1987) 139-41.
- [80] M. Sasase, S. Okayasu, H. Kurata and K. Hojou, *Physica C*, 357-360:2 (2001) 497-500.
- [81] D.M. Ginsberg, *Physical Properties of High Temperature Superconductors*, World Scientific, Singapore (1989).
- [82] R.L. Fleischer, *Prog. Mater. Sci.*, X (1981) 97.
- [83] C. Trautmann, S. Klaumunzer and H. Trinkaus, *Phys. Rev. Lett.*, 85:17 (2000) 3648-51.

- [84] R.L. Fleischer, P.B. Price and R.M. Walker, *Nuclear Tracks in Solids: Principles and Applications*, University of California Press, Berkeley (1975).
- [85] B.E. Fischer and R. Spohr, *Rev. Mod. Phys.*, 55:4 (1983) 907-48.
- [86] L. Civale, *Supercond. Sci. Technol.*, 10:7A (1997) A11-28.
- [87] L. Civale, A.D. Marwick, M.W. McElfresh, T.K. Worthington, A.P. Malozemoff, F.H. Holtzberg, J.R. Thompson and M.A. Kirk, *Phys. Rev. Lett.*, 65:9 (1990) 1164-7.
- [88] B.M. Vlcek, H.K. Viswanathan, M.C. Frischherz, S. Fleshler, K. Vandervoort, J. Downey, U. Welp, M.A. Kirk and G.W. Crabtree, *Phys. Rev. B*, 48:6 (1993) 4067-73.
- [89] M.J. Kramer, Q. Qian, D. Finnemore and L. Snead, *Physica C*, 203:1-2 (1992) 83-90.
- [90] J. Albrecht, S. Leonhardt, H.U. Habermeier, S. Bruck, R. Spolenak and H. Kronmuller, *Physica C*, 404:1-4 (2004) 18-21.
- [91] L. Wang, W. Wu, X.-G. Li, X. Liu, J. Zhu, L. Shi, Y. Jia, G. Zhou and Y. Zhang, *Jpn. J. Appl. Phys.*, 35:4A (1996) 2133-5.
- [92] S. Takamura, T. Aruga and T. Hoshiya, *Jpn. J. Appl. Phys.*, 28:7 (1989) L1118-L20.
- [93] S. Takamura, T. Hoshiya, T. Agura and M. Kobiyama, *Jpn. J. Appl. Phys.*, 28:8 (1989) 1395-7.
- [94] H.W. Neumuller, G. Ries, W. Schmidt, W. Gerhauser and S. Klaumunzer, *Journal of the Less-Common Metals*, 164/165:pt.B (1990) 1351-8.
- [95] Y. Kazumata, S. Okayasu, H. Kumakura and K. Togano, *Physica C*, 235-240:pt 5 (1994) 2825-6.
- [96] R. Gerbaldo, G. Ghigo, L. Gozzelino, E. Mezzetti, B. Minetti, P. Caracino and L. Gherardi, *Proceedings of Appl. Supercond.*, Institute of Physics Publishing (1997), p. 1101-4.
- [97] F. Laviano, D. Botta, A. Chiodoni, R. Gerbaldo, G. Ghigo, L. Gozzelino and E. Mezzetti, *Phys. Rev. B*, 68:1 (2003) 14507-17.
- [98] L. Klein, E.R. Yacoby, Y. Yeshurun, M. Konczykowski, F. Holtzberg and K. Kishio, *Physica C*, 209:1-3 (1993) 251-4.
- [99] L. Klein, E.R. Yacoby, Y. Wolfus, Y. Yeshurun, L. Burlachkov, B. Ya Shapiro, M. Konczykowski and F. Holtzberg, *Phys. Rev. B*, 47:18 (1993) 12349-52.
- [100] D. Zech, S.L. Lee, H. Keller, G. Blatter, B. Janossy, P.H. Kes, T.W. Li and A.A. Menovsky, *Phys. Rev. B*, 52:9 (1995) 6913-19.
- [101] R. Prozorov, A. Tsameret, Y. Yeshurun, G. Koren, M. Konczykowski and S. Bouffard, *Physica C*, 234:3-4 (1994) 311-7.
- [102] V. Hardy, A. Wahl, S. Hebert, A. Ruyter, J. Provost, D. Groult and C. Simon, *Phys. Rev. B*, 54:1 (1996) 656-64.
- [103] Y. Nakayama, T. Motohashi, K. Otszchi, J. Shimoyama, K. Kitazawa, K. Kishio, M. Konczykowski and N. Chikumoto, *Phys. Rev. B*, 62:2 (2000) 1452-6.
- [104] L. Civale, T.K. Worthington, L. Krusin-Elbaum, A.D. Marwick, F. Holtzberg, J.R. Thompson, M.A. Kirk and R. Wheeler, *JOM*, 44:10 (1992) 60-4.
- [105] M. Konczykowski, V.M. Vinokur, F. Rullier-Albenque, Y. Yeshurun and F. Holtzberg, *Phys. Rev. B*, 47:9 (1993) 5531-4.
- [106] M. Konczykowski, *Physica C*, 209:1-3 (1993) 247-50.
- [107] T. Schuster, M. Leghissa, M.R. Koblischka, H. Kuhn, M. Kraus, H. Kronmueller and G. Saemann-Ischenko, *Physica C*, 203:1-2 (1992) 203-22.
- [108] J.R. Thompson, Y.R. Sun, H.R. Kerchner, D.K. Christen, B.C. Sales, B.C. Chakoumakos, A.D. Marwick, L. Civale and J.O. Thomson, *Appl. Phys. Lett.*, 60:18 (1992) 2306-8.

- [109] J.R. Clem, Phys. Rev. B, 43:10 (1991) 7837-46.
- [110] H.W. Neumueller, W. Gerhaeuser, G. Ries, P. Kummeth, W. Schmidt, S. Klaumuenzer and G. Saemann-Ischenko, Cryogenics, 33:1 (1993) 14-20.
- [111] D.K. Christen, J.R. Thompson, H.R. Kerchner, B.C. Sales, B.C. Chakoumakos, L. Civale, A.D. Marwick and F. Holzberg, *Proceedings of 6th Annual Conference on Superconductivity and Applications*, Institute of Physics Conference Proceedings (1992), p. 24-36.
- [112] M. Konezykowski, Y. Yeshurun, L. Klein, E.R. Yacoby, N. Chikumoto, V.M. Vinokur and M.V. Feigel'man, J. Alloy. Compd., 195:1-2 (1993) 407-10.
- [113] V. Hardy, J. Provost, D. Groult, C. Simon, M. Hervieu and B. Raveau, J. Alloy. Compd., 195:1-2 (1993) 395-402.
- [114] K. Harada, H. Kasai, O. Kamimura, T. Matsuda, A. Tonomura, S. Okayasu and Y. Kazumata, Phys. Rev. B, 53:14 (1996) 9400-5.
- [115] V. Hardy, C. Simon, J. Provost and D. Groult, Physica C, 205:3-4 (1993) 371-6.
- [116] M. Sato, T. Shibauchi, S. Ooi, T. Tamegai and M. Konczykowski, Phys. Rev. Lett., 79:19 (1997) 3759-62.
- [117] J.T. Totty, G.K. Perkins, H.J. Jensen, R.A. Doyle and L.F. Cohen, Supercond. Sci. Technol., 11:9 (1998) 866-74.
- [118] M. Leghissa, L.A. Gurevich, M. Kraus, G. Saemann-Ischenko and L. Vinnikov, Phys. Rev. B, 48:2 (1993) 1341-4.
- [119] I.B. Khal'fin and B.Y. Shapiro, Physica C, 207:3-4 (1993) 359-65.
- [120] H. Raffy, S. Labdi, O. Laborde and P. Monceau, Physica C, 184:1-3 (1991) 159-64.
- [121] T. Tamegai, M. Sato, T. Shibauchi, S. Ooi, N. Katase and M. Konczykowski, Physica C, 293:1-4 (1997) 224-8.
- [122] W. Gerhaeuser, H.W. Neumueller, W. Schmidt, G. Ries, O. Eibl and G. Saemann-Ischenko, Physica C, 185-89:pt 4 (1991) 2339-40.
- [123] C.J. van der Beek, M. Konczykowski, V.M. Vinokur, T.W. Li, P.H. Kes and G.W. Crabtree, Phys. Rev. Lett., 74:7 (1995) 1214-17.
- [124] M. Konczykowski, N. Chikumoto, V.M. Vinokur and M.V. Feigelman, Phys. Rev. B, 51:6 (1995) 3957-60.
- [125] L. Miu, P. Wagner, A. Hadish, F. Hillmer, H. Adrian, J. Wiesner and G. Wirth, Phys. Rev. B, 51:6 (1995) 3953-6.
- [126] S.L. Lee, C.M. Aegerter, C. Ager, E.M. Forgan, S.H. Lloyd and H. Keller, J. Magn. Magn. Mater., 177-181:Pt (1998) 523-4.
- [127] P. Kummeth, H.W. Neumueller, G. Ries, M. Kraus, S. Klaumuenzer and G. Saemann-Ischenko, J. Alloy. Compd., 195:1-2 (1993) 403-6.
- [128] J.R. Thompson, D. Paul, Z.L. Wang, D.M. Kroeger and D.K. Christen, Appl. Phys. Lett., 67:7 (1995) 1007-9.
- [129] A.L. Crossley, J. Everett, G. Wirth, K. Kadowaki, C. Morgan, C. Eastell, C.R.M. Grovenor and A.D. Caplin, Appl. Supercond., 2:30 (1997) 1157-60.
- [130] S. Chu and M.E. McHenry, Physica C, 337:1 (2000) 229-33.
- [131] L. Civale, A.D. Marwick, R.I. Wheeler, M.A. Kirk, W.L. Carter, G.N. Riley, Jr. and A.P. Malozemoff, Physica C, 208:1-2 (1993) 137-42.
- [132] P. Kummeth, C. Struller, H.W. Neumueller, G. Ries, M. Kraus, M. Leghissa, G. Wirth, J. Wiesner and G. Saemann-Ischenko, J. Supercond., 7:5 (1994) 783-6.

- [133] H. Safar, J.H. Cho, S. Fleshler, M.P. Maley, J.O. Willis, J.Y. Coulter, J.L. Ullmann, P.W. Lisowski, G.N. Riley, Jr., M.W. Rupich, J.R. Thompson and L. Krusin-Elbaum, *Appl. Phys. Lett.*, 67:1 (1995) 130-2.
- [134] D.G. Marinaro, S.X. Dou, J. Horvat, J. Boldeman, R. Weinstein and R. Sawh, *IEEE Trans. Appl. Supercond.*, 11:1 Part 3 (2001) 3896-9.
- [135] T. Hwa, P. Le Doussal, D.R. Nelson and V.M. Vinokur, *Phys. Rev. Lett.*, 71:21 (1993) 3545-8.
- [136] G. Blatter, M.V. Feigelman, V.B. Geshkenbein, A.I. Larkin and V.M. Vinokur, *Rev. Mod. Phys.*, 66:4 (1994) 1125-388.
- [137] D.R. Nelson and V.M. Vinokur, *Phys. Rev. B*, 48:17 (1993) 13060-97.
- [138] T. Schuster, H. Kuhn, M. Indenbom, M. Leghissa, M. Kraus and M. Konczykowski, *Phys. Rev. B*, 51:22 (1995) 16358-70.
- [139] D.R. Nelson and V.M. Vinokur, *Phys. Rev. Lett.*, 68:15 (1992) 2398-401.
- [140] L. Krusin-Elbaum, A.D. Marwick, R. Wheeler, C. Feild, V.M. Vinokur, G.K. Leaf and M. Palumbo, *Phys. Rev. Lett.*, 76:14 (1996) 2563-6.
- [141] L. Civale, L. Krusin-Elbaum, J.R. Thompson, R. Wheeler, A.D. Marwick, M.A. Kirk, Y.R. Sun, F. Holtzberg and C. Feild, *Phys. Rev. B*, 50:6 (1994) 4102-5.
- [142] G. Kreiselmeyer, M. Muller, M. Kraus, B. Holzapfel, S. Bouffard and G. Saemann-Ischenko, *Physica C*, 235-240:pt.5 (1994) 3055-6.
- [143] P. Le Doussal and D.R. Nelson, *Physica C*, 232:1-2 (1994) 69-74.
- [144] R.L. Fleischer, *J. Mater. Sci.*, 28:16 (1993) 4518-29.
- [145] J. Schwartz and W. Shiming, *J. Appl. Phys.*, 73:3 (1993) 1343-7.
- [146] J.F. Ziegler, J.B. Biersack and U. Littlemark, *The Stopping Range of Ions in Solids*, Pergamon, New York (1985).
- [147] M.P. Maley, J.O. Willis, L.N. Bulaevskii, J.H. Cho, H.F. Safar, X.D. Wu, S.R. Foltyn and P.N. Arendt, *Proceedings of Physical Phenomena at High Magnetic Fields II*, World Scientific (1995), p. 467-83.
- [148] P. Bauer, C. Rossel, E.J. Williams, R. Berger, J. Daniel, B. Irmer, M. Kraus, G. Kreiselmeyer, G. Saemann-Ischenko and J. Karpinski, *Physica C*, 258:1-2 (1996) 84-94.
- [149] R.C. Budhani, J.O. Willis, M. Suenaga, M.P. Maley, J.Y. Coulter, H. Safar, J.L. Ullmann and P. Haldar, *J. Appl. Phys.*, 82:6 (1997) 3014-8.
- [150] Y. Zhu, X. Cai and D.O. Welch, *Philos. Mag. A*, 73 (1996) 1.
- [151] L. Krusin-Elbaum, J.R. Thompson, R. Wheeler, A.D. Marwick, C. Li, S. Patel, D.T. Shaw, P. Lisowski and D.T. Ullmann, *Appl. Phys. Lett.*, 64:24 (1994) 3331-3.
- [152] J.G. Ossandon and J.R. Thompson, *Superlattices Microstruct.*, 23:2 (1998) 543-50.
- [153] J.G. Ossandon, J.R. Thompson, L. Krusin-Elbaum, H.J. Kim, D.K. Christen, K.J. Song and J.L. Ullmann, *Supercond. Sci. Technol.*, 14:9 (2001) 666-71.
- [154] J.H. Cho, *Physica C*, 316:3 (1999) 287-92.
- [155] J.R. Thompson, J.G. Ossandon, L. Krusin-Elbaum, K.J. Song, D.K. Christen and J.L. Ullmann, *Physica B*, (2000) 877-8.
- [156] J.R. Thompson, J.G. Ossandon, L. Krusin-Elbaum, K.J. Song, H.J. Kim, D.K. Christen and J.L. Ullmann, *Physica C*, 335:1 (2000) 170-4.
- [157] J.H. Cho, H. Safar, M.P. Maley, J.O. Willis, J.Y. Coulter, D.G. Steel and K.E. Gray, *Physica C*, 302:2-3 (1998) 113-8.
- [158] J.H. Cho, *Physica C*, 361:2 (2001) 99-106.

- [159] L. Krusin-Elbaum, L. Civale, J.R. Thompson and C. Feild, *Phys. Rev. B*, 53:17 (1996) 11744-50.
- [160] M. Dhalle, F. Marti, G. Grasso, B. Hensel, E. Paschoud, M. Victoria and R. Fluekiger, *Physica C*, 282-287:3 (1997) 1305-6.
- [161] L. Krusin-Elbaum, D. Lopez, J.R. Thompson, R. Wheeler, K. Ullmann, C.W. Chu and W.M. Lin, *Nature*, 389:6648 (1997) 243-4.
- [162] L. Krusin-Elbaum, D. Lopez, J.R. Thompson, R. Wheeler, J. Ullmann, C.C. Tsuei, C.W. Chu and Q.M. Lin, *Physica C*, 282-287:pt 1 (1997) 375-8.
- [163] A. Schilling, M. Cantoni, J.D. Guo and H.R. Ott, *Nature*, 363:6424 (1993) 56-8.
- [164] Q. Xiong, Y. Cao, F. Chen, Y.Y. Xue and C.W. Chu, *J. Appl. Phys.*, 76:10 pt 2 (1994) 7127-9.
- [165] R. Weinstein, R.P. Sawh, R. Yanru, L. Jianxiong and D. Parks, *Proceedings of 1997 International Workshop on Superconductivity (The 3rd Joint ISTE/C/MRS Workshop)*, ISTE/C, Eishin Kaihatsu Bldg., 34-3 Shinbashi 5-chome, Minatoku, Tokyo, Japan; and MRS, 9800 KcKnight Road, Pittsburgh, PA 15237-6006, USA (1997), p. 108-11.
- [166] E. Babic, I. Kusevic, D. Marinaro, S.X. Dou, J. Boldeman and R. Weinstein, *Solid State Commun.*, 118:12 (2001) 607-10.
- [167] R.L. Fleischer, H.R. Hart, Jr., K.W. Lay and F.E. Luborsky, *Phys. Rev. B*, 40:4 (1989) 2163-9.
- [168] R. Weinstein, *Interaction of Radiation with Matter*, McGraw-Hill (1964).
- [169] R. Weinstein, R.P. Sawh, Y. Ren and J. Liu, *Proceedings of 9th International Symposium on Superconductivity: Advances in Superconductivity IX*, FIZ Karlsruhe (1997), p. 539-42.
- [170] R. Weinstein, A. Gandini, A. Ren, R. Sawh, D. Parks, Y.C. Guo, B. Zeimetz, S.X. Dou, S. Tonies, C. Klein and H.W. Weber, *Proceedings of The Ninth International Workshop On Critical Currents* (1999), p. 124-5.
- [171] Y. Ren, R. Weinstein, R.-P. Sawh and J. Liu, *Physica C*, 282-287:pt 4 (1997) 2301-2.
- [172] A. Gandini, R. Weinstein, Y.R. Ren, R.P. Sawh, D. Parks, Y.C. Guo, B. Zeimetz, S.X. Dou, S. Tonies, C. Klein and H.W. Weber, *Physica C*, 341-348:III (2000) 1453-4.
- [173] R. Weinstein, R. Sawh, Y.R. Ren, M. Eisterer and H.W. Weber, *Supercond. Sci. Technol.*, 11:10 (1998) 959-62.
- [174] R.-P. Sawh, R. Weinstein, Y. Ren, V. Obot and H. Weber, *Physica C*, 341-348:IV (2000) 2441-2.
- [175] S.X. Dou, *Physica C*, 341:Part 4 (2000) 2535-7.
- [176] C.P. Bean, R.L. Fleischer, P.S. Swartz and H.R. Hart, Jr., *J. Appl. Phys.*, 37 (1966) 2218.
- [177] R.L. Fleischer, P.B. Price and R.M. Walker, *J. Appl. Phys.*, 36 (1965) 3645.
- [178] O. Blunck and S. Leisegang, *Z. Phys.*, 128 (1950) 500.
- [179] H.J. Matzke, *Proceedings of First International Conference on 'Radiation Effects in Insulators'* (1981), p. 3-33.
- [180] M. Eisterer, S. Tonies, W. Novak, H.W. Weber, R. Weinstein and R. Sawh, *Supercond. Sci. Technol.*, 11:10 (1998) 1001-5.
- [181] F.E. Luborsky, R.H. Arendt, R.L. Fleischer, H.R. Hart, K.W. Lay, Jr., J.E. Tkaczyk and D. Orsini, *J. Mater. Res.*, 6:1 (1991) 28-35.
- [182] F.E. Luborsky, R.H. Arendt, R.L. Fleischer, H.R. Hart, Jr., K.W. Lay, J.E. Tkaczyk and D.A. Orsini, *J. Appl. Phys.*, 70:10 (1991) 5756-8.

- [183] R. Weinstein, R.P. Sawh and Y. Ren, *Proceedings of 9th International Symposium on Superconductivity: Advances in Superconductivity IX*, FIZ Karlsruhe (1997), p. 543-6.
- [184] Y. Ren, R. Weinstein and R.-P. Sawh, *Physica C*, 282-287:pt 4 (1997) 2275-6.
- [185] R.P. Sawh, Y. Ren, R. Weinstein, W. Hennig and T. Nemoto, *Physica C*, 305:3-4 (1998) 159-66.
- [186] J. Liu, I.-G. Chen, R. Weinstein and X. Jianchun, *J. Appl. Phys.*, 73:10, pt. 2B (1993) 6530-2.
- [187] I.-G. Chen, J. Liu, R. Weinstein and K. Lau, *J. Appl. Phys.*, 72:3 (1992) 1013-20.
- [188] R. Weinstein, R.-P. Sawh, D. Parks, M. Murakami, T. Mochida, N. Chikumoto, G. Krabbes and W. Bieger, *Physica C*, 383:3 (2002) 214-22.
- [189] F.E. Luborsky, R.H. Arendt, R.L. Fleischer, H.R. Hart, Jr., J.E. Tkaczyk and D.A. Orsini, *J. Mater. Res.*, 8:6 (1993) 1277-84.
- [190] G.W. Schulz, C. Klein, H.W. Weber, S. Moss, R. Zeng, S.X. Dou, R. Sawh, Y. Ren and R. Weinstein, *Appl. Phys. Lett.*, 73:26 (1998) 3935-7.
- [191] J. Chang, <http://atom.kaeri.re.kr>, *Table of Nuclides*, Nuclear Data Evaluation Lab., Korea Atomic Energy Research Institute (2001).
- [192] R.R. Kinsey and T.W. Burrows, <http://www.nndc.bnl.gov/nndc/nudat>, *National Nuclear Data Center Nuclear Data from NuDat*, National Nuclear Data Center (2003).
- [193] S. Tonies, C. Klein, H.W. Weber, B. Zeimetz, Y.C. Guo, S.X. Dou, R. Sawh, Y. Ren and R. Weinstein, *Proceedings of EUCAS 1999, the Fourth European Conference on Applied Superconductivity*, IOP Publishing (1999), p. 487-90.
- [194] S.X. Dou, Y.C. Guo, D. Marinaro, J.W. Boldeman, J. Horvat, P. Yao, R. Weinstein, A. Gandini, R. Sawh and Y. Ren, *Adv. Cryog. Eng.*, 46 (1999) 519-26.
- [195] S. Tonies, H.W. Weber, D. Milliken, Y.C. Guo, S.X. Dou, A. Gandini, R. Sawh, Y. Ren and R. Weinstein, *Physica C*, III:341-348 (2000) 1427-30.
- [196] S. Tonies, H.W. Weber, Y.C. Guo, S.X. Dou, R. Sawh and R. Weinstein, *IEEE Trans. Appl. Supercond.*, 11:1 (III) (2001) 3904-7.
- [197] S. Tonies, H.W. Weber, G. Gritzner, O. Heimpl and M. Eder, *Physica C*, 372-376:2 (2002) 755-8.
- [198] D. Marinaro, S.X. Dou, J. Horvat, Y.C. Guo, J. Boldeman, A. Gandini, R. Weinstein, R. Sawh and Y. Ren, *Physica C*, 341:Part 2 (2000) 1119-20.
- [199] D.G. Marinaro, J. Horvat, S.X. Dou, R. Weinstein and A. Gandini, *Phys. Rev. B*, 68:6 (2003) 064518-1-9.
- [200] L. Shan, H.H. Wen and S.X. Dou, *Physica C*, 390:1 (2003) 80-8.
- [201] D. Milliken and S.X. Dou, *Physica C*, 341:Part 3 (2000) 1411-4.
- [202] D.A. Milliken, J.H. Ahn and S.X. Dou, *IEEE Trans. Appl. Supercond.*, 11:1 (III) (2001) 3964-7.
- [203] D. Milliken, J.H. Ahn and S.X. Dou, *Physica C*, 354:1-4 (2001) 183-8.
- [204] Y.C. Guo, B. Zeimetz, S.X. Dou, A. Gandini, A. Ren, R. Sawh, R. Weinstein, G.W. Schultz, C. Klein and H.W. Weber, *Proceedings of The Ninth International Workshop On Critical Currents* (1999), p. 153-4.

STACKING MANNER OF CHARGE RESERVOIR BLOCKS IN SUPERCONDUCTING COPPER OXIDES

T. Nagai¹, T. Yokosawa^{2,3}, K. Kimoto², and Y. Matsui^{1,2}

¹) High Voltage Electron Microscopy Station, National Institute for Materials Science,
1-1 Namiki, Tsukuba 305-0044, Japan

²) Advanced Materials Laboratory, National Institute for Materials Science,
1-1 Namiki, Tsukuba 305-0044, Japan

³) Arrhenius Laboratory, Stockholm University, S-106 91, Stockholm, Sweden

1. INTRODUCTION

An enormous amount of data on crystal structures and mechanism of superconductivity has revealed that “charge reservoir blocks” and “conduction blocks” are alternately stacked along an unique direction in superconducting copper oxides. The blocks which are crucial with occurrence of high- T_c superconductivity are the latter, where CuO_2 layers are integrated with interstitial metal (A) layers such as $-\text{CuO}_2\text{-}A\text{-CuO}_2\text{-}A\text{-CuO}_2\text{-}$. Superconducting carriers, holes or electrons, are introduced into CuO_2 planes by charge reservoir blocks as well as A layers. A large number of compounds with different type of charge reservoir blocks (e.g. $\text{Sr}_2\text{Bi}_2\text{O}_4$, Ba_2HgO_x) were prepared so far. The structural variety of superconducting copper oxides is based on that of the blocks.

One of the key compounds in the development is well-known $\text{YBa}_2\text{Cu}_3\text{O}_7$ (Cu-1212 or so-called “123”). The crystal structure consists of BaO-CuO-BaO charge reservoir blocks and $\text{CuO}_2\text{-Y-CuO}_2$ conduction blocks. Since the Cu atoms in the CuO layers can be replaced by other various metal (M) atoms, such substitutions have resulted in discoveries of a number of charge reservoir blocks and related phases.

Among the phases, those with $M = \text{Ga, Al, or Co}$ have attracted significant interest as in the charge reservoir blocks oxygen atoms tetrahedrally coordinate the M atoms to form chains of corner-sharing MO_4 tetrahedra [1-6]. Lately, several authors have suggested the presence of complicated superstructures due to ordering of two types of MO_4 -tetrahedra chains, L - and R -chains, where the tetrahedra rotate in different ways [4-6]. Apart from these, considerable

concern has been raised about the phases with $M = \text{Ru}$, because ferromagnetism coexists with superconductivity in the phases [7-15]. A superstructure due to ordering of rotated RuO_6 octahedra, which might be related to occurrence of the ferromagnetism, has been recently suggested [13,14].

Here, we present recent transmission electron microscopy (TEM) studies of $M = \text{Ru}$ system (Yokosawa *et al.*, 2004 [16]) and $M = \text{Co}$ system (Nagai *et al.*, 2003 [17]). The investigations revealed superstructures in the charge reservoir blocks of the phases. The observed phases commonly belong to $M\text{-}12s2$ series: $\text{RuSr}_2\text{GdCu}_2\text{O}_8$ (Ru-1212), $\text{RuSr}_2\text{Gd}_{1.5}\text{Ce}_{0.5}\text{Cu}_2\text{O}_{10-\delta}$ (Ru-1222) in Ru-system, and $\text{CoSr}_2\text{YCu}_2\text{O}_{7-\delta}$ (Co-1212), $\text{CoSr}_2(\text{Y}_{3/4}\text{Ce}_{1/4})_2\text{Cu}_2\text{O}_{9-\delta}$ (Co-1222), $\text{CoSr}_2(\text{Y}_{1/3}\text{Ce}_{2/3})_3\text{Cu}_2\text{O}_{11-\delta}$ (Co-1232) in Co-system. Figure 1 shows schematic illustrations of $M\text{-}12s2$ fundamental structures. $M\text{-}1222$ and $M\text{-}1232$ structures are derived from $M\text{-}1212$ structure, where the CuO layer of the $\text{Cu}\text{-}1212$ phase is replaced by an MO_x layer. In $M\text{-}1222$ structure, instead of a single oxygen-free rare earth (R) layer, a three-layer fluorite-type $R\text{-O}_2\text{-}R$ block is inserted between the two CuO_2 planes of the $M\text{-}1212$ structure. In $M\text{-}1232$ structure furthermore, a five-layer fluorite-type $R\text{-O}_2\text{-}R\text{-O}_2\text{-}R$ block is inserted between them. With increasing number of s (from 1 to 3), the distance between the neighboring MO_x layers increases since the thickness of the rare-earth-containing block increases. This is a specific structural feature in the $M\text{-}12s2$ series.

Figures 2(a) and 2(b) show schematic diagrams of Ru-1212 structure model with tetragonal $P4/mmm$ (No.123) symmetry and Ru-1222 structure model with tetragonal $I4/mmm$ (No.139) symmetry, where octahedra and square pyramids indicate RuO_6 and CuO_5 , respectively. Average structures of Ru-1212 and Ru-1222 phases at room and low temperatures were refined by powder neutron diffraction [12,13] and synchrotron X-ray diffraction [14]. The structural refinements revealed that the basal and apical oxygen sites of the RuO_6 octahedra are statically displaced from the oxygen positions in the tetragonal structures ($I4/mmm$ and $P4/mmm$). A schematic illustration of the average structure of the RuO_6 octahedron is shown in the inset of Fig. 2, where the basal and apical oxygen sites are refined as split sites. The displacements of the basal and apical oxygen sites are considered to be due to rotations ($\sim 13\text{-}14^\circ$) of the RuO_6 octahedra around the c -axis and slight tilts ($\sim 4\text{-}6^\circ$) of the octahedra from the c -axis, respectively [12-14]. $\sqrt{2}a \times \sqrt{2}a \times c$ superstructure due to ordering of the rotated RuO_6 octahedra was first suggested for Ru-1212 phase based on selected-area electron diffraction (SAED) [14]. The space group of $P4/mbm$ (No. 127) was adopted on structural refinement of the superstructure by powder neutron diffraction [13]. On the other hand, the $\sqrt{2}a \times \sqrt{2}a \times c$ superstructure had not been observed for Ru-1222 phase [12,15]. Recently, Yokosawa *et al.* confirmed the superstructure for Ru-1222 phase ($\text{RuSr}_2\text{Gd}_{1.5}\text{Ce}_{0.5}\text{Cu}_2\text{O}_{10-\delta}$) by SAED technique. The authors found superstructural nm-size domains in the phase by several transmission electron microscopy (TEM) methods such as convergent-beam electron diffraction (CBED), dark-field transmission electron microscopy (DFEM), and high-resolution electron microscopy (HREM). Moreover, although the superstructural domains had not been confirmed for Ru-1212 phase [14], the authors also found somewhat larger nm-size domains in Ru-1212 phase ($\text{RuSr}_2\text{GdCu}_2\text{O}_8$) [16].

Figure 3 shows a schematic illustration of Co-1212 structure model with orthorhombic $Ima2$ (No.46) symmetry, where tetrahedra and square pyramids indicate CoO_4 and CuO_5 , respectively. The Co-1212 structure was studied by X-ray and neutron diffraction [3], and it was shown that the oxygen coordination around the Co atoms is tetrahedral, that is, basically

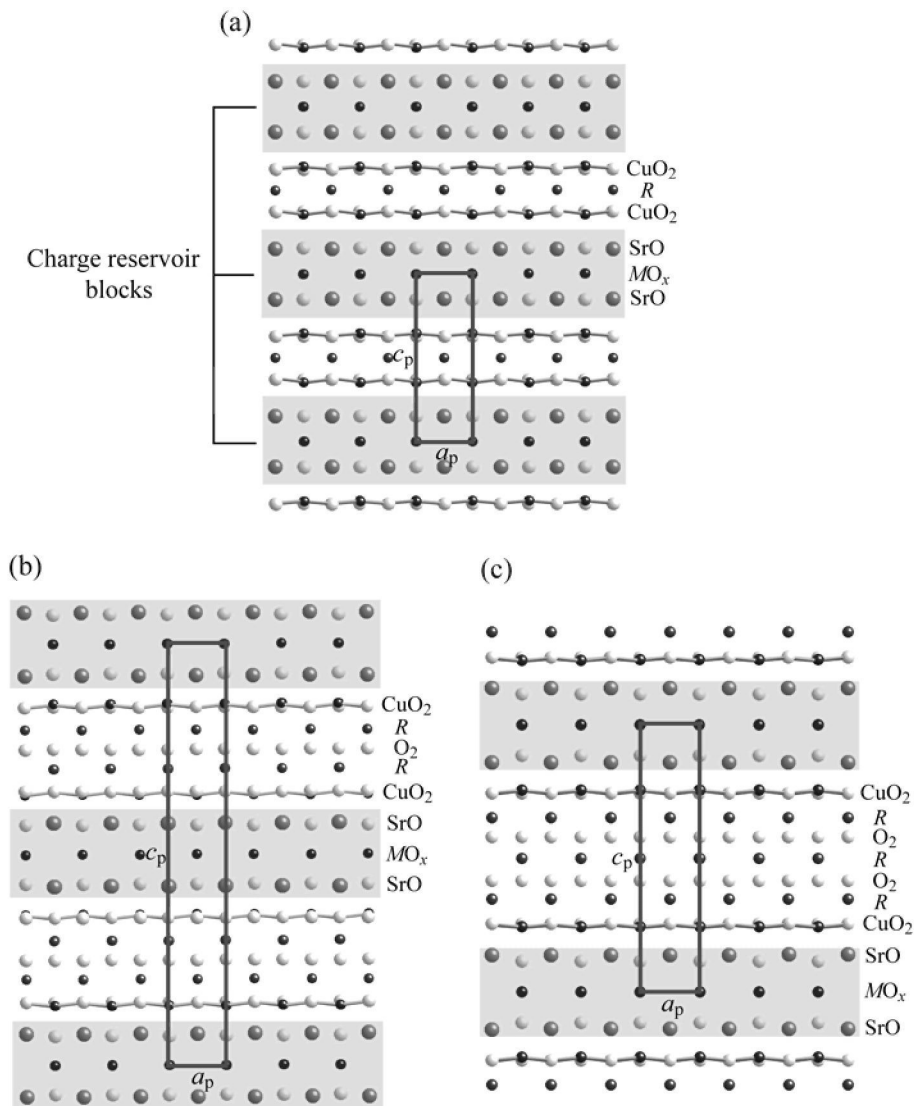


Fig. 1: Schematic illustrations of $M-12s2$ fundamental structures with the compositions of $MSr_2R_sCu_2O_{2s+x+4}$, (a) $s = 1$, (b) $s = 2$, and (c) $s = 3$.

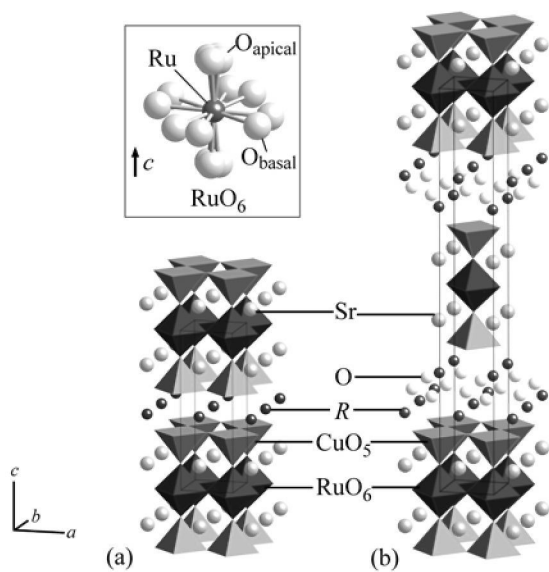


Fig. 2: Schematic diagrams of Ru-12s2 ($\text{RuSr}_2R_s\text{Cu}_2\text{O}_{2s+6}$) structure models, (a) $s = 1$ and (b) $s = 2$. The inset shows the average structure of RuO_6 octahedra.

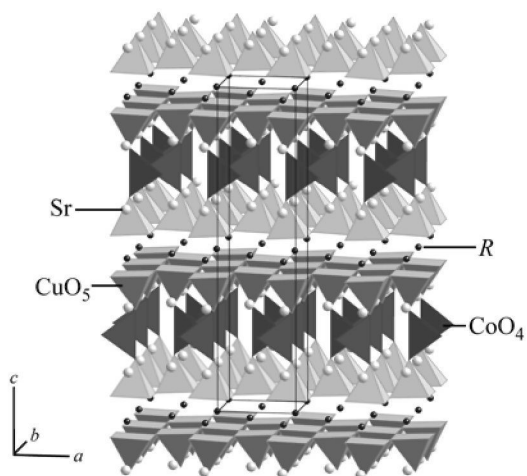


Fig. 3: Schematic diagram of Co-1212 ($\text{CoSr}_2R\text{Cu}_2\text{O}_7$) structure model.

different from the square planar configuration in Cu-1212 structure. Since $M = \text{Co, Ga, Al}$ ions have a strong tendency to be tetrahedrally coordinated by oxygen atoms, chains of corner-sharing MO_4 tetrahedra are formed in the M -1212 phases. However, SAED measurements revealed deviations from the orthorhombic $\text{Ima}2$ structure for the phases. The results indicated the existence of a long range ordered superstructure related to the MO_4 tetrahedra chains. Later, it was reported that MO_4 -tetrahedra can rotate in two different ways about the c -axis, giving rise to the formation of two kinds of zig-zag chains, L -chains and R -chains [4]. Recently, Nagai *et al.* revealed the superstructure due to ordering of the two types of CoO_4 chains for Co-1212 phase ($\text{CoSr}_2\text{YCu}_2\text{O}_7$) on the basis of TEM investigation. Furthermore, the authors found intralayer ordering and interlayer disordering of the chain arrangement in Co-1222 phase ($\text{CoSr}_2(\text{Y}_{3/4}\text{Ce}_{1/4})_2\text{Cu}_2\text{O}_9$) and Co-1232 phase ($\text{CoSr}_2(\text{Y}_{1/3}\text{Ce}_{2/3})_3\text{Cu}_2\text{O}_{11}$) [17].

The two works on the crystal structures of Ru-12s2 and Co-12s2 phases have revealed order and disorder in the structures of the charge reservoir blocks. The results are indicative of the presence of general phenomena on the structural order and disorder, which should be important for understanding the crystal chemistry of superconducting copper oxides. We further discuss the order and disorder with respect to the distance between the neighboring charge reservoir blocks and review the issue in terms of stacking manner of charge reservoir blocks.

2. EXPERIMENTAL

The $\text{RuSr}_2\text{GdCu}_2\text{O}_8$ (Ru-1212) compound was also synthesized through a solid-state reaction route from stoichiometric amounts of RuO_2 , SrO_2 , Gd_2O_3 and CuO . Calcinations were carried out on mixed powders at 1000 °C, 1020 °C and 1040 °C each for 24 hours with intermediate grindings. The pressed bar-shape pellets were annealed in flow of oxygen at 1060 °C for 40 hours and subsequently cooled slowly over a span of 20 hours to room temperature. The $\text{RuSr}_2\text{Gd}_{1.5}\text{Ce}_{0.5}\text{Cu}_2\text{O}_{10-\delta}$ (Ru-1222) compound was synthesized through a solid-state reaction route from RuO_2 , SrO_2 , Gd_2O_3 , CeO_2 and CuO . Calcinations were carried out on the mixed powder at 1000, 1020, 1040 and 1060 °C each for 24 hours with intermediate grindings. The pressed bar-shaped pellets were annealed in a flow of high-pressure oxygen (100 atm) at 420 °C for 100 hours and subsequently cooled slowly to room temperature. The bulk specimens were crushed into fine fragments, which were ultrasonically dispersed in CCl_4 and transferred onto carbon microgrids for transmission electron microscopy. The SAED and CBED patterns were taken at room temperature using an analytical transmission electron microscope (Hitachi HF-3000S) with a cold field emission gun operated at an accelerating voltage of 300 kV. The SAED and CBED patterns were taken from specimen areas with the diameter of about 100 and 8 nm, respectively. The dark-field images were taken by a Lorentz transmission electron microscope (Hitachi HF-3000L) with relatively larger magnification at the back focal plane operated at an accelerating voltage of 300 kV. The HREM images were taken using an ultra-high-voltage transmission electron microscope (Hitachi H-1500) [18] operated at an accelerating voltage of 800 kV.

The $\text{CoSr}_2(\text{Y,Ce})_3\text{Cu}_2\text{O}_{5+2s-\delta}$ (Co-12s2) compounds were synthesized through a solid-state reaction route from Co_2O_3 , SrO_2 , Y_2O_3 , CeO_2 and CuO . Calcinations were carried out on mixed powders at 975 °C and 1000 °C, each for 24 hours with an intermediate grinding. The

pressed bar-shape pellets were annealed in flowing oxygen at 1010 °C for 40 hours and subsequently cooled slowly over a span of another 20 hours to room temperature. For the Co-1222 and Co-1232 compounds, additional heat treatments at temperatures 10 to 20 °C higher than those for the Co-1212 compound were necessary at each heating step to obtain the desired phase. Previously the same samples were characterized by wet-chemical and thermogravimetric analyses, and found stoichiometric in terms of their oxygen contents [19]. The SAED patterns and HREM images were obtained using the ultra-high-voltage transmission electron microscope operated at an accelerating voltage of 800 kV. The TEM specimens were prepared by the crashing method. The SAED patterns were taken from specimen areas with the diameter of about 700 nm. Simulations of SAED patterns and HREM images based on dynamical diffraction theory were carried out with MacTempas software.

3. Ru-SYSTEM (Yokosawa *et al.* [16])

3.1. Physical properties

Transport and magnetic measurements of the present Ru-1212 ($\text{RuSr}_2\text{GdCu}_2\text{O}_8$) and Ru-1222 ($\text{RuSr}_2\text{Gd}_{1.5}\text{Ce}_{0.5}\text{Cu}_2\text{O}_{10.8}$) samples have already been reported elsewhere [15]. The Ru-1212 sample shows superconductivity transition around 20 K from the resistance data and the weak ferromagnetic transition at ~140 K from the DC magnetization data. The Ru-1222 sample shows superconductivity transition around 43 K from the resistance data and the weak ferromagnetic transition at ~90 K from the DC magnetization data.

3.2. SAED and HREM investigations

Figure 4(a) shows a SAED pattern of the Ru-1212 phase taken with [001] incidence. The reflections of hkl are corresponding to those in terms of the fundamental primitive tetragonal lattice which has already been reported as the 1212-type structure ($P4/mmm$: $a = 0.38337(6)$ nm and $c = 1.14926(9)$ nm) [15]. Superlattice reflections corresponding to $\sqrt{2}a \times \sqrt{2}a$ supercell are indicated by white and black arrowheads. The reflections of hkl_S (the suffix 'S' means the superlattice) are corresponding to those of the superlattice. Figures 4(b) and 4(c) show SAED patterns taken with [110] and [100] incidence, respectively. Figure 4(d) shows an HREM image of the phase taken with [100] incidence. The layers indicated by Ru, Sr, Cu and Gd are assumed to be corresponding to those of RuO_2 , SrO , CuO_2 and Gd, respectively. It is confirmed that the layers are stacked along the c -axis following 1212-type structure without any intergrowths [20].

SAED patterns of the Ru-1222 phase are shown in Figs. 5(a), 5(b), and 5(c) for [001], [110], and [100] incidence, respectively, although main reflections of hkl can be indexed on the fundamental body-centered tetragonal lattice which has already been reported as the 1222-type structure ($I4/mmm$: $a = 0.38327(7)$ nm, $c = 2.83926(8)$ nm) [15]. The superlattice reflections, which are corresponding to those caused by a $\sqrt{2}a \times \sqrt{2}a$ supercell, are also observed in Fig. 5(a) as indicated by the white and black arrowheads [14]. It is revealed from a detailed inspection that the superlattice reflections of $hk0_S$ with a condition of $k = h + 2n$ (n : integer) are extinctive as shown in the [001] SAED pattern. The extinction rule of the SAED pattern cannot be clearly involved in any crystallographic extinction rules. Therefore,

it is assumed that the SAED pattern is taken from a specimen area composed of superlattice domains. Detailed inspections of the superlattice domain will be shown later. Figure 5(d) shows an HREM image of the phase taken with $[100]$ incidence. The layers indicated by Ru, Sr and Cu are assumed to be corresponding to those of RuO_2 , SrO and CuO_2 , respectively. The two layers indicated by Gd and/or Ce are corresponding to parts of the fluorite-type block of $(\text{Gd}_{1.5}\text{Ce}_{0.5})_2\text{O}_2$. It is confirmed that the layers and the fluorite-type block are stacked along the c -axis following 1222-type structure without any intergrowths.

3.3. CBED and DFEM investigations

The superlattice reflections were observed along a direction perpendicular to the c -axis, the layer-stacking direction for the both phases. The SAED patterns are displayed in Figs. 6(a) and 6(b) for Ru-1212 and Ru-1222, respectively. The superlattice reflections with diffuse streaks along the c^* direction are observed in Fig. 6(a) as indicated by the white arrowheads. The superlattice reflections are corresponding to those indicated by the white arrowheads in the $[001]$ SAED pattern (Fig. 4(a)). The diffuse streaks suggest existence of domain structures or stacking disorders of the superlattice along the c direction in the Ru-1212 phase. The superlattice reflections with diffuse streaks along the c^* direction are also observed in Fig. 6(b) as indicated by white arrowheads. Here, it should be noted that the superlattice reflections of Ru-1222 are somewhat more streaked than those of Ru-1212.

Figure 7(a) shows a CBED pattern of Ru-1212, taken along $[310]$ from an area with the diameter of about 8 nm. Sharp superlattice reflections without diffuse streaks are observed at $l = n$ as indicated by a white arrowhead, while the diffuse streaks were observed in the $[310]$ SAED pattern, as already shown in Fig. 6(a). This indicates that the CBED pattern is taken from a single-domain area with the diameter of larger than about 8 nm. Figure 7(b) shows another CBED pattern of Ru-1212 taken also with $[310]$ incidence but from an illumination area other than that in the case of Fig. 7(a). Sharp superlattice reflections without diffuse streaks are observed at $l = (2n + 1)/2$ as indicated by a white arrowhead in the CBED pattern of Fig. 7(b), whereas at $l = n$ in the pattern of Fig. 7(a). These results indicate that superlattice domains giving such CBED patterns are stacked along the c direction in the Ru-1212 phase. Similar sets of $[310]$ CBED patterns of Ru-1222 are shown in Figs 8(a) and 8(b). The CBED pattern of Fig. 8(b) was taken from an illumination area other than that in the case of Fig. 8(a). Sharp superlattice reflections without diffuse streaks are observed at $l = 2n$ and $l = 2n + 1$ in Fig. 8(a) and 8(b), respectively. From the results, it is revealed that superlattice domains are stacked along the c direction in the Ru-1222 phase as well as in the Ru-1212 phase.

The superlattice domain structures were observed in dark-field images using a single superlattice reflection spot. Figures 9(a) and 9(b) show dark-field images of Ru-1212 and Ru-1222 by using the superlattice reflections at $l = n = 2$ and $l = 2n + 1 = 3$ as indicated by the white arrowheads in Figs. 7(a) and 8(b), respectively. The nm-size superlattice domains are clearly seen as many bright striated areas. It is important to note that the domain sizes in Ru-1222 are somewhat larger than those in Ru-1212, corresponding to the SAED patterns shown in Fig.6.

3.4. Structural considerations

Figure 10(a) shows a schematic diagram of the fundamental structure of Ru-1212 in which only RuO_2 planes are shown as indicated by filled squares. The rectangular parallelepiped

surrounded by solid lines represents the fundamental primitive tetragonal lattice. The rectangular parallelepipeds surrounded by the dotted lines are corresponding to the $\sqrt{2}a \times \sqrt{2}a \times c$ superlattice. It is assumed on the basis of the results by McLaughlin *et al.* [14] that the superlattice reflections observed for the Ru-1212 phase in this study are due to an ordering of the RuO₆ octahedra rotated about the *c*-axis. Here, we consider two possible arrangements of the rotated RuO₆ octahedra, P and I, as shown in Fig. 10(b). The rectangular parallelepipeds surrounded by the dotted lines and solid lines are corresponding to the fundamental lattice and $\sqrt{2}a \times \sqrt{2}a$ superlattice, respectively. Dark- and light-gray squares indicate right- and left-handed rotations of the RuO₆ octahedra about the *c*-axis, respectively. The rotated RuO₆ octahedra are ordered along the *c* direction with intervals of *c* and 2*c* in P and I arrangements, respectively. The different periodicities are caused by the differences of rotative direction of the RuO₆ octahedra indicated by arrowheads in Fig. 10(b). It is confirmed that the lattice types for P and I arrangements are primitive (*P*) and body-centered (*I*) tetragonal lattices, respectively. Further, possible space groups of the P and I superlattices can be assumed to be *P4/mbm* and *I4/mcm*, respectively. (The space group of the P superlattice is the same as that reported by Chmaissem *et al.* [13].) We propose that nm-size superlattice domains distinguished by the P and I superlattices are stacked along the *c* direction in the Ru-1212 phase.

Figure 11(a) shows a schematic diagram of a reproduced [001] SAED pattern based on the superlattice domain structure. The reflections of $hk0_s$ with the condition of $h + k = 2n + 1$ are extinctive in the case of the I superlattice structure. On the other hand, there exists no extinctive condition for the $hk0_s$ reflections in the case of the P superlattice structure. Although $h00_s$ and $0k0_s$ reflections with the condition of $h = 2n + 1$ and $k = 2n + 1$ are extinctive, the reflections are expected to be induced by multiple scattering of electron beam in the [001] projection. The P + I pattern, which is formed by superposing the pattern derived from the P superlattice on that from the I superlattice, is consistent with the experimental [001] SAED pattern shown in Fig. 4(a). Moreover, it is confirmed that the expectation concerning the $h00_s$ and $0k0_s$ reflections is realized. The superlattice reflections indicated by black arrowheads in the [001] SAED pattern (Fig. 4(a)) are absent in the [110] pattern (Fig. 4(c)). The fact indicates that the superlattice reflections are extinctive due to the glide planes of the P superlattice structure, but caused by multiple scattering of electron beam in the [001] pattern. Figure 11(b) shows a schematic diagram of the [310] CBED patterns for the P and I superlattice domains. These patterns are also consistent with the experimental ones in Fig. 7.

Figure 12(a) shows a schematic diagram of the fundamental structure of Ru-1222. The rectangular parallelepiped surrounded by solid lines represents the fundamental body-centered tetragonal lattice. The rectangular parallelepipeds surrounded by the dotted lines are corresponding to the $\sqrt{2}a \times \sqrt{2}a \times c$ superlattice. It is assumed on the basis of the result by Knee *et al.* [12] that the superlattice reflections observed for the Ru-1222 phase are also due to an ordering of the RuO₆ octahedra rotated about the *c*-axis. We consider two possible arrangements of the rotated RuO₆ octahedra, A and B, as shown in Fig. 12(b). The rectangular parallelepipeds surrounded by the dotted lines and solid lines are corresponding to the fundamental lattice and $\sqrt{2}a \times \sqrt{2}a$ superlattice, respectively. In both arrangements, the rotated RuO₆ octahedra are ordered along the *c* direction with the same interval of *c*, however, the rotative directions of the octahedra at (1/2, 1/2, 1/2) of the fundamental lattice are different as

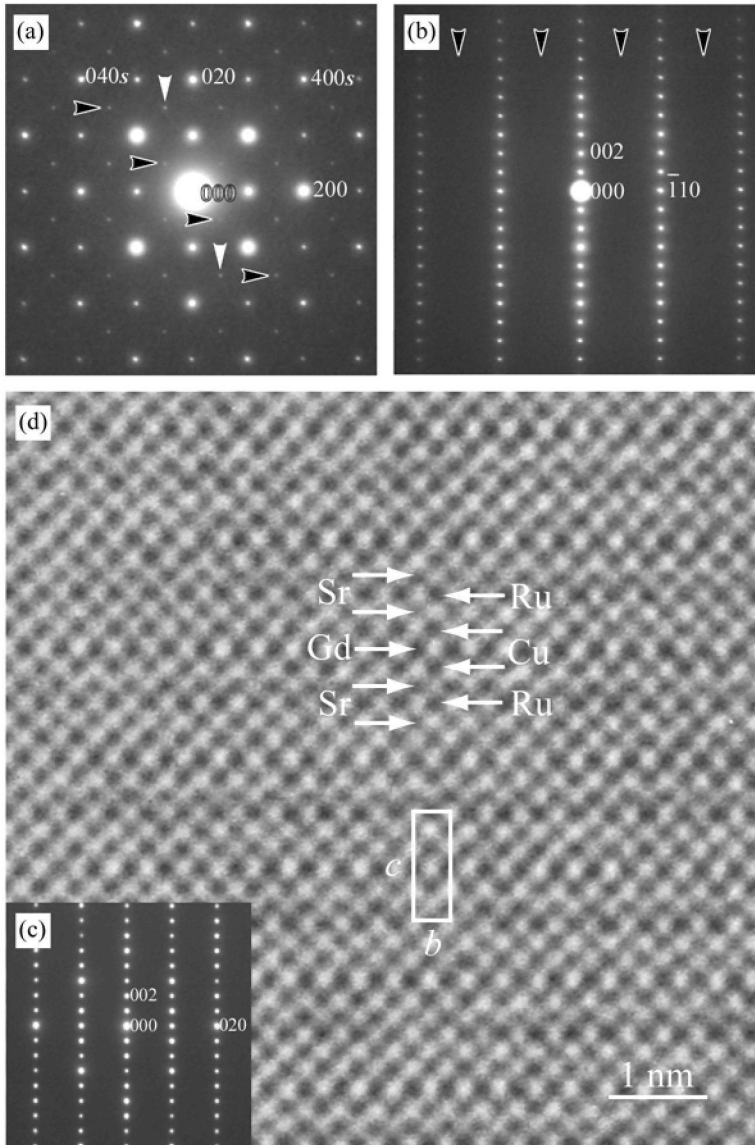


Fig. 4: SAED patterns taken with (a) [001], (b) [110], and (c) [100] incidence and (d) HREM image taken with [100] incidence for the Ru-1212 phase. hkl and hkl_s correspond to the indexes of reciprocal fundamental lattice and superlattice, respectively.

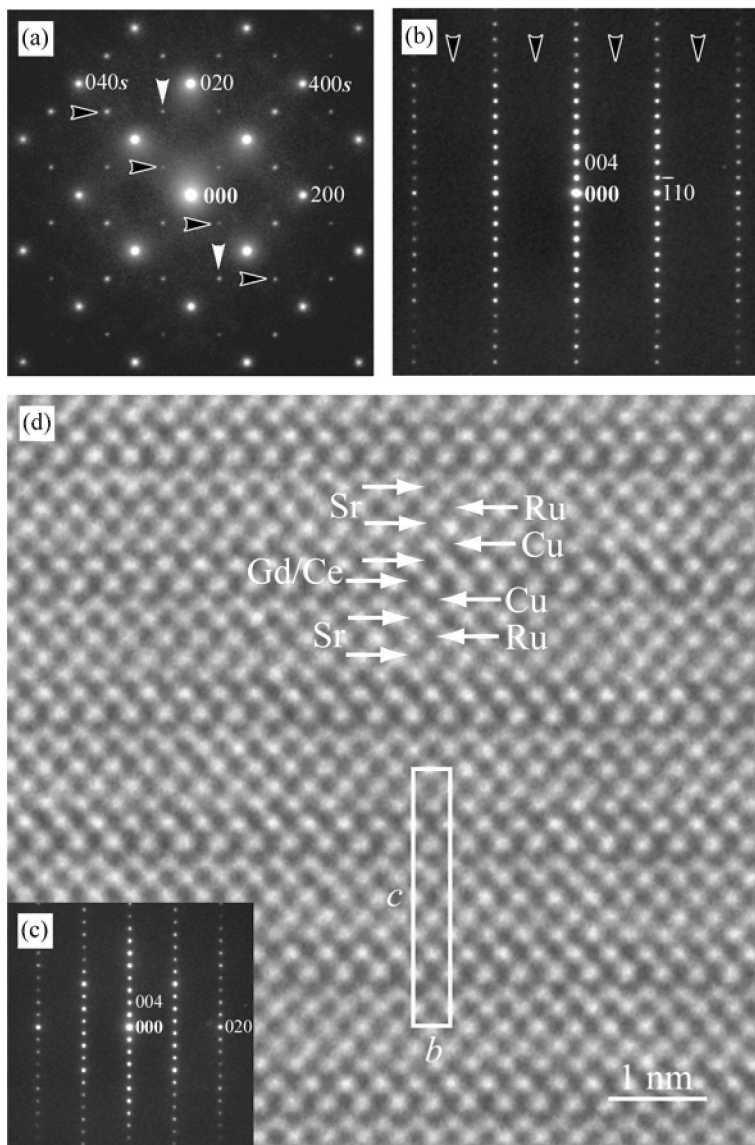


Fig. 5: SAED patterns taken with (a) [001], (b) [110], and (c) [100] incidence and (d) HREM image taken with [100] incidence for the Ru-1222 phase. hkl and hkl_s correspond to the indexes of reciprocal fundamental lattice and superlattice, respectively.

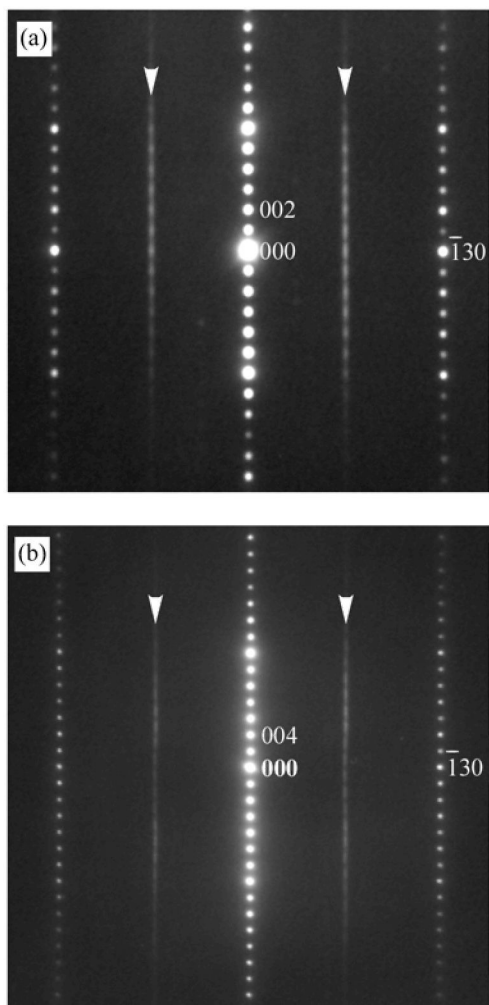


Fig. 6: SAED patterns taken with [310] incidence for (a) the Ru-1212 phase and (b) the Ru-1222 phase.

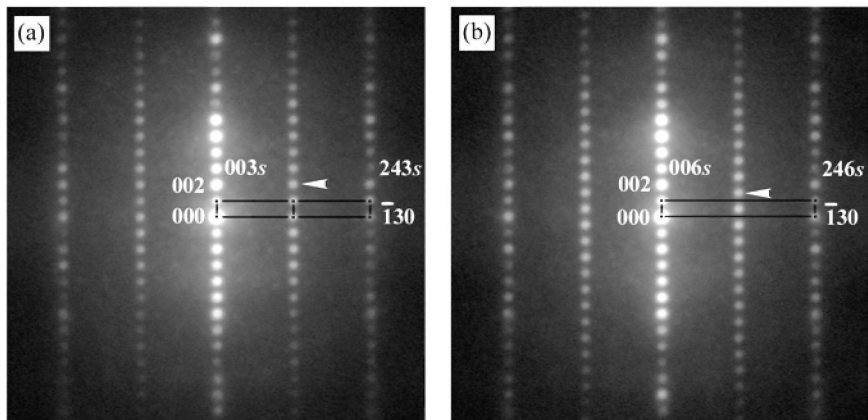


Fig. 7: CBED patterns taken with $[310]$ incidence for the Ru-1212 phase:
 (a) from one illumination area, superlattice reflections are seen at $l = n$ (n : integer),
 (b) from another illumination area, superlattice reflections are seen at $l = (2n + 1)/2$.

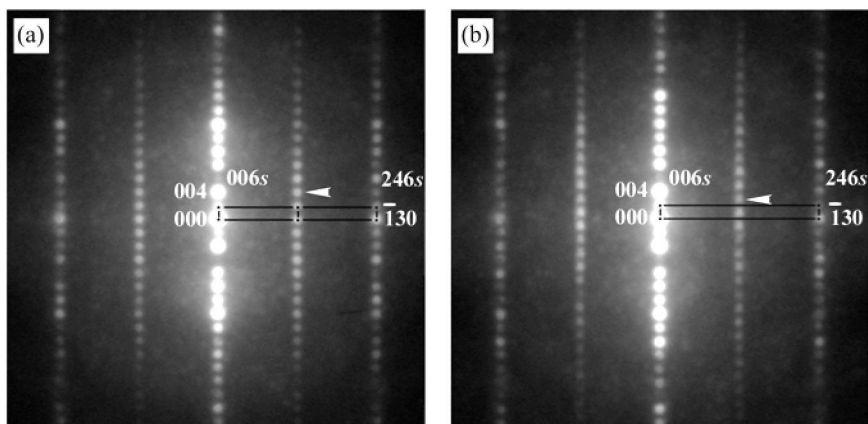


Fig. 8: CBED patterns taken with $[310]$ incidence for the Ru-1222 phase:
 (a) from one illumination area, superlattice reflections are seen at $l = 2n$ (n : integer),
 (b) from another illumination area, superlattice reflections are seen at $l = 2n + 1$.

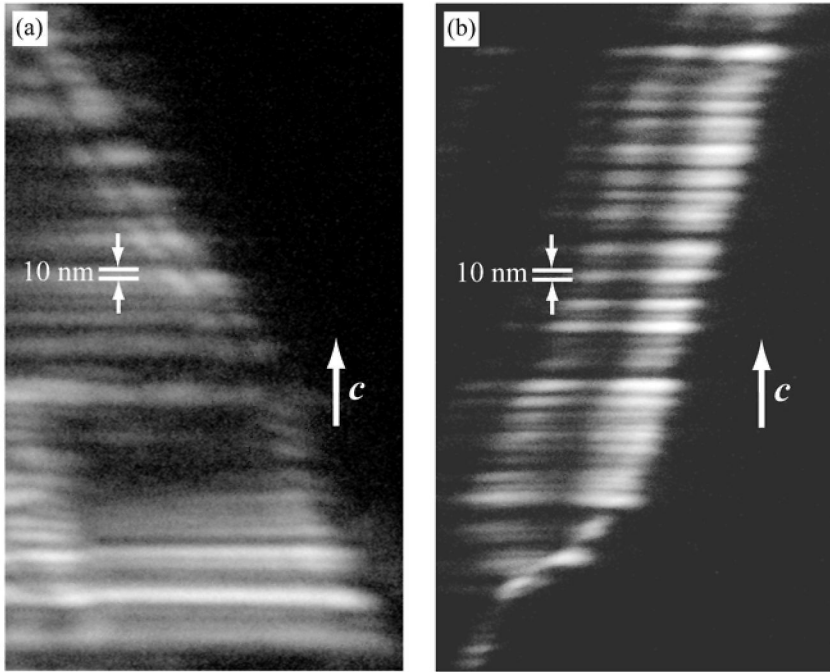


Fig. 9: Dark-field images for (a) the Ru-1212 phase and (b) the Ru-1222 phase by using the superlattice reflections at $l = 2$ and $l = 3$ as indicated by the white arrowheads in Figs. 7(a) and 8(b), respectively.

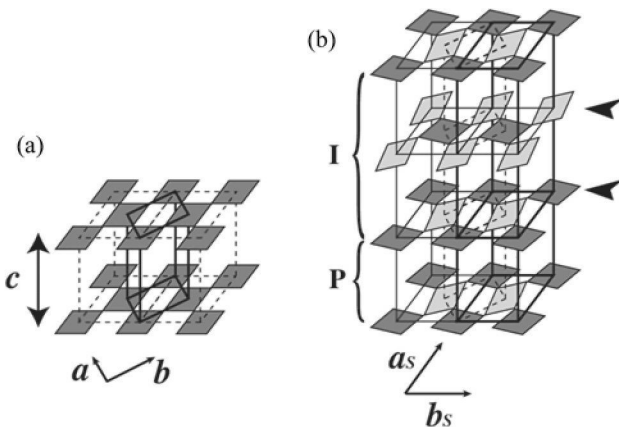


Fig. 10: Schematic diagrams of the fundamental lattice and superlattices for the Ru-1212 phase: (a) the fundamental lattice, only RuO₂ planes are shown as indicated by filled squares, (b) the two possible superlattices due to the arrangements of the rotated RuO₆ octahedra, P and I.

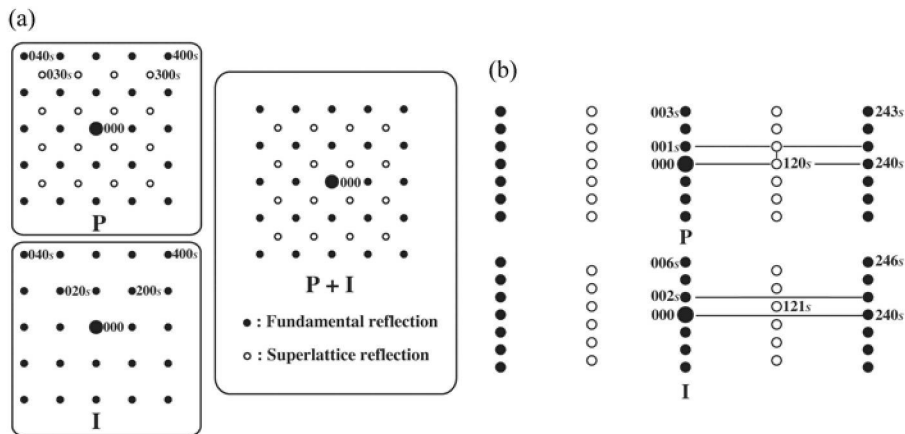


Fig. 11: Schematic diagrams of reproduced diffraction patterns for the Ru-1212 phase based on the superlattice domain structure due to the P and I arrangements: (a) [001] SAED patterns, (b) [310] CBED patterns.

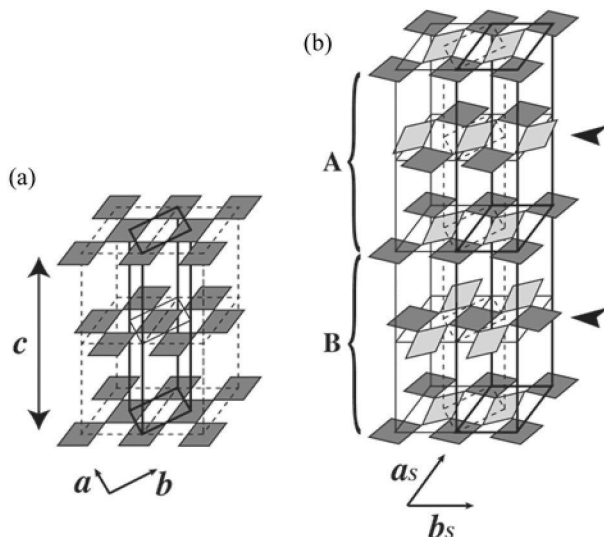


Fig. 12: Schematic diagrams of the fundamental lattice and superlattices for the Ru-1222 phase: (a) the fundamental lattice, only RuO_2 planes are shown as indicated by filled squares, (b) the two possible superlattices due to the arrangements of the rotated RuO_6 octahedra, A and B.

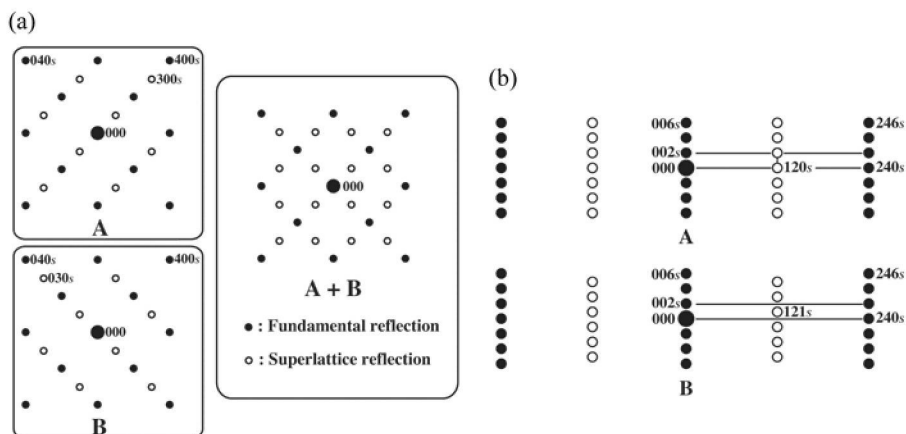


Fig. 13: Schematic diagrams of reproduced diffraction patterns for the Ru-1222 phase based on the superlattice domain structure due to the A and B arrangements: (a) $[001]$ SAED patterns, (b) $[310]$ CBED patterns.

indicated by arrowheads. It is confirmed that the lattice types for A and B arrangements are *A*-centered and *B*-centered orthorhombic lattices, respectively, if the axes of a_S and b_S are fixed as shown in the figure. (The A and B superlattices are crystallographically identical to each other, being mutually related by 90° rotation about the *c*-axis.) Further, possible space groups of the A and B superlattices can be assumed to be *Aeam* and *Bbem*, respectively. We propose that nm-size superlattice domains distinguished by the A and B superlattices are stacked along the *c* direction in the Ru-1222 phase.

Figure 13(a) shows a diagram of a reproduced [001] SAED pattern based on the superlattice domain structure. The reflections of $hk0_S$ with the condition of $k = 2n + 1$ and $h = 2n + 1$ are extinctive in the case of the A and B superlattice structures, respectively. The $h00_S$ reflections with the condition of $h = 2n + 1$ are extinctive in the case of the A superlattice structure, and the $0k0_S$ reflections with the condition of $k = 2n + 1$ are extinctive in the case of the B superlattice structure. However, these reflections are expected to be induced by multiple scattering of electron beam in the [001] projection. The A + B pattern, which is formed by superposing the pattern derived from the A superlattice on that from the B superlattice, is consistent with the experimental [001] SAED pattern shown in Fig. 5(a). Furthermore, the superlattice reflections indicated by black arrowheads in the [001] SAED pattern (Fig. 5(a)) are absent in the [110] pattern (Fig. 5(c)), which indicates that the expectation concerning the $h00_S$ and $0k0_S$ reflections is realized. Figure 13(b) shows a schematic diagram of the [310] CBED patterns for the A and B superlattice domains. These patterns are also consistent with the experimental ones in Fig.8.

4. Co-SYSTEM (Nagai *et al.* [17])

4.1. Physical properties

None of the three samples, $\text{CoSr}_2\text{YCu}_2\text{O}_7$ (Co-1212), $\text{CoSr}_2(\text{Y}_{3/4}\text{Ce}_{1/4})_2\text{Cu}_2\text{O}_9$ (Co-1222), and $\text{CoSr}_2(\text{Y}_{1/3}\text{Ce}_{2/3})_3\text{Cu}_2\text{O}_{11}$ (Co-1232), showed superconductivity. The magnetization data obtained for the samples are given and discussed elsewhere [19,22]. The data showed a general behavior common to all the three phases that is believed to originate from short-range low-dimensional correlations among the Co spins within the CoO layer. The lack of superconductivity in the samples is primarily attributed to the fact that appropriate doping of the CuO_2 planes with holes has not yet been achieved for the Co-12s2 phases. It should be noted that our preliminary Cu *L*-edge XANES (X-ray absorption near-edge structure) spectroscopy study revealed that the valence of Cu is very close to II in all the three samples [22].

4.2. SAED and HREM investigations

For the Co-1212 phase, all X-ray diffraction maxima could be indexed on the basis of *I2cm* (No.46) orthorhombic symmetry [1,3] and lattice parameters of $a = 0.5409$ nm, $b = 0.5452$ nm, and $c = 2.2799$ nm. Figure 14(a) shows a SAED pattern taken along [001] direction for the Co-1212 phase. The main spots are produced by the basic perovskite structure, and can be indexed on a rectangular quasi-square mesh, diagonal relative to the basic perovskite mesh (a $b = \sqrt{2}a_p$) [4]. In addition, superstructural spots are seen along the b^* -axis indicating double periodicity of $b_s = 2b$. The spots can be indexed as $(h, k \pm 1/2, 0)$. In Fig. 14(b) shown is a

SAED pattern of the same sample with $[100]$ incidence, where the $(0, k\pm 1/2, 0)$ superstructural spots which are clearly visible in Fig. 14(a) are absent. The $(0, k\pm 1/2, 0)$ superlattice reflections in Fig. 14(a) are kinematically forbidden but induced by multiple scattering of electron beam. The strong $0kl$ fundamental reflections with $k, l = \text{even}$ in Fig. 14(b) are caused by the primitive 1212 structure with a c -axis parameter of $c_{p1} = 3a_p$. The other relatively weak $0kl$ reflections with $k, l = \text{odd}$ in the figure indicate that the c -axis parameter of the Co-1212 phase is twice in length as compared with that of the primitive 1212 structure unit, $c = 2c_{p1} = 6a_p$. The extinction condition for the fundamental reflections due to the lattice type, $h + k + l = \text{odd}$, makes the basic lattice body-centered, which leads to a shift of the CoO_4 chain position by $[1/2, 1/2, 1/2]$ from the neighboring CoO layer. Figure 15 shows HREM images taken along (a) $[\bar{1}\bar{1}0]$ and (b) $[100]$ directions (in the subcell setting) for the Co-1212 phase. The $[\bar{1}\bar{1}0]$ SAED pattern is inset in Fig. 15(a). The 1212-type stacking of layers along the c -axis, $-\text{SrO}-\text{CoO}-\text{SrO}-\text{CuO}_2-\text{Y}-\text{CuO}_2-$, is clearly observed in Fig. 15(a). Figure 15(b) shows the relative shift of the CoO_4 chain position between neighboring CoO layers. In this figure, the white dot indicated by an arrow corresponds to a chain of oxygen vacancies between neighboring CoO_4 chains in a CoO layer. The superlattice reflections in Fig. 12(a) showing double periodicity along the b direction are indicative of a regular alternation of two different types of the CoO_4 -tetrahedra chains along the direction. The details are described in the next section.

For the Co-1222 phase, the lattice parameters of $a_{p2} = b_{p2} = 0.3832$ nm and $c_{p2} = 2.8170$ nm were given with use of $I4/mmm$ (No.139) tetragonal symmetry of primitive 1222 structure by X-ray diffraction analysis. The $[001]$, $[100]$ and $[\bar{1}\bar{1}0]$ zone-axis SAED patterns are shown in Figs. 16(a)-(c), where the main spots are indexed on a diagonal mesh in parallel to the case of Fig. 14. In Fig. 16(a), the reflections come from two different areas of the crystal, i.e. orientation variants differing by a 90° rotation about the c -axis. The striking difference between Fig. 14(a) and Fig. 16(a) is that the $hk0$ fundamental reflections with $h, k = \text{odd}$ are present in Fig. 14(a) but absent in Fig. 16(a). This is due to the presence of the three-layer fluorite-type block, causing a relative shift over $[1/2, 0, 0]$ or $[0, 1/2, 0]$ of the two neighboring blocks. There are the relatively weak $hk0$ fundamental reflections with $h = \text{odd}, k = \text{even}$ and the corresponding ones appear in the 90° -rotated positions because of the twin domain structure. Additionally, the weak superlattice reflections indicating the double periodicity of $b_s = 2b$ due to ordering of the CoO_4 -tetrahedra chains can be seen, and the corresponding ones appear in the rotated positions as well. In Fig. 16(b) only seen are the $0kl$ reflections with $k + l = \text{even}$, which indicates that the c -axis parameter of the Co-1222 phase is equal to that of the primitive 1222 structure unit, $c = c_{p2} = 6a_p + 2c_f$ (c_f : thickness of fluorite-type $R\text{-O}_2\text{-}R$ block), and the unit cell includes two CoO layers. The extinction condition for fundamental reflections due to the lattice type, $k + l = \text{odd}$, makes the basic lattice A -centered, which is indicative of a position shift of the CoO_4 chain by $[0, 1/2, 1/2]$ between the neighboring CoO layers. Figure 16(d) shows the HREM image taken along $[\bar{1}\bar{1}0]$ direction. The 1222-type stacking of layers is clearly seen, with a relative shift of the blocks due to the fluorite-type $(\text{Y}_{3/4}\text{Ce}_{1/4})\text{-O}_2\text{-}(\text{Y}_{3/4}\text{Ce}_{1/4})$ block.

For the Co-1232 phase, all X-ray diffraction maxima could be indexed on the basis of $I2cm$ (No.46) orthorhombic symmetry and lattice parameters of $a = 0.5417$ nm, $b = 0.5469$ nm, and $c = 3.3231$ nm. The SAED patterns along $[001]$, $[100]$, $[\bar{1}\bar{1}0]$ and the HREM image along $[\bar{1}\bar{1}0]$ are shown in Figs. 17(a)-(d), respectively. In Fig. 17(a), the reflections come from twin domains like in the case of the Co-1222 phase, and the pattern from the single domain is

identical to the one in Fig. 14(a), where superlattice reflections showing $b_s = 2b$ are seen. The five-layer fluorite-type block gives rise to no relative shift of the two neighboring blocks [23], which explains the prominent presence of the $hk0$ reflections with $h, k = \text{odd}$. The $0kl$ reflections with $k, l = \text{odd}$ indicate that the c -axis parameter of the Co-1232 phase is doubled as compared with that of the primitive 1232 structure unit, $c = 2c_{p3} = 6a_p + 4c_f$. Parallel to the case of the Co-1212 phase, the Co-1232 phase has a body-centered lattice of fundamental structure, indicating that the CoO_4 chain position shifts by $[1/2, 1/2, 1/2]$ between the neighboring CoO layers. We can see in Fig. 17(c) the 1232-type stacking of layers, with no relative shift due to the fluorite-type $(Y_{1/3}\text{Ce}_{2/3})\text{-O}_2\text{-}(Y_{1/3}\text{Ce}_{2/3})\text{-O}_2\text{-}(Y_{1/3}\text{Ce}_{2/3})$ block.

4.3. Structural considerations

As described above, superlattice reflections showing double periodicity along the b direction are seen for all the three phases. The superlattice reflections are indicative of a regular alternation of two different types of symmetry (L and R) of the CoO_4 -tetrahedra chains along the direction, which is shown in Fig. 18(a) [4]. It has been reported that MO_4 -tetrahedra can rotate in two different ways about the c -axis, giving rise to the formation of two kinds of zig-zag chains, L -chains and R -chains [4]. The L - R distinction is just relative because an L -chain is transferred into an R -chain by a mirror operation, and therefore the two types of chains are energetically equivalent, and would thus form with equal probabilities. The observed results indicate that the intralayer ordering of the two types of chains is a general phenomenon for all the three phases.

In order to reveal the arrangement of the chains along the layer-stacking direction (c direction) in the Co-1212 phase, the superlattice reflections were observed along a direction perpendicular to the c direction. The obtained SAED pattern for the Co-1212 phase is shown in Fig. 18(b). The superspots at $(1, 1/2, l)$ and $(3, 3/2, l)$ are only slightly streaked along the c^* direction, which indicates that the two types of chains are very nearly ordered along the c direction in the large specimen area with the diameter of about 700 nm. The interval between the neighboring superspots shows that the periodicity of the ordering is equal to the c -axis parameter, $c_s = c$. Figure 18(c) shows the proposed superstructure model with $P2cm$ (No.28) orthorhombic symmetry and lattice parameters of $a_s = a$, $b_s = 2b$, and $c_s = c$ for the Co-1212 phase. The positional parameters were adapted from those proposed for $\text{GaSr}_2\text{YCu}_2\text{O}_7$ (Ga-1212) by Roth *et al.* [1], which are on the basis of $Ima2$ (No.46) orthorhombic symmetry with cell setting of $b = c = \sqrt{2}a_p$. Simulated SAED patterns based on the superstructure model are consistent with the experimentally observed ones, as shown in Fig. 19. Particularly, Figs. 19(b) and 19(c) well produce the aforementioned feature that the $(0, k \pm 1/2, 0)$ superlattice reflections are induced in $[001]$ projection whereas they are not induced in $[100]$ projection. (It can be deduced that the local crystal areas have slight deviations from exact $[001]$ zone-axis orientation when the pattern shown in Fig. 14(a) is observed.)

Now, let us discuss the chain arrangement along the c direction in case of the Co-1222 and 1232 phases, which have the fluorite-type block between CuO_2 planes. The SAED patterns observed along a direction perpendicular to the c direction are shown in Fig. 20. For both phases, the superspots at $(1, 1/2, l)$ and $(3, 3/2, l)$ are completely streaked, that is, there exists no periodic variation along the c^* direction in intensity of the streaks. This feature indicates that the chains are completely disordered along the c direction. We display in Fig. 21 an HRE \approx image for the Co-1232 projected along $[1\bar{2}0]$, corresponding to the SAED pattern in

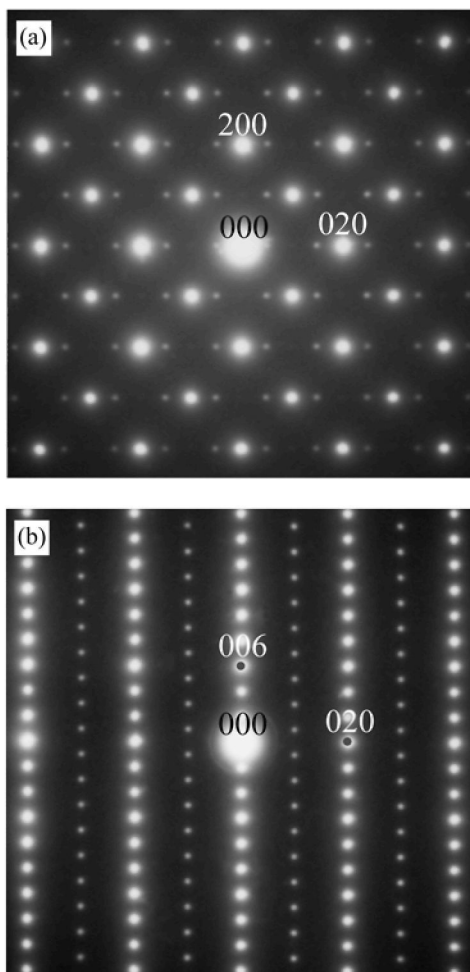


Fig. 14: SAED patterns taken along (a) [001] and (b) [100] direction for the Co-1212 phase. The main spots are indexed in the subcell.

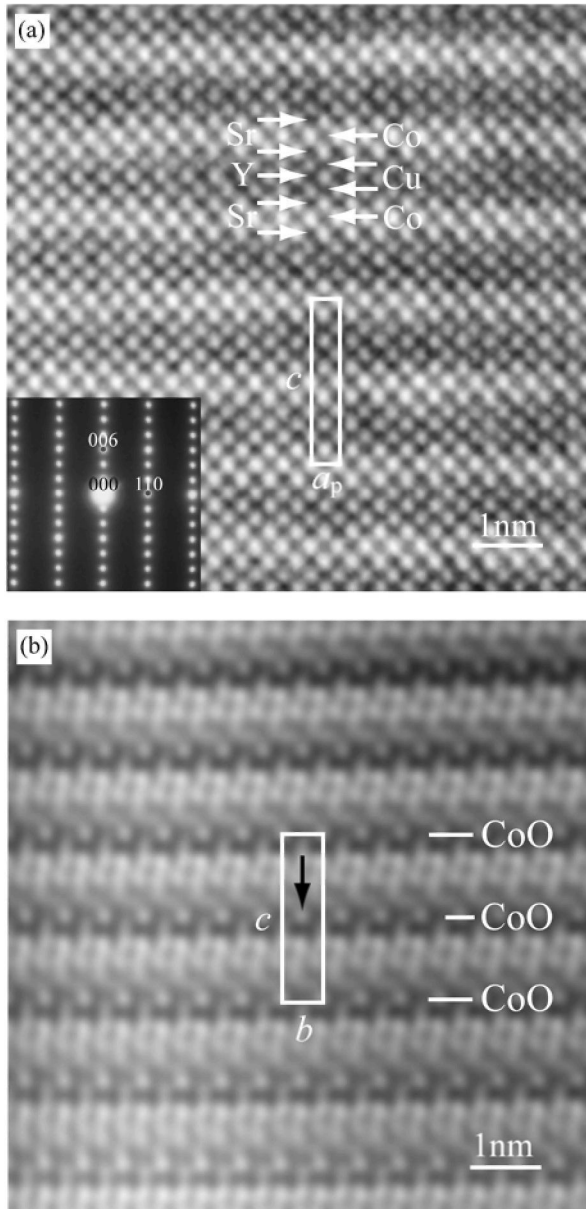


Fig. 15: HREM images taken along (a) $[1\bar{1}0]$ and (b) $[100]$ direction for the Co-1212 phase. The $[1\bar{1}0]$ SAED pattern is inset in figure (a).

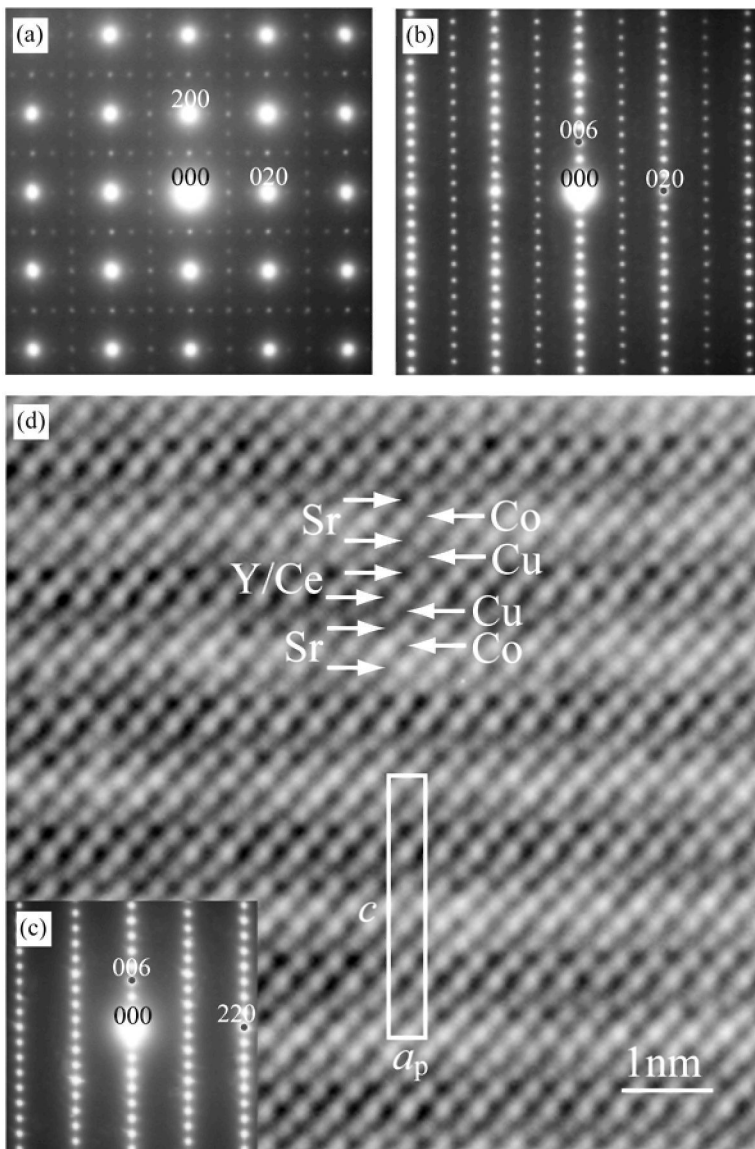


Fig. 16: SAED patterns taken along (a) $[001]$, (b) $[100]$, and (c) $[1\bar{1}0]$ and (d) HREM image taken along $[1\bar{1}0]$ for the Co-1222 phase. The main spots are indexed in the subcell.

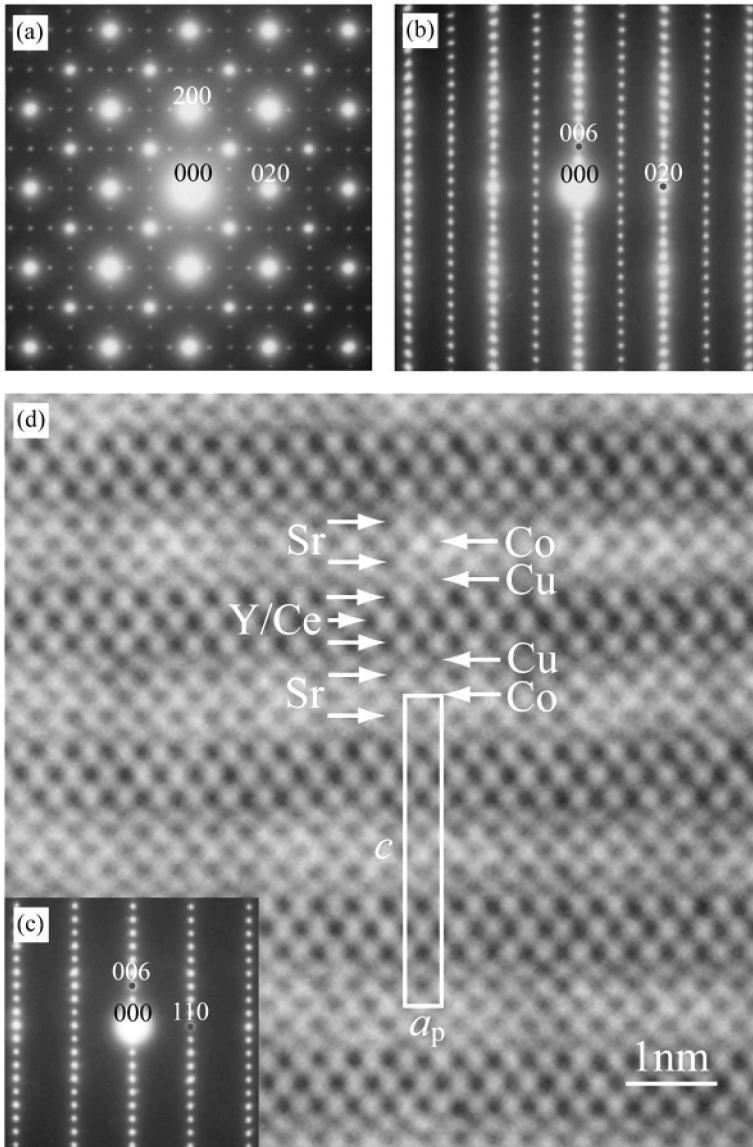


Fig. 17: SAED patterns taken along (a) $[001]$, (b) $[100]$, and (c) $[1\bar{1}0]$ and (d) HREM image taken along $[1\bar{1}0]$ for the Co-1232 phase. The main spots are indexed in the subcell.

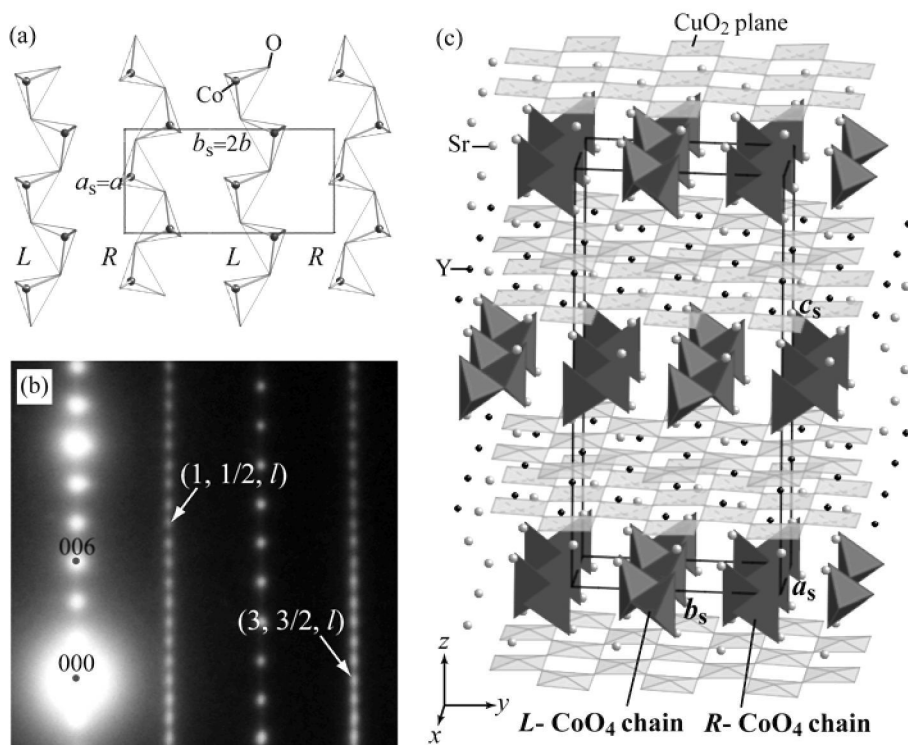


Fig. 18: (a) Illustration of a regular alternation of two types of CoO_4 -tetrahedra chains, L - and R -chains, along the b direction. (b) SAED pattern taken along $[1\bar{1}20]$ for the Co-1212 phase. (c) Superstructure model proposed for the Co-1212 phase with $P2cm$ (No.28) orthorhombic symmetry and lattice parameters of $a_s = a$, $b_s = 2b$, and $c_s = c$.

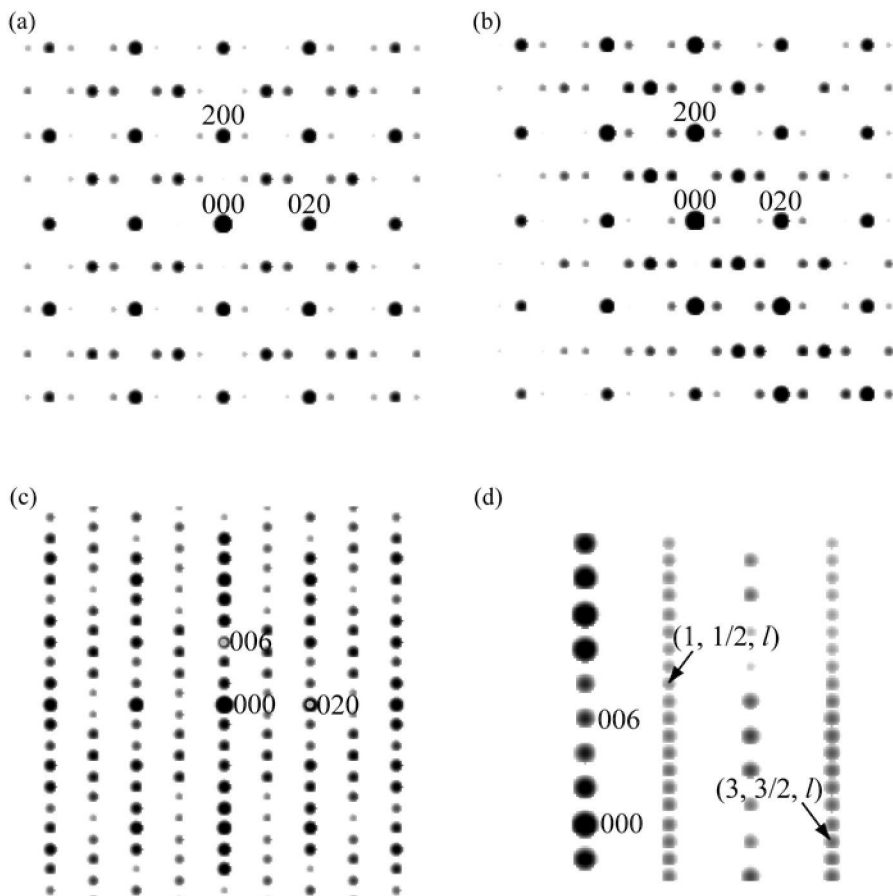


Fig. 19: Simulated SAED patterns based on the superstructure model in Fig. 18(c).

The main spots are indexed in the subcell. (a) [001] projection (in the subcell setting) with no crystal tilt, $h = k = 0$ mrad, (b) [001] projection with slight crystal tilt, $h = k = 20$ mrad, (c) [100] projection, (d) [$1\bar{2}0$] projection ((c), (d): with no crystal tilt). All the simulations were carried out with crystal thickness, $t = 10$ nm.

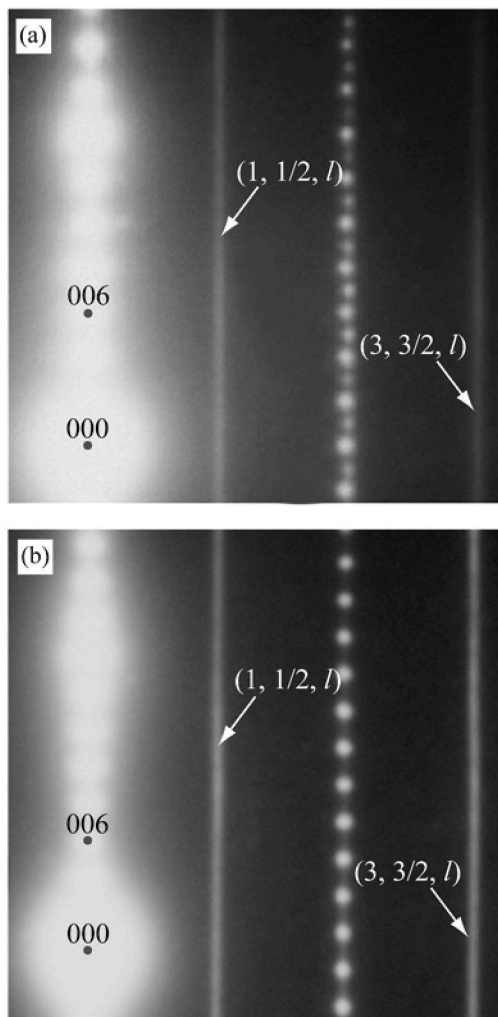


Fig. 20: SAED patterns taken along $[1\bar{2}0]$ for (a) the Co-1222 phase and (b) the Co-1232 phase.

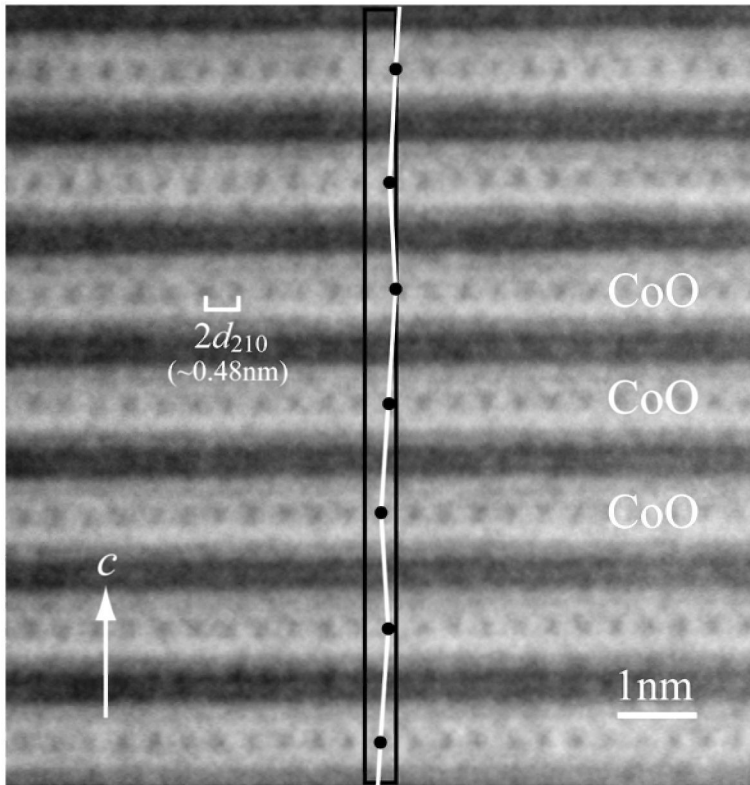


Fig. 21: HREM image for the Co-1232 phase projected along $[1\bar{2}0]$.
The arrangement of dots shows the intralayer ordering and interlayer disordering of the CoO₄ chains.

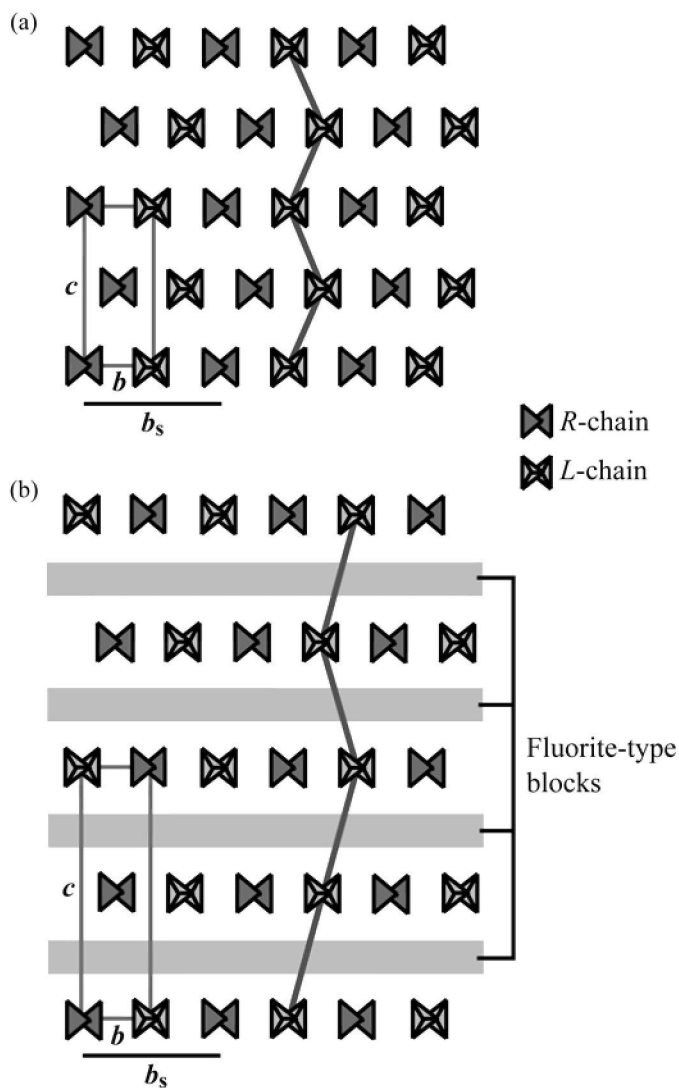


Fig. 22: Schematic representations of the arrangement of R - and L - CoO_4 chains for (a) the Co-1212 phase and (b) the Co-1222 and Co-1232 phases.

Fig. 20(b). The observed dot rows perpendicular to the c direction were formed by the completely streaked superlattice reflections, as judged by the regular interval of $2d_{210}$ between the neighboring dots. The arrangement of dots shows the intralayer ordering and interlayer disordering of the CoO_4 chains in the phase.

Ordering of the two types of chains presumably occurs so that the total lattice energy would be reduced. Schematic representations of CoO_4 chain arrangement for the present Co-12s2 phases are shown in Fig. 22. For all the three phases, the intralayer interaction between the chains is strong because of shortness of the distance between them. This is the reason for the general phenomenon of intralayer ordering of the two types of chains. On the other hand, the distance across the $\text{SrO-CuO}_2\text{-(Y,Ce)-(O}_2\text{-(Y,Ce))}_{s-1}\text{-CuO}_2\text{-SrO}$ block is long and the interlayer interaction thus weak. For the $s = 2$ and 3 phases, the distance is 1.41 nm (Co-1222) or 1.66 nm (Co-1232), and the interaction is especially weak, which probably causes the complete lack of interlayer order of the CoO_4 chains.

5. DISCUSSION AND CONCLUSIONS

The above two studies reveal structural order and disorder in the charge reservoir blocks of the Ru-12s2 and Co-12s2 phases. The structural order and disorder are based on the connection manner of RuO_6 octahedra for the Ru-system and that of CoO_4 tetrahedra for the Co-system. In the charge reservoir blocks, oxygen atoms octahedrally coordinate Ru atoms to form two-dimensional networks of corner-sharing RuO_6 octahedra for the Ru-system. On the other hand, oxygen atoms tetrahedrally coordinate Co atoms to form one-dimensional chains of corner-sharing CoO_4 tetrahedra for the Co-system.

In the Ru-system, superlattice reflections were commonly observed in SAED patterns taken along [001] direction, perpendicular to the RuO_2 layers. The reflections indicate intralayer superstructures due to ordering of two kinds of RuO_6 octahedra which rotate about the c -axis in different ways. Here, it should be noted that the superstructures formed in each charge reservoir block are crystallographically equivalent. However, as for the structural feature along the layer-stacking direction, it was confirmed that the superlattice reflections derived from ordering of RuO_6 octahedra are streaked along the c^* direction in the SAED patterns for the both phases. It was revealed by CBED and DFEM investigations that nm-size domains distinguished by different superlattices due to ordering of RuO_6 octahedra are stacked along the direction for both phases. Such structural states are regarded as disordered stacking of charge reservoir blocks. In the superlattice model of the Ru-1212 phase, charge reservoir blocks are stacked with constant position shifts perpendicular to the c direction by $[x, y]_s = [0, 0]_s$ (P-superlattice) or $[1/2, 1/2]_s$ (I-superlattice). In the model of the Ru-1222 phase, the constant shift vector is described as $[0, 1/2]_s$ (A-superlattice) or $[1/2, 0]_s$ (B-superlattice). The observed results indicate that the shifts of charge reservoir blocks in the Ru-12s2 phase are not constant, and consist of $[0, 0]_s$ and $[1/2, 1/2]_s$ (Ru-1212), or $[0, 1/2]_s$ and $[1/2, 0]_s$ (Ru-1222). Further, the DFEM investigations revealed that the sizes of the domains in Ru-1222 phase are somewhat larger than those in Ru-1212 phase. The results indicate that the degree of the stacking disorder in Ru-1222 phase is somewhat higher than that in Ru-1212 phase, and suggest that the degree might be related to the fundamental structure. Interestingly, a similar relation between the stacking manner of charge reservoir blocks and the fundamental structure is observed in the Co-12s2 phases.

In the Co-system, superlattice reflections were commonly observed in SAED patterns taken along [001] direction, perpendicular to the CoO layers. The reflections indicate intralayer superstructures due to ordering of two types of CoO₄ tetrahedra chains, *L*- and *R*-chains, where the tetrahedra rotate about the *c*-axis in different ways. The superstructures in each charge reservoir block are crystallographically equivalent like the case of the Ru-system. As for the structural feature along the layer-stacking direction, it was confirmed that the superlattice reflections derived from ordering of CoO₄ tetrahedra chains are only slightly streaked along the *c** direction for Co-1212 phase, and completely streaked for Co-1222 and Co-1232 phases. The SAED and HREM investigations revealed that the two types of chains are very nearly ordered along the *c* direction for Co-1212 phase whereas completely disordered for Co-1222 and Co-1232 phases. In the Co-1212 phase, charge reservoir blocks are stacked with regular position shifts as - *S*₁- *S*₂- *S*₁- *S*₂- *S*₁- *S*₂-, where *S*₁ = [1/2, 1/2] and *S*₂ = [-1/2, -1/2]. In the Co-1222 and 1232 phases, the blocks are stacked with irregular shifts such as - *S*₁- *S*₂- *S*₂- *S*₁- *S*₂- *S*₁-, where *S*₁ = [0, 1/2] and *S*₂ = [0, -1/2] (Co-1222), *S*₁ = [1/2, 1/2] and *S*₂ = [-1/2, -1/2] (Co-1232).

We can find an analogy between the structural features for the Ru-system and those for the Co-system. The degree of the stacking disorder of charge reservoir blocks in *M*-1212 phase is lower than that in *M*-1222 and *M*-1232 phases. It is deduced that the degree is related to the fundamental structure of the *M*-12*s*2 phase. As for the fundamental structure, there exists the specific feature that the distance between neighboring charge reservoir blocks increases with increasing number of *s*. Therefore, it is considered that the degree of the stacking disorder is related to the distance between neighboring charge reservoir blocks.

Stacking order of the charge reservoir blocks presumably occurs so that the total lattice energy would be reduced. As the distance between the charge reservoir blocks increases, the interlayer interaction between the blocks becomes weaker, which probably makes the degree of the stacking disorder in *M*-1232 and 1222 phases higher than that in *M*-1212 phase. It is expected that the relation between the stacking manner and the distance is general for superconducting and related copper oxides.

In conclusion, we have presented recent TEM studies on crystal structures of Ru-12*s*2 phases (*s* = 1-2) and Co-12*s*2 phases (*s* = 1-3). The studies revealed structural order and disorder in the charge reservoir blocks of the phases. The structural matter was discussed in terms of stacking manner of the charge reservoir blocks, and it was deduced that the stacking order and disorder is related to the distance between the neighboring charge reservoir blocks.

ACKNOWLEDGEMENTS

We collaborated on the present works with V. P. S. Awana, M. Karppinen, H. Yamauchi, S. K. Malik, W. B. Yelon, A. Yamazaki, and E. Takayama-Muromachi. We thank T. Asaka and C. Tsuruta for their skillful technical assistance and helpful discussions. The works were supported by the Nanotechnology Support Project of the MEXT, Japan.

REFERENCES

- [1] G. Roth, P. Adelman, G. Heger, R. Knitter, and T. Wolf, *J. de Physique I* (1991) 721.
- [2] J. T. Vaughey, J. P. Thiel, E. F. Hasty, D. A. Groenke, C. L. Stern, K. L. Poepelmeier, B. Dabrowski, P. Radaelli, A. W. Mitchell, and D. G. Hinks, *Chem. Mater.* 3 (1991) 935.
- [3] Q. Huang, R. J. Cava, A. Santoro, J. J. Krajewski, and W. F. Peck, *Physica C* 193 (1992) 196.
- [4] T. Krekels, O. Milat, G. Van Tendeloo, S. Amelinckx, T. G. N. Babu, A. J. Wright, and C. Greaves, *J. Solid State Chem.* 105 (1993) 313.
- [5] J. Ramirez-Castellanos, Y. Matsui, E. Takayama-Muromachi, and M. Isobe, *J. Solid State Chem.* 123 (1996) 378.
- [6] J. Ramirez-Castellanos, Y. Matsui, M. Isobe, and E. Takayama-Muromachi, *J. Solid State Chem.* 133 (1997) 434.
- [7] L. Bauenfeind, W. Widder, and H. F. Braun, *Physica C* 254 (1995) 151.
- [8] I. Felner, U. Asaf, Y. Levi, and O. Millo, *Phys. Rev. B* 55 (1997) R3374.
- [9] I. Felner and U. Asaf, *Int. J. Mod. Phys. B* 12 (1998) 3220.
- [10] C. Bernhard, J. L. Tallon, Ch. Niedermayer, Th. Blasius, A. Golnik, E. Brücher, R. K. Kremer, D. R. Noakes, C. E. Stronack, and E. J. Asnaldo, *Phys. Rev. B* 59 (1999) 14099.
- [11] J. W. Lynn, B. Keimer, C. Ulrich, C. Bernhard, and J. L. Tallon, *Phys. Rev. B* 55 (2000) R14964.
- [12] C. S. Knee, B. D. Reinfeld, and M. T. Weller, *J. Mater. Chem.* 10 (2000) 2445.
- [13] O. Chmaissem, J. D. Jorgensen, H. Shaked, P. Dollar, and J. L. Tallon, *Phys. Rev. B* 61 (2000) 6401.
- [14] A. C. McLaughlin, W. Zhou, J. P. Attfield, A. N. Fitch, and J. L. Tallon, *Phys. Rev. B* 60 (1999) 7512.
- [15] V. P. S. Awana, S. Ichihara, M. Karppinen, and H. Yamauchi, *Physica C* 378-381 (2002) 249.
- [16] T. Yokosawa, V. P. S. Awana, K. Kimoto, E. Takayama-Muromachi, M. Karppinen, H. Yamauchi, and Y. Matsui, *Ultramicroscopy* 98 (2004) 283.
- [17] T. Nagai, V. P. S. Awana, E. Takayama-Muromachi, A. Yamazaki, M. Karppinen, H. Yamauchi, S. K. Malik, W. B. Yelon, and Y. Matsui, *J. Solid State Chem.* 176 (2003) 213.
- [18] Y. Matsui, S. Horiuchi, Y. Bando, Y. Kitami, M. Yokoyama, and S. Suehara, *Ultramicroscopy* 39 (1991) 8.
- [19] M. Karppinen, V.P.S. Awana, Y. Morita, and H. Yamauchi, *Physica C*, 392 (2003) 82.
- [20] Y. Matsui, S. Horiuchi, H. Sawa, K. Obara, and J. Akimitsu, *Jpn. J. Appl. Phys.* 28 (1989) L1555.
- [21] V.P.S. Awana, S.K. Malik, W.B. Yelon, M. Karppinen, and H. Yamauchi, *Physica C* 378 (2002) 155.
- [22] M. Karppinen, Y. Morita, V.P.S. Awana, H. Yamauchi, R.S. Liu, and J.M. Chen, unpublished.
- [23] T. Wada, A. Nara, A. Ichinose, H. Yamauchi and S. Tanaka, *Physica C* 192 (1992) 181.

SUPERCONDUCTORS WITH NANOSCALE FLUX PINNING CENTRES

C.H. Cheng^{1,2}, Y. Zhao^{1,2*}, Y. Feng³, H. Zhang⁴, M. Nishiyama⁵,
N. Koshizuka⁵ and M. Murakami⁶

¹Superconductivity R&D Center, Southwest Jiaotong University
Chengdu, Sichuan, 610031 CHINA

²Superconductivity Research Group, School of Materials Science and Engineering,
University of New South Wales, Sydney, 2052 NSW, AUSTRALIA

³Northwest Institute for Nonferrous Metal Research,
P.O. Box 51, Xi'an, Shaanxi, 710016, CHINA

⁴State Key Lab for Mesophysics, Department of Physics
Peking University, Beijing 100871, CHINA

⁵Superconductivity Research Laboratory, International Superconductivity Technology Center,
1-10-13 Shinonome, Koto-ku, Tokyo, 135-0062, JAPAN

⁶Department of Materials Science and Engineering, Shibaura Institute of Technology,
Shibaura 3-9-14, Minato-ku, Tokyo 108-8548, JAPAN

1. INTRODUCTION

Revolutions in energy technology, information technology and biotechnology have been the main trend in the 21st century. Greatly increasing demand for energy has emerged due to the rapid development of the information technology revolution. In addition, energy conservation and related environmental issues will inevitably be the most serious problem of the 21st century. Superconductivity technology is the ultimate and environmentally-friendly

* Corresponding author: yzhao@home.swjtu.edu.cn or y.zhao@unsw.edu.au

technology for energy saving. It is expected to be the core technology of the 21st century, with its great impact on almost all of the aspects in our daily life.

Large-scale superconducting devices for power industry depend on the conductors with high critical current densities at temperatures where the costs for coolant are affordable. High-temperature cuprate superconductors (HTSs), such as (Bi,Pb)₂Sr₂Ca₂Cu₃O_x (Bi2223) and YBa₂Cu₃O_y (YBCO), and the newly discovered intermetallic compound superconductor MgB₂ are ideal candidates in the applications for this purpose [1]. For HTSs, although great progress in basic research and application development has been made since the discovery of HTS in 1986 [2], they have not been yet developed to the standard necessary for large-scale applications. The main scientific problem preventing commercialisation of HTSs is inadequate level of critical current density J_c at desirable temperatures and in expected magnetic fields. A J_c of 10^4 - 10^5 A/cm² for a superconducting wire or tape at a temperature range of 20-77 K and in a field of 0.3-5 T is necessary to fulfil most of the industrial applications [3,4]. The fundamental limit for J_c is the depairing critical current density, J_d , which is usually as high as 1.3×10^7 A/cm² at 77 K and 0 T for the typical HTSs [5]. Thus, in principle, the intrinsic J_d is sufficiently high for commercial applications.

However, only a sufficiently high J_d is not enough to guarantee a sufficiently high J_c for a superconductor to be a useful engineering conductor. Actually, superconductors can carry bulk current density only if there is a macroscopic fluxon density gradient [6], which can be sustained only by pinning the vortices at microstructural defects, this is the so-called flux pinning. Thanks to the flux pinning force F_p , which overcomes the Lorentz force $F_L = \mathbf{J} \times \mathbf{B}$ of the microscope current, a magnetically stable and energy dissipation-free state can be sustained. Tailoring the defect structure of the conductors will maximize the flux pinning force, and thus J_c .

Recently, it becomes more and more clear that structural defects with dimensions at nanoscale play important role for flux pinning in both low and high temperature superconductors [7-9]. For example, in low-temperature superconductors (LTSs) like Nb-Ti and Nb₃Sn, the most strong pinning is supplied by a dense lamellar structure of normal α -Ti ribbons, about 1 nm (0.2 ξ) thick and aligned parallel to the wire transport current in Nb-Ti [10], and by grain boundaries in Nb₃Sn [11-13]. In the newly discovered superconductor, MgB₂, the strong pinning may be also related to the nanoscale grain boundaries and nano-precipitates [14-19,]. In HTSs, due to a short coherence length and an extremely sensitive dependence of T_c on the hole-concentration in HTSs, a weak hole-depletion at crystalline defects can locally drive an HTS to an insulator. Such a local suppression of superconductivity has been observed near single-atom impurities (Ni and Zn) in doped Bi₂Sr₂CaCu₂O_x (Bi2212) single crystals [20], and on scale of 1-2 nm in pure crystals [21, 22]. This suggests that nanosize-defects in HTSs may also act as effective core pinning centres. Besides the point defects, other kinds of structure imperfections, such as dislocations [23,24], can also effectively pin the pancake vortices in HTSs at low temperatures. However, the performance of HTSs rapidly degrades with increasing field and temperature. Up to now, it is still no sure what kinds of pinning centres are suitable to pin the vortices in HTSs to guarantee a high performance at high temperatures (~77K) and high fields (4-5 T or higher).

It is well-known that HTSs have a layered structure in which superconducting layers (severed by CuO₂ planes) separated by non-superconducting layers are weakly Josephson coupled to each other. A vortex perpendicular to these layers, which would conventionally be considered a uniform cylinder of confined flux surrounded by circulating currents, is looked

upon in HTSs as a stacking of two-dimensional pancake-shaped vortices [25]. At a sufficiently low temperature, the coupling between the pancake vortices is rather strong, and making the vortices behave like a “flux line” that can be pinned by a limited number of pinning centres (see Fig.1 a). As the Josephson coupling energy decreases with increasing temperature ($E_J \sim (1-T/T_c)^2$ [26]), the “flux line” becomes very soft at higher temperatures and cannot be pinned by a few pinning centres (see Fig. 1b).

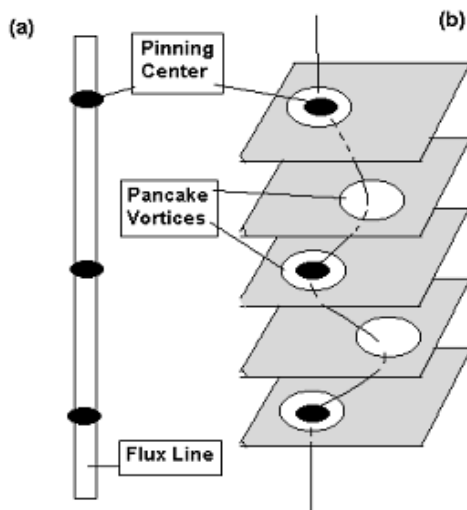


Fig. 1. Schematic of flux pinning. (a) A continuous, elastic flux line can be pinned by a limited number of pinning centres. Flux pinning of HTS at low temperatures may be described by this picture. (b) A series of pancake vortices cannot be pinned by the same pinning structure as shown in the (a). Flux pinning of HTS at high temperatures may be described by this picture.

Table 1. Basic parameters for practical superconductors. $\xi_{ab}(0)$ and $\lambda_{ab}(0)$ are in-plane coherence length and penetration depth at $T=0$ K, respectively. $J_d(0)$ is the depinning critical current density at $T=0$ K, a upper limit for J_c . H_{c2} is the upper critical field at or above which superconductivity vanishes. H_{irr} is the irreversibility field at or above which J_c vanishes.

| Material | T_c (K) | H_{c2} (T) | H_{irr} (T) | Anisotropy | $\xi_{ab}(0)$ | $\lambda_{ab}(0)$ | $J_d(0K)$ (A/cm ²) |
|--------------------|-----------|--------------|---------------|------------|---------------|-------------------|-----------------------------------|
| Nb-Ti | 9 | 12 at 4 K | 10.5 at 4K | ~1 | 4 nm | 240 nm | 3.6×10^7 |
| Nb ₃ Sn | 18 | 27 at 4 K | 24 at 4K | ~1 | 3 nm | 65 nm | 7.7×10^8 |
| MgB ₂ | 39 | 15 at 4 K | 8 at 4K | 2~3 | 6.5 nm | 140 nm | 7.7×10^7 |
| YBCO | 92 | >100 at 4 K | 5-7 at 77K | 7 | 1.5 nm | 150 nm | 3×10^8 |
| Bi2223 | 108 | >100 at 4 K | 0.2 at 77K | >50 | 1.5 nm | 150 nm | 3×10^8 |

Furthermore, as shown in Table 1, the typical value of HTS coherence length is about 1 nm, which allows point defects, such as isolated vacancies, substitutions, interstitials, etc., to be efficient pinning centres due to their sizes matching with the coherence length at low temperatures. Due to the fact that the coherence length increases with increasing temperature ($\xi = \xi(0) (1 - T/T_c)^{-1/2}$), and that at 77 K, it is about 3 nm for YBCO, most of the point defects in YBCO no longer operate as efficient pinning centres at 77 K due to the mismatch between the pinning size and the coherence length.

Recent experimental results in (Nd-Sm-Gd)Ba₂Cu₃O_y textured crystals suggest that clusters with dimensions of 3-10 nm strongly enhance the flux pinning [27]. We have also found that in Ho-doped YBCO textured crystals, stacking faults of a size around 10 nm and with a high density are the most likely to be responsible for a very high J_c [28,29]. All these results suggest that pinning centres of nanoscale may be the solution for efficient flux pinning in HTSs. Actually, as shown in Table 1, the coherence length of major engineering superconductors is in the nanoscale, therefore, the topic of flux pinning in these superconductors is in principle the interaction between flux lines (vortices) and defects at nanoscale. In this Chapter, more detailed results of the superconductors of nano-pinning centres will be given.

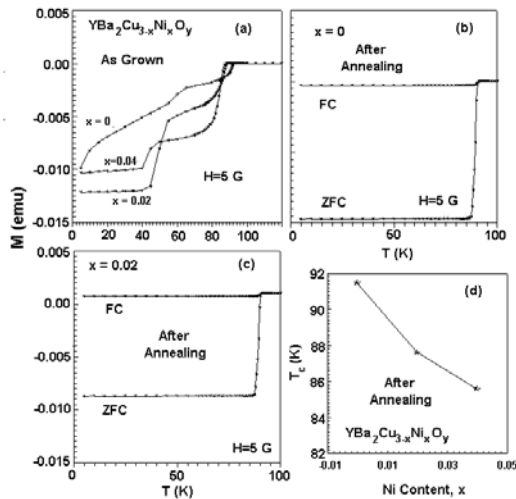


Fig. 2. (a) Temperature dependence of magnetization for the Ni-doped samples with different doping levels before oxygenation. (b) and (c) $M(T)$ curves for the samples with $x=0$ and $x=0.02$ after the annealing in flowing oxygen at 400 °C for 5 days. (d) The dopant concentration dependence of the T_c for the Ni-doped samples after the annealing in oxygen.

2. NIO INDUCED NANO-PINNING CENTRES IN MELT TEXTURED YBCO SUPERCONDUCTOR

The samples used for this study were prepared using the modified melt-textured-growth (MTG) method [30]. Presintered bars with a composition of YBa₂Cu_{3-x}Ni_xO_y ($x=0, 0.02$, and 0.04) and typical dimensions of 40x15x4 mm³ were prepared using high-purity (99.99%)

powders of Y_2BaCuO_5 (Y211), CuO , BaCuO_2 , and nano-sized NiO (~ 100 nm). Y211 substrate was used to absorb the unreacted liquid phase during the MTG process. Regular shapes with size of $1.2 \times 1.0 \times 0.3 \text{ mm}^3$ were cut from the as-grown crystal, annealed in flowing oxygen at 400°C for 120 hours. The microstructure and composition were determined by scanning electron microscope (SEM), transmission electron microscope (TEM), and energy dispersive x-ray (EDX) analysis. Micro-Raman spectroscopy, together with the temperature-pressure phase diagram of YBCO, was used to determine the oxygen content. DC SQUID magnetometer was used to measure the magnetization loops. J_c was deduced from the $M(H)$ loops (with H/c) by Bean Model.

The superconductivity of Ni-doped YBCO is affected by the doping level. As shown in Fig. 2, T_c of the Ni-doped crystals decreases monotonously from 91.7 K to 85.6 K with increasing the Ni doping level from $x=0$ to $x=0.04$. The transition width as well as the phase homogeneity of the samples is affected significantly by the post annealing in flowing oxygen atmosphere at 400°C for five days.

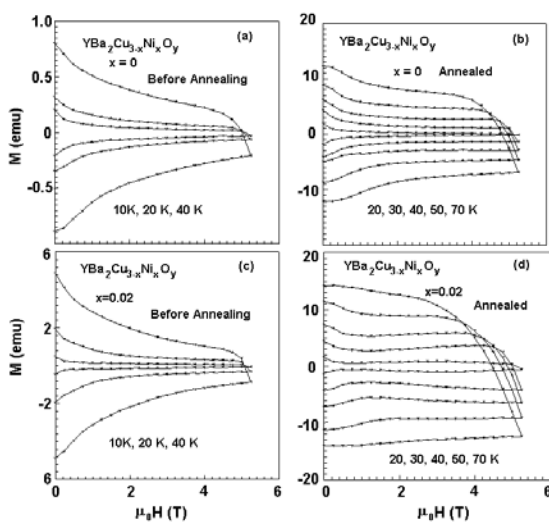


Fig. 3. Magnetic hysteresis loops at various temperatures for (a) the undoped sample before oxygenation; (b) the undoped sample after oxygenation; (c) the Ni-doped samples with $x=0.02$ before oxygenation; and (d) the Ni-doped samples with $x=0.02$ after oxygenation.

Fig. 3 presents the hysteresis loops at various temperatures for the samples of $x=0$ and $x=0.02$ before and after oxygenation. The oxygenated samples show much wide loops than the unannealed ones. For the undoped sample ($x=0$), the loop width decreases monotonously with the magnetic field at all temperatures, before and after oxygenation. However, the Ni-doped sample ($x=0.02$) exhibits a fishtail effect, i.e., a non-monotonous dependence of the hysteresis loop width with the applied field. The sample with $x=0.04$ shows a similar behavior (the results are not shown here) like the $x=0.02$. Because the fishtail effect only appears in the fully oxygenated, Ni-doped samples, it can be ruled out that the fishtail effect originates from

the oxygen deficient area in our Ni-doped samples. This also demonstrates that the fishtail effect can be induced by many different kinds of dopants, rather than only by oxygen vacancies.

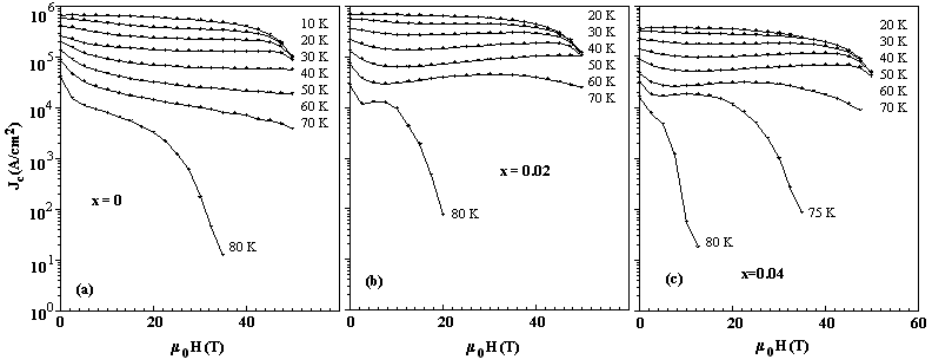


Fig. 4. Magnetic field dependence of J_c at various temperatures for (a) the undoped samples; (b) Ni-doped sample with $x=0.02$; and (c) Ni-doped sample with $x=0.04$. All these samples are oxygenated in flowing oxygen at 400 °C for 5 days.

Fig. 4 displays the field dependence of J_c deduced from the $M(H)$ curves for undoped and Ni-doped samples after oxygenation. Because of a higher T_c , the undoped sample exhibits a higher J_c and better J_c - H behavior than the Ni-doped samples at the temperatures above 70 K. When the temperature is slightly lower than 70 K, the Ni-doped samples exhibit a higher J_c and better J_c - H behavior than the undoped samples. Especially, Ni doping induces a dramatic fishtail effect, substantially increasing the J_c in the high magnetic fields.

The J_c - H relationship at 77 K for YBCO textured crystals containing 30 wt% Y211 (optimized addition of Y211) particles with various average particle sizes is shown in Fig. 4, and compared with the results of J_c at 70 K for Ni-doped sample with $x=0.02$. With decreasing particle size of Y211, the J_c increases steadily, as the average particle size reduces to submicron (0.5 μm), the J_c reaches 1.0×10^5 A/cm² at 77 K in zero-field and 4×10^3 A/cm² at 77 K in 5 T. The J_c may be further improved by further reducing the Y211 particle size, but it is not easy to achieve this goal using the conventional method. In a sense, submicron is a limited value of the Y211 average particle size for the samples made with most of the state-of-art techniques. However, the Ni-doped sample shows a much better result at slightly lower temperature (due to the lower T_c). As can be seen in Fig. 5, in the fields higher than 2 T, Ni doped sample exhibits much better performance than Y211-added YBCO samples. These results show that Ni (or Zn) doping is one of the most promising techniques to replace Y211 fine particles as the strong pinning centers. This chemical doping technique is easy to be adopted for introducing strong pinning centers during producing the 123-compound coated conductors.

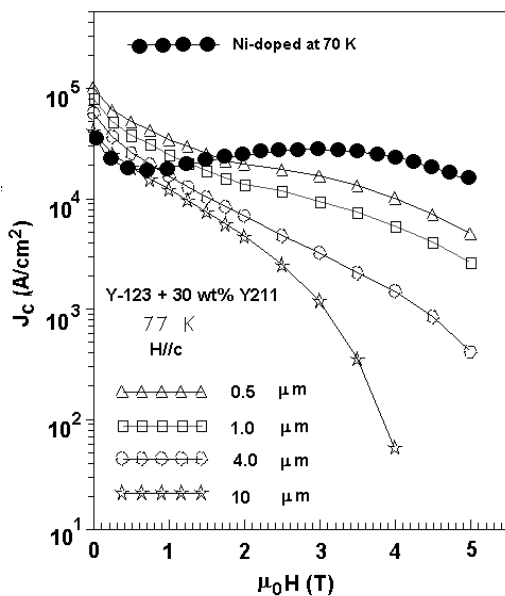


Fig. 5. Comparison of the field dependence of J_c (77 K) for Y211-added samples of different Y211 particle sizes with the field dependence of J_c for Ni-doped sample ($x=0.02$).

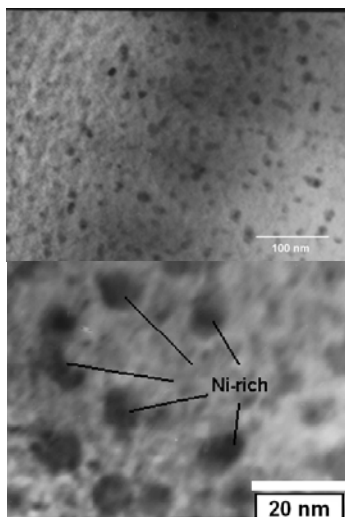


Fig. 6. Upper: TEM micrograph for the Ni-doped YBCO sample. Lower: enlarged Ni-rich nanoparticle in the sample with $x=0.02$.

Microstructure analysis shows that there are many nano-inclusion in Ni-doped YBCO samples (see Fig. 6). EDX analysis shows that these nano-inclusions are Ni-rich, indicating that they were induced by doping NiO. The grain size of the nano-inclusions is about 10 nm, thus approximately matches with the coherence length of YBCO at 77 K. This may be the reason why Ni doping can significantly increase the J_c of YBCO at relatively high temperatures.

It can be seen here that nano-pinning centres (~10 nm) have been successfully introduced into melt textured YBCO by doping NiO. The doping of NiO was realized by adding NiO nanoparticles into presintered YBCO and then followed by melt-textured processing. This method can reduce the substitution level of Ni in YBCO matrix and can create Ni-rich second-phase precipitates with a size around 10 nm. It is found that NiO-induced nano-pinning centres have a high pinning efficiency at a temperature around 70 K. The critical current density is significantly increased and the J_c - H behaviour is remarkably improved. Our results reveal that nano-pinning-centre is a feasible solution to solve the pinning-degradation at high temperature in YBCO.

3. NANOSCALE DEFECTS BY Y211 ADDITIONS IN MELT TEXTURED YBCO SUPERCONDUCTOR

In this study, high quality YBCO textured bulks with various number densities of flux pinning centers have been fabricated by a nanoparticle-powders-assisted MTG (melt-textured-growth) technique. The high density of flux pinning centers has been achieved by adding various proportions of Y211 nanoparticle powders (~50 nm) into the nano-precursors of YBCO. Microstructural and compositional analyses reveal that except for the presence of a high density of Y211 nanoparticles with a size around 100 nm, the YBCO matrix shows a high density of stress with dimensions about 10 nm, indicating that a nanoscale-defect-structure has been achieved in the YBCO bulk materials with a new processing technique. The critical current density at 77 K is systematically increased with increasing density of the nano-scale precipitates, indicating that the nanoscale defects are effective pinning centers in YBCO at 77 K.

The nanoscale YBCO and Y211-particles were prepared by citrate pyrolysis technique. The particle size for most of the YBCO and Y211 grains is around 50-100 nm as revealed by SEM (See Fig. 7). However, TEM analysis shows that the YBCO and Y211 nano-particles have some subgrain structure with a size between 10 to 40 nm. The mixture of precursor nano-powders (YBCO+20wt%Y211) were pressed into disks of a diameter 30 mm and thickness of 15 mm and then pressed again under hydrostatic pressure. The disks were then processed in an isothermal box furnace for a melt-textured growth processing with Sm123 as a seed on the top of the disk (a typical top-seeded melt-textured). The as-grown samples were annealed in flowing oxygen atmosphere at 300°C for 200 hours. DC SQUID magnetometer was used to measure the magnetization loops. J_c was deduced from the $M(H)$ loops (with $H//c$) by Bean Model.

Fig. 8 shows the J_c - H curves at 77 K for melt-textured YBCO prepared by the nanoparticles powders method with the Y211 percentage of 8 wt%, 15wt% and 25wt%, respectively. In the measurements the applied magnetic field is parallel to the c axis. It is

evident that the J_c - H behavior changes systematically with increasing Y211 weight percentage. The fishtail peak in the J_c - H curves shifts towards higher magnetic fields. At the same time, the degradation of J_c with increasing magnetic field becomes slow. For the samples of 25 wt% Y211, the J_c peak is located near the field of 3 T, much higher than the sample of 3 wt% Y211, indicating Y211 addition is also very important for creating flux pinning centers in YBCO, similar to the YBCO textured bulks prepared by the conventional MTG technique.

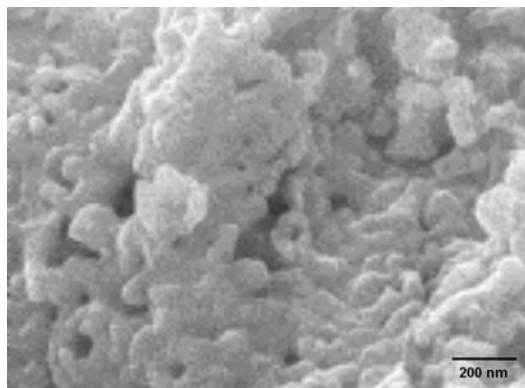


Fig. 7. SEM micrograph for Y123 nanoparticle-powders used as precursors for mel-textured growth.

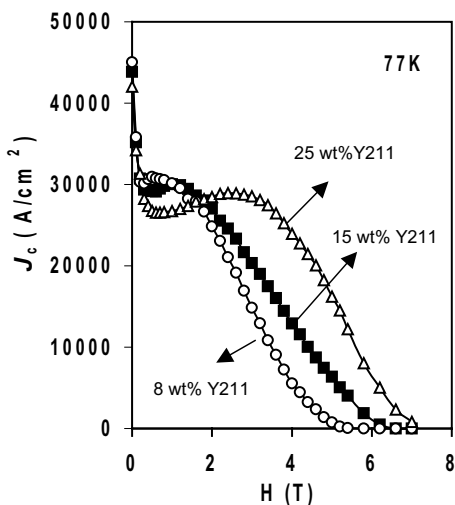


Fig. 8. J_c - H curves at 77 K for melt-textured YBCO prepared by the nanoparticles powders method with the Y211 percentage of 8wt%, 15wt% and 25wt%, respectively.

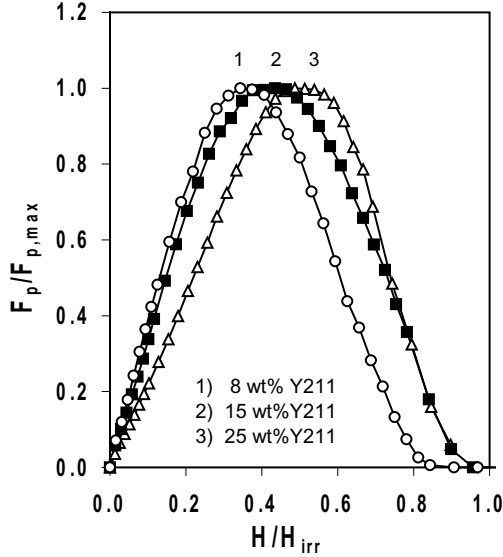


Fig 9. F_p - h curves at 77 K for melt-textured YBCO prepared by the nanoparticles powders method with the Y211 percentage of 3 wt%, 15wt% and 25wt%, respectively.

In order to understand the pinning mechanism of these samples, the scaling-law analysis proposed by Dew-Hughes¹⁸ was used, which has a general expression as

$$F_p/F_{p,max} \sim h^p (1-h)^q \quad (1)$$

where $F_{p,max}$ is the maximum volume pinning force, h the reduced field H/H_{irr} , and the parameters p and q the characteristics exponents reflecting flux pinning types. It is generally believed that the so-called core pinning (i.e., the flux pinning related to non-superconducting defects embedded in the superconducting matrix) is of a value of $h_{max} \sim 0.33$, but the so-called $\delta\kappa$ pinning (i.e., the flux pinning related to the spatial variation of the Ginzburg-Landau parameter κ in the superconductivity matrix) has a value of $h_{max} \sim 0.5$ [31]. As shown in Fig. 9, the sample of 25wt% Y211 has a value of $h_{max} \sim 0.5$, but the sample of 8 wt% Y211 has a $h_{max} \sim 0.34$, reflecting the pinning mechanisms are different in these samples.

The microstructural analysis revealed that these samples contain many Y211 particles with dimensions from 100 nm to 0.1 μm , as typically shown in Fig.10. In addition, there are a large density of twin boundaries and planar defects with dimensions around 100 nm. However, in the samples of $h_{max} \sim 0.5$, it is observed that there are a large density of stress-affected areas with dimensions about 10 nm (as shown in Fig.11). It is highly possible that the large pinning force at a field of 3T may be related with these nanoscale pinning centers.

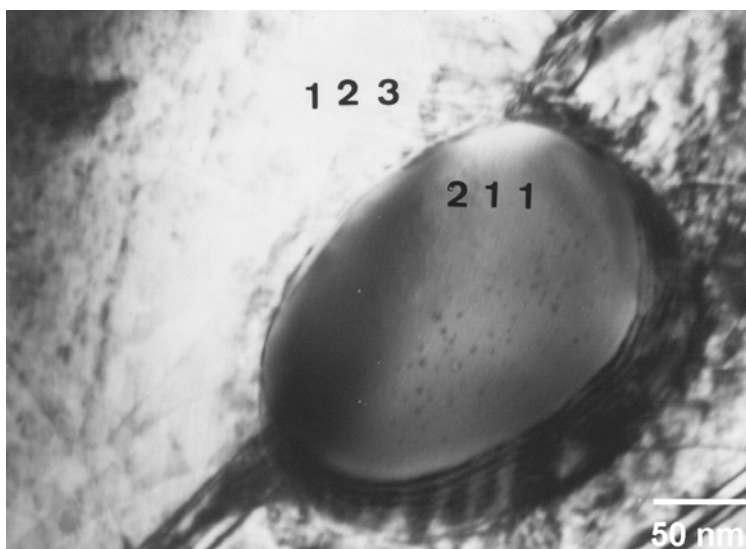


Fig. 10. TEM micrograph showing Y211 particle of a size about 200 nm in most of the samples prepared in this study.

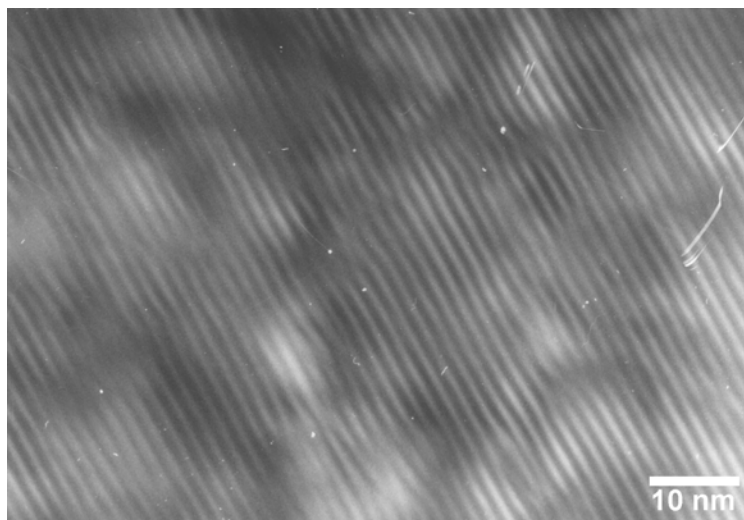


Fig. 11. The typical TEM micrograph for YBCO samples with $h_{\max} \sim 0.5$. It is evident that there is a high density of stress-affected areas of dimensions about 10 nm.

4. NANO-DIAMOND INDUCED FLUX PINNING IN MgB_2

Since the discovery of superconductivity at 39 K in MgB_2 [1], significant progress has been made in improving the performance of MgB_2 materials [17,32,33]. MgB_2 offers the possibility of wide engineering applications in the temperature range 20-30 K, where conventional superconductors, such as Nb_3Sn and Nb-Ti alloy, cannot play any roles due to their low T_c . However, the realization of large-scale applications for MgB_2 -based superconductivity technology essentially relies on the improvement of the pinning behaviour of MgB_2 in high fields. As it has poor grain connection and a lack of pinning centres, MgB_2 often exhibits a rapid decrease in critical current density, J_c , in high magnetic fields. Fortunately, through the formation of nanoparticle structures in bulk MgB_2 [17,32,33] and thin films [34], the problem of the poor grain connection can be solved, and the flux pinning force can also be significantly enhanced due to an increase of pinning centres served by grain boundaries. In order to improve further the performance of MgB_2 , it is necessary to introduce more pinning centres, especially those consisting of nanosized second-phase inclusions, which often provide strong pinning forces.

Nanodiamond, prepared by the detonation technique, has been widely used as an additive to improve the performance of various materials [35]. Yet, nanodiamond has never been used to increase the flux pinning force in MgB_2 superconductors until the present study. The high dispersibility of the nanodiamond powder makes it possible to form a high density of nano-inclusions in MgB_2 matrix. In this letter, we have prepared the MgB_2 -diamond nanocomposite, which consists of tightly-packed MgB_2 nanograins (~50-100 nm) with diamond nanoparticles (~10-20 nm) wrapped within the grains. This unique microstructure provides the composite with a good grain connection for the MgB_2 phase and a high density of flux-pinning centres served by the diamond nanoparticles. Compared to the MgB_2 bulk materials prepared with other techniques, the irreversibility line has been significantly improved and the J_c in high magnetic fields has been largely increased in the MgB_2 -diamond nanocomposite.

The MgB_2 -diamond nanocomposites with compositions of $\text{MgB}_{2-x}\text{C}_x$ ($x=0\%$, 5%, 8%, and 10%) were prepared by solid-state reaction at ambient pressure. Mg powder (99% purity, 325 meshes), amorphous B powder (99% purity, submicron-size), and nanodiamond powder (10-20 nm) were mixed and ground in air for 1 h. An extra 2% of Mg powder was added in the starting materials to compensate the loss of Mg caused by high temperature evaporation. The mixed powders were pressed into pellets with dimensions of $20 \times 10 \times 3 \text{ mm}^3$ under a pressure of 800 kg/cm^2 , sandwiched into two MgO plates, sintered in flowing Ar at $800 \text{ }^\circ\text{C}$ for 2 h, and then quenched to room-temperature in air. In order to compare the substitution effect of carbon in boron in MgB_2 with the additional effect of the nanodiamond in MgB_2 , a sample with an added 1.5 wt% of nanodiamond in MgB_2 was prepared. The sintering temperature and the sintering time for this sample were reduced respectively to $730 \text{ }^\circ\text{C}$ and 30 min in order to reduce the chemical reaction between the MgB_2 and the diamond. This sample has been referred to as "1.5wt%C".

The crystal structure was investigated by powder x-ray diffraction (XRD) using an X'pert MRD diffractometer with Cu $K\alpha$ radiation. The microstructure was analysed with a Philips CM200 field emission gun transmission electron microscope (FEGTEM). DC magnetization measurements were performed in a superconducting quantum interference device (SQUID, Quantum Design MPMS-7). J_c values were deduced from hysteresis loops

using the Bean model. The sample's dimensions with typical values of $0.7 \times 2.1 \times 2.7 \text{ mm}^3$ are used in the calculation of J_c . The values of the irreversibility field, H_{irr} , were determined from the closure of hysteresis loops with a criterion of 10^2 A/cm^2 .

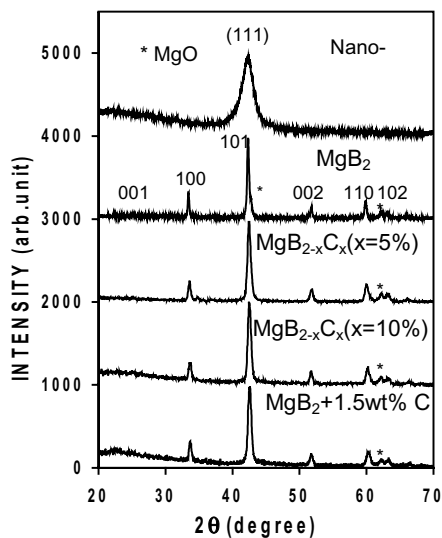


Fig. 12. Powder XRD patterns for MgB_2 -diamond nanocomposites. The pattern on the top row is for the nanodiamond.

Figure 12 shows the XRD patterns of the nanodiamond powder and the typical MgB_2 -diamond composites. The reflection (111) of the diamond is extremely broad and an amorphous-phase-like-background can be seen in the XRD pattern. The particle size of the nanodiamond powder is estimated to be about 20 nm according to the width of the reflection. In relation to the MgB_2 -diamond composites, one of the impurity phases is MgO , which may have formed during the mixing of raw materials in air. Diamond should be present as another impurity phase in the composites; however, its main reflection (111) cannot be seen in XRD patterns, due to an overlap with the MgB_2 (101) peak. As for the sample with the low doping level of $x=5\%$, its XRD pattern looks the same as that of the undoped MgB_2 , except for a decrease of the lattice parameter along the a -axis, indicating that a certain amount of carbon atoms have substituted for boron atoms in MgB_2 . This result is consistent with those reported by other groups, which show that partial substitution of boron by carbon results in a decrease of the lattice parameter [36,37]. With increasing doping level, an amorphous-phase-like background in the XRD pattern gradually appears, suggesting the existence of unreacted nanodiamond in the sample. As for the diamond-added MgB_2 sample (1.5wt% C), which contains an $x=5.4\%$ equivalent percentage of carbon atoms, the background of its XRD pattern shows some similarity to the background of the nanodiamond, suggesting that a substantial amount of unreacted nanodiamond exists within this sample.

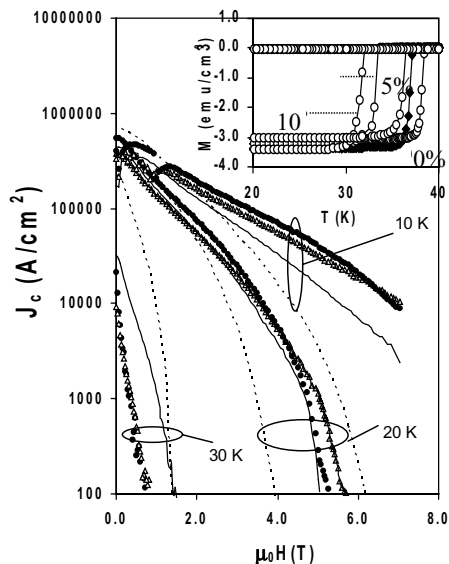


Fig. 13. Magnetic field dependence of J_c at 10, 20, and 30 K for $\text{MgB}_{2-x}\text{C}_x$ with $x=0\%$ (dashed lines), 5% (solid lines), 8% (solid circles), and 10% (open triangles). Inset: superconducting transition curves for the diamond-doped samples. The closed circles represent the results for the sample 1.5wt%C.

The substitution of boron by carbon in our MgB_2 can also be reflected by the gradual decrease of T_c with increasing carbon content (see the inset of Fig.13). The values of onset T_c for these carbon-substituted MgB_2 samples are 38.6 K for $x=0\%$, 36.1 K for $x=5\%$, 33.0 K for $x=8\%$, and 31.3 K for $x=10\%$. The T_c for the sample 1.5wt%C is 36.9 K, which is higher than that for the sample of $x=5\%$ ($T_c=36.1$ K), despite the former having a higher equivalent atomic percentage of carbon ($x=5.4\%$).

Figure 13 shows the magnetic field dependence of J_c at 10, 20, and 30 K for the carbon-substituted MgB_2 samples. At 30 K, the undoped MgB_2 exhibits the highest J_c and the slowest decrease of J_c with H ; whereas the sample of $x=10\%$ shows the lowest J_c and the quickest drop of J_c with H . It is evident that the J_c - H behaviour at 30 K for these samples is positively correlated to their T_c values. However, when the temperature decreases to the values far below T_c , a totally different situation appears. For example, at 10 K and 20 K, the diamond-doped samples show a much better J_c - H behaviour. The J_c drops much more slowly in diamond-doped samples than in pure MgB_2 . The best J_c at 20 K is found in the sample of $x=10\%$, reaching a value of 6×10^3 A/cm² in a 4 T field, indicating that a strong flux pinning force exists in these diamond-doped samples.

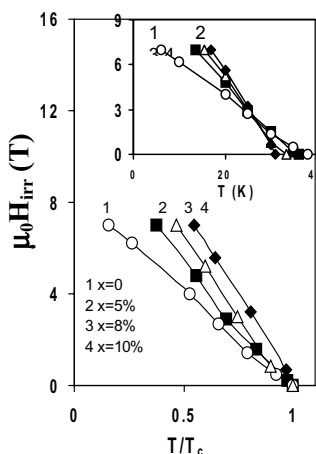


Fig. 14. Variation of H_{irr} with reduced temperature T/T_c for $MgB_{2-x}C_x$ with $x=0\%$, 5% , 8% , and 10% . Inset: $H_{irr}-T$ plot for the same data shown in the main figure.

The $H_{irr}-T$ relations for the diamond-substituted MgB_2 are shown in the inset of figure 14. The $H_{irr}(T)$ curves get steeper with increasing doping level. The best value of H_{irr} reaches 5.7 T at 20 K for the sample of $x=10\%$. As the T_c values vary with the diamond-doping level, only the $H_{irr}-T$ relation cannot directly reflect the intrinsic irreversibility behaviour for the samples of different doping levels. In the main panel of Fig.14, the temperature dependence of H_{irr} is replotted using a reduced temperature, T/T_c . It is evident that the irreversibility field shifts towards higher temperatures with the increase of the diamond-doping level. The result clearly shows that the diamond doping does enhance the flux pinning in MgB_2 significantly.

However, the effect of diamond doping on the enhancement of flux pinning in MgB_2 may be counterbalanced by its suppression on superconductivity, as clearly shown in the situation of $T=30$ K (see Fig.13). This counterbalancing effect may also exist at other temperatures, even when the effect of the J_c -enhancement is dominant. The further increase of J_c depends critically on reducing the T_c -suppression effect in the MgB_2 -diamond composite. This idea is confirmed by the results obtained in the diamond-added sample, 1.5wt% C, which has a higher T_c than other diamond-doped samples (see inset of Fig.13) and contains more nanodiamond inclusions as suggested by the XRD analysis (see Fig.12) and confirmed by our TEM analysis shown below. As shown in figure 15, the diamond-added sample shows a much better J_c-H behaviour than the carbon-substituted sample. Its J_c reaches 1×10^4 A/cm² at 20 K and 4 T, and its H_{irr} reach 6.4 T at 20 K. In fact, at all temperatures below 35 K, the J_c-H behaviour (results at 20 K are shown here only) and the $H_{irr}-T$ relation (see the inset of Fig.15) of the diamond-added sample are much better than those of other samples in this study.

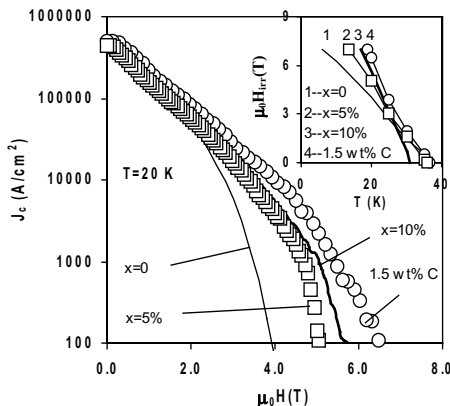


Fig.15. Comparison of J_c - H relations at 20 K for diamond-added MgB_2 sample 1.5wt%C with diamond-substituted MgB_2 . The atomic percentages of carbon in the sample 1.5wt%C and the sample of $x=5\%$ are almost the same. Inset: H_{irr} - T relations for the same samples shown in the main figure.

Fig.16 shows the typical results from microstructural analysis for the diamond-substituted MgB_2 and diamond-added MgB_2 samples. The diamond-substitutional sample mainly consists of relatively large MgB_2 grains (~ 1 micron or so in size) with a high density of dislocations. In some areas, discrete nanosized particles can be seen (Figs.16a , 16b). The diamond-added sample mainly consists of two kinds of nanoparticles: MgB_2 grains with a size of 50-100 nm and diamond particles with a size of 10-20 nm (see Fig.16c). In fact, this diamond-added MgB_2 forms a typical nanocomposite material. The nanodiamond particles are inserted into the MgB_2 grains. As the ab -plane coherence length of MgB_2 is about 6-7 nm [38], these 10- to 20-nm-sized diamond inclusions, with a high density, are ideal flux pinning centres and are responsible for the high performance in our samples.

The significant improvement of J_c and H_{irr} in the nanodiamond-added samples (1.5wt%) can be attributed to their nanocomposite structure which consists of two kinds of nanoparticles: MgB_2 grains with a size of 50-100 nm and diamond particles with a size of 10-20 nm. The enhanced number of grain boundaries associated with the smaller grain size can enhance the flux pinning, as reported previously [17,32-34]. However, only this factor cannot fully explain the experimental results because the enhancement of flux pinning in the nanodiamond-added samples (1.5wt%) is even much better than that in the Ti-doped MgB_2 [17,32,33] where the average grain size of MgB_2 reaches 8-10 nm. This indicates that there may be other mechanisms of flux pinning enhancement in the present system. One of the most likely candidates is the diamond nanoparticles which may play a similar role as Y_2O_3 nanoparticles did in Y_2O_3 -doped MgB_2 [39]. It is worth noting that, compared to the Y_2O_3 Y_2O_3 -doped MgB_2 , the nanodiamond-added samples (1.5wt%) has a higher J_c and H_{irr} . This may be due to the advantage of the nanodiamond whose lattice contact (for the cubic diamond $a=0.356$ nm) is very close to the c -axis of MgB_2 ($c=0.352$ nm). Therefore, these diamond nanoparticles may provide nucleation centres for MgB_2 and are tightly bound to them. It has

been reported that some undoped MgB_2 samples with a slight grain texture also show a high J_c and H_{irr} (see, for example, Narozhnyi et al [40]), suggesting that achieving a textured microstructure is another effective way to improve J_c of MgB_2 because of a slight anisotropy existing in this system. Accordingly, it is expected that the performance of the MgB_2 -diamond nanocomposite may be further improved by optimising the microstructure and the doping levels.

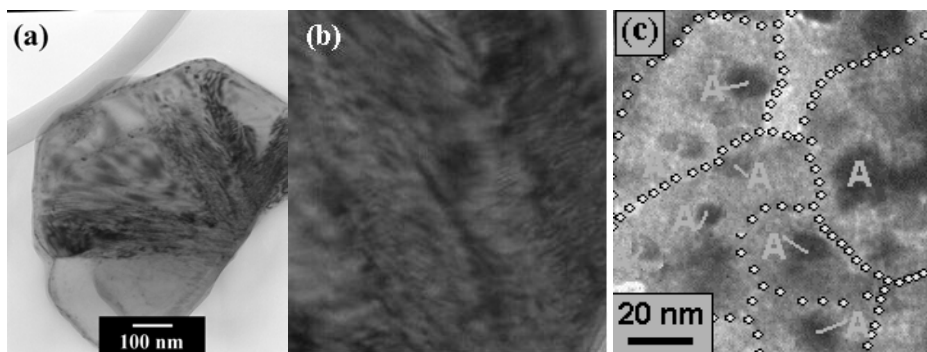


Fig 16. FEGTEM micrographs for (a) a typical grain ($\sim 1 \mu\text{m}$) of diamond-substituted MgB_2 with $x=5\%$ which shows the high density of dislocations (dark stripes) in the sample; (b) an enlarged view of the dislocations in Fig. 5a; (c) diamond-added MgB_2 with the carbon content of 1.5 wt%. The grain boundaries of MgB_2 are indicated by the guidelines. The diamond nanoparticles are marked by letter “A” beside it (for small ones) or on the particles (for big ones). The atomic percentages of carbon in these two samples are almost the same.

5. NANO-SiO₂ INDUCED FLUX PINNING IN MgB_2

Since the improvement of the pinning behaviour in MgB_2 has been one of the focuses in the superconductivity field, many approaches, such as high energy ion irradiation [41, 42], chemical doping using different elements [17,32,33,39,43] and nanoparticle addition [44–47] (which seems to be the best and most practical route), have proved successful to some degree. However, for most of the approaches, the enhancement of the flux pinning in MgB_2 is at the price of sacrificing other desirable superconducting properties, especially high T_c , and therefore the performance of MgB_2 at high temperatures is degraded. Hence, currently, there is an urgent need to develop a way to improve J_c and H_{irr} without depressing T_c for MgB_2 . In this work, we show that the addition of SiO_2 nanoparticles is a promising means for achieving this end.

MgB_2 pellets were prepared by solid-state reaction at ambient pressure. Powders of magnesium(99.9%pure) and amorphous B (99.9%, pure) were well mixed with SiO_2 nanopowder (10–20 nm) with the stoichiometry of $\text{MgB}_2(\text{SiO}_2)_x$, $x = 2\%, 5\%, 7\%, 10\%, 15\%$. An extra 2% of Mg powder was added to the reacting materials to compensate for the

loss of Mg caused by high temperature evaporation. Pellets with dimensions of 20 mm × 10 mm × 2 mm were made under a pressure of 20 MPa, packed in Ta foil, sealed in quartz tubes and heated at 650 °C for 45 min, 720 °C for 30 min, in flowing highly pure Ar, and quenched to room temperature in air. The crystalline structure was investigated by powder x-ray diffraction (XRD) analysis using an X'pert MRD diffractometer with Cu K α radiation. The microstructural analysis was carried out with a Philips CM200 field emission gun transmission electronic microscope. The DC magnetization of the samples was measured using a superconducting quantum interference device (SQUID; Quantum Design MPMS). The typical dimensions of the samples for the magnetization measurement were 0.21×0.21×0.21 mm³. The magnetic J_c was deduced from hysteresis loops using the Bean model. The irreversibility field (H_{irr}) was obtained from the closure of hysteresis loops with a criterion of 100 A cm⁻².

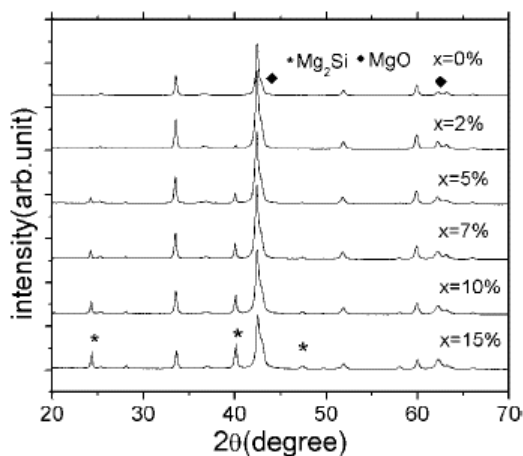


Fig. 17. X-ray diffraction patterns for the samples. MgSi₂ phase is found in specimens with SiO₂ addition.

Figure 17 shows the x-ray diffraction patterns for SiO₂-supplemented MgB₂ samples with different additive contents. MgO is the common impurity phase in these samples. In SiO₂-supplemented samples, another impurity phase is found: MgSi₂, whose content increases with increase of the content of the additive SiO₂. As revealed by x-ray diffraction analysis, there is no detectable sign of SiO₂ reflections. It is likely that SiO₂ has reacted with Mg, consuming SiO₂ and forming MgSi₂. This result is different from our original intended outcome: that SiO₂ would not react with other elements in MgB₂ samples, but only serve as an impurity phase. The main reflections of MgB₂ generally show a trend of moving towards low angles, implying an increase in the lattice parameters. As revealed by Rietveld refinement, the lattice parameter c of MgB₂ exhibits a significant increase at 2% content of the additive SiO₂. The lattice parameter c gradually saturates with further increasing content of the additive SiO₂, as shown in figure 18. In contrast, the lattice parameter a is nearly unchanged, with a

fluctuation between 3.0839 and 3.0847 Å. The partial substitution of Si for B may allow an increase of the lattice parameter c and stability of the lattice parameter a . The saturation for the c axis with additive content at 2% suggests that the solubility limit of Si in MgB₂ is relatively low ($x \ll 2$ wt%). The temperature dependence of the DC magnetization for these samples is shown in the inset of figure 18, from which the transition temperature (T_c) has been determined. T_c for the pure sample is 38 K, but it is almost the same ($T_c = 37.2$ K) for all of the SiO₂-supplemented samples, depressed only by 0.8K. This indicates that almost the same amount of Si is doped into the MgB₂ lattice although the nominal composition is quite different, consistent with the results of the phase analysis.

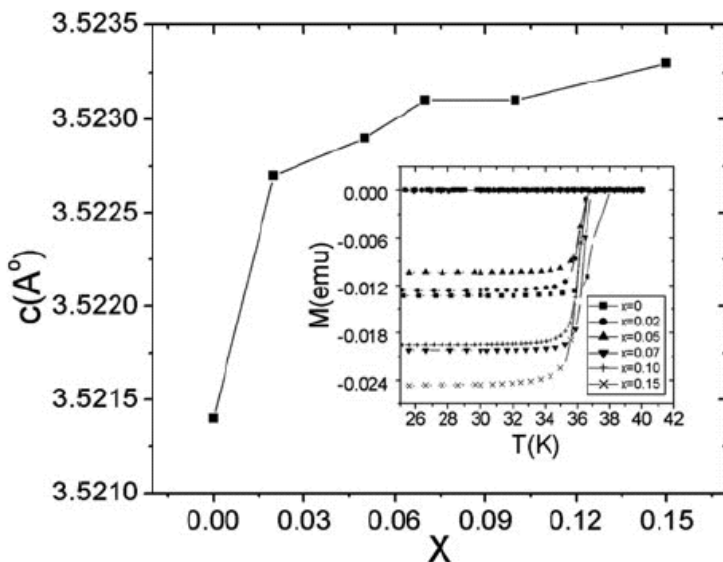


Fig.18. The change of the lattice parameter c for the samples with SiO₂ addition. Inset: temperature dependent magnetization curves measured in the ZFC condition in 20 Oe for the samples.

Figure 19 shows the magnetic field dependence of J_c at 10, 20 and 30 K for these samples. The $J_c(H)$ behavior exhibits a complex change with the additive content, x . In low magnetic fields, the J_c value of the SiO₂-supplemented MgB₂ samples increases with x in the low additive content region ($x < 7\%$), reaching a maximum near $x = 7\%$, then decreases with further increasing additive content and, at $x = 15\%$, drops to a value smaller than that for the pure MgB₂ sample. The best J_c is obtained for the 7% SiO₂-supplemented sample, reaching 2.5×10^5 A cm⁻² at 20 K and 1 T. In high magnetic fields, the improvement of J_c achieved by adding SiO₂ nanoparticles is not as significant as that in the low fields; as a result, the irreversibility field, H_{irr} , of the SiO₂-supplemented MgB₂ is not improved much.

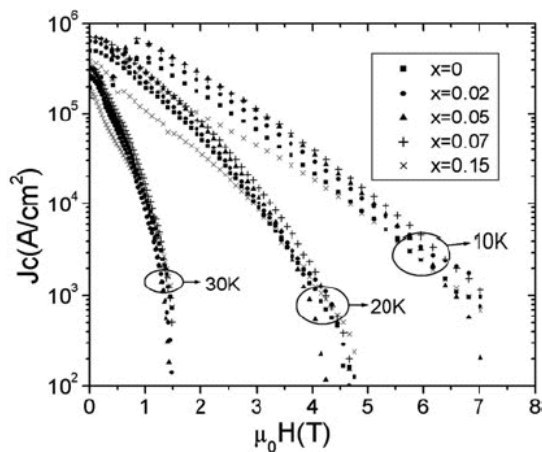


Fig. 19. J_c versus magnetic field at 10, 20 and 30 K for the samples with $x = 0, 2\%, 5\%, 7\%$ and 15% .

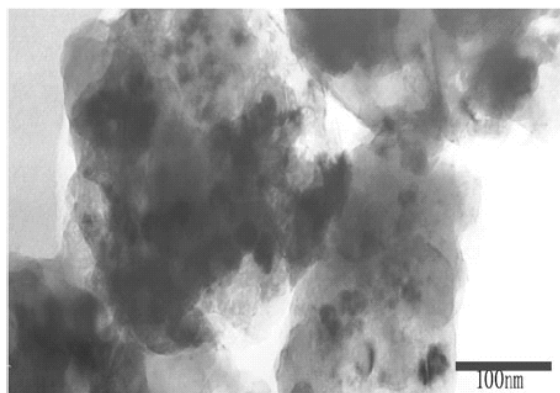


Fig. 20. A TEM image showing the second-phase particles in the MgB_2 matrix for 7% content of the additive.

As shown in figure 20, which presents a typical microstructure for the sample with $x = 7\%$, some fine particles (10–50 nm) of the second phase induced by the addition of SiO_2 are dispersed in the MgB_2 matrix with a thin and clear interface boundary. EDS analysis reveals that the grains are MgSi_2 , consistent with the results of XRD analysis. This unique microstructure has been observed in MgB_2 samples doped with nanodiamond particles [18,19], in which the nanopinning centres play a significant role in improving the J_c – H behaviour and the irreversibility field. There is more and more evidence that nanosized flux pinning centres are efficient in improving the J_c – H behaviour and directly increasing the J_c

value and the irreversibility field [17-19,32]. The improved J_c - H behaviour of MgB_2 achieved by SiO_2 nanoparticle addition can also be attributed to the formation of such nanosized pinning centres. However, the improvement of J_c , especially the improvement of H_{irr} , achieved by adding SiO_2 nanoparticles into MgB_2 is not as significant as that achieved by adding other dopants, for example by doping with nanodiamond powder [18,19], where a J_c value of $1 \times 10^4 \text{ A cm}^{-2}$ at 20K and 4T and a H_{irr} value of 6.4 T at 20K have been achieved. This discrepancy may be attributed to their different microstructures. The diamond-supplemented sample mainly consists of two kinds of nanoparticle: MgB_2 grains with a size of 50–100 nm and diamond particles with a size of 10–20 nm. These 10–20 nm sized diamond inclusions are inserted into the MgB_2 grains and work as effective pinning centres. In the present SiO_2 -supplemented MgB_2 samples, although MgSi_2 also forms nanosized pinning centres in MgB_2 grains, their size is about 50 nm, significantly larger than that of the nanodiamond particles. As the ab plane coherence length of MgB_2 is about 6–7 nm, pinning centres with a size about 10–20nm should have better pinning efficiency. Another possible reason for the discrepancy is the decrease in volume of the superconducting phase in SiO_2 -supplemented MgB_2 . Because of the formation of MgSi_2 and MgO , the amount of MgB_2 phase is accordingly decreased, which decreases the effective superconducting volume and, more seriously, some impurity phases must stay in the grain boundary region, resulting in a weak link effect in the system. The above results show that there is a great potential for further improving the performance of SiO_2 -supplemented

6. FLUX PINNING INDUCED BY COMPOSITION FLUCTUATIONS IN OVERDOPED CU-RICH $\text{Bi}_2\text{Sr}_2\text{CaCu}_2\text{O}_{8+x}$ SINGLE CRYSTALS

Short coherence length, large anisotropy and penetration depth are features of high temperature superconductors (HTSC's), especially of those with higher T_c and larger anisotropy like $\text{Bi}_2\text{Sr}_2\text{CaCu}_2\text{O}_{8+x}$ ($\text{Bi}2212$), resulting in giant thermal fluctuations and poor pinning behavior at high temperature (close to T_c) or in strong magnetic field. Irradiation with very energetic heavy ions or neutrons which yields the so-called columnar defects is expected to be an effective way to improve the flux pinning in Bi-systems [48,49]. Alternately, several recent reports[50-52] show that the pinning behavior has been significantly improved in the hole overdoped $\text{Bi}2212$, thus providing a more efficient, realistic, and economic way to improve the materials for practical applications. However, the mechanism of this improvement is not fully elucidated due to the combination of many possible factors involved, such as defect effect caused by cation-doping, columnar defects, reduction of the anisotropy parameter, variation of superconductivity, and possibly the inhomogeneous distribution of the cation dopants [49-52]. On the other hand, the explanation for the irreversibility line, which is an important mark for the pinning behavior, is still contradictory [48-56].

By using high quality single crystals in which no cation doping is involved, and all transitions (including superconducting-normal transition, dimensional crossover transition, etc.) are very sharp and clear, we investigate pinning behavior and irreversibility line in heavily overdoped Cu-rich Bi-2212 single crystals, and explore the mechanisms associated with the phenomena observed. For the overdoped crystals, the anisotropy parameter is significantly reduced, the second magnetization peak is largely heightened, and the crossover field is greatly shifted to a higher field.

The Cu-rich Bi2212 single crystals used in this study were grown by a traveling solvent floating zone method, as described elsewhere [57]. Compositional analysis made by inductively coupled plasma (ICP) method shows that the composition of Bi2212 single crystals is Cu-rich with the ration of Bi:Sr:Ca:Cu=2:2:0.9:2.1. Magnetic susceptibility and magnetization measurements with an applied field parallel to the c axis were carried out using a superconducting quantum interference device (SQUID) magnetometer. The irreversibility line was determined by checking the superposition of the susceptibility curves in zero field cooling (ZFC) and field cooling (FC), at different applied fields. The overdoped Bi2212 crystals with $T_c=72$ K were acquired by annealing the as-grown crystal at 400 °C in flowing oxygen for 7 days. The dimensions of the crystal used in this study are $0.7 \times 1.9 \times 0.01$ mm³.

The magnetic hysteresis loops of the overdoped Bi2212 crystal were measured at various temperatures from 10 K ($0.14 T_c$) to 65 K ($0.903 T_c$) with a field-sweeping rate of 0.1 mT/sec. Some typical results are shown in Fig. 21. In the high temperature region ($35 \text{ K} < T < T_c$), there is only one peak (first peak) observed in each hysteresis loop, which corresponds to the initial flux penetration. The position of the first peak is depicted as H_{p1} . As decreasing temperature, a giant second peak appears in the low temperature region ($10 \text{ K} < T < 35 \text{ K}$). Some features of the second peak in the present system are described below.

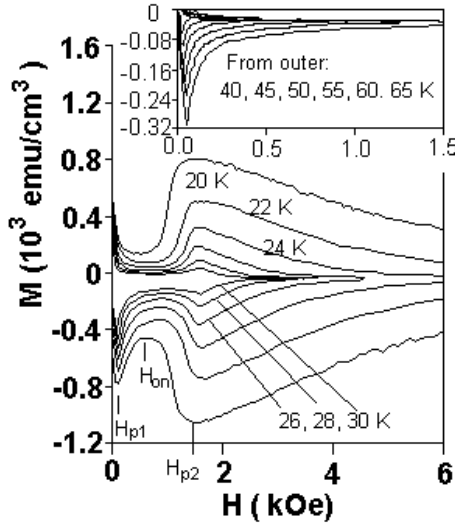


Fig. 21. Magnetic hysteresis loops for overdoped Bi2212 at low temperature region which show second peak. Inset: The loops at high temperature region.

First, the position of the second peak, denoted as H_{p2} , is temperature independent, same as that observed in optimally-doped Bi2212 [53]. This kind of phenomenon has been well explained as the crossover from three-dimensional (3D) to two-dimensional (2D) vortex system. At sufficient low temperature, the flux lines are supposed to decouple in a stack of vortex pancakes and form a 2D vortex solid [54]. The crossover field is expressed:

$$B_{cr} = 2\pi \frac{\phi_0 \ln(\gamma d / \xi_{ab}(0))}{\gamma^2 d^2} \quad (2)$$

where ϕ_0 is the flux quantum, γ the anisotropy parameter; $\xi_{ab}(0)$ the coherence length in ab planes, and d the spacing between superconducting layers. What the interesting is that the B_{cr} in overdoped Bi2212 is as high as about 0.16 T, close to the value of B_{cr} for the Bi2212 containing columnar defects [48], whereas the B_{cr} for optimally-doped system is usually around 0.04 T. According to Eq.(1) and using $d = 1.54$ nm, γ is roughly estimated as 70 for this overdoped Bi2212, which is very close to 66, the resistive anisotropy measured at 150 K for the same sample. The result indicates that the overdoped Bi2212 is much less anisotropic than the optimally-doped Bi2212.

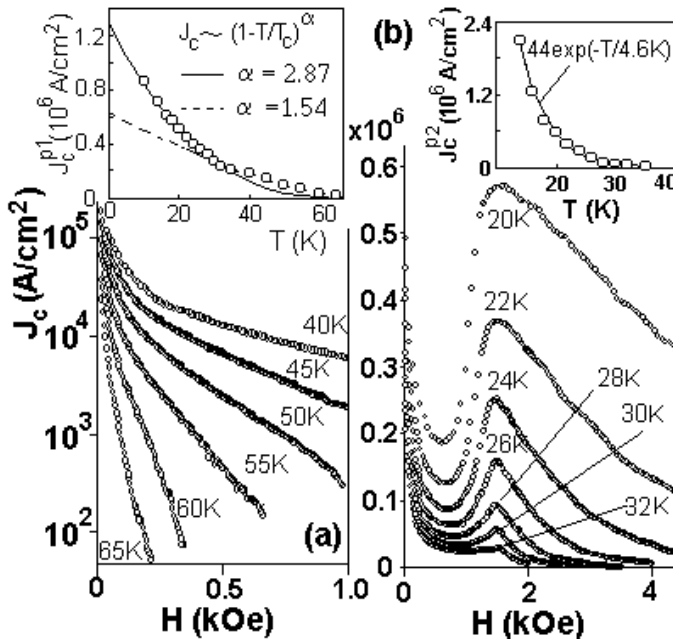


Fig. 22. (a) $J_c(H)$ curves in high temperature region. Inset: Temperature dependence of J_c^{p1} . (b) $J_c(H)$ curves in low temperature region. Inset: Temperature dependence of J_c^{p2} .

Second, the height of the second peak increases much faster than that of first peak with decreasing temperature, and exceeds the height of the first peak as $T < 25$ K. Such a phenomenon is usually observed in some less anisotropic systems [55,56], like $\text{YBa}_2\text{Cu}_3\text{O}_y$, $\text{Nd}_{2-x}\text{Ce}_x\text{CuO}_{4-y}$ etc, and seldom seen in the Bi2212 system. By using the modified Bean model, the critical current densities of the sample at different temperatures were deduced and illustrated in Fig.22. The temperature dependence of J_c at H_{p1} (denoted as J_c^{p1}) obeys a power

law of $J_c^{p1} \propto (1 - T/T_c)^\alpha$ with $T_c = 72$ K and $\alpha = 1.54$ in high temperature region and $\alpha = 2.87$ in low temperature region (see the inset of Fig.22a), whereas that of J_c at H_{p2} (denoted as J_c^{p2}) follows an exponential law of $J_c^{p2} = A \exp(-T/T_0)$ with $A = 4.4 \times 10^7$ A/cm² and $T_0 = 4.6$ K (see the inset of Fig.22b).

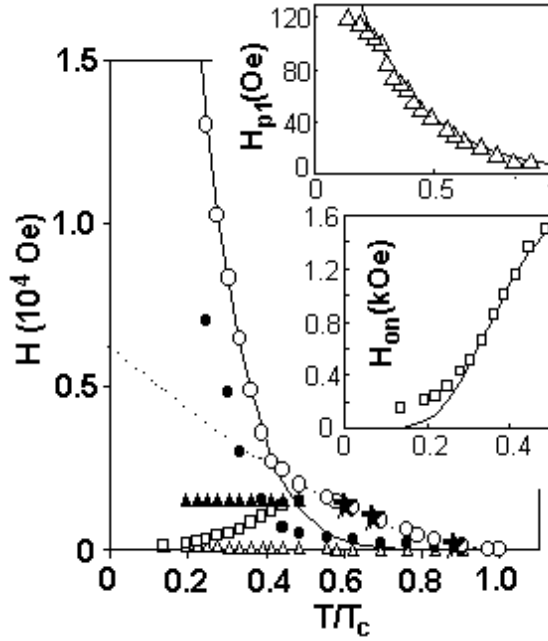


Fig. 23. H - T phase diagram. Open and solid circles are the data of H_{irr} for overdoped and optimally-doped Bi2212, respectively. Open and solid triangles are H_{p1} and H_{p2} , respectively. Square is H_{on} . The dotted and solid lines are power law and exponential law fits for $H_{irr}(T)$ in high and low temperature regions, respectively. Upper inset: $H_{p1}(T)$ and a fit with exponential law. Lower inset: $H_{on}(T)$ and a fit with $\exp(-T_e/T)$. The stars represent the vortex lattice melting points determined by resistive measurement.

In addition, the onset field for the second peak (denoted as H_{on}) exhibits an anomalous change with temperature--which increases with increasing temperature, opposite to the behavior of H_{on} observed in other overdoped systems [50,52,56].

The temperature dependences of H_{p1} , H_{p2} , and H_{on} , together with the irreversibility lines for optimally-doped and overdoped Bi2212, are shown in Fig.23. As can be seen in Fig.23, the irreversibility line of the overdoped Bi2212 shifts to higher temperatures compared with the optimally-doped Bi2212, indicating the enhancement of flux pinning. The temperature dependence of the irreversibility field exhibits a quite different behavior below and above the

crossover field. Below the crossover field, $H_{irr}(T)$ data are well fitted by a power law of $H_{irr} \sim (1-T/T_c)^n$ with $n=1.8$ and $T_c=72$ K. This behavior can be interpreted by the coincidence of the irreversibility line with the 3D vortex lattice melting, as observed by Schilling et al [58]. This coincidence is also confirmed by our resistive measurement (see the data represented by stars in Fig.23). Above the crossover field, the data are well fitted with an exponential law of $H_{irr} \sim \exp(-T/T_i)$ with $T_i=3.8$ K. This exponential behavior has been widely observed in HTSC's [51,56], however, the explanation of its origin is quite contradictory. For example, Schilling et al [58] suggested that the $H_{irr}(T)$ is the quasi-2D vortex lattice melting line, while Wen et al [51] explained it as the depinning line of a granular superconducting system. In $\text{Nd}_{2-x}\text{Ce}_x\text{CuO}_{4-y}$, it was interpreted as the consequence of surface barrier[56]. Our analyses below exclude these scenarios as a proper explanation for our data.

At first, according to the 2D melting theory[54], a field-independent melting temperature T_m^{2D} can be estimated by

$$T_m^{2D} \approx \frac{d \phi_0}{2 \sqrt{3} \mu_0 k_B (4 \pi \lambda_{ab}(0))^2} \quad (3)$$

With $\gamma=70$, $d=1.54$ nm, and $\lambda_{ab}(0)=150$ nm, the T_m^{2D} is found to be about 31 K, which is too high to fit our data at low temperatures. In addition, our data cannot also be fitted by the quasi-2D melting model, proposed by Scilling et al[58] and expressed as

$$B_m(T) \approx \frac{\phi_0}{d^2 \gamma^2} \exp\left(\frac{\phi_0^2 c_L^2 d}{2 \mu_0 \lambda_{ab}(0) k_B T}\right) \quad (4)$$

where c_L is the Lindemann number, and $\lambda_{ab}(0)$ the penetration depth in ab plane.

Recently, in order to explain the anomalous vortex pinning behavior in the vicinity of H_{c2} in Tl2201 single crystal, Geshkenbein et al[59] proposed that in a certain of granular superconducting system, the temperature dependence of the phase ordering field, B_G , obeys an exponential law as

$$B_G \propto (E_J^0 / T) \exp(-T / T^*) \quad (5)$$

where E_J^0 is the intergrain coupling energy and $T^*=v_F/2\pi A$, with v_F the Fermi velocity of the normal matrix and A the average intergrain spacing. The value of T^* can be deduced to be $T^*=9.95$ K from the experimental data and, accordingly, the value of A is estimated to be $A=200\text{\AA}$ by assuming $v_F=1\text{eV}$ as in Ref. 59. This value of A is one order of magnitude smaller than that obtain in Tl2201 system[59], indicating that the density of higher T_c grains in our Bi2212 system would be much higher. If it would be the case, the effect of these higher T_c grains would have been detected in the transport measurement as what we have observed in Bi2212/Bi2223 intergrowth single crystals which showed anomalous peak in a transformer configuration of the electrodes and a two-step transition in the normal 4-probe measurement[60]. However, no any trace of higher T_c phase have been observed in the transport measurement with both the 4-probe configuration and the transformer one. Therefore, we do not believe this granular superconducting model is the right explanation for our data.

We also checked the behaviors of $H_{p1}(T)$ and $J_c^{p1}(T)$ to test if the surface barrier model is suitable or not to explain our data. The $H_{p1}(T)$ curve can be well fitted by exponential law of $H_{p1} = H_{p1}(0)\exp(-T/T_s)$ with $H_{p1}(0)=270$ Oe and $T_s=19.5$ K (upper inset of Fig.23). This exponential behavior is the consequence of the Bean-Livingston surface barrier effect for thermally activated 2D pancake vortices[61], and similar to the behavior of $H_{irr}(T)$ in low temperature region. In $Nd_{2-x}Ce_xCuO_{4-y}$, a similar phenomenon was observed and used as the basis for the conclusion that the irreversibility line is controlled by the surface barrier[56]. If it is the case in our sample, $J_c^{p1}(T)$ should have a similar behavior because it is related to H_{p1} more directly and closely. Unfortunately, $J_c^{p1}(T)$ does not obey exponential law at all. In fact, H_{p1} is not sensitive to the dimension crossover—its behavior is not changed by the occurrence of the second peak and thus has very limited relation with the bulk pinning, while both $J_c^{p1}(T)$ and $H_{irr}(T)$ exhibit a change in their temperature dependences before and after the dimension crossover. Therefore, it is hard to conclude that the surface barrier is a dominant factor for the behavior of irreversibility line.

In our picture, the exponential behavior of the irreversibility line is the result of depinning of the 2D vortex lattice which obeys the collective pinning theory. As mentioned earlier, the behavior of $J_c^{p2}(T)$ also obeys an exponential law. This can be explained as the consequence of the collective pinning served by many weak pinning centers in the crystal. According to the general collective pinning theory[62], the creep of current density has a form as the following:

$$J_c(t) = J_c(0)[1 + (\beta T/U_0)\ln(1 + t/t_0)]^{-1/\beta} \quad (6)$$

where $J_c(0)$ is the critical current density at $T=0$, U_0 the barrier height, t_0 the relaxation time, $\beta=9/8$ for 2D system. As J_c approaches $J_c(0)$, Eq.(6) approaches an asymptotic form of $\exp(-T/T_0)$, which is the form that we have observed for both $J_c^{p2}(T)$ and $H_{irr}(T)$. In principle, both J_c and H_{irr} have a same origin—depinning of the vortex lattice, so the same temperature behavior of these two quantities convinces us that $H_{irr}(T)$ line here is only the vortex depinning line as $B > B_{cr}$.

The anomalous behavior of H_{on} mentioned earlier can also be interpreted according to the dimensional crossover of the layered superconducting system. The crossover occurs as the interlayer Josephson coupling vanishes. For HTSC's like Bi2212 in which the resistivity in c direction shows a semiconductive behavior, the interlayer Josephson coupling takes a form as[62]

$$E_c(T) = E_0(1 - T/T_c)^2 \exp(-T_E/T) \quad (7)$$

where E_0 is a constant for a given system, and T_E is a temperature related with the energy gap of the semiconducting layer between the superconducting layers, which is about 80 K for our system. According to Eq. (7), at the temperature below $T_c/2$, the temperature dependence of the coupling strength dominates by the exponential factor. As can be seen in the lower inset of Fig.23, H_{on} data can be roughly fitted by the $\exp(-T_E/T)$ law. If T_E is much lower than T_c , the power law factor in Eq.(7) will be dominant and a quite different temperature behavior can be observed, as reported by other groups [50,52,56].

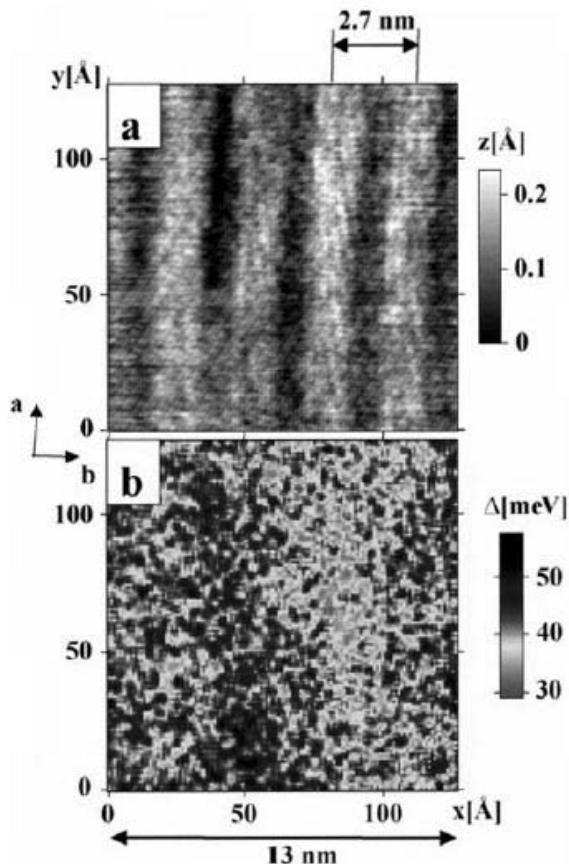


Fig. 24. STM/STS images of the Bi2212 cleaved surface at $T = 77$ K in an area of 13×13 nm². (a) Constant current STM topograph; $V_s = 0.1$ V and $I_t = 0.4$ nA. (b) The corresponding spatial map of the energy gap Δ estimated from differential conductance spectra. The STM image clearly shows the modulation whose wavelength \tilde{e} is about 2.7 nm. The gap map indicates an inhomogeneous distribution with a few nanometres scale but no correspondence to the modulation with $\lambda \ll 2.7$ nm.

From the above-mentioned results and discussion we can see that the origin of the second peak is the consequence of the switch of the flux pinning from 3D flux line pinning to 2D collective pinning. Because the defect structure in such a pure Bi2212 single crystal is dominated by many weak, point-typed defects associated with oxygen content, the pinning force is relatively low when the vortices are in the state of flux line lattice. As the flux lines are disassociated into 2D vortex pancakes, the total flux pinning force is suddenly increased by the 2D collective pinning effect and the second peak in magnetization curve appears. Our

results show that the pinning force of the point defects in both 2D and 3D vortex regions is enhanced as the anisotropy of the system decreases. Therefore, the $H_{irr}(T)$ curve shifts to higher temperatures and the second peak becomes more pronounced in overdoped system. It can be expected that with further decreasing anisotropy and increasing interlayer Josephson coupling, the crossover field will be pushed to higher field, and the pinning force will be further enhanced in Bi2212.

In order to further understand the pinning mechanism of the Cu-rich Bi2212, we have performed atomic-scale high-resolution scanning tunneling microscopy and spectroscopy measurements on the cleaved surface of single crystal $\text{Bi}_2\text{Sr}_2\text{CaCuO}_{8+y}$ superconductors with high critical current density J_c . The samples exhibited rugged structure about 15 nm in period, larger than the modulation of the BiO layer, which corresponded well to the energy gap distribution at 77 K. The presence of inhomogeneity from a nanometer to a micrometre scale, in the energy gap distribution, the structural modulation and the chemical composition fluctuation, may play an important role in improving J_c values in the $\text{Bi}_2\text{Sr}_2\text{CaCuO}_{8+y}$ crystals.

Nano-scale structures and local electronic density of states were studied with an ultrahigh-vacuum (UHV) low temperature STM instrument equipped with a low-temperature cleavage stage. The base pressure of the STM chamber was maintained below 2×10^{-10} Torr during measurements. All samples examined were cleaved *in situ* at 77 K to avoid oxygen loss from the sample surface. Mechanically sharpened Pt-Ir alloys were used as STM tips. The differential conductance dI/dV curves (tunneling spectra) as a function of the in-plane (x, y) tip position, where the tip-to-surface distance z is fixed after each STM imaging, is referred to as scanning tunneling spectroscopy (STS). This measurement mode allows us to obtain the topographic image as well as the spatial variation of the tunneling spectra. The STM and STS data acquisition was performed simultaneously.

Figure 24 shows STM/STS images at $T = 77$ K in an area of $13 \times 13 \text{ nm}^2$. Figure 24(a) is a constant current STM topograph. Figure 24(b) is the corresponding spatial map of the superconducting gap value Δ estimated from differential conductance spectra. The STM image clearly shows the modulation whose wavelength λ is about 2.7 nm. Although the gap map indicates some inhomogeneous distribution on a few nanometre scale as in [63–67], no correspondence to the modulation of $\lambda \ll 2.7$ nm is seen.

As mentioned above, we have observed that in the overdoped Bi2212 the crossover field increases to a value very close to that of the system containing columnar defects, the irreversibility line shifts to higher temperatures, and a more pronounced second peak appears. The origins of the second peak and the irreversibility line are qualitatively explained with the depinning of 2D collective pinning theory. The anomalous behavior of H_{on} can be interpreted with the Josephson coupling in layered superconducting system containing semiconducting layer. Our results also exclude other models including surface barrier, 2D melting, and granular superconductivity as a proper explanation for the overdoped Bi2212 system. Atomic-scale high-resolution scanning tunneling microscopy and spectroscopy measurements on the cleaved surface of single crystal $\text{Bi}_2\text{Sr}_2\text{CaCuO}_{8+y}$ superconductors revealed that similar to the composition fluctuation in YBCO with high J_c , a high J_c in Bi2212 may be also related to the compositional fluctuation at nanoscale which further show that imperfections at nanoscale is a very important resource for the strong flux pinning in both HTSs and MgB_2 .

7. SUMMARY

Our results reveal that nanoscale imperfections (including structure defects, compositional fluctuations, etc) are important resource for strong flux pinning in superconductors.

For HTSs, we can propose that an efficient pinning structure for HTSs should possess the features listed below:

- (1) high density of pinning centres, in order to pin the pancake vortices in different layers;
- (2) size around 3-10 nm for pinning centres, in order to match the coherence length at 77 K;
- (3) pinning centres being located in the CuO_2 planes, in order to directly interact with the vortices.

For other superconductor such as MgB_2 , 3-10 nanometers are also important scale for flux pinning. Although the general behaviour of these superconductors with nanoscale pinning centers possesses some features of the $\delta\kappa$ pinning mechanism, however, the detailed mechanism is still not so clear. We should keep it in mind that nanoparticles often have a strong surface effect in their physical and chemical properties. Therefore, it is likely that the strong pinning effect of nanoscale pinning centres is a consequence of this surface effect.

ACKNOWLEDGEMENT

The authors are grateful to Dr. J.A. Xia, Dr. C.H. Choi, Dr. M. Xu, Mr. X.F. Rui, Ms. R.P. Miao, Prof. P. Munroe and Prof. H.M. Zeng for their assistance and participation of part of the research. Zhao is grateful to the financial support of The Natural Science Foundation of China (No.50372502). Zhao and Cheng are grateful to the financial support of The University of New South Wales (Goldstar Award).

REFERENCES

1. J. Nagamatsu, N. Nakagawa, T. Muranaka, Y. Zenitani, J. Akimitsu, *Nature*, 410, 63 (2001)
2. J.G. Bednorz and K.A. Muller, *Z. Phys. B*, 64, 18 (1986).
3. S. Tanaka, *Bull. Ceram. Soc. Japan*, 33, 591 (1998); *Look Japan*, August Issue, 30 (2001).
4. D. Larbalestier, A. Gurevich, D. M. Feldmann, and A. Polyanskii, *Nature*, 414, 368 (2001).
5. D.C. Larbalestier, *IEEE Trans. Appl. Supercond.*, 7, 90 (1997).
6. A.M. Campbell & J.E. Evetts, *Adv. Phys.* 21 194 (1972).
7. Y. Zhao, C.H. Cheng, Y. Feng, L. Zhou, N. Koshizuka, and M. Murakami, *Studies on High Temperature Superconductors*, Vol. 44, edited by A. V. Narlikar, Published by NOVA Science Publishers, New York (2003).
8. Y. Zhao, C.H. Cheng, M. Xu, C.H. Choi, and X. Yao, *Studies on High Temperature Superconductors*, Vol. 41, pp45-74, edited by A. V. Narlikar, Published by NOVA Science Publishers, New York (2002).
9. M. Nishiyama, G. Kinoda, Y. Zhao, T. Hasegawa, Y. Itoh, N. Koshizuka and M. Murakami, *Supercond. Sci. Technol.*, 17 1406 (2003).
10. C. Meingast, & D.C. Larbalestier, *J. Appl. Phys.* 66 5971 (1989).
11. E.J. Kramer, *J. Appl. Phys.* 41, 621 (1970).
12. D. Dew-Hughes, *Phil. Mag.* 55 459 (1987).
13. L.D. Cooley, P.J. Lee, & D.C. Larbalestier. *Adv. Cryo. Eng.* (in press).
14. C.B. Eorn, et al. *Nature* 411, 558 (2001).
15. X. Song, et al.. *Supercond. Sci. Technol.* (in press).
16. S. Jin, H. Mavoori, C. Bower, and R.B. van Dover, *Nature* 411, 563 (2001).
17. Y. Zhao et al, *Appl. Phys. Lett* 79, 1154-1156 (2001).
18. Y. Zhao, X.F. Rui, C.H. Cheng, H. Zhang, P. Munroe, H.M. Zeng N. Koshizuka, and M. Murakami, *Appl. Phys. Lett.* 83 2916 (2003).
19. C.H. Cheng, H. Zhang, Y. Zhao, Y. Feng, X.F. Rui, P. Munroe, H.M. Zeng, N. Koshizuka, M. Murakami, *Supercond. Sci. Technol.*, 16 1182 (2003).
20. S.H. Pan, et al. *Nature* 403, 746 (2000).
21. S.H. Pan, et al, *Nature* 413, 282 (2001).
22. K.M. Lang, V. Madhavan, et al. *Nature*, 415, 412 (2002).
23. A. Diaz, I. Mechin, P.Berghuis, J.E. Evetts *Phys. Rev. Lett.* 80, 3855 (1998).
24. B. Dam, et al, *Nature* 399 439 (1999).
25. J.R. Chem, *Phys. Rev. B* 43, 1837 (1991).
26. Y. Zhao, et al, *Phys. Rev. B* 51, 3134 (1995).
27. M. Muralidhar, S. Nariki, M. Jirsa, Y. Wu, and M. Murakami, *Appl. Phys. Lett.*, 80, 1016 (2002).
28. Y Feng, AK. Pradhan, Y. Zhao, Y. Wu, N. Koshizuka, and L. Zhou, *Supercond. Sci. Technol.* 14, 224 (2001)
29. Y. Feng, A.K. Pradhan, Y. Zhao, S.K. Chen, Y. Wu, C.P. Zhang, G. Yan, et al, *Physica C* 385 363 (2003).
30. C.H. Choi, Y. Zhao, C.C. Sorrell, M. La Robina, C. Andrikidis, *Physica C*, 269, 306 (1996).

31. M. R. Koblischka, A. J. J. van Dalen, T. Higuchi, S. I. Yoo, and M. Murakami, *Phys. Rev. B* **58**, 2863 (1998).
32. Y. Zhao, D.X. Huang, Y. Feng, C.H. Cheng, T. Machi, N. Koshizuka, and M. Murakami, *Appl. Phys. Lett.* **80**, 1640 (2002).
33. Y. Zhao, Y. Feng, T. Machi, C.H. Cheng, D.X. Huang, Y. Fudamoto, N. Koshizuka, and M. Murakami, *Europhys. Lett.* **57**, 437 (2002).
34. C.B. Eorn, M.K. Lee, J.H. Choi, L.J. Belenky, X. Song, L.D. Cooley, M.T. Maus, S. Patnaik, J. Jiang, M. Rikel, A. Polyanskii, A. Gurevich, X.Y. Cai, S.D. Bu, S.E. Babcock, E.E. Hellstrom, D.C. Larbalestier, N. Rogado, K.A. Regan, M.A. Hayward, T. He, J.S. Slusky, K. Inumaru, M.K. Haas, and R.J. Cava, *Nature*, **411**, 558 (2001).
35. Q. Chen and S. Yun, *Mater. Res. Bull.* **35**, 1915 (2000).
36. T. Takenobu, T. Ito, D.H. Chi, K. Prassides, and Y. Iwasa, *Phys. Rev. B* **64**, 134513 (2001).
37. W. Mickelson, J. Cumings, W.Q. Han, and A. Zettl, *Phys. Rev. B* **65**, 052505 (2002).
38. M. Xu, H. Kitazawa, Y. Takano, J. Ye, K. Nishida, H. Abe, A. Matsushita, N. Tsujii, G. Kido, *Appl. Phys. Lett.*, **79**, 2779 (2001).
39. J. Wang, Y. Bugoslavsky, A. Berenov, L. Cowey, A.D. Caplin, L.F. Cohen, J.L. MacManus Driscoll, L.D. Cooley, X. Song, and D.C. Larbalestier, *Appl. Phys. Lett.* **81**, 2026 (2002).
40. V.N. Narozhnyi, G. Fucks, A. Handstein, A. Gumbel, J. Eckert, K. Nenkov, D. Hinz, O. Gutfleisch, A. Walte, L.N. Bogacheva, I.E. Kostyleva, K.-H. Muller, L. Schultz, condmat/0206513.
41. Y. Bugoslavsky *et al* *Nature* **411** 561 (2001).
42. M. Eisterer *et al*, *Supercond. Sci. Technol.* **15** L9 (2001).
43. Y. Feng, Y. Zhao, Y. P. Sun, F.C. Liu, B.Q. Fu, L. Zhou, C.H. Cheng, N. Koshizuka and M. Murakami, *Appl. Phys. Lett.* **79** 3983 (2001).
44. S.X. Dou, S. Soltanian, J. Horvat, X.L. Wang, P. Munroe, S.H. Zhou, M. Ionescu, H.K. Liu and M. Tomsic, *Appl. Phys. Lett.* **81** 3419 (2002).
45. Q. Li, G.D. Gu and Y. Zhu, *Appl. Phys. Lett.* **82** 2103 (2003).
46. X.L. Wang, S.H. Zhou, M.J. Qin, P.R. Munroe, S. Soltanian, H.K. Liu and S.X. Dou, *Physica C* **385** 461 (2003).
47. S. Soltanian, J. Horvat, X.L. Wang, P. Munroe and S.X. Dou, *Physica C* **390** 185 (2003).
48. N. Chikumoto, M. Kosugi, Y. Matsuda, M. Konczykowski, and K. Kishio, *Phys. Rev. B* **57**, 14507 (1998).
49. Y. Nakayama, T. Motohashi, K. Otschi, J. Shimoyama, K. Kitazawa, K. Kishio, M. Konczykowski, and N. Chikumoto, *Phys. Rev. B* **62**, 1452 (2000).
50. Y.P. Sun, Y.Y. Hsu, B.N. Lin, H.M. Luo, and H.C. Ku, *Phys. Rev. B* **61**, 11301 (2000).
51. H.H. Wen, S.L. Li, and Z.X. Zhao, *Phys. Rev. B* **62**, 716 (2000).
52. Y.P. Sun, W.H. Song, B. Zhao, J.J. Du, H.H. Wen, Z.X. Zhao, and H.C. Ku, *Appl. Phys. Lett.* **76**, 3795 (2000).
53. M. Kiuchi, H. Yamato, T. Hirano, T. Matsushita, and N. Koshizuka, *Physica C* **297**, 161 (1998).
54. L.I. Glazman, and A.E. Koshelev, *Phys. Rev. B* **43**, 2935 (1991).
55. S. Kokkaliaris, A.A. Zhukov, P.A. J. de Groot, R. Gagnon, L. Taillefer, and T. Wolf, *Phys. Rev. B* **61**, 3655 (2000).
56. M.C. de Andrade, N.R. Dilley, F. Ruess, and M.B. Maple, *Phys. Rev. B* **57**, R708 (1998).

57. Y. Zhao, Y. Feng, S. Shibata, and N. Koshizuka, *Proc. International Workshop on Critical Currents and Applications of HTS, Japan*, pp68-69 (2000).
58. A. Schilling, R. Jin, D. Guo, and H.R. Ott, *Phys. Rev. Lett.* 71, 1899 (1993).
59. V.B. Geshkenbein, L.B. Ioffe, and A.J. Millis, *Phys. Rev. Lett.* 80, 5778 (1998).
60. Y. Zhao, G.D. Gu, G.J. Russell, N. Nakamura, S. Tajima, J.G. Wen, K. Uehara, and N. Koshizuka, *Phys. Rev. B* 51, 3134 (1995).
61. V.N. Kopylov, A.E. Koshelev, I.F. Schegolev, and T.G. Togonize, *Physica C* 170, 291 (1990).
62. M.V. Feigel'man, V. B. Geshkenbein, V.M. Vinkur, *Phys. Rev. B* 43, 6263 (1991).
63. J.-X. Liu, J-C Wan, A. M. Goldman, Y.C. Chang and P.Z. Jiang, *Phys. Rev. Lett.* 67 2195 (1991).
64. K.M. Lang, V. Madhavan, J.E. Hoffman, E.W. Hudson, H. Eisaki, S. Uchida and J. C. Davis, *Nature* 415 412 (2002).
65. A. Matsuda, T. Fujii and T. Watanabe, *Physica C* 388-389 207 (2003).
66. K. Matsuba, H. Sakata, T. Mochiku, K. Hirata and N. Nishida, *Physica C* 388-389 281 (2003).
67. G. Kinoda, T. Hasegawa, S. Nakano, T. Hanaguri, K. Kitazawa, K. Shimuzu, J. Shimoyama and K. Kishio, *Phys. Rev. B* 67 224509 (2003).

PHYSICS AND CHEMISTRY OF THE COBALT OXIDE HYDRATE SUPERCONDUCTOR

K. Takada¹, H. Sakurai², and E. Takayama-Muromachi²

¹Advanced Materials Laboratory,

²Superconducting Materials Center,

National Institute for Materials Science, 1-1 Namiki, Tsukuba, 305-0044 Japan

1. INTRODUCTION

Discovery of high T_c superconductivity in layered copper oxides [1] brought about a major breakthrough in condensed matter science. Although, the mechanism of the high T_c superconductivity has not been elucidated yet, many researchers believe that it is related to the strong electron-electron correlation. Since the charge-transfer type insulator is expected for the oxides of a late $3d$ transition metal such as Co and Ni as well as Cu, intensive studies have been carried out on Ni and Co oxide systems for searching similar behavior. However, any oxide superconductors containing Ni or Co had not been discovered for more than 15 years, with the “consensus” that the CuO_2 plane was essential for high T_c superconductivity and could not be substituted by other transition metal plane.

Recently, the first Co oxide superconductor was discovered by Takada *et al* [2]. It is a quite unique superconductor in two aspects; (i) superconductivity is induced on a Co triangular lattice, and (ii) water molecules are inserted between the Co planes making the system strongly two-dimensional. The first aspect has attracted a great deal of attention of physicists including theorists because superconductivity in geometrically frustrated systems is one of the most interesting subjects of recent solid-state physics [3]. On the other hand, the second aspect has received much attention from chemists because soft-chemical processes at room temperature play an essential role in the synthesis of the superconductor. Thanks to the unique features of the superconductor, a lot of studies have been already carried out in spite of the short period since its discovery.

In this review paper, we will survey studies done on the system thus far, from both the chemical and physical points of view. We will describe not only the superconductor but also its parent oxide. In some cases, we need further studies to obtain conclusion because of serious discrepancies among available data. We will not omit such cases but refer to various results and try to make clear how they are discrepant.

2. LAYERED COBALT OXIDE SYSTEMS

2.1 Intercalation chemistry

Characteristic layered structures consisting of MO_2 layers are seen in alkali transition metal oxides with chemical formula of A_xMO_2 (A : alkali metal, M : transition metal such as Fe, Mn, Ni, Co, etc). The MO_2 layer is made of edge-sharing MO_6 octahedra with the M ions forming a triangular lattice. The MO_2 layers are stacked with alkali ions in the gallery between them as guest species. The Li^+ [4], Na^+ [5], and K^+ [6] ions can accommodate themselves into the gallery. In addition, protons [7] and noble metals [8] can also occupy the cation sites in the gallery. The manner of stacking of the MO_2 layers varies depending not only on the A and M atoms but also on synthesis conditions to give polymorphs.

The structures are categorized and named based on the number of the MO_2 sheets in unit cell and environment around the alkali metal ion [9]. As an example, polymorphs of a sodium cobalt oxide are shown in Fig. 1 where the P2 (γ), P3 (β), and O3 (α) phases are formed depending on the sodium content x and the synthesis temperature. The combination of the character and the number such as P2 stands for coordination polyhedron for the alkali ion (P: trigonal prism, O: octahedron, T: tetrahedron) and the number of the MO_2 sheets in unit cell. Thus, three CoO_2 layers are contained in the unit cell in the α - and β -phases, while two in the γ -phase. The Na^+ ions occupy trigonal prismatic sites in the β - and γ -phases while octahedral sites in the α -phase.

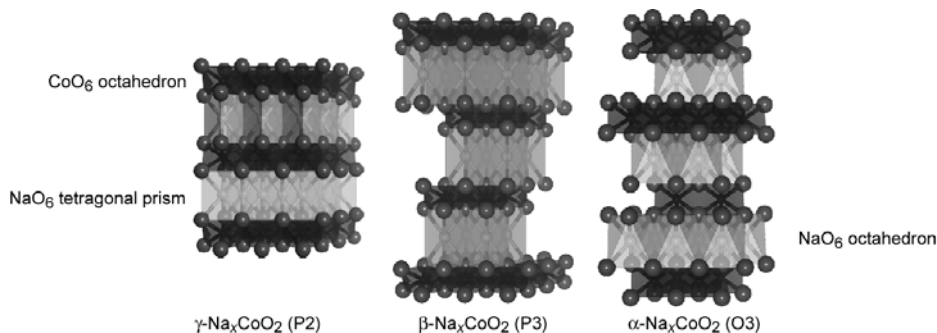


Fig. 1. Crystal structures of γ -, β -, and α - Na_xCoO_2 .

It is quite interesting from a chemical viewpoint that the guest species can be modified by softchemical procedures including ion-exchanging, intercalation, deintercalation, electrochemical reactions, etc. In the alkali transition metal oxides, the soft chemical reactions

are often accompanied by phase transformations. For instance, when the Na^+ ions are deintercalated from $\alpha\text{-Na}_x\text{CoO}_2$ with an O3 structure, the CoO_2 layers glide to change their relative positions as well as the Na coordination polyhedron from octahedron to trigonal prism. As a result, the α -phase is transformed into $\beta\text{-Na}_x\text{CoO}_2$ with a P3 structure via intermediate O'3 and P'3 structures, which are slightly distorted with monoclinic symmetries [10]. This kind of transformation is easy to understand if we use three kinds of triangular lattices, A, B, C. In the O3-type (ordered NaCl-type) structure, oxygen planes are stacked as ABCABC... in a way of cubic close packing, and both Co and Na occupy the octahedral sites between the O planes. The stacking sequence of the planes is $\text{A}_\text{O}\text{-C}_\text{Co}\text{-B}_\text{O}\text{-A}_\text{Na}\text{-C}_\text{O}\text{-B}_\text{Co}\text{-A}_\text{O}\text{-C}_\text{Na}\text{-B}_\text{O}\text{-A}_\text{Co}\text{-C}_\text{O}\text{-B}_\text{Na}$... in O3 while it is transformed to $\text{A}_\text{O}\text{-C}_\text{Co}\text{-B}_\text{O}\text{-A}$ (or C) $_x\text{Na}\text{-B}_\text{O}\text{-A}_\text{Co}\text{-C}_\text{O}\text{-B}$ (or A) $_x\text{Na}\text{-C}_\text{O}\text{-B}_\text{Co}\text{-A}_\text{O}\text{-C}$ (or B) $_x\text{Na}$... in P3 after the deintercalation. It is worth comparing the P3 structure with the P2 structure of the γ phase whose sequence is $\text{A}_\text{O}\text{-C}_\text{Co}\text{-B}_\text{O}\text{-A}$ (or C) $_x\text{Na}\text{-B}_\text{O}\text{-C}_\text{Co}\text{-A}_\text{O}\text{-B}$ (or C) $_x\text{Na}$...

LiCoO_2 has an O3 structure and in most cases, deintercalation of the Li^+ ions changes only the cell dimensions without changing the symmetry of the structure. (As an exception, the system undergoes a hexagonal to monoclinic transition when the deintercalation proceeds up to a composition of $\text{Li}_{0.5}\text{CoO}_2$ [11].) The deintercalation extracts electrons from the Co ions decreasing their ionic radii and shrinking CoO_6 octahedra and the a -axis. On the other hand, the deintercalation decreases the number of Li^+ ions. Since the positively-charged Li^+ ions attract the negatively-charged CoO_2 layers, deintercalation weakens a binding force between the layers to expand the interlayer distance and thus the c -axis. A notable feature of the deintercalation is that it takes place at a high potential of 4 V vs. Li^+/Li with high reversibility [12]. This is the reason why LiCoO_2 is used as cathode material in lithium ion cells.

Although only the O3 phase is thermodynamically stable in the Li_xCoO_2 system, metastable O2-type Li_xCoO_2 can be obtained by ion-exchange reaction [13]. When the Na^+ ions in $\gamma\text{-Na}_x\text{CoO}_2$ are exchanged by Li^+ ions, the CoO_2 layers glide changing the original trigonal prismatic sites into octahedral ones. Thus, P2 Na_xCoO_2 is transformed into O2 Li_xCoO_2 . Lithium deintercalation for this O2 phase yields various metastable phases with different stacking sequences depending on the degree of the deintercalation: phases appearing are $\text{T}^{\#2}$, $\text{T}^{\#2'}$, O6, and finally again O2 [14].

2.2 Physical properties of the layered cobalt oxides

The CoO_2 layer is quite interesting from a physical viewpoint because it is regarded as $S=1/2$ triangular lattice if every Co ion is tetravalent ($3d^5$) with a localized low spin state. Here, we will briefly introduce the physical properties originating in the CoO_2 layer taking $\gamma\text{-Na}_x\text{CoO}_2$ as an instance because it is one of the compounds which have been studied most intensively. The $\gamma\text{-Na}_x\text{CoO}_2$ has been attracting much attention because of its unusual high thermopower [15]. Spin- or valence-fluctuation has been suggested as the origin of this peculiar property of the γ -phase [15] but underlying physics has not been fully elucidated yet. For the sample with $x = 0.75$, a magnetic transition was observed at 22 K by Motohashi *et al* [16]. This transition is believed to be caused by a spin density wave formation [16, 17]. The Sommerfeld constant was estimated from the specific heat measurement to be $\gamma = 25.9 \text{ mJ/molK}^2$ [16], which is much larger than 10.5 mJ/molK^2 expected from band calculations [18], suggesting a heavy-

fermion-like nature. A heavy-fermion-like behavior was also reported by Miyoshi *et al* [19], who observed a broad maximum at 14 K in magnetic susceptibility data instead of the magnetic transition at 22 K. Sakurai *et al.* found that the physical properties of the system are very sensitive to the Na content x [20, 21] and the apparent inconsistency in the magnetic data is caused by a small difference in x [20]. Moreover, they suggested a phase separation model, like a separation to Na-rich and Na-poor domains, with the selective occurrence of the transition at 22 K in the former domains [20].

The electrical resistivity ρ of the system does not show a conventional temperature variation. The ρ - T curve (T : temperature) bends at around 120 K, and above ~ 120 K, T -linear variation is seen as in high T_c cuprates. The normal phonon scattering mechanism does not account for this T -linear variation because the temperature range in question is much lower compared with the Debye temperature [21]. On the other hand, ρ is proportional to $T^{-0.5}$ between 40 K and 120 K [21]. Although the origin of the bend at 120 K is not known, angle-resolved photoemission spectroscopy (ARPES) [22] and optical measurements [23] for $x = 0.7$ samples showed a certain anomaly at around 120 K, i.e., quasiparticle spectral weight near the Fermi level looked to disappear above 120 - 150 K [22].

A compound with $x < 0.7$ can not be prepared by the usual solid-state reaction [20] but only through processes under low temperature region such as a soft chemical process. It is expected for a compound with $x < 0.7$, a new magnetic phase appears in a low temperature region [21, 24, 25, 26]. In the case of $x = 0.5$, metal-insulator transition and antiferromagnetic order at 53 K has been reported [27, 28]. These results clearly indicate that Na_xCoO_2 is a strongly correlated electron (SCE) system. The SCE related behaviors are also seen in other compounds with the CoO_2 layers such as $\text{Bi}_2\text{Sr}_2\text{Co}_2\text{O}_z$, and $\text{Ca}_3\text{Co}_4\text{O}_9$, for instance, high thermopower and a magnetic transition are observed after partial substitution of Pb for Bi in the former compound [29]. The high thermopower and a magnetic transition are often seen in compounds with the CoO_2 layers [30].

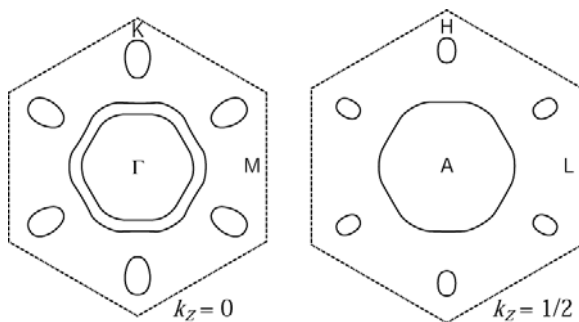


Fig. 2. Fermi surface of $\text{Na}_{0.5}\text{CoO}_2$ in the $k_z = 0$ (left) and $k_z = 0.5$ (right) planes calculated by Singh [18].

The triangular lattice of the Co atoms is, of course, the origin of the characteristic features of Na_xCoO_2 . Band structure of Na_xCoO_2 reflects six-fold symmetry of the triangular lattice, and in the case of $x = 0.5$, Fermi surface is composed of two components as shown in Fig. 2. Because of the rhombohedral distortion of CoO_6 octahedron, the degenerated t_{2g} orbitals of Co

$3d$ orbitals are split into a_{1g} and e_g' orbitals. Corresponding to this picture, the large Fermi surface section centered at Γ -point has mainly the a_{1g} character, while the small holelike sections have a mixed character between a_{1g} and e_g' . For superconducting $\text{Na}_x\text{CoO}_2 \cdot y\text{H}_2\text{O}$, six holelike pockets are also expected to exist [31, 32, 33], while two a_{1g} bands centered at Γ -point are almost degenerated due to a large interlayer separation [31, 34]. This difference may have some relevance to the appearance of superconductivity in $\text{Na}_x\text{CoO}_2 \cdot y\text{H}_2\text{O}$.

3. SUPERCONDUCTIVITY IN TWO DIMENSIONAL CoO_2 LAYERS

3.1 Chemistry of superconducting sodium cobalt oxide hydrate

3.1.1 Softchemical modification

The sodium cobalt oxide, $\gamma\text{Na}_{0.7}\text{CoO}_2$, was converted into the superconductor via a softchemical processes with chemical oxidation using bromine (Br_2) and immersion in water [2]. Two main reactions occurring in these processes are deintercalation of the Na^+ ions by Br_2 (oxidation) and intercalation of H_2O molecules (hydration). The H_2O intercalation results in an increase of the distance between the CoO_2 layers from 5.5 Å in the parent phase to 9.8 Å in the superconducting phase. The large separation of the layers enhances two-dimensional (2D) character of the system, which is believed to play an important role in inducing superconductivity.

The H_2O molecules coordinate to the Na^+ ions and form two water layers in the gallery sandwiching the Na plane, transforming the parent oxide into a bilayer-hydrate (BLH) as shown in Fig. 3. Exact chemical formula of the BLH-phase is $\text{Na}_x(\text{H}_3\text{O})_z(\text{H}_2\text{O})_n\text{CoO}_2$ as seen later, but a more simple formula of $\text{Na}_x\text{CoO}_2 \cdot y\text{H}_2\text{O}$ ($x \sim 0.35$, $y \sim 1.3$) has been used widely and we will also sometimes use this formula so long as it does not cause confusion.

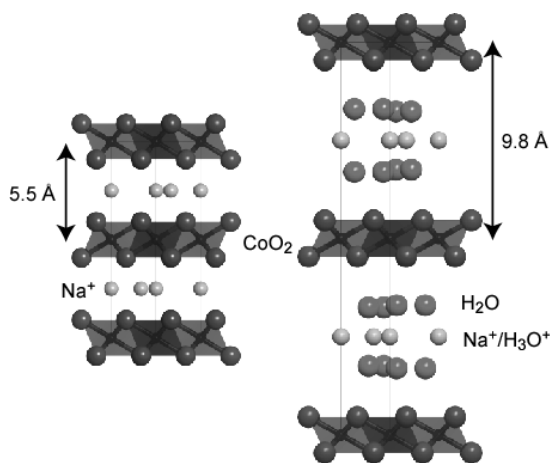


Fig. 3. Crystal structures of the superconducting phase (right) and its parent phase (left).

The CoO_2 layers in the parent oxide are attracted to each other through the Na^+ ions between them and the hydration does not occur when the parent oxide is immersed in water. The Br_2 oxidation extracts Na^+ ions from the gallery as well as electrons from the CoO_2 layers. Consequently, the charge density in the negatively-charged CoO_2 layer and the number of positively-charged Na^+ ions are both decreased, which weakens the attraction between the layers. This step seems to be indispensable for the following H_2O intercalation. In other words, the expansion of the interlayer distance looses the electrostatic energy, while the coordination of the H_2O molecules to the Na^+ ions gains hydration energy. Thus, the BLH-phase will be formed when the energy gain from the hydration is larger than the loss of the electrostatic energy.

If enough amount of Br_2 is not used in the Br_2 oxidation, less amount of Na^+ ion is deintercalated and an interlayer attraction would not be weakened sufficiently. This situation makes the intercalation of the H_2O molecules difficult and hinders the hydration process, to give an anhydrous (AH) phase. When the Br_2 amount is in an intermediate range, a sample obtained is mixed-phase of the AH and the BLH-phase which can be easily distinguished by the different interlayer distances of 5.5 Å (AH) and 9.8 Å (BLH) as shown in Fig. 4 [35]. The increasing amount of Br_2 increases the fraction of the BLH-phase and finally the single-phase sample of the BLH-phase is obtained with the disappearance of the AH-phase.

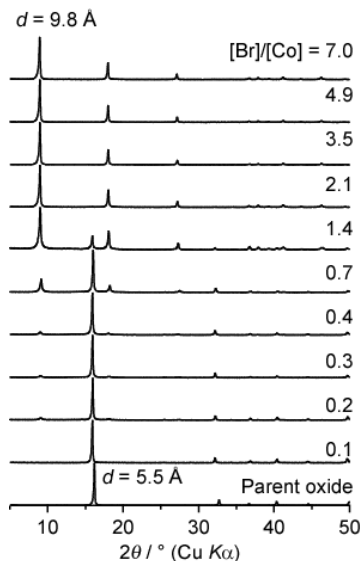


Fig. 4. Powder X-ray diffraction (XRD) patterns of the samples oxidized by different amounts of Br_2 . The amounts of dosed Br_2 are presented in the ratios to Co content in the parent $\text{Na}_{0.7}\text{CoO}_2$.

All the X-ray reflections of the BLH-phase are indexable on the basis of $P6_3/mmc$ which is the same space group as the parent oxide, consistent with the fact that the interlayer distance is increased without changing the basic manner of the stacking of the CoO_2 layers. In

other words, the BLH-phase has a P2-type structure as well as the parent oxide. It should be noted that the Na content cannot be decreased beyond a certain limit even when a very large amount of Br₂ is used. The redox potential of Co⁴⁺/Co³⁺ in Na_xCoO₂ increases with decreasing Na content, x , and the extraction of the Na⁺ ions is terminated when the Co⁴⁺/Co³⁺ redox potential becomes equal to that of Br₂/Br⁻. Indeed, in Fig. 4, the resultant phase is independent of the Br₂ amount if [Br]/[Co] ≥ 2.1. The BLH-phase shows bulk superconductivity below about 5 K as confirmed by steep decreases of magnetic susceptibility and electrical resistivity (Fig. 5).

Besides the Br₂ oxidation, several methods have been reported for the deintercalation of the Na⁺ ions in Na_xCoO₂, e.g. chemical oxidation using iodine [36] or KMnO₄ [37] and electrochemical oxidation [10, 38]. Recently, Park *et al.* reported a new synthetic route, in which Na₂S₂O₈ was used as an oxidizing agent [39]. They also claimed that the pH of the aqueous solution used for the hydration was crucial in the preparation of the superconducting phase. According to them, the optimum pH was ca. 10.5 though they did not give any explanation for the pH dependence. This point will be discussed later in connection with side reactions during the hydration.

Single crystals of the superconductor were obtained by several groups [40, 41, 42, 43]. Single crystals of γ -Na_xCoO₂ were grown by floating-zone or flux method, and Na⁺ ions were deintercalated from the crystals using the Br₂ oxidation technique or electrochemical way.

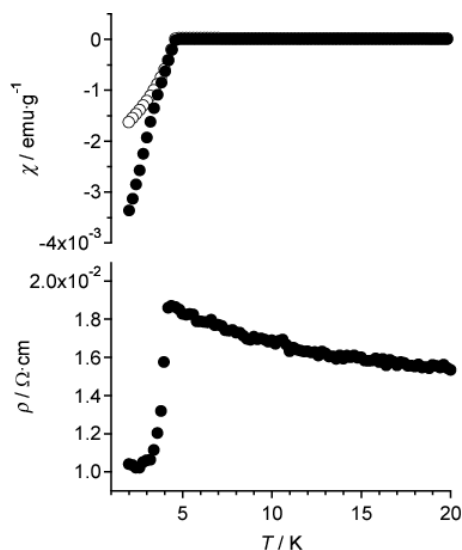


Fig. 5. Magnetic susceptibility (χ) and resistivity (ρ) of the BLH-phase. The closed and open circles indicate the susceptibilities by zero-field cooling (ZFC) and field cooling (FC) methods under 20 Oe, respectively. The resistivity was measured under zero magnetic field.

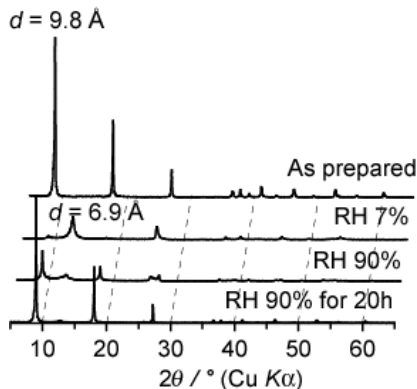


Fig. 6. XRD patterns of the sodium cobalt oxide hydrate sample changing relative humidity.

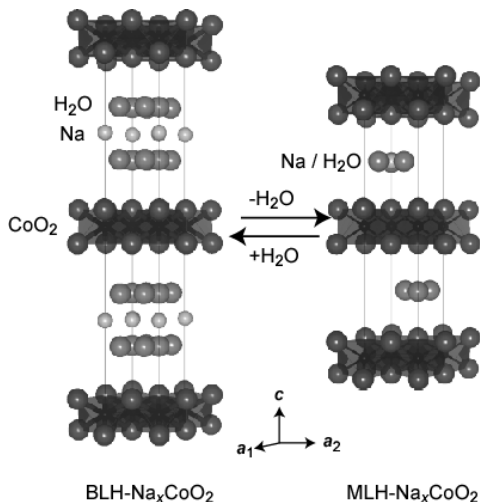


Fig. 7. Structural drawings of $\text{BLH-Na}_x\text{CoO}_2$ and $\text{MLH-Na}_x\text{CoO}_2$, where Na and H_2O sites are partially occupied.

The BLH-type structure is not unique for the cobalt oxide system but has been known for a manganese oxide called busserite. Partial dehydration for busserite yields a monolayer-hydrate (MLH) phase called birnessite with shrinkage of the $\text{MnO}_2\text{-MnO}_2$ interlayer distance from 10 Å in the BLH-phase to 7 Å in the MLH-phase [44]. Similar transformation takes place in the BLH cobalt oxide [45, 46]; storage of the BLH-phase under low relative humidity (RH) of 7% brought about a new phase with the $\text{CoO}_2\text{-CoO}_2$ interlayer distance of 6.9 Å at the expense of the original 9.8 Å phase (Fig. 6). Structure analysis of the 6.9 Å phase [45] confirmed a MLH-type structure similar to birnessite (see Fig. 7). When RH was increased again, the original BLH-phase was recovered reversibly. The approximate chemical

formulae for the BLH- and MLH-phases are $\text{Na}_x\text{CoO}_2 \cdot y\text{H}_2\text{O}$, $y = 1.3$ and 0.7 , respectively, i.e., the water content in the MLH-phase is about a half of that in the BLH-phase. In addition, phases with smaller y values, such as $y = 0.3$ and 0.1 , have been reported [41, 46, 47, 48].

In the MLH-phase, superconductivity completely disappears as shown in Fig. 8. Since the carrier (electron) density in the CoO_2 layer is kept unchanged through the BLH-MLH transformation, this fact strongly suggests that the adequate separation of the CoO_2 layers by the thick insulating layer of Na^+ ions and H_2O molecules is indispensable for the superconductivity. As a matter of course, this does not mean that the electron (carrier) density is an immaterial parameter, but it can be concluded that the optimum level of carrier doping into the CoO_2 layer alone is not enough for inducing the superconductivity.

Very recently, a novel cobalt oxide superconductor has been discovered [49]. Its chemical formula is essentially the same as that of the P2-type BLH-phase, but the stacking sequence of the CoO_2 layers is different. This compound is synthesized by the same soft chemical process as that used for the P2 superconductor, but by starting from a different parent oxide of $\alpha\text{-NaCoO}_2$. It has been already described that the α -phase has the O3-type structure and the P3-type phase is formed after the deintercalation of Na rather than the P2-type phase. The P3-type stacking is maintained after the hydration, and thus, the new superconductor belongs to the P3-type with space group of $R\bar{3}m$. In spite of the different manner of the stacking, hydration and dehydration processes are very similar to those in the P2 phase [50]. Moreover, T_c of the P3 superconductor is close to that of the P2 superconductor [51]. Since the P3 phase has just discovered and few experimental results are present, the P2-type BLH-phase will be mainly discussed below.

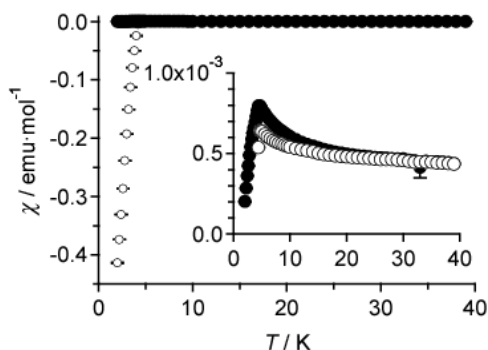


Fig. 8. Magnetic susceptibility (χ) of the BLH-phase (open circles) and the MLH-phase (closed circles). The susceptibilities were measured by ZFC method under 20 Oe.

3.1.2 Characterization of the superconducting phase

In the superconducting BLH-phase, the Co ion has a mixed-valence state between Co^{3+} and Co^{4+} . Determination of the valence state, or oxidation state, is very important because it corresponds to the carrier density. The oxidation state of Co had been simply evaluated as $4 - x$, where x is the Na content in the chemical formula of $\text{Na}_x\text{CoO}_2 \cdot y\text{H}_2\text{O}$. However, it was revealed recently that the Co oxidation state cannot be obtained only from the Na content because of the following complexity.

Table 1. Na content, x , and oxidation state of Co in the samples

| Sample | x | Oxidation state of Co | |
|--------------------------------|----------|-----------------------|--------------------------------------|
| $\text{Na}_{0.7}\text{CoO}_2$ | 0.695(5) | +3.30(2) | Data from ref. [53]. |
| AH- Na_xCoO_2 | 0.406(1) | +3.56(1) | |
| BLH- Na_xCoO_2 | 0.337(1) | +3.43(1) | |
| $\text{Na}_{0.72}\text{CoO}_2$ | 0.72(2) | +3.26(1) [3.25(1)] | Data from ref. [61]. The |
| AH- Na_xCoO_2 | 0.36(2) | +3.48(1) | oxidation states were determined |
| BLH- Na_xCoO_2 | 0.36(2) | +3.48(1) [3.44(1)] | by cerimetric titration (data in the |
| | | | left) and iodometric titration |
| | | | (data in the square brackets.) |

The Na content of the superconducting BLH-phase were reported to vary from $x = 0.25$ to 0.35 [52]. As stated above, the redox potential of Br_2/Br^- couple governs the maximum amount of Na^+ ions deintercalated from the parent oxide, or the minimum Na content in the as-oxidized phase. The composition dependence of the potential of $\gamma\text{-Na}_x\text{CoO}_2$ determined by electrochemical measurements [10] suggests that the minimum Na content that can be achieved by the Br_2 oxidation is 0.4. This value is obviously larger than the experimental Na content between 0.25 and 0.35. The most conceivable explanation for the low Na content is that the actual oxidation state of Co is lower than $4 - x$, and some cationic species other than Na^+ are accommodated in the gallery to compensate the difference. Since the sample was immersed in distilled water after the Br_2 oxidation, it seems likely that the Na^+ ions were exchanged by protons or oxonium ions (H_3O^+).

In Table 1, the Na content and the Co oxidation state reported by Takada et al. [53] are listed. They were determined by inductive-coupled plasma atomic emission spectroscopy (ICP-AES) and redox titration, respectively. The data are shown for three samples, the parent oxide of $\gamma\text{-Na}_{0.7}\text{CoO}_2$, as oxidized sample of AH- Na_xCoO_2 without hydration and the BLH-phase after the hydration. The x in the AH-phase was 0.41, which was consistent with that expected from the electrochemical data. On the other hand, the Co oxidation state in the AH-phase was +3.56 in consistent with the relation of $4 - x$ (the $4 - x$ relation is seen in the parent oxide, as well). Thus the Na^+ ions are only charge-balancing species before the hydration process.

The Na content decreased from 0.41 in the AH-phase to 0.34 in the BLH-phase. Indeed, Na was detected in the aqueous filtrate in which the AH-phase had been immersed and its amount corresponded to $\Delta x = 0.41 - 0.34$. Consequently, the decrease in the Na content can be explained by partial ion-exchange for the Na^+ ions with the protons or H_3O^+ ions in water. Raman spectroscopy indicated that the ingoing species is the H_3O^+ ion rather than the proton. The BLH-phase showed a peak at 1700 cm^{-1} and broad peaks overlapping each other in the wavenumber range from 2300 cm^{-1} to 3800 cm^{-1} , all of which were not detected for $\gamma\text{-Na}_{0.7}\text{CoO}_2$ (Fig. 9). The Raman peak at 1700 cm^{-1} is attributable to a bending mode of the H_3O^+ ion [54, 55], which can be distinguished from that of the H_2O molecule giving a bending mode at around 1600 cm^{-1} [56]. The poorly-resolved band observed in the wavenumber range from 2300 cm^{-1} to 3800 cm^{-1} was deconvoluted into several peaks, which should come from stretching vibration of OH. The most distinct peak at 2995 cm^{-1} was attributable to the stretching mode in H_3O^+ [56]. Its peak intensity was fairly strong, indicating that the BLH-phase accommodates a considerable amount of the H_3O^+ ions.

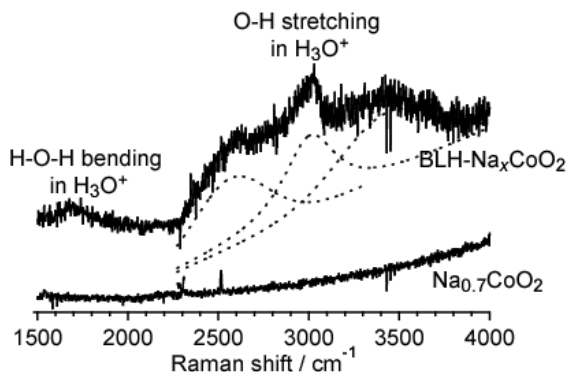


Fig. 9. Raman spectra for $\gamma\text{Na}_{0.7}\text{CoO}_2$ and $\text{BLH-Na}_x\text{CoO}_2$ in the wavenumber range from 1400 cm^{-1} to 4000 cm^{-1} . Dotted lines indicate the result of the deconvolution. The spectra were taken in a backward micro-configuration using the 514.5 nm line from an Ar^+ laser.

It should be noted in Table 1 that the Co oxidation state decreased from $+3.56$ of the AH-phase to $+3.43$ of the BLH-phase, which cannot be explained by the ion-exchange. The host should be reduced during the hydration process. An intercalation compound is sometimes reduced in an aqueous solution of alkali hydroxide accompanied by oxygen evolution and insertion of the cationic species [57, 58, 59, 60]. Similar reductive reaction was likely to take place in the present system, because the AH-phase was in contact with an aqueous solution of NaOH which was formed by the ion-exchange reaction as mentioned above. A host will be reduced when its electrochemical potential is higher than that of oxidation potential of water (oxygen evolution potential), which depends on pH of the solution [59]. The potential of $\text{AH-Na}_x\text{CoO}_2$ should be equal to that of Br_2/Br^- redox couple after the equilibrium was established during the oxidation process. The $\text{pH} = 11$ in the aqueous solution caused by the ion-exchange is high enough to make the oxidation potential of H_2O lower than the potential of the Br_2/Br^- redox couple, i.e., that of $\text{AH-Na}_x\text{CoO}_2$. Therefore, it is reasonable that the $\text{AH-Na}_x\text{CoO}_2$ was reduced when it was immersed in water.

Oxidation state of Co lower than $4 - x$ was also reported by Karppinen *et al.* [61] (see Table 1). However, analytical results for the AH-phase were somewhat different, i.e., deviation from $4 - x$ was already observed in the AH-phase before the hydration process. This discrepancy is open to discussion.

Formation process of the superconducting phase had been believed to involve only the oxidative extraction of the Na^+ ions and insertion of H_2O molecules. However, the actual process is much more complicated. A part of the Na^+ ions are exchanged by the H_3O^+ ions and further H_3O^+ ions are inserted reducing the Co ions as schematically displayed in Fig. 10. Most of studies for the BLH-phase have assumed the Co oxidation state of $+3.65$, which is deduced from the Na content of $x = 0.35$. However, the real Co oxidation state is much lower and reconsideration seems to be needed in some cases for previous studies.

Structural characterization of the BLH-phase has been carried out by several groups [2, 53, 62, 63]. But most of them considered only the Na^+ ions and the water molecules as the guest species. Full analysis has been done by Takada *et al.* for a synchrotron XRD pattern, taking

the H_3O^+ ions into account. First problem of the analysis was the positions of the H_3O^+ ions. The H_3O^+ ion is monovalent as the Na^+ ion, and therefore, it seems reasonable to expect that it shares the same crystallographic site with Na^+ . The comparison between the Raman spectra of $\gamma\text{-Na}_{0.7}\text{CoO}_2$ and the BLH-phase supported this idea. The spectrum of the BLH-phase has $E_{2g}(\text{Na})$ Raman mode at higher wavenumbers than that of the parent phase (Fig. 11). This shift toward higher wavenumbers suggests that the “Na sites” in the BLH-phase are occupied by species with an average mass smaller than that of Na, supporting the conjecture that the H_3O^+ ions occupy the “ Na^+ sites”.

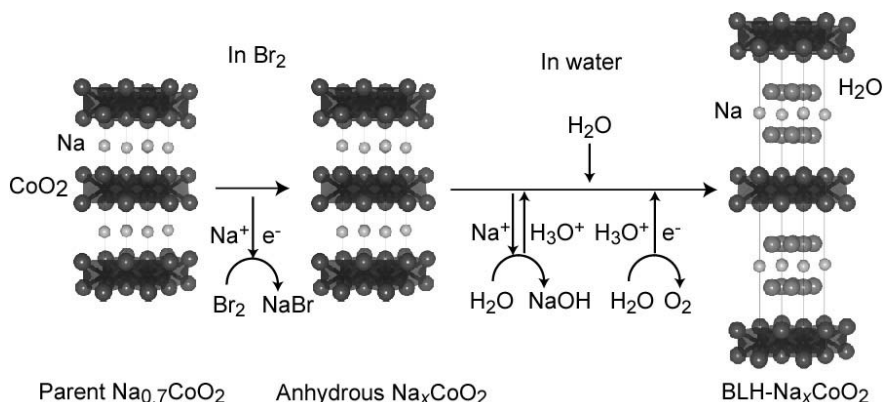


Fig. 10. A reaction schema in the formation of the BLH- Na_xCoO_2 .

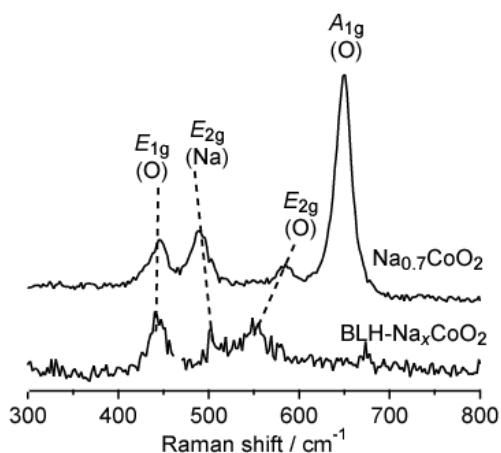


Fig. 11. Raman spectra for $\gamma\text{-Na}_{0.7}\text{CoO}_2$ and BLH- Na_xCoO_2 in the wavenumber range from 300 cm^{-1} to 800 cm^{-1} . Dotted lines are inserted to indicate the peak shift.

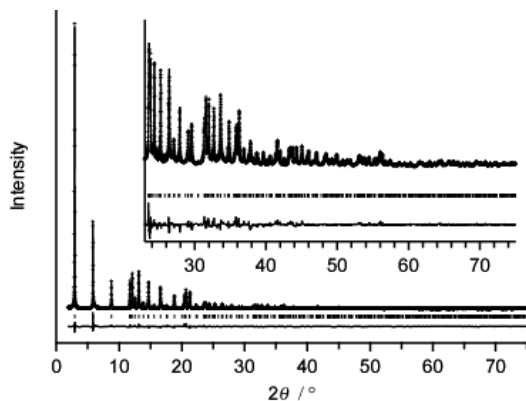


Fig. 12. Rietveld refinement patterns for the BLH- Na_xCoO_2 . The wavelength of the synchrotron radiation was 0.500971 Å. The Rietveld analysis was performed using a computer program, RIETAN-2000 [64].

On the basis of the above finding, the structure model for the BLH-phase was reconstructed with a chemical composition of $\text{Na}_x(\text{H}_3\text{O})_z(\text{H}_2\text{O})_n\text{CoO}_2$ instead of $\text{Na}_x\text{CoO}_2 \cdot y\text{H}_2\text{O}$. Fig. 12 shows Rietveld refinement XRD patterns and Table 2 lists the refined structure parameters based on this structure model. At the first step of the refinement, the Na/ H_3O mixed species were assumed to distribute at the $2b$ and $2d$ sites while they were further split into $4e$ and $2d$ sites in the final refinement.

Isotropic atomic displacement parameters U 's always converged at unreasonable values when the H_3O^+ ions were not considered. On the other hand, the refinement results in Table 2 are much improved; the U value reasonably increases in the order, for the heavy Co ion, for oxygen bonded to Co, and for guest species (Na^+ , H_3O^+ , and H_2O) bound loosely. These results are another evidence of the presence of the H_3O^+ ions.

Table 2. Fractional coordinates, occupancies, g , and isotropic atomic displacement parameters, U , for BLH- Na_xCoO_2 at room temperature

| Atom | Site | x | y | z | g | $U / \text{Å}^2$ |
|---|-------|----------|--------------------|-------------|----------|------------------|
| Co | $2a$ | 0 | 0 | 0 | 1 | 0.0062(2) |
| O | $4f$ | 1/3 | 2/3 | 0.04578(12) | 1 | 0.0091(5) |
| M1 (Na/ H_3O) [†] | $4e$ | 0 | 0 | 0.2413(12) | 0.182(3) | 0.047(4) |
| M2 | $2d$ | 2/3 | 1/3 | 1/4 | 0.216* | 0.030(4) |
| WO1 (H_2O) [†] | $12k$ | 0.137(2) | $=2x(\text{WO1})$ | 0.1700(5) | 0.111(5) | 0.026(5) |
| WO2 | $12k$ | 0.875(6) | $=x(\text{WO2})/2$ | 0.1757(6) | 0.088* | 0.023(8) |

Space group: $P6_3/mmc$ (No. 194); $a = 2.82374(10)$ Å and $c = 19.6576(8)$ Å; $R_{\text{wp}} = 5.10\%$ ($S = 2.67$), $R_{\text{p}} = 3.28\%$, $R_{\text{B}} = 1.75\%$, and $R_{\text{F}} = 1.70\%$. [†]WO denotes an H_2O molecule, whose atomic scattering factor was set equal to the sum of those of one O and two H atoms. M denotes a virtual chemical species having mean scattering amplitude of Na^+ ions and H_3O^+ ions. *The total contents of M and WO were fixed at 0.580 and 1.19 determined by the chemical analyses, respectively.

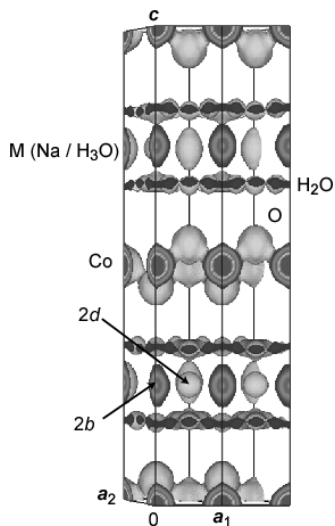


Fig. 13. Isosurface for number densities of electrons in BLH- Na_xCoO_2 at room temperature. Equidensity level: 0.8 \AA^{-3} . The density distribution was calculated by a MEM program, PRIMA [66].

In the BLH-phase, the guest species in the galleries are highly disordered. A maximum entropy method (MEM) is quite effective for detailed structure analysis of such an intercalation compound. In MEM-based whole pattern fitting (MPF) [65], crystal structures are expressed not by structure parameters such as fractional coordinates and atomic displacement parameters but by electron densities in unit cell. Therefore, MPF allows us to represent the disordered atomic configuration in a more appropriate way than the conventional Rietveld analysis adopting a split-atom model. Fig. 13 displays a three-dimensional representation of the charge-density distribution determined by MPF based on the aforementioned structure model [53]. The improvement of the refinement was confirmed by the fact that the R factors decreased from $R_{\text{wp}} = 5.10\%$, $R_{\text{B}} = 1.75\%$ and $R_{\text{F}} = 1.70\%$ in the Rietveld analysis to $R_{\text{wp}} = 4.99\%$, $R_{\text{B}} = 1.34\%$ and $R_{\text{F}} = 1.25\%$ in MPF.

Widely spread electrons around the $12k$ sites (H_2O sites) reflect the highly-disordered arrangement of the H_2O molecules. An interesting feature is seen in the charge-density distribution around the $2b$ site ($4e$ site in the final refinement of the Rietveld analysis). The isosurface surrounding this site suggests that the guest there is displaced largely along the c -axis. The marked difference in the shapes of isosurfaces around the $2b$ and $2d$ sites indicates that they correspond to different chemical species. Interatomic distances between the M and WO sites revealed that the species at the M1 ($4e$) sites are surrounded by H_2O molecules in distances shorter than those at the M2 ($2d$) sites. The arrangement of Na^+ , H_3O^+ ions and H_2O molecules co-intercalated between an oxide host framework was investigated for zeolites, and interatomic distances between the species were reported to be $2.49 \text{ \AA} - 2.72 \text{ \AA}$ for $\text{Na}^+ - \text{H}_2\text{O}$ and 2.94 \AA for $\text{H}_3\text{O}^+ - \text{H}_2\text{O}$ [67]. These interatomic distances imply that the $4e$ site is occupied mainly by the Na^+ ion rather than the H_3O^+ ion. The H_3O^+ ion makes a larger

hydrated group than the Na^+ ion owing to its larger ionic radius. When they are co-intercalated between CoO_2 layers, the larger H_3O^+ ion will work to enlarge the interlayer distance, leading to the large freedom of displacement for the smaller Na^+ ion along the c -axis in consistent with the isosurface of the $2b$ ($4e$) site in Fig. 13.

Another interesting feature is seen in the Co—O bond length. As stated above, it is very likely that the formation of the BLH-phase from the AH-phase involves reductive insertion of the H_3O^+ ions. The reduction donates electrons to the Co ions, which, in general, increases their ionic radii and thus elongates the Co—O bond length. However, the bond length decreased from 1.8875(15) Å in the AH-phase to 1.8622(12) Å in the BLH-phase. Correlation between a bond length and an oxidation state is evaluated by the bond valence sum rule [68], by which the bond length can be estimated from the oxidation state and vice versa. In the AH-phase, the bond valence sum for Co calculated from the Co—O distances and the bond valence parameter of 1.70 for the Co^{3+} ion [69] is +3.62, which is consistent with the experimental value determined by the redox titration. On the other hand, the observed Co—O bond length in the BLH-phase, 1.86 Å is much smaller than 1.91 Å estimated from the Co oxidation state of +3.42. That is, the Co—O bond length is unusually short. In the BLH-phase, electrostatic attraction between the O^{2-} ions in the CoO_2 layers and the Na^+ or H_3O^+ ions will be weakened by the H_2O molecules interposed between them. The weak attraction will result in the O^{2-} ions closely bound to the Co ions and the short Co—O bond length.

The shrinkage of the Co—O bond length caused by the hydration was also observed by a neutron diffraction study [62]; a Co—O bond length of 1.892(1) Å in the AH-phase was decreased to 1.872 Å in the BLH-phase. In addition, a similar short bond length of 1.8744(9) Å was obtained for the BLH-phase at 295 K in another neutron diffraction study [63]. The short Co—O bond length may enhance the correlation between the electrons and may have something to do with the appearance of superconductivity. In fact, a clear correlation was found between T_c and the lattice parameters [70].

The aforementioned structure analysis was based on the XRD data using synchrotron radiation. Neutron and electron diffractions are more powerful tools to determine the arrangements of the guest species. In neutron diffraction, deuterated samples must be used in order to suppress the inelastic scattering from the H atoms. Since D and O atoms have large scattering factors for neutron, D_2O molecules and D_3O^+ ions accommodated in the gallery are recognized much more easily in neutron diffraction than in XRD. In fact, additional superstructure reflections were more intense in the neutron diffraction pattern [63]. They are located at $d = 2.8 - 2.5$ Å and seem to be caused by a certain ordering of the guest species. Although they were assigned to an impurity phase in Ref. [62], it seems not the case because they were also observed, though with extremely weak intensities, in XRD diffraction. Superstructure was also confirmed by electron diffraction [71, 72]. Unfortunately, the H_3O^+ ions have not been considered in any neutron diffraction studies and serious discrepancies are present in the arrangements of the guest species. One group claimed that H_2O molecules have an ice structure (Fig. 14 left) [62]. Another proposed an arrangement in which H_2O molecules are hydrogen-bonded to oxygen atoms in the CoO_2 layers, and four H_2O molecules are coordinated to the Na^+ ion (Fig. 14 right) [63]. The discrepancies may be solved by considering the H_3O^+ ions.

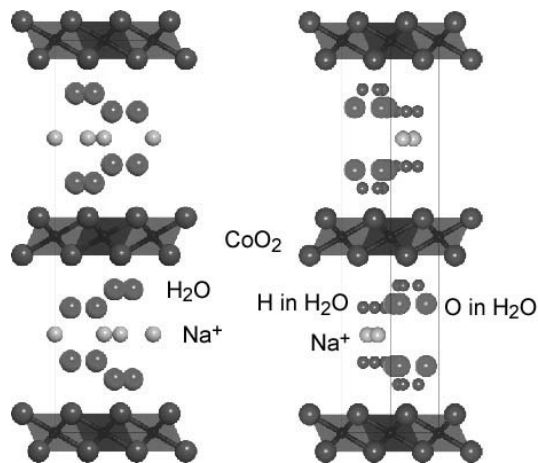


Fig. 14. Structure models proposed by Lynn *et al.* [62] (left) and Jorgensen *et al.* [63] (right).

3.2 Physics of superconducting sodium cobalt oxide hydrate

Superconductivity of the BLH-phase takes place on the triangular lattice of Co. Since the triangular lattice matches the idea of resonating-valence-bond (RVB) state [73], it was expected that superconductivity could be understood based on doped RVB model [74, 75, 76] as proposed for high T_c cuprates [77]. Based on single-band t - J model, chiral d -wave symmetry was proposed [74, 75, 76] for superconductivity of the BLH -phase, which is a natural development of the simple d -wave in high T_c cuprates [78]. However, the RVB view was questioned from the viewpoint of the carrier density, and instead, chiral p -wave symmetry was proposed based on simple fermiology, [79].

Now, it is widely believed that the RVB view is not suitable for the BLH-phase, because the carrier density of the system is too high. Although, under a certain condition, RVB superconductivity is expected to be restored in a heavily doped region [80], the present phase does not satisfy the condition. Moreover, it has been pointed out that single band model itself is not valid [81]. The mechanism of superconductivity is still open to discussion and recent papers by Yanase *et al.* and Kuroki *et al.* are useful to see the present situation of theoretical studies [82, 83].

Intensive and a variety of experimental studies have been carried out for the BLH- and related phases. However, there are still a lot of contradictions and further studies are needed to establish comprehensive physics for the present system. Thus, we cannot give clear-cut conclusion here, but instead, we will show various experimental results reported thus far and differences between them.

3.2.1 Phase diagram

The phase diagram of T_c vs. carrier density is quite important to understand superconductivity. Unfortunately, owing to the soft-chemical synthesis and the rather complicated chemical

reactions occurring in the soft-chemical process, the carrier density is hard to be controlled in the present system. Nevertheless, Schaak *et al.* reported a dome-shape phase diagram, which suggested that superconductivity appeared in the range of $1/4 < x < 1/3$ and the optimal $T_c \approx 4.5$ K was obtained at $x \approx 0.3$ [52]. However, this phase diagram is not very reliable because the presence of the H_3O^+ ions was not considered at all in spite that it should be taken into account to obtain the real carrier density. Indeed, Chen *et al.* have claimed that T_c was almost independent of x between 0.25 and 0.42 [41]. This apparent contradiction seems to be caused by the fact that the Na content x is not a good measure of the carrier (electron) density. Now, it is confirmed that the maximum T_c is around 4.6 K and it is given when the Co valence is $+3.42 - 3.43$ [53]. Strong dependency of T_c on the ratio of the lattice parameters is worth noting [70]; the maximum T_c is obtained for $c/a > 6.95$, while T_c decreases steeply for $c/a < 6.95$. Similar behavior is seen in the P3-type superconductor as well [51].

3.2.2 Critical fields

Upper-critical field, $H_{c2} = \Psi_0/2\pi\xi^2$ (ξ : coherence length), is one of the most important phenomenological superconducting parameters. In the present case, this is not only because ξ can be estimated from H_{c2} , but also because the value of H_{c2} influences interpretations of experiments carried out under high magnetic field, such as muon spin rotation/relaxation (μ SR) and nuclear magnetic resonance (NMR).

The superconducting behavior under high magnetic field is very sensitive to sample quality [84]. From $M/H-T$ curves in Fig. 15, the superconducting transition is clearly seen even under 7 T in the case of sample (a) with $T_c = 4.6$ K, the transition looks very broad and almost disappears under 7 T in sample (b) with $T_c = 4.2$ K. In specific heat data for a certain sample, bulk superconductivity is seen below 4 K at the lowest even under 8 T (Fig. 16(a)) [85]. The T_c of this sample under zero field is ca. 4.7 K [85] and is in good agreement with that of sample (a) in Fig. 15. Thus, the magnetic and thermal measurements give a consistent result as shown in Fig. 16(b) if samples with almost the same T_c are examined.

The initial slope of the $T_c = 4.6$ K sample in Fig. 15 (a) was estimated to be $dH_{c2}/dT|_{H=0} = -19.3$ T/K from the magnetic data as shown in Fig. 16 (b) which gives extremely high $H_{c2}(T=0)$ of 61 T [86] if the WHH formula [87] is applicable. However, many different results have been reported on H_{c2} and $dH_{c2}/dT|_{H=0}$ as listed in Table 3. $H_{c2}^{H/c}$ varies from ~ 1.7 T to 3.6 T, having a much smaller value than $H_{c2}^{H/ab}$ as expected from the 2D structure. ξ_{ab} is estimated to be 96 - 120 Å from the equation of $H_{c2}^{H/c} = \Psi_0/2\pi\xi_{ab}^2$. This value is much larger than a typical length in high T_c cuprates (20 - 30 Å). The H_{c2} determined for a powder sample reflects $H_{c2}^{H/ab}$ rather than $H_{c2}^{H/c}$. $H_{c2}^{H/ab}$ varies very largely from measurement to measurement and the discrepancy may come from the difference in the sample quality. However, the sample in Ref. [90] had T_c as high as 4.5 K (although the transition is rather broad) and showed relatively low $H_{c2}^{H/ab}$ [90]. As seen in Table 3, the electrical resistivity data tends to give smaller H_{c2} than the magnetic and thermal data. In the present compound, pinning force for vortex seems very weak resulting in a small irreversibility field comparable to that of the Bi cuprate [43, 91]. In such a case, it may be hard to determine H_{c2} by the resistivity measurement. Nevertheless, according to these $H_{c2}^{H/ab}$ values, ξ_c was estimated to be 5.4 - 22 Å by the equation of $H_{c2}^{H/c} = \Psi_0/2\pi\xi_{ab}\xi_c$, assuming $\xi_{ab} = 100$ Å. It is difficult to judge from this result whether ξ_c is larger than the distance between the CoO_2 layers (9.8 Å).

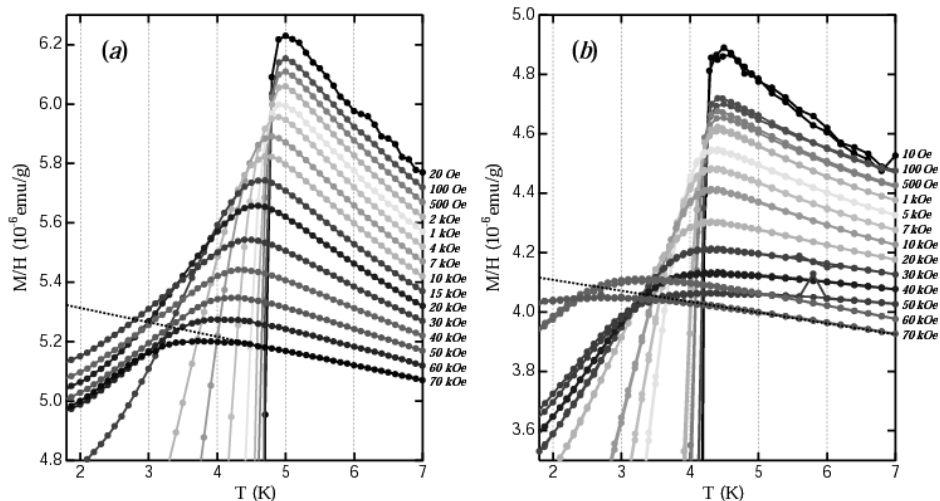


Fig. 15. Magnetic susceptibilities of two samples measured under various fields. Transition temperatures of sample (a) and (b) are $T_c = 4.6$ K and 4.2 K.

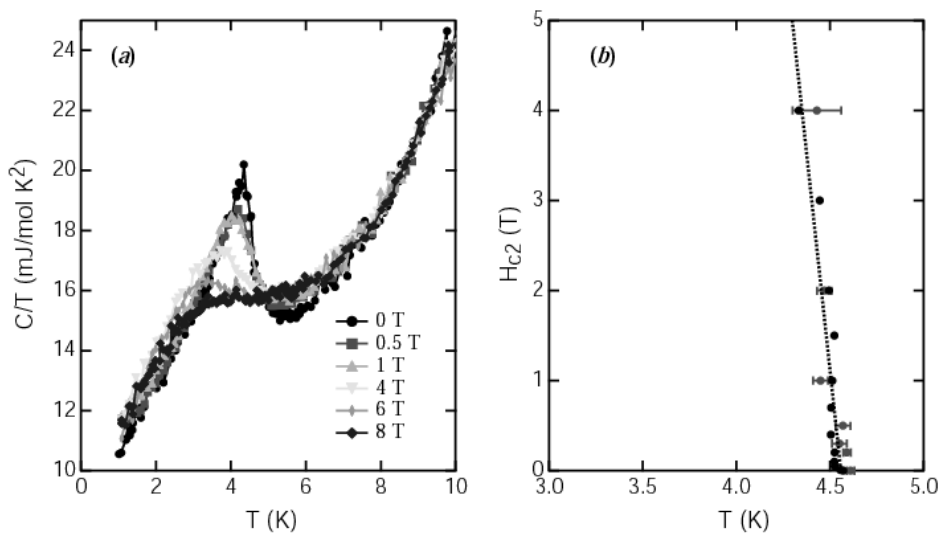


Fig. 16. (a) Specific heats measured under various fields. (b) Transition temperature under various fields estimated from the magnetic (black) and specific heat (red) measurements.

Table 3. Estimations of H_{c2} . IS is the initial slope of $-dH_{c2}/dT|_{H=0}$. H_p , M , ρ , and C represent Pauli limit ($H_p=1.84T_c$), no orientation because of powder sample, magnetic measurement, electrical resistivity measurement, specific heat measurement, respectively. WHH model is $H_{c2} = -0.7 \cdot dH_{c2}/dT|_{H=0} \cdot T_c$ [87].

| T_c [K] | IS [T/K] | $H_{c2}(0)$ [T] | orientation | measurement | estimation | Ref. |
|-----------|------------|-----------------|-------------|--------------------|-------------------|------|
| 4.6 | 19.3 | 61 | P | M | WHH model | [86] |
| 4.3 | 3.4 | 10 | P | ρ | WHH model | [88] |
| 4.6 | 5.8 | - | P | C ($H < 1T$) | - | [85] |
| | 16.3 | - | | average ($< 8T$) | | |
| 4.3 | 9.4 | 28 | $H//ab$ | M ($H > 1T$) | WHH model | [89] |
| | 1.7 | 5.2 | $H//c$ | M ($H < 0.1T$) | | |
| 4.2 | ~ 5.5 | ~ 8 | $H//ab$ | ρ | Estimated in | [40] |
| | ~ 1.0 | ~ 3 | $H//c$ | ρ | the present study | |
| 4.5 | 4.7 | H_p (8.3) | $H//ab$ | ρ | Extrapolation | [90] |
| | 0.53 | ~ 1.7 | $H//c$ | ρ | | |
| 3.7 | 6.12 | 15.6 | $H//ab$ | M | WHH model | [43] |
| | 1.41 | 3.6 | $H//c$ | M | | |

Lower-critical field, $H_{c1} = \Psi_0/2\pi\lambda^2 \ln \kappa$ (κ : penetration depth, and $\kappa = \lambda/\xi$: Ginzburg-Landau parameter), is also an important parameter and has been reported from three groups. Sakurai *et al.* estimated H_{c1} , $\lambda(0)$, and κ to be 28.1 Oe, 5680 Å, and 244 for a sample with $T_c = 4.6$ K, respectively [86]. According to Cao *et al.*, $H_{c1} = 13$ Oe, $\lambda = 7900$ Å, and $\kappa \sim 140$ for a sample with $T_c = 4.3$ K [88]. Badica *et al.* estimated $H_{c1}^{H//c}$ to be 17 Oe, and λ_{ab} and λ_c to be 6410 Å and 27560 Å, respectively for a rather low T_c sample with $T_c = 3.7$ K [43]. These λ values except for the λ_c value by Badica *et al.* are consistent with μ SR measurements which gave λ values of 9100 Å at 0.37 K under 400 Oe for a $T_c = 3.5$ K sample [92], 7000 Å at 2 K under 374 Oe for a $T_c = 4.6$ K sample [93], and 7200 Å at 0 K under 200 Oe for a $T_c = 4.5$ K sample [28]. From these facts, it is obvious that the present compound belongs to a family of extreme type II superconductors, as in the case of high T_c cuprates.

3.2.3 Magnetic and electrical properties above T_c

Normal-state magnetic susceptibilities χ above T_c are shown in Fig. 17 for the BLH- and MLH-phases with approximate compositions of $\text{Na}_x\text{CoO}_2 \cdot y\text{H}_2\text{O}$, $y = 1.3$ and 0.7 , respectively. Enhancement of the susceptibility is seen in a low temperature region in the BLH-phase with a broad minimum at ca. 130 K, which is much higher than 60 K in the MLH-phase. This suggests strongly that the enhancement is not due to a magnetic impurity phase but has an intrinsic origin [86, 94], which is consistent with μ SR, NQR and NMR measurements [93, 95, 96] (see below). Ferromagnetic fluctuation was proposed as the origin of the enhancement of χ [95]. Indeed, ferromagnetic tendency was expected by band calculations [33, 97, 98]. Related to this magnetic anomaly, it is notable that photoemission spectrum (PES) showed development of pseudogap near the Fermi level below 130 K [99]. The enhancement in χ may have important relevance to superconductivity as suggested by Ishida *et al.* and Ihara *et al.* [95, 100].

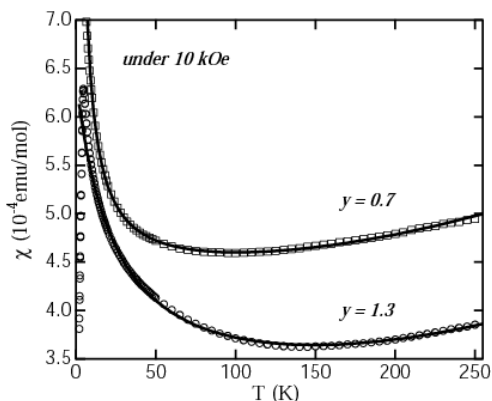


Fig. 17. Magnetic susceptibilities of BLH- and MLH- Na_xCoO_2 ($y = 1.3$ and 0.7 , respectively).

The χ of the BLH-phase has a value of $\sim 4 \times 10^{-4}$ emu/mol [40, 42, 86, 89, 90] which seems somewhat larger than the typical Pauli paramagnetic susceptibility. This seems to be explained by the ferromagnetic fluctuation even above 130 K. The Wilson ratio, $R = \pi^2/3 \times (k_B \mu)^2 \times \chi / \gamma$ (k_B : Boltzmann constant, μ_B : Bohr magneton, and γ : Sommerfeld constant), was calculated to be 1.5–2.9 using $\gamma = 10$ –20 mJ/molK² (see below), implying ferromagnetic correlation. Even much larger χ of $\sim 1.3 \times 10^{-3}$ and $\sim 1.9 \times 10^{-3}$ emu/mol have been reported [88, 101].

Only few data are available on the anisotropy of the normal-state magnetization. The information on the anisotropy may be useful to deduce the spin state of the Cooper pair. Chou *et al.* reported that $\chi^{H//ab}$ is approximately twice as large as $\chi^{H//c}$ and the anisotropy becomes larger with increasing the water content [40, 102]. The former result is consistent with the field orientation experiment for a powder sample [103]. The latter is probably related to the shrinkage of CoO_2 layer along the c -axis with the intercalation of the water molecules.

An anomalous kink has been observed in χ vs. T curves at 42 - 45 K in single-crystal measurements [40, 90, 102]. This anomaly is probably caused by oxygen existing inside the crystal as suggested by Sasaki *et al.* [90], although Chou *et al.* suggested that it was intrinsic [102]. Similar anomaly is sometimes seen even for a powder sample but it disappears when the sample is slowly cooled down from 250 K. Once the anomaly disappears, it is never seen in any thermal procedure below 250 K. As stated previously, oxygen gas will be evolved by the reductive reaction during the hydration process. Such oxygen seems to be confined inside a sample and affect the magnetism.

The electrical resistivities, ρ , of the BLH-phase in the ab plane show metallic behavior above T_c [40, 90]. Although the ρ - T curve seems to bend at 50 - 120 K as in the case of the parent oxide Na_xCoO_2 ($x = 0.70 - 0.78$) [21], detailed analysis has not been done on this point. Charge ordering into the Co^{3+} and Co^{4+} ions was claimed to occur at 15 K by PES [104], suggesting that the transport mechanism is not simple. The resistivity along the c -axis showed a broad maximum at approximately 200 K [40] and a similar behavior has been observed for the parent oxide of $\gamma\text{-Na}_x\text{CoO}_2$ [15], in spite of the doubled c -axis length in the BLH-phase. Upturn of ρ in a low temperature region is always seen in measurement for a powder sample

[2, 105, 106]. This anomaly looks to be due to grain boundary effect. However, we cannot rule out a possibility that the upturn reflects an intrinsic nature because it apparently corresponds to the rapid development of pseudogap below 40 - 45 K observed by PES and tunneling spectroscopy [99, 106] and such a behavior is expected from the t - J model on the electron-doped triangular lattice [107]. It should be noticed for the present system that single-crystal measurements does not always give more reliable results. It is easily imagined that guest species of the Na^+ ions, the water molecules and the H_3O^+ ions are not distributed uniformly throughout a single crystal after the soft-chemical synthesis process at room temperature. For instance, a metal-insulator transition was observed at 52 K in a single crystal [42], but it was probably caused by existence of domains of the AH-phase because a very similar metal-insulator transition has been observed at 53 K in an AH-sample with $x = 0.5$, [27].

3.2.4 Specific Heat

Specific heat data are expected to give useful information on the symmetry of superconducting gap function. Thus, many studies have been carried out on the BLH-phase, but phonon contribution and large residual Sommerfeld constant γ at 0 K make the analysis difficult.

Sommerfeld constant at normal state γ_n has been estimated simply by the function of $C/T = \gamma T + \beta T^2$ using C/T data between just above T_c and around 10 K. The values reported thus far are 16.1 mJ/mol \cdot K 2 (for a sample with $T_c = 4.5$ K) [42], 15.9 mJ/molK 2 ($T_c = 4.3$ K) [88], and 12.2 mJ/mol \cdot K 2 ($T_c = 4.2$ K) [108]. They are smaller than those reported for γ Na_xCoO_2 (26 - 31 mJ/mol \cdot K 2) [21], and are consistent with the result of band calculation [33]. However, it should be noted that entropy balance regarding the superconducting transition did not hold in these estimations, i.e., on the C/T - T curve, the positive and negative areas below T_c between the observed curve and the extrapolated one for the estimation were not compensated to null. In particular, in the case of Refs. [42] or [88], the positive area was much smaller than the negative one, and such a result cannot be explained by Schottky anomaly and/or other effects.

Analysis taking the entropy balance into account is possible and has been carried out by Yang *et al.* [85] and Lorenz *et al.* [109]. The γ_n and Debye temperature Θ reported by the two groups are $\gamma_n = 14.89$ mJ/molK 2 and $\Theta = 503$ K (for a sample with $T_c = 4.7$ K), and $\gamma_n = 10.8$ mJ/molK 2 and $\Theta \sim 280$ K ($T_c = 4.77$ K), respectively. There are large differences in two sets of data. The data of Yang *et al.* showed a large residual γ at 0 K of approximately 12 mJ/molK 2 , which is almost the same as the values by other groups [40, 42, 88, 108], while no residual γ in the data of Lorenz *et al.* In addition, the C/T value of Lorenz *et al.* at 10 K is approximately 58 mJ/molK, much larger than the values observed by other groups (~ 33 - 40 mJ/molK) [40, 42, 88, 108]. The origin of such large differences are not known at present, but probably not due to the sample quality because the Lorenz *et al.*'s sample had almost the same T_c as the Yang *et al.*'s, one.

Considering the superconducting volume fraction, Lorentz *et al.* strongly suggested the existence of line nodes on the Fermi surface. Yang *et al.* reached the same conclusion from T linear behavior of C_s/T (C_s : specific heat contributed by superconducting electrons). In addition, they observed specific heats consistent with the nodal superconducting symmetry at the entire T range below T_c for a sample with slightly lower T_c [110]. The nodal symmetry is

supported by μ SR and NQR measurements as discussed below. Lorenz *et al.* suggested the weak-coupling regime, while Yang *et al.* the strong-coupling regime, according to the normalized specific heat jump at T_c , $\Delta C/\gamma_n T_c$ of 0.99 and 1.96, respectively (Yang *et al.* have used $\gamma'_n = 3.96 \text{ mJ/molK}^2$ considering the superconducting volume fraction).

The residual γ is likely to be originated by non-superconducting portion which may be caused by sample inhomogeneity, and indeed, the superconducting volume fraction has been estimated from residual γ to be 18.1 - 26.6% [85, 88]. This range of the fraction seems rather small for a single-phase superconducting sample even the inhomogeneity is considered. As pointed out by Phillips [111], a similar phenomenon is seen in MgB_2 , for which an apparent residual γ of approximately 1 mJ/molK^2 would be estimated if only the data above 10 K are used [112, 113, 114]. In fact, the apparent residual γ disappears by further decrease of C/T below 8 K caused by a second superconducting gap. In the case of the present BLH-phase, the residual γ is relatively large compared with the specific heat jump at T_c and no steep decrease is observed in C/T down to 0.6 K [85]. These facts may suggest that in one of two types of Fermi surfaces, for example, in six holelike sections near K-point, superconducting gap does not develop. Namely, the non-superconducting volume fraction is possibly caused by the "non-superconducting" Fermi surface [111], although such a situation has not been found in other oxide superconductors. Such Fermi surface may cause large residual density of states (DOS) observed in $1/^{59}\text{Tl}T$ measurement in NQR, which is estimated to be 32% even for a good quality of sample [95].

It is notable that tail of the jump of C/T spreads above T_c in relatively wide temperature range and the range becomes much wider with increasing magnetic field as seen in Fig. 16(a). This fact suggests that the superconducting fluctuation develops in the wide temperature range above T_c and it is enhanced by magnetic field. Phillips pointed out that this is one of the evidences of the magnetic fluctuation [111].

3.2.5 μ SR

The μ SR is a powerful tool to detect a tiny internal field and one of the most important methods to determine whether the superconducting gap function has a chirality. On the other hand, one of the weak points is that the muon stopping site is sometimes difficult to be specified. In the case of the BLH-phase, Higemoto *et al.* [93] have determined the muon site to be around (02, 0.25, 0.12), which is located between the CoO_2 and water layers, by comparing dipolar widths of $\text{Na}_x\text{CoO}_2 \cdot y\text{H}_2\text{O}$ ($T_c = 4.6 \text{ K}$) and $\text{Na}_x\text{CoO}_2 \cdot y\text{D}_2\text{O}$ ($T_c = 4.6 \text{ K}$). Moreover, they have estimated the hyperfine coupling constant to be ${}^{\mu}\text{A}_{\text{hf}} = -0.20 \text{ kOe}/\mu_B$ from the ${}^{\mu}\text{K}$ - χ plot (${}^{\mu}\text{K}$: muon Knight shift) as described later. This value of ${}^{\mu}\text{A}_{\text{hf}}$ warrants that μ SR measurements reflect enough the electronic properties of the CoO_2 layer.

Zero-field (ZF) μ SR has indicated no internal field higher than 0.1 Oe at the muon site in the superconducting phase [93]. This means that there is no static magnetic moment larger than $0.002 \mu_B/\text{Co}$. Uemura *et al.* measured ZF- μ SR for an aligned powder sample of $\text{Na}_{0.35}\text{CoO}_2 \cdot 1.3\text{D}_2\text{O}$ ($T_c = 4.2 \text{ K}$) and observed no static internal field higher than 1 Oe, as well [28]. The chiral p - or d -wave superconducting state produces an internal field, and thus, it is not the case if we believe the μ SR results.

Transverse field (TF) μ SR data have been reported by three groups [28, 92, 93]. The temperature dependence of muon relaxation rate σ below T_c deviates from the line expected

from s -wave BCS weak-coupling model or two-fluid model, suggesting a nodal structure of the gap function [28, 92]. Uemura *et al.* observed no dependence of σ on TF in the field range of 0.1–2 kOe, which assures no involvement of 2D pancake vortex formation [28]. From the Uemura's plot, this compound belongs to a family which includes high T_c cuprates and other 2D superconductors [92, 28]. Kanigel *et al.* and Uemura *et al.* estimated the effective mass to be 75 - 100 times larger than the mass of the bare electron, assuming the carrier density equal to x [92, 28]. When we use the real carrier density taking account the H_3O^+ ions, the effective mass is still much larger than the mass of the bare electron.

Higemoto *et al.* estimated ${}^{\mu}\text{K}$ under 6 T [93] and found that it is proportional to the uniform magnetic susceptibility χ above 10 K. This indicates that the estimation of ${}^{\mu}\text{K}$ is reliable and that the enhancement of χ below approximately 130 K is intrinsic. Their enhancements are considered to reflect the ferromagnetic fluctuation as mentioned above, which is supported by NQR and NMR measurements. ${}^{\mu}\text{K}$ does not decrease below T_c with decreasing temperature. They claimed that this behavior was not explained by diamagnetic shift upon the formation of flux lattice and suggested the spin-triplet Cooper pair [93].

3.2.6 NQR

The nuclear quadrupole resonance (NQR) is one of the most useful techniques to investigate the superconducting state without magnetic field. The spin-lattice relaxation rate $1/T_1$ is a good probe to investigate the electronic state. When superconducting gap opens without nodes, Hebel-Schlichter peak (coherence peak) appears in $1/T_1$ - T plot and $1/T_1$ decays exponentially below T_c . On the other hand, in a case of anisotropic gap function with nodes, the coherence peak disappears and $1/T_1$ decays with a power-law dependence on temperature. Thus, the measurement of $1/T_1$ will lead to the elucidation of the superconducting gap symmetry.

The temperature dependence of $1/{}^{59}\text{T}_1$ reported by Ishida *et al.* is shown in Fig. 18 [95]. This figure clearly shows absence of the coherence peak and T^3 -dependence of $1/T_1$ from T_c to near 1 K. Fujimoto *et al.* reported similar result [115], although T_c of their sample (3.9 K) is lower than that of Ishida's (4.7 K), and, residual DOS (65%) is much larger than that in Ishida's data (32%). At the early stage of the research, presence of the coherence peak was claimed based on NMR and NQR measurements [101, 103]. At present, however, the peak observed by the NMR measurement is considered to be due to dynamics of vortices whose motions are slow comparable to NMR frequency [116]. The peak observed by the NQR measurement has not been reproduced [117]. Absence of the coherence peak and the T^3 -dependence of $1/{}^{59}\text{T}_1$ confirmed for the good quality of sample deny explicitly the s -wave symmetry which should show a large coherence peak. However, it is not easy to deny possibility of the chiral p - or chiral d -wave symmetry because the coherence peak could be too small to be detected in such a case. Fujimoto *et al.* suggested that their temperature dependency of $1/{}^{59}\text{T}_1$ could be explained by chiral p - or chiral d -wave taking an impurity effect into account [118, 119]. Although the superconducting gap function with line nodes on the Fermi surface is most probable at present, the possibility of the chiral p - or chiral d -wave still remains in spite of the μSR results.

Ishida *et al.* found that $1/{}^{59}\text{T}_1 T$ increases with decreasing temperature above T_c and is proportional to the uniform susceptibility [95]. This again indicates that the upturn of χ below 130 K is intrinsic and is likely caused by the ferromagnetic fluctuation. It was proved that T_c decreases as the enhancement is less pronounced [100]. Fujimoto *et al.* also reported the

upturn of $1/^{59}\text{T}_1$ (for a sample with $T_c = 3.9$ K), although they ascribed it to antiferromagnetic fluctuation. Fujimoto *et al.* estimated Weiss temperature to be -42 K. On the other hand, the uniform susceptibility for a $T_c = 4.6$ K sample gave Weiss temperature of -37.6 K [86], and it is expected to decrease with decreasing T_c [100]. Thus, the upturn observed by Fujimoto *et al.* seems to correspond to the upturn in the uniform susceptibility. The superconducting transition seems to be triggered by the ferromagnetic fluctuation. Of course, these results do not deny the existence of antiferromagnetic fluctuation. Antiferromagnetic fluctuation is likely to coexist as in the case of $\gamma\text{-Na}_x\text{CoO}_2$ [24], judging from the shape of the Fermi surface with many nesting vectors.

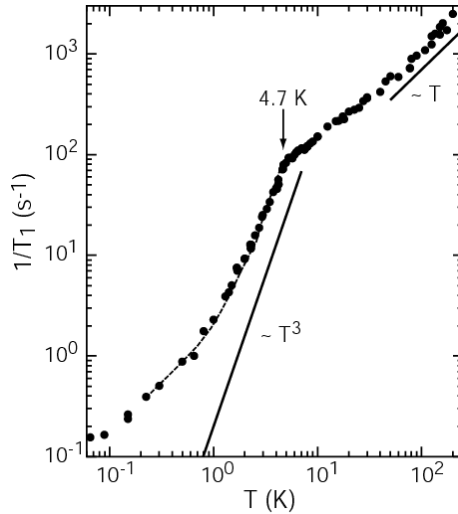


Fig. 18. $1/^{59}\text{T}_1T$ obtained by NQR measurement.

3.2.7 NMR

Knight shift is important because spin susceptibility can be estimated from it, and thereby it reflects the spin state of the Cooper pair. In the case of singlet pair, all the Knight shifts, K_x , K_y , and K_z , are expected to change below T_c , while, in the case of triplet pair, Knight shift along a certain direction is expected to be invariant.

Knight shift has been reported by two groups [103, 96, 120]. Waki *et al.* measured ^{59}K under 4.8 T and found that it had an almost constant value below T_c [103]. On the other hand, Kobayashi *et al.* reported a steep decrease of $^{59}\text{K}_y$ below T_c under 1.5 T and 2.8 T [120]. Later, it was confirmed that the apparent Knight shift below T_c depends on the magnetic field, and it is independent of temperature down to 2 K if it was measured under 7 T [96]. The Knight shift should be independent of the field and several possibilities are needed to be considered; (i) T_c under 7 T is lower than 2 K, (ii) superconducting volume fraction under 7 T is too small to detect the Knight shift of the superconducting state, (iii) the diamagnetic effect is large under low magnetic field causing the apparent decrease of the Knight shift, and (iv) a certain unknown phenomenon occurs, such as the change of the spin state of Cooper pair by field. (i)

and (ii) do not seem the case, because Michioka *et al*'s sample had a quality as good as the one seen in Fig. 15(a) and the $1/T_1$ measurements showed T_c to be around 4 K [116] even under 7 T. On the other hand, (iii) and (iv) are not ruled out. It is likely that the diamagnetic effect influences the estimation of ^{59}K to some extent. Indeed, from $^{59}\text{K}_y$ - χ plot above T_c , it was concluded that temperature independent term in $^{59}\text{K}_y$ is approximately 3.1% while the temperature dependent term (spin part) is only $\sim 0.1\%$ [96]. Thus, $^{59}\text{K}_y$ should not decrease so much as observed by Kobayashi *et al.* (down to 2.6%) [120], even assuming the spin singlet pairing. The temperature dependence of Knight shift is still open to discussion and further studies are needed to decide definitely the spin state of the Cooper pair. The ^{59}K - χ plot again indicated that the upturn of χ below 130 K is intrinsic.

3.2.8 Other topics

The pseudogap has been observed by PES [99] and tunneling spectroscopy [106]. The energy gap of ~ 20 meV is much larger than the superconducting gap of $\Delta \sim 1$ meV (estimated from the equation of $2\Delta/k_B T_c = 3.54$), while is close to that in magnetic interaction (10 – 20 meV) [99]. From Raman measurement, the magnetic interaction was expected to be approximately 130 K (= 11 meV) [121]. Thus, the pseudogap seems to reflect a certain magnetic state, although we cannot rule out the possibility of band pseudogap due to the fluctuation of charge disproportionation [33] in consideration of another PES result [104]. This pseudogap behavior seems to contradict NQR measurements [95,100] which indicated that DOS is enhanced in the low temperature region. At the present stage, the real origin of the pseudogap is unclear, but it may be notable that the field dependence of the pseudogap is different from the case of high T_c cuprates [106].

Pressure effect on T_c has been reported by Lorenz *et al* [122] to be $d\ln T_c/dp = -0.07 \sim -0.1$ G/Pa (p : pressure), which is close to the typical value of electron-doped high T_c cuprates [122]. Since the compressibility along the c -axis is much larger than that along the a -axis in the BLH-phase [39], the negative pressure dependence of T_c suggests the importance of the 2D character on superconductivity. This fact is consistent with the c/a dependence of T_c [70] mentioned previously. However, there is a report which suggested that T_c decreased with increasing the c -axis length [123].

Thermopower of the BLH-phase is saturated at approximately $S = 35$ $\mu\text{V}/\text{K}$ above about 130 K, which is much smaller than 80 $\mu\text{V}/\text{K}$ of $\text{Na}_{0.7}\text{CoO}_2$ at 300 K (thermopower continues to increase above 300 K) [105]. Since the saturation is considered to be caused by the narrow band, this fact indicates band narrowing in the BLH-phase compared with the parent γ - $\text{Na}_{0.7}\text{CoO}_2$ phase. The band narrowing tendency is in conflict with the carrier-density dependence of the band width [98], and is probably caused by the water molecules intercalated which are expected to make the a_{1g} band narrow [32].

Impurity effect on T_c has been reported by Yokoi *et al* [117]. The substitution of Ir or Ga for Co caused T_c reduction at the rate of ~ 1.0 K/1%Ir or ~ 2.0 K/1%Ga, respectively. They concluded that these small rates were consistent with the pair breaking by a non-magnetic impurity in the s -wave superconductivity, inconsistent with the non- s -wave superconductivity suggested by the specific heat, μSR , and NQR measurements. They deduced that the Ir ion was non-magnetic because the magnetic moment estimated by Curie-Weiss law did not increase with increasing the Ir content in parent $\text{Na}_{0.75}\text{Co}_{1-x}\text{Ir}_x\text{O}_2$. However, the Ir ion does not always take the trivalent state. The magnetic moment would not be changed by the

substitution of magnetic Ir^{4+} ions ($S=1/2$) for the Co^{4+} ions ($S=1/2$), even if $\text{Na}_{0.75}\text{CoO}_2$ was local moment system. Indeed, the Ir ion very often takes the tetravalent state ($5d^5$) or sometimes even higher states of +5 and +6 [124, 125]. Thus, the tetravalent state is most likely for the Ir ion in the BLH-phase in which Co valence is between +3 and +4. Yokoi *et al*'s results may imply no large difference between the non-magnetic and magnetic impurities in the suppression rate of T_c , although the reason for the small reduction rates is unknown.

The magnetic susceptibility of the MLH-phase (monolayer hydrated phase with $y = 0.7$) is larger than that of the BLH-phase with $y = 1.3$ [94,102], but the upturn begins at a much lower temperature near 60 K as shown in Fig. 17 [94]. In the BLH-phase, the upturn is intrinsic caused probably by the ferromagnetic fluctuation as mentioned previously. The upturn in the MLH-phase seems to have an extrinsic origin because almost temperature independent $1/^{59}\text{Tl}T$ was observed by NQR measurement for the MLH-phase [95]. However, muon Knight shift $^{\mu}\text{K}$ of the MLH-phase shows the upturn below 60 K down to approximately 20 K. In addition, $1/^{59}\text{Tl}T$ seems to show weak temperature dependence above 20 K. Thus, the ferromagnetic fluctuation seems to enhance the magnetic susceptibility, at least to some extent, in the MLH-phase as well, although the enhancement is much smaller compared with the BLH-phase. The enhancement of the susceptibility does not continue below 20 K in the MLH-phase according to the μSR study, in contrast to the BLH-phase. This may be related to the band narrowing and a reduction in the band splitting in the BLH-phase due to the intercalated water molecules, as suggested by band calculations [31, 32, 34]. Another difference between the two phases is seen in much less pronounced magnetic anisotropy in the MLH-phase [102].

Tunneling spectroscopy studies are desirable to elucidate the superconducting symmetry since spectrums corresponding to various symmetries have been already calculated theoretically [126, 127, 128, 129]. In addition, neutron scattering experiments seem also useful to solve the problem [130].

4. SUMMARY

The superconducting cobalt oxide hydrate is synthesized by the soft chemical technique from the parent oxide of $\gamma\text{-Na}_{0.7}\text{CoO}_2$. The soft chemical route includes two processes, the chemical oxidation using bromine (Br_2) and immersion in water. The former process can be substituted by oxidation by other chemicals such as $\text{Na}_2\text{S}_2\text{O}_8$ and KMnO_4 , as well as by electrochemical oxidation. Two main reactions occurring in these processes are deintercalation of the Na^+ ions (oxidation) and intercalation of H_2O molecules (hydration). The H_2O intercalation results in an increase of the distance between the CoO_2 layers from 5.5 Å in the parent phase to 9.8 Å in the superconducting phase. The H_2O molecules coordinate to the Na^+ ions and form two water layers sandwiching the Na plane, transforming the parent oxide into the bilayer-hydrate (BLH) phase.

Formation process of the superconducting phase had been believed to involve only the oxidative extraction of the Na^+ ions and insertion of H_2O molecules. However, the actual processes are much more complicated. A part of the sodium ions are exchanged by the H_3O^+ ions and further H_3O^+ ions are inserted reducing the Co ions. Thus, the exact chemical formula of the superconducting phase is $\text{Na}_x(\text{H}_3\text{O})_z(\text{H}_2\text{O})_n\text{CoO}_2$ rather than $\text{Na}_x\text{CoO}_{2-y}\text{H}_2\text{O}$ which has been used widely.

Physical and superconducting properties of the BLH-phase have been intensively studied thus far. Thanks to these studies, followings have become quite likely for the present system. (i) the compound belongs to the extreme type-II family, (ii) superconducting gap function is not *s*-wave but has line nodes on the Fermi surface, (iii) time-reversal symmetry is preserved, and (iv) magnetic susceptibility shows upturn below about 130 K due to the ferromagnetic fluctuation. On the other hand, there are various problems to be solved, such as (i) strong coupling or weak coupling, (ii) spin singlet pairing or triplet pairing, (iii) relationship between superconductivity and the ferromagnetic fluctuation, (iv) origin of the large residual Sommerfeld constant at 0 K, etc. Further studies are needed for understanding the physics of the system.

ACKNOWLEDGEMENTS

Special thanks to S. Takenouchi, Y. Yajima, and H. Komori (NIMS) for suggestions on composition analysis. We would like to thank T. Sasaki, M. Arai, A. Tanaka, H. Xu (NIMS), and all other collaborators for fruitful discussions and suggestions. This work is partially supported by CREST, Japan Science and Technology Agency and by Grants-in-Aid for Scientific Research (1634011, 16076209) from Japan Society for the Promotion of Science (JSPS). H. S. is a Research Fellow of JSPS.

REFERENCES

- [1] J. C. Bednorz and K. A. Müller. *Z. Phys. B* 64 (1986) 189.
- [2] K. Takada, H. Sakurai, E. Takayama-Muromachi, F. Izumi, R. A. Dilanian, and T. Sasaki, *Nature* 422 (2003) 53.
- [3] H. Aoki, *J. Phys.: Condens. Matter* 16 (2004) V1 and references therein.
- [4] W. D. Johnston, R. R. Heikes, and S. Sestrich, *J. Phys. Chem. Solids* 7 (1958) 1.
- [5] C. Fouassier, G. Matejka, J. -M Reau, and P. Hagenmuller, *J. Solid State Chem.* 6 (1973) 532.
- [6] V. H. Jansen and R. Hoppe, *Z. Anorg. Allg. Chem.* 408 (1974) 97.
- [7] R. G. Delaplane, J. A. Ibers, J. R. Ferraro, and J. J. Rush, *J. Chem. Phys.* 50 (1969) 1920.
- [8] R. D. Shannon, D. B. Rogers, and C. T. Prewitt, *Inorg. Chem.* 10 (1971) 713.
- [9] C. Delmas, C. Fouassier, and P. Hagenmuller, *Physica* 99B (1980) 81.
- [10] J. -J. Braconnier, C. Delmas, C. Fouassier, and P. Hagenmuller, *Mat. Res. Bull.* 15 (1980) 1797.
- [11] J. N. Reimers and J. R. Dahn, *J. Electrochem. Soc.* 139 (1992) 2091.
- [12] K. Mizushima, P. C. Jones, P. J. Wiseman, and J. B. Goodenough, *Mat. Res. Bull.* 15 (1980) 783.
- [13] A. Mendiboure, C. Delmas, and P. Hagenmuller, *Mat. Res. Bull.* 19 (1984) 1383.
- [14] D. Carlier, I. Saadoune, M. Ménétrier, and C. Delmas, *J. Electrochem. Soc.* 149 (2002) 1310.
- [15] I. Terasaki, Y. Sasago, and K. Uchinokura, *Phys. Rev. B* 56 (1997) R12685.
- [16] T. Motohashi, R. Ueda, E. Naujalis, T. Tojo, I. Terasaki, T. Atake, M. Karppinen, and H. Yamauchi, *Phys. Rev. B* 67 (2003) 064406.
- [17] J. Sugiyama, H. Itahara, J. H. Brewer, E. J. Ansaldo, T. Motohashi, M. Karppinen, and H. Yamauchi, *Phys. Rev. B* 67 (2003) 214420.
- [18] D. J. Singh, *Phys. Rev. B* 61 (2000) 13397.
- [19] K. Miyoshi, E. Morikuni, K. Fujiwara, J. Takeuchi, and T. Hamasaki, *Phys. Rev. B* 69 (2004) 132412.
- [20] H. Sakurai, S. Takenouchi, N. Tsujii, and E. Takayama-Muromachi, cond-mat/0407613, *J. Phys. Soc. Jpn.* 73 (2004) 2081.
- [21] H. Sakurai, N. Tsujii, and E. Takayama-Muromachi, cond-mat/0407614, *J. Phys. Soc. Jpn.* 73 No. 9, in print.
- [22] M. Z. Hasan, Y.-D. Chuang, D. Qian, Y.W. Li, Y. Kong, A. Kuprin, A. V. Fedorov, R. Kimmberling, E. Rotenberg, K. Rossnagel, Z. Hussain, H. Koh, N. S. Rogado, M. L. Foo, and R. J. Cava, *Phys. Rev. Lett.* 92 (2004) 246402.
- [23] N. L. Wang, P. Zheng, D. Wu, Y. C. Ma, T. Xiang, R. Y. Jin, and D. Mandrus, cond-mat/0312630.
- [24] Y. Ihara, K. Ishida, C. Michioka, M. Kato, K. Yoshimura, H. Sakurai, E. Takayama-Muromachi, cond-mat/0407195.
- [25] S. Y. Li, L. Taillefer, D. G. Hawthorn, M. A. Tanatar, J. Paglione, M. Sutherland, R. W. Hill, C. H. Wang, and X. H. Chen, *Phys. Rev. Lett.* 93 (2004) 056401.
- [26] F. Rivadulla, M. Bañbre-López, M. A. López-Quintela, and J. Rivas, cond-mat/0403687.
- [27] M. L. Foo, Y. Wang, S. Watauchi, H. W. Zandbergen, T. He, R. J. Cava, and N. P. Ong, *Phys. Rev. Lett.* 92 (2004) 247001.

- [28] Y. J. Uemura, P. L. Russo, A. T. Savici, C. R. Wiebe, G. J. MacDougall, G. M. Luke, M. Mochizuki, Y. Yanase, M. Ogata, M. L. Foo, and R. J. Cava, *cond-mat/0403031*.
- [29] T. Yamamoto, K. Uchinokura, and I. Tsukada, *Phys. Rev. B* 65 (2002) 184434.
- [30] J. Sugiyama, J. H. Brewer, E. J. Ansaldo, H. Itahara, T. Tani, M. Mikami, Y. Mori, T. Sasaki, S. Hébert, and A. Maignan, *Phys. Rev. Lett.* 92 (2004) 017602.
- [31] M. D. Johannes and D. J. Singh, *Phys. Rev. B* 70 (2004) 014507.
- [32] L.-J. Zou, J.-L. Wang, and Z. Zeng, *Phys. Rev. B* 69 (2004) 132505.
- [33] K. W. Lee, J. Kuneš, and W. E. Pickett, *Phys. Rev. B* 70 (2004) 045104.
- [34] C. A. Marianetti, G. Kotliar, and G. Ceder, *Phys. Rev. Lett.* 92 (2004) 196405.
- [35] K. Takada, H. Sakurai, E. Takayama-Muromachi, F. Izumi, R. A. Dilanian, and T. Sasaki, *Physica C* in press.
- [36] S. Kikkawa, S. Miyazaki, and M. Koizumi, *J. Solid State Chem.* 62 (1986) 35.
- [37] C.-J. Liu, C.-Y. Liao, L.-C. Huang, C.-H. Su, S. Neeleshwar, and Y.-Y. Chen, *cond-mat/0405244*.
- [38] S. Miyazaki, S. Kikkawa, and M. Koizumi, *Synth. Met.* 6 (1983) 211.
- [39] S. Park, Y. Lee, A. Moodenbaugh, and T. Vogt, *Phys. Rev. B* 68 (2003) 180505(R).
- [40] F. C. Chou, J. H. Cho, P. A. Lee, E. T. Abel, K. Matan, and Y. S. Lee, *Phys. Rev. Lett.* 92 (2004) 157004.
- [41] D. P. Chen, H. C. Chen, A. Maljuk, A. Kulakov, H. Zhang, P. Lemmens, and C. T. Lin, *Phys. Rev. B* 70 (2004) 024506.
- [42] R. Jin, B. C. Sales, P. Khalifah, and D. Mandrus, *Phys. Rev. Lett.* 91 (2003) 217001.
- [43] P. Badica, T. Kondo, K. Togano, and K. Yamada, *cond-mat/0402235*.
- [44] R. Chen, P. Zavalij, and M.S. Whittingham, *Chem. Mater.* 8 (1996) 1275.
- [45] K. Takada, H. Sakurai, E. Takayama-Muromachi, F. Izumi, R. A. Dilanian, and T. Sasaki, *J. Solid State Chem.* 177 (2004) 372.
- [46] M. L. Foo, R. E. Schaak, V. L. Miller, T. Klimczuk, N. S. Rogado, Y. Wang, G. C. Lau, C. Craley, H. W. Zandbergen, N. P. Ong, and R. J. Cava, *Solid State Commun.* 127 (2003) 33.
- [47] J. Cmaidalka, A. Baikalov, Y. Y. Xue, R. L. Meng, and C. W. Chu, *Physica C* 403 (2004) 125.
- [48] C. T. Lin, D. P. Chen, P. Lemmens, X. N. Zhang, A. Maljuk, and P. X. Zhang, *cond-mat/0407086*.
- [49] K. Takada, H. Sakurai, E. Takayama-Muromachi, F. Izumi, R. A. Dilanian, and T. Sasaki, *Adv. Mater.* (in press).
- [50] M. L. Foo, T. Klimczuk, L. Li, N. P. Ong, and R. J. Cava, *cond-mat/0406409*.
- [51] H. Sakurai, K. Takada, F. Izumi, D. A. Dilanian, T. Sasaki, and E. Takayama-Muromachi, *J. Phys. Soc. Jpn.* 73 (2004) No. 9 (in press).
- [52] R. E. Schaak, T. Klimczuk, M. L. Foo, and R. J. Cava, *Nature* 424 (2003) 527.
- [53] K. Takada, K. Fukuda, M. Osada, I. Nakai, F. Izumi, R. A. Dilanian, K. Kato, M. Takata, H. Sakurai, E. Takayama-Muromachi, and T. Sasaki, *J. Mater. Chem.* 14 (2004) 1448.
- [54] P. Fumagalli, L. Stixrude, S. Poli, and D. Snyder, *Earth Planet. Sci. Lett.* 186 (2001) 125.
- [55] K. K. Nash, K. J. Sully, and A. B. Horn, *J. Phys. Chem. A* 105 (2001) 9422.
- [56] R. W. T. Wilkins, A. Mateen, and G. W. West, *Am. Miner.* 59 (1974) 811.
- [57] K. Ooi, Y. Miyai, S. Katoh, H. Maeda, and M. Abe, *Langmuir* 5 (1989) 150.

- [58] H. Kanoh, Q. Feng, Y. Mayai, and K. Ooi, *J. Electrochem. Soc.* 140 (1993) 3162.
- [59] W. Li, W. R. McKinnon, and J. R. Darn, *J. Electrochem. Soc.* 141 (2310) 1994.
- [60] H. Arai and Y. Sakurai, *Denki Kagaku* 66 (1998) 1206.
- [61] M. Karppinen, I. Asako, T. Motohashi, and H. Yamaguchi, *Chem. Mater.* 16 (2004) 1693.
- [62] J. W. Lynn, Q. Huang, C. M. Brown, V. L. Miller, M. L. Foo, R. E. Schaak, C. Y. Jones, E. A. Mackey, and R. J. Cava, *Phys. Rev. B* 68 (2003) 214516.
- [63] J. D. Jorgensen, M. Avdeev, D. G. Hinks, J. C. Burley, and S. Short, *Phys. Rev. B* 68 (2003) 214517.
- [64] F. Izumi and T. Ikeda, *Mater. Sci. Forum* 321—324 (2000) 198.
- [65] F. Izumi, S. Kumazawa, T. Ikeda, W. -Z. Hu, A. Yamamoto, and K. Oikawa, *Mater. Sci. Forum* 378—381 (2001) 59.
- [66] F. Izumi and R. A. Dilanian, *Recent Research Developments in Physics vol 3*, Transworld Research Network, Trivandrum, (2002) pp. 699—726.
- [67] L. Zhu, K. Seff, D. H. Olson, B. J. Cohen, and R. B. V. Dreele, *J. Phys. Chem. B* 103 (1999) 291.
- [68] I. D. Brown and D. Altermatt, *Acta Crystallogr. Sect. B* 41 (1985) 244.
- [69] R. E. Brese and M. O’Keeffe, *Acta Crystallogr. Sect. B* 47 (1991) 192.
- [70] C. J. Milne, D. N. Argyriou, A. Chemseddine, N. Aliouane, J. Veira, and D. Alber, *cond-mat/0401273*.
- [71] Y. G. Shi, J. Q. Li, H. C. Yu, Y. Q. Zhou, H. R. Zhang, and C. Dong, *Supercond. Sci. Technol.* 17 (2004) 42.
- [72] D. N. Argyriou, C. J. Milne, N. Aliouane, P. G. Radaelli, L. C. Chapon, A. Chemseddine, J. Veira, S. Cox, N. D. Mathur, and P. A. Midgley, *cond-mat/0403661*.
- [73] P. W. Anderson, *Mater. Res. Bull.* 8 (1973) 153.
- [74] G. Baskaran, *Phys. Rev. Lett.* 91 (2003) 097003.
- [75] B. Kumer and B. S. Shastry, *Phys. Rev. B* 68 (2003) 104508 (69 (2004) 059901(E)).
- [76] Q.-H. Wang, D.-H. Lee, and P. A. Lee, *Phys. Rev. B* 69 (2004) 092504.
- [77] P. W. Anderson, *Science* 235 (1987) 1196.
- [78] M. Ogata, *J. Phys. Soc. Jpn.* 72 (2003) 1839.
- [79] A. Tanaka and X. Hu, *Phys. Rev. Lett.* 91 (2003) 257006.
- [80] O. I. Motrunich and P. A. Lee, *Phys. Rev. B* 69 (2004) 214516.
- [81] W. Koshibae and S. Maekawa, *Phys. Rev. Lett.* 91 (2003) 257003.
- [82] Y. Yanase, M. Mochizuki, and M. Ogata, *cond-mat/0407563*.
- [83] K. Kuroki, Y. Tanaka, and R. Arita, *cond-mat/0407587*.
- [84] H. Sakurai, K. Takada, T. Sasaki, and E. Takayama-Muromachi, *cond-mat/0408426*.
- [85] H. D. Yang, J.-Y. Lin, C. P. Sun, Y. C. Kang, K. Takada, T. Sasaki, H. Sakurai, and E. Takayama-Muromachi, *cond-mat/0308031*.
- [86] H. Sakurai, K. Takada, S. Yoshii, T. Sasaki, K. Kindo, and E. Takayama-Muromachi, *Phys. Rev. B* 68 (2003) 132507.
- [87] N. R. Werthamer, E. Helfand, and P. C. Hohenberg, *Phys. Rev.* 147 (1966) 250.
- [88] G. Cao, C. Feng, Y. Xu, W. Lu, J. Shen, M. Fang, and Z. Xu, *J. Phys., Condens. Matter* 15 (2003) L519.
- [89] M. M. Ma ka, M. Mierzejewski, B. Andrzejewski, M. L. Foo, T. Klimczuk, and R. J. Cava, *cond-mat/0402503*.

- [90] T. Sasaki, P. Badica, N. Yoneyama, K. Yamada, K. Togano, and N. Kobayashi, *J. Phys. Soc. Jpn.* 73 (2004) 1131.
- [91] P. Badica, T. Kondo, and K. Togano, *Appl. Phys. Lett.* 84 (2004) 559.
- [92] A. Kanigel, A. Keren, L. Patlagan, K. B. Chashka, P. King, and A. Amato, *Phys. Rev. Lett.* 92 (2004) 257007.
- [93] W. Higemoto, K. Ohishi, A. Koda, R. Kadono, K. Ishida, K. Takada, H. Sakurai, E. Takayama-Muromachi, and T. Sasaki, cond-mat/0310324, *Phys. Rev. B* in press.
- [94] H. Sakurai, K. Takada, F. Izumi, R. A. Dilanian, T. Sasaki, and E. Takayama-Muromachi, cond-mat/0310717, *Physica C*, in press.
- [95] K. Ishida, Y. Ihara, Y. Maeno, C. Michioka, M. Kato, K. Yoshimura, K. Takada, T. Sasaki, H. Sakurai, and E. Takayama-Muromachi, *J. Phys. Soc. Jpn.* 72 (2003) 3041.
- [96] C. Michioka, M. Kato, K. Yoshimura, K. Takada, H. Sakurai, E. Takayama-Muromachi, and T. Sasaki, cond-mat/0403293.
- [97] D. J. Singh, *Phys. Rev. B* 68 (2003) 020503(R).
- [98] J. Ni and G.-M. Zhang, *Phys. Rev. B* 69 (2004) 214503.
- [99] T. Shimojima, T. Yokoya, T. Kiss, A. Chainani, S. Shin, T. Togashi, C. Chen, S. Watanabe, K. Takada, T. Sasaki, H. Sakurai, and E. Takayama-Muromachi, cond-mat/0406632.
- [100] Y. Ihara, K. Ishida, C. Michioka, M. Kato, K. Yoshimura, K. Takada, T. Sasaki, H. Sakurai, and E. Takayama-Muromachi, cond-mat/0407192, *J. Phys. Soc. Jpn.* 73 (2004) 2069.
- [101] Y. Kobayashi, M. Yokoi, and M. Sato, *J. Phys. Soc. Jpn.* 72 (2003) 2161.
- [102] F. C. Chou, J. H. Cho, and Y. S. Lee, cond-mat/0404061.
- [103] T. Waki, C. Michioka, M. Kato, K. Yoshimura, K. Takada, H. Sakurai, E. Takayama-Muromachi, and T. Sasaki, cond-mat/0306036.
- [104] A. Chainani, T. Yokoya, Y. Takata, K. Tamasaku, M. Taguchi, T. Shimojima, N. Kamakura, K. Horiba, S. Tsuda, S. Shin, D. Miwa, Y. Nishino, T. Ishikawa, M. Yabashi, K. Kobayashi, H. Namatame, M. Taniguchi, K. Takada, T. Sasaki, H. Sakurai, and E. Takayama-Muromachi, *Phys. Rev. B* 69 (2004) 180508(R).
- [105] B. Fisher, K. B. Chashka, L. Patlagan, A. Kanigel, A. Knizhnik, G. Bazalitsky, and G. M. Reisner, *J. Phys., Condens. Matter* 15 (2003) L571.
- [106] L. Shan, H. Gao, Y. G. Shi, H. P. Yang, X. F. Lu, G. H. Cao, Z. A. Xu, and H. H. Wen, cond-mat/0311572.
- [107] B. Liu, Y. Liang, S. Feng, and W. Y. Chen, *Phys. Rev. B* 69 224506.
- [108] B. G. Ueland, P. Schiffer, R. E. Schaak, M. L. Foo, V. L. Miller, and R. J. Cava, *Physica C* 402 (2004) 27.
- [109] B. Lorenz, J. Cmaidalka, R. L. Meng, C. W. Chu, *Physica C* 402 (2004) 106.
- [110] H. D. Yang, J.-Y. Lin, C. P. Sun, Y. C. Kang, C. L. Huang, K. Takada, T. Sasaki, H. Sakurai, and E. Takayama-Muromachi, cond-mat/0407589.
- [111] N. E. Phillips, oral presentation at 2004 Taiwan International Conference on Superconductivity & the 7th Workshop on Low Temperature Physics.
- [112] F. Bouquet, R. A. Fisher, N. E. Phillips, D. G. Hinks, and J. D. Jorgensen, *Phys. Rev. Lett.* 87 (2001) 047001.
- [113] H. D. Yang, J.-Y. Lin, H. H. Li, F. H. Hsu, C. J. Liu, S.-C. Li, R.-C. Yu, and C.-Q. Jin, *Phys. Rev. Lett.* 87 (2001) 167003.
- [114] Y. Wang, T. Plackowski, and A. Junod, *Physica C* 355 (2001) 179.

- [115] T. Fujimoto, G.-q. Zheng, Y. Kitaoka, R. L. Meng, J. Cmaidalka, and C. W. Chu, *Phys. Rev. Lett.* 92 (2004) 047004.
- [116] M. Kato, C. Michioka, T. Waki, K. Yoshimura, K. Ishida, H. Sakurai, E. Takayama-Muromachi, K. Takada, and T. Sasaki, unpublished.
- [117] M. Yokoi, H. Watanabe, Y. Mori, T. Moyoshi, Y. Kobayashi, and M. Sato, *J. Phys. Soc. Jpn.* 73 (2004) 1297.
- [118] Y. Bang, M. J. Graf, and A. V. Balatsky, *Phys. Rev. B* 68 (2003) 212504.
- [119] Q. Han and Z. D. Wang, *cond-mat/0308160*.
- [120] Y. Kobayashi, M. Yokoi, and M. Sato, *J. Phys. Soc. Jpn.* 72 (2003) 2453.
- [121] P. Lemmens, V. Gnezdilov, N. N. Kovaleva, K. Y. Choi, H. Sakurai, E. Takayama-Muromachi, K. Takada, T. Sasaki, F. C. Chou, D. P. Chen, C. T. Lin, and B. Keimer, *J. Phys., Condens. Matter* 16 (2004) S857.
- [122] B. Lorenz, J. Cmaidalka, R. L. Meng, and C. W. Chu, *Phys. Rev. B* 68 (2003) 132504.
- [123] Y.G. Shi, Y.L. Liu, H.X. Yang, C. J. Nie, R. Jin, and J.Q. Li, *cond-mat/0404022*.
- [124] M. Wakeshima, D. Harada, and Y. Hinatsu, *J. All. Comp.* 287 (1999) 130.
- [125] S.-J. Kim, M. D. Smith, J. Darriet, and H.-C. zur Loye, *J. Solid State Chem.* 177 (2004) 1493.
- [126] Q. Han, Z. D. Wang, Q.-H. Wang, and T. Xia, *Phys. Rev. Lett.* 92 (2004) 027004.
- [127] Q.-H. Wang and Z. D. Wang, *Phys. Rev. B* 69 (2004) 092502.
- [128] J.-X. Zhu and A. V. Balatsky, *cond-mat/0306253*.
- [129] T. Pereg-Barnea and H.-H. Lin, *cond-mat/0407187*.
- [130] J.-X. Li and Z. D. Wang, *cond-mat/0310308*.

PROGRESS IN Na_xCoO_2 SINGLE CRYSTAL GROWTH

D. Prabhakaran and A.T. Boothroyd

Clarendon Laboratory, Department of Physics,
University of Oxford, Parks Road, Oxford OX1 3PU, UK.

1. INTRODUCTION

The discovery of new electronic phenomena such as superconductivity, colossal magnetoresistance, and effects associated with charge and orbital, especially in cuprates, manganites, nickelates and cobaltites, has rekindled interest among the research community in layered transition metal oxides. Alkaline cobaltite (A_xCoO_2) is a good example of this trend, having been studied over a long period of time for its interesting structural, thermoelectric and transport properties [1–3]. Recently, great attention has been paid to gamma phase Na_xCoO_2 , firstly because of its potential as a thermoelectric material [4], and second because of the discovery of a novel form of superconductivity in the hydrated compound ($\text{Na}_{0.3}\text{CoO}_2 \cdot 1.3\text{H}_2\text{O}$) [5].

Motivated by these recent discoveries, many groups have investigated the preparation and properties of Na_xCoO_2 for a range of x . Compositions near $\text{Na}_{0.7}\text{CoO}_2$ have been of particular interest since this is the usual starting material for the synthesis of the superconducting phase [4-7]. Single phase Na_xCoO_2 can be prepared in polycrystalline form by the conventional solid-state reaction technique. Different starting materials have been used during the preparation, including oxides [1], hydroxide [8] and nitride solutions [9]. Owing to the volatile nature of sodium, a ‘rapid heat-up’ technique [10] has been employed, and more recently, spark plasma sintering (SPS) has also been used to achieve high density single phase material [11]. Highly textured NaCo_2O_4 ceramic processing has been achieved by the reactive templated grain growth method using single crystal particles [12, 13]. It is very difficult to prepare the single phase material with $x < 0.5$, and often Co_2O_3 or CoO will

be present in the sample as an impurity phase. Magnetic and structural properties for these impurity phases have been reported elsewhere [14-16].

The Na_xCoO_2 compound has been classified into four different phases, namely α ($0.9 \leq x \leq 1$), α' ($x=0.75$), β ($0.55 \leq x \leq 0.6$), and γ - $\text{Na}_x\text{Co}_y\text{O}_2$ ($0.55 \leq x/y \leq 0.74$), each with different cell structures, rhombohedral, monoclinic, orthorhombic and hexagonal, respectively [1]. An early neutron powder diffraction study of $\text{Na}_{0.74}\text{CoO}_2$ reported a hexagonal structure with cell parameters $a=2.840 \text{ \AA}$ and $c=10.811 \text{ \AA}$, respectively, and also suggested that the Na ion can move freely between the cobalt-oxygen layers [17]. More recently, the structure of Na_xCoO_2 over a wider range of x has been studied by diffraction methods [18, 19]. Nevertheless, the c axis value of the gamma phase composition varies slightly with respect to the x concentration [10, 13, 18, 20]. Other interesting physical properties of this material are sodium ordering [21, 22] and $\text{Co}^{3+}/\text{Co}^{4+}$ charge ordering [23, 24].

Single crystals have been grown by the flux technique using NaCl as the flux medium [4, 25-27]. Flux-grown crystals are very thin, and the maximum size reported so far is $10 \times 10 \times 0.1 \text{ mm}^3$ [25]. Recently, single crystals have also been grown by the floating-zone technique [28-31]. This method offers the possibility of preparing large crystals for experiments where size is important, such as inelastic neutron scattering. Possible difficulties of this technique are Na evaporation during the melt growth, and changes in the physical properties depending on the atmosphere used during crystal growth. These issues have not been investigated in detail before now. In this paper we describe the preparation of large Na_xCoO_2 single crystals by the floating-zone method under different conditions. We investigated the composition $x = 0.75$ in some detail. We report the optimum crystal growth conditions (pressure and atmosphere), phase purity and some magnetic properties of the crystals. More detailed measurements of the magnetic properties of powder and single crystal Na_xCoO_2 for a wide range of x are given in ref. [30].

2. EXPERIMENTAL METHOD

Single phase polycrystalline samples of $\text{Na}_{0.75}\text{CoO}_2$ were prepared using high-purity (>99.98%) Na_2CO_3 and Co_3O_4 . The starting powders were first ground using a ball mill with acetone for homogenous mixing. The well mixed dry powder was spread on a platinum foil (instead of directly in an alumina boat to avoid reaction with Co_3O_4) and loaded into a preheated (>650°C) furnace. The use of a spread powder was found preferable to compressed pellets since the latter tended to leave an unreacted central core and hence needed more sintering. Rapid heating of the furnace to the desired maximum sintering temperature was employed to reduce the Na evaporation as reported previously [8]. To obtain single phase material, three different temperatures (850°C, 870°C and 890°C) were used for sintering the powders under oxygen flow with intermediate dry grinding. We avoided the use of solvents during the intermediate grinding since addition of acetone leads to absorption of moisture (converting unreacted Na_2O in to Na_2CO_3 and increasing the number of sintering cycles needed to obtain single phase material). All synthesized powders were analyzed carefully for Co_3O_4 and CoO impurities by powder X-ray diffraction (XRD) and magnetization measurements after each sintering process.

The feed material for the crystal growth process was prepared in the form of cylindrical rod of size 6-9 mm diameter and up to 14 cm length. Some of these feed rods were sintered at 900°C for 6-10 h under oxygen flow atmosphere. Single crystals were grown using a four-mirror optical floating-zone furnace (CSI System Inc.). Trials were made in which crystals were grown in different atmospheric composition and pressure as follows: flow of air, flow of oxygen, flow of argon, low pressure oxygen (2 atm), high pressure argon-rich (7.5 atm), and high pressure oxygen-rich (10 atm). The crystal growth speed also varied between 2 and 10 mm/hr accompanied by a counter-rotation of the feed and seed rods at 40 rpm.

Na_xCoO_2 was prepared with other Na concentrations ($x = 0.5-1.0$) using the same basic procedure as described above. However, the sintering temperature was varied with the Na content. For example, the sintering temperature for the $x = 1.0$ sample was 20°C less than that of $x = 0.75$ sample. The use of oxygen flow during sintering was found to reduce the number and period of the sintering cycles relative to air flow. However, the effect of oxygen annealing was found to change the magnetic properties of the material, especially at low temperature, as discussed in detail later. Normally, sintering performed on pellets improves the compound formation, but in this case Co_3O_4 impurity phase was observed in sintered pellets due to the slow reaction in the core of the pellet compared to the outer surface area. This may be due to the high densification during sintering which will prevent the oxygen flow to the centre core of the pellet.

Several techniques were used to characterize the grown crystals. Information on the crystal orientation and mosaic was obtained by neutron Laue diffraction. The chemical composition was analysed by electron probe micro-analysis (EPMA). The magnetization of the crystals was measured as a function of temperature and applied field with a superconducting quantum interference device (SQUID) magnetometer (Quantum Design).

3. RESULTS AND DISCUSSION

Compounds with $x < 0.5$ were found to have unreacted Co_3O_4 impurity phase irrespective of the number of sintering cycles or the sintering temperature. Hence, we were unable to achieve single phase material for $x < 0.5$. On the other hand, single phase compound was synthesized for $0.5 \leq x \leq 1.0$ without any detectable Co_3O_4 impurity phase. However, small amounts of CoO impurity phase (<5%) were observed in one or two cases. The amount of impurity was dependent on the sintering condition. Powder XRD studies indicated that the majority phase of the powder and single crystal samples was of a hexagonal structure. The measured a axis parameter for samples with nominally $x = 0.75$ was found to be $a = 2.83 \text{ \AA}$ virtually independent of preparation conditions, but the c axis parameter was found to vary with respect to the sample preparation. The results for c are given in Table 1. Our value for a for the γ phase hexagonal structure agrees well with that reported elsewhere, but the value of c for the composition $x = 0.75$ is reported to vary between 10.884 Å and 10.918 Å [20, 10]. The reported variation in c may be due to the difference in the Na/Co ratio, or absorption of moisture, or oxygen non-stoichiometry. The variation in c among our samples will be discussed in the following sections. The synthesised powders are very sensitive to moisture, and hence clean and dry storage is crucial. Since Co_3O_4 and CoO impurity phases show up clearly in XRD and magnetization measurements we used these two techniques to search for impurity phases in all our powder and single crystal samples.

During initial experiments we sintered the pressed feed rod used for crystal growth to improve its density and homogeneity, but after sintering the feed rod was found to contain traces of Co_3O_4 impurity phase which developed due to loss of Na during sintering. We believe this evaporation and the consequent decrease in the Na content accounts for the increase in c to 10.913 Å, since there is known to be a systematic increase in c with decreasing x [18]. Surprisingly, crystals grown using the impure feed rod did not contain any impurity. Since Na has a large solubility range in the γ phase ($0.55 \leq x/y \leq 0.74$) in this system, it seems that a small Na loss during sintering is corrected by homogeneous mixing in the molten zone interface. Subsequently we have used green (un-sintered) rods for the crystal growth in order to maintain the Na stoichiometry.

Crystals were grown with both polycrystalline and also single crystal seed rods. One reason for using a polycrystalline seed was to have the same Na composition both in the feed and seed rod. In some cases, Co_3O_4 impurity phase was thought to develop during slow heating of the seed crystal. However, under high pressure growth single crystal seeded runs yielded good quality crystals. The 'necking' technique was employed to improve the grain formation and the parallel platelet crystals were formed after 2–5 cm length of growth. The lower doped ($x \leq 0.65$) crystal growth ended up with small amounts of Co_3O_4 impurity phase despite having single phase starting powder. This was due to the loss of few percent of Na during crystal growth process. Moreover the size of the single crystal in the boule was very small (~1mm) and very difficult to separate from the grown rod. On the other hand, crystals with $x \geq 0.7$ are single phase and able to cleave large size single crystal from the grown rod. In the later sections we will describe the different conditions used for the growth of $x = 0.75$ crystals in detail. Similar optimum conditions were used for the higher doped crystal growth. Crystals grown under different conditions (named as Crystals A–E) are listed in Table 1. Even from the single-phase green feed rod crystals grown under flowing atmosphere at ambient pressure (Crystal A) or Ar rich atmosphere at high pressure (Crystal C) were found to contain a few percent of Co_3O_4 impurity phase due to Na evaporation or oxygen deficiency during crystal growth. We found that it was very difficult to stabilize the molten zone during atmospheric flow conditions (Crystal A), and hence crystal growth was unsuccessful. Due to the evaporation of Na (which condenses on the inner side of the quartz growth tube) at the time of melting, the molten region ends up being Co_3O_4 rich. Application of 2–3 atm pressure of (mainly) oxygen (Crystal B) during growth was found to reduce the Na evaporation a little. In this case the molten zone was stable for a short while but Co_3O_4 impurity phase was found to be present in the grown boule. A high growth rate (>10 mm/hr) was found to stabilize the molten zone, but it was not helpful to improve the quality or size of the grown crystal. Due to the presence of impurity phase in the grown rod, the separation of the plate-like crystals was very difficult. Application of higher pressure (7.5 atm) to reduce the Na loss, a moderate growth rate (3–5 mm/hr) to improve the crystal quality, and an Ar rich atmosphere (Crystal C — Ar/O₂ ratio = 4:1) enabled us to grow for up to 10 cm length with less Na loss, but a very small amount of Co_3O_4 impurity was still present. However, the c -axis parameter increased to 10.916 Å, which indicates Na loss in the grown crystal.

To investigate the influence of the atmosphere we next applied a gas ratio of O₂/Ar = 4:1 (Crystal D), and used a slightly lower growth rate (3 mm/hr) under the same 7.5 atm pressure. During this growth, Na evaporation was observed to be less compared with the Ar-rich 7.5 atm pressure (Crystal C) and the growth was found to be uniform. The c axis

Table 1. Conditions used to prepare the polycrystalline and single crystal samples of $\text{Na}_{0.75}\text{CoO}_2$.

| Material | Atmosphere | Growth rate | $\text{Co}_3\text{O}_4/\text{CoO}$ impurity | Na loss | <i>c</i> axis parameter value (Å) |
|--------------------|--|-------------|---|-------------|-----------------------------------|
| Synthesised powder | Flowing O_2 (20 cc/min) (890°C) | — | No | — | 10.896 |
| Sintered rod | Flowing O_2 (50 cc/min) (900°C) | — | Yes | Yes | 10.913 |
| Crystal A | Flowing O_2 (30 cc/min) | 7 mm/hr | Yes | Yes (heavy) | — |
| Crystal B | 2.5 atm pressure, $\text{O}_2/\text{Ar} = 8:1$ | 7 mm/hr | Yes | Yes | — |
| Crystal C | 7.5 atm pressure, $\text{O}_2/\text{Ar} = 1:4$ | 5 mm/hr | Yes | Yes | 10.916 |
| Crystal D | 7.5 atm pressure, $\text{O}_2/\text{Ar} = 4:1$ | 3 mm/hr | No | Minimum | 10.898 |
| Crystal E | 10 atm pressure, $\text{O}_2/\text{Ar} = 14:1$ | 4 mm/hr | Little | Yes | 10.889 |

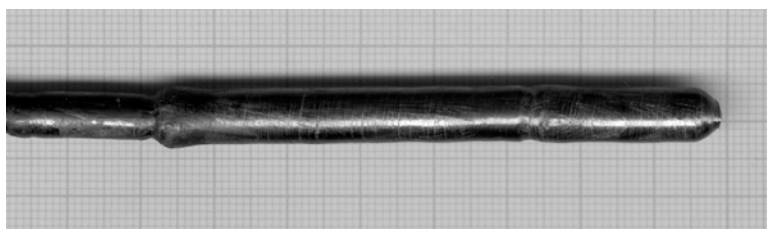


Fig. 1. As-grown seeded single crystal of $\text{Na}_{0.75}\text{CoO}_2$.

parameter (10.898 Å) was found to be consistent with that of the starting powder. Due to the layer growth mechanism the grown crystal was plate-like in nature along the growth direction, and the large faces were found to be parallel to the crystallographic *ab* plane. The central region of the grown crystal was cleaved and used as a seed for the next run. One such seeded crystal is shown in Fig.1.

Finally, we employed the maximum available oxygen-rich atmosphere (O_2/Ar ratio = 14:1) at a pressure of 10 atm. Several interesting effects were observed. First, we observed that the Na evaporation was slightly higher than during the growth of Crystal D, and secondly, a trace of Co_3O_4 impurity phase was found in the XRD patterns. However, the grown crystal was much more stable when stored in air under ambient conditions than any other of the crystals. The cleaved surface of the crystal was very shiny and stable under atmospheric condition in contrast to crystals grown under low applied pressure whose cleaved crystal surfaces became dull after a couple of hours due to the absorption of moisture. When

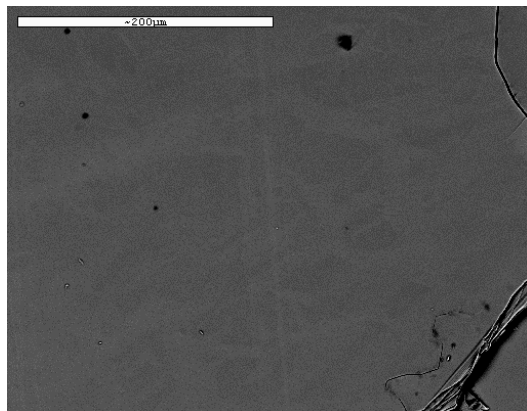


Fig. 2. (a) SEM image of $\text{Na}_{0.9}\text{CoO}_2$ single crystal grown under optimum conditions.

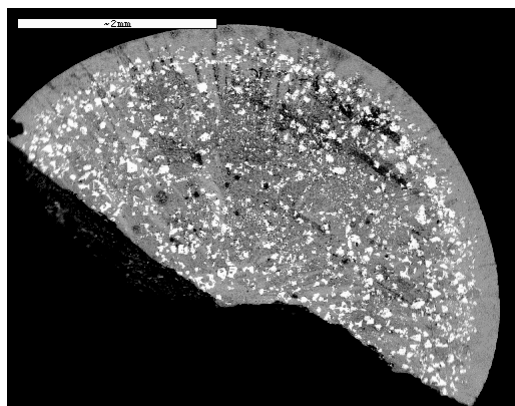


Fig. 2. (b) SEM image of cross section view of $\text{Na}_{0.65}\text{CoO}_2$ single crystal rod. The dark gray particles correspond to Co_3O_4 impurity intergrowths and white particle correspond to Na_2CO_3 .

conditions were close to optimum, very clear facets appeared on opposite sides of the crystal rod. These facets were found to be perpendicular to the c axis. Crystals grown under low applied pressure ($\sim 2\text{--}4$ atm) did not exhibit facets, but the surface of the crystal rod was observed to be very shiny immediately after growth, but turned white very quickly due to reaction with the atmosphere. Therefore, we assume that a deposition of Na_2O occurred on the outer surface during crystal growth.

The chemical compositions of the grown crystals were checked by electron microscopy combined with EPMA. We first performed compositional analysis at different points along the length of the crystal rod. These measurements did not reveal any variation in the Na/Co ratio along the growth direction. The rest of the measurements were performed on crystal grains cleaved from the top end of crystal rod. These revealed small inclusions of

Co_3O_4 on the surfaces (a few per cent of the area) of the lower doped samples ($x = 0.65$ and $x = 0.7$ crystals), but not on any of the higher Na-doped crystals. To illustrate this, a SEM image of the surface of the $x = 0.9$ crystal used for the EPMA measurement is shown in Fig. 2(a). For comparison, the SEM image for a $x = 0.65$ crystal is shown in Fig. 2(b). In the latter, the dark gray regions are Co_3O_4 impurity phase, and the white patches correspond to Na rich regions, probably Na_2CO_3 which formed due to the absorption of moisture. The EPMA analysis also revealed that the lower doped crystals ($x < 0.75$) showed some variation ($\sim 10\%$) in the Na content from point to point on the surface, whereas the crystals with higher doping ($x > 0.75$) were found to have very little variation in the Na:Co ratio over the surface ($\sim 1\%$). The average Na:Co ratio for the crystals found by EPMA did not always agree closely with the nominal value, but it was neither systematically high nor systematically low. These discrepancies, which in the worst cases were up to 20%, are difficult to understand given that the impurity content was very low. It is possible that the final Na content of the crystal is sensitive to the speed at which the crystal is grown or the growth atmosphere. Another interesting result that we observed was that the maximum Na content in the grown crystal was 0.87 irrespective of the composition of the single phase starting powder ($x \leq 1.0$). For example, we used single phase $x = 0.95$ starting material for the crystal growth and the grown crystal was found to have $x = 0.82$. It is very difficult to grow α phase ($0.9 \leq x \leq 1$) single crystal using this technique due to the thermodynamic stability [1]. But recently Takahashi et al., have been grown very thin ($\sim 0.1\text{mm}$) NaCoO_2 single crystal by using NaCl flux [27].

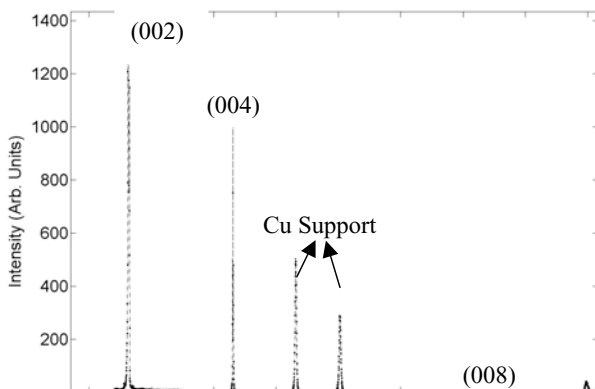


Fig. 3. Single crystal XRD pattern of $\text{Na}_{0.75}\text{CoO}_2$.

For magnetization and neutron diffraction measurements the crystals were cut into short cylinders perpendicular to the growth direction. The mosaic spread measured by neutron diffraction on a bulk piece of crystal of mass 1.3 g was found to be anisotropic. The in-plane mosaic (i.e. measured by monitoring a Bragg peak while rotating the crystal around the c axis) was found to be 2-3 deg, but the out-of-plane mosaic (measured by rotating the crystal

about an axis in the ab plane) was ~ 10 deg. Smaller crystals cleaved from the main boule had much narrower mosaics. Therefore, we conclude that the bulk crystals grown by the floating-zone method consist of an assembly of plate-like grains stacked together with the grains slightly mis-oriented with respect to one another. The maximum dimension of the cleaved single crystal was $50 \times 7 \times 2$ mm³. The XRD pattern for one such cleaved $\text{Na}_{0.75}\text{CoO}_2$ crystal oriented for the $(00l)$ reflections is shown in Fig. 3. The temperature dependence of the magnetization for the polycrystalline and single crystal samples grown under various conditions is shown in Fig. 4.

The magnetization is quite sensitive to the presence of Co_3O_4 and CoO which exhibit rounded peaks centred near 35 K and 290 K, respectively, as shown in the inset to Fig. 4. This impurity was found in all the crystals except crystal D (O_2/Ar ratio = 4:1). The presence of cobalt oxide impurities is most likely due to Na evaporation or oxygen non-stoichiometry.

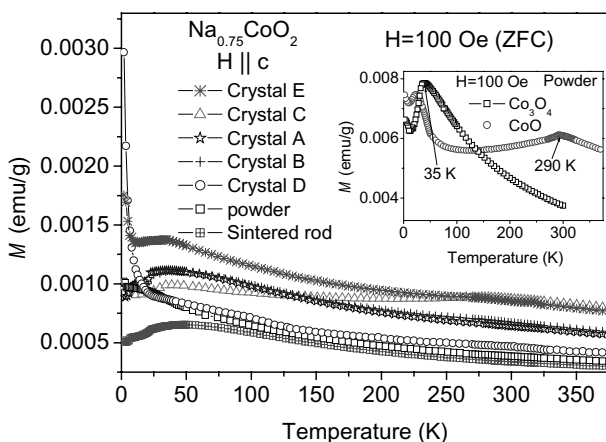


Fig. 4. Temperature dependence of the dc magnetization for $\text{Na}_{0.75}\text{CoO}_2$ polycrystalline and single crystal samples measured in an applied field of 100 Oe. The inset shows the magnetization of Co_3O_4 and CoO powders for reference. These contain peaks due to antiferromagnetic transitions at 35 K and 290 K, respectively.

In general, the use of a high pressure growth atmosphere reduces Na evaporation during growth, but it is also important to choose the correct composition of the atmosphere if the amount of impurity phase is to be a minimum. For example, Crystal E was grown under 10 atm pressure in an O_2 rich atmosphere and had very good crystal quality as described above, but the magnetization curve shows evidence that this crystal contains the Co_3O_4 impurity, in contrast to Crystal D which was grown at a lower pressure. We conclude from this that there is an optimum O_2/Ar ratio near 4:1 for good crystal quality and minimum Co_3O_4 impurity content.

Previously it has been reported that Na_xCoO_2 exhibits a weak ferromagnetic behaviour at low temperatures [32, 33]. This phase has since been observed over a wide range of x and at different temperatures [28-31]. However in a diluted Co_3O_4 system, spin-glass behavior has

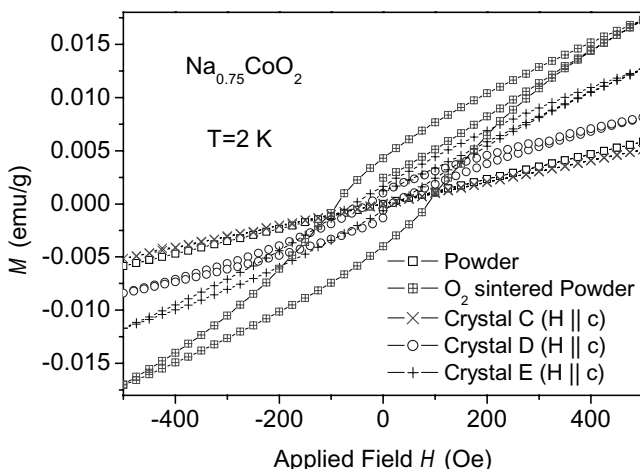


Fig. 5. *Dc* magnetization loop curves for polycrystalline and single crystal samples of $\text{Na}_{0.75}\text{CoO}_2$ prepared under different conditions.

been noticed below 30 K due to short-range interaction between dipole moments [34]. Our studies have shown that the magnetic irreversibility characteristic of this phase is quite sensitive to the nature and preparation of the sample. To examine this we carried out magnetization measurements as a function of applied field at a fixed temperature of 2 K. The effect of oxygen annealing on the single phase compound was studied by sintering the $x = 0.75$ single phase powder at $\sim 890^\circ\text{C}$ for 15 h under 20 cc oxygen flow and quenching from 750°C to room temperature. The annealed powder was single phase without any impurity. The field dependence (± 500 Oe) of the magnetization for the starting powder, oxygen-annealed powder, Crystal C, Crystal D and Crystal E are shown in Fig. 4. The starting powder is seen to be perfectly paramagnetic with no hysteresis, whereas the oxygen-annealed powder has a very prominent hysteresis loop. Of the crystals, C (grown under pressure in an Ar rich atmosphere) shows no hysteresis, whereas D and E (both grown in O_2 rich atmospheres) both show hysteresis, slightly greater in E than D. Notice also that there is a correspondence between the degree of hysteresis and the magnetization at fixed field above the hysteresis region, e.g. 500 Oe. Extra oxygen might be expected to increase the proportion of Co^{4+} , which carries a spin, relative to non-magnetic Co^{3+} , but this cannot be sufficient to explain the stronger hysteresis effect because samples with lower Na content (and therefore higher $\text{Co}^{4+}/\text{Co}^{3+}$ ratio) do not show increased magnetic irreversibility at low temperatures [30]. It is possible that the excess oxygen modifies the inter-planar magnetic coupling.

Magnetisation data for the $x = 0.95$ crystal measured with an applied field of 100 Oe parallel to the *ab* plane and *c* axis is shown in Fig. 6. The magnetization exhibits easy-plane anisotropy. The curves in Fig. 6 show a sharp anomaly at 22 K, corresponding to a magnetic transition that has been widely reported but whose nature is yet to be determined [31, 33]. This anomaly is strongest in the $H \parallel c$ data (both ZFC and FC). We have found that crystals of

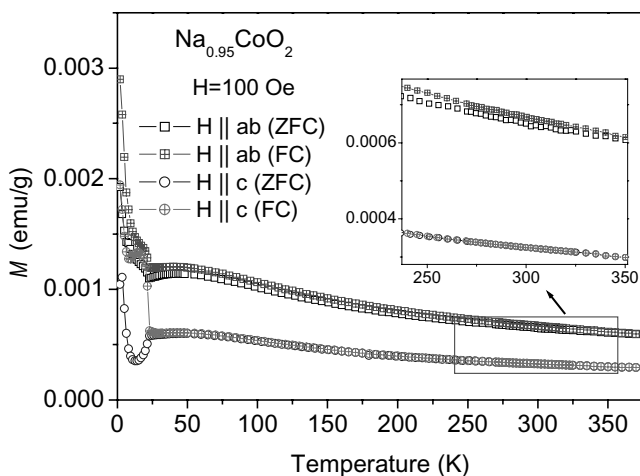


Fig. 6. Temperature dependence of the dc magnetization for $\text{Na}_{0.95}\text{CoO}_2$ single crystal measured in an applied field of 100 Oe along the ab and c planes. The inset shows the absence of high temperature (320 K) transition in both the planes.

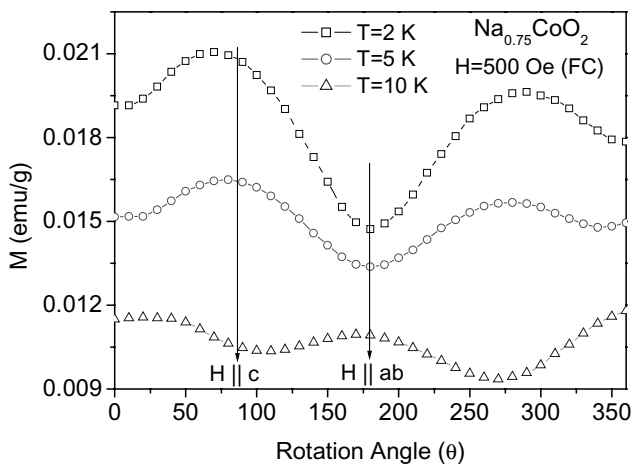


Fig. 7. dc magnetization versus rotation angle of a $\text{Na}_{0.75}\text{CoO}_2$ single crystal (Crystal D).

lower composition also show a high temperature anomaly near 320 K characterized by a sharp separation of the ZFC and FC magnetization curves [30]. The data in Fig. 6 for $x = 0.95$ do not show this feature for either field orientation. Similar high temperature anomalies have been reported in other bulk properties [23, 35], and these have been attributed to a small structural change associated with Na ordering between the CoO₂ layers. The absence of anomaly in the Fig. 6 data could be due to the reduced Na mobility at high Na doping. The this data with $H \parallel ab$ contains a small maximum centred near 40 K which may indicate a trace of Co₃O₄ impurity phase at a level too low to observed by powder XRD (i.e. < 5%).

Finally, we show a measurement in Fig. 7 of the magnetic anisotropy obtained by rotating Crystal D in the magnetometer relative to the applied field direction. What is interesting here is that the sense of the anisotropy switches between 5 K and 10 K. Thus, for $T \leq 5$ K the c axis is the easy direction of magnetization, whereas for $T \geq 10$ K the easy direction is in the ab plane. This indicates that with decreasing temperature below 10 K the spins have an increasing tendency to point along the c axis. However, no such anomaly was observed at low temperature for the higher doped crystals [31].

4. CONCLUSIONS

Our investigations and those of other groups have shown that bulk Na_xCoO₂ ($0.7 \leq x \leq 0.9$) single crystals can be grown by the floating-zone technique with only trace amounts of impurity phases (mainly cobalt oxides). The flux technique may be better to achieve crystals with higher Na content. Further work is needed to improve the mosaic spread of the largest crystals. A number of magnetic features are evident in the bulk magnetization of the crystals. The origins of the 22 K magnetic transition and the anomaly at ~320 K remain open questions. At very low temperatures weak ferromagnetism is observed which is enhanced in samples treated with oxygen. More work is needed to understand these observations.

ACKNOWLEDGMENT

We would like to thank Fred Wondre, Norman Charnley and Shamima Chaudhury for help with the crystal characterization. We are grateful to the Engineering and Physical Sciences Research Council of Great Britain for financial support.

REFERENCES

- [1] C. Fouassier, G. Matejka, J-M. Reau and P. Hagenmuller, *J. Solid State Chem.* 6 (1973) 532.
- [2] J. Molenda, C. Delmas and P. Dordor, *Solid State Ionics* 12 (1989) 473.
- [3] K. Mizushima, P.C. Jones, P.J. Wiseman and J.B. Goodenough, *Mat. Res. Bull.* 15 (1980) 783.
- [4] I. Terasaki, Y. Sasago, and K. Uchinokura, *Phys. Rev. B* 56 (1997) R12685.
- [5] K. Takada, H. Sakurai, E. Takayama-Muromachi, F. Izumi, R.A. Dilanian, and T. Sasaki, *Nature* 422 (2003) 53.
- [6] A.T. Boothroyd, R. Coldea, D.A. Tennant, D. Prabhakaran, L.M. Helme, and C.D. Frost, *Phys. Rev. Lett.* 92 (2004) 197201.
- [7] J. Sugiyama, J. H. Brewer, E. J. Ansaldo, B. Hitti, M. Mikami, Y. Mori, and T. Sasaki, *Phys. Rev. B* 69 (2004) 214423.
- [8] B.L. Cushing and J.B. Wiley, *J. Solid State chem.* 141 (1998) 385.
- [9] R. Ishikawa, Y. Ono, Y. Miyazaki and T. Kajitani, *Jpn. J. Appl. Phys.* 41 (2002) L337.
- [10] T. Motohashi, E. Naujalis, R. Ueda, K. Isawa, M. Karppinen, and H. Yamauchi, *Appl. Phys. Lett.* 79 (2001) 1480.
- [11] I. Matsubara, Y. Zhou, T. Takeuchi, R. Funahashi, M. Shikano, N. Murayama, W. Shin and N. Izu, *J. Ceram. Soc. Jpn.* 111 (2003) 238.
- [12] S. Tajima, T. Tani, S. Isobe and K. Koumoto, *Mater. Sci. Engg.* B86 (2001) 20.
- [13] H. Itahara, K. Fujita, J. Sugiyama, K. Nakamura and T. Tani, *J. Ceram. Soc. Jpn.* 111 (2003) 227.
- [14] W.L. Roth, *J. Phys. Chem. Solids* 25 (1964) 1.
- [15] J.R. Singer, *Phys. Rev.* 104 (1956) 929.
- [16] S. Greenwald, *Acta Cryst.* 6 (1953) 396.
- [17] R.J. Balsys and R. L. Davis, *Solid State Ionics* 93 (1996) 279.
- [18] Q. Huang, M.L. Foo, R.A. Pascal Jr., J.W. Lynn, B.H. Toby, Tao He, H.W. Zandbergen, and R.J. Cava, *Cond-Mat/0406570* (<http://arxiv.org/cond-mat/>).
- [19] J.D. Jorgensen, M. Avdeev, D.G. Hinks, J.C. Burley and S. Short, *Phys. Rev. B* 68 (2003) 214517.
- [20] J. Sugiyama, H. Itahara, J.H. Brewer, E.J. Ansaldo, T. Motohashi, M. Karppinen and H. Yamauchi, *Phys. Rev. B* 67 (2003) 214420.
- [21] H.W. Zandbergen, M. Foo, Q. Xu, V. Kumar and R.J. Cava, *Phys. Rev. B* 70 (2004) 24101.
- [22] Y.G. Shi, H.C. Yu, C.J. Nie and J.Q. Li, *Cond-Mat/0401052*. (<http://arxiv.org/cond-mat/>).
- [23] J. L. Gavilano, D. Rau, B. Pedrini, J. Hinderer, H.R. Ott, S. M. Kazakov and J. Karpinski, *Phys. Rev. B* 69 (2004) 100404.
- [24] C. Bernhard, A.V. Boris, N.N. Kovaleva, G. Khaliullin, A. Pimenov, L. Yu, D.P. Chen, C.T. Lin and B. Keimer, *Cond-Mat/0403155*(<http://arxiv.org/cond-mat/>).
- [25] K. Fujita, T. Mochida and K. Nakamura, *Jpn. J. Appl. Phys.* 40 (2001) 4644.
- [26] M. Mikami, M. Yoshimura, Y. Mori, T. Sasaki, R. Funahashi and I. Matsubara, *Jpn. J. Appl. Phys.* 41 (2002) L777.
- [27] Y. Takahashi, Y. Gotoh and J. Akimoto, *J. Solid State Chem.* 172 (2003) 22.
- [28] R. Jin, B.C. Sales, P. Khalifah, and D. Mandrus, *Phys. Rev. Lett.* 91 (2003) 217001.

- [29] F.C. Chou, J.H. Cho, P.A. Lee, E.T. Abel, K. Matan, and Y.S. Lee, Phys. Rev. Lett. 92 (2004) 157004.
- [30] D. Prabhakaran, A.T. Boothroyd, R.Coldea, L.M. Helme and D.A. Tennant, Cond-Mat/0312493 (<http://arxiv.org/cond-mat/>).
- [31] S. P. Bayrakci, C. Bernhard, D.P Chen, B. Keimer, R.K. Kremer, P. Lemmens, C.T. Lin, C. Niedermayer and J. Stremper, Phys. Rev. B 69 (2004) 100410.
- [32] T. Takeuchi, M. Matoba, T. Aharen and M. Itoh, Physica B 312-313 (2002) 719.
- [33] T. Motohashi, R. Ueda, E. Naujalis, T. Tojo, I. Terasaki, T. Atake, M. Karppinen, and H. Yamauchi, Phys. Rev. B 67 (2003) 064406.
- [34] Y. Hayakawa, S. Kohiki, M. Sato, Y. Sonda, T. Babasaki, H. Deguchi, A. Hidaka, H. Shimooka and S. Takahashi, Physica E 9 (2001) 250.
- [35] J. Wooldridge, D. McK. Paul, G. Balakrishnan and M.R. Lees, Cond-Mat/040651 (<http://arxiv.org/cond-mat/>).

DEVELOPMENT OF Nb-BASED CONDUCTORS

Bartek A. Glowacki^{1,2}

¹ Department of Materials Science and Metallurgy, University of Cambridge,
Pembroke Street, Cambridge CB2 3QZ, England

² IRC in Superconductivity, Cavendish Laboratory, University of Cambridge,
Madingley Road, Cambridge CB3 0HE, England

1. INTRODUCTION

The major usage of niobium is in the steel industry in production of ferro-niobium (85%), followed by superalloys (12%) where only 3% is shared between aerospace industry, nuclear energy, lighting and superconductivity. The well-established Nb-based low temperature superconductors, LTS, such as NbTi and Nb₃Sn represent 98% world production of superconducting materials, where the remaining 2% is shared between Nb₃Al, MgB₂ and Bi-based high temperature superconductors, (HTS).

The discovery of high temperature superconducting materials, HTS, and medium temperature superconducting material, MTS, (MgB₂), in 1986 and 2001 correspondingly does not eliminated the old well-established Nb-base conductors, but in contrary lack of the reliable strong, long lengths, high current at high magnetic field HTS and MTS conductors brought a renaissance to the Nb-based technologies for large-scale applications in 21 century. Only Magnetic Resonance Imaging magnets sector use approximately 200 tons of NbTi conductor per year, and this allows economies of large-scale production to be realized. The current consumption of the Nb₃Sn and Nb₃Al is much lower but demand is picking-up quickly due to the development of international applied projects on fusion reactors and on more importantly the new Hydron Colider. Presently the prototypes of the high field Nb₃Sn magnets >12T for high energy physics application are extensively being developed at several institutions in the world, including at FermiLab [1-4].

According to FermiLab the present Nb_3Sn conductor for high field application has a quite large effective filament diameter, in the order of 20 to 70 μm . It has quite a large magnetization, and causes a big persistent current, generating a substantial sextupole term at injection field. An extensive study in conjunction with the leading superconductor manufacturers are needed if required superconducting conductors are going to be delivered for this massive engineering project. There is also requirement for much smaller quantity but of a very advanced Nb-based conductors being able to generate fields of >23 Tesla for the application of 1GHz Nuclear Magnetic Resonance systems.

There are many technological issues must be adopted which are important from the point of view of quality of the final conductors which is usually cold drawn to yield long piece lengths. Independently from the production issues there is an important question to be answered if the fundamental pinning properties of Nb_3Sn and Nb_3Al and Nb_3Ga conductors can be improved by changing the pinning mechanism. For example in the case of Nb_3Sn conductors altering the typical grain boundary structure originated from a simple equiaxed grains to elongated ribbon-like grain-reinforced microstructure is the most plausible solution. Further improvement of intragranular pinning in rapidly quenched Nb_3Al and Nb_3Ga conductors by carefully optimised thermo-mechanical treatment looks promising. There is an urgent need to improve even further the high magnetic field performance of the LTS conductors for applications.

2. OUTLINE OF CRITICAL PARAMETERS AND GLOBAL PINNING FORCE Nb-BASED CONDUCTORS

The most important dependencies of superconducting parameters characterising the applicability of the particular materials are: $B_{c2}(T)$ Fig.1a), $J_c(B)$, Fig.1b), and obviously pinning force, F_p , see eq.(1).

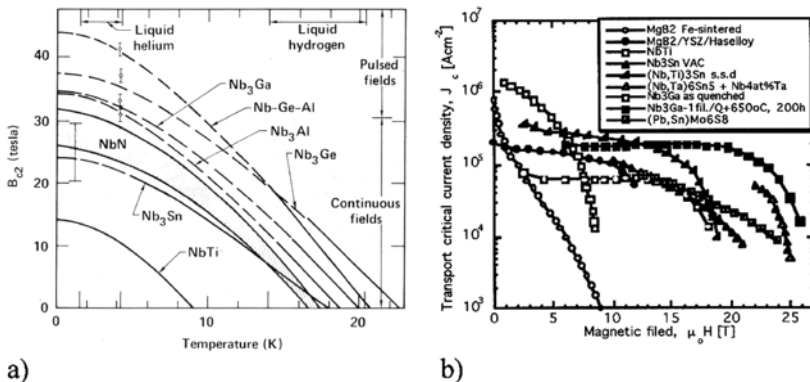


Fig. 1. a) The upper critical flux density versus temperature of Nb-based conductors after [5]; **b)** Transport critical current vs magnetic field for variety of LTS and also MTS [6], excluding Nb_3Al , which will be presented in the later chapter.

In most high pinning type II superconductors the global pinning force frequently exhibits scaling behaviour with reduced flux density $b=B/B_{c2}$, where constant G is a geometrical function of the microstructure, eq.(1), usually interpreted as a surface area of inclusion per unit volume of matrix. The significance of this equation is that if one measures F_p vs b at one temperature, then F_p at other temperatures can be predicted by scaling the results with a factor $[B_{c2}(T)]^n$.

Where n and m are fitting parameters and k is smoothing parameter defining maximum pinning value, p and q are pinning and materials related parameters.

$$F_p = J_c \cdot B = G \left[\frac{(B_{c2}(T))^n}{k^m} \right] \cdot f(b) \quad (1)$$

$$f(b) = b^p (1-b)^q \quad (2)$$

The position of the maximum of the pinning force on the coordinate axis of reduced flux density b , is defined by the ratio $p/(p+q)$. Kramer, [7] investigated the experimental data of several groups of hard superconductors such as NbZr, NbTa, NbTi, NbHf, Nb₃Sn, Nb₃Al and V₃Ga, and pointed out that eq.(1) can indeed describe the pinning force with the power n varying between 2 and 3, and with the function $f(b)$, eq.(2) depending on the microstructure and metallurgical treatment.

There are three main categories of Nb-based superconducting materials, which are described by the normalised pinning force dependencies versus normalised magnetic field, $f(b)$, eq.(2). Most of the Nb₃Sn conductors are close to $f(b)=b^{0.5}(1-b)^2$, Nb-Ti with the elongated grain boundaries can be describe by $f(b)=b(1-b)$ and finally Nb₃Al and Nb₃Ga (by rapid processing) with defects on the atomic scale has the best performance at very high magnetic field and therefore can be described by $f(b)=b^2(1-b)$ dependence, see Fig.2.

The difference between these three type of pinning mechanism is not in the crystallographic structure of the grains but more in the their morphology and intragranular defects, see Fig.3.

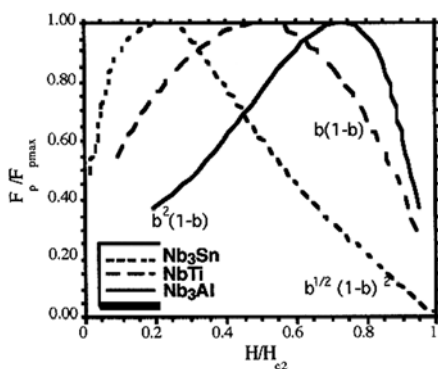


Fig. 2. Normalised pinning force vs normalised magnetic field dependences for Nb-based conductors: NbTi, Nb₃Sn, and Nb₃Al (rapidly quenched).

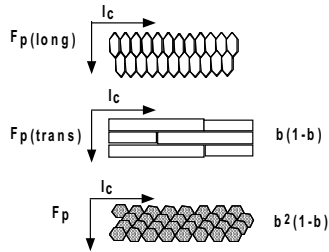


Fig. 3. Fragments of the cross-sectional grain structure of the superconducting filament along the wire and current direction, a) equiaxed grain structure characteristic for Nb₃Sn conductors b) elongated grain structure typical for NbTi conductors, c) Fine defect substructure typical for rapid quench Nb₃Al and Nb₃Ga.

3. NbTi CONDUCTORS

Nb-Ti was discovered soon after another superconducting alloy Nb-Zr in 1960. Once it was established that Nb-Ti possesses strong pinning at elevated magnetic fields ~ 5 Tesla, see Fig.1b, the industrial process originally developed by Teledyne Wah Chang to make filaments for light bulbs was developed. Even though it was possible to use a well-established technology, the price of the first 61 filament wire was 400£/kg during the first year of production and the performance was 70A at 5Tesla for the 0.4mm wire, Fig.4. After one year the price dropped to 200£/kg with minor improvements in current density. Interestingly enough the price of was stable for almost 20 years, because it was based on already mature technology. Taking into account the rate of inflation approx. 10% per year, the absolute price went down systematically. In time improved performance and involvement of other companies caused further reduction of price presented in Fig.4.

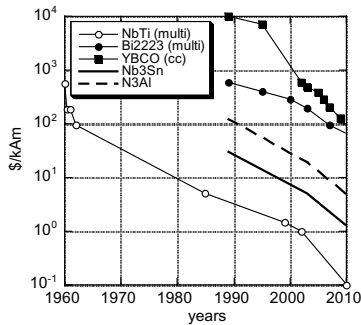


Fig. 4. Price reduction of the Nb-Ti superconducting wires since discovery in 1960. After J. Good, Cryogenics Ltd. For comparison prices of HTS Bi₂Sr₂Ca₂Cu₃O₈ and YBa₂Cu₃O₇ conductors are included.

Today the price of the simple Ni-Ti wire for MRI applications is at the level of 1\$/kAm where the price of the sophisticated ITER conductor is currently no more than 2\$/kAm. Further reduction of price can be realised by increase of performance by introduction of the Artificial Pinning Centres. The optimisation of the critical current density is part of the conductor fabrication process. J_c is determined by the microstructure and can therefore be manipulated largely during the wire fabrication process. Optimisation of J_c is achieved by introducing finely dispersed microstructural features acting as pinning centres. In the case of Nb-Ti the combination of the dislocation wells and normal conducting α -Ti precipitates in the superconducting β -phase are known to be most effective pinning centres. An optimum size and distribution of the precipitates is achieved by applying intermediate heat treatments (at about 400°C) during the wire fabrication process. After cold deformation of the Nb-Ti wires α -Ti precipitates forming flat noodles, which are lined flat along the wire axis, as a result of the marked texture of NbTi.

Interaction of the metallurgical treatment and flux pinning of NbTi superconductors is discussed in details by Hillmann [9]. The most intensive research and development into the process of the production of new class Nb-Ti superconducting materials characterised by the highest J_c values by introducing artificial pinning centres (APC), was carried out by Heussner et al. [8]. It was demonstrated, that the processes and manufactured articles under development have the following advantages by comparison to the conventional ones: a possibility of making and adjusting of APC material structure therefore to produce the strictly specified properties in superconductors; an economy-type achievement of the high level current-carrying capacity as compared to traditional materials; an opportunity of the essential increase (by a factor of 4 -5) of the superconductors current-carrying capacity. The experimental batches of highest J_c vs B superconducting Nb-Ti wires were produced by the University of Wisconsin in collaboration with USA Industry. Even further reduction of the cost can be achieved by exploitation of the new emerging technologies such as Direct Electroreduction of Oxides, DERO developed at University of Cambridge (see for example Fig.21) [10,11]. The cost of Nb-Ti alloys, by the use of the DERO process, is expected to be only between 4-7 times cheaper, Fig.4, because the Nb-Ti materials account for only 20-50% of the total cost of the final wire. The remaining cost covers all the other materials used in composite, deformation processes, electrical insulation and manpower.

The fabrication of a multifilamentary wire can be described as follows: in the case of a NbTi/Cu composite prefabricated NbTi and Cu parts are bundled inside a Cu tube to form a billet with an outer diameter of typically 100 to 250 mm. The billet is evacuated and warm extruded to a rod of 20 to 70 mm diameter. Further area reduction is achieved by cold working on drawing benches, bull blocks and multiple drawing machines. Twisting of the wire is performed close to the final dimension. The number of NbTi filaments and the copper to superconductor ratio is chosen according to the application. The composite wire can be further processed, e.g. into rectangular profiles or cables when required for special applications. The co-processing of NbTi and Cu in the ways described above is only possible because both materials are very ductile and behave fairly similarly with respect to hardness and resistance to deformation. In case of less favourable combinations other solutions had to be found. For example, stabilisation with ultra pure aluminium is desirable in some cases due to the very low residual resistance, the low weight and/or the transparency to nuclear radiation. Reliable cold working of a pure Al/NbTi has turned out to be very difficult. An

appropriate process to manufacture an Al-stabilised conductor is the co-extrusion of the Al onto a prefabricated NbTi/Cu composite wire or cable. Different applications require a specifically designed NbTi conductors of which examples are presented in Fig.5. There are also alloys from ternary or quaternary phase diagrams, which possess the best properties among Nb-based alloys, these are listed in Table 4 and Table 5.

The architecture and structure of any superconducting conductor is dictated by the application. Examples of Nb-Ti wires for different applications in Fig.5. The NbTi cable in Fig.5e) consist of 36 superconducting wires as in Fig.5(c), each wire being exactly 0.825 mm in diameter. Each wire houses 6300 superconducting filaments of niobium-titanium (NbTi). Each filament is about $6\mu\text{m}$ thick, Fig.5d). Around each filament there is a sub-micron $0.15\mu\text{m}$ layer of Nb and $0.5\mu\text{m}$ layer of high-purity copper. This Rutherford cable, Fig.5e), is 1.510 cm wide, 1.480 mm thick but tolerances are only a few micrometers. In the manufacture of such superconductor products the key know-how is to form 16 cm thick and about 70 cm long NbTi billets into filaments which are 512 000 km long and $6\mu\text{m}$ thick. It is not surprise that because such a high quality long length Nb-Ti conductors can be achieved reproducibly, the NbTi wires are treated as a commodity.

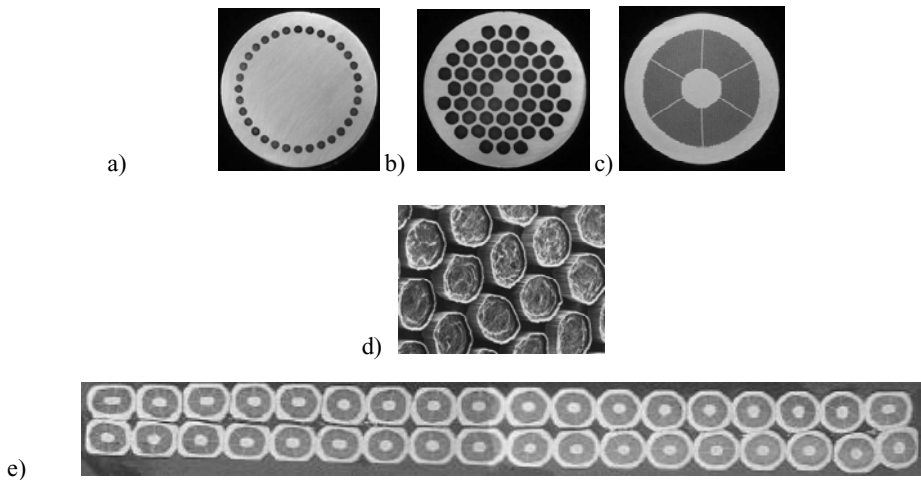


Fig. 5. Cross sections of the Nb-Ti superconducting wires; **a)** basic wire for MRI magnets; typical dimensions in the production 0.6 mm-1.94 mm, cryomagnetic stability of the wire is of paramount importance therefore there is a large amount of Cu, in the case of the failure of the superconductive state, copper acts as a highly conductive shunt transferring the electric current and the heat; **b)** wire to provide high background field in the NMR magnets where the core of the hybrid magnet is made from Nb_3Sn conductor, a typical dimensions in the production 0.4 mm-0.94 mm; **c)** wire for nuclear fusion OD = 0.787mm; **d)** magnified fragment of the wire in Fig.5c), where copper has been etched to show the end parts of the filaments; each Nb-47Ti filament is $6\mu\text{m}$ in diameter. Around each Nb-Ti filament there is $0.15\mu\text{m}$ thick niobium layer and $0.5\mu\text{m}$ thick layer of copper; **e)** Rutherford cable made from conductor presented in Fig.5c).

Table 1. Critical temperature for ternary Nb-based alloys.

| Alloy | Critical temperature T_c (K) |
|-------------------------|--------------------------------|
| Nb-(30-40%)Ti-(10-15%)W | 7.5 |
| Nb-43%Ti-8.4%Cu | 7.9 |
| Nb-50%Zr | 10.2 |
| Nb-40%Ti-10%Zr | 5.5 |
| Nb-5%Ti-45%Zr | 10.2 |
| Nb-10%Ti-40%Zr | 9.8 |
| Nb-25%Ti-25%Zr | 9.7 |
| Nb-45%Zr-5%Hf | 10.0 |
| Nb-47%Zr-3%W | 10.3 |

Table 2. Upper critical field of the selected multi element Nb-Ti based alloys.

| Alloy(wt%) | $\mu_0 H_{c2}$ (T) at 4.2K | $\mu_0 H_{c2}$ (T) at 2.2K |
|------------------|----------------------------|----------------------------|
| Nb-30Ti | 11.4 | |
| Nb-40Ti | 11.7 | |
| Nb-46.5Ti | 11.5 | 14.2 |
| Nb-49Ti | 12.2 | |
| Nb-22Ti-22Zr | 13.6 | |
| Nb-45Ti-16Zr | 12.4 | |
| Nb-43Ti-25Zr | 11.6 | 15.5 |
| Nb-41Ti-13Hf | 11.0 | 14.5 |
| Nb-38Ti-26Ta-6Hf | 11.3 | 15.3 |
| Nb-39Ti-24Ta-6Zr | 13.1 | |

4. Nb₃Sn CONDUCTORS

Intermetallic compounds including Nb-based were widely explored as potential superconducting materials in the 1950s and 1960s. The best intermetallic superconductors, based on niobium rich compounds with group IIIB and IVB elements (e.g., Nb₃Ga, Nb₃Al and Nb₃Sn), are still under continuous development and new discoveries of a cheaper and more reliable processes are described [10-12]. These are isotropic materials in which the conduction electrons travel in an electronic band made from niobium d states. The nature of the relation between the unique properties of the A15 intermetallic compound and the crystallographic structure was first pointed out by Weger [13]. The A15 structure is distinguished from other intermetallic phases in the Nb-Sn phase diagram by having three distinct families of Nb atoms arranged in chains parallel to the [100], [010] and [001] axes. The quasi-one-dimensional nature of the Nb lattice leads to unusual features in the electronic band structure, which are responsible for the unique properties. The atomic volume of the transition metal atoms such as Nb are smaller than that of non-transition-metal atoms such as Sn and thus have to be considered as the more decisive factor in determining the properties of these materials. The linear chain model, which expresses nearest-neighbour interaction was found to be quite

successful in explaining some of the elastic and magnetic (superconducting) properties of A15 alloys. The simple linear-chain model is quite successful despite the fact that the next-nearest-neighbour interaction is not negligible compared to the nearest-neighbour interaction.

Different physical parameters depend on quite different averages of the Fermi velocity v_F over a complex, many-branched Fermi surface: x_0 depends primarily on the mean value of $\langle v_F \rangle$ and to lesser extent on $\langle 1/v_F \rangle^{-1}$ through T_c , while $B_{c2}(t)$ depends on $\langle v_F^2 \rangle^{0.5}$ and anisotropy in $B_{c2}(0)$ relates to $\langle v_F^4 \rangle^{0.25}$. It was established that superconducting parameters such as T_c are more sensitive (degrade much faster) to substitution of the Nb sublattice than of the Sn sublattice. According to the Nb-Sn phase diagram, Fig.6(a) there are three intermetallic phases: Nb_3Sn ($T_c=18.2\text{K}$), Nb_6Sn_5 ($T_c=2.8\text{K}$), NbSn_2 ($T_c=2.6\text{K}$) and one solid solution $\alpha\text{-Nb}$ ($T_c=9\div 6\text{K}$) and also pure Sn ($T_c=3.2\text{K}$).

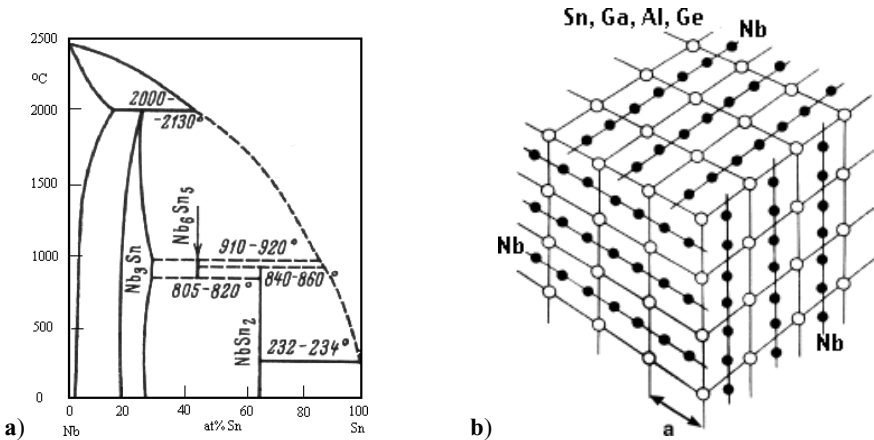
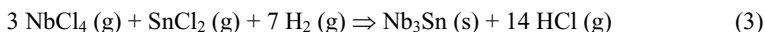


Fig. 6. a) A binary phase diagram of Nb-Sn system; **b)** Distribution of Nb and Al atoms in A15 structure of intermetallic compound Nb_3X (a -lattice parameter) demonstrating three orthogonal linear chains of Nb atoms, [15].

Unlike NbTi, Nb_3Sn is a brittle intermetallic compound having a well-defined stoichiometry, which is obtained in the practical multifilamentary wire form by long-term high temperature reactive diffusion. The Nb_3Sn intermetallic has a lattice parameter $a=0.518$ nm and an A15 type structure, A_3B , Fig.6b), which belongs to space group $\text{Pm}\bar{3}\text{n}$. The first single crystals of Nb_3Sn have been grown by Hanak et al. [14]. The Nb_3Sn coated conductor concept was developed through the two parallel routes: by reduction from the gaseous phase and by dip coating technique. The synthesis of this compound by the gas phase reaction on the metallic substrates appeared to be feasible because both Nb and Sn can be obtained by the hydrogen reduction of their gaseous chlorides at temperatures well below 1000°C . A simultaneous reduction of a mixture of these chlorides yields crystalline Nb_3Sn without the intermediate formation of the free metals or other Nb-Sn phases such as Nb_6Sn_5 and NbSn_2 . The overall reaction for the production of Nb_3Sn CVD coated conductors can be described by eq.(3) as:



Dip coated Nb_3Sn conductor was developed by passing the Nb-alloyed 20 μm thick tape through the liquid bronze bath in vacuum followed by isothermal on-line diffusion of Sn to Nb tapes from both sides allowing formation of the Nb_3Sn phase [16]. As it was proven by Mössbauer spectroscopy, this liquid-solid diffusion process allowed formation of the other intermetallic phases such as NbSn_2 and Nb_6Sn_5 but only in the coarse grain zone, (see for example Fig.25) [16,17].

Currently there are essentially three types of the Nb_3Sn superconducting conductors categorised by the architecture and initial composition: (i) bronze, (ii) internal tin and (iii) powder-in-tube. In all these cases formation of Nb_3Sn take place in then presence of Cu, which helps to achieve the fine grain structure. And facilitates formation of the Nb_3S at reaction temperature as low as 450°C [18]. Current progress in high current Nb_3Sn conductors by internal tin or powder-in- tube process is noticeable. The current density is reaching almost record values of 3000A/mm². Increase of the transport current by increasing the cross section of the Nb_3Sn layer is one of the obvious paths to continue development of the A15 conductors. Also there is another probably the most important path that could bring the largest further improvement of the wires performance by development of Nb_3Sn grain-structure with planar barriers normal to the Lorentz force. A typical technical superconductor consists of a composite of superconducting filaments, the stabilising matrix and insulation that may differ depends on the process adopted [19]. Each one of the suitable fabrication process listed in Table 3 must be capable of producing long lengths of composite conductors in a reliable and economic way. The process must allow the optimisation of the superconducting properties,

Table 3. List of manufacture processes and resulting properties of Nb_3Sn conductors

| PROCESS | % of overall cross section occupied by Nb_3Sn | J_c at 12T at 4.2K (A/cm ²) | Comments |
|--------------------------|---|---|---|
| Bronze | 15 | 1×10^5 | + uniform Nb_3Sn layer; - expensive; - low Sn content*; - multiple annealing |
| Internal Tin diffusion** | 18 | 1.5×10^5 | + cheap, easy deformation - non-uniform - filament bridging |
| Powder-in-Tube filaments | 33 | 1.8×10^5 | + ultrafine filaments - discontinuous - high ac losses*** |

* The amount of Nb_3Sn in the cross section is limited by the Sn content in the bronze, which above wt15% creates brittle Cu-Sn intermetallics, (see Fig.14a). ** The size of the filament diameter should be optimised in order to ensure that J_c value of the Nb_3Sn layer is maximised, the cross sectional inhomogeneities lower the local critical current density of the filament. *** The smaller the the filament size, the lower the hysteretic ac losses. The spacing between the filaments must be of order of 1 μm in order to electrically decouple the filament and therefore reduce the low-field ac losses.

especially the current carrying capacity. The completed composite wire must be processable into more complex conductor geometries, like cables, and into magnet coils. For applications with high currents and/or with large cooled conductor surface areas many individual strands are combined to form transposed cables or braids. Braids should be avoided because the many crossovers can lead to unacceptably large degradation of J_c . The cabled conductors allow an internal cooling of the conductor by forced flow of helium, provide good mechanical properties and allow vacuum impregnation of the coil winding pack. This yields the best electrical and mechanical performance of large superconducting coils while simultaneously allowing an efficient cool down and stable operation. Internally cooled conductors of the type shown are therefore generally adopted for large magnet systems.

Despite the fact that many superconducting materials are known, including high temperature superconductors, the complexity of all these requirements has led to only two materials being of technical relevance at the moment. These materials are: the ductile alloy NbTi and the brittle intermetallic compound Nb₃Sn. Due to its difficult handling Nb₃Sn is only used at high fields (>10 T) where the current carrying capacity of NbTi decreases very fast, see Fig.1b). The technology of multifilamentary Nb₃Sn wires is complex and requires the production of special kinds of high purity reshaped materials such as (niobium alloy rods, tin rods, large high tin concentration homogeneous bronze ingots, high purity copper tubes and foils, high purity Ta foils or tubes). Because Nb₃Sn superconductor is brittle, the processing of such intermetallic by warm and cold working has to be excluded. In this case the solution is to use a composite consisting of ductile precursor materials and to form the superconducting phase only after the deformation process. Nb₃Sn composite materials are manufactured by a solid state diffusion process (bronze process) or internal tin source process, see Table 3, where thin Nb filaments distributed in bronze (or copper plus tin) matrix, are separated from stabilised copper by diffusion barriers. The whole wire fabrication process includes: manufacture of bimetal precursors and sealing of them under vacuum by electron beam; extrusion of bimetal precursors at high temperature; cold deformation of bimetal rods to required size, assembling of multifilamentary rods and sealing; hot extrusion of multifilamentary rods; cold drawing of multifilamentary rods to required size; twisting of wire; final heat treatment to form intermetallic diffusion Nb₃Sn layers.

4.1 Nb₃Sn Bronze Process

The main reaction heat treatment to form the A15 layer is commonly an isothermal reactive diffusion in the range of 650°C to 750°C. At the lower end of this range the compound growth rate is very slow leading to unacceptably long reaction times [20] in addition the compound is disordered and has a high level of point defects exhibiting a degraded value of T_c and B_{c2} [21]. Above 750°C rapid grain growth and grain coarsening occurs [22], this is most apparent in the outermost region of the reaction layer which the first to form, Fig.7a). However for modern bronze processed ITER type strands with Nb filaments having diameter in the range of 2-3 μm and subjected to the standard ITER heat treatment (575°C 150h + 650°C 200h) Nb₃Sn grains were mainly equaxed but the grain size usually varied in relatively large interval from 30 nm to 250 nm, Fig.7b) and c). It contradicts to earlier accepted scheme of 3-layered structure of Nb₃Sn filaments that included two layers of equaxed grains with different sizes and one layer of the columnar grains, Fig 7a) [23]. The results obtained are in good

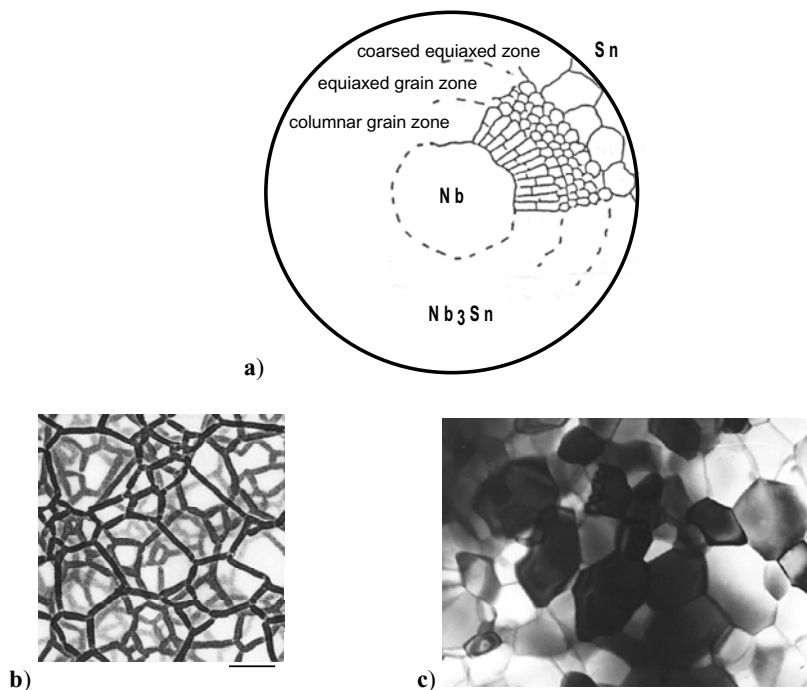


Fig. 7. a) Cross section of a single Nb-Nb₃Sn filament in the bronze matrix after solid state diffusion of Sn to Nb from the bronze matrix [25]; b) schematic projection of four 2D cuts through the Nb₃Sn layers of a grain boundaries of the fine equiaxed zone. Nb₃Sn layer growth direction, normal to the picture; c) TEM picture of the typical equiaxed zone; courtesy of V. Pantsyrnyi.

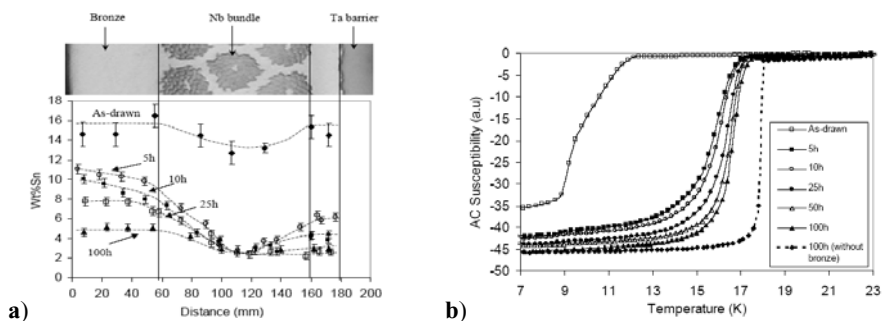


Fig. 8. Variation of tin concentration in bronze matrix across (a) NS6000 conductor for as-drawn, quenched, reacted at 725°C for 5, 10, 25, 50 and 100 hours as indicated in Fig.8 a) [28].

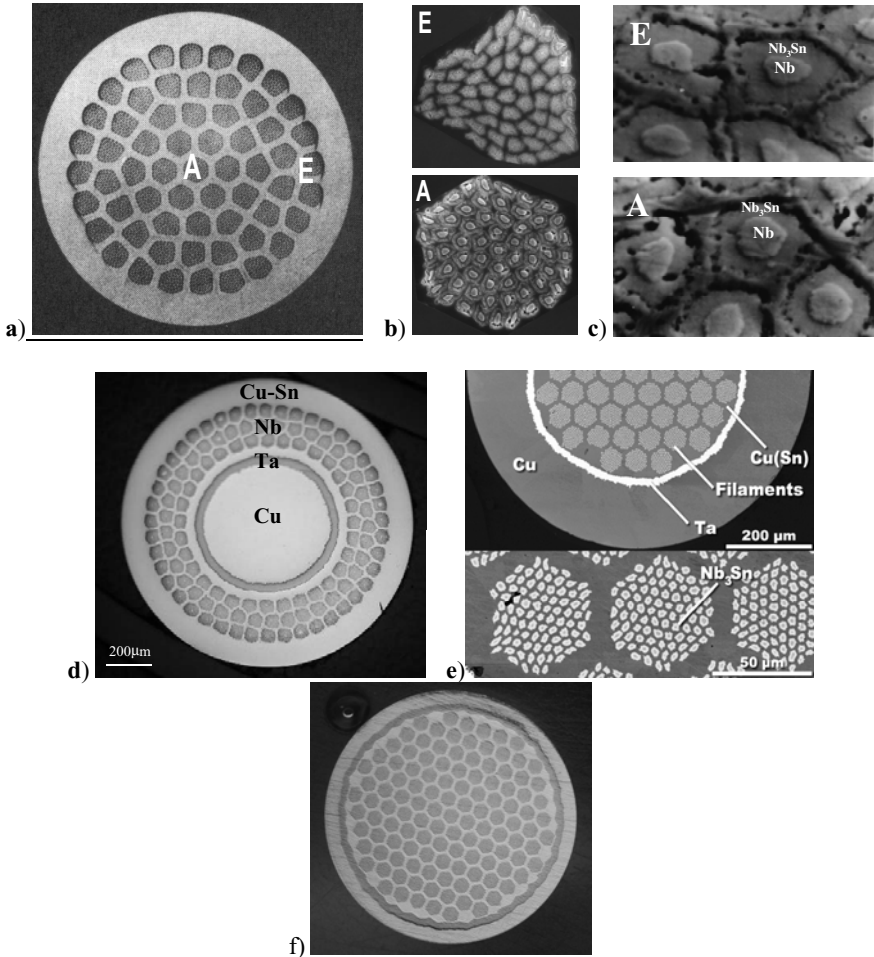


Fig. 9. SEM images of the cross-sections of the different types of Nb₃Sn conductors and corresponding filament details of: **(a)** bronze process conductor 64x64 filaments without Cu stabilization, central bundle is marked as A where the external bundle is marked as E; **(b)** marked bundles of the wire as in a) after isothermal diffusion [25]; **(c)** as **(b)** central regions of the marked bundles E and A after cycling diffusion process [27] (differences in Nb₃Sn layer thickness are negligible); **(d)** the bronze process ITER strand internal Cu stabilization Vacuumschmelze, Courtesy of H. Krauth; **(e)** the bronze process ITER strand external thick Cu stabilization, courtesy of D. C. Larbalestier [29]; **(f)** the bronze process ITER strand external thin Cu stabilization. The filament composition is Nb_{7.2}Ta, the bronze is 15.4wt% Sn; the diffusion barrier is Nb; Ti can be introduced either as artificial doping (1% in the filaments) or in the bronze (0.25%). Wire diameter is 1.25mm. courtesy of R. Flukiger and Vital Abaecherli [30,31].

correlation with the data of recent SEM investigation on Nb₃Sn grains morphology in other ITER type strands [24].

During the isothermal reactive diffusion of the multifilamentary conductor each filament follows its own layer growth pattern depending on the local variation in the tin concentration as the reaction proceeds [25], but the relation between the average grain size and the average intersept length is sensitive to the grain size distribution [26]. The tin concentration will vary spatially in a complex way across the composite as concentration gradients build up to drive the tin supply and as the localized 'sinks' for tin in the form of filaments undergoing reaction change their rate of tin uptake Fig.8 and Fig.9b). The practical consequence is that Nb₃Sn layer growth starts everywhere at the same rate determined by the initial bronze concentration and any additive present but rapidly falls to almost zero for the filaments remote from major sources of tin [30,31], Fig8a). A further consequence of tin depletion is the growth of off-stoichiometry Nb₃Sn with depressed values of T_c and B_{c2} . By using a multistage cyclic pumped diffusion (CDP) anneal which has to be optimised for each particular composite geometry, it is possible to achieve rapid uniform layer growth in a high tin bronze across the whole cross section of the thick external bronze reservoir conductors, compare Fig.9b) and c). The method is likely to be of particular value when a conductor contains substantial bronze reservoirs or is an external tin or internal tin composite design.

In the bronze route Nb rods are embedded in a Cu-15wt%Sn bronze and the Nb₃Sn phase is formed in the completed conductor by a solid state diffusion and reaction process at about 650°C–700°C [32]. It has to be mentioned that because of the high concentration of tin in bronze the stress-relief annealing process has to be repeated many times during wire drawing before the final conductor diameter can be reached. For this reason the configuration of Nb₃Sn conductors differs from that of NbTi conductors. To allow effective transformation of the Nb into Nb₃Sn within a reasonable time, the filament diameter is limited to about 3 to 5 μm. As a consequence, a high number of filaments is required (typically around 10000) therefore the bundling and deformation process has to be performed twice. In addition, the Cu-Sn matrix does not effectively stabilise and protect the conductor, requiring additional copper to be added, preferentially in the second bundling process. This pure Cu has to be protected from contamination by Sn during the reaction heat treatment by means of a diffusion barrier, e.g. of Ta, Fig.9d).

Superconducting wire in operational regimes is often exposed to sudden changes of external thermal or electromagnetic environment, which may cause the local development of the normal state in an Nb₃Sn superconductor. Since the bronze matrix has a high resistivity it is necessary to provide high-purity high-conductivity cladding by pure copper or aluminium to avoid the danger of destruction of the conductor in the heart of an expensive device and to provide an alternative route for the very high currents passing through the wire. The larger the number of discrete copper areas the more effective will be the stabilisation. The process of thermal and electrical stabilisation was extensively discussed by Wilson [33].

In the case of the reactive diffusion between Nb filaments and Sn from the bronze matrix the diameter of the Nb core is one of the very important elements in determining the time dependence of the intermetallic layer growth. The growth process is faster for fine filaments. The difference in this growth behaviour in the bronze-processed Nb₃Sn layer is attributed to the radial cracks formed during its growth. The source of the cracks in the layers appears to be due to the difference in the diffusion rate of Sn and Nb in Nb₃Sn layers. When cracks are

introduced in the layer, they will act as diffusion pipes for Sn and the limiting process will be the formation rate of Nb_3Sn at the Nb- Nb_3Sn interface. Additional evidence for Sn being the primary diffusion species is also provided in the observation of Kirkendal voids at the Nb- Nb_3Sn -(Cu-Sn) interface. The vacancies are being injected into the bronze, by Sn atoms being injected into the Nb_3Sn , faster than the vacancies can diffuse away to sinks in the bronze, thus forming the Kirkendal voids by supersaturation [34]. Additionally even multifilamentary bronze conductors during isothermal processing suffer from a significant depletion of Sn between the filaments, whereas the tin level in outside bronze tin reservoir is relatively unchanged. Such nonuniform diffusion is obviously reflected in a radial gradient of superconducting properties, which is the most undesired property of the conductor which will result in lower J_e and poorer cryomagnetic stability of conductors. To suppress formation of such non uniformities the modified multistage diffusion processes can be used successfully [27]. There is also gradient of the properties across an individual Nb_3Sn layer due to the gradient of concentration, which effect the superconducting parameters of such layers, Fig.10a [35]. It is evident from Fig.10b that the concentration of the Sn at the grain boundaries is higher than stoichiometric composition required by A-15 phase, therefore they should have a lower superconducting parameter, see Fig.10a). Because grain boundaries which are approximately 5-10 lattice constants wide $\sim (2.5\text{--}5\text{ nm})$ and are comparable to the coherence length, $\xi \sim 6\text{ nm}$ of Nb_3Sn they are most likely effective pinning centres.

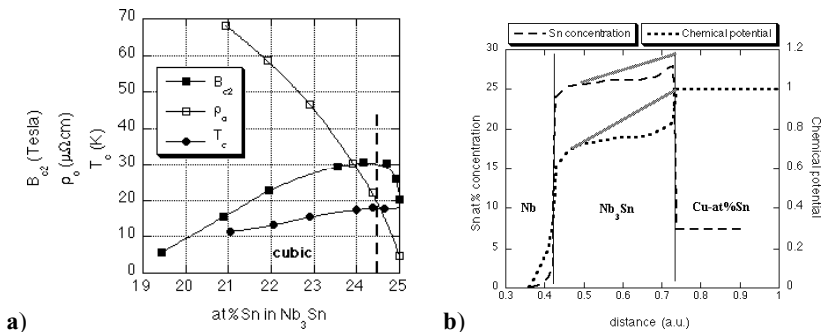


Fig. 10. a) Variation of B_{c2} , T_c and ρ_0 versus at% Sn content in Nb_3Sn . At low temperatures, binary Nb_3Sn transforms into the tetragonal phase at 24.5at%Sn. The tetragonal transformation from cubic structure is marked by the vertical broken line. Adapted after Flukiger [35]. The B_{c2} is related with other physical quantities as follows $B_{c2} = \gamma T_c \rho_0$ where γ is the electronic specific heat. This can explain why the additions of ternary elements to Nb_3Sn leads to a considerable increase of J_c at higher fields, which is due to a strong increase of ρ_0 . Enhanced B_{c2} and additional pinning centres originated from fine ternary precipitations improve high J_c vs B characteristics of such wires [35]; **b)** schematic diagram of the tin concentration and tin's chemical potential variations taking place at the Nb filament proximity in the Nb- Nb_3Sn -(Cu-Sn) diffusion system. The grey lines in the Nb_3Sn layer region represent the changes for the grain boundary, where the broken lines represent the intragrain properties; adopted after [38].

Based on the microstructural correlations in the Nb₃Sn a grain-boundary pinning mechanism is the dominant at moderated magnetic fields. It has been established that flux pinning force increases with decreasing grain size in other words J_c increases with a small-grained structure (recommended grains are if less than 40 nm in diameter [37,38]) Fig.11. We will now briefly mention the model of Pande and Suenaga [39] where grain size dependence is considered in detail, eq.(4). This model is based upon the following assumptions: (i) any grain boundary segment is regarded to be made up of a superposition of uniformly spaced dislocation walls. Spacing and other parameters are so chosen to satisfy all boundary conditions where on the average, the Burgers' vector are randomly distributed along all three axes; (ii) grains are made up of such segments.

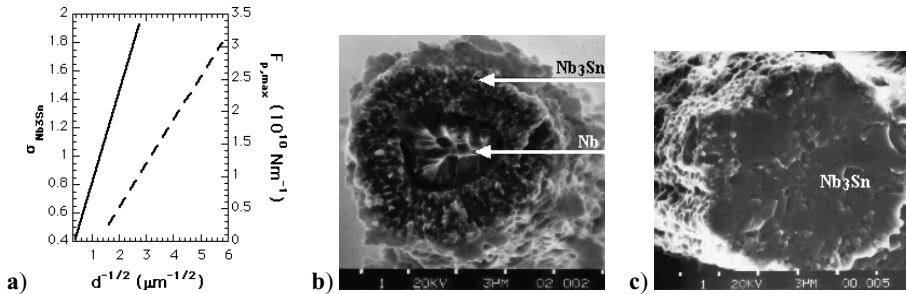


Fig. 11. (a) Dependence of the tensile strength and flux pinning force of the Nb₃Sn layer formed in the multifilamentary conductors expressed as a function of the grain size, to a first approximation [36]; (b) Fractured cross-section of the single filament selectively etched away from the multifilamentary conductor, radial thickness of the Nb₃Sn layer 2.9mm, reactive diffusion time 5.3hours, $F_p=2.3 \cdot 10^{10} \text{Nm}^{-3}$; (c) radial thickness of the Nb₃Sn layer 6mm, reactive diffusion time 100 hours, $F_p=0.57 \cdot 10^{10} \text{Nm}^{-3}$. There is a strong evidence of the Nb₃Sn grain growth after full conversion of Nb to Nb₃Sn resulting in lower pinning force and also lower critical current density [37].

The relation between the grain size D , and grain segment, d , will depend on geometry and shape of the grain, but on the average $D \approx kd$ where k parameter is of the order of two; and (iii) the flux pinning is primarily due to first order elastic interactions. Based on the above assumptions and after statistical summation of the elementary pinning forces, an expression for grain boundary pinning was obtained as, eq.(4) where P_0 is a constant

$$F_p(D) = \frac{P_0(1-b)^2}{D} \sin^2\left(\frac{\pi D}{\sqrt{3}ka_0}\right) \quad (4)$$

independent of grain size D , b is the “reduced” magnetic field and a_0 is the lattice constant of the fluxon line lattice which depends on the magnetic field [6]. Eq.(4) shows that the flux pinning and hence critical current is approximately inversely proportional to grain size as expected from experiments. However, eq.(4) also gives an oscillatory behaviour in F_p as function of grain size, but such oscillations are not observed experimentally although experimental results do show large scatter in the data, especially in thin films. It is believed

that such an oscillatory behaviour can be suppressed if a distribution in grain sizes is taken into account. Measurements of grain sizes in Nb₃Sn show that the distribution is roughly log-normal [40]. It is seen that the oscillations are smoothed out but there is a peak in the F_p at a value of $a_0/D = 1.83/k$. The exact location of the peak will depend on the value k used. This leads to the conclusion that flux pinning cannot be indefinitely increased by grain refining. Considering the other side of the grain size spectrum a prolonged heat treatment produces grain growth, see Fig.11 (b) and (c) and when the grain size is larger than the optimum than J_c value is dramatically suppressed [36,41] but J_c may still not reach the optimum value [37]. In this regard the bronze process is helpful thanks to the copper in bronze matrix that enables fine grain Nb₃Sn to form at lower temperatures than with reach Sn bronze. From the view of fracture behaviour of the brittle Nb₃Sn, fracture occurs at the grain boundary. Therefore it can be expected that the strength of Nb₃Sn compound have a strong inverse dependency on the grain size Fig.11a. A microstructure with fine grains is therefore required to get high J_c values. This is achieved by performing the reaction heat treatment at elevated temperature 650°C–700°C for a long time.

By treating such an arrangement of individual components Nb filaments, Nb₃Sn layer, bronze matrix, Ta diffusion barrier and Cu filaments—in the multifilamentary composite as a set of parallel resistors, the total resistance can be expressed by eq.5),

$$\frac{1}{R_T} = \sum_i \frac{1}{R_i(V, C, T, G)} \quad (5)$$

where R_T is the total resistance of the composite and R_i is the resistance of the individual components. During reactive diffusion processes, the resistance of the individual components depends on volume (V), composition (C), temperature (T) and grain morphology (G) (which includes stress/strain). A schematic indication of the possible resistance changes of individual components at different stages of the reactive diffusion processes is illustrated in Fig.12 [28].

During the first anneal cycle as in Fig.13, the non-linearity of the heating up curve might suggest some reactions occur along the heating up process. Hence, the derivative of resistance/length with respect to temperature was plotted against temperature to observe those tiny changes as shown in Fig.13b). The plot was then compared with the DTA results to show the relationship between both results. It was found that both graphs seem to agree with each other for most of the characteristic temperatures. At approximately 580°C, the $d(R/l)/dT$ curves start to decrease dramatically, which suggests the formation of Nb₃Sn layers and a corresponding sudden tin depletion of the bronze matrix near the Nb filaments. This results in a substantial decrease in the overall tin concentration of the bronze matrix and so decreases the resistivity of the whole wire in spite of the formation of Nb₃Sn, which has a higher resistivity. During the reactive diffusion processes a significant drop in the resistivity of the wire can be measured due to the formation of the Nb₃Sn layer using tin atoms from the bronze matrix Fig.13a).

In situ resistance measurements of multifilamentary composite conductors during the formation of the A15 layer proves to be a promising method to provide information about the details of the conductor at different stages of the reactive diffusion processes. The different results obtained from *in-situ* resistance measurements for different geometries and designs of the multifilamentary conductors show the capability of this technique to distinguish between different wires. It is the objective of this technique to monitor and optimise the formation of

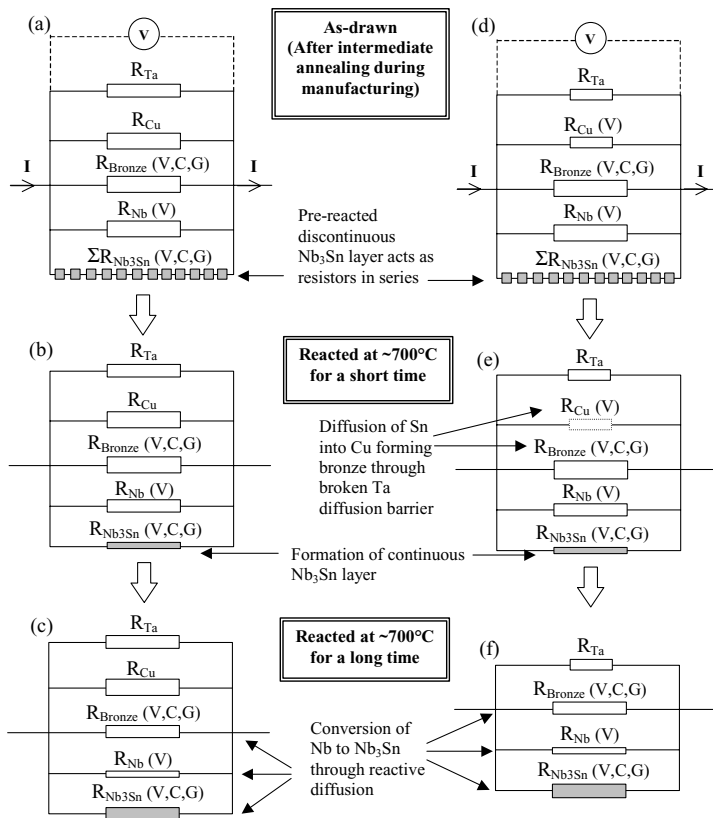


Fig. 12. An interpretation of the possible resistance changes of individual components of bronze process (a), (b), (c) stabilised and (d), (e), (f) unstabilised multifilamentary Nb-Sn-Cu-Ta conductors at different stages of reactive diffusion processes. The resistances of certain elements and compounds changes with volume (V), composition (C), and grain morphology (G) as indicated [28].

A15 layer using the *in-situ* resistance measurement technique. Although the grain size of the Nb_3Sn layer cannot be measured directly by this technique at the moment, it is hoped that by getting a better understanding of the resistivity changes in the bronze matrix and refining the experimental technique it will finally be possible to reveal the microstructure of the Nb_3Sn layer. This can enable the characterisation of multifilamentary composite conductors, probably even extracting the grain size development of the Nb_3Sn layer, during reactive diffusion processes, allowing optimisation to be performed simultaneously.

This technique can be used to monitor and optimise variety of Nb_3Sn multifilamentary composite conductors manufactured by the internal tin process or powder metallurgy and also other Nb-based conductors as it is described in the following chapters.

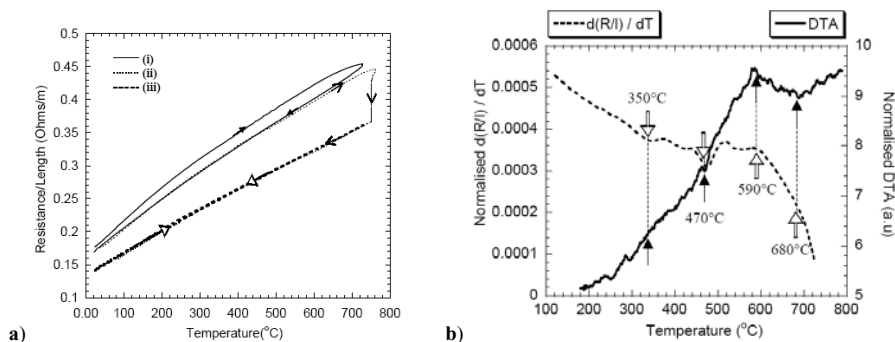


Fig. 13. In-situ resistance/length versus temperature measurements of NS6000 wire: **(a)** (i) heated at a rate of 300 K/h to 725°C then cooled slowly down to room temperature; (ii) wire as in (i) dwell for 50 hours at 750°C and cooled to room temperature and once again the same wire; (iii) the wire (ii) heated at a rate of 300 K/h to 725°C and cooled slowly to room temperature. **(b)** Comparison between derivative of the resistance/length versus temperature curve (i) in Fig.13a), and the DTA results. The open and closed arrows indicate the coinciding characteristic temperatures of curves $d(R/l)/dT$ and DTA respectively [28].

4.2 Nb₃Sn Internal Tin Process

The internal tin process is less complicated in respect of mechanical deformation because all initially used elements such as Nb, Sn, Ta, and Cu are very ductile and do not require intermediate stress-relief annealing as it does for the bronze technique. Generally the formation of the Nb₃Sn by the internal tin process requires a sequence of thermal processes such as: low temperature diffusion (LTD) at ~200°C, followed by intermediate temperature diffusion (ITD) at 200°C-340°C where Cu-Sn phases are formed, Fig.14. [42], followed by high temperature diffusion (HTD) at ~700°C where the formation of the intermetallic Nb₃Sn layer takes place [43]. After the low temperature diffusion process at 200°C a continuous rings of η -Cu₆Sn₅ (60 wt% Sn) and ϵ -Cu₃Sn (37.5 wt% Sn) phase are formed [44]. The further increase of the temperature from 200 °C to 340 °C induces a rapid conversion of the remaining tin core to η phase. Understanding of the correlation between the diffusion of tin from a high tin bronze reservoir to the niobium filaments and the properties of the intermetallic Nb₃Sn diffusion layers formed, is essential for further improvement of the superconducting electromagnetic properties of a conductor [43,46]. There is also a trend to increase the content of Sn in the conductor and number of the filaments to increase the overall critical current density of the conductor.

Computer design of the wire, require solving: diffusion equations, chemical equations, geometrical equations, electric equations, mechanic equations and thermal stability equations. Especially attractive from the point of view of high filling factor and uniformities of the undistorted Nb-based filament distribution in comparison to conventional extrusion processes of the drilled or stacked matrix, Fig.15a) is a modified tube, MT, technique used in the 'internal tin' process to manufacture large number of filaments in the individual bundles of the Nb₃Sn conductor Fig.15 [44].

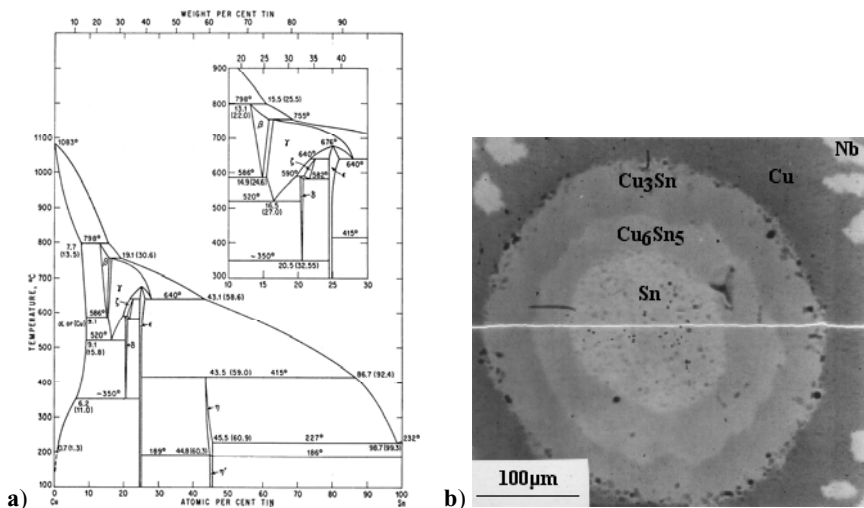


Fig. 14. a) Cu-Sn binary phase diagram; **b)** SEM micrograph revealing formation of the η -Cu₆Sn₅ and ϵ -Cu₃Sn phases at the Sn-Cu interface during low temperature diffusion process [44].

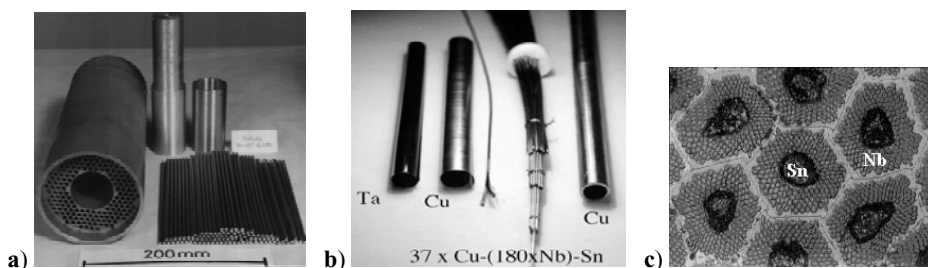


Fig. 15. Manufacture stages of the internal tin multifilamentary Nb₃Sn conductor: a) manufacture of the 180 filamentary Nb-Cu conductor, initial diameter of the copper matrix 120mm [44]; **b)** in the centre, the 180 Nb-filament Cu-Nb-Sn composite after reduction from diameter 120mm (Fig15a) to 1mm was restacked in the form of 37 bundle multifilamentary conductor inside the pure copper tube. The tantalum foil (far left) was used to prevent contamination of the external copper by the internal tin during a reactive diffusion process and subsequent increase of electric resistivity of the quench protection layer; **c)** central zone of the final superconducting Nb₃Sn 6660-filamentary composite conductor (180 x 37) before multistage reactive diffusion process between Cu-Sn followed by Nb-Sn reactive diffusion [45].

This MT technique [44] presented in Fig.15b) was adopted also by different companies for manufacture of the HTS superconducting Powder-in-Tube wires. The high engineering critical current value, eq.(6), is one of the most important parameter for the NMR and

accelerator magnets. A low value of the overall critical current density J_c is a particular problem with fully engineered conductors. The thickness of non-superconducting layers and the usual deterioration of J_c in the superconductor with increasing thickness t_s , eg.(7), lead to a maximum in J_c with t_s that can be expressed as:

$$J_c(t_s) = J_c(t_s) \cdot \left(\frac{t_s}{t_s + \sum_{i=1}^n t_i} \right) \quad (6)$$

here: $\sum_{i=1}^n t_i$ is a sum of the thicknesses of: matrix, unreacted Nb, diffusion barrier, stabilising (shunt) layer, insulating layer etc. (excluding superconductor). $J_c(t_s \approx 0)$ is a

$$J_c(t_s) = J_c(t_s \approx 0) \cdot t_s^w \cdot e^{k_j \cdot t_s} \quad (7)$$

current density independent of thickness if $w=0$ and $k=0$; parameter w defines the maximum position on the $J_c(t_s)$ curve where k_j parameter defines the J_c vs t_s dependence [37].

In respect of maximisation of the J_c , the filling factor, P , plays an important role in design of multifilamentary conductors, eq.(8). Filling factor, in multifilamentary composites by using modified tube technique, defined by the ratio of the cross-sections of Nb₃Sn to the remaining matrix, depends on the stacking number in the individual bundle arrangement, n_b , and the filling of the individually arranged bundle, P_i . Filling factor can be expressed as:

$$P = \frac{\prod_{i=1}^{n_b} P_i}{\left(\prod_{i=1}^{n_b} (P_i + 1) - \prod_{i=1}^{n_b} P_i \right)} \quad (8)$$

where

$$P_i = \frac{(N_e \cdot S_s)}{S_t} \quad (9)$$

and N_e is the number of sub-elements in an individual bundle; S_s is the cross-section of an individual sub-element; and S_t is the cross-section of the external tubes [44]. Usually the value of P changes from 0.05 for widely distributed filaments to 0.8 for densely distributed filaments. A dense distribution of Nb filaments is more suitable for high engineering critical current density, J_c , but requires a more careful adjustment of the cold deformation procedure to avoid interfilamentary bridging [43]. From the eq.(8) and eq.(9) it can be seen that the increase in the number of repeat stacking units, n_b , and the decrease in the number of sub-elements (in particular bundles) causes a decrease in final packing, P , Fig.15a). Increase of P requires reduction of number of steps, n , and an increase in the number of filaments in each step.

If the bundles are uniformly structured and filaments are widely distributed the formation of the Nb₃Sn layers across the bundles is rather uniform as in Fig.16. On the other hand if the bundles are not uniformly structured in conductor cross section the non uniform deformation

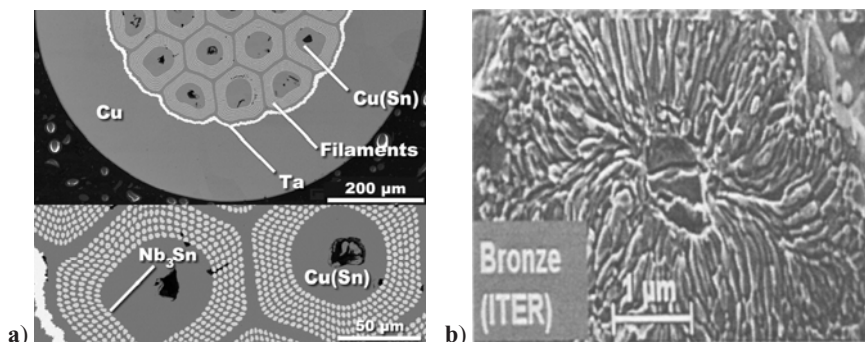


Fig. 16. Cross-sections of the different types of Nb_3Sn strand cross-section (SEM backscattered electron images) and corresponding filament details of: **a)** the internal Sn ITER strand, **b)** single filament as in Fig.16a) with radial grain structure, courtesy of D.C.Larbalestier [29].

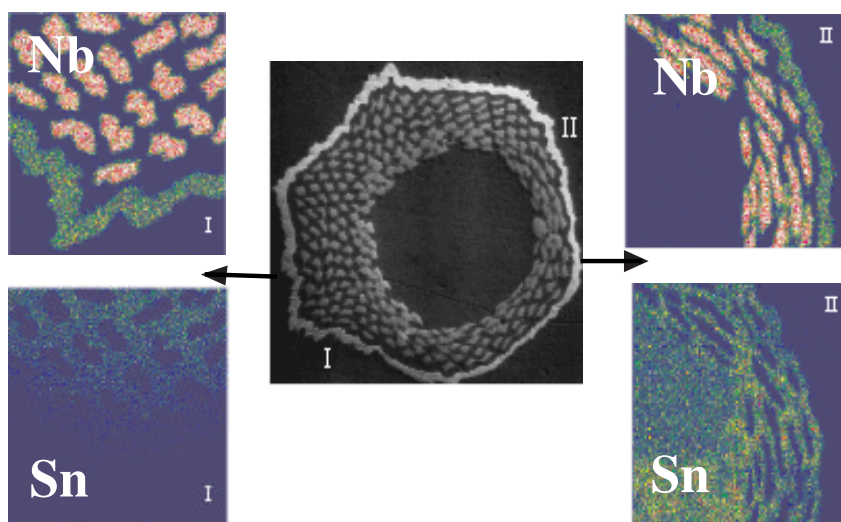


Fig. 17. EDAX mapping of the Nb and Sn distribution in the single bundle of the conductor used in CCIC cable. It is evident that the fragment I there is much less Sn than in fragment II and the filaments are more circular shape preventing rapid conversion of Nb to Nb_3Sn [43].

of the conductor take place and as a consequence rapid formation of the multiphase Cu-Sn and Nb-Sn layers leading to misplacement of the filaments inside the high Sn bronze matrix during high temperature diffusion formation as presented in Fig.17, [43]. There is a clear evidence in literature that to achieve a highest J_c value of the Nb_3Sn conductors the amount of evidence in literature that to achieve a highest J_c value of the Nb_3Sn conductors the amount of

Nb in the non copper region must approach 50at%, Fig.18b). In the case of the higher concentration of closely packed Nb filaments the bundles behave as a coils of superconducting material (during conversion from Nb to Nb₃Sn there is a 37% volume expansion) and Ta fins have to be introduced to allow the magnetic flux to penetrate to the non-superconducting centers of the bundles see Fig.19. It is obvious that further intensive research is required to optimise such conductors make them thermomagnetically stable and simultaneously of the highest J_c values.

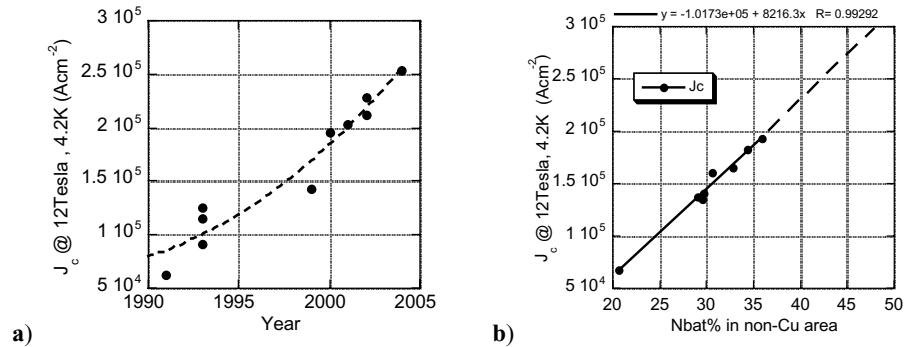


Fig. 18. Engineering critical current density of the non-Cu Nb₃Sn conductor: a) progress versus time; b) projected required atomic percentage of Nb in the non-Cu cross section of the conductor to achieve 300 kAcm⁻², after E.Barzi.

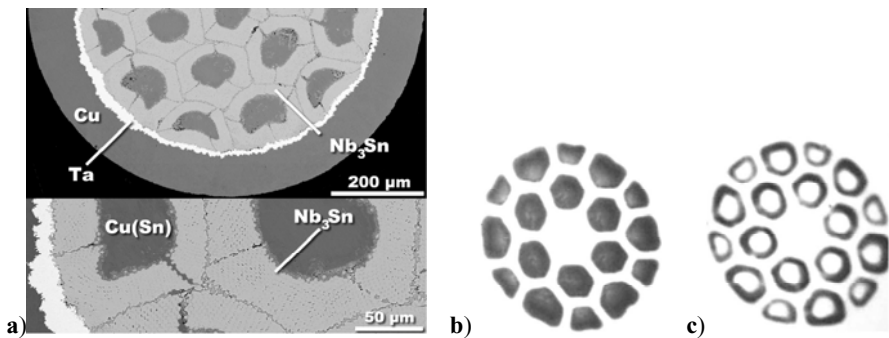


Fig. 19. Cross-sections of the internal tin ITER Nb₃Sn conductor: a) top figure fragment of the 'high J_c ' 19 bundle internal Sn conductor, the bottom part higher magnification where trans-filamentary radial Ta fins are visible; b) magneto-optic image of the cross section of the 18 bundle conductor without fins; c) magneto-optic image of the cross section of the 18 bundle conductor with fins, revealing the effectiveness of magnetic flux penetration of the bundles if fins are used. Courtesy of D.C.Larbalestier and P.Lee.

4.3 Nb₃Sn Powder in Tube Process

Wire produced by Powder-in-Tube process, known as a Kunzler method, [47] constitutes a tube of ductile material, Nb and Monel, with the core consisting of a mixture of original components in an almost stoichiometric ratio (3Nb+Sn), (Nb₆Sn₅+Nb) or (NbSn₂+Nb) in the form of powders. The sealed composite is swaged and cold drawn into a final wire, wound to the form of the solenoid and thermally processed at elevated temperatures to form Nb₃Sn core, Fig.20. The J_c of such wires exceeds that of ordinary Nb₃Sn bronze or internal tin conductors. This difference is due to the special filamentary structure of the core material. This consists of very thin regions of composition Nb₃Sn and thin intermediate regions of a different composition. This kind of structure is attributed to the degree of diffusion conversion of the initial phases during final heat treatment. The reactive diffusion treatment can either be performed before coil winding (React-and-Wind) or only after coil winding (Wind-and-React). Wind-and-React is mostly used for small sized Nb₃Sn magnets. Whereas React-and-Wind may be used for large magnets with low bending strain during coil winding [48], (see also Fig.40).

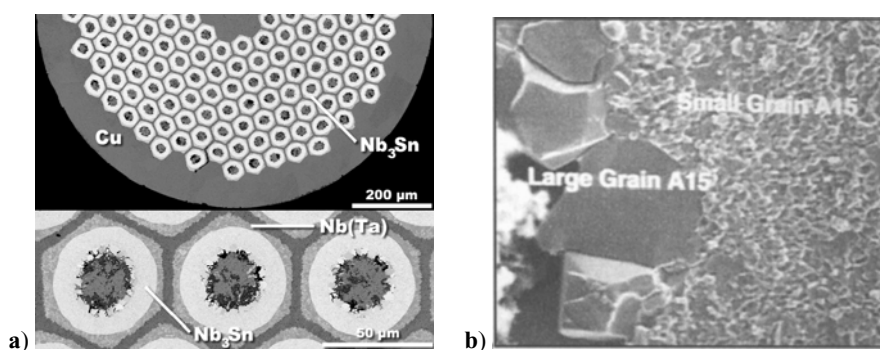


Fig. 20. Cross-sections of the different types of Nb₃Sn strand cross-section (SEM backscattered electron images) and corresponding filament details of: **a)** the high ' J_c ' PIT strands **b)** fragment of the bundle with gradiental changes of the tin atoms (from 25% at the Sn source side to 22% at Sn at the Nb side). The biggest gradient occurs at the Nb interface). Courtesy of D.C.Larbalestier and P.Lee [29].

4.5 Nb-based superconductors by Direct Electrochemical Reduction of Oxides

Technical superconductors based on NbTi and Nb₃Sn are now used routinely in many applications. The fabrication technology has reached a very high standard. Fabrication routes have been perfected to produce brittle Nb₃Sn compound in wire form for various high magnetic field applications. The Nb₃Sn conductor market is well developed but due to the mounting competition from the MgB₂ and (RE)Ba₂Cu₃O₇ conductors there is a pressure to improve the superconducting, cryomagnetic and mechanical properties of advanced Nb₃Sn. It is also continuous need to reduce the actual cost of the wire, Fig.4. There is new emerging technology, which was mentioned briefly already, where expensive Nb-alloyed metals can be

manufactured from electrochemically reduced Nb-based oxides using the Direct Electrochemical Reduction technique which will revolutionise the existing superconducting industry, enabling material costs reduction of an order of magnitude [49,50]. This electrochemical reduction route where Nb₂O₅ pellets or mixture of Nb-Ti oxides or even Nb-Sn oxides can be reduced to Nb, NbTi and Nb₃Sn in eutectic melts of CaCl₂-NaCl is much easier and quicker and a cheaper way to manufacture many superconducting metals and alloys than the established standard metallurgical routes [49], Fig.21.

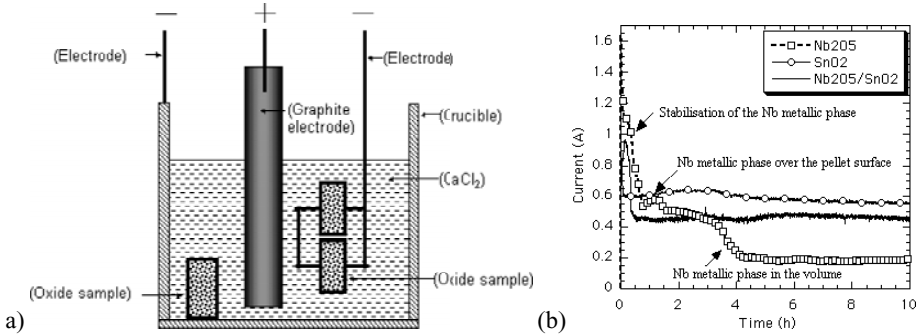


Fig. 21. Direct electrochemical reduction of oxides: (a) schematic diagram of reduction cell; (b) results of current vs time measurements of the pellets of the various pure and mixed oxides in a eutectic melt of CaCl₂-NaCl during a 10 hour electrolysis (potential 3.1V and temperature 900°C for Nb₂O₅ and SnO₂ and 935°C for Nb₂O₅/SnO₂ mixture) [49].



According to Nb-O phase diagram reduction of Nb_2O_5 to pure niobium metal should, in principle, take place through other oxides such as NbO_2 and NbO , whereas reduction of SnO_2 oxide to pure tin metal should, in principle, take place through other oxides such as Sn_3O_4 and SnO . Possible reactions: eq.(10) – eq.(22), which may take place during deoxidation process of Nb and Sn oxide mixture listed below. However the exact process of Nb-O and Sn-O reduction is not defined yet but may take place for Nb in the sequence eq.(10) \Rightarrow eq.(14) \Rightarrow eq.(16), and for Sn it may take place in the sequence eq.(17) \Rightarrow eq.(18) \Rightarrow eq.(22) or eq.(21) \Rightarrow eq.(22). Other electro-reduction sequences cannot be excluded due to the simultaneous in-situ formation of intermetallic Nb_3Sn phase.

Current versus time measurements of the various pure and mixed oxides pellets during oxide reduction in a eutectic melt are presented in Fig.21b). In case of pure niobium formation there are three distinguishing stages: (i) initial niobium formation at the so-called triple point between Nb_2O_5 – CaCl_2 electrode, (ii) fast conversion at the pellet surface and (iii) conversion of the Nb_2O_5 to niobium in the volume of the pellet. The situation is different in the case of tin conversion where due to the high temperature of electrolysis tin oxide, it is very rapidly converted to pure molten tin, Fig.21b), agglomerated at the bottom of the crucible. There are many factors influencing the grain size and morphology of the final product such as: conversion time, temperature, current, voltage, chemical composition of electrolyte and actual oxide and probably the most important factor is an initial density of oxide pellet, Fig.22.

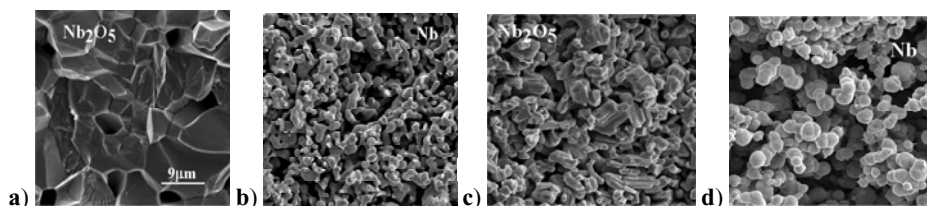


Fig. 22. SEM micrographs of the fractured cross sections of the different density pellets after the electrodeoxidation in a eutectic melt of CaCl_2 - NaCl ; **a)** The microstructure of the fractured cross section of the porous niobium pellet after electrolysis at 900°C for 24 hours followed 950°C for further 24 hours, initial Nb_2O_5 pellet compacted under $3.82 \cdot 10^7$ (kg/m^2) and sintered at 1400°C for 4 hours before electrolysis; **b)** The microstructure of the fractured cross section of the porous niobium pellet after electrolysis at 900°C for 24 hours followed 950°C for a further 24 hours the Nb_2O_5 pellet was only compacted and lightly sintered before electrolysis [49].

The complexity of in situ formation of the intermetallic Nb_3Sn compound at the interface between Nb-oxide/Sn-oxide results from the fact that oxide reaction is conducted at high temperatures above 800°C where melting temperature of pure tin is 232°C and the formation of Nb_3Sn takes place between solid niobium and liquid tin. It is not clear yet how exactly an in situ conversion to Nb_3Sn takes place. The speed of the reaction is probably due to the fact that some liquid tin is involved, Fig.21b). T_c transitions for the metallic products such as Nb, Nb-15%Ti, NbWZr and Nb_3Sn after DERO process are presented in Fig.23. The particle size of the Nb, Nb-Ti and Nb_3Sn powders prepared were determined to range from several hundred nanometres to about $100\mu\text{m}$, depending on how particle sizes of the initial oxides reacted and the experimental conditions utilised.

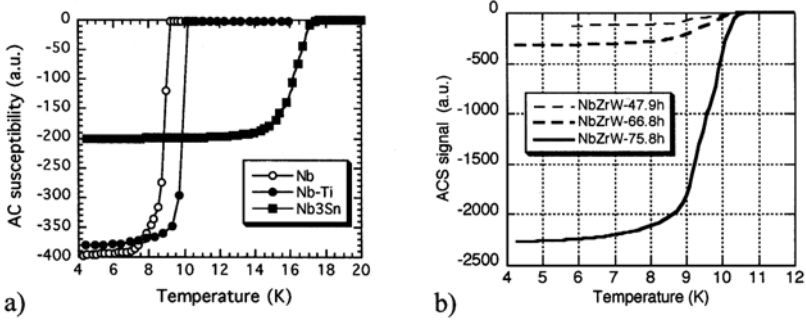


Fig. 23. AC susceptibility of the Nb-based materials produced by DERO process: **a)** Nb, Nb-50%Ti and Nb₃Sn compounds T_c equal 9.2K, 10.2K and 17.3K correspondingly; **b)** NbZrW alloy after different stages of reduction. $T_c > 10.3$ K, see Table 1.

This proven new, low cost method of reducing solid oxides to metals and alloys of the pre-defined alloy composition opens up a new opportunities for the highest quality, difficult to manufacture, best intermetallic LTS, (such as (NbTa)₃Sn, Nb₃(Al,Ge) and Nb₃Ga superconductors characterised by the highest J_c , B_{c2} , T_c values) for a fraction of the cost of the currently available Nb-Ti conductors which are treated more as a commodity Fig.4.

4.6 Improvement of Pinning

As it was pointed out by DewHuges [51], Gurevich et al. [52] and later by McDonald at al.[53] the best solution to achieve higher pinning force at higher magnetic field would be an introduction of the pinning walls extended along the filaments direction by an analogy to the Nb-Ti wires. The Nb₃Sn grain boundary network provide continuous path for the flux lines, therefore flux can move entirely within the grain boundary regions and the pinning force can be defined by the shear between grain boundary flux and the stationary flux line lattice. Resulting field dependence of the critical Lorentz force for the most of the Nb₃Sn conductors is can be described as $b^{0.5}(1-b)^2$. In Nb-Ti the grain boundaries, drawn out parallel to filament axis act as effective barriers to flux motion. Obviously there is also a contribution from α -Ti precipitation at the grain boundaries, dislocation tangles, sub-grain boundaries and interfaces with non-superconducting α -Ti precipitation but the overall morphology of the elongated grains has its strong influence which results in critical Lorentz force vs field dependence for the most of the Nb-Ti close to $b(1-b)$ eq.(2). For effective pinning the morphology of the noodle-shaped particles perpendicular to the wire axis is very important. Only those pins having their flat area perpendicular to the Lorentz force direction can be active [54].

Based on the earlier calculations of [51-53] the ‘transverse’ pinning, corresponding mainly to NbTi can be expressed as eq.(23)

$$J_{c,trans}(B,T) = \left[\frac{B_{c2}}{8\pi\mu_0 \kappa_1^2 D} \right] \cdot \left(1 - \frac{B}{B_{c2}} \right) \quad (23)$$

But ‘longitudinal’ pinning mainly describing Nb₃Sn conductors can be expressed as eq.(24).

$$J_{c,long}(B,T) = \left[\frac{2\alpha dB_c^2}{3\sqrt{3}\cdot\Phi_0\mu_0\kappa_1^2 D} \right] \cdot \left(\frac{\langle J_o \rangle}{J_d} \right)^2 \cdot \frac{\left(1 - \frac{B}{B_{c2}} \right)^2}{\sqrt{B}} \quad (24)$$

Parameter d is an effective size of the pinning site proportional to the effective boundary thickness, J_d is the depairing current density of the grains, $\alpha = \delta J_o / \langle J_o \rangle$ is the ratio of the decrement in J_o , δJ_o , to the average value, $\langle J_o \rangle$, D is a grain size, $1/D$ is the density of pinning sites, $k_1 = B_{c2}/2^{0.5} B_c$, $B_c(T) = B_c(0)[1 - (T/T_{co})^2]$.

Results of such calculations addressed to the possible conductors with the longitudinal and transversal pinning taking to account the actual material parameters: $\langle J_o \rangle / J_d = 0.7$, $B_{co} = 27T$, $T_{co} = 19K$, $T = 4.2K$, $\alpha = 0.25$, $d = 2nm$, $k_1 = 20$ and $D = 100nm$ are presented in Fig.24.

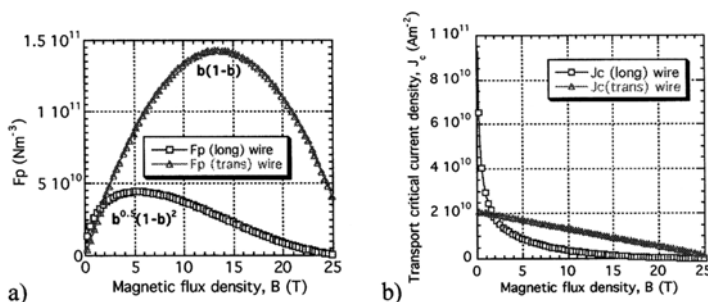


Fig. 24. a) Pinning force versus magnetic flux density for both types of pinning: ‘transverse’ pinning (elongated grains along the wire length and ‘longitudinal’ pinning (typical radial equiaxed grains) see Fig.3, Fig.7, Fig.16b) and Fig.25b); **b)** critical current density for longitudinal and transverse pinning.

Results presented in Fig.24 are very encouraging, suggesting that a substantial improvement of the future Nb_3Sn conductors could be possible if only with extended ribbon-like defects along the conductor axis would be produced. To study the influence of Nb_3Sn grain morphology on the pinning in the case of round multifilamentary conductors is rather difficult due to the round fibre symmetry of the filaments. There have been attempt to make a general calculation of the average Nb_3Sn grain size based on the computation of the large number of the experimental data [55]. Although such regression analysis with independent processing parameters such as diffusion time, diffusion temperature, number of niobium filaments, diameter of Nb filaments and volume ratio of the Cu-Sn matrix to Nb filaments provides correct results but only valid for the equiaxed-grain layers formed in a bronze wires see Fig.7.

The grain morphology and stoichiometry of the Nb_3Sn superconducting layers formed at different temperatures during liquid reactive diffusion, LRD, processes in long length conductors presented in Fig.25 differ noticeably and may provide additional information on the possible improvement of the pinning force described by eq.(23) and eq.(24). The diffraction patterns of the investigated Nb_3Sn layers were found not to differ from one another and they were practically the same as those in a randomly oriented Nb_3Sn polycrystalline material.

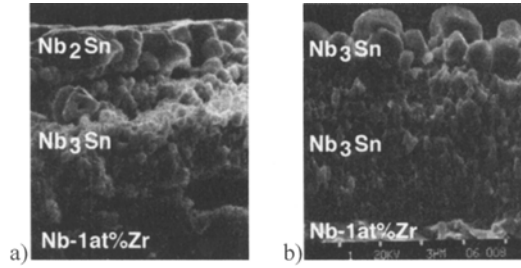


Fig. 25. Nb-Sn layers manufactured by Liquid Reactive Diffusion process: **a)** equiaxed grains and of the ellipsoidal shape with longer axis along the tape surface, 930°C, 11min; **b)** oval columnar grains partially perpendicular to the surface, 980°C, 11min. [56].

For the lower temperatures and shorter times of the LRD process the grains are smaller and ellipsoidal in shape with the longer axis parallel to the surface, therefore $F_p(H||S) \gg F_p(H\perp S)$, Fig. 25a) and Fig.26a) and b) whereas during diffusion at higher temperatures at also for longer time Nb_3Sn grains become bigger and grow more perpendicularly to the surface of the Nb1.5%Zr substrate. In this case the value of the $F_p(H||S) \cong F_p(H\perp S)$, Fig. 25b) and Fig. 26a) and c). This may look like simple case but there is an evidence that in other A15 coated conductors there is cross over between $F_p(H||S)$ and $F_p(H\perp S)$ versus external magnetic field. At higher magnetic fields it is possible that the mechanism may change and columnar grains may be more efficient for $F_p(B||S)$. The volume pinning force anisotropy measurements conducted on these tapes in external magnetic fields proved that the differences induced by the grain morphology are noticeable see Fig.26a) and confirm need for further study of the grain morphology improvement for better conductor performance in magnetic field.

Important pinning measurements results conducted for Nb_3Ge coated conductor, Fig.27a) suggest that possibly two different types of pinning mechanisms are measured for the same superconducting layer, depending on the magnetic field orientation to the film surface [14]. The Nb_3Ge layer was of columnar structure so the effective density of flux-pinning centres in the directions parallel and perpendicular to the growth direction of the columnar grains are very different. It can be assumed that “point-like” forces (pinning forces induced by the point defects) would be expected to dominate in the field perpendicular to the columnar grain axis, while “line-like” or “area-like” pinning forces may be caused by the grain boundary surfaces in the parallel to the film surface field. On the other hand at higher magnetic field where collective pinning on the intragrain defects dominates the effectiveness of the interconnected grain boundary, pinning will be reduce and the higher pinning force should be reached for $H||S$.

Despite the substantial differences in F_p observed for the tape conductor, result of pinning force summation Fig.27b) shown a limited improved of the overall performance of the wires because the calculated $F_p/F_{pmax}(b)$ dependence is very similar to $b^{0.5}(1-b)^2$. Successful simulation of the F_p vs B dependences in Fig.27 using eq.(23) and eq.(24) can be conducted assuming that only parameter to be change in eq.(24) is an effective grain boundary size parameter d . By increasing d from 2nm to 10nm in eq.(24) the results presented in Fig.28 are identical to those in Fig.27a).

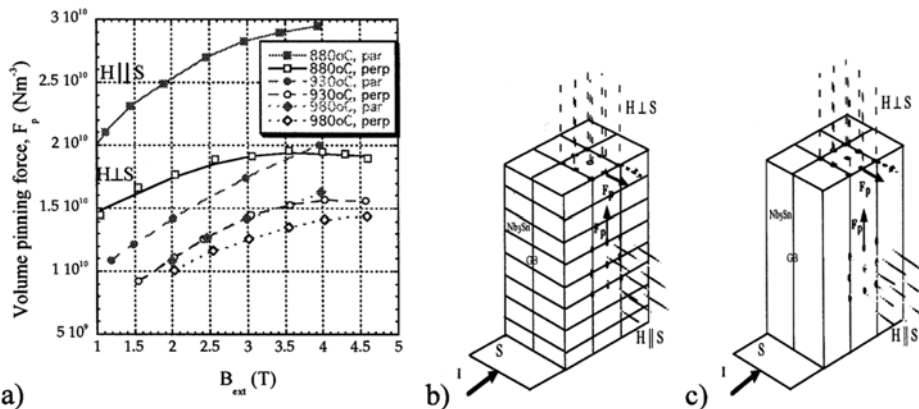


Fig. 26. a) Dependence of volume pinning force F_p vs B_{ext} for Nb_3Sn coated conductor manufactured by liquid reactive diffusion process, LRD, of tin atoms from the $Cu_{80}at\%Sn$ to $20\mu m$ thick, $1cm$ wide $Nb_{1.5}\%Zr$ tapes for 11 min in vacuum [57]; b) schematic representation of the grain boundary pinning for the Nb_3Sn flat-like grains see Fig.25a); c) Schematic representation of the grain boundary pinning for the Nb_3Sn columnar grains (see Fig.25b)). For simplification the square-like flux lattice was considered. It is evident that if the GB pinning dominates the higher pinning force should be reached for $H \perp S$. (Magnetic field was always perpendicular to the current flow direction).

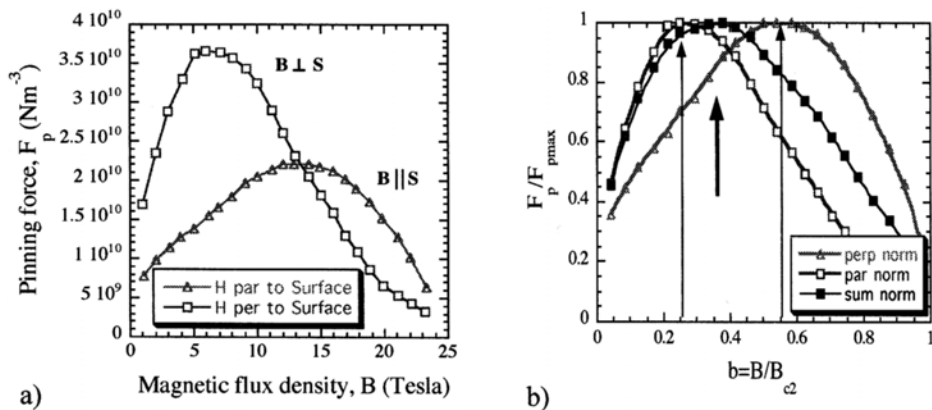


Fig. 27. a) Global pinning-force density of tape Nb_3Ge coated conductor manufactured by CVD [14]; $H \perp S$ represents magnetic field perpendicular to the tape surface but parallel to the columnar grains longer axis, $H \parallel S$ represents magnetic field parallel to the tape surface, but perpendicular to the columnar longer axis After Suzuki et al. [58]; b) Normalised pinning force for the data from the Fig.27a). An additional curve in Fig.27b) represent the expected resulting performance of the tape conductor which is very similar to $b^{0.5}(1-b)^2$ Fig.2.

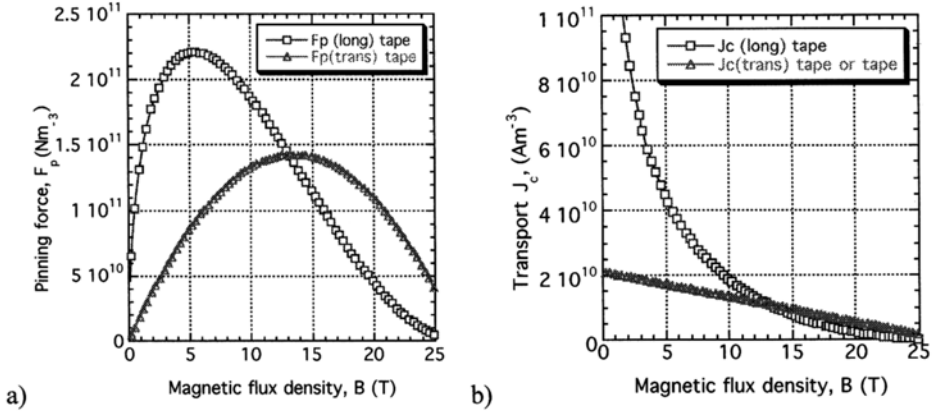


Fig. 28. a) Pinning force versus magnetic flux density for both types of pinning: ‘transverse’ pinning (elongated grains along the wire length and ‘longitudinal’ pinning (typical radial equiaxed grains) see Fig.25b); **b)** Normalised pinning force calculated from the data in Fig.28a).

In this case A-15 columnar grains for magnetic field perpendicular to substrates can be describe by eq.24 as a longitudinal pinning (along most of the grain boundaries) whereas for magnetic field parallel to substrates it can be describe by eq.23 as a transversal pinning (along smaller number of the grain boundaries).

Despite of clear evidence that eq.(23) and eq.(24) well describe a wide range of Nb₃Sn morphologies, more dramatic changes in the grain boundary structure are required if the Nb₃Sn wires are going to achieve the improved field performance, $f(b)=b(1-b)$ and also J_c vs B .

There are indications in the literature that controlled texture development of the Nb-based substrates/filaments may influence grain morphology of Nb₃Sn layer. Microstructural differences of Nb₃Sn superconducting diffusion layers grown by tin reaction with single niobium crystal substrate with faces parallel to the major b.c.c. planes (110),(100), (211) and (111) have been presented in literature [59,60]. The results shown that Nb₃Sn layers grown on the surfaces (211), (100) and (110) of Nb substrate have a similar morphology, minor variations in size and grain coverage, while layers grown on the Nb (111) surface have grains which are not only jagged but also highly irregular in size and distribution. The same grain morphology was observed for Nb₃Sn layers grown on a polycrystalline Nb substrate of (111) main texture [61].

The microscopical investigations revealed a well-defined planar fiber structure produced by the cold rolling. Transport critical current density was found lower when fibers are parallel to the direction of magnetic field than when they are perpendicular. This effect may be consequence of the interaction of flux movement with fiber boundaries [62]. Research on the effect of the pre-reaction of the bronze conductors on the properties of the Nb₃Sn composites reviled a significant circumferential differences in the grain morphology of the fine filaments which may be due to the crystallographic orientations developed during cold rolling of Nb filaments see Fig.29 [63].

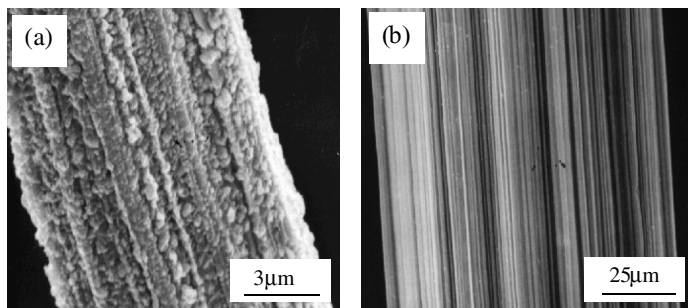


Fig. 29. The SEM images of Nb filaments: **a)** after multiple intermediate annealing at 500°C for 1 hour each in bronze process Nb-Sn multifilamentary; **b)** in the copper matrix in absence of tin atoms. Notice that nucleation and growth of the Nb₃Sn in the certain Nb groves differs substantially supporting the finding that the crystallographic orientation of Nb play an important role in Nb₃Sn layer growth.

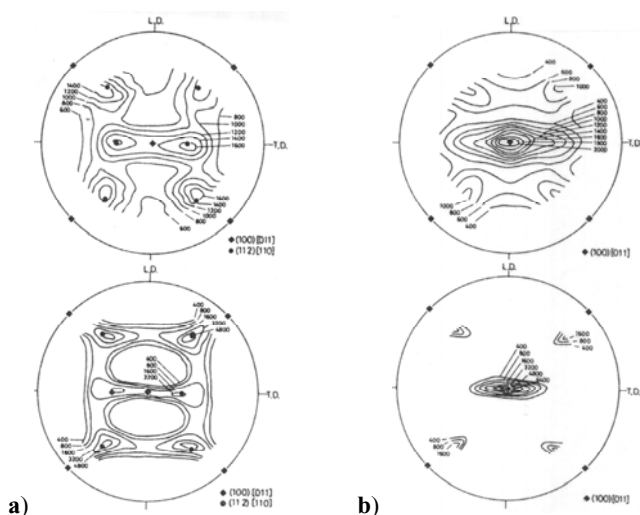


Fig. 30. Texture development in Nb₃Sn tape conductors **a)** liquid-solid diffusion Nb1%Zr/Sn; **b)** solid state diffusion Nb/Cu7at%Sn 800°C, 20h after [64]. The top figures correspond to Nb₃Sn layers formed on the Nb-based substrates characterized in the bottom figures.

There is a clear evidence in the literature which might suggest that texture induced growth of Nb₃Sn may play a role in further improvement of pinning. Pole figures indicate that the main feature of the texture in the Nb₃Sn layers is identical with that in the niobium substrate irrespectively of the processing technique, Fig.30 [64].

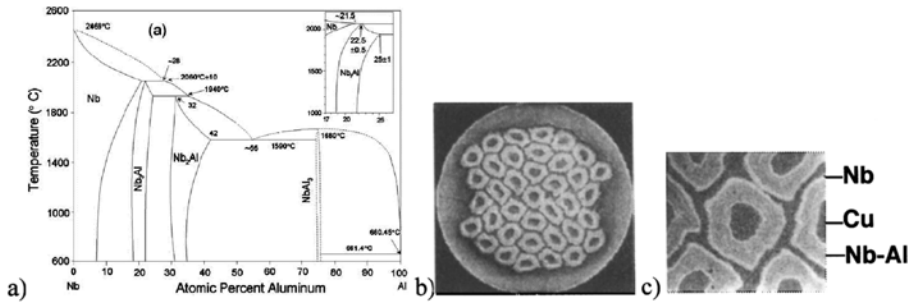


Fig. 31. a) Binary Nb-Al phase diagram; b) cross section of the jelly-roll jelly-roll Nb₃Al conductor containing 38 sub-jelly-roll bundles; c) close view of the individual jelly-roll bundles; courtesy of Europa Metalli. Each “jelly-roll rod” was prepared by winding a Nb sheet and Al sheet together on an oxygen free copper core and inserting into copper tube. [65]

5. Nb₃Al CONDUCTORS

Unfortunately there appears to be no equivalent of the bronze process for Nb₃Al superconducting wires due to lack of stoichiometry for Nb₃Al phase, see Fig.31. A way to achieve A-15 phase is to process elemental Nb and Al in a finely subdivided form known as a jelly-roll process, followed by solid state diffusion at elevated temperatures. In this process the jelly-roll composite is prepared by winding a Nb sheet and Al or Al-alloy sheet together on an oxygen-free copper core and inserting the wound cylinder into a copper tube for further cold drawing to the final wire diameter, or to a diameter suitable for restacking and redrawing.

Due to the continuous increase of the microhardness of Nb, there is a limit to which such a jelly-roll composite can be drawn without breaking the continuity of the conductor. Use of pure aluminium in this process has suffered from the poor workability of the composite caused by the large difference in hardness between pure aluminium and pure niobium. Alloy-hardening of the aluminium core with other elements, such as magnesium, silver, copper and zinc is very effective in matching the hardness between cores and matrix, and improving workability of the composite [65]. Unfortunately solid state diffusion of as drawn Nb-Al conductors does not provide the conductor with required high magnetic field performance, see Fig.32. Conflict between stoichiometry and grain size is severe in Nb₃Al.

The DTA and XRD studies of the Nb-Al conductor undergone only solid state diffusion show that the first phase to form is the NbAl₃ intermetallic phase, which is a two-stage process correspond to peak A and B in Fig.32. The first peak (A) has been identified as the three-dimensional nucleation and growth to coalescence of NbAl₃ in the plane of the Nb/Al interface. The second peak (B) is the one-dimensional growth of this NbAl₃ layer perpendicular to the interface (thickening of the planar layer). Peak (C) is attributed primarily to A15-Nb₃Al formation and followed by the thickening of the phase at higher temperatures or longer reaction times [66]. Coincidentally, the $d\rho/dT$ plot shows almost exactly the same shape as the DTA curve [67].

The way to achieve high magnetic field properties is to give the wire, at final size, a very rapid high temperature heat treatment followed by a quench into the gallium bath at room temperature, Fig.34, which forms bcc Nb-Al phase [68]. A subsequent heat treatment at lower

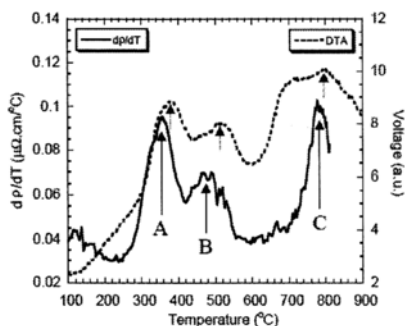


Fig. 32. Correlation between the first derivative of the resistivity with respect to temperature, $d\rho/dT$ and the DTA result for JR Nb-Al wire. The inset shows the TGA during the DTA measurements. Peaks A and B correspond to the formation of NbAl_3 planar layer by nucleation and growth to coalescence and the thickening of the planar layer respectively. Peak C is due to the $\text{A15-Nb}_3\text{Al}$ formation. The small discrepancies of each peak might due to the different ramp rate used in the DTA measurement (10K/min) and the heat treatment (5K/min) [67].

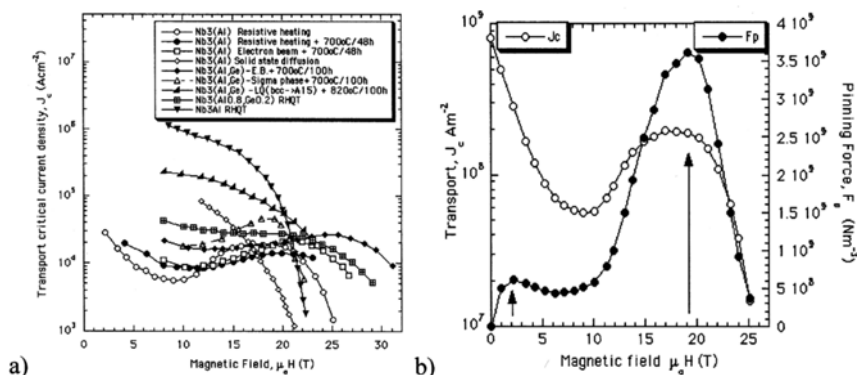


Fig. 33 a) Global pinning-force density of A15 (Nb_3Al) tape conductors manufactured by i) rapid ohmic heating and rapid cooling followed by subsequent annealing ii) solid state diffusion, and iii) other alternative processes; **b)** critical current density and Global pinning force versus magnetic field for conductor made by rapid ohmic heating and rapid cooling followed by subsequent annealing [65,68].

temperatures is used to order the structure and grow fine grains of the A15 phase with fine defects, therefore improving the J_c performance at highest magnetic fields, Fig.33 [69].

These general formulas, eq.(1) and eq.(2), fail where there is a change in basic pinning mechanism due, for instance, to matching effects, dimensional crossover or the onset of thermally activated processes. In such cases more appropriate descriptions of the pinning in the full field range can be given by the assumption of two pinning mechanisms and the eq.(1) can be rewritten as eq.5. Such an approach was adopted in describing flux pinning of

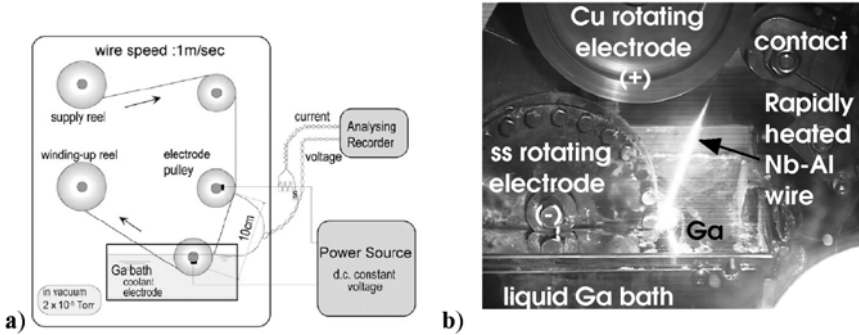


Fig. 34. a) Schematic of the reel-to-reel ohmic-heating and rapid-quenching apparatus to form RHQT Nb₃Al multifilamentary conductors [68], **b)** photo of the actual experiment in a dynamic vacuum chamber where the RHQ treatment for the Nb-Al precursor wires are carried. The precursor wires were continuously moving with a speed of 1m/sec on a reel-to-reel machine and heated up by resistive heating and held for 0.1s. The wires were subsequently quenched into the molten Ga bath at about 60°C. [70], courtesy of A. Kikuchi, NIMS, Japan.

intermetallic superconductors such as Nb₃(Al,Ge) and Nb₃Al where peak of the J_c vs B is observed at lower and in higher fields Fig.33b) [65,69]. The consequence of the peak effect of J_c vs B on the F_p vs B can be very nicely demonstrated on the base of resistively rapidly

$$F_p = J_c \cdot B = G \left[\frac{(B_{c2}(T))^{n'}}{k p^{m'}} \right] \cdot f(b) + G_1 \left[\frac{(B_{c2}(T))^{n''}}{k p^{m''}} \right] \cdot f(b)_1 \quad (25)$$

heated and quenched Nb₃Al wire, Fig.33, where two maxima occurs and the whole curve can be describe by coexistence of two pinning mechanisms by eq.(25). The lower maximum ~2T corresponds to grain boundary pinning where the maximum at 19T corresponds to finely distributed secondary phases, precipitations and stacking faults, Fig.35b).

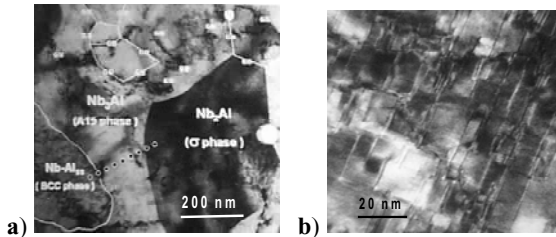


Fig. 35. TEM microstructure of the conductors manufactured by: a) Solid-state diffusion process; **(b)** Rapid Heating and Quenching process [68,69]. Courtesy of T.Takeuchi

Although the performance of the wires obtained by the Rapid Heating and Quenching technique is superior to any metallic superconductors, Fig.33, the technology is expensive and reproducibility over long lengths is the subject of intensive research mainly in Japan and USA. There is a need for the in situ resistometric measurements method to assess the phase formation and transformation processes to optimise Nb₃Al conductors if they are going to be competitive to currently available Nb₃Sn conductors [67]. During the actual rapid heating process the in situ resistivity measurements are conducted on the precursor wire shown in Fig.34 by control of Joule heating current and voltage. Usually the maximum heating temperatures are controlled by changing the dc voltage, which is applied to a distance of 10cm between the wire guide pulley and the liquid gallium bath, Fig.34. The phases formed after RHQ treatments under different applied voltages are summarised in Table 4. Post-quench annealing, solid-state diffusion process, was performed at 800°C for 10h in vacuum for the phase transformation to A15 and improvement of long-range order of the A15 crystal structures using in situ resistometric measurements.

Table 4. Nb-Al phases present under different applied voltages during RHQ of JR conductor presented in Fig.34. *The peak heating temperature increases with increasing applied voltages.

| Sample | dc applied voltage (V)* | Phases |
|--------|-------------------------|---------------------------------|
| 1 | 13.0 | A15, Nb ₂ Al, others |
| 2 | 13.5 | A15, Nb ₂ Al, others |
| 3 | 15.5 | A15, Nb ₂ Al, others |
| 4 | 16.0 | bcc, A15 |
| 5 | 17.0 | bcc |
| 6 | 18.0 | bcc |

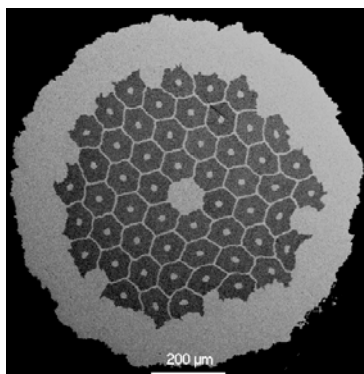


Fig. 36. SEM image of cross-section of the Nb-Al jelly-roll, JR, composite wire 0.89mm in diameter. It has 54 Nb-Al composite filaments with an average diameter of 80mm embedded in the Nb matrix. The Nb/Al atomic ratio in all the filaments is designed to be 3 and the ratio of Nb matrix to the filaments is 1.39.

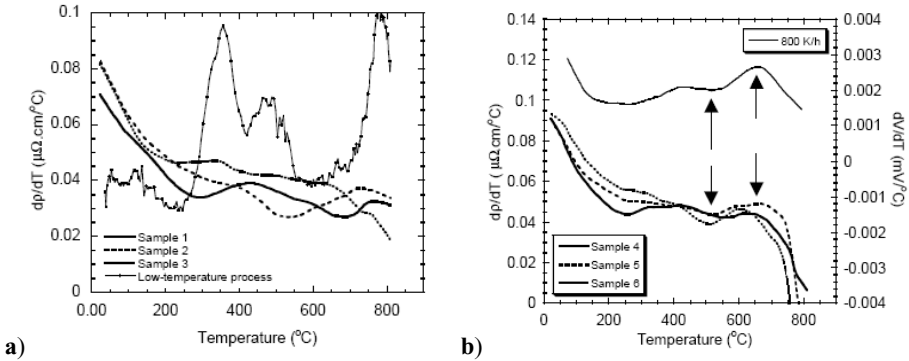


Fig. 37. First derivative of the resistivity with respect to temperature, $d\rho/dT$ against temperature plots for: **a)** low temperature process (same as in Fig.32) and sample 1, 2 and 3, (Table 4), which consists of multiphase (A15, σ -phase) in the as-quenched state; **b)** sample 4, 5 and 6, (Table 4), which consist of bcc Nb(Al)_{ss} in the as-quenched state and curve 800K/h represents RHQ JR Nb-Al wire adapted from [71,72]. Note that a ramp-up rate of 300K/h was used in all of the heat treatments of all the samples except for the one previous measurements where ramp-up rate of 800°C/h was used.

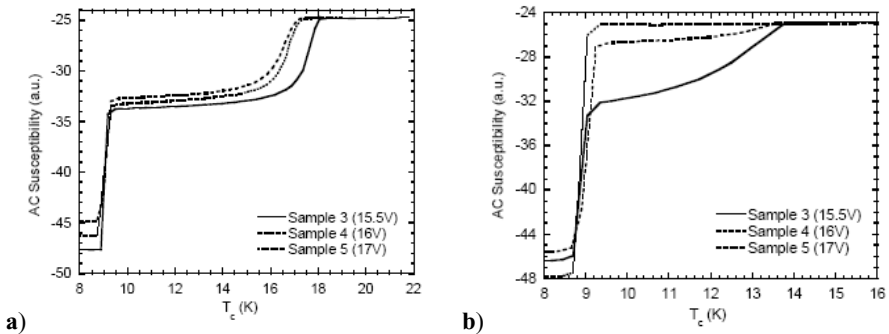


Fig. 38. AC susceptibility curves of the of the jelly-roll, JR, Nb-Al wires in the as-quenched state and after post-quench annealing at 800°C for 10 hours as a function of applied voltages during the RHQ treatment.

During the transformation heat treatment of the rapidly heated to lower T_{max} ($<15.5\text{V}$) and quenched JR Nb-Al wires, a more complex $d\rho/dT$ changes were observed due to the present of multiphase transformation, Fig.37a). Despite the lack of interest from the practical point of view in this region of the quenched wires, mainly due to the brittleness caused by direct formation of disordered-A15 phase, it would still be interesting to monitor the changes and have a better understanding of the multiphase transformation by further in situ resistometric studies supported by the DTA analysis during the initial heat treatment.

Rapidly heated to higher T_{\max} ($>16V$) and quenched JR Nb-Al wires show a very phase characteristic $d\rho/dT$ minimum at temperatures around $560^{\circ}C$ at which might indicates the ordering process of the bcc Nb(Al)_{ss} phase, followed by maximum at temperatures around $700^{\circ}C$ which is believed to be the initial transformation of the bcc Nb(Al)_{ss} to A15 Nb₃Al phase. The effect of ramp rates on the actual position of the minimum and maximum in the $d\rho/dT$ plot, and the transformation process during isothermal annealing monitored by the resistivity changes are the subjects of the current intensive study [73].

The analysis of the correlation between the resistivity changes and the optimum transformation heat treatment, enabling the formation of the optimal Nb₃Al A-15 phase characterised by an effective pinning centres such as a stacking faults and highest T_c , Fig.36 is a subject of an intensive research.

6. Nb₃Ga CONDUCTORS

All the alloys of the Nb-Ga system are superconducting. The solubility of gallium in niobium at $800^{\circ}C$ is approximately 9wt%; on raising the temperature the solubility increases and reaches 16% at the temperature of the peritectic reaction. With increasing gallium content in the α -Nb solid solution the value of T_c diminishes, and for the alloy with 5.4wt.%Ga it equals 7K. The analogous dependence is observed for alloying niobium with tin or vanadium with gallium. Apart from the intermetallic compound Nb₃Ga, which was originally reported as $T_c=14.5$, the Nb-Ga system forms three other compounds: Nb₅Ga₃, $T_c=7.5K$, Nb₂Ga₃, $T_c\sim 7K$ and NbGa₃, $T_c=7.5K$ [74]. Because low J_c and not very high T_c has been reported for all Nb₃Ga fabricated through various methods, this prevented development of Nb₃Ga conductors in the last thirty years. Recently Japanese researches who were successful in developing a RHQT (rapid heating, quenching, and transforming)-process of Nb₃Al conductors characterized by high J_c , applied the same RHQT-process to fabricate Nb₃Ga wires by making Nb/NbGa₃ micro-composite precursor wires. Externally alloyed Nb-Ga filaments were formed directly through the RHQ (rapid-heating and quenching) treatment, Fig.34. Although supersaturated Nb-Al bcc filaments were formed in the original RHQT-processed N₃Al wire, Nb-Ga supersaturated bcc phase may be too unstable to form in the RHQ-treatment. Post annealing at $600-750^{\circ}C$ was very effective to improve the superconducting properties of Nb₃Ga wire, which shows surprising results such as T_c of 19.7 K, $H_{c2}(4.2 K)=32$ T, and very high J_c vs B values as presented in Fig.1b. These values are much higher than those of the commercialised Nb₃Sn wires. The multifilamentary conductor was also successfully fabricated through the new process, however techniques to manufacture long lengths of such a conductor are currently under intensive development [75]. At present a stoichiometric Nb₃Ga with good long-range ordering shows high $T_c=20.7$ K and high $H_{c2}(4.2 K)$ above 30 T.

7. MECHANICAL STRAIN vs J_c in Nb-BASED CONDUCTORS

At the end of this chapter some consideration should be given to the relation between the mechanical stress and critical parameters of the practical conductors. Superconductor, during manufacture, has to sustain different mechanical stresses e.g. during cooling from diffusion

temperature ($\sim 700^\circ\text{C}$) to room temperature, during insulation coating and cabling. The same superconductor in a magnet has to accommodate different mechanical loads, e.g. during coil winding, cool down and operation at 4.2K (-268.8°C). Usually the stresses during operation due to Lorentz forces are dominating. The typical stress σ is given by eq.26 where J_e is an overall current density, B magnetic induction and

$$\sigma = J_e \cdot B \cdot R \quad (26)$$

R is a coil radius. The conductor must withstand these stresses without mechanical damage and without degradation of the critical current density. NbTi conductors show only little degradation of J_c as a function of stress and strain. Nb₃Sn based conductors are much more sensitive to strain especially in high magnetic fields. This has to be taken into account when measuring critical current densities of Nb₃Sn conductors and when designing Nb₃Sn conductors and Nb₃Sn magnets. Also Nb₃Sn conductors are very brittle after reaction and allow only low strain levels (<0.3%) for safe operation [19], whereas Nb₃Al is less susceptible to strain level, Fig.39 [76,77]. The tensile strength and flux pinning force of the Nb₃Sn layer formed in the multifilamentary conductor were expressed as a function of the grain size, to a first approximation in Fig.11a) [78]. This type of the relation of tensile strength vs grain size is known as the Hall-Petch relation [79,80], and has been derived on the basis of the mechanism that a crack is nucleated by a dislocation pile-up process against grain boundaries and therefore microscopic plastic flow is the cause of the fracture. For an increase tin content in bronze matrix it is desirable to reduce the reactive diffusion formation of A15 phase temperature to retain stability of the Nb₃Sn relative to tin rich compounds such as Nb₆Sn₅ and NbSn₂ [16]. Lack of copper-tin compounds isomorphous with Nb₃Sn and the absence of compounds in the niobium copper system suggest that Nb₃Sn is stable relative to a solid solution of tin in copper [81]. On the basis of Kramer's model [7] changes in the density of pinning sites should not greatly alter flux pinning efficiency at high fields. The reduction in J_c at high fields for low diffusion temperature or short times, indicates a change in the interaction energy between strongly pinned flux and pinning sites. Therefore introduction of the ultra-fine artificial pinning centres, APC, become more important in the high magnetic field region where the density of stacking faults and microdefects become comparable to fluxon lattice constant [6]. This also explains why additions of ternary elements to Nb₃Sn lead to a considerable increase of J_c at higher fields, Fig.1b). For high field strengths magnet applications above 12 T, wire made out of a ternary compound such as (NbTa)₃Sn or (NbTi)₃Sn, is commonly used due to improved J_c vs B characteristics (see Fig.1b)). The amount of Ta or Ti in the Nb is very low for these ternary compounds, a few atomic per cent only. (NbTa)₃Sn or (NbTi)₃Sn and Nb₃Sn conductors are identical except that the filaments are made of NbTa, NbTi or Nb.

The J_c of both A15 compounds and HTS oxides exhibits sensitivity to stress. Strain sensitivity increases with the magnetic field. The goal for the material is to withstand a tensile strain of 0.5% without permanent degradation. The use of wind-and-react coil fabrication, Fig.40, requires an insulation that withstands the reaction cycle (several hours at temperature higher than 650°C), like fibreglass or a ceramic. Wire (as opposed to tape) is the preferred strand due to adaptability to various cable designs. Moreover the co-winding of tape results in

large inductances (poor field quality and AC losses). Nevertheless there might be no other fabrication routes for some materials as for example HTS coated conductors. In certain constructions of superconducting solenoids, relatively bulky cylinders, tubes, plates and rings of superconducting material may be used. In view of the high superconducting parameters of A-15 compounds, their use for manufacturing such objects is very promising.

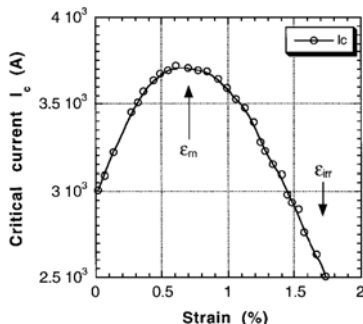


Fig. 39. Nb₃Al ($T_c = 20\text{K}$, $B_{c2} = 26\text{T}$) superconducting wires withstand a strain as high as 1%, [76,77].

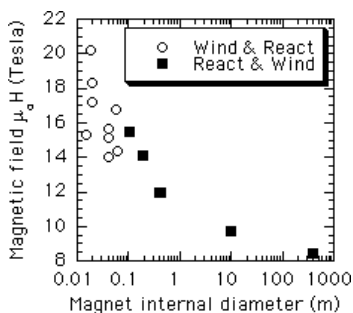


Fig. 40. Comparison of the possible electromagnet diameters and magnetic field generated in respect of the ‘wind and react’ or ‘react and wind’ manufacture techniques.

8. CONCLUSIONS

Although a model for A15 conductors that suggest that the flux pinning mechanism of Nb₃Sn can be modified to be the same as for NbTi paves the way to further technological improvements but also other following immediate issues require solving.

Further research is required to prevent the magnetic instabilities in high J_c PIT and ‘internal tin’ conductors, which cause premature quench at low fields. Study and optimisation of heat treatment should allow a reduction of reaction time preserving the largest superconducting phase volume and optimal microstructure. Future powders for 2-nd generation ($3 \cdot 10^9 \text{Am}^{-2}$ @ 12T at @ 4.2K of non-Cu regions) PIT conductors might be

manufactured by direct reduction of oxides process, DERO [49]. There is a big payback from flattening the Sn gradient across the Nb₃Sn layer, if large grain growth in the A15 grain size can be avoided. The progress in new generation of RQ processing of Nb₃Al and Nb₃Ga may define the future of low temperature superconductors considering growing competition from MgB₂ [82] conductors and even REBa₂Cu₃O₇, however the last one must be manufacture in the multifilamentary form of conductor [83].

REFERENCES

- [1] P. Limon, 'High Field Magnet R&D at Fermilab', Hadron Colliders Beyond the LHC, CERN/AC/95-05 (LHC), 20 October 1995.
- [2] A. D. McInturff, et al, 'Test Results for a High Field (13T) Nb₃Sn Dipole', PAC'97.
- [3] A. den Ouden, S. Wessel, E. Krooshoop and H. ten Kate, IEEE Transactions on Applied Superconductivity 7 (1997) 733.
- [4] <http://acwebimages.cern.ch/index.html>
- [5] L. T. Summers and J. R. Miller, IEEE Trans on Mag. 23 (1987) 1552.
- [6] B. A. Glowacki, Intermetallics 7 (1999) 117.
- [7] E. J. Kramer, J. Appl. Phys. 44 (1973) 360.
- [8] R. W. Heussner, J. D. Marquardt, P. J. Lee, and D. C. Larbalestier, Applied Physics Letters 70 (1997) 901.
- [9] H. Hillmann, Supercond. Science and Technol. 12 (1999) 348.
- [10] G. Z. Chen, D. J. Fray, and T. W. Farthing, Nature 407 (2000) 362.
- [11] B.A. Glowacki, X-Y. Yan, D.J. Fray, G. Chen, M. Majoros, and Y. Shi, Physica C 372-376 (2002) 1315.
- [12] K. Inoue, A. Kikuchi, Y. Yoshida, and Y. Iijima, Physica C 384 (2003) 267.
- [13] M. Weger, Rev. Modern Physics 36 (1964) 175.
- [14] J. J. Hanak, and H. S. Berman, J. Phys. Chem. Solids Suppl. C7 91967) 249.
- [15] L. R. Testardi, Physical Acoustics 10 (1973) 193.
- [16] B. A. Glowacki and J. Chojcan Phys. Stat. Sol. 80(1983) K93.
- [17] B. A. Glowacki, J. Mater. Sci. Lett. 4 (1985) 389.
- [18] G. Lefranc and A. Muller, J. Less-Common Metals 45 (1976) 339.
- [19] H. Krauth, in: *Superconducting Technology* ed. K. Fossheim, World Scientific, Singapore, New Jersey, London, Hong-Kong, (1991), p.149.
- [20] S. Ochiai, K. Osamura and M. Ryoji, Acta Metall. 35 (1987) 1433.
- [21] W. Schaure and W. Schelb, IEEE Trans on Mag 17 (1981) 374.
- [22] W. Schelb, J.Mat. Sci. 16 (1981) 2575.
- [23] W. Wu, D. R. Dietderich, J. T. Holthuis et al., J. Appl.Phys., v.54, (1983), 7139
- [24] P. J. Lee, C. M. Fisher, M. T. Naus et al., IEEE Trans. Appl. Supercond. 13 (2003) 3422.
- [25] N. J. Pugh, J. L. M. Robertson, E. R. Wallach, J. R. Cave, R. E. Somekh and J. E. Evetts, IEEE Trans on Mag. 21 (1985) 1129.
- [26] N. A. Haroun, J. Matt. Sci. 16 (1981)2257.
- [27] B. A. Glowacki and J. E. Evetts, IEEE Trans. Mag. 25 (1989) 2200.
- [28] K. S. Tan, S. C. Hopkins, B. A. Glowacki, M. Majoros and D. Astill, Superconductor Science and Technol. 17 (2004) 663.

- [29] M. C. Jewell, P. J. Lee and D. C. Larbalestier, *Supercond. Sci. Technol.* 16 (2003)1005.
- [30] V. Abaecherli, D. Uglietti, B. Seeber and R. Flukiger, *Physica C* 372-376 (2002) 1325.
- [31] V. Abaecherli, B. Seeber, E. Walker, R. Flukiger, W. Thiele and J. A. A. J. Perenboom, *IEEE-Transactions on Applied Superconductivity* 11 (2001) 3667.
- [32] H. Hillman, H. Pfister, E. Springer, M. Wilhelm, and K. Wohlleben, in: *Filamentary A-15 Superconductors*, eds. M. Suenaga and A. F. Clark, Plenum Press, New York and London, (1980), p.17.
- [33] M. N. Wilson, *Superconducting Magnets*, Clarendon Press, Oxford, (1983).
- [34] Von E. Starke, and H. Wever, *Z. Metallkde.* 55 (1964) 107.
- [35] R. Flükiger, in *Encyclopedia of Materials Science & Engineering*, ed. J.E. Evetts, Pergamon Press, Oxford, (1992), p.1.
- [36] R. M. Scanlan, W. A. Fietz, and E. F. Koch, *J. Appl. Phys.* 46 (1975) 2244.
- [37] B. A. Glowacki, and Z. Bukowski, *J. Materials Science*, 22 91987) 775.
- [38] M. Suenaga, in *Superconductor Materials Science , Metallurgy, Fabrication, and Applications*, ed. S. Foner, and B.B. Schwartz, NATO Advanced Study Institutes Series B: Physics, Plenum Press, New York and London. (1981), p.201.
- [39] C. S. Pande and M. Suenaga, *App. Phys. Lett.* 29 (1976) 443.
- [40] C. S. Pande, *Mater. Phys. Mech.* 2 (2000) 1.
- [41] J. D. Livingston, *Phys. Stat. Sol.* 44 (1977) 295.
- [42] J. H. Shim, C. S. Oh, B. J. Lee and D. N. Lee, *Z. Metallkde* 87 (1996) 205.
- [43] B. A. Glowacki, *IEEE Trans. Appl. Superconductivity* 7 (1997) 1520.
- [44] B. A. Glowacki and Z. M. Kosek, *Cryogenics* 27 (1987) 551.
- [45] B. A. Glowacki, *IEEE Trans. on Mag.* 32 (1996) 2768.
- [46] J. R. Cave and C. A. F. Weir, *IEEE Transactions on Magnetism*, MAG 19 (1983) 1120.
- [47] J. E. Kunzler, *Rev. Mod. Phys.* 33 501 (1961).
- [48] K. Noto, K. Watanabe and Y. Muto, in *Proc. Intern. Symp. on New Developments in Applied Superconductivity*, ed. Y. Murakami, World Scientific, Singapore, New Jersey, London, Hong Kong, (1989), p.628.
- [49] B. A. Glowacki, X. Y. Yan, D. J. Fray, G. Chen, M. Majoros, and Y. Shi, *Physica C* 372-376 1315 (2002).
- [50] S. C. Hopkins, A. Cox, B. A. Glowacki, D. J. Fray, *Proc. EUCHEM 2004 Molten Salts Conference*, 20-25 June 2004, Piechowice, Poland, PP36.
- [51] D. Dew-Huges, *IEEE Trans on Mag.* 23 (1987) 1172.
- [52] A. Gurevich and L. D. Cooley L.D. *Physical Rev. B* 50 (1994) 13563.
- [53] J. McDonald and E. Barzi, *IEEE Trans. on Applied Supercon.* 11 (2001) 3884.
- [54] H. Hillman, *Superconductor Sci. Technol.* 12 (1999) 348.
- [55] X. Aiying, H. Qingyong, S. Fengming and F. Juren, *Cryogenics* 25 (1985) 507.
- [56] B. A. Glowacki, *J. Mater. Sci. Lett.* 4 (1985) 389.
- [57] B. A. Glowacki and M. Horobiowski, *Phys. Stat. Sol. (a)* vol. 89 (1985) K13.
- [58] M. Suzuki, Y. Watanabe, T. Anayama, K. Watanabe, and K. Noto, *Japanese Journal of Applied Physics* 26 (1987) 881.
- [59] V. Diaduk, J. Bostock and M. L. A. MacVicar, *IEEE Trans. Magnetism* 15 (1979) 610.
- [60] B. Hillenbrand, Y. Uzel and K. Schmitzke, *Appl. Phys.* 23 (1980) 237
- [61] B. A. Glowacki, *Phys. Stat. Sol. (a)* 75 (1983) K103.

- [62] D. Kramer and C. G. Rhodes, *Trans. of The Metallurgical Society of AIME*, 233 (1965) 192.
- [63] D. B. Smathers, K. R. Marken, D. C. Larbalestier and R. M. Scanlan, *IEEE Trans. Mag.* 19 (1983) 1417.
- [64] K. Togano and K. Tachikawa *J. Appl. Phys.* 50 (1979) 3495.
- [65] B. A. Glowacki, *Intermetallics* 7 (1999) 117.
- [66] S. Ceresara, M. Ricci, N. Sacchetti and G. Sacerdoti, *IEEE Transactions on Magnetics* 11 (1975) 263.
- [67] K. S. Tan, S. C. Hopkins, B. A. Glowacki, A. Kikuchi, T. Takeuchi and K. Inoue, *International Conference Progress in Nb-based conductors*, Tsukuba, 2004.
- [68] T. Takeuchi, *Supercond. Sci. Technol.* 13 (2000) R101.
- [69] Y. Iijima, M. Kosuge, T. Takeuchi and K. Inoue, *Adv. Cryog. Eng.* 40 (1994) 899.
- [70] SCENET-2, DVD Lectures on Superconductivity <http://www.superconsultants.net>
- [71] T. Fukuzaki, T. Takeuchi, N. Banno, K. Tagawa, N. Tatsumi, H. Ogiwara and H. Wada, *Superconductor Science & Technology* 15 (2002) 1404.
- [72] T. Takeuchi, N. Banno, K. Tagawa, T. Kobayashi, K. Tsuchiya, N. Tatsumi, H. Kitaguchi, T. Fukuzaki, M. Kosuge, H. Wada, Y. Iijima, A. Kikuchi and K. Inoue, *IEEE Trans. on Appl. Supercon.* 2004 in press.
- [73] K. S. Tan, S. C. Hopkins, R. J. Stearn, B. A. Glowacki, A. Kikuchi, T. Takeuchi and K. Inoue, *IEEE on Applied Superconductivity* 2005.
- [74] V. V. Baron, L. F. Myzenkova, E. M. Savitskii and E. I. Gladyshevskii, in: *Metallography and Metal Physics of Superconductors*, Izd. Nauka, Moscow, (1965) p. 86.
- [75] K. Inoue, A. Kikuchi, Y. Iijima N. Banno, T. Takeuchi, and T. Fukuzaki. *IEEE on Applied Superconductivity* 14 (2005) 956.
- [76] Y. Yamada, N. Ayai, K. Takahashi, K. Sato, M. Sugimoto, T. Ando, Y. Takahashi, and M. Nishi, *Advances in Cryogenic Engineering*, 40 (1994) 907.
- [77] J. W. Ekin, *Advances Cryogenic Engineering*, 30 (1984) 823.
- [78] S. Ochiai, T. Uehara, and K. Osamura, *J. Materials Science* 2 (1986) 1020.
- [79] E. O. Hall, *Proc. Phys. Soc.* 64B (1951) 747.
- [80] N. J. Petch, *J. Iron, Steel Inst.* 173 (1953) 25.
- [81] I. L. MacDougal, *Proceedings 5-th Int. Mag. Tech. Conf. Frascati, Italy*, (1975) p.710.
- [82] B. A. Glowacki, M. Majoros, M. Vicker, M. Eisterer, S. Toenies, H. W. Weber, M. Fukutomi, K. Komori and K. Togano, *Supercond. Sci. Technol.*, 16 (2003) 297.
- [83] B. A. Glowacki, M. Majoros, N. A. Rutter and A. M. Campbell, *Physica C*, 357-360 (2001) 1213.

BI-BASED SUPERCONDUCTING CUPRATES: MATERIALS ASPECTS, CRYSTAL GROWTH AND PROPERTIES

E. Giannini⁽¹⁾, N. Clayton⁽¹⁾, N. Musolino⁽¹⁾, R. Gladyshevskii⁽²⁾, and R. Flükiger⁽¹⁾

⁽¹⁾ Department of Condensed Matter Physics (DPMC), University of Geneva
24, quai E.-Ansermet, CH-1211 Genève 4, Switzerland

⁽²⁾ Dept. Inorg. Chem., Ivan Franko National University of L'viv
Kyryla i Metodiya str. 6, UA-79005 L'viv, Ukraine.

1. INTRODUCTION

Among hundreds of superconducting compounds discovered since superconductivity was found to occur at high temperature in cuprates in 1986 [1], one of the most attractive families of materials is the Bi-based family described by the chemical formula $\text{Bi}_2\text{Sr}_2\text{Ca}_{n-1}\text{Cu}_n\text{O}_{4+2n+\delta}$ ($n = 1, 2, 3$). Three members with 1, 2 and 3 CuO_2 conducting layers belong to this family. Superconductivity in Bi-based cuprates was first found by Michel et al. [2] in 1987 in the $n = 1$ compound (from now on called Bi-2201) with $T_c \approx 10$ K, and shortly afterwards in the Bi-2212 ($n = 2$) and Bi-2223 ($n = 3$) with $T_c \approx 90$ K [3] and 110 K [4,5], respectively. In contrast to the Bi-2212 phase, which is rather easy to synthesise, the Bi-2223 phase was found to be extremely difficult to obtain single-phased. A partial substitution of Pb for Bi was found to improve its stability, thus facilitating the material preparation [6]. Due to the high transition temperature of the 2- and 3-layer compounds (higher than the boiling point of N_2) and the possibility to fabricate long conductors, the Bi-based superconducting cuprates have strongly stimulated both fundamental and applied research for more than 15 years.

In 1989, Mimura et al. [7] fabricated the first conductor based on the Bi,Pb-2223 material, consisting of a ceramic core inside a Ag-sheath and in 1991 Yamada et al. [8] performed the first study on the thermo-mechanical processing of this conductor achieving critical current values as high as $3 \cdot 10^4$ A/cm² at $T = 77$ K and zero field. This demonstrated

the clear commercial potential for power applications of Ag sheathed $(\text{Bi,Pb})_2\text{Sr}_2\text{Ca}_2\text{Cu}_3\text{O}_{10+\delta}$ tapes, which have constituted the first devices suitable for applications of superconductivity at liquid N_2 temperature. From then onwards, an enormous world-wide research effort has been done in order to improve the transport properties of Ag/Bi,Pb-2223 tapes and to increase the conductor length. Tapes and wires of Bi-2212 and Bi,Pb-2223 are nowadays produced at a large scale and commercialised by several companies in US, Japan, Europe and China and prototypes for power applications have been successfully manufactured.

However, in spite of the steady progress in Bi-based superconducting tapes over the last 17 years, market breakthrough has not been observed yet. In spite of the exciting goals achieved so far, we are far from fully exploiting the potential of these materials and fulfilling the economical requirements for widespread industrial applications. The reasons of this delay are correlated to the extreme complexity of the chemistry of the high- T_c superconducting materials and, in particular, of the Bi-based cuprates.

Processing conditions are difficult to control and the phase diagram of the Bi-Sr-Ca-Cu-O system still remains fairly obscure: as a consequence, bulk materials are porous and contain impurities, thus lowering the current carried in the superconducting state. As recently demonstrated by local magneto-optics studies, the macroscopic current density in Ag-sheathed Bi,Pb-2223 tapes is, at best, 5-6 times lower than the maximum current carried locally, of $>250 \text{ kA/cm}^2$ [9]. Flux pinning is very weak in Bi-based high- T_c superconductors, and strongly decreases with temperature, thus limiting the operation at 77 K to fields below 1 Tesla. Cryocoolers are needed in order to operate at lower temperatures (20-30 K). The intrinsic pinning properties of these compounds are still under investigation but the research has been strongly hindered for many years by the lack of high quality bulk single crystals and thin films.

Despite of all these difficulties and the lower superconducting performance of this material compared to the “second generation conductors” based on the $\text{YBa}_2\text{Cu}_3\text{O}_{7-\delta}$ material, Bi-based wires and tapes are at present the only high- T_c superconductors under production in long lengths and will remain the choice of the power industry in the next future. Many of the technical problems in manufacturing large power devices have been overcome and new processing routes have been successfully explored. Flux pinning has been artificially enhanced, and recently large and high quality single crystals of Bi-2223 and Bi,Pb-2223 have been grown. Based on these single crystals, structural features related to modulation and anisotropy have been understood. The slower improvement of the critical current values obtained in the last years, as compared to the past, should not deceive. Based on the recent knowledge and the experimental results of the last years, there is still room for future improvement in industrial applications.

The aim of this review is to summarise some of the results obtained in the last years in this field and the most recent knowledge acquired on Bi-2223 and Bi-2212. In Section 2, the structural aspects of these compounds will be presented and revisited. In Section 3 we will discuss the crystal growth of Bi-based cuprates, focussing on the recent single crystals of Bi-2223. The superconducting properties of Bi-2223 are described in Section 4. Section 5 is dedicated to the modulation-free Pb-doped Bi-2212 phase. In particular, the effect of strong Pb doping will be discussed, both on structure modulation and superconducting properties.

2. BI-BASED CUPRATES: GENERAL FEATURES AND CRYSTAL STRUCTURE

The structures of all the members of the homologous series $\text{Bi}_2\text{Sr}_2\text{Ca}_{n-1}\text{Cu}_n\text{O}_{4+2n+8}$ are formed by deficient perovskite-like blocks intercalated by rocksalt-like Bi-O bi-layers. In the $n = 1$ phase (“Bi-2201”) the perovskite-like block contains only one CuO_2 layer. In the $n = 2$ (“Bi-2212”) and $n = 3$ (“Bi-2223”) phases, the perovskite-like blocks contain 2 and 3 CuO_2 layers, respectively, separated by Ca atoms. The average structures are described by pseudo-tetragonal unit cells with parameters $a \approx b \approx 5.4 \text{ \AA}$ and $c \approx 24.4, 30.9$ and 37 \AA for Bi-2201, Bi-2212 and Bi-2223, respectively (Fig. 1, left). However, cation substitutions, oxygen off-stoichiometry, difference in translation periods of different layers, displacive and occupational modulation make the real structure of these compounds much more complicated. These compounds are extremely attracting, not only because of their superconducting properties but also because of the peculiarities of their crystal structure (a review of all the crystal structures of high- T_c superconductors is given in [10]). The structures of the three phases exhibit a characteristic incommensurate modulation, with a modulation vector $\mathbf{q} = \lambda_1 \mathbf{a}^* + \lambda_2 \mathbf{c}^*$. This feature has been studied and discussed in a number of reports [11-15], but its origin and its effect on the superconducting properties are still debated. Structure modulation was reported to be related to the mismatch between the BiO layer and the $\text{Sr}_2\text{Ca}_{n-1}\text{Cu}_n\text{O}_{2+2n}$ block which causes a displacement of the atoms and the insertion of additional oxygen atoms. A detailed study on the modulation in the Bi-based compounds was reported by Zandbergen et al. [13], who suggested extra oxygen atoms in BiO layers to be responsible for the structure modulation. In all the three phases oxygen is in excess: extra oxygen atoms are incorporated in the BiO layers, thus displacing the Bi atoms with respect to the $\text{Sr}_2\text{Ca}_{n-1}\text{Cu}_n\text{O}_{2+2n}$ blocks.

The structures of Bi-2201 and Bi-2212 were refined from single-crystal X-ray diffraction data [16,17] and the unit cells are described by monoclinic superlattices. Such modulated structures have also been refined by using an appropriate multi-dimensional formalism for aperiodic structures [15,18,19]. The refinement of the incommensurate structure of Bi-2212 was also carried out from single crystal neutron diffraction data by Miles et al. [20], who reported a slightly smaller unit cell and a lower oxygen content compared to XRD studies.

Structure refinement of Bi-2223 was not possible for long time because of the lack of single crystals of sufficient quality. High quality crystals of this compound have been recently grown [21-23] and the structure of both the Pb-free and Pb-doped phases successfully refined from single crystal X-ray diffraction, both with a supercell approach and 4-dimensional formalism for modulated structures [24]. The unit cell of the average structure of Bi-2223 is pseudo-tetragonal with $a = 5.4210(7)$, $b = 5.4133(6)$ and $c = 37.009(7) \text{ \AA}$ and a modulation vector $\mathbf{q} = 0.206 \mathbf{a}^*$ was defined. The modulated structure can be conveniently described in a supercell with 5-fold volume ($a = 27.105(4) \text{ \AA}$) and refined in an orthorhombic $P222$ group. With respect to the “non-modulated” structure, additional oxygen atoms (one O atom per translation unit of the modulation wave, i.e. one extra O for ten initial O) were found to be inserted into the BiO layers, so that regions with a distorted rocksalt-type atom arrangement and regions with chains of corner-linked BiO_3 ψ -tetrahedra are formed. Approximately 8% of Bi substitution was found on the Ca site, the refined composition being $\text{Bi}_{2.16}\text{Sr}_2\text{Ca}_{1.84}\text{Cu}_3\text{O}_{10.16}$. In the Pb-doped phase the orthorhombic distortion is enhanced and the c -axis is found to be slightly larger, like in the Bi,Pb-2212 phase [25], the refined cell

parameters being $a = 5.395(1)$, $b = 5.413(1)$ and $c = 37.042(11)$ Å. The modulation vector was found to be $\mathbf{q} = 0.20 \mathbf{a}^*$ and Bi was found to partially substitute for Ca but at lesser amount compared to the Pb-free structure ($\sim 5\%$). A projection along b -axis of the superstructure of Pb-free Bi-2223 is shown in Fig. 1 (right). Atom labels indicate the independent atomic positions in the refined supercell.

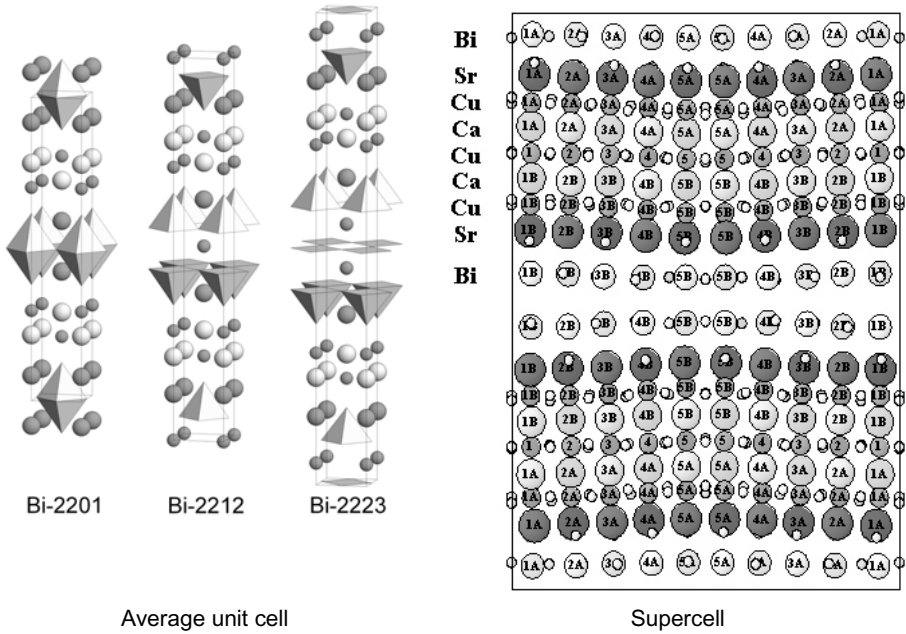


Fig. 1. (left) Average structures of Bi-2201, Bi-2212 and Bi-2223. (right) Modulated structure projected along the b -axis. Labels indicate the independent atoms in the orthorhombic supercell (as refined in [24])

Space groups and lattice constants of the three Bi-based superconducting phases are summarised in Table 1. In this table, chemical formulas generally refer to the refined composition. The components of the modulation vectors are specified when the refinement is performed in the multidimensional space for aperiodic structures. The average structures of Bi-2201 and Bi-2223 reported in [26] and [30], respectively, were refined from neutron powder diffraction data instead of single crystal X-ray diffraction data. The La-doped Bi-2201 compound is added in this table because of its high critical temperature: the very low T_c of the pure Bi-2201 phase can be enhanced by La doping on the Sr site up to $T_c = 33$ K for $\text{Bi}_2\text{Sr}_{1.6}\text{La}_{0.4}\text{CuO}_{6+d}$, as reported in [29]. The monoclinic distortion due to the systematic shift of the modulation waves in Bi-2201 and Bi-2212, becomes negligible in Bi-2223 in which the shift is approximately equal to π .

Table 1. Composition, space group, lattice constants and modulation vectors of the three members of the superconducting family $\text{Bi}_2\text{Sr}_2\text{Ca}_{n-1}\text{Cu}_n\text{O}_{4+2n+\delta}$. Average subcells, superlattices and modulated aperiodic structures in multidimensional space are reported.

| Chemical formula | Space Group | $a(\text{Å})$ | $b(\text{Å})$ | $c(\text{Å})$ | β° | Modulation wavevector \mathbf{q} | Ref |
|---|-------------------|---------------|---------------|---------------|---------------|------------------------------------|------|
| Bi-2201 | | | | | | | |
| $\text{Bi}_{1.86}\text{Sr}_{1.56}\text{Ca}_{0.83}\text{O}_{5.98}$ | <i>A2aa</i> | 5.375 | 5.378 | 24.377 | 90 | average structure | [26] |
| $\text{Bi}_{2.08}\text{Sr}_{1.84}\text{CuO}_6$ | <i>P:A2/a:11</i> | 5.3791(6) | 5.3811(9) | 24.589(3) | 89.93(1) | [0.2030, 0, 0.467] | [27] |
| $\text{Bi}_{2.26}\text{Sr}_{1.74}\text{CuO}_{6.19}$ | <i>P:A2/a:11</i> | 5.3874(5) | 5.3869(4) | 24.579(3) | 90.01(1) | [0.2105, 0, 0.538] | [28] |
| $\text{Bi}_2\text{Sr}_{1.7}\text{La}_{0.3}\text{CuO}_{6.28}$ | <i>P:A2/a:11</i> | 5.4015(2) | 5.3781(3) | 24.501(2) | 89.830(1) | [0.228, 0, 0.72] | [29] |
| Bi-2212 | | | | | | | |
| $\text{Bi}_{2.10}\text{Sr}_{1.78}\text{Ca}_{1.12}\text{Cu}_2\text{O}_8$ | <i>A2aa</i> | 5.4112(7) | 5.416(2) | 30.873(7) | 90 | average structure | [17] |
| $\text{Bi}_{2.15}\text{Sr}_{1.92}\text{Ca}_{0.75}\text{Cu}_2\text{O}_{8.1}$ | <i>M:A2aa:111</i> | 5.408(1) | 5.413(1) | 30.871(5) | 90 | [0.210, 0, 0] | [15] |
| $\text{Bi}_{2.09}\text{Sr}_{1.90}\text{CaCu}_2\text{O}_{8.22}$ | <i>Cc</i> | 37.754(7) | 5.4109(8) | 41.070(9) | 103.58(2) | supercell | [17] |
| Bi-2223 | | | | | | | |
| $\text{Bi}_1\text{Pb}_{2.3}\text{Sr}_2\text{Ca}_{1.7}\text{Cu}_3\text{O}_{10}$ | <i>A2aa</i> | 5.402(1) | 5.419(1) | 36.957(8) | 90 | average structure | [30] |
| | <i>A2aa</i> | 5.4210(7) | 5.4133(6) | 37.009(8) | 90 | average structure | [24] |
| $\text{Bi}_{2.16}\text{Sr}_2\text{Ca}_{1.84}\text{Cu}_3\text{O}_{10.16}$ | <i>P222</i> | 27.105(4) | 5.4133(6) | 37.009(8) | 90 | supercell | [24] |
| $\text{Bi}_1\text{Pb}_{2.12}\text{Sr}_2\text{Ca}_{1.87}\text{Cu}_3\text{O}_{10.12}$ | <i>A2aa</i> | 5.395(1) | 5.413(1) | 37.042(11) | 90 | average structure | [24] |
| | <i>P222</i> | 26.976(7) | 5.413(1) | 37.042(11) | 90 | supercell | [24] |

The incommensurate nature of the modulation is closely related with superconductivity. Modulation can induce strong distortions of the CuO_2 conducting layers, thus strongly affecting the superconducting properties of these compounds. Moreover, the charge carrier density depends on the oscillations of the polarisation charges in the Bi-O block layer. Hence, the structure modulation can be responsible for breaking the long-range phase coherence needed for superconductivity. The Bi-2201 phase, which exhibits the strongest modulation and monoclinic distortion, has a critical temperature ($T_c = 8\text{-}10\text{ K}$) much lower than the other 1-layer superconducting cuprates Tl-1201 ($T_c = 55\text{-}60\text{ K}$), Tl-2201 ($T_c = 90\text{ K}$), Hg-1201 ($T_c = 95\text{ K}$), and Pb-3201 ($T_c \sim 33\text{ K}$). The Bi-2212 and B-2223 phases also become superconducting at temperatures lower than other $n=2$ and $n=3$ superconducting compounds which don't exhibit any structure modulation or are only weakly modulated. As a matter of fact, structure modulation is an intrinsic limiting factor for superconductivity in layered cuprates [31].

Structure modulation can be modified by doping the phase in appropriate way either with cations or anions. Several studies about the reduction or even suppression of the modulation have been reported so far, and in many cases different structures have been found and improved superconducting properties have been measured. In Bi-2201, modulation is reduced by doping the Bi site with Pb [32], thus resulting in an enhancement of the critical temperature up to $T_c = 34\text{ K}$ ($T_{c\text{ onset}} = 41\text{ K}$) at the optimal oxygen doping. By simultaneously doping the Bi-site with Pb and the Sr site with La, the onset of superconductivity was measured to be as high as $T_{c\text{ onset}} = 47\text{ K}$ in Bi-2201 [33]. This is the highest T_c ever achieved so far in Bi-2201 and is a consequence of an optimised procedure for removal of the monoclinic distortion, reduction of the orthorhombic modulation and increase of the carrier concentration.

Structure modulation in Bi-2201 was successfully suppressed in fluorinated Bi-2201, in which the anionic exchange between one O^{2-} and two F^- ions take place in the Bi-O block layer [34]. The fluorinated phase was found to crystallise with a higher symmetry (*I*-centred

tetragonal unit cell, $I4/mmm$ space group), and the mismatch between the Bi-O rock salt layer and the perovskite layers was removed. Unfortunately, the fluorinated Bi-2201 phase was found not to be superconducting, probably because of the valence reduction of Cu in the CuO_2 layer. The anionic exchange between one O^{2-} and two F^- ions was observed also in the Bi-2212 and Bi-2223 phases, and confirmed by neutron powder diffraction [30]. In these compounds the fluorinated structure was also reported to be close to the tetragonal average structure, even though any investigation on the effect of fluorination on the modulation was impossible in that study.

Impressive consequences of the modulation suppression induced by strong cation doping of the Bi-O block layer can be observed in strongly Pb-doped Bi-2212 crystals [35]. In this compound, the complete disappearance of the structure modulation is responsible for a remarkable improvement of the pinning properties. The weak pinning properties of the Bi-2212 was the most limiting factor for practical applications of this superconducting compound: by controlling strong cation substitutions and adequately modifying the crystal structure the superconducting properties of the Bi-2212 phase can be improved. Because of the importance of this recent result, the modulation-free phase Bi,Pb-2212 will be described in a following section and its superconducting properties will be reviewed. It should be underlined, however, that the $\text{Bi}_{1.6}\text{Pb}_{0.4}\text{Sr}_2\text{CaCu}_2\text{O}_{8+\delta}$ phase has a different formation mechanism than pure Bi-2212, and could so far not be formed single phased in Ag-sheathed tapes.

Generally speaking, non-modulated structures with a higher symmetry have better superconducting properties. By doping, the intrinsic limiting factor for superconductivity in Bi-based superconducting compounds can be weakened or even removed. The recent results obtained on Bi-2201 and Bi-2212 lead to hope for similar improvements in the Bi,Pb-2223 compound, with a possibly strong impact on large scale applications.

3. CRYSTAL GROWTH OF BI-BASED SUPERCONDUCTORS

Growing large and pure crystals of Bi-based cuprates is in general not an easy task, and it becomes extremely difficult in the case of the 3-layer compounds Bi-2223 and Bi,Pb-2223. The main reason is the extreme complexity of the Bi-Sr-Ca-Cu-O phase diagram. All the members in the family of Bi-based cuprates melt incongruently and the primary phase field always contains several phases in equilibrium with each other [36]. The three Bi-based superconducting phases coexist in several multiphase pockets of the phase diagram and have similar crystal structures (as we have seen in the previous section): for this reason they can grow simultaneously one into the other, thus easily forming intergrowths and not pure crystals. The growth kinetics is strongly anisotropic, being much faster in the ab -plane than in the c -direction, and resulting in mica-like shaped crystals which are very thin in one direction and difficult to handle (the typical size is of the order of $1\text{-}10\text{ mm}^2$ in the ab -plane and only $10\text{-}50\text{ }\mu\text{m}$ in the c -direction). The early crystal growth activity in this field (until 1993) was exhaustively reviewed by Assmus and Schmidbauer [37], but the most interesting results have been obtained only very recently on crystals of higher quality. In particular, no crystals of the 3-layer phase have been available for many years, which constituted an obstacle to the research on high-temperature superconductivity in 3-layer cuprates. In the following, we will summarise the recent crystal growth activity in this field, mainly focussing on the very recent

results obtained in growing Bi-2223 and Bi,Pb-2223 crystals, which have represented the major challenge. It will be shown that the so-called Travelling Solvent Floating Zone method (TSFZ) is actually the most suitable technique for growing high quality crystals of Bi-based superconductors.

3.1. Growth of Bi-2201 crystals

Single crystals of the Bi-2201 phase have been grown by several techniques, namely the self-flux [38,39], alkali-chloride solution melt [40], and Travelling Solvent Floating Zone (TSFZ) method [41,42]. By the self-flux technique both pure and La-doped Bi-2201 crystals were grown in either Al_2O_3 [38] or Pt [39] crucibles, and large crystals (typically larger than $2 \times 1 \text{ mm}^2$ in the *ab*-plane, but very thin in the *c*-direction, $\sim 10\text{-}30 \mu\text{m}$) were obtained exhibiting superconducting transitions up to 36 K [39]. An excess of Bi was generally used in the nominal composition of the precursor mixture. Gorina et al. [40] succeeded in growing pure Bi-2201 crystals from solution-melt in KCl and in cavities formed in KCl. Critical temperatures up to 13 K and typical crystal size of $2 \times 2 \times 0.01 \text{ mm}^3$ were obtained by using this technique. The crystals obtained were used for measuring the electrical resistivity and investigating the structure modulation by TEM. However, by using the self-flux growth as well as the alkali-chloride solution-melt growth, one has to face the problem of sample contamination due to the reaction between the melt and the crucible material and the possible K^+ and Cl^- inclusions. In addition, these techniques provide small crystals, not large enough for many experimental studies.

The TSFZ technique has been successfully used for growing large and high-quality crystals of both pure and Pb-doped Bi-2201. Despite of the Pb losses occurring at high temperature, Chong et al. [41] were able to grow heavily Pb-doped Bi-2201 crystals using this technique in air. More recently, Liang et al. [42] reported the growth of very large undoped Bi-2201 crystals (up to $28 \times 6 \times 2.5 \text{ mm}^3$) by using the TSFZ method under oxygen overpressure. They studied in details the effect of the starting composition, oxygen pressure and travelling velocity on the size and the properties of the crystals. Sharp superconducting transitions ($\Delta T_c < 1.5 \text{ K}$) and T_c ranging between 3.5 K and 8.5 K were reported [42].

3.2. Growth of Bi-2212 crystals

Among the three members of the Bi family, Bi-2212 crystals are certainly the easiest ones to grow due to the large stability range in the temperature-composition phase diagram. A number of authors have described the successful growth of Bi-2212 crystals by various techniques, namely self-flux [43,44], KCl flux [45], Bridgman [46,47], Top-Seeded Solution Growth (TSSG) [48] and Travelling Solvent Floating Zone [49-51]. A review of the earlier activity in growing crystals of Bi-2212 can be found in [52].

The transition width of as-grown crystals is commonly quite broad, as a consequence of the inhomogeneity of the oxygen content in as-grown samples. By using the self-flux method, it is even more difficult to control the actual oxygen content in the melt. Crystals extracted from the same crucible exhibit quite a large distribution of T_c , and the structural quality differs strongly from one crystal to another. By using the self-flux method, the inhomogeneity of the starting precursor also plays an important role and the growth is

strongly dependent on local conditions which are difficult to keep under control. An interesting experiment was performed by Funabiki et al. [44], who grew Bi-2212 crystals by slow-cooling in Al_2O_3 crucibles without grinding and mixing the starting powder. By applying an overpressure on the melt, and the homogeneity of as-grown crystals was improved. Large ($4 \times 4 \text{ mm}^2$) crystals with T_c ($\rho = 0$) up to $\sim 88 \text{ K}$ and $\Delta T_c \approx 4 \text{ K}$ were obtained with this technique. The growth of heavily Pb-doped Bi-2212 crystals has been reported by Musolino et al. [35] by the self-flux method in a vertical 3-zone furnace. A home-made BaZrO_3 crucible was employed for avoiding melt contamination from the crucible. By continuously monitoring *in-situ* the weight of the crucible, they were able to control the Pb content in the melt and grow $\text{Bi}_{2-y}\text{Pb}_y\text{Sr}_2\text{CaCu}_2\text{O}_{8+\delta}$ crystals with a maximum nominal composition of $y = 0.8$. These crystals have been used for a systematic investigation of the pinning properties as a function of Pb content, and a structural study of the Pb-rich modulation-free phase. The results of this research will be reviewed in Section 5.

Large crystals were grown by using a vertical Bridgman method [46], but the quality of the samples obtained with this technique resulted to be lower than in crystals grown using other techniques, probably because of the difficulties encountered in controlling the composition and the oxygen content during growth.

As for the Bi-2201 phase, the crucible material can affect the quality of the crystals because of the interaction with the melt. Furthermore, a strong thermal gradient is generally found to favour the growth of crystals with a given orientation. Therefore, the largest and most pure Bi-2212 crystals are obtained by the TSFZ method in a mirror furnace, which is a crucible-free growth technique and makes it possible to control very strong temperature gradients at the liquid-solid interface. This is the most suitable technique for growing crystals of Bi-2212, and in general for growing crystals of many high- T_c superconducting compounds. Tanaka et al. [50] employed the TSFZ method by adding a Bi-rich solvent on the top of a gold crucibles and making it travel throughout the feed rod. Crystals with $3 \times 1 \text{ mm}^2$ large surfaces but broad superconducting transitions were obtained.

This technique was recently employed by Liang et al. [51] for growing underdoped Bi-2212 crystals. By changing the oxygen partial pressure inside the image furnace, the oxygen content could be controlled and the transition temperature of the as-grown crystals could be tuned. Crystals having the same cation composition but various oxygen contents were grown, exhibiting critical temperatures ranging from 91 K (optimal doping) to 76 K (underdoped regime). The transition widths were narrow at the optimal doping, but broadened with decreasing the oxygen content, showing that in the underdoped regime a homogeneous distribution of oxygen is difficult to achieve. The TSFZ method proved also to be suitable for growing large and thick crystals (up to $15 \times 5 \times 1 \text{ mm}^3$), more than 10 times as thick as crystals grown by any other technique. Structural quality is improved by using the TSFZ method, as confirmed by Bdikin et al. [53], who reported comparative X-ray topography and X-ray diffraction studies on Bi-2212 crystals grown using different techniques.

3.3. Growth of Bi-2223 crystals

Based on the chemical transport in a thermal gradient in molten KCl, the first successful growth of both Pb-free and Pb-doped Bi-2223 crystals was reported in 1994 by Balestrino et al. [54]. Still using a fused salt reaction of precursors in a KCl flux, Chu et al. [55] and

Gorina et al. [56] were able to grow Pb-doped and undoped Bi-2223 crystals, respectively. Crystals were very tiny, especially in the *c*-direction, contained spurious phases and exhibited broad superconducting transitions. The typical size of the Pb-doped crystals grown by this technique was $0.1 \times 0.1 \times 0.001\text{--}0.01 \text{ mm}^3$ ($T_{c(\rho=0)} = 105 \text{ K}$, 97% pure phase), and larger for the undoped ones, $1 \times 1 \times 0.003 \text{ mm}^3$ ($T_{c \text{ onset}} = 110 \text{ K}$, $\Delta T_c = 10 \text{ K}$). This was sufficient for measuring some transport properties of the Bi-2223 phase, such as *c*-axis and *ab*-plane electrical resistivity and the Hall effect [56]. However, these crystals contained a small amount ($\approx 3 \%$) of Bi-2212 phase, which obviously perturbs the measurement of the intrinsic properties of the Bi-2223 phase. A similar technique was used by Lee et al. [57], but without improving the size and the quality of the crystals (typical size $< 0.4 \times 0.4 \times 0.005 \text{ mm}^3$, $T_{c \text{ onset}} = 109 \text{ K}$, $\Delta T_c > 10 \text{ K}$). As a general remark, we note that alkali-chloride flux techniques have provided only small Bi-2223 and Bi,Pb-2223 crystals, which also contained impurities and were inhomogeneous. On the other side, no successful growth of Bi-2223 crystals have been reported by using the self-flux method.

Recently, successful growth experiments have been performed by Fujii et al. [21], Shimizu et al. [58] and Liang et al. [22], all using the TSFZ technique. Relatively large (up to $4 \times 2 \times 0.01 \text{ mm}^3$) Pb-free Bi-2223 crystals were grown by this technique, but the superconducting transitions reported were quite broad and even multiple. Both Pb-free and Pb-doped Bi-2223 single crystals were grown very recently by Giannini et al. [23] by means of a newly developed Vapour-Assisted Travelling Solvent Floating Zone method (VA-TSFZ), suitable for crystal growth in the presence of volatile elements such as Pb. This was the first successful experiment of growth of pure and large Pb-doped Bi-2223 crystals (up to $3 \times 2 \times 0.1 \text{ mm}^3$).

As already mentioned in the previous sections, the possibility of melting and crystallising without using any crucible allows one to grow pure samples. Furthermore, in the TSFZ method, the crystals grow at one point of the temperature-composition phase diagram, thus allowing crystal growth of even incongruently melting materials. A review of the floating zone method applied to the growth of high- T_c single crystals can be found in [59]. Growth conditions and transport properties of Bi-2212 and Bi-2223 crystals were recently reviewed in [60]. In the following, we will describe the VA-TSFZ technique as developed at the DPMC in Geneva [23]. The superconducting properties of the so obtained crystals will be described in Section 4.

3.4. Growth of Bi,Pb-2223 crystals by the VA-TSFZ technique

The so-called “feed” and “seed” rods of Pb-free and Pb-doped Bi-2223 precursors were prepared using either home-made or commercial powder (see [23] and references therein for details) with nominal cation ratios Bi:Sr:Ca:Cu = 2.1:1.9:2.0:3.0 and Bi:Pb:Sr:Ca:Cu = 1.84:0.32:1.84:1.97:3.00, respectively. The typical size of precursor rods was 6-7 mm in diameter and $\sim 8 \text{ cm}$ in length. High density and homogeneity of the precursor rods are required for good crystal growth conditions in the TSFZ technique.

TSFZ growth was performed in a home-made image furnace equipped with two 400 W halogen lamps, in which the atmosphere can be controlled. A mixture of 93%Ar-7%O₂, flowing at 0.5 l/h, was set instead of air or O₂-rich atmosphere as used in the other

works [21-22]. This particular oxygen composition was chosen in order to lower the melting temperature of the precursor and enlarging the stability range of the Bi-2223 phase [61].

For growing the Pb-doped crystals, the commonly used TSFZ/Image Furnace configuration was modified by adding an internal source of Pb. According to previously reported high pressure annealing experiments and *in situ* neutron diffraction studies [62,63], Pb losses which occur at high temperature must be minimised in order to keep the stoichiometry of the sample close to the nominal one, thus promoting equilibrium phase formation. In the Vapour-Assisted Travelling Solvent Floating Zone (VA-TSFZ), a Al_2O_3 ring crucible containing PbO and encircling the seed rod is placed inside the quartz tube close to the molten zone as shown in Fig. 2. The position of the PbO source has to be chosen accurately, so that the temperature of the ring crucible is the one needed for evaporation of PbO at a given rate ($\sim 2 \cdot 10^{-8}$ mole/hour at $T = 750^\circ\text{C}$). This allowed us to compensate for the Pb losses by means of a Pb release from the PbO source.

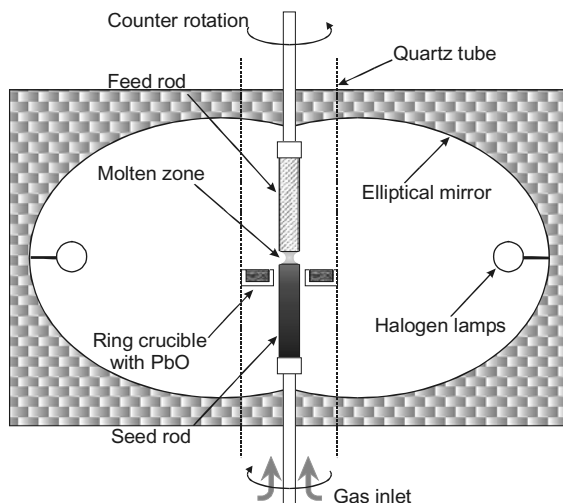


Fig. 2. Vertical cross section of the image furnace used for TSFZ in [23].

The feed rod has to be carefully densified prior to performing the crystal growth experiment. A fast pre-melting was performed at travelling velocity of 25 mm/h was chosen and the feed and the seed rod were counter-rotating at $\omega = 0.14 \text{ s}^{-1}$. The densification pre-melting is known to be a key step for keeping the molten zone stable during the whole experiment, and hence for growing large crystals. The crystal growth process was performed at very low travelling velocities, ranging from 30 to 200 $\mu\text{m/h}$, the best crystals being obtained at 50-60 μm . We notice that there is a general agreement about the optimum travelling and rotation velocities needed for good crystals of Bi-2223 among various authors. One of the main advantages of the TSFZ method is to set a high thermal gradient at the liquid-solid interface, thus providing very strong driving forces and favouring the growth of large crystals. The thermal gradient at the liquid-solid interface was measured to be as high as $\sim 50^\circ\text{C/mm}$ [23]. As-grown crystals need to be annealed under pure O_2 at pressures up to

10 MPa, at 500 °C for 10-200 h in order to increase and homogenise the oxygen content. Post-annealing at high pressure of O₂ was found to be more effective than long treatments at 1 bar for favouring the oxygen diffusion inside the Bi-2223 crystals. As a result, large (up to $3 \times 2 \times 0.1 \text{ mm}^3$) crystals of both the Pb-free and the Pb-doped Bi-2223 phase were obtained, having critical temperatures up to 111 K (in optimally doped Pb-free samples) and very narrow superconducting transitions ($\Delta T_c = 1 \text{ K}$ and 2-3 K for Pb-free and Pb-doped crystals, respectively). Superconducting properties of these samples will be reported in Section 4. Pb was found by EDX to be present in the Bi,Pb-2223 phase, the measured composition being $\text{Bi}_{2.16}\text{Pb}_{0.26}\text{Sr}_{2.08}\text{Ca}_{1.95}\text{Cu}_{2.55}\text{O}_{10+\delta}$. Pictures of these crystals are shown in Fig. 3.

In Fig. 4, the magnetic susceptibility of these crystals is shown. The crystals were annealed in oxidising atmosphere ($p(\text{O}_2) = 10 \text{ MPa}$, $T = 500^\circ\text{C}$) and very sharp superconductor transitions were obtained. We notice that the transition width of Pb-doped crystals is always larger than that of Pb-free crystals, which is likely to be due to a lesser homogeneity of the Pb-doped crystals.

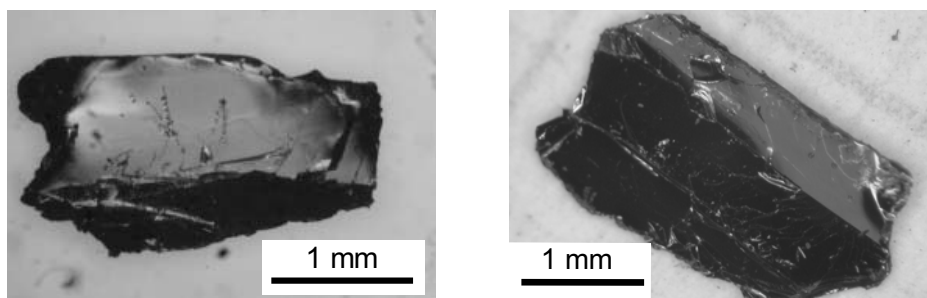


Fig. 3. Optical microscope images of a Pb-free (left) and a Pb-doped (right) Bi-2223 crystals.

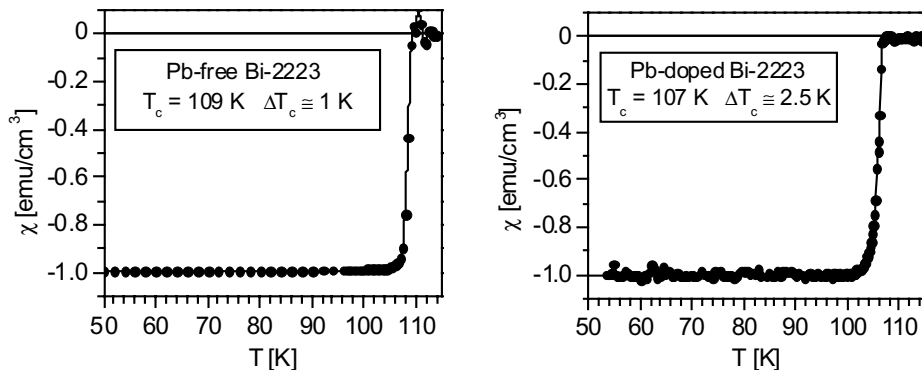


Fig. 4. Superconducting transitions of the crystals shown in Fig. 3, after annealing in oxidising atmosphere (from ref. [23, 86]). Very sharp transitions are obtained.

4. SUPERCONDUCTING PROPERTIES AND VORTEX PHASE DIAGRAM OF $\text{Bi}_2\text{Sr}_2\text{Ca}_2\text{Cu}_3\text{O}_{10}$

The very recent and limited availability of single crystals has yielded so far only a limited number of reports on the intrinsic superconducting properties of this material. Vortex phase diagram, anisotropy, penetration depth and magnetisation relaxation rate, have been investigated by Clayton et al. [64]. The improvement of vortex pinning induced by proton and heavy ion irradiation has been studied by Chu et al. [65] and Shimoyama et al. [66]. Transport properties, such as electrical resistivity, Hall effect, thermopower, have been studied by Gorina et al. [56], Shimizu et al. [58] and Fujii et al. [67]. Optical conductivity measurements have been reported by Boris et al. [68], Kovaleva et al. [69] and Carbone et al. [70] and STM experiments have been successfully performed by Kugler et al. [71]. This research activity has been carried out in the very last years and many questions still remain open about the superconducting properties of the Bi-2223 compound and the 3-layer superconducting cuprates in general. In this review, we will only recall the results of magnetic and transport measurements which are of interest in view of practical applications of this material.

4.1. Lower critical field, penetration depth and anisotropy of Bi-2223 crystals

The anisotropy is a key parameter for the understanding of the vortex phase diagram. The effectiveness of the pinning centres and the capability of the material of carrying high currents in the superconducting state are directly related to the anisotropy. The measurement of the anisotropy parameter γ needs single-crystalline samples. The first estimation of γ of Bi-2223 was obtained by measuring the higher critical fields H_{c2} with the applied field either parallel or perpendicular to the c -axis on Bi-2223 whiskers [72]. A value of $\gamma = H_{c2}(H // c) / H_{c2}(H // ab) = 31$ was obtained in this early study.

The superconducting anisotropy of Bi-2223 crystals has been recently obtained by measuring the ratio of the lower critical field, H_{c1} , with the magnetic field applied parallel to the c -axis and then to the ab -plane. A reliable measurement of the lower critical field in strongly anisotropic high- T_c superconductors requires very low field sweep rates, in order to avoid surface barrier effects which can impede the flux penetration [73]. At field sweep rates lower than $1 \times 10^{-4} \text{ Oe s}^{-1}$, the lower critical field could be measured in Bi-2223 crystals without any effect due to geometrical barriers and surface pinning, as reported in [64]. The anisotropy of Bi-2223 was measured to be $\gamma = H_{c1}(H // c) / H_{c1}(H // ab) \approx 50$ at $T = 30 \text{ K}$, and the corresponding values of H_{c1} are $H_{c1}(H // c) = 500 \text{ Oe}$ and $H_{c1}(H // ab) = 9.4 \text{ Oe}$. This γ value results to be intermediate if compared to Bi-2212 ($\gamma = 165$) and $\text{YBa}_2\text{Cu}_3\text{O}_{7-\delta}$ ($\gamma = 5-7$). However, the anisotropy in Bi-2223 is still higher than in strongly Pb-doped Bi-2212 ($\gamma = 25$), at the same temperature (see Section 5).

Higher values of the anisotropy parameter γ ($\gamma \approx 90-100$) of the Bi-2223 phase have been also reported [58], as obtained from the measurement of the second peak occurring in the magnetisation loops of Bi-2223 crystals, and under the assumption that the second peak coincides with the dimensional crossover 2D-3D of the vortex line lattice [74]. However, such an assumption is justified only in the case of very strong anisotropy, like in the Bi-2212 phase, in which the second peak appears at a field value close to the dimensional crossover, and does not apply to Bi-2223. As it will be shown in the next section (see Fig. 7), in Bi-2223

the crossover between a 2D and 3D behaviour occurs at a field higher than the second peak in the magnetisation loops. As a consequence, the determination of the anisotropy parameter γ from the position of the second peak is misleading and does not yield the correct estimation of the superconducting anisotropy.

The dependence of the lower critical field on temperature is plotted in Fig. 5(a). From the extrapolation of H_{c1} to $T=0$, one finds $H_{c1}(0) = 540$ Oe and, correspondingly, $\lambda_{ab}(0) = 1200$ Å, by assuming a coherence length $\xi_{ab}(0) = 10$ Å. The penetration depth λ_{ab} is found to be much shorter than in Bi-2212 ($\lambda_{ab}(0) = 3000$ Å). The London penetration depth λ_{ab} is plotted as a function of the temperature in Fig. 5(b). The previously reported value of $\lambda_{ab}(0) = 1240$ Å, measured in c -axis oriented polycrystalline Bi-2223 samples [75], is in good agreement with the most recent measurements on single-crystals. A comparison of γ , λ and ξ for the three Bi-based superconducting phases is given in Table 2. A strong reduction of the London penetration depth in the ab -plane is observed with increasing the number of conducting planes in Bi-based superconductors.

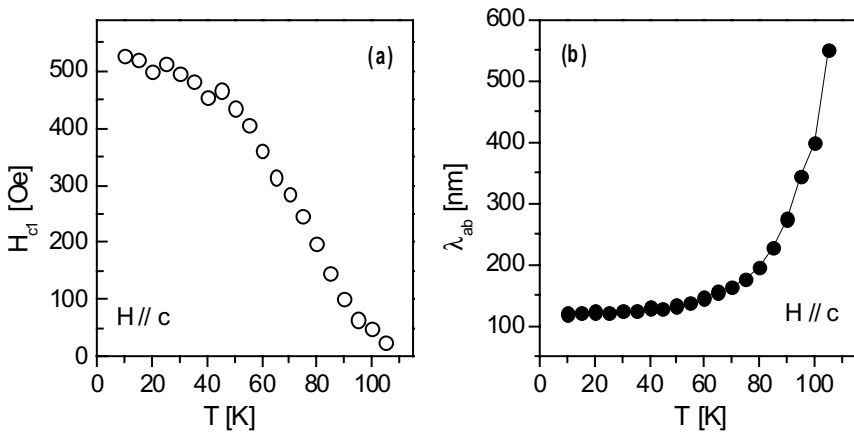


Fig. 5. (a) Lower critical field H_{c1} ($H // c$) of Bi-2223 as extracted from magnetisation measurements performed on single crystals [64]. (b) In-plane London penetration depth λ_{ab} as obtained from the H_{c1} values in 5(a) by using the anisotropic Ginzburg-Landau theory.

Table 2. Anisotropy, penetration depth and coherence length in Bi-based HTS cuprates.

| Compound | γ | $\lambda_{ab}(0)$ [Å] | $\xi_{ab}(0)$ [Å] | Comment | Ref |
|----------|----------|-----------------------|-------------------|-----------------------------|------|
| Bi-2201 | ~220 | 4000 | ~50 | La-doped polycryst. samples | [76] |
| Bi-2212 | 165 | 3000 | 17 | single crystal data | [77] |
| Bi-2223 | 50 | 1200 | 10 | single crystal data | [64] |

4.2. Irreversibility line and critical current in Bi-2223 crystals

The irreversibility line (IL) of Bi-2223 crystals has been recently measured [58, 64]. The IL determination was carried out from magnetic investigations by Clayton et al. [64], as the temperature at which a kink in the reversible magnetisation is observed, slightly above the merging of the ZFC and FC branches. On the other hand, Shimizu et al. [58] performed both magnetic and transport measurements in order to determine the irreversibility line. The results reported in [64] and [58] agree very well with each other.

The IL of Bi-2223 crystals is shown in Fig. 6(a), as a function of the reduced temperature, T/T_c , and is compared with the IL of Bi-2212 crystals measured with the same technique [64]. H_{irr} curves are plotted as a function of the normalised T/T_c instead of T , in order to directly compare the irreversible behaviour of Bi-2223 and Bi-2212 regardless of their different critical temperatures. One can easily notice the better superconducting performance of the Bi-2223 phase. The IL of Bi-2223 is translated to higher temperature than Bi-2212, due to its lower anisotropy and then to the higher effectiveness of pinning centres in Bi-2223. The irreversibility field is found to be $H_{irr} = 500$ Oe at $T = 77$ K, and $H_{irr} > 10000$ Oe at $T < 35$ K. (For comparison, in Ag-sheathed Bi,Pb-2223 tapes $H_{irr} \sim 2-4$ kOe at $T = 77$ K, and $H_{irr} = 70$ kOe at $T = 30$ K [78]).

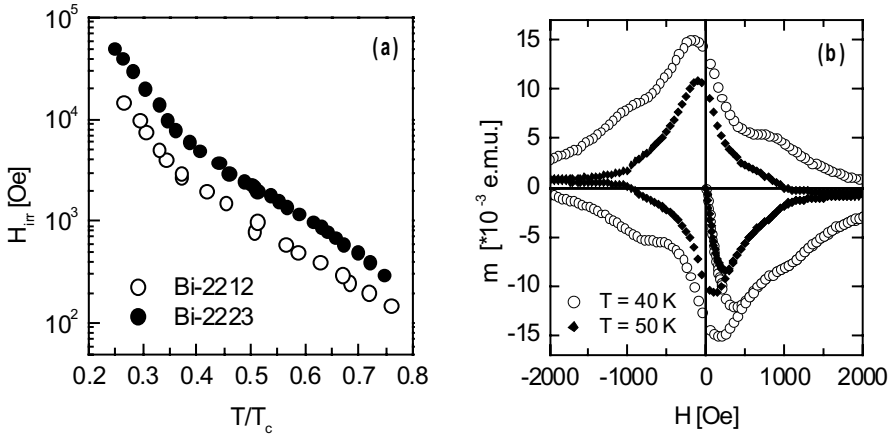


Fig. 6. (a) Irreversibility fields of Bi-2223 and Bi-2212 crystals plotted as a function of reduced temperature. (b) $m(H)$ loops at $T = 40$ and 50 K. The second peak is pronounced at 40 K but ($H_{peak} = 800$ Oe) and almost negligible at $T = 50$ K

The occurrence of the second peak in the magnetisation $m(H)$ loops have also been recently reported [58, 64, 66]. This phenomenon has been observed and widely investigated in many superconducting compounds (LSCO [79], Y-123 [80], RE-123 [81], Bi-2212 [82], Tl-2212 [83], Hg-1201 [84], Hg-1223 [85]), but it was not observed in Bi-2223 until high-quality single crystals became available. The second magnetisation peak is directly dependent on the amount of disorder in the crystal, and marks a transition of the vortex lattice from an ordered Bragg-glass to a disordered entangled glass state [86]. The second magnetisation peak

of Bi-2223 crystals is shown in Fig. 6(b). The second peak is visible in a limited range of field and temperature, $T \sim 25 - 45$ K and $H = 600 - 900$ Oe. The same H-T range for the occurrence of the second peak in the hysteresis loops is reported by Shimizu et al. [58] in Bi-2223 crystals grown also by the TSFZ method. This indicates that crystals grown by different groups by using a similar crucible-free TSFZ method exhibit a low and comparable amount of disorder. To the best of our knowledge, neither the IL nor the second peak effect of Bi-2223 crystals grown with other techniques have been reported in the literature.

The irreversibility line, the second peak effect and the lower critical field of Bi-2223 crystals are plotted together as a function of the temperature in Fig. 7 in order to trace the H-T phase diagram of this material, according to Giannini et al. [87]. The phase diagram of the Pb-free Bi-2223 phase is found to be qualitatively very similar to that of the Pb-free Bi-2212 phase (see Fig. 12 and ref. [88]), apart from the enlarged 3-dimensional region in the 3-layer compound. This is due to the reduced anisotropy of the Bi-2223 phase, as discussed in the previous section. The irreversibility line can be modelled as the melting of the vortex lattice based on the Lindemann criterion coupled with 2- and 3-dimensional fluctuation [89], at high and low magnetic fields, respectively. The result is shown by the solid and dashed curves in Fig. 7. The crossover from a 3D to a 2D behaviour of the vortex lattice, corresponding to the change in the concavity of the IL, occurs at a field higher than the second peak in the magnetisation loops and is marked by the horizontal dashed line in Fig. 7.

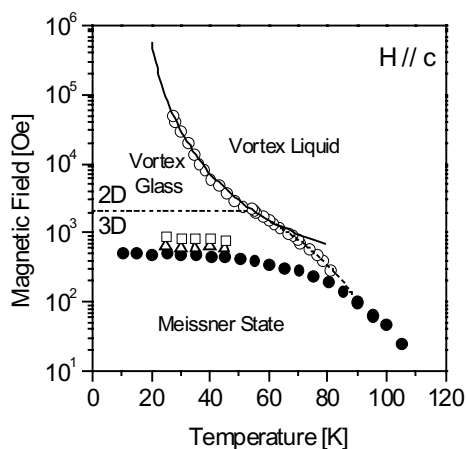


Fig. 7. *H-T* phase diagram of Pb-free Bi-2223. Symbols indicate (●) H_{c1} , (○) IL, (△) onset of the second magnetisation peak (SP), (□) peak of SP. The solid (dashed) line is the fit to the Lindemann melting model coupled with 2- (3-) dimensional vortex fluctuations. The horizontal dashed line marks the crossover from 3D to 2D vortex lattice.

The critical current density, J_c , was obtained from magnetisation measurements and is reported in Fig. 8(a). The comparison with J_c values measured in Bi-2212 crystals is shown by taking into account the different transition temperatures of the two compounds [64]. As expected, due to the lower anisotropy and the higher irreversibility fields, the critical current

density is always higher in Bi-2223 than in Bi-2212. As the temperature increases, J_c drops down to very low values, even if the decrease of J_c occurs more slowly than in Bi-2212. J_c was found to be $\approx 10^6$ A/cm² at $T = 10$ K and $\mu_0 H = 0$ T and $J_c > 10^5$ A/cm² at $\mu_0 H = 5$ T, but drops down at $J_c = 10^4$ A/cm² at $T = 60$ K and zero field. Similar results are reported by Shimizu et al. [58] and Shimoyama et al. [66].

Chu and McHenry [65] measured the critical current in small Pb-doped Bi-2223 crystals grown by the fused-salt reaction technique. An AC inductive method was employed for determining J_c and the dependence of J_c on the temperature was reported. The critical current density in zero field was found to be as high as 10^7 A/cm² at 5 K and to drop down to $\sim 2 \times 10^5$ A/cm² at 77 K. These values appear to be surprisingly large if compared to more recent reports (as reviewed above). This could be ascribed to a higher intrinsic disorder in Bi-2223 crystals grown using a KCl flux as a solvent.

The relaxation rate $S = d \ln M / d \ln t$ of the magnetisation was measured in Pb-free Bi-2223 crystals and is compared to the one of the Bi-2212 phase in Fig. 8(b) as a function of the applied field [35, 64]. The relaxation rate of Bi-2223 depends very weakly on the applied field, as a consequence of its reduced anisotropy. However, its average value remains close to the one of Bi-2212 at zero field. This result confirms the higher potential of Bi-2223 compared to Bi-2212 for magnet fabrication, even if lower values of S are needed for magnets operating in the persistent mode.

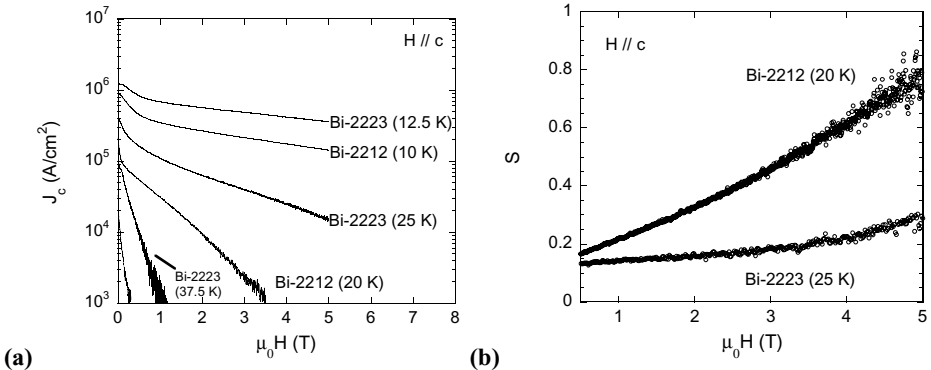


Fig. 8. (a) Critical current density $J_c(H)$ of Bi-2223 and Bi-2212 crystals compared at the same T/T_c (data from ref. [64]). **(b)** Magnetic relaxation rate of Bi-2223 and Bi-2212 crystals as reported by Clayton et al. [64]. These results show the better pinning properties of Bi-2223.

Even if the vortex pinning is more effective in Bi-2223 than in Bi-2212, one can generally state that intrinsic pinning in Bi-based HTS is weak. This is one of the most limiting factors for power applications of Bi-based superconducting wire and tapes, that makes these materials less suitable than second generation coated conductors based on Y-123 for carrying high currents in magnetic fields. The pinning properties of HTS materials can be improved by either proton or heavy ion irradiation. These techniques have been found to be suitable for increasing J_c and H_{irr} in Bi-2223 tapes [90, 91] and have been successfully employed for improving the pinning properties of Bi-2223 single crystals [65, 66].

In proton irradiated Bi-2223 crystals the critical current density was found to be enhanced by a factor of 2-3 (at zero field) with respect to non-irradiated crystals [65], but no field dependence of J_c was reported. A larger enhancement of the critical current density (by a factor of > 10) was observed in Bi-2223 crystals irradiated with Pb ions, and values of $J_c = 10^7$ A/cm² at $T = 10$ K, $\mu_0 H = 0$ T, and $J_c \approx 2 \times 10^5$ A/cm² at $T = 77$ K, $\mu_0 H = 0$ T were reported [66]. One should notice, however, that heavy ion irradiation is effective in adding strong pinning centres due to columnar defects in small crystals, but cannot be effectively used for artificially improving the transport properties of wires and tapes. Alternative techniques for artificially improving the pinning properties of Bi-based superconductors for industrial applications have to be found, either by adding chemical disorder due to atomic substitutions or by reducing the superconducting anisotropy thus stiffening the vortex lattice. This has been successfully done in Bi-2212 and will be the subject of the next section.

5. STRUCTURE AND SUPERCONDUCTING PROPERTIES OF MODULATION-FREE (Bi,Pb)₂Sr₂Ca₁Cu₂O_{8+ δ}

Partial substitution of Bi by Pb in the Bi-2212 phase was found to remarkably improve the flux pinning properties and enhance J_c above a critical Pb content by Chong et al. [92]. It is worth noting that the J_c enhancement due to strong Pb doping in Bi-2212 is even higher than that obtained by ion irradiation [93]. The transition temperature was also found to rise up to $T_c = 96$ K in strongly Pb-doped crystals at the optimal oxygen doping.

Heavy Pb doping was found to induce a phase separation inside the Bi,Pb-2212 crystals, into a Pb-rich (β) and a Pb-poor (α) phase, thus creating very effective pinning centres at the α - β phase interface. A characteristic microstructure of alternating stripes of 10-50 nm was observed by TEM, and modulation-free lamellae were identified as being made of the Pb-rich Bi-2212 phase [94]. A TEM picture showing the two-phase structure of a Bi_{1.4}Pb_{0.6}Sr₂CaCu₂O_{8+ δ} crystal grown at DPMC in Geneva is reported in Fig. 9(a) [35]. By progressively increasing the starting amount of doping Pb in the Bi-2212 phase, the volume of the Pb-rich phase increases and a systematic shift of the irreversibility line was observed, being more pronounced above $y = 0.4$ and at high temperatures. Correspondingly, J_c was strongly enhanced in crystals with high Pb content, as reported in [94] and [95] and shown in Fig. 9(b). By increasing the nominal Pb content (but without changing the crystal growth conditions from one Pb content to another), the wavelength of the modulation in Bi,Pb-2212 was found to increase, as observed by Hiroi et al. [94] in electron diffraction experiments. The reduction and even suppression of the modulation in Pb-doped Bi-2212 crystals was reported first by Fukushima et al. [96]. Inside β -phase regions of crystals with a nominal Pb content of $y = 0.7$ the modulation wavelength was found to be as large as $11b$ [94].

Single crystals of strongly Pb-doped Bi-2212 with a nominal Pb content up to $y = 0.8$ have been grown at the DPMC in Geneva by a slow cooling technique in homemade BaZrO₃ crucibles. The growth process was performed in a vertical 3-zone furnace under controlled atmosphere and the weight of the crucible was continuously monitored [35,88,95]. Such a growth technique reduces the Pb losses occurring at high temperature, thus allowing to grow crystals with high Pb content.

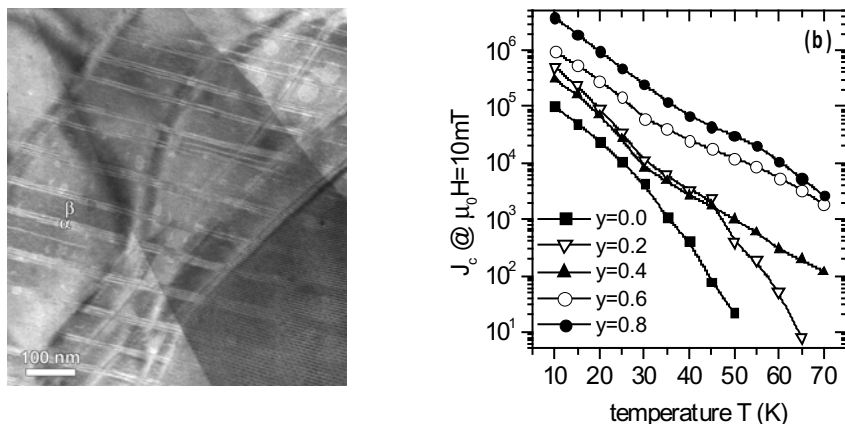


Fig. 9. (a) TEM image of a $y = 0.6$ crystal. Lamellae of Pb-rich modulation-free (β) and modulated Bi-poor domains (α) are visible [35]. (b) Critical current density J_c of Pb-doped crystals as a function of T for various nominal Pb doping, as reported by Dhallé et al. [95].

The actual Pb content corresponding to a nominal composition $\text{Bi}_{1.4}\text{Pb}_{0.8}\text{Sr}_2\text{CaCu}_2\text{O}_{8+\delta}$ was found to be $y^* = 0.4$.

In crystals with such a strong Pb doping an interesting phenomenon was observed, the disappearance of the lamellar microstructure as well as of the structure modulation, that provided a new key for understanding the origin of the pinning enhancement due to strong Pb doping in Bi-2212 [35]. In $y = 0.8$ doped crystals, the critical current density is higher than in crystals containing lower amounts of Pb, as shown in Fig. 9(b) and the critical temperature was measured to be $T_c = 93$ K. Neither electron diffraction (by TEM) nor single crystal X-ray diffraction (XRD) provided any evidence of satellites in the diffraction patterns, thus proving that the structure of these crystals does not exhibit any modulation. Both X-ray and electron diffraction patterns of modulated ($y = 0$) and modulation free ($y = 0.8$) crystals are compared in Fig. 10(a-d), as reported in [25] and [35]. It is worth noticing that the absence of satellites is commonly observed in TEM images of strongly Pb-doped Bi-2212 crystals, but it has been observed only recently in XRD patterns, that confirms the absence of modulation over the whole crystal.

The structure of the modulation-free Bi,Pb-2212 phase has been recently refined by Gladyshevskii et al. [25] in space group $A2aa$, with cell parameters $a = 5.3852(9)$, $b = 5.4286(9)$, and $c = 30.997(6)$. As reported in [25], the distance between two adjacent BiO layers is reduced in the modulation free phase as compared to the modulated one (from 3.22 \AA to 3.09 \AA), even if the c -axis parameter is slightly larger in the former. A shortening of the distance between BiO layers in modulation-free Y-doped Bi,Pb-2212 was also reported [97]. This has important implications on the superconducting properties of these material, because a shortening of the thickness of the block layer implies a large overlap of the order parameters and therefore a reduction of the superconducting anisotropy.

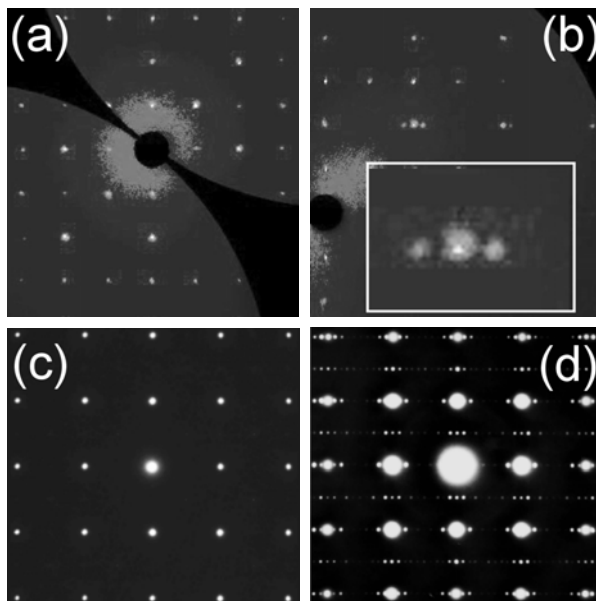


Fig. 10. (a) XRD pattern of a crystal of a refined composition $\text{Bi}_{1.7}\text{Pb}_{0.4}\text{Sr}_2\text{Ca}_{0.9}\text{Cu}_2\text{O}_{8+\delta}$ (corresponding to a nominal $y = 0.8$). No satellites are visible in the $[hk0]$ plane. (b) The XRD pattern of an undoped Bi-2212 crystal shows the satellites due to structure modulation. (c) TEM image of the same crystal as in (a). (d) TEM image of the same crystal as in (b).

The anisotropy of the modulation-free Pb-doped crystals was obtained from the measurement of the lower critical field, H_{c1} , with the applied field first parallel then perpendicular to the c -axis, as described in Section 4.1 for the Bi-2223 phase.

The anisotropy of the modulation-free Bi,Pb-2212 phase was found to be $\gamma = 25$, much lower than in modulated Pb-free crystals ($\gamma = 165$) and even lower than in Pb-free Bi-2223 ($\gamma \approx 50$) [35, 64]. As a consequence of the reduced anisotropy, the vortex lattice is stiffened and the region of the H - T phase diagram where the behaviour of the vortex lattice is 3D-like is enlarged. This is confirmed by the enhancement of the irreversibility field $H_{\text{irr}}(T)$ reported by Musolino et al. [35] in modulation-free Bi,Pb-2212 crystals. The irreversibility field is enhanced by a factor of ~ 5 at any temperature and becomes comparable to the IL of the Bi-2223 phase (see Section 4.2). At $T = 30$ K, H_{irr} was found to be $\sim 2 \times 10^4$ Oe in the modulation-free Bi-2212 phase, compared to $\sim 4 \times 10^3$ Oe in the modulated one. We can compare directly the two Bi-2212 phases (with and without modulation) to the Bi-2223 phases, as shown in Fig. 11 by plotting the three irreversibility lines as a function of the reduced temperature. One can immediately see the direct correlation between the irreversibility field and the superconducting anisotropy, which is $\gamma = 25$, 50, and 165 for Pb-doped Bi-2212, Pb-free Bi-2223, and Pb-free Bi-2212, respectively.

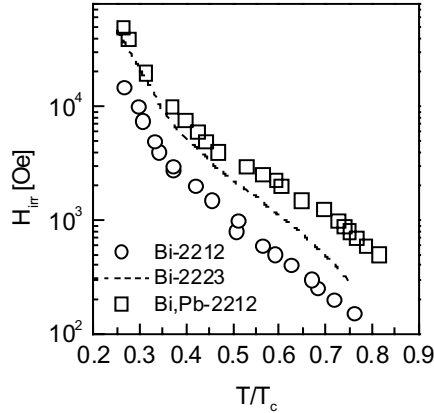


Fig. 11. Comparison of the irreversibility field $H_{irr}(t)$ of Pb-free Bi-2212, strongly Pb-doped Bi-2212 (not modulated) and Pb-free Bi-2223. Data are plotted as a function of T/T_c in order to compare phases with different critical temperatures.

The enhancement of the irreversibility line in modulation-free Bi-2212 is due to the strong reduction of anisotropy caused by the structural modification rather than to the addition of effective pinning centres.

These results provide a new key for the understanding of the role of the Pb doping in improving the superconducting properties of the Bi-2212 phase. The Pb doping is not only responsible for the formation of the lamellar structure and the phase separation between a Pb-rich and Pb-poor phase, thus creating additional pinning centres. The Pb doping has a strong influence on the structure of the block layer and leads to the formation of a Bi,Pb-2212 phase with better superconducting properties, if compared to the Pb-free modulated phase. In Bi,Pb-2212 crystals containing intermediate amount of Pb (nominal $y = 0.4 - 0.7$) and exhibiting the lamellar structure, the improvement of the pinning properties and the enhancement of J_c can be a consequence of both the stiffening of the vortex lattice and the addition of effective pinning centres at the α - β phase interface. This also suggests that improving the pinning properties of such superconducting materials via a chemical doping can be more effective than adding pinning centres artificially. In view of technological applications of conductors based on Bi-based cuprates, this is a very encouraging results, being the artificial methods for improving the flux pinning not suitable for the fabrication of long wires and technical devices.

Unfortunately, a similar improvement has not been observed so far either in polycrystalline tapes or in powder samples, and a strong research effort is still needed in order to scale up from small single crystals to large polycrystalline conductors.

The vortex phase diagram of the modulation-free Bi-2212 phase has been recently investigated and is reported in [88]. The H - T phase diagrams of Pb-free and Pb-doped Bi-2212 are shown in Fig. 12(a) and (b), respectively.

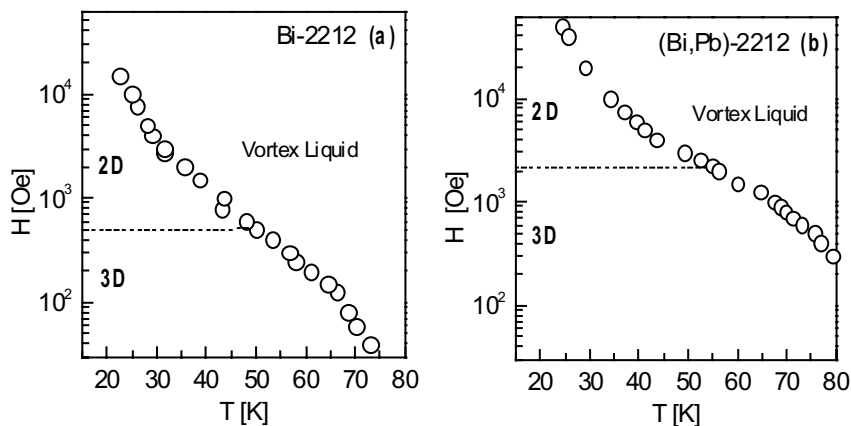


Fig. 12. H-T phase diagrams of the modulated (a) and modulation-free (b) Bi-2212 phases. The dimensional crossover (3D-2D) occurs at higher fields in modulation-free Bi-2212, as marked by the dashed horizontal lines.

The dimensional crossover of the vortex lattice from a 3D to a 2D behaviour (marked by dashed lines in Fig. 12 (a) and (b)) was found to shift to higher fields, even higher than in Bi-2223 (see Fig. 7). Moreover, in modulation-free Bi-2212, the dimensional crossover takes place at fields much higher than the second peak of the magnetisation loops. This confirms that the interpretation of the second peak as a dimensional crossover of the vortex lattice is not correct and can be accepted only in case of extreme anisotropy of the material. The second peak is related to the disorder in the crystal and the values of H_{pk} measured in Pb-free and Pb-doped Bi-2212 crystals are of the same order of magnitude ($\sim 5 \times 10^2$ Oe and $\sim 2 \times 10^2$ Oe, respectively). In modulation-free Bi,Pb-2212, a significant amount of disorder was found to be present [88].

6. CONCLUDING REMARKS

The structure and general features of Bi-based superconducting cuprates are reviewed with a particular emphasis on the recent results obtained on single crystals of Bi,Pb-2212, Bi-2223 and Bi,Pb-2223. Various growth processes employed for these crystals have been described, including the newly developed Vapour-Assisted Travelling Solvent Floating Zone (VA-TSFZ) method, particularly suitable for growing crystals containing volatile elements, like Bi,Pb-2223. Structural quality and superconducting properties of crystals grown using different techniques have been compared and discussed. Large and pure crystals of Bi-based superconducting cuprates are nowadays produced by means of TSFZ method.

So far, only the average structure of Bi-2223 and Bi,Pb-2223 was known, as determined by powder diffraction. The availability of large single crystals of high purity allowed to refine for the first time the crystal structure of the Bi,Pb-2212, Bi-2223 and

Bi,Pb-2223 compounds from single crystal XRD data and to determine the superstructure parameters.

The superconducting properties have been investigated and have been summarised in this article. Lower critical fields, anisotropy, penetration depth, irreversibility fields and critical current density of the three phases Bi,Pb-2212, Bi-2223 and Bi,Pb-2223 have been compared. In particular, the origin of the structure modulation and its effect on the superconducting properties has been discussed.

Thanks to the availability of crystals of sufficient quality of all the members of the Bi-based family, a general understanding of the fundamental features of these superconducting compounds is being achieved.

REFERENCES

- [1] J.G. Bednorz and K.A. Müller, *Z. Phys.* 64 (1986) 189.
- [2] C. Michel, M. Hervieu, M.M. Borel, A. Grandin, F. Deslandes, J. Provost, and B. Raveau, *Z. Phys. B* 68 (1987) 421.
- [3] J.M. Tarascon, Y. LePage, P. Barboux, B.G. Bagkley, L.H. Greene, W.R. McKinnon, G.W. Hull, M. Giroud, and D.M. Hwang, *Phys. Rev. B* 37 (1988) 9382.
- [4] H. Maeda, Y. Tanaka, M. Fukutomi, and T.Asano, *Jpn. J. Appl. Phys.* 27 (1988) L209.
- [5] H.W. Zandbergen, Y.K. Huang, M.J.V. Menken, J.N. Li, K. Kadowaki, A.A. Menovsky, G. vanTendeloo, and S. Amelinckx, *Nature* 332 (1988) 620.
- [6] S.A. Sunshine, T. Siegrist, L.F. Schneemeyer, D.W. Murphy, R.J. Cava, B. Batlogg, R.B. van Dover, R.M. Fleming, S.H. Glarum, S. Nakahara, J.J. Krajewski, S.M. Zahurak, J.V. Waszczak, J.H. Marshall, P. Marsh, L.W. Rupp Jr. and W.F. Peck, *Phys. Rev. B* 38 (1988) 893.
- [7] M. Mimura, H. Kumakura, K. Togano and H. Maeda, *Appl. Phys. Lett.* 54(16) (1989) 1582.
- [8] Y. Yamada, B. Obst and R. Flükiger, *Supercond. Sci. Technol.* 4 (1991) 165.
- [9] S. Patnaik, D.M. Feldmann, A. Polyanskii, Y. Yuan, J. Jiang, X.Y. Cai, E.E. Hellstrom, D.C. Larbalestier, and Y. Huang, *IEEE Trans. Appl. Supercond.* 13(2) (2003) 2930.
- [10] R. Gladyshevskii and P. Galez, *Crystal Structures of High-Tc Superconducting Cuprates*, Handbook of Superconductivity, Academic Press (2000) 267.
- [11] H. Leligny, S. Dur ok, P. Labbe, L. Ledesert, and B. Raveau, *Acta Cryst. B* 48 (1992) 407.
- [12] Y. Gao, P. Lee, P. Coppens, M.A. Subramanian, and A.W.Sleight, *Science* 241 (1988) 954.
- [13] H.W. Zandbergen, W.A. Groen, F.C. Mijlhoff, G. vanTendeloo, and S. Amelinckx, *Phys. C* 156 (1988) 325.
- [14] S. Ikeda, K. Aota, T. Hatano, and K. Ogawa, *Jpn. J. Appl. Phys.* 27 (1988) L2040.
- [15] V. Petricek, Y. Gao, P.Lee, and P.Coppens, *Phys. Rev. B* 41(1) (1990) 387.
- [16] M. Onoda and M.Sato, *Solid State Comm.* 67 (1988) 799.
- [17] R.E. Gladyshevskii and R. Flükiger, *Acta Cryst. B* 52 (1996) 38.
- [18] N. Jakubowicz, D. Grebille, M. Hervieu, and H. Leligny, *Phys. Rev. B* 63 (2001) 214511.
- [19] A.V. Mironov, A.M. Abakumov, and E.V. Antipov, *The Rigaku Journal* 19(2) - 20(1) (2003) 23.
- [20] P.A. Miles, S.J.Kennedy, G.J. McIntyre, G.D. Gu, G.J. Russel, and N. Koshizuka, *Phys. C* 294 (1998) 275.
- [21] T. Fujii, T. Watanabe, and A. Matsuda, *J. Cryst. Growth.* 223 (2001) 175.
- [22] B. Liang, C.T. Lin, P. Shang, and G. Yang, *Phys. C* 383 (2002) 75.
- [23] E. Giannini, V. Garnier, R. Gladyshevskii, and R. Flükiger, *Supercond. Sci. Technol.* 17 (2004) 220.
- [24] R. Gladyshevskii, R. Cerny, and E. Giannini, to be published.
- [25] R. Gladyshevskii, N. Musolino, and R. Flükiger, *Phys. Rev. B* (2004), at press.
- [26] H. Rajagopal, A. Sequeira, J. V. Yakhmi, P.V.P.S.S. Sastry, and R.M. Iyer, *Jpn. J. Appl. Phys.* 32 (1993) 1595.

- [27] H. Leligny, S. Dur ok, P.Labbe, M.Ledesert, and B. Raveau, *Acta Cryst. B* **48** (1992) 407-418.
- [28] A.V. Mironov, and E.V.Antipov, MSU-HTSC V Conference, March 24-29, 1998, Moscow, Russia.
- [29] N.R. Khasanova, and E.V. Antipov, *Phys. C* 246 (1995) 241.
- [30] E. Bellingeri, G. Grasso, R.E. Gladyshevskii, M. Dhallé, and R. Flükiger, *Phys. C* 329 (2000) 267.
- [31] S. Kuwata, and W. Kinase, *Jpn. J. Appl. Phys.* 32(2) (1993) 764.
- [32] Y. Zhang, J. Zhang, S. Tan, and G. Xu, *Phys. C* 341-348 (2000) 643.
- [33] J. Zhang, C. Zhang, S. Tan, G. Xu, and Y. Zhang, *Supercond. Sci. Technol.* 14 (2001) 599.
- [34] J. Hadermann, N. R. Khasanova, G. van Tendeloo, A.M. Abakumov, M.G.Rozova, A.M. Alekseeva, and E. V. Antipov, *J. Solid State Chem.* 156 (2001) 445.
- [35] N. Musolino, S. Bals, G. van Tendeloo, N. Clayton, E. Walker, and R. Flükiger, *Phys. C* 399 (2003) 1.
- [36] W. Wong-Ng, L.P. Cook, A. Kearsley, and W. Greenwood, *J. Res. Natl. Inst. Stand. Technol.* 104 (1999) 277.
- [37] W. Assmus and W. Schmidbauer, *Supercond. Sci. Technol.* 6 (1993) 555.
- [38] N.L. Wang, B. Buschinger, C. Geibel, and F. Steglich, *Phys. Rev. B* 54(10) (1996) 7449.
- [39] W.L. Yang, H.H. Wen, Y.M. Ni, J.W. Xiong, H. Chen, C. Dong, F. Wu, Y.L. Qin, and Z.X. Zhao, *Phys. C* 308 (1998) 294.
- [40] J.I. Gorina, G.A. Kaljuzhnaia, V.P. Martovitsky, V.V. Rodin, and N.N. Sentjurina, *Solid State Comm.* 108(5) (1998) 275.
- [41] I. Chong, T. Terashima, Y. Bando, M. Takano, Y. Matsuda, T. Nagaoka, and K. Kumagai, *Phys. C* 290 (1997) 57.
- [42] B. Liang, A. Maljuk, and C. T. Lin, *Phys. C* 361 (2001) 156.
- [43] X. Zhao, X. Sun, X. Fan, W. Wu, X.G. Li, S. Guo, Z. Zhao, *Phys. C* 307 (1998) 265.
- [44] H. Funabiki, K. Okanoue, C. Takano, and K. Hamasaki, *J. Cryst. Growth* 259 (2003) 85.
- [45] A. Thamizhavel, D.P. Paul, D. Prabhakaran, R. Jayavel, and C. Subramanian, *Phys. C* 288 (1997) 163.
- [46] S. Kishida, M. Nakamura, and W.Y Liang, *J. Cryst. Growth* 216 (2000) 220.
- [47] O. Nagashima, H. Tanaka, Y. Ebara and S. Kishida, *Phys. C* 392-396 (2003) 505.
- [48] A. Kulakov, I.G. Naumenko, S.A. Zver'kov, A.V. Kosenko, S.S. Khasanov, I.K. Bdikin, G.A. Emelchenko, M. Fehlmann, L.J.Gaukler, G. Yang, and J.S. Abell, *J. Cryst. Growth* 231 (2001) 194.
- [49] T.W. Li, P.H. Kes, N.T. Hien, J.J.M. Franse, and A.A. Menovski, *J. Cryst. Growth* 135 (1994) 481.
- [50] I. Tanaka, T. Iwamoto, A.T.M.N. Islam, and S. Watauchi, *Supercond. Sci. Technol.* 15 (2002) 458.
- [51] B. Liang, C.T. Lin, *J. Cryst. Growth* 237-239 (2002) 756.
- [52] T. Mochiku, *Bismuth-based High-temperature Superconductors*, (Ed. H. Maeda and K. Togano), Marcel Dekker, Inc. Publishers, NY (1996), 227.
- [53] I.K. Bdikin, A.N. Maljuk, A.B. Kulakov, C.T. Lin, P. Kumar, B. Kumar, G.C. Trignunayat, and G.A. Emel'chenko, *Phys. C* 383 (2003) 431.

- [54] G. Balestrino, E. Milani, A. Paoletti, A. Tebano, Y.H. Wang, A. Ruosi, R. Vaglio, M. Valentino, and P. Paroli, *Appl. Phys. Lett.* 64(13) (1994) 1735.
- [55] S. Chu and M. McHenry, *J. Mater. Res.* 13(3) (1998) 589.
- [56] J.I. Gorina, G.A. Kaljuzhnaia, V.P. Martovitsky, V.V. Rodin, N.N. Sentjurina, and V. Stepanov, *Solid State Commun.* 110 (1999) 287.
- [57] S. Lee, S. Yamamoto, and S. Tajima, *Phys. C* 357-360 (2001) 341.
- [58] K. Shimizu, T. Okabe, S. Horii, K. Otszchi, J. Shimoyama, and K. Kishio, *Mat. Res. Soc. Symp. Proc.* 689 (2002) 71.
- [59] A. Revcolevschi and J. Jegoudez, *Progress Mater. Sci.* 42 (1997) 321.
- [60] T. Watanabe, T. Fujii, and A. Matsuda, *Recent Res. Devel. Physics* 5 (2004) 51.
- [61] W. Zhu and P.S. Nicholson, *J. Appl. Phys.* 73(12) (1992) 8423.
- [62] M. Lomello-Tafin, E. Giannini, E. Walker, P. Cerutti, B. Seeber, and R. Flükiger *IEEE Trans. Appl. Supercond.* 11(1) (2001) 3438.
- [63] E. Giannini, I. Savvysuk, V. Garnier, R. Passerini, P. Toulemonde, and R. Flükiger, *Supercond. Sci. Technol.* 15 (2002) 1577.
- [64] N. Clayton, N. Musolino, E. Giannini, V. Garnier, and R. Flükiger, *Supercond. Sci. Technol.* 17 (2004) S563.
- [65] S. Chu and M.E. McHenry, *Phys. C* 337 (2000) 229.
- [66] J. Shimoyama, K. Shimizu, S. Ueda, S. Horii, K. Otszchi, K. Kishio, and N. Chikumoto, *Phys. C* 378-381 (2002) 457.
- [67] T. Fujii, I. Terasaki, T. Watanabe, and A. Matsuda, *Phys. Rev. B* 66 (2002) 024507.
- [68] A.V. Boris, D. Munzar, N.N. Kovaleva, B. Liang, C.T. Lin, A. Dubroka, A.V. Pimenov, T. Holden, B. Keimer, Y.-L. Mattis, and C. bernhard, *Phys. Rev. Lett.* 89 (2002) 277001.
- [69] N.N. Kovaleva, A.V. Boris, T. Holden, C. Ulrich, B. Liang, C.T. Lin, B. Keimer, C. Bernhard, J.L. Tallon, D. Munzar, A.M. Stoneham, *Phys. Rev. B* 69 (2004) 054511.
- [70] F. Carbone, H.J.A. Moelgraaf, A.B. Kuzmenko, E. van Heumen, E. Giannini, and D. van der Marel, *Phys. Rev. B*, submitted
- [71] M. Kugler, G. Levy de Castro, E. Giannini, A. Piriou, A. A. Manuel, C. Hess and Ø. Fischer, *J. Phys. Chem. Solids*, submitted.
- [72] I. Matsubara, H. Tanigawa, T. Ogura, H. Yamashita, and M. Kinoshita, *Phys. Rev B* 45 (1992) 7414.
- [73] M. Niederöst, R. Frassanito, M. Sallfrank, A.C. Mota, G. Blatter, V.N. Zavaritsky, W.T. Lin, and P.H. Kes, *Phys. Rev. Lett.* 81 (1998) 3231.
- [74] G. Blatter, M.V. Feigel'man, V.B. Geshkenbein, A.I. Larkin, and V.M. Vinokur, *Rev. Mod. Phys.* 66 (1994) 1125.
- [75] Y. Kopelevich, S. Moehlecke, and J. H. S. Torres, *Phys. Rev. B* 49 (1994) 1495.
- [76] G. Triscone, M.S. Chae, M.C. de Andrade, and M.B. Maple, *Phys. C* 290 (1997) 188.
- [77] J.W. Loram, J.L. Tallon, and W.Y. Liang, *Phys. Rev. B* 69 (2004) 060502(R).
- [78] J.G. Chandler, J. Jiang, X.Y. Cai, L.A. Schwartzkopf, and D.C. Larbalestier, *IEEE Trans. Appl. Supercond.* 13(2) (2003) 2945.
- [79] T. Kimura, K. Kishio, T. Kobayashi, Y. Nakayama, N. Motohira, K. Kitazawa, and K. Yamafuji, *Phys. C* 192 (1992) 247.
- [80] A.A. Zhukov, H. Kupfer, G. Perkins, L.F. Cohen, A.D. Caplin, S.A. Klestov, H. Claus, V.I. Voronkova, T. Wolf, and H. Wuhl, *Phys. Rev. B* 51(18) (1995) 12704.

- [81] M.R. Koblishka, A.J.J. van-Dalen, T. Higuchi, K. Sawada, S.I. Yoo, and M. Murakami, *Phys. Rev. B* 54(10) (1996) R6893.
- [82] C. Bernhard, C. Wenger, Ch. Niedermayer, D.M. Pooke, J.L. Tallon, Y. Kotaka, J. Shimoyama, K. Kishio, D.R. Noakes, C.E. Stronach, T. Sembiring, and E.J. Ansaldo, *Phys. Rev. B* 52(10) (1995) R7050.
- [83] P. Chowdhury, H.J. Kim, I.S. Jo, and S.I. Lee, *Phys. C* 384(3) (2003) 411.
- [84] M. Pissas, E. Moraitakis, G. Kallias, A. Terzis, D. Niarchos, and M. Charalambous, *Phys. Rev. B* 58(14) (1998) 9536.
- [85] S. Lee, T. Akao, H. Suematsu, H. Yamauchi, N.P. Kiryakov, D.A. Emelyanov, and M.S. Kuznetsov, *Appl. Phys. Lett.* 73(24) (1998) 3586.
- [86] T. Giamarchi, and P. Le Odussal, *Phys. Rev. B* 55(10) (1997) 6577.
- [87] E. Giannini, N. Clayton, N. Musolino, A. Piriou, R. Gladyshevskii, and R. Flükiger, presented at the ASC04 conference, October 3-8, 2004, Jacksonville, USA.
- [88] N. Musolino, N. Clayton, and R. Flükiger, *Phys. C* (2004), at press.
- [89] A. Schilling, R. Jin, J.D. Guo, and H.R. Ott, *Phys. Rev. Lett.* 71 (1993) 1899.
- [90] L. Civale, A.D. Marwick, R. Wheeler, M.A. Kirk, W.L. Carter, G.N. Riley, and A.P. Malozemoff, *Phys. C* 208(1-2) (1993) 137.
- [91] B. Hensel, F. Marti, G. Grasso, M. Dhalle, R. Flukiger, F. Paschoud, and M. Victoria, *IEEE Trans. Appl. Supercond.* 7(2) (1997) 2030-3.
- [92] I. Chong, Z. Hiroi, M. Izumi, J. Shimoyama, Y. Nakayama, K. Kishio, T. Terashima, Y. Ando, and M. Takano, *Science* 276 (1997) 770-773.
- [93] J. Shimoyama, Y. Nakayama, K. Kitazawa, K. Kishio, Z. Hiroi, I. Chong, and M. Takano, *Phys. C* 281 (1997) 69-75.
- [94] Z. Hiroi, I. Chong, and M. Takano, *J. Solid State Chem.* 138 (1998) 98-110.
- [95] M. Dhallé, C. Beneduce, N. Musolino, R. Gladyshevskii, E. Walker, and R. Flükiger, *IEEE Trans. Appl. Supercond.* 11(1) (2001) 3643-6.
- [96] N. Fukushima, H. Niu, S.H. Nakamura, S. Takeno, M. Hayashi, and K. Ando, *Phys. C* 159 (1989) 777-783.
- [97] G. Calestani, M.G. Francesconi, G. Salsi, and G.D. Andreotti, *Phys. C* 197 (1992) 283.

(RE)Ba₂Cu₃O₇ COATED CONDUCTORS FOR AC AND DC APPLICATIONS

Bartek A. Glowacki^{1,2}

¹ Department of Materials Science and Metallurgy, University of Cambridge,
Pembroke Street, Cambridge CB2 3QZ, England

² IRC in Superconductivity, Cavendish Lab. University of Cambridge,
Madingley Road, West Cambridge Site, Cambridge CB3 0HE, England

1. INTRODUCTION

Despite tremendous efforts in research and development after the discovery of high temperature perovskite-type layered superconductors, and high expectations expressed in market projection potential electrical commercial applications of these materials, they are taking off very slowly. Therefore the updated original comparative prediction of the market for the low temperature superconductors, LTS, and high temperature superconductors, HTS, is presented in Fig.1 where there is no cross over between the LTS and HTS if (RE)Ba₂Cu₃O₇ conductors are not going to be available commercially. This is because different applications of superconductivity require the simultaneous fulfilment of diverse thermal, mechanical and electromagnetic specifications; the potential to operate at higher temperatures is not the decisive factor except for transmission lines and transformers. Medical care which is mostly represented by magnetic resonance applications based on LTS will grow, and in 2010 should reach 15M€/year.

One of the biggest hurdles to the widespread application of the YBCO conductor is developing a manufacturing process that will produce it in long lengths and at prices competitive to copper for applications such as motors, generators, transmission cables, and other power systems. We have learned that the powder-in-tube process, PIT, which is successful in the manufacturing of low temperature superconductors like Nb₃Sn, medium

temperature superconductor MgB_2 and high temperature Bi-family superconductors cannot be used for YBCO conductors due to its granularity and ceramic-like mechanical bulk properties.

The long length coated conductors were developed successfully for the Nb_3Sn [1], Nb_3Ge , MgB_2 [2], $\text{Bi}_2\text{Sr}_2\text{CaCu}_2\text{O}_{8+x}$ [3] compounds, where $\text{YBa}_2\text{Cu}_3\text{O}_7$ with superior properties are under development. The increased performance of $\text{YBa}_2\text{Cu}_3\text{O}_7$ coated conductors in comparison to others is due to differences in materials rather than the processes, and it is important to notice that in all other cases the choice of industry are round multifilamentary Nb_3Sn , MgB_2 and $\text{Bi}_2\text{Sr}_2\text{CaCu}_2\text{O}_{8+x}$ wires, not flat coated conductors. However in the case of $\text{YBa}_2\text{Cu}_3\text{O}_7$ conductors, there are alternative processes for continuous formation of the $\text{YBa}_2\text{Cu}_3\text{O}_7$ in the form of fibres [4], but further development will probably take place once the coated conductor shows its final limitations. We have many examples of attempts to scale-up $\text{YBa}_2\text{Cu}_3\text{O}_7$ coated conductor processing but presently there is no infrastructure for making long length coated conductors due to the great uncertainty about which type and which deposition process should be used.

The primary focus of this chapter is on $\text{YBa}_2\text{Cu}_3\text{O}_7$ high temperature superconducting coated conductors for power engineering applications particularly the optimisation of processing routes for the production of coated conductors.

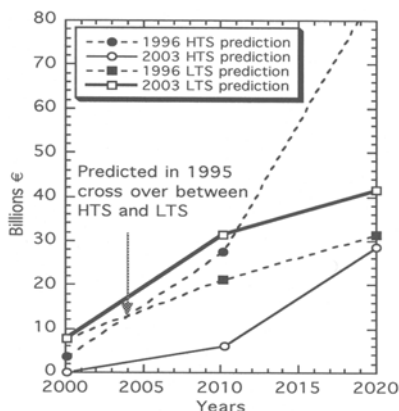


Fig.1. Projection of the LTS and HTS market, which is shared between electronics, power, industrial processing, medical care and transportation. 1995 estimation conducted at International Superconductivity Industry Summit, Yamanashi 1996, numbers corrected according to data in early 2003 (solid lines).

2. MATERIAL DESIGN AND PROCESSES CONSIDERATIONS

For more than 18 years thin films of yttrium barium copper oxide, $\text{YBa}_2\text{Cu}_3\text{O}_7$, (YBCO) have demonstrated promising superconducting properties for use at liquid nitrogen temperatures with critical current density, J_c , (at 77 K) higher than 10^6 Acm^{-2} , and high irreversibility field, H_{irr} (77 K), Fig.2. There are four major categories of so-called coated conductors: (i) rolling-assisted, biaxially textured substrate, RABiTS (the RABiTS process achieves texture by

mechanical rolling of a face-centered cubic metal and subsequent heat treatment on which the subsequent epitaxial layers are build (such process of texturing of tonnes of 20 μm thick NiFe tapes was developed by industry [5] Fig 3a) in 1950 and was used in traction transformers; (ii) ion beam-assisted deposition, IBAD (the IBAD technique achieves biaxial texture by means of a secondary ion gun that orients an oxide film buffer layer while it is being deposited onto the polycrystalline metallic substrate, or the inclined substrate deposition processes, ISD, The ISD process achieves texture by inclining the substrate to the oxide plume, Fig.(3b); (iii) liquid phase epitaxy, LPE (the LPE process enable formation of the superconductor from the under-cooled supersaturated liquid and (iv) thermo-magnetic processing, TM (the thermo-magnetic assisted processing enables formation of the highly textured superconducting layers without the necessity of textured substrates, Fig.3c). The actual deposition of the layers on the metallic substrates can be divided into physical methods and chemical methods as presented in Table 1. All the different types of deposition techniques of buffer and superconductor such as: pulse laser deposition, PLD [6]; ion-beam assisted-deposition, IBAD, [6,7]; sputtering [8], chemical vapour deposition, CVD [9]; metal organic deposition, MOD, [10,11]; metal organic chemical vapour deposition, MOCVD [12]; thermal evaporation [13]; sol-gel deposition [14,15]; ink-jet printing and coating [16]; dip coating [17]; and liquid phase processing [18,19], Tab.1, have been used to manufacture shorter or longer pieces of the high temperature superconducting tapes on a laboratory scale [20,21]. There is an additional aspect to the multifilamentary conductor preparation, which is needed for AC applications [22]. The outline of the two main conductor architectures for DC and AC applications are presented in Fig.4 and the aspects concerning computer design and processing will be discussed in later paragraphs.

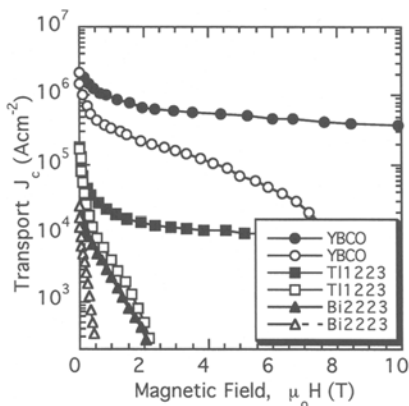


Fig.2. Critical current density versus magnetic field for $\text{YBa}_2\text{Cu}_3\text{O}_7$, $\text{Bi}_2\text{Sr}_2\text{CaCu}_2\text{O}_9$ and $\text{TlBa}_2\text{Ca}_2\text{Cu}_3\text{O}_9$. Solid symbols represent $B \parallel a-b$ where open symbols represent $B \perp a-b$. On the J_c vs ($B \perp a-b$) dependence three distinctive flux lattice pinning mechanisms can be observed: at lower fields a shear force of unpinned vortices around those strongly bound to defects takes place and the $J_c \sim B^{-1/2}$; at the intermediate fields there is a decrease in the elastic modulus of flux lattice and finally at the highest magnetic fields flux lattice melting is observed.

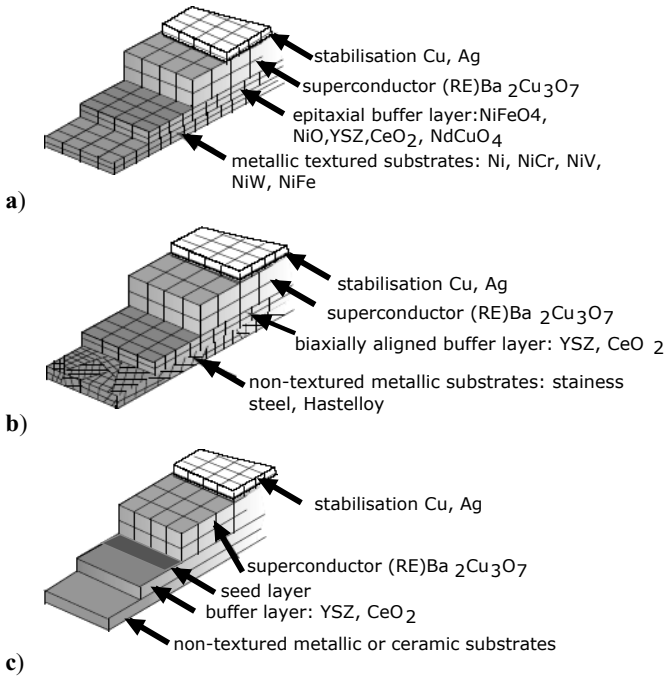


Fig.3. Schematic representation of different architectures of the coated conductors: **a)** RABiTS, such a tape is typically 10mm wide and is required to have a uniform high critical current over long lengths. The key conductor components are the metallic or ceramic substrate material, the buffer layer and the superconducting layer; the latter has to be biaxially textured throughout so that, although granular, the misorientation from grain to grain should be less than a few degrees; **b)** ion beam-assisted deposition, IBAD, or the inclined substrate deposition processes, ISD and; **c)** liquid phase epitaxy LPE or thermo-magnetic process. Adapted after ISTEC-SRL, Fujikura, Furukawa, Showa Electric.

The fundamental requirement relevant to all the architectural components of the fully engineered conductor is: they must be thin because important consideration in most applications is a flexibility and high value of engineering critical current density, J_e , defined as a critical current, I_c , carried by the superconducting layer divided by the total cross section of the conductor which includes the substrate and all the functional layers. Also the superconducting layer has to be highly textured along the ab-plane. A low value of the overall critical current density J_c will reduce the exploitation potential of fully engineered conductors. The thickness of non-superconducting layers and any deterioration of J_c in the superconductor with increasing thickness of the superconducting layer, t_{sup} , leads to a maximum in the dependence of J_e with t_{sup} which may occur at the higher t_{sup} than usually envisaged [23]. If the $J_c(t_{sup})$ dependence on the t_{sup} is expressed as $J_c(t_{sup}) = J_c(t_{sup} \approx 0) \exp[-Ct_{sup}]$, where C is an empirical fitting parameter, then the dependence of J_e on the thickness of the superconducting layer may be expressed as:

$$J_e(t_{\text{sup}}) = J_c(t_{\text{sup}}) \frac{t_{\text{sup}}}{\sum_{i=1}^n t_i} \quad (1)$$

where: $\sum_{i=1}^n t_i$ is a sum of thicknesses of the superconductor, t_{sup} , substrate, t_{sub} , buffer layer, t_{buf} , stabilising (shunt) layer, t_{stab} , and insulating layer, t_{ins} . Taking as an example the 1mm thick superconducting coatings characterised by $J_c(t_{\text{sup}}) \sim 10^6 \text{Acm}^{-2}$, but deposited on the 100 μm thick Ni-based substrates, this will not differ, in respect of the overall critical current density from the ordinary powder-in-tube (PIT) conductor which has $J_c(t_{\text{sup}}) \sim 10^4 \text{Acm}^{-2}$. The ultimate goal is that a future coated conductor may have a 20 μm thick metal substrate < 0.5 μm buffer layer, with 5 μm $\text{YBa}_2\text{Cu}_3\text{O}_7$ films on both sides and high technical and economic performance will eventually result in conductors with a high percentage of high J_c superconductor in the cross section. The stabilization layer need to be many tens of micrometers thick depends on the application and also the insulation, which again will depend on the application.

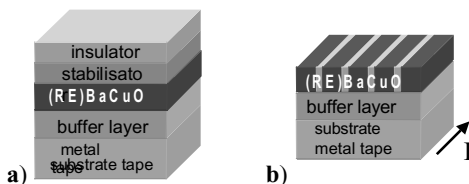


Fig.4. Schematic representation of the coated conductor architecture: **a)** typical DC conductor; **b)** one of the models of AC conductor where the superconducting layer has a parallel multifilamentary structure along its length, for better visualisation of the multifilamentary structure the top layers stabilisation and insulation layer have been removed.

Table 1. List of physical and chemical deposition methods of $\text{YBa}_2\text{Cu}_3\text{O}_7$ coatings; after [24].

| Physical Methods | Chemical Methods |
|--|--|
| Pulsed Laser Ablation/Deposition (PLA/PLD) | Sol-Gel |
| Electron Beam-Based Deposition | Chemical Vapor Deposition (CVD) |
| Electrophoresis | Metal Organic Chemical Vapor Deposition, (MOCVD) |
| Magnetron Beam-Based Deposition | Metal Organic Decomposition (MOD) |
| Thermal Evaporation | Electrodeposition |
| Sputtering | Aerosol/Spray Pyrolysis |

The actual dependencies of the J_c vs $\text{YBa}_2\text{Cu}_3\text{O}_7$ films thickness will be discussed later.

As major applications develop, close interaction is necessary between design engineers and materials producers. Following paragraphs summarises major design considerations for each of part of the coated conductor in terms of material specification and potential design requirements. There are distinct differences in the requirements for fully engineered conductors for DC and AC application area. Detailed design decisions must be reflected directly in the conductor specification [23,25].

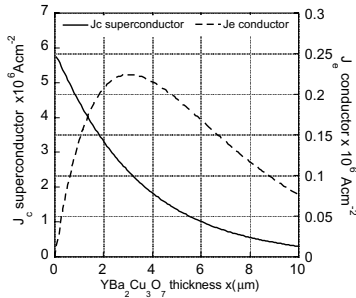


Fig. 5. Simulation of the J_c of superconductor and J_e engineering critical current density in the coated conductor; superconductor is 30 times thinner than the total thickness of the conductor. To achieve a full potential of this particular conductor thickness of the superconductor should be $3\mu\text{m}$.

3. METAL SUBSTRATES

There are two types of practical substrate used: untextured and textured. The untextured substrates are usually made of Hastelloy, stainless steel, silver or composite silver alloy [26]. The major substrate requirements are: chemical stability for high temperature process ($700\text{--}900^\circ\text{C}$), the high temperature strength ($\text{YBa}_2\text{Cu}_3\text{O}_7$ can withstand up to 0.5% strain in tension, more in compression), small thickness for high J_e , small width for low AC losses and a very important factor is a surface smoothness. The textured metal substrates required epitaxially transferred textured from the substrates to the superconducting layer. There is a range of Ni-based binary and ternary alloys that can be used as a substrate, Fig.6. Some of them are magnetic for example Ni [20], NiFe [5] and some of them are non-magnetic for example NiCu, NiV, NiCr, NiW [27-30] depending on the alloy composition, and of course, the temperature of the application envisaged. As we know NiFe and also Ni is a ferromagnetic material and may not be the best for ac applications. However the recently patented method of decoupling filaments by using magnetic-superconducting heterostructures may make some ac applications economically justified [31]. For the major magnet manufactures such as Oxford Instruments plc, since their applications are DC type, the magnetism of the metallic substrates is not a critical issue. The so-called 'cube' texture, with crystallographic axes parallel to the sample axes, forms an ideal textured metallic substrate. This can be obtained in most fcc metals by cold rolling to a reduction of greater than about 95% followed by heat treatment [32-34].

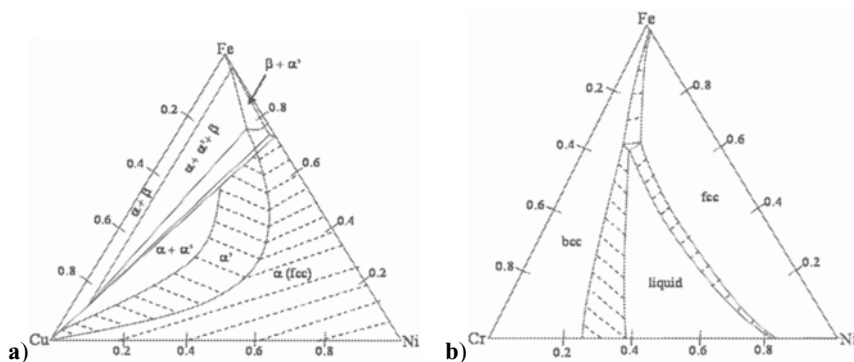

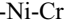


Fig. 6. Recrystallisation textures in Fe-Ni-Cr-Cu alloys: **a)** Fe-Ni-Cu alloy,  recrystallisation rolling texture,  cube texture; **b)** the ternary phase diagram Fe-Ni-Cr (the Ni-base substrates for future non-magnetic development).

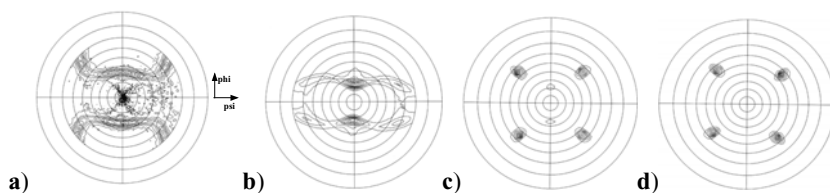


Fig. 7. X-ray pole figures of NiFe tape, 25 μ m thick: **a)** cold rolled (200) (linear scale $I_{\max} = 914$); **b)** cold rolled (111) (linear scale $I_{\max} = 3361$) all X-ray pole figures have roll direction vertical; **c)** annealed at 500°C; **d)** annealed 800°C.

Cold rolling gives a characteristic, but quite complex, texture described as (110)[112], (112)[111], (123)[422] and (146)[211], Fig.7a), b). (An ideal texture has (hkl) planes parallel to the sheet and the vector [uvw] parallel to the rolling direction.) Some of the work of deformation is stored as defects and this energy provides the driving force for recovery and recrystallisation [34,35]. The heat treatment is required to give the optimum highly oriented grains, Fig.7c), d). In general a cube texture is likely to depend on the grain size and the level of impurities. For this purpose the NiFe50% tape was cast in the form of 2 tonnes ingot and deformed and cold-rolled to the 3-5mm thin stripes, followed by the final rolling to thicknesses of 50 μ m, 25 μ m and 13 μ m and a width of 10cm. Each final roll weighed ~ 20kg and was approximately 1 km long. The deformation process and heat treatment in a protective atmosphere was conducted in a factory environment by Carpenter Technologies (UK). The final tape was slit to 25mm and 10 mm wide tapes for conductor development, see Fig.8. The NiFe tapes have superior mechanical and structural properties compared with pure Ni substrates and some of Ni-alloys, Fig.9a).

The important issue for the uninterrupted epitaxial growth of the buffer layers and superconducting layers on a highly textured tape is the smoothness of the sample surface. Therefore a continuous electropolishing technique was developed, which has greater

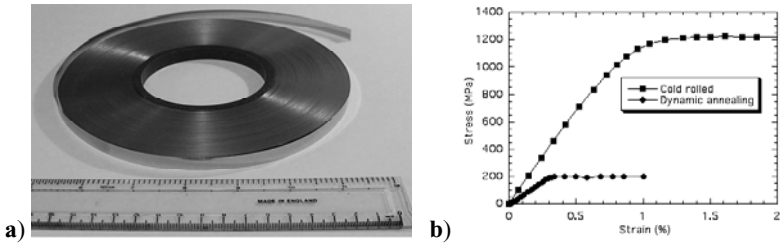


Fig. 8. NiFe flexible substrates for coated conductor: **a)** view of the NiFe tape, 760m long, 10mm wide and 25 μ m thick after continuous annealing; **b)** stress - strain curves of the cold rolled and dynamically annealed in protective atmosphere NiFe tape, 25 μ m thick tape [5].

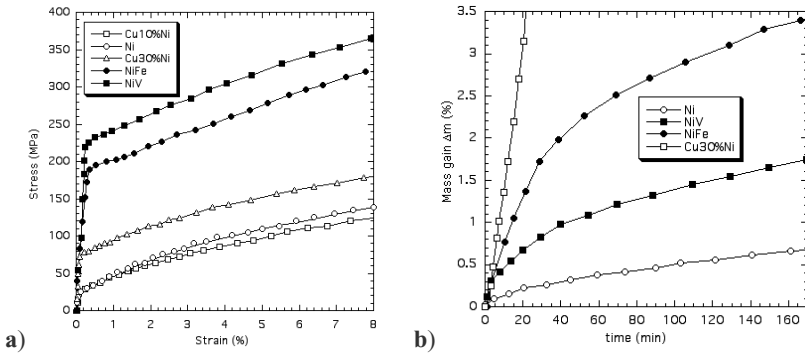


Fig. 9. Ni alloys: **a)** Stress-strain characteristics of the selected Ni-alloys developed in frame of Brite-Euram CONTEXT and MUST projects; **b)** thermogravimetric data representing oxidation of the different Ni-alloys the horizontal axis represent time during which the samples were exposed to oxygen at constant temperature 700°C.

flexibility and can be used on cube textured tapes. The electropolishing process conducted on Ni and NiFe tapes brought the roughness down from 0.20 μ m to < 0.1 μ m and formed the base for the development of the pilot continuous electropolishing treatment unit by Europa Metall, Italy. Trials indicated that to preserve uniform electric field distribution and to provide the optimum electropolishing, cleaning and drying conditions, the orientation of the tape should be vertical, see Fig.10i) and ii). From all these observations we can argue that the most reliable technique to achieve the roughness level requested over the longer lengths without microstructure interruption is electropolishing. The profilometric measurements along the length of the NiFe(50%50%) tapes are presented in Fig.10v).

The overall electron back-scattered patterns, EBSP, map of grain orientation as well as information about misorientation from grain to grain provides information about potential percolative current paths in the subsequent superconducting layer which can be derived on the base of the assumption that epitaxial growth of the subsequent buffer layers and superconducting layers will follow the original texture induced by substrates [36]. The EBSP data displayed in Fig.11 and Fig.12 showed that there is a clear percolative path at 6 degrees

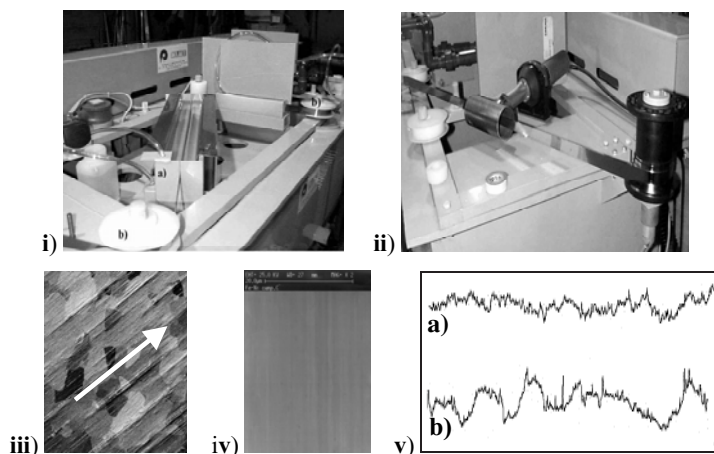


Fig. 10. Surface finish improvement: **i)** electropolishing unit at where long lengths of 25 mm wide and 25 μm thick NiFe tapes were electropolished: **ii):** (a) - view of the treatment tank, b) - cleaning and winding system, (c) on-line drying unit (courtesy of Europa Metalli S.p.a. Italy); **iii)** SEM picture of the NiFe tape surface before electropolishing (white arrow marks the rolling direction); **iv)** SEM picture of the tape surface after electropolishing; **v)** profilometric measurements of the dynamically annealed NiFe tape surface relief conducted by contact method: a) after electropolishing, b) before electropolishing.

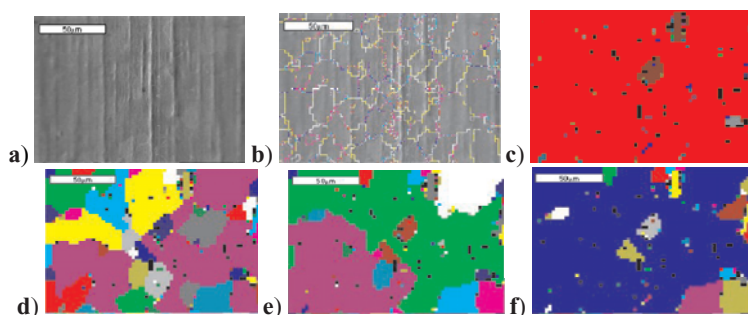


Fig. 11. The NiFe 25 μm thick tape dynamically annealed: **a)** SEM picture of the tape surface fragment; **b)** SEM picture of the tape surface fragment with superimposed combined EBSP misorientation map presented in the following pictures; **c)** outline of the strongly out of plane oriented substrate crystals **d)** misorientation EBSP map for 4 degrees; **e)** misorientation EBSP map for 5 degrees; **f)** misorientation EBSP map for 6 degrees; most of the grains are less than 6 degrees misaligned from normal to the surface of the substrate. Colours used for "decoration" of the individual grains or crystallites are arbitrary for each individual picture to emphasise the boundary of the given degree of misalignment. The bar on the pictures represents 50 μm distance.

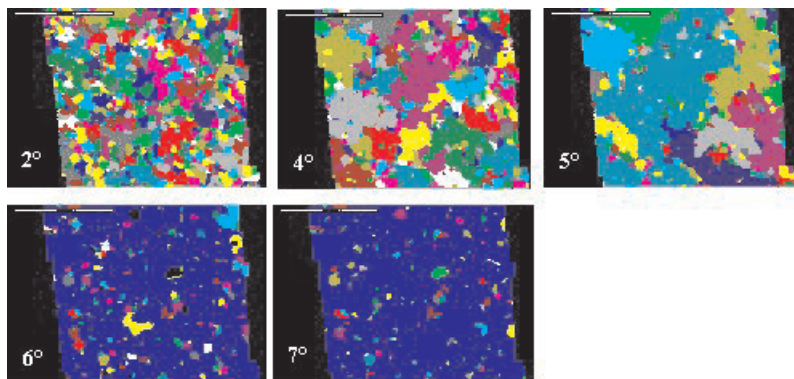


Fig. 12. Large area EBSD misorientation map for 2°, 4°, 5°, 6° and 7° respectively. The width of the investigated area $\sim 500\mu\text{m}$. (courtesy of E. Maher, EU ‘MUST’ Project [5]).

but there are unresolved areas / grains which are of a higher degree of misorientation and do not disappear after prolonged annealing. In Fig.11c) the unresolved grains which are oriented out of plane causing the strong misalignment of the subsequent epitaxially grown $\text{YBa}_2\text{Cu}_3\text{O}_7$ grains are represented by darker area.

4. BUFFER LAYER

The role of the buffer layer is to provide a chemically inert base to grow the superconductor on metallic substrates and to prevent chemical interdiffusion between substrates and superconducting coating. Most of the buffer layers are insulating but there is a need for conductive buffer layers which may allow the metallic substrates to serve as a current sharing stabilizer [37-39]. Since in most cases there is multi-component, multilayer architecture of the actual buffer layer, Fig.13a), the practical objective for the buffer development is reduction of the number of buffer layer components and also cost reduction. The ideal case would be a

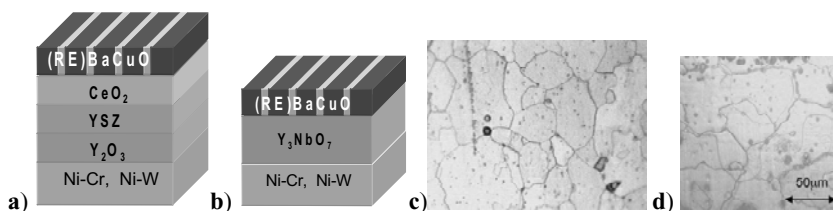


Fig. 13. Schematic representation of the buffer layer architecture of the coated conductor: **a)** multilayered buffer by PLD; **b)** single layer buffer by MOD technique; **c)** optical image of the surface of a transparent self oxide epitaxially, SOE, textured NiO/Ni grown at 1250°C in air (after removal of the native oxide layer) for 120 s, NiO thickness $\sim 2.5\mu\text{m}$; **d)** grown for 2 hours NiO thickness $\sim 15\mu\text{m}$.

Table 2. Accumulated list of the potential substrates their melting temperature, lattice parameter, a_0 , and relative misfit in % in respect to $\text{YBa}_2\text{Cu}_3\text{O}_7$ and Ni and NiO; courtesy of J.E. Evetts and A. Kursumovic. The lattice misfit for other Ni-based alloys is very similar to Ni because lattice parameter, a_0 , of Ni is equal 3.524\AA where for example for the Ni50at% Fe the $a_0 = 3.578\text{\AA}$. The L_m is matching distance in respect of a and b lattice parameter of $\text{YBa}_2\text{Cu}_3\text{O}_7$.

| Material | Structure | $T_m/^\circ\text{C}$ | a_0 (300K) | L_m | MisfitY BCO (%) | Misfit to Ni (%) | Misfit to NiO (%) |
|--|---------------------------------|----------------------|--------------|-------|-----------------|------------------|-------------------|
| Ni | fcc | 1455 | 3.52 | 3.52 | -9.38 | 0.00 | -18.47 |
| YSZ | cubic / fluorite | 2680 | 5.13 | 3.63 | -6.06 | 3.03 | -14.88 |
| $\text{Gd}_2\text{Zr}_2\text{O}_7$ | cubic / pyrochlore | | 10.52 | 3.72 | -3.49 | 5.38 | -12.10 |
| Y_2O_3 | cubic / Mn_2O_3 | >2400 | 10.6 | 3.75 | -2.67 | 6.13 | -11.20 |
| LaAlO_3 | rhombohedral / perovskite | 2100 | 5.36 | 3.79 | -1.58 | 7.12 | -10.03 |
| $\text{La}_2\text{Zr}_2\text{O}_7$ | cubic / pyrochlore | 2300 | 10.8 | 3.81 | -1.05 | 7.61 | -9.45 |
| Gd_2O_3 | cubic / Mn_2O_3 | >2400 | 10.81 | 3.82 | -0.79 | 7.85 | -9.16 |
| CaTiO_3 | orthorhombic / perovskite | | 5.38x5.44 | 3.82 | -0.79 | 7.85 | -9.16 |
| CeO_2 | cubic / fluorite | 2600 | 5.41 | 3.83 | -0.52 | 8.09 | -8.88 |
| Eu_2O_3 | cubic / Mn_2O_3 | >2300 | 10.87 | 3.84 | -0.26 | 8.33 | -8.59 |
| LaNiO_3 | rhombohedral / perovskite | | 5.45 | 3.84 | -0.26 | 8.33 | -8.59 |
| YBCO | orthorhombic | | 3.83x3.88 | 3.85 | 0.00 | 8.57 | -8.31 |
| $\text{Ca}_{0.6}\text{Sr}_{0.4}\text{TiO}_3$ | orthorhombic / perovskite | | 5.46x5.46 | 3.86 | 0.26 | 8.81 | -8.03 |
| NdGaO_3 | orthorhombic / perovskite | 1670 | 5.43x5.5 | 3.86 | 0.26 | 8.81 | -8.03 |
| Sm_2O_3 | cubic / Mn_2O_3 | >2300 | 10.93 | 3.86 | 0.26 | 8.81 | -8.03 |
| La_2NiO_4 | tetragonal | | 3.86 | 3.86 | 0.26 | 8.81 | -8.03 |
| Sr_2RuO_4 | tetragonal | | 3.87 | 3.87 | 0.52 | 9.04 | -7.75 |
| LSMO | rhombohedral / perovskite | | 5.49 | 3.88 | 0.77 | 9.28 | -7.47 |
| NdBCO | orthorhombic | | 3.87x3.92 | 3.89 | 1.03 | 9.51 | -7.20 |
| Pd | fcc | 1555 | 3.89 | 3.89 | 1.03 | 9.51 | -7.20 |
| Gd_2CuO_4 | tetragonal | | 3.89 | 3.89 | 1.03 | 9.51 | -7.20 |
| SrTiO_3 | cubic / perovskite | 2080 | 3.91 | 3.91 | 1.53 | 9.97 | -6.65 |
| LaMnO_3 | orthorhombic / perovskite | | 5.54x5.74 | 3.91 | 1.53 | 9.97 | -6.65 |
| Nd_2O_3 | cubic / Mn_2O_3 | >2300 | 11.08 | 3.92 | 1.79 | 10.20 | -6.38 |
| SrRuO_3 | orthorhombic / perovskite | | 5.57x5.54 | 3.93 | 2.04 | 10.43 | -6.11 |
| Nd_2CuO_4 | tetragonal | | 3.94 | 3.94 | 2.28 | 10.66 | -5.84 |
| BaTiO_3 | tetragonal / perovskite | | 3.99 | 3.99 | 3.51 | 11.78 | -4.51 |
| Ag | fcc | 961 | 4.09 | 4.09 | 5.87 | 13.94 | -1.96 |
| SrZrO_3 | orthorhombic / perovskite | 2800 | 5.79x5.82 | 4.10 | 6.10 | 14.15 | -1.71 |
| BaSnO_3 | cubic / perovskite | | 4.12 | 4.12 | 6.55 | 14.56 | -1.21 |
| NiO | cubic / rocksalt | 1984 | 4.17 | 4.17 | 7.67 | 15.59 | 0.00 |
| BaZrO_3 | cubic / perovskite | 2690 | 4.19 | 4.19 | 8.11 | 15.99 | 0.48 |
| MgO | cubic / rocksalt | 3100 | 4.21 | 4.21 | 8.55 | 16.39 | 0.95 |
| TiN | cubic / rocksalt | | 4.24 | 4.24 | 9.20 | 16.98 | 1.65 |

| | |
|--|---------------|
| | perovskite |
| | rocksalt |
| | fcc structure |
| | spinel |
| | fluorite |
| | C-type RE |
| | pyrochlore |

single buffer layer, for example Y_3NbO_7 or even NiO which will secure high J_c and I_c of the subsequent superconducting layer, Fig.13b),c) and d). The so-called native oxide buffer layers can be made by direct oxidation of the metallic substrates to simplify the deposition process. Such Ni-O layers are successfully used in LPE processing [18,19]. In the second generation AC conductors for small magnetic field $\sim 0.4T$, where interfilamentary decoupling is vital, magnetic buffer layer will be introduced [22,40,41].

There is a need for smoothness of the buffer layer to avoid the a -axis growth of $YBa_2Cu_3O_7$. There is also a desire for small-grained buffer layer to minimise the effect percolative effect in AC conductors. For the RABiTS processing where epitaxial growth is important the optimization of interfacial energy, lattice misfit, crystal structure, are extremely important. There is a wide choice of possible candidates listed just for $YBa_2Cu_3O_7$ in Table 2. Other (RE) $Ba_2Cu_3O_7$ superconductors are characterised by a slightly different a and b lattice constants.

5. SUPERCONDUCTING LAYER

Progress in the development of biaxially oriented epitaxial buffer layers [42,43] on untextured and biaxially oriented flexible Ni-alloy, Ag-alloy and Cu-based metallic substrates [44,45] has opened up possibilities for the application of $YBa_2Cu_3O_7$ in electric utility, Fig.14 and Fig.15 and also a high magnetic field dc devices such as MRI and NMR magnets. Despite the excellent existing demonstrators there is continuous development in many parallel directions to define economically viable and also reliable long length coated conductor technology, Table 3. Four different stages of such parallel development can be identified; (i) the near market design of fully engineered conductors for particular applications, (ii) incremental development of ‘established’ conductor processing routes, (iii) investigation of new routes for superconductor processing, and (iv) basic and enabling science to underpin materials processing [22,25]. Naturally the boundaries between these types of activity are processing [22,25]. Naturally the boundaries between these types of activity are blurred, however the different activities require different levels of interaction between industry and academia.

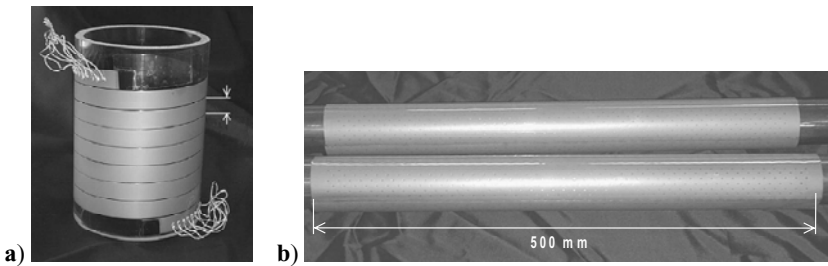


Fig. 14. Fully engineered $YBa_2Cu_3O_7$ coated conductor with stabilisation and insulation coatings prepared by IBAD/PLD technique on stainless steel substrate; **a)** 8-turn coil made for the 10mm wide and 2m long tape. The electric multi-contact current leads are also attached at the end of the coil; **b)** current leads 50cm long and 5cm with improved contact between the stabilisation layer and superconductor.



Fig. 15. a) The first 2nd generation demonstration cable (made by Southwire, from American Superconductor) uses second generation $\text{YBa}_2\text{Cu}_3\text{O}_7$ tape conductor prepared by RABiTS technique, tested by Oak Ridge National Lab.: $I_{dc} \sim 4.2$ kA at 77 K, 1.25m length, 24 total tapes, 50 μm of copper stabilizer (courtesy of American Superconductor); **b)** $\text{YBa}_2\text{Cu}_3\text{O}_7$ film was deposited by the PLD method on the biaxially textured Ag-Cu/Ag-Ni/Ag-Cu clad tape, substrates exhibits (110) $\langle 220 \rangle$ texture uniformly throughout the whole length, shows the uniform current distribution, $J_c > 10^5$ Acm^{-2} , in the 10 m-long tape, coil diameter 25cm [46]. Courtesy of Y. Shiohara.

Furthermore the type of research appropriate for a particular conductor processing route varies depending on the maturity of the technology and is driven by particular specifications. According to data presented in Table 3 The highest averaged value of the utility/merit can be assigned to non-vacuum processes.

There are numerous issues addressed throughout the chapter, which have to be considered by each of the proposed deposition techniques listed in Table 3:

- superconducting material choice and designing ($\text{RE}_x\text{Y}_{1-x}\text{Ba}_2\text{Cu}_3\text{O}_{7-d}$)
- buffer selection and simplification
- high deposition rate (for high production rate)
- high yield (for high production rate and for low cost)
- low cost process quasi-thermal equilibrium process; MOD, sol-gel)
- large deposition area for high production area
- Wide process window and low temperature process (temperature, $p\text{O}_2$, for reproducibility, long length uniformity and for simple buffer layer architecture)
- Thin film crystal growth mechanism optimised for high I_c , J_c and uniformity
- high J_c for thicker superconducting films (thickness dependence of J_c ; for high I_c , J_c as described in eq.(1). For YBCO of thickness higher than 5 μm , there are intrinsic obstacles since grains with a-axis perpendicular to the substrate start forming, there is insufficient oxygenation as thickness increases and defects accumulate and degrade J_c)
- Increase of H_{irr} and J_c by over-doping, appropriate oxygen content
- flux pinning improvement by introduction of artificial pinning centers (dislocations, defects, 211 phase particles, RE-Ba substitution)
- grain size control for RABiTS deposition for minimization of the current percolation path in long length coated conductors
- joining technology of coated conductor tapes for long length applications
- thermal properties
- mechanical properties

Table 3. Comparison of the deposition and utility/merit parameters of the deposition techniques of superconductor and buffer layers for coated conductor. (*- values concerned were: processing parameters; processing atmosphere; cost of chemicals and material utilisation efficiency; thickness and (RE)Ba₂Cu₃O₇ deposition rate; achieved J_c values. data adopted after [8,46].

| Deposition technique (long lengths) | Deposition speed | Utility/merit % | Comments main challenges |
|-------------------------------------|------------------|-----------------|---|
| Dip coating | 0.5cm/s | 60 | Speed and chemical stability |
| Ink-jet printing | 70cm/s | – | Ink formulation and deposition |
| Spray pyrolysis | 20cm/s | 59* | composition control, roughness |
| Sputtering | | | Speed, cost |
| Electrophoresis | | 38* | porosity |
| Electrodeposition | | 62* | porosity |
| E- beam | | 57* | |
| Sol-gel | | 79* | density and roughness |
| MOCVD | | 87* | thickness |
| PLD | | 63* | cost |
| MOD | | 91* | thickness, processing parameters (BF ₂) |
| CVD | | 49* | |
| LPE | | | corrosive environment |
| Web coating | | 78 | chemical stability, ink formulation |
| ISD | | 60 | cost, reproducibility |
| IBAD/IAD | | 65 | cost, reproducibility |

There are examples where the combination of two techniques is used for the deposition of the buffer, superconductor and stabiliser layers such as IBAD/PLD [47-49]. In some case even few techniques were used for deposition of conductor: buffer layers such as yttria stabilized zirconia (YSZ) or cerium oxide (CeO₂) were deposited by PLD combined with ISD to obtain in-plane alignment on this nontextured substrate. HoBa₂Cu₃O₇ was deposited by PLD on these buffer layers. Silver stabilizer was finally deposited by sputter method [50].

5.1 RABiTS - (RE)Ba₂Cu₃O₇ coated conductors

The current challenge is to find an economic route for large-scale production of the conductors including highly textured mechanically strong and thin metallic substrates in the form of a tape. The design of the final conductor under consideration consists of: (i) long lengths of well-oriented Ni-based substrate, (ii) an epitaxial buffer layer grown epitaxially on the metallic substrate, (iii) (RE)Ba₂Cu₃O₇ as the superconductor grown epitaxially on the

buffer layer, (iv) silver as a cryogenic and electric stabilisation layer and finally (v) polymer as the top layer for insulation and stress relief. This architecture is schematically presented in Fig.3a). Therefore for the complex coated conductor technique to gain a significant advantage, one has to use the thinnest possible substrates but simultaneously preserve their mechanical strength. The essential condition for development of biaxially oriented epitaxial buffer layers and superconducting layers on flexible metallic substrates is the degree of texture in the metallic substrate itself.

In order to overcome the problems with the NiFe tape oxidation, Fig.9b), and be able to proceed with coated conductor architecture as presented in Fig.3a), a series of depositions have been performed in a vacuum from a composite target consisting of a CeO_2 ceramic pellet and a piece of Pd sheet covering from 10 up to 50% of the laser ablated track. It is believed [51] that due to diffusion at elevated temperatures the effect of Pd gettering around various substrate defects (grooves, twins, surface irregularities) takes place similarly to the gettering of platinum by cavities in silicon recently reported by G.Mariani-Regula et al [52]. Such a gettering effect may suppress the high rate local oxidation caused by the severe oxygen diffusion through defects propagating in the overlying buffers. Such oxidation leads to distortion of the cube-on-cube texture and cracking. Probably the deposited Pd (lattice parameter $d = 3.89 \text{ \AA}$) also acts as an inhibitor suppressing NiO (111) formation and favoring NiO (200) ($d = 4.18 \text{ \AA}$) formation as a result of oxygen delivered to the NiFe ($d = 3.59 \text{ \AA}$) interface by solid state oxygen diffusion through the buffer layers. In confirmation of this scenario cross-section FIB microscopic images of the two samples deposited in forming gas and vacuum are presented on Fig.16a) and b) respectively. This analysis reveals the much clearer features of the CeO_2 :Pd-NiO interface in comparison with those of CeO_2 /NiO. All subsequently deposited layers preserve the quality of the first interface with voids and irregularities propagating towards and within the $\text{YBa}_2\text{Cu}_3\text{O}_7$. The region of relatively thick NiO formed during YBCO deposition is clearly seen on both samples suggesting strong oxygen diffusion through the buffer architecture. In the bottom part of the metal/oxide matrix the formation of Fe and NiFe oxide can be observed as darker regions while according to Schmalzried [53] Ni as a more noble metal oxidizes covering the outer region. The comparison of the in-plane texture quality of the buffer layers and superconductor layer deposited in forming gas on Ni50at%Ni substrate and vacuum is presented in Fig.17.

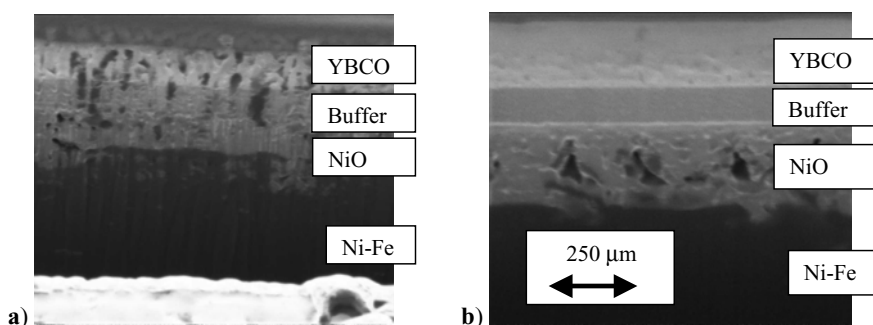


Fig. 16. Cross sectional FIB microscope images of the two complete coatings: a) CeO_2 layer deposited in forming gas; b) CeO_2 :Pd layer deposited in vacuum.

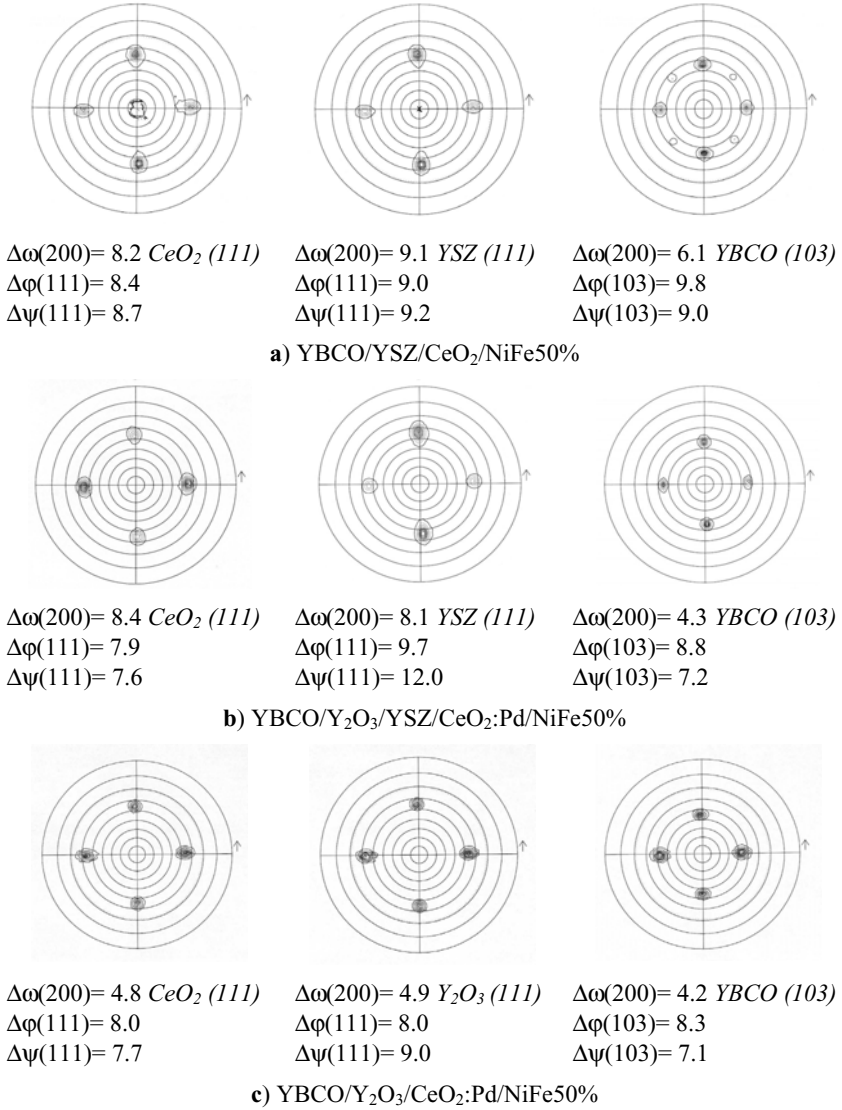


Fig. 17. In-plane and out-of-plane texture quality of buffers and YBa₂Cu₃O₇ superconductor:
a) YBa₂Cu₃O₇/Y₂O₃/YSZ/CeO₂:Pd/NiFe architecture deposited in forming gas;
b) YBa₂Cu₃O₇/Y₂O₃/YSZ/CeO₂:Pd/NiFe architecture deposited in vacuum;
c) YBa₂Cu₃O₇/Y₂O₃/CeO₂:Pd/NiFe deposited in vacuum [51].

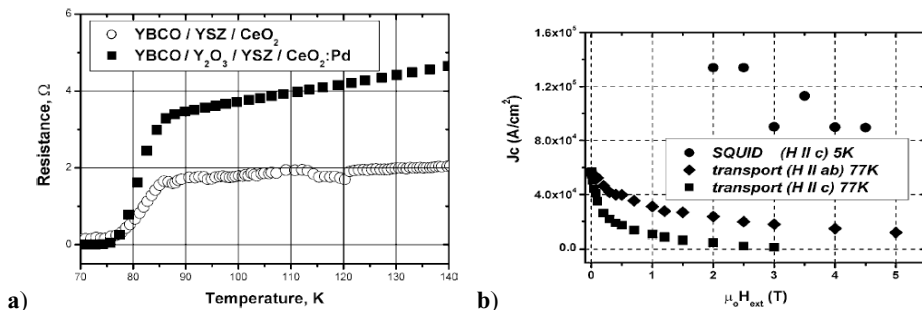


Fig. 18. Superconducting properties of the $\text{YBa}_2\text{Cu}_3\text{O}_7$ coated conductors deposited on the buffered NiFe50% 25 μm thick substrates: **a)** resistivity versus T ; **b)** J_c versus magnetic field. The magnetic field dependence of critical current density of $\text{YBa}_2\text{Cu}_3\text{O}_7/\text{Y}_2\text{O}_3/\text{YSZ}/\text{CeO}_2/\text{NiFe}$ tape evaluated by transport (at 77 K) and SQUID (at 5 K) current measurements.

The resistance vs. temperature measurements show $T_{c(\text{onset})}$ ranging between 87 and 90 K and a transition width from around 10 K for the $\text{CeO}_2:\text{Pd}$ sample to more than 20K for the CeO_2 sample (see Fig.18a), indicating the necessity of the optimisation of $\text{YBa}_2\text{Cu}_3\text{O}_7$ deposition.

The other possible reason for a reduced T_c and wide transition could be a partial replacement of Cu atoms with Ni due to the diffusion through the grain boundaries, which automatically leads to a degradation of T_c [54] Magnetic measurements were performed in a DC SQUID magnetometer. The sample was approximately hexagonal in shape and was placed in a perpendicular external magnetic field. Magnetic moments were measured as a function of temperature in zero-field-cooling and field-cooling conditions. Magnetisation characteristics were measured at 5 K in range of applied magnetic fields ± 6 T. The widths of the magnetisation loops were used to determine the critical current density, J_c . A standard relation, based on the Bean critical state model [55], suitable for thin films was used: $J_c = 3\Delta M(H)/(2R)$, where ΔM is the hysteresis loop width and R is an effective radius of the sample. A plateau value of J_c (5K) = $5.5 \times 10^8 \text{ A m}^{-2}$ in the magnetic field range of 3 to 5 T was observed (see Fig.18b). There are other more successful results of deposition on Ni-based alloys characterised by lower oxidation [56], but NiFe deserve attention due to its availability as a highly textured 13 μm and 25 μm thick substrates in tonnes.

In RABiT conductors, texture in the $\text{YBa}_2\text{Cu}_3\text{O}_7$ layer is developed by depositing upon a textured buffered metal tape. The preferential alignment is transferred from the substrate through the buffers into the superconductor. There is much evidence from transmission electron microscopy, Fig.19a), and magneto-optical (MO) measurements [57] that assignment of a critical current to each grain boundary requires knowledge of the relationship between the grain boundary angle and J_c as presented in Fig.20 and Fig.21. Despite this, all layers do not have exactly the same crystallographic alignment. While naturally occurring defects in $\text{YBa}_2\text{Cu}_3\text{O}_7$ are capable of providing high critical current J_c values, weak links such as high angle grain boundaries (GB's) can considerably affect the overall critical current [23], [58,59].

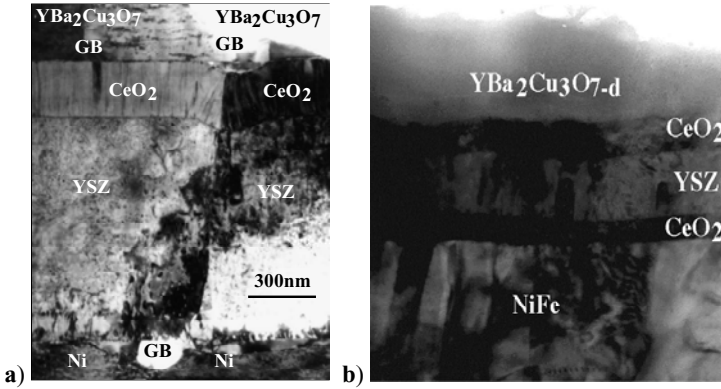


Fig. 19. Transmission Electron Microscopy, TEM micrograph of the superconducting multilayer composite coated conductor cross sections manufactured by RABiT process: **a)** the grain boundaries of textured buffered nickel substrate replicate the boundaries of $\text{YBa}_2\text{Cu}_3\text{O}_7$ in superconducting layer and also there is an additional grain boundary in $\text{YBa}_2\text{Cu}_3\text{O}_7$ layer probably induced by the imperfection in the CeO_2 layer induced; conductor structure: $\text{YBa}_2\text{Cu}_3\text{O}_7/\text{YSZ}/\text{CeO}_2/\text{Ni}$. The average grain size of $\text{YBa}_2\text{Cu}_3\text{O}_7$ is $20\mu\text{m}$. (Adopted after [60], courtesy of C. Prouteau,); **b)** $[\text{NiFe}-\text{CeO}_2-\text{YSZ}-\text{CeO}_2-\text{YBa}_2\text{Cu}_3\text{O}_7]$ the thickness of the various layers were about 50nm (1st CeO_2), 150nm (YSZ), 65nm (2nd CeO_2) and 250nm ($\text{YBa}_2\text{Cu}_3\text{O}_7$) respectively; $T_c \sim 90\text{K}$. The grain boundaries are not explicitly transmitted from the buffered NiFe substrates (courtesy of the Birmingham University, EU ‘MUST’ project).

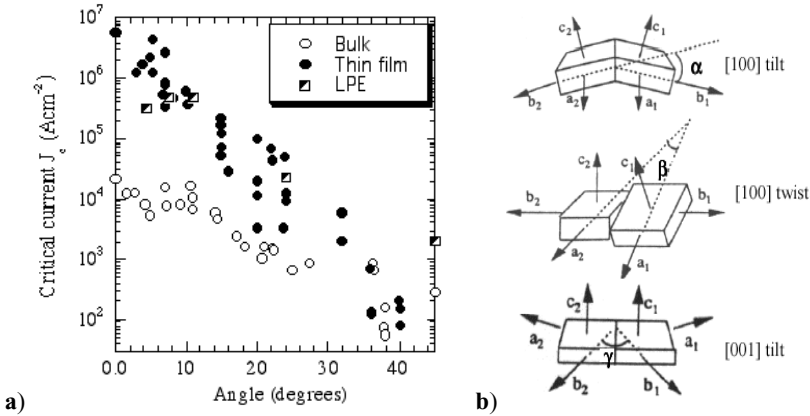


Fig. 20. Transport critical current density versus grain misalignment angle: **a)** J_c vs grain boundary angle data for [001] tilt boundaries in $\text{YBa}_2\text{Cu}_3\text{O}_7$ at 77K and zero external magnetic field: open symbols represent bulk samples, filled symbols thin films and crosses liquid phase epitaxy, LPE, coatings. Data adopted after [61,62]. Bulk data [67,68], thin film data [63-65], LPE data from [66]; **b)** schematic representation of the misalignment angles [69].

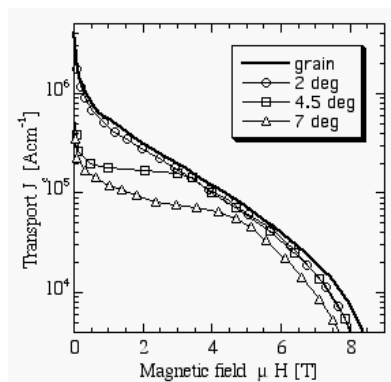


Fig. 21. Transport critical current density versus magnetic field parallel to *c* axis of $\text{YBa}_2\text{Cu}_3\text{O}_7$ grown epitaxially with different in plane misorientation [001] tilt, see Fig.20b); (adopted after [65], courtesy of C. Prouteau).

The grain size of the deposited buffer layers is usually smaller than that of the metallic tapes. This suggests that sub-grains develop during deposition as several growing film grains nucleate in different places within a single substrate grain. In addition, the overall crystallographic texture may improve or degrade in successive layers, depending upon substrate material, adopted architecture of the buffer layers. The grain size of the deposited buffer layers is usually smaller than that of the metallic tapes. This suggests that sub-grains develop during deposition as several growing film grains nucleate in different places within a single substrate grain. In addition, the overall crystallographic texture may improve or degrade in successive layers, depending upon substrate material, adopted architecture of the buffer layers and also deposition parameters such as temperature and deposition rate. Irrespective of the overall quality of textured metallic substrates some accidental high angle grains do exist, which may cause even growth of $\text{YBa}_2\text{Cu}_3\text{O}_7$ away from *a-b* plane, Fig.22 which obviously reduces the transport properties and amplifies transport current percolation. Such accidental crystals introduce a serious limitation to the overall current density of the conductors under development and should be avoided by optimisation of the cold rolling and heat treatment procedures during substrate development.

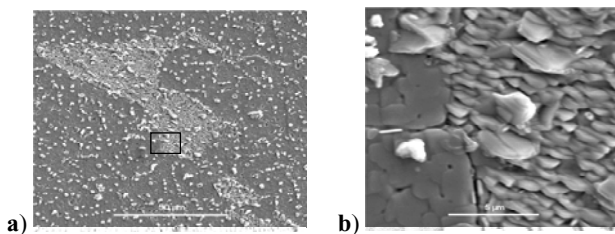


Fig. 22. SEM picture of the $\text{YBa}_2\text{Cu}_2\text{O}_7$ grown on buffered misaligned Ni-based grain $\text{Ni}_{0.1}\%\text{Mo}/\text{NiO}/\text{Ca}_{0.6}\text{Sr}_{0.4}\text{TiO}_3/\text{YBa}_2\text{Cu}_2\text{O}_7$: **a)** low magnification; **b)** magnification of the marked area on Fig.22a), courtesy R.H. Huhne.

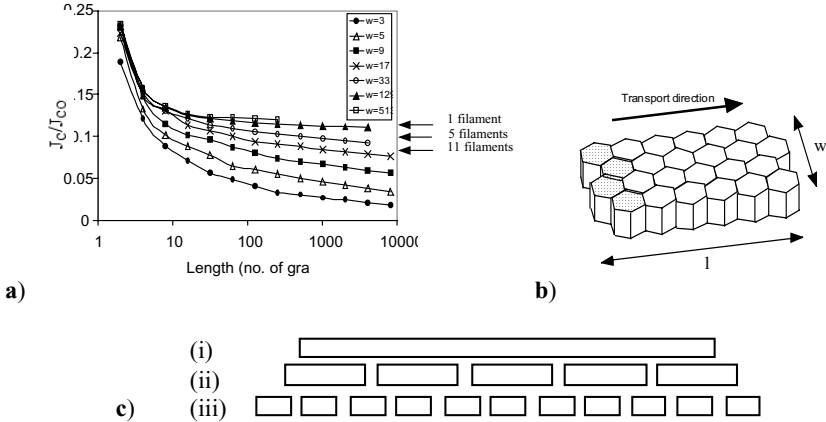


Fig. 23. a) The variation of J_c/J_{c0} with a sample length for prefixed sample width. The numbers assigned to length and width are given as a multiplication of chosen grain size. For example if the average size of the grain is of the order of $\sim 20 \mu\text{m}$, the curve ‘ $w=129$ ’ corresponds to the conductor path width, w , equal ($20\mu\text{m} \times 129 \text{ grains} = 0.35 \text{ mm}$). The shape of J_c/J_{c0} vs length and width dependencies have been calculated on the basis of the existing data correlating critical current of the grain boundaries vs misorientation angles. Arrows represent the level of current reached at the length of 10000 grains for the corresponding filamentary coated conductors presented in Fig.23c); **b)** schematic of the hexagonal grain array used for modelling of the J_c percolation in the coated conductor where l - length of the coated conductor or conductor strip and w – width of the superconducting path; **c)** model coated conductors cross-section (not to scale): i) monocoil - rectangular cross section $5.5\text{mm} \times 4\text{mm}$, ii) 5 filaments, each of rectangular cross-section $1.1\mu\text{m} \times 4\mu\text{m}$, separation between the filaments- 5mm , iii) 11 filaments, each of rectangular cross-section $0.5\mu\text{m} \times 4\mu\text{m}$, separation between the filaments- $5\mu\text{m}$. J_c decreases (approximately exponentially for $l \gg w$)

5.1.1. Current percolation in coated conductors - grain boundary engineering

Grain boundaries in oxide superconductors are of paramount importance both for engineering applications and for issues in fundamental science. Although closely studied for more than a decade there is still by no means a consensus on the properties of individual grain boundaries, or their collective behaviour when current percolates in a granular material. There are three components to this general problem, (i) the properties of individual grains and grain boundaries, (ii) the microstructure, grain texture and grain morphology of the conductor, and (iii) the macroscopic geometrical constraints such as conductor size and shape. An overview will be given of recent progress in characterizing and modelling current and flux percolation in $\text{YBa}_2\text{Cu}_3\text{O}_7$ coated conductor tapes.

The important problem of current percolation in granular superconductors can be addressed through the two different modeling approaches that are to an extent complementary, each making a particular contribution to the overall problem. ‘Limiting path analysis’ is particularly powerful for calculating the effect of conductor geometry, for instance

in complex conductors the need to be optimized for AC applications and cryomagnetic stability [70-79]. ‘Non-linear resistor network modeling’ provides a first estimate of the I - V transition and also I_c determining using a ‘voltage criterion’ [80,81]. The functional form of I - V for a coated conductor is an essential part of a full specification. At present there is little available data and possibly conflict between experimental observations and the scaling expected from classical percolation theory that considers the grains and grain boundaries as a ‘statistical ensemble’ with the grain boundaries state as the ‘statistical variable’[82].

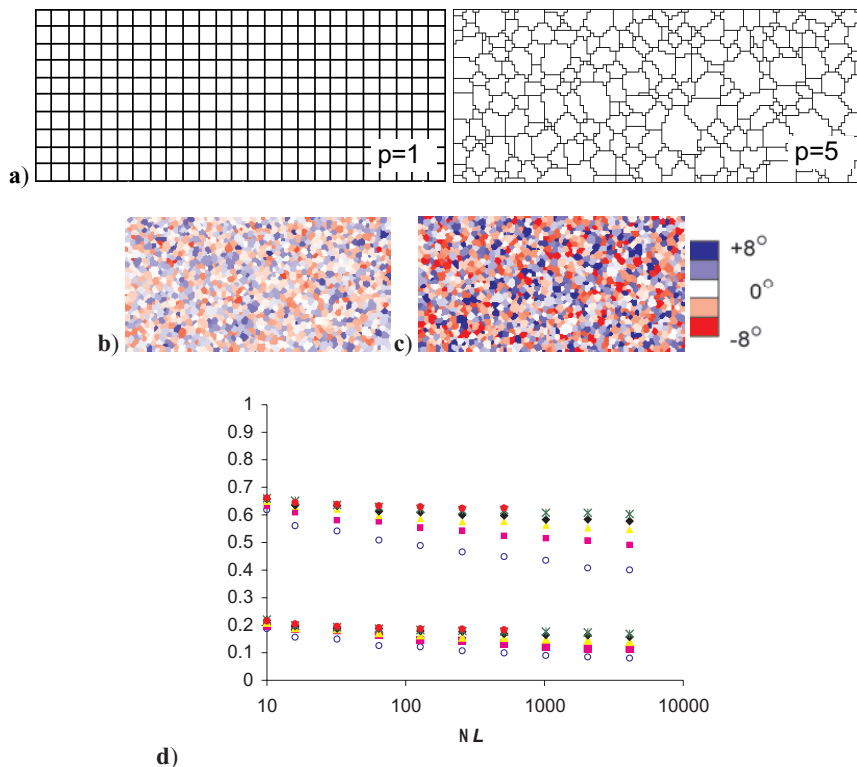


Fig. 24. Simulation of the realistic grain structure distribution for BABiTS deposition process **a)** grain structures for $p=1$ (simple square model) and $p=5$, both for samples 25 grains long and 10 grains wide. The average grain size in pixels (p) is related to Monte-Carlo simulation; **b)** Monte-Carlo simulation of the 4° misoriented grain structure; **c)** Monte-Carlo simulation of the 8° misoriented grain structure. It is apparent that at lower angle misoriented grains are more sensitive to the N_w parameter since the absolute value of the current density is more than 3 times lower for 8° GB misorientation angle; **d)** the normalised critical current density vs number of grains along the coated conductor N_L for two exemplary GB misorientation angles ω_{RD} , ω_{TD} , ω_{ND} where 4° is represented by top curves and 8° by the bottom curves. Courtesy of N. Rutter.

The typical dependence between the conductor width and the average grain size has been presented and analysed in order to predict the (grain size)/(filament-strip width) ratio influencing critical current density values in multifilamentary conductors [22], Fig.23. Also Fig.23 shows the degradation of the J_c/J_{c0} vs conductor length.

A Monte-Carlo grain growth model has been used to simulate more realistic grain structures in coated conductors and predict the actual J_c vs length dependence for the given misorientation angles as presented in Fig.24. The grains are initially made up of single square or hexagonal pixels. Each pixel has an energy based upon the number of neighbours, which are in the same grain. ‘High energy’ pixels are consumed by neighbouring grains. As the Monte-Carlo simulation progresses, grain structures such as those in Fig 24a) develop.

To visualise the actual reduction of the critical current I_c over the longer lengths of the coated conductor by RABiTS technique simulation was conducted for the range of widths and lengths of the conductor up to 1km, Fig.25.

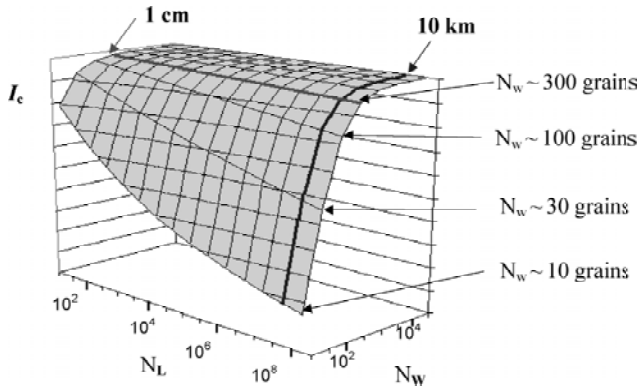


Fig. 25. Critical current density of the coated conductor versus number of grains along the length conductor N_L and along the width of conductor N_W . There is a useful relationship between critical current value and the number of grains along and across the conductor, eq.(2), courtesy of N.Rutter.

$$I_c \propto \left(\frac{1}{N_L}\right)^{\frac{1}{N_W}} \quad (2)$$

An important critical current density measurements was conducted at the University of Wisconsin on 1230 μ m long tracks of RABiT YBa₂Cu₃O₇ for the range of widths ranging from 10 times the average grain size of YBa₂Cu₃O₇ to on-grain wide case. As it was shown by Larbalestier et al [83] there is a characteristic field called transition field, H^* see Fig.26 above which $J_c(H)$ is width-independent so there is no GB-dissipation signature and the grain boundaries seems to not to be obstacles. Behaviour is single-crystal-like [84]. On the other hand for fields $H < H^*$; $J_c(H)$ is width-dependent which is in grain boundary controlled regime, Fig.26.

Recent study of the critical current angular dependences of the polycrystalline conductors carried out by scientists in Dresden [84] conclusively proved that at low magnetic fields, up to characteristic value H^* , the critical current is limited by the intergrain critical current. This is reflected in a power-law dependence of $J_c(B)$ and non-Ohmic linear differential-like signature of the V - J curves. At magnetic fields above H^* , $J_c(B)$ is limited by pinning within the $\text{YBa}_2\text{Cu}_3\text{O}_7$ grain (intergrain critical current) with a typical exponential decay dependence. It was found [92] that the transition from intergrain to intragrain critical current limitation is shifted to lower magnetic fields as the temperature is increased. This crossover behavior can have important implications for coated conductor applications. For applications that require the presence of higher magnetic fields, the intergrain critical current of the $\text{YBa}_2\text{Cu}_3\text{O}_7$ coated conductor does not limit the critical current and hence J_c is completely intragrain. The irreversibility field represents in this case the upper limit for applications in high magnetic fields with the intergrain critical current having no influence. A better in-plane texture of the coated conductor with smaller GB angles does not avoid this problem since the crossover field is only shifted to lower magnetic fields, leaving the exponential J_c decrease at high fields unchanged. Only in the case of applications that require magnetic fields lower than the crossover field, an improvement of the grain boundary angles in the samples can be useful [84]. It is interesting that as temperature decreases, H^* seems to increase linearly. This is good news for $>2\text{T}$ applications at 77K . The results if proven for longer lengths, will confirm the possibility of using a multifilamentary RABiTS coated conductor characterized by low FWHM of ω_{RD} , ω_{TD} , ω_{ND} for AC applications at higher fields and higher temperatures. However at 20K at LH_2 applications the field value may exceeded 10T .

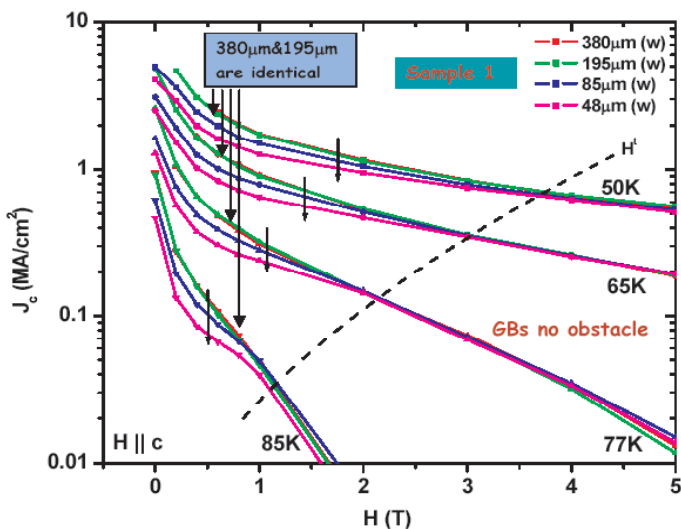


Fig. 26. Critical current density vs magnetic field of the 30-grains long tracks made on the MOD TFA RABiT coated conductor vs track width ranging from 10 grain width to one grain wide track. H^* is a characteristic critical field. Courtesy of D. Larbalestier [83].

5.1.2 Grain Boundary Engineering

There is also some hope that by engineering the grain boundary morphology of the actual RABiTS substrates it could be possible to improve the current performance of the future coated conductors. As recent research conducted on $\text{YBa}_2\text{Cu}_3\text{O}_7$ grown on SrTiO_3 bi-crystals with misalignment angle of 4 degrees shows [85,86] an in-plane orientation of magnetic field in respect of grain boundary has a strong influence on the actual performance of superconducting coating, Fig.27. There is the critical angle, ϕ_k at which the grain boundary does not degrade performance of such a conductor. Such an angle is a function of the temperature and field, which is described elsewhere in detail. [87,88].

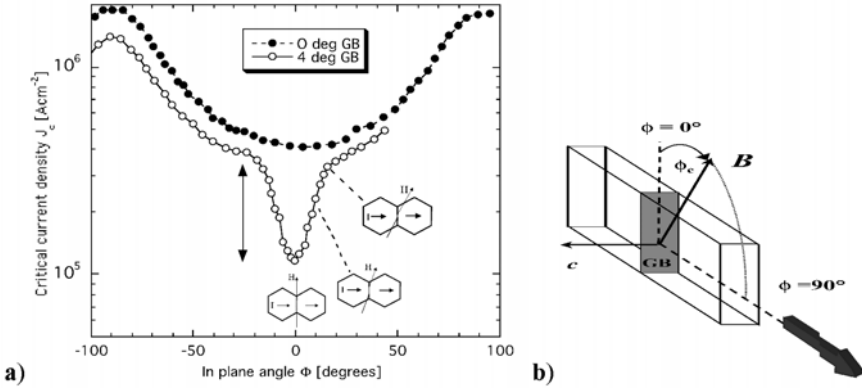


Fig. 27. In plane critical current vs magnetic field measurements on $\text{YBa}_2\text{Cu}_3\text{O}_7$ thin films: **a)** angular dependence of the critical current crossing low angle grain boundary at 8T. For the higher GB angle the minimum is wider and the absolute values are substantially lower; $\phi=90^\circ$ represents Lorentz force-free configuration. Hexagons represent grains whereas black outlines of hexagons represent grain boundaries (the vertical arrow marks the ϕ_k for the given temperature and applied magnetic field); **b)** schematic of the J_c vs (B, ϕ) in plain measurements. [86]. The critical current is only suppressed when the applied field is near parallel to the grain boundary.

At a grain boundary in $\text{YBa}_2\text{Cu}_3\text{O}_{7-d}$, the critical current behaviour is that of the grains unless the field is within an angle, ϕ_k , of the grain boundary [86,87,89]. The existence of this cross-over is a consequence of the fact that for low angle grain boundaries it is the structure and pinning of the lattice of Abrikosov-Josephson vortices which controls the critical current [90]. The part of an each flux line inside the weak pinning region at the grain boundary is small when f is large. It is only for $\phi < \phi_k$ that the small length of the flux lines at the grain boundary experience a Lorentz force in the grain boundary large enough to cut the flux line. Within the grain boundary dominated region j_c is

$$j_c(\phi) = f_{pin} \frac{1}{\Phi_0 \cos \phi} + f_{cut} \frac{1}{d_{gb} \Phi_0} \tan|\phi| \tag{3}$$

determined by the following eq.(3), where: f_{pin} is the pinning force per length, f_{cut} is the force required to cut a flux line, d_{gb} the width of the grain boundary and Φ_0 is the flux quantum. Outside the region defined by ϕ_k the critical current is simply determined by the pinning properties of the grains, the angular dependence of the critical current is simply due to the force free effect. In our previous measurements the minimum in j_c due to the current and magnetic field being perpendicular would be in the same place as the minimum attributed to the cross over into the grain-boundary limited regime. To separate out these two effects it is necessary to pattern a current track at an angle other than perpendicular to the grain boundary.

The $J_c(B, \phi)$ measurements conducted on one of the American Superconductor coated conductor at low fields shown in Fig.28a) the enhancement in critical current due to the force free effect is small at the magnetic fields studied, and the anisotropy of the current density reaches the maximum at field of < 2Tesla, Fig.28b). This data indicates that as the field is increased progressively more grain boundaries switch from the inter-grain limited to the intra-grain limited state. This results in the local current flow becoming progressively more and more aligned with the macroscopic current flow direction, which is required for a force free effect to be observed. Also a low value of the current density anisotropy at low values of magnetic flux density may be amplified by strong value of the self field generated in high current conductors.

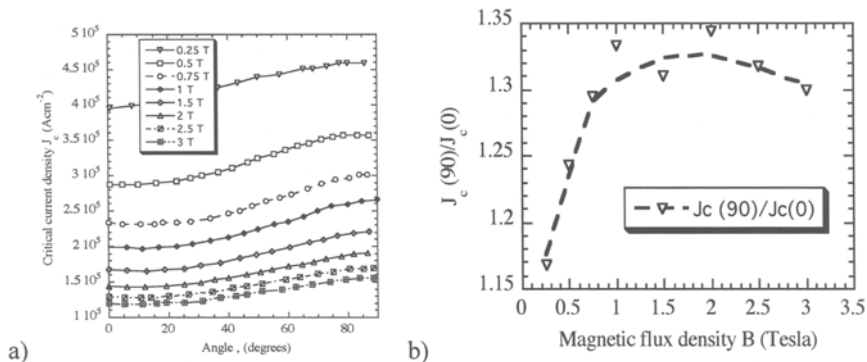


Fig. 28. a) Variation of critical current with rotated in-plane field in the coated conductor sample at 77K; b) the in plane current anisotropy $J_c(\phi=90^\circ)/J_c(\phi=0^\circ)$ in a coated conductor.

To minimise the exposure of the grain boundaries to the external magnetic field hexagonal-type grains should be aligned in the conductor as demonstrated in Fig.29(a). According to the percolation theory the elongated grains can be more efficient in current transfer reducing the probability of the transport current reduction. Additionally if the proposed grain elongation will coincide with grain boundary angles away from magnetic field direction as presented in Fig.29(b) such conductors will possess much better in field performance and versus temperature. The obvious application (not only), which will benefit from this finding are self standing HTS magnets and also hybrid magnets as presented in Fig.30. Therefore an intensive research on grain boundary engineering of the metallic substrates for RABiTS deposition technique is currently being conducted.

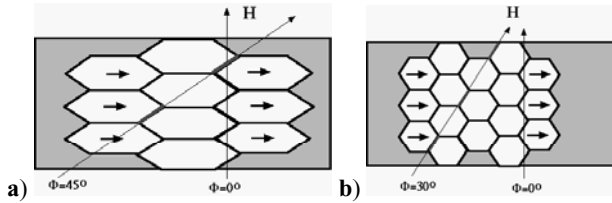


Fig. 29. Elongated hexagonal grains: **a)** have better percolative properties than the simple hexagonal ones; **b)** for the superconducting electromagnet applications is the advantageous response of grain boundaries of the hexagonal grains if all of them are aligned like in Fig.23b) not like in Fig.23b).

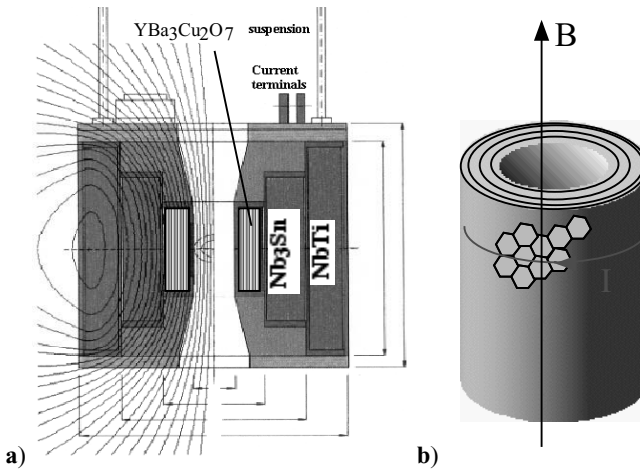


Fig. 30. High magnetic field superconducting electromagnet: **a)** schematic cross section of the multi-section hybrid electromagnet. The materials used are NbTi + Nb₃Sn + NbTi₃(Sn,Ta) resulting in 22.59 Tesla and if additional the magnetic field is generated by an internal coil in the centre it would generate an additional field. The total magnetic field in such a hybrid configuration, currently exceeds 24 Tesla; **b)** schematic outline of the favourable grain structure of the internal HTS coil made from the YBa₂Cu₃O₇ coated conductor.

There is a strong interest in chemical and structural modification of the grain boundaries to improve the electrical properties of higher angle grain boundaries. There are pronounced changes in the microstructure and improvement of the electrical properties of the small-angle GB and also high-angle GB that are induced by doping the boundaries with Ca. Ca doping provides a viable means of engineering the electrical structure of the grain boundaries themselves polycrystalline Y_{0.8}Ca_{0.2}Ba₂Cu₃O_{6+x}. One may accept also that J_c improvement of Ca doped YBa₂Cu₃O₇ coatings could change the level and shape of the J_c/J_{c0} (length, width) dependence shifting J_c/J_{c0} to higher values [91]. The downside of Ca doping is reduction of T_c .

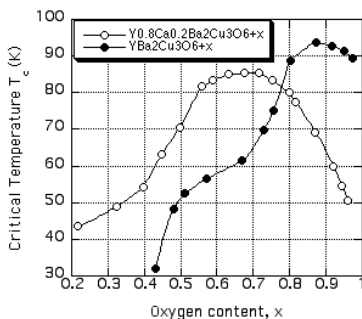


Fig. 31. Critical temperature versus oxygen content x in the $Y_{0.8}Ca_{0.2}Ba_2Cu_3O_{6+x}$ and $YBa_2Cu_3O_{6+x}$ superconductor, adopted after [92].

and also necessity of avoiding oxygen overdoping, Fig. 31. It is also possible to engineer the grain boundaries of the $(RE)_{0.8}Ba_2Cu_3O_7$ coatings with better connectivity by manipulating the composition of the GB using a mixture of the rear earth elements with different ion radiuses.

5.1.3 Intragrain pinning improvement

Because the detrimental effect of grain boundaries on the current percolation is limited to lower operation temperature and magnetic fields below H^* , see Fig.26 [83], it is therefore important that paths to further improvement of the intragrain J_c have to be researched along the Y_2O_3 -BaO-CuO phase diagram [4,93,94], Fig 32. The obvious objective of the introduction of the Y_2BaCuO_5 non-superconducting nanoparticles into the body of $YBa_2Cu_3O_7$ is to improve flux pinning therefore J_c by increasing the defect density, Fig.33b), but also it is probably more importantly to reduce an angular dependence of $J_c(H)$ without causing chemical degradation.

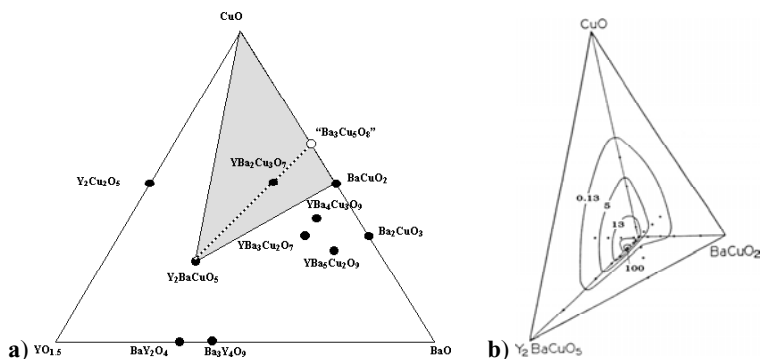


Fig. 32. a) simplified Y_2O_3 -BaO-CuO phase diagram [4,93] with outlined fragment presented in b); b) contour lines of J_c at 77K and 0 Tesla on the fragment of the Y_2BaCuO_5 -BaCuO₂-CuO phase diagram marked in Fig.32a) [94].

There is a strain surrounding the columnar defects induced by Y_2BaCuO_5 particles [95], which can be due to different lattice mismatch between lattice parameters of $Y_2BaCuO_5^*$ and $YBa_2Cu_3O_7$: $(a^*/a) - 6.9\%$, $(b^*/b) + 4.3\%$, $(c^*/c) - 3.2\%$, where $a^* = a/2$, $b^* = b/3$, $c^* = c \cdot 2$. In the case of Y_2BaCuO_5 it is advantageous that the interface between $Y_2BaCuO_5/YBa_2Cu_3O_7$ is sharp due to the lack of chemical reactivity or chemical demixing which is not the case for Y_2O_3 and CeO_2 . At 77K the Y_2BaCuO_5 particles size should be comparable to the $\xi_c \sim 4nm$.

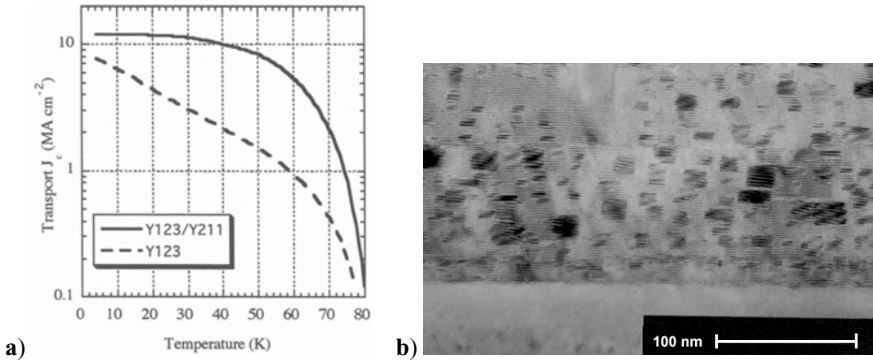


Fig. 33. $Y_2BaCuO_5/YBa_2Cu_3O_7$ multilayer coating by PLD: **a)** Comparison of the critical current density of the virgin $YBa_2Cu_3O_7$ broken line and in situ co-deposited $YBa_2Cu_3O_7/Y_2BaCuO_5$ 35 subsequent coating, solid line, $H_a = 1.6T$; **b)** TEM of the $(Y_2BaCuO_5$ 1.6nm/ $YBa_2Cu_3O_7$ 6.6nm)/35 multilayer system where Y_2BaCuO_5 density $\sim 3 \cdot 10^{11} cm^{-2}$, equivalent $H \sim 6T$. There is evidence of columnation from localized stress between Y_2BaCuO_5 defects. After T.Haugan [96,97].

5.1.4 Coated conductors for AC applications

Because of $(RE)Ba_2Cu_3O_7$ coated conductors are characterized by high irreversibility line and high J_c values in external magnetic fields they are one of the most promising candidates for power applications such as: generators or motors [98]. Advances in multifilamentary $YBa_2Cu_3O_7$ coated conductor technology such as laser grooving, ink-jet patterning and ink jet printing may allow the manufacture of narrow filaments with high critical current density on a thin non-magnetic metal alloy substrate which is separated from the superconductor by a thin dielectric or conductive or even magnetic buffers, Fig.34, see also Table 2.

Therefore there are many issues, which should be address during the design stage of the coated conductor for AC transport current and AC external field applications before actual optimisation of the deposition processes of the conductor takes place. The transverse resistivity across the filamentary structure, ρ_{tr} , depends: on the resistivity of YBCO/metal layer boundary, ρ_b , which affects the current transfer length, on the resistance of the metal layer covering the filaments per unit length, and finally on the width and J_c of YBCO filaments. In the case of the filaments with highly conductive stabilizers only on the top of the filaments, Fig 34c) transverse resistivity between filaments can be high.

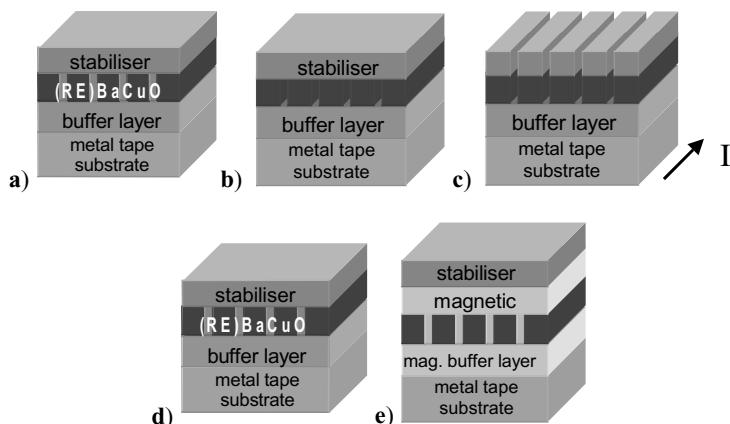


Fig. 34. Schematic representation of the variety of design of straight multifilamentary structures of the coated conductor, where: **a)** highly conductive stabilizer on the top of the filaments and in between filaments; **b)** highly conductive stabilizer interconnecting the filaments; **c)** highly conductive stabilizer only on the top of the filaments, (filaments are electrically decoupled). These tapes will exhibit minimized ac losses by subdividing the YBCO layer with barriers which exhibit high electrical resistance [100]; **d)** as on **a)** but with the conductive buffer layer providing additional stability from the metallic substrates (filaments are fully coupled in the conductive matrix); **e)** magnetic buffer and magnetic cap layer to provide magnetic decoupling and even electric decoupling of the filaments.



Fig. 35. Schematic of the fragment of the single filament and multifilamentary coating in external magnetic field.

It was established that for long tapes the average J_c increases for a smaller grain size (or larger sample) [71,101]. Therefore in this case, both high J_c and high uniformity of J_c are favoured for a small grain size (see paragraph on IBAD). This has significant consequences for coated conductor development. Since the multifilamentary coated conductors appeared to be favourable solution for low AC loss applications, the factors, which, affect the percolative nature of current flow in superconducting coated conductors, such as grain size and sample dimensions, have to be considered [102]. The hysteresis losses in perpendicular magnetic fields are about 2-3 orders of magnitude higher than in the parallel field as described in the eq.(4)-eq.(6):

for $H_{a\perp}$ at $H_o \gg H_{p\perp}$
$$Q_{h\perp} = \mu_o J_{c\perp} w H_o \left(1 - 2.772 \frac{H_{p\perp}}{\pi H_o}\right)$$
 (4)

H_o - amplitude of the applied magnetic field, w - tape width t - tape thickness

for $H_{a\parallel}$ at $H_o \gg H_{p\parallel}$
$$Q_{h\parallel} = \mu_o J_{c\parallel} t H_o \left(1 - 2 \frac{H_{p\parallel}}{3 H_o}\right)$$
 (5)

$$\lim_{H_o \gg H_{p\perp}, H_{p\parallel}} \frac{Q_{h\perp}}{Q_{h\parallel}} = \frac{J_{c\perp} w}{J_{c\parallel} t} = 10^4 \frac{J_{c\perp}}{J_{c\parallel}} = 10^3$$
 (6)

In the case $w=1\text{cm}$, $t=1\mu\text{m}$ the ratio $J_{c\perp}/J_{c\parallel} \cong 0.1$.

Initial calculations of the normalised magnetic moment $M/M_{\text{max(mono H}\parallel\text{c)}}$ of an exemplary multifilamentary coated conductor are presented in Fig.36. It is evident that division of the tape into filaments has little effect on the magnetic moment in the magnetic field parallel to the ab -planes of the conductor.

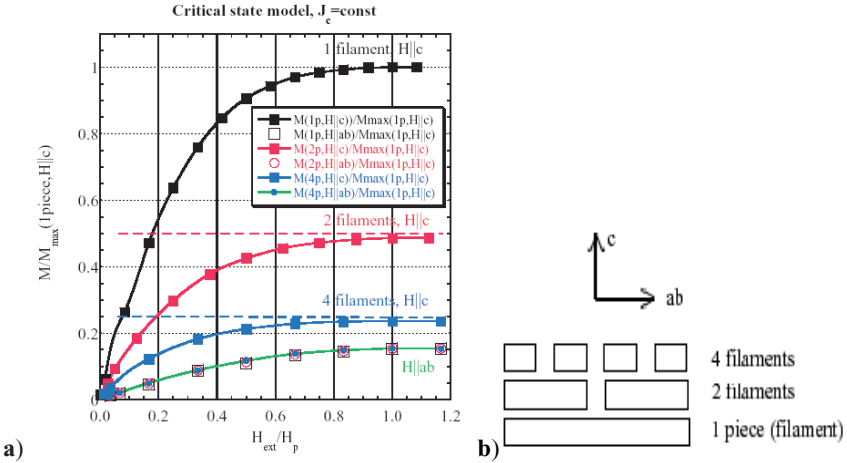


Fig. 36. a) calculated normalised magnetic moment of the YBa₂Cu₃O₇ filamentary tape for $H\parallel ab$ plane and $H\parallel c$ axis presented as outlined in b), division of the tape into filaments has little effect on the magnetic moment in the parallel field; **b)** schematic of the filamentary YBa₂Cu₃O₇ tape architecture.

The exemplary magnetic hysteric losses of the model variable widths filamentary YBa₂Cu₃O₇ coating deposited onto single-crystal LaAlO₃ substrates 3.2mm x12mm by the PLD process grooved by YAG laser at Mound Laser & Photonics Center, Inc. were recently measured and it confirmed the validity of the findings presented in Fig.36 [103], also recent energy loss measured on the actual multifilamentary and monofilamentary YBa₂Cu₃O₇ coated

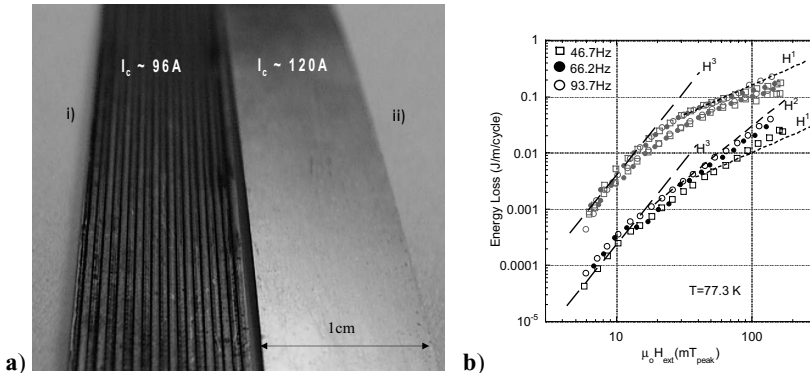


Fig. 37. a) An optical picture of the $\text{YBa}_2\text{Cu}_3\text{O}_7$ coated conductors by RABiTS technique: i) 20 filaments, single filament $\sim 400\mu\text{m}$ and the groove $\sim 100\mu\text{m}$, ii) single filament conductor (laser micromachining translation rate equal 0.10 mms^{-1}); **b)** AC losses due to the external magnetic field are reduced 10 times in the multifilamentary RABiT conductor in a perpendicular magnetic field. Red symbols IBAD monofilament, blue symbols RABiT monofilament, black symbols IBAD multifilament coated conductor.

conductors made by the RABiTS process, Fig.37. The comparison of AC losses measured for a 1 cm wide monofilamentary coated conductor manufactured by the RABiT and IBAD techniques is also presented in Fig.37b). The IBAD sample has slightly higher losses per unit length than RABiTS conductor, which may be due to the defect density of the fine grain structure of the superconducting layer.

It was established experimentally [103] that YBCO RABiTS non-striated (nonfilamentary) tape in perpendicular applied magnetic field linear extrapolation gives a loss value $\approx 0.55\text{ J/m/cycle}$ at $1T_{\text{peak}}$ (equivalent of $\approx 110\text{ W/m/cycle}$ at 200 Hz and $1T_{\text{peak}}$). AC losses follow H^3 and H^1 dependencies in accordance with the critical state model ($J_c = \text{const}$) for partial and full penetration regimes, respectively. The frequency dependence on the energy loss per cycle which is rather weak and the AC losses at different angles are governed mainly by the magnetic field component perpendicular to the ab -plane of the superconductor.

The multifilamentary RABiTS type coated conductor as presented in Fig.37 has roughly 1 order of magnitude lower losses than the monofilament one, Fig.37b). At magnetic fields nearly parallel to its ab plane of superconducting coated conductor AC losses in substrate start to dominate. AC losses in RABiTS multifilamentary conductor are dominated by losses in substrate at all angles of the applied magnetic field with respect to the ab plane of the superconductor. Presence of the magnetic substrate of RABiTS conductors may influence the loss behaviour at higher magnetic fields and different angles due to demagnetizing effects.

For DC applications at any field and for low frequency applications eddy current enabled current sharing will always be superior. For moderate and high frequency applications superconducting links which enables current sharing will have a better loss-sharing trade-off. For decoupled filaments AC loss reduction is directly proportional to the number of filaments eq.7 [104,105].

$$\frac{Q_{\perp mono}}{Q_{\perp multi}} \approx \frac{\pi}{2} N \tag{7}$$

where: N - number of filaments (limited by the smallest possible filament width from the point of view of current percolation).

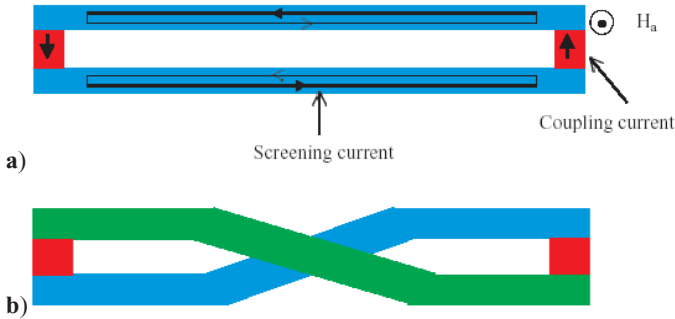


Fig. 38. Distribution of the coupling currents through the current leads in the model 2-filament coated conductor: **a)** untwisted conductor where currents are flowing along the low resistance current leads; **b)** twisted conductor where no coupling current is flowing between conductors.

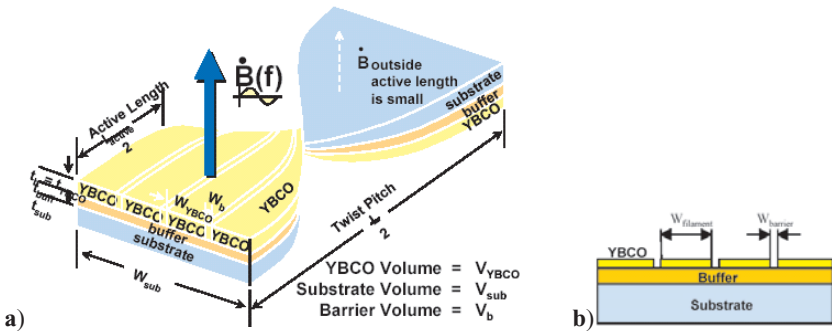


Fig. 39. a) schematic of the initial design of the multifilamentary twisted YBa₂Cu₃O₇ tape for a 1 MW superconducting generator armature, after Oberly [98] see also Fig.34c); **b)** schematic cross section of the conductor in Fig a).

Despite the electrically decouple filaments as in Fig.34c) and Fig.37a) a large circulating current can exist among the filaments due to obvious connections at the end (current leads). AC losses may increase by one order of magnitude or more depending on the distance between the filaments and the resistance at the end contacts.

Considering the presence of the coupling currents in an AC application, the filaments must be transposed (or twisted) at least one time in the middle of the length provided that the

magnetic field is exactly symmetric along both half lengths twisted decoupled filaments to achieve AC loss reduction, Fig 38a). Such a design is used in a 1MW superconducting generator, Fig.39.

5.1.5 Magnetically decoupled multifilamentary YBCO coated conductors

Presence of the magnetic material can have a detrimental and also beneficial influence on the reduction of AC losses and increase of J_c of superconductors. This problem is particularly important in the case of coated conductors and multifilamentary wires. The latest research on the multifilamentary conductors surrounded by magnetic material proved that losses can be reduced substantially according to eq.(8) by coating individual filaments with magnetic material.

By comparing losses in a standard multifilamentary superconductor, Q_{st} , to losses in a multifilamentary superconductor with the magnetic covers around individual filaments, Q_{cov} , at the same reduced current i , one can obtain magnetic decoupling loss reduction coefficient, K_{md} , (eq.8); where $i=I/I_c$, $I_{c1}=I_c/N$, N number of filaments. The parameters $k(i)$ and α are to be determined from experiments and represent individual filament [105].

$$K_{md} = \frac{Q_{st}}{Q_{cov}} = \frac{\alpha I_c^2 F(i)}{Nk(i)\alpha^2 I_{c1}^2 F(i)} = \frac{N^2 I_{c1}^2}{Nk(i)\alpha^2 I_{c1}^2} = \frac{N}{k(i)\alpha^2} \quad (8)$$

The numerical modelling of a model $YBa_2Cu_3O_7$ coated conductor with a different number of filaments of a rectangular cross-section covered with a magnetic layer schematically shown in Fig.34e) was performed using a Finite Element Method commercial package (QuickField) supported by a specially developed AC loss evaluation software [40,106]. As a magnetic material a soft iron was used with $B(H)$ characteristic and hysteretic losses. It was shown before that the best shielding effect and therefore the best decoupling of the filaments was obtained when also the buffer layer and cover layer was magnetic so that each filament was completely embedded in magnetic material. The modelled AC losses were calculated starting from a monocoil conductor, Fig.23b) which we then divided into 5 filaments and 11 filaments, keeping the amount of the superconducting material unchanged. In all cases the iron layer 1 μm thick covering each filament was considered and the separation between the covered filaments was always 5 μm . The critical current density $j_c=10^{10}\text{A/m}^2$ was chosen, a typical value for $YBa_2Cu_3O_7$ films at 77 K. The part of the losses dissipated in the iron layers was less than 0.5% of the losses dissipated in the superconductor, so only the losses in the superconductor are shown. With no magnetic cover ac losses practically do not depend on the number of the filaments in the geometrical configuration under study. Covering the filaments with iron layers decreases the ac loss level significantly. With 11 filaments an ac loss decrease of about 4 times was achieved. With increasing number of the filaments ac losses decrease. The lower curve in Fig.40 represents the losses of one filament multiplied by the corresponding number of filaments, i.e. it is a theoretical limit of totally decoupled filaments and it cannot be overcome. Again the two horizontal lines in Fig.40 represent two different goals ($0.45\text{mWA}^{-1}\cdot\text{m}^{-1}$ and $0.25\text{mWA}^{-1}\cdot\text{m}^{-1}$) for high temperature superconductors (HTS) to be competitive with copper wires. Only the coated conductor with 11 filaments covered with 1mm iron layers fulfils the weaker criterion $0.45\text{mWA}^{-1}\cdot\text{m}^{-1}$. To clarify the contribution of the individual filaments to overall ac losses in 11 filamentary coated conductors further analysis was performed. AC loss distribution among

the individual filaments is very inhomogeneous as can be seen in Figure 41, central filaments tend to have the lowest losses. The highest loss level is reached in the filaments positioned at the edges of the tape due to its high aspect ratio. Covering the filaments with iron layers smooths to some extent the ac loss gradients, but the filaments positioned at the edges of the tape still have the highest losses due to high aspect ratio of the filaments and due to the non-linear properties of the iron layers as well.

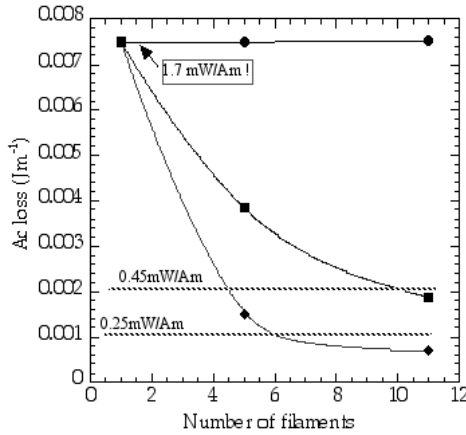


Fig. 40. AC loss in superconducting material of a model coated conductor ($j_c = 10^6 \text{ A cm}^{-2}$) versus number of filaments (constant amount of superconducting material, iron layer thickness $1\mu\text{m}$, separation between covered filaments $5\mu\text{m}$). (● - coupled filaments, i.e. no magnetic cover, ■ - magnetically screened filaments, ◆ - decoupled filaments, i.e. no magnetic cover but the filaments mutually independent). The curves are the guides for the eye. The two horizontal lines represent two different goals ($0.45 \text{ mW A}^{-1}\cdot\text{m}^{-1}$ and $0.25 \text{ mW A}^{-1}\cdot\text{m}^{-1}$) for HTS to be competitive with copper wires.

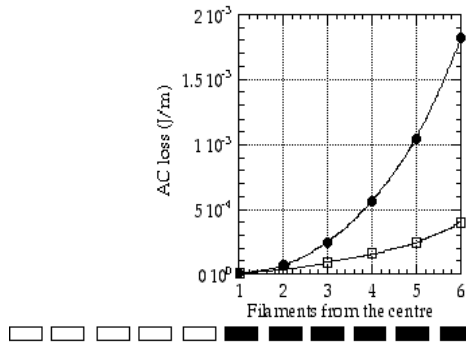


Fig. 41. AC loss contribution of the individual filaments in a half of the 11 coated conductor: ● - coupled filaments, □ - magnetically screened filaments.

The proposed method utilises the shielding effect of magnetic material. In an idealised case magnetic field of a current-carrying filament embedded in a ferromagnetic material propagates outside and is screened by ferromagnetic coverings of the neighbouring filaments, so that the current distribution of the filaments inside these ferromagnetic coverings remains unaffected by the magnetic field of the current-carrying filament. This effect is visualised by a numerical modelling Fig.42 performed on a model multifilamentary composite with 7 filaments of a rectangular cross-section embedded in a ferromagnetic material with different relative magnetic permeability μ when only one filament the upper left one carries the current.

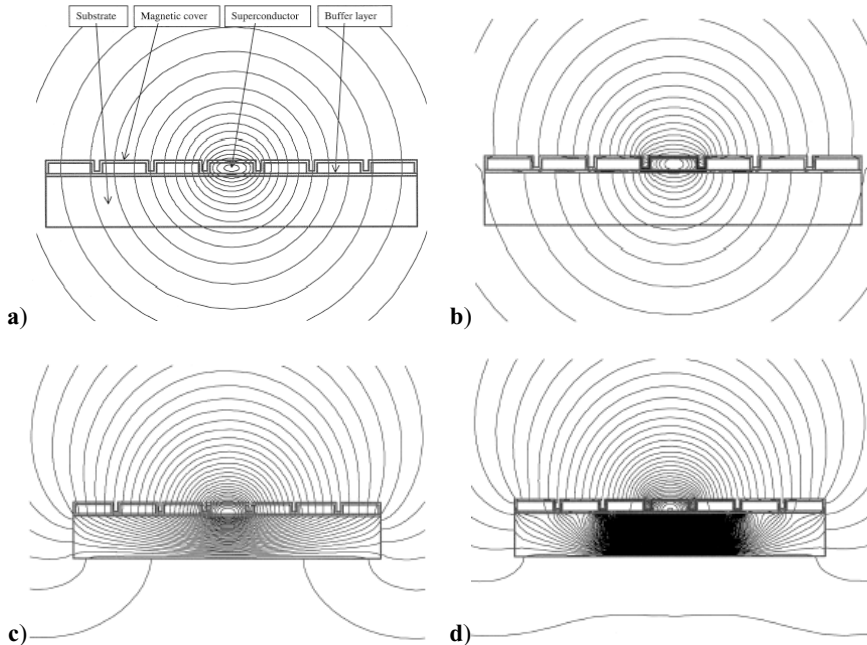


Fig. 42. Comparison of the magnetic flux profile in a superconducting multifilamentary YBCO coated conductor: **a)** Hastelloy substrate no-magnetic covers around the superconducting filaments, **b)** Hastelloy substrate magnetic covers around the superconducting filaments, **c)** NiFe substrate no-magnetic covers around the superconducting filaments, **d)** NiFe substrate magnetic covers around the filaments. The dimensions of the filaments are $8\ \mu\text{m}$ in width and $2\ \mu\text{m}$ in thickness. The thickness of the ferromagnetic layer in the case of **b)** and **d)** is $0.5\ \mu\text{m}$. The spacing between the filaments, covered with a magnetic layer, in both, horizontal and vertical directions, is $1\ \mu\text{m}$. The current with a current density of $10^9\ \text{A}\cdot\text{m}^{-2}$ passes only through the central filament [22,106].

6. ION-BEAM-ASSISTED-DEPOSITION, IBAD

All the results so far are based on achieving a crystallographic texture in the superconductor, which is exactly the same as that of a given metallic substrate using RABiTS technique. The best properties have so far been obtained by pulsed laser deposition, though there is much research into faster, more scalable techniques such as non-vacuum sol-gel technique with orientational epitactic crystallisation of the superconducting and buffer layers. One of the techniques of the coated conductor deposition which provides finer grains than the RABiT technique, is ion beam-assisted deposition, IBAD, inclined substrate deposition processes, ISD. A highly textured but fine grained superconducting layer is very important in terms of minimisation of the percolation effect for multifilamentary (RE)Ba₂Cu₃O₇ conductors for AC applications, Fig.21, Fig.23a), Fig.24d), Fig.25 and Fig.26. In IBAD and ISD processes, Fig.43 the superconducting layer is aligned according to the biaxially aligned buffer layer. This type of conductor is usually formed on a metallic substrate that is mechanically strong, but not textured. For example biaxially aligned yttrium-stabilised zirconia (YSZ) buffer layers can be deposited on untextured metallic substrates using the IBAD and ISD process. Using this technology, YBa₂Cu₃O₇ tapes with a length of a few meters has been fabricated in Japan and in Germany. Summarising, the YBa₂Cu₃O₇ layers produced by IBAD technique can be the finer grain size than that of RABiT process and can be therefore be formed into the finer filamentary conductors without so significant a reduction of the transport current as it is for RABiT conductors as presented in Fig.25.

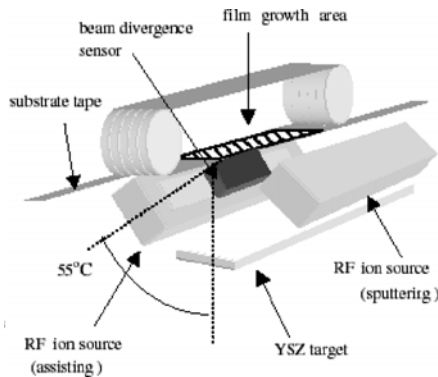


Fig. 43. Schematic diagram for reel-to-reel IBAD system to deposit biaxially textured template films on long metal tapes. A beam divergence sensor was applied to characterize the assisting ion beam. [107]; courtesy of I. Shirohara, see also Fig.3b)

Ion-beam-assisted-deposition (IBAD) is characterized as direct deposition of textured templates on non-textured substrates at quite low temperature [108]. No epitaxial relationships are required with metal tapes, Fig.44. Smooth and highly textured oxide template films of YSZ, Gd₂Zr₂O₇ can be obtained without any degradation that comes from grain boundaries of metal substrates. Recent progress of vacuum technologies makes it

possible to fabricate reliable long length substrates by IBAD [109,110] characterized by smaller grains than achievable by RABiTS technology.

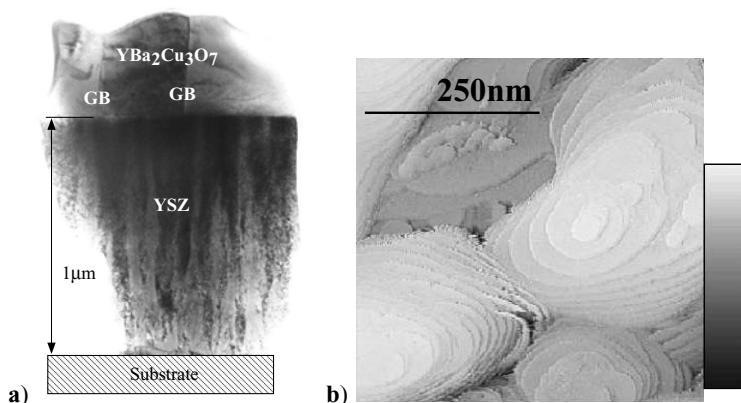


Fig. 44. IBAD of $\text{YBa}_2\text{Cu}_3\text{O}_7$ layer on untextured metallic substrates. **(a)** TEM, micrograph of the superconducting conductor cross section deposited on flexible metallic substrates by ion beam assisted deposition, IBAD. A highly textured YSZ buffer layer formed on the randomly oriented metallic substrates by the IBAD method has a columnar structure and fine nanometre scale grains. The subsequent highly textured $\text{YBa}_2\text{Cu}_3\text{O}_7$ layer, 300nm thick, has much larger grains with no correlation to the grain structure of the substrate but definitely suppressed the $\text{YBa}_2\text{Cu}_3\text{O}_7$ grain growth; courtesy of L.O. Kautschor and C. Jooss from Institute für Materialphysik, University of Goettingen; **(b)** the Scanning Tunneling Microscopy of the top surface of the $\text{YBa}_2\text{Cu}_3\text{O}_7$ superconducting grains showing a-b plains formed during island growth (courtesy of C. Jooss and V. Born). The average grain size is $0.2\mu\text{m}$.

7. METAL ORGANIC DEPOSITION

The fundamental difference between $\text{YBa}_2\text{Cu}_3\text{O}_7$ layers processed by MOD and PLD is that MOD provides a laminar microstructure and the defects are along the a-b plane whereas PLD provides a columnar microstructure with defects along the c-axis. These morphological differences also have influences on the pinning anisotropy in such materials. In some cases the design with magnetic field parallel to the *ab* planes can be more favourable than the $H\parallel ab$. The metal organic deposition process, MOD, (precursor based on metal trifluoroacetate ink [111-114]) can be used to facilitate the engineering of nanoparticle additions. There is a wide range of possible particulate additions such as: Y_2O_3 (coherent with the $\text{YBa}_2\text{Cu}_3\text{O}_7$ matrix), Y_2BaCuO_5 , $\text{Y}_2\text{Cu}_2\text{O}_5$, $\text{Y}_2\text{Cu}_2\text{O}_5$, BaCeO_3 and BaZrO_3 . The MOD process, through the precursor chemistry and process parameters, allows full control of nanoparticle density, size and composition. According to T. Holesinger, (LANL), nanoparticle doping by the MOD process shows improvement in I_c in all fields and temperatures and also provides very important reduction in angular critical current dependence $J_c(B, \phi)$.

8. SOL-GEL TECHNOLOGY

A sol is a colloidal dispersion of a solid in a liquid; it may be viewed as the intermediary stage between a liquid and a suspension. The discrete particles introduced into the solvent move randomly under Brownian motion and must be less than $1\mu\text{m}$ in size for stability; this is achieved by adjusting synthesis variables (such as time and temperature) as well as chemical variables (such as the choice of precursors, pH and concentration). The biggest advantage to sol-gel technology (known by many in the field of superconductivity as chemical solution deposition, CSD) is that the chosen metal ions in solution are mixed at a molecular level; this reduces the chances of chemical demixing/segregation and promotes chemically uniform coatings. Other advantages include low-cost fabrication (non-vacuum deposition methods when compared to other superconductor processes) and it also opens up the possibility for novel deposition methods as mentioned in paragraph 8.2.

8.1 Sol-Gel Synthesis

The main methods for the synthesis of sols can be divided into two sub-categories; aqueous and non-aqueous. Each synthesis route has its advantages and disadvantages but this is in terms of the method in which the sols are deposited, a critical overview of which is given in paragraph 8.2.

8.1.1 Aqueous Routes

A common aqueous form of REBCO formation via an aqueous route is by utilising acetate precursors. In this process, aqueous acetate solutions are mixed in their stoichiometric quantities and a complexing agent (commonly tartaric acid or succinic acid) is used to stabilise the sol.

The main advantages of this route are that it is relatively straightforward to synthesise and the precursors are non-toxic and low cost. The solutions created have a high surface tension and viscosity can be regulated to a certain degree by the addition or subtraction of the complexing agent.

Another popular aqueous route is the nitrate synthesis method. Here, metal nitrates are dissolved in water and complexed via citric acid. The solutions formed have a lower surface tension than that of the acetate route and the variation of viscosity can be done through the use of additives such as ethylene glycol (Pecchini method [115]). The biggest disadvantage to the nitrate route is the highly exothermic reactions caused by the removal of nitrogen (in the form of NO_x gases) during heat-treatment. This exothermic reaction hinders the morphology of the coating and therefore restricts it to the deposition of thin layers (in the order of nanometres as opposed to microns) as thinner layers involve the removal of less organic fraction. This method has become more popular and successful for the deposition of buffer layers (such as CeO_2 [116]) as opposed to superconducting layers as thinner layers are required from buffer materials. There are a number of other ways of forming superconducting and buffer layers from sol-gel technology via aqueous routes but the two most popular have been highlighted above.

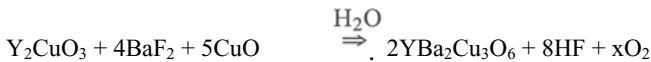
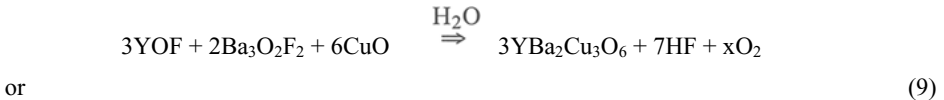
Table 4. List of synthesis sol-gel routes for preparation of the buffer and superconducting layers.

| Route | Synthesis | Comments | Properties |
|---|---|--|--|
| Aqueous Acetate [117] [118-120] | Aqueous acetate solutions. Complexing agent (such as succinic or tartaric acid). Yield a low viscosity sol with high surface tension. | Poor wetting on surface therefore unsuitable for deposition purposes such as dip-coating and ink-jet coating. Ideal for ink-jet printing. BaCO ₃ is known to form at the grain boundaries and hinder superconducting properties. | T_c : ~88K J_c : 3500 A/cm ² (77K) |
| Aqueous Nitrate [115] [121] [122-124] | Nitrate precursors Citric Acid. Addition of a polymerising agent such as ethylene glycol to increase viscosity | Good wetting means suitable for all deposition processes. Highly exothermic reaction involved in the removal of nitrogen. Formation of thick YBCO layers is difficult. Limited to thin buffer layer formation | T_c : ~90K J_c : 4·10 ⁶ A/cm ² (20K) |
| Non-Aqueous Alkoxide [15-20] [133] | Hydroxides dissolved in a non-aqueous solvent (such as methanol, isopropanol and/or hydrochloric acid). Aid of amines and xylenes to yield a sol with variable viscosities | Excellent wetting makes it very suitable for various deposition processes. Main drawback is the high cost of precursors | T_c : ~90K J_c : 10 ⁵ A/cm ² (77K) |
| Non-Aqueous Fluorine [111-114] [132] [131] | Metal precursor powders (for example acetates). Trifluoroacetic acid and methanol solvents. Produce sol with variable viscosities and low surface tension. | Fluorine content means that a barium fluoride complex is formed which stops the formation of barium carbonate. High quality YBCO may be formed. Conversion process is highly exothermic therefore thin layers must be built. Removal of fluorine is in the form of hydrofluoric acid | T_c : ~90K J_c : 2·10 ⁶ A/cm ² (77K) |

8.1.2 Non-Aqueous Routes

There are two main contenders to the field of non-aqueous sols in terms of REBCO production; the alkoxide and fluorine routes. The alkoxide route consists of the addition of metal hydroxides, as well as an amine, into an alcohol based solvent (such as methanol, isopropanol and/or hydrochloric acid). The reactions generated are very complex and involve a number of processes including polymerisation which yields high viscosities. As it is alcohol based, surface tensions are low and gelation (removal of solvent to create a gel network) is rapid. The main advantage to this process is that it is well established as one of the original sol-gel synthesis routes and hence is well covered in the literature. Its main disadvantages are that its precursors are generally expensive and its synthesis conditions are only stable in a narrow window.

Fluorine routes are becoming increasingly popular in the sol-gel synthesis of YBCO. An example of this process is the addition of acetate precursors dissolved in water, methanol and trifluoroacetic acid producing a highly viscous sol. The biggest advantage to this route is that the fluorine attaches itself to the barium ion complexes and this avoids the formation of barium carbonate, eq.(9), and produces high quality YBCO films. The biggest disadvantages are that the process produces hydrofluoric acid (during the removal of fluorine from the system) and is highly exothermic so heat-treatments must be very controlled.



Comments on the synthesis and processing issues for a range of applicable routes such as Acetate Tartaric Route [117,119,120], Nitrate Route [115,121,122-124], Alkoxide Route [125-130,133], Fluorine Route [111-114,132,131] discussed above are presented in Table 4.

8.2. Deposition Processes

There are a number of well established and new deposition processes for the formation of YBCO and buffer layer coatings via sol-gel technology. These can be divided into two categories; those that coat a uniform thin layer on the surface of the substrate in two dimensions and those that open up the possibility for the formation of structures and devices in three dimensions and patterns.

The chosen sol synthesis route greatly depends upon the deposition process as each sol behaves in a particular way (such as viscosity and surface tension) that may or may not be suitable for the deposition process of choice.

8.2.1 Two Dimensional Coatings

The most popular form of two dimensional coating depositions is that of dip-coating. In this process, the substrate is literally dipped into a bath of the desired sol and depending upon the sol and deposition parameters, a layer of the sol is coated over the substrate, Fig.45. The possibility to coat the surface of complex substrate structures (helical, spherical etc.) is now

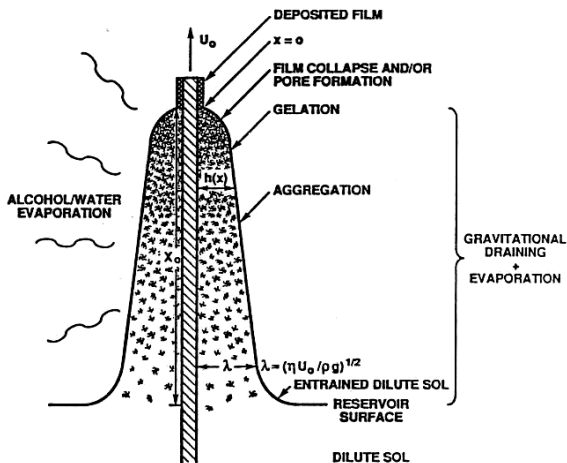


Fig. 45. Cross-sectional dip-coating schematic at bath-substrate surface [134].

possible as the entire surfaces of the substrates are immersed in the sol bath and coated upon removal.

In the dip-coating process, rheological properties of the sols have a large effect on the thickness, h , of the coating developed. The eq.(10) shows the balance between viscous drag ($\propto \eta U/h$) and gravitational forces ($\rho g h$) during deposition by dip coating. It summarises the parameters involved during the deposition of sols on surfaces during dip coating, where c_1 is a constant and h is governed by the viscosity of the sol, η , the speed of withdrawal of the substrate from the ink, U , the density of the sol, ρ , and the gravitational pull, g . As noticed, varying the withdrawal speed, density of the sol (i.e. concentration) and viscosity can have large effects on the coating deposited. Sols with viscosities that can be varied (nitrate, hydroxide and fluorine based sols) are of great advantage and sols with low surface tensions, γ , are crucial as adhesion, E_{Ad} , must be sufficiently high (non-aqueous sols are ideal) to produce low wetting angles, Ω_c , eq.(11).

$$h = c_1 \cdot ((\eta U) / (\rho g))^{-0.5} \quad (10)$$

$$E_{Ad} = \gamma_{LA} \cdot (1 + \cos(\Omega_c)) \quad (11)$$

The biggest advantage to dip-coating is that it opens up the possibility for an all CSD process for coated conductors. In a reel-to-reel deposition sequence, buffer layers can be deposited by CSD means onto textured substrates and superconducting layers can be deposited on top of that to form long length conductors. The only drawback is that both surfaces are coated and the process can be messy and limited to two-dimensional coatings.

Another reel-to-reel deposition process that rivals that of dip-coatings is ink-jet coating. In this process a number of droplets are printed onto the surface of the substrate via an ink-jet nozzle, the droplets then spread to cover the entire substrate surface on the chosen side (hence avoiding the use of scrubbers and reducing the quantity of sol waste). The sol properties required for ink-jet coating is similar to that of dip-coating; sols with low surface tensions

(non-aqueous). However, in order to enable the printing process and deposit through small nozzles (with dimensions in the order of a few microns) the viscosity of the sol must be as low as possible (similar to that of water at 1mPas) and therefore a dilute solution must be used. There are several other two-dimensional deposition processes, such as spray coating, that create uniform two-dimensional coating on flat or complex shaped substrates, however for the creation of three dimensional structures other deposition processes are required.

8.2.2 Two Dimensional Patterning and Three Dimensional Coatings

Ink-jet printing is the main contender in the rapid-prototyping of three-dimensional coatings of YBCO for the development of complex shapes and structures and the analysis of AC losses, Fig.46. In this process, well defined droplets are fired out of the nozzle onto the surface of the substrate, lines are printed and consecutive layers are built to form the desired pattern. In order to achieve these well defined drops, the sol or ink properties required are quite different to that of the two dimensional processes. Fig.46 illustrates the droplet profiles as deposited by ink-jet printing. The wetting angles created between the substrate and the ink has a large effect on the profiles. With angles close to zero, the velocity the droplets accumulate before interaction with the surface may cause it to spread, causing loss of resolution. With wetting angles within the 90-100° range, the resolution of the droplet is maintained and consequent droplets deposited alongside would form the desired pattern. On the other end of the scale, with wetting angles greater than 100°, the contact between the ink and the surface of the substrate is so small that the friction exerted on the droplet by the surface is virtually negligible. The droplet is mobile and therefore the next deposition by its side would be absorbed by it and a discontinuous print would be created.

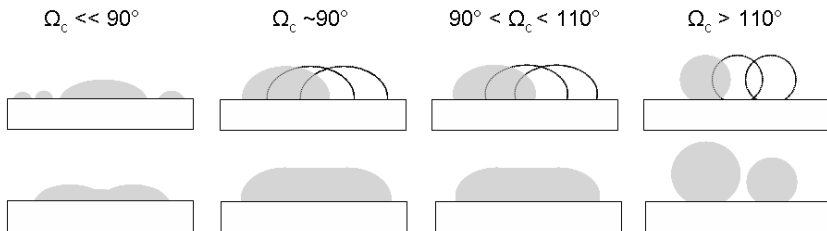


Fig. 46. Various profile created by droplets ink-jet printed onto a solid surface that exhibits a variety of wetting angles.

The optimal sols for this deposition process must have a sufficiently high surface tension to create well defined drops (such as the acetate-tartrate or acetate-succinic routes). In an ideal situation, Fig. 48, the wetting angles should lie in the range of 80-110° but in reality, surface friction exerted onto the droplet by the substrate would mean a whole range of synthesis routes are viable if droplet size can be decreased sufficiently.

Recent trends in the alternative development of coated conductors by non-vacuum techniques prompts questions concerning the high AC loss level of such mono-layer coated conductors. One way to reduce losses could be the division of the conductors to filamentary structures by laser patterning, see Fig.37a). However this adds an extra process to the already

expensive conductor manufacture procedure and may, more importantly, limit the actual transport current due to the intergranular current percolation between grains [101], Fig.25. Twisting or braiding of the sub-filaments of such conductors, Fig. 47a) and b) is impossible by a single coating procedure as it could pose problems on future AC applications. The proposed ink-jet printing technique will enable formation of braided and twisted coated conductors.

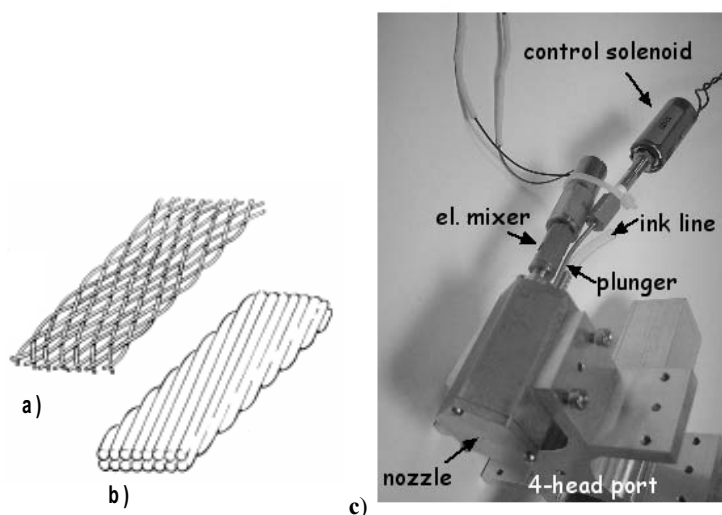


Fig. 47. a) schematic of transposed braided multifilamentary cable; b) schematic of twisted two layer Rutherford-type cable; c) photo of the ink-jet printing multi-head printer developed in Cambridge, which contains integrated mixer for deposition of inks with the $\text{YBa}_2\text{Cu}_3\text{O}_7$ and $\text{Y}_2\text{Ba}_4\text{Cu}_7\text{O}_{15}$ seeds for uniaxial and bi-axial alignment of $(\text{RE})\text{Ba}_2\text{Cu}_3\text{O}_7$ tracks [137].

The practical usage of the thin film coated conductor in AC applications very strongly depends on the level of the AC losses. Single layer superconducting coating on the cm wide metallic ribbons proved to have a very high AC losses in self-field and external field [99,105]. Division of the wide coatings to a narrower multifilamentary coating was proposed to reduce losses in the external magnetic field. Such a solution has almost no effect on self-field losses [135]. Recently proposed magnetic decoupling of the continuous parallel multistrip/multifilamentary conductors by usage of ferromagnetic coating around individual filaments proved to be successful and is very effective in self fields and partially effective in an external magnetic fields [31,136]. However such a technique required however extensive development of epitaxial magnetic buffer layers. None of the above solutions considered transposition of the filaments. Due to the nature of the deposition of kilometre long coated conductors, conventional transposition adopted from low temperature superconductors and even high temperature Bi-based multifilamentary powder-in-tube conductors for continuous twisting and braiding is impossible. Therefore a new sequential semi-continuous ink-jet printing technique of deposition is proposed to produce transposed conductors. A description

of the use of the developed ink-jet printing technique [138] adopted for sequential semi-continuous deposition of transposed braided and twisted multifilamentary coatings is presented in Fig. 48. There are essentially 3 stages of manufacture of transposed filaments in multifilamentary coated conductor as described in Fig.48. As a result of such ink-jet coated conductor preparation transport ac losses, in external magnetic field and also in self-field, can be reduced substantially.

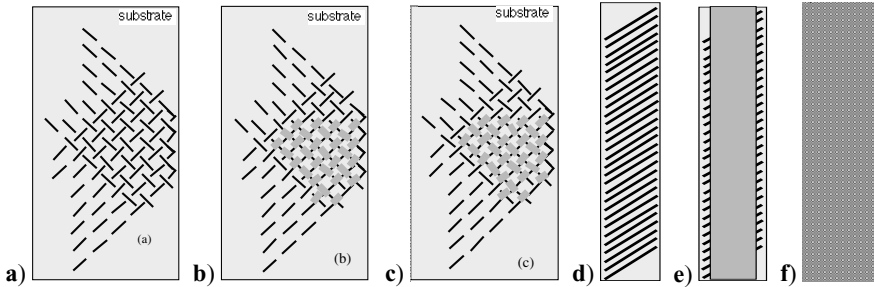


Fig. 48. (a–c) Stages of braided filaments manufacture for coated conductor: **a)** stage 1 where the outline of the first level of the superconducting paths is created; **b)** stage 2 where insulating or conductive or magnetic layer were deposited bridging uncompleted conductive paths over existing paths; **c)** stage 3, final superconducting coating was deposited over insulating or conductive or magnetic paths forming fully conductive network of transposed multifilamentary coated conductor. (**d–e**) Stages of manufacture of twisted filaments in multifilamentary coated conductor: **d)** stage 1 where the outline of the first level of the conductive/superconducting paths were created plain substrates metallic or buffered metallic or ceramic substrates in one direction; **e)** the stage 2 where insulating / conducting / magnetic layer were deposited covering uncompleted conductive paths leaving only the edge of the first layer uncovered; **f)** stage 3, the final coating of the conductive line array was deposited over layer two in a such a way that the edges of initially deposited superconducting paths are connected to the edges of the paths deposited in stage 3 forming fully conductive network of transposed ‘twisted’ multifilamentary coated conductor [16].

9. LIQUID PHASE EPITAXY

Among the major techniques researched for manufacture of the superconducting conductors is the liquid phase epitaxy method (LPE). This method was first developed for thin film growth of semiconductors and oxides for optoelectronics [139]. LPE involves the undercooling of a molten flux supersaturated with solutes and in the presence of a suitable substrate (e.g. small lattice mismatch), the desired phase would nucleate and grow. Growing HTS materials by the one-step LPE method was pioneered by Scheel et al. [140] who surveyed the essential problems and difficulties connected with the epitaxial growth of YBCO films. LPE of (RE)Ba₂Cu₃O₇ is more difficult than the traditional LPE of semiconductor and garnet films since the solubility of RE elements in the melt is very low, hence nucleation and growth is more difficult. The process of LPE has four stages: (i) Producing a solution containing a

quantity of solute corresponding to a saturation temperature T_S ; (ii) Cooling this solution to the growth temperature T_g producing an undercooling supersaturation corresponding to $\Delta T = (T_S - T_g)$; (iii) Bringing the solution and the substrate into contact for an appropriate period of time for the layer thickness required where the solution and/or substrate rotation can be used; (iv) Terminating the growth by separating the solution from the film. The order of stages (i) and (iii) can be interchanged and the cooling can be started (or continued) after the solution and the substrate are brought into contact. Cooling of the solution to promote supersaturation may be in continuous or in a single step mode, or a combination of these two. Stages (iii) and (iv) require certain mechanical movement of the solution and/or the substrate. After growing a layer with the desired thickness, the substrate is removed and it is important to ensure that the surface is free from any drops of excess solution. Knowledge of the phase relation, especially the primary crystallisation fields, PCF, and solubility curves, in the Y-Ba-Cu-O (or other RE) system is of fundamental importance for (Y,RE)Ba₂Cu₃O₇ crystal growth. Fig.49a) shows a ternary phase diagram of Y₂BaCuO₅-CuO-BaCuO₂ system exhibiting the PCF of YBa₂Cu₃O₇. For LPE (and crystal growth), the processing has to be performed within the PCF. Ternary phase diagrams of other REBCO systems are not fundamentally different but the areas of PCF may vary; for instance, the PCF of NdBa₂Cu₃O₇ is much wider than that of YBa₂Cu₃O₇. Fig.49b) illustrates the paths of liquid composition in cooling a melt of composition *p*. Upon cooling the liquid, solid phase Y₂BaCuO₅ crystallises out along p-q. From q to r, Y₂BaCuO₅ reacts with the liquid and forming YBa₂Cu₃O₇, i.e. peritectic reaction starts whereby Y₂BaCuO₅ reacts with liquid to form YBa₂Cu₃O₇ crystals around the Y₂BaCuO₅ particles. At r, all of Y₂BaCuO₅ has decomposed into YBa₂Cu₃O₇ but YBa₂Cu₃O₇ continues to crystallise from the liquid along r-s. Along s-t, YBa₂Cu₃O₇ and BaCuO₂ crystallise together and finally, at point *t*, the remaining liquid solidified via a eutectic reaction forming YBa₂Cu₃O₇, BaCuO₂ and CuO phases.

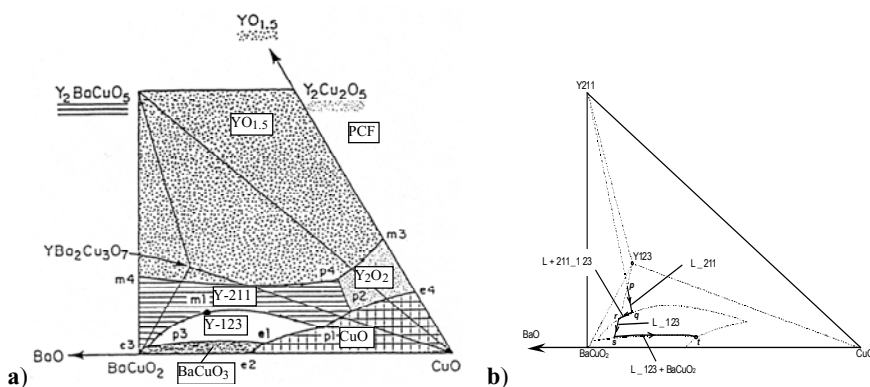


Fig. 49. Ternary phase diagram of Y₂BaCuO₅-CuO-BaCuO₂: **a)** underline of PCF of YBa₂Cu₃O₇ in air; after [141]; **b)** a schematic ternary phase diagram of Y₂BaCuO₅-CuO-BaCuO₂ showing the path in cooling a melt of composition *p*, indicated by arrows in the direction of falling temperature, adapted from [142].

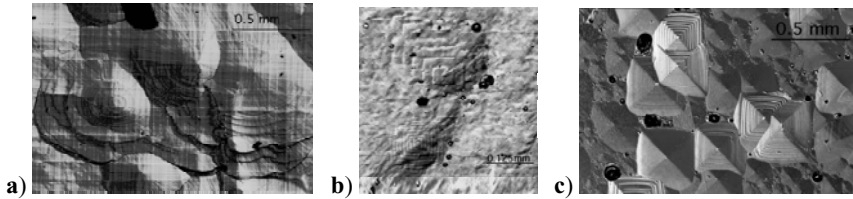


Fig. 50. Optical microscopy pictures of the surface of LPE $\text{YBa}_2\text{Cu}_3\text{O}_7$ layers grown at different patterns: (a) a-axis oriented film of $\text{YBa}_2\text{Cu}_3\text{O}_7$ grown on NdGaO_3 ; (b) c-axis oriented growth of $\text{YBa}_2\text{Cu}_3\text{O}_7$ on NdGaO_3 ; (c) c-axis oriented growth of $\text{YBa}_2\text{Cu}_3\text{O}_7$ on SrTiO_3 . After [144], courtesy of Cheng.

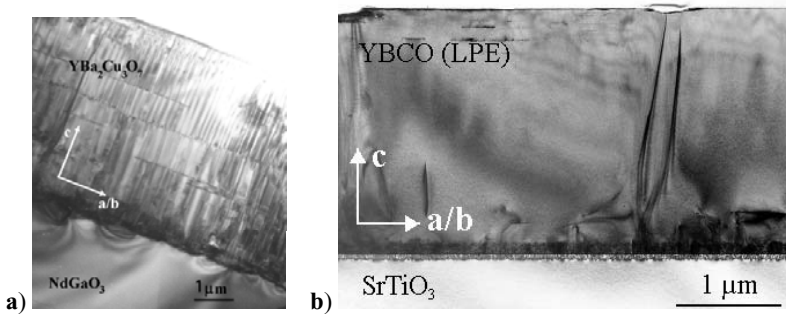


Fig. 51. Transmission Electron Microscopy images across the $\text{YBa}_2\text{Cu}_3\text{O}_7$ layer grown by LPE on different substrates showing high degree of epitaxy: **a)** NdGaO_3 , see Fig.50b) after [144]; **b)** MgO buffered SrTiO_3 substrate after [145], Fig.50c).

The liquid phase epitaxy, LPE, growth mechanism is a complex process that is initiated by multi-nucleation, followed by spiral-mediated growth around dislocation centres beyond a certain critical film thickness according to the BCF theory (Burton, Cabrera, and Frank) [143]. The film continued to grow in a nucleation-free manner and readily developed into elliptical or polygonised (straight edge) spirals that were associated with crystallographic orientations of the film as is demonstrated in Fig.50. Advantages of liquid phase epitaxy over the vacuum-base thin film techniques such as sputtering and pulse laser deposition (PLD) are evident. Such a process is characterised by fast growth rate, typically $1 \mu\text{m}/\text{min}$, texture of the superconducting coating and J_c do not degrade with increasing film thickness which is unique to LPE and the process is in-situ and non-vacuum (relatively low cost), Fig.52. The disadvantages are superconducting layer cracking above $5\mu\text{m}$ thickness dramatically degrading transport critical current. Also the process is conducted at a very high temperature in a corrosive atmosphere where most of the metallic substrates will corrode and the growth process is not exactly epitaxial and is sometimes called Liquid Phase Processing (LPP), therefore scalability and applicability of such a LPE technique to manufacture long lengths of tape from a conductor is problematic.

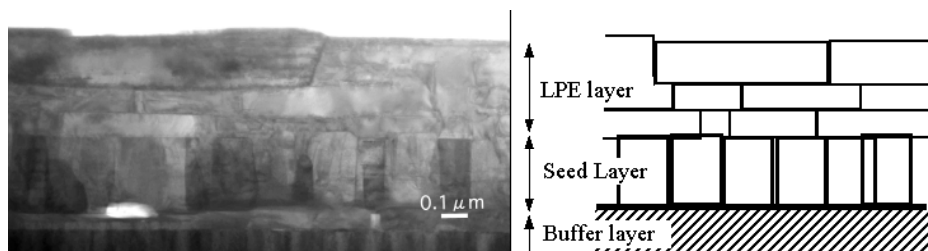


Fig. 52 Cross sectional Transmission Electron Microscopy observation of the LPE grown $\text{YBa}_2\text{Cu}_3\text{O}_7$ film on the $\text{YBa}_2\text{Cu}_3\text{O}_7$ seed layer on Y_2O_3 -YSZ buffer layer on Ni-Cr alloy; courtesy of Dr Y.Yamada.

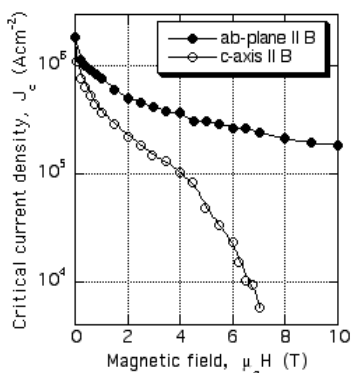


Fig. 53. Critical current density vs magnetic field for the $\text{YBa}_2\text{Cu}_3\text{O}_7$ superconducting LPE film presented in Fig.52.

Although the LPE fabrication process is complex, it provides excellent results in terms of production rate, texture, Fig.52 and film thickness and very high superconducting transport properties, Fig.53, when deposited on the flexible metallic tapes. To simplify the architecture of the conductor and reduce the cost of conductors, LPE fabrication of superconducting layers can be conducted directly on Ag substrates, which have a very low reactivity with $\text{YBa}_2\text{Cu}_3\text{O}_7$ and high conductivity ideal for cryomagnetic protection. Since the melting point of Ag is relatively low, the fabrication temperature of the LPE process must be lowered to around 900°C . The temperature of the LPE process can be lowered when BaF_2 is added to a Ba-Cu-O solution that is saturated with Ag. Using this procedure, $\text{YBa}_2\text{Cu}_3\text{O}_7$ films have been successfully fabricated on short Ag substrates by LPE process. Attempts are made to develop a continuous fabrication process that will allow longer tape conductors to be produced. The goal of this type of conductor is to produce a long tape with a superconducting layer at least $10 \mu\text{m}$ thick using a non-vacuum procedure. The only problem with the thicker $\text{YBa}_2\text{Cu}_3\text{O}_7$ layers is the minimum bending radius of such conductors which may restrict the usage of such conductors with superconductor thickness $> 5 \mu\text{m}$ to specific applications e.g. Fault Current Limiters.

9.1 Hybrid Liquid Phase Epitaxy

As was described in the previous paragraph in the case of classical LPE from a bath of molten flux, growth is controlled either by cooling of the melt from the undersaturated regime, or by spatial transport of flux from a high temperature saturated region to a lower temperature region at the substrate where it becomes supersaturated. In contrast, hybrid liquid phase epitaxy, HLPE growth is controlled by adjusting the rate of feeding of the liquid layer, with RE-rich material at constant temperature (RE)Ba₂Cu₃O₇, growth occurs by RE diffusive transport through a thin liquid BaO–CuO boundary layer); in this case σ , and the corresponding undercooling, adjust self-consistently to match the growth rate to the feeding rate [146].

For steady state growth the flux layer needs to be fed with stoichiometric (RE)Ba₂Cu₃O₇ material. Since the liquid flux layer can be as thin as 100 nm, the flux cannot dissolve a large amount of the substrate or seed layer, and the transit time for diffusion of RE through the layer is of the order of 0.1 ms, defining a time constant for equilibration of σ . It is found that nucleation of the (RE)Ba₂Cu₃O₇ phase is easier for HLPE than in the case of LPE where there is also a transition from *c*-axis oriented growth to *a*–*b* growth for increasing supersaturation (undercooling). It was reported that there exists a very narrow working window in temperature (~3°C) for growth of *c*-axis Ba₂Cu₃O₇ films on closely matched substrates such as NdGaO₃ [147]. We found a somewhat wider working window (~10°C) for LPE on NdGaO₃ [148,149]. However, in the case of HLPE this width is around 100°C. Also, while some degree of *a*–*b* misorientation was observed for lower deposition temperatures, this misorientation could be eliminated for reduced deposition rates. We believe that the origin of this fortunate behaviour lies in the liquid layer that promotes more thermodynamically stable *c*-axis growth rather than more kinetically favourable *a*–*b* growth [150]. Thus HLPE embodies all the advantages of LPE without the disadvantages of difficult nucleation and a large volume of aggressive liquid. YBCO films 1–2 μm thick with excellent epitaxial orientation, with $T_c \sim 90$ K and a critical current density $J_c > 2$ MA cm⁻² have been grown on a range of (100) textured nickel-alloy tapes buffered with NiO/SrTiO₃, and also on unbuffered (110) textured silver tape. Growth rates up to 10 nm s⁻¹ have been demonstrated with HLPE. Deposition of *c*-axis oriented epitaxial YBa₂Cu₃O₇ is reported on both seeded and non-seeded substrates; the process is tolerant of a high substrate mismatch. In marked contrast to LPE, it is possible to grow epitaxial *c*-axis oriented films without a seed layer even on significantly mismatched substrates such as MgO.

To enable continuous liquid phase deposition of the (RE)Ba₂Cu₃O₇ coatings on the metallic substrates a horizontal LPE continuous deposition technique of “drawing” the ribbon inside the crucible was developed in Cambridge. A split furnace arrangement was used for continuous coating of metallic tapes [151]. The arrangement of a uniquely designed “split” furnace (Fig.54) enables continuous deposition of an LPE film under precisely controlled parameters: temperature and RE supersaturation-rich fluid feed rotation system. Long metallic tapes were successfully coated, Fig.56b).

A part of the tape was immersed into the crucible in a similar manner as the rotating substrate. The submerged tape is kept in place by a ceramic holder over which can slide while being pulled (moved) through the melt. The stirring is accomplished by crucible rotation (resulting in a similar effect as the substrate rotation). In this case two stage mixing (boundary layer control is achieved), by tape movement at velocity $u \sim 0.1$ mm s⁻¹, and crucible rotation

at angular frequency (~ 100 rpm). The inert gas chamber used allowed growth to be carried out under reduced partial pressure of oxygen down to 0.1%, hence at much reduced temperatures ($\sim 850^\circ\text{C}$). However, reducing the growth temperature implies reduction of the solubility Fig.55.

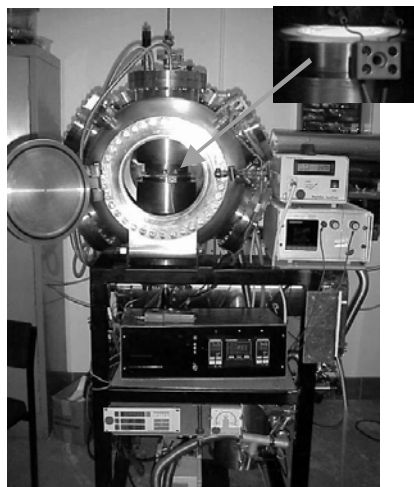
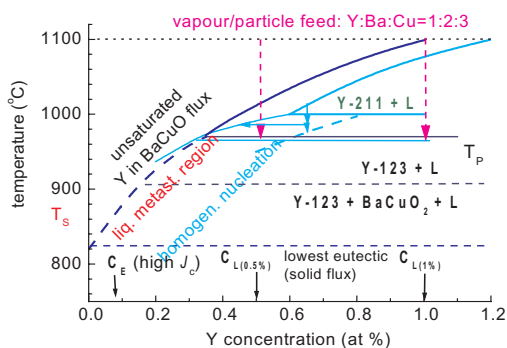
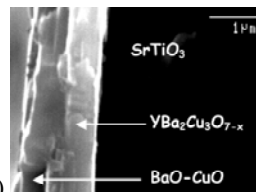


Fig. 54. Controlled atmosphere chamber used for reduced temperature LPE deposition. Inset is showing “split furnace” detail that enables horizontal continuous LPE coating of long metallic tapes [151,152].



a)



b)

Fig. 55. a) schematics of Y solubility in BaO-CuO flux in air (gray/cyan) and in 0.1% oxygen in 1 bar Ar (black/blue). The initial composition of the flux applied by HLPE is shown as $C_{L(0.5\%)}$ and $C_{L(1\%)}$ for respective Y concentration; **b)** Fractured cross section of the coating [146].

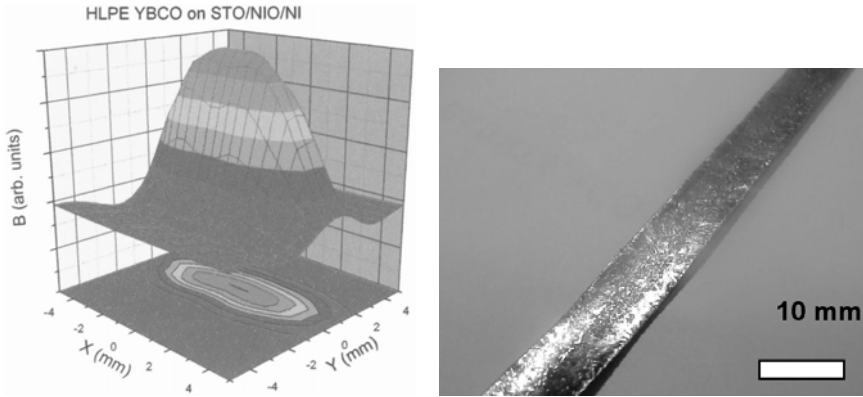


Fig. 56. The HLPE $\text{YBa}_2\text{Cu}_3\text{O}_7$ coated conductor: **a)** Trapped field mapping of HLPE $\text{YBa}_2\text{Cu}_3\text{O}_7$ on SrTiO_3 buffered NiO/Ni textured tape using Hall-probe scanner; **b)** view of the continuously deposited $(\text{RE})\text{Ba}_2\text{Cu}_3\text{O}_7$ from the RE supersaturated Ba-Cu-O flux by LPE on NiFe/ SrTiO_3 tape [153].

This drawback of lower solubility was researched with adding RE elements into the flux containing Y. The mixing of Y and RE was found to increase the overall solubility and supersaturation, hence the growth rate.

For lower deposition rates, the films have high crystalline perfection and correspondingly a low J_c ; when the deposition rate is high, J_c values of 2-4 MA cm^{-2} have been demonstrated consistently, Fig.56a). In this work we have achieved $T_c \sim 90$ K and $I_c \sim 400$ A per cm width in $\text{YBa}_2\text{Cu}_3\text{O}_7$ films on a range of substrates including single crystal substrates and RABiTS Ni-alloy tape with NiO/ SrTiO_3 buffers. The influence of substrate parameters and morphology on the controlled seeding process was investigated [152]. Rough vacuum deposition, high growth rates and easy composition control, with great flexibility in the feeding method are very attractive process characteristics. In addition, the process has a high efficiency of material utilization, and thick films can be produced with excellent crystallinity and high critical current densities. These features suggest that HLPE has the potential to be a robust high-rate low-cost process for coated conductor processing [18,151,154,155].

10. MAGNETIC ALIGNMENT AND THERMO - MAGNETIC GROWTH OF $(\text{RE})\text{Ba}_2\text{Cu}_3\text{O}_7$

In traditional, thermo-mechanical processing of grain-oriented superconducting oxides for applications, thermal treatment is combined with some method of mechanical alignment of grains, such as rolling or sequential pressing. An alternative to this approach involves applying a high magnetic field before or during thermal treatment to align grains. When a grain having an anisotropic paramagnetic susceptibility in its normal state is placed in a magnetic field, the grain rotates such that the axis of the minimum susceptibility is aligned

parallel to the field direction. Any anisotropic crystal placed in a uniform external magnetic field acting orientating force, F , defined by the difference of magnetic susceptibility for the perpendicular crystallographic axes $\Delta\chi$, magnitude of the applied magnetic field, H , volume of the crystal, V , and also orientation of the applied field (ϕ - angle between crystallographic axis at which c has a maximum value and the direction of external magnetic field), eq.12.

$$F = \Delta\chi \cdot V \cdot H^2 \cdot \sin(2\phi) \quad (12)$$

Because the paramagnetic susceptibility of the rare earths is anisotropic, an alternative alignment method is to use a static magnetic field to align crystals, which precipitate from a melt. The most effective texturing effect of the (RE)Ba₂Cu₃O₇ compounds in the external magnetic field is for such RE ions, which have the highest magnetic moment, Table 5.

Table 5. Magnetic moments of the RE ions and axis of (RE)Ba₂Cu₃O₇ alignment

| atomic number | atomic symbol | ionic radius (nm) | magnetic moment | Axis Parallel to H |
|---------------|---------------|----------------------|-----------------|--------------------|
| 21 | Sc | 0.083 | – | |
| 39 | Y | 0.106 | 0 | c |
| 57 | La | 0.122 | 0 | – |
| 58 | Ce | 0.118 | 2.56 | – |
| 59 | Pr | 0.116 | 3.62 | – |
| 60 | Nd | 0.115 | 3.68 | c |
| 61 | Pm | 0.114 | 2.83 | – |
| 62 | Sm | 0.113 | 1.55–1.65 | c |
| 63 | Eu | 0.113 | 3.40–3.50 | a |
| 64 | Gd | 0.111 | 7.94 | c |
| 65 | Tb | 0.109 | 9.7 | – |
| 66 | Dy | 0.107 | 10.6 | c |
| 67 | Ho | 0.105 | 10.6 | c |
| 68 | E | 0.104 | 9.6 | a |
| 69 | Tm | 0.104 | 7.6 | a |
| 70 | Yb | 0.1 | 4.5 | a |
| 71 | Lu | 0.99 | 0 | – |

Because YBa₂Cu₃O₇ contains no magnetic elements, its magnetic alignment results from anisotropy in the paramagnetic susceptibility associated with the Cu-O conducting planes. Since the susceptibility parallel to the c-axis is higher than that perpendicular to the c-axis, the compound aligns with the c-axis parallel to the applied field direction. In principle there are two contributing factors to the magnetic forces tending to align superconducting cuprates: the magnetic moment tending to align the longest dimension parallel to the field and the moment which aligns the axis of largest susceptibility along the field direction for a paramagnetic material. For spherical YBa₂Cu₃O₇ powder, the shape factor is small, and so the c-axis aligns along the direction of the field. For rare-earth doped (Y,RE)Ba₂Cu₃O₇ compounds, the paramagnetic susceptibility is dominated by the R³⁺ ion, and the source of anisotropy is

single-ion anisotropy associated with crystal fields at the rare-earth site. For Gd and Ho doped (Y,RE)Ba₂Cu₃O₇, the particles align with c-axis parallel to the magnetic field, while for Er-doped (Y,RE) YBa₂Cu₃O₇, the particles align perpendicular to the magnetic field. An addition of the Nd, and Eu to YBa₂Cu₃O₇ material causes density reduction of the sintered superconductor where Gd, Yb and especially Ho increase the density of the sintered YBa₂Cu₃O₇ coatings. There is a linear dependence between ionic radius of the rare earth elements and actual a and c lattice parameter of (RE)Ba₂Cu₃O₇ unit cell which is important for the magnetic alignment of the mixed rare earth, see Figure 57. The presence of a liquid phase such as binders and carriers in the superconducting oxide greatly facilitates grain alignment. Such a liquid phase can be attained through high temperature treatment of the oxide during simultaneous sintering, thereby eliminating the grain interface impurities or alternatively if the liquid phase has the similar composition to the superconducting oxide it may act as a interconnector between the individual particles during grain growth improving the grain interconnectivity and therefore minimising current percolation. The great advantage of the self-liquid approach for high or low temperature processing over the use of an organic solvent liquid is the significant decrease in impurity phases created at the grain boundaries by reaction of the (Y,RE)YBa₂Cu₃O₇ compound with the organic solvents and binders and low density of the final coating. Such impurities and voids degrade connection between grains, thereby severely limiting the J_c values achievable. When these materials are textured by a high magnetic field during melt-growth, not only is a textured, larger domain structure attained, but textured small grains with better connection between grains is achieved by liquid phase binding during the high temperature processing [156] as it is described under the two following headings.

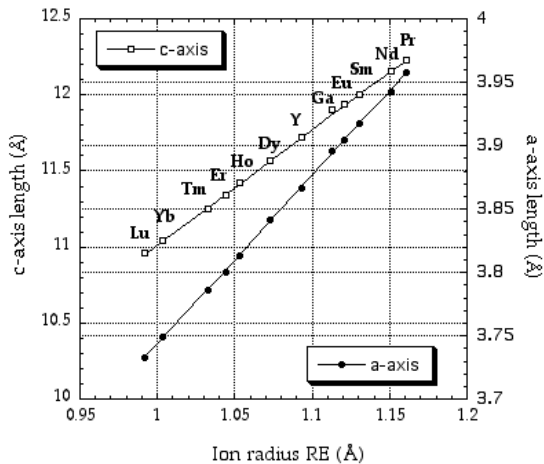


Fig. 57. Lattice parameters variations of the different (RE)Ba₂Cu₃O₇ crystals versus ionic radius of rear earth element.

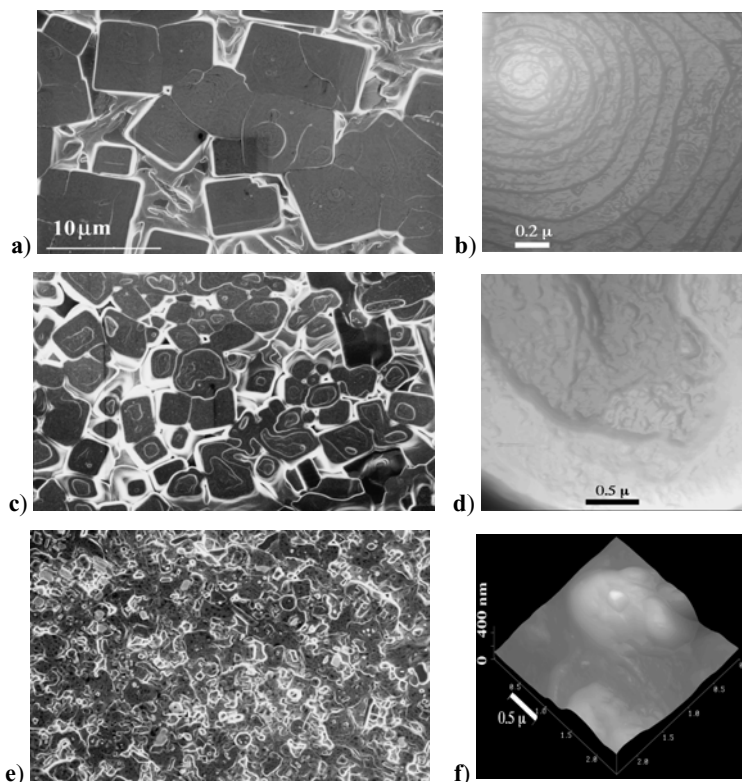


Fig. 58. SEM **a)**, **c)**, **e)** and high-resolution AFM images of the three CVD $\text{YBa}_2\text{Cu}_3\text{O}_7$ films grown at different magnetic fields: **(a)** 0T, large rectangular grains; **(b)** 0 T, A single-core spiral; **(c)** 2 T, irregular grains; **(d)** 2 T, 2D-growth behaviour; **(e)** 4 T, small interconnected grains; **(f)** 4T, the 3D growth mode.

10.1 Alignment During Slow Solidification of the $(\text{RE})\text{YBa}_2\text{Cu}_3\text{O}_7$

This alignment technique essentially based on the anisotropic magnetic susceptibility is very similar to the second technique [157]. In this particular case slow cooling through the solidification temperature maximise $(\text{RE})\text{Ba}_2\text{Cu}_3\text{O}_7$ grain size and simultaneously give enough time for the particles to rotate so that the direction in which the susceptibility is maximum aligns parallel with the direction of the applied magnetic field. Both calculations and experiments have shown that at temperatures which are sufficiently high to melt $(\text{RE})\text{Ba}_2\text{Cu}_3\text{O}_7$ in preparation for resolidification under field, this magnetic force is large enough to overcome disordering forces from thermal agitations or shape anisotropy. The successful thermal procedure is: $100^\circ\text{C}/\text{h} \Rightarrow 1085^\circ\text{C}$ 0.4h \Rightarrow fast cooling to 1035°C cooling $2^\circ\text{C}/\text{h} \Rightarrow 980^\circ\text{C}$ cooling $3^\circ\text{C}/\text{h} \Rightarrow 930^\circ\text{C} \Rightarrow 60^\circ\text{C}/\text{h} \Rightarrow 420^\circ\text{C}$ 72h $\Rightarrow 200^\circ\text{C}/\text{h} \Rightarrow \text{RT}$.

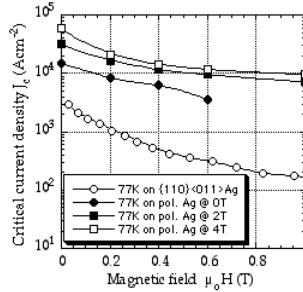


Fig. 59. J_c of $\text{YBa}_2\text{Cu}_3\text{O}_7$ superconducting non-vacuum coatings on silver substrates. Low values of the J_c of YBCO deposited by ultrasonic spray pyrolysis [159] on highly textured silver ribbons with a single component $\{110\}\langle 011\rangle$, FWHM smaller than 6° in comparison with CVD deposition on highly polished polycrystalline substrates [161] prove the point that smoothness of the substrate has a decisive role in high texture alignment of $\text{YBa}_2\text{Cu}_3\text{O}_7$ on silver not actual texture of the silver [160]. Similar comparative dependence was observed in the case of Tl1223 coatings [162].

Magnetically Assisted Nucleation and Growth of $\text{YBa}_2\text{Cu}_3\text{O}_7$ such a process conducted on polycrystalline untextured silver substrate by the chemical vapour deposition, CVD, appeared to possess much better J_c vs B characteristics through the improved grain connectivity [158] than that deposited on a highly textured silver substrates [159], Fig.58, Fig.59.

Images for the $\text{YBa}_2\text{Cu}_3\text{O}_7$ films deposited at different magnetic fields are presented in Fig.58. In the absence of a magnetic field, the films exhibit large rectangular grains, and large voids and poor interconnections are present. At 2 T, the grain shape seems similar to that of the 0T films, but the grain size is reduced. Under a field of above 2T, the crystallites of films were more homogeneous than an irregular grains; 1-2 μm were well connected to each other, compared with that without the magnetic field. Clearly, the intergrain connectivity and morphology were less influenced by fields over 4T. Thus, with increasing magnetic field, the grain size was reduced, but the grain connectivity was improved. Smoothness but not an actual texture of the silver-based substrate has a decisive role in nucleation of the preferentially align HTS coating [160]. The $\text{YBa}_2\text{Cu}_3\text{O}_7$ growth-mode change from the spiral growth mode at zero field to the two-dimensional or three dimensional island growth mode under an external magnetic field which is responsible for improvement of transport property of superconducting coatings [161], Fig.59. The thermo-magnetic process is very effective in yielding superconducting well-interconnected $\text{YBa}_2\text{Cu}_3\text{O}_7$ films on silver substrates with relatively high critical current densities, but without the use of any buffer layers. Such a novel technique may be used to produce texture in a bulk samples and in a low cost long lengths $\text{YBa}_2\text{Cu}_3\text{O}_7$ coated conductors, however further research is required to improve J_c vs B performance.

One can conclude that $\text{YBa}_2\text{Cu}_3\text{O}_7$ coatings on highly polished silver or silver plated Ni flexible metallic substrate (for better mechanical strength), can achieve good textured microstructure without any particular preferential texture development, is a promising

technique for conductors in long lengths. The J_c value compares well with the conventional superconducting tapes, e.g., Nb_3Sn . The microstructure and superconducting properties of the tape are very sensitive to the substrate parameters during the formation process which is a crucial parameter in maximising tape performance.

10.2 Dynamic Magnetic Alignment

As it was described earlier a static magnetic alignment by settling or immobilising monocrystal grains in a constant magnetic field is a common process to obtain uniaxially aligned $\text{YBa}_2\text{Cu}_3\text{O}_7$ [163]. In the case of the untwined $\text{Y}_2\text{Ba}_4\text{Cu}_8\text{O}_{16}$ or $\text{Y}_2\text{Ba}_4\text{Cu}_7\text{O}_{15}$ (or any rare earth-based) compound, advantage can be taken of their orthorhombic structure. The anisotropy of the structure leads to normal-state magnetic susceptibility with $b < a < c$ for $\text{Y}_2\text{Ba}_4\text{Cu}_7\text{O}_{15}$ and $\text{Y}_2\text{Ba}_4\text{Cu}_8\text{O}_{16}$ [164]. A constant magnetic field will align freely suspended grains along the c -axis. The rotation relaxation time as the time which a particle takes to rotate to its equilibrium orientation in a static magnetic field of given magnitude can be controlled. If the field is rotated from its initial orientation by 90° for a time shorter than the c -axis rotation relaxation time so that the c -axis alignment is not disturbed, the a -axis, with intermediate susceptibility, will tend to align along the rotated direction. The b -axis of the grain, with the minimum susceptibility, will align with the zero field direction. If such an alternating or dynamic field is applied to a powder in suspension in a medium of the appropriate viscosity, biaxial alignment will be achieved. The complete process is detailed elsewhere [137]. Fig.60a) illustrates the results of the process in the case of $\text{Y}_2\text{Ba}_4\text{Cu}_8\text{O}_{16}$. Clearly a significant fraction of the large melt-grown grains are aligned with one another and with the axes of the tape (parallel to the image's sides).

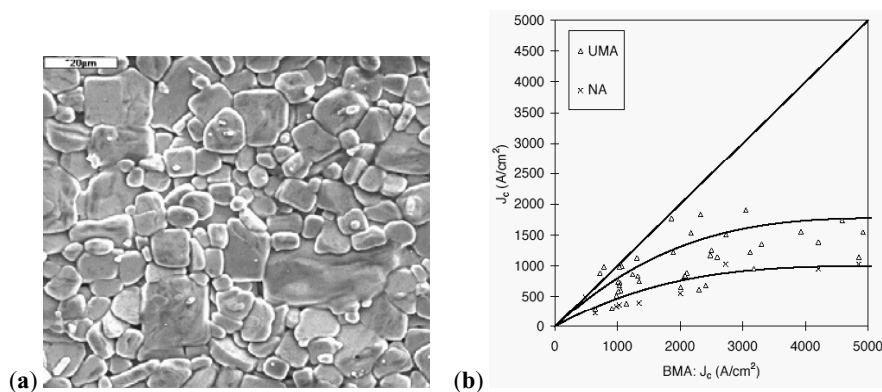


Fig. 60. The $\text{Y}_2\text{Ba}_4\text{Cu}_8\text{O}_{16}$ tape magnetically assisted melt-processed at 920°C , (a) SEM picture of the top surface of the tape [164]; (b) comparison of results J_c for biaxially aligned coating, BMA, uniaxially aligned coating, UMA and non-aligned coating, NA in respect to BMA coatings. However the lines are guides for the eye the benefit of biaxial alignment is obvious.

Using a dynamic alignment technique founded on similar ideas, Zhang and Budnick [165] demonstrated biaxial alignment of $\text{Sm}_2\text{Fe}_{17}$ particles with the a-axis and b-axes distributed within about 15° . In that case, they used an oscillating field and progressively decreased the amplitude of the oscillation, so that the process finished with the magnetic field fixed in direction. It is believed that maintaining the rotating field during the entire process is more appropriate to achieve in-plane anisotropy of the final superconducting coating. This is supported by the very high degree of texture obtained. Rocking curves on samples demonstrated FWHM to be as low as 2° .

The critical current results Fig.60b) demonstrate improvements due to the biaxial alignment process [164]. Benefit of biaxial alignment is presented in Fig.60b). The critical current densities of the uniaxially magnetically aligned, UMA, and non-aligned, NA, tapes are plotted as a function of the critical current density of the corresponding biaxially magnetically aligned, BMA, coating. The diagonal gives the limit below which a benefit is observed. The tapes compared were in the same batch and were melt processed at the same time. The only difference between them is the magnetic alignment process. All the data are situated in the bottom right part of Fig.60b) signifying a benefit from biaxial alignment.

11. CRYOMAGNETIC STABILISATION OF $\text{Ag}/\text{YBa}_2\text{Cu}_3\text{O}_7/\text{BUFFER}/\text{Ni}$ -BASED COATED CONDUCTOR

The highly conductive layer on the top superconductor has to provide cryomagnetic stability to the conductor and also protect it from the quench. Also this conductive layer helps to provide electrical contact to the current leads which have to be attached to the final product after construction, see Fig 14a). Once the current approaches the critical current value the current shering may take place and also the electric field can be generated. The problem of a voltage–current relation in a superconductor carrying a transport current is one of the most important for applications. There exist several theoretical models, which describe nonlinear voltage–current characteristics of type-II superconductors [166]. Particularly at high currents I ($I \leq I_c$) a power-law model, $E=(J/J_c)^n$ with $n=U_0/kT$ [167] is a good approximation of experimental data (I_c critical current, E electric field, E_c electric field at which the critical current density J_c is defined, U_0 a characteristic energy of bonding of the vortex to the pinning centre, k Boltzmann constant, T temperature). All the existing models are valid under isothermal conditions. In the real case non-isothermal conditions and resulting voltage (electric field) current relations of $\text{YBa}_2\text{Cu}_3\text{O}_7$ coated conductor immersed in liquid nitrogen have to be analysed. The 2-dimensional (2D) steady-state Poisson's heat transfer equation has to be solved using finite element method software with input parameters taken from experiment [73].

A $\text{YBa}_2\text{Cu}_3\text{O}_7$ coated conductor, 1 cm wide, of the cross-section given in Fig.60a) and b), was modeled for the case when immersed in a liquid nitrogen bath in the nucleate boiling regime. This regime is characterised by the saturation temperature $T_0 = 77.3$ K and approximately constant heat transfer coefficient $\alpha=4.06 \cdot 10^4 \text{ Wm}^{-2} \text{ K}^{-2}$ [168]. The boundary condition for the heat flux $F=-\kappa(T)\partial T/\partial n = \alpha(T-T_0)$ non the outer surface of the coated conductor was used. The validity of the regime is up to $(T-T_0)=5$ K [168]. The temperature dependence of the critical current density J_c was taken from measurements on a real

YBa₂Cu₃O₇ coated conductor and approximated by $J_c(T)=J_{c0}(12.106-0.14368T)$ (in SI units) with $J_{c0}=4\cdot 10^9$ Am⁻² [169]. The n -value of the power law voltage–current characteristics ($n=24$) was also taken from [169] for a real YBa₂Cu₃O₇ coated conductor. Its value was only weekly temperature dependent in the range of temperatures 77.3–85 K used in the modeling. Electrical conductivities (at 77.3–85 K), of the other materials used in the modeling were Ag: $\rho_{Ag}=1.1\cdot 10^{11}T^{1.32}$ [170] (in SI units), NiFe: $\rho_{NiFe}=1:33\cdot 10^6$ S/m [171]. Thermal conductivities (at 77.3–85 K), of the materials used in the modeling were for YBa₂Cu₃O₇: $\kappa(T)=9.295\div 0.044313T$ [168] (in SI units), Ag: $\kappa=400$ Wm⁻¹ K⁻¹, [170], NiFe: $\kappa=13$ Wm⁻¹ K⁻¹ [172], buffer layer: $\kappa=0.1$ Wm⁻¹ K⁻¹ [172]. The influence of a thin stabilising silver layer on top of YBa₂Cu₃O₇ film (Fig.61) was also modeled.

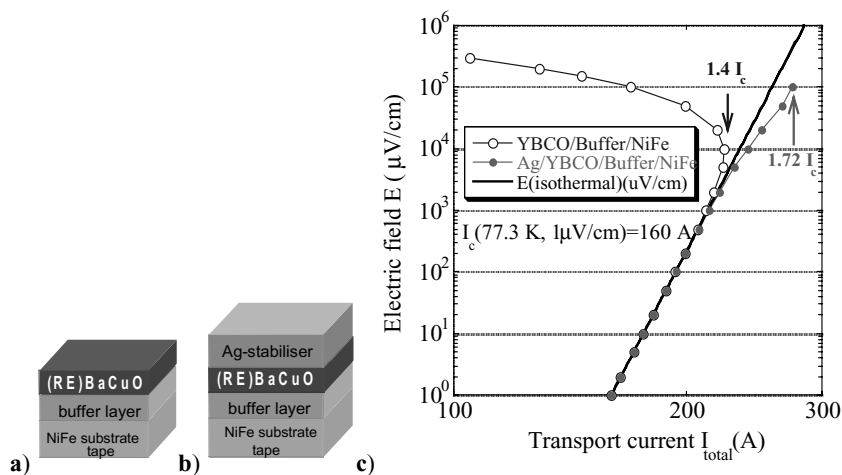


Fig. 61. Cross-sections of the conductors used in the E - I modeling: **a)** YBa₂Cu₃O₇/buffer/NiFe coated conductor 1 cm wide YBa₂Cu₃O₇ 4 μm thick, buffer layer 1 μm thick, NiFe 25 μm thick); **b)** Ag/YBa₂Cu₃O₇/buffer/NiFe coated conductor with Ag thickness 5 μm, other parameters as in a); **c)** calculated electric field – current characteristics (points) of the YBa₂Cu₃O₇ coated conductors as in (Fig.60a) and Fig.60b) immersed in liquid nitrogen in nucleate boiling regime. The straight line is the isothermal power-law voltage–current characteristic of the bare YBa₂Cu₃O₇ film at 77.3 K.

The calculated Electric field - current characteristics of the coated conductors YBa₂Cu₃O₇/buffer/NiFe and Ag/YBa₂Cu₃O₇/buffer/NiFe (Fig.61a) and Fig.61b) immersed in liquid nitrogen bath in nucleate boiling regime are shown in Fig.61c). The voltage–current characteristics of the composites follow the isothermal E - I curve of YBa₂Cu₃O₇ film up to an electric field $E=100\mu V/cm$. This means that in the experiments on composite materials in this electric field region the properties of the YBa₂Cu₃O₇ material itself are measured. The YBa₂Cu₃O₇/buffer/NiFe sample starts to be unstable (defined as the onset of negative differential resistance) at a current $I=1.4I_c$ and Ag/YBa₂Cu₃O₇/buffer/NiFe at $I=1.72I_c$. At $E=10^5$ μV/cm the Ag/YBa₂Cu₃O₇/ buffer/NiFe composite sample carries a total current

274.75 A of which the Ag layer carries 162.44 A, the $\text{YBa}_2\text{Cu}_3\text{O}_7$ film 108.98 A and the NiFe 3.33 A. Results of additional calculations conducted for the different thicknesses of the Ag stabilizing layer in a coated conductor are presented in Fig.62.

Detailed analysis of the $E-I$ curve around $E \approx 1 \mu\text{V}/\text{cm}$ showed that already at $E > 1 \mu\text{V}/\text{cm}$ the current starts to decrease with increasing electric field, i.e. the differential resistance of the sample starts to become negative. This implies an onset of thermal instability during a typical critical current measurement. At such a measurement a current power supply is usually used, which has a current feed back. The result of this is that such a power supply increases its voltage up to the maximum value in order to keep the pre-set current. At the point of the onset of negative differential resistance the power supply sets its maximum voltage. For a typical power supply with an output current of the order of 1 kA this maximum voltage is typically about 10 V. If we suppose that this voltage is applied over the measured length of a sample 1 cm long we obtain an electric field $E \approx 10 \text{V}/\text{cm} = 10^7 \mu\text{V}/\text{cm}$. Extrapolating the linear part of $E-I$ curve in the normal state ($T_{\text{max}} > T_c$) in the graph in Fig.62 to $E = 10^7 \mu\text{V}/\text{cm}$ one obtains roughly a power of about $5 \text{kW}/\text{cm}^2$, which usually results in damage to the sample. On the other hand in an experimental arrangement when a voltage power supply is used (with voltage feed back) the current is governed by the resistance of the sample. Under these conditions the sample works as a current limiting device suppressing the current.

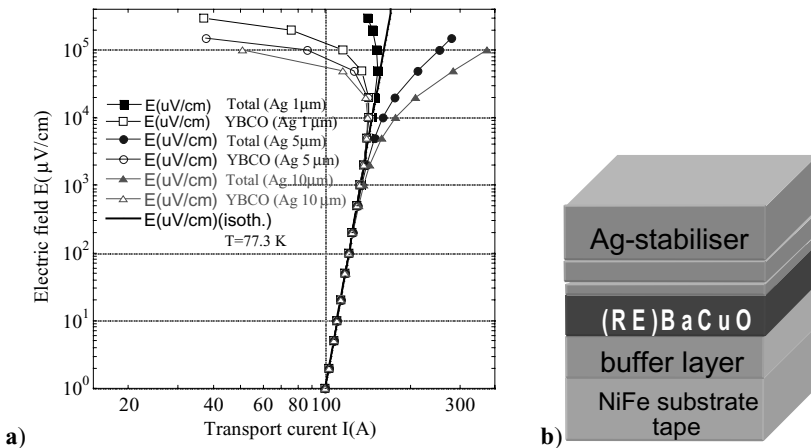
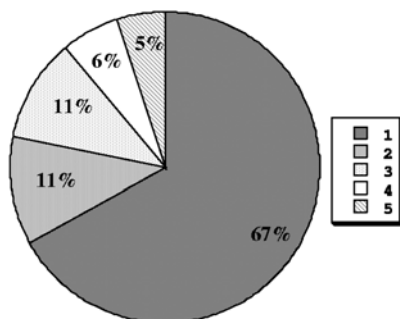


Fig. 62. a) Calculated voltage–current characteristics (points) of the $\text{Ag}/\text{YBa}_2\text{Cu}_3\text{O}_7/\text{buffer}/\text{NiFe}$ coated conductor immersed in liquid nitrogen in nucleate boiling regime. Series of curves represent variable Ag thickness 1, 5 and 10 μm , thickness of other components of coated conductors are kept constant: $\text{YBa}_2\text{Cu}_3\text{O}_7$ 10 μm , NiFe 25 μm and insulating buffer layer 0.5 μm . The broken straight line is the isothermal power-law voltage–current characteristic of the bare $\text{YBa}_2\text{Cu}_3\text{O}_7$ film at 77.3K. Open symbols represent extracted $E-I$ characteristic of the $\text{YBa}_2\text{Cu}_3\text{O}_7$ superconductor in the silver stabilized conductor, where the full symbols represent the $E-I$ characteristic of the actual conductor including silver; **b)** Schematic outline of the conductor architecture.

12. FINAL REMARKS

The relative contribution of the different $(\text{RE})\text{Ba}_2\text{Cu}_3\text{O}_7$ thin film applications to the total worldwide film market is depicted in Fig.62 [174]. As it is presented in Fig.62, only 11% of the thin film market is assigned to power applications like: resistive fault current limiters, transformers and cables, where $(\text{RE})\text{Ba}_2\text{Cu}_3\text{O}_7$ coated conductors are going to be used. The current status of the coated conductors across the world can be view on the following web page: <http://www.lanl.gov/superconductivity/score.shtml>.

There are alternative processes for continuous formation of the $\text{YBa}_2\text{Cu}_3\text{O}_7$ in the form of fibres [4], but further development will probably take place once the coated conductor shows its final limitations.



(RE)Ba₂Cu₃O₇ thin films market

Fig. 62. Relative contribution of film $(\text{RE})\text{Ba}_2\text{Cu}_3\text{O}_7$ applications to the total worldwide film market: 1) - the 67% share goes to RF-filters for mobile communications, 2 - power applications like resistive fault current limiters (11%), 3) - basic research (11%), 4) - medical applications such as Squid magnetometers or MRI / NMR – coils contribute only a minor share because such devices and sensors are small and engage only very little superconducting material (6%) 5) - superconducting electronics (5%). After W. Prusseit and M. Yoshida [174].

ACKNOWLEDGEMENTS

The author would like to thank the many colleagues who contributed to the preparation of this chapter. Acknowledgements are given to the production of DVD Lectures on Superconductivity for SCENET-2 for the picture source material provided <http://www.superconsultants.net>; the financial support of the Brite-Euram Project: “Multifunctional Flexible High Temperature Superconducting Tape” (MUST)-BRPR-CT97-0331; Brite-Euram Project: “Continuous High Rate Liquid Phase Epitaxy of Textured Coated Conductors” (CONTEXT)-PRPR-CT97-0607; EU F6 Project: “Coated Conductor by economic processing route” (COCON)-FP6-2002-SME-1; EPSRC Grant GR/R04423/01; EPSRC GR/R04386 ‘(RE)BCO on Coated Conductor Processing by Liquid Phase Epitaxy’; AFRL/PRPS Wright-Patterson Air Force Base, Ohio, USA “Low AC Loss $\text{YBa}_2\text{Cu}_3\text{O}_7$ Coated Conductor for 1MW Superconducting Generator”; ABB Corporate Research, Switzerland “Low Cost $\text{YBa}_2\text{Cu}_3\text{O}_7$ Coated Conductors by Continuous Liquid Phase Epitaxy”, is also gratefully acknowledged.

REFERENCES

- [1] B. A. Glowacki and J. Chojcan, *Phys. Stat. Sol.*, 80 (1983) K93.
- [2] B. A. Glowacki, M. Majoros, M. Vicker, M. Eisterer, S. Toenies, H. W. Weber, M. Fukutomi, K. Komori, and K. Togano, *Supercond. Sci. Technol.* 16 (2003) 297.
- [3] H. Noji, W. Zhou, B. A. Glowacki and A. Oota *Appl. Phys. Lett.*, 63 (1993) 833.
- [4] N. Ozkan, B. A. Glowacki, E. A. Robinson and P. A. Freeman, 6 (1991) 1829.
- [5] B. A. Glowacki, M. Vickers, N. Rutter, E. Maher, F. Pasotti, A. Baldini and R. Major, *Journal of Materials Science*, 37 (2002) 157.
- [6] A. Usoskin, H. C. Freyhardt, A. Issaev, J. Dzick, J. Knoke, M. P. Oomen, M. Leghissa, and H. W. Neumueller, *IEEE Trans. on Appl. Supercon.* 13 (2003) 2452.
- [7] Y. Iijima, K. Kakimoto, Y. Sutoh, S. Ajimura and T. Saitoh, *Supercond. Sci. Technol.* 17 (2004) S264.
- [8] J. Denul, I. Van Drissche, H. te Lintelo, R. De Gryse, A. Tsetsekou, S. Hoste, B. A. Glowacki, R. Garre, E. Maher, J. Good, E. Ranucci, E. Larrauri, *Inst. Phys. Conf. Ser.*, No.167 (2000) 335.
- [9] S. Donet, F. Weiss, P. Chaudouet, S. Beauquis, A. Abrutis, H. C. Freyhardt, A. Usokin, D. Selbmann, J. Eickemeyer, C. Jimenez, C. E. Bruzek and J. M. Saugrain, *IEEE Transactions on Applied Superconductivity* 13 (2003) 2524.
- [10] M. W. Rupich, U. Schoop, D. T. Verebelyi, C. Thieme, W. Zhang, X. Li, T. Kodendandath, N. Nguyen, E. Siegal, D. Buczek, J. Lynch, M. Jowett, E. Thompson, J. S. Wang, J. Scudiere, A. P. Malozemoff, Q. Li, S. Annavarapu, S. Cui, L. Fritze-meier, B. Aldrich, C. Craven, F. Niu, R. Schwall, A. Goyal, and M. Paranthaman, *IEEE Trans. on Appl. Supercon.* 13 (2003) 2458.
- [11] T. Izumi, T. Honjo, Y. Tokunaga, H. Fuji, R. Teranishi, Y. Iijima, T. Saitoh, Y. Nakamura and Y. Shiohara *IEEE Trans. on Appl. Supercon.* 13 (2003) 2500.
- [12] F. C. Yuan, Y. Y. Xie, J. P. Chen, G. W. Yang and B. J. Chen, *Supercond. Sci. Technol.* 9 (1996) 991.
- [13] R. Nemetschek, W. Prusseit, B. Holzapfel, J. Eickemeyer, U. Miller, and E. Maher, *IEEE Trans. on Appl. Supercon* 13 (2003) 2477.
- [14] I. H. Mutlu, E. Celik, and Y.S. Hascicek, *Physica C* 370 (2002)113.
- [15] A. Baranauskas, D. Jasaitis, and A. Kareiva, *Vibrational Spectroscopy* 28 (2002) 263.
- [16] B. A. Glowacki and T. Mouganie, 'Ink-jet printing of YBa₂Cu₃O₇ superconducting coatings on silver substrates for AC conductor applications' *Proc. EUCAS'03*.
- [17] I. H. Mutlu, Z. Aslanoglu, M. I. El-Kawni, E. Celik, H. Okuyucu, Y. Akin, W. Sigmund and Y. S. Hascicek, *Advances in Cryogenic Engineering* 48 (2002) 589.
- [18] A. Kursumovic, Y. S. Cheng, R. I. Tomov, R. Huhne, B. A. Glowacki, and J. E. Evetts, *Ceramic Transactions*, 140 (2003) 147.
- [19] A. Kursumovic, R. I. Tomov, R. Huhne, J. L. MacManus-Driscoll, B. A. Glowacki and J. E. Evetts, *Supercond. Sci. and Technol.* 17 (2004) 1215.
- [20] A. Goyal, D. P. Norton, D. M. Kroeger, D. K. Christen, M. Paranthaman, E. D. Specht, J. D. Budai, Q. He, B. Saffian, F. A. List, D. F. Lee, E. Hatfield, C. E. Klabunde, P. M. Martin, J. Mathis, C. Park, *J. Mater. Res.* 12 (1997) 2924.
- [21] Y. Yamada, *Supercond. Sci. and Technol.* 13 (2000) 82.
- [22] B. A. Glowacki, M. Majoros, N. A. Rutter and A. M. Campbell, *Cryogenics*, 41 (2001) 103.

- [23] J. E. Evetts and B. A. Glowacki, *Superconductor Science and Technology* 13 (2000) 443.
- [24] Coated Conductor Development Roadmap, 2001 US Department of Energy.
- [25] B. A. Glowacki 'High- T_c Superconducting Conductors for AC and DC Applications' in: *Studies of HTS superconductor applications (Advances in Research and Applications)*: ed. A.Narlikar, Springer Verlag, Volume1-Materials, 2003 p.239.
- [26] T. Watanabe, Y. Shiohara, and T. Izumi, *IEEE Trans. on Appl. Supercon.* 13 (2003) 2445.
- [27] A. Tuissi, R. Corti, E. Villa, A. P. Bramley, M. E. Vickers and J. E. Evetts, *Inst. Phys. Conf. Ser.* 167 (2000) 399.
- [28] E. Villa, A. Tuissi, R. Tomov, J. E. Evetts, *International Journal of Modern Physics B*, 14 (2000) 3145.
- [29] N. Reger, B. deBoer, J. Eickemeyer, R. Optiz, B. Holzapfel, and L. Schultz, *Inst. Phys. Conf. Ser.* No.167 (2000) 331.
- [30] J. Eickemeyer, D. Selbmann, R. Opitz, E. Maher and W. Prusseit, 'Effect of Ni purity on cube texture formation in RABiT-tapes', *Proceedings of 6th International Conference on Materials and Mechanisms of Superconductivity and High-Temperature Superconductors*, February 20-25, 2000, Houston, Texas, USA.
- [31] M. Majoros, B. A. Glowacki and A. M. Campbell, *Physica C* 334 (2000) 129.
- [32] C. S. Barrett "The Structure of Metals" (1952) and (1966) McGraw-Hill, Inc.
- [33] I. L. Dillamore *Metallurgical Reviews* 10 (1965) 271.
- [34] K. Lucke and O. Engler, *Materials Science and Technology* 6 (1990) 1113.
- [35] R. W. Cahn ed. "Materials Science and Technology" vol.15 "Processing Metals and Alloys" (1991) VCH Verlagsgesellschaft mbH.
- [36] B. M. Small, E. A. Giess, and R. Ghez, in *Handbook of Crystal Growth*, edited by D.T. J. Hurle, Vol. 3a, North-Holland, Amsterdam, (1994).
- [37] N. Rutter, M. Vickers, Z. Barber, A. Bramley, B. A. Glowacki, J. E. Evetts and E. Maher, *Inst. Phys. Conf. Ser.*, No.167 (2000) 403.
- [38] N. Rutter and B. A. Glowacki, *J. Materials Science*, 18 (1999) 1661.
- [39] T. Watanabe, Y. Ohashi, T. Maeda, M. Mimura and I. Hirabayashi *IEEE Trans. on Applied Supercon.* 13 (2003) 2484.
- [40] M. Majoros, B. A.Glowacki, in *Studies of HTS superconductors (Advances in Reserach and Applications) "AC losses and Flux Pinning and Formation of Stripe Phase"* ed. A.Narlikar, Nova Science Publishers, Inc., Huntington, New York, 32 (2000) 1.
- [41] B. A. Glowacki, M. Majoros, N. A. Rutter and A. M. Campbell 'A new method for decreasing transport ac losses in multifilamentary coated superconductors' *Physica C*, 357-360 (2001) 1213.
- [42] X. D. Wu, S. R. Foltyn, P. N. Arendt, W. R. Blumenthal, I. H. Campbell, J. D. Cotton, J. Y. Coulter, W. L. Hults, M. P. Maley, H. F. Safar, and J. L. Smith, *Appl. Phys. Lett.* 67 (1995) 2397.
- [43] M. Paranthaman, A. Goyal, F. A. List, E. D. Specht, D. F. Lee, P. M. Martin, Q. He, D. K. Christen, D. P. Norton, J. D. Budai, D. M. Kroeger, *Physica C* 275 (1997) 266.
- [44] A. Goyal, D. P. Norton, J. D. Budai, M. Paranthaman, E. D. Specht, D. M. Kroeger, D. K. Christen, Q. He, B. Saffian, F. A. List, D. F. Lee, P. M. Martin, C. E. Klabunde, E. Hartfield, and V. K. Sikka, *Appl. Phys. Lett.* 69 (1996) 1795.

- [45] T. Watanabe, Y. Shiohara, and T. Izumi *IEEE Trans. on Appl. Supercon.* 13 (2003) 2445.
- [46] A. Sheth, H. Schmidt and V. Lasrado, *Applied Superconductivity* 6 (1998) 855.
- [47] Y. Iijima, K. Kakimoto, Y. Sutoh, S. Ajimura and T. Saitoh, *Supercond. Sci. Technol.* 17 (2004) S264.
- [48] Y. Iijima, K. Kakimoto, and T. Saitoh, *IEEE Trans. on Appl. Supercon.* 13 (2003) 2466.
- [49] A. Usoskin, H. C. Freyhardt, A. Issaev, J. Dzick, J. Knoke, M. P. Oomen, M. Leghissa, and H. W. Neumueller, *IEEE Trans. on Appl. Supercon.* 13 (2003) 2452.
- [50] K. Ohmatsu, K. Muranaka, T. Taneda, K. Fujino, H. Takei, N. Hobara, S. Honjo, and Y. Takahashi, *IEEE Trans. on Appl. Supercon.* 13 (2003) 2462.
- [51] R. I. Tomov, A. Kursumovic, M. Majoros, D. J. Kang, B. A. Glowacki and J. E. Evetts, *Superconductor Science and Technology* 15 (2002) 598.
- [52] G. Mariani-Regula, B. Pichaud, S. Godey, E. Ntsoenzok, O. Perner, E. Bouayadi, *Materials Science and Engineering B71* (2000) 203.
- [53] H. Schmalzried, *Chemical Kinetics of Solids VCH* (1995) 211.
- [54] M. Quian, E.A. Stern, Y. Ma, R. Ingalls, M. Sarikaya, B. Thiel, R. Kurosky, C. Han, L. Hutter and I. Aksay, *Phys.Rev.B* 39 (1989) 9192.
- [55] C. P. Bean, *Rev. Mod. Phys.* 36 (1964) 31.
- [56] A. Tuissi, E. Villa, M. Zamboni, J. E. Evetts, R. I. Tomov, *Physica C* 372–376 (2002) 759.
- [57] D. M. Feldmann, J. L. Reeves, A. A. Polyanskii, G. Kozlowski, R. R. Biggers, R. M. Nekkanti, I. Maartense, M. Tomsic, P. Barnes, C. E. Oberly, T. L. Peterson, S. E. Babcock, and D. C. Larbalestier, *Appl. Phys. Lett.* 77 (2000) 18.
- [58] J. E. Evetts and B. A. Glowacki, *Cryogenics* 28 (1988) 641.
- [59] B. A. Glowacki, M. Vickers and E. Maher, *Materials World* 6 (1998) 683.
- [60] C. Prouteau, G. Duscher, D. K. Christen, N. D. Browning, S. J. Pennycook, M. F. Chisholm, D. P. Norton, A. Goyal, and C. Park., *Advances in Superconductivity X Proceedings of the 10th International Symposium on Superconductivity (ISS'97) Gifu, October 27-30 (1997) p.1015.*
- [61] K. E. Gray, M. B. Field, and D. J. Miller, *Phys. Rev. B.* 58 (1998) 9543.
- [62] J. G. Wen, T. Takagi, and N. Koshizuka, *Supercond. Sci. & Technol.* 13 (2000) 820.
- [63] Z. G. Ivanov, P. A. Nilsson, D. Winkler, J. A. Alarco, T. Claeson, E. A. Stepantsov, and A. Y. Tzalenchuk, *Appl. Phys. Lett.* 59 (1991) 3030.
- [64] N. F. Heinig, R. D. Redwing, I. F. Tsu, A. Gurevich, J. E. Nordman, S. E. Babcock, and D. C. Larbalestier, *Appl. Phys. Lett.* 69 (1996) 577.
- [65] D. T. Verebelyi, D. K. Christen, R. Feenstra, C. Cantoni, A. Goyal, D. F. Lee, M. Paranthaman, P. N. Arendt, R. F. DePaula, J. R. Groves, and C. Prouteau, *Appl. Phys. Lett.* 76 (2000) 1755.
- [66] N. Koshizuka, T. Takagi, J. G. Wen, K. Nakao, T. Usagawa, Y. Eltsev, and T. Machi, *Physica C* 337 (2000) 1.
- [67] V. R. Todt, X. F. Zhang, D. J. Miller, M. St. Louis Weber, and V. P. Dravid, *Appl. Phys. Lett.* 69 (1996) 3746.
- [68] M. B. Field, D. C. Larbalestier, A. Parikh, and K. Salama, *Physica C* 280 (1997) 221.
- [69] K. Salama, M. Mironova, S. Stolbov and S. Sathyamurthy, *Physica C*, 341-348 (2000) 1401.

- [70] N. A. Rutter and B. A. Glowacki, *Superconductor Science and Technology*, 14 (2001) 680.
- [71] N. A. Rutter and B. A. Glowacki, *IEEE Trans. Applied Superconductivity*, 11 (2001) 2730.
- [72] B. A. Glowacki "High- T_c Superconducting Conductors for AC and DC Applications" in: *Studies of HTS Superconductor Applications (Advances in Research and Applications)*: ed. A.Narlikar, Springer Verlag, Volume1-Materials, 2003 p.239.
- [73] M. Majoros A. M. Campbell, B. A. Glowacki, R. I. Tomov, *Physica C* 401 (2004) 140.
- [74] M. Majoros, R. I. Tomov, B. A. Glowacki, A. M. Campbell and C. E. Oberly, *IEEE Trans. on Appl. Supercon.* 13 (2003) 3626.
- [75] S. Iliescu, X. Granados, E. Bartolome, S. Sena, A. E. Carrillo, T. Puig, X. Obradors and J. E. Evetts, *Supercond. Sci. Technol.* 17 (2004) 182.
- [76] J. E. Evetts, *Supercond. Sci., Technol.*, 17 (2004) S315.
- [77] J. L. MacManus-Driscoll and X. Qi, *International Workshop on Superconductivity, Proceedings of ISTEC and MRS Conference, Honolulu, Hawaii, USA, June 24-27, 2001*, p.162.
- [78] A. Berenov, J. L. Driscoll, D. MacPhail and S. Foltyn, *Processing of High-Temperature Superconductors, Ceramic Transactions*, 140 (2003) 243.
- [79] M. J. Hogg, F. Kahlmann, Z. H. Barber and J. E. Evetts, *Supercon. Sci. Technol.* 14 (2001) 647.
- [80] B. Zeimetz, B. A. Glowacki and J. E. Evetts, *Physica C*, 372 (2002) 767.
- [81] B. Zeimetz, N. A. Rutter, B. A. Glowacki and J. E. Evetts, *Supercon. Sci. Technol.* 14 (2001) 672.
- [82] B. Zeimetz, B. A. Glowacki and J. E. Evetts, *Eur. Phys. J. B*, 29 (2002) 359.
- [83] S. I. Kim and D. C. Larbalestier, *J. Appl. Phys.* to be published.
- [84] L. Fernandez, B. Holzapfel, F. Schindler, B. de Boer, A. Attenberger, J. Hanisch, and L. Schultz, *Phys. Rev. B* 67 (2003) 052503.
- [85] M. Hogg, PhD Thesis, University of Cambridge, 2001.
- [86] J. H. Durrell, M. J. Hogg, F. Kahlmann, B. A. Glowacki, B. P. Zeimetz, M. G. Blamire, J. E. Evetts, M. P Dlamare, R. Rossler, J. D. Pedarnig, D. Bauerle, Presented at MRS Meeting, Boston, USA, 2-6 Dec. 2002, PM S5-9.
- [87] J. H. Durrell, M. J. Hogg, Z. Barber, B. A. Glowacki, M. G. Blamire, J. E. Evetts, presented at EUCAS'03 to be published.
- [88] J. H. Durrell, M. J. Hogg, N. A. Rutter, J. L. Driscoll, Z. H. Barber, B. A. Glowacki, M. G. Blamire and J. E. Evetts, *Mat. Res. Soc. Symp. Proc. Vol. EXS-3* © 2004 Materials Research Society EE4.7.1
- [89] J. H. Durrell, M. J. Hogg, F. Kahlmann, Z. Barber, M. G. Blamire and J. E. Evetts, *Phys. Rev. Lett.* 90 (2003) 247006.
- [90] A. Gurevich, M. S. Rzchowski, G. Daniels, S. Patnaik, et al., *Phys. Rev. Lett.* 8 (2002) 097001.
- [91] G. Hammer, A. Schmehl, R. R. Schulz, B. Goetz, H. Bieiefedt, C. W. Schneider, H. Hilgenkamp, and J. Mannhart, *Nature* 407 (2000) 162.
- [92] J. Loram, K.A. Mirza, and J.R. Cooper, *Research Review: High Temperature Superconductivity, IRC in Superconductivity, University of Cambridge 1998* p.77.
- [93] P. A. Freeman ,N. Ozkan, P. D. Honneyball and B. A. Glowacki, *Superconductors Science and Technology*, 4 (1991) S358.

- [94] Y. Wadayama, K. Kudo, A. Nagata, K. Ikeda, S. Hanada and O. Izumi, *J. Jap. Appl. Phys.* 27 (1990) L1221.
- [95] Y. Zhu, Z. X. Cai, R. C. Budhani, M. Suenaga and D. O. Welch *Phys. Rev. B* 48 (1993) 6436.
- [96] T. Haugan, P. N. Barnes I. Maartense, C. B. Cobb, E. J. Lee, M. Sumption, *J. Mater. Res.* 18 (2003) 2618.
- [97] T. Haugan, P. Barnes, R. Nekkanti, J. Evans, J. C. Tolliver, L. Brunke, J. P. Murphy, T. A. Campbell, A. Goyal and L. Heatherly, *EUCS 2003 Conf. Proceedings, Sorrento, Italy 2003* in press.
- [98] C. E. Oberly, L. Long, G. L. Rhoads, and W. J. Carr Jr., *Cryogenics*, 41 (2001) 117.
- [99] K. H. Müller, *Physica C* 312 (1999) 149.
- [101] N. A. Rutter, B. A. Glowacki and J. E. Evetts, *Supercond. Sci. Technol.*, 13 (2000) L25.
- [102] M. Majoros, B. A. Glowacki, A. M. Campbell, and C. E. Oberly, *IEEE Trans on Appl. Supercon.* (2005) to be published.
- [103] C. B. Cobb, P. N. Barnes, T. J. Haugan, J. Tolliver, E. Lee, M. Sumption, E. Collings, C. E. Oberly, *Physica C* 382 (2002) 52.
- [104] M. Majoros, R. I. Tomov, B. A. Glowacki, A. M. Campbell, and C. E. Oberly, *IEEE Trans on Appl. Supercon.* 13 (2003) 3626.
- [105] B. A. Glowacki and M. Majoros, *Supercon. Sci. Technol.*, 13 (2000) 971.
- [106] B. A. Glowacki, M. Majoros, *Superconductor Science and Technology*, 13 (2000) 483.
- [107] Y. Iijima, K. Kakimoto, Y. Sutoh, S. Ajimura and T. Saitoh, *Supercond. Sci. Technol.* 17 (2004) S264.
- [108] Y. Iijima, K. Onabe, N. Futaki, N. Tanabe, N. Sadakata and O. Kohno, *IEEE Trans. Appl. Supercond.* 3 (1993) 1510.
- [109] Y. Iijima, K. Kakimoto, M. Kimura, K. Takeda and T. Saitoh, *IEEE Trans. Appl. Supercond.* 12 (2001) 2816.
- [110] A. Usoskin, H. C. Freyhardt, A. Issaev, J. Dzick, J. Knoke, M. P. Oome, M. Leghissa and H. W. Neumueller, *IEEE Trans. Appl. Supercond.* 13 (2003) 2452.
- [111] Y. Xu, D. Shi, A. Goyal, N. A. Rutter, M. Paranthaman, P. M. Martin and D. M. Kroeger 'YBa₂Cu₃O_{7-d} films through a fluorine free TMAP MOD approach' Oak Ridge National Laboratory Reports, 2000.
- [112] D. T. Verebelyi, U. Schoop, C. Thieme, X. Li, W. Zhang, T. Kodenkandath, A. P. Malozemoff, N. Nguyen, E. Siegal, D. Buczek, J. Lynch, J. Scudiere, M. Rupich, A. Goyal, E. D. Specht, P. Martin and M. Paranthaman, *Superconductor Science & Technology*, 16 (2003) L19.
- [113] M. W. Rupich, U. Schoop, D. T. Verebelyi, C. Thieme, W. Zhang, X. Li, T. Kodenkandath, N. Nguyen, E. Siegal, D. Buczek, J. Lynch, M. Jowett, E. Thompson, J. S. Wang, J. Scudiere, A. P. Malozemoff, Q. Li, S. Annavarapu, S. Cui, L. Fritzemeier, B. Aldrich, C. Craven, F. Niu, R. Schwall, A. Goyal and M. Paranthaman, *IEEE Transactions on Applied Superconductivity*, 13 (2003) 2458.
- [114] X. Li, M. W. Rupich, W. Zhang, N. Nguyen, T. Kodenkandath, U. Schoop, D. T. Verebelyi, C. Thieme, M. Jowett, P. N. Arendt, S. R. Foltyn, T. G. Holesinger, T. Aytug, D. K. Christen and M. P. Paranthaman, *Physica C* 390 (2003) 249.
- [115] M. Kakihana, *Journal of Sol-Gel Science and Technology* 6 (1996) 7.

- [116] I. Van Driessche, G. Penneman, C. De Meyer, I. Stambolova, E. Bruneel and S. Hoste, Euro Ceramics VII, Pt 1-3. 2002. p. 479-482.
- [117] A. Baranuskas, D. Jasaitis, and A. Kareiva. *Vibrational Spectroscopy* 28 (2002) 263.
- [118] D. Marguillier, R. Cloots, A. Rulmont, J. F. Fagnard, P. Vanderbenden and M. Ausloos, *Physica C* 372 (2002) 715.
- [119] M. L. Kullberg, M. T. Lanagan, W. Wu and R. B. Poeppel, *Superconductor Science and Technology* 4 (1991) 337.
- [120] P. L. Steger and X. Z. Wang, *Physica C* 213 (1993) 433.
- [121] S. Fujihara, N. Yoshida, and T. Kimura, *Physica C* 276 (1997) 69.
- [122] R. S. Liu, R. Janes, M. J. Benet and P. P. Edwards, *Applied Physics Letters* 57 (1990) 920.
- [123] A. Aoki, S. Ohno, and Y. Muramatsu, *Journal of Non-Crystalline Solids* 147 & 148 (1992) 720.
- [124] J. McKittrick and R. Contreras, *Thin Solid Films* 206 (1991) 146.
- [125] I. Schildermans, M. VanBael, E. Knaepen, J. Yperman, J. Mullens and L. C. VanPoucke, *Physica C* 278 (1997) 55.
- [126] E. Benavidez, C. Oliver, R. Caruso and O. De Sanctis, *Materials Chemistry and Physics* 62 (2000) 9.
- [127] I. H. Mutlu, E. Celik, M. K. Ramazanoglu, Y. Akin and Y. S. Hascicek, *IEEE Transactions on Applied Superconductivity* 10 (2000) 1154.
- [128] L. F. Admaiai, P. Grange and B. Delmon, *Physica C* 247 (1995) 351.
- [129] S. Grigoryan, A. Manukyan, A. Hayrapetyan, A. Arzumanyan, A. Kuzanyan, Y. Kafadaryan and E. Vardanyan, *Superconducting Science and Technology* 16 (2003) 1202.
- [130] Sheth, A., H. Schmidt, and V. Lasrado, *Applied Superconductivity* 6 (1998) 855.
- [131] J. T. Dawley, P. G. Clem, M. P. Siegal, D. L. Overmyer and M. A. Rodriguez, *IEEE Transactions on Applied Superconductivity* 11 (2001) 2873.
- [132] M. Falter, K. Demmler, W. Hassler, B. Schlobach, B. Holzapfel and L. Schultz, *IEEE Transactions on Applied Superconductivity* 13 (2003) 2751.
- [133] V. F. Solov'yov, H. J. Wiesmann, L. J. Wu, Y. Zhu and M. Suenaga, *IEEE Transactions on Applied Superconductivity* 11 (2001) 2939.
- [134] L. Klein, *Sol-gel technology for thin films, fibers, preforms, electronics, and speciality shapes*: Noyes Publications, 1988.
- [135] K. H. Muller, N. Savvides, J. Herrmann, *Applied Superconductivity VI Conf Ser No 167* (1999) 939.
- [136] M. Majoros, B. A. Glowacki and A. M. Campbell, *Physica C* 338 (2000) 251.
- [137] M. Staines, J. Y. Genoud, A. Mawdsley and V. Manojlovic, *IEEE Trans. Appl. Supercond.* 9 (1999) 2284.
- [138] B. A. Glowacki, *Supercon.Sci.Technol.* 13 (2000) 584.
- [139] B. M. Small, E. A. Giess, and R. Ghez, in *Handbook of Crystal Growth*, edited by D. T. J. Hurle, Vol. 3a, North-Holland, Amsterdam, (1994).
- [140] H. J. Scheel, M. Berkowski, and B. Chabot, *J. Crystal Growth* 115 (1991) 19.
- [141] M. Kambara, PhD Thesis, University of Tokyo, Tokyo, 1999.
- [142] S. Kawabata, H. Hoshizaki, N. Kawahara, H. Enami, T. Shinohara, and T. Imura, *Jpn. J. Appl. Phys., Pt 2-Lett.* 29 (1990) L1490.

- [143] W. K. Burton, N. Cabrera, and F. C. Frank, *Philos. Trans. R. Soc. London A* 243 (1951) 299.
- [144] Y. S. Cheng, PhD Thesis, University of Cambridge, 2001.
- [145] Y. Yamada, *Supercond. Sci. Technol.* 13 (2000) 82.
- [146] A. Kursumovic, R. I. Tomov, R. Huhne, J. L. Driscoll, B. A. Glowacki and J. E. Evetts, *Supercond. Sci. Technol.* 17 (2004) 1215.
- [147] C. Klemenz and H. J. Scheel, *J. Cryst. Growth* 204 (1999) 62.
- [148] A. Kursumovic, Y. S. Cheng, B. A. Glowacki, J. Madsen and J. E. Evetts, *J. Cryst. Growth* 218 (2000) 4.
- [149] A. Kursumovic, Y. S. Cheng, A. Bramley, B. A. Glowacki and J. E. Evetts, *Inst. Phys. Conf. Ser. No. 167*, 1 (1999) 147.
- [150] X-Y. and P. Bennema *Phys. Rev. B* 53 (1996) 2314.
- [151] Y.S.Cheng, A.Kursumovic, R.I.Tomov, B.A.Glowacki, A.Tuissi, E.Villa, A.Vostner, H.E.Weber and J.E.Evetts, "Development of high critical current (RE)BCO coated conductors via low-cost high rate liquid phase epitaxy route", International Workshop on Superconductivity, Co-Sponsored by ISTEK and MRS, Honolulu, Hawaii, USA, June 24-27, 2001, p.185.
- [152] Y.S. Cheng, A.Kursumovic, B.A. Glowacki, H.W. Zandbergen, and J.E. Evetts, "Growth of Mixed $(Y_xRE_{1-x})Ba_2Cu_3O_{7-\delta}$ (RE = Sm, Nd) Thick Films by Liquid Phase Epitaxy, submitted to *J. Mater. Res.* in press.
- [153] <http://www.msm.cam.ac.uk/as>, <http://www.superconsultants.net>, <http://www.super-consultants.com>
- [154] J. L. MacManus-Driscoll, J. Nelstrop, A. Berenov and X. Qi, *Physica C*, 384 (2003) 507.
- [155] R. I. Tomov, A. Kursumovic, M. Majoros, R. Huhne, B. A. Glowacki, J. E. Evetts, A. Tuissi, E. Villa, S. Tonies, Y. Sun, A. Vostner, and H. W. Weber, *Ceramic Transactions* 140 (2003) 119.
- [156] J. V. Sande, MPC Industry Collegium, MIT Report. 13 (1996) 3.
- [157] M. R. Lees, D. Bourgault, D. Braithwaite, P. De Rango, P. Lejay, A. Sulpice, and R. Tourier, *Proceedings of ICMAS '91*, Paris, 1991, p.209.
- [158] Y. Ma, K. Watanabe, S. Awaji, and M. Motokawa, *Appl. Phys. Lett.*, 77 (2000) 3633.
- [159] J. J. Wells, N. Male, L. Cohen, M. J. Valler-Regi and J. L. MacManus-Driscoll, *Inst. Phys. Conf., Ser No.167* (1999) 319.
- [160] B. A. Glowacki, *Superconductor Sci. Technol.* 11 (1998) 989.
- [161] Y. Ma, K. Watanabe, S. Awaji, and M. Motokawa, *Phys. Rev. B*, 65 (2002) 174528.
- [162] T. J. Doi, T. Yuasa, T. Ozawa, and K. Higashiyama, 7th International Symposium on Superconductivity, November 8-11, 1994, Kitakyushu, Japan.
- [163] D. E. Farrell, S. Chandrasekhar, M. R. DaGuire, M. M. Fang, V. G. Kogan, J. R. Clem and D. K. Finnemore, *Phys. Rev. B*, 36 (1987) 4025.
- [164] J. Y. Genoud, M. Staines, A. Mawdsley, V. Manojlovic, and W. Quinton, *Supercond. Sci. Technol.* 12 (1999) 663.
- [165] Y.D. Zhang, and J.I. Budnick, *Appl. Phys. Lett.* 70 (1997) 1083.
- [166] M. Tinkham, *Introduction to Superconductivity*, second ed., McGraw-Hill, New York, 1996.
- [167] E. Zeldov, N. M. Amer, G. Koren, A. Gupta, M. W. McElfresh, *Appl. Phys. Lett.* 56 (1990) 680.

- [168] A. V. Gurevich, R. G. Mints and A. L. Rakhmanov, *The Physics of Composite Superconductors*, Begell House, Inc., New York, Wallingford (UK), 1997.
- [169] G. K. White and P. J. Meeson, *Experimental Techniques in Low-Temperature Physics*, fourth ed., Clarendon Press, Oxford, 2002.
- [170] M. Inoue, S. Nishimura, T. Kuga, M. Kiuchi, T. Kiss, M. Takeo, T. Matsushita, Y. Iijima, K. Kakimoto, T. Saitoh, S. Awaji, K. Watanabe and Y. Shiohara, *Physica C* 372–27 (2002) 794.
- [171] D. R. Lide (Ed.), *Handbook of Chemistry and Physics*, 71st ed., CRC Press, Inc., 1991.
- [172] A. J. Chapman, *Heat Transfer*, Macmillan Publishing Company, Collier Macmillan Publishers, New York, London, 1989.
- [173] W. Prusseit and M. Yoshida, *FSST News* 85 (2001) 10.

THALLIUM-BASED SUPERCONDUCTING CUPRATES

J-L. Jorda

Université de Savoie, LAIMAN-ESIA, Domaine Universitaire, B.P.806
F-74016 ANNECY cedex

1. INTRODUCTION

In the Editorial of the first issue of the review *"Superconductor Science & Technology"* J.E.Evetts noticed that "intense media attention has ensured that the one time specialist world of superconductivity is now firmly in the public mind" [1]. Sixteen years after, we have to admit that most of the dreams of the first age of High Temperature Superconductivity are not yet realities. Moreover, due to economic recession, the free data-base High T_c Update stopped its activity and the expression "superconductivity" is slowly disappearing of national and international research programs. Surprisingly, in the same time, the metallic superconductors especially the A15-type compounds Nb_3Sn , Nb_3Al and Nb_3Ga seems to find a new youth [2-8] while the interest for MgB_2 with a transition temperature about 40 K [9], claimed as promising solution in the fields of transport of current and electronic devices at the medium temperature range [10], is growing. It is an indication that the high temperature superconducting cuprates generated new problems not yet solved. Indeed, each class of superconducting materials has to clear a technological and economical barrier which postpones the date for large scale and home applications. The critical temperature lower than 25 K and the necessary cryogenic investment is unfavourable for metallic superconductors; the anisotropy of high temperature superconductors (HTS) questions about the ability of these materials to operate in high magnetic fields and to allow current flow through the grain boundaries. However, despite this quite depressing context, good news come from the "first generation" of the cuprates, $(Bi,Pb)_2Sr_2Ca_2Cu_3O_x$ with a critical temperature $T_c = 110K$, prepared by a powder-in-tube (PID) process. The studies of the phase formation, the understanding of the crucial role of the oxygen partial pressure during the sintering process

[11-14], the optimisation of the thermal treatments to improve the grain microstructure [15,16], the effects of the sheath material on the electrical and mechanical properties of the composite tapes [17] have been necessary ways for the development of conductors for practical use [18]. Long length, in the km range, wires and tapes are now commercially available. Power transmission lines, energy storage coils, transformers are under test (see for instance [19]) but the prohibitive cost of the Ag sheathed $(\text{Bi,Pb})_2\text{Sr}_2\text{Ca}_2\text{Cu}_3\text{O}_x$ cables and too high ac.losses are the limiting factors for a large scale transfer in the industries [20]. The birth of the "second generation" conductors based on coated $\text{YBa}_2\text{Cu}_3\text{O}_7$ with $T_c(\text{max})=92\text{ K}$ may be also considered as a good new. The anisotropy of the "historical" compound, which was the first to show a critical transition temperature above the boiling point of nitrogen [21], is less than that of $(\text{Bi,Pb})_2\text{Sr}_2\text{Ca}_2\text{Cu}_3\text{O}_x$. In addition, the emergence of low-cost film processes using Rolling Assisted Biaxially Textured substrates (RABiTS), associated with spray pyrolysis, Metal-Organic Deposition (MOD), Metal-Organic Chemical Vapor Deposition (MOCVD), screen-printing or sol-gel methods are expected to solve the problem of grain connectivity. A reel-to-reel system has been used to fabricate continuous ribbons of $\text{YBa}_2\text{Cu}_3\text{O}_7$ compatible with the industrial request, with a cost which is estimated to be two to five times lower than $\$50/\text{kA.m}$, the price of a wire prepared by the first generation powder in tube technique [22]. $\text{YBa}_2\text{Cu}_3\text{O}_7$ tapes with critical current densities J_c in the order of 10 MA/cm^2 have been prepared [23] and large-size films ($30\times 10\text{ cm}^2$) with a mean inductive J_c value of 2.6 MA/cm^2 have been obtained [24] by coating-pyrolysis process, opening the door of superconducting fault-current limiters and microwave applications. At this point of the listing of the principal activities in the field of superconducting materials, it is noteworthy that the two series of the cuprate superconductors $\text{Hg}_m\text{Ba}_2\text{Ca}_{n-1}\text{Cu}_n\text{O}_x$ and $\text{Tl}_m\text{Ba}_2\text{Ca}_{n-1}\text{Cu}_n\text{O}_x$, here referred as (Hg-Tl)- $m2(n-1)n$ having the highest critical temperature, $T_{c,\text{max}} = 135\text{ K}$ [25] and $T_{c,\text{max}} = 127\text{ K}$ [26], respectively do not appear as possible systems for applications of superconductivity. The volatility of mercury- and thallium oxides at high temperature and the subsequent health hazard that could result, is one of the problem for the production of (Hg-Tl)-based superconducting cables. However, the performances realized on Hg- or Tl- thin films presenting critical current densities close to or higher than 1 MA/cm^2 at 77 K [27-33] are attractive enough for the coated technology which, applied to these materials, could provide an alternative solution for future conductors and microwave devices [34,35]. Hg- and Tl-based superconducting cuprates may be compared for their high T_c and they have also a similar chemistry which favours partial substitution to improve the transport properties or to stabilise the phases [36-39]. But contradictory to the mercury-based system, the single and double TlO- layered compounds may be prepared at ordinary pressure and are thermodynamically stable at room temperature. Thus, beyond the applications, the thallium cuprate systems show an increased advantage from a basic research viewpoint. A great number of publications review the synthesis, the structural and the superconducting properties of the various Tl-compounds [35,40-43]. Recently we have reported on the formation and the stability of the unsubstituted phases and demonstrated that the knowledge of the phase equilibrium and the control of the pathway for the formation of the phases under interest are determinant elements for the preparation of compounds with similar, if not enhanced superconducting properties comparatively to the homologous substituted materials [44].

It is proposed here to review the thallium phases, mainly the effect of substitutions on the phase stability and on the superconducting properties in order to attempt to take stock of the work which still has to be done for better understanding of these compounds and to

discuss their potential for producing tapes open to become alternatives to $\text{YBa}_2\text{Cu}_3\text{O}_7$ or to $(\text{Bi,Pb})_2\text{Sr}_2\text{Ca}_2\text{Cu}_3\text{O}_x$.

2. STRUCTURAL AND CRYSTAL CHEMISTRY ASPECTS OF $\text{Tl}_m\text{Ba}_2\text{Ca}_{n-1}\text{Cu}_n\text{O}_x$

All members of the HTS $\text{Tl}_m\text{Ba}_2\text{Ca}_{n-1}\text{Cu}_n\text{O}_x$ have a tetragonal lattice, crystallising in the $P4/mmm$ or $I4/mmm$ space groups, depending on whether $m = 1$ or $m = 2$, respectively. An orthorhombic $\text{Tl}_2\text{Ba}_2\text{CuO}_4$, space group $Fmmm$ (and subgroups) can be also prepared with high thallium and/or oxygen content [45-47].

The two oxide families have been initially described in a general model which consists of an intergrowth of oxygen deficient perovskite blocks separated by insulating rock salt NaCl-type layers, leading to the general formulae $[\text{AO}]_m [\text{A}(\text{CuO}_{2.5})_{0.5}]_n$, $\text{A} = \text{Tl}, \text{Ba-Ca}$, = oxygen vacancy, derived from K_2NiF_4 or from the Ruddelsden-Popper $[\text{AO}][\text{ABO}_3]_n$ type structures [48-50]. In a "local charge" picture the perovskite blocks contain n CuO_2 planes, which may be considered as the superconducting element of the structure and the (AO) layer constitutes a kind of "charge reservoir" [51]. This description accounts for oxygen deficiency and possible order-disorder transitions, but encounters some difficulties to explain the formation of mixed valence state $\text{Cu}^{\text{II}}\text{-Cu}^{\text{III}}$ which is admitted to be the key for superconductivity. Because it is doubtful that extra oxygen could be inserted in the stoichiometric compounds, one way to generate Cu^{III} ions is to produce some thallium vacancies. The high temperature factors calculated for Tl on refining the crystal structure of the members of the series with $m = 2$ argues for this behaviour. Still remains to elucidate the case of the $m = 1$ series whose compounds have nearly stoichiometric $\text{Tl} = 1$ content. Another hard point of the model is the nature and therefore the role of the A cation to be placed in the rock-salt layer.

Early after the discovery in 1986 of the superconducting cuprates [52], Nardin et al. [53] proposed a unified description based on geometrical building but the first architecture for HTS which takes into account the bidimensional character of the supercurrents through sheets of the CuO_2 planes is due to R.Li [54]. The conductive CuO_2 planes are separated by "separators" layers S and connected by "connectors" C. A critical ionic radius ($r_c = 1.0\text{-}1.15 \text{ \AA}$) classifies the size of the cations and is useful to account for oxygen excess or deficiency. Taking advantage of possible arrangements of large and small ions surrounding the CuO_2 square planes, Li proposed a classification of the layered cuprate compounds in which blanks could be a good chance to discover new phases. It is proposed to induce superconductivity in known phases not yet superconducting, such as Tl-1222 or Tl-2222 by doping the CuO_2 layers, or to build new structures either using the known units of the cuprates, for instance $\text{LaBa}(\text{Nd,Ce})_2\text{Cu}_2\text{O}_y$, or by combining new separators and connectors as it was done for Tl-1232.

The more recent critical compilation of the crystallographic structures of HTS by R.Gladyshevskii and P.Galez [55] is based on a similar approach. The structure is built by stacking atoms layers following simple empirical rules based on more than 400 high- T_c superconducting cuprates known up to 1997. Four atom layers are defined: the "conducting" layer DO_2 representing the CuO_2 square planes, the "separating" layer C which is a single square mesh of metal atoms, Ca, Tl, Pb... separating the CuO_6 octahedra into two CuO_5 square pyramids, the "bridging" layer BO, for instance BaO, CaO.. and the "additional" layer

AO (A=Ti, Bi, Pb.), the "charge reservoir" in the classical perovskite-rock salt scheme, always separated from the CuO_2 planes by a bridging layer. This classification of the atom layers combined with related stacking rules induces the generation of a "family tree" for all HTS. The thallium series are included in this family represented by a stacking sequence such as $(\text{DO}_2)\text{-C-(DO}_2)\text{..BO-AO-BO}$ for the single TlO layer compounds. This layer model is more representative of the 2-dimensional superconductivity in cuprates than the block model. It offers a number of possibilities for intergrowth structures and, in the family tree, some branches still remain to be discovered. In addition, as it is the case for the block representation of HTS, the relations structure-composition makes clear the deviations from stoichiometric compositions and the doping of the CuO_2 plane may be interpreted in terms of valence fluctuation of thallium in the (TlO) layer. The correspondence between the block and the layer schemes for Tl-1223, written $(\text{TlO,BaO})[\text{BaCa}_2(\text{CuO}_{2.5-0.5})_2(\text{CuO}_2)]$ or $(\text{CuO}_2)\text{-Ca-(CuO}_2)\text{-Ca-(CuO}_2)\text{-BaO-TlO-BaO}$ respectively, is given as an example in figure 1.

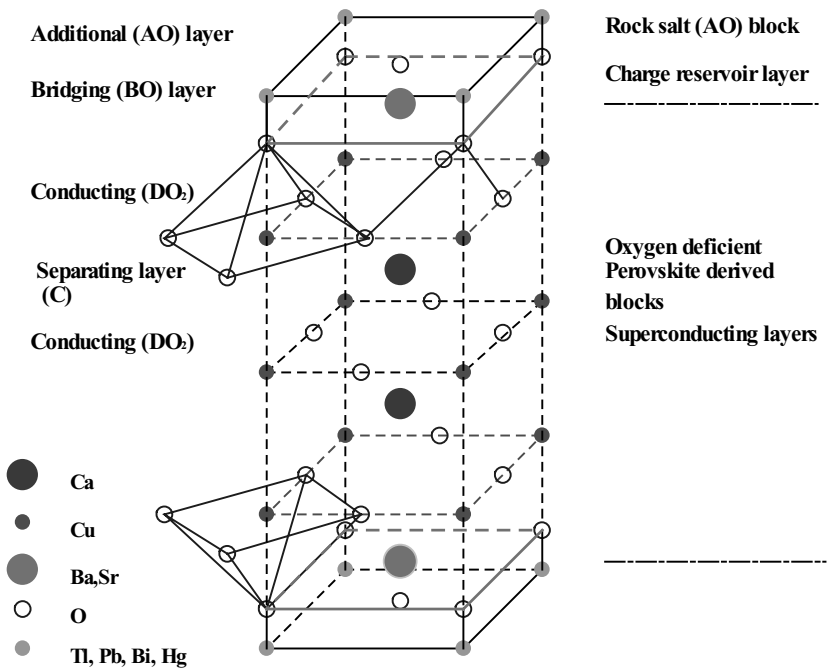


Fig. 1. The $\text{TlBa}_2\text{Ca}_2\text{Cu}_3\text{O}_9$ phase described as perovskite-rock salt intergrowth layers (right) or as a stacking of atoms layers (left). Only one group of pyramidal CuO_5 blocks has been represented for simplicity.

K.S.Aleksandrov and B.V.Beznosikov [56,57] included the HTS in their general studies on architecture and hierarchies of perovskite-like crystals for which a block description is preferred to a layered analysis. The model is based on BX_6 octahedra (named O), linked at their vertices. These blocks may be reduced to BX_5 pyramids (P) or BX_4 squares (Q) when the material is anion-deficient. The single TlO-layer cuprates are representative of such anion deficient multilayer Tl-12(n-1)n compounds with n up to 6 if Cu substitutes Tl [58]. As usually accepted, the double TlO-layer Tl-22(n-1)n series is representative of the Aurivillius phase-type: $(Tl_2O_2)(A_2Ca_{n-1}Cu_nO_{2n+4})$, A=Ba, Sr. The model suffers to be essentially geometric, but the systematic stacking of O, P and Q blocks, is an efficient "instrument" for the generation of new series of compounds with a perovskite-related structure.

The precedent representations, although based on crystal chemistry are essentially empirical so that the structure-properties relations cannot emerge. A more physical view is needed to be introduced. The first step is perhaps due to P.Ganguly and N.Shah [59] who proposed to apply the AX_3 close-packed description to the layered cuprates. It is known that the perovskite ABO_3 may be derived from a close-packed $L1_2$ ($Pm\bar{3}m$), $AuCu_3$ - type structure for AO_3 by placing the atom B in the centre of the cubic unit cell [60]. Inversely, when the perovskite is defined with the A atom in the central position, removing it gives the ReO_3 structure, DO_{22} -type, suggesting then to describe cation-deficient perovskites as A^*BX_3 , A^* representing a cation vacancy. The second important point is that AX_3 is also able to induce a DO_{22} closed-packed arrangement in the (112) plane [61]. P.Ganguly and N.Shah thus considered the rock-salt layers AO as derived from AX_3 in which X_2 rows have been removed.

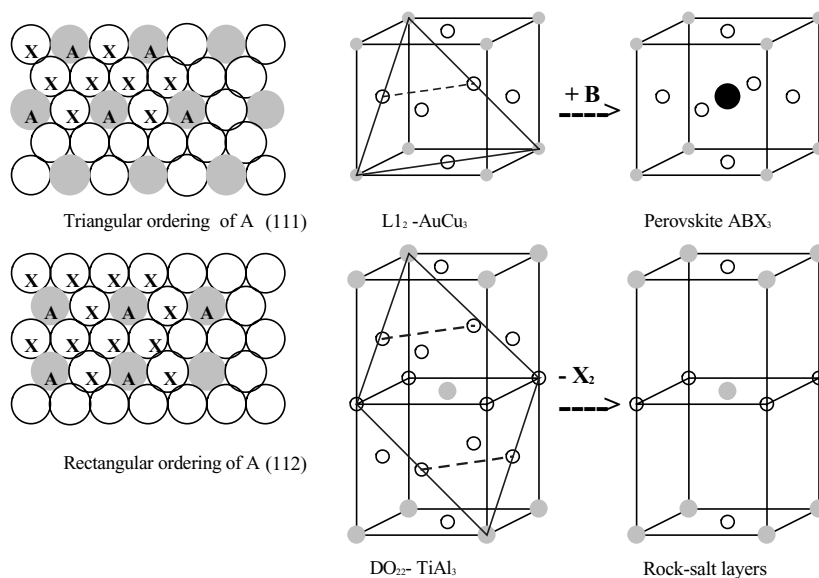


Fig. 2. The close-packing model for the perovskite ABX_3 - type structure and for a rock-salt layer (AX)

In figure 2 the close-packed structures with a triangular ordering of A atoms in the plane (111) and a rectangular ordering of the same atoms in the plane (112), leading to CuAu_3 and TiAl_3 respectively, have been represented. In outline, the route for the perovskite ABX_3 and the NaCl layers is also shown. Note that in the tetragonal distorted DO_{22} structure, the successive mixed AX layers are displaced by $[1/2, 1/2, 0]$. This close-packed description allowed P.Ganguly and N.Shah to use, for the layered cuprates, the results of the physical metallurgy, such as the existence of antiphase boundaries in incommensurated phases in intermetallics. The role of the A cation on the phase stability and on the critical temperature T_c of the cuprate superconductors may be estimated. For instance, an average size for the A atom, $r_A = 1.02 \text{ \AA}$, is found to be a constraint for the stability of the close-packed structure. This value may result from elements giving possibility for a mixed valence state or from substitution, or from vacancies in the site under consideration. With the thallium systems, using the Shannon-radii [62] for Tl^{1+} ($r_{\text{Tl}}^{1+} = 1.50 \text{ \AA}$) and Tl^{3+} ($r_{\text{Tl}}^{3+} = 0.885 \text{ \AA}$) in octahedral coordination, the ideal value for r_A is reached when the ratio $\text{Tl}^{1+}/\text{Tl}^{3+} = 0.28$. Then about 22 % of thallium ions in the TlO-layers should be monovalent. Similarly, when Pb^{2+} ($r_{\text{Pb}}^{2+} = 1.19 \text{ \AA}$) substitutes Tl^{3+} we find $\text{Pb}^{2+}/\text{Tl}^{3+} = 0.82$, meaning that thallium and lead would be nearly equally distributed to offer the greatest stability of the (Tl,Pb)-m2(n-1)n compounds. The size effect explains the number of possible substitutions on the Tl-site and also intersite exchange between Tl and Ca which are often reported in the Tl-22(n-1)n series, [63-67]. It has to be said that, even if the model cannot account for a complete understanding of the thallium superconductors, such as the existence of the single and double Tl-O layers, it presents some advantages comparatively to the stacking of blocks or of atoms layers, one of the most interesting being to clarify the coupling between the Tl-O and the CuO_2 layers, *via* the values of a tolerance factor for the stability of the close-packed structure. It is noteworthy that the close-packed representation of HTS, in the sense of equivalence between alloys and perovskite-like structures has been recently extended to a large variety of materials by J.Hauk and K.Mika [68,69], on the basis of the one-dimensional ising- model of the metal lattice and the oxygen positions.

Whatever the packing of the layers is described, one characteristic of the thallium cuprates is the presence of mixed valence states for Tl and Cu. For the latter, the coexistence of Cu^{3+} and Cu^{2+} i.e. the formation of holes in the (CuO_2) layers, is assumed to be the key for high temperature superconductivity. For $\text{YBa}_2\text{Cu}_3\text{O}_{7-\delta}$ and for the $\text{Bi}_2\text{Sr}_2\text{Ca}_{n-1}\text{Cu}_n\text{O}_x$ systems this p-doping is accepted to be due to the oxygen excess in the charge reservoir layers [70,72]. The hole concentration is related with the total amount of oxygen atoms in the materials and may be measured by iodometric titration [73,74] if the valency of all cations is unambiguously known. For the thallium series, the solution chemistry titration [75-78] cannot provide so clear relation between the liberated iodine during the chemical reduction and the hole concentration because (i) the thallium concentration in the superconducting phases is subjected to fluctuate depending on the preparation method and (ii) even if the thallium content is known, the two oxidation states Tl^{3+} and Tl^{1+} may coexist. Then, the total oxygen content in the system can be obtained only in materials with known Tl concentration, but individual oxidations in the CuO_2 and TlO layers cannot be distinguished [79]. In the early determination of the crystal structures of Tl-2212 and Tl-2223 the mutual substitution between the thallium and the calcium sites [65,80,81], suggested that the oxidation state of Tl is less than 3. The oxygen excess in between the double TlO layer (O4-position), possible substitutions of copper ions for thallium and thallium vacancies [82-84] are arguments for the

mixed valency of Tl in Tl-2201. Then, for the Tl-22(n-1)n series, it is of general agreement that holes in the CuO₂ sheets depends on the thallium content in the material. For samples with a thallium content close to 2 per formula unit, the p-doping occurs from an overlap of the initially empty Tl-6s band and the conduction band of the CuO₂ sheets. For the single TlO-layer series, the wet chemistry titration tends to indicate that thallium is at his highest oxidation state Tl³⁺ meaning there is no electrons in the Tl-6s band of Tl and thus the doping of the CuO₂ layers should be due to Tl vacancies and/or oxygen excess. However, detailed structural analysis of Tl-1223 single crystals [85] and recent X-ray photoemission investigations on the chemical bonding in Tl-1212, [86] gives a straightforward indication that Tl valency is close to, but not equal to 3.

Relying on the fact that Cu³⁺ ions never have been really observed in HTS, H.Oesterreicher proposed to see the superconducting cuprates as subperoxides containing O_q^{1-2q} anions, resulting of the mixture of O²⁻ and O⁻ [87-89]. The model is claimed to give a universal picture of HTS, also offering new interpretation of conventional results. For instance, the superconducting transition temperature T_c is found to scale with the O⁻/(O⁻+O²⁻) ratio, due to a subperoxide charge order which promotes hole propagation in the CuO₂ planes. The good agreement between calculated and observed T_c for the thallium systems is noticeable.

Table 1. Structural characteristics and critical temperature T_c for the thallium family members All distances are in Å

| Compounds | a (Å) | c(Å) | d(Cu-O _{ap}) | d | d' | T _c (K) | ref. |
|--|------------|------------|------------------------|--------|-------|--------------------|------|
| Tl _{1.2} Ba ₂ Cu _{0.7} O _{4.8} | 3.869(2) | 9.694(9) | | | 9.694 | ns | 48 |
| Tl _{0.9} Ba _{1.2} La _{0.8} CuO _{4.86} | 3.8479 | 9.0909 | 2.5 | | 9.091 | 52 | 90 |
| Tl _{1.17} Ba ₂ Ca _{0.83} Cu ₂ O _{6.75} | 3.8566(4) | 12.754(2) | 2.76 | 3.087 | 9.553 | 103 | 91 |
| TlBa ₂ Ca _{0.5} Nd _{0.5} Cu ₂ O _{6.86} | 3.87677(5) | 12.6045(3) | 2.626 | 3.287 | 9.317 | 40 | 92 |
| TlBa ₂ Ca _{0.8} Nd _{0.2} Cu ₂ O _{6.86} | 3.85638(5) | 12.6534(2) | 2.686 | 3.247 | 9.406 | 100 | 92 |
| TlSr ₂ CaCu ₂ O ₇ | 3.7859(1) | 12.104(1) | 2.31 | 3.3407 | 8.763 | ns | 93 |
| Tl _{1.2} Sr ₂ Ca _{0.8} Cu ₂ O _{6.86} | 3.79333(4) | 12.1259(2) | 2.389 | 3.332 | 8.794 | 60 | 94 |
| Tl _{0.5} Pb _{0.5} Sr ₂ CaCu ₂ O ₇ | 3.795(1) | 12.094(5) | 2.06 | 3.286 | 8.829 | 85 | 95 |
| Tl _{1.1} Ba _{1.88} Ca _{1.9} Cu ₃ O ₉ | 3.853 | 15.913 | 2.73 | 3.198 | 9.128 | 110 | 96 |
| TlBaSrCa ₂ Cu ₃ O ₉ | 3.8316(1) | 15.5926(5) | 2.54 | 3.287 | 9.019 | 103 | 97 |
| Tl _{0.5} Pb _{0.5} Sr ₂ Ca ₂ Cu ₃ O ₉ | 3.81265(8) | 15.2630(4) | 2.292 | 3.2602 | 8.761 | 118 | 98 |
| Tl _{0.5} Pb _{0.5} Sr _{1.6} Ba _{0.4} Ca ₂ Cu ₃ O ₉ | 3.81863(7) | 15.3511(4) | 2.456 | 3.2667 | 8.818 | 116 | 98 |
| Tl _{0.8} Bi _{0.2} Sr _{1.6} Ba _{0.4} Ca ₂ Cu ₃ O ₉ | 3.8211(2) | 15.4235(9) | 2.383 | 3.279 | 8.865 | 113 | 99 |
| TlBa ₂ Ca ₃ Cu ₄ O ₁₁ | 3.84809(5) | 19.000(3) | 2.638 | 3.201 | 9.451 | 114 | 100 |
| Tl _{1.85} Ba _{1.94} Cu _{1.15} O ₆ | 3.8608(4) | 23.1332(5) | 2.7 | | 11.57 | 12.4 | 101 |
| Tl _{1.7} Ba ₂ Ca _{0.9} Cu _{2.3} O ₈ | 3.857(1) | 29.39(1) | 2.646 | 3.231 | | 95 | 48 |
| Tl ₂ Ba ₂ CaCu ₃ O ₈ | 3.8550 | 29.318 | 2.700 | 3.166 | 11.49 | 110 | 102 |
| Tl ₂ Ba ₂ Ca ₂ Cu ₃ O ₁₀ | 3.85101(1) | 35.5824(1) | 2.656 | 3.199 | 11.39 | 102 | 103 |
| Tl ₂ Ba ₂ Ca ₃ Cu ₄ O ₁₂ | 3.85049(1) | 41.9668(2) | 2.729 | 3.233 | 11.46 | 109 | 104 |

It could be expected that the charge transfer between the reservoir layers and the CuO_2 planes affects the lattice parameters or some other characteristic lengths in the cell, such as the distance between the copper atoms and the oxygen atom in apical position in the CuO_6 or CuO_5 blocks. The separation distance d between two successive internal CuO_2 planes, as well as the thickness d' of the rock-salt type layers between two CuO_2 external planes, may also influence the transport properties, essentially the irreversibility line and the flux pinning. In table 1 the a- and c- cell parameters, the distance of the copper with the apical oxygen $d(\text{CuO}_2\text{-CuO}_2)$, the distance between two consecutive CuO_2 square-plane d , the distance between two consecutive CuO_6 octaedra or CuO_5 square-based pyramids d' , and T_c of the compounds of the thallium family are summarized.

The crystallographic parameters of samples reported in table 1 result from structure refinements by X-ray or neutron diffraction. Only the tetragonal lattice, with the $P4/mmm$ and $I4/mmm$ space groups for the $\text{Tl-12}(n-1)n$ and $\text{Tl-22}(n-1)n$ series, respectively has been considered. As it was already indicated, $\text{Tl}_2\text{Ba}_2\text{CuO}_5$ may also be prepared with an orthorhombic cell, $Fmmm$ space group. Reversible conversion from orthorhombic to tetragonal type structure depends on the thallium and of the oxygen contents of the phase. It is the unique example in the high T_c 's cuprates of a phase showing a superconducting critical temperature up to 90 K with two crystal symmetries. In addition to the data in table 1, it has to be noticed that for all thallium cuprates, the mean Cu-O distance in the CuO_2 squared planes is 1.92(1) Å and is not correlate with T_c and that the warping of the basal layers slightly increases with the number of copper layers, specially in the double TlO series, with a O-Cu-O angle of 175.2° for Tl-2212 and 178.4° for Tl-2234 . The Tl-O distance in the (001) direction is about 2 Å in all $\text{Tl-m2}(n-1)n$ compounds.

The a and c lattice parameters of the tetragonal cell of a large quantity of samples not substituted [48, 77, 81-83, 91, 96, 105-110], thallium- [98, 99, 111-120], barium- [93,94,95,97,121-123], and oxygen- [124,125] substituted, have been analysed. The most representative values are reported in figure 3 for the two series $m=1$ and $m=2$. It may be observed from this figure that the a cell parameter slightly decreases with the number of CuO_2 layers. In addition, the size of the square basal plane is dependent on the nature of the substituted atoms for Tl (Pb, Hg, Bi) but more significantly when Sr, Y or rare earths La, Nd substitute Ba, and fluorine replaces oxygen. For instance, a is reduced of about 2 % when strontium replaces barium in the two-copper-layers compound of the $m=1$ series. The effect of substitution on the cell size also decreases as the number of CuO_2 layers increases. Similar to a, for the two series $\text{Tl-12}(n-1)n$ and $\text{Tl-22}(n-1)n$, the size of the substituting ion has some influence on the c-parameter which is also distorted of about 3% comparatively to the non substituted phases and which increases linearly with n. For the single TlO layer compounds, it is found that $c_1 = 3.19(3).n + 6.31(9)$ and for $m=2$, $c_2 = 6.27(4).n + 16.9(1)$. For $m=1$, the relation simply describes the packing of the layers $c \sim (n-1)d_{\text{CuO-CuO}} + 2.d_{\text{Cu-Oap}} + 2 d_{\text{Tl-O}}$. In $m=2$ phases, c_2 is not exactly twice c_1 due to the addition of a TlO-layer and also to the change in the barium coordination number which is 12 in the single and 9 in the double TlO compounds. The relations above mentioned includes all anionic or cationic substituted phases, indicating that bonds in the c-direction can accommodate with a large range of ionic radii.

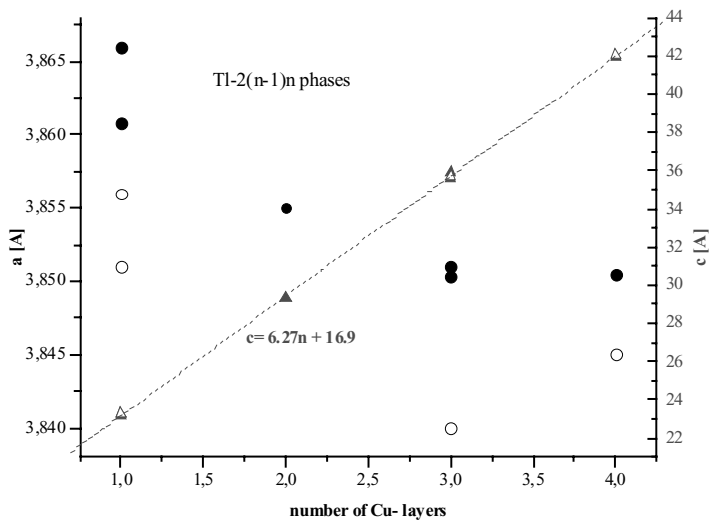
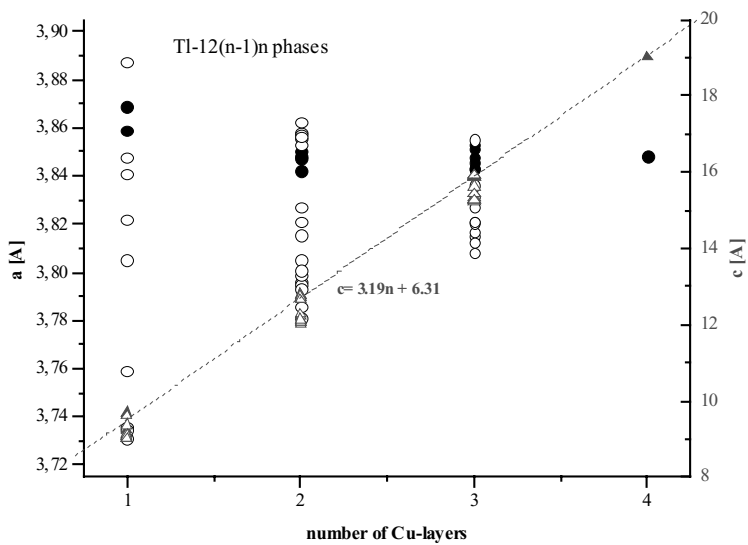


Fig. 3. Cell parameters a and c for Tl- $m2(n-1)n$ compounds; (\bullet, π) a and c for not substituted phases; (\circ, Δ) for substituted phases

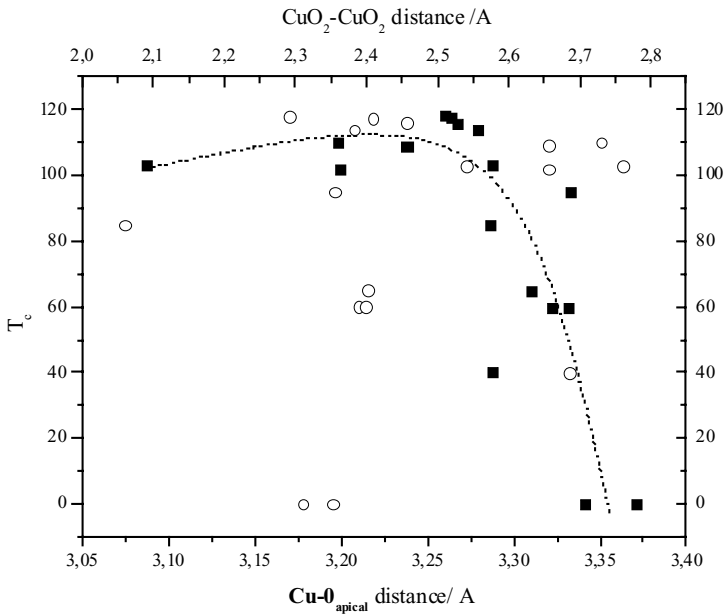


Fig. 4. The critical temperature for the Tl-cuprates as a function of the Cu-O_{apical} distance (■) and of the interlayer CuO₂-CuO₂ distance (○). The dotted line has been drawn as a guide for eyes

A common feature of the thallium superconducting phases with other cuprates is that the distance (CuO_{ap}) between the copper atoms and the apical oxygen in pyramidal CuO₅ or octahedral CuO₆ blocks, as well as the distance of two consecutive CuO₂ layers cannot be clearly related with T_c as may be seen in figure 4. For the latter however, a sharp drop in T_c is observed for d(CuO₂-CuO₂) > 3.30 Å. However, when considering the transport properties, the distance d' between the CuO₂ planes separated by the insulating and charge reservoir layers was found to be correlated with the irreversibility line, which is drastically displaced towards high values when d' is shortened [126,128].

In addition to these features, it is well known that for the two series m=1 and m=2, the critical temperature increases as the number of CuO₂ layers increases up to n=3 and then decreases for n=4. Even if not reflected on T_c, it is obvious that the selected distances Cu-O_{ap}, d(CuO₂-CuO₂) and d' are important parameters for the cohesive energy of the unit cells. For the two TlO layered phases Yang et al. [129] calculated the combinative energy of the perovskite and the rock-salt blocks and found it is closely related to T_c going through a minimum value (12.98 eV) as T_c is maximum (T_c = 128.5 K) for Tl-2223.

3. THE PHASE STABILITY OF THE SUBSTITUTED THALLIUM CUPRATES

The study of substitutions in the thallium cuprates was originated by the behaviour of the copper valence in the two families. Greenblatt et al.[41] noticed that the valence of copper for all the compounds of the single TlO-layer series, $TlBa_2Ca_{n-1}Cu_nO_{2n+3}$ is $(2+1/n)^+$ assuming thallium is 3^+ , as really observed. Then for Tl-1201, Tl-1212, Tl1223 and Tl-1234, we should find Cu^{3+} , $Cu^{2.5+}$, $Cu^{2.33+}$ and $Cu^{2.25+}$, respectively. The thermodynamic stability of the phases in this series was claimed to be affected by such high values of the copper valence and may explain the difficulties encountered to prepare pure samples. It is then suggested to replace thallium by metals with higher oxidation numbers. The behaviour of the double TlO materials, with the ideal stoichiometry $Tl_2Ba_2Ca_{n-1}Cu_nO_{2n+4}$ is on the opposite side with a valence of copper being strictly 2^+ . Accepting that the occurrence of superconductivity is related to a mixed valence state, high T_c 's for $m=2$ needs to generate some Cu^{3+} or Cu^{1+} ions, for instance by inducing a thallium deficiency or an oxygen excess. As for $m=1$, it is also possible to modify the hole or the electronic concentration in the CuO_2 layers by substitution: Pb^{2+} or Hg^{2+} on thallium sites, rare earth elements on the barium and calcium sites or fluorine on the oxygen site. Then substitutions in thallium cuprates have for main objective to study the change in the doping level of the CuO_2 sheets and to reach an optimum value of about 2.2-2.3 for the valence of the copper. *A posteriori* these substitutions have been found to make easier the preparation of some compounds essentially in the $m=1$ family. In table 2 are reported the Shannon radii [62] of the most used ions for substitution comparatively to the radii of initial ions: Tl^{3+} , Ba^{2+} , Ca^{2+} , Cu^{2+} and O^{2-} . For the lead and the bismuth ions, a mixed valence state may occur increasing the number of possible distributions on the thallium sites.

Table 2. Shannon radii of some substituting ions in the superconducting thallium cuprates . The coordination numbers are given in brackets

| | | | | | | | | |
|--------------|--------------|--------------|--------------|--------------|--------------|--------------|--------------|--------------|
| Tl 3+ | Tl 1+ | Pb 4+ | Bi 5+ | Hg 2+ | Ba 2+ | Sr 2+ | La 3+ | Ca 2+ |
| 0.885(6) | 1.5(6) | 0.775(6) | 0.76(6) | 1.02(6) | 1.47(9) | 1.31(9) | 1.216(9) | 1.12(8) |
| | | | | | 1.61(12) | 1.44(12) | 1.36(12) | |
| Y 3+ | Nd 3+ | Gd 3+ | Cd 2+ | Li 1+ | B 3+ | Rb 1+ | O 2- | F 1- |
| 1.019 | 1.108(8) | 1.053(8) | 1.10(8) | 0.76(6) | 0.27(6) | 1.52(6) | 1.4(6) | 1.33(6) |

3.1 Substitutions in the double Tl-O layered systems

In tetragonal Tl-2201, A.K.Ganguli and Subramanian [130] and Käll et al.[131] replaced Ba by Sr and found that superconductivity is suppressed for a substitution ratio $Ba/(Ba+Sr)$ of 30 % to 50 %, depending on the initial T_c , 55K and 90 K respectively. The introduction of Sr in the Ba sites results on a compression of the bond lengths round this site; in particular the $Cu-O_{ap}$ distance is shortened allowing an increased charge transfer from the charge reservoir layer to the CuO_2 planes which then becomes overdoped. La^{3+} was found to have a solubility limit $x=0.2-0.3$ in both tetragonal and orthorhombic $Tl_2Ba_{2-x}La_xCuO_5$ [81, 132,133]. There is no clear indication on the possibility to substitute oxygen by fluorine in Tl-2201 but Sun et al.[134] reported the formation of "near pure" phase by using a mixture of $xBaF_2$ and

(2-x)BaO₂ in the preparation process. For x=0.6 a critical temperature of 100 K was measured, which is about 8 K higher than that for the best Tl-2201 oxide material.

Because calcium (and possibly copper) is present on the thallium sites, it may be said that the Tl-2212 compound is a kind of "self-substituted" phase, but, if we restrict our investigation to ions different of the mother series, mercury has been reported to substitute thallium. Thopart et al.[66] replaced up to 18% thallium by Hg. No special ordering in the (Tl,Hg)O layers was observed. Hg substitution has poor influence on the critical temperature ($T_c=110$ K) and on the irreversibility lines. The (Tl,Hg)-2212 solid solution extends up to a value less than 50% Hg as may be seen on samples prepared by Tatsuki et al. [135] in their measurement of the thermoelectric power of (Tl_{0.5}Hg_{0.5})-2212. Interested to the relation between doping and crystallographic structure, and taking into account the work of Sequeira et al. [136] in which nearly 50% of Tl was replaced by K⁺ without incidence on the critical temperature, Morosin et al. [113] determined the structural parameters of Rb⁺-substituted Tl-2212. Due to the difference between the atomic number of Tl and Rb, the amount of rubidium determined by X-ray refinements cannot be given with high accuracy. It was estimated that 17% could be the limit for the uptake of Rb from more rich fluxes. The T_c onset of the resulting single phase samples was in the range of 107-112 K. E.A.Hayri and M.Greenblatt [137] found that the solid solution obtained by replacing Ba by Sr extends up to nearly 50%. As for Tl-2201, Käll et al.[131] explain the decrease of T_c from 110 K to 100K by a compression of the bonds near the (Ba,Sr) sites. In their study of the electrical resistivity of Tl₂Ba₂Ca_{1-x}R_xCu₂O_{8-δ}, R=Nd³⁺, Gd³⁺, Awad et al.[138] found that the c-parameter of the tetragonal cell decreases linearly with the rare earth content x with a slope $dc/dx = -0.056$ for Nd and -0.0524 for Gd. The solubility limit seems to be in the range of the compositions prepared by the authors, x=0.6 for Nd and x=0.4 for Gd. Superconductivity is suppressed at a critical composition $x_c = 0.369$ and $x_c=0.259$ and the samples become semiconductor at x=0.6 and x=0.4, for Nd and Gd, respectively. This behaviour is similar to that reported by Paranthaman et al. [139] for Y with x=0.3. To study the normal state pseudogap in the density of state at the Fermi level, Poddar et al. [140] examined the suppression of T_c by doping the CuO₂ planes by cobalt in Tl₂Ba₂Ca_{2-x}Y_x(Cu_{1-y}Co_y)₂O_{8+δ} and found that this suppression is more rapid in the underdoped region. An inverse power law with hole concentration is found for the magnitude of the pseudogap.

It is now established that Tl-2223 samples prepared with the stoichiometric ratio Tl:Ba:Ca:Cu = 2:2:2:3 are multiphase, containing Tl-2212 as main impurity but also the (Ca,Tl)CuO₂ solid solution and the Tl-rich binary phase Tl₂Ca₃O₆ [44]. Usually, thallium vacancies up to 12 % and about 10% calcium substitution on the thallium sites are conditions to prepare single phase Tl_{2-x-z}Ba₂Ca_{2+x}Cu₃O₁₀. A zero resistance temperature at $T_c = 127$ K (130 K for a diamagnetic response), the highest critical temperature in the thallium systems has been measured by Kaneko et al. [26] for a sample with the composition Tl_{1.7}Ba₂Ca_{2.3}Cu₃O₁₀. In agreement with R.S.Liu and P.P.Edwards [141], Paranthaman et al [142] reported that the solubility limit of Ca in the double TlO-layer is x=0.4. In reality, the composition of the sample, found by wet chemistry analysis is Tl_{1.33}Ba₂Ca_{2.4}Cu₃O_{9.67}. The authors demonstrated that introducing Ca in the Tl-sites contributed to the hole concentration optimisation. It must be noticed that Maignan et al. [143] have grown from the melt Tl-2223 single crystals of composition Tl_{1.95}Ba₂Ca_{2.05}Cu₃O_{10-δ} with typical superconducting properties ($T_c=124$ K and $J_c^{(a,b)} \sim 10^6$ A.cm⁻²), indicating that the doping is due essentially to the presence of Ca²⁺ in the Tl-sites and that pinning does not depend on punctual defects. In the

same register of "self-substituted" phase, copper was also claimed to partially occupied the thallium sites. Sinclair et al. [144] showed that Cu excess and calcium deficiency in $(\text{Tl}_{1.72}\text{Cu}_{2.8})\text{Ba}_2(\text{Ca}_{1.86}\text{Tl}_{0.14})\text{Cu}_3\text{O}_{10}$ favours the formation of a Tl-2223 phase with $T_c = 125$ K. Rubidium was also inserted in the double TlO layer by Morosin et al. [113] which encountered the same analytical difficulties than for Tl-2212. Nevertheless, it may be accepted that about 20% of the thallium sites are occupied by Rb. The T_c is not correlated with the Rb content and was found to range between 116 K to 120 K. From the work of Xin et al. [145] it is difficult to separate substitution from compositional effects in a series of $\text{Tl}_2\text{M}_{0.2}\text{Ba}_2\text{Ca}_2\text{Cu}_3\text{O}_x$, all multiphase samples, where M is an alkaline or a transition metal. Nevertheless, it is interesting to note that 95% to 98% Tl-2223 was prepared with $M = \text{Ti, Zn}$ and Hg with T_c of 115 K, 112 K and 120 K, respectively. Singh et al. [146] introduced Cd in the preparation of thin films by a spray pyrolysis process. The doping favours the formation of a single phase film and enhances the superconducting temperature up to 124 K for 0.2 Cd ions per formula unit. It is then deduced that Cd has similar effect than Ca, substituting Tl and/or filling the vacancies in the TlO-layers. Transport critical currents $j_c = 1.12 \cdot 10^5 \text{ A.cm}^{-2}$ have been measured at 77 K in self field and the films showed predominantly c-axis orientation. Starting from a mixture adjusted to form single phase $\text{Tl}_{1.8}\text{Ba}_2\text{Ca}_{2.2}\text{Cu}_3\text{O}_x$, Kayed et al. [146] added up to 3 mol.% of Li^+ . After a heat treatment (890°C for 3h in oxygen), appropriate to form preferably Tl-2212, the samples prepared with addition of 0.29 mol.% Li consisted mainly in Tl-2223. This behaviour at least indicates that small quantities of lithium may be used to improve the formation of Tl-2223, similarly as observed by the same author for 0.8-1 % boron additions [147]. Fluorination by a diffusion substrate-coating couple process using TlF as partial thallium source has been reported by Kikuchi et al. [148] who concluded that F-additions increases the critical transport current and shifts the irreversibility to higher temperature. The effect on phase formation is not clear due to the fact that the diffusion couple is multiphase.

3.2 Substitutions in the single Tl-O layered systems

It was already mentioned that in the single TlO-layered thallium cuprates the copper valence is between 2.2+ and 3+, so that holes in the CuO_2 sheets may control the superconducting state. The optimum doping value may be reached, as for the members of the $m=2$ series by changing the thallium or the oxygen content of the phases but the oxygen non stoichiometry has been more evidenced in the double TlO layer than in the single one. For instance, D.M.Ogborne and M.T.Weller [123] noticed that in Tl-2212, the O(3) sites of the in plane TlO layer are vacant up to 6% whereas in Tl-1212 only 1% change in oxygen stoichiometry may be observed. Then substitution appears to be most efficient procedure to optimise the superconducting properties. Usually, in this $m=1$ series, simultaneous substitution on the thallium and on the barium sites is claimed to result in the stabilization of both thermodynamic and superconducting properties. We observe that Pb^{4+} and Bi^{5+} for Tl^{3+} and trivalent rare earths for barium may be used to inject electrons in the CuO_2 layers whereas only size effects are expected when Sr is used instead of Ba. Studer et al.[149] by X-ray absorption spectroscopy showed that the lead valence is +4 in the series $\text{Tl}_{0.5}\text{Pb}_{0.5}(\text{Sr,Ca})_{n+1}\text{Cu}_n\text{O}_{2n+4+\delta}$ with $n=1-3$. One of the problems encountered when thallium and barium are respectively substituted by lead and strontium, is the reaction pathway through

stable barium plumbate perovskite and/or strontium-calcium cuprates which affects the kinetics of formation of the superconducting phases.

It is argued that the formal valence of copper (3+) in the first member of the $m=1$ family, $TlBa_2CuO_{5.8}$ is the reason why most of the samples are not superconducting ($\delta = 0$) or shows either a very low critical temperature (9.5 K) [121] or a "metastable" superconductivity around 25 K [122]. The Tl-1201 phase was stabilized by Letouzé et al. [112] who prepared a chromium-substituted single phase $Tl_{0.8}(CrO_4)_{0.2}Ba_2CuO_{4.3-8}$ in which chromate groups were evidenced, the Cr(6+) ions being on the Tl sites. The sample showed stable superconductivity at 42 K. A number of double substitutions (Pb,Bi) for Tl and Sr for Ba have been experimented. As a general trend if barium is completely replaced by strontium, in $TlSr_2CuO_5$, and in the solid solutions $(Tl_{1-x}Bi_x)Sr_2CuO_5$ and $(Tl_{1-x}Pb_x)Sr_2CuO_5$ superconductivity is difficult to be observed [150, 41,111]. A size effect on the band filling and the increased possibility for Ca^{2+} sites to accept thallium ions are presumably the reasons which promote superconductivity in $TlBaSrCuO_5$ where half of Ba^{2+} ions have been replaced by smaller Sr^{2+} and for which $T_c = 43$ K [121]. However, more enhancement of the critical temperature is obtained when La^{3+} is placed on the alkaline earth site independent on thallium substitution. Subramanian et al.[90] and Ku et al.[122] prepared $TlBa_{2-x}La_xCuO_5$ with x up to 0.8 and reproducible T_c from 45 K to 57 K. Shi et al. [151] obtained similar results in the $(Tl,Pb)(A,R)_2CuO_5$ systems with A= Ba, Sr and R= La, Pr and Nd. The highest critical temperature in the system has been measured in samples where some oxygen are supposed to be substituted by fluorine. M.A.Subramanian [124] used TlF as fluorine source to produce $TlBa_2CuO_{5-x}F_x$ single phase samples for $x \leq 0.5$ with T_c onset in the range 35-75 K. In such materials, the fluorine doping effect is not sufficient to explain such high T_c because the formal valence of copper (between 2.5+ and 2.8+) lies above the optimum value. Formation of oxygen vacancies during the preparation process is then expected.

Contradictory to Tl-1201, $TlBa_2CaCu_2O_7$ is easily prepared with a superconducting critical temperature of 103 K [91]. From a structural point of view the phase is very similar to $YBa_2Cu_3O_{7.8}$ which is the reference material for transport applications of superconductivity at 77 K. Then, with a T_c 10 K higher, Tl-1212 offers promising pinning properties and accounts for the large number of substitutions studies. From an electronic point of view, the formal valence of copper is 2.5. For not substituted quenched-annealed samples, Nakajima et al.[152] pointed out the extreme effect of the oxygen content on T_c . When oxygen-annealed specimens are heated at low temperature (500°C) in nitrogen, 0.5% of oxygen atoms are released and T_c jumps from 80 K to 110 K. Small changes in oxygen stoichiometry during the preparation process are probably responsible for the behaviour of samples where barium was fully replaced by strontium. $TlSr_2CaCu_2O_7$ has been found not superconducting [93] or with T_c ranging from 20 to 75 K [95,153]. Similarly to Tl-1201, the intermediate $TlBaSrCaCu_2O_7$ phase seems to take benefits of the substitution of Ba^{2+} by Sr^{2+} since T_c as high as 94 K was reported by Gopalakrishnan et al. [116]. Due to the difficulty to clearly identify the reasons for high critical temperature multi-site substitution has been extensively studied. We can summarize the main expectations: (i) lead, bismuth and chromium for thallium are supposed to increase the hole concentration in the CuO_2 planes; (ii) strontium from barium shrinks the cell decreasing substantially the d' distance between 2 consecutive CuO_5 or CuO_6 blocks, thus favouring charge transfer;(iii) The latter is however more efficient when trivalent rare earths partially occupy the Ca^{2+} site. A special mention has to be assigned to oxygen exchange by fluorine or chlorine due to experimental difficulties to quantify the substitution amount.

Table 3. Summary of superconducting properties of substituted Tl-1212 phase

| Compound | T _c (K) | Main | Ref. |
|---|--------------------|--|------|
| TlBa ₂ CaCu ₂ O _{7-δ} | 80-110 | δ=0.035; Optimum hole amount | 152 |
| TlBa ₂ CaCu ₂ O _{7-δ} | 100-116 | single crystal; anneal 400°C / Ar → T _c unchanged | 115 |
| TlBaSrCaCuO ₇ | 94 | after slow cooling in nitrogen | 116 |
| TlSr ₂ CaCu ₂ O _{7-δ} | 47 | about 90% of Tl-2212 | 95 |
| (Tl _{0.5} Pb _{0.5})Sr ₂ CaCu ₂ O ₇ | 85 69-77 | pure Tl-1212; lamellar crystals depending on the heat treatment; change in oxygen stoichiometry is around 1% | 123 |
| Tl _{0.961} Cr _{0.100} Sr ₂ Ca _{0.93} Cu ₂ O _y | 101 | nearly pure phase; Cr at high valence state | 114 |
| Tl _{0.55} Bi _{0.45} Sr ₂ CaCu ₂ | 94.9 | 10% of Ca sites substituted by Tl; platelet morphology- J _c (50K,2T) 10 ⁴ A/cm ² | 115 |
| Tl _{0.5} Pb _{0.5} Sr ₂ Ca _{1-x} Y _x Cu ₂ O _y | 110 | absence of oxygen effects on T _c | 154 |
| TlBa ₂ Ca _{1-x} Nd _x Cu ₂ O _{7-δ} x=0.2, 0.5 and 1 | 0-100 | all samples are single phase Tl-1212; x=1 not superconducting for x=0.2 and 0.5 → δ=0.14; holes governs superconductivity but not necessary due to the TlO layer | 92 |
| (TlPb)Ba _{0.4} Sr _{1.6} Ca _{0.8} R _{0.2} Cu ₂ O _x R= rare earths | 23.9- 100.1 | all samples are single phase; the low T _c is for Ce, the highest for Sm. | 155 |
| Tl(Sr _{2-x} Ce _x)CaCu ₂ O ₇ x<0.6 | 0-62 | single phase samples except for x=y=0; | 156 |
| TlSr ₂ (Ca _{1-y} Ce _y)Cu ₂ O ₇ x<0.7 | 80 | maximum T _c for x= y= 0.35; Transition metal-insulator for x= 0.6 at T=150K; | 157 |
| Tl(Sr _{2-x} R _x)CaCu ₂ O ₇ R=Sm, Eu, Dy; 0.1<x<1 | 90 | from resistivity Lnp~ T ⁿ , n=1/4→ 3D hopping mechanism | 158 |
| Tl(Sr _{2-x} R _x)CaCu ₂ O ₇ R=rare earth | 96 | (Ca,Y) complete solid solution; for x=0.3-0.5, T _c suppressed by inhomogeneous hole distribution; existence of a spin-gap | 159 |
| (Tl,Cr _{0.15})Sr ₂ (Ca _{0.9} Pr _{0.1})Cu ₂ O _{7-x} | 84-86 | Ag-sheathed tapes dominated by weak- links no significant anisotropic transport properties, comparatively to Bi-2223; Pr stabilizes the phase; Cr enhances T _c | 160 |
| TlA ₂ RCu ₂ O _{7-x} A= Ba,Sr; R= RE,Y,Ca | | coexistence superconductivity-magnetic ordering | 161 |
| TlSr ₂ CaCu ₂ O _{7-x} A _x A=F,Cl | 35-50 | SrF ₂ and CaCl ₂ used as F and Cl sources; single phase for F up to x<1.5; Cl prevents the Tl-1212 formation; | 162 |
| TlSr ₂ CaCu ₂ O _{7-x} F _x | 0-110 | CaF ₂ used as F source; x=0 is not superconducting; maximum T _c when CaO completely replaced by CaF ₂ ; optimum F content | 125 |

Some results of such substitutions on superconducting properties have been summarized in table 3 in which it may be noticed that, as a matter of fact, the highest critical temperatures (110-116) have been measured on non-substituted $TlBa_2CaCuO_{7-x}$ parent phase by optimising the heat treatment in order to produce the more efficient doping on the CuO_2 layers. The same result has been observed by using a fluorine component (SrF_2 or CaF_2) in the preparation process of the superconducting phase. Again, it is worth noting that fluorine was never directly observed on the oxygen sites but its effect on the superconducting properties, on the melting temperature and on the mechanical properties of the phase are arguments for giving some credibility to an effective substitution. The failure to form the Tl-1212 phase by chlorine doping, due to the large Cl^- ionic radius compared with F^- , may also induce similar conclusion. The effect of the replacement of oxygen by fluorine on the superconductivity of the thallium cuprates is to reduce the hole carrier number in the CuO_2 layers. This is also realized when Sr and Ca are substituted by trivalent rare earths with the insurance that substitution really occurs in the expected sites. Such cationic substitutions give rise to extended solid solutions in which transitions from non superconducting metallic to insulator state may be studied. We observe that substitutions on the thallium site, by lead or bismuth are always associated with at least partial replacement of Ba by Sr.

Considering now the stabilization of the phase by partial substitution, some comments are needed. Most of the papers in the literature mentions that the Tl-12(n-1)n compounds are more stable when they are substituted phases. As a matter of fact, it has to be understood that "more stable" here means that these substituted phases are easier to be formed due to their formation at a lower temperature than the parent compound and also appears as more pure materials. In any case this behaviour may account for thermodynamic stability. It more likely reflects the kinetics of the phase formation. To my knowledge, no systematic study of the thermodynamic properties of the substituted thallium cuprates has been reported, excepted for the $m=1, n=3$ member of the series that will be discussed in detail hereafter.

3.3 Phase stability of substituted Tl-1223 phase

The superconducting properties of the single layer $TlBa_2Ca_2Cu_3O_{9-\delta}$, with possible critical temperatures approaching 130 K, a high temperature irreversibility line with a 3D-like behaviour which well compares with $YBa_2Cu_3O_7$ and the infinite possibilities of substitutions which are expected to promote pinning centres, here are enough reasons to justify a special attention to the phase. Most of the reports on the compound concerns the substituted phase which was found to be more easily prepared than the parent material. Recently we have demonstrated that a careful analysis of the reaction path for the phase formation may help to prepare nearly pure $TlBa_2Ca_2Cu_3O_x$ (93%) with similar, if not enhanced superconducting properties. This is illustrated by the irreversibility field behaviour as a function of the temperature for $TlBa_2Ca_2Cu_3O_{9-\delta}$, $(Tl_{0.5}Pb_{0.5})(Sr_{1.6}Ba_{0.4})Ca_2Cu_3O_x$ [163], $(Tl_{0.6}Pb_{0.2}Bi_{0.2})Sr_{1.8}Ba_{0.2}Ca_2Cu_3O_x$ [164] and $YBa_2Cu_3O_{7-\delta}$ [165] (fig.5). We have found for some not substituted samples a high temperature irreversibility line very close to (Tl,Pb,Bi)-1223 but the most usual behaviour is similar to (Tl,Pb)-1223 [44,67]. It may argued, on the view of careful analysis of X-ray diffraction patterns and of the ac.susceptibility measurement of the T_c of $Tl_{1.05}Ba_2Ca_2Cu_3O_y$ (fig.6), that the high temperature irreversibility line is due to intergrowths of Tl-1223 and Tl-2223 phases [67,166]. Note in the inset of figure 6 the derivative of the ac. susceptibility which reveals the presence in the powdered sample of four superconducting

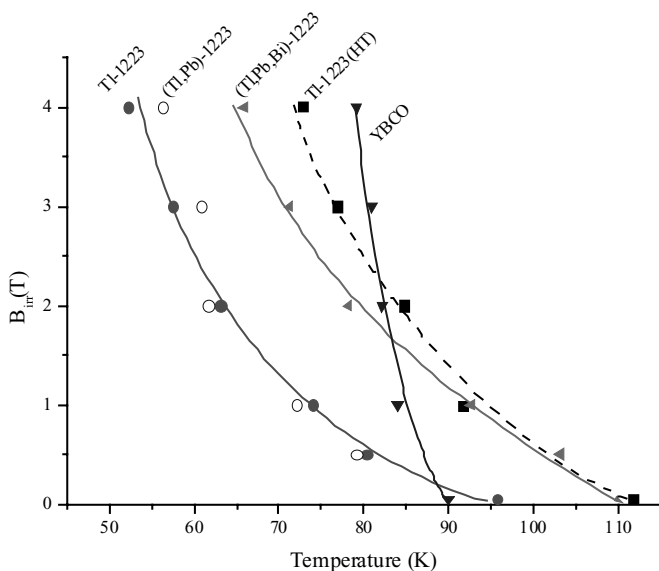


Fig. 5. Irreversibility field for thallium cuprates compared with YBCO

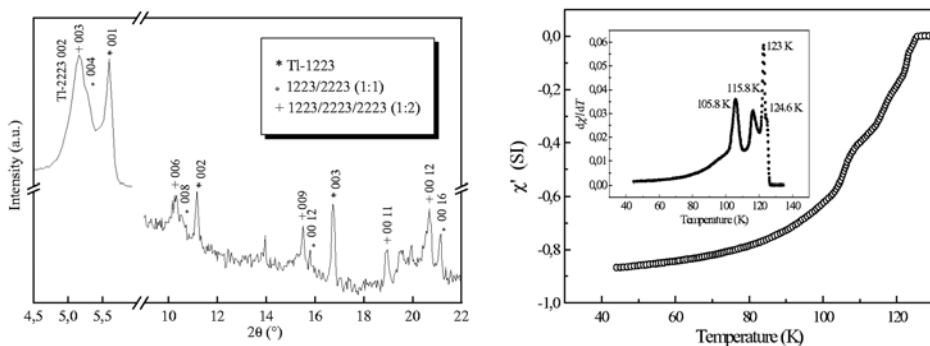


Fig. 6. Low angle part of the X-ray diffraction pattern of $\text{Tl}_{1.05}\text{Ba}_2\text{Ca}_2\text{Cu}_3\text{O}_y$ showing coexistence of Tl-1223 with 2 intergrowth phases (1223/2223) and (1223/2223/2223) (left) and the ac.susceptibility curve for the same powder sample which clearly shows in the inset 4 superconducting transitions (right)

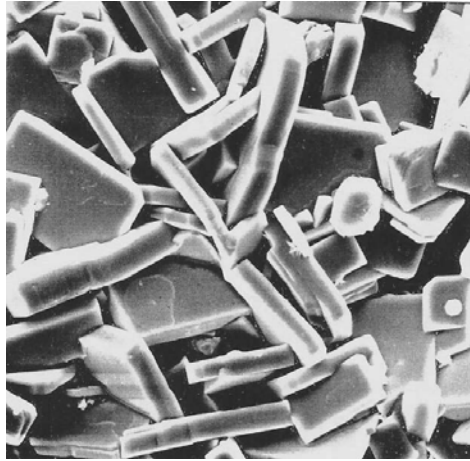


Fig. 7. Platelet-like grains of $\text{TlBa}_2\text{Ca}_2\text{Cu}_3\text{O}_{9.8}$. The mean size of the grains is $20\ \mu\text{m}$ and their thickness $5\ \mu\text{m}$

phases whereas the low angle X-ray diffraction pattern indicates Tl-1223 and two intergrowth phases (1223/2223) and (1223/2223/2223). However, it was found that the structure refinement is improved when (1223/2223/2223/2223) is also considered, in agreement with the 4 T_c signatures. Intergrowths are frequently encountered in the high temperature superconducting systems; in the thallium compounds their presence is favoured by the existence of the two series $m=1$ and $m=2$, by the pathway for the formation of Tl-1223 which implies Tl-2223 and therefore includes equilibrium state between the two phases, and finally, as recently showed by Iyo et al. [167,168] with samples prepared under high pressure (3.5 GPa), by carbon contamination which promotes the formation of Tl-2223. For the generation of "powder in tube" conductors, the transport properties however remained far from expected if we refer to the intrinsic superconducting properties and to the platelet-like Tl-1223 grains grown from Tl-2223 (figure 7) in the reaction pathway.

Returning to the hole doping description of the high temperature superconducting phases, the formal copper valence in Tl-1223 is +1.33, near the optimum value. As for Tl-1212, and for similar reasons replacement of Ba^{2+} by Sr^{2+} was attempted but only the use of high pressure (6GPa) allowed the preparation of single phase samples $\text{TlSr}_2\text{Ca}_2\text{Cu}_3\text{O}_{9.8}$ [169] with $T_c=86\ \text{K}$. Martin et al. [97] were more successful with $\text{TlBaSrCa}_2\text{Cu}_3\text{O}_{9.8}$ with $T_c=103\ \text{K}$ which may be increased up to 116 K after annealing at 280°C for very short times (15 min) in a reducing atmosphere. At so low annealing temperature, oxygen is removed from the cell, contributing to injects electrons in the CuO_2 layers and then to reduce the hole concentration. Substitution on the thallium site by Hg with a Ba-based phase with the objective to increase pinning effects have been reported [170,171] in $(\text{Tl}_{0.7}\text{Hg}_{0.3})\text{-1223}$. In a series of publications, Awad et al.[172] found that Ni and Zn may replace Tl with solubility limits of 0.3 and 0.4 respectively but with contradictory effects on T_c . The same author [173,174] reported activation energies for the flux motion in $(\text{Tl-Pr,Yb})\text{-1223}$, single phase up to 20-30% substitution. Tl-1223 is the major component of multiphase $[\text{Tl}_x\text{Cu}_{1-x}]\text{Ba}_2\text{Ca}_2\text{Cu}_3\text{O}_z$ samples

prepared under high pressures by Yamamoto et al [175] and Tanaka et al.[176] for the study of Tl-valence fluctuations. The impurity phases may be others thallium cuprates (Tl-1212, Tl-1234) or BaCuO₂, Ca_{0.8}CuO₂ and CuO depending on the applied pressure. Weight losses attributed to oxygen during annealing at 350°C indicate that 0.4 Tl³⁺ per formula unit are converted to Tl¹⁺ giving a T_c rise from 97.6 K for as synthesized samples to 125.6 K. Looking for a new superconducting phase, Chen et al. [177] discovered in the strontium-based TlSr₂Ca₂Cu₃O_z, than vanadium may be inserted in the thallium sites up to a ratio Tl:V = 1:1, but the most remarkable results are due to Liu et al. [178,179] who increased the critical temperature of (Tl_{0.5}Pb_{0.5})Sr₂Ca₂Cu₃O₉ up to 130 K after long evacuated anneal in vacuum and proved that such samples may transport currents as high as J_c = 1.24 10⁵ A.cm⁻² at 77 K under a 1 T field. The 3-D character of the irreversibility field which in this phase, is supposed to be responsible for high J_c, rather than creation of pinning centres, was observed from heat capacity measurements above T_c. The superconducting properties of such (Tl,Pb)-1223 then being comparable to YBCO but about 30 K higher, may be considered as the starting point of the credibility for thallium cuprates to be used in transport applications even if Doi et al. [180] first published interesting results on the formation of pinning centres not attributed to impurity precipitates, for double substituted (Tl_{0.5}Pb_{0.5})(Sr_{1.6}Ba_{0.4})Ca₂Cu₃O_x. Double substitution in the Tl-and Ba-sites have been extensively studied [98,99,119,181-187] in order to understand the phase formation, to determine its homogeneity range and to optimise the sample microstructure for the improvement of the superconducting properties.

The reaction pathway for the formation of the substituted Tl-1223 phase depends on the nature of the substitution element. In developing long length (Tl_{0.78}Bi_{0.22})Sr_{1.6}Ba_{0.4}Ca₂Cu₃O_x wires Miller et al.[188] reported the transitory or equilibrium precipitation of BaBiO_{2.77} and of (Ca,Sr)-Cu-O mixed oxides but the (TlBi)-1212 phase precedes the formation of (Tl,Bi)-1223 and all the bismuth atoms which will be further in the latter are already included in the former. K.Lebbou [163] and S.Trosset-Jarnieux [189] have extensively studied the reaction pathway, the kinetics for the phase formation and the phase equilibrium of substituted (Tl,Pb,Bi)(Sr,Ba)Ca₂Cu₃O_x. It is important here to point out the extreme complexity of the substituted systems because the (Tl,Pb)(Ba,Sr)-1223 phase belongs to a six component oxide system (TlO_{1.5})- (PbO)- (BaO)- (SrO)- (CaO)- (CuO), assuming that all metallic oxides are stable in the pressure-temperature field investigated. The knowledge of the equilibrium states requires the study of 57 equilibrium phase diagrams! We can restrict our investigation by focussing our attention to sections which contains the impurity phases formed in the ultimate step of the preparation of (Tl,Pb)-1223, namely the (Ca,Sr)_pCuO_x the perovskite (Tl,Pb)(Ba,Sr)O₃ phases, the calcium plumbate phase Ca₂PbO₄ and the two-CuO₂ layered neighbouring phase (Tl,Pb)(Ba,Sr)₂Ca₂Cu₃O_z. For kinetics studies, it is also important to understand the equilibrium implied in the precursor material which does not contain thallium "(Ba,Sr)₂Ca₂Cu₃O_x" but which may govern a reaction pathway as we have found for the unsubstituted Tl-1223 phase [44]. The ternary CaO-SrO-CuO system containing the precursor mixture "Sr₂Ca₂Cu₃O_x" for the preparation of the Sr-based (Tl,Pb)-1223 was revisited at 950°C by Lebbou [163, 190]. The precursor is two-phase (Sr,Ca)CuO₂ and (Sr,Ca)₂CuO₃. On substituting Ba for Sr, it is necessary to investigate the quaternary BaO-CaO-SrO-CuO system. On the "Ba₂Ca₂Cu₃O_x- Sr₂Ca₂Cu₃O_x" line the equilibrium states imply extended solid solutions of the binary compounds SrCuO₂ Sr₂CuO₃, BaCuO₂ as major components. Sr₁₄Cu₂₄O_x and Ba₄CaCu₃O_x were also found to participate to the equilibrium [189,191]. The solid state equilibrium in the field forming the perovskite compound

(Tl,Pb)(Ba,Sr)O₃ has been established [192]. No quaternary new phase could be detected in the Tl₂Ba₂O₅-Tl₂Sr₄O₇-PbSrO₃-PbBaO₃ section and the equilibrium diagram at 840°C shows an extended PbBaO₃ solid solution on Tl and Sr substitution for Pb and Ba, respectively.

The description of a single phase field in the six-component system needs 7 independent intensive thermodynamic variables! In order to limit this number, we can fix the temperature and the pressure of the equilibrium and add the compositional constraints for copper and calcium which are necessary $x_{\text{CuO}} = 0.375$ and $x_{\text{CaO}} = 0.25$. Then the Gibbs rule for the variance of the system becomes $v = 4 - \phi$ and a single phase field now belongs to a three-dimensional space. In this space all the (Tl_yPb_{1-y})(Sr_xBa_{1-x})-1223 stoichiometric compositions are located in a parallelogram with terminal vortexes TlBa-1223, TlSr-1223, PbBa-1223 and PbSr-1223. The homogeneity range at about 950°C of the (Tl,Pb)(Ba,Sr)-1223 phase has been represented in Fig.7

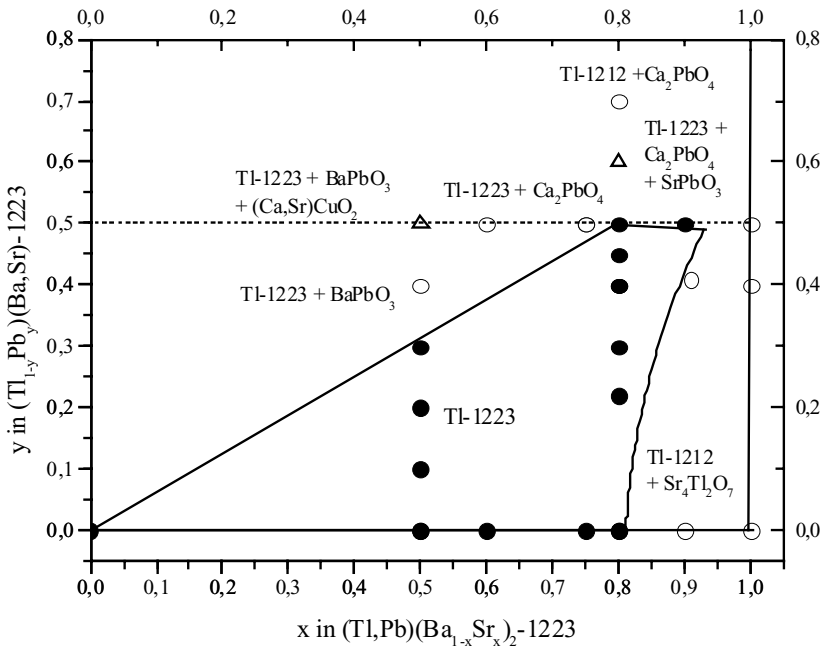


Fig. 8. The homogeneity range ($T=950^\circ\text{C}$) of $(\text{Tl}_{1-y}\text{Pb}_y)(\text{Ba}_{1-x}\text{Sr}_x)\text{Ca}_2\text{Cu}_3\text{O}_z$ ● single-phase, ○ two-phase and Δ- three phase samples

All the phases surrounding the (Tl,Pb)(Ba,Sr)-1223 field reported in Fig.7 are substituted (Tl,Pb)- and (Ba,Sr,Ca)-oxides. We note that the most usual composition for current transport studies, $(\text{Tl}_{0.5}\text{Pb}_{0.5})(\text{Ba}_{0.4}\text{Sr}_{1.6})\text{Ca}_2\text{Cu}_3\text{O}_x$ is at the limit of the single phase field which, in open system, is stable up to 820°C - 860°C , the temperature range at which thallium starts to

decompose. Studying the melting and the vaporization of the (Tl,Pb)(Ba,Sr)-1223 phase, Cook et al. [193] found by thermal and thermogravimetric analyses (DTA/TG) in oxygen flow, two main events on heating in the temperature ranges 920°C - 980°C. Other groups [163,189,194] confirmed the existence of two endothermic reactions but at temperatures slightly higher (960°C-1000°C). The temperatures discrepancy is probably due to the use of alumina for the sample container rather than MgO. In multiphase samples a third DTA signal, at about 860-880°C, not correlated to weight change, and with small intensity has to be attributed to solid state reactions between the impurity phases. The high temperature behaviour in the compositional field under interest has been represented in Fig.9.

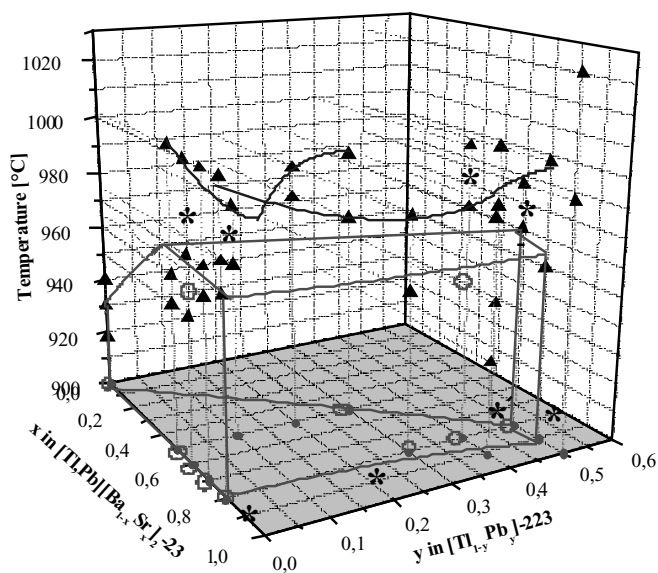


Fig. 9. Temperature stability of (Tl,Pb)(Ba,Sr)-1223. The single phase field is represented in red colour. ▲ is for multiphase samples and * for DTA/TG signals

The single phase limits are reduced at high temperature only in the barium-rich corner. Indeed, $TlBa_2Ca_2Cu_3O_x$ starts to decompose at 938°C, about 20°C below the strontium containing compounds. It is an argument for the highest stability of substituted phases. The first significant endothermic reaction occurs at 960°C for Tl-rich compositions and 980°C in the Pb-rich side. It corresponds to the decomposition of the (Tl,Pb)-1223 phase to (Tl,Pb)-

1212, perovskite $(\text{Ba,Sr})\text{PbO}_3$, calcium plumbate $(\text{Ca,Sr})_2\text{PbO}_4$ or (Ca,Sr) -cuprates, depending on the starting composition. It is not clearly established yet if a liquid phase participates to this decomposition but thallium (or thallium-lead) losses are strongly associated to the DTA signal and then could be significant of a peritectic-like reaction. The second DTA peak reported in Fig.9 reflects the liquidus surface which seems to form a kind of valley in the central part of the diagram, suggesting a eutectic reaction.

Contrary to $\text{TlBa}_2\text{Ca}_2\text{Cu}_3\text{O}_z$ the formation $(\text{Tl}_{1-x}\text{Pb}_x)(\text{Sr}_{1-y}\text{Ba}_y)_2\text{Ca}_2\text{Cu}_3\text{O}_z$, does not implies the double TlO layer series even in lead-free, barium substituted samples. This is due to the equilibrium composition of the precursor mixture which contains, as already mentioned, solid solutions of (Sr,Ca,Ba) -cuprates in which thallium is consumed to form $\text{Sr}_4\text{Tl}_2\text{O}_7$ during the thallination process. It is not expected that the first members of the double TlO series could be grown from this precursor. The first superconducting compound to be formed at 830°C in the reaction pathway is (Tl,Pb) -1212. The homogeneity field of this phase is very similar to that of (Tl,Pb) -1223 with the difference that the barium-free compound may be obtained easily for $0.3 < \text{Tl/Pb} < 0.5$.

To close this review on the substitution (Tl,Pb) - (Ba,Sr) effects on the thermal behaviour of the Tl-1223 phase, it is note worthy that bismuth may substitute thallium [163,182,183,185,187,194,195] but no more than 20% of bismuth atoms may be present in the thallium site for single phase samples. For $\text{Ba:Sr} = 0.4:0.6$ and a Bi content $0.2 < x < 0.4$ BaBiO_3 is found to coexist with Tl-1223 and the decomposition temperature in oxygen is 944°C , very close the value for the corresponding pure thallium compound. However Bi has been found to increase the kinetics for the phase formation due to the occurrence of a liquid phase in the reaction pathway at a temperature as low as 885°C which accelerates the grain growth. A benefit effect for texturing is then expected [194]. The results of cation substitution on the phase stability may be summarized as follows:

- Ba is necessary to form the substituted Tl-1223 phases but it was found to affect the microstructure of the samples so that high strontium contents are generally used, the key value being $\text{Sr}/(\text{Sr}+\text{Ba}) = 1.6/2$, for which a decrease of the thickness of the insulator layer is expected resulting in an increase of the Josephson coupling between adjacent CuO_2 layers; the irreversibility line is shifted towards high temperatures. A non negligible secondary effect of Sr on the barium sites is to shorten the Cu-O distances in the (a,b) plane and consequently crystal growth in this direction is enhanced.
- The optimum ratio Tl:Pb is 1:1 as predicted by the close-pack model for cuprates by Ganguly and Shah [59] but in (Tl,Pb) -1223 lead was found with an oxidation number Pb^{4+} ; the copper valence is thus reduced.
- Bismuth may also substitute thallium complementary with lead or not but the substitution ratio never excess 0.2 Bi atoms per formula unit. Bi seems to act as a catalyst for the formation of Tl-1223 due to liquid-phase sintering.
- Impurity phases always coexist with Tl-1223. Their nature depends on the content and on the nature of substituting element. Nevertheless, the barium perovskite BaPbO_3 , the calcium plumbate Ca_2PbO_4 , the mixed calcium-copper oxides $(\text{Ca,Sr})_2\text{CuO}_3$ and $(\text{Ca,Sr})\text{CuO}_2$ are the most current not superconducting phases encountered. Their quantity is drastically decreased if excess of Ca and Cu are used.

With the recurrent problem related to its analysis, fluorine substitution for oxygen has been claimed to improve the superconducting properties of Tl-1223. Handam et al.[196] using

CuF₂ as fluorine source enlarged the magnetization loop. Sung et al.[197] noticed that fluorine facilitates the formation of either Tl-1223 or Tl-2223 depending on the carbon impurity which induces superlattices (mTl-1223): nTl-2223). Kikuchi et al.[198] verified that the formation of Tl-1223 is enhanced when TlF is used as thallium source and argued that the observed decrease of the c-cell parameter when the annealing time at 850°C is increased is significant of fluorine inclusion in the phase. Trosset-Jarnieux included fluorination in her study of the stability of (Tl,Pb)(Ba,Sr)-1223 [189]. Based on pH titration of fluorinated solutions, it is concluded that F substitutes oxygen up to 0.15-0.2 atoms per formula unit but without influence on the homogeneity range and on the phase stability. On the contrary, Bellingeri [194] observed that (Tl_{0.57}Pb_{0.5})(Sr_{1.67}Ba_{0.2})Ca_{1.95}Cu₃O_yF_{0.47} prepared on high isostatic pressure (50 bar He) melted 10°C lower than the F-free corresponding compounds but Tl-1223 coexist with the liquid phase up to 995°C.

4. SUBSTITUTED OR UNSUBSTITUTED TlBa₂Ca₂Cu₃O_{9-δ}: COMPARATIVE SUPERCONDUCTING PROPERTIES

The TlBa₂Ca₂Cu₃O_{9-δ} phase received poor attention comparatively to (Tl,Pb)(Ba,Sr)-1223. As indicated, the reasons refers to the difficulties to produce single phase compounds and to transport high superconducting current. It is interesting here to rapidly compare the two systems. TlBa₂Ca₂Cu₃O_{9-δ} decomposes at 940°C, about 20°C lower than the substituted phase but it has been produced with a high degree of purity once the reaction path and the kinetics for the formation have been understood (see ref.[44] for detailed discussion).

All the samples analysed for this review showed a critical temperatures T_c ranging between 90 K and 130 K (Fig.10) depending on the thermal treatment. For unsubstituted phases, the most frequent T_c values are about 110 K-120 K. Iyo et al.[167] reported transitions as high 133.5 K for multiphase samples Tl_{1.05}Ba_{1.99}Ca_{1.96}Cu₃O_x prepared under 3.5 GPa which could contain carbon as impurity. It is not excluded that such high T_c could be related to intergrowths between Tl-1223 and Tl-2223. When preparing under a pressure of 4.5 GPa (Cu_{0.5}Tl_{0.5})-1223 with a large copper excess on the thallium sites, Tanaka et al.[176] also obtained T_c = 131 K after low temperature annealing (550°C). By XPS measurements, it was found that 40% of the occupied thallium sites are Tl¹⁺. So high critical temperatures are usual with the Tl-2223 phase which is in equilibrium with TlBa₂Ca₂Cu₃O_x for thallium contents from 1.4 to 0.9 per formula unit. A careful analysis of the X-ray diffraction pattern at low angles for testing the (00ℓ) lines (2<ℓ<8) is necessary to differentiate the two phases. Optimised heat treatment on Sr-substituted compounds gives T_c values comparable to the mother phase or slightly lower. The curve in the plane yOz in Fig.10 shows that the optimum doping composition for Pb or a mixture (Pb,Bi) replacing thallium is Tl/(Pb+Bi)=1/1 with T_c ~120 K

A general finding when fluorine is tentatively inserted in the cell is that fluorine has no significant effects on T_c, suggesting that the eventual substitution does not occurs in the CuO₂ planes but in the TlO-layer in such a way, the charges are equilibrated by partial reduction of Tl³⁺ to Tl¹⁺ [194]. Remembering the T_c of TlBa₂Ca₂Cu₃O_x, between 90 K and 120 K, it may be observed that the doping effect of substitutions remains relatively weak if compared with thallium deficiency, Tl-Ca intersite disorder and oxygen stoichiometry.

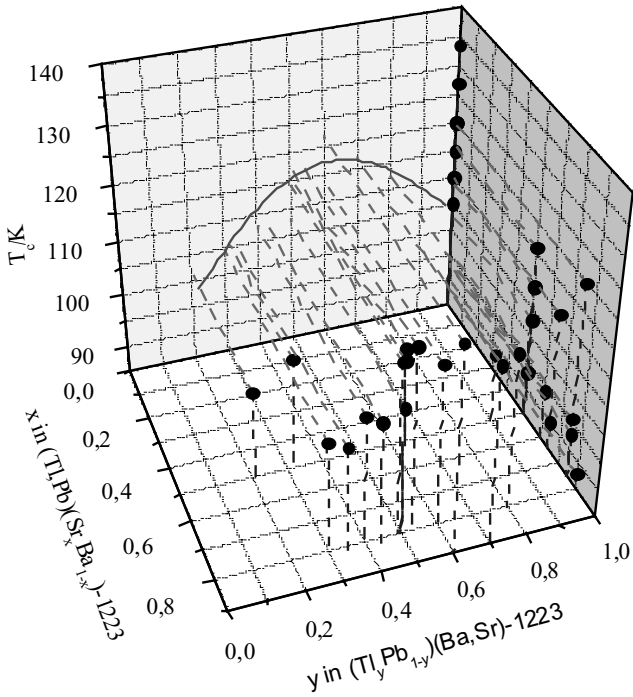


Fig. 10. The critical temperature T_c for the TI-1223 phase

The morphology of the powders is of interest for the superconducting properties. The ability to form orientated crystals for processing tapes obviously depends on the grain texture of the phases, which itself is related with the preparation conditions. In this context, $TlBa_2Ca_2Cu_3O_x$ is a good candidate due to the platelet-like grain morphology resulting from the reaction pathway (see Fig.7). Strontium or lead incorporation results in a more acicular morphology unfavourable to further preferential orientation and probably due to the number of intermediate compounds which participate to the phase formation and act as nucleation centres. With bismuth or fluorine substitutions the melting temperature of the TI-1223 phase are lowered comparatively to lead substituted compounds. For instance, $(Tl_{0.8}Bi_{0.22})Ba_{0.4}Sr_{1.6}Ca_2Cu_3O_z$ under 1 bar of oxygen melts at 944°C [185], nearly the same value than $TlBa_2Ca_2Cu_3O_x$ and about 50°C lower than the lead equivalent phase. The platelet like morphology of the grains is recovered due to rapid grain growth in presence of a liquid phase. It then appears that the synthesis of each material needs an optimised heat treatment; it

will be a compromise between the conditions to ensure complete reactivity of the components and these to avoid thallium vaporization.

Associated with the grain morphology the irreversibility lines are a clear indication of the potential qualities of the material for applications. If we neglect the high temperature line for $TlBa_2Ca_2Cu_3O_x$ which could be, as previously indicated a non equilibrium state, the irreversibility lines for the Tl-1223 phases represented in Fig.5 more display the role of substituted atoms. In particular it is observed that partial replacement of lead by bismuth in the thallium shifts the irreversibility line from 12 K towards high temperatures. Similar behaviour occurs when fluorine is used during the synthesis of the phase [189]. The irreversibility line reflects the flux pinning inside the grains which is enhanced when the distance d' between the CuO_2 planes of the perovskite blocks is shortened giving a tendency to a 3- dimensional superconductivity. Doi et al.[180] discovered that Tl-1223, as $YBa_2Cu_3O_7$ intrinsically contain pinning centres related to the coupling of the CuO_2 layers. The change from a 2-D character for the Tl- double layer to a 3-D behaviour for Tl-1223 is accompanied by a drastic reduction of d' from 11.40 Å to 9.40 Å.

Table 4. Crystal characteristics for some Tl-1223 phases

| Compound | a | c | d' | ref |
|---|---------|---------|--------|-------|
| $Tl_{0.9}Ba_2Ca_2Cu_3O_z$ | 3.84597 | 15.8681 | 9.4669 | [67] |
| $Tl_{0.5}Pb_{0.5}Ba_{0.4}Sr_{1.6}Ca_2Cu_3O_z$ | 3.8186 | 15.3511 | 8.8500 | [163] |
| $Tl_{0.5}Pb_{0.5}Sr_2Ca_2Cu_3O_z$ | 3.81265 | 15.2630 | 8.7440 | [163] |
| $Tl_{0.7}Pb_{0.2}Bi_{0.2}Ba_{0.2}Sr_{1.8}Ca_2Cu_3O_z$ | 3.8195 | 15.3335 | 8.8330 | [163] |
| $Tl_{0.8}Bi_{0.2}Ba_{0.4}Sr_{1.6}Ca_2Cu_3O_z$ | 3.8211 | 15.4235 | 8.8654 | [99] |
| $Tl_{0.5}Pb_{0.5}Ba_{0.4}Sr_{1.6}Ca_2Cu_3O_zF_{0.27}$ | 3.8256 | 15.356 | 8.8451 | [189] |

Inside the same family, here Tl-1223, the correlation between d' and the irreversibility field is not so clear. In table 4 the crystal characteristics of some Tl-1223 phases are summarized. The attempt to associate the results of Fig.5 and the data of this table, unfortunately fails. Indeed, it must be concluded that unsubstituted Tl-1223 and substituted (Tl,Pb)(Ba,Sr)-1223 may have the same flux pinning mechanism because they present the same irreversibility field . However, the pinning cannot only originate from better coupling between the CuO_2 blocks for which d' is, in the substituted phase, reduced by an amount of 6.5%. In bismuth and fluorine doped phases, the pinning mechanism is enhanced but it may be seen that d' is governed by the strontium size and not by Pb or Bi so that the CuO_2 coupling should be very similar in the lead and in the bismuth phases. In addition to punctual and linear defects which are the usual pinning centres, the shift of the irreversibility line towards high temperature could be due to small precipitates of impurity phases.

The weak-link problem between the grains of polycrystalline phases has been identified early after the discovery of high temperature superconductivity. The critical current densities J_c are limited by the defects produced during the fabrication process of the conductor. The mechanical damages, the porosity, the impurity segregations affects the connectivity between the grains of the superconducting powder. Including the use of high isostatic pressure in order to favour the alignment of the crystals was found to be efficient and

with platelet-like forming crystals, the problem is more easy to solve than for phases forming acicular-shaped grains. In the bismuth superconducting family, critical density currents as high as 41 kA/cm^2 at 77 K in self field, were obtained with $\text{Bi}_2\text{Sr}_2\text{Ca}_2\text{Cu}_3\text{O}_z$ [199], the competitive to YBCO material for large scale applications. Such performance is due to relatively good grain orientation, facilitated by combination of a high pressure, high temperature treatment. In this respect, Tl-1223, the bismuth and the fluorine substituted phases are promising materials. Kung et al. [165] in a study on the granularity of $\text{TlBa}_2\text{Ca}_2\text{Cu}_3\text{O}_x$ in Ag-sheathed tapes measured $J_c(77\text{K},0\text{T})$ values no higher than 6.5 kA/cm^2 . However, the constituting powder of the (PID) tapes presented a "cauliflower"- like morphology unfavourable to good intergrain connectivity. In a review on Tl-based superconductors for high current application, Jergel et al.[200] listed the best critical current densities obtained in Tl-1223 tapes. It is interesting to note that the highest critical current density at 77 K in self field (21 kA/cm^2) is found for Ag-sheathed pressed tapes $(\text{Tl}_{0.8}\text{Bi}_{0.22})\text{Ba}_{0.4}\text{Sr}_{1.6}\text{Ca}_2\text{Cu}_3\text{O}_z$ prepared by Ren et al.[201]. Recently lead containing $(\text{Tl}_{0.8}\text{Bi}_{0.2}\text{Pb}_{0.2})\text{Ba}_{0.4}\text{Sr}_{1.6}\text{Ca}_2\text{Cu}_3\text{O}_z$ tapes were just-rolled by Jeong et al.[202] with reproducible $J_c(77 \text{ K}, 0\text{T})= 18 \text{ kA/cm}^2$ further enhanced up to 25 kA/cm^2 with decreasing the barium content down to 0.2/ per formula unit. In these compounds, the grains were found to at least partly textured. The same author reported that highest J_c are obtained when tapes are prepared using unreacted precursors [203] rather than with partially reacted materials. It is an indication that the reaction pathway for the phase formation is a key parameter for obtaining optimised properties. On the basis of magnetization measurements Hamdan et al. [196,204] reported that incorporation of fluorine in Tl-1223 increases drastically the critical current density but the results are not confirmed in a systematic investigation by Trosset-Jarnieux [189] who found for $(\text{Tl}_{0.6}\text{Pb}_{0.3})\text{Ba}_{0.4}\text{Sr}_{1.6}\text{Ca}_2\text{Cu}_3\text{O}_z\text{F}_{1.5}$, $J_c(77\text{K},1\text{T}) = 6 \text{ kA/cm}^2$, nor by E.Bellingeri [194] who measured $J_c(77\text{K},0\text{T}) = 10 \text{ kA/cm}^2$ for a sample with a slightly different composition, $(\text{Tl}_{0.6}\text{Pb}_{0.5})\text{Ba}_{0.2}\text{Sr}_{1.8}\text{Ca}_{1.9}\text{Cu}_3\text{O}_z\text{F}_x$.

5. THALLIUM COATED SUPERCONDUCTORS

The problem of the grain connectivity may be attenuated by improving the preparation conditions. For instance, film processing of superconducting phases allows epitaxial grain growth and it is not a vogue reason if great number of the work on superconducting materials turned to the study of thin or thick layers . The actual technology may be divided into two main groups: physical processes include the most popular Ionic Beam Assisted Deposition (IBAD), generating films in the submicrometer scale, and chemical processes such as spray pyrolysis, electrochemical deposition, screen printing, MOCVD..which mostly provides thick films in the micrometer scale. This chemical route seems to be more easily adaptable to industrial applications of high temperature superconductor. In both case, the superconducting component is deposited onto a substrate which has to satisfy a number of chemical, crystallographic, mechanical and economic requirements. The substrate has to be chemically inert with the superconducting layer and lattice mismatch cannot exceed a few percents. Generally a multilayer architecture is proposed for coated conductors on RABiTS. As for bulk samples, the thallium-based cuprates, mainly Tl-1223, are found to be serious candidate for flexible cables, due to high critical currents densities developed in films.

The spray pyrolysis process is one of the methods most largely developed to produce thick films of good qualities. The method usually implies a double step procedure. The precursor oxides excluding thallium are deposited by spray pyrolysis and then thallinated *ex-situ*. DeLuca et al. [205], using a two-zone reactor for the thallination of precursors containing a small quantity of Ag sprayed on zirconia, yttrium oxide stabilized (YSZ) substrates measured a critical current $J_c(77\text{K},0\text{T}) = 105 \text{ kA/cm}^2$. The superconducting films have a "brick-wall" structure which allows percolating currents through paths of small (a,b) misorientation [206]. Koo et al. [207] noticed that the thallination by a bulk Tl-1223 sample may advantageously replace the two-zone reactor. Recently Phok et al. [32,208] produced $\text{TlBa}_2\text{Ca}_2\text{Cu}_3\text{O}_x$ films deposited on LaAlO_3 exhibiting a good c-axis orientation, an in-plane structure and $J_c(77\text{K},0\text{T}) = 750 \text{ kA/cm}^2$. The X-ray diffraction pattern and the grain microstructure are given in Fig. 11. In the inset of the $\theta/2\theta$ X-ray diffraction curve reveals that $\Delta\omega = 0.6^\circ$. A small quantity of unreacted BaCuO_2 and $(\text{Tl,Ca})_{1-x}\text{CuO}_2$ phases may be observed and we note, in the backscattered electron image the high density of the film. In addition, it is remarkable that the formation of the Tl-1223 phase is similar to that for bulk compounds, implying the double TlO-layers phases. A pseudo reaction order $n = 2.3$ for the conversion $\text{Tl-2223} \rightarrow \text{Tl-1223}$ reflects a 2D grain growth mechanism which is believed to correspond to the layer rearrangement as Tl and O atoms diffuse out of Tl-2223. The activation energy for such conversion, 160 kJ.mol^{-1} is significantly higher than those derived for the YBCO and Bi-based phases, and could be due to the reaction pathway which continuously, until completion forms the Tl-22(n-1)n phases [209].

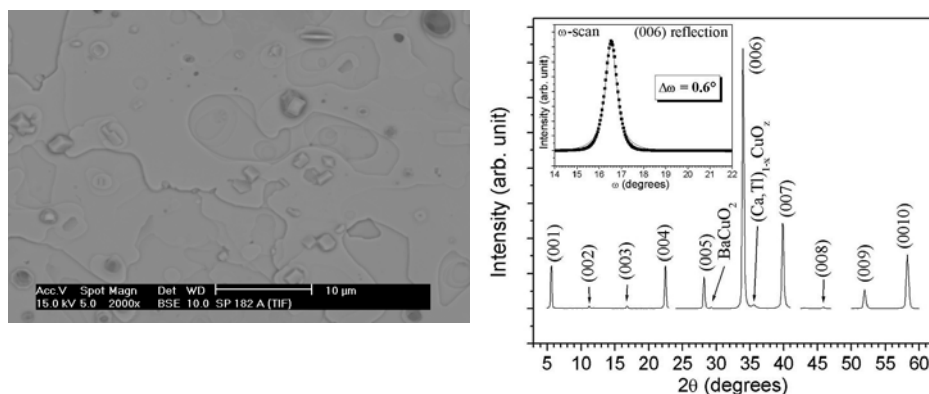


Fig. 11. Morphology (left) and $\theta/2\theta$ X-ray diffraction pattern (right) of Tl-1223 [32]

Electrodeposition was extensively used by Bhattacharya et al. [210-215] to prepare unsubstituted $\text{Tl}_2\text{Ba}_2\text{Ca}_2\text{Cu}_3\text{O}_x$ phase ($J_c(77\text{K},0\text{T}) = 44 \text{ kA/cm}^2$) and substituted (Tl,Pb,Bi)-1223 with optimum $J_c(77\text{K},0\text{T}) = 300 \text{ kA/cm}^2$ for samples electrodeposited on Ag-coated on single crystal LaAlO_3 . Higher values $J_c = 1.2 \text{ MA/cm}^2$ at 77 K in self field, are reported by the group of G. Gritzner [216-218] in $(\text{Tl}_{0.5}\text{Pb}_{0.5})\text{Ba}_{0.4}\text{Sr}_{1.6}\text{Ca}_2\text{Cu}_3\text{O}_z$ prepared by screen printing, a low cost, low polluting process. Malandrino and Fraga reviewed the preparation of Tl-Ba-

Ca-Cu-O superconducting films on ceramic substrates [29]. They were most interested by the double TlO-layer series but formation of the $Tl_{1+x}Ba_2Ca_2Cu_3O_z$ and $Tl_{1+x}Ba_2CaCu_2O_z$ metastable structures is interesting for further pinning studies.

The studies above mentioned on the film preparation confirm the promising properties of the thallium cuprates for large scale applications. As for bulk materials, Tl-1223 is competitive with YBCO but the challenge is now to transfer these properties from small samples deposited on single crystals to long RABiT coated conductors on low cost substrates.

6. CONCLUSION

This report is an attempt to review the major steps in the knowledge of the superconducting properties of the thallium base cuprates. Due to the number of publications mainly in the first period following their discovery by Sheng and Hermann [219] the literature cannot be exhaustive but the actual ideas on the system are the result of an impressive effort to understand the crystallographic structure, the chemistry, the physics and the thermodynamics of the two superconducting family series.

The crystal chemistry of the superconducting phases is a starting point for the understanding the doping behaviour, for conceiving possible new compounds and suggesting efficient substitutions for the improvement of the superconducting properties. In this respect, the intersite disorder between thallium and calcium, which is a kind of self substitution, the existence of thallium vacancies and the oxygen stoichiometry are the parameters in the thallium cuprate series which control the doping level and then the superconducting temperature. Substitutions on the thallium site by lead, bismuth, mercury and copper do not drastically modify T_c but they may influence the bulk transport properties, especially the critical current densities. The fluorine doping is not yet clearly understood even if the effect on H_c and J_c cannot be contested. It is not sure, however that the fluorine ions reach a high substitution level in the parent compounds. Its action on the superconducting properties must also be discussed in terms of phase relations and particularly the high temperature solid-liquid equilibrium remains to be precised.

The age of coated conductors which improves the grain connectivity offers a chance for thallium cuprates to become the future material for magnets and high current applications but more work is needed to solve the problem of high field behaviour. The more recent investigations here reported allow to have an optimistic point of view.

ACKNOWLEDGEMENTS

The author would like to thank all the students and colleagues at the University of Lyon and the University of Savoie who participate to this work. It is also a pleasure to thank the Region Rhône-Alpes for constant financial support.

REFERENCES

- [1] J. E. Evetts, *Supercond. Sci. Technol.* 1 (1988)
- [2] M. Takayasu, R. G. Ballinger, R. B. Goldfarb, A. A. Squitieri, P. J. Lee and D. C. Larbalestier, *AIP Conf. Proceedings-614B* (2002) 986
- [3] B. A. Glavacki, X. -Y. Yan, D. Fray, G. Chen, M. Majoros and Y. Shi, *Physica C* 372-376 (2002) 1315
- [4] V. Abächerli, D. Uglietti, B. Seeber and R. Flukiger, *Physica C* 372-376 (2002) 1325
- [5] T. S. Rong, D. N. Horspool, M. Aindow, *Intermetallics* 10 (2002) 1
- [6] N. Banno, T. Takeuchi, T. Fukusaki and H. Wada, *Supercond. Sci. Technol.* 15 (2002) 519
- [7] N. Banno, T. Takeuchi, A. Kikuchi, Y. Iijima, K. Inoue and H. Wada, *Supercond. Sci. Technol.* 17 (2004) 320
- [8] K. Inoue, A. Kikuchi, Y. Yoshida, Y. Iijima, *Physica C* 384 (2003) 267
- [9] J. Nagamatsu, N. Nakagawa, T. Muranaka, Y. Zenitani and J. Akimitsu, *Nature* 410 (2001) 63
- [10] C. Buzea, T. Yamashita, *Supercond. Sci. Technol.* 14 (2001) R115
- [11] Y. L. Chen, R. Stevens, *J. Amer. Ceram. Soc.* 75 (1992) 1142, 1140 and 1150
- [12] B. Hallstedt, D. Risold, L. J. Gauckler *J. Amer. Ceram. Soc.* 80 (1997) 2629
- [13] R. Flukiger, G. Grasso, J. C. Grivel, F. Marti, M. Dhallé, Y. Huang, *Supercond. Sci. Technol.* 10 (1997) A68
- [14] J. Muller, O. Eibl, B. Fischer and P. Herzog, *Supercond. Sci. Technol.* 11 (1998) 238
- [15] V. Garnier, I. Monot-Laffez, G. Desgardin, *Materials Science and Engineering B83* (2001) 48
- [16] Y. L. Tang, D. J. Miller, R. M. Baurceanu, V. A. Maroni and R. D. Parella, *Supercond. Sci. Technol.* 15 (2002) 1365
- [17] R. Navarro, *Supercond. Sci. Technol.* 13 (2000) -R147
- [18] See the review by R. Flukiger, this book
- [19] *Proceedings of the 5th European Conference on Applied Superconductivity, EUCAS 2001*, (Edt. M. Daumling) *Physica C* 372-376 (2002)
- [20] Y. Yamada, Y. Shiohara, *High Temperature Superconductivity 1*, (Ed. A. Narlikar), Springer-Verlag, Berlin Heidelberg (2004), pp. 291
- [21] M. K. Wu, J. R. Ashburn, C. J. Turng, P. H. Horr, R. L. Meng, L. Gao, Y. Q. Wang and C. W. Chu, *Phys. Rev. Lett.* 58 (1987) 908
- [22] L. J. Mansur, D. Buczek, E. Harley, T. Kodenkandath, X. Li, J. Lynch, N. Nguyen, M. Rupich, U. Schoop, J. Scudiere, E. Siegal, C. Thieme, D. Verebelyi, W. Zhang and J. Kellers, *Int. Symposium on Superconductivity, Yokohama, Japan, November 11-13, 2002*
- [23] T. Araki, K. Yamagiwa, I. Hirabayashi, K. Suzuki, S. Tanaka, *Supercond. Sci. Technol.* 14 (2001) L21
- [24] T. Manabe, M. Sohma, I. Yamagushi, W. Kondo, K. Tsukada, S. Mizuta, T. Kumagai, *Supercond. Sci. Technol.* 17 (2004) 354
- [25] K. Isawa, A. Tokiwa-Yamamoto, M. Itoh, S. Adachi and H. Yamauchi, *Physica C* 222 (1994) 33
- [26] T. Kaneko, H. Yamauchi, S. Tanaka, *Physica C* 178 (1991) 377
- [27] J. Z. Wu, Y. Y. Xie, Z. W. Xing, R. S. Aga, *Physica C* 382 (2002) 62

- [28] N. Inoue, A. Tsukamoto, Y. Moriwaki, T. Sugano, X. -J. Wu, A. Ogawa, S. Adachi, K. Tagagi and K. Tanabe, *High Temperature Superconductivity 1*, (Ed. A. Narlikar), Springer-Verlag (2004), pp213
- [29] G. Malandrino, I. Fragala, *High Temperature Superconductivity 1*, (Ed. A. Narlikar), Springer-Verlag, Berlin Heidelberg (2004), pp. 169
- [30] O. Heiml, G. Gritzner, *Supercond. Sci. Technol.* 15 (2002) 956
- [31] S. H. Pawar, P. M. Shirage, D. D. Shivagan, *Supercond. Sci. Technol.* 15 (2002) 1547
- [32] S. Phok, , P. Galez, J. L. Jorda, C. Peroz, C. Villard, D. De Barros and F. Weiss, *IEEE Trans. Appl. Supercond.* 13 (2003) 2864
- [33] A. Sundaresan, H. Asada, A. Crisan, J. C. Nie, H. Kito, A. Iyo, Y. Tanaka, M. Kusunoki, S. Ohshima, *Physica C* 388-389 (2003) 473
- [34] R. D. Blaugher, R. N. Bhattacharya, J. Chen, R. Padmanabhan, *Physica C* 382 (2002) 72
- [35] A. P. Bramlay, J. D. O'Connor and C. R. M. Grovenor, *Supercond. Sci. Technol.* 12 (1999) R57
- [36] A. Cigán, J. Ma ka, M. Mair, G. Gritzner, G. Plesch, V. Zrubec, *Physica C* 320 (1999) 267
- [37] R. N. Bhattacharya, Z. Xing, J. Z. Wu, J. Chen, S. X. Yang, Z. F. Ren, R. D. Blaugher, *Physica C* 377 (2002) 327
- [38] Q. L. Xu, F. Foong, S. H. Liou, L. Z. Cao and Y. H. Zhang, *Supercond. Sci. Technol.* 10 (1997) 218
- [39] S. Adachi, A. Tokiwa-Yamamoto, A. Fukuoka, R. Usami, T. Tatsuki, Y. Moriwaki and K. Tanabe, *Studies of High Temperature Superconductors*, Vol. 23 (Ed. A. Narlikar), Nova Sci. Publishers, NY (1997) pp163
- [40] M. Hervieu, C. Martin, C. Michel, J. Provost and B. Raveau, *J. Solid State Chem.* 75 (1988) 212
- [41] M. Greenblatt, S. S. Li, E. H. McMills, K. V. Ramanujachary, *Studies of High Temperature Superconductors*, Vol. 5 (Ed. A. Narlikar), Nova Sci. Publishers, NY (1990) pp 5
- [42] A. M. Hermann, J. V. Yakhmi, *Thallium Based High Temperature Superconductors*, Marcel Dekker Inc. , NY (1994)
- [43] M. P. Siegal, E. L. Venturini, M. Morosin, T. L. Aselage, *J. Mat. Research* 12 (1997) 2825
- [44] J. L. Jorda, P. Galez, S. Phok, Th. Hopfinger, T. K. Jondo, *High Temperature Superconductivity 1*, (Ed. A. Narlikar), Springer-Verlag Berlin Heidelberg (2004), pp. 29
- [45] Y. Shimakawa, *Physica C* 204 (1993) 247
- [46] J. L. Jorda, T. K. Jondo, R. Abraham, M. T. Cohen-Adad, C. Opagiste, M. Couach, A. Khoder, F. Sibieude, *Physica* 205 (1993) 177
- [47] C. Ström, S.-G. Eriksson, L. -G. Johansson, A. Simon, H. J. Mattausch and R. K. Kremer, *J. Solid State Chem.* 109 (1994) 321
- [48] S. S. Parkin, V. Y. Lee, A. I. Nazal, R. Savoy, T. C. Huang, G. Gorman and R. Beyers, *Phys. Rev. B* 38 (1988) 6531
- [49] B. Raveau, C. Michel *Annu. Rev. Mat. Sci.* , 19 (1989) 319
- [50] B. Raveau, C. Michel and M. Hervieu, *Materials Science and Engineering*, B3 (1989) 257

- [51] R. J. Cava, *Science* 247 (1990) 656
- [52] J. G. Bednorz, K. A. Muller, *Z. Phys. B*, 64 (1986) 189
- [53] B. G. Nardin, L. Randaccio and E. Zangrando, *Acta Cryst.* B45 (1989) 521
- [54] R. Li, *Appl. Phys. Comm.* 11 (1992) 295
- [55] R. Gladyshevskii, P. Galez, *Handbook on Superconductivity*, (Ed. C. P. Poole Jr.), S. Diego (2000)
- [56] K. S. Aleksandrov and B. V. Beznosikov, *Crystallography Reports* 42 (1997) 613
- [57] K. S. Alexandrov and B. V. Beznosikov, *Phys. Solid State* 39 (1997) 695
- [58] X. J. Wu, S. Adachi, C. Q. Jin, H. Yamauchi and S. Tanaka, *Physica C* 23 (1994) 243
- [59] P. Ganguly, N. Shah, *Physica C* 208 (1993) 307
- [60] F. S. Galasso, *Structure and properties of inorganic solids*, Pergamon Press (1970) pp. 162
- [61] H. J. Beattie Jr. *Intermetallic Compounds* (Ed. J. H. Westbrook), R. E. Krieger Publishing Huntington, New York (1977) pp. 144
- [62] R. D. Shannon, *Acta Cryst.* A32 (1976) 751
- [63] A. Maignan, C. Michel, M. Hervieu, C. Martin, D. Groult and B. Raveau, *Mod. Phys. Lett.* B2 (1988) 681
- [64] L. G. Johansson, C. Ström, S. Eriksson, I. Bryntse, *Physica C* 220 (1994) 295
- [65] C. C. Torardi, M. A. Subramanian, J. C. Calabrese, J. Gopalakrishnan, K. J. Morrissey, T. R. Askew, R. B. Flippen, U. Chowdhry, A. W. Sleight, *Science* 240 (1988) 631
- [66] D. Thopart, J. Hejmanek, D. Pelloquin, C. Martin, A. Maignan, *Physica C* 336 (2000) 143
- [67] Th. Hopfinger, PhD. Thesis, Université de Savoie, France, (1999)
- [68] J. Hauk and K. Mika, *Supercond. Sci. Technol.* 11 (1998) 614
- [69] J. Hauk and K. Mika, *Prog. Solid State Chem.* 28 (2000) 1
- [70] A. Manthiram, J. S. Swinnea, Z. T. Sui, H. Steinfink and J. B. Goodenough, *J. Am. Chem. Soc.* 109 (1987) 667
- [71] C. C. Torardi, J. B. Parise, M. A. Subramanian, J. Gopalakrishnan and A. W. Sleight, *Physica C* 157 (1989)
- [72] A. Manthiram and J. B. Goodenough, *Appl. Phys. Lett.* 53 (1988) 420
- [73] M. W. Shafer and T. Penney, *Eur. J. Solid State Inorg. Chem.* 27 (1990) 191
- [74] C. N. R. Rao, J. Gopalakrishnan, A. K. Santra, A. Manivannan, *Physica C* 174 (1991) 11
- [75] A. Manthiram, M. Paranthaman and J. B. Goodenough, *Physica C* 171 (1990) 135
- [76] M. Paranthaman, A. Manthiram and J. B. Goodenough, *J. Solid State Chem.* 87 (1990) 479
- [77] J. Gopalakrishnan, R. Vijayaraghavan, R. Nagarajan and C. Shivakumara, *J. Solid State Chem.* 93 (1991) 272
- [78] C. S. Gopinath, S. Subramanian, M. Paranthaman and A. M. Hermann, *Physica C* 214 (1993) 153
- [79] A. Manthiram, M. Paranthaman and J. B. Goodenough *J. Solid. State Chem.* 96 (1992) 464
- [80] B. Morosin, D. S. Ginley, E. I. Venturini, R. J. Baughman and C. P. Tigges *Physica C* 172 (1991) 413

- [81] M. Kikuchi, T. Kajitani, T. Suzuki, S. Nakajima, K. Hiraga, N. Kobayashi, H. Iwasaki, Y. Syono and Y. Muto *Jpn. J. Appl. Phys.* 28 (1989) L382
- [82] C. C. Torardi, M. A. Subramanian, J. C. Calabrese, J. Gopalakrishnan, E. M. McCarron, K. J. Morrissey, T. R. Askew, R. B. Flippen, U. Chowdhry, A. W. Sleight, *Phys. Rev. B* 38 (1988) 225
- [83] Y. Shimakawa, Y. Kubo, T. Manako and H. Igarashi, *Phys. Rev. B* 42 (1990) 10165
- [84] N. N. Kolesnikov, V. E. Korotkov, M. P. Kulakov, R. P. Shibaeva, V. N. Molchanov, R. A. Tamazyan and V. I. Simonov, *Physica C* 195 (1992) 219
- [85] M. P. Siegal, E. L. Venturini, B. Morosin, and T. L. Aselage *J. Mat. Res.* 12 (1997) 2825
- [86] R. P. Vasquez, M. P. Siegal, D. L. Overmyer, Z. F. Ren, J. Y. Lao and J. H. Wang, *Phys. Rev. B* 60 (1999) 4309
- [87] H. Oesterreicher, *J. Alloys and Compounds* 299 (2000) 264
- [88] H. Oesterreicher, *J. Alloys and Compounds* 319 (2001) 131
- [89] H. Oesterreicher, *J. Alloys and Compounds* 335 (2002) 95
- [90] M. A. Subramanian, G. H. Kwei, J. B. Parise, J. A. Goldstone and R. B. Von Dreele, *Physica C* 166 (1990) 19
- [91] B. Morosin, D. S. Ginley, P. F. Hlava, M. J. Carr, R. J. Baughman, J. E. Schirber, E. L. Venturini and J. F. Kwak, *Physica C* 152 (1988) 413
- [92] C. Michel, E. Suard, V. Caignaert, C. Martin, A. Maignan, M. Hervieu and B. Raveau, *Physica C* 178 (1991) 29
- [93] T. Doi, K. Usami and T. Kamo, *Jpn. J. Appl. Phys.* 29 (1990) L-57
- [94] Y. Shimakawa, J. D. Jorgensen, B. A. Hunter, H. Shaked, R. L. Hitterman, Y. Kubo, T. Kondo, T. Manako, H. Takahashi, N. Mori, *Physica C* 253 (1995) 71
- [95] C. Martin, J. Provost, D. Bourgault, B. Domengès, C. Michel, M. Hervieu and B. Raveau, *Physica C* 157 (1989) 460
- [96] M. A. Subramanian, J. B. Parise, J. C. Calabrese, C. C. Torardi, J. Gopalakrishnan and A. W. Sleight, *J. Solid State Chem.* 77 (1988) 192
- [97] C. Martin, M. Huvé, M. Hervieu, A. Maignan, C. Michel and B. Raveau, *Physica C* 201 (1992) 362
- [98] R. Gladyshevskii, Ph. Galez, K. Lebbou, J. Allemand, R. Abraham, M. Couach, R. Flukiger, J. L. Jorda, M. Th. Cohen-Adad, *Physica C* 267 (1996) 93
- [99] N. H. Hur, B. C. Chakoumakos, M. Paranthaman, J. R. Thompson, D. K. Christen, *Physica C* 253 (1995) 109
- [100] D. M. Ogborne and M. T. Weller, *Physica C* 230 (1994) 153
- [101] R. S. Liu, S. D. Hughes, R. J. Angel, T. P. Hackwell, A. P. Mackenzie and P. P. Edwards, *Physica C* 198 (1992) 203
- [102] M. A. Subramanian, J. C. Calabrese, C. C. Torardi, J. Gopalakrishnan, T. R. Askew, R. B. Flippen, K. J. Morrissey, U. Chowdhry and A. W. Sleight, *Nature* 332 (1988) 420
- [103] D. M. Ogborne, M. T. Weller and P. C. Lanchester, *Physica C* 200 (1992) 167
- [104] D. M. Ogborne, M. T. Weller, *Physica C* 223 (1994) 283
- [105] R. Beyers, S. S. P. Parkin, V. Y. Lee, A. I. Nazzal, R. Savoy, G. Gorman, T. C. Huang, and S. LaPlaca, *Appl. Phys. Lett.* 53 (1988) 432
- [106] S. S. P. Parkin, V. Y. Lee, A. I. Nazzal, R. Savoy and R. Beyers and S. LaPlaca, *Phys. Rev. Lett.* 61 (1988) 750

- [107] B. Morosin, D. S. Ginley, J. E. Schirber and E. L. Venturini, *Physica C* 156 (1988) 587
- [108] B. Morosin, E. L. Venturini and D. S. Ginley, *Physica C* 183 (1991) 90
- [109] M. A. Subramanian, J. C. Calabrese, C. C. Torardi, J. Gopalakrishnan, T. R. Askew, R. B. Flippen, K. J. Morrissey, U. Chowdhry and A. W. Sleight, *Nature* 332 (1988) 420
- [110] D. E. Cox, C. C. Torardi, M. A. Subramanian, J. Gopalakrishnan and A. W. Sleight, *Phys. Rev. B* 38 (1988) 6624
- [111] M. H. Pan and M. Greenblatt, *Physica C* 176 (1991) 80
- [112] F. Letouzé, C. Martin, M. Hervieu, A. Maignan, M. Daturi, C. Michel, B. Raveau, *Physica C* 292 (1997) 32
- [113] B. Morosin, E. L. Venturini, R. G. Dunn, P. Newcomer Provencio, N. Missert, R. R. Padilla *Physica C* 302 (1998) 119
- [114] Y. F. Li, O. Chmaisnen, Z. Z. Sheng, *Physica C* 248 (1995) 42
- [115] P. G. Wahlbeck, D. E. Peterson, J. O. Willis, E. J. Peterson, J. Y. Coulter, D. S. Phillips, K. V. Salazar, *Physica C* 256 (1996) 358
- [116] I. K. Gopalakrishnan, J. V. Yakhmi and R. M. Iyer, *Physica C* 172 (1991) 450
- [117] B. Morosin, E. L. Venturini, R. G. Dunn, P. P. Newcomer, *Physica C* 288 (1997) 255
- [118] M. Paranthaman, M. Foldeaki, R. Tello and A. M. Hermann, *Physica C* 219 (1994) 413
- [119] M. A. G. Aranda, D. C. Sinclair and J. P. Attfield, *Physica C* 221 (1994) 304
- [120] R. E. Gladyshevskii, A. Perin, B. Hensel, R. Flükiger, R. Abraham, K. Lebbou, M. Th. Cohen-Adad, J. L. Jorda, *Physica C* 255 (1995) 113
- [121] I. K. Gopalakrishnan, J. V. Yakhmi and R. M. Iyer, *Physica C* 175 (1991) 183
- [122] H. C. Ku, M. F. Tai, J. B. Shi, M. J. Shieh, S. W. Hsu, G. H. Hwang, D. C. Ling, T. J. Watson-Yang and T. Y. Lin *Jpn. J. Appl. Phys.* 28 (1989) L 923
- [123] D. M. Ogborne and M. T. Weller, *Physica C* 220 (1994) 389
- [124] M. A. Subramanian, *Mater. Res. Bull.* 29 (1994) 119
- [125] Y. Xin, K. W. Wong, G. F. Sun and D. F. Lu, *Solid State Comm.* 87 (1993) 1061
- [126] D. H. Kim, K. E. Gray, R. T. Kampwirth, J. C. Smith, D. S. Richeson, T. J. Marks, J. H. Kang, J. Talvacchio, M. Eddy, *Physica C* 177 (1991) 431
- [127] J. Shimoyama, *Physica C* 235-240 (1994) 2795
- [128] V. Hardy, A. Maignan, C. Martin, F. Warmont and J. Provost, *Phys. Rev. B* 56 (1997) 130
- [129] K. Yang, L. P. Yu, S. H. Han, H. Zhang, Y. Zhao, *Physica C* 357-360 (2001) 305
- [130] A. K. Ganguli and M. A. Subramanian *J. Solid State Chem.* 90 (1991) 382
- [131] M. Käll, L. Börjesson, M. Kakihama, C. Ström, L. G. Johansson, S. G. Eriksson, T. Larsson, *Physica C* 189 (1991) 821
- [132] C. Ström, M. Käll, L. G. Johansson, S. G. Eriksson L. Börjesson, *Physica C* 185-189 (1991) 625
- [133] S. Nakajima, T. Oku, R. Suzuki, M. Kikuchi, K. Hiraga and Y. Syono, *Physica C* 214 (1993) 80
- [134] G. F. Sun, Y. Xin, D. F. Lu, K. W. Wong, Y. Zhang, J. G. Stevens, *Solid State Comm.* 101 (1997) 849
- [135] T. Tatsuki, S. Adachi, T. Tamura, K. Tanabe, *Physica C* 320 (1999) 277

- [136] A. Sequeira, H. Rajogopal, I. K. Gopalakrishnan, P. V. P. S. S. Sastry, G. M. Phatak, J. V. Yakhmi and R. M. Iyer, *Physica C* 156 (1988) 599
- [137] E. A. Hayri and M. Greenblatt, *Physica C* 156 (1988) 775
- [138] R. Awad, A. I. Abou Aly, I. H. Ibrahim and W. A. Abdeen, *Supercond. Sci. Technol.* 17 (2004) 211
- [139] M. Paranthaman, A. Manthiram and J. B. Goodenough, *J. Solid State Chem.* 98 (1992) 343
- [140] A. Poddar, B. Bandyopadhyay, B. Cattopadhyay *Physica C* 390 (2003) 120
- [141] R. S. Liu and P. P. Edwards, *Physica C* 179 (1991) 353
- [142] M. Paranthaman, M. Foldeaki and A. M. Hermann, *Physica C* 192 (1992) 161
- [143] A. Maignan, C. Martin, V. Hardy, Ch. Simon, M. Hervieu and B. Raveau, *Physica C* 219 (1994) 407
- [144] D. C. Sinclair, M. A. G. Aranda, J. P. Attfield and J. Rodriguez-Carvajal, *Physica C* 225 (1994) 307
- [145] Y. Xin, Y. F. Li, D. X. Gu, D. O. Paderson, Z. Z. Sheng, *Physica C* 184 (1991) 185
- [146] T. S. Kayed, H. Özkan and N. M. Gasanly, *Supercond. Sci. Technol.* 14 (2001) 738
- [147] T. S. Kayed, *Mat. Res. Bull* 38 (2003) 533
- [148] A. Kikuchi, T. Kinoshita, N. Nishikawa, S. Komiya and K. Tachikawa *Jpn. J. Appl. Phys.* 34 (1995)L167
- [149] F. Studer, D. Bourgault, C. Martin, R. Retoux, C. Michel, B. Raveau, E. Dartyge and A. Fontaine, *Physica C* 159 (1989) 609
- [150] J. S. Kim, J. S. Swinnea and H. Steinfink, *J. Less Comm. Met.* 156 (1989) 347
- [151] J. B. Shi, M. J. Shieh, T. Y. Lin and H. C. Ku, *Physica C* 162-164 (1989) 721
- [152] S. Nakajima, M. Kikuchi, Y. Syono, K. Nagase, T. Oku, N. Kobayashi, D. Shindo, K. Hiraga *Physica C* 170 (1990) 443
- [153] S. Matsuda, S. Takeuchi, A. Soeta, T. Suzuki, K. Aihara and T. Kamo, *Jpn. J. Appl. Phys.* 27 (1988) 2062
- [154] J. L. Tallon, R. S. Liu, K. L. Wu, F. J. Blunt and P. T. Wu, *Physica C* 161 (1989) 523
- [155] Q. Hong and Jui. H. Wang, *Physica C* 214 (1991) 286
- [156] W. H. Lee, D. C. Wang, *Physica C* 253 (1995) 156
- [157] W. H. Lee, D. C. Wang, *Physica C* 289 (1997) 114
- [158] W. H. Lee, M. R. Yeh, L. R. Sung, *Physica C* 311 (1999) 297
- [159] Y. Kunii, T. Suzuki, A. Kakijima, T. Goto, S. Nakajima, T. Fukase, *Physica C* 388-389 (2003) 257
- [160] K. T. Lau, S. K. Chen, R. Abd-Shukor, *Physica C* 377 (2002) 547
- [161] E. P. Khlybov, I. E. Kostyleva, V. I. Nizhankovskii, T. Palewski, J. Warchulska, K. Nenkov, *Physica B* 294-295 (2001) 367
- [162] Z. Y. Chen, Z. Z. Sheng, Y. Q. Tang, Y. F. Li and D. O. Pederson, *Solid State Commun.* 83 (1992) 895
- [163] K. Lebbou, PhD thesis, University of Lyon (1996)
- [164] J. C. Wei, T. J. Yang, R. S. Liu, *Mat. Chem. Phys.* 43 (1996) 83
- [165] P. J. Kung, P. G. Wahlbeck, M. E. McHenry, M. P. Maley and D. E. Peterson, *Physica C* 220 (1994) 310
- [166] Th. Hopfinger, O. O. Shcherban, Ph. Galez, R. E. Gladyshevskii, M. Lomello-Tafin, J. L. Jorda, M. Couch, *J. Alloys and Compounds* 333 (2002) 237

- [167] A. Iyo, Y. A. Izawa, Y. Tanaka, M. Tokumoto, K. Tokiwa, T. Watanabe, H. Ihara, *Physica C* 357-360 (2001) 324
- [168] A. Iyo, Y. Ishiura, Y. Tanaka, R. Badica, K. Tokiwa, T. Watanabe, H. Ihara, *Physica C* 370 (2002) 205
- [169] S. Adachi, T. Shibata, T. Tatsuki, T. Tamura, K. Tanabe, S. Fujihara and T. Kimura, *Physica C* 324 (1999) 15
- [170] J. Z. Liu, I. C. Chang, M. D. Lan, P. Klavins and R. N. Shelton, *Physica C* 246 (1995) 203
- [171] I. C. Chang, J. Z. Liu, M. D. Lan, P. Klavins and N. R. Shelton, *J. Superconductivity* 9 (1996) 53
- [172] R. Awad, N. S. Aly, I. H. Ibrahim, A. I. Abou-Aly, A. I. Saad, *Physica B* 307 (2001) 72
- [173] R. Awad, *Supercond. Sci. Technol.* 15 (2002) 933
- [174] R. Awad, and N. H. Mohamed, *Supercond. Sci. Technol.* 17 (2004) 35
- [175] H. Yamamoto, K. Tanaka, K. Tokiwa, H. Hirabayashi, M. Tokumoto, N. A. Khan, H. Ihara, *Physica C* 302 (1998) 137
- [176] K. Tanaka, A. Iyo, N. Terada, K. Tokiwa, S. Miyashita, Y. Tanaka, T. Tsukamoto, S. K. Agarwal, T. Watanabe and H. Ihara, *Phys. Rev. B* 63 (01) 1
- [177] Z. Y. Chen, Z. Z. Sheng, Y. Q. Tang, Y. F. Li and D. O. Pederson, *Z. Phys. B* 93 (1994) 159
- [178] R. S. Liu, S. F. Hu, D. A. Jefferson, P. P. Edwards, *Physica C* 198 (1992) 318
- [179] R. S. Liu, D. N. Zheng, J. W. Loram, K. A. Mirza, A. M. Campbell, P. P. Edwards, *Appl. Phys. Lett.* 60 (1992) 101
- [180] T. Doi, M. Okada, A. Soeta, T. Yuasa, K. Aihara, T. Kamo, S. P. Matsuda, *Physica C* 183 (1991) 67
- [181] Z. F. Ren and J. H. Wang, *Physica C* 216 (1993) 199
- [182] M. Mair, W. T. Koenig and G. Gritzner, *Supercond. Sci. Technol.* 8 (1995) 894
- [183] R. S. Liu, S. F. Wu, D. S. Shy, S. F. Hu, D. A. Jefferson, *Physica C* 222 (1994) 278
- [184] X. D. Liu, H. T. Peng, S. H. Zhou, Q. Y. Peng, G. W. Yang, *Physica C* 256 (1996) 353
- [185] M. T. Lanagan, J. Hu, M. Foley, P. Kostic, M. R. Hagen, D. J. Miller, K. C. Goretta, *Physica C* 256 (1996) 387
- [186] W. Tian, J. S. Zhou, X. Jin, Z. M. Ye, Y. N. Wang, *Physica C* 258 (1996) 153
- [187] W. T. Koenig and G. Gritzner, *Physica C* 294 (1998) 22
- [188] D. J. Miller, J. G. Hu, Z. Ren, Q. Hong, J. H. Wang *J. Electronic Materials* 33 (1994) 1151
- [189] S. Trosset-Jarnieux, PhD thesis, Université Lyon (France) -1997
- [190] K. Lebbou, R. Abraham, S. Trosset, J. L. Jorda and M. T. Cohen-Adad, *Mater. Res. Bull.* 32 (1997) 1017
- [191] K. Lebbou, R. Abraham, S. Trosset and M. T. Cohen-Adad, *Mater. Res. Bull.* 32 (1997) 1027
- [192] J. L. Jorda, K. Lebbou, Ph. Galez, R. Abraham, *J. Alloys and Compounds* 256 (1997) 34
- [193] L. P. Cook, W. Wong-Ng and P. Paranthaman, *J. Res. of the NIST* 101 (1996) 675

- [194] E. Bellingeri, Handbook of superconducting Materials, Vol. 1 *Superconductivity, Materials and Processes*, Edt. D. Cardwell and D. Ginley IOP Publishing Ltd, Bristol and Philadelphia, (2003) 539
- [195] M. J. Tsai, S. F. Wu, S. W. Lu, Y. T. Huang and R. S. Liu, *Appl. Supercond.* 1 (1993) 527
- [196] N. M. Hamdan, Kh. A. Ziq and A. S. Al-Harhi, *Physica C* 314 (1999) 125
- [197] Y. S. Sung, X. F. Zhang, P. J. Kostic and D. Miller *Appl. Phys. Lett.* 69 (1996) 3420
- [198] A. Kukuchi, K. Inoue, K. Tachikawa, *Physica C* 337 (2000) 180
- [199] Y. Yuan, R. K. Williams, J. Jiang, D. C. Larbalestier, X. Y. Cai, M. O. Rikel, K. L. De Moranville, Y. Huang, Q. Li, E. Thompson, G. N. Riley Jr, E. E. Hellstrom *Physica C* 372-376 (2002) 88
- [200] M. Jergel, A. Conde Gallardo, C. Falcony Guajardo and V. Strbik, *Supercond. Sci. Technol* 9 (1996) 1
- [201] Z. F. Ren, C. A. Wang, D. H. Miller, K. C. Goretta, *Physica C* 247 (1995) 163
- [201] D. Y. Jeong, H. K. Kim, Y. C. Kim, *Physica C* 314 (1999)
- [202] D. Y. Jeong, M. H. Sohn, *Physica C* 297 (1998) 192
- [203] D. Y. Jeong, S. M. Baek, H. K. Kim, B. J. Kim, E. Y. Lee, Y. C. Kim, *Physica C* 377 (2002) 445
- [204] N. M. Hamdan, Kh. A. Ziq and A. S. Al-Harhi, *J. Low Temp. Phys.* 105 (1996) 1493
- [205] J. A. DeLuca, P. L. Karas, J. E. Tkaczyk, C. L. Briant, M. F. Garbaskas and P. J. Bednarczyc, *Physica C* 205 (1993) 21
- [206] E. D. Specht, A. Goyal, D. M. Kroger, J. A. DeLuca, J. E. Tkaczyk, C. L. Briant, J. A. Sutliff, *Physica C* 226 (1994) 7
- [207] H. S. Koo, G. C. Tu, T. Y. Tseng *J. Am. Ceram. Soc.* 77 (1994) 27
- [208] S. Phok, Ph. Galez, J. L. Jorda, Z. Supardi, D. De Barros, P. Odier, A. Sin, F. Weiss, *Physica C* 372-376 (2002) 876
- [209] S. Phok, Ph. Galez, J. L. Jorda, D. De Barros, C. Villard, F. Weiss, *Crystal Engineering* 5 (2002) 401
- [210] R. N. Bhattacharya, P. A. Parilla and R. D. Blaugher, *Physica C* 211 (1993) 475
- [211] R. N. Bhattacharya, and R. D. Blaugher, *Physica C* 229 (1994) 244
- [212] R. N. Bhattacharya, A. Duda, D. S. Ginley, J. A. DeLuca, Z. F. Ren, C. A. Wang and J. H. Wang, *Physica C* 229 (1994) 145
- [213] R. N. Bhattacharya, M. Paranthaman, *Physica C* 251 (1995) 105
- [214] R. N. Bhattacharya, R. D. Blaugher, Z. F. Ren, W. Li, J. H. Wang, M. Paranthaman, D. T. Verebelyi, D. K. Christen, *Physica C* 304 (1998) 55
- [215] R. N. Bhattacharya, H. L. Wu, Y. T. Wang, R. D. Blaugher, S. X. Yang, D. Z. Wang, Z. F. Ren, Y. Tu, D. T. Verebelyi and D. K. Christen, *Physica C* 333 (2000) 50
- [216] R. Zalecki, A. Kolodziejczyk, J. Chmista, W. König, G. Gritzner, *Physica C* 341-348 (2000) 2049
- [217] M. Eder and G. Gritzner, *Supercond. Sci. Technol.* 13 (2000) 1302
- [218] S. Tönies, H. W. Weber, G. Gritzner, O. Heiml, M. H. Eder, *IEEE Transactions on Appl. Supercond* 13 (2003) 2618
- [219] Z. Z. Sheng and A. M. Hermann, *Nature* 332 (1988) 55

MATERIALS DEVELOPMENTS AND APPLICATIONS OF BULK RE-Ba-Cu-O SUPERCONDUCTORS

Masato Murakami

Department of Materials Science and Engineering, Shibaura Institute of Technology,
Shibaura 3-9-14, Minato-ku, Tokyo 108-8548, Japan

1. INTRODUCTION

Before the discovery of high-temperature superconductors (HTSs), the applications of bulk superconductors were generally deemed not practical mainly due to their low cryostability [1]. However, the discovery of HTS changed such a situation. The thermal stability of HTS is extremely high because of their large thermal capacity. The stability is also greatly enhanced when they are used at higher temperatures. The simplicity of one of the earliest demonstrations of HTS, the levitation of a permanent magnet over a bulk Y-Ba-Cu-O, as shown in Fig. 1, started researchers seeking for their potential applications.

During the past fifteen years, researchers have made significant improvements in the materials properties of bulk HTSs and have investigated the feasibility of their use in various engineering applications. The combination of permanent magnets and HTS enabled us to construct magnetic bearings with a low-loss rotation that are installed in prototype high-efficiency flywheels. Bulk HTSs have demonstrated the ability to trap magnetic flux, and some samples have exhibited surface magnetic fields approximately an order of magnitude higher than presently used permanent magnets.

The performance of bulk HTS materials is given by the following equation:

$$M = A J_c r \quad (1)$$

where M is magnetization and stands for the performance of bulk materials, A is a geometrical constant, J_c the critical current density, and r the radius of single domain or the radius of a current loop. Thus in order to improve the performance of bulk HTS, one needs to increase J_c or the size of bulk HTS.

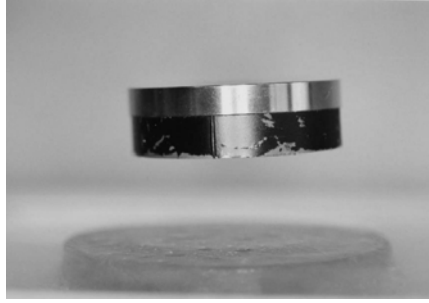
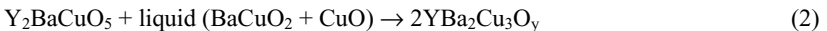


Fig. 1. Levitation of a Fe-Nd-B permanent magnet above bulk Y-Ba-Cu-O cooled by liquid nitrogen.

2. MATERIALS DEVELOPMENTS

2.1. Y-Ba-Cu-O

In the early stages of HTS research, bulk Y-Ba-Cu-O was synthesized via a solid-state reaction, which is a common ceramic processing route. However, due to its small coherence length and large anisotropy, high-angle grain boundaries acted as weak links and reduced critical currents below the level required for engineering applications. Sintered Y-Ba-Cu-O pellets were thus discarded as candidates for practical applications except a simple scientific toy for levitation experiment. Today, it is customary to fabricate bulk Y-Ba-Cu-O with controlled, melt processing based on the following peritectic solidification reaction.



The most common process is called “top-seeded melt growth” (TSMG), in which a $\text{NdBa}_2\text{Cu}_3\text{O}_y$ (Nd123) or Sm123 seed crystal with a higher melting temperature than Y123 is placed on top of a pre-sintered Y-Ba-Cu-O pellet (a mixture of Y123 and Y211) to promote heterogeneous grain nucleation, and the material is slowly cooled in the presence of a temperature gradient [2]. This process yields a highly textured structure with its c axis oriented perpendicular to the disk surface, as schematically shown in Fig. 2.

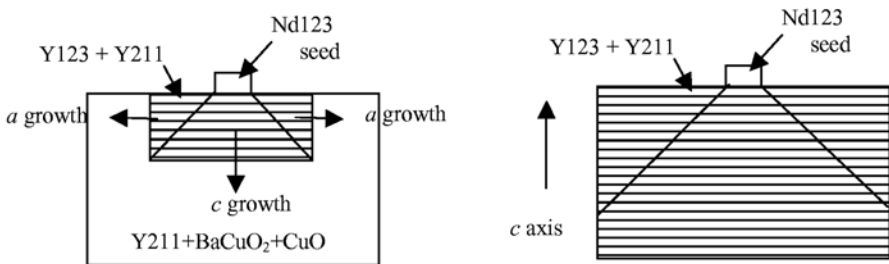


Fig. 2. Schematic illustration of the grain growth of Y123 during the top-seeded melt-growth process.

To impart superconductivity, melt-grown Y-Ba-Cu-O disks are subjected to annealing at 300-500°C in an oxygen atmosphere. The critical temperature (T_c) of TSMG-processed Y-Ba-Cu-O is in the range of 90-93 K, depending on the quality of the starting powders, the conditions of melt processing, and the oxygen-annealing treatment. Bulk Y-Ba-Cu-O has a microstructure in which small Y211 particles are distributed in the Y123 matrix.

The critical current densities (J_c) of Y-Ba-Cu-O are very sensitive to microstructure, particularly to the volume and size of dispersed Y211 particles [3] in that J_c is given by the following equation:

$$J_c = A \frac{V_f}{d} \quad (3)$$

where A is constant, V_f and d are the volume fraction and the average diameter of Y211 particles. Thus under constant volume of the second phase particles, J_c is inversely proportional to the size of the Y211 particles. It is thus common to add Pt or CeO₂ powders to the precursor to inhibit coarsening of Y211 particles, which leads to an enhancement of J_c values. Zero-field J_c at 77 K ranges from 10⁴ to 10⁵ A/cm², and J_c values at 77 K and 1 T for the $B//c$ axis are 5-30 kA/cm². The irreversibility field (B_{irr}) of Y-Ba-Cu-O is 3-5 T at 77 K for the $B//c$ axis. Although B_{irr} for the $B//ab$ plane exceeds 10 T at 77 K, B_{irr} for $B//c$ is more important for industrial applications that mainly use trapped fields or levitation forces.

Bulk Y-Ba-Cu-O disks can trap a large field due to flux pinning or induced supercurrents flowing persistently in the pellet. As presented in equation (1), the magnetization (M) or the trapped field (B_{trap}) increases with increasing grain size. At present, the maximum grain size of Y-Ba-Cu-O is 10 μ m [4]; however, due to contamination from the substrate materials, the superconducting properties of such a large grain degrade, and the B_{trap} at 77 K is only 0.8-1 T. A typical size of commercially available Y-Ba-Cu-O disks is 3-6 cm, for which the B_{trap} values at 77 K are 0.8-1.5 T. The trapped field increases with decreasing temperature and reaches 3-6 T at 50 K and even higher values at lower temperatures.

As the trapped field increases, the disk experiences a higher electromagnetic force, which sometimes causes cracking. The mechanical properties of Y-Ba-Cu-O are anisotropic but not so temperature dependent. The tensile strength along the c axis is 5-10 MPa, and that perpendicular to the c axis is 20-30 MPa [5]. It is important to realize that the maximum trapped field is limited by the tensile strength rather than the superconducting properties. Hence, an improvement of mechanical properties is critically important for enhancing the field trapping ability. The techniques to improve mechanical properties of bulk HTS will be described later.

2.2. RE-Ba-Cu-O

YBa₂Cu₃O₇ is a stoichiometric point compound, whereas RE-Ba-Cu-O (RE: Nd, Sm, Eu, or Gd) systems are known to have a RE_{1+x}Ba_{2-x}Cu₃O_y type solid solution (RE123ss) [6]. When RE-Ba-Cu-O is synthesized by melt processing in air, RE-rich RE123ss is formed, leading to a depression of T_c . This is because RE substitution on the Ba site decreases the hole concentration. Thus, RE-Ba-Cu-O had not been considered as a practical material until the oxygen-controlled melt-growth (OCMG) process [7] was invented. When RE-Ba-Cu-O is melt processed in a reduced oxygen atmosphere, the substitution of Ba by RE ion is significantly reduced. In addition, small clusters of RE-rich RE123ss 50 - 200 nm in size are

uniformly distributed in OCMG-processed RE-Ba-Cu-O. These RE-rich RE123ss clusters can act as field induced pinning centers, which causes a secondary peak effect in the J_c - B curve and thus relatively high J_c values at high fields as shown in Fig. 3 [8]. OCMG-processed Nd-Ba-Cu-O exhibits J_c values of 20-41 kA/cm² at 77 K and 2 T for $B//c$. J_c - B properties of RE-Ba-Cu-O are sensitive to chemical compositions and processing conditions. It is generally accepted that both J_c and B_{irr} values of properly processed RE-Ba-Cu-O are much superior to those of Y-Ba-Cu-O.

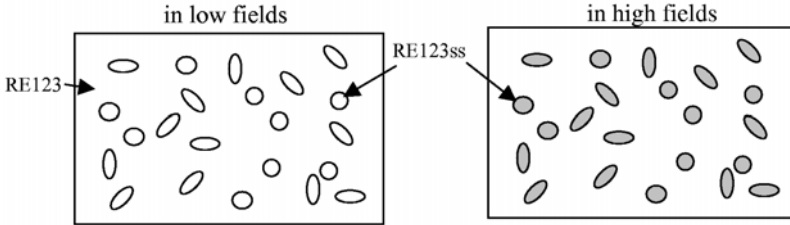


Fig. 3. Schematic illustration of field-induced pinning due to RE rich RE123ss cluster. They are superconducting in low fields, but are driven normal in high fields and thereby can act as effective pinning centers. This causes a secondary peak effect in J_c - B curves.

Recently, compounding the RE site with several rare earth ions was found to dramatically enhance flux pinning [9]. For example, (Nd, Eu, Gd)-Ba-Cu-O exhibits an extremely high B_{irr} of 15 T at 77 K for $B//c$ axis, with a J_c value exceeding 10 kA/cm² at 10 T [10]. Microstructural observation showed that RE-rich RE123ss clusters about 3-5 nm in size formed dense regular arrays in this material, as shown in Fig. 4, which was responsible for the high B_{irr} . This result shows that high-field superconducting applications are possible for RE-Ba-Cu-O even at 77 K.

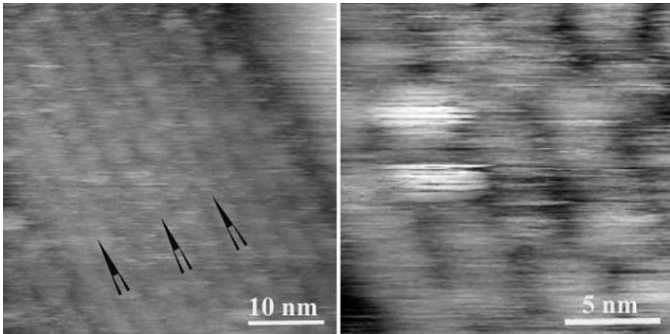


Fig. 4. Scanning tunneling micrograph of (Nd, Eu, Gd)-Ba-Cu-O sample with B_{irr} of 15T at 77K for $B//c$ axis. Regular arrays of RE rich RE123ss clusters observed in (Nd, Eu, Gd)-Ba-Cu-O. The average size of the clusters is 3 - 5 nm, which is almost comparable to the coherence length or the size of quantized fluxoid. Such a dense distribution of pinning centers is responsible for extremely high B_{irr} .

Because of their higher J_c and B_{irr} values, most researchers consider RE-Ba-Cu-O systems far superior to Y-Ba-Cu-O as trapped-field magnets. However, according to equation (1), trapped-field values also depend on grain size, and much present effort is devoted to developing processes for producing larger grain RE-Ba-Cu-O. Since these compounds are also peritectically formed like Y-Ba-Cu-O, the TSMG process can yield good-quality large-grain disks if oxygen partial pressure is controlled. The maximum grain size of RE-Ba-Cu-O systems is 3.0 cm for Nd-Ba-Cu-O, 6.0 cm for Sm-Ba-Cu-O, and 6.5 cm for Gd-Ba-Cu-O. The maximum trapped fields of these systems at 77 K are 1.8 T, 2.0 T, and 3.0 T, respectively. However, these values are affected by the aspect ratio, so that the trapped field between two Gd-Ba-Cu-O samples was found to be 4.1 T at 77 K after 90 min relaxation [11]. Like Y-Ba-Cu-O, the trapped-field values of RE-Ba-Cu-O are dramatically improved by lowering temperature, but again poor mechanical properties limit the field-trapping capability.

2.3. Mechanical properties

The field-trapping ability of bulk HTS material is essentially limited by its mechanical strength. The electromagnetic force in an energized trapped-field magnet is a hoop stress or a tensile stress, and tensile strength is quite low in bulk HTS. Thus, an improvement of the mechanical properties is critically important for high-field applications. Ag addition is well known to improve mechanical properties, since it distributes in a bulk and these clusters contribute to crack blunting [12]. However, in large-grain bulk HTS, crack initiation occurs at defects like voids and microcracks, and fracture strength is much smaller than what can be obtained in small samples. Y-Ba-Cu-O and RE-Ba-Cu-O undergo tetragonal to orthorhombic transformation during oxygen annealing, causing crystal deformation such that the c axis shrinks. Since there is no accommodation process for stress relaxation along the c axis, microcracks are introduced along (001) planes in a bulk body. The presence of such defects often causes serious cracking of bulk HTS materials during activation as shown in Fig. 5.

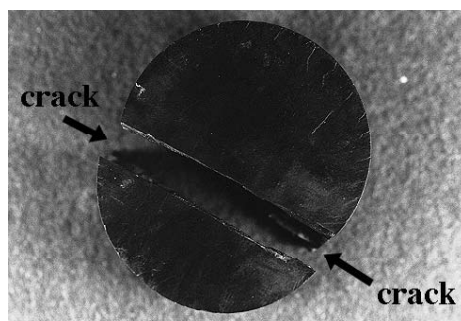


Fig. 5. Cracking in Y-Ba-Cu-O sample during the activation. The sample was field-cooled in 10 T and fractured when the external field reached 8T at 50K.

For large-grain samples, fracture strength improves from about 1 MPa to almost 10 MPa with the addition of Ag [13]. Therefore, Ag addition alone is not sufficient to ensure reliable mechanical stability or high trapped fields. Fortunately, compressional strengths of

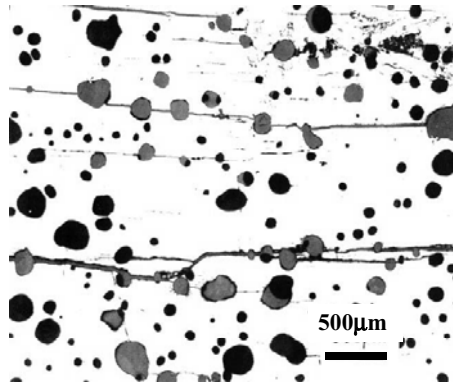


Fig. 6. Optical micrograph of a cross section of bulk Y-Ba-Cu-O treated with a resin impregnation. Note that resin can permeate into a bulk body through surface cracks and fills voids connected to the cracks.

bulk HTS exceed 200 MPa. Hence, encapsulation with metal rings was employed to improve mechanical properties [14]. When a bulk disk is surrounded by a metal ring, compressional stress acts on the disk on cooling to the operation temperature as the metal shrinks more than the disk. The resulting pre-compression force will accommodate the magnetically induced hoop stress and greatly enhances field-trapping ability.

Resin impregnation is also effective in improving the mechanical properties of bulk HTS [15]. When bulk disks are vacuum impregnated with epoxy, the resin can permeate into the bulk through surface cracks and fill internal voids, as shown in Fig. 6. This treatment increased the tensile strength of large-grain samples from several MPa to 100 MPa. In addition to enhanced mechanical strength, surface coating with resin improved the corrosion resistance against moisture. However, the resin can reach only 2-5 mm from the surface, and therefore the internal mechanical strength was not improved with resin impregnation. To overcome this problem, 0.5-1.0 mm diameter holes were mechanically drilled through the disk prior to resin impregnation, which allows the impregnation of resin into internal defects and thereby the improvement of the internal mechanical strength.

2.4. Cryostability

The stability of the current-carrying mode in type II superconductors has been a problem [16]. The low specific heat of LTS materials was responsible for their quenching. Multifilamentary structures solved this problem in that fine superconducting filaments generate less heat per unit volume due to flux motion and are embedded in a high thermal conductivity matrix that distributes the heat. The superconducting state in HTS materials is extremely stable due to their large heat capacity and high operating temperature. These are the principle characteristics that make the bulk HTS applications possible. However, another thermal instability intrudes when the bulk HTS magnet is activated. During activation, fluxoids in bulk HTS move, which generates heat. For stability, i.e., to avoid temperature rise, the cooling power of the system must be larger than local heat generation. Since the thermal

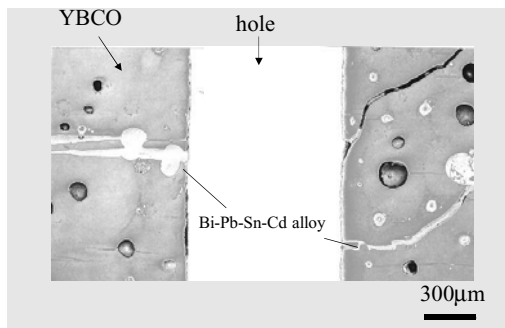


Fig. 7. Optical micrograph of the cross section of bulk Y-Ba-Cu-O drilled a center hole about 1mm in diameter followed by the impregnation treatment of Bi-Pb-Sn-Cd alloy. Note that the alloy can permeate into the artificial hole and furthermore it can fill the cracks and voids connected to the hole.

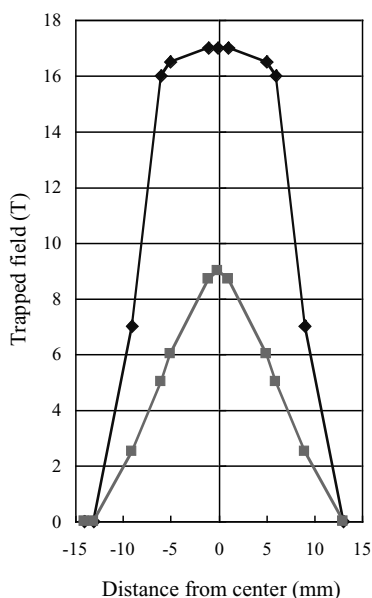


Fig. 8. Trapped field distribution.

effective in further enhancing the thermal stability. The alloy impregnation treatment also improved the internal mechanical strength of bulk HTS.

Fig.8 shows the trapped-field distribution of a 2.6-cm-diameter Y-Ba-Cu-O disk internally impregnated with Bi-Pb-Sn-Cd alloy. The disk was field cooled in 18 T to a target temperature, and the external field was removed. The trapped field for this disk was 9 T and 17 T at 46 K and 29 K, respectively [18]. Furthermore the distribution shows that the trapped field is not saturated at 29 K, indicating that the disk could trap much higher fields if a higher background field were available.

conductivity of HTS is small, cooling by cryogen at the bulk's surface is not sufficient to cool the interior region, leading to a local temperature rise. Regions with higher temperature are weaker superconductors or smaller in flux pinning, and surrounding fluxoids try to jump in. This phenomenon is called “flux avalanche” or “flux jumping” [17] and is more remarkable in larger samples. Once flux avalanche takes place in a superconductor, it is no longer stable, and bulk HTS is destroyed due to crack formation from the large electromagnetic forces.

Thermal stability in bulk HTS was improved by a simple treatment. An artificial hole about 1 mm in diameter was drilled through the disk, followed by impregnation of Bi-Pb-Sn-Cd alloy with melting temperature $< 100^{\circ}\text{C}$. Like resin, the alloy could permeate into the bulk body through cracks connected to the drilled hole, as shown in Fig. 7. This enhances the effective interface areas between the alloy and bulk material. The insertion of a highly conductive Al rod with its diameter slightly smaller than the hole was also

2.5. Joining

As already mentioned, it is possible to grow large-grain RE-Ba-Cu-O, 10 cm in diameter; however, J_c degrades with distance from the seed due to the presence of growth inhomogeneities and chemical contamination from the substrate materials. Consequently, the grain size of high-performance RE-Ba-Cu-O is limited to 3-6 cm. In principle, this limitation can be overcome by joining small RE-Ba-Cu-O blocks, and arbitrarily large monolithic structures should be fabricable once this technique is refined.

Several approaches have been used to obtain joints. These approaches can be grouped into two categories: (1) joining by using an HTS filler material that has a decomposition temperature lower than that of the RE-Ba-Cu-O blocks to be joined [19] and (2) direct-contact joining, which might include pressure loading of the joint [20]. For joining Y-Ba-Cu-O, fillers include Yb-Ba-Cu-O, Tm-Ba-Cu-O, Er-Ba-Cu-O, and Ag-doped Y-Ba-Cu-O. After oxygen annealing, the joined block exhibits superconductivity. However, the joining with filler materials often suffers from the segregation of residual liquid phase. This problem could be overcome by controlling the joined surface of the mother block parallel to be (110) [21]. Since the growth front is (100) facet, the liquid/solid interface is tilted by 45 degrees from the joined surface during the joining process. This will result in the formation of a zigzag-like liquid/solid interface, which prevents the layered segregation of un-reacted liquid phase along with an increase in the effective interfacial area. Fig. 9 shows magneto-optical images showing the distribution of the external fields exerted upon two joined samples. The left hand side is for the Y-Ba-Cu-O sample where (100) surfaces were joined using Er-Ba-Cu-O, and the right hand side for (110)/(110) joint. It is clear that the joint is not weakly linked for the sample in which (110) surfaces were welded.

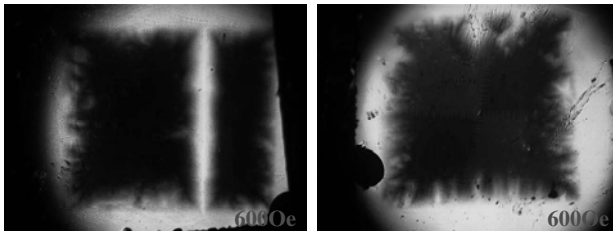


Fig. 9. Magneto-optical images for two Y-Ba-Cu-O samples joined with Er-Ba-Cu-O solder. (100)/(100) joint (left) and (110)/(110) joint (right).

3. APPLICATIONS OF BULK HTSs

When the magnetic fields change around electric conductors, electric currents are induced in the conductors as to oppose the change in the external fields according to Lenz's Law. In the case of a superconductor, the current that arises to counter the external change in flux can flow persistently. Thus, a superconducting material can act as a strong diamagnet or a strong quasi-permanent magnet depending on how the external changes. The magnetic applications of bulk HTS materials use these two properties and are classified into two categories: levitation and field trapping.

3.1. Levitation

One of the most popular applications of HTS levitation is the demonstration of the ability to levitate large masses, especially people [22] as shown in Fig. 10. Sumo wrestlers with total levitated mass (wrestler plus magnet) of 200 kg have also been levitated using the same device.

The use of magnetic levitation to avoid mechanical contact has special application to cryogenic structures. Most cryogenic tanks and transmission lines already have vacuum jackets, so the heat leak into the cryogen is through radiation and conduction paths. If a cryogenic storage tank or transmission line is magnetically levitated, then the conduction path disappears, and it is possible to reduce the heat leak significantly. Because a cryogenic environment already exists in this application, the use of an HTS to provide the levitation seems very reasonable. One of the earliest of these studies was the use of HTS levitation in hydrogen storage tanks for automobiles [23].

Bulk HTS could be used in dynamical levitational applications in several ways. The stable levitational force in HTS suggests application in magnetically levitated conveyor systems in clean rooms, where high-purity products can be transported without contact [24]. Trapped-field HTSs could be used to replace the superconducting coils aboard maglev vehicles traveling along normal-conducting guideways [25] (see Fig. 11). In this case, the trapped-field HTSs would act as very powerful PMs that allow much higher levitation heights than can be achieved with conventional PMs on maglev vehicles. Alternatively, the diamagnetic HTSs could be placed over a PM guideway [26].



Fig. 10. Levitation of a person.



Fig. 11. Man-loading vehicle on a Fe-Nd-B guideway.

3.1.1. Magnetic bearings

The combination of diamagnetic behavior as the superconductor attempts to negate any change in its internal magnetic field, together with the ability to lock magnetic field lines in pinning centers within the HTS, allows the stable levitation of a PM above or below an HTS [27]. If the PM is cylindrically symmetric, it freely rotates about its axis of symmetry and forms a low-loss magnetic bearing that is passively stable [28]. HTS bearings have seen considerable development and have been suggested for many applications [29, 30].

A dimensionless parameter that some have used to characterize HTS bearings is the coefficient of friction (COF), defined as the rotational drag force divided by the bearing load. A COF $< 10^{-7}$ has been obtained for several experimental HTS bearings [28], and the limit to obtaining lower values seems to depend on the ability to produce PMs of higher homogeneity. For comparison, mechanical roller bearings typically have a COF of the order of 10^{-3} . Damping time constants in directions other than the rotational one are typically of the order of seconds, so HTS bearings with such low rotational drag exhibit a remarkable anisotropy in damping.

3.1.2. Flywheel Energy Storage

The availability of HTS bearings that are so nearly friction-free naturally leads to their consideration for flywheel energy storage, and several major projects have investigated this application [30 - 33]. Flywheels with conventional bearings typically experience high-speed idling (that is, no power input or output) losses on the order of $\approx 1\%$ per hour. With HTS bearings, rotational losses as little as 0.001% per hour (of the energy in a full-speed rotor) have been achieved in laboratory experiments [34]. When conduction losses to the cryostat are included, and energy is taken from the flywheel to power the refrigerator that cools the HTSs, total parasitic energy losses for the bearing of 0.1% per hour are believed to be achievable. When coupled with efficient motors/generators and power electronics (capable of losses as low as 4% on input and output), the potential exists for constructing flywheels with a 90% diurnal storage efficiency. Probably only one other technology is capable of achieving such high diurnal storage efficiencies: superconducting coils hundreds of meters in diameter.

Electric utilities have a great need for efficient diurnal energy storage, such as flywheels, because the inexpensive base load capacity of the utilities is typically underutilized at night, and they must use expensive generating sources to meet their peak loads during the day. A distributed network of diurnal-storage devices could also make use of underutilized capacity in transmission lines at night and add robustness to the electric grid. These factors are expected to become more important in the forthcoming deregulation of the electric utility industry. Efficient energy storage would also be beneficial to renewable-energy technologies, such as wind turbines.

With modern graphite fiber/epoxy materials, the inertial section of a flywheel rotates with rim speeds well in excess of 1000 m/s and achieves energy densities greater than those of advanced batteries. The kinetic energy in a 0.3m-sized flywheel with this rim speed is ≈ 1 kWh, and a 1m-sized flywheel could store 20 - 41 kWh. Experimental versions of flywheels that employ HTS bearings have already stored > 2 kWh.

3.2. Trapped-field magnets

3.2.1. Experimental magnet system

Bulk superconducting magnets can be used as a magnetic source like PMs. The benefit of the superconductor is that the field strength is much greater than that of conventional PMs, although refrigeration is necessary. An experimental magnet system has been developed and already commercialized in that the trapped-field magnets generate fields [35]. Two types of experimental magnet systems are commercially available: a single-pole type and a double-pole type. Fig. 12 shows the latter. Here, two bulk RE-Ba-Cu-O disks are installed at the

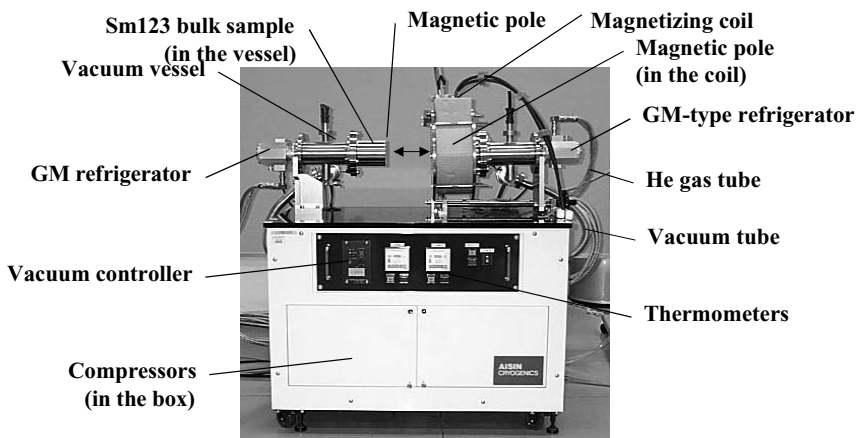


Fig. 12. Photograph of a double-pole bulk HTS magnet system for laboratory use. It is now commercially available.

heads, which are connected to a cryo-cooler and cooled down to the target temperature. As described in section III, one needs to apply high magnetic fields to magnetize bulk superconducting magnets. To make the operation simple, a pulse-field magnetization technique activates the bulk magnets in this system. At present, a magnetic field of 3 T can be obtained at the center of two trapped-field magnets in free space. An interesting feature of this magnet system is that the field configuration with like poles facing each other (e.g., N to N) can be easily produced by simply changing the direction of magnetization, in addition to the common field configuration of N to S.

3.2.2. Magnetic separation device

Purification of water is a very important technology. It is now common to use superconducting solenoids for magnetic separation of contaminants from polluted water. The force exerted on magnetic materials is given by

$$F = AB \frac{dB}{dr} \quad (4)$$

where A is constant, B magnetic induction, and dB/dr the field gradient. Hence, one needs a steep field gradient to achieve a large magnetic force for separation. Unfortunately, the field distribution of a large superconducting solenoid is quite uniform, so that steel wires are inserted in the bore of the magnet in order to achieve a steep field gradient. In contrast, the field created by a bulk superconducting magnet has a large dB/dr in addition to a large B . Thus, this material can be directly used for magnetic separation [36]. A commercialized magnetic separation device uses bulk HTS magnets to clean the filter of a membrane-type magnetic separator. In this type of separator, the membrane or the filter catches contaminants of polluted water. The polluted water is treated with coagulants that can flocculate small dirt particles to make flocs larger than the mesh size of the filter; thereby, the contaminants are caught by the filter. However, cleaning of the filter has been a problem, inhibiting continuous

operation. Thus, the possibility was raised to make magnetic flocs by adding ferromagnetic particles during the coagulation process; thereby, the dirt on the filter is detached by permanent magnets. The separation speed of such a system was very slow and was not commercially available due to small magnetic forces. The replacement of permanent magnets with bulk HTS magnets made the system powerful [37]. Fig. 13 shows a photo of a magnetic-separation device for water purification that is now commercially available. Here, several Y-Ba-Cu-O disks are cooled by a cryocooler down to 50 K and magnetized with a superconducting coil in the field-cooling process. The field strength of the trapped-field magnet is 5 T at the surface and 1 T at the working place where the dirt on the filter is detached. As shown in Fig. 14, the dirt on the filter is cleaned effectively and transported to a sludge pot with a rotating shell. The system can remove 98% of the contaminants from sewage. The density of recovered sludge is 41 g/l. Because the system is compact, it can be carried on vehicles. Mobile magnetic separation devices have already been developed and successfully used to clean ponds and rivers contaminated by green algae. This device can also be used to clean red tide, toxic planktons, and oil-contaminated seawater.

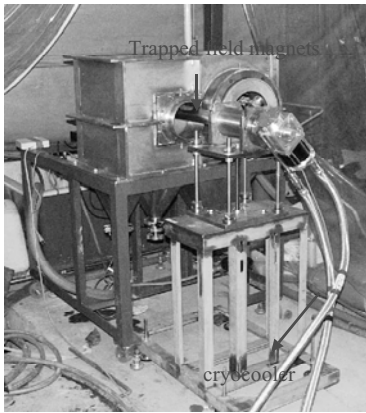


Fig. 13. Magnetic separation device.

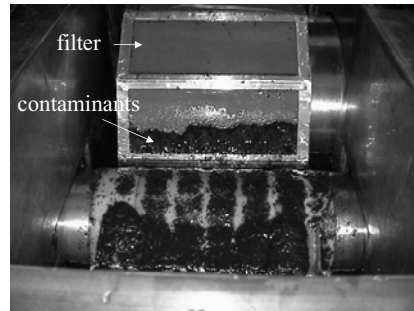


Fig. 14. Magnetic separation in operation.

3.2.3. Magnetron sputtering device

Magnetron sputtering is widely used to produce thin films for various industrial applications. In the sputtering process, a target or a cathode plate is bombarded by energetic ions generated in a glow discharge plasma. The bombardment process consists of removal of target atoms and subsequent deposition on a substrate. In this process, secondary electrons are also emitted from the target and maintain the plasma formation. PMs play a key role in the magnetron sputtering process. They are arranged such that one pole is positioned at the center of the target material, and the other in a ring shape covers the outer edge of the target. This arrangement creates magnetic closed loops starting from the center toward the edge. Soft magnetic materials are also used to form a ring along the periphery of the target. Secondary electrons are constrained along the loop due to the Lorentz force. If the field strength can be made higher, more dense plasma will be available near the target, which increases the deposition rate. It is also possible to maintain plasma even in high vacuum in large fields,

leading to the production of high-quality films. In addition, ferromagnetic thin films can be made with high-field magnetron sputtering. In conventional magnetron sputtering devices with permanent magnets, the field could not pass through ferromagnetic target materials. Hence, the idea was born to replace Fe-Nd-B magnets by trapped-field magnets [38]. Fig. 15 shows a schematic illustration of a magnetron sputtering device in which trapped-field magnets are installed as a magnetic source. A Sm-Ba-Cu-O disk, 65 mm in diameter, is used as a trapped-field magnet that can generate 6 T at 50 K. The parallel field of 0.6 T could be generated at the target surface using this trapped-field magnet. The experimental results show that a discharge current higher than 10 mA is achievable in the vacuum of 2×10^{-4} torr. It was also possible to deposit Fe particles using the high-field magnetron sputtering device. The system will be commercialized in the near future.

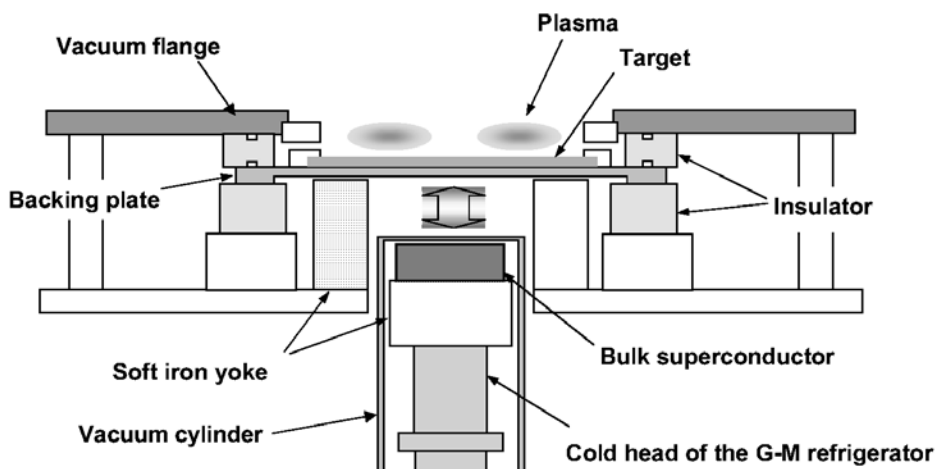


Fig. 15 Schematic illustration of a magnetron sputtering device in which trapped field magnets are installed as a magnetic source.

3.2.4. Motors

Shortly after the discovery of HTSs, work began on HTS motors. A result of this work was experimental devices of ever-increasing size [39]. The early devices used HTS wires and were analogs of conventional synchronous and homopolar motors that had been investigated earlier for LTS motors. More recently, motor designs that use bulk HTSs have been investigated as analogs to hysteresis, reluctance, and brushless PM designs. The expected benefits of HTS motors are greater efficiency and smaller motor size [40 - 43].

The ability of bulk HTSs to trap magnetic fields as high as 17 T [18] suggests their use in superconducting analogs to brushless synchronous motors that currently use PMs. In addition, the diamagnetic and hysteretic nature of bulk HTSs have suggested several new concepts for motors. For the most part, initial experiments with bulk HTS motors have allowed the entire motor to be situated in a liquid-nitrogen bath. If the application is cryogenic pumping, this condition is adequate. Slight modifications of these motors can easily be envisioned as operating in a liquid-hydrogen infrastructure. Also, there are several industrial

applications where compactness or low rotor inertia is the major parameter of interest. For these applications, the efficiency or type of cooling is not a major issue, and existing bulk HTS motor designs are already sufficient. However, in most power applications, the motor housing must be at ambient temperature, and the difficulties of cooling such motors must be addressed in the future.

4. SUMMARY AND FUTURE PROSPECTS

Since the discovery of HTSs, the advances in bulk HTS processing technologies have progressed to a level where these materials are used in some engineering applications, such as laboratory magnets, low-loss bearings, and motors.

There are two major areas in that bulk HTSs are presently used; those are magnetic levitation and trapped field magnets. A combination of permanent magnet and bulk HTS enabled us to levitate a heavy object. Five-man loading maglev vehicle has already been developed by a Chinese team. Flywheel energy storage system is now under development as a national project worldwide. But the load is limited by the field strength of a permanent magnet. Hence it is interesting to use a superconducting magnet as a magnetic source for magnetic levitation, which will allow the active control of the levitation and an increase in the load bearing capacity at least ten times higher than the present PM/HTS system.

Another interesting area of bulk HTS application is trapped fields. Bulk HTS can trap $>17\text{T}$ at 29K and can act as a very strong quasi-permanent magnet. Some commercial products installing bulk HTS magnets are now on the market. Those are field generators for laboratory experiments and magnetic separation devices. Superconducting motors and magnetron sputtering devices are almost ready to be brought to market. However, the activation of bulk HTS magnet requires another magnetic source. At present superconducting solenoids and pulse magnets are used to magnetize bulk HTS. A simple but powerful activation method must be developed to promote broad bulk HTS magnet applications.

Besides industrial applications, the field trapping ability of bulk HTS $> 20\text{T}$ is highly attractive for many scientific new areas. The application of such a high field to physical, chemical and biological processes will lead to the discovery of novel phenomena.

Acknowledgments

A part of this work was supported by the Center for Interconnecting Science and Technology at Research Organization for Advanced Engineering S. I. T. under the program of Frontier Research Center promoted by Ministry of Education, Culture, Sports, Science and Technology of Japan.

References

- [1] K. Tachikawa and K. Togano, *Proc. IEEE*, vol. 77, no. 8, pp. 1124-1130, 1989.
- [2] D. A. Cardwell, *Mater. Sci. & Eng. B*, vol. 53, pp. 1-10, 1998.
- [3] M. Murakami, *Melt processed high-temperature superconductors* (Singapore: World Scientific) 1991.
- [4] R. Tounier et al., *Supercond. Sci. & Technol.*, vol. 13, pp. 886-895, 2000.
- [5] N. Sakai, et al., *Supercond. Sci. & Technol.*, vol. 13, pp. 770-773, 2000.
- [6] M. Murakami, *Appl. Supercon.*, vol. 6, pp. 51-59, 1998.
- [7] S. I. Yoo, et al., *Appl. Phys. Lett.*, vol. 65, pp. 633-635, 1994.
- [8] T. Higuchi, et al., *Phys. Rev. B*, vol. 59, pp. 1514-1527, 1999.
- [9] M. Muralidhar, et al., *Supercond. Sci. & Technol.*, vol. 13, pp. 693 - 697, 2000.
- [10] M. Muralidhar, et al., *Phys. Rev. Lett.*, vol. 89, pp. 237001-1-4, 2002.
- [11] S. Nariki, et al., *Supercond. Sci. & Technol.* to be published.
- [12] P. Schaetzle, et al., *IEEE Trans. Appl. Supercond.*, vol. 9, pp. 2022-2025, 1999.
- [13] T. Miyamoto, J. Katagiri, K. Nagashima, and M. Murakami, *IEEE Trans. Appl. Supercond.*, vol. 9, pp. 2066-2069, 1999.
- [14] G. Fuchs, et al., *Appl. Phys. Lett.*, vol. 76, pp. 2107-2109, 2000.
- [15] M. Tomita and M. Murakami, *Supercond. Sci. & Technol.*, vol. 13, pp. 722-724, 2000.
- [16] S. L. Wipf, *Cryogenics*, vol. 31, pp. 936-948, 1991.
- [17] K. H. Muller & C. Andrikidis, *Phys. Rev. B*, vol. 49, pp. 1294-1307, 1994.
- [18] M. Tomita and M. Murakami, *Nature*, vol. 421, pp. 517-520, 2003.
- [19] J. Yoshioka et al., *Supercond. Sci. & Technol.*, vol. 15, pp. 712-716, 2002.
- [20] L. Chen et al., *Supercond. Sci. & Technol.*, vol. 15, pp. 672-674, 2000.
- [21] J. Yoshioka et al., *Physica C*, vol. 378-381, pp. 641-645, 2002.
- [22] M. Murakami, *Appl. Supercond.*, vol. 1, pp. 1157-1173, 1993.
- [23] H. Walter, et al., *IEEE Trans. Appl. Supercond.*, vol. 13, pp. 2150-2153, 2003.
- [24] H. Minami and J. Yuyama, *Jpn. J. Appl. Phys.*, vol. 34, pp. 346-349, 1995.
- [25] H. Kamijo, T. Higuchi, H. Fujimoto, H. Ichikawa, and T. Ishigohka, *IEEE Trans. Appl. Supercond.*, vol. 9, pp. 976-979, 1999.
- [26] J. S. Wang, et al., *Physica C*, vol. 386 pp. 431-437, 2003.
- [27] E. H. Brandt, *Am. J. Phys.*, vol. 58, pp. 43-49, 1990.
- [28] J. Hull, *Supercond. Sci. Technol.*, vol. 13, pp. R1-R14, 2000.
- [29] F. C. Moon, *Superconducting levitation* (New York: Wiley) 1994.
- [30] J. Hull, *Spectrum*, vol. 34, no. 7, pp. 20-25, 1997.
- [31] S. Nagaya, et al., *IEEE Trans. Appl. Supercond.*, vol. 11, pp. 1649-1652, 2001.
- [32] K. Matsunaga, et al., *Physica C*, vol. 378-381, pp. 883-887, 2002.
- [33] A. C. Day, et al., *IEEE Trans. Appl. Supercond.*, vol. 13, pp. 2179-2184, 2003.
- [34] J. R. Hull, T. M. Mulcahy, and J. F. Labataille, *Appl. Phys. Lett.*, vol. 70, pp. 655-657, 1997.
- [35] T. Oka, et al., *Physica C*, vol. 335, pp. 101-106, 2000.
- [36] J. H. P. Watson and I. Younas, *Mater. Sci. Eng.*, vol. B53, pp. 220-224, 1998.
- [37] N. Saho, et al., *Ceram. Trans.*, vol. 141, pp. 325-335, 2003.
- [38] U. Mizutani, et al., *Ceram. Trans.*, vol. 141, pp. 273-283, 2003.
- [39] D. Driscoll, V. Dombrovski, and B. Zhang, *IEEE Power Eng. Rev.*, vol. 20, no. 5, pp. 12-15, 2000.

- [40] L. K. Kovalev, et al., *IEEE Trans. Appl. Supercond.*, vol. 9, pp. 1261-1264, 1999.
- [41] B. Oswald, et al., *IEEE Trans. Appl. Supercond.*, vol. 9, pp. 1201-1204, 1999.
- [42] B. Oswald, et al., *Physica C*, vol. 372-376, pp. 1513-1516, 2002.
- [43] L. Kovalev, et al., *Supercond. Sci. Technol.*, vol. 15, pp. 817-822, 2002.

SYNTHESIS OF BULK SUPERCONDUCTORS AND THEIR PROPERTIES ON PERMANENT MAGNET GUIDEWAY

J.S. Wang and S.Y. Wang

Applied Superconductivity Laboratory, Southwest Jiaotong University,
Chengdu, Sichuan 610031, China

1. INTRODUCTION

Melt-textured rare-earth Ba-Cu-O (REBCO, RE=Nd, Sm, Eu, Gd etc) bulk has high critical current density and high critical magnetic flux, which can produce a strong levitation force and a stable equilibrium. The high temperature superconductor (HTS) REBCO bulk may be cooled using liquid nitrogen instead of liquid helium to reduce the initial construction and the running cost in practical application systems. This makes HTS particularly attractive for the applications such as magnetic bearings [1], rotating electrical machines [2], flywheel energy storage devices [3], and magnetic levitation (Maglev) vehicle [4-8], etc. The Maglev prototype using HTS bulk has been demonstrated by the Beijing Small Model [7]. In China, the first man-loading HTS Maglev test vehicle was tested successfully with up to five people at a net levitation gap > 20 mm on a 15.5 m long guideway consisting of two parallel permanent magnetic tracks [8].

The potential engineering applications mentioned above are based on high quality HTS bulks, and it is especially important to investigate the magnetic levitation properties between the YBCO bulk and the permanent magnet. The HTS bulk preparation is in great progress. The axial symmetry magnetic levitation properties are fully researched, and there are comprehensive review papers elsewhere [1, 9-13]. The Maglev properties between the YBCO bulk and the permanent magnet guideway are discussed in this paper. The contents include HTS bulk synthesis, HTS bulk levitation phenomenology, permanent magnetic guideway,

measurement system, magnetic levitation forces, magnetic guidance forces, dynamic experiment system, HTS Maglev vehicle and other applications.

2. HTS BULK SYNTHESIS

The important superconducting characteristic of the melt textured YBCO samples for the application is the magnetic levitation force. The Maglev force of the HTS bulk is determined by its critical current density J_c and the volume.

The rare-earth Ba-Cu-O (REBCO, RE=Y, La, Nd, Sm, Eu, Gd etc) HTS bulks have high critical current density J_c . The energy density associated with those so-called magnetized HTS bulks at 77 K is greater than that with HTS wires and tapes, because HTS bulks are able to support a large persistent eddy current. But for sintered YBCO HTS bulk, the J_c is low because of the existing weak link at large numbers of grain boundaries. To overcome the J_c limitations, due to weak link properties of the grain boundaries in sintered YBCO ceramics, Jin et al. developed a melt process called melt texture growth (MTG) in 1988 [14]. The melt textured YBCO bulk has been found to be able to carry J_c at least three orders of magnitude higher than those of sintered samples. Transport J_c values of the MTG samples obtained by Jin et al. [15] exceeded 10^4 A/cm² in zero magnetic field at the liquid nitrogen temperature 77 K. This result indicated that grain alignment may have extensively reduced the weak links and lead to a great material improvement. In order to improve J_c values in magnetic field, effective pinning centers must be introduced. In the following years this process was modified and improved by several researchers. The first improvement was achieved by Salama et al. [16] by introducing the liquid-phase processing technique. Murakami et al. [17,18] developed the melt powder melt growth (MPMG). The REYBCO prepared by MPMG have a high J_c at 77 K and high magnetic field. MPMG can increase domain size to cubic centimeter easily. Micro structural observations reveal that the size of the 211 phase is much finer and its distribution is much more uniform than that of classical MTG samples. MPMG also improves J_c values, especially under a magnetic field of 1 T. $J_c(B)$ variations calculated from magnetization measurements on MPMG processed samples exhibit $5\sim 6\times 10^4$ A/cm² in self field and over 2×10^4 A/cm² under 1 T.

A breakthrough in the inexpensive growth of large amounts of high quality YBCO samples was made by top seeded melt growth (TSMG) method [19]. In this TSMG technique, RE123 (Sm123 or Nd123) crystals with a higher melting temperature than Y123 are put on top of the precursor pellet. The processing conditions for the fabrication of NdBCO and SmBCO are considerably more complex than those for YBCO. A large number of single domain REBCO samples of various shapes are prepared with this method [20-23].

The melt process for the rare-earth Ba-Cu-O (LREBCO) systems (Nd, Sm, or Eu) under controlled oxygen partial pressure (p_{O_2}) is known as the oxygen-controlled melt growth (OCMG) process [24]. The OCMG-processed LREBCO superconductors exhibit a larger J_c in high magnetic fields and a much improved irreversibility field (H_{irr}) at 77 K, implying that stronger flux pinning can be realized in a commercially feasible way. The GdBCO sample

exhibits the highest zero-field critical current density of $88\,000\text{ A cm}^{-2}$ at 77 K for the $H \parallel c$ -axis, while the highest secondary peak J_c of $65\,000\text{ A cm}^{-2}$ was achieved in NdBCO at 1 T and 77 K for the $H \parallel c$ -axis [25].

The critical current density J_c value of melt processed YBCO superconductors was obtained above 10^5 A/cm^2 , especially under high magnetic fields. For an external field parallel to both a-b planes and the direction of the current flow, critical current densities of $16\,200\text{ A/cm}^2$ in self field and $11\,000\text{ A/cm}^2$ under 1 T were obtained [26].

In recent years, many efforts have been made to increase the textured domain size. The single bulk GdBCO 50 mm in diameter exhibited a trapped field of 2.6 T at 77 K, when the Hall sensor was in contact with the surface [27].

The single bulk GdBCO 65 mm in diameter exhibited the trapped field of 3.05 T at 77 K. And one measured the trapped field between two GdBCO bulks in order to minimize the demagnetizing effect and found that it reached 4.3 T at 77 K [28].

Another important superconducting characteristic of the melt textured YBCO samples for the application is trapping flux.

The trapping flux magnitude of the REBCO HTS bulks is proportional to its critical current density J_c and the volume. Krabbes et al. [29] prepared the cylindrical YBCO bulk with a modified melt crystallization process (MMCP) [30]. The maximum field 16 T was trapped at 24 K in the gap of a mini-magnet made of the two YBCO samples. B_0 on top of a single sample was 12.5 T at 20 K and 9 T at 40 K.

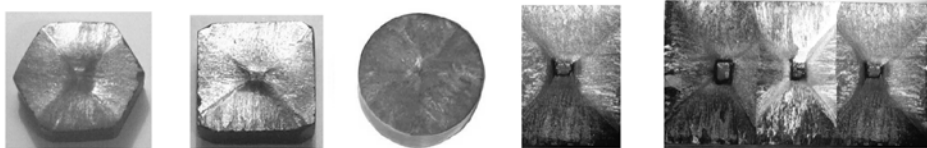


Fig. 1. Several shape of YBCO bulk HTS

Bulk YBCO superconductor as small as 2.4 cm in diameter covered with carbon fiber fabric can trap an extremely high static field of 13.55 T at 34 K, and bulk SmBCO superconductor as small as 2.4 cm in diameter can trap an extremely high static field of 13.69 T at 47 K [31]. Tomita and Murakami [32] prepared a YBCO bulk sample of high flux trapping after improving the mechanical stability and the thermal conductivity of the YBCO bulk. Their YBCO bulk is 2.65 cm diameter and traps magnetic field of 17.24 T at 29 K.

Several shape of YBCO bulk HTS used in Maglev were shown in Fig. 1. Fig. 1(a), (b), (c) are prepared by the Beijing General Research Institute for Non-Ferrous Metals, China, and Fig. 1(d) and (e) are prepared by the Institute of Solid State and Materials Research Dresden, Germany.

Microgravity experiment for growing large GdBCO bulks, which was 127 mm in diameter and 20 mm in thickness, was successfully performed on the space craft in 2003 [33]. Superconductor research colleagues are looking forward to good information of this large GdBCO bulk.

Recent progresses of melt texture REBCO exhibits a bright future for the application of HTS Maglev train operated on the permanent magnet guideway.

3. MAGNETIC LEVITATION OF HTS BULK

In January of 1987, the group of physicists at the University of Houston, led by C. W. Chu and his associate M. K. Wu of the University of Alabama at Huntsville, discovered ceramic YBCO superconductors with a critical temperature above the temperature of liquid nitrogen [34]. Therewith, Z.X.Zhao, L.Q.Chen et al. [35], of Institute of Physics of the Chinese Academy of Sciences, prepared YBCO high temperature superconductors in February of 1987.

The levitation of a NdFeB permanent magnet 0.7 cm^3 above a piece 2.5 cm-diameter, 0.6 cm thick disk of the YBCO bulk superconductor bathed in liquid nitrogen was observed by Hellman et al. [36]. While Peter et al. [37] had observed the very stable suspension of the YBCO samples in the divergent magnetic field, they discovered the suspending phenomenon below the permanent magnet.

The main drawback of the TR-07 electromagnetic levitation (EML) system using normal electromagnets in Germany is the small gap (8mm) between the vehicle and the guideway rail. The electrodynamic levitation (EDL) Maglev system using low T_c superconducting magnets in Japan has a large gap (100mm), but the operating temperature is very low and it is not a static suspension. The superconducting EML Maglev scheme with high T_c SCPMs possesses a number of the merits.

The superconducting YBCO bulk materials can trap higher magnetic fields than both Bi-based and Tl-based superconductors at liquid nitrogen temperature. So YBCO bulk as superconducting permanent magnets (PM) is particularly useful for magnetic levitation vehicles. A possibility of EML Maglev vehicles using high T_c superconducting PM is described [38].

The Maglev vehicles for high T_c superconductors may be realized by various schemes, for example, the magnetic levitation of high T_c bulk superconductor above the NPM, the EDS Maglev vehicle using high T_c superconducting PMs or superconducting wire material, the EMS Maglev vehicle using high temperature superconducting PMs, etc.

The Japanese have developed the EDL system using low T_c superconducting magnets at 4.2K. They have Nb-Ti superconducting magnet of 5T and on-board 8W G-M closed cycle refrigerator in the EDL Maglev train. The speed has reached 550km/h. This EDL Maglev system has a large gap (100mm), but the operating temperature is very low and it does not have static suspension. The cost of operating and maintenance is higher because the low temperature system uses a 4.2K refrigerator. Besides heavier weight and higher capital cost, more energy is consumed in this system. These shortcomings may limit its application.

A conceptual design of a superconducting magnet for Maglev using Bi-based high T_c superconducting wire has been discussed [39]. It is difficult to perform this scheme, because of the limited performance of high T_c superconducting wire.

The high T_c bulk superconductor is suited for making superconducting PM, because its flux jump fields are at least an order of magnitude larger than that of previously known type II superconductors. The superconducting PMs may reach an energy density of 1.8 MJ/m^3 [40], and this value is 3.5 times as high as NdFeB. The single bulk of GdBCO 65 mm in diameter exhibits the trapped field of 3.05 T at 77 K. Researchers measured the trapped field between two GdBCO bulks in order to minimize the demagnetizing effect and found that it reached 4.3 T at 77 K [28]. YBCO bulk of 2.65 cm diameter obtains trap magnetic field of 17.24 T at 29 K [32]. These data show that the bulk YBCO superconductors can be used as a superconducting PM, and have been studied for application in many fields [41]. It is possible to replace low T_c Nb-Ti superconducting magnets by high T_c superconducting PMs.

The higher magnetic field of superconducting PM produces larger magnetic levitation force. This means that vehicle could be levitated with the HTS bulk without superconducting wire.

The high T_c superconducting PMs can also be applied to the EML Maglev systems because of the simple structure and the large levitation force [6, 38]. The superconducting EML scheme with high T_c superconducting PMs has a number of benefits. For example, it not only provides static suspension, but also makes the suspension gap larger than the gap in the TR-07 electromagnetic levitation (EML) system using normal electromagnets in Germany.

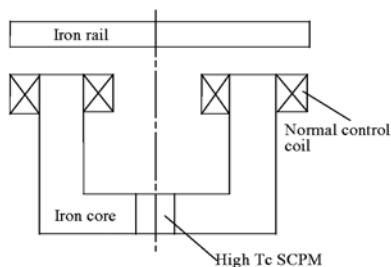


Fig. 2. Schematic diagram of Maglev vehicle with the high T_c bulk superconducting PM.

In this scheme, the high T_c superconducting PMs will replace the normal electromagnets as the suspension magnets of the Maglev vehicles.

The Grumman baseline EMS Maglev system consists of superconducting C-iron cored magnets on the vehicle [42]. These magnets are powered by Nb-Ti superconducting coils operating at 4.2K. An electromagnet consists of a C-core, a superconducting coil on the back leg of the C-core and a normal control coil on each leg of the C-core. In this scheme, the gap between the magnet poles and the rail is 40mm and it can provide static suspension. The superconducting PM can reach in

spite of higher field but experimental research for an EML system using a high T_c superconducting PM has shown that both the force and the gap of levitation are small [43]. The reason is a lower trapped field and worse field stability. The trapped field is limited by the mechanical tensile strength of the high T_c YBCO superconductors, but the maximum trapped field B_0 of 4.3 T at 77 K has been achieved in the bulk YBCO superconductors [28]. Therefore, the scheme of the Maglev transportation system using high T_c superconducting PMs should be considered. It is suitable to choose the trapped magnetic field of 2T for high T_c SCPMs, because the peak field in the iron is greater than 2 T.

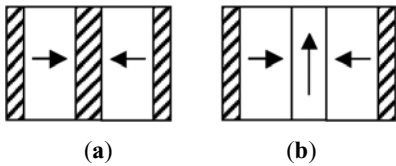
In order to implement the EDL Maglev system with the high T_c superconducting PM, it must achieve magnetic field of 5 T. The higher trapped field has been obtained below 77K

temperature in the some laboratory (ISTEC, IFW, and HPHT, etc). An on-board G-M or Stirling cryocooler of the temperature of 30 K-40 K can be used in this scheme. As a consequence, it also increases the weight and capital cost. So the scheme of EDL Maglev system using the high T_c superconducting PM is a challenge. Fujimoto et al. [44] presented this scheme of maglev train with the superconducting PM.

4. NORMAL PERMANENT MAGNETIC (NPM) GUIDEWAY

The levitation force of a quasi-crystal bulk YBCO superconductor is above 10 N/cm² (77 K). The disadvantages of the electrical magnet are the complex guideway and high electric energy consumption. If the applied magnetic field is provided by the normal permanent magnet (NPM), a larger levitation force between HTS and applied magnetic field can be achieved. The magnetic field of the NPM guideway can be increased by the application of a flux concentration scheme of the magnet arrangement. In order to increase the field strength on the top of the NPM guideway, ferromagnetic elements are introduced as magnetic conductors between two NPMs [5]. The aerial guideway of the NPM is used for some engineering applications in order to reduce the NPM’s effect on the environment.

Fig. 3 shows two construction cross-sectional drawings of the NPM guideway. The NPM guideway is composed of normal permanent magnets and iron plate. Arrowhead shows the magnetic pole .



The transverse distribution of magnetic field of a track is shown in Fig. 4. In Fig. 4, the magnetic field of the center of the NPM guideway is stronger than that of any other position, and it decreases fast with the increase of the gap from the surface of the NPM guideway. The surface magnetic field of a single permanent magnet is about 0.45T, and the surface concentrating magnetic flux density of the NPM guideway (a) is up to 1.2T. The magnetic flux

Fig. 3. The cross section of the NPM guideway iron → NdFeB

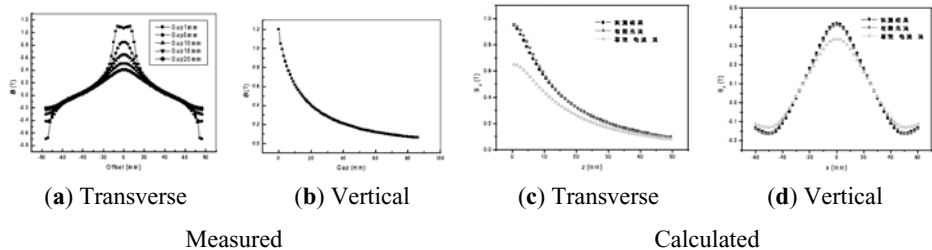


Fig. 4. Measured and calculated results of the magnetic field distribution of the NPM guideway along the transverse and the vertical direction

density is 0.4 T at 20mm gap from the surface of the guideway, and this value is close to the surface magnetic field. The NPM guideway (a) is used not only in the measurement of HTS Maglev properties but also in the HTS Maglev vehicle system [8].

Fig. 4 shows the measured and calculated results of the magnetic field distribution of the NPM guideway along the transverse and the vertical direction a track along the vertical direction [45, 46]. Fig.6 shows the distribution of magnetic line of force in the cross section of the NPM guideway in Fig. 3 [47].

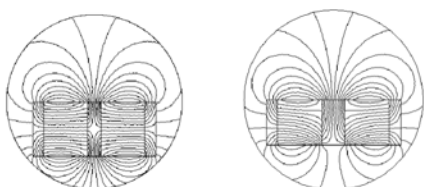


Fig. 5. The distribution of magnetic line of force in the cross section of the NPM guideway (a) (left) and (b) (right)

Table 1. Magnetic field of NPM guideway (a) along the vertical direction

| Height (mm) | Measured B_z (T) | Height (mm) | Measured B_z (T) |
|-------------|--------------------|-------------|--------------------|
| 0 | 1.2125 | 20 | 0.432 |
| 5 | 0.8388 | 25 | 0.363 |
| 10 | 0.6481 | 30 | 0.3089 |
| 15 | 0.5209 | | |

5. HTS MAGLEV MEASUREMENT SYSTEM

A HTS Maglev measurement system is developed [48, 49] in order to investigate magnetic levitation properties of the HTS YBCO bulk above NPM guideway. A series of the properties, for example, levitation force, guidance force, levitation stiffness, etc, of YBCO bulk HTS over a NPM guideway are investigated with this measurement system. The measurement system includes liquid nitrogen vessel, NPM guideway (Fig.3(a)), data collection and processing, mechanical drive and control system.

Fig. 3 is the construction cross-sectional drawing of the NPM guideway. The length of the NPM guideway is 920 mm, and the concentrating magnetic induction of NPM guideway (a) is up to 1.2 T at the guideway surface.

Fig. 6 shows the schematic diagram of the HTS Maglev measurement system. During the experiment, the YBCO is placed in the columnar liquid nitrogen vessel which is over the guideway. The YBCO is cooled in a zero magnetic field with liquid nitrogen and can move up and down at different speed. The horizontal drive platform 9 is used to measure the guiding force (stable equilibrium force along longitudinal orientation of guideway).

One of the important technologies in the high temperature superconducting onboard Maglev equipment is the thin wall liquid nitrogen vessel. The thickness of liquid nitrogen vessel wall is generally not considered, and its main feature is lower vapor rate. Because the bulk YBCO is levitated over a NPM guideway in the HTS Maglev measurement system, so a thin bottom wall of the vessel is needed. Only with a thin bottom wall, net levitation gap between outside wall of the vessel and the guideway can be high. A columnar liquid nitrogen

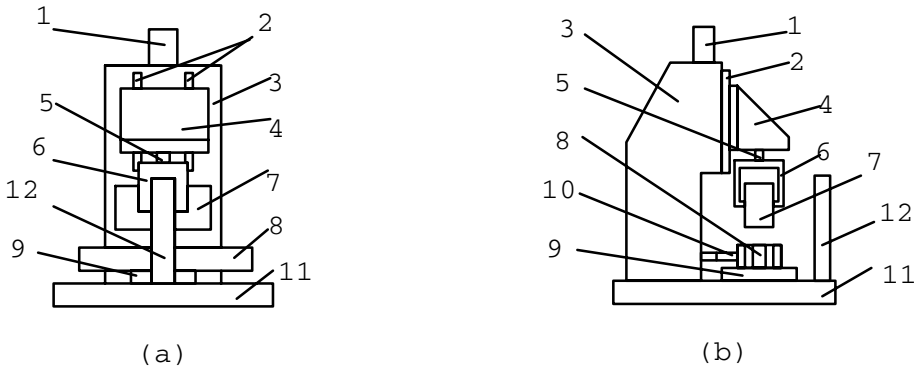


Fig. 6. Scheme of HTS Maglev measurement system. 1 – servo motor, 2 – vertical guided way, 3 – vertical column, 4 – cant lever, 5 – vertical sensor, 6 – fix frame of vessel, 7 – liquid nitrogen vessel, 8 – NPM guideway, 9 – horizontal drive platform, 10 – horizontal sensor, 11 – base, 12 – drive device of three dimension

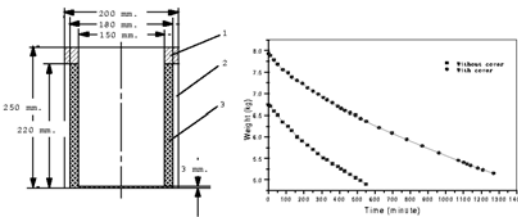


Fig 7. Schematic diagram and vapor rate of the liquid nitrogen vessel with thin wall

vessel with thin bottom wall has been developed [50] in order to verify the possibility of large size vessel with thin wall. Its bottom thickness is only 3.5 mm. Both schematic diagram and vapor rate of liquid nitrogen vessel are shown in Fig. 7.

The outline size of the vessel is an external diameter 200 mm, an internal diameter 150 mm, and height 250 mm. The liquid nitrogen vessel can operate continuously over 16 hours, and can place 7 blocks of YBCO samples of 30 mm in diameter. The vessel is used successfully to measure the levitation forces of YBCO bulk over a magnetic guideway. During the experiment, the YBCO is fixed on the bottom of the columnar liquid nitrogen vessel.

The outline size of the vessel is an external diameter 200 mm, an internal diameter 150 mm, and height 250 mm.

According to the experiment results mentioned above, the rectangle-shape liquid nitrogen vessel on board is developed [51]. The wall of the rectangle vessel is thinner, and bottom wall thickness is only 3 mm. The schematic diagram of the rectangle-shape liquid nitrogen vessel is shown in Fig. 8. Its outside outline size is 150 mm×516 mm. The inside size is 102 mm×470mm, and the height is 168 mm. The liquid nitrogen vessel can operate continuously over 6 hours. The rectangle-shape vessel is used in the measurement of the levitation force of tens of YBCO. The vessel is used successfully in HTS bulk Maglev measurement system.

The drive device of three dimensions can make scanning measurements of the magnetic field of the guideway and high T_c superconductor trapping flux. Fig. 9 is a photo of HTS Maglev measurement system.

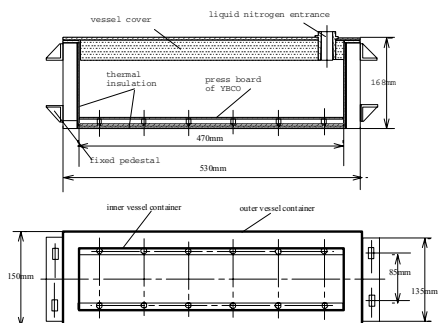
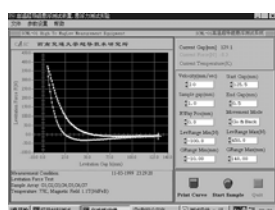


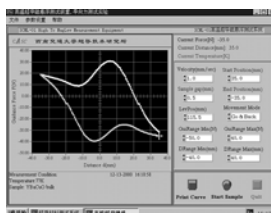
Fig. 8. Schematic diagram of the rectangle-shape liquid nitrogen vessel



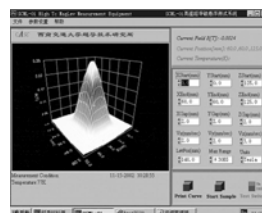
Fig. 9. Photo of HTS Maglev measurement system



(a) levitation force



(b) guidance force



(c) scanning trapping flux

Fig. 10. Main interfaces of the measurement results

The specification of the measurement system is: vertical 200 mm maximal displacement, ± 0.1 mm precision, ± 2000 N vertical maximal support force, 0.2% precision; 100 mm guideway horizontal maximal displacement, ± 0.1 mm precision, 1000 N horizontal maximal support force, and 0.1% precision. The trapping flux of high T_c superconductors and the magnetic induction of the guideway can be scanned in the range of 100 mm \times 100 mm. The system can make real time measurements of one or many superconductors. The measurement process is fully controlled by a computer. Main interfaces of the measurement results are shown in Fig. 10.

In the measurement, the YBCO HTS bulk is fixed at the bottom of the thin wall liquid nitrogen vessel, and then they are cooled into superconductivity state in a zero magnetic field. Secondly, the vessel is fixed at a connecting fixture with a servo electromotor. In order to avoid collision between the bottom of the vessel and the surface of NPM guideway, there is still a gap of 1.5 mm between the bottom of vessel and the surface of NPM guideway when the vessel moves to the lowest point, so the minimum gap is 5 mm between the bottom of the sample and the surface of NPM guideway. The vessel first moves downward, after reaching the lowest point, then moves upward at a speed of 2 mm/s, and the computer samples a data every 0.5 second. Measurement interface and results is shown in Fig. 10 (a).

6. MAGNETIC LEVITATION FORCE

6.1 LEVITATION FORCE OF YBCO ON SINGLE NPM DISK AND THE NPM GUIDEWAY

The levitation force of a HTS YBCO bulk over the NPM guideway is measured. The YBCO is cooled in a zero magnetic field with liquid nitrogen. The liquid nitrogen vessel can move up and down at different speed. Fig. 11 shows the measured results of the levitation forces over the NPM guideway (surface magnetic flux density is 1.2 T) and over the single NdFeB permanent magnet disk (surface magnetic flux density is 0.38 T), respectively [49].

Table 2 shows the levitation force at different position above the surface of magnets. F_{Lg} is the levitation force over the NPM guideway magnet and F_{LS} is the levitation force over the single NdFeB permanent magnet disk. The levitation force F_{Lg} between YBCO ($\phi=30$ mm, thick=17 mm) and the NPM guideway is 25 N, but the levitation force F_{LS} between the same YBCO and the single NdFeB permanent magnet disk is 0.1 N when the levitation gap is 25 mm. It is obvious that the levitation force over the NPM guideway is much larger than that over a single NdFeB permanent magnet disk. What's exciting is that there is still a large levitation force at higher levitation gaps.

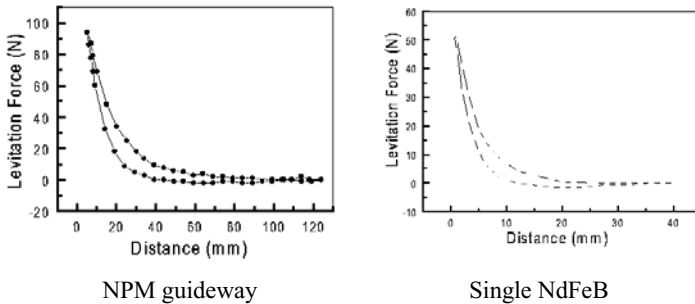


Fig. 11. Levitation force vs. levitation gap over the NPM guideway (left) and the single NdFeB (right)

Table 2. Levitation force vs. levitation gap over the single NdFeB and the NPM guideway

| Levitation gap (mm) | F_{Lg} (N) | F_{LS} (N) |
|---------------------|--------------|--------------|
| 5.0 | 94.0 | 18.4 |
| 10.0 | 68.9 | 7.0 |
| 15.0 | 47.9 | 2.8 |
| 20.0 | 34.4 | 0.5 |
| 25.0 | 25.0 | 0.1 |
| 30.0 | 18.1 | 0.0 |

F_{Lg} and F_{LS} are the levitation force over the guideway magnet and over the single NdFeB permanent magnet

This is very helpful for the design of the HTS Maglev vehicle system in which bulk superconductors are placed in the vessel on the vehicle.

Recently, a melt-textured YBCO bulk HTS sample that made in the Beijing General Research Institute for Non-Ferrous Metals is measured. The sample is a diameter of 30 mm and a thickness of 14 mm. In this case, there is 103.4 N (14.6 N/cm^2) levitation force at the 5 mm gap between this YBCO sample and the NPM guideway. The levitation force is larger.

6.2 LEVITATION FORCE vs. TEMPERATURE AND TRAPPED FLUX

In order to study temperature dependence of levitation force of YBCO bulk, a single YBCO bulk ($\Phi 30\text{mm} \times 17\text{mm}$) is fixed on the second stage cooling head of the G-M refrigerator rather than being immersed in liquid nitrogen (77K), whose temperature can be controlled by the deep cryogenic measurement system, ranging from 77K to 16K. A single permanent magnet (PM) NdFeB disk ($\Phi 30\text{mm} \times 15\text{mm}$) can be lifted vertically above HTS YBCO bulk with the gap between 100mm and 5mm. Levitation force of YBCO bulk at different gaps can be obtained at different temperatures under the control of the HTS Maglev measurement system [52].

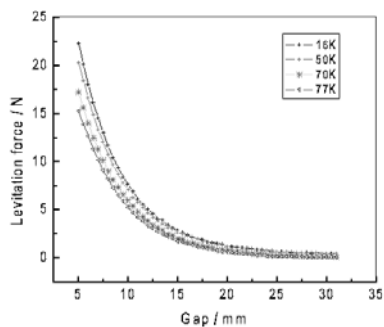


Fig. 12. Levitation force vs. gap at the temperature of 16 K, 50 K, 70 K, 77 K

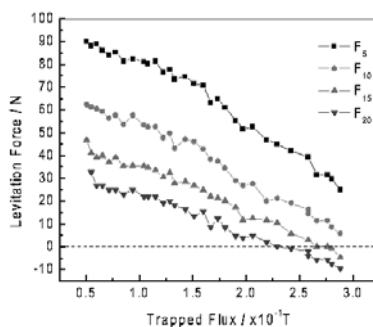


Fig. 13. Levitation force vs. trapped flux at different gaps

Fig. 12 shows levitation force of a single YBCO bulk under a single permanent magnet disk at 16 K, 50 K, 70 K, and 77 K, respectively. It is clear that temperature have much effect on the levitation force at small levitation gaps, for example, 22.3 N at 16 K and 15.2 N at 77K for the same gap of 5 mm [53]. However, the effect of temperature on levitation force is not obvious at larger levitation gaps. So if the levitation gap in practical applications is larger, cryogenic circumstance lower than 77 K is not economic.

In the experiment of trapped flux dependence of levitation force, the same YBCO bulk is used. Firstly, YBCO bulk is cooled by liquid nitrogen in applied field, which is provided by a permanent magnet. Trapped flux of YBCO bulk is controlled by changing the gap between the sample and the permanent magnet. Secondly, the levitation force of the YBCO bulk is

measured above the NPM guideway, whose central surface concentrating magnetic field is 1.2T and its field distribution in space is symmetrical about central vertical plane of the NPM guideway.

Fig. 13 is experimental results of levitation force of a single YBCO bulk with different trapped flux above the NPM guideway. From Fig. 13, levitation force decrease approximately linearly with increasing of trapped flux. It is well known that it is trapped flux that ensures stable levitation of YBCO bulk in applied field, but it weakens levitation force in the mean time, which can be seen clearly from Fig. 13. So an optimum trapped flux is very important in practical levitation systems, which shall make YBCO bulk provide both larger levitation force and guidance force.

Experimental results show that temperature and trapped flux affect levitation forces of YBCO in applied field and levitation force increases with decreasing of temperature and decreases approximately linearly with increasing of trapped flux. Guidance force of YBCO bulk exhibits much hysteresis; moreover, the hysteresis increases with decreasing of measurement height. Smaller lateral displacement may lead to the elastic lateral motion of the YBCO bulk arrays. So cryogenic circumstance and trapped flux in YBCO and effective lateral displacement need to be optimized according to requirements of practical levitation systems.

6.3 MULTI-YBCO BULK

6.3.1 ARRAY FOR FOUR-BLOCK YBCO [50]

The levitation force of different array of multi-block YBCO HTS over a NPM guideway is investigated with the NPM guideway in Fig. 3(a). The different arrays of multi-block YBCO HTS are shown in Fig. 14.

Fig. 15 shows that the levitation force of array 8 is the largest, but that of array 7 is the least. The levitation forces of different arrays at the same gap are list in table 3 for the convenient compare.

The levitation forces over NPM guideway (Fig. 3(a)) are 267.0 N, 221.1 N, 203.8 N, and 279.5 N for array 5, 6, 7, and 8 at 5 mm levitation gap, respectively. The levitation forces over NPM guideway (Fig. 3(a)) are 139.7 N, 119.6 N, 126.3 N, and 152.2 N for array 5, 6, 7, and 8 at 15mm levitation gap, respectively.

With the increase of the levitation gap, more and more YBCO bulks are in low magnetic field limit, and the effective area of different arrays is approximately equivalent. At 5 mm gap, the effective area of array 8 is maximum, array 5 and array 6 have smaller effect area, and array 7 has the smallest. Those effective area results in accordance with the levitation force at 5mm gap, that is, the levitation force of array 8 is maximal. At 40mm gap, levitation force is very close and consistent with the almost same effective area for different arrays.

6.3.2 COMPARE OF LEVITATION FORCE PER UNIT LENGTH [50]

Different arrays of multi-block YBCO HTS are shown in Fig. 14. The levitation force per unit length is defined by Newton per millimeter (N/mm) along the longitudinal direction of the

NPM guideway. The levitation forces of different arrays are listed in Table 3. Those data is measured at 20mm gap between YBCO HTS and NPM guideway.

Magnetic levitation force of YBCO is proportional to magnet field grads, and it depends on the inherent properties of YBCO bulk material. Table 3 shows that the levitation force of per unit length in array 4 is the largest.

Table 3. Levitation force of different arrays of YBCO bulk

| No | 1 | 2 | 3 | 4 | 5 | 6 | 7 | 8 |
|----------------------|------|------|------|------|------|------|------|------|
| Levitation force (N) | 145 | 193 | 177 | 163 | 105 | 123 | 136 | 118 |
| N/mm | 1.20 | 1.44 | 1.68 | 2.32 | 1.75 | 1.50 | 2.27 | 1.97 |
| Figure of merit | 8 | 7 | 5 | 1 | 4 | 6 | 2 | 3 |

6.3.3 COMBINATION LEVITATION FORCE OF MULTI-BLOCK YBCO [50]

The levitation force of seven-block YBCO HTS over a NPM guideway is investigated. Those melt-textured YBCO bulk HTS samples are made by the Beijing General Research Institute for Non-Ferrous Metals. The samples are a diameter of 30mm and a thickness of 14mm. The YBCO bulks are arrayed in the way of array 4 in Fig. 14. In this measurement, the HTS YBCO bulks are cooled into superconductivity state in a zero magnetic field. The levitation forces of the samples measurement results are shown in Fig. 16, including the levitation force of each YBCO sample (lift) and that of seven-block YBCO (right). The levitation forces of each sample approximate to each other.

The levitation force of 7 YBCO in array 4 over NPM guideway (Fig. 3(a)) is 264.1 N at 10 mm gap and the total levitation force of 7 block alone YBCO is 500.6 N at 10 mm gap. The levitation force of array 4 is smaller than one of the total levitation force of 7 single pieces of YBCO, because 4 pieces in array 4 are not in the center position of the NPM guideway lengthways direction when to measure the total force.

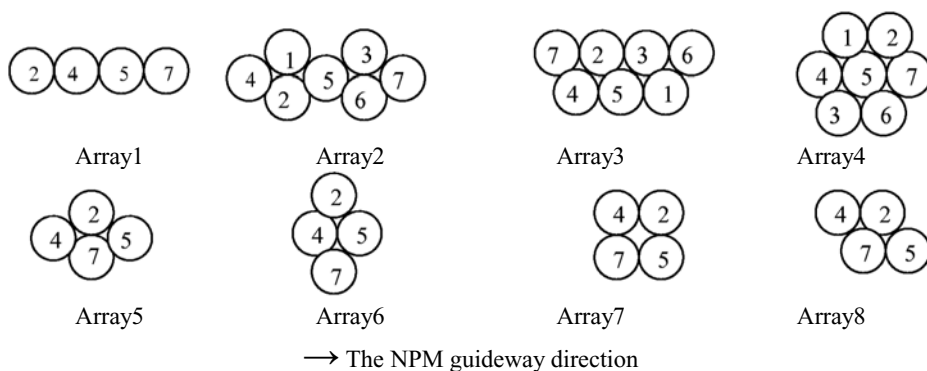


Fig 14. Different array of multi-block YBCO HTS

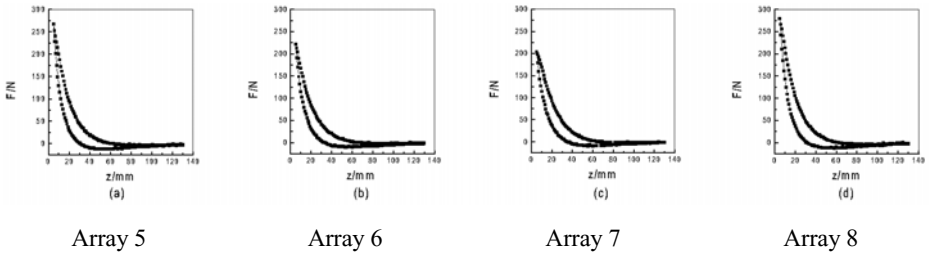


Fig. 15. The levitation force dependence on the gap of four different arrays

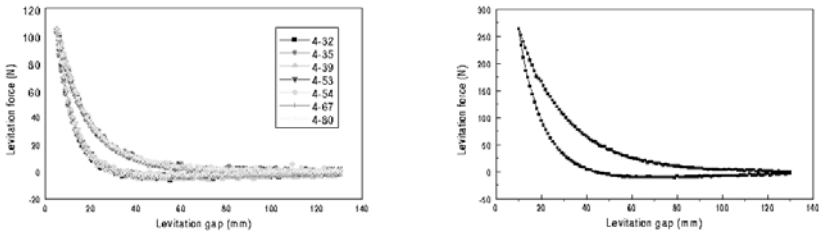


Fig 16. Levitation force of each YBCO sample (left) and the levitation force of seven-block YBCO in array 4 (right)

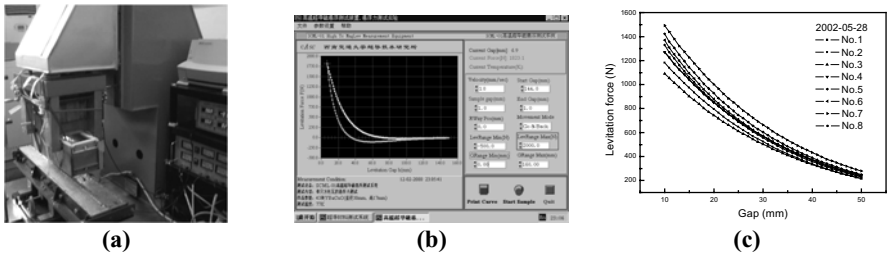


Fig 17. The rectangle-shape vessel in measurement (left), measured interface (center), and measured results (right) of on board single HTS magnetic levitation equipment (43 pieces of YBCO bulks)

The onboard HTS Maglev equipment is a key component of HTS Maglev vehicle. The onboard HTS Maglev equipment is composed of YBCO bulks and rectangle-shape liquid nitrogen vessel [51].

There are 43 pieces of YBCO bulks in the vessel. The YBCO bulks are 30 mm in diameter and 17-18 mm in thickness. All the YBCO bulks are fixed firmly in the rectangle-shape vessel. Fig 8 shows schematic diagram of the rectangle-shape vessel.

Fig. 17(a) shows a measuring system of the levitation forces of single onboard HTS Maglev equipment over the magnetic guideway. Fig. 17(b) shows that the levitation force of a single onboard HTS Maglev equipment over the magnetic guide way is 1227 N at the levitation gap of 15 mm, and the levitation force is 1593 N at the levitation gap of 8 mm. Fig. 17(c) shows that the levitation forces of 8 onboard Maglev equipment over the magnetic guideway are different. The levitation force of Maglev equipment No. 7 is 1493 N at the levitation gap of 10 mm, and 1227 N of 15 mm. The levitation force of Maglev module No. 3 is 1091 N at the levitation gap of 10 mm, and 902 N of 15 mm.

6.3.4 LEVITATION FORCE OF MULTIPLE SEEDED MELT GROWTH YBCO [54]

Schatzler [52] and Jee [53] proposed multiple seeded melt growth (MSMG) as the way to fabricate larger and well textured YBCO bulks. Song et al. [54] reported the experiment results of magnetic levitation force of TSMG YBCO bulks above the NPM guideway in parallel and perpendicular mode between the length directions of the NMP guideway and that of the MSMG bulks. All the TSMG bulk samples were fabricated by IFW, Dresden, Germany [52]. Each trisected part ($30 \times 35 \times 15 \text{ mm}^3$) (Fig. 1(d)) corresponds to one growth domain with one seeding crystal. They are stacked up as one bulk array ($90 \times 35 \times 15 \text{ mm}^3$). Moreover, there is a piece of MSMG bulk with the dimension ($90 \times 36 \times 15 \text{ mm}^3$) (Fig. 1(e)). The levitation forces are measured by the HTS Maglev measurement system [48, 49].

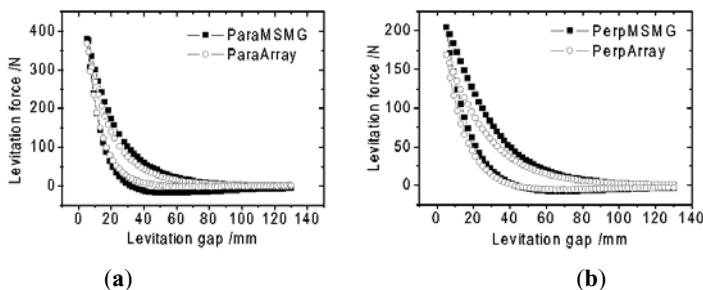


Fig. 18. Levitation force of the MSMG bulk and the stacked array consisting of bulk S01, S02 and S03 in the parallel mode (a) and perpendicular mode (b)

The levitation force of the MSMG bulk and the stacked array in parallel [Fig.18(a)] and perpendicular [Fig.18(b)] mode are compared. In the parallel mode hysteresis loss of the MSMG bulk is more obvious than the stacked array in [Fig.18(a)], and the weak-link GB give rise to hysteresis behavior. However, their maximum levitation forces are slightly different. The difference between them is 7.0 N with the percentage of 4.68%. But the difference rises up to 36.1 N with the percentage of 21.40% in the perpendicular mode though their maximum forces drop to 204.8 N and 168.7 N, respectively.

6.3.5 LEVITATION FORCE AND STIFFNESS [55]

The relationship between levitation force and stiffness in symmetrical and unsymmetrical applied fields is investigated by Song et al. [55]. Both the levitation force and stiffness are dependent on the displacement of a single YBCO bulk over the NPM guideway. Except for the applied field is symmetrical about the bulk axis, the levitation forces in unsymmetrical magnetic fields do not have linear relationship with the associated applied field or its gradient. Moreover levitation stiffness in FC is directly proportional to the levitation force in ZFC in both symmetrical and unsymmetrical applied field.

The magnetic levitation force of a YBCO bulk at different temperature from 100K to 40K is studied by He et al. [56].

7. MAGNETIC GUIDANCE FORCE

7.1 GUIDANCE FORCE OF ONE YBCO ON SINGLE NPM GUIDEWAY [57]

The guidance force (lateral force) depends on field-cooling height (FCH). Guidance forces of single YBCO bulk are measured in two FCH cases. In the first FCH case, YBCO bulk is cooled by liquid nitrogen at 50 mm above the center of the NPM guideway, where the applied field is 0.1575 T. Guidance forces of the YBCO bulk are measured at two different heights, i.e. 10 mm and 20 mm. In the second FCH case, YBCO bulk is cooled at 8 mm above center of the guideway, where the applied field is 0.6874 T, and then guidance forces of the YBCO bulk are measured at two different heights mentioned above.

Fig. 19 shows the guidance force of a single YBCO bulk above the NPM guideway in the first FC case, whose trapped flux is 0.092 T. The arrows indicate the moving direction of YBCO bulk during experiments. As shown in the Fig. 19, guidance forces exhibits much hysteresis, moreover, the hysteresis increases with decreasing of measurement height (MH). It is obvious that guidance force at MH 10 mm is much larger than that at MH 20 mm, especially near center of the guideway.

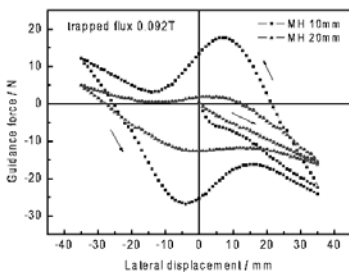


Fig. 19. Guidance force vs. lateral displacement in the first FC case

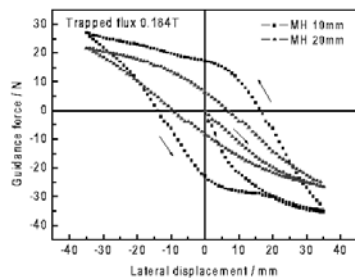


Fig. 20. Guidance force vs. lateral displacement in the second FC case

This is because guidance force depends not only on trapped flux in the YBCO bulk but also on the applied field. Although the trapped flux is the same, the applied field at MH 10 mm is stronger than that at MH 20 mm. In addition, it implies that YBCO bulk has better lateral stability at lower position above the NPM guideway.

Fig. 20 shows the guidance force of the same sample above the same NPM guideway in the second FC case, whose trapped flux is 0.184 T. Although its changing tendency is similar to that in the first FC case, there is also much difference between them. For example, the changing of guidance force is monotonous in Fig. 5; however, it is not monotonous in Fig. 4, especially at MH 10 mm. But there is no difference except trapped flux in YBCO bulk for the two groups of experiment results. So, trapped flux is very important for investigation of guidance force.

7.2 GUIDANCE FORCE OF YBCO ON PARALLEL TWO NPM GUIDEWAY [57]

The guidance forces of two YBCO bulk arrays above two parallel NPM guideways are measured. Each array includes 9 YBCO bulks arranging in a line and each sample is 30 mm in diameter and 17 mm in thickness, which are fixed on the bottom of the rectangular vessel.

Fig. 21 is the schematic diagram and photo of guidance force experiment of YBCO bulk arrays.

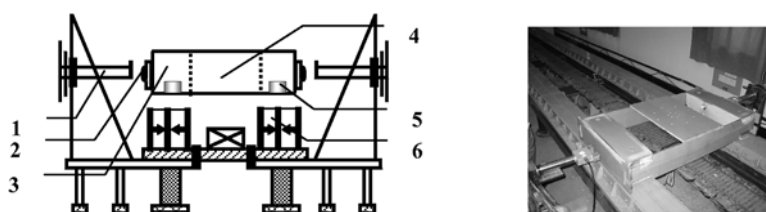


Fig. 21. Schematic diagram (left) and photo (right) of guidance force experiment of YBCO arrays on two parallel guideways (1.Horizontal propulsion arm; 2.Force transducer; 3.Liquid nitrogen vessel; 4.Rigid link; 5.HTS array; 6.NPM guideway)

Fig. 22 shows guidance forces of YBCO bulk arrays above two parallel NPM guideway when maximum lateral displacement (MLD) is 5mm and 15mm, respectively. When MLD is 5 mm, even though guidance forces are small, the place corresponding to zero guidance force is always original position, which implies that the YBCO bulk arrays can return to its original place freely after they leave their original place, i.e. the center of NPM guideway. Compared with guidance force of MLD=5mm, when MLD is 15mm, guidance forces are larger and raise fast with increasing lateral displacement, but the guidance force decreases fast to zero before it return to its original position. This is not beneficial to lateral stability of levitation system. So effective lateral displacement, that is maximum lateral displacement corresponding to levitation system being able to return to its original position after it leaves its original position, is very important to design of practical levitation systems.

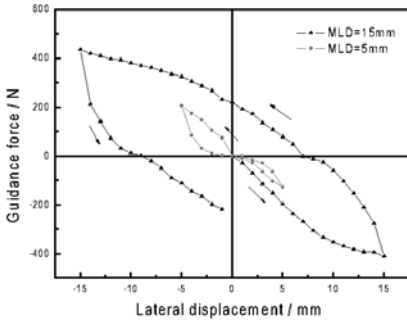


Fig. 22. Guidance forces of YBCO bulk arrays above two parallel NPM guideway with different maximum lateral displacement

8. INFLUENCE OF YBCO BULK SIZE AND SHAPE ON THE LEVITATION PROPERTIES

8.1 INFLUENCE OF YBCO BULK SHAPE ON THE PROPERTIES [58, 59]

The used samples include a hexagonal (Fig.1(a)) one with 26mm from side to side and 30mm from point to point and a cylindrical (Fig.1(c)) one with a diameter of 26mm. Their thickness is 11mm.

Table 4. Geometrical size and levitation force of samples

| sample | hexagon | cylinder |
|--------------------------------|---------|----------|
| Area (cm ²) | 6.1 | 5.1 |
| Thickness (mm) | 11 | 11 |
| Diameter (mm) | 26* | 26 |
| F_0 (N) | 66.5 | 55.6 |
| f_0 (N/cm ²) | 10.9 | 10.9 |
| F_{max} (N) | 40.2 | 44.9 |
| f_{max} (N/cm ²) | 6.6 | 8.8 |
| F_{15} (N) | 21.1 | 22.0 |
| F_{20} (N) | 16.3 | 15.3 |
| F_{min} (N) | -7.7 | -4.8 |
| * from side to side | | |

Table 4 lists the levitation forces of different case. F_{max} and F_{min} are the maximum levitation force and minimum levitation force over the NPM guideway, respectively; f_{max} is the value of F_{max} divided by cross section area of sample. F_{15} and F_{20} is the levitation force at the gap of 15 mm and 20 mm over the NPM guideway. From the results, we can see that the shape of samples affects levitation force of sample.

Although f_0 of two samples is the same, their f_{max} are different. This indicates that behavior of samples over the single magnet is different from that over the NPM guideway. It is well known that the levitation force is relevant with J_c , d and dB/dz . Here, d is the diameter of shield current

in a sample. Because the path of shield current of two samples is equal, levitation force difference is smaller at the levitation gap 15~20 mm of practical Maglev vehicle.

8.2 LEVITATION FORCE AND GUIDANCE FORCE OF RING YBCO BULK [46]

The levitation force of ring-shaped YBCO bulks above a NPM guideway is studied and the investigation focuses on the influence of the hole diameter of YBCO bulk on the levitation

force. In this experiment, three cylindrical YBCO bulks, one with a hole of 8 mm in diameter was made in BJ214, one with a hole of 12 mm in diameter for BJ215 and one with a hole of 18 mm in diameter for BJ216, were used, respectively (Fig. 23). The diameter is 30 mm and the height is 16 mm. First, the levitation force of each bulk was measured above the NPM guideway at FCH 40 mm, then as shown in Fig. 12. After that, the levitation force was measured at FCH 40 mm again.

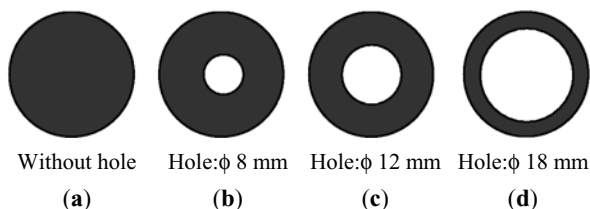


Fig. 23. Ring-shaped YBCO bulk with different holes

Fig. 24 shows the levitation force comparison of each bulk for with or without a hole. As shown in Fig. 24 (a) and (b), when the hole diameter is 8mm and 12 mm, it hardly has influence on the levitation force in the whole measuring range, i.e. gap from 40 mm to 3 mm. When the hole is enlarged to 18 mm in diameter, the levitation forces begin to decrease at lower levitation gap, but it still hardly has influence on the levitation force at larger levitation gap, for example, gaps more than 20 mm, as shown in Fig. 24 (c). This proves that the outer part of YBCO bulk contributes more than the inner part does to the levitation force. In some case, we can substitute the cylindrical YBCO bulk with a ring-shaped YBCO bulk in order to achieve a light weight Maglev system.

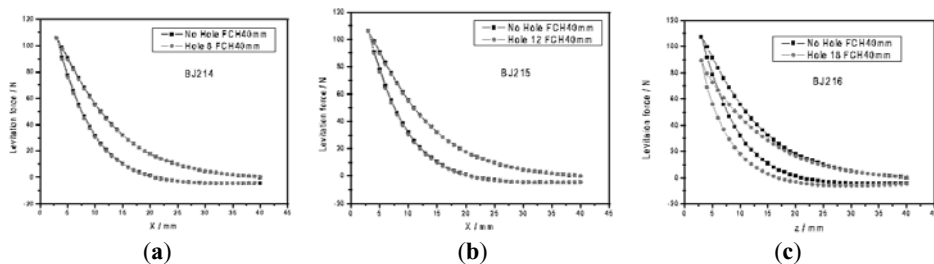


Fig. 24. Levitation force comparison of a YBCO bulk with a different hollow hole (a) a hole with 8 mm in diameter (b) a hole with 12 mm in diameter (c) a hole with 18 mm in diameter

While the hole doesn't cause much difference in levitation force, it has much influence on lateral force. But when the hole is enough small, like a hole with diameter of 4mm, the influence on lateral force is not obvious. As the diameter of the hole grows, the lateral force decreases fast [Fig. 25].

The reason is that lateral force results from interaction between trapped flux and applied field. Furthermore, trapped flux depends on pinning center. As the hole enlarges, the whole pinning center decreases, which results in smaller trapped flux and leads to smaller lateral force.

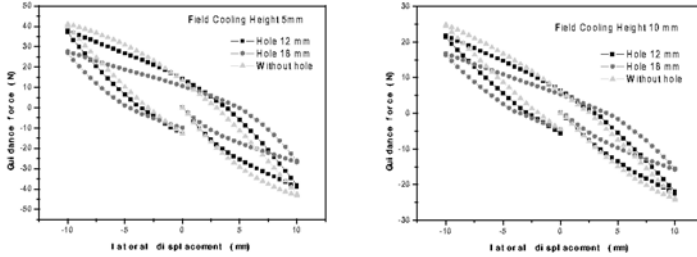


Fig. 25. Guidance force of vs. lateral displacement with different holes in field cooling height 5 mm (left) and 10 mm (right)

8.3 INFLUENCE OF YBCO BULK THICKNESS ON THE PROPERTIES

The melt-textured YBCO bulk sample with the diameter 30mm and thickness 13.7 mm is grinded by the method of reduced thickness 0.5 mm each time, and the levitation force is measured at the same time [58, 59]. The relationship between the thickness (from 13.7 mm to 2 mm) and the levitation force is presented in Fig. 26. It is shown that the levitation force does not change when the thickness decreases to 12 mm and will drop markedly after the thickness is 10 mm. It is well considered according to the trend of the curve that the levitation force may continue to increase if the thickness increases and similarly, the levitation force must become smaller when the thickness decreases. As a result, larger scale bulks are very useful to our Maglev transportation system.

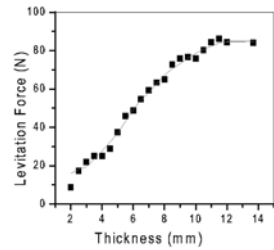


Fig. 26. Thickness vs. levitation force

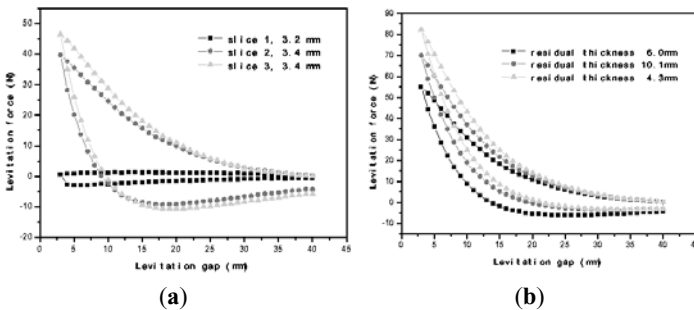


Fig. 27. Levitation force of slice thickness (a) and residual thickness (b) of YBCO sample

The levitation force of ground section YBCO is not measured in the grinding method of reduced thickness. Incising method of reduced thickness can measure the levitation force of incised section. The HTS bulk sample in this incising experiment is a MTG YBCO bulk with a diameter of 30 mm and high 18 mm. The sample is incised in turn 3.2 mm, 3.4 mm, and 3.4 mm from not seeded face. The residual thickness of sample is 14.3 mm, 10.1 mm, and 6 mm, respectively.

It can be seen from Fig. 27(b) that the influence of YBCO sample thickness on levitation force is larger when the levitation gap is smaller, but the levitation forces of different thickness YBCO samples are almost the same when levitation gap is bigger than 20 mm [46].

9. HTS MAGLEV TEST VEHICLE

9.1 LEVITATION FORCE OF HTS VEHICLE [8, 60-62]

The researchers in the Applied Superconductivity Laboratory, Southwest Jiaotong University (SWJTU), China, began synchronously to consider about the problem of HTS Maglev vehicle too in the early part of the 1990s. The SWJTU founded the research subject of HTS Maglev vehicle in 1994. In 1997, the research project of man-loading HTS maglev test vehicle is authorized by the National High Technology R & D Program (National 863 Program) in China. The first man-loading HTS Maglev vehicle in the world [8] was tested successfully on Dec.31, 2000. With five people standing on vehicle, the total weight is about 530kg, and the net levitation gap is more than 20mm (Fig. 29(b)).

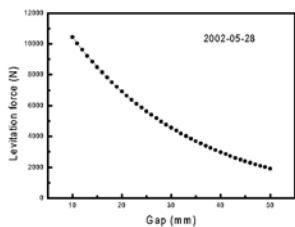


Fig. 28. (a) The total levitation force of 8 onboard HTS Maglev modules over the guideway

The guideway consists of two parallel permanent magnetic tracks, whose concentrating magnetic field on 20 mm height is about 0.5 T. The length of each NdFeB guideways is 15.5 m. The HTS Maglev provides inherent stability in both the vertical and the lateral directions, so there is no need to control in these two directions. The control system is only used as linear motors driving devices. The 8 onboard HTS Maglev equipments [51] are connected rigidly on the two sides of vehicle body, with 4 Maglev equipments on each side. The vehicle body (Fig. 29(b)) is 2268 mm long, 1038 mm wide and 120 mm high. Both the linear motor of the vehicle and permanent magnet guideways are under vehicle body.

Fig. 28 shows the total levitation force of 8 onboard HTS Maglev equipments over the guideway. The total levitation force of 8 on-board HTS Maglev equipments in the entire vehicle over the guideway is 10431 N at the levitation gap of 10 mm.

The total levitation force of entire Maglev vehicle is 7271 N at the levitation gap of 20 mm, and 8940 N at the levitation gap of 15 mm, respectively. The data are measured by the HTS Maglev measurement system, and they are the total levitation force of 8 onboard HTS

Maglev equipments in July 2001. In the measurement data, the levitation gap is the height between guideway upper surface and superconductors.

Net levitation gap is one between guideway upper surface and liquid nitrogen vessel bottom. The total levitation force of entire Maglev vehicle is 6351 N at the net levitation gap of 20 mm, and 7850 N at the net levitation gap of 15 mm in July 2001, respectively.

Fig. 29 (a) shows the photograph of filling liquid nitrogen. Fig. 29 (b) shows the net levitation gap of the HTS Maglev test vehicle body is more than 20mm when five people stand on vehicle, and the levitation height of the vehicle body is 33mm when the five people get off it. Fig. 29 (c) shows the photograph of HTS Maglev test vehicle with cabin. The external outline size of vehicle with shell is 3.5 m long, 1.2 m wide, and 0.8 m high. There are 4 seats in the HTS Maglev vehicle. The onboard Maglev equipments are used for man-loading HTS Maglev vehicle, and they are kept intact after they have been in operation over 3 years on vehicle body.

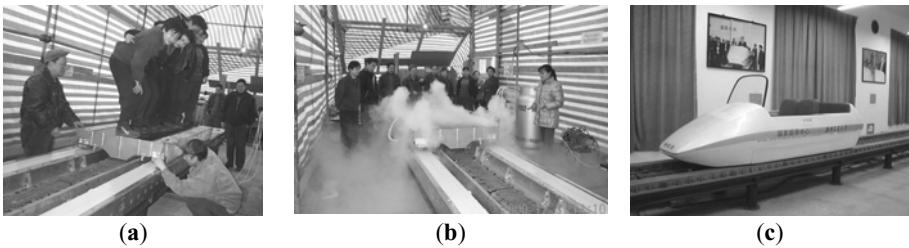


Fig. 29. (a) Photograph of the first pouring liquid nitrogen; (b) The net levitation gap of the HTS Maglev test vehicle body is more than 20mm when five people stand on vehicle; (c) Photograph of HTS Maglev test vehicle with outer casing.

9.2 GUIDANCE FORCE OF HTS MAGLEV VEHICLE [63]

The guidance force defines the lateral stability when Maglev vehicle is either still or moving. The lateral guidance force is dependent on the trapped flux in the bulk superconductors, and the stronger the trapped flux, the larger the guidance force. This is a distinctive character of the bulk HTS Maglev vehicle. This sort of Maglev vehicle with bulk HTS doesn't need any lateral stable control, which is superior to any other sort of Maglev vehicle. The guidance forces are enough large when large levitation forces are ensured.

The man-loading HTS maglev test vehicle is reported elsewhere [8]. The measuring equipment of guidance force of the entire HTS Maglev vehicle is manufactured (Fig. 30). It includes two sets of propulsion systems and two sets of force sensors. The force sensors are fixed on the vehicle. Each set of propulsion system can move in both horizontal and vertical directions so that it can measure guidance force of the entire vehicle at different levitation gaps. Two sets of propulsion systems are connected by a chain with a synchronization precision of 0.5mm. The moving range of the propulsion system in horizontal direction: 0~20cm, horizontal moving precision: 1mm; moving range in vertical direction: 0~10cm,

vertical moving precision: 1mm. A photograph of the measuring equipment of guidance force is showed in Fig 30.

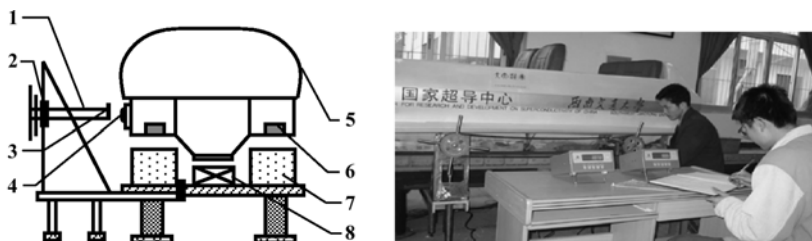


Fig. 30 Sketch (left) and Photograph (right) of measuring equipment of guidance force of vehicle: 1 Horizontal propulsion system; 2 Vertical propulsion system; 3 Screw of adjusting zero; 4 Force sensor; 5 vehicle body; 6 HTS; 7 Permanent magnetic railway; 8 Linear motor

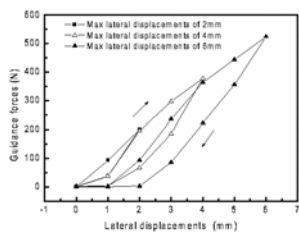


Fig. 31. Experimental results of guidance force of the entire vehicle under different maximum lateral distance

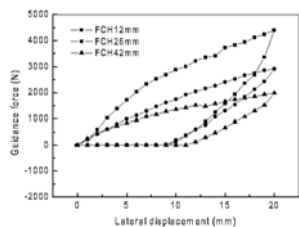


Fig. 32. Guidance force of the entire vehicle under different field cooling height (FCH)

The guidance forces of the entire vehicle are measured with the measuring equipment mentioned above. The experiment results of guidance force under maximum lateral distance 20mm are shown in Fig 32.

Fig 32 shows the lateral guidance forces have a large hysteresis effect. The guidance forces rise rapidly when the vehicle leaves its initial position, and the increase rate is smaller in the latter section of the curve in Fig. 32. The guidance forces drop rapidly when vehicle moves back to its initial positions from the maximum lateral displacement of 20 mm, and vanishes at about 10 mm. It indicates that the range of effective lateral displacement is smaller than 10 mm.

Those results and the following results are obtained with slow rate measurement. Therefore, the experiment results of guidance force of vehicle may have some limitations because trapped flux is changed at slow rate measurement.

Experimental results of guidance force of the entire vehicle under different maximum lateral distance are shown in Fig 31.

Fig. 31 shows the lateral guidance forces when the lateral displacement gradually increases from 0 mm to 2 mm, 4 mm, and 6 mm, respectively. It indicates that effective lateral guidance force can be achieved in the lateral

displacement of about 6 mm. The guidance forces are 337 N at lateral displacement of 4 mm and 524 N at 6 mm. Fig. 31 show the experiment results when levitation weight is 310 kg (no people loaded).

Fig. 32 shows the experiment results of guidance force of the entire vehicle under different field cooling heights (FCH). The data of the guidance forces are listed in Table 5. It can be seen from Table 1 and Fig 32 that the lateral guidance forces of the entire HTS Maglev vehicle are enough large. The guidance forces at displacement 20 mm are 4407 N, 2908 N, and 1980 N for field cooling height of 12 mm, 26 mm, and 42 mm, respectively.

When the lateral displacement is less than 6mm, the HTS Maglev vehicle is able to return to the initial position. But it can't go back to the initial position when the lateral displacement is greater than 6mm and less than 20mm. For example, there is zero guidance force at the displacement 9 mm when FCH is 26mm. Measured guidance pull force which makes the vehicle return to the initial rest position is 1214 N when FCH is 26 mm. This force is large enough.

Table 5. Guidance force under different field cooling height, Disp: Displacement, Forces unit: N, FCH: Field Cooling Height

| Disp mm | FCH (mm) | | | Disp mm | FCH (mm) | | |
|------------|----------|------|------|------------|----------|------|------|
| | 12 | 26 | 42 | | 12 | 26 | 42 |
| 1 | 215 | 207 | 250 | 16 | 3834 | 2517 | 1740 |
| 2 | 592 | 414 | 450 | 17 | 3941 | 2659 | 1785 |
| 3 | 1026 | 603 | 600 | 18 | 4117 | 2744 | 1845 |
| 4 | 1391 | 802 | 725 | 19 | 4246 | 2851 | 1930 |
| 5 | 1713 | 987 | 835 | 20 | 4407 | 2908 | 1980 |
| 6 | 2033 | 1122 | 945 | 19 | 3364 | 2422 | 1515 |
| 7 | 2330 | 1289 | 1085 | 18 | 2682 | 2120 | 1295 |
| 8 | 2521 | 1465 | 1165 | 17 | 2361 | 1834 | 1070 |
| 9 | 2685 | 1610 | 1275 | 16 | 1932 | 1533 | 885 |
| 10 | 2883 | 1734 | 1355 | 15 | 1580 | 1301 | 665 |
| 11 | 3003 | 1913 | 1420 | 14 | 1244 | 1073 | 470 |
| 12 | 3220 | 2038 | 1510 | 13 | 886 | 767 | 295 |
| 13 | 3350 | 2151 | 1475 | 12 | 590 | 606 | 120 |
| 14 | 3418 | 2263 | 1565 | 11 | 354 | 375 | 0 |
| 15 | 3726 | 2399 | 1660 | 10 | 110 | 190 | 0 |

9.3 LONG-TERM STABILITY OF HTS MAGLEV VEHICLE [62]

Fig. 33 and Table 6 show the total levitation forces of eight liquid nitrogen vessels over the NdFeB guideway in July 2001 are 8940 N at the levitation gap of 15 mm and 7271 N at the levitation gap of 20 mm, respectively. The total levitation force of eight liquid nitrogen vessels over the NdFeB guideway is 8000 N at the net levitation gap (deduct 3 mm bottom thickness of liquid nitrogen vessel) of 15 mm.

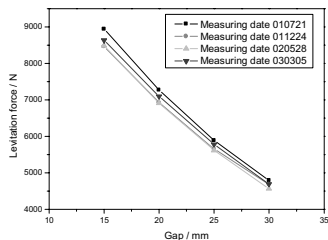


Fig. 33. The change of the total levitation force of entire HTS Maglev vehicle over the guideway

At first, the vehicle body is lifted by a hydraulic pressure until the gap between the bottom of liquid nitrogen vessels and the surface of the guideway is larger than 75 mm. Then HTS are cooled with liquid nitrogen. Fig. 29(c) is a photograph of HTS Maglev vehicle. From Fig. 29(c) we can see the two tracks and vehicle body.

Fig. 33 and Table 6 show the change of the total levitation force of 8 HTS Maglev equipments over the NdFeB guideway at different levitation gaps. The measurement results are measured by special experiment research equipment [8, 15] in July 2001, December 2001, May 2002, and March 2003, respectively.

Fig. 33 and Table 6 show the total levitation forces of the entire HTS Maglev vehicle are 8486 N at the levitation gap of 15 mm and 6908 N at the levitation gap of 20 mm, respectively in May 2002. The levitation force is 4561 N at the levitation gap of 30 mm, and this is a 46% decrease of levitation force compared with that at the levitation gap of 15 mm.

Table 6 Total levitation force of entire HTS Maglev vehicle

| gap (mm) | Levitation force (N) | | | |
|----------|----------------------|------------|------------|------------|
| | 07/21 2001 | 12/24 2001 | 05/28 2002 | 03/05 2003 |
| 15 | 8940 | 8457 | 8486 | 8633 |
| 20 | 7271 | 6927 | 6908 | 7094 |
| 25 | 5890 | 5656 | 5618 | 5782 |
| 30 | 4791 | 4685 | 4561 | 4693 |

The total levitation forces of the entire HTS Maglev vehicle are nearly the same from December 2001 to May 2002. The total levitation force is 7271 N at the levitation gap of 20 mm in July 2001, and the total levitation force is 6908 N at the levitation gap of 20 mm in May 2002. The levitation force has a 5.0 % decrease for a period of 10 months.

The change of the total levitation force of entire HTS Maglev vehicle over the guideway Measurement results of total levitation force in

March 2003 are slightly larger than one in December 2001, because the center line of HTS Maglev equipments and of NdFeB guideway are not laid to overlap accurately.

The comparison of total levitation forces of the entire HTS Maglev vehicle in July 2001 with one in May 2002 showed a levitation force decrease of a 5.1%, 5.0%, 4.6%, and 4.8% at the levitation gap of 15 mm, 20 mm, 25 mm, and 30 mm, respectively. All data are nearly the same, i.e., levitation force decrease is about 5.0% at different levitation gap.

It can be seen that the changes of levitation forces are small after about two year. Heretofore over 27000 passengers took the vehicle, and the total shuttle mileage is about 400 km. Experiment results indicate long-term stability of the HTS Maglev vehicle is better than experiment results mentioned above are obtained when HTS Maglev vehicle is at low speed operation. Behavior of HTS Maglev vehicle is very different at high speed. It is important to research the properties of high speed HTS Maglev vehicle. We shall investigate the dynamic properties of HTS maglev vehicle at high speed operation.

Trapped magnetic field of HTS Bulk has achieved 17.24 T at 29 K [22]. It implies that HTS Maglev vehicle has brilliant prospect and its real world application might appear sooner than we expect.

REFERENCES

- [1] J.R.Hull, *Supercond. Sci. Technol.* 13 (2000) R1
- [2] L.K.Kovalev, K.V.Ilyushin, V.T.Penkin, and K.L.Kavalev, *Electrical Technology* 2 (1994) 145
- [3] K.B.Ma, Y.V.Postrekhin, and W.K.Chu, *Rev. of Sci. Instruments* 74 (2003) 4989
- [4] H.Weih, H.Pahi, H.Hupe, A.Steingrver, and H.Way, *14th International Conference on Magnetically Levitated Systems and Liner Drives (Maglev'95)*, (1995), pp. 217-222
- [5] H.Weih, *Proceeding of Fifteenth International Conference on Magnet Technology*, (Ed. L. Z. Lin, G. L. Shen, L. G. Yan), Science Press, Beijing (1998), pp. 833-838
- [6] S. Y. Wang, J. S. Wang and J. S. Lian, *Proceeding of Fifteenth International Conference on Magnet Technology*, (Ed. L. Z. Lin, G. L. Shen, L. G. Yan), Science Press, Beijing (1998), pp. 767-769
- [7] Y. Zhang and S. G. Xu, *Proceeding of Fifteenth International Conference on Magnet Technology*, (Ed. L. Z. Lin, G. L. Shen, L. G. Yan), Science Press, Beijing (1998), pp. 763-766
- [8] Wang Jiasu, Wang Suyu, Zeng Youwen, Huang Haiyu, Luo Fang, Xu Zhipei, Tang Qixue, Lin Guobin, Zhang Cuifang, Ren Zhongyou, Zhao Guomin, Zhu Degui, Wang Shaohua, Jiang He, Zhu Min, Deng Changyan, Hu Pengfei, Li Chaoyong, Liu Fang, Lian Jisan, Wang Xiaorong, Wang Lianghui, Shen Xuming, Dong Xiaogang. The first man-loading high temperature superconducting maglev test vehicle in the world, *Physica C* 378-381 P1 (2002) 809
- [9] E.H.Brandt, *Science* 243 (1989) 349
- [10] F.C.Moon, *Superconducting Levitation*, New York: Wiley (1994)
- [11] J.R.Hull, and A. Cansiz, *J.of Appl. Phys.* 86 (1999) 6396
- [12] M.Murakami, *Inst. Phys. Conf. Ser.* 167(I) (2000) 7
- [13] K.B.Ma, Y.V.Postrekhin, and W.K.Chu, *Rev. of Sci. Instruments* 74 (2003) 4989
- [14] S.Jin, T.H. Tiefel, R.C, Sherwood, R.B. Van Dover, M.E. Davis, G.W.Kammlott, and R.A.Fastnacht, *Phys. Rev. B* 37 (1988) 7850
- [15] S.Jin, T.H.Tiefel, R.C, Sherwood, R.B. M.E. Davis, Van Dover, G.W.Kammlott, R.A.Fastnacht, and H.D.Kuth, *Appl. Phys. Lett.* 52 (1988) 2074
- [16] K.Salama, V.Selvamanicham, L.Gao, and K.Sun, *Appl. Phys. Lett.* 54 (1989) 2352 ; K.Salama and D.F.Lee, *Supercond. Sci. Technol.* 7 (1994) 177-193
- [17] M.Murakami, M.Mrita, K.Do, and K.Miyamoto, *Japan. J. Appl. Phys.* 28 (1989) 1189
- [18] M.Murakami, S.Gotoh, H.Fujimoto, K.Yamagushi, N.Koshizuka, and S.Tanaka, *Supercond. Sci. Technol.* 4 (1991) S49
- [19] D.F.Lee, C.S.Partsinevelos, R.G.Presswood Jr., and K.Salama, *J. Appl. Phys.*, 76 (1994) 603

- [20] G.Fuchs, P.Stoye, T.Staiger, G.Krabbes, P.Schätzle, W.Gawalek, P.Görnert, A.Gladun, IEEE Trans. Appl. Supercond. 7 (1997) 1949
- [21] A.W.Kaiser and H.J.B.R.Koch, Inst. Phys. Conf. Ser. 158 (1997) 837
- [22] D.A.Cardwell, W.Lo, H.D.E.Thorpe, and A.Roberts, J. Mater. Sci. Lett. 14 (1995) 1444
- [23] S.I.Yoo, N.Sakai, H.Takaichi, T.Higuchi, and M.Murakami, Appl. Phys. Lett. 65 (1994) 633
- [24] M.Murakami, S.I.Yoo, T.Higuchi, N.Skai, J.Weltz, N.Koshizuka, and S.Tanaka, Japan J. Appl. Phys. 33 (1994) L715
- [25] M.Muralidhar and M.Murakami, Supercond. Sci. Technol. 15 (2002) 683
- [26] M.R.Lees, D.Bourgault, P. De Rango, P.L.ejay, A.Sulpice, and R.Tournier, Physica C 191 (1992) 414
- [27] S.Nariki, N.Sakai, and M.Murakami, Supercond. Sci. Technol. 15 (2002) 648
- [28] S.Nariki, N.Sakai, and M.Murakami, *the 4th International PASREG workshop*, Jena, Germany, June 30-July 2, 2003
- [29] G.Krabbes, G.Fuchs, P.Verges, P.Diko, G.Stöver, and S.Gruss, Physica C 378~381 (2002) 636
- [30] P.Schätzle, G.Krabbes, S.Gruß, and G.Fuchs, IEEE Trans. Appl. Supercond. 9 (1999) 2022
- [31] M.Tomita and M.Murakami, IEEE Trans. Appl. Supercond., 13 (2003) 3095
- [32] M.Tomita and M.Murakami, Nature 421 (2003) 517
- [33] N.Sakai, K.Inoue, M.Murakami, and H.Hirata, *the 4th International PASREG workshop*, Jena, Germany, June 30-July 2, 2003
- [34] M.K.Wu, J.R.Ashburn, C.J.Torng, P.H.Hor, R.L.Meng, L.Gao, Z.J.Huang, and C.W.Chu, Phys. Rev. Lett. 58 (1987) 908
- [35] Z.X.Zhao, L.Q.Chen, C.G.Cui, Y.Z.Huang, J.X.Liu, G.H.Chen, S.L.Li, S.Q.Guo, and Y.Y.He, Kexue Tongbao 32 (1987) 412
- [36] F.Hellman, E.M.Gyorgy, D.W.Johnson, Jr.,H.M.O'Bryan, and R.C.Sherwood, J. Appl. Phys. 63 (1988) 447
- [37] P.N.Peters, R.C.Sisk, E.W.Urban, C.Y.Huang, and M.K.Wu, Appl. Phys. Lett. 52 (1988) 2066
- [38] Wang Jiasu, Wang Suyu, Ren Zhongyou, Lian Jisan, Lin Guobin, Zhang Cuifang, Huang Haiyu, Deng Changyan, and Zhu Degui, IEEE Trans. on Applied Superconductivity 9 (1999) 904
- [39] S.Yokoyama, K.Shimohata, T.Inaguchi, T.Kim, S.Nakamura, S.Miyashita, and F.Uchikawa, IEEE Trans on Applied Superconductivity 5 (1989) 610
- [40] S. L. Wipf and H. L. Laquer, IEEE Trans on Magnetics 25 (1989) 1877
- [41] Wang Jiasu and Wang Suyu, *Applications of superconducting technology*, Chengdu: The Press of Chengdu University of Science and Technology, (1995), pp.123-287 (in Chinese)
- [42] S. kalsi, R. Herbermann, C. Falkowski, M. Hennessy. A. Bourdillon. *13TH International Conference on Magnetically Levitated Systems and Liner Drives (Maglev'93)*, (1995) 153

- [43] A. Senba, H. Kitahara, H. Ohsaki, and E. Masada, *IEEE Trans on Magnetics* 32 (1996) 5049
- [44] H. Fujimoto, H. Kamijo, T. Higuchi, Y. Nakamura, K. Nagashima and M. Murakami and S. I. Yoo, *IEEE Trans. on Applied Superconductivity* 9 (1999) 301
- [45] X.R.Wang, Master's degree thesis, Southwest Jiaotong University, China, 2003
- [46] Z.Y.Ren, Doctor's degree thesis, Southwest Jiaotong University, China, 2004
- [47] X.Z.Wang, Technology Report, Southwest Jiaotong University, China, 2004
- [48] Wang Jiasu, Wang Suyu, Lin Guobin, Huang Haiyu, Zhang Cuifang, Zeng Youwen, Wang Shaohua , Den Changyan, Xu Zhipei, Tang Qixue, Ren Zhongyou, Jiang He, Zhu Min, *High Technology Letters*, 10 (2000) 55 (In Chinese)
- [49] Jiasu Wang, Suyu Wang, Zhongyou Ren, Min Zhu, He Jiang, and Qixue Tang, *IEEE Trans. on Applied Superconductivity* 11 (2001) 1801
- [50] Suyu Wang, Jiasu Wang, Zhongyou Ren, He Jiang, Min Zhu, and Qixue Tang, *IEEE Trans. on Applied Superconductivity* 11 (2001) 1808
- [51] S.Y. Wang, J.S. Wang, Z.Y. Ren, M. Zhu, H. Jiang, X.R. Wang, X.M. Shen, and H.H. Song, *Physica C*, 386 (2003) 531
- [52] P.Schätzle, G. Krabbes, G. Stover, G. Fuchs, and D. Schlafer, *Supercond. Sci.Technol.*, 12(1999) 69
- [53] Y.A. Jee, C.-J. Kim, T.H. Sung, and G.W. Hong, *Supercond. Sci. Technol.*, 13(2000) 195
- [54] H.H. Song a, O. De Haas, Z.Y. Ren, X.R. Wang, J. Zheng, X.Z. Wang, S.Y. Wang, J.S. Wang, Y. Zhao, *Physica C* (2004) (In press)
- [55] H.H. Song, J.S. Wang, S.Y. Wang, O. De Haas, et. al. *Supercond. Sci. Technol.*, (2004) (To be published)
- [56] Jiang He, Wang Jiasu, Wang Suyu, Ren Zhongyou, Zhu Min, Wang Xiaorong, Shen Xuming, *Physica C* 378-381 P1 (2002) 869
- [57] X.R. Wang, H.H. Song, Z.Y. Ren, M. Zhu, J.S. Wang, S.Y. Wang, and X.Z. Wang, *Physica C*, 386 (2003) 536
- [58] Zhongyou Ren, Jiasu Wang, Suyu Wang, He Jiang, Min Zhu, Xiaorong Wang, Honghai Song , *Physica C* 384/1-2 (2003) 159
- [59] Zhu Min, Ren Zhongyou, Wang Suyu, Wang Jiasu, Jiang He, Tang Qixue, *Proceedings of International Conference on Engineering and Technological Sciences 2000*, (Ed. Jian Song and Ruiyu Yin), Vol. 1, pp.578-581, Beijing, China, Oct. 11-13, 2000,
- [60] Suyu Wang, Jiasu Wang, Xiaorong Wang, Zhongyou Ren, Youwen Zeng, Changyan Deng, He Jiang, Min Zhu, Guobin Lin, Zhipei Xu, Degui Zhu, Honghai Song, *IEEE Trans. on Applied Superconductivity*, 13 (2003) 2134
- [61] J.S. Wang, S.Y. Wang, Z.Y. Ren, H. Jiang, M. Zhu, X.R. Wang, X.M. Shen, and H.H. Song, *Physica C* 386 (2003) 431
- [62] J.S. Wang, S.Y. Wang, Y.W. Zeng, C.Y. Deng, Z.Y. Ren, X.R. Wang, H.H. Song, X.Z. Wang, J. Zheng, Y. Zhao, *Superconductor Science and Technology*, 17 (2004) (In press)
- [63] Jiasu Wang, Suyu Wang, Zhongyou Ren, Xiaorong Wang, Min Zhu, He Jiang, Honghai Song, Xingzhi Wang, Jun Zheng, *IEEE Trans. on Applied Superconductivity*, 13 (2003) 2154

HIGH TC CUPRATES – THIN FILM PROCESSING, ATOMIC LAYER CONTROLLED DEPOSITION

Guus Rijnders and Dave H.A. Blank

Faculty Science & Technology, MESA+ Institute for Nanotechnology, University of Twente,
The Netherlands, P.O.Box 217, 7500 AE Enschede, NL

1. INTRODUCTION

The structural properties, i.e., defect structure, crystalline structure and surface morphology, of $\text{REBa}_2\text{Cu}_3\text{O}_{7-\delta}$ (RE123) thin films influence the electrical properties and determine the applicability in multilayer structures. For instance, structural defects, grain boundaries and anti-phase boundaries (APB's) play an important role in the flux pinning mechanism [1,2,3,4], whereas the surface morphology of RE123 thin films is important in multilayer structures which require smooth surfaces. Both, structural properties and surface morphology are a direct result of the thin film growth, influenced by deposition conditions and substrate properties. At the initial stage of the growth the stacking sequence of the individual atomic layers in RE123 at the interface with the substrate is influenced by the substrate surface properties, i.e., the terminating atomic layer and the crystalline structure. During subsequent deposition, the lattice mismatch between substrate and growing film becomes dominant.

Various deposition techniques, most frequently physical vapour deposition (PVD), are applied for the growth of RE123 thin films. Among them are reactive co-evaporation, molecular beam epitaxy (MBE), laser-MBE and pulsed laser deposition (PLD). Reflection high-energy electron reflection (RHEED) is most often used to study the growth of RE123 *in situ*. Independent of the deposition technique, oscillation of the RHEED intensity is observed caused by the two-dimensional (2D), unit cell layer by layer growth of RE123[5] when all constituents are provided simultaneously. It is found that the oscillation period corresponds precisely to the time necessary for deposition of one unit cell layer in the c-axis direction. In

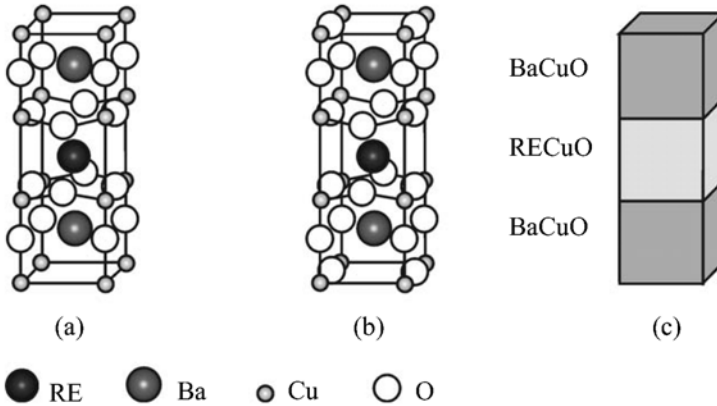


Fig. 1. Schematic representation of the unit cell of REBa₂Cu₃O₆ (a) and REBa₂Cu₃O₇ (b) consisting of three perovskite blocks (c). Note that the Cu-chain layer, i.e., the topmost layer in (b), is oxygen depleted in REBa₂Cu₃O₆.

general, it is believed that in epitaxial growth of ionic oxides the growth unit with a certain chemical composition has to satisfy charge neutrality. In the case of RE123 this minimum growth unit is the unit cell consisting of 6 atomic layers, see figure 1.

Growth in charge neutral unit cells has implications in the 2D epitaxial growth of RE123. First, a specific stacking sequence of the atomic layers should exist and, second, the growth unit should always terminate with the same atomic layer. Since the first atomic layer is determined by, both, substrate and film, the following questions arise:

- Is the charge neutral growth unit during the initial, hetero epitaxial growth, i.e., deposition of the first unit cell layer, also the unit cell of RE123 consisting of 6 atomic layers?
- Is the terminating atomic layer of the RE123 thin film depending on the terminating atomic layer of the substrate or is it thermodynamically determined by RE123 itself?
- Is the terminating atomic layer influenced by the deposition conditions?

In this chapter a state-of-the-art overview is given of the complex growth mechanisms of RE123 on SrTiO₃ substrates. Combined with experimental results, the questions mentioned above will be addressed and, if possible, answered. For this, *in situ* RHEED, *ex situ* atomic force microscopy (AFM), and high-resolution electron microscopy (HREM) have been applied to study the growth of RE123 on SrTiO₃ at typical PLD conditions.

2 NUCLEATION STAGE AND INITIAL GROWTH

Several groups have studied the initial growth of RE123 on SrTiO₃ in detail. The most important subjects of these studies were the interface between RE123 and SrTiO₃ and the terminating atomic layer of the first unit cell layer(s). Various techniques are applied like x-ray standing waves (XSW), HREM and surface sensitive ion scattering spectroscopy.

2.1 ATOMIC LAYER STACKING SEQUENCE AT THE INTERFACE BETWEEN RE123 AND SrTiO₃

Using HREM, Wen *et al.* [6] determined the stacking sequence of Y123, prepared by different techniques including evaporation, sputter deposition and PLD, on SrTiO₃. They found, independent of the growth technique, the stacking sequence to be: *bulk-SrO-TiO₂-BaO-CuO₂-Y-CuO₂-BaO-CuO-bulk*. To determine the proposed stacking sequence, the terminating atomic layer of the substrate was predetermined to be TiO₂. Without proper treatment, however, mixed terminated SrTiO₃ substrates is expected [7] enabling other stacking sequences. Still, from the high-resolution images it was found that the perovskite stacking sequence is preserved at the interface between Y123 and SrTiO₃. Using XSW the interface structure of c-axis oriented Gd123 and Eu123 films on SrTiO₃ substrates was determined by Nakanishi *et al.* [8]. The experimental results indicated that for Gd123 as well as Eu123 neither the CuO nor the CuO₂ layer can be the first atomic layer on TiO₂ terminated SrTiO₃ and, neither the BaO layer nor the oxygen depleted RE layer can be the first atomic layer on SrO terminated SrTiO₃. Therefore, a perovskite stacking sequence is proposed. Zegenhagen *et al.* [9] demonstrated, using soft XSW, that at the interface the stacking sequence of Y123 (prepared using evaporation) on SrTiO₃ to be perovskite-like.

2.2 TERMINATING ATOMIC LAYER OF RE123

The surface of a fully oxidised, orthorhombic RE123 ($\delta \sim 0$) crystal can have several atomic layers at the (001) surface: CuO₂, CuO, BaO and the oxygen deficient RE layer. These surfaces are differentiated by their composition and depend on the sequence of the underlying atomic layers.

Tanaka *et al.* [10] investigated the surface structure of Y123 deposited by ozone-assisted reactive co-evaporation on SrTiO₃ using *in situ* low-energy electron diffraction (LEED) and low-energy ion scattering spectroscopy (LEISS). From their LEED measurements it was concluded that the surface of the film is clean, crystalline and atomically flat. The films have an in-plane epitaxial relation of [100]YBCO//[100]STO and [110]YBCO//[110]STO. LEISS shows Cu and O atoms in the terminating layer of the surface. Through anneal experiments and measuring the O₂ desorption from the film it is concluded that the CuO chain layer is the terminating layer. Using depth profiling [11] the second layer is determined to be BaO. The stacking sequence of the top unit cell layer is found to be *BaO-CuO₂-Y-CuO₂-BaO-CuO*. Shimura *et al.* [12] confirmed this stacking sequence by cross sectional HREM.

Matijasevic *et al.* [13,14] studied the growth mechanism of co-evaporated (by reactive MBE) Sm123 thin films using atomic force microscopy (AFM) and high-resolution electron microscopy (HREM). AFM studies of less than one unit cell thick Sm123 films show preferential nucleation at the substrate steps. By changing the cation stoichiometry it was shown that irrespective of the composition, nucleation of molecular units with the same height occurred. Based on the height analysis of the Sm123 nucleation islands, a 1:3:3 cation stoichiometry for nucleation on TiO₂ terminated SrTiO₃ has been found, while x-ray photon spectroscopy (XPS) shows BaO termination. To match the proposed stacking sequence of the nucleated islands with AFM height measurements a reaction of the terminating BaO layer with air had to be taken into account. This reaction leads to a BaCO₃ top layer and, subsequently, to a height increase of 2 Å.

Behner *et al.* [15] studied Y123 prepared by DC-magnetron sputter deposition *in situ* using XPS and showed a uniform BaO termination. The proposed stacking sequence is: *bulk-BaO-CuO₂-Y-CuO₂-BaO-CuO-BaO*. From *ex situ* XPS it was concluded that carbonates are formed on the film surface within the first few hours due to reaction with CO₂ upon exposure in air.

Pennycook *et al.* [16] concluded from amorphization experiments, induced via oxygen ion implantation at room temperature, that Y123 films, deposited with PLD using molecular oxygen, terminate with the CuO chain plane. Z-contrast electron microscopy demonstrates growth to be unit cell by unit cell through sequential nucleation and coalescence of islands. It was concluded that the unit cell terminates with the CuO chain layer. They considered amorphization as the reverse of the growth process.

Badaye *et al.* [17,18] used atomic resolved AFM to determine the terminating layer of Nd123 [19] made by PLD. They found the CuO chain layer to be terminating layer, which was confirmed by total reflection angle X-ray spectroscopy (TRAXS) [20]. In order to perform these spectroscopic measurements the samples had to be cleaned *in situ* at 200 °C for 20 min with an atomic oxygen beam.

Rao *et al.* [21] determined the surface layer of Y123 with the glancing incident exit x-ray diffuse scattering (GIEXS) technique. It was shown that for a heat-treated PLD film the terminating layer is a mixture of BaO₂ and BaO. The topmost layer was shown to be the CuO plane after a heat treatment in a radical O* atmosphere.

Huibregtse *et al.* [22] concluded from AFM analysis of sub unit cell Y123 films the terminating atomic layer to be CuO on TiO₂ terminated SrTiO₃. The proposed stacking sequence for the first unit cell layer is *bulk-SrO-TiO₂-BaO-CuO₂-Y-CuO₂-BaO-CuO*. On SrO terminated SrTiO₃, on the other hand, BaO is expected to be the terminating layer. In this case the stacking sequence is *bulk-SrO -BaO-CuO₂-Y-CuO₂-BaO*. In the latter case the remaining CuO leads to the formation of CuO_x precipitates. Sub unit cell deposition, however, leads to nucleation of a cubic, (Y,Ba)CuO₃ phase [23] due to minimization of surface and interface energies. Determination of the terminating atomic layer of Y123 from AFM analysis is therefore not straightforward.

2.3 DISCUSSION

Both, the starting and terminating atomic layer of RE123 on SrTiO₃, deposited using various techniques, have been experimentally determined. In most cases a perovskite stacking sequence has been found at the interface. The starting atomic layer could only be determined assuming the terminating atomic layer of the SrTiO₃ substrate to be predetermined, i.e., either SrO or TiO₂. Without correct treatment of SrTiO₃ substrate surfaces, however, the termination is not well defined. Most of the experiments reported in literature concerning the first atomic layer of RE123 on SrTiO₃ have been performed on heat-treated substrates. Since a mixed termination is expected using heat treatments, the first atomic layer remains unclear. Nonetheless, a perovskite stacking sequence has been found in most cases. The first atomic layer of RE123 is, therefore, determined by the substrate terminating atomic layer.

The experimental results, reported in literature, concerning the terminating atomic layer of RE123 thin films are controversial and, therefore, the terminating layer remains ambiguous. Independent of the RE element, BaO [14,21,22,24,25,26] as well as the CuO [10,11,12,15,16,17,20,22] chain layer have been found as the terminating layer. Experimental

determination of the terminating layer, however, is not straightforward. The terminating layer will depend on the environment, i.e., temperature and oxygen pressure, during growth and post deposition treatments. *Ex situ* measurements usually involve surface treatments like annealing and/or ion bombardment to clean the surface prior to the measurement. Since modification of the surface is to be expected, determination of the terminating layer is difficult. For instance, a BaO termination was found after heat treatment, whereas treatment in radical O* environment a CuO was found to be the terminating layer [21].

Employing amorphization by oxygen ion implantation at room temperature [16], it was demonstrated that Y123 thin films, deposited by PLD in molecular oxygen, terminate with the CuO chain layer. Growth, however, takes place at elevated temperature and low oxygen pressure. Decomposition of the CuO chain plane is more likely at these temperatures compared to room temperature. Therefore, the terminating atomic layer during growth can be different from the terminating atomic layer of a treated RE123 film. The CuO chain layer has zero net charge and has been predicted [27] as the most stable surface. In the case of oxygen depleted, tetragonal RE123 ($\delta \sim 1$) the BaO surface possesses neutral charge and becomes the stable terminating atomic plane.

During growth, the oxygen content in the surface layer is in equilibrium with, both, the oxygen in the film and gas phase. To stabilize the RE123 film a certain amount of oxygen has to be incorporated in the surface. The deposition pressure during growth of RE123 depends on the deposition technique. While low pressures (typically below 10^{-2} Pa) are used in MBE and laser-MBE, higher pressures (between 1 and approximately 100 Pa) are used in PLD and sputter deposition. The oxidation power of molecular oxygen at these high pressures has been proven to be sufficient to stabilize the RE123 film [24,28] at deposition conditions. At low deposition pressures, however, more adequate oxidants like oxygen ions, atomic oxygen, ozone or nitrogen peroxide have to be used. Consequently, RE123 films can be stabilized at, both, low and high deposition pressure using suitable oxidation gasses. The termination layer, however, also depend on the oxidation power at deposition conditions. As mentioned earlier, at high temperatures, for example deposition temperatures, Cu-O bonds are easily broken resulting in desorption of oxygen. A high oxidant flux density is necessary to avoid the decomposition and, subsequently, to stabilize the CuO chain layer. Because of the different oxidation power used in the mentioned deposition techniques it is, therefore, expected that stabilization of the CuO chain layer depends on the deposition conditions. As a result the terminating layer of the as-deposited film will depend on the deposition conditions and is not always thermodynamically determined by the RE123 itself.

3 INFLUENCE OF SUBSTRATE PROPERTIES ON RE123 GROWTH

Not only the atomic stacking sequence at the substrate-film interface but also the growth mode is affected by the substrate properties. Especially the surface step density of SrTiO₃ substrates and lattice mismatch with RE123 have a large influence on the growth mode and will be discussed.

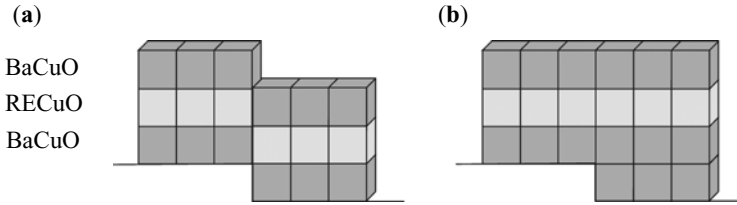


Fig. 2 . Schematic view of an anti-phase boundary (a) at a SrTiO₃ substrate step with displacement vector $[001/3]$ and the variable stacking sequence (b).

3.1 INFLUENCE OF VICINAL ANGLE SUBSTRATES ON THE GROWTH MODE

SrTiO₃ substrates used for deposition of RE123 typically have a miscut angle between 0.05° and 0.5°, resulting in a step-terrace surface morphology. Assuming 3.905 Å as the average step height, i.e., the lattice parameter of SrTiO₃, an average terrace length between ~500 and ~50 nm is to be expected. The step edges of the substrate act as a preferential adsorption site for atoms diffusing on the surface of the substrate. The nucleation and growth are, therefore, expected to depend on the relative distance of the terrace length l_T and the surface diffusion length l_D . If $l_D > l_T$, nucleation on the terrace is prevented resulting in step flow like growth [13,29,30,31,32]. On the other hand, if $l_D < l_T$, nucleation on the terrace occurs resulting in 2D growth. Nevertheless, preferential nucleation will also take place at the step edges [33,13].

The diffusion length of Y123 (at 0.2 mbar oxygen pressure and 760 C) in PLD is determined by STM studies [34] on vicinal substrates. The cross over from step flow like growth to 2D nucleation and growth is observed on substrates with 1.2° miscut. From this, a surface diffusion length $l_D \sim 20$ nm was determined.

3.2 INFLUENCE OF VICINAL ANGLE ON STRUCTURAL DEFECTS

At the initial growth, nucleation and growth towards steps in the substrate lead to the formation of anti-phase boundaries [13,29,30,35] (APB's). These APB's are perpendicular to the interface and can be described by a displacement vector $R = [00 \frac{1}{3}]$, see figure 2 (a).

Mechanisms preventing APB's to be formed at the substrate steps or annihilating APB's have been proposed in literature. A variable stacking mode [4] at the substrate steps during nucleation of Y123 creates the possibility of partial overgrowth at these steps, see figure 2 (b). Here, on the lower terrace, an additional BaCuO_x layer (~4Å) prevents the formation of the APB. This additional BaCuO_x layer can be seen as non-unit cell growth and changes the stacking sequence at the initial growth. As a result, the terrace length of the film is larger than that of the substrate. Due to the displacement vector $R = [00 \frac{1}{3}]$, however, not all APB's at the substrate steps are prevented by the proposed variable stacking sequence. Another stacking sequence is necessary to obtain $[00 \frac{2}{3}]$ displacement.

Non unit cell growth, like the variable stacking sequence, is not only observed at the initial growth. Also, annihilation [35] of APB's by non unit cell growth is observed at later stages of the growth. APB's in the film that originate from steps in the substrate can be eliminated enabling an energetically more favourable growth.

3.2 INFLUENCE OF STRAIN ON THE GROWTH

Lattice mismatch between film and substrate gives rise to epitaxial strain, which is relieved by the introduction of misfit dislocations above the critical thickness h_c . Several strain relieving mechanisms during hetero epitaxial growth of RE123 on SrTiO₃ (lattice mismatch ~1.6%) have been proposed [36,37,38,39,40,41]. Although the mechanisms for dislocation nucleation differ in nature, pseudomorphic growth has been found for layer thickness smaller than the critical thickness h_c . Values of h_c between 5 and 20 nm, i.e., between ~4 and ~16 unit cell layers [42,43,44,45,46,47], have been found for RE123 deposited on SrTiO₃ by PLD using molecular oxygen. Huijbrechtse *et al.* [22] found that the critical thickness depends strongly on the SrTiO₃ substrate termination. A value for h_c of 7.3 nm on SrO terminated substrates and 19 nm for TiO₂ terminated substrates was found. From this they concluded that the larger substrate-film interface energy for the TiO₂ termination enabled stabilization of a thicker pseudomorphic layer.

Not only the substrate termination but also the growth conditions determine the critical thickness h_c . The film surface morphology, which is a direct product of the growth process, has a large influence on the nucleation of dislocations. Stress relaxation via dislocation nucleation at the critical thickness depends, therefore, on the growth conditions. For instance, nucleation of dislocations in a structural perfect film with a smooth surface is extremely difficult. As a result, a large critical thickness h_c is expected. The large difference in the experimentally determined h_c values is, therefore, probably a result of the growth conditions. Note that control of the surface morphology during growth can be used to increase the critical thickness for pseudomorphic growth.

4 EXPERIMENTS: REBA₂CU₃O₇₋₈ ON SRTIO₃

The questions, presented in the introduction of this chapter, have been discussed in many papers in the last ten years. Most discussions, however, are based on RE123 films deposited on SrTiO₃ substrates with unknown termination. As a result the first atomic layer and stacking sequence of the individual atomic layers of the first unit cell layer of RE123 remains ambiguous.

In this study accurate control of the terminating layer of the SrTiO₃ substrate as well as *in situ* diagnostics by high pressure RHEED have been used. Chemical treatment followed by heat treatment has proven to be a suitable method to obtain single TiO₂ terminated SrTiO₃ with atomically smooth terraces. The use of these substrates enables the determination of the stacking sequence unambiguously with, for instance, HREM.

4.1 EXPERIMENTAL SETTINGS

The deposition conditions used in PLD of RE123 influences the growth significantly. This holds especially for the laser energy density at the target [48,49,50], the growth temperature and the oxygen deposition pressure [51,52] and these are, therefore, important parameters. Although a wide range of the parameter values have been investigated, only a small range have been found for optimised growth. As a result the parameter “space” converged to a typical set of values. The growth conditions used in this work are comparable to this set.

During growth of RE123, the substrate was heated to a temperature of 780°C and an oxygen background pressure of 18 Pa was applied. A sintered ceramic target was used which contained cation atoms in nominal ratio RE:Ba:Cu = 1:2:3. The energy density at the target [53,54,55] was set to 1.3 J/cm². Stoichiometric transfer from target to substrate is typically found above 1.3 J/cm². Lower densities leads to preferential ablation (between 1.0 and 1.3 J/cm²) or phase separation in the target (below 1.0 J/cm²). Phase separation at these low energy densities occurs due to the incongruent melting of RE123. Due to repetitive irradiation below the threshold of 1.3 J/cm², both, composition and morphology of the target surface is altered. As a consequence, the film characteristics during deposition change. The distance between substrate and target was set to 58 mm. At this position the substrate is placed just at the end of the visible plasma. Using these settings, films with transition temperatures of typically 90 K are produced. AFM measurements show surface morphologies resulting from a 2D growth mechanism. No growth spirals are observed at these growth conditions [56,57,58]. The thermalization of ejected particles from the target is heavily influenced by the deposition pressure and determines the impingement energy of the particles arriving at the substrate. Generally, 2D nucleation and growth is observed at typical PLD conditions for RE123 growth, i.e., pO₂ ~10-30 Pa and substrate placed at the end of the visible laser plasma. Higher deposition pressure decreases the impingement energy and, therefore, the diffusion length of the deposit. A transition from the 2D nucleation and growth mode to the spiral growth mode is observed when the diffusion length between the deposition pulses becomes sufficiently small. In the remainder of this chapter the mentioned growth conditions are referred to as *standard* growth conditions.

The RE123 films are deposited on TiO₂ terminated (001) SrTiO₃ substrates using the high pressure RHEED PLD equipment [59]. The typical miscut angle of the substrates is between ~0.05 and ~0.2°, yielding an average terrace length of ~400 to ~100 nm, respectively. All RHEED measurements are performed with 20 KV acceleration voltage. The angle of incidence was set to ~1°. The azimuthal angle was set to ~0° with respect to the [010] or [100] orientation of the SrTiO₃ substrate.

4.2. INITIAL GROWTH OF RE123 ON TIO₂ TERMINATED SRTIO₃

The RHEED patterns recorded after the deposition of 1 and 4 unit cell layers Y123 on TiO₂ terminated SrTiO₃ are depicted in figure 3 (a) and (b), respectively. Already at the initial growth, i.e., the deposition of the first few unit cells, the sharp 2D spots, originating from the SrTiO₃ substrate, are blurred into streaks. These streaks originate from the unit cell of Y123. The corresponding specular RHEED intensity shows a sharp decrease during deposition of the first unit cell without a large recovery, see figure 3 (c). Intensity oscillations are damped after approximately 4 unit cells. The observed streaks in the RHEED pattern and loss of RHEED

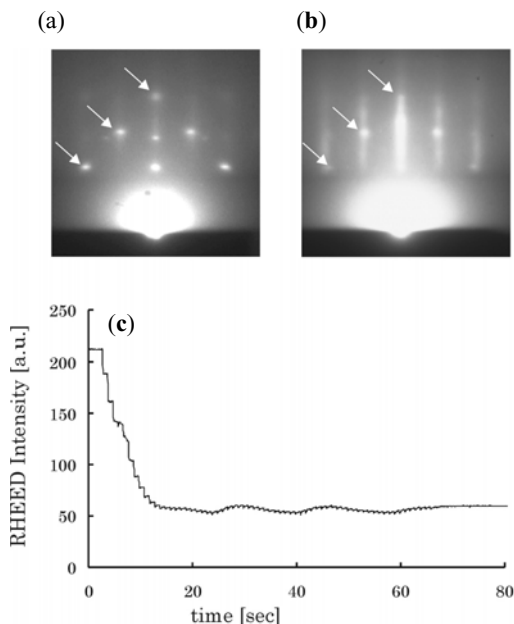


Fig. 3. RHEED patterns recorded after deposition of 1 (a) and 4 (b) unit cell layers of Y123 on TiO_2 terminated SrTiO_3 and the specular RHEED intensity recorded during initial growth (c).

intensity are indications of a roughened surface, i.e., the step density at the surface is increased. Bulk lattice parameters of substrate and film influence the specular RHEED intensity because of the small penetration depth of the electron beam and multiple scattering effects. The angle of incidence used in the experiments is set to $\sim 1^\circ$. At this angle, the specular RHEED intensity is maximal on SrTiO_3 . A small increase ($\sim 10\%$) of the specular RHEED is always observed by a small change of the angle of incidence of the electron beam after deposition.

This increase can be seen in the AFM micrographs depicted in figure 4 (a) and (b), showing the surface morphology of 4 and 20 unit cell thick Y123 layers, respectively. The insets show the cross section height analysis. Clearly the growth proceeds by 2D nucleation and subsequent spreading into larger 2D islands. Besides steps with heights corresponding to the c-axis unit cell parameter also smaller steps, corresponding to sub unit cell heights, are visible.

Note that the average island size is small compared to the terrace width of the vicinal substrate. The vicinal substrate steps are, therefore, not responsible for most of the sub unit cell steps at the surface of the Y123 film. The morphology of the 20 unit cell thick film is a result of 2D nucleation and growth. Here, nucleation and incorporation of adatoms at step edges is proceeding on an increasing number of unit cell levels. For example, in figure 4 (b) up to 4 unit cell levels can be seen.

In figure 3 (a) and (b), besides the observed streaks, clear 3D spots are visible as indicated by the arrows. From the intensity and sharpness of the spots one can conclude that on top of the Y123 film many small crystallites are formed. From the horizontal and vertical distance between the spots a lattice parameter of $\sim 4.3 \text{ \AA}$ can be determined. From the applied constituents, i.e., Dy, Ba, Cu and O, only cubic cuprite, Cu_2O , can be identified to be responsible for these 3D spots. The lattice parameter of Cu_2O is 4.27 \AA , which fits with the observed lattice parameter. The position of the spots revealed that the Cu_2O precipitates are aligned with the $[010]_{\text{Cu}_2\text{O}}//[010]_{\text{SrTiO}_3}$ and $[001]_{\text{Cu}_2\text{O}}//[001]_{\text{SrTiO}_3}$.

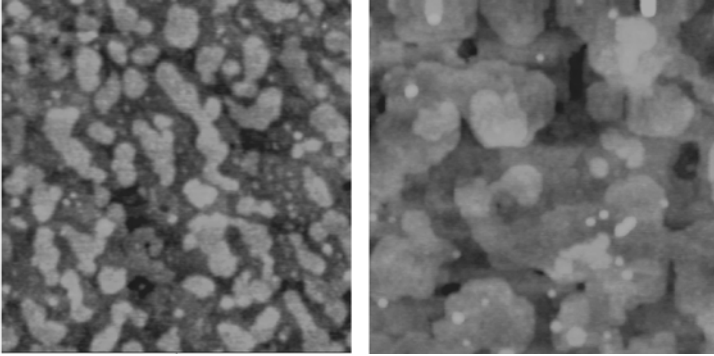


Fig. 4. AFM micrographs of a 4 (a) and 20 (b) unit cell thick Y123 on TiO_2 terminated SrTiO_3 .

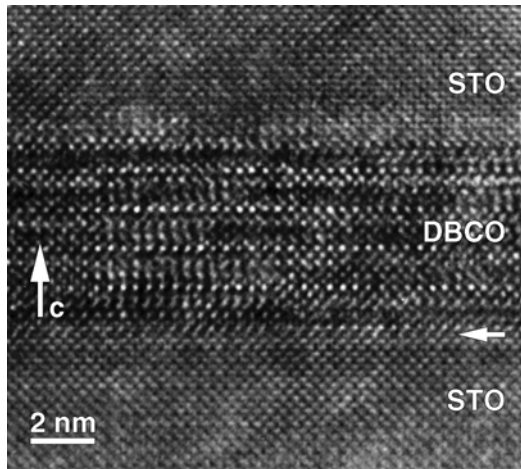


Fig. 5. Overview transmission electron micrograph of 4 unit cells Dy123 on TiO_2 terminated SrTiO_3 . The horizontal arrow indicates the interface. SrTiO_3 was deposited on top of the Dy123 layer to serve as a protection layer during HREM sample preparation.

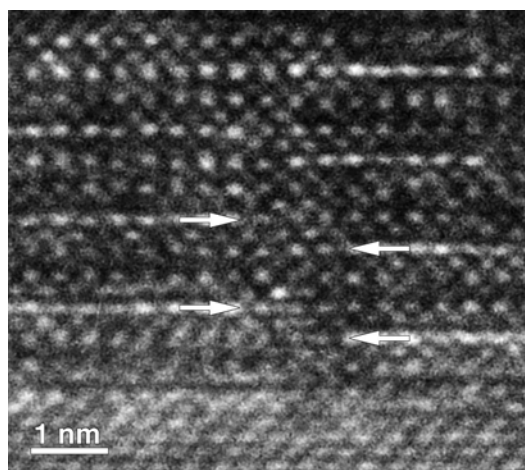


Fig. 6. HREM image of an anti-phase boundary in Dy123 film on TiO_2 terminated SrTiO_3 . The arrows indicate the CuO chain layers.

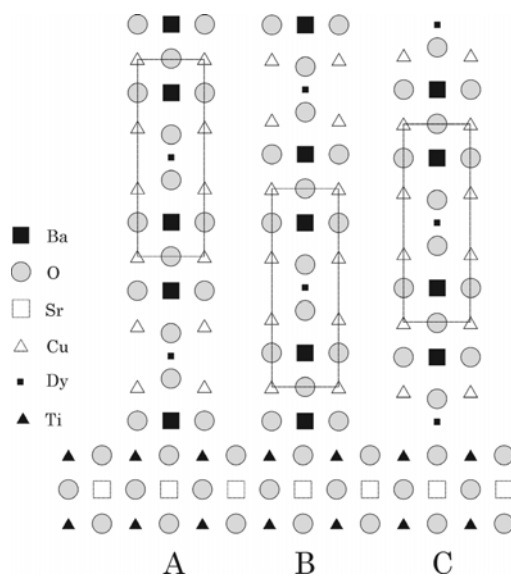


Fig. 7. Schematic of the three possible perovskite atomic layer stacking sequences of Dy123 on TiO_2 terminated SrTiO_3 .

Assuming a perovskite stacking sequence, stoichiometric deposition of Y123 on TiO₂ (B-site) terminated SrTiO₃ should lead to B-site terminated Y123, e.g., either a CuO₂ plane or the CuO chain layer. Furthermore, a symmetric unit cell with stacking sequence *bulk-BaO-CuO₂-Y-CuO₂-BaO-CuO_x-bulk* leads to the CuO chain layer as the terminating atomic layer. As mentioned earlier, it is expected that the small oxidation power at standard PLD conditions gives rise to an unstable CuO_x chain layer. As a consequence, BaO becomes the terminating atomic layer of Y123 and Cu₂O precipitates are formed. To comprehend the RHEED and AFM measurements of the first few unit cell layers on TiO₂ terminated SrTiO₃, high-resolution electron microscopy (HREM) was carried out [60]. HREM is performed along the perovskite cube directions; i.e. along [100] or [010] of the RE123 film. Imaging both the film and the substrate under ideal conditions is not straightforward; the lattice mismatch between film and substrate (about 1.6 %) causes local bending of the ultra-thin film. Figure 5 shows an overview HREM image of 4 unit cells Dy123. No interface dislocations or surface steps in the substrate have been noticed in this overview. The unit cells are clearly visible and the epitaxy is perfect all over the film with [001]Dy123//[001]SrTiO₃. The interface between film and substrate is atomically flat and no amorphous or secondary phases were observed.

The most prominent defects that occur are APB's. They start at the substrate-film interface and persist over the total film thickness. The average distance between the APB's is ~20 nm. An enlargement of an APB is shown in figure 6. The atomic layer sequence on both sides of the APB is determined using intensity line scans.

A perovskite stacking sequence is found at the substrate-film interface, allowing three possible atomic layer sequences at the interface of Dy123 on TiO₂ terminated SrTiO₃. These are visualized in figure 7. Because the size of a Ba-block (4.14Å) is larger than the size of a Dy-block (3.39Å), the position of the Dy-layer on both sides of the APB can be located. Figure 8 shows a detailed HREM image of the interface for a very small sample thickness and a defocus around -25nm. Image simulations indicate that the cations are imaged as dark dots and that oxygen columns are imaged as bright dots. Two arrowheads in figure 8 indicate the substrate-film interface; an APB is present in the middle of the figure, indicated by the vertical arrow.

Intensity scanning along the vertical [001] direction allows determining the first layer of the Dy123 film, see insets in figure 8. The first atomic layer of the Dy123 film was found to be at the same level on both sides of the APB; excluding a surface step as the reason for the APB formation

A clear shift of the Dy layer is observed over $R=[00\frac{1}{3}]$, leading to a structural misfit and, unavoidably, two different interface configurations. The structural misfit and the change in interatomic spacing at the APB also cause a relaxation and a slight bending of the atomic (001) planes close to the APB. This is clearly visible in the detailed HREM micrograph in figure 6. The interface stacking sequence is different on both sides of the APB. The interface stacking on the left side is determined to be: *bulk substrate-SrO-TiO₂-BaO-CuO-BaO-CuO₂-Dy-CuO₂-BaO-bulk film*. For the stacking of the layers at the interface on the right side the following sequence is found: *bulk substrate-SrO-TiO₂-BaO-CuO₂-Dy-CuO₂-BaO-CuO-BaO-bulk film*. These two interface configurations were observed throughout the complete film. Image simulations for both interface models were performed and the contrast could be matched with the experimental images. These simulated images are shown in figure 8 as insets.

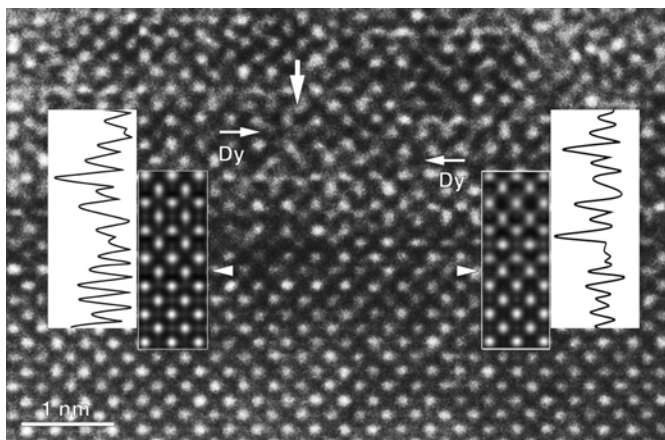


Fig. 8. Defocused HREM image. For, both, contrast and position, a focus value of 24 nm and a thickness of 2.4 nm was used for the left part of the image while a thickness of 3.2 nm was used for the right part.

The third possible interface stacking: *bulk substrate-SrO-TiO₂-Dy-CuO₂-BaO-CuO-BaO-CuO₂-Dy-bulk film* was never observed. Apparently, an interface with BaO as a first layer of the film is more stable than one with Dy as first layer.

The instability of an interface with Dy as the first atomic layer can be understood by taking into account the co-ordination environment of the Ti⁴⁺ cations. The *-SrO-TiO₂-Dy-CuO₂-* stacking sequence would imply an incomplete square-pyramid polyhedron for the Ti cation whereas it is favourably disposed towards an octahedral co-ordination. The absence of oxygen atoms in the Dy layer also results in an increase of the lattice energy associated with the interface due to a repulsion between the highly charged Ti⁴⁺ and Dy³⁺ cations. As a semiquantitative measure of the lattice energy and hence the stability of different interfaces one can use the Madelung's constant α . The Madelung energy is the electrostatic contribution to the binding energy of ionic crystals. It should be noted that an absolute value of the electrostatic energy is meaningless for RE123 compounds because of the strong covalent bonding in the (CuO₂) planes. Nevertheless, it is possible to compare α values for different types of interface configurations since the interaction between Ti⁴⁺, Dy³⁺, Ba²⁺ and oxygen can be considered as mostly ionic. The Madelung constant was computed using the Ewald's method of convergent series with an algorithm described by Popov *et al.* [61]. The charges associated with statistically occupied positions were chosen in accordance with the site occupancies. The unit cell constructed for these calculations consists of one unit cell of Dy123 and one unit cell of SrTiO₃. With this model the madelung constant have been computed for the three possible stacking sequences, depicted in figure 7, which contain equal amount of atomic layers of the same type and differ only by layer sequences. The α value is drastically lower for the interface C ($\alpha = 52.05$) compared to interfaces A ($\alpha = 64.18$) and B ($\alpha = 63.85$). This rough estimate suggests that the C interface is unstable in comparison with the interfaces A and B. Furthermore, similar lattice energies have been found for the interfaces A and B. As a consequence, formation probability of both interfaces is (almost) equal.

4.3 DISCUSSION

From the above presented data we can conclude that the initial growth of RE123 on TiO₂ terminated SrTiO₃ is dominated by two effects, i.e., the unstable terminating CuO chain layer at deposition conditions and the two possible stacking sequences at the substrate-film interface. The first effect will lead to BaO termination and Cu₂O precipitates, while the latter gives rise to the formation of APB's. Both hamper the unit cell layer by layer growth. The formation of Cu-rich precipitates on the surface of RE123 has been studied using PLD [62,63], MBE [64] and off-axis sputter deposition [65]. Especially the formation and growth kinetics were subject to the studies. Using light scattering technique [62] together with *ex situ* AFM it was demonstrated that at the initial stage of Y123 growth on TiO₂ terminated SrTiO₃ formation of CuO precipitates occur. These act as a nucleation site for BaCuO₂ and CuO by subsequent gettering of Ba and Cu. It was shown that deposition of CuO_x⁶³ on the surface of Dy123 using strong oxidizing conditions leads to the formation of Cu₂O precipitates, which act as an effective sink for the rest of the deposited CuO_x.

In general it is believed that, independent of the deposition technique, Cu-rich composition during deposition of RE123 will lead to the nucleation of CuO_x precipitates. At the initial growth stage, i.e., the deposition of the first unit cell layer, of Y123 on TiO₂ terminated SrTiO₃ the composition can be regarded as Cu-rich because of the BaO termination. In other words, the surplus of CuO_x, which is not incorporated in the first unit cell layer, leads to Cu enrichment. Due to the high reactivity [63] between the nucleated Cu₂O and BaO during subsequent deposition, BaCu_xO_y phases are formed. These stable phases hamper the reincorporation in the growing film. Consequently, the film will be Ba and Cu depleted.

From HREM measurements of Dy123 growth on TiO₂ terminated SrTiO₃, the following conclusions can be made:

- (1) The substrate-film interface is perovskite like. The first atomic layer on TiO₂ terminated SrTiO₃ is BaO.
- (2) The stacking sequence at the interface is either *SrO-TiO₂-BaO-CuO-BaO-CuO₂-Dy-CuO₂-BaO-bulk* or *SrO-TiO₂-BaO-CuO₂-Dy-CuO₂-BaO-bulk* resulting in formation of $[00\frac{1}{3}]$ APB's during deposition of first unit cell layer.
- (3) The diffusion length of the RE123 deposit during initial growth is ~20 nm, determined from the average distance between the APB's.

Various authors reported the presence of APB's in thin RE123 films, grown on SrTiO₃. However, in these cases the presence of the APB's was attributed to unit cell steps at the substrate. For instance, Dam *et al.* [35] concluded from cross section TEM analysis that the APB density is closely related to the substrate step density. They observed $[00\frac{1}{3}]$ APB's with average spacing ~10 to 20 nm on SrTiO₃ substrates with a miscut angle of 0.5° (9 average terrace length of ~50 nm).

In our case, however, the density of the APB's, is large compared to the density of substrate unit cell steps, determined from the miscut angle of the substrate surface. The density of substrate steps, observed in cross-section HREM, depends on the orientation of the step ledges with respect to the crystallographic orientation of the sample during observation.

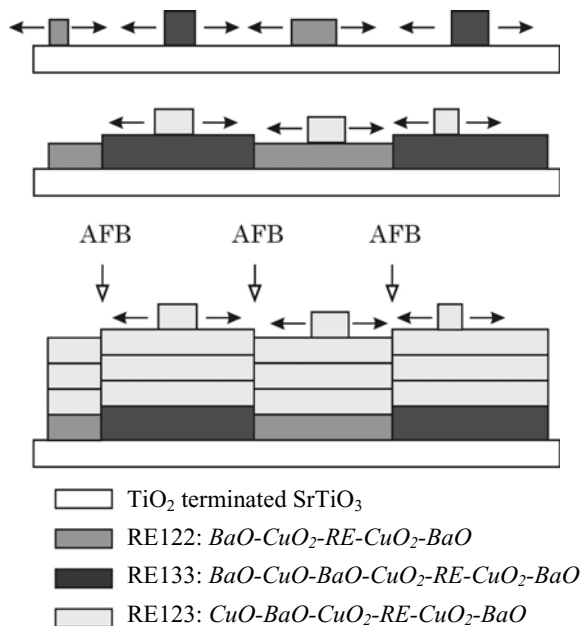


Fig. 9. Schematic representation of the initial RE123 growth on TiO_2 terminated SrTiO_3 . Coalescence of islands with different stacking sequence causes formation of anti-phase boundaries (APB's).

The maximum density is observed if the cross-section HREM sample is cut perpendicular the step ledges. The average terrace width, determined from the miscut angle ($<0.2^\circ$), is larger than 120 nm. From this one can conclude that APB's are formed on the atomically smooth terraces and not only at the substrate steps. Here, APB's are formed by the coalescence of neighbouring islands with a different stacking sequence. Consequently, the APB density is found to be larger than the substrate step density.

An APB will be formed at the substrate step if the stacking sequence on both terraces adjacent to the substrate step is identical. On the other hand, APB formation at the substrate step can be prevented by different stacking sequences on adjacent terraces. A large influence of the substrate steps on the growth of RE123 can be expected if the APB density becomes comparable to the substrate step density. This has been observed on high-miscut vicinal substrates by Haage *et al.* [34]. They attributed the presence of the variable stacking sequence to the substrate steps and proposed a model where partial overgrowth at the substrate steps occurs. This overgrowth leads to step flow like growth if the average terrace length of the substrates becomes comparable to or smaller than the surface diffusion length. They found that a miscut angle larger than 1° (The calculated average terrace length at 1° is 22 nm.) has to be used at typical PLD conditions, since a surface diffusion length of ~ 20 nm is expected [34].

The initial growth of Dy123 on TiO_2 terminated SrTiO_3 can be described qualitatively by the following sequence (see schematic view in figure 9):

- (1) 2D islands nucleate on the substrate surface until saturation in the density is reached. This density depends on the diffusion length of the deposit.
- (2) During subsequent deposition coalescence of the spreading islands occurs. Coalescence of islands with different stacking sequence at the substrate-film interface leads to the formation of $[00\frac{1}{3}]$ APB's. The surface step density is increased because of the height difference ($\sim 4\text{\AA}$) between the islands. Consequently, the RHEED intensity is decreased.
- (3) After coalescence of islands in the first unit cell layer, 2D unit cell by unit cell growth occurs indicated by the RHEED oscillations. The period of the observed oscillations equals the time necessary for deposition of one unit cell layer.

Thus, APB's are not only created at substrate step edges but also on the atomically smooth terraces of the substrate. As shown, precipitation of Cu_2O and, consequently, BaO (A-site) termination occur during growth of the first RE123 unit cell layer on TiO_2 (B-site) terminated SrTiO_3 . To avoid precipitation, substrates with SrO (A-site) termination can be an alternative. Here, stoichiometric deposition of RE123 leads to A-site termination and the supplied CuO

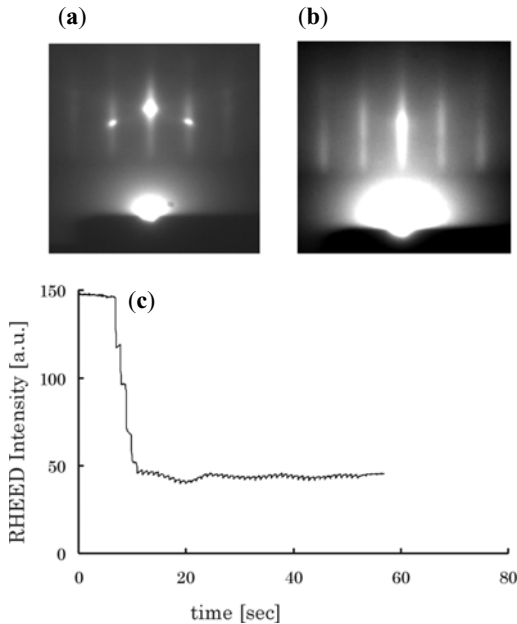


Fig. 10. RHEED patterns recorded after deposition of 1 ML SrO (a) and, subsequently, 4 unit cell layers of Y123 (b) on TiO_2 terminated SrTiO_3 and the specular RHEED intensity recorded during Y123 growth (c).

will be incorporated in the thin film. Hence, precipitation of Cu_2O is prevented. So far, however, no chemical treatments have been reported that produces single SrO terminated SrTiO_3 while heat treatment of SrTiO_3 usually results in a mixed termination. To obtain SrO termination we deposited a monolayer of SrO on TiO_2 terminated SrTiO_3 .

The RHEED patterns recorded after growth of SrO and, subsequently, 4 unit cell layers of Y123 are depicted in figure 10 (a) and (b), respectively. Now, only streaks, originating from the Y123 layer, can be seen. No indication of Cu_2O formation has been found, i.e., no 3D transmission spots have been observed. During the deposition of Y123 the supplied CuO_x is incorporated in the unit cell layer and A-site termination is preserved. Still a large drop in the RHEED intensity is observed without large recovery indicative for an increased step density, see figure 10 (c). In fact, the RHEED intensity resembles the RHEED intensity recorded during growth on TiO_2 terminated SrTiO_3 . So, no difference in the growth mode is expected. Here, also the occurrence of two stacking sequences is likely, i.e., *bulk substrate-SrO-TiO₂-SrO-CuO-BaO-CuO₂-Dy-CuO₂-BaO-bulk film* and *bulk substrate-SrO-TiO₂-SrO-CuO₂-Dy-CuO₂-BaO-CuO-BaO-bulk film*. Equal nucleation probability at the initial growth leads to an increase in the step density and formation of APB's. From, both, RHEED and AFM measurements we conclude that the growth mode on SrO terminated SrTiO_3 resembles the growth mode on TiO terminated SrTiO_3 .

4.4 MANIPULATING THE INITIAL GROWTH OF $\text{REBa}_2\text{Cu}_3\text{O}_{7-8}$

Stoichiometric deposition is a prerequisite at all stages during the film growth, to avoid precipitation of Cu_2O during the deposition of the first unit cell layer on TiO_2 terminated SrTiO_3 . The cation ratio RE:Ba:Cu of the first unit cell should be 1:2:2 or 1:3:3, see figure 9,

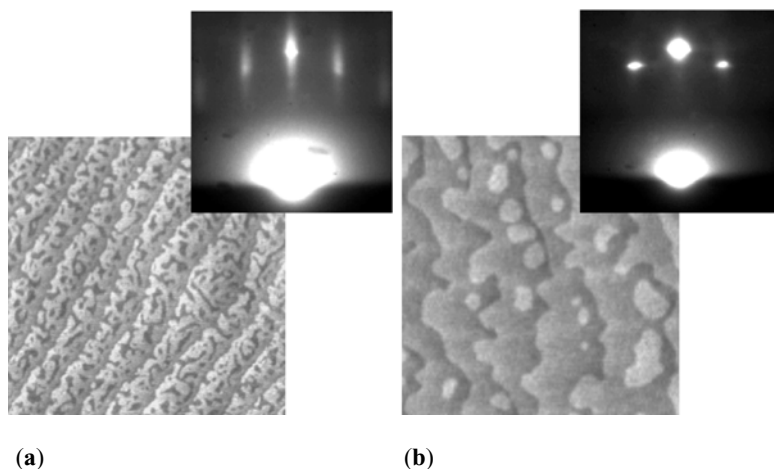


Fig. 11. AFM micrographs ($1 \mu\text{m}^2$) of Dy122 unit cell layer on TiO_2 terminated SrTiO_3 , at typical deposition conditions for RE123 (a) and optimised deposition conditions (b). The insets show the corresponding RHEED patterns.

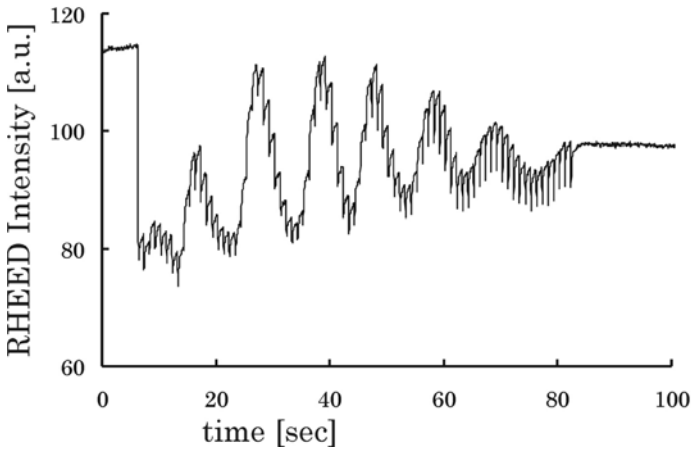


Fig. 12. Specular RHEED intensity recorded during growth of RE123 on RE122.

rather than 1:2:3. A 1:3:3 cation ratio, however, leads to the two observed stacking sequences. To avoid the latter we propose to use the 1:2:2 cation ratio.

4.4.1 INITIAL GROWTH OF $\text{REBa}_2\text{Cu}_2\text{O}_{7-8}$ ON TiO_2 TERMINATED SrTiO_3

Deposition was performed using a target with nominal 1:2:2 composition. Figure 11 (a) shows an AFM micrograph after deposition of approximately 1 unit cell layer using the standard deposition conditions. The inset shows the RHEED pattern after deposition. The terrace structure of the substrate is still visible in the AFM micrograph. The terraces consist of coalesced islands with height $\sim 4 \text{ \AA}$. The step density is clearly increased and, consequently the 2D spots in the RHEED pattern are somewhat blurred. Since no 3D spots are observed it is expected that nucleation of Cu_2O precipitates is prevented.

The intended stacking sequence is *bulk substrate-SrO-TiO₂-BaO-CuO₂-Dy-CuO₂-BaO*. Deposition of a single RE122 unit cell layer requires exact control of the supplied constituents. First, the amount of deposited material must exactly match to 1 unit cell layer. Second, the ratio between the constituents should be exactly 1:2:2. No improvement in the surface morphology has been observed by adjustment of the amount of deposited material. Excessive deposition leads to a more roughened surface. Obviously, supplying more material with a ratio close to 1:2:2 leads to nucleation of other phases. It is, therefore, expected that off stoichiometric deposition is the cause for the observed morphology. If the stacking sequence of the deposited Dy122 unit cell equals *BaO-CuO₂-Dy-CuO₂-BaO*, depletion of Ba and Cu is most probable. This can also be regarded as a surplus of Dy.

Several attempts were performed to obtain atomically smooth terraces by improving stoichiometry. Especially the energy density in the laser spot, the deposition temperature and

pressure have been optimised. Although islands were always found on the terraces and atomic smooth terraces were never observed, the step density is clearly diminished by the optimization, as shown by clear 2D RHEED spots. Figure 11 (b) shows an example of the AFM micrograph and corresponding RHEED pattern of a Dy122 unit cell layer deposited at an energy density of 7 J/cm^2 . Just after deposition the film was *in situ* annealed at a temperature of $880 \text{ }^\circ\text{C}$ for 1.5 h. The ledges of the terraces are roughened through coalescence of islands with the ledges.

4.4.2 INITIAL GROWTH OF $\text{DyBa}_2\text{Cu}_3\text{O}_{7-\delta}$ ON $\text{DyBa}_2\text{Cu}_2\text{O}_{7-\delta}$

Figure 12 shows the RHEED intensity during growth of Dy123 on top of a Dy122 unit cell layer. Clear intensity oscillations are observed indicating 2D nucleation and growth of the first unit cell layers. Compared to the initial growth on TiO_2 and SrO terminated SrTiO_3 the oscillations are more pronounced. Almost full recovery of the specular RHEED intensity is observed during deposition of the first few unit cell layers. Since the observed intensity is a direct measure of the surface step density, we conclude that no additional roughening takes place during initial growth. During subsequent growth, however, the oscillations are damped and the RHEED intensity decreases, indicating roughening of the surface.

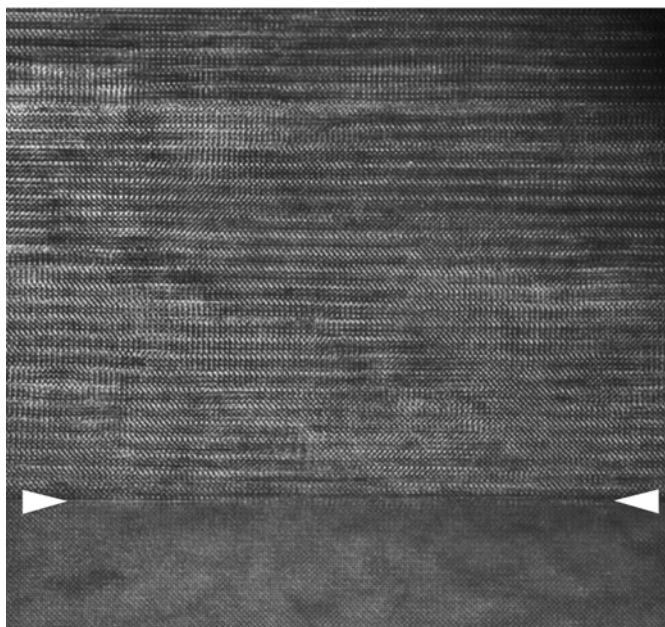


Fig. 13. Overview cross-section image of Dy123/Dy122 deposited on TiO_2 terminated SrTiO_3 . The arrowheads indicate the substrate-film interface.

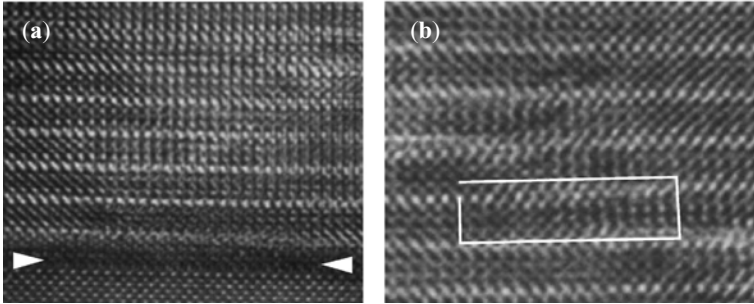


Fig. 14. Cross-section HREM images of the film-substrate interface of Dy123/Dy122 deposited on TiO₂ terminated SrTiO₃ (a). Non-unit cell growth during deposition of Dy123, indicated by the Burgers vector (b).

HREM analysis indicates the nucleation and initial growth mechanism to be different compared to Dy123 growth on TiO₂ terminated SrTiO₃. No APB's have been observed at the substrate-film interface, see cross-section image in figure 13 and HREM cross-section in figure 14 (a). However, non-unit cell growth has been observed remote from the interface, visualized by the Burgers vector in the HREM image in figure 14 (b).

4.4.3 DISCUSSION

As shown, deposition of the first unit cell layer with a cation ratio RE:Ba:Cu = 1:2:2 on TiO₂ terminated SrTiO₃ prevents Cu₂O precipitation. Apparently, it also prevents formation of APB's at the substrate-film interface. As discussed, APB's are formed during Dy123 deposition on TiO₂ as well as SrO terminated substrates by the coalescence of domains with different stacking sequence. The stacking sequence of the first unit cell layer in the domains is either *BaO(or SrO)-CuO₂-Dy-CuO₂-BaO* or *BaO(or SrO)-CuO-BaO-CuO₂-Dy-CuO₂-BaO*. The first can be considered as Dy122 whereas the latter can be considered as Dy133 (Dy133 can be considered as a Dy122 unit cell on top of a BaCuO block.). Formation of the Dy133 domains is suppressed in the case of Dy122 deposition, leading to one stacking sequence, i.e., *bulk substrate-SrO-TiO₂-BaO-CuO₂-Dy-CuO₂-BaO-bulk film*. Subsequently, formation of APB's is prevented.

5 CONCLUSIONS

Although in many studies a perovskite stacking sequence has been found at the interface of RE123 and SrTiO₃, the determination of the terminating atomic layer of the SrTiO₃ substrate as well as the starting atomic layer of RE123 remained ambiguous. Determination of the starting atomic layer with *ex situ* techniques like HREM and XSW requires the terminating layer of the substrate to be predetermined. The termination of SrTiO₃, however, can be SrO, TiO₂ or a mixture of both, depending on the surface treatment. Since most of the studies were

performed using thermally treated substrates, a mixed termination has to be expected. Reliable determination of the first atomic layer is, therefore, not straightforward.

The terminating atomic layer of RE123 have been studied extensively, using *in situ* and *ex situ* measurements. *Ex situ* determination usually requires surface cleaning by heat treatment and/or ion beam treatments. Modification of the surface is likely. Consequently, the measured termination layer may differ from the terminating layer during growth. Both, CuO_x and BaO have been found as the terminating layer. The growth conditions, especially the oxidation power during growth, determines the thermodynamically stable terminating layer at these conditions. Mostly, CuO_x termination is found at high oxidation power using ozone, atomic oxygen or other activated oxygen, whereas BaO is found at lower oxidation power using molecular oxygen. At standard PLD conditions the terminating atomic layer is BaO. Consequently, Cu_2O precipitation occurs during initial growth on TiO_2 terminated SrTiO_3 at these conditions.

Two methods have been successfully applied to avoid Cu_2O precipitation. In the first method, i.e., using SrO terminated SrTiO_3 substrates, A-site termination is preserved during deposition of the first unit cell layer and, hence, all CuO is incorporated in the thin film. The second method ensures “stoichiometric” deposition during the first unit cell layer. The exact amount of material, needed for the thermodynamically stable unit cell layer at deposition condition, is supplied. Since both the starting and terminating atomic layer of the first unit cell layer is BaO, a cation ratio of RE:Ba:Cu = 1:2:2 has to be used.

Ultra thin films of Dy123 prepared by PLD on TiO_2 -terminating SrTiO_3 apparently contain numerous APB's. Such boundaries were already observed in RE123 thin films and often related to unit cell steps on the substrate. The miscut-angle of the substrate used in this study was less than 0.2° , implying that the minimum width of a substrate terrace is 112 nm. Since HREM showed that the average width of an anti-phase domain is of the order of 20 nm, unit cell steps at the substrate cannot be the only reason for the formation of APB's, which are unavoidably created during the growth of the film. As a consequence two different stacking sequences at the interface are found. This causes a structural and chemical misfit and will lead to the formation of APB's, which will negatively influence the superconducting properties of the film.

A unique interface configuration is achieved by depositing the first unit cell layer with the cation ratio Y:Ba:Cu = 1:2:2, instead of 1:2:3, on single TiO_2 -terminated SrTiO_3 . Control of the stacking sequence at the interface has allowed us to study the influence of the density of APBs on the electrical transport properties of the superconducting film. It is found that the critical temperature T_c is depressed by increasing the in-plane ordering, which strongly indicates that the presence of APBs in the sample favors the oxygen indiffusion and the relaxation of the in-plane strain [66,67].

ACKNOWLEDGEMENTS

The authors like to acknowledge Mark Huijben, Matthijn Dekkers, Gertjan Koster, and Horst Rogalla for their discussions on the thin film preparation and characterization. Staf van Tendeloo and Sara Bals (EMAT, Belgium) for their contributions on the HREM images and accompanying discussions.

The authors like to devote this chapter in memory of Seve Currás.

REFERENCES

- [1] T.L. Hylton and M.R. Beasley, *Phys. Rev. B* **41** (1990) 11669
- [2] B. Dam, J.M. Huijbregtse, F.C. Klaassen, R.C.F. van der Geest, G. Doornbos, J.H. Rector, A.M. Testa, S. Freisem, J.C. Martinez, B. Stäuble-Pümpin and R. Griessen, *Nature* **399** (1999) 439
- [3] M. McElfresh, T.G. Miller, D.M. Schaefer, R. Reifenberger, R.E. Muenchausen, M. Hawley, S.R. Foltyn and X.D. Wu, *J. Appl. Phys.* **71** (1992) 5099
- [4] T. Haage, J. Zegenhagen, J.Q. Li, H.-U. Habermeier, M. Cardona, CH. Joos, R. Warthman, A. Forkl and H. Kronmüller, *Phys. Rev. B* **56** (1997) 8404
- [5] T. Terashima, Y. Bando, K. Iijima, K. Yamamoto, K. Hirata, K. Hayashi, K. Kamigaki and H. Terauchi, *Phys. Rev. Lett.* **65** (1990) 2684
- [6] J.G. Wen, C Traeholt and H.W. Zandbergen, *Physica C* **205** (1993) 354
- [7] G. Koster, B.L. Kropman, G.J.H.M. Rijnders, D.H.A. Blank and H. Rogalla, *Appl. Phys. Lett.* **73** (1998) 2920
- [8] M. Nakanishi, H. Hashizume, T. Terashima, Y. Bando, O. Michikami, S. Maeyama and M. Oshima, *Phys. Rev. B* **48** (1993) 10524
- [9] J. Zegenhagen, T. Siegrist, E. Fontes, L.E. Berman and J.R. Patel, *Solid State Comm.* **93** (1995) 763
- [10] S. Tanaka, T. Nakamura, H. Tokuda and M. Liyama, *Appl. Phys. Lett.* **62** (1993) 3040
- [11] T. Nakamura, S. Tanaka and M. Liyama, *Appl. Phys. Lett.* **66** (1995) 3362
- [12] K. Shimura, Y. Daitoh, Y. Yano, T. Terashima, Y. Bando, Y. Matsuda and S. Komiyama, *Physica C* **228** (1994) 91
- [13] B. Stäuble-Pümpin, V.C. Matijasevic, B. Ilge, J.E. Mooij, W.J.A.M. Peterse, P.M.L.O. Scholte, F. Tuinstra, H.J. Venvik, D.S. Wai, C. Træholt, J.G. Wen and H.W. Zandbergen, *Phys. Rev. B* **52** (1995) 7604
- [14] V.C. Matijasevic, B. Ilge, B. Stäuble-Pümpin, G. Rietveld, F. Tuinstra and J.E. Mooij, *Phys. Rev. Lett.* **76** (1996) 4765
- [15] H. Behner, K. Rührschopf, G. Wedler and W. Rauch, *Physica C* **208** (1993) 419
- [16] S.J. Pennycook, M.F. Chisholm, D.E. Jesson, D.P. Norton, D.H. Lowndes, R. Feenstra, H.R. Kerchner and J.O. Thomson, *Phys. Rev. Lett.* **67** (1991) 765
- [17] M. Badaye, W. Ting, K. Fukushima, N. Koshizuka, T. Morishita and S Tanaka, *Appl. Phys. Lett.* **67** (1995) 2155
- [18] M Badaye, J.G. Wen, K Fukushima, N Kohizuka, T, Morishita, T. Nishimura and Y Kido, *Supercond. Sci. Technol.* **10** (1997) 825
- [19] M. Badaye, F. Wang, Y. Kanke, K. Fukushima and T. Morishita, *Appl. Phys. Lett.* **66** (1995) 2131
- [20] Z. Liu, M. Badaye, S. Ogota and T. Morishita, *Appl. Surf. Sci.* **115** (1997) 180
- [21] J. Rao, T. Morishita, *Physica C* **291** (1997) 223
- [22] J.M. Huijbregtse, J.H. Rector, B. Dam, *Physica C* **351** (2001) 183
- [23] T. Haage, J. Zegenhagen, H.-U. Habermeier, C. Cardona, *Phys. Rev. Lett.* **80** (1998) 4225
- [24] M. Kawasaki and M. Nantoh, *MRS Bulletin* **IX** (1994) 33
- [25] G. Frank, Ch. Ziegler and W. Göpel, *Phys. Rev. B* **43** (1991) 2828

- [26] G.J.H.M. Rijnders, G. Koster, D.H.A. Blank and H. Rogalla, IEEE Transactions on Appl. Supercond. **9** (1999) 1547
- [27] R.C. Baetzhold and J. Mir, J. of Cryst. Growth **135**, (1994) 145
- [28] J.G. Lopez, D.H.A. Blank, H. Rogalla and J. Siejka, Physica C **307** (1998) 298
- [29] T. Haage, J. Zegenhagen, Ch. Jooss, R. Warthmann, J.Q. Li, H.-U. Habermeier, C. Cardona, Physica C **282-287** (1997) 557
- [30] T. Haage, J. Zegenhagen, C. Cardona, H.-U. Habermeier, J. of Alloys and Compounds **251** (1997) 23
- [31] F. Wellhöfer, P. Woodall, D.J. Norris, S. Johnson, D. Vassiloyannis, M. Aindow, M. Slaki and C.M. Muirhead, Appl. Surf. Sc. **127-129** (1998) 525
- [32] J. Kim, D.B. Chrisey, J.S. Horwitz, M.M. Miller and C.M. Gilmore, J. Mater. Res. **15** (2000) 596
- [33] M.G. Norton, C.B. Carter, J. Cryst. Growth **110** (1991) 641
- [34] T. Haage, H.-U. Habermeier, J. Zegenhagen, Surf. Sci. **370** (1997) L158
- [35] B. Dam, C. Træholt, B. Ståuble-Pümpin, J. Rector and D.G. de Groot, J. of Alloys. and Compounds. **251** (1997) 27
- [36] M. Yeadon, M. Aindow, F. Wellhöfer and J.S. Abell, J. of Cryst. Growth. **172** (1997) 145
- [37] J. Kim, D.B. Chrisey, C.M. Gilmore and J.S. Horwitz, Supercond. Sci. Technol. **13** (2000) 417
- [38] X.-Y. Zheng, D.H. Lowndes, S. Zhu, J.D. Budai and R.J. Warmack, Phys. Rev. B **45** (1992) 7584
- [39] J.-L. Maurice, O. Durand, M. Drouet and J.-P. Contour, Thin Solid Films **319** (1998) 211
- [40] I.A. Ovid'ko, J.Phys: Condens. Matter **13** (2001) L97
- [41] S.J. Pennycook, M.F. Chisholm, D.E. Jesson, R. Feenstra, S. Zhu, X.Y. Zheng and D.H. Lowndes, Physica C **202** (1992) 1
- [42] A. Abert, J.P. Contour, A. Défossez, D. Ravelosona, W. Schwegle and P. Ziemann, Appl. Surf. Sc. **96-98** (1996) 703
- [43] H.Y. Zhai and W.K. Chu, Appl. Phys. Lett. **76** (2000) 3469
- [44] D. Hüttner, O. Meyer, J. Reiner and G. Linker, Appl. Phys. Lett. **66** (1995) 1273
- [45] T.-S Gau, S.-L Chang, H.-H. Hung, C.-H. Lee, T.-W. Huang, H.-B. Lu, S.-J. Yang and S.-E Hsu, Appl. Phys. Lett. **65** (1994) 1720
- [46] L.X. Cao, J. Zegenhagen, E. Sozontov and M. Cardona, Physica C **337** (2000) 24
- [47] D.H. Lowndes, X.-Y Zheng, S. Zhu, J.D. Budai and R.J. Warmack, Appl.Phys. Lett. **61** (1992) 852
- [48] M.C.Foote, B.B. Jones, B.D. Hunt, J.B. Barner, R.P. Vasquez and L.J. Bajuk, Physica C **201** (1992) 176
- [49] B. Dam, J. Rector, M.F. Chang, S. Kars, D.G. de Groot and R. Griessen, Appl. Surf. Sc. **86** (1995) 13
- [50] R.I. Tomov, V.P. Manolov, P.A. Atanasov, V.N. Tsaneva, D.G. Ouzounov and V.I. Tsanev, Physica C **274** (1997) 187
- [51] R.H. Hammond and R. Bormann, Physica C **162-164** (1989) 703
- [52] A. Gupta, B.W. Hussey and M.Y. Chern, Physica C **200** (1992) 263

- [53] B. Dam, J.H. Rector, M.F. Chang, S. Kars, D.G. de Groot and R. Griessen, *Appl. Phys. Lett.* **65** (1994) 1581
- [54] B. Dam, J.H. Rector, J. Johansson, S. Kars and R. Griessen, *Appl. Surf. Sc.* **96-98** (1996) 679
- [55] M. Murakami, M. Morita, K. Doi, K. Miyamoto etc, *Jpn. J. Appl. Phys.* **28** (1989) L399
- [56] B. Dam, J.H. Rector, J.M. Huijbregtse and R. Griessen, *Physica C* **296** (1998) 179
- [57] B. Dam, B. Stäuble-Pümpin, *J. of Mat. Sc.* **9** (1998) 217
- [58] B. Dam, J.H. Rector, J. Huijbregtse and R. Griessen, *Physica C* **282-287** (1997) 559
- [59] A.J.H.M. Rijnders, G. Koster, D.H.A. Blank, H. Rogalla, *Appl. Phys. Lett.* **70** (1997) 1888
- [60] S. Bals, G. Rijnders, D.H.A. Blank and G. Van Tendeloo, *Physica C* **355** (2001) 225
- [61] S.G. Popov and V.A. Levitzky, *Zh. Phys. Khim (Russ.) LV* **87** (1981) 87
- [62] J.P. Gong, M. Kawasaki, F. Fujito, R. Tsuchiya, M. Yoshimoto and H. Koinuma, *Phys. Rev. B* **50** (1994) 3280
- [63] N. Kanda, M. Kawasaki, T. Kitajima, H. Koinuma, *Phys. Rev. B* **56** (1997) 8419
- [64] J-P. Locquet, Y. Jaccard, C. Gerber and E. Mächler, *Appl. Phys. Lett.* **63** (1993) 1426
- [65] Z. Han, T.I. Selinder and U. Helmersson, *J. Appl. Phys.* **75** (1994) 2020
- [66] J. M. Dekkers, G. Rijnders, S. Harkema, H.J.H. Smilde, H. Hilgenkamp, H. Rogalla, and D.H. A. Blank, *Appl. Phys. Lett.* **83** (2003) 5199
- [67] G. Rijnders, S. Curras, M. Huijben, D.H.A. Blank, and H. Rogalla, *Appl. Phys. Lett.* **84** (2004) 505

SUPERCONDUCTIVITY IN MgB_2

T. Muranaka¹, Y. Zenitani¹, J. Shimoyama², and J. Akimitsu¹

¹Department of Physics and Mathematics, Aoyama-Gakuin University
Fuchinobe 5-10-1, Sagamihara, Kanagawa 229-8558, Japan

²Faculty of Engineering, University of Tokyo
Hongo 7-3-1, Bunkyo-ku, Tokyo 113-8656, Japan

1. INTRODUCTION

Since the discovery of superconductivity in Hg, a huge number of superconductors were discovered among metal elements and intermetallic compounds, as shown in Fig. 1-1. In the early stage of material investigations, several intermetallic material groups with the AlB_2 -type structure were already recognized as candidate materials for superconductors, mainly by B.T. Matthias and J.K. Hulm in the 1950s. “Matthias’s rule” was derived as a result of the investigations of A15-type superconductors [1], and superconductors such as Nb_3Sn , V_3Ga , $\text{Nb}_3(\text{Al,Ge})$ [2] and Nb_3Ge [3], which were important materials for practical applications, were discovered. The superconductors that were discovered in this stage are called “BCS superconductors” because their behavior can be well explained within the framework of the BCS theory. However, the discovery of Cu-oxide high- T_c superconductors in 1986 [4] required a theoretical interpretation with a new key concept. The important point is that T_c was raised up to 138 K at ambient pressure [5], which is far above the highest T_c record of 23 K in Nb_3Ge [3]. With the high- T_c record being broken one after another by Cu-oxides, one of the most challenging questions in superconductivity has become “how much will T_c increase in non Cu oxide superconductors?” Up to 2001, the highest T_c in this class was 33 K in electron-doped $\text{Cs}_x\text{Rb}_y\text{C}_{60}$ [6] and the next highest T_c was 30 K in $\text{Ba}_{1-x}\text{K}_x\text{BiO}_3$ [7]. Within this background, we reported superconductivity at 39 K in MgB_2 [8] in 2001, which is the highest T_c among intermetallic superconductors and nearly twice the T_c previously reported. Although MgB_2 is a well-known popular material, its high- T_c superconductivity ($T_c=39$ K) had been hidden for about 50 years until our discovery. Because the limit of T_c in metallic superconductors had been believed to be ~ 30 K in the framework of the BCS theory, the discovery of unexpectedly high- T_c superconductivity in this simple binary intermetallic compound has triggered enormous interests in the world.

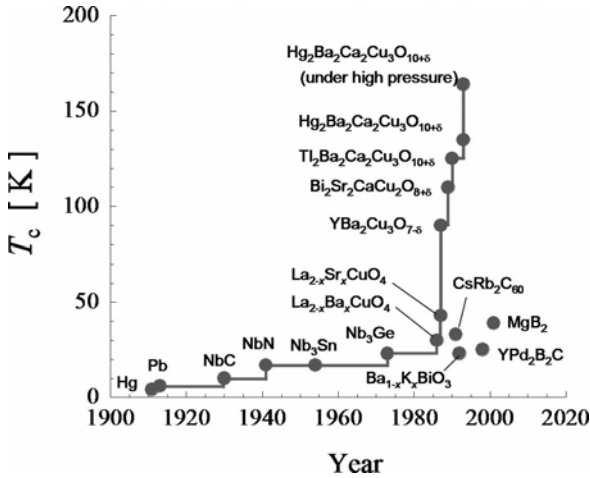


Fig. 1-1. Chronology of T_c .

derived from 3D π -bands and 2D σ -bands. Although multiple-gap superconductivity had been proposed by Suhl *et al.* [14] and since then, discussed in relation to other materials, for example, Nb-doped SrTiO₃ by Binnig *et al.* [15], MgB₂ is the first material containing intrinsic multiple gaps, and many basic elements of multiple-gap superconductivity have been investigated from various experimental and theoretical aspects. Moreover, its high T_c , simple crystal structure, large coherence length, high critical current density, high critical field, transparency of grain boundaries to current and low normal state resistivity promise that MgB₂ will be a good candidate material for both large scale applications and electronic devices. MgB₂ has already been fabricated in the form of bulk, single crystal, thin film, tape and wire [16,17], and shows potential for practical applications. Superconductivity in MgB₂ is one of the most fascinating topics in issues ranging widely from fundamental aspects to applications.

In this paper, we review the experimental results on MgB₂. In Sec. 2.1, we introduce the crystal structures of several families of boride compounds. In particular, we describe geometrical arrangements of boron atoms in borides. The boron atoms have a suitable size and electronic structure that allows them to form direct B-B bonds; that can form a boron network. The characteristic crystal and electronic structures of MgB₂ are introduced in Sec. 2.2. In Sec. 3 (Sec. 3.1, 3.2 and 3.3), we review the physical properties of MgB₂, particularly the electric, thermal and magnetic properties, and also the experimental results on electron-phonon (EP) coupling and multigap behavior. In Sec. 4, we review the potential of MgB₂ for practical applications. MgB₂ is expected to be a new candidate material for practical applications, such as superconducting wires and thin films. The critical current properties of MgB₂ in the form of single crystals, bulks and thin films are described in Sec. 4.1. In Sec. 4.2, we describe the doping effects on the critical current properties of MgB₂. In Sec. 4.3, we introduce the future prospects for MgB₂ materials. Finally, in Sec. 5, we will summarize the experimental results on MgB₂ and mention the future prospects for material development of related intermetallic compounds and for the application of superconducting wire and thin films. We note that there are some excellent reviews on MgB₂ [18,19].

MgB₂ has opened a new frontier of investigation into the physical properties of intermetallic superconductors. In the short period since the discovery of its high- T_c superconductivity, a large number of experimental and theoretical works have been performed [9-13], and the interpretation of this superconductivity focuses on the metallic nature of the 2D layer formed by B atoms. The discovery also prompts a search for other high- T_c materials in similar systems. Moreover, MgB₂ is a particularly attractive material for its multiple superconducting gaps which are caused by the characteristic electronic structure derived

2. CRYSTAL AND ELECTRONIC STRUCTURE OF MgB_2

2.1. Crystal Structure of Boride Compounds


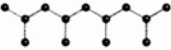
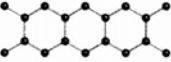
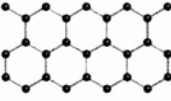
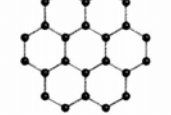
The boron atoms have a suitable size and electronic structure for forming direct B-B bonds that can form a boron network. The general chemical formulas of the borides correspond to the series M_4B , M_3B , M_7B_3 , $M_2B \rightarrow M_3B_2 \rightarrow MB \rightarrow M_{11}B_8 \rightarrow M_3B_4 \rightarrow M_2B_3 \rightarrow MB_2 \rightarrow MB_4$, $MB_6 \rightarrow MB_{12} \rightarrow MB_{15} \rightarrow M_3B_{12} \rightarrow MB_{66}$. The geometric arrangements of boron atoms in boride compounds are shown in Table 2-1 [20]. With increasing boron content, the network formed by boron atoms have a higher dimensionality.

In the metal-rich borides with the chemical formulas M_4B , M_7B_3 , M_3B and M_2B (Al_2Cu -type structure), the boron atoms are isolated. The crystal structures of Ni_3B and Co_3B are the same as that of Fe_3C . This group is called cementite. In this structure, the atomic radius of the metal element, such as Cr, Mn and Fe, is smaller than 1.3 Å. Re_3B is reported to be a superconductor ($T_c \sim 4.8$ K) in borides with the M_3B formula, [21,22], but the crystal structure of Re_3B is different from that of cementite (orthorhombic; $Cmcm$). Moreover, Re_7B_3 ($T_c = 3.5$ K) [22] and Ru_7B_3 ($T_c = 2.6$ K) [23] have been reported in borides with the M_7B_3 formula. The crystal structures of compounds with the M_2B formula are the same as the Al_2Cu -type structure. In the case of Fe_2B , the Fe-Fe distance is slightly smaller compared with that of pure metal iron. Many borides, Ta_2B , Mo_2B , W_2B , Mn_2B , Cr_2B , Fe_2B , Co_2B , Ni_2B , Be_2B and Re_2B , belong to M_2B -type compounds. Among these, Mo_2B ($T_c \sim 5$ K), Ta_2B ($T_c = 3.12$ K), W_2B ($T_c \sim 3.2$ K) and Re_2B ($T_c = 2.8$ K) are superconductors [23-25], however, the crystal structure of Re_2B is yet undetermined.

As the boron content increases, B-B bonds form in pairs with M_3B_2 -type borides. V_3B_2 , Nb_3B_2 and Ta_3B_2 belong to this type of boride, and crystal structures of these compounds are U_3Si_2 -type. In this crystal structure, B-B bonds form in pairs through the side shared by two M_6B triangular prisms. Similarly, in MB-type borides, the boron atom is surrounded by six metal atoms which form the M_6B triangular prism and B-B bonds form in zig-zag chains. In this class, FeB-, CrB- and MoB-type crystal structures are basically constructed of double metal layers including the M_6B triangular prisms, but crystal structures differ from each other. Among this class, TaB ($T_c = 4$ K), NbB ($T_c = 8.2$ K), ZrB ($T_c \sim 3$ K), HfB ($T_c = 3.1$ K) and MoB ($T_c = 0.5$ K) were reported to be superconductors [23,26-29]. Boron atoms in $M_{11}B_8$ -type borides are surrounded by metal atoms in triangle prisms, similar to M_3B_2 and MB. Also, boron atoms form branched chains. In M_3B_4 - and M_2B_3 -type borides, boron atoms form double and triple chains, respectively. Ta_3B_4 , Nb_3B_4 , Mn_3B_4 and Cr_3B_4 are listed as the former compounds, and the latter are V_2B_3 and Cr_2B_3 . The double or triple chain structure is considered to be just like the end of the honeycomb lattice or spin ladder compound seen in copper oxide. For example, in Ta_3B_4 , while the B-B distance in a pair is 1.54 Å between each chain, the B-B distance in a chain is 1.8 Å.

The many MB_2 -type borides have the AlB_2 -type structure (hexagonal; $P6/mmm$). In this structure, the characteristic 2D honeycomb layers formed by boron atoms are sandwiched by the triangular metal layers, like intercalated graphite, as shown in Fig. 2-1. The MB_2 -type structure is stable for a surprisingly wide range of metal atom sizes with a metal combination radius in the range of 1.3-1.8 Å. In these compounds, the transition metal electronic states are heavily involved in the Fermi energy [30,31]. Among metal diborides, ReB_2 has a strongly distorted boron honeycomb lattice, as shown in Fig. 2-2. This buckling obviously precludes superconductivity by the same phonon E_{2g} mode that mediates the superconductivity in MgB_2 [9]; and ReB_2 does not show superconductivity. On the other hand, theoretical calculation has

Table 2-1. Geometric arrangements of boron atoms in borides [20].

| Formula | Example | B-B bonds | |
|-------------|--------------|-----------------------|---|
| M_4B | Mn_4B | Isolated atoms | • • • |
| M_5B | Ni_5B | | |
| M_7B_3 | Ru_7B_3 | | |
| M_2B | Be_2B | | |
| M_3B_2 | V_3B_2 | pairs | •• •• |
| MB | NiB | zigzag chains |  |
| $M_{11}B_8$ | $Ru_{11}B_8$ | branched chains |  |
| M_3B_4 | Ta_3B_4 | double chains |  |
| M_2B_3 | Ta_2B_3 | triple chains |  |
| MB_2 | AlB_2 | 2-dimensional network |  |
| MB_4 | LaB_4 | 3-dimensional network | B_6 octahedron |
| MB_6 | LaB_6 | | |
| MB_{12} | YB_{12} | | B_{12} cubo-octahedron |
| MB_{15} | NaB_{15} | | B_{12} icosahedron |
| M_3B_{12} | B_4C | | |
| MB_{96} | YB_{96} | | $B_{12}(B_{12})_{12}$ icosahedron |

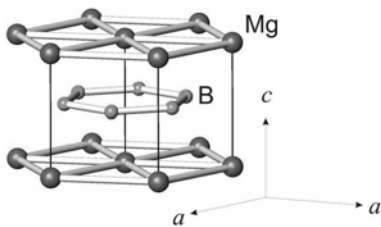


Fig. 2-1. Crystal structure of MgB_2 .

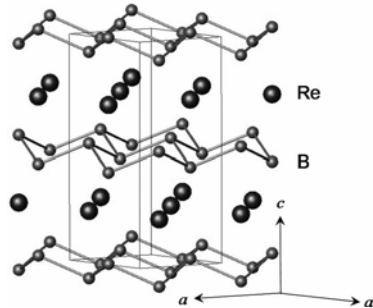


Fig. 2-2. Crystal structure of ReB_2 .

predicted that the density of states at the Fermi energy in ReB_2 assuming AlB_2 -type structure increased rather than ReB_2 with no assumption, leading to the possibility of superconductivity. Among AlB_2 -type borides, several superconductors have been reported, and their physical properties were investigated before the discovery of superconductivity in MgB_2 . In 1970, Cooper *et al.* reported superconductivity in B-rich NbB_2 ($\text{NbB}_{2.5}$) ($T_c=3.87$ K) and $\text{MoB}_{2.5}$ ($T_c=8.1$ K) in MB_2 (M: Y, Zr, Nb and Mo) compounds [32]. In $\text{NbB}_{2.5}$, the increase of T_c to 9.3 K and 7 K by slight Y and Th substitutions to Nb site was reported. T_c also increased by slight Y, Sc, Hf, Zr and Nb substitutions to Mo site, for example, $\text{Mo}_{0.85}\text{Zr}_{0.15}\text{B}_{2.5}$ ($T_c=11.2$ K). Although the crystal structure of the superconductor $\text{MoB}_{2.5}$ was the AlB_2 -type, it was confirmed to be the $\epsilon\text{-Mo}_2\text{B}_5$ -type structure (rhombohedral; $R3m$) with $a_{\text{hex}}=3.0152$ Å and $c_{\text{hex}}=20.971$ Å [33]. Similarly, WB_2 was first reported as the W_2B_5 phase, but its crystal structure was the “modified” AlB_2 -type (hexagonal, $P6/mmc$) with $a=2.982$ Å and $c=13.87$ Å [34]. In 1979, Leyarovska *et al.* reported superconductivity of NbB_2 ($T_c=0.62$ K) in MB_2 (M: Ti, Zr, Hf, V, Nb, Ta, Cr and Mo) compounds [35]. They reported that T_c changed from 0.62 to 6.4 K with increasing boron content from 2 to 2.5 in NbB_2 . Recently, however, $\text{Nb}_{1-x}\text{B}_2$ ($x=0.24$) prepared under 5 GPa revealed a maximum T_c of 9.2 K, and T_c changed from 7 to 9 K depending on the sintering pressure and nominal composition [36]. On the other hand, Gasparov *et al.* reported no sign of superconductivity in NbB_2 [37], so more precise investigation of the relationship between stoichiometry and crystal structure is needed.

Since the discovery of superconductivity in MgB_2 , the main issue in material development has been “whether MgB_2 is just a special example among diborides or not”. Hence AlB_2 -type borides have been extensively investigated both theoretically and experimentally. Experimentally, superconductivity in BeB_2 ($\text{BeB}_{2.75}$) [38], ZrB_2 [37], TaB_2 [39] and NbB_2 [36] has been reported one after another. From among similar systems, BeB_2 is the first natural candidate, since the lighter divalent Be atoms (atomic mass ratio of Mg to Be; $M_{\text{Mg}}/M_{\text{Be}}=2.25$) may provide higher phonon frequencies while retaining similar electronic properties. However, Felner reported no sign of superconductivity down to 5 K, on the basis of susceptibility measurements [40]. Young *et al.* reported that a superconducting phase ($T_c=0.72$ K) formed a complex structure in contrast to the simple AlB_2 -type structure, and that this structure has a chemical composition of $\text{BeB}_{2.75}$ [38]. Although Kaczorowski *et al.* reported superconductivity at 5.5 K in ZrB_2 [39], more detailed characterization of this superconducting phase is needed because their sample includes a small amount of an impurity phase, ZrB_{12} ($T_c=5.9$ K). Kaczorowski *et al.* also reported superconductivity at 9.5 K in TaB_2 , whereas Gasparov *et al.* reported no sign of superconductivity in it [37]. Therefore, it is not confirmed whether TaB_2 is a superconductor or not. From a theoretical point of view, it has been theoretically predicted that many isoelectronic boride systems such as CuB_2 , AgB_2 , AuB_2 , Li_xBC ($x\sim 0.5$) and related compounds should have a high T_c [41–43]. However, CaB_2 , AgB_2 and AuB_2 have not been synthesized yet. In particular, in the case of a monovalent metal, Ag or Au, the AlB_2 -type structure is unstable. In a theoretical study of the thermodynamic stability of the AlB_2 -type structure [44], the divalent metal diborides are at the minimum limit of stability, while the monovalent diborides (Na, Ag, Au, *etc.*) are clearly unstable. Therefore, AlB_2 -type structures including Ag or Au cannot be formed. Although the possibility of superconductivity in hole-doped MgB_2 or upon isoelectronic substitution of Mg (i.e., $\text{Mg}_{1-x}\text{M}_x\text{B}_2$ with $\text{M}=\text{Be}, \text{Ca}, \text{Li}, \text{Na}, \text{Cu}$ and Zn) has been suggested [45], the substitution of Li or Na to Mg site is also difficult for carrier doping and has not been reported. Fogg *et al.* reported the physical properties of Li_xBC ($x>0.5$), however, no superconductivity above 2 K was observed in this system [46].

In the last part of this section, the borides with a 3D B-network are described (MB_6 formula; hexaboride and MB_{12} formula; dodecaboride). The crystal structure of MB_6 -type borides is cubic (CaB_6 -type; $Pm\bar{3}m$), and characterized by a 3D skeleton composed of B_6 octahe-

dra, the interstices of which are occupied by a divalent or trivalent metal ion (see Fig. 2-3). The 3D frameworks of boron atoms and metal ions are arranged in a simple cubic lattice considering that the B_6 octahedron is one unit and this structure is described to be of the CsCl-type. The metal ions comprise the alkaline-earth metals (Ca, Sr and Ba), the rare-earth metals (La, Ce and Eu) and the actinium metals (Th and U). The lattice constants of hexaboride are increased linearly with increasing radius of these metal ions. However, the sizes of B_6 octahedra are unchanged and the distance between B_6 octahedra changes with changing lattice constant. In MB_6 -type borides including divalent metal ions, superconductivity was not confirmed, but among those with trivalent metal ions, YB_6 showed superconductivity ($T_c=6\sim 7$ K) [2,47,48]. As shown in Fig. 2-4, the crystal structure of MB_{12} dodecaborides is cubic (UB_{12} -type; $Fm\bar{3}m$). The arrangement of B_{12} cubo-octahedra and the rare earth atoms is the NaCl-type. Consequently, each metal atom is located at the center of a B_{24} cubo-icosahedron. This configuration is similar to the CaB_6 -type configuration. In this class, superconductivity was reported in YB_{12} ($T_c=4.7$ K), ScB_{12} ($T_c=0.39$ K), LuB_{12} ($T_c=0.48$ K) and ZrB_{12} ($T_c\sim 5.9$ K) [2,49].

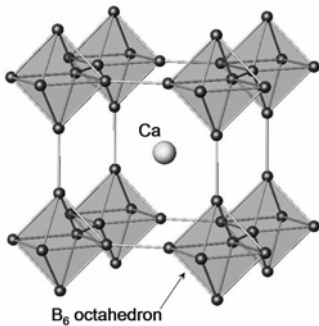


Fig. 2-3. Crystal structure of CaB_6 .

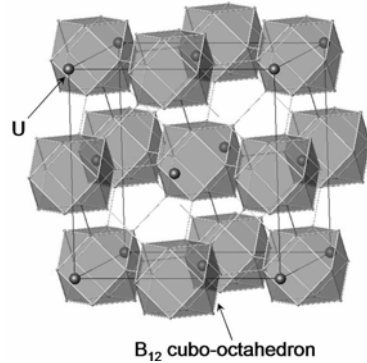


Fig. 2-4. Crystal structure of UB_{12} .

2.2. Crystal and Electronic Structures of MgB_2

2.2.1. Crystal structure of MgB_2

MgB_2 has an AlB_2 -type hexagonal structure with $a=3.08$ Å and $c=3.51$ Å ($P6/mmm$) [50]. The atomic position of Mg is $1a$ (0 0 0) and that of B is $2d$ ($1/2\pm\delta$ $1/2\pm\delta$ $1/2\pm\delta$). The structural arrangement can be described as an alternate stacking of boron honeycomb planes and Mg triangular planes. Each Mg atom is at the center of a hexagonal prism of boron atoms at a distance of ~ 2.5 Å. Each boron atom is surrounded by three other boron atoms, forming an equilateral triangle at a distance of $a/\sqrt{3}\sim 1.78$ Å, while the Mg-Mg distance in the plane is equal to the lattice constant a . Because lattice constants a and c in the AlB_2 -type structure are in the range of 3.0-3.2 Å and 3.0-4.0 Å, respectively, MgB_2 has the middle lattice constant in this type of structure. The crystal structure of MgB_2 has been investigated by high-resolution neutron powder diffraction [51-53] and x-ray diffraction [54-60]. These experiments mostly focused on the temperature dependence of lattice constants and the lattice compression versus external pressure.

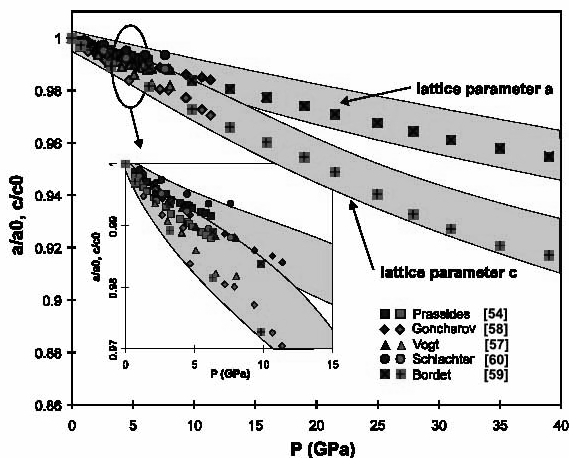


Fig. 2-5. Pressure dependence of normalized a and c . Inset shows the extension of lower pressure region (adopted from Ref. 18).

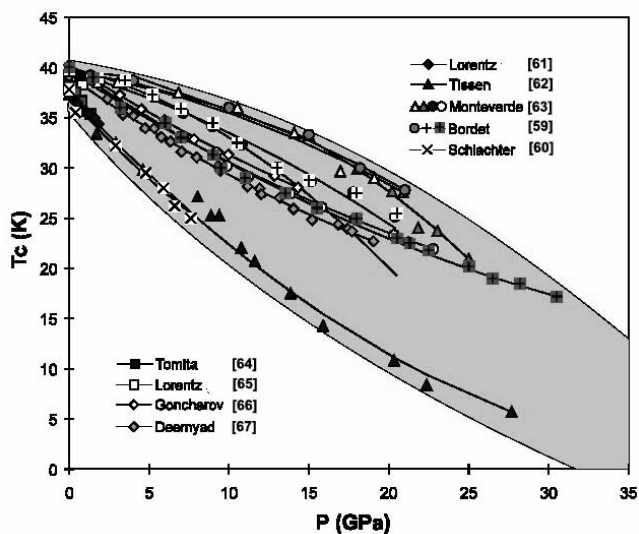


Fig. 2-6. Pressure dependence of T_c (adopted from Ref. 18).

Mg-B bonds. Jorgensen *et al.* also pointed out that there is a small hump in the variation of the lattice constant along the a -axis at around T_c ($\Delta a/a \approx 1.6 \times 10^{-5}$), while no hump exists along the c -axis. They speculated that these behaviors are related to the change of B-B bonding for superconductivity. On the contrary, Margadonna *et al.*, observed a slope discontinuity in the expansion along the c -axis just above T_c ($\Delta c/c \approx 4.0 \times 10^{-5}$), but not along the a -axis. They

The lattice constants, a and c , observed by several research groups are basically in good agreement; 3.085-3.090 Å and 3.520-3.529 Å, respectively, at room temperature. The tiny differences may reflect some uncontrollable displacement of the B atom from the ideal position and/or a slight defect at the Mg site. MgB₂ remains a hexagonal unit to the lowest temperature of 2 K or the highest pressure of 40 GPa, and no sign of structural transition was observed. Jorgensen *et al.* reported that the thermal expansion coefficient along the c -axis is two times larger than that along the a -axis ($\alpha_a \approx 5.4 \times 10^{-6} \text{ K}^{-1}$ and $\alpha_c \approx 11.4 \times 10^{-6} \text{ K}^{-1}$ at 11-297 K), on the basis of the temperature dependence of lattice constants [51]. This behavior is essentially consistent with the results reported by Margadonna *et al.* ($\alpha_a \approx 4 \times 10^{-6} \text{ K}^{-1}$ and $\alpha_c \approx 6.2 \times 10^{-6} \text{ K}^{-1}$ at 2-293 K) [52] and Oikawa *et al.* ($\alpha_a \approx 3.1 \times 10^{-6} \text{ K}^{-1}$ and $\alpha_c \approx 7.3 \times 10^{-6} \text{ K}^{-1}$ at 31-289 K) [53]. This anisotropy corresponds to a difference in the bond strength; the B-B bonds are more rigid than the

also argued that the anomaly in volume expansion ($(\Delta V)/T$) is consistent with the specific heat jump at T_c through the relationship $(\Delta V)/T = (dT_c/dP)(\Delta C/T_c)$. On the other hand, Oikawa *et al.* did not observe any anomaly in the temperature dependence of either lattice constant or the unit cell volume around T_c . The difference in these experimental results might be ascribed to the sample preparation process, which affects the stoichiometry, and structural properties such as imperfect stacking.

Many reports on the compressibility of lattice constants showed that the lattice parameter along the c -axis decreased rather than that along the a -axis with applied pressure (see Fig. 2-5). This anisotropic compressibility suggests that the out-of-plane Mg-B bonds are much weaker than the in-plane Mg-Mg bonds. In addition, dT_c/dP values were estimated to be -0.35 K/GPa [59] and -1.13 K/GPa [60]. These values are different from those estimated in other studies of the pressure-dependent properties (see Fig. 2-6) [61-67], for example, -1.6 K/GPa by Lorenz *et al.* [61]. The discrepancy among the compressibility values obtained in each study may arise from the difference in the pressure-transmitting medium such as silicone oil [54], methanol: ethanol: water (16:3:1) [57,62], helium [58,64-67], nitrogen [59], NaF [60], flourinert [61] and steatite [63]. The reduction of T_c under external pressure can be explained within the framework of BCS-type superconductivity mediated by high-frequency phonons. The behavior suggests the reduction of the density of states at E_F by contraction of both B-B and Mg-B bonds.

2.2.2. Electronic structure of MgB₂

Despite its crystal structure being similar to that of a graphite intercalated compound, MgB₂ has a qualitatively different and uncommon structure of the conducting states. The band structure has been calculated in several studies since the discovery of superconductivity [9,10,42,68] (see Fig. 2-7). The band structure of MgB₂ is similar to that of graphite, and is formed by three bonding σ bands (in-plane $sp_x p_y$ hybridization) and two π bands (bonding and antibonding; p_z hybridization). MgB₂ has two imperfectly filled σ bands, and these σ bands correspond to the sp^2 -hybrid bonding within the 2D honeycomb layer. The holes of σ bands along the ΓA line localized within the 2D boron layer manifest 2D properties. In contrast, the electrons and holes in 3D π bands are delocalized. The

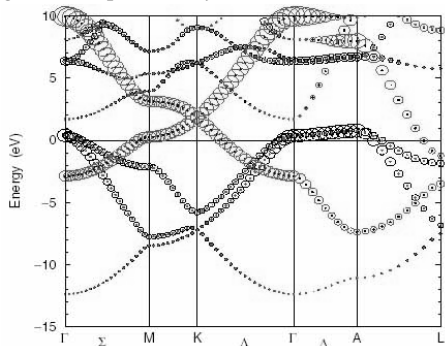


Fig. 2-7. Band structure of MgB₂ with B p character [9]. The radii of the red (black) circles are proportional to p_z ($p_{x,y}$) character.

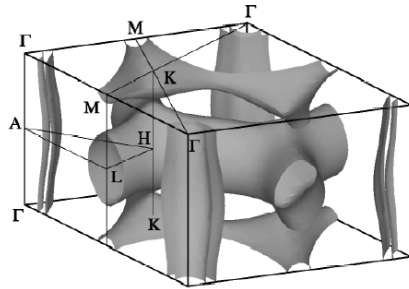


Fig. 2-8. Fermi surface of MgB₂ [9]. Green and blue cylinders (hole-like) come from the bonding $p_{x,y}$ bands, the blue tubular network (hole-like) from the bonding p_z bands, and the red (electron-like) tubular network from the antibonding p_z band.

2D σ bands and 3D π bands at E_F contribute equally to the total density of states, while 2D σ bands have a strong interaction with longitudinal vibrations within the 2D boron layer. Moreover, because k_z dispersion of σ bands is weak, two cylindrical sheets appear around the ΓA line (see Fig. 2-8). On the other hand, π bands form two tubular networks: an antibonding electron-type and a bonding hole-type sheet. These two sheets touch at one point on the KH line. Belashchenko *et al.* examined the relationship between the band structures of MgB_2 and graphite by comparing the following lattices; primitive graphite lattice with no displacement between layers, as in MgB_2 , using graphite lattice parameters; boron in the primitive graphite lattice with a as in MgB_2 , and c/a as in graphite (see Fig. 2-9) [68]. The band structure of the primitive graphite lattice with no displacement between layers is similar to that of graphite, and that of boron in the primitive graphite lattice shows a natural enhancement of the out-of-plane dispersion of the π bands when the interlayer distance is reduced. The distinct difference between MgB_2 and the primitive graphite lattice is the position of σ bands to E_F at the Γ point.

An investigation of the charge density distribution would give a better understanding of how the superconductivity is related to the electronic and crystal structures of MgB_2 . Precise x-ray structure analyses by Nishibori *et al.* (in a polycrystalline sample) [55], Lee *et al.* (in a single crystal) [56] and Mori *et al.* (in a single crystal; $Mg_{1-x}B_2$ $x=0.045$) [69] yielded accurate charge densities in MgB_2 .

The charge density obtained at room temperature revealed a strong B-B covalent bonding feature. On the other hand, there was no bond electron between Mg and B atoms, and Mg atoms were found to be fully ionized and in the divalent state. Nishibori *et al.* also reported that these characteristic density features were preserved in the charge density obtained at 15 K and were consistent with the calculated band structures indicating a two-band model [10]. Moreover, Nishibori *et al.* examined the valence of the atom by accumulating the number of electrons around a certain atom in the MEM

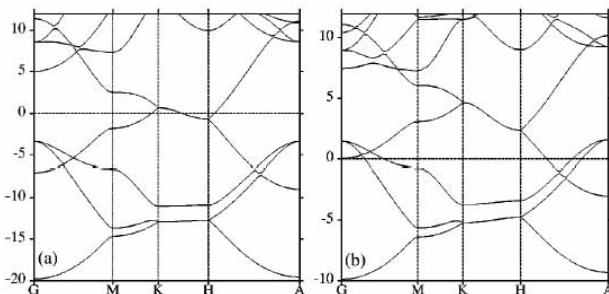


Fig. 2-9. Band structures of (a) primitive (AA stacking) graphite (PG), $a=2.456$ Å, $c/a=1.363$; (b) PG boron, $a=3.085$ Å, $c/a=1.142$ as in MgB_2 [68]

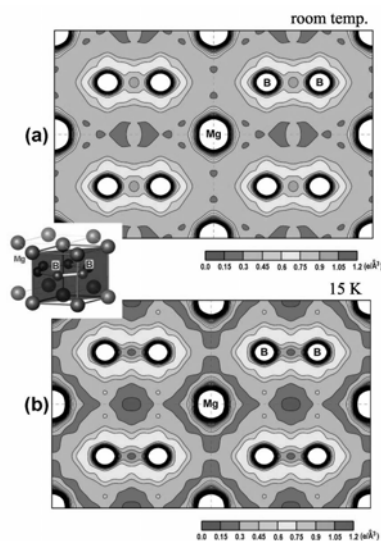


Fig. 2-10. The (110) sections of the MEM charge density of MgB_2 at room temperature (a) and 15K (b) [55].

density (see Fig. 2-10). The numbers of electrons at room temperature and 15 K were estimated to be $10.0(1)e$ and $10.0(1)e$ around the Mg atom and $9.9(1)e$ and $10.9(1)e$ around the boron 2D sheets, respectively. The values for Mg atoms are very close to the number of electrons around Mg^{2+} ions, so Mg atoms are fully ionized in the MgB_2 crystal at whole temperatures. On the other hand, the total numbers of electrons around boron 2D sheets show significant difference, which can be attributed to the valence of the whole boron 2D sheet changing from neutral to monovalent at 15 K. These results suggest that the electrons transfer from π bands (p_z orbitals) to in-plane σ bands (p_{xy} orbitals) at 15 K. However, these results do not agree with the valence electron distribution at room temperature determined by Wu *et al.* using synchrotron x-ray and electron diffraction techniques [70]. They reported that two electrons from each Mg atom moved to the B plane. Therefore, the boron layer had the same number of valence electrons, and these electrons were mainly located in the $p_x p_y$ orbitals between neighboring boron atoms. This disagreement is not yet resolved.

3. PHYSICAL PROPERTIES OF MgB_2

3.1. Transport and Magnetic Properties of MgB_2

3.1.1. Electric and thermal transport properties

Transport properties of MgB_2 determined by precise experiments using single crystals provide rich information to confirm the anisotropic band structure and phonon contribution to the electronic state that was estimated by band structure calculations [9,10,71]. In particular, the existence of two superconducting gaps in MgB_2 , a small one on the 3D tubular network and a large one on the 2D sheets, was predicted by Liu *et al.* using first-principles calculations [72]. The high T_c in MgB_2 originates from strong EP coupling [11,63]. Thus, an important question is whether the normal state transport properties can be described by the EP interaction alone. Most reports on transport properties support a phonon scattering scenario and anisotropy of the electronic state.

- Electric Resistivity -

As shown in Fig. 3-1, the in-plane resistivity ($\rho_{ab}(T)$) of MgB_2 is about 5-10 $\mu\Omega\text{cm}$ at room temperature [56,73-80]. The resistivity gradually deviates from a T -linear behavior with decreasing temperature. The residual resistivity (ρ_0) is 0.5-2 $\mu\Omega\text{cm}$ and the residual resistivity ratio (RRR) varies from 5 to 10, depending on the preparation conditions. Kim *et al.* reported $\rho_{ab}(T)$ under magnetic fields from 0 to 5 T ($H//ab$ and $H//c$) [75]. They analyzed the data in the normal state using the Bloch-Grüneisen (BG) formula [81],

$$R(T) = R_0 + R_{ph}(T),$$

where R_0 is the temperature independent residual part and $R_{ph}(T)$ is the phonon scattering contribution given by

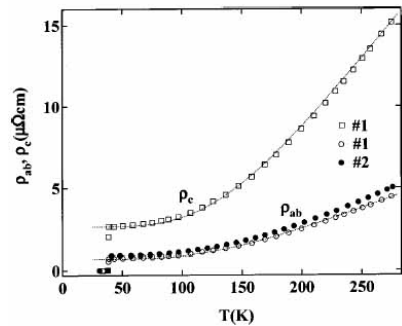


Fig. 3-1. Temperature dependence of in-plane and out-of-plane resistivities of MgB_2 [78]. Dotted lines show the fitted lines using B-G formula.

$$R_{ph}(T) = R_1 (T/\Theta_D)^m \int_0^{\Theta_D/T} \frac{z^m dz}{(1 - e^{-z})(e^z - 1)},$$

with R_1 being a proportionality constant. They reproduced the observed $\rho_{ab}(T)$ well with $m = 3.0$ and $\Theta_D \sim 1100$ K. This Θ_D value is comparable to those previously determined from specific heat and resistivity measurements using polycrystalline samples [11,82-84]. Their results suggest that the normal state transport properties are well described by an EP interaction without taking an electron-electron interaction into account. On the other hand, Masui *et al.* analyzed $\rho_{ab}(T)$ on the basis of the Boltzmann equation,

$$\rho(T) = \frac{(4\pi)^2 k_B T}{\omega_p^2 \hbar} \int_0^{\max} \frac{d\Omega}{\Omega} \alpha^2 F(\Omega) \times \left[\frac{\hbar\Omega / 2k_B T}{\sinh(\hbar\Omega / 2k_B T)} \right]^2 + \rho_0,$$

where ω_p is the plasma frequency and ρ_0 is the residual resistivity. In order to take account of the optical phonon contribution separately, they applied the model approximation [85] reported by Allen *et al.* In this model, the Eliashberg function, $\alpha^2 F(\Omega)$, is described as

$$\alpha^2 F(\Omega) = \alpha^2 F_D(\Omega) + \alpha^2 F_E(\Omega).$$

The first term is the Debye approximation part that gives the BG equation, and the second term represents the Einstein approximation,

$$\alpha^2 F_D(\Omega) = 2\lambda_D (\Omega/\Theta_D)^4 \theta(\Theta_D - \Omega)$$

$$\alpha^2 F_E(\Omega) = \lambda_E \omega_E \delta(\Omega - \omega_E) / 2$$

Here, ω_E is a characteristic Einstein phonon energy, and λ_D and λ_E are the electron-phonon coupling constants for each approximation. Masui *et al.* analyzed $\rho_{ab}(T)$ data by two approaches in order to estimate the contribution from the E_{2g} phonon mode. One approach is to assume a high Θ_D in the BG formula, and the other is to treat the E_{2g} phonon separately as an Einstein phonon. In the former treatment, they neglected the contribution of the $\alpha^2 F_E(\Omega)$ term. In the latter, the BG part represents the contribution of the low energy acoustic phonons. Both treatments reproduced $\rho_{ab}(T)$ data well, however, they concluded that the latter treatment seemed to be more reasonable because the Θ_D obtained roughly corresponded to the maximum frequency of the low energy phonon density of states for acoustic phonons [86], and the Θ_D value of 400 K was also reasonable for explaining the phonon drag peak observed in thermoelectric power [76].

Because the MgB₂ single crystal grows easily along the *ab*-direction, the thickness of the single crystal is insufficient for out-of-plane resistivity ($\rho_c(T)$) measurement. The electronic state of MgB₂ might be anisotropic because of the layered structure, so transport properties between in-plane and out-of-plane directions are expected to also be anisotropic. $\rho_c(T)$ was measured by Montgomery-type analysis [78] and four-probe methods [79,87]. As shown in Fig. 3-1, the temperature dependence of $\rho_c(T)$ is nearly the same as that of $\rho_{ab}(T)$, and the absolute value of $\rho_c(T)$ is higher than that of $\rho_{ab}(T)$, thus the resistivity ratio ρ_c/ρ_{ab} is about 3 just above T_c . However, the temperature dependence of ρ_c and ρ_{ab} suggests the existence of similar scattering mechanisms for in-plane and out-of-plane charge transfer. Eltsev *et al.* analyzed both ρ_c and ρ_{ab} using the BG formula, and they obtained the same value of $\Theta_D = 880$ K and in-plane and out-of-plane residual resistivities ρ_0 of 0.69 and 2.62 $\mu\Omega\text{cm}$, respectively. Thus, the basic agreement between the theoretical calculations [9,71,72] and the experimental data for the electronic structure and EP interaction is satisfactory, demonstrating the importance of EP scattering to both in-plane and out-of-plane resistivities.

- Hall effect -

On the basis of band calculations in MgB₂ [9], there are four bands near E_F, two hole-like σ-bands forming a 2D cylindrical Fermi surface, and hole- and electron-like 3D π-bands. Therefore, the normal state Hall coefficients (R_H) are strongly anisotropic [78,87] (see Fig. 3-2). The observed in-plane R_H is positive, as seen in reports on polycrystalline samples and thin films [88-90], while the out-of-plane R_H with H parallel to the ab-plane is negative. The R_H values in these reports were slightly temperature dependent. In order to understand two carrier behavior, Eltsev *et al.* analyzed R_H, assuming two parabolic bands with both holes and electrons as charge carriers [78]. R_H is a sum of the contributions from each band:

$$R_H = \frac{(p\mu_p^2 - n\mu_n^2)}{ec(p\mu_p + n\mu_n)^2},$$

where *e* is the carrier charge, *c* is the velocity of light, *n* and *p* are the densities of electrons and holes, and μ_n and μ_p are the mobilities of electrons and holes, respectively. The positive and negative signs of R_H are a result of the balance between the hole and electron terms. These behaviors can be expected within the framework of a two-band model, taking into account the possibility of different temperature dependence of the hole and electron mobilities. The upper limits of hole and electron densities were estimated to be *p*~2.6×10²² cm⁻³ and *n*~3.4×10²² cm⁻³ at 40 K. The Hall angle, cotθ_H=ρ_{xx}/ρ_{xy}, did not show the T²-dependence observed in high-T_c cuprates (see inset of Fig. 3-2). The scattering rates of σ and π bands differ considerably and σ-π scattering is extremely small [91]. Furthermore, in the temperature dependence of in-plane and out-of-plane longitudinal and Hall resistivities, no sign change was observed, unlike in MgB₂ films [89]. Therefore, the anomalous behavior in Hall effects of polycrystalline samples are due to an extrinsic origin. In conventional superconductors, the sign change of the Hall effects near T_c was reported in clean superconductors with *l*/ξ₀=0.1, where *l* is the electron mean free path, and ξ₀ is the coherence length. However, the sign of MgB₂ does not change in either the clean (*l*>>ξ₀) or dirty (*l*<<ξ₀) limit, where the in-plane and out-of-plane ξ₀ are ~68 Å and ~23 Å [78], and *l* are ~700 Å and ~180 Å, calculating the parameters for anisotropic resistivity, carrier density, and the Fermi velocity of 4.9×10⁷ cm/s (in-plane) and 4.76×10⁷ cm/s (out-of-plane) [9]. The ratio in-plane and out-of-plane *l*/ξ₀ is about 10. Therefore, Eltsev *et al.* concluded that the absence of the sign change of the Hall effect in MgB₂ is in good agreement with the empirical correlation between microscopic material parameters and mixed-state Hall-effect behavior reported for type-II superconductors [92].

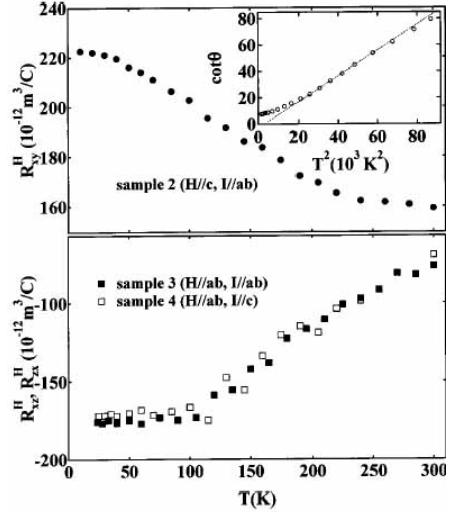


Fig. 3-2. Temperature dependence of in-plane and out-of-plane R_H of MgB₂ [78]. Inset shows temperature dependence of cotθ_H at 5 T.

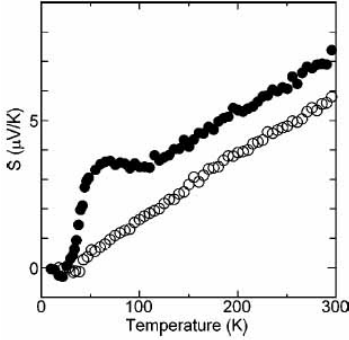


Fig. 3-3. Temperature dependence of S_{ab} (solid circles) and S of polycrystalline MgB_2 (open circles) [76,79].

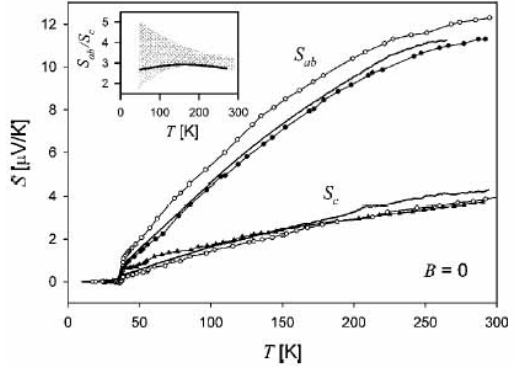


Fig. 3-4. Temperature dependence of in-plane and out-of-plane thermoelectric power, S_{ab} and S_c , measured on single-crystalline MgB_2 [100]. Inset shows anisotropy ratio of S_{ab}/S_c .

- Thermoelectric power -

Thermoelectric power, S , is an important parameter of the EP interaction. As shown by the electronic structure calculations [93], transport properties can be determined by the contribution from four sheets of the Fermi surface. The sign of S is positive in both polycrystalline and single crystal samples, reflecting the dominant contribution of σ -band holes [76,77,78,94-100], and S (S_{ab}) at 300 K is 7-12 $\mu\text{V}/\text{K}$. In particular, Masui *et al.* reported the temperature dependence of S_{ab} (in-plane) for a single crystal and S for a high quality polycrystalline sample. At high temperatures, S_{ab} reveals almost T -linear dependence and reaches ~ 7 $\mu\text{V}/\text{K}$. However, this behavior is contrary to that of polycrystalline samples (see Fig. 3-3). The difference is ascribed to the phonon mean free path because the sample with lower resistivity ($\rho(293\text{K})=38$ $\mu\Omega\text{cm}$, $RRR=2.5$) shows T -linear dependence. In the free-electron model, S is described as

$$S = \frac{\pi^2 k_B^2}{3e} \frac{N(E_F)}{n} T,$$

where $N(E_F)$ is the density of states at the Fermi level and n is the carrier density. The estimated value at room temperature is about 14 $\mu\text{V}/\text{K}$, using predicted values of $N(E_F)=0.25$ states/eV and $n=0.13$ holes/cell for σ -bands [10]. This value is two times larger than the observed one because of the negative contribution of the electron doped π -band. Masui *et al.* also discussed the contributions from acoustic and optical phonons to thermal transport properties. The temperature dependence of S_{ab} showed a broad maximum at around 70 K, while it was not observed in $S(T)$ of polycrystalline samples. This broad peak is attributed to the phonon drag effect; a phonon drag peak is usually observed at $T \sim 0.2\Theta_D$ when the mean free path of phonons is sufficiently long. The Θ_D estimated from $S_{ab}(T)$ is about 350 K and this value is close to that obtained from the resistivity by BG and Einstein analyses [76,79]. Plackowski *et al.* reported in-plane (S_{ab}) and out-of-plane (S_c) thermoelectric powers in a magnetic field up to 13 T [100] (see Fig. 3-4). S_c values in zero field (3.7-4.3 $\mu\text{V}/\text{K}$) are substantially lower than S_{ab} values (11.3-12.3 $\mu\text{V}/\text{K}$). The temperature dependence of S in both directions is similar,

and $S(T)$ increases almost linearly between T_c and 80 K, while at higher temperatures, the curvature becomes increasingly negative. The anisotropy ratio, S_{ab}/S_c , is on the order of 3-4 in the entire temperature region. The behavior of S_c is in contrast to the results reported in Refs. 76 and 79.

3.1.2. Magnetic properties of superconducting state

- Magnetic penetration depth -

The magnetic penetration depth, λ , in a mixed state provides useful information on the low-lying excitations in superconductors and hence that of the anisotropy of the superconducting energy gaps. Until now, several measurements by means of muon spin rotation (μ SR) [101-103], ac susceptibility [101,104], optical conductivity [105] and radio frequency (RF) technique [106,107] have been performed. Earlier experimental studies revealed that the temperature dependence of λ , $\lambda(T)$, followed a power law, that is, a T^2 -dependence [101,105] or/and $T^{2.7}$ -dependence [104], which was contrary to other results that indicate s -wave symmetry. However, later experiments confirmed the exponential temperature dependence of $\lambda(T)$ at low temperature, which is consistent with an s -wave behavior [102,103,106,107]. Carrington *et al.* reported $\lambda_{ab}(0) \approx 1100$ Å, $\xi_{ab}(0) \approx 55$ Å and the mean free path $l \approx 250$ Å from $\Delta\lambda(T)$ for $H//ab$ and $H//c$ on a single crystal (see Fig. 3-5) using the RF technique [106,107]. Although $\Delta\lambda_c(T)$ was shown to exhibit a similar temperature dependence to $\Delta\lambda_{ab}(T)$ and to be 1.4 times larger than $\Delta\lambda_{ab}(T)$, they did not exactly determine $\Delta\lambda_c$ because $\Delta\lambda_c(T)$ contained $\sim 20\%$ error in the absolute value due to the sample surface being uneven. $\Delta\lambda_{ab}(T)$ exhibited a clear exponential temperature dependence at low temperature and it was well fitted by the BCS behavior at $T \leq T_c/3$,

$$\Delta\lambda(T) \approx \lambda_0 \sqrt{\pi\Delta_0 / 2T} \exp(-\Delta_0 / T),$$

where Δ_0 is the energy gap at 0 K and $\lambda_0 = \lambda(0)$ in a weak coupling limit. Δ_0 values estimated by analysis below 12 K for both $\Delta\lambda_{ab}$ and $\Delta\lambda_c$ were 29 ± 2 K and 32 ± 2 K, respectively. The temperature dependence of λ was consistent with an s -wave symmetry, however, the gap was smaller than that in the BCS weak coupling limit. Kang *et al.* reported that $\lambda(T)$ could be represented by a two-gap model with $\Delta_S = 1.9$ meV, $\Delta_L = 6.1$ meV and $\lambda(0) = 76.4$ nm [108], on the basis of a magnetization analysis using the Hao-Clem model [109]. Ohishi *et al.*

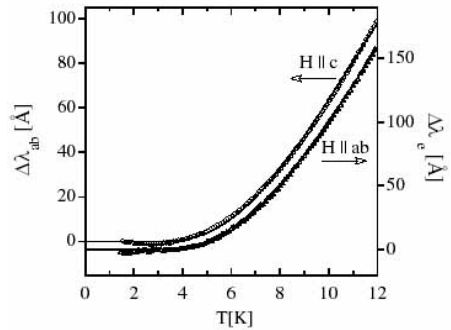


Fig. 3-5. Temperature dependence of penetration depth for $H//c$ and $H//ab$ [106,107]. The solid lines show fitted curves for BCS theory.

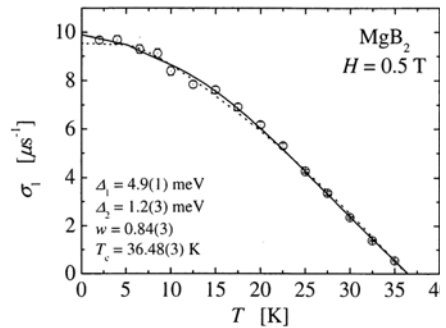


Fig. 3-6. Temperature dependence of σ_1 under 0.5 T [103]. The solid line is the fitted curve for two-gap model.

reported the temperature and magnetic field dependences of λ using μ SR measurements up to 5 T [103]. They measured $\lambda(T, H)$ with precaution in selecting field for the temperature dependence of λ in order to avoid the influence of random flux pinning near the lower critical field, H_{c1} . They analyzed the muon relaxation rate, σ [μs^{-1}], using a two-gap model [110] with Δ on σ -bands ($\Delta_\sigma = \Delta_1$) and Δ on π -bands ($\Delta_\pi = \Delta_2$),

$$\sigma(T) = \sigma(0) - w \cdot \delta\sigma(\Delta_1, T) - (1 - w) \cdot \delta\sigma(\Delta_2, T),$$

$$\delta\sigma(\Delta, T) = \frac{2\sigma(0)}{k_B T} \int_0^\infty f(\varepsilon, T) \cdot [1 - f(\varepsilon, T)] d\varepsilon,$$

$$f(\varepsilon, T) = \left(1 + e^{\sqrt{\varepsilon^2 + \Delta(T)^2} / k_B T} \right)^{-1},$$

where w is the gap energy ratio the two gaps, k_B is the Boltzmann constant, $f(\varepsilon, T)$ is the Fermi distribution function of quasiparticles and $\Delta(T)$ is the BCS gap energy. The obtained Δ_σ , Δ_π , w and T_c are 4.9(1) meV, 1.2(3) meV, 0.84(3) and 36.48(3) K, respectively (see Fig. 3-6). Although their results are consistent with those in other report [102], the value of Δ_π is considerably smaller than the reported value of 2.6(2) meV. λ can be deduced from σ using the following equation in the case of an ideal triangular FLL:

$$\sigma = 4.83 \times 10^4 (1 - h) \left[1 + 3.9(1 - h)^2 \right]^{1/2} \lambda^{-2},$$

where $h = H/H_{c2}$. Therefore, the relationship between σ and λ provides the field dependence of σ when λ is constant. As shown in Fig. 3-7, $\lambda(h)$ increases linearly with increasing h . This behavior is similar to those in $\text{YNi}_2\text{B}_2\text{C}$ [111], NbSe_2 [112] and high- T_c cuprate [113], where the increase of λ is attributed to the anisotropic order parameter and the associated nonlinear effect due to the Doppler shift of the quasiparticles in the nodal region. Fitting the relationship

$$\lambda(H) = \lambda(0) [1 + \eta \cdot h]$$

provides a dimensionless parameter η which represents the strength of the pair-breaking effect; η and $\lambda(0)$ are estimated to be 1.27 ± 0.29 and 116.1 ± 6.2 nm, respectively. The value of η is intermediate between those in $\text{YNi}_2\text{B}_2\text{C}$ ($\eta = 0.97$ at $0.2T_c$) [111] and NbSe_2 ($\eta = 1.61$ at $0.33T_c$) [112], while it is smaller than those in d -wave superconductors ($\eta = 5.5$ - 6.6 in high- T_c cuprates) [113]. These results indicate the existence of excess quasiparticle excitations outside the vortex cores, which strongly suggests an anisotropic structure of the order parameter in MgB_2 .

- Lower and upper critical fields, H_{c1} and H_{c2} -

Because of the unusual Fermi surface topology and the two-gap nature of the superconducting order parameter, peculiar physical properties have been observed [114]. H_{c2} at 0 K ($H_{c2}(0)$) in a single crystal for $H//ab$ plane and $H//c$ axis ($H_{c2//ab}(0)$ and $H_{c2//c}(0)$) were estimated to be ~ 14 - 19 T and ~ 3 - 4 T, respectively, by means of magnetotransport, ac susceptibility, torque

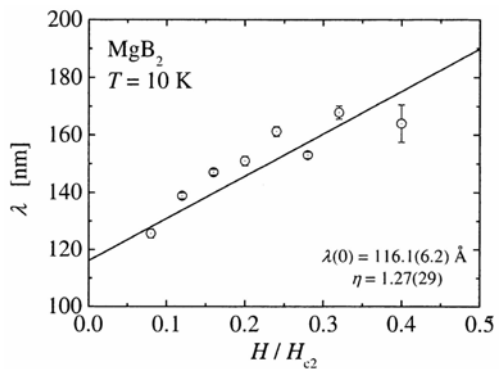


Fig. 3-7. Magnetic field dependence of λ at 10 K [103]. Solid line is a fitted curve.

magnetometry and specific heat measurements [115-123]. $H_{c2//c}(T)$ exhibited a classical linear temperature dependence near T_c , while $H_{c2//ab}(T)$ showed a positive curvature above 20 K (see Fig. 3-8). Moreover, the strong temperature dependence of the anisotropy of H_{c2} , $\Gamma_{Hc2}=H_{c2//ab}/H_{c2//c}$, was reported to be $\sim 5-6$ (0 K) and $\sim 1-2$ (near T_c). An upward curvature $H_{c2}(T)$ near T_c and a temperature-dependent anisotropy have been observed in layered superconductors including NbSe₂ [124] and borocarbide [125]. These behaviors cannot be accounted for by the standard Ginzburg-Landau theory incorporating effective mass anisotropy. These effects are addressed in various theoretical approaches involving gap anisotropy, the two-band model and strong coupling calculation. The use of the two-band model [126] seems appropriate for H_{c2} in MgB₂ because of the unusual Fermi surface and the two-band nature. In the region of low temperature and high field, H_{c2} was dominated by anisotropic 2D bands because the suppression of the 3D gap by high external fields was observed in specific heat measurement [83] and tunneling spectroscopy [127], and thus the anisotropy ratio was enhanced. On the other hand, the superconducting transition involved the entire Fermi surface, including the 3D band near T_c , so the anisotropy ratio was reduced. The temperature dependence of the anisotropy ratio in a lower critical field, $\Gamma_{Hc1}=H_{c1//ab}/H_{c1//c}$, was also reported by several groups. Caplin *et al.* suggested, on the basis of magnetization loops, that $\Gamma_{Hc1}\sim 2$ and independent of temperature [128], but their Γ_{Hc2} was different from those in other reports [115-120,123]. Lyard *et al.* found that $H_{c1//ab}(0)\approx H_{c1//c}(0)\sim 0.11$ T, resulting in $\Gamma_{Hc2}\sim 1$ at low temperature and negative curvature for $H_{c1//c}(T)$, which led to an increase of Γ_{Hc1} with increasing temperature [123] (see Fig. 3-9). The temperature dependence of Γ_{Hc1} is in contrast to that of Γ_{Hc2} , and the increase of Γ_{Hc1} is in good agreement with the theoretical prediction for a weakly coupled two-band superconductor [123,129-131] (see inset of Fig. 3-9), assuming that the anisotropy of each H_{c1} and London penetration depth are the same.

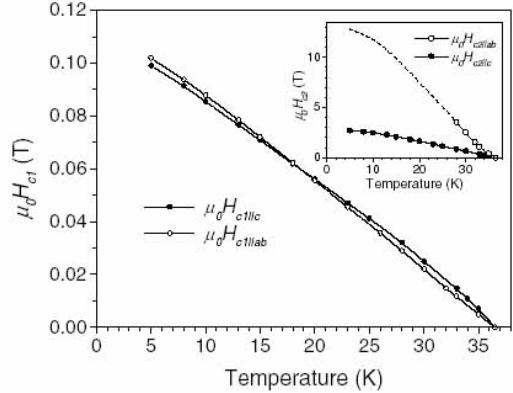


Fig. 3-8. Temperature dependence of $H_{c1//ab}$ and $H_{c1//c}$ [123]. Inset shows temperature dependence of $H_{c2//ab}$ and $H_{c2//c}$.

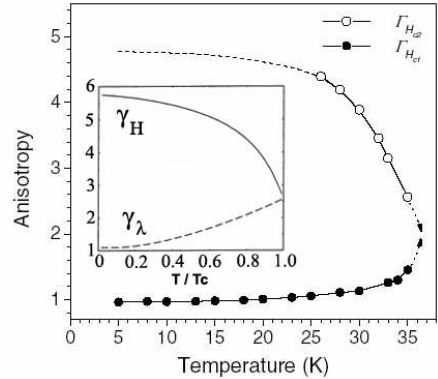


Fig. 3-9. Temperature dependence of Γ_{Hc1} and Γ_{Hc2} [123]. Inset shows temperature dependence of anisotropy ratios, $\gamma_H=H_{c2ab}/H_{c2c}$ and $\gamma_\lambda=\lambda_c/\lambda_{ab}$ [131].

3.2. Electron–Phonon (EP) Coupling in Superconductivity of MgB₂

The reported T_c (39 K) in MgB₂ seems to be the upper limit explained within the framework of phonon-mediated BCS superconductivity. The BCS theory has shown the important roles of high-frequency phonons, and therefore low atomic masses, in producing high T_c . From a fundamental point of view, the central issue of superconductivity in MgB₂ is whether the high T_c in this new system can be understood within the framework of a conventional EP mechanism, or whether a more exotic mechanism is responsible for the superconductive pairing. The isotope effect, dHvA (de Haas-van Alphen) effect, Raman scattering and inelastic neutron and x-ray scattering (INS and IXS) are effective probes for detecting the contributions of phonon modes in superconductivity. Actually, many groups have reported the important role of phonons on this superconductivity [19]. Several groups have calculated the phonon dispersion curve in MgB₂ and the phonon density of states (DOS) [9,10,42, 71,86,132,133]. There are four distinct optical phonon modes with calculated energies in the ranges of 40-42 meV (E_{1u} , in-plane B and Mg displacements), 48-52 meV (A_{2u} , out-of-plane B and Mg displacements), 58-82 meV (E_{2g} , B in-plane bond stretching), and 84-86 meV (B_{1g} , B out-of-plane bond bending) at the zone centre (Γ point) in MgB₂ (see Fig. 3-10). From the generalized phonon DOS (GDOS) based on the Born-von Karman (BvK) model, the contribution of light B atoms to the most weight to GDOS at high energies was calculated [132]. The strength and frequency dependence of EP coupling were determined from the EP spectral density, $\alpha^2(\omega)F(\omega)$, and the bare phonon DOS, $F(\omega)$. $\alpha^2(\omega)F(\omega)$ can be derived from the tunneling spectrum, while $F(\omega)$ can be derived from the INS law $S(Q, \omega)$. Usually, $\alpha(\omega)$ varies smoothly with frequency, so the bare phonon DOS provides an estimation of the frequency moments that determine the T_c value [134]. The calculations of the EP coupling constant indicated strong coupling of the electron to the E_{2g} optic phonon mode, while the coupling to the other optic phonon modes was weak [72].

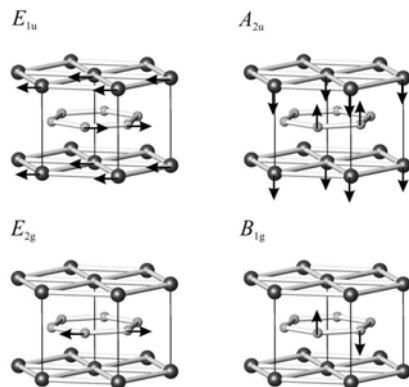


Fig. 3-10. Calculated phonon modes in MgB₂. Arrows show the direction of atom vibration.

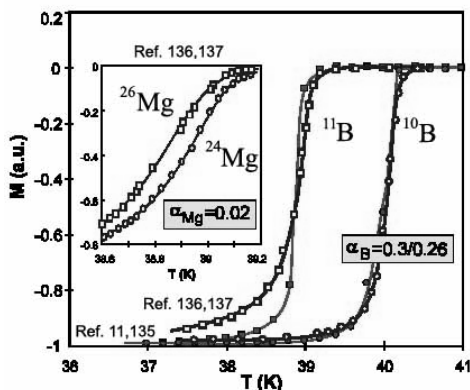


Fig. 3-11. Temperature dependence of relative magnetization of Mg¹⁰B₂ and Mg¹¹B₂. Inset shows Mg, ²⁴Mg and ²⁶Mg isotope effects, [11,135-137] (adopted from Ref. 18).

- Isotope effect -

In order to understand the role of phonons in superconductivity, the isotope effect is crucial information. The change of T_c with isotope mass suggests that phonons may play an important role in superconductivity. The isotope effect coefficient, α , is defined by the relationship, $T_c \propto M^{-\alpha}$, where M is the atomic mass. The boron isotope effect was reported by Bud'ko *et al.* who performed susceptibility and specific heat measurements (see Fig. 3-11) [11,135]. They reported that the increase of T_c upon substituting ^{10}B for ^{11}B is 1.0 K, and the boron isotope effect coefficient, α_B , is 0.26(3). This shift can be explained by the phonon-mediated BCS superconducting mechanism; therefore, the boron phonon modes play an important role in the pairing interaction. Hinks *et al.* reported that the estimated isotope effect coefficients for both B and Mg, α_B and α_{Mg} , are 0.30(1) and 0.02(1), respectively [136,137]. These results show that the phonons involved in superconductivity are primarily boron phonons. The Mg phonons apparently contribute little to overall pairing. Although α is experimentally found to be close to 0.5 for a simple metal such as Hg, Pb and Sn, α obtained for MgB_2 is much less than 0.5. Using the McMillan equation, α can be written as

$$\alpha = \frac{1}{2} \left[1 - \frac{1.04(1+\lambda)(1+0.62\lambda)\mu^{*2}}{(\lambda - \mu^*(1+0.62\lambda))^2} \right],$$

where λ is the coupling constant and μ^* is the screened Coulomb potential [138]. The coefficient α is obtained to be 0.5 in a phonon-mediated BCS superconductor with $\mu^*=0$ (corresponding to the weak-coupling limit). Therefore, MgB_2 is thought to be a strong-coupling superconductor.

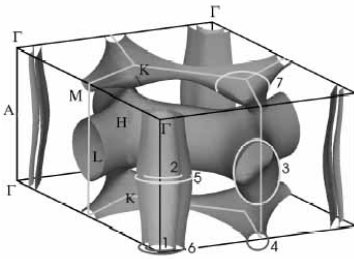


Fig. 3-12. Calculated Fermi surface topology with possible dHvA external orbits (for frequencies < 10 kT) [9,140].

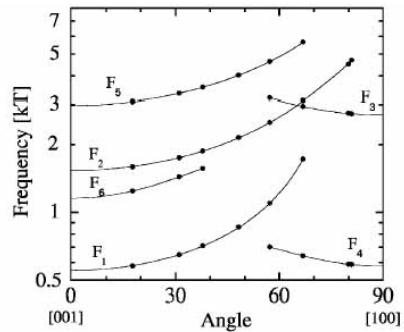


Fig. 3-13. Angular dependence of observed frequencies as sample rotation from $H//c$ to $H//a$ [140].

- de Haas-van Alphen (dHvA) effect -

Experimental studies on the dHvA effect provide crucial information on the electric properties of metals. The observations of quantum oscillations allow the determination of the shape of the Fermi surface and the effective masses of carriers on individual Fermi sheets. Then, EP coupling constants can be obtained through band structure calculations. Yelland *et al.* [139] and Carrington *et al.* [140] reported dHvA studies using a single crystal. Three dHvA frequencies were clearly resolved [139] for a rotation between [001] and [100], and these signals could be analyzed in the conventional manner using the Lifshitz-Kosevich expression [141]

for the oscillatory magnetization of a 3D Fermi liquid. Comparison between the temperature and angular dependences of the dHvA frequency and the temperature dependence of the dHvA amplitude with the band calculations strongly suggests that two of these frequencies originate from a single warped Fermi surface tube along the c direction and the third one is from cylindrical sections of an in-plane honeycomb network. The obtained effective mass was 0.44-0.68 m_e . Yelland *et al.* found that the EP coupling strength λ is ~ 3 times larger for the c -axis tube orbits than for the in-plane network orbit, upon comparison with calculated band masses. Carrington *et al.* detected dHvA orbits from all four sheets of the Fermi surface (see Fig. 3-12 and Fig. 3-13) [140], and they suggested an overall topology of the predicted electronic structure in MgB_2 . The EP interaction was larger on σ sheets and much smaller on π sheets, according to the calculations of the EP coupling constants for the different orbits.

- Raman scattering-

The phonon vibrational symmetry at the Γ point is specified as B_{1g} , E_{2g} , A_{2u} and E_{1u} modes. The E_{2g} phonon mode, which is ascribed to the in-plane B bond stretching mode in the honeycomb sheet, is responsible for EP coupling. Evidence of the EP interaction and two-gap nature has been supplied by several measurements [58,86,142-149]. The E_{2g} phonon frequency is estimated to be 590-660 cm^{-1} according to several theoretical calculations [9,10,36,71,72,133]. Raman scattering measurement is a powerful experimental technique for studying superconductors because it can provide direct information on the superconducting gap. The frequency and polarization dependence of the pair breaking peak can determine the magnitude and symmetry of the superconducting gap (2Δ). Quilty *et al.* reported the temperature and polarization dependence of the 2Δ pair breaking peak from in-plane and out-of-plane Raman shifts [144,145,148]. They suggested that the measured peak structure at around $105 \pm 1 \text{ cm}^{-1}$ in the in-plane spectrum showed BCS-like temperature dependence with slight anisotropy (see Fig. 3-14). This peak was associated with the clean-limit superconductivity on σ bands, and the average gap to T_c ratio $2\Delta/k_B T_c = 3.96 \pm 0.09$ indicated a strong-coupling superconductor. On the other hand, the measured peak structure at around 29 cm^{-1} in the out-of-plane spectrum indicated strongly damped superconductivity-induced renormalization on π bands. Two gaps in MgB_2 , a large gap on σ bands and a small one on π bands, could be distinguished from these behaviors. Both $2\Delta_\sigma$ and $2\Delta_\pi$ were consistent with the temperature dependence cal-

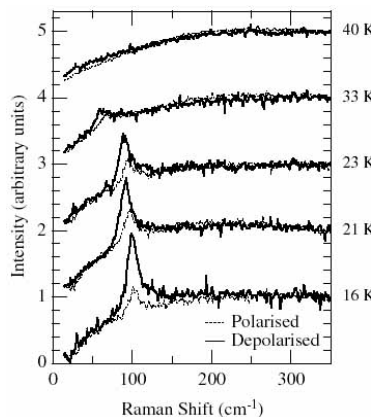


Fig. 3-14. Polarized and depolarized Raman spectra at $T < T_c$ [144].

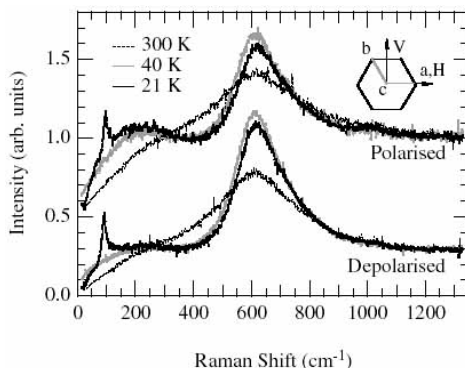


Fig. 3-15. Polarized (VV) and depolarized (HV) Raman spectra at 300 K, 40 K and 21 K [144]. Inset shows polarization orientation relative to MgB_2 crystallographic axis.

culated using the Eliashberg formula, and their magnitudes showed good agreement with the results of theoretical calculations [77,150]. They also reported that the E_{2g} mode was observed at around 620 cm^{-1} . This feature narrowed substantially with decreasing temperature (see Fig. 3-15), which is consistent with theoretical suggestions that the E_{2g} phonon is very unharmonic [133]. The spectrum had an unusually broad linewidth of almost 300 cm^{-1} , which was ascribed to an unharmonic character due to strong EP coupling. Martinho *et al.* pointed out that the temperature evolution of the E_{2g} linewidth was well fitted by 2-phonon unharmonic decay function throughout the entire temperature range, without any hardening or softening of the phonon mode [151].

- Inelastic neutron scattering (INS) measurement -

The investigation of phonons in MgB_2 is important as they play a crucial role in the superconductivity. In order to understand the phonon contribution to superconductivity in MgB_2 , several groups studied the phonon DOS by means of INS measurements on polycrystalline Mg^{11}B_2 [132,133,136,152]. The phonon DOS measured by each group are in agreement with the calculated phonon DOS (see Fig. 3-16) [86,133]. The acoustic phonon modes existed up to 35 meV and optical modes existed at higher energies of around 55, 70, 80, 90 and 100 meV. In particular, these optic phonon modes had a large width, which was due to dispersion curve features of the optic phonon branches. Yildirim *et al.* reported that no substantial changes were found in the temperature dependence of the spectrum from 7 up to 200 K, while a very modest softening mode was observed at around 325 K [133]. In addition, they theoretically predicted that E_{2g} in-plane modes are strongly coupled to the planar B σ bands near the Fermi level (see Fig. 3-17). Since the in-plane B motions change the boron orbital overlap, there is a significant splitting of the bands as well as shifts near the Fermi level, indicating strong EP coupling. Osborn *et al.* reported that the only difference in the temperature range between 8 K and 100 K was a slight suppression of the peak at 54 meV below T_c [132]. In a polycrystalline average, this change in phonon DOS is a very small effect, but it could still represent a significant change in an

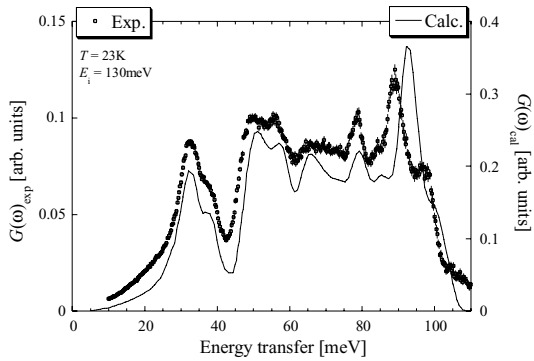


Fig. 3-16. Experimental result and theoretically calculated phonon DOS, $G(\omega)$, in MgB_2 [152]. The solid line shows the theoretical calculation from Ref. 90.

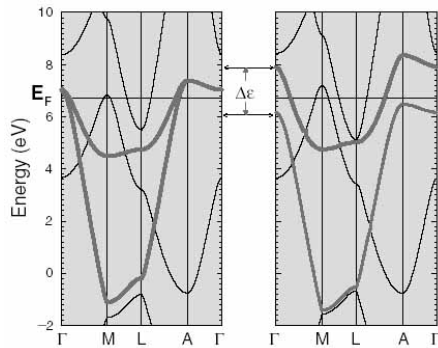


Fig. 3-17. Band structure undistorted (left) and distorted (right) by E_{2g} phonons [133].

individual phonon branch. This mode at around 54 meV was ascribed to the E_{2g} phonon mode and it was predicted to have the strongest EP coupling [10]. On the other hand, Muranaka *et al.* reported that the integrated intensity of phonon DOS increases with decreasing temperature in the energy ranges of 75 to 80 meV and 87 to 91 meV, assuming a multiphonon contribution [153]. Since these energy regions were close to the energies of E_{2g} and B_{1g} phonon modes at the Γ point, they suggested that this behavior could be interpreted as evidence of a strong relationship between these phonon states and superconductivity. However, such conclusions by Osbron *et al.* and Muranaka *et al.* require the measurement of phonon dispersion curves using a single crystal in order to be substantiated.

- Inelastic x-ray scattering (IXS) measurement -

INS and Raman scattering showed that the temperature dependence of phonon DOS in the energy range of the E_{2g} phonon mode revealed anomalous behavior [132,152] and that the optical E_{2g} phonon was strongly damped [58,86,142]. Phonon damping can be caused by EP coupling, i.e., mediated phonons decay into electron-hole pairs [153], or phonon-phonon interaction due to unharmonicity [154]. Many calculations suggest strong unharmonic effects in MgB_2 [72,133]. The INS experiments using polycrystalline samples [132,133,137,152] involve the integration of $Q(\omega)$ which does not allow easy specification of the each mode, and Raman scattering is limited in detecting every phonon (Raman active phonon; E_{2g} in MgB_2) at the Γ point [58,86,142-149]. Since the available single crystals of MgB_2 were too small for

INS measurements, IXS measurements were performed by two groups to obtain the phonon dispersion in MgB_2 and linewidth of phonons [155,156]. The linewidth (inverse of lifetime) of a given phonon is the sum of contributions from both EP coupling and unharmonic effects. Shukla *et al.* reported the phonon dispersion curves and linewidths along Γ -A, Γ -M and A-L in the Brillouin zone (BZ) (see Fig. 3-18) [155]. The measured phonon dispersion curves were in good agreement with their calculations, and the measured intrinsic linewidth of the E_{2g} branch was strongly anisotropic in the BZ. Along Γ -A, the linewidth of E_{2g} was large, while near the L and M points, it was within the experimental resolution. They suggested that the dominant contribution to broadening for all modes was EP coupling, because the unharmonic contribution was much smaller on comparison of the EP coupling constants obtained from experimental results and theoretical calculations. On the other hand, Baron *et al.* reported the softening and broadening of the crucial E_{2g} mode in the region of the Kohn anomaly along Γ -M [156]. They reported the presence of a longitudinal mode along Γ -A near the energy range of the E_{2g} mode, which was not predicted by theoretical calculations, but this anomalous intensity remains unexplained.

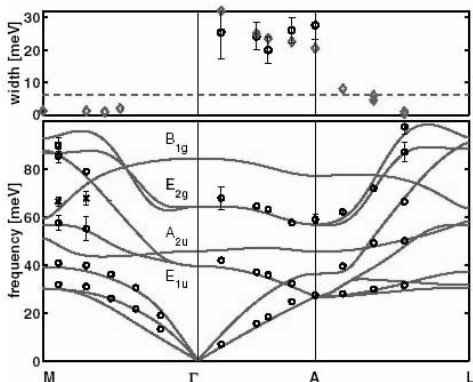


Fig. 3-18. Bottom: Experimental (circles) and theoretical phonon dispersion (solid line) along Γ -A, Γ -M and A-L [155]. Top: Intrinsic line width of E_{2g} mode.

3.3. Multigap in MgB₂

Soon after the discovery of MgB₂, it was basically classified as a conventional phonon-mediated BCS superconductor [13,18,157,158]. However, deviations from the BCS framework have been inferred from several experiments of, specific heat, photoemission spectroscopy (PES) and tunneling spectroscopy, using polycrystalline samples or single crystals [83,110,159-165]. The striking feature is the direct observation of two kinds of superconducting gaps in MgB₂. Theoretically, the two-band model was proposed to be appropriate for MgB₂ because the system consists of two qualitatively different charge carriers derived from 3D π and 2D σ bands [72]. Holes in σ bands are strongly coupled to phonons confined within the boron honeycomb plane. The large gap Δ_σ opens in σ bands, whereas a relatively small gap Δ_π opens in π bands due to the difference in the strength of EP coupling in each band. This scenario for superconductivity in MgB₂ is supported by an increasing number of experimental results. The concept of two-band superconductivity was first suggested by Suhl *et al.* [14] soon after the advocacy of the BCS theory, and has been discussed, since then, in relation to other superconductors, including Nb, Ta [166], doped SrTiO₃ [15] and borocarbide [125]. Several experimental reports presented clear signatures for two-gap superconductivity and offered the opportunity for comparison with theoretical predictions. Thus, MgB₂ is the first example of this model and opens up the possibility of interesting new phenomena.

- Specific heat -

In an early stage, specific heat measurements of a polycrystalline sample provided direct experimental evidence of the presence of a second gap in MgB₂ [83,110,159,167,168]. Several experimental results on higher quality polycrystalline samples and single crystals were subsequently reported [163,169,170]. Bouquet *et al.* reported the temperature dependence of specific heat, $C(T)$, under magnet fields [83,110,159,170]. In zero field, deviations from the BCS curve were observed in the amplitude and sharpness of the specific heat jump, and the large excess weight near $0.2T_c$ was a robust feature (see Fig. 3-19). Similar features were observed by other groups. Yang *et al.* and Bouquet *et al.* noted that the exponential decrease of $C(T)$ at low temperature is representative of a small gap, $\sim 1-1.5k_B T_c$, whereas Kremer *et al.* reported a larger gap of $\sim 4k_B T_c$ and strong coupling from specific heat jump [167-170]. These unusual behaviors were consequences of the anisotropic band structure of MgB₂. Two main bands cross the Fermi level. One consists of electrons and holes in the 3D π band and represents $\sim 56\%$ of the total DOS. The

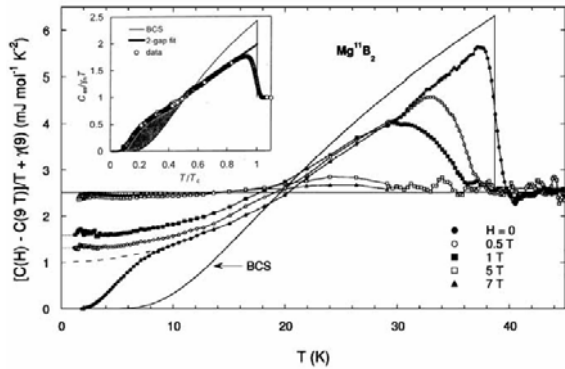


Fig. 3-19. Temperature dependence of specific heat in Mg¹¹B₂ $[C(H)-C(9T)]/T$ at various magnetic fields [83]. Inset shows temperature dependence of electric part of specific heat in superconducting state C_{es}/T normalized to γ_n [170]. The thick line is fitted two-gap line, and hatched area marks the low-temperature excess.

other consists of holes in the 2D σ band and represents $\sim 44\%$ of the total DOS. These different types of carriers induce two gaps at $T = 0$, $\Delta_{0\pi} \sim 2$ meV and $\Delta_{0\sigma} \sim 7$ meV; both gaps disappear at the same T_c [9,72,150]. The specific heat data were analyzed using the two-gap model (“ α model” [171]) with the gap values $\Delta_{0\pi}$ and $\Delta_{0\sigma}$, and relative weights of the Sommerfeld constant in each band, $\gamma_{\pi n}/\gamma_n$ and $\gamma_{\sigma n}/\gamma_n$ (see inset of Fig. 3-19). The superconducting state entropy is described by the following equation in the two-gap superconductor model:

$$S_{es} = -2k_B \sum_k \sum_n [f_k \ln f_k + (1 - f_k) \ln(1 - f_k)],$$

$$f_k = [1 + \exp(E_k/k_B T)]^{-1},$$

where the double sum is over the quasiparticle states in both bands, and E_k is the quasiparticle energy, which is different in the two bands. $E_{k1}^2 = \epsilon_{k1}^2 + \Delta_1^2$ and $E_{k2}^2 = \epsilon_{k2}^2 + \Delta_2^2$, where ϵ_k is the normal state quasiparticle energy, and $\Delta_1(T)$ and $\Delta_2(T)$ are gap functions. The temperature dependence of each gap follows the weak-coupling BCS behavior, but the amplitude is scaled by the parameter $\alpha = \Delta(0)/k_B T_c$: $\Delta_1(T) = (\alpha_1/\alpha_{\text{BCS}})\Delta_{\text{BCS}}(T)$ and $\Delta_2(T) = (\alpha_2/\alpha_{\text{BCS}})\Delta_{\text{BCS}}(T)$, where $\alpha_{\text{BCS}} = 1.764$, α_1 and α_2 are free parameters, and the reduced gaps, $\Delta_1(T)/\Delta_1(0) = \Delta_2(T)/\Delta_2(0) = \tilde{\Delta}(T)$, are assigned numerical values tabulated by Mühlshlegel [172]. Thus, $S_{es}(t)/\gamma_n T_c$ in Ref. 171 becomes

$$S_{es}/\gamma_n T_c = -\left(\frac{3}{\pi^2}\right)\alpha_1(\gamma_1/\gamma_n) \int [f_{x1} \ln f_{x1} + (1 - f_{x1}) \ln(1 - f_{x1})] dx$$

$$- \left(\frac{3}{\pi^2}\right)\alpha_2(\gamma_2/\gamma_n) \int [f_{x2} \ln f_{x2} + (1 - f_{x2}) \ln(1 - f_{x2})] dx,$$

where γ_1 and γ_2 represent the electron DOS in the two bands, and have the relationship

$$\gamma_1 + \gamma_2 = \gamma_n,$$

$$f_{x1} = \left\{ 1 + \exp\left[\alpha_1 t^{-1} (x^2 + \delta^2)^{1/2}\right] \right\}^{-1}$$

$$f_{x2} = \left\{ 1 + \exp\left[\alpha_2 t^{-1} (x^2 + \delta^2)^{1/2}\right] \right\}^{-1}.$$

Here $t \equiv T/T_c$, and the differential of $S_{es}(t)/\gamma_n T_c$ gives C_{es} . For a two-gap superconductor, C_{es} is the sum of two curves, one scaled by γ_1/γ_n and the other by γ_2/γ_n , and is obtained numerically. These parameters were estimated to be $\gamma_{\pi n}:\gamma_{\sigma n} \approx 45:55$, $2\Delta_{0\pi}/k_B T_c \approx 1.2$ -1.3 and $2\Delta_{0\sigma}/k_B T_c \approx 3.8$ -4.3 [110], which show good agreement with band calculations [72] and other spectroscopic measurements [144,161, 162]. Bouquet *et al.* also determined the Sommerfeld constant, γ_n , to be 2.6 mJ/mol·K², the Debye temperature, Θ , to be 1050 K, $[H_c(0)]^2/\gamma_n T_c^2$ to be 5.46 and $\Delta C(T_c)/\gamma_n T_c$ to be 1.32. From these results, they concluded that gap values $[H_c(0)]^2/\gamma_n T_c^2$ and $\Delta C(T_c)/\gamma_n T_c$ smaller than the BCS ones (5.95 and 1.43, respectively) can be ascribed to gap anisotropy or a multigap structure. In addition, they reported the results for a single crystal under magnetic fields up to 14 T ($H//ab$ and $H//c$). In the region of $H < 0.5$ T, no anisotropy of the Sommerfeld constant Γ (γ_{ab}/γ_c) was distinguished for the two directions, the ratio being ~ 1 . On the other hand, in the region of $H > 0.5$ T, Γ rapidly increased toward $\Gamma \sim 5$ with increasing H (see Fig. 3-20).

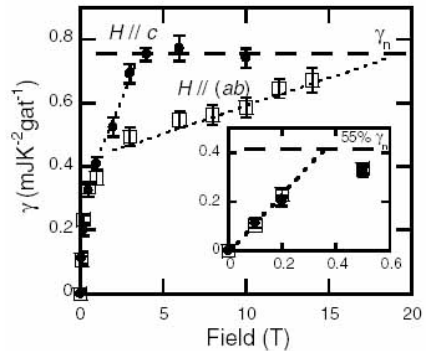


Fig. 3-20. Magnetic field dependence of Sommerfeld constant $\gamma(H)$ for $H//c$ and $H//ab$ [163]. Inset shows expanded view of the low-field region.

Similarly, Angst *et al.* reported that Γ increased linearly from ~ 2 under zero field up to 3.7 under 10 T [117,118].

- Photoemission spectroscopy (PES) -

In an early stage after the discovery of MgB_2 , the superconducting gap size Δ of 2-5.9 meV ($2\Delta/k_B T_c = 1.2-3.5$) was reported, as determined by spectroscopic measurements assuming an isotropic s -wave symmetry gap [128,157,158]. On the other hand, later experimental reports showed clear signatures for two-gap superconductivity. Theoretically, in MgB_2 , superconducting gaps with significantly different magnitudes were expected to open in the σ and π bands, as a result of the strong k dependence of EP coupling [72,150]. Because angle-resolved photoemission spectroscopy (ARPES) can observe the k -dependence of the superconducting gap, this technique is a powerful probe for measuring the superconducting gap in both σ and π bands in MgB_2 . ARPES of a high-density polycrystalline sample [161] and a single crystal [164,165,173] yielded experimental evidence of two-gap superconductivity and indicated the band structure of MgB_2 along $\Gamma K M$ (AHL), in studies by Uchiyama *et al.* and Souma *et al.* (see Fig. 3-21), and along $\Gamma \Sigma M$ in a study by Tsuda *et al.* The observed band structure showed considerable agreement with the results of band calculations [9,10]. However, Uchiyama *et al.* and Souma *et al.* observed a difference between experimental results and theoretical calculations. The difference was that a small electron-like pocket was observed around the $\Gamma(A)$ point, and they ascribed the observed band to a surface state. Tsuda *et al.* and Souma *et al.* reported Δ_π and Δ_σ to be 2.2 ± 0.4 and 5.5 ± 0.4 meV [164] and 1.5 ± 0.5 and 6.5 ± 0.5 meV [165] with s -wave symmetry. In the surface band observed by Souma *et al.*, the gap size was close to Δ_σ (6.0 ± 0.5 meV). Tsuda *et al.* reported that both gaps Δ_π and Δ_σ closed at the same temperature (see Fig. 3-22). These behaviors indicate the existence of strong interband pairing interaction in MgB_2 .

- Tunneling spectroscopy -

Tunneling spectroscopy traditionally is one of the most sensitive probes for observing the superconducting gap structure because the tunneling conductance (dI/dV) is equivalent to DOS near E_F [174]. Scanning tunneling microscopy (STM), point contact, planar junction and break junction are widely used in tunneling spectroscopy. At a finite temperature, the tunneling conductance in the S-I-N junction can be calculated from

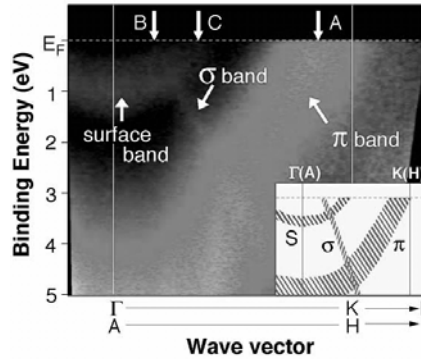


Fig. 3-21. Band structure near E_F along $\Gamma K M$ (AHL) at 45 K obtained by ARPES [165].

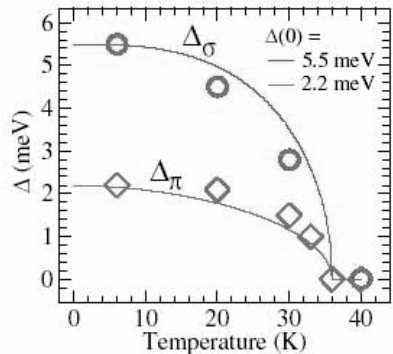


Fig. 3-22. Temperature dependence of superconducting gap $\Delta(T)$ [164]. Open circles and diamonds show the gap values on the σ and π bands.

$$dI/dV = -\sigma_N \int N(E) \partial f(E + eV) / \partial eV dE,$$

where $N(E)$ is the quasiparticle DOS and σ_N is the conductance of the junction in the normal state. To account for the experimentally observed broadening due to thermal smearing, the smearing parameter Γ is usually used in the BCS DOS [175].

$$N(E) = \text{Re} \left[\frac{|E - i\Gamma|}{\sqrt{(|E - i\Gamma|^2 - \Delta^2)}} \right]$$

To analyze the tunneling conductance of MgB_2 under the assumption of two-band superconductivity, an analytical model requires the solutions of two simultaneous equations for two gaps:

$$\Delta_1(E) = \frac{\Delta_1^0 + \Gamma_1 \Delta_2(E) / \sqrt{\Delta_2^2(E) - (E - i\Gamma_2^*)^2}}{1 + \Gamma_1 / \sqrt{\Delta_2^2(E) - (E - i\Gamma_2^*)^2}}$$

$$\Delta_2(E) = \frac{\Delta_2^0 + \Gamma_2 \Delta_1(E) / \sqrt{\Delta_1^2(E) - (E - i\Gamma_1^*)^2}}{1 + \Gamma_2 / \sqrt{\Delta_1^2(E) - (E - i\Gamma_1^*)^2}},$$

where $\Delta_{1,2}^0$ are the intrinsic pairing amplitudes in the two bands, $\Gamma_{1,2}$ are scattering rates related inversely to the times spent in each band prior to scattering to the other, and $\Gamma_{1,2}^*$ are smearing parameters in the two bands, which are added to account for lifetime effects.

Although many tunneling results for MgB_2 have been reported, the gap values are scattered in the range of $\Delta = 1.7$ -10, which indicated inconsistent results (see Table 3-1). This is probably due to the sensitivity of the sample surface state. However, these observed values have been categorized into two groups, Δ_π and Δ_σ [176], which had already been predicted theoretically [72,150]. Iavarone *et al.*, Guibileo *et al.* and Karpinski *et al.* reported two distinct gap structures in the STM spectrum [12,157,177,178-181]. With increasing temperature, this two distinct gap structures disappeared at T_c of the bulk MgB_2 . In particular, Iavarone *et al.* reported that temperature dependence of both gaps followed the BCS theory (see Fig. 3-23). This result confirmed the importance of Fermi-surface-sheet-dependent superconductivity in MgB_2 that was proposed in the multigap model [72]. The results of point contact were reported by Laube *et al.*, Li *et al.*, Lee *et al.*, Bugoslavsky *et al.*, Szabó *et al.* and Gonnelli *et al.* for MgB_2 -Cu [160], In [162,182], Pt [162,183,189], Nb [184,185] Au [162,186-189] junction. They also reported evidence for two distinct superconducting energy gaps, and temperature dependences of both gaps were in good agreement with the BCS theory. Schmidt *et al.*, Gonnelli *et al.* and Ekino *et al.* reported the tunneling spectrum obtained by the break junction method [127,176,189-193], and their results were in basic agreement with other results of STM, point contact and the break junction. However, the observed gaps revealed parallel contributions to the conductance from both bands because of the existence of the S-I-S junction. A subtle feature was observed near the $\Delta_\pi + \Delta_\sigma$ region, which was reminiscent of strong coupling effects. This feature provided important insight into the nature of two-gap superconductivity in MgB_2 .

Table 3-1. Energy gaps of MgB₂ determined by different tunneling spectroscopy methods (adopted from Ref. 176).

| | Energy gap (meV) | | Reference |
|----------------|-------------------|-----------------------|---------------|
| STM | $\Delta\pi=2.0$ | | [177] |
| | | $\Delta=5-7$ | [12] |
| | $\Delta\pi=2.3$ | $\Delta\sigma=7.1$ | [157,178] |
| | $\Delta\pi=3.5$ | $\Delta\sigma=7.5$ | [179] |
| | $\Delta\pi=2.2$ | $\Delta\sigma=6.9$ | [180,181] |
| Point contact | $\Delta\pi=2.6$ | | [182] |
| | $\Delta\pi=1.7$ | $\Delta\sigma=7$ | [183] |
| | $\Delta\pi=2.8$ | $\Delta\sigma=9.8$ | [184,185] |
| | $\Delta\pi=2.8$ | $\Delta\sigma=7.0$ | [160] |
| | $\Delta\pi=2-3$ | $\Delta\sigma=6-8$ | [186] |
| | $\Delta\pi=2.3$ | $\Delta\sigma=6.2$ | [187] |
| | | $\Delta=3-4$ | [188] |
| | $\Delta\pi=2.8$ | $\Delta\sigma=7.1$ | [162,189] |
| Break junction | $\Delta\pi=1.7-2$ | | [190] |
| | $\Delta\pi=2.5$ | $\Delta\sigma=7.6$ | [127,176,191] |
| | $\Delta\pi=2-2.5$ | $\Delta\sigma=8.5-10$ | [192,193] |

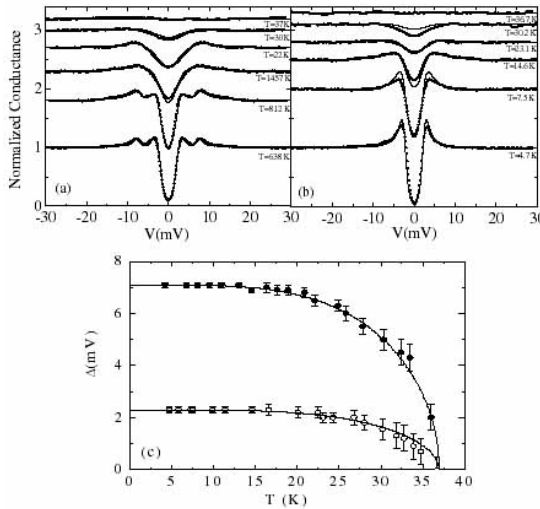


Fig. 3-23. Tunneling spectrum with theoretical curves (a), (b) and temperature dependence of the gap values (c) [178]. Solid lines show BCS curves.

4. POTENTIAL OF MgB_2 FOR PRACTICAL APPLICATIONS

4.1. Critical Current Properties of MgB_2 Single Crystals, Bulks and Thin Films

4.1.1. Attractive points of MgB_2 for practical applications

Since MgB_2 has the highest T_c of approximately 39 K among metallic superconductors and sufficient chemical stability, it is expected to be a new candidate material for practical applications, such as in superconducting wires and thin films, with operation at as high as 20 K, which can be easily attained using small cryocoolers or liquid hydrogen. The strongest point of MgB_2 is its high T_c , which is higher than twice that of the currently widely used metallic superconductor, Nb_3Sn ($T_c \sim 18$ K). Although T_c of MgB_2 is much lower than those of cuprate superconductors developed for practical applications, such as $\text{YBa}_2\text{Cu}_3\text{O}_y$ ($T_c \sim 92$ K) and $(\text{Bi,Pb})_2\text{Sr}_2\text{Cu}_3\text{O}_y$ ($T_c \sim 110$ K), MgB_2 has many advantages, such as strong grain coupling for superconducting current due to long coherence length and high carrier density, low electromagnetic anisotropy, and simple binary composition without expensive elements. These points are not well satisfied by cuprate superconductors that have short coherence length, high electromagnetic anisotropy requiring a grain alignment technique, and several constituent elements including some expensive and rare ones. In addition, it should be noted that MgB_2 is essentially a line compound free from the nonstoichiometric composition, which results in highly reproducible T_c , when it is prepared at moderately high temperatures under the thermodynamically equilibrium state. This point is quite favorable for the design and development of practical materials, in contrast to A15-type intermetallic compounds and cuprates having cation and/or oxygen nonstoichiometry.

T_c of pure MgB_2 is changed by lattice strain, crystallinity and possible magnesium deficiency. Lattice strain enhances T_c up to 41.8 K by slight expansion of the crystallographic c -axis. On the other hand, low crystallinity and magnesium deficiency, which occur with low-temperature processing, always decrease T_c . However, a decrease of T_c by several K can be allowed for practical applications at ~ 20 K.

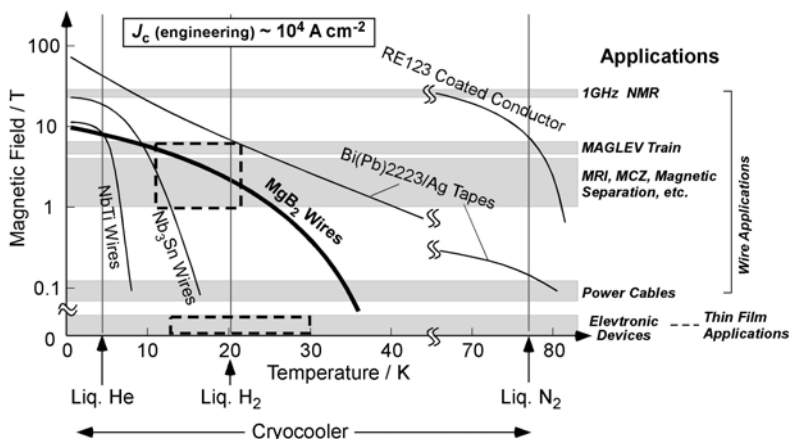


Fig. 4-1. Application fields of superconductors and $J_c(\text{engineering}) \sim 10^4 \text{ A cm}^{-2}$ lines for various superconducting materials. Expected applications for MgB_2 wires and thin films are represented by squares with dashed line.

For extensive application of MgB₂ wires, high critical current density, J_c , must be achieved even in high magnetic fields. This means that a high-irreversibility field, H_{irr} , and high J_c in the irreversible region are required for wire applications, such as magnets for MRI, MCZ and MAGLEV trains. For thin film device applications, homogeneous superconducting properties with high T_c and J_c as well as clean surfaces are required. Expected fields of application for MgB₂ materials are displayed in Fig. 4-1 together with those for other superconducting materials.

In the following section, critical current properties of undoped MgB₂ are summarized for single crystals, bulk and thin films in order to clarify the essential factors determining J_c of MgB₂.

4.1.2. Critical current properties of MgB₂ single crystals

Single crystals of MgB₂ were synthesized at high temperatures under high pressures in sealed BN capsules [56] or by heating in a metal container [73]. The crystals grown were plate-like with a c -axis vertical to the wide plane and smaller than 0.1 mm². Therefore, these tiny single crystals were not suitable for precise critical current measurements and were mainly used for studies on the fundamental physical properties. As was described in the previous section, the upper critical field, H_{c2} , of MgB₂ single crystals is low because of its long coherence length, and its anisotropy is small with $H_{c2}(//ab) / H_{c2}(//c) = 2\sim 5$ [119]. In particular, $H_{c2}(//c)$ is quite low, approximately 35 kOe at 0 K. Reported J_c 's for MgB₂ single crystals are $\sim 10^5$ A cm⁻² or less even at low temperatures below 10 K under low magnetic fields [116,194]. Furthermore, J_c of the single crystals rapidly decreases with increasing magnetic field. For example, J_c becomes $\sim 10^3$ A cm⁻² under an applied field of 20 kOe parallel to the c -axis. H_{irr} 's of single crystals are ~ 30 k and ~ 10 kOe at 5 and 20 K, respectively, under $H//c$. These mean that intragrain critical current properties of clean MgB₂ crystals are not sufficient for practical applications even at the liquid-He temperature.

4.1.3. Critical current properties of “*ex-situ*” processed MgB₂ bulk

Typical MgB₂ bulk shows much higher critical current performance than the single crystals. Many methods have so far been developed to synthesize MgB₂ bulk and the resulting bulk has exhibited various critical current properties. The “*ex-situ*” method is one of the main methods of producing MgB₂ bulk, in which commercial MgB₂ powder is used as a starting material. In this method, sintering under high pressures of several GPa is required for the fabrication of a well sintered bulk specimen [195] because MgB₂ grains are not strongly joined by sintering under ambient pressure. The high-pressure sintered bulk is highly dense having almost 100% the theoretical density of MgB₂, and is mainly composed of small grains 1~5 μm in diameter. J_c 's of the dense sintered bulk under low fields are $\sim 5 \times 10^2$ and 2×10^5 A cm⁻² at 5 and 20 K, respectively, which are several times higher than those of single crystals. In addition, the magnetic field dependence of J_c is greatly suppressed in the dense sintered bulk. High J_c of above 10^4 A cm⁻² is maintained up to ~ 50 kOe at 5 K and ~ 30 kOe at 20 K. H_{irr} is also improved to ~ 50 kOe at 20 K. Note that this H_{irr} is close to that of single crystals under $H//ab$. Therefore, these improved critical current properties of the dense sintered bulk are considered to be due to randomly oriented grains and the presence of grain boundaries.

The addition of small amounts of metals, such as Mg, In and Sn, is also effective for producing highly dense MgB₂ bulk or metal-sheathed tape [196,197]. Such bulk exhibits high J_c of over 10^5 A cm⁻² at 5 K under self-field, however, it quickly decreases with an increase of magnetic field, resulting in much lower H_{irr} than that of high-pressure synthesized bulk in

spite of the random grain orientations. This suggests that pinning force at grain boundaries is degraded by the addition of metals.

4.1.4. Critical current properties of “*in-situ*” processed MgB_2 bulk

In the case of the “*ex-situ*” method, the grain size of MgB_2 is usually larger than $1\ \mu\text{m}$. On the other hand, MgB_2 bulk synthesized by the “*in-situ*” method has fine grains smaller than $0.5\ \mu\text{m}$. In this method, Mg and B are used as starting materials. The most popular procedure is to start from a pressed powder mixture of Mg and B. The reaction between Mg and B occurs in a wide temperature range of $550\sim 1200^\circ\text{C}$. It should be noted that the melting and boiling points of Mg under ambient pressure are 650 and 1107°C , respectively, while the melting point of B is higher than 2000°C . Since the equilibrium vapor pressure of Mg is high at the reaction and/or sintering temperatures, as shown in Fig. 4-2, the synthesis of MgB_2 bulk by both “*in-situ*” and “*ex-situ*” methods must be

performed in sealed metal cells or under well controlled Mg vapor pressure. Synthesis of MgB_2 bulk starting from the pressed powder mixture of Mg and B has been performed with heating at $800\sim 1000^\circ\text{C}$ in the early stage, because hard MgB_2 bulk of almost a single phase can be obtained with a short heating time of less than 10 min. Such a rapid formation of the MgB_2 phase is due to the liquid (or gas)-solid reaction between Mg and B. Although, critical current properties of high-temperature processed “*in-situ*” bulk are dependent on heating conditions, there are few systematic studies on determining the optimal conditions as functions of temperature and heating time. Through the synthesis of a series of MgB_2 bulk by the powder-in-closed-tube (PICT) method using stainless tubes, which overcame the difficulty in the synthesis of MgB_2 bulk with reproducible J_c characteristics, the optimal heating conditions for the highest J_c at 20 K under self-field were found to be $825\sim 850^\circ\text{C}$ for 3 h [198]. Such optimal conditions are considered to be a result of the balance of improvement in grain coupling and grain growth, *i.e.*, the reduction of grain boundaries accompanied by heating. J_c of the MgB_2 bulk prepared by the PICT method under the optimized conditions is slightly higher than that of high-pressure synthesized “*ex-situ*” bulk, whereas the microstructure is porous with almost half the theoretical density.

On the other hand, the reaction forming MgB_2 requires a long heating time when synthesis is performed below the melting point of Mg, 650°C , where the solid-state reaction is predominant. In the low-temperature processing, grain size is mostly determined by that of the starting B powder, independent of heating temperature and time. J_c as high as that of the high-temperature processed “*in-situ*” bulk $\sim 4\times 10^5\ \text{A cm}^{-2}$ at 20 K under self-field is achieved by low-temperature heating [199]. The bulk density is also low, approximately half the theoretical value. Furthermore, J_c in magnetic fields and H_{irr} of low-temperature heated MgB_2 bulk are apparently higher than those of the high-temperature heated bulk. Higher H_{c2} , *i.e.*, shorter coherence length originating from the poor crystallinity of low-temperature heated MgB_2 bulk, is believed to contribute to the improvement of J_c characteristics. Low-temperature synthesis is always favorable for material development.

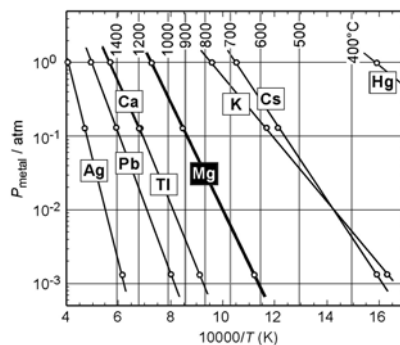


Fig. 4-2. Equilibrium vapor pressures of metals.

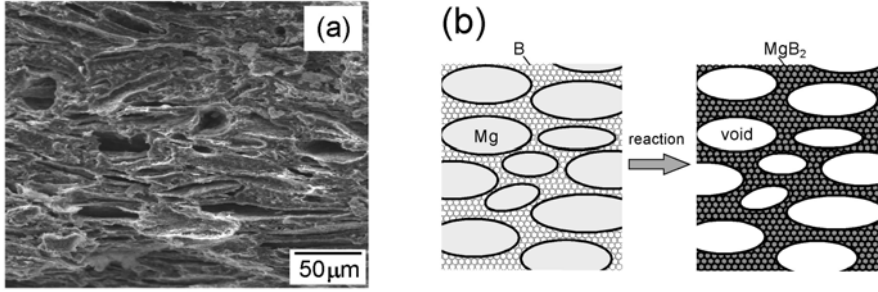


Fig. 4-3.: Typical secondary electron image of fractured surface of MgB_2 bulk (a) and concept of “*in-situ*” reaction of Mg and B (b).

4.1.5. Effect of porous microstructure on the J_c characteristics of “*in-situ*” MgB_2 bulk

The porous microstructure characterized in the “*in-situ*” method originates from the relatively high density of MgB_2 compared with those of Mg and B. Since the molar volumes of Mg, amorphous B and MgB_2 are 14.0, ~ 4.9 and 17.4 cm^3 , respectively, the reaction of $\text{Mg} + 2\text{B} = \text{MgB}_2$ is accompanied by a volume reduction of $\sim 27\%$. Considering that the initial packing density of the powder mixture of Mg and B is approximately 70%, the low density of the resulting MgB_2 bulk that is almost half of the theoretical value is quite reasonable. In the case of MgB_2 bulk, however, low density is not a very serious problem for limiting current passes because a strongly connected MgB_2 network with large pores is usually formed in the microstructure, as shown in Fig. 4-3(a). The large pores are initially occupied by the relatively large Mg particle that which diffuses into B to form MgB_2 or evaporates during the heating process. Although the B particle expands by ~ 80 vol% with the formation of MgB_2 , larger pores remain, as displayed in Fig. 4-3(b). It is clear that the densification of MgB_2 bulk is effective in enhancing J_c , as shown in Fig. 4-4. However, J_c can be almost doubled, at most, even in a desirably dense bulk synthesized by the diffusion method.

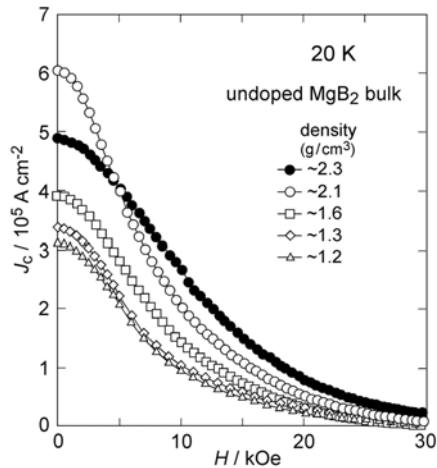


Fig. 4-4. Magnetic field dependence of J_c for MgB_2 bulks with various densities. The densest bulk sample was synthesized under a high pressure of 2 GPa.

4.1.6. Effects of particle size of MgB₂ and purity of starting powders on J_c characteristics of “*in-situ*” MgB₂ bulk

It must be pointed out that there are various commercial reagents of B powder with different purity, particle size and distribution. Low-purity B contains Fe, Si, C and other elements and results in slightly lower T_c of MgB₂. However, no clear systematic relationship between the critical current properties of MgB₂ bulk or tape and the purity of B has been found, because some impurity elements unexpectedly contribute to the enhancement of flux pinning, as described in the next section.

The dependence of J_c on the grain size of MgB₂ has not yet been quantitatively understood, however, improvement in J_c of MgB₂ bulk or tape upon using fine B powder has often been reported [196,200]. As is mentioned above, the grain size of MgB₂ is strongly affected by the size of the starting B powder unless heating is at high temperature for a long time. Therefore, small grain size of MgB₂ is preferable for enhanced J_c , similar to the case of Nb₃Sn materials where dense grain boundaries are believed to act as predominant flux pinning sites. Using fine B powder as a starting material has another advantageous point for the production of high- J_c MgB₂ bulk. Since the diffusion length of Mg in B in the formation reaction of MgB₂ is shortened when using fine B powder, MgB₂ bulk or tape can be synthesized by heating at lower temperatures and/or for shorter times, for example, at 630°C for 1 h [201]. These low-temperature and short-time heated samples have poor crystallinity and slightly lower T_c by 1~2 K and show higher J_c in high magnetic fields, while J_c is high in low magnetic fields, e.g., $\sim 3 \times 10^5$ A cm⁻² at 20 K. The dependence of J_c on magnetic field at 20 K for various MgB₂ bulk and single crystals is summarized in Fig. 4-5.

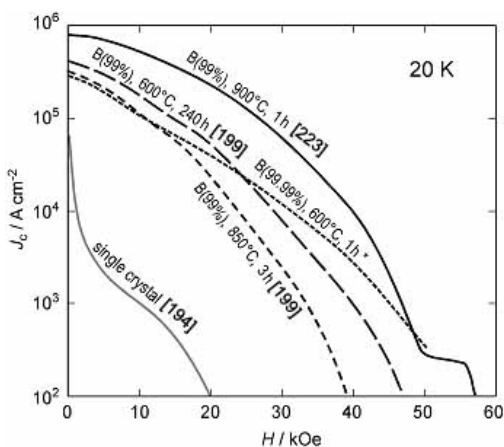


Fig. 4-5. J_c - H curves for various MgB₂ bulk samples and a single crystal at 20 K.

4.1.7. Critical current properties of MgB₂ thin films

To prepare MgB₂ thin films, there are three major methods: the two-step method of annealing B film in Mg vapor, the low-temperature “*in-situ*” method of coevaporation or sputtering, and the high-temperature “*in-situ*” method of hybrid physical-chemical vapor deposition (HPCVD) above 700°C. Details of MgB₂ thin films have been well summarized in a recent review [16].

The first method provides good *c*-axis-oriented thin films in terms of a clean surface, while the T_c of 37 K is slightly low even after moderate post-annealing, mainly due to poor crystallinity. Although these films consist of fine MgB₂ grains 20~40 nm in diameter, the reported J_c is not high, being 4×10^5 A cm⁻² at 4.2 K under self-field [202].

By the second method, thin films showing high T_c of ~ 39 K and high J_c exceeding 10^6 A cm^{-2} at 20 K under self-field were synthesized by several research groups [203-205]. The highest J_c 's at 15 K were 1.6×10^7 and 1×10^5 A cm^{-2} under self-field and 50 kOe ($H//c$), respectively, recorded for a c -axis-oriented thin film [205].

Thin films grown by the third method show significantly high T_c of up to 41.8 K due to lattice deformation and a large RRR (residual resistance ratio) even when compared with that of single crystals [206,207]. The highest J_c 's under low fields measured by the magnetization method are 1×10^8 A cm^{-2} at 5 K and 3×10^7 A cm^{-2} at 30 K [208]. The extremely high J_c at 5 K is comparable to the depairing current density. The films prepared by the HPCVD method are composed of columnar grains with an in-plane dimension of ~ 100 nm and, therefore, column boundaries parallel to the c -axis are considered to act as effective pinning sites under $H//c$. In fact, high J_c of over 10^6 A cm^{-2} is maintained up to 10 kOe at 20 K.

Critical current properties of various MgB_2 thin films are shown in Fig. 4-6. From the viewpoint of device applications, sufficiently high J_c has already been achieved up to 30 K under low fields, and the remaining subject is the fabrication of clean and highly reproducible junctions. Recent progress on the fabrication of MgB_2 junctions using thin films prepared by the low-temperature “*in-situ*” method [209,210] are promising in terms of practical device applications of MgB_2 in the near future.

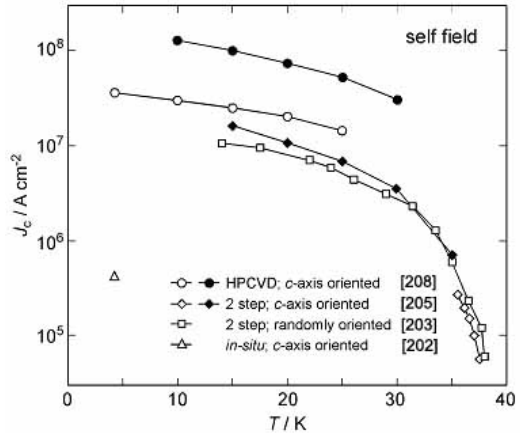


Fig. 4-6. Temperature dependence of J_c for various MgB_2 thin films.

4.2. Doping Effects on the Critical Current Properties of MgB_2

4.2.1. Effective pinning sites in MgB_2

Since the discovery of high T_c in MgB_2 , numerous efforts have been made to find new superconductors showing higher T_c by various substitutions of Mg and/or B sites. Unfortunately, no effective agent has so far been found that enhances T_c . However, many experimental results regarding the doping effect on the superconducting properties of MgB_2 have been accumulated. As described in the previous section, critical current properties of “*in-situ*”-processed undoped MgB_2 bulk are mainly determined by the crystallinity, grain size and density. Poor crystallinity accompanies higher H_{c2} ; smaller grain size is favorable for increasing the grain boundary pinning force, and high density directly increases current passes.

J_c of undoped MgB_2 bulk at low magnetic fields is high enough for practical applications, however, it rapidly decreases with an increase of magnetic field due to low H_{c2} and lack of effective pinning sites. Therefore, both the enhancement of H_{c2} and the introduction of effective pinning sites are needed to improve J_c under high magnetic fields for practical application

of MgB₂ wires in high fields. The best J_c for undoped MgB₂ bulk is 1×10^4 A cm⁻² at 20 K under 40 kOe [211], which was reported by one group in 2002. Other many groups reported much lower J_c 's under the same conditions, while those in low magnetic fields were sufficiently high, exceeding 10^5 A cm⁻² at 20 K. This implies that a common method of producing MgB₂ bulk with high J_c under magnetic field has not yet been established, in other words, the crucially important factor for improving flux pinning properties has not been identified up to now.

Doping of elements or compounds into MgB₂ accompanies element substitution and/or inclusion of impurity particles. In the former case, changes of electronic state, lattice constants and crystallinity are expected to occur. The latter impurity particles are expected to act as effective pinning sites if their grain size is moderately small and they are dispersed throughout the MgB₂ matrix. Another expected effect of doping is the suppression of the grain growth of MgB₂. In the following part of this section, effects of element substitution to Mg or B sites and compound substitution on the critical current properties will be described.

4.2.2. Substitution effect of Mg site

There are many elements that form metal diborides having the AlB₂ structure. The effects of partial substitution at Mg sites in MgB₂ have been reported for more than 15 of those elements, and three elements, Al, Ti and Zr, were found to be effective in the improvement of critical current properties. Unexpectedly, Ti and Zr do not substitute into the MgB₂ phase and they form thin TiB₂ or ZrB₂ layers less than 1 nm thick, resulting in very fine MgB₂ grains ~10 nm in diameter and dense microstructures including fine MgO particles [211,212]. Corresponding to the dramatic change in the microstructure, Ti- or Zr-doped MgB₂ bulk shows dramatically improved J_c , particularly under low magnetic fields. J_c is higher for Ti-doped samples and a sample with a nominal composition of Mg_{0.9}Ti_{0.1}B₂ exhibits the highest J_c for bulk of 1.3×10^6 A cm⁻² at 20 K under self-field. However, H_{irr} is not high even when compared with undoped MgB₂ bulk, ~70 kOe at 5 K and ~40 kOe at 20 K.

Although Al substitution at Mg site dramatically decreases T_c of MgB₂ due to the decrease of the hole carrier concentration, J_c under low magnetic fields is enhanced by 20~30% when the doping level is ~0.5% at Mg site. In this case, local weak superconducting regions around Al ions are considered to act as effective pinning sites. Similar dilute substitution effects are also found in cuprate superconductors [213,214].

4.2.3. Substitution effects at B site

Partial element substitution at B site has more significant effects on the superconducting properties of MgB₂, because superconductivity appears at the honeycomb B lattice. Substitution effects at B site of MgB₂ have been reported for Be, C, O, F and Si, all of which were found to essentially decrease T_c . Among them, C substitution effects have been eagerly studied to clarify the superconductivity mechanism and the improvement of critical current properties. Although there are numerous systematic studies on the relationship between the C substitution level and various physical properties, many inconsistencies concerning structural parameters and superconducting properties can be found. This problem originates from the difference in the C substitution level between nominal composition and the actual level in the resulting samples. In the case of single crystal growth at high temperatures of 1600~1700°C, the C substitution level is almost identical to the nominal one [215], while the actual C substitution level is usually much lower for polycrystalline bulk, even when they are heated at high

temperatures above 1000°C. Because C contains impurity phases, raw C, MgB₂C₂ and Mg₂C₃ often remain in the C-substituted MgB₂ bulk, resulting in a decrease in the actual C-substitution level in MgB₂. In the synthesis of C-substituted MgB₂ bulk, amorphous C, graphite, C₆₀, C nanotubes, nanodiamond and B₄C were used as starting materials.

The original high T_c of MgB₂ dramatically decreases with increasing C substitution level at B site, ~30 and ~2.5 K for 5 and 12.5%, respectively [215]. The temperature dependence of H_{c2} is, however steeper for C-substituted MgB₂ bulk [216,217] and, therefore, a small amount of C substitution into MgB₂ leads to higher H_{c2} at low temperatures. Corresponding to the enhancement of H_{c2} at low temperatures, J_c under high fields and H_{irr} below 20 K are higher for C-substituted MgB₂ bulk with moderate C concentrations than those of undoped bulk. This means that the pinning force in MgB₂ polycrystalline bulk is somehow enhanced when coherence length is shortened. Since the enhancement of H_{irr} is also observed for C-substituted single crystals [218], intragrain pinning is essentially improved by incorporating C.

For O substitution, unintentionally O-added thin films have attracted great interest due to their extremely high H_{c2} at low temperatures and improved J_c under high fields even at 20 K, although T_c is greatly lowered to ~30 K [219]. In the case of MgB₂ bulk, intentional substitution of O had been believed to be difficult, because O preferentially forms MgO and B₂O₃ during the high temperature heat treatment. However, several groups pointed out that small Mg(B,O)₂ regions are generated in the MgB₂ crystals [220], which suggests that O can substitute at B site even in a bulk specimen. Recently, O was found to dissolve into MgB₂ bulk resulting in improved H_{c2} , H_{irr} and J_c , as in the case of thin films, when the bulk was synthesized at low temperatures below 700°C [221]. Partial substitution of Si is reported to also be effective for improving the critical current properties under high fields [222].

It should be noted that substitutions of C, O or Si at B site are effective for improving critical current properties only under high magnetic fields, and J_c 's in low fields are usually lower than that of undoped MgB₂. On the contrary, as described above, substitutions of Ti, Zr or Al at Mg site are effective in enhancing J_c 's only under low fields.

4.2.4. Doping effect of compounds on critical current properties of MgB₂

The improvement of critical current properties of MgB₂ has been also attempted by doping various compounds, among which SiC fine powder is well known as one of the most effective dopants for improving H_{irr} and J_c [223]. A 10 wt % SiC-doped MgB₂ bulk showed H_{irr} ~80 kOe and J_c ~10⁵ A cm⁻² under 30 kOe at 20 K, while its density was almost half the theoretical value. These are the highest values obtained for MgB₂ bulk at the present stage and are almost comparable to those of commercial Bi(Pb)2223/Ag sheathed tapes. In the SiC-doped MgB₂ bulk, both Si and C are considered to contribute to the enhancement of H_{irr} and J_c by substituting at B site. In addition, J_c under low fields is not lowered by SiC doping. Highly dense dislocations and fine inclusions of Mg₂Si ~10 nm in size and unreacted SiC observed in the microstructure are believed to enhance J_c even under low fields. Recently, SiC-doped MgB₂ tape exhibited high H_{irr} of up to 230 kOe at 4.2 K [224], suggesting the possibility of practical applications for high magnetic field generation at the liquid He temperature.

Other effective dopants for the enhancement of J_c are fine powders of Y₂O₃ [225], SiO₂ [224] and metal carbonates, such as Li₂CO₃, Na₂CO₃ [226] and Mg₂CO₃. For Y₂O₃-doped MgB₂ bulk, very small YB₄ particles of 3~5 nm formed in MgB₂ grains are pointed out to act as effective pinning centers. In the case of metal-carbonate-doped MgB₂ bulk, C and O are

considered to substitute at B site, resulting in the enhancement of J_c under high magnetic fields.

An additional advantage of compound doping is the high reactivity at low temperatures. Although substitution with C is known to be effective for improving J_c under high fields, reaction of C to form $\text{Mg}(\text{B},\text{C})_2$ is nominal during low-temperature heating below 650°C , which is a desirable condition for enhancing both H_{irr} and J_c . On the other hand, C can substitute at B site in MgB_2 with low-temperature processing using SiC or B_4C as starting materials. A similar tendency is found for O substitution using B_2O_3 as a starting reagent.

4.3. Future Prospect of MgB_2 Materials

MgB_2 has various attractive points in terms of the development of wires and thin films for practical use. Its T_c is high enough for practical applications at 20 K, which can be easily realized using small cryocoolers, and its strong grain coupling and long coherence length are desirable for polycrystalline wires and thin films with homogeneous critical current performance. Although long coherence length suppresses H_{c2} and the resulting H_{irr} is not high enough for field generating applications using MgB_2 wires, various chemical dopants as well as low-temperature processing have been found to be effective for improving H_{c2} , H_{irr} and J_c under high magnetic fields. In addition, MgB_2 shows slow flux creep due to strong grain coupling compared with cuprate superconductors, as shown in Fig. 4-7. Several studies on the I - V characteristics of MgB_2 materials also revealed that the n -value in $V = I^n$ is large, particularly under low fields [227]. These mean that MgB_2 materials are suitable for fabricating a persistent current circuit, which is desirable for use in various magnet systems.

In the development of MgB_2 wires, the problem of the flux jump phenomenon must be solved before they can be put to practical use. In an extreme case of our studies, a SiC-doped MgB_2 bulk with dimensions of $0.7 \times 1.1 \times 1.8 \text{ mm}^3$ and high density of $\sim 2.2 \text{ g cm}^{-3}$ showed flux jumps up to 25 K. This particular bulk had a very high J_c of $4 \times 10^5 \text{ A cm}^{-2}$ at 25 K under 5 kOe. Therefore, the development of multi-filamentary wires with fine MgB_2 cores, which can prevent the flux jump phenomenon, is necessary for realizing reliable high- J_c wires.

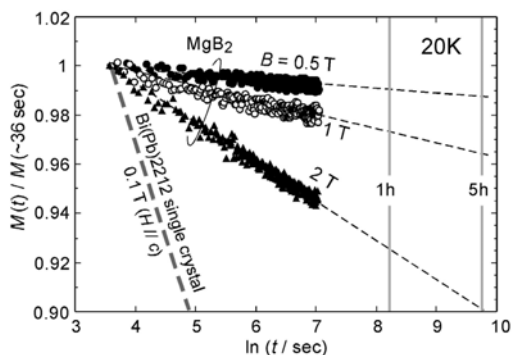


Fig. 4-7. Magnetization relaxation of MgB_2 bulk and $\text{Bi}(\text{Pb})2212$ single crystal at 20 K.

5. CONCLUSION

Since the discovery of superconductivity at 39 K in MgB_2 , the T_c of which is the highest record in intermetallic superconductors, a huge number of theoretical and experimental investigations have been reported in a short period because of its unexpectedly high T_c . In the framework of BCS theory, the theoretical interpretation of this superconductivity focuses on the metallic nature of a 2D layer formed by boron atoms and also on strong electron-phonon coupling caused mainly by the E_{2g} phonon mode (B in-plane bond stretching), which is supported by experimental results. Short after the discovery of the high T_c in MgB_2 , experimental results progressively accumulated as the sample quality become higher, for example, as the growth of single crystals became possible. The results have become consistent, except for small inconsistencies which are probably due to some disorder of the boron atom and/or a slight defect at the Mg site. In particular, the two-gap (on 2D σ band and 3D π band) nature in MgB_2 has been confirmed from the results of several spectroscopic measurements, and MgB_2 is now recognized as the first material to be found that containing intrinsic multigaps.

From the viewpoint of application, the high T_c , large coherence length, high J_c , high H_{c2} , transparency of grain boundaries to current and low normal state resistivity promise that MgB_2 will be a good candidate material for both large scale applications and electronic devices. Because MgB_2 has various merits for the development of wires and thin films for practical use, many trials have been performed for the improvement of J_c and H_{c2} in single crystals, bulk and thin films, involving the grain size effect, “*in-situ*” and “*ex-situ*” methods and the substitution effect for the introduction of effective pinning. Although the dependence of J_c on the grain size of MgB_2 has not been quantitatively explained, the improvement of J_c in MgB_2 bulk or tapes when using fine B powder has been reported. The slight substitution levels of C, O or Si at B site are effective for improving critical current properties only under high magnetic fields. Moreover, SiC fine powder is well known to be one of the most effective dopants for improving J_c , where J_c is not lowered under low fields. Highly dense dislocations and fine inclusions with Mg_2Si and/or unreacted SiC are believed to enhance J_c even under low magnetic fields. Although hurdles still remain, recent progress in the fabrication of MgB_2 bulk, wires, tapes and thin films is quite promising for the realization of practical device applications of MgB_2 in the near future.

The entire scenario of superconductivity in MgB_2 has essentially been clarified, and its potential for practical application has been shown. MgB_2 has opened up a new frontier of investigation of the physical properties of intermetallic superconductors. Now, one of the most exciting questions is “whether MgB_2 is merely a special example in the system of compounds including *p*-electron elements”. Actually, we have discovered new superconductors, for example, Y_2C_3 ($T_c=18$ K) [228], since the discovery of MgB_2 . Because the “BCS limit” has been broken by MgB_2 , the discovery of new higher T_c non Cu oxides is strongly expected. Unidentified superconductors may yet be waiting to be found.

ACKNOWLEDGEMENTS

This work was partly supported by a Grant-in-Aid for Scientific Research from The Ministry of Education, Culture, Sports, Science and Technology, Japan. TM, YZ and JA are thankful for a Grant-in-Aid for Science Research from the Ministry of Education, Culture, Sports, Science and Technology, Japan and the 21st COE program.

REFERENCES

- [1] For example; G. Hardy and H. Franz, *Phys. Rev.* **89** (1953) 884, B.T. Matthias, *Phys. Rev.* **92** (1953) 874
- [2] B.T. Matthias, T.H. Geballe, K. Andres, E. Corenzwit, G.W. Hull and J.P. Maita, *Science* **156** (1967) 645
- [3] J.R. Gavaler, *Appl. Phys. Lett.* **23** (1973) 480
- [4] J.G. Bednorz and K.A. Müller, *Z. Phys. B* **64** (1986) 189
- [5] S.N. Putilin, E.V. Antipov, A.M. Abakumov, M.G. Rozova, K.A. Lokshin, D.A. Pavlov, A.M. Balagurov, D.V. Sheptyakov, M. Marezio, *Physica C* **338** (2001) 52
- [6] K. Tanigaki, T.W. Ebbesen, S. Saito, J. Mizuki, J.S. Tsai, Y. Kubo and S. Kuroshima, *Nature* **352** (1991) 222
- [7] R.J. Cava, B. Batlogg, J.J. Krajewski, R.C. Farrow, L.W. Rupp Jr, A.E. White, K.T. Short, W.F. Peck Jr and T.V. Kometani, *Nature* **332** (1988) 814
- [8] J. Nagamatsu, N. Nakagawa, T. Muranaka, Y. Zenitani and J. Akimitsu, *Nature* **410** (2001) 63
- [9] J. Kortus, I.I. Mazin, K.D. Belashchenko, V.P. Antropov and L.L. Boyer, *Phys. Rev. Lett.* **86** (2001) 4656
- [10] J. M. An and W.E. Pickett, *Phys. Rev. Lett.* **86** (2001) 4366
- [11] S.L. Bud'ko, G. Lapertot, C. Petrovic, C.E. Cunningham, N. Anderson and P.C. Canfield, *Phys. Rev. Lett.* **86** (2001) 1877
- [12] A. Sharoni, I. Felner and O. Millo, *Phys. Rev. B* **63** (2001) 220508(R)
- [13] H. Kotegawa, K. Ishida, Y. Kitaoka, T. Muranaka and J. Akimitsu, *Phys. Rev. Lett.* **87** (2001) 127001
- [14] H. Suhl, B.T. Matthias and L.R. Walker, *Phys. Rev. Lett.* **3** (1959) 552
- [15] G. Binnig, A. Baratoff, H.E. Hoenig and J.G. Bednorz, *Phys. Rev. Lett.* **45** (1980) 1352
- [16] M. Naito and K. Ueda, *Supercond. Sci. Technol.* **17** (2004) R1
- [17] X.X. Xi, A.V. Pogrebnyakov, X.H. Zeng, J.M. Redwing, S.Y. Xu, Qi Li, Zi-Kui Liu, J. Lettieri, V. Vaithyanathan, D.G. Schlom, H.M. Christen, H.Y. Zhai and A. Goyal, *Supercond. Sci. Technol.* **17** (2004) S196
- [18] C. Buzea and T. Yamashita, *Supercond. Sci. Technol.* **14** (2001) R115
- [19] *Physica C*, Volume **385**, Issues 1-2, (2003)
- [20] J. Etourneau and P. Hagenmuller, *Philos. Mag. B* **52** (1985) 589
- [21] G.K. Strukova, V.F. Degtyareva, D.V. Shovkun, V.N. Zverev, V.M. Kiiko, A.M. Ionov and A.N. Chaika, cond-mat/0105293 (2001)
- [22] A. Kawano, Y. Mizuta, H. Takagiwa, T. Muranaka and J. Akimitsu, *J. Phys. Soc. Jpn.* **72** (2001) 1724
- [23] E.M. Savitskii, V.V. Baron, Y.V. Efimov, M.I. Bychkova and L.F. Myzenkova, *Superconducting materials*, Plenum Press, New York (1973)
- [24] E.E. Havinga, H. Damsma and J.M. Kanis, *J. Less-Common Met.* **27** (1972) 281
- [25] J.K. Hulm, *Phys. Rev.* **98** (1955) 1539
- [26] R. Kiessling, *Acta Chem. Scand.* **3** (1949) 603
- [27] O.I. Shulishova and I.A. Shcherback, *Inorg. Mater.* **3** (1967) 1304
- [28] H. Nowotny, F. Benesovsky and R. Kieffer, *Z. Metallk.* **50** (1959) 417
- [29] B.T. Matthias, T.H. Geballe and V.B. Compton, *Rev. Mod. Phys.* **35** (1963) 1
- [30] P. Vajeeston, P. Ravindran, C. Ravi and R. Asokamani, *Phys. Rev. B* **63** (2001) 045115

- [31] H. Rosner, W.E. Pickett, S.-L. Drechsler, A. Handstein, G. Behr, G. Fuchs, K. Nenkov, K.-H. Müller and H. Eschrig, *Phys. Rev. B* **64** (2001) 144516
- [32] A.S. Cooper, E. Corenzwit, L.D. Longinotti, B.T. Matthias and W.H. Zachariasen, *Proc. Natl. Acad. Sci. U.S.A.* **67** (1970) 313
- [33] I. Higashi, Y. Takahashi and S. Okada, *J. Less Common Met.*, **123** (1986) 277
- [34] T. Lundstrom, *Ark. Kemi.* **30** (1968) 115
- [35] L. Leyarovska and E. Leyarovski, *J. Less-Common Met.* **67** (1979) 249
- [36] A. Yamamoto, C. Takao, T. Masui, M. Izumi and S. Tajima, *Physica C* **383** (2002) 197
- [37] V.A. Gasparov, N.S. Sidorov, I.I. Zver'kova and M.P. Kulakov, *JETP Lett.* **73** (2001) 532
- [38] D.P. Young, R.G. Goodrich, P.W. Adams, J.Y. Chan, F.R. Fronczek, F. Drymiotis and L.L. Henry, *Phys. Rev. B* **65** (2002) 180518(R)
- [39] D. Kaczorowski, A.J. Zaleski, O.J. Zogal and J. Klamut, cond-mat/0103571 (2001)
- [40] I. Felner, *Physica C* **353** (2001) 11
- [41] S.K. Kwon, S.J. Youn, K.S. Kim and B.I. Min, cond-mat/0106483 (2001)
- [42] G. Satta, G. Profeta, F. Bernardini, A. Continenza, and S. Massidda, *Phys. Rev. B* **64** (2001) 104507
- [43] H. Rosner, A. Kitaigorodsky and W.E. Pickett, *Phys. Rev. Lett.* **88** (2002) 127001
- [44] T. Oguchi, *J. Phys. Soc. Jpn.* **71** (2002) 1495
- [45] For example ; N.I. Medvedeva, A.L. Ivanovskii, J.E. Medvedeva and A.J. Freeman, *Phys. Rev. B* **64** (2001) 020502
- [46] A.M. Fogg, J.B. Claridge, G.R. Darling and M.J. Rosseinsky, *Chem. Commun.* **12** (2003) 1348
- [47] B.T. Matthias, T.H. Geballe, K. Andres, E. Corenzwit, G.W. Hull and J.P. Maita, *Science* **159** (1968) 530
- [48] R.J. Sobczak and M.J. Sienko, *J. Less-Common Met.* **67** (1979) 167
- [49] Z. Fisk, A.C. Lawson, B.T. Matthias and E. Corenzwit, *Phys. Lett.* **37A** (1971) 251
- [50] M.E. Jones and R.E. Marsh, *JACSAT* **76** (1954) 1434
- [51] J.D. Jorgensen, D.G. Hinks and S. Short, *Phys. Rev. B* **63** (2001) 224522
- [52] S. Margadonna, T. Muranaka, K. Prassides, I. Maurin, K. Brigatti, R.M. Ibberson, M. Arai, M. Takata and J. Akimitsu, *J. Phys.: Condens. Matter* **13** (2001) L795
- [53] K. Oikawa, T. Kamiyama, T. Mochiku, H. Takeya, M. Furuyama, S. Kamisawa, M. Arai and K. Kadowaki, *J. Phys. Soc. Jpn.* **71** (2002) 2741
- [54] K. Prassides, Y. Iwasa, T. Ito, D.H. Chi, K. Uehara, E. Nishibori, M. Takata, M. Sakata, Y. Ohishi, O. Shimomura, T. Muranaka and J. Akimitsu, *Phys. Rev. B* **64** (2001) 012509
- [55] E. Nishibori, M. Takata, M. Sakata, H. Tanaka, T. Muranaka and J. Akimitsu, *J. Phys. Soc. Jpn.* **70** (2001) 2252
- [56] S. Lee, H. Mori, T. Masui, Y. Eltsev, A. Yamamoto and S. Tajima, *J. Phys. Soc. Jpn.* **70** (2001) 2255
- [57] T. Vogt, G. Schneider, J.A. Hriljac, G. Yang and J.S. Abell, *Phys. Rev. B* **63** (2001) 220505(R)
- [58] A.F. Goncharov, V.V. Struzhkin, E. Gregoryanz, H.K. Mao, R.J. Hemley, G. Lapertot, S.L. Bud'ko, P.C. Canfield and I.I. Mazin, cond-mat/0106258 (2001)

- [59] P. Bordet, M. Mezouar, M. Núñez-Regueiro, M. Monteverde, M.D. Núñez-Regueiro, N. Rogado, K.A. Regan, M.A. Hayward, T. He, S.M. Loureiro and R.J. Cava, *Phys. Rev. B* **64** (2001) 172502
- [60] S.I. Schlachter, W.H. Fietz, K. Grube and W. Goldacker, *Advances in Cryogenic Engineering: Proceedings of the International Cryogenic Materials Conference - ICMC*, **48** (2002) 809, cond-mat/0107205 (2001)
- [61] B. Lorenz, R.L. Meng and C.W. Chu, *Phys. Rev. B* **64** (2001) 012507
- [62] V.G. Tissen, M.V. Nefedova, N.N. Kolesnikov and M.P. Kulakov, *Physica C* **363** (2001) 194
- [63] M. Monteverde, M. Núñez-Regueiro, N. Rogado, K.A. Regan, M.A. Hayward, T. He, S.M. Loureiro and R.J. Cava, *Science* **292** (2001) 75
- [64] T. Tomita, J.J. Hamlin, J.S. Schilling, D.G. Hinks and J.D. Jorgensen, *Phys. Rev. B* **64** (2001) 092505
- [65] B. Lorenz, R.L. Meng and C.W. Chu, cond-mat/0104303 (2001)
- [66] A.F. Goncharov, V.V. Struzhkin, E. Gregoryanz, J. Hu, R.J. Hemley, H.K. Mao, G. Lapertot, S.L. Bud'ko and P.C. Canfield, *Phys. Rev. B* **64** (2001) 100509
- [67] S. Deemyad, J.S. Schilling, J.D. Jorgensen and D.G. Hinks, *Physica C* **361** (2001) 227
- [68] K.D. Belashchenko, M. van Schilfgaarde and V.P. Antropov, *Phys. Rev. B* **64** (2001) 092503
- [69] H. Mori, S. Lee, A. Yamamoto, S. Tajima and S. Sato, *Phys. Rev. B* **65** (2002) 092507
- [70] L. Wu, Y. Zhu, T. Vogt, H. Su and J.W. Davenport, *Phys. Rev. B* **69** (2004) 064501
- [71] Y. Kong, O.V. Dolgov, O. Jepsen and O.K. Anderson, *Phys. Rev. B* **64** (2001) 020501(R)
- [72] A.Y. Liu, I.I. Mazin and J. Kortus, *Phys. Rev. Lett.* **87** (2001) 087005
- [73] M. Xu, H. Kitazawa, Y. Takano, J. Ye, K. Nishida, H. Abe, A. Matsushita and G. Kodo, *Appl. Phys. Lett.* **79** (2001) 2779
- [74] A.K. Pradhan, Z.X. Shi, M. Tokunaga, T. Tamegai, Y. Takano, K. Togano, H. Kito and H. Ihara, *Phys. Rev. B* **64** (2001) 212509
- [75] K.H.P. Kim, J.-H. Choi, C.U. Jung, P. Chowdhury, H.-S. Lee, M.-S. Park, H.-J. Kim, J.Y. Kim, Z.Du, E.-M. Choi, M.-S. Kim, W.N. Kang, S.-I. Lee, G.Y. Sung and J.Y. Lee, *Phys. Rev. B* **65** (2002) 100510(R)
- [76] T. Masui, K. Yoshida, S. Lee, A. Yamamoto and S. Tajima, *Phys. Rev. B* **65** (2002) 214513
- [77] A.V. Sologubenko, J. Jun, S.M. Kazakov, J. Karpinski and H.R. Ott, *Phys. Rev. B* **66** (2002) 014504
- [78] Yu. Eltsev, K. Nakao, S. Lee, T. Masui, N. Chikumoto, S. Tajima, N. Yoshizuka and M. Murakami, *Phys. Rev. B* **66** (2002) 180504(R)
- [79] T. Masui and S. Tajima, *Physica C* **385** (2003) 91
- [80] Yu. Eltsev, *Physica C* **385** (2003) 162
- [81] Charles P. Poole, Jr., *Handbook of Superconductivity* (Academic Press, Florida, 2000), 31-32
- [82] Ch. Wälti, E. Felder, C. Degen, G. Wigger, R. Monnier, B. Delley and H. R. Ott, *Phys. Rev. B* **64** (2001) 172515
- [83] F. Bouquet, R.A. Fisher, N.E. Phillips, D.G. Hinks and J.D. Jorgensen, *Phys. Rev. Lett.* **87** (2001) 047001

- [84] M. Putti, E. Galleani d'Agliano, D. Marrè, F. Napoli, M. Tassisto, P. Manfrinetti, A. Palenzona, C. Rizzuto and S. Massidda, *Eur. Phys. J. B* **25** (2002) 439
- [85] P.B. Allen and W.W. Schulz, *Phys. Rev. B* **47** (1993) 14434
- [86] For example; K-P. Bohnen, R. Heid and B. Renker, *Phys. Rev. Lett.* **86** (2001) 5771
- [87] T. Masui, K. Yoshida, S. Lee, A. Yamamoto and S. Tajima, *Physica C* **378-381** (2002) 216
- [88] W.N. Kang, C.U. Jung, Kijoon H.P. Kim, Min-Soek Park, S.Y. Lee, Hyeong-Jin Kim, Eun-Mi Choi, Kyung Hee Kim, Mun Seog Kim and Sung-Ik Lee, *Appl. Phys. Lett.* **79** (2001) 982
- [89] R. Jin, M. Paranthaman, H.Y. Zhai, H.M. Christein, D.K. Christen and D. Mandrus, *Phys. Rev. B* **64** (2001) 220506
- [90] W.N. Kang, Heyong-Jin Kim, Eun-Mi Choi, Heon Jung Kim, Kijong H.P. Kim, H.S. Lee and Sung-Ik Lee, *Phys. Rev. B* **65** (2002) 134508
- [91] I.I. Mazin, O.K. Anderson, O. Jepsen, O.V. Dolgov, J. Kortus, A.A. Golubov, A.B. Kuz'menko and D. van der Marel, *Phys. Rev. Lett.* **89** (2002) 107002
- [92] S.J. Hagen, A.W. Smith, M. Rajeswari, J.L. Peng, Z.Y. Li, R.L. Greene, S.N. Mao, X.X. Xi, S. Bhattacharya, Qi Li and C.J. Lobb, *Phys. Rev. B* **47** (1993) 1064
- [93] For example; I.I. Mazin and V.P. Antropov, *Physica C* **385** (2003) 49
- [94] B. Lorentz, R. Meng, Y. Xue and C. Chu, *Phys. Rev. B* **64** (2001) 052513
- [95] T. Muranaka, J. Akimitsu and M. Sera, *Phys. Rev. B* **64** (2001) 020505(R)
- [96] W. Liu, J. Huang, Y. Wang, X. Wang, Q. Feng and A. Yan, *Solid State Commun.* **118** (2001) 575
- [97] M. Schneider, D. Lipp, A. Gladun, P. Zahn, A. Handstein, G. Fuchs, S.-L. Drechler, M. Richter, K.-H. Müller and H. Rosner, *Physica C* **363** (2001) 6
- [98] B. Fisher, K.B. Chashka, L. Patlagan and G.M. Reisner, *Physica C* **387** (2003) 10
- [99] D.C. Kim, J.S. Kim, B.H. Kim, Y.W. Park, C.U. Jung and S.I. Lee, *Physica C* **387** (2003) 313
- [100] T. Plackowski, C. Sułkowski, J. Karpinski, J. Jun and S.M. Kazakov, *Phys. Rev. B* **69** (2004) 104528
- [101] C. Panagopoulos, B.D. Rainford, T. Xiang, C.A. Scott, M. Kambara and I.H. Inoue, *Phys. Rev. B* **64** (2001) 094514
- [102] Ch. Niedermayer, C. Bernhard, T. Holden, R.K. Kremer and K. Ahn, *Phys. Rev. B* **65** (2002) 094512
- [103] K. Ohishi, T. Muranaka, J. Akimitsu, A. Koda, W. Higemoto and R. Kadono, *J. Phys. Soc. Jpn.* **72** (2003) 29
- [104] X.H. Chen, Y.Y. Xue, R.L. Meng and C.W. Chu, *Phys. Rev. B* **64** (2001) 172501
- [105] A.V. Promin, A. Pimenov, A. Loidl and S.I. Krasnosvobodtsev, *Phys. Rev. Lett.* **87** (2001) 097003
- [106] F. Manzano, A. Carrington, N.E. Hussey, S. Lee, A. Yamamoto and S. Tajima, *Phys. Rev. Lett.* **88** (2002) 047002
- [107] A. Carrington and F. Manzano, *Physica C* **385** (2003) 205
- [108] B. Kang, H.-J. Kim, M.-S. Park, K.-H. Kim and S.-I. Lee, *Phys. Rev. B* **69** (2004) 144514
- [109] Z. Hao, J.R. Clem, M.W. McElfresh, L. Civale, A.P. Malozemoff and F. Holtzberg, *Phys. Rev. B* **43** (1991) 2844

- [110] F. Bouquet, Y. Wang, R.A. Fisher, D.G. Hinks, J.D. Jorgensen, A. Junod and N.E. Phillips, *Europhys. Lett.* **56** (2001) 856
- [111] K. Ohishi, K. Kakuta, J. Akimitsu, W. Higemoto, R. Kadono, J.E. Sonier, A.N. Price, R.I. Miller, R.F. Kiefl, M. Nohara, H. Suzuki and H. Takagi, *Phys. Rev. B* **65** (2002) 140505
- [112] J.E. Sonier, R.F. Kiefl, J.H. Brewer, J. Chakhalian, S.R. Dunsiger, W.A. MacFarlane, R.I. Miller, A. Wong, G.M. Luke and J.W. Brill, *Phys. Rev. Lett.* **79** (1997) 1742
- [113] J.E. Sonier, J.H. Brewer and R.F. Kiefl, *Rev. Mod. Phys.* **72** (2000) 769
- [114] T. Dahm and N. Schopohl, *Phys. Rev. Lett.* **91** (2003) 017001
- [115] M. Zehetmayer, M. Eisterer, J. Jun, S.M. Kazakov, J. Karpinski, A. Wisniewski and H.W. Weber, *Phys. Rev. B* **66** (2002) 052505
- [116] L. Lyard, P. Samuely, P. Szabo, T. Klein, C. Marcenat, L. Paulius, K.H.P. Kim, C.U. Jung, H.-S. Lee, B. Kang, S. Choi, S.-I. Lee, J. Marcus, S. Blanchard, A.G.M. Jansen, U. Welp, G. Karapetrov and W.K. Kwok, *Phys. Rev. B* **66** (2002) 180502(R)
- [117] M. Angst, R. Puzniak, A. Wisniewski, J. Jun, S.M. Kazakov, J. Karpinski, J. Roos and H. Kreller, *Phys. Rev. Lett.* **88** (2002) 167004
- [118] M. Angst, R. Puzniak, A. Wisniewski, J. Roos, H. Kreller, P. Miranovi, J. Jun, S.M. Kazakov and J. Karpinski, *Physica C* **385** (2003) 143
- [119] U. Welp, A. Rydh, G. Karapetrov, W.K. Kwok, G.W. Crabtree, Ch. Marcenat, L.M. Paulius, L. Lyard, T. Klein, J. Marcus, S. Blanchard, P. Samuely, P. Szabo, A.G.M. Jansen, K.H.P. Kim, C.U. Jung, H.-S. Lee, B. Kang and S.-I. Lee, *Physica C* **385** (2003) 154
- [120] U. Welp, A. Rydh, G. Karapetrov, W.K. Kwok, G.W. Crabtree, Ch. Marcenat, L. Paulius, T. Klein, J. Marcus, K.H.P. Kim, C.U. Jung, H.-S. Lee, B. Kang and S.-I. Lee, *Phys. Rev. B* **67** (2003) 012505
- [121] Y. Machida, S. Sasaki, H. Fujii, M. Furuyama, I. Takeya and K. Kadowaki, *Phys. Rev. B* **67** (2003) 094507
- [122] Z.X. Shi, M. Tokunaga, T. Tamegai, Y. Takano, K. Togano, H. Kito and H. Ihara, *Phys. Rev. B* **68** (2003) 104513
- [123] L. Lyard, P. Szabó, T. Klein, J. Marcus, C. Marcenat, K.H. Kim, B.W. Kang, H.S. Lee and S.-I. Lee, *Phys. Rev. Lett.* **92** (2004) 057001
- [124] J.A. Woollam, R.B. Somoano and P. O'Connor, *Phys. Rev. Lett.* **32** (1974) 712
- [125] S.V. Shulga, S.-L. Drechsler, G. Fuchs, K.-H. Müller, K. Winzer, M. Heinecke, and K. Krug, *Phys. Rev. Lett.* **80** (1998) 1730
- [126] P. Miranovic, K. Machida and V. G. Kogan, *J. Phys. Soc. Jpn.* **72** (2003) 221
- [127] For example; H. Schmidt, J.F. Zasadzinski, K.E. Gray and D.G. Hinks, *Phys. Rev. B* **63** (2001) 220504(R)
- [128] A.D. Caplin, Y. Bugoslavsky, L.F. Cohen, L. Cowey, J. Driscoll, J. Moore and G.K. Perkins, *Supercond. Sci. Technol.* **16** (2003) 176
- [129] V.G. Kogan, *Phys. Rev. B* **66** (2002) 020509(R)
- [130] V.G. Kogan and S.L. Bud'ko, *Physica C* **385** (2003) 131
- [131] V.G. Kogan and N.V. Zhelezina, *Phys. Rev. B* **69** (2004) 132506
- [132] R. Osborn, E.A. Goremychkin, A.I. Kolesnikov and D.G. Hinks, *Phys. Rev. Lett.* **87** (2001) 017005

- [133] T. Yildirim, O. Gülseren, J.W. Lynn, C.M. Brown, T.J. Udovic, Q. Huang, N. Rogado, K.A. Regan, M.A. Hayward, J.S. Slusky, T. He, M.K. Haas, P. Khalifah, K. Inumaru and R.J. Cava, *Phys. Rev. Lett.* **87** (2001) 037001
- [134] J.P. Carbotte, *Rev. Mod. Phys.* **62** (1990) 1027
- [135] P.C. Canfield, S.L. Bud'ko and D.K. Finnemore, *Physica C* **385** (2003) 1
- [136] D.G. Hinks, H. Claus and J.D. Jorgensen, *Nature* **411** (2001) 457
- [137] D.G. Hinks and J.D. Jorgensen, *Physica C* **385** (2003) 98
- [138] W.L. McMillan, *Phys. Rev.* **167** (1968) 331
- [139] E.A. Yelland, J.R. Cooper, A. Carrington, N.E. Hussey, P.J. Meeson, S. Lee, A. Yamamoto and S. Tajima, *Phys. Rev. Lett.* **88** (2002) 217002
- [140] A. Carrington, P.J. Meeson, J.R. Cooper, L. Balicas, N.E. Hussey, E.A. Yelland, S. Lee, A. Yamamoto, S. Tajima, S.M. Kazakov and J. Karpinski, *Phys. Rev. Lett.* **91** (2003) 037003
- [141] A. Wasserman and M. Springford, *Adv. Phys.* **45** (1996) 471
- [142] J. Hlinka, I. Gregora, J. Pokorny, A. Plecenik, P. Kus, L. Satrapinsky and S. Benacka, *Phys. Rev. B* **64** (2001) 140503(R)
- [143] X.K. Chen, M.J. Konstantinovic', J.C. Irwin, D.D. Lawrie and J.P. Franck, *Phys. Rev. Lett.* **87** (2001) 157002
- [144] J.W. Quilty, S. Lee, A. Yamamoto and S. Tajima, *Phys. Rev. Lett.* **88** (2002) 087001
- [145] I. Loa, K. Kunc, K. Syassen and P. Bouvier, *Phys. Rev. B* **66** (2002) 134101
- [146] J.W. Quilty, S. Lee, S. Tajima and A. Yamanaka, *Phys. Rev. Lett.* **90** (2003) 207006
- [147] A.F. Goncharov and V.V. Struzhkin, *Physica C* **385** (2003) 117
- [148] J.W. Quilty, *Physica C* **385** (2003) 264
- [149] K.A. Yates, G. Burnell, N.A. Stelmashenko, D.-J. Kang, H.N. Lee, B. Oh, and M.G. Blamire, *Phys. Rev. B* **68** (2003) 220512(R)
- [150] H.J. Choi, D. Roundy, H. Sum, M.L. Cohen and S.G. Louie, *Nature* **418** (2002) 758
- [151] H. Martinho, C. Rettori, P.G. Pagliuso, N.O. Moreno and J.L. Sarrao, *condmat/0105204* (2001)
- [152] T. Muranaka, T. Yokoo, M. Arai, E. Margiolaki, K. Brigatti, K. Prassides, O. Petrenko and J. Akimitsu, *J. Phys. Soc. Jpn* **71** (2002) *Supple.* 338
- [153] P.B. Allen, *Phys. Rev. B* **6** (1972) 2577
- [154] J. Mene'ndez and M. Cardona, *Phys. Rev. B* **29** (1984) 2051
- [155] A. Shukla, M. Calandra, M. d'Astuto, M. Lazzeri, F. Mauri, C. Bellin, M. Krisch, J. Karpinski, S.M. Kazakov, J. Jun, D. Daghero and K. Parlinski, *Phys. Rev. Lett.* **90** (2003) 095506
- [156] A.Q.R. Baron, H. Uchiyama, Y. Tanaka, S. Tsutsui, D. Ishikawa, S. Lee, R. Heid, K.-P. Bohnen, S. Tajima and T. Ishikawa, *Phys. Rev. Lett.* **92** (2004) 197004
- [157] G. Karapetrov, M. Iavarone, W.K. Kwok, G.W. Crabtree and D.G. Hinks, *Phys. Rev. Lett.* **86** (2001) 4374
- [158] T. Takahashi, T. Sato, S. Souma, T. Muranaka and J. Akimitsu, *Phys. Rev. Lett.* **86** (2001) 4915
- [159] Y. Wang, T. Plackowski and A. Junod, *Physica C* **355** (2001) 179
- [160] P. Szabó, P. Samuely, J. Kamarik, T. Klein, J. Marcus, D. Fruchart, S. Miraglia, C. Marcenat and A.G.M. Jansen, *Phys. Rev. Lett.* **87** (2001) 137005
- [161] S. Tsuda, T. Yokoya, T. Kiss, Y. Takano, K. Togano, H. Kito, H. Ihara and S. Shin, *Phys. Rev. Lett.* **87** (2001) 177006

- [162] R.S. Gonnelli, D. Daghero, G.A. Ummarino, V.A. Stepanov, J. Jun, S.M. Kazakov and J. Karpinski, *Phys. Rev. Lett.* **89** (2002) 247004
- [163] F. Bouquet, Y. Wang, I. Sheikin, T. Plackowski, A. Junod, S. Lee and S. Tajima, *Phys. Rev. Lett.* **89** (2002) 257001
- [164] S. Tsuda, T. Yokoya, Y. Takano, H. Kito, A. Matsushita, F. Yin, J. Itoh, H. Harima and S. Shin, *Phys. Rev. Lett.* **91** (2003) 127001
- [165] S. Souma, Y. Machida, T. Sato, T. Takahashi, H. Matsui, S.-C. Wang, H. Ding, A. Kaminski, J.C. Campuzano, S. Sasaki and K. Kadowaki, *Nature* **423** (2003) 65
- [166] L. Shen, N. Senozan and N.E. Philips, *Phys. Rev. Lett.* **14** (1965) 1025
- [167] R.K. Kremer, B.J. Gibson and K. Ahn, cond-mat/0102432 (2001)
- [168] H.D. Yang, J.-Y. Lin, H.H. Li, F.H. Hsu, C.J. Liu, S.-C. Li, R.-C. Yu and C.-Q. Jin, *Phys. Rev. Lett.* **87** (2001) 167003
- [169] R.A. Fisher, G. Li, J.C. Lashley, F. Bouquet, N.E. Philips, D.G. Hinks, J.D. Jorgensen and G.W. Crabtree, *Physica C* **385** (2003) 180
- [170] F. Bouquet, Y. Wang, I. Sheikin, P. Toulemonde, M. Eisterer, H.W. Weber, S. Lee, S. Tajima and A. Junod, *Physica C* **385** (2003) 192
- [171] H. Padamasee, J.E. Neighbor and C.A. Schiffman, *J. Low Temp. Phys.* **12** (1973) 387
- [172] B. Mühlshlegel, *Z. Phys.* **155** (1959) 313
- [173] H. Uchiyama, K.M. Shen, S. Lee, A. Damascelli, D.H. Lu, D.L. Feng, Z.-X. Shen and S. Tajima, *Phys. Rev. Lett.* **88** (2002) 157002
- [174] I. Gieaver, *Phys. Rev. Lett.* **5** (1960) 147
- [175] R.C. Dynes, V. Narayanamurti and J.P. Garno, *Phys. Rev. Lett.* **41** (1978) 1509
- [176] For example, H. Schmidt, J.F. Zasadinski, K.E. Gray and D.G. Hinks, *Physica C* **385** (2003) 221
- [177] G. Rubio-Bollinger, H. Suderow and S. Vieira, *Phys. Rev. Lett.* **86** (2001) 5582
- [178] M. Iavarone, G. Karapetrov, A.E. Koshelev, W.K. Kwok, G.W. Crabtree and D.G. Hinks, W.N. Kang, E.-M. Choi, H.J. Kim, H.-J. Kim and S.I. Lee, *Phys. Rev. Lett.* **89** (2002) 187002
- [179] F. Guibileo, D. Roditchev, W. Sacks, R. Lamy, D.X. Thanh, J. Klein, S. Miraglia, D. Fruchart, J. Marcus and Ph. Monod, *Phys. Rev. Lett.* **87** (2001) 177008
- [180] M.R. Eskildsen, M. Kugler, S. Tanaka, J. Jun, S.M. Kazakov, J. Karpinski, and Ø. Fischer, *Phys. Rev. Lett.* **89** (2002) 187003
- [181] J. Karpinski, M. Angst, J. Jun, S.M. Kazakov, R. Puzniak, A. Winsniewski, J. Roos, H. Keller, A. Perucchi, L. Degiorgi, M. Eskildsen, P. Bordet, L. Vinnikov and A. Mironov, *Supercond. Sci. Technol.* **16** (2003) 221
- [182] A. Plecenik, Š. Be a ka, P. Kúš and M. Grajcar, *Physica C* **368** (2001) 251
- [183] F. Laube, G. Goll, J. Hagel, H.v. Löhneysen, D. Ernst and T. Wolf, *Europhys. Lett.* **56** (2001) 296
- [184] Z.-Z. Li, Y. Xuan, H.-J. Tao, Z.-A. Ren, G.-C. Che, B.-R. Zhao and Z.-X. Zhao, *Supercond. Sci. Technol.* **14** (2001) 944
- [185] Z.-Z. Li, H.-J. Tao, Y. Xuan, Z.-A. Ren, G.-C. Che and B.-R. Zhao, *Phys. Rev. B* **66** (2002) 064513
- [186] S. Lee, Z.G. Khim, Y. Chong, S.H. Moon, H.N. Lee, H.G. Kim, B. Oh and E. J. Choi, *Physica C* **377** (2002) 202

- [187] Y. Bugoslavsky, Y. Miyoshi, G.K. Perkins, A.V. Berenov, Z. Lockman, J.L. MacManus-Driscoll, L.F. Cohen, A.D. Caplin, H.Y. Zhai, M.P. Paranthaman, H.M. Christen and M. Blamire, *Supercond. Sci. Technol.* **15** (2002) 526
- [188] A. Kohen and D. Deutscher, *Phys. Rev. B* **64** (2001) 060506(R)
- [189] R.S. Gonnelli, A. Calzolari, D. Daghero, G.A. Ummarino, V.A. Stepanov, P. Fino, G. Giunchi, S. Ceresara and G. Ripamonti, *J. Phys. Chem. Solids* **63** (2002) 2319
- [190] R.S. Gonnelli, A. Calzolari, D. Daghero, G.A. Ummarino, V.A. Stepanov, G. Giunchi, S. Ceresara and G. Ripamonti, *Phys. Rev. Lett.* **87** (2001) 097001
- [191] H. Schmidt, J.F. Zasadzinski, K.E. Gray and D.G. Hinks, *Phys. Rev. Lett.* **88** (2002) 127002
- [192] T. Takasaki, T. Ekino, T. Muranaka, H. Fujii and J. Akimitsu, *Physica C* **378-381** (2002) 229
- [193] T. Ekino, T. Takasaki, T. Muranaka, J. Akimitsu and H. Fujii, *Phys. Rev. B* **67** (2003) 094504
- [194] Z.X. Shi, A.K. Pradhan, M. Tokunaga, K. Yamazaki, T. Tamegai, Y. Takano, K. Togano, H. Kito and H. Ihara, *Physica C* **378-381** (2002) 550
- [195] Y. Takano, H. Takeya, H. Fujii, H. Kumakura, T. Hatano, K. Togano, H. Kito and H. Ihara, *Appl. Phys. Lett.* **78** (2001) 2914
- [196] Qiang Li, L. Wu, A.R. Moodenbaugh, G.D. Gu, M. Suenaga, Z.X. Ye and D.A. Fischer, *IEEE Trans. on Appl. Supercond.* **13** (2003) 3051
- [197] K. Tachikawa, Y. Yamada, M. Enomoto, M. Aodai and H. Kumakura, *IEEE Trans. on Appl. Supercond.* **13** (2003) 3269
- [198] A. Yamamoto, J. Shimoyama, S. Ueda, Y. Katsura, S. Horii and K. Kishio, *Supercond. Sci. Technol.* **17** (2004) 921
- [199] A. Yamamoto *et al.*, submitted to *Supercond. Sci. Technol.*
- [200] P. Lezza, V. Abächerli, N. Clayton, C. Senatore, D. Uglietti, H.L. Suo and R. Flükiger, *Physica C* **401** (2004) 305
- [201] H. Fujii, K. Togano and H. Kumakura, *Supercond. Sci. Technol.* **15** (2002) 1571
- [202] K. Ueda and M. Naito, *Appl. Phys. Lett.* **79** (2001) 2046
- [203] S.H. Moon, J.H. Yun, H.N. Lee, J.I. Kye, H.G. Kim, W. Chung and B. Oh, *Appl. Phys. Lett.* **79** (2001) 2429
- [204] W.N. Kang, H.-J. Kim, E.-M. Choi, C.U. Jung and S.-I. Lee, *Science* **292** (2001) 1521
- [205] H.-J. Kim, W.N. Kang, E.-M. Choi, M.-S. Kim, K.H.P. Kim and S.-I. Lee, *Phys. Rev. Lett.* **87** (2001) 087002
- [206] X.H. Zeng, A.V. Pogrebnikov, A. Kotcharov, J.E. Jones, X.X. Xi, E.M. Lysczek, J.M. Redwing, S.Y. Xu, Q. Li, J. Lettieri, D.G. Schlom, W. Tian, X.Q. Pan and Z.-K. Liu, *Nature Materials* **1** (2002) 35
- [207] X.H. Zeng, A.V. Pogrebnikov, M.H. Zhu, J.E. Jones, X.X. Xi, S.Y. Xu, E. Wertz, Qi Li, J.M. Redwing, J. Lettieri, V. Vaithyanathan, D.G. Schlom, Z.-K. Liu, O. Trithaveesak and L. Schubert, *Appl. Phys. Lett.* **82** (2003) 2097
- [208] S.Y. Xu, Qi Li, E. Wertz, Y.F. Hu, A.V. Pogrebnikov, X.H. Zeng, X.X. Xi and J.M. Redwing, *Phys. Rev. B* **68** (2003) 224501
- [209] A. Saito, A. Kawakami, H. Shimakage, H. Terai and Z. Wang, *J. Appl. Phys.* **92** (2002) 7369
- [210] K. Ueda and M. Naito, *Physica C*, in press

- [211] Y. Feng, Y. Zhao, Y.P. Sun, F.C. Liu, B.Q. Fu, L. Zhou, C.H. Cheng, N. Koshizuka and M. Murakami, *Appl. Phys. Lett.* **79** (2001) 3983
- [212] Y. Zhao, Y. Feng, D.X. Huang, T. Machi, C.H. Cheng, K. Nakao, N. Chikumoto, Y. Fudamoto, N. Koshizuka and M. Murakami, *Physica C* **378-381** (2002) 122
- [213] G. Krabbes, G. Fuchs, P. Schätzle, S. Größ, J.W. Park, F. Hardinghaus, G. Stöver, R. Hyan, S.-L. Drechsler and T. Fahr, *Physica C* **330** (2000) 181
- [214] T. Okabe, J. Shimoyama, M. Shigemori, S. Horii and K. Kishio, *IEEE Trans. on Appl. Supercond.* **13** (2003) 3759
- [215] S. Lee, T. Masui, A. Yamamoto, H. Uchiyama and S. Tajima, *Physica C* **397** (2003) 7
- [216] S. Soltanian, J. Horvat, X.L. Wang, P. Munroe and S.X. Dou, *Physica C* **390** (2003) 185
- [217] C.H. Cheng, H. Zhang, Y. Zhao, Y. Feng, X.F. Rui, P. Munroe, H.M. Zeng, N. Koshizuka, and M. Murakami, *Supercond. Sci. and Technol.* **16** (2003) 1182
- [218] E. Ohmichi, T. Masui, S. Lee, S. Tajima and T. Osada, cond-mat/0312348 (2003)
- [219] C.B. Eom, M.K. Lee, J.H. Choi, L. Belenky, X. Song, L.D. Cooley, M.T. Naus, S. Patnaik, J. Jiang, M. Rikel, A. Polyanskii, A. Gurevich, X.Y. Cai, S.E. Babcock, E.E. Hellstrom, D.C. Labalestier, N. Rogado, K.A. Regan, M.A. Hayward, T. He, J.S. Slusky, K. Inumaru, M.K. Haas and R.J. Cava, *Nature* **411** (2001) 558
- [220] X.Z. Liao, A. Serquis, Y.T. Zhu, J.Y. Huang, L. Civale, D.E. Peterson, F.M. Mueller and H.F. Xu, *J. Appl. Phys.* **93** (2003) 6208
- [221] Y. Katsura *et al.*, in preparation
- [222] X.L. Wang, S.H. Zhou, M.J. Qin, P.R. Munroe, S. Soltanian, H.K. Liu and S.X. Dou, *Physica C* **385** (2003) 461
- [223] S.X. Dou, S. Soltanian, J. Horvat, X.L. Wang, S.H. Zhou, M. Ionescu, H.K. Liu, P. Munroe and M. Tomsic, *Appl. Phys. Lett.* **81** (2002) 3419
- [224] A. Matsumoto, H. Kumakura, H. Kitaguchi and H. Hatakeyama, *Supercond. Sci. Technol.* **16** (2003) 926
- [225] J. Wang, Y. Bugoslavsky, A. Berenov, L. Cowey, A.D. Caplin, L.F. Cohen, J. L. MacManus Driscoll, L.D. Cooley, X. Song and D.C. Larbalestier, *Appl. Phys. Lett.* **81** (2002) 2026
- [226] S. Ueda, J. Shimoyama, A. Yamamoto, S. Horii and K. Kishio, *Supercond. Sci. Technol.* **17** (2004) 926
- [227] For example; H. Kitaguchi, A. Matsumoto, H. Hatakeyama and H. Kumakura, *Physica C* **401** (2003) 246
- [228] G. Amano, S. Akutagawa, T. Muranaka, Y. Zenitani and J. Akimitsu, *J. Phys. Soc. Jpn.* **73** (2004) 530

SUPERCONDUCTIVITY OF MAGNESIUM DIBORIDE: THEORETICAL ASPECTS

Thomas Dahm

Institut für Theoretische Physik, Universität Tübingen, Auf der Morgenstelle 14,
D-72076 Tübingen, Germany

1. INTRODUCTION

Our theoretical understanding of superconductivity in magnesium diboride (MgB_2) has made rapid progress since its discovery by Nagamatsu et al. [1]. Unlike superconductivity in the high- T_c cuprates we are in a possession of a very clear picture of its superconducting state now [2]. It seems clear that superconductivity is driven by electron-phonon interaction in MgB_2 . More excitingly, it appears well established both theoretically and experimentally that the rare form of two gap superconductivity is realized in this compound. Two superconducting gaps of distinctively different size appear to exist on different disconnected parts of its Fermi surface. Since MgB_2 is the clearest example of two gap superconductivity to date, it makes it an interesting object for study and exploration. In the present work we want to review our present understanding of two gap superconductivity in MgB_2 from the theoretical perspective and discuss some of its consequences. The presence of these two different gaps gives rise to a number of anomalies and some of them shall be discussed here. Since the literature on superconductivity in MgB_2 has grown rapidly, no complete coverage of experimental and theoretical work can be made here. Instead, the theoretical results most crucial to our understanding in the authors view will be discussed and a selection of peculiar consequences will be presented.

Since much of our present understanding stems from band structure calculations and solutions of Migdal-Eliashberg equations, we are reviewing these results in the next section. The emergence and stability of two gap superconductivity in MgB_2 shall be discussed in section 3. In section 4 we will discuss consequences of this band structure picture for the upper critical field. Section 5 is finally devoted to the microwave conductivity.

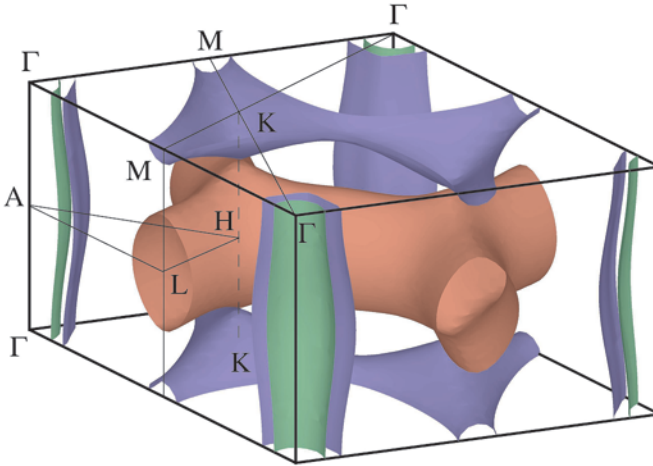


Figure 1: The Fermi surface of MgB_2 . (Adapted from Ref. [6], ©2001 The American Physical Society).

2. THE PICTURE SUGGESTED BY BAND STRUCTURE CALCULATIONS

Magnesium diboride possesses a comparatively high critical transition temperature compared with other conventional superconductors of about $T_c=40$ K. Presently only the high- T_c cuprates have higher transition temperatures. For that reason the natural question arises whether superconductivity in MgB_2 is of the conventional electron-phonon driven type or if its superconducting state has more similarities with the one in the high- T_c cuprates. In the high- T_c cuprates the superconducting state is of an unconventional d -wave type, possessing gap nodes, and electronic pairing mechanisms, like for example exchange of antiferromagnetic spin fluctuations, are discussed seriously. An ongoing discussion still concerns the role and importance of phonons in these compounds.

In contrast to optimally doped high- T_c cuprates MgB_2 shows a strong isotope effect. If the boron-11 isotope is replaced by the lighter boron-10 isotope, T_c increases by about one Kelvin, indicating an important phonon contribution to the pairing interaction [3]. Low temperature specific heat and penetration depth studies are consistent with an exponential decay, indicating the presence of a full gap without nodes [4, 5]. In addition, there are no indications of sizeable magnetic interactions in MgB_2 , again in contrast to the high- T_c cuprates. All these observations seem to place MgB_2 among the conventional s -wave electron-phonon driven superconductors. Then the question arises, why it has such a high transition temperature as compared with other conventional superconductors. Here, band structure calculations turned out to be elusive, which we want to review in the following.

The MgB_2 lattice structure consists of alternating layers of Boron and Magnesium atoms. The Boron atoms form a honeycomb lattice and the Magnesium atoms a triangular lattice halfway between the Boron layers. Calculations of the electronic band structure show four

bands crossing the Fermi energy leading to four topologically disconnected Fermi surface sheets shown in Fig. 1 [6]. Two of these bands are derived from Boron p orbitals. They form the so-called π bands seen as the red (electronlike) and blue (holelike) tubular networks in Fig. 1. The other two bands derive from Boron p_x and p_y orbitals and form the so-called σ bands, seen as the green and blue cylindrical Fermi surfaces centered around the Γ point (both holelike). These possess mainly two dimensional character. Interestingly, all these bands are dominated by Boron p orbitals and contributions from Magnesium orbitals are very small at the Fermi level. About 58 percent of the total density of states at the Fermi level is residing on the π bands making both σ and π bands about equally important for the electronic properties of MgB_2 .

Density-functional calculations of the phonon modes and the electron-phonon interaction strength can be found in Refs. [7], [8], and [9]. The highest phonon density of states is found in the energy range around 30 meV. However, these phonons only couple weakly to the electrons at the Fermi level and thus do not contribute very much to superconductivity. This can be nicely recognized in Fig. 1 of Ref. [7], where the interaction strength of the phonons is shown as the area of the black circles in the figure. In fact, the phonons that couple most strongly to the electrons at the Fermi level are found in the energy range around 70 meV. These phonon modes evolve from the E_{2g} mode at the Γ point and correspond to a Boron-Boron bond-stretching vibration of the Boron sub lattice. A comparison with the phonon modes in the isostructural but nonsuperconducting compound AlB_2 in Ref. [8] shows that these E_{2g} phonon modes are strongly softened in MgB_2 consistent with their strong coupling. Correspondingly, the so-called Eliashberg function $\alpha^2F(\omega)$, which weights the phonon density of states with the coupling strengths and appropriately describes the pairing interaction due to phonons, possesses a strong peak around 70 meV and significantly differs from the phonon density of states in contrast to conventional strong-coupling superconductors. The dimensionless electron-phonon coupling constant was found to lie between $\lambda \approx 0.7\text{-}0.9$ from these first-principles calculations. From this microscopic information we can obtain a qualitative understanding of why T_c is so high in MgB_2 by looking at the BCS T_c formula (which is of course a bad approximation in the present case, but can give us some qualitative tendencies):

$$k_B T_c = 1.13 \hbar \omega_c e^{-1/VN(0)} \quad (1)$$

Here, ω_c is a characteristic phonon frequency, V the interaction strength and $N(0)$ the density of states at the Fermi level, with $\lambda \sim VN(0)$. First of all, the characteristic phonon frequency is comparatively high, because Boron is a light element and the E_{2g} phonon modes in question only involve vibrations of the Boron sub lattice. Secondly, this high frequency phonon at the same time possesses a strong coupling to the electrons at the Fermi level. This means that in MgB_2 we have a favorable coincidence of two effects helping to raise T_c .

3. TWO GAP SUPERCONDUCTIVITY IN MAGNESIUM DIBORIDE

It was noted already early on that there is a problem with the superconducting gap size in MgB_2 . From the BCS gap ratio $\Delta_0 = 1.76 k_B T_c$ one should expect a gap of 6 meV or somewhat larger, if strong electron-phonon coupling effects are considered. However, experimental results obtained from different experimental techniques seemed to scatter between 2 meV and 8 meV with some clustering around 2.5 meV and 7 meV [10]. Initially, one might have attributed this to insufficient sample quality, however, by the end of 2001 high quality single

crystals became available and this problem remained. Also, values of the coherence length extracted by different means turned out to differ considerably. For example, STM tunneling measurements of the vortex core size by Eskildsen et al. [11] were consistent with a value of ≈ 50 nm, while the coherence length as determined from the upper critical field value on the same sample gave ≈ 10 nm. Since the coherence length is related to the superconducting gap via $\xi = \hbar v_F / \pi \Delta_0$ these differences can be related to differences in the gap value as well. These problems suggested studying the possibility of anisotropic or multiple gap structures in MgB_2 .

Again, important insight into this question was provided by Migdal-Eliashberg type calculations based on band structure calculations [9, 12, 13, 14]. Migdal-Eliashberg theory is a generalization of BCS-theory and allows to take into account the detailed properties of phonons and their coupling to the electrons at the Fermi level in the pairing interaction. Decomposing the electron-phonon coupling constant into contributions from the four bands Liu et al. [9] were able to show that the pairing interaction differs considerably on the σ and π bands. The pairing interaction on the σ bands turns out to be much stronger than the one on the π bands and the interband pairing strength. The reason for this is that the E_{2g} phonon mode being an in-plane vibration of the Boron atoms preferentially couples to the in-plane electrons on the more two dimensional σ bands, while its coupling to the three dimensional π bands is much weaker. Due to this anisotropy the resulting effective coupling constant was shown to increase to about $\lambda \approx 1$, being quantitatively more consistent with a T_c of 40 K.

A fully momentum dependent solution of Migdal-Eliashberg equations was presented by H. J. Choi et al in Refs. [13] and [14]. In this calculation the fully momentum dependent band structure, phonon modes, and electron-phonon couplings obtained from first principles density functional calculations were used as a starting point to solve Migdal-Eliashberg equations in the full Brillouin zone. The Coulomb pseudopotential was taken as a constant $\mu^* = 0.12$, which reproduces the experimental T_c . Neglecting impurity scattering, this procedure allowed to calculate the value of the superconducting gap at each point on the Fermi surface. The result is shown in Fig. 2, where the size of the gap is shown color coded on top of the Fermi surface structure. This picture impressively demonstrates the presence of a large gap value around 7 meV on the σ bands and a small gap value around 2 meV on the π bands.

Consistent with Ref. [9] the authors were able to demonstrate the important role of both anisotropy and anharmonicity of the phonons on T_c . When anisotropy was neglected and only the isotropic Migdal-Eliashberg equations were solved, T_c dropped from 39 K to 19 K. When anharmonicity on the phonon frequencies was neglected but anisotropy was kept, T_c was seen to increase from 39 K to 55 K [13]. This shows that phonon anharmonicity is harmful for superconductivity in MgB_2 , but anisotropy is helpful, and for a quantitative understanding of superconductivity in MgB_2 both are needed. Choi et al. were also able to show that the isotope exponent observed experimentally could be quantitatively reproduced, if the anharmonicity of the phonons was taken into account. Also, the temperature dependence of the specific heat from these calculations was in good agreement with the experimental results. All these results seem to show that we can obtain a complete understanding in terms of two gap superconductivity in MgB_2 based on the picture shown in Fig. 2.

An important question in this picture concerns the role of impurities and in particular interband impurity scattering, however. Conventionally one would expect that impurity scattering tends to equalize all gap values on the Fermi surfaces thereby reducing T_c . This is one of the

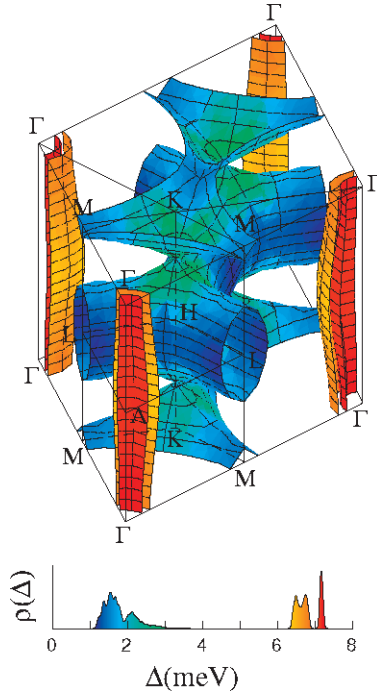


Figure 2: The energy gap distribution on the Fermi surface of MgB_2 (color coded). (Adapted from Ref. [14], ©2002 Nature Publishing Group).

reasons why two gap superconductivity or anisotropic s -wave superconductivity is rarely observed. This does not seem to be the case in MgB_2 . For example, samples with very different residual resistivities are observed to have essentially the same critical temperature T_c . This is a behavior that one would expect in a single gap s -wave superconductor due to Anderson's theorem. However, in a two gap superconductor a strong change of T_c with impurity concentration should be expected [15]. A very good answer to this question has been given by I. I. Mazin et al. in Ref. [16]: due to the particular electronic structure of MgB_2 the electronic wave functions on π bands and σ bands possess different parity symmetry. The π bands deriving from the Boron p orbitals are mainly antisymmetric with respect to the Boron plane, while the σ bands deriving from both Boron p and p orbitals are mainly symmetric. This disparity of σ and π bands makes the impurity scattering matrix element between these two types of bands exceptionally small as compared with the impurity scattering matrix element within each of these bands. Using density functional supercell calculations for various impurities Mazin et al were able to show that the interband scattering rate appears to be one to two orders of magnitude smaller than the intraband scattering rates due to this band disparity. This means that

impurity scattering will equalize the gaps within each of the two types of bands, but not very much between them. This makes the two gaps in MgB_2 exceptionally stable against impurity scattering. Only a very large amount of impurity scattering is expected to lead to a reduction of T_c due to interband scattering and an accompanied merging of the two gaps.

While signatures of the two gaps have been observed in several different experiments, so far direct experimental confirmation of the important role of the E_{2g} phonon for the pairing is still lacking. In principle, such a strong coupling phonon could produce observable structures in the tunneling density of states. However, there are difficulties in the case of MgB_2 as has been discussed by Dolgov et al [17]: on one hand the high frequency of the phonon mode leads to a strong reduction of the structures produced in the tunneling spectrum, on the other hand tunneling spectroscopy is mostly dominated by the π band phonons, which are not so important for the pairing interaction. This makes observation of the E_{2g} phonon and its coupling strength in tunneling spectroscopy difficult.

Concluding this section we can say that we seem to have a consistent and quantitative picture of two gap superconductivity in MgB_2 , which mainly arises from density functional calculations and solutions of Migdal-Eliashberg equations. The two gaps arise due to a strongly anisotropic electron-phonon interaction of the (anharmonic) E_{2g} phonon mode, which couples more strongly to the electrons on the σ bands than to the ones on the π bands. Due to the disparity of the two types of bands these two gaps appear to be very stable against impurity scattering, allowing T_c to remain large even in samples with large residual resistivities.

4. UPPER CRITICAL FIELD ANISOTROPY

In this section we want to explore the consequences of the two gap picture presented in the previous section on the temperature dependence of the upper critical field B_{c2} , particularly its anisotropy. Measurements of the upper critical field in MgB_2 single crystals have shown that not only B_{c2} is anisotropic, but also that this anisotropy is strongly temperature dependent [18, 19, 20, 21]. The anisotropy ratio Γ_{c2} is given by $\Gamma_{c2} = B_{c2}^{ab}/B_{c2}^c$, where B_{c2}^{ab} is the upper critical field, when the field is applied along the Boron planes, and B_{c2}^c the one for field along c -axis direction perpendicular to the Boron planes. At low temperatures Γ_{c2} reaches values around 5. It decreases with increasing temperature and reaches values around 2 at T_c (see the solid circles in Fig. 4 below). Close to T_c B_{c2}^c varies linearly with temperature, while B_{c2}^{ab} shows a pronounced upward curvature. This behavior is quite unusual, because in conventional single gap superconductors the anisotropy ratio is very much temperature independent, rarely changing by more than 10 to 20 percent. An upward curvature of the upper critical field has been observed in $\text{YNi}_2\text{B}_2\text{C}$ and attributed to two band behavior, however, in this case the upward curvature appeared in all spatial directions, in contrast to MgB_2 [22].

The first theoretical work addressing this unusual behavior in MgB_2 was a study within an anisotropic gap model by Posazhennikova et al. [23]. In this work a single anisotropic s -wave gap on an elliptical Fermi surface was considered. It was shown that the experimental data of the upper critical field in MgB_2 single crystals including both the strong temperature dependence of the anisotropy ratio as well as the upward curvature only appearing with field in ab -plane direction could be fitted within this model, if the gap was smaller in c -axis direction than in ab -plane direction. While this model can account for all experimental observations on the upper critical field in MgB_2 , it possesses some drawbacks, however, regarding its consistency with

other experimental results. One problem concerns the ratio of the maximum to the minimum gap value. Within this anisotropic s -wave model a gap ratio of about 1:10 was needed to explain the upper critical field data. This ratio seems too large compared with the about 1:3 ratio as observed in tunneling experiments, for example. In addition, measurements of the in-plane penetration depth clearly show an exponential decrease with the small gap [24, 25]. This suggests that the small gap is present within the Boron plane direction consistent with the picture in Fig. 2, but inconsistent with this anisotropic s -wave model.

Another problem concerns the anisotropy of the lower critical field B_{c1} . From anisotropic (single gap) Ginzburg-Landau theory one should expect that the upper critical field anisotropy is related to the lower critical field anisotropy via $B_{c2}^{ab}/B_{c2}^c = B_{c1}^c/B_{c1}^{ab}$. Recent experimental studies have established, however, that this relation is violated in MgB_2 [26, 27, 28], the upper critical field anisotropy decreasing with increasing temperature, while the lower critical anisotropy is found to increase. This is in agreement with expectations based on two gap models [29], but again inconsistent with an anisotropic s -wave model.

A first calculation within an anisotropic two band model was presented by Miranovic et al. [29] based on clean limit Eilenberger theory. The Fermi surface sheets of the two bands were taken as ellipsoids with very different anisotropies, while the two gaps were taken to be isotropic. Within this calculation it was also possible to qualitatively reproduce the experimentally observed upper critical field anisotropy as in the anisotropic s -wave model by Posazhennikova et al. In addition to that, however, this two band calculation did not suffer from the drawbacks mentioned above: more realistic values for the ratio of the two gaps could be taken, the small gap was present within the Boron plane direction, and the lower critical field anisotropy was found to increase with temperature.

In order to answer the question whether the picture in Fig. 2 is consistent with the upper critical field anisotropy the author and N. Schopohl presented a calculation within two band Eilenberger theory taking into account the detailed band structure Fermi surface topology based on Fig. 1 [30]. For that purpose a simple but realistic model of the Fermi surface was used as shown in Fig. 3. The upper panel of Fig. 3 shows one half of the Brillouin zone from Fig. 1. Using the periodicity of the lattice identical copies of the Brillouin zone may be attached to each other (center panel). Choosing a new Brillouin zone around the Γ point leads to the structure shown in the lower panel. This rearrangement shows that the σ band Fermi surface can be modeled by a distorted cylinder and the π band Fermi surface by a torus cut open half. Here, the two σ bands and the two π bands are assumed to be degenerate, for simplicity. This suggests the following parameterization of the Fermi surfaces for the σ band Fermi momentum [31]:

$$\vec{k}_{F,\sigma}(\varphi, k) = \begin{pmatrix} k_{F,\sigma} + \frac{\varepsilon_c}{c} \cos(ck) \cos \varphi \\ k_{F,\sigma} + \frac{\varepsilon_c}{c} \cos(ck) \sin \varphi \\ k \end{pmatrix} \quad (2)$$

and the π band Fermi momentum:

$$\vec{k}_{F,\pi}(\varphi, \vartheta) = \begin{pmatrix} k_{F,\pi} \left(\frac{1}{\kappa} + \cos \vartheta \right) \cos \varphi \\ k_{F,\pi} \left(\frac{1}{\kappa} + \cos \vartheta \right) \sin \varphi \\ k_{F,\pi} \sin \vartheta \end{pmatrix} \quad (3)$$

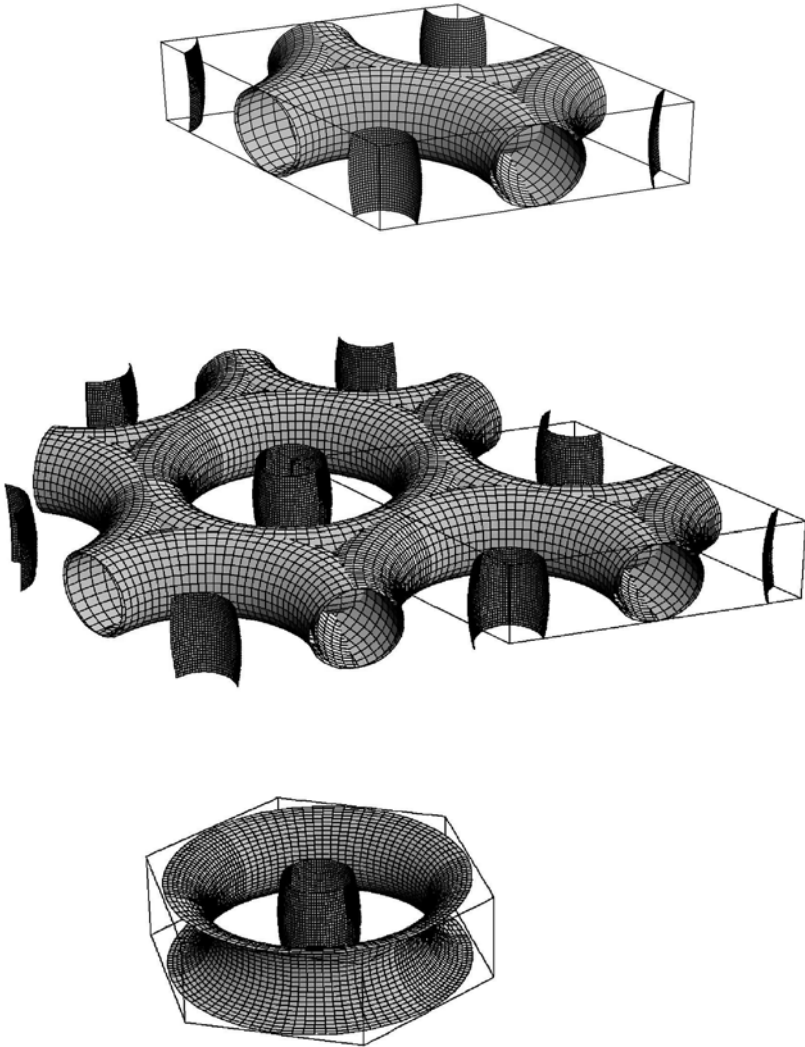


Figure 3: Simplification of the MgB_2 Fermi surface from Fig. 1. Rearranging the Fermi surface sheets around the Γ point shows that the σ band can be modeled as a distorted cylinder and the π band as a half-torus.

Here, φ is the in-plane angle, k the c -axis momentum, and ϑ the azimuthal angle of the half-torus running from $\pi/2$ to $3\pi/2$. The corresponding Fermi velocities are given by

$$\vec{v}_{F,\sigma}(\varphi, k) = v_{F,\sigma} \begin{pmatrix} \cos \varphi \\ \sin \varphi \\ \epsilon_c \sin c k \end{pmatrix} \quad \text{and} \quad \vec{v}_{F,\pi}(\varphi, \vartheta) = v_{F,\pi} \begin{pmatrix} \cos \varphi \cos \vartheta \\ \sin \varphi \cos \vartheta \\ \sin \vartheta \end{pmatrix} \quad (4)$$

Here, the dimensionless c -axis dispersion parameter ϵ_c has been assumed small. For MgB₂ the following parameter values have been extracted from band structure calculations [30]: $v_{F,\sigma} = 4.4 \times 10^5$ m/s, $v_{F,\pi} = 8.2 \times 10^5$ m/s, $\epsilon_c = 0.23$, and $\kappa = 0.25$.

Based on this model for the MgB₂ Fermi surface one can now calculate the upper critical field using the linearized two band Eilenberger equations. For $\omega_n > 0$ they read

$$\left\{ \omega_n + \vec{v}_{F,\alpha} \left[\frac{\hbar}{2} \vec{\nabla} - i \frac{e}{c} \vec{A}(\vec{r}) \right] \right\} f_\alpha(\vec{r}, \hat{k}; \omega_n) = -\Delta_\alpha(\vec{r}) \quad (5)$$

along with the gap equation

$$\Delta_\alpha(\vec{r}) = -\pi T \sum_{\alpha} \sum_{|\omega_n| < \omega_c} \lambda^{\alpha\alpha} \langle f_\alpha(\vec{r}, \hat{k}; \omega_n) \rangle_\alpha \quad (6)$$

Here, f_α is the anomalous Eilenberger propagator and $\Delta_\alpha(\vec{r})$ the (spatially dependent) gap function for the two bands $\alpha \in \{\pi, \sigma\}$. The pairing interaction $\lambda^{\alpha\alpha}$ becomes a two-by-two matrix in the band indices. The effective matrix elements have been calculated from band structure calculations in Ref. [9] and found to be

$$\begin{pmatrix} \lambda^{\sigma\sigma} & \lambda^{\sigma\pi} \\ \lambda^{\pi\sigma} & \lambda^{\pi\pi} \end{pmatrix} = \begin{pmatrix} 0.959 & 0.222 \\ 0.163 & 0.278 \end{pmatrix}. \quad (7)$$

Together Equations (5) and (6) establish an eigenvalue problem for the gap function $\Delta_\alpha(\vec{r})$. For a given temperature T one has to look for the solution $\Delta_\alpha(\vec{r})$ that solves both equations for the highest value of the magnetic field $\vec{B} = \vec{\nabla} \times \vec{A}$.

Eilenberger theory is a generalization of BCS theory to inhomogeneous superconducting states and contains Ginzburg-Landau theory as a limiting case for $T \rightarrow T_c$ [36, 37]. It holds in the limit $k_F \ll 1$, where ξ is the coherence length and k_F the Fermi momentum. Since Ginzburg-Landau theory is limited to the vicinity of T_c , Eilenberger theory is the method of choice, if one wants to calculate properties of type-II superconductors in the vortex state at lower temperatures from microscopic grounds. Near the upper critical field the gap function becomes small and therefore one can use the linearized Eilenberger equations to determine B_{c2} .

Equations (5) and (6) are usually solved using a Landau level expansion of $\Delta_\alpha(\vec{r})$ above the Abrikosov ground state of the vortex lattice [32]. For strongly anisotropic systems this procedure requires a high number of excited states, however. In addition, the calculation can only be done numerically. In Ref. [30] Equations (5) and (6) were solved using a variational method that had been introduced earlier by the author in Ref. [23]. This method does not require a high number of excited states and even allows to obtain analytical results in some limiting cases. The variational ansatz for $\Delta_\alpha(\vec{r})$ corresponds to a distorted Abrikosov ground state of the form

$$\Delta_\alpha(\vec{r}) = \Delta_\alpha \psi_\Lambda \left(e^{-\tau} x, e^\tau y \right) \quad (8)$$

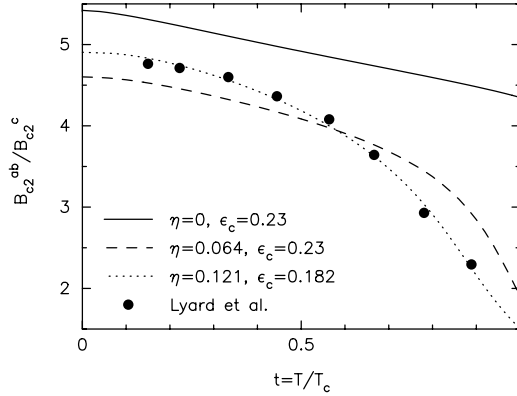


Figure 4: Temperature dependence of the anisotropy ratio $\Gamma_{c2} = B_{c2}^{ab}/B_{c2}^c$ for the band structure based two-band model of Ref. [30]. Results are shown for different interband pairing strengths η and c -axis dispersions ϵ_c . Solid circles are experimental results from Lyard et al. [20] (adapted from Ref. [30], ©2003 The American Physical Society).

where τ is used as a variational parameter and determined such as to maximize the upper critical field B_{c2} . Here, ψ_Λ is the usual (undistorted) Abrikosov ground state. More details about this variational method can be found in the appendix.

Using this method the temperature dependence of the anisotropy ratio was calculated from microscopic grounds based on band structure calculations in Ref. [30] as pointed out above. The result is shown in Fig. 4. Here, the parameter η is a dimensionless parameter describing the interband pairing strength and is given by

$$\eta = \frac{\lambda^{\pi\pi} - \lambda_-}{\lambda_+ - \lambda_-} \quad (9)$$

where λ_+ and λ_- are the larger and smaller eigenvalues of the matrix $\lambda^{\alpha\alpha}$ in Eq. (6), respectively. The dashed line shows the result for the parameters obtained from band structure calculations, the solid circles are experimental results on MgB_2 single crystals from Lyard et al. [20]. For comparison, also the result with no interband pairing $\eta = 0$ is shown as the solid line. In this case the upper critical field anisotropy is determined by the σ band only.

In Ref. [30] it was found that the two most important parameters determining the temperature dependence of the upper critical field anisotropy are η and the c -axis dispersion ϵ_c of the cylindrical σ band. All other parameters have only minor influence on the shape of the curves in Fig. 4. If these two parameters are allowed to vary from their band structure values, one can obtain an excellent fit of the experimental data shown as the dotted line in Fig. 4. In this (two parameter) fit the interband pairing strength η turns out to be somewhat larger and the c -axis dispersion ϵ_c a little bit smaller than expected from band structure calculations. Similar observations, that larger interband pairing strengths than found by band structure calculations are needed to fit experimental data, have been made also in Refs. [33] and [34]. Possible

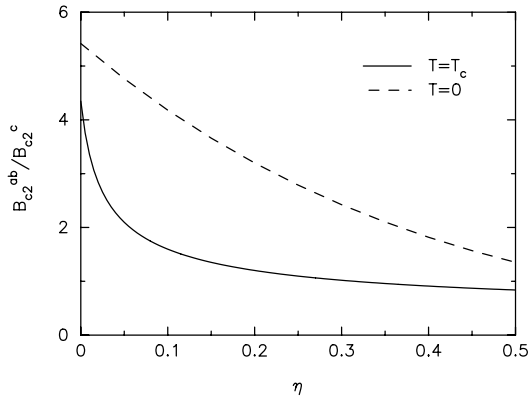


Figure 5: Anisotropy ratio $\Gamma_{c2} = B_{c2}^{ab}/B_{c2}^c$ as a function of interband pairing strength η for the band structure based two-band model of Ref. [30] at $T = 0$ (dashed line) and $T = T_c$ (solid line) (adapted from Ref. [30], ©2003 The American Physical Society).

explanations could be either that band structure calculations underestimate the interband pairing strength or that some small amount of interband impurity scattering or effects of strong electron-phonon coupling, which were neglected in the above calculations of the upper critical field, mimic a somewhat stronger interband pairing strength.

The result in Fig. 4 shows that indeed a strong temperature dependence of the upper critical field ratio consistent with experimental results has to be expected in the clean limit for the parameters found in band structure calculations for MgB_2 . As the solid line shows, the influence of both gaps is crucial here. The strong temperature dependence can be understood as follows: at low temperatures and high magnetic fields the σ band with the large gap is dominating leading to a strong anisotropy. When temperature is increased and thus the magnetic field reduced, the influence of the π band with the small gap becomes more and more important. Since the π band is more isotropic a reduction of the upper critical field anisotropy results.

It is instructive to look at the change of Γ_{c2} as a function of the interband pairing strength η at $T = 0$ and $T = T_c$. This is shown in Fig. 5. When $\eta = 0$ there is no strong temperature dependence of Γ_{c2} . When η is increased, Γ_{c2} decreases much more rapidly at $T = T_c$ than at $T = 0$, because the influence of the π band is more important at higher temperature. As a result the temperature dependence becomes stronger. However, when η is increased towards 0.5 (maximum coupling of the two bands), eventually Γ_{c2} becomes small also at low temperature and the temperature dependence becomes weak again. It appears that either for very weak or for very strong interband pairing interaction the system effectively behaves like a single gap superconductor with a weak temperature dependence of the upper critical field anisotropy. It is only in the intermediate regime around $\eta \sim 0.05 - 0.3$ where a strong temperature dependence of Γ_{c2} can be observed. This is just the regime in which MgB_2 appears to be according to band structure calculations.

In Ref. [35] further results of this model can be found: the temperature dependence of the upper critical field for field applied along the Boron plane direction shows an upward curvature, while for field applied in c -axis direction it does not, in good agreement with the experiments. Also, the magnetic field dependence of the zero energy density of states follows the experimental temperature dependence of the electronic specific heat coefficient.

The theories about the upper critical field in MgB_2 discussed so far are clean limit theories, e.g. impurity scattering was assumed to be small. However, even in the best MgB_2 single crystals available so far it is believed that in the π band the scattering rate is larger than the gap, while in the σ band the scattering rate might be smaller than the gap. This means that impurities are expected to affect the temperature dependence of the upper critical field and one might ask how this could affect the clean limit results discussed above. So far no calculations for general impurity scattering rates have been presented. However, calculations can be considerably simplified in the dirty limit. In Refs. [38, 39] such dirty limit theories of the upper critical field for MgB_2 were presented. The main simplification here is that the intraband scattering rates Γ_π and Γ_σ are assumed to be larger than the gaps, while the interband scattering rate is assumed to be negligible due to the parity argument by Mazin et al. [16] discussed in the previous section. Interestingly, the strong temperature dependence of the upper critical field anisotropy was shown to exist also in this dirty limit [39]. The physical reason for this behavior is the same as in the clean limit: an interband pairing interaction of intermediate strength and a strong anisotropy of the Fermi velocities in the σ band which results in a strong anisotropy of the diffusivities in this band. Therefore, the inclusion of impurities qualitatively does not change this behavior.

In Ref. [39] also the angular dependence of the upper critical field was studied. It was shown that this angular dependence shows strong deviations from the results expected from anisotropic Ginzburg-Landau theory. The reason for this is that the c -axis coherence lengths in the two bands strongly differ. As a result the validity of Ginzburg-Landau theory is reduced to a very narrow region near the critical temperature T_c [40].

To summarize this section we have seen that the unusually strong temperature dependence of the upper critical field anisotropy can be nicely understood in terms of the two gap model, if the particular Fermi surface topology of MgB_2 is taken into account. The essential ingredients for this effect are two Fermi surfaces with very different anisotropies and an interband pairing interaction with an intermediate strength. Too weak or too strong interband pairing would result in effectively single gap behavior. According to band structure calculations MgB_2 fulfils these requirements possessing a strongly anisotropic cylindrical σ band and a more isotropic toroidal π band. Parameters from band structure calculations can even reproduce the upper critical field anisotropy quantitatively. This shows that the behavior of the upper critical field is consistent with the band structure picture presented in the previous sections.

5. MICROWAVE CONDUCTIVITY

In this section we want to discuss the consequences of two gap superconductivity on the microwave conductivity in MgB_2 , particularly its temperature dependence at fixed frequency. In Ref. [33] the observation of an anomalous microwave conductivity peak in MgB_2 thin films has been reported and its interpretation in terms of two gap behavior shall be discussed here. We will first start with a review of conductivity peaks in conventional superconductors as well as in high- T_c cuprates and then compare them with the results in MgB_2 .

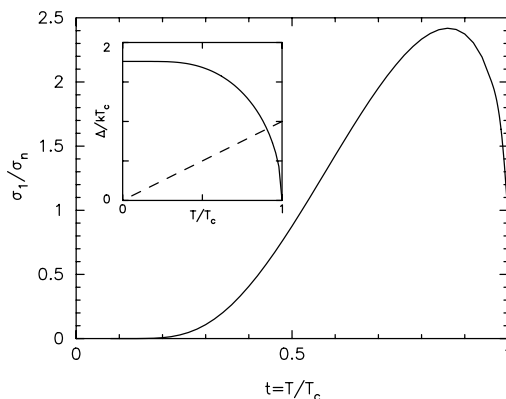


Figure 6: Temperature dependence of the microwave conductivity at a frequency of $\omega = 0.02k_B T_c$ for a conventional *s*-wave superconductor in the dirty limit. Inset: temperature dependence of the gap (solid line) along with the line $\Delta = k_B T$ (dashed line). The crossing point roughly determines the position of the peak in the conductivity.

In conventional dirty limit superconductors the microwave conductivity at frequencies sufficiently below the gap frequency shows a coherence peak as a function of frequency, which is related to the so-called Hebel-Slichter peak in the temperature dependence of the NMR spin relaxation rate. As shown in Fig. 6 the conductivity initially increases when entering the superconducting state going through a peak value near $0.9 T_c$ and finally being suppressed exponentially at lower temperatures. The peak naturally comes out of BCS theory and at the time was regarded as one of the key triumphs of BCS theory, because earlier theories based on two fluid models were not able to account for this effect. When the superconducting state is entered and the gap opens, a square-root singularity appears in the density of states at the gap edge. This singularity leads to increased contributions to the microwave conductivity. When the gap Δ increases upon lowering the temperature, it eventually becomes larger than $k_B T$. At this point quasiparticles are condensed out into the superfluid and the microwave conductivity is suppressed exponentially at lower temperatures. As a rule of thumb we can estimate the position of the coherence peak roughly at the point where $\Delta(T)$ becomes equal to $k_B T$, which is shown as the crossing point between the solid and the dashed line in the inset of Fig. 6. In contrast to the NMR Hebel-Slichter peak, the coherence peak in the microwave conductivity depends on the scattering rate, however. When the system becomes cleaner, the microwave coherence peak is gradually reduced, as has been discussed by Marsiglio [41]. The ultimate reason for this dependence on the scattering rate is lying in the fact that the conductivity is a nonlocal quantity in contrast to the NMR relaxation rate which is a local probe.

In the high- T_c cuprates the situation is completely different. In measurements of the NMR relaxation rate no Hebel-Slichter peak is observed. However, the microwave conductivity shows a huge peak at temperatures between $0.3 T_c$ and $0.6 T_c$ depending on frequency as shown in Fig. 7. The absence of the Hebel-Slichter peak can be easily understood as a consequence of the *d*-wave nature of the superconducting state. In a *d*-wave superconductor the singularity at

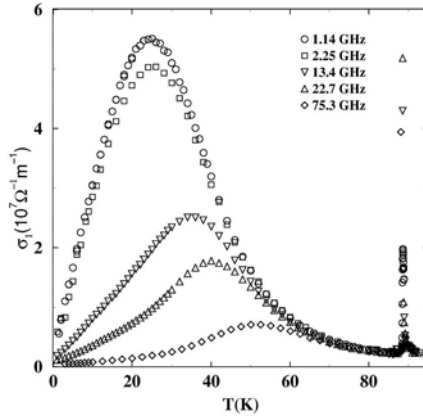


Figure 7: Temperature dependence of the microwave conductivity in YBCO showing a large conductivity peak (adapted from Ref. [42], ©1999 The American Physical Society).

the gap edge of the density of states is not a square-root singularity anymore, but a logarithmic singularity, having a much weaker influence on the NMR relaxation rate, as shown in Fig. 8. In addition, strong-coupling effects tend to wash out the singularities in the density of states, which leads to an additional suppression of the coherence peak as discussed in Ref. [41].

Since there is no coherence peak in the NMR relaxation rate, why is there a peak in the microwave conductivity? It has been suggested that this peak has a different physical origin and is related to a rapid suppression of the inelastic scattering rate in the superconducting state [43]. Such a drop of the inelastic scattering rate naturally appears when inelastic scattering in the normal state is dominated by electron-electron scattering, for example by spin fluctuations, because the superconducting gap is suppressing electron-electron scattering below the gap energy in the superconducting state. Detailed theoretical calculations by Hirschfeld et al [44] including *d*-wave superconductivity, strong impurity scattering, and inelastic spin fluctuation scattering were shown to be consistent with the experimental results.

In MgB_2 microwave conductivity measurements have shown a conductivity peak appearing at about $0.5 T_c$ as shown in Fig. 9. This peak position seems to be somewhat intermediate between conventional superconductors and high- T_c cuprates and the natural question arises, whether this is a coherence peak or a peak due to lifetime effects as in the cuprates. In order to address the question of lifetime effects a quick look at the temperature dependence of the resistivity in MgB_2 is useful. It has been shown that the temperature dependence of the resistivity can be fitted well by Bloch-Grüneisen formula with a temperature independent residual resistivity associated with impurity scattering and a temperature dependent phonon scattering part [45]. This seems to show that no large electron-electron scattering is present in the normal state of MgB_2 . Moreover, at T_c when superconductivity sets in, the resistivity is already in the saturation regime where phonon scattering is frozen out (due to the high frequency of the E_{2g}

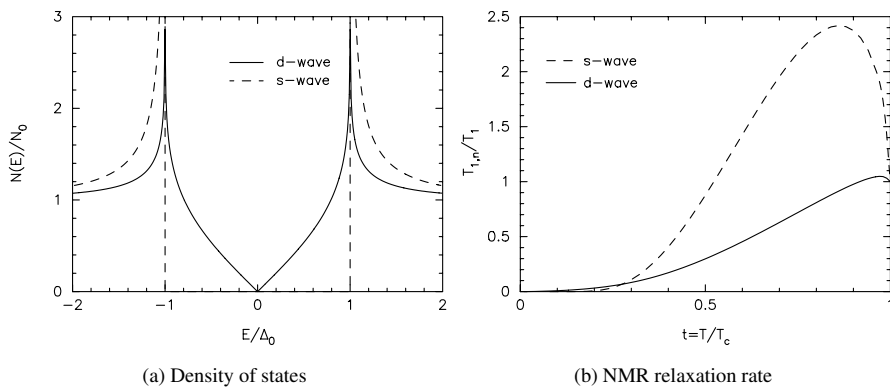


Figure 8: (a) Density of states in a d -wave superconductor (solid line) and an s -wave superconductor (dashed line). (b) Corresponding NMR relaxation rates for d -wave (solid line) and s -wave (dashed line). In the d -wave case no large Hebel-Slichter peak is visible anymore.

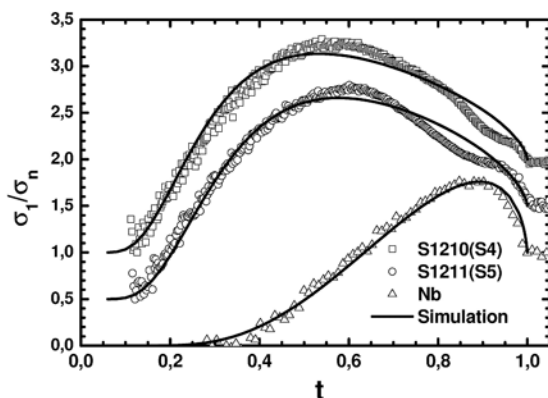


Figure 9: Temperature dependence of the microwave conductivity in MgB₂ thin films (circles and squares). For comparison, the microwave conductivity of a Niobium thin film in the dirty limit is also shown (triangles). (Adapted from Ref. [33], ©2003 The American Physical Society)

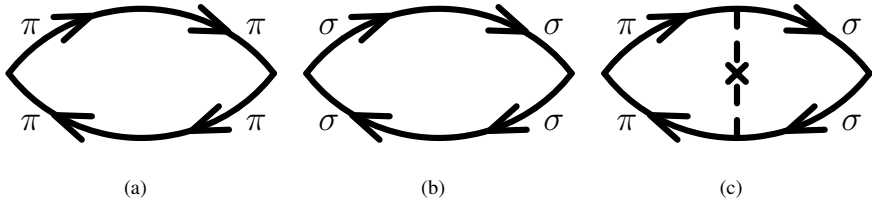


Figure 10: Diagrammatic contributions to the conductivity. (a) The main contribution to the π band. (b) The main contribution to the σ band. (c) The lowest order interband scattering contribution to the conductivity which is expected to be small in MgB_2 .

phonon mode). Therefore the resistivity at T_c seems to be dominated by elastic impurity scattering and thus no rapid drop of inelastic scattering can be expected in the superconducting state. Note that this is in contrast to the high- T_c cuprates, where resistivity varies linearly with temperature down to T_c and is not saturated. These arguments seem to exclude the interpretation of the conductivity peak in MgB_2 in terms of a lifetime effect.

In the following we therefore want to study the microwave conductivity of a dirty two gap superconductor. Dirty in the sense that the intraband impurity scattering rates in the two bands are assumed to be larger than the respective gaps, but interband scattering is neglected as suggested by the argument by Mazin et al. [16].

In a two band system like MgB_2 we can approximate the total conductivity as the sum of the two partial conductivities of the two bands (parallel resistor formula). This approximation neglects interband scattering events like the one shown diagrammatically in Fig. 10(c). However, these events are expected to give only small corrections, because interband impurity scattering is expected to be much weaker than intraband impurity scattering due to the argument by Mazin et al. [16].

If the intraband scattering rates in the two bands are sufficiently larger than their gaps, we can use the Mattis-Bardeen dirty limit formula for the conductivity in each band separately [46, 47]:

$$\frac{\sigma_\alpha(\omega)}{\sigma_{n,\alpha}} = \frac{1}{2\omega} \int_{-\infty}^{\infty} d\Omega \left(\tanh \frac{\Omega + \omega}{2T} - \tanh \frac{\Omega}{2T} \right) [N_\alpha(\Omega) N_\alpha(\Omega + \omega) + M_\alpha(\Omega) M_\alpha(\Omega + \omega)] \tag{10}$$

Here, the normal and anomalous densities of states are given by

$$N_\alpha(\Omega) = \text{Re} \left\{ \frac{|\Omega|}{\sqrt{\Omega^2 - \Delta_\alpha^2}} \right\} \quad \text{and} \quad M_\alpha(\Omega) = \text{Re} \left\{ \frac{\Delta_\alpha \text{sgn}(\Omega)}{\sqrt{\Omega^2 - \Delta_\alpha^2}} \right\} \tag{11}$$

The total conductivity under these assumptions is given by $\sigma_1(\omega) = \sigma_\pi(\omega) + \sigma_\sigma(\omega)$. The temperature dependence of the two gaps Δ_α has to be determined from a solution of the two by

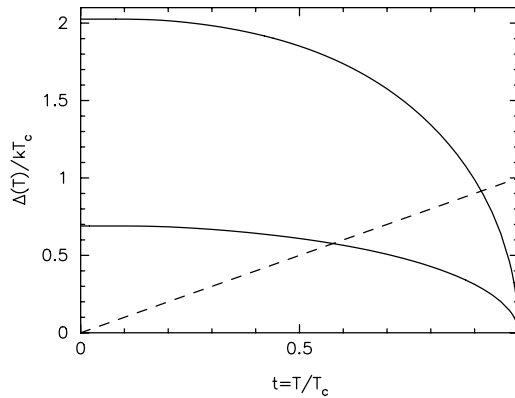


Figure 11: Temperature dependence of the two gaps in MgB_2 found from a solution of the two by two gap equation. The dashed line shows $\Delta = k_B T$. Its crossing point with the small gap appears at a much lower temperature than the one with the large gap.

two gap equation:

$$\Delta_\alpha = \sum_\beta \lambda^{\alpha\beta} \Delta_\beta \int_0^{\omega_c} dE \frac{\tanh \frac{\sqrt{E^2 + \Delta_\beta^2}}{2T}}{\sqrt{E^2 + \Delta_\beta^2}} \quad (12)$$

Here, ω_c is a characteristic phonon cut-off frequency and $\lambda^{\alpha\beta}$ the two by two coupling matrix. These parameters can be either taken from a band structure calculation or tried to be adjusted to the particular sample in question. In Ref. [33] an intermediate approach was taken: the partial densities of states and the cut-off frequency were taken from band structure calculations, while the remaining parameters were adjusted to the T_c of the sample and the value of the small gap, which could be extracted from the exponential fall-off of the temperature dependent change of the penetration depth. A typical temperature dependence of the two gaps found this way is shown in Fig. 11. One notices that the small gap reaches $k_B T$ at a much lower temperature than the large gap. According to the rule of thumb given above this would mean that the coherence peak in the π band is expected to appear at much lower temperature than in a conventional superconductor.

That this is indeed the case is shown in Fig. 12. Here, the temperature dependence of the Mattis-Bardeen conductivity is shown for different zero temperature gap values. In these calculations the BCS temperature dependence has been scaled to different gap values for simplicity. Clearly, the position of the coherence peak follows the crossing point of the gap with $k_B T$.

In Fig. 9 the fits to the two MgB_2 samples show the temperature dependence of the π band contribution to the conductivity obtained using the temperature dependence of the small gap in Fig. 11. Apparently there is good agreement between measurement and calculation. The fit to the Niobium sample was obtained using the BCS temperature dependence of the gap, as one should expect for a conventional superconductor.

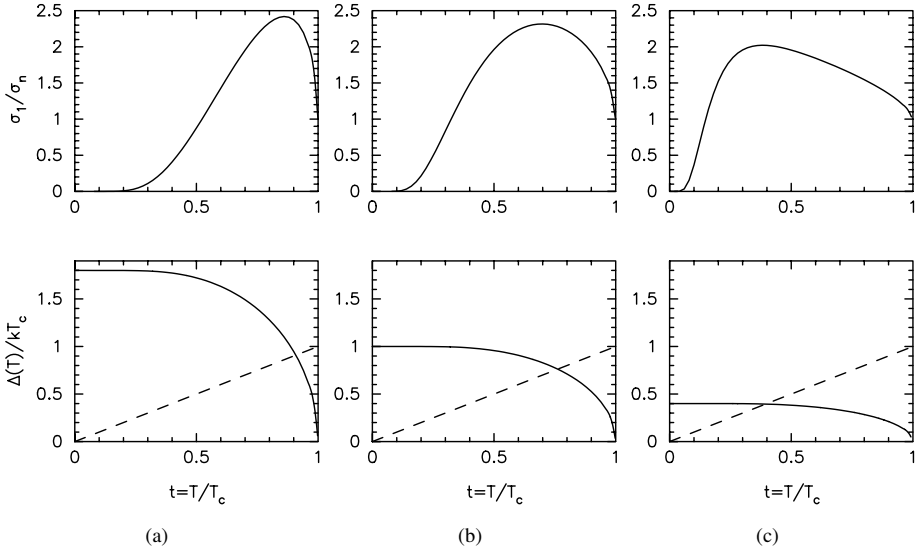


Figure 12: Temperature dependence of the microwave conductivity (upper panel) for different gap values (lower panel) at a frequency of $\omega = 0.02k_B T_c$.

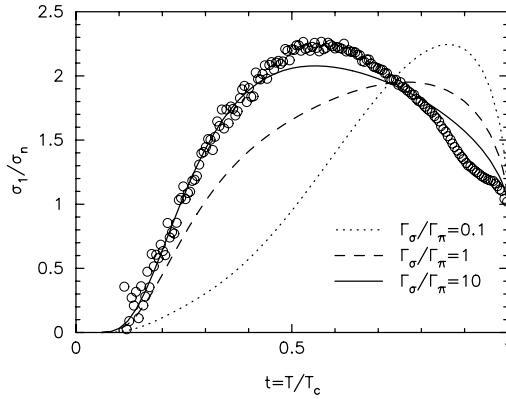


Figure 13: Temperature dependence of the microwave conductivity for different ratios of the scattering rates $\Gamma_\sigma/\Gamma_\pi=0.1, 1,$ and 10 along with the experimental results from Ref. [33].

Now one might ask where the contribution from the σ band in the MgB_2 samples is. According to Fig. 12 the σ band should produce a conventional coherence peak. The relative weight of the two contributions is determined by the partial normal state conductivities of the two bands, however. We have

$$\sigma_1(\omega) = \sigma_\pi(\omega) + \sigma_\sigma(\omega) = \sigma_{n,\pi} \frac{\sigma_\pi(\omega)}{\sigma_{n,\pi}} + \sigma_{n,\sigma} \frac{\sigma_\sigma(\omega)}{\sigma_{n,\sigma}} \quad (13)$$

where the conductivity ratios are given by Eq. (10). The normal state conductivities are related to the plasma frequencies $\omega_{p,\alpha}$ and the intraband scattering rates Γ_α via the expression

$$\sigma_{n,\alpha} = \hbar\epsilon_0 \frac{\omega_{p,\alpha}^2}{2\Gamma_\alpha} \quad (14)$$

Theoretical band structure values for the plasma frequencies have been given in Ref. [16]. According to these calculations we have $\omega_{p,\pi} = 5.89$ eV and $\omega_{p,\sigma} = 4.14$ eV for the in plane plasma frequencies. Therefore, if the scattering rates in the two bands are the same, the contribution of the π band is expected to be a factor of 2 larger than the one of the σ band. This is not sufficient to understand the apparent absence of a sizeable σ band contribution in the experimental data. A possible explanation could be a stronger scattering rate in the σ band at least in the thin film samples studied in Ref. [33]. To illustrate that, in Fig. 13 the temperature dependence of the conductivity is shown for different values of the relative ratio of the two scattering rates. These results suggest a at least 10 times larger scattering rate in the σ band than in the π band. In principle, the scattering rates in the two bands can be varied by selective doping, for example by doping with Aluminum for Magnesium or Carbon for Boron [48, 49, 16]. It would be interesting to see whether a cross-over like the one shown in Fig. 13 can be observed experimentally on a series of MgB_2 films with varying degree of doping.

Concluding this section we have seen that the anomalous microwave conductivity peak observed in MgB_2 thin films can be understood as a coherence peak due to the small gap. The peak appears at much lower temperatures than in conventional superconductors, because the small gap opens up more slowly upon reducing the temperature below T_c . As a result the condensation of excited quasiparticles and with it the exponential suppression of the conductivity sets in later. Again, this peculiar effect is consistent with two gap behavior and reinforces the picture presented in the previous sections.

6. SUMMARY

We have reviewed our present picture of superconductivity in magnesium diboride. Much of this picture stems from band structure calculations. We have seen that the high value of the critical temperature T_c is due to a high frequency phonon mode that couples strongly to the electrons at the Fermi level. This coupling is particularly strong to the electrons on the σ band and leads to a much larger superconducting gap on the σ band than on the π band. The different parity of the electronic wavefunctions of the σ band and the π band results in a strong reduction of the interband impurity scattering matrix element. This makes the two different gaps particularly stable against impurity scattering. For these reasons magnesium diboride appears to be the clearest example of an intrinsic two gap superconductor to date.

Two gap superconductivity in magnesium diboride leads to unusual behavior in a number of experimentally accessible quantities. Here, we have focused on the temperature dependence

of the upper critical field anisotropy and the microwave conductivity. The upper critical field anisotropy shows an unusual strong temperature dependence. This feature is related to the presence of the two gaps, but also to the very different anisotropy of the two bands. Here, the intermediate strength of the interband pairing interaction plays a crucial role as well. The temperature dependence of the microwave conductivity shows a peak at temperatures around $0.5T_c$. This peak can be understood as an anomalous coherence peak that is shifted downwards in temperatures because of the small gap.

In conclusion, the case of two gap superconductivity in magnesium diboride generated by strong electron-phonon coupling appears to be well established and can be consistently observed in very different experimental quantities such as the upper critical field or the microwave conductivity.

The author would like to thank O. V. Dolgov, S. Graser, C. Iniotakis, B. B. Jin, N. Klein, S.-I. Lee, K. Maki, A. I. Posazhennikova, and N. Schopohl for valuable discussions about this and related topics.

APPENDIX

In this appendix the variational method for the calculation of the upper critical field from Eqs. (5) and (6) shall be described. This method was used in Refs. [23, 30].

Defining the operator

$$L_\alpha = 2|\omega_n| + \text{sgn } \omega_n \vec{v}_{F,\alpha}(\hat{k}) \left[\hbar \vec{\nabla} - i \frac{2e}{c} \vec{A}(\vec{r}) \right] \quad (15)$$

where $\vec{v}_{F,\alpha}(\hat{k})$ is the Fermi velocity of band α , \vec{A} the vector potential due to the internal magnetic field within the system, and $\omega_n = (2n+1)\pi T$ the Matsubara frequencies, Eq. (5) can be inverted using the identity

$$L_\alpha^{-1} = \int_0^\infty ds e^{-sL_\alpha} \quad (16)$$

which leads to

$$f_\alpha(\vec{r}, \hat{k}; \omega_n) = -2 \int_0^\infty ds e^{-sL_\alpha} \Delta_\alpha(\vec{r}) \quad (17)$$

Introducing this into the gap equation Eq. (6) we can eliminate f_α :

$$\Delta_\alpha(\vec{r}) = 2\pi T \sum_\alpha \sum_{|\omega_n| < \omega_c} \lambda^{\alpha\alpha} \left\langle \int_0^\infty ds e^{-sL_\alpha} \Delta_\alpha(\vec{r}) \right\rangle_\alpha \quad (18)$$

This equation is a linear equation for $\Delta_\alpha(\vec{r})$.

As is usual in weak-coupling theory we can eliminate the cutoff frequency ω_c in favor of the critical temperature T_c . For this purpose we consider Eq. (18) in the absence of a magnetic field at T_c . Then the gap function $\Delta_\alpha(\vec{r})$ becomes homogeneous and we find

$$\begin{aligned} \Delta_\alpha &= 2\pi T_c \sum_{|\omega_n(T_c)| < \omega_c} \int_0^\infty ds e^{-2s|\omega_n(T_c)|} \sum_\alpha \lambda^{\alpha\alpha} \Delta_\alpha \\ &= 2\pi T_c \sum_{\omega_n(T_c) > 0}^{\omega_c} \frac{1}{\omega_n(T_c)} \sum_\alpha \lambda^{\alpha\alpha} \Delta_\alpha \end{aligned} \quad (19)$$

This is an eigenvalue equation for Δ_α and the largest eigenvalue λ_+ of the matrix $\lambda^{\alpha\alpha}$ determines T_c . Thus we find

$$\frac{1}{\lambda_+} = 2\pi T_c \sum_{\omega_n(T_c) > 0}^{\omega_c} \frac{1}{\omega_n(T_c)} \quad (20)$$

For $\omega_c \gg T_c$ the following relation holds:

$$2\pi T_c \sum_{\omega_n(T_c) > 0}^{\omega_c} \frac{1}{\omega_n(T_c)} - 2\pi T \sum_{\omega_n(T) > 0}^{\omega_c} \frac{1}{\omega_n(T)} \simeq \ln \frac{T}{T_c} \quad (21)$$

and thus we can write Eq. (20) in the form

$$\frac{1}{\lambda_+} - \ln \frac{T}{T_c} = 2\pi T \sum_{\omega_n(T) > 0}^{\omega_c} \frac{1}{\omega_n(T)} = 2\pi T \sum_{|\omega_n(T)| < \omega_c} \int_0^\infty ds e^{-2s|\omega_n(T)|} \quad (22)$$

Multiplying this equation by $\sum_{\alpha} \lambda^{\alpha\alpha} \Delta_{\alpha}(\vec{r})$ it can be subtracted from Eq. (18) leading to

$$\begin{aligned} \Delta_{\alpha}(\vec{r}) + \sum_{\alpha} \lambda^{\alpha\alpha} \Delta_{\alpha}(\vec{r}) \left(-\frac{1}{\lambda_{+}} + \ln \frac{T}{T_c} \right) \\ = \sum_{\alpha} \lambda^{\alpha\alpha} 2\pi T \sum_{|\omega_n| < \omega_c} \left\langle \int_0^{\infty} ds \left[e^{-sL_{\alpha}} - e^{-2s|\omega_n|} \right] \Delta_{\alpha}(\vec{r}) \right\rangle_{\alpha} \\ = \sum_{\alpha} \lambda^{\alpha\alpha} 4\pi T \sum_{\omega_n > 0}^{\omega_c} \int_0^{\infty} ds e^{-2s\omega_n} \left\langle \left[e^{-is\vec{v}_{F,\alpha} \cdot \vec{\Pi}} - 1 \right] \Delta_{\alpha}(\vec{r}) \right\rangle_{\alpha} \end{aligned} \quad (23)$$

Here, we have eliminated the $\text{sgn } \omega_n$ factor assuming inversion symmetry of the Fermi velocity $\vec{v}_{F,\alpha}(\hat{k}) = -\vec{v}_{F,\alpha}(-\hat{k})$ and introduced the operator

$$\vec{\Pi} = \frac{\hbar}{i} \vec{\nabla} - \frac{2e}{c} \vec{A}(\vec{r}) \quad (24)$$

In Eq. (23) we may now extend the ω_n summation to infinity and sum it up:

$$\begin{aligned} \sum_{\omega_n > 0} e^{-2s\omega_n} &= \sum_{n=0}^{\infty} e^{-2s(2n+1)\pi T} = e^{-2s\pi T} \sum_{n=0}^{\infty} \left(e^{-4s\pi T} \right)^n \\ &= e^{-2s\pi T} \frac{1}{1 - e^{-4s\pi T}} = \frac{1}{2 \sinh(2s\pi T)} \end{aligned} \quad (25)$$

Note that integration and summation in Eq. (23) may only be interchanged because the divergence for $s \rightarrow 0$ has been eliminated. (In Eq. (18) this summation was not possible). So we find from Eq. (23):

$$\begin{aligned} \Delta_{\alpha}(\vec{r}) + \sum_{\alpha} \lambda^{\alpha\alpha} \Delta_{\alpha}(\vec{r}) \left(-\frac{1}{\lambda_{+}} + \ln \frac{T}{T_c} \right) \\ = \sum_{\alpha} \lambda^{\alpha\alpha} \int_0^{\infty} \frac{du}{\sinh u} \left\langle \left[e^{-iu\vec{v}_{F,\alpha} \cdot \vec{\Pi}/(2\pi T)} - 1 \right] \Delta_{\alpha}(\vec{r}) \right\rangle_{\alpha} \end{aligned} \quad (26)$$

In the presence of an external magnetic field $\vec{B} = \vec{\nabla} \times \vec{A}$ it is convenient to choose the field direction as the z -axis of the coordinate system. In these coordinates $\Delta_{\alpha}(\vec{r})$ does not depend on z . Choosing the gauge $\vec{A} = Bx\hat{y}$ the operator $\vec{\Pi}$ simplifies to

$$\vec{\Pi} = \frac{\hbar}{i} \vec{\nabla} - \frac{2e}{c} \vec{A}(\vec{r}) = \begin{pmatrix} -i\hbar\partial_x & & \\ -i\hbar\partial_y - \frac{2e}{c}Bx & & \\ & 0 & \end{pmatrix} = \sqrt{\frac{eB}{c}} \begin{pmatrix} a + a^{\dagger} & & \\ & i(a - a^{\dagger}) & \\ & & 0 \end{pmatrix} \quad (27)$$

where we have introduced raising and lowering operators $2\sqrt{\frac{eB}{c}}a = -i\hbar\partial_x - \hbar\partial_y + 2i\frac{eB}{c}x$ and $2\sqrt{\frac{eB}{c}}a^{\dagger} = -i\hbar\partial_x + \hbar\partial_y - 2i\frac{eB}{c}x$. Thus, we see from Eq. (26) that only the components of the Fermi velocity perpendicular to the magnetic field direction play a role and we have

$$\vec{v}_{F,\alpha} \cdot \vec{\Pi} = \sqrt{\frac{eB}{c}} \left[(v_{x,\alpha} + iv_{y,\alpha}) a + (v_{x,\alpha} - iv_{y,\alpha}) a^{\dagger} \right] \quad (28)$$

where $v_{x,\alpha}$ and $v_{y,\alpha}$ are the components of the Fermi velocity perpendicular to the magnetic field \vec{B} . Note, that these components are not necessarily identical to the components of the Fermi velocity with respect to the crystal axes in Eq. (4).

It is useful to introduce a scaling of the x - and y -coordinates of the form

$$x = e^\tau \bar{x} \quad y = e^{-\tau} \bar{y} \quad (29)$$

Here e^τ is a scaling factor which scales the x - and y -coordinates in such a way as to preserve the area. Expressed in the new coordinates \bar{x} and \bar{y} the operator $\vec{\Pi}$ can be written:

$$\vec{\Pi} = \begin{pmatrix} -i\hbar e^{-\tau} \partial_{\bar{x}} & \\ -i\hbar e^\tau \partial_{\bar{y}} - \frac{2e}{c} e^\tau B \bar{x} & \\ 0 & \end{pmatrix} = \sqrt{\frac{eB}{c}} \begin{pmatrix} e^{-\tau} (\bar{a} + \bar{a}^\dagger) & \\ ie^\tau (\bar{a} - \bar{a}^\dagger) & \\ 0 & \end{pmatrix} \quad (30)$$

where the raising and lowering operators \bar{a} and \bar{a}^\dagger are also expressed in terms of these new coordinates. Using this result we find

$$\vec{v}_{F,\alpha} \cdot \vec{\Pi} = \sqrt{\frac{eB}{c}} \left[(e^{-\tau} v_{x,\alpha} + ie^\tau v_{y,\alpha}) \bar{a} + (e^{-\tau} v_{x,\alpha} - ie^\tau v_{y,\alpha}) \bar{a}^\dagger \right] \quad (31)$$

We can now write the exponential operator in Eq. (26) as follows:

$$e^{-iu\vec{v}_{F,\alpha} \cdot \vec{\Pi} / (2\pi T)} = e^{A+B} \quad (32)$$

with

$$\begin{aligned} A &= -i \frac{u}{2\pi T} \sqrt{\frac{eB}{c}} (e^{-\tau} v_{x,\alpha} - ie^\tau v_{y,\alpha}) \bar{a}^\dagger \\ B &= -i \frac{u}{2\pi T} \sqrt{\frac{eB}{c}} (e^{-\tau} v_{x,\alpha} + ie^\tau v_{y,\alpha}) \bar{a} \end{aligned} \quad (33)$$

Using the identity

$$e^{A+B} = e^{-[A,B]/2} e^A e^B \quad (34)$$

and calculating the commutator

$$[A, B] = u^2 \frac{eB}{c(2\pi T)^2} (e^{-2\tau} v_{x,\alpha}^2 + e^{2\tau} v_{y,\alpha}^2) \quad (35)$$

we can write

$$e^{-iu\vec{v}_{F,\alpha} \cdot \vec{\Pi} / (2\pi T)} = e^{-u^2 \frac{eB}{2c(2\pi T)^2} (e^{-2\tau} v_{x,\alpha}^2 + e^{2\tau} v_{y,\alpha}^2)} e^{-i \frac{u}{2\pi T} \sqrt{\frac{eB}{c}} (e^{-\tau} v_{x,\alpha} - ie^\tau v_{y,\alpha}) \bar{a}^\dagger} e^{-i \frac{u}{2\pi T} \sqrt{\frac{eB}{c}} (e^{-\tau} v_{x,\alpha} + ie^\tau v_{y,\alpha}) \bar{a}}$$

In principle, we can view Eq. (26) as an eigenvalue problem. The highest eigenvalue and its corresponding eigenfunction of the right hand side operator will determine the upper critical field $B_{c2}(T)$. We already know from Abrikosov's solution of Ginzburg-Landau theory that the

solution for an isotropic s -wave superconductor will be Abrikosov's vortex state wave function $\psi_\Lambda(\vec{r})$. This wavefunction has the property that it is destroyed by the operator a

$$a \psi_\Lambda(\vec{r}) = 0 \tag{36}$$

and has the form of the lowest Landau level wavefunction. In principle, one can try to solve Eq. (26) by making a Landau level expansion of $\Delta_\alpha(\vec{r})$ [32, 50]. However, for an anisotropic superconductor one should expect a distortion of the vortex lattice. Therefore here we will start from a variational ansatz to Eq. (26) by choosing a different wavefunction, which obeys the equation

$$\bar{a} \Delta_\alpha(\vec{r}) = 0 \tag{37}$$

This corresponds to the choice Eq. (8). Here, we can use the scaling parameter τ now as a variational parameter which has to be adjusted such as to yield the highest possible eigenvalue of Eq. (26). If we insert this variational wavefunction into Eq. (26) the e^B and e^A operators just drop out and we are left with the equation

$$\Delta_\alpha = \sum_\alpha \lambda^{\alpha\alpha} \left[\frac{1}{\lambda_+} - \ln \frac{T}{T_c} - l_\alpha \left(\tau, \frac{B_{c2}}{T^2} \right) \right] \Delta_\alpha \tag{38}$$

where the function l_α is given by the expression

$$l_\alpha \left(\tau, \frac{B_{c2}}{T^2} \right) = \int_0^\infty \frac{du}{\sinh u} \left\langle 1 - e^{-u^2 \frac{eB_{c2}}{8c\pi^2 T^2} (e^{-2\tau v_{x,\alpha}^2(\hat{k})} + e^{2\tau v_{y,\alpha}^2(\hat{k})})} \right\rangle_\alpha \tag{39}$$

Equation (38) is a 2×2 matrix equation and the upper critical field is determined by the criterion that the largest eigenvalue of the right hand side becomes 1. This criterion leads to the characteristic equation

$$(1 - \eta)l_\sigma + \eta l_\pi + \ln t = -\Lambda_\pm (l_\sigma + \ln t) (l_\pi + \ln t) \tag{40}$$

where $t = T/T_c$ and the parameters η and Λ_\pm are given by

$$\eta = \frac{\lambda^{\pi\pi} - \lambda_-}{\lambda_+ - \lambda_-} \quad \text{and} \quad \Lambda_\pm = \frac{\lambda_+ \lambda_-}{\lambda_+ - \lambda_-} \tag{41}$$

Here, λ_+ and λ_- are the larger and smaller eigenvalue of the matrix $\lambda^{\alpha\alpha}$, respectively. Note, that Eq. (40) means that only the two parameters η and Λ_\pm out of the four parameters $\lambda^{\alpha\alpha}$ determine the upper critical field of a two gap superconductor.

Equation (40) is a quadratic equation in $\ln t$ and allows to calculate t once l_π and l_σ are known. Therefore, calculation of B_{c2} from Eqs. (39) and (40) can proceed as follows: for given values of B_{c2}/T^2 and τ the quantities l_π and l_σ are calculated using Eq. (39) and the Fermi velocities given in Eq. (4). Then t can be calculated using Eq. (40) and the matrix elements given in Eq. (7). Now, the parameter τ is optimized such as to maximize t . From the maximized t and the given value of B_{c2}/T^2 finally B_{c2} can be calculated. This procedure is repeated for several values of B_{c2}/T^2 producing a $B_{c2}(T)$ curve.

In Eq. (39) the integration over u has a special form and it is useful to introduce the integral

$$I(y) = \int_0^\infty \frac{du}{\sinh u} (1 - e^{-yu^2}) \quad (42)$$

While this integral cannot be calculated analytically in the most general case, it at least possesses some simple limiting expressions for small and large arguments y . (Large y corresponds to the zero temperature limit in Eq. (39), while small y corresponds to $T \rightarrow T_c$, when $B_{c2} \rightarrow 0$.) These limiting expressions read

$$I(y) = \begin{cases} \frac{7}{2}\zeta(3)y - \frac{93}{4}\zeta(5)y^2 & \text{for } y \ll 1 \\ \frac{1}{2} \ln(4\gamma y) & \text{for } y \gg 1 \end{cases} \quad (43)$$

Here, $\zeta(n)$ is the Riemann Zeta function and $\ln \gamma = 0.577215$ Euler's constant. Using the integral $I(y)$ Eq. (39) can be written

$$l_\alpha \left(\tau, \frac{B_{c2}}{T^2} \right) = \left\langle I \left[\frac{eB_{c2}}{8c\pi^2 T^2} (e^{-2\tau} v_{x,\alpha}^2(\hat{k}) + e^{2\tau} v_{y,\alpha}^2(\hat{k})) \right] \right\rangle_\alpha \quad (44)$$

Using Eq. (43) this allows to find simple limiting expressions for l_α in the limits $T \rightarrow 0$ and $T \rightarrow T_c$. In particular, in the limit $T \rightarrow T_c$ we have in linear order in B_{c2}

$$l_\alpha = \frac{7}{2}\zeta(3) \frac{eB_{c2}}{8c\pi^2 T_c^2} (e^{-2\tau} \langle v_{x,\alpha}^2 \rangle_\alpha + e^{2\tau} \langle v_{y,\alpha}^2 \rangle_\alpha) \quad (45)$$

Since B_{c2} goes to zero for $T \rightarrow T_c$, both l_α and $\ln t$ decrease linearly and the right hand side of Eq. (40) can be neglected, because it becomes quadratic in $1 - t$. Thus in linear order we have

$$-\ln \frac{T}{T_c} = (1 - \eta)l_\sigma + \eta l_\pi = \frac{7\zeta(3)eB_{c2}}{16c\pi^2 T_c^2} \cdot \left\{ e^{-2\tau} [(1 - \eta) \langle v_{x,\sigma}^2 \rangle_\sigma + \eta \langle v_{x,\pi}^2 \rangle_\pi] + e^{2\tau} [(1 - \eta) \langle v_{y,\sigma}^2 \rangle_\sigma + \eta \langle v_{y,\pi}^2 \rangle_\pi] \right\} \quad (46)$$

Minimizing this expression with respect to τ one finds

$$e^{2\tau} = \sqrt{\frac{(1 - \eta) \langle v_{x,\sigma}^2 \rangle_\sigma + \eta \langle v_{x,\pi}^2 \rangle_\pi}{(1 - \eta) \langle v_{y,\sigma}^2 \rangle_\sigma + \eta \langle v_{y,\pi}^2 \rangle_\pi}} \quad (47)$$

Using this result we can calculate the slope of B_{c2} at T_c from Eq. (46):

$$\left. \frac{dB_{c2}}{dT} \right|_{T_c} = \frac{8c\pi^2 T_c}{7\zeta(3)e} \frac{1}{\sqrt{[(1 - \eta) \langle v_{x,\sigma}^2 \rangle_\sigma + \eta \langle v_{x,\pi}^2 \rangle_\pi] [(1 - \eta) \langle v_{y,\sigma}^2 \rangle_\sigma + \eta \langle v_{y,\pi}^2 \rangle_\pi]}} \quad (48)$$

REFERENCES

- [1] J. Nagamatsu, N. Nakagawa, T. Muranaka, Y. Zenitani, and J. Akimitsu, *Nature* 410 (2001) 63.
- [2] P. C. Canfield and G. W. Crabtree, *Physics Today* 56, No. 3 (2003) 34.
- [3] S. L. Bud'ko, G. Lapertot, C. Petrovic, C. E. Cunningham, N. Anderson, and P. C. Canfield, *Phys. Rev. Lett.* 86 (2001) 1877.
- [4] F. Bouquet, R. A. Fisher, N. E. Phillips, D. G. Hinks, and J. D. Jorgensen, *Phys. Rev. Lett.* 87 (2001) 047001.
- [5] R. Prozorov, R. W. Giannetta, S. L. Bud'ko, and P. C. Canfield, *Phys. Rev. B* 64 (2001) 180501(R).
- [6] J. Kortus, I. I. Mazin, K. D. Belashchenko, V. P. Antropov, and L. L. Boyer, *Phys. Rev. Lett.* 86 (2001) 4656.
- [7] Y. Kong, O. V. Dolgov, O. Jepsen, and O. K. Andersen, *Phys. Rev. B* 64 (2001) 020501(R).
- [8] K.-P. Bohnen, R. Heid, and B. Renker, *Phys. Rev. Lett.* 86 (2001) 5771.
- [9] A. Y. Liu, I. I. Mazin, and J. Kortus, *Phys. Rev. Lett.* 87 (2001) 087005.
- [10] For an early review see Fig. 35 in C. Buzea and Yamashita, *Superconductor Science and Techn.* 14 (2001) R115.
- [11] M. R. Eskildsen, M. Kugler, S. Tanaka, J. Jun, S. M. Kazakov, J. Karpinski, and Ø. Fischer, *Phys. Rev. Lett.* 89 (2002) 187003.
- [12] A. A. Golubov, J. Kortus, O. V. Dolgov, O. Jepsen, Y. Kong, O. K. Andersen, B. J. Gibson, K. Ahn, and R. K. Kremer, *J. Phys.: Condens. Matter* 14 (2002), 1353.
- [13] H. J. Choi, D. Roundy, H. Sun, M. L. Cohen, and S. G. Louie, *Phys. Rev. B* 66 (2002) 020513(R).
- [14] H. J. Choi, D. Roundy, H. Sun, M. L. Cohen, and S. G. Louie, *Nature (London)* 418 (2002) 758.
- [15] N. Schopohl and K. Scharnberg, *Solid State Comm.* 22 (1977) 371; N. Schopohl, *Diploma Thesis, University of Hamburg* (1977).
- [16] I. I. Mazin, O. K. Andersen, O. Jepsen, O. V. Dolgov, J. Kortus, A. A. Golubov, A. B. Kuz'menko, and D. van der Marel, *Phys. Rev. Lett.* 89 (2002) 107002.
- [17] O. V. Dolgov, R. S. Gonnelli, G. A. Ummarino, A. A. Golubov, S. V. Shulga, and J. Kortus, *Phys. Rev. B* 68 (2003) 132503.
- [18] M. Angst, R. Puzniak, A. Wisniewski, J. Jun, S. M. Kazakov, J. Karpinski, J. Roos, and H. Keller, *Phys. Rev. Lett.* 88 (2002) 167004.
- [19] Yu. Eltsev, S. Lee, K. Nakao, N. Chikumoto, S. Tajima, N. Koshizuka, and M. Murakami, *Phys. Rev. B* 65 (2002) 140501(R).
- [20] L. Lyard, P. Samuely, P. Szabo, T. Klein, C. Marcenat, L. Paulius, K. H. P. Kim, C. U. Jung, H.-S. Lee, B. Kang, S. Choi, S.-I. Lee, J. Marcus, S. Blanchard, A. G. M. Jansen, U. Welp, G. Karapetrov, and W. K. Kwok, *Phys. Rev. B* 66 (2002) 180502(R).
- [21] U. Welp, A. Rydh, G. Karapetrov, W. K. Kwok, and G. W. Crabtree, Ch. Marcenat, L. Paulius, T. Klein, J. Marcus, K. H. P. Kim, C. U. Jung, H.-S. Lee, B. Kang, and S.-I. Lee, *Phys. Rev. B* 67 (2003) 012505.
- [22] S. V. Shulga, S.-L. Drechsler, G. Fuchs, K.-H. Müller, K. Winzer, M. Heinecke, and K. Krug, *Phys. Rev. Lett.* 80 (1998) 1730.

- [23] A. I. Posazhennikova, T. Dahm, and K. Maki, *Europhys. Lett.* 60 (2002) 134.
- [24] B. B. Jin, N. Klein, W. N. Kang, Hyeong-Jin Kim, Eun-Mi Choi, Sung-Ik Lee, T. Dahm, and K. Maki, *Phys. Rev. B* 66 (2002) 104521.
- [25] T. Dahm, A. I. Posazhennikova, and K. Maki, *Acta Phys. Pol. B* 34 (2003) 549.
- [26] L. Lyard, P. Szabo, T. Klein, J. Marcus, C. Marcenat, K. H. Kim, B. W. Kang, H. S. Lee, and S. I. Lee, *Phys. Rev. Lett.* 92 (2004) 057001.
- [27] R. Cubitt, M. R. Eskildsen, C. D. Dewhurst, J. Jun, S. M. Kazakov, and J. Karpinski, *Phys. Rev. Lett.* 91 (2003) 047002.
- [28] M. Xu, H. Kitazawa, Y. Takano, J. Ye, K. Nishida, H. Abe, A. Matsushita, N. Tsujii, and G. Kido, *Appl. Phys. Lett.* 79 (2001) 2779.
- [29] P. Miranovic, K. Machida, and V. G. Kogan, *J. Phys. Soc. Japan* 72 (2003) 221.
- [30] T. Dahm and N. Schopohl, *Phys. Rev. Lett.* 91 (2003) 017001.
- [31] S. Graser, T. Dahm, and N. Schopohl, *Phys. Rev. B* 69 (2004) 014511.
- [32] C. T. Rieck, K. Scharnberg, and N. Schopohl, *J. Low Temp. Phys.* 84 (1991) 381.
- [33] B. B. Jin, T. Dahm, A. I. Gubin, Eun-Mi Choi, Hyun Jung Kim, Sung-IK Lee, W. N. Kang, and N. Klein, *Phys. Rev. Lett.* 91 (2003) 127006.
- [34] A. Rydh, U. Welp, A. E. Koshelev, W. K. Kwok, G. W. Crabtree, R. Brusetti, L. Lyard, T. Klein, C. Marcenat, B. Kang, K. H. Kim, K. H. P. Kim, H.-S. Lee, S.-I. Lee, *cond-mat/0308319*.
- [35] T. Dahm, S. Graser, and N. Schopohl, *Physica C* 408-410 (2004) 336 (*cond-mat/0304194*).
- [36] G. Eilenberger, *Z. Phys.* 214 (1968) 195.
- [37] A. I. Larkin and Yu. N. Ovchinnikov, *Zh. Eksp. Teor. Fiz.* 55 (1968) 2262 - engl. transl. *Sov. Phys. JETP* 28 (1969) 1200.
- [38] A. Gurevich, *Phys. Rev. B* 67 (2003) 184515.
- [39] A. A. Golubov and A. E. Koshelev, *Phys. Rev. B* 68 (2003) 104503.
- [40] A. E. Koshelev and A. A. Golubov, *Phys. Rev. Lett.* 92 (2004) 107008.
- [41] F. Marsiglio, *Phys. Rev. B* 44 (1991) 5373.
- [42] A. Hosseini, R. Harris, S. Kamal, P. Dosanjh, J. Preston, R. Liang, W. N. Hardy, and D. A. Bonn, *Phys. Rev. B* 60 (1999) 1349.
- [43] D. A. Bonn, P. Dosanjh, R. Liang, and W. N. Hardy, *Phys. Rev. Lett.* 68 (1992) 2390.
- [44] P. J. Hirschfeld, W. O. Putikka, and D. J. Scalapino, *Phys. Rev. B* 50 (1994) 10250.
- [45] Kijoon H. P. Kim, Jae-Hyuk Choi, C. U. Jung, P. Chowdhury, Hyun-Sook Lee, Min-Seok Park, Heon-Jung Kim, J. Y. Kim, Zhonglian Du, Eun-Mi Choi, Mun-Seog Kim, W. N. Kang, Sung-Ik Lee, G. Y. Sung, and J. Y. Lee, *Phys. Rev. B* 65 (2002) 100510(R).
- [46] D. C. Mattis and J. Bardeen, *Phys. Rev.* 111 (1958) 412.
- [47] S. B. Nam, *Phys. Rev.* 156 (1967) 470.
- [48] V. Braccini, A. Gurevich, J.E. Giencke, M.C. Jewell, C.B. Eom, D.C. Larbalestier, A. Pogrebnyakov, Y. Cui, B. T. Liu, Y. F.Hu, J. M. Redwing, Qi Li, X.X. Xi, R.K. Singh, R. Gandikota, J. Kim, B. Wilkens, N. Newman, J. Rowell, B. Moeckly, V. Ferrando, C. Tarantini, D. Marre, M. Putti, C. Ferdeghini, R. Vaglio, E. Haanappel, *cond-mat/0402001*.
- [49] M.Putti, C.Ferdeghini, M.Monni, I.Pallescchi, C.Tarantini, P.Manfrinetti, A.Palenzona, D.Daghero, R.S.Gonnelli, V.A. Stepanov, *cond-mat/0406377*.
- [50] Ye Sun and K. Maki, *Phys. Rev. B* 47, 9108 (1993); H. Won and K. Maki, *Phys. Rev. B* 53, 5927 (1996).

CRITICAL CURRENT DENSITY IN SUPERCONDUCTING MgB₂

S.X. Dou, A.V. Pan, M.J. Qin, and T. Silver

Institute for Superconducting and Electronic Materials, University of Wollongong,
Northfields Ave. Wollongong, NSW 2522, Australia,

1. INTRODUCTION

The discovery of superconductivity at 39K in a relatively common material, MgB₂ [1] has triggered a great deal of interest in the research community. MgB₂ exhibits the superconducting characteristics and physics of BCS-type LTS materials, as evidenced for example by a significant isotope effect; however, its critical temperature (T_c) is more than twice those of the presently used A15 superconductors Nb₃Sn and Nb₃Al, and more than four times that of the present LTS workhorse, NbTi. The importance of MgB₂ lies in its simple crystal structure, high T_c , high critical current (J_c), large coherence length and transparency of grain boundaries to current flow. These properties of MgB₂ offer the promise of important large-scale- and electronic device applications.

One of the most important applications of superconductors is in the areas of high current and high field where high J_c in magnetic fields is essential. During the past two years, MgB₂ has been fabricated in various forms, including single crystals, bulk, thin films, tapes and wires. In particular, enormous efforts have been directed to improvement of the critical current density through development and application of various novel techniques for fabrication of technical usable MgB₂ materials. Several groups have reported J_c values for MgB₂ as high as 10^6 A/cm² [2-9]. This gives proof that the performance of MgB₂ can rival and exceed that of conventional superconductors. However, the J_c of pristine MgB₂ drops rapidly with increasing magnetic field due to its low upper critical field (H_{c2}) and weak pinning strength. To take advantage of its high T_c of 39K, enhancement of H_{c2} and improvement of flux pinning are essential. Attempts to enhance H_{c2} and flux pinning have been made by using a number of techniques, including impurity scattering, addition and

substitution, irradiation, various thermo-mechanical processing techniques and magnetic shielding. Reports of increases in transport J_c , the irreversibility field (H_{irr}), and H_{c2} values are continually appearing, making a summary of this nature quickly dated. In this article, we review the progress on the central topic of critical current density of superconducting MgB_2 wires and bulk. In section 2, we provide a brief overview of the two-gap nature of the superconductivity of MgB_2 which has important implications for the H_{c2} and J_c . Background information on materials processing is then given in section 3 with an emphasis on bulk and wires. We discuss the effect of doping on the H_{c2} and $J_c - H$ performance of MgB_2 in detail in section 4. In section 5 we present the characteristics of vortex dynamics in MgB_2 in contrast to HTS. In section 6 we provide a phenomenological explanation on the extraordinary sample size effect on magnetization in MgB_2 . In section 7 we describe the beneficial effect of magnetic shielding on $J_c(H)$ performance. In section 8, we review the effects of various irradiation techniques on flux pinning.

2. TWO-GAP SUPERCONDUCTIVITY OF MgB_2

The compound MgB_2 forms a honeycomb-like stack of hexagonal networks. The B honeycomb dominates the electronic structure, which can be thought of as deriving from σ bonding within the B planes and π bonding orbitals out of the plane. In the MgB_2 crystal the in-plane σ orbitals lead to a corresponding 2-D σ band while the π space charge extends both out-of-plane and in-plane to form the 3-D π band. This partially covalent structure of the MgB_2 crystal gives rise to the Fermi surface with its two π and σ conduction bands. For dirty non-paramagnetically limited single-band low temperature superconductors a well known formula for the zero-temperature upper critical field $H_{c2}(0)$ is given by the frequently quoted expression:

$$H_{c2}(0) = 0.86T_c \left(\frac{-dH_{c2}}{dT} \right)_{T_c} \quad (2-1)$$

It is well established that for single band superconductors both $H_{c2}(0)/T_c$ and the slope $(-dH_{c2}/dT)_{T_c}$ scale with the normal state resistivity ρ , and hence that (for fixed T_c) both the low temperature H_{c2} and that near T_c benefit simultaneously from an increase in ρ . Equation (1) suggests an experimental method of obtaining $H_{c2}(0)$ that can be carried out at moderate fields, near T_c . Increases in H_{c2} can be expected to follow increases in the resistivity – a rule which has helped to guide the design of low temperature superconductors over the years. But for MgB_2 the simple rule has quantitative variants because the resistivity ρ depends on the electronic diffusivities D_π and D_σ associated with MgB_2 's two-band conductivity as follows [10]:

$$1/\rho = e^2 (N_{F\pi}D_\pi + N_{F\sigma}D_\sigma) \quad (2-2)$$

The introduction of two diffusivities results in pronounced departures from the single-band predictions. In particular (H_{c2}/T_c) and $(-dH_{c2}/dT)_{T_c}$ respond individually to D_π and D_σ rather than together and in proportion to $1/D$. Thus while increasing impurity scattering is beneficial to H_{c2} over the entire temperature range for both single-band and double-band superconductors, in the latter case it offers $H_{c2}(0)$ the opportunity to diverge to very large values in response to strong decreases in either D_σ or D_π .

The two-gap superconductivity has significant implications for the applicability of MgB₂ because it is the low H_{c2} which has mainly limited the potential applications of clean MgB₂, for which H_{c2} is even less than that of Nb-Ti. Efforts have thus been made to raise H_{c2} . Using nano-particle SiC doping into MgB₂, the authors' group has achieved a record high upper critical field, $H_{c2}(0)$, in bulk materials [2]. Recently, using high field transport measurements, Braccini et al. have reported the achievement of record high upper critical fields (H_{c2}) for textured films [11]. The observed remarkable H_{c2} enhancement to more than 74T for thin films is a consequence of the two-gap superconductivity of MgB₂, which has been established by many measurements and calculations [3,12]. There are three different impurity scattering channels in MgB₂ alloys: intraband scattering within each σ and π sheet and interband scattering between them. It is these multiple scattering channels which make it possible to increase H_{c2} of MgB₂ to a much greater extent than in one-gap superconductors, not only by the usual increase of the normal state resistivity, ρ , as in low-temperature superconductors, but also by optimizing the relative weight of the σ and π scattering rates by selective substitution of boron or magnesium.

3. MgB₂ MATERIAL AND WIRE DEVELOPMENT

Canfield first fabricated wires by exposing tungsten-core B filaments to Mg vapor [4]. This work was quickly followed by reports pursuing powder-in-tube (PIT) approaches [5,6]. Numerous institutions and researchers are involved in PIT wire, as it seems the most useful form for many applications. Grasso [7] fabricated Ni sheathed MgB₂ tapes using an *ex-situ* method; after filling the conductors were cold worked by groove rolling, drawing, and rolling. Flükiger *et al.* [8] found that ball milling did not increase B_{c2} , but did increase B_{irr} and J_c . Goldacker *et al.* compared *ex-situ* and *in-situ* wires constructed with Ta and Nb barriers and found that the *in-situ* wires showed inferior properties at higher fields. Goldacker et al. [9] also compared round strands and tapes made using the *ex-situ* route. They saw some anisotropy in the tapes, as have others. They found MgB₂ grain sizes ranging from 20 nm to 1 μ m. Oxygen was primarily present as MgO, and a small level of B-rich phases was found.

The authors' group has been deeply involved in MgB₂, producing some very useful and practical results [2,3, 13-15]. Early efforts by Dou et al., part of a collaborative effort between the University of Wollongong, Ohio State University and Hyper Tech Research, led to studies of pellet properties [16] and then to tape [5]. The authors' group has developed an *in-situ* fast formation technique for the fabrication of MgB₂ wire using the powder-in-tube technique [3]. A record high magnetic J_c of 10^6 A/cm² in zero field at 20K and a transport J_c of 20,000 A/cm² in 10T and 5K have been achieved for Fe-clad MgB₂ wires [15]. They have also identified Fe not only to be chemically compatible with MgB₂ but also ideal for the magnetic screening of external fields and hence the reduction of ac loss [17]. These results demonstrate clearly the great potential of the emerging superconductor for various applications. In a series of papers Dou et al. showed that the substantial enhancement in $J_c(H)$ by nano-SiC doping can be transferred to the properties of short wires [2,15]. Recently, Serquis et al. have reported construction of a 6-layer coil to generate a field of 1T at self-field at 25K, confirming that SiC doped MgB₂ is superior to the un-doped material, achieving $J_c > 10^4$ A/cm² at 7T [18].

As pointed out by Gurevich et al. [3], the use of MgB₂ will open a new domain of applications for superconducting magnets, one that is well outside the reach of Nb₃Sn. Its T_c of 39 K will permit safe operation in the temperature range from about 15 to 20 K, wherein its H_{c2} will, at the present time, drop from about 15 to 8T. However, if direct competition is called for, the $H_{c2}(T)$ of MgB₂ lies above that of Nb₃Sn all the way down to 0 K. Enhancements to H_{c2} will follow the judicious introduction of scattering impurities. In the past considerable effort was spent attempting to substitutionally modify the MgB₂ lattice in the quest for higher T_c . Perhaps some of this work could be revisited in the future, but from the standpoint of increasing H_{c2} , even at the expense of some lowering of T_c .

The key to magnet applications of superconductors lies in the rare combination of low cost and a ready wire fabrication route, which produces conductors with high H_{c2} and J_c . Due to recent advances in cryocoolers, many electric utilities may be best optimised at temperatures of 10 to 35K, a domain for which MgB₂ could provide the cheapest superconducting wires.

4. EFFECT OF SUBSTITUTION AND ADDITION

Oxygen alloying in MgB₂ thin films [19] and proton irradiation of MgB₂ powder [20] have resulted in useful improvements in irreversibility fields (H_{irr}) and $J_c(H)$. The great challenge is whether we can introduce effective pinning centres into MgB₂ by “conventional” chemical doping. Chemical doping has not been successful in HTS materials due to their short coherence lengths and high anisotropy. In contrast, MgB₂ has a relatively large coherence length and small anisotropy. Accordingly the fluxoids to be pinned are string-like and amenable to pinning by particles, precipitates, etc. This opens a window to the success of chemical doping in this material.

The numerous early studies that were made on the effect of elemental doping into MgB₂ focused on T_c measurement, mostly with negative results. On the other hand, attempts to improve flux pinning using chemical doping are only now gathering momentum. Chemical doping can be expected to influence T_c and H_{irr} , and may have secondary effects related to processing and crystal structure.

4.1 Carbon Doping

The effects of C-doping on superconductivity in MgB₂ compound have been studied by several groups [21-28]. The results on C solubility and the effects of C-doping on T_c reported so far vary significantly due to the precursor materials, fabrication techniques and processing conditions used. It appears that lower sintering temperatures and short sintering times result in an incomplete reaction and hence lower C solubility in MgB₂. Ribeiro et al. used Mg and B₄C as precursors to synthesize C doped MgB₂ by sintering at 1200°C for 24 hours [27]. A neutron diffraction study confirmed that the most likely solubility of C in MgB₂ ranges up to around 10% C in the boron sites, resulting in a large drop in both T_c and the a -axis lattice parameter [28]. Recently, Ohmichi et al. synthesised C-doped single crystalline MgB₂ at high pressure (5GPa) and high temperature (1600°C), obtaining a C solubility of 15% at the boron sites and T_c depression to below 3K [29]. Kazakov et al. have performed a systematic study on C-doped single-crystalline MgB₂ grown under high pressure and high temperature at 1900-

1950°C [30]. They found that the T_c can be tuned by adjustment of the nominal composition of $\text{Mg}(\text{B}_{1-x}\text{C}_x)_2$ with x varying from 0 to 0.15.

Most studies on C doping into MgB_2 have largely focused on the effect on superconductivity. From the applications point of view, the effect of C doping on the flux pinning properties is crucially important. The author's group has reported a significant improvement in $J_c(H)$ and H_{irr} in MgB_2 through nano-C [31], nano-carbon tube doping [32] and nano-SiC doping [2]. Recently, the effects of C doping on the flux pinning and critical current density in MgB_2 have been studied using amorphous carbon [31] and diamond [33], both showing improvement of J_c at elevated magnetic fields. It is clear from previous work that complete substitution of C for B causes a drastic depression in T_c , which is very undesirable for improving J_c at high temperatures. In order to explore the potential applications of MgB_2 around 20K or above it is essential to maintain the T_c and, at the same time, to enhance the J_c performance in magnetic fields. Soltanian et al. have designed compromise synthesis conditions that limit the degree of C substitution, which can cause disorder on B sites, and at the same time can promote the introduction of nano-additives to act as effective pinning centers in MgB_2 [31]. These authors prepared polycrystalline $\text{MgB}_{2-x}\text{C}_x$ samples with $x=0.05, 0.1, 0.2, 0.3, 0.4$ nano-particle carbon powder using an *in-situ* reaction method under well-controlled conditions to limit the extent of C substitution. They found that both the a -axis lattice parameter and the T_c decreased monotonically with increasing doping level. For the sample doped with the highest nominal composition of $x=0.4$ the T_c dropped only 2.7K. The nano-C-doped samples showed an improved field dependence of the J_c compared with the un-doped sample over a wide temperature range. X-ray diffraction results indicate that C reacted with Mg to form nano-size Mg_2C_3 and MgB_2C_2 particles. Nano-particle inclusions and substitution, both of which are observed, are proposed to be responsible for the enhancement of flux pinning in high fields.

Among various carbon precursors, carbon nano-tubes (CNT) are particularly interesting as their special geometry (high aspect ratio and nanometer diameter) may induce more effective pinning centres compared to other carbon-containing precursors. Wei et al. have studied the superconductivity of MgB_2 -carbon nano-tube composites [34]. However, the effect of carbon nano-tube doping on critical current density and flux pinning has not been reported. Dou et al. studied the effects of doping with carbon nano-tubes on the transition temperature, lattice parameters, critical current density and flux pinning of $\text{MgB}_{2-x}\text{C}_x$ with $x = 0, 0.05, 0.1, 0.2$ and 0.3 [32]. The carbon substitution for B was found to enhance J_c in magnetic fields but depress T_c . The depression of T_c , which is caused by the carbon substitution for B, increases with increasing doping level, sintering temperature and duration. Fig. 1 shows the T_c dependence on the sintering temperature of 10% CNT doped MgB_2 , indicating that the C substitution for B was clearly increased at 1000 °C. By controlling the extent of the substitution and the addition of carbon nano-tubes one can achieve the optimal improvement in critical current density and flux pinning in magnetic fields while maintaining the minimum reduction in T_c . Under these conditions, J_c was enhanced by two orders of magnitude at 8T and 5K and 7T and 10K. J_c was more than 10,000A/cm² at 20K and 4T and 5K and 8.5T, respectively, as shown in Fig. 2. The general trend is such that the $J_c(H)$ characteristic is improved with increasing sintering temperature. Although the sample sintered at 1000 °C has lower J_c values in the low field regime, its $J_c(H)$ curve crosses over the $J_c(H)$ for the other samples in higher fields. As a higher sintering temperature promotes the C substitution reaction for B, the improved field dependence of J_c measured at lower temperatures is clearly

attributable to the C substitution. However, because C substitution depresses T_c , the $J_c(H)$ behaviour for samples processed at high temperatures deteriorates above 20K. Thus, it is important to control the extent of C nano-tube substitution and addition to achieve the best combination of substitution induced flux pinning and C nano-tube additive pinning.

Partial C substitution for B causes disorder on B sites that can lead to intrinsic scattering and hence the enhancement of H_{c2} . Fig. 3 shows a comparison of H_{c2} for CNT doped and undoped MgB_2 as determined by transport measurements [35].

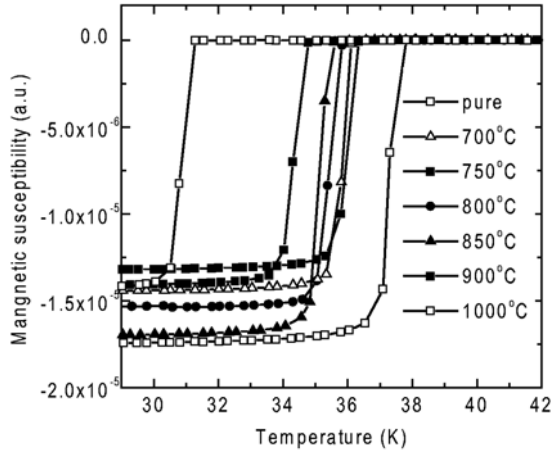


Fig. 1. Magnetic AC susceptibility as a function of temperature for $MgB_{1.8}C_{0.2}$ sintered at different temperatures for 30 minutes. Carbon added was in the form of carbon nano-tubes.

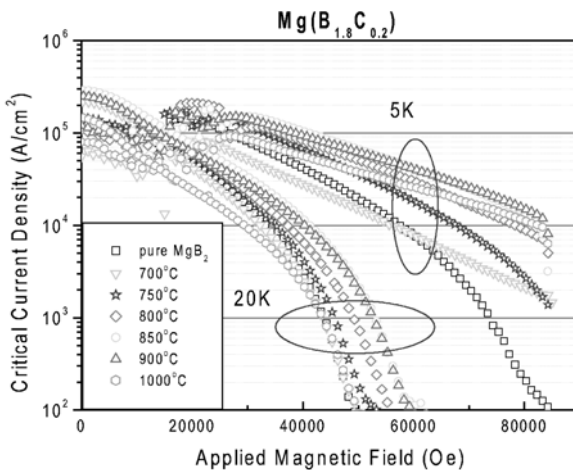


Fig. 2. Critical current density as a function of magnetic field at 5K and 20K for $MgB_{1.8}CNT_{0.2}$, sintered at different temperatures for 30 minutes.

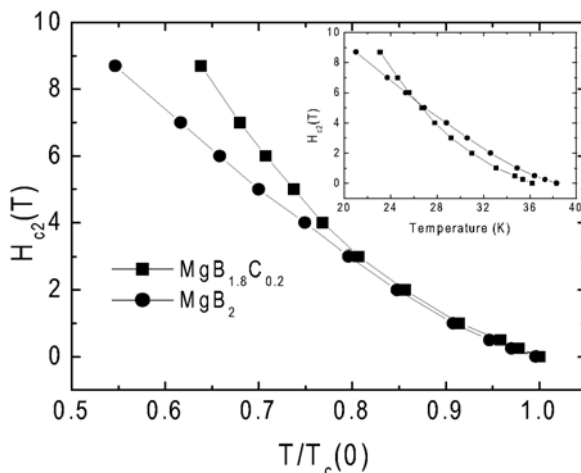


Fig. 3. Normalized temperature dependence ($T/T_c(0)$) of the upper critical field, H_{c2} , for pure MgB_2 and $MgB_{1.8}C_{0.2}$. The latter was sintered at 900 °C. Inset: the same dependence, but vs the temperature.

4.2 Nano-SiC Doping

The exceptional properties of SiC as a dopant have been systematically studied by the authors' group and collaborators over the past two years. Recently, we found that chemical doping of MgB_2 with nano-particle SiC can significantly enhance J_c in high fields with only slight reductions in T_c up to a doping level as high as 30% of B [14]. In fact we obtained the highest J_c values in magnetic fields at 20K ever reported for MgB_2 wires and bulk [2,15]. Compared to the un-doped sample, the J_c for the 10wt% SiC doped sample increased by a factor of 32 at 5K and 8T, 42 at 20K and 5T, and 14 at 30K and 2T, respectively (Fig. 4). Fig. 5 shows a comparison of magnetic $J_c(H)$ for a 10 wt% SiC doped sample at 20K with data reported in the literature. J_c for this sample exhibits better field performance and higher values in high field than any other element doped samples [36-37] and non-doped wires. The SiC doped MgB_2 samples are even better than the thin film MgB_2 , which has exhibited the strongest reported flux pinning and the highest J_c in high fields to date. At 20K, the best J_c for the 10wt% SiC doped sample was $10^5 A/cm^2$ at 3T, which exceeded the J_c of state-of-the-art Ag/Bi-2223 tapes. At 20K and 4T, J_c was $36,000 A/cm^2$, which is twice as high as for the best MgB_2 thin films [12] and an order of magnitude higher than for state-of-the-art Fe/ MgB_2 tapes [10].

Fig. 5 shows a comparison of J_c of the nano-SiC doped MgB_2 wire with those reported in the literature. Because of this high performance it is anticipated that in the future “ MgB_2 ” conductors will be made using the formula $MgB_xSi_yC_z$ instead of simple MgB_2 . This finding paves the way for this new compound to replace the current market leaders NbTi and HTS in many applications, as the chemical doping is a readily achievable, highly reproducible and economically viable process to introduce effective flux pinning.

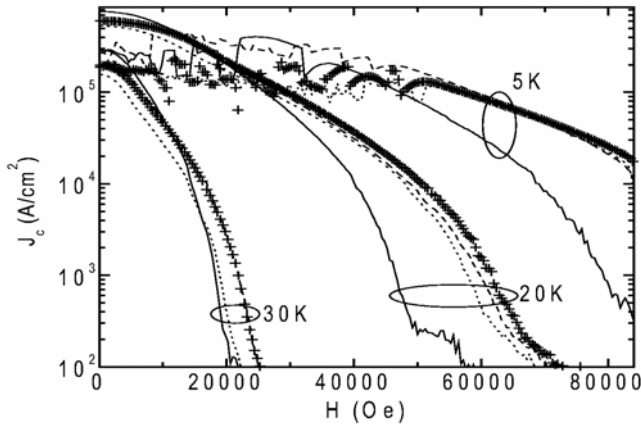


Fig. 4. The magnetic $J_c(H)$ dependence at 5, 20 and 30 K for un-doped and 10 mol%, 15 mol% and 10wt% SiC doped samples indicated by the solid line, dashed and dotted line, and crosses, respectively [2].

In comparison to all other doping reported so far, the special features of nano-scale SiC doping in MgB_2 can be described as follows: (1) the extent of enhancement in $J_c(H)$ is very large, by more than an order of magnitude above certain fields; (2) the enhancement of $J_c(H)$ extends to all temperatures up to T_c in contrast to most of the other doping studies, which only show that it is effective in enhancing $J_c(H)$ at low temperatures. These special features of the SiC doped samples can be explained in terms of impurity scattering in the framework of two gap superconductivity theory [3] and the improvement of flux pinning.

To understand the significant enhancement of J_c at higher fields with the nano-SiC doping, a set of four samples (Table 1) ranging from the clean limit to a very dirty state have wide variations of the normal state resistivity from $1 \mu\Omega\text{-cm}$ to $300 \mu\Omega\text{-cm}$ and significantly different electromagnetic properties, allowing us to understand the mechanisms behind the enhancement of $J_c(H)$. These include two Wollongong samples (un-doped, A, and 10% SiC doped, B), compared to two Madison samples, one being at the clean limit (sample C) and the second being this same sample exposed to Mg vapor (sample D) as described in detail elsewhere [39]. For comparison we also list some literature data on a pure sintered pellet in Table 1. The highest value of H_M^* correlates well to the highest value of resistivity, both being found in the SiC-doped sample for which the $J_c(H)$ characteristics are best too.

Role of impurity scattering

For sample D, the Mg vapor treatment caused the increase in resistivity from $1 \mu\Omega\text{-cm}$ for the clean limit sample C to $18 \mu\Omega\text{-cm}$. Because Mg vapor treatment will largely affect the Mg sites in the lattice, the disorder in Mg sites will induce out-of-plane π band scattering which will increase the resistivity and dH_{c2}/dT at low temperatures and hence the H_{c2} at low temperatures. This was indeed confirmed by the resistivity measurements in high field which gave the value of $H_{c2}(0)$ as about 29T [10]. As the Mg vapor treatment is unlikely to introduce impurities at grain boundaries, the increase in resistivity in this case can be considered tied to

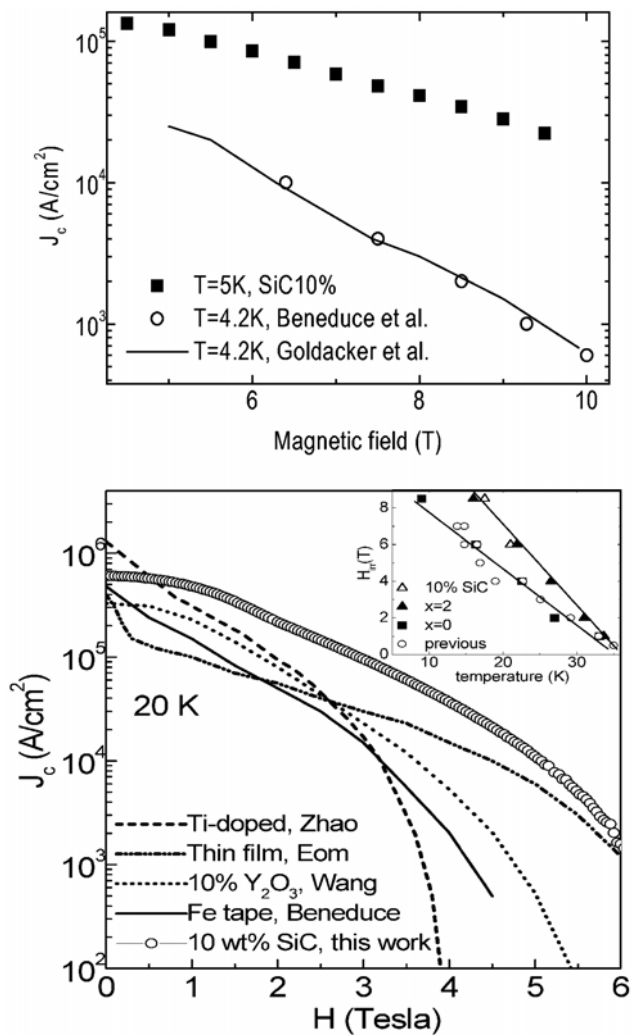


Fig. 5. A comparison of magnetic $J_c(H)$ at 4K (upper) and 20K (lower) for the 10wt% SiC doped sample and for Ti doped [36] and Y₂O₃ doped [37] bulks, as well as for thin film with strong pinning [19] and Fe/MgB₂ tape [9,38]. Inset: temperature dependence of the irreversibility field for SiC doped MgB₂ with different contents of SiC (triangles and squares) and for previously prepared non-doped MgB₂ (round symbols).

Table 1. Comparison of T_c , resistivity and irreversibility field data for samples A, B, C, D and one literature sample (pure sintered pellet made from ^{10}B [40]).

| Sample | A: Undoped | B: SiC doped | C: Clean limit | D: Mg vapor treated | Pure bulk |
|---|------------|--------------|----------------|---------------------|-----------|
| T_c (K) | 37.2 | 36.5 | 39 | 36.9 | 40.2 |
| ρ ($\mu\Omega\text{-cm}$) at 40K | 90 | 300 | 1 | 18 | 1 |
| RRR R(300K)/R(40K) | 2.1 | 1.74 | 14.7 | 3 | 19.7 |
| H_m^* (20K) (T) | 5.6 | 7.4 | 3.9 | 5.2 | 3.8 |

the improvement in H_{c2} . The improvement in H_{c2} at low temperatures leads to the improvement in $J_c(H)$ at low temperatures as shown from the J_c versus H results for sample D at 4.2K in Fig 6(a). The J_c of sample D is substantially larger than that of the clean limit sample C and also crosses over sample A in higher fields.

As for the SiC doped sample B, according to the two gap superconductivity theory [10], nano-SiC doping could lead to two different scattering channels. First, the partial C substitution for B or the formation of alloying between B and Si, B and C, and B and O in the close vicinity of B sites causes disorder on the B sites which will result in in-plane σ scattering. The alloying phases such as BC, BO_x and SiBO_x detected by the EELS analysis have dimensions well below 10nm. Their scattering will lead to an increase in dH_{c2}/dT at temperatures near T_c . Second, the formation of nano-domain structures is due to the variation of Mg-B spacing which in turn causes disorder at B and Mg sites. These nano-domains with a size of 2-3nm are also well below the 8-10nm coherence length of MgB_2 . These extensive nano-domain defects could result in strong in-plane and out-of-plane scattering and contribute to the increase of resistivity and H_{c2} over a wide temperature regime. This accounts for the enhancement of $J_c(H)$ over a wide temperature range for the SiC doped sample. Fig. 7 shows the record high $H_{c2}(0)$ value of 37T for a nano-SiC doped sample of bulk MgB_2 obtained from transport measurements as reported by Serquis et al. [41]. The strong upturn of $H_{c2}(T)$ at low temperatures indicates impurity scattering on the Mg sites.

Recently, Gurevich et al. [10] reported a record-high $H_{c2}(0) = 29\text{T}$ for (un-textured) sample C, with $H_{c2}^{\perp}(0) = 34\text{T}$ and $H_{c2}^{\parallel}(0) = 49\text{T}$ for a high resistivity film ($\rho(40\text{K}) = 220 \mu\Omega\text{cm}$) using direct, high-field resistivity measurements. It is consistent that the SiC-doped sample with the highest resistivity of $300 \mu\Omega\text{-cm}$ also has a very high H_{c2} .

Role of Flux Pinning

The additional impurities at nano-scale introduced by SiC doping can serve as strong pinning centers to improve flux pinning within a certain field region. This is clearly demonstrated by the superior $J_c - H$ performance of the SiC doped sample B as shown in Fig. 6. It is particularly interesting to note that the J_c for B is higher than for D by a factor of approximately 100 at 20K and 5T even though the H_{c2} for D is higher than for B. This result is further confirmed by the higher irreversibility line for B than for D, as shown in Fig. 8. The potential pinning centers introduced by SiC doping include inclusions such as highly dispersed MgSi_2 , BC, BO_x and SiBO_x , which are all at a scale below 10nm, match the coherence length very well and can act as strong pinning centers. In addition, the extensive network of nano-domain defects at a scale of 2-3nm would provide very effective collective pinning at all the temperatures up to T_c as shown in Fig. 9 [42]. These periodic regions trap

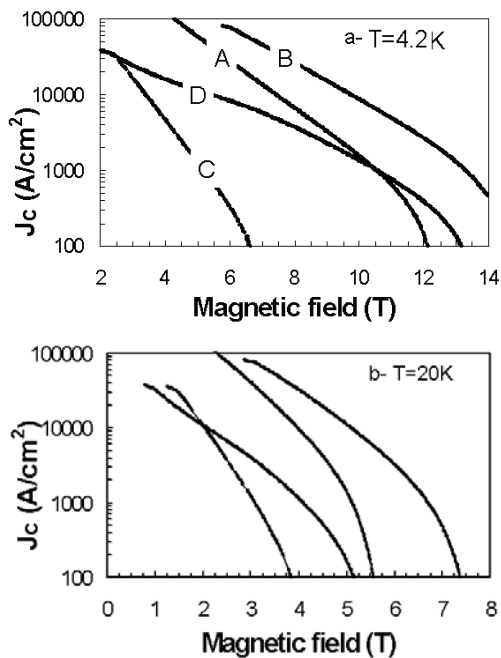


Fig. 6. A comparison of $J_c(H)$ for the un-doped (A), the 10wt% SiC doped (B), the clean limit (C) and the Mg vapor treated (D) samples at 4.2 K (a) and 20K (b).

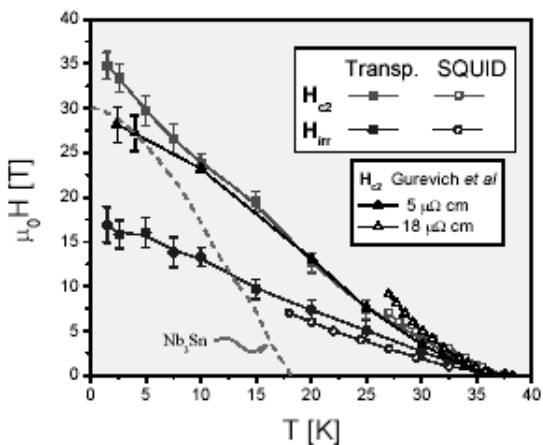


Fig. 7. Comparison of H_{c2} and H_{irr} for the SiC doped MgB_2 (squares) with the Mg-vapour treated MgB_2 (triangles) reported by Serquis et al. [41]. Note that $H_{c2}(0) = 37$ T for the SiC doped sample of Dou et al. [2].

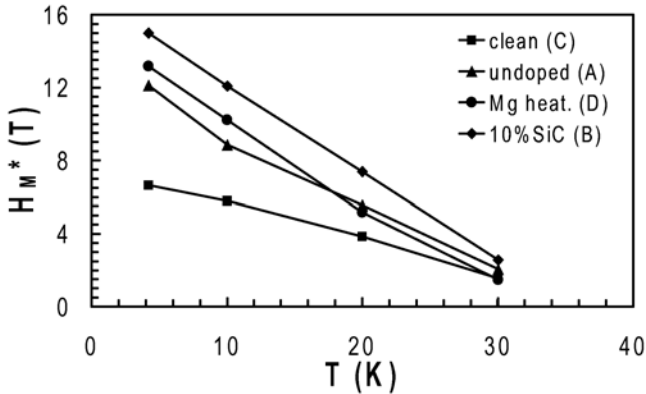


Fig. 8. The irreversibility field, H_M^* vs. temperature for clean limit, undoped, Mg vapour treated and 10% SiC doped samples.

numerous crystal defects migrating along nano-domain boundaries during self-alignment and act as intense vortex pinning centers that significantly enhance the high-field performance of MgB_2 . All these defects are absent in sample D as Mg vapor treatment would not introduce these impurities. Thus, the flux pinning in sample D is not as strong as in sample B, at least at higher temperatures. The fact that sample D has higher H_{c2} but lower H_m^* than sample B indicates that there are two closely related but distinguishable mechanisms that control the $J_c(H)$ characteristics: H_{c2} and flux pinning. The H_{c2} is the primary factor that sets the upper limit to H_m^* while the flux pinning is important to bring H_m^* close to H_{c2} and improve the $J_c(H)$ within certain field regimes. These results suggest that we can manipulate the processing parameters that could lead to the improvement of either H_{c2} or flux pinning or of both at the same time.

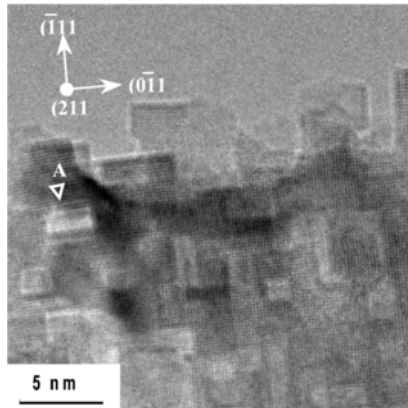


Fig. 9. HRTEM morphology shows that the majority of the nano-domains had rectangular shapes and were aligned along $[211]$ in self-aligned nano-structured MgB_2 [42].

The effect of SiC particle size and morphology

As a dopant, the SiC particle size and morphology were found to have a drastic effect on $J_c - H$ behavior, as shown in Figure 10 [43]. It is evident that the performance of the J_c field dependence was improved with decreasing grain sizes of the SiC precursor powder. The finer the SiC powders, the better the J_c field dependence is. For the coarse powders (37 μm), the J_c field dependence is slightly better than for the MgB_2 reference sample due to the limited reaction between the large grain size SiC powder and Mg+B . The sample doped with 100nm particles has a better J_c performance than the coarse particle doped one. The sample doped with 20nm particles shows very good J_c field dependence performance, as it contains fine particles, which can react strongly with Mg+B , and the resultant impurities or remaining SiC can embed in the MgB_2 grains to act as pinning centers. For this sample a J_c value of about 20000 A/cm^2 was achieved at 5K and 8T, which is more than one order of magnitude higher than that of the MgB_2 reference sample at the same field and temperature. The TEM results show that there are large numbers of nano-inclusions embedded inside MgB_2 grains. This is because the SiC is very fine and can easily form inclusions inside MgB_2 grains, as well as substituting in the lattice during the formation of MgB_2 as determined by EDS during TEM examination. However, the coarse SiC powders may distribute themselves around grain boundaries where they act as weak links due to their poor chemical activity.

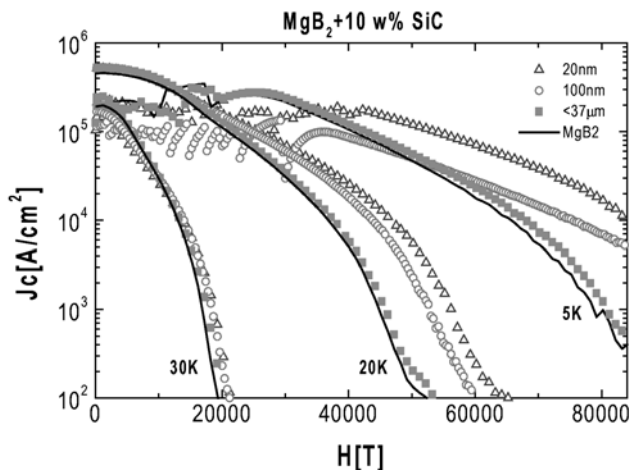


Fig.10. The J_c field dependence of MgB_2 samples doped with 10 wt % of different SiC powders as well as a pure reference sample at different temperatures of 5, 20 and 30K [43].

Confirmation of the effect of SiC doping

The significant enhancement of J_c , H_{irr} and H_{c2} by nano-SiC doping has been confirmed by a number of leading groups around the world in the last two years. Matsumoto et al. [44] has confirmed the effect of SiC doping in improving J_c , as well as increasing H_{irr} substantially. In their particular case, J_c was increased by an order of magnitude and H_{irr} went from about 17 T to about 23 T. The anomalous increase in H_{c2} and J_c is attributable to the unique feature of two-gap superconductivity in MgB_2 [10]. Figure 11 shows a comparison of the $J_c - H$

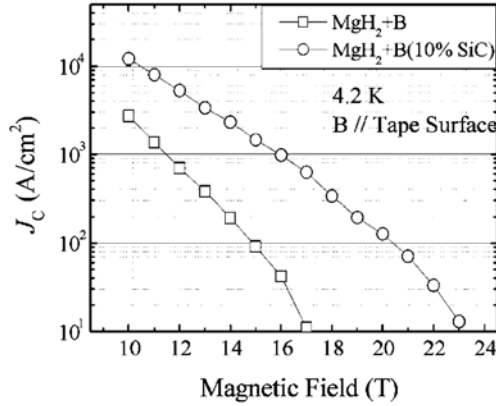


Fig. 11. The J_c - H curves in high magnetic fields of SiC doped and non-doped MgB_2 tapes (A. Matsumoto et al. [44]).

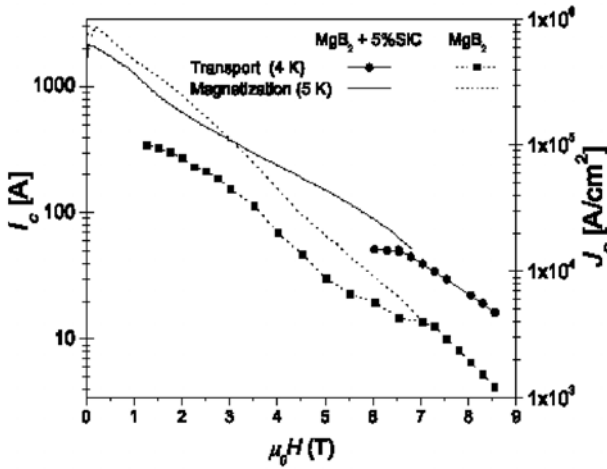


Fig. 12. Confirmation of the effect of SiC doping on MgB_2 by A. Serquis *et al.* at Los Alamos National Laboratory [18]. Critical current I_c (left axis) and critical current density J_c (right axis) versus magnetic field at 4K for a 1-layer SiC doped MgB_2 coil compared to a 6-layer coil made from non-doped MgB_2 .

behaviour of SiC doped MgB_2 wire with un-doped wires reported by Matsumoto et al. [44] at the National Institute for Materials Science in Japan. Figure 12 shows a comparison of SiC doped MgB_2 coil with un-doped MgB_2 coil reported by Serquis et al. [18]. The J_c values for the SiC doped coils are higher than for the un-doped one by a factor of two to three. Figure 13 shows pinning force density (from transport J_c) vs B at 4.2 K for MgB_2 wires, with and without SiC doping respectively, reported by Sumption et al. (Ohio State University) [45].

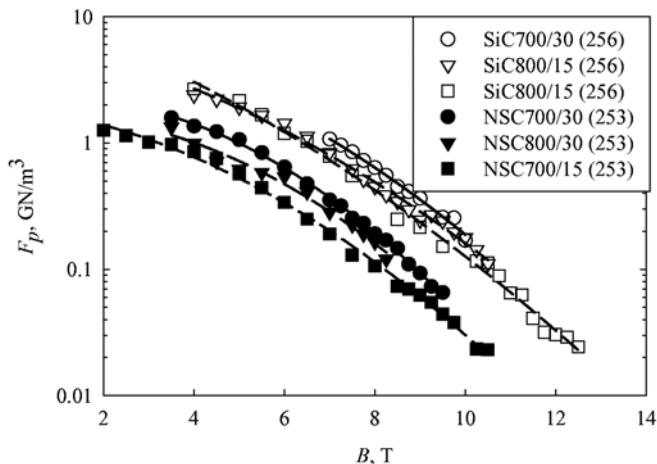


Fig. 13. Pinning force density (from transport J_c) vs B at 4.2 K for MgB_2 wires, with and without SiC doping (SiC/NSC), reported by M. Sumption et al. [45] (Ohio State University).

These results demonstrated that the enhancement effect on J_c - H performance from nano-SiC doping is highly reproducible. This significantly strengthens the position of MgB_2 as a competitor for both low and high temperature superconductors.

In summary, under the framework of two-gap superconductivity, the authors' group has discovered that nano-scale SiC doping into MgB_2 enhances both H_{c2} and flux pinning through multiple scattering channels. There are two closely related but distinguishable mechanisms that control the performance of $J_c(H)$: H_{c2} and flux pinning [46]. J_c for the nano-SiC doped samples increased by more than an order of magnitude at high fields and all temperatures compared to the un-doped samples. A record high $H_{c2}(0)$ value of 37T for bulk MgB_2 was achieved from transport measurements on a nano-SiC doped sample. Doping with SiC enhances the $J_c(H)$, H_{irr} and H_{c2} in a manner that helps make MgB_2 potentially competitive with both low and high- T_c superconductors.

4.3 Si and Silicide Doping

Si and silicides including WSi_2 , ZrSi_2 , MgSi_2 and SiO_2 as dopants for MgB_2 have been found to have positive effects on $J_c - H$ performance. Ma et al. have reported the effects of ZrSi_2 , WSi_2 , ZrB_2 , Mg_2Si and SiO_2 on the $J_c - H$ behaviour [47]. They found that J_c was enhanced by all these dopants except for SiO_2 . These compounds act as pinning centres in the form of additives. There are some reactions between these additives and Mg and B but there is no evidence that these elements are incorporated into the MgB_2 lattice. The extent of J_c enhancement depends on the additive content and processing conditions. However, the enhancement of J_c by these dopants is much less significant than that of SiC doping [2,44].

Cimerle et al. found that doping with a small amount of Li, Al or Si resulted in an increase in low-field J_c , but there was no improvement in H_{irr} [48]. Wang et al. studied the effect of nano-Si particle (<100nm) and coarse Si particle doping in MgB_2 on the $J_c - H$ performance

[49]. They found that the nano-particle doping enhanced the flux pinning while the coarse doping had a negative effect. A neutron diffraction study indicated that there is no substitution of Si in either B or Mg sites. The enhanced flux pinning is attributed to the impurity inclusions, including reaction products, Mg_2Si and un-reacted nano-Si particles.

4.4 Metal Element Doping

Jin et al. studied the effect of several metal elements including Fe, Mo, Cu, Ag and Y on the $J_c - H$ behaviour of MgB_2 . They found that these elements were not incorporated into the lattice and had negative effects on $J_c - H$ characteristics, with Fe being the least damaging element while Cu, Y and Ti were the most detrimental elements [50]. The elements Cu, Ag, Y and Ti react with Mg while Fe, Ag and Ti react with B to form intermetallics.

Fe doping was further studied by the author's group using nano-scale Fe powder and found to have a much stronger negative effect on $J_c - H$ behaviour, indicating that the magnetic properties of Fe damaged both the superconductivity and the J_c field dependence [51]. This is in contrast to work claiming that Fe addition acted to create effective pinning centres and improved the $J_c - H$ performance [52]. In Jin's study, they used an Fe particle size larger than $1\mu\text{m}$ so that the overall contact interface between MgB_2 and Fe or an Fe compound is relatively small. By using nano-scale Fe powder the interface area increased substantially, and the ferromagnetic effect of Fe on surrounding superconductor becomes more pronounced, resulting in a strong depression in T_c and superconductor volume, which in turn reduced J_c .

Zhao et al. doped MgB_2 with Ti and Zr. The J_c improved significantly at 4K, being attributable to the sintering-aid property and pinning centres of these additives [53]. However, there was no evidence for improved pinning at temperatures above 20K; the J_c dropped off rapidly with increasing field ($H_{irr} = 4\text{T}$ at 20K). Finnemore et al. used the CVD technique to co-deposit Ti with boron to form TiB and TiB_2 fibre [54]. When this fibre reacted in Mg vapor to transform boron into MgB_2 , the resulting conductor had a J_c of $5 \times 10^6 \text{ A/cm}^2$ at 5K and self-field. The samples show a fine dispersion of Ti without precipitation of TiB_2 at grain boundaries, in contrast to the precipitation of TiB_2 in the solid-state reaction route. However, as the un-doped sample is rather clean the $J_c - H$ characteristics for both Ti doped and un-doped samples showed strong field dependence. Prikhna et al. have achieved better $J_c - H$ performance of Ti doped MgB_2 using the high pressure of 2GPa [55]. The J_c for optimized Ti doped MgB_2 reached 10KA/cm^2 at 20K and 5T. Their interpretation was that the role of Ti addition is due to the absorption of hydrogen impurity to form TiH in the sample. However, for the normal un-pressured condition there is no hydrogen in the samples. Thus, the effect of Ti doping remains unclear.

Al substitution for Mg has been studied by a number of groups with the major emphasis on the effect on T_c . As Al substitution for Mg causes a serious deterioration in T_c it was expected that the effect on J_c would be negative too. However, recently, Berenov et al. used a low level of Al, 1-2.5 at% doping, to minimize the reduction in T_c . The J_c was enhanced by a factor of 20 for a doping level of 1 at% Al at 5K and 5T [56]. This may be attributable to the scattering at Mg sites as a result of Al substitution for Mg.

4.5 Oxide and Other Compound Doping

A group at Imperial College doped MgB_2 with nanoparticles of Y_2O_3 and obtained a significant improvement in the irreversibility field ($H_{irr} = 11.5\text{T}$) at 4.2K due to the introduction of dispersed inclusions such as YB_4 [37]. However, the improvement in H_{irr} for the doped samples is less significant at 20K ($H_{irr} = 5.7\text{T}$). Chen et al. have reported the results of ZrO_2 doping on the T_c and J_c of MgB_2 [57]. They found that ZrO_2 doping in conjunction with the *in-situ* reaction route caused detrimental effects on J_c while having only small effects on both T_c and J_c when the *ex-situ* reaction route was used.

The authors' group has studied the doping effect on T_c and $J_c - H$ behaviour using nitride compounds including Si_3N_4 and BN [58]. It was found that Si_3N_4 reacted with Mg to form MgSi_2 , causing degradation in both T_c and $J_c - H$ behaviour. In contrast, BN is highly compatible with MgB_2 . There is little effect on T_c and $J_c - H$ characteristics up to 20% addition, using an *in-situ* reaction route at an annealing temperature of 800°C.

5. ACTIVATION ENERGY

Since the discovery of the superconductivity of MgB_2 , the vortex dynamics of this superconductor has been the subject of intensive study, because of its importance in the evolution of our understanding of flux pinning. The critical current density is determined by the pinning properties of the sample as well as by the flux motion, because the motion of the vortices over pinning centers (flux creep) in the superconductor induces dissipation and reduces the critical current density. The activation energy against flux motion, especially its dependence on the current density, the magnetic field, and the temperature, is very important for understanding the underlying mechanism governing vortex motion in superconductors. From ac susceptibility measurements, the current-density dependent activation energy has been derived to be highly nonlinear $U(j) \propto j^{-0.2}$ (see Fig. 14). This result suggests that the $I-V$ curve of MgB_2 superconductors should also be highly non-linear, because using the Arrhenius rate equation, one has $E = Bv = Bv_0 \exp[-U(j)/k_B T] \propto \exp(-j^{-0.2})$. Nonlinear $I-V$ characteristics have been experimentally observed in MgB_2 [59]. On the other hand, the relaxation of the current density or the magnetization can be derived as $j(t) \propto [\ln(t/t_0)]^{-1/0.2}$, which is also a nonlinear function of $\ln(t/t_0)$. This non-logarithmic relaxation can be detected by means of dc magnetization relaxation measurements.

The activation energy as a function of the dc magnetic field $U(B)$ has also been derived and is shown in Fig. 15. It can be seen from Fig. 15 that a universal curve has been obtained by scaling the data by $j^{-0.21}$. This current density dependence is consistent with the result shown in Fig. 14. The solid line in Fig. 15 is a fit to the power law $U(B) \propto B^{-1.33}$. The obtained $U(B)$ is also consistent with the one derived from scaling in Fig. 14. The self-consistent scaling of $U(j, B)$ suggests that separation of the variables in the activation energy $U(j, B, T)$ is quite reasonable. The final expression for the temperature-, field-, and current-density dependent activation energy is given by

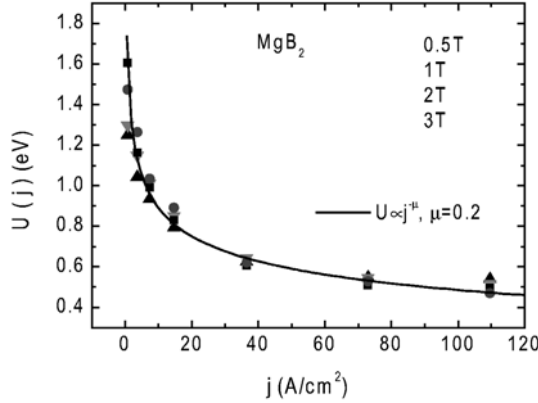


Fig. 14. Activation energy $U(j) \propto U(j, B_{dc}) \times B^{1.3}$ as a function of the current density for an MgB_2 bulk sample at various dc magnetic fields. Solid line is the fitting curve $U(j) \propto j^{-0.2}$.

$$U(B, T, j) = U_0 \left[1 - \left(\frac{T}{T_x} \right)^2 \right]^2 \left(\frac{B}{B_0} \right)^{-n} \left(\frac{j}{j_0} \right)^{-\mu} \quad (5-1)$$

where U_0 , j_0 , and B_0 are scaling values, and the exponents n and μ are determined to be 1.33 and 0.2, respectively.

As for the magnetic field dependence of the activation energy, a B^{-1} dependence has been previously derived using the Anderson-Kim model of the activation energy combined with the Ginzburg-Landau expressions for the coherence length, thermodynamic critical field, depairing critical current density, etc. [60,61]. Such a B^{-1} dependence has been observed in a $\text{La}_{1.86}\text{Sr}_{0.14}\text{CuO}_4$ single crystal with weak pinning centers by McHenry et al. [62]. In addition, for $\text{YBa}_2\text{Cu}_3\text{O}_x$ samples with strong pinning centers, such as twin planes, stacking faults or Y_2BaCuO_5 inclusions, a $U(B) \propto B^{-0.5}$ has been derived from both ac susceptibility and dc magnetization measurements [63,64]. For MgB_2 on the other hand, we find a $U(B) \propto B^{-1.33}$ dependence, showing that the activation energy decreases even faster with increasing magnetic field, compared to weakly pinned high temperature superconducting $\text{La}_{1.86}\text{Sr}_{0.14}\text{CuO}_4$ single crystal. The weakening of the activation energy with increasing magnetic field may be the reason why the critical current density drops steeply as the magnetic field increases, as has been observed by dc magnetization measurements [40,65-69]. This result is consistent with measurements of the flux creep rate S , defined as the logarithmic derivative of the magnetic moment m with respect to time t , $-\ln m / \ln t$, which has been derived to be small at low magnetic fields, but increases quasi-exponentially as the field approaches the irreversibility field H_{irr} . The energy U_0 , which measures the vortex pinning as modified by vortex-vortex interactions is found to decrease rapidly with increasing field. Taking into account the relatively low irreversibility line and the weakening of the activation energy with increasing magnetic field, the pinning properties of MgB_2 need to be enhanced

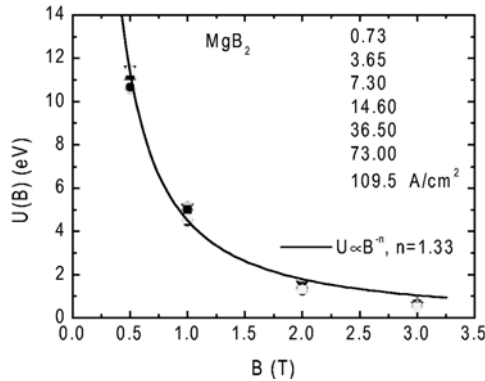


Fig. 15. Activation energy $U(B) \propto U(j, B_{dc}) \times j^{-0.21}$ as a function of the magnetic field for an MgB_2 bulk sample at various current densities. Solid line is the fitting curve $U(B) \propto B^{-1.33}$.

for practical applications. Chemical doping such as with SiC has been shown to be very effective in increasing both the critical current density and the irreversibility field.

6. SAMPLE SIZE DEPENDENCE OF THE MAGNETIC CRITICAL CURRENT DENSITY

It has been reported that the critical current density derived from magnetic measurements in MgB_2 superconductors depends on the sample size [70,71]. (See Fig. 16: a larger sample results in a higher critical current density at high fields.) If this were a true intrinsic property of this new superconductor, it would be advantageous to use MgB_2 in large-scale applications. Such a phenomenon has not been observed in either high temperature or low temperature superconductors. Explanations have been proposed to account for this observation [70,71]. Jin et al. [71] suggested that the vortices in MgB_2 are quite rigid at small sample lengths and break into segments as the sample length reaches the collective pinning length $L_c \approx (\epsilon_0^2 \xi^2 / \gamma)^{1/3}$, with ϵ_0 the basic energy scale, ξ the coherence length, and γ a parameter of disorder strength. Horvat et al. [70] proposed that different coupling mechanisms between the superconducting grains at different length scales are responsible for the sample size dependent critical current density for the entire field range.

In order to explain this observation, we start from the flux creep equation derived from Maxwell's equation $\nabla \times E = -\partial B / \partial t$ with $E = B \times v$ as discussed by Jirsa et al. [72] and Schnack et al. [73],

$$-\frac{dM}{dt} = \frac{\chi_0}{\mu_0} \frac{dB}{dt} - \frac{\Delta v_0 B}{\mu_0} \exp\left[-\frac{U(j, B, T)}{kT}\right] \quad (6-1)$$

The vortex velocity v is assumed to be thermally activated, i.e. $v = v_0 \exp[-U(j, B, T)/kT]$, where the attempt velocity $v_0 = x_0 \omega_0$ with attempt frequency ω_0 and attempt distance x_0 is

the velocity of vortices when $U(j) = 0$ (i.e. $j = j_c$). $U(j)$ is the activation energy and k the Boltzmann constant. The differential susceptibility χ_0 and the geometric factor Δ in Eq. (6-1) depend on the size and shape of the sample. Considering a disk with B parallel to its axis, one has $\chi_0 = \pi^2 R^3 / (3J)$ and $\Delta = 2\pi^2 R^2 / (3J)$, where R is the radius of the disk, and $\mu_0 R J$ the self-inductance of the disk. Eq. (6-1) can be solved for $U(j)$ as

$$U(j) = kT \ln \left[\frac{B\Delta v_0}{\mu_0 \frac{dM}{dt} + \chi_0 \frac{dB}{dt}} \right] \quad (6-2)$$

For a hysteresis loop measurement, we usually have $\mu_0 (dM/dt) \ll \chi_0 (dB/dt)$, and Eq. (6-2) can then be reduced to

$$U(j) = kT \ln \left(\frac{2Bv_0}{R\dot{B}} \right) \quad (6-3)$$

where $\dot{B} = dB/dt$. Eq. (6-3) is simply related to the current-voltage $I-V$ (or $j-E$) curves since for a cylinder of radius R , Faraday's law leads to $E = R\dot{B}/2$. Therefore, a larger sample size R will lead to a larger electric field in the sample, and therefore to a larger current density in the sample. This effect is similar to the effect of \dot{B} on the hysteresis loop in dynamical relaxation measurements [72,73].

According to Eq. (6-3), a different $U(j)$ will result in a different dependence of the current density on the sample size. The relaxation results of MgB_2 samples have led to a logarithmic dependence of the activation energy on the current density [74,75]

$$U(j) = U_0 \ln \frac{j_c}{j} \quad (6-5)$$

where U_0 is the energy scale and j_c the true critical current density at which $U(j_c) = 0$.

Combining Eq. (3) with Eq. (5), we obtain the sample size dependence of the current density as

$$j = j_c R^{1/n} \left(\frac{\dot{B}}{2Bv_0} \right)^{1/n} \quad (6-6)$$

where $n = U_0(B, T) / kT$ is the n-factor characterizing the $E-j$ relationship of the superconductor $E = E_c (j/j_c)^n$. The above analysis can also be applied to a rectangular rod with $R \approx ab/(a+b)$.

As can be seen from Eq. (6-6), the current density depends on the sample size as $j \propto R^{1/n}$, therefore the dependence is determined by the exponent n , which is a function of both temperature and magnetic field. If n is very large, there will be no sample size dependence as $R^{1/n} \rightarrow 1$, and this might be the reason why no sample size dependent current density has been reported in low temperature superconductors. Typical n factors in low temperature superconductors vary between 10 and 100 [76]. As an example, magnets which work in the

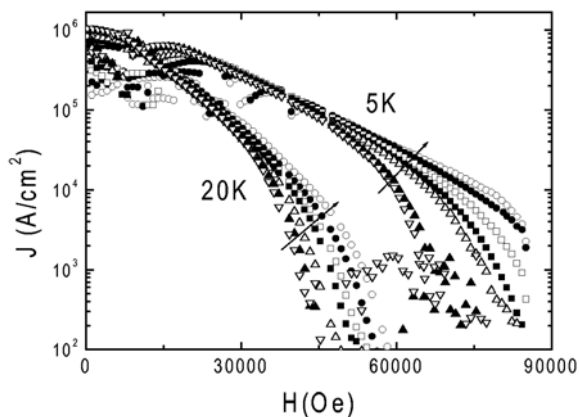


Fig. 16. The magnetic field dependent current density of MgB₂ samples at 5 K and 20 K. The arrows indicate the direction of increasing sample size.

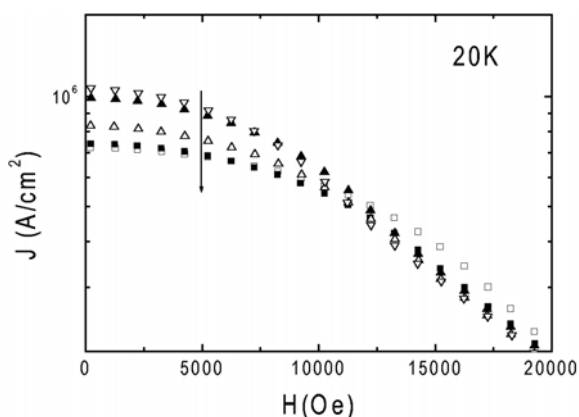


Fig. 17. The magnetic field dependent current density of MgB₂ samples at low magnetic field for 20 K. The arrows indicate the direction of increasing sample size.

persistent mode without a drift require wires with a high n factor, typically larger than 30 at the highest field [76]. In high temperature superconductors, n values as low as 5 in NdBa₂Cu₃O₇ [77] and 4 in YBa₂Cu₃O₇ [78] at high temperature and high magnetic field have been reported, indicating that a significant sample size dependent current density should be observed. However, weak-links in polycrystalline high temperature superconductors are very serious and prevail against the effects shown in Eq. (6-6), resulting in a lower critical current density in larger samples.

Although the activation energy was reported to be very high in MgB₂ at low temperature and low magnetic field, it drops sharply as the applied magnetic field and the temperature are increased [74]. The n factors in MgB₂/Fe tapes and wires have been reported [79,80] to be

around 60 at 4 T, but drop to below 10 at high fields. From the $I-V$ curves of MgB_2 high-density bulk samples reported by Pradhan et al. [81], the n factor is derived to be around 1.5 at 26.5 K and 5 T. Kim et al. [59] obtained a similar n factor around 1 from $I-V$ curves by at 30 K and 3 T. When the n factor is in this range, the sample size dependence of the current density is expected to appear as seen in Fig. 16. The power law dependence $R^{1/n}$ saturates as R is increased if n is larger than 1, which explains the reported saturation of the current density. No saturation is expected at very high temperatures and fields (where n may drop below 1), and the total current is limited by the irreversibility line as $B \rightarrow B_{irr}$.

On the other hand, as the n factor is very high at low fields [79,80] (more than 100), a sample size dependence of the current density is not expected ($R^{1/n} \rightarrow 1$). The decreasing current density as the sample size increases might result from the self-field effect. Because larger samples carry larger currents (even if the current density is almost the same), generating a larger self-field, this results in a smaller current density. Significant self-field has been observed in high temperature superconductors, especially in tapes with large critical currents [82,83]. MgB_2 is expected to show similar behavior. Another possible reason is due to the surface pinning effect [84]. In the presence of both bulk and surface pinning, the magnetization is just the sum of the bulk and surface contributions [85]. However, the surface component is only effective in the fields $H < H_p \approx \kappa H_{c1} / \ln \kappa$, with κ the Ginsburg-Landau parameter and H_{c1} the lower critical field [85]. For the rectangular rods in this study, the ratio between the surface area parallel to the applied magnetic field and the sample volume is $2(ac+bc)/abc \approx 2/R$, indicating a larger surface contribution as the sample size is decreased. This results in a larger current density in a smaller sample. The sample size dependence of the current density at low magnetic fields will be studied in more detail in our forthcoming work.

7. OVERCRITICAL CURRENTS IN MgB_2 WIRES WITH FERROMAGNETIC SHEATHING

In the previous chapters we have described an enormous effort to enhance pinning of vortices, which determines the maximum dissipation-free currents in superconductors in the Shubnikov state, by doping with various elements. The authors' group [86] has recently discovered a fundamentally different type of current-carrying enhancement in MgB_2 wire sheathed in ferromagnetic iron. It has turned out that this magnetic enhancement complements both intrinsic (bulk) pinning [87] and pinning gained by SiC doping. A critical current enhancement of more than one order of magnitude has been shown for round MgB_2 wires sheathed in iron compared to the same wires with their Fe-sheath stripped off [88]. This critical current enhancement is referred to as the *overcritical state*.

The existence of the overcritical state as a result of the magnetic interaction has been theoretically predicted by Genenko et al. [89,90] for thin 2D-like superconducting strips placed in the environment of a soft magnetic material (magnet). The main idea of this prediction is that magnets located near a current-carrying thin superconductor can strongly affect the spatial variation of the current-induced field and, consequently, the distribution of the transport current associated with this field [89]. For some magnet configurations the

supercurrent profile over the strip can be redistributed so that the supercurrent is pushed from the flux-filled strip edges to the central flux-free part of the strip, resulting in a total overcritical current $I_c^{oc} > I_c$ (the total critical current of the same strip having no magnetic environment) [90]. The field lines can be virtually removed from the edges of the strip, resulting in a suppression of the supercurrent near the edges and an enhancement of the supercurrent towards the centre of the strip. Effectively, the conventional \cup -like cross-sectional distribution in the magnet-free environment [91] transforms into a \cap -shaped supercurrent profile [5]. In the magnet-free environment, current singularities near the edges lead to a faster collapse of the superconductivity [91]. Such magnetically induced current redistribution (MICR) is possible and effective in thin strips since the (Meissner shielding) currents can flow over the entire surface (basically over the entire volume) of these thin 2D-like superconducting strips, remaining effectively flux-free. According to [89,90], the flux-free Meissner state is the physically important condition for overcritical currents to exist without violating the pinning-controlled critical current limitation mechanism. However, to achieve the highest predicted I_c^{oc} / I_c enhancement ratio (~ 7), the strips should be situated in a peculiar, “hard to fabricate” geometrical shape: an open convex magnetic cavity. This fabrication obstacle made it difficult to achieve and experimentally test this prediction.

In the only experiment on the overcritical state in thin films, Jarzina et al. [92] claimed that they had observed overcritical currents in YBCO samples with the magneto-optical (MO) imaging technique. These results, however, appear to be controversial for the following reason. Overcritical Meissner current densities ($J_c^{oc} \sim 1.5 \times 10^7$ A/cm²), which were up to 4-5 times larger than $J_c \sim 3 \times 10^6$ A/cm² at $T = 77$ K, were locally obtained by inversion of the Biot-Savart law in the film edge region next to the magnets, which were set perpendicular to the film. In contrast, the theory predicts that the currents should be suppressed near the edges adjacent to the magnet [90]. Moreover, no global investigations, such as magnetization or transport current measurements, were carried out.

The situation is fundamentally different in a 3D bulk superconductor-ferromagnet system such as MgB₂ superconducting wire sheathed in iron. In this case, the supercurrent flows only within the magnetic field penetration depth, unless the superconductor is filled with magnetic flux, which nominally violates the physical basis, predicted in [89,90], for the existence of the overcritical current. However, global magnetization experiments show that the overcritical state does exist in 3D bulk MgB₂ wire sheathed in iron [86-88].

Fig. 18 shows the normalized critical current density calculated from the corresponding magnetization measurements [88]. As can be clearly seen, if the magnetic field is applied perpendicular to the cylindrical wire axis (Fig. 18(a)) an enhancement of the critical current density is observed (overcritical current state) compared to the same wire without the Fe-sheath. The enhancement ratio J_c^{oc} / J_c at the maximum in $J_c^{oc}(H)$ is effectively constant and equals about 1.6 below $T/T_c \sim 0.8$ (Fig. 19). This temperature independent enhancement was shown to agree with the current increase predicted in [90]

$$\frac{J_c^{oc}}{J_c} = \left[\frac{1}{4\pi} \tan\left(\frac{\pi D}{4a}\right) \right]^{1/2} \quad (7-1)$$

if the wire diameter D and the distance between the magnetic sheath and the superconducting core a are taken into account [88]. However, at higher temperatures (approaching T_c) an

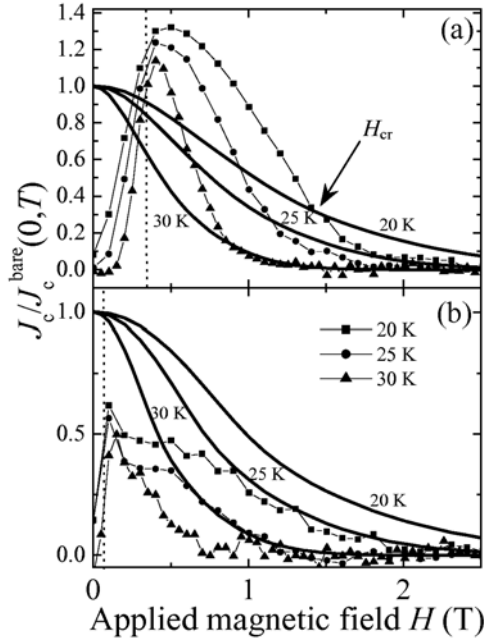


Fig. 18. The normalized critical current density of MgB₂ round wires for perpendicular (a) and parallel (b) field orientations relative to the cylindrical wire axis. The symbol curves show the comparative results for the Fe-sheathed wires. The bold solid curves exhibit the results for the bare wires with their Fe-sheath stripped off. The dashed lines denote the saturation fields H_s measured for the Fe-sheath above T_c for each orientation.

enhancement of more than one order of magnitude is achieved (Fig. 19). This dramatic enhancement was explained as a consequence of the interplay between the field dependence of J_c in the wire with its Fe-sheath stripped off (bare wire) and the magnetic screening effect for the Fe-sheathed wire. A similar enhancement behaviour was measured for some geometries of the wire cross section. An enhancement ratio of about 5 was obtained for a flat tape at $T = 35$ K [87].

If the field is applied parallel to the axis (Fig. 18(b)) of the wire, the critical current density of the wire in the sheath is slightly suppressed compared to the same wire without the sheath. A plausible attempt to explain the difference in the enhancement of the critical current density for the perpendicular and parallel field orientations has been made in Ref. [88]. The wire with the field applied parallel to its axis always exhibits a Bean-like field-current profile, independent of the presence or the absence of the magnetic sheath. In contrast, for the perpendicular configuration, the field-current profile is expected to be significantly modified due to the sheath magnetization and the well-known magnetic screening effect [93]. Therefore, the MICR has turned out to be a reasonable explanation for the overcritical state observation [88].

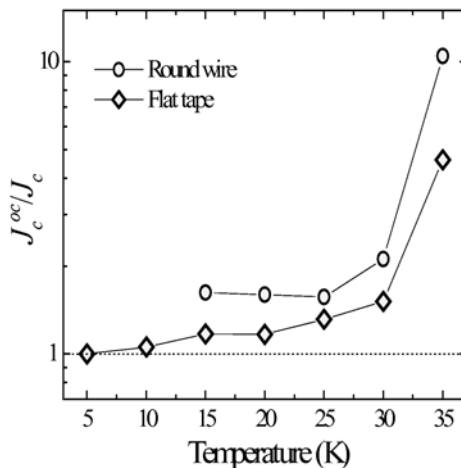


Fig. 19. The critical current density enhancement (J_c^{oc}/J_c) in the sheathed round wires relative to the same wires with the sheath removed measured at the field of the overcritical current density maximum (Fig. 1(a)) is indicated by the circles. The diamond symbols show the enhancement of a flat tape [87] for comparison.

The proposed supercurrent redistribution was further supported by the magnetic flux profile investigations over the superconducting MgB_2 wire sheathed in iron [94]. The experiments were carried out in different magnetic states, such as field cooled (FC) and zero-field cooled (ZFC), as well as with and without transport current applied. The extraction of the critical current profiles from the flux distributions has not been done yet since the Biot-Savart law inversion procedure is required to be modified to take into account the magnetic environment surrounding the superconducting core. However, a clear feature in the centre of the MgB_2 superconducting core consistent with a supercurrent redistribution from the sides towards the centre of the core was observed for the transport current applied in the FC case [94]. It is worthwhile noting that the overcritical current was also observed in the FC state from the global magnetization measurements [88].

The sheet supercurrent redistribution in a bulk round superconducting wire situated near a flat surface of a semi-infinite bulk magnet has been theoretically shown to change in the Meissner state [95]. The current is suppressed in the vicinity of the magnet and enhanced in the middle and on the opposite side of the wire, while the total current remains unchanged. The bulk flat magnet should act in a similar way as one side of the Fe-sheath does in MgB_2 wires if the field is applied perpendicular to the axis [86,88,93,94,96]. Hence, for two flat magnets on each side (or for the configuration of the sheathed wire), one can anticipate the sheet supercurrent flowing mainly in the middle region. A certain degree of agreement between the theoretical study and experiment was obtained by only comparing the partially flux-filled FC state with the field applied perpendicular and the transport current flowing in the superconductor [94]. In the case of only transport current applied to the wire, no redistribution in the middle of the superconducting core has been observed [86,94]. This

could be explained by the smallness of the possible enhancement in the middle between two magnets in the Meissner state. Therefore, more sensitive MO investigations are needed.

The superconducting signal subtraction procedure from a mixture of soft-magnetic and type II superconductor filament signals at low fields in the ZFC state has been developed on the basis of exact solutions of the London equation, and compared with experiment on MgB₂ wires sheathed in iron [97]. The comparison between the theory and the experiment indicated that the error, which might appear in the J_c calculation carried out in [86-88] due to not taking into account the increased magnetization of the iron from the superconducting shielding, could be only about 3% for the wire geometry used in the experiments. In experiments [86-88], a direct subtraction of the iron contribution measured above T_c from the mixed signal of the Fe/MgB₂ core measured below T_c has been employed. Moreover, above the saturation field H_s of the ferromagnetic iron [88], the error should be approaching zero.

The influence of the magnetic screening was also investigated by magnetization, transport and numerical finite element analysis methods (FEM) in Refs. [17,96,98]. Transport measurements carried out for the magnetic field applied parallel and perpendicular to the wire axis (and the current flow direction) showed that the shielding effect leads to considerable discrepancies in the critical current (I_c) dependence on the applied field [17]. For the perpendicular orientation, I_c was reduced by about 15% at $H_s^\perp = 0.2$ T and $T = 32$ K. At higher fields, within 0.2 T $< H < 0.6$ T, I_c remained constant. At $H > 0.6$ T, I_c dropped as $\propto \exp(-H/H_0)$, with $H_0 \sim 0.35$ T. For the parallel orientation, I_c dropped with the same exponential law starting from $H_s^\parallel = 0.025$ T. At $H = 0.4$ T, the critical current measured for the Fe-sheathed MgB₂ wire was up to 75% larger for the perpendicular orientation than for the parallel one. However, no overcritical currents were reported. It is worthwhile noting that at fields $< H_s$, nearly complete shielding was measured by inserting tiny pickup coils inside the sheath after removal of the superconducting core. The H_s values measured for both orientations are strongly consistent with the saturation fields of the ferromagnetic iron measured with the help of the magnetization measurements [86,88]. The saturation field value depends on the properties of iron and its mechanical (and likely thermal) treatment during the wire manufacturing process. For example, for Fe-sheathed MgB₂ multi-filamentary tapes H_s can be as high as 1 T [86,87]. However, the degree and the range of the magnetic shielding in the wires depend on the wire geometry. For flat samples the magnetic screening range is smaller than the measured H_s of the Fe-sheath [87]. This is also supported by the FEM diagrams calculated in [96,98]. Correspondingly, in the range over which the "pseudo" Meissner state of the wires is effectively extended by the magnetic screening [86,88,96]

$$H_{c1}^{ps} = H_{c1} + gH_s, \quad (7-2)$$

a geometry dependent parameter $g < 1$ has to be introduced.

A comparative study of MgB₂ wires sheathed in ferromagnetic iron and non-magnetic copper was performed by Kova et al. [98]. Transport measurements of the wires showed that the normalized critical current behaviour as a function of field has somewhat similar behaviour to the normalized $J_c(H)$ dependence exhibited in Fig.18(a). The critical current curves for the Cu-sheathed wire, to a large extent, resemble the behaviour of the stripped-off (bare) wires in Fig. 18(a), whereas the I_c curves for the Fe-sheathed wires behave similarly to the Fe-sheathed ones in Fig. 18(a) except for fields below ~ 0.4 T. This is because in the

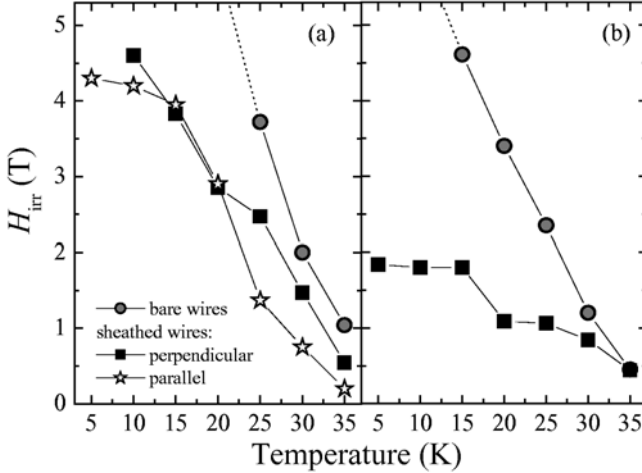


Fig. 20. The irreversibility field as a function of temperature for the Fe-sheathed and stripped off round wires (a) and flat tapes (b). The dotted lines show the expected irreversibility field lines, which could not be measured due to the field limitation of the magnetometer used.

magnetization experiments, J_c within $|H_s| < 0.4$ T for the round wires at the perpendicular orientation provides a vanishing superconducting signal due to the magnetic screening effect [86-88]. No overcritical currents were measured directly in [98], particularly taking into account the fact that critical current densities in Fe-sheathed MgB_2 wires are usually much higher than in Cu-sheathed ones [99]. However, from the results obtained in [98] one can anticipate that the overcritical state can be also measured not only by magnetization measurements as was done in [86-88], but also by the transport current technique. It is interesting to note that when the external field was applied at an angle of around 45° to the wire axis, a 15% larger I_c was measured at $H = 4$ T and $T = 4.2$ K than for the perpendicular and parallel orientations [98].

The magnetic screening effect imposed by the iron sheath has been shown to reduce and eliminate AC hysteretic losses induced by an external magnetic field [96,100]. Effectively zero and extremely small losses were measured below H_{cl}^{ps} , while above this field the hysteretic losses rise proportionally to $(H_m - H_{cl}^{ps})^3$.

At least one disadvantage of the Fe-sheath influence on the superconductivity of MgB_2 wires has been observed. The magnetized sheath suppressed J_c (i) for the parallel field orientation compared to that measured with the sheath stripped off (Fig. 18(b)); and (ii) at relatively high fields $> H_{cr}$ for the perpendicular orientation (Fig. 18(a)) [86,88]. Eventually, this suppression led to a significant reduction of the measured irreversibility fields for both orientations (Fig.20). A similar suppression effect at high fields can be found upon comparison of the normalized critical current for the Cu- and Fe-sheathed wires in [98].

8. J_c ENHANCEMENT BY IRRADIATION

Irradiation experiments on MgB_2 have involved the bombardment of this material with fast and thermal neutrons, protons, electrons, and heavy ions, as well as the U/n method, where the MgB_2 is doped with ^{235}U and then exposed to thermal neutrons to promote fission of the uranium, leading to the production of fission tracks. The earliest experiments began within months of the announcement of the superconducting properties of MgB_2 in early 2001. In some experiments the primary focus was on the disorder introduced by the irradiation, on how its effects compare with what is seen in other superconductors and how they affect the superconducting properties. Others were aimed at investigating such features as the two-gap structure of MgB_2 or flux pinning at grain boundaries. Still others have had a more technological focus, with an interest in the radiation hardness of the material or with introducing columnar defects to improve flux pinning.

8.1 Neutrons

Neutron irradiation is achieved by placing samples in the core of a nuclear reactor. With neutron irradiation the main damage is done by a nuclear reaction rather than by direct bombardment, although some displacements occur when high-energy neutrons collide with lattice atoms. MgB_2 made with natural boron has 19.9% of its boron atoms in the form of ^{10}B , which has the enormous cross-section of 3837 barn for the $^{10}B(n,\alpha)^7Li$ nuclear reaction at thermal neutron energies. The ^{10}B nucleus and the neutron react to form an α particle with a kinetic energy of 1.47 MeV and a 7Li nucleus with a kinetic energy of 0.84 MeV. The reaction products produce the atomic displacements along the ranges of 4.8 μm and 2.1 μm , respectively. Because of the low penetration range and extremely large reaction cross-section for thermal neutrons, they only induce defects at the surface of the sample. The reaction cross-section decreases with $E_n^{-0.5}$ behaviour up to neutron energies of 10^5 eV [101] as the penetration range increases. A 0.5 mm cadmium shield will absorb almost all of the low energy neutrons, reducing the self-shielding effects and thus the inhomogeneity.

A collaboration led by a group at the Institute of Metal Physics, Ekaterinburg, did not screen out the thermal neutrons, but achieved a relatively homogeneous distribution of defects by using a very high neutron fluence of 1×10^{19} n/cm² on bulk MgB_2 produced by an *ex situ* method, corresponding to a damaging dose of 10 displacements per atom [102,103]. The irradiation increased the unit cell volume by 1.4%, mostly by increasing the *c* parameter, and decreased the occupancy of Mg sites. However, the symmetry of the original structure was maintained. The critical temperature T_c decreased to 5 K, but was progressively restored to the pre-irradiation value of 39K by annealing at higher and higher temperatures, being almost completely restored by annealing at 700°C. There was very little broadening in the transition width, indicating a relatively homogeneous distribution of defects, and little change in dH_{c2}/dT . On the basis of the nuclear magnetic resonance (NMR) line shift and nuclear spin-lattice relaxation, [102] ascribes the drop in T_c to a substantial decrease in the density of states (DOS) of boron $2p_{x,y}$ states due to the irradiation. The electronic states of Mg near E_F were not affected.

Babic et al. (2001) irradiated bulk and powder MgB_2 with fluences of thermal neutrons ranging up to 4.5×10^{15} n/cm². The highest fluence only produced a drop in T_c of 0.3 K, and

this group also noted the absence of transition broadening. Modest enhancements of magnetisation loops were observed at the highest fluence and attributed to flux pinning at ion tracks [104]. Eisterer et al. [101] (2002) irradiated bulk MgB_2 with a fast neutron fluence of $2 \times 10^{15} \text{ cm}^{-2}$ together with a thermal neutron fluence of $1.6 \times 10^{15} \text{ n/cm}^2$. In some of their experiments they used a cadmium shield to absorb the thermal neutrons. This increased the centre to surface ratio of defects from about 5×10^{-4} to 7%. T_c was only modestly reduced after irradiation, particularly in the unshielded sample, but they did report significant broadening in the unshielded sample due to inhomogeneous distribution of defects.

Unlike Kar'kin et al. [102], Eisterer et al. observed an increased upper critical field H_{c2} at lower temperatures with a steeper dH_{c2}/dT in the unshielded sample. This was linked to an increase in the normal state resistivity and hence a decrease in the mean free path and decreased coherence length. $H_{c2}(0)$ increased from 17 T to 24 T. The ratio between H_{c2}^{\parallel} and the irreversibility field was about 2 before irradiation and remained unchanged by it, leading to an increased H_{irr} for the unshielded sample in particular. The low ratio of H_{irr} to H_{c2} was attributed to anisotropy and the random orientation of the crystal grains with respect to the applied field. Modest improvements in the critical current J_c were observed at higher fields, but this was attributed to the increased H_{c2} rather than to flux pinning on radiation-induced defects.

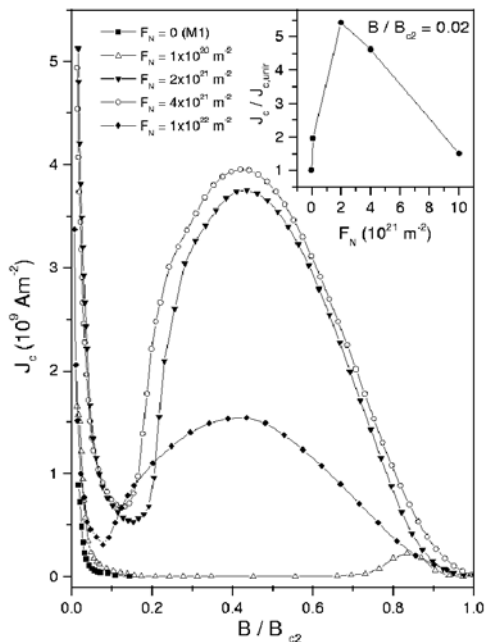


Fig. 21. Critical current density in MgB_2 single crystal as a function of the reduced magnetic induction for several (fast) neutron fluences at 5 K. Inset: Enhancement of J_c with neutron irradiation at small inductions $B/B_{c2} = 0.02$. After M. Zehetmayer et al. [106].

The same group (Zehetmayer et al. [105,106] (2003, 2004)) also examined radiation effects in single crystal material irradiated with fast neutrons at fluences up to 1×10^{16} n/cm². Transmission electron microscopy (TEM) revealed spots of defect contrast 5 nm in diameter (comparable to the coherence length). These indicated locally bent lattice planes due to the strain field associated with defects. As in the bulk, T_c and ΔT_c were not much affected. $\mu_0 H_{c2}^c(0)$ increased from 3 to 7 T. The irreversibility line was dramatically increased, becoming almost identical to H_{c2} . J_c increased by up to a factor of up to 5 at low magnetic fields. In magnetisation measurements, a very pronounced fishtail effect appeared at fluences from 1×10^{14} n/cm², as shown in Fig. 21. The effect first appears near H_{c2} , but extends over almost the entire mixed state as the fluence increases, and there are history dependent effects on J_c on the low energy side. The authors attribute this to an order-disorder transition where the pinning energy competes with the energy of the vortex lattice as the magnetic field increases, resulting in a more disordered lattice, but better adaptation of flux lines to the pinning environment and hence higher J_c .

In a collaboration led by a group at the University of Geneva, Bouquet et al. [107] and Wang et al. [108], both in 2003, were able to closely model the specific heat of polycrystalline MgB₂ from the point of view of the two-gap theory, which explains some of the MgB₂ properties from the presence of two superconducting gaps which open on different parts of the Fermi surface. The smaller arises from three-dimensional π orbitals, and the larger from nearly cylindrical sheets arising from the σ band. The workers investigated whether a total fast neutron irradiation up to a fluence of 3×10^{16} n/cm², sufficient to strongly depress T_c , would cause the gaps to converge as predicted by theory. This was measured by heat capacity measurements before and after irradiation. At the highest fluence irradiation was able to suppress T_c from 37 to 30 K. As reported by earlier workers, there were strong enhancements of H_{c2} and in the residual resistivity. However, the low-temperature specific heat remained unchanged after irradiation, implying that the Sommerfeld normal state coefficient was unaffected and thus that the irradiation was producing its effects on T_c and H_{c2} by merely enhancing scattering rather than by reducing the density of states, in contrast to the conclusions of [103]. The fact that T_c was affected rather than just the normal state resistivity implied that the irradiation was causing interband scattering between the π and the σ bands. The workers found a suppression of the larger σ gap after irradiation, while the π gap remained substantially unchanged, with convergence slower than predicted by theory. They noted that large increases in H_{c2} could be achieved without sacrificing more than a few degrees of T_c , indicating the technological potential of tuned disorder to improve MgB₂.

8.2 Protons

Experiments involve irradiation with proton beams from accelerators, with proton kinetic energies ranging up to 6 MeV. A TRIM simulation showed that at 6 MeV the protons penetrate to 258 μm in MgB₂, depositing most of their energy between 225 and 258 μm [109]. This profile is characteristic of protons so that achieving a reasonably homogeneous distribution of defects within a thin depth requires irradiating with a range of proton energies. The protons do not participate in a nuclear reaction in MgB₂ and produce their damage by displacing Mg and B atoms directly, creating a variety of defects. The ageing effects reported by a collaboration led by the Imperial College group [110] suggests that the main defects are

vacancies, which can diffuse easily. The protons remaining at the ends of tracks can also react with Mg to create MgH_2 or B to create boranes. Damage similar to that reported for neutrons has been reported.

Mezzetti et al. [109] irradiated bulk MgB_2 with protons at energies up to 6 MeV and a fluence of 0.8×10^{16} p/cm². They noted very little change after irradiation and concluded that MgB_2 is a good candidate for space applications where exposure to low and medium energy protons is unavoidable. The Imperial College collaboration [20,110] did see significant effects on small polycrystalline (PX) fragments and single crystals irradiated at lower proton energies and about the same fluence. These involved the same sorts of effects that have mostly already been described for neutrons: for the polycrystalline (PX) sample there were modest decreases in T_c (here on the order of 2K), increased H_{irr} at lower temperatures and higher dH_{irr}/dT , as shown in Fig. 22. J_c in the PX sample is slightly decreased at low magnetic fields but increased at higher magnetic fields, so that it falls off much more slowly with increasing field. Aging causes a slow reversion to the virgin behaviour. In the single crystal sample there is a fishtail effect similar to that described for neutron-irradiated single crystals, with J_c significantly increased in the peak. The fishtail effect strongly increases with aging, possibly because of diffusion of the defects responsible. H_{c2} is approximately doubled at low temperatures, and the critical temperature decreased by 2K. The explanations given are similar to those for neutrons and relate to scattering, which decreases the mean free path so as to increase the normal state resistivity and H_{c2} . The decreases in T_c are ascribed to interband scattering in particular. The fishtail effect is due to an order-disorder transition, and it does not appear in the PX sample because in that case the defects (probably vacancies) can rapidly diffuse away along grain boundaries.

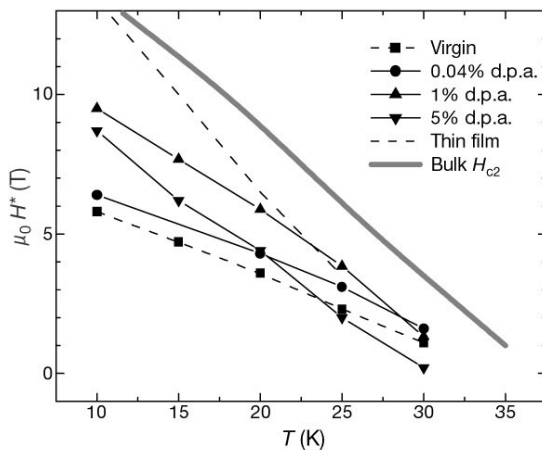


Fig. 22. Temperature dependence of the irreversibility field H^* for different levels of irradiation damage as defined by displacements per atom. The damage was caused by irradiation with protons at a range of energies up to 2 MeV. The irreversibility field is that at which J_c becomes immeasurably small; here a criterion of 1 kA cm^{-2} was used. There is a systematic increase of the slope of the $H^*(T)$ curve with increasing dose. After Bugoslavsky et al. [20].

8.3 Electrons

Okayasu et al. [111, 112] irradiated *in-situ* grown MgB_2 with electrons accelerated to 2.5 MV at a fluence of 5×10^{17} e/cm². They observed little effect on T_c . Critical currents were not affected at lower fields, but values were slightly lower after irradiation at higher fields. Sudden flux jumps of the zero-field-cooled susceptibility were more likely to occur near T_c in the irradiated sample, suggesting that vortices could suddenly move into the interior of the sample without trapping by pinning centres. These changes were attributed to degradation at the electron-irradiated grain boundaries, which tend to be much more affected than the interior of grains due to the smaller binding energies at grain boundaries. If the coupling at grain boundaries is degraded, then flux vortices can penetrate more easily. Conversely, these results support the importance of flux pinning at grain boundaries in MgB_2 .

8.4 Heavy Ions

Heavy ion irradiation is of particular interest because of the possibility of creating columnar defects. These are of special technological importance because they can allow a number of vortices to be pinned on the same defect. Spectacular increases in J_c have been achieved with columnar defects in highly anisotropic cuprate superconductors where pancake vortices can move independently on the different copper oxide planes, but significant results have also been achieved with less anisotropic materials such as $\text{Yb}_2\text{Cu}_3\text{O}_{7.5}$ (YBCO) [113]. The Coulomb explosion and thermal spike models give alternative explanations for how tracks are created. In the Coulomb explosion model [114] the damage is done by a cylindrical shock wave. Due to the slow response of the conduction electrons with respect to the time required for the bombarding ion to cross an atomic site, a long cylinder of positively charged ions is created. The cylinder explodes in a radial direction due to violent Coulomb repulsion. In the more commonly invoked thermal spike model [115, 116, 117] the defects are tracks (possibly discontinuous) of amorphous material resulting from melting in a highly localised volume along the track of the high-energy ion followed by cooling that is too rapid to allow re-crystallisation. The presence or otherwise of the tracks depends on whether the electronic stopping power S_e is above a threshold value that depends on the target materials and ions [118, 119]. Energy transfer from the ions to the crystal electrons must occur on timescales that allow melting of the lattice, and the heat conductivity required for freezing the molten volume must be high enough that there is no time for re-crystallisation. It is difficult, although not impossible, to create ion tracks in metals because the large number of mobile conduction electrons screen any space charge and rapidly spread the deposited energy [120]. Computer modeling indicates that it ought to be possible for at least discontinuous tracks to occur in MgB_2 [121,122]. However, the assumptions on which the models are based might not be correct, as there are strong differences in the literature as to whether columnar defects are created in this material. Determining the necessary parameters has been hampered by difficulties in growing large single crystals for experiments. There is disagreement in the reports as to whether any significant effects occurred as a result of the ion bombardment, and only one group has claimed to image columnar defects. The changes that were reported are consistent with point defects resulting from the irradiation.

In experiments performed a few months after the discovery of MgB_2 , Narayan et al. [121] irradiated polycrystalline MgB_2 with a beam of 200 MeV ^{107}Ag ions from an accelerator up to

a dose of 10×10^{20} ions/cm². They then used scanning tunnelling microscopy (STM) to image the irradiated surface. The results indicated amorphous tracks with diameters ranging from 50 to 80 Å. Scanning tunnelling spectroscopy indicated that the amorphous tracks and grain boundaries both had a metallic nature. Although Narayan et al. were of the view that the tracks would enhance pinning and J_c , no experiments to determine this were done. Okayasu et al. [112] irradiated polycrystalline MgB₂ with 3.54 GeV Xe ions from a ring cyclotron to a dose of 1×10^{11} ions/cm². They claimed that J_c was not enhanced in the lower field region, but that the irreversibility field was shifted to a higher field region so that there was some improvement in J_c at higher fields. This was ascribed to columnar defects. Chikumoto et al. [123,124] irradiated very dense polycrystalline MgB₂ with 5.8 GeV Pb-ions with fluences ranging up to 2×10^{11} ions/cm². The samples initially had a sharp T_c transition at 39K, and there were no significant changes after irradiation. J_c decreased at low magnetic fields, but increased at high fields, particularly at low temperatures. Magneto-optical imaging showed slight changes after irradiation that could be attributed to increased pinning. The defects responsible for the pinning were identified from TEM as spherical amorphous defects about 20 nm in size in [123], and not columnar defects as had been suggested in [121].

Olsson *et al.* [122] reported only slight shifts to higher temperature in the irreversibility and upper critical field in *c*-axis oriented MgB₂ films after irradiation with 1.2 GeV U⁵⁷⁺ to 2×10^{11} ions/cm² and 1.4 GeV Au³²⁺ to a somewhat smaller fluence. These workers also reported an increase in J_c at high temperatures near T_c but not at low temperatures. They could find no evidence for anisotropic pinning and no evidence for columnar defects from STM. Ghigo et al. [125] irradiated high-density MgB₂ bulk samples with 4.2 GeV Au ions at a fluence of 3.75×10^{10} ions/cm². They found no significant change in T_c , the irreversibility line, or any other values or behaviours as a result of irradiation. Like [109] they suggested that the radiation hardness of this material might make it suitable for space applications. Gupta et al. [126] found no changes (apart from a slight increase in T_c) after irradiation of electron beam evaporation (EBE) grown MgB₂ film in terms of irreversibility or J_c , but severe degradation in a pulsed laser deposition (PLD) grown film with much smaller grain boundaries. Irradiation was with 200 MeV Ag⁺¹⁷ ions at a dose of 1×10^{11} ions/cm². The results are explained by irradiation-induced effects at grain boundaries in the context of a flux line shear model.

8.5 U/n method

The U/n method [127,128] involves doping a superconductor with ²³⁵U atoms and then irradiating with thermal neutrons. The uranium atoms absorb the neutrons and fission. The two fission products recoil in opposite directions with a total kinetic energy of approximately 160 MeV. In cuprate materials this creates two randomly oriented, discontinuous fission tracks of amorphous material like the columnar defects due to heavy ions. Silver et al. [129] attempted to use this method on bulk MgB₂ that had been made by a reaction *in situ* method from Mg powder and very fine crystalline isotopically pure ¹¹B. The ¹¹B was used to avoid the nuclear reaction discussed above under neutron irradiation. The samples were 1 wt% U in the form of uranium oxide 93% enriched with ²³⁵U. EDS mapping showed a reasonably even distribution of uranium oxide particles. Irradiation was in a nuclear reactor at a variety of fluences up to 2×10^{16} n/cm². There were no significant changes as a result of irradiation in J_c .

or T_c , and there was no evidence of fission tracks in TEM, even though gamma ray spectroscopy showed that fission had occurred to the extent expected. This result, like [122] and [125], suggests that columnar defects probably do not form in MgB_2 ,

ACKNOWLEDGEMENTS

The authors thank J. Horvat, X.L. Wang, S. Soltanian, S.H. Zhou, M. Ionescu, H.K. Liu, A. Serquis, M. Sumption, M. Tomsic and E.W. Collings for their help in various aspects of this work. The work in Wollongong was supported by the Australian Research Council, Hyper Tech Research Inc, OH, USA, Alphatech International Ltd, NZ, and the University of Wollongong.

REFERENCES

- [1] J. Nagamatsu, N. Nakagawa, T. Muranaka, Y. Zenitani and J. Akimitsu, *Nature* 410 (2001) 63.
- [2] S. X. Dou, S. Soltanian, J. Horvat, X. L. Wang, P. Munroe, S. H. Zhou, M. Ionescu, H. K. Liu and M. Tomsic, *Appl. Phys. Lett.* 81 (2002) 3419.
- [3] X. L. Wang, S. Soltanian, J. Horvat, A. H. Li, M. J. Qin, H. K. Liu and S. X. Dou, *Physica C* 361 (2001) 149.
- [4] P.C. Canfield, D.K. Finnemore, S.L. Bud'ko, J.E. Ostenson, G. Lapertot, C.E. Cunningham and C. Petrovic, *Phys.Rev. Lett.* 86 (2001) 2423.
- [5] S. Soltanian, X.L. Wang, I. Kusevic, E. Babic, A.H. Li, M.J. Qin, J. Horvat, H.K. Liu, E.W. Collings, E. Lee, M.D. Sumption and S.X. Dou, *Physica C* 361 (2001) 84.
- [6] B.A. Glowacki, M. Majoros, M. Vickers, J.E. Evetts, Y. Shi and I. McDougall, *Supercond. Sci. Technol.* 14 (2001) 193.
- [7] G. Grasso, A. Malagoli, M. Modica, A. Tumino, C. Ferdeghini, A.S. Siri, C. Vignola, L. Martini, V. Previtali and G. Volpini, *Supercond. Sci. Technol.* 16 (2003) 271.
- [8] R. Flükiger, H.L. Suo, N. Musolino, C. Beneduce, P. Toulemonde and P. Lezza, *Physica C* 385 (2003) 286.
- [9] W. Goldacker, S.I. Schlachter, S. Zimmer and H. Reiner, *Supercond. Sci. Technol.* 14 (2001) 787.
- [10] A. Gurevich, S. Patnaik, V. Braccini, et al., *Supercond. Sci Technol.* 17 (2004) 278.
- [11] V. Braccini, A. Gurevich, J.E. Giencke, et al., *cond-mat/0402001* (2004).
- [12] A.Y. Liu, I.I. Mazin and J. Kortus, *Phys. Rev. Lett.* 87 (2001) 087005.
- [13] S.X. Dou, A.V. Pan, S. Zhou, M. Ionescu, H.K. Liu and P.R. Munroe, *Supercond. Sci. Technol.* 15 (2002) 1587.
- [14] S.X. Dou, A.V. Pan, S. Zhou, M. Ionescu, X.L. Wang, J. Horvat, H.K. Liu and P.R. Munroe, *J. Appl. Phys.* 94 (2003) 1850.
- [15] S.X. Dou, J. Horvat, S. Soltanian, X.L. Wang, M.J. Qin, S.H. Zhou, H.K. Liu and P.R. Munroe, *IEEE Trans. Appl. Supercond.* 13 (2003) 3199.
- [16] S.X. Dou, X.L. Wang, J. Horvat, D. Milliken, A.H. Li, K. Konstantinov, S. Zhou, E.W. Collings, M.D. Sumption and H.K. Liu, *Physica C* 361 (2001) 79.
- [17] J. Horvat, X.L. Wang, S. Soltanian and S.X. Dou, *Appl. Phys. Lett.* 80 (2002) 829.
- [18] A. Serquis, L. Civale, J.Y. Coulter, D.L. Hammon, X.Z. Liao, Y.T. Zhu, D.E. Peterson, F.M. Mueller, V.F. Nestorenko and S.S. Indrakanti, *cond-m*
- [19] C.B. Eom, M.K. Lee, J.H. Choi, et al., *Nature* 411 (2001) 558.
- [20] Y. Bugoslavsky, L.F. Cohen, G.K. Perkins, M. Polichetti, T.J. Tate, R. Gwilliam and A.D. Caplin, *Nature* 411 (2001) 561.

- [21] T. Takenobu, T. Ito, D.H. Chi, K. Prassides and Y. Iwasa, Phys. Rev. B 64 (2001) 134513.
- [22] M. Paranthaman, J.F. Thompson, D.K. Christen, Physica C 355 (2001) 1.
- [23] A. Bharathi, S. Jemina Balaselvi, S. Kalavathi, G.L.N. Reddy, V. Sankara Sastry, Y. Haritharan and T.S. Radhakrishnan, Physica C 370 (2002) 211.
- [24] I. Maurin, S. Margadonna, K. Prassides, T. Takenobu, T. Ito, D.H. Chi, Y. Iwasa and A. Fitch, Physica B 318 (2002) 392.
- [25] W. Mickelson, J. Cumings, W.Q. Han and A. Zettl, Phys. Rev. B 65 (2002) 052505.
- [26] Z.H. Cheng, B.G. Shen, J. Zhang, S.Y. Zhang, T.Y. Zhao and H.W. Zhao, J. Appl. Phys. 91 (2002) 7125.
- [27] R.A. Ribeiro, S. Bud'ko, C. Petrovic and P.C. Canfield, Physica C 382 (2002) 166.
- [28] M. Avdeev, J.D. Jorgensen, R.A. Ribeiro, S.L. Bud'ko and P.C. Canfield, Cond-Mat/0301025 (2003).
- [29] E. Ohmichi, T. Masui, S. Lee, S. Tajima and T. Osada, Cond-mat/0312348 (2003).
- [30] S.M. Kazakov, R. Puzniak, K. Rogacki, A.V. Mironov, N.D. Zhigadlo, J. Jun, Ch. Soltmann, B. Batlogg and J. Karpinski, Cond-Mat/0405060 (2004).
- [31] S. Soltanian, J. Hirvat, X.L. Wang, P. Munrow and S.X. Dou, Physica C 390 (2003) 185.
- [32] S.X. Dou, W.K. Yeoh, J. Horvat and M. Ionescu, Appl. Phys. Lett. 83 (2003) 4996
- [33] C.H. Cheng, H. Zhang, Y. Zhao, Y. Feng, X.F. Rui, P. Munroe, H.M. Zeng, N. Koshizuka and M. Murakami, Cond-Mat/0302202 (2003).
- [34] J. Wei, Y. Li, C. Xu, B. Wei and D. Wu, Mater. Chem. Phys. 78 (2003) 785.
- [35] W.K. Yeoh et al., submitted to Supercond. Sci. Technol.
- [36] Y. Zhao, Y. Feng, C.H. Cheng, L. Zhou, Y. Wu, T. Machi, Y. Fudamoto, N. Koshizuka and M. Murakami, Appl. Phys. Lett. 79 (2001) 1154.
- [37] J. Wang, Y. Bugoslavsky, A. Berenov, L. Cowey, A.D. Caplin, L.F. Cohen and J.L. MacManus Driscoll, Appl. Phys. Lett. 81 (2002) 2026.
- [38] C. Beneduce, H.L. Suo, P. Toulemonde, N. Musolino and R. Flükiger, Cond-mat/0203551 (2002).
- [39] V. Braccini, L.D. Cooley, S. Patnaik, D.C. Larbalestier, P. Manfrinetti, A. Palenzona and A.S. Siri, Appl. Phys. Lett. 81 (2002) 4577
- [40] D. K. Finnemore, J. E. Ostenson, S. L. Bud'ko, G. Lapertot, and P. C. Canfield, Phys. Rev. Lett. 86 (2001) 2420.
- [41] A. Serquis, L. Civale, X.Z. Liao, J.Y. Coulter, D.L. Hammon, Y.T. Zhu, D.E. Peterson, F.M. Mueller and V.F. Nesterenko, *Frontiers in Superconducting Materials - New Materials and Applications Symposium (Mater. Res. Soc. Symposium Proceedings Vol. EXS-3)*. Mater. Res. Soc., Warrendale, PA, USA (2004), pp 161.
- [42] S.Li, T. White, K. Laursen, T.T. Tan, C.Q. Sun, Z.L. Dong, Y. Li, S.H. Zhou, J. Horvat and S.X. Dou, Appl. Phys. Lett. 83 (2003) 314.
- [43] S. Soltanian, X.L. Wang, J. Horvat, M.J. Qin, H.K. Liu, P.R. Munroe and S.X. Dou, IEEE Trans. Appl. Supercond. 13 (2003) 3273.
- [44] A. Matsumoto, H. Kumakura, H. Kitaguchi and H. Hatakeyama, Supercond. Sci. Technol. 16 (2003) 926.
- [45] M. Sumption, M. Bhatia, S.X. Dou, M. Rindfliesch, M. Tomsic, L. Arda, M. Ozdemir, Y. Hascicek and E.W. Collings, Supercond. Sci. Technol. 17 (2004) 1180.
- [46] S.X. Dou, V. Braccini, S. Soltanian, R. Klie, Y. Zhu, S. Li, X.L. Wang and D. Larbalestier, Cond-mat/0308265 (2003), J. Appl Phys., in press.
- [47] Y. Ma, H. Kumakura, A. Matsumoto, H. Hatakeyama and K. Togano, Supercond. Sci. Technol. 16 (2003) 852.

- [48] M.R. Cimberle, M. Novak, P. Manfrinetti and A. Palenzona, *Supercond. Sci. Technol.* **15** (2002) 43.
- [49] X.L. Wang, S.H. Zhou, M.J. Qin, P.R. Munroe, S. Soltanian, H.K. Liu and S.X. Dou, *Physica C* **385** (2003) 461.
- [50] S. Jin, H. Mavoori, C. Bower and R.B. van Dover, *Nature* **411** (2001) 563.
- [51] S.X. Dou et al., unpublished work
- [52] T. Prozorov, R. Prozorov, A. Snezhko, K.S. Suslick, *Cond-mat/0305303* (2003).
- [53] Y. Zhao, Y. Feng, D.X. Huang, T. Machi, C.H. Cheng, K. Nakao, N. Chikumoto, Y. Fudamoto, N. Koshizuka and M. Murakami, *Physica C* **378-381** (2002) 122.
- [54] D.K. Finnemore, W.E. Straszheim, S.L. Bud'ko, P.C. Canfield, N.E. Anderson Jr. and R.J. Suplinskas, *Cond-mat/0302242* (2003).
- [55] T.A. Prikhna, W. Gawalek, Ya.M. Savchuk, et al., *Physica C* **386** (2003) 565.
- [56] A. Berenov, A. Serquis, X.Z. Liao, Y.T. Zhu, D.E. Peterson, Y. Bugoslavsky, K.A. Yates, M.G. Blamire, L.F. Cohen and J.L. MacManus-Driscoll, *Cond-mat/0405567* (2004).
- [57] S.K. Chen, B.A. Glowacki, J.L. MacManus-Driscoll, M.E. Vickers and M. Majoros, *Supercond. Sci. Technol.* **17** (2004) 243.
- [58] Soltanian et al., unpublished work
- [59] K. H. P. Kim, W. N. Kang, M.-S. Kim, C. U. Jung, H.-J. Kim, E.-M. Choi, M.-S. Park and S.-I. Lee, *cond-mat/0103176*.
- [60] Y. Yeshurun and A. P. Malozemoff, *Phys. Rev. Lett.* **60** (1988) 2202.
- [61] M. Tinkham, *Phys. Rev. Lett.* **61** (1988) 1658.
- [62] M. E. McHenry, S. Simizu, H. Lessure, M. D. Maley, Y. Coulters, I. Tanaka and H. Kojima, *Phys. Rev. B* **44** (1991) 7614.
- [63] P. J. Kung, M. P. Maley, M. E. McHenry, J. O. Wills, J. Y. Coulter, M. Murakami and S. Tanaka, *Phys. Rev. B* **46** (1992) 6427.
- [64] P. J. Kung, M. P. Maley, M. E. McHenry, J. O. Wills, J. Y. Coulter, M. Murakami and S. Tanaka, *Phys. Rev. B* **48** (1993) 13922.
- [65] D. C. Larbalestier, L. D. Cooley, M. O. Rikel, A. A. Polyanskii, J. Y. Jiang, S. Patnaik, X. Y. Cai, D. M. Feldmann, A. Gurevich, A. A. Squitieri, M. T. Naus, C. B. Eom, E. E. Hellstrom, R. J. Cava, K. A. Regan, N. Rogado, M. A. Hayward, T. He, J. S. Slusky, P. Khalifah, K. Inumaru and M. Haas, *Nature* **410** (2001) 186.
- [66] Y. Takano, H. Takeya, H. Fujii, H. Kumakura, T. Hatano, K. Togano, H. Kito and H. Ihara, *cond-mat/0102167*.
- [67] Y. Bugoslavsky, G. K. Perkins, X. Qi, L. F. Cohen and A. D. Caplin, *cond-mat/0102353*.
- [68] X. H. Chen, Y. Y. Xue, R. L. Meng and C. W. Chu, *cond-mat/0103029*.
- [69] H. H. Wen, S. L. Li, Z. W. Zhao, Y. M. Ni, Z. A. Ren, G. C. Che and Z. X. Zhao, *cond-mat/0103521*.
- [70] J. Horvat, S. Soltanian, X. L. Wang and S. X. Dou, *Appl. Phys. Lett.* **84** (2004) 3109, *cond-mat/0304004* (2003); J. Horvat, S. Soltanian, A.V. Pan and X.L. Wang, *J. Appl. Phys.* **Oct. 2004**, in press, *cond-mat/0402353*.
- [71] H. Jin, H.-H. Wen, H.-P. Yang, Z.-Y. Liu, Z.-A. Ren, and G.-C. Che, *Appl. Phys. Lett.* **83** (2003) 2626.
- [72] M. Jirsa, L. Pust, H. G. Schnack and R. Griessen, *Physica C* **207** (1993) 85.
- [73] H. G. Schnack, R. Griessen, J. G. Lensink, C. J. van der Beek and P. H. Kes, *Physica C* **197** (1992) 337.
- [74] M. J. Qin, X. L. Wang, S. Soltanian, A. H. Li, H. K. Liu and S. X. Dou, *Phys. Rev. B* **64** (2001) 060505.

- [75] Y. S. Han, M. J. Qin, J. K. F. Yau, H. K. Liu, S. X. Dou, C. M. Lee and X. Jin, *Physica C* 386 (2003) 631.
- [76] B. Seeber, *Handbook of Applied Superconductivity*, Institute of Physics Publishing, Bristol and Philadelphia (1998).
- [77] K. Inoue, N. Sakai, K. Waki and M. Murakami, *Physica C* 357-360 (2001a) 531.
- [78] K. Inoue, N. Sakai, K. Waki, and M. Murakami, *Physica C* 378-381 (2001b) 503.
- [79] H. L. Suo, P. Lezza, D. Uglietti, C. Beneduce, V. Abächerli, and R. Flükiger, *IEEE Trans. Appl. Supercond.* 13 (2002) 3265.
- [80] R. Flükiger, H. L. Suo, N. Musolino, C. Beneduce, P. Toulemonde and P. Lezza, *Physica C* 385 (2003) 286.
- [81] A. K. Pradhan, Z. X. Shi, M. Tokunaga, T. Tamogai, Y. Takano, K. Togano, H. Kito and H. Ihara, *Phys. Rev. B* 64 (2001) 212509.
- [82] L. A. Schwartzkopf, J. Jiang, X. Y. Cai, D. Apodaca and D. C. Larbalestier, *Appl. Phys. Lett.* 75 (1999) 3168.
- [83] S. Spreafico, L. Gherardi, S. Fleshler, D. Tatelbaum, J. Leone, D. Yu, G. Snitchler, L. Masure, P. Miles and D. Parker, *IEEE Trans. Appl. Supercond.* 9 (1999) 2159.
- [84] C. P. Bean and J. D. Livingston, *Phys. Rev. Lett.* 12 (1964) 14.
- [85] L. Burlachkov, V. B. Geshkenbein, A. E. Koshelev, A. I. Larkin and V. M. Vinokur, *Phys. Rev. B* 50 (1994) 16770.
- [86] A. V. Pan, S. Zhou, H. K. Liu and S. X. Dou, *Supercond. Sci. Technol.* **16** (2003) L33, also cond-mat/0205253 (2002).
- [87] A. V. Pan, S. Zhou and S. X. Dou, *Supercond. Sci. Technol.* 17 (2004) S410.
- [88] A. V. Pan and S. X. Dou, *J. Appl. Phys.* 96 (2004) 1146.
- [89] Yu. A. Genenko, A. Usoskin and H. C. Freyhardt, *Phys. Rev. Lett.* 83 (1999) 3045.
- [90] Yu. A. Genenko, A. Snezhko and H. C. Freyhardt, *Phys. Rev. B* 62 (2000) 3453.
- [91] E. H. Brandt, *Phys. Rev. B* 46 (1992) 8628.
- [92] H. Jarzina, Ch. Jooss and H. C. Freyhardt, *J. Appl. Phys.* **91** (2002) 3775.
- [93] J. D. Jackson, *Classical Electrodynamics* (John Wiley & Sons, New York, 1975).
- [94] A. V. Pan S. X. Dou, and T. H. Johansen, *NATO Science Series II: Mathematics, Physics and Chemistry*, Vol.142: *Magneto-Optical Imaging* (Ed. T.H. Johansen and D.V. Shantsev), Kluwer A. P., Dordrecht, Boston, London (2004), pp. 141.
- [95] S. V. Yampolski and Yu. A. Genenko, 'Current distributions in a magnetically shielded superconducting filament', Proc. of 6th European Conference on Applied Superconductivity (EUCAS-03), 14-18 September, 2003, Sorrento, Italy.
- [96] M.D.Sumption, E. Lee, X.L. Wang, et al., *Adv. Cryog. Eng. (Materials)* 48 (2001) 824.
- [97] Yu. A. Genenko, S. V. Yampolski and A. V. Pan, *Appl. Phys. Lett.* 84 (2004) 3921.
- [98] P. Kova , M. Ahoranta, T. Melišek, J. Lehtonen and I. Hušek, *Supercond. Sci. Technol.* 16 (2003) 793.
- [99] S. Zhou, A. V. Pan, M. Ionescu, H. Liu and S. Dou, *Supercond. Sci. Technol.* 15 (2002) 236.
- [100] M.D. Sumption, E. W. Collings, E. Lee, X.L. Wang, S. Soltanian and S.X. Dou, *Physica C* 378-381 (2002) 894.
- [101] M. Eisterer, M. Zehetmayer, S. Tönies and H.W. Weber, *Supercond. Sci. Technol.* 15 (2002) L9.
- [102] A.E. Kar'kin, V.I. Voronin, T.V. D'yachkova, N.I. Kadyrova, A.P. Tyutyunik, V.G. Zubkov, Yu. G. Zaimulin, M.V. Sadovskii and B.N. Goshchitskii, *JETP Lett.* 73 (2001) 640.

- [103] A.P. Gerashenko, K.N. Mikhalev, S.V. Verkhovskii, A.E. Karkin and B.N. Goshchitskii, *Phys. Rev. B* 65 (2002) 132506.
- [104] E. Babic, D. Miljanic, K. Zadro, I. Kusevic, Z. Marohnic, D. Drobac, X.L. Wang and S.X. Dou, *Fizika A* 10 (2001) 87.
- [105] M. Zehetmayer, M. Eisterer, H.W. Weber, J. Jun, S.M. Kazakov and J. Karpinski, *Physica C* 388-389 (2003) 159.
- [106] M. Zehetmayer, M. Eisterer, J. Jun, S.M. Kazakov, J. Karpinski, B. Birajadar, O. Eibl and H.W. Weber, *Phys. Rev. B* 69 (2004) 054510.
- [107] F. Bouquet, Y. Wang, I. Sheikin, P. Toulemonde, M. Eisterer, H.W. Weber, S. Lee, S. Tajima and A. Junod, *Physica C* 385 (2003) 192.
- [108] Y. Wang, F. Bouquet, I. Sheikin, P. Toulemonde, B. Revaz, M. Eisterer, H.W. Weber, J. Hinderer and A. Junod, *J. Phys.: Condens. Matter* 15 (2003) 883.
- [109] E. Mezzetti, D. Botta, R. Cherubini, A. Chiodoni, R. Gerbaldo, G. Ghigo, G. Giunchi, L. Gozzelino and B. Minetti, *Physica C* 372-376 (2002) 1277.
- [110] G.K. Perkins, Y. Bugoslavsky, A.D. Caplin, J. Moore, T.J. Tate, R. Gwilliam, J. Jun, S.M. Kazakov, J. Karpinski and L.F. Cohen, *cond-mat/0305255*, unpublished.
- [111] S. Okayasu, H. Ikeda and R. Yoshizaki, *Physica C* **378-381** (2002) 462.
- [112] Okayasu, M. Sasase, K. Hojou, Y. Chimi, A. Iwase, H. Ikeda, R. Yoshizaki, T. Kambara, H. Sato, Y. Hamatani and A. Maeda, *Physica C* **382** (2002) 104.
- [113] M. Eisterer, S. Tönies, H.W. Weber, R. Weinstein, R. Sawh and Y. Ren, *Physica C* 341-348 (2000) 1439.
- [114] D. Leuser and A. Dunlop, *Radiation Effects and Defects in Solids* 126 (1993) 163.
- [115] G. Szenes, *Phys. Rev. B* 51 (1995) 8026.
- [116] F. Seitz and J.F. Koehler in *Solid State Physics: Advances in Research and Applications*, vol.2 (Ed. F. Seitz and D. Turnbull), Academic, NY (1995), pp. 305.
- [117] M. Toulemonde, C. Dufour and E. Paumier, *Phys. Rev. B* 46 (1992) 14 362.
- [118] Y. Zhu, Z.X. Cai, R.C. Budhani, M. Suenaga and D.O. Welch, *Phys. Rev. B* 48 (1993) 6436.
- [119] J. Provost, Ch. Simon, M. Hervieu, D. Groult, V. Hardy, F. Studer and M. Toulemonde, *Mater. Res. Soc. Bulletin* 20 (1995) 22.
- [120] D. Kanjilal, *Current Science* 80 (2001) 1560 and references therein.
- [121] H. Narayan, S.B. Samanta, A. Gupta, A.V. Narlikar, R. Kishore, K.N. Sood, D. Kanjilal, T. Muranaka and J. Akimitsu, *Physica C* 377 (2002) 1.
- [122] R.J. Olsson, W.-K. Kwok, G. Karapetrov, M. Iavarone, H. Claus, C. Peterson and G.W. Crabtree, *cond-mat/0201022*, unpublished.
- [123] N. Chikumoto, A. Yamamoto, M. Konczykowski and M. Murakami, *Physica C* 378-381 (2002) 466.
- [124] N. Chikumoto, A. Yamamoto, M. Konczykowski and M. Murakami, *Physica C* 388-389 (2003) 167.
- [125] G. Ghigo, D. Andreone, D. Botta, A. Chiodoni, R. Gerbaldo, L. Gozzelino, F. Laviano, M. Negro, E. Mezzetti and B. Minetti, *IEEE Trans. Appl. Supercond.* 13 (2003) 3518.
- [126] Gupta, H. Narayan, D. Astill, D. Kanjilal, C. Ferdeghini, M. Paranthamam and A.V. Narlikar, *Supercond. Sci. Technol.* 16 (2003) 951.
- [127] R. Weinstein, Y. Ren, J. Liu, I. Chen, R. Sawh, C. Foster and C. Obot, *Proc. Int. Symp. Superconductivity, Hiroshima, 1993*. Springer Verlag, Berlin (1993), pp. 285.
- [128] G.W. Schulz, C. Klein, H.W. Weber, S. Moss, R. Zeng, S.X. Dou, R. Sawh, Y. Ren and R. Weinstein, *Appl. Phys. Lett.* 73 (1998) 3935.
- [129] T.M. Silver, J. Horvat, M. Reinhard, P. Yao, S. Keshavarzi, P. Munroe and S.X. Dou, *IEEE Trans. Appl. Supercond.* 14 (2004) 33.

PREPARATION AND PROPERTIES OF ADVANCED MgB₂ WIRES AND TAPES

W. Goldacker and S.I. Schlachter

Forschungszentrum Karlsruhe, Institut für Technische Physik,
P.O. Box 3640, 76021 Karlsruhe, Germany

1. INTRODUCTION

The discovery of superconductivity at 39 K [1] in MgB₂, a material which is known since about 50 years, has initiated strong activities to investigate the fundamental and applied aspects of this material. The burst of activities was quite early reviewed by an article from Buzea and Yamashita [2]. Meanwhile it is well established that the physical properties of MgB₂ are more comparable with the conventional LTS superconductors than with the high temperature superconductor (HTS) systems. A quite large coherence length of >5 nm explains the weak-link free grain boundaries [3]. In self field this leads to high transport current densities of the order of $J_c > 10^6$ Acm⁻² and above in bulk material [4–6], thin films [7–9] and wires and tapes [10–19], even at temperatures raising to 20 K and above. However, the hexagonal AlB₂-type structure (space group P6/mmm) of MgB₂ is responsible to significant intrinsic anisotropic properties, similar to the HTS systems, in particular with respect to thermal expansion, compressibility [20, 21], resistivity [7], irreversibility field and upper critical field [22, 23]. This has important consequences for the application of MgB₂ in wires, tapes and films at high background fields and will presumably lead in future to the desire of textured materials to achieve the best possible superconducting transport currents.

Quite low material costs, the already achieved high current densities and the possibility of a low cost powder-in-tube (PIT) wire and tape preparation route favours the chances of MgB₂ to come into competitiveness with NbTi with the advantageous operation of a higher operation temperature around 20 K. Cryogen free cooling techniques as Gifford-McMahon

(GM) and pulse-tube coolers (PTC) made an enormous progress with respect to cooling power and reliability during the last years, last not least influenced from the progress in the HTS research. This situation gives MgB_2 good prospects for a row of applications in intermediate fields as fault current limiters (FCL), magnetic resonance imaging magnets (MRI), motors, generators and devices for space application, operated at temperatures around 20 K. The absence of granularity does not require a texture in MgB_2 for high intergranular currents. This is an important aspect for the preparation of superconducting joints and their application in persistent mode coils.

The recent progress in increasing the upper critical field in textured MgB_2 films, accompanied by a much more profound theoretical understanding of superconductivity in the two gap system MgB_2 , in particular from band structure calculations, gives profound prospects that at low temperatures (4.2 K) even high background fields above 20 Tesla could be tolerated in the most advanced samples. In films with non-magnetic C-doping $H_{c2}(0)$ values up to 49 T (perpendicular field) and 29 T (parallel field) were found [24]. These samples are close to the dirty limit for enhanced flux pinning (corresponding to high resistivity ρ) which is caused by impurity scattering on an atomic scale within the quite large coherence length of 5-10 nm. In addition microstrains in the scale of the coherence length are considered as pinning effective disturbance but are not yet confirmed. A systematic correlation between ρ , a reduction of T_c and an improvement of H_{c2} could not be established yet due to the contribution from macroscopic secondary phase or impurity inclusions to the values of ρ [24]. In MgB_2 wires and tapes transport currents are limited through the irreversibility field H^* which is actually at about 60-80% of the H_{c2} level. For MgB_2 bulk samples with SiC particles as artificial flux pinning centres, a detailed discussion about relations between T_c , ρ and H_{c2} or H^* was given in Ref. [25].

After the discovery of superconductivity in MgB_2 , first MgB_2 fibres were prepared by Canfield *et al.* via Mg vapour infiltration into the Boron layer of coated Tungsten-wires [26]. Inductively measured J_c values of 10^5 Acm^{-2} were achieved. However, nearly from the beginning round wires and flat tapes were also prepared applying the PIT technique, which is a quite simple low cost technique well known from the HTS BSCCO-conductors [10–19]. A variety of methods were applied for wire and tape fabrication as reviewed by Flükiger *et al.* [27] recently. Wires and tapes with reacted MgB_2 powder as precursor (*ex-situ* route) proved to carry already reasonable transport supercurrents after cold deformation [17, 28], although the commonly applied heat treatment at temperatures of 850-950°C, which reaches the decomposition regime of MgB_2 , was established to be favourable for an improved core density with well connected grains [15, 17, 29, 30]. The high annealing temperature, however, reduced the choice of sheath materials due to chemical reactions with the filament which have to be avoided in future multifilamentary wires with much smaller filament dimensions. The thickness of the reaction layer is typically in the range of 1-25 microns depending on the used sheath and applied heat treatment temperature. Much more flexible was the choice of unreacted Magnesium + Boron powder mixtures as precursor (*in-situ* route) with phase formation during a heat treatment of the final wire or tape [12, 15]. In this case much lower heat treatment temperatures in the range of 550-650°C are sufficient to achieve high critical current densities which extends the choice of applicable sheath materials. The main impurity in both precursor routes is oxygen forming MgO as secondary phase with a content of up to a

few percent. For the *in-situ* route also Boron rich phases are present due to not completely reacted precursor [24]. For further improvements alternative precursors were examined as $\text{MgH}_2 + \text{B}$ [31], mixtures of Mg_2Cu and B [32] or mixtures of Mg and B_6Si [33]. It was found that the particle size of the precursors plays an important role to achieve high critical currents [34], as the filament homogeneity and small MgB_2 grains are favoured. For reacted MgB_2 planetary ball milling got a crucial preparation step to crack agglomerates and the surrounding shell like MgO layers and to reduce the majority of the powder particles into the micron and submicron regime [34–36]. In Mg + B powder mixtures, extensive milling [37, 38] or use of small plasma sprayed Mg particles [39] led to an improved fine grained MgB_2 phase. For all preparation routes a MgB_2 grain size as small as possible in the submicron regime is one of the most crucial goals to enhance the flux pinning properties of the samples and the transport critical current densities in high fields.

Due to thermal instabilities, transport currents are commonly quenched far below the critical current at low fields and at low temperatures. As practised for technical LTS conductors, future technical MgB_2 conductors require a low resistive component in the sheath composite to carry the transport current in the normal state. In addition a separation of the superconductor into a multifilamentary structure has to be done to have a stable current sharing with the sheath. First investigations of mono- and multifilamentary tapes and wires with small filament size led to reduced current densities due to an irregular filament geometry (sausaging) and chemical reactions with the sheath [40, 41].

This review for MgB_2 wires and tapes is focussed on the most advanced recent results. For a broader insight in the evolution of wire and tape R&D, the reader should study the given citations or in particular review articles already published earlier [2, 27]. The authors like to distinguish explicitly between wires and tapes since the preparation techniques are significantly different. Round or nearly square wires are much more suitable and preferred for application in windings or coils. Tapes, however, have some advantages to achieve a dense MgB_2 filament, texture and a large contact surface to the sheath which is important for thermal stability as outlined below.

2 PREPARATION OF MgB_2 WIRES AND TAPES

2.1 *In-situ* phase formation

Precursors of the *in-situ* route are mainly mixtures of Mg and Boron powders with grain sizes as small as available (typically –325 mesh) with the option of additional ball milling. Alternative approaches apply MgH_2 and Boron [31] with the goal to reduce the oxygen contamination. The extraction mechanism for the hydrogen during annealing a closed long length wire is not finally clear at the moment.

Also for the *in-situ* route the main impurity is oxygen which is introduced in the conductors as oxides from both powder components. DTA traces of the MgB_2 phase formation indicate that the B_2O_3 impurities melt at 450°C and form MgO, the main secondary phase in MgB_2 powders beside not completely reacted Boron rich phases (see Figure 1).

The DTA exothermal dip minimum of the MgB_2 formation is localized at 650°C , which coincides with the melting point of Mg [42]. Melted Mg strongly promotes the kinetics of the

MgB₂ formation. Meanwhile it is a commonly accepted fact that fine powder particles are a supposition for the formation of small final MgB₂ grains. However, fine grained Mg powders require handling in noble gas atmosphere (Ar filled glove boxes). When using fine precursor particles the reduced inter diffusion lengths improves the completeness of the phase formation and the damped grain growth of MgB₂ at low temperatures favours small final MgB₂ grains. A recently published advanced preparation method took advantage of these relationships applying nano-scaled Mg powder particles made via plasma spraying into Ar atmosphere [39]. The resulting small MgB₂ grains led to significantly improved critical current densities and upper critical fields. For nano-scaled powders special care has to be spent to a contamination from surface oxygen. The formation of MgO shifts the composition of the filament due to consumption of Mg.

An alternative method to reduce the grain size of the initial powders is mechanical alloying performed by means of long term ball milling of Mg/B powder mixtures. The intensive admixture of the elements in a submicron scale reduces the phase formation temperature in *in-situ* processed tapes to values around 500°C [37, 38]. The observed broadening and reduction of T_c might be an indication of a possible contamination from the milling container and of induced strains in the powder particles.

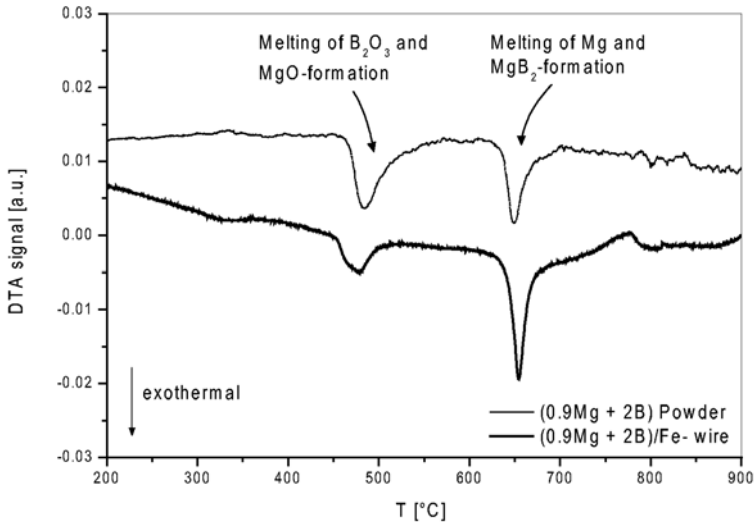


Fig. 1. DTA characterisation of a MgB₂/Fe wire and the corresponding Mg + B precursor powder mixture

A lowered phase formation temperature avoids or minimizes chemical reactions with the sheath and favours the use of high conductive sheath materials like Cu and Ni which are suitable to improve the thermal stability of the conductor. A quite low phase formation temperature of 430 - 490°C has been observed by Chen et al. [43] in high temperature resistance measurements on bulk samples when using nanometer-sized Mg powder instead of

micrometer-sized material. Taking advantage of the lower melting point of Mg_2Cu (568°C) compared to pure Mg (650°C) a reduction of the phase formation temperature in *in-situ* MgB_2 wires and tapes was achieved by replacing pure Mg with Mg_2Cu as starting material [32]. In another route Cooley *et al.* were able to produce MgB_2 at temperatures as low as 450°C applying the ternary mixture of Mg and B_6Si [33]. For identical annealing temperature and time the reactions were completed to a higher degree using the ternary system compared to the binary mixture of Mg and B, as indicated by higher diamagnetic shielding and larger X-ray diffraction peak intensities of MgB_2 in relation to those of Mg as reference. The question of the most suitable precursor for the *in-situ* route is still open.

In-situ preparation routes offer the advantage to add nano-sized particles of a secondary phase to the powder mixture which are distributed in the microstructure of MgB_2 and which primarily hinder the grain growth during MgB_2 formation. Secondary phases improving J_c of MgB_2 wires or tapes are SiC, TiB_2 , W or carbon nanotubes. Practically all substitutionally implemented additions as Li, Na, Ag, Ca, Cu, Al, Zn, Ti, Mn, Fe, Co, C occupy Boron sites (except Al) and decrease the critical temperature T_c [44, 45]. Up to now SiC is the most effective additive added with 10 mol% in form of about 10 nm small particles [46].

2.2 *Ex-situ* route (reacted MgB_2 precursors)

Commercially available reacted MgB_2 formed from the elements exhibits a broad particle range from the sub micron scale to >100 microns including agglomerates [35]. The main secondary phase is MgO with a content between 2 and 5 %. MgO can be found as cover layer on grains and agglomerates which originates from a reaction of MgB_2 with moisture of the atmosphere, forming toxic Borane gas and MgO. Planetary bowl milling of the precursors tends out to be very favourable to crush the agglomerates and reduce the mean particle size for increased transport critical current densities and upper critical fields [35]. Heavily worked or milled MgB_2 shows a strong broadening of the T_c transition due to strain effects. A heat treatment is necessary to recover the superconducting properties. MgB_2 starts to decompose above $860\text{-}870^\circ\text{C}$ and shows no defined melting temperature. For a good grain connection and strain release it is favourable to anneal the samples for a short time in the decomposition regime of $860\text{-}950^\circ\text{C}$, reforming the phase upon slow cooling. This high annealing temperature however favours chemical reactions with the sheath material.

3 SHEATH MATERIALS AND COMPOSITE STRUCTURE OF MONOFILAMENTARY CONDUCTORS

Several aspects are important for the selection of the sheath material. Most crucial is to avoid the already mentioned chemical reaction of sheath and filament. Formed reaction layers hinder the realisation of small filament diameters and an effective current sharing between filament and sheath. Depending on the precursor route, *in-situ*, *ex-situ* and mechanically alloyed *in-situ*, the choice of the sheath material meets different phase formation temperatures of about 900°C , 600°C and 500°C , respectively. Generally reduced phase formation

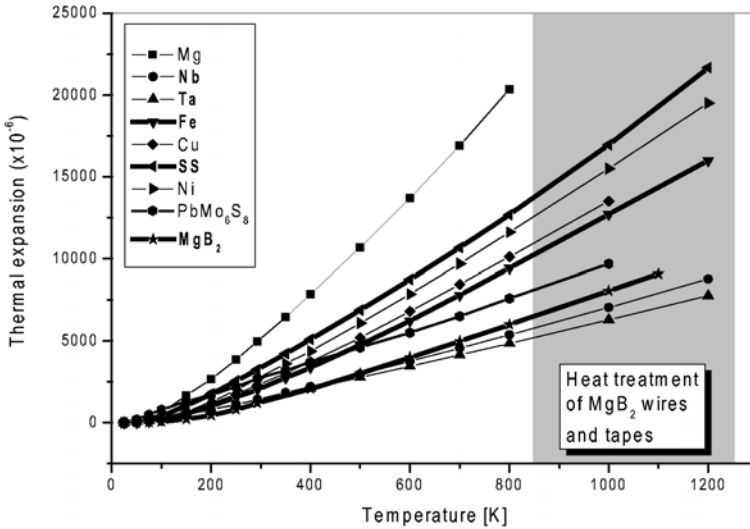


Fig. 2. Thermal expansion of MgB₂ and different sheath materials normalised to $T = 10$ K. For comparison the values for Chevrel phase PbMo₆S₈ are added. SS = stainless steel

temperatures give a chance to consider a wider selection of favourable sheath materials like Cu, Cu alloys, Ag or Ni being suited as thermal stabilisation.

An important aspect for the design of a conductor composite is the match of the thermal expansion of the conductor components, which should always give a compressive pre-stress state in the filament upon cooling from the phase formation or sinter temperature. Precompression of the filament avoids crack formation but affects the superconducting properties. In Figure 2 the thermal expansion of selected sheath materials and MgB₂ are shown [47]. The thermal expansion of MgB₂ was calculated from temperature dependent neutron diffraction data of the lattice parameters in single crystals [20]. For sheath materials with a smaller thermal expansion than MgB₂, as Nb and Ta, a composite with a steel clad is necessary for compressive pre-stress.

Sheath materials which are applied were Cu [12, 17, 48], Ni [11, 17, 34], Ag [17, 48], Fe [10, 11, 41, 46, 49–51], Cu-Ni [52] and stainless steel (SS) [31, 52, 53]. The option of a mechanically stainless steel reinforced composite sheath was realized for the materials Nb(Ta)/Cu/SS [15] and Fe/SS [41, 42, 51]. Fe was so far the most suitable one-component sheath which leads to restricted reaction layers of only 1-3 microns depending on the route (*in-situ* or *ex-situ*) and the heat treatment temperature applied [41, 54]. A disadvantage of Fe is the limited cold deformation due to strain hardening which requires for long conductor lengths intermediate annealing steps around 600°C to release work hardening strains. The intermediate heat treatment comes in conflict with the efforts to reduce the phase formation temperature well below 600°C for the *in-situ* routes. A pre-reaction of MgB₂ during deformation is the consequence. Sheath composites with 2 or 3 material compounds might be suitable to solve either the reaction problems between sheath and filament and the

requirements for thermal and mechanical stabilisation, but introduce a much more complex deformation behaviour of the composite. Additionally increased costs of the conductor fabrication result.

Round wires as well as flat tapes were under development from the beginning. Round wires are generally preferred performing layered windings of coils. Tapes offer in principle the option to achieve a texture in MgB_2 to take advantage of the anisotropy of H^* and H_{c2} .

4 THE PIT PROCESS

The first preparation step of the PIT process is powder filling into a tube (see Figure 3). This happens preferably in glove boxes under protecting gas atmosphere (Ar, N_2) to avoid ingot of oxygen and moisture. Actually no prior densification steps as CIP pressed rods are reported. Usually the powder has 50-60% density at the beginning, depending on particle shape and size. Before deformation, sheath tubes have typical diameters between 5 and 20 mm (10-15% wall thickness). The starting diameter is an important aspect for the applied deformation ratio which is in particular important for an extrapolation of the applied method to an industrial long length route. Starting at 10 mm outer diameter, Fe sheaths require an intermediate recovery annealing at about 2-3 mm diameter, whereas Ni and Cu need no intermediate heat treatment at all.

For deformation, laboratory and material specific methods are applied as wire drawing, wire swaging and groove rolling. In the tape route flat rolling starts at about 2 - 2.5 mm diameter of the round wire and is processed to a final thickness of the tape of about 0.25 - 0.35 mm thickness and a width of 2 - 5 mm. It was shown by a systematic investigation that the rolling process favours a high densification of the filament due to the short deformation zone (depending on roll diameter) and the related high deformation pressure [51]. Therefore, the grain connectivity is improved by the rolling process and also some c -axis texturing is observed with reduced tape thickness for the *ex-situ* route by mechanically oriented MgB_2 grains (although the texture degree still remains relatively low and limited to the filament surface layer) [55]. To achieve comparable densities in round wires, preferably the *in-situ* route is chosen.

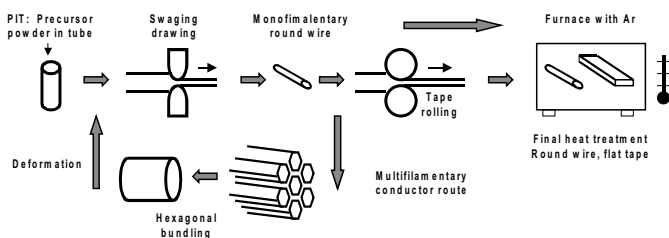


Fig. 3. Schematic sketch of the PIT wire and tape preparation mechanism

Multifilamentary wires and tapes are processed by different approaches. The conventional technical method starts with a bundle of monocoresh with hexagonal cross section inserted into a tube of sheath material (see Figure 3). The hexagonal arrangement leads to filament numbers of 7, 19, 37, 85, 126, etc. This technique requires a good compaction and contact between the components to avoid slipping and deformation failure. The alternative approach starts with a cylinder with drilled holes in the hexagonal arrangement, which need to be filled with the MgB_2 precursor [37]. For tapes rectangular bundling of monocoresh tapes can be applied with the advantage of a more regular geometry of the filaments [35, 56]. Until now conductors with up to 37 filaments have been reported.

5 ALTERNATIVE PREPARATION ROUTES

A variation of the PIT preparation route was the continuous tube forming/filling procedure (CTFF) to prepare monocoresh wires [57]. Long sheath strips, 23 mm wide and 0.2 mm thick, from Fe or Nb are formed continuously into a tube with overlapping the strip sides and in parallel filled with the MgB_2 powder or preferably with Mg/B precursor powder mixture. The closed tube (5.9 mm diameter) was introduced into another tube as Monel and deformed to a round wire. Both, binary and SiC doped conductors were fabricated with success [57].

Another technique starts with a steel clad thin Nb tube filled with a Mg rod surrounded by Boron powder [58]. After deformation and annealing the composite forms inside the Nb tube a layer from MgB_2 . Due to the shrinkage of the precursor during forming MgB_2 a hole remains inside the now "hollow wire".

6 SUPERCONDUCTING PROPERTIES OF MgB_2 WIRES AND TAPES

6.1 Strain effects on the critical temperature T_c

After deformation of *ex-situ* PIT MgB_2 wires and tapes commonly a strong broadening of the T_c transition and a decrease of the T_c onset is observed [59, 60]. The main reasons are strains and stresses induced from deformation. However, nearly full recovery can be obtained by strain release upon annealing. Investigations of pressure effects on T_c investigating MgB_2 powder samples showed irreversible degradations of T_c with a strong decrease for non-hydrostatic stress states [61, 62]. After release of the applied pressure only a partial recovery of T_c is observed [61]. Remaining lowered T_c values have to be attributed to residual strain states in the sample. Residual lattice strains of 0.2% were found from neutron diffraction experiments still after high temperature annealing [87]. Lattice strains could reach values up to 1% in deformed tapes which correlates with a decrease of T_c down to 31 K. From the fact of an anisotropic thermal expansion of the lattice axis of MgB_2 in conjunction with an anisotropic compressibility, the presence of residual strains is expected in general, but so far not investigated in detail with respect to an influence on all the superconducting properties.

6.2 Transport critical current density, irreversibility field and upper critical field

The critical current density in MgB_2 is determined by many factors, e.g. the preparation route (*in-situ* or *ex-situ*), choice of sheath material, heat treatment conditions, MgB_2 grain size and connectivity and presence of secondary phases, additions and defects.

In self field at 4.2 K, the critical current density J_c of the best undoped MgB_2 conductors exceeds values of 10^6 A/cm^2 (magnetic measurements or extrapolated transport measurements). However, with increasing magnetic fields or with increasing temperatures, J_c of undoped MgB_2 conductors decreases drastically due to poor flux pinning properties. Crushing and milling of the precursor powder [36] (*ex-situ*) or mechanical alloying of Mg and Boron [37], low annealing heat treatment temperatures [42] and use of nano-sized Mg powders [39] (*in-situ*) led to improved critical current densities at high fields due to a reduced MgB_2 grain size. Reported transport critical current densities of undoped MgB_2 wires and tapes at $T = 4.2 \text{ K}$ and $\mu_0 H = 8 \text{ T}$ were approximately $5 \cdot 10^3 \text{ Acm}^{-2}$ for undoped *ex-situ* [36] and $2.8 \cdot 10^4 \text{ Acm}^{-2}$ for undoped *in-situ* wires and tapes [39] (see Figure 4).

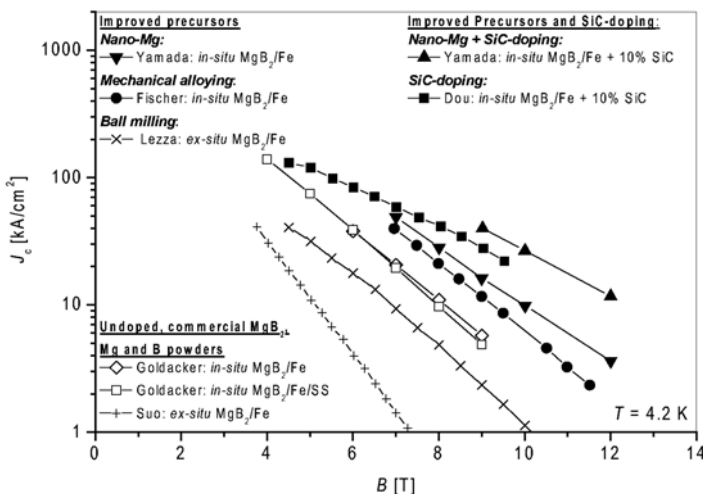


Fig. 4. $J_c(B)$ of undoped MgB_2/Fe wires and tapes made from commercial MgB_2 , Mg and Boron powders (Suo *et al.* [40], Goldacker *et al.* [42]) in comparison to $J_c(B)$ of MgB_2/Fe wires with improved precursors. The improvement of precursors and resulting increase of J_c especially in high magnetic fields was achieved by milling (Lezza *et al.* [36]), mechanical alloying (Fischer *et al.* [37]), use of Mg powder with nano grain size (Yamada *et al.* [39]), and SiC-doping (Dou *et al.* [63] and Yamada *et al.* [39]).

In undoped MgB_2 wires and tapes the main flux pinning mechanism is grain boundary or defect pinning. In addition also secondary phases and impurities like MgO work as pinning sites [64]. The increase of upper critical field and irreversibility field of MgB_2 bulk samples and wires after neutron irradiation indicate the effectiveness of defects in nano-scale dimensions [65]. Therefore, the achieved critical fields strongly depend on different

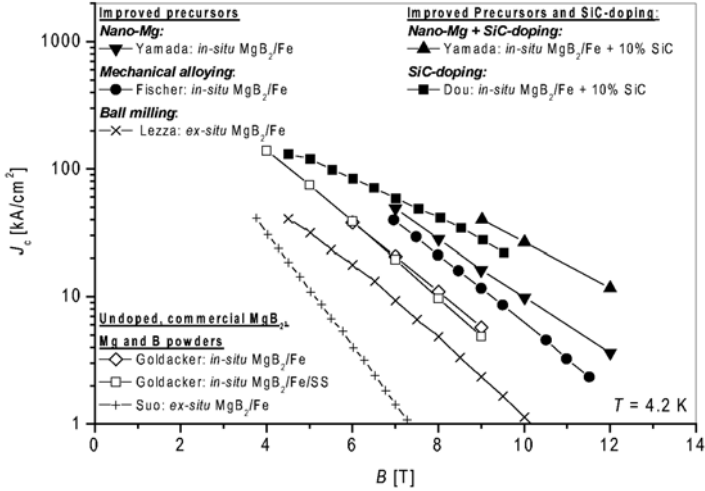


Fig. 5. Comparison of the temperature dependence of the irreversibility fields $\mu_0 H^*$ of PIT wires (Eisterer *et al.* [65], Schlachter *et al.* [66]), PIT tapes (Flückiger *et al.* [29]) and thin films (Gurevich *et al.* [24])

parameters, e.g. the preparation route (*ex-situ* or *in-situ*), the resulting microstructure of the filament including strains and the resulting grain size, homogeneity and composition of MgB₂. The irreversibility field H^* can be improved by increasing the density of pinning centers through reduction of the MgB₂ grain size, applying irradiation or doping. As shown in Figure 5 and Figure 6 in *in-situ* MgB₂/Fe wires prepared with commercial Mg and B powders and a low temperature annealing process linear extrapolated values of $H^*(0\text{ K}) = 18\text{ T}$ and $H_{c2}(0\text{ K}) = 22\text{ T}$ [42] were achieved. Neutron irradiation of such MgB₂ wires raised $H^*(0\text{ K})$ to 23 T and $H_{c2}(0\text{ K})$ to 28 T [66].

A further improvement of the critical fields was achieved applying the *in-situ* route using plasma sprayed nano-sized Mg powders and amorphous Boron powder with 1 μm particle size [39]. The reduced grain size in MgB₂ was about 0.2 μm . In order to show the high potential for usage of MgB₂ conductors in high magnetic fields in Figure 5 and Figure 6 also the critical fields of different thin films are included.

The addition of dopands to MgB₂ was found to be a very effective alternative way to insert defects and to limit the grain size. The so far optimised high critical current densities obtained for undoped *in-situ* processed MgB₂ wires and tapes give the bench mark to evaluate the effects of dopands on transport currents and critical fields. Therefore, we restrict our report on results with superior performance. A more detailed review of other doping efforts is given in Ref. [27]. The most successful addition so far was 10 at% nano-scaled SiC which improved the critical current densities in high fields significantly [46]. At 8 T about $4.1 \cdot 10^4\text{ Acm}^{-2}$ (4.2 K) were achieved which is approximately 4 times the value for *in-situ* MgB₂/Fe wires with commercial Precursor powders and optimised heat treatment [42] and 50 % higher than the value for *in-situ* MgB₂/Fe tapes with improved nano-sized precursor powders [39].

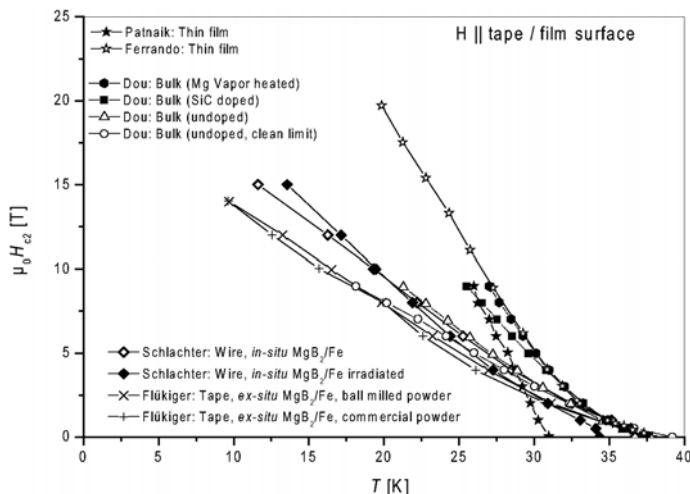


Fig. 6. Comparison of the temperature dependence of the upper critical fields $\mu_0 H_{c2}$ of PIT wires (Schlachter *et al.* [66]), PIT tapes (Flükiger *et al.* [29]), bulk samples (Dou *et al.* [25]) and thin films (Patnaik *et al.* [23] and Ferrando *et al.* [67])

Applying the SiC doped *in-situ* Mg/B precursor to the alternative CTFF preparation route, a significant further improvement of the critical current density to values slightly above 10^5 Acm^{-2} (4.2 K, 8 T) was reported [57]. Applying SiC additions increases ρ and leads to a further improvement of H^* and H_{c2} . For the CTFF method H^* of about 18 T (4.2 K) and 9 T (15 K) was analysed [57].

Values of $H^* \approx 15 \text{ T}$ (4.2 K) and 7.4 T (20 K) were found for the PIT route of SiC doped bulk samples [25]. Values for the upper critical field H_{c2} at 0 K or 4.2 K determined from the field dependency of resistive T_c transitions are less accurate due to the necessary extrapolation and the uncertainty how the critical fields scale with temperature. For the mostly progressed wires and tapes H_{c2} values around or slightly above 30 T (4.2 K) can be estimated, which is superior to technical Nb_3Sn wires (25 - 28 T at 4.2 K).

Towards self field all transport J_c values of the different wires extrapolate to a current density around $2 \cdot 10^6 \text{ Acm}^{-2}$ (4.2 K). Towards high fields the discrepancy between the transport currents of un-doped and doped conductors becomes strongly different due to the increased H^* of doped materials.

Also at higher temperatures as 20 K, the critical currents were improved significantly with doping reaching J_c values of up to 10^4 Acm^{-2} at $B = 4 \text{ T}$ and $T = 21.5 \text{ K}$ [57] as best values. The gain of increased critical fields at about 20 K however is partly compensated through a reduced critical temperature T_c . Table 1 gives a selection of the best values achieved for H_{irr} , H_{c2} and J_c .

6.3 Multifilamentary wires and tapes

Multifilamentary wires and tapes were reported for Fe and Cu and composite sheaths for both the *ex-situ* and *in-situ* route, having filament numbers up to 19 [37, 40, 56, 58, 68]. Multifilamentary wires in general carry lower critical transport currents and have reduced irreversibility fields compared to the respective monocoresh. This can be attributed to several reasons. Depending on the deformation ratio and the final conductor diameter, irregularities of the filament cross sections become effective, the so called "sausaging". A second important influence comes from the reaction layers at the filament/sheath interface which increase in relative volume for reduced filament sizes. Filament diameters of about 50-80 microns were realized. The mostly approached preparation of 19-filamentary tapes using mechanically alloyed precursors in Fe sheath could realize critical current densities even slightly above the values of the monocoresh tapes, reaching about $3 \cdot 10^4 \text{ Acm}^{-2}$ at 4.2 K in $B = 8 \text{ T}$ [37] which is a very promising result for this route.

Table 1. Superconducting properties for a selection of different MgB_2 wires and tapes made by different approaches. The critical current densities are obtained from transport measurements. Critical fields are usually determined from resistive T_c measurement in varied fields. (*) wire was irradiated with neutrons, (**) MgB_2 doped with SiC, (***) calculated from Kramer plot

| Type | Prep. route | sheath | T [K] | J_c (5 T) kAcm^{-2} | J_c (8 T) kAcm^{-2} | $\mu_0 H^*$ [T] | $\mu_0 H_{c2}$ [T] | Ref. |
|--------|----------------|----------|---------|--------------------------------|--------------------------------|-----------------|--------------------|------|
| wire | <i>In-situ</i> | Fe | 4.2 | 70 | 10 | | | [42] |
| | | | 20 | | | 7.5 | 9.5 | [42] |
| wire* | <i>In-situ</i> | Cu | 4.2 | 20 | 2.5 | 12 | | [65] |
| | | | 20 | | | 4.5 | | [65] |
| wire | <i>In-situ</i> | Steel/Nb | 4.2 | 25 | 2 | 10-12 | | [58] |
| | | | 20 | | | 6-7.5 | | [58] |
| wire** | <i>In-situ</i> | Fe | 4.2 | 300 | 200 | 18 | | [57] |
| | | | 21.5 | | | 4.5*** | | [57] |
| tape** | <i>In-situ</i> | Fe | 5 | 120 | 41 | | | [63] |
| | | | 20 | 10 | | | | [63] |
| tape | <i>In-situ</i> | Fe | 4.2 | | 280 | | | [39] |
| tape** | <i>In-situ</i> | Fe | 4.2 | | >400 | | | [39] |
| | | | 24 | | | 6.4 | 7 | [69] |
| tape | <i>In-situ</i> | Fe | | 100 | 28 | | | [37] |
| wire | <i>Ex-situ</i> | steel | 4.2 | | 3 | | | [70] |
| tape | <i>Ex-situ</i> | Fe | 4.2 | 30 | 5 | | | [77] |
| | | | 20 | 1 | | 8 | 8 | [77] |

6.4 Effect of axial strain or bending on the critical current density

For the possible application of MgB_2 conductors the mechanical performance plays an important role. Standard experiments apply axial stress to the samples and monitor strain and critical currents by means of quite different strain rig techniques. Besides a conventional linear arrangement [47], a U-shaped sample holder [72, 72], a new developed so called Pacman device [72] and a Walters spring [73] are used. Only in the linear arrangement the sample is free standing and not soldered to a support. During the experiment the pre-compression of the filament is successively compensated through the externally applied strain

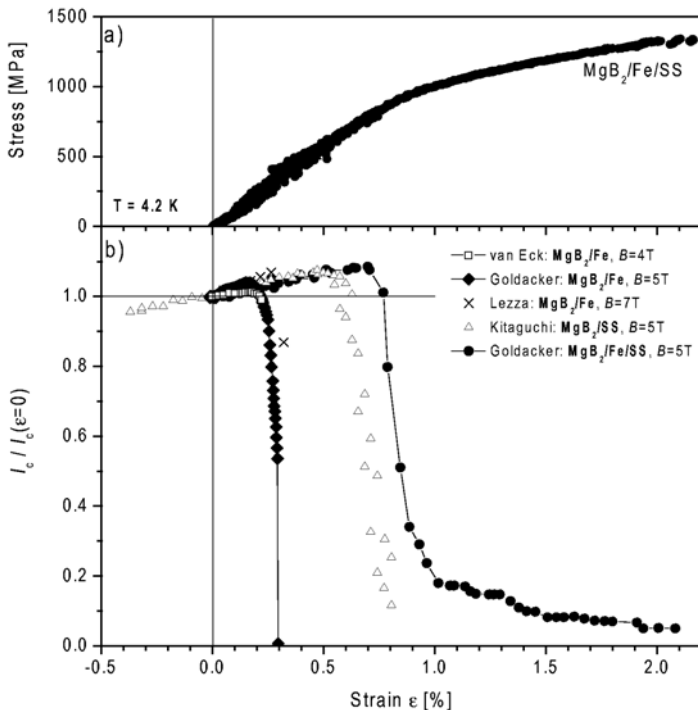


Fig. 7. a) Stress/Strain dependence for a MgB₂/Fe/SS wire [42] and **b)** normalized critical current $I_c/I_c(\epsilon=0)$ versus strain for MgB₂/Fe wires and tapes (Lezza *et al.* [36], Goldacker *et al.* [47], and van Eck *et al.* [72]), for a MgB₂/SS tape (Kitaguchi *et al.* [71]) and a MgB₂/Fe/SS wire (Goldacker *et al.* [42])

and an increase of the critical current is observed. This observation illustrates that the critical current depends on elastic lattice distortions induced by the pre-strain, quite similar as observed for technical LTS Nb₃Sn wires.

Measurements on the U-shaped sample holder allow strain application on the compressive side which confirm the current degradation with increasing pre-strain amount [71, 72]. Crossing a maximum in I_c an irreversible sample degradation occurs in the tensile regime through the formation of cracks in the brittle filament with the consequence of current degradations.

The amount of filament pre-compression and the strength of the sheath material determines the achievable tolerable stress and strain range of the sample. It was shown by systematic studies that varied steel reinforcements of the sheath are suitable to improve the filament pre-compression and lead to different tolerable strain regimes of the samples up to 0.7 % strain [47]. The best performance so far was achieved in a steel reinforced MgB₂/Fe/SS *in-situ* wire of only 310 μm diameter, developed for space application and annealed at quite low

temperature of 640°C which keeps the steel clad nearly as hard as deformed [42]. The tolerable stress and strain values were at remarkable 800 MPa and 0.8% respectively (Figure 7). The application of higher annealing temperatures of 800-950°C leads to softer sheaths and reduced mechanical performance, tolerable stress/strain ranges are limited to 0.2-0.3% strain for non reinforced Fe-clad samples [36, 47, 72]. Cold deformed ex-situ MgB₂ tapes with stainless steel sheaths withstand strains up to 0.5 – 0.6% [69, 71]. Bending strain effects were studied by means of an innovative bending strain rig operating at 4.2 K and allowing a continuous change of the bending radius [74]. For a steel reinforced MgB₂/Fe wire of 310 µm diameter, the tolerable bending radius was found to be 15 mm which is consistent with the results from the axial stress/strain experiment.

6.5 Thermal stability and *n*-factors

For high current carrying MgB₂ wires and tapes a still non sufficient thermal stabilisation leads to burn through effects for high transport currents (low background fields and low operation temperature) already below the true I_c . The characteristics of the $E(I)$ transitions of the transport critical currents is influenced by a variety of intrinsic and extrinsic factors and can give indications about the degree of thermal stabilisation of the superconductor [75]. $E(I)$ transitions are commonly described by means of a power law equation, which defines a characteristic exponent, the so called *n*-value. Reaching high *n*-values is important for technical application of superconductors, especially regarding coils operated in persistent mode with minimised long-term drift of the field. Very high *n*-values above 100 were observed for MgB₂ conductors at low fields [76–80]. Like J_{cs} , $\log(n)$ scales roughly linear with the background field at a given temperature. A double logarithmic plot of *n*-value vs. I_c show in the low current regime a linear relationship, but at high currents a deviation to higher *n*-values indicating already the contribution of thermal effects [79].

From earlier research on LTS-conductors it is well known that a variety of fundamental conductor properties as microstructure, homogeneity, filament size, geometry problems, sheath material and current sharing between filaments, have a strong influence on the stabilisation of the conductor and the characteristics of the $E(I)$ transition, in particular the occurring *n*-value [75, 81–84]. Therefore, the observed very high *n*-values in the still quite imperfect MgB₂ conductors have to be considered with care to be addressed as an intrinsic property or being more likely dominated by extrinsic parameters.

A detailed investigation of the whole $E(I)$ transition in MgB₂ conductors gave some information about the onset and contribution of thermal effects to the transition. Such effects were found at all current levels and background fields and depend strongly on the transport current density level [76]. At high transport currents, thermal effects can significantly change and increase the slope of $E(I)$, quite similar as was analysed for Nb₃Sn wires [85]. Such a contribution of successive energy dissipation to the shape of the $E(I)$ transition is very difficult to extract especially for small *E*-values. In actual MgB₂ conductors heat fluctuations are observed already at *E*-values of a few µV/cm which is close to the commonly used I_c criterion. Calculations and modelling of the stability and current sharing situation of a typical but ideal MgB₂/Fe composite filament led to expected instabilities at *E*-values above 200 µV/cm [86]. Considerations and modelling of the quench propagation in ideal filament/sheath composites confirm these results [87].

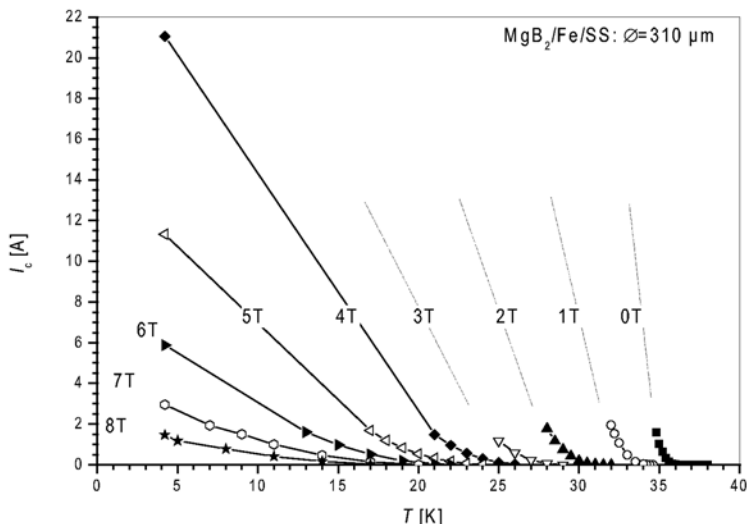


Fig 8. Transport critical currents of $\text{MgB}_2/\text{Fe}/\text{SS}$ ($\varnothing=310 \mu\text{m}$) current lead wires with field and temperatures. At $T > 4.2 \text{ K}$ the currents were measured with a Quantum Design PPMS device (I limited to $I_{\text{max}} = 2 \text{ A}$)

Imperfections of actual conductors are mainly responsible for the discrepancy of results from modelling and experimental observations. The comparison of different MgB_2 monofilamentary wires indicate that both a homogeneous microstructure and a high current carrying percolation path may have a significant influence on the intra-filamentary thermal stabilisation, the occurrence of hot spots and the dissipation of the energy approaching I_c [41]. The local distribution of the critical current density, a consequence of the inhomogeneous microstructure, obviously plays an important role for the complete quench. For the low temperature heat treatment of *in-situ* wires surprising low n -values of only 15 not depending on background field were observed in one sample batch with very high current densities [41]. The interpretation was the presence of an effective percolation path and an intra-filamentary current sharing at I_c .

For a thin $\text{MgB}_2/\text{Fe}/\text{Steel}$ wire with an only 160 micron thick filament, transport critical currents at higher temperatures and in fields were measured (Figure 8) and n -values determined from the I - V curves (Figure 9). Plotting the n -values versus transport currents indicates the presence of thermal effects through the deviation from a linear behaviour (left side of Figure 9) even for such small filament diameters. At 4.2 K and self field these wires also burn through at current levels up to 30 Amps. Similar results were obtained by Kitaguchi et al. [79]. They observed nonlinear deviations in the $\log(n)/\log(I_c)$ plot, the influence of thermal effects, at critical currents exceeding about 40-50 Amperes.

For a final statement about the true intrinsic n -values of MgB_2 filaments and for the development of a stabilised technical conductor, a multifilamentary structure with thin filaments, homogeneous microstructure, regular filament geometry and a sufficient external thermal stabilisation is absolutely necessary to eliminate the contribution of a local heat

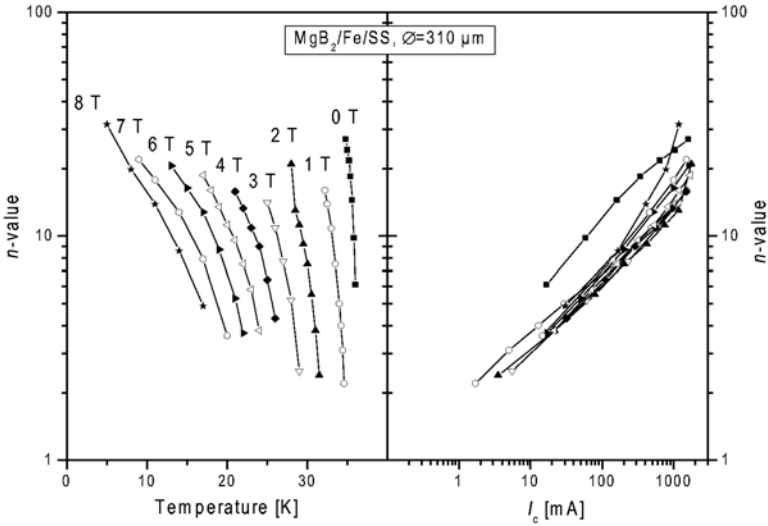


Fig. 9. n -values calculated from $E(I)$ transitions in the range $0.5\text{--}5\ \mu\text{V}/\text{cm}$ for the critical current data of Figure 8, plotted versus temperature (left side) and transport critical current (right side).

generation to the I_c transition in the filaments. For monocoil wires filament diameters of 50–160 microns and for multifilamentary wires with about 80 microns were realised. In both cases a thermal stabilisation of the critical currents in the high current regime (self field or low fields of a few Tesla at 4.2 K) was not yet achieved.

7 TECHNICAL APPLICATION OF MgB_2 CONDUCTORS

Although many problems have still to be solved after 3 ½ years of MgB_2 conductor development, first demonstrators for technical applications of MgB_2 are on the way. Small coils with magnetic fields exceeding 1 Tesla at 4.2 K and even at 25 K have been prepared by Sumption *et al.* [88] and Serquis *et al.* [89]. This demonstrates that with advanced MgB_2 conductors magnetic fields can be achieved approaching the requirements for superconducting transformers or some magnet applications such as low-field MRI.

As first real technical application thin, stainless steel reinforced monofilamentary $\text{MgB}_2/\text{Fe}/\text{SS}$ wires (Figure 10) have been developed as low thermal conduction current leads between a magnet (operation temperature 1.3 K) and the power supply ($T = 17\ \text{K}$) in an x-ray spectrometer (XRS) on the American–Japanese research satellite ASTRO-E2 [42]. An excellent mechanical performance of the wires was proven measuring I_c as a function of applied tensile strain. Tolerable strains of 0.8% without current degradation, corresponding to stresses of about 800 MPa provided a mechanical strength of the wires to withstand the vibrations during the launch of the satellite being scheduled for February 2005. Despite of the small filament diameter (160 μm) that makes the filament susceptible to inhomogeneities and

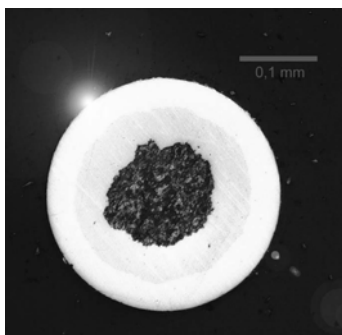


Fig. 10. Optical micrograph of a $\text{MgB}_2/\text{Fe}/\text{SS}$ current lead wire cross section.

reaction layers between filament and sheath, the thin wires showed the same critical current densities as comparable MgB_2/Fe wires with much bigger filament diameter.

8 CONCLUSIONS

During the short time of three and a half year after discovery of superconductivity in MgB_2 a remarkable and for a new superconductor uniquely rapid R&D progress towards technical conductors took place. At 4.2 K the critical current densities of MgB_2 tapes reached a performance which is already competitive with NbTi. With the achieved knowledge about the flux pinning mechanism and applying improved suitable and sophisticated preparation techniques, as artificial pinning centres, the irreversibility fields and the upper critical fields of wires and tapes were improved to values much higher compared to NbTi and a further improvement is expected. This opens the chance for future applications at elevated operation temperatures around 20 K and the use of cryogen free cryocoolers in future devices made from MgB_2 conductors. At 4.2 K MgB_2 conductors reached upper critical fields around 30 T which is superior to technical Nb_3Sn wires. The corresponding irreversibility fields close to 20 T indicate the potential of the further possible improvement of the MgB_2 conductor performance and the small chance to come possibly into competition with Nb_3Sn conductors at 4.2 K.

Despite this very optimistic prospects, actually a lot of unsolved problems remain and are under investigation. Multifilamentary wires and tapes with a high number of thin filaments in combination with a thermal stabilizing low resistive sheath are actually not achieved. Presently all high current carrying conductors overheat below the critical current at low fields or self field at 4.2 K. The PIT wire and tape preparation technique is well known to have limitations in reaching a perfect geometric conductor structure with very thin filaments of a few microns. Consequently very high demands are addressed to the precursor quality with respect to particle size spectrum and purity including the additions. Intensive research from powder developers and suppliers is asked to achieve the required progress. The design of the conductor composite and the choice of the sheath materials has to meet several important technical conductor specifications which actually cannot be fulfilled from one single sheath

material. Composite sheaths are required. Last but not least sufficient mechanical stability is necessary to withstand handling actions during coil winding, thermal stresses and Lorentz forces in magnetic fields.

The anisotropy of superconductivity in MgB_2 offers the option to further increase the transport currents in textured MgB_2 . This is already seen for very high transport currents in c -axis textured thin films and their weaker field dependence [90]. In PIT conductors texturing was only observed occasionally at the surface layer of filaments and was so far not realised as volume effect. Future very thin filaments may give a chance for a texture in the major volume fraction

Towards an industrial fabrication all efforts in conductor development need to be applicable for high deformation ratios and industrial techniques to reach conductor lengths of several km. Economic conductor routes are required to achieve an economic competition with commercial NbTi wires, taking into account reduced cooling costs from the expected higher operation temperature around 20 K. For an application of MgB_2 conductors realistic prospects for an operation temperature of 20-25 K and fields up to 5 T are already given. Application prospects focus mainly on magnetic resonance imaging (MRI) magnets with fields of 2-5 T, fault current limiters (FCL) in form of coils and windings for transformers, motors and generators. For space application, MgB_2 is of extraordinary interest as a quite light material which meets easy cooling conditions in space for application at 20-25 K.

ACKNOWLEDGEMENT

We dedicate this article to our colleague Silke Zimmer who passed away in April 2004 after fighting against a serious illness. Silke Zimmer supported our efforts in conductor development by performing numerous tests and measurements in our cryogenic laboratory. We owe her a great debt of gratitude and keep her in memory as a hard-working, accurate and nice colleague.

REFERENCES

- [1] J. Nagamatsu, N. Nakagawa, T. Muranka, Y. Zenitani, J. Akimitsu, *Nature* 410 (2001)
- [2] C. Buzea, T. Yamashita, *Supercond. Sci. Technol.* 14 (2001) R115
- [3] D.C. Larbalestier, L.D. Cooley, M.O. Rikel, A.A. Polyanskii, J. Jiang, S. Patnaik, X.Y. Cai, D.M. Feldmann, A. Gurevich, A.A. Squitieri, M.T. Naus, C.B. Eom, E.E. Hellstrom, R.J. Cava, K.A. Regan, N. Rogado, M.A. Hayward, T. He, J.S. Slusky, P. Khalifah, K. Inumaru, M. Haas; *Nature* 410 (2001) 186.
- [4] M. Kambara, N.H. Babu, E.S. Sadki, J.R. Cooper, H. Minami, D.A. Cardwell, A.M. Campbell, I.H. Inoue; *Supercond. Sci. Technol.* 14 (2001) L5.
- [5] Y. Takano, H. Takeya, H. Fujii, H. Kumakura, T. Hatano, K. Togano; *Appl. Phys. Lett.* 78 (2001) 2914.
- [6] M. Dhallé, P. Toulemonde, C. Beneduce, N. Musolino, M. Decroux, R. Flükiger, *Physica C* 363 (2001) 155
- [7] C.B. Eom, M.K. Lee, J.H. Choi, L. Belenky, X. Song, L.D. Cooley, M.T. Naus, S. Patnaik, J. Jiang, M. Rikel, A. Polyanskii, A. Gurevich, X.Y. Cai, S.D. Bu, S.E. Babcock, E.E. Hellstrom, D.C. Labalestier, N. Rogado, K.A. Regan, M.A. Hayward, T. He, J.S. Slusky, K. Inumaru, M.K. Haas, R.J. Cava, *Nature* 411 (2001) 558.
- [8] M. Paranthaman, C. Cantoni, H.Y. Zhai, H.M. Christen, T. Aytug, S. Sathyamurthy, E.D. Specht, J.R. Thompson, D.H. Lowndes, H.R. Kerchner, D.K. Christen, *Appl. Phys. Lett.* 78 (2001) 3669.
- [9] W.N. Kang, E.-M. Choi, H.-J. Kim, H.-J. Kim, S.-I. Lee; *Physica C* 385 (2003) 24.
- [10] H.L. Suo, C. Beneduce, M. Dhallé, N. Musolino, X.D. Su, R. Flükiger; *Advances in Cryogenic Engineering*, vol. 48B (2002) 872;
- [11] H.L. Suo, C. Beneduce, M. Dhallé, N. Musolino, J. Genoud, and R. Flükiger; *Applied Physics Letters* 79 (2001) 3116
- [12] B. A. Glowacki, M. Majoros, M. Vickers, J. E. Evetts, Y. Shi and I McDougall; *Supercond. Sci. Technol.* 14 (2001) 193.
- [13] S. Jin, H. Mavoori, C. Bower, R.B. van Dover; *Nature* 411 (2001) 563.
- [14] S. Soltanian, X.L. Wang, I. Kusevic, E. Babic, A.H. Li, H.K. Liu, E.W. Collings, S.X. Dou; *Physica C* 361 (2001) 84.
- [15] W. Goldacker, S. I. Schlachter, S. Zimmer and H. Reiner; *Supercond. Sci. Technol.* 14 (2001) 787.
- [16] A.K. Pradhan, Y. Feng, Y. Zhao, N. Koshizuka; *Appl. Phys. Lett.* 79 (2001) 1649.
- [17] G. Grasso A. Malagoli, C. Ferdeghini, S. Roncallo, V. Braccini, A.S. Siri, M.R. Cimberle; *Appl. Phys. Lett.* 79 (2001) 230.
- [18] H. Kumakura, A. Matsumoto, H. Fujii, K. Togano, *Appl. Phys. Lett.* 79 (2001) 2435.
- [19] K.J. Song, N.J. Lee, H.M. Jang, H.S. Ha, D.W. Ha, S.S. Oh, M.H. Sohn, Y.K. Kwon, K.S. Ryu, cond-mat/0106124.
- [20] J. D. Jorgensen, D. G. Hinks, and S. Short; *Physical Review B* 63, 224522.
- [21] J.S. Schilling, J.D. Jorgensen, D.D. Hinks, S. Deemyad, J. Hamlin, C.W. Looney and T. Tomita, "Studies of High Temperature Superconductors" 38, ed. by A. Narlikar (Nova Science Publishers, N.Y. 2001)

- [22] C. Ferdeghini, V. Ferrando, G. Grassano, W. Ramandan, E. Bellingeri, V. Braccini, D. Marré, P. Manfrinetti, A. Palenzona, F. Borgatti, R. Felici, T.-L. Lee, *Supercond. Sci. Technol.* 14 (2001) 952.
- [23] S. Patnaik, L.D. Cooley, A. Gurevich, A.A. Polyanskii, J. Jiang, X.Y. Cai, A.A. Squitieri, M.T. Naus, M.K. Lee, J.H. Choi, L. Belenky, S.D. Bu, J. Letteri, X. Song, D.G. Schlom, S.E. Babcock, C.B. Eom, E.E. Hellstrom, D.C. Larbalestrier, *Supercond. Sci. Technol.* 14 (2001) 315.
- [24] A. Gurevich, S. Patnaik, V. Braccini, K.H. Kim, C. Mielke, X. Song, L.D. Cooley, S.D. Bu, D.M. Kim, J.H. Choi, L.J. Belenky, J. Giencke, M.K. Lee, W. Tian, X.Q. Pan, A. Siri, E.E. Hellstrom, C.B. Eom, D.C. Larbalestrier *Supercond. Sci. Technol.* 17 (2004) p.278
- [25] S.X. Dou, V. Braccini, S. Soltanian, P. Klie, Y. Zhu, S. Li, X.L. Wang, D. Larbalestrier, *Cond-mat/0308265*
- [26] P.C. Canfield, D.K. Finnemore, S.L. Bud'ko, J.E. Ostenson, G. Lapertot, C.E. Cunningham, and C. Petrovic; *Phys. Rev. Lett.* 86 (2001) 2423.
- [27] R. Fluekiger, H.L. Suo, N. Musolino, C. Beneduce, P. Toulemonde, P. Lezza; *Physica C* 385 (2003) 286-305
- [28] G. Grasso, A. Malagoli, D. Marré, E. Bellingeri, V. Braccini, S. Roncallo, N. Scati, S. Siri, *Physica C* 378–381 (2002) 899.
- [29] R. Flükiger, P. Lezza, C. Beneduce, N. Musolino, H.L. Suo; *Supercond. Sci. Technol.* 16 (2003) 264
- [30] X.L. Wang, S. Soltanian, J. Horvat, M.J. Qin, H.K. Liu, S.X. Dou, *Physica C* 361 (2001) 149.
- [31] A. Matsumoto, H. Kumakura, H. Kitaguchi and H. Hatakeyama; *Supercond. Sci. Technol.* 16 (2003) 926.
- [32] A. Kikuchi, Y. Yoshida, Y. Iijima, N. Banno, T. Takeuchi, K. Inoue; *Supercond. Sci. Technol.* 17 (2004) 781.
- [33] L.D. Cooley, K. Kang, R.F. Klie, Q. Li, A.M. Moodenbaugh, R.L. Sabatini; *Supercond. Sci. Technol.* 17 (2004) 942
- [34] H. L. Suo, C. Beneduce, X. D. Su and R. Flükiger; *Supercond. Sci. Technol.* 15 (2002) 1058.
- [35] H. L. Suo, P. Lezza, D. Uglietti, C. Beneduce, V. Abächerli, and R. Flükiger; *IEEE Transactions on Applied Supercond.* 13, (2003) 3265.
- [36] P. Lezza, V. Abächerli, N. Clayton, C. Senatore, D. Uglietti, H.L. Suo, R. Flükiger; *Physica C* 401 (2004) 305.
- [37] C. Fischer, W. Häßler, C. Rodig, O. Perner, G. Behr, M. Schubert, K. Nenkov, J. Eckert, B. Holzapfel, L. Schultz; *Physica C* 406 (2004) 121.
- [38] W. Häßler, C. Rodig, C. Fischer, B. Holzapfel, O. Perner, J. Eckert, K. Nenkov and G. Fuchs; *Supercond. Sci. Technol.* 16 (2003) 281.
- [39] H. Yamada, M. Hirakawa, H. Kumakura, A. Matsumoto, and H. Kitaguchi; *Appl. Phys. Lett.* 84 (2004) 1728.
- [40] H. L. Suo, C. Beneduce, M. Dhallé, P. Toulemonde, and R. Flükiger ; *IEEE Transactions On Applied Supercond.* 12 (2002) 1079.

- [41] W. Goldacker, S. I. Schlachter, B. Obst, B. Liu, J. Reiner and S. Zimmer; *Supercond. Sci. Technol.* 17 (2004) 363.
- [42] W. Goldacker, S. I. Schlachter, B. Obst and M. Eisterer; *Supercond. Sci. Technol.* 17 (2004) 490.
- [43] C. Chen, Z.-j. Zhou, X.-G. Li, J. Xua, Y.-h. Wang, Z.-X. Gao, Q.-r. Feng; *Solid State Communications* 131 (2004) 275.
- [44] P. Toulemonde, N. Musolino, R. Flükiger; *Supercond. Sci. Technol.* 16 (2003) 231.
- [45] J.S. Slusky, N. Rogado, K.A. Regan, M.A. Hayward, P. Khallfah, T. He, K. Inumaru, S.M. Loureiro, M.K. Haas, H.W. Zandbergen, R.J. Cava; *Nature* 410 (2001) 343.
- [46] S.X. Dou, J. Horvat, S. Soltanian, X.L. Wang, M.J. Qin, S.H. Zhou, H.K. Liu, P.G. Munroe, *IEEE Trans. Appl. Superc.* Vol.13, 2 (2003) p.3199
- [47] W. Goldacker, S.I. Schlachter, H. Reiner, S. Zimmer, B. Obst, H. Kiesel, A. Nyilas, "Studies of High Temperature Superconductors" Vol.44, (2003) 169 ed. by A.Narlikar (Nova Science Publishers, N.Y. 2003).
- [48] B.A. Glowacki, M. Majoros, M.E. Vickers, B. Zeimetz; *Physica C* 372-376 (2002) 1254.
- [49] P. Ková , I. Hušek, W. Pachla, T. Melišek, R. Diduszko, K. Fröhlich, A. Morawski, A. Presz, D. Machajdik; *Supercond. Sci. Technol.* 15 (2002) 1127.
- [50] W. Goldacker and S.I. Schlachter; *Physica C* 378–381 (2002) 889.
- [51] R. Nast, S.I. Schlachter, S. Zimmer, H. Reiner, W. Goldacker; *Physica C* 372–376 (2002) 1241.
- [52] H. Kumakura, A. Matsumoto, H. Fujii, H. Kitaguchi, K. Togano, *Physica C* 182 (2002) 93.
- [53] A. Serquis, L. Civale, D.L. Hammon, J.Y. Coulter, X.Z. Liao, Y.T. Zhu, D.E. Peterson, F.M. Mueller, *Appl. Phys. Lett.* 82 (2003) 1754.
- [54] P. Ková , I. Hušek, Ch. Grovenor and Ch. Salter; *Supercond. Sci. Technol.* 16 (2003) 292.
- [55] V. Beilin, E. Dul'kin, E. Yashchin, E. Galstyan, Y. Lapides, M. Tsindlekht, I. Felner, M. Roth; *Physica C* 405 (2004) 70.
- [56] P.Kovac, I.Husek, T.Melisek, *Physica C* 401 (2004) 282.
- [57] M.D. Sumption, M. Bathia, S.X. Dou, M. Rindfliesch, M. Tomsic, L. Arda, M. Ozdemir, Y. Hascicek, E.W. Collings, *Supercond. Sci. Technol.* 17 (2004) 1180.
- [58] G. Giunchi, S. Ceresara, G. Ripamonti, A Di Zenobio, S. Rossi, S. Chiarelli, M. Spadoni, R. Wesche, P.L. Bruzzone; *Supercond. Sci. Technol.* 16 (2003) 285.
- [59] H.L. Suo, C. Beneduce, M. Dhallé, N. Musolino, X.D. Su, R. Flükiger; *Advances in Cryogenic Engineering* 48B (2002) 872.
- [60] S.I. Schlachter, W. Goldacker, J. Reiner, S. Zimmer, B. Liu, and B. Obst; *IEEE Transactions of Applied Superconductivity* 13 (2003) 3203.
- [61] S.I. Schlachter, W.H. Fietz, K. Grube, W. Goldacker; *Advances in Cryogenic Engineering* 48B (2002) 809.
- [62] S. Deemyad, T. Tomita, J.J. Hamlin, B.R. Beckett, J.S. Schilling, D.G. Hinks, J.D. Jorgensen, S. Lee, S. Tajima; *Physica C* 385 (2003) 105.

- [63] S. X. Dou, S. Soltanian, J. Horvat, X. L. Wang, S. H. Zhou, M. Ionescu, H. K. Liu, P. Munroe, M. Tomsic; *Applied Physics Letters* 81 (2002) 3419
- [64] P. Kovac, I. Husek, T. Melisek, J.C. Grivel, W. Pachla, V. Strbik, R. Diduszko, J. Horneyer, N.H. Andersen; *Supercond.Sci.Technol.* 17 (2004) L41.
- [65] M. Eisterer, B.A. Glowacki, H.W. Weber, L.R. Greenwood, M. Majoros, *Supercond. Sci. Technol.* 15 (2002) 1088.
- [66] S.I. Schlachter, W. Goldacker, M. Eisterer, H.W. Weber; to be published.
- [67] V. Ferrando, C. Tarantini, E. Bellingeri, P. Manfrinetti, I. Pallecchi, D. Marré, O. Plantevin, M. Putti, R. Felici and C. Ferdeghini, *cond-mat/0406539*
- [68] G. Grasso, WAMS "workshop on Accelerator Magnet Superconductors" 22.-24.3.2004 Archamps - France, to be published in *Proceedings*
<http://amt.web.cern.ch/amt/activities/workshops/WAMS2004>
- [69] H. Kitaguchi, A. Matsumoto, H. Hatakeyama and H. Kumakura; *Supercond. Sci. Technol.* 17 (2004) S486.
- [70] A. Serquis, L. Civale, D.L. Hammon, X.Z. Liao, J.Y. Coulter, Y.T. Zhu, M. Jaime, D.E. Peterson, and F. M. Mueller, V. F. Nesterenko, Y. Gu; *Appl. Phys. Lett.* 82 (2003) 2847.
- [71] H. Kitaguchi, H. Kumakura, K. Togano; *Physica C* 363 (2001) 198.
- [72] H.J.N. van Eck, D.C. van der Laan, M. Dhalle, B. tenHaken and H.H.J. tenKate., *Supercond. Sci. Technol.* 16, 9 (2003) 1026.
- [73] D. Uglietti, B. Seeber, V. Abächerli, A. Pollini, D. Eckert, R. Flükiger., *Supercond. Sci. Technol.* 16, (2003) 1000.
- [74] W. Goldacker, S.I. Schlachter, R. Nast, H. Reiner, S. Zimmer, H. Kiesel, A. Nyilas *Advances in Cryogenic Engineering* 48 (2002) 469.
- [75] W. H. Warnes, L.D. Cooley, D.C. Larbalestier, *Adv. Cryog. Eng. Mater.* 34 (1988) 1009.
- [76] W. Goldacker, S.I. Schlachter, B. Liu, B. Obst, E. Klimenko, *Physica C* 401 (2004) 80.
- [77] P. Lezza, V. Abächerli, N. Clayton, C. Senatore, D. Uglietti, H.L. Suo, R. Flükiger, *Physica C* 401 (2004) 305.
- [78] P. Kovac, I. Husek, T. Melisek, *Physica C* 401 (2004) 282.
- [79] H. Kitaguchi, A. Matsumoto, H. Hatakeyama, H. Kumakura; *Physica C* 401 (2004) 346.
- [80] G. Giunchi, S. Raineri, R. Wesche, P. L. Bruzzone; *Physica C* 401 (2004) 310.
- [81] W. H. Warnes, D. C. Larbalestier, *Cryogenics* 26 (12) (1986) 643.
- [82] W. H. Warnes, *J. Appl. Phys.* 63 (5) (1988) 1651.
- [83] D. P. Hampshire, H.Jones ; *Cryogenics* 27 (1987) 608.
- [84] J. Ekin, *Cryogenics* 27 (1987) 603
- [85] R. Kimmich, F. Hornung, A. Rimikis, T. Schneider, P. Lee; *IEEE Trans. Appl. Superc.* 11 (1) (2001) 3675.
- [86] M. Majores, A.M. Campbell, B.A. Glowacki, R.I. Tomov; *Physica C* 401 (2004) 140
- [87] H. vanWeeren, N. van den Eijnden, J.J.Rabbers, Y.Ilyin, M.Dhalle, A.den Ouden, to be published in *Supercond Sci. Technol.*

- [88] M.D. Sumption, M. Tomsic, M. Bhatia, Y. Hascieck, S.X. Dou, E. W. Collings; Presented at the ICMC Topical Conference Feb. 10-13 2004, Wollongong, Australia
- [89] A. Serquis, L. Civale, J. Y. Coulter, D. L. Hammon, X. Z. Liao, Y. T. Zhu, D. E. Peterson, F.M. Mueller, V. F. Nesterenko, S. S. Indrakanti; *Supercond. Sci. Technol.* 17 (2004) L35.
- [90] K. Komori, K. Kawagishi, Y. Takano, S. Arisawa, H. Kumakura, M. Fukutomi, K. Togano, *Appl. Phys. Lett.* 81 (2002) 1047.
- [91] E. Belingeri, M. Modia, V. Braccini, A.S. Siri, G. Graso, *Supercond.Sci.Technol.* 16 (2003) p.276

MgB₂ THIN FILM

X.X. Xi

Department of Physics, Department of Materials Science and Engineering, and
Materials Research Institute, The Pennsylvania State University, University Park,
Pennsylvania 168 02, USA xxx4@psu.edu

1 INTRODUCTION

Magnesium diboride, MgB₂, which was discovered to be a superconductor with a transition temperature T_c of 39 K in 2001 [1], shows a unique property of being a clear example of a “two gap” superconductor [2, 3, 4]. There are two qualitatively different Fermi surfaces in MgB₂ giving rise to the σ band and π band, and their different pairing strengths with the B-B stretch modes of E_{2g} symmetry result in two different energy gaps [5, 6]. MgB₂ also has great potentials in high magnetic-field [7] as well as Josephson junction and integrated circuit applications [8]. In particular, high critical current density J_c near the depairing limit has been observed in MgB₂ [9], and unlike high temperature superconductors grain boundaries in MgB₂ do not behave like weak links [7]. Although clean MgB₂ shows low upper critical field H_{c2} [10], in high resistivity MgB₂ films H_{c2} is substantially higher [11]. Like the conventional superconductor Nb, MgB₂ is a phonon-mediated superconductor [12] with a relatively long coherence length [13], making the prospect of fabricating reproducible uniform MgB₂ Josephson junctions much brighter than for high temperature superconductors. The possibility of 2-K operation and potentially higher speeds than Nb-based integrated circuits make MgB₂ digital circuits very attractive.

Superconducting integrated circuits require multilayers of superconducting, insulating and resistive films. Therefore, a thin film technology, preferably an *in situ* process, in which multilayers of MgB₂ and other materials are formed directly on the substrate, needs

to be developed. For basic studies of normal-state and superconducting properties of MgB_2 , high-quality single-crystalline thin films are also very desirable, in particular when large-size, high quality MgB_2 single crystals are difficult to produce [14, 15]. Thin films with controlled degrees of interband and intraband scattering will facilitate research in the unique properties of MgB_2 due to its two-gap nature. Even for high-field applications, research in thin films is important as it can shed lights on the mechanisms of enhancing H_{c2} and J_c , and thin film techniques can be used to make coated-conductor tapes.

Nearly four years after the discovery of superconductivity in MgB_2 , great progress has been made in the area of MgB_2 thin films. Several deposition techniques have been successfully developed to grow MgB_2 thin films with good superconducting properties. In the process, a series of major difficulties were recognized and overcome, which include the volatility of Mg and phase stability of MgB_2 [16, 17], the low sticking coefficients of Mg at elevated temperatures [18], and the reactivity of Mg with oxygen [19, 20]. This article will give an up-to-date summary of how these challenges have been met by different deposition techniques, and discuss the results on clean and dirty MgB_2 films and on MgB_2 thin-film devices.

2 DIFFICULTIES IN DEPOSITING MgB_2 FILM

2.1 REQUIREMENT OF HIGH Mg VAPOR PRESSURE

The biggest challenge to the deposition of MgB_2 is the volatility of Mg. For materials containing a volatile constituent, such as GaAs in which As is volatile [21], and $\text{YBa}_2\text{Cu}_3\text{O}_{7-x}$ in which O is volatile [22], thermodynamics is often very helpful in identifying the phase stability conditions that are suitable for film growth. A thermodynamic analysis by Liu *et al.* [16, 17] has provided critical insights into the issue. In Fig. 1 (left), the pressure-temperature phase diagram for $x_{\text{Mg}}/x_{\text{B}} \geq 1 : 2$ is shown. In the practice of MgB_2 film deposition, the formation of the MgB_2 phase should take place within the window marked by “Gas + MgB_2 ” where the thermodynamically-stable phases are MgB_2 and gas phases. Note that the Mg pressures for this growth window are very high. For example, at 75 °C a Mg pressure greater than 44 mTorr is necessary to keep the MgB_2 phase thermodynamically stable. This is very high for most vacuum deposition techniques.

Fan *et al.* has shown that a significant kinetic barrier to the thermal decomposition of MgB_2 exists [18, 23]. In other words, MgB_2 does not decompose as easily as predicted by the thermodynamics. However, the mass spectrometry-Knudsen effusion experiment seems to support the thermodynamic predictions [24]. Practically, the existence of a kinetic barrier is very important: as long as the MgB_2 phase is formed in the films, they can be subject to heating during the subsequent device processing without degrading as easily as predicted by the thermodynamic calculations.

The volatility of Mg also brings a benefit for the *in situ* MgB_2 film deposition: the automatic composition control that accompanies the adsorption-controlled growth of films containing volatile species. The pressure-composition phase diagram at 85 °C is also shown in Fig. 1 (right) and the growth window is marked by “Gas + MgB_2 ”. Again, the Mg partial pressure has to be high (above 34 mTorr) to keep MgB_2 thermodynamically

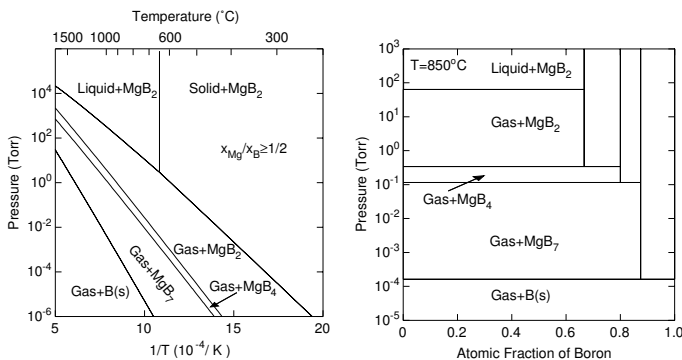


Fig. 1. Phase diagrams for the Mg-B system. Left: The pressure-temperature phase diagram for the Mg:B atomic ratio $x_{Mg}/x_B \geq 1/2$. The region of “Gas + MgB₂” represent the growth window for MgB₂ films. Right: The pressure-composition phase diagram of the Mg-B system at 85 °C. (From Ref. [16]).

stable. In terms of the Mg:B ratio, however, as long as it is above the stoichiometric 1:2 any amount of extra Mg above the stoichiometry will be in the gas phase and be evacuated and the desired MgB₂ phase will result. This is why the pressure-temperature phase diagram is identical for all $x_{Mg}/x_B \geq 1 : 2$.

2.2 LOW TICKING COEFFICIENT OF Mg

Another issue in the deposition of MgB₂ films is the low sticking coefficient of Mg at elevated temperatures. Kim *et al.* showed that the sticking coefficient of Mg onto the substrate and onto the deposited B film drops to near zero above 25 °C, whereas that of B does not change [18]. Similar results have been shown by Ueda and Naito [25, 26] in MgB₂ films prepared by molecular beam epitaxy. As a consequence, at preferred temperatures for *in situ* epitaxial growth of MgB₂ there is only a small probability that Mg sticks to the substrate and reacts with B to form MgB₂. The remedy for this problem is to provide an abundance of Mg supply during the deposition, by an extremely high Mg pressure or a large Mg flux, to compensate for the low Mg sticking coefficient. Incidentally, this is consistent with the requirement for MgB₂ phase stability described above.

2.3 U CEPTIBILITY TO CONTAMINATION

The susceptibility of MgB₂ to contamination is another serious problem. Mg reacts strongly with oxygen to form MgO. For example, an oxygen pressure of 10^{-6} Torr is sufficient for the deposition of MgO films at 3 °C [27]. For *in situ* deposition of MgB₂ at 25 - 30 °C, a background pressure of 3×10^{-8} Torr leads to insulating films [2, 25, 26]. The detrimental effects of the oxidation of Mg include the reduction of the effective Mg vapor pressure as well as the formation of insulating grain boundaries that prevents grain growth of MgB₂, resulting in nanocrystalline structure [19, 28], poor connectivity [29], and

poor superconducting properties. It has been suggested by Eom *et al.* that some level of oxygen contamination may help to enhance the flux pinning in MgB₂ films [19]. However, the level of oxygen contamination is difficult to control, and its detrimental effects outweigh its possible benefits.

Carbon is another common contaminant. Most often it comes from the source materials such as in sputter or laser ablation targets. Carbon doping reduces T_c of MgB₂ [3]. Left uncontrolled, the carbon contamination prevents the deposition of clean MgB₂ films. It should be pointed out that carbon doping can enhance the upper critical field of MgB₂ [31, 32]. Even for this purpose, it is preferred that the carbon doping is done in a controlled manner.

3 DEPOSITION TECHNIQUE FOR MgB₂

Typically, a growth temperature about one half of the melting temperature, T_m (in Kelvin), is optimal for epitaxy and high crystallinity in thin films, although the minimum temperature can be much lower [33], for example, about $T_m/8$ for metals [34]. For MgB₂, T_m is 243 °C (~ 27 K) under an equilibrium vapor pressure exceeding 49 Torr [16]. Therefore, the deposition of MgB₂ could take place between ~ 18 °C (135 K) and ~ 7 °C (34 K). The lower deposition temperature often results in poor crystallinity and degraded transport and superconducting properties, but it does not require very high Mg vapor pressure. For higher deposition temperatures favored for epitaxial growth and good crystallinity, a high Mg vapor pressure is needed. For example, for deposition at 18 °C, a Mg vapor pressure of at least 11 Torr is needed according to thermodynamic stability conditions [16]. Different deposition techniques used for MgB₂ approach this problem in different temperature regimes.

3.1 EX SITU HIGH-TEMPERATURE ANNEALING IN Mg VAPOR

This approach generates high Mg vapor pressures by heating Mg bulk in an enclosure. Precursor films of B or Mg-B mixture are deposited at lower temperatures by pulsed laser deposition [35, 36, 37, 38], magnetron sputtering [19, 39, 40, 41], electron-beam evaporation [42, 43], thermal evaporation [44, 45], chemical vapor deposition [46, 47, 48], or screen printing [49]. The precursor films are then sealed into a Ta tube in an Ar atmosphere together with high-purity Mg metal pieces, and annealed above 85 °C. The high Mg vapor pressure in the enclosure allows the high processing temperature according to the thermodynamic stability conditions. A variation of the technique seals the precursor film and Mg in a Nb box *in situ* in the vacuum chamber before annealing at 83 °C [4]. Because of the high annealing temperature, the MgB₂ thin films grown by this process are epitaxial [38, 39]. The superconducting properties are also excellent, showing $T_c \sim 39$ K [35, 36, 42] and very high J_c exceeding 10^7 A/cm² at zero field [43, 5]. By carefully adjusting the annealing conditions, it is possible that little Mg is deposited on the surface of the MgB₂ films. However, it is difficult to eliminate oxygen and carbon contamination, which is the result of the precursor film deposition, either due to the low background vacuum or to the carbon in the source materials.

3.2 IN SITU ANNEALING AT INTERMEDIATE TEMPERATURE

The two-step *i situ* annealing technique generates the Mg vapor pressure locally and temporarily. Precursor films or multilayers of MgB₂, Mg+MgB₂, or Mg+B, are deposited at room temperature to 300 °C, by pulsed laser deposition [18, 28, 36, 51, 52, 53, 54, 55, 56], sputtering [57, 58, 59], thermal evaporation [44], or e-beam evaporation [60, 61, 62]. They are then annealed *i situ* in the growth chamber. During the annealing, a Mg vapor pressure is generated by the sublimation or evaporation of excess Mg in the films while the formation of the MgB₂ phase takes place. At the same time, the Mg vapor pressure changes and eventually drops, and MgB₂ decomposes. Clearly, a careful balancing between all these processes is critical. Kim *et al.* [18] and Zhao *et al.* [63] have studied the interplay between the annealing temperature and duration. For example, Kim *et al.* found that one may either anneal at 55 °C for 30 minutes or at 800 °C for a very short period. Because of the lower temperature used, films produced by the two-step *i situ* annealing technique have poor crystallinity and are often nanocrystalline [28]. The T_c ranges from the early reports of around or below 25 K [36, 51, 52, 53] to about 34 K [18, 28]. Oxygen contamination is very severe, which also contributes to the nanocrystalline microstructure.

3.3 ONE STEP DEPOSITION AT LOW TEMPERATURE

The low temperature deposition of MgB₂ avoids the requirement of high Mg vapor pressure by lowering the temperature. For example, the Mg pressure required for phase stability can be greatly reduced to 10⁻⁸ Torr at 300 °C [16], easily achievable by vacuum deposition techniques. Still, oxygen contamination problem needs to be solved as it has been shown that a background pressure of 3 × 10⁻⁸ Torr leads to insulating films [20, 25, 26]. A UHV background is critical. It is also important that pure Mg metal source is used to avoid oxygen and carbon contamination. This approach has been successfully demonstrated by several groups [18, 20, 25, 26, 64, 65, 66, 67, 68]. Using molecular beam epitaxy, superconducting MgB₂ films were obtained for substrate temperatures between 150 – 320 °C, and $T_c \sim 36$ K for 320 °C [25, 26]. The films show clear MgB₂ peaks in x-ray diffraction [25, 26, 64, 69] and the grains can be as large as 400 Å [64, 69]. The low deposition temperature is not ideal for epitaxial growth and leads to more defects in the films. This may or may not be critical for Josephson devices, and the low temperature is advantageous for device processing.

3.4 IN SITU DEPOSITION UNDER HIGH Mg PRESSURE

The key steps to generate a high Mg pressure and reduce oxygen contamination during *i situ* deposition have been achieved by several techniques. Using a reactive co-evaporation (RCE) technique similar to those used for high temperature superconductor thin films [70], Moeckly *et al.* succeeded in creating a high Mg vapor pressure locally in a “pocket heater”, which at the same time overwhelms the residual oxygen in the background pressure inside the “pocket heater” [71]. The substrate rotates periodically from an opening on the “pocket” to deposit B layer by e-beam evaporated into the “pocket” to react with Mg and form the MgB₂ phase. Very high quality films of MgB₂ have been reported using this

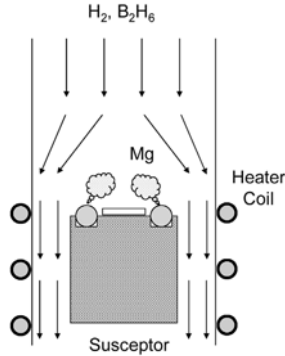


Fig. 2. Schematic of the HPCVD reactor. (From Ref. [73]).

technique to deposit at 55 °C. Schneider *et al.* reported a similar scheme in which the substrate and pure Mg pieces are placed in an oven and B is sputtered through a hole on the oven [72]. Deposition at 44 °C has been reported.

The most successful of this type of technique is the hybrid physical-chemical vapor deposition (HPCVD). It combines physical vapor deposition (heated bulk Mg is used as the Mg source) with chemical vapor deposition (diborane, B_2H_6 , in hydrogen is used as the boron precursor gas). The schematic of the system is shown in Fig. 2 and the details have been described elsewhere [73, 74]. The total pressure during the deposition can be high. For example, Zeng *et al.* used a H_2 carrier gas pressure of 1 Torr at 4 sccm, allowing a high Mg vapor pressure in the vicinity of the substrate to be generated when the bulk Mg pieces are heated. The HPCVD technique solves all the three problems discussed above. The high Mg vapor pressure satisfies the thermodynamic phase stability condition at the high deposition temperature and provides an abundance of Mg to react with B. The reducing hydrogen ambient in the deposition process suppresses the oxidation of Mg and the high purity sources of Mg and B greatly reduce the oxygen and carbon contamination. The deposition temperature used in the HPCVD setup in Fig. 2 vary from 55 °C to around 7 °C [75]. Using a high concentration of B_2H_6 in H_2 as the B precursor gas, Chen *et al.* has demonstrated that the deposition rate of HPCVD can be as high as 17 Å/s [76].

4 PROPERTIES OF CLEAN EPITAXIAL HPCVD FILM

The MgB_2 films deposited by HPCVD have shown the best overall structural and superconducting properties among films by all the deposition techniques. The high deposition temperatures result in excellent epitaxy and crystallinity [74, 77]. The highly reducing H_2 ambient and the high purity sources lead to very clean MgB_2 thin films [78]. In the following, we focus the discussion of film properties on the HPCVD deposited MgB_2 films.

The HPCVD films are epitaxial. Figure 3 shows (a) a $\theta - 2\theta$ scan and (b) a ϕ scan of x-ray diffraction from a MgB_2 film on a (1×1) 4H-SiC substrate. The $\theta - 2\theta$ scan shows

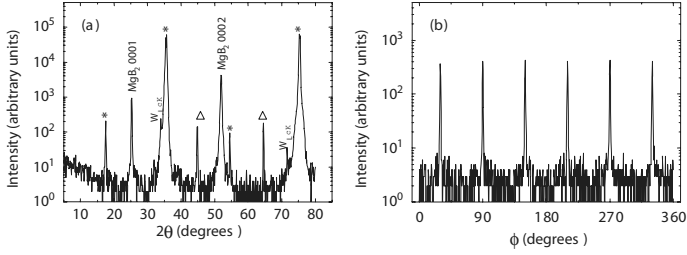


Fig. 3. X-ray diffraction spectra of a MgB_2 thin film on a (111) 4H-SiC substrate. (a) $\theta - 2\theta$ scan and (b) ϕ scan of the 112 MgB_2 reflection. The substrate peaks are marked by *, while the unidentifiable substrate peaks are marked as Δ . (From Ref. [77]).

a c -axis orientation, and the ϕ scan shows that the films are in-plane aligned with the substrate lattice. The rocking curves for both $\theta - 2\theta$ and ϕ scans are sharp, indicating good crystallinity. The MgB_2 film on SiC has its hexagonal lattice directly aligned with that of the substrate [77]. Similar epitaxy is also obtained on (111) sapphire substrate, however the hexagonal lattice of the film is rotated by 3° around the c axis to reduce the large lattice mismatch with the sapphire substrate [74].

The HPCVD films are clean. Figure 4 shows a resistivity versus temperature curve for a MgB_2 thin film on 4H-SiC substrate. It shows a high T_c , low residual resistivity ρ_0 , and high residual resistivity ratio RRR . The best values reported for the HPCVD films are $T_{c0}=41.8\text{ K}$, $\rho_0 = .26\mu\Omega\text{cm}$, and $RRR > 3$ [78]. Using the Drude expression for the electron mean free path, $l = 3/[\rho N(\epsilon)v_F e^2]$, the average Fermi velocity $v_F = 4.8 \times 10^7$ cm/s, and the density of state $N(\epsilon) = .7/(\text{eV unit cell})$ [79], one obtains $l \sim 6$ Å. The residual resistivity is lower than the reported values for single crystals [14] and bulk samples [8]. Compared to the first-principle calculations of the temperature-dependent resistivity for the clean and dirty limit, based on the two-band picture [81], the HPCVD film shown in Fig. 4 is clearly in the clean limit.

The critical current density J_c of the HPCVD films is high. A transport measurement of the self-field J_c in a patterned bridge of $2\ \mu\text{m}$ width reveals a value of 3.4×10^7 A/cm² at 4.2 K [77]. This value is close to the depairing critical current density in MgB_2 [82]. However, J_c in such films is suppressed quickly by the applied magnetic field indicating a lack of pinning, a natural consequence of the cleanness of the films. Another indication of the cleanness of the films is the low upper critical field H_{c2} . A value of $H_{c2}^\perp = 4$ T has been reported for an HPCVD films when the applied field is perpendicular to the film surface [83].

Figure 4 clearly shows a T_c higher than that in the bulk MgB_2 [1]. By depositing MgB_2 films of different thicknesses and on different substrates, it is found that T_c increases with tensile strain in the films [84]. The highest zero-resistance T_c obtained in the HPCVD films is 41.8 K, which is well above the bulk value. In the HPCVD films, the tensile strain increases with the film thickness, which is caused primarily by the coalescence of initially nucleated discrete islands (the Volmer-Weber growth mode) [85, 86]. First-principles

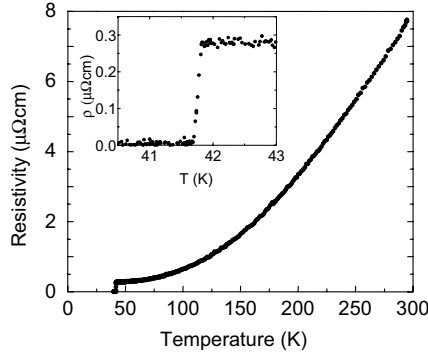


Fig. 4. Resistivity versus temperature for a 225 Å-thick MgB₂ film on 4H-SiC. The inset shows details at the superconducting transition. (From Ref. [78]).

calculations show that the T_c increase is due to the softening of the bond-stretching E_{2g} phonon mode, which is confirmed by Raman scattering measurements. The decrease in the E_{2g} phonon frequency leads to a large increase in the electron-phonon coupling strength, which more than compensates the lowering of the temperature/energy scale that is proportional to T_c . The result points to the E_{2g} phonon softening as a possible avenue to achieve higher T_c in MgB₂.

5 PROPERTIES OF CARBON-DOPED HPCVD FILM

Although clean MgB₂ has low H_{c2} [1], in high resistivity MgB₂ films H_{c2} is substantially higher [11]. Because of the multiple impurity scattering channels and the two-gap nature of superconductivity in MgB₂, H_{c2} can be enhanced well above the estimate $H_{c2}(\text{)} = .69T_c H_{c2}'(T_c)$ of one-gap theory. It has been recently shown that carbon doping can substantially enhance H_{c2} of MgB₂ [32, 87]. As mentioned above, carbon doping very often occurs in the film deposition process through contamination, or in other words, unintentionally. What is desirable is a controlled way of carbon doping that can optimize the high field properties of MgB₂. The HPCVD technique achieves this by adding a carbon-containing magnesium precursor, bis(methylcyclopentadienyl)magnesium ((MeCp)₂Mg) to the H₂ carrier gas [83]. The carbon content in the carbon-doped MgB₂ films is conveniently controlled by the flow rate of a secondary hydrogen flow that passes through the (MeCp)₂Mg bubbler.

The structure of the carbon-doped HPCVD MgB₂ films consists of columnar nanograins of Mg(B_{1-x}C_x)₂ with a preferential c -axis orientation. The individual columnar grains show deviations of their c -axis from the film normal much broader than in undoped films. In plane the carbon-doped films show an equiaxial morphology of the columnar grains, and an amorphous phase is observed between the grains. X-ray diffraction spectra show peaks most likely due to B₄C, B₈C, or B₁₃C₂, which may be the amorphous phases in the grain boundaries. Unlike the carbon-doped single crystals, where the a axis lattice

constant decreases but that of c axis remains almost constant for all the carbon concentration [31], both the c and a axes expand in the carbon-doped HPCVD films until about a nominal carbon concentration of 3 at.%, above which the c lattice constant decreases and the a lattice constant increases dramatically [83].

As the MgB_2 films are doped with carbon, the resistivity increases dramatically and the T_c of the film is suppressed much more slowly with increasing carbon concentration. For example, with a carbon concentration of 24 at.%, the residual resistivity increases from the undoped value of less than $1 \mu\Omega\text{cm}$ to $\sim 2 \mu\Omega\text{cm}$, and T_c decreases from over 41 K to 35 K. The suppression of T_c is much slower and the increase of resistivity much faster than in carbon-doped single crystals [31] and filaments [32]. This indicates that only a small portion of the carbon in the films is doped into the MgB_2 structure and the rest forms high resistance grain boundaries. It has been pointed out by Rowell [88] that the widely-varying resistivity of MgB_2 in the literature reflects reduced cross sections of the samples that carry current. This scenario applies perfectly to the carbon-doped HPCVD MgB_2 films. As the carbon concentration increases, the conduction area between the MgB_2 grains is reduced to 2 % of the total cross section before it is completely blocked by the grain boundaries around a nominal carbon concentration of ~ 29 at.% [89].

The H_{c2} values of the carbon-doped MgB_2 films are much higher than that in the undoped films. Figure 5 shows the results for an undoped, 7.4 at.%, and 22 at.% carbon doped films. Carbon doping changes the downward curvature in $H_{c2}^{\perp}(T)$ for the undoped film to an upward curvature in the carbon-doped films, and H_{c2} increases with carbon concentration. Recently, Braccini *et al.* have shown that the carbon-doped HPCVD MgB_2 films have $H_{c2}(\)$ values as high as 7 T [87]. The measurement of the transport $J_c(H)$ show that although the self-field J_c is lower in carbon-doped films, it remains relatively high in much higher magnetic fields. This indicates a significantly enhanced vortex pinning in carbon-doped MgB_2 films. These results are very encouraging for using MgB_2 in high-magnetic-field applications.

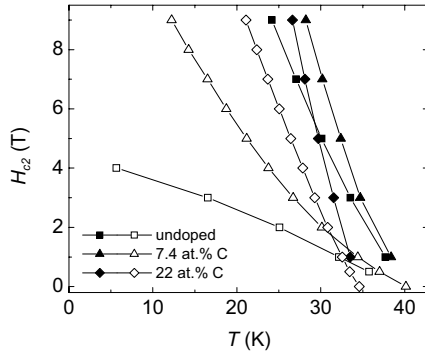


Fig. 5. Upper critical field as a function of temperature for an undoped film and two doped films with 7.4 at.% and 22 at.% nominal carbon concentrations, respectively. The solid symbols are for parallel field (H_{c2}^{\parallel}) and the open symbols are for perpendicular field (H_{c2}^{\perp}). (From Ref. [83].)

6 UB TRATE AND HETERO STRUCTURE

6.1 UB TRATE FOR MgB₂ FILM

The substrate materials for MgB₂ thin films need to be sufficiently stable chemically against the reaction with Mg, which is encountered in all the deposition techniques albeit at different temperatures. Liu *et al.* carried out a calculation of thermodynamic reactivity of magnesium vapor with various substrate materials and found that MgO, SiC, AlN and TaN are stable in high Mg pressures [9]. Si, ZrO₂, and TiN can also be stable at low Mg vapor pressures. Experimentally, He *et al.* showed that ZrO₂, MgO, TiN, TaN, and AlN do not react with MgB₂ at 8 °C [91]. Practically, as long as the reaction between a material with MgB₂ is slow enough, it can still be a viable substrate for MgB₂. Indeed, sapphire has been used as a substrate material for epitaxial MgB₂ films, although oxide layers have been observed at the film/substrate interface [39, 74, 92]. On the other hand, the epitaxial interface between MgB₂ film and SiC substrate is often free from oxides [93].

For epitaxial growth, lattice match is also a consideration. MgB₂ has a hexagonal structure with $a = 3.86 \text{ \AA}$ and $c = 3.524 \text{ \AA}$ [1]. For epitaxial growth of c -axis oriented MgB₂ films, both (111)4H-SiC ($a = 3.73 \text{ \AA}$) and (111)6H-SiC ($a = 3.81 \text{ \AA}$) offer a perfect lattice match [77]. Therefore, c -axis films with the hexagonal lattice of MgB₂ directly on top of the hexagonal lattice of SiC have been obtained (Fig. 3). For sapphire ($a = 4.765 \text{ \AA}$), on the other hand, the lattice mismatch is large and the hexagonal MgB₂ lattice is rotated by 3 ° to match the hexagonal lattice of sapphire [38, 39, 74]. The triangular lattice of (111)MgO has also been used to generate highly c -axis oriented films [94]. The orientation of the films can also be affected by other conditions during the growth. For example, Chen *et al.* showed (111) oriented MgB₂ films on sapphire by HPCVD, most likely due to the very high deposition rate (17 Å/s) during the film growth [76].

If epitaxy or texture in the films are not required, many materials can be used as the substrate for MgB₂. Using the RCE technique, Moeckly *et al.* have shown MgB₂ films with T_c around 39 K on c -, r -, and m -cut sapphire, SiC, MgO, LaAlO₃, NdGaO₃, LaGaO₃, (LaAlO₃)_{0.3}(Sr₂AlTaO₆)_{0.7}, SrTiO₃, and yttrium-stabilized ZrO₂ [71]. Even polycrystalline alumina, buffered Si, as well as stainless steel have been successfully used for the RCE MgB₂ films. Using HPCVD, Feng *et al.* have grown 1 μm-thick MgB₂ films on stainless steel substrates [95].

6.2 MULTILAYER OF MgB₂ WITH OTHER MATERIAL

Integrated circuits using MgB₂ Josephson junctions require multilayers of MgB₂ with other insulating and metallic materials. There have been reports of epitaxial MgB₂ multilayers with materials of hexagonal structures. For example, Fig. 6 show the results of a bilayer of MgB₂ with TiB₂ [96]. TiB₂ is a highly conductive material with excellent mechanical, tribological, chemical, and thermal properties [97]. On top of a 15 Å-thick TiB₂ layer grown by pulsed laser deposition [98], a MgB₂ film of 12 Å was grown with HPCVD. The $\theta - 2\theta$ scan in Fig. 6(a) shows that both layers are c -axis oriented. The ϕ scans in

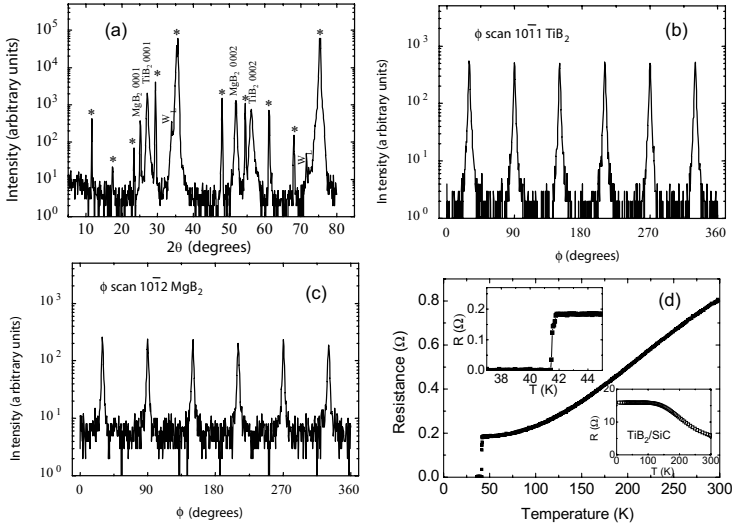


Fig. 6. X-ray diffraction spectra and R vs. T curve of a $\text{MgB}_2/\text{TiB}_2$ bilayer on a $(1\ \bar{1})$ 6H-SiC substrate. (a) The $\theta - 2\theta$ scan, (b) the ϕ scan of the $1\ \bar{1}$ TiB_2 reflection, (c) the ϕ scan of the $1\ \bar{2}$ MgB_2 reflection, and (d) the R vs. T curve. The insets to (d) are the details near the superconducting transition and the resistance of the TiB_2 layer. (From Ref. [96].)

Fig. 6(b) for the TiB_2 layer, of the $1\ \bar{1}$ reflection, and Fig. 6(c) for the MgB_2 layer, of the $1\ \bar{2}$ reflection, indicate that both layers are in-plane aligned with each other and with the substrate. The resistivity versus temperature curve in Fig. 6(d) shows a superconducting transition at above 4 K. After etching off the MgB_2 layer, the resistance of the TiB_2 layer is measured and plotted in the inset, which shows a low resistance.

Other materials that have been grown in multilayers with MgB_2 include AlN [96, 99, 1] and MgO [1], both for barrier layers in MgB_2 Josephson junctions. The HPCVD MgB_2 films on epitaxial AlN layers deposited by MOCVD are epitaxial [96], and those on c -axis textured AlN layers are c -axis textured as well [1]. Abe *et al.* sputtered AlN layers on c -axis textured sputtered MgB_2 films and found that the AlN layers are also c -axis textured [1 1]. The $\text{MgB}_2/\text{MgO}/\text{MgB}_2$ trilayers, grown by HPCVD *in situ* are epitaxial [1]. The superconducting properties of both the top and bottom MgB_2 layers in HPCVD $\text{MgB}_2/\text{MgO}/\text{MgB}_2$ and $\text{MgB}_2/\text{AlN}/\text{MgB}_2$ trilayers are excellent, which is promising for all- MgB_2 Josephson junctions using MgO and AlN as the barrier materials.

7 MgB₂ THIN FILM DEVICE

7.1 JOSEPHSON JUNCTION AND SQUID

A major goal of the MgB₂ thin film research is to fabricate MgB₂/barrier/MgB₂ trilayers Josephson junctions and circuits that can operate above 2 K. So far, no such Josephson junction has been reported. However, many other types of junctions consisting of MgB₂ films have been successfully produced. These include MgB₂ nanobridges formed by focused ion beam [1 2, 1 3], planar MgB₂ junctions created by local ion damage [1 4, 1 5, 1 6], MgB₂/Ag/MgB₂ step-edge junctions [1 7], and ramp-type junctions [1 8]. Planar trilayer junctions with one electrode being MgB₂ and the other a low temperature superconductor (S/I/S' junctions) have been reported by several groups. These include Nb/Al₂O₃/Al/MgB₂ [1 9], NbN/AlN/MgB₂ [99, 11], and V/Al₂O₃/MgB₂ junctions [111]. Well defined junction characteristics as well as near ideal Fraunhofer pattern have been observed in such junctions [11 , 111]. Also, SIN-type Au/MgO/MgB₂ junctions have been reported [112]. Although only one electrode is MgB₂, these planar trilayer junctions demonstrated the viability of AlN, Al₂O₃, and MgO as the barrier materials and the high quality of their interfaces with MgB₂. With the progress in MgB₂ heterostructures, we can confidently expect that MgB₂/barrier/MgB₂ trilayer junctions will be produced.

The impact of the two-gap nature of MgB₂ on the Josephson tunneling has been discussed by Brinkman *et al.* (MgB₂/I/MgB₂ junctions) [113] and Agterberg *et al.* (MgB₂/I/S' junctions, where S' is a single-gap superconductor) [114]. The energies of the two gaps in MgB₂ are ~ 7 meV and ~ 2 meV, respectively [2], and the tunneling experiment senses the smaller gap. Brinkman *et al.* showed that a large $I_c R_n$ product that would result from the larger energy gap of MgB₂ can only be achieved when the tunneling occurs between *ab* planes of the MgB₂ electrodes [113]. From materials science point of view, this is a serious challenge.

Using the MgB₂ junctions described above, superconducting quantum interference devices (SQUIDs) have been demonstrated [1 2, 115, 116]. In MgB₂ nanobridge SQUIDs made from HPCVD films, Mijatovic showed that the voltage modulation by an applied magnetic field can be observed up to 38.8 K, an outstanding performance by a MgB₂ SQUID [117].

7.2 MICROWAVE PROPERTIES

Applications of MgB₂ in microwave devices have not been prominently considered because of the extra cooling required compared to high temperature superconductors. However, given the larger than expected nonlinearity in high temperature superconductors [118], MgB₂ may be attractive if it has superior nonlinear properties because it is a conventional superconductor. The microwave surface resistance of MgB₂ films has been measured by several groups [119, 12 , 121, 122]. Although low surface resistance has been observed [121, 123], the nonlinearity measurements of MgB₂ films reported so far have not shown better properties than high temperature superconductors [124, 125].

7.3 DEGRADATION

A critical issue for any MgB_2 thin film devices is the stability of the film against degradation in the environments necessary for device processing. This includes the exposure to solvents, water, photoresist, and developer. It has been found that MgB_2 is sensitive to water and moisture. Zhai *et al.* reported that MgB_2 prepared by the *ex situ* high temperature annealing degrade when exposed to water [126]. Cui *et al.* found that HPCVD MgB_2 films degrade in water faster at room temperature than at $^\circ\text{C}$. The effects of the exposure to other solvents and photoresist were also studied, and it was found that isopropanol does not cause MgB_2 films to degrade [127].

X-ray photoelectron spectroscopy (XPS) study shows that the degradation of MgB_2 is related to the surface decomposition [128]. Serquis *et al.* suggested that the degradation product in the MgB_2 from air exposure is $\text{Mg}(\text{OH})_x$, and also possibly some components of MgO and Mg oxycarbon in addition to Mg hydroxide [128]. Wong-Ng *et al.* have found that when MgB_2 was exposed to water vapor and the resultant material was annealed in Ar atmosphere, $\text{Mg}_2\text{B}_2\text{O}_5$ peaks were observed in the x-ray diffraction spectrum [129]. It has also been reported that grain boundary seems to degrade much faster than the MgB_2 grain itself [128, 13]. Doping of Ti into MgB_2 has been reported to enhance the stability of MgB_2 against degradation [131].

8 CONCLUSION

The research on MgB_2 thin films has made very impressive progress since the discovery of superconductivity in MgB_2 . The critical problems in depositing MgB_2 films have been understood and overcome; successful deposition techniques, in particular the HPCVD technique, have been developed; epitaxial films with high degrees of crystallinity have been deposited; clean MgB_2 films as well as films doped to different degrees of dirtiness have been produced; very high H_{c2} have been achieved in carbon-doped MgB_2 films; Josephson devices, either planar or with MgB_2 as one electrode, have been produced; and MgB_2 heterostructures have been achieved. There is no doubt that MgB_2 /barrier/ MgB_2 trilayer Josephson junctions will soon be demonstrated. The high quality films also provide an ideal materials system for basic solid-state research. These achievements in the areas of MgB_2 thin films will help to place MgB_2 to a prominent position in the practical applications of superconductors.

ACKNOWLEDGMENT

I would like to thank my many colleagues and collaborators, and our graduate students, undergraduate students, and postdocs, for their invaluable contributions to our work on MgB_2 thin films, in particular related to the HPCVD technique, which have allowed me to gain insights into various aspects of the exciting field of MgB_2 thin films. This work is supported in part by ONR under grant No. N 14- 1- 294, and by NSF under grant No. DMR- 3 6746.

References

- [1] J. Nagamatsu, N. Nakagawa, T. Muranaka, Y. Zenitani, and J. Akimitsu, *Nature (London)* 41, 63 (2 1).
- [2] H. J. Choi, D. Roundy, H. Sun, M. L. Cohen, and S. G. Louie, *Nature (London)* 418, 758 (2 2).
- [3] W. Pickett, *Nature (London)* 418, 733 (2 2).
- [4] S. Souma, Y. Machida, T. Sato, T. Takahashi, H. Matsui, S.-C. Wang, H. Ding, A. Kaminski, J. C. Campuzano, S. Sasaki, and K. Kadowaki, *Nature (London)* 423, 65 (2 3).
- [5] A. Y. Liu, I. I. Mazin, and J. Kortus, *Phys. Rev. Lett.* 87, 87 5 (2 1).
- [6] J. M. An and W. E. Pickett, *Phys. Rev. Lett.* 86, 4366 (2 1).
- [7] D. C. Larbalestier, L. D. Cooley, M. O. Rikel, A. A. Polyanskii, J. Jiang, S. Patnaik, X. Y. Cai, D. M. Feldmann, A. Gurevich, A. A. Squitieri, M. T. Naus, C. B. Eom, E. E. Hellstrom, R. J. Cava, K. A. Regan, N. Rogado, M. A. Hayward, T. He, J. S. Slusky, P. Khalifah, K. Inumaru, and M. Haas, *Nature (London)* 41, 186 (2 1).
- [8] J. Rowell, *Nature Materials* 1, 5 (2 2).
- [9] S. Y. Xu, Q. Li, E. Wertz, Y. F. Hu, A. V. Pogrebnayakov, X. H. Zeng, X. X. Xi, and J. M. Redwing, *Phys. Rev. B* 68, 2245 1 (2 3).
- [10] P. C. Canfield and G. Crabtree, *Physics Today* 56(3), 34 (2 3).
- [11] A. Gurevich, S. Patnaik, V. Braccini, K. H. Kim, C. Mielke, X. Song, L. D. Cooley, S. D. Bu, D. M. Kim, J. H. Choi, L. J. Belenky, J. Giencke, M. K. Lee, W. Tian, X. Pan, A. Siri, E. E. Hellstrom, C. B. Eom, and D. Larbalestier, *Supercond. Sci. Technol.* 17, 278 (2 4).
- [12] S. L. Bud'ko, G. Lapertot, C. Petrovic, C. E. Cunningham, N. Anderson, and P. C. Canfield, *Phys. Rev. Lett.* 86, 1877 (2 1).
- [13] D. K. Finnemore, J. E. Ostenson, S. L. Bud'ko, G. Lapertot, and P. C. Canfield, *Phys. Rev. Lett.* 86, 242 (2 1).
- [14] S. Lee, *Physica C* 385, 31 (2 3).
- [15] J. Karpinski, S. M. Kazakov, J. Jun, M. Angst, R. Puzniak, A. Wisniewski, and P. Bordet, *Physica C* 385, 42 (2 3).
- [16] Z. K. Liu, D. G. Schlom, Q. Li, and X. X. Xi, *Appl. Phys. Lett.* 78, 3678 (2 1).
- [17] Z.-K. Liu, Y. Zhong, D. Schlom, X. X. Xi, and Q. Li, *CALPHAD* 25, 299 (2 1).
- [18] J. Kim, R. K. Singh, N. Newman, and J. M. Rowell, *IEEE Trans. Appl. Supercond.* 13, 3238 (2 3).
- [19] C. B. Eom, M. K. Lee, J. H. Choi, L. Belenky, X. Song, L. D. Cooley, M. T. Naus, S. Patnaik, J. Jiang, M. O. Rikel, A. A. Polyanskii, A. Gurevich, X. Y. Cai, S. D. Bu, S. E. Babcock, E. E. Hellstrom, D. C. Larbalestier, N. Rogado, K. A. Regan, M. A. Hayward, T. He, J. S. Slusky, K. Inumaru, M. Haas, and R. J. Cava, *Nature (London)* 411, 558 (2 1).
- [20] A. J. M. van Erven, T. H. Kim, M. Muenzenberg, and J. S. Moodera, *Appl. Phys. Lett.* 81, 4982 (2 2).
- [21] R. Heckingbottom, G. Davies, and K. Prior, *Surf. Sci.* 132, 375 (1983).
- [22] R. H. Hammond and R. Bormann, *Physica C* 162, 7 3 (1989).

- [23] Z. Y. Fan, D. G. Hinks, N. Newman, and J. M. Rowell, *Appl. Phys. Lett.* 79, 87 (2 1).
- [24] S. Brutti, A. Ciccioi, G. Balducci, G. Gigli, P. Manfrinetti, and A. Palenzona, *Appl. Phys. Lett.* 8 , 2892 (2 2).
- [25] K. Ueda and M. Naito, *Appl. Phys. Lett.* 79, 2 46 (2 1).
- [26] K. Ueda and M. Naito, *J. Appl. Phys.* 93, 2113 (2 3).
- [27] T. Ishiguro, Y. Hiroshima, and T. Inoue, *Japn. J. Appl. Phys.* 35(6A), 3537 (1996).
- [28] X. H. Zeng, A. Sukiashyan, X. X. Xi, Y. F. Hu, E. Wertz, Q. Li, W. Tian, H. P. Sun, X. Q. Pan, J. Lettieri, D. G. Schlom, C. O. Brubaker, Z.-K. Liu, and Q. Li, *Appl. Phys. Lett.* 79, 184 (2 1).
- [29] J. Rowell, S. Y. Xu, X. H. Zeng, A. V. Pogrebnnyakov, Q. Li, X. X. Xi, J. M. Redwing, W. Tian, and X. Pan, *Appl. Phys. Lett.* 83, 1 2 (2 3).
- [3] R. A. Ribeiro, S. L. Bud'ko, C. Petrovic, and P. C. Canfield, *Physica C* 384, 227 (2 3).
- [31] S. Lee, T. Masui, A. Yamamoto, H. Uchiyama, and S. Tajima, *Physica C* 397, 7 (2 3).
- [32] R. H. T. Wilke, S. L. Bud'ko, P. C. Canfield, D. K. Finnemore, R. J. Suplinskas, and S. T. Hannahs, *Phys. Rev. Lett.* 92, 217 3 (2 4).
- [33] M. H. Yang and C. P. Flynn, *Phys. Rev. Lett.* 62, 2476 (1989).
- [34] C. P. Flynn, *J. Phys. F* 18, L195 (1988).
- [35] W. N. Kang, H.-J. Kim, E.-M. Choi, C. U. Jung, and S.-I. Lee, *Science* 292, 1521 (2 1).
- [36] S. R. Shinde, S. B. Ogale, R. L. Greene, T. Venkatesan, P. C. Canfield, S. Bud'ko, G. Lapertot, and C. Petrovic, *Appl. Phys. Lett.* 79, 227 (2 1).
- [37] C. Ferdeghini, V. Ferrando, G. Grassano, W. Ramadan, E. Bellingeri, V. Braccini, D. Marré, P. Manfrinetti, A. Palenzona, F. Borgatti, R. Felici, and T.-L. Lee, *Supercond. Sci. Technol.* 14, 952 (2 1).
- [38] A. Berenov, Z. Lockman, X. Qi, J. L. MacManus-Driscoll, Y. Bugoslavsky, L. F. Cohen, M.-H. Jo, N. A. Stelmashenko, V. N. Tsaneva, M. Kambara, N. H. Babu, D. A. Cardwell, and M. G. Blamire, *Appl. Phys. Lett.* 79, 4 1 (2 1).
- [39] S. D. Bu, D. M. Kim, J. H. Choi, J. Giencke, S. Patnaik, L. Cooley, E. E. Hellstrom, D. C. Larbalestier, C. B. Eom, J. Lettieri, D. G. Schlom, W. Tian, and X. Pan, *Appl. Phys. Lett.* 81, 1851 (2 2).
- [4] R. Vaglio, M. G. Maglione, and R. Di Capua, *Supercond. Sci. Technol.* 15, 1236 (2 2).
- [41] M. G. Maglione, F. Chiarella, R. di Capua, R. Vaglio, M. Salvato, L. Maritato, and S. L. Prischepa, *Int. J. Mod. Phys. B* 17, 779 (2 3).
- [42] M. Paranthaman, C. Cantoni, H. Y. Zhai, H. M. Christen, T. Aytug, S. Sathya-murthy, E. D. Specht, J. R. Thompson, D. H. Lowndes, H. R. Kerchner, and D. K. Christen, *Appl. Phys. Lett.* 78, 3669 (2 1).
- [43] S. H. Moon, J. H. Yun, H. N. Lee, J. I. Kye, H. G. Kim, W. Chung, and B. Oh, *Appl. Phys. Lett.* 79, 2429 (2 1).
- [44] A. Plecenik, L. Satrapinsky, P. Kúš, Š. Gaži, Š. Beňačka, I. Vávra, and I. Kostič, *Physica C* 363, 224 (2 1).

- [45] S. Schiestel, C. Carosella, J. Horwitz, M. Osofsky, C. Kendziora, S. Qadri, and D. Knies, *Surf. Coat. Techn.* 158, 2 3 (2 2).
- [46] X. H. Fu, D. S. Wang, Z. P. Zhang, and J. Yang, *Physica C* 377, 4 7 (2 2).
- [47] S.-F. Wang, Y.-B. Zhu, Z. Liu, Y.-L. Zhou, Q. Zhang, Z.-H. Chen, H.-B. Lu, and G.-Z. Yang, *Chinese Phys. Lett.* 2 , 1356 (2 3).
- [48] S. F. Wang, Y. L. Zhou, Y. B. Zhu, Q. Zhang, Z. H. Chen, H. B. Lu, S. Y. Dai, and G. Z. Yang, *J. Supercond.* 16, 585 (2 3).
- [49] M. Kühberger, K. R. S. Gerhard Gritzner and, H. W. Weber, Å. A. F. Olsen, and T. H. Johansen, *Supercond. Sci. Technol.* 17, 764 (2 4).
- [5] H.-J. Kim, W. N. Kang, E.-M. Choi, M.-S. Kim, K. H. P. Kim, and S.-I. Lee, *Phys. Rev. Lett.* 87, 87 2 (2 1).
- [51] D. H. A. Blank, H. Hilgenkamp, A. Brinkman, D. Mijatovic, G. Rijnders, and H. Rogalla, *Appl. Phys. Lett.* 79, 394 (2 1).
- [52] H. Christen, H. Zhai, C. Cantoni, M. Paranthaman, B. Sales, C. Rouleau, D. Norton, D. Christen, and D. Lowndes, *Physica C* 353, 157 (2 1).
- [53] H. Y. Zhai, H. M. Christen, L. Zhang, C. Cantoni, M. Paranthaman, B. C. Sales, D. K. Christen, and D. H. Lowndes, *Appl. Phys. Lett.* 79, 26 3 (2 1).
- [54] Y. Hikita, T. Fukumura, T. Ito, M. Kawasaki, and H. Takagi, *J. Low Temp. Phys.* 131, 1187 (2 3).
- [55] V. Ferrando, S. Amoruso, E. Bellingeri, R. Bruzzese, P. Manfrinetti, D. Marre, R. Velotta, X. Wang, and C. Ferdeghini, *Supercond. Sci. Technol.* 16, 241 (2 3).
- [56] T. Uchiyama, H. Koga, and I. Iguchi, *Jpn. J. Appl. Phys.* 43, 121 (2 4).
- [57] S. N. Ermolov, M. V. Indenbom, A. N. Rossolenko, I. K. Bdikin, L. S. Uspenskaya, N. S. Stepanov, and V. G. Glebovskii, *JETP Lett.* 73, 557 (2 1).
- [58] Z. Mori, K. Eitoku, D. Toshiya, S. ichiro Koba, and Y. Hakuraku, *Physica C* 388-389, 115 (2 3).
- [59] J.-R. Ahn, S.-G. Lee, Y. Hwang, G. Y. Sung, and D. K. Kim, *Physica C* 388-389, 127 (2 3).
- [6] P. Kus, A. Plecenik, L. Satrapinsky, Y. Xu, and R. Sobolewski, *Appl. Phys. Lett.* 81, 2199 (2 2).
- [61] R. Rogai, V. Galluzzi, A. Mancini, G. Celentano, T. Petrisor, A. Rufoloni, E. Varesi, G. Grassano, V. Boffa, and U. Gambardella, *Int. J. Mod. Phys. B* 17, 7 3 (2 3).
- [62] M. Jergel, E. Andrade, Š. Chromik, M. Jergel, C. Falcony, V. Štrbík, M. Rocha, and E. Zavalá, *Physica C* 383, 287 (2 3).
- [63] Y. Zhao, M. Ionescu, A. V. Pan, S. X. Dou, and E. W. Collings, *Supercond. Sci. Technol.* 16, 1487 (2 2).
- [64] W. Jo, J.-U. Huh, T. Ohnishi, A. F. Marshall, M. R. Beasley, and R. H. Hammond, *Appl. Phys. Lett.* 8 , 3563 (2 2).
- [65] A. Saito, A. Kawakami, H. Shimakage, and Z. Wang, *Jpn. J. Appl. Phys.* 41, L127 (2 2).
- [66] A. Saito, A. Kawakami, H. Shimakage, and Z. Wang, *Jpn. J. Appl. Phys.* 41, L127 (2 2).
- [67] H. Shimakage, A. Saito, A. Kawakami, and Z. Wang, *IEEE Trans. Appl. Supercond.* 13, 33 9 (2 3).

- [68] S. Yata, G. Shimizu, Y. Yamada, S. Kubo, and A. Matsushita, *Physica C* 388-389, 155 (2-3).
- [69] W. Jo, M. R. Beasley, and R. H. Hammond, *IEEE Trans. Appl. Supercond.* 13, 3257 (2-3).
- [70] P. Berberich, B. Utz, W. Prusseit, and H. Kinder.
- [71] B. H. Moeckly and W. S. Ruby, in *2003 Fall Meeting Technical Program*, 759 (Materials Research Society) (2-3).
- [72] R. Schneider, J. Geerk, F. Ratzel, G. Linker, and A. Zaitsev, submitted to *Appl. Phys. Lett.*
- [73] X. X. Xi, X. H. Zeng, A. V. Pogrebnyakov, S. Y. Xu, Q. Li, Y. Zhong, C. O. Brubaker, Z.-K. Liu, E. M. Lysczek, J. M. Redwing, J. Lettieri, D. G. Schlom, W. Tian, and X. Q. Pan, *IEEE Trans. on Appl. Supercond.* 13, 3233 (2-3).
- [74] X. H. Zeng, A. V. Pogrebnyakov, A. Kotcharov, J. E. Jones, X. X. Xi, E. M. Lysczek, J. M. Redwing, S. Y. Xu, Q. Li, J. Lettieri, D. G. Schlom, W. Tian, X. Q. Pan, and Z. K. Liu, *Nature Materials* 1, 35 (2-2).
- [75] B. T. Liu, X. X. Xi, V. Vaithyanathan, and D. G. Schlom, submitted to *IEEE Trans. Appl. Supercond.*
- [76] C. P. Chen, X. F. Wang, Y. Lu, Z. Jia, J. P. Guo, X. N. Wang, M. Zhu, X. Y. Xu, J. Xu, and Q. R. Feng, *cond-mat/46325* (1999).
- [77] X. H. Zeng, A. V. Pogrebnyakov, M. H. Zhu, J. E. Jones, X. X. Xi, S. Y. Xu, E. Wertz, Q. Li, J. M. Redwing, J. Lettieri, V. Vaithyanathan, D. G. Schlom, Z. K. Liu, O. Trithaveesak, and J. Schubert, *Appl. Phys. Lett.* 82, 297 (2-3).
- [78] A. V. Pogrebnyakov, J. M. Redwing, J. E. Jones, X. X. Xi, S. Y. Xu, Q. Li, V. Vaithyanathan, and D. G. Schlom, *Appl. Phys. Lett.* 82, 4319 (2-3).
- [79] J. Kortus, I. I. Mazin, K. D. Belashchenko, V. P. Antropov, and L. L. Boyer, *Phys. Rev. Lett.* 86, 4656 (2-1).
- [80] P. C. Canfield, D. K. Finnemore, S. L. Bud'ko, J. E. Ostenson, G. Lapertot, C. E. Cunningham, and C. Petrovic, *Phys. Rev. Lett.* 86, 2423 (2-1).
- [81] I. I. Mazin, O. K. Andersen, O. Jepsen, O. V. Dolgov, J. Kortus, A. A. Golubov, A. B. Kuz'menko, and D. van der Marel, *Phys. Rev. Lett.* 89, 172 (2-2).
- [82] M. N. Kunchur, S.-I. Lee, and W. N. Kang, *Phys. Rev. B* 68, 64516 (2-3).
- [83] A. V. Pogrebnyakov, J. M. Redwing, J. E. Giencke, C. B. Eom, V. Vaithyanathan, D. G. Schlom, A. Soukiassian, S. B. Mi, C. L. Jia, J. Chen, Y. F. Hu, Y. Cui, Q. Li, and X. X. Xi, submitted to *IEEE Trans. Appl. Supercond.*
- [84] A. V. Pogrebnyakov, D. A. Tenne, A. Soukiassian, X. X. Xi, J. M. Redwing, V. Vaithyanathan, D. G. Schlom, S. Y. Xu, Q. Li, M. D. Johannes, D. Kasinathan, and W. E. Pickett, to appear in *Phys. Rev. Lett.*
- [85] J. A. Floro, E. Chason, R. C. Cammarata, and D. J. Srolovitz, *MRS Bulletin* 27(1), 19 (2-2).
- [86] R. Koch, *J. Phys.: Condens. Matter* 6, 9519 (1994).
- [87] V. Braccini, A. Gurevich, J. Giencke, M. Jewell, C. Eom, D. Larbalestier, A. Pogrebnyakov, Y. Cui, B. T. Liu, Y. F. Hu, J. M. Redwing, Q. Li, X. X. Xi, R. Singh, R. Gandikota, J. Kim, B. Wilkens, N. Newmann, J. Rowell, B. Moeckly, V. Ferrando, C. Tarantini, D. Marré, M. Putti, C. Ferdeghini, R. Vaglio, and E. Haanappel, unpublished.

- [88] J. Rowell, *Supercond. Sci. Tech.* 16, R17 (2 3).
- [89] A. V. Pogrebnnyakov, X. X. Xi, J. M. Redwing, V. Vaithyanathan, D. G. Schlom, A. Soukiassian, S. B. Mi, C. L. Jia, J. Giencke, C. B. Eom, J. Chen, Y. F. Hu, Y. Cui, and Q. Li, *Appl. Phys. Lett.* 85, 2 17 (2 4).
- [9] Z.-J. Liu, S. Zhou, X. Xi, and Z.-K. Liu, *Physica C* 397, 87 (2 3).
- [91] T. He, R. J. Cava, and J. M. Rowell, *Appl. Phys. Lett.* 8 , 291 (2 2).
- [92] W. Tian, X. Q. Pan, S. D. Bu, D. M. Kim, J. H. Choi, S. Patnaik, and C. B. Eom, *Appl. Phys. Lett.* 81, 685 (2 2).
- [93] J. S. Wu, N. Jiang, B. Jiang, J. C. H. Spence, A. V. Pogrebnnyakov, J. M. Redwing, and X. X. Xi, *Appl. Phys. Lett.* 85, 1155 (2 4).
- [94] S. F. Wang, Z. Liu, Y. B. Zhu, Y. L. Zhou, Z. H. Chen, H. B. Lu, and G. Z. Yang, *Chin. Phys.* 13, 112 (2 4).
- [95] Q. R. Feng, C. P. Chen, Y. Lu, Z. Jia, J. P. Guo, X. N. Wang, M. Zhu, J. Xu, and Y. Z. Wang, *cond-mat/* 4 8597 .
- [96] X. X. Xi, A. V. Pogrebnnyakov, X. H. Zeng, J. M. Redwing, S. Y. Xu, Q. Li, Z.-K. Liu, J. Lettieri, V. Vaithyanathan, D. G. Schlom, H. M. Christen, H. Y. Zhai, and A. Goyal, *Supercond. Sci. Technol.* 17, S196 (2 4).
- [97] R. G. Munro, *J. Res. Natl. Inst. Stand. Technol.* 1 5, 7 9 (2).
- [98] H. Y. Zhai, H. M. Christen, C. Cantoni, A. Goyal, and D. H. Lowndes, *Appl. Phys. Lett.* 8 , 1963 (2 2).
- [99] A. Saito, A. Kawakami, H. Shimakage, H. Terai, and Z. Wang, *IEEE Trans. Appl. Supercond.* 13, 1 67 (2 3).
- [1] P. Orgiani, Y. Cui, A. V. Pogrebnnyakov, J. M. Redwing, V. Vaithyanathan, D. G. Schlom, and X. X. Xi, submitted to *IEEE Trans. Appl. Supercond.* .
- [1 1] H. Abe, M. Naito, W.-J. Moon, K. Kaneko, A. Saito, and Z. Wang, *J. Appl. Phys.* 96, 2343 (2 4).
- [1 2] A. Brinkman, D. Veldhuis, D. Mijatovic, G. Rijnders, D. H. A. Blank, H. Hilgenkamp, and H. Rogalla, *Appl. Phys. Lett.* 79, 242 (2 1).
- [1 3] A. Malisa, M. Valkeapää, L.-G. Johansson, and Z. Ivanov, *Supercond. Sci. Technol.* 17, S345 (2 4).
- [1 4] G. Burnell, D.-J. Kang, H. N. Lee, S. H. Moon, B. Oh, and M. G. Blamire, *Appl. Phys. Lett.* 79, 3464 (2 1).
- [1 5] D.-J. Kang, N. H. Peng, R. Webb, C. Jeynes, J. H. Yun, S. H. Moon, B. Oh, G. Burnell, E. J. Tarte, D. F. Moore, and M. G. Blamire, *Appl. Phys. Lett.* 81, 36 (2 2).
- [1 6] D. A. Kahler, J. Talvacchio, J. M. Murduck, A. Kirschenbaum, R. E. Brooks, S. B. Bu, J. Choi, D. M. Kim, and C.-B. Eom, *IEEE Trans. Appl. Supercond.* 13, 1 63 (2 3).
- [1 7] J.-I. Kye, H. N. Lee, J. D. Park, S. H. Moon, and B. Oh, *IEEE Trans. Appl. Supercond.* 13, 1 75 (2 3).
- [1 8] D. Mijatovic, A. Brinkman, I. Oomen, G. Rijnders, H. Hilgenkamp, H. Rogalla, and D. Blank, *Appl. Phys. Lett.* 8 , 2141 (2 2).
- [1 9] G. Carapella, N. Martucciello, G. Costabile, C. Ferdeghini, V. Ferrando, and G. Grassano, *Appl. Phys. Lett.* 8 , 2949 (2 2).

- [11] A. Saito, A. Kawakami, H. Shimakage, H. Terai, and Z. Wang, *J. Appl. Phys.* 92, 7369 (2 2).
- [111] T. H. Kim and J. S. Moodera, *Appl. Phys. Lett.* 85, 434 (2 4).
- [112] K. Ueda and M. Naito, *IEEE Trans. Appl. Supercond.* 13, 3249 (2 3).
- [113] A. Brinkman, A. A. Golubov, H. Rogalla, O. V. Dolgov, J. Kortus, Y. Kong, O. Jepsen, and O. K. Andersen, *Phys. Rev B* 65, 18 517 (2 2).
- [114] D. F. Agterberg, E. Demler, and B. Janko, *Phys. Rev. B* 66, 2145 7 (2 2).
- [115] G. Burnell, D.-J. Kang, D. A. Ansell, H. N. Lee, S. H. Moon, E. J. Tarte, and M. G. Blamire, *Appl. Phys. Lett.* 81, 1 2 (2 2).
- [116] A. Brinkman, D. Mijatovic, H. Hilgenkamp, G. Rijnders, I. Oomen, D. Veldhuis, F. Roesthuis, H. Rogalla, and D. H. A. Blank, *Supercond. Sci. Technol.* 16, 246 (2 3).
- [117] D. Mijatovic, *MgB₂ thin films and Josephson devices*, Ph.D. thesis, University of Twente (2 4).
- [118] T. Dahm, D. J. Scalapino, and B. A. Willemsen, *J. Supercond.* 12, 339 (1999).
- [119] S. Y. Lee, J. H. Lee, J. H. Lee, J. S. Ryu, J. Lim, S. H. Moon, H. N. Lee, H. G. Kim, and B. Oh, *Appl. Phys. Lett.* 79, 3299 (2 2).
- [12] A. A. Zhukov, A. Purnell, Y. Miyoshi, Y. Bugoslavsky, Z. Lockman, A. Berenov, H. Y. Zhai, H. M. Christen, M. P. Paranthaman, D. H. Lowndes, M. H. Jo, M. G. Blamire, L. Hao, J. Gallop, J. L. MacManus-Driscoll, and L. F. Cohen, *Appl. Phys. Lett.* 8 , 2347 (2 2).
- [121] N. Hakim, C. Kusko, S. Sridhar, A. Soukiassian, X. H. Zeng, and X. X. Xi, *Appl. Phys. Lett.* 81, 36 3 (2 2).
- [122] B. B. Jin, N. Klein, W. Kang, H.-J. Kim, E.-M. Choi, S.-I. Lee, T. Dahm, and K. Maki, *Supercond. Sci. Technol.* 16, 2 5 (2 3).
- [123] B. B. Jin, T. Dahm, C. Iniotakis, A. I. Gubin, E.-M. Choi, H. J. Kim, S.-I. Lee, W. N. Kang, S. F. Wang, Y. L. Zhou, G. Z. Yang, A. V. Pogrebnyakov, J. M. Redwing, X. X. Xi, and N. Klein, submitted to *Appl. Phys. Lett.* .
- [124] A. Andreone, E. DiGennaro, G. Lamura, M. Salluzzo, A. Purnell, L. F. Cohen, L. Hao, J. Gallop, C. Cantoni, and M. Paranthaman, *Supercond. Sci. Technol.* 16, 26 (2 3).
- [125] A. J. Purnell, L. F. Cohen, H. Y. Zhai, H. M. Christen, M. P. Paranthaman, D. H. Lowndes, L. Hao, and J. C. Gallop, *Supercond. Sci. Technol.* 17, 681 (2 4).
- [126] H. Y. Zhai, H. M. Christen, L. Zhang, M. Paranthaman, P. H. Fleming, and D. H. Lowndes, *Supercond. Sci. Technol.* 14, 425 (2 1).
- [127] Y. Cui, J. E. Jones, A. Beckley, R. Donovan, D. Lishego, E. Maertz, A. V. Pogrebnyakov, P. Orgiani, J. M. Redwing, and X. X. Xi, submitted to *IEEE Trans. Appl. Supercond.* .
- [128] A. Serquis, Y. T. Zhu, D. E. Peterson, F. M. Mueller, R. K. Schulze, V. F. Nesterenko, and S. S. Indrakanti, *Appl. Phys. Lett.* 8 , 44 1 (2 2).
- [129] W. Wong-Ng, private communication .
- [13] C. H. Cheng, Y. Zhao, Y. Feng, X. T. Zhu, N. Koshizuka, and M. Murakami, *Supercond. Sci. Technol.* 16, 125 (2 3).
- [131] Y. Zhao, C. H. Cheng, T. Machi, N. Koshizuka, and M. Murakami, *Appl. Phys. Lett.* 8 , 2311 (2 2).

SUBJECT INDEX

- Activation energy to inhibit flux motion, 1027–1029
- Alkaline cobaltite ($A_x\text{CoO}_2$), 683
- Alternative preparation routes for MgB_2 , 1056
- Amorphous disorder and superconductivity in simple metals, 500–503
- Amorphous disorder and superconductivity in transition metals, alloys and metallic glasses, 503–506
- Angle resolved photoemission spectroscopy (ARPES), 654
- Anomaly (magnetic) at 22K for Na_xCoO_2 , 691
- Applications of bulk HTS, 876–878
- Levitation, 876–878
 - , – Fly-wheel energy storage, 878
 - , – Magnetic bearings, 877–878
 - Trapped field magnets, 878–882
 - , – Experimental magnet system, 878–879
 - , – Magnetic separation device, 879–880
 - , – Magnetron sputtering device, 880–882
 - , – Motors, 881
- Applications of superconductors, 4–6
- Atomic layer controlled thin film deposition of HTS cuprates, 913–936
- Auger spectroscopy, 232
- Basic parameters for practical superconductors, 621
- BCS theory, 2, 184, 500, 505
- McMillan's extension of, 500
- Bean-Livingston type (surface) energy barrier for vortices, 427
- Bi-based superconducting cuprates, 739–764
- Bi-layer hydrate phase (of sodium cobalt oxide), 656–663
- Magnetic susceptibility, 657, 667
 - Raman spectroscopy, 660, 662
 - Resistivity, 657
 - Specific heat under various fields, 667
 - XRD, 657, 663
- Borides and borocarbides, 46–48
- Borocarbide superconductors, 4
- Buffer layer in the processing of coated conductors, 774–776
- Bulk HTS and applications, 885–911
- C_{60} molecule and lattice models, 235–237
- C_{60} molecules, 235–236
 - Model for C_{60} solid, 236–237
- C_{60} solid doped with alkali metals, 3
- Calculation of series, 452–454
- Ce-based HF superconductors, 120–149
- A-phase and electronic structure of CeCu_2Si_2 , 125–126
 - Coexistence of superconductivity and A-phase in CeCu_2Si_2 , 129–134
 - High pressure mixed-valent phase transition, 126–127
 - Non-fermi liquid state and quantum critical behaviour, 129
 - Quantum critical behaviour and superconductivity in CeCu_2Si_2 and alloy series $\text{CeCu}_2(\text{Si}_{1-x}\text{Ge}_x)_2$, 122–123
 - Quantum critical points and the B-T phase diagram, 123–125
 - the almost ideal NFL compound CeNi_2Ge_2 , 123
 - Superconductivity and quantum criticality under pressure in CePd_2Si_2 and CeRh_2Si_2 , 135–139

- Unconventional superconductivity and the two QCPs, 127–129
- Change in c-parameter of MgB_2 with SiO_2 addition, 637
- Charge/carrier distribution, 278–285
 - Bi-2212, 281–284
 - Bi-2223, 284–285
 - Cu 1212: $\text{CuBa}_2\text{RCu}_2\text{O}_{6.93}$, 279–280
 - (Cu, Mo)1232: $(\text{Cu}_{0.75}\text{Mo}_{0.25})\text{Sr}_2(\text{Ce}_{0.67}\text{R}_{0.33})_3\text{Cu}_2\text{O}_{11+\delta}$, 280–281
 - XANES spectroscopy, 278–279
- Charge reservoir blocks, 589
- Chemical design of copper oxide superconductors, 255–294
- Chronology of Tc, 937
- Close packing model of perovskite ABX_3 , 837
- Coated conductors of $\text{REBa}_2\text{Cu}_3\text{O}_7$, 765–831
- Cobalt oxide hydrate superconductor, 651–681
 - Intercalation chemistry of, 652–653
 - Physical properties of, 653–655
- Coherence length, 4
- Collver and Hammond's systematics, 503–504
- Comparative superconducting properties of pure and substituted Tl-1223, 855–858
- Conduction blocks, 589
- Critical current density of MgB_2 , 1011–1047
- Critical current properties of MgB_2 thin films, 967–968
- Critical temperature for ternary Nb-based alloys, 702–703
- Cryomagnetic stabilization of Ag/YBCO/buffer/Ni based coated conductor, 820–822
- Crystal and electronic structure of MgB_2 , 939–946
 - Crystal structure of boride compounds, 939–942
- Crystal characteristics of some Tl-1223 phases, 857
- Crystalline and amorphous disorders, 499
 - In A-15 compounds, 506–508
 - Amorphous disorder, 508
 - Crystalline, 506–508
- Crystalline disorder in high Tc cuprates, 508–550
- Crystal structure and occurrence of Rutheno-cuprates, 369–370
- Crystal structure of α , β and γ Na_xCoO_2 , 652
- Crystal structure of A-15 compounds, 507
- Crystal structure of MgB_2 , 942–944
- Crystal structure of sodium cobalt oxide, before and after water intercalation, 655
- Crystal structure of Tl-1223, 836
- Crystal structure of YBCO, 509
- Debye-Waller factor, 503
- de Haas van Alphen (dHvA) oscillations in $\text{LuNi}_2\text{B}_2\text{C}$, 400
- Depairing critical current density, 620
- Dependence of critical field on nuclear magnetization in nuclear paramagnets, 91–97
 - Al, 92–93
 - Au- Al_2 , 92
 - AuIn_2 , 94
 - In, 94–96
 - Rh, 96–97
 - Sn, 94
 - TiH_{2+y} as a future candidate, 97
- Deposition techniques for MgB_2 , 1076–1078
 - Ex-situ high temperature annealing in Mg vapor, 1076
 - In-situ deposition under high Mg pressure, 1077–1078
- Difficulties encountered in depositing MgB_2 thin films, 1074–1076
 - Low sticking coefficient of Mg, 1075
 - Requirement of high Mg vapor pressure, 1074–1075
 - Susceptibility to contamination, 1075–1076
- Disordered superconductors, 499–454

- Distribution of superconducting elements in periodic table, 2
- Doping in cuprates, 301–306
 - Control of doping state, 301–302
 - Doping phase diagram, 302–303
 - Measuring the doping level, 303–306
- Doping effects of J_c properties of MgB_2 , 967–968, 970–971
 - Doping at B-site, 969–970
 - Doping at Mg site, 969
 - Effective pinning sites in MgB_2 , 968–969
- DTA characterization of MgB_2 /Fe wire, 1052
- Dynamical mean field theory (DMFT), 238, 239

- Effect of porous microstructure on J_c characteristics of in-situ MgB_2 bulk, 966–967
- Effect of substitution and addition on MgB_2 properties, 1014–1027
 - Carbon doping, 1014–1015
 - Metal- element doping, 1026
 - Nano-SiC doping, 1017–1025
 - Oxide and other compound doping, 1026
 - SiC and silicide doping, 1025
- Effective electron-electron interaction, 232
- Electronic structure of cuprates, 300–301
- Electronic structure of MgB_2 , 944–946
- Electron irradiation, 556
- Electron-phonon coupling, 234
- Electron-phonon coupling in MgB_2 , 953–958
 - Calculated phonon modes, 953
 - dHvA effect, 954–955
 - Inelastic neutron scattering, 956–957
 - Inelastic X-ray scattering, 956–957
 - Isotope effect, 953–954
 - Raman spectroscopy, 955
- Electron phonon interaction strength, 501
- Energy parameters for C_{60} solid system, 233
- EPMA, 685
- ESR (EPR), 350
- Evolution of organic superconductivity, 183–186
- Excitonic mechanism of superconductivity, 184

- Experimental findings in superconducting fullerenes, 234–235
- Experimental methods at micro-kelvin temperatures, 73–75

- Fault current limiter (FCL), 1050
- Fermi surface of $Na_{0.5}CoO_2$, 653
- Ferromagnetic resonance (FMR), 350
- Field cooled magnetic susceptibility, 334
- Field emission gun transmission electron microscope (FEGTEM), 630
- Field independent lattice melting temperature, 643
- Fine-structure and superconductivity, 286–287
- Fission irradiation methods for J_c enhancement, 565–570
- Flux creep, 644
- Flux pinning force, 620
- Flux pinning induced by composition fluctuations in over-doped Cu-rich BSCCO single crystals, 639–646
- FM dot on SC film 433–438
- FM-SC bilayers, 438–448
 - Continuum regime, 439–444
 - Discrete regime, 444
- Four phased of Na_xCoO_y , 684
- F_p -h curves at 77K for YBCO with nanoparticles, 628
- Fullerenes, 3
- Future prospects in bulk HTS applications, 882

- Gamma ray irradiation for J_c enhancement, 555–556
- Gap coefficient, 501
- General features of crystal structure of Bi-based cuprates, 741–744
- Growth of BSCCO single crystals, 744–749
 - Growth of Bi 2201, 745
 - Growth of Bi 2212, 745–746
 - Growth of Bi 2223, 746–747
 - Growth of (Bi, Pb) 2223 by VA-TSFZ technique, 747–750
- H_{c2} (upper critical field), 4, 5
- $H_{c2}(T)$ for YNi_2B_2C , 410

- Heat capacity of borocarbides, 403
- Heavy substitutional disorder, 295
- Heterogeneous magnetic superconducting systems (HMSS), 425–457
- High pressure effects on superconductivity, 459–497
- High temperature cuprate superconductors, 2, 6–32
- Basic physics of, 19–29
 - Metallurgical aspects of, 9–14
 - Structural aspects of, 8–9, 11
 - Superconductive coupling in, 17–19
 - Symmetry of superconducting order parameter for, 15–16
 - Technical applications of, 30–32
- Heavy fermion quaternary borocarbide: $\text{YbNi}_2\text{B}_2\text{C}$, 403–404
- Heavy fermion (HF) superconductors, 3, 35–38
- Ce-based, 39
 - Rare-earth skutterudites, 43–44
 - U-based, 40–42
- HMSS theory, 427–433
- Finite systems, 433
 - Periodic systems, 432–433
 - Two dimensional textures and vortices, 429–432
 - Three dimensional systems, 428–429
- HTS bulk synthesis, 886–888
- HTS maglev measurement system, 891–894
- HTS maglev test vehicle, 905–910
- Guidance force of HTS maglev vehicle, 906–908
 - Levitation force of HTS vehicle, 905–906
 - Long term stability of HTS maglev vehicle, 908–910
- Hyperfine enhanced nuclear magnetism, 73, 98–104
- Images of diffraction pattern from the vortex lattice in $\text{YNi}_2\text{B}_2\text{C}$ under magnetic field, 407
- Impact Of hyperfine enhanced nuclear magnetism on superconductivity of $\text{Pr}_{0.50}\text{La}_{0.50}\text{Te}$, 98–101
- Impurity phase Co_3O_4 in single crystals of sodium cobalt oxide, 685
- Inequivalent CuO_2 planes, 286
- Influence of YBCO bulk size and shape on levitation properties, 902–905
- Influence of substrate properties on RE-123 growth, 917–919
- Influence of strain on growth, 919
 - Influence of vicinal angle on structural defects, 918
 - Influence of vicinal angle substrates on the growth mode, 917–918
- Integrals of Bessel functions, 449–452
- Interplay between ferromagnetism and superconductivity, 425
- Interplay of hyperfine enhanced nuclear magnetism and superconductivity, 98–104
- Interplay of magnetism and superconductivity, 365
- Interplay of van Vleck paramagnetism and superconductivity in $\text{Pr}_{1-x}\text{La}_x\text{Te}$, 98
- Ion beam assisted deposition (IBAD), 800–801
- Ion irradiation for J_c enhancement, 558–560
- High energy ions, 561–565
 - Low energy ions, 560–561
- Irradiation of HTS for enhancement of J_c , 555–588
- Isotope effect, 234
- Jahn Teller coupling, 237, 240
- Jahn-Teller phonons, 236, 240
- J_c enhancement of MgB_2 by irradiation, 1038–1044
- Electrons, 1042
 - Heavy ions, 1042–1043
 - Neutrons, 1038–1040
 - Protons, 1040–1041
 - U/n method, 1043
- J_c -H behaviour, 624, 626, 627, 632, 634, 638, 641
- Josephson junctions, 5

- Knight shift measured in Na_xCoO_2 , 674
- Large scale use of superconductivity, 620
- Lindemann number, 643
- Liquid phase epitaxy, 808–814
- Hybrid, 812–814
- Local pairing via local quantum fluctuations, 240–249
- Attractive pairing interaction, 241–245
 - Doping dependence of T_c , 247–249
 - Local pairing mechanism, 245–247
- Lorentz force, 4
- LUMO, of C_{60} , 232, 234
- Magnesium diboride, 4, 48–49
- Magnetic alignment and thermomagnetic growth of $(\text{RE})\text{Ba}_2\text{Cu}_3\text{O}_7$, 814–820
- Alignment during slow solidification, 816–819
 - Dynamic magnetic alignment, 819–820
- Magnetic field dependence of electronic thermal conductivity of borocarbide sample, 412
- Magnetic field dependence of J_c , 624
- Magnetic guidance force, 900–901
- Magnetic levitation force, 894–900
- Magnetic levitation of HTS bulk, 888–890
- Magnetic properties of MgB_2 , 949–952
- H_{c1} and H_{c2} , 951–952
 - Magnetic penetration depth, 949–951
- Magnetic quaternary borocarbide superconductors $\text{RNi}_2\text{B}_2\text{C}$ (R: Tm, Er, Ho, Dy), 401–402
- Magnetic resonance imaging (MRI), 5
- Magnetic susceptibility and resistivity studies of rutheno-cuprate samples, 331–342
- Magnetism of rutheno-cuprates, 350–358
- Mass renormalization factor, 237
- Matthias' rules, 503
- Mechanical strain vs J_c in Nb-based conductors, 733–735
- Meissner effect, 1
- Meissner state and spontaneous vortex phase, 359–360
- MgB_2 /diamond composite, 631
- Material and wire development of MgB_2 , 1013
- Materials aspects and crystal growth of BSCCO system, 739–764
- Materials design and process considerations for coated conductors, 766–770
- Materials development and applications of bulk RE-Ba-Cu-O superconductors, 869–883
- Materials development, 870–876
- Cryostability, 874–876
 - Mechanical properties, 873–874
 - RE-Ba-Cu-O, 871–873
 - Y-Ba-Cu-O, 870–871
- Metal organic chemical vapor deposition (MOCVD), 834, 858
- Metal-organic deposition, 801, 834
- for coated conductors, 801
- Metal substrates for coated conductors, 770–774
- MgB_2 thin films, 1073–1091
- M-H hysteresis loops at different temperatures, 623, 640
- Microscopic superconducting pairing mechanism in HF compounds, 149–155
- Magnetic excitation mechanism for superconductivity in U-based HF compounds, 154–155
 - Spin-fluctuation mechanism for cerium-based HF compounds, 150–152
 - T_c dependence on spectral properties of spin fluctuations, 152–154
- Microstructural studies of Co-system, 604–616
- Physical properties, 604
 - SAED and HREM, 604–606
 - Structural considerations, 606–616
- Microstructure studies of rutheno-cuprate system, 594–604
- CBED and DFEM, 595–604
 - Physical properties, 594–595
 - SAED and HREM, 594
 - Structural considerations, 595–596
- Migdal approximation 232

- Mott insulator transition, 232, 238–240
- MRI, 697, 700
- Multigap in MgB_2 , 958–962
- Photoemission spectroscopy, 960–961
 - Specific heat studies, 958–960
 - Tunneling spectroscopy, 961–962
- Nano-diamond, 630
- Nano-diamond induced flux pinning in MgB_2 , 630–635
- Nano-scale defects by 211 addition in melt textured YBCO, 626–629
- Nano- SiO_2 induced flux pinning in MgB_2 , 635–639
- Nb-Al phase diagram, 728
- Nb-based conductors, 697–738
- Critical parameters for, 698–700
 - Nb_3Al , 728–733
 - DTA, 728
 - TEM of, 730
 - XRD of, 729
- Nb_3Al by Jelly Roll process, 728, 731–733
- Nb_3Ga , 733
- Nb-Sn phase diagram, 704
- Nb_3Sn conductors, 703–727
- By bronze process, 706–714
 - By direct electro-chemical reduction of oxides, 719–722
 - By internal tin process, 714–718
 - By PIT process, 718–719
 - Improvement of flux pinning, 722–727
 - Manufacturing of, 705
 - Texture developed in, 727
- Nb-Ti conductors, 700–702
- Price reduction over the years, 700
- Neutron irradiation, 556–558
- Neutron powder diffraction, 350
- New Ce115 and Ce 218 class of HF superconductors, 139–146
- AF quantum critical points and superconductivity, 140–142
 - Basics of the electronic structure, 139–140
 - NFL anomalies in field and pressure induced QCPs, 142–143
 - Superconducting gap function in CeCoIn_5 , 143–144
 - Vortex state and FFLO phase in CeCoIn_5 , 145–146
- NiO induced nano pinning-centres in melt textured YBCO, 622–626
- NMR, 350
- Noble metals Cu, Ag and Au; search for superconductivity, 77–83
- Ag, 77
 - Au, 75–77
 - Cu, 77
- Nonmagnetic quaternary borocarbides, 399–400
- Normalised pinning force vs normalized magnetic field for Nb-based conductors, 699
- Normal permanent magnetic (NPM) guideway, 890–891
- Normal state resistivity, striped phase and cationic disorder, 527–550
- Co-doped $\text{ErBa}_2\text{Cu}_{3-x-y}\text{Zn}_x\text{Fe}_y\text{O}_{7-\delta}$, 527–537
 - $\text{Y}_{1-x}\text{Pr}_x\text{BaSrCu}_3\text{O}_{7-\delta}$, 544–550
 - $\text{Yb}_{1-x}\text{Pr}_x\text{Ba}_2\text{Cu}_3\text{O}_{7-\delta}$, 537–544
- Nuclear ferromagnetism and its interplay with superconductivity in AuIn_2 , 83–86
- Impact of nuclear FM on SC of AuIn_2 , 86–90
 - Nuclear FM ordering of In nuclei in AuIn_2 , 83–86
- Nucleation stage and initial growth, 914–917
- Atomic layer stacking, 915
 - Terminating atomic layer of RE 123, 915–916
- ^{17}O NMR, 314–322
- AF fluctuations, 317
 - Knight shift, 315
 - Phase separation, 321–322
 - Pseudogap, 316–317
 - Single-spin fluid, 316
- Spin-lattice relaxation, 315–316

- One dimensional organic superconductors, 183–230
- One-D physics, high temperature regime, 192–194
- Charge ordering in insulating state of $(\text{TMTSF})_2\text{X}$, 195–196
 - Dimensionality crossover under pressure, 199–200
 - Longitudinal vs transverse transport, 196–198
 - Pseudogap and zero frequency mode, 203–204
 - Symmetry of anions, 204–206
 - $(\text{TM})_2\text{X}$ compounds with $\frac{1}{2}$ or $\frac{1}{4}$ filled band, 200–204
 - $(\text{TMTTF})_2\text{PF}_6$ phase diagram, 198–199
- Organic and other carbon-based superconductors, 3, 44–45
- Organic superconductivity in $(\text{TMTSF})_2\text{X}$, 186–188
- Other oxide superconductors, 33–34
- Over-critical currents in wire with ferromagnetic sheathing, 1032–1037
- Oxygen and superfluid density, 311–314
- Chain-layer superfluid density, 312–313
 - Irreversibility field, 313–314
 - Uemura relation, 311
- Oxygen diffusion, 309–311
- Oxygen engineering of copper oxide superconductors, 255–294
- Oxygen in high Tc cuprate superconductors, 295–329
- Oxygen isotope effect, 322–326
- Effect of pseudogap, 322–324
 - Site selective isotope effect, 325–326
- Oxygen ordering, 306–309
- CuO chain ordering in Y-123, 306–308
 - Other ordered phases, 308
 - Y-247 and (Y, Ca)-123, 308–309
- Oxygen vacancy disorder in CuO_2 planes, 509–527
- In substituted $\text{ErBa}_2\text{Cu}_{3-x}\text{M}_x\text{O}_{7-\delta}$ (M: Fe, Co, Ni and Ga), 523–524
 - In substituted $\text{R}_{1-x}\text{Ca}_x\text{Ba}_2\text{Cu}_3\text{O}_{7-\delta}$ (R: Er, Y, Sm, Nd), 516–523
 - In substituted $\text{Y}_{1-x}\text{Pr}_x\text{Ba}_2\text{Cu}_3\text{O}_{7-\delta}$, 509–515
- Pancake (shaped) vortices, 621, 640
- Pearl vortex, 448–449
- Peculiarities of the superconducting coupling in $(\text{TM})_2\text{X}$, 215
- Pairing symmetry, 215–219
 - Superconductivity and nonmagnetic defects, 219–221
- Penetration depth, 4
- Phase diagram approach to magnetic superconductors, 365–391
- Phase diagram and phase properties, 366–369
- Multinary systems, 367–368
 - Superconducting and magnetic properties, 368–369
- Phase equilibria in Sr-Gd-Ru-Cu-O system, 370–372
- Pseudoternary subsolidus phase diagram, 372–375
- Phase stability of substituted Tl-cuprates, 843–855
- Phonon density of states at fermi surface, 501
- Platinum metals Rh, Pd and Pt; search for superconductivity, 77–83
- Pd, 78–80
 - Pt, 81
 - Pt powder, 81–83
 - Rh, 77–78
- Potential of MgB_2 for practical applications, 963–971
- Attractive features for applications, 963–964
 - Critical current properties of ex-situ processed MgB_2 bulk, 964–965
 - Critical current properties of in-situ processed MgB_2 bulk, 965–966
 - Critical current properties of MgB_2 single crystals, 964
- Powder in tube (PIT) route for MgB_2 , 1049, 1055–56
- $\text{Pr}_{1-x}\text{La}_x\text{Cu}_6$, a future candidate to study interplay of nuclear magnetism and superconductivity, 102–104

- Preparation and properties of advanced MgB₂ wires and tapes, 1049–1071
- Preparation and properties of Rutheno cuprates, 377–378
- Ru-1222, 377–378
 - Ru-1212, 378–384
- Preparation of MgB₂ wires and tapes, 1051–1053
- Ex-situ route, 1053
 - In-situ phase formation, 1051–1053
- Pressure dependence of intra- and intergrain transition temperatures for Ru1212/Gd, 345
- Pressure effects in HTS, 469–483
- Increase of T_c to new records under imposed pressure, 469–473
 - Pressure induced redistribution of mobile oxygen in HTS, 475–483
 - Unified phase diagram and the charge transfer model to understand pressure effects, 473–475
- Pressure effects in LTS, 461–469
- Nonlinear T_c(P) of thallium and rhenium revealing fermi surface instabilities, 464–465
 - Pressure dependence of T_c in BCS and strong coupling theory, 462–463
 - Superconductivity and structural transformation, 466–469
- Pressure effects in unconventional superconductors, 483–489
- Competition of superconducting and magnetic orders in superconducting ferromagnets as revealed by high pressure experiments, 487–489
 - In MgB₂ and isostructural intermetallics, 483–486
 - Pressure control of dimensionality in Na_xCoO₂·H₂O, 486–487
- Properties of clean epitaxial HPCVD films of MgB₂, 1078–1080
- Properties of carbon doped HPCVD films of MgB₂, 1080–1081
- Quantum interference devices, 5
- Quantum Monte Carlo technique, 238
- Reaction scheme in the formation of BLH phase, 661–662
- REBa₂Cu₃O_{7-d} on SrTiO₃, 919–932
- Experimental settings, 919–920
 - Initial growth of RE-123 on TiO₂ terminated SrTiO₃, 920–926
- Redox tailoring, 277–277
- Hole doping level, 277
 - Layer-matching and redox characteristics, 274–277
 - Oxygen nonstoichiometry, 272–274
- Reversible magnetization of Ru-1212, 344
- Rolling assisted biaxially textured substrates (RABiTS), 834
- Rutheno-cuprates; superconducting ferromagnets, 331–363
- Crystal structure of Ru-1212 and Ru-1222, 334
 - Synthesis of, 333–342
- Sample size dependence of the magnetic critical current density in MgB₂, 1029–1032
- Schematic molecular energy levels of an isolated C₆₀ molecule, 236
- Schematic picture of alkali doped C₆₀ solid, 232
- SC rf cavities, 5
- Shannon radii of substituting ions, 843
- Sheath materials and composite structure of monofilamentary conductors of MgB₂, 1053–1055
- Single crystals of Na_xCoO₂, 683–695
- Grown using four mirror optical floating zone furnace, 685–689
 - Grown by flux method, 684–685
- Sol-gel technique, 802–808, 834
- Sol-gel synthesis, 802
 - , – Aqueous routes, 802
 - , – Non-aqueous routes, 802–804

- Deposition process, 804–814
- , - Two dimensional coatings, 804–806
- , - Two dimensional patterning and three dimensional coatings, 806–808
- Spontaneous vortex state, 332
- SQUID (Magnetometer), 630, 685
- Stacking manner of charge reservoir blocks in superconducting copper oxides, 589–618
- STM/STS of cleaved BSCCO surface, 645, 646
- Strong coulomb correlation effects, 4
- Strongly correlated electron (SCE) system, 654
- Structural and crystal chemistry aspects of $Tl_mBa_2Ca_{n-1}Cu_nO_x$, 835–842
- Structural categorization of HTS cuprates, 256–271
 - Homologous series of category-A, 256–265
 - , - M-m2(n-1)n:RS phase, 259–260
 - , - M-m2(n-1)n:P phase, 260
 - , -“Zero” 02(n-1)n phase and their water derivatives, 260–264
 - , -“Zero” 01(n-1)n phase, 264–265
 - Homologous series of category-B, 265–269
 - , - Non-superconductive M-12s2 phases, 269
 - , - Ru-12s2 magneto-superconductors, 268–269
 - , - Superconductive M-12s2 phases, 267–268
 - , - Zaro phases, 266–267
 - Infinite layer phases, 269–270
 - Other types of layered copper oxides, 271
- Structural chemistry and Tc of Tl-cuprate family, 839
- Structure and materials of quaternary borocarbide family, 396–399
- Structure and superconducting properties of modulation-free $(Bi, Pb)_2Sr_2CaCu_2O_{8+\delta}$, 755–759
- Structure of HTS cuprate series, 296–300
 - BSCCO family, 299–300
 - YBCO family, 296–299
- Substitution in double Tl-O layered systems, 843–845
- Substitution in single Tl-O layered systems, 845–848
- Substrates and hetero-structures with MgB_2 thin films, 1080–1081
 - Multilayers of MgB_2 without other materials, 1080–1081
 - Substrates for deposition, 1080
- Superconducting anisotropy of borocarbides, 404–415
 - Anisotropy and symmetry of SC gap function, 409–415
 - Flux lattice and its structural phase transition, 405–409
- Superconducting elements in periodic table, 72
- Superconducting gap, 234
- Superconducting layer in coated conductors, 776–799
 - Coated conductors for AC applications, 792–797
 - Current percolation in coated conductors, 783–787
 - Grain boundary engineering, 788–790
 - Intergrain pinning improvement, 791–792
 - Magnetically decoupled multifilamentary YBCO coated conductors, 797–799
 - RABiTS, $(RE)Ba_2Cu_3O_7$ coated conductor, 778–782
- Superconducting parameters of amorphous simple metals and alloys, 502
- Superconducting properties and vortex phase diagram of Bi-2223, 750–755
 - Irreversibility line and critical current, 752–755
 - Lower critical field, penetration depth and anisotropy, 750–751
- Superconducting properties of wires and tapes of MgB_2 , 1056–1064
 - Effect of axial strain or bending on Jc, 1060
 - Multifilamentary wires and tapes, 1059–1060
 - Strain effects on Tc, 1056

- Thermal stability, 1062–1064
- Transport Jc, irreversibility field and H_{c2} , 1056–1059
- Superconducting properties of substituted TI-1212, 847
- Superconducting quaternary borocarbides, 393–423
 - crystal structure of 396
 - discovery of, 394–396
- Superconducting state in $(TM)_2X$ compounds, 206–215
 - Superconducting transition, 206–208
 - Superconductivity under pressure, 208–215
- Superconductivity and granularity of rutheno-cuprates, 342–349
- Superconductivity at ultra-low temperatures, 71–108
 - And its interplay with nuclear magnetism, 83–108
- Superconductivity in fullerides, 231–253
- Superconductivity in heavy fermion (HF) compounds, 109–182
- Superconductivity in MgB_2 , 937–981
- Superconductivity in two dimensional CoO_2 layers, 655–676
 - Chemistry of superconducting sodium cobalt-oxide hydrate, 655
 - , – Characterization of superconducting phase, 659–665
 - , – Soft chemical modification, 655–659
 - Physics of sodium Cobalt Oxide Hydrate, 666–676
 - , – Critical fields, 667
 - , – Magnetic and electrical properties above T_c , 669–671
 - , – μ SR, 672–673
 - , – NMR, 674
 - , – NQR, 673–674
 - , – Phase diagram, 666–667
 - , – Pressure effects, 675–676
 - , – Pseudogap, 675
 - , – Specific heat, 667, 671–672
- Superconductors with nanoscale flux pinning centers, 619–649
- Technical applications of MgB_2 conductors, 1064–1065
- TEM, 590
 - At ultra high voltage of 800 kV, 594
 - Dark field (DFEM), 590
 - High resolution (HREM/HRTEM), 590, 593
- Temperature dependence of DC magnetization of $Na_{0.75}CoO_2$ polycrystalline and single crystals, 691
- Thallium based superconducting cuprates, 833–868
- Thallium coated superconductors, 858–860
- Theories for the normal HF state, 111–120
 - Dual model for U-based systems, 113–118
 - Renormalized band theory for the Ce compounds 111–113
 - The NFL state and its scaling laws, 118–120
- Theoretical aspects of Superconductivity of MgB_2 , 983–1009
 - Anisotropy of H_{c2} , 988–994
 - Band structure calculations, 984–985
 - Microwave conductivity, 994–1001
 - Two gap superconductivity, 985–988
- Thermopower studies of rutheno-cuprate, 341–342
- The $(TM)_2X$ period, 186–221
- Thin film devices of MgB_2 , 1081–1082
 - Degradation of, 1082
 - Josephson junctions and SQUID, 1081–1082
 - Microwave properties, 1082
- $(TM)_2X$ at high temperature, 192–194
- Transport properties of MgB_2 , 946–962
 - Electrical resistivity, 946–947
 - Hall effect, 947–948
 - Thermoelectric power, 948–949
- Two-D vortex lattice melting theory, 643
- Two gap superconductivity of MgB_2 , 1012–1013
- Type-II superconductors, 4, 698

U-based HF superconductors, 155–167

- $U_{1-x}Th_xBe_{13}$, 156–157
- , – Electronic structure and NFL-like normal state, 157
- UPd_2Al_3 , 159–167
- , – Electronic structure- the dual model, 161–163
- , – Mass enhancement and superconducting pairing due to magnetic excitations, 163–164
- , – Physical properties, 160–161
- , – Symmetry of the superconducting gap function and Eliashberg theory, 165–167

U/n method (irradiation) for J_c increase, 570–579

Upper critical field, H_{c2} , 666, 668

Upper critical field vs temperature for Nb-based conductors, 698

Uranium-BSCCO interaction, 579

Variety of ground states in $(TM)_2X$ series, 188–192

Weak ferromagnetic behaviour of Na_xCoO_2 , 691

Weiss mean field theory, 238

XANES, 350

XRD, 334, 335, 336, 342, 631, 636, 656, 657, 685, 690

Zero field cooled magnetic susceptibility, 334

Zero field NMR (ZFNMR), 350, 351, 352